Cover Picture

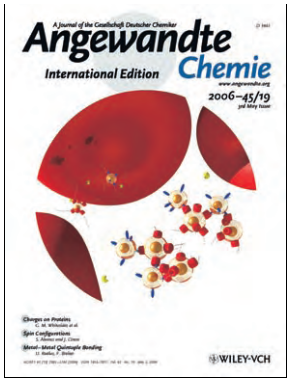

Todd J. Harris, Geoffrey von Maltzahn, Austin M. Derfus, Erkki Ruoslahti, and Sangeeta N. Bhatia*

Sterically shielded nanoparticles diffuse freely in solution and biological fluids until proteases expressed by cancer cells trigger them to self-assemble. In their Communication on page 3161 ff., S. N. Bhatia and co-workers show that complimentary Fe_3O_4 nanoparticle binding is inhibited by the attachment of protease-cleavable polymers. Cleavage of these polymers triggers "latent" nanoparticles to form multimeric assemblies with emergent properties.

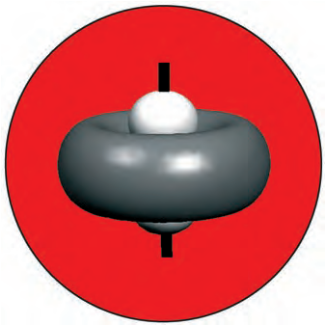

Hybridization and Electron Configuration
In their Essay on page 3012 ff., S. Alvarez and J. Cirera describe how the splitting of the d-orbital manifold and the existence of low-spin states in putative tetrahedral complexes can be explained by the hybridization of the orbitals.

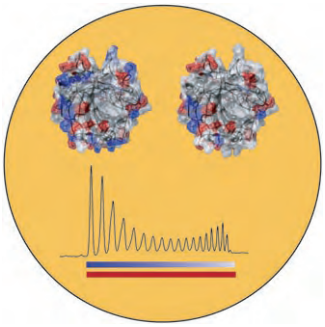

Charges on Proteins
G. M. Whitesides and co-workers consider in their Review on page 3022 ff. the question of the function of charged amino acids on proteins, and present techniques that have proved useful in the search for the answer.

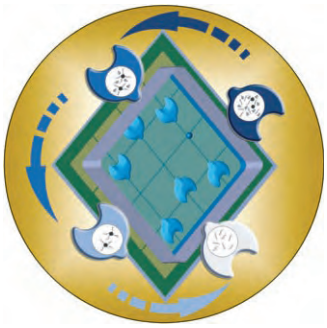

Miniaturization
A method for DNA purification on a chip has been developed by U. Lehmann et al. This system employs magnetic microparticles and is suitable for dilute concentrations of raw cell samples (see their Communication on page 3062 ff.).

Contents

The following Communications have been judged by at least two referees to be "very important papers" and will be published online at www.angewandte.org soon:

*C. Burke, Y. Shi**
Regio- and Enantioselective Epoxidation of Dienes by a Chiral Dioxirane: Synthesis of Optically Active Vinyl *cis*-Epoxides

Cheuk-W. So, H. Roesky, J. Magull, R. Oswald*
Synthesis and Characterization of [{PhC(NtBu)$_2$}SiCl]: A Stable Monomeric Chlorosilylene

S. Harder, J. Brettar*
Rational Design of a Well-Defined Soluble Calcium Hydride Complex

*H. Yu, S. Huang, H. Chokhawala, M. Sun, H. Zheng, Xi Chen**
Highly Efficient Chemoenzymatic Synthesis of Naturally Occurring and Non-Natural α2,6-Linked Sialosides: A *P. damsela* α2,6-Sialyltransferase with Extremely Flexible Donor Substrate Specificity

*V. Lavallo, Y. Canac, B. Donnadieu, W. Schoeller, G. Bertrand**
CO Fixation to Stable Acyclic and Cyclic Alkyl Amino Carbenes: Stable Amino Ketenes with a Small HOMO–LUMO Gap

*D. Rohde, C.-J. Yan, Hui-J. Yan, Li-J. Wan**
From Lamellar to Hexagonal Self-Assembly of Bis(dioxaborin) Molecules

Meeting Reviews

Natural Products Research: Renaissance with Strengthened Integration of Biology and Chemistry — *W. Maison* — **3000**

Books

TTF Chemistry — Jun-ichi Yamada, Toyonari Sugimoto — *reviewed by C. Rovira* — **3003**

Principles of Inorganic Materials Design — John N. Lalena, David A. Cleary — *reviewed by L. Qi* — **3004**

Highlights

Bond Theory

U. Radius,* F. Breher* — **3006 – 3010**

To Boldly Pass the Metal–Metal Quadruple Bond

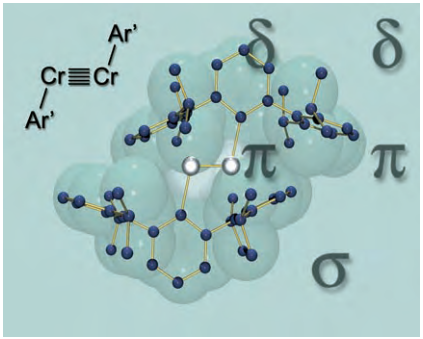

The metal–metal quintuple bond: Minimizing the number of sterically demanding ligands increases the number of valence orbitals available to form metal–metal bonds. Following this concept, Power et al. have recently synthesized and structurally characterized a dinuclear chromium–chromium-bonded complex with one ligand per metal atom (see picture) featuring a metal–metal quintuple bond. Driving this concept to an extreme, even larger bond orders than five should be feasible.

InterScience

© 2006 Wiley-VCH Verlag GmbH & Co. KGaA, Weinheim

Essays

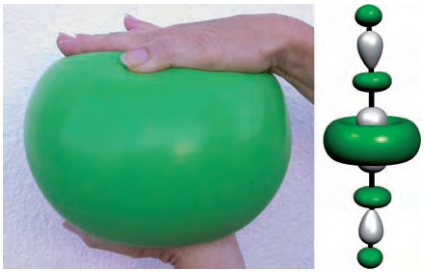

How *high* is high and how *low* is low? With respect to transition-metal complexes of different coordination numbers and stereochemistry, high-, low-, and intermediate-spin states may mean different things. The hybridization of the d orbitals, similar to the deformation of a balloon subjected to pressure (see picture), provides a rationale for the splitting of the d manifold and, hence, for the allowed spin states in a given complex.

Spin Configurations

S. Alvarez,* J. Cirera ——— **3012 – 3020**

How High the Spin? Allowed and Forbidden Spin States in Transition-Metal Chemistry

Reviews

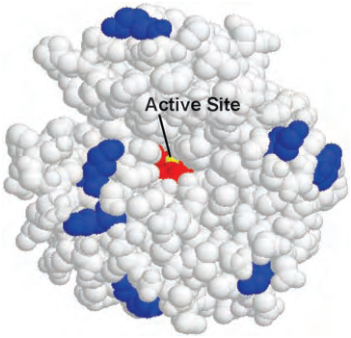

Electrostatic effects in proteins are complicated: The charged groups form a network of interactions in which the members can influence each other at long distances. Sets of derivatives in which variable numbers of charges are removed or added by chemical reactions (protein charge ladders) together with capillary electrophoresis comprise a tool with which to examine the character of this network.

Proteins

I. Gitlin, J. D. Carbeck, G. M. Whitesides* ——— **3022 – 3060**

Why Are Proteins Charged? Networks of Charge–Charge Interactions in Proteins Measured by Charge Ladders and Capillary Electrophoresis

Communications

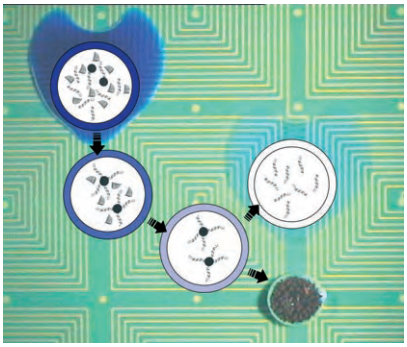

Merge, mix, split, and transport are the main manipulation steps used for on-chip droplet-based DNA purification (see figure). The system is able to extract genomic material from dilute raw cell samples by using the actuation of magnetic microparticles within the droplets through a matrix of coils.

Microfluidics

U. Lehmann,* C. Vandevyver, V. K. Parashar, M. A. M. Gijs **3062 – 3067**

Droplet-Based DNA Purification in a Magnetic Lab-on-a-Chip

For the USA and Canada: ANGEWANDTE CHEMIE International Edition (ISSN 1433-7851) is published weekly by Wiley-VCH PO Box 191161, D 69451 Weinheim, Germany. Air freight and mailing in the USA by Publications Expediting Inc. 200 Meacham Ave., Elmont, NY 11003. Periodicals postage paid at Jamaica NY 11431. US POSTMASTER: send address changes to *Angewandte Chemie*, Wiley-VCH, 111 River Street, Hoboken, NJ 07030. Annual subscription price for institutions: US$ 5685/5168 (valid for print and electronic / print or electronic delivery); for individuals who are personal members of a national chemical society prices are available on request. Postage and handling charges included. All prices are subject to local VAT/sales tax.

© 2006 Wiley-VCH Verlag GmbH & Co. KGaA, Weinheim

The best in chemistry –

for more than a hundred years

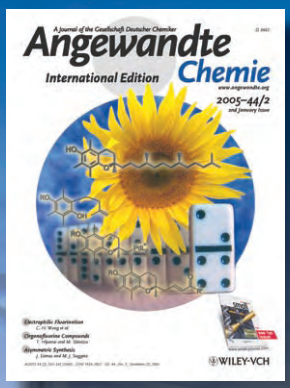

A Journal of the Gesellschaft Deutscher Chemiker

Angewandte
International Edition **Chemie**

www.angewandte.org

1888: ***The beginning of a success story***

Constant Innovations

1962: *First issue of the International Edition*
1976: *Graphical abstracts*
1979: *Cover pictures*
1988: *Centenary of Angewandte*
1989: *Routine use of color*
1991: *New section: Highlights*
1992: *Computerized editorial tracking system*
1995: *Internet service for readers*
1998: *Regular press service; full-text online*
2000: *New section: Essays; EarlyView: Communications available online ahead of the printed version*
2001: *New section: Minireviews*
2002: *Online submission of manuscripts*
2003: *Weekly publication; new section: News; new layout*
2004: *Backfiles (1962-1997); ManuscriptXpress: Online system for authors and referees*

Angewandte's advisors...

Rainer Metternich
Schering AG, Berlin

*»**Angewandte Chemie** keeps me up to date on the top new developments in chemistry. I am engaged in drug discovery, and this high-quality journal covering breakthrough discoveries in interdisciplinary research, particularly in bioorganic chemistry, is of the highest relevance to me. Each issue of Angewandte provides an outstanding source for innovations.«*

Angewandte Chemie International Edition *is a journal of the German Chemical Society (GDCh)*

GDCh

WILEY InterScience® DISCOVER SOMETHING GREAT

WILEY-VCH

18041502_gu

Out of the brew! Four new antibiotics were isolated from a fermentation broth of *Steptomyces lydicus* (strain HKI0343). The 13-membered-ring peptides (see formula, X–Y: CH_2–NH, CH=NH; R1, R2: H, OH) are cyclized through a lactone function at serine and also contain the nonproteinogenic amino acid piperazic acid (or a derivative thereof). The peptides show promising activity against various mycobacteria without being cytotoxic.

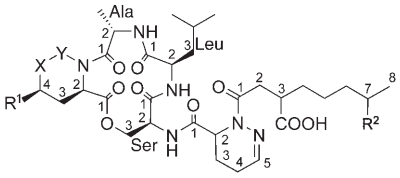

Antibiotics

X. Huang, E. Roemer, I. Sattler,*
U. Moellmann, A. Christner,
S. Grabley ——— **3067 – 3072**

Lydiamycins A–D: Cyclodepsipetides with Antimycobacterial Properties

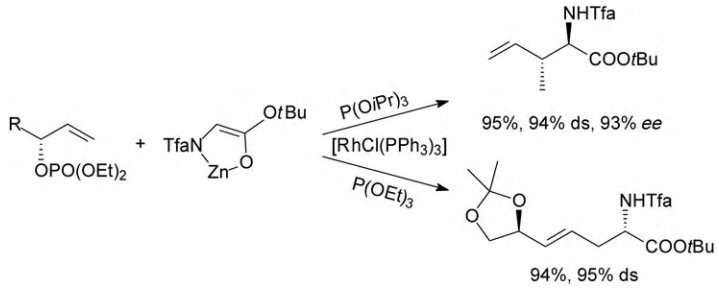

Rehabilitated: The rhodium-catalyzed allylic alkylation is indeed a viable alternative to the better-known palladium-catalyzed version. Rhodium complexes show a different regioselectivity and have a low tendency for isomerization. The allylations proceed with excellent chirality transfer for both branched and linear products (see scheme; Tfa = trifluoroacetyl).

Asymmetric Catalysis

U. Kazmaier,* D. Stolz ——— **3072 – 3075**

Regio- and Stereoselective Rhodium-Catalyzed Allylic Alkylations of Chelated Enolates

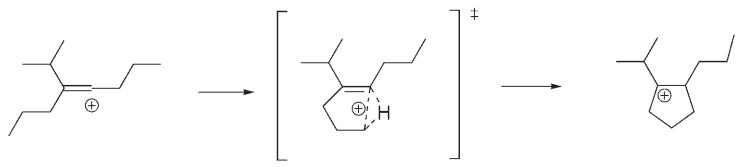

Tying the knot: In analogy to singlet carbenes, vinyl cations insert into C–H bonds in a concerted intramolecular reaction, as shown by experimental investigations and quantum mechanical calculations. This reaction is useful for the synthesis of cyclopentane derivatives.

C–H Insertion

U. Biermann, R. Koch,
J. O. Metzger* ——— **3076 – 3079**

Intramolecular Concerted Insertion of Vinyl Cations into C–H Bonds: Hydroalkylating Cyclization of Alkynes with Alkyl Chloroformates To Give Cyclopentanes

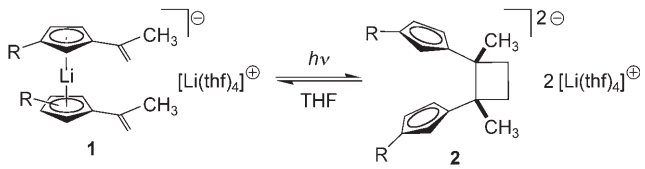

Li and light: Alkenyl-substituted lithium cyclopentadienides, which are in equilibrium with the substituted lithocene anion structure **1**, undergo a photochemical [2+2] cycloaddition to yield selectively the carbon–carbon coupling product **2**. This is a rare case of organic functional-group chemistry for a reactive organolithium compound.

Organolithium Compounds

J. Paradies, G. Erker,*
R. Fröhlich ——— **3079 – 3082**

Functional-Group Chemistry of Organolithium Compounds: Photochemical [2+2] Cycloaddition of Alkenyl-Substituted Lithium Cyclopentadienides

© 2006 Wiley-VCH Verlag GmbH & Co. KGaA, Weinheim

Contents

Inorganic Polymers

M. Raab, G. Schick, R. Fondermann, M. Dolg, W. Henze, U. Weynand, R. M. Gschwind, K. Fischer, M. Schmidt, E. Niecke* ——— **3083 – 3086**

A PH-Functionalized Polyphosphazene: A Macromolecule with a Highly Flexible Backbone

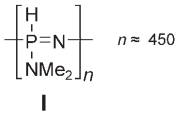

I

The simplest side group: The first example of a completely H-substituted polyphosphazene **I** is obtained by the polycondensation of $(Me_2N)_2PNH_2$ in solution at low temperature. NMR investigations and light-scattering experiments substantiate the constitution of the polymer. The conformation and a reaction pathway to **I** are proposed on the basis of ab initio calculations.

Chemical Memory

A. Kaminaga, V. K. Vanag, I. R. Epstein* ——— **3087 – 3089**

A Reaction–Diffusion Memory Device

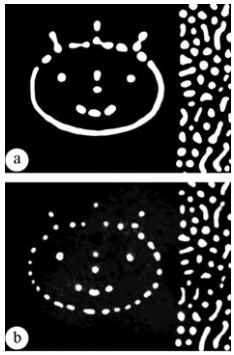

A face to remember: A photoimprinted image in a reactive microemulsion persisted for more than an hour. Such localized patterns in reaction–diffusion systems could find application in memory-storage devices. The picture shows the image of a face immediately following illumination (a) and after 1 h (b). The area at the right shows the evolution of a spontaneous Turing pattern.

Zeolites

F.-S. Xiao,* L. Wang, C. Yin, K. Lin, Y. Di, J. Li, R. Xu, D. S. Su, R. Schlögl, T. Yokoi, T. Tatsumi ——— **3090 – 3093**

Catalytic Properties of Hierarchical Mesoporous Zeolites Templated with a Mixture of Small Organic Ammonium Salts and Mesoscale Cationic Polymers

Holey zeolites! Hierarchical mesoporous zeolites (see SEM image) were prepared by a one-step hydrothermal reaction using both a small organic ammonium salt and a mesoscale cationic polymer as templates. The zeolites thus obtained reveal excellent catalytic properties relative to conventional zeolites, indicating the importance of their mesoporous structure for industrial catalysis.

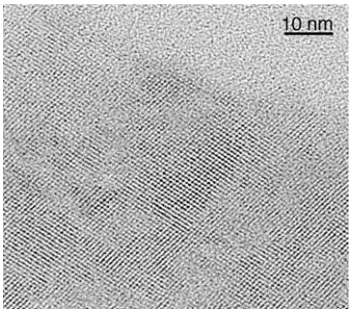

Chiral Ionic Liquids

S. Luo,* X. Mi, L. Zhang, S. Liu, H. Xu, J.-P. Cheng* ——— **3093 – 3097**

Functionalized Chiral Ionic Liquids as Highly Efficient Asymmetric Organocatalysts for Michael Addition to Nitroolefins

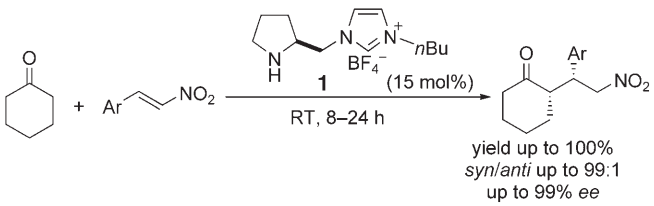

Catalytic combination: By combining the advantages of organocatalysts and ionic liquids, a functionalized chiral ionic liquid such as **1** can act as a highly efficient and reusable organocatalyst for the asymmetric Michael addition reaction of ketones and aldehydes with nitroalkenes.

© 2006 Wiley-VCH Verlag GmbH & Co. KGaA, Weinheim

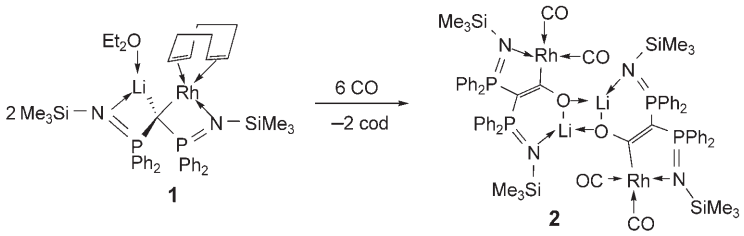

Metals helping metals: The bimetallic spirocyclic bridged-carbene complex **1** reacts almost quantitatively with CO by formal "insertion" into the Rh–C(Li) bond to form the dimeric complex **2**, the first example of a μ_2,η^2-(O,C) lithium–rhodium ketene complex (see scheme). Complex **2** reacts with water to transform the ketene ligand into a methine group by CO elimination.

Bimetallic Complexes

M. Fang, N. D. Jones, R. Lukowski, J. Tjathas, M. J. Ferguson, R. G. Cavell* ——— **3097 – 3101**

A Bimetallic, Coordinated-Ketene Complex Formed from a Bimetallic Lithium–Carbon Spirocycle by Lithium-Mediated Insertion of CO into a Rhodium–Carbon Bond

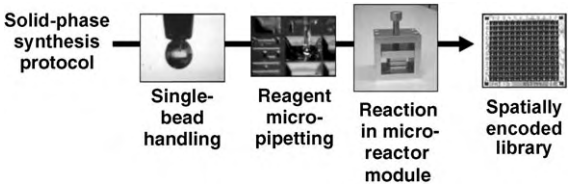

Miniature labs: A microstructured silicon wafer was used as a microreactor array for single-bead synthesis on a nanovolume scale. Products were prepared by combinatorial synthesis and spatially encoded by their position in the array. Three-component Biginelli condensations were carried out at 100 °C for 14 h and therefore required the development of a specially sealed reactor device.

Microscale Synthesis

G. A. Groß,* G. Mayer, J. Albert, D. Riester, J. Osterodt, H. Wurziger, A. Schober* ——— **3102 – 3106**

Spatially Encoded Single-Bead Biginelli Synthesis in a Microstructured Silicon Array

Exceptional activity in carbon oxidation is displayed by a zeolite-supported ruthenium catalyst (see diagram; *Y* = carbon weight loss) that unlike platinum catalysts does not require the presence of NO_x in the gas stream. This catalyst opens up a new route for catalytic soot oxidation in diesel engine exhaust filters.

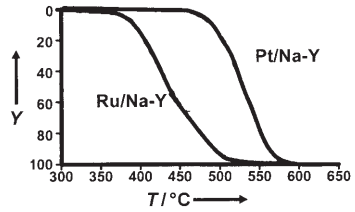

Heterogeneous Catalysis

K. Villani, C. E. A. Kirschhock, D. Liang, G. Van Tendeloo, J. A. Martens* ——— **3106 – 3109**

Catalytic Carbon Oxidation Over Ruthenium-Based Catalysts

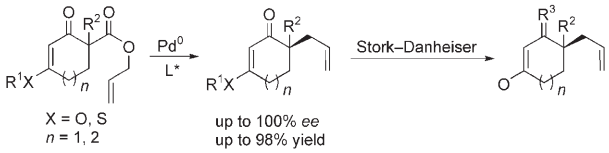

Excellent yields and enantioselectivities were achieved for the palladium-catalyzed asymmetric allylic alkylation of vinylogous thioesters. The close-to-neutral reaction conditions ensure that this reaction can tolerate a wide range of functionalities. Furthermore, this approach provides a convenient protocol for the synthesis of synthetically important α,α- and γ,γ-disubstituted cycloalkenones.

Asymmetric Synthesis

B. M. Trost,* R. N. Bream, J. Xu ——— **3109 – 3112**

Asymmetric Allylic Alkylation of Cyclic Vinylogous Esters and Thioesters by Pd-Catalyzed Decarboxylation of Enol Carbonate and β-Ketoester Substrates

© 2006 Wiley-VCH Verlag GmbH & Co. KGaA, Weinheim

Contents

Noncovalent Interactions

X. Zhang, P. Xie,* Z. Shen, J. Jiang, C. Zhu, H. Li, T. Zhang, C. C. Han, L. Wan, S. Yan,* R. Zhang* _____ **3112 – 3116**

Confined Synthesis of a *cis*-Isotactic Ladder Polysilsesquioxane by Using a π-Stacking and H-Bonding Superstructure

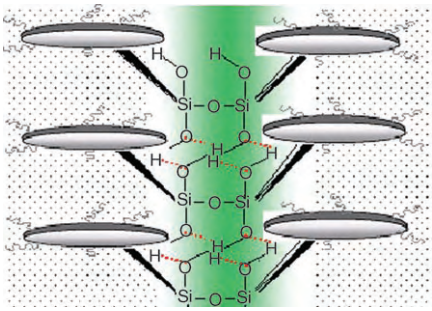

On the rung way: Concerted self-organization of an α,ω-bis(triphenylenetetrahydroxy)disiloxane through π–π-stacking and H-bonding interactions generates a supramolecular channel in which silanol groups are entrapped between two hydrophobic columns. Ordered polycondensation leads to a high-molecular-weight, soluble, ladder *cis*-isotactic polysilsesquioxane (see picture).

Synthetic Methods

N. T. McDougal, S. E. Schaus* _____ **3117 – 3119**

Highly Diastereoselective Synthesis of Bicyclo[3.2.1]octenones through Phosphine-Mediated Condensations of 1,4-Dien-3-ones

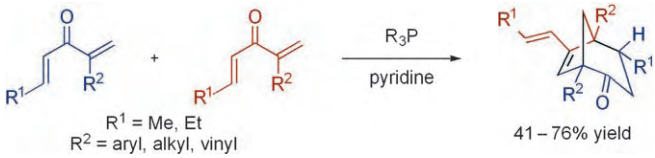

Making rings: A highly diastereoselective synthesis of bicyclo[3.2.1]octenones from 1,4-dien-3-ones occurs through a domino phosphine-mediated formal [4+2] cycloaddition followed by an intramolecular Wittig olefination.

Fuel Cells

S. Yamazaki,* T. Ioroi, Y. Yamada, K. Yasuda, T. Kobayashi ___ **3120 – 3122**

A Direct CO Polymer Electrolyte Membrane Fuel Cell

A good source of energy: The reformation of hydrocarbons generates CO as well as H_2. Despite its high reducing activity, CO is not suitable as a fuel in polymer electrolyte membrane fuel cells (PEMFCs) because it is a strong poison for the Pt catalyst used as the anode. A new fuel cell has now been developed with a rhodium octaethylporphyrin ([Rh(oep)]) anode catalyst that uses neat CO as a fuel, and delivers high performance (see graph).

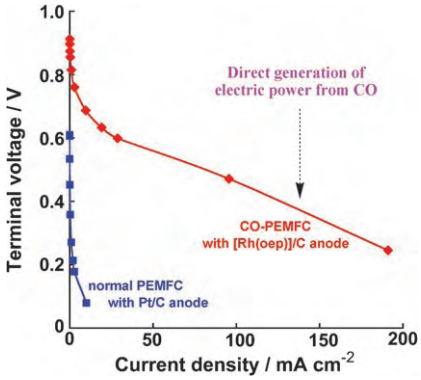

Molecular Recognition

S. Le Gac, J. Marrot, O. Reinaud,* I. Jabin* _____ **3123 – 3126**

Allosterically Coupled Double Induced Fit for 1+1+1+1 Self-Assembly of a Calix[6]trisamine, a Calix[6]trisacid, and Their Guests

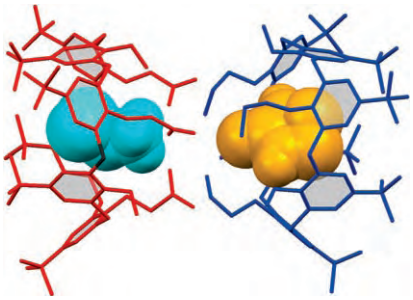

Special guests: A cooperative double induced-fit process leads to the 1+1+1+1 self-assembly of quaternary complexes comprising two complementary calix[6]-arene-based hosts and their specific guests (see picture). The guests direct self-assembly by shaping their hosts. Such allosteric control involves multiple recognition levels reminiscent of those in biology.

© 2006 Wiley-VCH Verlag GmbH & Co. KGaA, Weinheim

Open channels: Chemical modulators are developed to convert a naturally occurring channel protein into a pH-actuated nanovalve. The pH interval, sensitivity, and activation of the valve by channel opening are tunable through the design of the modulators. The valve is useful for releasing or mixing the contents of liposomes at a desired location, time, and dosage, for example, in micro/nanosensory and delivery devices (see picture).

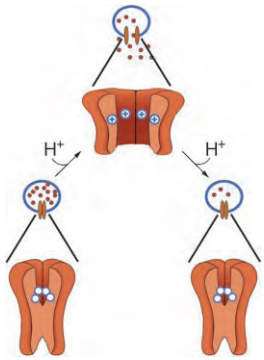

Biosensors

A. Koçer, M. Walko, E. Bulten, E. Halza, B. L. Feringa,* W. Meijberg* **3126 – 3130**

Rationally Designed Chemical Modulators Convert a Bacterial Channel Protein into a pH-Sensory Valve

A rare methyleneimine complex of ruthenium(II), *cis*-[Ru(NH=CH_2)($NCCH_3$)-$(bpy)_2$]$^{2+}$ (see structure), was obtained from the reaction of *cis*-[Ru$(N_3)_2$-$(bpy)_2$]·H_2O (bpy = 2,2′-bipyridine) with CH_3I in CH_3CN at room temperature in the dark. The reaction of such azido complexes will be useful in the synthesis of nitrogen-containing ligands.

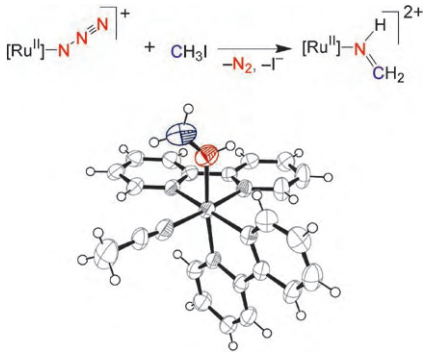

Azides

H. Nagao,* T. Kikuchi, M. Inukai, A. Ueda, T. Oi, N. Suzuki, M. Yamasaki **3131 – 3133**

Formation of a Methyleneimine Moiety by Reaction of a Ru^{II}-Coordinated Azide Ion with Methyl Iodide

Pool view preferred: In agreement with recent theoretical work, a new line of experimental evidence was obtained in support of the controversial claim that direct mechanisms do not couple methanol to ethylene in the catalyzed methanol-to-olefin process. The results preclude carbene routes and oxonium ylide mechanisms, among others (see picture), in favor of the hydrocarbon pool mechanism.

Methanol-to-Olefin Process

VIP

D. M. Marcus, K. A. McLachlan, M. A. Wildman, J. O. Ehresmann, P. W. Kletnieks, J. F. Haw* **3133 – 3136**

Experimental Evidence from H/D Exchange Studies for the Failure of Direct C–C Coupling Mechanisms in the Methanol-to-Olefin Process Catalyzed by HSAPO-34

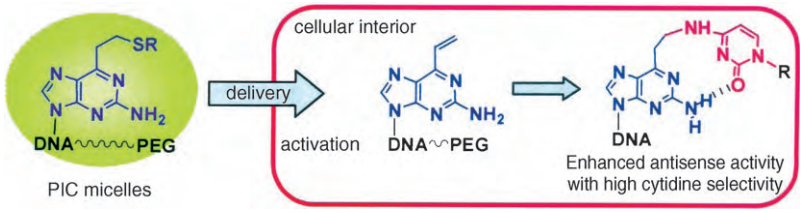

One mismatch is discriminated in a target mRNA sequence by an inducible alkylation system based on sulfide precursors to the nucleoside 2-amino-6-vinylpurine (see scheme). The reactive oligonucleotides were delivered into the cell as poly(ethylene glycol) (PEG) conjugates in polyion-complex (PIC) micelles and showed antisense activity of high selectivity and greater potency than that of the natural antisense oligonucleotide.

Biological Chemistry

M. M. Ali, M. Oishi, F. Nagatsugi, K. Mori, Y. Nagasaki, K. Kataoka, S. Sasaki* **3136 – 3140**

Intracellular Inducible Alkylation System That Exhibits Antisense Effects with Greater Potency and Selectivity than the Natural Oligonucleotide

© 2006 Wiley-VCH Verlag GmbH & Co. KGaA, Weinheim

Contents

Carbocyclization

J. Barluenga,* M. Trincado, E. Rubio, J. M. González ——— **3140 – 3143**

Direct Intramolecular Arylation of Aldehydes Promoted by Reaction with IPy_2BF_4/HBF_4: Synthesis of Benzocyclic Ketones

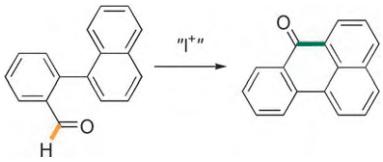

Iodine helps: Aldehydes acylate arenes upon treatment at low temperature with IPy_2BF_4 and HBF_4. This reaction is exploited in a novel intramolecular approach to the preparation of benzocyclic ketones (see scheme). A plausible mechanistic rational is also given.

Molecular Logic Gates

L. F. O. Furtado, A. D. P. Alexiou, L. Gonçalves, H. E. Toma,* K. Araki* ——— **3143 – 3146**

TiO_2-Based Light-Driven XOR/INH Logic Gates

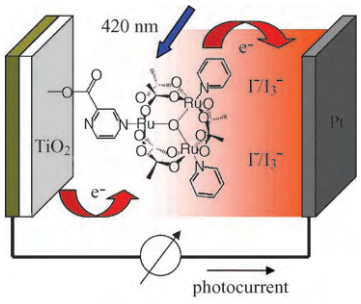

Logical progression: Optoelectronic XOR and INH logic gates based on two light inputs and an electrical output were demonstrated using a nanocrystalline TiO_2 dye-sensitized solar cell. The Grätzel-type cell was generated using a ruthenium complex as dye, with reverse injection of electrons at the semiconductor/dye interface (see picture).

Nucleophilic Reactions

H. Morimoto, S. H. Wiedemann, A. Yamaguchi, S. Harada, Z. Chen, S. Matsunaga,* M. Shibasaki* ——— **3146 – 3150**

Trichloromethyl Ketones as Synthetically Versatile Donors: Application in Direct Catalytic Mannich-Type Reactions and the Stereoselective Synthesis of Azetidines

Chemical transformers! Catalytic nucleophilic activation of trichloromethyl ketones allows applications in intermolecular carbon–carbon bond-forming reactions. Mannich adducts such as azetidines can be obtained from the primary products in high yield and *syn* selectivity. PG = protecting group.

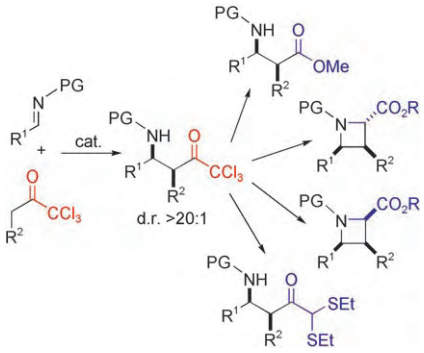

Expanded Porphyrins

X. Zhu, S. Fu, W.-K. Wong,* J.-P. Guo, W.-Y. Wong ——— **3150 – 3154**

A Near-Infrared-Fluorescent Chemodosimeter for Mercuric Ion Based on an Expanded Porphyrin

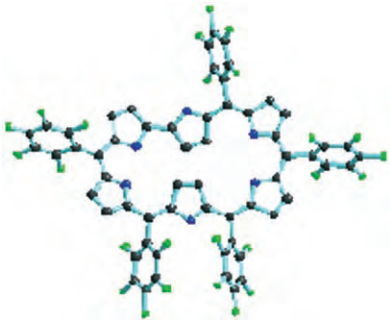

Running rings around mercuric ions: A [26]hexaphyrin(1.1.1.1.1.0), comprising an α,α′-bipyrrole unit and four pyrrolic and five pentafluorophenyl rings, was prepared and characterized by X-ray crystallography (see picture; N blue, F green, C black). The expanded porphyrin displays near-infrared luminescence above 900 nm and may serve as a highly sensitive and selective chemodosimeter for Hg^{2+} ions.

© 2006 Wiley-VCH Verlag GmbH & Co. KGaA, Weinheim

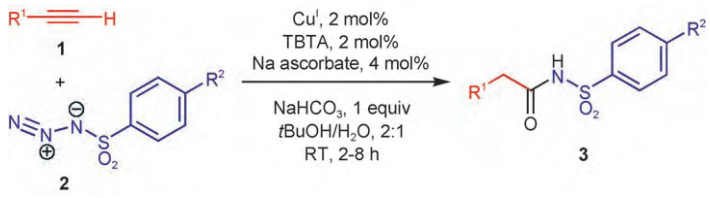

A direct, simple, and efficient route from terminal alkynes to amides is achieved by their copper(I)-catalyzed reaction with sulfonyl azides (see scheme). The reaction proceeds with the in situ generation of copper(I) acetylides and represents a one-step formal oxidative hydration of a triple bond.

Synthetic Methods

M. P. Cassidy, J. Raushel, V. V. Fokin* ——— 3154 – 3157

Practical Synthesis of Amides from In Situ Generated Copper(I) Acetylides and Sulfonyl Azides

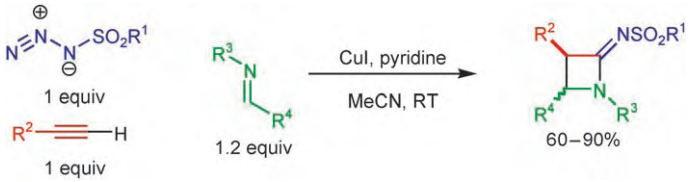

Selective conversion, take three: Densely functionalized azetidine derivatives are formed in an experimentally simple three-component catalytic procedure through the highly selective reaction of readily available terminal alkynes under mild conditions (see scheme). The azetidin-imine products are remarkably stable to a wide range of reaction conditions and readily undergo further functionalization.

Synthetic Methods

M. Whiting, V. V. Fokin* ——— 3157 – 3161

Copper-Catalyzed Reaction Cascade: Direct Conversion of Alkynes into *N*-Sulfonylazetidin-2-imines

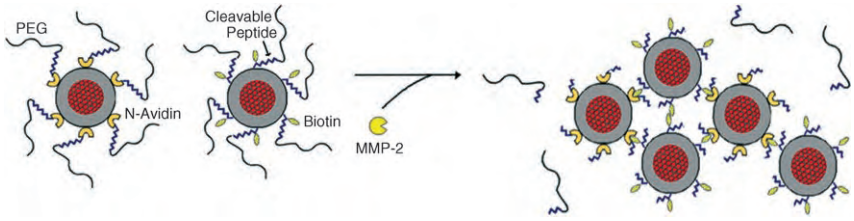

Sleeping giant: Inorganic nanoparticles are synthesized to exist in a latent form until proteolytic activation drives them to self-assemble into nanostructures with amplified magnetic properties. Binding of complimentary Fe_3O_4 nanoparticles is blocked by the attachment of inhibitory polymers that may be removed by proteases involved in cancer-cell invasion and metastasis.

Nanostructures

T. J. Harris, G. von Maltzahn, A. M. Derfus, E. Ruoslahti, S. N. Bhatia* ——— 3161 – 3165

Proteolytic Actuation of Nanoparticle Self-Assembly

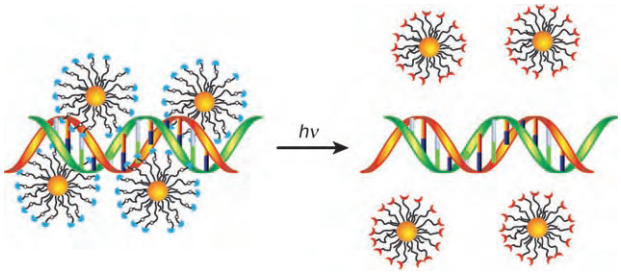

Light and life: A photolabile gold nanoparticle has been constructed to serve as a DNA carrier. UV irradiation causes the reversal of the nanoparticle surface charge, resulting in effective DNA release and reactivation of suppressed DNA transcription in vitro. This effect was also observed in living cells, together with efficient internalization of DNA into the nucleus.

DNA Carriers

G. Han, C.-C. You, B. J. Kim, R. S. Turingan, N. S. Forbes, C. T. Martin, V. M. Rotello* ——— 3165 – 3169

Light-Regulated Release of DNA and Its Delivery to Nuclei by Means of Photolabile Gold Nanoparticles

© 2006 Wiley-VCH Verlag GmbH & Co. KGaA, Weinheim

Contents

Molecular Electronics

A. Wakamiya, T. Taniguchi, S. Yamaguchi* ——— **3170 – 3173**

Intramolecular B–N Coordination as a Scaffold for Electron-Transporting Materials: Synthesis and Properties of Boryl-Substituted Thienylthiazoles

Stacking the deck: Incorporation of boryl groups into the thienylthiazole system fixes the π-conjugated framework in a planar fashion by intramolecular B–N coordination. The dimer of boryl-substituted thienylthiazole forms a unique packing structure with offset face-to-face π stacking (see picture; B orange, N blue, S yellow, C turquoise) and films of it show high electron mobility.

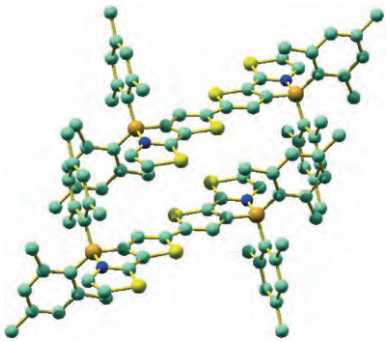

Fluorescence Spectroscopy

A. Cannizzo, F. van Mourik, W. Gawelda, G. Zgrablic, C. Bressler, M. Chergui* ——— **3174 – 3176**

Broadband Femtosecond Fluorescence Spectroscopy of $[Ru(bpy)_3]^{2+}$

It's sizzling! Femtosecond fluorescence-upconversion studies of aqueous $[Ru(bpy)_3]^{2+}$ show a short-lived vibrationally hot emission of the singlet metal-to-ligand charge-transfer state, with an ultrafast intersystem crossing (≈10 fs) to the triplet state at constant energy (the colors indicate the luminescence intensity).

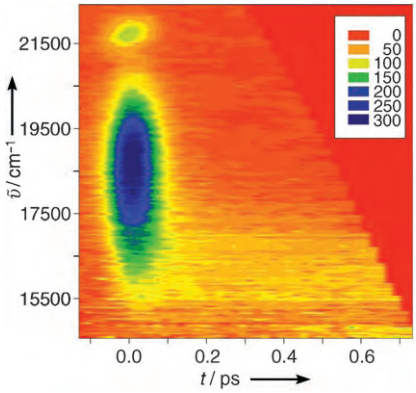

Host–Guest Chemistry

C.-F. Lin, Y.-H. Liu, C.-C. Lai, S.-M. Peng, S.-H. Chiu* ——— **3176 – 3181**

Precise Facial Control in Threading Guests into a Molecular Cage and the Formation of a Turtlelike Supramolecular Complex

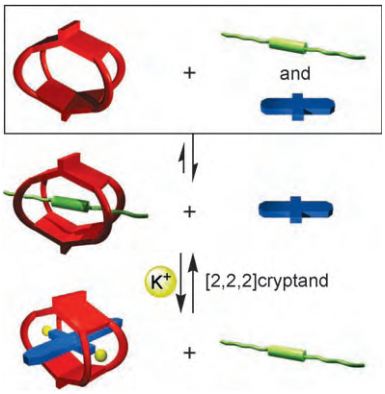

Caught in a cage: Two different thread components and a molecular cage generate different [2]pseudorotaxane-like complexes, which represent a new type of molecular machinery. An unprecedented type of molecular motion is generated by the addition of K^+ ions and [2,2,2]cryptand units to this mixture and their removal from it, in which the rodlike components penetrate the molecular cage alternately through its different faces.

Looking for outstanding employees?

Do you need another expert for your excellent team?
... Chemists, PhD Students, Managers, Professors, Sales Representatives...

Place an advert in the printed version and have it made available online for 1 month, free of charge!

Angewandte Chemie International Edition
Advertising Sales Department: Marion Schulz
Phone: 0 62 01 - 60 65 65
Fax: 0 62 01 - 60 65 50
E-Mail: MSchulz@wiley-vch.de

Service

Keywords ——— *3182*

Authors ——— *3183*

Vacancies ——— *2999*

Preview ——— *3185*

© 2006 Wiley-VCH Verlag GmbH & Co. KGaA, Weinheim

Natural Products Research: Renaissance with Strengthened Integration of Biology and Chemistry**

Wolfgang Maison

Natural products research covers a vast area that spans isolation and identification, biosynthesis, the investigation of effects, and the chemical synthesis and applications of natural products and derived analogues. Right at the outset, the question of the isolation and identification of natural products arises. Where should one search to find new structures with interesting biological properties? In this respect, it is becoming apparent that less researched organisms and habitats are often particularly rich in novel structures. Different centers of expertise have been formed for the isolation and testing of natural products. The institute for biotechnological research (GBF) in Brunswick is one of these, and last year in Irsee Gerhard Höfle lectured on the enormous pool of new compounds from myxobacteria, of which the epothilones are merely a prominent example.[1] Further such centers of expertise are located at the IBWF in Kaiserslautern (Heidrun and Timm Anke), which is concerned mainly with fungal metabolites, and in the Hans-Knöll-Institut (Axel Brakhage) in Jena. In addition to fungi and bacteria, marine organisms are a rich source of natural products that is being exploited by Axel Zeeck in Göttingen (Niedersächsischen Forschungsschwerpunkt Meeresbiotechnologie) and by Werner Müller in Mainz (Kompetenzzentrum Biotec Marin, supported by the BMBF). The isolation, identification, and utilization of natural products in chemical biology (targeted manipulation of biological phenomena with small molecules) and chemical ecology (investigation of the communication between living species by means of chemical compounds) often go hand in hand.

In pharmaceutical and plant protection research, in particular, large compound libraries have been developed through the increasing automation of synthesis and combinatorial chemistry; these libraries have frequently replaced those based on natural product extracts in the screening for active compounds. Meanwhile, however, the prevailing view is that the success of a screening project depends primarily on the quality and not quantity of the investigated library.[2] Thus it is necessary to test small, intelligent collections of biologically validated structures for their activity, as Tilman Spelling (Schering) elaborated last year in Irsee. Over millions of years the structures of natural products have been optimized with respect to their interactions with receptors. Hit ratios are correspondingly high in the screening for active compounds in pharmaceutical and plant protection research, an area that was covered in Irsee in a lecture by Joachim Rheinheimer (Pflanzenschutz, BASF).

The challenge for synthetic chemistry that arises from these requirements is of the synthesis and structural optimization of often complex, chiral, and highly functionalized, but for all that, biologically validated parent frameworks based upon natural products. "Biology-orientated synthesis" (BIOS) has been shaped to a large extent by the work of the group of Herbert Waldmann (MPI Dortmund),[3] who lectured in Irsee on the BIOS concept for the design of focused libraries. An integral part of this concept is the structural mapping of natural products (Scheme 1). This allows reduction of complex compounds to smaller scaffolds, essential for biological activity.[4] The value of the concept has already been established by a number of model studies, and offers an approach for the design of focused libraries of natural product-like compounds. The Analyti-Con Discovery company (Potsdam) is already using BIOS for building natural product-like libraries, as reported by Lutz Müller-Kuhrt in Irsee. A further center of expertise on this topic is located at the universities of Hanover and Göttingen (SFB 416 (Lutz Tietze) on the chemical and biological synthesis and transformation of natural products and analogues).

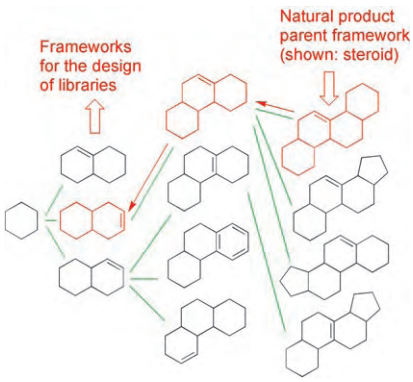

Scheme 1. Section of the natural products family tree. The red pathway illustrates exemplarily the reduction of complex natural product structures with known biological activities to smaller frameworks for the design of libraries.

A complementary approach for the introduction of diversity in natural product frameworks is provided by biological methods such as combinatorial biosynthesis based upon the reengineering of

[*] Dr. W. Maison
Universität Hamburg
Institut für Organische Chemie
Martin-Luther-King-Platz 6
20146 Hamburg (Germany)
E-mail: maison@chemie.uni-hamburg.de

[**] Symposium: 18th Irseer Naturstofftage of DECHEMA, February 22–24, 2006, Irsee (Germany).

WILEY InterScience DISCOVER SOMETHING GREAT
© 2006 Wiley-VCH Verlag GmbH & Co. KGaA, Weinheim

biosynthetic pathways. This approach allows the utilization of biological concepts, such as gene shuffling as an evolutive process, as well as chemical concepts, for example, the variation of reactants within the biosynthetic pathways. The attractiveness of this concept is reflected by the support of project 1152 "Evolution of metabolic diversity" (Toni M. Kutschan) by the German Research Foundation (DFG). Here a general trend is revealed: Approaches to solve the pressing questions in the area of natural products research stem in the meantime from the most diverse areas of the life sciences. Representative of this is the work of Christian Hertweck (HKI Jena), who last year in Irsee reported amongst other things on the mutasynthesis of aureothin analogues and who in 2005 was awarded the DECHEMA young researcher award for natural products research (Nachwuchswissenschaftler-Preis für Naturstoff-Forschung).[5] Through the exchange of *para*-nitrobenzoate, the natural initiator for polyketide biosynthesis, with *para*-cyanobenzoate it was possible to obtain the unnatural aureonitrile, a derivative with an interesting cytotoxic profile (Scheme 2).

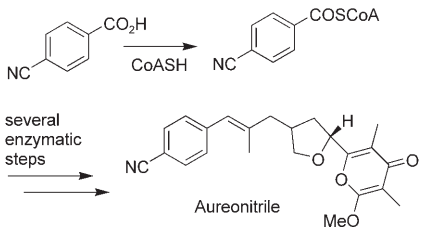

Scheme 2. Mutasynthesis of aureonitrile.

In natural products research much attention is currently being focused on the areas of oncology and infectious diseases. The immense social significance of infectious diseases (most frequent cause of death worldwide) and the withdrawal of many pharmaceutical companies from this (in part, unprofitable) business area have been the motivation for a series of academic research projects, including SFB 630 (Gerhard Bringmann) for the "Recognition, isolation, and functional analysis of compounds active against infectious diseases" and project 1160 (Axel Brakhage, HKI Jena) "Human pathogenic fungi". In this connection the area of tropical infectious diseases formed a subject area in Irsee, and August Strich (Universität Würzburg) and Martin Schlitzer (LMU Munich) reported on the sobering status quo in the treatment of tropical diseases; it is here that government support could provide critical impulse.

A trend in the area of oncology is the development of selective active compounds and diagnostics based upon mostly complex natural products such as oligosaccharides and peptides that specifically recognize tumor surface structures. One example is the work of Horst Kunz on synthetic tumor vaccines. A highly specific immune reaction could be produced in mice with a fully synthetic glycopeptide that contained the building block of a tumor-specific mucin (MUC1) in a tandem repeat sequence,[6] an important step on the way to nontoxic tumor vaccines.

Work on chemical ecology contributes fundamentally to the understanding of the communication between life forms through chemical compounds, and is also relevant for the utilization of natural products in plant protection and in pharmaceuticals. In this context, Wittko Francke (Universität Hamburg) reported on his extensive work on the investigation of the complex chemical communication of insects. Centers of Expertise on chemical ecology are located in Halle (Leibnitz-Institut für Pflanzenbiochemie) and in Jena (MPI für Chemische Ökologie). This area also includes the work of Georg Pohnert (ETH Lausanne) on wound closure of the alga *Caulerpa taxifolia*, for which he was awarded the DECHEMA young researcher award in Irsee this year. Wound closure of this single cell alga is remarkable from many points of view: it prevents leakage of the alga upon damage, it is essential for reproduction, and it follows a previously unknown mechanism of protein cross-linking with bisaldehydes formed enzymatically in situ. This mechanism can be used in vivo for enzyme-triggered polymerization, and thus it forms a bridge between chemical ecology and materials science.[7]

Karl Gademann (ETH Zürich) presented his work on anachelin H, a side-

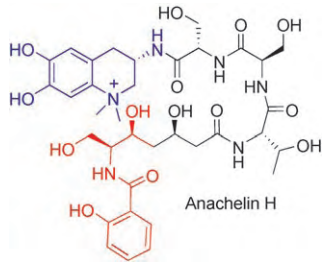

rophore from the cyanobacterium *Anabaena cylindrica,* which made possible the synthesis of the natural product as well as corresponding fragments and derivatives. This permitted the complete characterization and the investigation of extensive structure–activity relationships, which led to the identification of a dual mode of action of the natural product: Part of the molecule (shown in blue) is a growth factor for the cyanobacteria, and another part (shown in red) inhibits the growth of competitive green algae; both factors are supposed to play a key role in algal blooms caused by toxic *cyanobacteria*. Owing to its very good coordination to metals, the catechol residue (blue) can be used for the anchoring of functional molecules onto the surface of metal oxides, which can prevent the biofouling of artificial surfaces.[8]

Natural products research profits manifoldly from interdiscplinary approaches, for which new approaches to scientific education are required; graduate schools already exist in a number of localities, for example, for chemical biology in Dortmund (MPI and Universität Dortmund, Universität Bochum), and for chemical ecology in Jena (MPI, HKI, and Universität Jena), which is a step in the right direction. The considerable advances in recent years in the areas of isolation, identification, and synthesis shows that, after years of declining importance, the search for active compounds from natural products is undergoing a renaissance. The structural complexity of natural products is no longer considered a disadvantage but is being profitably exploited for the most-diverse applications—what influence this outcome of natural products research will exert in the future on, for example, the search for active compounds and materials science will be followed with anticipation.

© 2006 Wiley-VCH Verlag GmbH & Co. KGaA, Weinheim

[1] G. Höfle, H. Reichenbach in *Anticancer Agents from Natural Products* (Eds.: G. M. Cragg, D. G. I. Kingston, D. J. Newman), Taylor & Francis Group, Boca Raton, **2005**, p. 413 – 450.
[2] F. E. Koehn, G. T. Carter, *Nature Rev. Drug. Disc.* **2005**, *4*, 206 – 220.
[3] R. Breinbauer, I. R. Vetter, H. Waldmann, *Angew. Chem.* **2002**, *114*, 3002 – 3015; *Angew. Chem. Int. Ed.* **2002**, *41*, 2878 – 2890.
[4] M. A. Koch, A. Schuffenhauser, M. Schreck, S. Wetzel, M. Casaulta, A. Odermatt, P. Ertl, H. Waldmann, *Proc. Natl. Acad. Sci. U.S.A.* **2004**, *101*, 16721 – 16726.
[5] M. Ziel, J. He, H.-M. Dahse, C. Hertweck, *Angew. Chem.* **2005**, *117*, 1226 – 1230; *Angew. Chem. Int. Ed.* **2005**, *44*, 1202 – 1205.
[6] S. Dziadek, A. Hobel, E. Schmitt, H. Kunz, *Angew. Chem.* **2005**, *117*, 7803 – 7808; *Angew. Chem. Int. Ed.* **2005**, *44*, 7630 – 7635.
[7] S. Adolph, V. Jung, J. Rattke, G. Pohnert, *Angew. Chem.* **2005**, *117*, 2866 – 2869; *Angew. Chem. Int. Ed.* **2005**, *44*, 2806 – 2808.
[8] S. Zürcher, D. Wäckerlin, Y. Bethuel, B. Malisova, M. Textor, S. Tosatti, K. Gademann *J. Am. Chem. Soc.* **2006**, *128*, 1064 – 1065.

DOI: 10.1002/anie.200601297

Unique – Comprehensive – Fascinating

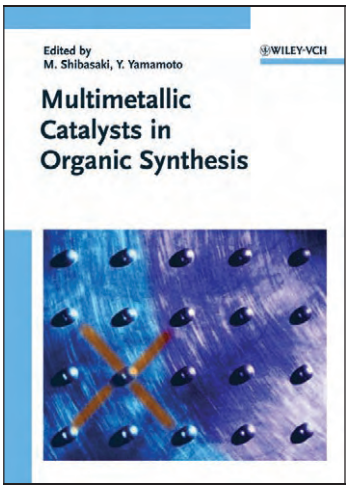

2004. XV, 295 pages, 173 figures, 66 tables. Hardcover. ISBN 3-527-30828-8 € 135.- /£ 90.- /US$ 194.-

MASAKATSU SHIBASAKI and YOSHINORI YAMAMOTO, (Eds.)

Multimetallic Catalysts in Organic Synthesis

This first book to comprehensively cover this hot topic presents the information hitherto scattered throughout smaller reviews or single book chapters to provide an introduction to this rapidly expanding field.
In ten chapters, the international team of expert authors treats asymmetric syntheses, new transformations, and organometallic reactions using homo- and hetero-bimetallic catalysts. Written for advanced researchers, this very timely publication is of significant benefit to organic and organometallic chemists in both academia and industry.

22530509_kn

Register now for the free
WILEY-VCH Newsletter!
www.wiley-vch.de/home/pas

WILEY-VCH • P.O. Box 10 11 61 • D-69451 Weinheim, Germany
Fax: +49 (0) 62 01 - 60 61 84
e-mail: service@wiley-vch.de • http://www.wiley-vch.de

WILEY-VCH

 © 2006 Wiley-VCH Verlag GmbH & Co. KGaA, Weinheim

Bond Theory

DOI: 10.1002/anie.200504322

To Boldly Pass the Metal–Metal Quadruple Bond

Udo Radius and Frank Breher**

Keywords:
arene ligands · bond theory · metal–metal interactions · multiple bonds

Dedicated to Professor Hansgeorg Schnöckel on the occasion of his 65th birthday

The theory of chemical bonding is intriguing and of fundamental importance. Bonding concepts were developed and rules were established over the years to describe and subdivide molecular compounds consisting of either single, double, or triple bonds. The latter was believed to be the highest accessible bond order for a long time. Although compounds that contain quadruple bonds between transition metals were already prepared in the 19th century, for example $[Cr_2(\mu\text{-}O_2CMe)_4(H_2O)_2]$),[1] it was not until 1964, when Cotton et al. reported on the crystal structure of $K_2[Re_2Cl_8]\cdot 2H_2O$ featuring a surprisingly short Re–Re distance of 2.24 Å,[2] that such a quadruple bond between two transition-metal atoms was confirmed unequivocally. The $[Re_2Cl_8]^{2-}$ ion has become the prototype for this type of complexes, and a new era of inorganic chemistry and a rich chemistry has evolved around this class of transition-metal complexes.[3]

The well-known qualitative description of a $\sigma^2\pi^4\delta^2$ quadruple bond is elegant and deceptively simple (and familiar), but it is based on a one-electron model and the inherent assumption that four bonding orbitals are doubly occupied. Today we know that this is not entirely true for weak intermetallic bonds. The small overlap between δ orbitals results in a relatively weak interaction, thus making a simple molecular orbital (MO) description of the quadruple bond inappropriate.[4] A more accurate, but less transparent description of the quadruple bond requires an approach that goes beyond single configuration methods inherent to simple MO formalisms. To properly describe systems already in the ground state, treatments must include correlation effects. A bond order analysis of $[Re_2Cl_8]^{2-}$ relying on CASSCF (complete active-space self-consistent field) calculations,[5] for example, has shown, that the Re–Re bond has an effective (calculated) bond order of 3.2 and the net bond order contribution of the δ bond is about 0.5. The reason is mainly a partial occupation of the antibonding δ* orbitals. Whether it should be called a triple or a quadruple bond or whether the δ bond should be called a weak bond or half a bond is more or less a matter of definition of the term "bond" or "bond order". The alternatives here are to describe the bonding as a "weak" quadruple bond (four orbitals with relevant overlap) or as a bond involving four electron pairs with an effective bond order of about three.

Various orbitals contribute to a different extent to metal–metal bonding, as demonstrated by intriguing compounds such as the silicon analogue of an alkyne, RSi≡SiR, reported by Sekiguchi et al. or Wiberg et al.[6] and the corresponding germanium, tin, and lead compounds REER (E = Ge–Pb) comprising bulky aryl ligands (Ar′ and Ar*)[7] described not long before by Power et al.[8] For the REER compounds, the term alkyne analogue does not imply that each of the three valences available for the Group 14 element contribute equally to chemical bonding to retain a triple bond featuring an integer bond order of three. As a result of the gradually increasing, nonlinear, *trans*-bent geometries on descending the group, a considerable weakening of one component of the degenerate π bonding was suspected. Although the structural data, as well as quantum-chemical calculations point towards bond orders approaching three for Si, approximately two for Ge and Sn, and one for Pb, the correlation of bond length and bond order is questionable and should be treated with care, especially when counterions are involved. This has led to controversial discussions in the past, for example, whether $[Ar^*GaGaAr^*]^{2-}$ (formally isoelectronic to neutral RGeGeR) is the first experimentally proven gallium–gallium triple bond or not.[9] Although not capable of distinguishing between covalent and electrostatic contributions, the best experimental tool for a classification of such bonds might be the force constant of the metal–metal bond.[10]

A milestone for multiple-bond chemistry involving transition metals was recently reported by Power and co-workers, who impressively succeeded in isolating "a stable compound with fivefold bonding between two chromium(I) centers".[11] To achieve the highest bond order possible in an isolable compound, the number of ligands has to be minimized, since their binding reduces the number of valence orbitals available to form metal–metal bonds. Furthermore, the steric requirements for the ligand system is of crucial importance since large ligands prevent oligomerization and undesirable bridging motifs are usually disfavored for steric reasons. Relying on their background in main group chemistry,[8] Power et al. have synthesized and characterized a dinuclear metal–metal-bonded complex with one ligand per metal atom in the ligand

[*] Priv.-Doz. Dr. U. Radius, Prof. Dr. F. Breher
Institut für Anorganische Chemie
Universität Karlsruhe (TH)
Engesserstrasse 15
76131 Karlsruhe (Germany)
Fax: (+49) 721-608-8440
E-mail: radius@aoc1.uni-karlsruhe.de
breher@aoc1.uni-karlsruhe.de

InterScience
© 2006 Wiley-VCH Verlag GmbH & Co. KGaA, Weinheim

sphere. The reduction of [{Cr(μ-Cl)Ar′}$_2$][7] with a slight excess of potassium graphite afforded the thermally robust complex [Ar′CrCrAr′] (**1**) in 41 % yield.

Following the simplified picture developed for $[Re_2Cl_8]^{2-}$, the bonding in a (hypothetical) linear complex [RCrCrR] (R = monoanionic ligand) can be described as a quintuple (ten-electron–two-center) Cr–Cr bond formed by a fivefold overlap between metal d orbitals (Figure 1). Five electron

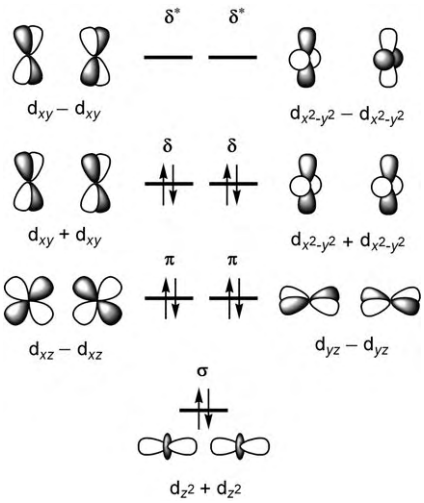

Figure 1. Schematic MO picture for linear [R-CrCr-R].

pairs play a dominant role in holding the metal atoms together, but it does not necessarily imply that the bond order is five or that the bonding is very strong. As pointed out for $[Re_2Cl_8]^{2-}$, the ground state of the molecule possibly involves mixing of other higher energy configurations with less bonding character.

The molecular structure of [Ar′Cr-CrAr′] (**1**) (Figure 2) reveals a planar

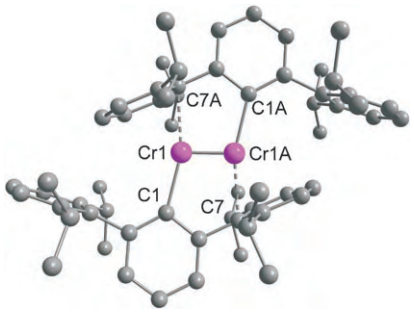

Figure 2. Molecular structure and numbering scheme of [Ar′CrCrAr′] (**1**).

core geometry with a Cr–Cr bond length of 1.8351(4) Å. The chromium–chromium distance is slightly longer than the bond length reported for a quadruply bonded, but ligand-bridged Cr^{II} dimer $[Cr_2(\mu^2\text{-OMe-5-Me}C_6H_3)_4]$ (1.828(2) Å), which has the shortest metal–metal bond distance observed so far.[12] The atoms C1, Cr1, Cr1A, and C1A of the central Cr_2C_2 unit in **1** are aligned in a plane, but deviate significantly from linearity (angle Cr1A-Cr1-C1 102.78(3)°), adopting a *trans*-bent structure. Each chromium atom is bonded to the *ipso*-carbon atom (Cr1–C1 2.131(1) Å) of the Ar′ ligand and through a somewhat weaker interaction (Cr1–C7A 2.2943(9) Å) to an *ipso*-carbon atom of a flanking dipp ring (dipp = C_6H_3-2,6-*i*Pr_2) of the ligand. The interaction of the dipp moiety with the chromium atom can also be considered as that with a distorted η^6-coordinated arene ligand; the chromium–carbon distances range from 2.29 to 2.97 Å.

The simple bonding model given above, therefore, has to be adjusted to the geometry observed. Additionally, mixing of orbitals can occur due to the lower symmetry of the complex. DFT single-point calculations on the experimentally verified structure presented by the authors support the view that there are five orbital interactions (one σ, two π, and two δ) between the Cr^{I} ions (Figure 3). HOMO and HOMO–1, which differ in energy by 0.41 eV, correspond to δ bonds, and the LUMO, which is 2.01 eV higher in energy than the HOMO, corresponds to a δ* orbital. The chromium–chromium σ-binding orbital (HOMO–2) that emerges from the single-point DFT calculations on **1** is comparatively high in energy, above the two π-binding orbitals (HOMO–3 and HOMO–4). This might be due to significant orbital mixing and/or due to reduced overlap along the chromium–chromium axis. Although the authors provided first results on CASSCF calculations in the Supplementary Material of the original article, the meaning of this feature for metal–metal bonding remains to be evaluated in a more thorough theoretical treatment of **1** or models of this compound.

Before entering into a further discussion of the bonding in complex **1**, it is most instructive to briefly outline the

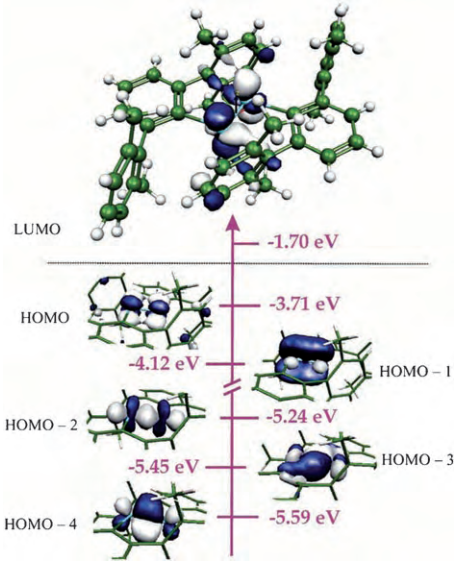

Figure 3. Electron density surfaces and energies for the Cr–Cr frontier orbitals in [Ar′CrCrAr′] (**1**)[11a] (reprinted with permission from *Science* **2005**, *310*, 844. Copyright 2005 AAAS).

bonding situation in the dichromium dimer, Cr_2, which has attracted considerable interest in recent years.[13] By continuing with the concept of minimizing the number of metal ligands to maximize the number of free metal valence orbitals available to form metal–metal bonds to an extreme, even larger bond orders than five should be feasible. The bare dimers of the open d-shell transition metals provide an opportunity to examine multiple bonds between metal atoms in the absence of ligand effects. Among the dimers of the first transition series, Cr_2 potentially provides one of the most intriguing examples of multiple metal–metal bonding. Since the chromium atom has a high-spin ^7S ground state (a $(3d)^5(4s)^1$ valence electron configuration with one electron in each of six valence orbitals), closely spaced energy levels result. The spin pairing of two ground-state atoms results in a $^1\Sigma_g^+$ Cr_2 molecule with a valence electron configuration $(4s\sigma)^2(3d\sigma)^2(3d\pi)^4(3d\delta)^4$ comprising two σ, two π, and two δ bonds giving formal chromium–chromium bond order of six. The complexity of the bonding in Cr_2, however, was for a long time a challenge for ab initio quantum chemistry because of this "hextuple" bond and the unusual shape of the Cr_2 potential energy curve (Figure 4).

© 2006 Wiley-VCH Verlag GmbH & Co. KGaA, Weinheim

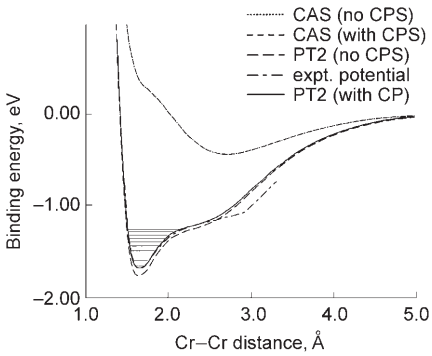

Figure 4. Experimental and calculated potential energy curves for Cr_2 using CASSCF and CASPT2 according to Roos[13d] (reproduced from reference [13d] with permission of the Institute of Organic Chemistry and Biochemistry, Academy of Sciences of the Czech Republic).

At a short internuclear Cr–Cr distance ($r_e = 1.6788$ Å), the molecule is multiply bonded and exhibits a relatively deep potential. As the atoms separate, the rapid loss of bonding between the compact 3d orbitals is partially compensated by increased interatomic exchange stabilization, as well as by 4s–4s bonding. As a result, the potential curve rises more slowly with increased internuclear separation than would be expected, which renders the curve highly anharmonic with a shelf or a shallow minimum at intermediate chromium–chromium separations. The nature of the Cr–Cr interaction changes qualitatively with increased internuclear separation, from multiple 3d–3d bonding at short distances to single 4s–4s bonding (with the 3d electron cores of the two atoms antiferromagnetically coupled to give a singlet state) at long distances. The Cr_2 potential provides a beautiful illustration of this phenomenon. Using highly correlated CASSCF and CASPT2 calculations, Anderson and Roos et al.[13d–h] gave a qualitatively correct description of the Cr_2 potential energy surface and calculated a total chromium–chromium bond order of 4.4 at equilibrium distance. Accordingly, the chromium–chromium bond consists of one σ bond of primarily 4s and 3d contributions, two π bonds totally 3d in character, two δ bonds totally 3d in character, and one antiferromagnetically coupled electron pair. This assignment avoids the rather counterintuitive description of two chromium–chromium σ bonds. The distinction between antiferromagnetic coupling and bonding, however, is in this case not clearly defined.

As with Cr_2, the chromium–chromium bond in the complex **1** presented by Power et al. might alternatively be described as a quadruple bond with two antiferromagnetically coupled electrons residing in chromium-localized orbitals. Magnetic measurements on [Ar′Cr-CrAr′] revealed a temperature-independent weak paramagnetism of 0.000112(5) emu per mol Cr, which is consistent with strongly coupled paired electrons ($S = 0$) and an first excited state ($S = 1$) relatively high in energy, without a significant population of $S > 0$ states at room temperature. The most common metrics used to gauge the quality of calculations of the electronic structure of quadruple bonds are the geometry-optimized metal–metal bond length and the δ–δ* excitation energy. The electronic absorption spectrum of [Ar′CrCrAr′] displays a broad absorption at 488 nm, which lies in the range observed for δ–δ* transitions of compounds with metal–metal quadruple bonds.

Without doubt, the analysis of the bonding situation in [Ar′CrCrAr′] as well as those for the iron and cobalt analogues, briefly mentioned by Power and co-workers, will be an interesting topic among theoreticians. It is very interesting to note that the structurally related [Ar′FeFeAr′] (+4 electrons) and [Ar′CoCoAr′] (+6 electrons) dimers have much longer metal–metal contacts (2.53 Å (Fe–Fe) and 2.80 Å (Co–Co)). Assuming the classical bonding picture, this would imply an increase of the bond length of approximately 0.7 Å due to occupation of two antibonding δ* orbitals. A bonding distance as long as 2.53 Å would result for a formal iron–iron triple bond!

Going one step further to f block elements, the uranium atom holds, similarly to a chromium atom, six electrons in its valence shell. However, whereas chromium has exactly six valence orbitals, there are 16 such orbitals close in energy available for uranium; that is the seven 5f, five 6d, one 7s, and three 7p orbitals. Gagliardi and Roos recently presented calculations on hypothetical diuranium U_2 using CASSCF calculations.[14a] As the authors stated, the maximum flexibility for describing electronic structures and the capability of handling arbitrary spin as offered by the CASSCF method is important, because "we cannot assume anything concerning the final number of paired electrons in U_2". Indeed, when considering heavy actinide elements, metal–metal bonds proved to be particularly complicated. Although the ground-state electronic configuration of an uranium atom is $(5f)^3(6d)^1(7s)^2$ (quintet ground state), the energy cost of unpairing the 7s electrons is low, revealing in principle six electrons available for each U atom to form chemical bonds. The bonding situation for uranium, however, is considerably more complex than the situation found for Cr_2—in fact unique, as reported by Gagliardi and Roos.[14a]

Their calculations revealed that three (two-electron–two-center) electron pair bonds are formed by hybrid orbitals with predominantly 7s and 6d character, that is one σ-type and a degenerate set of π-type orbitals (Figure 5, first row). Furthermore, two singly occupied orbitals of σ-type ($6d\sigma_g$) and of δ-type ($6d\delta_g$), which show mainly d-orbital character, give rise to two one-electron–two-center bonds between the two uranium atoms. Two singly occupied orbitals of δ- and π-type ($5f\delta_g/5f\pi_u$ and $5f\delta_u/5f\pi_g$, respectively), with predominantly f character, form two additional one-electron bonds. Finally, two electrons occupy a localized 5f orbital ($5f\phi_u$ and $5f\phi_g$) equally distributed over both uranium atoms with the electron spins aligned parallel. To summarize, the bonding in U_2 arises from three two-electron–two-center electron pair bonds ($\sigma + 2\pi$), four one-electron–two-center bonds ($\sigma + \pi + 2\delta$), and two localized electrons. For U_2, all single spins are predicted to be parallel ("ferromagnetically" coupled) and the $S = 3$ septet state is the ground state of the molecule.[15] The calculated (CASPT2-SO, including spin-orbit coupling, SO) equilibrium bond length of (2.43 ± 0.05) Å and a harmonic vibrational frequency of 265 cm^{-1} suggests comparability of the strength of the U_2 bond to that of other multiple bonds between transition metals. Overall, the unprecedented ground state of U_2 is expressed as $\sigma^2\pi^4\sigma^1\delta^1\delta^1\pi^1\phi^1\phi^1$ (with ϕ^1 = localized 5f orbital, $S = 3$, $\Lambda = 11$, ground state

 © 2006 Wiley-VCH Verlag GmbH & Co. KGaA, Weinheim

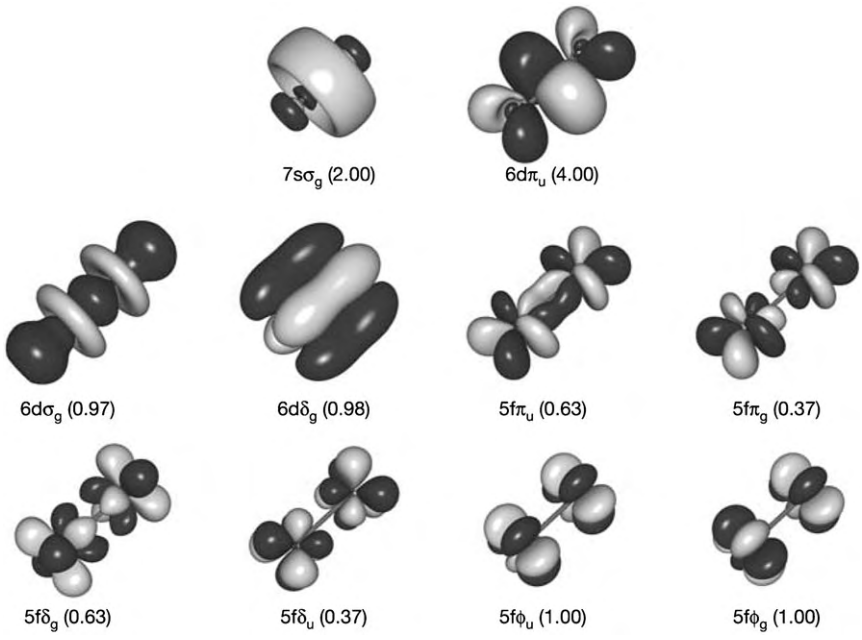

Figure 5. The molecular orbitals forming the chemical bond between two uranium atoms in U_2. Orbital labels are given below each orbital, together with the number of electrons occupying this orbital or pair of orbitals in the case of degeneracy[14a] (reprinted by permission from Macmillan Publishers Ltd: *Nature* **2005**, *433*, 848, copyright 2005).

$^{7}11_{14}$), and is more complex than any other known diatomic bond.

If two of the twelve electrons of U_2 were removed, some simplifications of the electronic structure are predicted.[14b] Quantum-chemical calculations, based on multiconfigurational wave functions and including relativistic effects, show that the U_2^{2+} system has a large number of low-lying electronic states with $S = 0$–2 and Λ ranging from zero to ten. A bond length of approximately 2.30 Å (cf. 2.43 Å for neutral U_2) is common for these states. The lowest electronic state corresponds to an electron configuration $(\sigma_g)^2(\pi_u)^4$ and suggests a triple bond. The σ orbital is a hybrid comprising 7s, 6dσ, and 5fσ atomic orbitals, and the π_u orbitals are mainly 6d in character. The next four electrons, two localized on each of the uranium atoms, occupy 5fδ and 5fϕ orbitals, which are essentially nonbonding.

Recently, a related theoretical paper presented model calculations on linear singlet [HTh≡ThH], which should be a likely candidate for the so far unknown multiple, in this particular case triple, bond between f elements.[14c] The orbital picture and the bonding analyses suggest substantial f character in the Th–Th bond in linear $^{1}\Sigma_g$-[HTh≡ThH] bonding orbitals. The molecular orbitals of this compound correspond to σ(Th–H) bonds, one σ(Th–Th) bond (HOMO−1), and a double π(Th–Th) bond (HOMO) featuring up to 22% f character in the bond. According to the calculations the f-orbital participation stabilizes the linear geometry of the molecule.

The model of the two-electron–two-center bond, as introduced by G. N. Lewis in 1916, which features a single bond to be formed by one pair of electrons, is one of the most important concepts in chemistry. This also covers multiple bonds since they are regarded as composed of two, three or four two-electron components. The last few years have witnessed an in depth discussion on multiple bonding between main group elements, which has revealed that simple concepts mainly emerging from the peculiarities of carbon (or the second period of elements) chemistry are not valid for heavier elements. Apparently, the models, which are consistent and clear for the lighter main group elements, become considerably more complicated than anticipated when applied to their heavier counterparts. The same holds true for the term "bond order", which is in fact more or less a matter of definition—not trivial if reasonable at all. The decrease of orbital overlap and increase of nonbonding lone-pair character for molecules of multiply bonded main group elements, and hence the deviation from planarity (for R_2EER_2) or linearity (REER) has shown that the concepts developed for elements of the second period are certainly not appropriate to describe the nature of an element–element "multiple" bond. The involvement of d orbitals certainly complicates the situation due to moderate overlap for δ-type d orbitals. The work of Power et al., in unraveling the quintuple bond in *trans*-bent [Ar′CrCrAr′] (**1**), has added a further dimension to the concept of multiple bonding in transition-metal chemistry. It is likely, however, that the bonding situation in [Ar′CrCrAr′] is not fully understood and that the *trans*-bending of this complex will add an additional level of complexity to the analysis of bonding. The current state of the bond description for **1** is that five pairs of overlapping orbitals are more or less involved in metal–metal bonding; a situation that chemists usually would describe as a quintuple bond.[16] A detailed theoretical analysis of the nature of the chemical bond in **1** will certainly be undertaken in the future and it is likely that there will be a renewed debate about metal–metal multiple bonding. To fully understand the bonding in this complex is of crucial significance and many fundamental questions remain to be answered. Whatever the conclusion turns out to be regarding the bond multiplicity in the newly synthesized compound [Ar′CrCrAr′], this work undoubtedly inspires scientists from a theoretical and experimental point of view.

The greatest achievement here is the preparative work, which has opened a new area previously considered nonexistent. This work will certainly encourage others to investigate transition-metal complexes bearing "ultralarge" ligands in more detail. The combination of both the isolation of further compounds of the type [RMMR] on the one hand, and their precise characterization on the other, may facilitate an accurate experimental assessment of the bonding situation and the bond strength in these

 © 2006 Wiley-VCH Verlag GmbH & Co. KGaA, Weinheim

types of complexes. The main objective for experimental as well as theoretical chemists is undoubtedly to work together to develop an understanding of this unusual bonding situation between d-block metals—and similar compounds comprising f-block metals are not out of reach!

[1] E. Peligot, *C. R. Hebd. Seances Acad. Sci.* **1844**, *19*, 609.

[2] a) F. A. Cotton, N. F. Curtis, C. B. Harris, B. F. G. Johnson, S. J. Lippard, J. T. Mague, W. R. Robinson, J. S. Wood, *Science* **1964**, *145*, 1305; b) F. A. Cotton, N. F. Curtis, B. F. G. Johnson, W. R. Robinson, *Inorg. Chem.* **1965**, *4*, 326; c) F. A. Cotton, C. B. Harris, *Inorg. Chem.* **1965**, *4*, 330; d) F. A. Cotton, *Inorg. Chem.* **1965**, *4*, 334.

[3] F. A. Cotton, L. A. Murillo, R. A. Walton, *Multiple Bonds Between Metal Atoms*, 3rd ed., Springer, Berlin, **2005**.

[4] F. A. Cotton, D. G. Nocera, *Acc. Chem. Res.* **2000**, *33*, 483.

[5] a) L. Gagliardi, B. O. Roos, *Inorg. Chem.* **2003**, *42*, 1599; b) F. Ferrante, L. Gagliardi, B. E. Bursten, A. P. Sattlberger, *Inorg. Chem.* **2005**, *44*, 8476.

[6] a) A. Sekiguchi, R. Kinjo, M. Ichinohe, *Science* **2004**, *305*, 1755; b) N. Wiberg, W. Niedermayer, G. Fischer, H. Nöth, M. Suter, *Eur. J. Inorg. Chem.* **2002**, 1066; c) N. Wiberg, S. K. Vasisht, G. Fischer, P. Mayer, *Z. Anorg. Allg. Chem.* **2004**, *630*, 1823; d) M. Weidenbruch, *Angew. Chem.* **2005**, *117*, 518; *Angew. Chem. Int. Ed.* **2005**, *44*, 514 (Highlight); e) M. Weidenbruch in *The Chemistry of Organic Silicon Compounds*, *Vol. 3* (Ed.: Z. Rappoport, Y. Apeloig), Wiley, Chichester, **2001**; f) N. Takagi, S. Nagase, *Eur. J. Inorg. Chem.* **2002**, 2775; Recently, Passmore and co-workers impressively succeeded in isolating the $S_2I_4^{2+}$ cation featuring a sulfur sulfur bond with a high bond order, which is comparable to that of RSiSiR: g) S. Brownridge, T. S. Cameron, H. Du, C. Knapp, R. Köppe, J. Passmore, J. M. Rautiainen, H. Schnöckel, *Inorg. Chem.* **2005**, *44*, 1660; h) S. K. Ritter, *Chem. Eng. News* **2005**, *83*, 49.

[7] Ar′: -C_6H_3-2,6-$dipp_2$ (dipp = C_6H_3-2,6-iPr$_2$); Ar*: -C_6H_3-2,6-$trip_2$ (trip = C_6H_2-2,4,6-iPr$_3$).

[8] a) M. Stender, A. D. Phillips, R. J. Wright, P. P. Power, *Angew. Chem.* **2002**, *114*, 1863; *Angew. Chem. Int. Ed.* **2002**, *41*, 1785; b) A. D. Phillips, R. J. Wright, M. M. Olmstead, P. P. Power, *J. Am. Chem. Soc.* **2002**, *124*, 5930; c) L. Pu, B. Twamley, P. P. Power, *J. Am. Chem. Soc.* **2000**, *122*, 3524; d) P. P. Power, *Appl. Organomet. Chem.* **2005**, *19*, 488; e) C. Cui, M. M. Olmstead, J. C. Fettinger, G. H. Spikes, P. P. Power, *J. Am. Chem. Soc.* **2005**, *127*, 17530; for selected reviews see: f) P. P. Power, *Chem. Rev.* **1999**, *99*, 3463; g) M. Weidenbruch, *Organometallics* **2003**, *22*, 4348; h) P. P. Power, *Chem. Commun.* **2003**, 2091.

[9] a) Y. Xie, R. S. Grev, J. Gu, H. F. Schaefer, P. v. R. Schleyer, J. Su, X.-W. Li, G. H. Robinson, *J. Am. Chem. Soc.* **1998**, *120*, 3773; b) G. H. Robinson, *Chem. Commun.* **2002**, 2175; c) F. A. Cotton, A. H. Cowley, X. Feng, *J. Am. Chem. Soc.* **1998**, *120*, 1795; d) M. M. Olmstead, R. S. Simons, P. P. Power, *J. Am. Chem. Soc.* **1997**, *119*, 11705; e) T. L. Allen, W. H. Fink, P. P. Power, *J. Chem. Soc. Dalton Trans.* **2000**, 407; f) N. J. Hardman, R. J. Wright, A. D. Phillips, P. P. Power, *J. Am. Chem. Soc.* **2003**, *125*, 2667; g) R. Ponec, G. Yuzhakov, X. Gironés, G. Frenking, *Organometallics* **2004**, *23*, 1790; h) J. Grunenberg, N. Goldberg, *J. Am. Chem. Soc.* **2000**, *122*, 6045; i) N. Takagi, M. W. Schmidt, S. Nagase, *Organometallics* **2001**, *20*, 1646.

[10] See for example: a) R. Köppe, H. Schnöckel, *Z. Anorg. Allg. Chem.* **2000**, *626*, 1095; b) see also ref. [9h].

[11] a) T. Nguyen, A. D. Sutton, M. Brynda, J. C. Fettinger, G. J. Long, P. P. Power, *Science* **2005**, *310*, 844; b) G. Frenking, *Science* **2005**, *310*, 796.

[12] F. A. Cotton, S. A. Koch, M. Millar, *Inorg. Chem.* **1978**, *17*, 2084.

[13] For the potential energy curve of Cr_2 see: a) S. M. Casey, D. G. Leopold, *J. Phys. Chem.* **1993**, *97*, 816; for theoretical calculations on Cr_2 see for example: b) N. E. Schultz, Y. Zhao, D. G. Truhlar, *J. Phys. Chem. A* **2005**, *109*, 4388; c) E. A. Baudreaux, E. Baxter, *Int. J. Quantum Chem.* **2004**, *100*, 1170; d) B. O. Roos, *Collect. Czech. Chem. Commun.* **2003**, *99*, 265; e) G. L. Gutsev, C. W. Bauschlicher, Jr., *J. Phys. Chem. A* **2003**, *107*, 4755; f) B. O. Roos, K. Anderson, *Chem. Phys. Lett.* **1995**, *245*, 215; g) K. Anderson, *Chem. Phys. Lett.* **1995**, *237*, 212; h) K. Anderson, B. O. Roos, P.-Å. Malmqvist, P.-O. Widmark, *Chem. Phys. Lett.* **1994**, *230*, 391; i) M. M. Goodgame, W. A. Goddard III, *Phys. Rev. Lett.* **1985**, *54*, 661.

[14] a) L. Gagliardi, B. Roos, *Nature* **2005**, *433*, 848; b) L. Gagliardi, P. Pyykkö, B. O. Roos, *Phys. Chem. Chem. Phys.* **2005**, *7*, 2415; c) M. Stratka, P. Pyykkö, *J. Am. Chem. Soc.* **2005**, *127*, 13090.

[15] Note the difference to Cr_2 featuring "antiferromagnetic" coupling, which causes spin-pairing of the electrons and usually provides some additional small bonding contributions and some extra stabilization. In the particular case of U_2, this ferromagnetic coupling can be attributed to favorable exchange stabilization, that is interaction between nonbonding 5f electrons and one-electron bonds.

[16] Bonding pictures might also be totally unexpected, as experienced in the case of U_2; see also: M.-M. Rohmer, M. Bénard, *Chem. Soc. Rev.* **2001**, *30*, 340

 © 2006 Wiley-VCH Verlag GmbH & Co. KGaA, Weinheim

Spin Configurations

DOI: 10.1002/anie.200503492

How High the Spin? Allowed and Forbidden Spin States in Transition-Metal Chemistry**

Santiago Alvarez and Jordi Cirera*

Keywords:
coordination compounds · ligand field theory · molecular orbital theory · spin states · transition metals

> *"When I use a word," Humpty Dumpty said in rather a scornful tone, "it means just what I choose it to mean—neither more nor less."*
> *"The question is," said Alice, "whether you can make words mean different things."*
> Lewis Carroll, *Through The Looking Glass* (1871)

Introduction

The quest for new homoleptic complexes (those with identical ligands) is a common target of several research groups in the field of synthetic transition-metal chemistry. For instance, Menjón, Forniés, and co-workers have prepared a series of organometallic $[MR_x]$ complexes (M = transition metal; R = polyhalophenyl group; $x = 4$–6)[1] that cover almost all the d^n electron configurations and in most cases are paramagnetic. Even simpler in composition, a variety of homoleptic complexes with methyl ligands were reported by Seppelt and co-workers.[2] Homoleptic cyano compounds have been known for a long time,[3] but some new elegant examples were recently reported[4–6] in view of their potential use as building blocks for polynuclear and extended structures with interesting magnetic properties.[7] Even such large families of complexes as the metal carbonyls[8] and alkoxides[9] are continuously expanding. To date, hundreds of thousands of transition-metal complexes have been structurally characterized, and the mainstream lines of research in that area are concerned with the self-assembly of large polynuclear systems that contain hundreds of atoms, tens or even hundreds of which can be transition-metal atoms.[10] The question is thus asked: Why then is there a renaissance of the chemistry of mononuclear complexes with only one type of relatively simple ligand?

Clearly, there is a synthetic challenge as the preparation of compounds with only one type of ligand is not always an easy task. In our view, though, there is also the perception that the stereochemistry, electronic structure, and chemical properties of such compounds are not so well understood, despite the tremendous advances in our capabilities to analyze them both crystallographically and computationally. Especially for those electron configurations that allow for more than one spin state, it is not always easy to predict which will be the ground state for a given combination of metal ion and ligands. The concepts of high-spin and low-spin states, and the related classification of low- and high-field ligands, derived from the crystal-field treatment of an octahedral compound, are usually extrapolated to other cases in a straightforward way, leading in some instances to ambiguities.

The case of the homoleptic cyano complexes illustrates the problems and lack of a unified use of the low-spin and high-spin labels. The $[Mn(CN)_4]^{2-}$ anion reported recently by Miller and coworkers is a textbook example of the general tendency of tetrahedral complexes to have their d electrons arranged with parallel spins, resulting in the highest possible spin state (Figure 1 a).[4] (We will see in the last section of the Essay

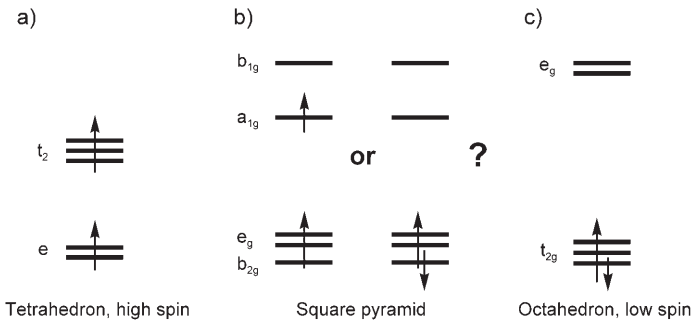

Figure 1. Splitting of d orbitals in a) a tetrahedral high-spin complex, $[Mn(CN)_4]^{2-}$, b) a square-pyramidal complex, $[Cr(CN)_5]^{3-}$, with high-spin (left) or low-spin configuration (right), and c) an octahedral low-spin complex, $[Cr(CN)_6]^{4-}$.

[*] Prof. S. Alvarez, J. Cirera
Departament de Química Inorgànica and
Centre Especial de Recerca en Química Teòrica (CeRQT)
Universitat de Barcelona
Martí i Franquès 1–11
08028 Barcelona (Spain)
Fax: (+34) 93-490-7725
E-mail: santiago@qi.ub.es

[**] Financial support of this work was provided by the Ministerio de Ciencia y Tecnología (project no. CTQ2005-08123-C02-02/BQU) and through an MECD doctoral grant to J.C. The authors thank R. Poli and R. Hoffmann for illuminating discussions.

InterScience
© 2006 Wiley-VCH Verlag GmbH & Co. KGaA, Weinheim

that low-spin tetrahedral complexes do exist under certain circumstances.) Such a tendency is explained by the small splitting of the d orbitals in a tetrahedral environment, even in the presence of strong-field ligands such as cyanide. The octahedral $[Cr(CN)_6]^{4-}$ anion, on the other hand, presents a low-spin configuration with $S=1$ (Figure 1c),[4] which can be explained by the large splitting of the d orbitals due to an octahedral environment of strong-field ligands. In both of these cases, two different factors determine the magnitude of the d-orbital splitting and, hence, the choice of the spin state: the molecular (coordination) geometry and the nature of the ligands. (Another factor, which we will comment on later, is the interelectronic repulsion.)

If we consider yet a third type of structure, such as the square-pyramidal or trigonal-bipyramidal geometries reported recently for the $[Cr(CN)_5]^{3-}$ anion,[5] should we expect all electrons to have parallel spins or not? Should the relevant energy gap between the a_{1g} and e_g orbitals in the presence of strong ligands such as cyanide be large (Figure 1c) or small (Figure 1a)? It has been shown experimentally that the high-spin electron configuration is preferred (Figure 1b).[5] However, could we have predicted the spin state beforehand by using qualitative molecular-orbital arguments? Moreover, if the $[Mn(CN)_5]^{3-}$ anion with an extra electron could be prepared, should we expect the fifth electron to lie parallel (occupying a b_{1g} orbital) or antiparallel (occupying a b_{2g} orbital)? Similarly, we could turn to lower coordination numbers and ask if the high-spin configurations found for three-coordinated d^7-Fe^{I} and d^6-Fe^{II} cations with the diketiminate bidentate ligand[11] is something we could have predicted without calculations or experiment.

Another possible source of ambiguity comes from labeling some compounds as having "intermediate" spin states. This label has been applied to Jahn–Teller-distorted six-coordinated metal ions, such as Co^{III} in $LaCoO_3$,[12] to Fe^{II} and Fe^{III} porphyrin complexes in which the Fe ion is four-, five-, or six-coordinated,[13–15] and to a square-planar Fe^{II} dithiolato complex.[16] In the case of a square-planar Fe^{II} complex, taking into account the typical d-orbital splitting pattern,[17] two alternative spin states can be expected in the presence of weak-field ($S=2$) or strong-field ligands ($S=1$; Figure 2). A ground spin

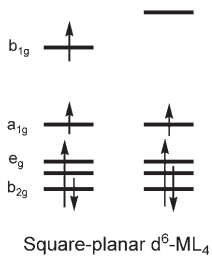

Figure 2. Splitting of d orbitals in a square-planar d^6-ML_4 complex and its high-spin (left) or low-spin (right) configurations.

state with all electrons paired ($S=0$) could be conceived, but, to the best of our knowledge, there is no experimental evidence for such a spin state in a square-planar d^6-metal complex. Should the configuration as shown on the right in Figure 2 be termed the low-spin state or the intermediate-spin state? Is the diamagnetic state possible?

The correct characterization and description of the spin state of a transition-metal complex is very important given the different magnetic, structural, and chemical properties associated with different spin states.[18] However, in the most-recent revision of the IUPAC's *Nomenclature of Inorganic Chemistry*[19] the naming of spin configurations or states is completely overlooked. Therefore, we believe that it is timely to reflect on when and why are high-, intermediate-, or low-spin configurations possible. It would be convenient that the scientific community establishes some naming convention to avoid ambiguities and misunderstandings. For this reason, we present herein a qualitative revision of the orbital principles underlying the choice of spin states in transition-metal compounds. As the interplay of d-orbital splitting and electron repulsion determines the spin configuration, we start by looking at some general rules that govern the relative magnitude of these two effects. We present a general molecular-orbital scheme that provides a sound qualitative description of the relative energies of the metal d orbitals in complexes with any coordination number and geometry and establish accordingly the possible spin states for different coordination geometries and d^n configurations. Last, we address the possibility of less-common orbital-splitting situations and provide some rationale for known exceptions to the rules proposed.

Splitting of the d Orbitals

The use of high-spin and low-spin labels for electron configurations is associated with the well-known splitting pattern of the metal d orbitals into two degenerate sets in octahedral and tetrahedral complexes (Figure 1), when crystal-field or molecular-orbital theories are applied. In both cases, there are only two distinct choices of electron configuration, characterized by the highest and lowest possible spin for n electrons in the five d orbitals. However, the situation is less clear for other coordination geometries, for which more than two sets of symmetry-equivalent orbitals can be found, as in square-planar (Figure 2) and square-pyramidal complexes (Figure 1b). Therefore, let us try to establish some rules that allow us to treat these less symmetric cases in a simple but reliable way. We do so by considering the molecular orbitals of an idealized complex with predominant metal d character.

When d orbitals interact with the symmetry-adapted linear combinations (SALC)[20] of ligand orbitals, they form bonding and antibonding molecular orbitals for each symmetry representation. Atomic d orbitals that do not match the symmetry of the SALCs are strictly nonbonding, as is the case for the t_{2g} metal set in an octahedral environment (assuming only σ-donor ligands) or for the b_{2g} and e_g orbitals in a square-planar four-coordinate complex (Figure 3a). For the purpose of the present discussion, we focus on the antibonding combinations, whose largest contribution comes in most cases from the metal d orbitals, such as the d_{z^2} and $d_{x^2-y^2}$ orbitals in a square-planar complex. For simplicity, we refer to these molecular orbitals as d-MOs to differentiate them from the unperturbed atomic d orbitals. Thus, now we can classify the d-MOs into two sets: those

 © 2006 Wiley-VCH Verlag GmbH & Co. KGaA, Weinheim

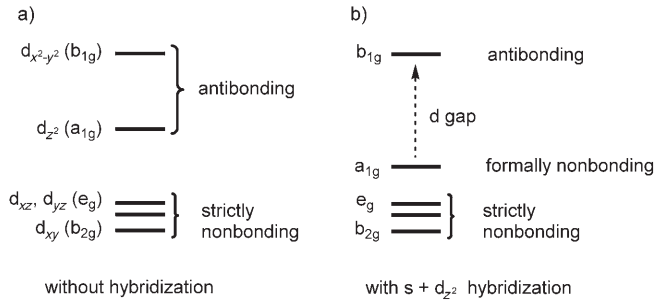

Figure 3. d Molecular orbitals in square-planar ML_4 complexes: a) without hybridization; b) with s+d_{z^2} hybridization.

with antibonding character and those with strictly nonbonding character (Figure 3a).

However, there are two different situations regarding the antibonding d-MOs, depending on whether or not there are valence s or p metal orbitals of the same symmetry. In the presence of symmetry-matched valence s or p orbitals, energy minimization of the system imposes extensive mixing of orbitals of the same symmetry, in such a way as to make the lower one as little metal–ligand antibonding as possible, while the upper, unoccupied one (formerly s or p), accumulates most of the antibonding character. Such a hybridization converts the corresponding d-MOs into *formally* nonbonding orbitals, as happens with d_{z^2} in the case of a square-planar complex; it is hybridized with the s orbital (both being A_{1g}-symmetric; Figure 4a). Conversely, in a linear complex hybridization occurs with the opposite sign (Figure 4b). A similar situation appears, for example, for the t_2 set of d-MOs in a tetrahedral complex which hybridize with metal p orbitals that have the same symmetry (Figure 4c).

In those cases the d-MOs are hybridized such that their electron density is concentrated away from the ligands, appearing similar to a balloon when subject to pressure. The effect of pressing a balloon in axial and equatorial directions (Figure 5a,b) can be compared with the hybridization found for the d_{z^2} orbital in ML_2 and ML_4 complexes (Figure 5c,d). In summary, we should expect the d-MO manifold to be split into two distinct sets, with the lower energy set containing the nonbonding (both strictly and formally) orbitals and the higher energy set comprising the metal–ligand antibonding orbitals. The sets of orbitals are separated by a significant d-orbital energy gap.

Let's pretend that the splitting between nonbonding and antibonding d-MOs is much larger than the energy differences within each of these two orbital sets; it is therefore this energy gap that should be taken into account when considering alternative spin configurations.[21] There are good reasons for this assumption, as illustrated by the splitting of the d orbitals in different homoleptic cyano complexes (Figure 6) according to density functional theory (DFT) calculations.[22] In each case, the symmetry of the coordination sphere determines which orbitals belong to each of these two sets (see Table 1). It can be seen that the number of antibonding d-MOs corresponds to the number of d orbitals that participate in the valence-bond hybridization

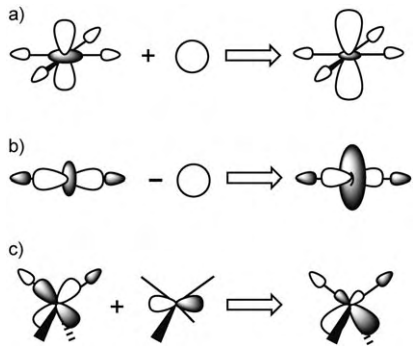

Figure 4. Minimization of antibonding character through hybridization of d-MOs: s+d_{z^2} hybridization in a) square-planar ML_4 and b) linear ML_2 complexes, and c) p+d hybridization in tetrahedral complexes.

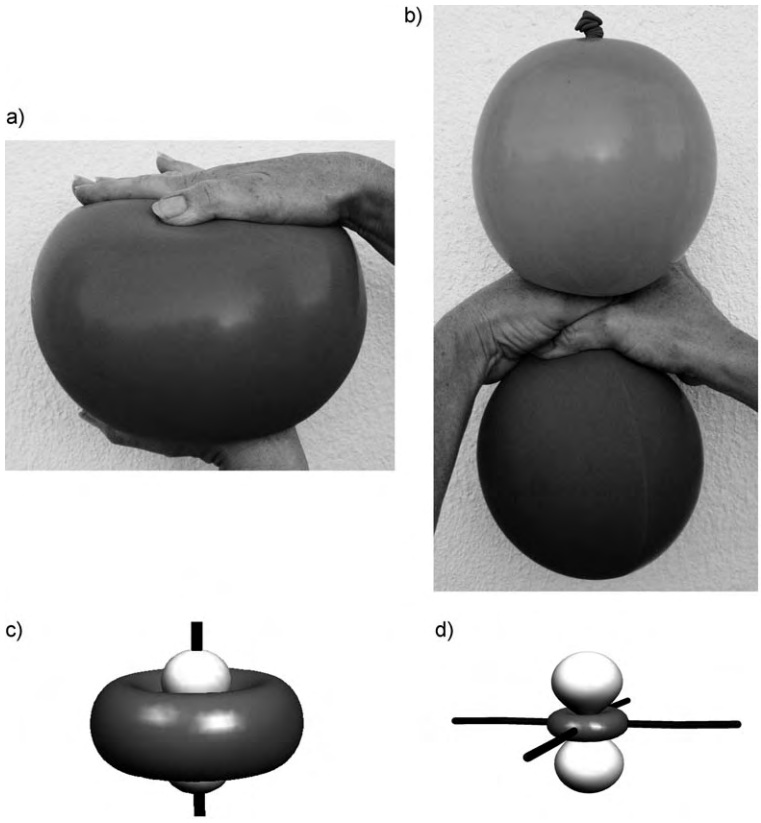

Figure 5. Effect of applying pressure to a balloon along the *z* axis (a) and circularly in the *xy* plane (b), compared to the shape of the d_{z^2} orbital (see Figure 4a,b) in linear $[Ag(CN)_2]^-$ (c) and in square-planar $[Ni(CN)_4]^{2-}$ (d), as obtained from DFT calculations.

 © 2006 Wiley-VCH Verlag GmbH & Co. KGaA, Weinheim

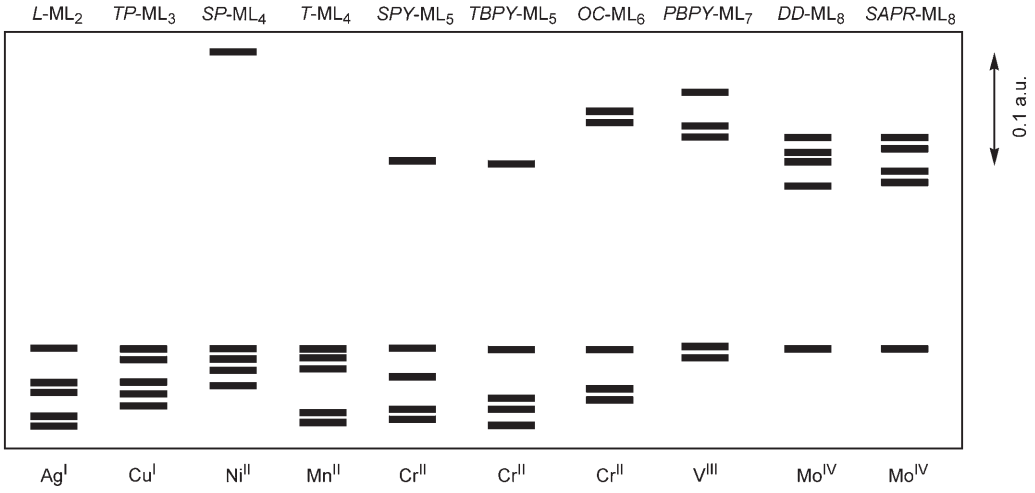

Figure 6. Relative energies of the d molecular orbitals in several homoleptic cyano complexes, from left to right: linear $[Ag(CN)_2]^-$, trigonal-planar $[Cu(CN)_3]^{2-}$, square-planar $[Ni(CN)_4]^{2-}$, tetrahedral $[Mn(CN)_4]^{2-}$, square-pyramidal $[Cr(CN)_5]^{2-}$, nearly trigonal-bipyramidal $[Cr(CN)_5]^{2-}$, octahedral $[Cr(CN)_6]^{4-}$, pentagonal-bipyramidal $[V(CN)_7]^{4-}$, and dodecahedral and square-antiprismatic $[Mo(CN)_8]^{4-}$. To facilitate comparison of the energy gaps, the orbital energies of each compound are referred to that of the highest formally nonbonding d-MOs (0.1 a.u. $= 2.19\times10^4$ cm^{-1}).

Table 1: Expected hybridization of the metal atom in ML_n complexes and formal bonding nature of the metal d orbitals when considering metal–ligand σ interactions only.

Symbol[a]	Geometry	Hybridization	Nonbonding[b]	Antibonding
L-ML_2	linear	sp	all	none
TP-ML_3	trigonal plane	sp^2	all	none
T-ML_4	tetrahedron	sp^3	all	none
SP-ML_4	square plane	dsp^2	d_{z^2}, d_{xy}, d_{xz}, d_{yz}	$d_{x^2-y^2}$
TBPY-ML_5	trigonal bipyramid	dsp^3	d_{xz}, d_{yz}, $d_{x^2-y^2}$, d_{xy}	d_{z^2}
SPY-ML_5	square pyramid	dsp^3	d_{xz}, d_{yz}, d_{xy}, d_{z^2}	$d_{x^2-y^2}$
OC-ML_6	octahedron	d^2sp^3	d_{xy}, d_{xz}, d_{yz}	$d_{x^2-y^2}$, d_{z^2}
TPR-ML_6	trigonal prism	d^2sp^3	d_{xy}, $d_{x^2-y^2}$, d_{z^2}	d_{xz}, d_{yz}
PBPY-ML_7	pentagonal bipyramid	d^3sp^3	d_{xz}, d_{yz}	d_{z^2}, $d_{x^2-y^2}$, d_{xy}
OCF-ML_7	capped octahedron	d^3sp^3	$d_{x^2-y^2}$, d_{xy}	d_{z^2}, d_{xz}, d_{yz}
TPRS-ML_7	capped trigonal prism	d^3sp^3	$d_{x^2-y^2}$, d_{xy}	d_{z^2}, d_{xz}, d_{yz}
CU-ML_8	cube	d^3sp^3	$d_{x^2-y^2}$, d_{xy}	d_{z^2}, d_{xz}, d_{yz}
DD-ML_8	dodecahedron	d^4sp^3	$d_{x^2-y^2}$	d_{z^2}, d_{xy}, d_{xz}, d_{yz}
SAPR-ML_8	square antiprism	d^4sp^3	d_{z^2}	d_{xy}, d_{xz}, d_{yz}, $d_{x^2-y^2}$

[a] IUPAC polyhedral symbol. [b] The metal atomic orbitals identified as "nonbonding" may be strictly so, as imposed by symmetry (e.g., the t_{2g} set in octahedral complexes), or only formally nonbonding as discussed in the text.

scheme.[23] As an example, the dsp^2 hybridization expected for a square-planar complex is translated into a molecular-orbital scheme with only one antibonding d orbital, whereas the d^4sp^3 hybridization expected for a dodecahedral, eight-coordinated metal corresponds to a splitting into one nonbonding and four antibonding d-MOs.

High-Spin and Low-Spin Configurations

The size of the d-energy gap is determined by the strength of the orbital interaction between the metal center and the donor atoms, and is controlled by the overlap and difference in electronegativity of both σ- and π-type metal–ligand interactions. Its magnitude obtained from visible spectra, for example, is empirically expressed through the spectrochemical series of the ligands and of the metal ions.[24] On the basis of such information, cyanide, phosphines, or CO are considered strong ligands, while O-donor ligands (including water) and halides are referred to as weak ligands. (The nature of the metal also has an effect on the magnitude of the gap; it increases with the oxidation state of the metal and also upon descending a periodic group.)

The choice of the spin state in a particular case, however, depends on both the d-orbital energy gap and the electron repulsion associated with the occupation of the same orbital by two electrons with opposed spins ("pairing energy"). Thus, a large gap and a small pairing energy favor a low-spin state, whereas a small gap combined with large pairing energy favors a high-spin state. Intermediate situations are harder to predict and are best exemplified with spin-crossover complexes, which can change their spin state through changes in temperature or pressure or by irradiation.[25] To get a feel for how much the pairing energy can change from one metal to another and with oxidation state, one can take a look at the values of the Racah electron-repulsion parameters for free ions.[26] The following trends are observed: 1) for metal ions with the same oxidation state, the pairing energy increases with atomic number along a transition series; 2) for metal ions belonging to the same group, the pairing energy decreases down the group; and 3) for the same metal atom, the pairing energy increases with increasing oxidation state. In Figure 7, the factors that influence the magnitudes of these two parameters are summarized according to the magnitudes of the pairing energy and the d-orbital energy gap. A qualitative map is also shown that indicates the

 © 2006 Wiley-VCH Verlag GmbH & Co. KGaA, Weinheim

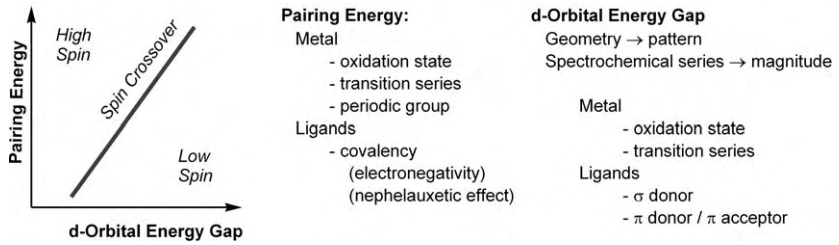

Figure 7. Factors that influence the magnitudes of the pairing energy and the d-orbital energy gap.

regions of high- and low-spin states, separated by a region in which spin crossover can occur. With so many factors in action, it is not easy to predict the most-stable spin configuration for a given complex. However, we can try to predict at least which spin states can be reasonably expected in the limiting cases of strong and weak fields.

Taking into account the classification of d orbitals in nonbonding and antibonding sets, we can establish the possible spin configurations for a given coordination number and geometry (Table 2). As an example, let us consider the case of a d^5 ion in tetrahedral and octahedral geometries, for which three spin states can be envisaged: $S = 5/2, 3/2$, or 1/2. For the octahedron (*OC*-ML_6), the highest spin ($S = 5/2$) is attained if the d-orbital splitting (energy gap) is small compared to the pairing energy, and the lowest spin ($S = 1/2$) is obtained in the opposite case. In contrast, the $S = 3/2$ state is forbidden because the pairing of the fourth and fifth electrons in t_{2g} orbitals is either favorable for both ($S = 1/2$ preferred) or unfavorable for both ($S = 5/2$ preferred), but cannot be preferred for one electron and unfavorable for the other one (as required for $S = 3/2$ to be the ground state). For the tetrahedron (*T*-ML_4), both the $S = 3/2$ and $S = 1/2$ spin states are forbidden because the energy difference between the e and t_2 orbital sets is small regardless of the nature of the metal and ligands. The experimental realization of these cases is exemplified by $[Fe(H_2O)_6]^{3+}$, $[Fe(CN)_6]^{3-}$, and $[Mn(CN)_4]^{2-}$. For the two octahedral complexes, the $S = 5/2$ ($[Fe(H_2O)_6]^{3+}$) and $S = 1/2$ ($[Fe(CN)_6]^{3-}$) states observed correspond to the two allowed situations at the extremes of weak-field (H_2O) and strong-field (CN^-) ligands. The $S = 5/2$ spin state observed for $[Mn(CN)_4]^{2-}$, even with a strong ligand, corroborates the negligible effect of the splitting within nonbonding orbitals on the electron configuration. Thus, for the case of a d^5 metal ion, it is sensible to refer to the $S = 5/2$ and $S = 1/2$ states of octahedral complexes as the high-spin and low-spin configurations, respectively, while for isoelectronic tetrahedral compounds there is no need to refer to a "high-spin" situation as there is only one observed spin state. The intermediate spin for that configuration is not expected to exist as a ground state, at least not for homoleptic complexes.

Table 2: Allowed spin configurations (√) for different coordination geometries and numbers of d electrons, considering only an energy gap between formally nonbonding and σ-antibonding orbitals.[a]

Configuration	Spin	*T*-ML_4	*SP*-ML_4	*SPY*-ML_5	*OC*-ML_6	*PBPY*-ML_7	*DD*-ML_8
d^2	1	√	√	√	√	√	√
	0	–	–	–	–	–	√
d^3	3/2	√	√	√	√	√	√
	1/2	–	–	–	–	√	√
d^4	2	√	√	√	√	√	√
	1	–	–	–	√	–	√
	0	–	–	–	–	√	–
d^5	5/2	√	√	√	√	√	√
	3/2	–	√	√	–	–	√
	1/2	–	–	–	√	√	–
d^6	2	√	√	√	√	√	√
	1	–	√	√	–	√	–
	0	–	–	–	√	–	–
d^7	3/2	√	√	√	√	√	√
	1/2	–	√	√	√	–	–
d^8	1	√	√	√	√	√	√
	0	–	√	√	–	–	–

[a] The forbidden cases correspond to spin configurations that imply electron pairing within the set of (formally and strictly) nonbonding d orbitals. Polyhedral symbols as reported in Table 1.

With a "map" in hand of the possible spin states for a variety of coordination geometries and different d-electron configurations, and considering only the splitting of the d orbitals in two broad sets of nonbonding and antibonding orbitals (Table 2), we can establish some generalities as well as some specificities.

a) Three spin states are possible only for the d^4, d^5, and d^6 electron configurations. Nevertheless, for a given coordination geometry only two or even just one of those spin states are allowed, if we disregard spin-pairing within the nonbonding set, before it is half-filled.
b) For d^2, d^3, d^7, and d^8 configurations, only two spin states are possible, but in many instances the spin state with the highest multiplicity only is allowed.
c) From Table 2, a general rule for tetrahedral complexes (*T*-ML_4) is that only the highest spin state should be expected in all cases (see the discussion in the next section).
d) The highest spin state should be expected also for linear two-coordinate (*L*-ML_2) and trigonal-planar three-coordinate (*TP*-ML_3) complexes. In these cases, all the d molecular orbitals are formally nonbonding (Figure 6) and a negligible d-orbital energy gap should be expected. Recently reported examples

 © 2006 Wiley-VCH Verlag GmbH & Co. KGaA, Weinheim

of two-coordinate complexes with d^4 to d^8 electron configurations all presented high-spin states.[27] Similarly, three-coordinate complexes seem in most cases to appear in their high-spin configurations.[28,29] (Exceptions are discussed in the next section.)

e) For eight-coordinate complexes with four or more d electrons (*DD*-ML_8 or *SAPR*-ML_8), the state with the lowest spin multiplicity is always forbidden because it would imply unnecessary electron-pairing within the antibonding orbitals (Figure 6).

f) Given the different d-orbital splitting patterns, the allowed spin states change with the coordination number. Thus, for the d^6 configuration the state with all spins paired is forbidden in square-planar (*SP*-ML_4), square-pyramidal (*SPY*-ML_5), and pentagonal-bipyramidal (*PBPY*-ML_7) complexes, while it is allowed for octahedral geometries. On the contrary, the $S=1$ state is allowed in the former cases but forbidden in the latter. A similar situation arises for the d^5 configuration.

g) A spin-paired configuration is forbidden for octahedral complexes of d^2 or d^3 metals. However, the high–low spin state dichotomy exists for seven- and eight-coordinated metal ions with these electron configurations, and d^2-configured octacyanometallates are indeed low-spin complexes.

Electron-Pairing within the Nonbonding Orbital Set

So far, we have relied on the assumption that differences in energy within the set of nonbonding d orbitals are not large enough as to induce spin pairing. However, we have neglected metal–ligand π interactions in our arguments. Let us now consider some examples in which π bonding may invalidate such a hypothesis. The exceptions correspond mostly to pseudotetrahedral Fe^{II} and Co^{II} complexes of the type $[M(BE_3)X]$, where BE_3 represents tridentate ligands such as trispyrazolylborates (E = N),[30] triphosphineborates (E = P),[31,32] trithioborates (E = S),[33] or tris(carbene)borates[34] (see **1**–**3**, Figure 8). These compounds adopt a low-spin configuration when the fourth ligand, X, is a π donor. A somewhat different case is that of diamagnetic tetrahedral Ni^{IV} compound, [NiBr(norbornyl)$_3$],[35] in which all ligands are monodentate. In all these compounds there are varying degrees of umbrella-type distortions of the tetrahedron. This distortion is in contrast to the more commonly found spread distortion path[36] that ultimately leads to a square-planar complex. Such distortions can be calibrated by the sum of the E-M-E bond angles (Σ), which is expected to be 328.4° for the ideal tetrahedron but is found to be 300.2° for the Ni^{IV} complex and between 264° and 298° in the compounds with tridentate ligands.

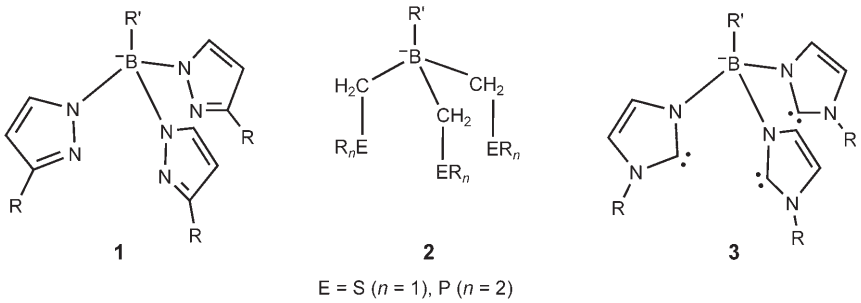

Figure 8. Tridentate ligands that appear, supplemented with a monodentate π-donor ligand, in pseudotetrahedral Fe^{II} and Co^{II} complexes with low-spin configurations.

An explanation for the stability of the low-spin state in these systems was proposed on the basis of DFT calculations by Peters and co-workers.[32] The distortion of the coordination tetrahedron results in the splitting of the t_2 set of d orbitals (Figure 9), and the a_1 (d_{z^2}) orbital thereby loses its antibonding character as the E donor atoms approach its nodal cone (at Σ = 270°). In addition, the π-donor nature of X adds π-antibonding character to the 2e (d_{xz}, d_{yz}) degenerate pair. Such a π interaction is enhanced as a result of the balloon effect discussed before (Figure 4c). Note also that such a hybridization increases with the umbrella distortion, as the overlap between the ligand lone pairs and metal d_{xz} or

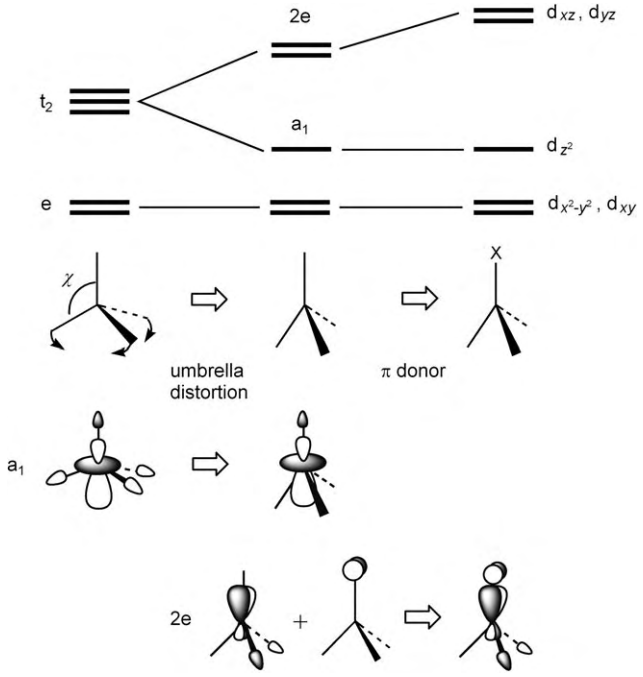

Figure 9. Effect of an umbrella distortion and of a π-donor apical ligand X on the d-orbital splitting. The loss of σ overlap in the a_1 orbital and the enhanced π overlap in the 2e orbital explain the deviation of the orbital splitting from the $e+t_2$ pattern of the tetrahedron.

© 2006 Wiley-VCH Verlag GmbH & Co. KGaA, Weinheim

d_{yz} orbitals increases. In summary, the umbrella distortion stabilizes the a_1 (d_{z^2}) orbital, while the presence of a π-donor ligand X combined with the umbrella distortion strongly destabilizes the 2e set. The resultant wide energy gap stabilizes the low-spin configuration.

Consistent with the orbital picture just discussed, all the d^6 and d^7 complexes of ligands **1**–**3** with a σ-donor or π-acceptor ligand X appear in their high-spin configurations, as the 2e orbitals lack the π-antibonding character that leads to a significant d-orbital energy gap. On the other hand, those complexes in which X is a π-donor ligand present a good correlation between the degree of umbrella distortion and the spin of the ground state: Compounds with strong distortions have a low-spin ground state, whereas those with weaker distortions appear in their high-spin configuration. The borderline appears at $\Sigma \approx 277°$.

If we turn now to the pseudotetrahedral complex [NiBr(norbornyl)$_3$],[35] we note that it has two of the requisites to present a low-spin state: an umbrella distortion and a π-donor ligand. However, as the umbrella distortion is not strong ($\Sigma = 300°$) it does not comply with the third requisite. Current studies in our research group indicate that even with four σ-donor ligands (e.g., alkyl groups), a tetrahedrally coordinated metal in its +IV oxidation state presents a large enough gap between the t_2 and e orbitals as to favor the low-spin state. This behavior has been experimentally found for the $[Co(norbornyl)_4]^y$ complexes ($y = -1, 0, +1$), which appear in their low-spin states.[37]

We have already noted above that the d-orbital splitting depends not only on the donor ability of the ligands but also increases with the metal oxidation state. Hence, the different behavior of the tetrahedral $[Mn(CN)_4]^{2-}$ and [NiBr(norbornyl)$_3$] complexes, which present high- and low-spin configurations, respectively, are well accounted for by the general rules of d-orbital splitting if we assume that for metal oxidation states of +IV or higher the metal–ligand interaction is so strong that the p+d hybridization is insufficient to make the t_2 orbitals formally nonbonding. In other words, they become effectively antibonding. Another interesting recent case is that of a four-coordinate d^4-Ru^{IV} nitrido complex with a tridentate ligand that adopts an approximately square-planar geometry (*SP*-ML_4) but a low-spin state ($S = 0$).[38] Three factors that favor the unusual low-spin state can be identified in that compound: a second-series transition metal, a high oxidation state, and asymmetric π bonding.

Three-coordinate complexes also present exceptions that require closer inspection. According to the discussion above, all the d orbitals should be nonbonding in such a case (*TP*-ML_3 in Table 1 and Figure 6). In fact, most three-coordinate complexes for which magnetic moments have been reported present their maximum spin multiplicity.[28] However, there are a few with a spin-paired configuration, such as $[Rh(PPh_3)_3]^+$,[39] $[Ni(mesityl)_3]^-$,[40] [M(mesityl)$_3$] (M = Rh, Ir),[41] or d^2 imido complexes.[42] The coordination geometry in the $[Rh(PPh_3)_3]^+$ and $[Ni(mesityl)_3]^-$ complexes should be described as T-shaped rather than trigonal planar, and therefore the orbital scheme that applies[28] is similar to that found for square-planar complexes (*SP*-ML_4 in Figure 6). A singlet state should be expected for d^8 ions. In the case of the Rh and Ir mesityl complexes the coordination sphere is far from planar, and agostic interactions with methyl groups of the ligands have been identified. These account for an effective octahedral ligand field for which an $S = 0$ situation is conceivable (*OC*-ML_6 in Table 2). Such a situation has been shown through computational studies for a Cr^{II} alkoxy complex, in which the $d_{x^2-y^2}$ orbital is strongly destabilized by π interactions, even if in this case the d^4 configuration precludes a low-spin state.[43] As for the d^2 imido complexes, again the strong π-donor character of the ligands in an anisotropic arrangement, combined with high oxidation states in those W^{IV}, Re^{V}, and Os^{VI} complexes, should result in a strong destabilization of both the e′ and e″ sets of orbitals (Figure 10). As discussed above for the case of pseudotetrahedral complexes with one π-donor ligand, the hybridization required to alleviate the σ-antibonding nature of some d orbitals enhances the π-antibonding effect.

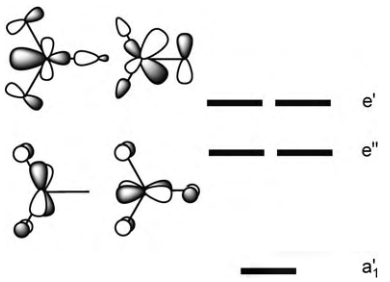

Figure 10. Destabilization of the e′ and e″ sets by strong π-donor ligands in d^2 tricoordinate imido complexes.

Some Final Considerations

The general tendency to label spin states as either high or low spin reflects the duality of the choice of spin state that is rooted in the general rules that govern the energy patterns for the d-MOs in transition-metal complexes. These orbitals can, in general, be divided into two subsets with nonbonding and antibonding character relative to the metal–ligand bonds. These two subsets are separated by a significant energy gap, the magnitude of which, together with the electron-pairing energy, ultimately determines the relative energies of the allowed spin states. Although some of the formally nonbonding MOs have antibonding contributions, these are minimized by hybridization with metal s and p orbitals of the same symmetry, resulting in only a small increase in energy relative to the strictly nonbonding orbitals. As a consequence, electron pairing within the nonbonding subset is forbidden before all its orbitals are half-occupied. This simplified orbital scheme, which is strongly dependent on the coordination number and geometry and disregards π interactions in a first approximation, allows us to qualitatively predict two or three allowed spin states for a variety of electron configurations and coordination geometries (Table 2). Exceptions to these rules arise from the promotion of one or more of the formally nonbonding orbitals to the antibonding set and are caused by one or more of three possible causes: 1) Severe distortions from the ideal geometries, 2) strongly anisotropic interaction with π-donor ligands, and 3) a high oxidation state of the metal atom in combination with strong σ-donor ligands.

 © 2006 Wiley-VCH Verlag GmbH & Co. KGaA, Weinheim

Eventual references to intermediate-spin states are not in contradiction with the dual nature of the spin state but lies with the fact that three spin states are conceivable for some d^n configurations. Then, it is the specific geometrical and bonding situation of each compound that determines which of these are the two allowed spin states. References to intermediate-spin states are found mostly in metal porphyrin complexes. If two additional ligands are coordinated to the metal atom besides the porphyrin ligand, only the highest and lowest spin states should be expected for a strictly octahedral coordination sphere (*OC*-ML_6 in Table 2). However, when the two axial ligands are much weaker donors compared to the porphyrin ring (e.g., tetrahydrofuran, ethanol, or water),[14] the d-orbital splitting pattern is closer to that of the square-planar complexes, for which the allowed spin states are different for d^5 and d^6 electron configurations (*SP*-ML_4 in Table 2). A similar situation is found in $LaCoO_3$, for which the intermediate-spin state is stabilized by a tetragonal, Jahn–Teller-driven distortion of the coordination octahedron.[12]

It is clear that the traditional way of naming spin states for octahedral and tetragonal complexes, referring to the two allowed spin states as high and low, leads to inconsistencies when dealing with these systems, because one does not know beforehand whether a particular compound should be considered as octahedral or tetragonal from the orbital point of view. Other inconsistencies result from the traditional labeling of spin states. Consider, for example, the lowest allowed spin states of d^5-ML_5 and d^5-MXL_5 complexes, which are related by ligand association/dissociation. Even if we refer to a low-spin configuration in both cases, we are actually talking about different spin states, $S = 3/2$ and $S = 1/2$, respectively (see *SPY*-ML_5 and *OC*-ML_6 in Table 2).

To avoid the above inconsistencies in the naming of spin states, maybe some convention could be established that considers all the situations discussed here as well as potential new developments. Because in all cases there are, at most, three possible spin states, one could refer to high- and low-spin states for those electron configurations with only two possibilities (d^2, d^3, d^7, and d^8), and to high-, intermediate-, and low-spin states for the d^4, d^5, and d^6 cases, regardless of whether such states in different geometries are allowed. There are some precedents for referring to square-pyramidal[15] or square-planar[16] complexes as having intermediate spin, but it would certainly change the way we usually name spin states in, for example, octahedral complexes. For instance, all known octahedral "low-spin" d^4-metal complexes should be renamed as "intermediate spin". In return, such nomenclature should allow for a clearer correlation between complexes that are related by association or dissociation of a ligand, and the name of the spin state would be unequivocally associated to the *S* value.

Experience shows that changes in nomenclature are rarely smoothly and universally adopted, and it may well be that the introduction of a new naming convention for the spin states finally brings about more confusion than it avoids. In any case, we hope that the reflections presented in this essay may help clarify the concepts that describe spin states and that more data and new ideas can be proposed in the near future by other researchers along these lines. Whatever convention is adopted in each particular case, to avoid ambiguities and misinterpretations the most important point is to be aware of the strong interdependence of spin states and coordination geometry and to be sure to have at hand a clear picture of the splitting pattern of the d molecular orbitals and of the factors that affect the choice of spin state. No matter how high or low one considers the spin of a given compound, probably the wisest choice is to specify in all cases the total spin or the spin multiplicity.

Published online: April 10, 2006

[1] R. Usón, J. Forniés, M. Tomás, B. Menjón, K. Sünkel, R. Bau, *J. Chem. Soc. Chem. Commun.* **1984**, 751; J. Forniés, B. Menjón, R. M. Sanz-Carrillo, M. Tomás, N. G. Connelly, J. G. Crossley, A. G. Orpen, *J. Am. Chem. Soc.* **1995**, *117*, 4295; P. J. Alonso, L. R. Falvello, J. Forniés, A. Martín, B. Menjón, G. Rodríguez, *Chem. Commun.* **1997**, 503; P. J. Alonso, L. R. Falvello, J. Forniés, M. A. García-Monforte, A. Martín, B. Menjón, G. Rodríguez, *Chem. Commun.* **1997**, 1721; P. J. Alonso, J. Forniés, M. A. García-Monforte, A. Martín, B. Menjón, *Chem. Commun.* **2001**, 2138; P. J. Alonso, J. Forniés, M. A. García-Monforte, A. Martín, B. Menjón, C. Rillo, *Chem. Eur. J.* **2002**, *8*, 4056; P. J. Alonso, J. Forniés, M. A. García-Monforte, A. Martín, B. Menjón, *Chem. Commun.* **2002**, 728; P. J. Alonso, L. R. Falvello, J. Forniés, M. A. García-Monforte, B. Menjón, *Angew. Chem.* **2004**, *116*, 5337; *Angew. Chem. Int. Ed.* **2004**, *43*, 5225; I. Ara, J. Forniés, M. A. García-Monforte, A. Martín, B. Menjón, *Chem. Eur. J.* **2004**, *10*, 4186; P. J. Alonso, J. Forniés, M. A. García-Monforte, A. Martín, B. Menjón, *Organometallics* **2005**, *24*, 1269; P. J. Alonso, J. Forniés, M. A. García-Monforte, A. Martín, B. Menjón, *Chem. Eur. J.* **2005**, *11*, 4713; J. Forniés, A. Martín, L. F. Martín, B. Menjón, *Organometallics* **2005**, *24*, 3266.

[2] S. Kleinhenz, V. Pfennig, K. Seppelt, *Chem. Eur. J.* **1998**, *4*, 1687; S. Kleinhenz, K. Seppelt, *Chem. Eur. J.* **1999**, *5*, 3573; B. Toessler, S. Kleinhenz, K. Seppelt, *Chem. Commun.* **2000**, 1039.

[3] K. Dunbar, R. A. Henitz, *Prog. Inorg. Chem.* **1997**, *45*, 283.

[4] W. E. Buschmann, A. M. Arif, J. S. Miller, *Angew. Chem.* **1998**, *110*, 813; *Angew. Chem. Int. Ed.* **1998**, *37*, 781.

[5] K. J. Nelson, I. D. Giles, W. W. Shum, A. M. Arif, J. S. Miller, *Angew. Chem.* **2005**, *117*, 3189; *Angew. Chem. Int. Ed.* **2005**, *44*, 3129.

[6] W. R. Entley, C. R. Treadway, S. R. Wilson, G. S. Girolami, *J. Am. Chem. Soc.* **1997**, *119*, 6251.

[7] M. Verdaguer, G. S. Girolami in *Magnetism: Molecules to Materials, Vol. V* (Eds.: J. S. Miller, M. Drillon), Wiley-VCH, Weinheim, **2005**, p. 283; L. M. C. Beltran, J. R. Long, *Acc. Chem. Res.* **2005**, *38*, 325.

[8] E. Bernhardt, C. Bach, B. Bley, R. Wartchow, U. Westphal, I. H. T. Sham, B. von Ahsen, C. Wang, H. Willner, R. C. Thompson, F. Aubke, *Inorg. Chem.* **2005**, *44*, 4189; M. Finke, E. Bernhardt, H. Willner, C. W. Lehmann, F. Aubke, *Inorg. Chem.* **2005**, *44*, 4206; H. Willner, F. Aubke, *Organometallics* **2003**, *22*, 3612; J. E. Ellis, *Organometallics* **2003**, *22*, 3322.

[9] M. V. Metz, Y. Sun, C. L. Stern, T. L. Marks, *Organometallics* **2002**, *21*, 3691; T. C. Rosen, K. Kirschbaum, D. M. Giolando, *Dalton Trans.* **2003**, 120; M. C. Buzzeo, A. H. Iqbal, C. M. Long, D. Millar, A. Patel, M. A. Pellow, S. A. Saddoughi, A. L. Smenton, J. F. C. Turner, J. D. Wadhawan, R. G. Compton, J. A. Golen, A. L. Rheingold, L. H. Doerrer, *Inorg. Chem.* **2004**, *43*, 7709.

 © 2006 Wiley-VCH Verlag GmbH & Co. KGaA, Weinheim

[10] N. T. Tran, D. R. Powell, L. F. Dahl, *Angew. Chem. Int. Ed.* **2000**, *39*, 4121; A. Müller, P. Kögerler, C. Kuhlmann, *Chem. Commun.* **1999**, 1347; S. Dehnen, A. Eichhofer, D. Fenske, *Eur. J. Inorg. Chem.* **2002**, 279.

[11] S. A. Stoian, Y. Yu, J. M. Smith, P. L. Holland, E. L. Bominaar, E. Münck, *Inorg. Chem.* **2005**, *44*, 4915.

[12] K. Knízek, P. Novák, Z. Jirák, *Phys. Rev. B* **2005**, *71*, 054420; J. Wang, Z. D. Wang, W. Zhang, D. Y. Xing, *Phys. Rev. B* **2002**, *66*, 064406.

[13] S. Obara, H. Kashiwagi, *J. Chem. Phys.* **1982**, *77*, 3155; T. Ikeue, T. Saitoh, T. Yamaguchi, Y. Ohgo, M. Nakamura, M. Takahashi, M. Takeda, *Chem. Commun.* **2000**, 1989; H. Goff, G. N. La Mar, C. A. Reed, *J. Am. Chem. Soc.* **1977**, *99*, 3641.

[14] J.-P. Simonato, J. Pécaut, L. Le Pape, J.-L. Oddou, C. Jeandey, M. Shang, W. R. Scheidt, J. Wojaczynski, S. Wolowiec, L. Latos-Grazynski, J.-C. Marchon, *Inorg. Chem.* **2000**, *39*, 3978; T. Sakai, Y. Ohgo, T. Ikeue, M. Takahashi, M. Takeda, M. Nakamura, *J. Am. Chem. Soc.* **2003**, *125*, 13028.

[15] K. M. Barkigia, M. W. Renner, J. Fajer, *J. Porphyrins Phthalocyanines* **2001**, *5*, 415.

[16] K. Ray, A. Begum, T. Weyhermüller, S. Piligkos, J. van Slageren, F. Neese, K. Wieghardt, *J. Am. Chem. Soc.* **2005**, *127*, 4403.

[17] T. A. Albright, J. K. Burdett, W.-H. Whangbo, *Orbital Interactions in Chemistry*, Wiley, New York, **1985**.

[18] R. Poli, *Chem. Rev.* **1996**, *96*, 2135; R. Poli, J. N. Harvey, *Chem. Soc. Rev.* **2003**, *32*, 1; J. N. Harvey, R. Poli, K. M. Smith, *Coord. Chem. Rev.* **2003**, *238–239*, 347; R. Poli, *J. Organomet. Chem.* **2004**, *689*, 4291.

[19] *Nomenclature of Inorganic Chemistry. IUPAC Recommendations 2005* (Eds.: N. G. Connelly, T. DAmhus, R. M. Hartshorn, A. T. Hutton), Royal Society of Chemistry, **2005**.

[20] F. A. Cotton, *Chemical Applications of Group Theory*, 3rd ed., Wiley-Interscience, New York, **1990**.

[21] "*And here I wish I could tell you half the things Alice used to say, beginning with her favourite phrase 'Let's pretend'.*" Lewis Carroll, *Through The Looking Glass* (1871).

[22] The orbital patterns shown in Figure 6 were obtained from DFT-B3LYP calculations on the low-spin states of the compounds indicated at their experimental structures by using the Gaussian package (Gaussian 03 (Revision B.4), M. J. Frisch, G. W. Trucks, H. B. Schlegel, G. E. Scuseria, M. A. Robb, J. R. Cheeseman, J. A. Montgomery, Jr., T. Vreven, K. N. Kudin, J. C. Burant, J. M. Millam, S. S. Iyengar, J. Tomasi, V. Barone, B. Mennucci, M. Cossi, G. Scalmani, N. Rega, G. A. Petersson, H. Nakatsuji, M. Hada, M. Ehara, K. Toyota, R. Fukuda, J. Hasegawa, M. Ishida, T. Nakajima, Y. Honda, O. Kitao, H. Nakai, M. Klene, X. Li, J. E. Knox, H. P. Hratchian, J. B. Cross, C. Adamo, J. Jaramillo, R. Gomperts, R. E. Stratmann, O. Yazyev, A. J. Austin, R. Cammi, C. Pomelli, J. W. Ochterski, P. Y. Ayala, K. Morokuma, G. A. Voth, P. Salvador, J. J. Dannenberg, V. G. Zakrzewski, S. Dapprich, A. D. Daniels, M. C. Strain, O. Farkas, D. K. Malick, A. D. Rabuck, K. Raghavachari, J. B. Foresman, J. V. Ortiz, Q. Cui, A. G. Baboul, S. Clifford, J. Cioslowski, B. B. Stefanov, G. Liu, A. Liashenko, P. Piskorz, I. Komaromi, R. L. Martin, D. J. Fox, T. Keith, M. A. Al-Laham, C. Y. Peng, A. Nanayakkara, M. Challacombe, P. M. W. Gill, B. Johnson, W. Chen, M. W. Wong, C. Gonzalez, J. A. Pople, Gaussian, Inc., Pittsburgh, PA, **2003**). A test calculation for the high-spin state of $[Cr(CN)_6]^{4-}$ indicates that the d-orbital energy gap is only slightly reduced and the semiquantitative picture of Figure 6 is still valid.

[23] J. E. Huheey, E. A. Keiter, R. L. Keiter, *Inorganic Chemistry: Principles of Structure and Reactivity*, 4th ed., Harper Collins, New York, **1993**.

[24] M. Gerloch, E. C. Constable, *Transition Metal Chemistry*, VCH, Weinheim, **1994**.

[25] J. A. Real, A. B. Gaspar, M. C. Muñoz, *Dalton Trans.* **2005**, 2062.

[26] J. S. Griffith, *Theory of Transition Metal Ions*, Cambridge University Press, Cambridge, **1961**.

[27] T. Nguyen, A. Panda, M. M. Olmstead, A. F. Richards, M. Stender, M. Brynda, P. P. Power, *J. Am. Chem. Soc.* **2005**, *127*, 8545; W. M. Reiff, A. LaPointe, E. H. Witten, *J. Am. Chem. Soc.* **2004**, *126*, 10206.

[28] S. Alvarez, *Coord. Chem. Rev.* **1999**, *193–195*, 13.

[29] J. Vela, J. M. Smith, Y. Yu, N. A. Ketterer, C. J. Flaschenriem, R. J. Lachicotte, P. L. Holland, *J. Am. Chem. Soc.* **2005**, *127*, 7857.

[30] J. L. Detrich, R. Konecny, W. M. Vetter, D. Doren, A. L. Rheingold, K. H. Theopold, *J. Am. Chem. Soc.* **1996**, *118*, 1703; J. D. Jewson, L. M. Liable-Sands, G. P. A. Yap, A. L. Rheingold, K. H. Theopold, *Organometallics* **1999**, *18*, 300; O. M. Reinaud, A. L. Rheingold, K. H. Theopold, *J. Am. Chem. Soc.* **1994**, *116*, 1703; N. Shirasawa, M. Akita, S. Hikichi, Y. Moro-oka, *Chem. Commun.* **1999**, 417; N. Shirasawa, T. T. Nguyet, S. Hikichi, Y. Moro-oka, M. Akita, *Organometallics* **2001**, *20*, 3582.

[31] T. A. Betley, J. C. Peters, *J. Am. Chem. Soc.* **2003**, *125*, 10782; T. A. Betley, J. C. Peters, *J. Am. Chem. Soc.* **2004**, *126*, 6252; S. D. Brown, T. A. Betley, J. C. Peters, *J. Am. Chem. Soc.* **2003**, *125*, 322; S. D. Brown, J. C. Peters, *J. Am. Chem. Soc.* **2004**, *126*, 4538.

[32] S. D. Brown, J. C. Peters, *J. Am. Chem. Soc.* **2005**, *127*, 1913; D. M. Jenkins, J. C. Peters, *J. Am. Chem. Soc.* **2005**, *127*, 7148.

[33] P. J. Schebler, B. S. Mandimutsira, C. G. Riordan, L. M. Liable-Sands, C. D. Incarvito, A. L. Rheingold, *J. Am. Chem. Soc.* **2001**, *123*, 331; P. J. Schebler, C. G. Riordan, I. A. Guzei, A. L. Rheingold, *Inorg. Chem.* **1998**, *37*, 4754.

[34] I. Nieto, F. Cervantes-Lee, J. M. Smith, *Chem. Commun.* **2005**, 3811.

[35] V. Dimitrov, A. Linden, *Angew. Chem.* **2003**, *115*, 2735; *Angew. Chem. Int. Ed.* **2003**, *42*, 2631.

[36] J. Cirera, P. Alemany, S. Alvarez, *Chem. Eur. J.* **2004**, *10*, 190.

[37] E. K. Byrne, K. H. Theopold, *J. Am. Chem. Soc.* **1989**, *111*, 3887.

[38] A. Walstrom, M. Pink, X. Yang, J. Tomaszewski, M.-H. Baik, K. G. Caulton, *J. Am. Chem. Soc.* **2005**, *127*, 5330.

[39] Y. W. Yared, S. L. Miles, R. Bau, C. A. Reed, *J. Am. Chem. Soc.* **1977**, *99*, 7076; C. B. Knobler, T. B. Marder, E. A. Mizusawa, R. G. Teller, J. A. Long, P. E. Beehnken, M. F. Hawthorne, *J. Am. Chem. Soc.* **1984**, *106*, 2990.

[40] R. Hay-Motherwell, G. Wilkinson, T. K. Sweet, M. B. Hursthouse, *Polyhedron* **1996**, *15*, 3163.

[41] D. M. Roddick, T. D. Tilley, A. L. Rheingold, S. J. Geib, M. B. Hursthouse, G. Wilkinson, *J. Chem. Soc. Chem. Commun.* **1990**, 1242; R. S. Hay-Motherwell, G. Wilkinson, B. Hussain-Bates, M. B. Hursthouse, *J. Chem. Soc. Dalton Trans.* **1992**, 3477.

[42] D. F. Eppley, P. T. Wolczanski, G. D. Van Duyne, *Angew. Chem.* **1991**, *103*, 616; *Angew. Chem. Int. Ed. Engl.* **1991**, *30*, 584; J. T. Anhaus, T. P. Kee, M. H. Schofield, R. R. Schrock, *J. Am. Chem. Soc.* **1990**, *112*, 1642; D. S. Williams, R. R. Schrock, *Organometallics* **1993**, *12*, 1148; D. S. Williams, J. T. Anhaus, M. H. Schofield, R. R. Schrock, W. M. Davis, *J. Am. Chem. Soc.* **1991**, *113*, 5480.

[43] O. L. Sydora, P. T. Wolczanski, E. B. Lobkovsky, C. Buda, T. R. Cundari, *Inorg. Chem.* **2005**, *44*, 2606.

 © 2006 Wiley-VCH Verlag GmbH & Co. KGaA, Weinheim

DOI: 10.1002/anie.200502530

Proteins

Why Are Proteins Charged? Networks of Charge–Charge Interactions in Proteins Measured by Charge Ladders and Capillary Electrophoresis

*Irina Gitlin, Jeffrey D. Carbeck, and George M. Whitesides**

Keywords:
capillary electrophoresis · charge networks · charge regulation · electrostatic interactions · proteins

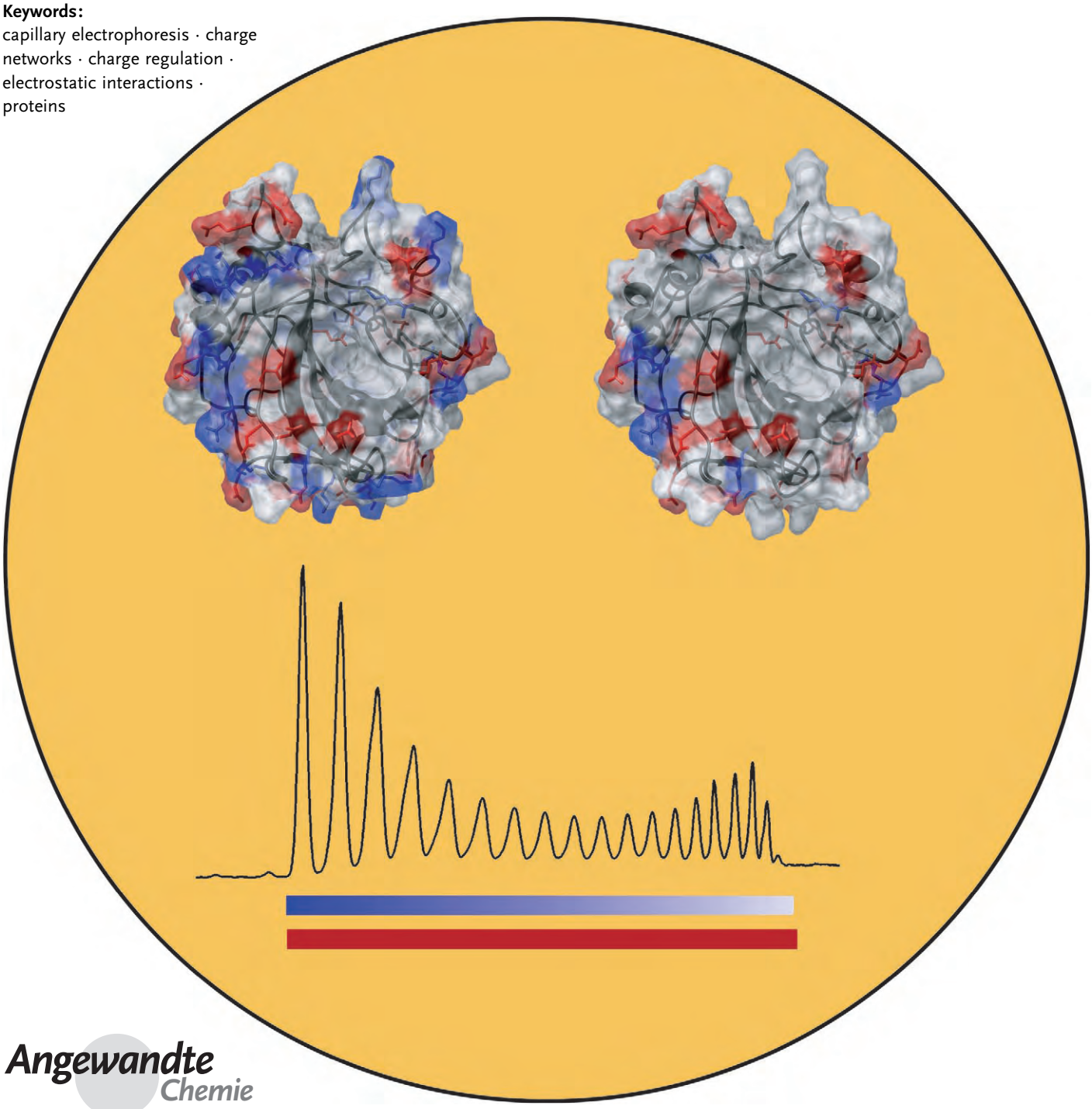

© 2006 Wiley-VCH Verlag GmbH & Co. KGaA, Weinheim

Almost all proteins contain charged amino acids. While the function in catalysis or binding of individual charges in the active site can often be identified, it is less clear how to assign function to charges beyond this region. Are they necessary for solubility? For reasons other than solubility? Can manipulating these charges change the properties of proteins? A combination of capillary electrophoresis (CE) and protein charge ladders makes it possible to study the roles of charged residues on the surface of proteins outside the active site. This method involves chemical modification of those residues to generate a large number of derivatives of the protein that differ in charge. CE separates those derivatives into groups with the same number of modified charged groups. By studying the influence of charge on the properties of proteins using charge ladders, it is possible to estimate the net charge and hydrodynamic radius and to infer the role of charged residues in ligand binding and protein folding.

From the Contents

1. Introduction	3023
2. Electrostatic Free Energies of Proteins	3026
3. Methods of Studying Electrostatic Interactions in Proteins	3036
4. Protein Charge Ladders—A New Approach to Probing Networks of Interactions among Charged Groups on Proteins	3037
5. Model Proteins in Studies with Charge Ladders	3037
6. Synthesis and Characterization of Protein Charge Ladders	3037
7. Models for the Analysis of Data from Capillary Electrophoresis	3041
8. Charge Ladders for Measuring the Net Charge and Hydrodynamic Drag of a Protein	3042
9. Influence of the Net Charge of Proteins (Z_{CE}) on Binding of Ligands: Combining Charge Ladders with Affinity Capillary Electrophoresis	3047
10. Study of Electrostatic Contributions to Protein Folding and stability by Using Charge Ladders	3050
11. The Net Charge of Proteins in the Gas Phase	3053
12. Using Charge Ladders to Study the Role of Electrostatics in Bioprocessing	3053
13. Summary and Outlook	3054

1. Introduction

Why do proteins include amino acids with charged side chains? Charged groups are often found at the active site of proteins, where they interact electrostatically with substrates, transition states, and products. Most efforts to study the role of charged groups in the biological activity of proteins have focused on these groups, and in many cases the mechanisms of their action are understood qualitatively, if not quantitatively.[1,2]

Charged groups on proteins are not restricted to active sites: they are found over the entire surface of proteins: approximately one third of the amino acids on the protein–water interface of a typical globular protein are charged.[3] Charged functional groups are also present in the interior of proteins (although they are concentrated on the surface; Scheme 1). The influence of "non-active site" charged residues on the structure, stability, and activity of proteins is not well understood. This Review focuses on these non-active site charges.

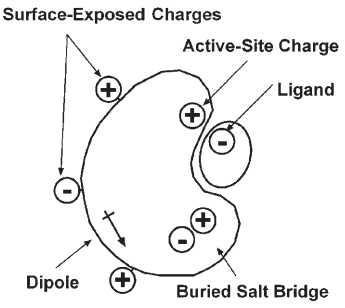

Scheme 1. Schematic diagram of a protein, showing surface, active site, and buried charges. The shape of the dielectric cavity seen by the charges, and the overall distribution of charge, may depend on whether a ligand is or is not bound at the active site.

Interactions between charged groups are often referred to simply as "electrostatics" in protein biochemistry and biophysics. This term is misleading: the charges are not static, and charged side chains, substrates, and ions in the solution all

[*] Dr. I. Gitlin, Prof. Dr. G. M. Whitesides
Department of Chemistry and Chemical Biology
Harvard University
12 Oxford St., Cambridge, MA 02138 (USA)
Fax: (+1) 617-495-9857
E-mail: gwhitesides@gmwgroup.harvard.edu
Dr. J. D. Carbeck
Department of Chemical Engineering
Princeton University
A-319 Engineering Quadrangle, Princeton, NJ 08544 (USA)

 © 2006 Wiley-VCH Verlag GmbH & Co. KGaA, Weinheim

move. The charged groups on proteins are also predominantly acids and bases that exchange protons with water; they are thus in dynamic equilibrium with their uncharged states. The term "electrostatics" is, however, convenient when referring to charge–charge, charge–dipole, and dipole–dipole interactions in proteins, and we use the term in this sense in this Review.

1.1. The Role of Charged Groups in Biochemistry

Charged groups can unquestionably play important roles in protein biochemistry. Processes that are influenced by electrostatic interactions include:

1) association of receptors with charged ligands;[4–6]
2) binding of substrates by enzymes, and catalysis of reactions;[1,7]
3) formation of protein–protein[8–11] and protein–nucleic acid[12] complexes;
4) transfer of electrons between biological reaction centers;[13]
5) selective transport of ions in protein channels;[14]
6) folding and stability of proteins;[15–19]
7) denaturation of proteins at high and low pH values;[20,21]
8) solubilization and precipitation of proteins;[22]
9) incorporation of proteins into amyloid fibers.[23]

The importance of charged groups in protein biochemistry has been studied extensively using site-directed mutagenesis as the primary tool, and with an emphasis on mutations in the active site.[2] This approach measures the contribution of the side chain of a specific amino acid to the stability and/or activity of a protein. Theoretical models of electrostatic interactions, both microscopic and continuum,[24–26] have complemented these experimental studies.

We have developed protein charge ladders as an alternative experimental approach to study charged groups in proteins; this approach is complementary to site-directed mutagenesis. Protein charge ladders clarify the contributions of charges to the stability of proteins, and to their interactions with ligands. Studies with charge ladders provide a different type of information than do those with site-directed mutagenesis, in that they allow the measurement of average contributions of a particular type of charged group (e.g., NH_3^+ or COO^- groups) on the exterior of the protein to stability or binding. This Review focuses on this subject.

Understanding electrostatic interactions will help to understand many processes in which proteins are involved. This understanding may, in turn, allow the design of molecules that bind to proteins (that is, potential drug leads) and the engineering of proteins for improved activity, stability, and processability, and for new functionality. There is also the opportunity to understand more about structure–function relationships in a way that might be used to design new molecules that mimic its properties.

1.2. The Free Energy of Proteins

The net changes in free energy as proteins fold or bind to molecules are often the result of large and opposing contributions,[27–29] and comprised of both enthalpic and entropic terms. For example, the native state of proteins is stabilized primarily by the unfavorable free energy of solvation of nonpolar side chains by water (that is, the "hydrophobic effect"); the hydrophobic effect causes these side chains to form the hydrophobic core of the native state. The less-ordered denatured state is stabilized by the favorable configurational free energy of the peptide backbone and side chains.[30,31]

Hydrophobic interactions are the main driving force for protein folding.[27,28,32] The relative contributions of enthalpy and entropy to the hydrophobic effect vary with temperature, but at 25 °C the free energy of hydrophobic interactions is dominated by the entropy of solvation of nonpolar solutes by water ($\Delta G_{\text{hydrophob}} \approx -T\Delta S_{\text{hydrophob}}$).[28,33] Although hydrophobic interactions are still a challenge to describe theoretically,[34] good empirical correlations exist between the hydrophobic free energy of solvation and solvent-exposed surface area,[35] or number of C–H bonds.[36] These correlations allow reasonable estimates of the overall contribution of hydrophobic interactions to protein stability.[37]

The contributions of configurational free energy to protein stability have been more difficult to quantify.[31] Translational, vibrational, rotational, and configurational entropies of small molecules can be estimated using simple models from statistical mechanics.[38] The configurational entropy and low frequency vibrational modes of proteins

Jeffrey D. Carbeck is a chemical engineer and materials scientist with expertise in biomaterials, biophysical and bio-analytical chemistry, molecular simulations, and theory. He gained his B.S.E from the University of Michigan, and his PhD from MIT. Both degrees were in materials science. He then spent two years as a postdoctoral researcher with G. M. Whitesides at Harvard University. He was a member of the faculty of Princeton University in the Department of Chemical Engineering from 1998 to 2006. In 2005, he co-founded the biomaterials company WMR, Inc.

Irina Gitlin received a BS in chemical engineering from the University of Illinois at Urbana-Champaign in 2000. She has recently completed her PhD in chemistry with G. M. Whitesides. Her research in the area of protein chemistry explores the role of electrostatic interactions in protein stability, binding of ligands, and susceptibility to denaturation by surfactants. She has also worked in the area of microfluidics.

 © 2006 Wiley-VCH Verlag GmbH & Co. KGaA, Weinheim

are, however, difficult to treat because they are numerous and poorly characterized; they are also difficult to measure experimentally, and molecular dynamics simulations are typically restricted to time-scales too short to capture these modes. Finally, proteins in the denatured state often do not resemble random coils, for which polymer physics has provided useful models of configurational entropy.[39]

The changes in configurational free energy and free energy of solvation that accompany protein denaturation are both on the order of 100 kcal mol^{-1}.[40] In contrast, the net difference in free energy between native and denatured states (that is, the standard state change in Gibbs free energy of denaturation, ΔG°_{D-N}; D: denatured, N: native) under conditions at which most proteins are stable (25 °C, neutral pH, and without chemical denaturants) is of the order of 10 kcal mol^{-1}.[33] This difference is equivalent in free energy to the formation of approximately 10 hydrogen bonds, a net hydrophobic interaction of perhaps 10 CH_3 groups, or electrostatic interaction between two charges in low ($\varepsilon \approx 5$) dielectric separated by a distance of less than 1 nm. Since these large and opposing contributions to the total free energy nearly cancel, other noncovalent interactions influence and may in certain cases determine the net stability of proteins.

Van der Waals interactions, through a combination of repulsion and attraction, provide selectivity to noncovalent interactions. When a pair of molecules has shapes that are complementary, numerous atoms from each of the molecules come in close contact simultaneously; this contact allows the attractive part of the interaction to make a significant contribution to the specificity of the interaction.[41]

Hydrogen bonds stabilize the secondary structure of proteins (e.g., α helices and β sheets). They are a particular type of electrostatic interactions between a weak acid donor group (e.g., N–H, O–H) and an acceptor group with a lone pair of electrons (e.g., N, O). For a hydrogen bond to form, the distance between the donor and acceptor group must be about 3 Å with the donor–H bond preferably pointing along the axis of the lone pair orbital of the acceptor.[42] Although most hydrogen bonds are electrostatic, there is some controversy over the presence and possible importance in enzymatic catalysis of short hydrogen bonds that are characterized by two energy minima with low energy barriers (low-barrier hydrogen bonds) and which may have a covalent component.[43]

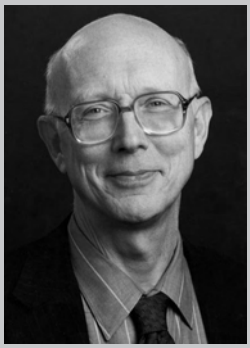

George M. Whitesides received his AB degree from Harvard University in 1960, and his PhD from the California Institute of Technology in 1964. He was a Mallinckrodt Professor of Chemistry from 1982–2004, and is now a Woodford L. and Ann A. Flowers University Professor. Prior to joining the Harvard faculty in 1992, he was a member of the chemistry faculty of the Massachusetts Institute of Technology. His research interests include physical and organic chemistry, materials science, biophysics, complexity, surface science, microfluidics, self-assembly, micro- and nanotechnology, and cell-surface biochemistry.

1.3. Measuring and Understanding Electrostatic Interactions in Proteins

Electrostatic interactions between charged groups in proteins in aqueous solution are difficult to understand and quantify for four reasons:

1) Electrostatic interactions are long-range. The electrostatic free energy of a protein includes interactions between charged groups that are separated by distances comparable to the dimensions of the protein.[28] Large numbers of interactions must thus be considered in calculating the total electrostatic free energy.
2) Acid–base equilibria are cooperative. The apparent pK_a value of a particular ionizable group on a protein may depend significantly on its interactions with other charged and polar groups, both on the protein and in solution.[44,45] Thus, a protein must be described as a network of interdependent charges. The quantitative description of a nonlinear network with a number of nodes (that is, charges) is not straightforward.
3) The dielectric properties of protein/solvent systems are heterogeneous. There is no single, well-defined parameter that describes the dielectric properties of proteins and the surrounding solutions.[46] A common simplifying approximation is to consider three separate regions of the system, each with a different dielectric constant: a) the core of the protein has a low dielectric constant ($\varepsilon = 2$–4), b) the bulk solvent (water, buffer, or biological fluid) has a high dielectric constant (typically taken to be that of bulk water: $\varepsilon \approx 80$), and c) the surface of the protein and surrounding layer of solvent has intermediate values of dielectric constant ($\varepsilon \approx 10$–20).[47] The dielectric constant of solvent-exposed regions of the protein is higher than that of the interior as a consequence of the presence and configurational mobility of polar side chains.[47] The dielectric constant of water near the surface of proteins is lower than bulk water because of the reduced mobility—and perhaps enhanced structure—of water in this region. These differences in dielectric properties are important because both the free energy of interaction between charges, and the free energy of solvation of individual charges, depend on the local dielectric properties of the medium the charges experience.[48] Average dielectric constants of the interiors of proteins may vary not only with heterogeneities within a protein but also with their stability to temperature.[49]
4) In biological systems, electrostatic interactions are supplemented by specific ion effects. The background electrolyte can affect the properties of proteins in solutions through forces other than simple electrostatics: the Hofmeister series and related classifications reflect the complexity of interactions involving proteins, ions, and water.[50] These effects are incompletely understood and are omitted in most descriptions of protein-containing solutions. Ninham and co-workers have pointed out that specific ion effects can in part be accounted for by dispersion forces between ions.[51,52] While we do not explicitly review this subject here, we emphasize that a

© 2006 Wiley-VCH Verlag GmbH & Co. KGaA, Weinheim

complete picture of protein–ion or protein–protein interactions must ultimately include those forces.

The most common method used by biologists to explore stability or activity of proteins is site-directed mutagenesis—that is, changing the identity of single amino acids and attempting to measure changes in the free energy or in the activity between the mutant and the wildtype.[2,53] This approach successfully identifies individual amino acids that make major contributions to the process of interest. We demonstrate in this Review that there are important interactions among charged groups on proteins that are best, and perhaps only, described by considering the charged groups as a network, rather than as electrostatically non-interacting charges.

1.4. Protein Charge Ladders

The protein charge ladder method uses chemical modifications that target charged groups on the surface of a protein (e.g. acetylation of a Lys-NH_3^+ residue) to annihilate the charge associated with that group (Figure 1 A).[54] It has the advantage that it produces large numbers of derivatives of a protein—perhaps several thousand—in a single experimental step. It has the disadvantage that these derivatives are characterized only by their net charge, not by knowledge of the detailed location of the charges. Relative to site-specific mutagenesis, it substitutes numbers of derivatives and experimental ease for knowledge of the detailed structure of these mutants.

This approach to producing large numbers of derivatives of a protein was first described by Hollecker and Creighton[19] and further developed by Goto and co-workers.[55] This earlier work was also based on the acylation of amines, and is similar in spirit to the work described in this Review. Hollecker and Creighton used urea-gradient gel electrophoresis to examine effects of reversing the charge of amino groups on protein stability.[19] Conversion of the first several Lys-ε-NH_3^+ groups of cytochrome *c* to negatively charged species (ε-$NHCOCH_2CH_2CO_2^-$) with succinic anhydride produced little effect on stability; succinylation of the final lysine group, however, caused unfolding even in the absence of urea. The limited resolution of gel electrophoresis prevented quantitative measurement of the effects of incremental changes in the net charge on stability.

The mixture of protein derivatives was analyzed by capillary electrophoresis (CE). This analytical technique separates the derivatized proteins into separate bands composed of families of proteins that all have the same number of modified charged groups and, therefore, approximately the same net charge (Figure 1 B, details of the analysis are described in Section 6.2). We call the protein derivatives separated in this way a "protein charge ladder," and each peak of the "ladder" we call a "rung". The resolution of CE allows quantitative measurement of the effects of changes in charge on protein folding[56] and ligand binding[4,5] that result from adding or subtracting a unit of charge by modification of a charged group. The combination of charge ladders and CE also makes it possible to isolate net charge[57] and hydrodynamic drag[58] in physiologically relevant solutions.

We have used three well-characterized proteins—carbonic anhydrase, α-lactalbumin, and lysozyme—for most of our studies. Charge ladders can, however, be generalized to many,[54] although not all, proteins. Charge ladders can also be used to count the number of modifications on a protein, and thus to study other properties of the protein surface: in this Review we describe changes in the hydrodynamic size of the protein and surface hydrophobicity produced by using this same approach of incremental chemical modifications.

The objective of this Review is to describe the use of protein charge ladders to address questions in the physical chemistry of proteins, especially the long-range interactions between charged groups. Section 2 is an overview (or tutorial) of the various contributions to the electrostatic free energy of proteins, with an emphasis on the concept of proteins as networks of charges.

We do not describe in detail theoretical methods for calculating the electrostatic free energies of proteins.[59] We also do not review the literature on experiments carried out using site-directed mutagenesis to measure the role of charged groups.[60] Excellent reviews of these topics exist already.[24,61]

2. Electrostatic Free Energies of Proteins

This section provides a short explanation of electrostatic contributions to the free energies of proteins. We start by describing the different definitions of the net charge of proteins, and discuss why the net charge is a useful parameter for characterizing the electrostatic properties of proteins. We classify individual charged groups on proteins in terms of their location, and of the character of their interactions with other charged groups. We introduce relevant basic ideas concerning proton equilibria, and describe charge regulation. We describe the simplest electrostatic interaction— two charges interacting with one another—and extend this description to the interaction between multiple charges; this description emphasizes that both enthalpy and entropy are important in determining the overall free energy of electrostatic interactions. We describe the contributions of solvation of charged groups to the electrostatic free energy of protein folding or binding to other molecules. Finally, we discuss how the electrostatic interactions contribute to both the strength and the specificity of molecular recognition events involving proteins.

2.1. Definitions of Net Charge of a Protein: Z_{H^+}, Z_{seq}, $Z_{protein}$, and Z_{CE}

Net charge is defined most generally as the sum over all charged groups that are covalently or tightly associated with a protein. We consider four definitions of net charge. Proton titrations measure the total number of protons bound to the protein as a function of the pH value and provide one measure of net charge, Z_{H^+}.[45] Proteins often change struc-

 © 2006 Wiley-VCH Verlag GmbH & Co. KGaA, Weinheim

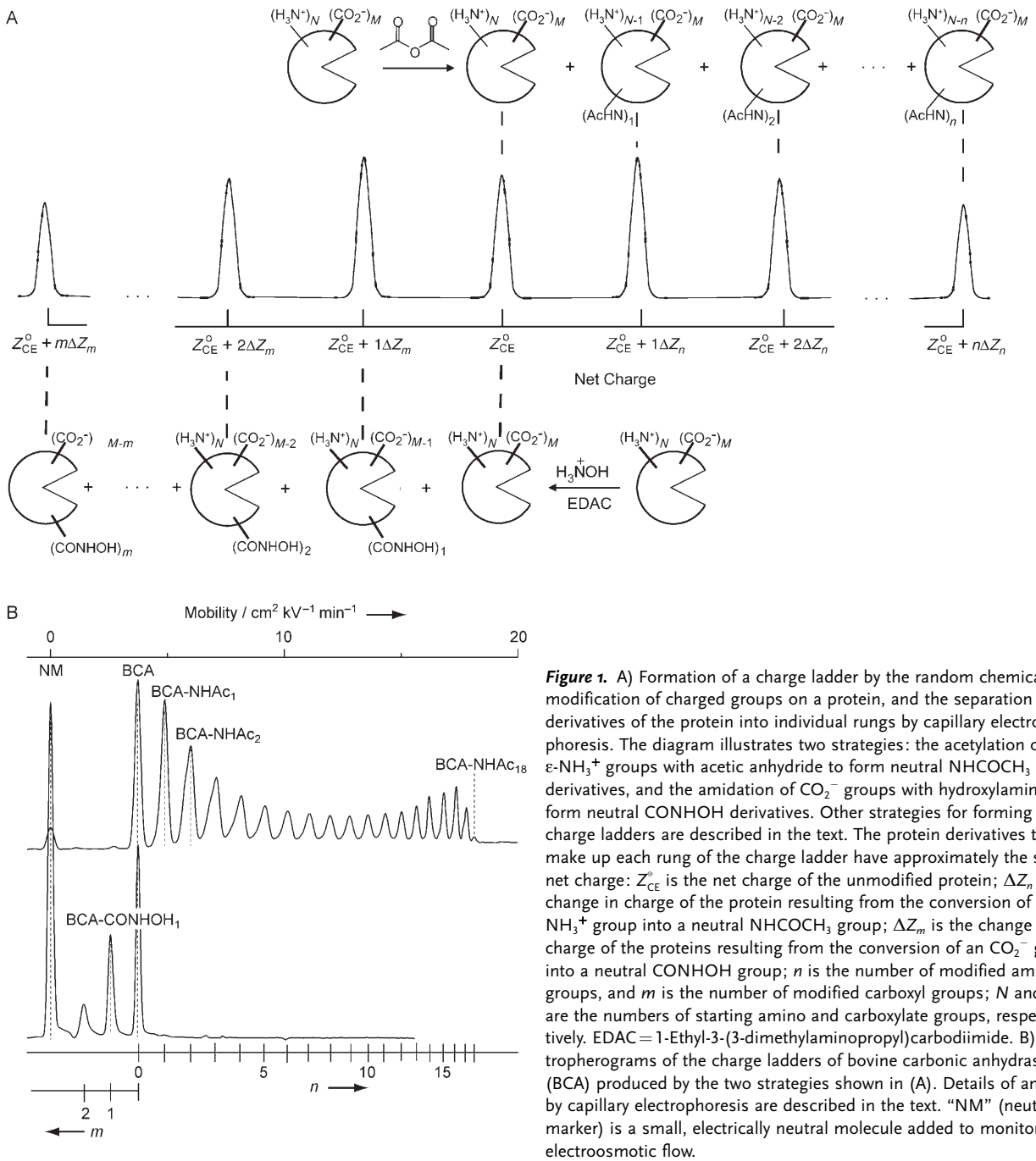

Figure 1. A) Formation of a charge ladder by the random chemical modification of charged groups on a protein, and the separation of the derivatives of the protein into individual rungs by capillary electrophoresis. The diagram illustrates two strategies: the acetylation of Lys ε-NH_3^+ groups with acetic anhydride to form neutral $NHCOCH_3$ derivatives, and the amidation of CO_2^- groups with hydroxylamine to form neutral CONHOH derivatives. Other strategies for forming charge ladders are described in the text. The protein derivatives that make up each rung of the charge ladder have approximately the same net charge: Z°_{CE} is the net charge of the unmodified protein; ΔZ_n is the change in charge of the protein resulting from the conversion of an NH_3^+ group into a neutral $NHCOCH_3$ group; ΔZ_m is the change in charge of the proteins resulting from the conversion of an CO_2^- group into a neutral CONHOH group; *n* is the number of modified amino groups, and *m* is the number of modified carboxyl groups; *N* and *M* are the numbers of starting amino and carboxylate groups, respectively. EDAC = 1-Ethyl-3-(3-dimethylaminopropyl)carbodiimide. B) Electropherograms of the charge ladders of bovine carbonic anhydrase II (BCA) produced by the two strategies shown in (A). Details of analysis by capillary electrophoresis are described in the text. "NM" (neutral marker) is a small, electrically neutral molecule added to monitor electroosmotic flow.

ture, aggregate, or denature when the pH value of the solution changes, and so values of Z_{H+} can be difficult (or impractical) to measure experimentally. Proton titrations also require large quantities of proteins. Net charge can also be estimated starting with the sequence of the protein (Z_{seq}), where the charge on each ionizable group is approximated using a standard value of its ionization constant (that is, its pK_a value) and the pH value of the solution. Values of Z_{seq} are usually inaccurate because they neglect both the roles of the local dielectric environment on the pK_a values, and the cooperativity inherent to proton equilibria in proteins.

Values of Z_{H+} and Z_{seq} also ignore the contribution of other charged species (e.g. buffer ions) that are noncovalently associated with the protein. The "true net charge" of a protein ($Z_{protein}$) is defined as the charge determined from the actual values of charge of the ionized groups of the amino acids making up the protein, and—when appropriate—any ionic species tightly associated with the protein; there has, in the past, been no practical method to measure $Z_{protein}$.

The combination of protein charge ladders and CE provides a method for the measurement of the net charge of proteins (Section 8). This approach measures the change in

 © 2006 Wiley-VCH Verlag GmbH & Co. KGaA, Weinheim

electrophoretic mobility that results from incremental changes in the number of charged groups present on the surface of a protein and extrapolates to the number n of charged groups that would have to be added to or subtracted from the protein to make its electrophoretic mobility, and therefore its value of net charge, zero. If we know or can estimate the value of the change in charge ΔZ that results from the addition or subtraction of one fully charged group to the protein, then the value of net charge of the unmodified protein Z_{CE} is $-n\Delta Z$. The value of ΔZ depends on the group that is modified and the pH value and ionic strength of the solution. With an accurate estimate of ΔZ, we believe that Z_{CE} is closer to the true value $Z_{protein}$ than Z_{H+} and Z_{seq}. In Section 8, we describe several ways of estimating ΔZ.

2.2. Why is Net Charge Important?

The net charge of a protein is a fundamental physical property,[62] and its value directly influences the solubility,[22] aggregation,[63] and crystallization[64,65] of the protein. These influences can all be described in terms of the value of the second virial coefficient (B_{22}) of proteins; B_{22} is a measure of two-body interactions between solutes in a solution,[66] and can be determined experimentally by static light scattering, membrane osmometry, or self-interaction chromatography.[67] Positive values of B_{22} represent net repulsive interactions between proteins, while negative values represent net attractive interactions.

The net charge of proteins modulates the second virial coefficient.[62,68] It is known empirically that crystallization of proteins occurs most readily over a narrow range of negative values of B_{22}, that is, when there is a net attractive force between proteins in solution.[65,69,70] If the attraction becomes too strong (that is, the value of B_{22} is too negative), the proteins aggregate and precipitate, rather than crystallize. If the proteins have a net repulsion in solution (a positive B_{22} value), the solution is stable and crystallization does not occur. Doye et al.[71] argued that proteins have evolved with a negative design principle that avoids crystallization, because crystallization or aggregation would compromise the viability of the cell and cause disease.[72] Studies of the effects of mutations on the crystallizability of proteins indicate that Lys residues, which present positively charged primary ammonium groups, when present on the surface of proteins may play an important role in inhibiting crystallization.[64] It is not known at this time whether or not this inhibition of crystallization is primarily an effect of electrostatic interactions, or of some other property of the side chain of this amino acid.

The connection between net charge and second virial coefficient is not fully understood. Simple models of charged colloids that can predict values of the second virial coefficient as a function of net charge do not always accurately predict the behavior of proteins in solution.[73] This occurs in part because the models treat small ions in solution by using continuum electrostatic theory, which neglects the excluded volume and dispersion interactions of the ions.[51,74,75] The relationship between net charge, the second virial coefficient, the structure of the surface of a protein, and its tendencies toward solubility, aggregation, or crystallization is an area of active interest in structural biology and bioengineering.[70,76]

Both experiments and theoretical models suggest that net charge can influence the rates of protein–protein association[10,11,77,78] and enzymatic catalysis.[79,80] Long-range electrostatic interactions between the two molecules involved are thought to enhance their rate of association; this effect can result in rates of association that exceed the limits of diffusion.[80] The net charge of proteins can also influence their equilibrium properties: that is, the free energy of their interactions with ligands,[4,5] and their thermal stability.[56,81]

Net charge values are also important in the processes that lead to the separation and purification of proteins. Filtration,[82–85] chromatography,[86,87] and two-phase extraction[88] are all techniques that can be used to separate proteins on the basis of net charge. The net charge also influences the electrophoretic mobility of proteins in solution, a fact which we take considerable advantage of in the work described in this Review.

2.3. Classification of Charged Groups on Proteins

The charges on proteins result from the reversible exchange of protons with water and other acids or bases in solution. Table 1 lists ionizable groups encountered in proteins. Cofactors (e.g., Zn^{2+}, ATP, NADPH) or modifications of proteins (e.g., phosphorylation) must also be considered.

Table 1: Average and anomalous values of pK_a of ionizable residues encountered in proteins.

Residue	Average pK_a[a]	Anomalous residue in a protein	pK_a of that residue	Reason	Ref.
Asp	4.0	RNase T1: Asp76	0.5	buried, 3 intramolecular H bonds, 1 H bond to buried water	[91]
Glu	4.5	Staph.[c] nuclease: Glu66[b]	8.8	buried	[92]
His	6.4	T4 lysozyme: His31	9.1	involved in salt bridge with Asp70	[93]
Cys	9.1	papain Cys25	4.0	interacts with imidazole group of His159	[94]
Lys	10.4	Staph. nuclease: Lys66[b]	5.7	buried	[92]
Tyr	9.7	glutathione *S*-transferase A1-1	8.1	stabilized by conserved Arg and by electropositive ring edge of Phe10	[95]
Arg	12.0	n/a			
N-term. NH_3^+	7.8	n/a			
C-term. COOH	3.6	n/a			

[a] Ref. [2]. [b] Introduced by site-directed mutagenesis (Val66Glu and Val66 Lys); n/a: examples not found. [c] Staph. = Staphylococcal.

 © 2006 Wiley-VCH Verlag GmbH & Co. KGaA, Weinheim

The type and location of the functional group is important (Scheme 1). Charged groups are located in the active site, on the surface, or in the interior of the protein. Charges may exist in pairs or groups, or may be isolated. We categorize interactions between charged groups in macromolecules as either local or long-range (Scheme 2), based on the distance between them. If two charged groups are sufficiently close (≤ 4 Å) that a water molecule cannot fit between them, we consider the interaction between those charges as local. If two oppositely charged groups with local interactions are in sufficient proximity that they can form a hydrogen bond, they are referred to as a salt bridge.[15] If two charges can accommodate water or other species between them, their interaction is long-ranged.

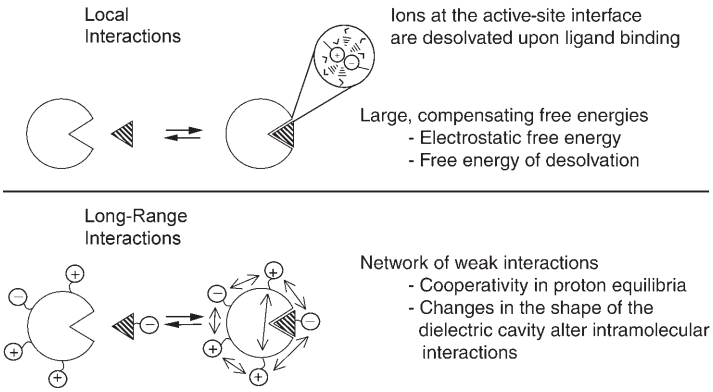

Scheme 2. Schematic diagram illustrating the difference between local and long-range interactions among charged groups on proteins.

The location of charged groups plays a role in determining the types of interactions in which they participate, and the contributions they make to the electrostatic free energy of the protein. For example, a buried salt bridge that is surrounded by the low dielectric interior of the protein has a very different electrostatic free energy than two charged groups on the surface of the protein that are exposed to water and dissolved ions. Table 1 illustrates the effects of the environment on the ionization of amino acids through examples of anomalous values of pK_a encountered in proteins; they can differ by as much as three units from the average values.

Another classification of charged groups is based on whether the interactions among them are pair-wise additive or cooperative. In general, the charge on one ionizable group influences the charge on other ionizable groups in its vicinity by shifting proton equilibria.[44] We describe cooperativity in proton equilibria in greater detail in Sections 2.4 and 2.5. This interdependence means that we cannot, in general, represent the total electrostatic free energy of a protein as the sum of pair-wise charge–charge interactions.

There are conditions, however, when this interdependence can be neglected: for example, when the charged groups are separated by large distances (e.g., >20 Å in water). This distance, of course, depends on the local dielectric environment as well as on the concentration of salts and other charged species in solution. Also, if the pK_a values of two groups differ both from each other and from the pH value of the solution by several (ca. 3) pH units, cooperativity is normally not important. For example, at pH 7, interactions between Arg groups on proteins (p$K_a \approx 12$) and phosphate groups on the backbone of DNA (p$K_a \approx 2$) can be treated as occurring between groups of fixed charge. Both groups are fully ionized at this pH value, and even if interactions between them were to shift their apparent pK_a values, their extent of ionization would be largely unaffected.

In addition to charges associated with ionized groups, the total electrostatic free energy of proteins must also account for the fact that many covalent bonds have significant dipole moments. In modeling studies of the interactions between charges and bond dipoles, it is often convenient to treat the dipole as comprising equal and opposite point charges (either whole units of charge or fractions) separated by the length of the bond. By using this convention, polar bonds and groups may be treated within the same system as charged groups. This approach is embodied in the development of a number of different sets of charge parameters[89,90] used in molecular simulations and continuum electrostatic models.

2.4. Proton Equilibria

This section starts with the simplest picture of proton equilibria: acid–base equilibria involving individual monovalent acids and bases. It then describes the simplest system—glycine—that demonstrates cooperativity of proton equilibria. Finally it extends this picture to describe the essential elements of proton equilibria of ionizable groups on proteins where there is cooperativity within a network of ionizable groups.

2.4.1. Proton Equilibria in Molecules with a Single Ionizable Site: Monovalent Acids and Bases

The average extent of protonation v [Eq. (1)] of an acid

$$v = \frac{[HA]}{[HA]+[A^-]} = \frac{K_a[H^+]}{1+K_a[H^+]} = \frac{1}{1+10^{(pH-pK_a)}} \quad (1)$$

(HA) is determined by the dissociation constant $K_a = [H^+][A^-]/[HA]$[90] of the ionizable group, and by the pH value of the medium. The same equations describe proton equilibria for a monovalent base by replacing [HA] with [HB^+] and [A^-] with [B]. The charge associated with a particular ionizable group i as a result of proton equilibria is $Z = q - v$, where $q = 1$ if the molecule is a base, or $q = 0$ if it is an acid. The rate at which proton equilibrium is reached is normally fast relative to the rates of protein folding, ligand binding, and electrophoresis;[2] thus we assume that ionizable groups are always at thermodynamic equilibrium with protons (hydronium ions) in solution.

The value of v, and therefore the value of Z, depends on the difference between the pH and pK_a values. Changes in Z can be the result of a shift in either of these values.

© 2006 Wiley-VCH Verlag GmbH & Co. KGaA, Weinheim

2.4.2. *Proton Equilibria in Molecules with Two Ionizable Sites: Glycine*

Glycine contains both a carboxylic acid group ($pK_a = 2.3$) and an amine ($pK_a = 9.7$). For pH values between 4 and 8, the carboxylic acid group is assumed to be completely deprotonated and the amine fully protonated; under these conditions glycine is a zwitterion. Scheme 3, however, shows that in this range of pH values there are in principle four (and in practice, three) different species in equilibrium.[96]

At a fixed pH value, the extent of deprotonation of the carboxylic acid group is greater when the amino group is protonated than when it is deprotonated; analogously, the extent of protonation of the amino group is lower when the carboxylic acid group is protonated than when it is deprotonated. These changes in proton equilibria can be interpreted in two ways: 1) Differences in the extent of protonation are due to shifts in the pK_a values of the molecule in response to local values of electrostatic potential, which reflect the other charges on the molecule.[97,98] 2) Differences in extent of protonation result from local pH values that differ from bulk values, because electrostatic fields caused by the molecule locally concentrate or deplete protons. Both interpretations lead to the same prediction of the effects of cooperativity in proton equilibria, since local pH values also reflect the local value of electrostatic potential.

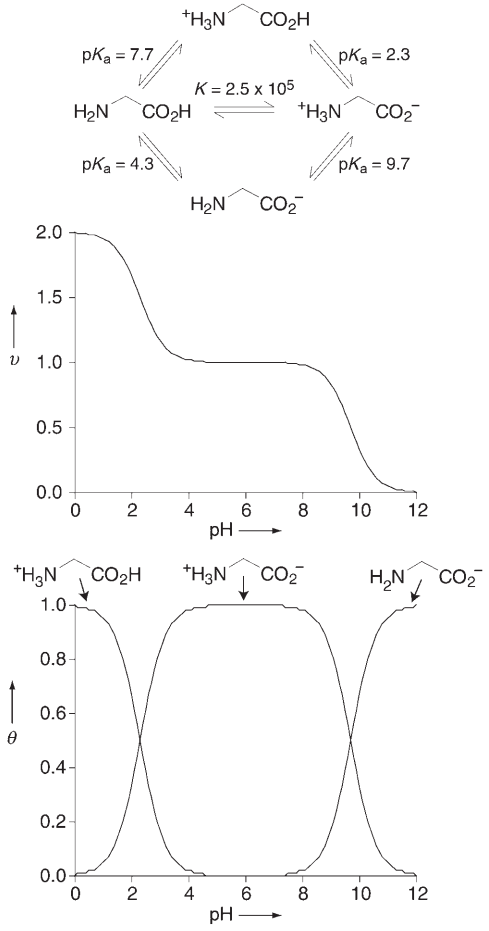

Scheme 3. Cooperativity of proton equilibria in glycine. The pK_a value of the CO_2H group is lower when the NH_2 group is protonated than when deprotonated. The plot of extent of protonation ν versus pH value shows two transitions. The plot of the relative populations θ of the different species as a function of the pH value shows that the transitions in the proton titration curve correspond primarily to ^+H_3N-CH_2-$CO_2H \rightleftharpoons {}^+H_3N$-$CH_2$-$CO_2^-$ (centered at pH ≈ 2.3), and ^+H_3N-CH_2-$CO_2^- \rightleftharpoons H_2N$-$CH_2$-$CO_2^-$ (centered at pH ≈ 9.7). Favorable electrostatic interactions between the NH_3^+ and CO_2^- groups increases the difference in the pK_a values between these groups, and the neutral species H_2N-CH_2-CO_2H is never populated significantly.

Scheme 3 implies there are five separate constants that describe proton equilibria in glycine. In fact, when we distinguish the two sites for protonation, there are only three independent equilibrium constants. If we do not distinguish the sites and just count the number of protons associated (as is done with proton titration), there are only two. To demonstrate these two cases, we use two different approaches to derive expressions for the extent of protonation υ.[48] In doing so, we also clarify the idea of cooperativity.

First we consider the approach that distinguishes the two sites for protonation: the carboxylate group and the amine. There are three possibilities for protons (H^+) to equilibrate with glycine (G): protonation only of the carboxylate (site a) with equilibrium constant K_a [Eq. (2)], protonation only of

$$G + H^+ \rightleftharpoons G_aH;\ K_a = \frac{[G_aH]}{[G][H^+]} \tag{2}$$

the amine (site b) with equilibrium constant K_b [Eq. (3)], or

$$G + H^+ \rightleftharpoons G_bH;\ K_b = \frac{[G_bH]}{[G][H^+]} \tag{3}$$

simultaneous protonation at both sites with equilibrium constant K_c [Eq. (4)].

$$G + 2H^+ \rightleftharpoons G_{ab}H_2;\ K_c = \frac{[G_{ab}H]}{[G][H^+]^2} \tag{4}$$

The extent of protonation (the average number of protons associated with a molecule of G as a function of $[H^+]$) is given by Equation (5). If the two sites are independent, then $K_c = K_aK_b$, and there is no cooperativity in the proton equilibria, and υ is defined completely by two equilibrium constants [Eq. (6)].

$$\upsilon = \frac{(K_a + K_b)[H^+] + 2K_c[H^+]^2}{1 + (K_a + K_b)[H^+] + K_c[H^+]^2} \tag{5}$$

$$\upsilon = \frac{K_a[H^+]}{1 + K_a[H^+]} + \frac{K_b[H^+]}{1 + K_b[H^+]} \tag{6}$$

When $K_c \neq K_aK_b$, the equilibria are cooperative: when $K_c > K_aK_b$, the cooperativity is positive and when $K_c < K_aK_b$, it is negative (sometimes referred to as anti-cooperative). A free energy that describes the interactions between sites (that is, the cooperativity) ΔG_c° is given in Equation (7). For the

$$\Delta G_c^\circ = -RT\ln\left(\frac{K_c}{K_aK_b}\right) \tag{7}$$

 © 2006 Wiley-VCH Verlag GmbH & Co. KGaA, Weinheim

case of glycine, a model based on Coulomb's law may provide a reasonable estimate of ΔG_c°.

A shortcoming of the site-based approach is that values of K_a and K_b cannot be determined uniquely by fitting Equation (5) to titration data. The terms involving K_a and K_b in Equation (5) always appear as sums. Without an independent measure of K_a, K_b, and K_c (e.g. by NMR experiments that distinguish the extent of protonation of individual sites on the molecules), the proton equilibria can only be described by two equilibrium constants.

These two independent equilibrium constants can be obtained by using an approach based on the stoichiometry of the proton equilibria, where two protons can bind to glycine with equilibrium constants K_1 and K_2 [Eqs. (8) and (9)],

$$G + H^+ \rightleftharpoons GH;\ K_1 = \frac{[GH]}{[G][H^+]} \tag{8}$$

$$GH + H^+ \rightleftharpoons GH_2;\ K_2 = \frac{[GH_2]}{[GH][H^+]} = \frac{[GH_2]}{K_1[G][H^+]^2} \tag{9}$$

consistent with the stoichiometry. The extent of protonation as a function of $[H^+]$ is given by Equation (10).

$$\upsilon = \frac{K_1[H^+] + 2K_1K_2[H^+]^2}{1 + K_1[H^+] + K_1K_2[H^+]^2} \tag{10}$$

The stoichiometric approach, which does not distinguish between sites, requires only two parameters to describe the titration data of glycine. This approach yields values of $K_1 = 2\times10^2\,\text{M}^{-1}$ ($pK_1 = 2.3$) and $K_2 = 5\times10^9\,\text{M}^{-1}$ ($pK_2 = 9.7$).[96] Even though it is tempting to do so, it is not appropriate to assign these values explicitly to the carboxylic acid and amine groups. By comparing Equations (5) and (10), we see that $K_1 = K_a + K_b$ and $K_2 = cK_aK_b/(K_a+K_b)$ where $c = K_c/(K_aK_b)$. Scheme 3 gives $K_a = 5\times10^9\,\text{M}^{-1}$ and $K_b = 2\times10^4\,\text{M}^{-1}$. Therefore, $K_1 \approx K_a$ and $K_2 \approx cK_b$. By comparing the values of K_a, K_b, K_1, and K_2, we infer that $c = 10^{-2}$ and, from Equation (7), $\Delta G_c^{\circ} = 2.7\,\text{kcal mol}^{-1}$ at 25 °C. This value of free energy indicates a negative cooperativity that results from a repulsive electrostatic interaction between the sites (the positive charge associated with the ammonium group creates a potential at the carboxylate group that makes the protonation of this group less favorable than protonation in the absence of charge). These ideas can be extended to a molecule with an arbitrary number of sites for association by using the concept of binding polynomials, as pioneered by Wyman and Gill.[48,96]

2.4.3. Proton Equilibria in Molecules with Networks of Ionizable Groups: Proteins

When there are multiple ionizable groups on a molecule, the interdependence of proton equilibria described for the simple case of glycine in Section 2.4.2 results in a picture of the molecule as a network of ionizable groups. The quantitative model developed for glycine can be used to understand proton equilibria in proteins qualitatively.

When discussing proteins, it is useful to assign an average extent of protonation υ_i to each residue. Residues of a particular kind (e.g. Lys or Glu) in a protein do not necessarily all have the same values of υ_i at a given value of pH, or a value of υ_i equal to that of model compounds. These differences in the υ_i values are usually interpreted in terms of a model that postulates differences in pK_a values. The pK_a values are also influenced by solvent accessibility and by the presence of other charged and polar residues on the protein.

There are three important implications of this picture of proteins as networks of ionizable groups:

1) The pK_a values of ionizable groups in proteins can differ from model compounds by several pH units (see Table 1).
2) Not all ionizable groups of a particular kind (e.g., carboxylic acid groups of Glu) on a protein have the same pK_a value.
3) The pK_a values of of charged groups will, in general, be different in folded and unfolded protein,[99] as well as in free protein and protein bound to other proteins.[11]

These dependencies mean that the free energies of folding and binding can be linked thermodynamically to the pH value of the solution.

Lysozyme provides a good example of the link between proton equilibria and protein stability. This protein has a maximum in stability at about pH 7. As the solution is made more acidic, the protein becomes less stable, and denatures spontaneously when the pH value is less than 2 (at 25 °C).[97] Denaturation under either acidic or alkaline conditions has been documented for many proteins, with detailed studies conducted with lysozyme,[93,100] various ribonucleases,[101] α-lactalbumin,[102] myoglobin,[18,103] and cytochrome *c*.[103,104]

In all of these cases, differences in proton equilibria between the native and denatured states influence (and may determine) the dependence of the stability on the pH value.[21] Section 10 shows how charge ladders and CE can determine the difference in the number of protons associated with α-lactalbumin in the native and denatured states, and thus can predict the dependence of the stability of this protein on the pH value of the solution.

2.5. Charge Regulation Is a Useful Model for the Network of Ionizable Groups on a Protein

A change in the extent of the protonation of one group of a molecule can cause an adjustment in the extent of protonation of the other ionizable groups on this molecule. This process is called "charge regulation"[105–107] and reflects the fact that the charges comprise a network. Linderstrøm-Lang first modeled this phenomenon in the context of pH titrations of proteins.[108] Linderstrøm-Lang's model treats a protein as a sphere with the charge distributed uniformly over its surface. A change in the extent of protonation of one residue changes the density of the charge on the sphere, and thereby the electrostatic potential at the surface of the sphere. This change in potential shifts the state of protonation of the other ionizable groups. In this model (Section 8.1), the net charge is determined by iteratively calculating the protonation state of all the residues on the protein sphere. This process makes the Linderstrøm-Lang model a mean-field model. Despite its lack of molecular detail, this model is

 © 2006 Wiley-VCH Verlag GmbH & Co. KGaA, Weinheim

qualitatively useful for understanding charge regulation in proteins.

As in glycine, the shift in the protonation state of one group because of another can be interpreted equivalently by either of the two mechanisms: 1) a change in the local proton concentration, or 2) a shift in the pK_a values of ionizable residues. From the expression for equilibrium of a single acidic group, $K_a/[H^+] = [A^-]/[HA]$, the change in the ratio of ionized to unionized acid can be interpreted either as a change in K_a or in the local value $[H^+]$.

Other, more complex models of proton equilibria exist that use more realistic representations of the protein.[109] These representations explicitly include the positions of ionizable groups, based on the crystal structure of the protein, and calculate the net charge of ionizable groups by averaging over the ensemble of different possible protonation states of the protein, rather than by using the mean-field approach of Linderstrøm-Lang.

Charge regulation is relevant to the analysis of protein charge ladders. Acetylation of a charged ε-NH_3^+ group of Lys removes a positive charge, and thus perturbs the network of charges on the protein. Other ionizable residues will adjust their average extent of protonation in response to this perturbation. For quantitative analysis of experiments with charge ladders, we need to know the change in the net charge of the protein ΔZ that results from the annihilation of charge on a particular group on the protein. Our initial work on charge ladders[4,110,111] did not consider charge regulation, and assumed $\Delta Z = -1$: that is, we assumed the change in net charge of the protein to be just the change in the charge of the particular group that was modified. Menon and Zydney pointed out that this assumption was wrong.[105] Estimates by Menon and Zydney, and subsequently by us,[106,107] showed that values of ΔZ for the acetylation of Lys ε-amino groups ranged from −0.6 to −0.95 (depending on pH value, ionic strength, and position of acetylation) and suggested that the error in net charge associated with earlier analyses (assuming $\Delta Z = -1$ at pH 8.4) was approximately 10%.

2.6. Enthalpic and Entropic Contribution to the Electrostatic Free Energy

The aim of this section is to describe the electrostatic free energy of proteins, starting from a given distribution of charges. We begin with a simple description of the interactions between two point charges and extend this discussion to proteins as arrays of point charges.

The models used in this section to predict electrostatic free energy, enthalpy, and entropy of charge–charge interactions are highly simplified. We use Coulomb's law and Debye–Hückel theory to calculate the work done in taking two point charges from infinity to some finite distance of separation. Other researchers have developed more rigorous approaches to describe the interactions of charges in solution by using statistical mechanics.[112,113] These approaches, which are part of a more general theory of noncovalent binding,[114] predict equilibrium association constants between ions, from which standard-state free energies can be determined. Although our models are simplified relative to these more rigorous approaches, the conclusions reached are essentially the same:[113] that is, both enthalpy and entropy contribute in unexpected ways to the free energy of interaction between charges in water.

2.6.1. Interactions between Two Charges

Coulomb's law in a vacuum [Eq. (11)] describes the work

$$\Delta E_{vac} = \frac{e^2 z_1 z_2}{4\pi\varepsilon_0(1/r_0 - 1/\infty)} \tag{11}$$

required to bring two point charges from infinity to a finite separation r_0 in a vacuum (ε_0 is the dielectric permittivity of a vacuum; Scheme 4A). Equation (11) gives the difference in energy (in this case, enthalpy; Coulomb's law in a vacuum does not describe entropy) between charges at $r = \infty$ and $r = r_0$.

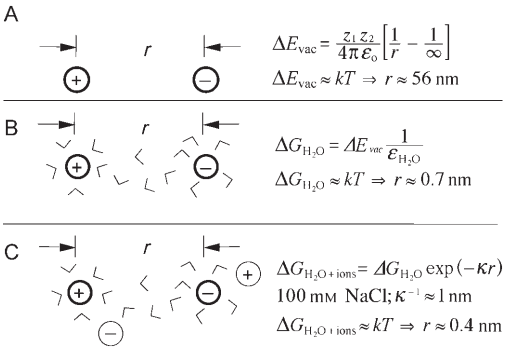

Scheme 4. Diagram describing differences in electrostatic energies in vacuum (A), water (B), and in the presences of dissolved ions (C). The free energy of interaction between two, singly charged groups in water is smaller than between isolated charges in a vacuum because of the presence of water with a large dielectric constant and ions that tend to shield interactions. κ is the inverse Debye screening length.

There is no temperature dependence to this interaction; it is not a free energy. Values of ΔE_{vac} are favorable (negative) if the two charges are opposite in sign, and unfavorable if they have the same sign. The value of ΔE_{vac} approaches the value of thermal energy (RT) when $r \approx 56$ nm at 298 K. Clearly, electrostatic interactions are long-range in a vacuum relative to the dimensions of a protein; a typical protein has a diameter of 5 nm.

In a uniform dielectric with dielectric constant ε, the Coulombic interaction energy is just $\Delta E_{vac}/\varepsilon$ (Scheme 4B). Since values of ε are always greater than 1, the effect of the medium is to reduce the magnitude of the interaction. The value of ε is dependent on temperature, and thus the energy of interaction is now a free energy: for example, in water $\Delta G_{H_2O} = \Delta E_{vac}/\varepsilon_{H_2O}$, where $\varepsilon_{H_2O} \approx 80$ at 25 °C. The temperature dependence of ε reflects the fact that enthalpic and entropic contributions are included in the work of polarizing the medium by the charges. In this discussion, we ignore all the

 © 2006 Wiley-VCH Verlag GmbH & Co. KGaA, Weinheim

molecular details of water. We treat it as a uniform continuum described by a single (temperature-dependent) parameter ε: the larger the ε value of the medium, the smaller in magnitude is the free energy of interaction for a particular value of r. For water, ΔG_{H_2O} approaches the value of thermal energy (RT) at 298 K when $r \approx 0.7$ nm. The large dielectric constant of water plays a significant role in establishing the magnitude of the electrostatic free energy of interactions between charged groups in biological systems.

A charge in a solution containing other dissolved ions tends to repel ions of the same charge, and to attract ions of the opposite charge. Therefore, the local concentration of oppositely charged ions in the vicinity of a charged group is higher than that in the bulk and the concentration of like-charged ions is lower than in the bulk. The electrostatic potential produced by the charge is therefore weakened, or "screened" (Scheme 4C).

The Debye–Hückel model describes the reduction in the free energy of interaction between charges resulting from the presence of dissolved ions. In this model, the free energy of interaction is $\Delta G_{H_2O+ions} = \Delta G_{H_2O}\exp(-\kappa r)$, where κ^{-1} is the characteristic distance of the screening of the potential, known as the Debye length. Values of κ are temperature dependent, and reflect the work done (involving both enthalpic and entropic contributions) in the creation of a localized concentration gradient of ions surrounding the two charges (that is, the creation of an "ion atmosphere"). As in the case of the dielectric constant, Debye–Hückel theory ignores all the molecular details of the ions—they are treated as a continuum charge density described by a single (temperature-dependent) parameter κ. A typical ionic strength of a biological solution is 150 mM. Under these conditions, $\kappa^{-1} \approx 1$ nm and $\Delta G_{H_2O+ions}$ approaches the value of the thermal energy (RT) at 298 K when $r \approx 0.4$ nm.

2.6.2. Enthalpy and Entropy of Interaction between Two Ions

The free energy of interaction between charged groups in a vacuum is entirely enthalpic: that is, this value is independent of temperature. However, the free energy of interaction between charged groups in water is often dominated by entropy. Changes in entropy reflect the way in which water and ions in solution reconfigure in response to the presence of the charges. These effects are described by the dielectric constant (ε) and by the Debye length (κ^{-1}).

Two charges interact in a uniform dielectric with a free energy described by Equation (12). Since the dielectric

$$\Delta G = \frac{e^2 z_1 z_2}{4\pi\varepsilon_0 \varepsilon r} \tag{12}$$

constant depends on temperature, the interaction described by Equation (12) is a free energy. The entropy is defined in Equation (13), and the enthalpy of interaction by Equation (14). Values of $(\partial\varepsilon/\partial T)$ are typically less than zero:

$$\Delta S = -\left(\frac{\partial \Delta G}{\partial T}\right)_{p,N} = \Delta G\left(\frac{1}{\varepsilon}\frac{\partial \varepsilon}{\partial T}\right) \tag{13}$$

$$\Delta H = \Delta G + T\Delta S = \Delta G\left(1 + \frac{T}{\varepsilon}\frac{\partial \varepsilon}{\partial T}\right) \tag{14}$$

$(T/\varepsilon)(\partial\varepsilon/\partial T) \approx -0.26$ for hexane, and ≈ -1.37 for water at 25 °C.[115] Therefore, $\Delta H \cong 0.74\Delta G$ for hexane, but $\Delta H \cong -0.37\Delta G$ for water: that is, at all distances the enthalpy of interaction between oppositely charged ions in the lower dielectric hexane is favorable ($\Delta H < 0$), while the enthalpy of interaction in water is unfavorable ($\Delta H > 0$). For both cases the entropy of interaction is favorable ($\Delta S > 0$).

This result is surprising: we usually think about a statement "unlike charges attract" in terms of the favorable enthalpic component of the interaction. In fact, in water, unlike charges do attract—but not because of enthalpic interactions between ions; rather, they attract because the entropy of ion–solvent interactions (as described by the temperature-dependence of the dielectric constant of water) becomes increasingly more positive (favorable) as ions approach one another. This result also indicates that bringing two ions of the *same* charge together in water releases heat ($\Delta H < 0$) even though the free energy increases.[116] These characteristics are the result of four unique properties of water: its large ε value, its large and negative value of $\partial\varepsilon/\partial T$, its small molar volume, and its ability to form a network of hydrogen bonds in the liquid state.

Equation (15) gives the free energy of interaction of two

$$\Delta G = \frac{e^2 z_1 z_2}{4\pi\varepsilon_0 \varepsilon r}\exp(-\kappa r) \tag{15}$$

charges in a uniform dielectric that contains dissolved ions, as predicted by the Debye–Hückel model with the concentration of ions described by κ. Equations (16) and (17) give the

$$\Delta S = \Delta G\left(\frac{1}{\varepsilon}\frac{\partial \varepsilon}{\partial T}\right) \tag{16}$$

$$\Delta H = \Delta G\left(1 + \frac{T}{\varepsilon}\frac{\partial \varepsilon}{\partial T} + rT\frac{\partial \kappa}{\partial T}\right) \tag{17}$$

entropy and enthalpy of interaction predicted by this model. The values of $(\partial\kappa/\partial T)$ are also less than zero, and therefore also contribute to the favorable entropy of interaction between oppositely charged groups.

Figure 2 compares the contributions to the free energy of interaction between two singly charged groups as they are brought from infinite to finite separation distance r in pure hexane (a low dielectric medium: $\varepsilon = 2$) and in water ($\varepsilon = 80$) containing 100 mM NaCl. In hexane, it is the favorable enthalpy of interaction that makes the largest contribution to the favorable electrostatic free energy of interaction of opposite charges as they approach the point of contact. In water with dissolved ions, the enthalpy of interaction between opposite charges is actually unfavorable (the enthalpy includes the contributions of the polarized water and ion atmospheres surrounding the charges, as well as the interaction between the charges themselves). It is instead the

 © 2006 Wiley-VCH Verlag GmbH & Co. KGaA, Weinheim

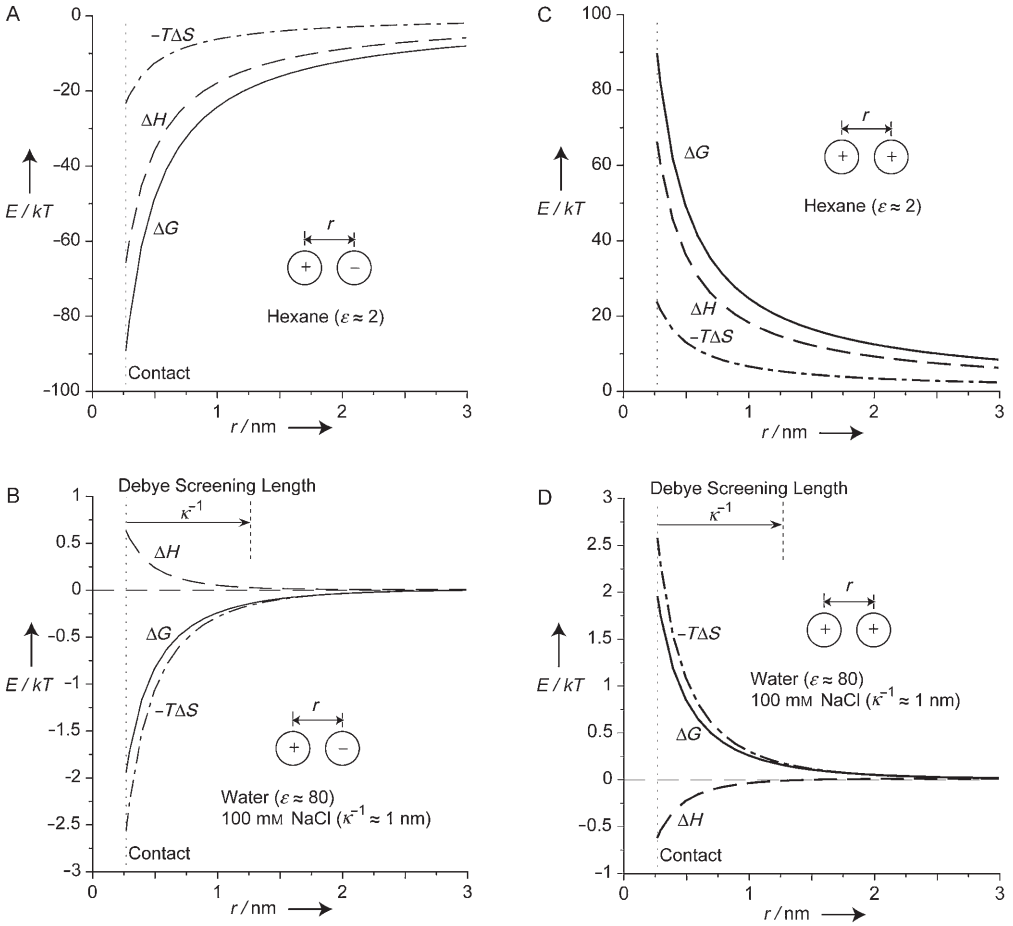

Figure 2. The electrostatic free energy, enthalpy, and entropy of interaction between two ions of the opposite (A, B) and of the same (C, D) charge in hexane (A, C) and water (B, D) containing 100 mM NaCl depends on the distance between the ions. Values of the free energy of interaction in this simplified, isothermal, one-dimensional system (ΔG, in units of kT) were calculated at 25 °C using Equations (12)—(14) for hexane, and Equations (15)–(17) for water with salt.

entropic contribution to the free energy that makes the interactions between opposite charges favorable.

This conclusion—that plus and minus charges do attract in aqueous solutions, but for entropic and not enthalpic reasons—is one of the almost endless, counterintuitive properties of water. The answer to the question "Why?" is "because the value of the dielectric constant decreases steeply with increasing temperature," which is more a statement of experimental fact than molecular-level explanation. The dielectric constant reflects the static polarization of water, both between the plates of a capacitor and around an ion. The structure of the water, which influences this polarizability, becomes disordered as the temperature increases, and releases water molecules as ions approach one another.

The nature of electrostatic interactions in water, and the partitioning of these interactions between enthalpic and entropic terms, is one surprise about water. There are others. For example, Ninham and co-workers have shown that electrostatic interactions do not always dominate the total free energy of interactions between ions. As the concentrations of ions increases, dispersion forces among ions and water have to be included in accurate thermodynamic descriptions of solutions of electrolytes.[75] A striking, counterintuitive result of the study by Ninham and co-workers is that the net interaction between some ions of like charge is attractive when dispersion forces are included.[75] For example, in a 1 M aqueous solution of $NaNO_3$, the ion–ion pair distribution function shows that NO_3^- ions prefer to be next to other NO_3^- ions rather than Na^+ ions; Na^+ ions, however, do not show an analogous preference.

2.7. From a Pair of Charges to Proteins

There are two ways of describing the distribution of charges on a protein mathematically: One, which can be applied to whole proteins or to individual side chains, is through a multipole expansion. In this approach, the electrostatic free energy of interaction between two molecules is represented as a sum of charge–charge, charge–dipole, dipole–dipole, and higher-order interactions. The multipole expansion requires evaluations of large numbers of terms, and is cumbersome when describing large molecules such as proteins.

 © 2006 Wiley-VCH Verlag GmbH & Co. KGaA, Weinheim

An alternative to using the multipole expansion focuses on the density of charge $\rho(\mathbf{r})$ [$C\,m^{-3}$]. If all the charge is localized on individual atoms, then $\rho(\mathbf{r})$ corresponds to an array of point charges, with z_i as the charge associated with atom i. Values of z_i can be whole or fractional units of charge. The total electrostatic free energy of a particular distribution of charge is the work done in assembling an array of charges from a reference state of infinite separation [Eq. (18)], where

$$\Delta G = \sum_i z_i \varphi(\mathbf{r}_i) \tag{18}$$

the sum is over all charges in the array, and $\varphi(\mathbf{r}_i)$ is the electrostatic potential at the position $\mathbf{r}_i$ ar a consequence of the other charges in the array.

The problem of calculating the electrostatic free energy is that of calculating the electrostatic potential $\varphi(\mathbf{r}_i)$. This calculation can be done for proteins by using the Poisson–Boltzmann equation, which is described briefly in Section 3.2.

2.7.1. The Free Energy of Solvation of Charges

Interactions between charges during protein folding, ligand binding, and protein–protein interaction often involve changes in their solvation. The free energy of transferring a charged group from a medium with a larger value of ε to one with a smaller value of ε is always positive (that is, unfavorable);[48,117] this effect is often referred to as desolvation in biophysics, as it typically occurs when a charged group moves from a more-solvated to a less-solvated state.

The free energy of solvation of a charged group is the result of the polarization induced in the dielectric medium surrounding the group.[48] The polarization produces a local electric field (called the "reaction field", or sometimes the "self field"). The larger the value of ε, the greater is the magnitude of the reaction field. The free energy of interaction between a charged group and its reaction field is always negative (that is, favorable). This free energy of solvation is a major driving force in the dissolution of ionic solids in water.

The transfer of a charged group from a region with a large ε value to a region with a smaller ε value reduces the magnitude of the reaction field of the ion, and results in a positive free energy of transfer. These changes in solvation can have interesting consequences on protein stability and activity. For example, in the absence of a ligand, charges on the surface of the active site of a protein are exposed to solvent. The binding of a ligand to the protein expels solvent from the interface; the charged group is transferred from an environment with a high dielectric constant ($\varepsilon \approx 20$–80) to the interior of the complex where the dielectric constant is much lower ($\varepsilon \approx 4$). The consequence of this transfer is that charged groups in active sites do not always contribute to the strength of the interaction between the protein and the ligand. Davis et al.[8] argued in a study of the binding of two cell-surface proteins CD2 and CD48 that charged residues on CD2 contribute little to the *affinity* of binding of CD48 because of the trade-off between the unfavorable energy of desolvation of charges and the favorable energy of forming electrostatic contacts. Instead, these charged residues contributed primarily to the *specificity* of interactions because of electrostatic complementarity of the two surfaces.

Desolvation plays a major role in the energetics of buried charges. The formation of a buried salt bridge can actually be destabilizing if the favorable free energy of electrostatic interactions between two oppositely charged groups is smaller than the unfavorable free energy of desolvation of the individual charges. Hendsch and Tidor estimated this effect in protein folding.[17] Calculations based on continuum electrostatic theory indicated that the majority of buried salt bridges are destabilizing in the folded state, relative to interactions between amino acids that are the same size, form hydrogen bonds, but are not charged; this destabilization by salt bridges is due to the large penalty of desolvation.

From the work of Hendsch and Tidor[17] as well as others,[15,118] it is clear that the free energy of desolvation is similar in magnitude to the free energy of electrostatic interactions in the formation of buried salt bridges. The net free energy for the formation of buried salt bridges is still uncertain, because these interactions offset each other. For example, Baker and co-workers[118] have argued that the free energy of electrostatic interactions between charges more than compensates for the free energy of desolvation in most cases. Kumar and Nussinov[15] surveyed the free energy of formation for a large number of salt bridges predicted by continuum electrostatic calculations, and suggested, based on their calculations, that only a minority (34%) of buried salt bridges were destabilizing. Kumar and Nussinov attributed the discrepancy between their work and the work of Hendsch and Tidor[17] to differences in the distance of charge–charge interactions used to define a salt bridge: while the study of Hendsch and Tidor included many salt bridges with separation distances greater than 4 Å, Kumar and Nussinov defined salt bridges as having separations of ≤ 4 Å.

2.7.2. The Influence of Ionic Strength on Electrostatic Interactions in Proteins

It is a common belief that increasing the ionic strength of a solution minimizes the free energy of the electrostatic interactions by shielding charged groups by the Debye layer. In proteins, however, the electrostatic free energy is not necessarily reduced by ionic strength for three reasons:

1) The energy of desolvation is only weakly dependent on ionic strength. If desolvation dominates the contribution of the electrostatic interactions to the free energy, then the net free energy will be fairly insensitive to the ionic strength.[17]
2) The distances between many charged groups in proteins (especially those involved in salt bridges) are significantly smaller than the Debye screening lengths ($\kappa(I{=}100\text{ mM}) \approx 1$ nm; I = ionic strength); the effect of changing the screening length on the free energy of the interaction is therefore insignificant for these groups.
3) Charges on the surface of a protein also interact through the low dielectric interior of the protein; free ions in solution should have little effect on this type of interaction.

© 2006 Wiley-VCH Verlag GmbH & Co. KGaA, Weinheim

2.7.3. Conclusions

The charged groups on a protein constitute a network with interdependent, cooperative proton equilibria. The variety of environments in which charged groups are found—on the surface or in the interior, proximal to other charges or not—make it impossible to generalize the contributions of electrostatic interactions to many processes in proteins. As a result, experimental work and new experimental methods are required.

3. Methods of Studying Electrostatic Interactions in Proteins

3.1. Experimentally, by Site-Directed Mutagenesis

The most common strategy for exploring the contribution of charged groups to the stability and activity of proteins is site-directed mutagenesis. This approach identified key amino acids that contribute substantially to stability or activity.[119,120] Double mutant cycles have also been used to estimate the free energy of interactions between two charged groups on a protein[121,122] or between two proteins.[11] This approach focuses on local interactions, and identifies the roles of particular charged residues—often the ones in the active site, at the area of contact with another macromolecule or a ligand, or forming a salt bridge.

Fersht and co-workers pioneered the use of site-directed mutagenesis to examine the role of charged groups in proteins with studies on barnase and subtilisin.[2,121,123] A classic example is the work of Anderson et al. on the role of charged groups on the stability of T4 lysozyme.[93] This study demonstrated that a specific salt bridge (Asp70-His31) contributed 3–5 kcal mol^{-1} to the stability of the protein. Dao-pin et al.[122] measured the stability of 13 different single, double, triple, and quadruple mutants of T4 lysozyme produced by site-directed mutagenesis, and concluded that long-range electrostatic interactions contributed, on average, little to stability. In another example, which reached a different conclusion, Perl et al. replaced a single negatively charged amino acid (Glu) on the surface of a mesophilic cold-shock protein by a positively charged amino acid (Arg); this mutation increased the thermal stability of the protein by more than 2.8 kcal mol^{-1}, and rendered the mutated mesophilic protein nearly equal in stability to its thermophilic counterpart.[119] Analysis of the structure of these proteins showed this change in stability was not due to the formation of an ion pair involving Arg and a specific negatively charged group on the protein, but a result of many long-range, but generally favorable interactions. Significant changes in stability can thus result from the change in the electrostatic free energy of interactions on mutation of a single charged amino acid, but understanding and predicting these changes may not be simple.

Benkovic and Hammes-Schiffer used site-directed mutagenesis to explore the mechanisms of the catalytic activity of dihydrofolate reductase.[124] This elegant, extensive work demonstrated that residues that are neither in direct contact with ligands in the active site, nor able to make contact after substantial conformational rearrangements, are still able to influence catalytic activity. The authors concluded that these conserved residues act as a coupled network that determines protein structure and, perhaps more importantly, coordinates intramolecular motions of the protein central to its catalytic activity.

Site-directed mutagenesis has two major limitations. First, the expression and purification of protein mutants is time consuming. Second, the individual or pair-wise interactions targeted by this technique can be too weak to detect or quantify. As we describe later, CE and charge ladders circumvent some of these limitations (while introducing others).

3.2. Theoretically, by Calculations of Continuum Electrostatics

The Poisson–Boltzmann equation is a second-order, nonlinear differential equation that relates values of electrostatic potential to the density of charge that is embedded in a nonuniform dielectric continuum. In this equation, values of electrostatic potential, charge density, and dielectric constant are all functions of position. Numerical solutions of the Poisson–Boltzmann equation, first applied to proteins by Warwicker and Watson[125] and then by Honig and co-workers,[59,126] are the method of choice for calculating electrostatic free energies between proteins and between charged groups on a protein, for representing potential surfaces, for calculating free energies of solvation of charged groups as well as the pK_a values of ionizable residues, and for other applications.[24,26] This approach is semimacroscopic: the distribution of charges on the macromolecule is treated explicitly on the basis of crystallographic data, while the solvent is treated as a continuum, with a density of charge to represent dissolved ions.[24] The protein is represented as a cavity of low dielectric constant—either uniform or as a function of position[47]—embedded in a high dielectric medium.

Numerical solutions of the Poisson–Boltzmann equation predict the electrostatic potentials present at protein surfaces, and can clarify the role of electrostatics in protein–protein and protein–nucleic acid interactions.[24] For example, trypsin and bovine pancreatic trypsin inhibitor form a strong complex, even though both proteins have a large positive net charge. The Poisson–Boltzmann equation revealed a local domain of negative potential at the binding site of trypsin that probably contributes to the affinity of the two proteins.[24]

Solutions to the Poisson–Boltzmann equation are computationally intensive, and therefore cannot be easily coupled to dynamic simulations. There are also uncertainties in the parameters of the model (e.g. atomic radii that define the boundary between the protein and solvent, dielectric constants of the protein and solvent at the interface, and the "intrinsic" pK_a values used to determine proton equilibria).

Calculations using the Poisson–Boltzmann equation indicate that many electrostatic interactions that are likely to be encountered in proteins and complexes of proteins and ligands are sufficiently weak that they are currently undetectable by experiment. As an example, we calculated the

 © 2006 Wiley-VCH Verlag GmbH & Co. KGaA, Weinheim

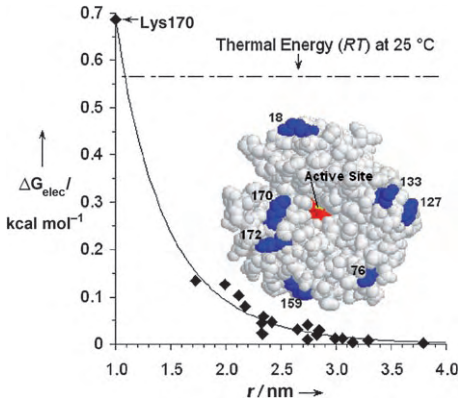

Figure 3. The electrostatic free energy ΔG_{elec} of interactions between the positive charge on each Lys ε-NH_3^+ group of human carbonic anhydrase II (HCAII), and a positive "test" charge situated at the active site of the enzyme, as a function of distance r between the charges. The electrostatic free energy is calculated using numerical solutions of the linearized Poisson–Boltzmann equation. The solvent surrounding the protein is modeled with a dielectric constant of $\varepsilon = 80$; the interior of the protein is modeled with $\varepsilon = 4$. The solid line is a fit of a screened Coulombic potential [Eq. (28) in the text]) with both ε and κ varied to fit the data. The inset shows the structure of HCAII: the active site is colored red with the Zn^{2+} ion in yellow; the 7 of the 21 total Lys residues that are visible in this view are colored blue; the number indicates their position in the sequence of the protein.

electrostatic free energy of interaction between each Lys ε-NH_3^+ residue of carbonic anhydrase and a positive "test" charge situated at the active site of the enzyme (Figure 3). All but one interaction are below the thermal energy (RT).

4. Protein Charge Ladders—A New Approach to Probing Networks of Interactions among Charged Groups on Proteins

Protein charge ladders are formed by chemical modifications of charged groups which alter the charge state of that group, (e.g. -NH_3^+→NHCOCH$_3$; -CO_2^-→-CO_2CH_3). The reactions are, we believe, generally relatively nonspecific in their position—most or all of the Lys residues in a protein may, in principle, react with similar probability. As a result, the reaction mixture contains protein derivatives with different numbers and sites of modifications. The mixture of the protein derivatives can be separated into distinct bands by capillary electrophoresis (CE). CE readily measures and separates molecules on the basis of electrophoretic mobility (μ [$m^2 V^{-1} s^{-1}$])—a property that depends on the ratio of two fundamental biophysical characteristics of proteins: net charge and hydrodynamic drag.[127] Each peak consists of a mixture of regio-isomers of approximately the same net charge.

The combination of protein charge ladders and CE makes it possible to measure or estimate the electrostatic properties and interactions of proteins. The following sections review the synthesis, characterization, and the use of charge ladders and CE to examine the following properties of proteins: 1) the net charge, 2) the extent of charge regulation upon acetylation of a Lys residue, 3) the electrostatic contributions to the free energy of binding of ligands, 4) the electrostatic contributions to the free energy of folding and stability, and 5) the role of the charge of a protein and of the electrostatic interactions in bioprocessing (in particular in ultrafiltration). Two other subjects that we review that do not fall in to the realm of electrostatics, but can nevertheless be addressed using charged ladders and CE, are: 1) determination of the hydrodynamic drag of proteins, and 2) the effects of surface charge on the pattern of protein ionization in electrospray mass spectrometry.

5. Model Proteins in Studies with Charge Ladders

The development of a new technique often requires a system that is straightforward to handle. In protein biophysics, the models used have included barnase[128] for folding, acylphosphatase for studies of in vitro aggregation and amyloid formation,[129] and triosphosphate isomerase and dihydrofolate reductase[124] for catalysis. We have used carbonic anhydrase (CA, EC 4.2.1.1) as the model protein in our studies. Both the bovine CA (BCA) with 18 Lys ε-NH_3^+ groups and the human CA (HCA) with 21 Lys ε-NH_3^+ groups are commercially available and their structures are determined. Both proteins have naturally acetylated N-terminal α-amino groups. CA is stable (T_m(HCA) = 60 °C; T_m(BCA) = 65 °C)[130] and therefore easy to handle. More importantly, the charge ladders of CA are well-resolved by CE (see Figures 1b and 4), and acetylation of CA does not disrupt its tertiary structure.[131] CA does not interact with the walls of the capillary when the electrophoresis buffer has a pH value of greater than 7.5. In addition, a variety of well-characterized inhibitors to CA (almost all aryl sulfonamides) are commercially available or easy to synthesize.[132] We have also used insulin,[133] lysozyme,[107,134] and α-lactalbumin[56] in studies with charge ladders. Many proteins other than these few form well-resolved charge ladders,[54] but we have not carried out detailed analysis of their electrostatic properties by using this technique.

6. Synthesis and Characterization of Protein Charge Ladders

6.1. Preparation of Protein Charge Ladders

The reactions used to form charge ladders convert residues that are charged at the pH value of interest (e.g the Lys ε-NH_2 group, which is ε-NH_3^+ at physiological pH values) into neutral species; certain modifications—for example, acylation of amines with succinic or glutaric anhydride—reverse the charge (Table 2).[19,54] When the reactions are not carried to completion, they result in statistical mixtures of derivatives of the protein; these derivatives differ in the extent of modification, and thus in the number of charged groups. We refer to the set of derivatives with the same number of modifications as a "rung" of the ladder. The

© 2006 Wiley-VCH Verlag GmbH & Co. KGaA, Weinheim

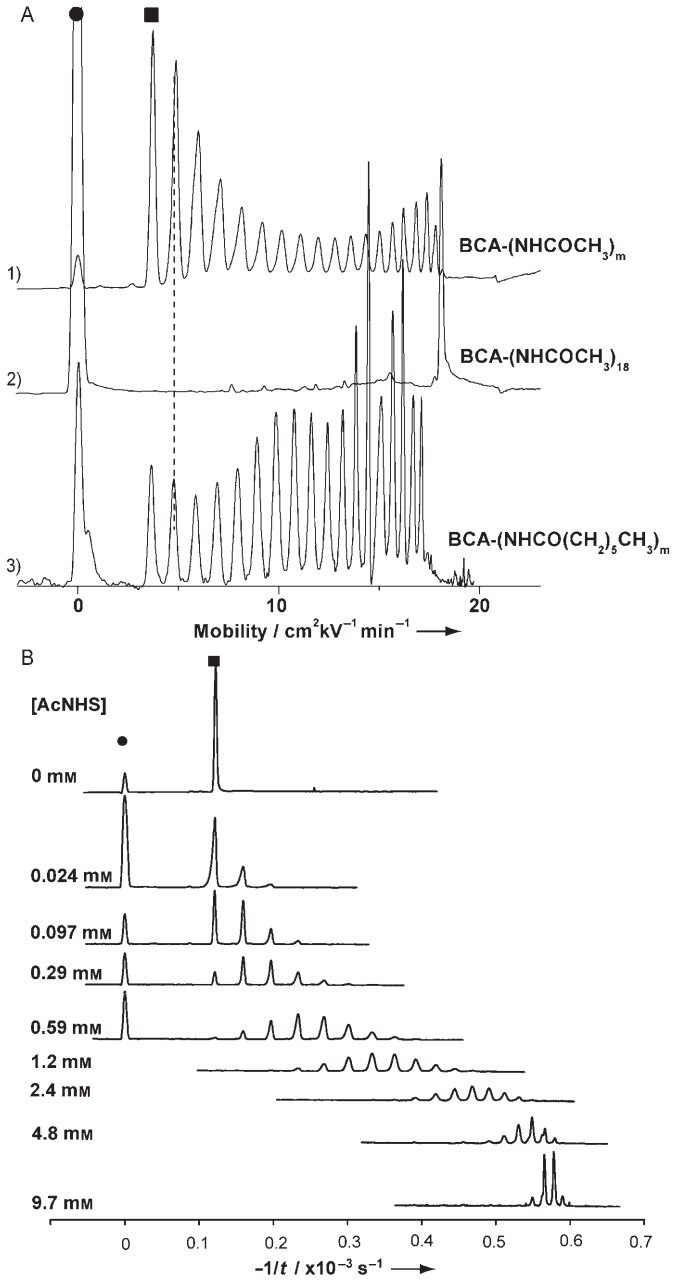

Figure 4. A) Electropherograms of charge ladders of bovine carbonic anhydrase II. 1) Charge ladder of BCAII generated with acetic anhydride (BCA-$(NHCOCH_3)_m$). 2) The reaction can be driven to completion to generate peracetylated protein (BCA-$(NHCOCH_3)_{18}$). 3) Charge ladder generated with hexanoic anhydride (BCA-$(NHCO(CH_2)_4CH_3)_m$). ● indicates native protein, and ■ indicates an electrically neutral marker (mesityl oxide or *p*-methoxybenzyl alcohol) used to monitor electroosmotic flow. A dashed vertical line indicates that the mobilities of the first rung of the acetyl and hexanoyl ladder are indistinguishable. Late rungs of the hexanoyl ladder show the influence of (probably) increasing drag. All separations are done in 25 mM Tris/192 mM Gly buffer on a capillary 47 cm long. B) High-resolution electropherograms of BCAII charge ladders generated with the *N*-hydroxysuccinimide ester of acetic acid. The acetylation reactions were conducted in borate buffer of pH 8.56 and analyzed in D_2O-based Tris-Gly buffer on a capillary 117 cm long. The scale of $-1/t$ is proportional to mobility μ [Eq. (30)]. (Adapted from Ref. [137].)

Table 2: Examples of possible modifications of the Lys, Asp, Glu, and Arg residues of a protein that result in a change in the charge of the residue.

Residue	Reagent	Product	ΔZ
$-(CH_2)_4NH_3^+$	$(CH_3CO)_2O$	$-(CH_2)_4NHCOCH_3$	−1
$-(CH_2)_4NH_3^+$	$(CH_3(CH_2)_4CO)_2O$	$-(CH_2)_4NHCO(CH_2)_4CH_3$	−1
$-(CH_2)_4NH_3^+$	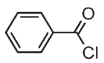	$-(CH_2)_4NHCOC_6H_5$	−1
$-(CH_2)_4NH_3^+$	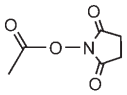	$-(CH_2)_4NHCOCH_3$	−1
$-(CH_2)_4NH_3^+$	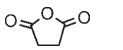	$-(CH_2)_4NHCO(CH_2)_2COO^-$	−2[a]
$-(CH_2)_4NH_3^+$	$N\equiv C-O^-$	$-(CH_2)_4NHCONH_2$	−1
$-CH_2COO^-$ or $-(CH_2)_2COO^-$	CH_2N_2	$-CH_2COOCH_3$ or $-(CH_2)_2COOCH_3$	+1
$-CH_2COO^-$ or $-(CH_2)_2COO^-$	EDAC[b]/ $NH_2OH\cdot HCl$	$-CH_2CONHOH$ or $-(CH_2)_2CONHOH$	+1
	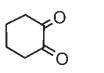	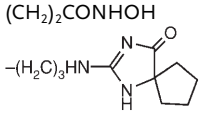	−1[c]

[a] In some circumstances, the reaction can form the cyclic, neutral intermediate. [b] 1-Ethyl-3-(3-dimethylaminopropyl)carbodiimide. [c] This product results when the reaction is carried out at pH > 12. Reactions carried out at pH 7–9 results in *N*,*N*-(1,2-dihydroxycyclohex-1,2-ylene)arginine (no change in charge), and pH 10–11 in multiple uncharacterized products.[142]

literature on protein modifications[135,136] lists many additional reactions that might be used to form charge ladders.

Acylation of ε-NH_3^+ residues of Lys by anhydrides or *N*-hydroxysuccinimide (NHS) esters of carboxylic acids annihilates a positive charge (ε-$NH_3^+ \rightarrow$ε-NHCOR) and makes the protein more negatively charged with each modification. Acylation of N-terminal α-NH_3^+ groups also occurs, but the difference in the pK_a values of α-NH_3^+ and ε-NH_3^+ groups allows for preferential acylation of one group over another at certain pH values, if necessary.[133]

The procedure for forming charge ladders by acylation of lysines usually involves the addition of 5–25 equivalents of an anhydride or an NHS ester (relative to the protein) to the solution of a protein in 10% v/v 0.1N NaOH (pH ≈ 10).[54,133] An excess of the reagent is required because the acylation reaction proceeds in competition with aqueous hydrolysis. For proteins with large numbers of lysine groups, we typically generate protein charge ladders showing complete sets of rungs by combining two batches of modified protein, one prepared using 10 equivalents of acylating agent, and one using 25 equivalents. This dual procedure favors the formation of the early and late rungs of the charge ladder; their combination gives a mixture containing all rungs. The reactions can also be carried out in buffers,[137] but the buffer must have low nucleophilicity so that reaction with the buffer does not compete with acylation. Carbamylation

 © 2006 Wiley-VCH Verlag GmbH & Co. KGaA, Weinheim

reactions using potassium cyanate can also be used to neutralize lysine residues by converting them into homocitrulline.[138]

Reactions of carboxylic acid residues (Glu-COOH, Asp-COOH) with diazo compounds[136,139] or with nucleophiles such as hydroxylamine[111] or glycine methyl ester[140] result in the annihilation of a complete or partial negative charge, and make the overall charge of a protein more positive. Another possibility is the reaction between arginine and α-dicarbonyl compounds.[141] The products of this reaction, however, vary depending on the pH value of the reaction, and have not been thoroughly characterized.[142]

Another class of acylating reagents that can be used to form charge ladders comprises reagents that themselves generate charge, such as succinic anhydride, 1,2,4-benzenetricarboxylic anhydride, and 1,2,4,5-benzenetetracarboxylic dianhydride.[54,143] Upon reaction and subsequent hydrolysis, these reagents introduce one, two, and three carboxylic acid groups, respectively, in place of a positively charged lysine residue. We use these reagents primarily to improve the resolution of the rungs of charge ladders of proteins of high molecular weight.

The reactions of Lys ε-NH_3^+ residues with anhydrides or NHS esters of large, more hydrophobic groups, such as hexanoyl or benzoyl (Figure 4), result in what we call "hydrophobic charge ladders." Here, we use the change in the charge of the Lys residue upon acylation primarily to count the number of hydrophobic groups added to the protein, and the main objective of acylation is to modify the hydrophobicity of the protein rather than the charge. We have also extended the idea of a ladder to hydrodynamic drag.[144] Hydrodynamic ladders are generated by reactions of lysine residues with NHS-activated poly(ethylene glycol) (PEG) chains (see Section 8.3).

We have driven some of these reactions to more than 90% completion in an aqueous phase by using an excess of the reagents and carefully controlling the reaction conditions:[145] these procedures generate a single species (the perfunctionalized proteins), rather than a mixture. The ability to generate a single, perfunctionalized version of a protein makes it possible to use analytical techniques other than capillary electrophoresis to characterize it.[131,146] Figure 1b and 4 show electropherograms of different ladders of BCA, made with acetic anhydride, hexanoic anhydride, and hydroxylamine, as well as a demonstration of a peracetylated BCA.

6.2. Characterization and Analysis of Charge Ladders by Capillary Electrophoresis

We analyze protein charge ladders by capillary electrophoresis (CE) in free solution. CE separates molecules on the basis of competition between electrokinetic and hydrodynamic forces.[127] In comparison to other techniques for separating biomolecules based on charge—such as isoelectric focusing (IEF), poly(acrylamide) gel electrophoresis (PAGE), or ion exchange chromatography—CE offers high resolving power, minute consumption of material, rapid analysis, and ease of operation.

The basics of CE and its application to charge ladders have been reviewed extensively,[57,127,147] and thus we describe it here only briefly. The electrophoretic mobility of an analyte (μ [$m^2 V^{-1} s^{-1}$]), which is defined as the steady-state velocity per unit applied field, results from the balance of two opposing forces: an electrokinetic force that accelerates the charged molecule and a hydrodynamic drag force that slows it. The mobility μ can be expressed by Equation (19), where Z

$$\mu = \frac{eZ}{f_{\mathrm{eff}}} \tag{19}$$

(with no units) is the net charge of the molecule, e [C] is the charge of an electron, and f_{eff} [$N s m^{-1}$] is the effective hydrodynamic drag coefficient. The value of f_{eff} is a complex function of the shape and size (molecular weight) of the protein and the properties of the electrophoretic buffer (viscosity and ionic strength).

The experimentally observed mobility μ_{obs} of a molecule is the sum of two terms: the electrophoretic mobility μ of the molecule itself and the electroosmotic velocity (the velocity of the buffer) per unit field strength μ_{os}. Electroosmotic flow can be measured by adding an electrically neutral marker to the solution of the protein injected into the capillary.

The electrophoretic mobility of an analyte is thus calculated from the measured values of the migration times of the analyte and a neutral marker from Equation 20, where

$$\mu = \mu_{\mathrm{obs}} - \mu_{\mathrm{os}} = \frac{L_t L_d}{V}\left(\frac{1}{t} - \frac{1}{t_m}\right) \tag{20}$$

V [V] is the applied voltage, L_t [m] is the total length of the capillary, L_d [m] is length of the capillary from the inlet to the detector, t_{nm} [s] is the time that the neutral molecule takes to reach the detector, and t [s] is the time that the analyte takes to reach the detector. The mobility of the neutral marker is thus set to zero.[148]

CE separates the collection of derivatives of a protein charge ladder in free solution into the individual peaks or "rungs" of the ladder, with each rung containing the same number of modifications, and approximately the same net charge. Since small reagents such as acetic anhydride add <1% of mass or volume to the protein, they do not significantly alter the hydrodynamic drag (Figure 4), and the rungs of the charge ladder are separated by CE primarily on the basis of charge. Values of mobilities of the nth rung of the ladder, μ_n, for all the rungs of the charge ladder are measured in a single experiment; typical times for separation range from 3 to 30 minutes.

Capillary electrophoresis can resolve changes in μ of about 1×10^{-9} $m^2 V^{-1} s^{-1}$. The ability of CE to resolve the rungs of a particular charge ladder depends on the difference in the mobility caused by a change in a single unit of charge. We found empirically that proteins with molecular weights below 50 kDa form resolvable charge ladders in which the rungs differ by about 1 unit of charge.[54] In larger proteins (> 50 kDa), the change in one unit of charge does not change the μ value sufficiently to give resolvable rungs of the ladders. In this case, reagents that change the charge by more than one

© 2006 Wiley-VCH Verlag GmbH & Co. KGaA, Weinheim

unit per modification can be used to resolve the rungs of the ladder.[54]

For small proteins such as insulin (MW = 3 kDa), regioisomers with different acetylation patterns can sometimes be resolved and assigned.[133] The assignment of the acetylation patterns in insulin can be done by exploiting the differences in the pK_a values of the lysine group and the two N-terminal α-NH_2 groups, and by carrying out acetylation reactions in buffers of different pH values. Such assignments would be hard to carry out in a larger protein containing multiple lysine residues of similar reactivities.

Interactions between proteins and the walls of the capillary can complicate the analysis of charge ladders by CE. We usually analyze negatively charged proteins (that is, proteins analyzed at values of pH > p*I*; p*I* = isoelectric point of the protein) on bare silica capillaries. Such capillaries are negatively charged because of the ionization of silanol to siloxide groups ($SiOH \rightleftharpoons SiO^- + H^+$, $pK_a \approx 2.2$).[127] To analyze basic proteins (p*I* > pH of the electrophoresis buffer), it is necessary to reverse the charge of the capillaries to minimize the adsorption of positively charged proteins onto the negatively charged capillary wall. A variety of chemical methods can be used to modify and screen the negative charge on the wall of the capillary through covalent chemical modification[149] or physical adsorption of polymers.[134,150] We choose the straightforward and convenient method of noncovalent adsorption of a cationic polymer such as polybrene (Poly(*N*,*N*,*N*′,*N*′-tetramethyl-*N*-trimethylenehexamethylenediammonium dibromide)) to reverse the charge of the capillary to analyze basic proteins.[134,147] A technical difficulty in analysis arises when the charge ladder of a protein contains both net positively and negatively charged species: the rungs having charge opposite to that of the capillary tend to adsorb to its walls.

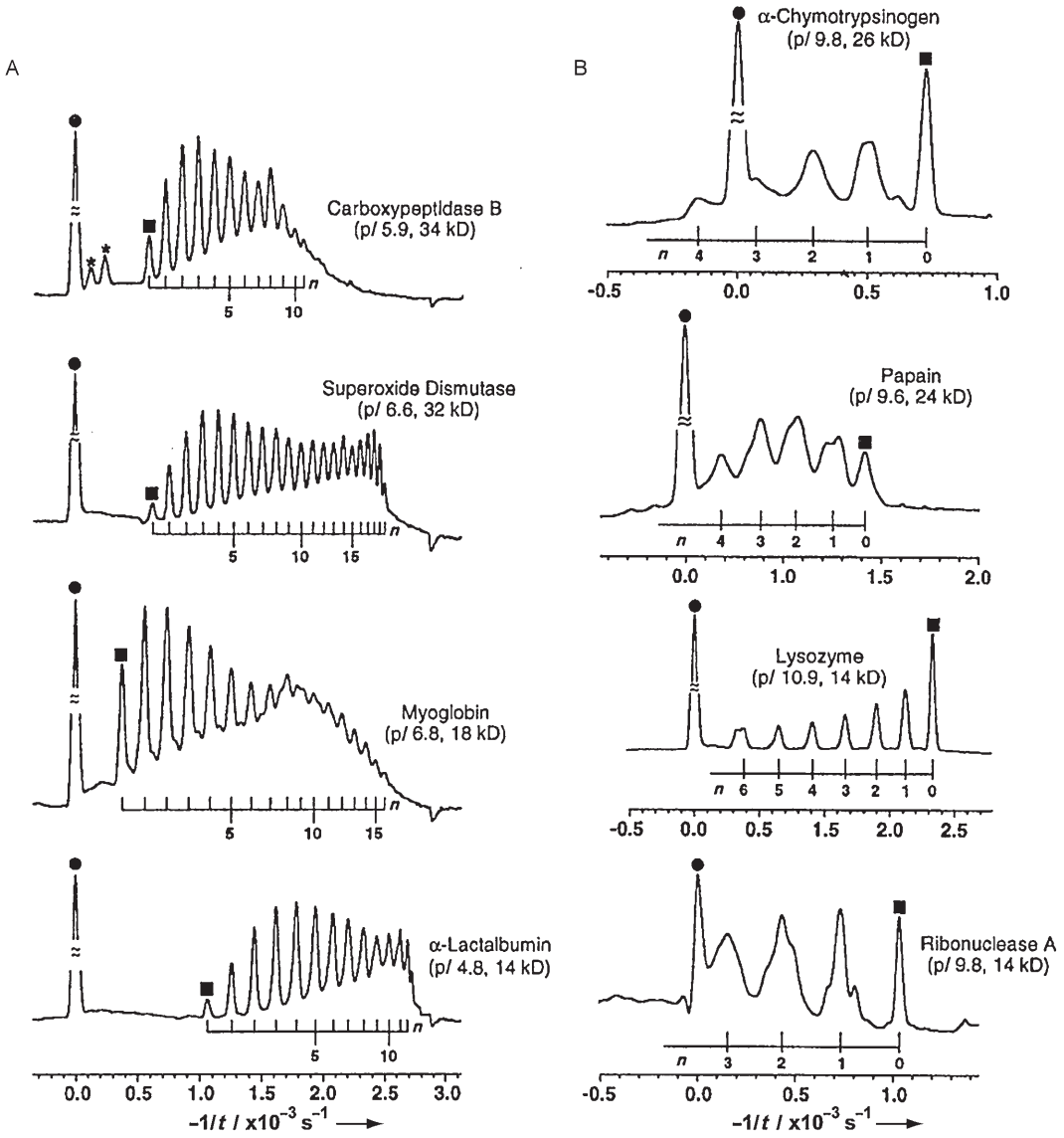

Figure 5. Examples of charge ladders formed by acetylation of Lys ε-NH_3^+ residues. ●: neutral marker, ■: native protein, and *: impurities in the starting sample. The number of acetylated Lys groups (*n*) is indicated below each electropherogram. A) Charge ladders of proteins having values of p*I* < 8.4, analyzed on an uncoated negatively charged capillary. B) Charge ladders of proteins having values of p*I* > 8.4, analyzed on a polybrene-coated (positively charged) capillaries. (Reproduced with permission from Ref. [54].)

 © 2006 Wiley-VCH Verlag GmbH & Co. KGaA, Weinheim

Figure 5 shows a survey of different proteins—both basic and acidic, of various molecular weights, and containing various numbers of lysine residues—for their ability to form resolvable charge ladders. While many proteins form useful charge ladders, some (e.g. myoglobin) show the rungs of the ladder superimposed on a broad background; we do not understand the shape of those electropherograms. We believe we can form charge ladders of most proteins, unless acylation of lysine residues spontaneously denatures the protein or causes the derivatives to aggregate.

Increased resolution of the rungs of the charge ladder can be achieved by carefully choosing the conditions of the separation. We have worked out the conditions for baseline separation of the rungs of a charge ladder of carbonic anhydrase by using a long (117 cm) capillary and D_2O-based Tris-Gly buffer.[137] We believe that the D_2O-based buffer increases the resolution of the separation by increasing the viscosity of the buffer in comparison to the H_2O-based buffer. Figure 4B shows high-resolution electropherograms of early and late rungs.

7. Models for the Analysis of Data from Capillary Electrophoresis

Electrokinetic models, such as those used in colloidal science, can aid in the analysis of data from charge ladders, and can help to characterize the physical properties of proteins (that is, values of net charge and effective hydrodynamic size). As we show, a priori prediction of electrophoretic mobilities of proteins is challenging because it requires the combination of two models: an electrostatic one, to predict the distribution of charges and values of the electrostatic potential in the vicinity of the protein, and an electrokinetic one, which uses the values of electrostatic potential, information about the size and shape of the protein and properties (viscosity, concentration of different ions) of the solution to predict values of electrophoretic mobility.

The values of mobility of the rungs of a charge ladder with the smallest magnitude of net charge typically correlate linearly with the number of modifications and with the charge, if we assume the change in charge ΔZ between the rungs to be constant. One of the more useful and straightforward models for the analysis of the mobility data from a capillary electrophoresis experiment is that of Hückel,[151] with subsequent modification by Henry.[152] This model relates the mobility (μ [$m^2V^{-1}s^{-1}$]) of a particle to its surface potential (ψ_s [V]) through Equation (21), where ε_0 [$CV^{-1}m^{-1}$] is the permittivity of a vacuum, ε is the dielectric constant of the solution medium, η [Pa s] is the viscosity of the solution, κ [m^{-1}] is the inverse Debye length, and R [m] is the radius of the particle of interest. The function $f(\kappa R)$[153] added by Henry ranges in value from 1.0 to 1.5 and extends the applicability of the model of Hückel to particles of arbitrary size with respect to the Debye length.

$$\mu = \frac{2\varepsilon\varepsilon_0\psi_s}{3\eta} f(\kappa R) \tag{21}$$

The Debye model relates the surface potential ψ_s to the charge Z [Eq. (22)] and comes from the solution to the linearized Poisson–Boltzmann equation for a spherical object assuming a low average absolute surface potential ($|\psi_s| < 25$ mV; this assumption is known as the Debye–Hückel approximation[154]) and uniform charge distribution. Combining Equations (21) and (22) results in a simple expression that relates mobility directly to net charge [Eq. (23)]. The mobilities extracted from a capillary electrophoresis experiment for the rungs of a protein charge ladder can be analyzed, using Equation (23) to extract the values of charge of each rung, provided that the parameters η, κ, and R are known.

$$\psi_s = \frac{eZ}{4\pi\varepsilon_0\varepsilon R(1+\kappa R)} \tag{22}$$

$$\mu = \frac{eZ}{6\pi\eta R(1+\kappa R)} f(\kappa R) \tag{23}$$

Alternatively, Henry's model can be used in conjunction with mobilities from protein charge ladders to extract values of the hydrodynamic radius of a protein.[58] The procedure requires estimating or assuming the value of ΔZ, and involves a linear least-squares fit of the values of mobility of the first several rungs of a charge ladder to Equation (23). This procedure provides a value of the effective hydrodynamic radius R of the protein, which can be interpreted as the radius of a sphere that would have the same hydrodynamic drag as the protein.

The assumptions that underlie these colloid models do not describe proteins accurately. The Debye model assumes that the charge on the surface of a protein is uniformly distributed; since charged groups on proteins are clearly localized, this assumption is an approximation. Proteins are also only approximately spherical; theoretical predictions of the effective hydrodynamic radius R of a protein based on its real shape is an involved task that requires atomic-level structural data, and consideration of the effects of layers of hydration by the solvent.[155] Both the electrokinetic models of Henry and Hückel and the electrostatic model of Debye are valid only when the absolute average surface potential of the protein is less than about 25 mV.[151] As the magnitude of the charge on the protein increases beyond this value, the use of the Debye–Hückel approximation is no longer valid. Also, the ionic atmosphere surrounding the protein can no longer be assumed to be at its equilibrium value: the applied field can distort (that is, polarize) the ion atmosphere, and the finite mobility of these ions results in a distortion of this atmosphere as the protein moves (ion relaxation). The models of Hückel and Henry are, however, straightforward to use and can provide quick estimates of the net charge of a protein Z°_{CE} (defined in Section 2.1) under a particular set of conditions, provided there is some estimate of R.

There have been multiple extensions of the model of Henry and Hückel to address these approximations.[156–158] Yoon and Kim[156] relaxed the assumption that the protein is a sphere, and instead treated the protein as an ellipsoid with uniform surface potential; the electrostatics are still treated with the Debye–Hückel approximation, and ion relaxation

 © 2006 Wiley-VCH Verlag GmbH & Co. KGaA, Weinheim

and polarization are ignored. If this model is parameterized with experimental protein diffusivities, and with some estimate of the shape of the ellipsoid from crystallographic data, it accurately predicts experimental mobilities for charge ladders[159] if the net absolute protein charge is low and the average absolute surface potential is less than approximately 25 mV.

O'Brien and White[157] treated the protein as a sphere with charge uniformly distributed on the surface; this model uses the nonlinear Poisson–Boltzmann equation and includes the effects of polarization and relaxation of ions. Since this model treats the electrokinetic problem for a uniformly charged sphere and its ion atmosphere exactly, and without further approximation, it is referred to in the colloids literature as the "Standard model" of electrokinetics.[160]

To assess the limits of Henry's model for describing the mobility of proteins in charge ladders, we compared experimental values of electrophoretic mobility of the charge ladder of HCAII with predictions from the models of O'Brien and White and the model of Henry using the electrostatic potential calculated with the Debye–Hückel theory [Eq. (22)].[58] Calculations with the Standard model were carried out using two values of ΔZ: a value of -1.0 to represent the "ideal" case and a value of -0.9 to approximate the effects of charge regulation (see Section 8.1). Figure 6 shows that both models give values that agree with the experimental mobilities for the rungs of the charge ladder with the smallest absolute values of net charge. The net charge of the protein becomes increasingly more negative with increasing number n of acetylated lysine ε-NH_3^+ groups, and the values of mobility no longer correlate linearly with n. The onset of nonlinearity at $n = 8$ in the experimental data coincides with deviation of the nonlinear Standard model from the linear model of Henry. Thus, both the nonlinear electrostatics and ion polarization and relaxation contribute to the observed nonlinearity. The fact that the experimental data fall between the two theoretical curves is consistent with other estimates of ΔZ for HCAII (Section 8.1).

The boundary element (BE) model of Allison et al.[161] requires the fewest approximations in modeling the electrokinetics of proteins. This approach uses the crystal structure of the protein to construct its hydrodynamic shear surface (that is, the particle–solution interface where the local viscosity changes from a high to the bulk value[161]) and to calculate its electrostatic potential. The BE model is thus an extension of the Standard model to particles with shapes and distribution of charge that more accurately describe the protein than does the Standard model.

In collaboration with Allison, we compared values of mobility calculated by the BE model with experimental mobilities of the charge ladders produced from five different proteins (bovine α-lactalbumin, hen egg-white lysozyme, bovine superoxide dismutase, human carbonic anhydrase II, and hen ovalbumin).[159] All calculated mobilities were in good-to-excellent agreement with experiments. The BE model also allowed the prediction of the change in mobility resulting from an incremental change in the charge of one unit. Comparison of these predicted changes in mobility with measured changes arising from modification of the charged

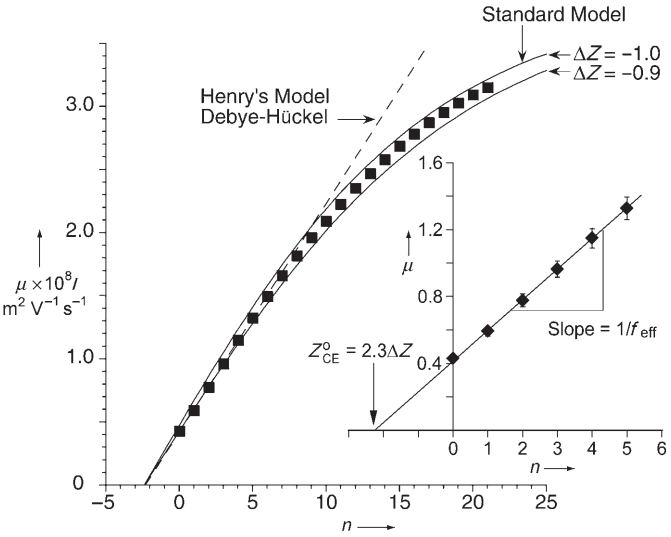

Figure 6. Values of the electrophoretic mobility μ of the rungs of the acetyl charge ladder of HCAII, plotted as a function of the number n of $NHCOCH_3$ groups on the protein. -----: values of μ predicted by Henry's equation using the electrostatic potential calculated from the Debye–Huckel equation; ——: values of μ predicted by the standard model of O'Brien and White, determined using values of $\Delta Z = -1.0$ and $\Delta Z = -0.9$. The inset shows the linear section of the graph of μ versus n. The solid line is a linear least-squares fit of these data: the intercept of the x-axis gives the number of amine groups that would have to be modified to make the electrophoretic mobility of the protein, and by inference the net charge of the protein, zero. The intercept indicated by the arrow in the inset shows that 2.3 amine groups would have to be added to the protein in this case. The net charge of the unmodified protein determined by CE is $Z^{\circ}_{CE} = 2.3\Delta Z$; here ΔZ is the change in net charge as a result of the acetylation of a Lys ε-NH_3^+ group. The value of ΔZ must be determined or estimated by some other means to assign a quantitative value to Z°_{CE}. The slope of the line gives the reciprocal of the effective hydrodynamic drag coefficient $1/f_{eff}$ of the protein.

groups provided estimates of ΔZ that were in reasonable agreement with values calculated using models of charge regulation (Section 8.1).[159] The main limitations to the BE calculations are that they are not yet available in an easily distributed software package, and are expensive computationally. This approach also requires knowledge of the crystal structure of the protein and an independent measure of the translational diffusion coefficient of the protein.

We found that the main challenge to the accurate prediction of electrophoretic mobilities of proteins is in the modeling of the electrostatics—the distribution of charged groups on the protein—and not in modelling the electrokinetics. Comparison of measured electrophoretic mobilities with predictions from electrokinetic models may be a useful approach to the development and testing of new models of electrostatics and proton equilibria in proteins.

8. Charge Ladders for Measuring the Net Charge and Hydrodynamic Drag of a Protein

Charge ladders provide a self-calibrating tool useful for the estimation of certain basic physical parameters of a

 © 2006 Wiley-VCH Verlag GmbH & Co. KGaA, Weinheim

protein such as charge and hydrodynamic radius, both of which can be related to the electrophoretic mobility. Plots of the values of electrophoretic mobilities of the rungs of a protein charge ladder versus the number n of modifications typically shows a linear correlation, at least for small values of n (inset of Figure 6). If we know the change in charge ΔZ per modification of an ε-NH_3^+ group, and replot the mobility of the rungs versus the change in charge of each rung $n\Delta Z$, we are then able to determine the net charge of the unmodified protein Z°_{CE} by extrapolation of the best-fit line to the intersection with the x-axis. Equation (24) expresses the mobility of rung n as a function of Z°_{CE} and ΔZ.

$$\mu_n = \frac{eZ^n_{CE}}{f_{eff}} = \frac{e(Z^{\circ}_{CE} + n\Delta Z)}{f_{eff}} \tag{24}$$

This analysis (inset of Figure 6) allows the determination of the net charge of a protein in the absence of any models of electrophoresis and underlying assumptions. It requires, however, a value of ΔZ—the change in charge upon acetylation—to calibrate the x-axis.

8.1. Estimating the Change in Charge ΔZ upon Acetylation

The value of ΔZ depends both on the initial extent of protonation of the charged group being modified, that is, on the pK_a value of the group and on the pH value of the solution, and on the response of the protein to the modification. The Lys ε-NH_3^+ groups (nominal p$K_a = 10.4$) are 99% protonated at pH 8.4 while the Glu and Asp -COO^- groups (p$K_a \approx 4$) are more than 99% deprotonated. The elimination of charge on the Lys ε-NH_3^+ groups or the Glu/Asp -COO^- groups would then be expected to result in $|\Delta Z| = 1$ at, or close to, this pH value. The discussion in Section 2 of the protein as a network of ionizable groups rather than as a collection of independent charges emphasizes, however, that $|\Delta Z| < 1$. Other ionizable groups on the protein adjust to a change of electrostatic potential on the surface by shifting their charges. This shift reduces the magnitude of the change in net charge. Whether this shift is considered to reflect changes in pK_a values or in local concentration of protons at the protein–solvent interface is immaterial: these two mechanisms are equivalent both mathematically, and in their effect.[106] It is also possible that the adjustment take place through binding of the buffer ions. This type of charge adjustment is, however, more likely to be specific to the structure of the protein and composition of the buffer, rather than is that due to proton equilibria, and thus difficult to generalize or model.

8.1.1. The Linderstrøm-Lang Model

A simple model to use in analyzing this cooperative interaction among ionizable groups is that of Linderstrøm-Lang,[108] which was developed originally to interpret the curves of pH titrations of solutions of proteins. Menon and Zydney were the first to apply this model to the analysis of charge ladders.[105] The two key assumptions of the Linderstrøm-Lang model (which we abbreviate as the "LL model") are that 1) the protein is spherical and has no detailed structure and 2) the distribution of electrostatic potential on the surface of this spherical protein is uniform. The model assumes that the concentration of the protons near the surface $[H^+_{surface}]$ follows the Boltzmann distribution, described by Equation (25), where $[H^+]$ is the concentration of protons in the bulk solution.

$$[H^+_{surface}] = [H^+]\exp\left(\frac{-e\psi_s}{k_B T}\right) \tag{25}$$

The ionization state υ_I of each ionizable amino acid is determined by Equation (26), where $pH_{surface}$ is defined as $-\log[H^+_{surface}]$ and p$K_{a,i}$ is the ionization constant of the residue i in the absence of an electrostatic potential. The net charge Z°_{LL} of the protein is determined by summing all charges [Eq. (27)].

$$\upsilon_i = \frac{1}{1 + 10^{(pH_{surface} - pK_{a,i})}} \tag{26}$$

$$Z^{\circ}_{LL} = \sum_{\text{basic groups}} \upsilon_i - \sum_{\text{basic groups}} (1 - \upsilon_i) \tag{27}$$

The net charge Z°_{LL} of a protein calculated using the LL model can be related to its surface potential ψ_s by the Debye equation [Eq. (22)], and calculations are repeated iteratively using Equations (25)–(27) and (22) until the solution converges to a final value of Z°_{LL}. This calculation can be applied to the unmodified protein, and to the consecutive rungs of the protein charge ladder derived from it, in order to estimate the net charges Z°_{LL} and Z^n_{LL}, and thus the difference in charge upon a modification $\Delta Z = {}^1_{LL}\text{-}Z^{\circ}_{LL}$.

Menon and Zydney[105] applied the LL model to the acetyl charge ladders of bovine carbonic anhydrase to calculate the net charge of the rungs. They compared the results of the calculations to the values of net charge estimated from the measured values of electrophoretic mobility using Henry's model of electrophoresis. They concluded that cooperativity had a significant effect on the value of ΔZ, changing it from the ideal value of -1 to -0.86 in buffer of pH 8.4, $I = 10$ mM. We[106] compared values of net charge measured from the linear regression analysis with the LL calculations and with the charge calculated from experimental mobilities using the Hückel model of electrophoresis, and concluded that the value of ΔZ for the early rungs of the ladder of BCA was -0.93 at pH 8.4, $I = 10$ mM.[106] The difference in the value of ΔZ between our calculation and those of Menon and Zydney results from our consideration of details of the structure of BCA—post-translational acetylation of the N-terminus, coordination of three histidine residues and water to the Zn^{II} cofactor, and ionization of the water ($ZnOH_2^{2+} \rightleftharpoons ZnOH^+ + H^+$, p$K_a \approx 7$).[162] With these inclusions, the calculations agree that $\Delta Z \approx 0.9$, and perhaps more importantly, that the combination of the LL and Henry models provide a useful and reliable method to estimate ΔZ.

We have also studied the dependence of ΔZ for the acetyl charge ladder of BCA on the ionic strength and pH value of

© 2006 Wiley-VCH Verlag GmbH & Co. KGaA, Weinheim

the solution (Figure 7). The ability of each type of residue to participate in charge regulation depends on the pH value of the solution: as the pK_a value of a residue and the pH value of

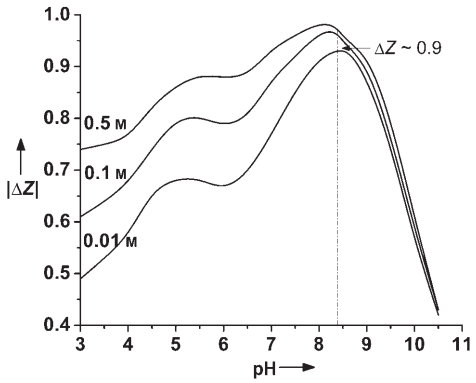

Figure 7. Plot of Linderstrøm-Lang calculated change in charge $|\Delta Z|$ upon acetylation, for a low number of modifications, for BCAII at three different ionic strengths. The vertical line indicates the pH value of the Tris-Gly buffer used in the CE. Increasing ionic strength diminishes the effect of charge regulation, and brings $|\Delta Z|$ close to unity at pH 8. (Reproduced with permission from Ref. [106].)

the solution approach one another, large adjustments in the ionization state of that residue can occur upon a change in the local electrostatic potential at the protein–solution interface. At physiologically relevant pH values of 7–8, among the major functional groups, the histidine residues (p$K_a \approx 6.5$) are most sensitive to electrostatic interactions and most prone to adjust their extent of ionization.[163] Other amino acids (Lys, Arg, Tyr, Glu, Asp) can also adjust to the change in the electrostatic potential, albeit to a lesser extent. BCAII, for example, contains the following numbers of ionizable groups: 18 Lys, 30 Asp/Glu, 9 Arg, 8 Tyr, 11 His, 1 C-terminal α-CO_2^-, 1 $ZnOH^+$. The range of pH values at which the deviation of the value of $|\Delta Z|$ from the nominal value of 1.0 is minimal is pH 8.0–8.5 (Figure 7). At high pH values, the lysine ε-NH_3^+ groups deprotonate, and at low pH values, the aspartate and glutamate CO_2^- groups easily protonate, thus reducing the magnitude of ΔZ. Increasing the ionic strength diminishes the effect of charge regulation through more efficient shielding of charges. Although the LL model makes several important simplifying assumptions, and neglects the explicit distance dependence of the electrostatic force between charged residues, it clarifies the cooperativity among ionizable groups and factors that influence it.

8.1.2. *Poisson–Boltzmann Monte Carlo (PBMC) Simulations*

We also used CE and charge ladders to measure the pK_a values of the N-terminal α-NH_3^+ group of two forms of lysozyme:[107] the native protein (with no $NHCOCH_3$ groups) and the modified protein with all six of its Lys ε-NH_3^+ groups acetylated (Figure 8A). If the ionization states of the Lys ε-NH_3^+ groups influence the ionization of the α-NH_3^+ group, then the pK_a value of NH_3^+ group in the native lysozyme will differ from that in the modified protein. We then compared the experimentally determined pK_a values with those determined by the LL model, and with those from Monte Carlo

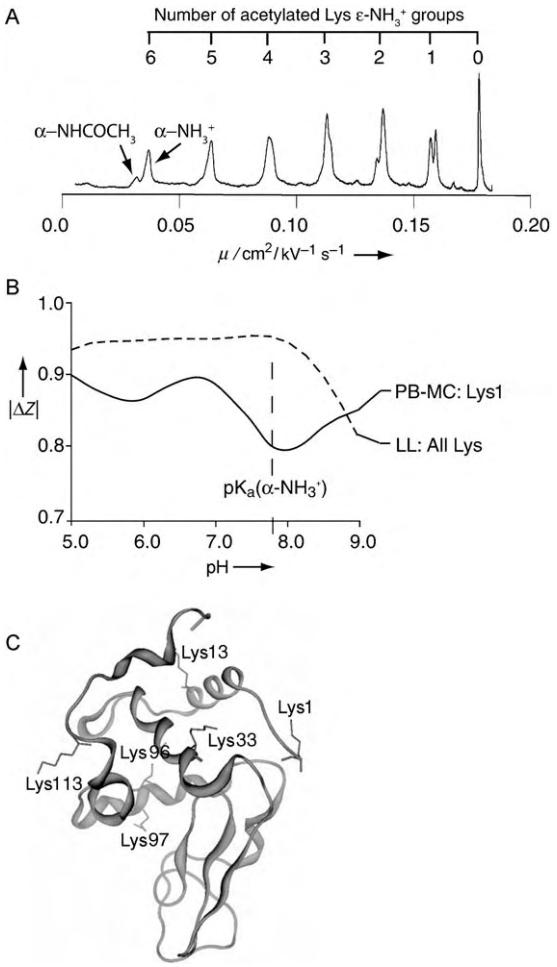

Figure 8. A) High-resolution electropherogram of the charge ladder of lysozyme showing the splitting of the rungs because of the presence of species with and without acetylated N-terminal α-NH_3^+ groups. B) The change in net charge ΔZ of lysozyme predicted by the PB-MC model as a result of the specific acetylation of Lys1 as a function of pH, and average ΔZ value calculated with the LL model. The LL model does not differentiate between different Lys ε-NH_3^+ groups. C) A ribbon diagram showing the position of the different lysine residues.

sampling of protonation states based on electrostatic potentials from numerical solutions of the linearized Poisson–Boltzmann equation (PB-MC model). Lysozyme is a good model for this kind of detailed study, because the pK_a values of all of its ionizable groups have been determined experimentally[100] and calculated by using continuum methods.[164]

The experimental measurements of the pK_a values of the α-NH_3^+ group in native and modified lysozyme showed that the pK_a values of the α-NH_3^+ group differed by 0.3 units at low ionic strength ($I = 33$ mM; pK_a(α-NH_3^+, native) $= 7.5 \pm 0.1$, pK_a(α-NH_3^+, peracetylated) $= 7.8 \pm 0.1$). The values of these two pK_a values at high ionic strength ($I = 108$ mM) were the same (p$K_a = 7.9$). This observation indicates that high salt concentrations can screen the cooperative interactions among charged groups in this small protein sufficiently that they become undetectable.

The LL model predicts that $\Delta Z = -0.94$ upon acetylation of a Lys group at any position at pH 8.4 ($I = 33$ mM), and is

 © 2006 Wiley-VCH Verlag GmbH & Co. KGaA, Weinheim

approximately constant between pH 5.5 and 8 (Figure 8B). By using the PB-MC model, we were able to study in detail the response of lysozyme to the acetylation of a specific lysine residue.[107] We found that values of ΔZ upon acetylation of Lys13, Lys33, Lys97, and Lys116 agreed well with the value of ΔZ predicted by the LL model; the values of ΔZ upon acetylation of Lys1 and Lys96 differed significantly from the results from the LL model: The ΔZ value decreases to about 0.8 at pH 8 in the case of Lys1, and decreases to approximately 0.7 at pH 6 for Lys96. The reason behind these differences is, we believe, the proximity of other ionizable residues to the lysines of interest. For example, the α-NH_3^+ group of lysozyme and the ε-NH_3^+ group of Lys1 are only 0.7 nm apart in the crystal. The α-NH_2 group would therefore be expected to change its extent of protonation significantly under the influence of a change in charge on the Lys1 residue. A similar argument can be applied to His15, which is located only 0.8 nm away from Lys96.

In general, we found that significant cooperativity in ionization states only exists between acetylated lysine residues and other titratable groups on lysozyme separated by less than about 1.5 nm. This specific cooperativity can contribute up to approximately 0.2 units to the reduction in magnitude of ΔZ per pair of closely spaced residues. Interactions of lysine residues with a number of other distant titratable groups can contribute about 0.1 units to the reduction in magnitude of ΔZ.

The results of the detailed PB-MC model can be expressed by a simple empirical relationship, originally developed by Lee et al.[165] [Eqs. (28) and (29)]. This relationship describes the cooperativity in proton binding between titratable groups in terms of a shift of the pK_a value by using a screened Coulombic potential (SCP) that depends explicitly on the distance r_{ij} between the two groups on the protein. The cooperativity between groups is modeled by using the Debye–Hückel model with the dielectric constant ε_{eff} as a fitting parameter. This relationship should be useful for the quick analysis of cooperative interactions between specific groups i and j to identify those large enough to influence the values ΔZ.

$$\Delta\psi_{ij} = \frac{e}{4\pi\varepsilon_0\varepsilon_{eff}}\frac{\Delta Z_j}{r_{ij}}\exp(-\kappa r_{ij}) \quad (28)$$

$$\Delta pK_{a,ij} = \frac{e\Delta\psi_{ij}}{2.303 k_B T} \quad (29)$$

8.1.3. Determination of ΔZ though Independent Measure of the Hydrodynamic Radius of Proteins (The Linear Regression–Taylor Dispersion Method, LR-TD)

We propose another method for calibrating the value of ΔZ for the analysis of charge ladders.[166] This method involves independent measurement of the diffusivities of proteins by using the analysis of the dispersion of the analyte sample in pressure-driven flows through thin capillaries.[167,168] The concentration profile of the analyte, which is shaped by the axial convection and radial diffusion, is related to the diffusivity of the protein through the expression of Taylor,[169] and then to the hydrodynamic radius R through the Stokes–Einstein equation. Conveniently, the concentration profile of the analyte can be measured in a standard capillary electrophoresis setup, equipped with pressure flow capability.[166,168]

With the experimentally determined values of R, one can determine the effective hydrodynamic drag f_{eff} of proteins by Henry's law of electrophoresis, and thus ΔZ [Eq. (24)]. Table 3 shows the results for the measurement of diffusivity D_0 for several proteins by using analysis of dispersion, calculation of R from the D_0 value, and subsequent estimation of the ΔZ value through linear regression (abbreviated as the LR-TD method). The Table also compares the ΔZ values from the LR-TD approach with those calculated by the model of Linderstrøm-Lang and by the screened Coulombic potential approach. In most cases, the values of ΔZ agree well among the three methods for most proteins and conditions, although there is no consistency in over- or under-estimation of ΔZ by one method or another. It is possible that the large discrepancy in the case of α-lactalbumin is due to the partial denaturation of the protein.[170]

Table 3: Comparison of ΔZ found by linear regression/Taylor dispersion method (LR-TD) with ΔZ calculated by Linderstrøm-Lang (LL) and screened Coulombic potential (SCP) models.

Protein	D_0[a] [$\times 10^6$ cm s^{-1}]	R [Å]	I [mM]	ΔZ, LL-TD	ΔZ, LL[b]	ΔZ, SCP
BCAII	0.939 ± 0.009	26.1 ± 0.2	8	-0.87 ± 0.01	-0.91	-0.93
BCAII			33	-0.97 ± 0.01	-0.93	-0.95
BCAII			133	-0.97 ± 0.01	-0.95	-0.97
α-lactalbumin	1.10 ± 0.01	22.3 ± 0.2	8	-0.81 ± 0.02	-0.93	
α-lactalbumin			28.1	-0.96 ± 0.02	-0.95	
lysozyme	1.19 ± 0.02	20.6 ± 0.2	8	-0.86 ± 0.02	-0.91	-0.86
lysozyme			33	-0.93 ± 0.02	-0.94	-0.92
lysozyme			108	-0.98 ± 0.02	-0.96	-0.95
myoglobin	1.21 ± 0.02	20.2 ± 0.3	8	-0.82 ± 0.02	-0.91	
ovalbumin[c]	0.730 ± 0.002	33.5 ± 0.1	8	$+0.91 \pm 0.01$	$+0.91$	

[a] No dependence of D_0 and thus R on ionic strength was found. [b] Values of R, used for LL calculations are the experimentally determined values obtained by the Taylor dispersion method. [c] Positive charge ladder formed by amidation of carboxylic acid residues.

8.1.4. Conclusions concerning the Change in Charge ΔZ upon Acetylation

Charge regulation, or cooperativity in proton equilibria, must be included in the analysis of charge ladders. Annihilation of charge on one group of a protein perturbs the extent of protonation of other groups, in the direction that tends to decrease the net change in charge $|\Delta Z|$. Calculations of accurate values of ΔZ will increase the accuracy of the parameters extracted from charge ladders.[107] PB-MC mod-

© 2006 Wiley-VCH Verlag GmbH & Co. KGaA, Weinheim

eling or the empirical relation [Eqs. (28), (29)] requires the crystal structure to estimate the value of ΔZ. If only the sequence of a protein is known, the LL model can quickly provide an estimate of ΔZ. The LR-TD method provides an experimental way of determining both R and ΔZ values at any value of pH or ionic strength without requiring that the crystal structure or sequence of the protein be known. For most proteins, however, we believe that using a value of $\Delta Z = 0.9 \pm 0.05$ at pH 8.4 and $I = 10$ mM will minimize the error in calculations based on charge ladders.

8.2. Determination of Net Charge and Hydrodynamic Drag

When we have a value of ΔZ, we can determine the net charge of the protein under the conditions of electrophoresis by linear extrapolation (Figure 6). For HCAII in Tris-Gly buffer (25 mM Tris, −192 mM Gly, pH 8.4, $I = 10$ mM, 25 °C) with the ΔZ value estimated as −0.90, $Z^{\circ}_{CE} = -2.1$. This value differs from the value of charge calculated from the sequence of the protein Z_{seq} by almost a full unit of charge, with $Z_{seq} = -1.2$. This difference results from the fact that values of Z_{seq} are calculated using standard values of pK_a that neglect the unique electrostatic environment—including the effects of charge regulation—of the particular protein.

The slope of the linear regression line through the values of mobility of the charge ladder depending on the number of rungs n provides the value of the effective hydrodynamic drag f_{eff} of the protein [Eq. (24)].[58] The effective hydrodynamic drag can then be converted into the hydrodynamic radius R of the protein by using Henry's model of electrophoresis (Section 7). Such analysis, of course, would be of interest only if ΔZ is estimated by a method other than LR-TD or simply assumed. The value of R for HCAII was estimated to be 2.5 nm when a value of $\Delta Z = 0.90$ was used.[58] Thus, this approach allows the charge and size of a protein to be determined in aqueous solutions that mimic biological environments in a single experiment.

8.3. PEG Ladders: Ladders of Hydrodynamic Drag

Hydrodynamic ladders are formed by grafting chains of poly(ethyleneglycol) (PEG), rather than acetyl groups, to the surface of a protein by acylation; each reaction changes both the charge and the hydrodynamic drag of the protein.[144] This type of experiment uses the charges measured by the ladder to count the number of PEG groups attached to the protein. We determined the electrophoretic mobilities of the rungs of PEG ladders of lysozyme by using CE, and calculated the hydrodynamic radius R of each rung using Henry's model of electrophoresis.[58,152] Figure 9 addresses the effects of chain density by showing that the increase in the hydrodynamic radius of lysozyme modified with short PEG (2 kD) chains is smaller than the increase in the radius of lysozyme modified with the longer (5 kD) PEG chain.

It is not directly apparent whether the R values of each protein-PEG construct would be accurately predicted by Henry's model, as the model describes the behavior of smooth, uniformly charged spheres. To test the accuracy of Henry's model, we related the values of R to the partition coefficient of these proteins into neutral gels by using Ogston's model,[171] and compared those partition coefficients with experimentally measured ones.[144] We found excellent agreement between the predicted and measured partition coefficients for all rungs of the PEG ladder. This agreement shows that the analysis of hydrodynamic ladders can be done by using Henry's model of electrophoresis. We believe that the hydrodynamic ladders will be useful in studies of the effects of hydrodynamic size on the transport properties of proteins.

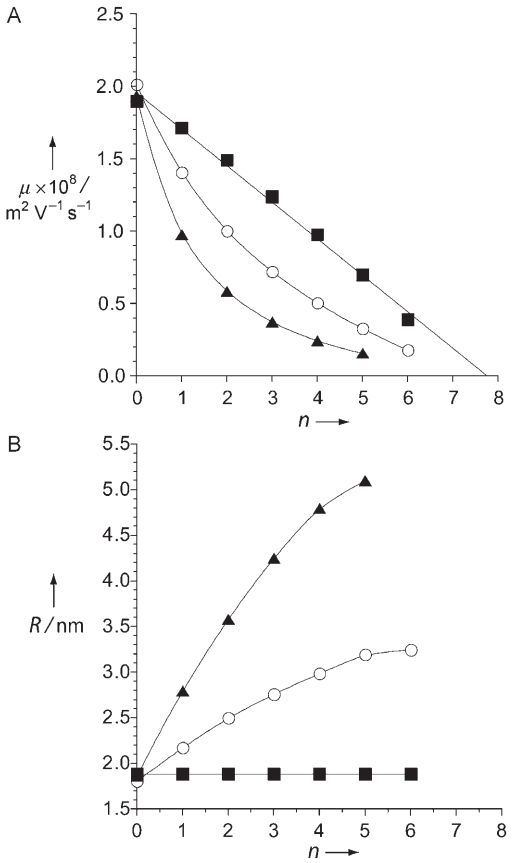

Figure 9. A) Electrophoretic mobility μ of protein charge and radius ladders of lysozyme produced by the partial modification of Lys ε-NH_3^+ groups with polyethylene glycol chains functionalized with *N*-hydroxysuccinimide ester (HO-PEG-OCH_2COO-NHS): molecular weight 2 kDa (○) and 5 kDa (▲). Each acylation results in a change in mobility because of the neutralization of an ε-NH_3^+ group and the increase in the hydrodynamic drag of the protein. The mobilities are compared with values of the charge ladders produced by modification with acetic anhydride (■). B) The hydrodynamic radius R of the rungs of the charge and radius ladders of lysozyme calculated using Henry's model. The values were calculated by assuming differences in mobility of each rung between the PEG and acetyl-modified protein in (A) are due entirely to effects of the PEG on the effective hydrodynamic radius. The hydrodynamic radii of free 2- and 5-kDa PEG chains are 1.4 and 2.2 nm, respectively.

 © 2006 Wiley-VCH Verlag GmbH & Co. KGaA, Weinheim

9. Influence of the Net Charge of Proteins (Z_{CE}) on Binding of Ligands: Combining Charge Ladders with Affinity Capillary Electrophoresis

Molecular recognition events involving proteins—for example, ligand binding or folding—in general result in changes in the net charge and/or hydrodynamic drag of proteins. CE detects these changes as a shift in the electrophoretic mobility, and can therefore be used to monitor them.[172] Since protein charge ladders allow the net charge of proteins to be isolated as an independent variable, biophysical studies using charge ladders and CE can also provide measurements of the role of net charge and electrostatics in molecular recognition events involving proteins.[4]

9.1. Affinity Capillary Electrophoresis

The measurement of the binding of ligands to proteins by capillary electrophoresis (affinity CE or ACE) is well described in the literature,[172,173] and we give only a brief description of the technique here. In an ACE experiment, a sample of the receptor is injected onto a capillary and the electrophoretic mobility is measured as a function of the concentration of the ligand in the electrophoresis buffer. The binding of a charged, low-molecular-weight ligand to a protein causes a shift in the electrophoretic mobility of the protein. The shift is due to the fact that the protein and the protein–ligand complex differ (to a first approximation) by the charge of the ligand, but have similar hydrodynamic drag. Measuring the mobility of the protein at different concentrations of the ligand present in the electrophoresis buffer makes it possible to measure binding constants and thus free energies of binding. Affinities of neutral ligands can be measured by using competitive assays against a charged ligand with known binding constant.[174] By using this approach it is straightforward to measure the binding of ligands to multiple proteins (isozymes, homologous proteins, members of a charge ladder) at the same time. For example, ACE makes it possible to measure the mean binding constant for all proteins in each rung of a charge ladder in one set of experiments.[4,5]

9.2. Dependence of the Free Energy of Binding of Charged Ligands on the Net Charge of Carbonic Anhydrase

The binding of a charged ligand to the proteins that make up the rungs of a charge ladder shifts their mobilities.[4,5] Figure 10A shows representative electropherograms of the charge ladder of HCAII measured with different concentrations of the benzene sulfonamide inhibitor **1** in the electrophoresis buffer. As the concentration of this ligand increases, the fraction of the protein–ligand complex also increases. As this ligand carries a net positive charge, the effect of binding is a shift in the positions of the peaks in the electropherograms to the left (that is, to decreasing values of mobility as the protein is negatively charged under the conditions of the experiments). The mobilities of the rungs of the charge ladder measured at 10 μM of the ligand **1** represent the saturated or fully bound state of the protein.

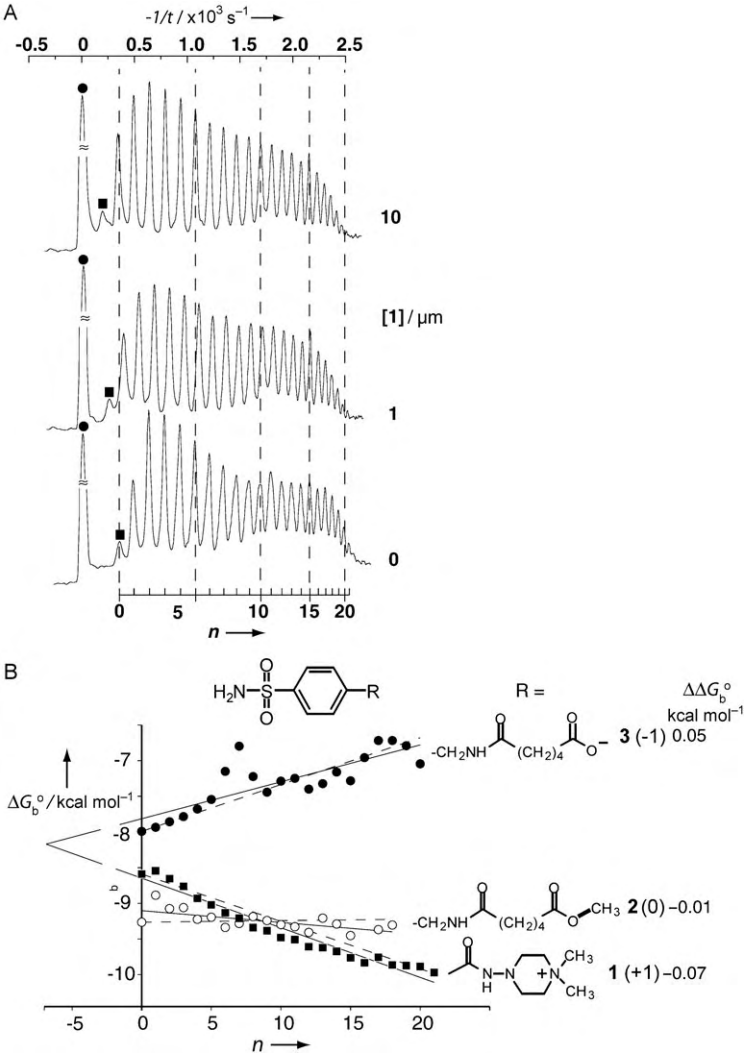

Figure 10. A) Electropherograms demonstrating the changes in the electrophoretic mobility of the rungs of the charge ladder of human carbonic anhydrase II as a result of the binding of ligand **1**. ●: electrically neutral markers of electroosmotic flow, ■: the unmodified protein. The number of acetylated Lys ε-NH_3^+ groups (n) is indicated below the electropherogram. The ACE experiment was performed with inhibitors **1**–**3** in 25 mM Tris/192 mM Gly (pH 8.4). B) Dependence of the standard-state free energy of binding ΔG_b° on the number n of $NHCOCH_3$ groups of the charge ladder of HCAII, and on the charge on the ligands. ——: least-squares fit to the data; -----: results of the continuum electrostatics calculations. The slopes ($\Delta\Delta G_b^\circ/n$) from the linear regression analyses of ΔG_b° versus n yielded the magnitudes of the influence of the charges of the Lys ε-NH_3^+ groups on the HCAII–ligand interactions. The lines from the continuum electrostatics calculations are just the average of the calculated contributions of the 21 different Lys ε- NH_3^+ groups to the free energies of binding of the different sulfonamides. (Reproduced with permission from Ref. [5].)

We carried out experiments, analogous to those in Figure 10A, with three different ligands—each a benzene sulfonamide substituted in the *para* position with a charged or neutral pendant group—and analyzed the data to determine the binding affinities of the rungs of the charge ladder for

 © 2006 Wiley-VCH Verlag GmbH & Co. KGaA, Weinheim

those ligands. HCAII becomes more negatively charged as the number of acetylations increases. Figure 10B shows values of the free energies of binding (ΔG_b°) of these ligands as a function of the number of modifications on HCAII. These data allow comparison of the binding affinities of unmodified HCAII for each of these different ligands; they also provide a direct measure of the effects of long-range electrostatic interactions on the binding affinities. Values of ΔG_b° for the neutral ligand are approximately independent of the net charge on the protein. These results imply that the modifications to the amino acids that produced the charge ladders had little effect on the structure of the active site of this enzyme.

For the charged ligands, we observed an approximately linear relationship between the free energy of binding and the net charge of the protein: increasing the net negative charge of the protein resulted in more favorable binding of the positively charged inhibitor **1**, and less favorable binding of the negatively charged inhibitor **3**. This linear relationship implies that the effect of increasing net charge on binding affinity is, in this case, approximately additive.

9.2.1. *Modified Carbonic Anhydrase with Selectivity for Charged Ligands that Increases with Net Charge*

The acetylation of Lys ε-amino groups results in a change in the free energy of interaction between the protein and charged ligands that reflects the collective effects of long-range electrostatic interactions. These interactions, which are less than 0.1 kcal mol^{-1} per unit increment of charge of the protein (that is, 10–20% of RT), are individually too weak to be measured by most biophysical techniques. Increasing the net charge on HCAII by eliminating the positive charge on 21 Lys ε-NH_3^+ groups resulted in an affinity for the anionic inhibitor **3** that was more than 100 times (corresponding to approximately 3 kcal mol^{-1}) that of cationic inhibitor **1**. It is surprising that the most highly charged species follow the linear trends in affinity observed for proteins with lower net charge.

9.2.2. *Modified Carbonic Anhydrase with Large Values of Net Charge without Loss of Stability*

Figure 10B indicates that acetylating all 21 Lys ε-NH_3^+ groups does not change the active site: the affinity of HCAII for the electrically neutral inhibitor is essentially insensitive to increasing numbers of acetylations. Carbonic anhydrase is a particularly stable protein (with a free energy of denaturation at 25 °C of ca. 20 kcal mol^{-1}),[175] and one must be concerned that this conclusion might apply only to such proteins. This conclusion may, however, be applicable to at least some other proteins. For example, Pace and co-workers[22] demonstrated that as many as five charge-reversal mutations (that is, the conversion of five Asp or Glu residues into Lys residues) had only a modest influence on the stability of ribonuclease Sa, and reduced the free energy of denaturation at 25 °C by approximately 0.5 kcal mol^{-1}. Quantitative measurements of the dependence of the thermal stability of α-lactalbumin on the net charge measured by using CE and charge ladders[56] also suggest that net charge is not an important determinant of stability in this protein (Section 10).

9.3. *Comparison of Experimental Values with Predictions by Continuum Electrostatic Modeling Studies*

Continuum electrostatics calculations, which are based on numerical solutions of the linearized Poisson–Boltzmann equation,[24] provided a detailed analysis of the contributions of individual Lys ε-NH_3^+ groups to the electrostatic free energy of binding that is impossible to detect experimentally.[5] We calculated values of ΔG_{elec}°, the contribution of electrostatic free energy to the total free energy of binding, as the difference in the electrostatic free energy of the protein in the presence of a sulfonamide ligand bound to the zinc ion at the active site, and in the absence of ligand (where a hydroxide ion is bound to the zinc ion).[5] We defined the contribution of each Lys ε-NH_3^+ group to the electrostatic free energy of binding as $\Delta\Delta G_i^\circ$, the difference in ΔG_{elec}° when Lys ε-NH_3^+ group i carried a charge of $+1$, and when it had been converted into an $NHCOCH_3$ group with a charge of 0. These calculations made the simplifying assumption that $\Delta Z = -1$. The values of $\Delta\Delta G_i^\circ$ [kcal mol^{-1}] from calculations, averaged over all 21 Lys ε-NH_3^+ groups, were -0.07 for inhibitor **1**, 0.00 for inhibitor **2**, and $+0.05$ for inhibitor **3**. The dashed lines in Figure 10B are plotted with these values as slopes.

These calculations suggested that values of $\Delta\Delta G_i^\circ$ could be divided into three parts (illustrated in Scheme 5): 1) the direct

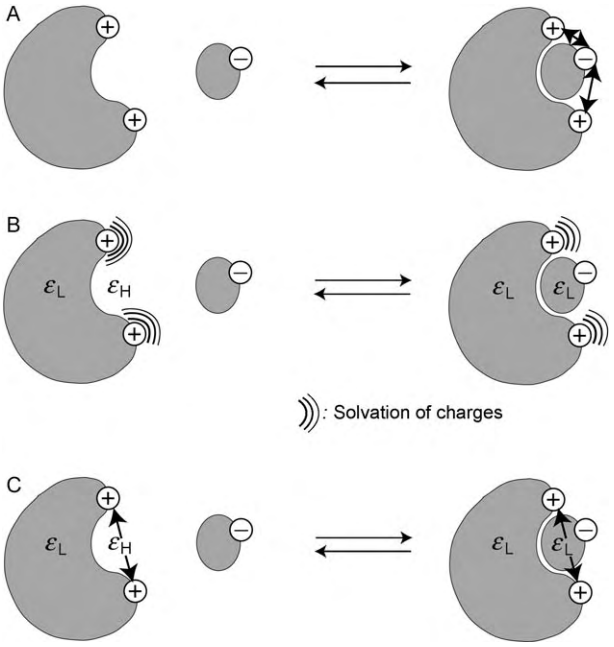

Scheme 5. Schematic diagram illustrating three contributions to $\Delta\Delta G_{elec}^\circ$ (see text); A) direct effect, B) solvation effect, C) indirect effect. The gray interiors of the protein and ligand are regions of low dielectric ($\varepsilon_L = 2$–4), the regions surrounding the protein and ligand are water with high dielectric ($\varepsilon_H \approx 80$); ↔: electrostatic interaction between charges. (Adapted from Ref. [5].)

 © 2006 Wiley-VCH Verlag GmbH & Co. KGaA, Weinheim

effect, $\Delta\Delta G^{\circ}_{dir}$, is the intermolecular Coulombic interactions between charged groups on the protein and charged groups on the ligand or hydroxide ion bound to the zinc ion; 2) the effect of solvation, $\Delta\Delta G^{\circ}_{solv}$, is the change in the free energy of solvation of charged groups on the protein and ligand when the hydroxide ion is replaced by the ligand in the active site; 3) the indirect effect, $\Delta\Delta G^{\circ}_{indir}$, is the change in the intramolecular Coulombic interactions between charged groups on the protein and the ligand when the hydroxide ion, and a significant volume of water in the active site, is replaced by the ligand. Values of $\Delta\Delta G^{\circ}_{solv}$ and $\Delta\Delta G^{\circ}_{indir}$ reflect the changes in screening by the solvent and the ionic atmosphere that result from the change in the shape of the interface between regions of low dielectric constant (the protein and bound ligand, if present), and of high dielectric solvent (water) in the bound and the unbound state.

Values of $\Delta\Delta G^{\circ}_{solv}$ were small (less than 4×10^{-4} kcal mol^{-1} for all lysine groups, except Lys170) because the region of the protein that is desolvated on ligand binding is far from all of the lysines except Lys170 (which had a $\Delta\Delta G^{\circ}_{solv}$ value of 0.02 kcal mol^{-1}). Figure 11 compares the direct and indirect

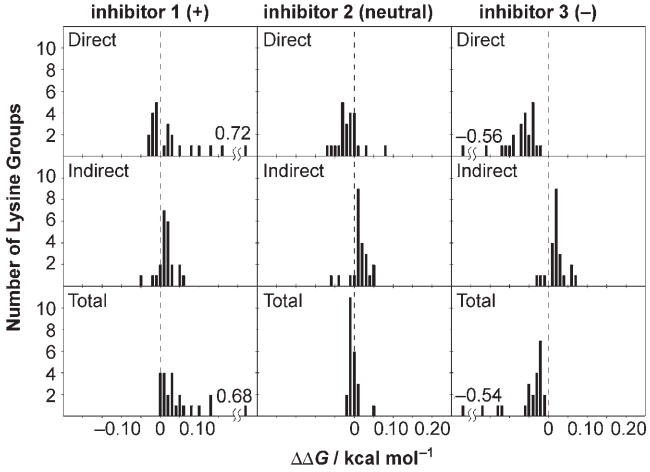

Figure 11. Histograms of $\Delta\Delta G^{\circ}_{dir}$, $\Delta\Delta G^{\circ}_{indir}$, and the total $\Delta\Delta G^{\circ}_{elec}$ (including $\Delta\Delta G^{\circ}_{solv}$) as calculated for each of the three inhibitors from Figure 10B. Each bar indicates the number of Lys ε-NH_3^+ groups on HCAII that contribute an amount of free energy, given by the *x*-axis, to $\Delta\Delta G^{\circ}_{elec}$. The values of $\Delta\Delta G^{\circ}_{dir}$ and the total $\Delta\Delta G^{\circ}_{elec}$ calculated for Lys170 in the presence of inhibitors **1** and **3** are much larger in magnitude than the values for the other Lys residues. The four values for Lys170 are printed explicitly on the histograms. (Reproduced with permission from Ref. [5].)

contributions of different Lys ε-NH_3^+ groups to $\Delta\Delta G^{\circ}_{elec}$. Most previous analyses have focused only on the direct effect; this study shows that both direct and indirect interactions can be of similar magnitude.

How do we reconcile the complex distribution of interaction free energies (shown in Figure 11) with the relatively simple dependence of the ΔG°_{b} value on the number of acetylations (shown in Figure 10B)? It may be that these details are obscured when values of $\Delta\Delta G^{\circ}_{elec}$ are averaged over the different protein derivatives that make up each rung of the charge ladder. To test this idea we performed Monte Carlo simulations to examine the influence of different patterns of acetylation on the average binding free energies of the different rungs of the ladder.[5] These simulations showed that a large number of different patterns of acetylation gave results that were in good agreement with the experimental results.

What do these results tell us about the ability of ACE and charge ladders to resolve changes in the electrostatic free energy of binding that result from changes in the net charge of the protein? There are two issues: 1) the ability of ACE to measure differences in values of ΔG°_{b} between adjacent rungs, and 2) the ability of ACE to resolve the presence of species with different values of ΔG°_{b} within a single rung. The results in Figure 10 show that ACE can measure differences in the ΔG°_{b} values between adjacent rungs of the ladder that are as small as 0.1 kcal mol^{-1}. This accuracy, combined with the large number of rungs of the ladders that are simultaneously monitored for binding by CE, provides an accurate measure of the average value for $\Delta\Delta G^{\circ}_{elec}$ over a large number of derivatives. (It would be very difficult to estimate energetic terms of this magnitude using site-directed mutagenesis.)

These results cannot rule out the existence of outliers from the measured average values of $\Delta\Delta G^{\circ}_{elec}$ in the pool of derivatives within a single rung. Calculated contributions to the free energy of binding of different lysine groups ranged from 0.01 to 0.15 kcal mol^{-1}, except for one residue in HCAII, Lys170, which contributed between 0.54 and 0.72 kcal mol^{-1}. If we assume that the derivatives acetylated at Lys170 represent the only outliers, then these derivatives will make up only approximately 5% of the population in a rung. The resolution of CE (defined as the ability to resolve species with different values of electrophoretic mobility into separate peaks) also limits this kind of experiment. The difference in mobility between adjacent rungs (ca. 2×10^{-9} m^2 V^{-1} s^{-1}; Figure 10A) represents the maximum shift in mobility from the binding of a ligand that presents a single unit of charge (+ or −) μ_{PL}-μ_P. From Figure 10A, we estimate a peak width to correspond to the difference in mobility of about 0.8×10^{-9} m^2 V^{-1} s^{-1}: a reasonable estimate of the resolution of CE.

We use these estimates to determine the ability of ACE to resolve differences in the values of K_d among different species within the same rung of the ladder. The maximum difference in mobilities will occur at concentrations of ligand near the value of K_d. We assume a rung of the ladder is composed of two populations: the first population includes those derivatives where Lys170 is not acetylated and has a value of $\Delta G^{\circ}_{b} = -8$ kcal mol^{-1} at 25 °C (which corresponds to a value of $K_d = 1.36$ μM); the second population includes those derivatives acetylated at Lys170 and has a value of $\Delta G^{\circ}_{b} = -8.5$ kcal mol^{-1} at 25 °C (which corresponds to a value of $K_d = 0.58$ μM). With the concentration of ligand of 1.36 μM, the first population will be half-saturated, while the fraction of second population with bound ligand will be 0.7. From our previous estimate of μ_{PL}-$\mu_P = 2\times10^{-9}$ m^2 V^{-1} s^{-1}, we estimate that these two populations will differ in electrophoretic mobility by about 0.4×10^{-9} m^2 V^{-1} s^{-1}, a value smaller than the width of a single peak of the charge ladder. Therefore, we do not expect the presence of different populations that differ in values of

© 2006 Wiley-VCH Verlag GmbH & Co. KGaA, Weinheim

ΔG_b° on the order of 0.5 kcal mol^{-1} to result in the presence of detectable shoulders or splitting of peaks during an ACE experiment. This estimate was supported by simulations of the ACE experiment.[5] The relatively uniform behavior observed with CE and charge ladders may in fact be masking more complex behavior, which is homogenized through the combined effects of averaging over a population of different protein derivatives and limited resolution of CE.

9.4. Conclusions

The modification of as many as 21 primary amino groups on HCAII does not alter its binding to neutral inhibitors; we infer that the binding pocket of this enzyme is not altered by these modifications. Large numbers of weak (< 0.1 kcal mol^{-1} per unit of charge), long-range electrostatic interactions contribute significantly to the free energy of binding of charged ligands to proteins and can influence the selectivity of binding. These weak interactions can be measured accurately by the combination of ACE and charge ladders because of the large number of derivatives that are studied simultaneously.

Continuum electrostatic theory accurately predicts the average contributions of long-range electrostatics to the free energy of binding of charged ligands to HCAII. There is a distribution in the contribution of different charged groups to the free energy of binding; ACE usually does not resolve these differences within individual rungs of a ladder. These calculations also show that changes in the shape of the boundary between regions of low and high dielectric constant that accompany the binding of a ligand to the protein contribute an amount to the electrostatic free energy of binding that is similar in magnitude to the Coulombic interactions between charged groups on the protein and ligand. Detailed models that include explicitly the molecular shape of the protein and protein–ligand complex are required to capture this effect.

The combination of charge ladders, ACE, and continuum electrostatic theory is a useful method for studying the contributions of charged groups to the free energy of ligand binding. ACE and protein charge ladders measure the average effects of long-range electrostatic interactions, and can serve as a check of models based on continuum electrostatic theory that, in turn, provide the details of the contributions individual charged groups make to the free energy of binding.

10. Study of Electrostatic Contributions to Protein Folding and stability by Using Charge Ladders

10.1. The Role of Net Charge in Protein Stability

Our use of protein charge ladders to study the role of net charge on protein stability to thermal denaturation was motivated by two questions: 1) Do charged groups on proteins influence stability in a way that is similar to their influence on affinity for charged ligands?[81] 2) What is the role of charged groups in the pH-dependent stability of proteins?[21]

Many proteins denature under acidic and alkaline conditions.[2] There are two explanations for this instability at extremes of pH values. 1) At values of pH far from the isoelectric point, proteins will develop a large net excess of positive charge (at low pH) or negative charge (at high pH). This large net charge will destabilize the compact, native state, relative to that of the more extended denatured state, by increasing the repulsion between like-charged groups. 2) Values of pK_a change when the protein denatures; differences in pK_a values would link charge regulation directly to thermal denaturation, and would result in differences in the net charge of proteins in the native and denatured states. Previously, these two possibilities could not be disentangled.

The combination of CE and charge ladders provides both the thermodynamics (that is, the free energy of denaturation $\Delta G_{D\text{-}N}^\circ$, D: denatured, N: native) and structural changes (that is, the net charge Z_{CE} and effective hydrodynamic radius R of proteins in both the native and denatured states) associated with protein denaturation, and hence it is well suited to study protein stability. Measurements of the temperature at which different rungs of the ladder denature provide values of $\Delta G_{D\text{-}N}^\circ$ for those rungs and demonstrate the effects of net charge on stability. The Z_{CE} and R values of the native and denatured species reflect the changes in the number of bound protons and in the hydrodynamic size that accompany denaturation.

10.2. Using CE to Measure the Free Energy of Protein Denaturation

The procedure for measuring the free energy of protein denaturation by using CE is similar to ACE. Rather than using different concentrations of ligand, we measure values of electrophoretic mobility at different temperatures or concentrations of chemical denaturants (e.g. urea) in the electrophoresis buffer. Changes in mobility are proportional to the equilibrium distribution of proteins between native and denatured states, and thus can be used to calculate the equilibrium constant $K_{D\text{-}N}$ for denaturation.[176] The details of the procedure and the relationships between the melting temperature and free energy of denaturation $\Delta G_{D\text{-}N}^\circ$ are described elsewhere.[56,147]

10.3. Monitoring the Thermal Denaturation of a Charge Ladder of α-Lactalbumin by CE

α-Lactalbumin (α-LA, MW = 14,200 Da, pI = 4.8) denatures under mildly acidic and alkaline conditions.[177] We were interested in the role that proton binding and long-range electrostatic interactions play in the thermal stability of this protein. Figure 12 shows electropherograms of the charge ladder of α-LA produced by the partial acetylation of Lys ε-NH_3^+ groups, measured at different temperatures and corrected for changes in the viscosity resulting from increasing temperature.[56] Shifts in the position of peaks thus reflect only

 © 2006 Wiley-VCH Verlag GmbH & Co. KGaA, Weinheim

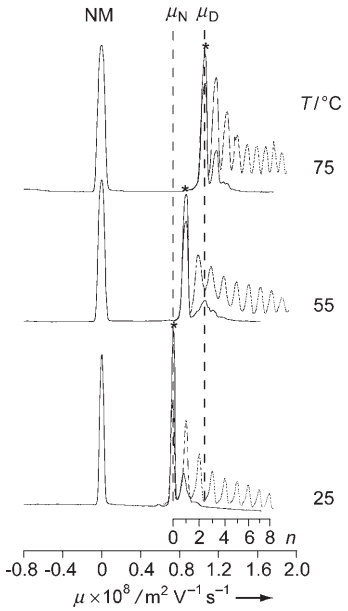

Figure 12. Electropherograms of the charge ladder of α-LA (-----) superimposed on those of the unmodified protein (——) at different values of temperature; NM: neutral marker. The separations were done in a buffer composed of 25 mM Tris/192 mM Gly (pH 8.4), 20 mM NaCl, and 35 μM $CaCl_2$. The peak marked with (*) corresponds to unmodified protein; the number of acetylated Lys ε-NH_3^+ groups *n* is indicated below the corresponding peak. The vertical dashed lines indicate the electrophoretic mobilities of unmodified α-LA ($n=0$) in the native (μ_N) and denatured (μ_D) states. The rungs of the charge ladder, as well as the peak that corresponds to the unmodified protein, broaden near the melting temperature of α-LA (ca. 56 °C). This broadening may reflect the finite rate of interconversion of the native and denatured states or heterogeneity in the free energies of unfolding of different derivatives of α-LA that have the same number of acetylated Lys ε-NH_3^+ groups. (Reproduced with permission from Ref. [56].)

changes in the charge and hydrodynamic drag of the protein with increasing temperature. The impurity to the right of the main peak in the unmodified sample has approximately the same mobility as the first rung of the charge ladder; it is possible that this peak corresponds to α-LA with a deamidated asparagine or glutamine side chain, with a change in charge similar to that produced by the acetylation of a Lys ε-NH_3^+ group.[178]

α-LA forms a compact denatured state, known as a molten globule, with a melting temperature of 56 °C under the conditions of these separations (pH 8.4 Tris-Gly buffer containing 25 mM NaCl and 35 μM $CaCl_2$).[102,179] Individual rungs of the charge ladder were resolved at all temperatures as the protein was denatured. We assume that all the proteins in all the rungs have completed the transition to the compact denatured state at 75 °C. An interesting feature of these data is that the mobility of the proteins increases upon denaturation. We expected the configuration of the protein in the molten globule to be more extended than the native state and, therefore, the value of f_{eff} to increase as the protein denatured. Since the mobility is the ratio of Z_{CE} to f_{eff}, the observed increase in mobility must be due to an increase in the magnitude of the net charge of the protein: that is, changes in Z_{CE} outweigh effects of changes in f_{eff} on the mobility of α-LA as it denatured.

To quantify these effects we analyzed the data in Figure 12 by using the methods described in Section 8.2 to determine *R* and Z_{CE} of α-LA as it denatured thermally. Figure 13 A shows

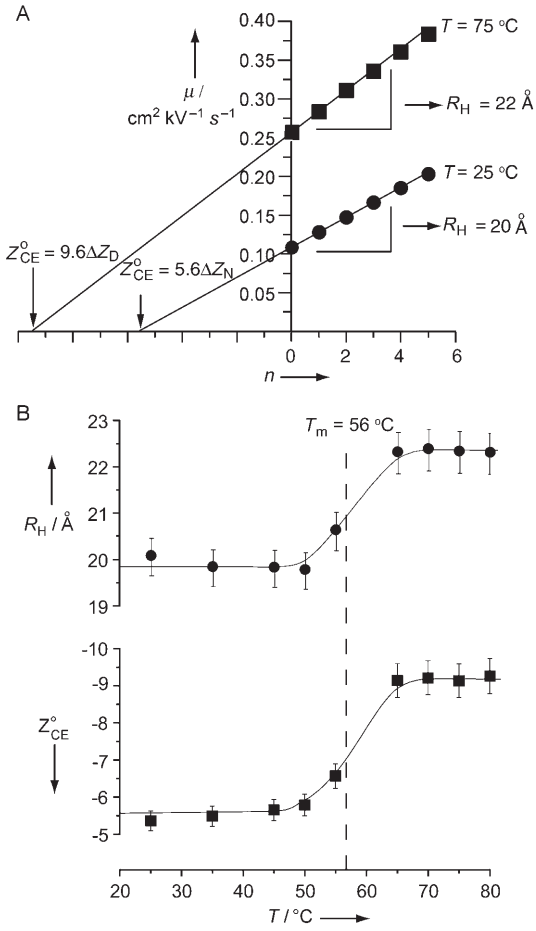

Figure 13. A) Determination of the charge Z°_{CE} and hydrodynamic radius *R* of proteins in the native and denatured state. Values of the electrophoretic mobility of the rungs of the charge ladder of α-LA from Figure 12 are plotted as a function of *n*. ●: native protein at 25 °C, ■: compact denatured state at 75 °C. The net charges $Z^\circ_{CE,N} = -5.4$ (native protein) and $Z^\circ_{CE,D} = -9.2$ (denatured protein), were calculated assuming $\Delta Z_N = \Delta Z_D = -0.96$. The hydrodynamic radius *R* is determined from the slope of the line using Henry's model. B) Values of the hydrodynamic radius *R* and net charge Z°_{CE} of α-LA determined at different temperatures from analysis of the data in (A). The dashed line indicates the melting temperature of this protein (56 °C). (Reproduced with permission from Ref. [56].)

plots of mobility versus *n* for the charge ladder of α-LA measured in the native state (25 °C) and thermally denatured states (75 °C). Linear least-squares analysis of these data yielded values of Z_{CE} and *R* for the unmodified protein at different temperatures (Figure 13 B). We measured an increase in *R* of approximately 0.2 nm or 11 %, relative to the native state, as α-LA transformed from the native to the compact denatured state. A large change in the magnitude of the net charge accompanied this relatively small change in hydrodynamic size: the value of Z°_{CE} nearly doubled from

 © 2006 Wiley-VCH Verlag GmbH & Co. KGaA, Weinheim

-5.4 ($Z^{\circ}_{CE,N} = 5.6\Delta Z$, $\Delta Z_N = -0.96$) in the native state to -9.2 ($Z^{\circ}_{CE,D} = 9.6\Delta Z$, $\Delta Z_D = -0.96$) in the denatured state. We calculated the value of ΔZ for the native state by using the LL model (Section 8.1.1). Since charge regulation is expected to be less significant in the denatured state than in the native state, ΔZ_D was assumed to be the same as ΔZ_N. Figure 13B shows that values of Z°_{CE} and R of the unmodified protein could be measured throughout the transition from the native to the denatured states, and the melting temperature of a protein can be estimated from that set of data.

Similar denaturation experiments carried out with the neutral denaturant urea indicated an increase in R of approximately 0.5 nm on denaturation: this value is approximately twice that measured for thermal denaturation. The change in net charge from $5.6\Delta Z$ in the native state to $9.0\Delta Z$ in the denatured state measured with urea denaturation was similar to that measured with thermal denaturation. These results suggest the significant change in the Z°_{CE} value that accompanies denaturation is independent of the denaturant in the case of α-LA.

10.4. The Role of Proton Equilibria in the Thermal Stability of α-Lactalbumin

The measured change in the Z°_{CE} value that accompanied thermal denaturation of α-LA indicated that several titratable residues had shifted their extents of protonation in the denatured ensemble from their values in the native state. This observation implies that proton equilibria were linked energetically to denaturation, and values of $\Delta G^{\circ}_{D\text{-}N}$ should depend on the pH value.[21] This dependence was quantified by Wyman and Gill[96] as a thermodynamic identity [Eq. (30)].

$$\frac{\partial \Delta G^{\circ}_{D\text{-}N}}{\partial \mathrm{pH}} = 2.303\, RT(Q_n - Q_D) \qquad (30)$$

This expression describes the contribution of differences in proton equilibria between the native and denatured states to the pH-dependence of the free energy of unfolding, where Q_N is the number of protons associated with the protein in the native state, and Q_D is the number in the denatured state.

We used CE to measure values of $\Delta G^{\circ}_{D\text{-}N}$ for unmodified α-LA at different values of pH, and determined a value of $\partial \Delta G^{\circ}_{D\text{-}N}/\partial \mathrm{pH} = 5.3$ kcal mol^{-1} per unit of pH.[56,147] From Equation (30), this value corresponds to a $\Delta Q_{D\text{-}N} = -3.9$—a value similar to $\Delta Z_{CE,D\text{-}N} = -3.8$ measured by using CE and charge ladders. We conclude that at pH 8.4, values of $\Delta Z_{CE,D\text{-}N}$ reflect primarily a difference in the extent of protonation between native and denatured states of α-LA arising from differences in pK_a values, dielectric constants, and electrostatic potentials of the protein in the native and denatured states.

10.5. The Role of Net Charge in the Thermal Stability of α-Lactalbumin

To quantify the effects of long-range electrostatics on the thermal stability, we determined the value of $\Delta G^{\circ}_{D\text{-}N}$ for the rungs of the charge ladder of α-LA by determining the fraction of denatured protein for each rung as a function of temperature.[56] Figure 14 compares values of $\Delta G^{\circ}_{D\text{-}N}$ for the

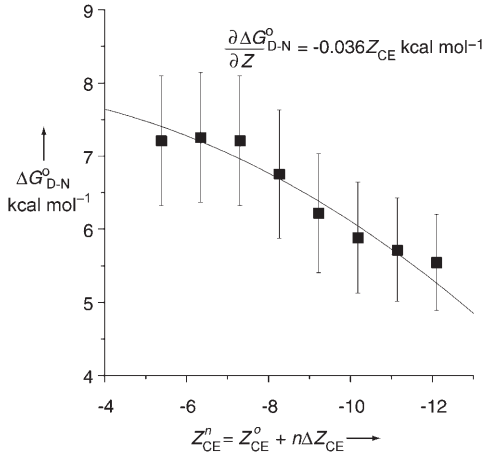

Figure 14. Dependence of free energy of unfolding $\Delta G^{\circ}_{D\text{-}N}$ on the net charge Z^{n}_{CE} of the rungs of charge ladders of α-LA. (Reproduced with permission from Ref. [56].)

members of ladders of α-LA as a function of the net charge measured by CE (using $\Delta Z = -0.96$, calculated by the LL model). The solid line is a quadratic regression fit of the data. We chose this functional form for the dependence of $\Delta G^{\circ}_{D\text{-}N}$ on the net charge because it is consistent with a simple model, in which the electrostatic free energy of protein denaturation is proportional to the free energy of charging a sphere, with the charge distributed evenly on the surface. This charging free energy is proportional to the square of net charge.[180] The fact that this quadratic equation fits the data implies that this model is consistent with the results for α-LA.

The slope of the curve in Figure 14 provides the differential dependence of $\Delta G^{\circ}_{D\text{-}N}$ of α-LA on the net charge $\partial \Delta G^{\circ}_{D\text{-}N}/\partial Z_{CE} = -0.036\, Z_{CE}$ kcal mol^{-1} per unit increase in net charge. The effect of acetylation on the thermal stability of α-LA therefore increases as more amino groups are acetylated (that is, as the protein becomes more negatively charged). This differential provides a direct measure of the average effects of long-range electrostatic interactions to the free energy of folding of α-LA. In the case of α-LA, the difference in $\Delta G^{\circ}_{D\text{-}N}$ between the native and the peracetylated protein is not large (ca. 2 kcal mol^{-1}): this particular protein can accommodate changes in several charged groups without significant loss of stability.

10.6. Conclusions

This section has illustrated the quantitation of contributions of both proton binding and long-range electrostatic interactions to the stability of a representative protein, α-LA. The primary influence of the pH value on the stability of α-LA was a shift in the proton equilibria between the native and denatured states (namely, a shift in the pK_a values of several groups that result in a change in the number of bound protons between the native and denatured states). Increasing the net

 © 2006 Wiley-VCH Verlag GmbH & Co. KGaA, Weinheim

charge on the protein by chemical modification has comparably little effect on stability. As in the case of ligand binding, the average contribution that a single lysine amino group makes to the stability of a protein is small, although not zero. In contrast to ligand binding, the influence of charged groups on stability is not simply additive: the larger the net charge already on a protein, the greater the influence of an additional charge.

11. The Net Charge of Proteins in the Gas Phase

Electrospray ionization mass spectrometry (ESI-MS) is an important analytical tool for characterizing proteins and protein–ligand complexes.[181] The factors that influence the formation and relative abundance of ions in ESI-MS are not completely understood. We wanted to determine whether the net charge of a protein in solution determines its net charge in the gas phase. Charge ladders of BCAII (Figure 15) provide an excellent system with which to solve this, since each rung of the ladder differs in charge, but not in any other important parameter, such as sequence or state (native versus denatured).[182]

The separation of the charge ladder by CE followed by analysis by ESI-MS confirmed the previous assignment of the composition of the rungs of the charge ladder: each rung is composed of derivatives that have the same number of modified charged groups. The fact that only a few charge states are observed in the gas phase is also consistent with the retention of the compact structure of the native protein (denatured proteins typically demonstrate a different distribution of charge states in the gas phase[183]). More significant in terms of the physical chemistry of ESI is the observation that both the magnitude and distribution of charged states of the ions generated in the gas phase do not correlate with the net charge of the protein derivatives in solution (that is, the number of Lys ε-NH_3^+ groups they contain).

An interesting correlation found through the examination by ESI-MS of charge ladders of BCAII, lysozyme, and bovine pancreatic trypsin inhibitor is that the magnitude of charge states increases with the surface area of the proteins in such a way that the surface density of charge is retained over a fairly narrow range of 0.9–1.5 units of charge per 1000 Å^2. This observation suggests that proton binding to the proteins in the gas phase is determined largely by electrostatic interactions among charged groups, and not by the intrinsic affinity of basic functional groups of the protein for protons as measured, for example, by values of proton affinity of amino acids in the vapor phase.

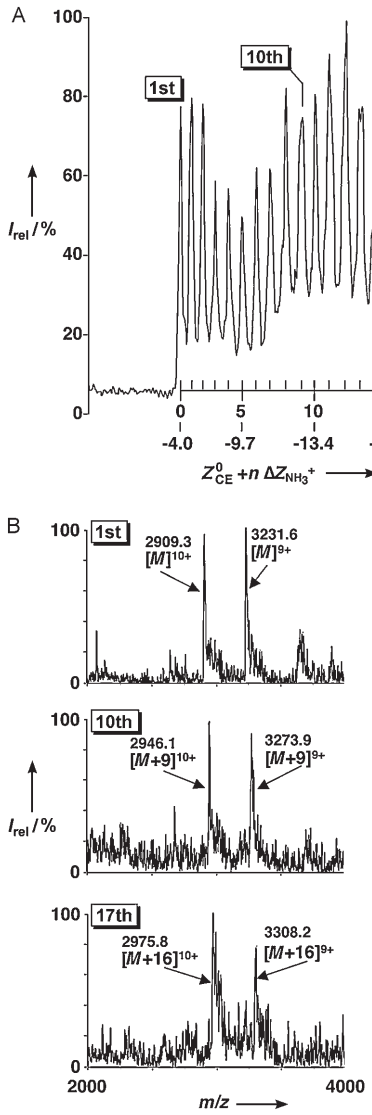

Figure 15. A) CE-ESI-MS electropherogram of an acetyl charge ladder of BCAII. The number of acetylated Lys ε-NH_3^+ groups n, as well as the estimated charge $Z^0_{CE}+n\Delta Z$ of the proteins that make up each of the rungs of the ladder, are indicated below the electropherogram. B) ESI mass spectra obtained from the accumulation of scans for the 1st, 10th, and 17th peaks to emerge after separation by CE. Each peak is labeled with its value of m/z and identified using the notation $[M+n]^{\pm z}$. The quantity in brackets represents the net mass of the ion, where M is the mass of the native protein; the superscript $\pm z$ represents the charge of the ion in the gas phase. (Reproduced from Ref. [182].)

12. Using Charge Ladders to Study the Role of Electrostatics in Bioprocessing

Ultrafiltration is a common technique for the purification of proteins. The selectivity of an ultrafiltration membrane for a particular protein is measured by its value of sieving coefficient S, the ratio of concentration of the protein in the filtrate and the retentate. The values of the sieving coefficient depend both on the size of a protein and on the electrostatic interactions between the protein and the membrane.[82] Thus, for a particular combination of protein and membrane, the sieving coefficient is a function of both the ionic strength and the pH value of the solution. Changes in the pH value can alter the density of charged groups on both the protein and the membrane.[83] Changes in ionic strength can alter the electrostatic free energy of interaction between the charged protein and charged membrane.[184] If there is significant charge regulation between charged groups on either the protein or the membrane, then the density of charged groups

 © 2006 Wiley-VCH Verlag GmbH & Co. KGaA, Weinheim

can also change with ionic strength. It has therefore been difficult to determine directly the effects of net charge of the protein in the ultrafiltration process.

Menon and Zydney[84,85] used charge ladders of BCAII and myoglobin to measure the contributions of net charge to the ultrafiltration selectivity of these proteins, and to test models of this process. At the pH value of their experiments (pH 7), both unmodified proteins were negatively charged. The values of S decreased with increasing magnitude of net (negative) charge for charge ladders of both proteins through a negatively charged membrane (Figure 16). Selectivity also

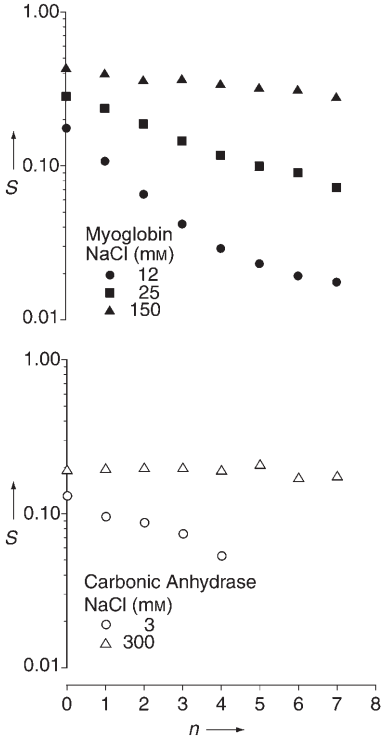

Figure 16. Effect of charge of myoglobin and BCAII on S through negatively charged polyethersulfone (Biomax) ultrafiltration membranes at different ionic strengths. (Reproduced with permission from Ref. [85].)

depended on the ionic strength of the solution. In the presence of 150 mM NaCl, the value of S for the different rungs of the charge ladder of myoglobin went from about 0.45 for the unmodified protein to 0.30 for the rung composed of proteins with eight acetylated amino groups; in the presence of 12 mM NaCl, the value of S went from approximately 0.2 to 0.02 for the same proteins. At a concentration of 300 mM NaCl, there was no measurable difference in the values of S for the rungs of the charge ladder of BCAII.

Menon and Zydney[85] rationalized these changes in S as resulting from an increase in the exclusion of the protein from the membrane as a result of the repulsion between the negatively charged walls of the pores of the membrane and the negatively charged proteins. Increases in ionic strength effectively screened these interactions, decreased the magnitude of the electrostatic free energy of interaction between the protein and membrane, and thereby reduced the dependence of S on the net charge of the protein. The authors calculated the effects of charge on S by using an equilibrium model of partitioning of proteins into charged, cylindrical pores.[185] This model predicted values of S accurately for the first four rungs of the charge ladder of myoglobin at an ionic strength of 12 mM. The later rungs of the charge ladder, which had the largest magnitude of net charge, showed significant deviations between the model and experiments.

Menon and Zydney[85] pointed out that CE and charge ladders should also be useful in measuring electrostatic interactions involving membrane systems in much the same way that solutions of dextran with different distributions in molecular weight have been useful in measuring the effects of steric interactions.[186] The combination of charge ladders and CE can also be extended to other bioprocessing techniques. Examples would include ion-exchange chromatography (where proteins are separated on the basis of their affinity for charged surfaces[187]) and aqueous two-phase extraction (where proteins are separated on the basis of their relative solubility in the two immiscible solutions of polymers.[188]).

The development of models that predict the selectivity of these different bioprocessing strategies on the basis of charge is an on-going, fundamental research effort in chemical engineering.[82–86,88,105,184,189] The value of such models is that they could lead to strategies for the engineering of proteins by manipulating their composition to improve processability, similar to the way in which proteins are currently engineered for improved stability and activity. Charge ladders, and their extensions to other properties of proteins such as hydrodynamic size and surface hydrophobicity, will help to improve our understanding of the fundamental interactions that serve as the basis for bioprocessing techniques.

13. Summary and Outlook

13.1. Summary

This Review describes the procedures used to form, characterize, and manipulate protein charge ladders, and to use them to explore problems in the physical chemistry of proteins. The combination of protein charge ladders and CE provides internally self-consistent data (in the form of electrophoretic mobilities) for a large number of derivatives of a protein—which differ incrementally in number of charged groups—in a single, simple experiment. These data permit the extraction of net charge[111,190] and hydrodynamic radius[58] of the parent, native protein.

The chemical modifications used to generate charge ladders are performed on folded proteins, and thus involve charged residues on their exterior. There is currently no way to target groups in specific locations, so charge ladders are not appropriate for studying the roles of specific residues, such as those buried in the interior of the protein or those in its active site; questions concerning these roles are best addressed by site-directed mutagenesis. Charge ladders are, however, very useful for examining collective effects of charged residues, and for studying phenomena that originate on the surface of a

 © 2006 Wiley-VCH Verlag GmbH & Co. KGaA, Weinheim

protein. Electrostatic interactions in proteins are often relatively weak ($< RT$, Figure 3), but numerous, and are thus difficult to quantify individually. Charge ladders and CE allow simultaneous analysis of a large number of charge variants, and thus provide a way to begin to quantify those interactions.

We have examined the effect of net charge on ligand binding[4] (with carbonic anhydrase, Figure 11), on thermal stability[56] (with α-lactalbumin, Figure 14), and on ion formation in the vapor phase[182] (with carbonic anhydrase, Figure 15). Zydney and co-workers have used charge ladders to study the effects of the net charge of proteins on their transport through charged ultrafiltration membranes[84,85] (Figure 16). Other phenomena that are likely to be dependent on the surface charges—aggregation, crystallization, protein–protein association, catalytic activity—have not been yet examined, but their examination should be facilitated by experiments using protein charge ladders.

We have also combined experimental data from CE and charge ladders with continuum electrostatic theory to validate the ability of the theory to predict the effects of net charge on the binding of charged and neutral ligands;[5] the theory provided details of electrostatic interactions that could not be revealed experimentally (Figure 11). This combination of theory and experiment circumvents some of the limitations of both charge ladders and site-directed mutagenesis alone. It can provide information on the role of individual charges in specific locations and can analyze the electrostatic interactions in proteins with many permutations of charges.

The ability to extract the values of net charge of the native protein, and of its derivatives, depends on the ability to estimate the value of ΔZ—the difference in charge between successive rungs of a ladder, or between proteins differing by one modification. The value of ΔZ is influenced not only by the charge of the group that is modified, but also by the cooperative interactions among other ionizable groups on the protein. Although we cannot measure ΔZ directly, we can estimate it theoretically by using three different models:

1) The Linderstrøm-Lang model. This model requires knowing the composition of amino acids of the protein and the pK_a values of ionizable residues, and an estimate of the effective hydrodynamic radius of the protein.[105,106]
2) Poisson–Boltzmann calculations with Monte Carlo simulations of proton equilibria. This technique requires knowledge of the three-dimensional structure of the protein and significant numerical computation.[107]
3) Screened Coulombic potential model. This simple model also requires knowing the three-dimensional structure of the protein (especially the distances between ionizable groups), but does not require significant computation: it can be solved on a spreadsheet.[107]

Values of ΔZ can also be estimated experimentally by combining measured electrophoretic mobilities of charge ladders with an independent measurement of hydrodynamic radius; this measurement can be accomplished conveniently on a CE instrument by using analysis of Taylor's dispersion.[168] At pH values of about 8.5 and low (ca. 10 mM) ionic strengths, the value of ΔZ per acetylation of a lysine lies between −0.8 and −0.9, based on the analysis of several proteins. At high ionic strengths (ca. 100 mM), the value of ΔZ approaches −1.

The concept of "ladders" can also be extended to properties of proteins other than charge. We have described derivatives of proteins with incremental changes in hydrodynamic size (Figure 9) and proposed how the surface hydrophobicity of proteins can be altered by successive acylation of amino groups (Figure 4). In these experiments, CE serves primarily to count the number of modifications of the protein, not to estimate the charge.

13.2. Outlook

Protein charge ladders, site-directed mutagenesis, and theory allow us to begin to ask sophisticated, focused questions about roles of charged groups in macromolecules. Here we give several representative questions, and sketch experimental evidence relevant to their eventual answer; in no case do we have a complete answer, and in no case can these questions be easily answered with one experimental technique.

13.2.1. Is it the Value of Net Charge of a Protein that is Important in the Intracellular and Extracellular Environments, or Is it the Distribution of Charges on a Protein That Is Important?

To start to address this question, we analyzed the structure of charges and net charge of 20 isoforms of carbonic anhydrase (CA).[131] This analysis showed that the net charge Z_{seq} calculated from the sequence of amino acids varied from +1.8 to −2.3, with 90% of the isoforms falling between $Z = +1.5$ and −1.5, even though the total number of charges (positive and negative) ranged from 36 to 75. These results imply that there is evolutionary pressure to maintain the net charge of CA between +1 and −2, even if the total number of charged groups is not conserved. It would be interesting to extend the analysis to other families of proteins.

It is possible that retaining a small net charge on proteins both reduces the osmotic pressure[191] and, at the same time, prevents phase separation inside the cell[192] and minimizes nonspecific protein–protein interactions in an environment crowded with ions, nucleic acids, and proteins.[193] Sear has started to explore this subject by calculating the net charge Z_{seq} of all proteins (ca. 4000) in the genome of *E. Coli*.[191] The distribution of net charge is approximately Gaussian, centered around −3, with a standard deviation of 8. Few proteins (< 1%) had magnitudes of charge greater than 30. Such analysis, done on the proteome of an organism, supports the idea that net charge, as a parameter, is important for the function of a cell.

The distribution of charge in proteins is certainly involved in formation of protein–protein complexes,[8] binding of highly charged nucleic acids,[24] and may be important in more subtle phenomena, such as electrostatic steering.[10,78] Thus, the conservation of both net charge and of charge distribution are likely to occur in some circumstance. We

© 2006 Wiley-VCH Verlag GmbH & Co. KGaA, Weinheim

therefore cannot yet answer the question of the relative importance of net charge and charge distribution.

13.2.2. Are Charged Groups on Proteins Involved in "Negative Design"?

In the complex environment of a cell, specific interactions required for life must be balanced against other interactions detrimental to life;[194,195] the latter may result in crystallization and homogeneous or heterogeneous aggregation. Charged groups on the surfaces of proteins may be involved in the "negative design", where the presence of charge does not necessarily improve the function of an enzyme, but instead reduces undesirable, noncatalytic interactions (such as the protein–protein interactions involved in crystallization or aggregation).

Richardson and Richardson described a specific example of the role of charges in negative design in β-sheet proteins.[195] Naturally occurring β-sheet proteins are usually soluble, but fragments or mutants of these proteins can aggregate and, in some cases, form amyloid fibers. An analysis of 75 proteins having β-sheet structures led the authors to conclude that the presence of a single charged group on one edge of the β sheet was one of the most common natural features associated with inhibition of aggregation; the authors also argued that out of all available charged residues, Lys would be the best choice because of its flexibility. These arguments, supported by experiments done by Wang and Hecht,[196] showed that this design principle was effective in converting proteins, designed de novo to form β sheets and to assemble into amyloid-like fibers, into proteins that remained as soluble monomers in solution.

13.2.3. Do Cells Utilize Electrostatics To Control the Activity and Stability of Proteins?

Cells actively regulate the concentration of ions and protons in compartmentalized volumes: for example, endosomes and lysosomes are quite acidic (pH 5–6), while the cytosolic pH value is close to neutral (ca. 7.2).[197] During apoptosis, cells undergo acidification of their intracellular pH value by 0.3–0.4 units,[198] sometimes with a transient alkalinization. The cytosolic pH values of tumor and multidrug resistant cells are different from those of normal cells.[199] Cells utilize these pH differences, and thus differences in protonation states of proteins, to activate certain enzymes and pathways only where and when necessary.

One example of such control is the transport of proteins to the lysosomes. Proteins to be transported to the lysosome are tagged with a marker, mannose-6-phosphate, in the Golgi complex (at neutral pH). Vesicles containing a receptor for mannose-6-phosphate bind the marked proteins. These carriers then fuse with pre-lysosomal vesicles that are acidic; lowering of pH value causes the marked protein to dissociate from the receptor and continue its way to the lysosome.[41]

Another question that rises immediately is: "*How do lysosomal enzymes refrain from uncontrolled, and likely destructive, activity en route to the lysosome?*" Heikinheimo et al.[200] proposed the following mechanism for the activation of lysosomal α-mannosidase at a low pH value: at cytosolic pH values, multiple salt bridges stiffen the loops near the active site of the enzyme, thus reducing the catalytic activity; at the acidic pH value of the lysosome, protonation of glutamic and aspartic acids breaks the network of salt bridges and allows for the necessary plasticity of the enzyme required for catalysis. There are many other examples of pH-activated events (activation of hemagglutinin at low pH values in influenza infection may be another well-known one[201]), and all cannot be listed here. The point is that the forces that are modulated by a change in the pH value are in part electrostatic.

13.2.4. Can One Make "Better" Proteins—That is, Proteins with Improved Stability, Greater Activity, or New Functionality—by Designing an Appropriate Pattern of Charge?

Changing the patterns of charge on protein surfaces may be a strategy to achieve desired properties of proteins for applications in biotechnology: for example, in organic synthesis, diagnostics and sensing applications, and protein therapy. Leist et al. have recently demonstrated an excellent example of an improved charge-modified therapeutic with erythropoietin (EPO). Carbamylation of lysine residues on EPO did not interfere with its binding to the tissue-protective receptors, but interfered with its binding to the receptor responsible for the hematopoietic activity of EPO.[202] Thus, EPO-stimulated tissue-protective pathways could be activated without the unwanted effects of up-regulated production of red blood cells.

Sarkar et al. demonstrated a clever utilization of the difference in electrostatic interactions between a therapeutic protein and its receptor at two different pH values to control the lifetime of the therapeutic.[203] The authors engineered a cytokine GCSF (granulocyte colony-stimulating factor) to contain a His residue at the binding interface to its receptor (GCSFR). At the extracellular pH value of about 7 when the His is deprotonated, GCSF maintained its tight binding to the receptor. At the endosomal pH value of 5–6, unfavorable electrostatic interactions resulting from the protonation of His reduced the affinity of GCSFR to bind GCSF by several fold. As a result of the weakened interaction of the cytokine with its receptor in the endosome, the cytokine was recycled back to the surface of the cell rather than being sent for degradation in the lysosome. This increased recycling of the engineered GCSF increased the lifetime and, thereby, the activity of the cytokine, relative to the wild-type. The authors believe that modulation of binding affinity between ligands and receptors by carefully engineered "histidine switches" may be a general strategy for the enhancement of endosomal recycling.

13.2.5. What Are the Energetics of Interaction and Forces between Ions and Charged Macromolecules in Solution?

Before we are able to answer any questions about the role of charges on proteins in complex mixtures, we need to understand better the behavior of ions in solution. Interestingly, we do not understand the behavior of even simple ions

 © 2006 Wiley-VCH Verlag GmbH & Co. KGaA, Weinheim

in solutions,[50,74,75] especially at biologically relevant concentrations.

In contrast to a vacuum, where the electrostatic free energy of interaction between charged groups is entirely enthalpic, the free energy of interaction between charged groups in biological fluids is often dominated by the contributions of entropy. It is the entropic contribution to the electrostatic free energy that can make the electrostatic interactions between opposite charges favorable. The electrostatic enthalpy of interaction between opposite charges can actually be unfavorable in aqueous solutions.

Ninham and co-workers[74,75] have shown that charge–charge interactions do not always dominate the total free energy of interactions between ions. Dispersion forces among ions and water must be included in accurate thermodynamic descriptions of solutions of electrolytes. A striking, counterintuitive result of the studies by Ninham and co-workers is that the net interaction between some ions of *like* charge is *attractive* when dispersion forces are included.[75] The dispersion force depends on the size and polarizability of the ions, and therefore, may play an important role in describing the effects of specific ions in experimentally measured osmotic coefficients and surface tensions. The authors have also argued that dispersion forces can explain such observations as the dependence of net charge and ionization constants of a protein on the background electrolyte,[51] and the "salting-in" and "salting-out" of proteins by different salts (also known as Hofmeister effect).[204] These specific ion effects, which are still incompletely understood, are omitted in most models of protein solutions. A more complete picture of protein–ion interactions will need to include these effects.

In addition, if we are to understand fully electrostatic interactions in biology, we must measure more than just equilibrium constants and the associated standard state free energies of interaction; we must also know the individual contributions of enthalpy and entropy to this free energy. To see a complete picture, we will need to measure the thermodynamic parameters that describe molecular recognition directly, by using techniques such as calorimetry.

While experiments with protein charge ladders by themselves will not be able to directly answer the questions we have posed, and others of a similar character, they will certainly advance our understanding of electrostatic interactions involving proteins in solutions. Complimentary calculations with continuum electrostatic theory will add to this understanding. Protein charge ladders, and extensions to other ladders that systematically alter the surface chemistry of proteins, will, we believe, also aid in the development of tools for protein separation and characterization.

This work was supported by the National Institute of Health (grant GM 51559 (G.M.W.)), the National Science Foundation (grant CTS-0134429), and the Camille and Henry Dreyfus Foundation (J.D.C.). We thank Katie Gudiksen, Demetri Moustakas, Logan McCarty, and Max Narovlyansky for helpful discussions.

Received: July 20, 2005
Published online: April 18, 2006

[1] M. Garcia-Viloca, J. Gao, M. Karplus, D. G. Truhlar, *Science* **2004**, *303*, 186.
[2] A. R. Fersht, *Structure and Mechanism in Protein Science: A Guide to Enzyme Catalysis and Protein Folding*, *3rd ed.*, Freeman, New York, **1998**.
[3] S. Miller, J. Janin, A. M. Lesk, C. Chothia, *J. Mol. Biol.* **1987**, *196*, 641.
[4] J. M. Gao, M. Mammen, G. M. Whitesides, *Science* **1996**, *272*, 535.
[5] J. A. Caravella, J. D. Carbeck, D. C. Duffy, G. M. Whitesides, B. Tidor, *J. Am. Chem. Soc.* **1999**, *121*, 4340.
[6] D. F. Green, B. Tidor, *J. Mol. Biol.* **2004**, *342*, 435.
[7] C. Park, R. T. Raines, *J. Am. Chem. Soc.* **2001**, *123*, 11472.
[8] S. J. Davis, E. A. Davies, M. G. Tucknott, E. Y. Jones, P. A. van der Merwe, *Proc. Natl. Acad. Sci. USA* **1998**, *95*, 5490.
[9] F. Dong, M. Vijayakumar, H. X. Zhou, *Biophys. J.* **2003**, *85*, 49; F. B. Sheinerman, B. Honig, *J. Mol. Biol.* **2002**, *318*, 161; L. P. Lee, B. Tidor, *Nat. Struct. Biol.* **2001**, *8*, 73.
[10] G. Schreiber, A. R. Fersht, *Nat. Struct. Biol.* **1996**, *3*, 427.
[11] G. Schreiber, A. R. Fersht, *J. Mol. Biol.* **1995**, *248*, 478.
[12] I. Moarefi, D. Jeruzalmi, J. Turner, M. O'Donnell, J. Kuriyan, *J. Mol. Biol.* **2000**, *296*, 1215; D. Tworowski, A. V. Feldman, M. G. Safro, *J. Mol. Biol.* **2005**, *350*, 866.
[13] I. Muegge, P. X. Qi, A. J. Wand, Z. T. Chu, A. Warshel, *J. Phys. Chem. B* **1997**, *101*, 825; R. G. Alden, W. W. Parson, Z. T. Chu, A. Warshel, *J. Am. Chem. Soc.* **1995**, *117*, 12284; K. K. Rodgers, S. G. Sligar, *J. Am. Chem. Soc.* **1991**, *113*, 9419.
[14] Y. X. Jiang, V. Ruta, J. Y. Chen, A. Lee, R. MacKinnon, *Nature* **2003**, *423*, 42; D. A. Doyle, J. M. Cabral, R. A. Pfuetzner, A. L. Kuo, J. M. Gulbis, S. L. Cohen, B. T. Chait, R. MacKinnon, *Science* **1998**, *280*, 69; R. S. Eisenberg, *J. Membr. Biol.* **1996**, *150*, 1.
[15] S. Kumar, R. Nussinov, *J. Mol. Biol.* **1999**, *293*, 1241.
[16] H. X. Zhou, F. Dong, *Biophys. J.* **2003**, *84*, 2216; S. Kumar, R. Nussinov, *Proteins Struct. Funct. Genet.* **2000**, *41*, 485; S. Kumar, B. Y. Ma, C. J. Tsai, R. Nussinov, *Proteins Struct. Funct. Genet.* **2000**, *38*, 368; S. Spector, M. H. Wang, S. A. Carp, J. Robblee, Z. S. Hendsch, R. Fairman, B. Tidor, D. P. Raleigh, *Biochemistry* **2000**, *39*, 872.
[17] Z. S. Hendsch, B. Tidor, *Protein Sci.* **1994**, *3*, 211.
[18] D. Stigter, D. O. V. Alonso, K. A. Dill, *Proc. Natl. Acad. Sci. USA* **1991**, *88*, 4176.
[19] M. Hollecker, T. E. Creighton, *Biochim. Biophys. Acta* **1982**, *701*, 395.
[20] A. H. Elcock, *J. Mol. Biol.* **1999**, *294*, 1051; M. Schaefer, M. Sommer, M. Karplus, *J. Phys. Chem. B* **1997**, *101*, 1663.
[21] A. S. Yang, B. Honig, *J. Mol. Biol.* **1993**, *231*, 459.
[22] K. L. Shaw, G. R. Grimsley, G. I. Yakovlev, A. A. Makarov, C. N. Pace, *Protein Sci.* **2001**, *10*, 1206.
[23] J. P. Schmittschmitt, J. M. Scholtz, *Protein Sci.* **2003**, *12*, 2374; F. Chiti, M. Stefani, N. Taddei, G. Ramponi, C. M. Dobson, *Nature* **2003**, *424*, 805.
[24] B. Honig, A. Nicholls, *Science* **1995**, *268*, 1144.
[25] A. Warshel, A. Papazyan, *Curr. Opin. Struct. Biol.* **1998**, *8*, 211; Y. Y. Sham, Z. T. Chu, A. Warshel, *J. Phys. Chem. B* **1997**, *101*; T. Simonson, *Curr. Opin. Struct. Biol.* **2001**, *11*, 243; N. Sinha, S. J. Smith-Gill, *Curr. Protein Pept. Sci.* **2002**, *3*, 601.
[26] F. B. Sheinerman, R. Norel, B. Honig, *Curr. Opin. Struct. Biol.* **2000**, *10*, 153.
[27] W. Kauzmann, *Adv. Protein Chem.* **1959**, *12*, 1.
[28] K. A. Dill, *Biochemistry* **1990**, *29*, 7133.
[29] K. A. Dill, S. Bromberg, K. Z. Yue, K. M. Fiebig, D. P. Yee, P. D. Thomas, H. S. Chan, *Protein Sci.* **1995**, *4*, 561.
[30] H. S. Chan, K. A. Dill, *Annu. Rev. Biophys. Biophys. Chem.* **1991**, *20*, 447.
[31] K. A. Dill, *Protein Sci.* **1999**, *8*, 1166.

 © 2006 Wiley-VCH Verlag GmbH & Co. KGaA, Weinheim

[32] C. N. Pace, B. A. Shirley, M. McNutt, K. Gajiwala, *FASEB J.* **1996**, *10*, 75.
[33] P. L. Privalov, S. J. Gill, *Adv. Protein Chem.* **1988**, *41*, 191.
[34] G. Hummer, S. Garde, A. E. Garcia, M. E. Paulaitis, L. R. Pratt, *J. Phys. Chem. B* **1998**, *102*, 10469.
[35] C. Hansch, *Acc. Chem. Res.* **1993**, *26*, 147.
[36] J. Kyte, *Biophys. Chem.* **2003**, *100*, 193.
[37] N. T. Southall, K. A. Dill, A. D. J. Haymet, *J. Phys. Chem. B* **2002**, *106*, 521.
[38] D. A. McQuarrie, *Statistical Mechanics*, Harper & Row, New York, **1975**.
[39] P. G. de Gennes, *Scaling concepts in polymer physics*, Cornell University Press, Ithaca, NY, **1979**.
[40] K. A. Dill, *Biochemistry* **1985**, *24*, 1501.
[41] L. Stryer, *Biochemistry, 4th ed.*, Freeman, New York, **1995**.
[42] D. Voet, J. G. Voet, *Biochemistry, 3rd ed.*, Wiley, New York, **2004**.
[43] B. Schiott, B. B. Iversen, G. K. H. Madsen, F. K. Larsen, T. C. Bruice, *Proc. Natl. Acad. Sci. USA* **1998**, *95*, 12799; A. Warshel, *J. Biol. Chem.* **1998**, *273*, 27035; W. W. Cleland, P. A. Frey, J. A. Gerlt, *J. Biol. Chem.* **1998**, *273*, 25529; J. G. Chen, M. A. McAllister, J. K. Lee, K. N. Houk, *J. Org. Chem.* **1998**, *63*, 4611; E. L. Ash, J. L. Sudmeier, E. C. DeFabo, W. W. Bachovchin, *Science* **1997**, *278*, 1128; A. Warshel, A. Papazyan, *Proc. Natl. Acad. Sci. USA* **1996**, *93*, 13665; J. P. Guthrie, *Chem. Biol.* **1996**, *3*, 163; A. Warshel, A. Papazyan, P. A. Kollman, *Science* **1995**, *269*, 102; W. W. Cleland, M. M. Kreevoy, *Science* **1994**, *264*, 1887; P. A. Frey, S. A. Whitt, J. B. Tobin, *Science* **1994**, *264*, 1927.
[44] D. Bashford, M. Karplus, *Biochemistry* **1990**, *29*, 10219.
[45] C. Tanford, *Adv. Prot. Chem.* **1962**, *17*, 69.
[46] C. N. Schutz, A. Warshel, *Proteins* **2001**, *44*, 400.
[47] T. Simonson, C. L. Brooks III, *J. Am. Chem. Soc.* **1996**, *118*, 8452.
[48] K. A. Dill, S. Bromberg, *Molecular Driving Forces*, Garland, New York, **2003**.
[49] B. N. Dominy, H. Minoux, C. L. Brooks, *Proteins Struct. Funct. Genet.* **2004**, *57*, 128.
[50] K. D. Collins, M. W. Washabaugh, *Q. Rev. Biophys.* **1985**, *18*, 323.
[51] M. Bostrom, D. R. M. Williams, B. W. Ninham, *Biophys. J.* **2003**, *85*, 686.
[52] M. Bostrom, D. R. M. Williams, B. W. Ninham, *Eur. Phys. J. E* **2004**, *13*, 239.
[53] F. H. Arnold, G. Georgiou in *Methods in Molecular Biology, Vol. 230*, Humana, Totowa, NJ, **2003**.
[54] I. J. Colton, J. R. Anderson, J. Gao, R. G. Chapman, L. Isaacs, G. M. Whitesides, *J. Am. Chem. Soc.* **1997**, *119*, 12701.
[55] Y. Hagihara, Y. Tan, Y. Goto, *J. Mol. Biol.* **1994**, *237*, 336.
[56] R. S. Negin, J. D. Carbeck, *J. Am. Chem. Soc.* **2002**, *124*, 2911.
[57] J. D. Carbeck, I. J. Colton, J. Gao, G. M. Whitesides, *Acc. Chem. Res.* **1998**, *31*, 343.
[58] J. D. Carbeck, R. S. Negin, *J. Am. Chem. Soc.* **2001**, *123*, 1252.
[59] K. Sharp, B. Honig, *J. Phys. Chem.* **1990**, *94*, 7684; W. Rocchia, E. Alexov, B. Honig, *J. Phys. Chem. B* **2001**, *105*, 6507.
[60] A. R. Fersht, S. E. Jackson, L. Serrano, *Philos. Trans. R. Soc. Lond. A* **1993**, *345*, 141; A. R. Fersht, L. Serrano, *Curr. Opin. Struct. Biol.* **1993**, *3*, 75.
[61] H. Nakamura, *Q. Rev. Biophys.* **1996**, *29*, 1; T. Simonson, *Rep. Prog. Phys.* **2003**, *66*, 737; K. Sharp, B. Honig, *Annu. Rev. Biophys. Biophys. Chem.* **1990**, *19*.
[62] D. J. Winzor, *Anal. Biochem.* **2004**, *325*, 1.
[63] L. R. Deyoung, A. L. Fink, K. A. Dill, *Acc. Chem. Res.* **1993**, *26*, 614.
[64] G. H. Iyer, S. Dasgupta, J. A. Bell, *J. Cryst. Growth* **2000**, *217*, 429.
[65] A. George, W. W. Wilson, *Acta Crystallogr. Sect. D* **1994**, *50*, 361.
[66] T. Hill, *An Introduction to Statistical Thermodynamics*, Dover, **1986**.
[67] P. M. Tessier, A. M. Lenhoff, S. I. Sandler, *Biophys. J.* **2002**, *82*, 1620; P. M. Tessier, A. M. Lenhoff, *Curr. Opin. Biotechnol.* **2003**, *14*, 512.
[68] P. B. Warren, *J. Phys. Condens. Matter* **2002**, *14*, 7617; A. H. Elcock, J. A. McCammon, *Biophys. J.* **2001**, *80*, 613; W. C. K. Poon, S. U. Egelhaaf, P. A. Beales, A. Salonen, L. Sawyer, *J. Phys. Condens. Matter* **2000**, *12*, L569; R. C. Chang, D. Asthagiri, A. M. Lenhoff, *Proteins Struct. Funct. Genet.* **2000**, *41*, 123; C. J. Coen, H. W. Blanch, J. M. Prausnitz, *AIChE J.* **1995**, *41*, 996.
[69] B. L. Neal, D. Asthagiri, O. D. Velev, A. M. Lenhoff, E. W. Kaler, *J. Cryst. Growth* **1999**, *196*, 377.
[70] B. Guo, S. Kao, H. McDonald, A. Asanov, L. L. Combs, W. W. Wilson, *J. Cryst. Growth* **1999**, *196*, 424.
[71] J. P. K. Doye, A. A. Louis, M. Vendruscolo, *Phys. Biol.* **2004**, *1*, 9.
[72] A. Pande, J. Pande, N. Asherie, A. Lomakin, O. Ogun, J. King, G. B. Benedek, *Proc. Natl. Acad. Sci. USA* **2001**, *98*, 6116; P. G. Vekilov, A. R. Feeling-Taylor, D. N. Petsev, O. Galkin, R. L. Nagel, R. E. Hirsch, *Biophys. J.* **2002**, *83*, 1147.
[73] J. Z. Wu, D. Bratko, J. M. Prausnitz, *Proc. Natl. Acad. Sci. USA* **1998**, *95*, 15169.
[74] M. Bostrom, B. W. Ninham, *J. Phys. Chem. B* **2004**, *108*, 12593.
[75] W. Kunz, L. Belloni, O. Bernard, B. W. Ninham, *J. Phys. Chem. B* **2004**, *108*, 2398.
[76] P. M. Tessier, A. M. Lenhoff, *Curr. Opin. Biotechnol.* **2003**, *14*, 512.
[77] A. H. Elcock, D. Sept, J. A. McCammon, *J. Phys. Chem. B* **2001**, *105*, 1504.
[78] C. J. Camacho, Z. Weng, S. Vajda, C. DeLisi, *Biophys. J.* **1999**, *76*, 1166.
[79] A. Warshel, *Annu. Rev. Biophys. Biomol. Struct.* **2003**, *32*, 425; A. Warshel, *Acc. Chem. Res.* **2002**, *35*, 385.
[80] A. Warshel, J. Florian, *Proc. Natl. Acad. Sci. USA* **1998**, *95*, 5950; A. H. Elcock, M. J. Potter, D. A. Matthews, D. R. Knighton, J. A. McCammon, *J. Mol. Biol.* **1996**, *262*, 370; J. Antosiewicz, S. T. Wlodek, J. A. McCammon, *Biopolymers* **1996**, *39*, 85.
[81] J. M. Sanchez-Ruiz, G. I. Makhatadze, *Trends Biotechnol.* **2001**, *19*, 132.
[82] D. B. Burns, A. L. Zydney, *AIChE J.* **2001**, *47*, 1101.
[83] D. B. Burns, A. L. Zydney, *Biotechnol. Bioeng.* **1999**, *64*, 27.
[84] M. F. Ebersold, A. L. Zydney, *Biotechnol. Bioeng.* **2004**, *85*, 166.
[85] M. K. Menon, A. L. Zydney, *J. Membr. Sci.* **2001**, *181*, 179.
[86] D. Nagrath, B. W. Bequette, S. M. Cramer, A. Messac, *AIChE J.* **2005**, *51*, 511; C. A. Brooks, S. M. Cramer, *AIChE J.* **1992**, *38*, 1969.
[87] Y. Yao, A. M. Lenhoff, *Anal. Chem.* **2004**, *76*, 6743; J. Stahlberg, *J. Chromatogr. A* **1999**, *855*, 3.
[88] C. A. Haynes, F. J. Benitez, H. W. Blanch, J. M. Prausnitz, *AIChE J.* **1993**, *39*, 1539; A. P. Sassi, A. J. Shaw, S. M. Han, H. W. Blanch, J. M. Prausnitz, *Polymer* **1996**, *37*, 2151.
[89] W. L. Jorgensen, D. S. Maxwell, J. TiradoRives, *J. Am. Chem. Soc.* **1996**, *118*, 11225; W. D. Cornell, P. Cieplak, C. I. Bayly, I. R. Gould, K. M. Merz, D. M. Ferguson, D. C. Spellmeyer, T. Fox, J. W. Caldwell, P. A. Kollman, *J. Am. Chem. Soc.* **1995**, *117*, 5179; D. Sitkoff, K. A. Sharp, B. Honig, *J. Phys. Chem.* **1994**, *98*, 1978; M. E. Davis, J. D. Madura, B. A. Luty, J. A. McCammon, *Comput. Phys. Commun.* **1991**, *62*, 187; B. H. Besler, K. M. Merz, P. A. Kollman, *J. Comput. Chem.* **1990**, *11*, 431; B. R. Brooks, R. E. Bruccoleri, B. D. Olafson, D. J. States, S. Swaminathan, M. Karplus, *J. Comput. Chem.* **1983**, *4*, 187.

 © 2006 Wiley-VCH Verlag GmbH & Co. KGaA, Weinheim

[90] A. D. MacKerell, D. Bashford, M. Bellott, R. L. Dunbrack, J. D. Evanseck, M. J. Field, S. Fischer, J. Gao, H. Guo, S. Ha, D. Joseph-McCarthy, L. Kuchnir, K. Kuczera, F. T. K. Lau, C. Mattos, S. Michnick, T. Ngo, D. T. Nguyen, B. Prodhom, W. E. Reiher, B. Roux, M. Schlenkrich, J. C. Smith, R. Stote, J. Straub, M. Watanabe, J. Wiorkiewicz-Kuczera, D. Yin, M. Karplus, *J. Phys. Chem. B* **1998**, *102*, 3586.
[91] A. Giletto, C. N. Pace, *Biochemistry* **1999**, *38*, 13379.
[92] B. E. Garcia-Moreno, J. J. Dwyer, A. G. Gittis, E. E. Lattman, D. S. Spencer, W. E. Stites, *Biophys. Chem.* **1997**, *64*, 211.
[93] D. E. Anderson, W. J. Becktel, F. W. Dahlquist, *Biochemistry* **1990**, *29*, 2403.
[94] L. Polgar, *Euro. J. Biochem.* **1973**, *33*, 104.
[95] C. A. Ibarra, B. S. Nieslanik, W. M. Atkins, *Biochemistry* **2001**, *40*, 10614.
[96] J. Wyman, S. J. Gill, *Binding and Linkage: The Functional Chemistry of Biological Macromolecules*, University Science Books, Mill Valley, CA, **1990**.
[97] C. Tanford, R. Roxby, *Biochemistry* **1972**, *11*, 2192.
[98] R. Roxby, C. Tanford, *Biochemistry* **1971**, *10*, 3348.
[99] Y. Tan, M. Oliveberg, A. R. Fersht, *J. Mol. Biol.* **1995**, *254*, 980.
[100] S. Kuramitsu, K. Hamaguchi, *J. Biochem.* **1980**, *87*, 1215.
[101] A. L. Fink, L. J. Calciano, Y. Goto, M. Nishimura, S. A. Swedberg, *Protein Sci.* **1993**, *2*, 1155.
[102] S. Kim, J. Baum, *Protein Sci.* **1998**, *7*, 1930.
[103] Y. Goto, N. Takanashi, A. L. Fink, *Biochemistry* **1990**, *29*, 3480.
[104] Y. Goto, L. J. Calciano, A. L. Fink, *Proc. Natl. Acad. Sci. USA* **1990**, *87*, 573.
[105] M. K. Menon, A. L. Zydney, *Anal. Chem.* **2000**, *72*, 5714.
[106] I. Gitlin, M. Mayer, G. M. Whitesides, *J. Phys. Chem. B* **2003**, *107*, 1466.
[107] U. Sharma, R. S. Negin, J. D. Carbeck, *J. Phys. Chem. B* **2003**, *107*, 4653.
[108] K. C. Linderstrom-Lang, *C. R. Trav. Lab. Carlsberg* **1924**, *15*, 1.
[109] M. Lund, B. Jonsson, *Biochemistry* **2005**, *44*, 5722; T. Simonson, J. Carlsson, D. A. Case, *J. Am. Chem. Soc.* **2004**, *126*, 4167; T. Grycuk, *J. Phys. Chem. B* **2002**, *106*, 1434.
[110] J. M. Gao, F. A. Gomez, R. Harter, G. M. Whitesides, *Proc. Natl. Acad. Sci. USA* **1994**, *91*, 12027.
[111] J. D. Carbeck, I. J. Colton, J. R. Anderson, J. M. Deutch, G. M. Whitesides, *J. Am. Chem. Soc.* **1999**, *121*, 10671.
[112] M. C. Justice, J. C. Justice, *J. Solution Chem.* **1976**, *5*, 543; H. Yokoyama, H. Yamatera, *Bull. Chem. Soc. Jpn.* **1975**, *48*, 1770.
[113] J. E. Prue, *J. Chem. Educ.* **1969**, *46*, 12.
[114] M. Mihailescu, M. K. Gilson, *Biophys. J.* **2004**, *87*, 23.
[115] D. R. Lide, *Handbook of Chemistry and Physics*, *84th ed.*, CRC, Boca Raton, **2003**.
[116] D. F. Evans, H. Wennerstrom, *The colloidal domain: Where physics, chemistry, biology and technology meet*, *1st ed.*, VCH, New York, **1994**.
[117] J. Israelachvili, *Intermolecular and Surface Forces: With Applications to Colloidal and Biological Systems*, *2nd ed.*, Academic Press, New York, **1992**.
[118] A. V. Morozov, T. Kortemme, D. Baker, *J. Phys. Chem. B* **2003**, *107*, 2075.
[119] D. Perl, U. Mueller, U. Heinemann, F. X. Schmid, *Nat. Struct. Biol.* **2000**, *7*, 380.
[120] P. Barth, I. Guillouard, P. Setif, B. Lagoutte, *J. Biol. Chem.* **2000**, *275*, 7030.
[121] R. Loewenthal, J. Sancho, T. Reinikainen, A. R. Fersht, *J. Mol. Biol.* **1993**, *232*, 574.
[122] S. Dao-pin, U. Sauer, H. Nicholson, B. W. Matthews, *Biochemistry* **1991**, *30*, 7142.
[123] S. E. Jackson, A. R. Fersht, *Biochemistry* **1993**, *32*, 13909.
[124] S. J. Benkovic, S. Hammes-Schiffer, *Science* **2003**, *301*, 1196.
[125] J. Warwicker, H. C. Watson, *J. Mol. Biol.* **1982**, *157*, 671.
[126] A. Nicholls, B. Honig, *J. Comput. Chem.* **1991**, *12*, 435.
[127] P. D. Grossman, J. C. Colburn, *Capillary Electrophoresis. Theory and Practice*, Academic Press, San Diego, CA, **1992**.
[128] A. R. Fersht, *FEBS Lett.* **1993**, *325*, 5; A. R. Fersht, *Philos. Trans. R. Soc. Lond. B* **1995**, *348*, 11.
[129] F. Chiti, M. Calamai, N. Taddei, M. Stefani, G. Ramponi, C. M. Dobson, *Proc. Natl. Acad. Sci. USA* **2002**, *99*, 16419.
[130] D. Matulis, J. K. Kranz, F. R. Salemme, M. J. Todd, *Biochemistry* **2005**, *44*, 5258.
[131] K. Gudiksen, I. Gitlin, J. Yang, A. R. Urbach, D. T. Moustakas, G. M. Whitesides, *J. Am. Chem. Soc.* **2005**, *127*, 4707.
[132] C. T. Supuran, A. Scozzafava, A. Casini, *Med. Res. Rev.* **2003**, *23*, 146.
[133] J. Gao, M. Mrksich, F. Gomez, G. M. Whitesides, *Anal. Chem.* **1995**, *67*, 3093.
[134] E. Cordova, J. Gao, G. M. Whitesides, *Anal. Chem.* **1997**, *69*, 1370.
[135] J. E. Coligan, B. M. Dunn, H. L. Ploegh, D. W. Speicher, P. T. Wingfield, *Current Protocols in Protein Science*, Wiley, New York, **2003**.
[136] A. N. Glazer, *Annu. Rev. Biochem.* **1970**, *39*, 101.
[137] J. R. Anderson, O. Cherniavsky, I. Gitlin, G. S. Engel, L. Yuditsky, G. M. Whitesides, *Anal. Chem.* **2002**, *74*, 1870.
[138] S. Rimon, G. E. Perlmann, *J. Biol. Chem.* **1968**, *243*, 3566; V. V. Loladze, G. I. Makhatadze, *Protein Sci.* **2002**, *11*, 174.
[139] I. Gitlin, J. Yang, G. M. Whitesides, unpublished results.
[140] D. G. Hoare, D. E. Koshland, Jr., *J. Biol. Chem.* **1967**, *242*, 2447.
[141] K. Toi, E. Bynum, E. Norris, H. A. Itano, *J. Biol. Chem.* **1967**, *242*, 1036.
[142] L. Patthy, E. L. Smith, *J. Biol. Chem.* **1975**, *250*, 557; L. Patthy, E. L. Smith, *J. Biol. Chem.* **1975**, *250*, 565.
[143] A. A. Vinogradov, E. V. Kudryashova, V. Y. Grinberg, N. V. Grinberg, T. V. Burova, A. V. Levashov, *Protein Eng.* **2001**, *14*, 683.
[144] U. Sharma, J. D. Carbeck, *Electrophoresis* **2005**, *26*, 2086.
[145] J. Yang, I. Gitlin, V. M. Krishnamurthy, J. A. Vazquez, C. E. Costello, G. M. Whitesides, *J. Am. Chem. Soc.* **2003**, *125*, 12392.
[146] S. Julka, F. E. Regneir, *Anal. Chem.* **2004**, *76*, 5799.
[147] U. Sharma, J. D. Carbeck, *Methods Mol. Biol.* **2004**, *276*, 189.
[148] M. Mammen, I. J. Colton, J. D. Carbeck, R. Bradley, G. M. Whitesides, *Anal. Chem.* **1997**, *69*, 2165.
[149] S. Hjerten, *J. Chromatogr.* **1985**, *347*, 191; J. Horvath, V. Dolnik, *Electrophoresis* **2001**, *22*, 644.
[150] H. Katayama, Y. Ishihama, N. Asakawa, *Anal. Chem.* **1998**, *70*, 5272; T. W. Graul, J. B. Schlenoff, *Anal. Chem.* **1999**, *71*, 4007.
[151] R. J. Hunter, *Foundations of Colloid Science*, *Vol. 1*, Oxford University Press, New York, **1991**.
[152] D. C. Henry, *Proc. R. Soc. London Ser. A* **1931**, *133*, 106.
[153] $f(\kappa R) = (1 + \frac{\kappa^2 R^2}{16} - \frac{5\kappa^3 R^3}{48} - \frac{\kappa^4 R^4}{96} + \frac{\kappa^5 R^5}{96} - \frac{11}{98} e^{\kappa R} \int_{\infty}^{\kappa R} \frac{e^{-r}}{r} dr)$;
in this expression, κ [m^{-1}] is the Debye screening parameter, r is a dimensionless distance (namely, distance multiplied by κ) and R [m] is the radius of the particle.
[154] This assumption comes from the linearization of the Poisson–Boltzmann equation which involves expanding the exponential and retaining only the term linear in potential. Doing so is valid when $e\psi_s/kT$ and $|\psi_s| < 25$ mV at 25 °C.
[155] J. G. De la Torre, M. L. Huertas, B. Carrasco, *Biophys. J.* **2000**, *78*, 719.
[156] B. J. Yoon, S. Kim, *J. Colloid Interface Sci.* **1989**, *128*, 275.
[157] R. W. O'Brien, L. R. White, *J. Chem. Soc. Faraday Trans. 2* **1978**, *74*, 1607.
[158] M. V. Piaggio, M. B. Peirotti, J. A. Deiber, *Electrophoresis* **2005**, *26*, 3232.
[159] S. A. Allison, J. D. Carbeck, C. Y. Chen, F. Burkes, *J. Phys. Chem. B* **2004**, *108*, 4516.
[160] W. B. Russel, D. A. Saville, W. R. Schowalter, *Colloidal Dispersions*, Cambridge University Press, Cambridge, UK, **1999**.

 © 2006 Wiley-VCH Verlag GmbH & Co. KGaA, Weinheim

[161] S. A. Allison, V. T. Tran, *Biophys. J.* **1995**, *68*, 2261; S. A. Allison, *Macromolecules* **1996**, *29*, 7391; S. A. Allison, M. Potter, J. A. McCammon, *Biophys. J.* **1997**, *73*, 133.
[162] L. L. Kiefer, S. A. Paterno, C. A. Fierke, *J. Am. Chem. Soc.* **1995**, *117*, 6831.
[163] M. Raghavan, V. R. Bonagura, S. L. Morrison, P. J. Bjorkman, *Biochemistry* **1995**, *34*, 14649; W. L. Martin, A. P. West, L. Gan, P. J. Bjorkman, *Mol. Cell* **2001**, *7*, 867; E. R. Sprague, W. L. Martin, P. J. Bjorkman, *J. Biol. Chem.* **2004**, *279*, 14184.
[164] P. Beroza, D. A. Case, *J. Phys. Chem.* **1996**, *100*, 20156.
[165] K. K. Lee, C. A. Fitch, B. E. Garcia-Moreno, *Protein Sci.* **2002**, *11*, 1004.
[166] U. Sharma, J. D. Carbeck, unpublished results.
[167] M. S. Bello, R. Rezzonico, P. G. Righetti, *Science* **1994**, *266*, 773.
[168] U. Sharma, N. J. Gleason, J. D. Carbeck, *Anal. Chem.* **2005**, *77*, 806.
[169] G. Taylor, *Proc. R. Soc. London B* **1953**, *140*, 219.
[170] E. A. Permyakov, L. A. Morozova, E. A. Burstein, *Biophys. Chem.* **1985**, *21*, 21.
[171] A. G. Ogston, *Trans. Faraday Soc.* **1958**, *54*, 1754.
[172] I. J. Colton, J. D. Carbeck, J. Rao, G. M. Whitesides, *Electrophoresis* **1998**, *19*, 367.
[173] Y.-H. Chu, L. Z. Avila, J. Gao, G. M. Whitesides, *Acc. Chem. Res.* **1995**, *28*, 461; R. M. Guijt-van Duijn, J. Frank, G. W. van Dedem, E. Baltussen, *Electrophoresis* **2000**, *21*, 3905.
[174] L. Z. Avila, Y.-H. Chu, E. C. Blossey, G. M. Whitesides, *J. Med. Chem.* **1993**, *36*, 126.
[175] R. Lavecchia, M. Zugaro, *FEBS Lett.* **1991**, *292*, 162.
[176] V. J. Hilser, E. Freire, *Anal. Biochem.* **1995**, *224*, 465.
[177] F. M. Robbins, F. E. Andreotti, L. G. Holmes, M. J. Kronman, *Biochim. Biophys. Acta* **1967**, *133*, 33.
[178] S. J. Wearne, T. E. Creighton, *Proteins Struct. Funct. Genet.* **1989**, *5*, 8.
[179] C. Redfield, B. A. Schulman, M. A. Milhollen, P. S. Kim, C. M. Dobson, *Nat. Struct. Biol.* **1999**, *6*, 948.
[180] C. Tanford, *Physical Chemistry of Macromolecules*, Wiley, New York, **1961**.
[181] F. Rusconi, R. Guillonneau, D. Praseuth, *Mass Spectrom. Rev.* **2002**, *21*, 5; M. Mann, R. C. Hendrickson, A. Pandey, *Annu. Rev. Biochem.* **2001**, *70*, 437.
[182] J. D. Carbeck, J. C. Severs, J. Gao, Q. Wu, R. D. Smith, G. M. Whitesides, *J. Phys. Chem. B* **1998**, *102*, 10596.
[183] J. A. Loo, R. R. Loo, H. R. Udseth, C. G. Edmonds, R. D. Smith, *Rapid Commun. Mass Spectrom.* **1991**, *5*, 101.
[184] N. S. Pujar, A. L. Zydney, *Ind. Eng. Chem. Res.* **1994**, *33*.
[185] F. G. Smith, W. M. Deen, *J. Colloid Interface Sci.* **1980**, *78*, 444.
[186] L. Zeman, A. L. Zydney, *Microfiltration and Ultrafiltration: Principles and Applications*, Marcel Dekker, New York, **1996**.
[187] F. E. Regneir, *Science* **1987**, *238*, 319.
[188] A. D. Diamond, J. T. Hsu, *Adv. Biochem. Eng./Biotechnol.* **1992**, *47*.
[189] N. S. Pujar, A. L. Zydney, *J. Chromatogr. A* **1998**, *796*, 229.
[190] J. Gao, G. M. Whitesides, *Anal. Chem.* **1997**, *69*, 575.
[191] R. P. Sear, *J. Chem. Phys.* **2003**, *118*, 5157.
[192] R. P. Sear, J. A. Cuesta, *Phys. Rev. Lett.* **2003**, *91*; B. L. Neal, D. Asthagiri, A. M. Lenhoff, *Biophys. J.* **1998**, *75*, 2469.
[193] R. J. Ellis, A. P. Minton, *Nature* **2003**, *425*, 27; D. Hall, A. P. Minton, *Biochim. Biophys. Acta* **2003**, *1649*, 127.
[194] J. S. Richardson, D. C. Richardson, N. B. Tweedy, K. M. Gernert, T. P. Quinn, M. H. Hecht, B. W. Erickson, Y. B. Yan, R. D. McClain, M. E. Donlan, M. C. Surles, *Biophys. J.* **1992**, *63*, 1186; M. J. Nohaile, Z. S. Hendsch, B. Tidor, R. T. Sauer, *Proc. Natl. Acad. Sci. USA* **2001**, *98*, 3109.
[195] J. S. Richardson, D. C. Richardson, *Proc. Natl. Acad. Sci. USA* **2002**, *99*, 2754.
[196] W. Wang, M. H. Hecht, *Proc. Natl. Acad. Sci. USA* **2002**, *99*, 2760.
[197] B. Alberts, J. Alexander, J. Lewis, M. Raff, K. Roberts, P. Walter, *Molecular Biology of the Cell*, *4th ed.*, Garland, New York, **2002**.
[198] D. Lagadic-Gossmann, L. Huc, V. Lecureur, *Cell Death Differ.* **2004**, *11*, 953.
[199] S. Simon, D. Roy, M. Schindler, *Proc. Natl. Acad. Sci. USA* **1994**, *91*, 1128.
[200] P. Heikinheimo, R. Helland, H. K. S. Leiros, I. Leiros, S. Karlsen, G. Evjen, R. Ravelli, G. Schoehn, R. Ruigrok, O. K. Tollersrud, S. McSweeney, E. Hough, *J. Mol. Biol.* **2003**, *327*, 631.
[201] M. Lakadamyali, M. J. Rust, X. W. Zhuang, *Microb. Infect.* **2004**, *6*, 929.
[202] M. Leist, P. Ghezzi, G. Grasso, R. Bianchi, P. Villa, M. Fratelli, C. Savino, M. Bianchi, J. Nielsen, J. Gerwien, P. Kallunki, A. K. Larsen, L. Helboe, S. Christensen, L. O. Pedersen, M. Nielsen, L. Torup, T. Sager, A. Sfacteria, S. Erbayraktar, Z. Erbayraktar, N. Gokmen, O. Yilmaz, C. Cerami-Hand, Q. W. Xie, T. Coleman, A. Cerami, M. Brines, *Science* **2004**, *305*, 239.
[203] C. A. Sarkar, K. Lowenhaupt, T. Horan, T. C. Boone, B. Tidor, D. A. Lauffenburger, *Nat. Biotechnol.* **2002**, *20*, 908.
[204] M. Bostrom, V. S. J. Craig, R. Albion, D. R. M. Williams, B. W. Ninham, *J. Phys. Chem. B* **2003**, *107*, 2875; M. Bostrom, W. Kunz, B. W. Ninham, *Langmuir* **2005**, *21*, 2619; M. C. Gurau, S. M. Lim, E. T. Castellana, F. Albertorio, S. Kataoka, P. S. Cremer, *J. Am. Chem. Soc.* **2004**, *126*, 10522.

 © 2006 Wiley-VCH Verlag GmbH & Co. KGaA, Weinheim

Communications

DOI: 10.1002/anie.200503624

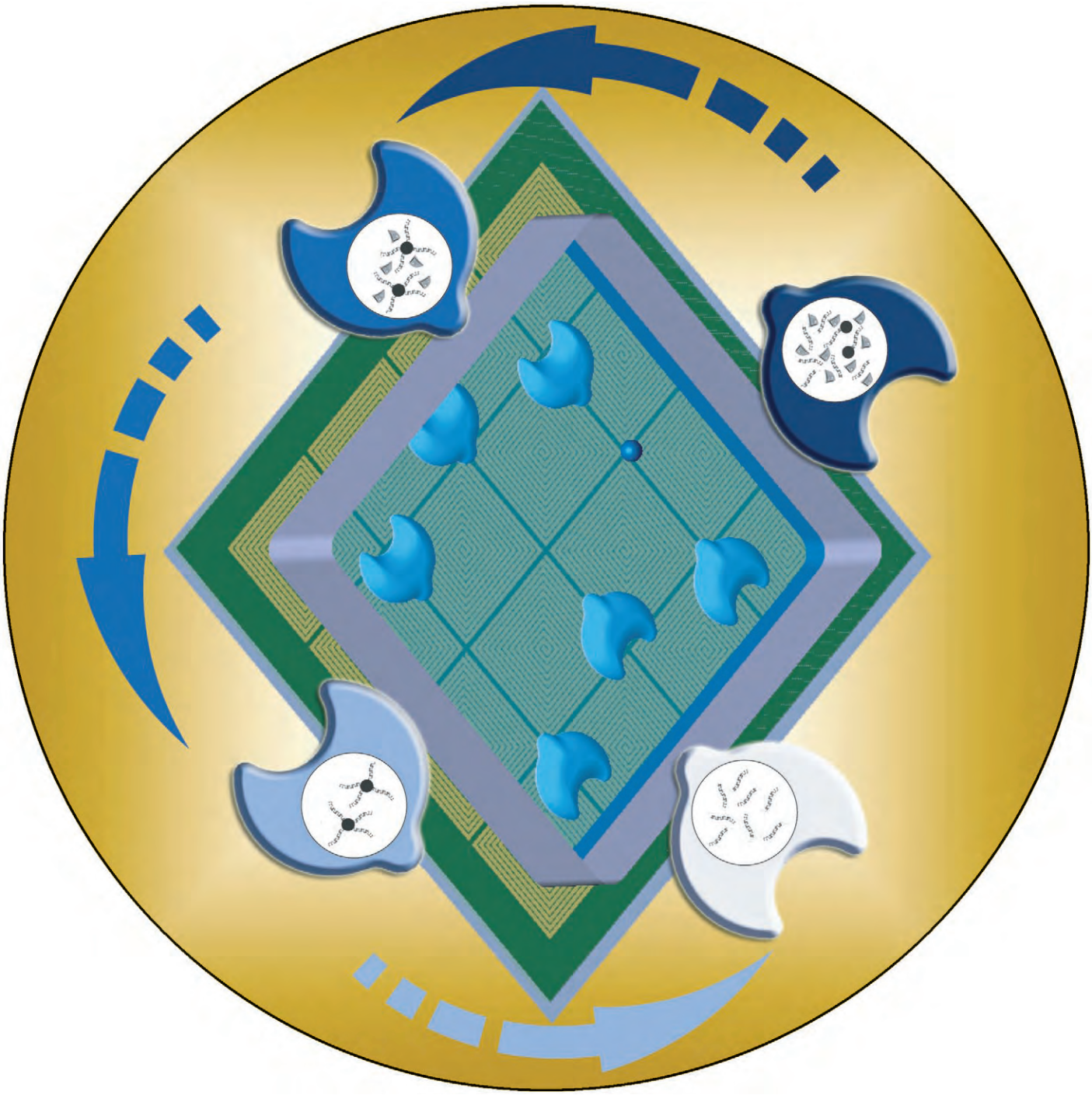

The manipulation of small droplets through magnetic particles and an array of coils offers new possibilities for the miniaturization of bioanalytical and biochemical applications. In their Communication on page ff., U. Lehmann et al. present an on-chip process for the purification of DNA, making it possible to extract the DNA from as little as 10 cells.

WILEY InterScience DISCOVER SOMETHING GREAT
© 2006 Wiley-VCH Verlag GmbH & Co. KGaA, Weinheim

Microfluidics

DOI: 10.1002/anie.200503624

Droplet-Based DNA Purification in a Magnetic Lab-on-a-Chip**

Ulrike Lehmann, Caroline Vandevyver, Virendra K. Parashar, and Martin A. M. Gijs*

The handling of small liquid volumes is an important task in miniaturized analytical systems where decreased sample sizes can reduce analysis times and costs.[1,2] Herein, we describe a microfluidic system based on the two-dimensional magnetic manipulation of free aqueous droplets. The drops are suspended in silicone oil and contain magnetic microparticles that serve both as force mediators for the magnetic actuation and as a mobile substrate for the molecules.[3–6]

When the interfacial tension between the droplet and the oil medium is carefully adjusted, a matrix of simple coils can be used for the actuation; external moving magnets are not required high operational flexibility is possible. The increased degrees of freedom in fluid handling and the capability to work with small sample volumes makes our system an ideal platform for molecular diagnostics, especially for DNA purification. With this system, we demonstrate an integrated on-chip DNA-purification process where DNA can be extracted from a raw cell lysate. This method is of high interest for miniaturized bioanalysis applications, as current chip-based PCR devices require pure DNA samples for successful DNA amplification.[7]

Several promising adsorption-based separation techniques that employ the binding of DNA to silica surfaces have been reported as alternatives to laborious traditional methods, such as phenol extraction procedures.[8–11] These devices are mainly based on microfluidic channels that have limited flexibility with respect to scale and reconfiguration.[11] Here, the manipulation of liquids in small discrete volumes (microdroplets) can provide an alternative,[12,13] especially when the droplets are not confined by microchannels, thus introducing additional degrees of freedom and reducing problems of adsorption on the channel walls.[14,15] Moreover, it has been shown that additives to the oil medium surrounding the droplet can decrease adsorption at liquid–liquid interfaces through the formation of a monolayer of molecules around the droplet surface.[16] Recent reports, based on a variety of principles, demonstrate the manipulation of droplets without microfluidic channels.[17–21] Among these, magnetic actuation offers the advantages of long-range and large forces,[19] which allows droplet manipulation with very limited surface contact. A further advantage is the weak interaction between the magnetic field and the aqueous droplet media, which extends the system's compatibility towards polar and ionic samples.

Herein, we present a magnetic droplet manipulation system (Figure 1) in which aqueous droplets are actuated through a multilayer set of coils on a printed circuit board (PCB). The PCB generates a changeable magnetic-field topology over the chip surface that allows variation in the force that acts on the magnetic particles inside the droplets. This magnetic force is strongly enhanced when the whole system is placed in an external homogeneous magnetic field, thus increasing the magnetic moment of the particles.[22] On top of the PCB, we place a reservoir containing silicone oil. The density of the oil is adjusted such that an aqueous droplet can sink to the bottom of the reservoir where its spherical shape is approximately retained. This is important as the magnetic force created within the droplet depends strongly on its distance to the PCB and thus allows an optimal use of the field energy. The submerged and nearly spherical droplets slide, driven by the field gradient, over the reservoir bottom, which consists of a very thin hydrophobic teflon layer (12.5 μm). This layer keeps the droplet and the coil multilayer a small distance apart and prevents adhesion-related problems. If a fixed position of the droplet is desired, the friction between the droplet and the reservoir bottom can be increased by locally modifying the surface of the teflon layer with oxygen plasma.[23] The resultant hydrophilic pattern serves as a droplet immobilization site for droplet merging and splitting operations. The hydrophilicity of the plasma-treated teflon areas does not degrade during experiments, and the zones exposed to the oxygen plasma display a clear hydrophilic behavior even several months after treatment. The plasma treatment is generally done directly before the use of the reservoir, which provides stable hydrophilic conditions for the droplet manipulation. The fact that the teflon foil is the only part that is replaced between experi-

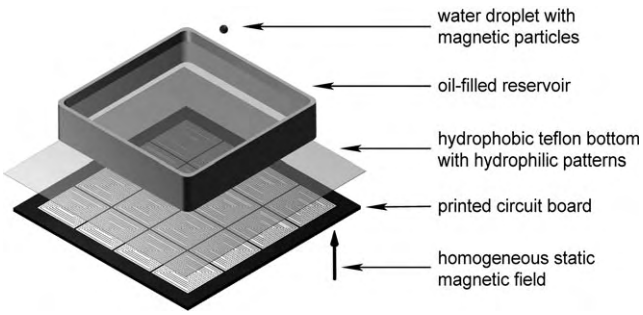

Figure 1. Schematic diagram of the droplet-manipulation system.

[*] U. Lehmann, Dr. V. K. Parashar, Prof. M. A. M. Gijs
Institute of Microelectronics and Microsystems
Ecole Polytechnique Fédérale de Lausanne (EPFL)
1015 Lausanne (Switzerland)
Fax: (+41) 21-693-5950
E-mail: ulrike.lehmann@epfl.ch
Dr. C. Vandevyver
Laboratory of Chemical Biotechnology
Ecole Polytechnique Fédérale de Lausanne (EPFL)
1015 Lausanne (Switzerland)

[**] We thank the Swiss National Science Foundation (Grant 200020-107372) for financial support of this research. We also acknowledge Dr. A. Rida and S. Hadjidj for their advice and support in the initial phase of the project, M. Friedrich for assistance with the experiments, A. Tschersich for determination of the oil properties, and F. Fenter for critical reading of the manuscript.

 © 2006 Wiley-VCH Verlag GmbH & Co. KGaA, Weinheim

ments results in a highly flexible and user-friendly system. Among the different droplet-manipulation steps, extracting a small liquid volume from an immobilized droplet (droplet splitting) presents the most challenging task because sufficient energy is required to overcome the interfacial tension. The tension can be lowered by careful adjustment of the oil composition. As the energy needed to deform and split a droplet is directly related to the change in droplet surface area,[24] the splitting process can be facilitated by taking advantage of the hydrophilic patterning of the teflon bottom where well-defined hydrophilic shapes allow the deformation of the naturally semispherical immobilized droplet. Figure 2 shows a splitting sequence starting with a deformation of an initially heart-shaped immobilized droplet of 12 μL and ending with the release of a second 2-μL droplet containing the magnetic particles. The combination of optimized hydrophilic/hydrophobic surface patterning and adjusted oil properties enables us to perform all droplet-manipulation steps, such as transport, merging, mixing, and splitting, in an easy-to-construct system.

By combining droplet-manipulation steps, we could design a DNA-purification procedure in which the magnetic particles are used as carriers for the DNA while the protocol for macroscopic bead-based DNA-purification procedures is followed.[25] Our on-chip DNA purification employs six stages of droplet merging, mixing, and splitting. The buffer solutions for binding, washing, and elution are present on the chip in the form of immobilized 10-μL droplets. Figure 3 is a schematic summary of the complete procedure, which involves DNA-to-particle binding (a), washing (b), and elution of the DNA from the particles (c). Following the chosen protocol, the sample DNA was bound to the silica beads after chemical cell lysis in a colored guanidinium thiocyanate (GuSCN) binding buffer solution (position 1). The sample DNA binds preferentially to the silica surface of the magnetic beads owing to the presence of chaotropic salts like guanidinium or sodium iodide.[8] Other molecules, such as proteins and lipids, remain free in the solution.[26] The DNA binding is driven by three major effects: 1) shielding of intermolecular electrostatic forces, 2) dehydration of DNA and silica surfaces, and 3) formation of intermolecular hydrogen bonds in the DNA–silica contact layer. After binding, a small droplet containing the DNA–particle complex was extracted from the binding site and passed through a series of immobilized droplets of wash solutions (positions 2–4) to remove cellular debris, proteins, and lipids (Figure 3b). The first washing site

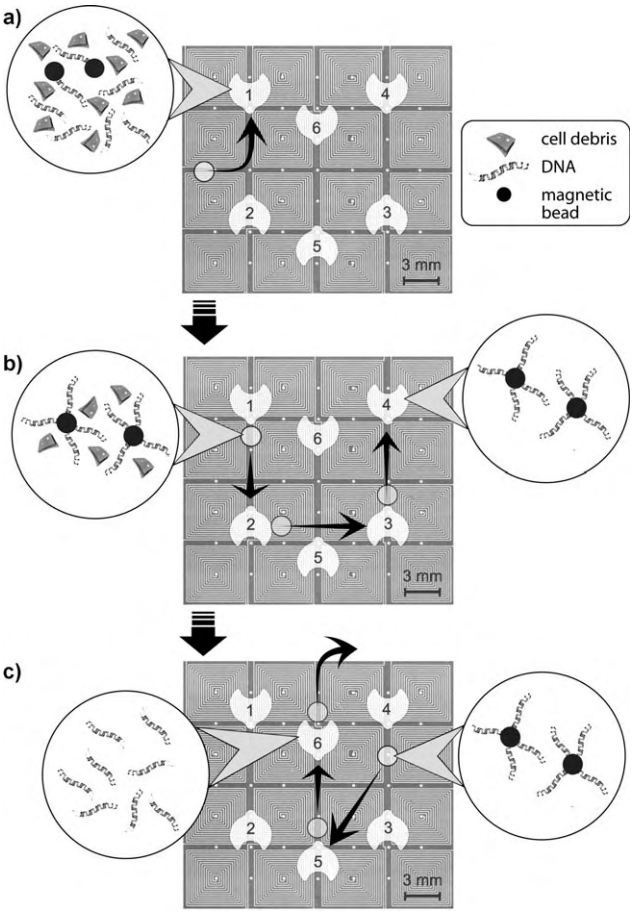

Figure 3. Schematic representation of DNA purification from a lysed cell sample solution: a) the binding of the DNA to the magnetic particles in the binding/lysis buffer (position 1); b) a series of three washing steps to remove any transferred cell debris, proteins, and lipids (positions 2–4); and c) removal of DNA from the magnetic beads through magnetic agitation in two immobilized droplets of elution buffer solution (positions 5–6) and, subsequently, removal of the magnetic particle from the chip.

(position 2) contains ethanol, water, and guanidinium chloride, whereas the following two hold only ethanol and water (positions 3 and 4). Finally, the cleaned particle-bound DNA was mixed with droplets of low-ionic-strength elution buffer solution or water (positions 5 and 6) to remove the DNA from the particles (Figure 3c). The particles were then subsequently extracted from the system.

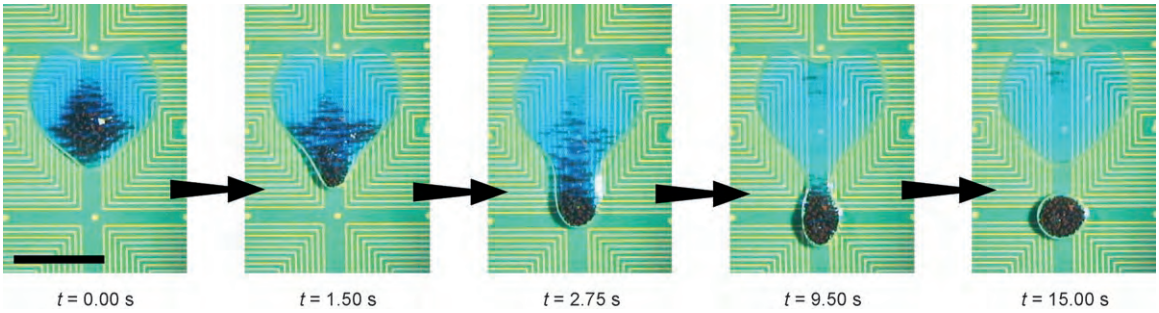

Figure 2. Photographs of a droplet splitting sequence, starting from a deformed droplet of 12 μL. Scale bar: 3 mm.

 © 2006 Wiley-VCH Verlag GmbH & Co. KGaA, Weinheim

The eluted DNA can be detected on- or off-chip through a fluorescent marker, or used for subsequent amplification. Off-chip detection offers the advantage of a standardized read-out protocol, whereas on-chip detection avoids additional pipetting and dilution and results in a higher sensitivity and recovery. Figure 4a shows the reservoir after a complete procedure including extraction of the separated magnetic droplet. The washing efficiency can be clearly seen through the fading of the color introduced by the binding buffer in position 1. A typical on-chip detection by using a fluorescent marker is shown in Figure 4b.

We evaluated the bioanalytical performance characteristics of our system by using three different types of genomic material of increasing complexity, *HinD* III-digested λ-phage DNA, human genomic DNA fragments (> 50 kb), and mammalian Jurkat ATCC TIB-152 cells. In experiments with the λ-phage DNA, we detected off-chip 20–25% of the initial DNA content (Figure 5a), which is comparable to the performance of macroscopic bead-based purification systems and miniaturized purification devices that are based on other principles. With direct on-chip fluorescence analysis, we measured up to 50% recovery (see Figure 4b), which demonstrates the increased efficiency of on-site detection.

As a second step, we examined the performance of the system for the purification of human genomic DNA fragments whose strands are longer than the λ-phage DNA. Samples with different concentrations of DNA were processed, and after elution, collected for off-chip analysis. The measured DNA recovery was in the range of 25% (Figure 5b), which is similar to the value obtained for the shorter stranded λ-phage DNA, therefore demonstrating that the system is not dependent on the length of the DNA strand. To

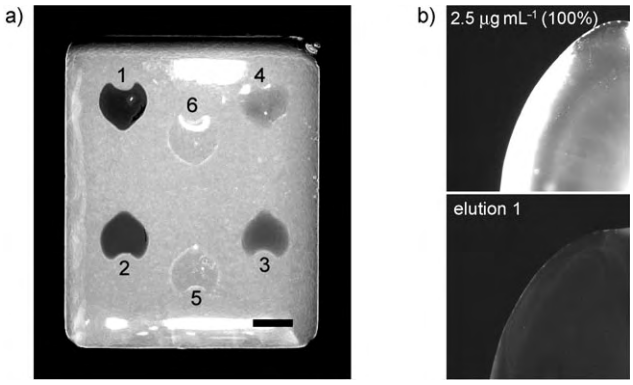

Figure 4. Different stages of DNA purification and detection. a) Photograph of the chip after DNA purification, showing immobilized droplets of lysis/binding buffer (1), washing solutions (2–4), and DNA-containing elution buffers (5, 6). The fading of the color between steps 1 and 5 indicates the efficiency of the washing procedure. b) On-chip fluorescent detection of the droplet containing the eluted λ-phage DNA indicates a recovery of 25% of DNA in the first elution, compared to a 100% reference solution. Scale bar: 3 mm.

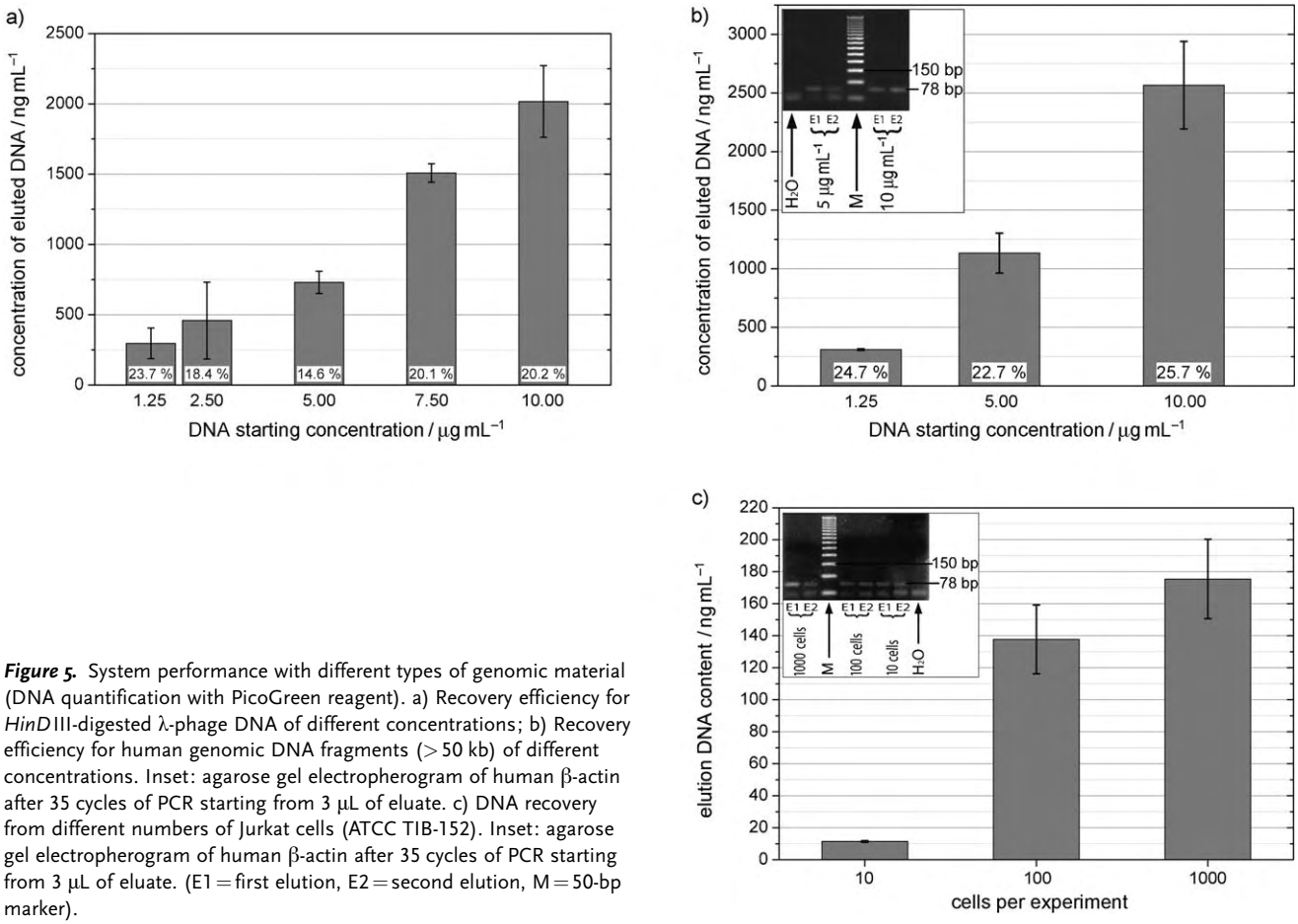

Figure 5. System performance with different types of genomic material (DNA quantification with PicoGreen reagent). a) Recovery efficiency for *HinD* III-digested λ-phage DNA of different concentrations; b) Recovery efficiency for human genomic DNA fragments (> 50 kb) of different concentrations. Inset: agarose gel electropherogram of human β-actin after 35 cycles of PCR starting from 3 μL of eluate. c) DNA recovery from different numbers of Jurkat cells (ATCC TIB-152). Inset: agarose gel electropherogram of human β-actin after 35 cycles of PCR starting from 3 μL of eluate. (E1 = first elution, E2 = second elution, M = 50-bp marker).

 © 2006 Wiley-VCH Verlag GmbH & Co. KGaA, Weinheim

ensure that no inhibitory compounds, such as the GuSCN binding buffer, were present in eluted samples, an additional off-chip PCR procedure was performed. The inset of Figure 5b shows the successful amplification of a selected DNA fragment, indicating both the absence of PCR inhibitors in the eluate and the intactness of DNA after capture, washing, and elution. After the demonstration of the system's ability to provide PCR-amplifiable human genomic DNA from pure samples, the process was extended to the purification of DNA from real biological samples such as mammalian cells. Samples containing 10 to 1000 Jurkat cells were lysed in GuSCN buffer solution (10 μL), loaded onto the microchip, and processed as described in the experiment above. The values of DNA recovery (Figure 5c) demonstrate the high sensitivity of our system, which allows DNA detection starting from only 10 cells per 10 μL. This detection limit is almost one order of magnitude better than the performance of high-end macroscopic bead-based systems.[27] Again, the amplification of a selected DNA fragment demonstrates successful DNA extraction and purification (inset of Figure 5c). The amounts of unconsumed primers that constitute the lowest band in the columns of the electropherogram also show the difference in DNA contents for the higher cell concentration. This difference is less visible with fluorescence detection (Figure 5c) owing to saturation effects. Finally, a comparison of the results of the direct fluorescence detection indicates a good interchip reproducibility of the experiments with an average standard deviation of 10%. Thus, we can conclude that our experiments clearly demonstrate the potential of our system to isolate DNA from a crude matrix, such as a cell lysate.

In summary, we have demonstrated a new droplet-manipulation system in which magnetic microparticles act both as force mediators and mobile substrates for biomolecules. Compared to other droplet-manipulation devices, our system permits easy DNA handling as there is no direct interaction between the actuating magnetic field and the dielectric properties of the DNA. Our actuation method, which is based on a switchable matrix of simple coils, avoids the use of external moving magnets and allows a high operational flexibility. Furthermore, the modularity of our system requires only a small part, namely the teflon foil, to be exchanged between experiments. With our system, we successfully extracted and purified different types of genomic material on-chip and with a good interchip reproducibility. This proved that the protocol is independent of the length of the DNA strand. In addition, we demonstrated on-chip DNA purification from whole cell samples down to 10 cells per 10 μL, which is an order of magnitude better than that achievable with high-end macroscopic bead-based systems. This combination of good DNA recovery and high sensitivity makes our system a very promising platform for DNA analysis in a miniaturized format, including purification, PCR amplification, and detection.

Experimental Section

Synthesis of the silicone oil medium: The hydrophobic biocompatible medium contains octamethyltrisiloxane (OMTS) as a basis. The OMTS is thoroughly mixed with poly(dimethyl-co-methyl phenyl)-siloxane and a phthalic ester (plasticizer; dioctylphthalate) to achieve a density of $\rho = 877.86\ \mathrm{kg\,m^{-3}}$, a dynamic viscosity of $\mu = 3.8$–$4.2\ \mathrm{mPa\,s^{-1}}$, and an interfacial tension towards water of $\gamma = 1.52\ \mathrm{mN\,m^{-1}}$. The small difference in density between the droplet and the oil medium results in a droplet position close to the actuation coils. The small surface tension γ and low viscosity μ facilitate distortion, splitting, and transport of the submersed droplet. Pure OMTS forms a stable layer around the water droplet, obstructs merging and splitting of droplets, and is permeable to water.[27] Surfactants, which lower the interfacial tension, were often used to enable merging and splitting operations. However, as biological molecules can easily react with these surfactants,[16] they are not the best choice for bioanalytical systems. In our setup, the presence of the phthalic ester in the silicone oil promotes the formation of a slightly deformable protective monolayer between the aqueous droplet and the OMTS. This layer prevents direct contact between the oil and the droplet media, thus permitting the introduction of saline buffer as well as water–ethanol droplets, both of which are required by the purification protocol, into the system. This also prevents the permeation of water into the oil medium.

Reagents and DNA preparation: All reagents used for DNA isolation were taken from the MagNA Pure LC DNA isolation kit I from Roche Diagnostics (Penzberg, Germany). Guanidinium chloride, tris(hydroxymethyl)aminomethane (Tris), Triton X-100, ethylenediaminetetraacetic acid (EDTA), and ethanol were purchased from Sigma-Aldrich (St. Louis, MO). *HinD* III-digested λ-phage DNA was from GibcoInvitrogen Cell Culture (Carlsbad, CA), and human genomic DNA was from Promega (Madison, WI). Stock solutions of DNA were prepared in lysis/binding buffer (guanidinium thiocyanate (1–5%) and Triton X-100 (1–5%); Roche, MagNA Pure LC DNA isolation kit I) and TE buffer solution ($500\ \mathrm{ng\,mL^{-1}}$; Tris-HCl (10 mM), EDTA (1 mM); pH 8.0). λ-DNA samples of different concentrations were made by serial dilution of this stock solution into the lysis/binding buffer for DNA extraction experiments and in TE buffer for use as standards in the DNA-quantization assay. Cell lysates were prepared from various concentrations of Jurkat cells (ATCC TIB-152). The cells were grown in RPMI 1640 medium supplemented with fetal calf serum (FCS; 10%), L-glutamine (2 mM), sodium pyruvate (1 mM), nonessential amino acids (1%) and HEPES (4-(2-hydroxyethyl)-1-piperazineethanesulfonic acid) buffer solution (1%) (all from GibcoInvitrogen Cell Culture). Finally, the cells were centrifuged at 900 rpm for 3 min and resuspended in phosphate-buffered saline solution (PBS).

On-chip DNA-purification procedure: All processing was done at room temperature. As a first step in all of the experiments, an immobilized 10-μL droplet containing genomic material was merged and mixed on-chip with a second droplet, which was carrying magnetic particles. Prior to injection into the system, the magnetic particles were washed twice with PBS (phosphate buffer (0.01 M), NaCl (0.138 M), and KCl (0.0027 M); pH 7.4). For DNA binding, the lysis/binding buffer containing the DNA or cell lysate and the magnetic beads were mixed thoroughly for 3 min by using magnetic actuation. Proteins and possible PCR inhibitors were removed by passing the particle–DNA droplet through a first droplet of washing buffer I (ethanol (30–40%) and guanidinium chloride (1–5%)) and then through two droplets of washing buffer II (ethanol (50%)) to further remove impurities (cellular debris) and reduce the chaotropic salt concentration. Finally, the DNA was eluted in two immobilized droplets of low-ionic-strength TE buffer through magnetic mixing for 5 min per droplet. From the injection of the DNA or cell lysate to the extraction of the magnetic particles after elution, the complete purification process takes about 20 min. The captured and eluted DNA was either quantified on- or off-chip by using fluorescence, or it was transferred to an amplification protocol. All of the experiments were repeated at least three times, with a change in the reservoir bottom after every experiment to prevent cross-contamination.

 © 2006 Wiley-VCH Verlag GmbH & Co. KGaA, Weinheim

DNA quantification: DNA present in the eluted fractions was quantified by using the PicoGreen ds-DNA Quantitation kit (Molecular Probes). For off-chip detection, the eluate (3 μL) was diluted in TE buffer solution (15 μL) and an equal volume of PicoGreen reagent. These samples were prepared in 96-well plates and read in a microplate fluorometer (Cytofluor series 4000, Perceptive Biosystems) by using wavelengths of 485 nm and 530 nm for excitation and emission, respectively. The results of the fluorescence measurements were quantified through standard curves that were generated with λ-phage DNA. For on-chip detection, PicoGreen reagent (10 μL) was added to the elution droplet (10 μL) on the chip, where the fluorescence was detected by using a CCD camera (Hamamatsu, ORCA-C4742-95ER) mounted on a fluorescence microscope platform. Data acquisition and processing were performed with the AquaCosmos software (Hamamatsu). For quantification, we compared the on-chip fluorescence signal with that of a droplet containing a reference DNA concentration.

Polymerase Chain Reaction (PCR) amplification: Extracted DNA samples were amplified by using PCR with a Biometra Thermocycler (Göttingen, Germany) and a standard PCR protocol. A fragment with 78 base pairs (bp) from the human β-actin gene was amplified by using the following primers: β-actin-For: 5′-AAGCCACCCCACTTCTCTCTAA-3′; β-actin-Rev: 5′-AATGCTATCACCTCCCCTGTGT-3′. PCR reactions were based on 10 × Taq polymerase buffer solution with Mg^{2+} (25 mM), primer (15 μM of each), dNTP (100 μM), and the collected fractions (1–5 μL) in a total volume of 50 μL (all reagents were purchased from Promega). The thermal cycler program was 94 °C for 2 min, followed by 35 cycles of 94 °C for 30 s/60 °C for 1 min/72 °C for 2 min. A final extension step was used for 7 min at 72 °C. All of the amplified samples were analyzed by agarose gel electrophoresis.

Received: October 13, 2005
Revised: December 23, 2005
Published online: March 23, 2006

Keywords: DNA · fluorescence · magnetic particles · microfluidics

[1] T. Vilkner, D. Janasek, A. Manz, *Anal. Chem.* **2004**, *76*, 3373.
[2] P. A. Auroux, D. Iossifidis, D. R. Reyes, A. Manz, *Anal. Chem.* **2002**, *74*, 2637.
[3] M. A. M. Gijs, *Microfluid. Nanofluid.* **2004**, *1*, 22.
[4] E. Verpoorte, *Lab Chip* **2003**, 3, 60N.
[5] J. Baudry, E. Bertrand, N. Lequeux, J. Bibette, *J. Phys. Condens. Matter* **2004**, *16*, R469.
[6] K. B. Lee, S. Park, C. A. Mirkin, *Angew. Chem.* **2004**, *116*, 3110; *Angew. Chem. Int. Ed.* **2004**, *43*, 3048.
[7] L. J. Kricka, P. Wilding, *Anal. Bioanal. Chem.* **2003**, *377*, 820.
[8] H. Tian, A. F. R. Hühmer, J. P. Landers, *Anal. Biochem.* **2000**, *283*, 175.
[9] K. A. Wolfe, M. C. Breadmore, J. P. Ferrance, M. E. Power, J. F. Conroy, P. M. Norris, J. P. Landers, *Electrophoresis* **2002**, *23*, 727.
[10] M. C. Breadmore, K. A. Wolfe, I. G. Arcibal, W. K. Leung, D. Dickson, B. C. Giordano, M. E. Power, J. P. Ferrance, S. H. Feldman, P. M. Norris, J. P. Landers, *Anal. Chem.* **2003**, *75*, 1880.
[11] J. W. Hong, V. Studer, G. Hang, W. F. Anderson, S. R. Quake, *Nat. Biotechnol.* **2004**, *22*, 435.
[12] B. Zheng, R. F. Ismagilov, *Angew. Chem.* **2005**, *117*, 2576; *Angew. Chem. Int. Ed.* **2005**, *44*, 2520.
[13] M. Joanicot, A. Ajdari, *Science* **2005**, *309*, 887.
[14] P. Aussillous, D. Quere, *Nature* **2001**, *411*, 924.
[15] K. Jensen, A. Lee, *Lab Chip* **2004**, *4*, 31N.
[16] L. S. Roach, H. Song, R. F. Ismagilov, *Anal. Chem.* **2005**, *77*, 785.
[17] S. K. Cho, H. Moon, C.-J. Kim, *J. Microelectromech. Syst.* **2003**, *12*, 70.
[18] J. R. Dorvee, A. M. Derfus, S. N. Bhatia, M. J. Sailor, *Nat. Mater.* **2004**, *3*, 896.
[19] M. Shikida, K. Inouchi, H. Honda, K. Sato in *17th IEEE International Conference on Micro Electro Mechanical Systems (MEMS 2004)*, Maastricht, The Netherlands, **2004**, pp. 359.
[20] O. D. Velev, B. G. Prevo, K. H. Bhatt, *Nature* **2003**, *426*, 515.
[21] A. Wixforth, C. Strobl, C. Gauer, A. Toegl, J. Scriba, Z. von Guttenberg, *Anal. Bioanal. Chem.* **2004**, *379*, 982.
[22] A. Rida, V. Fernandez, M. A. M. Gijs, *Appl. Phys. Lett.* **2003**, *83*, 2396.
[23] N. Inagaki, K. Narushim, N. Tuchida, K. Miyazaki, *J. Polym. Sci. Part B* **2004**, *42*, 3727.
[24] A. Frohn, N. Roth, *Dynamics of Droplets*, Springer, Berlin, **2000**.
[25] M. M. Exner, M. A. Lewinski, *Diagn. Microbiol. Infect. Dis.* **2003**, *46*, 235.
[26] K. A. Melzak, C. S. Sherwood, R. F. B. Turner, C. A. Haynes, *J. Colloid Interface Sci.* **1996**, *181*, 635.
[27] S. M. Williams, C. A. Meadows, E. Lyon, *Clin. Chem.* **2002**, *48*, 1629.

 © 2006 Wiley-VCH Verlag GmbH & Co. KGaA, Weinheim

Antibiotics

DOI: 10.1002/anie.200503381

Lydiamycins A–D: Cyclodepsipetides with Antimycobacterial Properties**

Xueshi Huang, Ernst Roemer, Isabel Sattler, Ute Moellmann, Arnulf Christner, and Susanne Grabley*

Dedicated to Professor Axel Zeeck on the occasion of his 65th birthday

In the course of our investigations of natural products from microorganisms for drug discovery,[1] we studied *Streptomyces lydicus* (strain HKI0343) by physico-chemical analysis of its

[*] Dr. X. Huang,[+] Dr. E. Roemer,[$] Dr. I. Sattler, Dr. U. Moellmann, Dr. A. Christner, Prof. Dr. S. Grabley
Leibniz Institute for Natural Product Research and Infection Biology
Hans-Knöll-Institute
Beutenbergstrasse 11a, 07745 Jena (Germany)
Fax: (+49) 3641-656-679
E-mail: isabel.sattler@hki-jena.de

[+] Current address:
Syntheses & Biomimetic Drugs Research Center
China Medical University
Liaoning (P.R. China)

[$] Current address:
Leibniz Institute of Plant Biochemistry
Halle (Germany)

[**] We thank our colleagues at the HKI department of Biomolecular Chemistry for providing NMR and MS data. We are grateful to Dr. L. P. Martinova, Central Research Institute of Tuberculosis of the Russian Academy of Science, for biological testing. Financial support by the German Ministry for Education and Research (BMBF, CHN 02/322) is gratefully acknowledged.

Supporting information for this article is available on the WWW under http://www.angewandte.org or from the author.

© 2006 Wiley-VCH Verlag GmbH & Co. KGaA, Weinheim

metabolite pattern.[2,3] Four new secondary metabolites, lydiamycins A–D (**1**–**4**; PBB = piperazic acid, PSA = 2-pentylsuccinic acid), were discovered in the fermention broth of this strain by thin-layer chromatography (visualization by UV absorption and staining with anisaldehyde/H_2SO_4). The cyclodepsipeptides lydiamycins A (20 mg), B (15 mg), C (10 mg), and D (7 mg) were obtained as white solids by standard chromatographic procedures from a 300-L fermentation of the strain. Herein we report the structure determination of each metabolite using a combination of CID ESIMS/MS data (CID = collision-induced dissociation) and 1D and 2D NMR techniques such as DEPT, COSY, HMBC, TOCSY, and ROESY, the assignment of the absolute configurations, and, finally, the biological properties.

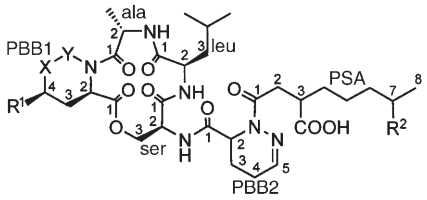

	R^1	R^2	X-Y
1	H	H	-CH_2-NH-
2	OH	H	-CH_2-NH-
3	H	H	-CH=N-
4	H	OH	-CH_2-NH-

High-resolution ESIMS of the Na adduct of lydiamycin A (**1**) indicated a molecular formula of $C_{31}H_{49}NaN_7O_9$ ($[M+Na]^+$, *m*/*z*: found 686.3495, calcd. 686.3489). Like the IR spectrum with characteristic absorption bands of amide carbonyls at 1663 and 1539 cm^{-1} and ester carbonyls at 1745 cm^{-1}, the NMR data showed typical characteristics of peptides, for example, resonances for amide carbonyls in the ^{13}C NMR spectrum and for amide and α protons in the ^1H NMR spectrum (Tables 1 and 2). Signals for five amino acid α carbons (δ_C = 50.5, 50.7, 51.4, 52.7, 55.6 ppm) and seven carbonyls, either of amide or carboxylic acid origin (δ_C = 169.1, 169.3, 169.7, 170.9, 174.3, 175.9, 177.3 ppm) were found. As fragment ion peaks commonly observed for acyclic peptides were not noted in the CID ESIMS/MS data, a cyclic oligopeptide structure was proposed for **1**.

Based on analysis of the 2D NMR data, **1** was determined to contain alanine (Ala), leucine (Leu), Serine (ser), PBB (piperazic acid building block 1, PBB1), dehydropiperazic acid (piperazic acid building block 2, PBB2), and 2-pentylsuccinic acid (PSA) moieties. The two unusual heterocyclic amino acids were confirmed by comparison to literature data.[4,5] The presence of long-range couplings ($^nJ_{C,H}$, HMBC, Figure 1) suggested amide linkages between the leucine carbonyl and the alanine amine, between the alanine carbonyl and the piperazic acid δ-amine, between the serine carbonyl and the leucine amine, and between the dehydropiperazic acid carbonyl and the serine amine. This data, combined with indication of an ester linkage between the piperazic acid carbonyl and the serine β-OH, established the structure as a thirteen-membered cyclic depsipeptide, with the dehydropiperazic acid moiety located peripheral to the ring.

Table 1: ^{13}C NMR data (δ_C, 75 MHz, CD_3Cl) of lydiamycins A (**1**), B (**2**), C (**3**), and D (**4**).

Position		**1**	**2**	**3**	**4**
Ala	C-1	174.3	174.6	172.8	174.3
	C-2	50.5	50.5	50.8	50.5
	C-3	18.2	18.2	19.3	18.3
PBB1	C-1	169.1	171.2	169.9	169.1
	C-2	52.7	49.06	50.0	52.7
	C-3	24.4	32.1	18.8	24.4
	C-4	21.4	61.3	21.3	21.4
	C-5	47.1	52.4	146.9	47.1
Ser	C-1	169.7	169.2	168.0	169.7
	C-2	50.7	50.8	50.6	50.7
	C-3	68.2	68.9	68.6	68.2
PBB2	C-1	170.9	170.8	170.8	170.9
	C-2	55.6	55.5	55.3	55.6
	C-3	19.4	19.3	19.2	19.4
	C-4	20.6	20.6	20.6	20.6
	C-5	142.6	142.7	142.6	142.9
Leu	C-1	169.3	169.3	170.4	169.3
	C-2	51.4	51.2	50.7	51.4
	C-3	36.6	36.6	36.6	36.6
	C-4	24.6	24.6	24.5	24.6
	C-5	22.7	22.8	22.9	22.8
	C-6	22.2	22.2	22.2	22.2
PSA	C-1	175.9	175.9	176.2	175.9
	C-2	36.5	36.5	36.5	36.6
	C-3	46.0	46.0	46.0	45.9
	C-4	31.6	31.6	31.6	31.6
	C-5	26.8	26.9	26.9	30.3
	C-6	31.5	31.5	31.5	38.8
	C-7	22.4	22.4	22.4	67.6
	C-8	13.9	13.9	13.9	24.4
	C-9	177.3	177.2	176.9	177.2

HMBC spectra of **1** did not provide unambiguous proof for the point of attachment of the 2-pentylsuccinic acid unit. However, CID ESIMS/MS data indicated that it was incorporated as an amide with the secondary amine of the dehydropiperazic acid unit (Figure 2). Specifically, a fragment at *m*/*z* 516, caused by the α fission of the postulated amide bond, and its daughter fragment at *m*/*z* 460 $[437+Na]^+$ formed by subsequent retro-Diels–Alder reaction were detected. Moreover, the fragment at *m*/*z* 558.3 $[535+Na]^+$ in the daughter spectrum of the molecular ion at *m*/*z* 686 $[M+Na]^+$ enabled assignment of the regiochemistry of the attachment as the C-1 carboxy group of the dicarboxylic acid building block.

For the determination of the absolute configurations, an acidic hydrolysate was generated according to the Marfey protocol.[6–8] Subsequent HPLC analysis indicated the presence of L-alanine, D-leucine, and L-serine. However, piperazic acid derivatives could not be detected in the hydrolysate. Instead, the stereochemistry of the piperazic acid moiety PBB1 was determined through conformational analysis and computation with an MM+ force field. The assignment of H-2 (δ_H = 5.15 ppm, brd, 3.1 Hz in $[D_4]$methanol) in the equatorial position, as well as discrimination between H_{ax} and H_{eq} at C-5 was possible through their $^3J_{H,H}$ coupling data and NOE correlations of H-2 with H_{eq}-3 (δ_H = 2.35 ppm) and

 © 2006 Wiley-VCH Verlag GmbH & Co. KGaA, Weinheim

Table 2: [1]H NMR data[a] of lydiamycins A (**1**), B (**2**), C (**3**), and D (**4**).

Position			**1**[b]	**1**[c]	**2**[c]	**3**[d]	**4**[d]
Ala	C-2	4.55, 1H, cov	4.83, 1H, dq, 7.25, 10.5	4.85, 1H, dq, 7.2, 11.0	4.98, 1H, m	4.83, 1H, m	
	C-3	1.51, 3H, d, 8.0	1.43, 3H, d, 7.25	1.45, 3H, d, 7.2	1.43, 3H, d, 7.2	1.43, 3H, d, 7.2	
	NH	–	7.27, 1H, d, 10.5	7.39, 1H, d, 11.0	7.48, 1H, d, 9.9	7.29, 1H, d, 10.4	
PBB1	C-2	5.15, 1H, brd, 3.1	5.28, 1H, m cov	5.15, 1H, brd, 5.3	5.44, 1H, brs	5.29, 1H, brd	
	C-3	1.76, 1H, m	1.77, 1H, m	2.05, 1H, m	1.86, 1H, m	1.77, 1H, m	
		2.27, 1H, m	2.35, 1H, m	2.55, 1H, m	2.52, 1H, m	2.35, 1H, m	
	C-4	1.57, 2H, m	1.60, 2H, m	3.95 1H, brs	2.30, 1H, m	1.60, 2H, m	
					2.25, 1H, m		
	C-5	3.08, 1H, brd, 14.0	H_{eq}: 3.12, 1H, brd, 13.5,	3.10, 1H, brd, 14.6	7.16H, brs	3.14, 1H, brd, 14.0	
		2.73, 1H, m cov	H_{ax}: 2.75, 1H, brdq, 3.8, 13.5[e]	2.88, 1H, brt, 14.1		2.77, 1H, m	
	NH	–	4.31, 1H, brd	5.29 brd, 11.7		4.33, 1H, m	
Ser	C-2	4.64, 1H, t, 5.9	5.28, 1H, m cov	5.32, 1H, m	5.20, 1H, dd, 4.5, 9.9	5.29, 1H, m	
	C-3	4.07, 1H, dd, 5.9, 11.0	4.03, 1H, brd, 11.4	4.28, 1H, brd, 11.2	4.01, 1H, brs, 11.5	4.03, 1H, brd, 11.5	
		4.75, 1H, dd, 5.9, 11.0	4.75, 1H, dd, 4.4, 11.4	4.62, 1H, dd, 4.5, 11.2	4.64, 1H, dd, 4.5, 11.5	4.76, 1H, dd, 4.3, 11.5	
	NH	–	8.25, 1H, d, 9.85	8.28, 1H, d, 9.9	8.20, 1H, d, 9.9	8.25, 1H, d, 9.8	
PPB2	C-2	4.96, 1H, brt	4.65, 1H, brt, 5.7	4.70, 1H, brt, 5.5	4.72, 1H, brt, 5.7	4.66, 1H, brt	
	C-3	2.01, 1H, m	1.93, 1H, m	1.93, 1H, m	1.90, 1H, m	1.95, 1H, m	
		2.27, 1H, m	2.35, 1H, m	2.39, 1H, m	2.39, 1H, m	2.35, 1H, m	
	C-4	2.13, 1H, m	1.92, 1H, m	1.93, 1H, m	1.93, 1H, m	1.90, 1H, m	
		2.26, 1H, m	2.15, 1H, m	2.19, 1H, m	2.15, 1H, m	2.15, 1H, m	
	C-5	6.98, 1H, brs	6.90, 1H, brs	6.91, 1H, brs	6.90, 1H, brs	6.93, 1H, brs	
Leu	C-2	4.55, 1H, m cov	4.33, 1H, m cov	4.40, 1H, m	4.45, 1H, m	4.33, 1H, m	
	C-3	1.60, 2H, m	1.77, 2H, m	1.78, 2H, m	1.75, 2H, m	1.77, 2H, m	
	C-4	1.59, 1H, m	1.63, 1H, m	1.65, 1H, m	1.64, 1H, m	1.63, 1H, m	
	C-5	0.94, 3H, d, 6.7	0.93, 3H, d, 6.5	0.95, 3H, d, 6.6	0.93, 3H, d, 6.4	0.93, 3H, d, 6.5	
	C-6	0.91, 3H, d, 6.6	0.87, 3H, d, 6.5	0.87, 3H, d, 6.5	0.87, 3H, d, 6.4	0.87, 3H, d, 6.5	
	NH	–	7.43, 1H, d, 7.8	7.42, 1H, d, 9.7	7.25, 1H, d	7.42, 1H, 9.8	
PSA	C-2	2.45, 1H, dd, 5.0, 16.5	2.60, 1H, dd, 5.3, 16.8	2.60, 1H,dd, 5.5, 12.4	2.64, 1H, dd 5.5, 16.9	2.60, 1H, dd, 16.8, 5.3	
		2.78, 1H, dd, 10.1, 16.5	3.30, 1H, dd, 12.2, 16.8	3.31, 1H, dd, 12.4, 16.8	3.30, 1H, dd, 12.1, 16.9	3.32, 1H, dd, 12.6, 16.8	
	C-3	3.74, 1H, m	3.02, 1H, m	3.01, 1H, m	3.01, 1H, m	3.05, 1H, m	
	C-4	1.45, 1H, m	1.52, 1H, m	1.55, 1H, m	1.52, 1H, m	1.60, 1H, m	
		1.67, 1H, m	1.71, 1H, m	1.75, 1H, m	1.72, 1H, m	1.80, 1H, m	
	C-5	1.26–1.35, 2H, m	1.24, 1H, m	1.24, 1H, m	1.24, 1H, m	1.42, 2H, m	
			1.35, 1H, m	1.35, 1H, m	1.35, 1H, m		
	C-6	1.26–1.35, 2H, m	1.26–1.27, 2H, m	1.26–1.27, 2H, m	1.26–1.27, 2H, m	1.45, 2H, m	
	C-7	1.26–1.35, 2H, m	1.26–1.27, 2H, m	1.26–1.27, 2H, m	1.26–1.27, 2H, m	3.75, 1H, m	
	C-8	0.89, 3H, t, 7.3	0.85, 3H, t, 6.5	0.85, 3H, t, 6.6	0.85, 3H, t, 6.4	1.15, 3H, d, 6.2	

[a] δ_H, intensity, multiplicity, *J* [Hz]; cov = covered. [b] 500 MHz, [D_4]methanol. [c] 500 MHz, $CDCl_3$. [d] 300 MHz, $CDCl_3$. [e] 2.69, ddd 13.9, 13.9, 3.9 in $CDCl_3$/10% [D_4]methanol, 500 MHz.

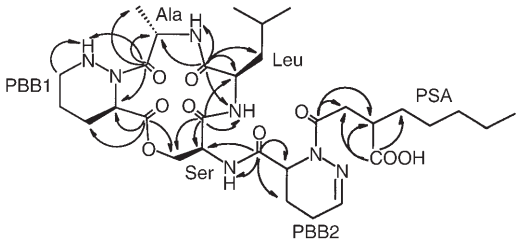

Figure 1. Long-range couplings ($^nJ_{C,H}$) of **1** as deduced from HMBC NMR data.

H_{ax}-3 ($\delta_H = 1.77$ ppm) and between H_{ax}-5 ($\delta_H = 2.75$ ppm, br dq, 3.8 and 13.5 Hz in $CDCl_3$) and H_{ax}-3 ($\delta_H = 1.77$ ppm; Table 2 and Figure 3). Based on this information along with X-ray results of other piperazic acid containing depsipetides, we assumed a chair conformation for PBB1 in **1** (Figure 3).[9] Molecular dynamic force field calculations and subsequent ab initio calculations were carried out for the peptide core (including PBB2) for both possible configurations of C-2 in PBB1 (Figure 4).[10] The lowest energy conformation for each diastereomer was confirmed after intermediate annealing processes. Owing to the small size of the peptide ring, the two three-dimensional structures are almost planar, which is consistent with the lack of NOEs between nonvicinal amino acids. The two diastereomeric structures can be distinguished by noting the significant difference in the distance between 5-H_{ax} and Ala-CH_3: 4.06 Å in the case of the 2*R* of PBB1 and 2.65 Å in the case of 2*S* (Figure 4). A rough estimate of the distance between H_{ax}-5 ($\delta_H = 2.75$ ppm) and Ala-CH_3 ($\delta_H =$ 1.43 ppm) by the ROESY peak volumina, when calibrated against the correlation between H-2 and CH_3 of the alanine residue, yielded a distance of 4.1 Å (5% intensity). Thus, the 2*R* configuration was suggested for PBB1. The absolute configuration at C-2 of PBB2 could not be assigned. The configuration cannot be rationalized by biosynthetic relationships, as related compounds include two piperazic acid building blocks with different configurations.[4]

Structure determinations of lydiamycins B–D (**2**–**4**) were conducted by analogy to that of **1**. Absolute configurations

 © 2006 Wiley-VCH Verlag GmbH & Co. KGaA, Weinheim

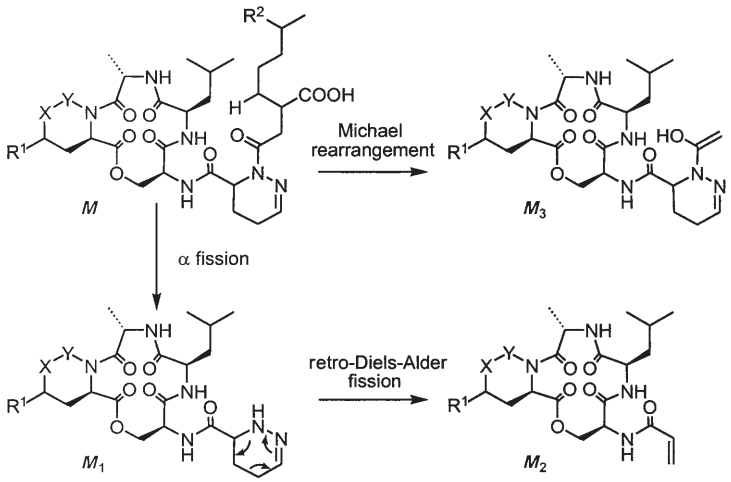

	-X-Y-	R^1	R^2	$[M+Na]^+$	$[M_1+Na]^+$	$[M_2+Na]^+$	$[M_3+Na]^+$
1	$-CH_2$-NH-	H	H	686	516	460	558
2	$-CH_2$-NH-	OH	H	702	532	476	574
3	-CH=N-	H	H	684	514	458	556
4	$-CH_2$-NH-	H	OH	702	516	460	558

Figure 2. Fragments identified by CID ESIMS/MS data of **1**–**4**.

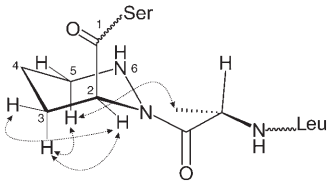

Figure 3. Schematic presentation of the PBB1–Ala fragment of lydiamycin A (**1**) showing NOE correlations (ROESY, dotted line).

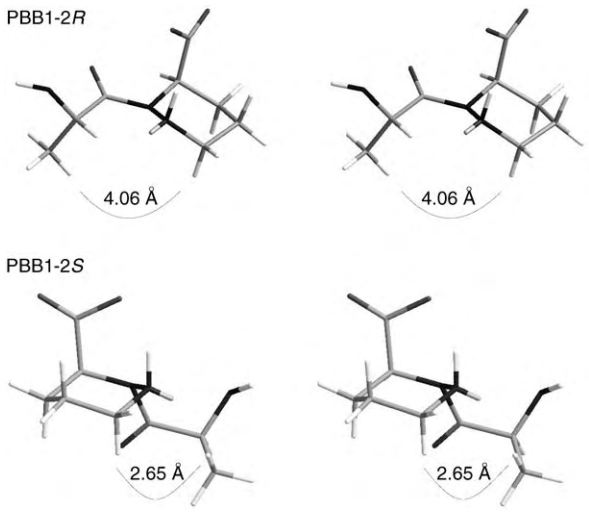

Figure 4. Three-dimensional projection of the two possible diastereomers of the PBB1–Ala fragment in **1** as obtained by molecular modeling (the diagrams are rotated relative to the view in Figure 3 in order to visualize the crucial distance between Ala-methyl and 5-H_{ax} of PBB1).

were assumed to be identical to those in lydiamycin A (**1**). Thus, in the following section, we discuss only the elucidation of altered structural features. The molecular formula $C_{31}H_{49}N_7O_{10}$ of lydiamycin B (**2**) differed from that of **1** by one additional oxygen atom. The analogous fragment ion peaks in the CID ESIMS/MS indicated that this additional oxygen was located in the depsipeptide core of **2** (Figure 2). ^{1}H and ^{13}C NMR data of **2** were very similar to those of **1** except for a missing methylene group ($\delta_C = 21.4$ ppm in **1**) and an additional oxymethine group ($\delta_C = 61.3$ ppm) in PBB1. TOCSY and HMBC NMR data revealed the piperazic acid of **1** to be replaced by 4-hydroxypiperazic acid in **2**.[11] As the remaining methine proton (H-4) appears as the broad singlet of an equatorial proton in the ^{1}H NMR data ($\delta_H = 3.95$ ppm, Table 2), the hydroxy substituent was assigned an axial position. Thus, PBB1 of **2** is suggested to be 2*R*,4*R*-configured.

The molecular formula of lydiamycin C (**3**), $C_{31}H_{47}N_7O_9$, suggested that it is a dehydro analogue of **1**. Consistent with this, in the ^{13}C spectra of lydiamycin C (**3**) one CH_2 signal is replaced by a signal for an sp^2-hybridized carbon ($\delta_C = 146.9$ ppm). An additional double bond between C-5 and the neighboring nitrogen of the piperazic acid moiety (PBB1) could readily be assigned based on the altered spin systems detected in COSY and TOCSY spectra.

Compounds **3** and **1** show identical fragmentation sequences in the CID ESIMS/MS data, which confirms the position of the double bond in **3**. As for **2**, the molecular formula of $C_{31}H_{49}N_7O_{10}$ indicated that lydiamycin D (**4**) is an oxygenated analogue of **1**. Since the fragment-ion peaks of **4** in the CID ESIMS/MS spectra were identical to those of **1**, the oxygenation site had to be located in the 2-pentylsuccinic acid moiety. The regiochemistry of the hydroxylation was determined by HMBC and COSY experiments.

In our biological profiling program of new natural products, lydiamycins A–C (**1**–**3**) were shown to selectively inhibit *Mycobacterium smegmatis* SG 987, *M. aurum* SB66, and *M. vaccae* IMET 10670 in a panel of Gram-positive and Gram-negative bacteria, yeasts, and fungi (Table 3). No cytotoxicity was found against L929, K562, HeLa, MDCK, and GMK cell lines.[12] Further studies on the antibiotic activity of lydiamycin A against slow-growing and pathogenic mycobacteria, including the *M. tuberculosis* standard strain (H37Rv) and a multiresistant clinical isolate, confirmed its antimycobacterial properties (Table 4). Interestingly, activity against the multiresistant strain of *M. tuberculosis* suggests a mechanism of action different from that of available ther-

Table 3: Antibacterial activities of lydiamycins A–C (**1**–**3**).

Organism	MIC [$\mu g\,mL^{-1}$][a]		
	1	**2**	**3**
Bacillus subtilis ATCC 6633	100.1	100.1	100.1
Mycobaterium smegmatis SG 987	25.0	25.0	25.0
Mycobacterium aurum SB66	6.3	6.3	12.5
Mycobacterium vaccae IMET 10670	3.1	3.1	3.1
Mycobacterium fortuitum B.	100.1	100.1	100.1

[a] MIC = minimal inhibitory concentration; mean of three independent experiments.

 © 2006 Wiley-VCH Verlag GmbH & Co. KGaA, Weinheim

Table 4: Activity of lydiamycin A (**1**) against *M. tuberculosis* strains

Strains	Cmpds.	MIC [μg mL^{-1}]	MBC [μg mL^{-1}][a]
H37Rv	**1**	12.5	25
# 246[b]		25	50
H37Rv	control[c]	1.17	1.56
# 246		>100	>100

[a] Minimal bactericidal concentration. [b] Clinical isolate resistant against main antituberculosis drugs. [c] Isoniazid.

apeutics like isoniazid, rifampicine, etambutol, and streptomycin.

From a structural point of view, the lydiamycins represent a novel class of small cyclodepsipeptides.[13,14] Among the several hundred cyclodepsipeptides of natural origin, only 34 thirteen-membered cyclic depsipeptides, representing four structural families, are known.[15] The largest group among them, 16 beauverolides, recently attracted interest because of their antiatherogenic activity, as demonstrated by inhibition of acyl-CoA-cholesterol acyltransferase (ACAT).[16] Altogether, the thirteen-membered ring depsipetides cover a wide range of biological activities, including antibiotic,[17] antifungal,[18] insecticidal,[19] and immunosuppressant properties.[20] Like the lydiamycins, none of them are known to display significant cytotoxic activity which is a very common characteristic of larger cyclodepsipetides. Next to their small ring size, the most outstanding structural feature of the lydiamycins is the presence of the piperazic acid building blocks, which are not found in any of the other small congeners. However, two piperazic acid building blocks are the major characteristic of the 19-membered cyclodepsipeptides of the azinothricin family, for example, aurantimycins[4] and verucopeptin.[21] A common feature of the azinothricin family and some other cyclodepsipeptides, as well as with the lydiamycins, is the presence of one polyketide chain of varying complexity and length.

Since the unique structural features of the lydiamycins are obviously linked to their biosynthetic origin, studies on the genetic and regulatory setup of their biosynthesis are underway.[22] Together with the observed biological activity profile, our results might be a promising basis for the development of a novel class of antituberculosis agents.

Experimental Section

General experimental procedures were performed and materials were obtained as previously described in the literature.[23]

Strain and cultivation: *Streptomyces lydicus*, isolated from a soil sample, was classified according to 16*S* RNA analysis with 99.9% identity. The isolate was deposited as DSM16701 at the Deutsche Sammlung von Mikroorganismen und Zellkulturen GmbH (DSMZ, Braunschweig, Germany). The cultivation was performed in 300 L of soybean/mannitol medium (soybean flour 20 g L^{-1}, mannitol 20 g L^{-1}, pH 7.5) at 28 °C with stirring for 4 d.

Isolation of **1**–**4**: The filtrate of the culture broth (300 L) was adsorbed on Amberchrom 161CG (column 20 × 20 cm, 6 L). The resin was washed with deionized water then eluted with a MeOH/water gradient (flow rate 1 L min^{-1}, 0–4 min 40% MeOH, 4–52 min 40%–80% MeOH, 52–54 min 80–100% MeOH, 54–74 min 100% MeOH). The fractions collected at 34–66 min were concentrated to an aqueous residue and lyophilized to obtain 7.0 g of a crude brown material which upon silica gel column chromatography ($CHCl_3$/MeOH, gradient 9:1 to 4:1) gave nine fractions. The first fraction was purified again by silica gel chromatography (petroleum ether/EtOAc gradient, 2:1 to 1:1) and subsequent chromatography on Sephadex LH20 ($CHCl_3$) to yield lydiamycin A (20 mg), lydiamycin B (15 mg), lydiamycin C (10 mg), and lydiamycin D (7 mg). TLC analysis on silica gel eluting with $CHCl_3$/MeOH 9:1 gave R_f values of 0.54 (A), 0.18 (B), 0.31 (C), and 0.23 (D).

Lydiamycin A (**1**): $[\alpha]_D^{20} = -19.8°$ (c=0.23 in CH_3Cl); ESIMS: m/z: 686.8 $[M+Na]^+$, 681.9 $[M+NH_4]^+$, 664.9 $[M+H]^+$, 662.6 $[M-H]^-$; HRESIMS: m/z: 686.3495 ($C_{31}H_{49}NaN_7O_9$ calcd 686.3489); IR (film): $\tilde{\nu}_{max}$ = 3295, 2954, 2359, 2341, 2163, 2051, 1745, 1663, 1539, 1408, 1218, 793, 667, 629 cm^{-1}; for ^{1}H and ^{13}C NMR data see Table 1 and Table 2.

Lydiamycin B (**2**): $[\alpha]_D^{20} = -34.5°$ (c=0.17 in CH_3Cl); ESIMS: m/z: 702.8 $[M+Na]^+$, 698.0 $[M+NH_4]^+$, 680.8 $[M+H]^+$, 678.6 $[M-H]^-$; HR ESIMS: m/z: 702.3444 ($C_{31}H_{49}NaN_7O_{10}$ calcd 702.3439); IR (film): $\tilde{\nu}_{max}$ = 3299, 2932, 2358, 2324, 2163, 2073, 1754, 1662, 1538, 1415,1260, 1218, 1093, 773, 630 cm^{-1}; for ^{1}H and ^{13}C NMR data see Tables 1 and 2.

Lydiamycin C (**3**): $[\alpha]_D^{20} = -16.2°$ (c=0.20 in CH_3Cl); ESIMS: m/z: 684.8 $[M+Na]^+$, 662.9 $[M+H]^+$, 679.9 $[M+NH_4]^+$, 660.6 $[M-H]^-$; HRESIMS: m/z: 684.3325 ($C_{31}H_{47}NaN_7O_9$ calcd 684.3333); IR (film): $\tilde{\nu}_{max}$ = 3301, 2954, 2359, 2341, 2164, 2049, 1746, 1718, 1666, 1627, 1539, 1416, 1261, 1218, 1048, 988, 960, 772, 630 cm^{-1}; for ^{1}H and ^{13}C NMR data see Tables 1 and 2.

Lydiamycin D (**4**): $[\alpha]_D^{20} = -21.2°$ (c=0.32 in CH_3Cl); ESIMS: m/z: 702.8 $[M+Na]^+$, 680.9 $[M+H]^+$, 697.8 $[M+NH_4]^+$, 678.6 $[M-H]^-$; HRESIMS: m/z: 702.3453 ($C_{31}H_{49}NaN_7O_{10}$ calcd 702.3439); IR (film): $\tilde{\nu}_{max}$ = 3280, 2933, 2867, 2359, 2163, 1744, 1721, 1657, 1629, 1563, 1535, 1442, 1408, 1309, 1253, 1206, 1181, 1054, 1033, 1011, 912, 869, 696 cm^{-1}; for ^{1}H and ^{13}C NMR data see Tables 1 and 2.

Hydrolysis of lydiamycin A (**1**) and HPLC analysis: A solution of lydiamycin A (**1**) (0.5 mg, 0.77 μmol) in 10 drops of 10 N HCl was heated (100 °C bath temperature) for 15 h, and the solution turned clear after 3 h. For the workup, the solution was frozen and lyophilized. The resulting white residue was derivatized with 1-fluoro-2,4-dinitrophenyl-5-L-alanine amide (FDAA) as described in the literature.[6–8] The L and D enantiomers of serine, alanine, and leucine were converted into their DAA derivatives as well. HPLC analysis was performed using a reversed-phase C-8 silica gel column (4.6 mm i.d. × 250 mm length) eluting with a gradient consisting of water/0.05% formic acid (A) and methanol (B) [0 min 10%, 30 min 30%, 35 min 50%, 45 min 100% B] flow rate 1 mL min^{-1}, 25 °C, 254 nm. The HPLC peaks of the amino acid derivatives obtained from lydiamycin A (**1**) were assigned by comparison with the control samples.

Molecular modeling of **1**: The computational investigations on the three-dimensional structure of **1** were carried out using HyperChem Release 7.52. As a starting structure, **1** was truncated at the PSA moiety and the 2*R* configuration was chosen for PBB2. From that theoretical derivative, two diastereomers were created around the C-2 stereocenter of PBB1. The calculation was conducted by a series of alternating processes of geometry minimization and simulated annealing to obtain the global energy minimum. We used the MM+ force field with the Polak–Ribière algorithm. Ten cycles of molecular dynamic processes were run (heating time 0.1 ps, running time 0.5 ps, step size 0.0005 ps, starting temperature 100 K, simulation temperature 300 K, temperature step 30 K.), followed by five cycles of annealing at 600 K. Finally, an ab initio calculation using STO-3G as minimal basis set was performed.

Biological testing: Antimicrobial activity was determined in a primary screen by the agar diffusion assay against a series of Gram-positive and Gram-negative bacteria, yeasts, and fungi.[24,25] For *Bacillus subtilis* ATCC 6633, *Mycobacterium smegmatis* SG 987 (HKI0056), *M. aurum* SB66, *M. vaccae* IMET 10670, and *M. fortuitum* B, minimal inhibitory concentrations (MIC) were determined

 © 2006 Wiley-VCH Verlag GmbH & Co. KGaA, Weinheim

according to the NCCLS guidelines using the microbroth dilution method.[26,27]

For *M. tuberculosis* strains, inoculae of 0.2 mL of 5×10^8 cells mL^{-1} were suspended in tubes with 2 mL of liquid Shkol'nikova medium (Middelbrook H9 medium supplemented with human serum and egg albumin) containing twofold serial dilutions of the compounds, from 100.0 to 0.195 μg mL^{-1}. After 14 days of incubation at 37 °C, the tubes were centrifuged for 15 min at 3000 rpm. The sediment was resuspended in 0.8 mL of sterile 0.9 % NaCl solution. A 0.1-mL sample of the suspension was used to prepare smears subsequently stained by the Ziehl–Neelsen method. The remaining sediment was inoculated in 0.2-mL volumes into three tubes with solid Loewenstein–Jensen medium. The results were read after 21–28 days of cultivation at 37 °C. MICs were characterized by the presence of individual mycobacteria in a smear and a decrease in the number of colonies grown on solid media compared to controls. MBC (minimal bactericidal concentration) of drugs were considered as the drug concentration completely inhibiting the growth of mycobacteria on the solid medium.

Received: September 23, 2005
Revised: December 2, 2005
Published online: April 18, 2006

Keywords: antibiotics · mycobacteria · natural products · peptides · structure elucidation

[1] S. Grabley, I. Sattler in *Modern Methods of Drug Discovery* (Eds.: R. Hilgenfeld, A. Hillisch), Birkhäuser, Basel, **2001**, pp. 87 – 107.
[2] S. Grabley, R. Thiericke in *Drug Discovery from Nature* (Eds.: S. Grabley, R. Thiericke), Springer, Berlin, **1999**, pp. 124 – 148.
[3] I. Schmid, I. Sattler, S. Grabley, R. Thiericke, *J. Biomol. Screening* **1999**, *4*, 13 – 23.
[4] U. Gräfe, R. Schlegel, M. Ritzau, W. Ihn, K. Dornberger, C. Stengel, W. F. Fleck, W. Gutsche, A. Härtl, E. F. Paulus, *J. Antibiot.* **1995**, *48*, 19 – 25.
[5] M. Chu, R. Mierzwa, L. He, L. Xu, F. Gentile, J. Terracciano, M. Patel, L. Miesel, S. Bohanon, C. Kravec, C. Cramer, T. O. Fischman, A. Hruza, L. Ramanathan, P. Shipkova, T.-M. Chan *Tetrahedron Lett.* **2001**, *42*, 3549 – 3551.
[6] K. Fujii, Y. Ikai, T. Mayumi, H. Oka, M. Suzuki, K. Harada, *Anal. Chem.* **1997**, *69*, 3346 – 3352.
[7] D. E. Williams, M. Craig, C. F. B Holmes, R. J. Andersen, *J. Nat. Prod.* **1996**, *59*, 570 – 575.
[8] Product information 48895 from Pierce (Rockford, IL).
[9] CCDC GNANVOG, NUDWIS, VAFPEX, and ZEMHEE contain the complete crystallographic data for compounds cited in comparison. The data can be obtained free of charge from the Cambridge Crystallographic Data Centre via http://www.ccdc.cam.ac.uk/data_request/cif.
[10] The *R* configuration was assigned arbitrarily for C-2 of PBB2. The configuration of this stereocenter should have no significant influence on the conformational arrangement of the peptide core, in particular the PBB1—Ala unit.
[11] K. Umezawa, K. Nakazawa, Y. Ikeda, H. Naganawa, S. J. Kondo, *J. Org. Chem.* **1999**, *64*, 3034 – 3038.
[12] H. M. Dahse, B. Schlegel, U. Gräfe, *Pharmazie* **2000**, *55*, 489 – 491.
[13] F. Sarabia, S. Chammaa, A. S. Ruiz, L. M. Ortiz, F. J. Herrera, *Curr. Med. Chem.* **2004**, *11*, 1309 – 1332.
[14] C. E. Ballard, H. Yu, B. Wang, *Curr. Med. Chem.* **2002**, *9*, 471 – 498.
[15] Dictionary of Natural Products on CD-ROM, Version 14.1, Chapmann & Hall, London, **2005**.
[16] I. Namatame, H. Tomoda, S. Ishibashi, S. Omura, *Proc. Natl. Acad. Sci. USA* **2004**, *101*, 737 – 742.
[17] J. Shoji, H. Hinoo, T. Hattori, K. Hirooka, Y. Kimura, T. Yoshida, *J. Antibiot.* **1989**, *42*, 1460 – 1464.
[18] Y. Hathout, Y. P. Ho, V. Ryzhov, P. Demirev, C. Fenselau, *J. Nat. Prod.* **2000**, *63*, 1492 – 1496.
[19] K. Mochizuki, K. Ohmori, H. Tamura, Y. Shizuri, S. Nishiyama, E. Miyoshi, S. Yamamura, *Bull. Chem. Soc. Jpn.* **1993**, *66*, 3041 – 3046.
[20] T. Morino, A. Masuda, M. Yamada, M. Nishimoto, T. Nishikiori, S. Saito, N. Shimada, *J. Antibiot.* **1994**, *47*, 1341 – 1343.
[21] K. Sugawara, S. Toda, T. Moriyama, M. Konishi, T. Oki, *J. Antibiot.* **1993**, *46*, 928 – 935.
[22] D. Schwartz, personal communication.
[23] L. Han, X. Huang, I. Sattler, H. M. Dahse, H. Fu, W. Lin, S. Grabley, *J. Nat. Prod.* **2004**, *67*, 1620 – 1623.
[24] Deutsches Arzneibuch, 9th ed., Deutscher Apotheker Verlag, Stuttgart, **1986**, pp. 47–48 and 424 – 430.
[25] S. Afonin, R. W. Glaser, M. Berditchevskaja, P. Wadhwani, K.-H. Gührs, U. Möllmann, A. Perner, A. S. Ulrich, *ChemBioChem* **2003**, *4*, 1151 – 1163.
[26] L. Heinisch, S. Wittmann, T. Stoiber, A. Berg, D. Ankel-Fuchs, U. Möllmann, *J. Med. Chem.* **2002**, *45*, 3032 – 3040.
[27] National Committee for Clinical Laboratory Standards. Methods for Dilution Antimicrobial Susceptibility Tests for Bacteria that Grow Aerobically, Approved Standard. NCCLS Document M7A4, *5th ed*. National Committee for Clinical Laboratory Standards, Villanova, PA, **2000**.

 © 2006 Wiley-VCH Verlag GmbH & Co. KGaA, Weinheim

Asymmetric Catalysis

DOI: 10.1002/anie.200600100

Regio- and Stereoselective Rhodium-Catalyzed Allylic Alkylations of Chelated Enolates**

Uli Kazmaier and Daniel Stolz*

Dedicated to Professor Dieter Enders on the occasion of his 60th birthday

The development of organometallic chemistry during the last 40 years has had a strong impact on organic synthesis.[1] Of the various transition metals used, the noble metals are especially important for catalytic processes, and palladium has long played a dominant role.[2] But recently, the neighboring elements such as ruthenium[3] and rhodium[4] have moved

[*] Prof. Dr. U. Kazmaier, Dipl.-Chem. D. Stolz
Universität des Saarlandes
Institut für organische Chemie
Im Stadtwald, Geb. C4.2, 66123 Saarbrücken (Germany)
Fax: (+49) 681-302-2409
E-mail: u.kazmaier@mx.uni-saarland.de

[**] This work was supported by the Deutsche Forschungsgemeinschaft and the Fonds der Chemischen Industrie.

WILEY InterScience DISCOVER SOMETHING GREAT
© 2006 Wiley-VCH Verlag GmbH & Co. KGaA, Weinheim

more into the limelight. Since the introduction of Wilkinson's catalyst,[5] asymmetric hydrogenations in the presence of chiral ligands, in particular, have initiated a boom in rhodium catalysis.[6] In the meantime a wide range of synthetic applications of Wilkinson's catalyst have been developed, for example, for allylic alkylations.[7]

Like iridium,[8] molybdenum,[9] and tungsten,[10] rhodium's reactivity is different from that of palladium,[11] which makes this metal and its complexes interesting from a synthetic point of view. Back in 1985 Tsuji et al. compared the Rh- and Pd-catalyzed allylic alkylations of β-keto esters using allylic substrates **A** and **B** (Scheme 1).[12] While with Pd, the product distribution (**C**–**E**) was nearly independent of the substrate used, the Rh-catalyzed reaction provided preferentially the product in which the incoming substituent takes the position of the previous leaving group. For the Pd-catalyzed reaction, the product distribution can be explained by the formation of a π-allyl complex which undergoes fast π–σ–π isomerization. This complex is preferentially attacked by the nucleophile at the sterically least hindered position. In contrast, for the Rh-catalyzed reaction, Tsuji postulated the formation of a σ-allyl rhodium complex instead of a π-allyl complex. In comparing these two processes they noted that Pd-catalyzed reaction proceeds faster and under milder conditions than the Rh-catalyzed reaction.

For a time interest in the Rh-catalyzed allylation waned, until Evans et al. in 1998 recognized that phosphite ligands significantly improve the reaction rate as well as the regioselectivity.[13] Phosphites are better π acceptors than phosphanes. Therefore the rhodium–allyl intermediate is more electrophilic, and nucleophilic attack occurs preferentially at the sterically more hindered position. This effect, which was also observed for Pd-catalyzed reactions, can be explained by a switch of the reaction mechanism from an S_N2- to an S_N1-type attack.[14] If optically active substrates such as **F** are used, in the Rh-catalyzed version the chiral information can be transferred more or less completely to the product **G** (Scheme 1). This is not possible with Pd catalysts because of the very fast π–σ–π isomerization. With soft nucleophiles the reaction apparently proceeds with double inversion via intermediate **H**, which undergoes slow interconversion into σ-allyl intermediate **I**.[15]

This tendency for interconversion of the rhodium–allyl complexes seems to depend on the substrate used. Pregosin et al.[16] and Hayashi et al.[17] were able to show that under suitable conditions racemic aryl-substituted substrates **K** can be converted into nearly enantiomerically pure products **M** in the presence of chiral ligands (Scheme 1). This clearly indicates that π–σ–π isomerization can also occur in Rh complexes and that the Rh-catalyzed allylic alkylation is considerably less well understood than the Pd-catalyzed version.

Since some time our group has been investigating Pd-catalyzed allylic alkylations of chelated enolates obtained from amino acid esters (Scheme 2).[18] Owing to their high reactivity, these enolates react under much milder conditions than the generally used stabilized enolates do, offering new synthetic options.[19] For example, at −78 °C the π–σ–π isomerization of the π-allyl Pd intermediates can be suppressed completely.[20] Nevertheless, the regioselectivity of the reactions of the terminal allyl complexes remains unsatisfactory. Although linear substitution products such as **3** can be obtained readily, the branched products **2** are not accessible.

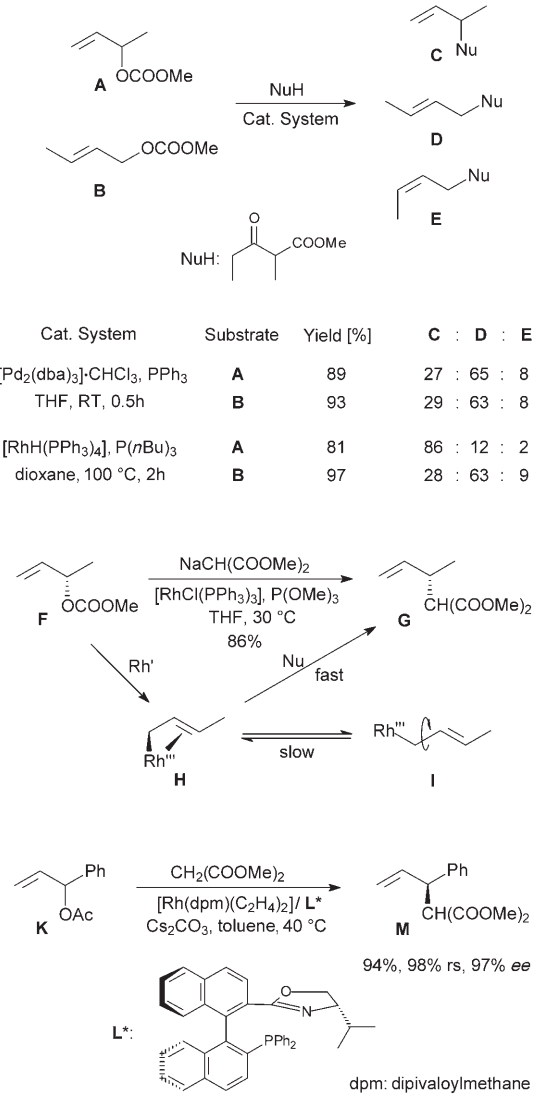

Cat. System	Substrate	Yield [%]	C : D : E
$[Pd_2(dba)_3]\cdot CHCl_3$, PPh_3	**A**	89	27 : 65 : 8
THF, RT, 0.5h	**B**	93	29 : 63 : 8
$[RhH(PPh_3)_4]$, $P(n\text{Bu})_3$	**A**	81	86 : 12 : 2
dioxane, 100 °C, 2h	**B**	97	28 : 63 : 9

Scheme 1. Rhodium-catalyzed allylic alkylations. dba = dibenzylideneacetone, rs = regioselectivity, *ee* = enantiomeric excess.

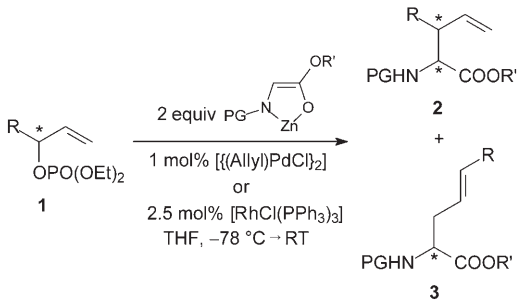

Scheme 2. Allylic alkylations of chelated amino acid ester enolates; PG = protecting group.

 © 2006 Wiley-VCH Verlag GmbH & Co. KGaA, Weinheim

In addition, if chiral substrates such as **1** are used, complete epimerization is observed as a consequence of the fast isomerization.

We therefore shifted our focus to the Rh-catalyzed version. To compare our results with those of Evans et al., we started our investigations with substrate *rac*-**1a** so that we could evaluate the effect of the reaction parameters (ligand, temperature etc.) on the regio- and stereoselectivity (Table 1). In general, best results were obtained with an excess of the nucleophile and with phosphate as the leaving group, which proved to be superior to other leaving groups (e.g. acetate, carbonates). That is why these parameters were not changed, and also the amount of Rh-catalyst was kept constant.

We first examined the influence of the phosphite ligand (Table 1, entries 1–3). When *N*-trifluoroacetylated (Tfa) *tert*-butyl glycinate was used as the nucleophile, the regioselectivity towards the branched product improved with increasing steric demand of the ligand. In the presence of $P(OiPr)_3$ the branched product **2** was obtained in a highly selective fashion and almost quantitative yield.[21] When the racemic phosphate was replaced by an optically active one, nearly perfect chirality transfer was observed (entry 4).

With the phenyl-substituted derivative **1b** even in the presence of $P(OMe)_3$ the branched product was obtained exclusively with perfect chirality transfer, although the diastereoselectivity was lower than expected (entry 5). In this case the less reactive acetate had to be used, because the corresponding phosphate is not stable and undergoes fast isomerization to the linear allyl phosphate. Increasing the steric demand of the alkyl substituent (entries 6–8) resulted in a shift of regioselectivity more towards **3**, and in case of the isobutyl derivative **1e** the linear product was formed nearly exclusively. Very surprising was the high degree of chirality transfer, which was observed for all linear products. This might result from the very slow isomerization of the allyl–rhodium intermediates formed.

For analytical purposes we subjected **1e** to the same reaction, also with a Pd catalyst. In this case only racemic products (linear as well as branched) were obtained (Table 1, entry 9). To prove that the low reaction temperature has a beneficial effect on the outcome, we also performed a control experiment at room temperature (entry 10). The yield and chirality transfer was significantly worse, which clearly indicates that isomerization is also a factor in Rh-catalyzed allylations at higher temperatures, but that this process is much slower than in the Pd-catalyzed reaction.

Although the regioselectivities obtained with alkyl substrates **1a**, **1b**, and **1e** are very high, other alkyl-substituted derivatives seem to react less selectively. Therefore, we also investigated the influence of the protecting groups (PG and R′) on the glycine enolate. Replacement of the sterically demanding *tert*-butyl ester by a small methyl ester resulted in lower yield, but the selectivity towards the branched product increased (Table 1, entry 11). The same was true when the *N*-trifluoroacetyl group (Tfa) was replaced by the carbamate protecting group Boc (entry 12). With Cbz-protected methyl glycinate the branched product was formed nearly exclusively (entry 13). This tendency seems to be generally valid. For example, the branched allylic substrate **1e** still provided the linear product preferentially, but the proportion of **2** was significantly higher than that obtained with the Tfa ester (entries 14 and 8). Remarkable is the excellent chirality transfer observed, which was superior even to that obtained with the Tfa ester.

From a synthetic point of view the stereoselective formation of the linear product is of special interest, and therefore we investigated allylations with several other, also functionalized substrates (Scheme 3). In all the examples evaluated so far, only the linear product was obtained.

In conclusion one can say that the Rh-catalyzed allylic alkylation is as efficient and versatile as the Pd-catalyzed version. In reactions of chelated enolates with suitable protecting groups, high yields and selectivities were obtained, and the regioselectivity can be directed by the reaction parameters. The chirality transfer from the allyl substrate to the attacking nucleophile is excellent.

Table 1: Rhodium-catalyzed allylic alkylations of chelated amino acid ester enolates (see Scheme 2).

Entry	Substr.	% *ee*	R	PG[a]	R′	Ligand	Yield [%][b]	**2/3**	**2**			**3**	
									% ds	% *ee*	Config.	% *ee*	Config.
1	*rac*-**1a**		Me	Tfa	*t*Bu	10% $P(OMe)_3$	84	87:13	92				
2	*rac*-**1a**		Me	Tfa	*t*Bu	10% $P(OEt)_3$	85	89:11	91				
3	*rac*-**1a**		Me	Tfa	*t*Bu	10% $P(OiPr)_3$	98	99:1	94				
4	(*S*)-**1a**	95	Me	Tfa	*t*Bu	10% $P(OiPr)_3$	95	98:2	94	93	(2*S*,3*S*)		
5	(*R*)-**1b**[c]	99	Ph	Tfa	*t*Bu	10% $P(OMe)_3$	52	99:1	59	99	(2*R*,3*R*)		
6	*rac*-**1c**		Et	Tfa	*t*Bu	10% $P(OEt)_3$	98	47:53	87				
7	(*R*)-**1d**	99	*n*Pr	Tfa	*t*Bu	10% $P(OEt)_3$	97	71:29	92	98	(2*R*,3*R*)	83	(2*S*)
8	(*R*)-**1e**	99	*i*Bu	Tfa	*t*Bu	10% $P(OEt)_3$	95	7:93	88	98	(2*R*,3*R*)	89	(2*S*)
9	(*R*)-**1e**	99	*i*Bu	Tfa	*t*Bu	4.5% PPh_3[d]	76	14:86	89	*rac*		*rac*	
10	(*R*)-**1d**[e]	99	*n*Pr	Tfa	*t*Bu	10% $P(OEt)_3$	80	69:31	94	87	(2*R*,3*R*)	67	(2*S*)
11	(*R*)-**1d**	99	*n*Pr	Tfa	Me	10% $P(OEt)_3$	76	85:15	92	95	(2*R*,3*R*)	75	(2*S*)
12	(*R*)-**1d**	99	*n*Pr	Boc	*t*Bu	10% $P(OEt)_3$	55	87:13	89	93	(2*R*,3*R*)	n.d.[f]	
13	(*R*)-**1d**	99	*n*Pr	Cbz	Me	10% $P(OEt)_3$	65	97:3	90	99	(2*R*,3*R*)		
14	(*R*)-**1e**	99	*i*Bu	Cbz	Me	10% $P(OEt)_3$	60	33:67	95	90	(2*R*,3*R*)	93	(2*S*)

[a] Tfa = trifluoroacetyl, Boc = *tert*-butoxycarbonyl, Cbz = benzyloxycarbonyl. [b] Yield of isolated product. [c] Allyl acetate was used instead of allyl phosphate. [d] The catalyst was 1 mol% $[\{(allyl)PdCl\}_2]$. [e] Reaction was carried out at room temperature. [f] Not determined.

 © 2006 Wiley-VCH Verlag GmbH & Co. KGaA, Weinheim

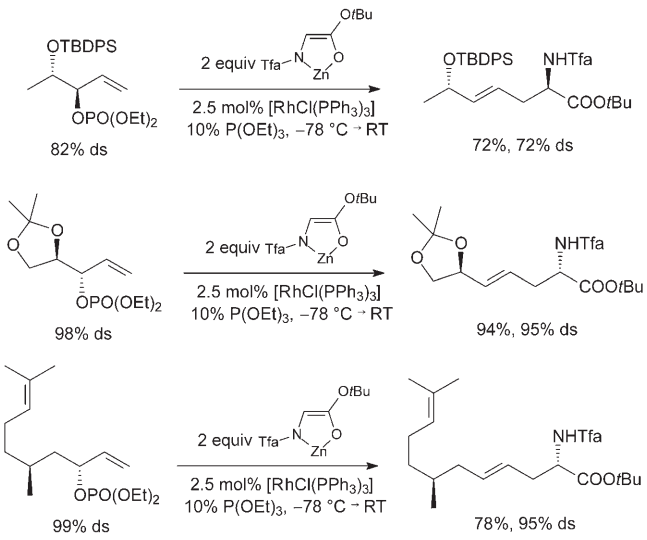

Scheme 3. Syntheses of functionalized linear amino acids; TBDPS = *tert*-butyldiphenylsilyl.

Experimental Section

General procedure for rhodium-catalyzed allylic alkylations: A solution of hexamethyldisilazane (223 mg, 1.38 mmol) in freshly distilled THF (1.0 mL) under argon was prepared in a Schlenk flask. After the solution had been cooled to −20 °C, a solution of *n*-butyllithium (1.6 M, 0.78 mL, 1.25 mmol) was added slowly. The cooling bath was removed, and stirring was continued for further 10 min. In a second Schlenk flask the *N*-protected glycinate (0.50 mmol) was dissolved in freshly distilled THF (1 mL). The solution was cooled to −78 °C before the freshly prepared LHMDS solution was added. After 10 min a solution of dried $ZnCl_2$ (75 mg, 0.55 mmol) in THF (1.0 mL) was added, and stirring was continued for 30 min at −78 °C.

A solution was prepared from Wilkinson's catalyst (5.8 mg, 6.25 μmol) and the trialkyl phosphite (25.0 μmol) in THF (1 mL). The solution was stirred for 5 min at room temperature during which time it turned yellow. The allyl substrate (0.25 mmol) was added to the yellow solution, and the resulting solution was added slowly to the chelated enolate at −78 °C. The mixture was allowed to warm to room temperature overnight. The solution was diluted with diethyl ether before 1 M $KHSO_4$ was added. After separation of the layers, the aqueous layer was extracted three times with diethyl ether and the combined organic layers were dried over Na_2SO_4. The solvent was evaporated in vacuo, and the crude product was purified by flash chromatography.

Received: January 10, 2006
Revised: February 9, 2006
Published online: April 5, 2006

Keywords: allylation · amino acids · chelates · chirality transfer · rhodium

[1] a) *Transition Metals in the Synthesis of Complex Organic Molecules* (Ed.: L. S. Hegedus), University Science Books, Herndon, **1999**; b) *Transition Metals for Organic Synthesis* (Eds.: M. Beller, C. Bolm), Wiley-VCH, Weinheim, **2004**; c) *Metal-Catalyzed Cross Coupling Reactions* (Eds.: A. de Meijere, F. Diederich), Wiley-VCH, Weinheim, **2004**.

[2] a) J. Tsuji, *Organic Syntheses with Palladium Compounds*, Springer, Heidelberg, **1980**; b) *Palladium Reagents in Organic Syntheses* (Ed.: R. F. Heck), Academic Press, London, **1985**; c) *Handbook of Palladium-Catalyzed Organic Reactions* (Eds.: J. L. Malleron, J. C. Fiaud, J. Y. Legros), Academic Press, San Diego, **1997**.

[3] *Ruthenium in Organic Synthesis* (Ed.: S. I. Murahashi), Wiley-VCH, Weinheim, **2004**.

[4] *Modern Rhodium-Catalyzed Organic Reactions* (Ed.: P. A. Evans), Wiley-VCH, Weinheim, **2005**.

[5] J. A. Osborne, F. H. Jardine, J. F. Young, G. Wilkinson, *J. Chem. Soc. A* **1966**, 1711.

[6] Y. Chi, W. Tang, X. Zhang in *Modern Rhodium-Catalyzed Organic Reactions* (Ed.: P. A. Evans), Wiley-VCH, Weinheim, **2005**, pp. 1–31.

[7] D. K. Leahy, P. A. Evans, in *Modern Rhodium-Catalyzed Organic Reactions* (Ed.: P. A. Evans), Wiley-VCH, Weinheim, **2005**, pp. 191–214.

[8] a) R. Takeuchi, M. Kashio, *Angew. Chem.* **1997**, *109*, 268–270; *Angew. Chem. Int. Ed. Engl.* **1997**, *36*, 263–265; b) J. P. Janssen, G. Helmchen, *Tetrahedron Lett.* **1997**, *38*, 8025–8026; c) B. Bartels, G. Helmchen, *Chem. Commun.* **1999**, 741–742; d) R. Takeuchi, K. Tanabe, *Angew. Chem.* **2000**, *112*, 2051–2054; *Angew. Chem. Int. Ed.* **2000**, *39*, 1975–1978.

[9] a) B. M. Trost, C. Merlic, *J. Am. Chem. Soc.* **1990**, *112*, 9590–9600; b) B. M. Trost, S. Hildbrand, K. Dogra, *J. Am. Chem. Soc.* **1999**, *121*, 10416–10417; c) N. F. Kaiser, U. Bremberg, M. Larhed, C. Moberg, A. Hallberg, *Angew. Chem.* **2000**, *112*, 3741–3744; *Angew. Chem. Int. Ed.* **2000**, *39*, 3595–3598.

[10] a) G. C. Lloyd-Jones, A. Pfaltz, *Angew. Chem.* **1995**, *107*, 534–536; *Angew. Chem. Int. Ed. Engl.* **1995**, *34*, 462–464; b) A. V. Malkov, I. R. Baxendale, D. Dvořák, D. J. Mansfield, P. Kočovský, *J. Org. Chem.* **1999**, *64*, 2737–2750.

[11] U. Kazmaier, M. Pohlman, in *Metal-Catalyzed Cross Coupling Reactions* (Eds.: A. de Meijere, F. Diederich), Wiley-VCH, Weinheim, **2004**, pp. 531–583.

[12] I. Minami, I. Shimizu, J. Tsuji, *J. Organomet. Chem.* **1985**, *296*, 269–280.

[13] a) P. A. Evans, J. D. Nelson, *Tetrahedron Lett.* **1998**, *39*, 1725–1728; b) P. A. Evans, L. J. Kennedy, *J. Am. Chem. Soc.* **2001**, *123*, 1234–1235.

[14] R. Prétôt, A. Pfaltz, *Angew. Chem.* **1998**, *110*, 337–339; *Angew. Chem. Int. Ed.* **1998**, *37*, 323–325.

[15] P. A. Evans, J. D. Nelson, *J. Am. Chem. Soc.* **1998**, *120*, 5581–5582.

[16] K. Selvakumar, M. Valentini, P. S. Pregosin, A. Albinati, *Organometallics* **1999**, *18*, 4591–4597.

[17] T. Hayashi, A. Okada, T. Suzuka, M. Kawatsura, *Org. Lett.* **2003**, *5*, 1713–1715.

[18] a) U. Kazmaier, F. L. Zumpe, *Angew. Chem.* **1999**, *111*, 1572–1574; *Angew. Chem. Int. Ed.* **1999**, *38*, 1468–1470; b) U. Kazmaier, S. Maier, F. L. Zumpe, *Synlett* **2000**, 1523–1535; c) T. D. Weiß, G. Helmchen, U. Kazmaier, *Chem. Commun.* **2002**, 1270–1271; d) U. Kazmaier, *Curr. Org. Chem.* **2003**, 317–328.

[19] a) U. Kazmaier, T. Lindner, *Angew. Chem.* **2005**, *117*, 3368–3371; *Angew. Chem. Int. Ed.* **2005**, *44*, 3303–3306; b) T. Lindner, U. Kazmaier, *Adv. Synth. Catal.* **2005**, *347*, 1687–1695.

[20] a) U. Kazmaier, F. L. Zumpe, *Angew. Chem.* **2000**, *112*, 805–807; *Angew. Chem. Int. Ed.* **2000**, *39*, 802–804; b) U. Kazmaier, M. Pohlman, *Synlett* **2004**, 623–626.

[21] The regio- and stereoselectivities were determined before workup by GC using the chiral column Chirasil-L-Val.

 © 2006 Wiley-VCH Verlag GmbH & Co. KGaA, Weinheim

C–H Insertion

DOI: 10.1002/anie.200504288

Intramolecular Concerted Insertion of Vinyl Cations into C–H Bonds: Hydroalkylating Cyclization of Alkynes with Alkyl Chloroformates To Give Cyclopentanes**

*Ursula Biermann, Rainer Koch, and Jürgen O. Metzger**

C–H insertions with formation of a new C–C bond are of topical interest.[1] At present, great efforts are devoted to developing the transition-metal-catalyzed C–H insertion.[2] The insertion of carbenes into C–H bonds proceeds by direct attack of a nonactivated C_{sp^3}–H bond and formation of a new C–C bond in a concerted one-step reaction.[3] Theoretical studies[4,5] as well as experimental investigations in the gas phase[6] have shown that the vinyl cation $C_2H_3^+$ can insert into the H–H bond by formation of the ethyl cation[4,6] and into the C–H bond of methane and of ethane by formation of the 2-propyl cation[6] and the 2-butyl cation,[5] respectively.

Recently we reported on the hydroalkylation of alkenes with alkyl chloroformates induced by ethylaluminum sesquichloride ($Et_3Al_2Cl_3$).[7] The reaction of the Lewis acid, for example, with isopropyl chloroformate (**1a**) gives the isopropyl cation, which adds across the alkene. Transfer of a hydride ion from an ethylaluminum sesquichloride species to the adduct carbenium ion takes place by formation of the hydroalkylation product (Scheme 1).

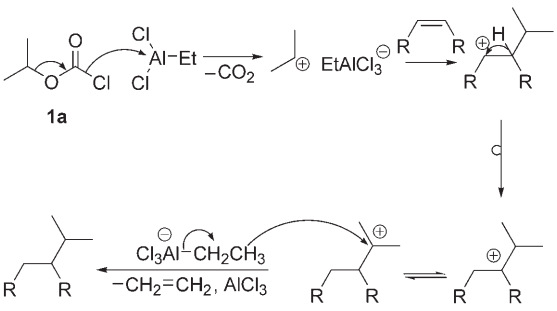

Scheme 1. Mechanism of the hydroalkylation of alkenes with isopropyl chloroformate (**1a**) induced by ethylaluminum sesquichloride. R = alkyl.

The application of this reaction to alkynes was expected to give analogously alkylated alkenes. The reaction of 4-octyne (**2a**) and **1a** under similar reaction conditions in the presence of $Et_3Al_2Cl_3$ and with Et_3SiH as an additional hydride donor[8] was expected to proceed via vinyl cation **3a** to give 4-isopropyl-4-octene (**4a**) (Scheme 2). To our surprise this

	a	b	c	d
R^1	Pr	Bu	Et	H
R^2	Pr	Bu	Et	Hex

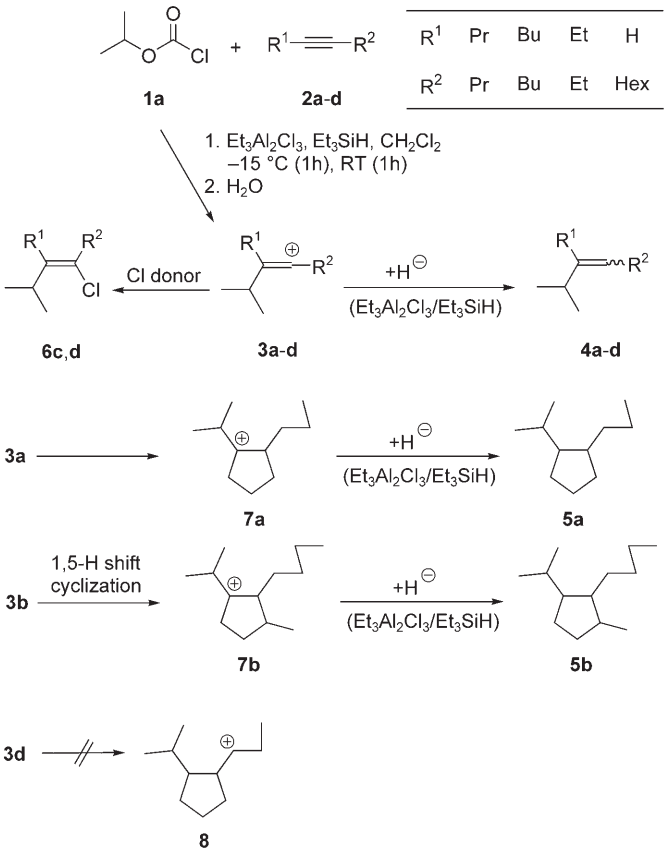

Scheme 2. Reactions of alkynes **2a–d** with **1a** in the presence of $Et_3Al_2Cl_3/Et_3SiH$ proceeding via vinyl cations **3a–d**. Products **5a,b** and **6c,d** as well as the side products **4a–d** were obtained as mixtures of diastereomers. Products derived from the exocyclic cyclopentyl cation **8** were not observed.

product was formed only as a side product (< 5%). We isolated 1-isopropyl-2-propylcyclopentane (**5a**) in 79% yield as a mixture of two diastereomers in a ratio of 4.6:1. The analogous reaction of 5-decyne (**2b**) afforded the 1,2,3-trialkyl-substituted cyclopentane **5b** in 74% yield as a mixture of four diastereomers in a ratio of 11:6:1:1. In this case, too, the hydroalkylation product **4b** was formed in only trace amounts (< 2%). The analogous reaction of 3-hexyne (**2c**) gave chloroalkene **6c** as a diastereomeric mixture (1.3:1) in 38% yield. The hydroalkylation product **4c** was obtained in about 12% yield. Reaction of 1-octyne (**2d**) with **1a** in the presence of $Et_3Al_2Cl_3$ afforded the chloroalkylation product **6d** in 40% yield as a diastereomeric mixture and about 5% of the hydroalkylation product **4d**. A cyclopentane derivative or another cyclic product was not observed in either reaction.

[*] Dr. U. Biermann, Dr. R. Koch, Prof. Dr. J. O. Metzger
Institute of Pure and Applied Chemistry
University of Oldenburg
P.O. Box 2503, 26111 Oldenburg (Germany)
Fax: (+49) 441-798-3618
E-mail: juergen.metzger@uni-oldenburg.de

[**] This work was supported financially by the German Research Foundation (DFG, ME 722/14-1).

Supporting information for this article is available on the WWW under http://www.angewandte.org or from the author.

InterScience
© 2006 Wiley-VCH Verlag GmbH & Co. KGaA, Weinheim

The formation of products **4**–**6** can be explained as follows: The initially formed 2-propyl cation adds across the C–C triple bond to give vinyl cations **3**. If a C–H bond is available in position 5 of **3** an intramolecular 1,5-hydride shift takes place to give cyclopentyl cations **7a** and **7b**, respectively, with formation of a new C–C bond. Finally, intermolecular hydride transfer leads to the products **5a** and **5b**, respectively.[9] The intramolecular 1,5-hydride shift is definitely faster than the intermolecular hydride transfer from $Et_3Al_2Cl_3$ or Et_3SiH yielding hydroalkylation products **4**. In the case of alkyne **2c** a 1,5-hydride shift is not possible. Therefore vinyl cation **3c** is mainly trapped by transfer of a chloride ion from chloroformate **1a** or an $EtAlCl_3^-$ species to give chloroalkenes **6c**. Apparently the transfer of a chloride ion to the vinyl cation intermediate is faster than the transfer of a hydride ion. Marcuzzi and Melloni reported on the chloroalkylation of alkynes using chloroalkanes in the presence of Lewis acids.[10]

In analogy, the cyclization of vinyl cation **3d** should be possible by formation of the exocyclic carbenium ion **8**. However, products derived from **8** were not observed, giving evidence that a fast 1,5-hydride shift takes place only if an endocyclic carbenium ion such as **7a**,**b** is formed. Thus, alkynes **2c** and **2d** were treated with 2-butyl chloroformate (**1b**) in the presence of $Et_3Al_2Cl_3$ and Et_3SiH. As expected, we observed the formation of the cyclopentane derivatives **10c** and **10d** via vinyl cations **9c** and **9d**, respectively (Scheme 3). The diastereomeric mixtures of compounds **10c** and **10d** were obtained in yields of 26% (GC) and 13% (GC), respectively. Interestingly, the reaction of alkyne **2a** with alkyl chloroformate **1b** via vinyl cation **9a** gave cyclopentane **10a** as well as **11** (total yield: 52%) in a ratio of 1:3.

There are some questions concerning the mechanism of the formation of the cyclopentanes. Schegolev et al. reported on the formation of cyclopentenone derivatives by additions of acyl cations to alkynes. They discussed a 1,5-hydride shift of the initially formed acyl vinyl cation followed by an addition–elimination reaction A_DE or alternatively an intramolecular electrophilic substitution S_Ei.[11] In our case both mechanistic alternatives can be excluded with certainty. Cyclopentene derivatives formed as products of a S_Ei reaction were not observed even in trace amounts. The alternative 1,5-hydride transfer followed by an addition reaction to give a cyclopentyl cation, which under our reaction conditions could be trapped by a hydride donor, can be excluded, too, because in this case the vinyl cation intermediates **3a** and **3b** should give initially a primary and secondary alkyl carbenium ion, respectively. Our investigations of hydroalkylations of alkenes have shown that 1,2-H shifts of the alkyl carbenium ion intermediates are always faster than all kinds of possible inter- and intramolecular trapping reactions.[7] However, products of these rearranged carbenium ions, such as cyclobutanes, were not observed. Thus, the 1,5-H shift and the cyclization must proceed in a concerted reaction (Scheme 4).

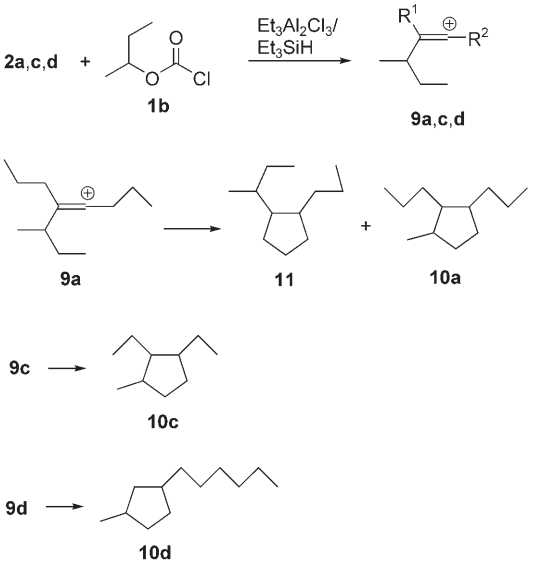

Scheme 3. Reaction of alkynes **2a**,**c**,**d** with **1b** in the presence of $Et_3Al_2Cl_3/Et_3SiH$ proceeding via vinyl cations **9a**,**c**,**d** to give the products of a hydroalkylating cyclization **10a**,**c**,**d** and **11**. Cyclopentanes **10a** and **11** are formed in a ratio of 1:3 via vinyl cation **9a**. The cyclopentanes were obtained as mixtures of diastereomers. For R^1, R^2, see Scheme 2.

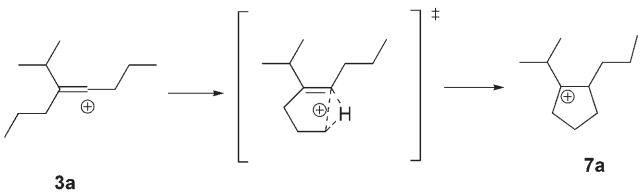

Scheme 4. Concerted intramolecular insertion of vinyl cation **3a** into a primary C–H bond to give the cyclopentyl carbenium ion **7a**.

Our quantum-mechanical calculations (MP2/6-311 + G(d,p)//MP2/6-31G(d) + ZPVE)[12] predict that this concerted insertion of vinyl cation **3a** into a C–H bond is a possible pathway. After the exothermic formation of **3a** ($-197\ kJ\,mol^{-1}$), the reaction proceeds via the transition state of the concerted process (Figure 1), leading directly to the cyclopentyl cation **7a**. While the latter is stabilized by about $130\ kJ\,mol^{-1}$ relative to **3a**, the activation energy for the cyclization and simultaneous hydrogen transfer is only $8\ kJ\,mol^{-1}$. The formation of a primary alkyl carbenium ion by 1,5-hydride shift followed by C–C bond formation can be ruled out because the carbenium ion is not a minimum on the potential energy surface but rearranges by a 1,2-hydrogen shift to give a secondary alkyl carbenium ion, which cannot form cyclopentanes. Analysis of the transition state's single imaginary frequency reveals a motion of the bond-forming carbon atoms towards each other, while the hydrogen atom is moving above the ring system. The relevant distances are in accordance with those of an insertion of the ethenyl cation into the C–H bond of ethane[5] and those of comparable C–H insertion reactions of carbenes.[13–15]

Surprisingly, vinyl cation **3d** does not form an exocyclic secondary cyclopentyl cation **8**. The reason could be that the generation of a secondary cation is energetically less favorable than formation of a tertiary endocyclic carbenium ion. Our calculations with the model vinyl cation **3e** (R^1 = Pr, R^2 = Bu) demonstrate that the formation of the exocyclic carbenium ion **12** is in particular kinetically disfavored (Scheme 5).

 © 2006 Wiley-VCH Verlag GmbH & Co. KGaA, Weinheim

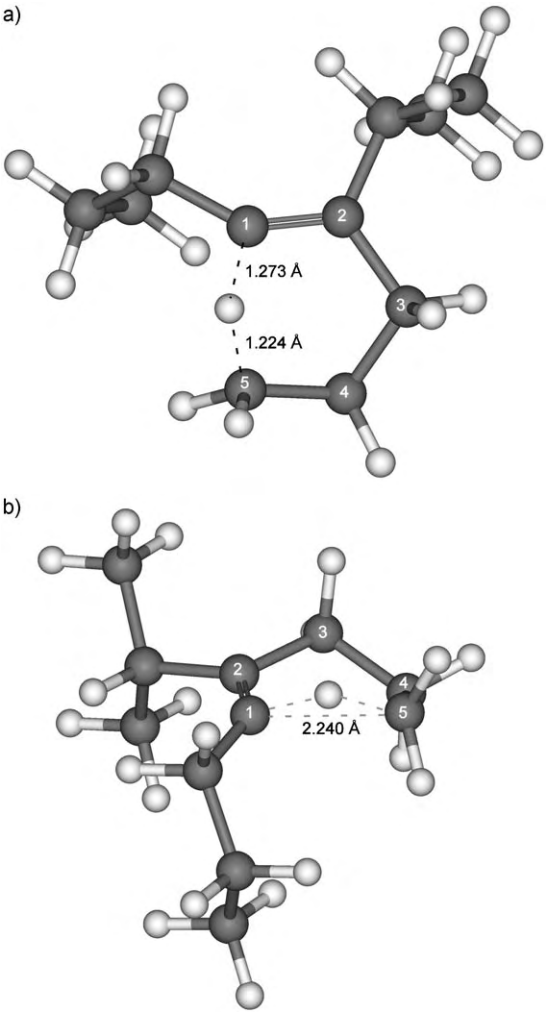

Figure 1. Transition state for the concerted formation of cyclopentyl cation **7a** from vinyl cation **3a**. Relevant C–H and C–C distances are given. a) View of the forming cyclopentane ring in the plane. b) The view of the forming cyclopentane ring perpendicular to the plane reveals a boatlike orientation; carbon atoms 2–4 lie above the C1-H-C5 plane. The C1-H-C5 angle is 127.5°.

While the cyclopentyl cation **7e** as the *endo* product is as stable as the corresponding *exo* product **12**, there is a significant difference in the transition states. The formation of the exocyclic carbenium ion **12** is no longer a concerted process, but its transition state corresponds more to a hydride transfer transition state.[16] Its barrier is calculated to be about 20 kJ mol^{-1} higher in energy than that for the formation of the observed endocyclic cation **7e**.

Our experimental results and the quantum mechanical calculations clearly indicate that 1,5-H shift and cyclization of vinyl cations **3a,b** as well as **9a**,**c**,**d** should be concerted processes, allowing the preparatively useful intramolecular insertion of a vinyl cation into C–H bonds[4–6] in solution, in analogy to the insertion of singlet carbenes.[3,17]

Received: December 2, 2005
Published online: April 5, 2006

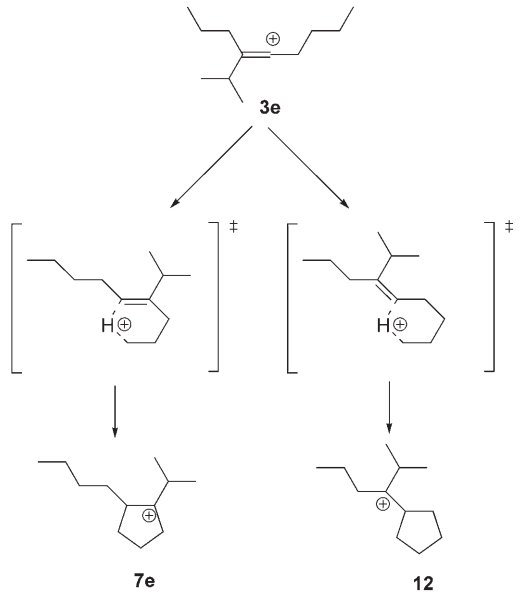

Scheme 5. Model reaction of vinyl cation **3e** by endo- and exocyclic pathways to give the cyclopentyl cations **7e** and **12**.

Keywords: alkylation · alkynes · C–H insertion · cyclopentanes · vinyl cations

[1] *Handbook of C-H Transformations: Applications in Organic Synthesis* (Ed.: G. Dyker), Weinheim, Wiley-VCH, **2005**.
[2] a) H. M. L. Davies, R. E. J. Beckwith, *Chem. Rev.* **2003**, *103*, 2861–2904; b) M. Lersch, M. Tilset, *Chem. Rev.* **2005**, *105*, 2471–2526; c) V. Ritleng, C. Sirlin, M. Pfeffer, *Chem. Rev.* **2002**, *102*, 1731–1769.
[3] a) W. Kirmse, *Carbene Chemistry*, Academic Press, New York, **1971**; b) *Carbene (Carbenoide) (Houben-Weyl) Vol. E19b* (Ed.: M. Regitz), Thieme, Stuttgart, **1989**.
[4] H. Kollmar, H. O. Smith, *Angew. Chem.* **1972**, *84*, 680–682; *Angew. Chem. Int. Ed. Engl.* **1972**, *11*, 635–636.
[5] P. Campomanes, D. Suárez, T. L. Sordo, *J. Phys. Chem. A* **1999**, *103*, 5996–6002.
[6] S. Fornarini, M. Speranza, *J. Phys. Chem.* **1987**, *91*, 2154–2160.
[7] a) U. Biermann, J. O. Metzger, *J. Am. Chem. Soc.* **2004**, *126*, 10319–10330; b) U. Biermann, J. O. Metzger, *Angew. Chem.* **1999**, *111*, 3874–3876; *Angew. Chem. Int. Ed.* **1999**, *38*, 3675–3677.
[8] H. Mayr, N. Basso, G. Hagen, *J. Am. Chem. Soc.* **1992**, *114*, 3060–3066.
[9] As a result of rapid 1,2-H shifts, cations **7** exist in an equilibrium as a mixture of three (**7a**) and four (**7b**) isomeric tertiary carbenium ions.[7] Consequently, deuterium labeling cannot yield unambiguous information on the underlying mechanism.
[10] a) F. Marcuzzi, G. Melloni, *J. Am. Chem. Soc.* **1976**, *98*, 3295–3300; b) F. Marcuzzi, G. Melloni, *J. Chem. Soc. Perkin Trans. 2* **1976**, 1517–1522.
[11] a) A. A. Schegolev, W. A. Smit, V. F. Kucherov, R. Caple, *J. Am. Chem. Soc.* **1975**, *97*, 6604–6606; b) A. A. Schegolev, W. A. Smit, G. V. Roitburd, V. F. Kucherov, *Tetrahedron Lett.* **1974**, *15*, 3373–3376; c) M. I. Kanischev, A. A. Schegolev, W. A. Smit, R. Caple, M. J. Kelner, *J. Am. Chem. Soc.* **1979**, *101*, 5660–5671.
[12] All calculations were performed employing the program package Gaussian 03. Structures were optimized at the perturbation theory level MP2/6-31G(d), as were also the zero-point vibrational energies, which are scaled with the factor 0.967. More

 © 2006 Wiley-VCH Verlag GmbH & Co. KGaA, Weinheim

reliable energies are obtained from MP2 single-point calculations with the valence triple-zeta basis set 6-311 + G(d,p) with inclusion of diffuse and polarized functions. Gaussian 03, Revision C.02, M. J. Frisch, G. W. Trucks, H. B. Schlegel, G. E. Scuseria, M. A. Robb, J. R. Cheeseman, J. A. Montgomery, Jr., T. Vreven, K. N. Kudin, J. C. Burant, J. M. Millam, S. S. Iyengar, J. Tomasi, V. Barone, B. Mennucci, M. Cossi, G. Scalmani, N. Rega, G. A. Petersson, H. Nakatsuji, M. Hada, M. Ehara, K. Toyota, R. Fukuda, J. Hasegawa, M. Ishida, T. Nakajima, Y. Honda, O. Kitao, H. Nakai, M. Klene, X. Li, J. E. Knox, H. P. Hratchian, J. B. Cross, V. Bakken, C. Adamo, J. Jaramillo, R. Gomperts, R. E. Stratmann, O. Yazyev, A. J. Austin, R. Cammi, C. Pomelli, J. W. Ochterski, P. Y. Ayala, K. Morokuma, G. A. Voth, P. Salvador, J. J. Dannenberg, V. G. Zakrzewski, S. Dapprich, A. D. Daniels, M. C. Strain, O. Farkas, D. K. Malick, A. D. Rabuck, K. Raghavachari, J. B. Foresman, J. V. Ortiz, Q. Cui, A. G. Baboul, S. Clifford, J. Cioslowski, B. B. Stefanov, G. Liu, A. Liashenko, P. Piskorz, I. Komaromi, R. L. Martin, D. J. Fox, T. Keith, M. A. Al-Laham, C. Y. Peng, A. Nanayakkara, M. Challacombe, P. M. W. Gill, B. Johnson, W. Chen, M. W. Wong, C. Gonzalez, J. A. Pople, Gaussian, Inc., Wallingford CT, **2004**.

[13] N. Yoshikai, E. Nakamura, *Adv. Synth. Catal.* **2003**, *345*, 1159 – 1171.

[14] E. Nakamura, N. Yoshikai, M. Yamanaka, *J. Am. Chem. Soc.* **2002**, *124*, 7181 – 7192.

[15] H. M. Schulzbach, E. Bolton, D. Lenoir, P. v. R. Schleyer, H. F. Schaefer III, *J. Am. Chem. Soc.* **1996**, *118*, 9908 – 9914.

[16] The 1,4-hydride shift in 2,5-dimethyl-2-hexyl cation shows a similar transition state: I. V. Vrèek, V. Vrèek, H. U. Siehl, *J. Phys. Chem. A* **2002**, *106*, 1604 – 1611.

[17] P. S. Skell, R. C. Woodworth, *J. Am. Chem. Soc.* **1956**, *78*, 4496; W. v. E. Doering, H. Prinzbach, *Tetrahedron* **1959**, *6*, 24 – 30.

 © 2006 Wiley-VCH Verlag GmbH & Co. KGaA, Weinheim

Organolithium Compounds

DOI: 10.1002/anie.200503726

Functional-Group Chemistry of Organolithium Compounds: Photochemical [2+2] Cycloaddition of Alkenyl-Substituted Lithium Cyclopentadienides**

Jan Paradies, Gerhard Erker, and Roland Fröhlich*

Organolithium compounds are among the most important reagents in organic and organometallic synthesis.[1] Because of their high reactivity and sensitivity, functional-group chemistry at the stage of the active organolithium nucleophiles is virtually nonexistent.[2] All the desired structural and functional-group variations, therefore, need to be made in synthetic sequences either before or after the organolithium stage.[3] This is also true for syntheses that involve substituted or functionalized lithium cyclopentadienide reagents. Derivatization of cyclopentadienyl (Cp) ligand frameworks in metallocene syntheses, for example, practically never takes place at the stage of the cyclopentadienyllithium reagent; it is mostly done prior to the actual lithiation step or in some rarer cases after the final transmetalation.[4] We have now found a useful method for carrying out organic functional-group chemistry at the stage of suitably substituted lithium cyclopentadienides. This method demonstrates the principal feasibility of utilizing organic functional-group transformations at active organolithium nucleophiles and at the same time provides a new entry to the synthesis of very useful organic ligand systems.

In our work we focused on the photochemical [2+2] cycloaddition reaction between alkenyl substituents attached to the lithium cyclopentadienides. We had previously shown that the intramolecular [2+2] cycloaddition reaction of bis(alkenylcyclopentadienyl) ligands complexed to Group 4 metals constitutes a viable synthetic pathway to ansa metallocenes.[5] It had been demonstrated that this reaction could even be extended to the construction of ansa calcocenes and related systems (Scheme 1).[6,7] Since it was known that

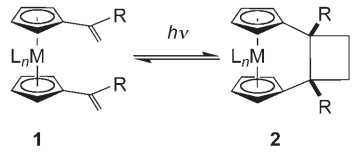

Scheme 1.

lithium cyclopentadienides undergo facile ligand disproportionation of the donor-ligand-stabilized monomer to give the corresponding anionic lithiocene structures (Scheme 2),[8,9]

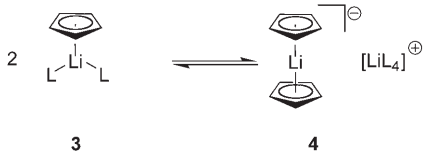

Scheme 2.

we decided to use this feature to extend the typical metallocene photocycloaddition reaction to the corresponding alkenyl-functionalized lithiocenes.

We synthesized a series of lithium (alkenyl)cyclopentadienides by means of the fulvene route.[10] As a typical example *tert*-butylcyclopentadiene (**5e**) was treated with acetone in the presence of pyrrolidine[11] to yield the 3-*tert*-butyl-substituted 6,6-dimethylpentafulvene **6e**, which was

[*] Dr. J. Paradies, Prof. Dr. G. Erker, Dr. R. Fröhlich[+]
Organisch-Chemisches Institut
Universität Münster
Corrensstrasse 40, 48149 Münster (Germany)
Fax: (+49) 251-833-36503
E-mail: erker@uni-muenster.de
[+] Röntgenstrukturanalyse

[**] Financial support from the Deutsche Forschungsgemeinschaft and the Fonds der Chemischen Industrie is gratefully acknowledged.
Supporting information for this article is available on the WWW under http://www.angewandte.org or from the author.

 © 2006 Wiley-VCH Verlag GmbH & Co. KGaA, Weinheim

then treated with lithium diisopropylamide (LDA) in diethyl ether to cleanly yield **7e** in 78% yield (Scheme 3). The (alkenyl-Cp)–Li compound **7e** was characterized spectroscopically and by C,H elemental analysis. Treatment with

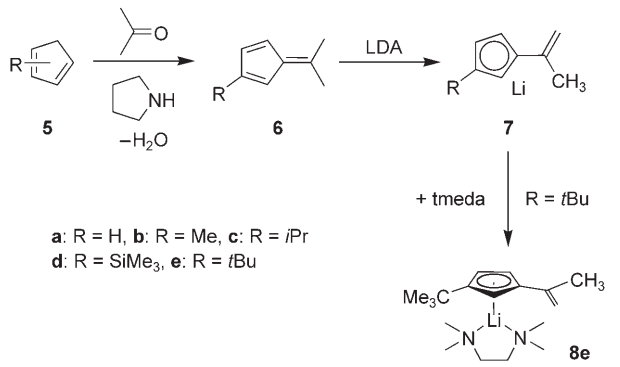

Scheme 3.

tetramethylethylenediamine (tmeda) gave [{$(H_2C{=}C\text{-}Me)C_5H_3(t\text{Bu})$}Li(tmeda)] (**8e**), which was characterized by an X-ray crystal structure analysis (see Figure 1, for details

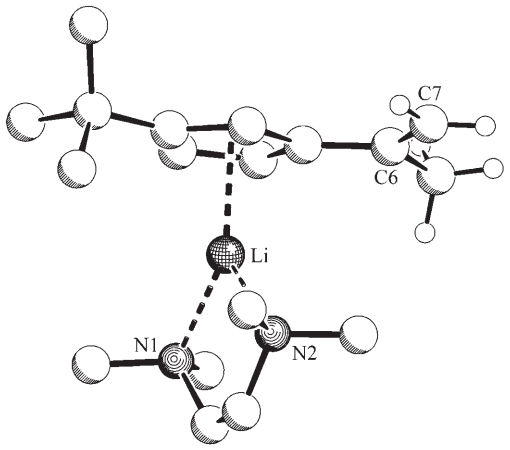

Figure 1. X-ray crystal structure of **8e**.

see the Supporting Information). It features a monomeric structure in which the C=C bond of the alkenyl substituent (d(C6–C7) = 1.332(4) Å) is coplanar with the central 1,3-disubstituted Cp ring. The electrostatic Li–Cp interaction results in uniform (η^5-$C_5H_3R^1R^2$)Li coordination with Li–C distances being in a narrow range between 2.257(5) Å and 2.299(5) Å. The Li–N bond lengths are slightly shorter at 2.125(5) Å (Li–N2) and 2.155(4) Å (Li–N1).[12]

The lithiocene equilibration can best be monitored by temperature-dependent ^{7}Li NMR spectroscopy.[8] A solution of **7e** in [D_8]THF at ambient temperature features a single sharp resonance at $\delta = -7.5$ ppm. Upon cooling the sample, the signal rapidly broadens and splits into two broad resonances of almost equal intensity at $\delta = -12.2$ and -12.3 ppm (at 168 K), which we attribute to a mixture of the diastereomeric lithiocenes *rac*-**9e** and *meso*-**9e**. The very broad low-field signal stays broad for a much larger temperature range. It decreases in intensity with decreasing temperature and shifts its maximum continuously to lower field. At the lowest temperature (168 K) a single slightly broadened ^{7}Li NMR resonance remains at $\delta = -1.1$ ppm which is approximately equal in intensity to the pair of signals at $\delta = -12.2$/12.3 ppm (see Figure 2). The interpretation of this typical

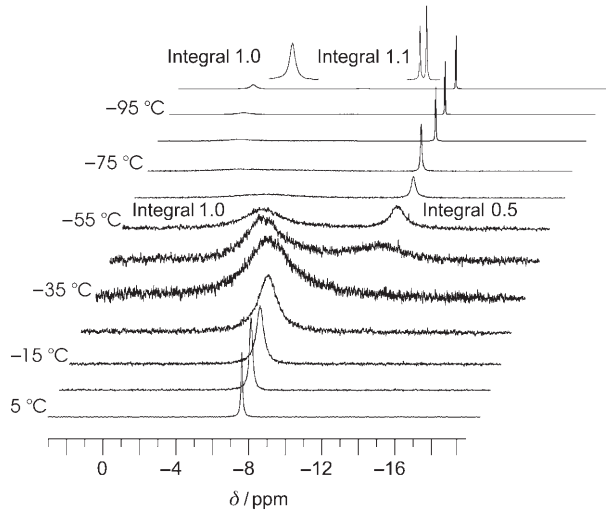

Figure 2. Temperature-dependent ^{7}Li NMR spectra (233.1 MHz, [D_8]THF) of the **7e**/*meso*-**9e**/*rac*-**9e** equilibrium.

NMR behavior is straightforward: we have most likely monitored the consequences of a rapid equilibration between the THF-stabilized monomer [**7e**$(thf)_n$] with the corresponding lithiocene anion **9e** and its [Li$(thf)_m]^+$ ion. The [Li$(thf)_m]^+$ ion equilibrates with the **7e** monomer under our NMR conditions, and the equilibration 2**7e**⇌**9e** + [Li$(thf)_m]^+$ is strongly temperature dependent and shifted almost completely to the right at low temperature (Scheme 4; for further details see the Supporting Information).

We have made use of these characteristic equilibrium features for the photochemical [2+2] cycloaddition at the stage of the functionalized lithiocene. A solution of **7e** in [D_8]THF in a quartz NMR tube was placed in a Schlenk tube (2 cm i.d.) that was filled with acetone. This was placed in a

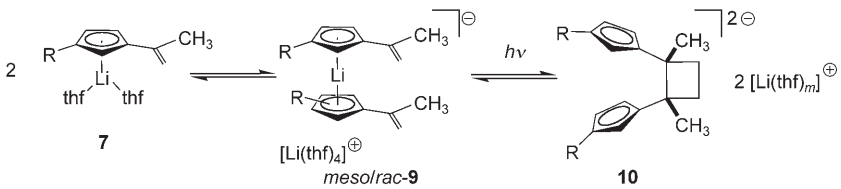

a: R = H, **b**: R = Me, **c**: R = *i*Pr
d: R = $SiMe_3$, **e**: R = *t*Bu

Scheme 4.

 © 2006 Wiley-VCH Verlag GmbH & Co. KGaA, Weinheim

cooling bath (THF) and irradiated at −90 °C with a water-cooled HPK 125 lamp (quartz filter) from a distance of 3 cm. Under these specific conditions a slow [2+2] cycloaddition reaction took place that in the course of two days resulted in the clean formation of the cyclized product **10e** (95 % yield along with 5 % starting material; Scheme 5). The obtained

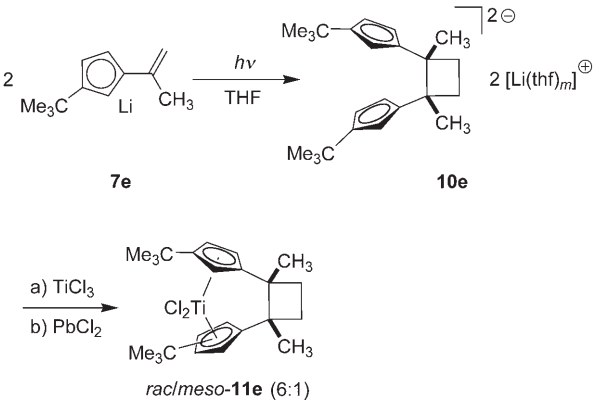

Scheme 5.

mixture seems to represent the photostationary equilibrium under these specific conditions. Further irradiation at −90 °C through a THF filter instead of the acetone filter led to a slow conversion to a 70:30 mixture of **7e** and **10e**, similar to the mixture found upon direct irradiation of pure **7e** at −90 °C under these conditions with purely THF-filtered light. Photolysis of the reaction mixture after cyclization (95 % **10e**) at room temperature with pyrex-filtered UV light converted it cleanly back to **7e**. Complex **10e** was isolated from several experiments and characterized spectroscopically (see the Experimental Section) and by a transmetalation reaction (see below).

The photochemical [2+2] cycloaddition of the lithiocene is not limited to the example **7e**→**10e** but has been observed with other substituted lithium (alkenyl)cyclopentadienides as well. Thus the low-temperature irradiation of the trimethylsilyl-substituted (methylethenyl)Cp–lithium derivative **7d** (HPK 125, quartz, acetone filter, −90 °C) gave 83 % yield of the cyclized product **10d** after 3 days. The isopropyl derivative **7c** cyclized similarly to give 61 % yield of **10c** after 3 days, whereas the methyl-substituted system **7b** was much less efficient in this reaction. The cyclized product **10b** was obtained in a yield of only 39 % of after 4 days of irradiation at −90 °C under our typical conditions, and the parent compound (**7a**) did not cyclize at all.

Qualitatively, the observed efficiencies for the [2+2] cycloadditions seem to parallel the **7**⇌**9** equilibrium reached at low temperature. Whereas formation of the lithiocene anion seems to be close to complete at 168 K in the case of the *tert*-butyl derivative 2**7e**→**9e**, a substantial quantity (ca. 50 %) of the isopropyl-substituted monomer is present under the same conditions in the equilibrium as judged by its prominent ^{7}Li NMR feature at $\delta = -6.8$ ppm (**9d** lithiocene signal observed at $\delta = -12.2/-12.3$ ppm, $[Li(thf)_m]^+$ resonance at $\delta = -1.2$ ppm in [D$_8$]THF at 168 K). This trend of shifting the 2**7**⇌**9** equilibrium to the monomer side increases steadily with decreasing steric bulk of the substituent R attached to the Cp ring (for details see the Supporting Information).

We have used this method for the preparation of a new ansa titanocene system. The (alkenyl)Cp–lithium reagent **7e** was irradiated under our typical reaction conditions (see above) and the resulting cyclobutylene-linked biscyclopentadienide reagent **10e** was transmetalated by treatment with $[TiCl_3(thf)_3]$. Subsequent oxidative chlorination by treatment with $PbCl_2$[13] eventually gave the ansa titanocene complex **11e** in 82 % yield as a 6:1 mixture of the *rac* isomer with one of the two possible *meso* diastereomers (Scheme 5).[14]

Single crystals were obtained of the minor compound of the mixture, namely *meso*-**11e**. The X-ray crystal structure analysis shows the presence of the cyclobutylene-bridged *ansa*-metallocene framework (Figure 3). The C–C σ bonds of the bridging four-membered carbocycle amount to 1.584(5) Å (C10A–C10B) and 1.529(5) Å (C11A–C11B); *d*(C10A–C11A) = 1.543(5) Å, *d*(C10B–C11B) = 1.550(5) Å (for further details see the Supporting Information).

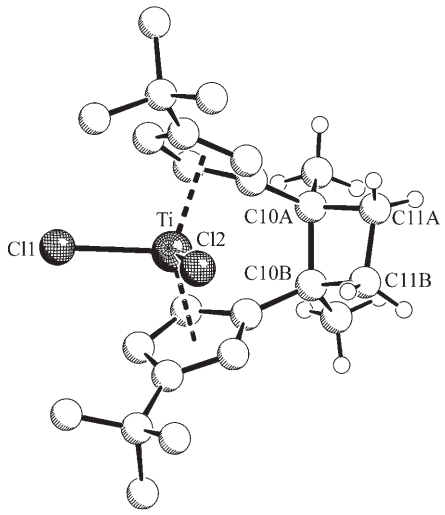

Figure 3. X-ray crystal structure of the *meso*-titanocene dichloride **11e**.

Experimental Section

10e: A Philipps HPK lamp (125 W) placed in a water-cooled vacuum-jacketed quartz vessel was used for UV irradiation. A 0.26 M solution of **7e** (prepared by deprotonation of **6e**[15] with LDA in diethyl ether) in [D$_8$]THF in a 5-mm quartz NMR tube and was placed in a 2-cm i.d. Schlenk tube filled with acetone (10 mL) serving as a filter and for heat transfer. The Schlenk tube was placed at a distance of 3 cm from the light source. The sample was irradiated in a THF-filled cooling bath at −90 °C for 2 days. For a preparative reaction **7e** (300 mg, 1.78 mmol) was dissolved in THF (20 mL) (2-cm i.d. Schlenk tube) and photolyzed under similar conditions as described above for 2 days. The solvent was removed in vacuo to give a white solid. The solid was suspended in diethyl ether and the supernatant liquid removed by syringe to separate unreacted starting material. This procedure was repeated twice (2 × 10 mL diethyl ether). The remaining solid was dried in vacuo to yield 211 mg (71 %) of **10e**. ^{1}H NMR (599.8 MHz, [D$_8$]THF), 75 °C): $\delta = 5.23$ (m, 2H), 5.17 (m, 2H), and 5.15 (m, 2H; C_5H_3), 2.49 (m, 2H), and 1.83 (m, 2H; CH_2), 1.47 (s, 6H; CH_3), 1.09 ppm (s, 18H; CH_3); ^{13}C NMR (150.8 MHz, [D$_8$]THF,

 © 2006 Wiley-VCH Verlag GmbH & Co. KGaA, Weinheim

75 °C): $\delta = 129.4$ (C-q), 127.1 (C-q), 102.9 (CH), 101.3 (CH), 97.6 (CH), 48.3 (C-q), 33.3 (CH_3), 32.1 (C-q), 31.3 (CH_2), 25.9 ppm (CH_3).

11e: A mixture of [$TiCl_3(THF)_3$] (232 mg) and **10e** (211 mg, 0.63 mmol) was dissolved in 15 mL of precooled THF at −78 °C. The solution was stirred overnight and then warmed to room temperature. The vigorously stirred solution was treated with solid anhydrous lead dichloride (105 mg, 0.38 mmol, 0.6 equiv). The reaction mixture was stirred for an additional 4 h before the solvent was removed in vacuo. The residue was suspended in pentane and the insoluble material removed by filtration through a plug of celite. The solid was washed with pentane until the filtrate was colorless, and the combined filtrates were concentrated in vacuo at −50 °C to give a red precipitate. The supernatent solution was removed by syringe and the solid dried in vacuo. The solution was further concentrated to yield a second fraction of the product (total yield: 227 mg, 82 %, *rac*/*meso*-A/*meso*-B: 6/1/–); m.p. 202 °C (decomp 319 °C); *meso*-**11e**: ^{1}H NMR (599.8 MHz, [D_6]benzene, 25 °C): $\delta = 6.78$ (m, 2H), 6.20 (m, 2H) and 5.90 (m, 2H, C_5H_3), 2.11 (m, 2H) and 1.54 (m, 2H; CH_2), 1.54 (s, 18H; CH_3), 0.99 ppm (s, 6H; CH_3); ^{13}C NMR (150.8 MHz, [D_6]benzene, 25 °C): $\delta = 143.3$ (C-q), 140.5 (C-q), 130.6 (CH), 117.1 CH), 108.0 (CH), 50.4 (C-q), 34.5 (C-q), 31.6 (CH_3), 30.0 (CH_2), 25.8 ppm (CH_3); *rac*-**11e**: ^{1}H NMR (599.8 MHz, [D_6]benzene, 25 °C): $\delta = 6.60$ (m, 1H), 6.39 (m, 1H), 6.37 (m, 1H), 6.28 (m, 1H), 6.07 (m, 1H), and 6.02 (m, 1H; C_5H_3), 2.11 (m, 2H), and 1.54 (m, 2H; CH_2), 1.53 (s, 9H) and 1.32 (s, 9H; CH_3), 1.01 ppm (s, 6H; CH_3); ^{13}C NMR (150.8 MHz, [D_6]benzene, 25 °C): $\delta = 155.8$ (C-q), 144.4 (C-q), 143.3 (C-q), 140.7 (C-q), 127.9 (CH), 120.2 (CH), 117.1 (CH), 116.2 (CH), 109.7 (CH), 106.7 (CH), 50.5 (C-q), 49.8 (C-q), 34.8 (C-q), 34.6 (C-q), 31.5 (CH_3), 30.4 (CH_3), 29.9 (CH_2), 29.9 (CH_2), 25.6 (CH_3), 25.3 ppm (CH_3); elemental analysis: calcd (%) for $C_{24}H_{34}TiCl_2$: C 65.32, H 7.77; found: C 64.93, H 7.73. Slow concentration of a solution of *rac*/*meso*-**11e** in diethyl ether gave red crystals of *meso*-**11e** suitable for the X-ray crystal structure analysis.

Received: October 20, 2005
Published online: March 29, 2006

Keywords: cycloaddition · lithium · metallocenes · photochemistry

[1] M. Schlosser, *Organometallics in Synthesis*, Wiley, New York, **2001**; B. J. Wakefield, *Organolithium Methods*, Academic Press, London, **1998**; J. Clayden, J. E. Baldwin, *Organolithiums: Selectivity for Synthesis*, Pergamon, New York, **2002**; *Lithium Chemistry, A Theoretical and Experimental Overview* (Eds.: A.-M. Sapse, P. von R. Schleyer), Wiley, New York, **1995**, and references therein.

[2] For rare exceptions see, for example, H. J. Reich, J. E. Holladay, T. G. Walker, J. L. Thompson, *J. Am. Chem. Soc.* **1999**, *121*, 9769 – 9780; W. F. Bailey, M. J. Mealy, *J. Am. Chem. Soc.* **2000**, *122*, 6787 – 6788; X. Wei, R. J. K. Taylor, *Angew. Chem.* **2000**, *112*, 419 – 422; *Angew. Chem. Int. Ed.* **2000**, *39*, 409 – 412; D. Cheng, K. R. Knox, T. Cohen, *J. Am. Chem. Soc.* **2000**, *122*, 412 – 413.

[3] See, for example, T. Hense, D. Hoppe, *Angew. Chem.* **1997**, *109*, 2377 – 2410; *Angew. Chem. Int. Ed. Engl.* **1997**, *36*, 2283 – 2316.

[4] G. Erker, G. Kehr, R. Fröhlich, *J. Organomet. Chem.* **2004**, *689*, 1402 – 1412.

[5] G. Erker, S. Wilker, C. Krüger, R. Goddard, *J. Am. Chem. Soc.* **1992**, *114*, 10983 – 10984; G. Erker, S. Wilker, C. Krüger, M. Nolte, *Organometallics* **1993**, *12*, 2140 – 2151; W.-L. Nie, G. Erker, G. Kehr, R. Fröhlich, *Angew. Chem.* **2004**, *116*, 313 – 317; *Angew. Chem. Int. Ed.* **2004**, *43*, 310 – 313; N. Iwama, T. Kato, T. Sugano, *Organometallics* **2004**, *23*, 5813 – 5817.

[6] P.-J. Sinnema, P. J. Shapiro, B. Höhn, T. E. Bitterwolf, B. Twamley, *Organometallics* **2001**, *20*, 2883 – 2888.

[7] For a recent review on organometallic photochemistry see T. E. Bitterwolf, *J. Organomet. Chem.* **2004**, *689*, 3939 – 3952; see also Q. Chu, D. C. Swenson, L. R. MacGillivray, *Angew. Chem.* **2005**, *117*, 3635 – 3638; *Angew. Chem. Int. Ed.* **2005**, *44*, 3569 – 3572, and references therein.

[8] L. A. Paquette, W. Bauer, M. R. Sivik, M. Bühl, M. Feigel, P. von R. Schleyer, *J. Am. Chem. Soc.* **1990**, *112*, 8776 – 8789; K. Kunz, J. Pflug, A. Bertuleit, R. Fröhlich, E. Wegelius, G. Erker, E.-U. Würthwein, *Organometallics* **2000**, *19*, 4208 – 4216; K. Kunz, G. Erker, G. Kehr, R. Fröhlich, *Organometallics* **2001**, *20*, 392 – 400.

[9] Reviews: P. Jutzi, *J. Organomet. Chem.* **1990**, *400*, 1 – 17; P. Jutzi, *Pure Appl. Chem.* **1990**, *62*, 1035 – 1038; P. Jutzi, *Pure Appl. Chem.* **1989**, *61*, 1731 – 1736; P. Jutzi, *Adv. Organomet. Chem.* **1986**, *26*, 217 – 295; E. Weiss, *Angew. Chem.* **1993**, *105*, 1565 – 1587; *Angew. Chem. Int. Ed. Engl.* **1993**, *32*, 1501 – 1523; D. Stahlke, *Angew. Chem.* **1994**, *106*, 2256 – 2259; *Angew. Chem. Int. Ed. Engl.* **1994**, *33*, 2168 – 2171; P. Jutzi, N. Burford, *Chem. Rev.* **1999**, *99*, 969 – 990; P. Jutzi, G. Reumann, *Dalton Trans.* **2000**, 2237 – 2244; P. H. M. Budzelaar, J. J. Engelberts, J. H. van Lenthe, *Organometallics* **2003**, *22*, 1562 – 1576.

[10] K. Ziegler, W. Schäfer, *Justus Liebigs Ann. Chem.* **1934**, *511*, 101 – 109; K. Ziegler, H.-G. Gellert, H. Martin, K. Nagel, J. Schneider, *Justus Liebigs Ann. Chem.* **1954**, *589*, 91 – 121; M. F. Sullivan, W. F. Little, *J. Organomet. Chem.* **1967**, *8*, 277 – 285; P. Renaut, G. Tainturier, B. Gautheron, *J. Organomet. Chem.* **1978**, *148*, 43 – 51; J. Okuda, *Chem. Ber.* **1989**, *122*, 1075 – 1077; G. Erker, R. Nolte, Y.-H. Tsay, C. Krüger, *Angew. Chem.* **1989**, *101*, 642 – 644; *Angew. Chem. Int. Ed. Engl.* **1989**, *28*, 628 – 629; G. Erker, R. Nolte, R. Aul, S. Wilker, C. Krüger, R. Noe, *J. Am. Chem. Soc.* **1991**, *113*, 7594 – 7602; R. R. Squires, *Acc. Chem. Res.* **1992**, *25*, 461 – 467.

[11] K. J. Stone, R. D. Little, *J. Org. Chem.* **1984**, *49*, 1849 – 1853.

[12] See for a comparison: A. Hammel, W. Schwarz, J. Weidlein, *Acta Crystallogr. Sect. C* **1990**, *46*, 2337 – 2339.

[13] G. A. Luinstra, J. H. Teuben, *J. Chem. Soc. Chem. Commun.* **1990**, 1470 – 1471.

[14] This synthesis is especially useful since we could not prepare complex **11e** in analogy to the zirconium analogue[5] by photochemical [2+2] cycloaddition of the corresponding (alkenylCp)$_2$$TiCl_2$ system.

[15] T. J. Clark, T. A. Nile, *Synlett* **1990**, 589 – 590.

 © 2006 Wiley-VCH Verlag GmbH & Co. KGaA, Weinheim

Inorganic Polymers

DOI: 10.1002/anie.200504208

A PH-Functionalized Polyphosphazene: A Macromolecule with a Highly Flexible Backbone**

*Michael Raab, Gerold Schick, Rebecca Fondermann, Michael Dolg, Wolfram Henze, Ulrike Weynand, Ruth M. Gschwind, Karl Fischer, Manfred Schmidt, and Edgar Niecke**

Dedicated to Professor Herbert W. Roesky on the occasion of his 70th birthday

Polyphosphazenes are macromolecules with a phosphorus–nitrogen backbone carrying a wide range of organic side groups. These "hybrid" inorganic–organic polymers represent the most extensively studied class of inorganic macromolecules besides silicones and have considerable scientific and applicative relevance.[1] Advanced commercial applications range from membranes to solid electrolytes, from biomedical to electro-optical materials, and from elastomers to flame retardants.[2]

Most polyphosphazenes are linear open-chain species described by the general formula $X[P(R^1)(R^2)=N]_nY$, in which the groups X and Y terminate the PN backbone of the polymer. The material properties of the phosphazene polymers highly depend on the phosphorus-bound side groups R^1 and R^2. Such side groups can easily be introduced by nucleophilic substitution of the halogen atoms of poly(dichlorophosphazene) $[Cl_2PN]_n$ (PCP),[3] which is one of the most versatile building blocks for the development of new hybrid materials. This well-established synthetic pathway affords polymers with a wide range of side-group combinations (R^1, R^2 = alkyl, aryl, alkoxy, aryloxy, etc.). High-molecular-weight, non-cross-linked PCP with $n \geq 10^4$ is commonly obtained by ring-opening polymerization of the cyclotriphosphazene $(Cl_2PN)_3$ at elevated temperatures (> 250 °C).[3,4]

In the last decade, the transformation of the phosphoraneimine $Cl_3P{=}NSiMe_3$[5] to PCP has gained increasing attention.[6] This solution-state "living" cationic polymerization leads to polyphosphazenes with controlled molecular weight and narrow polydispersity.[7] Application of this polycondensation to organophosphoraneimines allows access to a nongeminal arrangement of two different side groups along the chain as a basis for block copolymers.[8]

Although a large number of side-group modifications are described in the literature, hydrogen substitution has not yet been mentioned for polyphosphazenes.[9] Access to multiply PH-functionalized polyphosphazenes $[P(R^1)(R^2){=}N]_n$ (with $R^1 = H$, R^2 = heteroatom substituent) would extend the reaction diversity of linear open-chain polyphosphazenes with respect to PH insertions or nucleophilic substitution of side groups R^2 with retention of the PH functionality. In this context, it has to be emphasized that PH-functionalized polyphosphazenes are isolobal to polyhydridosiloxanes $[Si(H)(R)O]_n$, which are well-established compounds with versatile industrial applications.[10]

Recently, we reported the synthesis, X-ray structure determination, and reactivity of dialkylamino(amino)phosphines $(R_2N)_2PNH_2$ (R = Cy, *i*Pr).[11] An outcome of this work was the first isolable tris(hydrido)cyclotriphosphazene $(P(H)(NCy_2){=}N)_3$, which was obtained by elimination of amine and formation of further uncharacterized polymeric by-products.[12]

Considering these findings, we have now focused our interest on the kinetically controlled polycondensation process. To prevent the formation of cross-linked polymeric networks and to obtain polyphosphazenes with narrow polydispersities, we studied the condensation reaction of the sterically less protected aminophosphine $(Me_2N)_2PNH_2$ (**2**) in solution at low temperatures. Since **2** is not available in pure form, we generated this compound in situ by ammonolysis of the corresponding chlorophosphine **1** (Scheme 1).

In a typical experiment,[13] bis(dimethylamino)chlorophosphine **1** was dissolved in diethyl ether at −78 °C and added to dry liquid ammonia. The vanishing ^{31}P NMR signal at $\delta = 108.4$ ppm in the course of the reaction indicates the

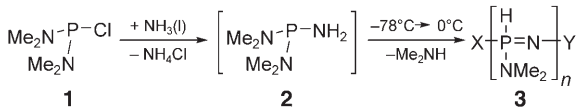

1 2 3

Scheme 1. Formation of **3** by polycondensation.

[*] Dr. M. Raab, Dr. G. Schick, Prof. E. Niecke
Institut für Anorganische Chemie
Rheinische Friedrich-Wilhelms-Universität Bonn
Gerhard-Domagk-Strasse 1, 53121 Bonn (Germany)
Fax: (+49) 228-735-327
E-mail: e.niecke@uni-bonn.de
Dipl.-Chem. R. Fondermann, Prof. M. Dolg
Institut für Theoretische Chemie
Universität zu Köln
Greinstrasse 4, 50939 Köln (Germany)
Dipl.-Chem. W. Henze, U. Weynand
Kekulé-Institut für Organische Chemie und Biochemie
Rheinische Friedrich-Wilhelms-Universität Bonn
Gerhard-Domagk-Strasse 1, 53121 Bonn (Germany)
Prof. R. M. Gschwind
Institut für Organische Chemie
Universität Regensburg
Universitätsstrasse 31, 93053 Regensburg (Germany)
Dr. K. Fischer, Prof. M. Schmidt
Institut für Physikalische Chemie
Johannes Gutenberg Universität Mainz
Welderweg 11, 55099 Mainz (Germany)

[**] This work was supported by the Deutsche Forschungsgemeinschaft and the Fonds der Chemischen Industrie. We also thank Prof. D. Gudat, University of Stuttgart, for preliminary NMR experiments and valuable discussions as well as M. Özmen for support in the synthetic work.

Supporting information (including experimental details) for this article is available on the WWW under http://www.angewandte.org or from the author.

 © 2006 Wiley-VCH Verlag GmbH & Co. KGaA, Weinheim

transient formation of the intermediate **2**.[14] After 30 minutes of stirring at −78 °C, the excess ammonia was removed at 0 °C, and the precipitate was separated by filtration. Evaporation of all volatiles yielded pure **3** as a colorless oil.[15]

The ^{31}P NMR spectrum of **3** in diethyl ether shows an intense signal at $\delta = -4.3$ ppm with characteristic doublet splitting (^1J(P,H) = 554 Hz) as a result of a hydrogen atom attached to each tetracoordinate phosphorus atom. The ^{1}H NMR spectrum (10 % in [D$_{10}$]Et$_2$O) of **3** exhibits two intense doublets centered at $\delta = 7.07$ (br, 1H, ^1J(P,H) = 554 Hz) and 2.63 ppm (6H, ^3J(P,H) = 11.5 Hz) and thus confirms the constitution of a *P*-hydrido(dimethylamino)-phosphazene unit, [P(H)(NMe$_2$)=N]$_n$. The simplicity of the spectra with respect to the main signals indicates a high mobility of the polymer in a planar *cis*,*trans* conformation or twisted helical conformation, which are the optimal geometries for an attractive 1,4 interaction in the chain.[2] In addition to the intense signals of **3**, both spectra show a few small signals, which are assigned to a terminating group along with small amounts of six-membered-ring products[12] and oxidized species. After three to five hours, signals assigned to the cross-linked phosphazene polymer are also observed (see Figure 1 a, b). The ^{1}H and ^{31}P chemical shifts of these compounds are obtained by a combination of one-dimensional ^{1}H, ^{1}H{^{31}P}, ^{31}P, and ^{31}P{^{1}H} NMR spectra as well as two-dimensional ^{1}H,^{31}P HMBC, ^{1}H,^{31}P HMQC, and ^{1}H DOSY spectra.[13]

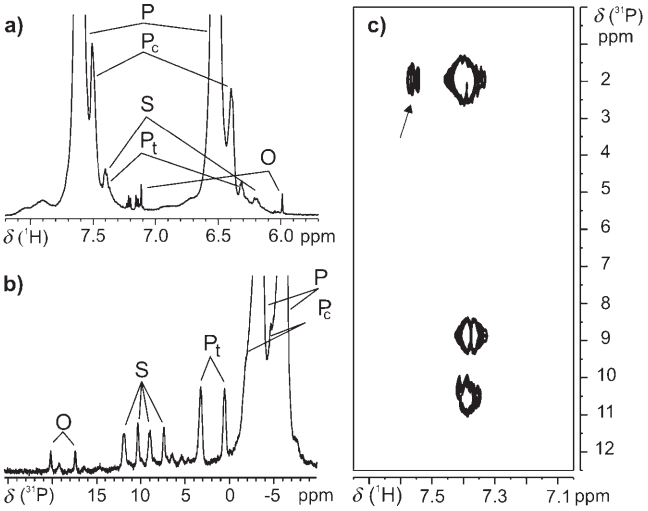

Figure 1. Selected sections of a ^{1}H NMR spectrum (a), a ^{31}P NMR spectrum (b), and a ^{1}H,^{31}P HMBC spectrum without a low-pass *J* filter of **3** (10 % in [D$_{10}$]Et$_2$O) at 273 K. For the peak assignments, the following abbreviations are used: P = polymeric **3**, P$_c$ = cross-linked polymeric **3**, P$_t$ = terminating group of polymeric **3**, S = six-membered rings, O = oxidized monomers. In (c) the long-range correlation is indicated by an arrow.

The terminating groups in low-molecular-weight polyphosphazenes can readily be identified by ^{31}P NMR spectroscopy.[16] However, this method generally does not apply for higher analogues because of their poor solubility as a result of their crystallinity. The lack of crystallinity of **3** permitted us for the first time to obtain information on the nature of one terminating group of a phosphazene polymer with about 500 repeating units. The ^{1}H,^{31}P HMBC spectra of **3** show long-range correlations between the ^{1}H chemical shift of the PH protons of the polymeric species and the ^{31}P chemical shift of one terminating group, thus indicating a direct connection (Figure 1 c). The ^{1}H,^{31}P HMBC and ^{1}H,^{31}P HMQC spectra show a PH moiety ($\delta(^1\text{H}) = 6.86$ ppm, $\delta(^{31}\text{P}) = 1.9$ ppm, ^1J(P,H) = 542 Hz) together with one NMe$_2$ group ($\delta(^1\text{H}) = 2.60$ ppm, ^3J(P,H) = 11.5 Hz) as characteristics of this terminating group, indicating a Me$_2$N(HN=)P(H) unit as one terminating group of the polymer.[13] Taking into account the constitution of the starting material and a conceivable reaction mechanism for the formation of **3** (see below), we propose a (Me$_2$N)$_2$P(H)=N group as the second terminating group. However, a corresponding ^{31}P NMR signal for this second group was not detected. It seems reasonable that the appropriate NMR shift is hidden in the region of the broad ^{31}P NMR signal of the polymeric moiety, thus inhibiting detection in the NMR spectra. This assumption is supported by ^{31}P NMR chemical shifts reported for comparable low-molecular P(V) species (R$_2$N)$_2$P(H)=NR′, which show $\delta(^{31}\text{P})$ values in the range of −10 to 0 ppm.[17]

Furthermore, from ^{1}H PFG DSE (pulse field gradient, double stimulated echo) experiments,[18] an assessment of the relative hydrodynamic radius of cross-linked polymeric **3** compared to polymeric **3** is possible. The relative diffusion coefficients determined in diethyl ether at 273 K several hours after preparation of polymeric **3** ($D = 2.8 \times 10^{-10}$ m^{2}s^{-1}, $R_h = 2.5$ nm) and cross-linked polymeric **3** ($D = 1.0 \times 10^{-10}$ m^{2}s^{-1}, $R_h = 7$ nm) reveal an approximately threefold difference in their hydrodynamic radii.

The absolute molar mass of **3** was determined by static light scattering in benzene at 283.15 K to be M_w = 41 000 g mol^{-1}. The radius of gyration was too small to be measured ($R_g < 10$ nm). The value of the second virial coefficient ($A_2 = 5 \times 10^{-4}$ mol cm^3 g^{-2}) demonstrates that benzene is a moderately good solvent for **3** (Figure 2).[13] Dynamic light scattering did not reveal any *q* or *c* dependence of the apparent diffusion coefficient which was determined by cumulant analysis of the electric-field autocorrelation functions. The *z*-average diffusion coefficient was determined to be $D_z = 5.74 \times 10^{-11}$ m^{2}s^{-1}, which leads to a hydrodynamic radius of $R_h = 4.7$ nm by formal application of Stokes' law.

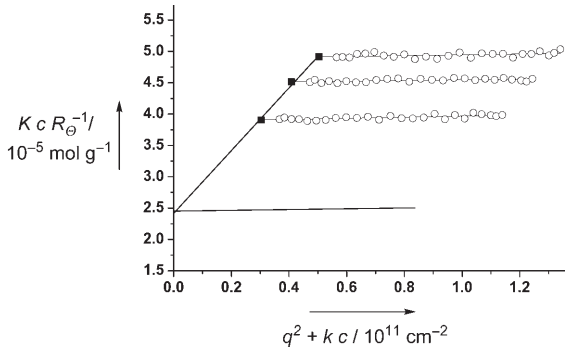

Figure 2. Zimm plot of **3** in benzene at 283.15 K (c = 15, 20, 25 g L^{-1}; $k = 2.0 \times 10^{12}$ cm g^{-1}).

 © 2006 Wiley-VCH Verlag GmbH & Co. KGaA, Weinheim

The normalized second cumulant ($\mu_2 = 0.1$) indicates considerable polydispersity, which is estimated to be $1.5 \leq M_w/M_n \leq 2$, the range expected for a polycondensation. From the degree of polymerization ($P_w = 455$), the contour length of **3** is calculated to be $L_w = 130$ nm, assuming an extended *cis,trans* conformation (monomer length $l = 0.24$ nm). Taking the hydrodynamically effective cross section of the chain as $d = 0.93$ nm and considering the polydispersity, the Kuhn statistical segment length is determined from the hydrodynamic radius to be $l_K = 2.3 \pm 0.2$ nm by use of the Kratky–Porod wormlike chain model.[19,20] The variance in l_K originates primarily from uncertainties in d (± 0.1 nm) and in the polydispersity ($1.5 \leq M_w/M_n \leq 2$).

Based on ab initio calculations, **3** might be expected to form a helix rather than a random coil. In this case, the contour length is reduced to $L_w = 455 \times 0.15$ nm $= 68.3$ nm with the pitch of the helix per monomer unit $l = 0.15$ nm. Taking $d = 1.01$ nm, the Kuhn length is determined to be $l_K = 4.2 \pm 0.2$ nm; thus, the formed helix would be significantly more flexible than DNA ($l_K = 100$ nm) or polyhexylisocyanates ($l_K = 20$–40 nm).[21,22] However, the obtained measurements do not allow a clear assignment of one of the two conformers.

It is known from various studies that polyphosphazenes tend to crystallize in a planar *cis,trans* conformation with minor P–N bond-length alternations. In contrast, recent theoretical studies of several phosphazene oligomers suggest that isolated polyphosphazenes preferentially form a twisted helical conformation.[23] Our ab initio calculations using a finite-cluster approach[13,24] on $[P(H)(NH_2)=N]_n$ as a model for the methyl-substituted analogue $[P(H)(NMe_2)=N]_n$ reveal the twisted helical conformation to be slightly lower in energy than the *cis,trans* conformation by 2.3 kcal mol^{-1} per repeated PN unit (at Møller–Plesset second-order perturbation theory). However, according to these calculations, the *cis,trans* conformation is favored in the solid state.[25]

A well-established reaction mechanism for the formation of small rings and higher linear polymers from organophosphoraneimines that bear an electropositive leaving group at the nitrogen atom (for example, trimethylsilyl) and an electronegative group at the phosphorus atom (for example, alkoxy) is the anionic polymerization, which is initiated by anionic or neutral bases.[26] Assuming such a reaction mechanism in the case discussed here, the initial step for the polymerization should be the tautomerization of the aminophosphine $(Me_2N)_2PNH_2$ (**2**) to its PH form, $(Me_2N)_2P(H)=NH$.[27] Abstraction of the NH-hydrogen atom by the solvent ammonia (or dimethylamine) leads to the phosphazene anion $[(Me_2N)_2P(H)=N]^-$, which attacks the phosphorus atom of the starting aminophosphine **2** through the negatively charged nitrogen atom. Elimination of amine yields the aminophosphanyl(hydrido)phosphazene, $(Me_2N)_2P(H)=NP(NMe_2)NH_2$. The tautomerization of this species to the diphosphazene, $(Me_2N)_2P(H)=NP(H)(NMe_2)=NH$, followed by deprotonation to the diphosphazene anion and subsequent reaction with aminophosphine **2**, propagates the chain to give **3**.

Ab initio calculations were carried out to underline the experimental findings. Starting from the parent triaminophosphine $P(NH_2)_3$ (**2′**), the relative stabilities of corresponding aminophosphine–phosphazene tautomers for the idealized polycondensation reaction were compared. This idealized reaction mechanism is based on several condensation/elimination steps. The results derived from these calculations are shown in Scheme 2 and demonstrate the energy balance for the aminophosphine–phosphazene equilibrium with progressive chain propagation. While the aminophosphine form is energetically more favored than the corresponding phosphazene form for the tautomers **2′**/**4′** and **5′**/**6′**, the energetic situation is nearly balanced for the three-PN units **7′**/**8′**.[28]

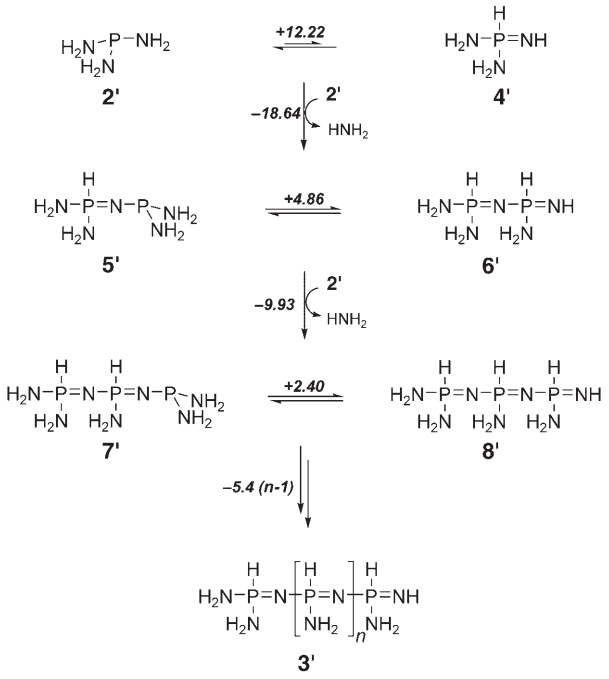

Scheme 2. Idealized reaction mechanism for polycondensation of the parent compound $P(NH_2)_3$ (**2′**) (ΔE in kcal mol^{-1}).

Under the conditions of chain propagation, the formation of an iminophosphorane moiety is energetically more favorable than the formation of an aminophosphine unit. Extrapolation for the formation of an infinite polymer chain **3′** shows a stabilization energy of 5.4 kcal per PN unit, which indicates the presence of a conjugative effect. A detailed analysis of the bonding in analogous λ^5-P=C bond systems revealed a similar stabilizing conjugative effect, which was attributed to an effective one-way P–C interaction.[29]

Further investigations of **3** are in progress with respect to addition and elimination reactions or substitution of the $N(alkyl)_2$ side groups under retention of the PH functionality.

Received: November 25, 2005
Revised: January 6, 2006
Published online: April 3, 2006

Keywords: ab initio calculations · phosphazenes · polycondensation · polymerization

 © 2006 Wiley-VCH Verlag GmbH & Co. KGaA, Weinheim

[1] M. Gleria, R. de Jaeger, *Top. Curr. Chem.* **2005**, *250*, 165 – 251.
[2] H. R. Allcock, *Chemistry and Application of Polyphosphazenes*, Wiley-Interscience, New York, **2003**.
[3] H. R. Allcock, R. L. Kugel, *J. Am. Chem. Soc.* **1965**, *87*, 4216 – 4217.
[4] High-molecular-weight poly(dichlorophosphazenes) were also obtained by thermal condensation of $Cl_3P{=}NP(O)Cl_3$: M. Helioui, R. de Jaeger, M. Puskaric, J. Heubel, *Macromol. Chem.* **1982**, *183*, 1137 – 1143; R. de Jaeger, M. Helioui, M. Puskaric, U. S. Patent 4.377.558.
[5] E. Niecke, W. Bitter, *Inorg. Nucl. Chem. Lett.* **1973**, *9*, 127 – 129.
[6] B. Wang, E. Rivard, I. Manners, *Inorg. Chem.* **2002**, *41*, 1690 – 1691.
[7] C. H. Honeyman, I. Manners, C. A. Morrissey, H. R. Allcock, *J. Am. Chem. Soc.* **1995**, *117*, 7035 – 7036.
[8] H. R. Allcock, J. M. Nelson, S. D. Reeves, C. H. Honeyman, I. Manners, *Macromolecules* **1997**, *30*, 50 – 56.
[9] A PH-substitution pattern is reported for a poly(phosphinoborane); see: H. Dorn, R. A. Singh, J. A. Massey, A. J. Lough, I. Manners, *Angew. Chem.* **1999**, *111*, 3540 – 3543; *Angew. Chem. Int. Ed.* **1999**, *38*, 3321 – 3323.
[10] H.-H. Moretto, M. Schulze, G. Wagner, *Ullmann's Encyclopedia of Industrial Chemistry*, *5th ed.*, Wiley-VCH, Weinheim, **1993**, pp. 57 – 93 and references therein.
[11] G. Schick, A. Loew, M. Nieger, K. Airola, E. Niecke, *Chem. Ber.* **1996**, *129*, 211 – 217.
[12] G. Schick, M. Raab, D. Gudat, M. Nieger, E. Niecke, *Angew. Chem.* **1998**, *110*, 2486 – 2488; *Angew. Chem. Int. Ed.* **1998**, *37*, 2390 – 2392.
[13] Further information on materials and methods is available in the Supporting Information.
[14] Comparable results were obtained for the reaction of bis(diethylamino)chlorophosphine with dry ammonia. The transient formation of both tris(amino)phosphines $(R_2N)_2PNH_2$ (R = Me (**2**), Et) in the course of the condensation reactions was verified by complexation with tetracarbonylnickel: M. Raab, Diploma Thesis, University of Bonn (Germany), **1998**.
[15] An early report on the ammonolysis of the chlorophosphine **1** predicts the formation of tris(hydrido)cyclotriphosphazenes on the basis of spectroscopic investigations: A. Schmidpeter, H. Rossknecht, *Chem. Ber.* **1974**, *107*, 3146 – 3148.
[16] H. R. Allcock, S. D. Reeves, J. M. Nelson, I. Manners, *Macromolecules* **2000**, *33*, 3999 – 4007.
[17] L. N. Markovski, V. L. Romanenko, A. V. Ruban, *Phosphorus and Sulfur* **1980**, *9*, 221 – 226.
[18] A. Jerschow, N. Müller, *J. Magn. Reson.* **1997**, *125*, 372 – 375.
[19] M. Schmidt, *Macromolecules* **1984**, *17*, 553 – 560.
[20] O. Kratky, G. Porod, *Recl. Trav. Chim. Pays-Bas* **1949**, *68*, 1106 – 1122.
[21] T. Itou, H. Chikiri, A. Teramoto, S. M. Aharoni, *Polym. J.* **1988**, *20*, 143 – 151.
[22] Attempts to measure the molecular weight of **3** by size exclusion chromatography (SEC) in toluene by using styragel columns and polystyrol standards for calibration failed as a result of adsorption interactions or thermal decomposition on the column. Analyzable data could not be obtained.
[23] H. Sun, *J. Am. Chem. Soc.* **1997**, *119*, 3611 – 3618.
[24] M. Yu, S. Kalvoda, M. Dolg, *Chem. Phys.* **1997**, *224*, 121 – 131.
[25] R. Fondermann, M. Dolg, M. Raab, E. Niecke, *Chem. Phys.*, in press.
[26] M. White, K. Matyjaszewski, *Macromol. Chem. Phys.* **1997**, *198*, 665 – 671.
[27] Although attempts to detect the PH form by NMR experiments failed, experimental/computational studies, for example, on the influence of electronic effects of the substituents on the equilibrium between the NH-phosphanylamido form and the tautomeric PH-iminophosphorane form, strongly suggest the occurrence of these species in the course of the reaction; see, for example: M. Raab, A. Sundermann, G. Schick, A. Loew, M. Nieger, W. W. Schoeller, E. Niecke, *Organometallics* **2001**, *20*, 1770 – 1775.
[28] The intramolecular amine elimination from triphosphazene **8′** to yield the cyclotriphosphazene, $[P(H)(NH_2){=}N]_3$, is energetically favored by about 2.5 kcal per PN unit.
[29] L. Nyulászi, T. Vespremi, *J. Phys. Chem.* **1996**, *100*, 6456 – 6462.

 © 2006 Wiley-VCH Verlag GmbH & Co. KGaA, Weinheim

Chemical Memory

DOI: 10.1002/anie.200600400

A Reaction–Diffusion Memory Device**

*Akiko Kaminaga, Vladimir K. Vanag, and Irving R. Epstein**

Any computer consists of processor and memory elements. Patterns and waves in excitable or oscillatory reaction–diffusion media are able to perform such processor tasks as counting,[1] logical operations,[2] signal transformation,[3] and finding the shortest path through a maze.[4] Since the brain may be thought of as a reaction–diffusion system, these capabilities are perhaps not so remarkable, though the simplicity of the systems employed is striking. Kuhnert et al.[5] demonstrated that the photosensitive Belousov–Zhabotinsky (BZ) oscillating chemical reaction is capable of briefly (for a few periods of oscillation, that is, several minutes) storing and smoothing an image as complex as a human face. However, practical applications require the ability to store information for longer periods of time, ideally indefinitely. Localized patterns in reaction–diffusion systems have been suggested as media for memory-storage devices.[6] The BZ system dispersed in a water-in-oil microemulsion (ME) with the surfactant sodium bis(2-ethylhexyl)sulfosuccinate (BZ-AOT system) exhibits a rich variety of pattern formation,[7] including several types of localized structures.[8] Herein we show that a photosensitive BZ-AOT system can store spatial information for up to an hour, even without replenishment of reactants. Simulation of this behavior with simple reaction–diffusion models reveals the likely mechanism of this information-storage capacity.

We recently reported the existence of localized stationary and oscillatory patterns in the BZ-AOT system.[8,9] In a system with tris(2,2′-bipyridine)ruthenium ($[Ru(bpy)_3]^{2+}$) catalyst, patterns can be suppressed by sufficiently intense illumination, which leads to photogeneration of bromide, an inhibitor of the reaction.[10] We have found conditions under which this system displays hysteresis and bistability (between a homogeneous steady state and stationary Turing patterns). Turing patterns, which are often invoked as a mechanism for biological morphogenesis, are spatially periodic concentration variations that arise as a result of the interaction between nonlinear reaction kinetics and diffusion.[11] Turing patterns form spontaneously in our system in the dark. If the light intensity (I) is slowly increased, the patterns initially change only slightly, but at a critical intensity (I_{sc}), they suddenly vanish, and a homogeneous steady state (SS) is observed. If we then slowly decrease I, the Turing patterns spontaneously reemerge at a lower intensity (I_c). For $I_c < I < I_{sc}$, the system is bistable, which is a characteristic feature of subcritical Turing instability. In this bistable range of I, localized patterns generated by a local perturbation can be stable, and Turing patterns cannot emerge spontaneously elsewhere in the medium, since the SS is also stable. First, we attempted to photoimprint an image and maintain it as long as possible for I within the bistable region, and then to develop a model that reproduces this phenomenon.

Since our BZ-AOT system is operated in a batch (closed system) mode, we first sought conditions under which stationary Turing patterns can survive for long periods of time (an hour or more) and the system displays significant photosensitivity. These criteria are fulfilled when $[MA]_0 = 0.1\,\text{M}$, $[H_2SO_4]_0 = 0.3\,\text{M}$, $[NaBrO_3]_0 = 0.25\,\text{M}$, $[Ru(bpy)_3]_0 = 0.004\,\text{M}$, $\omega = 10$, and $\varphi_d = 0.45$ (MA is malonic acid, $\omega \equiv [H_2O]/[AOT]$ determines the radius of water droplets in the microemulsion, and φ_d is the volume fraction of the droplets). The radius of the water droplets, measured by dynamic light scattering, is 2 nm, and the microemulsion is below the percolation threshold, as shown by conductivity measurements in the range $\varphi_d = 0.4$–0.7. Under such conditions, the diffusion coefficient of small, oil-soluble molecules, such as the inhibitor Br_2, is significantly larger than that of water-soluble molecules, such as the activator $HBrO_2$, that diffuse with entire water droplets.[12]

When I is in the bistable region, the image of the mask imprinted in the layer of reactive ME can persist essentially unchanged for approximately 30 min. Since our system is closed, the concentrations of BZ reactants and intermediates evolve, and the photosensitivity, as characterized by, for example, the values of I_c and I_{sc}, also changes with time. To maintain the image of the mask for longer we must change the light intensity accordingly. This procedure extends the lifetime of the image to more than an hour, which is roughly the lifetime of the reactive ME in our batch configuration.

Figure 1 presents snapshots taken from a typical experiment. The image in Figure 1 A, which is taken shortly after decreasing I to within the bistable region, is essentially identical to the "face" mask through which the reactor is illuminated. The "face" image remains for about 1 h, but the continuous lines transform into dotted lines (Figure 1 A and B). Similar behavior is observed in the Turing patterns in the unilluminated area: most of the stripes that emerge initially mutate into spotlike Turing patterns after 30–60 min. If we increase I briefly (2–7 min) to suppress the image and then decrease it back to within the bistable region, the original image slowly reappears. Longer exposure to strong light erases the memory of the medium. If we decrease I below the bistable region, new spots begin to emerge around and within the "face" and eventually cover the entire area. Figure 1 C shows a space–time plot made from a cross section of Figure 1 B taken immediately after the light intensity was decreased. The emergence of new stationary spots is seen as the advent of vertical white bands.

[*] Dr. A. Kaminaga, Dr. V. K. Vanag, Professor I. R. Epstein
Department of Chemistry and
Volen Center for Complex Systems, MS 015
Brandeis University
Waltham, MA 02454 (USA)
Fax: (+1) 781-736-2516
E-mail: epstein@brandeis.edu

[**] This work was supported by grant CHE-0306262 from the Chemistry Division of the National Science Foundation and by the donors of the American Chemical Society Petroleum Research Fund.

 © 2006 Wiley-VCH Verlag GmbH & Co. KGaA, Weinheim

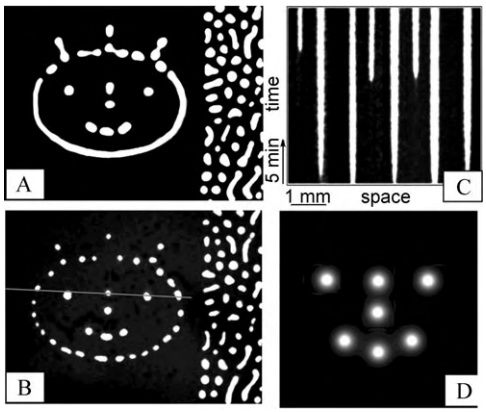

Figure 1. Images of the mask shown in Scheme 1 in the BZ-AOT system (A, B). Size of snapshots A and B is 7.7 mm × 5.8 mm. The time between frames A and B is 1 h. $I = I_0/5$, $I_0 = 28$ mW cm^{-2}. The right-hand side of the reactor (with Turing stationary spots) was not illuminated. C) Space–time plot for the experiment shown in A and B along the cross-sectional line marked in B taken immediately after the light intensity was decreased (bottom of frame C shows time = 0). New spots appear at roughly 10 (2 spots) and 14 min. D) Localized spots in the model described by Equations (1) and (2) with parameters $f = 2$, $q = 0.001$, $m = 200$, $\varepsilon_1 = 0.1$, $i_0 = 0.025$, $\varepsilon = 0.2$, $D_v = 1$, $D_Z = 20$, size = 100 × 100.

Various patterns in the BZ-AOT system, including Turing patterns, have been successfully simulated by several two-, three-, and four-variable models.[8,9,13] We have found localized patterns in all of these models with broad, but different, ranges of parameters.[14] Our simplest model is obtained by augmenting the two-variable Oregonator model[15] by a term i_0 that accounts for the photoinduced production of bromide ion (inhibitor of autocatalysis)[16] and by introducing an additional term mz [Eqs. (1) and (2)].

$$\partial v/\partial \tau = ([fz + i_0(1-mz)](q-v)/(q+v) + v(1-mz)/(1-mz+\varepsilon_1) - v^2)/\varepsilon + D_v \nabla^2 v \quad (1)$$

$$\partial z/\partial \tau = v(1-mz)/(1-mz+\varepsilon_1) - z + D_Z \nabla^2 z \quad (2)$$

In this model, v and z are dimensionless concentrations of activator ($HBrO_2$) and oxidized catalyst, ($[Ru(bpy)_3]^{3+}$), respectively; D_v and D_Z are dimensionless diffusion coefficients of activator and catalyst, respectively; and f, ε, and q are parameters of the Oregonator model.[15] The term $mz = [Z]/C_0$ ([Z] and C_0 are the concentrations of oxidized and total (reduced plus oxidized) catalyst, respectively) takes into account that only the oxidized state of the catalyst is photosensitive and that autocatalysis ceases if mz approaches 1 ($0 < \varepsilon_1 < 1$).[9]

We assume $D_v \ll D_Z$, since the inhibitor bromine diffuses much more rapidly in the oil phase than the activator v, and its concentration is almost linearly related to that of the catalyst z through mass exchange and chemical transformations.[9,13,17] Figure 1 D shows a set of localized stationary spots (analogues of the "eyes", "nose", and "mouth" of our imprinted image) modeled by Equations (1) and (2).

Computer simulations of Equations (1) and (2) reveal that the behavior of the localized spots as i_0 is varied depends on D_Z ($D_v = 1$). The parametric diagram in Figure 2 A shows that

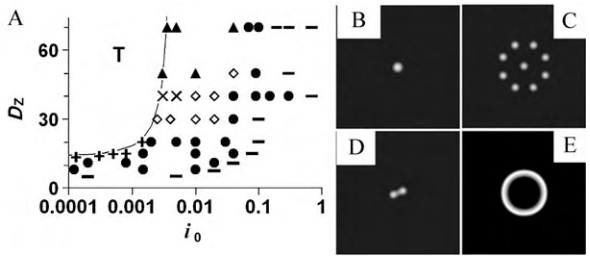

Figure 2. Parametric diagram in the i_0–D_Z plane (A) for Equations (1) and (2). Symbols: localized stationary spot ●; homogeneous SS −. Turing instability occurs in domain T (calculated by linear stability analysis). The localized initial spot (B) can lose stability by producing new spots at radius R from the center (+) (C), by splitting into two spots (◇) (D), or by emitting a circular wave (▲) (E). The circular smooth wave loses its circular symmetry as it approaches the boundaries and transforms first into a dashed wave[20] and then emits backward waves. In a narrow parameter region (×), the circular wave is segmented into dashes. Parameters: $f = 1.85$, $q = 0.004$, $m = 10$, $\varepsilon_1 = 0.02$, $\varepsilon = 0.4$, $D_v = 1$, size = 100 × 100.

at a small D_Z value an initial localized spot (Figure 2 B) generates new spots lying on a circle when i_0 is decreased (Figure 2 C); at a larger D_Z value, the localized spot splits into two new spots (self-replication scenario)[18] (Figure 2 D); and at an even larger D_Z value, the localized spot emits a circular wave (Figure 2 E). For all D_Z values examined, the final stationary pattern for small values of i_0 consists of spots occupying the entire area, whereas larger values of i_0 lead to the homogeneous SS. Comparison with the experimental results (Figure 1 C), in which a decrease in i_0 leads to the emergence of new spots without affecting the existing ones, demonstrates that the scenario that corresponds to our experiments is the generation of new spots at small D_Z values.

We have shown that the BZ reaction can be used not only for image processing[5] but also for image storage, if the BZ-AOT system is employed to enable bistability between the homogeneous steady state and localized stationary (Turing) patterns. Our results imply that images can be stored indefinitely if the BZ reactants are continuously replenished, which can be accomplished with various types of unstirred flow reactors.[19] This photosensitive system can thus be used to create readable and rewriteable chemical memory. From a practical point of view, these findings should be of most importance in three-dimensional media, which have a large enough information capacity to accomplish significant tasks. Although it is uncertain whether a mechanism resembling that involved in the BZ-AOT system is employed for memory storage in living systems, the potential for artificial computational devices created using reaction–diffusion systems is clear.

 © 2006 Wiley-VCH Verlag GmbH & Co. KGaA, Weinheim

Experimental Section

The reactive ME was prepared in the usual way[7,8] by mixing two stock microemulsions (ME1 and ME2) containing MA with H_2SO_4, and $NaBrO_3$ with $[Ru(bpy)_3]^{2+}$, respectively, and enough pure octane to give the desired value of φ_d. A small drop of the reactive ME was placed between two optical windows separated by an annular teflon gasket (Zefluor membrane) of thickness 80 μm, inner diameter 25 mm, and outer diameter 47 mm. This arrangement constitutes our reactor (sandwich S in Scheme 1). Patterns were observed at room temperature (24 °C) through a microscope equipped with a digital CCD camera connected to a computer.

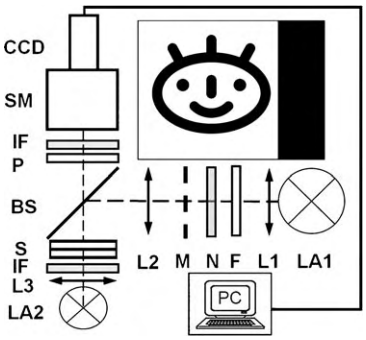

Scheme 1. Block scheme of the experimental setup. LA1 500 W actinic arc lamp; LA2 tungsten 100 W lamp; L1, L2, L3 lenses; F band-pass filter (400–500 nm) with maximum transparency at 450 nm; N neutral density filter; M mask (the "face" mask used in our experiments is shown in the top right corner); S sandwich with photosensitive BZ-AOT system; BS beam splitter; P polarizer; IF interference filter (450 nm); SM stereo microscope; CCD camera; PC computer. The mask was printed onto a transparency film with a laser printer.

The reactive ME in the reactor was kept in darkness for about 1 hour because of the long induction period for the autocatalytic oxidation of $[Ru(bpy)_3]^{2+}$ by $NaBrO_3$. After autocatalysis began, stationary Turing patterns emerged within 1–2 min in the right-hand portion of the reactor, which was kept in darkness throughout the experiment. At 10 min before the end of the induction period (which was measured in advance), the reactor was illuminated through a mask (M) (Scheme 1) at the maximum light intensity I_0, which suppresses the emergence of patterns in all illuminated areas. As soon as an image of the mask (like that shown in Figure 1 A) appeared, the mask was removed, and neutral density filters N were inserted to reduce I.

Received: January 30, 2006
Published online: March 29, 2006

Keywords: imprinting · localized patterns · memory · reaction–diffusion systems

[1] J. Gorecki, K. Yoshikawa, Y. Igarashi, *J. Phys. Chem. A* **2003**, *107*, 1664–1669.
[2] I. N. Motoike, A. Adamatzky, *Chaos Solitons Fractals* **2005**, *24*, 107–114.
[3] N. G. Rambidi, K. E. Shamayaev, G. Y. Peshkov, *Phys. Lett. A* **2002**, *298*, 375–382.
[4] O. Steinbock, A. Toth, K. Showalter, *Science* **1995**, *267*, 868–871.
[5] L. Kuhnert, K. I. Agladze, V. I. Krinsky, *Nature* **1989**, *337*, 244–247.
[6] a) S. Barland, J. R. Tredicce, M. Brambilla, L. A. Lugiato, S. Balle, M. Giudici, T. Maggipinto, L. Spinelli, G. Tissoni, T. Knodl, M. Miller, R. Jager, *Nature* **2002**, *419*, 699–702; b) P. Coullet, C. Riera, C. Tresser, *Chaos* **2004**, *14*, 193–198.
[7] V. K. Vanag, I. R. Epstein, *Phys. Rev. Lett.* **2001**, *87*, 228301.
[8] V. K. Vanag, I. R. Epstein, *Phys. Rev. Lett.* **2004**, *92*, 128301.
[9] A. Kaminaga, V. K. Vanag, I. R. Epstein, *J. Chem. Phys.* **2005**, *122*, 174706.
[10] H. J. Krug, L. Pohlmann, L. Kuhnert, *J. Phys. Chem.* **1990**, *94*, 4862–4866.
[11] A. M. Turing, *Philos. Trans. R. Soc. London Ser. B* **1952**, *237*, 37–72.
[12] L. J. Schwartz, C. L. DeCiantis, S. Chapman, B. K. Kelley, J. P. Hornak, *Langmuir* **1999**, *15*, 5461–5466.
[13] V. K. Vanag, I. R. Epstein, *Phys. Rev. Lett.* **2002**, *88*, 088303.
[14] Numerical simulations were carried out with the FlexPDE package (http://www.pdesolutions.com) with zero-flux boundary conditions. FlexPDE refines the triangular finite-element mesh until the estimated error in any variable is less than a specified tolerance, which we chose as 5×10^{-5}, at every cell of the mesh. Smaller tolerances did not change the results.
[15] J. P. Keener, J. J. Tyson, *Phys. D* **1986**, *21*, 307–324.
[16] S. Kadar, T. Amemiya, K. Showalter, *J. Phys. Chem. A* **1997**, *101*, 8200–8206.
[17] Taking into account the reactions Br_2 + malonic acid $\rightarrow Br^-$ + bromomalonic acid and $Br_2 + H_2O \rightleftharpoons HOBr + Br^- + H^+$, we can write $Br_2 \rightleftharpoons Br^-$, and in addition $y \cong fz/(q+v)$, in which y is the dimensionless concentration of bromide ion.
[18] K. J. Lee, W. D. McCormick, J. E. Pearson, H. L. Swinney, *Nature* **1994**, *369*, 215–218.
[19] a) Z. Noszticzius, W. Horsthemke, W. D. McCormick, H. L. Swinney, W. Y. Tam, *Nature* **1987**, *329*, 619–620; b) Q. Ouyang, J. Boissonade, J. C. Roux, P. De Kepper, *Phys. Lett. A* **1989**, *134*, 282–286; c) W. Y. Tam, W. Horsthemke, Z. Noszticzius, H. L. Swinney, *J. Chem. Phys.* **1988**, *88*, 3395–3396.
[20] V. K. Vanag, I. R. Epstein, *Phys. Rev. Lett.* **2003**, *90*, 098301.

 © 2006 Wiley-VCH Verlag GmbH & Co. KGaA, Weinheim

Zeolites

DOI: 10.1002/anie.200600241

Catalytic Properties of Hierarchical Mesoporous Zeolites Templated with a Mixture of Small Organic Ammonium Salts and Mesoscale Cationic Polymers**

Feng-Shou Xiao, Lifeng Wang, Chengyang Yin, Kaifeng Lin, Yan Di, Jixue Li, Ruren Xu, Dang Sheng Su, Robert Schlögl, Toshiyuki Yokoi, and Takashi Tatsumi*

Crystals of zeolites with intricate micropores have been widely used in industry as heterogeneous catalysts, in particular as solid acid catalysts in the fields of oil refining and petrochemistry. However, relatively small individual micropores in zeolites such as Beta, ZSM-5, and Y strongly influence mass transport to and from the active sites located within them, severely limiting the performance of industrial catalysts.[1,2] To overcome this problem, various strategies have been successfully pursued, such as the synthesis of nanosized zeolites,[3] ultralarge-pore zeolites and zeolite analogues (VPI-5,[4] JDF-20,[5] UTD-1,[6,7] CIT-5,[8] SSZ-53,[9] ECR-34,[10] UCSB,[11] ITQ-21,[12] IM-12,[13] and SU-M,[14,15] among others), and ordered mesoporous materials (e.g. MCM-41,[17] SBA-15,[18] and FSM-16,[19]). However, the use of these materials is rather limited owing to the difficult separation of nanosized zeolite crystals from the reaction mixture,[3] the complexity of the templates used for the synthesis of ultralarge-pore zeolites,[6–9] and the relatively low thermal and hydrothermal stability of ordered mesoporous materials.[17–28] More recently, mesoporous zeolites from nanosized carbon templates have also been successfully synthesized,[29–32] but their industrial applications are still limited by the complexity of the synthetic procedure involved and the hydrophobicity of the carbon templates.

Herein, we demonstrate a facile, controllable, and universal route for the synthesis of hierarchical mesoporous zeolites templated from a mixture of small organic ammonium salts and mesoscale cationic polymers. The route involves a one-step hydrothermal synthesis, and the templated mixture is homogeneously dispersed in the synthetic gel. Importantly, these novel zeolites exhibit excellent catalytic properties compared with conventional zeolites. This work may give an entry to the synthesis of hierarchical mesoporous zeolites that reveal fast mass transport, with potential application in industrial catalysis.

Beta zeolite is generally synthesized from a small organic template of tetraethylammonium hydroxide (TEAOH). In the present strategy, hierarchical mesoporous Beta zeolite (Beta-H) was crystallized in the presence of TEAOH and a mesoscale cationic polymer, polydiallyldimethylammonium chloride (PDADMAC). For comparison, conventional Beta zeolite was prepared in the absence of cationic polymer by a similar procedure.

The X-ray diffraction (XRD) pattern of calcined Beta-H (Figure 1a) shows well-resolved peaks in the 4–40° range,

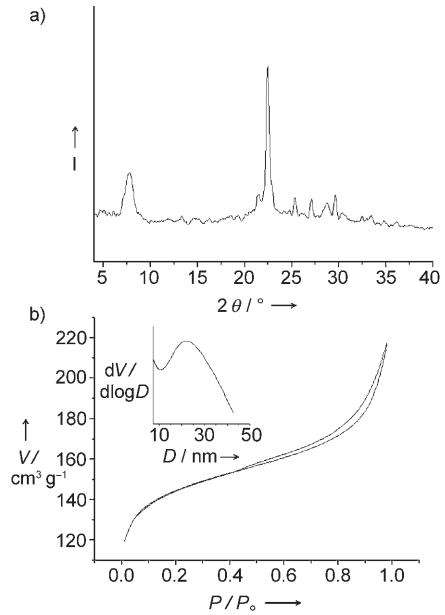

Figure 1. Analyses of the sample of calcined Beta-H: a) XRD pattern; b) N_2 adsorption/desorption isotherms and pore-size distribution curve (inset).

characteristic for the Beta zeolite structure.[33] Interestingly, N_2 adsorption/desoption isotherms of calcined Beta-H exhibit a step at a relative pressure, P/P_0, of 0.8–0.95, as a result of the presence of mesostructures (Figure 1b). Correspondingly, the pore-size distribution for calcined Beta-H shows mesopores at 5–40 nm (Figure 1b, inset). These results indicate that the Beta-H sample contains mesostructures, which may be of importance for mass transport.[1,2]

Low-magnification scanning electron microscopy (SEM) images of the calcined sample of Beta-H (see Figure 2a and

[*] Prof. F.-S. Xiao, L. Wang, C. Yin, K. Lin, Y. Di, Prof. J. Li, Prof. R. Xu
State Key Laboratory of Inorganic Synthesis and Preparative Chemistry
College of Chemistry
Jilin University
Changchun 130012 (P.R. China)
Fax: (+86) 431-516-8624
E-mail: fsxiao@mail.jlu.edu.cn
Dr. D. S. Su, Prof. R. Schlögl
Abteilung für Anorganische Chemie
Fritz-Haber-Institut der Max-Planck-Gesellschaft
Faradayweg 4–6, 14195 Berlin (Germany)
Dr. T. Yokoi, Prof. T. Tatsumi
Chemical Resources Laboratory
Tokyo Institute of Technology
4259 Nagatsuta-cho, Midori-ku, Yokohama 226-8503 (Japan)

[**] This work was supported by the National Natural Science Foundation of China (20573044, 20373018, 20233030), the State Basic Research Project of China (2004CB217804 and 2003CB615802), and the Ministry of Education, China. We thank Prof. D. Z. Jiang and Prof. S. J. Ma for helpful discussions.

Supporting information for this article is available on the WWW under http://www.angewandte.org or from the author.

InterScience DISCOVER SOMETHING GREAT
© 2006 Wiley-VCH Verlag GmbH & Co. KGaA, Weinheim

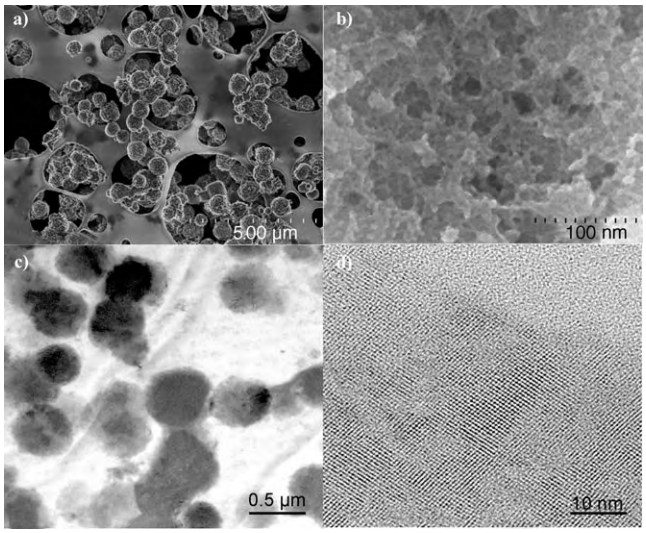

Figure 2. Electron microscopy images of calcined Beta-H: a, b) SEM images at low and high magnification, respectively (the separation between each marker represents 5 µm and 100 nm, respectively); c, d) TEM images at low and high magnification, respectively.

Supporting Information) reveal the presence of almost uniformly sized particles (size about 600 nm) with similar morphology. Furthermore, SEM images under high magnification (see Figure 2b and Supporting Information) clearly show hierarchical mesoporosity in the range of 5–40 nm. Partial connections between these hierarchical pores were observed that could be beneficial for the mass transfer of reactants and products in catalysis. For comparison, the SEM image of the sample of Beta zeolite reveals uniform particles of 300 nm in size (see Supporting Information), about half the size of the particles in Beta-H.

The transmission electron microscopy (TEM) image of the calcined sample of Beta-H (Figure 2c) also shows uniformly sized particles, confirming the pure phase of the sample. TEM images under high magnification (see Figure 2d and Supporting Information) show both hierarchical mesopores (5–20 nm) and ordered micropores in the sample of Beta-H. Note that the micropores with a size of around 0.8 nm, which are related to typical pores of Beta zeolite crystals, are ordered.[34] Hierarchical mesopores are partially continuous and open at the external surface of the sample, and crystal walls are partially connected to each other. Relative to conventional ordered mesoporous materials, the pore size of the mesopores in the Beta-H sample is relatively wide, which confirms hierarchical mesoporosity and is again of importance for mass transport.[1,2]

Thermogravimetric analysis (TGA) of the sample of Beta-H shows a weight loss of 32.9% owing to the removal of the organic templates, TEAOH and the cationic polymer (see Supporting Information). In contrast, the sample of conventional Beta zeolite exhibits a total weight loss of 22.2%. The larger weight loss in Beta-H is assigned reasonably to the removal of the cationic polymer in the sample, and the results also suggest that Beta-H reveals a larger pore volume and more-complex porosity.

The alkylation of benzene with propan-2-ol over various Beta zeolites was investigated as a model catalytic reaction. Figure 3 shows the dependence of the catalytic activity and selectivity on the reaction time in the alkylation reaction.

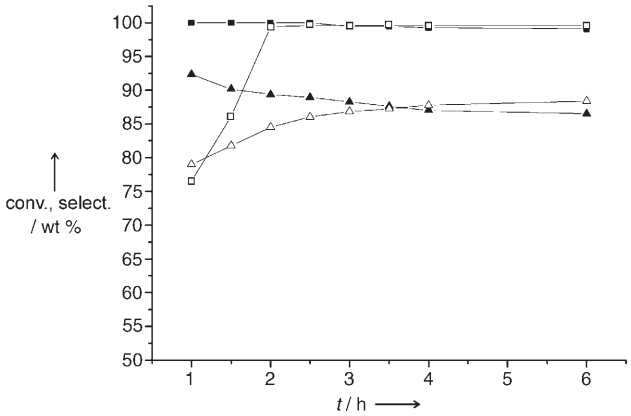

Figure 3. Catalytic conversions (conv. [wt%]) and selectivities (select. [wt%]) in the alkylation of benzene with propan-2-ol with various zeolites samples as a function of reaction time (reaction temperature: 200°C; 4:1 benzene/ propan-2-ol; reaction pressure: 2.0 MP, weight hourly spare velocity (WHSV): 10 h^{-1}). Conversion on Beta-H (■); selectivity on Beta-H (□); conversion on Beta zeolite (▲); selectivity on Beta zeolite (△).

Surprisingly, the Beta-H sample shows a high activity and selectivity as a catalyst, as well as a long catalyst life relative to the sample of conventional Beta zeolite. The similarities of Beta-H to conventional Beta zeolite in terms of Si/Al ratios, aluminum distribution, and acidic strength, as well as the larger particle size of Beta-H than that of Beta zeolite indicate that the higher catalytic activity of Beta-H in the model alkylation reaction relates to the mesoporosity in the Beta-H sample. These results also show that the presence of hierarchical mesopores in the sample of Beta-H is important for the mass transport of the reactants and products in the alkylation of benzene with propan-2-ol.

The presence of hierarchical mesoporosity in the Beta-H sample is attributed to the use of the molecular and aggregated cationic polymer PDADMAC. The molecular weight of the cationic polymer lies in the range 1×10^5–1×10^6, and its size is estimated at 5–40 nm, which is in good agreement with the dimensions of the mesopores obtained from high-resolution (HR)TEM studies (Figure 2d). The cationic polymers could effectively interact with negatively charged inorganic silica species in alkaline media, resulting in the hierarchical mesoporosity. The addition of a greater amount of cationic polymer in the synthetic gel yields Beta zeolite with larger mesoporosity, indicating the controllable mesoporosity of the zeolite sample.

The synthesis of hierarchical mesoporous zeolites is not limited to the Beta variety, which was obtained through use of TEAOH with PDADMAC, but other mixtures of organic amine salts and cationic polymer templates may be used if they effectively interact with inorganic species in alkaline media under conditions to crystallize the zeolites. This method opens the door for the syntheses of a variety of

 © 2006 Wiley-VCH Verlag GmbH & Co. KGaA, Weinheim

hierarchical mesoporous zeolites, such as ZSM-5, Y, TS-1, and so on. For example, hierarchical mesoporous ZSM-5 zeolite (ZSM-5-H) was obtained using a mixture of tetrapropylamine hydroxide and dimethyldiallyl ammonium chloride acrylamide copolymer (10 wt %), and its hierarchical mesoporosity was characterized by XRD, N_2 adsorption/desorption isotherms, SEM, and HRTEM techniques (see Supporting Information). Particularly, use of the hierarchical mesoporous sample ZSM-5-H in the catalytic cracking of 1,3,5-triisopropylbenzene showed that it is much more active a catalyst than conventional ZSM-5 under the same reaction conditions (see Supporting Information).

Experimental Section

In a typical synthesis of hierarchical mesoporous Beta zeolite (Beta-H), NaOH (0.16 g) and $NaAlO_2$ (0.30 g) were mixed with tetraethylammonium hydroxide (TEAOH; 25–35 mL, 20–25 wt %), and fumed silica (SiO_2, 4.8 g) was then added. After stirring the mixture for 1 h at room temperature, cationic polymer polydiallyldimethylammonium chloride (PDADMAC; 0.4–4.0 g, 40 wt %) was added. After stirring for 10–24 h at room temperature, the mixture was transferred into an autoclave at 140 °C for 120–240 h for further crystallization. The product was collected by filtration, dried in air, and calcined at 550 °C for 5 h to remove the template. For comparison, conventional Beta zeolite was synthesized by the same procedure except for the absence of cationic polymer.

In a typical synthesis of hierarchical mesoporous ZSM-5 zeolite (ZSM-5-H), $NaAlO_2$ (0.08 g), tetrapropylammonium hydroxide (TPAOH; 4–12 mL, 20–25 wt %), and tetraethyl orthosilicate (TEOS; 7.0 mL) were mixed with H_2O (20.0 mL) under stirring and aged at 100 °C for 1.5–3 h. Then, cationic polymer dimethyldiallyl ammonium chloride acrylamide copolymer (PDD-AM; 0.5–8.0 g, 10 wt %) was added to the reaction mixture. After stirring for 12–48 h at room temperature, the mixture was transferred into an autoclave at 180 °C for 120–240 h for further crystallization. The product was collected by filtration, dried in air, and calcined at 550 °C for 5 h to remove the template. For comparison, standard ZSM-5 zeolite was synthesized under the same conditions except for the absence of cationic polymer. Furthermore, larger crystals of ZSM-5 zeolite (ZSM-5-F) were synthesized by a similar procedure with the addition of NH_4F (1.2 g) and in the absence of cationic polymer.

XRD patterns were obtained with a Siemens D5005 diffractometer using $Cu_{K\alpha}$ radiation. Nitrogen adsorption and desorption isotherms at 77 K were measured using a Micromeritics ASAP 2010 M system. The samples were degassed for 10 h at 300 °C before the measurements. SEM experiments were performed on Hitachi S-5200 and Hitachi S-4000 electron microscopes. TEM experiments were performed on a Philips CM 200 LaB_6 operating at 200 kV and a JEM-3010 electron microscope (JEOL, Japan) with an acceleration voltage of 300 kV. Differential thermal analysis and TGA studies were performed with Perkin-Elmer TGA 7 and DTA-1700 apparatus, respectively. ^{27}Al MAS NMR measurements were performed on a Varian Infinity plus 400 spectrometer. Ratios of Si/Al in the samples were determined by the results of inductively coupled plasma analysis (ICP, Perkin-Elmer 3300DV) and chemical analysis. Temperature-programmed desorption of ammonia (NH_3-TPD) curves were obtained in the range 120–600 °C, where the temperature was increased at a rate of 15 °C min^{-1}.

Received: January 19, 2006
Revised: February 22, 2006
Published online: March 30, 2006

Keywords: amines · heterogeneous catalysis · polymers · template synthesis · zeolites

[1] M. E. Davis, *Nature* **2002**, *417*, 813 – 821.
[2] M. Hartmann, *Angew. Chem.* **2004**, *116*, 6004 – 6006; *Angew. Chem. Int. Ed.* **2004**, *43*, 5880 – 5882.
[3] B. J. Schoeman, J. Sterte, J. E. Otterstedt, *Zeolites* **1994**, *14*, 110 – 116.
[4] M. E. Davis, C. Saldarriaga, C. Montes, C. Garces, C. Crowder, *Nature* **1988**, *331*, 698 – 699.
[5] Q. Huo, R. Xu, S. Li, Z. Ma, J. M. Thomas, R. Jones, A. Chippindale, *J. Chem. Soc. Chem. Commun.* **1992**, 875 – 876.
[6] C. C. Freyhardt, M. R. Tsapatsis, F. Lobo, K. J. Balkus, M. E. Davis, *Nature* **1996**, *381*, 295 – 298.
[7] a) T. Wessels, C. Baerlocher, L. B. McCusker, *Science* **1999**, *284*, 477 – 479; b) T. Wessels, C. Baerlocher, L. B. McCusker, E. J. Creyghton, *J. Am. Chem. Soc.* **1999**, *121*, 6242 – 6247.
[8] P. Wagner, M. Yoshikawa, T. Katsuyuki, M. E. Davis, M. Lovallo, M. Taspatsis, *Chem. Commun.* **1997**, 2179 – 2180.
[9] A. Burton, S. Elomari, C.-Y. Chen, R. C. Medrud, I. Y. Chan, L. M. Bull, C. Kibby, T. V. Harris, S. I. Zones, E. S. Vittoratos, *Chem. Eur. J.* **2003**, *9*, 5737 – 5748.
[10] K. G. Strohmaier, D. W. Vaughan, *J. Am. Chem. Soc.* **2003**, *125*, 16035 – 16039.
[11] X. Bu, P. Feng, G. D. Stucky, *Science* **1997**, *278*, 2080 – 2085.
[12] A. Corma, M. Diaz-Cabanas, J. Martinez-Triguero, F. Rey, J. Rius, *Nature* **2002**, *418*, 514 – 517.
[13] J.-L. Paillaud, B. Harbuzaru, J. Patarin, N. Bats, *Science* **2004**, *304*, 990 – 992.
[14] X. Zou, T. Conradsson, M. Klingstedt, M. S. Dadachov, M. O'Keeffe, *Nature* **2005**, *437*, 716 – 719.
[15] H. Gies, *Nature* **2005**, *437*, 633 – 633.
[16] J. Zhu, X. Bu, P. Feng, G. D. Stucky, *J. Am. Chem. Soc.* **2000**, *122*, 11563 – 11564.
[17] C. T. Kresge, M. E. Leonowicz, W. J. Roth, J. C. Vartuli, J. S. Beck, *Nature* **1991**, *352*, 710 – 712.
[18] D. Zhao, J. Feng, Q. Huo, N. Melosh, G. H. Fredrickson, B. F. Chmelka, G. D. Stucky, *Science* **1998**, *279*, 548 – 552.
[19] S. Inagaki, Y. Fukushima, K. Kuroda, *J. Chem. Soc. Chem. Commun.* **1993**, 680 – 682.
[20] A. Corma, *Chem. Rev.* **1997**, *97*, 2373 – 2420.
[21] K. Landskron, G. A. Ozin, *Science* **2004**, *306*, 1529 – 1532.
[22] S. A. Johnson, P. J. Ollivier, T. E. Mallouk, *Science* **1999**, *283*, 963 – 965.
[23] a) Y. Liu, W. Zhang, T. J. Pinnavaia, *J. Am. Chem. Soc.* **2000**, *122*, 8791 – 8792; b) Y. Liu, W. Zhang, T. J. Pinnavaia, *Angew. Chem.* **2001**, *113*, 1295 – 1298; *Angew. Chem. Int. Ed.* **2001**, *40*, 1255 – 1258.
[24] a) Z. Zhang, Y. Han, L. Zhu, R. Wang, Y. Yu, S. Qiu, D. Zhao, F.-S. Xiao, *Angew. Chem.* **2001**, *113*, 1298 – 1302; *Angew. Chem. Int. Ed.* **2001**, *40*, 1258 – 1262; b) F.-S. Xiao, Y. Han, X.-J. Meng, Y. Yu, M. Yang, S. Wu, *J. Am. Chem. Soc.* **2002**, *124*, 888 – 889.
[25] H. Gies, S. Grabowski, W. Grunert, *Stud. Surf. Sci. Catal.* **2004**, *154*, 2869 – 2875.
[26] a) D. T. On, S. Kaliaguine, *Angew. Chem.* **2001**, *113*, 3348 – 3351; *Angew. Chem. Int. Ed.* **2001**, *40*, 3248 – 3251; b) D. T. On, S. Kaliaguine, *J. Am. Chem. Soc.* **2003**, *125*, 618 – 619.
[27] a) C. E. A. Kirschhock, S. P. B. Kremer, J. Vermant, G. Van Tendeloo, P. A. Jacobs, J. A. Martens, *Chem. Eur. J.* **2005**, *11*, 4306 – 4313; b) S. P. B. Kremer, C. E. A. Kirschhock, A. Aerts, K. Villani, J. A. Martens, O. I. Lebedev, G. Van Tendeloo, *Adv. Mater.* **2003**, *15*, 1705 – 1707.
[28] F. Schüth, *Angew. Chem.* **2003**, *115*, 3730 – 3750; *Angew. Chem. Int. Ed.* **2003**, *42*, 3604 – 3622.
[29] C. J. H. Jacobsen, C. Madsen, J. Houzvicka, I. Schmidt, A. Carlsson, *J. Am. Chem. Soc.* **2000**, *122*, 7116 – 7117.

 © 2006 Wiley-VCH Verlag GmbH & Co. KGaA, Weinheim

[30] Y. Tao, H. Kanoh, K. Kaneko, *J. Am. Chem. Soc.* **2003**, *125*, 6044 – 6045.
[31] Z. Yang, Y. Xia, R. Mokaya, *Adv. Mater.* **2004**, *16*, 727 – 732.
[32] W.-C. Li, A.-H. Lu, R. Palkovits, W. Schmidt, B. Spliethoff, F. Schüth, *J. Am. Chem. Soc.* **2005**, *127*, 12595 – 12600.
[33] M. M. J. Treacy, J. B. Higgins, *Collection of Simulated XRD Powder Patterns for Zeolites*, *4th ed.*, Elsevier, Amsterdam, **2001**.
[34] M. K. Rubin, European Patent 0159846, **1985**.

 © 2006 Wiley-VCH Verlag GmbH & Co. KGaA, Weinheim

Chiral Ionic Liquids

DOI: 10.1002/anie.200600048

Functionalized Chiral Ionic Liquids as Highly Efficient Asymmetric Organocatalysts for Michael Addition to Nitroolefins**

Sanzhong Luo, Xueling Mi, Long Zhang, Song Liu, Hui Xu, and Jin-Pei Cheng**

Ionic liquids, especially functional ionic liquids (FIL; or task-specific ionic liquids, TSIL), have received growing attention recently due to their tuneable features for various chemical tasks and their advantages as reusable homogeneous supports, reaction media, and reagents with "green" credentials.[1] In general, FILs are designed and synthesized by attachment of functional groups onto the side chains of ionic liquids. Such chemical functionalization usually enhances the versatility of ionic liquids, thereby leading to a large number of diverse FILs with improved properties.[1i,2] Important progress along this line has been made with the development of chiral ionic liquids (CILs).[3] Following the initial work of Seddon and co-workers,[4] a number of CILs were employed as chiral-resolution reagents, chiral solvents, or chiral additives.[3c] Although it has been shown that chiral ionic liquids employed as chiral additives indeed helped to induce moderate enantioselectivity in some cases, such as in photoisomerization,[5] the Baylis–Hillman reaction,[6] and Michael additions,[7] the full potential of CILs in asymmetric synthesis still remains undisclosed. Compared to the extensive works on the achiral ionic-liquid catalysts,[8] essentially no highly efficient catalyst of the CIL type has been reported up to now. Here, we present our recent discovery of a new class of distinctly functionalized CILs that act as highly efficient asymmetric organocatalysts.

This work was inspired by the extraordinary success of chiral pyrrolidines and imidazolines as highly enantioselective organocatalysts (Scheme 1, left and middle).[9] Since the seminal works of List et al.[10] and MacMillan and co-workers,[11] a great number of pyrrolidine- and imidazoline-type asymmetric organocatalysts have been reported. The cyclic five-membered secondary amine structure of these compounds is now regarded as one of the "privileged" backbones for asymmetric catalysis.[9a] Thus, our design for functionalized CILs (for example, **2a** in Scheme 1) comprises such a "privilieged" chiral pyrrolidine unit covalently tethered to an IL moiety, so that the former can serve as a catalytic site and the latter as both the phase tag and a chiral-induction group. Previous studies have shown that the use of ionic liquids as reaction media or phase tags for organocatalysts facilitated catalyst recycling and offered enhanced reactivity and enantioselectivity.[12] In this work, we envisaged that ionic-liquid-type organocatalysts such as **2a** would still maintain the unique properties of an ionic liquid and would also serve as an efficient catalyst for judiciously selected reactions. The role of imidazolium as a chiral-induction group may be rationalized by considering that 1) the bulky and planar organic cation may impart space shielding to the reaction intermediate and 2) the proximity of the ionic-liquid unit to the active site may create a microenvironment that is favorable for the reaction. In fact, the high polarity and ionic character of the ILs exert synergistic effects on many organic reactions.[1i,13]

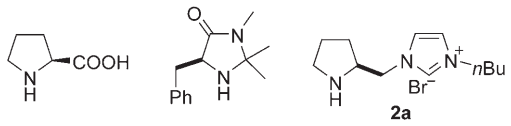

Scheme 1. Privileged organic catalysts.

A series of the pyrrolidine-type CILs were synthesized from the "chiral pool" using L-proline as a starting material (Scheme 2). The synthetic procedures were quite straightforward and afforded the product (for example, **2a**) in 45% total yield from L-proline. All the CILs obtained are viscous liquids at room temperature and are soluble in moderately polar solvents, such as chloroform, dichloromethane, and methanol, but insoluble in less polar solvents, such as diethyl ether, ethyl acetate, and hexane. These properties, together with the straightforward synthesis, suffice for practical applications in asymmetric synthesis.

We next examined the applications of these CILs in asymmetric catalysis, where the asymmetric Michael reaction

[*] Dr. S. Luo, H. Xu, Prof. Dr. J.-P. Cheng
Centre for Molecular Science
Institute of Chemistry
Chinese Academy of Sciences
Beijing, 100080 (P.R. China)
Fax: (+86) 10-6255-4449
E-mail: luosz@iccas.ac.cn
chengjp@mail.most.gov.cn
X. Mi, L. Zhang, S. Liu, Prof. Dr. J.-P. Cheng
Department of Chemistry and State-key Laboratory of Elemento-organic Chemistry
Nankai University
Tianjin, 300071 (P.R. China)
Fax: (+86) 10-5888-1878

[**] This work was supported by the Natural Science Foundation of China (grant nos.: NSFC 20452001, 20421202, and 20542007), the Ministry of Science and Technology (MoST), and the Institute of Chemistry, Chinese Academy of Sciences (ICCAS). We thank Prof. D. Wang, Prof. Q. H. Fan, and Dr. L. Liu for the HPLC instrument.

Supporting information for this article is available on the WWW under http://www.angewandte.org or from the author.

 © 2006 Wiley-VCH Verlag GmbH & Co. KGaA, Weinheim

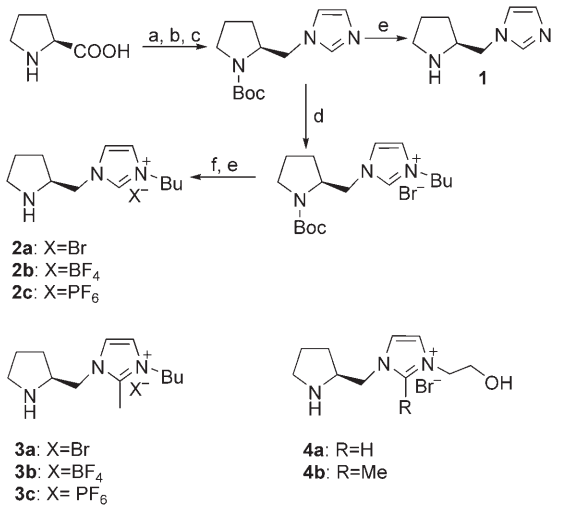

Scheme 2. Synthesis of functionalized chiral ionic liquids. Conditions: a) $LiAlH_4$, THF, 75%; b) 1. Boc_2O, NaOH; 2. TosCl, pyridine, 90% for 2 steps; c) NaH, imidazole, 83%; d) *n*BuBr, toluene, 70°C, 93%; e) HCl/EtOH; then sat. $NaHCO_3$, 90%; f) NaX, acetone/acetonitrile, room temperature. Boc = *tert*-butoxycarbonyl, THF = tetrahydrofuran, Tos = toluene-4-sulfonyl.

Table 1: The effect of chiral ionic-liquid catalysts in asymmetric Michael additions of cyclohexanone and *trans*-β-nitrostyrene.[a]

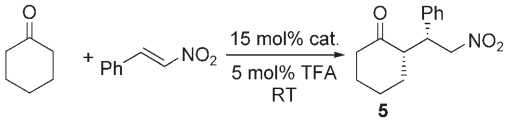

Entry	Catalyst	*t* [h]	Yield [%][b]	*syn*/*anti*[c]	*ee* [%][d]
1	**1**	18	97	97:3	91
2	**2a**	10	99	99:1	98
3[e]	**2a**	20	99	99:1	97
4	**2b**	8	100	99:1	99
5[f]	**2b**	8	97	97:3	94
6[g]	**2b**	24	99	96:4	91
7[h]	**2b**	48	96	97:3	93
8	**2c**	12	86	98:2	87
9	**3a**	20	97	97:3	97
10	**3b**	16	100	96:4	94
11	**3c**	12	40	96:4	82
12	**4a**	18	86	97:3	89
13	**4b**	18	25	94:6	70

[a] TFA = trifluoroacetic acid. [b] Yield of isolated product. [c] Determined by ^{1}H NMR spectroscopy. [d] Determined by HPLC analysis (chiralcel AD-H column). [e] 10 mol% of catalyst was used. [f]–[h] Second, third, and fourth reuses of the catalyst, respectively.

was selected as our initial focus. As one of the most important carbon–carbon bond-forming reactions, Michael addition has been the subject of considerable research efforts aimed at developing efficient asymmetric catalysts, especially environmentally friendly, metal-free organocatalysts.[14] Proline derivatives such as pyrrolidinyltetrazole,[15] aminomethylpyrrolidine,[16] and 2,2′-bipyrrolidine[17] have been shown to serve as useful asymmetric catalysts for the Michael addition of ketones or aldehydes. Recently, Kotsuki and co-workers developed a pyrrolidine–pyridine conjugate base as a highly selective catalyst for Michael reactions of ketones.[18] Wang et al.[19] and Hayashi et al.[20] have independently reported excellent catalysts for the asymmetric Michael reaction of aldehydes. Intrigued by the success of chiral pyrrolidines as asymmetric Michael addition catalysts, we investigated pyrrolidine-type CILs in the Michael addition of cyclohexanone to *trans*-β-nitrostyrene.

As can be seen from the results summarized in Table 1, all synthesized CILs catalyzed the asymmetric Michael addition. The corresponding catalytic and enantioselective activities varied significantly with different ionic-liquid units. With regard to the ionic-liquid-cation moiety, CILs with an imidazolium core (**2a**–**c** and **4a**) are superior to their 2′-methyl counterparts (**3a**–**c** and **4b**) in terms of both activities and enantioselectivities (Table 1, entries 2–13). Incorporation of a protic group in the side chain of the cation, as in **4a** and **4b**, led to a decrease in both the catalytic activity and selectivity (Table 1, entries 12 and 13). As for the anion, while the swap of Br^- to BF_4^- provided comparable catalysts with slightly enhanced activities (Table 1, entry 2 versus 4 and entry 9 versus 10), the exchange of Br^- for PF_6^- had a detrimental effect on both the activities and selectivities (Table 1, entries 8 and 11). The functionalized CILs tested in this work performed much better than previously reported chiral pyrrolidine catalysis in ionic liquids as the reaction media.[12d,h] For example, 40 mol% of L-proline was required to catalyze cyclohexanone addition to nitrostyrene in ionic liquids with 75% yield after 60 h (d.r. = 95:5 and 75% *ee* for the *syn* diastereomer).[12h] These observations, together with the comparatively lower efficiencies of non-ionic-liquid pyrrolidine–imidazole conjugate **1** (Table 1, entry 1), clearly indicate the critical role of the ionic-liquid moieties for asymmetric catalysis. Overall, pyrrolidine–imidazolium bromide and tetrafluoroborate, **2a** and **2b**, respectively, demonstrate the best performances with nearly quantitative yields and high diastereoselectivity (*syn*/*anti* = 99:1) and enantioselectivity (98% *ee*).

In general, the reactions were carried out in neat mixtures with 15 mol% of catalyst and 5 mol% of TFA as the co-catalyst. (These were observed to be the optimal conditions; see the Supporting Information.) A reduction in the amount of catalyst (**2a**) to 10 mol% resulted in a relatively slow reaction but still gave quantitative yield and 97% *ee* within 20 h (Table 1, entry 3). This result is comparable to that of the experiment by Kotsuki and co-workers with a pyrrolidine–pyridine catalyst (24 h, 95%, *syn*/*anti* 98:2, 99% *ee*).[18] In agreement with previous reports,[16,17] the use of an acidic co-catalyst was essential in our catalytic system. In the absence of co-catalyst, the reaction became very sluggish and only afforded 33% yield after 40 h.

The synthetic functionalized CILs still maintained the biphasic property of ionic liquids and could be easily recycled by precipitation with diethyl ether. Recycled CIL **2b** was directly used in the next run and demonstrated identical activity with slightly decreased selectivities (Table 1, entry 5; Table 2, entry 1). Loss of activity was observed for the third and fourth reuse of the CIL, but excellent yields and *ee* values could still be achieved (Table 1, entries 6 and 7; Table 2, entry 1).

 © 2006 Wiley-VCH Verlag GmbH & Co. KGaA, Weinheim

Table 2: CIL-catalyzed asymmetric Michael addition to nitroalkenes.

Entry	Product	CIL	*t* [h]	Yield [%][a]	*syn*/*anti*[b]	*ee* [%][c]	Entry	Product	CIL	*t* [h]	Yield [%][a]	*syn*/*anti*[b]	*ee* [%][c]
1	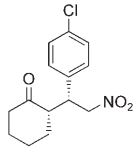 **6**	**2a**	12	92	98:2	95	7	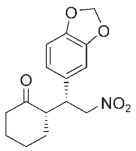 **12**	**2a**	42	99	98:2	94
		2b	10	100	99:1	99			**2b**	24	99	99:1	97
		2b[d]	10	92	96:4	94							
		2b[e]	24	93	97:3	93							
2	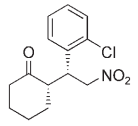 **7**	**2a**	12	99	99:1	96	8	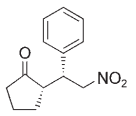 **13**	**2a**	80	61	75:25	83/80
		2b	12	100	99:1	99			**2b**	60	87	63:37	79/82
3	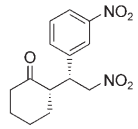 **8**	**2a**	15	76	98:2	96	9	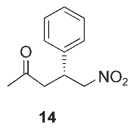 **14**	**2a**	12	77	–	45
		2b	10	94	98:2	96			**2b**	12	83	–	43
4	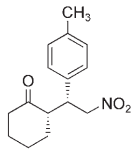 **9**	**2a**	16	94	99:1	92	10	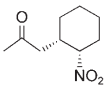 **15**	**2a**	24	57	83:17	79/81
		2b	12	99	99:1	95			**2b**	24	92	85:15	76/80
5	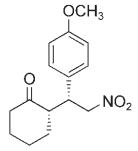 **10**	**2a**	20	94	99:1	94	11	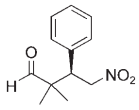 **16**	**2a**	96	51	–	89
		2b	12	99	99:1	95			**2b**	96	70	–	86
6	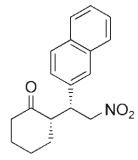 **11**	**2a**	12	99	99:1	95	12	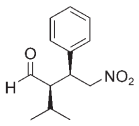 **17**	**2a**	60	73	90:10	77
		2b	10	99	99:1	97			**2b**	60	100	90:10	72

[a] Yield of isolated product. [b] Determined by ^{1}H NMR spectroscopy. [c] Determined by HPLC analysis (chiralpak AD-H or AS-H columns). [d] and [e] Second and third reuses of the catalyst, respectively.

We next probed the scope of the reaction for a variety of Michael donors and nitroalkenes with the identified optimal catalysts **2a** and **2b** (Table 2). The reactions worked extremely well with cyclohexanone to generate Michael adducts in nearly quantitative yields, high diastereoselectivities (d.r. $\geq$ 97:3), and excellent enantioselectivities (92–99% *ee*). Both electron-rich and electron-deficient nitrostyrenes were excellent Michael acceptors for cyclohexanone (Table 2, entries 1–7). With regard to the Michael donors, the reaction with cyclopentanone occurred smoothly and showed moderate diastereoselectivity and enantioselectivity for both diastereomers (Table 2, entry 8). Acetone also served as an efficient Michael donor to produce the desired adduct with good yield and moderate enantioselectivity (Table 2, entry 9). In the presence of **2a**, the reaction of acetone with cyclic nitroolefin afforded the desired Michael adducts with high yields and good enantioselectivities (Table 2, entry 9, *syn*: 76% *ee*, *anti*: 80% *ee*).

Our preliminary studies demonstrated that CILs **2a** and **2b** could also catalyze the Michael addition of aldehydes (Table 2, entries 11 and 12). Under the optimized conditions, the addition of isobutyraldehyde to *trans*-β-nitrostyrene gave the desired adduct in good yields and up to 89% *ee* (Table 2, entry 11). Valeraldehyde also worked well to afford the desired product with quantitative yield and moderate selectivity (Table 2, entry 12, *syn*/*anti* = 90:10, 72% *ee*). In most of the cases examined, CIL tetrafluoroborate **2b** performed slightly better than CIL bromide **2a**.

 © 2006 Wiley-VCH Verlag GmbH & Co. KGaA, Weinheim

The relative and absolute configurations of the Michael adducts were determined by ^{1}H NMR spectroscopic analysis and comparison of the optical rotations with those of known compounds. The high diastereoselectivities and excellent enantioselecitivities of CIL catalysis in the Michael additions reported here may be explained by the concept of an acyclic synclinal transition state, as proposed by Seebach and Golinski[21] and in other previous studies.[15–20] In this model, the ionic-liquid moiety would effectively shield the *Si* face of the enamine double bond in the ketone donor and the reaction would occur through a *Re–Re* approach (Scheme 3).[22] The ionic and highly polar nature of the imidazolium group may also contribute in the transition state and this feature is currently under investigation.

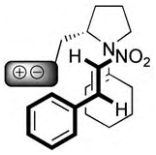

Scheme 3. Transition-state model for ketone donors.

In summary, we have developed a novel asymmetric catalytic system with functionalized CILs and demonstrated their potential as highly efficient asymmetric organocatalysts for Michael reactions. The pyrrolidine–ionic-liquid conjugates have several noteworthy features: 1) they can very efficiently catalyze the Michael additions for a broad range of Michael donors (both ketones and aldehydes) and Michael acceptors (nitroolefins) with high yields (up to 100%), excellent enantioselectivity (up to 99% *ee*), and very good diastereoselectivity (*syn*/*anti* up to 99:1); 2) the ionic-liquid moiety can not only act as a phase tag to facilitate recycling and reuse of the catalyst but can also function as an efficient chiral-induction group to ensure high selectivity; and 3) the modular and tuneable features of ionic liquids promise further developments. Further improvements of the present catalysts (reusability) and the application of the CILs to other types of reactions are currently underway in our laboratory.

Experimental Section

Typical experimental procedure: Nitrostyrene (37 mg, 0.25 mmol) and **2b** (12 mg, 15 mol%) were mixed with cyclohexanone (0.5 mL, 5 mmol) at room temperature. After stirring at room temperature for 8 h, the homogeneous reaction mixture was diluted with ethyl ether to precipitate the catalyst. The organic layer was separated and loaded onto a silica gel column for purification, to afford the Michael adduct (61 mg, 99%) as a white solid: *syn*/*anti* 99:1, 99% *ee* (by HPLC on a chiralpak AD-H column, $\lambda = 254$ nm, eluent *i*PrOH/hexane (10:90), flow rate $= 0.5\ mL\,min^{-1}$; $t_R = 21.4$ (minor), 27.2 min (major)). The catalyst was used directly for the next run after removing the residual solvent.

Received: January 5, 2006
Published online: April 4, 2006

Keywords: asymmetric catalysis · ionic liquids · Michael addition · nitroalkenes · organocatalysis

[1] For reviews, see: a) J. H. Davis, *Chem. Lett.* **2004**, *33*, 1072 – 1077; b) P. Wasserscheid, W. Keim, *Angew. Chem.* **2000**, *112*, 3926 – 3946; *Angew. Chem. Int. Ed.* **2000**, *39*, 3772 – 3789; c) T. Welton, *Chem. Rev.* **1999**, *99*, 2071 – 2083; d) R. Sheldon, *Chem. Commun.* **2001**, 2399 – 2407; e) J. Dupont, R. F. de Souza, P. A. Z. Suarez, *Chem. Rev.* **2002**, *102*, 3667 – 3692; f) J. S. Wikes, *J. Mol. Catal. A* **2004**, *214*, 11 – 17; g) T. Welton, *Coord. Chem. Rev.* **2004**, *248*, 2459 – 2477; h) C. E. Song, *Chem. Commun.* **2004**, 1033 – 1043; i) N. Jain, A. Kumar, S. Chauhan, S. M. S. Chauhan, *Tetrahedron* **2005**, *61*, 1015 – 1060.

[2] Z. Fei, T. J. Geldbach, D. Zhao, P. J. Dyson, *Chem. Eur. J.* **2006**, *12*, 2122 – 2130.

[3] For reviews, see: a) C. Baudequin, J. Baudoux, J. Levillain, D. Cahard, A.-C. Gaumont, J.-C. Plaquevent, *Tetrahedron: Asymmetry* **2003**, *14*, 3081 – 3093; b) J. Ding, D. W. Armstrong, *Chirality* **2005**, *17*, 281 – 292; c) C. Baudequin, D. Brégeon, J. Levillain, F. Guillen, J.-C. Plaquevent, A.-C. Gaumont, *Tetrahedron: Asymmetry* **2005**, *16*, 3921 – 3945.

[4] M. J. Earle, P. B. McCormac, K. R. Seddon, *Green Chem.* **1999**, *1*, 23 – 25.

[5] J. Ding, V. Desikan, X. Han, T. L. Xiao, R. Ding, W. S. Jenks, D. W. Armstrong, *Org. Lett.* **2005**, *7*, 335 – 337.

[6] B. Pégot, G. Vo-Thanh, A. Loupy, *Tetrahedron Lett.* **2004**, *45*, 6425 – 6428.

[7] Z. Wang, Q. Wang, Y. Zhang, W. Bao, *Tetrahedron Lett.* **2005**, *46*, 4657 – 4660.

[8] For achiral ionic-liquid catalysts, see: acidic catalysts: a) A. Cole, J. Jensen, I. Ntai, K. Loan, T. Tran, K. Weaver, D. Forbes, J. Davis, *J. Am. Chem. Soc.* **2002**, *124*, 5962 – 5963; b) Y. Gu, F. Shi, Y. Deng, *Catal. Commun.* **2003**, *4*, 597 – 601; c) D. C. Forbes, K. J. Weaver, *J. Mol. Catal. A* **2004**, *214*, 129 – 132; d) Y. Gu, F. Shi, Y. Deng, *J. Mol. Catal. A* **2004**, *212*, 71 – 75; e) J. Gui, H. Ban, X. Cong, X. Zhang, Z. Hu, Z, Sun, *J. Mol. Catal. A* **2005**, *225*, 27 – 31; f) J. Gui, Y. Deng, Z. Hu, Z. Sun, *Tetrahedron Lett.* **2004**, *45*, 2681 – 2683; g) D. Li, F. Shi, J. Peng, S. Guo, Y. Deng, *J. Org. Chem.* **2004**, *69*, 3582 – 3585; h) S. Kitaoka, K. Nobuoka, Y. Ishikawa, *Chem. Commun.* **2004**, 1902 – 1903; i) Z. Fei, D. Zhao, T. J. Geldbach, R. Scopelliti, P. J. Dyson, *Chem. Eur. J.* **2004**, *10*, 4886 – 4893; basic catalysts: j) B. C. Ranu, S. Banerjee, *Org. Lett.* **2005**, *7*, 3049 – 3052; k) S. Abelló, F. Medina, X. Rodríguez, Y. Cesteros, P. Salagre, J. E. Sueiras, D. Tichit, B. Coq, *Chem. Commun.* **2004**, 1906 – 1907; l) A. Zhu, T. Jiang, D. Wang, B. Han, L. Liu, J. Huang, J. Zhang, D. Sun, *Green Chem.* **2005**, *7*, 514 – 517; nucleophilic catalysts: m) D. W. Kim, C. E. Song, D. Y. Chi, *J. Am. Chem. Soc.* **2002**, *124*, 10278 – 10279; n) D. W. Kim, C. E. Song, D. Y. Chi, *J. Org. Chem.* **2003**, *68*, 4281 – 4285; o) D. W. Kim, Y. S. Choe, D. Y. Chi, *Nucl. Med. Biol.* **2003**, *30*, 345 – 350; p) D. W. Kim, D. Y. Chi, *Angew. Chem.* **2004**, *116*, 489 – 491; *Angew. Chem. Int. Ed.* **2004**, *43*, 483 – 485; q) L.-W. Xu, Y. Gao, J.-J. Yin, L. Li, C.-G. Xia, *Tetrahedron Lett.* **2005**, *46*, 5317 – 5320; r) B. C. Ranu, S. S. Dey, *Tetrahedron* **2004**, *60*, 4183 – 4188; s) L.-W. Xu, J.-W. Li, S.-L. Zhou, C.-G. Xia, *New J. Chem.* **2004**, *28*, 183 – 184.

[9] For selected reviews of organocatalysis, see: a) P. I. Dalko, L. Moisan, *Angew. Chem.* **2004**, *116*, 5248 – 5286; *Angew. Chem. Int. Ed.* **2004**, *43*, 5138 – 5175; b) A. Berkessel, H. Groger, *Asymmetric Organocatalysis*, Wiley-VCH, Weinheim, **2005**; c) J. Seayad, B. List, *Org. Biomol. Chem.* **2005**, *3*, 719 – 724; d) S. T. Handy, *Chem. Eur. J.* **2003**, *9*, 2938.

[10] B. List, R. A. Lerner, C. F. Barbas III, *J. Am. Chem. Soc.* **2000**, *122*, 2395.

[11] K. A. Ahrendt, C. J. Borths, D. W. C. MacMillan, *J. Am. Chem. Soc.* **2000**, *122*, 4243 – 4244.

 © 2006 Wiley-VCH Verlag GmbH & Co. KGaA, Weinheim

[12] a) P. Kotrusz, I. Kmentova, B. Gotov, Š. Toma, E. Solčániová, *Chem. Commun.* **2002**, 2510 – 2511; b) T.-P. Loh, L.-C. Feng, H.-Y. Yang, J.-Y. Yang, *Tetrahedron Lett.* **2002**, *43*, 8741 – 8743; c) N. S. Chowdari, D. B. Ramachary, C. F. Barbas III, *Synlett* **2003**, 1906 – 1909; d) P. Kotrusz, S. Toma, H.-G. Schmalz, A. Adler, *Eur. J. Org. Chem.* **2004**, 1577 – 1583; e) H. M. Guo, L. F. Cun, L. Z. Gong, A. Q. Mi, Y. Z. Jiang, *Chem. Commun.* **2005**, 1450 – 1452; f) P. Kotrusz, S. Alemayehu, T. Toma, H. G. Schmalz, A. Adler, *Eur. J. Org. Chem.* **2005**, 4904 – 4911; g) A. Córdova, *Tetrahedron Lett.* **2004**, *45*, 3949 – 3952; h) M. S. Rasalkar, M. K. Potdar, S. S. Mohile, M. M. Salunkhe, *J. Mol. Catal. A* **2005**, *235*, 267 – 270; i) X. L. Mi, S. Z. Luo, J.-P. Cheng, *J. Org. Chem.* **2005**, *70*, 2338 – 2341; j) R. T. Dere, R. R. Pal, P. S. Patil, M. M. Salunkhe, *Tetrahedron Lett.* **2003**, *44*, 5351 – 5353.

[13] a) S. T. Handy, *Curr. Org. Chem.* **2005**, *9*, 959 – 988; b) J. Habermann, S. Ponzi, S. V. Ley, *Mini-Rev. Org. Chem.* **2005**, *2*, 125 – 137.

[14] For a review, see: a) J. Christoffers, A. Baro, *Angew. Chem.* **2003**, *115*, 1726 – 1728; *Angew. Chem. Int. Ed.* **2003**, *42*, 1688 – 1690. For imidazoline-type organocatalysts for Michael additions, see: b) N. Halland, P. S. Aburel, K. A. Jørgensen, *Angew. Chem.* **2004**, *116*, 1292 – 1297; *Angew. Chem. Int. Ed.* **2004**, *43*, 1272 – 1277, and references therein; c) M. T. H. Fonseca, B. List, *Angew. Chem.* **2004**, *116*, 4048 – 4050; *Angew. Chem. Int. Ed.* **2004**, *43*, 3958 – 3960; d) Y. Hayashi, H. Gotoh, T. Tamura, H. Yamaguchi, R. Masui, M. Shoji, *J. Am. Chem. Soc.* **2005**, *127*, 16028 – 16029.

[15] a) A. J. A. Cobb, D. A. Longbottom, D. M. Shaw, S. V. Ley, *Chem. Commun.* **2004**, 1808 – 1809; b) A. J. A. Cobb, D. M. Shaw, D. A. Longbottom, J. B. Gold, S. V. Ley, *Org. Biomol. Chem.* **2005**, *3*, 84 – 96; c) C. E. T. Mitchell, A. J. A. Cobb, S. V. Ley, *Synlett* **2005**, 611 – 614.

[16] a) B. List, P. Pojarliev, H. J. Martin, *Org. Lett.* **2001**, *3*, 2423 – 2425; b) J. M. Betancort, C. F. Barbas III, *Org. Lett.* **2001**, *3*, 3737 – 3740; c) N. Mase, R. Thayumanavan, F. Tanaka, C. F. Barbas III, *Org. Lett.* **2004**, *6*, 2527; d) J. M. Betancort, K. Sakthivel, R. Thayumanavan, F. Tanaka, C. F. Barbas III, *Synthesis* **2004**, 1509 – 1521.

[17] a) A. Alexakis, O. Andrey, *Org. Lett.* **2002**, *4*, 3611 – 3614; b) O. Andrey, A. Alexakis, G. Bernardinelli, *Org. Lett.* **2003**, *5*, 2559 – 2561; c) O. Andrey, A. Alexakis, A. Tomassini, G. Bernardinelli, *Adv. Synth. Catal.* **2004**, *346*, 1147 – 1168.

[18] T. Ishii, S. Fujioka, Y. Sekiguchi, H. Kotsuki, *J. Am. Chem. Soc.* **2004**, *126*, 9558 – 9559.

[19] W. Wang, J. Wang, H. Li, *Angew. Chem.* **2005**, *117*, 1393 – 1395; *Angew. Chem. Int. Ed.* **2005**, *44*, 1369 – 1371.

[20] Y. Hayashi, H. Gotoh, T. Hayashi, M. Shoji, *Angew. Chem.* **2005**, *117*, 4284 – 4287; *Angew. Chem. Int. Ed.* **2005**, *44*, 4212 – 4215.

[21] D. Seebach, J. Golinski, *Helv. Chim. Acta* **1981**, *64*, 1413 – 1423.

[22] For aldehyde donors, *anti*-enamine intermediates would be formed and the reactions would occur through a *Si–Si* approach.[15–17]

 © 2006 Wiley-VCH Verlag GmbH & Co. KGaA, Weinheim

Bimetallic Complexes

DOI: 10.1002/anie.200503814

A Bimetallic, Coordinated-Ketene Complex Formed from a Bimetallic Lithium–Carbon Spirocycle by Lithium-Mediated Insertion of CO into a Rhodium–Carbon Bond**

*Min Fang, Nathan D. Jones, Robert Lukowski, Jim Tjathas, Michael J. Ferguson, and Ronald G. Cavell**

Bimetallic complexes play a large role in organometallic chemistry in part because of the potential for cooperative catalytic applications. Of particular interest in this context are hetero-bimetallic systems constructed around a single-carbon (methylene) bridge (sometimes also classified as a "bridging carbene"). Most hetero-bimetallic systems are either "A-frame" complexes that are bridged by bis(phosphine) ligands or compounds containing a direct M–M bond.[1]

The use of lithium reagents as organic and organometallic synthetic precursors[2–5] is also relevant to the system described herein, and the importance of such reagents has warranted extensive interest from synthetic, structural, and theoretical perspectives.[6] There are, however, few structurally characterized lithium systems which contain a carbon-bridged Li–C–precious-metal assembly, and only three of these cases involve Rh.[7,8] None of these bridged-carbene Rh complexes carries a phosphorus substituent on the central carbon atom.

A final facet of the system described herein is the insertion of CO into a metal–carbon bond, which is an important organometallic transformation.[9] In particular, metal ketene complexes (which can formally be considered as the derivatives of such insertion processes) are considered to play important roles in industrial Fischer–Tropsch syntheses[1e,10] as well as in CO_2 fixation and functionalization,[11] and may be intermediates in the thermal and photochemical reactions of carbene/CO complexes.[12] In most cases, the existence of the intermediate ketene complex is only inferred because the general instability of such complexes hampers direct observation. Nevertheless, over the years, a number of ketene complexes has been prepared and structurally characterized. The varied chemistry of ketene complexes has been reviewed;[10f] it was noted that up to nine coordination modes

[*] Dr. M. Fang, Dr. N. D. Jones, R. Lukowski, J. Tjathas, Dr. M. J. Ferguson,[+] Prof. Dr. R. G. Cavell
Department of Chemistry
University of Alberta
Edmonton, Alberta T6G 2G2 (Canada)
Fax: (+1) 780-492-8231
E-mail: ron.cavell@ualberta.ca

[+] X-Ray Crystallography Laboratory

[**] We are indebted to the Natural Sciences and Engineering Research Council of Canada and the Killam Trust (postdoctoral fellowship to N.D.J.) for financial support.

Supporting information for this article is available on the WWW under http://www.angewandte.org or from the author.

 © 2006 Wiley-VCH Verlag GmbH & Co. KGaA, Weinheim

have been identified. A few X-ray crystal structures of μ_2,η^2-(O,C) M^1–M^2 ketene complexes have been reported;[10f,13] however, none of these early examples contained Rh. The isolation and characterization of stable η^2-(C,O) and η^2-(C,C) ketene complexes of iridium(I) and rhodium(I)[14,15] have renewed interest in ketene complexes in general.[15–18]

Herein, we report a chemical sequence which combines the above major themes and derives from the unusual lithiated spirocyclic bridging-carbene complex **1** initially formed by the 1:1 reaction[19] of [{Rh(cod)Cl}$_2$] (cod = 1,5-cyclooctadiene) with [{$Li_2C(Ph_2P{=}NSiMe_3)_2$}$_2$] ([$(Li_2L)_2$],[20,21] Scheme 1). Although **1** is moisture sensitive, it can be isolated

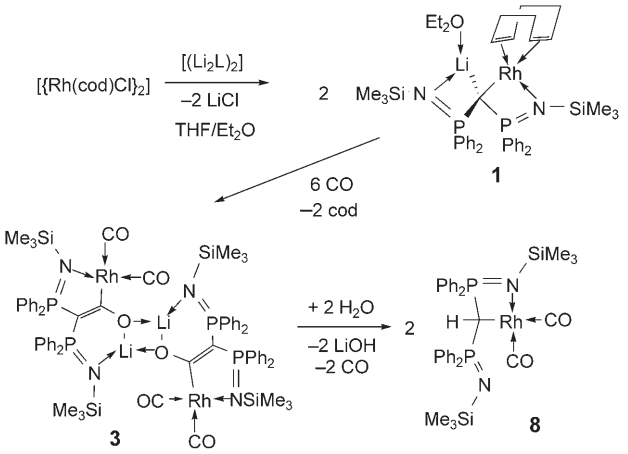

Scheme 1. Synthesis of complexes **1**, **3**, and **8** (L = $C(Ph_2P{=}NSiMe_3)_2$).

and stored for several weeks without apparent change at −20 °C in a drybox freezer. Subsequent reaction of this complex with other metallic precursors leads to a series of bimetallic (or hetero-bimetallic) complexes of the form **2** (Scheme 2).[22] More significantly, **1** combines with CO by

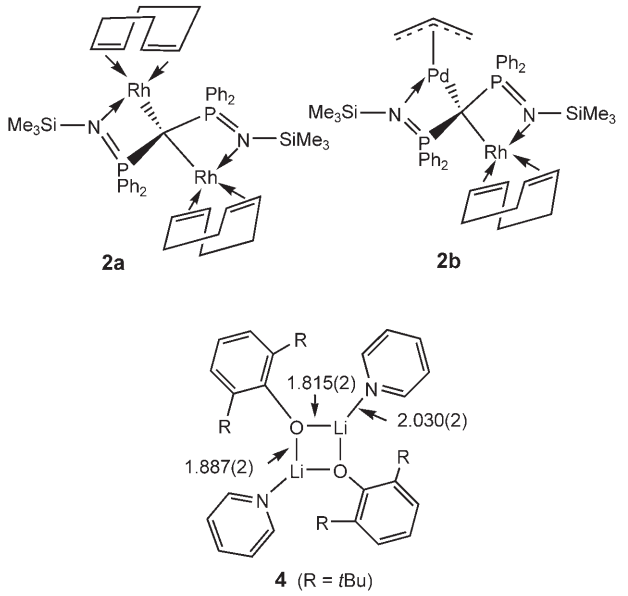

Scheme 2. Spirocyclic bimetallic complexes **2** and the Li dimer **4**. Bond lengths are in Å.

insertion to yield the stable dimeric ketene complex **3** (Scheme 1).[23]

The molecular structure of **1**[24] is shown in Figure 1. The complex is monomeric, presumably as a result of the

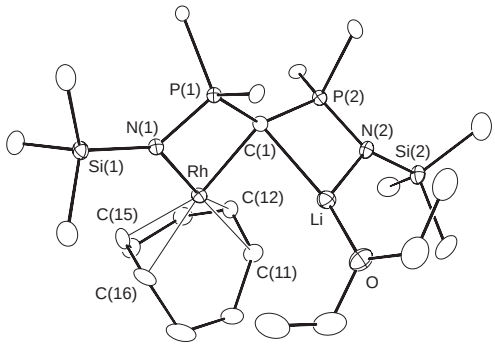

Figure 1. X-ray crystal structure of **1**. Non-hydrogen atoms are represented by Gaussian ellipsoids set at 20% probability. Only the *ipso*-carbon atom of each phenyl ring is shown, and hydrogen atoms are not shown. Selected bond lengths [Å] and angles [°]: Rh–C(1) 2.105(6), P(1)–C(1) 1.706(6), P(2)–C(1) 1.695(6), P(1)–N(1) 1.611(4), Rh–N(1) 2.160(4), P(2)–N(2) 1.579(5), Li–N(2) 2.02(1), Li–O 1.89(1), Li–C(1) 2.20(1); P(1)-C(1)-Rh 91.8(2), C(1)-P(1)-N(1) 101.5(2), P(1)-N(1)-Rh 92.6(2), N(1)-Rh-C(1) 74.1(2), P(2)-C(1)-Li 81.5(4), C(1)-Li-N(2) 77.7(4), Li-N(2)-P(2) 90.4(4), N(2)-P(2)-C(1) 108.1(3), P(1)-C(1)-P(2) 135.4(3); torsion angles [°]: Rh-C(1)-P(1)-N(1) 1.0(3), C(1)-Li-N(2)-P(2) 10.1(3).

substantial bulk of the substituents. The coordination geometry around the Rh atom in **1** is nearly planar with a Rh-C(1)-P(1)-N(1) ring torsion angle of 1.0(3)°. The Rh atom is bonded to the cod ligand in the normal fashion with typical distances from the metal to the centroids of the two olefin bonds, and the metal lies 0.073 Å below the plane defined by the C=C centroids, C(1), and N(1) (torsion angle: 2.2(3)°). The Rh–C(1) and Rh–N(1) bond lengths are within the normal ranges, but the former is shortened, which, along with the relatively short P–C(1) bonds, gives relatively large P-C(1)-Rh and N-P-C(1) angles. The geometry around C(1) is distorted tetrahedral, with angles ranging from 81.5(4) (∢P(2)-C(1)-Li) to 135.4(3)° (∢P(1)-C(1)-P(2)). This distortion could be a result of one or all of the following: the short P–C(1) bond lengths, the repulsion between the positively charged Rh and Li atoms, and steric crowding. The C(1)-Li-N(2)-P(2) ring is also nearly planar (torsion angle: 10.1(3)°). The bond angles and lengths in **1** are generally in good agreement with those found for other four-membered CLiNP rings,[25] all of which are nearly planar (C-Li-N-P torsion-angle range: −12.4(2)–6.74(8)°). The Rh–Li separation (2.88(1) Å) is larger than the sum of covalent radii of the individual atoms (1.35+1.34 = 2.69 Å), thus indicating that there is no Rh–Li bonding. The Li–C(1) bond length (2.20(1) Å) in **1**, in which the Li atom is tricoordinate, is substantially shorter than those with tetracoordinate Li atoms (2.29–2.39 Å).[25a,e] The P–C(1) bond lengths (1.695(6), 1.706(6) Å) lie between typical P–C single-bond (1.80 Å) and P–C double-bond (1.57 Å) lengths.[26] The P–N bond lengths (1.611(4), 1.579(5) Å) are closer to typical

 © 2006 Wiley-VCH Verlag GmbH & Co. KGaA, Weinheim

P–N double-bond (1.57 Å) than to P–N single-bond (1.77 Å) values. The Si–N bond lengths (1.693(5), 1.706(4) Å) are indicative of Si–N single bonds (1.70 Å). Overall, this structure is best formulated with an ylidic P-C-P backbone.

Complex **1** reacts smoothly with CO by replacement of the cod ligand and formal C–C bond formation upon "insertion" of CO into the Rh–C bond to yield **3**, which has been fully characterized by elemental analysis, NMR spectroscopy (^{1}H, ^{7}Li, ^{13}C, and ^{31}P),[23] and X-ray structural analysis.[24] The molecular structure of **3** (Figure 2) reveals a

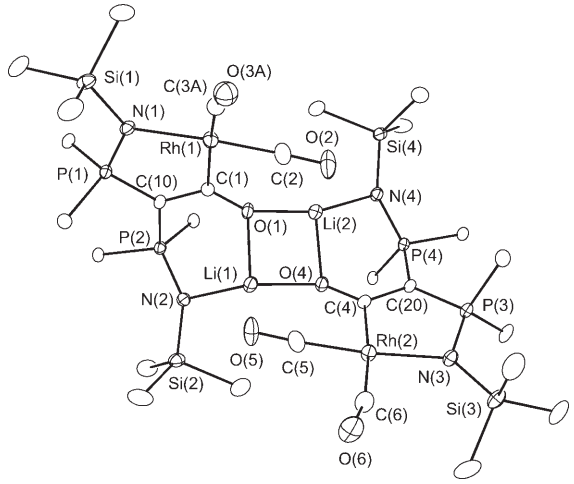

Figure 2. X-ray crystal structure of **3**. Non-hydrogen atoms are represented by Gaussian ellipsoids set at 20% probability. Only the *ipso*-carbon atom of each phenyl ring is shown, hydrogen atoms are not shown, and only one part of the disordered carbonyl ligand (C(3A),O(3A)) on Rh(1) is shown. Selected interatomic separations [Å] and bond angles [°]: Si(1)–N(1) 1.742(4), N(1)–P(1) 1.611(4), P(1)–C(10) 1.745(4), P(1)–C(11) 1.815(5), P(1)–C(21) 1.811(4), C(10)–C(1) 1.396(6), C(1)–O(1) 1.296(5), Rh(1)–C(1) 2.057(4), Rh(1)–C(2) 1.816(6), Rh(1)–C(3A) 1.922(10), C(3A)–O(3A) 1.152(13), C(2)–O(2) 1.159(7), C(10)–P(2) 1.785(4), P(2)–N(2) 1.575(4), N(2)–Li(1) 1.995(9), O(1)–Li(1) 1.933(9), Li(1)–O(4) 1.880(9), O(4)–Li(2) 1.924(9), O(1)–Li(2) 1.819(9), N(2)–Si(2) 1.699(4), Li(1)···Li(2) 2.582(13), Li(1)···O(5) 2.360(9), Li(2)···O(2) 2.715(10); Li(1)-O(1)-Li(2) 86.9(4), O(1)-Li(2)-O(4) 94.2(4), Li(2)-O(4)-Li(1) 85.5(4), O(4)-Li(1)-O(1) 92.0(4), C(10)-C(1)-O(1) 118.0(4), C(10)-C(1)-Rh(1) 118.3(3), Rh(1)-C(1)-O(1) 123.5(3); torsion angles [°]: O(4)-Li(1)-O(1)-Li(2) 8.9(4), Rh(2)-C(4)-C(20)-P(3) −0.5(4), P(2)-C(10)-C(1)-O(1) 3.4(5), P(2)-N(2)-Li(1)-O(1) 6.5(4).

central dilithium-core structure formed by two bridging ketene moieties. The geometries around the O*C*RhC carbon atoms C(1) and C(4) (sum of angles around each C atom (av): 359.9(4)°) as well as around the PCP carbon atoms C(10) and C(20) (sum of angles around each C atom (av): 359.8(3)°) are planar, thus suggesting sp^2 hybridization. The Rh–$C_{C=C}$ bond lengths in **3** (av: 2.058(5) Å) fall within the range of typical Rh^{I}–C(sp^2) single-bond lengths (2.057(3)[27] to 2.123(5) Å[28]). The Rh–C_{CO} bonds *trans* to the carbon atoms are much longer (bond length (av): 1.923(5) Å) than the Rh–C_{CO} bonds *trans* to the nitrogen atom (bond length (av): 1.817(6) Å) as a result of the higher *trans* influence of carbon compared to nitrogen. The O(1)–C(1) (1.296(5) Å), C(1)–C(10) (1.396(6) Å), C(10)–P(1) (1.745(4) Å), and P(1)–N(1) (1.611(4) Å) bond lengths all lie between typical single- and double-bond lengths (C–O 1.43, C=O 1.20, C–C 1.48, C=C 1.34, P–C 1.80, P=C 1.57, P–N 1.77, P=N 1.57 Å), thus indicating electron delocalization in the O(1)-C(1)-C(10)-P(1)-N(1) and the corresponding O(4)-C(4)-C(20)-P(3)-N(3) regions. The central Li_2O_2 ring is nearly planar with a O(4)-Li(1)-O(1)-Li(2) torsion angle of 8.9(4)°. The Li···Li separation of 2.58(1) Å suggests some bonding interaction (covalent radius of Li: 1.34 Å). The Li–N and Li–O bond lengths of **3** are comparable to those observed in complex **4** (Scheme 2).[29] The Li(1)···O(5) contact (2.360(9) Å) is shorter than the Li(2)···O(2) (2.715(10) Å) contact and is probably the reason why the Li(1)–O(4) bond is much longer than the Li(2)–O(1) bond. These contact separations are much smaller than the sum of the van der Waals radii of Li and O (3.32 Å).[30]

The metrical details for **3** suggest that resonance structures **3a**–**3d** (see the Supporting Information) all contribute to the overall bonding in this complex. The resonance structure **3c** (Scheme 4) suggests that the complex could also be viewed as a rhodium-substituted enolate. Very few metal enolate MC(=O)CR_2^- complexes, except for a few iron complexes,[13] have been structurally characterized. The solution NMR spectroscopic chemical shifts are consistent with the structure of complex **3**. The ^{31}P NMR spectrum resonance signal at $\delta = 9.1$ ppm was assigned to the PNRh phosphorus atom and showed a two-bond coupling ($^{2}J_{P,Rh} =$ 6 Hz) to Rh through mediation by the N atom. The Rh*C*C carbon atoms of **3** appeared at $\delta = 238.8$ ppm in the ^{13}C NMR spectrum with a $^{1}J_{C,Rh}$ coupling constant of 33 Hz.

We presume that **3** is formed from a Li-mediated insertion reaction, which follows the normal substitutional replacement of the cod ligand with CO on the Rh center to give **5** (Scheme 3). In the second step, a CO ligand on Rh inserts into the Rh–C bond to form **6**, and the bridging CO ligand then attacks at the Li atom and opens the Li–C bond to form the Li–O bond, which is likely to be stronger due to the oxophilicity of the Li atom, in **7**. The coordinative unsaturation at Rh which is created by this process is readily satisfied by an additional equivalent of CO. The overall result is that one CO molecule has "inserted" into the Rh–$C_{carbene}$ bond.

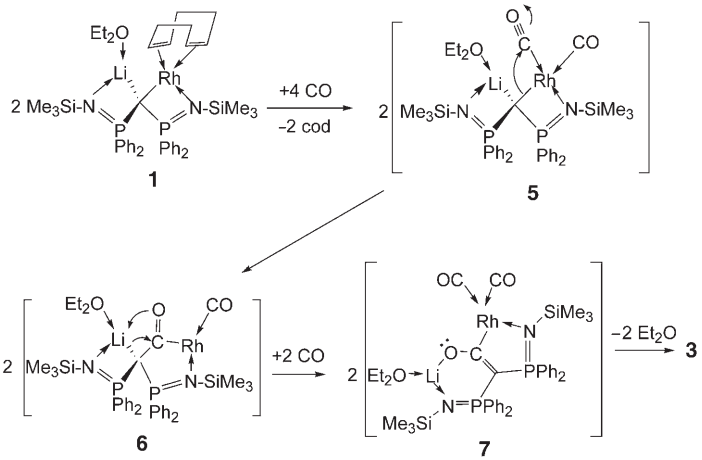

Scheme 3. A possible route to **3** from **1** and CO.

 © 2006 Wiley-VCH Verlag GmbH & Co. KGaA, Weinheim

Elimination of diethyl ether and dimerization yield **3**, and this process probably enhances the stability of the final product. There is no evidence for the formation of any lithium–carbonyl intermediate.[10g]

Notably, complexes analogous to **1**, such as complexes **2a** and **2b** (Scheme 2) which have weaker Rh–$C_{carbene}$ bonds (bond lengths: 2.148(2) (**2a**), 2.137(3) (**2b**), 2.105(6) Å (**1**)), do not undergo insertion reactions with CO.[22] This situation suggests that the Li atom plays a key role in promoting the CO insertion reaction of **1**, probably by inducing a higher nucleophilicity of the proximal carbon through increased polarity at the bridging carbene center. The nearly quantitative formation of **3** also implies that a direct CO insertion into the Li–C bond is not operative because such reactions are generally nonspecific at room temperature.[31,32]

Complex **3** reacts with H_2O at room temperature according to Scheme 1 (experimental details given in the Supporting Information) to give complex **8** with a bidentate methine ligand. No intermediate was observed in the reaction.[22] A possible reaction pathway is illustrated in Scheme 4. Consid-

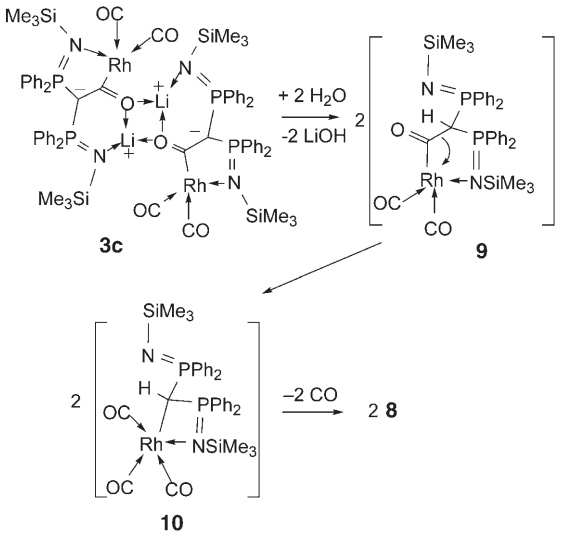

Scheme 4. Hydrolysis of complex **3**. Experimental details are given in the Supporting Information.

ering that the PCP carbon atoms in **3** possess significant negative charge, as suggested by one resonance structure **3c**, it is likely that the first step of the hydrolysis involves attack at the Li atoms to form LiOH, and protonation of the carbene center gives intermediate **9**, which then rearranges to form intermediate **10**. Subsequent elimination of excess CO from the Rh center affords **8**.

In summary, the first μ_2,η^2-(O,C) lithium–rhodium ketene complex **3** was synthesized at room temperature in high yield by insertion of CO into the spirocyclic carbene center of the Li/Rh complex **1** by a reaction pathway in which CO first coordinates then inserts. Hydrolysis of **3** gives **8** under elimination of CO. The preparation of **3** suggests that a new synthetic route to μ_2,η^2-(O,C) lithium–metal ketene complexes could be developed through the application of "insertions" of free CO into Li-C-M bimetallic complexes of the type exemplified by **1**.

Received: October 27, 2005
Revised: January 30, 2006
Published online: March 30, 2006

Keywords: bimetallic compounds · bridging ligands · lithium · rhodium · spiro compounds

[1] a) S. Tsutsumiani, N. Komine, M. Hirano, S. Komiya, *Organometallics* **2004**, *23*, 44–53; b) S. Tsutsumiani, N. Komine, M. Hirano, S. Komiya, *Organometallics* **2003**, *22*, 4238–4247; c) M. A. Rida, A. K. Smith, *J. Mol. Catal. A* **2003**, *202*, 87–95; d) M. Zhou, Y. Xu, A.-M. Tan, P.-H. Leung, K. F. Mok, L.-L. Koh, T. S. A. Hor, *Inorg. Chem.* **1995**, *34*, 6425–6429; e) C. P. Casey, J. D. Audett, *Chem. Rev.* **1986**, *86*, 339–352; f) J. R. Moss, L. G. Scott, *Coord. Chem. Rev.* **1984**, *60*, 171–190; g) J. E. Hahn, *Prog. Inorg. Chem.* **1984**, *31*, 205–264; h) W. A. Herrmann, *J. Organomet. Chem.* **1983**, *250*, 319–343; i) W. A. Herrmann, *Adv. Organomet. Chem.* **1982**, *20*, 159–263.

[2] D. M. Huryn in *Comprehensive Organic Synthesis*, *Vol. 1* (Ed.: S. L. Schreiber), Pergamon, Oxford, **1991**, pp. 49–75.

[3] M. A. Beswick, D. S. Wright in *Comprehensive Organometallic Chemistry (II)*, *Vol. 1* (Eds.: E. W. Abel, F. G. A. Strone, G. Wilkinson), Pergamon, Oxford, **1995**, pp. 1–34.

[4] G. Boche, *Angew. Chem.* **1989**, *101*, 286–306; *Angew. Chem. Int. Ed. Engl.* **1989**, *28*, 277–297.

[5] D. Seebach, *Angew. Chem.* **1988**, *100*, 1685–1715; *Angew. Chem. Int. Ed. Engl.* **1988**, *27*, 1624–1654.

[6] a) E. D. Jemmis, G. Subramanian, A. J. Kos, P. von R. Schleyer, *J. Am. Chem. Soc.* **1997**, *119*, 9504–9512; b) R. P. Davies, P. R. Raithby, R. Snaith, *Angew. Chem.* **1997**, *109*, 1261–1263; *Angew. Chem. Int. Ed. Engl.* **1997**, *36*, 1215–1217; c) K. Sorger, P. von R. Schleyer, R. Fleischer, D. Stalke, *J. Am. Chem. Soc.* **1996**, *118*, 6924–6933; d) A. Sygula, F. R. Fronczek, P. W. Rabideau, *J. Organomet. Chem.* **1996**, *526*, 389–391; e) S. Harder, M. Lutz, A. Streitwieser, *J. Am. Chem. Soc.* **1995**, *117*, 2361–2362; f) A. J. Ashe III, J. W. Kampf, P. M. Savla, *Organometallics* **1993**, *12*, 3350–3353; g) M. Ludvig, R. J. Lagow, *J. Org. Chem.* **1990**, *55*, 4880–4883; h) H. Kawa, B. C. Manley, R. J. Lagow, *Polyhedron* **1988**, *7*, 2023–2025; i) S. Harder, J. Boersma, L. Brandsma, J. A. Kanters, *J. Organomet. Chem.* **1988**, *339*, 7–15.

[7] M. A. Kulzick, R. A. Andersen, E. L. Muetterties, V. W. Day, *J. Organomet. Chem.* **1987**, *336*, 221–236.

[8] J. Cipot, D. Wechsler, M. Stradiotto, *Organometallics* **2003**, *22*, 5185–5192.

[9] G. W. Parshall, S. D. Ittel in *Homogeneous Catalysis* (Eds.: G. W. Parshall, S. D. Ittel), Wiley-Interscience, New York, **1992**.

[10] a) M. M. Dell'Amico, S. J. Trepanier, R. McDonald, M. Cowie, *Organometallics* **2001**, *20*, 88–99; b) B. D. Rowsell, S. J. Trepanier, R. Lam, R. McDonald, M. Cowie, *Organometallics* **2002**, *21*, 3228–3237; c) D. Ristic-Petrovic, D. J. Anderson, J. R. Torkelson, R. McDonald, M. Cowie, *Organometallics* **2003**, *22*, 4647–4657; d) S. J. Trepanier, J. N. L. Dennett, B. T. Sterenberg, R. McDonald, M. Cowie, *J. Am. Chem. Soc.* **2004**, *126*, 8046–8058; e) B. D. Rowsell, R. McDonald, M. Cowie, *Organometallics* **2004**, *23*, 3873–3883; f) G. L. Geoffroy, S. L. Bassler, *Adv. Organomet. Chem.* **1988**, *28*, 1–83; g) M. Tacke, R. Leyden, L. P. Cuffe, *J. Mol. Struct. (Theochem)* **2004**, *684*, 211–215.

[11] P. Hofmann, L. A. Perez-Moya, O. Steigelmann, J. Riede, *Organometallics* **1992**, *11*, 1167–1176.

[12] L. S. Hegedus in *Comprehensive Organometallic Chemistry II* (Eds.: E. W. Abel, F. G. A. Stone, G. Wilkinson), Pergamon, Oxford, **1995**, pp. 549–576.

 © 2006 Wiley-VCH Verlag GmbH & Co. KGaA, Weinheim

[13] P. Berno, P. Braunstein, C. Floriani, A. Chiesi-Villa, C. Gaustini, *Inorg. Chem.* **1991**, *30*, 1407 – 1410.

[14] D. B. Grotjahn, H. C. Lo, *Organometallics* **1995**, *14*, 5463 – 5465.

[15] D. B. Grotjahn, L. S. B. Collins, M. Wolpert, G. A. Bikzhanova, H. C. Lo, D. Combs, J. L. Hubbard, *J. Am. Chem. Soc.* **2001**, *123*, 8260 – 8270.

[16] H. C. Lo, D. B. Grotjahn, *J. Am. Chem. Soc.* **1997**, *119*, 2958 – 2959.

[17] D. B. Grotjahn, G. A. Bikzhanova, L. S. B. Collins, T. Concolino, K.-C. Lam, A. L. Rheingold, *J. Am. Chem. Soc.* **2000**, *122*, 5222 – 5223.

[18] D. B. Grotjahn, G. A. Bikzhanova, *Organometallics* **1999**, *18*, 5614 – 5619.

[19] Synthesis of **1**: [{RhCl(cod)}$_2$] (0.253 g, 0.513 mmol) was added as a solid in a single portion to a suspension of [(Li$_2$L)$_2$] (0.590, 0.517 mmol) in THF (15 mL) at room temperature. The resulting suspension was stirred at room temperature for 3 h, over which time the solution turned to a deep red color. The in situ yield (^{31}P NMR) of **1** was 89 %. The solvent was removed under dynamic vacuum, and the resultant solids were extracted with diethyl ether (10 mL). The insoluble portion (LiCl) was removed by centrifugation. The red solution was reduced in vacuo to approximately 2 mL and kept at −20 °C overnight in the dry box to yield 0.548 g of a crystalline orange solid. The supernatant liquid was decanted, further reduced in volume, and cooled again to obtain a second crop (0.095 g) of **1**. The overall yield of **1** was 0.643 g (73.8 %). Elemental analysis (%) calcd for $C_{43}H_{60}LiN_2OP_2RhSi_2$: C 60.8, H 7.1, N 3.3; found: C 60.2, H 7.2, N 3.2. Selected NMR spectral data (full data are given in the Supporting Information): ^{31}P{^{1}H} NMR (161.9 MHz, C_6D_6, 298 K, 85 % H_3PO_4): $\delta = 42.4$ (dd, $^2J_{P,P} = 80.4$ Hz, $^2J_{P,Rh} = 19.4$ Hz; PNRh), 15.3 ppm (d, $^2J_{P,P} = 79.8$ Hz, $^2J_{P,Li} = 5.7$ Hz; PNLi); ^{7}Li{^{1}H} NMR (155.4 MHz, C_6D_6, 298 K, LiCl/D_2O): $\delta = 1.03$ ppm (d, $^2J_{P,Li} = 5.7$ Hz).

[20] A. Kasani, R. P. K. Babu, R. McDonald, R. G. Cavell, *Angew. Chem.* **1999**, *111*, 1580 – 1582; *Angew. Chem. Int. Ed.* **1999**, *38*, 1483 – 1484.

[21] C. M. Ong, D. W. Stephan, *J. Am. Chem. Soc.* **1999**, *121*, 2939 – 2940.

[22] M. Fang, N. D. Jones, K. Friesen, G. Lin, M. J. Ferguson, R. McDonald, R. Lukowski, R. G. Cavell, unpublished results.

[23] Synthesis of **3**: An orange benzene solution (7 mL) of complex **1** (0.247 g, 0.291 mmol) was exposed to CO (1 atm) in a closed Pyrex glass vessel (50 mL) at room temperature with a gas-entry stopcock. The solution was stirred for 2 h, and the orange solution gradually turned green. The ^{31}P NMR spectrum of the solution which was extracted from the vessel showed complex **3** (89 % P) and small amounts of two unidentified species: **X1** at $\delta = 52.4$ (dd, $J_{P,P} = 66$ Hz, $J_{P,Rh} = 20$ Hz), 15.4 ppm ($J_{P,P} = 61$ Hz, $J_{P,Rh} = 0$ Hz) (10 % P) and **X2** at $\delta = 17.9$ ppm (0.9 % P). No further reaction occurred according to ^{31}P NMR monitoring after the mixture was exposed to additional CO (1 atm) and stirred for 2 h further. The CO and solvent were removed under dynamic vacuum, and the residue was redissolved in diethyl ether. The diethyl ether solution was concentrated to 1–2 mL and then kept at −20 °C overnight in a drybox to afford **3** as a yellow-green crystalline solid (0.127 g). The supernatant liquid was decanted, further reduced in volume, and cooled again to obtain a second crop (0.041 g) of **3**. The overall yield of **3** was 0.168 g (73.3 %). Elemental analysis (%) calcd for $C_{68}H_{76}Li_2N_4O_6P_4Rh_2Si_4 \cdot 0.5\,Et_2O$: C 54.89, H 5.50, N 3.56; found: C 54.65, H 5.31, N 3.64. Selected NMR spectral data (full data are given in the Supporting Information): ^{31}P{^{1}H} NMR (161.9 MHz, C_6D_6, 298 K, 85 % H_3PO_4): $\delta = 50.6$ (d, $^2J_{P,P} = 90$ Hz; PNLi), 9.1 ppm (dd, $^2J_{P,P} = 90$ Hz, $^2J_{P,Rh} = 6$ Hz; PNRh); ^{7}Li{^{1}H} NMR (155.4 MHz, [D_8]THF, 298 K, LiCl/D_2O): $\delta = -0.25$ ppm (s).

[24] a) Crystallographic data for **1**: $C_{43}H_{60}LiN_2OP_2RhSi_2$, $M_r = 848.90$, yellow plates, $0.15 \times 0.13 \times 0.05$ mm^3, monoclinic, space group $P2_1$ (No. 4), $a = 10.8558(7)$, $b = 18.8081(12)$, $c = 10.9412(7)$ Å, $\beta = 99.5810(10)°$, $V = 2202.8(2)$ Å^3, $Z = 2$; $\rho_{calcd} = 1.280$ g cm^{-3}, $\mu(Mo_{K\alpha}) = 0.548$ mm^{-1}, $T = 193$ K, R_1 (F) = 0.0540 [6633 reflections, $F_o^2 \geq 2\sigma(F^2_{ACHTUNGTRENNUNGo})$], $wR_2 = 0.1046$ for all 8597 unique data; b) Crystallographic data for **3**·Et_2O: $C_{72}H_{86}Li_2N_4O_7P_4Rh_2Si_4$, $M_r = 1575.39$, orange plates, $0.42 \times 0.38 \times 0.07$ mm^3, monoclinic, space group $P2_1/n$ (an alternate setting of $P2_1/c$ [No. 14]), $a = 15.6713(9)$, $b = 17.2388(9)$, $c = 31.3524(17)$ Å, $\beta = 92.7650(10)°$, $V = 8460.1(8)$ Å^3, $Z = 4$, $\rho_{calcd} = 1.237$ g cm^{-3}, $\mu(Mo_{K\alpha}) = 0.570$ mm^{-1}, $T = 193$ K, R_1 (F) = 0.0504 [11650 reflections, $F_o^2 \geq 2\sigma(F_o^2)$], $wR_2 = 0.1692$ for all 17367 unique data. CCDC-277956 (**1**) and CCDC-285955 (**3**·Et_2O) contain the supplementary crystallographic data for this paper. These data can be obtained free of charge from The Cambridge Crystallographic Data Centre via www.ccdc.cam.ac.uk/data_request/cif.

[25] a) M. Said, M. Thornton-Pett, M. Bochmann, *Organometallics* **2001**, *20*, 5629 – 5635; b) F. López-Oritiz, E. Peláez-Arango, B. Tejerina, E. Pérez-Carreño, García-Granda, *J. Am. Chem. Soc.* **1995**, *117*, 9972 – 9981; c) A. Müller, B. Neumüller, K. Dehnicke, *Chem. Ber.* **1996**, *129*, 253 – 257; d) P. B. Hitchcock, M. F. Lappert, Z. Wang, *Chem. Commun.* **1997**, 1113 – 1114; e) P. B. Hitchcock, M. F. Lappert, P. G. H. Uiterweerd, Z. Wang, *J. Chem. Soc. Dalton Trans.* **1999**, 3413 – 3417.

[26] P. Imhoff, R. van Asselt, C. J. Elsevier, K. Vrieze, K. Goubitz, K. F. van Malssen, C. H. Stam, *Phosphorous Sulfur* **1990**, *47*, 401 – 415.

[27] K. T. K. Chan, L. P. Spencer, J. D. Masuda, J. S. J. McCahill, P. Wei, D. W. Stephan, *Organometallics* **2004**, *23*, 381 – 390.

[28] A. A. H. van der Zeijden, G. van Koten, R. A. Nordemann, B. Kojic-Prodic, A. L. Spek, *Organometallics* **1988**, *7*, 1957 – 1966.

[29] T. J. Boyle, D. M. Pedrotty, T. M. Alam, S. C. Vick, M. A. Rodriguez, *Inorg. Chem.* **2000**, *39*, 5133 – 5146.

[30] A. Bondi, *J. Phys. Chem.* **1964**, *68*, 441 – 451.

[31] L. S. Trzupek, T. L. Newirth, E. G. Kelly, N. E. Sbarbati, G. M. Whitesides, *J. Am. Chem. Soc.* **1973**, *95*, 8118 – 8133.

[32] N. S. Nudelman in *The Chemistry of Double-bonded Functional Groups*, *Vol. 2*, *Part 2* (Ed.: S. Patai), Wiley, New York, NY, **1989**.

 © 2006 Wiley-VCH Verlag GmbH & Co. KGaA, Weinheim

Microscale Synthesis

DOI: 10.1002/anie.200503041

Spatially Encoded Single-Bead Biginelli Synthesis in a Microstructured Silicon Array**

G. Alexander Groß, Günther Mayer, Jens Albert, Daniel Riester, Jens Osterodt, Hanns Wurziger, and Andreas Schober**

Microreaction technology has become a field of wide scientific and industrial interest as it allows an increased overall efficiency through savings in labor, materials, time, and costs. The advantages of miniaturization have been discussed in the context of the "lab-on-a-chip" concept.[1,2] For combinatorial chemistry, microfluidic approaches have to cope with many reagent solutions with different fluid properties, vapor pressures, wettabilities, and other factors.[3] Despite the many technical problems to be solved, the use of microfluidic devices seems promising.[4] Owing to the distinct architecture of such systems, the identity of products manufactured in a continuous process is always secured. Solid-phase synthesis is used for the preparation of libraries with large numbers of compounds. The bead-based "split-and-recombine" process is technically less demanding and very efficient in terms of the number of products versus the number of synthetic steps.[5,6] However, a major disadvantage is inherent in this process: the information on the reaction sequence of each individual bead is lost. The necessary product information has to be retrieved afterwards by encoding or decoding strategies, which is a serial and time-consuming process. This problem can be overcome by using a spatially resolved approach. In this case, the prepared compounds are encoded by their position. Most of these approaches are restricted to chemical protocols similar to those used in peptide chemistry.[7,8] Microstructured silicon nanotiter plates[2c] charged with a single bead per compound allow the application of nearly all solid-phase chemistry protocols, resulting in a bead array with immobilized substances with known processing history for each compound.[7–9]

The miniaturization of solid-phase chemistry to the nanovolume scale is difficult and requires much effort to solve the technical difficulties. Evaporation of solvents must be avoided, even with long reaction times. This is exacerbated even more if the necessary reaction temperatures increase the vapor pressures of the solvents used. Cross-contamination must also be avoided during filling, sealing, and reaction steps. This is particularly important for the condensed 200-nL-volume reactor arrays with 12×12 wells on a 16×16-mm^2-sized chip. Such a format equates to 4700 wells on the MTP footprint. It is amenable to selection, excision, and manipulation of individual beads and solutions by simple handling steps in an automated setup.

Herein we describe the first miniaturized parallel organic synthesis in nanoliter volumes on single beads at 100 °C for 14 h as a "proof-of-concept experiment". Evaporation and "cross-talk" was excluded by using a combination of a pressurized sealing device (at the end a vice) and a specially designed chip module with two covering stamps. Only silicon and PTFE come into contact with chemicals. The brittle silicon nanochips with their integrated reactor wells withstand a sealing pressure of 3000 N because the lateral gasket deformation was hindered by the setup used (Figure 1).[10] In this way each single reaction well was sealed reliably even at temperatures up to 100 °C.

The nanochips are made up from three microstructured silicon wafers, which are stacked and secured by PDMS (polydimethylsiloxane) bonding (Figure 2). The chip stack is flanked by the two gasket layers 1 and 3 (Figure 2, types b–d) at the top and bottom. The silicon layer 2 inbetween contains the actual reaction wells with microsieves. These sieves allow the removal of reaction or washing solutions under vacuum[2c]). Figure 2 shows different chip designs that have been optimized with respect to tightness and reusability. This means that there will be no permanent connection between the chip, the gasket, and the cover, even if the vice force of 3000 N acts on the 2.56-cm^2 chip. One major problem had to be solved. In filled chambers of types a and b (Figure 2) all inner surfaces are wetted up to the upper rim owing to the surface tension of the solvent. If the gasket comes into contact with the surface of the liquid, capillary forces cause contamination of all wells. In types c and d, additional inner rims

[*] Dr. A. Schober
Center for Micro- and Nanotechnologies
Technical University of Ilmenau
98693 Ilmenau (Germany)
Fax: (+49) 367-769-3499
E-mail: andreas.schober@tu-ilmenau.de
Dr. G. A. Groß
Department of Physical Chemistry and Microreaction Technology
Technical University of Ilmenau
Weimarerstrasse 32, 98693 Ilmenau (Germany)
Fax: (+49) 367-769-3179
E-mail: alexander.gross@tu-ilmenau.de
Dr. G. Mayer, J. Albert
Microsystems Division
Institute for Physical High Technology e.V. Jena
Albert-Einstein-Strasse 9, 07745 Jena (Germany)
Dr. D. Riester
Institute of Microbiology and Genetics
University of Göttingen
Grisebachstrasse 8, 37077 Göttingen (Germany)
Dr. J. Osterodt, Dr. H. Wurziger
Merck KGaA
Frankfurterstrasse 250, 64298 Darmstadt (Germany)

[**] The authors thank Dr. P. Raddatz and Dr. I. Lues for the pleasant working conditions. The technical assistance of Jörg Heisiep and Stephan Niedziella with microanalysis is gratefully acknowledged, as well as the assistance and engineering support by Michael Schmelz and Günther Brenner. We particularly thank our colleagues at the IPHT Jena for the microstructuring support and Dr. Andreas Schwienhorst (University of Göttingen) for helpful discussions. Funding was provided by BMBF grant 0311766 with contributions from Merck KgaA Darmstadt (BMBF grant 0311765) and partial support by a grant of the Thüringer Ministerium für Kultur (TKM) and the European Community (B 678-03001).

Supporting information for this article is available on the WWW under http://www.angewandte.org or from the author.

InterScience
© 2006 Wiley-VCH Verlag GmbH & Co. KGaA, Weinheim

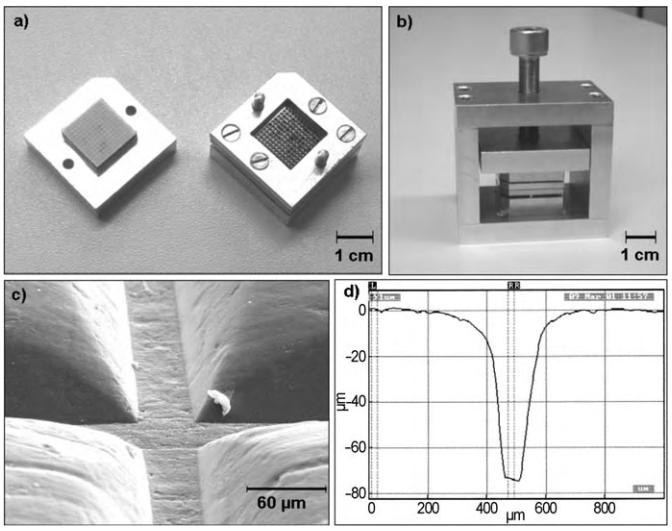

Figure 1. Synthesis module composed of the chip carrier with gaskets and the closing vice. a) Chip carrier modules with PTFE gaskets. b) Closed vice with the assembled chip module inside. c) SEM image of a PTFE gasket molded by the chip after 24 h. d) Profile across the used PTFE gasket (≈75 µm deep).

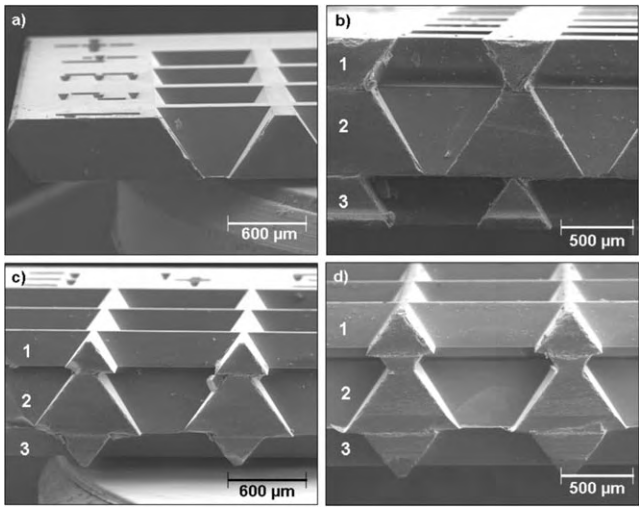

Figure 2. SEM images of cross-sections of different types of reaction chips. a) Microstructured 14×14 chip. b), c), d) Three layer sandwich chip assemblies, PDMS bonded. Type d is equipped with an internal rim. Layer captions: 1 and 3 are gasket-bearing layers, 2 contains the reaction chambers.

prevent the wetting of the gasket-bearing layer. Type d in Figure 2 best fulfils all the criteria.

The Biginelli reaction was chosen to test the parallel synthesis on the nanovolume scale. This reaction requires temperatures of near 100 °C for more than 12 h.[11] 4,6-Diaryl 1,3-dihydropyrimidin-2(1*H*)-ones (DHPMs) **4** are formed in a three-component condensation of immobilized *N*-3-aryl-3-oxopropanamides **1**, aldehydes **3**, and thiourea (**2**) (Scheme 1). DHPMs are regarded as privileged structures for drug research. They have been described as calcium-channel modulators, α_{a1}-adrenergic-receptor antagonists, mitotic kinesin inhibitors, antibacterial and fungicidal compounds, and others.[12]

Nine copies of a DHPM library with 16 members was synthesized copies on a single chip by following an adapted macroscopic protocol.[11] The recommended solvent mixture 1,4-dioxane/*i*PrOH was changed to triglyme/*i*PrOH to obtain a higher vapor pressure and boiling point. Appropriate *N*-3-aryl-3-oxopropanamide beads were prepared before by addition of aryl lithium enolates to immobilized 4-nitrophenyl carbamates according to a literature protocol.[13] During transfer of these beads into the chip wells, swollen beads were sorted according to their horizontal diameter (350 ± 10 µm) by using the image processor of the *x*,*y*,*z* manipulation and pipetting robot (Figure 3). The loaded beads were placed

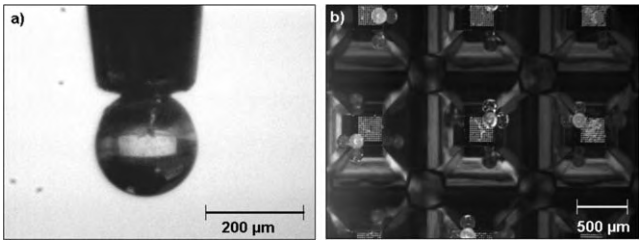

Figure 3. Bead handling. a) Partially swollen bead fixed through a vacuum needle during the transfer and sorting process. b) Top view into a chamber with one bead placed on the sieve bottom (there are four reflections of the bead at the angular silicon walls).

in columns, and the necessary reagent solutions (0.5 mmol L^{-1}) were then added in lines to the chip to yield the pattern outlined in Figure 4.

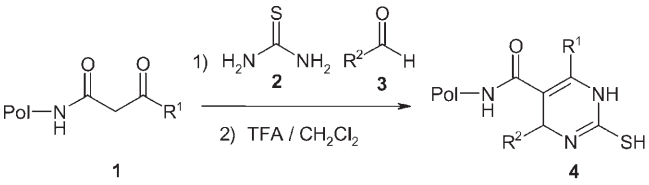

Scheme 1. The Biginelli reaction. TFA = trifluoroacetic acid.

A fused silica capillary connected to a syringe pump was used for pipetting. The chip inside the holding device was mounted onto the bottom gasket stamp and adjusted next to a 96-well storage plate at the pipetting robot. Reagent solutions (150 µL) were aspirated from this plate and dispensed in 150-nl portions into the target wells on the silicon chip by contact pipetting. The wetting properties of the surfaces and the geometry of the chip wells aid their precise filling into the middle chip (see Figure 5).[14]

After dosing, the capillary was removed with only a very small droplet remaining at the tip. This was removed by rinsing the syringe system twice. The liquid transfer required approximately 35 min, after which the cover stamp was adjusted, fixed, and pressed together within the vice. The sealed "synthesis module" was then placed in an incubator set to 100 °C for 14 h. Afterwards, the setup was allowed to cool to ambient temperature. To determine the tightness of the

 © 2006 Wiley-VCH Verlag GmbH & Co. KGaA, Weinheim

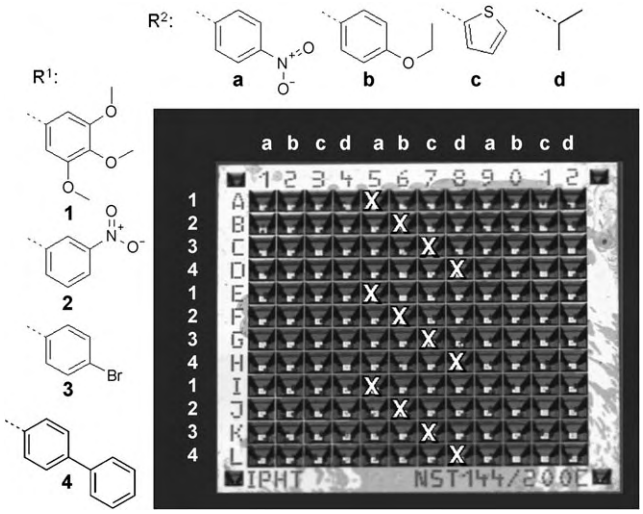

Figure 4. Spatially encoded library inside the silicon chip and building blocks used. A library of 16 DHPM derivatives was prepared in nine copies inside a single silicon chip. Aldehydes (R^2 = **1**–**4**) were used in columns, polymer-bound β-ketoamides (R^1 = **a**–**d**) were used in rows. The spatial position encoding is etched into the silicon surface at the top and left border of the chip (A1–L12). HPLC analysis of marked product positions is shown in Figure 6.

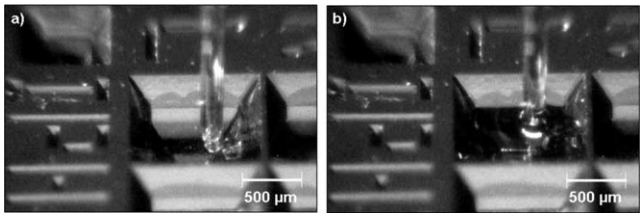

Figure 5. Contact pipetting of reagent solution into a silicon reaction chamber. a) Fused silica capillary placed inside the reaction chamber. b) Chamber with fused silica capillary after a dosage of 150 nL.

system, it was weighed before and after the experiment. On average, a weight loss of less than 2 % was observed.

The chemical conversion was done by heating and subsequent cooling of the reagent solutions. Due to solvent evaporation and condensation, the surfaces of the gasket-bearing lids became moist. The dismantling and removal of the cover lid led to cross-contamination. When the vice is released, capillary forces move the reagent solution into the opening slit between the lid and the silicon chip, thus contaminating the entire chip. This, however, is of no influence when the immobilized starting materials in all wells are consumed. The subsequent washing steps remove excess reagents.

The beads were washed five times with triglyme/*i*PrOH (3:2), 1,2-dichloroethane (DCE), and finally with *i*PrOH by using the vacuum station next to the pipettor. Deliberate overfilling (300 µL) ensured the cleaning of all possibly contaminated surfaces and beads. In the last step, the beads were dried under vacuum for 10 min. The PDMS-bonded chip stack withstands all experiments. This is due to the very small contact area between PDMS and solvents as well as the high vice force acting on the stack during the high-temperature synthesis.

For reference purposes, 100 mg of the appropriate *N*-3-aryl-3-oxopropionaminde beads were converted into 16 DHPM derivatives in standard glassware. Single-bead products of chip-processed and macroscopic-batch beads were analyzed and compared. Therefore chip-processed beads of four different products were chosen from three different positions each. Analyzed chip positions marked in Figure 4 belong to the chromatograms shown in Figure 6.

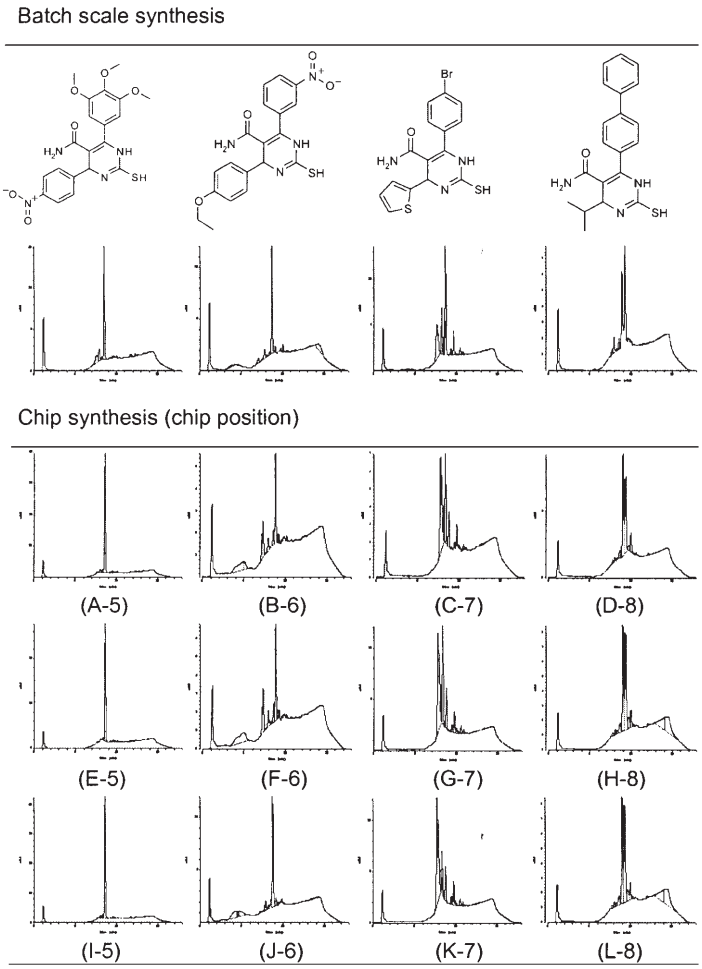

Figure 6. Comparison of product chromatograms.

To cleave the products from the beads, single beads were treated in HPLC vials for 1 h with 30 µL of the cleavage solution (DCE/TFA 1:1). The solvents were carefully evaporated from the cleavage products, and the resulting residues were dissolved at least for one hour in acetonitrile/water (10 µL; 95:5). These solutions were analyzed by HPLC (LC-Packings Instruments) in the presence of the beads. The chromatograms of the macroscopic batch and chip synthesis showed no significant differences (Figures 6 and 7). As a spot check, the collected material from 10 beads was analyzed by LC–MS in more detail. Masses of precursors and main products were as expected. However, the precursor/product ratio varies depending on the dissolving time after cleavage.

 © 2006 Wiley-VCH Verlag GmbH & Co. KGaA, Weinheim

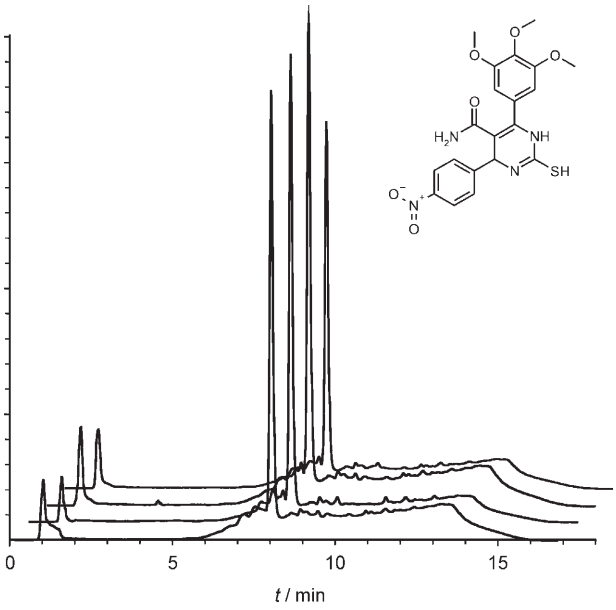

Figure 7. Chromatogram comparison of identical single-bead products (arranged in ascending order): 1. batch-scale reference; 2. chip position A-5; 3. chip position E-5; 4. chip position I-5.

This indicates a rebinding process of the product to the beads (i.e. Figure 6, chromatograms C-7 and K-7). The intensity of the measured chromatograms of identical substances varies by up to 50% (peak area). This is a reflection of differences in the sizes of the selected beads, dosing errors during liquid handling, before and during injection into the HPLC system, or a varying solubility of the received products. A comparison of chromatograms of products from neighboring chip wells indicates no cross-contamination. We conclude that each individual reaction well of the silicon chip of type D (Figure 2) was sealed properly during reaction.

We demonstrated the feasibility of a novel approach for miniaturized parallel solid-phase synthesis of a library in 200-nl volumes. Individual, spatially segregated synthesis beads were addressed by a combination of silicon wafer technology and system engineering. Hereby the problems of evaporation, leakage, and cross-contamination in the small volume could be solved by a specially designed chip and covering system. The approach proved to be versatile for a solid-phase Bigginelli synthesis at 100 °C for 14 h and should be feasible for chemical protocols under less-demanding conditions.

As shown in the proof-of-concept experiment, standard pipettor techniques can be used. Solvents with high vapor pressures can be used (up to pressures of $\approx$150 mbar inside the chamber). In this way individual reaction vessel could be closed to allow the use of common organic solvents at temperatures up to 120 °C. Generic solid-phase protocols can be used in this setup.

The approach seems to be a promising alternative to miniaturization for chemical synthesis, particularly for solid-phase synthesis. The bead loading, pipetting, and washing steps were carried out by one robotic system, thus the complete process is suitable for automation. Our single-bead synthesis approach could potentially be used for the "on demand synthesis" of potential drug derivatives upstream to screening procedures. The technological gap between high-throughput synthesis (HTS) and high-content screening procedures can be overcome. Nanotiter plates on common HTS equipment allows the production of enough material on a single bead for several biological tests. The technology is currently under development for automatic, large-scale parallel combinatorial synthesis.

Received: August 26, 2005
Revised: December 19, 2005
Published online: March 30, 2006

Keywords: combinatorial chemistry · microreactors · nanochip · solid-phase synthesis · synthesis miniaturization

[1] a) D. J. Harrison, K. Fluri, K. Seiler, Z. Fan, C. S. Effenhauser, A. Manz, *Science* **1993**, *261*, 895–897; b) M. A. Burns, *Science* **2002**, *296*, 1818–1819; c) "Microsystems for independent parallel chemical and biological processing": A. Schober, A. Schwienhorst, J. M. Köhler, M. Fuchs, R. Günther, M. Thürk, *Microsystems Technologies*, (Eds.: H. Reichel, A. Heuberger), VDE-Verlag, Berlin, **1994**, pp. 381–390; d) for a recent example, see: B. Zheng, R. F. Ismagilov, *Angew. Chem.* **2005**, *117*, 2576–2579; *Angew. Chem. Int. Ed.* **2005**, *44*, 2520–2523.

[2] a) *Microreactors* (Eds.: W. Ehrfeld, V. Hessel, H. Löwe), Wiley-VCH, Weinheim, **2000**, pp. 154–162; b) K. Jähnisch, V. Hessel, H. Löwe, M. Baerns, *Angew. Chem.* **2004**, *116*, 410–451; *Angew. Chem. Int. Ed.* **2004**, *43*, 406–446; c) "Nanotiterplates for screening and synthesis": G. Mayer, K. Wohlfahrt, A. Schober, J. M. Köhler in *Microsystem Technology: A Powerful Tool for Biomolecular Studies in Biomethods* (Ed.: H. P. Saluz), Birkhäuser, Basel, **1999**, pp. 75–128; d) N. Schwesinger, O. Marufke, F. Qiao, R. Devant, H. Wurziger, *Process Miniaturization-IMRET 2: 2nd International Conference on Microreaction Technology. Topical Conference Reprints*, **1998**, New Orleans, p. 124; e) A. Schober, G. Schlingloff, G. Mayer, A. Groß, J. Albert, T. Henkel, H. Wurziger, *Microsyst. Technol.* **2004**, *10*, 281–292; f) E. Gottwald, A. Schober, *Eur. Pharm. Rev.* **2004**, *4*, 35–44.

[3] For recent examples of combinatorial microfluidics, see the special issue: *QSAR Comb. Sci.* **2005**, *24*, 699–767.

[4] a) P. Watts, S. J. Haswell, *Chem. Soc. Rev.* **2005**, *34*, 235–246; b) for instance see T. Kawaguchi, H. Miyata, K. Ataka, K. Mae, J. Yoshida, *Angew. Chem.* **2005**, *117*, 2465–2468; *Angew. Chem. Int. Ed.* **2005**, *44*, 2413–2416.

[5] a) A. Furka, F. Sebestyén, M. Asgedom, G. Dibó, *Int. J. Pept. Protein Res.* **1991**, *37*, 487–493; b) M. A. Gallop, R. W. Barrett, W. J. Dower, S. P. A. Fodor, E. M. Gordon, *J. Med. Chem.* **1994**, *37*, 1233–1251; c) E. M. Gordon, R. W. Barret, W. J. Dower, S. P. A. Fodor, M. A. Gallop, *J. Med. Chem.* **1994**, *37*, 1385–1401.

[6] J. R. Schullek, J. H. Butler, Z. -J. Ni, D. Chen, Z. Yuan, *Anal. Biochem.* **1997**, *246*, 20–29.

[7] S. P. A. Fodor, J. L. Read, M. C. Pirrung, L. Stryer, A. T. Lu, D. Solas, *Science* **1991**, *251*, 767–773.

[8] M. Meldal, C. B. Holm, G. Bojeson, M. H. Jacobsen, A. Holm, *Int. J. Pept. Protein Res.* **1993**, *41*, 250–260.

[9] R. Frank, *Tetrahedron* **1992**, *48*, 9217–9232.

[10] Sealing conditions were determined experimentally (data not shown); for details, see patent: B. Diefenbach, H. Deppe, H. Wurziger, A. Gross, G. Schlingloff, A. Schober, D. Tomandl (Merck), **2000**, WO 2001089680 [*Chem. Abstr.* **2001**, 868299].

[11] G. A. Groß, H. Wurziger, A. Schober, *J. Comb. Chem.* **2006**, *8*, 153–155.

 © 2006 Wiley-VCH Verlag GmbH & Co. KGaA, Weinheim

[12] For examples of solution-phase, polymer-supported, fluorous, and soluble-polymer-supported DHPM syntheses, see: C. O. Kappe, *QSAR Comb. Sci.* **2003**, *22*, 630–645 and references therein; for a discussion on soluble- versus insoluble-polymer-assisted synthesis, see: J. J. V. Eynde, O. Watte, *Arkivoc* **2003**, *4*, 93–101.
[13] G. A. Groß, H. Deppe, A. Schober, *Tetrahedron Lett.* **2003**, *44*, 3939–3942.
[14] An accuracy of 3% was determined by optical measurement of the filling level.

 © 2006 Wiley-VCH Verlag GmbH & Co. KGaA, Weinheim

Heterogeneous Catalysis

DOI: 10.1002/anie.200503799

Catalytic Carbon Oxidation Over Ruthenium-Based Catalysts**

*Kenneth Villani, Christine E. A. Kirschhock, Duoduo Liang, Gustaaf Van Tendeloo, and Johan A. Martens**

The redox chemistry of ruthenium has been exploited in many catalytic redox processes, for example in low-temperature carbon monoxide oxidation,[1,2] steam reforming of methane,[3,4] methanation of carbon monoxide,[5,6] Fisher–Tropsch synthesis,[7,8] and the water gas shift reaction.[9,10] Despite the high activity of ruthenium catalysts in oxidation reactions,[1,2,11–13] however, little research has been done on the possibility of using ruthenium catalysts for catalytic carbon oxidation.[14] We report here the exceptional activity of supported ruthenium metal in the oxidation of solid carbon in the presence of oxygen and water vapor. The finding is particularly relevant to the development of catalytically regenerated soot filters for the purification of diesel engine exhaust.

Diesel engines are prevalent power sources for vehicles owing to their efficiency, reliability, and durability, although they present the environmental drawback of soot and NO_x formation as combustion by-products. This calls for efficient exhaust gas treatment systems for diesel engines. A common approach for soot removal involves trapping of the particles on a filter,[15] although regeneration of these soot filters, and controlled oxidation of the trapped carbon in particular, is technically challenging. In principle, catalysts offer a means to control combustion and to decrease the light-off temperature. The use of a mobile catalyst has been investigated to achieve catalytic activity in the conversion of solid carbon.[16–19] The mobility of molten salts allows wetting and effective contacting of the carbon surfaces but also makes loss of catalyst from the filter probable and technically difficult to avoid.[18,19]

In the continuously regenerating particulate trap (CRT),[20–22] a platinum-based catalyst positioned upstream of the filter catalyses oxidation of NO to the more powerful oxidant NO_2. In this and similar catalytic concepts,[23] the NO_2 acts as an efficient mobile oxidizing agent that accesses the carbon particles and causes light-off to occur in an appropriate temperature range. The dependence of this technology on the presence of environmentally harmful NO_x molecules in the exhaust gas, however, limits its applicability. Technical developments of diesel engines strive to suppress raw NO_x emissions, which calls for a catalyst system that accelerates carbon oxidation in the absence of NO_x. Several catalyst formulations have been evaluated for the oxidation of carbon in the presence of oxygen,[24] but with limited success.

Carbon black was mixed with Na-Y zeolite loaded with ruthenium (Ru/Na-Y) or platinum (Pt/Na-Y). The weight loss of the carbon/catalyst mixture owing to carbon oxidation was determined in a thermogravimetric setup (Figure 1). Under conditions that are suitable for platinum-based catalysts (a gas stream with 500 ppm NO in addition to 10% O_2 and 5% water), ruthenium on Na-Y zeolite performs similarly to platinum on the same support (Figure 1, conditions a). The onset of carbon combustion, as indicated by the temperature at 10% carbon weight loss ($T10$), is reduced by more than 100 °C in the presence of these catalysts (Figure 1, curves c). Surprisingly, with the Ru/Na-Y catalyst omission of NO_x from the gas stream had hardly any influence on the carbon

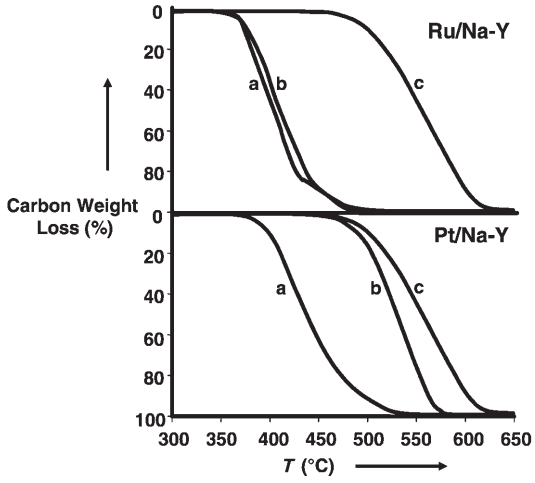

Figure 1. Carbon weight loss in the presence of Ru/Na-Y and Pt/Na-Y catalyst versus temperature. Gas composition: a) 500 ppm NO, 10% O_2, and 5% H_2O; b) 10% O_2 and 5% H_2O; c) 500 ppm NO, 10% O_2, and 5% H_2O without catalyst. Heating rate: 5 °C min^{-1}.

[*] K. Villani, Prof. C. E. A. Kirschhock, Prof. J. A. Martens
Centre for Surface Chemistry and Catalysis, K.U. Leuven
Kasteelpark Arenberg 23, 3001 Leuven (Belgium)
Fax: (+32) 1632-1998
E-mail: johan.martens@biw.kuleuven.be
D. Liang, Prof. G. Van Tendeloo
Centre for Electron Microscopy for Materials Science
University of Antwerp
Groenenborgerlaan 171, 2020 Antwerp (Belgium)

[**] This work was performed in the framework of the Comet project sponsored by the European Community. The authors appreciate their many useful discussions with their Comet partners. J.A.M. and C.E.A.K. acknowledge the Flemish government for a concerted research action (GOA) and the FWO for financing a collaboration project.

WILEY InterScience DISCOVER SOMETHING GREAT
© 2006 Wiley-VCH Verlag GmbH & Co. KGaA, Weinheim

oxidation temperatures, whereas such experimental conditions rendered the platinum catalyst almost inactive (Figure 1, conditions b). A carbon oxidation experiment in dry air revealed that the catalytic effect of Ru/Na-Y is only slightly dependent on the presence of water. Water tolerance of a ruthenium catalyst has previously been observed in the oxidation of CO by humid air at room temperature.[2]

The Ru/Na-Y catalyst used in the experiment of Figure 1 was prepared by ruthenium autoreduction under nitrogen at 500 °C. Pretreatment of the Ru-exchanged Na-Y zeolite under hydrogen at the same temperature resulted in a similar carbon oxidation performance. TEM investigations revealed the Ru metal to be finely dispersed, especially over the external surface of the zeolite particles (Figure 2 a). In view of

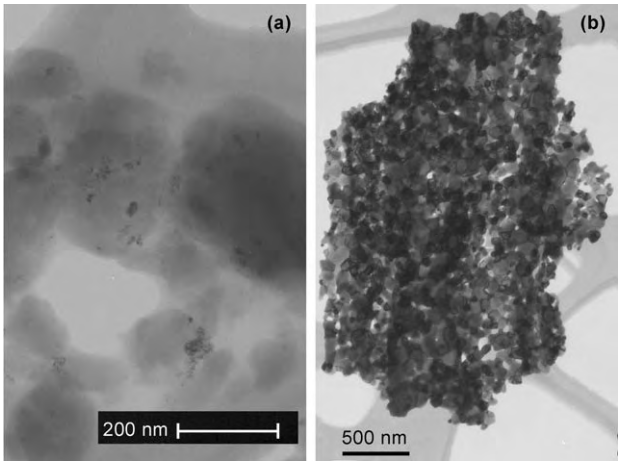

Figure 2. TEM images of Ru/Na-Y (a) and Ru nanopowder (b).

the literature on catalytic oxidation with ruthenium, it is unlikely that ruthenium metal surfaces are responsible for the observed carbon oxidation activity.[25] Using surface science approaches, Aßmann et al. have recently formulated a core–shell model to explain the catalytic activity of ruthenium particles in CO oxidation.[26] Active ruthenium particles have an ultrathin, 1–2 nm thick RuO_2 layer supported on a metallic ruthenium core. Under oxidizing conditions, the stability of these RuO_2/Ru core–shell particles is limited to temperatures below 375 °C, above which a transformation into less active, bulk RuO_2 occurs. The low-temperature part of our temperature-programmed carbon oxidation experiment provides suitable conditions for ruthenium surface oxidation.

To pinpoint the active state of ruthenium, the reduced Ru/Na-Y catalyst was exposed to dry air at temperatures between 300 and 500 °C and the phase composition determined by XRD and Rietveld refinement (Figure 3). Ruthenium is present as the metal and as a RuO_2 phase, and with increasing temperature the amount of RuO_2 increases at the expense of ruthenium metal. No change of the total Ru content of the samples was detected upon exposure to dry air at these temperatures. The transformation of Ru metal into RuO_2 is accompanied by a gradual decrease of the catalytic activity, as seen by an increase of $T10$ (Figure 4). Under the conditions of the carbon oxidation experiment, the catalytic activity is

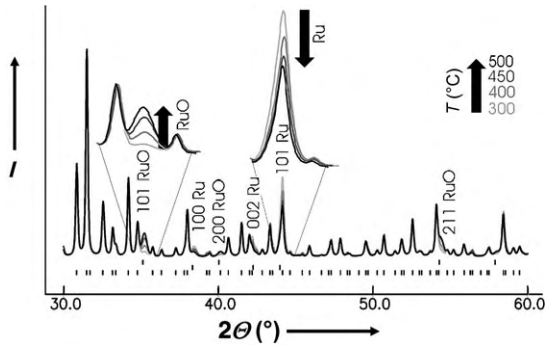

Figure 3. XRD patterns of Ru/Na-Y treated in dry air at temperatures between 300 and 500 °C.

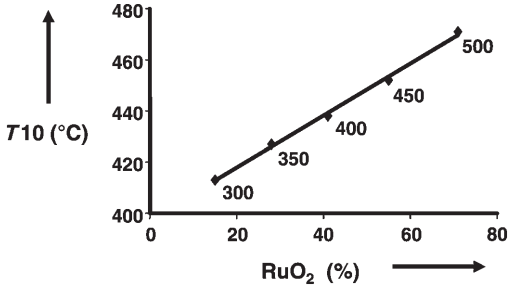

Figure 4. Temperature at 10% carbon oxidation versus percentage of ruthenium present as RuO_2 in the Ru/Na-Y catalyst pretreated at 300, 350, 400, 450, and 500 °C in dry air.

linked to the presence of ruthenium metal rather than bulk RuO_2: the RuO_2 particles and thick RuO_2 layers on Ru metal formed in dry air at these temperatures are catalytically inactive.[26]

After the carbon oxidation experiment of Figure 1 a, the ruthenium phase-composition of Ru/Na-Y, as determined by XRD, was 60% Ru metal and 40% RuO_2. When mixed with carbon and tested again, $T10$ was found to be 460 °C, which is much higher than with fresh, entirely reduced catalyst, which has a $T10$ value of 375 °C. The possibility of recovering maximum catalytic activity was therefore explored. Reducing the catalyst at 400 °C under hydrogen restored the initial activity as RuO_2 is quantitatively reduced to ruthenium metal under such conditions.[27] Surprisingly, the catalyst could also be regenerated by heating at 500 °C under nitrogen. The Ru/Na-Y catalyst maintained its performance over at least four carbon oxidation/catalyst regeneration cycles under nitrogen. The reused catalyst contained 38% RuO_2 and 62% Ru, similar to the catalyst used only once. After regeneration at 500 °C under nitrogen only Ru metal could be detected, thus indicating that residual carbon in the catalyst assumes the role of reducing agent in the regeneration procedure.

The carbon oxidation activity of Ru/Na-Y is related to the Ru content. Thus, the $T10$ values of Ru/Na-Y with Ru loadings of 0.3, 3, and 7.5 wt% are 396, 373, and 356 °C, respectively. The degree of dispersion of Ru in these samples is similar, which shows the importance of a Ru surface for the catalytic activity.

 © 2006 Wiley-VCH Verlag GmbH & Co. KGaA, Weinheim

To optimize the supported ruthenium catalyst, various ruthenium precursors and support materials were tested. The nature of the Ru compound ($RuCl_3$, $[Ru(NH_3)_6Cl_3]$, ruthenium red, $[Ru(NO)(NO_3)_3]$) used in the catalyst preparation did not make a marked difference.

Ruthenium catalysts were prepared using a variety of zeolite supports and alumina and evaluated as catalysts. All catalysts were active. The observed *T*10 order was:

$$\begin{aligned} &\text{Ru/AlPO-11 (350}^{o}\text{C)} < \text{Ru/Na-Y (375}^{o}\text{C)} \\ &< \text{Ru/ferrierite (380}^{o}\text{C)} < \text{Ru/Al}_2\text{O}_3\text{ (415}^{o}\text{C)} \end{aligned} \quad (1)$$

The low *T10* values obtained with the zeolites can be related to the significant external surface areas of these materials (22, 10, and 6 $m^2 g^{-1}$ for AlPO-11, ferrierite, and Na-Y zeolite, respectively).

The catalytic activity of ruthenium metal nanoparticles was evaluated as follows. $RuCl_3$ powder was pretreated at 500 °C under nitrogen—XRD confirmed the transformation of the ruthenium chloride into Ru metal—to give an aggregated nanopowder with a particle size of about 50 nm, according to TEM (Figure 2b). An amount of Ru nanopowder equivalent to the amount of Ru used in the experiments with supported catalysts was mixed with carbon and its catalytic activity evaluated. The *T*10 value was 385 °C, which is in the range of temperatures obtained with the supported ruthenium catalysts [Eq. (1)], thereby revealing that Ru metal nanoparticles are responsible for the catalytic activity. AlPO-11, with its narrow pores of 0.63×0.39 nm^2, has the capacity to sustain free radical autoxidation catalysis better than wider-pore zeolites, such as Na-Y, or mesoporous supports, such as alumina, as demonstrated in cyclohexane autoxidation.[28]

Na-Y-supported iridium, palladium, platinum, and rhodium metals were also screened for carbon oxidation activity; none of them proved to be better than ruthenium. In the absence of a physical contact between carbon and catalyst, the ruthenium surface is most likely a generator of active oxygen species that then migrate to the carbon surface. Oxygen chemisorption on under-coordinated Ru atoms of oxidized ruthenium metal surfaces generates weakly bonded atomic oxygen with an unusually high chemical reactivity.[29,30] Furthermore, ruthenium surfaces have the capacity to homolytically dissociate water molecules.[31]

Higher oxides of ruthenium formed at elevated temperatures are volatile and toxic.[32] The volatilization of ruthenium upon exposing reduced Ru/Na-Y to dry air was evaluated by thermogravimetric analysis (Figure 5). The weight increase starting around 400 °C of about 500 μg for an initial catalyst weight of about 49 mg corresponds to that (460 μg) theoretically required for stoichiometric conversion of Ru metal into RuO_2. The weight loss ascribed to ruthenium volatilization sets in around 900 °C. This temperature is the upper limit in practical applications of ruthenium catalysts.

In conclusion, we have discovered that zeolite-supported ruthenium catalyzes carbon oxidation in the absence of NO_x at temperatures where platinum catalysts require the presence of NO_x in the gas stream. In oxidizing gas, there is a progressive conversion of Ru into bulk RuO_2, which causes deactivation of the catalyst and necessitates a reactivation through reductive treatment. In a practical application in a diesel particulate filter, ruthenium reduction could be realized using hydrogen from on-board reforming of diesel fuel or by generating lambda spikes, which nowadays can be realized in diesel engines.[33]

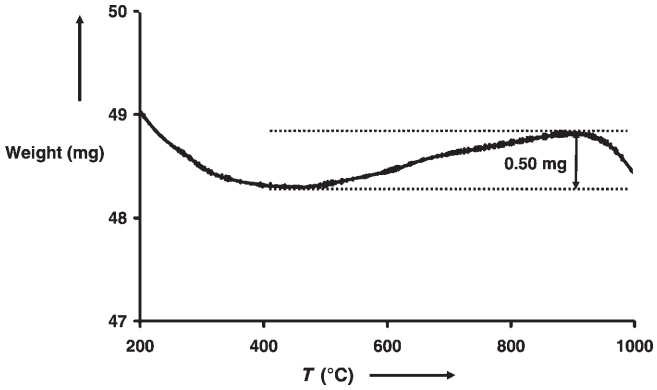

Figure 5. Thermogravimetric analysis of Ru/Na-Y in dry air. Heating rate: 5 °C min^{-1}.

Experimental Section

The supports used for ruthenium were Na-Y zeolite (Zeocat, Si/Al = 2.7), AlPO-11 (synthesized according to the literature[34]), ferrierite (TSZ-710, Toyo Soda, Si/Al = 8.4), and alumina (A-201, La Roche). Supports were loaded with 3 wt% ruthenium by making a slurry of the support powder in an aqueous ammonia solution of $RuCl_3$ (Alfa Aesar) at 80 °C and pH 8.5. The catalyst powder was filtered, washed with deionized water, and dried at 60 °C. Platinum (0.5 wt%) was loaded on Na-Y by the incipient wetness impregnation method using an aqueous solution of $[Pt(NH_3)_4Cl_2]\cdot H_2O$ (Alfa Aesar). The catalyst powder was pelletized by compression into particles (0.25–0.50 mm) for pretreatment in a fixed bed. The ruthenium catalyst was pretreated by heating under nitrogen at 500 °C for 2 h. The platinum catalyst was oxidized at 400 °C under oxygen and reduced under hydrogen at the same temperature after intermittent cooling. The pretreated catalyst was ground manually in a mortar. Carbon black (Degussa AG Printex-U) and the catalyst were carefully mixed with a spatula to obtain realistic contact conditions.[35] An aliquot of ethanol was added to obtain a paste, which was dried at 60 °C for 2 h and then crushed. The catalyst:carbon ratio was 2:1 by weight. Carbon oxidation was performed in a Magnetic Suspension Balance (Rubotherm) with 270 mg of the catalyst/carbon mixture. The gas flow rate was 150 mL min^{-1} and the heating rate 5 °C min^{-1}. The temperature was recorded with a thermocouple positioned in the immediate vicinity of the catalyst/carbon mixture. X-ray diffraction was performed with a STOE Stadi P instrument in transmission mode using $Cu_{K\alpha}$ radiation. TEM images were recorded with a Philips CM20 electron microscope equipped with an Oxford EDX attachment, operating at 200 kV.

Received: October 27, 2005
Revised: February 15, 2006
Published online: March 30, 2006

Keywords: carbon · oxidation · ruthenium · supported catalysts

 © 2006 Wiley-VCH Verlag GmbH & Co. KGaA, Weinheim

[1] J. Aßmann, V. Narkhede, L. Khodeir, E. Löffler, O. Hinrichsen, A. Birkner, H. Over, M. Muhler, *J. Phys. Chem. B* **2004**, *108*, 14634.
[2] L. Zang, H. Kisch, *Angew. Chem.* **2000**, *112*, 4075; *Angew. Chem. Int. Ed.* **2000**, *39*, 3921.
[3] L. S. Lobo, D. L. Trimm, J. L. Figueiredo, *Proceedings of the Fifth International Congress on Catalysis*, Palm Beach, **1972**, Vol. 2, North Holland, Amsterdam, **1973**, p. 1125.
[4] J. R. Rostrup-Nielsen, J.-H. Hansen, *J. Catal.* **1993**, *144*, 38.
[5] R. A. Dalla Betta, A. G. Piken, M. Shelef, *J. Catal.* **1974**, *35*, 54.
[6] P. A. Jacobs, H. H. Nijs, J. B. Uytterhoeven, *Prepr. Div. Petrol. Chem. Am. Chem. Soc.* **1978**, *23*, 469.
[7] H. H. Nijs, P. A. Jacobs, J. B. Uytterhoeven, *J. Chem. Soc. Chem. Commun.* **1979**, 180.
[8] P. C. Das, N. C. Pradhan, A. K. Dalai, K. A. Dalai, N. N. Bakhshi, *Fuel Process. Technol.* **2004**, *85*, 1487.
[9] J. Verdonck, P. A. Jacobs, J. B. Uytterhoeven, *J. Chem. Soc. Chem. Commun.* **1979**, 181.
[10] A. Basińska, W. Jóźwiak, J. Góralski, F. Domka, *Appl. Catal. A* **2000**, *190*, 107.
[11] J. Aßmann, E. Löffler, A. Birkner, M. Muhler, *Catal. Today* **2003**, *85*, 235.
[12] I. Balint, A. Miyazaki, K. Aika, *J. Catal.* **2003**, *220*, 74.
[13] P. V. Snytnikov, V. A. Sobyanin, V. D. Belyaev, P. G. Tsyrulnikov, N. B. Shitova, D. A. Shlyapin, *Appl. Catal. A* **2003**, *239*, 149.
[14] W. S. Rahayu, L. Monceaux, B. Taouk, P. Courtine, *Stud. Surf. Sci. Catal.* **1995**, *96*, 563.
[15] J. P. A. Neeft, M. Makkee, J. A. Moulijn, *Fuel Process. Technol.* **1996**, *47*, 1.
[16] D. W. McKee, *Carbon* **1997**, *35*, 587.
[17] G. Mul, J. P. A. Neeft, F. Kapeteijn, M. Makkee, J. A. Moulijn, *Appl. Catal. B* **1995**, *6*, 339.
[18] B. A. A. L. Van Setten, S. J. Jelles, M. Makkee, J. A. Moulijn, *Appl. Catal. B* **1999**, *21*, 35.
[19] B. A. A. L. Van Setten, R. van Dijk, S. J. Jelles, M. Makkee, J. A. Moulijn, *Appl. Catal. B* **1999**, *21*, 51.
[20] B. J. Cooper, J. E. Thoss, *SAE Paper 890404*, **1989**.
[21] P. N. Hawker, *Platinum Met. Rev.* **1995**, *39*, 2.
[22] P. Hawker, N. Myers, G. Hüthwohl, H. T. Vogel, B. Bates, L. Magnusson, P. Bronnenberg, *SAE Paper 970182*, **1997**.
[23] C. Görsmann, *Monatsh. Chem.* **2005**, *136*, 91.
[24] B. A. A. L. Van Setten, M. Makkee, J. A. Moulijn, *Catal. Rev. Sci. Eng.* **2001**, *43*, 489.
[25] C. H. F. Peden, D. W. Goodman, *J. Phys. Chem.* **1986**, *90*, 1360.
[26] J. Aßmann, D. Crihan, M. Knapp, E. Lundgren, E. Löffler, M. Muhler, V. Narkhede, H. Over, M. Schmid, A. P. Seitsonen, P. Varga, *Angew. Chem.* **2005**, *117*, 939; *Angew. Chem. Int. Ed.* **2005**, *44*, 917.
[27] R. Ryoo, S. J. Cho, C. Pak, J.-G. Kim, S.-K. Ihm, J. Y. Lee, *J. Am. Chem. Soc.* **1992**, *114*, 76.
[28] D. L. Vanoppen, D. De Vos, M. J. Genet, P. G. Rouxhet, P. A. Jacobs, *Angew. Chem.* **1995**, *107*, 637; *Angew. Chem. Int. Ed. Engl.* **1995**, *34*, 560.
[29] H. Madhavaram, H. Idriss, S. Wendt, Y. D. Kim, M. Knapp, H. Over, J. Aßmann, E. Löffler, M. Muhler, *J. Catal.* **2001**, *202*, 296.
[30] H. Over, *Appl. Phys. A* **2002**, *75*, 37.
[31] K. Andersson, A. Nikitin, L. G. M. Pettersson, A. Nilsson, H. Ogasawara, *Phys. Rev. Lett.* **2004**, *93*, 196101.
[32] E. A. Seddon, K. R. Seddon, *The Chemistry of Ruthenium*, Elsevier, Amsterdam, **1984**.
[33] A. Tsolakis, A. Megaritis, M. L. Wyszynski, *Fuel* **2004**, *83*, 1837.
[34] S. T. Wilson, B. M. Lok, C. A. Messina, T. R. Cannan, E. M. Flannigen, *J. Am. Chem. Soc.* **1982**, *104*, 1146.
[35] B. A. A. L. van Setten, J. M. Schouten, M. Makkee, J. A. Moulijn, *Appl. Catal. B* **2000**, *28*, 253.

 © 2006 Wiley-VCH Verlag GmbH & Co. KGaA, Weinheim

Asymmetric Synthesis

DOI: 10.1002/anie.200504421

Asymmetric Allylic Alkylation of Cyclic Vinylogous Esters and Thioesters by Pd-Catalyzed Decarboxylation of Enol Carbonate and β-Ketoester Substrates**

Barry M. Trost, Robert N. Bream, and Jiayi Xu*

β-Alkoxy α,β-unsaturated ketones are versatile synthons for organic synthesis, as they serve as masked 1,3-dicarbonyl compounds in which the two ketone groups and adjacent carbon atoms may be selectively functionalized. Polysubstituted cyclic vinylogous esters are particularly useful for the synthesis of terpene, alkaloid, and steroidal natural products;[1] a practical method for their synthesis in enantioenriched form is therefore eminently desirable. The catalytic enantiomeric protocol to synthesize enones, such as **3**, was reported recently by Fuchs and co-workers, but was limited to monosubstituted enones ($R^2 = H$), and the relatively harsh conditions may further limit the access to highly functionalized enones.[2] Our strategy aimed to take advantage of an asymmetric allylic alkylation (AAA)/Stork–Danheiser addition sequence to furnish γ,γ-disubstituted cycloalkenones **3** [Eq. (1)].[3]

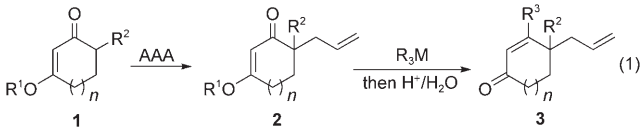

We initially attempted to access **2** with our previously reported method by alkylating the kinetically generated enolate of **1** with a combination of Pd^0, methyl allyl carbonate, and a chiral bidentate phosphine ligand.[4] The use of lithium diisopropyl amide (LDA) as the base (Li is essential for regiospecific enolate formation and alkylation) allowed quantitative formation of allylated products. However, we could not improve enantioselectivity beyond 30%. We there-

[*] Prof. Dr. B. M. Trost, Dr. R. N. Bream, J. Xu
Department of Chemistry
Stanford University
Stanford, CA 94305-5080 (USA)
Fax: (+1) 650-725-0002
E-mail: bmtrost@stanford.edu

[**] We thank the National Science Foundation and the National Institutes of Health, General Medical Sciences (Grant GM13598) for their generous support. J.X. was supported by Abbott Laboratories Fellowships. Mass spectra were provided by the Mass Spectrometry Regional Center of the University of California—San Francisco supported by the NIH Division of Research Resources. We thank Chirotech (now Dow) for their generous gifts of ligands and Johnson Matthey for gifts of Pd salts.

Supporting information for this article is available on the WWW under http://www.angewandte.org or from the author.

© 2006 Wiley-VCH Verlag GmbH & Co. KGaA, Weinheim

fore set about investigating an asymmetric variant of the Tsuji protocol for allylation, pioneered by Muzart and co-workers[5] and developed recently by us and others.[6] This strategy requires the preliminary synthesis of either allyl β-ketoesters or allyl enol carbonates of ketone **1**. Whereas efforts to synthesize the desired enol carbonates **4** gave only by-product **6** [Eq. (2); HMDS = hexamethyldisilazane, TMEDA = *N*,*N*,*N*',*N*'-tetramethyl-1,2-ethanediamine] or a low yield of **4** [Eq. (3); R^1 = Bn], the related β-ketoesters were available in excellent yields [Eq. (4)]. We then submitted these substrates to our decarboxylative alkylation conditions and were delighted to see product formation with excellent enantiomeric excess. Enol carbonate **4** was completely converted into the product. However, the conversion of the β-ketoesters was much worse, reflecting the additional energy

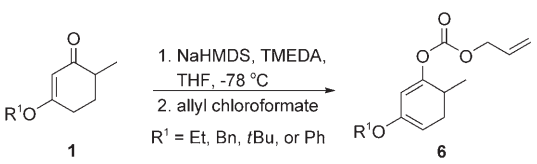

(2)

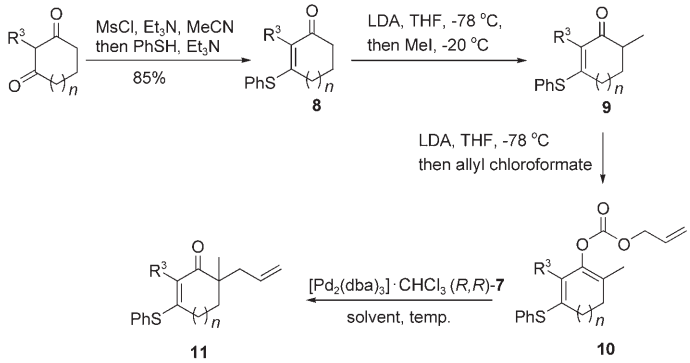

Scheme 1. The preparation of allyl carbonate **10** and the Pd-catalyzed asymmetric Tsuji reaction.

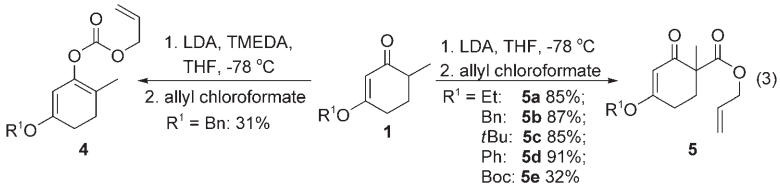

(3)

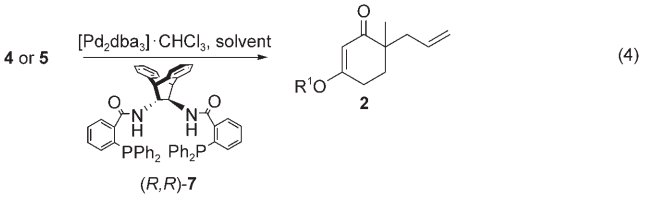

(4)

required to break a C–C bond in the decarboxylation step. This effect is exacerbated by the π-donating ability of the ether oxygen atom (Table 1, entries 2 and 4). Heating the reaction or addition of oxophilic Lewis acids failed to improve the conversion.[7] *O*-*tert*-Butyloxycarbonyl (Boc) and *O*-phenyl derivatives (Table 1, entries 5 and 6), in which the electron-donating power of the oxygen atom is attenuated,

Table 1: The optimized results for the reaction of **4** or **5**.[a]

Entry	Substrate	Solvent	Yield [%][b]	*ee* [%][c]
1	**4**	toluene	87	85
2	**5a**	1,4-dioxane	26	94
3	**5b**	THF	51	91
4	**5c**	1,4-dioxane	29	97
5	**5d**	1,4-dioxane	70	96
6	**5e**	THF	66	94

[a] All reactions were performed on a 0.1-mmol scale at 0.1 M at 23 °C overnight with 2.5 mol% of $[Pd_2dba_3]\cdot CHCl_3$ and 6 mol% of ligand. [b] Yield of the isolated products. [c] The *ee* values were determined by chiral HPLC on Chiralcel columns.

gave better conversions, although the synthesis of these substrates was achieved in much lower yield.

We reasoned that the poorer orbital overlap between sulfur and carbon would make the β-ketoesters or enol carbonates of vinylogous thioethers more reactive substrates. The generation of **9** proceeded as expected (Scheme 1).[8]

Surprisingly, the attempted formation of the β-ketoesters under the previously optimized conditions [Eq. (3)] predominantly afforded the allyl enol carbonates **10** instead. These proved to be excellent substrates for the allylation reaction (Table 2). Dioxane or THF at lower temperature were superior to other solvents for this reaction, an observation consistent with tight ion pairs as intermediates. Allylated products **11** containing five-, six-, and seven-membered rings are produced in excellent yield and enantioselectivity. Substitution at the 2-position is tolerated as well (Table 2, entries 2–4): the vinyl bromide is particularly useful for further functionalization. Remarkably, disubstitution at the 5-position is also tolerated (Table 2, entry 5), thus allowing the formation of adjacent quaternary centers in good enantiomeric excess.

The related β-ketoesters were also available through a slightly modified route. Accordingly, the enolization of **8** with two equivalents of LDA in toluene at −78 °C followed by the addition of allyl chloroformate yielded β-ketoester **12** as the major product in 75% yield of the isolated product. Alkyla-

Table 2: The reaction of various allyl enol carbonates.[a]

Entry	*n*	R^3	R^4	Solvent	*T* [°C][b]	Yield [%][c]	*ee* [%][d]
1	1	H	H	THF	−20	100	98
2	1	CH_3	H	THF	0–4	100	99
3	1	Br	H	dioxane	23	97	86
4	1	Ph	H	dioxane	23	100	97
5	1	H	Me_2	THF	0–4	91	79
6	2	H	H	THF	0–4	100	94
7	0	Me	H	THF	0–4	96	80

[a] All reactions were performed on a 0.1-mmol scale at 0.1 M overnight with 2.5 mol% of $[Pd_2dba_3]\cdot CHCl_3$ and 6 mol% of ligand. [b] Optimized temperature for the best *ee* value and conversion. [c] Yield of the isolated products. [d] The *ee* values were determined by chiral HPLC on Chiralcel columns.

 © 2006 Wiley-VCH Verlag GmbH & Co. KGaA, Weinheim

tion by either S_N2 substitution or conjugate addition gave **13** in excellent yields (Scheme 2). These compounds were also excellent substrates for the decarboxylative alkylation reaction and products were formed in excellent yields and with generally excellent enantioselectivities (Table 3). The reaction tolerates a wide range of functionalities at R^2. We believe the reaction to proceed through an inner-sphere mechanism, in which the final bond-forming event occurs by reductive elimination of a Pd-bound enolate and π-allyl moiety.[6c,f] The successful reaction given in entry 15 lends further credence to this theory: the free enolate would undoubtedly deprotonate the tethered malonate, which could then be alkylated. We suggest that coordination of the side-chain functionality (Table 3, entry 5: C≡C; entries 8, 11, and 15: C=O) disrupts the transition state of the enantiorecognition step, thus resulting in the lower observed *ee* values (Scheme 3). Shorter (Table 3, entries 9 and 10) or longer (Table 3, entry 12) tethers to the coordinating group or increased steric congestion (Table 3, entry 6) disfavor this interaction and the *ee* values of the products return to ≥90%.

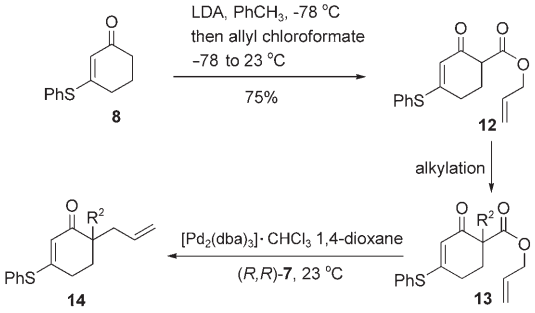

Scheme 2. The preparation of vinylogous thioester **13** and the Pd-catalyzed asymmetric Tsuji reaction.

Table 3: The reaction of various β-ketoesters **13** and **14**.[a]

Entry	R^2	*T* [h]	Yield [%][b]	*ee* [%][c]
1	CH_3	16	75	100
2	CH_2Ph	16	78	92
3	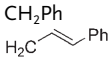	2	98	95
4		16	84	91
5		4	83	72
6		1	89	91
7	CH_2CH_2CN	0.5	98	83
8	$CH_2CH_2C(O)CH_3$	6	75	57
9	$CH_2C(O)CH_3$	2	97	85
10	CH_2CO_2Et	1	80	92
11	$CH_2CH_2CO_2Et$	4	90	73
12	$CH_2(CH_2)_2CO_2Et$	2	86	94
13	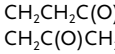	0.5	87	95
14	$CH_2(CH_2)_2OBn$	16	65	93
15	$CH_2CH(CO_2tBu)_2$	2	97	36

[a] All reactions were performed on a 0.2-mmol scale at 0.1 M in 1,4-dioxane at 23 °C with 2.5 mol% of $[Pd_2dba_3]\cdot CHCl_3$ and 5.5 mol% of ligand. [b] Yield of the isolated products. [c] The *ee* values were determined by chiral HPLC on Chiralcel columns. TMS = trimethylsilyl.

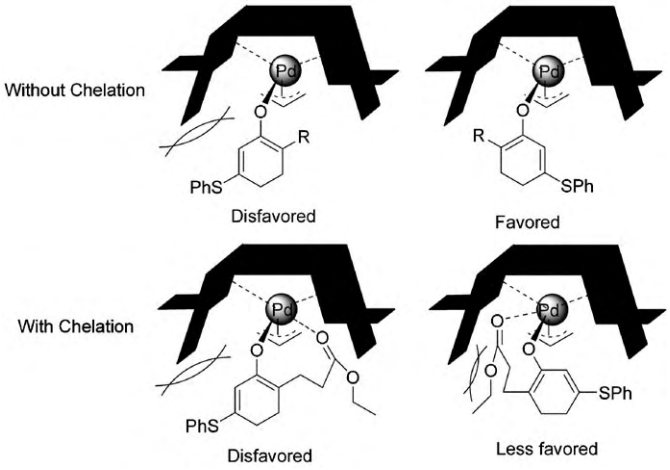

Scheme 3. Schematic representation of the mechanism of the enantiorecognition step with or without chelation.

The synthetic utility of the alkylated products was briefly investigated (Schemes 4 and 5). The addition of alkyllithium reagents[9] or diisobutylaluminium hydride (DIBAL-H) occurs selectively in a 1,2-fashion to afford γ,γ-disubstituted cyclohexenones on aqueous acidic work up. Conversion into the corresponding vinylogous methyl ester occurs readily on treatment with sodium methoxide in refluxing methanol,[10] to which Grignard reagents may be added directly. Along these lines, **14** was manipulated to afford known compounds **15** and **20**.[11] Comparison of optical rotation allowed us to assign the absolute stereochemistry of **14** as *R*, which is consistent with our previous results.[6c]

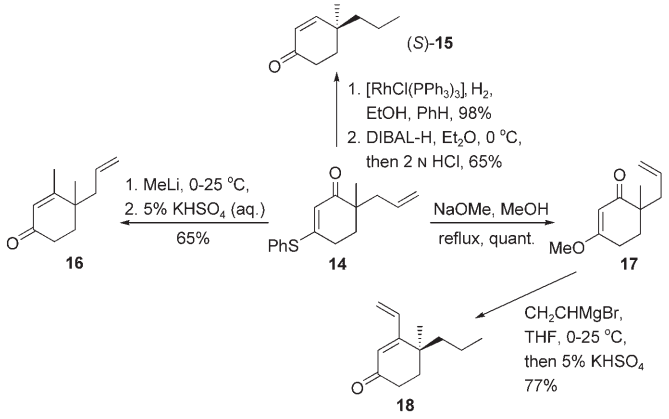

Scheme 4. Transformations of **14** to γ,γ-disubstituted cyclohexenones.

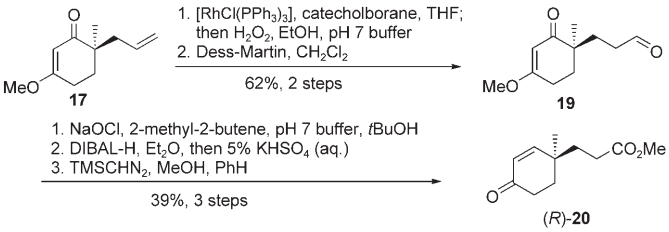

Scheme 5. Confirmation of the configuration of **17**.

 © 2006 Wiley-VCH Verlag GmbH & Co. KGaA, Weinheim

In summary we have achieved the palladium-catalyzed asymmetric allylic alkylation of vinylogous thioesters in excellent yield and enantiomeric excess under neutral conditions. Both allyl enol carbonates and allyl β-ketoesters are competent substrates. However, the β-ketoesters react more sluggishly and therefore show a greater dependency on the choice of the 3-heteroatom substituent, to which the difference in the rate of decarboxylation is attributed. These compounds are readily transformed into γ,γ-disubstituted cycloalkenones, the utility of which will be demonstrated in synthetic endeavors in due course.

Experimental Section

Typical experimental procedures for the reaction of **13**: Two oven-dried test tubes were connected with a double-ended needle. One test tube was loaded with $[Pd_2(dba)_3]\cdot CHCl_3$ (dba = dibenzylideneacetone; 5.2 mg, 0.005 mmol) and (*R*,*R*)-**7** (9.2 mg, 0.011 mmol), and the other tube was loaded with **13** ($R^2 = CH_3$; 0.20 mmol, 60.5 mg). The system was evacuated and flushed with argon three times, at which point dry degassed 1,4-dioxane (1.0 mL) was added to both of the test tubes. After being stirred for 20 min, the orange catalyst solution was transferred into the test tube containing the substrate. The color of the reaction solution turned to light yellow within a few minutes and then back to orange, thus indicating the completion of the reaction. The reaction mixture was concentrated in vacuo and purified by column chromatography on silica gel eluted with diethyl ether/petroleum ether (30:70, v/v) to afford **14** as a colorless oil (39 mg, 75 %).

Received: December 13, 2005
Published online: April 5, 2006

Keywords: alkylation · asymmetric catalysis · ketones · palladium

[1] a) M. G. Banwell, D. W. Lupton, *Org. Biomol. Chem.* **2005**, *3*, 213 – 215; b) H. Liu, J. Zhu, I. Chen, R. Jankowska, Y, Han, K. Shia, *Angew. Chem.* **2003**, *115*, 1895 – 1897; *Angew. Chem. Int. Ed.* **2003**, *42*, 1851 – 1853; c) M. Toyata, M. Sasaki, M, Ihara, *Org. Lett.* **2003**, *5*, 1193 – 1195; d) J. Wu, K. Shia, H. Liu, *Tetrahedron Lett.* **2001**, *42*, 4207 – 4209; e) D. Desmaële, J. d'Angelo, *J. Org. Chem.* **1994**, *59*, 2292 – 2303; f) A. I. Meyers, D. Berne, *J. Org. Chem.* **1989**, *54*, 4673 – 4676.

[2] J. Evarts, E. Torres, P. L. Fuchs, *J. Am. Chem. Soc.* **2002**, *124*, 11093 – 11101.

[3] G. Stork, R. L. Danheiser, *J. Org. Chem.* **1973**, *38*, 1775 – 1776.

[4] B. M. Trost, G. M. Schroeder, *J. Am. Chem. Soc.* **1999**, *121*, 6759 – 6760.

[5] a) F. Hénin, J. Muzart, *Tetrahedron: Asymmetry* **1992**, *3*, 1161 – 1164; b) S. J. Aboulhoda, F. Hénin, J. Muzart, C. Thorey, *Tetrahedron: Asymmetry* **1994**, *5*, 1321 – 1326.

[6] a) E. C. Burger, J. A. Tunge, *Org. Lett.* **2004**, *6*, 4113 – 4115; b) D. C. Behenna, B. M. Stoltz, *J. Am. Chem. Soc.* **2004**, *126*, 15044 – 15045; c) B. M. Trost, J. Xu, *J. Am. Chem. Soc.* **2005**, *127*, 2846 – 2847; d) J. T. Mohr, D. C. Behenna, A. M. Harned, B. M. Stoltz, *Angew. Chem.* **2005**, *117*, 7084 – 7087; *Angew. Chem. Int. Ed.* **2005**, *44*, 6824 – 6927; e) M. Nakamura, A. Hajra, K. Endo, E. Nakamura, *Angew. Chem.* **2005**, *117*, 7414 – 7417; *Angew. Chem. Int. Ed.* **2005**, *44*, 7248 – 7251; f) B. M. Trost, J. Xu, *J. Am. Chem. Soc.* **2005**, *127*, 17180 – 17181; g) J. A. Tunge, E. C. Burger, *Eur. J. Org. Chem.* **2005**, *9*, 1715 – 1726.

[7] $[In(OTf)_3]$ (OTf = trifluoromethanesulfonate), $[Sc(OTf)_3]$, $[Ho(OTf)_3]$, BEt_3, and $B(OMe)_3$ have been investigated.

[8] a) J. B. Hendrichson, M. A. Walker, *Org. Lett.* **2000**, *2*, 2729 – 2731; b) B. M. Trost, P. Seoane, S. Mignani, M. Acemoglu, *J. Am. Chem. Soc.* **1989**, *111*, 7487 – 7500.

[9] Grignard reagents give a mixture of 1,2- and 1,4-addition products.

[10] T. H. Chan, C. V. C. Prasad, *J. Org. Chem.* **1987**, *52*, 110.

[11] a) S. Yamada, G. Otani, *Tetrahedron Lett.* **1969**, *10*, 4237 – 4240; b) G. Otani, S. Yamada, *Chem. Pharm. Bull.* **1973**, *21*, 2125 – 2129; c) D. I. Schuster, R. H. Brown, B. M. Resnick, *J. Am. Chem. Soc.* **1978**, *100*, 4504 – 4512.

 © 2006 Wiley-VCH Verlag GmbH & Co. KGaA, Weinheim

Noncovalent Interactions

DOI: 10.1002/anie.200504474

Confined Synthesis of a *cis*-Isotactic Ladder Polysilsesquioxane by Using a π-Stacking and H-Bonding Superstructure**

Xiaojing Zhang, Ping Xie, Zhongrong Shen, Jinqiang Jiang, Chuanfeng Zhu, Huihui Li, Taoyi Zhang, Charles C. Han, Lijun Wan, Shouke Yan,* and Rongben Zhang**

Ladder polymers are of particular interest in the field of advanced materials because of their incontestable superiority in terms of their thermo- or radiation-resistant and mechan-

[*] X. Zhang, Prof. P. Xie, Z. Shen, Dr. J. Jiang, Dr. H. Li, Dr. T. Zhang, Prof. C. C. Han, Prof. S. Yan, Prof. R. Zhang
State Key Laboratory of Polymer Physics and Chemistry
The Joint Laboratory of Polymer Sciences and Materials
Institute of Chemistry
Chinese Academy of Sciences
Beijing 100080 (China)
Fax: (+86) 10-6255-9373
E-mail: skyan@iccas.ac.cn
zhangrb@iccas.ac.cn

X. Zhang
Graduate School of the Chinese Academy of Sciences
Beijing 100039 (China)

Prof. C. Zhu, Prof. L. Wan
State Key Laboratory of Molecular Nanostructure and Nanotechnology
Institute of Chemistry
Chinese Academy of Science
Beijing 100080 (China)

[**] This project was supported by the National Nature Science Foundation of China (Nos. 20174047, 20204016, 50273043, 29974036, 50073028), the Outstanding Youth Fund (No. 20425414), the National Center for Nanoscience and Technology, China, the Polymer Chemistry Laboratory, Chinese Academy of Sciences, and the China Petrochemical Corporation. We would like to express our gratitude to Prof. Y. Wang and Prof. G. Xu for their valuable help in proof-reading the manuscript and for discussions.

Supporting information for this article is available on the WWW under http://www.angewandte.org or from the author.

WILEY InterScience DISCOVER SOMETHING GREAT
© 2006 Wiley-VCH Verlag GmbH & Co. KGaA, Weinheim

ical properties.[1] The preparation of a perfect stereoselective ladder polysilsesquioxane (LPS) has been a particularly tantalizing target of polymer scientists for over four decades since Brown et al.[2] first reported the synthesis of a soluble high-molecular-weight ladder polyphenylsilsesquioxane (PPSQ) by "equilibration polycondensation". However, its structure was disputed later by Frye and Klosowski,[3] who concluded that PPSQ was not a real ladder polymer, but actually "partially opened polycyclic cages". In fact, the structure of polysilsesquioxanes depends a great deal on the methods used for their preparation. As Bailey pointed out,[1] there are many problems in making a perfect ladder polymer, such as insolubility, reversible cross-linking reactions, and statistical considerations. As far as we know, only a few real ladder oligomers, such as a Diels–Alder carbocyclic oligomer, a carbocyclic oligomer, and a pentacyclic ladder siloxane have been synthesized.[1,4] Theoretically, the most desirable pattern of reaction for the formation of a perfect ladder is one in which both sides of the ladder are either formed simultaneously or no reaction occurs.[1] Accordingly, we proposed a supramolecular template strategy, by which a series of ordered organo-bridged ladder polysiloxanes (OLPSs) have been successfully prepared in recent years.[5–8] However, the perfect LPS has not yet been prepared because of the absence of an efficient template to control the synthetic mechanism. As Brook stated, ladder polysiloxanes may result under certain conditions (namely, a bioprocess).[9]

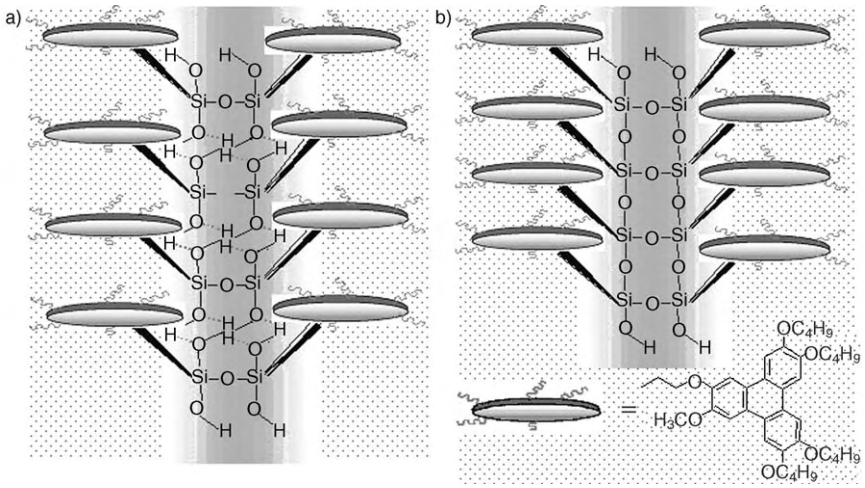

Figure 1. Schematic representation for the confined polycondensation of the monomer **3** in ladder structure **5** (a) to form the covalent ladder polymer **6** (b).

Here we report a confined synthesis method by using a supramolecular approach, which is based on the self-organization of α,ω-di(triphenylenetetrahydroxy)disiloxane (**4**) by concerted π-π stacking and H bonding to yield a ladder superstructure (LS). A soluble, high-molecular-weight triphenylene-containing ladder polymer (LP) is then formed by dehydration condensation to realise the aforementioned long-awaited target. In contrast to the general method to achieve spatially confined polymerization,[10,11] it is the first time a self-assembled "supramolecular channel" has been employed to direct the ordered polycondensation of multifunctional monomers. This is in fact an advanced step in the field of supramolecular template-directed polymerization.[12–16] We also present an efficient way to control the configuration of condensation polymers derived from achiral monomers. Moreover, the ladder polymer with densely stacked discotic side groups can be potentially used as a functional nanowire.

Interestingly, this method is based on the knowledge that electron-rich disclike triphenylene units tend to self-assemble into hydrophobic columns through π-π stacking, and that hydrophilic silanol groups tend to associate through H-bonding interactions.[17] Hence, the two kinds of interactions could act in a cooperative manner to form a channel (Figure 1 a), while the hydrolyte (**4**) of the monomer (**3**) would be readily self-assembled into the LS. Condensation of the silanol groups entrapped within the channel would then be dictated by the H-bonding wire. As a result, the high-molecular-weight LP shown in Figure 1 b would be generated under conditions that ensure the formation of a stable LS. Moreover, the interactions between the π-conjugated discotic side groups of adjacent ladder rungs make them arrange in a *cis*-isotactic configuration.

A synthetic route to the LP is shown in Scheme 1. A key factor in the molecular design of the momomer (**3**) has been emphasized: according to molecular simulation, the length of the Si-O-Si segment along the ladder chain should just match the intercore distances (which range from 3.5 to 4.0 Å) in a typical columnar structure assembled with discotic triphenylene units. The obtained LP (**6**) is a brown solid and has high solubility in common solvents such as *n*-hexane, toluene, tetrahydrofuran (THF), and chloroform, but is insoluble in highly polar solvents such as acetonitrile and ethanol. The molecular weight ($M_w = 8.2 \times 10^5$) of the polymer was determined by static light scattering (SLS) studies in THF solution. The dependence of the intrinsic viscosity $[\eta]$ on molecular weight is given by the expression $[\eta] = 2.25 \times 10^{-6} M^{1.24}$.[18] The higher value of the conformation index $\alpha = 1.24$ compared with that of general flexible polymers ($\alpha = 0.5$–0.9) clearly indicates the greater stiffness of the chain. Differential scanning calorimetry (DSC) measurements showed a T_g at 255.9 °C,[18] which is much higher than those of the LPSs previously reported. The densely stacked discotic side groups seem to set the ladder chain in a splint and consequently greatly increase the rigidity of the chain.

Two important structural features can be found from ^{29}Si NMR spectroscopic analysis that verify the extreme order of the ladder structure (Figure 2): Firstly, it is known that the higher the regularity of the LP, the narrower is the resonance signal.[2,5–8] Clearly, the extremely sharp signal at $\delta = -18.67$ ppm corresponding to the $RSiO_{3/2}$ unit (R = triphenylene group) with a half-peak width $\Delta_{1/2} < 0.3$ ppm indicates that **6** only consists of regular $RSiO_{3/2}$ units, without the noticeable presence of any branched moieties. Secondly, compared with the signals of the general $RSiO_{3/2}$ units located at $\delta = -70$ ppm, this resonance signal is remarkably shifted to a very low field ($\delta = -18.67$ ppm), thus inferring that the huge

 © 2006 Wiley-VCH Verlag GmbH & Co. KGaA, Weinheim

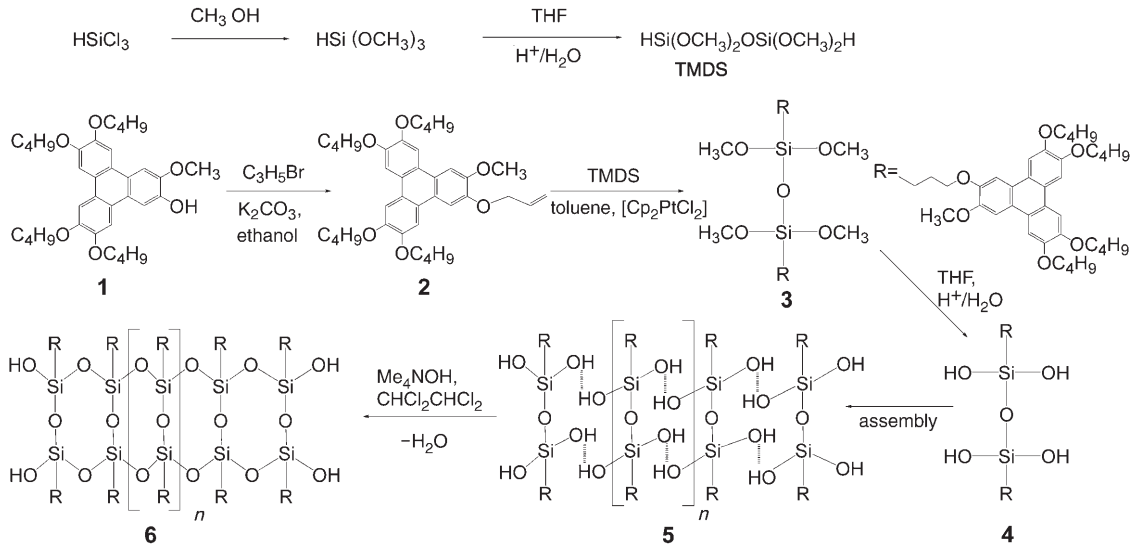

Scheme 1. Synthetic route to the ladder polymer.

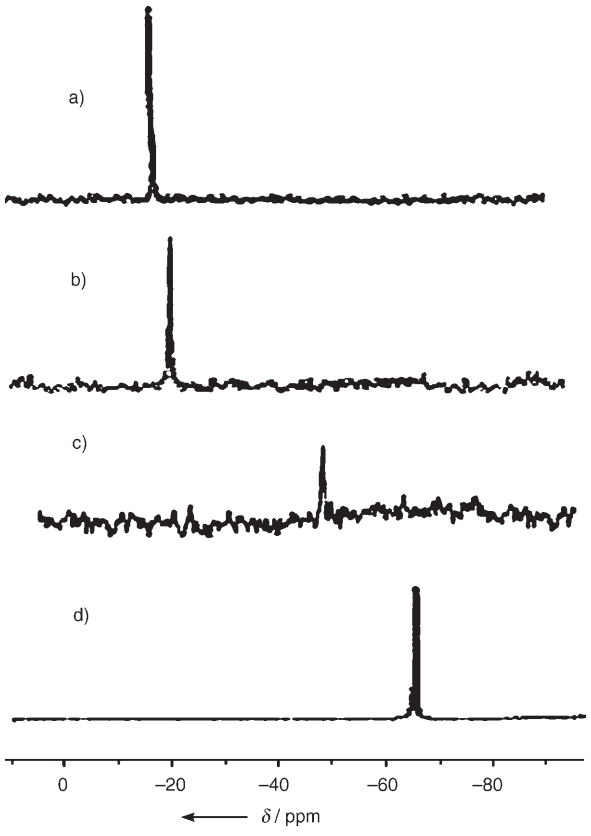

Figure 2. ^{29}Si NMR spectra of: a) **6**, b) **5**, c) **3**, and d) TMDS in toluene.

α,ω-ditriphenylene side groups are rolled up as a consequence of the *cis*-isotactic configuration. As a result, the deshielding effect of the circular current results in the signal remarkably being shifted downfield by over 50 ppm. Furthermore, it is also found that the resonance signal of the LS **5** occurs at $\delta = -21.40$ ppm, very near the resonance signal of the LP **6** ($\delta = -18.67$ ppm) but far from that of the monomer **3** ($\delta = -50.50$ ppm), which indicates that the chemical environments of the Si atoms in **5** and **6** are also similar, and that the ladder superstructure truly exists.

The X-ray diffraction (XRD) spectrum of **6** (Figure 3a) shows three distinct peaks. According to literature reports,[2,5–8] two peaks ($d_1 = 3.23$ nm; $d_2 = 1.38$ nm), which coincide with the simulated molecular width and thickness of the ladder chain, in the small-angle region is characteristic of a ladder structure and indicates that the semirigid ladder chains tend to form a lamella structure, and another peak in the wide-angle region ($d_3 = 0.36$ nm) corresponds to the disc–disc spacing. Thus, the disc plane should be almost perpendicular to the chain, but with a slight tilt. The top view of the molecular simulation of the chain (Figure 3b) also shows that all the triphenylene units are arranged on the same side of the ladder backbone (*cis*-isotactic). In addition, the XRD pattern of a freeze-dried sample of **5** obtained from its benzene solution, in which it maintains its original configuration, also shows the characteristic lamella structure similar to that of **6**, with only minor differences in the diffraction peaks (Table 1). This observation further verifies the presence of a preorganized ladder superstructure in solution.

A linear single-chain polymer (SP) with two triphenylene groups, $\{[R^1(CH_2)_3][R^1O(CH_2)_3]SiO\}_n$, ($R^1$ = 3-methoxy-6,7,10,11-tetrabutoxy-2-yloxytriphenylene) was synthesized as a reference polymer of the LP **6**. This reference polymer also shows a similar XRD pattern consistent with a lamellar structure (Table 1), which is a common characteristic of discotic side-chain polymers[19,20] as well as semirigid ladder polymers.[2,5–8] In other words, such similarity in the XRD patterns also demonstrates that **6** is a linear ordered polymer.

The regular stereoconfiguration of **6** is also supported by fluorescence emission spectra. In comparison to **3**, a new emission band at 493 nm appears in the spectrum of **6** (Figure 4), which is attributed to the excimer formed by the face to face π-π stacking of the triphenylene side groups.[21] It is also found that the ratio of the fluorescence emission

 © 2006 Wiley-VCH Verlag GmbH & Co. KGaA, Weinheim

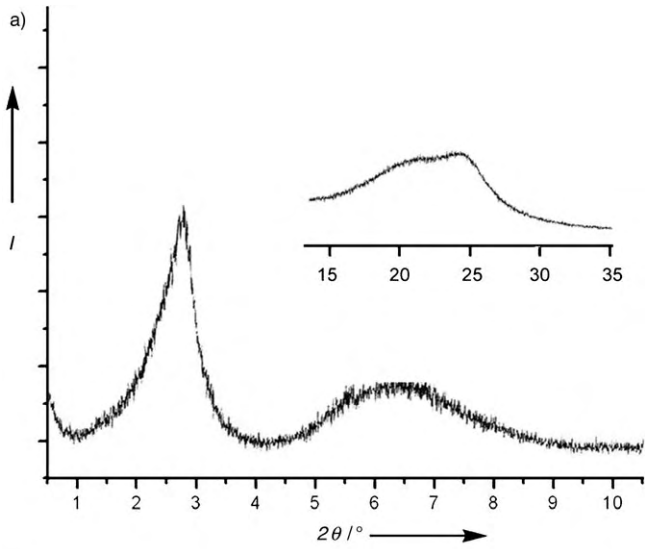

Figure 3. a) XRD spectrum of **6**. b) Top view of the molecular simulated ladder chain with six repeat units (Hyper Chem7.0 geometry optimization with RMS gradient of 0.1 kcal mol^{-1}).

Table 1: Comparison of the data for **3**, **5**, **6**, and SP.

Sample	Formula	^{29}Si NMR δ [ppm]	XRD [Å]			λ_F emission peak [nm]
			d_1	d_2	d_3	
3	$RSi(OCH_3)_2OSi(OCH_3)_2R$[a]	−50.50	–	16.0	3.5	372
5	supramolecular assembly	−21.89	34.6	15.6	3.7	382,462
6	$[R_2Si_2O_3]_n$	−18.67	32.3	13.8	3.6	387,493
SP	$\{[R^1(CH_2)_3][R^1O(CH_2)_3]SiO\}_n$[b]	−21.40	30.0	14.8	3.9	390

[a] R refers to Scheme 1. [b] R^1 = 3-methoxy-6,7,10,11-tetrabutoxy-2-yloxytriphenylene.

intensities (I_m/I_e) at 390 nm (I_m) and at 493 nm (I_e) is independent of the concentration of **6**, and no red-shift of the emission spectra occurs as the concentration is changed. The existence of the intramolecular excimer further confirms the *cis*-isotactic structure. As expected, **5** also shows an additional emission band similar to **6.** Unlike the LP **6** or LS **5**, however, the fluorescence spectrum of the SP does not show a distinct emission peak arising from the formation of the excimer. The reason for this may be attributed to a highly free rotation of the triphenylene groups that are linked to the single polysiloxane chain through a flexible spacer. Comparative data of a series of control experiments between **3**, **5**, **6**, and SP are summarized in Table 1.

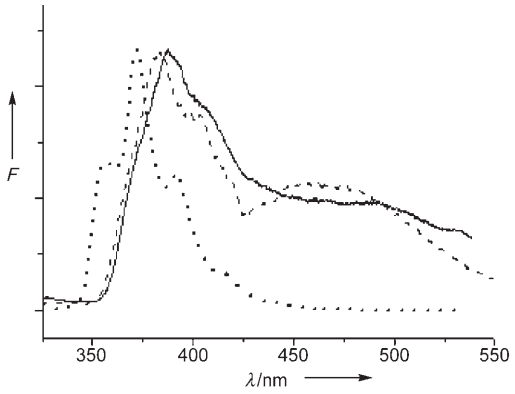

Figure 4. Fluorescence emission spectra of **3** (dotted line), **5** (dashed line), and **6** (solid line) in *n*-hexane solution (10^{-6} M).

To investigate the hydrogen-deuterium (H-D) exchange activity of the LS **5** by ^{1}H NMR spectroscopy, two model compounds, $Ph(OH)_2SiOSi(OH)_2Ph$ and $Ph_2Si(OH)_2$, with silanol groups in different (confined/opened) H-bonding environments were also studied at the same concentration (10 mmol L^{-1}) in [D$_6$]acetone. The H-D exchange rate denoted by the exchange half-life ($t_{1/2}$) for **5** ($t_{1/2} \approx 45$ min) is much lower than those of the comparative compounds ($t_{1/2} \leq 5$ min), thus indicating the presence of strong H-bonding interactions in the confined ladder geometry.

The transmission electronic microscopy (TEM) image (Figure 5a) shows domains with dark lamellas with widths of about 2.5 nm (in agreement with the XRD results), but it is still very difficult to obtain an image of the actual single chain even at very dilute concentrations because of the extremely high tendency of the polymer chain to aggregate. However, high-resolution atomic force microscopy (AFM) images of a spin-coated film of **6** on mica (Figure 5b,c) show clear features (three parallel bright lines) of extended ladder chains (shown schematically in Figure 5d): double chains align on the surface with the triphenylene side groups at the edge—the bright lines of two sides correspond to stacked triphenylene cores, and the middle one corresponds to the main chain of the ladder silsesquioxane. Careful observation shows the disc plane is aligned tilted to the chain axis. Section analysis gave the width of the repeat ladder unit $w = 1.30 \pm 0.08$ nm, which is reasonable for the distance between the centers of the triphenylene cores at the two sides.

We have shown here an example of the confined synthesis of a ladder polymer, where a supramolecular channel is formed by concerted self-organization through π–π stacking and H-bonding which dictates the ordered polycondensation of the silanols entrapped in the channel between two hydrophobic columns. This strategy demonstrates a significant advantage over other synthesis processes by which it is difficult to produce high-molecular-weight ladder chains. We have also shown an efficient way to control the stereo-

 © 2006 Wiley-VCH Verlag GmbH & Co. KGaA, Weinheim

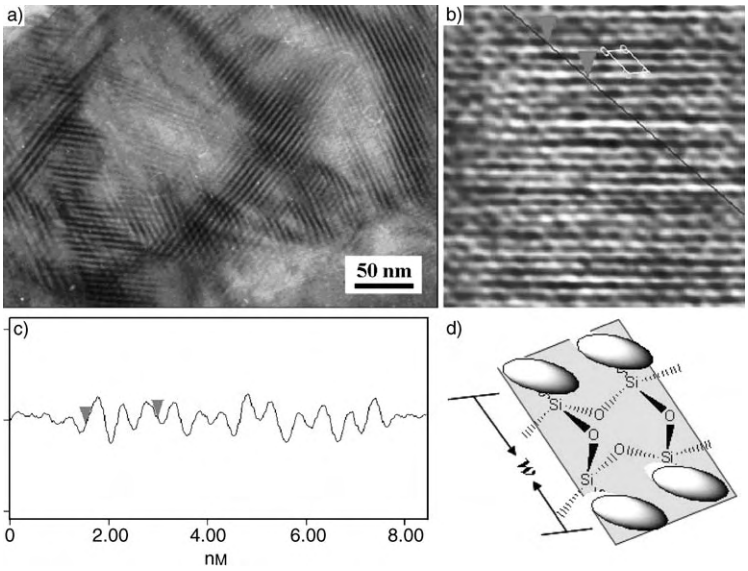

Figure 5. TEM and AFM images of **6**: a) A bright-field TEM image obtained by freeze-drying a benzene solution (10^{-14} M); b) high-resolution AFM image of a spin-coated film obtained from benzene solution; c) AFM section analysis; d) schematic representation of the ladder structure observed by AFM and the average value of w is 1.30 nm.

configuration of condensation polymers by utilizing the interaction between triphenylene side groups. Hence, successful synthesis of a high-molecular-weight, stereoregular ladder polymer would help to clarify the formation, evolution, and function of ladder biopolymers, such as DNA etc. Furthermore, the highly ordered and densely stacked discotic side groups along the ladder backbone form a well-ordered columnar structure, which could potentially be used as a functional nanowire.

Experimental Section

3 was synthesized by a hydrosilylation reaction of **2**[18] with 1,1,3,3-tetramethoxy disilazane (TMDS) using $[Cp_2PtCl_2]$ as a catalyst and toluene as the solvent in a dry argon atmosphere. **3** was hydrolyzed under very mild conditions to form **4**, which readily self-organized into a *cis*-isotactic ladder superstructure **5** and underwent polycondensation in a concentrated solution of 1,1,2,2-tetrachloroethane under mild conditions (slowly stirring at 60–80 °C) using Me_4NOH as the catalyst. The water released was removed by azeotropic distillation under vacuum. Finally the polycondensation was continued in the solid phase at gradually elevated temperatures of 100–130 °C in a vacuum to increase the molecular weight. The crude polymerized product **6** was purified and fractionated by repeated precipitation from petroleum ether solution by cautious addition of a 1:1 mixture of methanol and ethanol. The obtained LP **6** was a brown solid and had good solubility in ordinary solvents.

Received: December 16, 2005
Published online: April 4, 2006

Keywords: nanowires · noncovalent interactions · polymers · self-assembly · silsesquioxanes

[1] W. J. Bailey, *Concise Encyclopedia of Polymer Science & Engineering* (Ed.: J. I. Kroschwitz), Wiley, New York, **1990**, pp. 516–528.
[2] J. F. Brown, Jr., L. H. Vogt, Jr., A. Katchman, J. W. Eustane, K. M. Kiser, K. W. Krantz, *J. Am. Chem. Soc.* **1960**, *82*, 6194–6195.
[3] C. L. Frye, J. M. Klosowski, *J. Am. Chem. Soc.* **1971**, *93*, 4599–4601.
[4] M. Unno, A. Suto, H. Matsumoto, *J. Am. Chem. Soc.* **2002**, *124*, 1574–1575.
[5] H. Tang, J. Sun, J. Jiang, T. Hu, P. Xie, R. Zhang, *J. Am. Chem. Soc.* **2002**, *124*, 10482–10488.
[6] C. Liu, H. Zhao, P. Xie, R. Zhang, *J. Polym. Sci. Part A* **2000**, *38*, 2702–2710.
[7] G. Guo, Y. Zhang, H. Li, P. Xie, R. Zhang, *Macromol. Rapid Commun.* **2002**, *23*, 366–369.
[8] H. Li, C. Liu, G. Guo, X. Zhou, P. Xie, S. Yu, R. Zhang, *J. Polym. Sci. Part A* **2002**, *40*, 3161–3170.
[9] M. A. Brook, *Silicon in Organic, Organometallic, and Polymer Chemistry*, Wiley, New York, **2000**, pp. 321–324.
[10] T. Keisuke, A. Takuzo, *Chem. Commun.* **2000**, *24*, 2399–2412.
[11] I. Schmidt, C. Madsen, C. J. H. Jacobsen, *Inorg. Chem.* **2000**, *39*, 2279–2283.
[12] S. I. Stupp, V. Lebonheur, K. Walker, L. S. Li, K. E. Huggins, M. Keser, A. Amstutz, *Science* **1997**, *276*, 384–389.
[13] a) R. J. P. Corriu, *Angew. Chem.* **2000**, *112*, 1432–1455; *Angew. Chem. Int. Ed.* **2000**, *39*, 1376–1398; b) R. J. P. Corriu, *Chem. Eur. J.* **2005**, *11*, 1109–1121.
[14] H. Muramatsu, R. J. P. Corriu, B. Boury, *J. Am. Chem. Soc.* **2003**, *125*, 854–855.
[15] S. Nagahama, T. Tanaka, A. Matsumoto, *Angew. Chem.* **2004**, *116*, 3899–3902; *Angew. Chem. Int. Ed.* **2004**, *43*, 3811–3814.
[16] a) J. J. E. Moreau, B. P. Pichon, M. W. C. Man, C. Bied, H. Pritzkow, J.-L. Bantignies, P. Dieudonne, J.-L. Sauvajol, *Angew. Chem.* **2004**, *116*, 205–208; *Angew. Chem. Int. Ed.* **2004**, *43*, 203–206; b) J. J. E. Moreau, L. Vellutini, M. W. C. Man, C. Bied, P. Dieudonne, J.-L. Bantignies, J.-L. Sauvajol, *Chem. Eur. J.* **2005**, *11*, 1527–1537.
[17] a) M. Kakudo, T. Watase, *J. Chem. Phys.* **1953**, *21*, 167–168; b) N. Kasai, M. Kakudo, *Bull. Chem. Soc. Jpn.* **1954**, *27*, 605–608.
[18] See the Supporting Information.
[19] M. Werth, H. W. Spiess, *Makromol. Chem. Rapid. Commun.* **1993**, *14*, 329–338.
[20] C. Ba, Z. Shen, H. Gu, G. Guo, P. Xie, R. Zhang, C. Zhu, L. Wan, F. Li, C. Huang, *Liq. Cryst.* **2003**, *30*, 391–397.
[21] F. Hirayama, *J. Chem. Phys.* **1965**, *42*, 3163–3171.

 © 2006 Wiley-VCH Verlag GmbH & Co. KGaA, Weinheim

Synthetic Methods

DOI: 10.1002/anie.200600126

Highly Diastereoselective Synthesis of Bicyclo-[3.2.1]octenones through Phosphine-Mediated Condensations of 1,4-Dien-3-ones**

*Nolan T. McDougal and Scott E. Schaus**

New methods for the construction of highly substituted carbocycles with a defined configuration are important for the synthesis of natural products and drugs.[1] The synthesis of cyclic compounds that possess all-carbon quaternary centers is a challenge that has been primarily addressed by the alkylation of enolates,[2] the Diels–Alder reaction,[3] and radical cyclizations.[4] One elegant approach is the [4+3] cycloaddition of oxyallyl cations with substituted dienes and furans to afford bicycles that contain quaternary carbon centers.[5] Complementary approaches to simple carbocycles from acyclic precursors include phosphine-mediated methods such as [3+2] annulations[6] as well as intramolecular Rauhut–Currier,[7] Morita–Baylis–Hillman,[8] and S_N2 reactions.[9] Despite the myriad approaches afforded by these reactions,[10] few synthetic methods that produce quaternary carbon-containing bicyclic structures by using nucleophilic promoters exist.[11] Herein we report the phosphine-mediated highly diastereoselective synthesis of bicyclo[3.2.1]octenones[12] that bear two bridgehead quaternary carbon centers from 1,4-dien-3-ones by a formal [4+2] cycloaddition–Wittig reaction process.

1,4-Dien-3-ones are useful multifunctional building blocks in the synthesis of carbocyclic compounds. A recent report illustrated their utility in the synthesis of cyclohexenones through an electrocyclic ring closure following base-mediated formation of the corresponding hexatriene.[13] Intermolecular Diels–Alder reactions[14] of 1,4-dien-3-ones as electron-deficient dienophiles also afford carbocyclic structures. Cyclopentenones and highly substituted bicycles are readily accessed through another type of electrocyclic ring closure of dienones, the Nazarov reaction.[5a–d,15] On the basis of the multifunctional nature of 1,4-dien-3-ones, we believed that they could serve as latent 1,3-dienes in [4+2] annulation reactions.

[*] N. T. McDougal, Prof. Dr. S. E. Schaus
Department of Chemistry
Metcalf Center for Science and Engineering
Boston University
590 Commonwealth Avenue, Boston, MA 02215 (USA)
Fax: (+1) 617-353-6466
E-mail: seschaus@bu.edu

[**] The authors acknowledge Dr. J. P. Lee (Boston University) for assistance with key NMR spectroscopy experiments and Dr. E. B. Lobkovsky (Cornell University) for X-ray crystallographic analysis. This research was supported by a NSF CAREER grant (CHE-0349206) and Amgen, Inc.

Supporting information for this article is available on the WWW under http://www.angewandte.org or from the author.

We began our investigations with the reaction of phosphines with 1,4-dien-3-ones to determine the feasibility of a phosphine-catalyzed all-carbon [4+2] annulation (Scheme 1). When styryl vinyl ketone (R = H) is mixed with Ph_3P in THF,

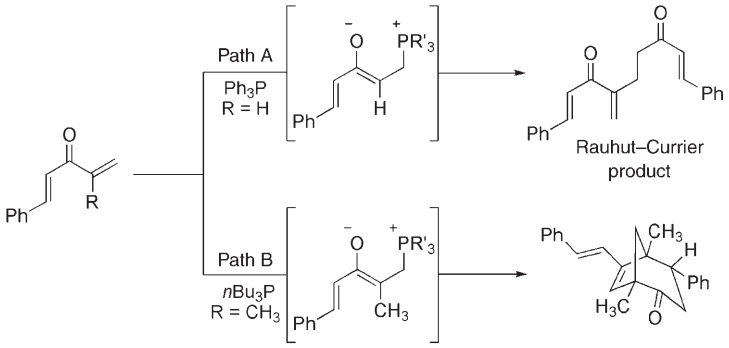

Scheme 1. Phosphine-promoted reactions of 1,4-dien-3-ones.

the Rauhut–Currier product is formed in 53% yield (Path A). Although this result confirms that the enolate can be generated in situ, α-proton transfer leads to the Rauhut–Currier reaction pathway. To investigate other reaction pathways of this type of latent 1,3-diene, we synthesized α-substituted 1,4-dien-3-ones (Path B). When styryl isopropenyl ketone (**1a**) was treated with nBu_3P in CH_2Cl_2 at room temperature, we found that bicyclo[3.2.1]octenone **2a** formed as a single diastereomer in 15% yield (Table 1, entry 1). Bicyclo[3.2.1]octanes are subunits of a variety of biologically active terpenes, including the scopadulcic acids,[16] gibberellins,[17] and aphidicolane diterpenes.[18] We screened various electronically and sterically different phosphines[19] and found that 1 equivalent of Et_2PhP mediated the condensation reaction in 65% yield after 20 h (Table 1, entry 3). Substoichiometric amounts of phosphine resulted in extended reaction times and lower yields. Although the reaction proceeded in most polar, non-ether solvents ($CHCl_3$, $PhCF_3$,

Table 1: Phosphine-mediated synthesis of bicyclo[3.2.1]octenone **2a**.[a]

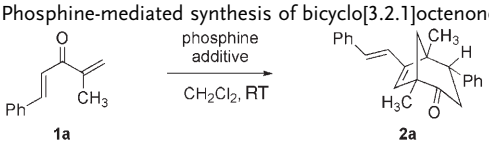

1a **2a**

Entry	Phosphine	Additive	Yield [%][b]
1	nBu_3P	–	15[c]
2	Cy_3P	–	–[d]
3	Et_2PhP	–	65
4	$EtPh_2P$	–	–[e]
5	Ph_3P	–	–[e]
6	Et_2PhP	DBU	44
7	Et_2PhP	Et_3N	65
8	Et_2PhP	pyridine	76

[a] Reactions were run with ketone (0.3 mmol), phosphine (0.3 mmol), and additive (0.3 mmol) in CH_2Cl_2 (0.5 M) at room temperature for 20 h under Ar, followed by flash chromatography on silica gel. [b] Yield of isolated product. [c] Reaction time was 5 min. [d] Decomposition of **1a**. [e] No reaction observed by ^1H NMR spectroscopy. Cy = cyclohexyl, DBU = 1,8-diazabicyclo[5.4.0]undec-7-ene.

 © 2006 Wiley-VCH Verlag GmbH & Co. KGaA, Weinheim

CH_3CN), the best yields were obtained with anhydrous CH_2Cl_2. Basic additives affected the reaction yield (Table 1, entries 6–8). The use of 1 equivalent of pyridine improved the yield to synthetically useful levels while maintaining the high diastereoselectivity (Table 1, entry 8); no reaction was observed when pyridine was used in the absence of phosphine.[20] Therefore, we selected 1 equivalent each of Et_2PhP and pyridine in CH_2Cl_2 at room temperature as general reaction conditions.

These reaction conditions proved general for a variety of 1,4-dien-3-ones (Table 2). Halogen- and alkyl-substituted aryl substrates **1b–d** cleanly underwent condensation in yields greater than 70%. Heteroaromatic and electron-donating aromatic dienones afforded the bicyclo[3.2.1]octenone products in good yields, although gentle heating was required for the 4-methoxy derivative **1h** (Table 2, entries e–h). Substitutional effects were more pronounced at other positions of the 1,4-dien-3-one backbone. The condensation of 2-ethyl-1,4-dienone **1i** resulted in lower yields, although heating to 50°C in $CHCl_3$ afforded the desired product in 41% yield after 20 h (Table 2, entry i). Substrates bearing alkyl substituents (Table 2, entries j,k) did not react under the general conditions; however, the use of more-nucleophilic phosphines such as nBu_3P resulted in effective condensation of these less-electrophilic enones to afford the bicyclic products. Dienones **1l–n** underwent condensation under similar reaction conditions; Et_2PhP was the nucleophilic promoter for aromatic **1l** and **1m** [Eq. (1)], whereas geranal-derived **1n** required nBu_3P for optimal yields [Eq. (2)]. In an experiment designed to explore the reactivity of the dienones, the reaction of **1e** with Et_2PhP and pyridine in the presence of a stoichiometric amount of **1n** resulted in the exclusive formation of **2e**, the condensation product of 2 equivalents of **1e**. The heterodimer product, afforded by the reaction of 1 equivalent each of **1e** and **1n**, was not observed. This might have been due to the higher electrophilicity of aromatic over aliphatic substrates toward both the nucleophilic addition of Et_2PhP and the reaction of the resulting 1,3-diene.

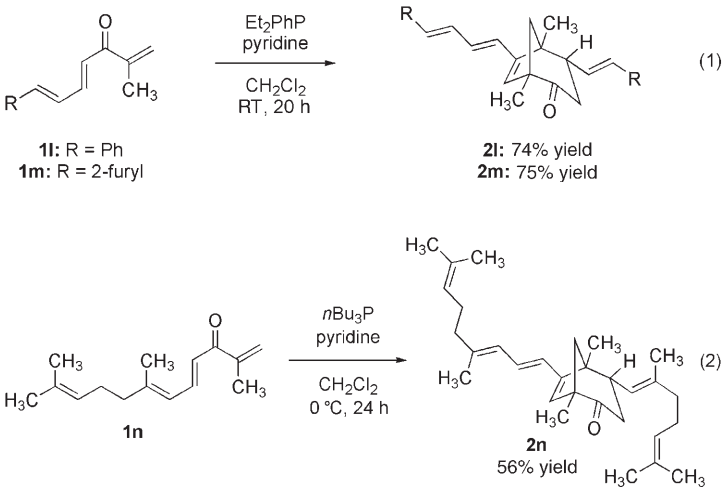

Table 2: Phosphine-mediated synthesis of bicyclo[3.2.1]octenes.[a]

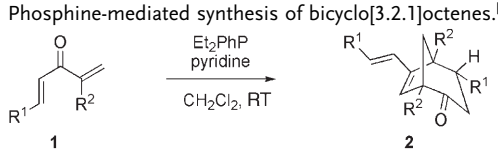

Entry	R^1	R^2	Yield [%][b]
a	C_6H_5	CH_3	76
b	4-F-C_6H_4	CH_3	70
c	4-Br-C_6H_4	CH_3	70
d	4-Me-C_6H_4	CH_3	75
e	2-furyl	CH_3	75
f[c]	2-MeO-C_6H_4	CH_3	70
g	3-MeO-C_6H_4	CH_3	73
h[d]	4-MeO-C_6H_4	CH_3	66
i[e]	C_6H_5	CH_2CH_3	41
j[f]	$H_3C(CH_2)_6$	CH_3	60
k[f]	2-furyl-$(CH_2)_2$	CH_3	60

[a] Reactions were run with ketone (0.3 mmol), pyridine (0.3 mmol), and Et_2PhP (0.3 mmol) in CH_2Cl_2 (0.5 M) at room temperature for 20 h under Ar, followed by flash chromatography on silica gel. [b] Yield of isolated product. [c] Reaction time was 30 h. [d] Reaction was run at 30°C. [e] Reaction was run in $CHCl_3$ at 50°C. [f] nBu_3P, added over 6 h, was used at 0°C.

We propose herein a mechanism for the condensation reaction in which the phosphine fulfills two roles (Scheme 2).[21] Nucleophilic addition of the phosphine to **1** affords diene **3**.[22] A formal [4+2] cycloaddition of **3** with another 1 equivalent of **1** in an *endo* fashion yields cycloadduct **4** as one diastereomer. We postulate that pyridine facilitates the proton transfer to protonate enolate **4** and form phosphorus ylide **5**.[23] When the reaction of **1a** was conducted in $CDCl_3/D_2O$ (9:1), we observed deuterium incorporation at the methylene α to the carbonyl group and at the cyclic-olefin methine positions of **1b** (both 82% D incorporation), suggesting that the protonation of **4** may occur by an intermolecular process and that formation of **5** is reversible. Notably, deuterium incorporation was not observed at the bridgehead methylene or the exocyclic vinyl hydrogen atoms,

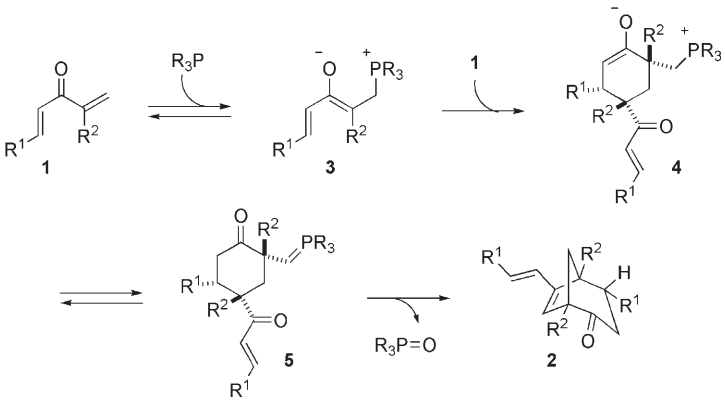

Scheme 2. Proposed mechanism for the phosphine-mediated synthesis of bicyclo[3.2.1]octenones.

 © 2006 Wiley-VCH Verlag GmbH & Co. KGaA, Weinheim

which indicates that the [4+2] cycloaddition may not be reversible. Finally, intramolecular Wittig olefination[24] of **5** and the α,β-unsaturated carbonyl group located on the same face of the cyclohexanone ring afforded the bicyclo-[3.2.1]octenone **2** and phosphine oxide, as observed by ^{31}P NMR spectroscopy. Given this proposed mechanism, we conducted experiments to test whether **5** could undergo intermolecular Wittig olefinations with aldehydes in situ. The reaction of **1a** with Et_2PhP in the presence of benzaldehyde, acetaldehyde, or paraformaldehyde resulted solely in the formation of the bicyclic product **2a**. Intermolecular Wittig olefination products were not formed, suggesting a fast intramolecular olefin-formation step.

In summary, we have developed a highly diastereoselective phosphine-mediated synthesis of bicyclo[3.2.1]octenones that contain two quaternary carbon centers by a domino [4+2] cycloaddition–Wittig reaction process. The phosphine acts as both a nucleophilic promoter to generate a 1,3-diene and a mediator of intramolecular olefination. Experiments designed to explore the scope and limitations of this reaction are ongoing and will be reported in due course.

Received: January 11, 2006
Published online: April 5, 2006

Keywords: carbocycles · cyclization · phosphanes · synthetic methods · Wittig reactions

[1] Reviews: a) K. Fuji, *Chem. Rev.* **1993**, *93*, 2037 – 2066; b) E. J. Corey, A. Guzman-Perez, *Angew. Chem.* **1998**, *110*, 402 – 415; *Angew. Chem. Int. Ed.* **1998**, *37*, 388 – 401; c) J. Christoffers, A. Mann, *Angew Chem.* **2001**, *113*, 4725 – 4732; *Angew. Chem. Int. Ed.* **2001**, *40*, 4591 – 4597; d) C. J. Douglas, L. E. Overman, *Proc. Natl. Acad. Sci. USA* **2004**, *101*, 5363 – 5367.

[2] Recent examples: a) E. J. Park, M. H. Kim, D. Y. Kim, *J. Org. Chem.* **2004**, *69*, 6897 – 6899; b) A. G. Doyle, E. N. Jacobsen, *J. Am. Chem. Soc.* **2005**, *127*, 62 – 63; c) A. H. Mermerian, G. C. Fu, *J. Am. Chem. Soc.* **2005**, *127*, 5604 – 5607.

[3] Reviews: a) K. A. Jørgensen, *Angew. Chem.* **2000**, *112*, 3702 – 3733; *Angew Chem. Int. Ed.* **2000**, *39*, 3558 – 3588; b) E. J. Corey, *Angew. Chem.* **2002**, *114*, 1724 – 1741; *Angew. Chem. Int. Ed.* **2002**, *41*, 1650 – 1667; c) K. C. Nicolaou, S. A. Snyder, T. Montagnon, G. Vassilikogiannakis, *Angew. Chem.* **2002**, *114*, 1742 – 1773; *Angew. Chem. Int. Ed.* **2002**, *41*, 1668 – 1698.

[4] B. B. Snider, *Chem. Rev.* **1996**, *96*, 339 – 364.

[5] a) J. A. Bender, A. E. Blize, C. C. Browder, S. Giese, F. G. West, *J. Org. Chem.* **1998**, *63*, 2430 – 2431; b) Y. Wang, A. M. Arif, F. G. West, *J. Am. Chem. Soc.* **1999**, *121*, 876 – 877; c) C. C. Browder, F. P. Marmsäter, F. G. West, *Org. Lett.* **2001**, *3*, 3033 – 3035; d) M. Harmata, S. K. Ghosh, X. Hong, S. Wacharasindhu, P. Kirchhoefer, *J. Am. Chem. Soc.* **2003**, *125*, 2058 – 2059; e) Y. Wang, B. D. Schill, A. M. Arif, F. G. West, *Org. Lett.* **2003**, *5*, 2747 – 2750; f) J. Juang, R. P. Hsung, *J. Am. Chem. Soc.* **2005**, *127*, 50 – 51.

[6] a) Y. Du, X. Lu, Y. Yu, *J. Org. Chem.* **2002**, *67*, 8901 – 8905; b) J.-C. Wang, S.-S. Ng, M. J. Krische, *J. Am. Chem. Soc.* **2003**, *125*, 3682 – 3683.

[7] a) L.-C. Wang, A. L. Luis, K. Agapiou, H.-Y. Jang, M. J. Krische, *J. Am. Chem. Soc.* **2002**, *124*, 2402 – 2403; b) S. A. Frank, D. J. Mergott, W. R. Roush, *J. Am. Chem. Soc.* **2002**, *124*, 2404 – 2405; c) P. M. Brown, N. Käppel, P. J. Murphy, *Tetrahedron Lett.* **2002**, *43*, 8707 – 8710.

[8] a) F. Roth, P. Gygax, G. Fráter, *Tetrahedron Lett.* **1992**, *33*, 1045 – 1048; b) F. Dinon, E. Richards, P. J. Murphey, D. E. Hibbs, M. B. Hursthouse, K. M. A. Malik, *Tetrahedron Lett.* **1999**, *40*, 3279 – 3282; c) G. E. Keck, D. S. Welch, *Org. Lett.* **2002**, *4*, 3687 – 3690.

[9] a) M. E. Krafft, T. F. N. Haxell, *J. Am. Chem. Soc.* **2005**, *127*, 10168 – 10169; b) M. E. Krafft, K. A. Seibert, T. F. N. Haxell, C. Hirosawa, *Chem. Commun.* **2005**, 5772 – 5774.

[10] a) X. Lu, C. Zhang, Z. Xu, *Acc. Chem. Res.* **2001**, *34*, 535 – 544; b) J. L. Methot, W. R. Roush, *Adv. Synth. Catal.* **2004**, *346*, 1035 – 1050.

[11] a) C. Zhang, X. Lu, *J. Org. Chem.* **1995**, *60*, 2906 – 2908; b) M. Couturier, F. Ménard, J. A. Ragan, M. Riou, E. Dauphin, B. M. Andresen, A. Ghosh, K. Dupont-Gaudet, M. Girardin, *Org. Lett.* **2004**, *6*, 1857 – 1860; c) R. K. Thalji, W. R. Roush, *J. Am. Chem. Soc.* **2005**, *127*, 16778 – 16779; see also: d) R. B. Grossman, D. S. Pendharkar, B. O. Patrick, *J. Org. Chem.* **1999**, *64*, 7178 – 7183; e) C. Gimbert, M. Lumbierres, C. Marchi, M. Moreno-Mañas, R. M. Sebastián, A. Vallribera, *Tetrahedron* **2005**, *61*, 8598 – 8605.

[12] For a review on bicyclo[3.2.1]octane synthesis, see: M.-H. Filippini, J. Rodriguez, *Chem. Rev.* **1999**, *99*, 27 – 76.

[13] N. A. Magomedov, P. L. Ruggiero, Y. Tang, *Org. Lett.* **2004**, *6*, 3373 – 3375.

[14] J. D. Winkler, *Chem. Rev.* **1996**, *96*, 167 – 176.

[15] Reviews: a) K. L. Habermas, S. E. Denmark, T. K. Jones, *Org. React.* **1994**, *45*, 1 – 158; b) H. Pellissier, *Tetrahedron* **2005**, *61*, 6479 – 6517.

[16] a) T. Hayashi, M. Kishi, M. Kawasaki, M. Arisawa, M. Shimizu, S. Suzuki, M. Yoshizaki, N. Morita, Y. Tezuka, T. Kikuchi, L. H. Berganza, E. Ferro, I. Basualdo, *Tetrahedron Lett.* **1987**, *28*, 3693 – 3696; b) M. E. Fox, C. Li, J. P. Marino, Jr., L. E. Overman, *J. Am. Chem. Soc.* **1999**, *121*, 5467 – 5480.

[17] L. N. Mander, *Chem. Rev.* **1992**, *92*, 573 – 612.

[18] M. Toyota, M. Ihara, *Tetrahedron* **1999**, *55*, 5641 – 5679.

[19] a) W. C. Davies, W. P. G. Lewis, *J. Chem. Soc.* **1934**, 1599; b) W. A. Henderson, Jr., S. A. Buckler, *J. Am. Chem. Soc.* **1960**, *82*, 5794 – 5800.

[20] For amine-catalyzed conjugate additions of highly unsaturated zwitterionic enolates, see: C. A. Evans, S. J. Miller, *J. Am. Chem. Soc.* **2003**, *125*, 12394 – 12395.

[21] Notable examples: a) C.-K. Jung, J.-C. Wang, M. J. Krische, *J. Am. Chem. Soc.* **2004**, *126*, 4118 – 4119; b) K. H. Low, N. A. Magomedov, *Org. Lett.* **2005**, *7*, 2003 – 2005.

[22] C. K. McClure, P. K. Mishra, *Tetrahedron Lett.* **2002**, *43*, 5249 – 5253.

[23] For examples of ylides formed from activated alkenes and phosphines, see: a) R. Oda, T. Kawabata, S. Tanimoto, *Tetrahedron Lett.* **1964**, *5*, 1653 – 1657; b) J. D. McClure, *Tetrahedron Lett.* **1967**, *8*, 2401 – 2405; c) E. Hedaya, S. Theodoropulus, *Tetrahedron* **1968**, *24*, 2241 – 2254; d) S. W. McCombie, C. A. Luchaco, *Tetrahedron Lett.* **1997**, *38*, 5775 – 5776; e) A. Ramazani, A. Bodaghi, *Tetrahedron Lett.* **2000**, *41*, 567 – 568.

[24] K. B. Becker, *Tetrahedron* **1980**, *36*, 1717 – 1745.

 © 2006 Wiley-VCH Verlag GmbH & Co. KGaA, Weinheim

Fuel Cells

DOI: 10.1002/anie.200504379

A Direct CO Polymer Electrolyte Membrane Fuel Cell**

Shin-ichi Yamazaki, Tsutomu Ioroi, Yusuke Yamada, Kazuaki Yasuda, and Tetsuhiko Kobayashi*

The reformation of natural gases, coal gases, and biomass-derived gases generates a considerable amount of CO. The ideal method for the generation of energy from CO would be the direct use of CO as a fuel in polymer electrolyte membrane fuel cells (PEMFCs). However, its use as a fuel is restricted, despite it being a strong reducing agent, because it is a strong poison for the Pt catalyst of PEMFCs. The presence of only 100 ppm CO results in the oxidation of H_2 on the Pt catalyst decreasing to 25% of that without CO in.[1] Direct electrochemical oxidation of CO is very sluggish even at high temperatures;[2] hence the realization of a low-temperature direct CO fuel cell has been regarded as an impossible task.

Recently, a novel CO utilization system operating at low temperature was proposed.[3] In this system, CO is oxidized by a polyoxometalate with the aid of an Au catalyst, and the reduced polyoxometalate serves as a fuel for the PEMFC. This report demonstrated that CO could act as an energy source "indirectly". However, the system requires electron transfer from CO to the polyoxometalate, and hence is essentially equal to the water gas shift reaction (electron transfer from CO to H_2O).[4] Many different processes are needed for the use of CO, and, as a result, the system becomes complex. The performance of this cell is limited by the redox activity of the polyoxometalate, and irrespective of the strong reducing power of CO. The reported cell performance remains much lower than those of H_2-PEMFCs and direct methanol fuel cells.

Although systems for the conversion of CO into fuels (H_2, reduced polyoxometalate, and so on) have been reported,[3,4] a direct CO-PEMFC, in which neat CO is supplied to a membrane electrode assembly (MEA), has not yet been developed. The difficulty in the development of such a system is based on the fact that current noble-metal catalysts are strongly poisoned by CO, as mentioned above. However, certain kinds of metalloporphyrins can catalyze the electrochemical oxidation of CO.[5–7] We focused on a carbon-supported Rh porphyrin which has been reported to oxidize CO electrochemically.[5–7] In a previous study we demonstrated that carbon-supported Rh octaethylporphyrin ([Rh(oep)]) gave a steady-state current during the oxidation of CO at very low potentials.[7] On the basis of the high performance of the carbon-supported [Rh(oep)],[7] we planned to use this material as an anode catalyst for the oxidation of CO and to construct a direct CO-PEMFC.

Herein, we report for the first time a direct CO-PEMFC. The CO-PEMFC cell delivers a much improved performance than the previous PEMFC that used a fuel reduced by CO.[3] Our cell is very specific in that it can use neat CO without oxidation of H_2.

The performances of the PEMFC with [Rh(oep)]/C and a standard PEMFC with Pt/C as the anode catalyst are depicted in Figures 1 and 2 when CO and H_2 were used as the anode gases, respectively. Figure 1A shows an *I–V* curve for a PEMFC in which the anode catalyst is [Rh(oep)]/C. Neat CO gas and neat O_2 gas were used as the anode and cathode gases, respectively. The cell delivered a good performance: the cell voltage at 96 mA cm^{-2} reached 0.47 V, and the maximum power exceeded 45 mW cm^{-2} at 80 °C. This is the first example of a direct CO-PEMFC. In typical PEMFCs with a Pt catalyst, the oxidation of H_2 by Pt is dramatically suppressed, even in the presence of 100 ppm CO,[1]. In fact, PEMFCs with a Pt/C anode catalyst generate virtually no power when neat CO is used as a fuel (Figure 1B). In contrast, surprisingly, a cell with [Rh(oep)]/C can use neat CO very efficiently. The anode and cathode reactions are shown in Equations (1) and (2), respectively.

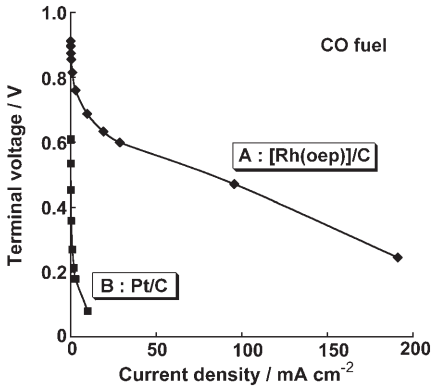

Figure 1. *I–V* curves for PEMFC with A) [Rh(oep)]/C and B) Pt/C (40%, Johnson–Matthey) anode catalysts using neat CO as the anode gas. Neat O_2 was used as the cathode gas. The gases were supplied at a rate of 100 cm^3 min^{-1}. The cell operation and gas humidification were performed at 80 °C.

$$CO + H_2O \rightarrow CO_2 + 2H^+ + 2e^- \quad (1)$$

$$O_2 + 4H^+ + 4e^- \rightarrow 2H_2O \quad (2)$$

[*] Dr. S. Yamazaki, Dr. T. Ioroi, Dr. Y. Yamada, Dr. K. Yasuda, Dr. T. Kobayashi
Research Institute for Ubiquitous Energy Devices
National Institute of Advanced Industrial Science and Technology (AIST)
1-8-31, Midorigaoka, Ikeda, Osaka 563-8577 (Japan)
Fax: (+81) 72-751-9629
E-mail: s-yamazaki@aist.go.jp

[**] We thank researchers of the Advanced Fuel Cell Research Group (National Institute of Advanced Industrial Science and Technology) for their fruitful discussions.

Supporting information for this article is available on the WWW under http://www.angewandte.org or from the author.

InterScience DISCOVER SOMETHING GREAT
© 2006 Wiley-VCH Verlag GmbH & Co. KGaA, Weinheim

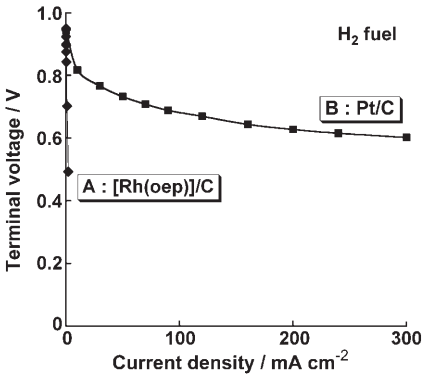

Figure 2. *I–V* curves for a PEMFC with A) [Rh(oep)]/C and B) Pt/C (40%, Johnson–Matthey) anode catalysts using neat H_2 as the anode gas. Neat O_2 was used as the cathode gas. The gases were supplied at a rate of 100 $cm^3 min^{-1}$. The cell operation and gas humidification were performed at 80°C.

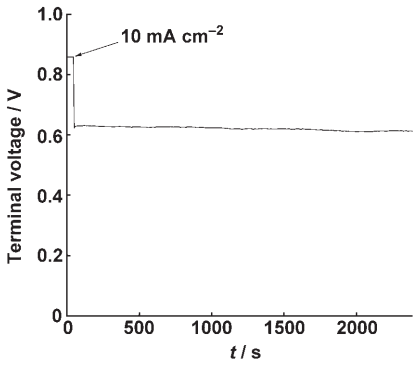

Figure 3. Time-courses of the voltage of the PEMFC with [Rh(oep)]/C using neat CO as the anode gas. The current density was changed from 0 to 10 mA cm^{-2} at $t = 50$ s. The other conditions were the same as in Figure 1.

While the cell performance is worse than that of a typical PEMFC (Figure 2B), it is much higher (by a factor of about 15) than that of the previous PEMFC in which a fuel reduced by CO is used.[3] The design of our cell with [Rh(oep)]/C is very simple and in contrast to previous systems that utilize CO, and furthermore it can be made by the same procedure as normal PEMFCs.

Evaluation of the performance of the PEMFC with [Rh(oep)]/C in which H_2 is used as an anode gas (Figure 2A) shows that only a small amount of power is generated using H_2. However, the power and performance are virtually zero compared to those obtained when CO is used as the fuel (Figure 1A). Thus, the PEMFC with [Rh(oep)]/C is unprecedented and very specific in that the cell uses CO in preference to H_2, while a normal PEMFC with a Pt/C anode catalyst uses H_2 in preference to CO. This contrast is clearly seen in Figures 1 and 2. A large amount of CO is generated concomitant with H_2 during the reformation of hydrocarbons. The PEMFC with [Rh(oep)]/C uses CO, while the PEMFC with a Pt/C anode uses H_2. When using the CO-PEMFC, it should be placed in the anode gas line upstream relative to the H_2-PEMFC. Ideally, the CO in the CO/H_2 gas mixture is consumed as a fuel by the CO-PEMFC. The resulting CO-free H_2 gas can then then used by the H_2-PEMFC. Thus, the CO-PEMFC can be used as an anode gas cleaner concomitant with generation of power. When the CO concentration decreases, the current generated would also decrease. However, only a small amount of current is required for the removal of a low concentration of CO. This situation would allow the possibility of using this cell for the removal of a low concentration of CO in hydrogen gas steams in PEMFCs.

The time-course of the potential at 10 mA cm^{-2} in the CO-PEMFC with [Rh(oep)]/C is shown in Figure 3. A steady-state power output is observed, thus indicating that power generation is stable over the time range of the measurement. However, for a prolonged use of this cell, the possibility that the Rh porphyrin could leak into the acidic electrolyte from the carbon should be taken into consideration. A long-term stability study on the CO-PEMFC is underway.

These novel characteristics of the CO-PEMFC with [Rh(oep)]/C are derived from the catalytic effect of [Rh(oep)]/C, which was examined in detail in our previous report.[7] The open circuit voltage (OCV) of the CO-PEMFC with [Rh(oep)]/C is 0.91 V (Figure 1A). This value is somewhat smaller than the theoretical cell voltage of CO-PEMFC (1.35 V). The difference (0.44 V) cannot be explained by cathode overpotential alone. In general, the cathode overpotential of Pt/C (40%) is estimated to be approximately 0.2–0.3 V. Thus the difference (ca. 0.14–0.24 V) reflects the overpotential of the anodic oxidation of CO. We have already demonstrated that an observable electrochemical oxidation of CO by [Rh(oep)]/C starts at a potential about 0.2 V higher than the redox potential of reaction (1).[7] The OCV of CO-PEMFC can be explained by the properties of the [Rh(oep)]/C catalyst.

In our previous study,[7] an almost diffusion-limited steady-state current was observed for the electrocatalytic oxidation of CO by [Rh(oep)]/C under electrode rotation conditions. The steady-state current of CO oxidation is a characteristic property of [Rh(oep)]/C. This catalytic effect of the [Rh(oep)]/C can explain the high current density (Figure 1A) and steady-state power output (Figure 3) of the CO-PEMFC with [Rh(oep)]/C.

The possible influences of impurities such as light alcohol (methanol), aldehyde (formaldehyde), and acid (formic acid) in the anode gas were examined using a rotating disk electrode. However, the effects of these gases on CO oxidation were negligible up to 0.1 mM. The level of impurities in the anode gas is thought to be much lower, and hence the effects of impurities on the CO-PEMFC would be negligible.

Many attempts have been made to use organic-based metal complexes as an anode catalyst. However, these complexes appear to be catalytically active only in alkaline solution.[8] In the acidic electrolyte of the PEMFC, their application is limited to being promoters for a Pt anode catalyst.[9] Hence, this report on a CO-PEMFC is the first example of the use of organic-based metal complexes as an anode catalyst for a PEMFC.

 © 2006 Wiley-VCH Verlag GmbH & Co. KGaA, Weinheim

In conclusion, we have reported for the first time a direct CO-PEMFC. Surprisingly, the cell uses neat CO as a fuel, which is in contrast to the performance of PEMFCs with CO-tolerant Pt catalysts[10–19] which are dramatically suppressed even in the presence of a low concentration of CO. The success of this direct CO-PEMFC arose from the catalytic effect of [Rh(oep)]/C; the cell performance can be explained by the catalytic effect of the [Rh(oep)]/C system, which was examined in our previous study.[7]

[Rh(oep)]/C exhibits the best catalytic effect among other electrocatalysts for CO oxidation at 25 °C.[7] However, it is known that certain kinds of Ru catalysts have relatively high activity for the electrooxidation of CO.[20] Our design of a CO-PEMFC might lead to the development of various CO-PEMFCs with CO oxidation catalysts based on ruthenium.

A mixture of CO and H_2 is generated by the reformation of hydrocarbons. More CO is generated from biomass-derived gases and coal gases. Thus, the CO-PEMFC might make it possible to use biomass-derived gases and coal gases as a power source for PEMFCs.

Another prominent property of this cell is that it uses CO without effecting H_2 oxidation. This property, which is not observed in the conventional anode catalyst (Pt/C), may enable two important applications. One application is the assembly of an apparatus for the electrochemical removal of CO and the generation of power. Currently, selective oxidation catalysts as well as water gas shift catalysts are widely used to decrease the CO concentration in the anode gas.[4] However, the inevitable oxidation of H_2 by O_2 by selective oxidation processes lowers the efficiency of the PEMFC. An apparatus with a PtRu catalyst for the electrochemical removal of CO was developed by Maeda et al.[21] However, this apparatus requires an energy supply and, furthermore, oxidizes H_2 concomitantly. In marked contrast to this, the CO-PEMFC can eliminate CO selectively from a CO/H_2 gas mixture. Our CO-PEMFC does not require energy to drive electrochemical CO oxidation, and moreover, it can generate power from this reaction. The CO-PEMFC is more favorable as an apparatus for CO removal in that it does not need energy and O_2 to remove the CO, and has high selectivity. The other application is as a CO sensor, since the selectivity of the CO-PEMFC enables the detection of CO even in CO/H_2 mixtures.

Experimental Section

Full experimental details are described in the Supporting Information. Briefly, carbon-supported [Rh(oep)] was prepared as described in the literature.[7,22,23] Carbon-supported [Rh(oep)] or carbon-supported platinum (40%, Johnson–Matthey Co. Ltd.) was used as the anode catalyst. Throughout the experiments, carbon-supported platinum (40%, Johnson–Matthey Co. ltd.) was used as the cathode catalyst. Nafion solution (5%, Aldrich) was added to the catalyst materials, and mixed thoroughly. The suspension was then made into a thin layer as described in the literature.[10,11] The thin layers of anode and cathode catalysts were hot-pressed on both sides of the pre-treated nafion membrane to form the MEA. Nafion 117 was used for the electrolyte membrane unless otherwise stated. The cell performance was measured at 80 °C. Fully hydrated gases were supplied at a flow rate of 100 $cm^3 min^{-1}$ to MEA.

Received: December 9, 2005
Published online: March 29, 2006

Keywords: carbon monoxide · electrochemistry · fuel cells · porphyrinoids · rhodium

[1] M. Götz, H. Wendt, *Electrochim. Acta* **1998**, *43*, 3637–3644.
[2] C.-G. Lee, K.-S. Ahn, H.-C. Lim, J.-M. Oh, *J. Power Sources* **2004**, *125*, 166–171.
[3] W. B. Kim, T. Voitl, G. J. Rodriguez-Rivera, J. A. Dumesic, *Science* **2004**, *305*, 1280–1283.
[4] T. Kobayashi, A. Ueda, Y. Yamada, H. Shioyama, *Appl. Surf. Sci.* **2004**, *223*, 102–108, and references therein.
[5] J. F. van Baar, J. A. R. van Veen, N. de Wit, *Electrochim. Acta* **1982**, *27*, 57–59.
[6] J. F. van Baar, J. A. R. van Veen, J. M. van der Eijk, T. J. Peters, N. de Wit, *Electrochim. Acta* **1982**, *27*, 1315–1319.
[7] S. Yamazaki, Y. Yamada, K. Yasuda, *Inorg. Chem.* **2005**, *44*, 6512–6514.
[8] A. N. Golikand, S. Shahrokhian, M. Asgari, M. G. Maragheh, L. Irannejad, A. Khanchi, *J. Power Sources* **2005**, *144*, 21–27.
[9] J. S. Bett, H. R. Kunz, A. J. Aldykiewicz, Jr., J. M. Fenton, W. F. Bailey, D. V. McGrath, *Electrochim. Acta* **1998**, *43*, 3645–3655.
[10] T. Ioroi, K. Yasuda, Z. Siroma, N. Fujiwara, Y. Miyazaki, *J. Electrochem. Soc.* **2003**, *150*, A1225–A1230.
[11] T. Ioroi, N. Fujiwara, Z. Siroma, K. Yasuda, Y. Miyazaki, *Electrochem. Commun.* **2002**, *4*, 442–446.
[12] S. Gottesfeld, J. Pafford, *J. Electrochem. Soc.* **1988**, *135*, 2651–2652.
[13] T. Lei, M. S. Zei, G. Ertl, *Surf. Sci.* **2005**, *581*, 142–154.
[14] H.-F. Oetjen, V. M. Schmidt, U. Stimming, F. Trila, *J. Electrochem. Soc.* **1996**, *143*, 3838–3842.
[15] H. A. Gasteiger, N. M. Markovic, P. N. Ross, *J. Phys. Chem.* **1995**, *99*, 8945–8949.
[16] H. A. Gasteiger, N. M. Markovic, P. N. Ross, *J. Phys. Chem.* **1995**, *99*, 16757–16767.
[17] B. N. Grgur, G. Zhuang, N. M. Markovic, P. N. Ross, *J. Phys. Chem. B* **1997**, *101*, 3910–3913.
[18] S. J. Lee, S. Mukerjee, E. A. Ticianelli, J. McBreen, *Electrochim. Acta* **1999**, *44*, 3283–3293.
[19] A. Ueda, Y. Yamada, T. Ioroi, N. Fujiwara, K. Yasuda, Y. Miyazaki, T. Kobayashi, *Catal. Today* **2003**, *84*, 223–229.
[20] H. A. Gasteiger, N. M. Markovic, P. N. Ross, *J. Phys. Chem.* **1995**, *99*, 8290–8301.
[21] H. Maeda, H. Fukumoto, K. Mitsuda, *Electrochemistry* **2002**, *70*, 615–621.
[22] S. Yamazaki, Y. Yamada, K. Yasuda, *Inorg. Chem.* **2004**, *43*, 7263–7265.
[23] S. Yamazaki, Y. Yamada, T. Ioroi, N. Fujiwara, Z. Siroma, K. Yasuda, Y. Miyazaki, *J. Electroanal. Chem.* **2005**, *576*, 253–259.

 © 2006 Wiley-VCH Verlag GmbH & Co. KGaA, Weinheim

Molecular Recognition

DOI: 10.1002/anie.200503906

Allosterically Coupled Double Induced Fit for 1+1+1+1 Self-Assembly of a Calix[6]trisamine, a Calix[6]trisacid, and Their Guests**

Stéphane Le Gac, Jérôme Marrot, Olivia Reinaud, and Ivan Jabin**

Recognition systems with allosteric guest responses have the greatest importance in biology, as they are involved in activation, regulation, and information-transmission phenomena.[1] The simplest case is a compound that presents different binding sites which are conformationally coupled through hydrogen bonds, dipole orientations, metal-ion complexation, and so forth. Classical biological examples[2] include allosteric binding sites associated with a receptor,[2a] thus triggering a particular piece of information, as well as the allosteric control of the activity of an enzyme. Various degrees of sophistication can be found, such as ligand-induced closure in enzymes,[2b] synergism between coenzyme and substrate binding,[2c] ordered substrate binding combined with a domain-closure-facilitating catalysis,[2d] and mutual induced fit during recognition between two large protagonists.[2e]

All these fascinating phenomena have long motivated the difficult and challenging design of artificial systems that could reproduce such allosteric control.[3] The classical systems are based on intramolecular conformational changes in a single unit presenting ditopic receptor sites that are sterically[4] or electronically[5] coupled for cooperative recognition processes. This concept, in some instances, has been exploited for selective catalysis.[6] Calix[4]arene proved to be a very interesting scaffold for the design of cooperative systems.[7] A recent sophisticated example reports the successive cooperative binding of three different guests.[8] Coupled multiple induced fit represents yet another level of sophistication and remains a real challenge.

In contrast to self-assembled systems involving calix[4]arenes, systems involving the larger calix[6]arenes are rare.[9] This is mainly because of their higher conformational flexibility, which must be restricted to obtain well-preorganized subunits. We are involved in the design of calix[6]arene-based biomimetic receptors, and have recently discovered that a calix[6]arene bearing three amino arms at the small rim ($\mathbf{1}^{NH_2}$, Scheme 1) could be efficiently structured by trifluoroacetic acid (HTFA) into a polarized receptor $\mathbf{1}^{NH_3^+,TFA^-}$ that displays an impressive affinity for polar neutral guests such as amides, alcohols, or nitriles in chloroform.[10,11] Its efficiency results from the self-assembly of an ion-paired cap that closes the cavity, freezes the calixarene core in a cone conformation, and stabilizes the neutral guests through hydrogen bonding and charge–dipole interactions. We were interested in replacing the three molar equivalents of HTFA by a tripodal triscarboxylic acid that would be preorganized for guest binding. Herein, we report the cooperative assembly and host properties of calix[6]trisamine $\mathbf{1}^{NH_2}$[12] and calix[6]trisacid $\mathbf{2}^{CO_2H}$[13] (Scheme 1).

The ability of calix[6]trisacid $\mathbf{2}^{CO_2H}$ to shape calix[6]trisamine $\mathbf{1}^{NH_2}$ in a trisammonium conical host $\mathbf{1}^{NH_3^+}$ was investigated first. The addition of an equimolar amount of $\mathbf{2}^{CO_2H}$ to a solution of $\mathbf{1}^{NH_2}$ in $CDCl_3$ led to broad ^1H NMR spectra in the 223–293-K temperature range, which indicates the formation of ill-defined, partially aggregated species (Figure 1a).[14] Upon addition of an excess of a small polar guest G such as DMF or ethanol, the NMR profiles remained quasi-unchanged (Figure 1b), and no guest inclusion could be detected under conditions in which receptor $\mathbf{1}^{NH_3^+,TFA^-}$ was effective. This result indicates that, in contrast to HTFA, $\mathbf{2}^{CO_2H}$ is inefficient at structuring $\mathbf{1}^{NH_2}$ into a molecular receptor.

We reasoned that this finding was partly a consequence of the overflexibility of $\mathbf{2}^{CO_2^-}$,[15] and thought of rigidifying the latter with an ammonium guest. When propylammonium picrate ($PrNH_3^+Pic^-$, 1 equiv) was added to the ternary mixtures, the NMR spectra sharpened remarkably and new peaks in the high-field region attested to the formation of two C_{3v}-symmetrical *endo* complexes, $\mathbf{2}^{CO_2^-}\supset PrNH_3^+$ and $\mathbf{1}^{NH_3^+}\supset G$ (Figure 1c). Similar experiments carried out with an alkyl urea (imidazolidin-2-one (IMI), 1–6 equiv), which is a more polar guest G,[16] and $PrNH_3^+Pic^-$ led to the *endo* complexation of exactly one equivalent of each guest (Figure 1d). Each calixarene core presents sharp doublets for its $ArCH_2$ protons, which indicates a rigidified, flattened-cone conformation with methoxy groups expelled from the cavity (δ_{OMe} = 3.82 and 3.90 ppm). Hence, the addition of $PrNH_3^+$ to the ill-defined ternary mixtures induced the structuring of both calixarene modules and the inclusion of the first guest G, in addition to its own inclusion.

Such complexes were also obtained with $EtNH_3^+Pic^-$ in place of $PrNH_3^+Pic^-$, and their formation was under thermodynamic control since it was independent of the introduction order of the partners.[17] Thus, all these results highlight a cooperative self-assembly process that leads to the formation

[*] Prof. O. Reinaud
Laboratoire de Chimie et Biochimie Pharmacologique et Toxicologique
UMR CNRS 8601, Université René Descartes
45 rue des Saints Pères, 75270 Paris cedex 06 (France)
Fax: (+33) 142-868-387
E-mail: Olivia.Reinaud@univ-paris5.fr
S. Le Gac, Dr. I. Jabin
URCOM
Université du Havre
25 rue Philippe Lebon, BP 540, 76058 Le Havre cedex (France)
Fax: (+33) 232-744-391
E-mail: ivan.jabin@univ-lehavre.fr
Dr. J. Marrot
Institut Lavoisier
UMR CNRS 8637, Université de Versailles St-Quentin en Yvelines
45 av. des Etats-Unis, 78035 Versailles cedex (France)

[**] We thank the French Ministry of Research and New Technologies and the CNRS for financial support. We also gratefully acknowledge Dr. Gildas Bertho and Prof. Jean-Pierre Girault (UMR CNRS 8601) for fruitful discussions and help with the NMR studies.

Supporting information for this article is available on the WWW under http://www.angewandte.org or from the author.

 © 2006 Wiley-VCH Verlag GmbH & Co. KGaA, Weinheim

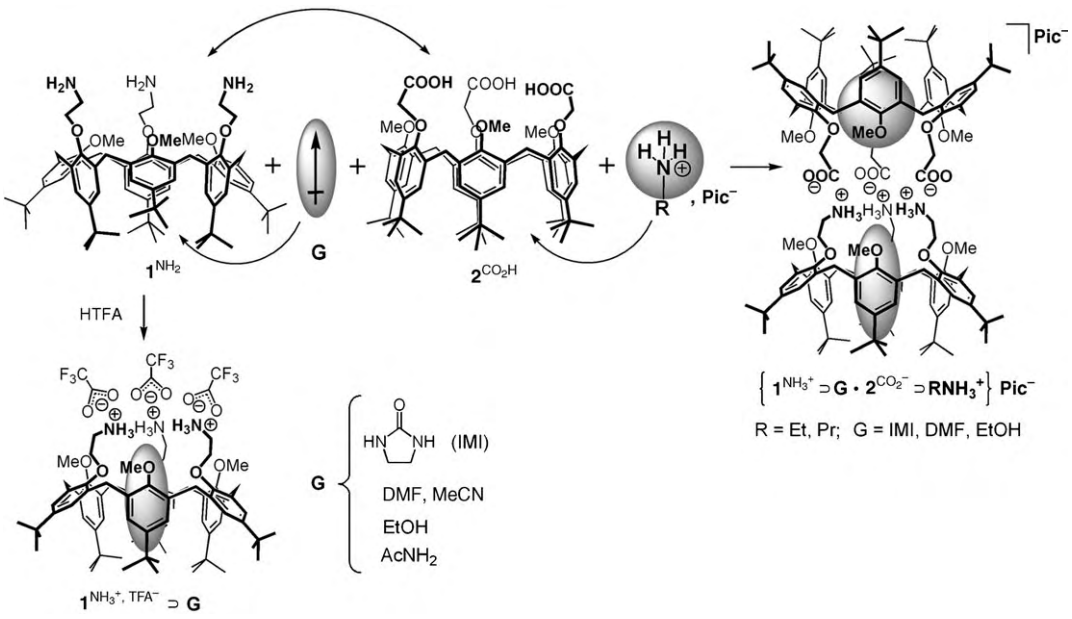

Scheme 1. Complexation of polar neutral guests G by calix[6]trisamine $\mathbf{1}^{NH_2}$ in the presence of HTFA and cooperative self-assembly of the quaternary complex $\{\mathbf{1}^{NH_3^+}\supset G\cdot\mathbf{2}^{CO_2^-}\supset RNH_3^+\}$ in chloroform. Pic^- = picrate, DMF = *N*,*N*-dimethylformamide.

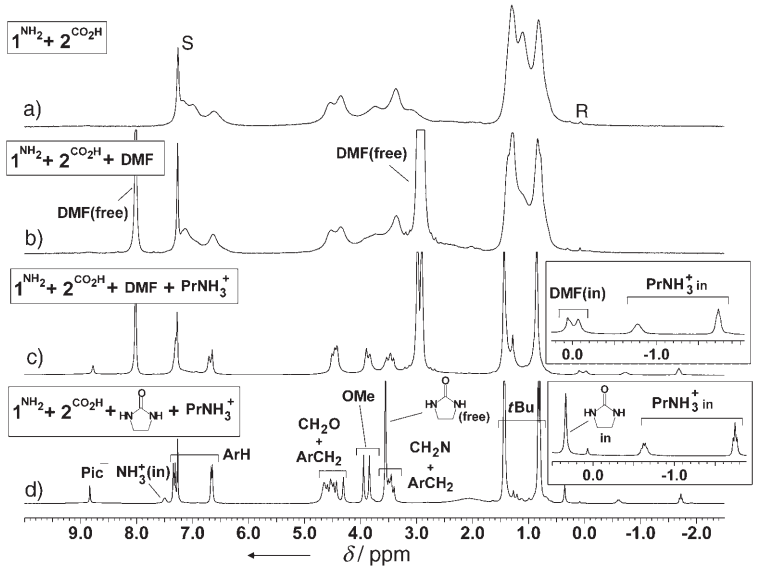

Figure 1. ^{1}H NMR spectra ($CDCl_3$, room temperature) of a 1:1 mixture of $\mathbf{1}^{NH_2}$ and $\mathbf{2}^{CO_2H}$ (4.3×10^{-3} M): a) before and b) after addition of G = DMF (30 equiv); c) after subsequent addition of $PrNH_3^+Pic^-$ (1 equiv); d) with G = IMI (6 equiv) instead of DMF. S = residual solvent; R = reference.

of quaternary complexes $\{\mathbf{1}^{NH_3^+}\supset G\cdot\mathbf{2}^{CO_2^-}\supset RNH_3^+\}$ according to Scheme 1.[18,19]

Crystals of $\{\mathbf{1}^{NH_3^+}\supset IMI\cdot\mathbf{2}^{CO_2^-}\supset PrNH_3^+\}$ suitable for X-ray analysis[20] were obtained by slow diffusion at 4 °C of diethyl ether into a solution of $\mathbf{1}^{NH_2}$ and $\mathbf{2}^{CO_2H}$ (1:1) in $CDCl_3$ in the presence of IMI (3 equiv) and $PrNH_3^+Pic^-$ (1 equiv; Figure 2). In agreement with the solution study, the solid-state structure shows two calixarene subunits in a flattened-cone conformation with the *tert*-butyl substituents of the anisole units closing the entrance of each cavity. The narrow rims of the two calixarenes are assembled through triple ion pairing between the complementary carboxylate and ammonium arms of $\mathbf{2}^{CO_2^-}$ and $\mathbf{1}^{NH_3^+}$. Each calixarene subunit deeply includes its specific guest in the heart of its hydrophobic cavity. Three carboxylate oxygen donors of $\mathbf{2}^{CO_2^-}$ specifically point toward the ammonium group of $PrNH_3^+$ at hydrogen-bonding distances. $\mathbf{1}^{NH_3^+}$ and the imidazolidin-2-one are strongly bound as well by four hydrogen bonds that link the urea carbonyl and NH groups with two ammonium arms and the corresponding two phenoxy oxygen donors, respectively.

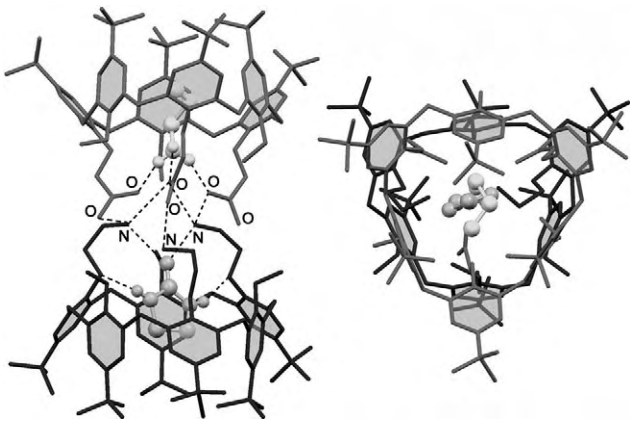

Figure 2. Crystal structure of $\{\mathbf{1}^{NH_3^+}\supset IMI\cdot\mathbf{2}^{CO_2^-}\supset PrNH_3^+\}$ (side and top views). The calixarene hosts and the guests are depicted in capped-stick and ball-and-stick models, respectively. Only the hydrogen atoms belonging to the NH groups of the guests are displayed in the side view (their locations were calculated). Other hydrogen atoms, the picrate counter anion, free IMI, and solvents of crystallization are omitted for clarity. Each dashed line denotes a hydrogen bond with $2.65 < d(N\cdots O) < 2.98$ Å.

 © 2006 Wiley-VCH Verlag GmbH & Co. KGaA, Weinheim

As previously observed with the parent 1:1 host–guest complexes, the supramolecular structure is further stabilized by CH–π interactions between the guest alkyl groups and the aromatic walls of the calixarene cavities (d(C···Ar) = 3.3–3.5 Å and 3.4–3.6 Å for IMI and $PrNH_3^+$, respectively) and charge–dipole interactions within the polycharged sites. Hence, the IMI and $PrNH_3^+$ guests display remarkable complementarities in terms of size, shape, and electronic structure with their hosts, which leads to an optimized hydrogen-bonding network.[21]

The quaternary complex $\{\mathbf{1}^{NH_3^+} \supset IMI \cdot \mathbf{2}^{CO_2^-} \supset PrNH_3^+\}$ proved to be exceptionally stable. In $CDCl_3$, its ^1H NMR signature did not change over a large temperature range (223–330 K) and down to a concentration of 70 μM. After the addition of a quarter volume of a polar protic solvent such as CD_3OD, 50% of the quaternary complex survived. It also appeared insensitive to the presence of a large excess of IMI (≈30 equiv), which demonstrates the high selectivity of the recognition process. In contrast, upon the addition of complementary counterions ($PrNH_3^+Pic^-$, ≈5 equiv), the quaternary edifice was split into two 1:1 complexes, as the characteristic NMR patterns of $\mathbf{1}^{NH_3^+,Pic^-} \supset IMI$ and $\mathbf{2}^{CO_2^-,PrNH_3^+} \supset PrNH_3^+$ were obtained.

All these results highlight a rare case of spontaneous 1+1+1+1 self-assembly thanks to the specific interaction between two different calixarene hosts ($\mathbf{1}^{NH_3^+}$ and $\mathbf{2}^{CO_2^-}$) shaped by their specific guest, a neutral polar molecule (G), and an ammonium ion (RNH_3^+). The recognition process involves several cooperative events:

1) To act as a host, each calixarene must be shaped and polarized. Thus, a prerequisite is the triple proton exchange between $\mathbf{1}^{NH_2}$ and $\mathbf{2}^{CO_2H}$ that allows both calixarene cores to self-assemble into polarized cones with opposite binding properties. One of them ($\mathbf{1}^{NH_3^+}$) presents a cationic cap with hydrogen-bond donors, whereas the other ($\mathbf{2}^{CO_2^-}$) is anionic with hydrogen-bond acceptors.
2) Conversely, the presence of each guest (G and RNH_3^+) is crucial for the self-assembly. Indeed, their inclusion increases the preorganization and the directionality of the ionic arms involved in the recognition of the two calixarene subunits. Hence, the guests act as "shoe trees" that direct the self-assembly process through triple ion pairing.[22]
3) Lastly, the structural modification induced by the presence of a first guest is efficiently sensed by the other calixarene host and the binding of the second guest is favored, which denotes a positive heterotropic allosteric control.

In summary, the formation of these quaternary complexes with four different components is a very selective process. Indeed, no "error" was detectable by NMR spectroscopy. The process involves multiple recognition levels that are chemically (acid–base) and conformationally (host–guest) coupled. Carboxylate and ammonium groups are classical effectors for recognition and self-assembly in biology (e.g., substrate in the active site of an enzyme) and are often used in artificial constructions. In the present example, three levels of positive cooperativity, with two guest bindings and one assembly of the hosts, were effective: a first guest binding favors the calixarene assembly that favors the second guest binding; or, in a different way, the (imperfect) assembly of the calixarenes favors the first guest (weak) binding that favors the second guest binding, which, ultimately, optimizes the shaping and the noncovalent bonds of the whole edifice! This is a rare and interesting case of an allosterically coupled double induced-fit process that could be useful for the elaboration of double recognition devices of molecules, or for the construction of sophisticated periodic networks.

Received: November 4, 2005
Published online: April 3, 2006

Keywords: allosterism · calixarenes · host–guest systems · self-assembly · supramolecular chemistry

[1] J. M. Berg, J. L. Tymoczko, L. Stryer in *Biochemistry*, 5th ed., W. H. Freeman, New York, **2002**.
[2] For selected examples, see: a) N. J. M. Birdsall, S. Lazareno, *Mini-Rev. Med. Chem.* **2005**, *5*, 523–543; b) S. Hayward, *J. Mol. Biol.* **2004**, *339*, 1001–1021; c) P. Andersson, J. Kvassman, B. Olden, G. Pettersson, *Eur. J. Biochem.* **1984**, *144*, 317–324; d) J. Wang, K. A. Stieglitz, J. P. Cardia, E. R. Kantrowitz, *Proc. Natl. Acad. Sci. USA* **2005**, *102*, 8881–8886; e) B. Delagoutte, D. Moras, J. Cavarelli, *EMBO J.* **2000**, *19*, 5599–5610.
[3] L. Kovbasyuk, R. Krämer, *Chem. Rev.* **2004**, *104*, 3161–3187.
[4] J. Rebek, Jr., T. Costello, L. Marshall, R. Wattley, R. C. Gadwood, K. Onan, *J. Am. Chem. Soc.* **1985**, *107*, 7481–7487.
[5] H. Sato, K. Tashiro, H. Shinmori, A. Osuka, Y. Murata, K. Komatsu, T. Aida, *J. Am. Chem. Soc.* **2005**, *127*, 13086–13087.
[6] a) J. Kang, J. Rebek, Jr., *Nature* **1997**, *385*, 50–52; b) M. Yoshizawa, Y. Takeyama, T. Okano, M. Fujita, *J. Am. Chem. Soc.* **2003**, *125*, 3243–3247.
[7] M. Takeuchi, M. Ikeda, A. Sugasaki, S. Shinkai, *Acc. Chem. Res.* **2001**, *34*, 865–873.
[8] T. Nabeshima, T. Saiki, J. Iwabuchi, S. Akine, *J. Am. Chem. Soc.* **2005**, *127*, 5507–5511.
[9] a) A. Arduini, L. Domiano, L. Ogliosi, A. Pochini, A. Secchi, R. Ungaro, *J. Org. Chem.* **1997**, *62*, 7866–7868; b) J. J. Gonzales, R. Ferdani, E. Albertini, J. M. Blasco, A. Arduini, A. Pochini, P. Prados, J. de Mendoza, *Chem. Eur. J.* **2000**, *6*, 73–80; c) A. M. Rincon, P. Prados, J. de Mendoza, *Eur. J. Org. Chem.* **2002**, 640–644.
[10] U. Darbost, M. Giorgi, N. Hucher, I. Jabin, O. Reinaud, *Supramol. Chem.* **2005**, *17*, 243–250.
[11] For another example of polarization of a calix[6]arene by protonation of its aza cap for the selective and efficient binding of neutral dipolar guests, see: U. Darbost, M.-N. Rager, S. Petit, I. Jabin, O. Reinaud, *J. Am. Chem. Soc.* **2005**, *127*, 8517–8525.
[12] For the preparation of $\mathbf{1}^{NH_2}$, see: U. Darbost, M. Giorgi, O. Reinaud, I. Jabin, *J. Org. Chem.* **2004**, *69*, 4879–4884.
[13] For the preparation of $\mathbf{2}^{CO_2H}$, see: A. Castani, P. Minari, A. Pochini, R. Ungaro, *J. Chem. Soc. Chem. Commun.* **1991**, 1413–1414.
[14] The spectrum displayed in Figure 1a was recorded after dissolving $\mathbf{1}^{NH_2}$ (3 mg, 2.6 μmol) and $\mathbf{2}^{CO_2H}$ (3 mg, 2.5 μmol) in $CDCl_3$ (0.6 mL, neutralized with basic alumina) at 293 K. It is different from those of the separated species.
[15] This finding is also due to the weaker acidity of $\mathbf{2}^{CO_2H}$ relative to HTFA. Indeed, addition of AcOH to $\mathbf{1}^{NH_2}$ did not lead to its structuration and no inclusion of the guest was observed.
[16] IMI is a much better guest for $\mathbf{1}^{NH_3^+,TFA^-}$ than DMF (this specific point will be discussed elsewhere). Its relative affinity, which has

 © 2006 Wiley-VCH Verlag GmbH & Co. KGaA, Weinheim

been determined through a competitive NMR binding experiment in $CDCl_3$ at 263 K, is about 400 times higher than that of DMF (see the Supporting Information for the detailed procedure).

[17] In the ternary mixtures containing both calixarenes but only one good guest (either $PrNH_3^+$ or IMI in large excess), partial inclusion of the guest could be detected. Interestingly, the chemical shifts observed for the included guest were different from those observed with the quaternary adducts. See the Supporting Information for selected ^1H and 2D NMR spectra of the ternary or quaternary adducts and for the resonances of the included guests.

[18] The formation of the 1+1+1+1 complex $\{\mathbf{1}^{NH_3^+}\supset IMI\cdot\mathbf{2}^{CO_2^-}\supset PrNH_3^+\}$ in solution is further substantiated by T_1 measurements. Indeed, all groups of protons belonging to its calixarene skeletons displayed T_1 values 30 to 100% higher than those for the monomeric species $\mathbf{1}^{NH_3^+,TFA^-}\supset IMI$ (260 K, 500 MHz, 4.3 mM, OCH_3: 1.2 vs. 0.6 s; $ArCH_2$: 0.75 vs. 0.4 s; H_{Ar}: 1.35 vs. 1.1 s). As a result of their high molecular weights, both compounds were found in the same regime, namely $\omega\tau_c > 1$ (over the extreme narrowing limit). Indeed, the NOE crosspeaks were negative at 500 MHz ($\tau_m = 800$ ms).

[19] Accurate determination of the equilibrium constants for the formation of the quaternary complexes is not possible, as "free" calixarenes are partially aggregated. However, the values were estimated based on the NMR data ($CDCl_3$) with $PrNH_3^+Pic^-$, by considering $[\mathbf{1}\text{ or }\mathbf{2}]_{free} = [\mathbf{1}\text{ or }\mathbf{2}]_{total} - [\{\mathbf{1}^{NH_3^+}\supset G\cdot\mathbf{2}^{CO_2^-}\supset PrNH_3^+\}]$: $K_{DMF} \approx 10^6\,M^{-3}$ and $K_{IMI} > 10^{16}\,M^{-3}$ for G = DMF and IMI, respectively.

[20] Crystal data for $\{\mathbf{1}^{NH_3^+}\supset IMI\cdot\mathbf{2}^{CO_2^-}\supset PrNH_3^+\}$: yellow platelet of dimensions $0.30\times0.25\times0.08$ mm, triclinic, space group $P\bar{1}$ (no. 2), $a = 21.733(2)$, $b = 22.133(2)$, $c = 23.987(2)$ Å, $\alpha = 115.851(2)$, $\beta = 107.189(3)$, $\gamma = 96.818(3)°$, $V = 9500(2)$ Å^3, $Z = 2$, $\rho_{calcd} = 1.029\,g\,cm^{-3}$; X-ray intensity data were collected on a Bruker X8-APEX2 CCD area-detector diffractometer with $Mo_{K\alpha}$ radiation ($\lambda = 0.71073$ Å) at $T = 100$ K. Five sets of narrow data frames (30 s per frame) were collected at different values of θ for two and three initial values of ϕ or ω, respectively, by using 0.5° increments of ϕ or ω. Data reduction was accomplished with SAINT V7.03.[23] The redundancy in data allowed a semiempirical absorption correction (SADABS V2.10)[23] to be applied, on the basis of multiple measurements of equivalent reflections. The structure was solved by direct methods, developed by successive difference Fourier syntheses, and refined by a full-matrix least-squares method on all F^2 data by using SHELXTL V6.14.[24] Hydrogen atoms were included in calculated positions and allowed to ride on their parent atoms; total reflections collected: 214162; independent reflections: 44205 (29578 with $F_o > 4\sigma(F_o)$); $2\theta_{max} = 55.37°$ (99.3% coverage). Number of variables: 1987; $R_1 = 0.0748$, $wR_2 = 0.2271$, $S = 1.100$; highest residual electron density: $1.494\,e\,Å^{-3}$. CCDC-287821 contains the supplementary crystallographic data for this paper. These data can be obtained free of charge from the Cambridge Crystallographic Data Centre via www.ccdc.cam.ac.uk/data_request/cif.

[21] Additional intermolecular hydrogen bonding involving the picrate counter anion or a free IMI molecule are observable in the lattice. Thus, in the solid state, the whole self-assembled structure $\{\mathbf{1}^{NH_3^+}\supset IMI\cdot\mathbf{2}^{CO_2^-}\supset PrNH_3^+\}$ is stabilized through a total of 15 cooperative hydrogen bonds.

[22] C. L. D. Gibb, B. C. Gibb, *J. Supramol. Chem.* **2001**, *1*, 39–52.

[23] APEX2 version 1.0-8, Bruker AXS, Madison, WI, **2003**.

[24] SHELXTL version 6.14, Bruker AXS, Madison, WI, **2001**.

 © 2006 Wiley-VCH Verlag GmbH & Co. KGaA, Weinheim

Biosensors

DOI: 10.1002/anie.200503403

Rationally Designed Chemical Modulators Convert a Bacterial Channel Protein into a pH-Sensory Valve**

Armağan Koçer, Martin Walko, Erna Bulten, Erik Halza, Ben L. Feringa, and Wim Meijberg**

Small-molecule modulators are very promising tools for the exploration and manipulation of biological systems beyond the limits of genetics. The modern molecular biology toolkit provides a variety of methods that aid in exploring and understanding the structure and function of biological molecules. However, these methods have limitations, especially in the range of changes and responses that they can accomplish. In this regard, chemical modification provides a complementary approach. Variations can be introduced to the protein to confer features not achievable with the 20 amino acids that are genetically encoded. This is especially true when a combination of properties, such as reversibility, tunability, target specificity, sensitivity to external stimuli, and control over the timescale of the effect, are desired all at the same time.

A particularly interesting property to control at the molecular level is transport across barriers such as biological membranes, as such control could easily lead to applications in, for example, sensing and detection and drug delivery. This effect has been pursued in a number of studies on the construction of functional nanopores with either synthetic molecules or naturally occurring channels, the latter mainly as β-barrel structures.[1] Herein, we describe the rational design

[*] M. Walko,[+] E. Halza, Prof. Dr. B. L. Feringa
Department of Organic and Molecular Inorganic Chemistry
Stratingh Institute and Material Science Center
University of Groningen
Nijenborgh 4, 9747 AG, Groningen (The Netherlands)
Fax: (+31) 50-363-4296
E-mail: b.l.feringa@rug.nl

Dr. A. Koçer,[+] E. Bulten, Dr. W. Meijberg
BiOMaDe Technology Foundation
Nijenborgh 4, 9747 AG, Groningen (The Netherlands)
Fax: (+31) 50-363-4429
E-mail: meijberg@biomade.nl

[+] These authors contributed equally to this work.

[**] We acknowledge Dr. R. Friesen for early contributions to the work, Prof. Dr. G. T. Robillard and Prof. Dr. Bert Poolman for fruitful discussions, C. M. Jeronimus-Stratingh and A. van Dam for the ESI-MS analyses, and the Neurobiophysics Group at the University of Groningen for patch-clamp facilities. This work was supported by the Netherlands Organization for Scientific Research (NWO-CW; B.L.F.), the Materials Science Center (MSC plus), University of Groningen (M.W. and B.L.F), and Nanoned, a national nanotechnology program coordinated by the Dutch Ministry of Economic Affairs.

Supporting information for this article is available on the WWW under http://www.angewandte.org or from the author.

WILEY InterScience DISCOVER SOMETHING GREAT
© 2006 Wiley-VCH Verlag GmbH & Co. KGaA, Weinheim

and engineering of a semisynthetic α-helical channel protein by altering its intrinsic properties, such that it senses changes in ambient pH and converts this signal into the opening of a pore (Figure 1). To do so, chemical modulators were developed that allow tuning of the pH interval and sensitivity of the response (that is, steepness of the transition). Furthermore, the introduction of a photocleavable protecting group results in a light-activated pH-sensitive valve.

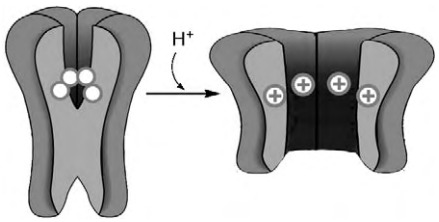

Figure 1. Protonation-induced opening of a mechanosensitive channel, which shows four of the five subunits in the pentamer (conceptual drawing). Protonation of a hydrophobic pore region of the MscL results in conformational changes and channel opening.

The protein we used is one of the best-studied channel proteins to date, that is, the mechanosensitive channel of large conductance (MscL) from *Escherichia coli*.[2] In nature, this homopentameric protein is embedded in the cytoplasmic membrane[3,4] and protects the bacterial cell against severe osmotic shocks.[5] Under hypo-osmotic conditions, cell turgor leads to tension in the membrane and an altered lateral-pressure profile, which in turn triggers large conformational changes.[6] The result is a 3-nm nonselective pore,[7] through which molecules can flow to balance the osmotic difference between the interior and exterior of the cell.[8]

An important parameter that influences the gating transitions of the MscL is the polarity of the hydrophobic constriction zone.[9] An increase in the polarity or hydrophilicity of the amino acid residue 22, located in this part of the protein, shifts the tension threshold for channel opening to lower values.[10] The introduction of a cysteine residue at this position followed by chemical modification with charged sulfhydryl-reactive compounds caused the channel to gate spontaneously.[11] Recently, we used covalently attached photosensitive modulators to induce charge at this position, thus leading to a channel in which gating could be switched on and off in the absence of any applied tension in response to radiation of an appropriate wavelength.[12]

Herein, we coupled charge-induced channel opening of the MscL to the ambient pH. In vivo this parameter varies depending on the health status of the surrounding tissue and/or cellular compartment. Around solid tumors, sites of inflammation, endosomes, and lysosomes the pH is lower (pH 6.8 to 5)[13] than under normal physiological conditions (pH 7.4). The incorporation of pH-controlled membrane channels in drug-carrying liposomes will allow selective release at diseased sites only. This might increase the effectiveness of the drug-delivery device, which is our ultimate goal. In previous studies it has been shown that a glycine-22-to-histidine (G22H) mutant exhibited increased sensitivity toward membrane tension but did not open spontaneously in response to pH.[10] To achieve pH-induced opening we modified the channel with specifically designed pH-responsive chemical modulators. The pH-sensitivity interval of the channel could be tuned by varying the pK_a and hydrophobicity of the modulators. Further control over the timing, location, and amplitude of the channel opening was obtained through the use of caged modulators, in which the pH modulator was protected by a photoremovable group. Channels thus modified are inert to the environmental pH until exposure to long-wavelength UV irradiation, at which point the pH responsiveness is immediately regained. This additional feature resulted in more flexibility and precision with respect to external control over the channel opening and the associated release of molecules from carrier devices.

To selectively attach the chemical modulators to the protein, glycine-22 was mutated into cysteine (G22C).[11] This change resulted in five identical modification sites within the hydrophobic constriction zone of the homopentameric protein. The chemical modulators were designed as sulfhydryl-reactive molecules (Table 1) and were covalently attached to detergent-solubilized MscL-G22C. It is known that the constriction zone of the protein is not fully accessible to chemical modification when the MscL is in its natural membrane environment.[20] ESI-MS analyses (see Supporting Information) indicate that in detergent-solubilized systems under our conditions all five subunits of the protein are modified simultaneously, and that the modification proceeds specifically and quantitatively within the detection limits of the mass spectrometry measurements. Our results are indicative of a more relaxed conformation of the channel in detergent solution compared to the natural membrane environment. In this regard, it is interesting to recall the arguments about whether the *Mycobacterium tuberculosis* crystal structure,[21] which was obtained in the presence of detergent, represents a fully or partially closed conformation

Table 1: The structure and properties of synthetic pH modulators.

	Compound	pK_a	Mass[a]	
			calcd	exptl
1	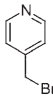	5.23[14]	15 786	15 789
2	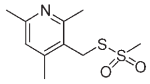	7.10[15]	15 860	15 860
3	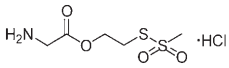	7.75[16]	15 828	15 830
4	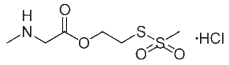	7.85[b]	15 842	15 841
5	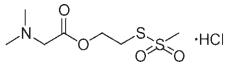	7.35[b]	15 856	15 855

[a] The masses refer to the monomer of MscL-G22C covalently modified with the corresponding compound. [b] The pK_a values were estimated on the basis of similar molecules found in the literature.[17–19].

 © 2006 Wiley-VCH Verlag GmbH & Co. KGaA, Weinheim

of the protein.[6,22,23] Our results support the latter interpretation.

The effects of chemical modification of MscL have been followed under isoosmotic conditions in a straightforward liposomal efflux assay, by using fluorescence changes upon the release of a reporter (see Supporting Information). Briefly, chemically modified channels were incorporated in liposomes consisting of synthetic lipids by a detergent-mediated reconstitution method[24] in the presence of calcein, a self-quenching fluorescent dye. After chromatographic removal of external dye, the resulting proteoliposomes (average size 200 nm, as determined by dynamic light scattering) were analyzed for channel activity at different pH values. Channel opening led to the release of the dye from the liposomal interior, and the resulting concentration decrease and dequenching upon entering the surrounding buffer could be monitored as an increase in fluorescence. Controls with liposomes lacking MscL-G22C, or containing unmodified MscL-G22C or wild-type MscL (with the C-terminal His tag that is present in all proteins described here), did not show any release activity (see Supporting Information).

pH-induced release through MscL modified with **1** could not be observed by the assay described above between pH 6 and 8, the pH limits of the assay. To access lower pH ranges, pyridine-modified channels were analyzed at the single-molecule level by measuring the ionic current flowing through the channel in response to the pH in patch-clamp experiments. Spontaneous channel opening was observed at pH 5.2, but at higher pH values the channels still required tension to open (see Supporting Information). Modulator **2** was designed to have a higher pK_a value, within the physiological range as well as the pH interval of the efflux assay. Channels modified with **2** did indeed show pH-dependent activity in efflux assays (Figure 2a), a result confirmed with patch-clamp measurements (Figure 2b and c). Thus, we showed for the first time that it is possible to open the channel in response to pH in synthetic lipids without applying any tension, in both patch-clamp and liposomal efflux setups.

It is known that the gating behavior of MscL channels can be correlated with the hydrophilicity of the residues present in the pore constriction.[10] From this point of view, the pyridine derivatives are not ideal modulators as they are quite hydrophobic. To address this issue and improve the liposomal efflux efficiency, pH modulators based on a different structural motif (**3**–**5**) were designed. We aimed specifically at increased hydrophilicity, a pK_a value tunable in the range pH 6–8, synthetic availability, and specific and efficient coupling to the protein.

Proteoliposomes containing channels modified with modulators **3**–**5** responded to pH and released more calcein at pH values below the pK_a of the modulator used. In contrast, control liposomes without MscL were stable at all pH values analyzed (Figure 3). The pH interval in which the channel is activated is dependent on the pK_a and hydrophobicity of the modulator. When the hydrophobicity of the pH modulator was higher as a result of the additional methyl groups, the modified channel was harder to open at higher pH values, where the modulator is mainly in its uncharged form. A particularly interesting case is the channel modified with **5** (Figure 3c), which has the highest hydrophobicity of the three modulators as well as the lowest pK_a. At pH 7.4, the

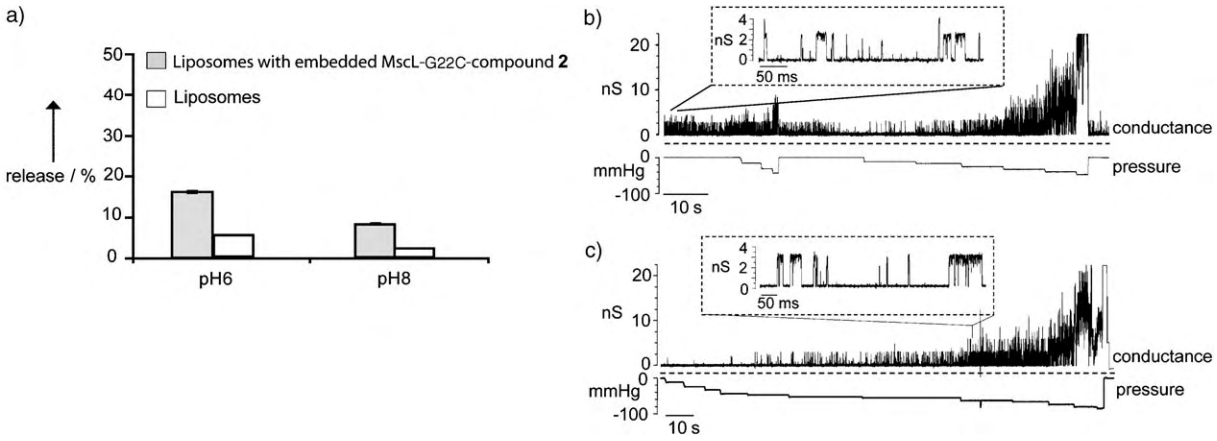

Figure 2. Activity of MscL-G22C modified with **2**. Modified MscL was reconstituted in 1,2-dioleoyl-*sn*-glycero-3-phosphocholine (DOPC) liposomes at a protein/lipid ratio of 1:120 (wt/wt) with a detergent-mediated reconstitution method. The fluorescent dye calcein (final concentration 50 mM) was added to the lipid–protein mixture and the detergent was removed with biobeads. External calcein was removed by column chromatography on Sephadex G50 and the liposomal fraction was used in the efflux assay. Depending on the concentration, about 10 μL of liposomes were diluted in 2 mL isoosmotic buffer (330 mosm) with varying pH values, and the increase in fluorescence was monitored for 45 min. Maximum release was reached within 30 min and is reported here relative to the release obtained after bursting the liposomes with excess Triton X100. Error bars indicate the standard deviation of two separate experiments. a) pH-induced release in calcein efflux assays. At pH 8, the proteoliposomes released about 8% of the dye, but at pH 6 the release increased to 16%. Patch-clamp measurements at b) pH 5.8 and c) at pH 8. Insets: typical channel openings in an enlarged form. The channel opened spontaneously without applied tension at pH 5.8. The observed conductance was about 2.5 nS, but if tension was applied gradually, the channel also gated to its full conductance of 3 nS with as little as 15 mm Hg applied negative pressure. Conversely, at pH 8 spontaneous gating was absent and only the tension-dependent openings were observed. At lower tensions (up to −50 mm Hg pressure in the patch) the channel opened to lower subconducting states (1 and 2 nS), whereas at higher levels of applied tension the full conductance was reached. Further application of tension resulted in the opening of more than one channel.

 © 2006 Wiley-VCH Verlag GmbH & Co. KGaA, Weinheim

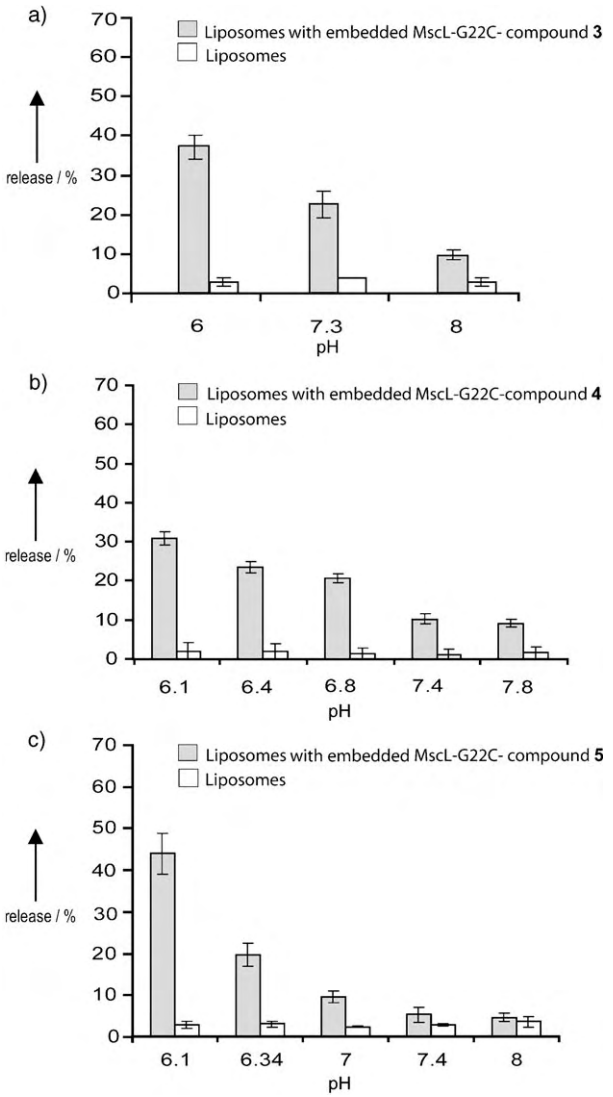

Figure 3. pH-dependent activity of modified MscL in calcein efflux assays. Modified MscL was reconstituted in DOPC/cholesterol/DSPE-PEG2000 (70:20:10 M) liposomes in the presence of calcein. The activity of the channel at different pH values was monitored to determine the maximum release values. Release was invariably completed within 30 min. Error bars indicate the standard deviation from four independent experiments. MscL-G22C modified with a) **3**, b) **4**, and c) **5**. DSPE = 1,2-distearoyl-*sn*-glycero-3-phosphoethanolamine; PEG = polyethylene glycol.

physiological pH for humans, liposomes with these channels retain their content at levels comparable to those of liposomes without protein, but start to open and release content at lower pH values, such as those found at cancerous and inflammation sites. The results were confirmed by patch-clamp measurements (see Supporting Information). As in the case of modification with **2**, the channel opened to a subconducting state in response to pH in the absence of tension, and to its full conducting state after the application of a small amount of tension. It has been reported that transition from the closed to the subconducting state represents the opening of the main gate of the channel and is associated with the highest energy barrier.[9] Our results, in particular the dramatic increase in channel activity upon a small amount of suction, appear to be in agreement with this model.

Further control over the pH-induced opening process was gained by chemically protecting the pH-sensitive group of the modulator. This allows activation on command. It was achieved by coupling the amino group of modulator **4** to a photolysable group that can be removed by irradiation with long-wavelength UV light (**6**; Figure 4a). In the dark, the

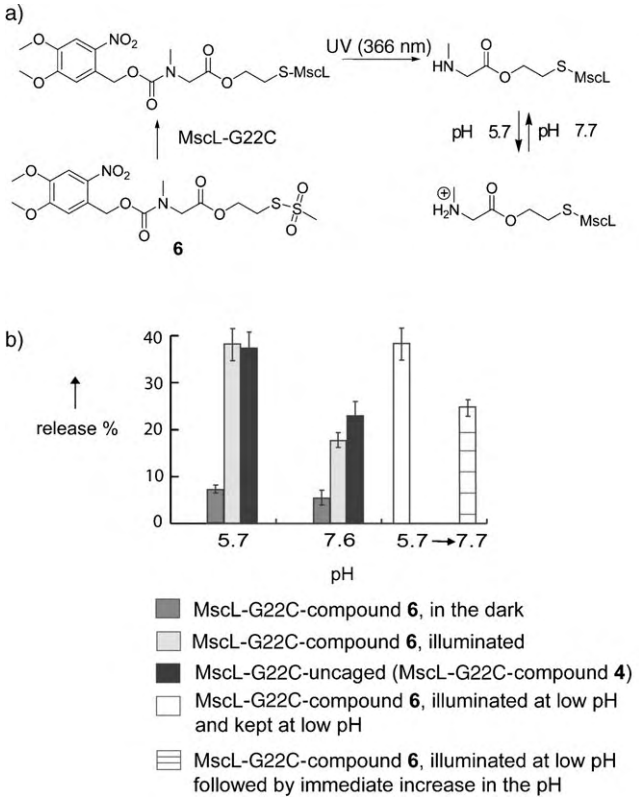

Figure 4. MscL-G22C modified with a caged pH modulator. a) Structure of **6** and removal of the protecting group by illumination. b) Activity of the modified MscL-G22C channels in the efflux assay. Channels modified with caged modulator **6** did not open at any pH value in the dark (dark gray bars). After deprotection by irradiation at 366 nm for 10 min (spectroline long-life filter, 365 mW cm^{-2}), channels became activated and released the liposomal content in dependence on the ambient pH (light gray bars). If the pH of the protein sample, which was illuminated at low pH, was immediately raised to 7.7 ± 0.1, the release of dye stopped (white bar with horizontal lines) because of closing of the channel; if the pH was kept constant at a low value, the channel stayed open (white bar) and release continued. Channels modified with uncaged modulator **4** opened in response to pH (black bar). Error bars indicate the standard deviation from three independent experiments.

modified channel remains closed and consequently calcein efflux experiments show no release of dye, irrespective of the environmental pH (Figure 4b, dark gray bars). After removal of the protecting group at the amine moiety by UV irradiation, the channel becomes responsive again to the pH of the environment, which results in high release of the liposomal content at low pH (Figure 4b, light gray bars).

 © 2006 Wiley-VCH Verlag GmbH & Co. KGaA, Weinheim

Comparison of the performance of the illuminated sample with an uncaged sample at the same pH (Figure 4b, black bars) indicated that the expected activity of **4** after removal of its protecting group was recovered, and therefore that photocleavage was complete.

The caged modulator was also used to address the reversibility of the pH-induced opening of the channel. To this end, duplicate samples were illuminated at pH 5.7. Subsequently, the pH of one of the samples was raised to 7.7. Although release started during illumination in both samples, the process was arrested immediately after the pH was raised to 7.7 (Figure 4b, white bar with horizontal lines), while continuing at low pH (Figure 4b, white bar). This experiment shows that the modified pH-sensitive channels can be closed through a protonation reaction. Unfortunately, the time course and sensitivity of the liposomal release experiment do not allow this cycle to be repeated a number of times with the same sample. Therefore, further investigation is required to conclusively prove that the pH-induced opening of the channel is reversible, that is, that the closed state at high pH after removal of the cage is identical to the closed state after a cycle of low and high pH.

The pH modulators described herein were able to confer pH responsiveness to the channel, as shown from patch-clamp and efflux measurements. However, the measurements also show that complete release of enclosed calcein was not achieved. Although this effect is not fully understood, a number of explanations can be put forward. For example, the reconstitution procedure does not guarantee that an active channel is associated with every liposome. Furthermore, in the case of the pH modulators, the ionization of one group will depress the pK_a of its neighbors in close proximity in the homopentameric protein. The accumulation of five positive charges will therefore only be achieved at much lower pH values, and hence the overall activity of the protein will appear to be lower. This proposal was confirmed by showing that modification of the protein with [2-(trimethylammonio)ethyl]methanethiosulfonate ($MTSET^+$), which carries a charge under all experimental conditions used here and thus results in five positive charges in the channel constriction, leads to maximum release values close to 100% (see Supporting Information). Finally, it has been reported that when the number of MscLs was low in the patches, the channel activity was followed by irreversible inactivation.[25] A combination of the latter two effects, that is, reduced activity and inactivation with time, will lead to release values below 100%.

In summary, we have converted a bacterial channel protein into a pH-sensitive valve. When embedded in liposomes, the modified channels sense the ambient pH and conditionally release the liposomal content. The sensitivity and pH interval for channel opening were tuned by varying the hydrophobicity and pK_a of the modulators. Additional control over pH response was gained through the introduction of a photosensitive caging group. Gaining control over MscL channel activity as presented herein is valuable for further investigations into the mechanism of the channel function. The pH-activated channel or caged channels can also serve as control valves to release or mix the contents at a desired location, time, and dosage, for example, in micro/nanosensory and delivery devices.

Received: September 26, 2005
Revised: December 7, 2005
Published online: April 4, 2006

Keywords: biosensors · drug delivery · membrane proteins · protein modifications · protonation

[1] H. Bayley, O. Braha, S. Cheley, L. Gu in *Nanobiotechnology* (Eds.: C. M. Niemeyer, C. A. Mirkin), Wiley-VCH, Weinheim, **2004**, pp. 93–112.
[2] S. I. Sukharev, P. Blount, B. Martinac, F. R. Blattner, C. Kung, *Nature* **1994**, *368*, 265–268.
[3] C. Berrier, A. Coulombe, C. Houssin, A. Ghazi, *FEBS Lett.* **1989**, *259*, 27–32.
[4] P. Blount, S. I. Sukharev, P. C. Moe, M. J. Schroeder, H. R. Guy, C. Kung, *EMBO J.* **1996**, *15*, 4798–4805.
[5] N. Levina, S. Totemeyer, N. R. Stokes, P. Louis, M. A. Jones, I. R. Booth, *EMBO J.* **1999**, *18*, 1730–1737.
[6] E. Perozo, A. Kloda, D. M. Cortes, B. Martinac, *Nat. Struct. Biol.* **2002**, *9*, 696–703.
[7] C. C. Cruickshank, R. F. Minchin, A. C. Le Dain, B. Martinac, *Biophys. J.* **1997**, *73*, 1925–1931.
[8] B. Ajouz, C. Berrier, A. Garrigues, M. Besnard, A. Ghazi, *J. Biol. Chem.* **1998**, *273*, 26670–26674.
[9] A. Anishkin, C. S. Chiang, S. Sukharev, *J. Gen. Physiol.* **2005**, *125*, 155–170.
[10] K. Yoshimura, A. Batiza, M. Schroeder, P. Blount, C. Kung, *Biophys. J.* **1999**, *77*, 1960–1972.
[11] K. Yoshimura, A. Batiza, C. Kung, *Biophys. J.* **2001**, *80*, 2198–2206.
[12] A. Koçer, M. Walko, W. Meijberg, B. L. Feringa, *Science* **2005**, *309*, 755–758.
[13] K. Ulbrich, V. Šubr, *Adv. Drug Delivery Rev.* **2004**, *56*, 1023–1050.
[14] A. Fischer, M. J. Kung, F. P. Robinson, *Can. J. Chem.* **1978**, *56*, 3072–3077.
[15] E. C. Kornfeld, *J. Am. Chem. Soc.* **1955**, *77*, 4425–4427.
[16] S. Glasstone, E. F. Hammel, *J. Am. Chem. Soc.* **1941**, *63*, 243–248.
[17] J. Martin, R. Mendez, T. Alemany, *J. Chem. Soc. Perkin Trans.* **1989**, 223–226.
[18] J. Hine, C. D. Fischer, *J. Am. Chem. Soc.* **1975**, *97*, 6513–6521.
[19] J. Hine, M. S. Cholod, R. A. King, *J. Am. Chem. Soc.* **1974**, *96*, 835–845.
[20] J. L. Bartlett, G. Levin, P. Blount, *Proc. Natl. Acad. Sci. USA* **2004**, *101*, 10161–10165.
[21] G. Chang, R. H. Spencer, A. T. Lee, M. T. Barclay, D. C. Rees, *Science* **1998**, *282*, 2220–2226.
[22] I. Iscla, G. Levin, R. Wray, R. Reynolds, P. Blount, *Biophys. J.* **2004**, *87*, 3172–3180.
[23] G. Levin, P. Blount, *Biophys. J.* **2004**, *86*, 2862–2870.
[24] J. L. Rigaud, B. Pitard, D. Levy, *Biochim. Biophys. Acta* **1995**, *1231*, 223–246.
[25] C. C. Häse, A. C. Le Dain, B. Martinac, *J. Biol. Chem.* **1995**, *270*, 18329–18334.

 © 2006 Wiley-VCH Verlag GmbH & Co. KGaA, Weinheim

Azides

DOI: 10.1002/anie.200504157

Formation of a Methyleneimine Moiety by Reaction of a Ru^{II}-Coordinated Azide Ion with Methyl Iodide**

Hirotaka Nagao, Takehiro Kikuchi, Minako Inukai, Akihiro Ueda, Takao Oi, Noriyuki Suzuki, and Mikio Yamasaki*

It has been reported that an azide ion coordinated to a metal center photochemically and thermally decomposes to afford a nitrogen-containing compound(s), which retain(s) a nitrogen atom of the azido ligand. The reaction proceeds via a reactive intermediate such as a nitrene and nitride complex, and N_2 is generated.[1–5] Although azide compounds are explosive as a result of rapid dinitrogen evolution, azido–metal complexes can potentially to be converted into various nitrogen-containing complexes such as imido and cycloaddition compounds.[2–6] Di(azido)bis(2,2′-bipyridine) complexes of Ru^{II} and Ru^{III} have been synthesized[1,7] and investigated in thermal and photochemical reactions.[1,8]

Methyleneimine is known to be a reactive molecule and its existence can be recognized only at low temperatures by IR spectroscopy.[9] A few metal complexes containing a methyleneimine moiety ($NH{=}CH_2$) have been synthesized by the reaction of a methylhydrazine or methylimido complex.[10] The $NH{=}CH_2$ ligand coordinates through two coordination modes; one is the N-monodentate mode (κN) of a rhenium complex[10a–c] and another the *N*,*C*-bidentate one ($\kappa^2 N,C$) of an osmium complex.[10d] Only one rhenium complex containing an methyleneimine-κN moiety has been characterized by X-ray crystallography.[10c] Herein, we describe the reaction of *cis*-$[Ru(N_3)_2(bpy)_2]\cdot H_2O$ (bpy = 2,2′-bipyridine) with CH_3I in CH_3CN to give a rare methyleneimine complex of ruthenium(II) ($Ru{-}NH{=}CH_2$) and its characterization by IR and NMR spectroscopy and X-ray crystallography.

cis-$[Ru(NH{=}CH_2)(NCCH_3)(bpy)_2](PF_6)_2$ was synthesized by the reaction of *cis*-$[Ru(N_3)_2(bpy)_2]\cdot H_2O$ with CH_3I in CH_3CN (Scheme 1). Red needle crystals were obtained by recrystallization from CH_3CN/H_2O. The IR spectrum shows

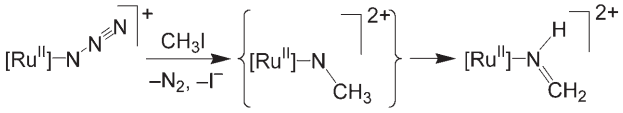

Scheme 1. Reaction of the azido ligand with CH_3I.

characteristic bands at $\tilde{\nu} = 3283$ and 2186 cm^{-1}, which were assigned to ν(NH) and ν(CN), respectively, as well as some bands of bpy ligands and PF_6. After the complex was recrystallized from D_2O/CH_3CN (1:1 *v*/*v*), the band at 3283 cm^{-1} shifted to 2430 cm^{-1} (see Supporting Information). This indicates that the proton of the NH moiety is exchangeable with a solvent proton.

The ^1H NMR spectrum in $(CD_3)_2CO$ shows a broad signal for the hydrogen atom of the imine function ($NH{=}CH_2$) at $\delta =$ 12.14 ppm as a doublet of doublets owing to coupling with two signals at $\delta = 7.98$ and 7.81 ppm ($NH{=}CH_2$). These two signals overlap with the bpy signals in the aromatic region and were characterized by H,H COSY. The δ value of the hydrogen atom of the imine is similar to that of the $CH_2{=}NH$-κN and -$\kappa^2 N,C$.[10] The ^{13}C NMR spectrum shows a signal at 172.42 ppm, which was assigned to the carbon atoms of the methyleneimine, analogously to that of the known Os complex.[10d]

The structure of the cation, *cis*-$[Ru(NH{=}CH_2)(NCCH_3)(bpy)_2]^{2+}$ is shown in Figure 1. The methyleneimine and the acetonitrile ligands are positioned *cis* to each other. The methyleneimine ligand coordinates to the ruthenium center in a bent fashion with Ru-N1-C1 = 135.4(7)° and with Ru–N1 = 2.083(10) and N1–C1 = 1.202(16) Å. This coordination fashion is similar to that of the reported κN-mode coordination rhenium complex.[10c] The N1–C1 bond length, 1.202(16) Å, is

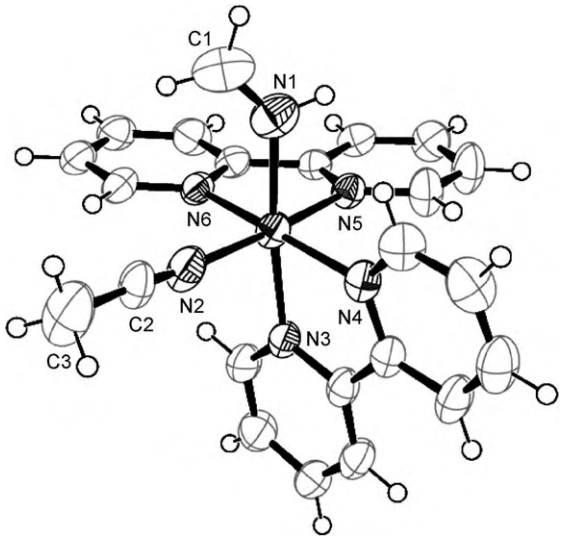

Figure 1. Structure of *cis*-$[Ru(NH{=}CH_2)(NCCH_3)(bpy)_2]^{2+}$ with 50% probability for thermal ellipsoids.

[*] Prof. Dr. H. Nagao, T. Kikuchi, M. Inukai, A. Ueda, Prof. Dr. T. Oi
Department of Chemistry
Faculty of Science and Technology, Sophia University
7-1 Kioi-cho, Chiyoda-ku, Tokyo 102-8554 (Japan)
Fax: (+81) 3-3238-3361
E-mail: h-nagao@sophia.ac.jp
Dr. N. Suzuki
RIKEN
Wako, Saitama 351-0198 (Japan)
Dr. M. Yamasaki
Application Laboratories, Rigaku Corporation
3-9-12 Matsubara-cho, Akishima, Tokyo 196-8666(Japan)

[**] This work was supported by a Grant-in-Aid for Scientific Research (no. 14540520) from the Ministry of Education, Culture, Sports, Science, and Technology, Japan. We thank Professor James M. Mayer (University of Washington) for his helpful discussion.

Supporting information for this article is available on the WWW under http://www.angewandte.org or from the author.

 © 2006 Wiley-VCH Verlag GmbH & Co. KGaA, Weinheim

shorter than those of other structurally characterized imine moieties coordinated to a metal center (1.25–1.31 Å).[10c,11] The acetonitrile ligand linearly coordinates to the metal center, as in previously reported Ru^{II} complexes.[11b] The structural parameters of two bpy ligands are similar to those of the previously reported ruthenium complexes.[11b,12]

The cyclic voltammogram (CV) of the complex in CH_3CN containing tetraethylammonium perchlorate (0.1 mol dm^{-3}) shows irreversible and reversible oxidation waves at $E_{pa} =$ 0.86 and $E_{1/2} = 1.10$ V versus Fc/Fc^+ at room temperature (see Supporting Information). The first irreversible oxidation potential is higher than those of Ru^{II} complexes containing polypyridine ligands and that of the imine complex of Ru^{II}, $[Ru(NH{=}CMe_2)(bpy)(trpy)]^{2+}$.[13] The first irreversible wave corresponds to a one-electron process by a controlled potential electrolysis. After the electrolysis, the CV shows only one reversible couple at 1.10 V. The profile of the CV does not change, even at low temperature (−40 °C). The oxidized form of this complex is very unstable and decomposes rapidly.

The UV/Vis spectrum of the starting diazido complex of Ru^{II} in CH_3CN shows two bands at $\lambda = 560$ and 387 nm. The spectrum in the presence of CH_3I in CH_3CN changes to show new bands at $\lambda = 496$ and 356 nm. The band at $\lambda = 496$ nm then decreases in intensity and a new band appears at $\lambda =$ 442 nm (see Supporting Information). However, in absence of CH_3I, the spectrum does not change for at least 4 days. The spectral change in CH_3NO_2 is the same as that in CH_3CN at the first stage, but no further change is observed for at least a few hours. A reaction intermediate like $[Ru(NH{=}CH_2)(N_3)(bpy)_2]^+$ and $[Ru(NH{=}CH_2)_2(bpy)_2]^{2+}$, which shows a characteristic band at 496 nm, develops during the formation of the methyleneimine complex. Attempts to isolate the product in CH_3NO_2 were all unsuccessful. We believe that the methyleneimine ligand is formed by the reaction of CH_3I with the negatively charged nitrogen atom of the azido ligand on Ru^{II} via a methylimido intermediate with N_2 evolution and proton transfer from the methyl group to the imido nitrogen atom, as in the formation of a methyleneimine-κ^2N,C osmium complex from a methylimido-κN analogue.[10d]

In this reaction of the azido complex, the nitrogen atom of the coordinated azide ion remains on the ruthenium center. The reaction of azido complexes will be useful in the synthesis of nitrogen-containing ligands for metal complexes. Detailed studies on the reaction of the azido complex and further reactions and properties of the methyleneimine ligand on the ruthenium complex are in progress.

Experimental Section

cis-$[Ru(NH{=}CH_2)(NCCH_3)(bpy)_2](PF_6)_2$: A suspension of *cis*-$[Ru(N_3)_2(bpy)_2]\cdot H_2O$ (200 mg, 0.388 mmol) and CH_3I (3 cm^3) in CH_3CN (100 cm^3) was stirred in the dark until the starting complex dissolved to form a dark red solution. A red oily reaction product was obtained after addition of KPF_6 (200 mg, 1.09 mmol) as a precipitant and concentration of the resultant solution. The red product obtained was recrystallized from CH_3CN/H_2O (1:1, 100 cm^3) through concentration by slow evaporation to form red needles (138 mg, 46 %). Elemental analysis: calcd for $C_{23}H_{22}N_6P_2F_{12}Ru$ (%): C 35.72, H 2.87, N 10.87; found: C 35.64, H 2.70, N 10.72; FAB MS: 629(M-PF_6); ^{1}H and ^{13}C NMR spectra were recorded on JEOL EX-270, AL-400 and ECP-500 spectrometers. The signals of the complex were characterized by ^{1}H, ^{1}H{^{1}H}, ^{13}C{^{1}H}, DEPT, COSY, C,H-COSY NMR spectroscopy (see Supporting Information). ^{1}H NMR (400 MHz, [D$_6$]acetone, TMS): $\delta = 2.50$ (s, 3H; CH_3CN), 7.41–7.44 (m, 2H; bpy), 7.81 (d, $J = 21$ Hz, 1H; CH_2), 7.89–7.94 (m, 4H; bpy), 7.98 (d, $J = 13$ Hz, 1H; CH_2), 8.04–8.09 (m, 2H; bpy), 8.32–8.36 (m, 2H; bpy), 8.61–8.70 (m, 2H; bpy), 8.74–8.81 (m, 2H; bpy), 9.15–9.17 (m, 1H; bpy), 9.52–9.54 (m, 1H; bpy), 12.14 ppm (br dd, $J = 13$ Hz, $J = 21$ Hz, 1H; NH); ^{13}C NMR (67.8 MHz, [D$_6$]acetone, TMS): $\delta = 4.04$ (CH_3CN), 124.49, 124.71, 124.90, 124.98, 127.82 (CH_3CN, overlapped with 2,2′-bipyridyl), 127.98, 128.46, 128.77, 138.73 (2C), 139.00, 139.27, 152.89, 153.16, 153.41, 154.09, 158.00 (q), 158.28 (q), 158.49 (q), 159.07 (q), 172.42 ppm (CH_2).

Crystal structure determination: Intensity data were collected on a Rigaku RAXIS RAPID imaging plate area detector, using graphite-monochromated $Mo_{K\alpha}$ radiation (0.71075 Å). All the calculations were carried out with the Crystal Structure software package. Structures were solved by SHELXL, expanded by using Fourier techniques, and refined by using full-matrix least-squares techniques on F^2. Crystallographic data: $C_{23}H_{22}F_{12}N_6P_2Ru$, $M_w = 773.47$, monoclinic, $P2_1/c$, $a = 17.078(6)$ Å, $b = 17.847(5)$ Å, $c = 11.825(3)$ Å, $\beta = 127.266(14)°$, $V = 2868.3(15)$ Å^3, $Z = 4$, ρcalcd $= 1.791$ g cm^{-3}, $\mu(Mo_{K\alpha}) = 7.63$ cm^{-1}, $T = 103$ K, 26072 reflections collected, 6523 unique ($R_{int} = 0.0330$), $R1\{I>2\sigma(I)\} = 0.0909$, $wR2$ (all data) $=$ 0.2458, GOF $= 1.052$; two PF_6 ions are disordered: P–F bonds and F-P-F angles of each PF_6 ion were restrained and refined. CCDC-289365 contains the supplementary crystallographic data for this paper. These data can be obtained free of charge from The Cambridge Crystallographic Data Centre via www.ccdc.cam.ac.uk/data_request/cif.

Received: November 22, 2005
Published online: April 4, 2006

Keywords: azides · imines · N ligands · ruthenium · synthetic methods

[1] G. M. Brown, R. W. Callahan, T. J. Meyer, *Inorg. Chem.* **1975**, *14*, 1915–1921.
[2] L. A. P. Kane-Maguire, P. S. Sheridan, F. Basolo, R. G. Pearson, *J. Am. Chem. Soc.* **1970**, *92*, 5865–5872.
[3] R. T. Weaver, F. Basolo, *Inorg. Chem.* **1974**, *13*, 1535–1538.
[4] a) T. Suzuki, A. G. DiPasquale, J. M. Mayer, *J. Am. Chem. Soc.* **2003**, *125*, 10514–10515; b) C. A. Grapperhaus, B. Mienert, E. Bill, T. Weyhermüller, K. Wieghardt, *Inorg. Chem.* **1974**, *39*, 5306–5317; c) J. L. Reed, H. D. Gafney, F. Basolo, *J. Am. Chem. Soc.* **1974**, *96*, 1363–1369; d) G. Ferraudi, J. F. Endicott, *Inorg. Chem.* **1973**, *12*, 2389–2396; e) H. D. Gafney, J. L. Reed, F. Basolo, *J. Am. Chem. Soc.* **1973**, *95*, 7998–8005.
[5] a) S. D. Brown, J. C. Peters, *J. Am. Chem. Soc.* **2005**, *127*, 1913–1923; b) T. R. Weaver, B. C. Lane, F. Basolo, *Inorg. Chem.* **1972**, *11*, 2277–2279; c) B. C. Lane, J. W. McDonald, F. Basolo, R. G. Pearson, *J. Am. Chem. Soc.* **1972**, *94*, 3786–3793.
[6] a) Y.-J. Kim, S.-H. Lee, S.-H. Lee, S. I. Jeon, M. S. Lim, S. W. Lee, *Inorg. Chim. Acta* **2005**, *358*, 650–658; b) Y.-J. Kim, X. Chang, J.-T. Han, M. S. Lim, S.-W. Lee, *Dalton Trans.* **2004**, 3699–3708; c) S.-C. Hsu, Y.-C. Lin, S. L. Huang, Y.-H. Liu, Y. Wang, H. Liu, *Eur. J. Inorg. Chem.* **2004**, 459–462; d) Y.-J. Kim, Y.-S. Joo, J.-T. Han, W.-S. Han, S.-W. Lee, *J. Chem. Soc. Dalton Trans.* **2002**, 3611–3618; Y.-J. Kim, Y.-S. Kwak, Y.-S. Joo, S.-W. Lee, *J. Chem. Soc. Dalton Trans.* **2002**, 144–151.
[7] W. M. Wallace, P. E. Hoggard, *Inorg. Chem.* **1979**, *18*, 2934–2935.
[8] a) K.-W. Lee, P. E. Hoggard, *Inorg. Chem.* **1993**, *32*, 1877–1878; b) D. M. Martin, P. E. Hoggard, *J. Chem. Soc. Chem. Commun.* **1989**, 100–101.

 © 2006 Wiley-VCH Verlag GmbH & Co. KGaA, Weinheim

[9] a) M. S. Platz in *Reactive Intermediate Chemistry* (Eds.: R. A. Moss, M. S. Platz, M. Jones, Jr.) Wiley, **2004**, pp. 507 – 508; b) A. Reiser, H. M. Wagner in *The chemistry of the azido group* (Ed.: S. Patai), Intersceience, New York, **1971**, p. 468; c) D. Milligan, M. E. Jacox, *J. Chem. Phys.* **1963**, *39*, 712 – 715; d) D. E. Milligan, *J. Chem. Phys.* **1961**, *35*, 1491 – 1497.

[10] a) G. Albertin, S. Antoniutti, A. Bacchi, B. Fregolent, G. Pelizzi, *Eur. J. Inorg. Chem.* **2004**, 1922 – 1938; b) G. Albertin, S. Antoniutti, M. T. Giorgi, *Eur. J. Inorg. Chem.* **2003**, 2855 – 2866; c) G. Albertin, S. Antoniutti, A. Bacchi, E. Bordignon, M. T. Giorgi, G. Pelizzi, *Angew. Chem.* **2002**, *114*, 2296 – 2298; *Angew. Chem. Int. Ed.* **2002**, *41*, 2192 – 2194; d) P. A. Shapley, J. M. Shusta, J. L. Hunt, *Organometallics* **1996**, *15*, 1622 – 1629.

[11] a) J. Zhang, T. B. Gunnoe, J. L. Petersen, *Inorg. Chem.* **2004**, *44*, 2895 – 2907; b) D. A. Garnovskii, A. J. L. Pombeiro, M. Haukka, P. Sobota, V. Y. Kukushkin, *Dalton Trans.* **2004**, 1097 – 1103; c) H. Nagao, T. Hirano, N. Tsuboya, S. Shiota, M. Mukaida, T. Oi, M. Yamasaki, *Inorg. Chem.* **2002**, *41*, 6267 – 6273; d) R. Castarlenas, M. A. Esteruelas, E. Gutiérrez-Puebla, E. Onate, *Organometallics* **2001**, *20*, 1545 – 1554, and references therein.

[12] a) F. Xobi, M. Hohl, I. Zimmermann, R. Alberto, *Inorg. Chem.* **2004**, *43*, 2771 – 2772; b) M. G. Mellace, F. Fagalde, N. E. Katz, I. G. Crivelli, A. Delgadillo, A. M. Leiva, B. Loeb, M. T. Garland, R. Baggio, *Inorg. Chem.* **2004**, *43*, 1100 – 1107; c) K. Sakai, Y. Uchida, T. Kajiwara, T. Ito, *Acta Crystallogr. Sect. C* **2004**, *60*, m65 – m68.

[13] a) P. A. Adcock, F. R. Keene, R. S. Smythe, M. R. Snow, *Inorg. Chem.* **1984**, *23*, 2336 – 2343; b) P. A. Adcock, F. R. Keene, *J. Am. Chem. Soc.* **1981**, *103*, 6494 – 6495.

 © 2006 Wiley-VCH Verlag GmbH & Co. KGaA, Weinheim

Methanol-to-Olefin Process

DOI: 10.1002/anie.200504372

Experimental Evidence from H/D Exchange Studies for the Failure of Direct C–C Coupling Mechanisms in the Methanol-to-Olefin Process Catalyzed by HSAPO-34**

*David M. Marcus, Kelly A. McLachlan, Mark A. Wildman, Justin O. Ehresmann, Philip W. Kletnieks, and James F. Haw**

The conversion of methanol to ethylene and propene on microporous solid acid catalysts[1,2] such as the silicoaluminophosphate HSAPO-34 at temperatures of 573 K and above remains a stimulus to mechanistic progress in heterogeneous catalysis. The general features of this reaction on a working catalyst (i.e., following a kinetic induction period) are widely accepted as a hydrocarbon pool mechanism on the basis of experimental[3–6] and theoretical work.[7,8] Prior to recognition of the hydrocarbon pool mechanism, speculation centered on any of a dozen or more "direct" mechanisms in which, typically, an activated single carbon fragment reacted with methanol or dimethyl ether (DME) to form ethylene, methyl ethyl ether, or some other species with a "first" carbon–carbon bond.[1] Note that there are still important additional contributions that theory can make, such as a thorough comparison of detailed hydrocarbon pool reaction steps to putative direct reaction steps. Previously,[9] we used highly purified reagents to call into question whether "direct" mechanisms occur at all, even at very low rates during the kinetic induction period. In this view, the original hydrocarbon pool forms from impurities rather than a "direct" route, and a mature hydrocarbon pool then develops from side reactions of propene or other products.

Very recently, a pair of theoretical papers[10,11] examined essentially all direct pathways from methanol to species with a first C–C bond. Those studies concluded that no combination of direct steps exist that is capable of linking methanol with ethylene, even at a temperature of 720 K. Some of the direct routes examined involved the intermediacy of framework-bound methoxy groups, Z(O)-CH_3, which indisputably form from a fraction of acid sites in the equilibration of methanol, dimethyl ether, and water on the catalyst (Scheme 1).[6,12] The

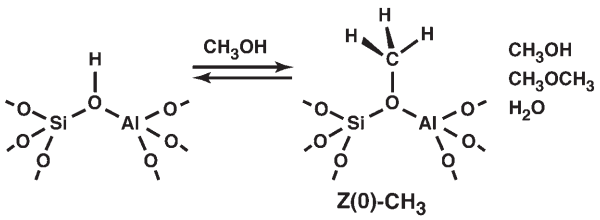

Scheme 1. Equilibration of methanol over framework acid sites in the MTO catalyst, HSAPO-34.

ease with which Z(O)-CH_3 can be observed by spectroscopy has probably contributed to the attraction of framework methoxy groups as key intermediates in proposals of direct reactions of methanol on HSAPO-34[13] or methyl halides on basic catalysts.[14]

In their theoretical study,[11] Waroquier and co-workers reject equilibration of Z(O)-CH_3 with carbene (Scheme 2) as

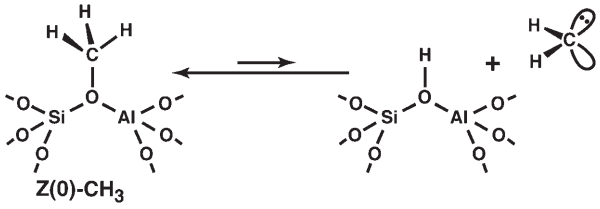

Scheme 2. Putative dissociation of Z(O)-CH_3 to carbene. Carbene could also insert into an O–D bond[15] to form Z(O)-CH_2D, and H/D exchange would be evident.

[*] D. M. Marcus, K. A. McLachlan, M. A. Wildman, J. O. Ehresmann, P. W. Kletnieks, Prof. J. F. Haw
Department of Chemistry
University of Southern California
Los Angeles, CA 90089-1661 (USA)
Fax: (+1) 213-740-0930
E-mail: jhaw@usc.edu

[**] This work was supported by the US Department of Energy (DOE) Office of Basic Energy Sciences (BES; grant no. DE-FG03-99ER14956).

Supporting information for this article is available on the WWW under http://www.angewandte.org or from the author.

© 2006 Wiley-VCH Verlag GmbH & Co. KGaA, Weinheim

a possible direct route owing to a theoretical barrier of 242.1 kJ mol^{-1} and a theoretical rate constant of 5.3×10^{-7} at 720 K (reaction J1 in reference [11]). A second possibility involving the conversion of Z(O)-CH_3 and dimethyl ether to trimethyloxonium ylide (Scheme 3, reaction X1 and analogous reaction X2 in reference [11]) was also shown not to exist.

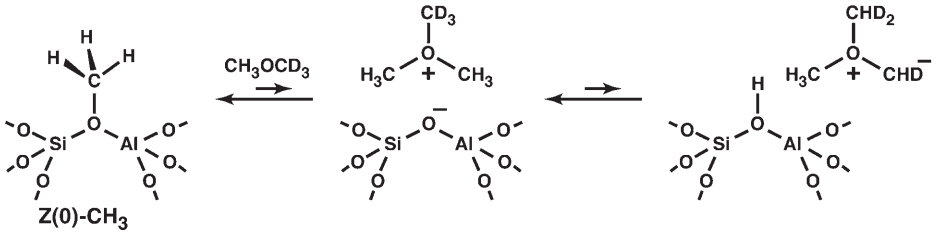

Scheme 3. Putative formation of trimethyloxonium ylide from Z(O)-CH_3 and [D_3]DME. Exchange of H/D labels would be facile if the ylide formed at all.

As all possible routes from Z(O)-CH_3 to species with a C–C bond must involve C–H bond activation, we devised a simple and conclusive test of Scheme 2 and, by extension, many other direct reaction mechanisms, based on the measurement of H/D exchange between Z(O)-CH_3 and Z(O)-CD_3 groups that coexist on the catalyst. Note that observation of exchange would not prove any of these mechanisms, but the opposite would be decisive.

The essence of our simple experiment is shown in Scheme 4. By pulsing a particular isotopomer of [D_3]DME

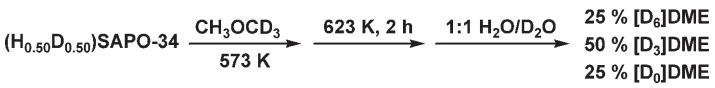

Scheme 4. Formation of framework-bound methoxy groups and their removal without H/D exchange.

(CH_3OCD_3) onto the preferred methanol-to-olefin (MTO) catalyst, HSAPO-34, at 573 K we were able to convert about 30% of the acid sites in a catalyst bed to methoxy groups, equally Z(O)-CH_3 and Z(O)-CD_3. For the experiment depicted in Scheme 4 we raised the reactor temperature to 623 K and gave the intimate mixture of Z(O)-CH_3 and Z(O)-CD_3 two hours to exchange labels, prior to sweeping the methyl groups out of the catalyst as mixed isotopomers of [D_n]DME using a pulse of HOD (i.e., 50% D_2O). To ensure an equal balance of hydrogen and deuterium, the catalyst bed was also first treated with 50% D_2O prior to activation and formation of methoxy groups. As with our previous work,[9] the use of highly purified reagents strongly suppressed the formation of hydrocarbons in these experiments.

The mixture of [D_n]DME isotopomers released from the catalyst was quantified using online GC-MS. Figure 1 reports three hypothetical, simulated ion mass distributions for such an experiment, corresponding to interesting exchange conditions. Figure 1a shows the case of no exchange. As suggested in Scheme 4, a distribution of 25% [D_0]DME, 50% [D_3]DME, and 25% [D_6]DME arises from the chance pairing of equal amounts of Z(O)-CH_3 and Z(O)-CD_3, and the absence of C–H activation is reflected in the absence of [D_1], [D_2], [D_4], and [D_5] isotopomers. Figure 1b is the opposite case, with complete, random H/D exchange resulting in a statistical distribution of all isotopomers and a very characteristic mass pattern. Figure 1c shows the case of blending 90% no exchange and 10% complete exchange, allowing for the possibility of exchange at a hypothetical "minority site". This case demonstrates the accuracy of our fits—HSAPO-34 is a highly uniform material and there is no evidence of any site diversity. The experimental mass pattern observed for the experiment in Scheme 4 as well as the fit to the data are shown in

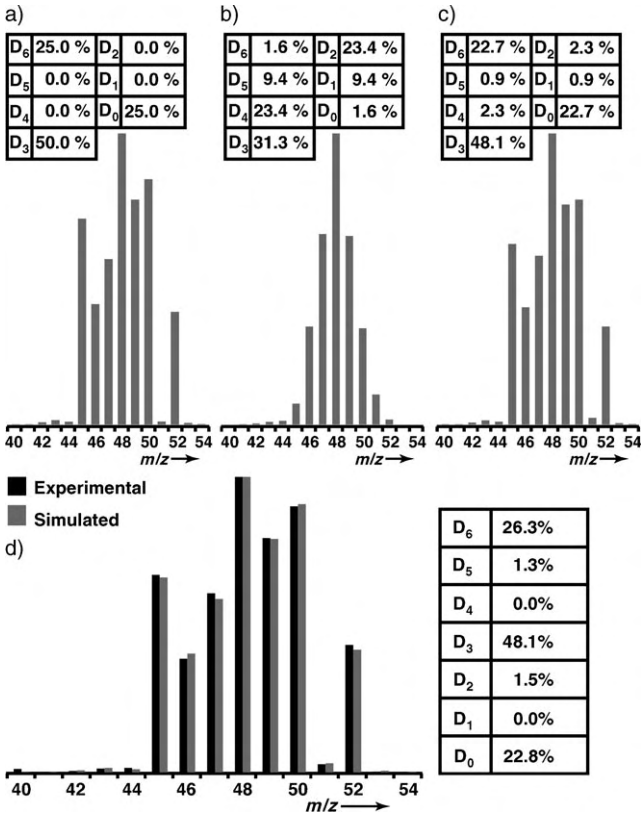

Figure 1. Ion mass distributions for specific mixtures of partially deuterated dimethyl ether, modeling the experiment suggested in Scheme 4. a) Simulated distribution for a mixture of 25% [D_0]DME, 50% [D_3]DME, and 25% [D_6]DME (i.e., the case of no H/D exchange beyond recombination of intact methyl and [D_3]methyl groups to dimethyl ether). b) Simulated distribution for complete randomization of hydrogen and deuterium by C–H bond activation. c) Simulated distribution assuming that only 10% of methoxy groups undergo complete exchange. d) Experimental distribution (and best-fit simulation) for dimethyl ether liberated after 120 minutes at 623 K from a catalyst bed deuterated to 50% and then treated with 0.50 equivalents of CH_3OCD_3 to form equal concentrations of [D_0]methoxy and [D_3]methoxy species. It is estimated that our detection limit for methoxy H/D exchange corresponds to 1% of the acid sites in the catalyst bed. The fit in Figure 1d is in excellent agreement with experimental data and shows no evidence of H/D exchange whatsoever.

 © 2006 Wiley-VCH Verlag GmbH & Co. KGaA, Weinheim

Figure 1d. The experimental data in Figure 1d are in outstanding agreement with the prediction for no H/D exchange in Figure 1a. Indeed, measurements performed at various times and temperatures (see Table 1) show that the low entries for $[D_5]$DME and $[D_2]$DME in Figure 1d are fitting

Table 1: H/D exchange as a function of time in framework-bound methoxy groups on $H_{0.50}D_{0.50}$SAPO-34.

$[D_n]$DME	Distribution [%] at various times and temperatures					
	6 min, 573 K	15 min, 573 K	30 min, 573 K	60 min, 573 K	120 min, 573 K	120 min, 623 K
$[D_6]$	26.5	26.8	26.9	26.9	26.9	26.3
$[D_5]$	1.4	1.3	1.3	0.8	0.6	1.3
$[D_4]$	0.3	0.0	0.0	0.0	0.3	0.0
$[D_3]$	48.0	48.4	48.2	48.7	49.1	48.1
$[D_2]$	1.5	1.0	1.4	0.7	1.0	1.5
$[D_1]$	0.0	0.0	0.0	0.0	0.0	0.0
$[D_0]$	22.4	22.5	22.2	22.9	22.2	22.8

errors caused by minor variations in the experimental spectra and constraints in the model to preclude negative concentrations. The upper limit on the rate constant for the process in Scheme 2 (J1 in reference [11]) at 623 K is estimated to be 2×10^{-6}, but it could also be much lower.

We also used GC-MS to determine that neither the methanol or dimethyl ether that exit the reactor in the seconds following the CH_3OCD_3 pulse showed unexpected isotope exchange. Hence, methoxy groups are not deprotonated by methanol, dimethyl ether, or water at 573 K. Indeed, these observations show that C–H bonds are not broken or made in any reaction step that is reversibly coupled to methoxy formation (see Scheme 3, or either X1 or X2 in reference [11]).

We conclude that the only valid mechanisms for the methanol-to-olefin conversion are hydrocarbon pool mechanisms that describe primary synthesis of olefins on organic reaction centers, such as methylbenzenes, coupled with well-known secondary reactions of olefins. This is true not only for a working catalyst but also for initiation reactions during the kinetic induction period. All conceivable direct mechanisms based on or in equilibrium with the formation of $Z(O)\text{-}CH_3$ are invalidated by the failure of framework-bound methoxy groups to undergo H/D exchange at high temperatures. In agreement with recent theoretical studies, our experimental studies preclude both the carbene route (Scheme 2) and the methoxonium ylide route (Scheme 3). The conclusion of both theory and experiment is that the direct mechanisms fail, and chance introduction of a primordial hydrocarbon pool is the only mechanism for MTO initiation in agreement with these findings. The present work in combination with references [10] and [11] disproves the central claims of reference [13] that were recently reiterated in reference [16].

Experimental Section

HSAPO-34 was synthesized using standard procedures,[17] followed by calcination at 873 K. $[D_3]$DME (specifically CH_3OCD_3) was obtained from Cambridge isotopes (lot number R-444, PSO 4C-117), as was D_2O (99.9% deuterium content).

See Supporting Information for a schematic and detailed description of our reactor. We used 300-mg catalyst beds of HSAPO-34 catalyst, rigorously calcined (873 K, 100 standard cubic centimeters per minute (sccm) flowing air) for 1 h just prior to use. The carrier gas was then switched to flowing He (600 sccm), and the temperature was lowered to 648 K. Then, three pulses (3.3 equiv, 20 μL) of 50% D_2O in H_2O were applied at five-minute intervals to bring the catalyst bed to 50% deuteration. The catalyst bed was held at 648 K with He gas flow for 30 minutes to ensure complete removal of water. At 573 K we loaded the catalyst with an equimolar mixture of $[H_3]$- and $[D_3]$methoxy groups by pulsing two aliquots (0.25 equiv per aliquot) of CH_3OCD_3 onto the catalyst bed. The reactor temperature was then immediately raised to 623 K and gas flow was maintained for 2 hours (the temperature was lowered back to 573 K just prior to the end of this period), or the temperature was maintained at 573 K for a variable time between 6 minutes and 2 hours, before hydrolyzing the chemisorbed methoxy species with a single pulse (5 equiv) of 50% D_2O in H_2O to liberate dimethyl ether for isotopic analysis by GC-MS. (Note: DME was chosen for this analysis to avoid the complication of the readily exchangeable hydroxy proton of methanol; i.e. CH_3OD versus CH_2DOH.)

An Agilent gas chromatograph equipped with dual 50-m Supelco DH columns and both mass spectrometric and flame-ionization detectors (FID) was used to analyze the reactor effluent gases. The temperarture of the oven was held at 308 K (isothermal). The mass spectrometer was used to obtain isotope distributions as needed, while the FID provided quantified peak integrations (using published response factors) as well as significantly lower detection limits.

Received: December 8, 2005
Revised: February 16, 2006
Published online: March 29, 2006

Keywords: heterogeneous catalysis · isotopic labeling · methanol-to-olefin process · zeolites

[1] M. Stöcker, *Microporous Mesoporous Mater.* **1999**, *29*, 3–48.
[2] J. F. Haw, W. Song, D. M. Marcus, J. B. Nicholas, *Acc. Chem. Res.* **2003**, *36*, 317–326.
[3] I. M. Dahl, S. Kolboe, *J. Catal.* **1994**, *149*, 458–464.
[4] B. Arstad, S. Kolboe, *J. Am. Chem. Soc.* **2001**, *123*, 8137–8138.
[5] P. W. Goguen, T. Xu, D. H. Barich, T. W. Skloss, W. Song, Z. Wang, J. B. Nicholas, J. F. Haw, *J. Am. Chem. Soc.* **1998**, *120*, 2650–2651.
[6] W. Song, J. F. Haw, J. B. Nicholas, C. S. Heneghan, *J. Am. Chem. Soc.* **2000**, *122*, 10726–10727.
[7] J. F. Haw, J. B. Nicholas, W. Song, F. Deng, Z. Wang, C. S. Heneghan, *J. Am. Chem. Soc.* **2000**, *122*, 4763–4775.
[8] B. Arstad, J. B. Nicholas, J. F. Haw, *J. Am. Chem. Soc.* **2004**, *126*, 2991–3001.
[9] W. Song, D. M. Marcus, H. Fu, J. O. Ehresmann, J. F. Haw, *J. Am. Chem. Soc.* **2002**, *124*, 3844–3845.
[10] D. Lesthaeghe, V. Van Speybroeck, G. B. Marin, M. Waroquier, *Chem. Phys. Lett.* **2005**, *417*, 309–315.
[11] D. Lesthaeghe, V. Van Speybroeck, G. B. Marin, M. Waroquier, *Angew. Chem.* **2006**, *118*, 1746–1751; *Angew. Chem. Int. Ed.* **2006**, *45*, 1714–1719.
[12] T. R. Forester, R. F. Howe, *J. Am. Chem. Soc.* **1987**, *109*, 5076–5082.
[13] W. Wang, A. Buchholz, M. Seiler, M. Hunger, *J. Am. Chem. Soc.* **2003**, *125*, 15260–15267.
[14] D. K. Murray, J.-W. Chang, J. F. Haw, *J. Am. Chem. Soc.* **1993**, *115*, 4732–4741.

 © 2006 Wiley-VCH Verlag GmbH & Co. KGaA, Weinheim

[15] a) W. Kirmse, *Carbene Chemistry*, *2nd ed.*, Academic Press, New York, **1971**; b) *Carbenes Vol. I and II*, (Eds.: R. A. Moss, M. Jones, Jr.), Wiley, New York, **1974** and **1975**.
[16] Y. J. Jiang, W. Wang, V. R. R. Marthala, J. Huang, B. Sulikowski, M. Hunger, *J. Catal.* **2006**, *238*, 21—27.
[17] HSAPO-34 was prepared according to a patented procedure: B. M. Lok, C. A. Messina, R. L. Patton, R. T. Gajek, T. R. Cannan, E. M. Flanigen, US Patent 4,440,871, **1984**. X-ray diffraction studies showed a pure crystalline phase with the CHA structure. The product was calcined in static air at 873 K for 10 h to remove the template agent and pressed into 10–20 mesh pellets without binder or other additives.

 © 2006 Wiley-VCH Verlag GmbH & Co. KGaA, Weinheim

Biological Chemistry

DOI: 10.1002/anie.200504441

Intracellular Inducible Alkylation System That Exhibits Antisense Effects with Greater Potency and Selectivity than the Natural Oligonucleotide**

*Md. Monsur Ali, Motoi Oishi, Fumi Nagatsugi, Kenya Mori, Yukio Nagasaki, Kazunori Kataoka, and Shigeki Sasaki**

Synthetic oligonucleotides (ODNs) that incorporate a chemically reactive appendage have been widely investigated in the endeavor to create new functions through specific reactivity toward a target sequence. A number of biotechnological approaches have been invented based on sequence-selective alkylation,[1] cross-linking,[2,3] strand cleavage,[4–7] chemical ligation,[8] signal amplification,[9] and other techniques. Cross-linking oligonucleotides have been used to stabilize complexes with the cellular target mRNA by covalent-bond formation, and have been shown to be useful in enhancing antisense effects. Emerging knowledge about the fundamental role of micro-RNAs (miRNAs) in gene regulation has led to great interest in efficient antisense oligonucleotides against miRNAs as a tool for specifically knocking down particular miRNAs.[10,11] Psoralen derivatives are activated by UV irradiation and are the only reagents applicable to in vitro and in vivo studies. They not only enhance antisense effects[12,13] but also induce specific mutations at the sites of the reaction within the triplex DNA.[14,15] However, until now the use of alkylating oligonucleotides in biological studies has been hampered by the lack of an efficient cross-linking agent. As alkylating or cross-linking agents tend to be unstable under physiological conditions, the use of stable precursors with inducible reactivity was expected to provide a solution to this problem.[2,16] We recently proposed a new concept of inducible reactivity, in which a phenylsulfide derivative used as a stable precursor to a 2-amino-6-vinylpurine nucleoside analogue is automatically activated in the proximity of the target cytidine residue to form a covalent bond selectively (Scheme 1).[17–20] The selectivity of this inducible alkylation system for cytidine is so high that a single nucleotide difference can be discriminated in the alkylation. Herein we describe the capacity of the inducible alkylation system to exhibit antisense effects in an intracellular environment with greater potency and selectivity than the corresponding unmodified oligonucleotide.

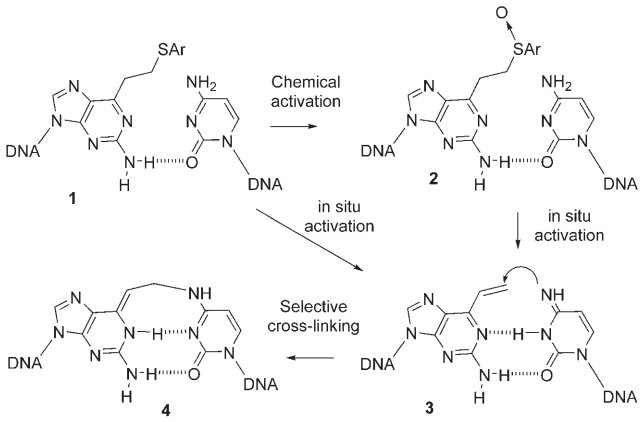

Scheme 1. In situ activation of the sulfide precursor **1** to the 2-amino-6-vinylpurine **3** for selective cross-linking with cytidine to give **4**.[17] The vinyl compound **3** can be generated selectively in the hybrid with the complementary sequence from the sulfoxide **2** or the sulfide precursor **1**. As intermediary formation of **2** has not been detected, it is anticipated that activation from **1** to **3** takes place directly.

In a previous study, the phenylsulfide derivative **1** was oxidized chemically to produce the sulfoxide derivative **2**, which was activated selectively to the vinyl compound **3** by hybridization with the complementary sequence. It has been shown that the cytidine residue at the target site enhances the elimination step from **2** to **3**, which is followed by efficient

[*] Dr. M. M. Ali, Prof. Dr. F. Nagatsugi, Prof. Dr. S. Sasaki
Graduate School of Pharmaceutical Sciences
Kyushu University
3-1-1 Maidashi, Higashi-ku, Fukuoka 812-8582 (Japan)
Fax: (+81) 92-642-6615
E-mail: sasaki@phar.kyushu-u.ac.jp
Dr. M. Oishi, Prof. Dr. Y. Nagasaki
Institute of Materials Science
Tsukuba University
1-1-1 Ten-nodai, Tsukuba, Ibaraki 305–8573 (Japan)
Dr. K. Mori
GeneAct Ltd.
2432-3 Kawaimachi, Kurume, Fukuoka 839-0861 (Japan)
Prof. Dr. K. Kataoka
Department of Materials Science and Engineering
Graduate School of Engineering
The University of Tokyo
7-3-1 Hongo, Bunkyo-ku, Tokyo 113-8656 (Japan)

[**] This work was supported by a Grant-in-Aid for Scientific Research (A) from the Japan Society for the Promotion of Science (JSPS) and CREST of the Japan Science and Technology Agency (JST).

Supporting information for this article is available on the WWW under http://www.angewandte.org or from the author.

InterScience © 2006 Wiley-VCH Verlag GmbH & Co. KGaA, Weinheim

alkylation to produce **4**.[17] The vinyl compound **3** can also be generated selectively from the sulfide precursor **1** in the hybrid with the complementary sequence. In this case it is anticipated that activation from **1** to **3** takes place directly. The elimination of the sulfide group is also accelerated by the cytidine residue at the target site. As the sulfide derivative **1** is chemically stable, we viewed it as a potential candidate for an alkylating agent with inducible reactivity for use in living systems.

Herein, we have applied polyion-complex (PIC) micelles of PEG conjugates of oligonucleotides for both the protection of ODNs from enzymatic digestion and their efficient delivery into the cellular interior.[21–23] Scheme 2 summarizes the

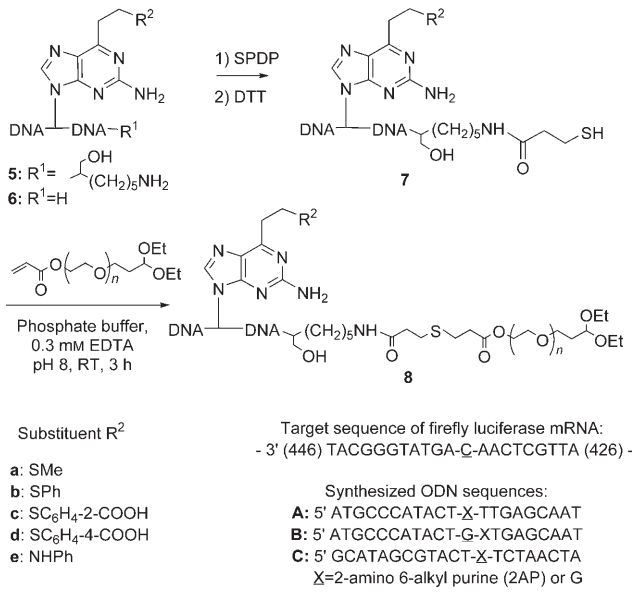

Scheme 2. Synthesis of the antisense PEG conjugates in which 2-amino 6-alkyl purine is incorporated. The sequence **A** has X at the complementary site to the cytidine residue of the target mRNA sequence, **B** contains X at the adjacent site, and **C** is a random sequence. The description **6A** refers to species with the ODN sequence **A** that are not conjugated with PEG; **8B** (X = AP, R^2 = SMe) is the PEG conjugate with the ODN sequence **B** in which a 2-amino-6-(2-methylthioethyl)purine derivative is incorporated adjacent to the complementary site to the cytidine residue of the target sequence. EDTA = ethylenediaminetetraacetic acid.

synthesis of PEG conjugates of the functional oligonucleotides. The antisense sequence to firefly-luciferase mRNA (sequence **A** in Scheme 2) was designed according to a reported technique.[24] The methylsulfide derivative of a 2-amino 6-alkyl purine was incorporated into the natural-type ODN (**5a** and **6a**),[17] and was then transformed into the phenylsulfide (**5b**, **6b**), 2-carboxyphenylsulfide (**5c**, **6c**), 4-carboxyphenylsulfide (**5d**, **6d**), and phenylamino derivatives (**5e**) by sequential reactions with magnesium monoperphthalate (MMPP) and aqueous NaOH, following the addition of the corresponding thiol or amine. The amino group of the 3′ terminus of **5** was modified with *N*-succimidyl-3-(2-pyridyldithio)propionate (SPDP), followed by reduction with dithiothreitol (DTT) to form the thiol-containing ODN **7**. Finally, the β-thiopropionate linkage of the corresponding ODN–PEG conjugates **8** was formed by a Michael reaction with a PEG polymer bearing a diethylacetal group at one terminus and an acrylate group at the other (M_n = 4460). The conjugates **8** were isolated in good yields by purification by reversed-phase column chromatography. Sequence **A** has X at the complementary site to the cytidine residue of the target mRNA sequence, **B** contains X at the adjacent site, and **C** is a random sequence. The structures of the ODNs and the PEG conjugates were confirmed by MALDI-TOF MS. The PEG–ODN conjugates obtained were mixed with poly-L-lysine (PLL) in a 1:1 molar ratio with respect to the phosphate group in the PEG–ODN conjugate and the amino group in PLL to form the PIC micelles (N/P = 1).

Antisense effects of the reactive ODNs (**6A**, R^1 = H) were first evaluated in a transcription and translation assay without cells. The following order was found for the cross-linking rates of the derivatives of 2-aminopurine in the nonbiological system: phenyl sulfoxide > 2-carboxyphenylsulfide ≫ phenylsulfide > methylsulfide.[17] However, as the phenyl sulfoxide derivatives were found to be unstable in the biological assay, the sulfide-functionalized ODNs were used in this study. Transcription, followed by translation, of firefly luciferase was performed by using ODN **6** (X = G or a sulfide derivative of 2-aminopurine) and firefly-luciferase DNA in a wheat-germ extract. Production of luciferase was monitored by measuring luminescence (Figure 1). All ODNs **6A** showed dose-dependent antisense inhibition. It should be noted that all sulfide-functionalized ODNs showed higher antisense effects than the corresponding natural antisense ODN.

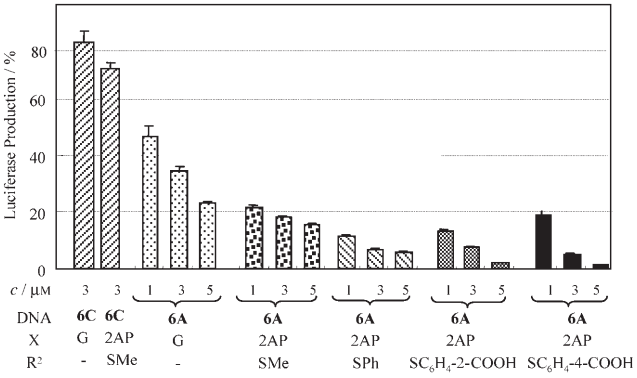

Figure 1. Antisense effects on luciferase production in an assay without cells. Transcription and translation were performed in vitro for 90 min at 30 °C by using DNA (0.3 μg) in the absence or presence of the ODN in TNT coupled wheat germ extract system (Promega). The extent of luciferase production relative to that in the control is shown in the ordinate.

To check whether or not in situ activation would take place in a cell lysate, we mixed the reactive ODN **6A** (X = AP, R^2 = SMe) and the ODN with the target sequence in a cell lysate, and the reaction mixture was analyzed by HPLC.[25] Although the cross-linked adduct was not detected clearly, the formation of 2-amino-6-vinylpurine was evidenced by its intrinsic fluorescence. This vinyl derivative of ODN **6** was

 © 2006 Wiley-VCH Verlag GmbH & Co. KGaA, Weinheim

only clearly observed in the presence of the ODN with the target cytidine, which suggests that the activation is dependent on cytidine.

The biological stability of the ODNs was investigated in a cell lysate and in the presence of DNase I. It was shown that the modified ODN **6A** (X = AP, R^2 = SMe) was slightly more stable than the natural ODN **6A** (X = G), and that the PEG conjugate **8A** (X = G) exhibits high stability in a cell lysate (Figure 2a). To rule out the possibility that the higher activity

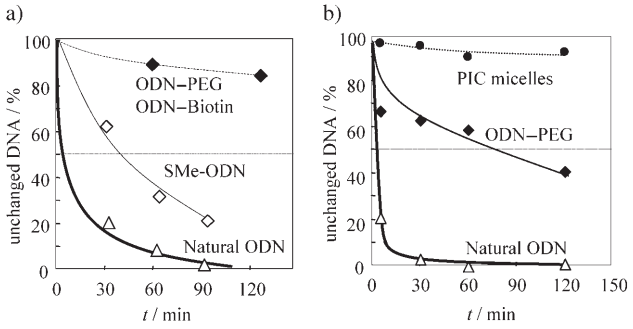

Figure 2. Comparison of the stability of the ODN derivatives in a cell lysate (a) and in the presence of DNase I (b) at 30°C. Natural ODN: **6A** (X = G), SMe-ODN: **6A** (X = AP, R^2 = SMe), ODN–PEG: **8A** (X = G), ODN–biotin: biotin amide of **5A** (X = G), PIC micelles: B-PEI + **8A** (X = G) (N/P = 1; B-PEI: M_w = 25 000, DP = 580). B-PEI = branched polyethyleneimine, DP = degree of polymerization.

of the modified ODNs is merely an effect of higher biostability induced by the modification, we next investigated the antisense effect of the PEG conjugates. The ODN–PEG conjugates were incubated with mRNA of firefly luciferase for 30 min in a buffer, and translation was performed by treatment with an amino acid mixture in a cell lysate for 90 min at 30°C. It was clearly demonstrated that the PEG conjugate with the modified ODN, **8A** (X = 2AP, R^2 = SMe), exhibited a higher inhibitory effect than the conjugate with the natural ODN, **8A** (X = G), and that the biostability of the modified ODN is not a major factor in the enhancement of the antisense effect.[25]

Hybridization of the ODN with the luciferase mRNA following a cross-linking reaction was next investigated by reverse-transcription polymerase chain reaction (RT-PCR). When primers were used for the upstream and downstream regions of the antisense target site, it was expected that the PCR with cross-linked mRNA would produce shorter PCR products than that with unmodified mRNA. First, ODN **6A** (X = G or 2AP, R^2 = SPh) was mixed with mRNA in a buffer, the mixture was subjected to RT-PCR, and the products were analyzed by gel electrophoresis (Figure 3). The RT-PCR products corresponding to a 223-mer nucleotide of the full length were formed as the major product (Figure 3, lanes 2 and 3), thus indicating that neither covalent nor noncovalent hybridized complexes were formed effectively in a buffer. We next attempted to form complexes with mRNA in cell lysates, so that we could isolate the complexes by using streptavidin affinity beads. mRNA and biotin-conjugated ODN were incubated in a cell lysate, and the hybridized complexes were separated with streptavidin beads. (**5A**–biotin is as biostable

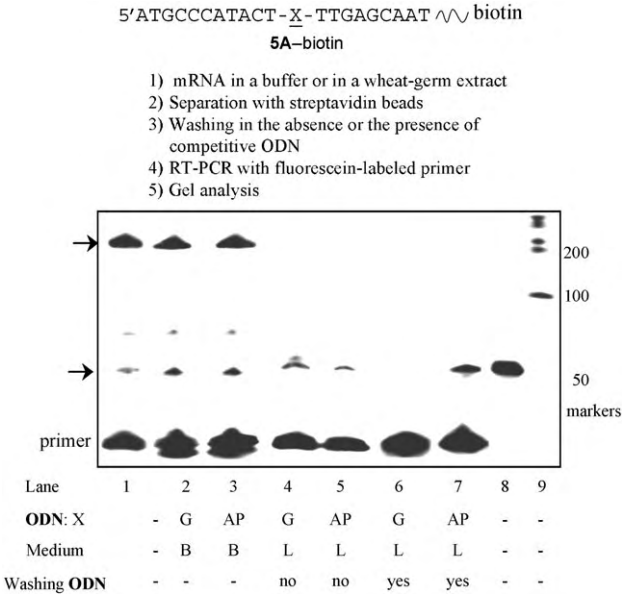

Figure 3. Analysis of RT-PCR products (denoted by arrows) of the reaction of the ODN and luciferase mRNA. Lane 1: control; lane 2: ODN **6A** (X = G) and mRNA were subjected to RT-PCR; lane 3: ODN **6A** (X = 2AP, R^2 = SPh) was used in the same procedure as that for lane 2; lane 4: ODN **5A**–biotin (X = G) and mRNA complexes were separated with streptavidin beads then washed several times with a buffer in the absence of the competitive ODN; lane 5: ODN **5A**–biotin (X = 2AP, R^2 = SPh) was used in the same procedure as that for lane 4; lane 6: washing was done in the presence of the competitive ODN in otherwise the same procedure as that used for lane 4; lane 7: washing was done in the presence of the competitive ODN in otherwise the same procedure as that used for lane 5; lanes 8 and 9: markers. G is guanosine and AP is 2-amino-6-(2-phenylthioethyl)purine (R^2 = SPh; see Scheme 2). Medium B is a buffer and medium L is lysate. The ODN **5A**–biotin has a biotin unit at its 3′ amino end. The sequence of the washing ODN (21 mer) is the sense sequence 3′-TACGGGTATGA-C-AACTCGTTA-5′: the target sequence of firefly-luciferase mRNA.

as the ODN–PEG conjugate, as shown in Figure 2a.) The PCR in which separated streptavidin beads were used afforded shorter RT-PCR products of approximately 50-mer length (Figure 3, lanes 4 and 5), which showed that the RT reaction was inhibited before the site of cross-linking with both the natural ODN (X = G) and the cross-linking ODN (X = 2AP, R^2 = SPh). These results also clearly indicate that tight ODN–mRNA complexes are formed in cell lysates, but not in a buffer, in the case of both the natural and the modified ODN. When the separated streptavidin beads were washed in the presence of the competitive ODN, the short RT-PCR products disappeared in lane 6 and were retained in lane 7, thus demonstrating that covalently bound ODN–mRNA complexes are formed with the cross-linking ODN (X = 2AP, R^2 = SPh). These results, together with the fact that the sulfide derivative is transformed into a 2-amino-6-vinylpurine derivative in cell lysates,[25] strongly suggest that the ODN with the reactive 2-aminopurine residue forms the covalent bond with the target mRNA in the cell lysate to enhance the antisense effect.

We next evaluated the intracellular antisense activity of the reactive ODN–PEG conjugates by a dual-luciferase-

 © 2006 Wiley-VCH Verlag GmbH & Co. KGaA, Weinheim

reporter assay. The PIC micelles of the reactive ODN–PEG conjugates exhibit high stability toward enzymatic digestion (Figure 2b) and were therefore used as the system for the delivery of the ODN into the cellular interior. [21,22,25] HuH-7 cells were cotransfected with plasmids of firefly and renilla luciferases in amounts at which both luciferases are expressed to a similar extent. The cells were incubated for 24 h in the presence of the reactive ODN–PEG as the PIC micelles and then for 24 h in a fresh medium. The PEG–ODN conjugates were mixed with PLL (poly-L-lysine, DP = 100, M_w = 20900) with a 1:1 molar ratio of the phosphate group in the PEG–ODN conjugate and the amino group in PLL (N/P = 1) to form the PIC micelles. The luciferase expression was monitored by measuring luminescence with the dual luciferase assay kit. Antisense effects are summarized in Figure 4.

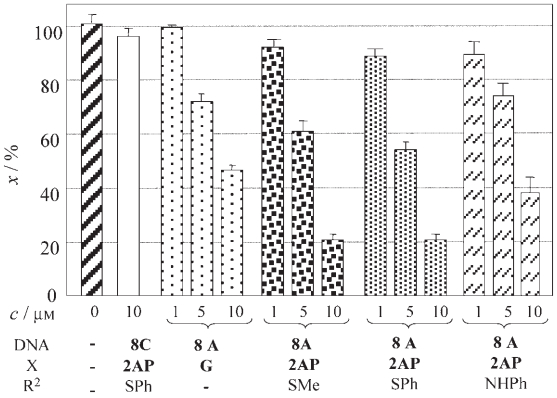

Figure 4. Antisense effects with PEG–ODN/PLL PIC micelles against gene expression of firefly luciferase in cultured HuH-7 cells. Normalized ratios *x* of firefly-luciferase activity to that of renilla luciferase are shown in the ordinate. G and 2AP represent guanosine and the 2-amino 6-alkyl purine nucleoside; substituents R^2 are shown in Scheme 2.

Neither the antisense ODN **6A** nor the PEG–ODN **8A** alone showed antisense inhibition.[21,22] Under conditions under which the PIC micelles of the PEG–ODN **8C** with the random sequence did not show an antisense effect, the micelles of the natural PEG–ODN **8A** clearly showed potent antisense effects of about 50% inhibition at 10 μM. Although higher concentrations of the PIC micelles were needed for potent inhibition than those required in the antisense experiments in cell lysates (compare Figures 1 and 4), the PIC micelles formed with the ODN–PEG conjugates and PLL did not cause cytotoxicity at concentrations of 10 μM.[25] Thus, the inhibitory effects summarized in Figure 4 result from selective antisense effects of **8A**. The sulfide derivatives of 2-aminopurine (**8A**, X = AP, R^2 = SMe and SPh) showed greater antisense effects than the PEG conjugate with the natural antisense oligonucleotide (**8A**, X = G). At a concentration of 10 μM in the sulfide derivative, luciferase expression was inhibited to 20% of that in the control. This degree of expression corresponds to a background level. The ODN containing the aniline derivative (**8A**, X = AP, R^2 = NHPh) was used as an unreactive antisense control. In the presence of this ODN, less effective antisense inhibition was observed, which again supports the hypothesis that the 2-aminopurine derivative in the reactive ODN enhances antisense inhibition.

The consequences of one mismatched site on the antisense effects are compared in Figure 5 for the natural antisense

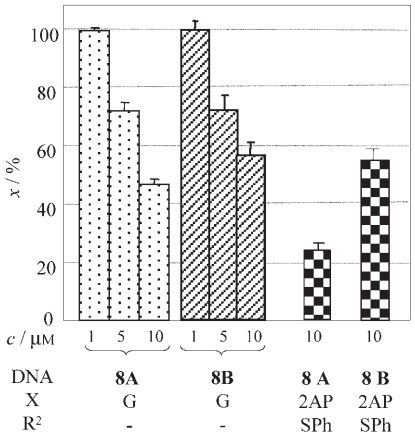

Figure 5. Comparison of the consequences of one mismatched site on the antisense effects. Systems were assayed for their antisense effect in a similar way to that described in the footnote of Figure 4. G and 2AP represent guanosine and the 2-amino 6-alkyl purine nucleoside; substituents R^2 are shown in Scheme 2. *x* = normalized ratios of firefly-luciferase activity to that of renilla luciferase. Target mRNA sequence: -3′-TACGGGTATGA-C-AACTCGTTA-; antisense sequences: **8A**: 5′-ATGCCCATACT-X-TTGAGCAAT-PEG, **8B**: 5′-ATGCCCATACT-G-XTGAG-CAAT-PEG.

ODNs (**8A** and **8B**, X = G) and the reactive ODNs (**8A** and **8B**, X = 2AP, R^2 = SPh). The natural ODN with one mismatched site (**8B**, X = G) exhibited similar inhibition to that of the fully matched ODN (**8A**, X = G), which demonstrates a disadvantage to the use of natural ODNs in terms of antisense inhibition. In marked contrast, the reactive ODN (**8B**, X = AP, R^2 = SPh), in which the 2-aminopurine derivative is at the position adjacent to the target cytidine, was much less efficient than the fully matched ODN (**8A**, X = AP, R^2 = SPh), thus demonstrating the superiority of the reactive ODN over the natural antisense ODN in discriminating a single nucleoside difference in cells. As the 2-amino-6-(2-phenylthioethyl)purine nucleoside is highly selective to cytidine at the complementary position,[17,18] the high sensitivity to a single mismatch site can also be reasonably interpreted as a result of selective cross-linking with the 2-amino-6-vinylpurine derivative.

In this study, we have applied the inducible alkylating system that has been developed by our research group to intracellular antisense oligonucleotides. It was found that the sulfide derivative of the 2-amino-6-vinylpurine nucleoside exhibited high reactivity in a cell lysate, in striking contrast to the chemical reactivity investigated in simple model systems. Detailed investigations of the reaction product of the reactive ODN with mRNA in a cell lysate strongly suggest that the reactive ODN that incorporates the 2-aminopurine nucleoside analogue forms a covalent bond with the target mRNA. The reactive ODN was subsequently applied in intracellular antisense inhibition of luciferase by using polyion-complex

 © 2006 Wiley-VCH Verlag GmbH & Co. KGaA, Weinheim

(PIC) micelles of the PEG–ODN conjugate. In conclusion, we have successfully shown that the inducible alkylation system functions in an intracellular environment to promote efficient and selective antisense activity against luciferase production. A unique benefit of this alkylating agent is reflected in its high selectivity, which may permit the discrimination of a single nucleotide difference in cells. As the sulfide precursors to the 2-amino-6-vinylpurine derivative, unlike psoralen, do not need UV irradiation for activation, they are expected to be useful for further in vivo applications. This type of inducible alkylation system combined with the delivery system of PIC micelles for PEG conjugates opens new opportunities for the use of reactive oligonucleotides in vivo.

Received: December 14, 2005
Revised: February 3, 2006
Published online: March 30, 2006

Keywords: alkylation · antisense oligonucleotides · biological chemistry · cross-linking · inducible reactivity

[1] K. B. Grant, P. B. Dervan, *Biochemistry* **1996**, *35*, 12313 – 12319.
[2] For a recent review, see: S. Sasaki, *Eur. J. Pharm. Sci.* **2001**, *13*, 43 – 51; see also references therein.
[3] Q. B. Zhou, S. E. Rokita, *Proc. Natl. Acad. Sci. USA* **2003**, *100*, 15452 – 15457.
[4] Y. Yamamoto, W. Tsuboi, M. Komiyama, *Nucleic Acids Res.* **2003**, *31*, 4497 – 4502.
[5] T. Fukuma, C. M. Walton, C. H. Wu, G. Y. Wu, *Bioconjugate Chem.* **2003**, *14*, 295 – 301.
[6] R. N. Zuckermann, D. R. Corey, P. G. Schultz, *J. Am. Chem. Soc.* **1988**, *110*, 1614 – 1615.
[7] K. Nagai, S. M. Hecht, *J. Biol. Chem.* **1991**, *266*, 23994 – 24002.
[8] S. Sando, H. Abe, E. T. Kool, *J. Am. Chem. Soc.* **2004**, *126*, 1081 – 1087.
[9] M. P. van de Corput, R. W. Dirks, R. P. M. van Gijlswijk, E. van Binnendijk, C. M. Hattinger, R. A. de Paus, J. E. Landegent, A. K. Raap, *J. Histochem. Cytochem.* **1998**, *46*, 1249 – 1259.
[10] G. Meister, M. Landthaler, Y. Dorsett, T. Tuschl, *RNA* **2004**, *10*, 544 – 550.
[11] G. Hutvagner, M. J. Simard, C. C. Mello, P. D. Zamore, *PLoS Biol.* **2004**, *2*, e98.
[12] A. Murakami, A. Yamayoshi, R. Iwase, J. Nishida, T. Yamaoka, N. Wake, *Eur. J. Pharm. Sci.* **2001**, *13*, 25 – 34.
[13] J. M. Kean, A. Murakami, K. R. Blake, D. D. Cushman, P. S. Miller, *Biochemistry* **1988**, *27*, 9113 – 9121.
[14] N. Puri, A. Majumdar, B. Cuenoud, P. S. Miller, M. M. Seidman, *Biochemistry* **2004**, *43*, 1343 – 1351.
[15] A. Majumdar, A. Khorlin, N. Dyatkina, F. L. Lin, J. Powell, J. Liu, Z. Fei, Y. Khripine, K. A. Watanabe, J. George, P. M. Glazer, M. M. Seidman, *Nat. Genet.* **1998**, *20*, 212 – 214.
[16] Q. B. Zhou, S. E. Rokita, *Proc. Natl. Acad. Sci. USA* **2003**, *100*, 15452 – 15457.
[17] T. Kawasaki, F. Nagatsugi, Md. M. Ali, M. Maeda, K. Sugiyama, K. Hori, S. Sasaki, *J. Org. Chem.* **2005**, *70*, 14 – 23.
[18] F. Nagatsugi, T. Kawasaki, D. Usui, M. Maeda, S. Sasaki, *J. Am. Chem. Soc.* **1999**, *121*, 6753 – 6754.
[19] F. Nagatsugi, K. Uemura, S. Nakashima, M. Maeda, S. Sasaki, *Tetrahedron* **1997**, *53*, 3035 – 3044.
[20] F. Nagatsugi, K. Uemura, S. Nakashima, M. Maeda, S. Sasaki, *Tetrahedron Lett.* **1995**, *36*, 421 – 424.
[21] M. Oishi, S. Sasaki, Y. Nagasaki, K. Kataoka, *Biomacromolecules* **2003**, *4*, 1426 – 1432.
[22] M. Oishi, F. Nagatsugi, S. Sasaki, Y. Nagasaki, K. Kataoka, *ChemBioChem* **2005**, *6*, 1 – 6.
[23] For a similar method, see: J. H. Jeong, S. W. Kim, T. G. Park, *Bioconjugate Chem.* **2003**, *14*, 473 – 479.
[24] M. Mishra, J. R. Bennett, G. Chaudhuria, *Biochem. Pharmacol.* **2001**, *61*, 467 – 476.
[25] See the Supporting Information.

 © 2006 Wiley-VCH Verlag GmbH & Co. KGaA, Weinheim

Carbocyclization

DOI: 10.1002/anie.200504448

Direct Intramolecular Arylation of Aldehydes Promoted by Reaction with IPy_2BF_4/HBF_4: Synthesis of Benzocyclic Ketones**

José Barluenga, Mónica Trincado, Eduardo Rubio, and José M. González*

Dedicated to Professor K. Peter C. Vollhardt on the occasion of his 60th birthday

The Friedel–Crafts acylation of arenes is a prevailing reaction for accessing aryl ketones.[1] However, conditions for carrying out the desired arene acylation directly from an aryl-substituted aldehyde have not yet been described. Herein, an intramolecular version of such a process is presented. Thus arenecarboxaldehydes are converted into benzocyclic ketones[2,3] in a straightforward one-pot process.

The iodoarylation of alkenes and alkynes is an efficient tool for the modular assembly of heterocycles with rapid generation of diversity.[4] During the course of these iodoarylation studies, we discovered by chance that the advanced intermediate **1** underwent not only the expected arylation of the alkyne functionality, but also conversion into the benzocyclic ketone **2** [Eq. (1), Py = pyridine]. In this conceptually attractive transformation, an aryl aldehyde acts formally as a proper acylating agent in a novel intramolecular reaction sequence triggered by iodonium ions. We decided to further

[*] Prof. Dr. J. Barluenga, Dr. M. Trincado, Dr. E. Rubio, Dr. J. M. González
Instituto Universitario de Química Organometálica "Enrique Moles"
Unidad Asociada al C.S.I.C.
Universidad de Oviedo
Julián Clavería, 8, 33006-Oviedo (Spain)
Fax: (+34) 98-510-3450
E-mail: barluenga@uniovi.es

[**] This research was partially supported by the Spanish M.E.C. (Grant CTQ 2004-08077-C02-01). M.T. thanks the Spanish M.E.C. for a fellowship. Generous support from Merck Sharp & Dohme is gratefully acknowledged. The authors thank the referees for helpful and clarifying suggestions. Py = pyridine.

Supporting information for this article is available on the WWW under http://www.angewandte.org or from the author.

WILEY InterScience DISCOVER SOMETHING GREAT
© 2006 Wiley-VCH Verlag GmbH & Co. KGaA, Weinheim

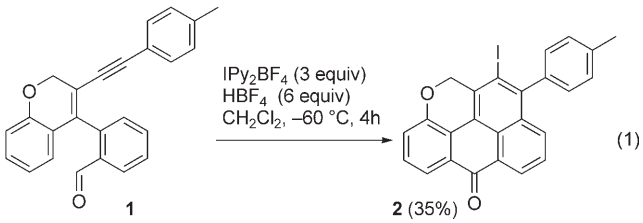

(1)

explore the generality of this formal C–H functionalization to produce ketones. We chose 2-(1-naphthyl)benzenecarboxaldehyde (**3**) as a suitable starting material to test the feasibility of this challenging reaction with simpler compounds [Eq. (2)].

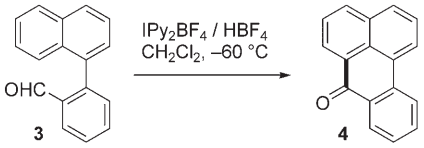

(2)

An initial optimization procedure revealed that the desired process was most efficient when a 2:1 molar ratio of HBF_4 to the iodinating reagent and a 2:1 ratio of the latter with respect to **3** were used (Table 1). When the ratio of IPy_2BF_4 was increased, the yield of **4** was not improved. However, the use of more electrophilic conditions gave better results (Table 1, entry 6). For entries 1–5, **3** was added to a cooled solution that contained the iodinating reagent and the acid. However, in the case of entry 6, a different experimental protocol was adopted. First, the iodinating agent and the acid were mixed at −80 °C, and the pyridinium salts generated in the neutralization were removed to a great extent by filtration at low temperature under an inert atmosphere. After **3** had been added to this solution,[5] the temperature was allowed to rise to −60 °C and was kept constant while the mixture was stirred for the time stated.

Table 1: Optimization of conditions for the direct conversion of **3** into **4** [Eq. (2)].

Entry	IPy_2BF_4 [equiv]	HBF_4 [equiv]	*t* [h]	Conversion[a] [%]	Yield[b] [%]
1	1	1	24	5	–
2	1	2	24	20	17
3	2	4	18	50	46
4	–	4	24	–	–
5	3	6	18	75	48[c]
6[d]	2	4	15	94	61[e]

[a] Determined by ^1H NMR spectroscopic analysis of the crude reaction mixture with respect to **3**. [b] Of isolated **4** with respect to **3**. [c] An iodinated derivative of **3** was formed in 19% yield. [d] The reaction was conducted by following the modified experimental protocol discussed in the text; see also the Experimental Section. [e] Iodinated derivatives of **3** (28%) and **4** (4%) were also formed.

We explored the scope and the selectivity of the process by preparing and screening the reactivity of the set of aromatic aldehydes **5**–**15** (Tf = trifluoromethanesulfonyl).[6] The arylation reactions were conducted under the modified experimental conditions described for entry 6 of Table 1, unless otherwise specified. The structures of the aromatic polycyclic ketones obtained as well as the yields and the reaction times are depicted in Scheme 1.

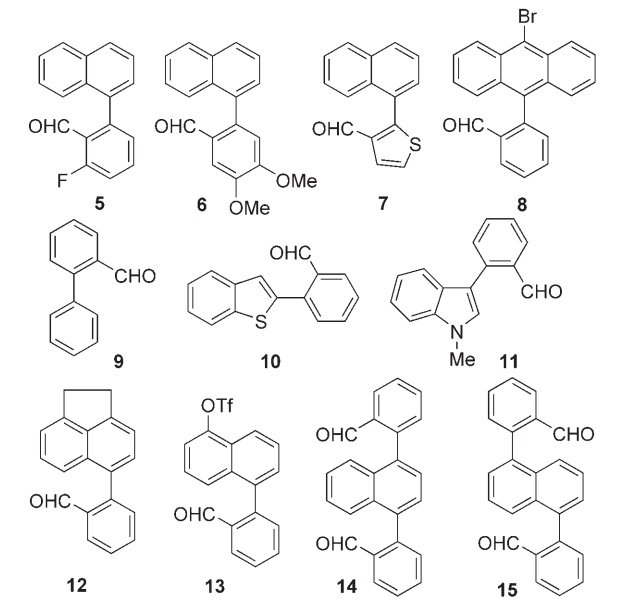

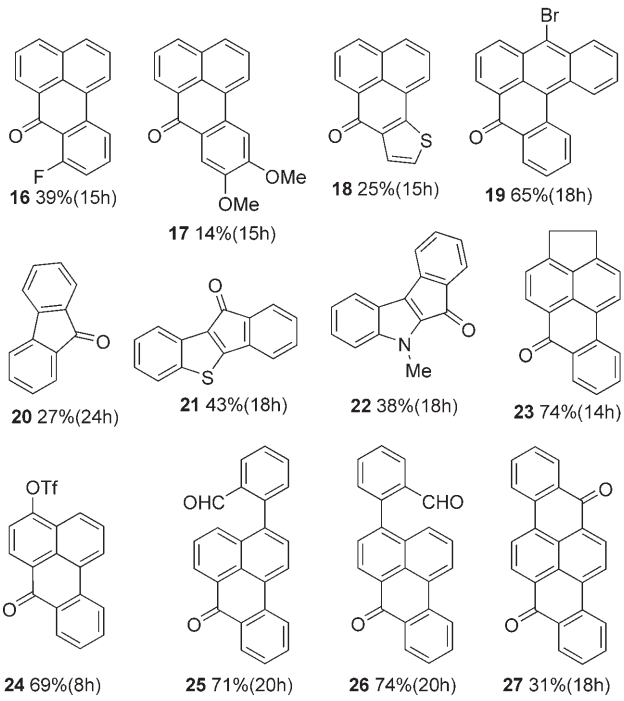

Scheme 1. Polycyclic aromatic ketones obtained in the formal Friedel–Crafts acylation of arenes **5**–**15** with aldehydes, yields, and reaction times.

The formation of a single isomer was observed consistently for the cyclization of compounds **5**–**15**. However, the reaction of 2-(9-phenanthrenyl)benzenecarboxaldehyde (**28**) gave mixtures of **29** and **30** [Eq. (3)]. When the reaction was

 © 2006 Wiley-VCH Verlag GmbH & Co. KGaA, Weinheim

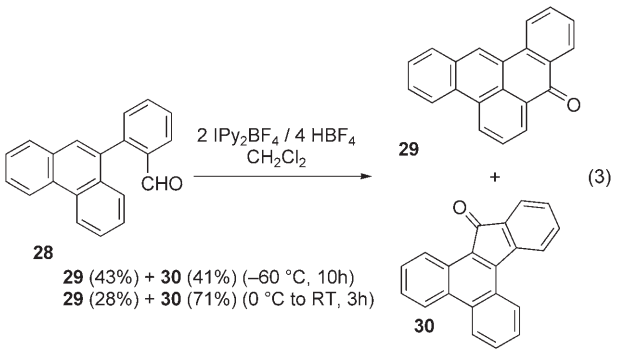

carried out under the standard conditions, the two compounds were isolated in nearly a 1:1 ratio. Interestingly, a larger amount of **30** was obtained when the reaction was carried out at 0°C.

For the other systems tested, six-membered rings were formed exclusively when the formation of both six- and five-membered carbocycles from a given precursor was feasible. One exception to this trend was found for the indole derivative **11**, which probably reflects the preference for the attack of electrophilic intermediate species at C2 to that at C4. Five-membered rings were formed in the reactions of **9** and **10**, though the products were only obtained in low to moderate yields. In the case of six-membered rings, the yields could reach 74%; however, they were lower when side reactions were observed, as in the case of product **17** (iodinated **6** was recovered in 81% yield), or for clean reactions with low conversion, as in the case of **16** (45% conversion; most of the recovered material was unaltered **5**). In an interesting process, the cyclization of **15** gave **26** smoothly in 74% yield; this product can also be seen as an attractive substrate for further cyclization. Consequently, **26** was transformed subsequently into the aromatic diketone structure **27**. Overall, **27** is derived from **15** through a formal double C–H functionalization process.

A mechanistic proposal to account for the formation of the ketones from the aldehydes is outlined in Scheme 2. Two alternative pathways are compatible with the observed effect of additional substituents on the aromatic rings and with the possible occurrence of competing aromatic iodination when electronically activated aromatic rings are present; this side reaction has been observed for some substrates.

First, the acid protonates the pyridine molecules, which are initially associated with the iodonium species. The pyridinium salt formed precipitates at low temperature and is removed by filtration to give rise to a more reactive mixture.[5] The interaction of the resulting solution with the starting aldehyde would give species **A**. Such a complex could then further react to yield the ketone product in two different ways. As depicted on the left-hand side of Scheme 2, it could undergo formal addition of IF to form intermediate **B**. Further oxidation[7] would give **C** and liberate HI into the solution, thus accounting for the use of two equivalents of IPy_2BF_4. One equivalent is decomposed by reaction with HI to form I_2. In situ activation of the resulting acyl fluoride by the BF_3 present in the reaction medium would lead to an acyl cation, which could undergo cyclization to form the benzocyclic ketone product according to the characteristics of an electrophilic process, as discussed above.

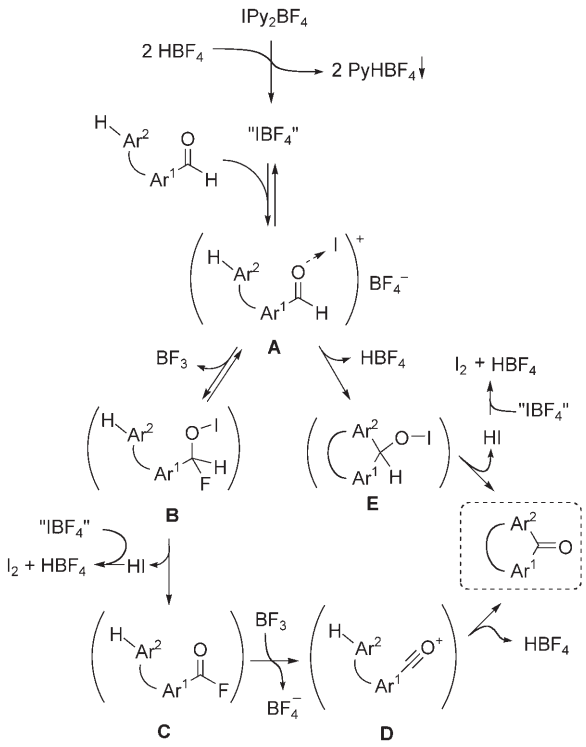

Scheme 2. Proposed mechanistic pathways that account for the observed aldehyde-to-ketone conversion.

Alternatively, as outlined in the right-hand part of Scheme 2, a direct addition of the arene to the activated carbonyl group can not be ruled out at present. Subsequent loss of HI would give the ketone and would also account for the need for a second equivalent of the iodinating reagent. Both mechanistic pathways are plausible and compatible with the formation of the observed products and the available information on the process.

In short, a new reaction promoted by the presence of iodonium ions has been reported. The reaction makes it possible to use aldehydes as acylating agents for arenes in a straightforward synthesis of ketones.

Experimental Section

Typical procedure: IPy_2BF_4 (0.74 g, 2 mmol, 2 equiv) was dissolved in dry CH_2Cl_2 (10 mL) and the resulting solution was stirred for 5 min at room temperature. It was then cooled to −80°C, and HBF_4 (542 μL, 54% solution in diethyl ether, 4 mmol, 4 equiv) was added. After 10 min the mixture was filtered under nitrogen. The aldehyde was added to the filtrate at −60°C, and the resulting mixture was stirred until the starting material had disappeared or until no further evolution of the reaction was observed. The reaction mixture was then poured onto crushed ice (100 g) and vigorously stirred until the temperature of the mixture had risen to room temperature. The organic layer was washed with a 5% aqueous solution of $Na_2S_2O_3$ (50 mL), dried over sodium sulfate, and concentrated under reduced pressure. The ketone product was purified by column chromatography (silica gel, hexane/EtOAc).

 © 2006 Wiley-VCH Verlag GmbH & Co. KGaA, Weinheim

Experimental procedures for the preparation of the starting aldehydes, as well as characterization data for ketones **2**, **4**, **16**–**27**, **29**, and **30**, are provided in the Supporting Information.

Received: December 14, 2005
Published online: March 30, 2006

Keywords: aldehydes · C—H activation · electrophilic aromatic substitution · iodonium ions · ketones

[1] For recent studies, see: a) A. Fürstner, D. Voigtländer, W. Schrader, D. Giebel, M. T. Reetz, *Org. Lett.* **2001**, *3*, 417–420; b) L. J. Gooßen, K. Ghosh, *Angew. Chem.* **2001**, *113*, 3566–3568; *Angew. Chem. Int. Ed.* **2001**, *40*, 3458–3460; c) M. H. Sarvari, H. Sharghi, *J. Org. Chem.* **2004**, *69*, 6953–6956; d) H. Firouzabadi, N. Iranpoor, F. Nowrouzi, *Tetrahedron* **2004**, *60*, 10843–10850; for an elegant application of α-fluoro carbocations in a related Friedel–Crafts cyclization reaction, see: e) J. Ichikawa, H. Jyono, T. Kudo, M. Fujiwara, M. Yokota, *Synthesis* **2005**, 39–46; for studies on the "photo-Friedel–Crafts acylation" of 1,4-naphthoquinones, see: f) M. Oelgemöller, C. Schiel, R. Fröhlich, J. Mattay, *Eur. J. Org. Chem.* **2002**, 2465–2474.

[2] Polycyclic aromatic ketone scaffolds found in natural products show remarkable profiles of biological activity; for example, in hypericin: a) D. Meruelo, G. Lavie, D. Lavie, *Proc. Natl. Acad. Sci. USA* **1988**, *85*, 5230–5234; b) A. M. Prince, D. Pascual, D. Meruelo, L. Liebes, Y. Mazur, E. Dubovi, M. Mandel, G. Lavie, *Photochem. Photobiol.* **2000**,*71*, 188–195; c) S. Rahimipour, C. Palivan, F. Barbosa, I. Bilkis, Y. Koch, L. Weiner, M. Fridkin, Y. Mazur, G. Gescheidt, *J. Am. Chem. Soc.* **2003**, *125*, 1376–1384; d) M. Van de Putte, T. Roskams, J. R. Vandenheede, P. Agostinis, P. A. M. de Witte, *Br. J. Cancer* **2005**, *92*, 1406–1413; and in resistomycin: e) K. Jakobi, C. Hertweck, *J. Am. Chem. Soc.* **2004**, *126*, 2298.

[3] For recent syntheses of diaryl ketones by metal-catalyzed coupling reactions of aldehydes with iodoarenes and with trifluoroarene borates, see: a) Y.-C. Huang, K. K. Majumdar, C.-H. Cheng, *J. Org. Chem.* **2002**, *67*, 1682–1684; b) M. Pucheault, S. Darses, J.-P. Genet, *J. Am. Chem. Soc.* **2004**, *126*, 15356–15357; c) S. Ko, B. Kang, S. Chang, *Angew. Chem.* **2005**, *117*, 459–461; *Angew. Chem. Int. Ed.* **2005**, *44*, 455–457; for syntheses of diaryl ketones by metal-catalyzed addition reactions to arenecarboxylic acid derivatives of aryl magnesium halides and aryl zinc reagents, see: d) C. Duplais, F. Bures, I. Sapountzis, T. J. Korn, G. Cahiez, P. Knochel, *Angew. Chem.* **2004**, *116*, 3028–3030; *Angew. Chem. Int. Ed.* **2004**, *43*, 2968–2970; e) Y. Zhang, T. Rovis, *J. Am. Chem. Soc.* **2004**, *126*, 15964–15965; f) X.-j. Wang, L. Zhang, X. Sun, Y. Xu, D. Krishnamurthy, C. H. Senayake, *Org. Lett.* **2005**, *7*, 5593–5595.

[4] a) J. Barluenga, M. Trincado, E. Rubio, J. M. González, *J. Am. Chem. Soc.* **2004**, *126*, 3416–3417; b) J. Barluenga, M. Trincado, M. Marco-Arias, A. Ballesteros, E. Rubio, J. M. González, *Chem. Commun.* **2005**, 2008–2010.

[5] It had already been shown that the resulting solution was more active for the iodofluorination of electron-deficient alkenes, see: J. Barluenga, P. J. Campos, J. M. González, J. L. Suárez, G. Asensio, *J. Org. Chem.* **1991**, *56*, 2234–2237.

[6] The aldehydes were prepared by well-established metal-catalyzed cross-coupling reactions; see the Supporting Information for more details.

[7] For the oxidation of aldehydes to acyl fluorides by reaction with $CsSO_4F$ in CH_3CN at 35 °C, see: S. Stavber, Z. Planinšek, M. Zupan, *J. Org. Chem.* **1992**, *57*, 5334–5337.

 © 2006 Wiley-VCH Verlag GmbH & Co. KGaA, Weinheim

Molecular Logic Gates

DOI: 10.1002/anie.200600076

TiO_2-Based Light-Driven XOR/INH Logic Gates**

Luis F. O. Furtado, Anamaria D. P. Alexiou, Léia Gonçalves, Henrique E. Toma, and Koiti Araki**

The ever-growing demand for faster and smaller devices has been successfully fulfilled by the semiconductor industry through formidable scientific and technological advances in the manufacturing of ever-smaller silicon-based devices. However, this astonishing progress is almost reaching its physical limits[1] as the size of the components goes further into the nanoscale world, requiring the urgent development of devices with innovative architectures. Efforts are underway to identify and develop alternative systems to the current complementary metal oxide semiconductor (CMOS) technology, such as quantum cellular automata,[2] single-electron transistors (SETs),[3] and quantum computing[4] and molecular systems.[5]

Molecular systems are interesting candidates for the storage, processing, and communication of information/data. Recently, several examples have been reported that emulate the functions of memories, transistors, rectifiers, switches, and wires.[6–9] Great attention is also being given to the construction of molecular logic gates that mimic the functions of present silicon devices. Accordingly, several systems using electrical, chemical, optical, or mechanical signals as inputs and outputs[5,10–13] have been described that generally involve complicated arrangements, equipment, or processes.

One of the biggest challenges to the development of a viable technology based on molecular systems is the external addressability and compatibility with present-day electronic/nanoelectronic devices and circuits. Generally, conceptual models that explore molecular junction properties involve one or more steps in which a solution is injected into the system. Consequently, function of the device is compromised by long washout times. Herein, we report the first molecular optoelectronic XOR logic gate that operates exclusively with

[*] Dr. L. F. O. Furtado, Dr. A. D. P. Alexiou, L. Gonçalves, Prof. H. E. Toma, Prof. K. Araki
Instituto de Química
Universidade de São Paulo
Caixa Postal 26077, CEP 05513–970 São Paulo, SP (Brazil)
Fax: (+55) 11-3815-5579
E-mail: koiaraki@iq.usp.br

[**] This research was supported by Fundação de Amparo à Pesquisa do Estado de São Paulo (FAPESP), Conselho Nacional de Desenvolvimento Científico e Tecnológico (CT-Energ/CNPq 400.804/2003-4), Instituto do Milênio de Materiais Complexos (IMMC), and Rede de Nanotecnologia Molecular e Interfaces (RENAMI). We also thank Degussa for kindly supplying titanium dioxide P-25 and Prof. Ivo A. Hümmelgen for helpful discussions.

Supporting information for this article is available on the WWW under http://www.angewandte.org or from the author.

© 2006 Wiley-VCH Verlag GmbH & Co. KGaA, Weinheim

optical inputs and an electric output, making the system easily addressable and compatible with present electronic systems.

The device is based on a TiO_2 dye-sensitized Grätzel-type cell,[14,15] which has attracted widespread interest for the conversion of sunlight into electricity. A typical Grätzel cell consists of a thin nanocrystalline TiO_2 film on a conductive glass electrode (fluorine-doped tin oxide, FTO) covered with a chemisorbed chromophore such as $[Ru(dcb)_2(SCN)_2)]^{2+}$ ("N3"; dcb = 2,2′-bipyridine-4,4′-dicarboxylic acid). The circuit is closed and made regenerative by connecting it with a platinized FTO cathode and filling the space in between them with a hole-conducting electrolyte such as a solution of I_3^-/I_2 in CH_3CN. The photosensitizer molecules absorb light and inject electrons into the *n*-type nanocrystaline semiconductor layer, leading to charge separation and consequent generation of electric power. However, direct absorption of light by TiO_2 ($\lambda_{exc} < 400$ nm; Figure 1B, curve b) also produces a similar photoinduced charge separation, such that the dye is used to extend the range of harvested light into the visible region.

By using a dye that accepts rather than injects electrons into the semiconductor layer when in the excited state, the direction of the photocurrent output can be modulated by the wavelength of the incident light, making possible the generation of a light-driven logic gate. For this purpose, the molecular dye should be reductively quenched by the nanocrystalline semiconductor layer. Consequently, the ground-state reduction potential should be more positive than about 0.0 V to satisfy this requirement when 2.5-eV photons ($\lambda_{exc} \approx 500$ nm) are used for excitation, as the energy of the TiO_2 valence band (upper limit) and the standard hydrogen electrode referenced to vacuum level are 6.8[16] and 4.44 eV, respectively. Generally, the reduction potential of organic compounds and ruthenium polypyridine complexes such as N3 is more negative than −1.0 V, and they are well-known electron injectors. However, ruthenium acetate trinuclear clusters reveal reduction potentials that lie in a suitable range. For example, the complex $[Ru_3O(Ac)_6(py)_2(pzCO_2H)]PF_6$ (**1**; Ac = acetyl, py = pyridine, pz = pyrazine) exhibits favorable characteristics and was used to demonstrate our hypothesis (see Figure 1 and Supporting Information).

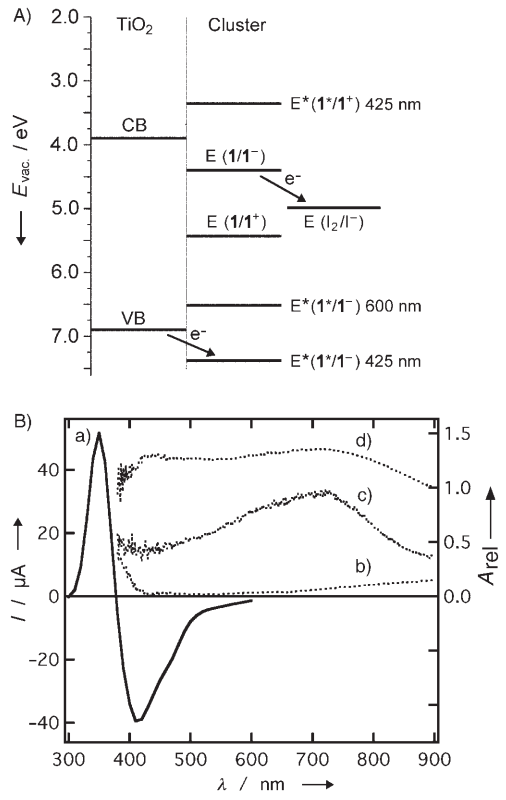

Figure 1. A) Diagram showing the energy levels of TiO_2 and the Ru cluster complex adsorbed on the surface (the asterisk represents an excited complex). The energy levels of the ground ($E(E) = E_{redox} +$ 4.44 eV) and excited states ($E(E^*) = E_{redox} \pm E_{h\nu} + 4.44$ eV) referenced to the vacuum level were calculated from the redox potentials. CB = conduction band; VB = valence band. B) a) Photoaction response of the assembled device; b, c) reflectance spectra of the nanocrystalline TiO_2 film on FTO (b) and in the presence of a cluster sensitizer (c); and d) reflectance spectrum of a solid (powder) cluster complex.

Recently, Biancardo et al.[5] reported a photonic NOR gate based on a TiO_2 photoelectrochemical cell. However, their cell was based on a completely different design and concept in which potential and Cu^{II} ions were used as inputs and the luminescence of $[Ru(dcb)_2(CN)_2]$ dye was used as the output.

The photoaction spectrum of a cell assembled with the ruthenium cluster dye is shown in Figure 1B, curve a. A photocurrent maximum is observed around $\lambda = 350$ nm, passes through zero at 375 nm, and remains negative up to $\lambda = 600$ nm, with a peak negative photocurrent value at 410 nm, where the absorption band of the adsorbed **1** is localized (Figure 1B, curve d). Note that the spectrum of the sensitized TiO_2 film is similar to that of the sum of the nanocrystalline semiconductor and complex **1** and that the contribution of this species decreases below $\lambda = 400$ nm, indicating that at least two processes are driving the photocurrent in opposite directions as shown in Figure 2. One is the direct absorption of light by the *n*-type TiO_2 layer and the second is the abstraction of electrons by the excited cluster complex. The first process is predominant at $\lambda_{exc} < 375$ nm and the current should increase sharply as λ_{exc} decreases, but the filtering effect by glass also increases rapidly, giving rise to the maximum at 350 nm (Figure 2A). This peak is the sole feature observed in a similar device assembled with a nonsensitized nanocrystalline TiO_2 film. Above 375 nm the photocurrent becomes dependent on the excited-state properties of the adsorbed dye. The adsorbed complex **1** displays a broad charge-transfer band at 420 nm (Figure 1B, curves c and d), at the negative peak in the photoaction spectrum, but the intracluster band at 700 nm is the most intense one. Electron injection from "hot" excited states are known to be responsible for the high efficiency of Grätzel cells, but this is the first report on electron injection in the reverse direction, that is, from the TiO_2 film to the excited dye sensitizer.

The excited complex **1*** ($E^*(\mathbf{1}^*/\mathbf{1}^+)$ for oxidation/electron injection to TiO_2 and $E^*(\mathbf{1}^*/\mathbf{1}^-)$ for reduction/electron removal from TiO_2) can inject electrons to the semiconductor layer, but this cannot be the main process because current flows in the opposite direction (Figure 2B). Also, a mechanism in which there is first oxidative quenching of **1*** by I_2 was also ruled out because TiO_2 cannot reduce the $\mathbf{1}^+$ species.

 © 2006 Wiley-VCH Verlag GmbH & Co. KGaA, Weinheim

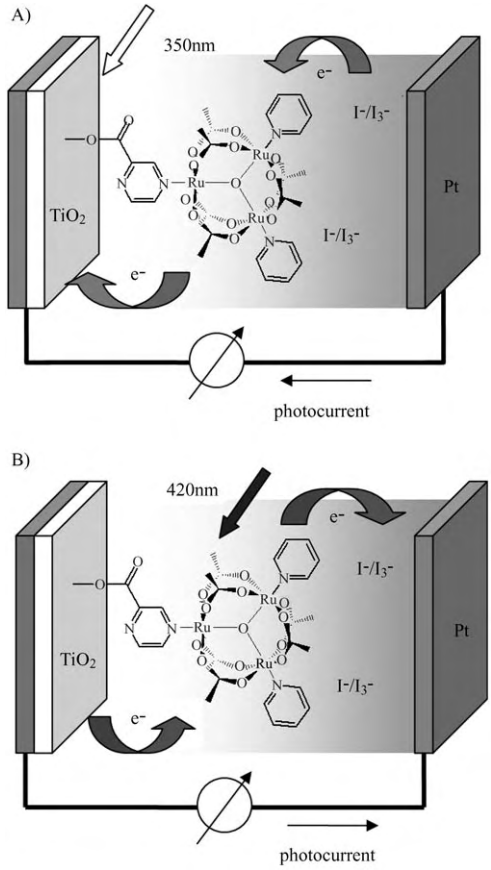

Figure 2. Scheme showing the mechanisms of photocurrent generation with inputs of A) 1-0 and B) 0-1. See text for details.

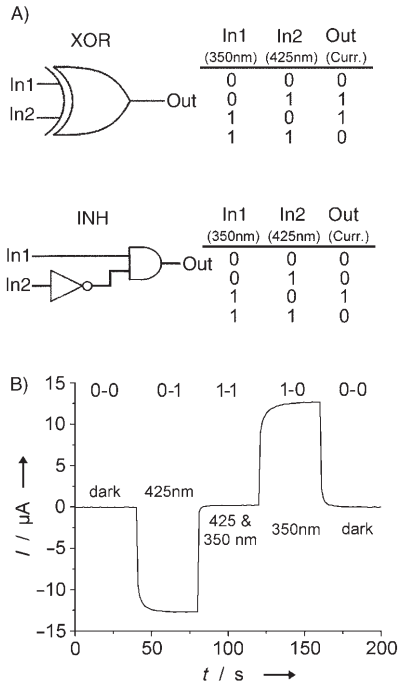

Figure 3. A) Symbolic representation and truth table for the XOR and INH logic gates. B) Photoresponses for the combinations of inputs In1 and In2 corresponding to the XOR logic-gate device.

Table 1: Summary of the response of the optoelectronic device corresponding with the truth table of XOR and INH devices shown in Figure 3A.

Input	In1-In2[a]	Photocurrent	Output XOR	Output INH
none	0-0	–	0	0
425 nm	0-1	cathodic	1	0
350 nm	1-0	anodic	1	1
425 and 350 nm	1-1	no current	0	0

[a] In1: $\lambda_{exc} = 350$ nm; In2: $\lambda_{exc} = 425$ nm.

Consequently, the reverse photocurrent should be generated by the mechanism depicted in Figure 2A, involving the reductive quenching of **1*** by the TiO_2 layer, followed by reduction of I_2 to I^- by $\mathbf{1}^-$ species and migration of electrons to the counterelectrode, closing the circuit.

Such a photoelectrochemical response can be readily exploited in the design of a XOR logic gate, which has proven difficult to emulate on the molecular scale.[17,18] Generally, these devices have two inputs and one output that follow the truth table shown in Figure 3A. The photocurrent output (Out) obtained by exciting with light at 350 and 425 nm as inputs (In1 and In2, respectively) are shown in Figure 3B. When In1 and In2 are equal to 0 (i.e. no light, 0-0), no photocurrent is generated (Out = 0). When $\lambda_{exc} = 425$ nm (0-1), a cathodic photocurrent is recorded and Out = 1. An anodic photocurrent is recorded when light at 350 nm hits the cell (1-0) and again Out = 1. However, if the cell is irradiated simultaneously at both excitation wavelengths (i.e. 350 and 420 nm, 1-1), no net current flows as they are canceled out (Out = 0). The truth table matches that for the XOR gate, as shown in Table 1. Once the binary logic is based on threshold values,[12] the INH gate also can be obtained simply by changing the intensity or the excitation wavelength of one of the inputs in such a way as to decrease the absolute output signal and establish a threshold in between Out1 and Out2. For example, one can set 7 and 13 μA as the outputs and 10 μA as the threshold to realize the INH logic gate, whose logic responses are summarized in Table 1.

In summary, optoelectronic XOR and INH logic gates based on two light inputs and a current output were demonstrated for the first time by using a nanocrystalline TiO_2 dye-sensitized solar Grätzel-type cell with reverse injection of electrons at the semiconductor/dye interface. These findings should give helpful insights for the development of new light-driven devices and the realization of more intricate systems. Further investigations in this direction are currently underway.

Experimental Section

$[Ru_3O(Ac)(py)_2(pzCO_2H)]PF_6$ (**1**) was obtained from treatment of $[Ru_3O(Ac)_6(py)_2(CH_3OH)]PF_6$ (**2**), which was prepared according to an adapted procedure,[19] with carboxypyrazinic acid ($pzCO_2H$) in CH_3OH/CH_2Cl_2 (1:5 v/v). The reaction mixture was left for 20 h at 25 °C, filtered free of any solids, and added dropwise into diethyl ether. The resultant precipitate was purified by multiple recrystalli-

 © 2006 Wiley-VCH Verlag GmbH & Co. KGaA, Weinheim

zation steps in CH_2Cl_2/acetone mixtures to afford dark green crystals (0.33 g, 42%); elemental analysis (%) calcd for $Ru_3C_{27}H_{38}O_{15}N_4$: C 29.46, H 2.93, N 5.09; found: C 29.43, H 3.02, N 5.08.

The photoelectrochemical cell was prepared according to the procedure described by Grätzel and co-workers (method B therein).[15,20] A viscous dispersion obtained by grinding Degussa P25 TiO_2 nanoparticles (30% rutile/70% anatase, mean particle size: 30 nm) with Triton-X 100 and acetylacetone, was spread onto a fluorine-doped SnO_2 conducting glass slide (TEC15 FTO glass, $\approx 15\ \Omega\,cm^{-2}$). The film was deposited over a 1-cm^2 area, limited by the use of Scotch tape on the center of a 2 cm × 2 cm square piece. After drying, the samples were fired at 450°C in air to give films with an average thickness of 14 μm. After cooling, the electrode was soaked in a solution of **1** ($1x10^{-4}$ M) in acetonitrile for 6 h and assembled with a Pt-coated FTO glass counterelectrode form a sandwich-type cell. The circuit was closed by filling the space between the electrodes with an electrolyte solution containing I_2 (0.05 M), tetrabutylammonium iodide (0.8 M), LiI (0.1 M), and *tert*-butylpyridine (0.5 M) in acetonitrile.

The photoaction spectrum was recorded using an Oriel Spectral Luminator (model 69050) as light source and a Hung Chang Building CDM digital multimeter (model HC608).

The logic gates were demonstrated by using the Spectral Luminator and an Applied Photophysics 150-W Xe lamp with a Czern-Turner monochromator as light sources, irradiating at 350 and 425 nm, respectively. The light from the former was brought to the cell by using a bundle fiber-optics cable ($\varphi = 3$ mm) in a 45° arrangement. The light intensities measured through a FTO plate at the cell position was 2.9 (350 nm) and 4.3 $\mu W\,cm^{-2}$ (420 nm). The output was measured with the multimeter as before. A much simpler arrangement using light sources with band-pass filters can also be used.

Received: January 9, 2006
Revised: February 13, 2006
Published online: March 30, 2006

Keywords: molecular devices · nanotechnology · optoelectronics · sensitizers · titanium

[1] M. Schulz, *Nature* **1999**, *399*, 729.
[2] I. Amlani, A. O. Orlov, G. Toth, G. H. Bernstein, C. S. Lent, G. L. Snider, *Science* **1999**, *284*, 289.
[3] R. H. Chen, A. N. Korotkov, K. K. Likharev, *Appl. Phys. Lett.* **1996**, *68*, 1954.
[4] V. Cerletti, W. A. Coish, O. Gywat, D. Loss, *Nanotechnology* **2005**, *16*, R27.
[5] M. Biancardo, C. Bignozzi, D. C. Hugh, G. Redmond, *Chem. Commun.* **2005**, 3918.
[6] S. Auvray, V. Derycke, M. Goffman, A. Filoramo, O. Jost, J. P. Bourgoin, *Nano Lett.* **2005**, *5*, 451.
[7] A. R. Pease, J. O. Jeppesen, J. F. Stoddart, Y. Luo, C. P. Collier, J. R. Heath, *Acc. Chem. Res.* **2001**, *34*, 433.
[8] J. M. Tour, *Acc. Chem. Res.* **2000**, *33*, 791.
[9] C. Joachim, J. K. Gimzewski, A. Aviram, *Nature* **2000**, *408*, 541.
[10] P. Ball, *Nature* **2000**, *406*, 118.
[11] A. P. de Silva, N. D. McClenaghan, *J. Am. Chem. Soc.* **2000**, *122*, 3965.
[12] F. M. Raymo, *Adv. Mater.* **2002**, *14*, 401.
[13] Y. Weizmann, R. Elnathan, O. Lioubashevski, I. Willner, *J. Am. Chem. Soc.* **2005**, *127*, 12666.
[14] B. Oregan, M. Grätzel, *Nature* **1991**, *353*, 737.
[15] M. K. Nazeeruddin, A. Kay, I. Rodicio, R. Humphrybaker, E. Muller, P. Liska, N. Vlachopoulos, M. Grätzel, *J. Am. Chem. Soc.* **1993**, *115*, 6382.
[16] J. H. Snook, L. A. Samuelson, J. Kumar, Y. G. Kim, J. E. Whitten, *Org. Electron.* **2005**, *6*, 55.
[17] V. Balzani, A. Credi, M. Venturi, *Molecular Devices and Machines*, Wiley-VCH, Weinheim, **2003**.
[18] M. Conrad, K.-P. Zauner, *Molecular Computing*, MIT Press, Boston, **2003**, chap. 1.
[19] J. A. Baumann, D. J. Salmon, S. T. Wilson, T. J. Meyer, W. E. Hatfield, *Inorg. Chem.* **1978**, *17*, 3342.
[20] A. F. Nogueira, A. L. B. Formiga, H. Winnischofer, M. Nakamura, F. M. Engelmann, K. Araki, H. E. Toma, *Photochem. Photobiol. Sci.* **2004**, *3*, 56.

 © 2006 Wiley-VCH Verlag GmbH & Co. KGaA, Weinheim

Nucleophilic Reactions

DOI: 10.1002/anie.200600227

Trichloromethyl Ketones as Synthetically Versatile Donors: Application in Direct Catalytic Mannich-Type Reactions and the Stereoselective Synthesis of Azetidines**

Hiroyuki Morimoto, Sean H. Wiedemann, Akitake Yamaguchi, Shinji Harada, Zhihua Chen, Shigeki Matsunaga, and Masakatsu Shibasaki**

The catalytic generation of metal enolates in situ and their use in stereoselective carbon–carbon bond-forming reactions are subjects of vigorous current research.[1] This strategy is superior in terms of atom economy to conventional methods that employ stoichiometric amounts of strong base.[2] Although various metal catalysts have proven effective in this regard, and enantioselective variants have been reported during the last decade, nucleophiles have been mostly limited to ketones.[3] Catalytic generation in situ of metal enolates derived from carboxylic acid derivatives is still a formidable task owing to the high pK_a value of the α protons. The development of a suitably activated carboxylic acid derivative and/or a new catalyst capable of promoting catalytic ester enolate formation in situ would thus be of considerable significance. Recently, Evans et al. reported highly diastereo-

[*] H. Morimoto, Dr. S. H. Wiedemann, A. Yamaguchi, S. Harada, Z. Chen, Dr. S. Matsunaga, Prof. Dr. M. Shibasaki
Graduate School of Pharmaceutical Sciences
The University of Tokyo
Hongo, Bunkyo-ku, Tokyo 113-0033 (Japan)
Fax: (+81) 3-5684-5206
E-mail: smatsuna@mol.f.u-tokyo.ac.jp
mshibasa@mol.f.u-tokyo.ac.jp

[**] We thank Prof. S. Kobayashi, H. Kiyohara, and T. Ogino at the University of Tokyo for their kind help in X-ray crystallographic analysis. This work was supported by Grant-in-Aid for Specially Promoted Research and Grant-in-Aid for Encouragements for Young Scientists (B) (for SM) from JSPS and MEXT.

Supporting information for this article is available on the WWW under http://www.angewandte.org or from the author.

WILEY InterScience DISCOVER SOMETHING GREAT
© 2006 Wiley-VCH Verlag GmbH & Co. KGaA, Weinheim

and enantioselective catalytic aldol reactions by using *N*-acyloxazolidinones and *N*-acylthiazolidinethiones as donors.[4] Shair and co-workers have also developed remarkable diastereo- and enantioselective aldol reactions with malonic acid half-thioesters.[5] We have in turn contributed an aldol reaction with nitriles.[6] On the other hand, methods applicable to the direct Mannich-type reaction[1b] of ester-equivalent donors are rare. We previously reported the use of an *N*-acylpyrrole as an ester-equivalent donor in Mannich-type reactions;[7] however, the reaction was limited to an α-hydroxy-substituted nucleophile. A direct catalytic Mannich-type reaction with an alkyl-substituted ester-equivalent donor has not been reported.[8] Herein we investigate the utility of trichloromethyl ketones **1** (Scheme 1) as Mannich donors. A catalytic amount of *p*-MeO-C_6H_4OLi promotes the direct Mannich-type reaction of **1** with high diastereoselectivity (*syn*/*anti* = 6:1–> 20:1) and in good yield (up to 96%). Trichloromethyl ketones not only serve as ester and amide synthetic equivalents, but also enable unique transformations. Conversions of Mannich adducts, including the stereoselective synthesis of trisubstituted azetidine-2-carboxylates, are demonstrated herein.

Trichloromethyl carbinols[9] and trichloromethyl ketones[10] are versatile building blocks in synthesis. The trichloromethyl group is a good leaving group;[11] thus, trichloromethyl ketones can be readily converted into carboxylic acids,[10a] esters,[10b] and amides.[10c] Furthermore, the strong inductive effect of the trichloromethyl group lowers the pK_a value of the α protons of trichloromethyl ketones sufficiently to allow catalytic deprotonation. These properties make **1** a promising ester-equivalent donor. Nonetheless, to our knowledge, there are no reports of **1** being used for stereoselective intermolecular carbon–carbon bond-forming reactions, probably owing to stability problems under basic conditions.[12] The requisite selectivities for utilizing enolates of **1** are summarized in Scheme 1. Careful selection of base and reaction conditions is important to promote the desired catalytic enolate formation a) while preventing undesired haloform C–C bond cleavage[10] b). It is well-known that Favorskii rearrangements of trichloromethyl ketones readily proceed under basic conditions.[13] Therefore, the desired intermolecular reaction with electrophiles c) must proceed faster than intramolecular Favorskii rearrangement d). We hypothesized that, in the presence of a suitably activated electrophile, the intermolecular path c) could be favored because the Favorskii rearrangement generates a strained cyclopropanone intermediate.

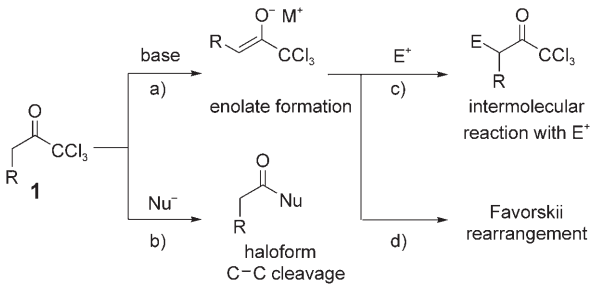

Scheme 1. Possible reaction pathways of trichloromethyl ketones under basic conditions.

We investigated Mannich-type reactions of trichloromethyl ketone **1a**[14] with imines **2a–d** bearing different protecting groups (Table 1, entries 1–4) at −40 °C in the presence of *p*-MeO-C_6H_4OLi (10 mol%) as a base.[15] With **2a** and **2b**, no Mannich adduct was observed (Table 1, entries 1 and 2). Imines **2c** and **2d**, which bear electron-withdrawing substituents, produced the desired Mannich adducts in good yield and with high *syn* selectivity (Table 1, entry 3: 12 h, 95% yield, *syn*/*anti* = 14:1; entry 4: 1 h, 88% yield, *syn*/*anti* > 20:1). Because the *N*-diphenylphosphinoyl (*N*-Dpp) imine **2d** had the best reactivity and *syn* selectivity,[16] it was used for further optimization. As shown in Table 1, entries 5 and 6, 3-Å molecular sieves were effective in allowing the molar excess of **1a** to be decreased while maintaining high reaction yield. The reaction of **1a** (2 equiv) proceeded smoothly in the presence of 3-Å molecular sieves, affording the Mannich adduct **3da** after 3 h in 96% yield with an excellent d.r. (> 20:1). The reaction proceeded equally well with only 5 mol% of base (Table 1, entry 7). The success of the Mannich reaction with 5–10 mol% catalyst loading implies that side reactions such as the Favorskii rearrangement, which quenches catalytic base by production of HCl, are negligible.

Table 1: Optimization of reaction conditions.

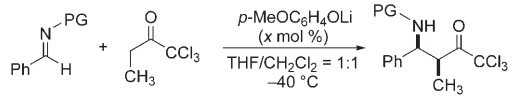

Entry	PG (imine)	Catalyst [mol%]	**1a** [equiv]	Additive	*t* [h]	Yield [%][a]	Product	*syn*/*anti*[b]
1	Bn (**2a**)	10	5	–	24	0	**3aa**	–
2	*p*-$MeOC_6H_4$ (**2b**)	10	5	–	24	0	**3ba**	–
3	*p*-Ts (**2c**)	10	5	–	12	95	**3ca**	14:1
4	$Ph_2P(O)$ (**2d**)	10	5	–	1	88	**3da**	> 20:1
5	$Ph_2P(O)$ (**2d**)	10	2	–	3	84	**3da**	> 20:1
6	$Ph_2P(O)$ (**2d**)	10	2	M.S. 3 A[c]	3	96	**3da**	> 20:1
7	$Ph_2P(O)$ (**2d**)	5	2	M.S. 3 A[c]	3	95	**3da**	> 20:1

[a] Yield of isolated product. [b] Determined by ^{1}H NMR spectroscopic analysis. [c] 200 mg mmol^{-1} of **2d** was used. M.S. 3 A = 3-Å molecular sieves, PG = protecting group.

As summarized in Table 2, Mannich-type reactions proceeded well using various aryl (Table 2, entries 1–4), heteroaryl (Table 2, entries 5–6), alkenyl (Table 2, entry 7), and alkyl[17] *N*-Dpp imines (Table 2, entries 8–10). In all examples, the reactions were complete within 1–6 h, and good to excellent diastereoselectivity (*syn*/*anti* = 6:1–> 20:1)[18] was obtained. Notably, the reaction proceeded in good yield when using readily isomerizable aliphatic *N*-Dpp imines. The low pK_a value of **1a**, ascribed to the inductive effects of the

 © 2006 Wiley-VCH Verlag GmbH & Co. KGaA, Weinheim

Table 2: Catalytic direct *syn*-selective Mannich-type reactions of trichloromethyl ketones **1a–1d** with *N*-Dpp imines **2d–2m**.[a]

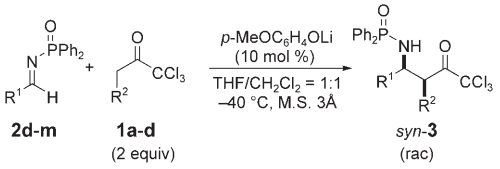

Entry	R^1 (Imine)	R^2 (**1**)	*t* [h]	Yield [%][b]	**3**	*syn*/*anti*[c]
1	Ph (**2d**)	CH_3 (**1a**)	3	96	**3da**	>20:1
2	*p*-Cl-C_6H_4 (**2e**)	CH_3 (**1a**)	4	93	**3ea**	>20:1
3	*p*-Me-C_6H_4 (**2f**)	CH_3 (**1a**)	6	89	**3fa**	>20:1[d]
4	*p*-$MeOC_6H_4$ (**2g**)	CH_3 (**1a**)	5	68	**3ga**	>20:1[d]
5	2-furyl (**2h**)	CH_3 (**1a**)	1	88	**3ha**	6:1
6	2-thienyl (**2i**)	CH_3 (**1a**)	2	89	**3ia**	8:1
7	(*E*)-PhCH=CH (**2j**)	CH_3 (**1a**)	1	81	**3ja**	7:1
8[e]	cyclohexyl (**2k**)	CH_3 (**1a**)	2	78	**3ka**	>20:1[d]
9[e]	$(CH_3)CHCH_2$ (**2l**)	CH_3 (**1a**)	3	71	**3la**	>20:1[d]
10[e]	*n*-Bu (**2m**)	CH_3 (**1a**)	3	73 (61)[f]	**3ma**	>20:1[d]
11[g]	Ph (**2d**)	CH_3CH_2 (**1b**)	2	87	**3db**	14:1
12[h]	Ph (**2d**)	$PhCH_2$ (**1c**)	6	90	**3dc**	>20:1
13	Ph (**2d**)	$BnO(CH_2)_2$ (**1d**)	1	89	**3dd**	11:1

[a] 2 equivalents of **1** was used unless otherwise noted. [b] Yield of isolated product after column chromatography unless otherwise noted. [c] Determined by ^{1}H NMR spectroscopic analysis of the crude mixture. [d] Minor isomer was not detected. [e] Reaction was performed in the absence of 3-Å molecular sieves using **1a** (5 equiv). [f] Product was isolated by crystallization ($CHCl_3$/hexane) without chromatography. [g] 3 equivalents of **1b** was used. [h] Reaction was performed at −60 °C.

trichloromethyl group, allowed chemoselective nucleophilic activation. Furthermore, Mannich adducts are quite crystalline and can be isolated without chromatography after extractive workup. For example, diastereomerically pure **3ma** was isolated in 61% yield by crystallization of a crude mixture from $CHCl_3$/hexane (Table 2, entry 10). Besides **1a**, trichloromethyl ketones with longer side chains (**1b** and **1c**) and oxygen functionality (**1d**) were applied (Table 2, entries 11–13); they afforded Mannich adducts in 87–90% yield with good diastereoselectivity (11:1–>20:1). The Mannich-type reaction of **1c** was performed at −60 °C to prevent side reactions.

A postulated catalytic cycle and a transition-state model that explains the observed *syn* selectivity are illustrated in Scheme 2. *p*-MeO-C_6H_4OLi first deprotonates the α proton of **1**. Trichloromethyl ketones favor the formation of *Z* enolate **II** because of steric pressure from the bulky trichloromethyl group.[19] The observed high *syn* selectivity is accounted for by the *Z*-enolate transition state **III**. Protonation of **IV** by *p*-MeO-C_6H_4OH regenerates the catalyst and affords **3**.

The synthetic utility of the trichloromethyl ketone moiety was demonstrated by the transformations shown in Scheme 3. Mannich adducts **3da** and **3la** were readily converted into esters **4da** and **4la** in 100% and 94% yield, respectively, by treatment with NaOMe in MeOH for 15 min, during which no epimerization was observed. Treatment of **3da** with NaOH followed by coupling with Gly-O*t*Bu gave amide **5da** in 84%

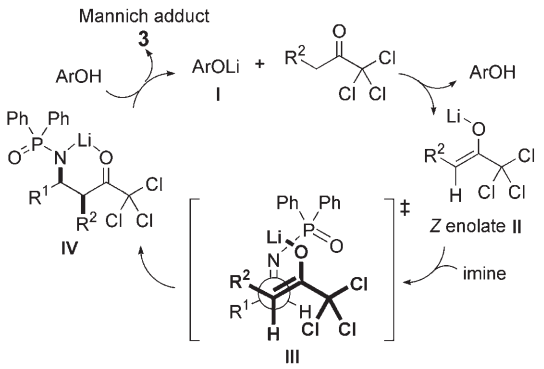

Scheme 2. Postulated catalytic cycle and transition-state model for *syn* selectivity.

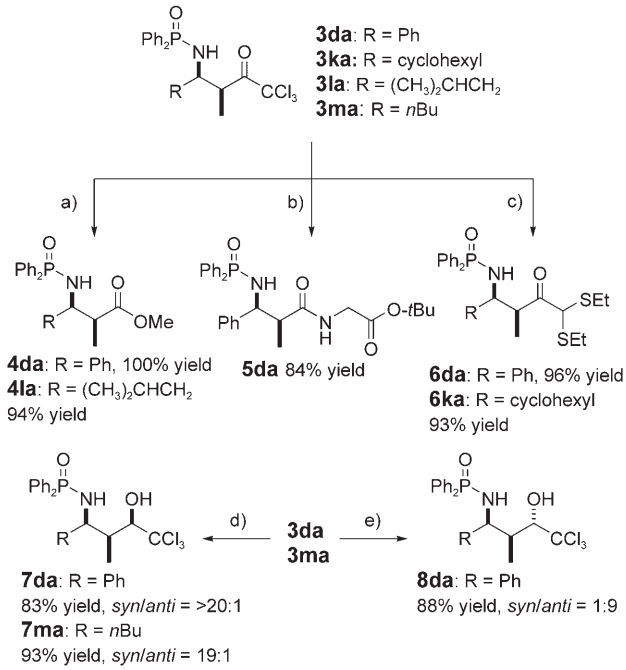

Scheme 3. Transformations of the trichloromethyl ketone moiety. Reagents and conditions: a) NaOMe, MeOH, 0→25 °C, 15 min; b) 1. NaOH, THF/H_2O, 0 °C, 20 min; 2. Gly-O*t*Bu·HCl, HOAt, EDC·HCl, Et_3N, 0 °C→RT, 14 h; c) EtSLi, EtSH, THF, 0 °C, 15 min; d) $LiAl(OtBu)_3H$, THF/CH_2Cl_2, −40 °C, 5 h; e) $Zn(BH_4)_2$, THF/Et_2O, −78 to −40 °C, 16 h. EDC = 1-ethyl-3(3-dimethylaminopropyl)carbodiimide.

yield (two steps). The trichloromethyl ketone unit functions not only as a synthetic equivalent for esters and amides, but also as a unique template for further transformations. Treatment of **3da** and **3ka** with basic ethanethiol for 15 min afforded dithianes **6da** and **6ka** in 96% and 93% yield, respectively.[10d] In this case, the thiol acts as both a nucleophile and a reductant to give synthetically useful protected aldehydes. *syn*-Selective reduction of the Mannich adducts with $LiAl(O\text{-}tBu)_3H$ afforded the N-protected amino alcohols **7da** and **7ma**, whereas *anti*-selective reduction with $Zn(BH_4)_2$ afforded the N-protected amino alcohol **8da**.[20] The synthetic versatility of **7** and **8** can potentially be utilized in stereoselective transformations as reported by Corey and

 © 2006 Wiley-VCH Verlag GmbH & Co. KGaA, Weinheim

Link.[9a,b] Furthermore, we also succeeded in the highly stereocontrolled synthesis of azetidines (Scheme 4). By treating **7da** with aqueous NaOH in 1,2-dimethoxyethane (DME), we obtained the azetidine-2-carboxylic acid **9da**. The

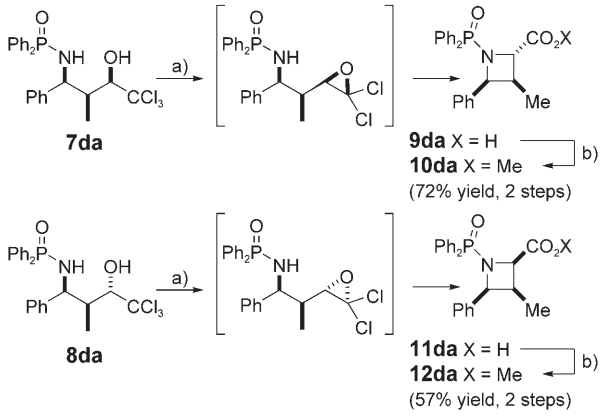

Scheme 4. Stereoselective synthesis of azetidines from trichloromethyl carbinols. Reagents and conditions: a) aq. NaOH, DME, 25 °C, 24 h; b) $TMSCHN_2$, MeOH/hexane, 25 °C. TMS = trimethylsilyl.

reaction is considered to proceed via a *gem*-dichlorooxirane intermediate.[9a] Intramolecular ring opening affords the azetidine ring. After conversion into the corresponding methyl esters, methyl azetidine-2-carboxylate **10da** was isolated in 72% yield (two steps).[21] From **8da**, *all-syn*-substituted methyl azetidine-2-carboxylate **12da** was obtained, albeit in moderate yield (57% in two steps). The relative configuration of **12da** was confirmed by single-crystal X-ray crystallographic analysis (Figure 1).[21,22] Because stereoselective syntheses of 3,4-*syn*-substituted azetidine-2-carboxylic acids, particularly sterically hindered *all-syn*-substituted azetidines, are rare, the present stereoselective method should prove useful to medicinal chemists studying nonnatural amino acid motifs.[23]

In summary, we successfully developed a chemoselective catalytic nucleophilic activation of trichloromethyl ketones and applied this method to intermolecular C–C bond-forming reactions. Direct Mannich-type additions of trichloromethyl ketones to various *N*-Dpp imines in the presence of catalytic amounts of a weak Brønsted base proceeded in good yield and high *syn* selectivity (62–96%, *syn*/*anti* = 6:1–>20:1). Transformations of the Mannich adducts formed were demonstrated, including a highly stereoselective synthesis of azetidines. Efforts toward the use of trichloromethyl ketones in conjunction with chiral catalysts in Mannich and other addition reactions are ongoing.

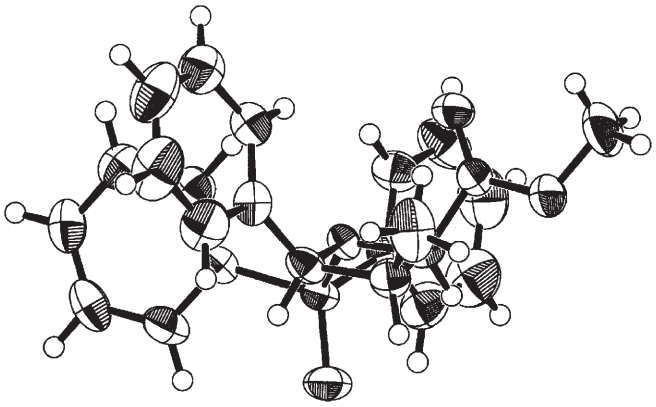

Figure 1. X-ray crystallographic structure of azetidine **12da**. Ellipsoids drawn at the 50% probability level.

Received: January 19, 2006
Published online: April 5, 2006

Keywords: asymmetric catalysis · azetidines · diastereoselectivity · Mannich reaction · trichloromethyl ketones

[1] For a review of the direct aldol reaction, see: a) B. Alcaide, P. Almendros, *Eur. J. Org. Chem.* **2002**, 1595; for reviews of direct Mannich(-type) reactions, see: b) A. Córdova, *Acc. Chem. Res.* **2004**, *37*, 102; c) M. M. B. Marques, *Angew. Chem.* **2006**, *118*, 356; *Angew. Chem. Int. Ed.* **2006**, *45*, 348.

[2] B. M. Trost, *Science* **1991**, *254*, 1471.

[3] For selected recent examples of direct catalytic asymmetric Mannich-type reactions using metal catalysts and ketone nucleophiles, see: a) K. Juhl, N. Gathergood, K. A. Jørgensen, *Angew. Chem.* **2001**, *113*, 3083; *Angew. Chem. Int. Ed.* **2001**, *40*, 2995; b) B. M. Trost, L. R. Terrell, *J. Am. Chem. Soc.* **2003**, *125*, 338; c) S. Matsunaga, N. Kumagai, S. Harada, M. Shibasaki, *J. Am. Chem. Soc.* **2003**, *125*, 4712; d) S. Matsunaga, T. Yoshida, H. Morimoto, N. Kumagai, M. Shibasaki, *J. Am. Chem. Soc.* **2004**, *126*, 8777, and references therein.

[4] a) D. A. Evans, J. S. Tedrow, J. T. Shaw, C. W. Downey, *J. Am. Chem. Soc.* **2002**, *124*, 392; b) D. A. Evans, C. W. Downey, J. T. Shaw, J. S. Tedrow, *Org. Lett.* **2002**, *4*, 1127; c) D. A. Evans, C. W. Downey, J. L. Hubbs, *J. Am. Chem. Soc.* **2003**, *125*, 8706.

[5] a) G. Lalic, A. D. Aloise, M. D. Shair, *J. Am. Chem. Soc.* **2003**, *125*, 2852; b) D. Magdziak, G. Lalic, H. M. Lee, K. C. Fortner, A. D. Aloise, M. D. Shair, *J. Am. Chem. Soc.* **2005**, *127*, 7284.

[6] a) Y. Suto, R. Tsuji, M. Kanai, M. Shibasaki, *Org. Lett.* **2005**, *7*, 3757, and references therein; b) N. Kumagai, S. Matsunaga, M. Shibasaki, *J. Am. Chem. Soc.* **2004**, *126*, 13632; c) N. Kumagai, S. Matsunaga, M. Shibasaki, *Chem. Commun.* **2005**, 3600.

[7] a) S. Harada, S. Handa, S. Matsunaga, M. Shibasaki, *Angew. Chem.* **2005**, *117*, 4439; *Angew. Chem. Int. Ed.* **2005**, *44*, 4365; for other exceptional examples of Mannich-type reactions using readily enolizable substrates, see: malonates and ketoesters as donors: b) M. Marigo, A. Kjærsgaard, K. Juhl, N. Gathergood, K. A. Jørgensen, *Chem. Eur. J.* **2003**, *9*, 2359; c) Y. Hamashima, N. Sasamoto, D. Hotta, H. Somei, N. Umebayashi, M. Sodeoka, *Angew. Chem.* **2005**, *117*, 1549; *Angew. Chem. Int. Ed.* **2005**, *44*, 1525; d) S. Lou, B. M. Taoka, A. Ting, S. E. Schaus, *J. Am. Chem. Soc.* **2005**, *127*, 11256; glycine Schiff base as a donor: e) L. Bernardi, A. S. Gothelf, R. G. Hazell, K. A. Jørgensen, *J. Org. Chem.* **2003**, *68*, 2583; f) T. Ooi, M. Kameda, J. I. Fujii, K. Maruoka, *Org. Lett.* **2004**, *6*, 2397.

[8] For reactions of alkyl-substituted ketones and aldehydes promoted by organocatalysts, see reference [1b, c]; for selected examples, see: a) B. List, *Acc. Chem. Res.* **2004**, *37*, 548; b) W. Notz, F. Tanaka, C. F. Barbas III. *Acc. Chem. Res.* **2004**, *37*, 580; c) A. Córdova, *Chem. Eur. J.* **2004**, *10*, 1987; d) D. Enders, C. Grondal, M. Vrettou, G. Raabe, *Angew. Chem.* **2005**, *117*, 4147; *Angew. Chem. Int. Ed.* **2005**, *44*, 4079, and references therein; e) T. Kano, Y. Yamaguchi, O. Tokuda, K. Maruoka, *J. Am. Chem. Soc.* **2005**, *127*, 16408, and references therein.

[9] a) E. J. Corey, J. O. Link, *J. Am. Chem. Soc.* **1992**, *114*, 1906; b) E. J. Corey, J. O. Link, *Tetrahedron Lett.* **1992**, *33*, 3431; c) T. Fujisawa, T. Ito, K. Fujimoto, M. Shimizu, H. Wynberg, E. G. J.

 © 2006 Wiley-VCH Verlag GmbH & Co. KGaA, Weinheim

Staring, *Tetrahedron Lett.* **1997**, *38*, 1593; d) Z. Wang, S. Campagna, K. Yang, G. Xu, M. E. Pierce, J. M. Fortunak, P. N. Confalone, *J. Org. Chem.* **2000**, *65*, 1889; e) B. Jiang, Y.-G. Si, *Adv. Synth. Catal.* **2004**, *346*, 669; f) R. Bejot, S. Tisserand, L. M. Reddy, D. K. Barma, R. Baati, J. R. Falck, C. Mioskowski, *Angew. Chem.* **2005**, *117*, 2044; *Angew. Chem. Int. Ed.* **2005**, *44*, 2008.

[10] a) Haloform reaction: M. B. Smith, J. March, *Advanced Organic Chemistry*, 5th ed., Wiley, New York, **2001**, p. 813; b) B. M. Trost, J. M. Balkovec, M. K. T. Mao, *J. Am. Chem. Soc.* **1986**, *108*, 4974; c) J. R. Salim, F. Nome, M. C. Rezende, *Synth. Commun.* **1989**, *19*, 1181; d) S. C. Hess, F. Nome, C. Zucco, M. C. Rezende, *Synth. Commun.* **1989**, *19*, 3037; e) M. Romero-Ortega, H. Reyes, A. Covarruvias-Zuñiga, R. Cruz, J. G. Avila-Zarraga, *Synthesis* **2003**, 2765, and references therein.

[11] For systematic studies on the leaving ability of the CCl_3 group, see: a) C. Zucco, C. F. Lima, M. C. Rezende, J. F. Vianna, F. Nome, *J. Org. Chem.* **1987**, *52*, 5356; b) M. Uieara, C. Zucco, D. Zanette, M. C. Rezende, F. Nome, *J. Chem. Soc. Perkin Trans. 2* **1987**, 175; for structural aspects of trichloromethyl ketones, see: c) E. J. Corey, J. O. Link, S. Sarshar, Y. Shao, *Tetrahedron Lett.* **1992**, *33*, 7103.

[12] For exceptional results with methyl trichloromethylacetoacetate and 4,4,4-trichloromethyl-3-oxobutanal as nucleophiles in Knoevenagel condensations, see: a) L. F. Tietze, H. Meier, H. Nutt, *Chem. Ber.* **1989**, *122*, 643; b) J. P. Chupp, L. R. Smith, *J. Heterocycl. Chem.* **1988**, *25*, 1785.

[13] For recent reports of Favorskii rearrangements and related reactions of acyclic trihalomethyl ketones, including trichloromethyl ketones under basic conditions, see: a) S. Braverman, M. Cherkinsky, E. V. K. S. Kumar, H. E. Gottlieb, *Tetrahedron* **2000**, *56*, 4521; b) B. Föhlisch, T. Franz, G. Kreiselmeier, *Eur. J. Org. Chem.* **2005**, 4687, and references therein.

[14] For the synthesis of trichloromethyl ketones **1a**–**d**, see: a) E. J. Corey, J. O. Link, Y. Shao, *Tetrahedron Lett.* **1992**, *33*, 3435, and references therein; although trichloromethyl carbinols were oxidized mainly by using stoichiometric amounts of chromium(VI) reagents in the original report, we utilized the catalytic oxidation method reported by workers at Merck: b) M. Zhao, J. Li, Z. Song, R. Desmond, D. M. Tschaen, E. J. J. Grabowski, P. J. Reider, *Tetrahedron Lett.* **1998**, *39*, 5323; Swern oxidation is also applicable, see Supporting Information.

[15] We selected a phenoxide base for its relevance to ongoing studies of the development of catalytic asymmetric reactions with chiral metal phenoxides such as 1,1′-bi-2-naphthol (binol) derivatives. Other bases with low nucleophilicity, such as Li{N-$(SiMe_3)_2$} (10 mol%), also promoted the Mannich reaction of imine **2d** with **1a** (5 equiv) at −40 °C in comparable yield (conv. 89%), albeit with lower *syn* selectivity (*syn*/*anti* = 13:1) and longer reaction time (13 h) than the corresponding reactions in Table 1.

[16] The *N*-Dpp group is useful because it is readily removed; for a review on the use of *N*-Dpp imines in organic synthesis, see: S. M. Weinreb, R. K. Orr, *Synthesis* **2005**, 1205.

[17] For the synthesis of enolizable alkyl *N*-Dpp imines **2k**–**2m**, see: a) A. Côté, A. A. Boezio, A. B. Charette, *Proc. Natl. Acad. Sci. USA* **2004**, *101*, 5405; b) J.-N. Desrosiers, A. Côté, A. B. Charette, *Tetrahedron* **2005**, *61*, 6186; for related enolizable alkyl *N*-Ts (Ts = *p*-toluenesulfonyl) imines, see: c) F. Chemla, V. Hebbe, J.-F. Normant, *Synthesis* **2000**, 75.

[18] The relative configuration of **3fa** was unequivocally determined by single-crystal X-ray crystallographic analysis;[22] the relative configurations of **3da** and **3la** were determined after conversion into known compounds; see Supporting Information.

[19] For discussions on steric effects of the trichloromethyl group, see: M. B. Smith, J. March, *Advanced Organic Chemistry*, 5th ed., Wiley, New York, **2001**, chap. 9, p. 374; see also reference [11c].

[20] The relative configuration of **8da** was determined by X-ray crystallographic analysis of the corresponding cyclic carbamate; see Supporting Information.

[21] For the determination of the relative configurations of **10da** and **12da**, see Supporting Information.

[22] CCDC 295183–295185 (**12da**, **3fa**, cyclic carbamate derived from **8da**, respectively) contain the supplementary crystallographic data for this paper. These data can be obtained free of charge from The Cambridge Crystallographic Data Centre via www.ccdc.cam.ac.uk/data_request/cif.

[23] For the synthesis of azetidine-2-carboxylic acids (L-aze analogues) and their incorporation into peptides, see the review: a) F. Couty, G. Evano, D. Prim, *Mini-Rev. Org. Chem.* **2004**, *1*, 133, and references therein; for selected recent examples, see: b) D. Enders, J. Gries, *Synthesis* **2005**, 3508, and references therein; c) F. Couty, G. Evano, N. Rabasso, *Tetrahedron: Asymmetry* **2003**, *14*, 2407; d) S. Hanessian, N. Bernstein, R.-Y. Yang, R. Maguire, *Bioorg. Med. Chem. Lett.* **1999**, *9*, 1437; e) A. P. Kozikowski, Y. Liao, W. Tückmantel, S. Wang, S. Pshenichkin, A. Surin, C. Thomsen, J. T. Wroblewski, *Bioorg. Med. Chem. Lett.* **1996**, *6*, 2559.

 © 2006 Wiley-VCH Verlag GmbH & Co. KGaA, Weinheim

Expanded Porphyrins

DOI: 10.1002/anie.200600248

A Near-Infrared-Fluorescent Chemodosimeter for Mercuric Ion Based on an Expanded Porphyrin**

Xun-Jin Zhu, Shi-Tao Fu, Wai-Kwok Wong, Jian-Ping Guo, and Wai-Yeung Wong*

In recent years, there has been an upsurge of interest in the development of expanded porphyrins with five or more

[*] X. Zhu, S. Fu, Prof. W.-K. Wong, Dr. W.-Y. Wong
Department of Chemistry and
Centre for Advanced Luminescence Materials
Hong Kong Baptist University
Waterloo Road, Kowloon Tong, Hong Kong (P.R. China)
Fax: (+852) 3411-7348
E-mail: wkwong@hkbu.edu.hk

S. Fu
Department of Chemistry
Wuhan University
Wuhan, Hubei (P.R. China)

Dr. J.-P. Guo
Department of Chemistry
Shanxi Universtiy
Taiyuan, Shanxi (P.R. China)

[**] This work was supported by a CERG Grant from the Research Grants Council of the Hong Kong SAR, P.R. China (Project HKBU2021/03P), and Hong Kong Baptist University.

Supporting information for this article is available on the WWW under http://www.angewandte.org or from the author.

WILEY InterScience DISCOVER SOMETHING GREAT
© 2006 Wiley-VCH Verlag GmbH & Co. KGaA, Weinheim

conjugated pyrrolic rings, because of their spectral and electronic features, their interesting and often unprecedented cation-coordination properties, and, in many cases, their ability to bind anions in certain protonation states.[1–3] Continuing research efforts have culminated in the synthesis of a variety of large pyrrole-containing macrocycles such as corrole (**1**), N-confused porphyrin (**2**), sapphyrin (**3**), rubyrin (**4**), rosarin (**5**), hexaphyrin **6**, heptaphyrin **7**, octaphyrin **8**, nonaphyrin **9**, and higher homologues.[4–10] Recently, the X-ray crystal structure of an N-confused pentaphyrin was also reported.[11] Among these macrocycles, a significant subset shares the structural motif of one or more direct α,α′-bipyrrole linkages (e.g. **1**, **3**, **4**, **5**) and display interesting and potentially useful properties.[12]

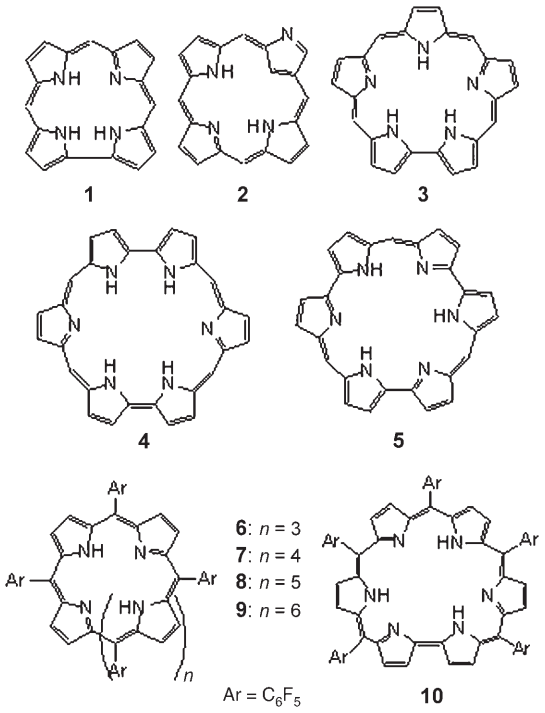

Recently, an improved "[3+1+1]" procedure to sapphyrin with a high yield was reported by Sessler and co-workers.[6b] However, the similar presumed structure of a [26]hexaphyrin(1.1.1.1.1.0) (**10**) is not yet known and inspired us to reinvestigate the cyclization reaction under different conditions. Herein, we report the chemistry of the new expanded porphyrin **10**, which contains one α,α′-bipyrrole, four pyrrolic rings, and five pentafluorophenyl rings. The porphyrinoid exhibits near-infrared (NIR) luminescence with $\lambda_{em} > 900$ nm, a region that is free of optical interference from commonly used matrix and other organic compounds under assay conditions. We describe how **10** may serve as a chemodosimetric tool with high sensitivity and selectivity for Hg^{2+} ions. Many efforts have been devoted to the development of sensors for Hg^{2+} ions, and promising results were obtained with,[13] for example, some water-soluble porphyrins that can be used for sensing heavy-metal ions by purely optical means or reversed-phase HPLC.[14] However, to our knowledge, there are very few reports dealing with the use of NIR-fluorescent expanded porphyrins for the accurate and rapid determination of trace amounts of mercury(II) ions.[15]

The synthesis of **10** was carried out under modified Lindsey conditions, at relatively low reactant concentrations (10 mM) of both pentafluorobenzaldehyde and unsubstituted pyrrole in CH_2Cl_2 in the presence of methanesulfonic acid (7 mM). After oxidation of the product with 2,3-dichloro-5,6-dicyano-1,4-benzoquinone (DDQ), repeated chromatography over a silica gel column led to the isolation of normal tetra(pentafluorophenyl)porphyrin and two expanded porphyrins **6** and **10**, besides traces of other porphyrin derivatives. The absorption spectrum of **10** in MeOH shows broad bands at $\lambda = 543$ nm ($\varepsilon = 2.64 \times 10^5$ $cm^{-1}M^{-1}$), 704 nm ($\varepsilon = 1.6 \times 10^4$ $cm^{-1}M^{-1}$), and 768 nm ($\varepsilon = 1.21 \times 10^4$ $cm^{-1}M^{-1}$). Upon photoexcitation at $\lambda = 514$ nm, porphyrinoid **10** shows intense NIR emission peaks at 959 and 1085 nm.

The crystal structure of **10** was confirmed by X-ray analysis (Figure 1).[16] This macrocycle displays a nonplanar conformation with four *exo* pyrrolic rings and two *endo* rings. π-Electron delocalization in the macrocyclic core is apparent from the observed bond lengths: 1.327(6)–1.383(6) Å for the N–C_α bond and 1.385(7)–1.427(7) Å for the C_α–C_{meso} bonds. On the other hand, the bond lengths observed for the C–C bonds in the pyrrole rings suggest double and single bond character for these bonds: 1.316(7)–1.366(7) Å for the C_β–C_β bonds and 1.383(7)–1.463(7) Å for the C_α–C_β bonds. The five pentafluorophenyl rings are tilted by 56.3–82.5° relative to the least-square plane defined by the atoms of the macrocyclic core. Consequently, the average bond length of 1.4854 Å between the *meso* carbon atoms and the pentafluorophenyl rings indicates the absence of interactions between those rings

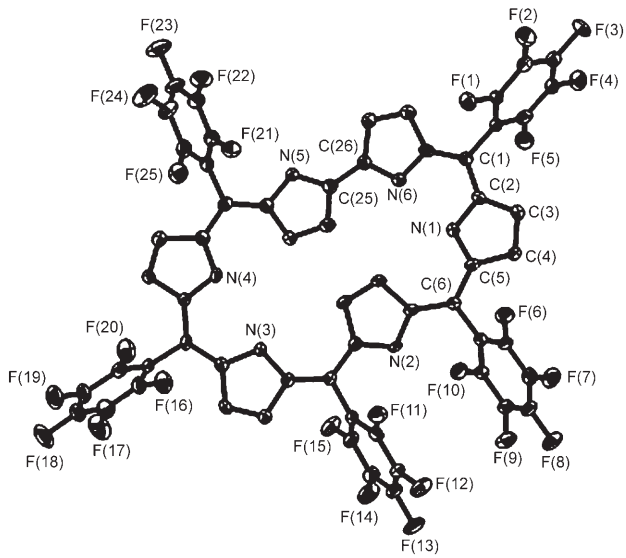

Figure 1. X-ray crystal structure for *meso*-pentafluorophenyl[26]hexaphyrin(1.1.1.1.1.0) (**10**). Thermal ellipsoids are shown at the 30% probability level; hydrogen atoms are omitted for clarity; labels for N, F, and selected C atoms are shown. Selected bond lengths [Å]: N–C_α 1.327(6)–1.383(6), C_α–C_{meso} 1.385(7)–1.427(7), C_β–C_β 1.316(7)–1.366(7), C_α–C_β 1.383(7)–1.463(7), C1–C30 1.484(7), C1–C2 1.408(7), C2–C3 1.401(7), C3–C4 1.364(7).

 © 2006 Wiley-VCH Verlag GmbH & Co. KGaA, Weinheim

and the macrocyclic core. These structural features are consistent with a 26π-electron aromatic current ring extended over the nitrogen atoms, the α-pyrrolic carbon atoms, and the *meso* carbon atoms of the macrocyclic ring. The nonplanarity of the macrocycle in **10** is presumably attributed to the large molecular dimensions of the six pyrrole rings as compared to four pyrrole rings in regular porphyrin, together with the steric bulk of the five *meso*-pentafluorophenyl rings. To minimize the steric interactions, the macrocycle loses the planarity of its core, leading to an average deviation of 0.3064 Å from the least-square plane defined by the atomic positions of the macrocycle.

We next investigated the affinity of **10** for a series of acetate salts of transition-metal ions (Mn^{2+}, Co^{2+}, Cd^{2+}, Zn^{2+}, Fe^{3+}, Ag^{+} and Hg^{2+}) and some Group 1 (Li^{+} and K^{+}) and Group 2 (Ca^{2+} and Ba^{2+}) metal ions in methanol. Generally, only minor changes in the UV/Vis spectra were observed when 2 equiv of the metal ions were used with the exception of the Hg^{2+} ion, for which marked hyperchromic shifts were observed. The bright red solution of **10** turned purple and then deep blue upon complexation with Hg^{2+}, and the color changes were clearly visible to the naked eye (see Supporting Information). Analogous to the previous observation,[13] the complexation process caused notable changes in the absorption spectrum of **10** upon the addition of an increasing amount of Hg^{2+} ion. A marked bathochromic shift in its λ_{max} value was apparent (see Supporting Information). The absorption maximum at 543 nm gradually decreased in intensity and was accompanied by the formation of a new absorption band at 568 nm ($\Delta\lambda_{max} = 15$ nm). A distinct decrease in the integrated NIR emission was observed upon addition of Hg^{2+}. It is likely that the fluorescence quenching of **10** results from the cation interactions between the heavy atom and the electron-rich aromatic ring.[11] Metal-binding titration experiments indicate that **10** forms a 1:2 porphyrin/metal complex with Hg^{2+} in MeOH (Figure 2). The cumulative association constant for the complexation event of **10** with Hg^{2+} was evaluated by the spectroscopic titration method to be $1.62 \times 10^{9}\,M^{-1}$ (see Supporting Information).[17]

The fluorescent response of **10** to various cations and its selectivity for Hg^{2+} is illustrated in Figure 3. The response of **10** towards Hg^{2+} was unaffected in a background of environ-

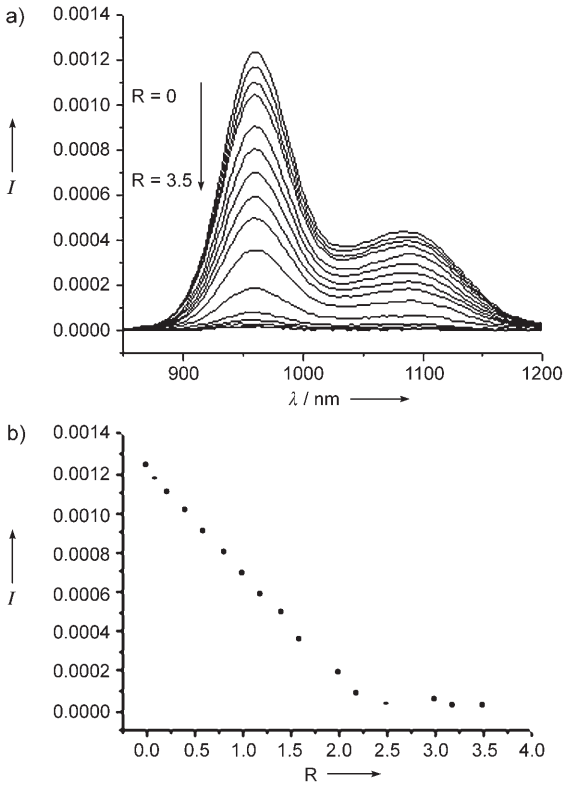

Figure 2. a) NIR fluorescence response of **10** (2 μM, $\lambda_{ex} = 514$ nm) to the addition of Hg^{2+} ion in methanol. [Hg^{2+}]/[**10**] = R = 0, 0.1, 0.2, 0.4, 0.6, 1.0, 1.2, 1.4, 1.6, 2.0, 2.2, 2.5, 3.0, 3.2, and 3.5. b) NIR fluorescence intensity values ($\lambda_{ex} = 514$ nm) versus the number of equivalents of Hg^{2+} ions added.

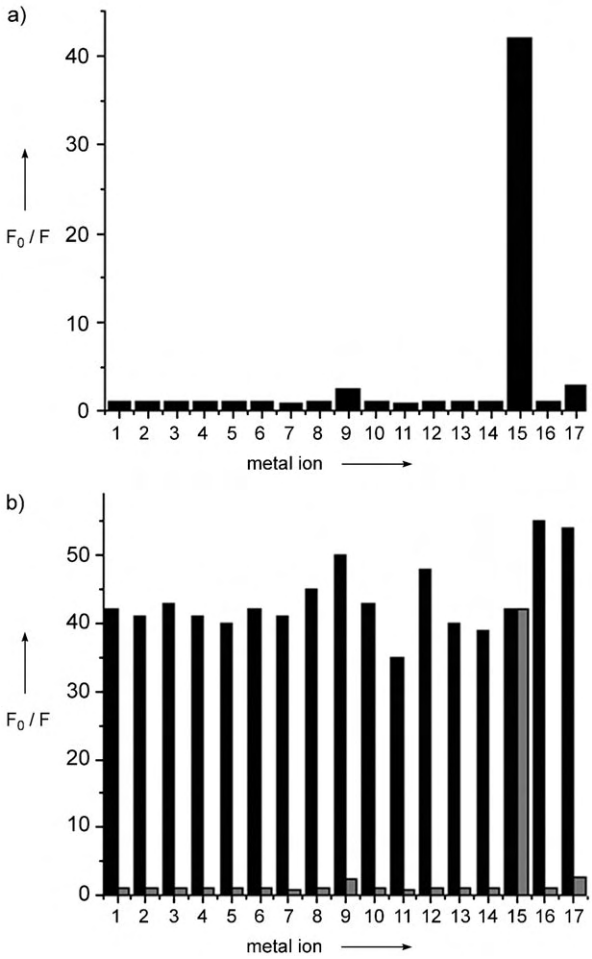

Figure 3. a) Fluorescence response (F) of **10** to various cations in methanol; F_0 is the response for the free expanded porphyrin. The bars represent the NIR fluorescence of **10** (2 μM) in the presence of 40 equiv of the cation of interest: 1) Li^{+}; 2) Na^{+}; 3) Rb^{+}; 4) Mg^{2+}; 5) Ca^{2+}; 6) Sr^{2+}; 7) Ba^{2+}; 8) Cr^{3+}; 9) Ag^{+}; 10) Co^{2+}; 11) Pd^{2+}; 12) Ni^{2+}; 13) Zn^{2+}; 14) Cd^{2+}; 15) Hg^{2+}; 16) K^{+}; 17) Pb^{2+}. b) The selectivity of **10** for Hg^{2+} ions in the presence of other cations in methanol. The gray bars represent the NIR fluorescence of **10** (2 μM) in the presence of 40 equiv of the cation of interest. The black bars represent the change in integrated NIR fluorescence that occurs upon subsequent addition of 40 equiv of Hg^{2+} ion to a solution containing **10** and a cation of interest (1–17).

 © 2006 Wiley-VCH Verlag GmbH & Co. KGaA, Weinheim

mentally relevant alkali and alkaline earth metal ions including Li^+, Na^+, K^+, Rb^{2+}, Mg^{2+}, Ca^{2+}, Sr^{2+}, and Ba^{2+}. The Group 12 Zn^{2+} and Cd^{2+} ions, in addition to Cr^{3+} and Pb^{2+}, did not inhibit the fluorescence response of **10** to Hg^{2+}. From Figure 3, it is seen that **10** reveals a high selectivity and sensitivity for Hg^{2+} ion. Furthermore, at the concentrations of the probe employed in our studies, Hg^{2+} could be detected down to a concentration of 10^{-7} M, that is, at concentrations in the ppb range.[13c,d,e] We also investigated the possible interference owing to the counteranion(s) used. The results showed that the selected anions have almost no interaction with **10** in methanol (see Supporting Information).

In summary, we have prepared and structurally characterized a new expanded porphyrin, which can be exploited as a highly sensitive near-infrared-fluorescent chemodosimeter selective for the detection of Hg^{2+} ions.

Experimental Section

A solution of pentafluorobenzaldehyde (1.23 mL, 0.01 mmol) and pyrrole (715 μL, 0.01 mmol) in dichloromethane (1.0 L) was placed in a 2.0-L round-bottomed flask under nitrogen. Methanesulfonic acid (MSA; 450 μL, 7.0 mmol) was added to this solution, and the mixture was stirred for 30 min. After adding 2,3-dichloro-5,6-dicyano-1,4-benzoquinone (DDQ), the solution was stirred for another 30 min and then passed through a short column of basic alumina. The crude reaction mixture was separated by column chromatography over silica gel with CH_2Cl_2/petroleum ether (2:1 v/v). Three different colored fractions were obtained, first violet, second red, and last deep violet, which afforded the regular porphyrin (9–12% yield), the [26]hexaphyrin(1.1.1.1.1.1) (15–20% yield), and **10** (8–12% yield), respectively. The violet band was purified by preparative thin-layer chromatography eluting with CH_2Cl_2/petroleum ether (7:3 v/v), followed by protonation with CF_3COOH and recrystallization from a $CHCl_3$/MeOH mixture to give another batch of pure product **10** with satisfactory NMR spectroscopic data. **10**: m.p. > 300 °C (decomp); ^{1}H NMR (400 MHz, CD_3OD): $\delta = 10.10$ (d, $J = 4.8$ Hz, 1H), 9.75 (d, $J = 4.8$ Hz, 1H), 9.59–9.48 (m, 5H), 9.42 (d, $J = 4.8$ Hz, 1H), −3.18 (d, $J = 4.8$ Hz, 1H), −3.30 (d, $J = 4.8$ Hz, 1H), −3.82 (d, $J = 4.8$ Hz, 1H), −4.26 ppm (d, $J = 4.8$ Hz, 1H); ^{19}F NMR (CF_3COOH, 376.33 MHz, CD_3OD): $\delta = -139.26$, −139.54, −140.12, −149.88, −150.39, −151.73, −151.89, −161.83, −162.38, −162.67 ppm; HR-MS (ESI): m/z calcd for $[M+H]^+$: 1283.1862; found: 1283.1864.

Received: January 20, 2006
Published online: April 3, 2006

Keywords: fluorescence · mercury · nitrogen heterocycles · porphyrinoids · sensors

[1] a) J. L. Sessler, A. Gebauer, S. J. Weghorn, *The Porphyrin Handbook*, *Vol. 2* (Eds.: K. M. Kadish, K. M. Smith, R. Guilard), Academic Press, San Diego, **2000**, p. 421; b) T. D. Lash, *Angew. Chem.* **2000**, *112*, 1833–1837; *Angew. Chem. Int. Ed.* **2000**, *39*, 1763–1767; c) B. Franck, A. Nonn, *Angew. Chem.* **1995**, *107*, 1941–1957; *Angew. Chem. Int. Ed. Engl.* **1995**, *34*, 1795–1811; d) A. Srinivasan, T. Ishizuka, A. Osuka, F. Furuta, *J. Am. Chem. Soc.* **2003**, *125*, 878–879; e) J. L. Sessler, D. Seidel, A. E. Vivian, V. Lynch, B. L. Scott, D. W. Keogh, *Angew. Chem.* **2001**, *113*, 611–614; *Angew Chem. Int. Ed.* **2001**, *40*, 591–594.

[2] a) J. L. Sessler, M. J. Cyr, V. Lynch, E. MaGhee, J. A. Ibers, *J. Am. Chem. Soc.* **1990**, *112*, 2810–2813; b) J. L. Sessler, T. Morishima, V. Lynch, *Angew. Chem.* **1991**, *103*, 1018–1020; *Angew. Chem. Int. Ed. Engl.* **1991**, *30*, 977–980; c) J. L. Sessler, S. J. Weghorn, V. Lynch, M. R. Johnson, *Angew. Chem.* 1994, 106, 1572–1575; *Angew. Chem. Int. Ed. Engl.* **1994**, *33*, 1509–1512; d) J. Setsune, S. Maeda, *J. Am. Chem. Soc.* **2000**, *122*, 12405–12406; e) V. G. Anand, S. K. Pushpan, S. Venkatraman, A. Dey, T. K. Chandrashekar, B. S. Joshi, R. Roy, W. Teng, K. R. Senge, *J. Am. Chem. Soc.* **2001**, *123*, 8620–8621; f) N. Sprutta, L. Latos-Grażyński, *Chem. Eur. J.* **2001**, *7*, 5099–5112.

[3] a) S. Shimizu, V. G. Anand, R. Taniguchi, K. Furukawa, T. Kato, T. Yokoyama, A. Osuka, *J. Am. Chem. Soc.* **2004**, *126*, 12280–12281; b) S. Mori, A. Osuka, *J. Am. Chem. Soc.* **2005**, *127*, 8030–8031.

[4] a) J. L. Sessler, D. Seidel, *Angew. Chem.* **2003**, *115*, 5292–5333; *Angew. Chem. Int. Ed.* **2003**, *42*, 5134–5175; b) A. Ghosh, *Angew. Chem.* **2004**, *116*, 1952–1965; *Angew. Chem. Int. Ed.* **2004**, *43*, 1918–1931; c) R. Paolesse, L. Jaquinod, D. J. Nurco, S. Mini, F. Sagone, T. Boschi, K. M. Smith, *Chem. Commun.* **1999**, 1307–1308; d) Z. Gross, N. Galili, I. Saltsman, *Angew. Chem.* **1999**, *111*, 1530–1533; *Angew. Chem. Int. Ed.* **1999**, *38*, 1427–1429.

[5] a) H. Furuta, T. Asano, T. Ogawa, *J. Am. Chem. Soc.* **1994**, *116*, 767–768; b) P. J. Chmielewski, L. Latos-Grażyński, K. Rachlewicz, T. Głowiak, *Angew. Chem.* **1994**, *106*, 805–808; *Angew. Chem. Int. Ed. Engl.* **1994**, *33*, 779–781.

[6] a) P. J. Chmielewski, L. Latos-Grażyński, K. Rachlewicz, *Chem. Eur. J.* **1995**, *1*, 68–73; b) S. V. Shevchuk, J. M. Davis, J. L. Sessler, *Tetrahedron Lett.* **2001**, *42*, 2447–2450.

[7] a) J. L. Sessler, T. Morishima, V. Lynch, *Angew. Chem.* **1991**, *103*, 1018–1020; *Angew. Chem. Int. Ed. Engl.* **1991**, *30*, 977–980; b) S. Shimizu, R. Taniguchi, A. Osuka, *Angew. Chem.* **2005**, *117*, 2265–2269; *Angew. Chem. Int. Ed.* **2005**, *44*, 2225–2229; c) S. K. Pushpan, V. R. G. Anand, S. Venkatraman, A. Srinivasan, A. K. Gupta, T. K. Chandrashekar, *Tetrahedron Lett.* **2000**, *41*, 3391–3394.

[8] J. L. Sessler, S. J. Weghorn, T. Morishima, M. Rosingana, V. Lynch, V. Lee, *J. Am. Chem. Soc.* **1992**, *114*, 8306–8307.

[9] M. G. P. M. S. Neves, R. M. Martins, A. C. Tome, A. J. D. Silvestre, A. M. S. Silva, V. Felix, M. G. B. Drew, J. A. S. Cavaleiro, *Chem. Commun.* **1999**, 385–386.

[10] Y. Shin, H. Furuta, K. Yoza, S. Igarashi, A. Osuka, *J. Am. Chem. Soc.* **2001**, *123*, 7190–7191.

[11] Y. Shin, H. Furuta, A. Osuka, *Angew. Chem.* **2001**, *113*, 639–641; *Angew. Chem. Int. Ed.* **2001**, *40*, 619–621.

[12] a) S. K. Pushpan, S. Venkatraman, V. G. Anand, J. Sankar, H. Rath, T. K. Chandrashekar, *Proc. Indian Acad. Sci. Chem. Sci.* **2002**, *114*, 311–338; b) J. L. Sessler, P. J. Melfi, D. Seidel, A. E. V. Gorden, D. K. Ford, P. D. Palmer, C. D. Tait, *Tetrahedron* **2004**, *60*, 11089–11097.

[13] a) L. Wang, X. Zhu, W.-Y. Wong, J. Guo, W.-K. Wong, Z. Li, *Dalton Trans.* **2005**, 3235–3240; b) J. V. Ros-Lis, M. D. Marcos, R. R. Martínez-Máñez, K. Rurack, J. Soto, *Angew. Chem.* **2005**, *117*, 4479–4482; *Angew. Chem. Int. Ed.* **2005**, *44*, 4405–4407; c) R. Metivier, I. Leray, B. Valeur, *Chem. Eur. J.* **2004**, *10*, 4480–4490; d) E. M. Nolan, S. J. Lippard, *J. Am. Chem. Soc.* **2003**, *125*, 14270–14271; e) A. B. Descalzo, R. Martínez-Máñez, R. Radeglia, K. Rurack, J. Soto, *J. Am. Chem. Soc.* **2003**, *125*, 3418–3419; f) A. Caballero, R. Martinez, V. Lloveras, I. Ratera, J. Vidal-Gancedo, K. Wurst, A. Tarraga, P. Molina, J. Veciana, *J. Am. Chem. Soc.* **2005**, *127*, 15666–15667; g) M. Matsushita, M. M. Meijler, P. Wirsching, R. A. Lerner, K. D. Janda, *Org. Lett.* **2005**, *7*, 4943–4946; h) E. M. Nolan, S. J. Lippard, *J. Mater. Chem.* **2005**, *15*, 2778–2783.

[14] a) B. Tatineni, S. Manickam, M. Hideyuki, *Analyst* **2005**, *130*, 1162–1167; b) H. Otto, V. Zsolt, V. Arnd, *Inorg. Chem. Commun.* **2004**, *7*, 854–857; c) K. Krzysztof, P. Krystyna, *Talanta* **2003**, *60*, 669–678; d) X. Zhang, C. Guo, Z. Li, G. Shen, R. Yu,

 © 2006 Wiley-VCH Verlag GmbH & Co. KGaA, Weinheim

Anal. Chem. **2002**, *74*, 821 – 825; e) D. Delmarre, R. Meallet, C. Bied-Charreton, R. B. Pansu, *J. Photochem. Photobio. A* **1999**, *124*, 23 – 28.

[15] C. Zhu, L. Li, F. Fang, J. Chen, Y. Wu, *Chem. Lett.* **2005**, *34*, 898 – 899.

[16] Crystal data for **10** ($C_{60.5}H_{21}Cl_3F_{25}N_6O_{1.5}$): $M_w = 1437.18$, crystal dimensions: $0.40 \times 0.20 \times 0.20$ mm^3, monoclinic, space group: $P\bar{1}$, $a = 14.505(2)$, $b = 14.639(2)$, $c = 16.434(2)$ Å, $a = 78.480(2)°$, $\beta = 74.718(2)°$, $\gamma = 62.232(2)°$, $V = 2966.4(8)$ Å^3, $Z = 2$, $\rho_{calcd} = 1.609$ g cm^{-3}, $\mu(Mo_{K\alpha}) = 0.283$ mm^{-1}, $F(000) = 1428$, $T = 203$ K, $2\theta_{max} = 50.02°$. 12230 reflections measured, of which 10195 were unique ($R_{int} = 0.0329$). Final $R_1 = 0.0773$ and $wR_2 = 0.1797$ for 4369 observed reflections with $I > 2\sigma(I)$. CCDC-295258 contains the supplementary crystallographic data for this paper. These data can be obtained free of charge from The Cambridge Crystallographic Data Centre via www.ccdc.cam.ac.uk/data_request/cif.

[17] a) H. Tsukube, H, Furuta, A. Odani, Y. Kudo, Y. Takeda, Y. Inoue, H. Sakamoto, K. Kimura, Y. Liu in *Comprehensive Supramolecular Chemistry*, *Vol. 8* (Eds.: J.-M. Lehn, J. E. D. Davies, J. A. Ripmeester), Pergamon, New York, **1996**, p. 426; b) Y. Pocker, J. C. Ciula, *J. Am. Chem. Soc.* **1989**, *111*, 4728 – 4735; c) J. Bourson, J. Pouget, B. Valeur, *J. Phys. Chem.* **1993**, *97*, 4552 – 4557; d) J. Raker, T. E. Glass, *J. Org. Chem.* **2001**, *66*, 6505 – 6512.

 © 2006 Wiley-VCH Verlag GmbH & Co. KGaA, Weinheim

Synthetic Methods

DOI: 10.1002/anie.200503805

Practical Synthesis of Amides from In Situ Generated Copper(I) Acetylides and Sulfonyl Azides**

*Michael P. Cassidy, Jessica Raushel, and Valery V. Fokin**

Copper(I) efficiently catalyzes the "fusion" of organic azides with terminal alkynes to produce regioselectively 1,4-disubstituted-1,2,3-triazoles.[1] The very broad scope, simple experimental conditions, and exceptional reliability of this transformation have placed it among the most reliable "stitching" reactions[2] available today. It has resulted in applications in organic synthesis, molecular biology, macromolecular chemistry, and materials science. A stepwise mechanism involving the coordination of the azide to the copper(I) acetylide through the proximal nitrogen atom, followed by formation of a (1,2,3-triazol-5-yl)copper species has been proposed.[1] This mechanism is supported by computational studies, which indicate that the activation barrier for this catalytic version of the Huisgen cycloaddition is reduced by as much as 11 kcal mol^{-1}, which corresponds to the experimentally observed rate acceleration of seven to eight orders of magnitude.[3]

1,2,3-Triazoles are among the most stable nitrogen heterocycles: they are exceedingly resistant to severe hydrolytic, reductive, and oxidative conditions. However, 5-lithiated-1,2,3-triazoles have been shown to spontaneously eliminate dinitrogen at temperatures ranging from −78 to +60 °C.[4] Recently, Chang and co-workers have shown that sulfonyl azides react with copper(I) acetylides and secondary amines to form amidines.[5] Intrigued by their findings and interested in its mechanistic underpinnings, we undertook a study of reactions of sulfonyl azides with copper(I) acetylides. Herein we report that copper(I) ions efficiently catalyze the direct formation of *N*-acylsulfonamides from terminal alkynes and sulfonyl azides in aqueous solvents (Scheme 1). The process

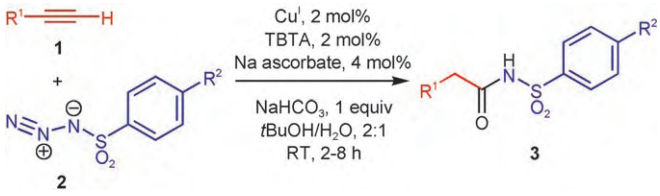

Scheme 1. Synthesis of amides from alkynes and sulfonyl azides.

appears to have a broad scope with respect to both components, is experimentally simple, and furnishes pure *N*-acylsulfonamide products in good yield without complicated purification steps. Different copper(I) sources, such as CuI, CuBr, $[Cu(CH_3CN)_4]PF_6$, and $CuSO_4$/ascorbate, could be used for the reaction. Aqueous *tert*-butanol was commonly employed as a solvent, although other aqueous systems can be utilized. The pH value was found to have a pronounced effect on the outcome of the reaction: highest conversions into *N*-acylsulfonamides were observed under mildly basic conditions, which were easily achieved by buffering the reaction mixture with one equivalent of sodium bicarbonate. Additionally, we found that addition of only 1–2 mol% of tris[(1-benzyl-1*H*-1,2,3-triazol-4-yl)methyl]amine (TBTA)[6] strongly accelerates the reaction, and when TBTA is bound to a resin it greatly simplifies the purification of the products.

After screening various combinations of reagents, we arrived at a convenient procedure which performs well with different sulfonyl azides and terminal alkynes. Thus, a combination of 2 mol% $[Cu(CH_3CN)_4]PF_6$, 2 mol% TBTA,[7] 4 mol% sodium ascorbate (to prevent formation of oxidation by-products), and 1 equiv sodium bicarbonate in *tert*-butanol/water (2:1) as a solvent gave near quantitative conversions in 2–8 h. *N*-Acylsulfonamide products were obtained in good yields as pure materials by precipitation and filtration.

[*] Dr. M. P. Cassidy, J. Raushel, Prof. V. V. Fokin
Department of Chemistry
The Scripps Research Institute
10550 North Torrey Pines Road, La Jolla, CA 92037 (USA)
Fax: (+1) 858-784-7562
E-mail: fokin@scripps.edu

[**] We thank the National Institutes of Health, the National Institute of General Medical Sciences (GM28384), the Skaggs Institute for Chemical Biology, and Pfizer, Inc. for financial support. We also thank Prof. K. B. Sharpless, Prof. M. G. Finn, and Dr. M. Whiting for valuable advice and stimulating discussions.

Supporting information for this article is available on the WWW under http://www.angewandte.org or from the author.

InterScience
© 2006 Wiley-VCH Verlag GmbH & Co. KGaA, Weinheim

Representative examples of this convenient amide synthesis are shown in Table 1. Terminal alkynes with various functional groups—including alcohols (entry 1), carbamates (entry 4), ethers (entry 6), and carboxylic acids (entry 8), as well as ethynyl estradiol, a sterically demanding tertiary propargyl alcohol (entry 9)—participated readily in the transformation. Although 4-acetamidobenzenesulfonyl azide was commonly employed, because it is commercially available and amenable to further derivatization (see below), other sulfonyl azides also participate in this transformation (entries 11 and 12). However, 4-nitrobenzenesulfonyl azide (entry 11) resulted in markedly lower yields.

Table 1: Amides obtained from terminal alkynes and sulfonyl azides.

Entry	Amide product	Procedure[a]	Yield [%][b]	M.p. [°C]
1	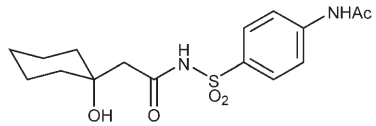	A	60	225–227
2	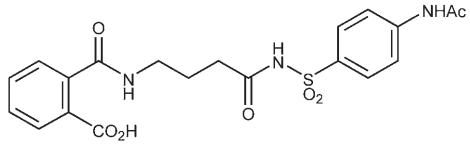	A	67	113–115 (decomp)
3	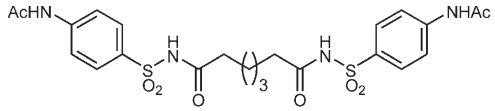	A[c]	74	226 (decomp)
4	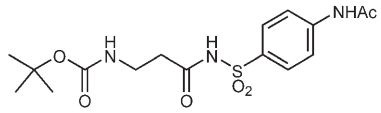	B	83	203–205 (decomp)
5	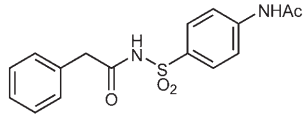	A	64	232–234 (decomp)[d]
6	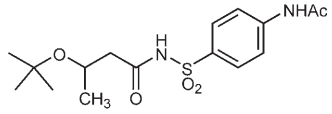	A	83	204–206 (decomp)
7	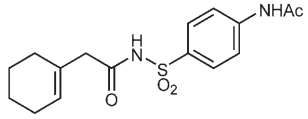	A	54	227 (decomp)
8	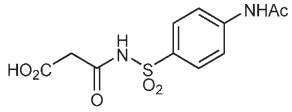	A	75	261 (decomp)
9	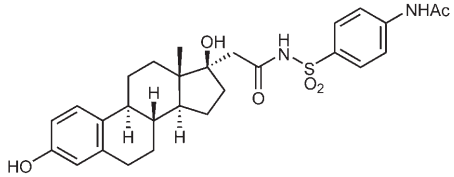	A	68	175 (decomp)
10	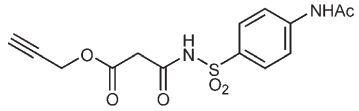	B	62	195–197 (decomp)
11	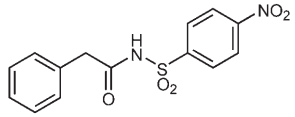	A	27	170–171[e]
12	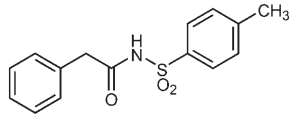	B	69	142–144[f]

[a] Representative experimental procedures are described in the Experimental Section. [b] Yield of isolated product after precipitation and filtration. [c] 2 equiv of the sulfonyl azide were used. [d] Lit. 239 °C.[8] [e] Lit. 172–173 °C.[9] [f] Lit. 149 °C.[8]

Although a detailed understanding of the mechanism of this process will require additional studies, we propose the mechanism outlined in Scheme 2. Similar to the copper(I)-catalyzed triazole synthesis,[1,3] copper(I) acetylides are first converted into the (1,2,3-triazol-5-yl)copper species **4**, which normally undergoes proteolysis to release the triazole product **5**. However, in the presence of a strongly electron-withdrawing group at N-1, **4** may eliminate a molecule of dinitrogen, thereby producing a transient alkynamide **6**. A similar transformation of 5-lithiated-1,2,3-triazoles has been reported before.[4] The alkynamide **6** is then protonated to give the highly reactive ketenimine **8**, which is immediately trapped by water to form the *N*-acylsulfonamide **3**. An alternative route to **8** is through a ring-opening pathway resembling the well-known Dimroth rearrangement.[10] Thus, intermediate **4** can be shunted off into this pathway to form the diazoimine **7**.[11] Although the stability of **4** is primarily controlled by the substituent at N-1, other factors, such as the acidity of the reaction medium[12] and the nature of the functional groups at C-4 and C-5,[13] are known to influence ring-chain isomerizations. Thus, the strongly electronegative sulfonyl functionality at N-1 and basic conditions favor **7** which, upon release of a molecule of dinitrogen, collapses into the keteneimine **8**.

N-acylsulfonamides are very resistant to hydrolytic cleavage and thus can be viewed as perma-

 © 2006 Wiley-VCH Verlag GmbH & Co. KGaA, Weinheim

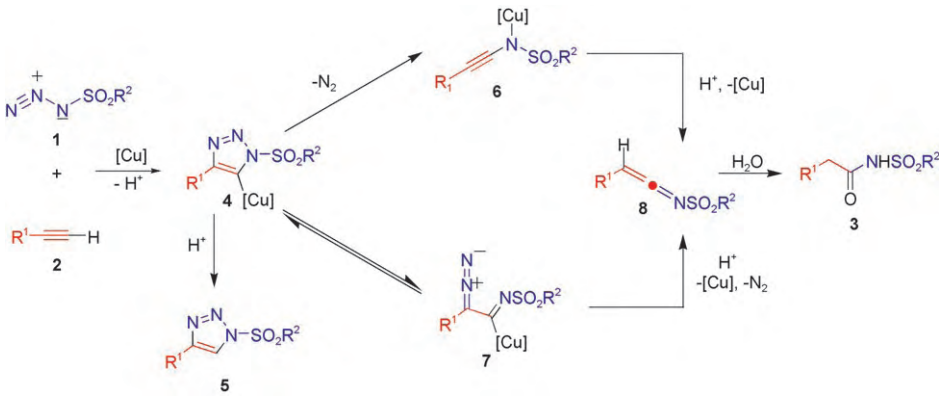

Scheme 2. Proposed intermediates in the copper(I)-catalyzed synthesis of *N*-acylsulfonamides from alkynes and sulfonyl azides.

nent connectors that tolerate various transformations of other functional groups in the molecule (of course, they are also competent hydrogen-bond donors and acceptors, and are indeed known pharmacophores[14]). For example, acetanilides are readily cleaved under either basic or acidic conditions and liberate free anilines that can be further converted into other functional groups. Furthermore, *N*-acylsulfonamides can be activated by N-methylation with methyl iodide, thereby activating the amide bond to nucleophilic cleavage.[15] Thus, free carboxylic acids (**13**) and carboxamides (**12**) are readily obtained from alkynes in a straightforward fashion (Scheme 3).

The copper(I)-catalyzed sequence described here provides a direct, simple, and efficient route to carboxamides from terminal alkynes, thus representing a formal oxidative hydration of a triple bond. This latest addition to the growing list of examples of strikingly unique reactivity of in situ generated copper(I) acetylides is, to the best of our knowledge, the first general method for a one-step conversion of alkynes into amides under mild conditions.[16] This transformation of alkynes to thermally and chemically stable *N*-acylsulfonamides should prove useful whenever near-permanent, biologically benign connections between structural units with diverse functionality are required. Additional studies directed at better understanding the mechanism of this process and at further exploring its utility are currently underway and will be published in due course.

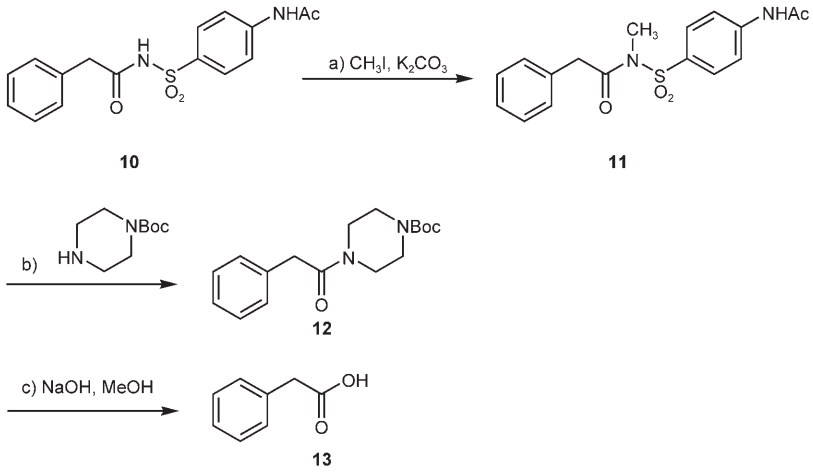

Scheme 3. Synthesis of carboxylic derivatives from alkynes. Reagents and conditions: a) CH_3I (10 equiv), K_2CO_3 (2 equiv), CH_3CN, RT, 81%; b) *tert*-butylpiperazine-1-carboxylate (1.1 equiv), toluene, 100°C, 8 h, 97%; c) NaOH (4 equiv), MeOH, RT, 6 h, HCl workup, 60%. Boc = *tert*-butoxycarbonyl.

Experimental Section

Procedure A, as exemplified for the synthesis of *N*-(4-acetamidophenylsulfonyl)-2-phenylacetamide (Table 1, entry 5): Phenylacetylene (1 mmol) and 1M sodium bicarbonate solution (1 mL), followed by 4-acetamidobenzenesulfonylazide (1 mmol) and 1M sodium ascorbate solution (0.05 mL, 0.05 mmol) were added to a solution of TBTA (0.02 mmol) and $[Cu(CH_3CN)_4]PF_6$ (0.02 mmol) in *t*BuOH/water (2:1, 5 mL). The vial was loosely capped and stirred until the starting materials had completely disappeared, as evident by LC/MS analysis. *tert*-Butanol was removed in vacuo, and the remaining aqueous solution was stirred with Cuprisorb resin and 10% NH_4OH (3 drops) for 30 minutes, then filtered through celite, and the filtered resin washed with MeOH. The filtrate was made slightly acidic with 1M HCl, and the MeOH was removed in vacuo. The product was collected by suction filtration and dried in vacuo to afford 0.25 g (74%) of the product as an off-white solid.

Procedure B, as exemplified for prop-2-ynyl 3-(4-acetamidophenylsulfonamido)-3-oxopropanoate (Table 1, entry 10): TBTA/[Cu] resin (100 mg, 0.02 mmol, based upon 0.19 mmol g^{-1} loading), 1M sodium bicarbonate solution (1 mL) and 1M sodium ascorbate solution (0.05 mL) were added to a solution of sulfonyl azide (1 mmol) and alkyne (1 mmol) in *t*BuOH/water (2:1, 5 mL). The work-up was as described for Procedure A and afforded 0.21 g (62%) of the product as a white solid.

Received: October 27, 2005
Published online: March 29, 2006

Keywords: alkynes · azides · copper · oxidation · synthetic methods

[1] a) V. V. Rostovtsev, L. G. Green, V. V. Fokin, K. B. Sharpless, *Angew. Chem.* **2002**, *114*, 2708; *Angew. Chem. Int. Ed.* **2002**, *41*, 2596; b) C. W. Tornøe, C. Christensen, M. Meldal, *J. Org. Chem.* **2002**, *67*, 3057.
[2] H. C. Kolb, M. G. Finn, K. B. Sharpless, *Angew. Chem.* **2001**, *113*, 2056; *Angew. Chem. Int. Ed.* **2001**, *40*, 2004.
[3] F. Himo, T. Lovell, R. Hilgraf, V. V. Rostovtsev, L. Noodleman, K. B. Sharpless, V. V. Fokin, *J. Am. Chem. Soc.* **2005**, *127*, 210.
[4] a) R. Raap, *Can. J. Chem.* **1971**, *49*, 1792–1798; b) T. L. Gilchrist, *Adv. Heterocycl. Chem.* **1987**, *41*, 41; c) M. Whiting, V. V. Fokin, *Angew. Chem.* **2006**, *118*, 3229; *Angew. Chem. Int. Ed.* **2006**, *45*, 3157.
[5] I. Bae, H. Han, S. Chang, *J. Am. Chem. Soc.* **2005**, *127*, 2038.
[6] T. R. Chan, R. Hilgraf, K. B. Sharpless, V. V. Fokin, *Org. Lett.* **2004**, *6*, 2853.
[7] TBTA can be immobilized on a tentagel resin and then preloaded with $[Cu(CH_3CN)_4]PF_6$. This resin is a convenient replacement for the free TBTA/$CuSO_4$/

 © 2006 Wiley-VCH Verlag GmbH & Co. KGaA, Weinheim

ascorbate combination, especially for an automation-assisted parallel synthesis. Another benefit is the reduced contamination of the products with copper ions; see Procedure B and T. R. Chan, PhD thesis, The Scripps Research Institute, **2005** for details.

[8] D. P. van Leeuwen, A. F. Arnold, C. G. Hartland, A. Siedsma (PLIVA, Zagreb), Netherlands patent 298391, **1965** [*Chem. Abstr.* **1966**, *64*, 12604c].

[9] R. Dohmori, *Chem. Pharm. Bull.* **1964**, *12*, 591.

[10] O. Dimroth, *Justus Liebigs Ann. Chem.* **1909**, *364*, 183; for reviews see G. L'abbé, *Bull. Chem. Soc. Belg.* **1990**, *99*, 281; E. S. H. El Ashry, Y. El Kilany, N. Rashed, H. Assafir, *Adv. Heterocycl. Chem.* **1999**, *75*, 79.

[11] *N*-sulfonyltriazoles are formed under neutral to slightly acidic pH values in 20–25% yield. For example, performing the reaction between 4-acetamidobenzenesulfonylazide and phenylacetylene in *t*BuOH/H_2O (1:1, 0.1M) in the presence of $CuSO_4$ (2 mol%) and Na ascorbate/ascorbic acid (10 mol% each) results in the formation of 42% of the 1-sulfonyltriazole product. Likewise, intermediate **4** can be captured with electrophiles other than protons. For example, 1-sulfonyl-5-allyltriazole is isolated in 51% yield by using allyl iodide (10 equiv) in anhydrous acetonitrile.

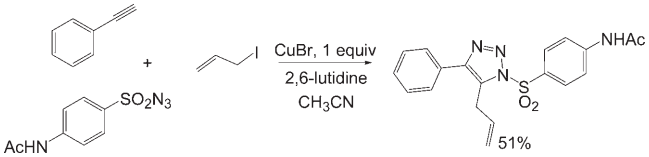

[12] D. J. Brown, T. Nagamatsu, *Aust. J. Chem.* **1977**, *30*, 2515.

[13] a) R. E. Harmon, F. Stanley, Jr., S. K. Gupta, J. Johnson, *J. Org. Chem.* **1970**, *35*, 3444; b) G. Himbert, M. Regitz, *Justus Liebigs Ann. Chem.* **1973**, *9*, 1505.

[14] Currently, there are 4 drugs on the market that contain the *N*-acylsulfonamide functionality, while over 600 are currently in different stages of development: MDDR database, Elsevier MDL Information Systems, 2005.

[15] a) H. Nagashima, N. Ozaki, M. Washiyama, K. Itoh, *Tetrahedron Lett.* **1985**, *26*, 657; b) B. J. Backes, J. A. Ellman, *J. Am. Chem. Soc.* **1994**, *116*, 11171.

[16] While this manuscript was under review, the following account describing a similar transformation of alkynes to amides was published: S. H. Cho, E. J. Yoo, I. Bae, S. Chang, *J. Am. Chem. Soc.* **2005**, *127*, 16046.

 © 2006 Wiley-VCH Verlag GmbH & Co. KGaA, Weinheim

Synthetic Methods

DOI: 10.1002/anie.200503936

Copper-Catalyzed Reaction Cascade: Direct Conversion of Alkynes into *N*-Sulfonylazetidin-2-imines**

*Matthew Whiting and Valery V. Fokin**

As part of our ongoing research into the discovery and development of highly efficient, versatile reactions,[1] and inspired by the success of the copper-catalyzed 1,3-dipolar cycloaddition reaction between terminal alkynes and azides,[2] we became interested in the unusual reactivity of copper(I) acetylides towards sulfonyl azides. This initially surprising reactivity is illustrated by their conversion into *N*-sufonylamidines when the reaction is conducted in the presence of amines[3] and *N*-acylsulfonamides in the presence of water.[4] Herein, we describe the direct, stereoselective conversion of alkynes to *N*-sulfonylazetidin-2-imines by the initial reaction of copper(I) acetylides with sulfonyl azides, followed, in situ, by the formal [2+2] cycloaddition of a postulated *N*-sulfonylketenimine intermediate with a range of imines.

We began our investigations by looking into the copper(I)-catalyzed reaction of phenylacetylene with *para*-toluenesulfonyl azide. With the expectation of forming the 1-sulfonyl-4-phenyl-1,2,3-triazole, the reaction was carried out in the absence of a nucleophile, under conditions that were known to promote dipolar cycloaddition between alkynes and alkyl or aryl azides.[2a] We were therefore surprised to find that the only isolated product was the cyclobutene derivative **1** (Scheme 1). The results of extensive NMR studies correlate with the proposed structure.

Compound **1** could result from the dimerization of an initially formed toluenesulfonylketenimine intermediate fol-

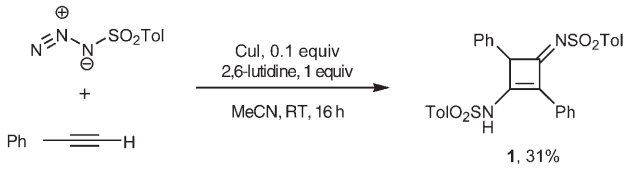

Scheme 1. Formation of ketenimine dimer **1**. Tol = *p*-tolyl.

[*] Dr. M. Whiting, Prof. V. V. Fokin
Department of Chemistry
The Scripps Research Institute
10550 North Torrey Pines Road, La Jolla, CA 92037 (USA)
Fax: (+1) 858-784-7562
E-mail: fokin@scripps.edu

[**] We thank the National Institutes of Health, the National Institute of General Medical Sciences (GM28384), the Skaggs Institute for Chemical Biology, and Pfizer, Inc. for financial support. We also thank Prof. K. B. Sharpless for valuable advice and stimulating discussions.

Supporting information for this article is available on the WWW under http://www.angewandte.org or from the author.

© 2006 Wiley-VCH Verlag GmbH & Co. KGaA, Weinheim

lowed by tautomerization, through a sequence proposed below. Initial cycloaddition of the copper acetylide and sulfonyl azide would give the (1-sulfonyl-4-phenyltriazol-5-yl)copper intermediate **2**. Direct elimination of dinitrogen, as previously reported for a range of 5-lithiated-triazoles,[5] would generate copper alkynamide **3**. Protonation of this species would then furnish the requisite sulfonylketenimine **4** with concomitant liberation of the copper catalyst. Alternatively the cuprated triazole **2** could undergo ring-chain isomerization, which is known to be rapid for electron-deficient triazoles, especially those with an electron-withdrawing group at N-1.[6] This route would give rise to the cuprated diazoimine **5**, which upon loss of dinitrogen and protonation would again generate the *N*-sulfonylketenimine **4** and regenerate the copper catalyst (Scheme 2).

The isolation of **1** was significant in itself, as there are very few reports of ketenimine dimerization and all proceed across at least one of the cumulenic C=N bonds,[7] as opposed to both C=C bonds observed herein. Of greater synthetic interest was

Table 1: *N*-sulfonyl azetidinimine synthesis: effect of ligands.

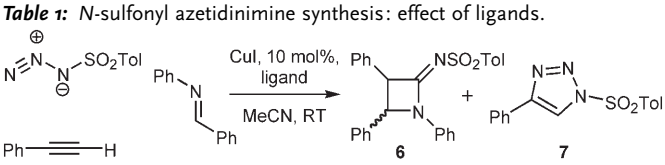

Entry	Ligand[a]	*t* [h]	*trans*-**6**:*cis*-**6**:**7**[b]
1	2,6-lutidine	3	80:13:7
2	none	16	56:11:33
3	pyridine	3	95:5:0
4	2,6-di-*tert*-butylpyridine	16	45:10:45
6	neocuproine	no reaction	–
7	Et_3N	3	94:6:0
8	TMEDA	3	83:17:0[c]
9	TBTA[d]	< 2	42:58:0

[a] 1 equiv of ligand used. [b] Determined from the ^{1}H NMR spectra of the crude reaction product. [c] The oxidatively coupled di-alkyne was also observed. [d] 0.1 equiv of ligand used. TMEDA = *N*,*N*,*N*′,*N*′-tetramethylethylenediamine, TBTA = tris[(1-benzyl-1*H*-1,2,3-triazol-4-yl)methyl]amine.

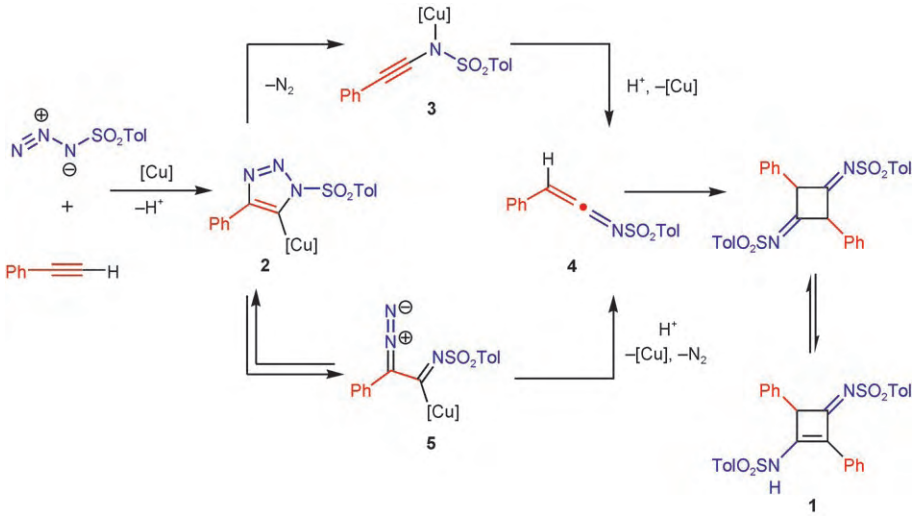

Scheme 2. Possible mechanistic pathways leading to **1**.

the possibility of capturing the *N*-sulfonylketenimine intermediates by alternative means. Ketenimines with *N*-alkyl or -aryl substituents are considerably less reactive than their oxygen analogues, ketenes, although they are still known to undergo a range of useful transformations,[7a,8] particularly in an intramolecular fashion.[7a] Introduction of an *N*-sulfonyl substituent leads to a marked increase in reactivity. For example, *N*-sulfonylketenimines have been shown by Ghosez and co-workers to readily undergo intermolecular Staudinger-type [2+2] cycloadditions with imines to furnish azetidinimines.[9]

We were pleased to find that carrying out the reaction in the presence of *N*-benzylideneaniline gave the expected azetidinimine product **6** as a 6:1 mixture of the *trans* and *cis* isomers, along with a small amount of the 1,4-disubstituted triazole **7** (Table 1, entry 1). The use of alternative ligands/bases in the reaction gave greatly altered selectivities. For example, the reaction proceeded much more slowly in the absence of an added ligand and furnished an increased amount of triazole by-product (entry 2). The use of pyridine completely suppressed triazole formation and gave the desired azetidinimine as a 95:5 ratio of isomers in favor of the *trans* product (entry 3). A number of other ligands were screened, but all gave a reduction in the selectivity or the rate of reaction (entries 4–9). Interestingly TBTA,[10] a potent ligand for the Cu^I-catalyzed azide/alkyne cycloaddition, not only increased the rate of azetidinimine formation, but also reversed the selectivity, giving a slight excess of the *cis* isomer (entry 9). The observed dependence of the reaction selectivity upon the additive is not yet fully understood and is the subject of continued investigation. It does however imply that the amine, either itself directly or as a ligand for copper, is involved in promotion of the [2+2] process.

Reducing the amount of pyridine resulted in a slight reduction in the stereoselectivity, while increasing it to two equivalents gave an even more selective reaction that furnished the azetidinimine with greater than 95:5 selectivity in favor of the *trans* isomer. With regard to the reaction solvent, more polar solvents tended to give reduced *trans*:*cis* selectivity, and less polar solvents generally required longer reaction times. None of those tested, however, were as efficient or resulted in as high a selectivity as acetonitrile. Under the optimal conditions (1 equiv sulfonyl azide, 2 equiv pyridine, 1 equiv alkyne, 1.2 equiv imine, 10 mol% CuI, RT, 16 h), **6** was obtained in 90% yield and in greater than 95% purity by simple dilution of the reaction mixture with 1M HCl and collection of the precipitated product by filtration (Table 2, entry 1).

A brief survey of the scope with regard to the alkyne component revealed that both alkyl and aryl alkynes gave the

 © 2006 Wiley-VCH Verlag GmbH & Co. KGaA, Weinheim

Table 2: Synthesis of azetidinimines: scope with respect to the alkyne component.

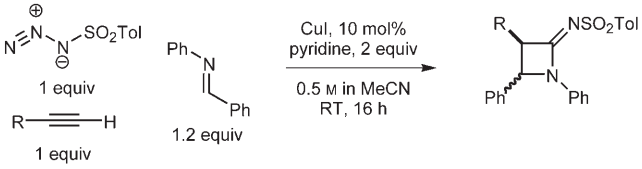

Entry	R	Yield [%][a]	*trans*:*cis*[b]
1	Ph	90	>95:5
2	4-BrC_6H_4	90	>95:5
3	2-$(CF_3)C_6H_4$	79	>95:5
4	4-$(MeO)C_6H_4$	69	90:10
5	3-Pyr	81	>95:5
6	Bn	62	92:8
7	$PhthCH_2$	60	>95:5
8	$CH_2Cl(CH_2)_2$	55	>95:5
9	$MeO_2C(CH_2)_3$	55	>95:5
10	TMS	48	25:75

[a] Yield of the isolated isomeric mixture. [b] Determined from the ^{1}H NMR spectra of the crude reaction product. Bn = benzyl, Phth = phthalimido, TMS = trimethylsilyl.

desired product, generally with high *trans* selectivity (Table 2). The electron-rich (*para*-methoxyphenyl)acetylene (entry 4) and 3-phenyl-1-propyne (entry 6) gave slightly reduced selectivities, and in the case of trimethylsilylacetylene the selectivity was reversed to give a 3:1 *cis*:*trans* ratio of products (entry 10), possibly as the silyl substituent promotes a more concerted [2+2] reaction that leads to a greater amount of the kinetic product. A wide range of functionality was accepted; however incorporation of nucleophilic groups tended to give mixtures of products arising from intra- or intermolecular nucleophilic trapping of the ketenimine intermediate.

We have also examined the scope with regard to the imine and the azide components (Tables 3 and 4, respectively). The reactivity of imines derived from electron-rich or -poor

Table 3: Synthesis of azetidinimines: scope with respect to the imine component.

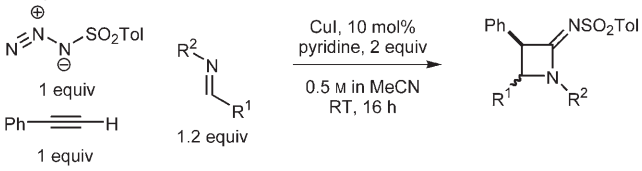

Entry	R^1	R^2	Yield [%][a]	*trans*:*cis*[b]
1	4-FC_6H_4	Ph	87	>95:5
2	4-$(MeO)C_6H_4$	Ph	79	>95:5
3	Ph	Bn	80	89:11
4	Ph	4-$(MeO)C_6H_4$	77	92:8
5	4-$(MeO_2C)C_6H_4$	4-$(MeO)C_6H_4$	73	86:14
6	4-$(TMSC{\equiv}C)C_6H_4$	4-$(MeO)C_6H_4$	65	77:23
7	Ph	SO_2Ph	ca. 5[b]	–
8	EtO_2C	Ph	53	<5:95
9	EtO_2C	4-$(MeO)C_6H_4$	63	<5:95

[a] Yield of isolated isomeric mixture. [b] Determined from the ^{1}H NMR spectra of the crude reaction product.

aromatic aldehydes appeared to be similar, and equally high selectivities were observed (Table 3, entries 1 and 2). Incorporation of the readily cleavable benzyl (entry 3) or *para*-methoxyphenyl (PMP, entry 4) groups on the nitrogen atom led to slightly reduced selectivities, with PMP being the more selective of the two. The use of more elaborate *N*-PMP imines gave rise to highly functionalized products in good yield, albeit with slightly reduced selectivities (entries 5 and 6). As expected, the electron-deficient benzylidenebenzenesulfonamide (entry 7) did not participate in the reaction, presumably because of the low nucleophilicity of its nitrogen atom. The use of aldimines and ketimines bearing α protons gave rise to alternative modes of reaction; however, imines derived from ethyl glyoxylate gave the desired products with inverted selectivity of <5:95 *trans*:*cis* (entries 8 and 9).

From our initial studies the reaction appears to be amenable to the use of a wide range of sulfonyl azides (Table 4). For example, the desired azetidinimines product

Table 4: Synthesis of azetidinimines: scope with respect to the sulfonyl azide component.

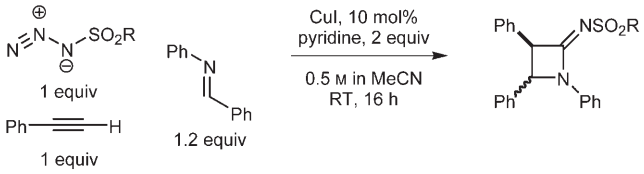

Entry	R	Yield [%][a]	*trans*:*cis*[b]
1	4-$(NO_2)C_6H_4$	63	>95:5
2	4-BrC_6H_4	77	>95:5
3	4-IC_6H_4	76	>95:5
4	Me	68	95:5

[a] Yield of isolated isomeric mixture. [b] Determined from the ^{1}H NMR spectra of the crude reaction product.

bearing a readily cleavable nitrobenzenesulfonyl (nosyl, Ns) group on the imino nitrogen atom was obtained from *p*-nitrobenzenesulfonyl azide with high selectivity (entry 1). The use of *para*-bromobenzenesulfonyl azide and *para*-iodobenzenesulfonyl azide gave equally selective conversion into the expected halogenated products (entries 2 and 3). The reaction also proceeded well when alkylsulfonyl azides were used (entry 4).

Further support for the proposed mechanism was obtained by conversion of the isolated 1-sulfonyltriazole **8** into the corresponding azetidinimine product **9** (the triazole **8** was isolated as a minor product (17%) from the reaction of benzenesulfonyl azide with phenylacetylene and *N*-benzylideneaniline, carried out in the presence of one equivalent of 2,6-di-*tert*-butylpyridine.[11]) Although **8** was stable when resubjected to the reaction conditions, metalation at the 5-position using *n*BuLi in THF resulted in the immediate extrusion of N_2, even at −78 °C, presumably with formation of the relatively stable metalated ketenimine **10**.[12] Addition of *N*-benzylideneaniline and one equivalent of anhydrous HCl gave rise to the azetidinimine product **9** which could be isolated in 20% yield as an 85:5 mixture of isomers favoring the *cis* product (Scheme 3).

 © 2006 Wiley-VCH Verlag GmbH & Co. KGaA, Weinheim

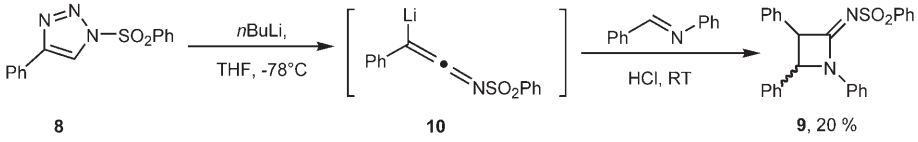

Scheme 3. Conversion of 1-sulfonyl-4-phenyltriazole **8** into azetidinimine **9**.

The sulfonyl azetidinimne products described above can be viewed as β-lactam analogues, and as such they have potential applications as therapeutic agents.[13] They are highly stable under acidic conditions: the starting material was quantitatively recovered after stirring in HCl (2 M, dioxane/water) overnight. Moderately basic conditions (K_2CO_3 in dioxane/water) did not cause any degredation either. However, prolonged exposure to KOH under similar conditions led to various hydrolysis products.

The stability of azetidinimines to a wide range of reaction conditions makes them valuable synthetic intermediates. Several examples of their selective functionalization (see below) illustrate their synthetic utility. Thus, deprotonation of **6** with KH followed by quenching with allyl bromide furnished **11** in 92% yield as a single diastereomer, presumably that with the *cis* configuration (Scheme 4).

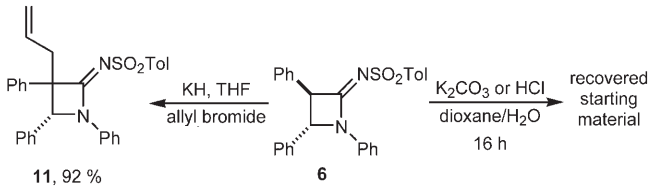

Scheme 4. Acid/base stability and allylation of **6**.

Cleavage of the *p*-Ns group[14] from **12** furnished the NH imine **13** which reacts readily with activated carbonyl compounds. For example, carbamate **14** was obtained in 66% yield over the two steps (Scheme 5).

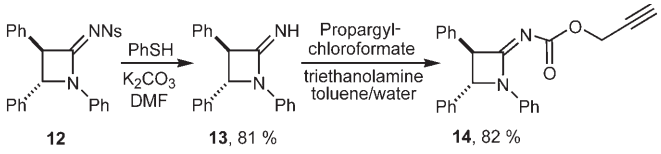

Scheme 5. Cleavage of the *p*-nitrobenzenesulfonyl (Ns) group and formation of a carbamate.

Aryl halide functionality can be easily converted into a range of alternative products. As an example, iodide **15** was converted into azide **16** by copper-catalyzed azidation,[15] or to the biaryl derivative **17** by using a Suzuki coupling with a boronic acid (Scheme 6).[16] 1*H*-Azetidinimines, such as **19**, are easily accessible from *N*-1-PMP derivatives (**18**) by treatment with ceric ammonium nitrate (CAN) (Scheme 7).[17]

In summary, we have developed an experimentally simple catalytic procedure for the highly selective conversion of alkynes into *N*-sulfonylazetidin-2-imines under mild conditions. This three component process is thought to proceed through the initial reaction of in situ generated copper(I) acetylides with sulfonyl azides to give transient (1-sulfonyltriazolyl)copper intermediates which, upon extrusion of dinitrogen, generate *N*-sulfonylketenimines. The azetidinimine products are remarkably stable to a wide range of reaction conditions and readily undergo further functionalization. This newly discovered reaction sequence rapidly constructs densely functionalized azetidine derivatives from readily available terminal alkynes in just one simple step and should prove useful for exploring the utility of these four-membered heterocycles.

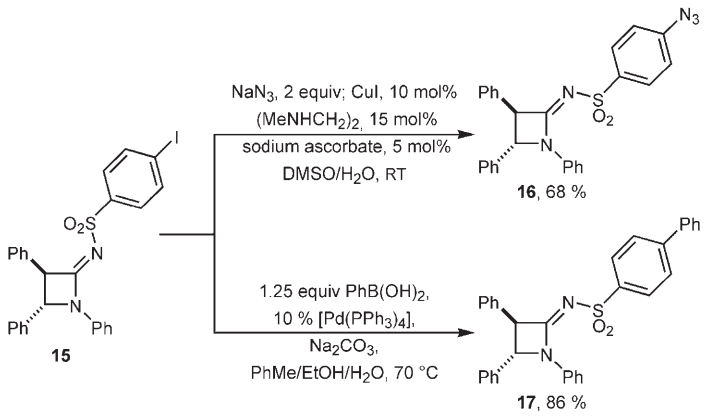

Scheme 6. Further functionalization of **15**.

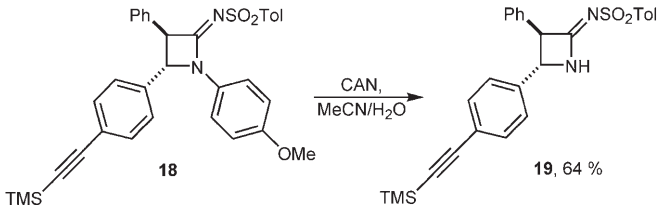

Scheme 7. Cleavage of the *N*-1-PMP group.

Received: November 7, 2005
Published online: March 29, 2006

Keywords: alkynes · azides · cycloaddition · homogeneous catalysis · small ring systems

[1] H. C. Kolb, M. G. Finn, K. B. Sharpless, *Angew. Chem.* **2001**, *113*, 2056–2075; *Angew. Chem. Int. Ed.* **2001**, *40*, 2004–2021.
[2] a) V. V. Rostovtsev, L. G. Green, V. V. Fokin, K. B. Sharpless, *Angew. Chem.* **2002**, *114*, 2708–2711; *Angew. Chem. Int. Ed.*

 © 2006 Wiley-VCH Verlag GmbH & Co. KGaA, Weinheim

2002, *41*, 2596 – 2599; b) C. W. Tornøe, C. Christensen, M. Meldal, *J. Org. Chem.* **2002**, *67*, 3057 – 3064.
[3] I. Bae, H. Han, S. Chang, *J. Am. Chem. Soc.* **2005**, *127*, 2038 – 2039.
[4] a) S. H. Cho, E. J. Yoo, I. Bae, S. Chang, *J. Am. Chem. Soc.* **2005**, *127*, 16046 – 16047; b) M. Cassidy, J. Raushel, V. V. Fokin, *Angew. Chem.* **2006**, *118*, 3226; *Angew. Chem. Int. Ed.* **2006**, *45*, 3154.
[5] a) R. Raap, *Can. J. Chem.* **1971**, *49*, 1792 – 1798; b) T. L. Gilchrist, *Adv. Heterocycl. Chem.* **1987**, *41*, 41 – 74.
[6] W.-Q. Fan, A. R. Katritzky in *Comprehensive Heterocyclic Chemistry II*, *Vol. 4* (Eds: A. R. Katritzky, C. W. Rees, E. F. V. Scriven), Pergamon, Oxford, **1996**, chap. 1.
[7] a) M. Alajarin, A. Vidal, F. Tovar, *Targets Heterocycl. Syst.* **2000**, *4*, 293 – 326, and references therein; b) E. Langhals, R. Huisgen, K. Polborn, *Chem. Eur. J.* **2004**, *10*, 4353 – 4357.
[8] For leading references see: a) G. R. Krow, *Angew. Chem.* **1971**, *83*, 455; *Angew. Chem. Int. Ed. Engl.* **1971**, *10*, 435 – 449; b) G. Barbaro, P. Giorgianni, D. Giacomini, *Tetrahedron* **1993**, *49*, 4293 – 4306; c) A. H. Mermerian, G. C. Fu, *Angew. Chem.* **2005**, *117*, 971 – 974; *Angew. Chem. Int. Ed.* **2005**, *44*, 949 – 952.
[9] A. Van Camp, D. Goosens, M. Moya-Portuguez, J. Marchand-Brynaert, L. Ghosez, *Tetrahedron Lett.* **1980**, *21*, 3081 – 3084.
[10] T. R. Chan, R. Hilgraf, K. B. Sharpless, V. V. Fokin, *Org. Lett.* **2004**, *6*, 2853 – 2855.
[11] The major product, *N*-(1,3,4-triphenyl-azetidin-2-ylidene)-benzenesulfonamide, was obtained in 71 % yield as a 90:10 mixture of isomers in favor of the *trans* product. The regiochemistry of the triazole by-product was confirmed by unambiguous synthesis of the 1,5-regioisomer and comparison of their spectral data. See the Supporting Information for further details.
[12] K. Sung, *J. Chem. Soc. Perkin Trans. 2* **1999**, 1169 – 1173.
[13] a) *Comprehensive Heterocyclic Chemistry II*, *Vol. 1* (Eds: A. R. Katritzky, C. W. Rees, E. F. V. Scriven), Pergamon, Oxford, **1996**, chap. 18–20; b) *Chemistry and Biology of* β*-Lactam Antibiotics*, *Vol. 1–3* (Eds: R. B. Morin, M. Goldman), Academic Press, New York, **1982**.
[14] T. Fukuyama, C.-K. Jow, M. Cheung, *Tetrahedron Lett.* **1995**, *36*, 6373 – 6374.
[15] a) W. Zhu, D. Ma, *Chem. Commun.* **2004**, 888; b) J. Andersen, U. Madsen, F. Björkling, X. Liang, *Synlett* **2005**, 2209 – 2213.
[16] N. Miyaura, A. Suzuki, *Chem. Rev.* **1995**, *95*, 2457 – 2483.
[17] D. R. Kronenthal, C. Y. Han, M. K. Taylor, *J. Org. Chem.* **1982**, *47*, 2765 – 2768.

 © 2006 Wiley-VCH Verlag GmbH & Co. KGaA, Weinheim

Nanostructures

DOI: 10.1002/anie.200600259

Proteolytic Actuation of Nanoparticle Self-Assembly**

*Todd J. Harris, Geoffrey von Maltzahn, Austin M. Derfus, Erkki Ruoslahti, and Sangeeta N. Bhatia**

Nature has evolved elegant strategies to temporally and spatially control the initiation of protein activity, including the synthesis of subunits that self-assemble to form a functional unit and the synthesis of proteins with prodomains that require cleavage for activation. Nanomaterials that exploit bio-inspired self-assembling motifs have been used for sensitive detection of DNA,[1,2] proteins,[3,4] viruses,[5] and pH changes[6] in vitro. In general, these systems employ complementary chemistries that are constitutively exposed and lack elements of temporal control that could broaden their applicability. Herein, inspired by the biological motif of initiating assembly by enzymatic removal of inhibitors, we demonstrate with peptide–polymer chemistry that inorganic nanoparticles may be functionalized to exist in a "latent" state until triggered by a protease to self-assemble.

We inhibit the binding of biotin and neutravidin coated superparamagnetic Fe_3O_4 nanoparticles with polyethylene glycol (PEG) polymers that may be proteolytically removed to initiate assembly by matrix metalloproteinase-2 (MMP-2), a protease correlated with cancer invasion, angiogenesis, and metastasis.[7–9] We demonstrate that MMP-2 initiated assembly amplifies the transverse (T2) relaxation of nanoparticle

[*] T. J. Harris,[+] G. von Maltzahn,[+] Prof. S. N. Bhatia
Harvard-MIT Division of Health Sciences and Technology
Massachusetts Institute of Technology
E19-502D Cambridge, MA 02139 (USA)
Fax: (+1) 617-324-0710
E-mail: sbhatia@mit.edu

Prof. S. N. Bhatia
Electrical Engineering and Computer Science/MIT
Brigham & Women's Hospital
Boston, MA (USA)

A. M. Derfus
Department of Bioengineering
University of California
San Diego, La Jolla, CA (USA)

E. Ruoslahti
Burnham Institute
La Jolla, CA (USA)

[+] These authors contributed equally

[**] This work was supported by NCI/NASA (N01-CO37117) and NCI (U54 CA119349 and U54 CA119335). T.J.H. acknowledges support from the NIH-NIBIB (EB 006324). G.v.M. acknowledges support from the Whitaker Foundation. We thank Dr. Daniel Sodickson and Dr. Aaron Grant for assistance with MRI, Dr. Deborah Burstein at the Beth Israel Deaconess Medical Center for the use of the 4.7T MRI, Yusuke Nagai for help with atomic force microscopy, and Dr. Michael Sailor for helpful discussions.

© 2006 Wiley-VCH Verlag GmbH & Co. KGaA, Weinheim

solutions in magnetic resonance imaging (MRI), enables magnetic manipulation with external fields, and allows MRI detection of tumor-derived cells that produce the protease. In the future, this general approach may enable site-selective immobilization and enhanced image contrast in regions of tumor invasion in vivo.

The synthesis of proteolytically actuated, self-assembling nanoparticles involves modifying them to be self-complementary but rendered latent by protease-cleavable elements (Figure 1). Briefly, 50 nm dextran-coated Fe_3O_4 nanoparticles, sized by analytical ultracentrifugation (Micromod, Germany), were modified with either biotin or neutravidin (Pierce, Rockford, IL) to generate two populations of particles. When combined in solution, these particles self-assemble through highly stable biotin–neutravidin interactions. To allow enzymatic control of particle assembly, the nanoparticle surfaces of both populations are modified with the MMP-2 peptide substrate, GPLGVRGC,[10] which serves as an anchor for linear PEG chains. PEG is a highly mobile, hydrophilic polymer with a large sphere of hydration that has been widely used to deter adsorption of proteins or cells on surfaces and to extend therapeutic circulation times in vivo.[11,12] We hypothesized that linear PEGs of appropriate lengths would inhibit association of 50 nm nanoparticles but still allow MMP-2 proteases (<9 nm[13]) to cleave peptide linkers. To explore this idea, we conjugated PEGs of varying molecular weights (2, 5, 10, and 20 kDa) to biotin and neutravidin particles through MMP-2-cleavable linkers, and tested their ability to assemble with and without MMP-2. The rate and extent of assembly was measured by monitoring changes in the solution extinction at 600 nm (Figure 2a). Assembly of PEG-coated biotin and neutravidin particles without MMP-2 was found to be inversely related to PEG molecular weight with almost complete inhibition of particle assembly at lengths of 10 kDa or higher. Nanoparticles incubated with MMP-2 also aggregated at a rate inversely related to PEG chain length, likely owing to a similar steric repulsion of MMP-2. A comparison of the change in extinction of particles incubated with MMP-2 with those without MMP-2 incubation at 3 h showed that the 5 kDa and 10 kDa PEGs allow the highest MMP-2-catalyzed assembly enhancement (Figure 2b). However, because the 5 kDa PEG cannot completely inhibit particle interaction in their latent state, the 10 kDa PEG was chosen as the optimum surface modification.

To further verify that the particle assembly was due to the sequence-specific release of PEG by MMP-2, a scrambled linker with low cleavage specificity by MMP-2, GPVGLRGC,[14] was generated and conjugated to the particles. The nanoparticles with the scrambled peptide exhibit markedly decreased assembly compared with the specific peptide sequence (Figure 2c). At 3 h, following MMP-2 addition, assemblies of nanoparticles with specific MMP-2 substrates, examined by AFM, were as large as 0.5—1 μm. This suggests assembly of 10s to 100s of particles. The nanoparticles that are not incubated with MMP-2 remained dispersed with diameters of ≈75 nm (Figure 2d).

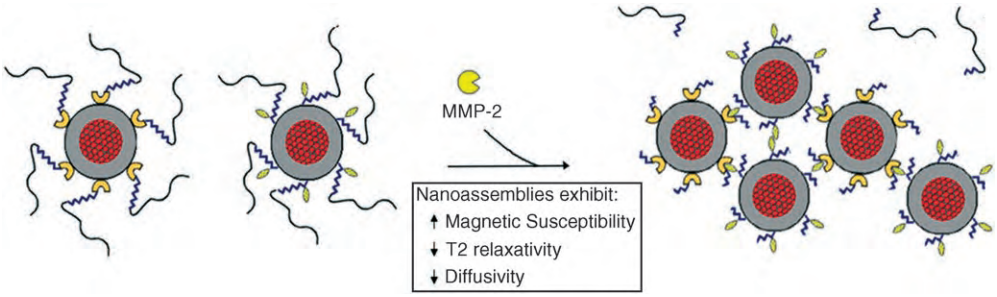

Figure 1. Schematic representation of a proteolytic actuation of self-assembly. Neutravidin- and biotin-functionalized superparamagnetic iron oxide nanoparticles are inhibited by the attachment of PEG chains that are anchored by MMP-2-cleavable peptide substrates (GPLGVRGC). Upon proteolytic removal of PEG through cleavage of the peptides, biotin and neutravidin particles self-assemble into nanoassemblies with enhanced magnetic susceptibility, T2 magnetic resonance relaxation, and lowered diffusivity.

Nanoassemblies of iron oxide particles that form upon proteolytic activation acquire emergent magnetic properties that may be remotely detected with MRI. The coordination of superparamagnetic Fe_3O_4 magnetic dipoles in assembled nanoparticles amplifies the diffusional dephasing of surrounding water molecules and causes shortening of T2 relaxation times in MRI.[15,16] We demonstrate that measurement of T2 changes allows sensitive, remote detection of protease-triggered assembly across a tenfold variation in particle concentration (Figure 3). The concentrations used correspond to 0.7–7 mg Fe/kg of solution, spanning the working concentrations typically utilized for tumor and lymphatic targeting in vivo (2.6 mg Fe/kg body weight).[17] Nanoparticle solutions were incubated with varying concentrations of MMP-2 in a 384-well plate, and their T2 relaxation times were mapped by using a Carr-Purcell-Meiboom-Gill (CPMG) sequence on a 4.7T Bruker MRI. T2 shifts of greater than 150 ms were observed by MMP-2-triggered assembly in a 3.2 pM nanoparticle solution. For 10 pM and 32 pM concentrations, a T2 shortening of approximately 50% of the starting value was observed after incubation with MMP-2. Nanoparticles at a 10 pM concentration were sensitive to at least 170 ng mL^{-1} (9.4 U mL^{-1}) of MMP-2, which compares favorably with levels found in tumor tissue of MMP-2-expressing cancer cells (435 U/g MMP-2).[14]

Next, the utility of the protease-triggered nanoparticles was explored in complex biological specimens in which nonspecific protein adsorption is often problematic. Specifically, latent nanoparticles were incubated in cell-culture medium above living human fibrosarcoma cells, HT-1080s, which constitutively express and activate MMP-2.[18,19] MMP-2 is a zinc-binding protease with cleavage specificity for Type IV collagen, the principal constituent of basement membranes. Upregulation of MMP-2 activity leads to invasive proliferation and metastases of cancer cells by breaking down

 © 2006 Wiley-VCH Verlag GmbH & Co. KGaA, Weinheim

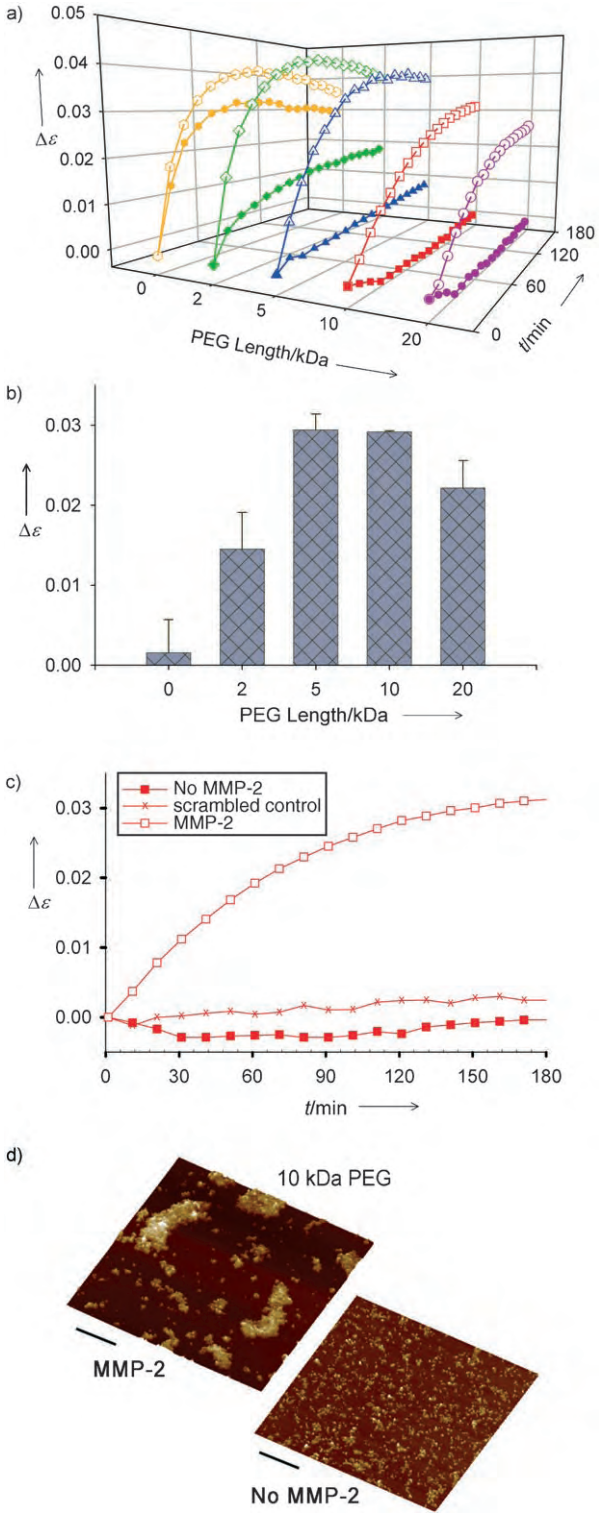

Figure 2. The role of PEG length and characterization of assembly. a) Changes in light scattering of nanoparticles over time with MMP-2 (11 μg mL^{-1}; hollow) or without MMP-2 (solid) shows the influence of PEG length on particle aggregation kinetics. b) The difference between extinction of particles with and without MMP-2 after 3 h reveals an optimal PEG chain length of 10 kDa. c) Nanoparticles with a specific MMP-2 substrate aggregate in the presence of MMP-2 (11 μg mL^{-1}), whereas particles with a scrambled peptide do not. d) Atomic force micrographs of particle solutions in (c) confirm aggregation of particles in the presence of MMP-2. Scale bars are 500 nm.

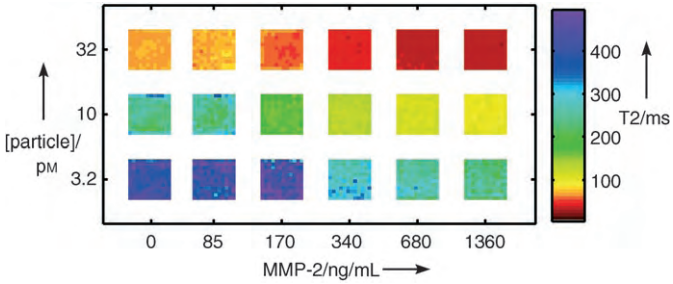

Figure 3. The triggered self-assembly of MMP-2 results in detectable changes in T2 relaxation times. T2 maps generated by a 4.7T Bruker MRI shows detectable aggregation after 3 h with the addition of 85, 170, 340, 680, and 1360 ng mL^{-1} MMP-2 for nanoparticle concentrations of 32 pM, 10 pM, and 3.2 pM.

tissue barriers.[7,8] Nanoparticles (10 pM) were incubated over HT-1080 cells for 5 h, and T2 maps of media samples were generated with MRI. A substantial shortening in T2 was detected in the media over HT-1080 cells compared with media over cells incubated with the broad-spectrum MMP inhibitor Galardin (Figure 4a).

Triggered assembly of the nanoparticles can also be used to magnetically target nanoassemblies to cells. As the magnetic domains of coalesced nanoparticles coordinate to form an amplified cumulative dipole, they become more susceptible to long-range dipolar forces.[20] This phenomenon, similar to the T2 relaxivity enhancement in MRI, allows manipulation of the nanoassemblies with imposed magnetic fields, whereas isolated particles remain unaffected. By using a high-gradient permanent magnet, MMP-2 triggered assemblies of iron oxide particles (1.5 nM) can be visually drawn out of solution, whereas nonactivated particles remain disperse (Figure 4b). To demonstrate that this can be extended towards targeting particles onto cancer cells, HT-1080 cultures were placed over a strong permanent magnet and incubated with nanoparticles at a 150 pM concentration. After 3 h, the media was removed and the cells were washed, fixed, and stained for aggregates by using a biotinylated fluorescent probe. Bright fluorescent staining of particle assemblies is seen over HT-1080 cells, whereas weak diffuse staining, indicating little to no targeting, is seen over cells incubated with the inhibitor Galardin (Figure 4c).

To the best of our knowledge, this report represents the first demonstration of protease-triggered nanoparticle self-assembly. This system differs from the reported use of enzymatic cleavage to prevent assembly,[2,21,22] rather it exploits proteolytic activity to construct multimeric assemblies with emergent properties. Previously, our laboratories have demonstrated that peptide-modified semiconductor quantum dots could precisely target tumors in whole animals[23] and subcellular organelles in living cells.[24] This report extends the ability of nanoparticles not only to target sites of interest, but to interact with the processes of disease by harnessing biological machinery to assemble nanomaterials with amplified properties. We show that polymeric protection can temporarily shield dissimilar complementary ligands, including both small molecules (biotin) and tetrameric proteins (neutravidin). Accordingly, in contrast to recent

 © 2006 Wiley-VCH Verlag GmbH & Co. KGaA, Weinheim

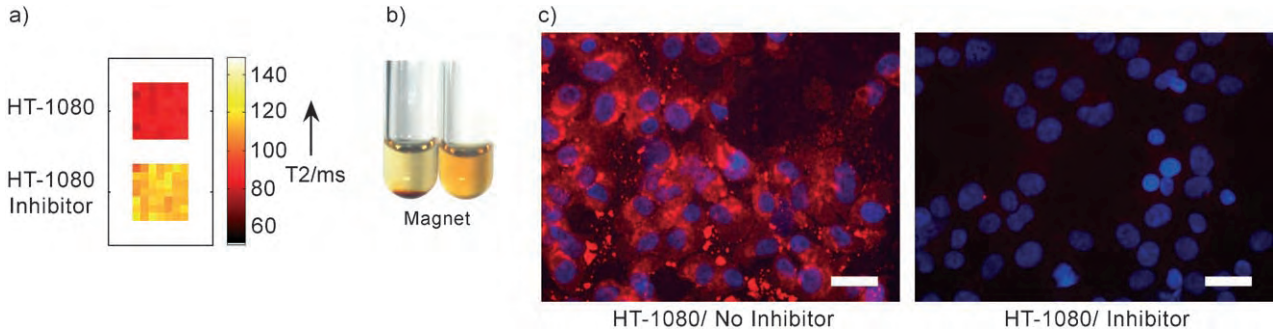

Figure 4. Triggered self-assembly of nanoparticles by HT-1080 Tumor-derived cells. a) T2 mapping of Fe_3O_4 nanoparticles incubated for 5 h over HT-1080 cells that secrete active MMP-2 in a complex medium. Nanoparticle assembly amplifies T2 relaxation over cancer cells relative to cells incubated with the MMP inhibitor Galardin at 25 μM. b) Activated nanoparticles are drawn out of solution by a strong magnet (left) whereas inactive nanoparticles (right) are not. c) Nanoparticles activated by MMP-2-secreting tumor cells for 3 h are drawn out of solution onto cells by a magnetic field. Available neutravidins on aggregates are stained with biotin-quantum dots (emission: 605 nm) and imaged by epifluorescent microscopy. Assemblies are not targeted to cells if an MMP inhibitor is used. Scale bar represents 50 μm.

reports of proteolytic activation of cell-penetrating peptides[19] and peroxidase-initiated nanoparticle assembly,[4,25] our approach can be considered entirely modular and thereby generalizable. Therefore, key features, for example, biochemical triggers and molecular recognition, may be altered without significant re-engineering. Formulations with new functionalities could be easily developed by substituting the complementary binding pairs, cleavable substrates (e.g. glycans, lipids, oligonucleotides), or multivalent nanoparticle cores (e.g. gold, quantum dot, dendrimer) to extend the capabilities of existing modalities.

Experimental Section

Synthesis of nanoparticle probes: Protease-triggered, self-assembling nanoparticles were synthesized by using amine-functionalized, dextran-coated iron-oxide nanoparticles (50 nM; 6.25 pmol/mg Fe), sized by analytical ultracentrifugation (Micromod (Germany)). All peptides were obtained at >90% purity (Synpep), and all reagents were obtained from Sigma unless otherwise specified. A high-gradient magnetic-field filtration column was used between each conjugation (Miltenyi Biotec) and all conjugations were performed at room temperature unless stated. Peptides were synthesized to sequentially contain a lysine (for the attachment of polyethylene glycol polymers), an MMP-2 cleavage sequence (or scrambled version), and a terminal cysteine (for linkage onto amines in the dextran coat or lysines on neutravidin proteins). Phosphate-buffered saline buffer solution (PBS; Na_2PO_4 (0.1M), NaCl buffer (0.15M)). For biotin probes, *N*-Succinimidyl-3-[2-pyridyldithio]-propionamido (SPDP; 0.25 mg mL^{-1}) was treated with particle amines (2.5 mg Fe; PBS (1 mL), pH 7.2; 1 hr), after which cysteine-containing peptides (acetyl-KGPLGVRGC-X-Biotin (1 mg mL^{-1})) were added to displace pyridine-2-thione leaving groups (PBS (1 mL) with EDTA (10 mM), pH 7.2; 12 h under N_2; 4 °C). Polyethylene glycol polymers with a terminal methoxy cap at one end and an opposing amine-reactive succimidyl α-methylbutanoate (mPEG-SMB) (Nektar; 2.5 mM) were then attached to peptide lysines (PBS (1 mL), pH 7.2; 3 h). Neutravidin (Pierce) nanoparticles were formed by modifying particles (2.5 mg Fe) with biotinamidohexanoyl-6-amino-hexanoic acid *N*-hydroxy-succinimide ester (0.5 mg mL^{-1}; PBS (1 mL); pH 7.2; 1 h) and then coated with a saturating concentration of neutravidin (850 μg neutravidin per 2.5 mg nanoparticles; (PBS (5 mL), pH 7.2; >3 h). The extinction of the solution at 600 nm was measured during incubation to ensure no aggregate formation. Additionally, neutravidin-coated particles were passed through a 0.1 μm filter to confirm monodispersity. By using the same conditions described for biotin particle conjugations, peptides (KGPLGVRGC) were linked to available lysine amines on neutravidin-coated nanoparticles with SPDP, after which mPEG-SMB polymers were linked to peptide lysines. Scrambled sequences used for control experiments contained GVRLGPG instead of GPLGVRG. Extinction, AFM, and magnetic field migration measurements: For all assembly experiments, equimolar ratios of particles were used. All extinction measurements were performed in duplicate in 384-well plates by using a SpectraMax Plus spectrophotometer (Molecular Devices, Sunnyvale CA). Biotin and neutravidin probes (0.5 mg mL^{-1}; 2-[4-(2-hydroxyethyl)-1-piperazinyl]ethanesulfonic acid (HEPES; 0.1M), $CaCl_2$ (5 mM); pH 7.2) were mixed at equal ratios and 0.5 μg of the recombinant catalytic domain of MMP-2 (Biomol,) (6 μL Tris-Cl (50 mM), $CaCl_2$ (5 mM), Brij-35 (0.005%); pH 7.5) was added to 40 μL probe solution at time zero. For controls, 6 μL of buffer without MMP-2 was added. The same probe and MMP-2 concentrations were used for AFM and solution phase magnetic precipitation experiments. AFM measurements were performed by using a multimode, Digital Instruments AFM (Santa Barbara CA) operating in tapping-mode by using FESP Tips (Veeco Nanoprobe TM, Santa Barbara CA). AFM reactions were incubated for 3 h, diluted, and evaporated on freshly cleaved mica for analysis. In magnetic precipitation experiments, probe solutions were incubated with or without MMP-2 overnight and placed over a strong magnet for 2.5 min.

MRI detection of self-assembly: MRI images were taken on a Bruker 4.7T magnet, 7 cm bore. Biotin–peptide-P-EG and neutravidin–peptide–PEG nanoparticles were mixed together and serially diluted in 384-well plate. Serial dilutions of recombinant MMP-2 in 6 μL of buffer solution (Tris-Cl (50 mM), $CaCl_2$ (5 mM), Brij-35 (0.005%); pH 7.5) were added to each well. After 3 h, a CPMG sequence of 16 images with multiples of 10.45 ms echo times and a relaxation time of 5000 ms were acquired. T2 maps were obtained for each well by fitting images on a pixel by pixel basis to the equation $y = M^* \times 10^{(-TE/T2)}$ by using MATLAB.

Cell culture: HT-1080 human fibrosarcoma cells (ATCC) were cultured in 24-well plates by using minimum essential medium eagle (Invitrogen) with fetal bovine serum (10%; Invitrogen) and penicillin/streptomycin (1%). For MRI experiments, the media was replaced with serum-free dubelcco's modified eagle medium (DMEM; Invitrogen) with a 10 pM nanoparticle concentration. The broad-spectrum MMP-2 inhibitor Galardin (Biomol) was added at a concentration of 25 μM in control cultures. Samples of 40 μL were taken at 5 h for MRI imaging by using the same procedures for T2 mapping described above. For fluorescent labeling experiments, media was replaced with serum-free DMEM with a 200 pM nanoparticle concentration and cells were placed over a strong magnet.

 © 2006 Wiley-VCH Verlag GmbH & Co. KGaA, Weinheim

After 3 h, the media was removed and the cells fixed with paraformaldehyde (2%). The cells were permeabilized with Triton-X (0.1%) in PBS and incubated with biotin quantum dots (emission = 605 nm; Quantum Dot Corp). Nuclear staining was performed by incubating with Hoescht (0.001%) for 1 min.

Received: January 20, 2006
Revised: March 11, 2006

Keywords: magnetic properties · nanostructures · proteases · self-assembly · triggered assembly

[1] C. A. Mirkin, R. L. Letsinger, R. C. Mucic, J. J. Storhoff, *Nature* **1996**, *382*, 607.
[2] J. M. Perez, L. Josephson, T. O'Loughlin, D. Hogemann, R. Weissleder, *Nat. Biotechnol.* **2002**, *20*, 816.
[3] D. G. Georganopoulou, L. Chang, J. M. Nam, C. S. Thaxton, E. J. Mufson, W. L. Klein, C. A. Mirkin, *Proc. Natl. Acad. Sci. USA* **2005**, *102*, 2273.
[4] J. M. Perez, F. J. Simeone, A. Tsourkas, L. Josephson, R. Weissleder, *Nano Lett.* **2004**, *4*, 119.
[5] J. M. Perez, F. J. Simeone, Y. Saeki, L. Josephson, R. Weissleder, *J. Am. Chem. Soc.* **2003**, *125*, 10192.
[6] M. M. Stevens, N. T. Flynn, C. Wang, D. A. Tirrell, R. Langer, *Adv. Mater.* **2004**, *16*, 915.
[7] G. Giannelli, J. FalkMarzillier, O. Schiraldi, W. G. StetlerStevenson, V. Quaranta, *Science* **1997**, *277*, 225.
[8] D. R. Edwards, G. Murphy, *Nature* **1998**, *394*, 527.
[9] J. M. Fang, Y. Shing, D. Wiederschain, L. Yan, C. Butterfield, G. Jackson, J. Harper, G. Tamvakopoulos, M. A. Moses, *Proc. Natl. Acad. Sci. USA* **2000**, *97*, 3884.
[10] J. L. Seltzer, K. T. Akers, H. Weingarten, G. A. Grant, D. W. Mccourt, A. Z. Eisen, *J. Biol. Chem.* **1990**, *265*, 20409.
[11] J. M. Harris, R. B. Chess, *Nat. Rev. Drug Discovery* **2003**, *2*, 214.
[12] R. Gref, Y. Minamitake, M. T. Peracchia, V. Trubetskoy, V. Torchilin, R. Langer, *Science* **1994**, *263*, 1600.
[13] E. Morgunova, A. Tuuttila, U. Bergmann, M. Isupov, Y. Lindqvist, G. Schneider, K. Tryggvason, *Science* **1999**, *284*, 1667.
[14] C. Bremer, C. H. Tung, R. Weissleder, *Nat. Med.* **2001**, *7*, 743.
[15] R. A. Brooks, F. Moiny, P. Gillis, *Magn. Reson. Med.* **2001**, *45*, 1014.
[16] P. Gillis, F. Moiny, R. A. Brooks, *Magn. Reson. Med.* **2002**, *47*, 257.
[17] M. G. Harisinghani, J. Barentsz, P. F. Hahn, W. M. Deserno, S. Tabatabaei, C. H. van de Kaa, J. de la Rosette, R. Weissleder, *N. Engl. J. Med.* **2003**, *348*, 2491.
[18] C. Bremer, S. Bredow, U. Mahmood, R. Weissleder, C. H. Tung, *Radiology* **2001**, *221*, 523.
[19] T. Jiang, E. S. Olson, Q. T. Nguyen, M. Roy, P. A. Jennings, R. Y. Tsien, *Proc. Natl. Acad. Sci. USA* **2004**, *101*, 17867.
[20] Y. Lalatonne, J. Richardi, M. P. Pileni, *Nat. Mater.* **2004**, *3*, 121.
[21] M. Zhao, L. Josephson, Y. Tang, R. Weissleder, *Angew. Chem.* **2003**, *115*, 1413; *Angew. Chem. Int. Ed.* **2003**, *42*, 1375.
[22] J. M. Perez, T. O'Loughin, F. J. Simeone, R. Weissleder, L. Josephson, *J. Am. Chem. Soc.* **2002**, *124*, 2856.
[23] M. E. Akerman, W. C. W. Chan, P. Laakkonen, S. N. Bhatia, E. Ruoslahti, *Proc. Natl. Acad. Sci. USA* **2002**, *99*, 12617.
[24] A. M. Derfus, W. C. W. Chan, S. N. Bhatia, *Adv. Mater.* **2004**, *16*, 961.
[25] A. Bogdanov, Jr., L. Matuszewski, C. Bremer, A. Petrovsky, R. Weissleder, *Mol. Imaging* **2002**, *1*, 16.

 © 2006 Wiley-VCH Verlag GmbH & Co. KGaA, Weinheim

DNA Carriers

DOI: 10.1002/anie.200600214

Light-Regulated Release of DNA and Its Delivery to Nuclei by Means of Photolabile Gold Nanoparticles**

*Gang Han, Chang-Cheng You, Byoung-jin Kim, Rosemary S. Turingan, Neil S. Forbes, Craig T. Martin, and Vincent M. Rotello**

Gene therapy is one of the most promising prospects in biomedical and bioorganic realms.[1] The success of gene therapy benefits mainly from having effective gene-delivery vectors for transporting plasmid DNA, small interfering RNA, or antisense oligonucleotides into target cells. The delivery of therapeutic nucleotides using nanomaterials such as polymeric micelles,[2] dendrimers,[3] nanorods,[4] nanotubes,[5] and nanoparticles[6] is attracting increasing attention as a consequence of their unique dimensions and properties.[7–10]Despite much progress, unpacking DNA inside target cells in a spatiotemporally controlled fashion is a major limiting factor in designing these artificial carriers.[11] Although several intracellular release strategies have been employed, including low pH,[12] high enzyme concentration,[13] and redox materials inside the cells,[14] the use of light as an external stimulus represents a unique site- and time-specific means of unloading DNA. As such, photosensitive synthetic DNA carriers will provide new directions for gene delivery owing to the potential for versatile and facile chemical modifications and the modularity of the carrier–DNA complex.

As a highly orthogonal external stimulus, photochemical processes enjoy wide use in surface patterning,[15] advanced materials,[16] biochemistry,[17] and drug-delivery systems.[18,19] Light-regulated methods uniquely limit the resultant biological effects to the illuminated areas with temporal control.[20] For example, biologically active molecules can be modified with photosensitive groups to be essentially bioinert; they can then be reactivated by photointervention.[21] Such caged compounds have shown tremendous applications in chemical

[*] G. Han, Dr. C.-C. You, R. S. Turingan, Prof. Dr. C. T. Martin, Prof. Dr. V. M. Rotello
Department of Chemistry, University of Massachusetts
710 North Pleasant Street, Amherst, MA 01003 (USA)
Fax: (+1) 413-545-4490
E-mail: Rotello@Chem.umass.edu
B. J. Kim, Prof. Dr. N. S. Forbes
Department of Chemical Engineering, University of Massachusetts
Amherst, MA 01003 (USA)

[**] This research was supported by the NIH (EB 004503(VR) and GM55002 (CTM)). Confocal images were taken at the Central Microscopy Facility at the University of Massachusetts at Amherst, which is supported by a grant from the National Science Foundation (NSF BBS 8714235).

Supporting information for this article is available on the WWW under http://www.angewandte.org or from the author.

 © 2006 Wiley-VCH Verlag GmbH & Co. KGaA, Weinheim

biology, such as the control of DNA hybridization,[22] DNA transcription,[23] RNA ribosome function,[24] and modulation of aptamer function.[25] Recently, the delivery of caged DNA or proteins into cells by microinjection followed by uncaging with light at desired times or locations has become a valuable tool for studying living organisms.[26] However, construction of the caged genetic materials can be costly and involves complicated handling, purification, and storage. Furthermore, the microinjection approach is limited in allowing high-throughput DNA delivery, as only one cell can be manipulated at a time, and the DNA itself may suffer degradation inside cells. Caged-delivery vectors bearing light-controlled DNA-binding functionality provide a means for overcoming these challenges. Systems of this type can be easily constructed and manipulated in a modular fashion and provide potential protection for DNA. Thus, they offer a simple and novel approach for the functional delivery of DNA in a well-regulated fashion.

Our recent studies demonstrated that cationic gold nanoparticles provide an efficient platform for DNA surface binding. These nanoparticles display a high affinity for electrostatic interactions with DNA, which results in the suppression of DNA transcription by T7 RNA polymerase in vitro[27] and effective DNA delivery in mammalian cells.[28] Herein, we construct a positively charged gold nanoparticle bearing a photoactive *o*-nitrobenzyl ester linkage, which allows temporal and spatial release of DNA by light. These cationic photocleavable nanoparticles (NP-PC) initially associate with DNA through charge pairing (Figure 1a). Near-UV irradiation (> 350 nm) cleaves the nitrobenzyl linkage, releasing the positively charged alkyl amine and leaving behind a negatively charged carboxylate group (NP-TCOOH). This reversal in electrostatics leads to the efficient release of DNA from the nanoparticle, resulting in a high level of recovery of DNA transcription in vitro. Moreover, effective DNA delivery and release in living cells with significant nuclear localization of the DNA were obtained with this system, thus providing an important proof of concept for the development of light-regulated biological-macromolecule and drug-delivery systems.

Photolabile gold nanoparticles (NP-PC, Figure 1b) were prepared by place exchange of 1-pentanethiol-capped 2-nm gold clusters with *o*-nitrobenzyl ester functionalized thiol ligands.[29] The *o*-nitrobenzyl ester group is a commonly used biocompatible species that is photocleavable. It has long-term stability under ambient light, but can be removed quickly and efficiently by UV light (> 350 nm) with minimal adverse effects on biological systems.[30] The positively charged dimethylethylammonium functionalities at the periphery of the nanoparticles provide good water solubility and allow interaction with DNA through complementary charges. Furthermore, tetraethylene glycol (TEG) was incorporated as a tether to increase both the biocompatibility and water solubility of the particles.[31]

A solution of NP-PC was irradiated with UV light ($\lambda =$ 350 nm), and the course of the photochemical reaction was monitored by UV/Vis spectroscopy to establish the cleavage of the *o*-nitrobenzyl ester linkage. Irradiation led to a decrease in absorption at 304 nm and an increase at 342 nm

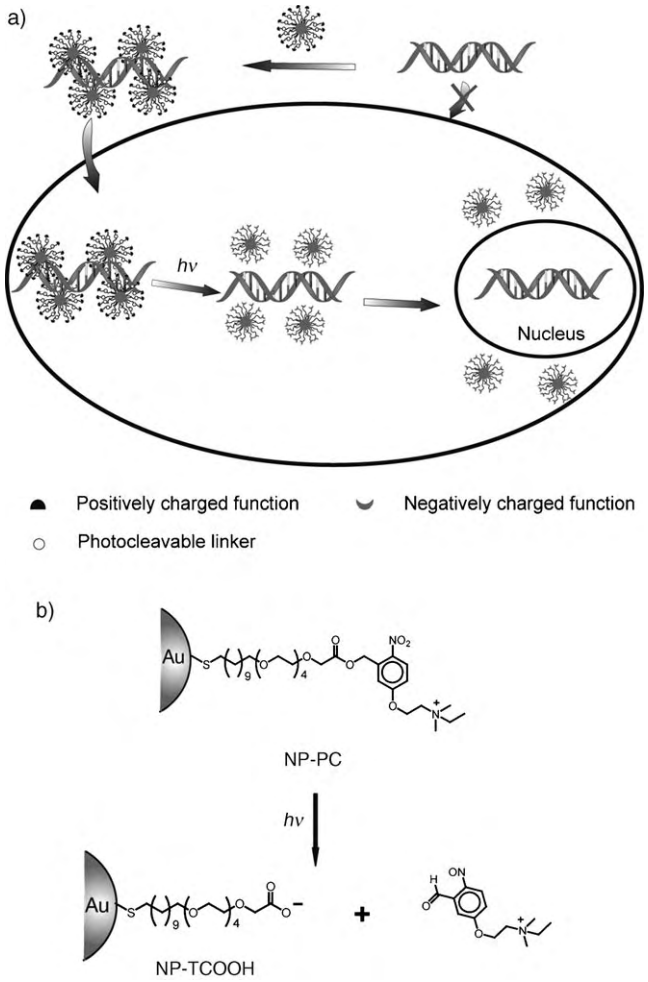

Figure 1. a) Schematic illustration of the release of DNA from the NP-PC–DNA complex upon UV irradiation within the cell; b) schematic presentation of light-induced surface transformation of NP-PC.

over time (Figure 2), thus indicating the breakage of the photolabile ester bond and the generation of *o*-nitrobenzaldehyde concomitant with charge conversion on the NP-PC

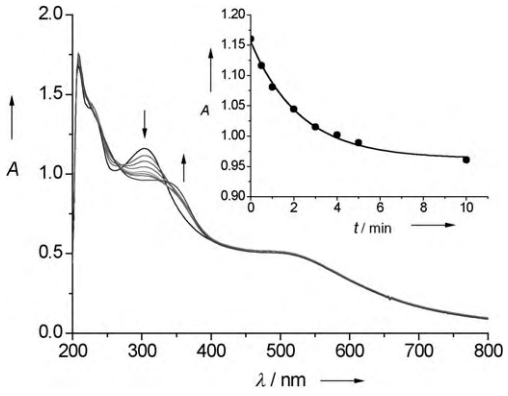

Figure 2. UV/Vis spectral changes of NP-PC (1.0 μM) upon irradiation with UV light ($\lambda = 350$ nm). Inset: The plot of absorbance at 304 nm against irradiation time shows that the photochemical reaction approached maximum conversion within 10 min.

 © 2006 Wiley-VCH Verlag GmbH & Co. KGaA, Weinheim

monolayer. The photochemical conversion on the monolayer of the gold particles approached maximum within 10 min.

An ethidium bromide (EtdBr) fluorescence assay was used to follow the interaction between NP-PC and DNA. EtdBr is weakly fluorescent in aqueous solution but exhibits strong fluorescence upon intercalation into the DNA duplex.[32] It is expected that the complementary electrostatic interaction of NP-PC with DNA would block the hydrophobic grooves of DNA and thus diminish the EtdBr–DNA interaction, which should be reflected by fluorescence changes in EtdBr. Indeed, drastic fluorescence quenching was observed when NP-PC was added to a solution of DNA and EtdBr, suggesting that EtdBr is expelled from the DNA duplex, and its intrinsic fluorescence is quenched by the bulk water molecules.[25,28,33] Because anionic gold nanoparticles cannot bind with negatively charged DNA molecules, the absorption effect of the gold core on fluorescence quenching was subtracted with NP-TCOOH as a reference. The corrected fluorescence titration curve shows that the fluorescence quenching due to complex formation is dependent on nanoparticle concentration, and a plateau is reached at a NP-PC/37-mer DNA ratio of 6:1 (see Supporting Information), indicating a binding stoichiometry of 6:1.

DNA transcription by T7 RNA polymerase was studied in vitro to determine the impact of complex formation on DNA function and the functional efficiency of DNA release.[34] Premixed (5 min) 37-mer DNA/NP-PC (1:6) solutions were exposed to UV light ($\lambda = 350$ nm) for varying periods of time followed by a T7 RNA polymerase transcription assay.[27] The product 20-mer RNA transcripts were subjected to gel electrophoresis for quantitative determination of the extent of reaction, with the transcription level obtained in the absence of nanoparticles set to 100%. Before UV irradiation, the transcription was less than 5% of the control (Figure 3). Upon irradiation, however, the transcription level increased significantly, reaching a maximum of about 75% recovery in 8 min (Figure 3). A control experiment showed that DNA alone irradiated by UV light for 10 min has essentially identical levels of transcription to that without UV irradiation, which suggests that DNA function is retained in the presence of UV light. Such a high level of restoration of DNA-transcription ability indicates that the DNA–NP-PC complexes are efficiently dissociated upon irradiation. As discussed previously, the cationic NP-PC electrostatically associates with DNA to afford DNA–nanoparticle supramolecular complexes. Therefore, the initially observed transcription inhibition is ascribed to competition between the nanoparticles and the RNA polymerase for binding to the DNA. Upon UV irradiation, the cationic NP-PC is converted into the anionic NP-TCOOH, which is no longer able to associate with DNA molecules, thus releasing the DNA for transcription. This result not only provides evidence for functional DNA release in vitro through the light regulation of our photolabile nanoparticles, but also demonstrates the feasibility of NP-PC as a novel photocontrolled bioactive system.

Next, light-triggered DNA delivery and release were investigated in living cells by fluorescence microscopy. Gold nanoparticles are reported to quench conjugated fluorophores effectively through energy transfer.[35] Once detached from the nanoparticles, the fluorophores "light up" as the energy-transfer pathway is removed. Herein, as a model system, we used fluorescein (FAM)-labeled 37-mer DNA (F-DNA), which bears the same sequence as that used in the T7 RNA polymerase assay, to detect DNA delivery and release in vivo. On the basis of the 6:1 binding stoichiometry, NP-PC–F-DNA complexes were prepared at a slight molar excess of 10:1 for optimal cellular internalization.[24,36] Mouse embryonic fibroblast cells were incubated with NP-PC–F-DNA for 6 h in 96-well plates and then washed with phosphate-buffered saline (PBS) to remove the uninternalized nanoparticles. The cells were irradiated for 2 h with a hand-held low-power UV lamp, and fluorescence-microscopy images were taken before and after irradiation. Significant fluorescence with UV irradiation was observed inside most cells (Figure 4, right), whereas the control experiment without irradiation did not show observable fluorescence (Figure 4, left). No fluorescence was observed in cells incubated with merely F-DNA, thus indicating that the cellular uptake of naked DNA is inefficient. Furthermore, untreated cells with and without NP-PC incubation also showed no observable fluorescence after irradiation; autofluorescence from nanoparticles or cells is therefore precluded.[29] Taken together, the results clearly show that cationic NP-PC can effectively carry DNA into the cells and that the DNA is successfully unloaded

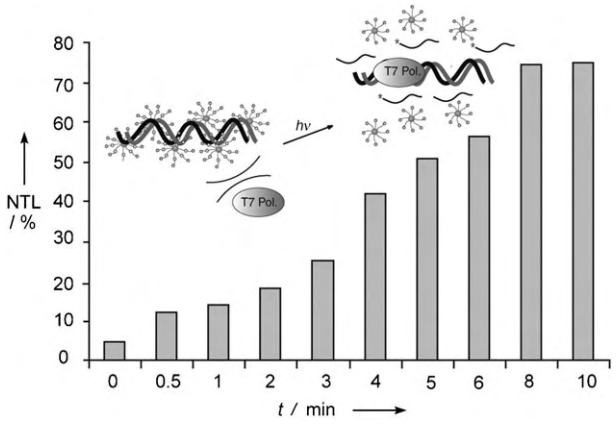

Figure 3. Normalized transcription level (NTL) of 20-mer RNA products upon irradiation at 350 nm for different times, showing the efficient transcription restoration by T7 RNA polymerase (T7 Pol.). Inset: Proposed mechanism of light-triggered transcription recovery.

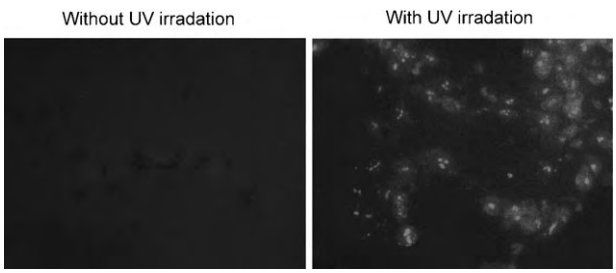

Figure 4. Representative fluorescence-microscopy images showing the phototriggered DNA release from the NP-PC–F-DNA complex.

 © 2006 Wiley-VCH Verlag GmbH & Co. KGaA, Weinheim

from gold nanoparticles with the intervention of UV light, thus demonstrating that light provides effective spatiotemporal control.

Effective accumulation of DNA in the nucleus after dissociation from transporting vectors is an essential step in gene delivery, as gene expression takes place inside the cell nucleus.[37] To evaluate the subcellular distribution of the released DNA, specifically with respect to its nuclear localization within cells after UV irradiation, the nuclear stain 4′,6-diamidino-2-phenylindole (DAPI) was used. A sample of the NP-PC–F-DNA complex (10:1) was incubated with mouse embryonic fibroblast cells for 6 h in glass-bottomed dishes and washed with PBS buffer. After UV irradiation for 2 h, fluorescence-microscopy images were taken immediately. Although some F-DNA molecules were found in the cytoplasm, significant nuclear localization of the DNA is clearly demonstrated by colocalization of F-DNA (red) and DAPI (yellow) (Figure 5a). In accord with the fluorescence-microscopy results, confocal microscopic studies further confirmed that the unloaded F-DNA accumulated inside the nucleus (Figure 5b).

In summary, we have developed a photolabile gold nanoparticle that provides effective light-regulated control over DNA–nanoparticle interactions. We have demonstrated that light is effective in triggering DNA release from gold clusters both in vitro and in vivo. These cationic nanoparticles bind with DNA through complementary surface electrostatic interactions; upon UV irradiation, the electrostatic nature of the surface of the nanoparticles is converted, thus resulting in effective DNA release. We have demonstrated that such release leads to a high level of DNA-transcription recovery in vitro. Most importantly, effective DNA delivery and release were also observed in cells, with significant nuclear localization of the DNA molecules. This light-mediated release strategy paves a simple and unique way for delivering therapeutic materials into cells in a spatiotemporally controlled fashion. Furthermore, versatile surface modification of gold nanoparticles combined with the controlled interactions of biomolecules could be used to enhance the transfection of genetic materials as well as protein and drug delivery.

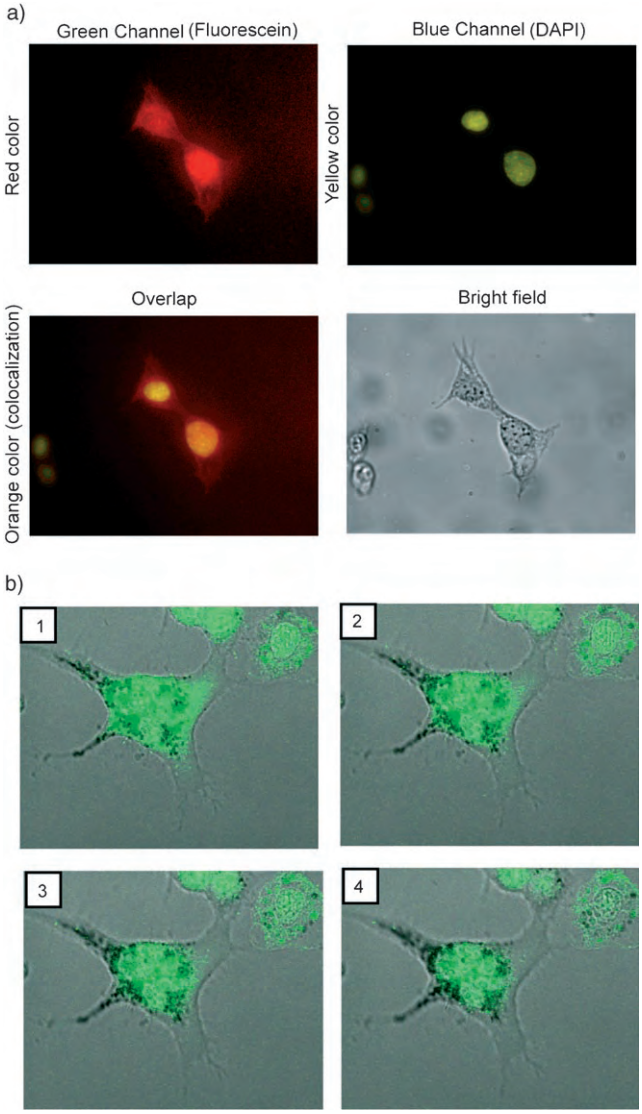

Figure 5. a) Fluorescence- and bright-field-microscopy images illustrating nuclear localization of DNA released from the NP-PC–DNA complex by photo-triggering. For an improved observation of overlapping F-DNA and nuclei stained with DAPI, we colored the green (fluorescein) and blue (DAPI) channels red and yellow, respectively. b) Confocal-microscopy images showing that the photoreleased DNA effectively accumulates inside the nucleus of cells. Panels 1–4 show four consecutive slices of the middle sections of z-series confocal images (interval = 1.0 μm).

Experimental Section

All chemicals were obtained from Sigma–Aldrich (St. Louis, MO, USA) unless otherwise noted. Two complementary 37-mer unlabeled DNA single strands **S1** (5′-TAATACGACTCACTATAGGGAGACCACAACGGTTTCC-3′) and **S2** (3′-ATTATGCTGAGTGATATCCCTCTGGTGTTGCCAAAGG-5′) were synthesized and purified according to the method reported previously.[30] The FAM-labeled DNA single strand **S3** (5′-(FAM)TAATACGACTCACTATAGGGAGACCACAACGGTTTCC(FAM)-3′) was purchased from Integrated DNA Technologies, Inc (Coralville, IA, USA). Concentrations of single-stranded DNA stock solutions in tris-EDTA (TE) buffer (pH 7.8, tris = tris(hydroxymethyl)aminomethane (10 mM), EDTA = ethylenediaminetetraacetate (1 mM)) were calculated using the weighted sums of the different measured molar-extinction coefficients for each base at 253, 259, and 267 nm. **S2** was annealed with **S1** and **S3** separately by combining equivalent molar amounts of the individual sequences (final concentration 50 μM), heating to 90 °C for 5 min, and slowly cooling to room temperature. DNA was stored at −20 °C. The detailed experimental procedure for the synthesis of the photolabile thiol ligand and the corresponding NP-PC is described in the Supporting Information.

UV: Samples were irradiated in quartz cuvettes using a Rayonet photochemical reactor (Southern N.E. Ultraviolet Co., Middletown, CT, USA) at the wavelength of 350 nm. UV/Vis spectra of NP-PC were recorded with a HP 8452A spectrophotometer.

EtdBr: This assay was modified from a reported procedure.[33] Samples were prepared in PBS buffer (pH 7.8, potassium phosphate (20 mM), sodium chloride (100 mM)) unless otherwise noted. Fluorescence spectra were recorded in a conventional quartz cuvette ($10 \times 10 \times 35$ mm^3) on a Shimadzu RF-5301 PC spectrofluorometer with excitation at 545 nm. Both the excitation and emission slit widths were 5 nm. During the titration, a mixture (2 mL) of 37-mer DNA (0.1 μM) and EtBr (1 μM) was placed in the cuvette, and the initial

 © 2006 Wiley-VCH Verlag GmbH & Co. KGaA, Weinheim

emission spectrum was recorded. Aliquots (10 μL) of a solution of 37-mer DNA (0.1 μM), EtBr (1 μM), and NP-PC (3.5 μM) or NP-TCOOH (3.5 μM, as control) were subsequently added to the solution in the cuvette. After each addition, a fluorescence spectrum was recorded. The normalized fluorescence intensities calibrated by respective controls at a selected wavelength (589 nm) were plotted against the ratio [NP-PC]/[DNA] (see Supporting Information).

T7 RNA Polymerase: This assay was modified according to that previously described.[34] The assay was carried out in PBS buffer. To mediate the reversal of inhibition of transcription, DNA/NP-PC (1:6) solutions were premixed for 5 min and then irradiated at 350 nm for different times (0, 0.5, 1, 2, 3, 4, 5, 6, 8, and 10 min) in a Rayonet photochemical reactor. DNA solutions irradiated for 0 and 10 min served as controls. T7 RNA polymerase (enzyme/DNA = 5:1, [DNA] = 0.1 μM) and excess nucleotide triphosphates were then added to the mixture. The nucleotide triphosphates included ^{32}P-labeled guanosine 5′-triphosphate (GTP) for isotopic detection. The enzymatic reaction proceeded for 5 min at 37 °C before being quenched with EDTA (15 mM) in formamide (95 %). The 20-mer RNA transcripts were resolved by electrophoresis in a polyacrylamide (20 %) and urea (7 M) gel (Supporting Information) and visualized and quantified with a Storm 840 phosphorimager to determine the extent of reaction. Transcription levels obtained in the absence of NP-PC were set to 100 %.

Cell culture: Mouse embryonic fibroblast cell lines were gifts from Dr. R. Johnson, University of California, San Diego. Cells were grown in a cell-culture flask in high-glucose Dulbecco's Modified Eagle Medium (DMEM; glucose (4.5 g L^{-1})) containing 4-(2-hydroxyethyl)-1-piperazineethanesulfonic acid (HEPES) buffer (pH 7.4, 25 mM) supplemented with fetal bovine serum (FBS; 10 %). Cultures were maintained at 37 °C under a humidified condition with CO_2 (5 %).

Images: All fluorescence images were obtained with an Olympus X71 inverted microscope with excitation at 470 nm and emission at 525 nm for the green (fluorescein) channel, and with excitation at 360 nm and emission at 460 nm for the blue (DAPI) channel. Confocal images were obtained with a Zeiss LSM510 microscope equipped with a 40× objective lens. An argon laser (488 nm) was used to provide the excitation for fluorescein-labeled DNA.

Plates (96-well): Mouse embryonic fibroblast cells (12000 cells/well) were incubated with the NP-PC–F-DNA complex (10:1, [F-DNA] = 0.2 μM) for 6 h on the culture plates followed by washing with PBS buffer. Fluorescence-microscopy images were taken (magnification 20×, exposure time 500 ms) before and after 2 h of irradation at 365 nm using a hand-held low-power Spectroline ENF-240C UV lamp.

Glass-bottomed dishes: Mouse embryonic fibroblast cells (3000 cells/dish) were plated overnight, then incubated with the NP-PC–F-DNA complex (10:1, [F-DNA] = 0.2 μM) for 6 h on the dishes followed by washing with PBS buffer. After 2 h of irradiation with a hand-held UV lamp, fluorescence-microscopy images were taken (magnification 40×, exposure time 1000 ms). The confocal-microscope image was taken by using the parameters noted above.

Received: January 18, 2006
Published online: March 30, 2006

Keywords: DNA · gold · nanoparticles · photochemistry · transcription

[1] W. F. Anderson, *Science* **1992**, *256*, 808 – 813.
[2] D. W. Pack, A. S. Hoffman, S. Pun, P. S. Stayton, *Nat. Rev. Drug Discovery* **2005**, *4*, 581 – 593.
[3] U. Boas, P. M. H. Heegaard, *Chem. Soc. Rev.* **2004**, *33*, 43 – 63.
[4] A. K. Salem, P. C. Searson, K. W. Leong, *Nat. Mater.* **2003**, *2*, 668 – 671.
[5] W. Wu, S. Wieckowski, G. Pastorin, M. Benincasa, C. Klumpp, J. P. Briand, R. Gennaro, M. Prato, A. Bianco, *Angew. Chem.* **2005**, *117*, 6516 – 6520; *Angew. Chem. Int. Ed.* **2005**, *44*, 6358 – 6362.
[6] D. Luo, W. M. Saltzman, *Nat. Biotechnol.* **2000**, *18*, 893 – 895.
[7] E. Katz, I. Willner, *Angew. Chem.* **2004**, *116*, 6166 – 6235; *Angew. Chem. Int. Ed.* **2004**, *43*, 6042 – 6108.
[8] C. M. Niemeyer, *Angew. Chem.* **2001**, *113*, 4254 – 4287; *Angew. Chem. Int. Ed.* **2001**, *40*, 4128 – 4158.
[9] L. Pasquato, P. Pengo, P. Scrimin, *J. Mater. Chem.* **2004**, *14*, 3481 – 3487.
[10] A. Verma, V. M. Rotello, *Chem. Commun.* **2005**, 303 – 312.
[11] D. Luo, *MRS Bull.* **2005**, *30*, 654 – 658.
[12] W. J. Li, Z. H. Huang, J. A. MacKay, S. Grube, F. C. Szoka, *J. Gene Med.* **2005**, *7*, 67 – 79.
[13] C. A. H. Prata, Y. X. Zhao, P. Barthelemy, Y. G. Li, D. Luo, T. J. McIntosh, S. J. Lee, M. W. Grinstaff, *J. Am. Chem. Soc.* **2004**, *126*, 12196 – 12197.
[14] S. Giri, B. G. Trewyn, M. P. Stellmaker, V. S. Y. Lin, *Angew. Chem.* **2005**, *117*, 5166 – 5172; *Angew. Chem. Int. Ed.* **2005**, *44*, 5038 – 5044.
[15] a) D. Ryan, B. A. Parviz, V. Linder, V. Semetey, S. K. Sia, J. Su, M. Mrksich, G. M. Whitesides, *Langmuir* **2004**, *20*, 9080 – 9088; b) A del Campo, D. Boos, H. W. Spiess, U. Jonas, *Angew. Chem.* **2005**, *117*, 4785 – 4791; *Angew. Chem. Int. Ed.* **2005**, *44*, 4707 – 4712.
[16] K. N. Plunkett, A. Mohraz, R. T. Haasch, J. A. Lewis, J. S. Moore, *J. Am. Chem. Soc.* **2005**, *127*, 14574 – 14575.
[17] H. Bayley, *Nat. Chem. Biol.* **2006**, *2*, 11 – 13.
[18] N. Nishiyama, A. Iriyama, W. D. Jang, K. Miyata, K. Itaka, Y. Inoue, H. Takahashi, Y. Yanagi, Y. Tamaki, H. Koyama, K. Kataoka, *Nat. Mater.* **2005**, *4*, 934 – 941.
[19] N. K. Mal, M. Fujiwara, Y. Tanaka, *Nature* **2003**, *421*, 350 – 353.
[20] K. Berg, P. K. Selbo, L. Prasmickaite, A. Hogset, *Curr. Opin. Mol. Ther.* **2004**, *6*, 279 – 287.
[21] H. Ando, T. Furuta, R. Y. Tsien, H. Okamoto, *Nat. Genet.* **2001**, *28*, 317 – 325.
[22] B. Ghosn, F. R. Haselton, K. R. Gee, W. T. Monroe, *Photochem. Photobiol.* **2005**, *81*, 953 – 959.
[23] L. Krock, A. Heckel, *Angew. Chem.* **2005**, *117*, 475 – 477; *Angew. Chem. Int. Ed.* **2005**, *44*, 471 – 473.
[24] S. G. Chaulk, A. M. MacMillan, *Nucleic Acids Res.* **1998**, *26*, 3173 – 3178.
[25] A. Heckel, G. Mayer, *J. Am. Chem. Soc.* **2005**, *127*, 822 – 823.
[26] J. P. Pellois, T. W. Muir, *Angew. Chem.* **2005**, *117*, 5859 – 5863; *Angew. Chem. Int. Ed.* **2005**, *44*, 5713 – 5717.
[27] C. M. McIntosh, E. A. Esposito, A. K. Boal, J. M. Simard, C. T. Martin, V. M. Rotello, *J. Am. Chem. Soc.* **2001**, *123*, 7626 – 7629.
[28] K. K. Sandhu, C. M. McIntosh, J. M. Simard, S. W. Smith, V. M. Rotello, *Bioconjugate Chem.* **2002**, *13*, 3 – 6.
[29] See Supporting Information for details.
[30] D. M. Rothman, M. E. Vazquez, E. M. Vogel, B. Imperiali, *J. Org. Chem.* **2003**, *68*, 6795 – 6798.
[31] R. Hong, N. O. Fischer, A. Verma, C. M. Goodman, T. Emrick, V. M. Rotello, *J. Am. Chem. Soc.* **2004**, *126*, 739 – 743.
[32] J. Olmsted III, D. R. Kearns, *Biochemistry* **1977**, *16*, 3647 – 3654.
[33] D. L. Boger, B. E. Fink, S. R. Brunette, W. C. Tse, M. P. Hedrick, *J. Am. Chem. Soc.* **2001**, *123*, 5878 – 5891.
[34] P. Gong, E. A. Esposito, C. T. Martin, *J. Biol. Chem.* **2004**, *279*, 44277 – 44285.
[35] C. H. Fan, S. Wang, J. W. Hong, G. C. Bazan, K. W. Plaxco, A. J. Heeger, *Proc. Natl. Acad. Sci. USA* **2003**, *100*, 6297 – 6301.
[36] H.-T. Song, J.-S. Choi, Y.-M. Huh, S. Kim, Y.-W. Jun, J.-S. Suh, J. Cheon, *J. Am. Chem. Soc.* **2005**, *127*, 9992 – 9993.
[37] a) O. Zelphati, F. C. Szoka, *Pharm. Res.* **1996**, *13*, 1367 – 1372; b) O. Zelphati, F. C. Szoka, *Proc. Natl. Acad. Sci. USA* **1996**, *93*, 11493 – 11498.

 © 2006 Wiley-VCH Verlag GmbH & Co. KGaA, Weinheim

Molecular Electronics

DOI: 10.1002/anie.200504391

Intramolecular B–N Coordination as a Scaffold for Electron-Transporting Materials: Synthesis and Properties of Boryl-Substituted Thienylthiazoles**

*Atsushi Wakamiya, Takuhiro Taniguchi, and Shigehiro Yamaguchi**

The exploration of new and excellent electron-transporting materials is a current topic in the field of organic electronics, including organic light-emitting diodes (OLEDs) and organic thin-film transistors (OTFTs).[1] A crucial issue in their molecular design is the creation of a π-conjugated framework that has a reasonably high electron affinity as well as a suitable solid-state structure for facilitating an efficient carrier transport. The employment of C=N double-bond-containing N-heteroaromatic rings as building units is a widely accepted and effective design because of their intrinsically high electron affinity. In fact, various types of fascinating materials have already been developed along this line.[2–11] We now disclose a new concept for the further structural and electronic modification of N-heteroaromatic ring-based materials by exploiting the Lewis acidity of the boron atom.[12] Thus, our idea is to incorporate boryl groups at the appropriate positions of a nitrogen-containing π-conjugated framework to allow intramolecular coordination from the Lewis basic nitrogen atom to the boron atom, as shown in Figure 1. This interaction between the Lewis acid and Lewis base would not only constrain the π-conjugated framework in a planar fashion,[13] but would also affect the electronic structure by lowering the LUMO level. Therefore, we have designed the (3-boryl-2-thienyl)-2-thiazole **1** as a key building unit. The use of the thienylthiazole skeleton[14] would allow us to achieve regioselective and stepwise metallations at the 5-positions of the thiazole and thiophene rings in **1**, which would be a significant advantage for synthesizing a wide range of compounds derived from this key skeleton.

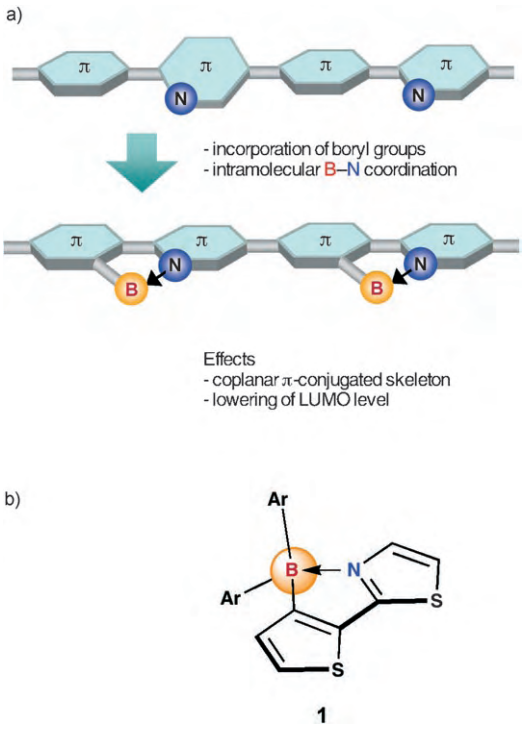

Figure 1. a) Schematic representation of electronic and structural modification of N-heteroaromatic ring-based π-electron systems by intramolecular B–N coordination. b) Boryl-substituted thienylthiazole **1** as a key building unit.

The dimesitylboryl-substituted thienylthiazole **1a** was prepared in 75% yield from (3-bromo-2-thienyl)-2-thiazole by lithiation with *n*BuLi and subsequent treatment with Mes_2BF (Mes = 2,4,6-$Me_3C_6H_2$; Scheme 1). Compound **1a** is stable in air and water and can be purified by column chromatography on silica gel. The X-ray crystal structure analysis of **1a** reveals a B–N bond length of 1.67 Å, thus demonstrating that the intramolecular coordination between the nitrogen atom and the boron atom actually occurs in this skeleton. This coordination constrains the thienylthiazole skeleton in the s-*cis* conformation with a dihedral angle of 7.4°

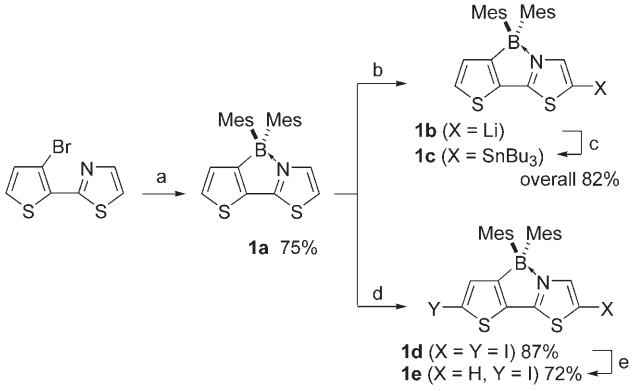

Scheme 1. Reagents and conditions: a) *n*BuLi (1 equiv), diethyl ether, −78 °C, then Mes_2BF; b) *n*BuLi (1 equiv), THF, −78 °C; c) Bu_3SnCl; d) *n*BuLi (2 equiv), THF, −78 °C, then I_2; e) *n*BuLi (1 equiv), THF, −78 °C, then H_2O.

[*] Dr. A. Wakamiya, T. Taniguchi, Prof. Dr. S. Yamaguchi
Department of Chemistry
Graduate School of Science
Nagoya University
Chikusa, Nagoya 464-8602 (Japan)
Fax: (+81) 52-789-5947
E-mail: yamaguchi@chem.nagoya-u.ac.jp

[**] We thank Mr. T. Tanaka, Mr. M. Nishiyama, and Dr. H. Eguchi (TOSOH Co.) for the measurements of TOF carrier mobility. This work was supported by a Grant-in-Aid (No.12CE2005 for Elements Science) from the Ministry of Education, Culture, Sports, Science, and Technology, Japan. A.W. thanks the Mitsubishi Chemical Corporation Fund and TOSOH Award in Synthetic Organic Chemistry.

Supporting information for this article is available on the WWW under http://www.angewandte.org or from the author.

InterScience
© 2006 Wiley-VCH Verlag GmbH & Co. KGaA, Weinheim

between the thiophene plane and thiazole plane (see the Supporting Information).[15]

The functionalization of **1a** was examined as shown in Scheme 1. The monolithiation of **1a** with one equivalent of *n*BuLi proceeded regioselectively at the 5-position of the thiazole ring. The resultant monolithiated derivative **1b** was treated with Bu_3SnCl to give the thiazole-monofunctionalized derivative **1c** in 82% yield. The dilithiation of **1a** was achieved by treatment with two equivalents of *n*BuLi, and subsequent treatment with iodine gave the diiodide derivative **1d** in 87% yield. Additionally, the further monolithiation of **1d** with one equivalent of *n*BuLi proceeded at the 5-position of the thiazole ring, and quenching with water afforded the thiophene-monofunctionalized derivative **1e** in 72% yield.

To demonstrate the utility of these functionalized derivatives as precursors for extended π-electron systems, we synthesized a series of regioisomeric dimers, including the head-to-head (H–H), head-to-tail (H–T), and tail-to-tail (T–T) dimers **2**–**4** (Scheme 2), in which the thiophene ring is

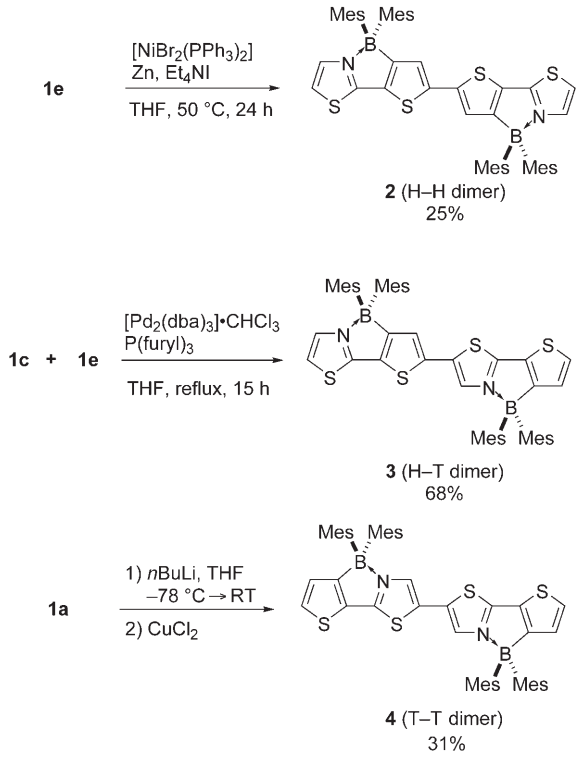

Scheme 2. Synthesis of head-to-head (H–H), head-to-tail (H–T), and tail-to-tail (T–T) dimers **2**–**4**.

denoted as the head and thiazole as the tail. Thus, while the nickel-catalyzed homocoupling of **1e** gave the H–H dimer **2** in 25% yield,[16] the palladium-catalyzed cross-coupling of **1c** and **1e** afforded the H–T dimer **3** in 68% yield.[17] The T–T dimer **4** was obtained in 31% yield by the $CuCl_2$-promoted oxidative coupling of the monolithiated derivative **1b**, which was generated in situ from **1a**.[18]

The photophysical and electrochemical data for the monomer **1a** and dimers **2**–**4** are summarized in Table 1, in which the corresponding data for 2-thienyl-2-thiazole (the parent molecule of **1a** without the boryl group), tris(8-hydroxyquinoline)aluminum (Alq_3), and 2-(4-biphenyl)-5-(4-*tert*-butylphenyl)-1,3,4-oxadiazole (PBD) are included for comparison. While the monomer **1a** displays an absorption band at 333 nm, the dimers **2**–**4** display absorption maximum wavelengths in the range 414–443 nm. The boryl-substituted thienylthiazoles **1a** and **2**–**4** show weak fluorescence emissions in the range 452–492 nm. Electrochemical data were determined by cyclic voltammetry and showed an irreversible reduction wave with a peak potential at $E_{pc} = -2.95$ V for the parent 2-thienyl-2-thiazole. In contrast, boryl-substituted **1a** exhibited a reversible reduction wave, as evident from the areas and proximity of the anodic and cathodic peaks, at a less negative peak potential ($E_{pc} = -2.41$ V). This result demonstrates that the formation of the intramolecular B–N coordination not only decreases the reduction potential but also stabilizes the produced radical anion. In addition, the extension of the π conjugation on going from the monomer **1a** to the dimers **2**–**4** also shifts the reduction potential to more positive values by about 0.3–0.4 V (E_{pc}: **2** −2.00 V, **3** −2.08 V, **4** −2.06 V); however, the regiochemistry of the dimer structure does not significantly affect the reduction potential. Notably, the reduction potentials of the dimers **2**–**4** are less negative than those of Alq_3 ($E_{pc} = -2.36$ V)[19a] and PBD ($E_{pc} = -2.40$ V),[19b] which is indicative of the possible application of **2**–**4** as electron-transporting materials.

Table 1: Photophysical[a] and electrochemical[b] data.

Compound	Absorption λ_{abs} [nm]	log ε	Fluorescence λ_{em} [nm]	Φ_F	CV E_{pc} [V][c]	$E_{1/2}$ [V][c]
2-thienyl-2-thiazole	313	4.15	373	0.11[d]	−2.95	
1a	333	4.11	452	0.09[d]	−2.41	−2.30
2 (H–H)	443	4.42	492	0.06[e]	−2.00	−1.94
3 (H–T)	427	4.55	486	0.07[e]	−2.08	−2.00
4 (T–T)	414	4.51	472	0.09[e]	−2.06	−1.99
Alq_3					−2.36[f]	
PBD					−2.40[g]	−2.37[g]

[a] In THF. [b] In THF with $Bu_4N^+PF_6^-$ at a scan rate of 100 mV s^{-1}. [c] Potentials vs. ferrocene/ferrocenium. [d] Determined with quinine sulfate as a standard. [e] Determined with perylene as a standard. [f] Ref. [19a] (determined under conditions similar to those described above). [g] Ref. [19b] (determined in *N*-methylpyrrolidine with $Bu_4N^+BF_4^-$). CV = cyclic voltammetry.

We conducted density functional theory (DFT) calculations (B3LYP/6-31G(d) level) on the H–H dimer **2** and its parent analogue, the thienylthiazole dimer **5**. Boryl-substituted **2** has a lower-lying LUMO (by 0.33 eV) than that of **5**. Notably, while both of these compounds have a similar LUMO shape over the entire π-conjugated framework, a difference is observed in their electrostatic-potential maps (Figure 2). In the skeleton of **2**, the thiazole moiety is clearly electronically more positive than the thiophene moiety, thus demonstrating that the B–N coordination enhances the electron-accepting nature of the thiazole ring.

X-ray crystallographic analyses on **2**–**4** revealed that all the dimers have highly π-conjugated coplanar frameworks, each with a dihedral angle of 0° between the monomer units, thus indicative of effective π conjugation extended through

 © 2006 Wiley-VCH Verlag GmbH & Co. KGaA, Weinheim

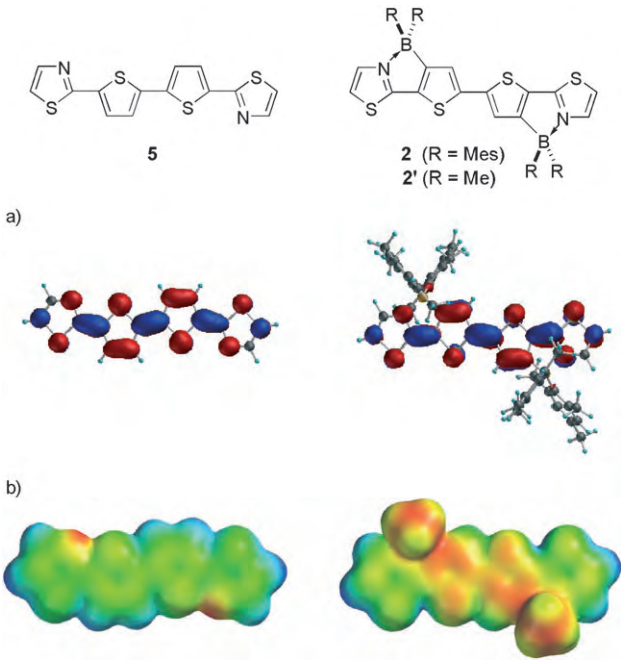

Figure 2. Comparison of electronic structure between **2** and its parent analogue **5**: a) Pictographic drawings of LUMOs and b) electrostatic-potential maps, in which a dimethylboryl analogue **2′** is employed as a model of **2**, clearly show the difference in the electrostatic nature between the thiazole and thiophene rings in **2′**.

the dimer skeletons. The H–H dimer **2** forms an interesting π-stacking structure (Figure 3).[15] In this structure, the molecules are arranged in an offset face-to-face π-stacking array with an interplanar distance of 3.60 Å, such that the thiophene moiety and the thiazole moiety are facing each other (Figure 3a). The intermolecular electrostatic interaction might be partly responsible for the formation of this packing structure since the thiophene and the thiazole moieties in the skeleton of **2** can be regarded as electron-donating and electron-accepting moieties, respectively. In conjunction with this solid-state structure, it is noteworthy that **2** has a relatively high electron mobility of $\mu = 1.5 \times 10^{-4}\ cm^2\,V^{-1}\,s^{-1}$,[20] while this compound did not show any hole-transporting ability, according to a preliminary time-of-flight (TOF) carrier-mobility measurement on its vacuum-deposited film.

In summary, the boryl-substituted thienylthiazole **1a** was designed and synthesized as a new building unit for electron-transporting materials. On the basis of the regioselective functionalization of **1a**, a series of regioisomeric dimers was also prepared. The studies of their structures and properties showed that the intramolecular B–N coordination effectively fixes the π-conjugated framework in a planar fashion and substantially affects the electronic structure through an increase in the electron affinity. These results clearly demonstrate the potential of this molecular design for electron-transporting materials. Importantly, the present concept is simple and general, and should be applicable to other N-heteroaromatic ring-based π-electron systems. Further development of new n-type semiconducting materials along this line is now in progress.

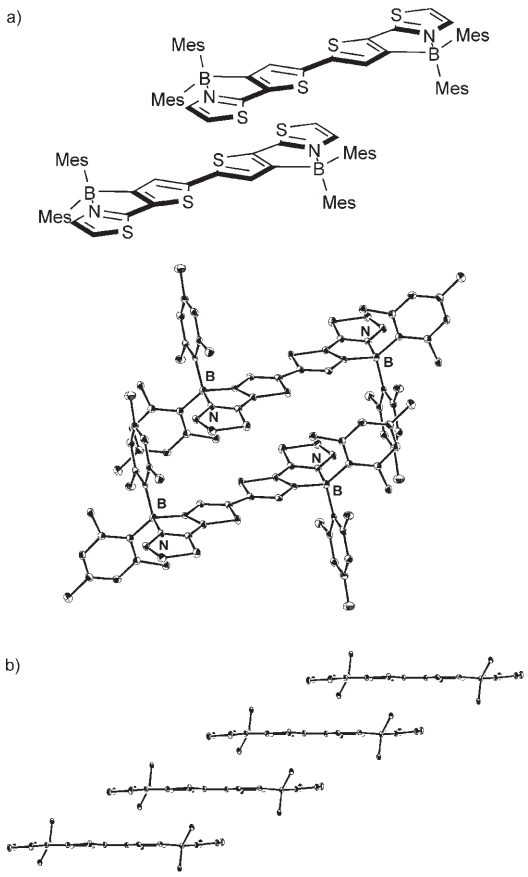

Figure 3. a) Structural formula and perspective view of the crystal packing in **2** and b) side view of the one-dimensional π stacking in **2**. Hydrogen atoms are omitted for clarity, and only the *ipso*-carbon atom from each mesityl group is shown in (b).

Experimental Section

Full experimental details and analytical data can be found in the Supporting Information.

1a: A solution of *n*BuLi (16.8 mL, 1.60 M in hexane, 26.9 mmol) was added dropwise to a solution of (3-bromo-2-thienyl)-2-thiazole (6.61 g, 26.9 mmol) in diethyl ether (150 mL) at −78 °C. After the mixture was stirred at −78 °C for 1.5 h, a solution of dimesitylfluoroborane (7.27 g, 26.9 mmol) in diethyl ether (50 mL) was added to the mixture by cannula. The reaction mixture was gradually warmed to room temperature and stirred for 4 h. The solvent was removed under reduced pressure, and the mixture was purified by silica gel column chromatography (CH_2Cl_2, $R_f = 0.53$). Recrystallization from a mixed solvent of CH_2Cl_2/hexane gave 8.36 g (20.1 mmol) of **1a** as pale yellow crystals in 75 % yield. M.p. 233–235 °C; ^{1}H NMR (270 MHz, $CDCl_3$): $\delta = 7.69$ (d, $J_{HH} = 5.2$ Hz, 1H), 7.46 (d, $J_{HH} = 6.8$ Hz, 1H), 7.25 (d, $J_{HH} = 6.8$ Hz, 1H), 6.99 (d, $J_{HH} = 5.2$ Hz, 1H), 6.67 (s, 4H), 2.21 (s, 6H), 1.88 ppm (s, 12H); ^{13}C NMR (100 MHz, $CDCl_3$): $\delta =$ 166.6, 139.9, 137.2, 134.0, 133.3, 130.7, 129.4, 129.1, 116.3, 24.3, 20.8 ppm (two peaks for the boron-bound carbon atoms are not observed as a result of quadrupolar relaxation); ^{11}B NMR (128 MHz, $CDCl_3$): $\delta = 3.52$ ppm; EI-MS: *m*/*z*: 415 [M^+]. Elemental analysis calcd (%) for $C_{25}H_{26}BNS_2$: C 72.28, H 6.31, N 3.37; found: C 72.26, H 6.25, N, 3.28.

Received: December 10, 2005
Published online: March 29, 2006

 © 2006 Wiley-VCH Verlag GmbH & Co. KGaA, Weinheim

Keywords: boron · conjugation · cyclic voltammetry · electron transport · heterocycles

[1] For recent reviews, see: a) G. Hughes, M. R. Bryce, *J. Mater. Chem.* **2005**, *15*, 94; b) A. P. Kulkarni, C. J. Tonzola, A. Babel, S. A. Jenekhe, *Chem. Mater.* **2004**, *16*, 4556; c) C. R. Newman, C. D. Frisbie, D. A. da Silva Filho, J.-L. Brédas, P. C. Ewbank, K. R. Mann, *Chem. Mater.* **2004**, *16*, 4436; d) C. D. Dimitrakopoulos, P. R. L. Malenfant, *Adv. Mater.* **2002**, *14*, 99.

[2] a) C. Adachi, T. Tsutsui, S. Saito, *Appl. Phys. Lett.* **1989**, *55*, 1489; b) M. Meier, E. Buchwald, S. Karg, P. Pösch, M. Greczmiel, P. Strohriegl, W. Rieß, *Synth. Met.* **1996**, *76*, 95; c) J. Bettenhausen, P. Strohriegl, *Adv. Mater.* **1996**, *8*, 507; d) N. Tamoto, C. Adachi, K. Nagai, *Chem. Mater.* **1997**, *9*, 1077; e) Z. Peng, Z. Bao, M. E. Galvin, *Adv. Mater.* **1998**, *10*, 680; f) H.-C. Yeh, R.-H. Lee, L.-H. Chan, T.-Y. J. Lin, C.-T. Chen, E. Balasubramaniam, Y.-T. Tao, *Chem. Mater.* **2001**, *13*, 2788; g) C. Wang, G.-Y. Jung, Y. Hua, C. Pearson, M. R. Bryce, M. C. Petty, A. S. Batsanov, A. E. Goeta, J. A. K. Howard, *Chem. Mater.* **2001**, *13*, 1167.

[3] a) J. Kido, C. Ohtaki, K. Hongawa, K. Okuyama, K. Nagai, *Jpn. J. Appl. Phys.* **1993**, *32*, L917; b) M. Strukelj, F. Papadimitrakopoulos, T. M. Miller, L. J. Rothberg, *Science*, **1995**, *267*, 1969; c) M. Strukelj, T. M. Miller, F. Papadimitrakopoulos, S. Son, *J. Am. Chem. Soc.* **1995**, *117*, 11976.

[4] a) S. E. Tunney, J. Suenaga, J. K. Stille, *Macromolecules* **1983**, *16*, 1398; b) T. Kanbara, N. Saito, T. Yamamoto, K. Kubota, *Macromolecules* **1991**, *24*, 5883; c) T. Kanbara, T. Yamamoto, *Macromolecules* **1993**, *26*, 3464; d) J. Bettenhausen, M. Greczmiel, M. Jandke, P. Strohriegl, *Synth. Met.* **1997**, *91*, 223; e) M. Jandke, P. Strohriegl, S. Berleb, E. Werner, W. Brütting, *Macromolecules* **1998**, *31*, 6434; f) C. J. Tonzola, M. M. Alam, S. A. Jenekhe, *Adv. Mater.* **2002**, *14*, 1086; g) Y. Zhu, M. M. Alam, S. A. Jenekhe, *Macromolecules* **2003**, *36*, 8958.

[5] a) T. Yamamoto, T. Maruyama, Z. Zhou, T. Ito, T. Fukuda, Y. Yoneda, F. Begum, T. Ikeda, S. Sasaki, H. Takezoe, A. Fukuda, K. Kuboda, *J. Am. Chem. Soc.* **1994**, *116*, 4832; b) C. Wang, M. Kilitziraki, J. A. H. MacBride, M. R. Bryce, L. E. Horsburgh, A. K. Sheridan, A. P. Monkman, I. D. W. Samuel, *Adv. Mater.* **2000**, *12*, 217.

[6] J. A. Osaheni, S. A. Jenekhe, *Chem. Mater.* **1992**, *4*, 1282.

[7] T. Kanbara, T. Yamamoto, *Chem. Lett.* **1993**, 419.

[8] a) Y. Saitoh, T. Yamamoto, *Chem. Lett.* **1995**, 785; b) S. Naka, H. Okada, H. Onnagawa, T. Tsutsui, *Appl. Phys. Lett.* **2000**, *76*, 197.

[9] a) R. Fink, C. Frenz, M. Thelakkat, H.-W. Schmidt, *Macromolecules* **1997**, *30*, 8177; b) R. Fink, Y. Heischkel, M. Thelakkat, H.-W. Schmidt, C. Jonda, M. Hüppauff, *Chem. Mater.* **1998**, *10*, 3620.

[10] C. J. Tonzola, M. M. Alam, W. Kaminsky, S. A. Jenekhe, *J. Am. Chem. Soc.* **2003**, *125*, 13548.

[11] a) K. Tamao, M. Uchida, T. Izumizawa, K. Furukawa, S. Yamaguchi, *J. Am. Chem. Soc.* **1996**, *118*, 11974; b) M. Uchida, T. Izumizawa, T. Nakano, S. Yamaguchi, K. Tamao, K. Furukawa, *Chem. Mater.* **2001**, *13*, 2680.

[12] For recent reviews of organoboron materials, see: a) C. D. Entwistle, T. B. Marder, *Chem. Mater.* **2004**, *16*, 4574; b) C. D. Entwistle, T. B. Marder, *Angew. Chem.* **2002**, *114*, 3051; *Angew. Chem. Int. Ed.* **2002**, *41*, 2927.

[13] For planarization using intramolecular hydrogen bonding, see: A. P. Monkman, L.-O. Pålsson, R. W. T. Higgins, C. Wang, M. R. Bryce, A. S. Batsanov, J. A. K. Howard, *J. Am. Chem. Soc.* **2002**, *124*, 6049.

[14] For thienylthiazole-based π-electron systems, see, for example: a) I. H. Jenkins, P. G. Pickup, *Macromolecules* **1993**, *26*, 4450; b) U. Mitschke, E. M. Osteritz, T. Debaerdemaeker, M. Sokolowski, P. Bäuerle, *Chem. Eur. J.* **1998**, *4*, 2211; c) U. Mitschke, T. Debaerdemaeker, P. Bäuerle, *Eur. J. Org. Chem.* **2000**, 425; d) X. M. Hong, H. E. Katz, A. J. Lovinger, B.-C. Wang, K. Raghavachari, *Chem. Mater.* **2001**, *13*, 4686; e) M.-K. Ng, L. Yu, *Angew. Chem.* **2002**, *114*, 3750; *Angew. Chem. Int. Ed.* **2002**, *41*, 3598; f) M.-K. Ng, D.-C. Lee, L. Yu, *J. Am. Chem. Soc.* **2002**, *124*, 11862; g) J. Cao, J. W. Kampf, M. D. Curtis, *Chem. Mater.* **2003**, *15*, 404; h) J. Cao, M. D. Curtis, *Chem. Mater.* **2003**, *15*, 4424; i) T. Yamamoto, M. Arai, H. Kokubo, S. Sasaki, *Macromolecules* **2003**, *36*, 7986; j) P. Jiang, G. M. Morales, W. You, L. Yu, *Angew. Chem.* **2004**, *116*, 4571; *Angew. Chem. Int. Ed.* **2004**, *43*, 4471; k) M. D. Curtis, J. Cao, J. W. Kampf, *J. Am. Chem. Soc.* **2004**, *126*, 4318; l) J. Lee, B.-J. Jung, S. K. Lee, J.-I. Lee, H.-J. Cho, H.-K. Shim, *J. Polym. Sci. Part A* **2005**, *43*, 1845; m) S. Ando, R. Murakami, J. Nishida, H. Tada, Y. Inoue, S. Tokito, Y. Yamashita, *J. Am. Chem. Soc.* **2005**, *127*, 14996.

[15] Crystal data for **1a**: $C_{25}H_{26}BNS_2$, $M_r = 415.40$, crystal dimensions $0.20 \times 0.20 \times 0.20$ mm^3, triclinic, space group $P\bar{1}$, $a = 8.1921(18)$, $b = 10.118(2)$, $c = 13.205(3)$ Å, $\alpha = 90.093(5)$, $\beta = 91.356(5)$, $\gamma = 90.159(5)°$, $V = 1094.3(4)$ Å^3, $Z = 2$, $\rho_{calcd} = 1.261$ g cm^{-3}, $\lambda(Mo_{K\alpha}) = 0.71070$ Å, $T = 173(2)$ K, $2\theta_{max} = 50.0°$, 7314 measured reflections, 3775 independent reflections ($R_{int} = 0.0199$), $R_1 = 0.0406$, $wR_2 = 0.1026$ ($I > 2\sigma(I)$), GOF = 1.043. Crystal data for **2**: $C_{50}H_{50}B_2N_2S_4$, $M_r = 828.78$, crystal dimensions $0.20 \times 0.10 \times 0.10$ mm^3, monoclinic, space group $P2_1/c$, $a = 7.8642(15)$, $b = 15.824(3)$, $c = 17.361(3)$ Å, $\beta = 100.0793(9)°$, $V = 2127.2(7)$ Å^3, $Z = 2$, $\rho_{calcd} = 1.294$ g cm^{-3}, $\lambda(Mo_{K\alpha}) = 0.71070$ Å, $T = 100(2)$ K, $2\theta_{max} = 50.0°$, 14103 measured reflections, 3715 independent reflections ($R_{int} = 0.0333$), $R_1 = 0.0412$, $wR_2 = 0.0956$ ($I > 2\sigma(I)$), GOF = 1.073. Crystal data for **4**: see the Supporting Information. CCDC-292025 (**1a**), CCDC-292026 (**2**), and CCDC-292027 (**4**) contain the supplementary crystallographic data for this paper. These data can be obtained free of charge from The Cambridge Crystallographic Data Centre via www.ccdc.cam.ac.uk/data_request/cif.

[16] M. Iyoda, H. Otsuka, K. Sato, N. Nisato, M. Oda, *Bull. Chem. Soc. Jpn.* **1990**, *63*, 80.

[17] V. Farina, B. Krishnan, *J. Am. Chem. Soc.* **1991**, *113*, 9585.

[18] a) T. Kauffmann, *Angew. Chem.* **1974**, *86*, 321; *Angew. Chem. Int. Ed. Engl.* **1974**, *13*, 291; b) J. Kagan, K. Arora, *Heterocycles* **1983**, *20*, 1937.

[19] a) Y. Sakamoto, T. Suzuki, A. Miura, H. Fujikawa, S. Tokito, Y. Taga, *J. Am. Chem. Soc.* **2000**, *122*, 1832; b) S. Janietz, A. Wedel, *Adv. Mater.* **1997**, *9*, 403.

[20] For comparison, reported electron mobilities for the representative materials by means of TOF measurements: Alq_3 ($\mu = \approx 1 \times 10^{-5}$ cm^2 V^{-1} s^{-1}),[20a] PBD ($\mu = 1.9 \times 10^{-5}$ cm^2 V^{-1} s^{-1}),[20b] silole derivatives ($\mu \approx 2 \times 10^{-4}$ cm^2 V^{-1} s^{-1}),[20c] 1,10-phenanthroline ($\mu = 5.2 \times 10^{-4}$ cm^2 V^{-1} s^{-1}),[8b] and ter(9,9-diarylfluorene)s ($\mu \approx 1.2 \times 10^{-3}$ cm^2 V^{-1} s^{-1});[20d] see: a) S. Barth, P. Müller, H. Riel, P. F. Seidler, W. Rieß, H. Vestweber, H. Bässler, *J. Appl. Phys.* **2001**, *89*, 3711; b) T. Yasuda, Y. Yamaguchi, D.-C. Zou, T. Tsutsui, *Jpn. J. Appl. Phys.* **2002**, *41*, 5626; c) H. Murata, G. G. Malliaras, M. Uchida, Y. Shen, Z. H. Kafafi, *Chem. Phys. Lett.* **2001**, *339*, 161; d) C.-C. Wu, T.-L. Liu, W.-Y. Hung, Y.-T. Lin, K.-T. Wong, R.-T. Chen, Y.-M. Chen, Y.-Y. Chien, *J. Am. Chem. Soc.* **2003**, *125*, 3710.

 © 2006 Wiley-VCH Verlag GmbH & Co. KGaA, Weinheim

Fluorescence Spectroscopy

DOI: 10.1002/anie.200600125

Broadband Femtosecond Fluorescence Spectroscopy of $[Ru(bpy)_3]^{2+}$**

*Andrea Cannizzo, Frank van Mourik, Wojciech Gawelda, Goran Zgrablic, Christian Bressler, and Majed Chergui**

The excited-state dynamics of metal–polypyridine complexes are of great importance in applications as diverse as solar-energy conversion[1–3] and information storage[4] because they can be photo- and redox-triggered. Ruthenium trisbipyridine ($[Ru(bpy)_3]^{2+}$) is the prototype for this class of complexes, the study of which has formed the basis for most photochemical applications. These complexes exhibit transitions due to charge transfer between the metal-centered d orbital and the ligand π orbital, commonly known as metal-to-ligand charge transfer (MLCT). Femtosecond transient-absorption studies on $[Ru(bpy)_3]^{2+}$ have shown that upon excitation of the singlet ^{1}MLCT state (absorption maximum 450 nm), ultrafast intersystem crossing (ISC) occurs in < 100 fs, leading to the formation of the triplet ^{3}MLCT state with near-unity quantum yield.[5,6] From 300 fs onwards, the transient-absorption spectrum remains unchanged.[5] The ^{3}MLCT state decays radiatively to the ground state with a lifetime of ≈ 600 ns in aqueous solution at room temperature.[2,3,7] However, the issue of energy disposal and vibrational relaxation within the complex is still a subject of debate. Indeed, a 400-nm excitation corresponds to an excess energy of ≈ 8500 cm^{-1} above the vibrationally relaxed ^{3}MLCT state,[8] which would be dissipated in ≈ 300 fs, according to the literature.[5,6]

To address this issue, Bhasikuttan et al.[9] carried out a fluorescence-upconversion study at single wavelengths that correspond to those at which the ^{1}MLCT (500 and 575 nm) and the ^{3}MLCT (620 nm) emissions are expected. Their results were interpreted in terms of fast ISC to the ^{3}MLCT state followed by vibrational cooling on a timescale of 0.6 to 1 ps. The emission by the ^{3}MLCT state could not be observed in their experiment owing to its low radiative rate. However, single-wavelength detection does not produce a complete picture of the relaxation dynamics. Consequently, Browne et al.[10] implemented a picosecond broadband detection technique and observed an emission band centered at 520 nm, which they attributed to the ^{1}MLCT state. Unfortunately, they could not capture the details of the relaxation dynamics within the ^{3}MLCT state with the time resolution (≈3 ps) used.

Herein we report for the first time a polychromatic femtosecond fluorescence-upconversion experiment in the 440–690 nm range, with a resolution of 110 ± 10 fs to capture the early relaxation processes leading to the steady-state emission of the ^{3}MLCT state of $[Ru(bpy)_3]^{2+}$. The experimental procedure and the data analysis are explained in reference [11] and in the Supporting Information.

Figure 1a shows a typical 2D spectrum obtained upon excitation at 400 nm (25000 cm^{-1}). The spot at ≈ 21600 cm^{-1} is the Raman line of water. Although fluorescence in the 15000–20000-cm^{-1} region was present at $t = 0$, it was very short-lived, converging within 200 fs to a weak emission in the 16000–17500-cm^{-1} (575–680 nm) region. Spectra at fixed

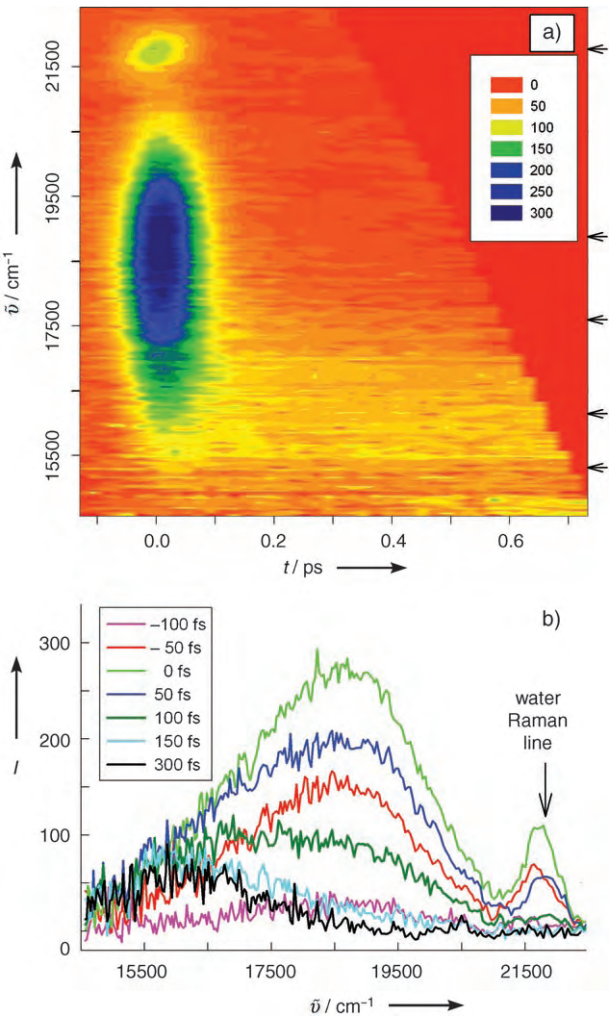

Figure 1. a) 2D time-resolved luminescence spectrum of aqueous $[Ru(bpy)_3]^{2+}$ under excitation at 25000 cm^{-1} (intensities (0–300) in arbitrary units). The red area on the right is due to GVD (group velocity dispersion) correction (see Supporting Information). The signal at ≈ 21600 cm^{-1} is the Raman line of water. Arrows indicate the wavelengths corresponding to the kinetic traces in Figure 2. b) Luminescence spectra recorded at different time delays.

[*] Dr. A. Cannizzo, Dr. F. van Mourik, W. Gawelda, G. Zgrablic, Prof. Dr. C. Bressler, Prof. Dr. M. Chergui
Laboratoire de Spectroscopie Ultrarapide, ISIC, FSB-BSP
Ecole Polytechnique Fédérale de Lausanne
EPFL SB ISIC LSU, Ch-1015 Lausanne-Dorigny (Switzerland)
Fax: (+41) 21-693-0422
E-mail: majed.chergui@epfl.ch

[**] This work was supported by the Swiss NSF via the NCCR: Quantum Photonics.

Supporting information for this article is available on the WWW under http://www.angewandte.org or from the author.

InterScience
© 2006 Wiley-VCH Verlag GmbH & Co. KGaA, Weinheim

time delays (Figure 1b) allow us to follow the evolution of the luminescence. Between $t=-50$ and $+50$ fs, the spectrum is centered at 19230 cm^{-1} (520 nm). At $t>50$ fs, the band displays a red shift with time, while a shoulder appears at about 16500 cm^{-1}. By 200 fs, the 19230-cm^{-1} band has disappeared, leaving only the red wing, which is centered at the same energy (16100 cm^{-1}) as the steady-state ^{3}MLCT emission. The band has a slight broadening on its blue wing, which disappears within 300 fs (see Supporting Information), and the width of this band then remains unchanged for longer time delays, as checked by a scan of t up to 250 ps. As the broadening seems to affect only the blue wing, it is most probably due to a remnant of the ^{1}MLCT fluorescence.

Characteristic kinetic traces at fixed emission wavelengths are shown in Figure 2. It is clear that the fluorescence rises

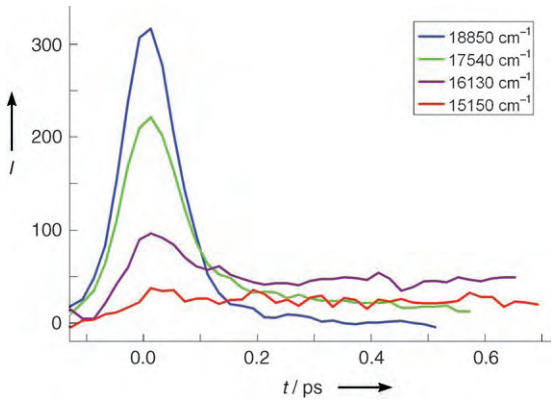

Figure 2. Time traces at different wavelengths after 25000-cm^{-1} pulsed excitation. Time delays were taken with respect to the water Raman line (Figure 1a).

and decays within the cross-correlation time of our experiment ($\approx$110 fs). In fact, by convoluting with the latter, fits of the kinetic traces that correspond to the range of the ^{1}MLCT emission suggest a decay time of 15 ± 10 fs for the singlet state, which is significantly shorter than the ultrafast decays reported in previous transient-absorption[5] and femtosecond fluorescence-upconversion experiments.[9] As the detection is tuned towards red wavelengths, the initial peak disappears, and the background signal rises. The latter eventually appears distinctly at the extreme-red wavelength of 660 nm (15150 cm^{-1}). It remained constant over the longest time delay of our experiment and is evidently due to the ^{3}MLCT emission. The rise of the extreme-red signal corresponds to the excitation pulse width, thus implying a population time of the ^{3}MLCT state of at most a few tenths of a femtosecond.

The above results show a number of remarkable features: a) The ^{1}MLCT fluorescence appears to undergo a Stokes shift of $\approx$0.74 eV at $t=0$; b) the ^{3}MLCT state is populated at a time delay that is within the resolution of our experiment ($\approx$110 fs); c) the shape of the emission band of the ^{3}MLCT state resembles that of the steady-state emission from 200–300 fs onwards, that is, there seems to be no hint of a vibrationally hot emission, which would manifest itself in a broadening of the emission band. This finding contradicts that of reference [9], which reported a 0.6–1-ps vibrational-relaxation time in the ^{3}MLCT state from kinetic traces at 620 nm. However, as these results were extracted after the subtraction of the background signal, we believe that errors may have been introduced into the treatment of the data. Furthermore, the authors used a laser with a repetition period that was much shorter than the lifetime of the ^{3}MLCT state, which would cause buildup effects. This is not the case herein, as the kinetic trace at $\approx$16000 cm^{-1} (620 nm) can be fitted easily with a sharply rising and decreasing component, which is identical to the signal at 18900 cm^{-1} (530 nm), superimposed on the purely rising background signal, which is identical to that at 15150 cm^{-1} (Figure 2).

Concerning point a) above, the $t=0$ Stokes shift can be interpreted in terms of vibrationally hot ^{1}MLCT emissions. Indeed, the ^{1}MLCT absorption band is dominated by a progression of the skeletal mode at 1607 cm^{-1} of the bpy ligands in the $^2A'_2$ electronic state,[12] with a Huang–Rhys factor of 0.74 (see Supporting Information). A 400-nm pulse mainly excites the $v=2$ level of this Franck–Condon active mode. Consequently, the emission will stem from this level, giving rise to a Franck–Condon distribution of a vibrationally hot state. This is shown in Figure 3, in which the $t=0$ spectrum

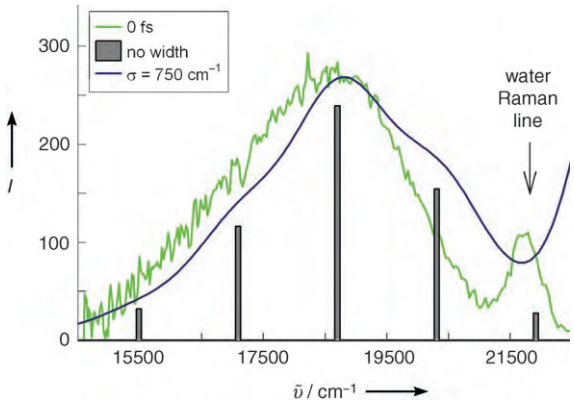

Figure 3. Comparison of the emission spectrum at $t=0$ (green line) with the simulated hot emission from the $v=2$ vibrational level of the ^{1}MLCT state to the ground state (see Supporting Information). The bars show the distribution of emission probabilities (final levels $v''=2$–6), and the solid blue line is the simulated spectrum, assuming that the bandwidth of the individual vibronic lines are the same as that in the fit of the absorption band.

is compared with a simulated spectrum that was obtained from the calculated intensities from the Franck–Condon factors of the harmonic potential associated with the 1607-cm^{-1} mode, with the v^3 dependence of the emission taken into account. In the region of interest, the spectrum exhibits two maxima, one on either side of the $0\rightarrow0$ transition at $\approx$22000 cm^{-1}. As our filter excludes wavenumbers $\geq$22200 cm^{-1} (450 nm), the higher-frequency maximum is not visible. The good agreement of experiment with simulation (Figure 3) allows us to attribute the 19200-cm^{-1} band to the vibrationally hot and short-lived emission of the ^{1}MLCT state. The rationale of this result is that the ^{1}MLCT state undergoes ISC to the ^{3}MLCT state at constant energy (i.e. in a "horizontal" process).

 © 2006 Wiley-VCH Verlag GmbH & Co. KGaA, Weinheim

A related and remarkable observation is that the ^{3}MLCT state is formed in 15 ± 10 fs with an emission lineshape that is identical to that of the vibrationally relaxed state. For an ISC, this timescale is unusual as it corresponds to the vibrational period of a high-frequency mode (incidentally, the 1607-cm^{-1} mode period lies in this range), which would point to a strongly nonadiabatic process. This effect, however, is not observed in the fit of the absorption[12] and emission[8] bands with the 1607-cm^{-1} mode. Rather, the latter results from electron injection into the bpy ligands, and the occurrence of the 1607-cm^{-1} mode in the absorption spectrum (see Supporting Information) suggests that the electron is already localized on a single ligand. A large spin-orbit coupling constant could account for the very efficient ISC, and the calculated value of ≈ 1200 cm^{-1} for the 4d electrons of Ru[13] is of the right order of magnitude.

The dissipation of ≈ 8500 cm^{-1} of energy in less than 300 fs within the manifold electronic and vibrational levels of the ^{3}MLCT state is unlikely to occur by transfer to the solvent. Rather, we believe that ultrafast intramolecular vibrational-energy redistribution (IVR) transfers the energy stored in the high-frequency modes to the low-frequency modes. Such an impulsive IVR has been reported for the case of bacteriorhodopsin, in which the high-frequency skeletal (C=C and C–C) and hydrogen out-of-plane (HOOP) modes, in the 1000–1500-cm^{-1} range of frequencies, decay in ≈ 200 fs, thus giving rise to low-frequency torsional modes[14,15] of the order of 150 cm^{-1}. The steady-state ^{3}MLCT emission band has a width of ≈ 3500–4000 cm^{-1} and is, like the absorption lineshape, nicely fitted with a progression of the 1607-cm^{-1} mode.[8] However, important activity of the low-frequency metal–ligand modes between 100 and 500 cm^{-1} is observed at low temperatures.[16] Under these circumstances, if energy redistribution to the low-frequency modes is very rapid, their contribution to the total linewidth is likely to be negligible, and the ^{3}MLCT state will not show broadening at early times, in agreement with our observations.

Experimental Section

The experimental setup is described in detail in reference [11]. Briefly, the sample was excited by 400-nm pulses (typical width 40 fs, power 80 μJ/pulse, focal spot 50 μm (FWHM), repetition rate 250 Hz). The luminescence, collected in forward-scattering geometry, was upconverted in a 250-μm thick β-barium borate (BBO) crystal by mixing with a gate pulse at 800 nm. The upconverted signal was spatially filtered and detected with a spectrograph and a liquid-N_2-cooled charge-coupled device (CCD) camera in polychromatic mode.[1] Schott filters GG420 and UG-11 (Schott Glass Technologies, Mainz, Germany) were used to attenuate the remaining 400- and 800-nm light. This greatly improved the signal-to-noise ratio but limited the detectable spectral range to the 440–690-nm region. The upconverted Raman line of water was used to determine $t = 0$ in situ (Figure 1). See Supporting Information for details.

Received: January 11, 2006
Published online: April 4, 2006

Keywords: charge transfer · fluorescence · hot emission · intersystem crossing · ruthenium

[1] K. Kalyanasundaram, *Coord. Chem. Rev.* **1982**, *46*, 159.
[2] V. Balzani, A. Juris, M. Venturi, S. Campagna, S. Serroni, *Chem. Rev.* **1996**, *96*, 759.
[3] V. Balzani, S. Campagna, G. Denti, A. Juris, S. Serroni, M. Venturi, *Acc. Chem. Res.* **1998**, *31*, 26.
[4] V. Balzani, L. de Cola (eds.), *Supramolecular Chemistry*, Kluwer Academic, Dordrecht, **1992**.
[5] N. H. Damrauer, G. Cerullo, A. Yeh, T. R. Boussie, C. V. Shank, J. K. McCusker, *Science* **1997**, *275*, 54.
[6] A. T. Yeh, C. V. Shank, J. K. McCusker, *Science* **2000**, *289*, 935.
[7] V. Balzani, N. Sabbatini, F. Scandola, *Chem. Rev.* **1986**, *86*, 319.
[8] P. Hartmann, M. J. P. Leiner, S. Draxler, M. E. Lippitsch, *Chem. Phys.* **1996**, *207*, 137.
[9] A. C. Bhasikuttan, M. Suzuki, S. Nakashima, T. Okada, *J. Am. Chem. Soc.* **2002**, *124*, 8398.
[10] W. R. Browne, C. G. Coates, C. Brady, P. Matousek, M. Towrie, S. W. Botchway, A. W. Parker, J. G. Vos, J. J. McGarvey, *J. Am. Chem. Soc.* **2003**, *125*, 1706.
[11] G. Zgrablic, K. Voitchovsky, M. Kindermann, S. Haacke, M. Chergui, *Biophys. J.* **2005**, *88*, 2779.
[12] T. Schonherr, J. Degen, E. Gallhuber, G. Hensler, H. Yersin, *Chem. Phys. Lett.* **1989**, *158*, 519.
[13] W. Gawelda, M. Johnson, F. M. F. de Groot, R. Abela, C. Bressler, M. Chergui, *J. Am. Chem. Soc.*, in press.
[14] T. Kobayashi, T. Saito, H. Ohtani, *Nature* **2001**, *414*, 531.
[15] D. W. McCamant, P. Kukura, R. A. Mathies, *J. Phys. Chem. B* **2005**, *109*, 10449.
[16] H. Yersin, W. Humbs, J. Strasser, *Coord. Chem. Rev.* **1997**, *159*, 325.

 © 2006 Wiley-VCH Verlag GmbH & Co. KGaA, Weinheim

Host–Guest Chemistry

DOI: 10.1002/anie.200600336

Precise Facial Control in Threading Guests into a Molecular Cage and the Formation of a Turtlelike Supramolecular Complex**

*Chi-Feng Lin, Yi-Hung Liu, Chien-Chen Lai, Shie-Ming Peng, and Sheng-Hsien Chiu**

The synthesis of functional interlocked molecules continues to attract attention because these machinelike molecules[1] have potential applicability in mesoscale molecular electronic

[*] C.-F. Lin, Y.-H. Liu, Prof. S.-M. Peng, Prof. S.-H. Chiu
Department of Chemistry
National Taiwan University
No. 1, Sec. 4, Roosevelt Road, Taipei (Taiwan)
Fax: (+886) 2-3366-1677
E-mail: shchiu@ntu.edu.tw
Prof. C.-C. Lai
Department of Medical Genetics and Medical Research
China Medical University Hospital
Taichung (Taiwan)

[**] This study was supported by the National Science Council, Taiwan (NSC-94-2113M-002-011 and NSC-94-2752M-002-002-PAE).

Supporting information for this article is available on the WWW under http://www.angewandte.org or from the author.

WILEY InterScience DISCOVER SOMETHING GREAT

© 2006 Wiley-VCH Verlag GmbH & Co. KGaA, Weinheim

devices.[2] On the other hand, some interlocked molecules are of considerable interest not for their specific function but as synthetic challenges or for their aesthetic appeal.[3] Although many different macrocycles, including crown ethers,[4] cyclophanes,[5] and cyclodextrins,[6] have been used for the construction of a range of interlocked molecules, their molecular structures are quite similar in that they present only two open faces for guest penetration. In contrast, molecular cages[7] containing internal voids may possess more than two openings for the threading of rodlike components. Conceptually, different [2]pseudorotaxane complexes can be generated from a cubic molecular cage[8] by threading the guest species through its different faces, but such supramolecular systems have not been constructed previously, possibly because of synthetic difficulties (e.g., the number of macrocyclization reactions required) and the less-predictable nature of guest complexation by the host.

Recently, we demonstrated that molecular cage **1** forms an extremely stable supramolecular complex with the dimethyldiazapyrenium (DMDAP) ion (Scheme 1).[9] Herein, we

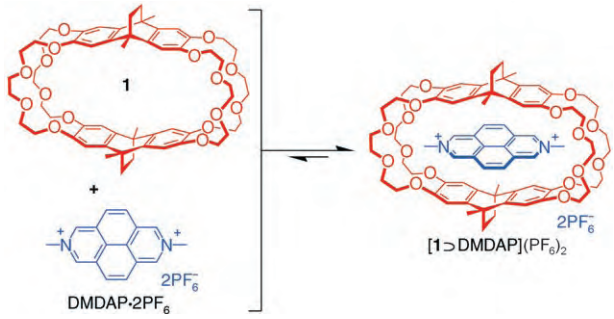

Scheme 1. Complexation of molecular cage **1** with DMDAP.

report that two different thread components are capable of selectively penetrating **1** through its two different sets of open faces (namely, the 24-[10] and 34-membered rings, respectively) to result in two different [2]pseudorotaxane-like complexes. The mixture of these two thread components and **1** represents a new type of molecular machinery; the two thread components alternate between their corresponding [2]pseudorotaxane complexes upon threading through the different faces of the molecular cage under the control of K^+ ions. A small tetrasubstituted macrocycle forms a unique turtle-like supramolecular complex with **1**; in this complex, the four substituent groups penetrate though the four opening faces of the molecular cage.

Previously, we demonstrated that the methyl and α-pyridinium protons of the DMDAP dication form multiple C–H···O hydrogen bonds with the oxygen atoms in the ethylene glycol chains of **1**. Based on this finding, we synthesized the rod-shaped salt **2**·2 PF_6 by reaction of commercially available 1,2-bis(4-pyridyl)ethane and 1-bromopentane. We expected that the 2^{2+} ions would form [2]pseudorotaxane complexes with **1** upon the threading of two pentyl groups through the two 24-membered ring faces of **1**. This complex should be stabilized not only through C–H···O hydrogen bonds between the α-pyridinium protons and the oxygen atoms of the ethylene glycol chains but also through π stacking of the two pyridinium rings with the concave aromatic surfaces of the molecular cage (Scheme 2).[11]

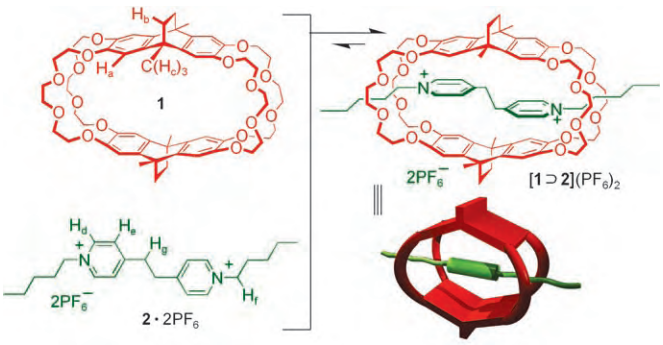

Scheme 2. Complexation of molecular cage **1** with **2**·2 PF_6.

The ^{1}H NMR spectrum of an equimolar mixture of **1** and thread **2**·2PF_6 in $CDCl_3/CD_3CN$ (9:1, 3 mM) at room temperature displays significant changes in the chemical shifts of the protons of the complex relative to those of its free components (Figure 1). To confirm that the disappearance of the

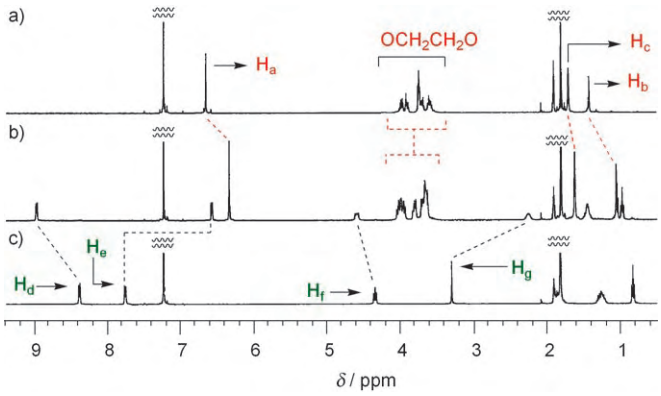

Figure 1. Partial ^{1}H NMR spectra (400 MHz, $CDCl_3/CD_3CN$ (9:1), 298 K) of a) **1**, b) an equimolar mixture of **1** and **2**·2 PF_6 (3 mM), and c) **2**·2 PF_6.

signals of the free species in the spectrum is due to complete complexation of the two components, rather than being the result of fast rates of exchange for the complexation/decomplexation processes under these conditions, we obtained the ^{1}H NMR spectrum of a non-stoichiometric mixture of **1** (2 mM) and **2**·2 PF_6 (3 mM) in $CDCl_3/CD_3CN$ (9:1). We observed two sets of signals, which integrated in a 2:1 ratio, with the weaker absorption set corresponding to the signals of free **2**·2 PF_6 (see the Supporting Information). This result suggests that the binding stoichiometry of **1** to **2**·2 PF_6 is 1:1 and that the exchange rates for their complexation and decomplexation are slow under these conditions. We did not observe any signals of the free species in the ^{1}H NMR spectra upon diluting equimolar mixtures of **1** and **2**·2 PF_6 from 1 mM

 © 2006 Wiley-VCH Verlag GmbH & Co. KGaA, Weinheim

to 20 μM (see the Supporting Information), thus suggesting that the binding between **1** and **2**·2 PF_6 is extremely tight.

The spectrum of the complex displays shifts downfield of the signals of the methylene protons H_f adjacent to the pyridinium center and the α-pyridinium protons H_d of **2**·2 PF_6 (Figure 1), in conjunction with weak, but discernable, shifts in the signals of the ethylene glycol protons of **1**. These shifts suggest the existence of C–H···O hydrogen bonds in the complex.[9,12] The considerable upfield shifts of signals for aromatic protons of both components (namely, H_a and H_e) and of the ethylene protons of **2**·2 PF_6 (H_g) imply that π stacking of the aromatic rings occurs in the complex. We grew single crystals suitable for X-ray crystallography through liquid diffusion of isopropyl ether into an equimolar solution of **1** and **2**·2 BF_4 in CH_3CN.[13] The solid-state structure reveals a [2]pseudorotaxane-like molecular geometry for the complex $[\mathbf{1}\supset\mathbf{2}]^{2+}$ (Figure 2),[14,15] in which the rodlike component $\mathbf{2}^{2+}$ penetrates through the two 24-membered rings of the molecular cage.

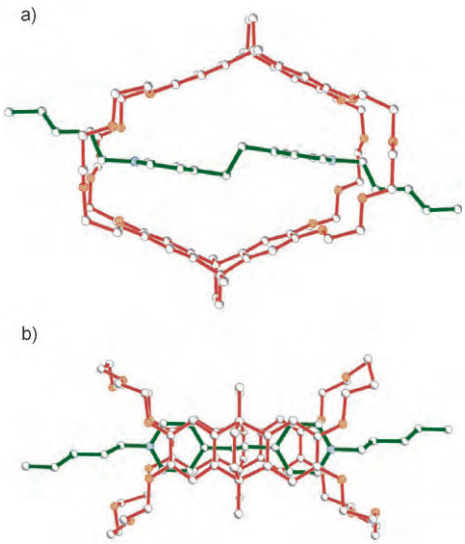

Figure 2. Ball-and-stick representations of the solid-state structure of $[\mathbf{1}\supset\mathbf{2}]^{2+}$: a) side and b) top views. C gray, O red, N blue.

The addition of four equivalents of KPF_6 to a solution of **1** and **2**·2 PF_6 in $CDCl_3/CD_3CN$ (9:1, 3 mM) led to the appearance of characteristic absorptions of free **2**·2 PF_6 in the ^{1}H NMR spectrum (see the Supporting Information), which suggests that complex $[\mathbf{1}\supset\mathbf{2}]^{2+}$ dissociated through competitive binding of K^+ ions to **1**.

Previously, we demonstrated that a complex formed between **1** and two K^+ ions involved the cooperation of each triethylene glycol loop (namely, each K^+ ion binds to all of the oxygen atoms of a 24-membered-ring crown ether). In that solid-state structure, two acetonitrile solvent molecules behaved as ligands for the K^+ ions and were positioned within the molecular cage.[9] We suspected that a suitable bidentate ligand, such as anthraquinone, would bind to the two K^+ ions, in place of the two labile acetonitrile ligands, to result in an additional supramolecular complex stabilized through ion–dipole interactions. Because each K^+ ion would be bound to the oxygen atoms of both the anthraquinone and the 24-membered rings, the two aryl rings of the anthraquinone thread would extend out of the complex through the two 34-membered rings of the molecular cage to result in a [2]pseudorotaxane-like complex (Scheme 3).

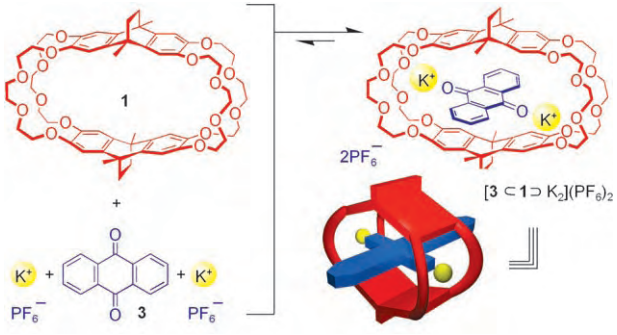

Scheme 3. The complexation of molecular cage **1** with K^+ ions and **3**.

As indicated in Figure 3b, the signals of the protons of an equimolar mixture of **1** and anthraquinone (**3**) in $CDCl_3/CD_3CN$ (50:1, 5 mM) at room temperature do not undergo

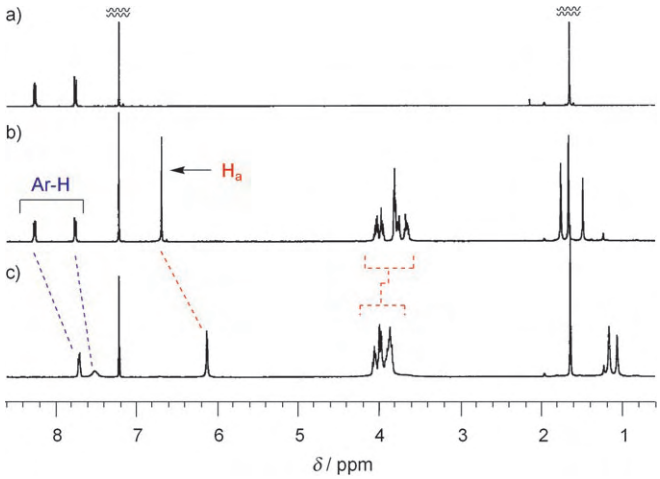

Figure 3. Partial ^{1}H NMR spectra (400 MHz, $CDCl_3/CD_3CN$ (50:1), 298 K) of a) **3**, b) an equimolar (5 mM) mixture of **1** and **3**, and c) the mixture obtained after adding KPF_6 (2 equiv) to solution (b).

significant shifts relative to those of the free species. This observation suggests that the binding affinity between the two species is negligible under these conditions. After the addition of two equivalents of KPF_6 to the solution, however, the ^{1}H NMR spectrum displays significant shifts for the signals of both of the organic components (Figure 3c). In particular, the upfield shifts of the signals of the aromatic protons of both components imply that stacking of the aromatic rings occurs within this supramolecular complex.

We grew single crystals suitable for X-ray crystallography through liquid diffusion of isopropyl ether into a solution of **1**, KPF_6, and **3** (1:2:1) in CH_3CN. The solid-state structure (Figure 4) reveals the expected [2]pseudorotaxane binding

 © 2006 Wiley-VCH Verlag GmbH & Co. KGaA, Weinheim

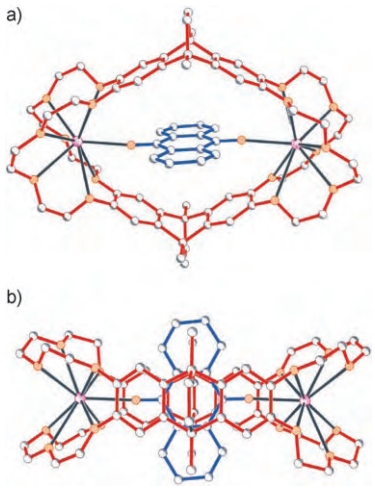

Figure 4. Ball-and-stick representations of the solid-state structure $[\mathbf{3}\subset\mathbf{1}\supset K_2]^{2+}$: a) side and b) top views. C gray, O red, N blue, K purple.

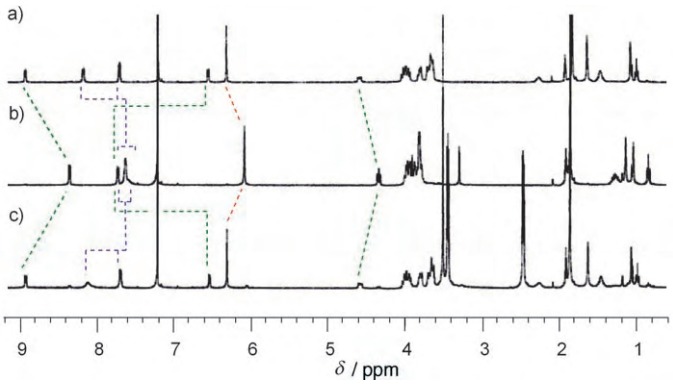

Figure 6. Partial ^{1}H NMR spectra (400 MHz, $CDCl_3/CD_3CN$ (9:1), 298 K) of a) an equimolar (3 mM) mixture of **1**, **2**·2 PF_6, and **3**; b) the mixture obtained after adding KPF_6 (4 equiv) to solution (a); and c) the mixture obtained after adding [2,2,2]cryptand (4 equiv) to solution (b).

geometry of the complex $[\mathbf{3}\subset\mathbf{1}\supset K_2]^{2+}$.[16] The rodlike **3** penetrates the two 34-membered rings, whereas the two oxygen atoms coordinate to the two K^+ ions. Thus, we can form [2]pseudorotaxane complexes from **1** with precise facial control (namely, threading through either the 24- or 34-membered rings) by using the rod-shaped salt **2**·2 PF_6 or a combination of K^+ ions and **3**.

Because K^+ ions not only template the formation of the [2]pseudorotaxane complex $[\mathbf{3}\subset\mathbf{1}\supset K_2]^{2+}$ but also cause dissociation of complex $[\mathbf{1}\supset\mathbf{2}]^{2+}$ in solution, the addition and removal of K^+ ions from a solution of **1**, **2**·2 PF_6, and **3** could be used to mediate an unprecedented type of machinelike molecular motion,[17] in which the rodlike components penetrate the molecular cage alternately through its different faces (Figure 5).

The ^{1}H NMR spectrum of an equimolar mixture of **1**, **2**·2 PF_6, and **3** in $CDCl_3/CD_3CN$ (9:1) indicates the formation of the [2]pseudorotaxane complex $[\mathbf{1}\supset\mathbf{2}]^{2+}$ exclusively (Figure 6a). The addition of four equivalents of K^+ ions to this solution not only leads to the dissociation of most of the $[\mathbf{1}\supset\mathbf{2}]^{2+}$ but also to the generation of the other [2]pseudorotaxane complex $[\mathbf{3}\subset\mathbf{1}\supset K_2]^{2+}$ (Figure 6b). The subsequent addition of [2,2,2]cryptand (4 equiv), which is a very strong binder of K^+ ions, to the solution leads to the disappearance of the signals that are diagnostic of $[\mathbf{3}\subset\mathbf{1}\supset K_2]^{2+}$ and the reappearance of the signals of $[\mathbf{1}\supset\mathbf{2}]^{2+}$. Thus, sequential addition of K^+ ions and [2,2,2]cryptand to a mixture of **1**, **2**·2 PF_6, and **3** in solution controls the mechanical threading of the different rodlike components within the molecular cage through selective formation of $[\mathbf{1}\supset\mathbf{2}]^{2+}$ and $[\mathbf{3}\subset\mathbf{1}\supset K_2]^{2+}$ (Figure 5).

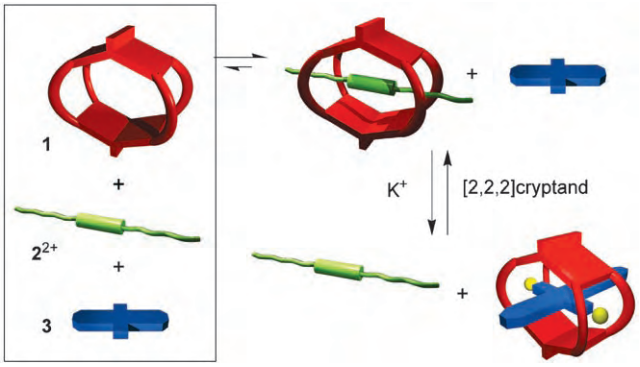

Figure 5. K^+ ion and [2,2,2]cryptand-controlled threading and dethreading processes associated with the alternate formation of [2]pseudorotaxane complexes $[\mathbf{1}\supset\mathbf{2}]^{2+}$ and $[\mathbf{3}\subset\mathbf{1}\supset K_2]^{2+}$.

Having proven that precise facial control is achievable in the formation of [2]pseudorotaxane complexes from **1** and that machinelike molecular motion can occur with these supramolecular systems, we turned our attention to the construction of a supramolecular complex in which each of the four macrocyclic openings in **1** encircles a rodlike unit. We synthesized the four-armed salt **5**·2 PF_6 through the reaction of the bipyridine **4**[18] with 1-bromopropane. We expected that the complexation of **5**·2 PF_6 with **1** would lead to the formation of a symmetrical complex $[\mathbf{1}\supset\mathbf{5}](PF_6)_2$, in which each of the four substituting groups of **5**·2 PF_6 would thread through a different opening of the **1** (Scheme 4).

The ^{1}H NMR spectrum (see the Supporting Information) of an equimolar mixture (2.6 mM) of **1** and **5**·2 PF_6 in $CDCl_3/CD_3CN$ (3:17) displays three sets of resonances—one set for free **1**, one for free **5**·2 PF_6, and one for the 1:1 complex formed between **1** and **5**·2 PF_6—which suggests that the rates of complexation and decomplexation are both slow on the ^{1}H NMR timescale at 400 MHz and 298 K. Using a single-

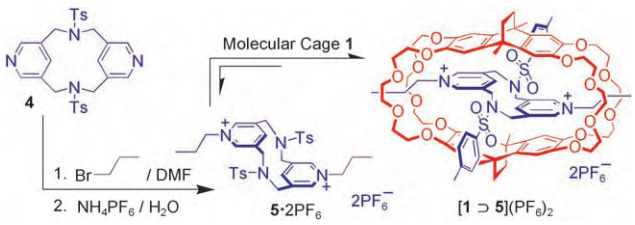

Scheme 4. Complexation of molecular cage **1** with **5**·2 PF_6. DMF = dimethylformamide, Ts = toluenesulfonyl.

 © 2006 Wiley-VCH Verlag GmbH & Co. KGaA, Weinheim

point method,[19] we determined the association constant (K_a) of this system at 298 K to be 300 M^{-1} in $CDCl_3/CD_3CN$ (3:17).

We grew single crystals suitable for X-ray crystallography through liquid diffusion of isopropyl ether into an equimolar solution of **1** and **5**·2 BF_4 in CH_3CN.[13] The solid-state structure reveals a binding geometry for the complex $[\mathbf{1}\supset\mathbf{5}]^{2+}$ [20] in which the *n*-propyl groups penetrate through the 24-membered rings and the two tosyl groups emerge from the 34-membered rings of **1** (Figure 7). The structure of $[\mathbf{1}\supset\mathbf{5}]^{2+}$ is unique, which may be correlated to a turtle's four legs protruding from its hard shell.

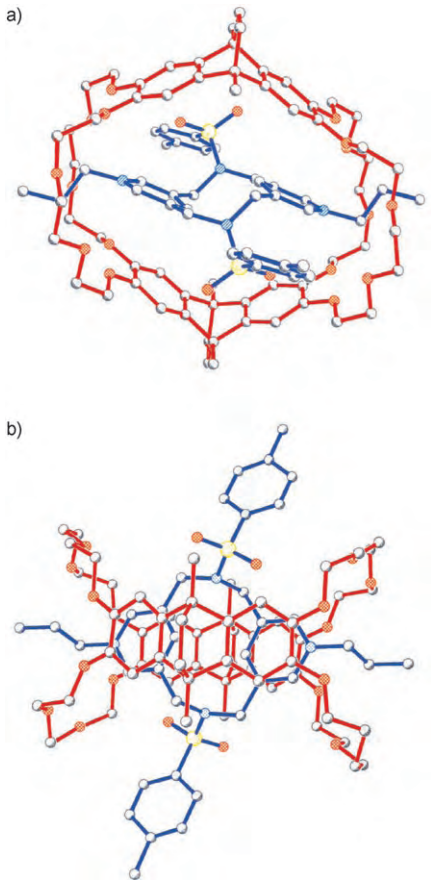

Figure 7. Ball-and-stick representation of the solid-state structure of $[\mathbf{1}\supset\mathbf{5}]^{2+}$: a) side and b) top views. C gray, O red, N blue, S yellow.

We have demonstrated that two different types of thread component (based on a bispyridinium ion and quinone) can be applied to molecular cage **1** to generate different [2]pseudorotaxane-like complexes with precise facial control. A mixture of the two threading components and **1** in solution undergoes a new type of molecular motion, powered through the addition and removal of K^+ ions and [2,2,2]cryptand units, in which the rodlike components penetrate the molecular cage alternately through its different faces. In addition, the four-armed macrocyclic guest **5**·2 PF_6 forms a complex with **1**, in which each of the limbs of the guest protrudes from a unique macrocyclic face of the host to result in a turtlelike supramolecular complex. We believe that the molecular recognition properties of this molecular cage will be useful in various fields, such as the construction of molecular machinery, supramolecular polymers, and supramolecular catalytic systems, which we are presently investigating.

Experimental Section

2·2 PF_6: 1-Bromopentane (403 μL, 3.2 mmol) was added to a solution of 1,2-di(4-pyridyl)ethane (100 mg, 0.54 mmol) in DMF (2 mL) at ambient temperature. The solution was stirred for 12 h before being poured into CH_2Cl_2 (5 mL) to provide a precipitate, which was collected and dissolved in MeCN (10 mL). Saturated aqueous NH_4PF_6 (10 mL) was added, and then the organic solvent was evaporated under reduced pressure. The precipitate was collected, washed with H_2O (20 mL), and dried to give **2**·2 PF_6 as a pale-yellow solid (246 mg, 74%). ^{1}H NMR (400 MHz, CD_3CN): $\delta = 0.91$ (t, $J =$ 7 Hz, 6H), 1.23–1.42 (m, 8H), 2.08–2.21 (m, 4H), 3.28 (s, 4H), 4.45 (t, $J = 7$ Hz, 4H), 7.85 (d, $J = 6$ Hz, 4H), 8.54 ppm (d, $J = 6$ Hz, 4H); ^{13}C NMR (100 MHz, CD_3CN): $\delta = 14.0$, 22.6, 28.5, 31.3, 35.0, 61.8, 128.3, 143.9, 160.3 ppm; HR-MS (FAB): $C_{22}H_{34}F_6N_2P^+$ ($[\mathbf{2}\cdot PF_6]^+$) calcd *m*/*z* 471.2363; found *m*/*z* 471.2403.

5·2 PF_6: 1-Bromopropane (50 μL, 0.53 mmol) was added to a solution of the dipyridine **4** (25 mg, 0.05 mmol) in DMF (1 mL) at ambient temperature. The solution was stirred at 90 °C for 12 h before being poured into diethyl ether (10 mL) to give a precipitate, which was dissolved in MeCN (10 mL). Saturated aqueous NH_4PF_6 (10 mL) was added, and then the organic solvent was evaporated under reduced pressure. The precipitate was collected, washed with H_2O (20 mL), and dried to give **5**·2 PF_6 as a pale-yellow solid (41 mg, 98%). ^{1}H NMR (400 MHz, CD_3CN): $\delta = 0.84$ (t, $J = 7$ Hz, 6H), 1.77–1.85 (m, 4H), 2.51 (s, 6H), 4.29 (t, $J = 7$ Hz, 4H), 4.66 (s, 8H), 7.54 (d, $J =$ 8 Hz, 4H), 7.88 (d, $J = 8$ Hz, 4H), 8.27 (s, 4H), 8.75 ppm (s, 2H); ^{13}C NMR (100 MHz, CD_3CN): $\delta = 10.6$, 21.7, 25.1, 51.1, 64.1, 127.4, 130.7, 135.6, 137.5, 143.2, 145.4, 147.7 ppm; HR-MS (FAB): $C_{34}H_{42}F_6N_4O_4PS_2^+$ ($[\mathbf{5}\cdot PF_6]^+$) calcd *m*/*z* 779.2289; found *m*/*z* 779.2305.

Received: January 26, 2006
Published online: March 29, 2006

Keywords: host–guest chemistry · molecular cages · molecular devices · molecular recognition · pseudorotaxanes

[1] a) V. Balzani, A. Credi, F. M. Raymo, J. F. Stoddart, *Angew. Chem.* **2000**, *112*, 3484–3530; *Angew. Chem. Int. Ed.* **2000**, *39*, 3348–3391; b) J.-P. Collin, C. Dietrich-Buchecker, P. Gaviña, M. C. Jiménez-Molero, J.-P. Sauvage, *Acc. Chem. Res.* **2001**, *34*, 477–487; c) D. A. Leigh, J. K. Y. Wong, F. Dehez, F. Zerbetto, *Nature* **2003**, *424*, 174–179; d) J. D. Badjić, V. Balzani, A. Credi, S. Silvi, J. F. Stoddart, *Science* **2004**, *303*, 1845–1849; e) J. Berna, D. A. Leigh, M. Lubomska, S. M. Mendoza, E. M. Perez, P. Rudolf, G. Teobaldi, F. Zerbetto, *Nat. Mater.* **2005**, *4*, 704–710.

[2] a) *Molecular Electronics: Science and Technology* (Eds.: A. Aviram, M. Ratner), New York Academy of Sciences, New York, **1998**; b) C. P. Collier, G. Mattersteig, E. W. Wong, Y. Luo, K. Beverly, J. Sampaio, F. M. Raymo, J. F. Stoddart, J. R. Heath, *Science* **2000**, *289*, 1172–1175; c) H. Yu, Y. Luo, K. Beverly, J. F. Stoddart, H.-R. Tseng, J. R. Heath, *Angew. Chem.* **2003**, *115*, 5884–5889; *Angew. Chem. Int. Ed.* **2003**, *42*, 5706–5711; d) A. H. Flood, R. J. A. Ramirez, W.-Q. Deng, R. P. Muller, W. A. Goddard III, J. F. Stoddart, *Aust. J. Chem.* **2004**, *57*, 301–322.

[3] a) K. Kim, *Chem. Soc. Rev.* **2002**, *31*, 96–107; b) K. S. Chichak, S. J. Cantrill, A. R. Pease, S.-H. Chiu, G. W. V. Cave, J. L. Atwood, J. F. Stoddart, *Science* **2004**, *304*, 1308–1312; c) L. Wang, M. O. Vysotsky, A. Bogdan, M. Bolte, V. Böhmer, *Science* **2004**, *304*, 1312–1314; d) L.-E. Perret-Aebi, A. von Zelewsky, C.

 © 2006 Wiley-VCH Verlag GmbH & Co. KGaA, Weinheim

Dietrich-Buchecker, J.-P. Sauvage, *Angew. Chem.* **2004**, *116*, 4582 – 4585; *Angew. Chem. Int. Ed.* **2004**, *43*, 4482 – 4485; e) X.-Z. Zhu, C.-F. Chen, *J. Am. Chem. Soc.* **2005**, *127*, 13158 – 13159.

[4] a) G. W. Gokel, *Crown Ethers and Cryptands*, The Royal Society of Chemistry, Cambridge, **1991**; b) *Crown Ethers and Analogous Compounds* (Ed.: M. Hiraoka), Elsevier, Amsterdam, **1992**; c) M. C. T. Fyfe, J. F. Stoddart, in *Advances in Supramolecular Chemistry*, *Vol. 5* (Ed.: G. W. Gokel), JAI, London, **1999**, pp. 1 – 53.

[5] a) F. Diederich, *Cyclophanes*, The Royal Society of Chemistry, Cambridge, **1991**; b) M. Gómez-López, J. A. Preece, J. F. Stoddart, *Nanotechnology* **1996**, *7*, 183 – 192.

[6] a) S. A. Nepogodiev, J. F. Stoddart, *Chem. Rev.* **1998**, *98*, 1959 – 1976; b) C. J. Easton, S. F. Lincoln, *Modified Cyclodextrins — Scaffolds and Templates for Supramolecular Chemistry*, Imperial College Press, London, **1999**; c) A. Harada, *Acc. Chem. Res.* **2001**, *34*, 456 – 464.

[7] Noncovalent molecular cages have been prepared; see: a) M. Kim, G. W. Gokel, *J. Chem. Soc. Chem. Commun.* **1987**, 1686 – 1688; b) J. M. C. Kerckhoffs, F. W. B. van Leeuwen, A. L. Spek, K. Kooijman, M. Crego-Calama, D. N. Reinhoudt, *Angew. Chem.* **2003**, *115*, 5895 – 5900; *Angew. Chem. Int. Ed.* **2003**, *42*, 5717 – 5722; c) M. Yoshizawa, S. Miyagi, M. Kawano, K. Ishiguro, M. Fujita, *J. Am. Chem. Soc.* **2004**, *126*, 9172 – 9173; cryptand-type host molecules may be considered as the simplest covalently linked molecular cages; see: d) K. A. Nielsen, J. O. Jeppesen, E. Levillain, N. Thorup, J. Becher, *Org. Lett.* **2002**, *4*, 4189 – 4192; e) D. F. Perkins, L. F. Lindoy, G. V. Meehan, P. Turner, *Chem. Commun.* **2004**, 152 – 153; f) M. Bonizzoni, L. Fabbrizzi, G. Piovani, A. Taglietti, *Tetrahedron* **2004**, *60*, 11159 – 11162; cryptophanes, carcerands, and hemicarcerands may also be considered as covalently linked molecular cages; see: g) A. Collet, J.-P. Dutasta, B. Lozach, J. Canceil, *Top. Curr. Chem.* **1993**, *165*, 103 – 130; h) A. Jasat, J. C. Sherman, *Chem. Rev.* **1999**, *99*, 931 – 967; i) R. Warmuth, *Acc. Chem. Res.* **2001**, *34*, 95 – 105.

[8] A cylindrical host comprising two linked bis(*meta*-phenylene[26]crown-8) moieties has been prepared; the two crown ether units form complexes with two paraquat guests independently; see: F. Huang, L. N. Zakharov, A. L. Rheingold, M. Ashraf-Khorassani, H. W. Gibson, *J. Org. Chem.* **2005**, *70*, 809 – 813.

[9] C.-F. Lin, Y.-H. Liu, C.-C. Lai, S.-M. Peng, S.-H. Chiu, *Chem. Eur. J.*, DOI: 200600090.

[10] The 24-membered ring faces are dibenzo[24]crown-8 (DB24C8)-like openings; for the chemistry of DB24C8, see: a) S. J. Cantrill, A. R. Pease, J. F. Stoddart, *J. Chem. Soc. Dalton Trans.* **2000**, 3715 – 3734; b) T. Clifford, A. Abushamleh, D. H. Busch, *Proc. Natl. Acad. Sci. USA* **2002**, *99*, 4830 – 4836.

[11] The cation–dipole interaction may also exist between the pyridinium ions and the oxygen atoms of the ethylene glycol chains and help to stabilize the complex.

[12] a) P. L. Anelli, P. R. Ashton, R. Ballardini, V. Balzani, M. Delgado, M. T. Gandolfi, T. T. Goodnow, A. E. Kaifer, D. Philp, M. Pietraszkiewicz, L. Prodi, M. V. Reddington, A. M. Z. Slawin, N. Spencer, J. F. Stoddart, C. Vicent, D. J. Williams, *J. Am. Chem. Soc.* **1992**, *114*, 193 – 218; b) P.-T. Chiang, P.-N. Cheng, C.-F. Lin, Y.-H. Liu, C.-C. Lai, S.-M. Peng, S.-H. Chiu, *Chem. Eur. J.* **2006**, *12*, 865 – 876.

[13] The ^{1}H NMR spectra displayed similar shifts of signals when macrocycle **1** was mixed with the PF_6 or BF_4 salt of this guest under the same conditions (see the Supporting Information).

[14] Crystal data for [**1**⊃**2**]·MeCN·0.5 CH_2Cl_2·0.5 $CHCl_3$·2 BF_4: $[C_{85}H_{114.5}O_{16}N_3Cl_{2.5}][BF_4]_2$, $M_r = 1696.54$, monoclinic, space group $p2_1/n$, $a = 20.80500(10)$, $b = 20.28900(10)$, $c = 23.22970(10)$ Å, $V = 9087.18(7)$ Å^3, $\rho_{calcd} = 1.240$ g cm^{-3}, $\mu(Mo_{K\alpha}) = 0.165$ mm^{-1}, $T = 295(2)$ K, light-yellow plates; 15996 independent measured reflections, F^2 refinement, $R_1 = 0.1308$, $wR_2 = 0.3733$.

[15] CCDC-296094–296096 ([**1**⊃**5**]$(BF_4)_2$, [**1**⊃**2**]$(BF_4)_2$, and [**3**⊂**1**⊃K_2]$(PF_6)_2$, respectively) contain the supplementary crystallographic data for this paper. These data can be obtained free of charge from The Cambridge Crystallographic Data Centre via www.ccdc.cam.ac.uk/data_request/cif.

[16] Crystal data for [**3**⊂**1**⊃K_2]·2 MeCN·0.5 $CHCl_3$·H_2O·2 PF_6: $[C_{78.5}H_{90.5}O_{19}N_2Cl_{1.5}][PF_6]_2$, $M_r = 1787.34$, monoclinic, space group $C2/c$, $a = 31.5201(4)$, $b = 16.3152(3)$, $c = 19.0614(3)$ Å, $V = 9784.3(3)$ Å^3, $\rho_{calcd} = 1.213$ g cm^{-3}, $\mu(Mo_{K\alpha}) = 0.252$ mm^{-1}, $T = 295(2)$ K, deep-yellow plates; 11101 independent measured reflections, F^2 refinement, $R_1 = 0.1235$, $wR_2 = 0.3002$.

[17] The addition and removal of metal ions is an efficient method for switching supramolecular systems between different states, see: a) J.-P. Collin, C. Dietrich-Buchecker, P. Gavina, M. C. Jimenez-Molero, J.-P. Sauvage, *Acc. Chem. Res.* **2001**, *34*, 477 – 487; b) G. Kaiser, T. Jarrosson, S. Otto, Y.-F. Ng, A. D. Bond, J. K. M. Sanders, *Angew. Chem.* **2004**, *116*, 1993 – 1996; *Angew. Chem. Int. Ed.* **2004**, *43*, 1959 – 1962; c) T. Iijima, S. A. Vignon, H.-R. Tseng, T. Jarrosson, J. K. M. Sanders, F. Marchioni, M. Venturi, E. Apostoli, V. Balzani, J. F. Stoddart, *Chem. Eur. J.* **2004**, *10*, 6375 – 6392; d) G. W. Gokel, W. M. Leevy, M. E. Weber, *Chem. Rev.* **2004**, *104*, 2723 – 2750; e) P.-N. Cheng, P.-T. Chiang, S.-H. Chiu, *Chem. Commun.* **2005**, 1285 – 1287; f) D. S. Marlin, D. G. Cabrera, D. A. Leigh, A. M. Z. Slawin, *Angew. Chem.* **2006**, *118*, 1413 – 1418; *Angew. Chem. Int. Ed.* **2006**, *45*, 1385 – 1390.

[18] T. Satou, T. Shinmyozu, *J. Chem. Soc. Perkin Trans. 2* **2002**, 393 – 397.

[19] a) P. R. Ashton, E. J. T. Chrystal, P. T. Glink, S. Menzer, C. Schiavo, N. Spencer, J. F. Stoddart, P. A. Tasker, A. J. P. White, D. J. Williams, *Chem. Eur. J.* **1996**, *2*, 709 – 728; b) P. R. Ashton, M. C. T. Fyfe, S. K. Hickingbottom, J. F. Stoddart, A. J. P. White, D. J. Williams, *J. Chem. Soc. Perkin Trans. 2* **1998**, 2117 – 2124; c) W.-C. Hung, K.-S. Liao, Y.-H. Liu, S.-M. Peng, S.-H. Chiu, *Org. Lett.* **2004**, *6*, 4183 – 4186.

[20] Crystal data for [**1**·**5**]·2 MeCN·2 BF_4: $[C_{98}H_{124}O_{20}N_6S_2][BF_4]_2$, $M_r = 1943.77$, monoclinic, space group $p2_1/n$, $a = 14.12900(10)$, $b = 15.2950(2)$, $c = 23.4410(2)$ Å, $V = 5021.35(9)$ Å^3, $\rho_{calcd} = 1.286$ g cm^{-3}, $\mu(Mo_{K\alpha}) = 0.138$ mm^{-1}, $T = 295(2)$ K, light-yellow plates; 8806 independent measured reflections, F^2 refinement, $R_1 = 0.0873$, $wR_2 = 0.2579$.

 © 2006 Wiley-VCH Verlag GmbH & Co. KGaA, Weinheim

Cover Picture

Frank Hoffmann, Maximilian Cornelius, Jürgen Morell, and Michael Fröba*

Like Honeycomb is how the pore structures of silica-based mesoporous organic–inorganic hybrid materials often appear. In the Review on page 3216 ff., M. Fröba and co-workers give an overview of their preparation. The cover picture shows hybrids whose pores are functionalized with cyclam (ligand), sulforhodamine B (laser die), and a cinchona derivative (for heterogeneous asymmetric catalysis). Particular attention is given to the class of periodic mesoporous organosilicas (PMOs).

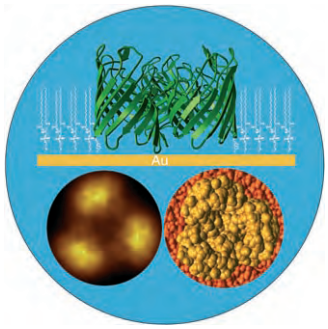

Membrane Proteins
In their Communication on page 3252 ff., J. H. Lakey and co-workers report that a membrane protein can be fixed in a defined orientation on flat gold surfaces. Coassembly with thiolipids gives clearly defined, immobilized proteins.

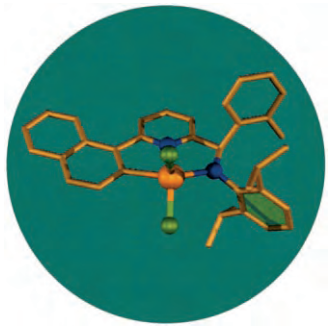

Polymerization Catalysts
V. Murphy, J. C. Stevens, V. Busico, and co-workers describe the discovery, optimization, and commercial application of a class of Hf-based non-metallocene olefin polymerization catalysts in their Communication on page 3278 ff.

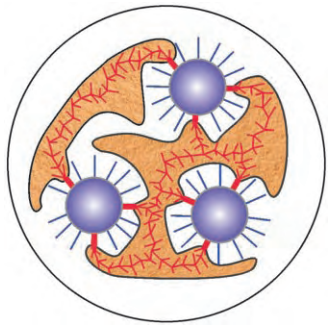

Supported Gold Catalysts
Calcination of a three-component material containing Au nanoparticles produces a highly active catalyst for the oxidation of CO at low temperatures, as reported by A. Corma and G. Budroni in their Communication on page 3328 ff.

Contents

VIP ***The following Communications have been judged by at least two referees to be "very important papers" and will be published online at www.angewandte.org soon:***

*C. Burke, Y. Shi**
Regio- and Enantioselective Epoxidation of Dienes by a Chiral Dioxirane: Synthesis of Optically Active Vinyl *cis*-Epoxides

Cheuk-W. So, H. Roesky, J. Magull, R. Oswald*
Synthesis and Characterization of [{PhC(NtBu)$_2$}SiCl]: A Stable Monomeric Chlorosilylene

S. Harder, J. Brettar*
Rational Design of a Well-Defined Soluble Calcium Hydride Complex

*H. Yu, S. Huang, H. Chokhawala, M. Sun, H. Zheng, Xi Chen**
Highly Efficient Chemoenzymatic Synthesis of Naturally Occurring and Non-Natural α2,6-Linked Sialosides: A *P. damsela* α2,6-Sialyltransferase with Extremely Flexible Donor Substrate Specificity

*V. Lavallo, Y. Canac, B. Donnadieu, W. Schoeller, G. Bertrand**
CO Fixation to Stable Acyclic and Cyclic Alkyl Amino Carbenes: Stable Amino Ketenes with a Small HOMO–LUMO Gap

*D. Rohde, C.-J. Yan, Hui-J. Yan, Li-J. Wan**
From Lamellar to Hexagonal Self-Assembly of Bis(dioxaborin) Molecules

Web Sites

http://www.gdch.de/fofue and http://dgr.rints.com — Finding a Chemist in a Haystack — *A. Mills* — ***3202***

Books

Organic Reaction Mechanisms — A. C. Knipe — *reviewed by D. Lenoir* — **3204**

Highlights

Catalytic Oxidation

D. Lenoir* — **3206 – 3210**

Selective Oxidation of Organic Compounds—Sustainable Catalytic Reactions with Oxygen and without Transition Metals?

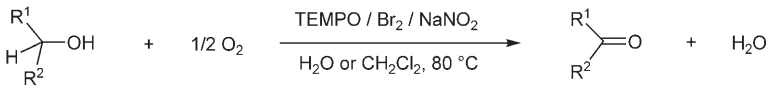

Going without: Alcohols can be oxidized with oxygen and without transition-metal complexes (see scheme; TEMPO = 2,2,6,6-tetramethylpiperidine-N-oxide). Conventional methods are compared with new catalytic variants developed for this reaction and for the complete oxidation of pollutants with regard to sustainability.

Correspondence

Higher-Coordinate Si Compounds

X. Kästele, P. Klüfers,* R. Tacke — **3212 – 3214**

Not Unhydrolyzed at pH 8

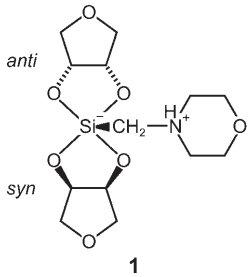

1

Contrary to a recent claim that the zwitterionic bis(diolato)silicate **1** exhibits remarkable hydrolytic stability at pH 7–8, a closer look at ^{29}Si and ^{13}C NMR spectroscopic data of **1** under various conditions (solvent, pH, concentration) reveals that hydrolysis products are the predominant species in solution.

© 2006 Wiley-VCH Verlag GmbH & Co. KGaA, Weinheim

Reviews

Pores for thought: The modification of mesoporous silica phases with organic components extends this class of materials and their potential application in areas such as the production of insulators in the chip industry. Periodic mesoporous organosilicas (PMOs) occupy a special position in this respect, as the organic component is an integral part of the framework. The figure shows a PMO with a crystal-like structure of the pore wall.

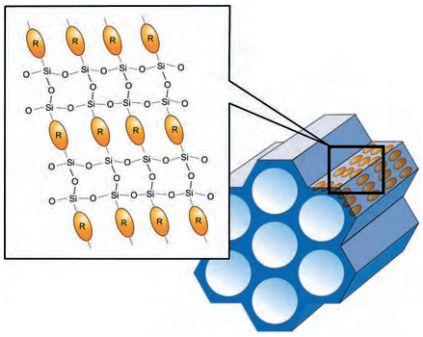

Mesoporous Materials

F. Hoffmann, M. Cornelius, J. Morell, M. Fröba* _____ **3216 – 3251**

Silica-Based Mesoporous Organic–Inorganic Hybrid Materials

Communications

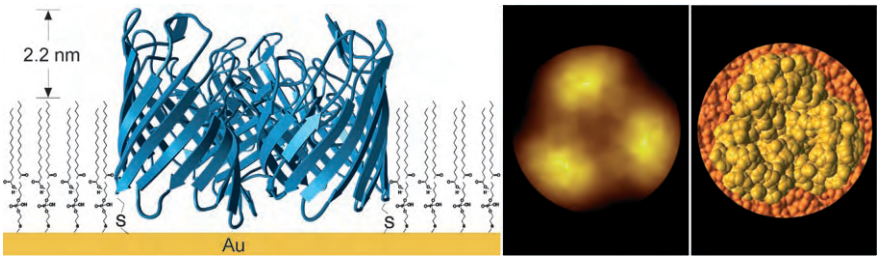

Observed from above: A cysteine mutation in a membrane protein enables it to be fixed in a defined orientation on flat gold surfaces (see picture, left). Subsequent coassembly with thiolipids produces clearly defined, immobilized proteins. Analysis by atomic force microscopy provides topographs of similar quality to those revealed from 2D crystals.

Topography

D. A. Cisneros, D. J. Muller, S. M. Daud, J. H. Lakey* _____ **3252 – 3256**

An Approach To Prepare Membrane Proteins for Single-Molecule Imaging

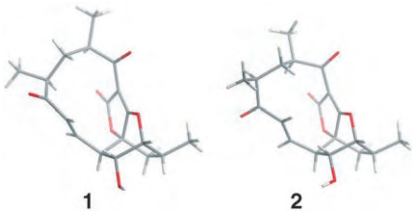

Into the abyss: A total synthesis of abyssomicin C (**1**) through a metathesis-based strategy offers a highly convergent approach to the construction of analogues. A novel and potent atropisomer of the natural product **1** was thus discovered, namely atrop-abyssomicin C (**2**), which reveals subtle yet important structural differences to **1** (see structures; O red, C gray, H white).

Natural Product Synthesis

K. C. Nicolaou,* S. T. Harrison _____ **3256 – 3260**

Total Synthesis of Abyssomicin C and atrop-Abyssomicin C

For the USA and Canada:
ANGEWANDTE CHEMIE International Edition (ISSN 1433-7851) is published weekly by Wiley-VCH PO Box 191161, D 69451 Weinheim, Germany. Air freight and mailing in the USA by Publications Expediting Inc. 200 Meacham Ave., Elmont, NY 11003. Periodicals postage paid at Jamaica NY 11431. US POSTMASTER: send address changes to *Angewandte Chemie*, Wiley-VCH, 111 River Street, Hoboken, NJ 07030. Annual subscription price for institutions: US$ 5685/5168 (valid for print and electronic / print or electronic delivery); for individuals who are personal members of a national chemical society prices are available on request. Postage and handling charges included. All prices are subject to local VAT/sales tax.

© 2006 Wiley-VCH Verlag GmbH & Co. KGaA, Weinheim

The best in chemistry –

for more than a hundred years

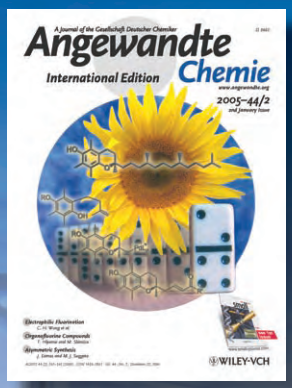

A Journal of the Gesellschaft Deutscher Chemiker

Angewandte
International Edition **Chemie**

www.angewandte.org

1888: ***The beginning of a success story***

Constant Innovations

1962: *First issue of the International Edition*
1976: *Graphical abstracts*
1979: *Cover pictures*
1988: *Centenary of Angewandte*
1989: *Routine use of color*
1991: *New section: Highlights*
1992: *Computerized editorial tracking system*
1995: *Internet service for readers*
1998: *Regular press service; full-text online*
2000: *New section: Essays; EarlyView: Communications available online ahead of the printed version*
2001: *New section: Minireviews*
2002: *Online submission of manuscripts*
2003: *Weekly publication; new section: News; new layout*
2004: *Backfiles (1962-1997); ManuscriptXpress: Online system for authors and referees*

Angewandte's advisors...

Martin Jansen
Max-Planck-Institut für Festkörperforschung, Stuttgart

»Professional presentation of the latest research in all fields of chemistry is the distinguishing characteristic that makes ***Angewandte Chemie*** *indispensable. This journal leads students to the cutting edge of chemical knowledge.«*

Angewandte Chemie International Edition *is a journal of the German Chemical Society (GDCh)*

GDCh

WILEY InterScience® DISCOVER SOMETHING GREAT

WILEY-VCH

1894504_gu

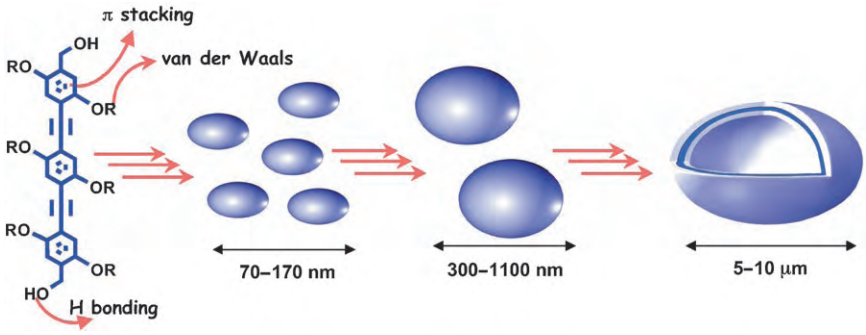

Wires to particles: A subtle balance of H-bonding, π-stacking, and van der Waals interactions facilitates the concentration-controlled self-assembly of a short molecular wire (see figure) into nanoparticles and fluorescent microspheres in nonpolar hydrocarbon solvents. Above a critical concentration, a blue-light emitting organogel is formed.

Light-Emitting Organogel

A. Ajayaghosh,* R. Varghese, V. K. Praveen, S. Mahesh — **3261 – 3264**

Evolution of Nano- to Microsized Spherical Assemblies of a Short Oligo-(*p*-phenyleneethynylene) into Superstructured Organogels

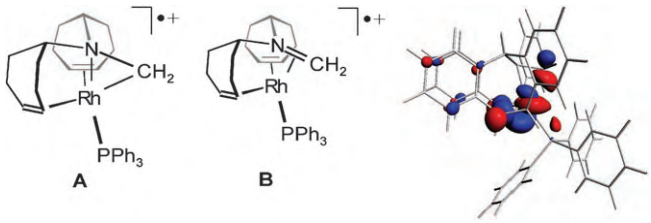

Rh steps into the ring: The radical cation shown is best described as a rhodaazacyclopropane (**A**) rather than as a Rh^{I} iminium ion complex (**B**). EPR and DFT data indicate that the delocalization of the unpaired electron into the ligand framework contributes to the stability of **A** (see plot of the singly occupied molecular orbital).

Metallacycles

P. Maire, A. Sreekanth, T. Büttner, J. Harmer,* I. Gromov, H. Rüegger, F. Breher, A. Schweiger, H. Grützmacher* — **3265 – 3269**

Synthesis of a Rhodaazacyclopropane and Characterization of Its Radical Cation by EPR Spectroscopy

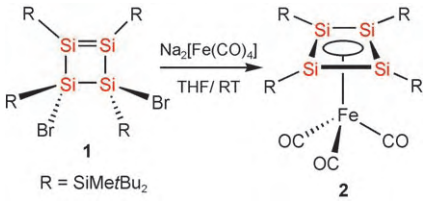

All in the family: $[(\eta^4\text{-}R_4Si_4)Fe(CO)_3]$ **2** ($R = SiMe_tBu_2$) represents a neutral silicon congener of a (cyclobutadiene)tricarbonyliron complex and was synthesized by the reaction of the dibromocyclotetrasilene $R_4Si_4Br_2$ **1** with $Na_2[Fe(CO)_4]$. The tetrasilacyclobutadiene ligand in **2** has stronger π-donating properties than the cyclobutadiene ligand in the parent complex $[(\eta^4\text{-}H_4C_4)Fe(CO)_3]$.

Silicon Ligands

K. Takanashi, V. Ya. Lee, M. Ichinohe, A. Sekiguchi* — **3269 – 3272**

A (Tetrasilacyclobutadiene)tricarbonyliron Complex $[\{\eta^4\text{-}(tBu_2MeSi)_4Si_4\}Fe(CO)_3]$: The Silicon Cousin of Pettit's (Cyclobutadiene)tricarbonyliron Complex $[(\eta^4\text{-}H_4C_4)Fe(CO)_3]$

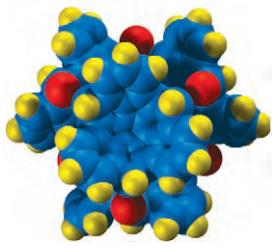

Charging hemifullerene $C_{30}H_{12}$ with potassium metal gives the hexaanion $C_{30}H_{12}^{6-}$ ($\mathbf{1}^{6-}$). The NMR data, which indicate high symmetry, high charge density, and pyramidalization of the C-4 positions, as well as DFT calculations, are consistent with a tetramer $[\mathbf{1}^{6-}]_4/24\,K^+$, in which six K^+ ions bridge four hexaanions (see picture; red K^+, yellow H, blue C; the remaining 18 solvent-separated K^+ ions are not shown).

Hemifullerenes

N. Treitel, T. Sheradsky, L. Peng, L. T. Scott,* M. Rabinovitz* — **3273 – 3277**

$C_{30}H_{12}^{6-}$: Self-Aggregation, High Charge Density, and Pyramidalization in a Supramolecular Structure of a Supercharged Hemifullerene

© 2006 Wiley-VCH Verlag GmbH & Co. KGaA, Weinheim

Contents

Polymerization Catalysts

T. R. Boussie, G. M. Diamond, C. Goh, K. A. Hall, A. M. LaPointe, M. K. Leclerc, V. Murphy,* J. A. W. Shoemaker, H. Turner, R. K. Rosen, J. C. Stevens,* F. Alfano, V. Busico,* R. Cipullo, G. Talarico _____ **3278 – 3283**

Nonconventional Catalysts for Isotactic Propene Polymerization in Solution Developed by Using High-Throughput-Screening Technologies

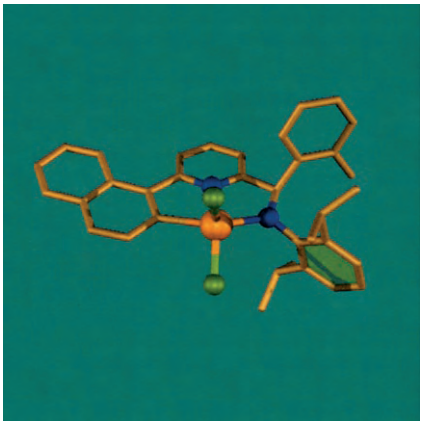

A textbook example of catalyst discovery, optimization, and commercial implementation is provided with the discovery of a class of Hf-based non-metallocene olefin polymerization catalysts (see picture; Hf orange sphere, N blue, C(Me) green, C orange), their advanced high-throughput screening, and their industrial application in a high-temperature solution process for the production of highly isotactic polypropylene based materials.

Chemical Protein Synthesis

E. C. B. Johnson, T. Durek, S. B. H. Kent* _____ **3283 – 3287**

Total Chemical Synthesis, Folding, and Assay of a Small Protein on a Water-Compatible Solid Support

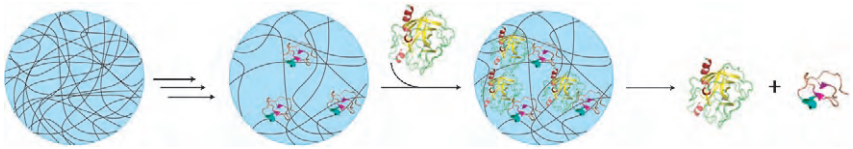

All wrapped up: A protein was assembled inside a beaded polymer, then folded with concomitant formation of disulfide bonds, and assayed for biochemical activity while still bound to the water-compatible polymer.

Zeolite Analogues

Z.-X. Wang, X.-F. Shen, J. Wang, P. Zhang, Y.-Z. Li, E. N. Nfor, Y. Song,* S.-i. Ohkoshi, K. Hashimoto,* X.-Z. You* **3287 – 3291**

A Sodalite-like Framework Based on Octacyanomolybdate and Neodymium with Guest Methanol Molecules and Neodymium Octahydrate Ions

Heavy-metal sodalite: Nd^{III} reacts with $[Mo^{V}(CN)_8]^{3-}$ in methanol to form a new 3D framework consisting of cyanide-bridged Nd^{III} and Mo^{IV} ions. The anionic framework (red and blue in the picture) has a cage structure similar to that of the zeolite sodalite and contains hexagonal channels filled by methanol molecules and $[Nd^{III}(H_2O)_8]^{3+}$ ions (green spheres).

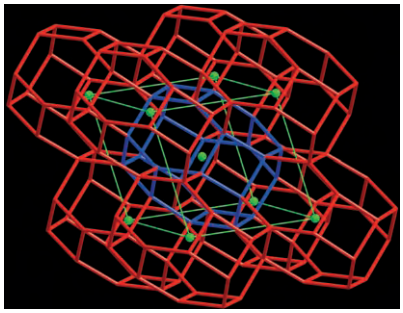

Dinitrogen Activation

A. R. Fout, F. Basuli, H. Fan, J. Tomaszewski, J. C. Huffman, M.-H. Baik, D. J. Mindiola* _____ **3291 – 3295**

A Co_2N_2 Diamond-Core Resting State of Cobalt(I): A Three-Coordinate Co^{I} Synthon Invoking an Unusual Pincer-Type Rearrangement

Unmasking the truth: The dimer $[\{(\mu_2\text{-PNP})Co\}_2]$ (Co light blue, N dark blue, P green, C gray, only one carbon atom of the isopropyl groups shown; PNP = $[N\{2\text{-}P(CHMe_2)_2\text{-}4\text{-}MeC_6H_3\}_2]^-$) contains a Co_2N_2 diamond core and bridging PNP ligands. Upon reaction with $ClCPh_3$, CO, or N_2, rearrangement of the PNP ligands to a terminal chelating mode is observed to give four-coordinate Co complexes such as $[\{(PNP)Co\}_2(\mu_2\text{-}N_2)]$.

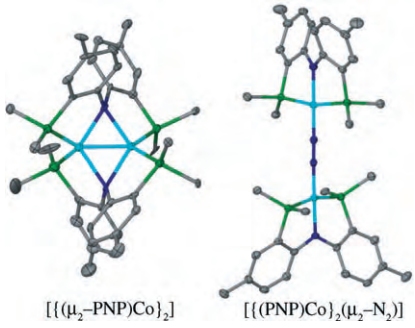

© 2006 Wiley-VCH Verlag GmbH & Co. KGaA, Weinheim

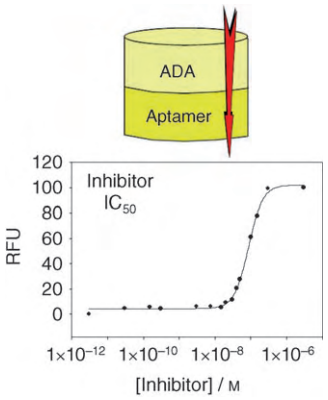

Layered enzyme assays: The use of a layered sol-gel based material allows for spatial separation of coimmobilized enzyme and fluorescent aptamer reporter species. This provides a route for facile assaying of enzyme activity and inhibition in cases where the aptamer signals the presence of the enzyme substrate. This then results in accurate IC_{50} determinations.

Enzyme Assays

N. Rupcich, R. Nutiu, Y. Li,*
J. D. Brennan* ——— **3295 – 3299**

Solid-Phase Enzyme Activity Assay Utilizing an Entrapped Fluorescence-Signaling DNA Aptamer

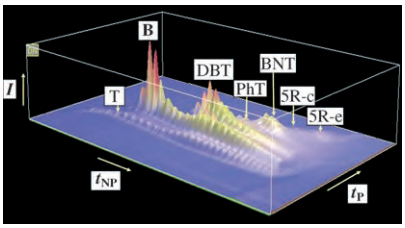

Heavy-oil desulfurization is an important process for the production of clean (ultra-low sulfur) transportation fuels. The relative reactivities of the sulfur compounds present in heavy oils (the graphic shows retention times for thiophenes (T) and annulated thiophenes on nonpolar and polar columns) are strongly dependent on the conditions of the desulfurization process.

Heavy-Oil Desulfurization

T. V. Choudhary,* J. Malandra, J. Green,
S. Parrott, B. Johnson ——— **3299 – 3303**

Towards Clean Fuels: Molecular-Level Sulfur Reactivity in Heavy Oils

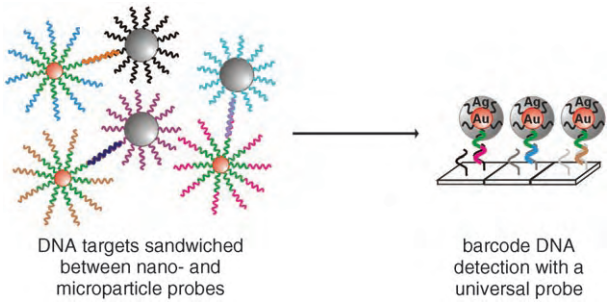

Sorting the mail: A highly selective assay for the detection of multiple DNA targets in solution was developed based on gold nanoparticles with oligonucleotide reporters. Four DNA targets associated with infectious viruses were detected simultaneously without enzymatic amplification at mid-femtomolar concentrations.

DNA Assays

S. I. Stoeva, J.-S. Lee, C. S. Thaxton,
C. A. Mirkin* ——— **3303 – 3306**

Multiplexed DNA Detection with Biobarcoded Nanoparticle Probes

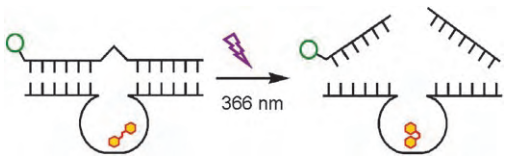

Lights, camera, action! Photoswitchable nucleoside analogues containing *o*-, *m*-, or *p*-azobenzenes can be inserted in the catalytic core of RNA-cleaving 10–23 deoxyribozymes by replacing a nonconserved residue (see picture). Irradiation of the modified deoxyribozymes at 366 nm enhances RNA cleavage rates up to ninefold, thus achieving the rates observed for the unmodified deoxyribozyme.

RNA Cleavage

S. Keiper, J. S. Vyle* ——— **3306 – 3309**

Reversible Photocontrol of Deoxyribozyme-Catalyzed RNA Cleavage under Multiple-Turnover Conditions

© 2006 Wiley-VCH Verlag GmbH & Co. KGaA, Weinheim

Contents

Molecular Recognition

J. Kondo, B. François, A. Urzhumtsev, E. Westhof* ——— **3310 – 3314**

Crystal Structure of the *Homo sapiens* Cytoplasmic Ribosomal Decoding Site Complexed with Apramycin

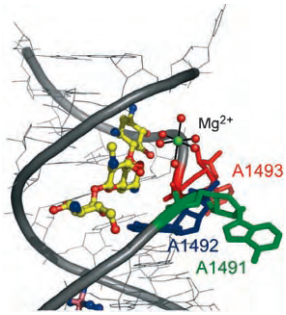

On target: The crystal structure of the complex formed between apramycin and the cytoplasmic ribosomal decoding sites of human cells (see picture; complex in yellow, adenine residues numbered) was studied and compared with that of the analogous bacterial complex. The studies provide insight into apramycin toxicity in humans.

Synthetic Methods

N. Nishina, Y. Yamamoto* ——— **3314 – 3317**

Gold-Catalyzed Intermolecular Hydroamination of Allenes with Arylamines and Resulting High Chirality Transfer

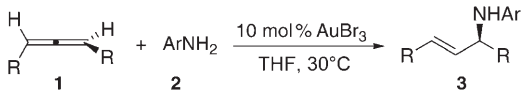

Au contraire! Contrary to the relatively well-studied metal-catalyzed intramolecular hydroamination of allenes, the intermolecular reaction is rare and is here accomplished with a gold(III) catalyst. Aryl amines **2** react with chiral allenes **1** in the presence of $AuBr_3$ at ambient temperature to produce chiral allylamines **3** (Ar = Ph; *o*-, *m*-, *p*-$CH_3C_6H_4$) in good yields with high *ee* values.

Protein Identification

V. An Thieu, D. Kirsch, T. Flad, C. Müller, B. Spengler* ——— **3317 – 3319**

Direct Protein Identification from Nonspecific Peptide Pools by High-Accuracy MS Data Filtering

Validate your results! High-accuracy mass spectrometric analysis and composition-based de novo sequencing (CBS) combined with database(DB)-assisted protein identification allows for the rapid production of validated analytical results in proteome research. A simplified sample preparation scheme is sufficient to provide for reliable identification of proteins even when following nonspecific and unknown degradation processes.

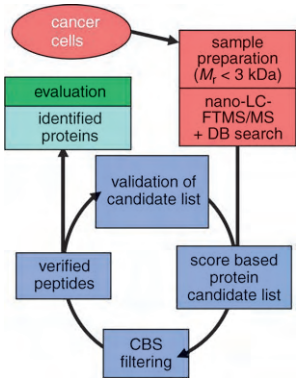

Natural Product Synthesis

Y.-G. Wang, R. Takeyama, Y. Kobayashi* ——— **3320 – 3323**

Total Synthesis of Phoslactomycin B and Its Biosynthetic Deamino Precursor

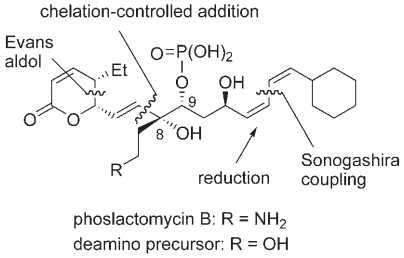

The implicated intermediate in the biosynthesis of phospholine (phoslactomycin B, see picture), namely its deamino precursor, as well as phospholine itself are synthesized. The phoslactomycins show antitumor, antibacterial, and antifungal activities, however, it is not yet known which part of the skeleton contributes to the activities.

© 2006 Wiley-VCH Verlag GmbH & Co. KGaA, Weinheim

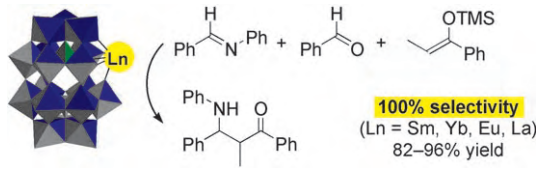

Catalytic cornerstone: Lanthanide(III) complexes of a lacunary Dawson-type polyoxometalate catalyze Lewis acid mediated reactions (see figure, TMS = trimethylsilyl). The compounds $(NBu_4)_5H_2[\alpha_1\text{-}Ln(H_2O)_4P_2W_{17}O_{61}]$ (Ln = Yb, Sm, Eu, La) are much more chemoselective than the lanthanide triflates. Furthermore, the polyoxotungstic framework can play a role, presumably through H-bonding to the substrates.

Polyoxometalate Catalysts

C. Boglio, G. Lemière, B. Hasenknopf, S. Thorimbert,* E. Lacôte,* M. Malacria* ——— **3324 – 3327**

Lanthanide Complexes of the Monovacant Dawson Polyoxotungstate $[\alpha_1\text{-}P_2W_{17}O_{61}]^{10-}$ as Selective and Recoverable Lewis Acid Catalysts

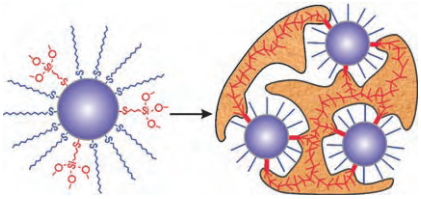

Heart of gold: A three-component material composed of 2-nm Au nanoparticles (see picture; blue spheres) capped with alkanethiols that are partially functionalized with alkoxysilane groups and then incorporated into an "open shell" of silica was prepared. Upon calcination, the sample is a highly active catalyst for the oxidation of CO at low temperatures, being an order of magnitude more active than Au on structured mesoporous materials.

Supported Gold Catalysts

G. Budroni, A. Corma* ——— **3328 – 3331**

Gold–Organic–Inorganic High-Surface-Area Materials as Precursors of Highly Active Catalysts

Tubes or cages? Quantum chemical calculations provide new evidence that methylaluminoxanes prefer nanotubular shapes with diameters of approximately 1 nm (see picture). These nanotubes are capable of adopting several structures, of which zigzag (4,0) is energetically favored.

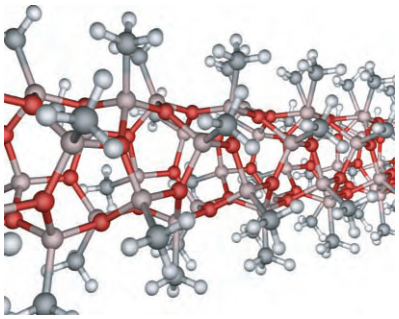

Polymerization Catalysts

M. Linnolahti,* J. R. Severn, T. A. Pakkanen ——— **3331 – 3334**

Are Aluminoxanes Nanotubular? Structural Evidence from a Quantum Chemical Study

Self-assembled transporter: Self-association of a partial-cone calixarene amide provides membrane-active aggregates that enable the transport of chloride anions across phospholipid membranes (see picture). Additionally, a regulatory system is described, wherein an inactive calixarene analogue inhibits the active chloride transporter.

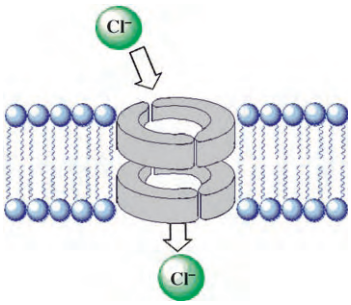

Anion Transporters

J. L. Seganish, P. V. Santacroce, K. J. Salimian, J. C. Fettinger, P. Zavalij, J. T. Davis* ——— **3334 – 3338**

Regulating Supramolecular Function in Membranes: Calixarenes that Enable or Inhibit Transmembrane Cl^- Transport

© 2006 Wiley-VCH Verlag GmbH & Co. KGaA, Weinheim

Contents

DNA Sensing

M. J. Schmid, K. Manthiram, S. M. Grayson, J. C. Willson, J. E. Meiring, K. M. Bell, A. D. Ellington, C. G. Willson* ——— **3338 – 3341**

Feature Multiplexing—Improving the Efficiency of Microarray Devices

So much information: An exponential increase in information density for sensor microarrays is enabled through the development of a new multiplexed probe distribution approach to form a feature-multiplexed array. The picture shows a fluorescence micrograph of the sensor response during a detection assay.

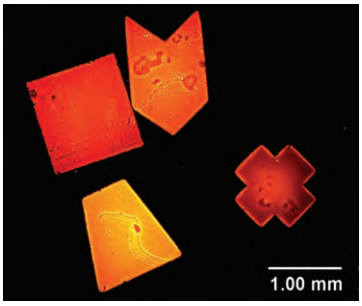

Molecular Transport

R. Schmuhl, A. van den Berg, D. H. A. Blank, J. E. ten Elshof* ——— **3341 – 3345**

Surfactant-Modulated Switching of Molecular Transport in Nanometer-Sized Pores of Membrane Gates

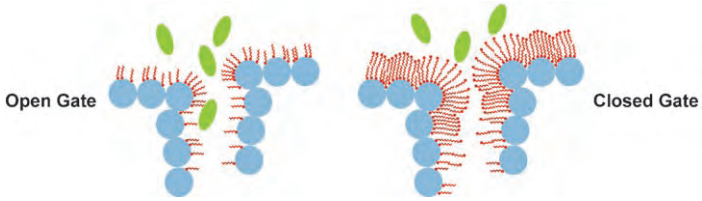

An open-and-shut case: A switchable membrane gate for ionic species that operates by co-addition and removal of surfactant molecules is demonstrated (see picture). The permeability of the gate to specific ions can be manipulated and tuned by changing the nature and concentration of the surfactant.

Peptide Enrichment

W. Jia, X. Chen, H. Lu,* P. Yang* ——— **3345 – 3349**

$CaCO_3$–Poly(methyl methacrylate) Nanoparticles for Fast Enrichment of Low-Abundance Peptides Followed by $CaCO_3$-Core Removal for MALDI-TOF MS Analysis

An octopus for observation: A $CaCO_3$–poly(methyl methacrylate) (PMMA) nanoparticle that has a destroyable core of $CaCO_3$ was applied to the enrichment of low-abundance peptides and proteins. The linear chains of PMMA linked on the $CaCO_3$ core spread out into the solution like the tentacles of an octopus, and the resulting nanoparticle-adsorbed peptides or proteins are analyzed by MALDI-TOF MS (see scheme).

Cross-Coupling

A. L. Hansen, J.-P. Ebran, M. Ahlquist, P.-O. Norrby,* T. Skrydstrup* ——— **3349 – 3353**

Heck Coupling with Nonactivated Alkenyl Tosylates and Phosphates: Examples of Effective 1,2-Migrations of the Alkenyl Palladium(II) Intermediates

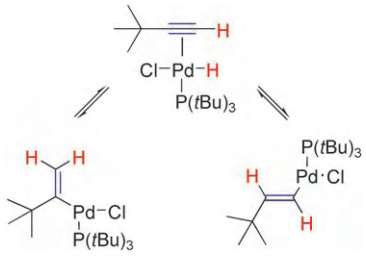

What the Heck! A catalytic system composed of a Pd complex with a basic, hindered alkyl phosphine ligand is capable of promoting Heck coupling of nonactivated vinyl tosylates and phosphates with electron-deficient olefins. An unexpected 1,2-migration of the alkenyl Pd^{II} intermediates (see Scheme) leads to the isomerized Heck coupling product.

© 2006 Wiley-VCH Verlag GmbH & Co. KGaA, Weinheim

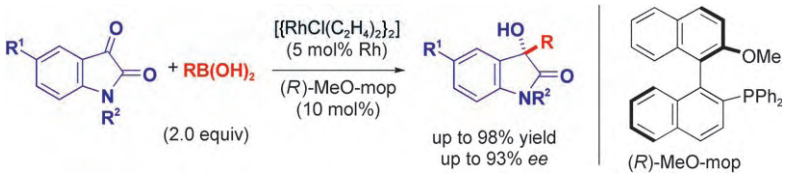

Mopping up the rhodium: A rhodium-catalyzed asymmetric addition of arylboronic acids to isatins has been developed to produce biologically relevant 3-aryl-3-hydroxy-2-oxindoles in high yield (see scheme). High enantioselectivity was observed with (*R*)-MeO-mop as a ligand, and the reaction could be extended to the addition of alkenyl groups.

Asymmetric Catalysis

R. Shintani, M. Inoue, T. Hayashi* ——— **3353 – 3356**

Rhodium-Catalyzed Asymmetric Addition of Aryl- and Alkenylboronic Acids to Isatins

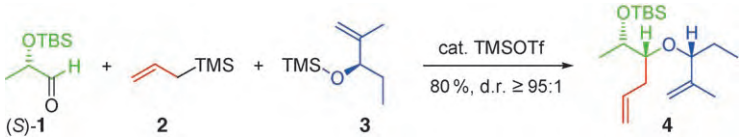

The more the merrier: A multicomponent Sakurai reaction has been developed in which an efficient, highly diastereoselective three-component condensation of an aldehyde **1**, allyl silane **2**, and silylated alcohol **3** is mediated by trimethylsilyl triflate (TMSOTf). Products such as **4** can serve as direct precursors to dihydropyran skeletons, which is demonstrated by the synthesis of a portion of (+)-ambruticin. TBS = *tert*-butyldimethylsilyl.

Synthetic Methods

J. Pospíšil, T. Kumamoto, I. E. Markó* ——— **3357 – 3360**

Highly Diastereoselective Silyl-Modified Sakurai Multicomponent Reaction

Everything just clicks into place: Alkyne-group functionalized polymer films that are deposited from the gas phase allow spatially defined immobilization of biomolecules, such as biotin, through the 1,3-dipolar cycloaddition click reaction with azide derivatives (see scheme). Such biofunctional surfaces have applications in diagnostics and biosensors.

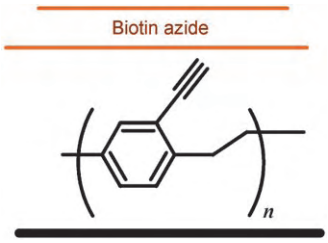

Bioactive Surfaces

H. Nandivada, H.-Y. Chen, L. Bondarenko, J. Lahann* ——— **3360 – 3363**

Reactive Polymer Coatings that "Click"

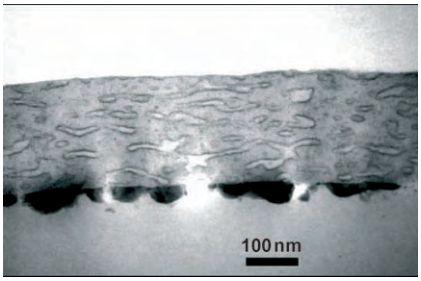

Proper percolation of charges in solar cells is possible with the self-assembled nanostructure of a block-copolymer film (see the TEM cross section of a solar cell). A photovoltaic device made from such a block copolymer exhibits a ten-times higher short circuit current and a considerably larger photovoltage than its polymer-blend analogue.

Polymer Solar Cells

S. M. Lindner, S. Hüttner, A. Chiche, M. Thelakkat,* G. Krausch* **3364 – 3368**

Charge Separation at Self-Assembled Nanostructured Bulk Interface in Block Copolymers

© 2006 Wiley-VCH Verlag GmbH & Co. KGaA, Weinheim

Contents

Electron Transfer

J. Dannhäuser, W. Donaubauer, F. Hampel, M. Reiher, B. Le Guennic, B. Corzilius, K.-P. Dinse, A. Hirsch* ____ **3368 – 3372**

σ-Donor and π-Acceptor Stacking Interactions in a *trans*-2-Linked C_{60}–Cobalt(II) Tetraphenylporphyrin Diad

Hold me close: A *trans*-2-linked molecular diad displays both σ-donor and π-acceptor interations (see picture). The crystal structure reveals linear stacking arrangements in which the fullerene moiety is located directly above the porphyrin moiety of the neighboring molecule.

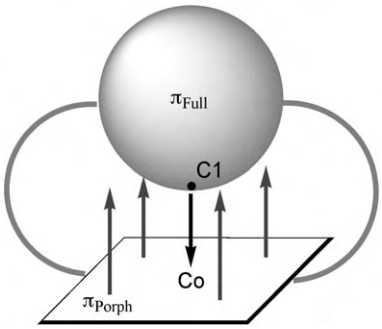

Fluorescent Probes

E. Mayer-Enthart, H.-A. Wagenknecht* ____ **3372 – 3375**

Structure-Sensitive and Self-Assembled Helical Pyrene Array Based on DNA Architecture

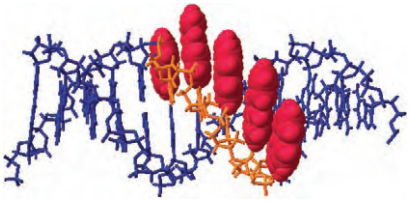

Five times is more than fivefold: The helical π-stacked array of pyrene-modified uridine shows a strong fluorescence enhancement that is structure sensitive to base mismatches. As the fluorescence is highly sequence dependent, it can serve as a structure-sensitive probe for DNA.

WILEY InterScience®
DISCOVER SOMETHING GREAT

"**Hot Papers**" are chosen by the Editors for their importance in a rapidly evolving field of high current interest. A preview with the graphical abstracts of these articles can be found on the *Angewandte Chemie* homepage in Wiley InterScience at www.angewandte.org.

All articles in *Angewandte Chemie* are published online several weeks ahead of print. They are found under the "**EarlyView**" link on the journal's homepage in Wiley InterScience.

Service

Keywords ____ *3376*

Authors ____ *3377*

Angewandte's Sister Journals ____ *3378 – 3379*

Preview ____ *3381*

For more information on ChemMedChem see www.chemmedchem.org

© 2006 Wiley-VCH Verlag GmbH & Co. KGaA, Weinheim

Catalytic Oxidation

DOI: 10.1002/anie.200502702

Selective Oxidation of Organic Compounds—Sustainable Catalytic Reactions with Oxygen and without Transition Metals?**

*Dieter Lenoir**

Keywords:
dioxygen · environmental chemistry · oxidation · pollutants · sustainability

Oxidation reactions belong to the repertoire of organic chemistry.[1] Over the past few years a series of sustainable[2] oxidation methods have been developed in which tailor-made transition-metal complexes serve as catalysts.[3] In these reactions the chemo-, regio-, stereo-, and enantioselectivity can be controlled under relatively mild reaction conditions and the products obtained with optimal yield.[3] Recent results from research focusing on two important reactions are discussed here: 1) the selective homogeneously catalyzed oxidation of alcohols to give aldehydes/ketones and 2) the complete oxidation of pollutants. Although every synthesis begins in the laboratory, oxidation reactions also play a very important role in industrial chemistry. However, these large-scale industrial production processes will not be considered here.

Selective Oxidation of Alcohols

The selective oxidation of alcohols is an important preparative method in organic chemistry. The textbook classic by J. March[1a] lists 65 references to classical oxidation methods. The databank "ISI Web of Science" provides 4715 entries on this topic for the period January 1996 to July 2005. In Table 1 three familiar oxidation methods and five more recent approaches are compared with respect to their sustainability parameters.[2] In each case the reactions result in yields of 80–98%. In methods 1–4 the oxidation agent is a metal oxide or non-metal oxide in a high oxidation state, methods 5–8 are more recent catalytic oxidations with hydrogen peroxide or dioxygen.

Atom economy[2a] and the environmental factor E[2b] are measures for the amount of waste produced in a reaction relative to the amount of desired product. The heading atom economy in Table 1 refers to the reaction stoichiometry; the environmental factor E also takes into account the solvent and auxiliaries that must be disposed of. The ecotoxicity of the reaction must also be considered: toxic compounds are used in the Jones and Swern oxidations (methods 1 and 2 in Table 1). The assessment in terms of the atom economy and the environmental factor E is particularly poor for the Swern and Dess–Martin oxidations owing to the large amount of waste produced. In oxidations with hydrogen peroxide and oxygen (methods 5–8 in Table 1) only water is formed in addition to the desired carbonyl compound, and it is not waste in a strict sense. The cost of the oxidizing agent listed in Table 1 is calculated for a one-mole scale. The price of chemicals reflects the cost of their preparation from basic compounds including energy requirements.[2] If one assumes that the costs for auxiliaries are similarly high for all eight methods, the price of the oxidizing agent is then a measure for the economy and the ecology. It can be seen from Table 1 that the price for one oxidation equivalent (removal of two electrons) is highly dependent upon the oxidation agent used and ranges from 185 Euro for the Swern reagent to 0.038 Euro for dioxygen. An improvement with respect to atom economy and cost is particularly recognizable for catalytic methods with molecular oxygen or air. In past years such methods have been developed on the laboratory scale, mainly with transition-metal complexes based on copper, palladium, and ruthenium,[3,5] and they are clearly superior with respect to sustainability parameters such as atom economy, cost of the oxidizing agent, and (eco)toxicity of the starting compounds and reaction products. In Table 1 the sustainability of the methods listed improves from top to bottom, also because the amount of waste decreases significantly.

Molecular oxygen does indeed have considerable oxidation potential, but at room temperature it does not react with most organic compounds owing to high activation barriers. At higher temperatures, oxygen, which exists as diradical in the ground state, takes part preferably in nonselective radical reactions, for example, the autooxidation of hydrocarbons. To achieve selective oxidations with oxygen, transition-metal complexes have been developed as homogeneous catalysts.[3,5] Method 7 in Table 1 illus-

[*] Prof. Dr. D. Lenoir
Institut für Ökologische Chemie
GSF-Forschungszentrum für Umwelt und Gesundheit
Postfach 1129
85778 Neuherberg bei München (Germany)
Fax: (+49) 89-3187-3371
E-mail: lenoir@gsf.de

[**] I am grateful to Dr. M. Eissen and Dr. C. Wattenbach for their cooperation and assistance in the preparation of this manuscript.

WILEY InterScience DISCOVER SOMETHING GREAT
© 2006 Wiley-VCH Verlag GmbH & Co. KGaA, Weinheim

Table 1: Comparison of the sustainability of eight selective oxidation methods with benzyl alcohol as example.[a]

Method	Name	Reagent	Catalyst	Solvent	*T* [°C]	Atom economy [%]	Environmental factor E [kg kg^{-1}]	Cost [€][b]	(Eco)toxicity
1[4a]	Jones oxidation	CrO_3/H_2SO_4	no	acetone	0–20	38.8	ca. 6	17	CrO_3 is carcinogenic
2[4b]	Swern oxidation	$(CH_3)_2SO, (COCl)_2, N(C_2H_5)_3$	no	CH_2Cl_2	−60	20.6	ca. 58	185	toxic reactants and products
3[4c]	Dess–Martin oxidation	periodinane (DMP) 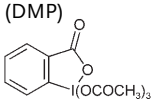	no	CH_2Cl_2/H_2O	−20	19.9	ca. 1800	160	DMP is unstable and explosive
4[4d]	according to Anelli et al.	NaOCl/NaBr	TEMPO[c]	CH_2Cl_2/H_2O	0	58.1	ca. 58	110	low
5[4e]	according to Sasson et al.	H_2O_2 (30%)	$RuCl_3$/phase-transfer cat.	CH_2ClCH_2Cl/toluene	80	74.7	ca. 12	20	low
6[4f]	according to Sheldon et al.	O_2	TEMPO	various	80	85.5	–	0.038	low
7[5]	see Ref. [5]	O_2	Complexes of Cu, Pd, Ru	different	80	85.5	ca. 26	0.038	none
8[6]	according to Liu et al.	O_2 or air	TEMPO, Br_2, $NaNO_2$	H_2O or CH_2Cl_2	80	85.5	ca. 15	0.038	low

[a] Stoichiometric equations can be found in Ref. [1a] and the respective literature citations. [b] Prices for pure chemicals from the Aldrich catalogue (2003), Price from the company Linde for O_2 (50 L, 99.95% purity). [c] TEMPO = 2,2,6,6-tetramethyl-1-piperidinyloxy.

trates the diversity of more recent, sustainable oxidation methods.

Since compounds of the transition metals described are expensive and often not available commercially and also potentially (eco)toxic (Table 1), the Chinese research group lead by X. Hu and X. Liang at the Dalian Institute of Chemical Physics has introduced the combination of TEMPO/bromine/sodium nitrite as an alternative catalyst (method 8 in Table 1).[6] A variant of this new method uses 1,3-dibromo-5,5-dimethylhydantoin or *N*-bromosuccinimide in place of bromine.[6b] Benzyl alcohols (eight examples), aliphatic alcohols (four examples), and an allyl alcohol may be oxidized selectively with air in aqueous solution or CH_2Cl_2 to give the corresponding carbonyl compounds in high yield (Scheme 1). A pyridine-3-carbinol was oxidized to the aldehyde without the addition of acid. Reaction times were 1–5 h. However, one disadvantage of this method is the high cost of the apparatus: an autoclave is required to achieve the oxygen partial pressure necessary (0.4 Mpa). Working in water as solvent[7] can be an advantage for the process, but organic solvents are preferable since contaminated aqueous solutions are more difficult to dispose of.

A three-stage catalytic reaction cascade has been suggested as the mechanism (Scheme 2). Coupled cyclic processes of redox pairs of different catalysts can explain many oxidation reactions such as method 7 (Table 1).[3,8] It is known that TEMPO itself can react as a stoichiometric oxidant,[4f] but as a cocatalyst with sodium bromide it can also bring about the oxidation of alcohols with sodium hypochlorite (method 4 in Table 1).

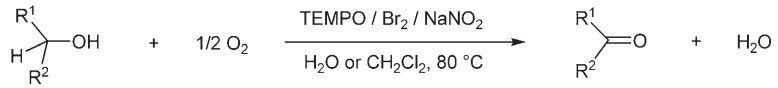

Scheme 1. Selective oxidation of alcohols with the system TEMPO/Br_2/$NaNO_2$.[6]

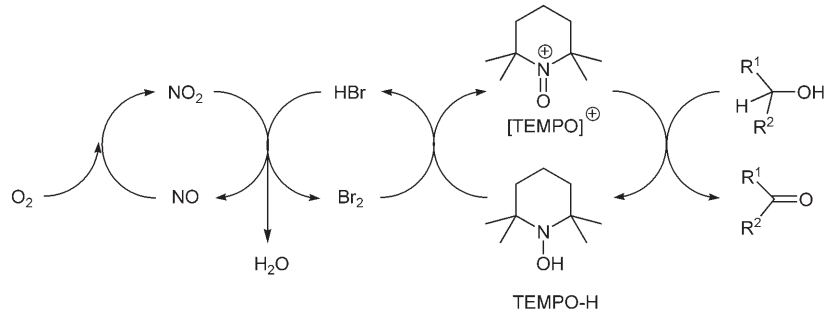

Scheme 2. Reaction cascade for the oxidation of alcohols.[6]

 © 2006 Wiley-VCH Verlag GmbH & Co. KGaA, Weinheim

In addition to the desired selectivity, turnover number and frequency (TON and TOF values), the substrate/catalyst ratio and the formation of toxic by-products must also be considered in the assessment of catalytic reactions.[3] The data given in Table 1 are a criterion for the efficiency of a method and should therefore be taught in chemistry courses. In the Jones oxidation, which is indeed convenient and relatively inexpensive, a carcinogenic oxidizing agent (CrO_3) is used. Since there are better, more environmentally friendly methods that do not require toxic reagents, two alternative methods are given in the Introduction of the Sustainable Organic Laboratory Course (NOP).[2h] In special cases such as the Dess–Martin reaction (method 3 in Table 1) very poor sustainability parameters are disregarded in favor of milder reaction conditions (oxidation in the presence of sensitive groups). Of the methods listed in Table 1 both method 7 and method 5 (oxidation with H_2O_2/$RuCl_3$ described by Sasson) are particulary advantageous, because all of the reagents and cheap and readily available.

Sustainability plays an important role in industrial oxidations of alcohols on a large scale.[9] Moreover, the global effects of competing industrial processes can be compared based on an ecoefficiency analysis. This was demonstrated recently with the comparison of five alternative indigo syntheses by a group at BASF.[10] In a detailed evaluation of the reactions listed in Table 1 by the EATOS method[2d] the mass flows of all starting compounds and reaction products and auxiliaries are balanced (the E value in Table 1 is an approximate summation parameter for this). The values given in Table 1 show a clear trend with respect to the sustainability of the different oxidation processes on a laboratory scale; they are indicative for synthesis on an industrial scale.

Oxidation of Pollutants (Complete Oxidation)

Most dissolved contaminants are mineralized in the environment, in other words, they undergo complete oxidative degradation to carbon dioxide and water. (S, N, and Cl compounds also give rise to sulfate, nitrate, and chloride, respectively.) For most materials in waste water this takes place by the microbiocenosis of the sewage plant. Only contaminants such as perhalogenated compounds, the so-called persistent organic pollutants (POPs), resist biological oxidation.[11] Therefore a plurality of chemical oxidation processes (advance oxidation processes, AOPs) have been developed in which hydrogen peroxide and dioxygen play a pivotal role.[12] The Fenton reagent consisting of iron(II) salts and hydrogen peroxide[13] is not selective enough for effective oxidation because the most of the H_2O_2 is converted into water and unreactive oxygen by redox disproportionation (catalase activity). This is also true for the use of H_2O_2 in the oxidation of alcohols (method 5 in Table 1). For this reason H_2O_2 is combined with metal catalysts such as complexed metal salts of iron and manganese, which have lower catalase activity.[14] None of the known oxidation processes converts organic compounds and H_2O_2 to CO_2 and H_2O quantitatively—the degree of mineralization lies at only 40%.

Selected isomers of chlorophenols, the five key compounds earmarked by the U.S. Environmental Protection Agency as "priority pollutants", have been used as models for the oxidation of persistent impurities with H_2O_2 or oxygen in the presence of metal catalysts. Meunier et al. have employed iron phthalocyanine and iron porphin catalysts in the oxidation of 2,4,6-trichloro- and pentachlorophenol with H_2O_2,[15] and Lente and Espensen have recently described reactions with five different iron cyclam complexes.[14] Application of these processes is made difficult in that the organic solvents must be added to the aqueous solutions. To address this problem the group lead by Collins has developed the Fe-TAML catalyst (Figure 1; TAML = macrocyclic tetraamido ligand).[16] The oxidation of 2,4,6-trichloro- and pentachlorophenol with hydrogen peroxide and this system was recently investigated in detail.[17] The mass balance for carbon showed for TCP that CO_2 and CO account for 35% in addition to six low-molecular-weight, readily biodegradable organic acids:

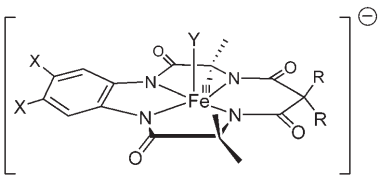

Figure 1. The Fe-TAML catalyst: Variant 1: X = Cl, Y = H_2O, R = CH_3; Variant 2: X = H, Y = Cl, R = CH_3; Variant 3: X = H, Y = H_2O, R = F; Li^+ or $(C_2H_5)_4N^+$ are present as cations.

oxalic acid (11%), formic acid (5%), chloromaleic acid (16%), malonic acid (7.5%), hydroxymalonic acid (6.5%), and chloromalonic acid (4.5%). Organically bound chlorine is mineralized to about 85%. Unlike other oxidation processes for chlorophenols, toxic chlorinated dibenzodioxins and dibenzofurans are not detectable even in trace amounts.[17]

Other pollutants such as azo dyes and alkyl sulfides or effluent from paper and pulp production can be decomposed oxidatively and thus disposed of with this method.[18] According to the Daphnia test, the reaction products from the oxidation of "Orange II", a widely used azo dye, are less toxic than the starting compound.[18a] The mechanism of the oxidation with H_2O_2/Fe-TAML is still not completely understood, but it probably proceeds via iron(IV) complexes.[16]

In analogy to their work on selective oxidations of alcohols without heavy metals (method 8 in Table 1)[6] the same Chinese group succeeded in the oxidation of 2,4,6-trichlorophenol (TCP) with dioxygen as the oxidant and sodium nitrite as the catalyst[19] in an autoclave at a pressure of 0.5 Mpa. Possibly the chlorophenol acts through the phenol/phenoxyl radical redox pair with nitrite (redox pair NO_2/NO) as cocatalyst. The intermediate formation of peroxynitrite or nitrate would offer an alternative explanation, but there are no indications of the formation of these species based on the results of NO and O_2 in atmospheric chemistry. The method was optimized with respect to the reaction conditions, whereby equimolecular amounts of substrate and nitrite were used. Oxidation of TCP at 210°C leads after six hours to mineralization (CO_2 and CO) of 75% besides the four acids: formic acid (4.3%), acetic acid (5.3%),

 © 2006 Wiley-VCH Verlag GmbH & Co. KGaA, Weinheim

pyruvic acid (2.4%), and succinic acid (2.5%). Organically bound chlorine was mineralized to about 90%. The new method[18] is thus an interesting alternative to the method of Collins, as sodium nitrite is significantly cheaper than TAML, although on an industrial scale it would be necessary to recycle or dispose of it. The relatively high energy requirement and the apparatus expenditure must also be taken into account. The method of Collins et al. with H_2O_2/Fe-TAML requires 10–30 min at room temperature with a catalyst/substrate ratio of 1:2000. However, hydrogen peroxide is a more expensive oxidant than oxygen (Table 1). Therefore a detailed comparison that includes the energy balance of both methods would be of interest for industrial application.

Conclusion

A number of catalytic oxidation reactions of organic substrates with molecular oxygen are possible even without transition metals,[6,19] but transition metals cannot (yet) be dispensed with in most oxidations.[3] The (eco)toxicological assessment of metal-catalyzed reactions is currently possible only as an approximation, for the toxicity of a metal is essentially dependent upon its speciation (bonding state).[20] The toxicity of the most frequently used transition-metal catalysts is not known. Since many compounds may be toxic, they should not come into contact with personnel or the environment in the laboratory or in industrial operations, and after use they must be disposed of (which involves additional costs for metal-contaminated effluent).

If there is a choice between different catalysts and reagents in a catalytic reaction, the less toxic alternative should be given preference. The new methods described here[6,19] can contribute. The Fe-TAML catalyst[16,17] for total oxidations exhibits very low toxicity, and the system with oxygen and sodium nitrite for the total oxidation of chlorophenols is characterized by a high degree of mineralization.[19]

Note added in proof: A new review describes the application for the bleaching of textiles and pulp (R. Hage, A. Lienke, *Angew. Chem.* **2006**, *118*, 212–229; *Angew. Chem. Int. Ed.* **2006**, *45*, 206–222).

[1] a) M. B. Smith, J. March, *Advanced Organic Chemistry, Reactions, Mechanisms, and Structure*, 5th ed., Wiley-Interscience, New York, **2001**, chap. 19; b) M. Hudlicky, *Oxidations in Organic Chemistry*, American Chemical Society, Washington, DC, **1990**; c) R. C. Larock in *Comprehensive Organic Transformations*, 2nd ed., Wiley-VCH, New York, **1999**, p. 1197.

[2] On concepts of sustainable chemistry: a) B. M. Trost, *Angew. Chem.* **1995**, *107*, 285–307; *Angew. Chem. Int. Ed. Engl.* **1995**, *34*, 259–281 and B. M. Trost, *Angew. Chem.* **2005**, *117*, 6788–6825; *Angew. Chem. Int. Ed.* **2005**, *44*, 6630–6666; b) R. A. Sheldon, *CHEMTECH* **1994**, *3*, 38–47; c) P. T. Anastas, J. C. Warner, *Green Chemistry: Theory and Praxis,* Oxford University Press, New York, **1998**; d) M. Eissen, J. O. Metzger, *Chem. Eur. J.* **2002**, *8*, 3580–3585; e) M. Eissen, J. O. Metzger, E. Schmidt, U. Schneiderwind, *Angew. Chem.* **2002**, *114*, 402–425; *Angew. Chem. Int. Ed.* **2002**, *41*, 414–436; f) S. Boeschen, D. Lenoir, M. Scheringer, *Naturwissenschaften* **2003**, *90*, 93–103; g) *Green Chemistry, Nachhaltigkeit in der Chemie* (Ed.: Gesellschaft Deutscher Chemiker), Wiley-VCH, Weinheim, **2003**; h) *NOP*, an Internet book in German, English, and Italian: www.oc-praktikum.de; i) M. Lancaster, *Green Chemistry: An Introductory Text*, Royal Chemical Society, Cambridge, UK, **2002**.

[3] *Modern Oxidation Methods* (Ed.: J.-E. Bäckvall), Wiley-VCH, Weinheim, **2004**.

[4] a) K. Bowden, I. M. Heilbron, E. R. H. Jones, B. C. L. Weedon, *J. Chem. Soc.* **1946**, 39; b) Y. Liu, J. C. Vederas, *J. Org. Chem.* **1996**, *61*, 7856–7859; c) S. D. Meyer, S. L. Schreiber, *J. Org. Chem.* **1994**, *59*, 7549–7552; d) P. L. Anelli, C. Biffi, F. Montanari, S. Quici, *J. Org. Chem.* **1987**, *52*, 2559–2562; e) G. Barak, J. Dakka, Y. Sasson, *J. Org. Chem.* **1988**, *53*, 3553–3555; f) R. A. Sheldon, I. W. C. Arends, G.-J. ten Brink, A. Dijksman, *Acc. Chem. Res.* **2002**, *35*, 774–781.

[5] a) On copper-catalyzed oxidations: I. E. Marko, A. Gautier, R. Dumeunier, K. Doda, F. Philipart, S. M. Brown, C. J. Urch, *Angew. Chem.* **2004**, *116*, 1614–1617; *Angew. Chem. Int. Ed.* **2004**, *43*, 1588–1591, loc. cit.; b) on palladium-catalyzed oxidations: S. S. Stahl, *Angew. Chem.* **2004**, *116*, 3480–3501; *Angew. Chem. Int. Ed.* **2004**, *43*, 3400–3420, amd references therein; c) on ruthenium-catalyzed oxidations: B.-Z. Zhan, M. A. White, T.-K. Sham, J. A. Pincock, R. J. Doucet, R. K. V. Ramana, K. N. Robertson, T. S. Cameron, *J. Am. Chem. Soc.* **2003**, *125*, 2195–2199, and references therein.

[6] a) R. Liu, X. Liang, C. Dong, X. Hu, *J. Am. Chem. Soc.* **2004**, *126*, 4112–4113; b) R. Liu, C. Dong, X. Liang, X. Wang, X. Hu, *J. Org. Chem.* **2005**, *70*, 729–731.

[7] C.-J. Li, T. H. Chan, *Organic Reactions in Aqueous Media*, Wiley, New York, **1997**.

[8] C. L. Hill, *Angew. Chem.* **2004**, *116*, 406–408; *Angew. Chem. Int. Ed.* **2004**, *43*, 402–404, and references therein.

[9] *Applied Homogenic Catalysis with Organometallic Compounds*, *Vol. 1* (Eds.: B. Cornils, W. Herrmann), VCH, Weinheim, **1996**, chap. 2.4.

[10] a) P. Saling, A. Kicherer, B. Dittrich-Krämer, R. Wittlinger, W. Zombik, I. Schmidt, W. Schrott, S. Schmidt, *Int. J. Life Cycle Assess.* **2002**, *7*, 203–218; b) D. R. Shonnard, A. Kicherer, P. Saling, *Environ. Sci. Technol.* **2003**, *37*, 5340–5348.

[11] a) B.-U. Hildebrandt, U. Schlottmann, *Angew. Chem.* **1998**, *110*, 1382–1393, *Angew. Chem. Int. Ed. Engl.* **1998**, *37*, 1316–1326; b) S. Ramamoorthy, S. Ramamoorthy, *Chlorinated Organic Compounds in the Environment*, CRC Press, Boca Raton, Fl, USA, **1999**.

[12] a) T. Hatta, O. Nakano, N. Imai, N. Takizawa, H. Kiyohara, *J. Biosci. Bioeng.* **1999**, *87*, 267–272; b) M. Pera-Titus, V. Garcia-Molina, M. A. Banos, J. Giminez, S. Esplugas, *Appl. Catal. B* **2004**, *47*, 219–256.

[13] a) C. Walling, *Acc. Chem. Res.* **1975**, *8*, 125–131; b) C. Walling, *Acc. Chem. Res.* **1998**, *31*, 155–157, loc. cit.

[14] G. Lente, J. H. Espenson, *Green Chem.* **2005**, *7*, 28–34, and references therein.

[15] a) G. Labat, J. L. Seris, B. Meunier, *Angew. Chem.* **1990**, *102*, 1488–1490; *Angew. Chem. Int. Ed. Engl.* **1990**, *29*, 1471–1473; b) A. Sorokin, J. L. Series, B. Meunier, *Science* **1995**, *268*, 1163–1166, and references therein; c) B. Meunier, A. Sorokin, *Acc. Chem. Res.* **1997**, *30*, 470–476; d) A. Hadasch, A. Sorokin, A. Rabion, B. Meunier, *New J. Chem.* **1998**, *22*, 45–51.

[16] a) T. J. Collins, *Acc. Chem. Res.* **2002**, *35*, 782–790; b) A. Gosh, T. T. Oliveira, T. Yano, T. Nishioka, E. S. Beach, I. Kinoshita, E. Münck, A. D. Ryabov, C. P. Horwitz, T. J. Collins, *J. Am. Chem. Soc.* **2005**, *127*, 2505–2513.

[17] S. Sen Gupta, M. Stadler, C. A. Noser, A. Gosh, B. Steinhoff, D. Lenoir, C. P. Horwitz, K.-W. Schramm, T. J. Collins, *Science* **2002**, *296*, 326–328.

[18] a) Azo dyes: N. Chahbane, D. Lenoir, K.-W. Schramm, D. A. Mitchell, D.-L. Popercu, A. Chanda, A. D. Ryabov,

 © 2006 Wiley-VCH Verlag GmbH & Co. KGaA, Weinheim

T. C. Collins, unpublished results; b) alkyl sulfides: T. J. Collins, D. Banerjee, S. K. Khetan, *Abstracts of Papers of the American Chemical Society* **2004**, *228*, U796–U796 (133-Inor Part 1, Aug 22); c) Effluent from pulp and paper production: C. P. Horwitz, T. J. Collins, J. Spatz, *Abstracts of papers of the American Chemical Society* **2004**, *227*, U293–U293 (094-Cell Part 1, March 28).

[19] X. Liang, D. Fu, R. Liu, Q. Zhang, T. Y. Zhang, X. Hu, *Angew. Chem.* **2005**, *117*, 5656–5659; *Angew. Chem. Int. Ed.* **2005**, *44*, 5520–5523.

[20] D. M. Templeton, F. Ariese, R. Cornelis, G. Danielson, H. Muntau, H. P. van Leeuwen, R. Lobinski, *Pure Appl. Chem.* **2000**, *72*, 1453–1470.

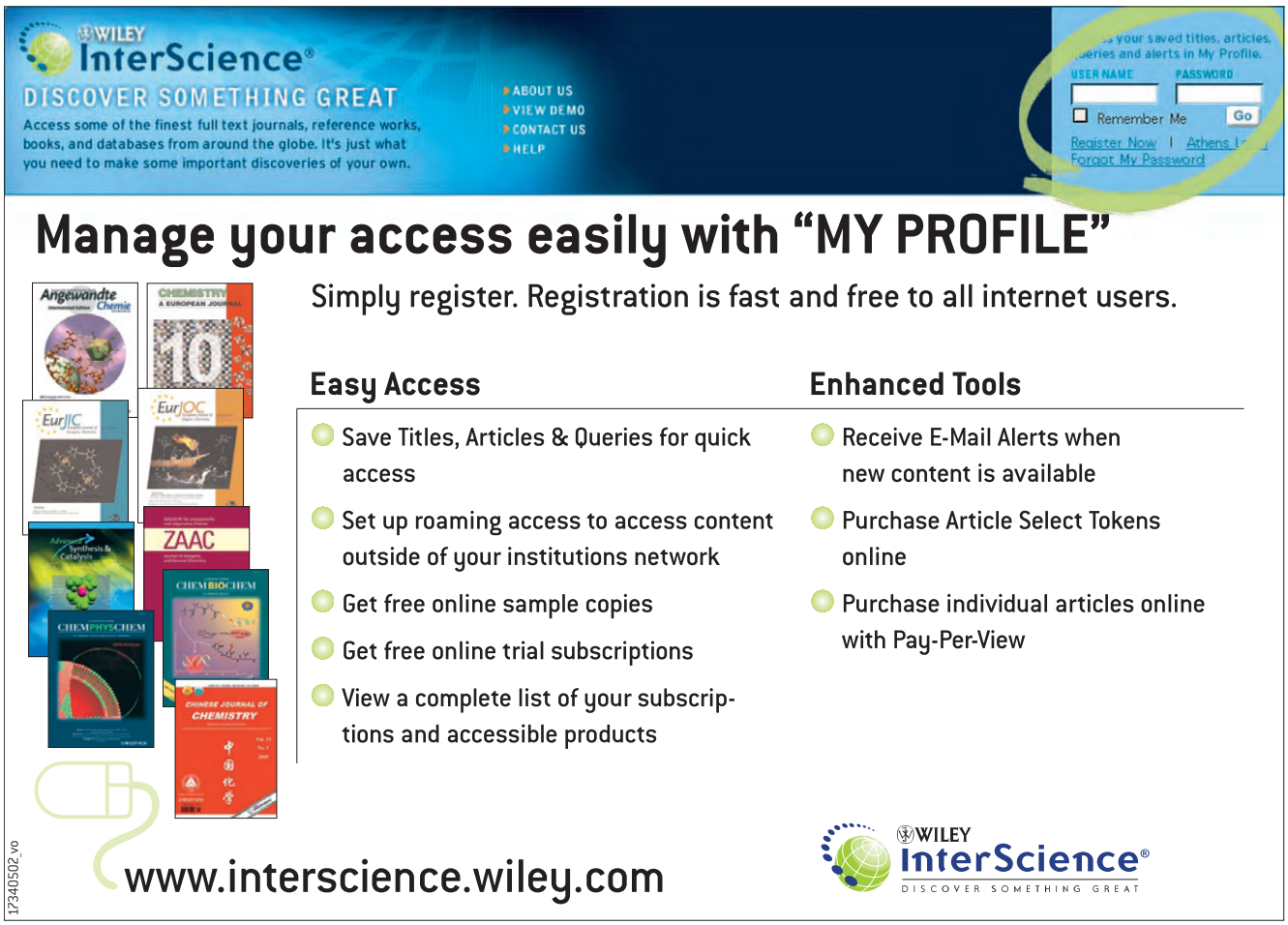

 © 2006 Wiley-VCH Verlag GmbH & Co. KGaA, Weinheim

Higher-Coordinate Si Compounds

DOI: 10.1002/anie.200503534

Not Unhydrolyzed at pH 8**

Xaver Kästele, Peter Klüfers, and Reinhold Tacke*

Keywords:
higher-coordinate compounds · silicates · silicon · zwitterions

The search for silicon complexes that exhibit hydrolytic stability in neutral aqueous solution is a major challenge in contemporary silicon chemistry and has both technical and biochemical relevance. The recently published claim by one of us[1] that a zwitterionic bis(diolato)silicate, derived from anhydroerythritol (*meso*-oxolane-3,4-diol; AnEryt) is hydrolytically stable at pH 7–8, thus appeared to be a milestone. The compound in question is bis[*meso*-oxolane-3,4-diolato(2−)](morpholiniomethyl)silicate (**1** (originally labeled **10** in Ref. [1]); see Figure 1). It was reported that no tetracoordinate silicon species could be detected upon dissolution of **1** in water; that is, no hydrolytic decomposition occurred.

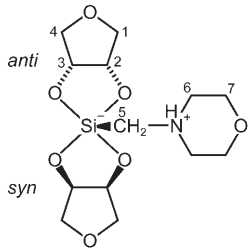

1

Figure 1. The zwitterionic (oxolanediolato)silicate **1**. The orientation of an oxolane ring with respect to the monovalent substituent at the silicon center defines *syn* or *anti* bonding. The numbering of the oxolane carbon atoms corresponds to that for a furanose.

[*] X. Kästele, Prof. Dr. P. Klüfers
Department Chemie und Biochemie
Ludwig-Maximilians-Universität
Butenandtstrasse 5–13, 81377 München (Germany)
Fax: (+49) 89-2180-77407
E-mail: kluef@cup.uni-muenchen.de
Prof. Dr. R. Tacke
Institut für Anorganische Chemie
Universität Würzburg
Am Hubland, 97074 Würzburg (Germany)

[**] A correction to "A Zwitterionic Spirocyclic Pentacoordinate Silicon Compound Synthesized in Water by Si–O and Si–C Bond Cleavage".[1]

The hydrolytic stability that was claimed would have meant that **1** is drastically different from pentacoordinate bis[*meso*-oxolane-3,4-diolato(2−)]-silicates, which do not have the morpholiniomethyl group as their fifth substituent. An example is the analogous pentacoordinate anionic species, bis[*meso*-oxolane-3,4-diolato(2−)]hydroxosilicate. On the one hand, its alkali salts share with **1** a convenient synthetic accessibility from aqueous solution by simple evaporation of the solvent.[2] On the other hand, these hydroxosilicates and the related phenylsilicates show partial hydrolysis in aqueous solution at high pH values, typically at about pH 12, and complete hydrolysis in neutral aqueous environment, as observed by NMR spectroscopy.

Though it appears to be a reasonable hypothesis that the introduction of a positive charge close to the silicon center may suppress hydrolytic decomposition, the first step of which may be the protonation of a silicon-bonded alkoxide O atom, the claimed extent of stabilization of **1** seemed highly unlikely in light of a report by Kästele et al. on anionic pentacoordinate oxolanediolatosilicates.[3] It thus appeared sensible to connect the areas of anionic and zwitterionic silicates in a step-by-step procedure in order to identify the origin of the apparent inconsistencies.

The experimental procedure chosen is summarized in Figure 2. Starting from the well-known area of pentacoordinate oxolanediolatosilicate anions under non-hydrolyzing conditions,[3] the experiments eventually approach the conditions reported in Ref. [1]. The NMR spectra of the anionic morpholinomethyl homologue of a bis(oxolanediolato)-phenylsilicate or -hydroxosilicate in methanolic solution are shown in Figure 2a. Under these basic, non-hydrolyzing conditions, the conjugate base of **1**, the anion $[(AnErytH_{-2})_2SiCH_2NC_4H_8O]^-$, was expected to be the only reaction product. In fact, the signal patterns in both the ^{29}Si and ^{13}C NMR spectra (Figure 2a) consistently resembled the spectra of the analogous phenyl- or hydroxosilicates. The spectra in Figure 2a thus show all the typical features related to the characteristic *syn*/*anti* isomerism.[3] First, the ^{29}Si NMR spectrum consists of three signals that span a typical chemical shift range of some 3–8 ppm. The signal of the minor component, tentatively the *syn*/*syn* isomer, appeared, as expected, most upfield. The *syn*/*anti* and *anti*/*anti* isomers were the main species. Crystals of $K[(AnErytH_{-2})_2SiCH_2NC_4H_8O]\cdot MeOH$ grown from such solutions accordingly contained one of the two main isomers, namely the *anti*/*anti*-configured anion.[4]

Second, the ^{13}C NMR spectrum (Figure 2a) revealed a spectral feature corresponding to the phenylsilicate analogue: The ^{13}C NMR signals of the monovalent substituent at the silicon center mirrored the pattern of the ^{29}Si NMR signals. The signals assigned to C6 and C7 showed the *syn*/*syn* minor component clearly separated and shifted upfield by about 1 ppm from a pair of signals corresponding to the main isomers. The signal for C5, corresponding to one carbon atom only, appears to be a less suitable probe owing to its lower intensity, a situation that parallels the difference in usefulness of the C_{ipso} and C_{ortho} signals of phenylsilicates.[3]

InterScience
© 2006 Wiley-VCH Verlag GmbH & Co. KGaA, Weinheim

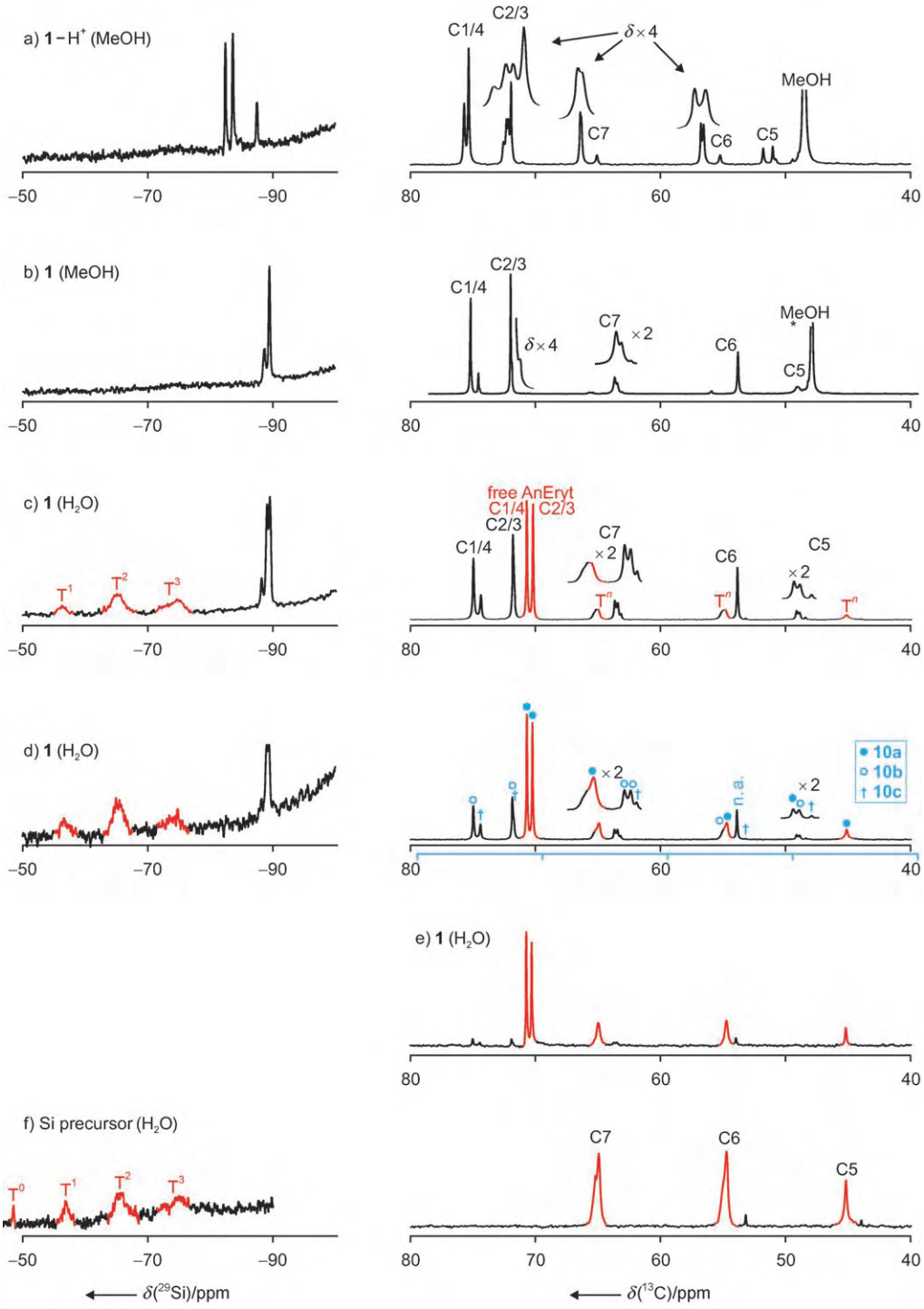

Figure 2. ^{29}Si (left) and $^{13}C\{^1H\}$ NMR spectra (right) for **1** (a–e) under various conditions. a) 1:2:1 molar ratio of $(MeO)_3SiCH_2NC_4H_8O$/AnEryt/KOMe in methanol; [Si] = 0.48 mol kg^{-1}. b) As for Figure 2a but without KOMe. The ^{13}C NMR spectrum was recorded at −30 °C and is shifted such that the signal for C6 is aligned with that in Figure 2c for comparison (the original position of the signal is marked by an asterisk). c) Aqueous solution of **1** (1.04 mol kg^{-1}) at pH 8.2. Signals corresponding to hydrolysis products of **1** are shown in red, and those assigned to free AnEryt resemble those for a sample of pure AnEryt in water. d) Aqueous solution of **1** (0.45 mol kg^{-1}; 0.47 mol L^{-1}) at pH 8.0. The assignment of signals, the scale, and compounds labels **10a–c**, according to Ref. [1] are shown in blue (n.a. = not assigned in Ref. [1]). e) Aqueous solution of **1** (0.1 mol kg^{-1}) at pH 7.8. The ^{29}Si NMR spectrum was not recorded as a result of the low total concentration. f) Aqueous solution of trimethoxy(morpholinomethyl)silane (0.58 mol kg^{-1}). A stock solution (1.5 mol kg^{-1}) in water was left for 3 days and diluted prior to the measurement. Inserts labeled "$\delta \times 4$" show the respective signals with fourfold magnification along the δ axis, while those labeled "×2" show the respective signals with double magnification along both axes. The numbering scheme for carbon atoms corresponds to that shown in Figure 1. See text for details.

 © 2006 Wiley-VCH Verlag GmbH & Co. KGaA, Weinheim

Third, *syn*/*anti* isomerism was clearly recognizable in the signal pattern in the ^{13}C NMR region corresponding to AnEryt. As a result of symmetry considerations, one strong signal (the *anti*/*anti* isomer), two signals of equal intensity (the *syn*/*anti* isomer), and a weak signal (the *syn*/*syn* isomer) were expected and indeed observed for the pair of chemically equivalent diol carbon atoms (C2/3). Because of accidental signal overlap, less than four separate signals were observed, as usual, for the carbon atoms adjacent to the diol moiety (C1/4). Quite reliably, the signals for AnEryt are characteristically shifted with respect to free AnEryt by about 1 ppm for the diol carbon atoms (C2/3) and by about 4 ppm for those lying adjacent (C1/4). These shifts are close to the respective mean values of 2 and 5 ppm observed for a series of furanoidic ligands with the AnEryt partial structure.[3]

In the next step (Figure 2b), one equivalent of protons was added to obtain the zwitterionic species while maintaining the non-hydrolyzing solvent methanol (in practice, the addition of methoxide was omitted). At room temperature, the NMR spectra shown in Figure 2b displayed unexpectedly few signals; for instance, in the ^{13}C NMR spectrum only one signal was observed for each type of carbon atom. However, upon cooling to −30 °C, some signals split and adopted the same shape as observed in aqueous media (see below). Note that some spectral features that indicate *syn*/*anti* isomerism are missing. First, the range of the splitting of the ^{29}Si NMR signal is unusually narrow. Second, the splitting of the mirror signals (C5, C6, C7) is small or absent. Third, the typical pattern for atoms C2/3 is missing. Nevertheless, a thorough analysis of the peculiarities of zwitterion isomerization is outside the scope of the present contribution. Though questions regarding isomerism remain open, AnEryt is clearly bonded to silicon, as indicated by the typical differences in chemical shift values. The spectra in Figure 2b thus correspond to pure, non-hydrolyzed **1**.

Next, the solvent was changed from methanol to water. Figure 2c shows the distribution of species in an aqueous solution (1M) of the zwitterionic **1**. Additional signals of hydrolytic species appeared (drawn in red) which could be observed separately in blank experiments using solutions of pure AnEryt and pure trimethoxy(morpholinomethyl)silane in water. Typical spectra for the latter are shown in Figure 2f: at pH ≈8.5, hydrolysis of the pure silicon precursor yielded four groups of signals in the ^{29}Si NMR spectrum which were tentatively assigned to T^0 to T^3 groups of silsesquioxane species (see Ref. [5] for details of the T^n nomenclature and typical ranges of ^{29}Si NMR chemical shifts). As is clear from Figure 2f, the relatively broad ^{13}C NMR signals of C5, C6, and C7 are no longer usable mirrors of the ^{29}Si NMR signals. In the second blank experiment, AnEryt gave rise to two signals, as expected.

The influence of the concentration of silicate is illustrated in Figure 2d and e. The lower the concentration, the more pronounced the hydrolysis. The conditions used in Figure 2d most closely resemble those given in Ref. [1], and thus the spectral assignment used therein is applied here. A comparison of the ^{13}C NMR spectrum (Figure 2d) with the revised assignment given in Figure 2c shows that the hydrolysis products are assigned to the main pentacoordinate species (labeled as **10a** in Ref. [1]). At the same time, the related ^{29}Si NMR signals of the silsesquioxane part had been overlooked. The pronounced hydrolytic instability of **1** at a pH value close to neutrality is made particularly clear by further dilution. Figure 2e shows the ^{13}C NMR spectrum recorded at a concentration of silicon of 0.1 mol kg^{-1}; the small amount of residual **1** is clear.

As a result, the statement made in Ref. [1] that **1** (**10**) experiences no hydrolytic decomposition upon dissolution in water is not supported by the correctly assigned NMR spectra shown herein. Contrary to the conclusions made previously,[1], hydrolysis products dominate the spectra of aqueous solutions, particularly at higher dilution. Despite this troublesome result, it should be noted that, in fact, the hydrolytic stability of a pentacoordinate silicate increases if the silicon center is part of a zwitterion instead of an anion. Moreover, hydrolysis may be increasingly suppressed, as observed by ^{29}Si NMR spectroscopy, when increasing amounts of excess oxolanediol are present in the solution equilibrium.

[1] R. Tacke, R. Bertermann, C. Burschka, S. Dragota, *Angew. Chem.* **2005**, *117*, 5426–5429; *Angew. Chem. Int. Ed.* **2005**, *44*, 5292–5295.

[2] K. Benner, P. Klüfers, J. Schuhmacher, *Z. Anorg. Allg. Chem.* **1999**, *625*, 541–543.

[3] X. Kästele, P. Klüfers, F. Kopp, J. Schuhmacher, M. Vogt, *Chem. Eur. J.* **2005**, *11*, 6326–6346, and references therein.

[4] X. Kästele, P. Klüfers, unpublished results.

[5] S. Altmaier, P. Behrens in *Silicon Chemistry* (Eds.: P. Jutzi, U. Schubert), Wiley-VCH, Weinheim, **2003**, p. 460–474.

 © 2006 Wiley-VCH Verlag GmbH & Co. KGaA, Weinheim

Mesoporous Materials

DOI: 10.1002/anie.200503075

Silica-Based Mesoporous Organic–Inorganic Hybrid Materials

*Frank Hoffmann, Maximilian Cornelius, Jürgen Morell, and Michael Fröba**

Keywords:
amphiphiles · materials science · mesoporous materials · organic–inorganic hybrid materials · template syntheses

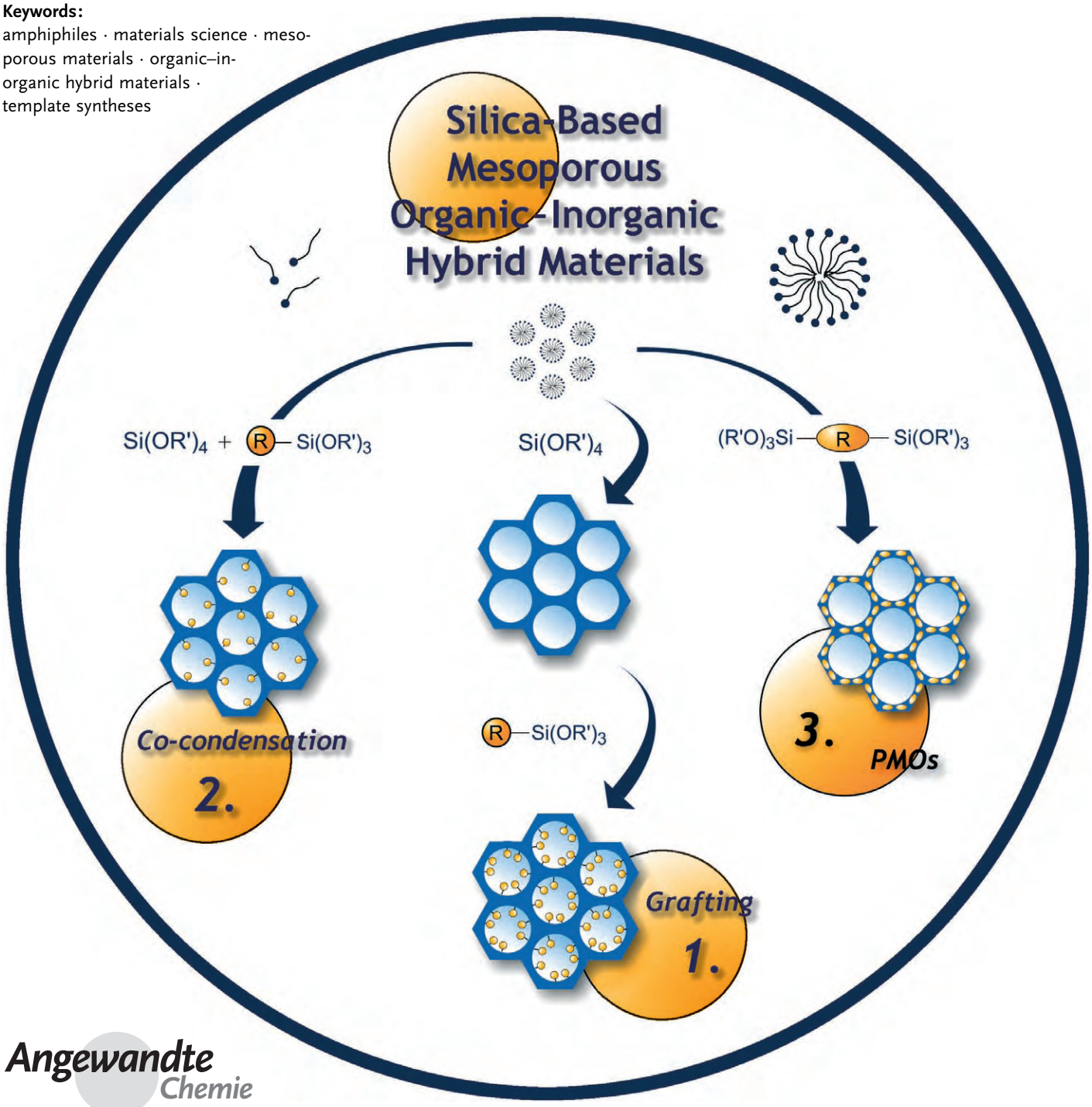

© 2006 Wiley-VCH Verlag GmbH & Co. KGaA, Weinheim

Mesoporous organic–inorganic hybrid materials, a new class of materials characterized by large specific surface areas and pore sizes between 2 and 15 nm, have been obtained through the coupling of inorganic and organic components by template synthesis. The incorporation of functionalities can be achieved in three ways: by subsequent attachment of organic components onto a pure silica matrix (grafting), by simultaneous reaction of condensable inorganic silica species and silylated organic compounds (co-condensation, one-pot synthesis), and by the use of bissilylated organic precursors that lead to periodic mesoporous organosilicas (PMOs). This Review gives an overview of the preparation, properties, and potential applications of these materials in the areas of catalysis, sorption, chromatography, and the construction of systems for controlled release of active compounds, as well as molecular switches, with the main focus being on PMOs.

From the Contents

1. Introduction 3217
2. Organically Functionalized Mesoporous Silica Phases 3220
3. Postsynthetic Functionalization of Silica (Grafting) 3221
4. Co-Condensation (One-Pot Synthesis) 3226
5. PMOs 3229
6. Outlook 3246

1. Introduction

The development of porous materials with large specific surface areas is currently an area of extensive research, particularly with regard to potential applications in areas such as adsorption, chromatography, catalysis, sensor technology, and gas storage. An upsurge began in 1992 with the development by the Mobil Oil Company of the class of periodic mesoporous silicas known as the M41S phase. These materials superseded zeolite molecular sieves, which were restricted to a pore size of around 15 Å.[**] Like the microporous crystalline zeolites, this class of materials is characterized by very large specific surface areas, ordered pore systems, and well-defined pore radius distributions. Unlike the zeolites, however, the M41S materials have pore diameters from approximately 2 to 10 nm[***] and exhibit amorphous pore walls. The most well-known representatives of this class include the silica solids MCM-41 (with a hexagonal arrangement of the mesopores, space group *p6mm*), MCM-48 (with a cubic arrangement of the mesopores, space group $Ia\bar{3}d$), and MCM-50 (with a laminar structure, space group *p*2) (Figure 1).[1,2] The use of supramolecular aggregates of ionic surfactants (long-chain alkyltrimethylammonium halides) as structure-directing agents (SDAs) was groundbreaking in the synthesis of these materials. These SDAs, in the form of a lyotropic liquid-crystalline phase, lead to the assembly of an ordered mesostructured composite during the condensation of the silica precursors under basic conditions. The mesoporous materials are obtained by subsequent removal of the surfactant by extraction or calcination.

In-depth investigations into the formation process of these composite materials have found that two different mechanisms are involved: On the one hand, in true liquid-crystal templating (TLCT), the concentration of the surfactant is so high that under the prevailing conditions (temperature, pH) a lyotropic liquid-crystalline phase is formed without requiring the presence of the precursor inorganic framework materials (normally tetraethyl- (TEOS) or tetramethylorthosilica (TMOS)).[4] On the other hand, it is also possible that this phase forms even at lower concentrations of surfactant molecules, for example, when there is cooperative self-assembly of the SDA and the already added inorganic species, in which case a liquid-crystal phase with hexagonal, cubic, or laminar arrangement can develop (Figure 2).[5]

In the meantime, the original approach has been extended by a number of variations, for example, by the use of triblock copolymer templates[****] under acidic conditions by which means the so-called SBA silica phases may be synthesized.

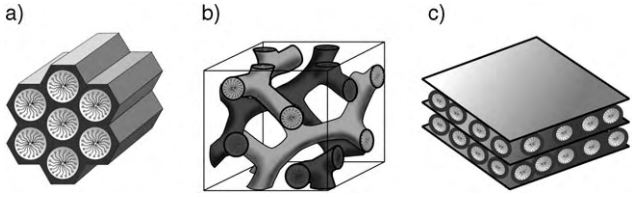

Figure 1. Structures of mesoporous M41S materials: a) MCM-41 (2D hexagonal, space group *p6mm*), b) MCM-48 (cubic, space group $Ia\bar{3}d$), and c) MCM-50 (lamellar, space group *p*2).

[*] Dr. F. Hoffmann, M. Cornelius, J. Morell, Prof. Dr. M. Fröba
Institut für Anorganische und Analytische Chemie
Justus-Liebig-Universität Giessen
Heinrich-Buff-Ring 58, 35392 Giessen (Germany)
Fax: (+49) 641-34-109
E-mail: michael.froeba@anorg.chemie.uni-giessen.de

[**] Independently of the researchers at Mobil, Yanagisawa et al.[3] discovered somewhat earlier another method to prepare mesoporous silicon dioxide by the intercalation of surfactants into lamellar silicas, the so-called FSM materials. However, this is not an actual template mechanism; rather, the preparation involves a "swelling" of lamellar silicas from which the three-dimensional structures were eventually obtained.

[***] According to the definition of IUPAC, porous materials are divided into three different classes, depending on their pore sizes. Mesoporous materials are described as materials whose pore diameters lie in the range between 2 and 50 nm. Solids with a pore diameter below 2 nm or above 50 nm belong to the class of micro- and macroporous materials, respectively.

[****] The term template is used in zeolite synthesis to mean those molecules that have a definite structure-directing function in the construction of composite materials. Meanwhile, however, the meaning of this term has changed to such an extent that it is frequently used in the general sense of a structure-determining agent even when it relates to supramolecular aggregates and when several structural types can be produced by the same agent.

© 2006 Wiley-VCH Verlag GmbH & Co. KGaA, Weinheim

A fundamental condition for this method is that an attractive interaction between the template and the silica precursor is produced to ensure inclusion of the structure director without phase separation taking place. Figure 3 illustrates the different interactions that can take place between the inorganic components and the head groups of the surfactants. According to the suggestion of Huo et al.,[6,7] these interactions are classified as follows: If the reaction takes place under basic conditions (whereby the silica species are present as anions) and cationic quaternary ammonium surfactants are used as the SDA, the synthetic pathway is termed S^+I^- (Figure 3a; S: surfactant; I: inorganic species). The preparation can also take place under acidic conditions (below the isoelectric point of the Si–OH-bearing inorganic species; $pH \approx 2$), whereby the silica species are positively charged. To produce an interaction with the cationic surfactant, it is necessary to add a mediator ion X^- (usually a halide) ($S^+X^-I^+$; pathway (b)). Conversely, when negatively charged surfactants (e.g., long-chain alkyl phosphates) are used as the SDA, it is possible to work in basic media, whereby again a

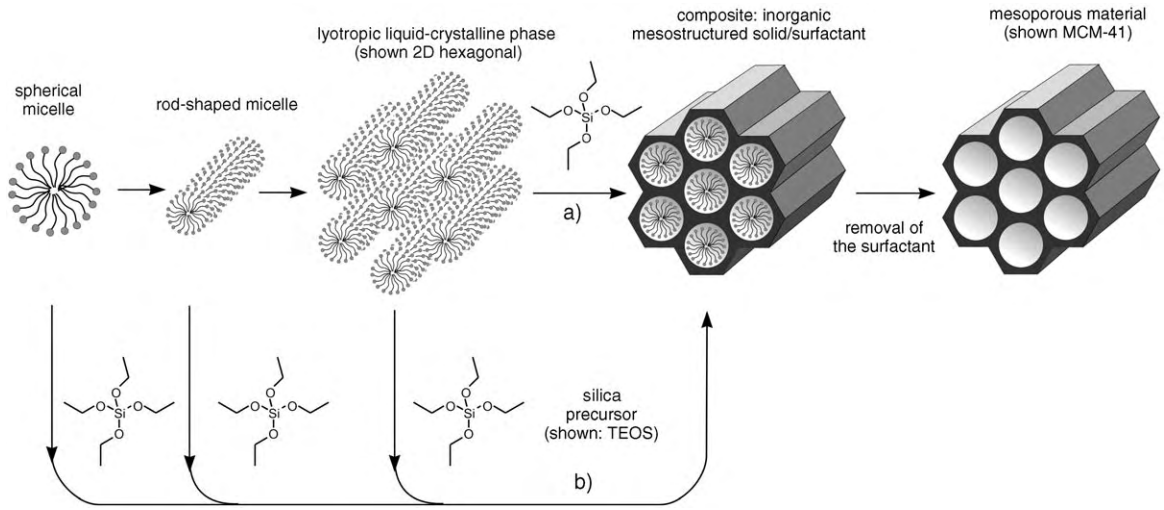

Figure 2. Formation of mesoporous materials by structure-directing agents: a) true liquid-crystal template mechanism, b) cooperative liquid-crystal template mechanism.

Frank Hoffmann studied chemistry at the Institute of Organic Chemistry in Hamburg and received his doctorate for work on the topic "Interactions in chiral Langmuir films" under the direction of Prof. H. Hühnerfuss. Since 2002, he has undertaken postdoctoral research in the group of Prof. M. Fröba in Giessen. His main interest is the theoretical understanding of aggregation- and structure-forming phenomena during the synthesis of mesostructured materials.

Jürgen Morell studied chemistry at the Justus Liebig University of Giessen. He received his diploma in 2003 in the group of Prof. M. Fröba at the Institute of Inorganic and Analytical Chemistry in Giessen. Since then he has been working towards his doctorate on the synthesis and characterization of new PMOs.

Maximilian Cornelius studied chemistry first in Giessen and then in Marburg and received his diploma in 2003 for work on "Photoinduced ring-opening polymerization in the synthesis of polyesters" at the Institute of Macromolecular Chemistry. He then began his doctorate work in the group of Prof. M. Fröba at the Justus Liebig University of Giessen on the synthesis of new organosilica precursors for the preparation of PMOs with special coordination sites.

Michael Fröba studied chemistry in Würzburg and Hamburg and received his doctorate in 1993 from the Institute of Physical Chemistry, where he worked with Prof. W. Metz on graphite intercalation compounds. From 1994 to 1996, he was a Feodor Lynen research fellow in the group of Dr. J. Wong at the Lawrence Livermore National Laboratory. After his habilitation at the University of Hamburg in 2000, he was appointed Professor for Inorganic Chemistry at the Friedrich Alexander University of Erlangen–Nuremberg. Since 2001, he has been Professor for Inorganic Chemistry with a focus on solid-state and materials chemistry at the Justus Liebig University of Giessen.

 © 2006 Wiley-VCH Verlag GmbH & Co. KGaA, Weinheim

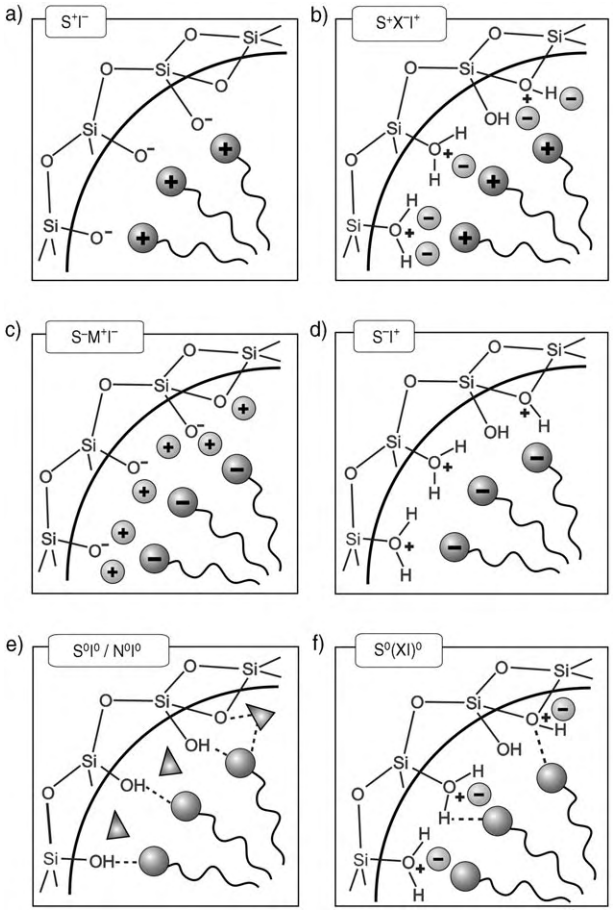

Figure 3. Interactions between the inorganic species and the head group of the surfactant with consideration of the possible synthetic pathway in acidic, basic, or neutral media. Electrostatic: S^+I^-, $S^+X^-I^+$, $S^-M^+I^-$, S^-I^+; through hydrogen bonds: S^0I^0/N^0I^0, $S^0(XI)^0$.

mediator ion M^+ must be added to ensure interaction between the equally negatively charged silica species ($S^-M^+I^-$; pathway (c)); a mediator ion is not required in acidic media (S^-I^+; pathway (d)). Thus, the dominating interactions in pathways (a–d) are of an electrostatic nature. Moreover, it is still possible for the attractive interactions to be mediated through hydrogen bonds. This is the case when nonionic surfactants are used (e.g., S^0: a long-chained amine; N^0: polyethylene oxide), whereby uncharged silica species (S^0I^0; pathway (e)) or ion pairs ($S^0(XI)^0$; pathway (f)) can be present.

Meanwhile template-synthetic routes have also been used successfully in the preparation of non-silica mesoporous metal oxides (e.g., titanium,[8–11] aluminum,[11,12] zirconium,[11] tin,[11] manganese,[13] niobium[14]), metal sulfides (e.g., germanium[15]), and metal phosphates (e.g., aluminum,[16] zirconium[17]).

The syntheses of ordered mesoporous solids described above are classified as endotemplate methods ("soft-matter templating"). In exotemplate methods ("nanocasting"), a porous solid is used as the template in place of the surfactant. Thus, this method is also known as "hard-matter templating". The hollow spaces that provide the exotemplate framework are filled with an inorganic precursor, which is then transformed (cured) under suitable conditions. In this way, the pore system of the template is copied as a "negative image". After removal of the now-filled exotemplate framework, the incorporated material is obtained with a large specific surface area. An example of periodic porous solids employed as exotemplates are ordered mesoporous silica phases (e.g., MCM-48 and SBA-15 types). This replication method was used for the first time by Ryoo et. al.[18] for the synthesis of mesoporous carbon (CMK-1). A short time later, Hyeon and co-workers[19] independently presented very similar approaches for the preparation of mesoporous carbon materials, known as SNU-X materials. (Note that the terms endo- and exotemplate are formally derived from the terms endo- and exoskeleton used in biology. An excellent overview of the concepts and their concrete use has been presented by Schüth.)[20]

A series of review articles cover the syntheses of mesoporous materials, whether they be pure silica phases or other metal oxides, and their applications.[21–28] Considerable efforts have been undertaken to incorporate organic components within an inorganic silica framework to achieve symbiosis of the properties of both components. Herein we give an overview of the synthesis and properties as well as the prospects for application of organically modified silica phases that are accessible by the endotemplate method (a review article that specifically covers catalytic applications is found in reference [29]). The main focus will be on periodic mesoporous organosilicas (PMOs) that in the eyes of the authors have a special position in this class of hybrid materials.[*] Metal-substituted silica phases and materials that are functionalized with metal complexes or organometallic compounds are not considered. The three fundamental principles for the preparation of organically modified or functionalized silica phases will be introduced together with a discussion of the respective advantages and disadvantages of the synthetic routes and the resulting properties of these materials. Selected examples of the postsynthetic functionalization of silicas and the direct methods of co-condensation as well as a comprehensive overview of the state of research in the area of PMOs and their potential applications will be given.

[*] We use the term hybrid material in a strict sense that implies a *covalent* bond between the organic and inorganic components within the material. In contrast, the term composite materials is used to describe systems composed of two or more distinctively different components that exhibit an interface; in this case, the interactions between organic and inorganic components are provided by hydrogen bonds, van der Waals forces, and π interactions, or are electrostatic in nature. In this way we are following the definition that has been given by, for example, Schubert and Hüsing in their updated monograph.[30] An alternative definition is used by Gómez-Romero and Sanchez, who use the term hybrid materials in both cases and classify those materials in which a covalent bond is present as "class II hybrids" and all other materials as "class I hybrids".[31]

 © 2006 Wiley-VCH Verlag GmbH & Co. KGaA, Weinheim

2. Organically Functionalized Mesoporous Silica Phases

The combination of the properties of organic and inorganic building blocks within a *single* material is particularly attractive from the viewpoint of materials scientists because of the possibility to combine the enormous functional variation of organic chemistry with the advantages of a thermally stable and robust inorganic substrate. This is particularly applicable to heterogeneous catalysis. The symbiosis of organic and inorganic components can lead to materials whose properties differ considerably from those of their individual, isolated components.

Adjustment of the polarity of the pore surfaces of an inorganic matrix by the addition of organic building blocks extends considerably the range of materials that can be used, for example, in chromatography. Equally interesting is modification with organic functionalities such as C–C multiple bonds, alcohols, thiols, sulfonic and carboxylic acids, and amines, etc., which allow, for example, localized organic or biochemical reactions to be carried out on a stable, solid inorganic matrix.

Three pathways are available for the synthesis of porous hybrid materials based on organosilica units: 1) the subsequent modification of the pore surface of a purely inorganic silica material ("grafting"), 2) the simultaneous condensation of corresponding silica and organosilica precursors ("co-condensation"), and 3) the incorporation of organic groups as bridging components directly and specifically into the pore walls by the use of bissilylated single-source organosilica precursors ("production of periodic mesoporous organosilicas").

2.1. Postsynthetic Functionalization of Silicas ("Grafting")

Grafting refers to the subsequent modification of the inner surfaces of mesostructured silica phases with organic groups. This process is carried out primarily by reaction of organosilanes of the type $(R'O)_3SiR$, or less frequently chlorosilanes $ClSiR_3$ or silazanes $HN(SiR_3)_3$, with the free silanol groups of the pore surfaces (Figure 4). In principle, functionalization with a variety of organic groups can be realized in this way by variation of the organic residue R. This method of modification has the advantage that, under the synthetic conditions used, the mesostructure of the starting silica phase is usually retained, whereas the lining of the walls is accompanied by a reduction in the porosity of the hybrid material (albeit depending upon the size of the organic residue and the degree of occupation). If the organosilanes react preferentially at the pore openings during the initial stages of the synthetic process, the diffusion of further molecules into the center of the pores can be impaired, which can in turn lead to a nonhomogeneous distribution of the organic groups within the pores and a lower degree of occupation. In extreme cases (e.g., with very bulky grafting species), this can lead to complete closure of the pores (pore blocking).

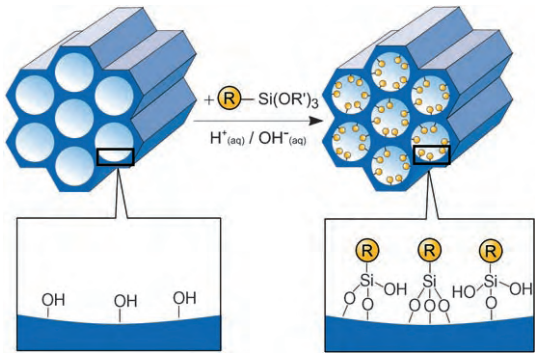

Figure 4. Grafting (postsynthetic functionalization) for organic modification of mesoporous pure silica phases with terminal organosilanes of the type $(R'O)_3SiR$. R = organic functional group.

The process of grafting is frequently erroneously called immobilization, which is a term that we believe should be reserved for adsorptive methods (e.g., the removal of toxic or environmentally relevant contaminants by adsorbent materials, or the separation of proteins and biocatalysts by restriction of the freedom of movement).

2.2. Co-Condensation (Direct Synthesis)

An alternative method to synthesize organically functionalized mesoporous silica phases is the co-condensation method (one-pot synthesis). It is possible to prepare mesostructured silica phases by the co-condensation of tetraalkoxysilanes $[(RO)_4Si$ (TEOS or TMOS)] with terminal trialkoxyorganosilanes of the type $(R'O)_3SiR$ in the presence of structure-directing agents leading to materials with organic residues anchored covalently to the pore walls (Figure 5). By using structure-directing agents known from the synthesis of

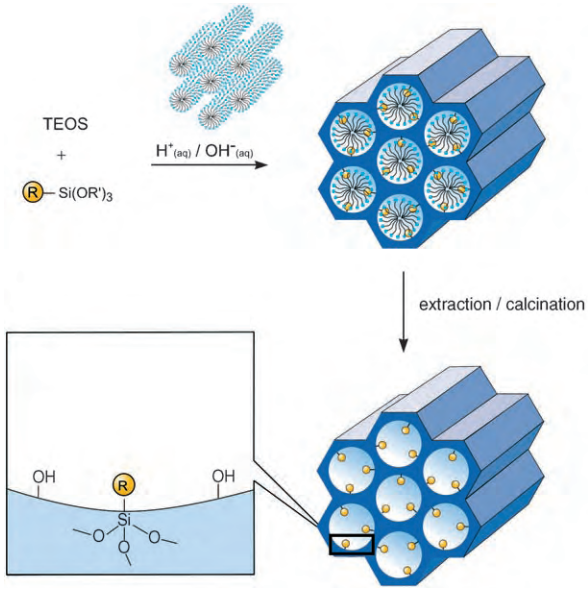

Figure 5. Co-condensation method (direct synthesis) for the organic modification of mesoporous pure silica phases. R = organic functional group.

 © 2006 Wiley-VCH Verlag GmbH & Co. KGaA, Weinheim

pure mesoporous silica phases (e.g., MCM or SBA silica phases), organically modified silicas can be prepared in such a way that the organic functionalities project into the pores.

Since the organic functionalities are direct components of the silica matrix, pore blocking is not a problem in the co-condensation method. Furthermore, the organic units are generally more homogeneously distributed than in materials synthesized with the grafting process. However, the co-condensation method also has a number of disadvantages: in general, the degree of mesoscopic order of the products decreases with increasing concentration of $(R'O)_3SiR$ in the reaction mixture, which ultimately leads to totally disordered products. Consequently, the content of organic functionalities in the modified silica phases does not normally exceed 40 mol%. Furthermore, the proportion of terminal organic groups that are incorporated into the pore-wall network is generally lower than would correspond to the starting concentration of the reaction mixture. These observations can be explained by the fact that an increasing proportion of $(R'O)_3SiR$ in the reaction mixture favors homocondensation reactions—at the cost of cross-linking co-condensation reactions with the silica precursors. The tendency towards homocondensation reactions, which is caused by the different hydrolysis and condensation rates of the structurally different precursors, is a constant problem in co-condensation because the homogeneous distribution of different organic functionalities in the framework cannot be guaranteed. Moreover, an increase in loading of the incorporated organic groups can lead to a reduction in the pore diameter, pore volume, and specific surface areas. A further, purely methodological disadvantage that is associated with the co-condensation method is that care must be taken not to destroy the organic functionality during removal of the surfactant, which is why commonly only extractive methods can be used, and calcination is not suitable in most cases.

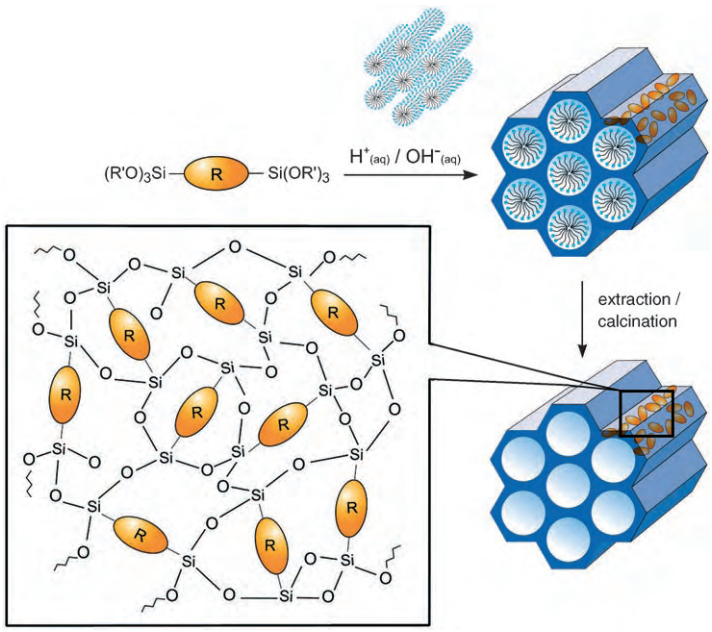

Figure 6. General synthetic pathway to PMOs that are constructed from bissilylated organic bridging units. R = organic bridge.

2.3. Preparation of Periodic Mesoporous Organosilicas (PMOs)

The synthesis of organic–inorganic hybrid materials by hydrolysis and condensation reactions of bridged organosilica precursors of the type $(R'O)_3Si{-}R{-}Si(OR')_3$ has been known for a long time from sol–gel chemistry.[32,33] In contrast to the organically functionalized silica phases, which are obtained by postsynthetic or direct synthesis, the organic units in this case are incorporated in the three-dimensional network structure of the silica matrix through two covalent bonds and thus distributed totally homogeneously in the pore walls. These materials, which are obtained as porous aero- and xerogels, can have large inner surface areas of up to 1800 $m^2 g^{-1}$ as well as high thermal stability but generally exhibit completely disordered pore systems with a relatively wide distribution of pore radii.

The transfer of the concept of the structure-directed synthesis of pure silica mesophases by surfactants to the bissilylated organosilica precursors described above allows the construction of a new class of mesostructured organic–inorganic hybrid materials—periodic mesoporous organosilicas (PMOs)—in which the organic bridges are integral components of the silica network (Figure 6). In contrast to amorphous aero- and xerogels, PMOs are characterized by a periodically organized pore system and a very narrow pore radius distribution. The first PMO was synthesized in 1999 by three research groups working independently of one another.[34–36]

PMO materials are considered as highly promising candidates for a series of technical applications, for example, in the areas of catalysis, adsorption, chromatography, nanoelectronics, or the preparation of active compound release systems.

3. Postsynthetic Functionalization of Silica ("Grafting")

Probably, one of the most spectacular works in the area of subsequent organic functionalization of silica phases was done by Mal et al.,[37,38] who successfully constructed a photochemically controlled system for compound uptake and release by anchoring coumarin to the pore openings of MCM-41 silica phases. The construction strategy was to use first an MCM-41 preparation in which the SDA was still present so that coumarin reacted only with the silanol groups at the pore openings and the outer surface. The SDA was removed by extraction only after successful modification. This method allows active compounds such as cholestane derivatives to be inserted into the pores. Irradiation of the samples with UV light ($\lambda > 310$ nm) led to dimerization of the coumarin, which resulted in sealing of the pore openings and enabled permanent incorporation. Final irradiation of the samples with UV light at around 250 nm led in turn to cleavage of the coumarin dimers, which allows diffusion-controlled release of the enclosed active compounds (Figure 7).

© 2006 Wiley-VCH Verlag GmbH & Co. KGaA, Weinheim

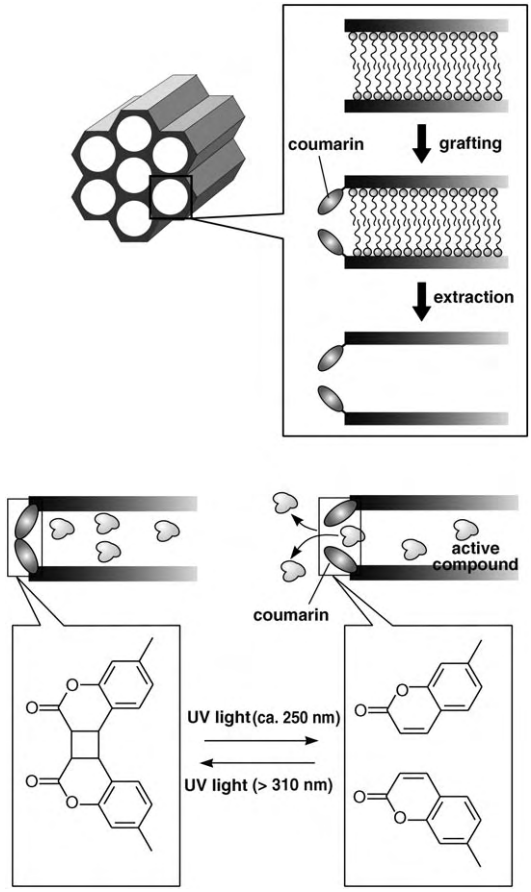

Figure 7. Top: Postsynthetic functionalization of silica phases with coumarin. Bottom: A system for the controlled release of active compounds based thereupon.

Tourné-Péteilh et al.[39] constructed another potential active-compound transport system by chemically anchoring ibuprofen to the inner surface of MCM-41 materials. In this case, the release mechanism is less sophisticated; it simply involves the cleavage of the labile ester bond through which the ibuprofen is bound to the silica phase. However, no such experiments have been reported.

Similar work aimed at the construction of controlled molecular transport systems or molecular sensors has been carried out by Fu et al.,[40] Radu et al.,[41] Descalzo et al.,[42] and Rodman et al.[43] Fu et al.[40] developed a transport system that reacts to thermal stimuli. This system is based on chains of poly-*N*-isopropylacrylamide (a known thermosensitive polymer), which exist in a collapsed, hydrophobic state when exposed to heat, but an expanded, hydrophilic state in the cold. In this way, samples of mesoporous, spherical silica particles (particle diameter 10 μm) that were lined and coated with the thermosensitive polymer by atom transfer radical polymerization could take up greater or lesser amounts of the dye fluoroscein. This transport process was followed spectrometrically.

The development of an MCM-41-based receptor that is able to differentiate between neurotransmitters with different amino acid functionalities is particularly noteworthy. For this purpose, Radu et al. initially synthesized by co-condensation thiol-functionalized MCM-41 material in the form of spherical particles with approximately 300-nm diameters.[41] Epoxyhexyl groups were attached to the outer surface of the nanoparticles prior to the removal of the template, and the samples were treated with MeOH/HCl, whereby not only was the template removed but the epoxy groups were also converted into dihydroxy groups. The thiol groups inside the pores were treated with *o*-phthalaldehyde to obtain 2-((ethylthio)(hydroxy)methyl)benzaldehyde groups; a poly-L-lactic acid layer was polymerized onto the outer surface. The 2-((ethylthio)(hydroxy)methyl)benzaldehyde groups form the probe for the neurotransmitters in that they begin to fluoresce upon reaction with primary amines. The sensor can differentiate between three different neurotransmitters, namely dopamine, tyrosine, and glutamic acid, on the basis of the variation in the fluorescence intensity. This selectivity is caused by the outer polylactic acid layer, which functions as a gatekeeper in this system and exhibits differential permeability for the three neurotransmitters.

Descalzo et al.[42] produced an adenosine triphosphate (ATP) sensor based on MCM-41 by treating amino-functionalized samples with 9-anthraldehyde to form *N*-propylanthracene-10-amino groups. These materials display a significantly reduced fluorescence signal (quenching) in the presence of ATP, and hence concentrations as low as 0.5 ppm could be detected in aqueous solution.

Rodman et al.[43] developed an optical sensor based on mesoporous silica monoliths for the quantitative analysis of Cu^{II} ions in aqueous solutions. This sensor relies on the formation of a copper tetraamine complex upon diffusion of Cu^{II} ions into the pores, which were lined with amino groups.

The postsynthetic functionalization of mesoporous silica phases is also used for the development of adsorbents. For the uptake of nonpolar substances, the walls are lined with hydrophobic compounds; for the adsorption of polar substances or (metal) ions, they are lined with hydrophilic groups, that is, Lewis bases or acids. Thus, MCM-41, MCM-48, and SBA-15 silica materials have been functionalized with, for example, amino or aminopropyl groups,[44–50] diamino,[51,52] triamino,[52] ethylenediamine,[53] malonamide,[54] carboxy,[46,49] thiol,[44,48,55] 1-allyl,[56] 1-benzoyl-3-propylthiourea,[57,58] dithiocarbamate,[59] and imidazole groups,[60–62] as well as saccharides.[63]

Mercier et al.[55] reported the high affinity of mercury(II) for thiol-functionalized MCM-41 phases, and Liu et al.[48] reported its affinity for thiol-functionalized SBA-15 samples, as well as the preferential adsorption of Cu^{2+}, Zn^{2+}, Cr^{3+}, and Ni^{2+} by amino-functionalized materials. The preferential adsorption of Hg^{2+} and Cu^{2+} to analogously functionalized MCM-41/48 materials could be reproduced by Walcarius et al.[44] Trens et al. reported[54] the successful heterogeneous extraction of the radionuclide ions americium(III) (^{241}Am) and europium(III) (^{152}Eu) by malonamide-functionalized MCM-41 materials. The preparation of 1-allyl- and 1-benzoyl-3-propylthiourea-derivatized phases was achieved by a two-stage reaction in which amino-functionalized materials were obtained in the first step and then treated with allyl and benzoyl isothiocyanate, respectively, in the second step. These

 © 2006 Wiley-VCH Verlag GmbH & Co. KGaA, Weinheim

materials also proved to be efficient mercury(II) adsorbents.[56–58] Kang et al. reported that imidazole- and thiol-functionalized SBA-15 phases show high selective affinity for Pd^{2+} and Pt^{2+} in the presence of other cations (Ni^{2+}, Cu^{2+}, Cd^{2+}), even when they were present in high excess.[60,61] Yoshitake et al. [47] showed that amino-functionalized MCM-41 and SBA-1 samples are also suitable for the removal of toxic oxyanions such as arsenate and chromate from contaminated effluent. Saccharide-functionalized MCM-41 materials proved to be highly efficient borate ion adsorbents.[63] Ho et al.[46] demonstrated the ability of amino-functionalized MCM-41 phases in the selective adsorption of large amounts of the dye anthraquinone blue in the presence of another dye, namely, methylene blue, whereas carboxy-functionalized materials absorb methylene blue selectively from this dye mixture.

Pure mesoporous silica phases were hydrophobized principally by reaction of chloroalkyl-, trialkoxysilane, or silazane derivatives with the free silanol groups on the inner (and occasionally also the outer) surfaces (silylation reactions).[45,64–68] Alkyl, chloroalkyl, and bromoalkyl residues of various hydrocarbon chain lengths as well as aryl residues have been used as hydrophobic groups. The materials modified in this way are more resistant towards hydrolysis[45,65,68] and have high adsorption capacities for alkylanilines and 4-nonylphenol (the latter can interact unfavorably with the hormone balance of mammals and is thus a representative of the class of hormone-active compounds (endocrine disruptors)).[64,66] Martin et al.[67] developed a method for the preparation of octyl-functionalized, spherical MCM-41 particles, which they used as packing materials in reverse-phase HPLC columns that in some aspects exhibited separation superior to conventional reverse silica phases. Anwander et al.[65] silylated the inner surfaces of MCM-41 phases with disilazanes of the type $HN(SiRR'_2)_2$ (R, R′ = H, Me, Ph, vinyl, *n*-butyl, *n*-octyl), whereby the degree of silylation depended naturally on the spatial requirements of the silylating reagent. Complete passivation could be achieved with hexamethyldisilazane, which can be used to determine the number of free silanol groups. The vinyl-functionalized MCM-41 samples proved to be very amenable to subsequent consecutive surface modification by hydroboration.

At this point the strategy for functionalization of Mal et al. should be remembered (see above): one possibility for specific control of the polarity of extra- and intraporous materials and thus the transport properties of potential guest molecules is stepwise functionalization. In the first step, the outer surface of the material, which still contains the SDA, is modified. After removal of the SDA, the inner surface can be provided with the desired functionality. Such a method has been described, for example, by Park et al.[69] and de Juan and Ruiz-Hitzky.[70]

3.1. Thin Films

In the past there have also been isolated reports of the postsynthetic functionalization of thin films of ordered mesoporous silica phases. These morphological variants are suitable for many technical applications, for example, sensors. Carboxy-,[71] amino-, and thiol-functionalized[72] films (among others) have been prepared by conventional spin- and dip-coating procedures. Tanaka et al.[73] have also recently prepared thin mesostructured silica films by spin coating but used for the functionalization a new vapor-infiltration technique in which the samples were exposed to the vapor of the organosilica functionalization reagents (methyltriethoxysilane, dimethyldiethoxysilane) at 180 °C for several hours in an autoclave. Interestingly, in contrast to conventional postsynthetic functionalization or functionalization by co-condensation, this process did not lead to a decrease in pore diameter.

3.2. Complex Organic Compounds and Photochemistry

The postsynthetic functionalization of mesoporous silica phases is not by any means limited to small organic functional groups. The size of the pores, especially in SBA-15, allows the construction of far-more-complex structures within them. This was demonstrated, for example, in the work of Acosta et al.,[74] who reported the construction of dendrimer-like structures in the pores of amino-functionalized SBA-15 materials. Melamine-like structures were produced within the pores by means of a stepwise alternating treatment of the substrate with 2,4,6-trichlorotriazine and 4-aminomethylpiperidine (Figure 8).

Equally impressive is the work of the Kuroda group[75,76] on the creation of FRET systems based on chlorophyll in the pores of FSM materials (FRET = fluorescence resonance energy transfer). They first functionalized the FSM samples with 3-aminopropyl groups to guarantee an ideal position of the macroscopic chlorin units (in the pore center) and prevent their denaturation. They then ligated chlorophyll derivatives that possess 3-(triethoxysilyl)-*N*-methylpropan-1-amine groups to the pore walls. Zinc (a fluorescence donor) and copper (a fluorescence acceptor) were chosen as the central ions of the chlorins, which made it possible to initiate and record an efficient FRET process (Figure 9).

By mere thermal treatment of a mixture of C_{60} and C_{70} fullerenes with FSM-16 particles in vacuo at 773 K for 100–150 hours, Fukuoka et al.[77] were able to anchor the fullerenes permanently in the channels, such that they were well distributed and isolated from one another (Figure 10). These hybrid materials were highly effective in the allylic oxidation of cyclohexene by oxygen under the influence of UV irradiation.

In a similar vein, but at significantly lower temperatures, Subbiah und Mokaya[78] were able to insert fullerenes and zinc phthalocyanines into the channel system of mesoporous MCM-41-like silica films, either individually or both species together. In this case, the guest molecules were also well separated. The formation of charge-transfer complexes could not be observed. The authors can imagine that such materials could form the basis for future optical limiters, although nonlinear optical (NLO) effects could not be detected.

Chen et al.[79] observed a 20-fold increase in the photoluminescence (PL) of pure MCM-41 upon functionalization with triethoxy-3-ethylenediaminopropylsilane (TEEDPS);

 © 2006 Wiley-VCH Verlag GmbH & Co. KGaA, Weinheim

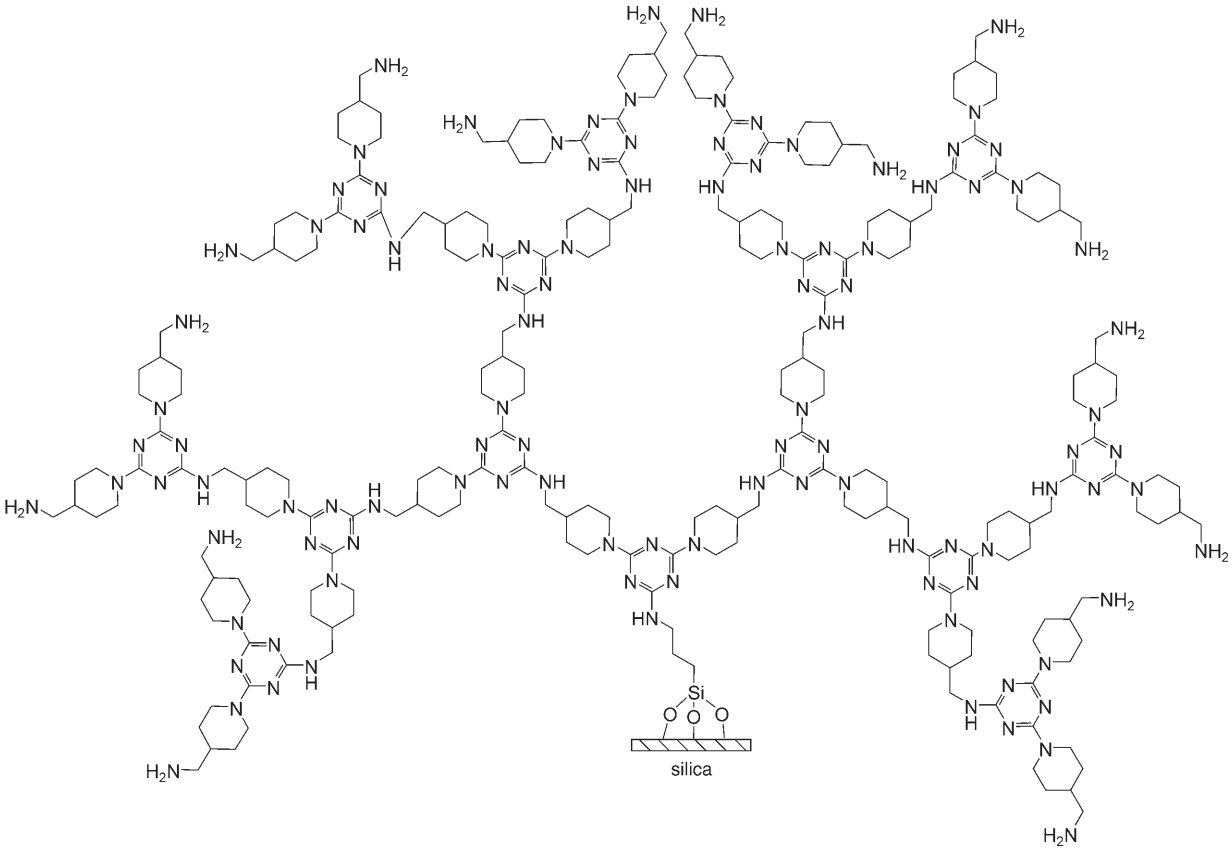

Figure 8. Melamine-like structure within the pores of a mesoporous SBA-15 silica phase constructed by stepwise alternating treatment of the substrate with 2,4,6-trichlorotriazine and 4-aminomethylpiperidine.

the PL of pure MCM-41 as well as TEEDPS are essentially negligible.

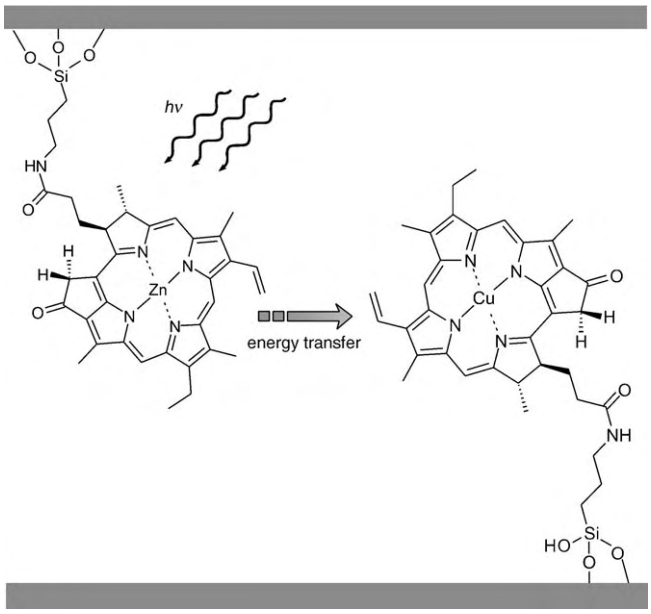

Figure 9. FRET system within the pores of an FSM silica phase; the energy transfer is initiated by irradiation with light and takes place from the fluorescence donor (Zn as central atom) to the fluorescence acceptor (Cu as central atom).

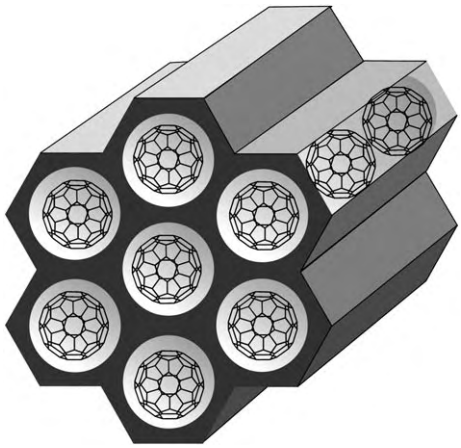

Figure 10. Embedded fullerene in the pore system of FSM materials.

3.3. Acid Catalysis

Notable in the context of catalysts based on mesoporous silica phases are efforts to create solid-state acids that could be used a heterogeneous acid catalysts, in analogy to Brønsted acidic zeolites, but as they possess larger pores they should be able to incorporate larger substrates. Hitherto, mainly sulfonic acid derivatives were anchored by using both one- and two-step functionalization strategies. Das et al.[80,81] functionalized MCM-41 and MCM-48 materials postsynthetically with

 © 2006 Wiley-VCH Verlag GmbH & Co. KGaA, Weinheim

propylthiol groups initially, so as to be able to convert them into propylsulfonic acid groups under mild oxidative conditions with H_2O_2. This pathway was also pursued for the corresponding functionalization of FSM-16[82] and SBA-15 materials.[83] An interesting approach to the introduction of sulfonic acid groups into SBA-15 phases was also pursued by Dufaud et al.,[84] who obtained materials by functionalization with a bissilylated disulfide reagent followed by cleavage of the disulfide bridges and oxidation of the resulting thiols into sulfonic acid groups. This results in a material in which each two of the sulfonic acid groups possess a specific spatial separation from one another. Mbaraka and Shanks[85] anchored hydrophobic alkyl residues to the remaining free silanol groups so as to keep the disruptive water produced during esterification of fatty acids away from the immediate neighborhood of the catalytic center. Also of note is the production of a Nafion analogue by Alvaro et al.,[86] who lined MCM-41 and SBA-15 phases with perfluorosulfonic acid groups in a single-stage functionalization reaction.

These solid-state acids led to good yields and selectivities in the condensation of phenol and acetone to bisphenol A,[80,81,84] and high activities were recorded in the acetalation of acetophenone with ethylene glycol[82] as well as in the preparation of dibutyl ether from 1-butanol in a dehydration reaction.[83]

3.4. Base Catalysts

Mesoporous silica materials have also been employed in the development of heterogeneous base catalysts. A comprehensive survey of work up to 2000 may be found in a review by Weitkamp et al.[87] Two more recent studies have dealt with the role of the solid support materials of the actual active catalytic species and the effectiveness of these species in relation to the quality of their dispersion in the support material. Corma et al.[88] have studied MCM-41 samples functionalized with 1,8-bis(dimethylaminonaphthalene) which have proven to be highly efficient catalysts in the Knoevenagel condensation of benzaldehyde with activated methylene compounds and in the Claison–Schmidt condensation of benzaldehyde with 2-hydroxyacetophenone. Macquarrie et al.[89] investigated the role of the distribution of aminopropyl groups in correspondingly functionalized MCM-41 phases in the catalysis of classical C–C coupling reactions such as the nitroaldol condensation of nitromethane with benzaldehyde and the Michael addition of nitromethane with 2-cyclohexene-1-one.

3.5. Oxidative Catalysis

A number of studies on heterogeneous oxidation catalysts based on mesoporous silica phases have been devoted to materials doped with metals, metal complexes, or organometallic compounds. However, these will not be discussed further herein. The number of reports on purely organically functionalized phases that were utilized in oxidative catalysis is extremely small. One of the very few examples is the work of Brunel et al.,[90] who functionalized MCM-41 samples with the 2,2,6,6-tetramethylpiperidine-*N*-oxyl (TEMPO) radical by different anchoring procedures and tested the catalytic potential of this material by means of the oxidation of primary alcohols.

3.6. Chiral Catalysis

Organically functionalized mesoporous silica phases are in principle suitable candidates for the creation of efficient heterogeneous catalysts. In addition to the numerous studies on the catalytic properties of silica materials functionalized with metal salen complexes (e.g., Mn^{III},[91–96] Co^{II},[97] and vanadyl salen;[98] H_2salen = *N*,*N*′-bis(salicylidene)ethylenediamine), there are purely organic studies involving functionalization with alkaloids and alkaloid derivates (cinchona,[99–101] ephedrine[102,103]), bis(oxazoline),[104] amino alcohols,[105] as well as proline and benzylpenicillin derivatives.[106]

Motorina and Crudden[99] used an SBA-15 phase functionalized with a cinchona derivative for the asymmetric dihydroxylation of olefins under Sharpless conditions and were able to achieve enantioselectivities (*ee* values up to 99%) almost identical to those that are obtained with the corresponding homogeneous system. The catalyst could be recovered without difficulty and used several times without critical loss in yield and selectivity. Identical results were obtained by H. M. Lee et al.,[100] who investigated the same system. Corma et al.[101] examined the catalytic properties of cinchonidine- and cinchonine-functionalized MCM-41 phases in the Michael addition of ethyl-2-oxocyclopentanecarboxylate with 3-butene-2-ol; although the yields were good, the *ee* values were only 20–50%. Abramson et al.[102,103] studied the influence of the (−)-ephedrine residue anchored to the inner surfaces of mesoporous silica phases as chiral auxiliaries in the enantioselective alkylation of benzaldehyde with diethylzinc. A. Lee et al.[104] anchored a chiral bis(oxazoline) ligand (BOX) onto SBA-15 samples and tested this catalytic species in the nitro-Mannich reaction of *(E)*-ethyl-2-(4-methoxyphenylimino)acetate with nitroalkanes of differing chain lengths. They obtained enantioselectivities that, depending upon the chain length, were comparable to the analogous homogeneous system, and diastereoselectivities that were even higher. The best values were obtained with nitrohexane: *syn*/*anti* 98:2, 93% *ee syn* isomer, 82% *ee anti* isomer. For the recovered catalyst, the values for both the diastereoselectivity and the enantioselectivity fell progressively with each cycle. Whang et al.[105] investigated the catalytic potential of a series of chiral amino alcohols anchored to MCM-41 supports in the asymmetric reduction of aromatic ketones to alcohols. MCM-41 phases as supports for proline and benzylpenicillin derivatives were tested for their catalytic potential in the direct aldol reaction of acetone with 4-nitro- and 4-fluorobenzaldehyde. Unfortunately, the yields and *ee* values were only average.[106]

© 2006 Wiley-VCH Verlag GmbH & Co. KGaA, Weinheim

3.7. Enzyme Immobilization and Biocatalysis

The pore systems of mesoporous silica phases have sizes that can accommodate at least small enzymes or proteins; this applies to a lesser extent for MCM-41/48-like phases and to a greater extent for SBA-15-like phases. The immobilization can involve physisorption or actual chemical bonding of the enzyme/protein to the surface of the pore walls, although in the latter case there is always the risk of partial or total denaturation and hence a considerable decrease in activity. Conversely, it is expected that the stronger bonding will result in a smaller amount of material washed away during recycling. Chemisorption is generally carried out with functionalized phases. A few selected examples are illustrated below; a more comprehensive overview on this topic can be found in the recent publications of Hartmann[107] and Yiu and Wright.[108]

Unmodified MCM-41/48 and SBA-15 phases,[109] as well as carboxy-, aminopropyl-, thiol-, cyano-, and phenyl-modified SBA-15 phases[110] have been used by Yiu et al. for the immobilization of trypsin. The activity of the trypsin was measured on the basis of the hydrolysis of *N*-α-benzoyl-DL-arginine-4-nitroanilide. The thiol-functionalized phases proved to be highly promising. Lei et al.[49] successfully used amino- and carboxy-functionalized SBA-15 phases to immobilize the enzyme organophosphorus hydrolase, which in this state had double the activity of that in the free state. Ma et al.[111] carried out studies on the activity of porcine pancreas lipase immobilized on the surface of MCM-41 samples solely by hydrogen bonds. The strong decrease in activity following recovery (simply because of leaching of the enzyme from the pores) could not be prevented even by functionalization with vinyl groups after immobilization of the enzyme, which was anticipated to lead to stronger binding of the enzyme to the surface. Salis et al.[112] immobilized *Mucor javanicus* lipase in the channel system of SBA-15 materials at different pH values (pH 5–8). The loading and hydrolysis activity (in the hydrolysis of tributyrin and trolein) were highest at pH 6. Chemical adsorption was achieved by functionalization of the support medium with glutardialdehyde (pentaldial); however, hydrolysis activity was lost in the case of triolein. Also, the immobilization of conalbumin,[113] cytochrome *c*,[114] subtilisin,[115] (chloro-) peroxidases,[115,116] and lysozyme[117] in SBA-15 phases has been reported.

4. Co-Condensation (One-Pot Synthesis)

Since the initial work of the groups of Mann,[118] Macquarrie,[119] and Stein,[120] a number of organically modified silica phases have been synthesized by co-condensation. Through the use of the respective organosilane, organic functionalities such as alkyl,[118,121] thiol,[121–124] amino,[52,119,122,125–130] cyano/isocyano,[119,126,131] vinyl/allyl,[120–122,126,132–135] organophosphine,[131,136] alkoxy,[122] or aromatic groups[118,122,131,137,138] can be incorporated into the pore walls of the silica network. However, care must always be taken that the organic group remains intact when the SDA is removed. The mesoporous materials obtained by direct synthesis can to some extent exhibit interesting catalytic and adsorption properties, or, by subsequent chemical transformation of the organic groups on the pore surfaces, can act as starting compounds for the synthesis of new organically modified silica phases. A few examples will be presented here.

Vinyl-modified silicas have proved to be very interesting owing to the reactivity of the C=C bond. Asefa et al.[139] successfully transformed the vinyl groups into alcohols by hydroboration and into the corresponding diols by epoxidation. Furthermore, the accessibility of the C=C bond in vinyl-functionalized silicas has been established by bromination reactions.[120]

Another area of research is the construction of systems for heterogeneous base or acid catalysis. In base-catalyzed reactions, amino-functionalized mesoporous silicas can act as heterogeneous catalysts. In this context, the investigations of Macquarrie et al.[140,141] on the catalytic activity of amino-functionalized silicas in Knoevenagel condensation reactions of aldehydes or ketones with ethyl cyanoacetate is particularly noteworthy. As mentioned in Section 3, thiol-functionalized silicas serve as a basis for the construction of solid-state acids, as the SH groups in the pore channels can be transformed into sulfonic acid groups by suitable oxidizing agents such as HNO_3 or H_2O_2.[142–145] Stucky and co-workers[146] have shown that the oxidation of thiol groups need not necessarily be carried out after the synthesis of the mesostructured products, but can take place in situ by the addition of H_2O_2 to the reaction mixture of the co-condensation reactants. The catalytic activities of sulfonic acid functionalized silicas have been determined, for example, by means of esterifications and ether syntheses.[147–149] Apart from the previously mentioned sulfonic acid functionalized silicas, hybrid materials that contain other acid groups are also known. Schüth and co-workers[150] showed that the cyano group in 2-cyanoethyl-functionalized SBA-15 can be converted into the corresponding carboxylic acid by hydrolysis with H_2SO_4. Functionalization with phosphoric acid groups by ester hydrolysis of a diethyl phosphonate has been realized by Corriu et al.[151]

Thiol-functionalized mesoporous silicas show interesting adsorption properties. The high affinity of these compounds for thiophilic heavy metals, especially toxic Hg^{2+} ions, has been demonstrated by several authors,[152–154] and size-selective protein immobilization has also been reported.[155] Thiol groups are also able to complex $AuCl_4^-$ ions, and gold nanoparticles can be formed in the pores by subsequent reduction of these embedded species.[156–158]

It is possible to functionalize silicas with far-more-complex organic groups by means of co-condensation reactions, which opens up the path to further materials with interesting chelating or adsorbing properties. Corriu et al.[159] anchored chelating cyclam molecules by substitution of the chlorine atoms on previously synthesized 3-chloropropyl-functionalized silicas and showed that almost all cyclam units were localized on the pore surface and were thus freely accessible to complexation by Cu^{II} and Co^{II} ions (Figure 11 a; cyclam = 1,4,8,11-tetraazacyclotetradecane).

Jia et al.[160] were successful in functionalizing silicas with the chelate ligand 3-(2-pyridyl)-1-pyrazolylacetamide. After subsequent complexation of $MoO(O_2)_2$, the samples showed

 © 2006 Wiley-VCH Verlag GmbH & Co. KGaA, Weinheim

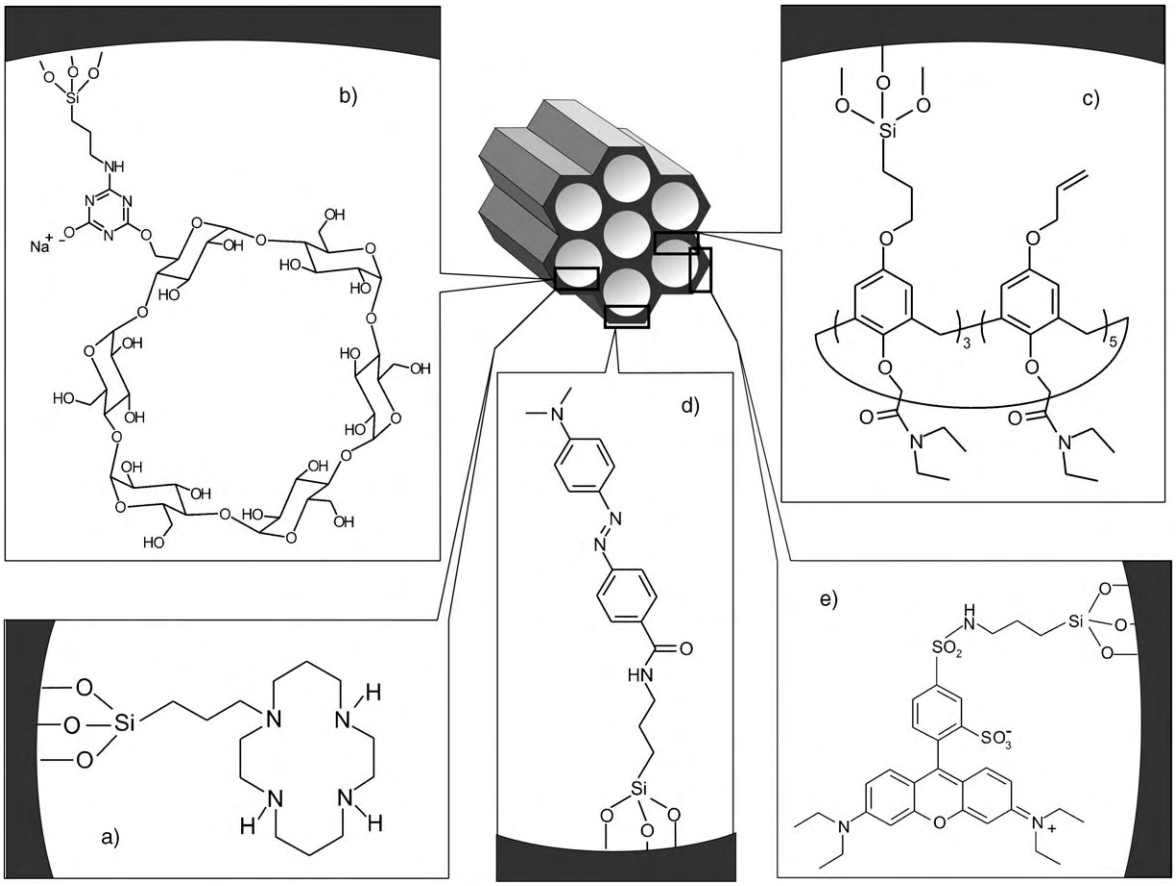

Figure 11. Selected organic functionalities anchored by co-condensation on the pore surface of silica phases (see text for details).

catalytic activity in the epoxidation of cyclooctene with *t*BuOOH. Huq and Mercier[161] synthesized cyclodextrin-modified silicas by first coupling the cyclodextrin units to 3-aminopropyltriethoxysilane (APTS) and then co-condensed with TEOS (Figure 11b). All attempts at subsequent modification of thiol silicas by grafting cyclodextrin units onto the surface have been unsuccessful. It has also been demonstrated that the cyclodextrin units on the surface of the silicas obtained by direct synthesis are able to adsorb *p*-nitrophenol from aqueous solutions.

Liu et al.[162] synthesized silicas functionalized with calix[8]arene amide (Figure 11c) and showed that they were suitable for the adsorption of humic acid from aqueous solutions. The synthesis of spherical mesostructured particles modified with the dipeptide carnosine (β-alanyl-L-histidine) has been published by Walcarius et al.[163] The peptide units of the ordered mesoporous materials obtained were more accessible than those of analogously functionalized amorphous porous particles, as was demonstrated by complexation reactions with Cu^{II} ions.

Further works focus on the modification of silica matrices with different chromophores. Mann and co-workers[164,165] synthesized 3-(2,4-dinitrophenylamino)propyl-functionalized MCM-41 and obtained materials in the form of powders, thin films, and monoliths. Ganschow et al.[166] anchored the photochromic azo dye 4-[(4-dimethylaminophenyl)azo]benzoic acid and the fluorescent laser dye sulforhodamine B into 3-aminopropyl-MCM-41 (Figure 11d,e). The coupling of the dye molecules to the amino group of the organosilane through the carboxylic and sulfonic acid groups, respectively, and the actual co-condensation reaction with the inorganic precursor could be carried out simultaneously in a microwave apparatus. The reaction time could be significantly reduced by microwave-supported synthesis relative to conventional methods, and thus degradation of the dye molecules during hydrothermal treatment could be reduced.

Brinker and co-workers[167] synthesized nanocomposite films bearing photosensitive azobenzene units; 4-(3-triethoxysilylpropylureido)azobenzene, synthesized by the coupling of triethoxysilylpropylisocyanate with 4-phenylazoaniline, was used as an organosilane precursor in the co-condensation reaction. The photoisomerization of the *trans* into the *cis* form, initialized by UV irradiation, should theoretically lead to a decrease in the pore size by approximately 6.8 Å, but this was difficult to establish experimentally. The "switching" of the azobenzene units back into the *trans* form was achieved by irradiation with light of greater wavelengths or by thermal treatment (Figure 12).

Further functionalization of mesoporous films with the pH-sensitive dye fluorescein was accomplished by Wirnsberger et al.[168] The organosilane used for the actual co-condensation reaction was first prepared by reaction of

 © 2006 Wiley-VCH Verlag GmbH & Co. KGaA, Weinheim

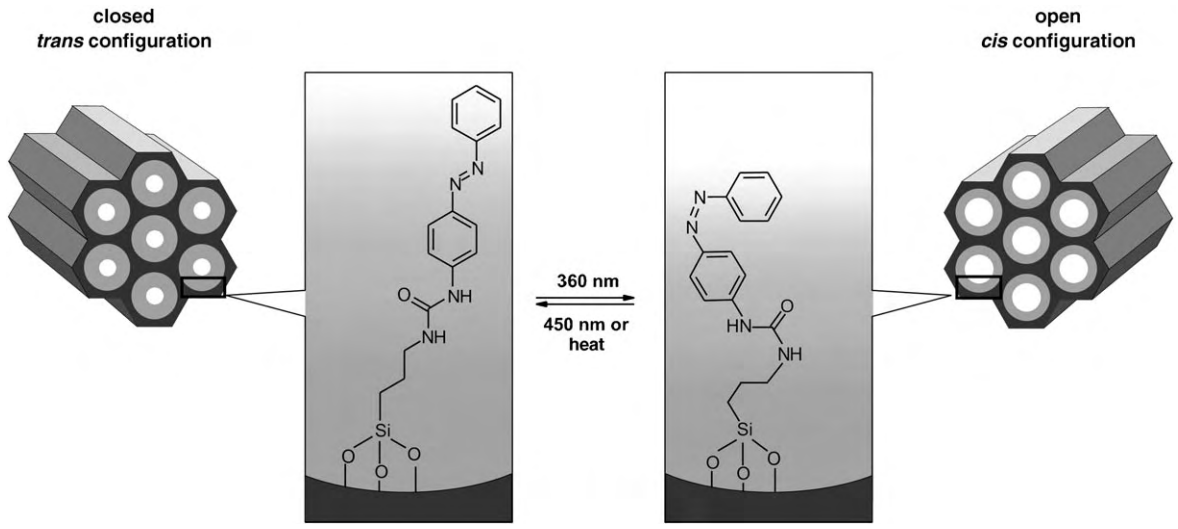

Figure 12. Construction of a photosensitive switch based on azobenzene in the pore system of mesoporous silica.

fluorescein isocyanate (FITC) with APTS. The possible use of the dye-modified films as pH sensors was investigated by measurement of the fluorescence after excitation with an Ar-ion laser (488 nm); a dramatic change in fluorescence intensity was observed around pH 8 with a response time of a few seconds.

Dye-functionalized silicas can also possess molecular sensing properties, as demonstrated by Lin et al.[169] They synthesized—in a principally analogous manner to the work of Radu et al.[41] described in Section 3—amine-sensitive *o*-phthalhemithioacetal-modified MCM-41 silicas by the reaction of *o*-phthalaldehyde with mesoporous thiol-functionalized silicas whose free silanol groups on the pore surfaces had been previously functionalized with propyl-, pentyl-, and pentafluorophenyl groups. The sensor properties of the product thus obtained were demonstrated by the selective fluorescence detection of amine guest molecules such as dopamine and glucosamine. Lin and co-workers[170] also reported a system based on spherical MCM-41 silica particles functionalized with thiol groups and CdS nanocrystals for the controlled release of active compounds, which was demonstrated for a number of neurotransmitters and pharmaceutical products.

Ji et al.[171] synthesized methacrylate-functionalized silicas and, by subsequent in situ polymerization with 3-trimethoxysilylpropylmethacrylate, obtained a polymer-silica nanocomposite material with increased mechanical and thermal stability. Finally, Che et al.[172] synthesized mesoporous silicas with helical chirality by calcination of ammonium-functionalized silicas that were prepared by using the chiral anionic surfactant *N*-acyl-L-alanate (Figure 13).

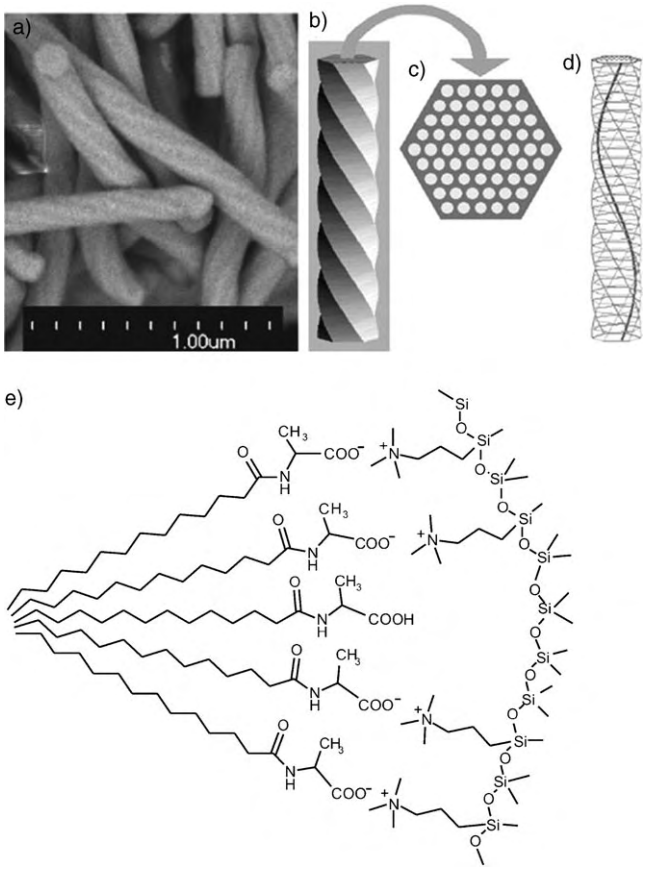

Figure 13. a–d) SEM image and schematic representation of a mesoporous, rod-shaped 2D hexagonal silica phase that exhibits a chiral helical external topology formed by calcination of ammonium-functionalized silicas that were obtained previously by the use of the chiral anionic surfactant *N*-acyl-L-alanate (Reproduced with permission from the Nature Publishing Group). e) Interaction between the chiral surfactant and the ammonium-functionalized silica surface.

 © 2006 Wiley-VCH Verlag GmbH & Co. KGaA, Weinheim

5. PMOs

5.1. Synthesis of PMOs by Structure Direction with Ionic Surfactants

5.1.1. Alkyltrimethylammonium and Hexadecylpyridinium Halides

The most frequently used ionic structure-directing agents are the bromide and chloride salts of long-chain alkyltrimethylammonium compounds and the corresponding salts of long-chain alkylpyridinium derivatives (hexadecyltrimethylammonium bromide/chloride (CTAB/CTAC), octadecyltrimethylammonnium bromide/chloride (OTAB/OTAC), hexadecylpyridinium bromide/chloride (CPB/CPC)). Under certain conditions (temperature, concentration, solvent, pH, etc.) and in the presence of organosilica precursors, these surfactants self-assemble to form a lyotropic liquid-crystalline phase. The hydrolysis and condensation of the precursors in this phase produce the ordered periodic hybrid material, which after removal of the surfactant exhibits accessible pores of uniform size and shape (Figure 6).

The year of birth of PMOs was 1999. In that year, three different research groups were successful in applying the concept for the synthesis of ordered pure mesoporous silica phases through structuring with ionic surfactants to organosilica hybrid phases, by assembling bridged dipodal alkoxysilane [$(RO)_3Si{-}R'{-}Si(OR)_3$] precursors. Scheme 1 shows the precursors successfully converted into PMOs thus far.

Inagaki et al.[34] were able to prepare a new organic–inorganic hybrid material by the conversion of 1,2-bis(trimethoxysilyl)ethane (BTME; **2**) under basic conditions in the presence of OTAC as SDA. The symmetry of the pore arrangement depended on the mixture ratios of the components in the reaction mixture. Materials with a 2D hexagonal (2D hex) pore arrangement as well as those with 3D hexagonal (3D hex) periodicity were obtained. Nitrogen physisorption measurements revealed specific inner surface areas of 750 (2D hex) and 1170 m^2g^{-1} (3D hex) and pore diameters of 3.1 (2D hex) and 2.7 nm (3D hex). ^{29}Si MAS NMR measurements showed that the Si–C bond is not cleaved during the synthesis. Both materials decompose only at temperatures above 400 °C.

In the same year, the group of Ozin reported the synthesis of a PMO that contained an unsaturated organic spacer.[36] They used 1,2-bis(triethoxysilyl)ethene (**3**) as a precursor, which was transformed under basic conditions in the presence of CTAB as SDA to obtain an ethene-bridged[*] PMO material with a 2D hexagonally ordered pore system (specific surface area $S_{BET} = 640\ m^2g^{-1}$, $\varnothing = 3.9$ nm). Bromination reactions were carried out to test the accessibility to the C=C bonds incorporated into the silica framework. Elemental analysis showed a degree of bromination of 10% relative to the C=C bond content.

Around the same time, Stein and co-workers[35] published the synthesis of an ethene-bridged PMO material that was obtained under similar reaction conditions and with the same precursor and surfactant. The material exhibited a very high specific surface area of approximately 1200 m^2g^{-1} but a comparably low long-range order. Transmission electron microscopic (TEM) investigations suggested the presence of wormlike rather than strictly parallel 2D hexagonally arranged pores with diameters of 2.2–2.4 nm.

A more recent report on the synthesis of an ethene-bridged PMOs comes from Nakajima et al.,[173] who prepared long-range-ordered material with a 2D hexagonal pore system by structuring with OTAC under basic conditions.

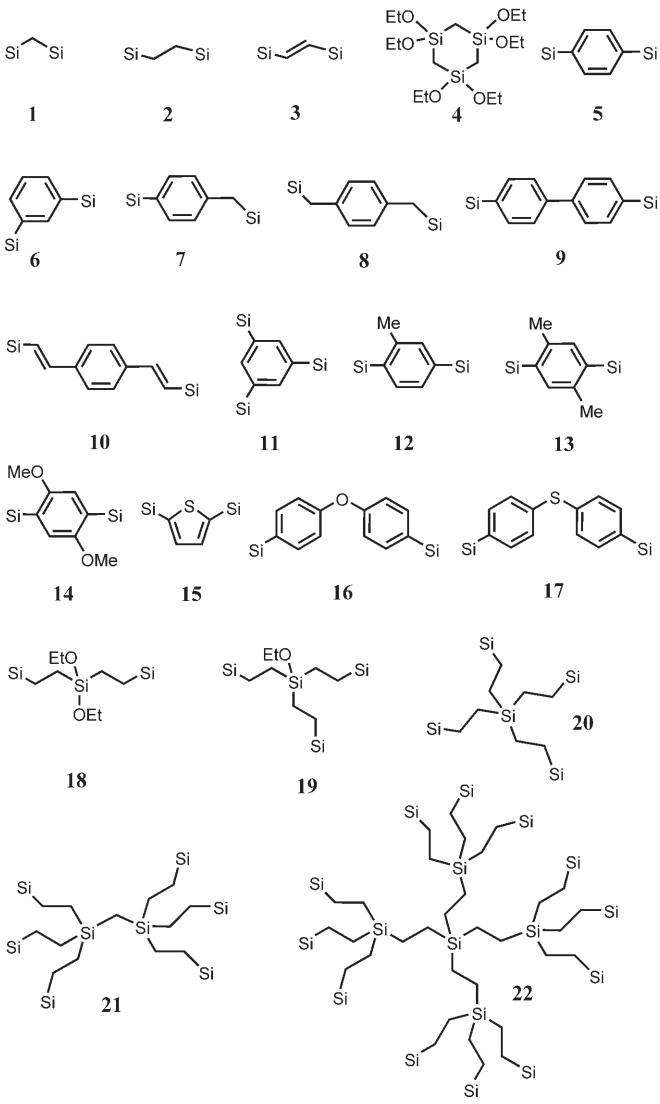

Scheme 1. Overview of the organosilica precursors that have been converted into PMOs. Terminal Si atoms: $Si = Si(OR)_3$ with $R = CH_3$, C_2H_5.

[*] The nomenclature of PMOs has not yet been uniformly standardized. Following the practice within the research community (with the exception of the methylene bridge, for which the bridging unit is correctly named according to the IUPAC recommendations), the parent name of the respective precursor is for simplicity also used as the name for the bridging unit. The fact that, for example, an ethane or benzene unit (C_2H_6 and C_6H_6, respectively) cannot occur as a bridging component but would have to be correctly named as an ethylene or phenylene bridge (C_2H_2 and C_6H_4, respectively) may understandably appear unfortunate in this respect. However, since the ethene molecule, for example, is commonly called "ethylene", the risk of confusion is minimized in this way.

 © 2006 Wiley-VCH Verlag GmbH & Co. KGaA, Weinheim

An ethane-bridged PMO material with cubic symmetry ($Pm\bar{3}n$)—the analogous mesoporous pure silica phase with identical symmetry is SBA-1—has been synthesized for the first time by Guan et al.[174] and by Sayari et al.,[175] who in each case used BTME (**2**) as organosilica source in the presence of CTAC as SDA in basic media. The crystal-like external morphology of the particle, determined by scanning electron microscopy (SEM), was described as 18 faced, consisting of 6 squares and 12 hexagons.

In a further study, Sayari and co-workers[176] investigated the influence of the chain length of the surfactant on the synthesis of ethane-bridged PMOs whereby the length of the hydrocarbon chain varied between 10 and 18 carbon atoms. They also compared two different synthetic pathways: in one, the last step comprised merely aging at room temperature, whereas the second included hydrothermal treatment at 95 °C in an autoclave. As expected, the pore diameter increased with increasing length of the surfactant used. In contrast, the specific surface areas followed no clear trend. With but one exception the PMO materials were always obtained with a 2D hexagonal pore system. The exception was the sample that was synthesized with CTAC as SDA and treated hydrothermally; this sample exhibited a cubic structure.

Asefa et al.[177] investigated the thermally induced transformation processes that could occur with a methylene-bridged PMO (2D hexagonal pore system, $\varnothing = 3.1$ nm) at higher temperatures. With combined thermogravimetric analysis (TGA)/NMR investigations they were able to show that the bridging methylene unit transformed above 400 °C into a terminally bonded methyl group. In this process, an Si–C bond is cleaved, a proton is transferred from a silanol group to a neighboring $SiCH_2$ group, and a new Si–O–Si bridge is formed—this process is presumed to take a highly concerted course (Scheme 2).

Ethane-bridged PMOs could also be synthesized under acidic reaction conditions ($S^+X^-I^+$ pathway). Ren et al.[178] used 1,2-bis(triethoxysilyl)ethane (BTEE, **2**) as a precursor in the presence of CPB as the structure-directing agent. This synthetic approach, however, gave only poorly ordered material for the ethane-bridged PMO. In spite of this, the product showed relatively high specific surface areas of 800–1200 $m^2 g^{-1}$ (dependent upon the pH and temperature during synthesis). The TEM images suggested the presence of predominantly wormlike channels. The extent to which the ethane bridges remained intact under the synthetic conditions is not clear, but this was assumed by the authors on the basis of the IR spectroscopic investigations.

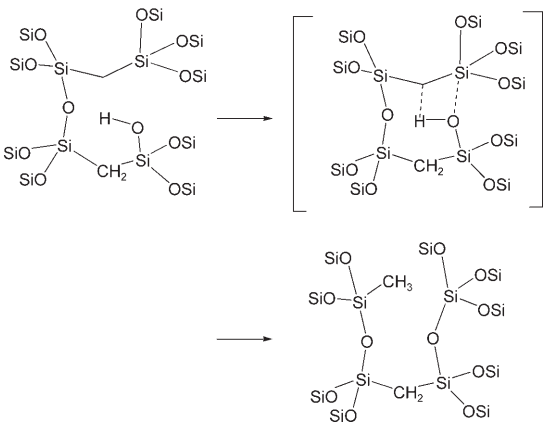

Scheme 2. Heat-induced rearrangement of methylene-bridged organosilicas to form a new Si–O–Si bridge by a hydrogen transfer from a neighboring silanol group onto a bridging methylene unit, which is transformed into a terminal methyl group in a concerted process.

5.1.1.1. *Aromatic PMOs*

All PMOs described previously contain only saturated aliphatic or ethene bridges. Interestingly, the hydrocarbon chain of the organosilica precursors can be at most just two carbon atoms long to produce periodic ordered mesoporous materials—a clear indication that the organic bridge must not be too flexible if pure PMO materials and not disordered hybrid materials are desired. This requirement is fulfilled by (hetero)aromatic compounds; thus, numerous attempts have been made to introduce aromatic bridges, and thus a form of functionality, into PMOs.

The first synthesis of PMO materials with aromatic bridges was reported by Yoshina-Ishii et al.[179] as early as 1999. They used 1,4-bis(triethoxysilyl)benzene (BTEB, **5**) and 2,5-bis(triethoxysilyl)thiophene (BTET; **15**) as precursors in the presence of CTAB as structure-directing agent. Interestingly, synthesis in the presence of ammonia led to cleavage of the Si–C bonds, thus almost all the organic bridges were cleaved in the reaction products obtained. Only in mild acidic conditions, which could be realized by the use of hexadecylpyridinium chloride as SDA, led to well-ordered products ($\varnothing = 2.0$ nm) with a high degree of structural integrity of the organic bridges, and even under these conditions Si–C bond cleavage could not be avoided entirely.

Temtsin et al.[180] prepared the aromatic precursors 1,4-bis(triethoxysilyl)-2-methylbenzene (**12**), 1,4-bis(triethoxysilyl)-2,5-dimethylbenzene (**13**), and 1,4-Bis(triethoxysilyl)-2,5-dimethoxybenzene (**14**) by Grignard reaction of the respective brominated compounds with chlorotriethoxysilane and were able to use these precursors to obtain PMO materials. They used hexadecylpyridinium chloride as SDA under acidic reaction conditions, neutralized the reaction mixture, and then treated the experiments with ammonium fluoride, which acted as catalyst. 2D hexagonal products were obtained with pore diameters of 2.3 nm and specific surface areas between 560 and 1100 $m^2 g^{-1}$. Thermogravimetric analyses showed that the aryl bridges are cleaved from the silica framework only at temperatures above 360 °C.

5.1.1.2. *PMOs with Crystal-like Pore Walls*

Meanwhile several research groups have produced PMO materials that as well as having periodic, ordered mesopores also show crystal-like organization of the organic bridges within the pore walls. This means that the mass centers of the molecules or inversion centers of the organic bridges exhibit long-range order; the bridges themselves, however, because of their free rotation of the Si–C bond around the molecular longitudinal axis have alternating orientations in relation to

 © 2006 Wiley-VCH Verlag GmbH & Co. KGaA, Weinheim

the bordering silica layers and thus do not possess any strict translational symmetry. Figure 14 shows schematically the preparation of PMOs with crystal-like pore walls.

The first report of PMOs with crystal-like pore walls comes from Inagaki et al.,[181] who, like Yoshina-Ishii et al., used **5** as a precursor in the presence of OTAC as SDA under basic conditions. The powder X-ray diffraction (XRD) pattern of the benzene-bridged PMO showed, as well as reflections that were assigned to the highly ordered 2D hexagonal mesophase (*p6mm*), four reflections (10, 20, 30, 40) in the wide-angle range ($2\theta > 10°$) that showed the existence of a periodicity of 7.6 Å on the molecular scale (Figure 15). This crystal-like organization of the organic bridges within the pore walls (a model of the pore walls is shown in Figure 16) was confirmed by HRTEM images, which showed numerous lattice fringes along the pore axis and also indicated a separation distance of 7.6 Å. The product ($\varnothing = 3.8$ nm, $S_{BET} = 818\ m^2 g^{-1}$) was thermally stable up to 500 °C.

Bion et al.[182] also synthesized 1,4-benzene-bridged PMO materials with crystal-like pore walls. The pore diameter could be varied between 2.3 and 2.9 nm by variation of the length of the hydrocarbon chain (C_{14} to C_{18}) of the trimethylammonium halide surfactant used.

Another aromatic PMO system that shows both periodic ordered mesoporosity and a periodicity at a molecular level was prepared by Inagaki and co-workers,[183] who used 4,4′-bis(triethoxysilyl)biphenyl (BTEBP, **9**) as the organosilica source in the presence of OTAC under basic conditions. The material obtained ($\varnothing = 3.5$ nm, $S_{BET} = 869\ m^2 g^{-1}$), because of the periodicity of its mesopores, showed one reflection in the low-angle region of the powder XRD pattern and five additional reflections in the wide-angle region that can be attributed to a crystal-like arrangement of the biphenyl units within the pore walls. The periodicity of the organic bridges (11.6 Å) derived from the diffraction pattern was confirmed by a corresponding separation of the lattice fringes in the HRTEM images.

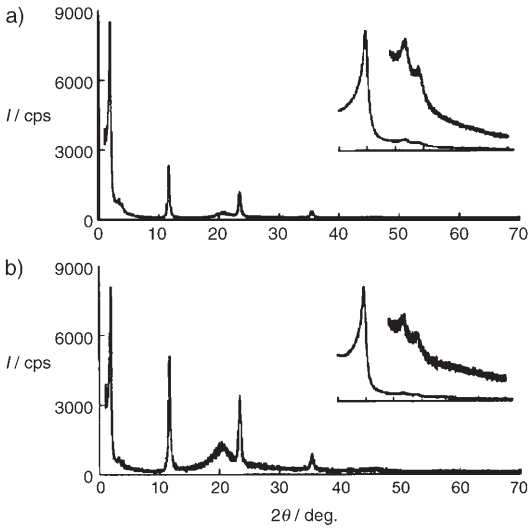

Figure 15. Powder X-ray diffraction pattern of a mesoporous benzene-bridged PMO. a) Sample after removal of the surfactant. b) Composite sample that still contains the surfactant. Insets: Reflections in the small-angle area ($1 < 2\theta < 7$). This material shows periodicity both on the mesoscopic ($d = 45.5$, 26.0, and 22.9 Å) and on the molecular scale ($d = 7.6$, 3.8, and 2.5 Å). Reproduced with permission from the Nature Publishing Group.

The series of organosilica precursors that produce PMO products with crystal-like arrangement of organic bridges was extended by one representative recently by Sayari and Wang.[184] They used 1,4-bis[(*E*)-2-(triethoxysilyl)vinyl]-benzene (BTEVB, **10**) as a precursor and OTAC as SDA under basic conditions to obtain 2D hexagonal PMO materials that also possess crystalline pore walls. This was also the first synthesis of a PMO material with a bridge whose conjugation extended beyond the benzene unit. This precursor could also be used with conventional sol–gel methods (without the addition of SDAs) to obtain materials that, as expected, exhibited no mesoscopic order but, interestingly, showed periodicity at the molecular level. At the same time, Cornelius et al.[185] synthesized 1,4-divinylbenzene-bridged PMOs ($\varnothing = 2.7$ nm, $S_{BET} = 800\ m^2 g^{-1}$) to investigate the possibility for further functionalization of the double bonds in this PMO. The goal here is the postsynthetic hydroboration for the formation of (chiral) diols, and cycloaddition reactions.

The synthesis of aromatic PMOs with crystal-like organization of the organic bridges within the pore walls is not restricted to symmetrically substituted precursors, as Kapoor et al.[186] demonstrated with the formation of PMO product from the nonsymmetric precursor 1,3-bis(triethoxysilyl)benzene (**6**).

It is worth noting that mesoporous materials with ethane or methylene bridges do not show any periodicity at the molecular level, even when they possess

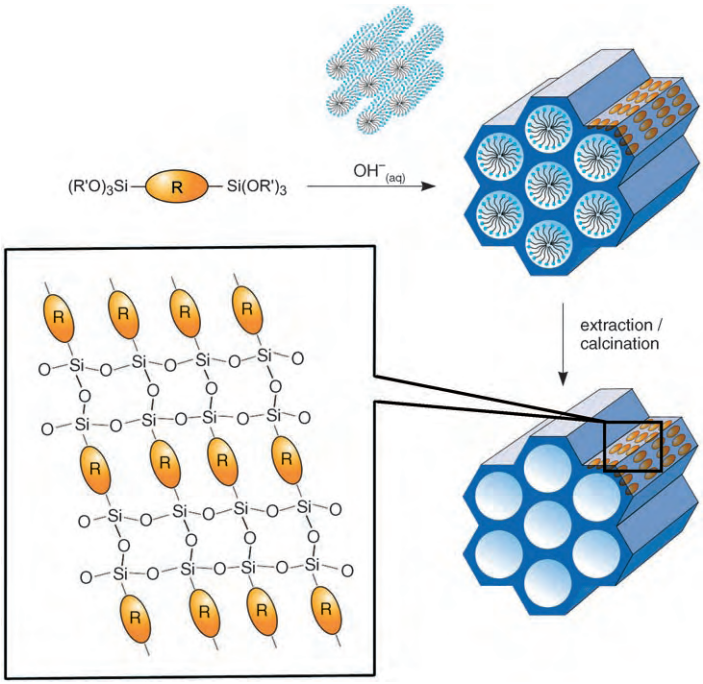

Figure 14. Synthesis of PMOs with a crystal-like arrangement of the bridging organic units R in the pore walls. This representation is idealized: the bridges can be slightly tilted or twisted with respect to each other.

© 2006 Wiley-VCH Verlag GmbH & Co. KGaA, Weinheim

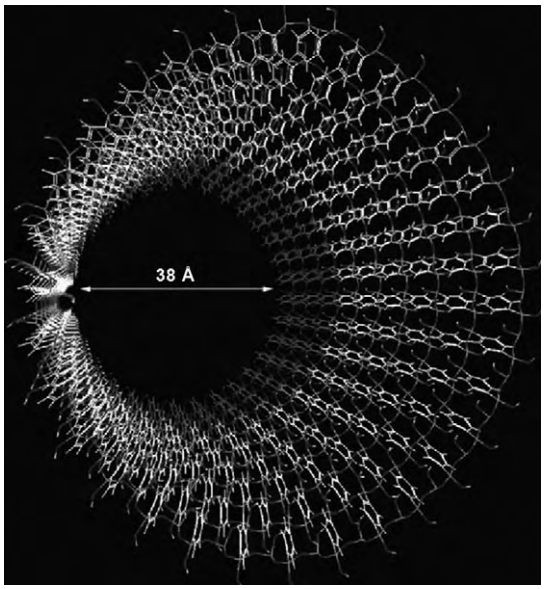

Figure 16. Model of the pore surface of a mesoporous benzene-bridged organosilica. The benzene molecules are arranged circularly along the pore and are embedded between the silica layers bordering both sides. The pore surface of the silica is saturated with silanol groups. The benzene and silica layers are arranged alternately along the pore axis with a separation of 7.6 Å; Si orange, O red, C white, H yellow. Reproduced with permission from the Nature Publishing Group.

highly ordered mesostructures, and that rigid aromatic bridges only show crystal-like organization within the channels when the corresponding synthesis is carried out in the presence of a structure-directing agent, but not when a simple sol–gel process (without SDA) is used. Nevertheless, Corriu and co-workers[187,188] observed organization in isotropic solutions of rigid, rod-shaped, mainly aromatic or heteroaromatic organosilica precursors that exhibited anisotropic domains after a sol–gel process without SDA, that is, domains in which the organic units were each oriented in a preferred direction with respect to each other; this phenomenon was confirmed by the birefringence of the nonporous materials obtained. This raises the question of how and to what extent the self-assembly of the SDA favors the formation of periodicity on a molecular scale, and whether the development of micelles (with the associated aggregation of the precursors) and the crystal-like arrangement of the organic bridges are two mutually independent processes.

This question has not yet been fully answered; however, Morell et al.[189] were able to show from in situ SAXS measurements (with synchrotron radiation) of the formation process of biphenyl-bridged PMO (under basic conditions, OTAC as SDA) that the mesophase and the periodicity within the pore walls forms simultaneously, presumably in a highly cooperative process during hydrothermal treatment. After formation of the initially spherical micelles, the X-ray reflections caused by the formation of the mesophase/mesopore (low-angle region) and the molecular scale periodicity appear and grow simultaneously in the corresponding diffraction pattern (Figure 17).

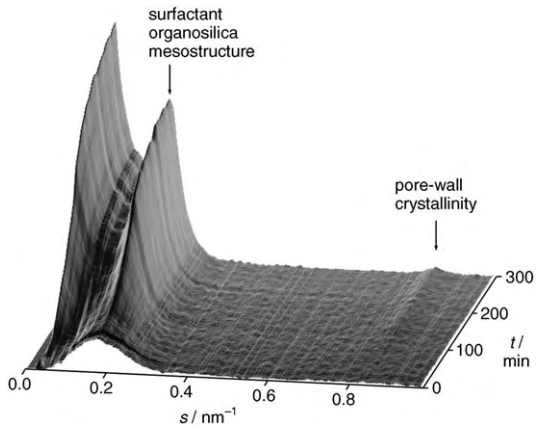

Figure 17. Temporal development of the SAXS/XRD pattern during the synthesis of the mesoscopically ordered biphenyl-bridged PMOs with a crystal-like arrangement of the biphenyl bridges; the corresponding reflections appear almost simultaneously. Reproduced with permission from ACS Publishing.

5.1.2. Gemini Surfactants and Ionic Liquids

Some of the structure-directing agents that are used in the synthesis of PMOs belong to the class of gemini surfactants. The term gemini surfactant was coined by Menger and Littau,[190] and a summary of research in this area can be found in a review article by Menger and Keiper.[191] Gemini surfactants are made up of at least two conventional surfactants that are connected covalently by a spacer. All gemini surfactants consist of at least two hydrophobic chains and two ionic or polar head groups; the spacer can consist of alkyl chains of different lengths (C_2 to C_{12}), can be flexible or rigid (aromatic), and can be polar (polyethers) or nonpolar (aliphatic, aromatic); the head group can be nonionic (saccharides), or positively (ammonium) or negatively (phosphate, sulfonate) charged. Both symmetric and nonsymmetric gemini surfactants are known, that is, those with identical chains and head groups and those that differ in at least one component.

Cationic gemini surfactants have been used in the synthesis of high-quality MCM-48 silica phases that exhibit very large specific surface areas and very narrow pore radii distributions.[192] The use of (cationic) gemini surfactants has two advantages: 1) The doubly charged head group is expected to interact more strongly in basic media with the deprotonated silanol groups of the precursor, which could have favorable effects on the degree of order of the mesophase. 2) The packing parameter g[193] of the SDAs can be adjusted relatively simply by variation of the chain length of the spacer of the gemini surfactant, which allows better control over the symmetry of the resulting mesophase.

Liang and Anwender[194] synthesized ethane-bridged PMOs from BTEE (**2**) in the presence of a binary surfactant mixture under basic conditions whereby the mixture consisted of the gemini surfactant $[CH_3(CH_2)_{17}NMe_2(CH_2)_3NMe_3]^{2+}2\,Br^-$ (abbreviated as $C_{18\text{-}3\text{-}1}$) and CTAB. The products had only a relatively low degree of order, but by adding

 © 2006 Wiley-VCH Verlag GmbH & Co. KGaA, Weinheim

typical swelling agents such as 1,3,5-trimethylbenzene (mesitylene) or 1,3,5-triisopropylbenzene to the binary surfactant mixture, the authors were able at the same time to increase the pore diameter considerably. The materials prepared with swelling agents exhibited pore diameters up to 11 nm.

By using the same organosilica source (BTEE, **2**) and a gemini surfactant of the same type but with a somewhat shorter alkyl chain ($C_{16\text{-}3\text{-}1}$), Liang et al.[195] were able to synthesize the corresponding PMO material in a hitherto unknown form with cubic symmetry ($Fm\bar{3}m$).

A special gemini surfactant that belongs to the interesting class of organic salts from which ionic liquids can be obtained was used by Lee et al. in the synthesis of ethane-bridged PMOs.[196] Under basic conditions, they used the imidazolium-based surfactants 1-hexadecane-3-methylimidazolium bromide and 1-hexadecane-2,3-dimethylimidazolium bromide as SDAs. Mesoporous products with hexagonal symmetry and a pore diameter of 2.1 nm were obtained but which showed no pronounced long-range order. The authors also synthesized a propylimidazolium-bridged mesoporous organosilica by using the aforementioned imidazolium SDAs and the precursor *N*-(3-triethoxysilylpropyl)-*N'*-(trimethoxysilylpropyl)-4,5-dihydroimidazolium iodide, which is also regarded as an ionic liquid. The product obtained also showed no highly ordered mesostructure, but displayed a high uptake capacity for ReO_4^- ions as a consequence of anion exchange.[197] In spite of the low degree of order that the products have hitherto exhibited, this approach to the synthesis of PMOs or mesoporous organosilicas is a promising alternative, since the gemini surfactants have different stereochemical and electronic properties from those of the surfactants normally used. It is thus conceivable that their use will open up the way to new types of organosilica materials; whether success is achieved in actually obtaining periodic ordered pore systems remains to be seen.

5.2. Synthesis of PMOs through Structure Direction by Nonionic Surfactants

5.2.1. PMOs with Large Pores

After the initial reports on the syntheses of PMOs, considerable effort was made to enlarge the pore diameters of these materials with a view to potential applications in such areas as catalysis, sorption, and host–guest chemistry. The pore diameters of the PMOs prepared by structure-directing agents with ionic alkyl ammonium surfactants (with chain lengths from C_{12} to C_{20}) were restricted to the range between 2 and 5 nm. This limitation was finally surmounted by using different nonionic triblock copolymers such as P123 ($EO_{20}PO_{70}EO_{20}$), F127 ($EO_{106}PO_{70}EO_{106}$), or B50-6600 ($EO_{39}BO_{47}EO_{39}$) as SDAs under acidic conditions (EO = ethylene oxide, PO = propylene oxide, BO = butylene oxide). These triblock copolymers were used previously in the synthesis of large-pore mesoporous pure silica phases such as SBA-15 (*p6mm*), SBA-16 ($Im\bar{3}m$), und FDU-1 ($Fm\bar{3}m$).[198–201] The synthesis takes place by the $S^+X^-I^+$ pathway when nonionic surfactants in acidic media are used (Figure 3).

The first syntheses of large-pore PMOs by structuring with triblock copolymers was reported by Muth et al. in 2001.[202] BTME (**2**) was used as precursor in the presence of P123 as supramolecular template under acidic conditions to synthesize the corresponding ethane-bridged silica, which exhibited a 2D hexagonal pore structure analogous to SBA-15 ($\varnothing$ = 6.5 nm, $S_{BET} = 913\ m^2 g^{-1}$).

Burleigh et al.[203] used BMTE (**2**) and P123, and the reaction mixtures were treated with various amounts of the swelling agent 1,3,5-trimethylbenzene (TMB). The pore diameters increased from 6 to 20 nm with increasing concentrations of TMB, while the pore structure changed from wormlike motifs to a hexagonal arrangement of spherical pores.

The degree of order of these materials structured by triblock copolymers could be improved by the addition of inorganic salts such as NaCl to the reaction mixture. The salts have a specific effect on the interaction between the positively charged head group of the surfactant and the inorganic species. In this way, Guo et al.[204] were able to obtain a highly ordered large-pore ($\varnothing = 6.4$ nm), ethane-bridged PMO with 2D hexagonal symmetry (*p6mm*).

Bao et al.[205–207] investigated the influence of the ratio of the organosilica precursor and P123 in the reaction mixture in the synthesis of ethane-bridged PMOs, as well as the effect of acid concentration on the degree of structural order and the external morphology of the products. By optimization of the synthetic conditions, they were able to obtain highly ordered materials without needing to add inorganic salts. In contrast to the corresponding pure silica phases, the pore properties and the external morphologies of the ethane-bridged PMOs were considerably dependent on the acid concentration in the polymer solution.

Zhu et al.[208] reported the synthesis of a large-pore ethane-bridged silica phase by the TLCT approach. As SDA they used a lyotropic liquid-crystalline phase formed from the binary P123/water mixture to which the precursor was added, and they obtained well-organized monolithic 2D hexagonal PMO materials ($\varnothing = 7.7$ nm, $S_{BET} = 957\ m^2 g^{-1}$). The synthesis of 2D hexagonal (*p6mm*) ethane-bridged silica with large pores could also be achieved by the use of the triblock copolymer poly(ethylene oxide)-poly(DL-lactic acid-*co*-glycolic acid)-poly(ethylene oxide) ($EO_{16}(L_{28}G_3)EO_{16}$; LGE53) as SDA, as reported by Cho et al.[209] The product showed high hydrothermal stability: the structural integrity of the material was almost entirely intact even after a 25-day hydrothermal treatment in boiling water. In contrast, a pure silica phase synthesized under the same conditions for comparison and an ethane-bridged PMO synthesized with OTAC as SDA lost their mesoscopic order after hydrothermal treatment for 48 and 24 hours, respectively.

2D hexagonal phases are usually obtained in the synthesis of large-pore PMOs with P123. If instead F127 or B50-6600 is used as the SDA, large-pore PMOs with cubic structure are obtained under certain conditions. A number of authors have high hopes of the advantage of a three-dimensional pore structure with regard to catalytic applications, since this structure would ensure more-efficient material transport—a prediction that would first have to be substantiated. Thus, Cho

 © 2006 Wiley-VCH Verlag GmbH & Co. KGaA, Weinheim

et al.[210] attempted to synthesize an ethane-bridged silica analogous to SBA-16 by co-condensation of BTEE (**2**) and TEOS in the presence of the triblock copolymer F127, but found that products of cubic structure were only then obtained when the BTEE content was no more than 10% by weight. Guo et al.[211] were the first to prepare a pure large-pore ethane-bridged silica with cubic symmetry ($Im\bar{3}m$, $\varnothing =$ 9.8 nm, $S_{BET} = 989\ m^2 g^{-1}$). They used BTME (**2**) as the organosilica precursor and F127 as the SDA under acidic conditions with the addition of K_2SO_4 to increase the interaction between the head group of the triblock copolymer and the organosilica species. Without the addition of K_2SO_4, only amorphous gel-like substances were obtained. Another ethane-bridged silica with cubic symmetry and up to 10-nm large cagelike pores, similar to the structure of the pure silica phase FDU-1, was synthesized by Matos et al.,[212] who used the more hydrophobic triblock copolymer B50-6600 ($EO_{39}BO_{47}EO_{39}$) as a template. Zhao et al.[213] recently published the synthesis of a highly ordered ethane-bridged PMO material with a $Fm\bar{3}m$-symmetric cagelike pore system ($\varnothing = 5.6$ nm, $S_{BET} = 796\ m^2 g^{-1}$) with the use of BTME (**2**) and F127 under acidic conditions and with the addition of KCl.

Most of the large-pore PMOs that have been reported are ethane-bridged materials, which may be because of the commercial availability of the respective precursors BTME and BTEE (**2**). Unfortunately the ethane bridge offers few possibilities for further chemical modification. Only a few syntheses of large-pore PMO materials with complex organic bridges have been reported so far.

The first benzene-bridged PMO with large pores was synthesized by Goto und Inagaki.[214] They obtained well-ordered material with 2D hexagonal symmetry ($\varnothing = 7.4$ nm, $S_{BET} = 1029\ m^2 g^{-1}$). However, unlike the corresponding benzene-bridged silicas synthesized under basic conditions in the presence of alkylammonium surfactants, this material showed no reflections in the wide-angle region of the powder XRD pattern, and thus exhibited no crystal-like pore walls. Thermogravimetric analysis showed that the material was stable up to 550 °C and thus exceeded the thermal stability of the benzene-bridged silicas prepared with the help of alkylammonium surfactants by 50 °C.

The integration of a further unsaturated organic bridge into large-pore PMOs was achieved by Sayari and co-workers,[215] who used **3** as the precursor, and by the addition of butanol to the polymeric reaction solution arrived at well-structured ethene-bridged PMO materials with narrow pore-radius distributions ($\varnothing = 8.0$ nm). Subsequent bromination showed that approximately 30% of the ethene bridges were accessible for chemical reaction.

Recently, Morell et al.[216] reported the synthesis of a highly ordered thiophene-bridged PMO material with a SBA-15-analogous mesostructure ($\varnothing = 5$–6 nm, $S_{BET} = 550\ m^2 g^{-1}$) that was stable in air up to 400 °C. In contrast to works under alkaline conditions, which leads to a high degree of Si–C bond cleavages, ^{29}Si MAS NMR and Raman spectroscopy showed that less than 4% of the Si–C bonds were cleaved under the strongly acidic conditions used. Interestingly, the bridging thiophene group is the only heteroarene that has been incorporated into PMO materials so far. A model of the pore wall structure of this PMO type is shown in Figure 18.

The number of large-pore PMOs with complex organic units described in the literature thus far is indeed small, but this could change in the future thanks to synthetic approaches with the aid of triblock copolymers.

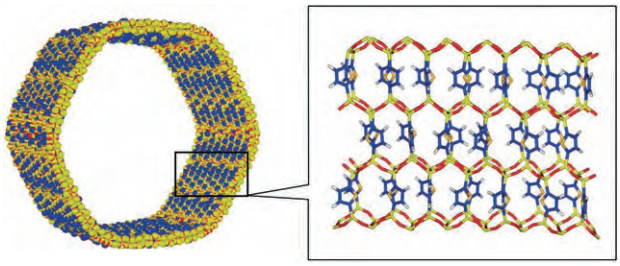

Figure 18. CPK model of part of the pore of a thiophene-bridged PMO and enlarged representation of a section of the pore-wall structure as a stick model; Si yellow, O red, C blue, S orange, H white. CPK stands for the modeling system of Corey, Pauling, and Koltun, which is based on the van der Waals radii of the atoms.

5.2.2. PMOs with Small Pores

In 2002, another highly promising synthetic route for PMO materials was established in which nonionic polyoxyethylene alkyl ethers composed of hydrophobic hydrocarbon chains and hydrophilic PEO blocks, such as polyoxyethylene-(10)-hexadecyl ether ($C_{16}H_{33}(EO)_{10}OH$) and polyoxyethylene-(10)-octadecyl ether ($C_{18}H_{37}(EO)_{10}OH$) (Brij 56 and Brij 76), were used as structure-directing agents. Like those with the triblock copolymers, the syntheses with the Brij surfactants are also carried out in acidic media, and hence they also follow the $S^+X^-I^+$ mechanistic pathway. This pathway generally leads to higher hydrolysis and condensation rates for the precursor, higher product yields, and a tendency towards thicker pore walls, which is desirable with respect to thermal stability. The advantages of Brij surfactants over triblock copolymers are that they are cheap, nontoxic, and biodegradable. However, the pore diameters of the PMO materials that can be synthesized with Brij surfactants are restricted to around 5.5 nm; the values of the specific surface areas are correspondingly higher.

Burleigh et al.[217] reported the syntheses of ethane-bridged PMOs that were structured with the aid of Brij 56 and Brij 76 under marked variation in acid concentrations. The PMOs structured with Brij 76 exhibited highly ordered 2D hexagonal ($p6mm$) pore systems with pore diameters between 4.3 and 4.5 nm, whereas the degree of order of the products structured with Brij 56 was lower, and the pore diameters were also somewhat lower (3.6–3.9 nm), in keeping with the shorter alkyl chain. All products exhibited a specific surface area of approximately $1000\ m^2 g^{-1}$. Interestingly, the degree of order and the symmetry of the mesostructure proved to be almost independent of the acid concentration; in

 © 2006 Wiley-VCH Verlag GmbH & Co. KGaA, Weinheim

comparison, the ethane-bridged PMOs synthesized with CTAC in acid showed a very low degree of order, and changes in pH significantly affected the resulting mesophase.

In a further work, Burleigh et al.[218] reported a new protocol based on Brij 76 for the synthesis of 2D hexagonal PMO materials with long-range order, which included methylene-, ethane-, ethene-, and benzene-bridged systems. These materials showed considerable mechanical and hydrothermal stability and even outperformed pure silica phases synthesized under the same conditions.[,219] Successful syntheses of Brij-structured ethane-bridged PMO materials have also been reported by Hamoudi and Kaliaguine[220] and Sayari and Yang.[221] Sayari and co-workers[215,222] were also able to obtain well to very well ordered ethene- and benzene-bridged PMOs with the aid of Brij surfactants. The ethene-bridged PMO contained a good 20% more accessible C=C bonds than the corresponding material structured with P123. In contrast to the materials prepared in basic media with alkyltrimethylammonium surfactants and the benzene-bridged silicas structured with P123, the benzene-bridged PMO with 2D hexagonal symmetry showed no crystal-like arrangement of the organic bridges within the pore walls, which was concluded from the absence of reflections in the wide-angle region of the powder XRD pattern. According to the authors, Fourier transform TEM images indicated partial but novel order of the benzene units, which were not oriented parallel to the pore axis, but at an angle of 57°.

Hunks and Ozin[223,224] used the two organosilica sources bis-4-(triethoxysilyl)phenyl ether (**16**) and bis-4-(triethoxysilyl)phenyl sulfide (**17**) in the presence of Brij 76, along with the addition of small amounts of NaCl, to synthesize the respective PMOs bridged with 4-phenyl ether and 4-phenyl sulfide. They obtained the precursors by Grignard reaction of TEOS with the corresponding bromo derivatives of 4-phenyl ether and 4-phenyl sulfide. The 4-phenyl ether bridged material exhibited a wormlike mesoporous structure, whereas the 4-phenyl sulfide bridged PMO was less well structured, which the authors attributed to a less-efficient packing of the sterically more demanding and rotationally restricted sulfur bridge within the pore walls. The pore diameters of these new PMO derivatives varied between 2 and 3 nm, and the specific surface areas were 637 $m^2 g^{-1}$ for the 4-phenyl ether and 432 $m^2 g^{-1}$ for the 4-phenyl sulfide PMO. Both products were stable in air up to about 500 °C and thus achieved thermal stabilities that are comparable with the rigid benzene- and biphenyl-bridged PMOs.

By structuring with Brij surfactants, Hunks and Ozin[224] were also able to prepare PMO materials with arylmethylene bridges by starting from the corresponding organosilica precursors with bridges of the type 1,4-$(CH_2)_nC_6H_4$ ($n = 0$–2; **5**, **7**, **8**) under acid catalysis and with the addition of NaCl. The 1,4-benzene-bridged PMO was already known, the PMOs with 4-benzyl and *p*-xylene bridges, however, were described for the first time. All products showed a 2D hexagonal arrangement of the mesopores with comparably restricted long-range order and pore diameters of 2 to 3 nm, although the *p*-xylene-bridged material exhibited noticeably smaller pores, an appreciably smaller pore volume, and smaller specific surface areas. The thermal stability of the products decreased with increasing number of methylene units of the organic bridges, that is, **5** > **7** > **8**.

Zhang et al.[225] demonstrated that, unlike the syntheses described previously, the synthesis of the PMO compounds could also be realized under neutral conditions. They synthesized 2D hexagonal ethane-bridged PMOs with BTME (**2**) in the presence of Brij 76 as structure-directing agent, whereby small amounts of fluoride ion were added as a catalyst for the hydrolysis of the organosilica precursor. It emerged that the formation of an ordered 2D hexagonal mesostructure under neutral conditions is only possible with the addition of bivalent inorganic salts such as $NiCl_2$ or in the presence of the previously described hydrolysis catalysts.

A further interesting synthetic route to PMOs comes from Kapoor and Inagaki,[226] who used a binary surfactant mixture formed from OTAC and Brij 30 ($C_{12}H_{25}(EO)_4OH$) as SDA under basic conditions. They obtained from the precursor BTME (**2**) a highly ordered ethane-bridged silica phase ($\varnothing$ = 2.8 nm, $S_{BET} = 744\ m^2 g^{-1}$) with cubic symmetry ($Pm\bar{3}n$) similar to the pure silica phase SBA-1. SEM investigations showed that the material consisted of particles of uniform size (5 μm) and well-defined dodecahedral morphology. Notable during the synthesis was the sensitivity relative to the composition of the surfactant: the optimal Brij 30/OTAC ratio was 15:85, and even the smallest deviation from this ratio led to very poorly ordered products.

5.3. PMOs from Tri- and Multisilylated Precursors—the Creation of New PMO Classes

PMO materials that are constructed from bissilylated precursors may be perceived as MCM-41/SBA-15 phases in which, in the ideal case (although impossible in practice), a quarter of all Si–O–Si units are replaced by Si–R–Si units, which corresponds to a formal molecular formula of $[R_{0.5}SiO_{1.5}]$. Unlike the bivalent oxygen atom, however, the organic bridges can in principle form bonds to more than two silicon atoms. In this way, the structure motifs already realized in PMOs can be extended considerably, especially when the multifarious possibilities that arise from the use of mixtures of tris-, bis-, and monosilylated precursors are considered. At the same time, the mechanical and thermal stability of PMOs can be increased, since tris- and multisilylated precursors can act as cross-linkers.

It remains to be seen whether the thermal stabilities of existing PMO materials will be adequate for use in industrial applications. For example, many catalytic reactions in the area of inorganic chemistry and above all in the petrochemical industry require temperatures of 500 °C or even considerably higher, which suggests that their use in this area is unlikely. In contrast, the stabilities appear sufficiently large for use in the catalysis of organic reactions—especially the production of active pharmaceutical compounds, agrochemicals, flavorings and fragrances, as well as other chiral organic synthetic components and to an even greater extent the especially temperature-sensitive biocatalysis reactions. Nevertheless, a highest possible thermal stability is desirable for two reasons: 1) To ensure adequate long-term stability at elevated process

 © 2006 Wiley-VCH Verlag GmbH & Co. KGaA, Weinheim

temperatures, the decomposition point must lie at temperatures far above the working temperature; 2) Even if the planned or envisaged application itself does not demand very high temperatures, high temperatures may occur during certain fabrication processes, for example, in the production and processing of thin films with low dielectric constants (low-*k* thin films, see Section 5.8.3) that are used as insulators in components in the semiconductor industry, in which temperatures of up to 450 °C are necessary.[227]

It was the Ozin group that introduced this innovative approach of using multisilylated precursors. This was at the same time an important step to increase the complexity of the organic components to bestow new properties onto the representatives of this class of materials.

In 2002, Kuroki et al.[228] published the synthesis of an aromatic PMO material that was obtained from the three-point coupling precursor 1,3,5-tris(triethoxysilyl)benzene (**11**). The nitrogen physisorption measurements, however, suggested the existence of a microporous rather than a mesoporous material. Benzene groups began to separate from the 1,3,5-benzene-bridged PMO above around 600 °C (under a nitrogen atmosphere), whereas xerogels of 1,3-bis- and 1-monobenzene-bridged silicas prepared for comparison began to decompose at 500 and 450 °C, respectively.

Another structurally interesting motif was constructed by Landskron et al.,[229] who used the cyclic precursor 1,1,3,3,5,5-hexaethoxy-1,3,5-trisilacyclohexane (**4**), which eventually led to linked $\{Si(CH_2)\}_3$ ring structures. This PMO (pore diameter 2.2 nm) showed no decomposition at temperatures up to 500 °C (under a nitrogen atmosphere), and the mesoporous system remained ordered and without a decrease in pore diameter even up to 600 °C. It was also shown that the materials could be obtained as an oriented thin film that exhibited an unusually low dielectric constant (see Section 5.8.3).

In 2004, Landskron and Ozin [230] transferred a structure-building concept from organic chemistry—the dendrimer concept—to PMO chemistry. Self-assembly of dendrimer building blocks (Scheme 1, **20**–**22**) with hydrolyzable alkoxysilyl groups at the outer edge through ionic (with OTAC) and the nonionic (with triblock copolymers) synthetic pathways gave highly ordered periodic mesoporous dendrisilicas (PMDs) with pore diameters and wall strengths that are typical for the respective synthetic routes. ^{29}Si MAS NMR measurements showed that essentially none of the SiC_4 building blocks were cleaved during the synthesis.

Hunks and Ozin[231] introduced the most recent representative of a new class of bifunctional PMOs that were formed from single-source precursors and contained either siloxane-disilsesquioxane (DT^2 type; formed from **18**) or siloxy-trisilsesquioxane units (MT^3 type; formed from **19**). A note on nomenclature: "Classical" PMOs that are built up from silsesquioxanes and are anchored at two points in the network belong to the T^2 type. The organosiloxane compounds are classified according to the number of oxygen atoms that are grouped around the silicon core. The silicon atom can form one to four siloxane bridges whereby mono-, di-, tri-, and tetrasubstitution is named with the letters M, D, T, and Q, respectively.

Hunks and Ozin used a nonionic triblock copolymer synthetic route under strongly acidic conditions to obtain 2D hexagonally ordered mesoporous materials with pore diameters of 6.2 (DT^2 type) and 5.8 nm (MT^3 type) and a wall thickness of about 5.7 nm. Despite their relatively thick pore walls, these materials proved to have below average thermal stability (stable to ca. 250 °C in air).

An overview of the described PMO syntheses with ionic and nonionic SDAs is given in Table 1.

5.4. Other PMO Derivatives

An interesting approach of Kuroda and co-workers[232] involved no added structure-directing agent. Instead, they simply use a newly developed siloxane-based surfactant-like organosilica source that consists of a long-chain alkylsilane nucleus and three trimethoxysilyl groups branching from it ($C_nH_{2n+1}Si(OSi(OMe)_3)_3$, $n = 10$ or 16). In this method, the precursor itself functions also as a surfactant. For $n = 16$ a layered interlocked hybrid material was obtained, whereas a 2D hexagonally ordered phase whose presence was supported by TEM images was obtained for $n = 10$ (Figure 19). The materials were calcined to remove the covalently bound alkyl chain from the product. This led to collapse of the structure in the case of the layered product; the structure of the 2D hexagonally ordered product was retained, although the *d* value for the lattice spacing decreased slightly, and a microporous solid was obtained (pore diameter of 1.7 nm).

5.4.1. PMAs

In 2003, Ozin and co-workers[233] reported the synthesis of periodic mesoporous aminosilicas (PMAs), in which amino groups are anchored in the framework of the mesoporous network. These materials were prepared by the thermal ammonolysis of PMOs in a stream of gaseous ammonia, which resulted in substitution of the organic components and siloxane coupling sites of the PMOs by amino and nitride groups. The number of amino groups that could be incorporated was strongly dependent upon the temperature at which the ammonolysis was carried out. The highest loading with amino groups (20% by weight) was achieved by a 4-h treatment of a well-ordered cubic methylene-bridged PMO material with ammonia at 850 °C. The degree of nitrogen incorporation is thus similarly high or even higher than with corresponding syntheses of mesoporous silicon oxynitrides that could be obtained by ammonolysis from the pure silica phases SBA-15[234] or MCM-41.[235] In the case of the methylene-bridged PMOs, the mesoscopic order of the materials was retained during ammonolysis, and the pore diameter decreased only slightly. However, the mesostructure of the ethane-bridged PMO materials collapsed. The ammonolysis was incomplete at lower ammonolysis temperatures (400–550 °C), and a large number of the organic bridges remained intact. This method opens up highly promising opportunities to develop new multifunctional mesoporous organoaminosilica materials.

 © 2006 Wiley-VCH Verlag GmbH & Co. KGaA, Weinheim

Table 1: Overview of PMO syntheses in the presence of ionic or nonionic surfactants as structure-directing agents.[a]

Precursor	Surfactant	pH	Mesophase	Pore size [nm]	Ref.
	CTAB	basic	2D hex	3.1	[177]
	Brij 76	acidic	2D hex	5.0	[218]
	OTAC	basic	a) 3D hex b) 2D hex	a) 3.1 b) 2.7–3.3	[34, 175]
	CTAC	basic	cubic	2.9–4.0	[174, 175]
	C_{10}–C_{18} TMACl	basic	2D hex	3.0–4.4	[176]
	CPB	acidic	C_{16}: cubic wormlike	2.8–3.1	[178]
	CTAB	acidic→basic	2D hex/wormlike	2.2	[35]
	P123	acidic	2D hex/wormlike	6.0–20.0	[202–208]
	F127	acidic	cubic	5.6; 9.8	[211, 213]
	LGE53	acidic	2D hex	7.9	[209]
	B50-6600	acidic	FDU-1-like	10.0	[212]
	Brij 76	acidic	2D hex	4.3–5.5	[217–219, 175]
		neutral $NiCl_2/NH_4F$	2D hex	3.9–4.7	[225]
	Brij 56	acidic	2D hex	3.6–4.5	[217, 220]
	Brij 30/OTAC	basic	cubic	2.8	[226]
	CTAB	basic	2D hex	3.9	[36]
	CTAB	acidic→basic	n.d.	2.4	[35]
	OTAC	basic	2D hex	3.3	[173]
	P123	acidic	2D hex	8.0–8.6	[215]
	Brij 76	acidic	2D hex	3.9–5.1	[215, 218]
	Brij 56	acidic	2D hex	4.0	[215]
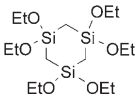	CTAC	basic	n.d.	2.2	[229]
	CPC	acid	2D hex	2.0	[179]
	OTAC	basic	2D hex cryst.	3.8	[181]
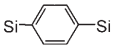	C_{14}–C_{18} TMABr/TMACl	basic	2D hex cryst.	3.2–3.9	[182]
	P123	acidic	2D hex	7.4	[214]
	Brij 76	acidic	2D hex	3.5–3.9	[218, 222]
	Brij 56	acidic	2D hex	3.5	[222]
	OTAC	basic	2D hex cryst.	3.0	[186]
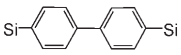	OTAC	basic	2D hex cryst.	3.5	[183]
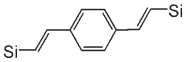	OTAC	basic	2D hex cryst.	2.7–3.1	[184, 185]
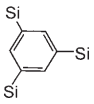	CPC	acidic	2D hex	< 2.2	[228]
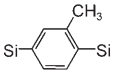	CPC	acidic→neutral	2D hex	2.3	[180]
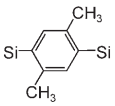	CPC	acidic→neutral	2D hex	2.3	[180]
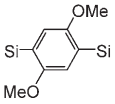	CPC	acidic→neutral	low order	2.3	[180]

© 2006 Wiley-VCH Verlag GmbH & Co. KGaA, Weinheim

Table 1: (Continued)

Precursor	Surfactant	pH	Mesophase	Pore size [nm]	Ref.
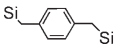	Brij 56	acidic	low order	2.9	[224]
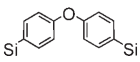	Brij 56	acidic	low order	2.4	[224]
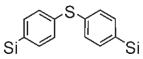	Brij 76	acidic	wormlike	2.0–3.0	[223]
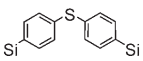	Brij 76	acidic	wormlike	2.0–3.0	[223]
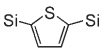	CPC P123	acid acidic	2D hex 2D hex	n.d. 5.0–6.0	[179]] [216]
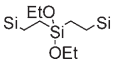	P123	acidic	2D hex	6.2	[231]
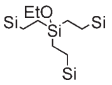	P123	acidic	2D hex	5.8	[231]
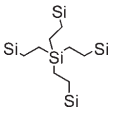	OTAC	basic	n.d.	2.5	[230]
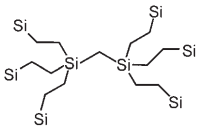	P123	acidic	n.d.	8.2	[230]
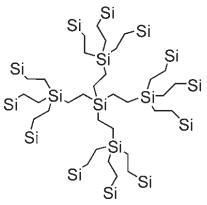	P123	acidic	n.d.	9.1	[230]

[a] Terminal Si: $Si=Si(OR)_3$ (n.d. = not determined, hex = hexagonal, cryst. = crystal-like pore walls, TMABr/Cl = trimethylammonium bromide/chloride).

5.4.2. *Carbon/Silica Nanocomposites*

A further possibility for the transformation of PMOs into other mesoporous materials has been described by Pang et al.[236] By heating a mesostructured benzene-bridged PMO with crystal-like pore walls for 4 h at 900 °C in a stream of nitrogen, they obtained mesoporous carbon/silica nanocomposite materials with pores walls uniformly constructed from molecular carbon and silica units. During this "carbonization process", the surfactant still contained within mesostructured starting material decomposed, and the benzene units in the pore walls were transformed into carbon. Thermogravimetric analysis showed that the carbon in the composite materials originated almost exclusively from the aromatic units of the PMO and not from the surfactant. The order of the mesostructure in the end product was essentially retained after the "carbonization", but crystal-like regions were only partially present in the pore walls. The mesostructure following thermal treatment was contracted, as evidenced by both a reduction in the *d* value (from 4.8 to 4.0 nm) and in the pore size (from 2.5 to 2.0 nm). Interestingly, by removal of the silica components from the composite material, mesoporous carbon with a positive image of the mesostructure of the starting compound could be obtained (in contrast to conventional 2-stage synthesis), although the degree of order was significantly lower.

 © 2006 Wiley-VCH Verlag GmbH & Co. KGaA, Weinheim

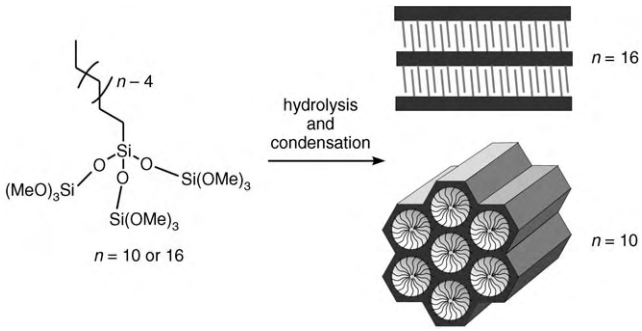

Figure 19. Synthesis of a PMO derivative with the use of a siloxane-based oligomer that consists of an alkylsilane nucleus and three branching trimethyoxysilyl groups ($C_nH_{2n+1}Si(OSi(OMe)_3)_3$, $n=10$ or 16). This precursor acts simultaneously both as organosilica source and surfactant. For $n=10$, a 2D hexagonal composite is formed; for $n=16$, a lamellar phase is formed.

5.5. PMOs from Mixtures of Bis- and Monosilylated Precursors

As can be seen from Scheme 1, the number of PMO materials synthesized so far is very limited. The reason for this is primarily that not all organosilica precursors can be converted into mesostructured products, since they lack the necessary structural requirements, especially adequate rigidity of the organic bridges. A further reason is that the syntheses of those precursors that are not available commercially are often by no means trivial. However, the variability of PMOs can be extended by the construction of bifunctional PMOs by co-condensation reactions of mixtures of bridged bis(trialkoxysilyl)organosilanes $[(RO)_3Si{-}R'{-}Si(OR)_3]$ and terminal trialkoxysilylorganosilanes $[(RO)_3SiR'']$ in the presence of a structure-directing agent (in analogy to the co-condensation reactions of TEOS/TMOS and terminal trialkoxysilylorganosilanes $[(RO)_3SiR'']$). The resulting bifunctional PMOs then consist of a combination of bridging organic units and terminal organic groups whose ends point into the pore interiors and are thus accessible for further chemical reactions. The syntheses of these bifunctional PMOs are carried out with the established ionic alkylammonium, or nonionic Brij or triblock-copolymer surfactants as SDA.

Reports are found in the literature on syntheses in which the bridging components consist of, for example, ethane, ethene, benzene, or biphenyl species, while the terminal functionalities include different alkyl, amino, thiol, cyano, vinyl, alkoxy, aromatic, and heteroaromatic groups. A summary of the published syntheses of bifunctional PMOs is provided in Table 2.[237–249] In principle, the same negative effects in relation to the degree of mesoscopic order and porosity of the products appear in these co-condensation reactions as those already discussed in Section 4.

In a few cases, the terminal organic groups of the bifunctional PMOs were further chemically modified, for example, by selective transformation of terminal vinyl groups into hydroxyl groups by hydroboration and subsequent oxidation,[240] or by oxidative conversion of thiol groups into sulfonic acid groups.[242,243,247] Moreover, Inagaki and co-workers[244] prepared sulfonic acid functionalized benzene-bridged PMOs with crystal-like pore walls by co-condensation of BTEB (**5**) with 3-mercaptopropyltrimethoxysilane (MPTMS) in the presence of OTAC under basic conditions and subsequent conversion of the terminal thiol groups into sulfonic acid groups by oxidation. Even though the degree of mesoscopic order decreased continuously with increasing MPTMS content, the molecular periodicity within the pore walls was retained up to a content of 67 mol% in the starting solution and 24 mol% in the final product. Following this synthetic protocol, the authors could also construct the corresponding bifunctional PMO with a biphenyl unit (**9**) as bridging component; in this case, molecular periodicity could be observed within the pore walls with up to a content of 70 mol% MPTMS in the reaction mixture.[245]

5.6. PMOs from Mixtures of Two Different Bissilylated Precursors

A further possibility for the synthesis of bifunctional PMOs is to allow a mixture of two different bridged bis(trialkoxysilyl) precursors to co-condense in the presence of an SDA. The PMOs obtained then consist of two different organic bridges that are bonded covalently within the framework of the pore walls, in contrast to with mixtures of nonbridged trialkoxy organosilanes, with which the functional groups subsequently point into the pore interiors, which as already discussed has disadvantages with respect to mesoscopic order and porosity.

Zhu et al.[250] synthesized a PMO whose pore walls were functionalized with ethane and propylethylenediamine bridges. This material was obtained by co-condensation of BTEE (**2**) and Cu^{II}-complexed *N*,*N*′-bis[(3-trimethoxysilyl)-propyl]ethylenediamine (BTSPED) by means of the TLCT approach (P123). The preformed Cu^{II} complex was chosen to reduce the flexibility of the ethylenediamine group, which was expected to favor the formation of a mesophase. By increasing the molar ratio of BTSPED to BTEE (**2**) from 0.1 to 0.3, the pore diameter of the functionalized material increased from 11 to 21 nm. The embedded Cu^{2+} ions could be removed reversibly from the pore wall framework and exchanged for Zn^{2+} ions.

Wahab et al.[251] reported a further attempt to prepare bridged amine-functionalized ethane-silica materials by co-condensation of BTEE (**2**) and bis[(3-trimethoxysilyl)propyl]amine (BTMSPA) in the presence of CTAB. Regrettably, they obtained only poorly ordered materials with a content of BTMSPA in the reaction mixture up to 18 mol%; a further increase in the amine content worsened the mesostructure further. An interesting transition of the mesostructure of this system with increasing BTMSPA content in the starting mixture was observed by Rebbin and Fröba[252] in the co-condensation of BTME (**2**) and BTMSPA in the presence of OTAC: Upon changing the BTME/BTMSPA ratio from 90:10 to 55:45, a change from a 2D hexagonal (*p6mm*) to a cubic ($Pm\bar{3}n$) mesophase took place. Even higher BTMSPA concentrations in the reaction mixture led to a collapse of the structure.

Recently Burleigh et al.[253] succeeded in preparing a new family of bifunctional PMOs that contain ethane and benzene bridges and were obtained by co-condensation of the

 © 2006 Wiley-VCH Verlag GmbH & Co. KGaA, Weinheim

Table 2: Overview of the syntheses based on bissilylated and monosilylated precursors in the presence of ionic or nonionic surfactants as structure-directing agents.[a]

Monosilylated precursor	Bissilylated precursor	Surfactant	pH	Content/reaction mixture [mol%]	Content/Product [mol%]	Ref.
	2	CTAB/Brij 30	basic	25	n.d.	[248]
	2	CTAB/Brij 30	basic	25	n.d.	[248]
	3	CTAB	basic	33	n.d.	[240]
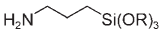	**2**	CTAC	basic	25	17–18	[237]
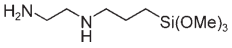	**2**	CTAC	basic	25	13	[237, 238, 241]
	2	CTAC	acidic	30	16	[239]
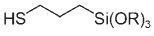	**2**	CTAC	basic	25	21	[237]
	2	Brij 76	acidic	40	n.d.	[249]
	2	P123	acidic	30	n.d.	[249]
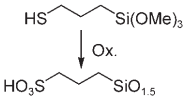	**2**	Brij 76	acid	30	1.72 H^+ mmol g^{-1}	[247]
	2	CTAC	basic	50	33 (-SH) 15 (-SO_3H)	[242]
	2	OTAC	basic	25	n.d.	[243]
	5	OTAC	basic	67	24	[244]
	9	OTAC	basic	70	n.d.	[245]
	2	CTAB	basic	50	n.d.	[246]
	2	CTAB/Brij 30	basic	25	n.d.	[248]
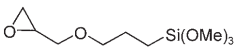	**2**	CTAB/Brij 30	basic	25	n.d.	[248]
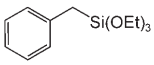	**2**	CTAC	basic	25	23	[237]
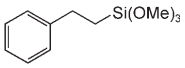	**2**	CTAC	basic	25	22	[237]
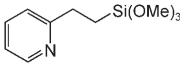	**2**	CTAC	basic	25	16	[237]
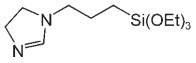	**2**	CTAC	basic	25	10	[237]

[a] n.d. = not determined.

corresponding bridged organosilanes in the presence of Brij 76. Interestingly, they always obtained well-ordered 2D hexagonal (*p6mm*) phases with almost identical porosities regardless of the molar ratio of the two precursors in the starting mixture.

Elemental analysis showed that owing to different hydrolysis and condensation rates, the proportion of benzene bridges incorporated into the resulting material was always higher than the ratio in the starting mixture. Moreover, multifunctional PMOs that contained up to four different organic bridges, including methylene, ethane, ethylene, and benzene units, could also be prepared by using the same synthetic procedure.

Jayasundera et al.[254] recently synthesized 2D hexagonal bifunctional benzene- and chelating ethylenediamine-bridged PMOs with Brij 76. The materials obtained were able to adsorb both *p*-chlorophenol and Cu^{II} ions; the adsorption was just as efficient for binary *p*-chlorophenol/Cu^{II} solutions. Moreover, the adsorption amounts increased by a factor of 2.5 by substitution of a small number of benzene bridges in the pore walls of the PMOs by diethylbenzene functionalities (5% of the respective precursor).

Despite the general problems that occur in co-condensation reactions, this approach should be pursued and optimized. A worthwhile goal could be, for example, a bifunctional PMO with two bridging organic units for which the content of both components could be adjusted precisely. Figure 20 shows such an example of a hypothetical PMO material constructed with thiophene and benzene bridges. The initial work towards the synthesis of such bifunctional aromatic PMOs has already been carried out in our research group.[255]

 © 2006 Wiley-VCH Verlag GmbH & Co. KGaA, Weinheim

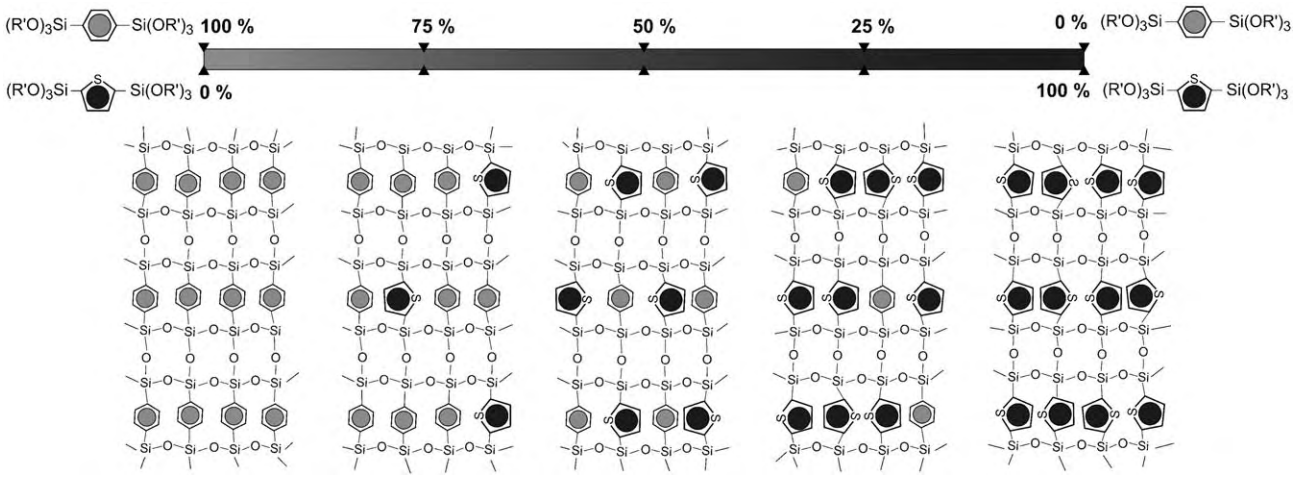

Figure 20. A hypothetical bifunctional PMO material that consists of two different organic bridging groups and whose content is freely adjustable (thiophene black, benzene: gray).

5.7. PMOs from Mixtures of Tetra(m)ethoxysilane and Bis- as well as Multisilylated Organic Precursors

In this section, we wish to address a number of methods to synthesize organic–inorganic hybrid materials in which not only bissilylated organosilica precursors, but also mixtures of precursors for pure silica phases, such as TMOS and TEOS, and bissilylated organosilanes are used. An overview of the precursors that have been used in co-condensation reactions with TEOS is found in Table 3 and Scheme 3.

As already explained in Section 4, owing to the different reactivities, the co-condensation of TMOS/TEOS with bissilylated organic precursors can lead to an inhomogeneous distribution of the organic bridge units within the framework of the hybrid material. Nevertheless, these materials still typically exhibit highly ordered pore systems, large specific surface areas, and a high thermal stability so long as the content of bissilylated organic bridges remains low. As the content of organic units increases, however, the degree of structural order decreases. It is therefore usually necessary to use an excess of TEOS as a "source" of the self-assembly from which the ordered backbone of the hybrid material can form.

In 2001, García and co-workers[256] synthesized a silica material ($\varnothing = 3.8$ nm, $S_{BET} = 930\ m^2 g^{-1}$) that contained viologen **23** in the pore walls. They obtained a material in which up to 15% of the viologen formed a highly ordered 2D hexagonal phase. It is notable that the viologen units of this material can be almost completely transformed into bipyridinium radical cations upon irradiation or thermal treatment, which showed lifetimes up to one month. In further work, they studied the electrochemical behavior and the catalytic potential of the viologen in the electrochemical oxidation of hydroquinone.[257]

A further article in 2002 dealt with the construction of organic chemical switches from organically modified M41S phases.[258] For this purpose, 1.5% *trans*-1,2-bis(4-pyridylpropyl)ethene units (**24**) were inserted into the channels of a MCM-41 silica framework, and a change of the configuration of the C=C bond from *trans* to *cis* was induced by irradiation with light of a suitable wavelength. This photochemically induced switching is associated with a decrease of the pore diameter from 3.9 to 3.5 nm and an increase in the specific surface area from 350 to 470 $m^2 g^{-1}$.

Corriu et al.[259–261] incorporated large chelating agents into mesoporous silica matrices. They introduced the cyclam derivative **25** into the framework of the silica materials through the neutral synthetic route with the triblock copolymers P123 and F127 as SDA, and with the addition of NaF. The materials obtained exhibited only relatively low mesoscopic order, but were able to bind large amounts of the transition-metal ions Cu^{2+} and Co^{2+} selectively. The Cu^{II} cyclam complex was also formed quantitatively by the direct incorporation of $CuCl_2$ into the hybrid material, by which the complete accessibility of Cu^{II} to the cyclam residue within the framework was demonstrated. Chemical lining (grafting) of the inner pore wall with a metal *N*-triethoxysilylpropylcyclam complex followed by the incorporation of a further metal salt into the network of the of the pore wall gave a hybrid material that contained two different metal chelate complexes of which one was anchored within the framework and the other in the pore channels.

An alternative route to the incorporation of metals by complexation into a mesoporous solid was reported recently by Olkhovyk and Jaroniec,[262] who synthesized a hybrid material by co-condensation of TEOS with the trissilylated precursor tris[3-(trimethoxysilyl)propyl]isocyanurate (**26**) which contained 25% of the organic components within the organosilica framework and was suitable for the adsorption of divalent mercury.

5.7.1. Chirality and PMOs

Chirality is an interesting topic in the context of mesoporous solids in general and PMOs in particular, both in regard to the fundamental aspects of chirality and in relation to possible applications. For example, the synthetic pathway by which these materials are formed in a highly cooperative many-particle self-assembly process could conceivably form

© 2006 Wiley-VCH Verlag GmbH & Co. KGaA, Weinheim

Table 3: Overview of the syntheses based on TEOS and bis- or multisilylated precursors in the presence of ionic or nonionic surfactants.[a]

Bis- or multisilylated precursor	Surfactant	pH	Content/reaction mixture [mol%]	Content/product [mol%]	Ref.
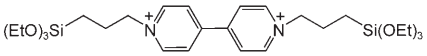	CTAB	basic	1–15	n.d.	[256]
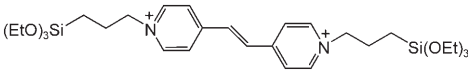	CTAB	basic	1.5–18	31	[258]
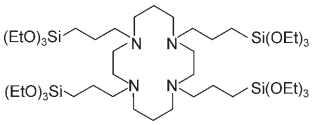	P123	neutral (NaF)	10	11	[259]
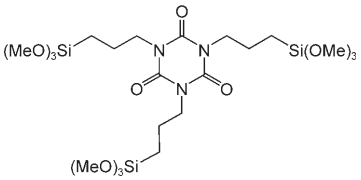	P123	acidic	10–90	90	[262]
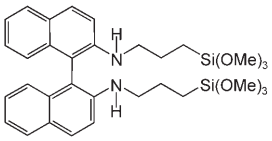	CTAB	basic	5–50	7	[263]
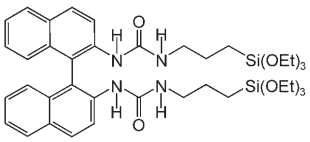	CTAB	basic	5–50	5	[263]
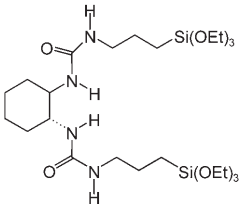	CTAB	basic	5–50	6	[263]
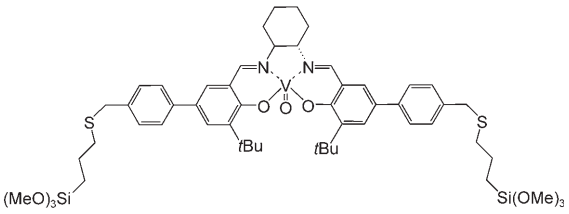	CTAB	basic	5–15	3	[264]

[a] n.d. = not determined.

the basis of studies of the mechanism of chirality transfer. Within this context, as already noted in Section 4, the work of Che et al.,[172] who produced a MCM-41-analogous silica material whose channels showed a helical twist in the direction of the pore axis is notable. This syntheses was achieved not by the use of chiral precursors, but with chiral enantiomerically pure surfactants of the *N*-acyl-L-alanine type. In view of this result, it is possible here to speak of a special type of crystal engineering, even though periodicity at a molecular level is absent.

Another interesting approach, especially with PMOs, would be the direct anchoring of chiral building blocks into the mesoporous framework; this could be relatively easy implemented by the use of chiral organic bridges as integral part of the bissilylated precursors. This was realized in 2004 by García and co-workers,[263] although not for pure PMOs, but for those that are constructed from mixtures with TEOS. The authors integrated chiral organic bridges into MCM-41-analogous hybrid materials by using mixtures of bissilylated binaphthyl or cyclohexadiyl precursors (**27**–**29**) and TEOS. The maximum content of chiral precursor in the reaction mixture that did not lead to a significant reduction in mesoscopic order of the resulting products was 15%. The authors were able to confirm the optical activity of the solid directly by measurement of the rotation of the plane of linearly polarized light. Moreover, the material displayed a

 © 2006 Wiley-VCH Verlag GmbH & Co. KGaA, Weinheim

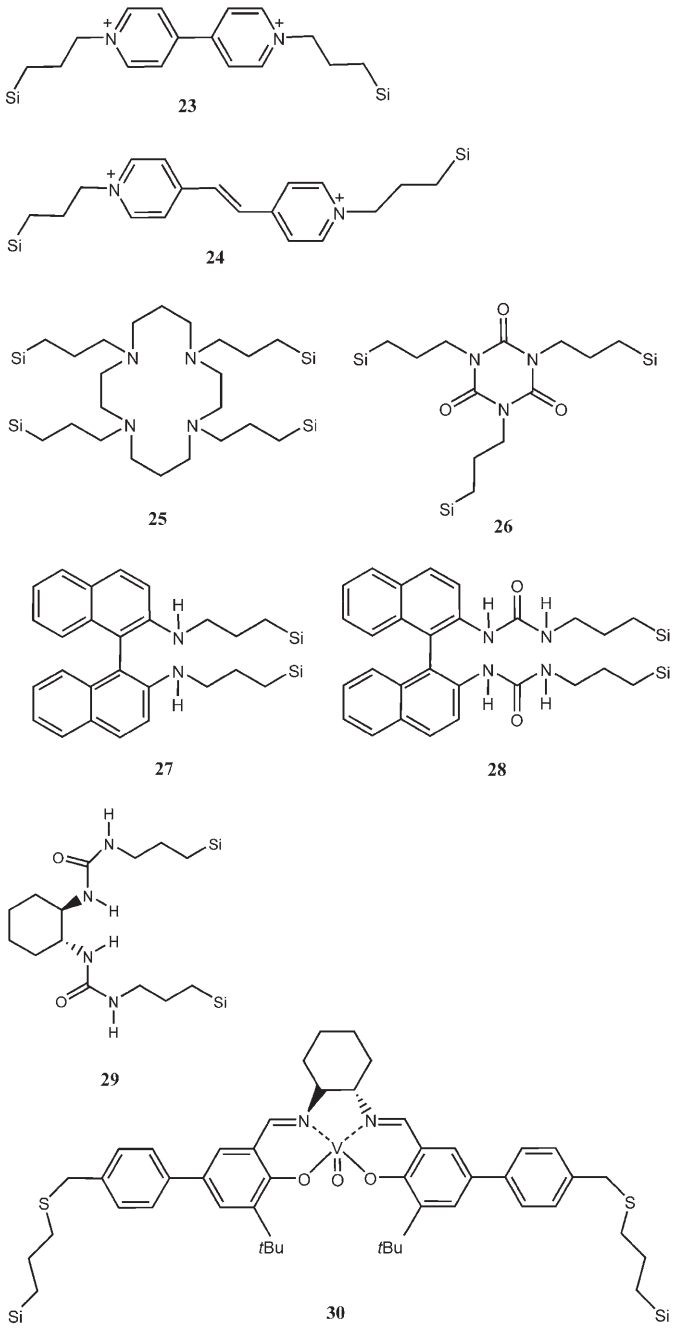

Scheme 3. Bissilylated organosilica precursors that were used in the co-condensation reactions with TEOS/TMOS. Terminal Si atoms: $Si=Si(OR)_3$ with $R=CH_3$, C_2H_5.

certain degree of ability to discriminate chiral compounds; the addition of enantiomerically pure 1,2-cyclohexadiamine to a suspension of the binapthyl-bridged solid led to an increase in fluorescence.

MCM41- and SBA-15-analogous materials with chiral organic groups anchored to the surface and PMOs consisting of chiral organic bridging units are undoubtedly suitable candidates for heterogeneous asymmetric catalysis. There are still a few obstacles to overcome. For example, there must be the highest possible transfer of chirality from the chiral precursor to the end product; that is, any racemization during the synthesis must be avoided. Initial steps have already been taken in the desired direction. For example, Baleizao et al.[264] have integrated large chiral metal complexes into the framework of MCM-41-analogous material. They prepared a chiral vanadyl salen complex (**30**) and coupled it with TEOS in a co-condensation reaction under basic conditions in the presence of OTAC. They were able to incorporate up to 2.5% of the salen complex into the material, which still displayed an average degree of mesoscopic order. Further conceivable applications for chiral PMOs lie in the area of enantioselective chromatography or their use as sensors for smaller, biologically relevant molecules such as chiral peptides.

5.8. Morphologies and Applications of PMOs

The conventional syntheses of PMOs usually lead to powders that are composed of particles of non-uniform size and irregular external form. For their use in special applications, however, it would be highly desirable to be able to influence their morphology. As an example, for chromatographic applications such as HPLC, spherical particles with an average size of about 10 μm and a very narrow size distribution are ideal. In contrast, films of uniform thickness are necessary for applications in the area of sensors. An important aspect in the development of applications based on PMOs is the adjustment of their morphologies to the required mass-transport properties.

A number of fundamental investigations into the influence of various synthetic parameters and conditions on the morphology of ethane-bridged PMOs (synthesis in base, OTAB as SDA, space group *p6mm*, pore diameter 3.3 nm) as well as their changes with aging have been carried out by Lee et al. and Park et al.[265–267] They observed a whole series of different complex morphologies: short broken rods, small fibroid aggregates, larger hexagonally shaped platelets and strands, as well as spiral, gyroid-, and wormhole-like particles, all of which exhibited a hexagonal basal plane. The convoluted morphologies, the authors presume, are probably formed from linear topological defects, whereby disclinations along the traverse lead to bended structures and those along the longitudinal axis lead to twisted structures. These studies underline the fact that the symmetry of the micellar arrangement also determines the outer shape of the PMO particles. This factor is reflected in the difficulties in preparing PMO particles with other morphologies, especially spherical particles. The advances in achieving this objective will be reported in this section.

5.8.1. Spherical PMO Particles and Chromatography

Most attempts to produce monodispersed, spherical PMO particles are based on variants of the Stoeber reaction,[268] that is, very mild basic synthetic conditions are employed through the use of dilute ammonia solutions in ethanol rather than the usual aqueous sodium hydroxide solutions.

Kapoor and Inagaki[269] prepared benzene-bridged PMO particles ($\varnothing = 1.8$ to 2.0 nm) with spherical morphology and

 © 2006 Wiley-VCH Verlag GmbH & Co. KGaA, Weinheim

particle diameters between 0.6 and 1.0 μm (average: 0.8 μm). However, the pore walls exhibited a rather disordered structure at the molecular level. On the basis of electron microscopy investigations at different times during the growth of the particles, the authors deduced that mild basicity and very low reaction and condensation rates are necessary conditions for the formations of spherical morphologies. These conditions are required for the nuclei to form simultaneously and for each individual nucleus to grow uniformly at a constant but slow rate until all particles have achieved simultaneously their final size and adjust their growth on the basis of the consumed condensation material.

Rebbin et al.[270] employed the same modified Stoeber reaction conditions to prepare almost perfectly spherical particles from ethane-bridged PMO materials with diameters between 0.4 and 0.5 μm and a narrow particle-size distribution. Meanwhile considerably larger benzene-bridged PMO particles with average diameters tunable between 3 and 15 μm and acceptably narrow size distributions have been prepared—with this, the objective of producing PMO materials suitable for HPLC has been achieved.[271] This synthesis was not carried out according to the modified Stoeber reaction; instead, a mixture of P123 and CTAB in a hydrochloric acid solution with ethanol as co-solvent was used in a two-stage hydrothermal treatment (5 h at 80 °C, followed by 12 h at 130 °C). An SEM image of spherical particles with diameters of approximately 5 μm is shown in Figure 21. First, HPLC measurements were carried out. The separation of three different mixtures containing up to four components with different polarities was accomplished with the new material.

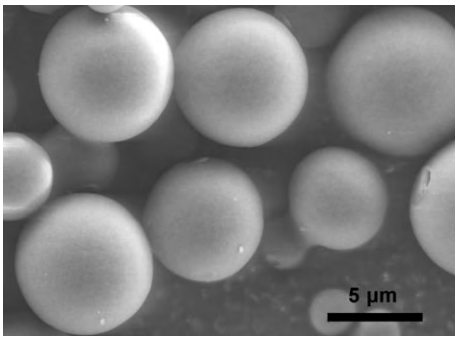

Figure 21. Exemplary SEM image of spherical, benzene-bridged PMO particles with a diameter of approximately 5 μm.

Kim et al.[272] synthesized PMO particles (ethane-bridged, pore diameter 3.2 nm) with spherical morphology and narrow size distributions with diameters between 1.5 and 2.5 μm—the lower limit for materials for application in HPLC. They used the basic synthetic route (aqueous NaOH solution, CTAC as SDA), but instead of following the conventional hydrothermal treatment (after stirring the reaction mixture for 19 h at room temperature), they applied a treatment for various periods of time (between 2 and 6 h) in a microwave oven at different temperatures (95 to 135 °C). The material was tested for its separation capabilities as a packing material in a micro-HPLC column: The quality of the separation of a mixture of eight substances of medium to high hydrophobicity with this column was compared with that of a column packed with conventionally-prepared ethane-bridged PMO particles (octadecahedral morphology, average size 8 μm). Separation of the eight substances was achieved with both columns, but the particles produced by the microwave method proved to be a significantly better separating medium with complete baseline separation observed for at least three of the eight compounds.

5.8.2. ***Adsorbents***

The large inner surface area of PMO materials, their excellent pore accessibility, and the possibility to functionalize them with different chelating or complexing agents make these materials ideal for use in the area of sorption, for example, in waste water treatment.

Zhang et al.[273] used the bridged tetrasulfide precursor $(EtO)_3Si(CH_2)_3S–S–S–S(CH_2)_3Si(OEt)_3$ in combination with TEOS to obtain a PMO-like material that showed a high affinity for Hg^{II} ions and was able to remove them selectively from aqueous solutions that contained the competitive cations Pb^{2+}, Cd^{2+}, Zn^{2+}, or Cu^{2+}. The amount of adsorbed mercury varied between 627 mg g^{-1} for the material that contained only 2 % of the tetrasulfide and 2710 mg g^{-1} for the material in which 15 % was incorporated.

Lee et al.[274] developed an anion-exchange resin based on PMOs for relatively bulky ions such a perrhenate, perchlorate, and pretechnetate, which are significant environmental contaminants. They integrated *N*-((trimethoxysilyl)propyl)-*N*,*N*,*N*-trimethylammonium chloride and *N*-((trimethoxysilyl)propyl)-*N*,*N*,*N*-tri-*n*-butylammonium chloride into the networks of ethane- and benzene-bridged PMO materials. The adsorption capacity proved to be dependent upon pH: the adsorption was highest for neutral solutions (99.9 % Re^{VII} could be extracted from 10^{-4} M $NaReO_4$ solution, which corresponds to a capacity of 1.86 mg Re^{VII} g^{-1}), but decreased with decreasing pH value (67.8 % extraction, corresponding to 1.26 mg Re^{VII} g^{-1} at pH 1). The amount adsorbed decreased only slightly in the presence of competitive sulfate ions, which demonstrates that this PMO-based anion-exchange resin can be used effectively in solutions of mixed anions.

5.8.3. ***Thin Films and Low-k Materials***

Many applications require the preparation of materials in the form of thin layers or films that can also be lithographically microstructured, for example, for sensors or biomedical coatings. One application for which PMO films are particularly suited is as insulators in the semiconductor industry. The continually increasing density of electronic components, switching elements, and circuit paths in modern highly integrated circuits require insulators that have sufficiently small k values (k: relative permittivity or relative dielectric constant, also known as ε_r) to prevent transfer of charge and signal losses that can arise through undesirable charge accumulation between the switching elements and

 © 2006 Wiley-VCH Verlag GmbH & Co. KGaA, Weinheim

circuit paths. Currently the chip industry is working intensely on the development of materials that are suitable for the new, increasingly more efficient and fast chips of the coming generation. These insulating materials must have relative permittivity values significantly lower than that of silicon dioxide ($\varepsilon_r \approx 3.8$)—the term low-*k* dielectric is used here—and for components smaller than the typical size of 0.1 μm, even materials with ε_r values less than 2 are necessary (ultralow-*k* materials).

Owing to their large pore volumes ($\varepsilon_r(\text{air}) \approx 1$) and their comparatively high organic fraction, PMO films, whose atoms are lighter and less extensively polarizable than those of silicon dioxide, are in principle very suitable as low-*k* dielectrics. As the materials must be moisture repellent, the free silanol groups on the surface of the film are generally hydrophobized with hexamethyldisilazane (HMDS) or trimethylsilyl chloride (TMSC).

Other than the typical spin- and dip-coating methods, the evaporation-induced self-assembly method (EISA) introduced by Brinker's group[275] for producing pure silica mesophases is particularly suitable for the production of PMO films. In the EISA approach, an excess of a volatile solvent is used to ensure that the initial concentration of SDA remains below the critical micellar concentration (CMC). Upon addition of the reaction solution to the substrate, the rapid evaporation of the solvent induces self-assembly of the components involved.

Brinker and co-workers[276] were also the first to transfer the EISA approach to PMO films. They prepared ethane-bridged PMO films that were co-condensed with different fractions of TEOS. To remove the silanol groups from the surface, the films were treated with hexamethyldisilazane following calcination. Capacitance measurements showed that dielectric values decreased with increasing organic fraction; the lowest value obtained was $\varepsilon_r = 1.98$.

A similar technique was used by Dag et al.,[277] who prepared ethane-, ethene-, thiophene-, and benzene-bridged PMO films by applying a heated or highly diluted, clear, homogeneous solution containing the corresponding precursors and the nonionic SDA $C_{12}H_{25}(EO)_{10}H$ in methanol onto a glass substrate. The channels of the PMO film thus obtained (which all displayed 3D hexagonal symmetry) were oriented vertically with respect to the surface of the glass substrate. Unfortunately, the films were not mechanically robust enough to be scratched from the glass surface without destruction of the mesostructure.

Another approach to prepare PMO films was taken by Park and Ha.[278,279] They produced oriented, free-standing ethane-bridged PMO films (2D hexagonal symmetry, C_{12}-, C_{16}-, and C_{18}TAB as SDAs, pore diameters 2.4, 2.6, and 3.3 nm, respectively) of high quality that formed by template structuring without a solid substrate at the air/water interface. In this way they obtained continuous transparent films of uniform thicknesses between 180 and 780 nm. Interestingly, unlike the films of Dag et al., the pores were oriented parallel to the interface. However, no charge capacitance measurements on the products were carried out.

The PMO material described in Section 5.3, consisting of connected $\{Si(CH_2)_3\}$ rings, could also be obtained as an oriented thin film by spin coating onto glass plates.[229] For comparison, films with various organic content were synthesized from mixtures of the precursors TMOS and the cyclohexane derivative $[(EtO)_2SiCH_2]_3$. These films, which were calcined at 300 or 400 °C in a nitrogen atmosphere, showed a linear decrease in the dielectric values with increasing organic content. The values for the films prepared completely from the cyclohexane derivative were 2.5 and 2.0 for the samples calcined at 300 and 400 °C, respectively.

The previous attempts to prepare PMO films with low permittivities for use as insulators in microelectronic applications are very promising. Even lower permittivity values could be achieved by even better control of the structure and porosity; a further possibility in this context is the use of precursors with a higher organic fraction.

5.8.4. Nanowires and Catalysis

PMOs are promising candidates for applications in catalysis, materials separation, and sensor technologies owing to the properties that result from their organic–inorganic hybrid nature, their easily accessible, large inner surface area, and their defined pore geometry. The potential advantages in catalysis of PMOs over microporous zeolites are described in almost every publication. Although the number of reports on promising catalytic applications of PMOs is still very small, if it is considered that PMOs were introduced only six years ago and that it is not rare for a period of at least ten years between development of a technology to its readiness for market, the hope of achieving the pursued targets in the coming years is not totally unfounded.

In 2001, Fukuoka et al.[280] reported the incorporation of pure Pt, Rh, and Pt/Rh and Pt/Pd mixtures into ethane-bridged 2D hexagonal PMOs (pore diameter 3.1 nm). The nanowires prepared in this way exhibit bead-chain-like morphologies (in contrast to the cylindrical rodlike nanowires that form in the pure silica phases FSM-16, MCM-41, and SBA-15), which was attributed to the repulsive interaction of the solution of (polar) metal salt precursor with the (nonpolar) organic components of the PMO walls. The nanowires were incorporated into the channels by impregnation of dried, calcinated PMOs with aqueous solutions of $H_2[PtCl_6]\cdot 6H_2O$, $H_2[PdCl_4]$, and $RhCl_3\cdot 3H_2O$, followed by photochemical reduction (by irradiation with a mercury lamp for 24 h) and drying in vacuo. An alternative, chemical reduction step with H_2 led to separated nanoparticles within the channels. From energy-dispersive X-ray analysis (EDX), the authors concluded the presence of a true, uniform alloy in the case of Pt/Rh mixtures, whereas impregnation of Pt/Pd led to a bicontinuous phase. The Pt/Rh and especially the Pt/Pd PMOs exhibited interesting magnetic properties: the magnetic susceptibilities at temperatures below 90 °C were two and three times (for Pt/Rh and Pt/Pd, respectively) the sum of the values for the two individual component metals. This unusual behavior was attributed to the low dimensionality of the metal topology within the channels , which means that they showed a quantum size effect, as can be often noticed for metallic nanoparticles.

© 2006 Wiley-VCH Verlag GmbH & Co. KGaA, Weinheim

The photoreductive mechanism for the formation of the Pt nanowire was investigated in more detail by Sakamoto et al.[281] with the aid of TEM, X-ray absorption fine structure (XAFS) spectroscopy, and powder XRD. They isolated the platinum wires by removal of the PMO framework with diluted aqueous HF solution. The isolated wires tended to agglomerate, but they could be stabilized as individual wires by the addition of ligands such as $[N(C_{18}H_{37})(CH_3)_3]Cl$ or $P(C_6H_5)_3$. In further work by Sakamoto and co-workers,[282] the ability of palladium nanowires embedded in PMOs to act as catalysts in the oxidation of CO to CO_2 in the presence of excess O_2 was studied. The turnover number (TON) was somewhat higher than for Pd nanowires that were embedded into the pure silica phase FSM-16.

Apart from nanowires, whose effective use in catalysis must still be proven, intensive efforts have been devoted to the development of solid-state acids that, by analogy with microporous zeolites, could extend the area of heterogeneous catalysis. However, unlike with the zeolites, which possess intrinsic (Brønsted) acid centers, with PMOs the acid functional groups must be specifically incorporated. There are in principle two ways that may be pursued with pure PMOs for this purpose. The first—and better—is for the precursors to bear an acid functionality already. The second possibility, the subsequent anchoring of acidic groups onto the surface (grafting), is associated with the disadvantages already described for the grafting method.

Yuan et al.[243] synthesized ethane-bridged PMOs functionalized with sulfonic acid groups to obtain a highly ordered mesoporous solid-state acid with a specific surface area of $873\ m^2 g^{-1}$ and an acid capacity of up to $0.93\ mmol\,g^{-1}$. The catalytic activity was evaluated by alkylation of phenol with 2-propanol and compared with that of ZSM-5 and the sulfonic acid modified MCM-41 (MCM-41-SO_3H). Far higher turnover was achieved with the two functionalized mesoporous materials (PMO-SO_3H and MCM-41-SO_3H) than with ZSM-5. Whereas the activity of MCM-41-SO_3H began to decrease slightly after 10 h, the PMO-SO_3H material showed almost constant activity over a period of 25 h (the turnover was constant at about 60 %).

The ability of PMO-SO_3H to function as acid catalyst was also studied by Yang et al.[247] They prepared PMOs with a high density of sulfonic acid groups by co-condensation of ethane- and benzene-bridged organosilanes with MPTMS in acidic media in the presence of H_2O_2 and Brij 76 as SDA (in situ oxidation) and compared the products with those formed from MPTMS-functionalized PMOs by subsequent oxidative conversion (with 65 % HNO_3). Both materials were shown to be efficient catalysts for the condensation of phenol and acetone to form bisphenol A. In both cases, the ethane-bridged PMO-SO_3H material showed higher catalytic activity than the corresponding benzene-bridged material, and, although the PMO-SO_3H material synthesized by in situ oxidation had a higher specific surface area, larger pore diameters, and a higher number of acid groups per gram, the turnover number with the subsequently functionalized PMO-SO_3H was higher. The authors attributed this finding mainly to the better accessibility of the reactants to the sulfonic acid groups, since in the subsequently functionalized material these are localized preferentially on the outer surface of the pore entrances; this could point to a key role of limited diffusion capability.

In further work by Yang et al.,[283] the catalytic activity of subsequently functionalized PMO-SO_3H materials in the esterification of acetic acid with ethanol was investigated. The reaction rate exceeded that achieved with the commercially available solid-state acid Nafion-H, which is used, for example, as a heterogeneous catalysis in the aldol condensation. However, after the first recovery of the used material, approximately 25 % of the catalytic activity was lost, presumably a result of the weak bonding of the propylsulfonic acid group ($Si(CH_2)_3SO_3H$) to the silicon.

Hamoudi et al.[284] prepared an arylsulfonic acid functionalized ethane-bridged PMO material by co-condensation of BTME (**2**) and 2-(4-chlorosulfonylphenyl)ethyltrimethoxysilane. The acid capacity and proton conductivity were determined to be $1.38\ milliequiv.\,g^{-1}$ and $1.6\times10^{-2}\,S\,cm^{-1}$, respectively. On the basis of these results, the authors claim that this material is exceptionally suitable as a catalyst in fuel cell technology; however, no evidence was provided.

Nevertheless, these initial reports show that PMO materials, especially the analogous heterogeneous solid-state acids, could become very promising alternatives to existing heterogeneous catalysts.

6. Outlook

Research on mesoporous silica phases and on hybrid PMOs is still in its early stages. A goal in the coming years will be to convert the acquired knowledge into technical applications. In view of the interdisciplinary nature of the topic, the growing number of research groups involved, and the diversity of the building blocks deployed, it is difficult to predict which (possibly substantial) expansions of this field must be reckoned with.

A fundamental question that also arises is whether it is at all necessary to construct periodic, ordered pore systems for the envisaged applications, or whether non-ordered porous materials, such as the analogous, more thoroughly researched aero- and xerogels, would fulfill the intended purpose equally well. In particular with regard to PMOs, it must not be forgotten that the synthesis of the precursors and SDAs is laborious and costly, in particular on an industrial scale.

Ordered and oriented pore systems, especially those with narrow pore radius distributions, have advantages in aspects such as their transport properties, which in principle make these materials more suitable for active compound release and transport (of insecticides, pesticides, or pharmaceuticals) than their disordered, non-oriented counterparts. One could imagine, for example, stents (vessel supports) that are coated with mesoporous silica or organosilica phases whose pore systems form the reservoir for an adsorbed medicament, which is successively released to prevent restenosis (new formation) of tissue that would lead to repeated closure of the constriction. Particularly promising is the work of drug delivery systems that react to an external stimulus by releasing an active compound (stimulus-response behavior);

 © 2006 Wiley-VCH Verlag GmbH & Co. KGaA, Weinheim

in the broadest sense, these are systems that depend on switchable porous materials, such as the work of Mal et al.[37,38] on the grafting of silica phases with coumarin and the work of Brinker and co-workers[167] on switchable azobenzene units described in Section 4.

One of the interesting characteristics of PMOs is that their polarity, that is, their hydrophobicity or hydrophilicity, can be tuned within a certain range by the choice of the organic component, and hence their ability to adsorb other materials can at least be partly controlled. Moreover, it is possible to use chiral organic bridges. Thus, it is conceivable that new materials based on PMOs for enantioselective chromatography and new catalysts for heterogeneous catalysis will be developed.

If host–guest systems based on organically functionalized mesoporous silica phases are considered, the possibility arises to construct anisotropic systems with interesting properties, especially with PMOs: If organic bridges with a permanent dipole are used and care taken that they are anchored within the pore walls with uniform orientation, they could be the basis of quite novel materials with NLO properties.

These are just a few of many topics that could play a role in the future. We look ahead with excitement on the further development of this field of research and will endeavor to make a contribution to this development.

Abbreviations

∅	pore diameter
APTS	3-aminopropyltriethoxysilane
BET	Brunauer–Emmett–Teller
BTEB	1,4-bis(triethoxysilyl)benzene
BTEBP	4,4′-bis(triethoxysilyl)biphenyl
BTEE/BTME	1,2-bis(triethoxysilyl)ethane/1,2-bis(trimethoxysilyl)ethane
BTET	2,5-bis(triethoxysilyl)thiophene
BTEVB	1,4-bis[(*E*)-2-(triethoxysilyl)vinyl]benzene
BTEY	1,2-bis(triethoxysilyl)ethylene
CMC	critical micellar concentration
CPB/CPC	hexadecylpyridinium bromide/chloride
CP-MAS NMR	cross-polarized magic angle spinning nuclear magnetic resonance
CTAB/CTAC	hexadecyltrimethylammonium bromide/chloride
FSM	folded sheet mechanism
FT-IR	Fourier transform infrared
GS	gemini surfactants
HPLC	high-performance liquid chromatography
HRTEM	high-resolution transmission electron microscopy
MCM	Mobil composition of matter
MPTMS	3-mercaptopropyltrimethoxysilane
OTAB/OTAC	octadecyltrimethylammonium bromide/chloride
PMO	periodic mesoporous organosilica
S_{BET}	specific BET surface area ($m^2 g^{-1}$)
SAXS	small-angle X-ray scattering
SDA	structure-directing agent
SEM	scanning electron microscopy
TEM	transmission electron microscopy
TEOS	tetraethoxysilane (tetraethylorthosilica)
TG	thermogravimetry
TLCT	true liquid-crystal templating
TMOS	tetramethoxysilane (tetramethylorthosilica)
TON	turnover number
XAFS	X-ray absorption fine structure
XRD	X-ray diffrraction

We thank the ABCR GmbH & Co. KG and the Fonds der Chemischen Industrie for financial support and S. Wenzel for the very careful review of the manuscript.

Received: August 30, 2005

[1] C. T. Kresge, M. E. Leonowicz, W. J. Roth, J. C. Vartuli, J. S. Beck, *Nature* **1992**, *359*, 710–712.
[2] J. S. Beck, J. C. Vartuli, W. J. Roth, M. E. Leonowicz, C. T. Kresge, K. D. Schmitt, C. T.-W. Chu, D. H. Olson, E. W. Sheppard, S. B. McCullen, J. B. Higgins, J. L. Schlenker, *J. Am. Chem. Soc.* **1992**, *114*, 10834–10843.
[3] T. Yanagisawa, T. Shimizu, K. Kuroda, C. Kato, *Bull. Chem. Soc. Jpn.* **1990**, *63*, 988–992.
[4] G. S. Attard, J. C. Glyde, C. G. Göltner, *Nature* **1995**, *378*, 366–368.
[5] A. Monnier, F. Schüth, Q. Huo, D. Kumar, D. Margolese, R. S. Maxwell, G. Stucky, M. Krishnamurty, P. Petroff, A. Firouzi, M. Janicke, B. Chmelka, *Science* **1993**, *261*, 1299–1303.
[6] Q. Huo, D. I. Margolese, U. Ciesla, P. Feng, T. E. Gier, P. Sieger, R. Leon, P. M. Petroff, F. Schüth, G. D. Stucky, *Nature* **1994**, *368*, 317–321.
[7] Q. Huo, D. I. Margolese, U. Ciesla, D. G. Demuth, P. Feng, T. E. Gier, P. Sieger, A. Firouzi, B. F. Chmelka, F. Schüth, G. D. Stucky, *Chem. Mater.* **1994**, *6*, 1176–1191.
[8] D. M. Antonelli, J. Y. Ying, *Angew. Chem.* **1995**, *107*, 2202–2206; *Angew. Chem. Int. Ed. Engl.* **1995**, *34*, 2014–2017.
[9] D. M. Antonelli, *Microporous Mesoporous Mater.* **1999**, *30*, 315–319.
[10] K. L. Frindell, J. Tang, J. H. Harreld, G. D. Stucky, *Chem. Mater.* **2004**, *16*, 3524–3532.
[11] P. Yang, D. Zhao, D. I. Margolese, B. F. Chemlka, G. D. Stucky, *Chem. Mater.* **1999**, *11*, 2813–2826.
[12] S. A. Bagshaw, T. J. Pinnavaia, *Angew. Chem.* **1996**, *108*, 1180–1183; *Angew. Chem. Int. Ed. Engl.* **1996**, *35*, 1102–1105.
[13] Z.-R. Tian, W. Tong, J.-Y. Wang, N.-G. Duan, V. V. Krishnan, S. L. Suib, *Science* **1997**, *276*, 926–930.
[14] D. M. Antonelli, J. Y. Ying, *Angew. Chem.* **1996**, *108*, 461–464; *Angew. Chem. Int. Ed. Engl.* **1996**, *35*, 426–430.
[15] M. J. MacLachlan, N. Coombs, G. A. Ozin, *Nature* **1999**, *397*, 681–684.
[16] M. Tiemann, M. Fröba, *Chem. Mater.* **2001**, *13*, 3211–3217.
[17] U. Ciesla, S. Schacht, G. D. Stucky, K. K. Unger, F. Schüth, *Angew. Chem.* **1996**, *108*, 597–600; *Angew. Chem. Int. Ed. Engl.* **1996**, *35*, 541–543.
[18] R. Ryoo, S. H. Joo, S. Jun, *J. Phys. Chem. B* **1999**, *103*, 7743–7746.
[19] J. Lee, S. Yoon, T. Hyeon, S. M. Oh, K. B. Kim, *Chem. Commun.* **1999**, 2177–2178.
[20] F. Schüth, *Angew. Chem.* **2003**, *115*, 3730–3750; *Angew. Chem. Int. Ed.* **2003**, *42*, 3604–3622.
[21] N. K. Raman, M. T. Anderson, C. J. Brinker, *Chem. Mater.* **1996**, *8*, 1682–1701.

 © 2006 Wiley-VCH Verlag GmbH & Co. KGaA, Weinheim

[22] D. M. Antonelli, J. Y. Ying, *Curr. Opin. Colloid Interface Sci.* **1996**, *1*, 523 – 529.
[23] P. Behrens, *Angew. Chem.* **1996**, *108*, 561 – 564; *Angew. Chem. Int. Ed. Engl.* **1996**, *35*, 515 – 518.
[24] X. S. Zhao, G. Q. Lu, G. J. Millar, *Ind. Eng. Chem. Res.* **1996**, *35*, 2075 – 2090.
[25] A. Sayari, *Chem. Mater.* **1996**, *8*, 1840 – 1852.
[26] J. Y. Ying, C. P. Mehnert, M. S. Wong, *Angew. Chem.* **1999**, *111*, 58 – 82; *Angew. Chem. Int. Ed.* **1999**, *38*, 56 – 77.
[27] G. J. de A. A. Soler-Illia, C. Sanchez, B. Lebeau, J. Patarin, *Chem. Rev.* **2002**, *102*, 4093 – 4138.
[28] A. Stein, *Adv. Mater.* **2003**, *15*, 763 – 775.
[29] A. P. Wight, M. E. Davis, *Chem. Rev.* **2002**, *102*, 3589 – 3614.
[30] U. Schubert, N. Hüsing, *Synthesis of Inorganic Materials, 2nd ed.*, Wiley-VCH, Weinheim, **2005**.
[31] "Hybrid Materials, Funcional Applications. An Introduction": P. Gómez-Romero, C. Sanchez in *Functional Hybrid Materials* (Eds.: P. Gómez-Romero, C. Sanchez), Wiley-VCH, Weinheim, **2004**.
[32] D. A. Loy, K. J. Shea, *Chem. Rev.* **1995**, *95*, 1431 – 1442.
[33] K. J. Shea, D. A. Loy, *Chem. Mater.* **2001**, *13*, 3306 – 3319.
[34] S. Inagaki, S. Guan, Y. Fukushima, T. Ohsuna, O. Terasaki, *J. Am. Chem. Soc.* **1999**, *121*, 9611 – 9614.
[35] B. J. Melde, B. T. Holland, C. F. Blanford, A. Stein, *Chem. Mater.* **1999**, *11*, 3302 – 3308.
[36] T. Asefa, M. J. MacLachlan, N. Coombs, G. A. Ozin, *Nature* **1999**, *402*, 867 – 871.
[37] N. K. Mal, M. Fujiwara, Y. Tanaka, *Nature* **2003**, *421*, 350 – 353.
[38] N. K. Mal, M. Fujiwara, Y. Tanaka, T. Taguchi, M. Matsukata, *Chem. Mater.* **2003**, *15*, 3385 – 3394.
[39] C. Tourné-Péteilh, D. Brunel, S. Bégu, B. Chiche, F. Fajula, D. A. Lernera, J.-M. Devoisselle, *New J. Chem.* **2003**, *27*, 1415 – 1418.
[40] Q. Fu, G. V. R. Rao, L. K. Ista, Y. Wu, B. P. Andrzejewski, L. A. Sklar, T. L. Ward, G. P. López, *Adv. Mater.* **2003**, *15*, 1262 – 1266.
[41] D. R. Radu, C.-Y. Lai, J. W. Wiench, M. Pruski, V. S.-Y. Lin, *J. Am. Chem. Soc.* **2004**, *126*, 1640 – 1641.
[42] A. B. Descalzo, D. Jimenez, M. D. Marcos, R. Martínez-Máñez, J. Soto, J. El Haskouri, C. Guillém, D. Béltran, P. Amorós, M. V. Borrachero, *Adv. Mater.* **2002**, *14*, 966 – 969.
[43] D. L. Rodman, H. Pan, C. W. Clavier, X. Feng, Z.-L. Xue, *Anal. Chem.* **2005**, *77*, 3231 – 3237.
[44] A. Walcarius, M. Etienne, B. Lebeau, *Chem. Mater.* **2003**, *15*, 2161 – 2173.
[45] A. Matsumoto, K. Tsutsumi, K. Schumacher, K. K. Unger, *Langmuir* **2002**, *18*, 4014 – 4019.
[46] K. Y. Ho, G. McKay, K. L. Yeung, *Langmuir* **2003**, *19*, 3019 – 3024.
[47] H. Yoshitake, T. Yokoi, T. Tatsumi, *Chem. Mater.* **2002**, *14*, 4603 – 4610.
[48] A. M. Liu, K. Hidajat, S. Kawi, D. Y. Zhao, *Chem. Commun.* **2000**, 1145 – 1146.
[49] C. Lei, Y. Shin, J. Liu, E. J. Ackerman, *J. Am. Chem. Soc.* **2002**, *124*, 11242 – 11243.
[50] H. Y. Huang, R. T. Yang, D. Chinn, C. L. Munson, *Ind. Eng. Chem. Res.* **2003**, *42*, 2427 – 2433.
[51] R. A. Khatri, S. S. C. Chuang, Y. Soong, M. Gray, *Ind. Eng. Chem. Res.* **2005**, *44*, 3702 – 3708.
[52] T. Yokoi, H. Yoshitake, T. Tatsumi, *J. Mater. Chem.* **2004**, *14*, 951 – 957.
[53] F. Zheng, D. N. Tran, B. J. Busche, G. E. Fryxell, R. S. Addleman, T. S. Zemanian, C. L. Aardahl, *Ind. Eng. Chem. Res.* **2005**, *44*, 3099 – 3105.
[54] P. Trens, M. L. Russell, L. Spjuth, M. J. Hudson, J.-O. Liljenzin, *Ind. Eng. Chem. Res.* **2002**, *41*, 5220 – 5225.
[55] L. Mercier, T. J. Pinnavaia, *Environ. Sci. Technol.* **1998**, *32*, 2749 – 2754.
[56] V. Antochshuk, M. Jaroniec, *Chem. Commun.* **2002**, 258 – 259.
[57] V. Antochshuk, O. Olkhovyk, M. Jaroniec, I.-S. Park, R. Ryoo, *Langmuir* **2003**, *19*, 3031 – 3034.
[58] O. Olkhovyk, V. Antochshuk, M. Jaroniec, *Colloids Surf. A* **2004**, *236*, 69 – 72.
[59] K. A. Venkatesan, T. G. Srinivasan, P. R. Vasudeva Rao, *J. Radioanal. Nucl. Chem.* **2003**, *256*, 213 – 218.
[60] T. Kang, Y. Park, K. Choi, J. S. Lee, J. Yi, *J. Mater. Chem.* **2004**, *14*, 1043 – 1050.
[61] T. Kang, Y. Park, J. Yi, *Ind. Eng. Chem. Res.* **2004**, *43*, 1478 – 1484.
[62] G. S. Armatas, C. E. Salmas, M. Louloudi, G. P. Androutsopoulos, P. J. Pomonis, *Langmuir* **2003**, *19*, 3128 – 3136.
[63] G. Rodríguez-López, M. D. Marcos, R. Martínez-Máñez, F. Sancenón, J. Soto, L. A. Villaescusa, D. Beltrán, P. Amorós, *Chem. Commun.* **2004**, 2198 – 2199.
[64] K. Inumaru, J. Kiyoto, S. Yamanaka, *Chem. Commun.* **2000**, 903 – 904.
[65] R. Anwander, I. Nagl, M. Widenmeyer, G. Engelhardt, O. Groeger, C. Plam, T. Röser, *J. Phys. Chem. B* **2000**, *104*, 3532 – 3544.
[66] K. Inumura, Y. Inoue, S. Kakii, T. Nakano, S. Yamanaka, *Phys. Chem. Chem. Phys.* **2004**, *6*, 3133 – 3139.
[67] T. Martin, A. Galarneau, F. Di Renzo, D. Brunel, F. Fajula, *Chem. Mater.* **2004**, *16*, 1725 – 1731.
[68] H. Yang, G. Zhang, X. Hong, Y. Zhu, *Microporous Mesoporous Mater.* **2004**, *68*, 119 – 125.
[69] M. Park, S. Komarneni, *Microporous Mesoporous Mater.* **1998**, *25*, 75 – 80.
[70] F. de Juan, E. Ruiz-Hitzky, *Adv. Mater.* **2000**, *12*, 430 – 432.
[71] N. Liu, R. A. Assink, C. J. Brinker, *Chem. Commun.* **2003**, 370 – 371.
[72] N. Petkov, S. Mintova, B. Jean, T. Metzger, T. Bein, *Mater. Sci. Eng. C* **2003**, *23*, 827 – 831.
[73] S. Tanaka, J. Kaihara, N. Nishiyama, Y. Oku, Y. Egashira, K. Ueyama, *Langmuir* **2004**, *20*, 3780 – 3784.
[74] E. J. Acosta, C. S. Carr, E. E. Simanek, D. F. Shantz, *Adv. Mater.* **2004**, *16*, 985 – 989.
[75] S. Murata, H. Hata, T. Kimura, Y. Sugahara, K. Kuroda, *Langmuir* **2000**, *16*, 7106 – 7108.
[76] H. Furukawa, T. Watanabe, K. Kuroda, *Chem. Commun.* **2001**, 2002 – 2003.
[77] A. Fukuoka, K. Fujishima, M. Chiba, A. Yamagishi, S. Inagaki, Y. Fukushima, M. Ichikawa, *Catal. Lett.* **2000**, *68*, 241 – 244.
[78] S. Subbiah, R. Mokaya, *J. Phys. Chem. B* **2005**, *109*, 5079 – 5084.
[79] H. G. Chen, J. L. Shi, H. R. Chen, Y. S. Li, Z. L. Hua, D. S. Yan, *Appl. Phys. B* **2003**, *77*, 89 – 91.
[80] D. Das, J.-F. Lee, S. Cheng, *Chem. Commun.* **2001**, 2178 – 2179.
[81] D. Das, J.-F. Lee, S. Cheng, *J. Catal.* **2004**, *223*, 152 – 160.
[82] K. Shimizu, E. Hayashi, T. Hatamachi, T. Kodama, T. Higuchi, A. Satsuma, Y. Kitayama, *J. Catal.* **2005**, *231*, 131 – 138.
[83] B. Sow, S. Hamoudi, M. H. Zahedi-Niaki, S. Kaliaguine, *Microporous Mesoporous Mater.* **2005**, *79*, 129 – 136.
[84] V. Dufaud, M. E. Davis, *J. Am. Chem. Soc.* **2003**, *125*, 9403 – 9413.
[85] I. K. Mbaraka, B. H. Shanks, *J. Catal.* **2005**, *229*, 365 – 373.
[86] M. Alvaro, A. Corma, D. Das, V. Fornés, H. García, *Chem. Commun.* **2004**, 956 – 957.
[87] J. Weitkamp, M. Hunger, U. Rymsa, *Microporous Mesoporous Matter.* **2001**, *48*, 255 – 270.
[88] A. Corma, S. Iborra, I. Rodríguez, F. Sánchez, *J. Catal.* **2002**, *211*, 208 – 215.
[89] D. J. Macquarrie, R. Maggi, A. Mazzacani, G. Sartori, R. Sartorio, *Appl. Catal. A* **2003**, *246*, 183 – 188.

 © 2006 Wiley-VCH Verlag GmbH & Co. KGaA, Weinheim

[90] D. Brunel, F. Fajula, J. B. Nagy, B. Deroide, M. J. Verhoef, L. Veum, J. A. Peters, H. van Bekkum, *Appl. Catal. A* **2001**, *213*, 73 – 82.
[91] G.-J. Kim, D.-W. Park, J. M. Ha, *Korean J. Chem. Eng.* **2000**, *17*, 337 – 343.
[92] G.-J. Kim, J.-H. Shin, *Tetrahedron Lett.* **1999**, *40*, 6827 – 6830.
[93] D.-W. Park, S.-D. Choi, S.-J. Choi, C.-Y. Lee, G.-J. Kim, *Catal. Lett.* **2002**, *78*, 145 – 151.
[94] S. Xiang, Y. Zhang, Q. Xin, C. Li, *Chem. Commun.* **2002**, 2696 – 2697.
[95] J. S. Choi, D. J. Kim, S. H. Chang, W. S. Ahn, *Appl. Catal. A* **2003**, *254*, 225 – 237.
[96] X. M. Zheng, Y. X. Qi, X. M. Zhang, J. S. Suo, *Chin Chem. Lett.* **2004**, *15*, 655 – 658.
[97] G.-J. Kim, J.-H. Shin, *Catal. Lett.* **1999**, *63*, 205 – 212.
[98] C. Baleizão, B. Gigante, D. Das, M. Alvaro, H. Garcia, A. Corma, *Chem. Commun.* **2003**, 1860 – 1861.
[99] I. Motorina, C. M. Crudden, *Org. Lett.* **2001**, *3*, 2325 – 2328.
[100] H. M. Lee, S.-W. Kim, T. Hyeon, B. M. Kim, *Tetrahedron: Asymmetry* **2001**, *12*, 1537 – 1541.
[101] A. Corma, S. Iborra, I. Rodríguez, M. Iglesias, F. Sánchez, *Catal. Lett.* **2002**, *82*, 237 – 242.
[102] S. Abramson, N. Bellocq, M. Laspéras, *Top. Catal.* **2000**, *13*, 339 – 345.
[103] S. Abramson, M. Laspéras, D. Brunel, *Tetrahedron: Asymmetry* **2002**, *13*, 357 – 367.
[104] A. Lee, W. Kim, J. Lee, T. Hyeon, B. M. Kim, *Tetrahedron: Asymmetry* **2004**, *15*, 2595 – 2598.
[105] M. S. Whang, Y. K. Kwon, G.-J. Kim, *J. Ind. Eng. Chem.* **2002**, *8*, 262 – 267.
[106] D. Dhar, I. Beadham, S. Chandasekaran, *Proc. Indian Acad. Sci. Chem. Sci.* **2003**, *115*, 365 – 372.
[107] M. Hartmann, *Chem. Mater.* **2005**, *17*, 4577 – 4593.
[108] H. H. P. Yiu, P. A. Wright, *J. Mater. Chem.* **2005**, *15*, 3690 – 3700.
[109] H. H. P. Yiu, P. A. Wright, N. P. Botting, *Microporous Mesoporous Mater.* **2001**, *44–45*, 763 – 768.
[110] H. H. P. Yiu, P. A. Wright, N. P. Botting, *J. Mol. Catal. B* **2001**, *15*, 81 – 92.
[111] H. Ma, J. He, D. G. Evans, X. Duan, *J. Mol. Catal. B* **2004**, 30, 209 – 217.
[112] A. Salis, D. Meloni, S. Ligas, M. F. Casula, M. Monduzzi, V. Solinas, E. Dumitriu, *Langmuir* **2005**, *21*, 5511 – 5516.
[113] Y.-J. Han, G. D. Stucky, A. Butler, *J. Am. Chem. Soc.* **1999**, *121*, 9897 – 9898.
[114] L. Washmon-Kriel, V. L. Jimenez, K. J. Balkus, Jr., *J. Mol. Catal. B* **2000**, *10*, 453 – 469.
[115] H. Takahashi, B. Li, T. Sasaki, C. Miyazaki, T. Kajino, S. Inagaki, *Microporous Mesoporous Mater.* **2001**, *44–45*, 755 – 762.
[116] Y.-J. Han, J. T. Watson, G. D. Stucky, A. Butler, *J. Mol. Catal. B* **2002**, *17*, 1 – 8.
[117] A. Vinu, V. Murugesan, M. Hartmann, *J. Phys. Chem. B* **2004**, *108*, 7323 – 7330.
[118] S. L. Burkett, S. D. Sims, S. Mann, *Chem. Commun.* **1996**, 1367 – 1368.
[119] D. J. Macquarrie, *Chem. Commun.* **1996**, 1961 – 1962.
[120] M. H. Lim, C. F. Blanford, A. Stein, *J. Am. Chem. Soc.* **1997**, *119*, 4090 – 4091.
[121] L. Mercier, T. J. Pinnavaia, *Chem. Mater.* **2000**, *12*, 188 – 196.
[122] C. E. Fowler, S. L. Burkett, S. Mann, *Chem. Commun.* **1997**, 1769 – 1770.
[123] R. Richer, L. Mercier, *Chem. Commun.* **1998**, 1775 – 1776.
[124] A. Walcarius, C. Delacôte, *Chem. Mater.* **2003**, *15*, 4181 – 4192.
[125] A. S. M. Chong, X. S. Zhao, *J. Phys. Chem. B* **2003**, *107*, 12 650 – 12 657.
[126] S. Huh, J. W. Wiench, J.-C. Yoo, M. Pruski, V. S.-Y. Lin, *Chem. Mater.* **2003**, *15*, 4247 – 4256.
[127] D. J. Macquarrie, D. B. Jackson, J. E. G. Mdoe, J. H. Clark, *New J. Chem.* **1999**, *23*, 539 – 544.
[128] T. Yokoi, H. Yoshitake, T. Tatsumi, *Chem. Mater.* **2003**, *15*, 4536 – 4538.
[129] S. Che, A. E. Garcia-Bennett, T. Yokoi, K. Sakamoto, H. Kunieda, O. Terasaki, T. Tatsumi, *Nat. Mater.* **2003**, *2*, 801 – 805.
[130] N. Liu, R. A. Assink, B. Smarsly, C. J. Brinker, *Chem. Commun.* **2003**, 1146 – 1147.
[131] F. Cagnol, D. Grosso, C. Sanchez, *Chem. Commun.* **2004**, 1742 – 1743.
[132] S. R. Hall, C. E. Fowler, B. Lebeau, S. Mann, *Chem. Commun.* **1999**, 201 – 202.
[133] M. H. Lim, A. Stein, *Chem. Mater.* **1999**, *11*, 3285 – 3295.
[134] Y. Q. Wang, C. M. Yang, B. Zibrowius, B. Spliethoff, M. Lindén, F. Schüth, *Chem. Mater.* **2003**, *15*, 5029 – 5035.
[135] Y. Wang, B. Zibrowius, C. M. Yang, B. Spliethoff, F. Schüth, *Chem. Commun.* **2004**, 46 – 47.
[136] R. J. P. Corriu, C. Hoarau, A. Mehdi, C. Reyé, *Chem. Commun.* **2000**, 71 – 72.
[137] C. M. Bambrough, R. C. T. Slade, R. T. Williams, *J. Mater. Chem.* **1998**, *8*, 569 – 571.
[138] R. C. T. Slade, C. M. Bambrough, R. T. Williams, *Phys. Chem. Chem. Phys.* **2002**, *4*, 5394 – 5399.
[139] T. Asefa, M. Kruk, M. J. MacLachlan, N. Coombs, H. Grondey, M. Jaroniec, G. A. Ozin, *Adv. Funct. Mater.* **2001**, *11*, 447 – 456.
[140] D. J. Macquarrie, D. B. Jackson, *Chem. Commun.* **1997**, 1781 – 1782.
[141] D. J. Macquarrie, D. B. Jackson, S. Tailland, K. A. Utting, *J. Mater. Chem.* **2001**, *11*, 1843 – 1849.
[142] M. H. Lim, C. F. Blanford, A. Stein, *Chem. Mater.* **1998**, *10*, 467 – 470.
[143] W. M. Van Rhijn, D. E. De Vos, B. F. Sels, W. D. Bossaert, P. A. Jacobs, *Chem. Commun.* **1998**, 317 – 318.
[144] I. Diaz, C. Márquez-Alvarez, F. Mohino, J. Pérez-Pariente, E. Sastre, *J. Catal.* **2000**, *193*, 283 – 294.
[145] V. Ganesan, A. Walcarius, *Langmuir* **2004**, *20*, 3632 – 3640.
[146] D. Margolese, J. A. Melero, S. C. Christiansen, B. F. Chmelka, G. D. Stucky, *Chem. Mater.* **2000**, *12*, 2448 – 2459.
[147] I. Diaz, C. Márquez-Alvarez, F. Mohino, J. Pérez-Pariente, E. Sastre, *J. Catal.* **2000**, *193*, 295 – 302.
[148] W. D. Bossaert, D. E. De Vos, W. M. Van Rhijn, J. Bullen, P. J. Grobet, P. A. Jacobs, *J. Catal.* **1999**, *182*, 156 – 164.
[149] J. G. C. Shen, R. G. Herman, K. Klier, *J. Phys. Chem. B* **2002**, *106*, 9975 – 9978.
[150] C. Yang, B. Zibrowius, F. Schüth, *Chem. Commun.* **2003**, 1772 – 1773.
[151] R. J. P. Corriu, L. Datas, Y. Guari, A. Mehdi, C. Reyé, C. Thieuleux, *Chem. Commun.* **2001**, 763 – 764.
[152] J. Brown, R. Richer, L. Mercier, *Microporous Mesoporous Mater.* **2000**, *37*, 41 – 48.
[153] R. I. Nooney, M. Kalyanaraman, G. Kennedy, E. J. Maginn, *Langmuir* **2001**, *17*, 528 – 533.
[154] A. Bibby, L. Mercier, *Chem. Mater.* **2002**, *14*, 1591 – 1597.
[155] H. H. P. Yiu, C. H. Botting, N. P. Botting, P. A. Wright, *Phys. Chem. Chem. Phys.* **2001**, *3*, 2983 – 2985.
[156] Y. Guari, C. Thieuleux, A. Mehdi, C. Reyé, R. J. P. Corriu, S. Gomez-Gallardo, K. Philippot, B. Chaudret, R. Dutartre, *Chem. Commun.* **2001**, 1374 – 1375.
[157] Y. Guari, C. Thieuleux, A. Mehdi, C. Reyé, R. J. P. Corriu, S. Gomez-Gallardo, K. Philippot, B. Chaudret, *Chem. Mater.* **2003**, *15*, 2017 – 2024.
[158] A. Ghosh, C. R. Patra, P. Mukherjee, M. Sastry, R. Kumar, *Microporous Mesoporous Mater.* **2003**, *58*, 201 – 211.
[159] R. J. P. Corriu, A. Mehdi, C. Reyé, C. Thieuleux, *Chem. Mater.* **2004**, *16*, 159 – 166.
[160] M. Jia, A. Seifert, M. Berger, H. Giegengack, S. Schulze, W. R. Thiel, *Chem. Mater.* **2004**, *16*, 877 – 882.

 © 2006 Wiley-VCH Verlag GmbH & Co. KGaA, Weinheim

[161] R. Huq, L. Mercier, *Chem. Mater.* **2001**, *13*, 4512 – 4519.
[162] C. Liu, N. Naismith, L. Fu, J. Economy, *Chem. Commun.* **2003**, 2472 – 2473.
[163] A. Walcarius, S. Sayen, C. Gérardin, F. Hamdoune, L. Rodehüser, *Colloids Surf. A* **2004**, *234*, 145 – 151.
[164] C. E. Fowler, B. Lebeau, S. Mann, *Chem. Commun.* **1998**, 1825 – 1826.
[165] B. Lebeau, C. E. Fowler, S. R. Hall, S. Mann, *J. Mater. Chem.* **1999**, *9*, 2279 – 2281.
[166] M. Ganschow, M. Wark, D. Wöhrle, G. Schulz-Ekloff, *Angew. Chem.* **2000**, *112*, 167 – 170; *Angew. Chem. Int. Ed.* **2000**, *39*, 161 – 163.
[167] N. Liu, Z. Chen, D. R. Dunphy, Y.-B. Jiang, R. A. Assink, C. J. Brinker, *Angew. Chem.* **2003**, *115*, 1773 – 1776; *Angew. Chem. Int. Ed.* **2003**, *42*, 1731 – 1734.
[168] G. Wirnsberger, B. J. Scott, G. D. Stucky, *Chem. Commun.* **2001**, 119 – 120.
[169] V. S.-Y. Lin, C.-Y. Lai, J. Huang, S.-A. Song, S. Xu, *J. Am. Chem. Soc.* **2001**, *123*, 11 510 – 11 511.
[170] C.-Y. Lai, B. G. Trewyn, D. M. Jeftinija, K. Jeftinija, S. Xu, S. Jeftinija, V. S.-Y. Lin, *J. Am. Chem. Soc.* **2003**, *125*, 4451 – 4459.
[171] X. Ji, J. E. Hampsey, Q. Hu, J. He, Z. Yang, Y. Lu, *Chem. Mater.* **2003**, *15*, 3656 – 3662.
[172] S. Che, Z. Liu, T. Ohsuna, K. Sakamoto, O. Terasaki, T. Tatsumi, *Nature* **2004**, *429*, 281 – 284.
[173] K. Nakajima, D. Lu, J. N. Kondo, I. Tomita, S. Inagaki, M. Hara, S. Hayashi, K. Domen, *Chem. Lett.* **2003**, *32*, 950 – 951.
[174] S. Guan, S. Inagaki, T. Ohsuna, O. Terasaki, *J. Am. Chem. Soc.* **2000**, *122*, 5660 – 5661.
[175] A. Sayari, S. Hamoudi, Y. Yang, I. L. Moudrakovski, J. R. Ripmeester, *Chem. Mater.* **2000**, *12*, 3857 – 3863.
[176] S. Hamoudi, Y. Yang, I. L. Moudrskovski, S. Lang, A. Sayari, *J. Phys. Chem. B* **2001**, *105*, 9118 – 9123.
[177] T. Asefa, M. J. MacLachlan, H. Grondey, N. Coombs, G. A. Ozin, *Angew. Chem.* **2000**, *112*, 1878 – 1881; *Angew. Chem. Int. Ed.* **2000**, *39*, 1808 – 1811.
[178] T. Ren, X. Zhang, J. Suo, *Microporous Mesoporous Mater.* **2002**, *54*, 139 – 144.
[179] C. Yoshina-Ishii, T. Asefa, N. Coombs, M. J. MacLachlan, G. A. Ozin, *Chem. Commun.* **1999**, 2539 – 2540.
[180] G. Temtsin, T. Asefa, S. Bittner, G. A. Ozin, *J. Mater. Chem.* **2001**, *11*, 3202 – 3206.
[181] S. Inagaki, S. Guan, T. Ohsuna, O. Terasaki, *Nature* **2002**, *416*, 304 – 307.
[182] N. Bion, P. Ferreira, A. Valente, I. S. Goncalves, J. Rocha, *J. Mater. Chem.* **2003**, *13*, 1910 – 1913.
[183] M. P. Kapoor, Q. Yang, S. Inagaki, *J. Am. Chem. Soc.* **2002**, *124*, 15 176 – 15 177.
[184] A. Sayari, W. Wang, *J. Am. Chem. Soc.* **2005**, *127*, 12 194 – 12 195.
[185] M. Cornelius, F. Hoffmann, M. Fröba, *Chem. Mater.* **2005**, *17*, 6674 – 6678.
[186] M. P. Kapoor, Q. Yang, S. Inagaki, *Chem. Mater.* **2004**, *16*, 1209 – 1213.
[187] F. Ben, B. Boury, R. J. P. Corriu, V. Le Strat, *Chem. Mater.* **2000**, *12*, 3249 – 3252.
[188] G. Cerveau, R. J. P. Corriu, E. Framery, F. Lerouge, *Chem. Mater.* **2004**, *16*, 3794 – 3799.
[189] J. Morell, C. V. Teixeira, M. Cornelius, V. Rebbin, M. Tiemann, H. Amenitsch, M. Fröba, M. Lindén, *Chem. Mater.* **2004**, *16*, 5564 – 5566.
[190] F. M. Menger, C. A. J. Littau, *J. Am. Chem. Soc.* **1991**, *113*, 1451 – 1452.
[191] F. M. Menger, J. S. Keiper, *Angew. Chem.* **2000**, *112*, 1980 – 1996; *Angew. Chem. Int. Ed.* **2000**, *39*, 1906 – 1920.
[192] Q. Huo, R. Leon, P. M. Petroff, G. D. Stucky, *Science* **1995**, *268*, 1324 – 1327.
[193] J. N. Israelachvili, D. J. Mitchell, B. W. Ninham, *J. Chem. Soc. Faraday Trans. 2* **1976**, *72*, 1525 – 1568.
[194] Y. Liang, R. Anwander, *Microporous Mesoporous Mater.* **2004**, *72*, 153 – 165.
[195] Y. Liang, M. Hanzlik, R. Anwander, *Chem. Commun.* **2005**, 525 – 527.
[196] B. Lee, H. Luo, C. Y. Yuan, J. S. Linc, S. Dai, *Chem. Commun.* **2004**, 240 – 241.
[197] B. Lee, H.-J. Im, H. Luo, E. W. Hagaman, S. Dai, *Langmuir* **2005**, *21*, 5372 – 5376.
[198] D. Zhao, Q. Huo, J. Feng, B. F. Chmelka, G. D. Stucky, *J. Am. Chem. Soc.* **1998**, *120*, 6024 – 6036.
[199] G. J. de A. A. Soler-Illia, E. L. Crepaldi, D. Grosso, C. Sanchez, *Curr. Opin. Colloid Interface Sci.* **2003**, *8*, 109 – 126.
[200] S. Förster, *Top. Curr. Chem.* **2003**, *226*, 1 – 28.
[201] C. Yu, Y. Yu, D. Zhao, *Chem. Commun.* **2000**, 575 – 576.
[202] O. Muth, C. Schellbach, M. Fröba, *Chem. Commun.* **2001**, 2032 – 2033.
[203] M. C. Burleigh, M. A. Markowitz, E. M. Wong, J.-S. Lin, B. P. Gaber, *Chem. Mater.* **2001**, *13*, 4411 – 4412.
[204] W. Guo, J.-Y. Park, M.-O. Oh, H.-W. Jeong, W.-J. Cho, I. Kim, C.-S. Ha, *Chem. Mater.* **2003**, *15*, 2295 – 2298.
[205] X. Y. Bao, X. S. Zhao, X. Li, P. A. Chia, J. Li, *J. Phys. Chem. B* **2004**, *108*, 4684 – 4689.
[206] X. Bao, X. S. Zhao, X. Li, J. Li, *Appl. Surf. Sci.* **2004**, *237*, 380 – 386.
[207] X. Y. Bao, X. S. Zhao, S. Z. Qiao, S. K. Bhatia, *J. Phys. Chem. B* **2004**, *108*, 16 441 – 16 450.
[208] H. Zhu, D. J. Jones, J. Zajac, J. Rozière, R. Dutartre, *Chem. Commun.* **2001**, 2568 – 2569.
[209] E. B. Cho, K. Char, *Chem. Mater.* **2004**, *16*, 270 – 275.
[210] E. B. Cho, K.-W. Kwon, H. Char, *Chem. Mater.* **2001**, *13*, 3837 – 3839.
[211] W. Guo, I. Kim, C.-S. Ha, *Chem. Commun.* **2003**, 2692 – 2693.
[212] J. R. Matos, M. Kruk, L. P. Mercuri, M. Jaroniec, T. Asefa, N. Coombs, G. A. Ozin, T. Kamiyama, O. Terasaki, *Chem. Mater.* **2002**, *14*, 1903 – 1905.
[213] L. Zhao, G. Zhu, D. Zhang, Y. Di, Y. Chen, O. Terasaki, S. Qiu, *J. Phys. Chem. B* **2005**, *109*, 765 – 768.
[214] Y. Goto, S. Inagaki, *Chem. Commun.* **2002**, 2410 – 2411.
[215] W. Wang, S. Xie, W. Zhou, A. Sayari, *Chem. Mater.* **2004**, *16*, 1756 – 1762.
[216] J. Morell, G. Wolter, M. Fröba, *Chem. Mater.* **2005**, *17*, 804 – 808.
[217] M. C. Burleigh, M. A. Markowitz, M. S. Spector, B. P. Gaber, *J. Phys. Chem. B* **2002**, *106*, 9712 – 9716.
[218] M. C. Burleigh, S. Jayasundera, C. W. Thomas, M. S. Spector, M. A. Markowitz, B. P. Gaber, *Colloid Polym. Sci.* **2004**, *282*, 728 – 733.
[219] M. C. Burleigh, M. A. Markowitz, S. Jayasundera, M. S. Spector, C. W. Thomas, B. P. Gaber, *J. Phys. Chem. B* **2003**, *107*, 12 628 – 12 634.
[220] S. Hamoudi, S. Kaliaguine, *Chem. Commun.* **2002**, 2118 – 2119.
[221] A. Sayari, Y. Yang, *Chem. Commun.* **2002**, 2582 – 2583.
[222] W. Wang, W. Zhou, A. Sayari, *Chem. Mater.* **2003**, *15*, 4886 – 4889.
[223] W. J. Hunks, G. A. Ozin, *Chem. Commun.* **2004**, 2426 – 2427.
[224] W. J. Hunks, G. A. Ozin, *Chem. Mater.* **2004**, *16*, 5465 – 5472.
[225] L. Zhang, Q. Yang, W.-H. Zhang, Y. Li, J. Yang, D. Jiang, G. Zhu, C. Li, *J. Mater. Chem.* **2005**, *15*, 2562 – 2568.
[226] M. P. Kapoor, S. Inagaki, *Chem. Mater.* **2002**, *14*, 3509 – 3514.
[227] D. Shamiryan, T. Abell, F. Iacopi, K. Maex, *Mater. Today* **2004**, *7*, 34 – 39.
[228] M. Kuroki, T. Asefa, W. Whitnal, M. Kruk, C. Yoshina-Ishii, M. Jaroniec, G. A. Ozin, *J. Am. Chem. Soc.* **2002**, *124*, 13 886 – 13 895.

 © 2006 Wiley-VCH Verlag GmbH & Co. KGaA, Weinheim

[229] K. Landskron, B. D. Hatton, D. D. Perovic, G. A. Ozin, *Science* **2003**, *302*, 266 – 269.
[230] K. Landskron, G. A. Ozin, *Science* **2004**, *306*, 1529 – 1532.
[231] W. J. Hunks, G. A. Ozin, *Adv. Funct. Mater.* **2005**, *15*, 259 – 266.
[232] A. Shimojima, K. Kuroda, *Angew. Chem.* **2003**, *115*, 4191 – 4194; *Angew. Chem. Int. Ed.* **2003**, *42*, 4057 – 4060.
[233] T. Asefa, M. Kruk, N. Coombs, H. Grondey, M. J. MacLachlan, M. Jaroniec, G. A. Ozin, *J. Am. Chem. Soc.* **2003**, *125*, 11662 – 11673.
[234] K. Wan, Q. Liu, C. Zhang, *Chem. Lett.* **2003**, *32*, 362 – 363.
[235] J. El Haskouri, S. Cabrera, F. Sapina, J. LaTorre, C. Guillem, A. Beltrán-Porter, D. Beltrán-Porter, M. D. Marcos, P. Amorós, *Adv. Mater.* **2001**, *13*, 192 – 195.
[236] J. Pang, V. T. John, D. A. Loy, Z. Yang, Y. Lu, *Adv. Mater.* **2005**, *17*, 704 – 707.
[237] M. C. Burleigh, M. A. Markowitz, M. S. Spector, B. P. Garber, *J. Phys. Chem. B* **2001**, *105*, 9935 – 9942.
[238] M. C. Burleigh, M. A. Markowitz, M. S. Spector, B. P. Garber, *Chem. Mater.* **2001**, *13*, 4760 – 4766.
[239] M. C. Burleigh, M. A. Markowitz, M. S. Spector, B. P. Garber, *Langmuir* **2001**, *17*, 7923 – 7928.
[240] T. Asefa, M. Kruk, M. J. MacLachlan, N. Coombs, H. Grondey, M. Jaroniec, G. A. Ozin, *J. Am. Chem. Soc.* **2001**, *123*, 8520 – 8530.
[241] M. C. Burleigh, S. Dai, E. W. Hagaman, J. S. Lin, *Chem. Mater.* **2001**, *13*, 2537 – 2546.
[242] S. Hamoudi, S. Kaliaguine, *Microporous Mesoporous Mater.* **2003**, *59*, 195 – 204.
[243] X. Yuan, H. I. Lee, J. W. Kim, J. E. Yie, J. M. Kim, *Chem. Lett.* **2003**, *32*, 650 – 651.
[244] Q. Yang, M. P. Kapoor, S. Inagaki, *J. Am. Chem. Soc.* **2002**, *124*, 9694 – 9695.
[245] M. P. Kapoor, Q. Yang, Y. Goto, S. Inagaki, *Chem. Lett.* **2003**, *32*, 914 – 915.
[246] M. A. Wahab, I. Kim, C.-S. Ha, *Microporous Mesoporous Mater.* **2004**, *69*, 19 – 27.
[247] Q. Yang, J. Liu, J. Yang, M. P. Kapoor, S. Inagaki, C. Li, *J. Catal.* **2004**, *228*, 265 – 272.
[248] M. A. Wahab, I. Imae, Y. Kawakami, C.-S. Ha, *Chem. Mater.* **2005**, *17*, 2165 – 2174.
[249] Q. Yang, J. Liu, J. Yang, L. Zhang, Z. Feng, J. Zhang, C. Li, *Microporous Mesoporous Mater.* **2005**, *77*, 257 – 264.
[250] H. Zhu, D. J. Jones, J. Zajac, R. Dutartre, M. Rhomari, J. Rozière, *Chem. Mater.* **2002**, *14*, 4886 – 4894.
[251] M. A. Wahab, I. Kim, C.-S. Ha, *J. Solid State Chem.* **2004**, *177*, 3439 – 3447.
[252] V. Rebbin, M. Fröba, unpublished results.
[253] M. C. Burleigh, S. Jayasundera, M. S. Spector, C. W. Thomas, M. A. Markowitz, B. P. Gaber, *Chem. Mater.* **2004**, *16*, 3 – 5.
[254] S. Jayasundera, M. C. Burleigh, M. Zeinali, M. S. Spector, J. B. Miller, W. Yan, S. Dai, M. A. Markowitz, *J. Phys. Chem. B* **2005**, *109*, 9198 – 9201.
[255] J. Morell, M. Güngerich, G. Wolter, J. Jiao, M. Hunger, P.J. Klar, M. Fröba *J. Mater. Chem.*, **2006**, in press.
[256] M. Alvaro, B. Ferrer, V. Fornés, H. García, *Chem. Commun.* **2001**, 2546 – 2547.
[257] A. Doménech, M. Alvaro, B. Ferrer, H. García, *J. Phys. Chem. B* **2003**, *107*, 12781 – 12788.
[258] M. Alvaro, B. Ferrer, H. García, F. Rey, *Chem. Commun.* **2002**, 2012 – 2013.
[259] R. J. P. Corriu, A. Mehdi, C. Reyé, C. Thieuleux, *Chem. Commun.* **2002**, 1382 – 1383.
[260] R. J. P. Corriu, A. Mehdi, C. Reyé, C. Thieuleux, *Chem. Commun.* **2003**, 1564 – 1565.
[261] R. J. P. Corriu, A. Mehdi, C. Reyé, C. Thieuleux, *New J. Chem.* **2003**, *27*, 905 – 908.
[262] O. Olkhovyk, M. Jaroniec, *J. Am. Chem. Soc.* **2005**, *127*, 60 – 61.
[263] M. Alvaro, M. Benitez, D. Das, B. Ferrer, H. García, *Chem. Mater.* **2004**, *16*, 2222 – 2228.
[264] C. Baleizao, B. Gigante, D. Das, M. Alvaro, H. García, A. Corma, *Chem. Commun.* **2003**, 1860 – 1861.
[265] C. H. Lee, S. Soo Park, S. Joon Choe, D. H. Park, *Microporous Mesoporous Mater.* **2001**, *46*, 257 – 264.
[266] S. S. Park, C. H. Lee, J. H. Cheon, S. J. Choe, D. H. Park, *Bull. Korean Chem. Soc.* **2001**, *22*, 948 – 952.
[267] S. S. Park, C. H. Lee, J. H. Cheon, D. H. Park, *J. Mater. Chem.* **2001**, *11*, 3397 – 3403.
[268] W. Stoeber, A. Fink, E. Bohn, *J. Colloid Interface Sci.* **1968**, *26*, 62 – 69.
[269] M. P. Kapoor, S. Inagaki, *Chem. Lett.* **2004**, *33*, 88 – 89.
[270] V. Rebbin, M. Jakubowski, S. Pötz, M. Fröba, *Microporous Mesoporous Mater.* **2004**, *72*, 99 – 104.
[271] V. Rebbin, R. Schmidt, M. Fröba, *Angew. Chem. Int. Ed.*, **2006**, in press.
[272] D.-J. Kim, J.-S. Chung, W.-S. Ahn, G.-W. Kang, W.-J. Cheongy, *Chem. Lett.* **2004**, *33*, 422 – 423.
[273] L. Zhang, W. Zhang, J. Shi, Z. Hua, Y. Li, J. Yan, *Chem. Commun.* **2003**, 210 – 211.
[274] B. Lee, L.-L. Bao, H.-J. Im, S. Dai, E. W. Hagaman, J. S. Lin, *Langmuir* **2003**, *19*, 4246 – 4252.
[275] Y. Lu, R. Ganguli, C. A. Drewien, M. T. Anderson, C. J. Brinker, W. Gong, Y. Guo, H. Soyez, B. Dunn, M. H. Huang, J. Zink, *Nature* **1997**, *389*, 364 – 368.
[276] Y. Lu, H. Fan, N. Doke, D. A. Loy, R. A. Assink, D. A. LaVan, C. J. Brinker, *J. Am. Chem. Soc.* **2000**, *122*, 5258 – 5261.
[277] Ö. Dag, C. Yoshina-Ishii, T. Asefa, M. J. MacLachlan, H. Grondey, N. Coombs, G. A. Ozin, *Adv. Funct. Mater.* **2001**, *11*, 213 – 217.
[278] S. S. Park, C. S. Ha, *Chem. Commun.* **2004**, 1986 – 1987.
[279] S. S. Park, C. S. Ha, *Chem. Mater.* **2005**, *17*, 3519 – 3523.
[280] A. Fukuoka, Y. Sakamoto, S. Guan, S. Inagaki, N. Sugimoto, Y. Fukushima, K. Hirahara, S. Iijima, M. Ichikawa, *J. Am. Chem. Soc.* **2001**, *123*, 3373 – 3374.
[281] Y. Sakamoto, A. Fukuoka, T. Higuchi, N. Shimomura, S. Inagaki, M. Ichikawa, *J. Phys. Chem. B* **2004**, *108*, 853 – 858.
[282] A. Fukuoka, H. Araki, Y. Sakamoto, S. Inagaki, Y. Fukushima, M. Ichikawa, *Inorg. Chim. Acta* **2003**, *350*, 371 – 378.
[283] Q. Yang, M. P. Kapoor, S. Inagaki, N. Shirokura, J. N. Kondo, K. Domen, *J. Mol. Catal. A* **2005**, *230*, 85 – 89.
[284] S. Hamoudi, S. Royer, S. Kaliaguine, *Microporous Mesoporous Mater.* **2004**, *71*, 17 – 25.

© 2006 Wiley-VCH Verlag GmbH & Co. KGaA, Weinheim

Communications

DOI: 10.1002/anie.200504506

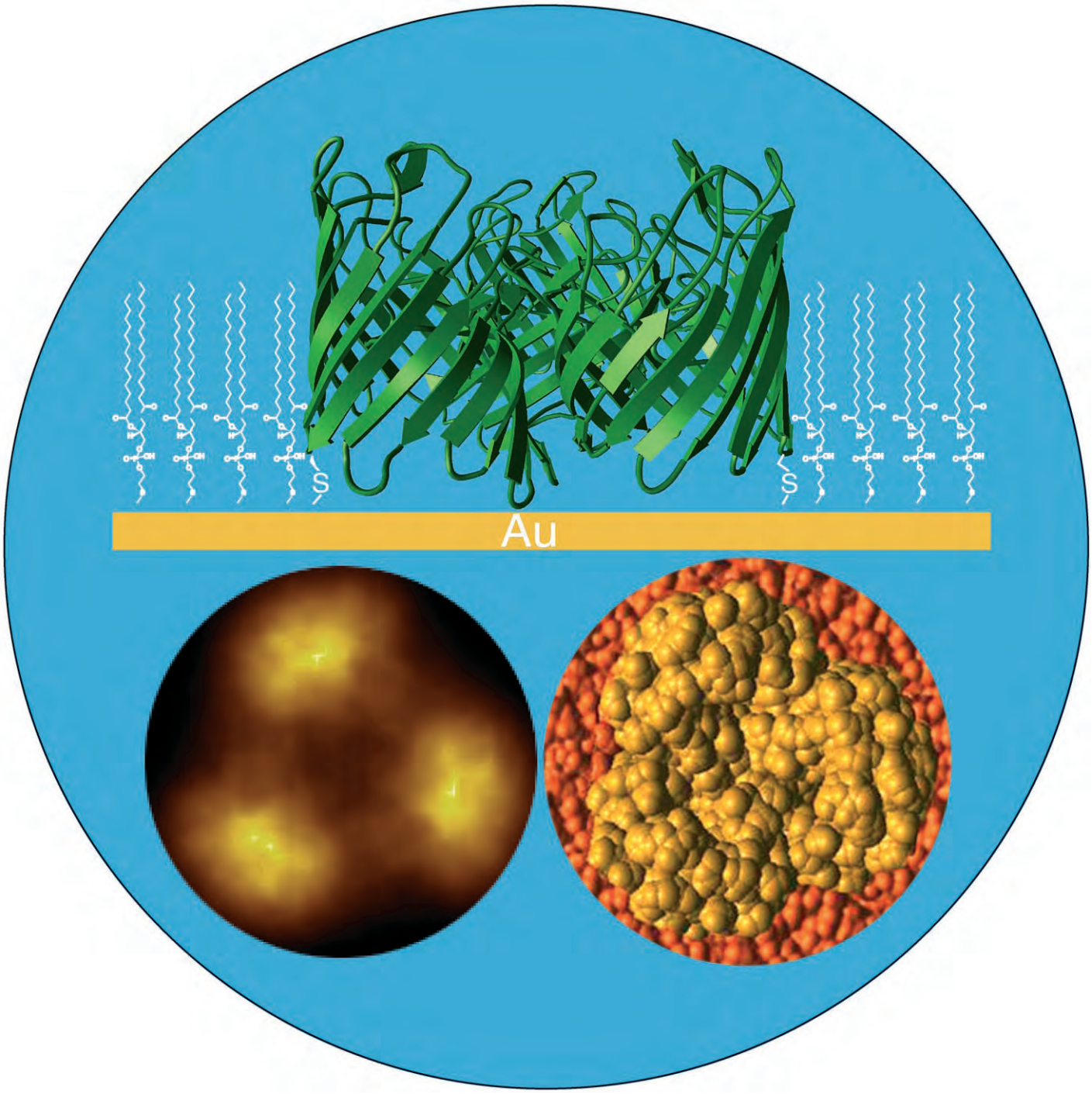

A membrane protein with a cysteine mutation, fixed in a defined orientation on a flat gold surface, can be used to obtain high-quality AFM images under aqueous conditions without 2D crystallization. Details can be found in the Communication of J. H. Lakey and co-workers on the following pages.

WILEY InterScience DISCOVER SOMETHING GREAT
© 2006 Wiley-VCH Verlag GmbH & Co. KGaA, Weinheim

Topography

DOI: 10.1002/anie.200504506

An Approach To Prepare Membrane Proteins for Single-Molecule Imaging**

*David A. Cisneros, Daniel J. Muller, Sofian M. Daud, and Jeremy H. Lakey**

Membrane proteins are under represented in the database of high-resolution structures obtained from X-ray crystallographic and NMR spectroscopic methods.[1] Furthermore, they often form large and sometimes transient supramolecular complexes. Alternative approaches such as cryo-electron microscopy (EM) and Atomic force microscopy (AFM) are essential tools that are able to provide complementary information on the structure–function relationship of membrane proteins embedded in the lipid membrane. Two approaches increase the resolution of these methods, 2D crystallization and single-particle reconstruction. In EM, crystals provide electron diffraction data which can increase resolution, whereas single-particle averaging can be used for proteins > 200 kDa. High-resolution AFM topographs can reveal structural details of single native membrane proteins but, as a prerequisite, the proteins must be adsorbed to atomically flat mica and densely packed in a membrane to restrict their lateral mobility.[2] Although averaging of single particles shows their common structures, selected examples can be used to characterize structural flexibility, variability, and conformational changes.[3] Many examples of AFM analysis of self-assembled monolayers on gold have been published,[4] and thiolipids have been developed to create membrane mimetic surfaces on gold.[5–7] However, these have not yet been combined as a means to image membrane proteins.

Herein we demonstrate a covalent assembly approach to membrane protein imaging that avoids crystallization. Atomically flat gold, engineered proteins, and chemically modified lipids are combined to rapidly assemble immobile and fully oriented samples (Figure 1). The resulting tapping-mode AFM topographs of single membrane proteins, set against a

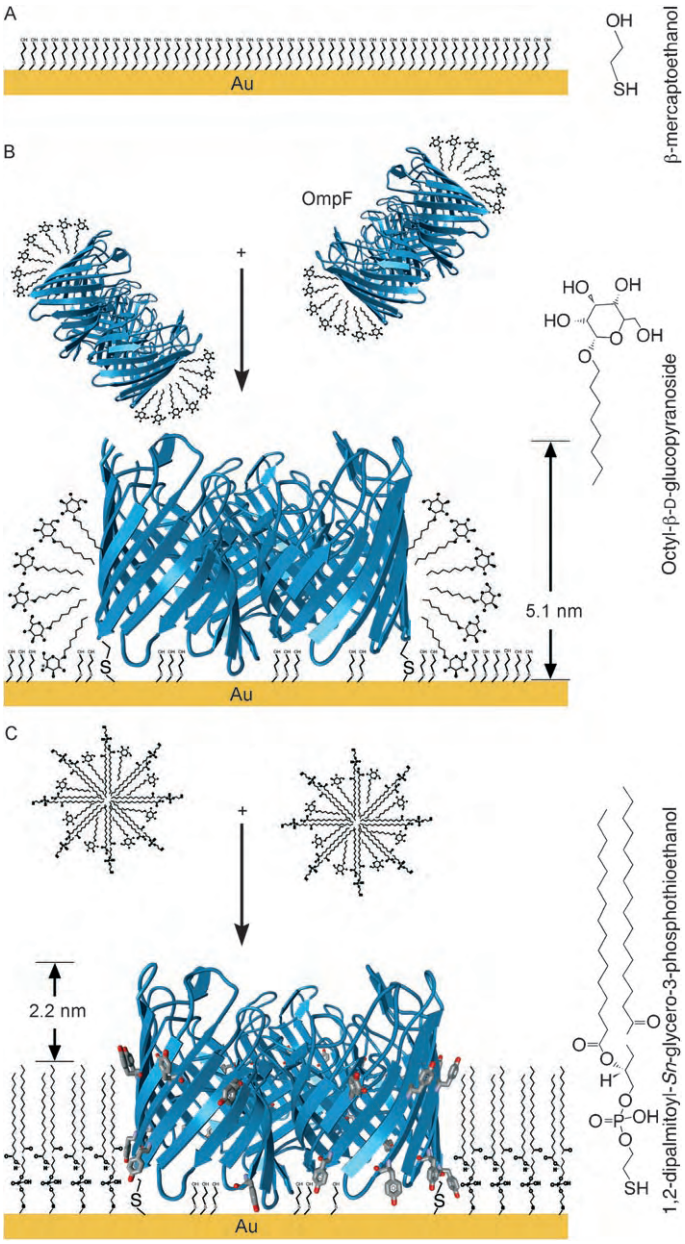

Figure 1. The attachment of OmpF porin trimers to a gold surface. A) The gold surface is passivated by β-mercaptoethanol. B) OmpF trimers in OG micelles attach to gold surfaces through cysteine mutation E183C. C) Mixed OG/thiolipid micelles are added to assemble a thiolipid monolayer. Subsequent washing with OG-containing, and later detergent-free, buffer solution removes free lipid and detergent leaving a hydrophobic half bilayer. Owing to the relatively thin cross section of outer-membrane proteins, the hydrophobic belt of the OmpF protein (indicated by the aromatic residues) is effectively stabilized by the 3-nm thick lipid monolayer. All compounds shown in the scheme are to scale.

[*] Prof. J. H. Lakey
Institute for Cell and Molecular Biosciences
University of Newcastle upon Tyne
Newcastle upon Tyne, NE2 4HH (UK)
Fax: (+44) 191-222-8865
E-mail: j.h.lakey@ncl.ac.uk

D. A. Cisneros, Prof. D. J. Muller
Biotechnologisches Zentrum
Technische Universität Dresden
Tatzberg 49, 01307 Dresden (Germany)

S. M. Daud
Institute for Nanoscale Science and Technology
University of Newcastle
Newcastle upon Tyne, NE2 4HH (UK)

[**] This work was supported by the BBSRC (ISIS Travel Grant, and Research Development Fellowship & Project Grant E19051 to J.H.L.), the DFG (GK864 to D.A.C.), the European Union, the BMBF, and the state of Saxony (D.J.M.). We thank Helen Ridley for excellent technical assistance and Neil Keegan for helpful discussions.

Supporting information for this article is available on the WWW under http://www.angewandte.org or from the author.

© 2006 Wiley-VCH Verlag GmbH & Co. KGaA, Weinheim

hydrophobic background, are used to create averaged structures with a resolution approaching that of 2D crystals.

The major outer-membrane porin OmpF, from *E. coli*, is a well-characterized member of a large and widespread group of β-barrel proteins.[8,9] We have previously shown that OmpF can be covalently assembled on gold surfaces if a single cysteine residue is inserted into the intracellular face of this protein trimer.[7] The assembly process consists of passivating the gold surface with a short chain thiol, adding OmpF–Cys in detergent solution and then completing the remaining surface with a layer of thiolipid in which the headgroup contains a thiol that is able to chemisorb to the gold surface. FTIR, surface plasmon resonance (SPR), electrochemistry,[7] neutron reflection (NR),[10] and CD[11] have shown that surface pretreatment (Figure 1A) and thiolipid (Figure 1C) assembly are critical in maintaining protein structure.

Template stripped gold (TS-Au)[12] covered with a thiolipid monolayer provided a control background (Figure 2A). This half bilayer of immobilized phospholipid probably acts like hydrophobic self-assembled monolayers (SAM) of methyl terminated alkane thiols.[13] Recent studies show that interaction forces of the hydrophilic Si_3N_4 tips with hydrophobic SAM layers are very low,[14] thus enabling the acquisition of clear AFM topographs.

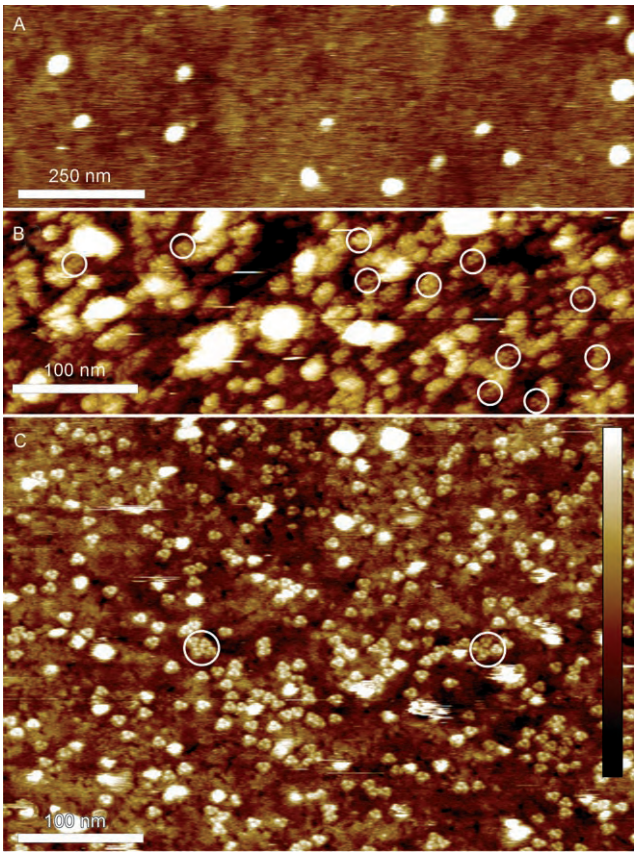

Figure 2. Assembly of porin on flat TS-Au surfaces. A) Control surface of thiolipid assembled on TS-Au surface without OmpF. B) OmpF assembled on TS-Au. Individual trimers are circled. C) Sample as in (B) followed by overnight thiolipid assembly. OmpF trimers are clearly resolved and areas of apparent intermolecular organization are circled. The vertical height scale given in (C) corresponds to 10 nm and is the same for all topographs.

OmpF–Cys on gold without thiolipid remains stable in detergent-free buffer solution (buffer B) possibly owing to the remaining tightly bound surfactant.[15] Under these conditions, (Figure 2B) we observed poorly defined OmpF trimers with, nevertheless, the expected height of 5.5 ± 1.3 nm ($n = 18$) corresponding to that of their 3D structure (Figure 3D–E).[16] However, after incubation with thiolipid, the topographs were greatly improved (Figure 2C) and revealed highly reproducible individual trimers protruding by 2.2 ± 0.4 nm ($n = 17$). The height difference of ≈ 3.3 nm confirmed that the trimers were embedded by the thiolipid monolayer (Figure 2C and Figure 3A–C). From our measurements, we do not know whether a screening layer of tightly bound detergent may have resisted the washing with detergent-free buffer solutions. Such remaining detergents may shield hydrophobic surfaces that would otherwise be exposed to water. It has been shown, however, that detergents like octylglucopyranoside (OG) dissociate from similar hydrophobic surfaces after being diluted below their critical micellar concentration.[17]

The improvement of the sample background after thiolipid assembly may be due to two effects, the removal of poorly attached OmpF–Cys after competition with thiolipid, and the reduction of possible lateral displacements by a rigid thiolipid layer. Although the protein solution used contains non-aggregated individual trimers (gel filtration chromatography,[9] data not shown), we observed small groups (25% of 393 trimers) of closely contacting trimers arranged as in 2D crystals. This possibly implies a cooperative assembly of OmpF trimers at the surface (Figure 2C, white circles). The SPR, FTIR,[7] and NR[10] data were collected on evaporated and therefore rougher gold surfaces. Comparable topographs from these samples are presented in the Supporting Information.

Topographs of single OmpF trimers assembled on TS-Au were averaged (Figure 3F–G) by using the same approach as used previously on 2D crystals (Figure 3H,I). The resulting topographs clearly resolve the three individual protrusions of the extracellular OmpF trimer surface.[16] The majority (>90%) of structures observed in our topographs were trimeric. All of these structures showed the characteristic structural appearance of the extracellular surface of the OmpF porin trimer as identified in previous work.[18] Therefore, these data show that the cysteine mutation ensures 100% orientation of the proteins in the final sample (as in Figure 1). Additionally, the exposed hydrophobic face of the thiolipid monolayer provided a smooth noninteracting background for AFM imaging. Although the method is immediately applicable to many outer-membrane proteins, it could be extended to the study of other types. In particular, by avoiding crystallization, the tiny quantities required make the study of hard-to-purify complexes more attractive. The limiting step would be to purify the membrane protein and keep it stable in detergent solution. Here, the proteins are fixed close to the surface but thiolipids with hydrophilic spacers could be used to stabilize the proteins with water-soluble domains.[5] Finally, the engineering scaffold properties of the β-barrel proteins suggests that these oriented layers are

 © 2006 Wiley-VCH Verlag GmbH & Co. KGaA, Weinheim

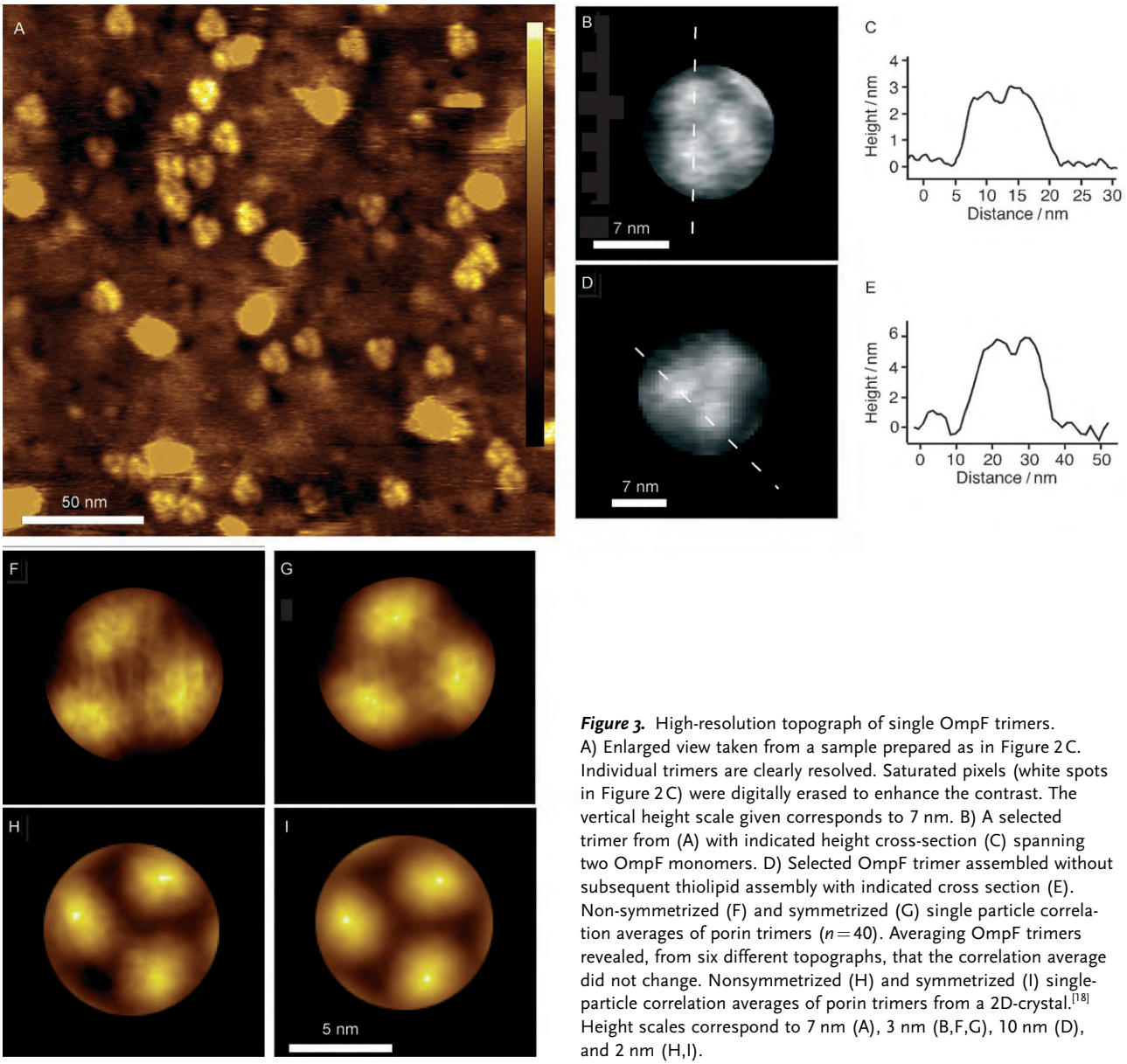

Figure 3. High-resolution topograph of single OmpF trimers. A) Enlarged view taken from a sample prepared as in Figure 2C. Individual trimers are clearly resolved. Saturated pixels (white spots in Figure 2C) were digitally erased to enhance the contrast. The vertical height scale given corresponds to 7 nm. B) A selected trimer from (A) with indicated height cross-section (C) spanning two OmpF monomers. D) Selected OmpF trimer assembled without subsequent thiolipid assembly with indicated cross section (E). Non-symmetrized (F) and symmetrized (G) single particle correlation averages of porin trimers ($n = 40$). Averaging OmpF trimers revealed, from six different topographs, that the correlation average did not change. Nonsymmetrized (H) and symmetrized (I) single-particle correlation averages of porin trimers from a 2D-crystal.[18] Height scales correspond to 7 nm (A), 3 nm (B,F,G), 10 nm (D), and 2 nm (H,I).

capable of contributing to the development of precise nanoscale biointerfaces.[7,19]

Experimental Section

OmpF–Cys was purified as described previously[7] except that buffer solution A contained NaCl (300 mM), Tris-HCl (50 mM; pH 7.5), and OG (1%; Melford, UK). TS-Au surfaces[12] were treated with β-mercaptoethanol (10 mM) for 20 min before washing and incubation with protein (0.25 mg mL^{-1} in buffer solution A plus tris(2-carboxyethyl)phosphine hydrochloride (1 mM)). Protein incubations were for a minimum of 1 h. After this, the samples were washed with buffer solution A before incubation with buffer solution A containing thiolipid (1,2-Dipalmitoyl-sn-Glycero-3-Phosphothioethanol; 0.5 mg mL^{-1}; Avanti Polar Lipids, USA) for at least 1 h at 45 °C. To remove loosely bond proteins, thiolipids, and detergent the sample was repeatedly (3x) washed with buffer solution A followed by buffer solution B (NaCl (150 mM), Tris-HCl (50 mM); pH 7.8). The AFM (MultiMode, DI-Veeco, CA) was operated in buffer solution B by using a fluid cell. The piezoelectric scanner had a scan range of $\approx 120 \times 120\ \mu m^2$. Oxide sharpened Si_3N_4 cantilevers had a nominal force constant of 0.08 N m^{-1} (OMCL TR400PS, Olympus Ltd, Tokyo). Imaging was performed in tapping mode with a drive frequency close to the resonance frequency of the cantilevers (9.5 kHz) immersed in buffer solution B. The drive amplitude of the cantilever was set to a root-mean-square (RMS) value of 18–30 nm. All samples were imaged in buffer solution at room temperature (23 °C). Single particles extracted from the topograph (trace and retrace) shown in Figure 3A were aligned and correlation averaged by using the software Semper. The final average was threefold symmetrized. This procedure was identical for the topographs from 2D crystals.[18]

Received: December 19, 2005
Revised: March 10, 2006
Published online: April 24, 2006

Keywords: lipids · membrane proteins · porin OmpF · protein structures · scanning force microscopy

 © 2006 Wiley-VCH Verlag GmbH & Co. KGaA, Weinheim

[1] S. H. White, *Protein Sci.* **2004**, *13*, 1948.
[2] D. J. Müller, H. Janovjak, T. Lehto, L. Kuerschner, K. Anderson, *Prog. Biophys. Mol. Biol.* **2002**, *79*, 1.
[3] A. Engel, D. J. Müller, *Nat. Struct. Biol.* **2000**, *7*, 715; S. Scheuring, D. J. Müller, H. Stahlberg, H. A. Engel, A. Engel, *Eur. Biophys. J.* **2002**, *31*, 172.
[4] G. J. Leggett, *Anal. Chim. Acta* **2003**, *479*, 17; A. Tinazli, J. Tang, R. Valiokas, S. Picuric, S. Lata, J. Piehler, B. Liedberg, R. Tampe, *Chemistry* **2005**, *11*, 5249; J. C. Love, L. A. Estroff, J. K. Kriebel, R. G. Nuzzo, G. M. Whitesides, *Chem. Rev.* **2005**, *105*, 1103; P. Wagner, F. Zaugg, P. Kernen, M. Hegner, G. Semenza, *J. Vac. Sci. Technol. B* **1996**, *14*, 1466; P. Wagner, P. Kernen, M. Hegner, E. Ungewickell, G. Semenza, *FEBS Lett.* **1994**, *356*, 267.
[5] H. Lang, C. Duschl, H. Vogel, *Langmuir* **1994**, *10*, 197.
[6] S. Terrettaz, T. Stora, C. Duschl, H. Vogel, *Langmuir* **1993**, *9*, 1361; T. Stora, J. H. Lakey, H. Vogel, *Angew. Chem.* **1999**, *111*, 402; *Angew. Chem. Int. Ed.* **1999**, *38*, 389; R. Naumann, S. M. Schiller, F. Giess, B. Grohe, K. B. Hartman, I. Karcher, I. Koper, J. Lubben, K. Vasilev, W. Knoll, *Langmuir* **2003**, *19*, 5435; K. Tamada, M. Hara, H. Sasabe, W. Knoll, *Langmuir* **1997**, *13*, 1558.
[7] S. Terrettaz, W.-P. Ulrich, H. Vogel, Q. Hong, L. G. Dover, J. H. Lakey, *Protein Sci.* **2002**, *11*, 1917.
[8] M. P. Bos, J. Tommassen, *Curr. Opin. Microbiol.* **2004**, *7*, 610; A. Bateman, L. Coin, R. Durbin, R. D. Finn, V. Hollich, S. Griffiths-Jones, A. Khanna, M. Marshall, S. Moxon, E. L. L. Sonnhammer, D. J. Studholme, C. Yeats, S. R. Eddy, *Nucleic Acids Res.* **2004**, *32*, D138.
[9] V. Visudtiphole, M. B. Thomas, D. A. Chalton, J. H. Lakey, *Biochem. J.* **2005**, *392*, 375.
[10] S. A. Holt, J. H. Lakey, S. M. Daud, N. Keegan, *Aust. J. Chem.* **2005**, *58*, 674.
[11] N. Keegan, N. G. Wright, J. H. Lakey, *Angew. Chem.* **2005**, *117*, 4879; *Angew. Chem. Int. Ed.* **2005**, *44*, 4801.
[12] M. Hegner, P. Wagner, G. Semenza, *Surf. Sci.* **1993**, *291*, 39; P. Wagner, M. Hegner, H. J. Guntherodt, G. Semenza, *Langmuir* **1995**, *11*, 3867.
[13] C. D. Bain, G. M. Whitesides, *Science* **1988**, *240*, 62.
[14] G. Yang, N. A. Amro, Z. B. Starkewolfe, G. Y. Liu, *Langmuir* **2004**, *20*, 3995; S. Subramanian, S. Sampath, *Pramana* **2005**, *65*, 753.
[15] R. K. Thomas, *Annu. Rev. Phys. Chem.* **2004**, *55*, 391; J. L. Popot, E. A. Berry, D. Charvolin, C. Creuzenet, C. Ebel, D. M. Engelman, M. Flotenmeyer, F. Giusti, Y. Gohon, P. Herve, Q. Hong, J. H. Lakey, K. Leonard, H. A. Shuman, P. Timmins, D. E. Warschawski, F. Zito, M. Zoonens, B. Pucci, C. Tribet, *Cell. Mol. Life Sci.* **2003**, *60*, 1559.
[16] S. W. Cowan, T. Schirmer, G. Rummel, M. Steiert, R. Ghosh, R. A. Paupit, J. N. Jansonius, J. P. Rosenbush, *Nature* **1992**, *358*, 727.
[17] G. B. Sigal, M. Mrksich, G. M. Whitesides, *Langmuir* **1997**, *13*, 2749.
[18] D. J. Müller, A. Engel, *J. Mol. Biol.* **1999**, *285*, 1347.
[19] H. Lang, *Int. J. Med. Microbiol.* **2000**, *290*, 579.

 © 2006 Wiley-VCH Verlag GmbH & Co. KGaA, Weinheim

Natural Product Synthesis

DOI: 10.1002/anie.200601116

Total Synthesis of Abyssomicin C and atrop-Abyssomicin C**

K. C. Nicolaou and Scott T. Harrison*

Abyssomicin C (**1**) is a recently discovered antibiotic with a novel molecular architecture and unique mechanism of action.[1] Isolated from the actinomycete *Verrucosispora* strain AB 18-032 cultivated from a sediment sample collected from the depths of the Sea of Japan, this deftly named natural product inhibits the biosynthesis of *p*-aminobenzoic acid in bacteria, a pathway that is absent in human physiology. The intriguing structural topology of abyssomicin C coupled with its reported activity against both methicillin-resistant *Staphylococcus aureus* (MRSA, 4 $\mu g\,mL^{-1}$) and vancomycin-resistant *Staphylococcus aureus* (VRSA, 13 $\mu g\,mL^{-1}$) prompted immediate interest from the synthetic community, culminating in a total synthesis by Sorensen and co-workers[2] and several approaches toward its structure by a number of other groups.[3] Herein, we report our efforts in this field which led not only to a total synthesis of abyssomicin C (**1**) but also to the recognition of atrop-abyssomicin C (**2**), a novel isomer of the naturally occurring product **1** that exhibits even more potent antibiotic activity than its originally isolated twin.

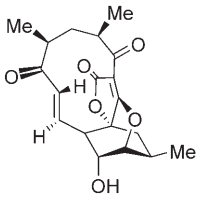

1 (abyssomicin C)

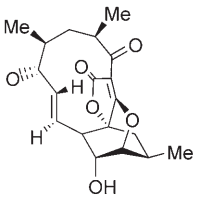

2 (atrop-abyssomicin C)

Aiming for maximum molecular diversity in the subsequent construction of analogues, our strategy for the total synthesis of the abyssomicins was based on the highly convergent retrosynthetic analysis depicted in Figure 1.

[*] Prof. Dr. K. C. Nicolaou, S. T. Harrison
Department of Chemistry and
The Skaggs Institute for Chemical Biology
The Scripps Research Institute
10550 North Torrey Pines Road, La Jolla, CA 92037 (USA)
Fax: (+1) 858-784-2469
E-mail: kcn@scripps.edu
and
Department of Chemistry and Biochemistry
University of California, San Diego
9500 Gilman Drive, La Jolla, CA 92093 (USA)

[**] We thank Dr. D. H. Huang and Dr. R. Chadha for assistance with NMR spectroscopic and X-ray crystallographic analyses, respectively. Financial support for this work was provided by the Skaggs Institute for Research (predoctoral fellowship to S.T.H.).

WILEY InterScience DISCOVER SOMETHING GREAT
© 2006 Wiley-VCH Verlag GmbH & Co. KGaA, Weinheim

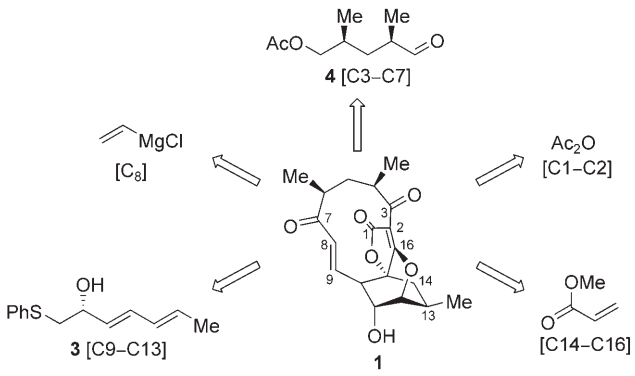

Figure 1. Retrosynthetic analysis of abyssomicin C (**1**).

Thus, construction of the oxabicyclo[2.2.2]octane core of the molecule was expected from a Diels–Alder reaction between the hydroxy diene **3** and methyl acrylate. An acetate unit, the acetoxy aldehyde **4**,[4] and vinyl magnesium chloride were chosen to provide the remaining carbon atoms with their appropriate functionalities as needed for the target molecule. Finally, a ring-closing metathesis reaction was projected as the means to forge the strained 11-membered ring of the abyssomicin skeleton.

The [4+2] cycloaddition-based construction of the enantiomerically enriched oxabicyclo[2.2.2]octane core **12** is summarized in Scheme 1. The required hydroxy diene **3** was prepared from the known and readily available Weinreb amide **5**[5] by reaction with the lithium derivative of thioanisole[6] (80% yield), followed by asymmetric reduction of the resulting dienone with (*R*)-CBS (cat.)/catecholborane[7] (89% yield, 90% *ee*[8]). The Diels–Alder reaction of **3** with methyl acrylate needed considerable refinement before becoming a practical process to produce the desired adduct **8**. Reaction of **3** with methyl acrylate in the presence of MeMgBr in toluene at room temperature according to the precedent of Ward and Abaee[9] failed to yield any cycloadducts. Warming the mixture to 55 °C led primarily to decomposition of the diene, although some product **8** was obtained (25% yield based on the diene). After further experimentation[10] we discovered that mixing 1 equivalent of **3** with 3 equivalents of ligand **6**[11] and 4 equivalents of MeMgBr (3.0 M solution in ether) in toluene at 0 °C, followed by the addition of 10 equivalents of methyl acrylate and warming to 55 °C for 24 h, furnished the desired cycloadduct **8** as a single diastereomer and in 80% yield. Despite the excess of reagents, the isolation of **8** was simple, requiring only an acid wash (to remove both the ligand and the magnesium salts) and flash chromatography. The scope of this remarkable Lewis acid templated Diels–Alder reaction, whose postulated transition state (**7**) is depicted in Scheme 1, merits further investigation as we envision potential applications in chemical synthesis in general and particularly in asymmetric catalysis.[10]

Returning to the sequence toward the targeted oxabicyclo system **12** (Scheme 1), generation of the enolate by deprotonation of the γ-lactone **8** with LiHMDS at −78 °C, followed by quenching with O_2 and $(EtO)_3P$ furnished α-hydroxy lactone **9** (74% yield), whose configuration was supported by its spectroscopic data and unambiguously proven by its eventual

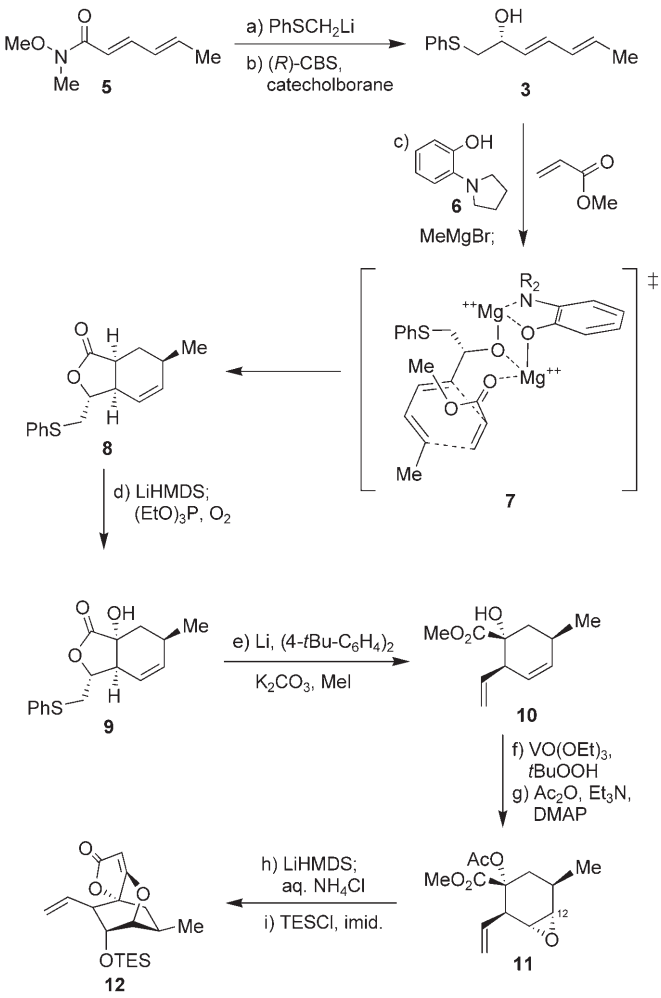

Scheme 1. Synthesis of TES-protected oxabicyclo[2.2.2]octane intermediate **12**. Reagents and conditions: a) thioanisole (1.3 equiv), DABCO (1.3 equiv), *n*BuLi (1.3 equiv), THF, 0 °C, 1 h; then −78 °C; then **5**, 45 min, 80%; b) (*R*)-CBS (0.1 equiv), catecholborane (1.25 equiv), CH_2Cl_2, −78 °C, 24 h, 89%, 90% *ee*;[8] c) **6** (3.0 equiv), MeMgBr (4.0 equiv), $PhCH_3$, 0 °C; then methyl acrylate (10 equiv), 55 °C, 24 h; 0 °C, wash with 3 N aq. HCl, 80%; d) LiHMDS (1.5 equiv), THF, −78 °C, 0.5 h; then $(EtO)_3P$ (2.0 equiv), bubbling O_2, 74%; e) 4,4′-di-*tert*-butylbiphenyl (0.5 equiv), Li (10 equiv), THF, 0 °C, 2 h; −40 °C; then **9**, 3 h; then MeOH quench, remove excess Li, concentrate; add DMF, K_2CO_3 (2.0 equiv), MeI (10 equiv), 60 °C, 10 min, 97%; f) $VO(OEt)_3$ (0.2 equiv), *t*BuOOH (3.0 equiv), CH_2Cl_2, 25 °C, 3 h, 90%; g) Ac_2O (10 equiv), DMAP (0.05 equiv), Et_3N, 25 °C, 3 h, 93%; h) LiHMDS (2.5 equiv), THF, −78 to 25 °C; then sat. aq. NH_4Cl, reflux, 2 h; i) TESCl (1.3 equiv), imid. (2.6 equiv), DMAP (0.05 equiv), DMF, 25 °C, 2 h, 97%, two steps. TES = triethylsilyl, DABCO = 1,4-diazabicyclo[2.2.2]octane, (*R*)-CBS = (*R*)-(+)-2-methyl-CBS-oxazaborolidine, LiHMDS = lithium bis(trimethylsilyl)amide, DMF = *N*,*N*-dimethylformamide, DMAP = 4-(dimethylamino)pyridine, imid. = imidazole.

conversion to the abyssomicins C (**1** and **2**). Further processing of the phenylthiomethyl γ-lactone **9** with the radical anion species derived from catalytic amounts of 4,4′-di-*tert*-butylbiphenyl and Li metal resulted in the opening of the lactone ring with concomitant olefin formation, which led, upon quenching the carboxylate anion with methyl iodide, to α-hydroxy methyl ester **10** in 97% overall yield. A vanadium-directed epoxidation (*t*BuOOH) of the hydroxy diene **10** was

 © 2006 Wiley-VCH Verlag GmbH & Co. KGaA, Weinheim

then achieved, with exclusive delivery of the oxygen atom to the bottom face of the molecule. This highly regio- and stereoselective reaction proceeded in 90% yield when the rarely utilized $VO(OEt)_3$[12] catalyst was employed instead of the more traditional $VO(acac)_2$,[13] whose performance in this case resulted in only 55–60% yield. Standard acetylation of the so-obtained hydroxy epoxide then furnished acetate **11** (93% yield), which served admirably as a precursor to the targeted intermediate **12**. Thus, deprotonation of **11** (LiHMDS, THF) at −78 °C, followed by warming to ambient temperature, addition of saturated aqueous NH_4Cl (25 °C),[3c] and heating at reflux for two hours, allowed first Dieckmann cyclization[3a,c,14] to occur and then regioselective epoxide opening[2,3a,c] (at C12) to give, after standard silylation, compound **12** in 97% overall yield.

The elaboration of the oxabicyclo[2.2.2]octane system **12** to atrop-abyssomicin C (**2**) is summarized in Scheme 2. Thus, lithiation of **12** with *t*BuLi at −78 °C, followed by quenching with the known aldehyde **4** (90% *ee*),[4a] which was obtained through a facile enzymatic desymmetrization,[4b] led to a mixture of epimeric alcohols (ca. 1:1 ratio, 75% yield) which was smoothly oxidized with IBX to afford ketone **13** in 90% yield. Exposure of the **13** to excess 1,2-ethanedithiol and $BF_3{\cdot}OEt_2$ resulted in thioketalization and concomitant desilylation to afford the corresponding hydroxy thioketal (90% yield), from which the acetate group was removed by the action of K_2CO_3 in methanol to furnish diol **14** (97% yield). A shorter route from **12** to **14** was also developed. Therein, the lithio derivative obtained from **12** as described above was quenched with enantiomerically enriched lactone **15**,[15] and the crude lactol so-obtained was subjected to thioketalization with 1,2-ethanedithiol and TMSOTf to afford **14** in 75% overall yield. Compound **14** was homogeneous according to ^1H NMR spectroscopy ($CDCl_3$, 500 MHz), indicating over 98% diastereomeric purity at this stage of the synthesis.

Chemoselective oxidation of the primary hydroxy group within **14** with IBX in DMSO, followed by addition of vinylmagnesium chloride to the crude aldehyde so-obtained led to the diastereomeric mixture (ca. 3:2) of alcohols **16** in 65% overall yield. The much anticipated ring-closing metathesis of compound **16** proceeded smoothly under the initiating influence of the Grubbs catalyst II (**17**)[16] in refluxing CH_2Cl_2 to afford a mixture of diastereomeric products (ca. 3:2), which were *trans*-configured about the newly formed double bond (^1H NMR spectroscopic analysis). The corresponding *cis* isomer, which was considered unlikely on the basis of molecular models, was not observed. A second chemoselective oxidation performed with IBX in DMSO then converted the two allylic alcohols into a single hydroxy enone (**18**, 50% yield; Table 1), whose precise conformational geometry (*transoid* versus *cisoid*) around the enone functionality remains unknown. Seemingly, only a single step separated this intermediate, **18**, from our targeted molecule, abyssomicin C (**1**). Indeed, treatment of **18** with $PhI(OTFA)_2$ cleaved, as expected, its thioketal protecting group and afforded a stable crystalline compound (EtOH, m.p.: 220 °C (decomp.)), whose spectroscopic data were consistent with the overall structure of the expected compound (Table 1), however, these data did not exactly match those reported[1,2]

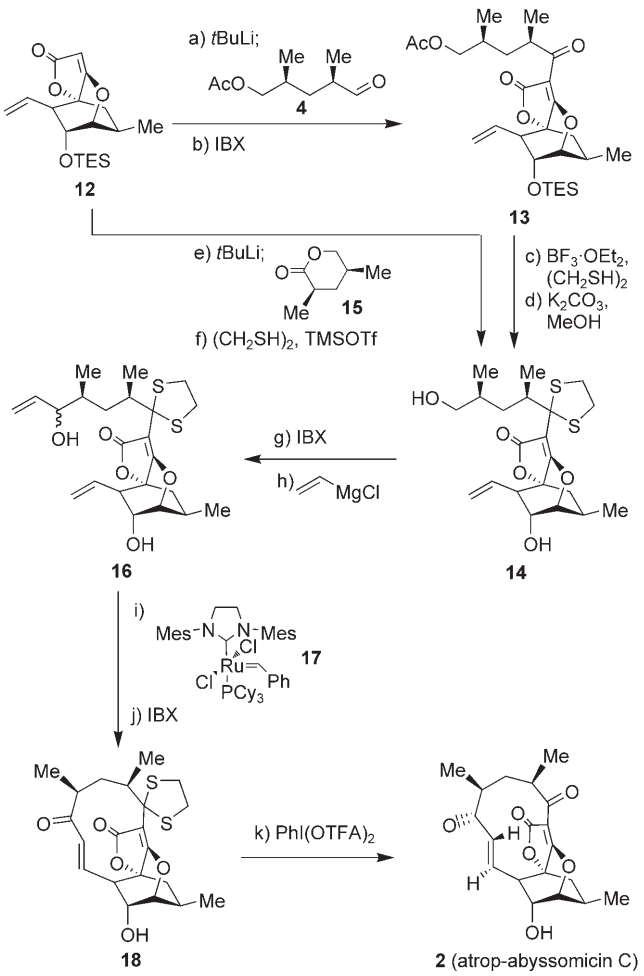

Scheme 2. Completion of the total synthesis of atrop-abyssomicin C (**2**). Reagents and conditions: a) *t*BuLi (1.2 equiv), THF, −78 °C, 0.5 h; then **4** (1.1 equiv), 10 min, 75%; b) IBX (1.5 equiv), DMSO, 25 °C, 1 h, 90%; c) 1,2-ethanedithiol (4.0 equiv), $BF_3{\cdot}OEt_2$ (4.0 equiv), CH_2Cl_2, 0→25 °C, 12 h, 90%; d) K_2CO_3 (5.0 equiv), MeOH, 4 h, 25 °C, 97%; e) *t*BuLi (1.2 equiv), THF, −78 °C, 0.5 h; then **15** (1.1 equiv), 10 min; f) 1,2-ethanedithiol (4.0 equiv), CH_2Cl_2, −78 °C; then TMSOTf (1 equiv), 30 min; then 1 N aq. HCl, −78 to 25 °C, 30 min, 75%, two steps; g) IBX (1.5 equiv), DMSO, 25 °C, 1.5 h; h) vinyl MgCl (3.0 equiv), THF, −78 °C, 65%, two steps; i) **17** (0.05 equiv), CH_2Cl_2 (0.002 M), reflux, 1 h, 85%; j) IBX (1.5 equiv), DMSO, 25 °C, 1.5 h, 50%; k) $PhI(OTFA)_2$ (2.0 equiv), CH_3CN/H_2O (5:1), 50%. IBX = *o*-iodoxybenzoic acid, DMSO = dimethyl sulfoxide, TMSOTf = trimethylsilyl trifluoromethanesulfonate, TFA = trifluoroacetyl.

for natural abyssomicin C (**1**), suggesting a close relationship between the two compounds. The conundrum was solved by X-ray crystallographic analysis of the synthetic compound (**2**):[17] its structure was revealed as an atropisomer[18] of abyssomicin C (**1**)[1] (see Figure 2a for ORTEP structures).

Comparison of the reported X-ray crystal structural data of abyssomicin C (**1**)[1] to those of atrop-abyssomicin C (**2**) reveals subtle but important structural differences (Figure 2b). Chiefly, the carbonyl group at C7 adopts a more *transoid* conformation with the C8–C9 double bond in the natural product **1** (dihedral angle O=C7-C8=C9 144.8°), whereas the conformation of this group in **2** is more *cisoid* (dihedral angle O=C7-C8=C9 26.4°). Because **2** exhibits an

 © 2006 Wiley-VCH Verlag GmbH & Co. KGaA, Weinheim

Table 1: Selected physical properties for synthetic dithiolane abyssomicin C **18**, atrop-abyssomicin C (**2**), and abyssomicin C (**1**).[a]

18: $R_f = 0.31$ (silica gel, EtOAc/hexanes 3:2); $[\alpha]_D^{25} = -39.4$ ($c = 0.18$, $CHCl_3$); IR (film): $\tilde{\nu}_{max} = 3449, 2964, 2927, 2871, 1749, 1727, 1694, 1658, 1626, 1455\ cm^{-1}$; ^1H NMR (500 MHz, $CDCl_3$): $\delta = 6.48$ (dd, $J = 16.7$, 4.1 Hz, 1H), 6.44 (d, $J = 16.7$ Hz, 1H), 4.57 (dd, $J = 4.6$, 1.6 Hz, 1H), 4.53 (dd, $J = 4.5$, 1.9 Hz, 1H), 3.36–3.28 (m, 1H), 3.27–3.18 (m, 1H), 3.17–3.07 (m, 2H), 3.05 (dd, $J = 3.7$, 2.1 Hz, 1H), 2.83–2.74 (m, 1H), 2.65 (dd, $J = 12.6$, 11.0 Hz, 1H), 2.40 (ddd, $J = 10.3$, 7.0, 3.1 Hz, 1H), 1.92–1.82 (m, 2H), 1.37 (dd, $J = 12.6$, 2.5 Hz, 1H), 1.32 (ddd, $J = 14.7$, 7.9, 3.0 Hz, 1H), 1.20 (d, $J = 6.6$ Hz, 3H), 1.14 (d, $J = 7.1$ Hz, 3H), 1.13 ppm (d, $J = 7.2$ Hz, 3H); ^{13}C NMR (125 MHz, $CDCl_3$): $\delta = 203.4$, 171.0, 169.5, 138.4, 129.1, 107.7, 81.2, 79.1, 71.1, 65.9, 49.2, 47.8, 41.8, 40.9, 39.7, 38.6, 34.6, 24.8, 18.6, 17.9, 17.3 ppm; HRMS (ESI-TOF): calcd for $C_{21}H_{27}O_5S_2^+$ $[M+H^+]$: 423.1294; found: 423.1297.

2: $R_f = 0.21$ (silica gel, EtOAc/hexanes 3:2); colorless crystals (EtOH), m.p.: 220 °C (decomp.); $[\alpha]_D^{25} = -71.4$ ($c = 0.33$, MeOH); IR (film): $\tilde{\nu}_{max} = 3442, 2967, 2933, 2866, 1757, 1690, 1637, 1457\ cm^{-1}$; ^1H NMR (600 MHz, MeOD): $\delta = 6.66$ (dd, $J = 16.5$, 5.8 Hz, 1H), 6.53 (d, $J = 16.6$ Hz, 1H), 4.63 (dd, $J = 4.3$, 1.5 Hz, 1H), 4.42 (dd, $J = 4.2$, 3.0 Hz, 1H), 3.20 (dd, $J = 5.8$, 2.9 Hz, 1H), 2.85–2.76 (m, 1H), 2.71 (dd, $J = 12.5$, 11.1 Hz, 1H), 2.67–2.61 (m, 1H), 2.54 (dqd, $J = 14.3$, 7.1, 3.6 Hz, 1H), 1.88 (ddd, $J = 15.7$, 12.1, 2.5 Hz, 1H), 1.49–1.43 (m, 2H), 1.17 (d, $J = 7.3$ Hz, 3H), 1.15 (d, $J = 7.2$ Hz, 3H), 1.13 ppm (d, $J = 6.7$ Hz, 3H); ^{13}C NMR (150 MHz, MeOD): $\delta = 203.5$, 200.5, 179.4, 170.8, 140.2, 129.0, 106.2, 84.5, 81.1, 67.0, 50.6, 49.1, 43.5, 38.6, 33.7, 25.7, 18.2, 17.5, 16.3 ppm; HRMS (ESI-TOF): calcd for $C_{19}H_{23}O_6^+$ $[M+H^+]$: 347.1489; found: 347.1484.

1: $R_f = 0.28$ (silica gel, EtOAc/hexanes 3:2); $[\alpha]_D^{25} = -43.1$ ($c = 0.1$, MeOH); colorless crystals (MeOH), m.p.: 180 °C (decomp.) [lit. m.p.: 180 °C (decomp.)][1]; IR (film): $\tilde{\nu}_{max} = 3461, 2968, 2933, 2876, 1757, 1686, 1615, 1457, 1434\ cm^{-1}$; ^1H NMR (600 MHz, MeOD): $\delta = 6.53$ (d, $J = 13.6$ Hz, 1H), 5.97 (dd, $J = 13.6$, 9.6 Hz, 1H), 5.05 (dd, $J = 6.1$, 3.4 Hz, 1H), 4.56 (dd, $J = 3.4$, 0.7 Hz, 1H), 3.50 (dqd, $J = 13.4$, 6.7, 2.7 Hz 1H)), 2.97 (dd, $J = 9.6$, 6.1 Hz, 1H), 2.93 (ddd, $J = 10.8$, 7.2, 1.5 Hz, 1H), 2.75–2.69 (m, 1H), 2.69–2.64 (m, 1H), 1.99 (td, $J = 14.1$, 11.1 Hz, 1H), 1.41 (ddd, $J = 14.1$, 2.6, 1.6 Hz, 1H), 1.25 (dd, $J = 11.8$, 4.8 Hz, 1H), 1.17 (d, $J = 7.0$ Hz, 3H), 1.09 (d, $J = 7.2$ Hz, 3H), 1.06 ppm (d, $J = 6.7$ Hz, 3H); ^{13}C NMR (150 MHz, MeOD): $\delta = 206.2$, 200.5, 187.5, 171.5, 135.3, 135.1, 104.6, 86.8, 78.9, 73.8, 48.1, 49.4, 43.1, 40.2, 37.3, 25.9, 21.0, 19.3, 17.2 ppm; HRMS (ESI-TOF): calcd for $C_{19}H_{23}O_6^+$ $[M+H^+]$: 347.1489; found: 347.1485.

[a] We assume that the systematic differences (≈ 2 ppm) between the originally reported ^{13}C NMR data[1] and those of our synthetic abyssomicin C (**1**) are a consequence of differing calibration. We used the signal for CD_3OD at $\delta = 49.05$ ppm as reference. The data provided above are consistent with those reported by Sorensen and co-workers for their synthetic material.[2]

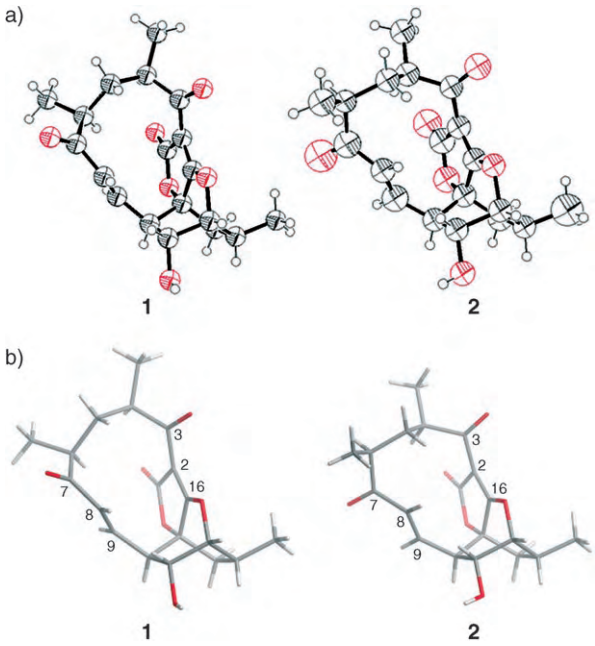

Figure 2. a) ORTEP drawings of abyssomicin C (**1**)[1] and atrop-abyssomicin C (**2**)[15] generated from X-ray crystallographic analysis. Spheres are drawn at a 50% probability level. b) Computer-generated stick models of **1** and **2** based on X-ray crystallographic data.

increased degree of conjugation between the carbonyl group and the double bond moiety, it was anticipated that it might be a more powerful Michael acceptor than **1**. This change in conformation at C7 has structural ramifications throughout the rest of the macrocyclic system, most notably the orientation of the carbonyl group at C3. In the natural compound **1** the O=C3-C2=C16 dihedral angle is 33.8°, whereas in atrop-abyssomicin C (**2**) the corresponding angle is 56.2°.

Thermally induced conversion of **2** into **1** (refluxing MeOH or toluene) was unsuccessful, leading either to no reaction or decomposition at higher temperatures (180 °C, xylenes, microwave irradiation). Surprisingly, however, while obtaining NMR spectroscopic data for **2** in unstabilized $CDCl_3$, it was observed that compound **2** slowly converted into **1**, cleanly affording a 2:1 mixture of **1**/**2** after 24 h. The same equilibrium (**1**/**2** 2:1) was reached from pure **1** ($CDCl_3$, 25 °C, 5 days). This phenomenon may be explained by either of two hypothetical scenarios (Scheme 3). The first (path a) postulates that catalytic amounts of hydrochloric acid present in $CDCl_3$ provides activation such that the tetronate becomes a sufficiently good leaving group, allowing the hydroxy group at C11 to initiate an attack upon C12 to generate the epoxide proposed for the biogenesis of the natural product.[2] This intermediate may then exhibit enhanced torsional freedom, allowing interconversion between the two atropisomers before retrapping the epoxide that would freeze them in stable conformations. Alternatively (path b), acid-catalyzed activation of the tetronate core would leave C16 electron-deficient and capable of drawing π-electron density from the suitably poised double bond at C2 (C2–C16 3.19 Å in **2** and 3.27 Å in **1** from X-ray crystallographic analysis). This bridging interaction would draw C2 even closer to C16 of the tetronate, relieving torsional strain in the macrocycle, and thus lowering the energy barrier to rotation of the σ bond as needed for the atropisomer interconversion. Synthetic abyssomicin C (**1**) was chromatographically separated from its atropisomer **2** and fully characterized (Table 1). Its physical properties were identical to those reported for the natural product.[1,2]

Preliminary minimal inhibitory concentration (MIC) assays of **1**, **2**, and **18** for antibacterial activity against MRSA revealed that they all exhibit activity, with the non-natural atropisomer **2** being the most potent (3.5 $\mu g\,mL^{-1}$) as compared to **1** (5.2 $\mu g\,mL^{-1}$) and **18** (17 $\mu g\,mL^{-1}$).[19] Our

 © 2006 Wiley-VCH Verlag GmbH & Co. KGaA, Weinheim

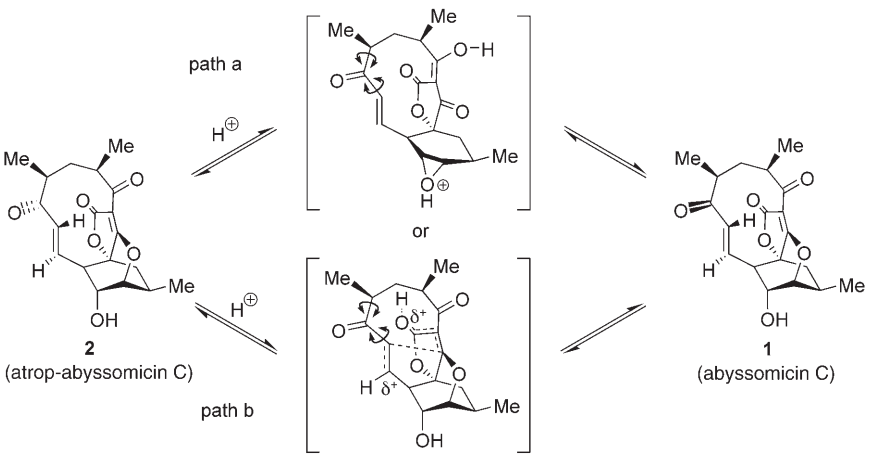

Scheme 3. Total synthesis of abyssomicin C (**1**) and postulated mechanisms (path a, involving epoxide participation; path b, involving enone participation) for the interconversion of **1** and **2**. Reagents and conditions: $CDCl_3$, 25 °C, 24 h, quantitative, **2**/**1** 1:2.

current hypothesis is that the difference in activity is due to **2** being a more powerful Michael acceptor than **1** as discussed above.

The chemistry described above offers the opportunity for a structure–activity relationship program within the abyssomicin structural motif, while revealing an intriguing and rare form of atropisomerism in medium-sized rings[16] of natural or designed origin. Studies directed toward the discovery of novel antibacterial agents through exploitation of these findings are continuing.

Received: March 21, 2006
Published online: April 24, 2006

Keywords: abyssomicin · antibiotics · atropisomerism · natural products · total synthesis

[1] a) B. Bister, D. Bischoff, M. Strobele, J. Riedlinger, A. Reicke, F. Wolter, A. T. Bull, H. Zahner, H. P. Fiedler, R. D. Sussmuth, *Angew. Chem.* **2004**, *116*, 6828; *Angew. Chem. Int. Ed.* **2004**, *43*, 2574; b) J. Riedlinger, A. Reicke, H. Zahner, B. Krismer, A. T. Bull, L. A. Maldonado, A. C. Ward, M. Goodfellow, B. Bister, D. Bischoff, R. D. Sussmuth, H. P. Fiedler, *J. Antibiot.* **2004**, *57*, 271.

[2] C. W. Zapf, B. A. Harrison, C. Drahl, E. J. Sorensen, *Angew. Chem.* **2005**, *117*, 6691; *Angew. Chem. Int. Ed.* **2005**, *44*, 6533.

[3] a) J. P. Rath, S. Kinast, M. E. Maier, *Org. Lett.* **2005**, *7*, 3089; b) B. B. Snider, Y. Zou, *Org. Lett.* **2005**, *7*, 4939; c) A. L. Zografos, A. Yiotakis, D. Georgiadis, *Org. Lett.* **2005**, *7*, 4515.

[4] Aldehyde **4** was derived from oxidation of the corresponding alcohol and prepared in ca. 90% *ee* (as determined by $[\alpha]_D^{25} = +10.5°$, $CDCl_3$, $c = 3.0$); see: a) S. V. Ley, R. T. Guy, M. A. Palomero, A. Polara, F. Rodriguez, T. D. Sheppard, *Org. Biomol. Chem.* **2004**, *2*, 3618; b) G.-Q. Lin, W.-C. Xu, *Bioorg. Med. Chem.* **1996**, *4*, 375.

[5] T. Hiyama, G. B. Reddy, T. Minami, T. Hanamoto, *Bull. Chem. Soc. Jpn.* **1995**, *68*, 350.

[6] E. J. Corey, D. Seebach, *J. Org. Chem.* **1966**, *31*, 4097.

[7] E. J. Corey, C. J. Helal, *Angew. Chem.* **1998**, *110*, 2092; *Angew. Chem. Int. Ed.* **1998**, *37*, 1987.

[8] Determined by HPLC using a Chiracel OD-H column and eluting with a solvent gradient of hexane to 5% *i*PrOH in hexane over 35 min.

[9] D. E. Ward, M. S. Abaee, *Org. Lett.* **2000**, *2*, 3937.

[10] The use of BINOL in conjunction with Me_2Zn (2.0 equiv) and MeMgBr (1.0 equiv) heated to 55 °C furnished **7** in less than 5% yield, albeit with 80% recovery of the diene; see: D. E. Ward, M. S. Souweha, *Org. Lett.* **2005**, *7*, 3533.

[11] Commercially available from a number of sources. However, we prepared it on an 85 g scale under the following conditions: 2-aminophenol (1.0 equiv), 1,4-dibromobutane (1.05 equiv), diisopropylethylamine (3.0 equiv), toluene (1.3 M), 65 °C, 12 h (80%).

[12] For an example of homoallylic alcohol directed epoxidation with $(n\mathrm{PrO})_3VO$, see: J. M. Evans, J. Kallmerten, *Synlett* **1992**, 269. We thank Professor K. B. Sharpless for suggesting the use of $(EtO)_3VO$ in this reaction.

[13] S. Tanaka, H. Yamamoto, H. Nozaki, K. B. Sharpless, R. C. Michaelson, J. D. Cutting, *J. Am. Chem. Soc.* **1974**, *96*, 5254.

[14] For other examples of Dieckmann cyclizations of this type, see: a) K. Takeda, Y. Shibata, Y. Sagawa, M. Urahata, K. Funaki, K. Hori, H. Sasahara, E. Yoshii, *J. Org. Chem.* **1985**, *50*, 4673; b) W. R. Roush, M. L. Reilly, K. Koyama, B. B. Brown, *J. Org. Chem.* **1997**, *62*, 8708.

[15] Prepared according to the sequence reported for *ent*-**15** by using (*R*)-(+)-α-methylbenzylamine; see: L. A. Paquette, S. L. Boulet, *Synthesis* **2002**, 888.

[16] M. Scholl, S. Ding, C. W. Lee, R. H. Grubbs, *Org. Lett.* **1999**, *1*, 953.

[17] CCDC-602361 (**2**) contains the supplementary crystallographic data for this paper. These data can be obtained free of charge from The Cambridge Crystallographic Data Centre via www.ccdc.cam.ac.uk/data_request/cif.

[18] For examples of medium ring compounds that lack a biaryl axis and exhibit atropisomerism, see: a) D. Anastasiou, E. M. Campi, H. Chaouk, W. R. Jackson, *Tetrahedron* **1992**, *48*, 7467; b) W. H. Pearson, E. J. Hembre, *J. Org. Chem.* **1996**, *61*, 5546; c) E. A. Anderson, J. E. P. Davidson, J. R. Harrison, P. T. O'Sullivan, J. W. Burton, I. Collins, A. B. Holmes, *Tetrahedron* **2002**, *58*, 1943.

[19] MIC values were determined with serial dilutions in 96-well plates against 1:10000 dilution in nutrient broth of a 24 h culture of methicillin-resistant *Staphylococcus aureus* (ATCC 33591) at 35 °C. We thank Ms. Desiree Thayer for assistance in performing these assays.

 © 2006 Wiley-VCH Verlag GmbH & Co. KGaA, Weinheim

Light-Emitting Organogel

DOI: 10.1002/anie.200600256

Evolution of Nano- to Microsized Spherical Assemblies of a Short Oligo(*p*-phenyleneethynylene) into Superstructured Organogels**

Ayyppanpillai Ajayaghosh, Reji Varghese, Vakayil K. Praveen, and Sankarapillai Mahesh*

The self-assembly of linear π-conjugated molecules to form nanoarchitectures of different morphologies is important in various fields of nanoscience and technology, particularly in the emerging field of supramolecular electronics.[1,2] In this context, oligo(*p*-phenyleneethynylene)s (OPEs), a class of conjugated molecules often referred as "molecular wires" has attracted much attention, particularly for the design of molecular electronic devices.[3] Although *meta*- and *para*-linked oligo- and poly(*p*-phenyleneethynylene)s (PPEs) are known to form solvophobically induced assemblies in solvent mixtures of different polarities,[4–6] the creation of stable supramolecular self-assemblies of short OPEs with different shapes and sizes from a single solvent of choice continues to be challenging. Herein, we report an unprecedented hierarchical self-assembly of a short OPE into nanoparticles, microspheres, and superstructures of different size and morphology that eventually result in stable blue-light emitting organogels.

Alhough the design of organic nanoparticles of small molecules[7,8] and polymers[9] are known, linearly conjugated oligomers are only rarely exploited for this purpose; however, a few reports have been published recently.[10] π-Extended molecules preferably self-assemble, with a few exceptions,[10a,d,g] to form elongated structures; for example, the self-assembly of oligo(*p*-phenylenevinylene)s (OPVs) results in the formation of supramolecular tapes and helices.[11,12] We have now targeted OPEs, the dehydrogenated analogues of OPVs in an attempt to understand the self-assembly processes of conjugated systems. For this purpose, **OPE1** and **OPE2** were synthesized by using multistep synthetic strategies involving palladium-catalyzed Sonogashira–Hagihara cross-coupling reactions (Scheme 1).[13] These molecules were characterized by ^{1}H NMR and ^{13}C NMR spectroscopy as well as by MALDI-TOF mass spectrometry.[14]

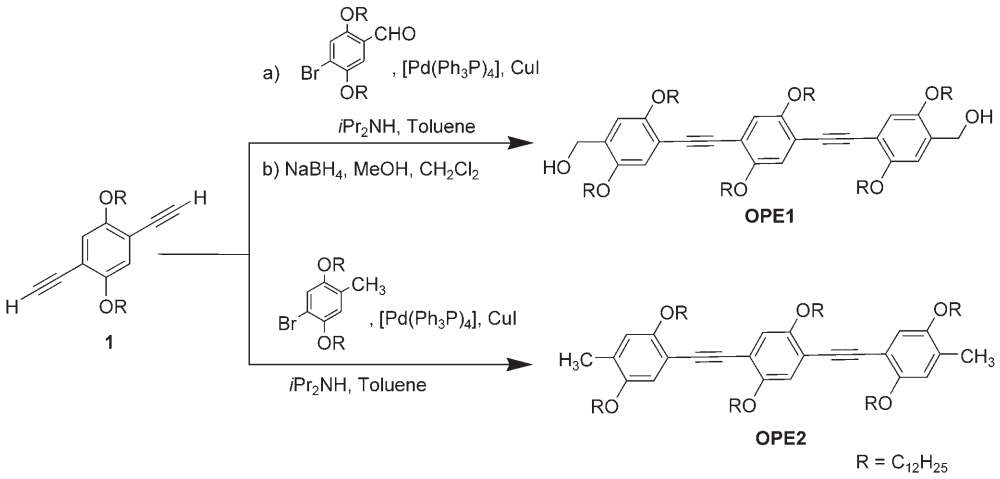

Scheme 1. Synthesis of **OPE1** and **OPE2**.

The UV/Vis spectrum of **OPE1** in chloroform (1×10^{-5} M) at 25 °C showed a strong π–π* absorption band at 377 nm. In decane, the absorption maximum is red-shifted to 385 nm and the formation of an additional band at 419 nm was observed. The emission maximum in chloroform was at 414 nm, which was significantly red-shifted towards 443 nm in decane but with decreased intensity.[14] These observations are attributed to the J-type aggregation of **OPE1** in decane. Variable-temperature UV/Vis absorption spectra recorded in decane (1.1×10^{-5} M) showed there was a reversible transition of the aggregates to isotropic species between 20 and 70 °C (Figure 1a). A plot of the fraction of the aggregates (α) versus temperature revealed a sharp transition between 30 and 40 °C as well as a broad transition in the range of 45–55 °C, thus indicating the presence of aggregates of different thermal stabilities (Figure 1a, inset). Furthermore, the absorption spectrum of **OPE1** (1.1×10^{-5} M) in decane at room temperature showed a time-dependent decrease in the absorption maximum, which reached a stable state after 4 h (Figure 1b).

[*] Dr. A. Ajayaghosh, R. Varghese, V. K. Praveen, S. Mahesh
Photosciences and Photonics Unit
Chemical Sciences and Technology Division
Regional Research Laboratory, CSIR
Trivandrum 695019 (India)
Fax: (+91) 471-249-0186
E-mail: aajayaghosh@rediffmail.com

[**] This work was supported by the Department of Science and Technology (DST), Government of India, New Delhi, and the Council of Scientific and Industrial Research (CSIR, Task Force Programme, CMM 10). The authors thank S. G. K Pillai for optical microscopy, P. Rao for SEM, and P. Gurusamy for XRD measurements. Prof. T. Pradeep of the Indian Institute of Technology, Madras, is acknowledged for providing the HR-TEM pictures. R.V. and V.K.P. thank the CSIR, and S.M. acknowledges the University Grants Commission (UGC), Government of India, for fellowships. This is manuscript No. RRLT-PPU-216.

Supporting information for this article is available on the WWW under http://www.angewandte.org or from the author.

 © 2006 Wiley-VCH Verlag GmbH & Co. KGaA, Weinheim

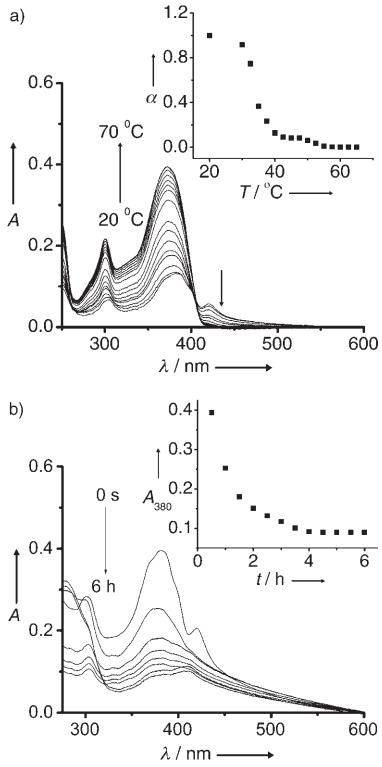

Figure 1. a) Temperature- and b) time-dependent absorption changes of **OPE1** in decane (1.1×10^{-5} M). The insets show a) the plot of the fraction of aggregates (α) versus temperature (absorption monitored at 380 nm) and b) the changes in the absorbance at 380 nm versus time.

Increasing the temperature at this point resulted in the original spectrum of the molecularly dissolved **OPE1**. These observations support the initial formation of kinetically controlled aggregates that undergo slow transformation to thermodynamically stable species through first-order kinetics, with a rate constant of $k = 47.41\ \text{min}^{-1}$ (Figure 1b, inset). The kinetically controlled aggregates are stable only up to 40 °C whereas the thermodynamically controlled aggregates are stable up to 55 °C. Interestingly, no considerable differences in the absorption spectra of solutions of **OPE2** in chloroform and decane were observed, thus indicating that this molecule fails to self-aggregate because of the absence of the H-bonding end functional groups.

The atomic force microscopy (AFM) pictures of the self-assemblies of 1×10^{-6} and 1×10^{-5} M solutions of **OPE1** in decane at different magnifications are shown in Figure 2. These images reveal the concentration-dependent self-assembly of **OPE1** to individually dispersed particles of different size. The average diameter of the particles was estimated from the fitted histograms of the size distribution curves (Figure 2c,f) after subtracting the tip-broadening parameters.[15] The histograms, which were obtained from the individual diameters of 500 particles, show a Lorentzian distribution ($R^2 = 0.9103$) with an average diameter of 94 ± 2 nm and a height of 4 ± 1 nm at 1×10^{-6} M (full-width at half maximum = 34 nm). The corresponding analysis of the particles formed at 1×10^{-5} M revealed an average diameter of 535 ± 10 nm and a height of 20 ± 5 nm ($R^2 = 0.9003$, full-width at half maximum = 226 nm). Comparison of the heights and diameter indicates a flattening of the spheres when transferred to the mica surface. Although there could be several causes of this flattening, it is likely that the removal of the solvent after the transfer of the soft particles to the mica surface and the high local force applied by the AFM tip may be the major reasons.[8c,e,10b] The vesicular nature of the sphere is clear from the high-resolution transmission electron microscopy (HR-TEM) image (Figure 2g). The wall thickness of the vesicle is approximately 10 nm and has a bilayer morphology, with each layer having a thickness of about 4 nm. Further increase of the concentration (1×10^{-4} M) resulted in the formation of fluorescent microspheres with diameters as large as 10 μm (Figure 3a). These microspheres can be seen to be agglom-

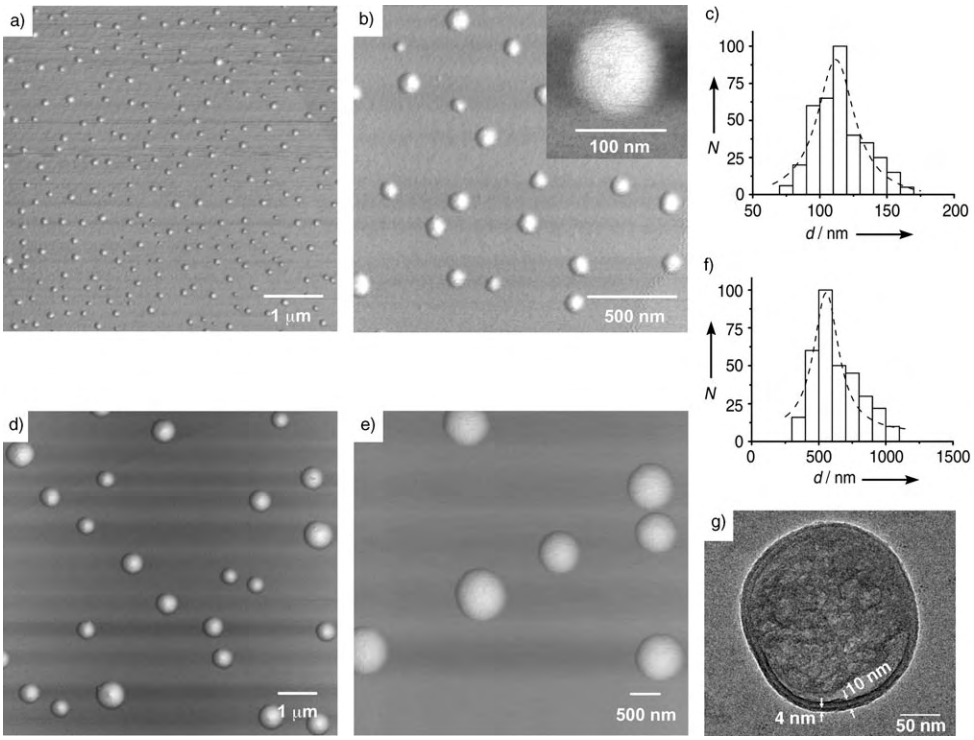

Figure 2. AFM tapping mode height images of **OPE1** in decane, and the corresponding histograms (Lorentzian fit) at different concentrations. a–c) 1×10^{-6} M and d–f) 1×10^{-5} M (blank experiments were conducted with only decane on mica to rule out any artefacts). g) HR-TEM image of a sphere of **OPE1** from decane at 5×10^{-6} M without staining.

 © 2006 Wiley-VCH Verlag GmbH & Co. KGaA, Weinheim

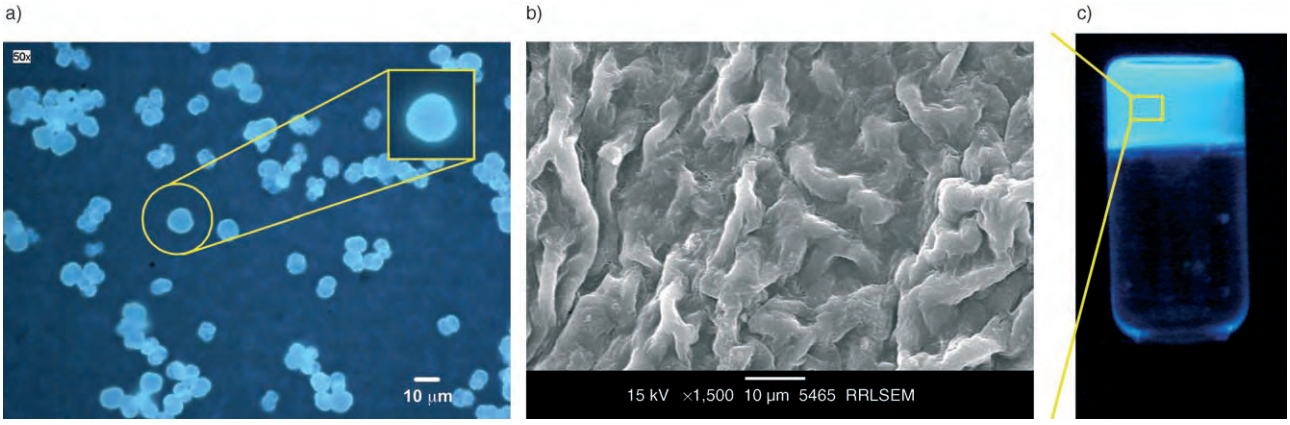

Figure 3. a) Optical microscopic picture of **OPE1** (1×10^{-4} M in decane) under illumination with light of wavelength 365 nm. b) SEM image of **OPE1** gel (3.4×10^{-3} M) in decane. c) Photograph of the gel in decane (5×10^{-3} M) under illumination (365 nm).

erated and fused in many places, which is in contrast to the individual nanospheres obtained at low concentrations. A self-supporting gel with strong blue fluorescence ($\lambda_{max}=$ 443 nm, Figure 3c) is obtained at 3.4×10^{-3} M. It is important to note that there are no reports on short OPEs that form organogels through intermediate spherical assemblies, although there are a few reports on the direct gelation of polymeric, macrocyclic, and hybrid phenyleneethynylene systems.[16]

The scanning electron microscopy (SEM) image of a dried **OPE1** gel (Figure 3b) obtained from decane (3.4×10^{-3} M) reveals the formation of superstructures of micrometer size. The morphological features indicate that these extended structures could be formed from fused microspheres at higher concentrations. Furthermore, the **OPE1** gel obtained from decane exhibited birefringent textures when viewed through crossed polarizers, thus indicating molecular anisotropy of the aggregates. X-ray powder diffraction (XRD) analysis of a dried gel showed intense reflections with *d* spacings of 31.3, 21.2, 4.6, 4.1, and 3.7 Å.[14] These spacings are characteristic of a π-stacked lamellar packing of the individual molecules in the self-assembled structure.

The morphological features of the self-assembly of **OPE1** is remarkably different from those of the analogous OPVs.[11] The latter prefers to form an extended tapelike morphology irrespective of the concentration gradient. This result is attributed to the differences in the π interactions which are responsible for the stacking of the molecules. These interactions are expected to be strong in planar OPVs relative to that in the nonplanar **OPE1**. Thus, at low concentrations **OPE1** forms less-stable aggregates that undergo a slow time-dependent transformation into thermodynamically favored spherical assemblies. However, at higher concentrations (above the critical gelator concentration (CGC)), the initially formed aggregates prefer to form extended superstructures that lead to gelation. A reasonable representation of these processes is shown in Figure 4.

In conclusion, we have shown the unprecedented evolution of nanoparticles and microspheres of a short molecular wire below the CGC and giant fibrillar assemblies above the CGC. The current method has the advantage of generating self-assemblies of different size and shape simply by variation of the concentration of the building blocks in a single solvent, which is in contrast to the induced assemblies in solvent

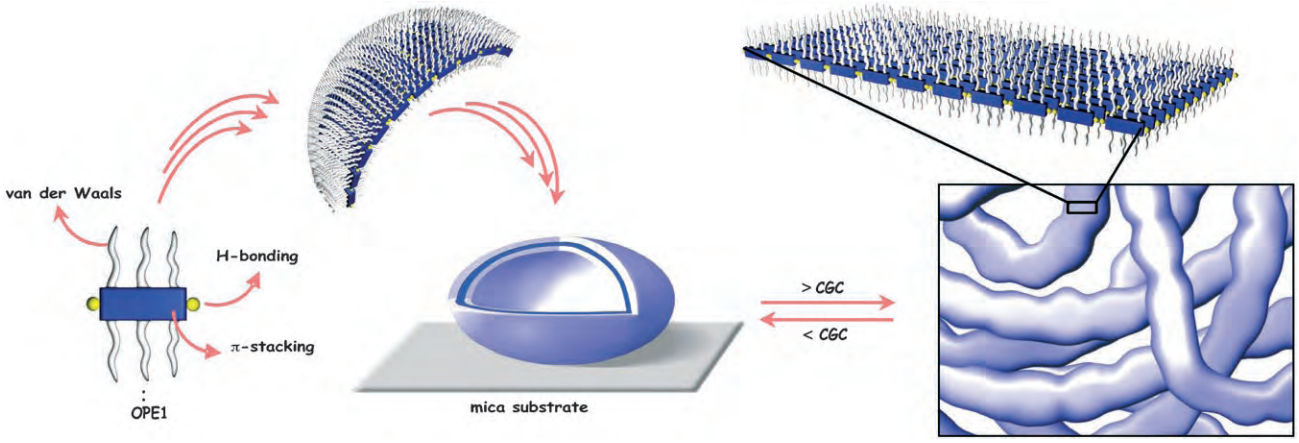

Figure 4. Schematic representation of the self-assembly processes. The mode of molecular arrangements in a single layer of the spherical and the extended self-assemblies are also shown.

 © 2006 Wiley-VCH Verlag GmbH & Co. KGaA, Weinheim

mixtures reported previously by other research groups. To our knowledge, this is the first report on the self-assembly of a short linear OPE with a tunable size and morphology from a single solvent that results in nanoparticles, microspheres, and super-structured blue-light emitting organogels.

Received: January 20, 2006
Published online: April 18, 2006

Keywords: gels · nanostructures · self-assembly · supramolecular chemistry

[1] a) A. P. H. J. Schenning, E. W. Meijer, *Chem. Commun.* **2005**, 3245 – 3258; b) E. W. Meijer, A. P. H. J. Schenning, *Nature* **2002**, *419*, 353 – 354.

[2] M. V. D. Auweraer, F. C. De Schryver, *Nat. Mater.* **2004**, *3*, 507 – 508.

[3] a) R. L. Carroll, C. B. Gorman, *Angew. Chem.* **2002**, *114*, 4556 – 4579; *Angew. Chem. Int. Ed.* **2002**, *41*, 4378 – 4400; b) J. M. Tour, *Acc. Chem. Res.* **2000**, *33*, 791 – 804; c) J. Chen, M. A. Reed, A. M. Rawlett, J. M. Tour, *Science* **1999**, *286*, 1550 – 1552; d) K. Müllen, G. Wegner, *Electronic Materials. The Oligomer Approach*, Wiley-VCH, Weinheim, **1998**.

[4] a) D. J. Hill, M. J. Mio, R. B. Prince, T. S. Hughes, J. S. Moore, *Chem. Rev.* **2001**, *101*, 3893 – 4011; b) J. S. Moore, *Acc. Chem. Res.* **1997**, *30*, 402 – 413.

[5] J. Xu, C.-Z. Zhou, L. H. Yang, N. T. S. Chung, Z.-K. Chen, *Langmuir* **2004**, *20*, 950 – 956.

[6] a) R. B. Breitenkamp, G. N. Tew, *Macromolecules* **2004**, *37*, 1163 – 1165; b) Q. Chu, Y. Pang, *Macromolecules* **2003**, *36*, 4614 – 4618; c) S. Zahn, T. M. Swager, *Angew. Chem.* **2002**, *114*, 4399 – 4404; *Angew. Chem. Int. Ed.* **2002**, *41*, 4226 – 4230; d) U. H. F. Bunz, *Acc. Chem. Res.* **2001**, *34*, 998 – 1010; e) U. H. F. Bunz, *Chem. Rev.* **2000**, *100*, 1605 – 1644; f) P. Samorí, V. Francke, K. Müllen, J. P. Rabe, *Chem. Eur. J.* **1999**, *5*, 2312 – 2317; g) P. Samorí, I. Sikharulidze, V. Francke, K. Müllen, J. P. Rabe, *Nanotechnology* **1999**, *10*, 77 – 80.

[7] a) M. Han, M. Hara, *J. Am. Chem. Soc.* **2005**, *127*, 10951 – 10955; b) Z. Tian, Y. Chen, W. Yang, J. Yao, L. Zhu, Z. Shuai, *Angew. Chem.* **2004**, *116*, 4152 – 4155; *Angew. Chem. Int. Ed.* **2004**, *43*, 4060 – 4063; c) R. Charvet, D.-L. Jiang, T. Aida, *Chem. Commun.* **2004**, 2664 – 2665; d) D. Xiao, L. Xi, W. Yang, H. Fu, Z. Shuai, Y. Fang, J. Yao, *J. Am. Chem. Soc.* **2003**, *125*, 6740 – 6745; e) H. Fu, B. H. Loo, D. Xiao, R. Xie, X. Ji, J. Yao, B. Zhang, L. Zhang, *Angew. Chem.* **2002**, *114*, 1004 – 1007; *Angew. Chem. Int. Ed.* **2002**, *41*, 962 – 965; f) Y. J. Jeon, P. K. Bharadwaj, S. Choi, J. W. Lee, K. Kim, *Angew. Chem.* **2002**, *114*, 4654 – 4656; *Angew. Chem. Int. Ed.* **2002**, *41*, 4474 – 4476; g) H.-B. Fu, J.-N. Yao, *J. Am. Chem. Soc.* **2001**, *123*, 1434 – 1439.

[8] a) T. Akutagawa, K. Kakiuchi, T. Hasegawa, S.-i. Noro, T. Nakamura, H. Hasegawa, S. Mashiko, J. Becher, *Angew. Chem.* **2005**, *117*, 7449 – 7453; *Angew. Chem. Int. Ed.* **2005**, *44*, 7283 – 7287; b) T. Nakanishi, W. Schmitt, T. Michinobu, D. G. Kurth, K. Ariga, *Chem. Commun.* **2005**, 5982 – 5984; c) M. Yang, W. Wang, F. Yuan, X. Zhang, J. Li, F. Liang, B. He, B. Minch, G. Wegner, *J. Am. Chem. Soc.* **2005**, *127*, 15107 – 15111; d) M. Lee, S.-J. Lee, L.-H. Jiang, *J. Am. Chem. Soc.* **2004**, *126*, 12724 – 12725; e) S. Zhou, C. Burger, B. Chu, M. Sawamura, N. Nagahama, M. Toganoh, U. E. Hackler, H. Isobe, E. Nakamura, *Science* **2001**, *291*, 1944 – 1947.

[9] a) M. Oh, C. A. Mirkin, *Nature* **2005**, *438*, 651 – 654; b) E. Hittinger, A. Kokil, C. Weder, *Angew. Chem.* **2004**, *116*, 1844 – 1847; *Angew. Chem. Int. Ed.* **2004**, *43*, 1808 – 1811; c) O. Uzun, A. Sanyal, H. Nakade, R. J. Thibault, V. M. Rotello, *J. Am. Chem. Soc.* **2004**, *126*, 14773 – 14777; d) D. M. Vriezema, J. Hoogboom, K. Velonia, K. Takazawa, P. C. M. Christianen, J. C. Maan, A. E. Rowan, R. J. M. Nolte, *Angew. Chem.* **2003**, *115*, 796 – 800; *Angew. Chem. Int. Ed.* **2003**, *42*, 772 – 776.

[10] a) N. Zhou, E. F. Merschrod, S. Y. Zhao, *J. Am. Chem. Soc.* **2005**, *127*, 14154 – 14155; b) I. O. Shklyarevskiy, P. Jonkheijm, P. C. M. Christianen, A. P. H. J. Schenning, E. W. Meijer, O. Henze, A. F. M. Kilbinger, W. J. Feast, A. D. Guerzo, J.-P. Desvergne, J. C. Maan, *J. Am. Chem. Soc.* **2005**, *127*, 1112 – 1113; c) B.-S. Kim, W.-Y. Yang, J.-H. Ryu, Y.-S. Yoo, M. Lee, *Chem. Commun.* **2005**, 2035 – 2037; d) S.-J. Lim, B.-K. An, S. D. Jung, M.-A. Chung, S. Y. Park, *Angew. Chem.* **2004**, *116*, 6506 – 6510; *Angew. Chem. Int. Ed.* **2004**, *43*, 6346 – 6350; e) Y.-S. Yoo, J.-H. Choi, J.-H. Song, N.-K. Oh, W.-C. Zin, S. Park, T. Chang, M. Lee, *J. Am. Chem. Soc.* **2004**, *126*, 6294 – 6300; f) L. Jiang, R. C. Hughes, D. Y. Sasaki, *Chem. Commun.* **2004**, 1028 – 1029; g) B.-K. An, S.-K. Kwon, S.-D. Jung, S. Y. Park, *J. Am. Chem. Soc.* **2002**, *124*, 14410 – 14415.

[11] a) A. Ajayaghosh, S. J. George, A. P. H. J. Schenning, *Top. Curr. Chem.* **2005**, *258*, 83 – 118; b) S. J. George, A. Ajayaghosh, *Chem. Eur. J.* **2005**, *11*, 3217 – 3227; c) A. Ajayaghosh, S. J. George, V. K. Praveen, *Angew. Chem.* **2003**, *115*, 346 – 349; *Angew. Chem. Int. Ed.* **2003**, *42*, 332 – 335; d) A. Ajayaghosh, S. J. George, *J. Am. Chem. Soc.* **2001**, *123*, 5148 – 5149.

[12] a) A. Ajayaghosh, R. Varghese, S. J. George, C. Vijayakumar, *Angew. Chem.* **2006**, *118*, 1159 – 1162; *Angew. Chem. Int. Ed.* **2006**, *45*, 1141 – 1144; b) A. Ajayaghosh, C. Vijayakumar, R. Varghese, S. J. George, *Angew. Chem.* **2006**, *118*, 470 – 474; *Angew. Chem. Int. Ed.* **2006**, *45*, 456 – 460; c) S. J. George, A. Ajayaghosh, P. Jonkheijm, A. P. H. J. Schenning, E. W. Meijer, *Angew. Chem.* **2004**, *116*, 3504 – 3507; *Angew. Chem. Int. Ed.* **2004**, *43*, 3422 – 3425.

[13] J.-F. Nierengarten, T. Gu, G. Hadziioannou, D. Tsamouras, V. Krasnikov, *Helv. Chim. Acta* **2004**, *87*, 2948 – 2966.

[14] See the Supporting Information.

[15] The image broadening arising from the AFM tip convolution effect is estimated as reported in: a) H.-J. Butt, R. Guckenberger, J. P. Rabe, *Ultramicroscopy* **1992**, *46*, 375 – 393; b) P. Samori, V. Francke, T. Mangel, K. Müllen, J. P. Rabe, *Opt. Mater.* **1998**, *9*, 390 – 393; the radius of the tip (Veeco probes, MPP-11100–10) is taken as 12.5 nm. At 1×10^{-6} M, the measured height of the particles is 4 ± 1 nm, and the calculated tip broadening is 18 ± 2 nm. Therefore, the actual average diameter is estimated by subtracting the broadening from the measured diameter (112 nm) which is 94 ± 2 nm. Similarly, at 1×10^{-5} M, the calculated actual diameter of the particles of height 20 ± 5 nm is 535 ± 10 nm after accounting for the tip-broadening effect of 20 ± 10 nm.

[16] a) W. Y. Huang, S. Matsuoka, T. K. Kwei, Y. Okamoto, *Macromolecules* **2001**, *34*, 7166 – 7171; b) C.-H. Lin, J. Tour, *J. Org. Chem.* **2002**, *67*, 7761 – 7768; c) C.-C. Tsou, S.-S. Sun, *Org. Lett.* **2006**, *8*, 387 – 390.

 © 2006 Wiley-VCH Verlag GmbH & Co. KGaA, Weinheim

Metallacycles

DOI: 10.1002/anie.200504382

Synthesis of a Rhodaazacyclopropane and Characterization of Its Radical Cation by EPR Spectroscopy**

Pascal Maire, Anandaram Sreekanth, Torsten Büttner, Jeffrey Harmer, Igor Gromov, Heinz Rüegger, Frank Breher, Arthur Schweiger, and Hansjörg Grützmacher**

Cyclopropane and its derivatives $(ER_2)_3$ (E = C, Si, Ge, Sn), bicyclobutanes, and other strained hydrocarbons have remarkably low oxidation potentials when compared to their unstrained linear counterparts.[1–3] Can this property be translated to transition-metal complexes, such that small rings incorporating the transition metal lead to more facile oxidation? With this question in mind, we characterized a d^8 Rh complex that has a metal center incorporated in a three-membered ring. Furthermore, we report the results from high-resolution pulse EPR spectroscopy, which, in combination with density functional theory (DFT) calculations, allowed us to characterize in detail the electronic structure of the corresponding radical cation.

In analogy to the preparation of $trop_2NH$[4] (trop = tropylidenyl = 5*H*-dibenzo[*a*,*d*]cyclohepten-5-yl), we prepared the *N*-methyl derivative $trop_2NMe$ (**1**) from $(Me_3Si)_2NMe$ and tropCl (Scheme 1). Subsequently, **1** was treated with $[Rh_2(\mu_2\text{-}Cl)_2(cod)_2]$ (cod = 1,5-cyclooctadiene) to yield $[Rh_2(\mu_2\text{-}Cl)_2(trop_2NMe)_2]$, which was treated with PPh_3 to give $[RhCl(trop_2NMe)(PPh_3)]$ (**2**). Addition of AgOTf ($OTf^- = CF_3SO_3^-$) led to the isolation of $[Rh(trop_2NMe)(PPh_3)]OTf$ (**3**) as red needles in 78% overall yield (for details, see the Supporting Information). The ^{13}C- and D_3-labeled iodide complexes [^{13}C]**5** and [D_3]**5** were prepared from the reactions of the rhodium(I)amide **4**[5] with $^{13}CH_3I$ and CD_3I, respectively. The NMR data indicate that **2** and **5** form trigonal bipyramidal 18-electron complexes in $CDCl_3$ solution with the halide atoms and the $C{=}C_{trop}$ units in the equatorial positions. Complex **3** forms an ion pair in solution, such that the OTf^- ion binds remotely from the metal in a pocket between the NMe group and the benzylic protons of the $trop_2NMe$ ligand.

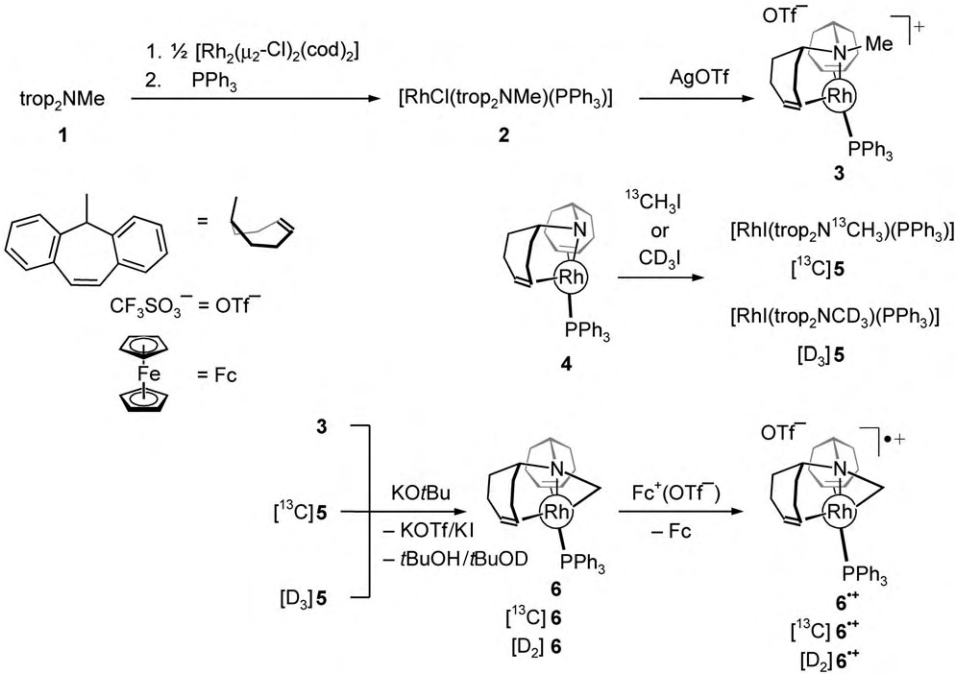

Scheme 1. Synthesis of complexes **3**, [^{13}C]**5**, [D_3]**5**, **6**, [^{13}C]**6**, [D_2]**6**, and radical cations $\mathbf{6}^{\bullet+}$, [^{13}C]$\mathbf{6}^{\bullet+}$, and [D_2]$\mathbf{6}^{\bullet+}$.

An ion pair is also observed for **3** in the solid state, again with the OTf^- ion bound remotely from the metal center and embedded between the arene groups of the tropylidenyl and PPh_3 ligands (Figure 1b).[6] The $[Rh(trop_2NMe)(PPh_3)]^+$ ion has an unusual "saw-horse" structure (Figure 1a) which is nonplanar and resembles a trigonal bipyramid with one equatorial ligand missing (selected bond lengths and angles are listed in Table 1). Structures of this type have rarely been observed for stable 16-electron complexes; some examples include the neutral amide **4**[5] and the Ru complexes $[Ru(CO)_2L_2]$ (**I**) and $[Ru(CO)(NO)L_2]^+$ (**II**; L = P*t*Bu_2Me).[7] The N-Rh-P bond angle in **3** (158.2(1)°) and the P-Ru-P bond angle in **II** (157.3°) are slightly more acute than the corresponding bond angles in the neutral complexes **4** (166.2°) and **I** (165.6°). The ct-Rh-ct angle (134.5(2)°; ct = centroid of the coordinated double bond) is similar to the corresponding angles in **4** and **I** (ca. 135°), but larger than that

[*] Dr. A. Sreekanth, Dr. J. Harmer, Dr. I. Gromov, Prof. Dr. A. Schweiger[†]
Laboratorium für Physikalische Chemie
Departement Chemie und Angewandte Biowissenschaften
ETH Zürich
8093 Zürich (Switzerland)
Fax: (+41) 44-632-1021
E-mail: harmer@phys.chem.ethz.ch
Dr. P. Maire, Dr. T. Büttner, Dr. H. Rüegger, Dr. F. Breher, Prof. Dr. H. Grützmacher
Laboratorium für Anorganische Chemie
Departement Chemie und Angewandte Biowissenschaften
ETH Zürich
8093 Zürich (Switzerland)
Fax: (+41) 44-633-1418
E-mail: gruetzmacher@inorg.chem.ethz.ch
[†] Deceased on January 4, 2006

[**] This work was supported by the Swiss National Science Foundation.
Supporting information for this article is available on the WWW under http://www.angewandte.org or from the author.

 © 2006 Wiley-VCH Verlag GmbH & Co. KGaA, Weinheim

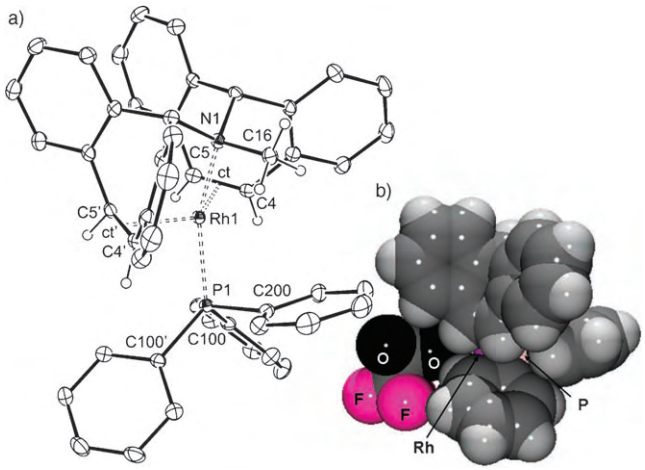

Figure 1. Structure of **3**·3 CH_2Cl_2. a) Thermal ellipsoids are set at 30% probability. The three CH_2Cl_2 molecules, the OTf^- counteranion, and the hydrogen atoms, apart from those in the *N*-methyl group and at the olefinic carbon atoms, are omitted for clarity. Selected bond lengths and angles are listed in Table 1 (ct = centroids of the C=C_{trop} units). Additional angles [°]: C100-P1-C100′ 102.4(3), C200-P1-C100/100′ 108.0(2), Rh-P1-C100/100′ 124.4(1). b) Space-filling model of **3** showing the position of the anion.

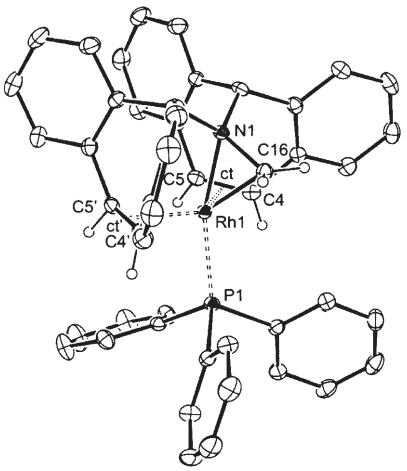

Figure 2. Structure of **6**·toluene. Thermal ellipsoids are set at 30% probability. The toluene molecule and hydrogen atoms, apart from those in the methylene bridge and at the olefinic carbon atoms, are omitted for clarity. Selected bond lengths and angles are listed in Table 1 (ct = centroids of the C=C_{trop} units).

in the nitrosyl complex **II** (120°). The small Rh1-P1-C200 angle (86.1(2)°) and relatively short Rh···C200 distance (2.80 vs. > 3.6 Å for the other Rh···C_{phenyl} distances) in **3** are especially noteworthy and indicate a hyperconjugative interaction between the P–C bond and the metal center.

The triflate complex **3** reacts cleanly with KO*t*Bu to give complex **6**. The compounds [^{13}C]**6** and [D_2]**6**, in which the *N*-methylene group is ^{13}C- and D-labeled, were obtained from the respective iodide complexes [^{13}C]**5** and [D_3]**5**. The result of an X-ray structure analysis on orange crystals of **6** is shown in Figure 2; selected bond lengths and angles are given in Table 1.

Interactions between a metal M and an unsaturated ligand X=Y can be considered with regard to the limiting cases represented by the heterocyclic metallacyclopropane form (type **A**, Scheme 2) and a X=Y→M donor–acceptor complex (type **B**).[8] Complex **6** can be described either as a rhodaazacyclopropane **6A** or a rhodium iminium ion complex **6B**. In the first case, the Rh center has a formal oxidation state of +1, and in the latter case a formal oxidation state of −1.

The Rh–N bond in **6** (2.059(3) Å) is shorter than in **3** (2.131(5) Å). Also, the N–CH_2 bond in **6** (1.446(5) Å) is significantly shorter than the N–CH_3 bond in **3** (1.505(7) Å), but considerably longer than the N=C bonds in iminium ions (1.274–1.301 Å)[9] and close in length to the N–C bonds in aziridines (1.440–1.471 Å).[10] Hence, the structural data favor

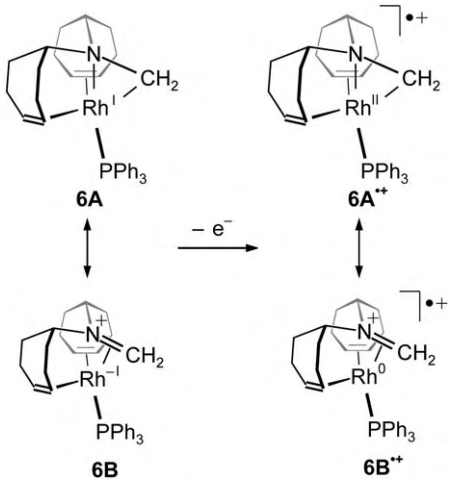

Scheme 2. Selected resonance structures for **6** and **6**$^{\bullet+}$.

the rhodaazacyclopropane description **6A**, which is expected in view of the energetically low-lying π* orbital of the N–C bond and the consequently strong metal-to-ligand back donation. N–C bond lengths similar to that in **6** have been observed in the few comparable metalla-aza-cyclopropanes.[11] The large change in the ^{13}C NMR spectroscopic resonances ($\Delta\delta = \delta_{complex} - \delta_{ligand}$) of the C=$C_{trop}$ units ($\Delta\delta$ = −75.8 and −67.0 ppm) on coordination to the Rh center in **6** is particularly noteworthy, thus indicating significant cyclopropane character for the RhC_2 units.

Table 1: Selected bond lengths [Å] and angles [°] of **3** (experimental), **6** (experimental), and **6**$^{\bullet+}$ (calculated by DFT).[a]

Compound	Rh-C16	Rh-N	N-C16	Rh-P	Rh-ct	C=C_{trop}	N-Rh-P	ct-Rh-ct	Rh-N-C16	N-C16-Rh	C16-Rh-N
$\mathbf{3}_{exp}$	–	2.131(5)	1.505(7)	2.254(1)	2.075(4)	1.413(6)	158.2(1)	134.5(2)	103.1(3)	–	–
$\mathbf{6}_{exp}$	2.117(4)	2.059(3)	1.446(5)	2.254(1)	2.065(3)	1.419(4)	160.35(9)	132.6(1)	71.9(2)	67.6(2)	40.5(1)
$\mathbf{6}^{\bullet+}_{calcd}$	2.090	2.164	1.417	2.367	2.179	1.422	158.50	136.05	67.75	73.37	38.88

[a] ct indicates the midpoint of the coordinated C=C_{trop} bond.

 © 2006 Wiley-VCH Verlag GmbH & Co. KGaA, Weinheim

A cyclic voltammogram recorded in a THF solution (0.1 M nBu$_4$NPF$_6$ electrolyte, $T = 298$ K, Pt electrode, scan rate 100 mV s^{-1}) of the rhodaazacyclopropane **6** showed one reversible wave at a remarkably low potential ($E^{o}_{1/2} = -0.510$ V vs. the ferrocenium/ferrocene couple), corresponding to the oxidation **6**→**6**$^{\bullet+}$.[12] The high stability of **6**$^{\bullet+}$ allowed the first detailed study of the electronic structure of a rhodaazacyclopropyl radical cation by continuous-wave (CW) and pulse EPR spectroscopy.[13] For this study, **6** as well as the ^{13}C- and D$_2$-labeled derivatives [^{13}C]**6** and [D$_2$]**6** were oxidized with ferrocenium triflate to give the radical cations **6**$^{\bullet+}$, [^{13}C]**6**$^{\bullet+}$, and [D$_2$]**6**$^{\bullet+}$, respectively. The half-life of **6**$^{\bullet+}$ in THF solution (ca. 0.1 mM) is about five hours at room temperature.[14]

The frozen-solution X-band CW-EPR spectra of **6**$^{\bullet+}$ and [^{13}C]**6**$^{\bullet+}$ are shown in Figure 3a. Both spectra are well-resolved at the high-field end ($g_2 = 2.0155$, $g_3 = 2.0145$) and show splittings from the ^{103}Rh nucleus ($I = 1/2$) for **6**$^{\bullet+}$ and from the ^{103}Rh and ^{13}C nuclei ($I = 1/2$) for [^{13}C]**6**$^{\bullet+}$. At the low-field end ($g_1 = 2.121$), the spectra are poorly resolved.[15] Pulse ENDOR (electron nuclear double resonance) and HYSCORE (hyperfine sublevel correlation) spectroscopies were used to determine the complete set of hyperfine parameters of the ^{103}Rh and ^{13}C nuclei of the methylene unit, as well as of the two methylene ^{1}H nuclei, the weakly coupled ^{14}N nucleus, the olefinic ^{13}C nuclei, the olefinic protons, and the ^{31}P nucleus (see the Supporting Information). To assign the methylene proton signals unambiguously, the corresponding spectra of [D$_2$]**6**$^{\bullet+}$ were also recorded (Supporting Information).

In Figure 3b, a representative hyperfine-correlated ENDOR (HYEND) spectrum of [^{13}C]**6**$^{\bullet+}$ is displayed which contains ^{103}Rh and ^{13}C ENDOR frequencies (ν_{ENDOR} axis) that are correlated with their corresponding hyperfine frequencies (ν_{HF} axis). In Figure 3c, a representative Q-band HYSCORE spectrum of **6**$^{\bullet+}$ is shown which contains peaks from the ^{103}Rh nucleus, the ^{13}C nuclei of the olefinic C5 atoms, and the ^{14}N and ^{31}P nuclei. The EPR parameters were obtained from the spectrum by matching the position of the experimental cross-peaks with those calculated from the relevant spin Hamiltonian. A complete set of experimentally derived parameters is given in Table 2, along with the data obtained from DFT calculations.[16] The experimental spin populations were calculated from their respective hyperfine couplings.[17]

Overall, the agreement between experimentally derived and calculated EPR parameters and spin populations is excellent. According to the DFT calculations, the main part of the spin density is located on the rhodium center (47%), the methylene carbon atom (14%), and the four olefinic carbon atoms (C5 2×15%, C4 2×−3%). This distribution of spin density can be seen by inspection of the spin-density plot

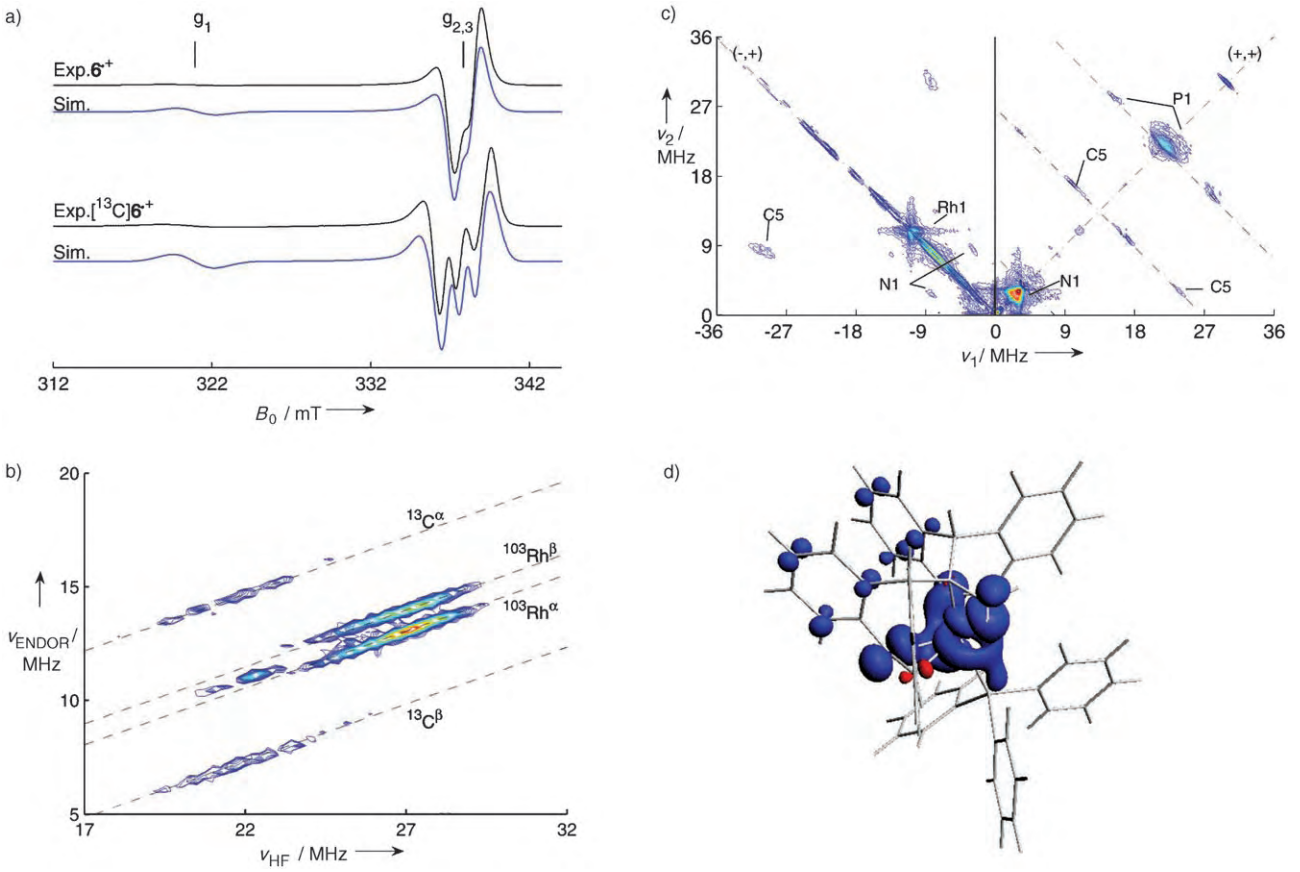

Figure 3. a) Experimental (Exp.) and simulated (Sim.) second-derivative X-band CW-EPR spectra of **6**$^{\bullet+}$ and [^{13}C]**6**$^{\bullet+}$ in THF measured at 115 K. b) X-band HYEND spectrum of [^{13}C]**6**$^{\bullet+}$ in THF measured at 15 K at the observer position g_2. The dashed lines are separated by twice the nuclear Zeeman interaction ($2\nu_I$) of ^{103}Rh and ^{13}C, and cross the ν_{ENDOR} and ν_{HF} axes at ν_I(^{103}Rh) and ν_I(^{13}C), respectively. c) Q-band HYSCORE spectrum of **6**$^{\bullet+}$ in THF measured at 15 K near to the g_3 observer position. Cross-peaks from ^{13}C (in natural abundance), ^{103}Rh, ^{31}P, and ^{14}N are labeled. d) Spin density of compound **6**$^{\bullet+}$, plotted with an isosurface level of 0.004.

 © 2006 Wiley-VCH Verlag GmbH & Co. KGaA, Weinheim

Table 2: EPR parameters and spin populations of compound $\mathbf{6}^{\bullet+}$. DFT values are given in brackets.[a]

Group	Nucleus	A_1 [MHz]	A_2 [MHz]	A_3 [MHz]	Spin population
–	Rh1	29 ± 2 (26.3)	25 ± 2 (22.6)	−18 ± 2 (−12.2)	– (47%)
methylene	C16	19 ± 2 (16.3)	20 ± 2 (16.8)	66 ± 2 (47.8)	15% (14%)
methylene	H16	−11 ± 1 (−7.9)	0 ± 2 (0.1)	3 ± 1 (4.2)	2×−0.2% (2×−0.1%)
amine	N1	−1.6 ± 0.2 (−1.6)	−0.9 ± 0.2 (−0.8)	0.2 ± 0.2 (0.4)	−0.5% (−0.5%)
PPh_3	P1	0 to 15 (0.4)	0 to 15 (4.3)	0 to 15 (17)	– (2.5%)
olefin	C5	21 ± 5 (−0.2)	21 ± 5 (−0.1)	55 ± 5 (40.3)	2×11% (2×15%)
	C4	(−8.6)	(−4.2)	(−2.7)	(2×−3%)
olefin	H5	−11 ± 1 (−10.8)	4 ± 2 (1.3)	4 ± 1 (2.3)	2×−0.1% (2×−0.2%)
	H4	5 ± 1 (3.5)	5 ± 2 (5.2)	10 ± 1 (9.3)	2×0.5% (2×0.3%)

[a] The signs of the experimental hyperfine couplings $A_{1,2,3}$ are assigned according to the DFT results; principal axis directions are given in the Supporting Information. $g_1 = 2.121 \pm 0.001$ (2.1050), $g_2 = 2.0155 \pm 0.0005$ (2.0174), $g_3 = 2.0145 \pm 0.0005$ (2.0163).

given in Figure 3d. There is some spin delocalization to the two benzo moieties (2×6%) of the trop ligand, with the alternating sign of the hyperfine couplings of adjacent carbon nuclei indicating a spin-polarization (hyperconjugation) mechanism. Both experimental and calculated data show small hyperfine couplings and thus small spin populations on the nitrogen and phosphorus nuclei. A comparison of **6** and $\mathbf{6}^{\bullet+}$ shows that the gross structural features are retained.

In summary, X-ray, NMR, and EPR spectroscopic data strongly support the proposal that **6** and $\mathbf{6}^{\bullet+}$ are best formulated as RhNC metallacycles. In such a formulation, the interaction of the filled π(C–N) orbital (polarized towards the N atom) with unoccupied metal orbitals represents the Rh–N bond, and the interaction of the unoccupied π*(C–N) orbital (polarized towards the C atom) with occupied metal orbitals represents the Rh–C bond, which lies higher in energy. Therefore, oxidation of **6** mainly affects the Rh–C bond, and consequently the spin population at the carbon atom in $\mathbf{6}^{\bullet+}$ is significant, but very low at the nitrogen atom.

It has been convincingly demonstrated that constraints imposed by the ligand sphere can be used to control the redox potential of transition-metal complexes,[18] and we have reported that four-coordinate d^8 Rh complexes have large negative reduction potentials when the ligand sphere is not flexible enough to allow for a tetrahedral distortion.[19] However, as a result of a lack of suitable reference compounds, the present study does not allow the firm conclusion that small-ring metalla-heterocycles are more easily oxidized than corresponding larger-ring complexes or comparable acyclic compounds, and it remains an open question whether compounds such as **6** are strained molecules. Certainly, the coordination of the $C{=}C_{trop}$ units to the metal center also contributes to the low oxidation potential of **6** and the high stability of its radical cation $\mathbf{6}^{\bullet+}$.[20] An assignment of an oxidation state to the metal center in $\mathbf{6}^{\bullet+}$ is not meaningful,[21] and this complex is best described as a radical with a delocalized unpaired electron.

Experimental Section

Selected spectroscopic data of diagnostic value are given; for details, see the Supporting Information.

3: CH_2Cl_2 (10 mL) and THF (10 mL) were added to [RhCl(trop$_2$NMe)(PPh_3)] (162 mg, 0.200 mmol) and $AgSO_3CF_3$ (51 mg, 0.200 mmol). The resulting red suspension was stirred at room temperature for 1 h and filtered over celite to remove AgCl. The solvents were evaporated in vacuo, and the residue was recrystallized from CH_2Cl_2/hexanes to yield **3** (175 mg, 0.189 mmol, 94%) as red needles. M.p. > 190 °C (decomp); ^{1}H NMR (300.1 MHz, CD_2Cl_2): $\delta =$ 1.85 (d, $^4J_{PH} = 2.9$ Hz, 3H, NCH_3), 4.88 (dd, $^3J_{HH} = 8.9$ Hz, $^3J_{PH} =$ 2.0 Hz, 2H, CH_{olefin}), 6.61 ppm (ddd, $^3J_{HH} = 8.9$ Hz, $^3J_{PH} = 2.9$ Hz, $^2J_{RhH} = 2.9$ Hz, 2H, CH_{olefin}); ^{13}C NMR (75.5 MHz, CD_2Cl_2): $\delta = 44.6$ (s, NCH_3), 78.6 (d, $^1J_{RhC} = 7.3$ Hz, CH_{olefin}), 88.5 ppm (d, $^1J_{RhC} =$ 13.1 Hz, CH_{olefin}); ^{31}P NMR (121.5 MHz, CD_2Cl_2): $\delta = 39.2$ ppm (d, $^1J_{RhP} = 138$ Hz); ^{103}Rh NMR (12.6 MHz, $CDCl_3$): $\delta = 1272$ ppm (d, $^1J_{RhP} = 138$ Hz); HRMS (MALDI): *m/z*: 776.1975 (calcd for $C_{49}H_{40}NPRh^+$: 776.1948).

6: A solution of KO*t*Bu (18.2 mg, 0.162 mmol) in THF (2 mL) was added to a suspension of **3** (150 mg, 0.162 mmol) in THF (5 mL). The resulting orange solution was filtered over a plug of alumina and concentrated to 1 mL under reduced pressure. The product crystallized upon addition of toluene (1 mL) and hexanes (10 mL). The mother liquor was decanted, and orange crystals of **6** were dried in vacuo. Yield: 88 mg (0.114 mmol, 70%); m.p. > 165 °C (decomp); ^{1}H NMR (400.1 MHz, [D_8]THF): $\delta = 2.89$ (dd, $^3J_{PH} = 3.3$ Hz, $^2J_{RhH} =$ 2.0 Hz, 2H, CH_2), 3.83 (ddd, $^3J_{HH} = 9.5$ Hz, $^3J_{PH} = 8.5$ Hz, $^2J_{RhH} =$ 1.5 Hz, 2H, CH_{olefin}), 4.37 ppm (dd, $^3J_{HH} = 9.5$ Hz, $^2J_{RhH} = 2.0$ Hz, 2H, CH_{olefin}); ^{13}C NMR (62.9 MHz, [D_8]THF): $\delta = 54.7$ (d, $^1J_{RhC} =$ 9.7 Hz, CH_{olefin}), 62.4 (d, $^1J_{RhC} = 17.0$ Hz, CH_2), 63.5 ppm (d, $^1J_{RhC} =$ 8.7 Hz, CH_{olefin}); ^{31}P NMR (162.0 MHz, [D_8]THF): $\delta = 63.8$ ppm (d, $^1J_{RhP} = 185$ Hz); ^{103}Rh NMR (12.6 MHz, [D_8]THF): $\delta = -229$ ppm (d, $^1J_{RhP} = 185$ Hz); HRMS (MALDI): *m/z*: 776.1937 (calcd for $C_{49}H_{40}NPRh^+$: 776.1948); EPR samples of $\mathbf{6}^{\bullet+}$ were prepared by adding a solution containing one equivalent of ferrocenium triflate (5 mM in THF) to a solution of **6** (5 mM in THF). Sample tubes were degassed by three freeze-pump-thaw cycles, sealed, and stored in liquid nitrogen.

Received: December 9, 2005
Revised: January 16, 2006
Published online: April 18, 2006

Keywords: density functional calculations · EPR spectroscopy · heterocycles · redox chemistry · rhodium

[1] Cyclopropanes and strained hydrocarbons: a) P. G. Gassmann, R. Yamaguchi, *Tetrahedron* **1982**, *38*, 1113; b) P. G. Gassmann, R. Yamaguchi, *J. Am. Chem. Soc.* **1979**, *101*, 1308.

[2] Cyclotrisilane: a) Z.-R. Zhang, J. Y. Becker, R. West, *J. Appl. Electrochem.* **1998**, *28*, 517; b) cyclotristannane: I. S. Orlov, A. A. Moiseeva, K. P. Butin, L. R. Sita, M. P. Egorov, O. M. Nefedov, *Mendeleev Commun. Electronic Version* **2002**, *4*, 1; I. S. Orlov, M. P. Egorov, O. M. Nefedov, A. A. Moiseeva, K. P. Butin, D. Ostendorf, M. Weidenbruch, *Mendeleev Commun. Electronic Version* **2002**, *3*, 1.

[3] a) H. Bock, *Angew. Chem.* **1989**, *101*, 1659; *Angew. Chem. Int. Ed. Engl.* **1989**, *28*, 1627; b) M. Driess, H. Grützmacher, *Angew. Chem.* **1996**, *108*, 901; *Angew. Chem. Int. Ed. Engl.* **1996**, *35*, 828.

 © 2006 Wiley-VCH Verlag GmbH & Co. KGaA, Weinheim

[4] T. Büttner, F. Breher, H. Grützmacher, *Chem. Commun.* **2004**, 2820.

[5] P. Maire, T. Büttner, F. Breher, P. Le Floch, H. Grützmacher, *Angew. Chem.* **2005**, *117*, 6477; *Angew. Chem. Int. Ed.* **2005**, *44*, 6318.

[6] **3**·3 CH_2Cl_2: $C_{53}H_{44}Cl_6F_3NO_3PRhS$, red needles, orthorhombic, space group *Pnma*, $a = 23.791(4)$, $b = 17.642(3)$, $c = 12.192(2)$ Å, $V = 5117(1)$ Å^3, $Z = 4$, $\rho_{calcd} = 1.530$ Mg m^{-3}, $Mo_{K\alpha}$, 200 K, $2\theta_{max} = 52.74°$, 30414 reflections, 5403 independent ($R_{int} = 0.0679$), Patterson, empirical absorption correction SADABS (version 2.03), refinement against full matrix (versus F^2) with SHELXTL (version 6.12) and SHELXL-97, 341 parameters, $R1 = 0.0598$, $wR2 = 0.1568$ (all data), max./min. residual electron density 1.339/−1.624 e Å^{-3}. **6**·toluene: $C_{56}H_{47}NPRh$, orange crystals, orthorhombic, space group *Pnma*, $a = 25.397(1)$, $b = 13.634(1)$, $c = 12.052(1)$ Å, $V = 4173.0(4)$ Å^3, $Z = 4$, $\rho_{calcd} = 1.381$ Mg m^{-3}, $Mo_{K\alpha}$, 250 K , $2\theta_{max} = 52.74°$, 25675 reflections, 4450 independent ($R_{int} = 0.0711$), direct methods, refinement against full matrix (versus F^2) with SHELXTL (version 6.12) and SHELXL-97, 291 parameters, $R1 = 0.0415$, $wR2 = 0.0933$ (all data), max./min. residual electron density 0.823/−0.594 e Å^{-3}. CCDC-290105 (**3**) and CCDC-290104 (**6**) contain the supplementary crystallographic data for this paper. These data can be obtained free of charge from The Cambridge Crystallographic Data Centre via www.ccdc.cam.ac.uk/data_request/cif. For further details, see also the Supporting Information.

[7] a) M. Ogasawara, D. Huang, W. E. Streib, J. C. Huffman, N. Gallego-Planas, F. Maseras, O. Eisenstein, K. G. Caulton, *J. Am. Chem. Soc.* **1997**, *119*, 8642, and references therein; related C_{2v} structures were found by IR spectroscopy and calculations for the carbonyl complexes $[M(CO)_4]$ (M = Fe, Ru, Os; isolated only at very low temperatures in inert matrices): b) M. Poliakoff, J. J. Turner, *J. Chem. Soc. Dalton Trans.* **1974**, 2276; c) M = Ru: P. L. Bogdan, E. Weitz, *J. Am. Chem. Soc.* **1989**, *111*, 3163; d) J. Li, G. Schreckenbach, T. Ziegler, *J. Am. Chem. Soc.* **1995**, *117*, 486; also for $[RhH(CO)_3]$ and *trans*-$[RhH(CO)_2(PH_3)]$, possible intermediates in hydroformylation reactions, nonplanar structures were calculated, but the distortions are much smaller: e) R. Schmid, W. A. Herrmann, G. Frenking, *Organometallics* **1997**, *16*, 701.

[8] For a recent review, see: G. Frenking, K. Wichmann, N. Fröhlich, C. Loschen, M. Lein, J. Frunzke, V. M. Rayón, *Coord. Chem. Rev.* **2003**, *238–239*, 55.

[9] See, for example: S. Hollenstein, T. Laube, *Angew. Chem.* **1990**, *102*, 194; *Angew. Chem. Int. Ed. Engl.* **1990**, *29*, 188.

[10] See, for example: S. Brückner, L. Malpezzi, A. V. Prosyanik, S. V. Bondarenko, *Acta Crystallogr. Sect. C* **1985**, *41*, 215.

[11] CoNC heterocycles: a) R. Dreos, A. Felluga, G. Nardin, L. Randaccio, G. Tauzher, *Organometallics* **2003**, *22*, 2486, and references therein; b) R. M. Hartshorn, S. G. Telfer, *J. Chem. Soc. Dalton Trans.* **2000**, 2801; c) D. M. Tonei, L.-J. Baker, P. J. Brothers, G. R. Clark, D. C. Ware, *Chem. Commun.* **1998**, 2593; d) L. G. Marzilli, S. M. Polson, L. Hansen, S. J. Moore, P. A. Marzilli, *Inorg. Chem.* **1997**, *36*, 3854; e) ZrNC heterocycle: J. Pflug, A. Bertuleit, G. Kehr, R. Fröhlich, G. Erker, *Organometallics* **1999**, *18*, 3818; f) PdNC heterocycle: C. C. Lu, J. C. Peters, *J. Am. Chem. Soc.* **2004**, *126*, 15818.

[12] For comparison, the neutral pentacoordinate 18-electron complex **2** is oxidized at +0.33 V (in THF, 0.1 M nBu_4NPF_6), the cationic complex **3** at +0.26 V (in 5:1 THF/CH_2Cl_2, 0.1 M nBu_4NPF_6), and the labile pentacoordinate 18-electron complex $[Rh(MeCN)(trop_2NMe)(PPh_3)]^+$ ($K \approx 4$ L mol^{-1}) at +0.753 V (in MeCN, 0.1 M nBu_4NPF_6).

[13] A. Schweiger, G. Jeschke, *Principles of Pulse Electron Paramagnetic Resonance*, Oxford Press, Oxford, **2001**.

[14] The decomposition of $\mathbf{6}^{\bullet+}$ gives about 20% $[Rh(trop_2NMe)(PPh_3)]OTf$ (**3**) and three other rhodium phosphane complexes of unknown structure.

[15] The poor resolution is probably a result of considerable g strain caused by a distribution of different molecular conformations and poor glass formation in frozen solution.

[16] DFT calculations were performed with the Amsterdam Density Functional (ADF 2005.01) package. Details are given in the Supporting Information.

[17] J. R. Morton, K. F. Preston, *J. Magn. Reson.* **1978**, *30*, 577.

[18] The classical way to influence the redox potential of a transition-metal complex is to destabilize the ground-state structure of one partner in a redox couple. For examples of this strategy, see: a) C. O. Dietrich-Buchecker, J. Guilhem, J.-M. Kern, C. Pascard, J.-P. Sauvage, *Inorg. Chem.* **1994**, *33*, 3498, and references therein; b) C. Dietrich-Buchecker, J.-P. Sauvage, J.-M. Kern, *J. Am. Chem. Soc.* **1989**, *111*, 7791.

[19] C. Laporte, F. Breher, J. Geier, J. Harmer, A. Schweiger, H. Grützmacher, *Angew. Chem.* **2004**, *116*, 2621; *Angew. Chem. Int. Ed.* **2004**, *43*, 2567.

[20] Olefins as non-innocent ligands in Ir^{II} compounds: D. G. H. Hetterscheid, J. Kaiser, E. Reijerse, T. P. J. Peters, S. Thewissen, A. N. J. Blok, J. M. M. Smits, R. de Gelder, B. de Bruin, *J. Am. Chem. Soc.* **2005**, *127*, 1895; D. G. H. Hetterscheid, M. Bens, B. de Bruin, *Dalton Trans.* **2005**, *5*, 979.

[21] Formally, $\mathbf{6}^{\bullet+}$ could be described as a Rh^{II} complex, but the g values of such complexes are significantly different: K. K. Pandey, *Coord. Chem. Rev.* **1992**, *121*, 1.

 © 2006 Wiley-VCH Verlag GmbH & Co. KGaA, Weinheim

Silicon Ligands

DOI: 10.1002/anie.200600338

A (Tetrasilacyclobutadiene)tricarbonyliron Complex [{η^4-(tBu$_2$MeSi)$_4$Si$_4$}Fe(CO)$_3$]: The Silicon Cousin of Pettit's (Cyclobutadiene)tricarbonyliron Complex [(η^4-H$_4$C$_4$)Fe(CO)$_3$]**

*Kazunori Takanashi, Vladimir Ya. Lee, Masaaki Ichinohe, and Akira Sekiguchi**

The story of the (cyclobutadiene)tricarbonyliron complex is one of the most intriguing in the field of transition-metal chemistry.[1] The existence of this complex was perspica-

[*] Prof. Dr. A. Sekiguchi
Department of Chemistry
Graduate School of Pure and Applied Sciences
University of Tsukuba
Tsukuba, Ibaraki 305-8571 (Japan)
Fax: (+81) 29-853-4314
E-mail: sekiguch@staff.chem.tsukuba.ac.jp
Dipl.-Chem. K. Takanashi, Dr. V. Ya. Lee, Dr. M. Ichinohe
Department of Chemistry
Graduate School of Pure and Applied Sciences
University of Tsukuba
Tsukuba, Ibaraki 305-8571 (Japan)

[**] This work was supported by Grants-in-Aid for Scientific Research (Nos. 14078204, 16205008, 17655014) from the Ministry of Education, Culture, Sports, Science, and Technology and the COE (Center of Excellence) program.

© 2006 Wiley-VCH Verlag GmbH & Co. KGaA, Weinheim

ciously predicted by Longuet-Higgins and Orgel in 1956,[2a] and its tetraphenyl derivative $[(Ph_4C_4)Fe(CO)_3]$ (**1a**) was

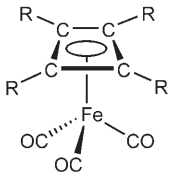

1a: R = Ph
1b: R = H
1c: R = $SiMe_3$

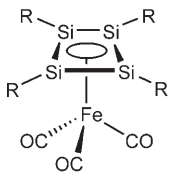

2a: R = $SiMetBu_2$
2b: R = $SiMe_3$

synthesized in 1959 by Hübel and Braye.[2b] The crystal structure of **1a** was determined by Dodge and Schomaker in 1960.[2c] The saga of the cyclobutadiene complexes reached its culmination in 1965, when Pettit and co-workers reported the brilliant discovery of the parent unsubstituted compound $[(H_4C_4)Fe(CO)_3]$ (**1b**).[2d] As another breakthrough development in the chemistry of this stable 18-electron complex, Pettit and co-workers subsequently reported the remarkable aromaticity of **1b**, as manifested in a number of its electrophilic aromatic-substitution reactions.[2e] Moreover, the oxidation of **1b** with ceric ammonium nitrate resulted in the generation of the transient free cyclobutadiene, an elusive antiaromatic 4π-electron species.[2f] Since these findings, the chemistry of **1b** and its derivatives has been developed extensively in all its aspects. However, its analogues incorporating the heavier Group 14 elements into the cyclobutadiene skeleton have remained unknown.[3] Herein, we report the discovery of the (tetrasilacyclobutadiene)tricarbonyliron complex $[\{\eta^4\text{-}(tBu_2MeSi)_4Si_4\}Fe(CO)_3]$ (**2a**), which represents the first heavy analogue of Pettit's complex $[(H_4C_4)Fe(CO)_3]$ (**1b**) and also the first neutral transition-metal complex featuring a η^4-tetrasilacyclobutadiene ligand.

For the synthesis of the target iron complex, the key precursor 3,4-dibromo-1,2,3,4-tetrakis(di-*tert*-butylmethylsilyl)cyclotetrasilene $R_4Si_4Br_2$ (**3**, R = $SiMetBu_2$) was prepared in 81% yield by the reduction of the tetrabromocyclotetrasilane $R_4Si_4Br_4$ **4**[4] with 2.1 equivalents of KC_8 in THF (Scheme 1). The ^{29}Si NMR spectrum of **3** revealed a characteristic downfield resonance of the endocyclic double-bonded Si atoms at $\delta = 141.4$ ppm.[5] The subsequent reaction of **3** with an excess of $Na_2[Fe(CO)_4]$ in THF at room temeperature for two days resulted in the formation of the desired complex $[(\eta^4\text{-}R_4Si_4)Fe(CO)_3]$ **2a**, which was isolated as air- and moisture-sensitive pale yellow crystals in 42% yield (Scheme 1). The ^1H and ^{13}C NMR spectra of **2a** both exhibited only one set of signals for each of the Me and *t*Bu groups, thus indicating the magnetic equivalence of all the tBu_2MeSi substituents, which can be attributed to the free (or very low-energy-barrier) rotation about the axis formed by the Si_4 ring center and the Fe atom. The resonance of the CO ligands was observed in the ^{13}C NMR spectrum of **2a** at $\delta = 221.1$ ppm, which is shifted slightly downfield from corresponding resonance signals of typical iron carbonyl complexes.[6] The skeletal Si atoms of the tetrasilacyclobutadiene ligand resonate in the ^{29}Si NMR spectrum at $\delta = -15.8$ ppm, which is far outside the low-field region anticipated for a conjugated tetrasilacyclobutadiene system.[7] Such great shielding can be attributed to an appreciable degree of 3d(Fe)–$\pi^*(Si_4)$ π back donation, which is facilitated by the low-lying LUMO of the Si_4 ligand. GIAO calculations produced a similar value of $\delta = -21.9$ ppm for the ^{29}Si NMR resonance signal of the skeletal Si atoms in the model compound **2b**.[8]

The crystal structure of **2a** is presented in Figure 1 and exhibits several unusual structural features.[9] First, the Si_4 ring is tetrahapto-coordinated to the Fe atom and is nearly planar,

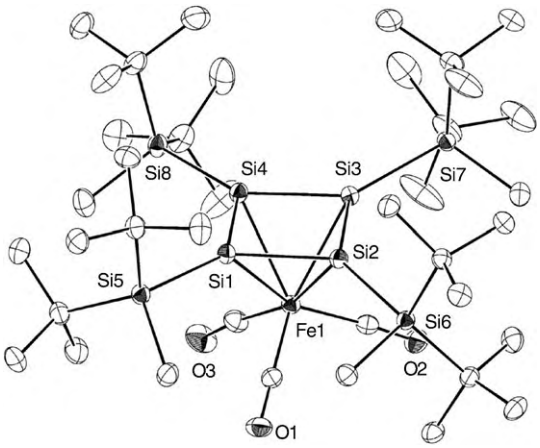

Figure 1. Crystal structure of **2a** (ORTEP plot; thermal ellipsoids are shown at 30% probability; hydrogen atoms are omitted). Selected bond lengths [Å] and angles [°]: Si1-Si2 2.2802(7), Si2-Si3 2.2702(7), Si3-Si4 2.2610(7), Si1-Si4 2.2742(7), Si1-Fe1 2.4976(6), Si2-Fe1 2.5130(6), Si3-Fe1 2.5050(6), Si4-Fe1 2.4853(6), Si1-Si5 2.3883(7), Si2-Si6 2.3937(7), Si3-Si7 2.3835(7), Si4-Si8 2.3926(7); Si2-Si1-Si4 90.65(3), Si1-Si2-Si3 88.85(2), Si2-Si3-Si4 91.24(3), Si1-Si4-Si3 89.23(3). Dihedral angle [°]: Si1-Si2-Si3/Si1-Si3-Si4 1.79(2).

with the sum of the interior bond angles being 359.97° (folding angle: 1.79°). The endocyclic Si–Si bond lengths in the Si_4 ring range from 2.2610(7) to 2.2802(7) Å; these values lie between the typical Si–Si single-bond lengths (av: 2.34 Å) and Si–Si double-bond lengths (av: 2.20 Å).[10] The Si–Fe bonds in **2a** (2.4853(6)–2.5130(6) Å) are longer than those in silyl–iron complexes (2.197(3)–2.360(2) Å)[11] as well as in the recently reported complex $[\{\eta^2\text{-}(tBu_2MeSi)ClSi{=}SiCl\text{-}(SiMetBu_2)\}Fe(CO)_4]$ (2.4269(7) and 2.4447(5) Å),[12] and this difference can be explained in terms of the higher coordination hapticity of the R_4Si_4 ligand in **2a**. The Si_4 skeleton has a nearly regular square shape, with

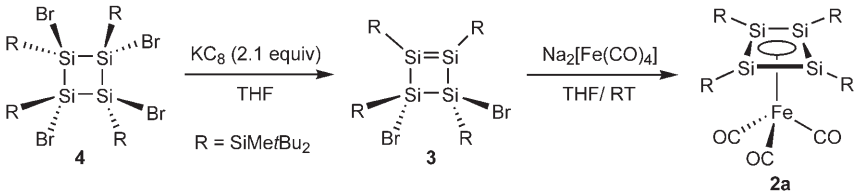

Scheme 1. Synthesis of **3** and **2a**.

© 2006 Wiley-VCH Verlag GmbH & Co. KGaA, Weinheim

one of the skeletal Si–Si bonds longer (Si1–Si2 2.2802(7) Å) and another slightly shorter (Si3–Si4 2.2610(7) Å) than the other two (Si2–Si3 2.2702(7), Si1–Si4 2.2742(7) Å; Figure 1, Table 1). Such a small departure of the tetrasilacyclobutadiene ring from square geometry likely results from the staggered conformation (12.7°, Figure 2) of the CO ligands and Si_4 ring atoms in **2a**, in which the Si1–Si2 bond is superimposed by one of the carbonyl groups. In contrast, the calculated structure **2b** has an eclipsed conformation (3.5°) of the CO ligands and Si_4 ring atoms as a result of the lower degree of steric bulk of the Me_3Si substituents (Figure 2).[13,14] The spatial orientation of the bulky tBu_2MeSi substituents in **2a** is dictated by the degree of their steric interactions with the CO ligands; the smaller Me group of each of the tBu_2MeSi substituents is uniformly directed toward the carbonyl groups to minimize steric repulsion. The silyl Si atoms are situated insignificantly outside the mean plane of the Si_4 ring (Si5 0.179, Si7 0.403, Si8 0.047 Å above the mean plane; Si6 0.246 Å below the mean plane).

Table 1: Experimental and calculated bond lengths [Å] and angles [°] of the Si_4 skeleton of complexes **2a** and **2b**.

Bond lengths	2a	2b	Bond angles	2a	2b
Si1–Si2	2.2802(7)	2.265	Si2-Si1-Si4	90.65(3)	90.1
Si2–Si3	2.2702(7)	2.266	Si1-Si2-Si3	88.85(2)	89.7
Si3–Si4	2.2610(7)	2.258	Si2-Si3-Si4	91.24(3)	90.1
Si4–Si1	2.2742(7)	2.258	Si1-Si4-Si3	89.23(3)	90.1

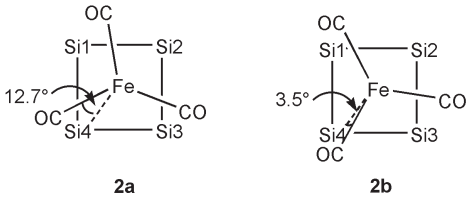

Figure 2. Comparison of ligand conformations in **2a** and **2b**.

The nearly square-planar geometry exhibited by the Si_4 ligand is quite typical for the cyclobutadiene transition-metal complexes.[1] In sharp contrast, the ionic complex $[\{K(diglyme)_2(thf)\}^+\{(R_4Si_4)Co(CO)_2\}^-]$ (**5**, $R = SiMetBu_2$)[3k] previously reported by us is a very particular case in which the geometry is greatly affected by the presence of a negative charge. Thus, the geometry of the same R_4Si_4 ligand in the Co complex has been forced to change from the common square-planar geometry to the rather unusual rectangular-planar geometry as a result of the partial delocalization of the negative charge over the R_4Si_4 ligand. This observation is consistent with the ^{29}Si NMR resonances of the skeletal Si atoms in each complex ($\delta = -43.2$ ppm for **5**, $\delta = -15.8$ ppm for **2a**). Such partial charge transfer is also clearly evident from the higher degree of π back donation from the transition-metal center to the CO ligands in the case of previously reported Co complex **5** compared to the newly synthesized Fe complex **2a**, as revealed by the lower value of the CO stretching frequency for **5** (1870 cm^{-1}) in comparison to those of **2a** (1922 and 1973 cm^{-1}). Another important factor affecting the overall geometry of the R_4Si_4 ligand in the Co complex **5**[3k] is the spatial orientation of the two CO groups, which are superimposed by the two opposite skeletal Si–Si bonds. Undoubtedly, such a conformation would result in the stretching of the eclipsed Si–Si bonds and, consequently, in the occurrence of the R_4Si_4 ligand in the preferential rectangular form.[15]

As in the parent complex $[(H_4C_4)Fe(CO)_3]$,[1] one of the most important ligand-to-metal interactions in the model compound **2b** between the singly occupied π orbitals of the tetrasilacyclobutadiene ligand and the d_{xz} and d_{yz} orbitals of the Fe atom results in the formation of two pairs of doubly degenerate bonding (HOMO−1 and HOMO) and antibonding (LUMO and LUMO+1) orbitals (Figure 3). The HOMO and LUMO energy levels of **2b** are higher and lower, respectively, than the corresponding levels of the hypothetical carbon-ring analogue $[\{(Me_3Si)_4C_4\}Fe(CO)_3]$ (**1c**; HOMO: **2b** −5.59, **1c** −6.30 eV; LUMO: **2b** −0.98, **1c** −0.66 eV). This result gives rise to the smaller HOMO–LUMO energy gap for **2b** (4.61 eV) compared with that of **1c** (5.64 eV). The higher HOMO level of the Si_4 ligand compared with its carbon counterpart is the likely reason for the stronger π-donating ability of the tetrasilacyclobutadiene ligand, which in turn brings about the enhanced π back donation from the Fe atom to the carbonyl ligands. This difference is clearly apparent in the lower CO stretching frequencies in the IR spectrum of **2a** (1922 and 1973 cm^{-1}) compared with those of **1b** (1985 and 2055 cm^{-1}).

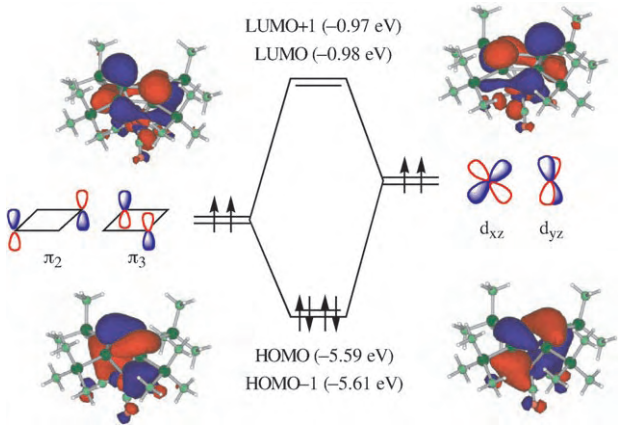

Figure 3. Calculated frontier molecular orbitals of **2b** (B3PW91/6-31G(d) level).

The novel complex **2a** possesses some degree of aromaticity, which was estimated by nucleus-independent chemical shift (NICS)[16] calculations. The NICS(1) for the model compound **2b** was calculated at 1 Å above the Si_4 ring center (on the side opposite to the Fe center) to be −12.5, which points to the inclusion of this complex in the class of organometallic compounds featuring three-dimensional aromaticity, as in Pettit's complex $[(H_4C_4)Fe(CO)_3]$.

 © 2006 Wiley-VCH Verlag GmbH & Co. KGaA, Weinheim

Experimental Section

3: Compound **4**[4] (80 mg, 0.075 mmol) and KC_8 (22 mg, 0.163 mmol) were placed in a reaction tube with a magnetic stirrer. Oxygen-free, dry THF (2 mL) was introduced into the reaction tube by vacuum transfer, and the reaction mixture was stirred at room temperature to produce a yellow solution over 3 h. The solvent was removed in vacuo, and the residue was extracted with degassed hexane. The mixture was filtered to remove the graphite and inorganic salt, and the solution was cooled to −30 °C to produce yellow crystals of **3** (55 mg, 81 %). M.p. 153–155 °C; ^{1}H NMR (400.2 MHz, [D$_6$]benzene, TMS): $\delta = 0.40$ (s, 6H), 0.51 (s, 6H), 1.15 (s, 18H), 1.17 (s, 18H), 1.32 (s, 18H), 1.40 ppm (s, 18H); ^{13}C{^{1}H} NMR (100.6 MHz, [D$_6$]benzene, TMS): $\delta = -5.1$, −4.1, 21.6, 21.9, 22.66, 22.72, 29.7, 30.1, 30.5, 30.7 ppm; ^{29}Si{^{1}H} NMR (79.5 MHz, [D$_6$]benzene, TMS): $\delta = -23.2$ (skeletal Si), 18.2, 26.8, 141.4 (skeletal Si); UV/Vis (hexane): $\lambda_{max}(\varepsilon) =$ 432 (3300), 326 (4700), 288 (5400), 277 nm (47 000). Elemental analysis (%) calcd for $C_{36}H_{84}Br_2Si_8$: C 47.96, H 9.39; found: C 47.71, H 9.22.

2a: Compound **3** (67 mg, 0.074 mmol) and $Na_2[Fe(CO)_4]$ (80 mg, 0.374 mmol) were placed in a reaction tube with a magnetic stirrer. THF (2 mL) was introduced into the reaction tube by vacuum transfer, and the reaction mixture was stirred at room temperature for 2 days to produce an orange solution. The solvent was removed in vacuo, and the residue was extracted with degassed hexane. The mixture was filtered to remove the salt and residual $Na_2[Fe(CO)_4]$, and the solution was cooled to −30 °C to produce pale yellow crystals of **2a** (28 mg, 42 %). M.p. > 184 °C (decomp); ^{1}H NMR (400.2 MHz, [D$_8$]THF, TMS): $\delta = 0.32$ (s, 12H), 1.18 ppm (s, 72H); ^{13}C{^{1}H} NMR (100.6 MHz, [D$_8$]THF, TMS): $\delta = -3.6$, 22.3, 30.5, 221.1 ppm; ^{29}Si{^{1}H} NMR (79.5 MHz, [D$_8$]THF, TMS): $\delta = -15.8$ (skeletal Si), 24.6 ppm; IR (KBr): $\tilde{\nu}_{CO} = 1973$, 1922 cm^{-1}. Elemental analysis (%) calcd for $C_{39}H_{84}FeO_3Si_8$: C 53.13, H 9.60; found: C 53.56, H 9.61.

Received: January 26, 2006
Revised: February 24, 2006
Published online: April 19, 2006

Keywords: aromaticity · iron · silicon · small ring systems · structure elucidation

[1] a) A. Efraty, *Chem. Rev.* **1977**, *77*, 691; b) D. Seyferth, *Organometallics* **2003**, *22*, 2.

[2] a) H. C. Longuet-Higgins, L. E. Orgel, *J. Chem. Soc.* **1956**, 1969; b) W. Hübel, E. H. Braye, *J. Inorg. Nucl. Chem.* **1959**, *10*, 250; c) R. P. Dodge, V. Schomaker, *Nature* **1960**, *186*, 798; d) G. F. Emerson, L. Watts, R. Pettit, *J. Am. Chem. Soc.* **1965**, *87*, 131; e) J. D. Fitzpatrick, L. Watts, G. F. Emerson, R. Pettit, *J. Am. Chem. Soc.* **1965**, *87*, 3254; f) L. Watts, J. D. Fitzpatrick, R. Pettit, *J. Am. Chem. Soc.* **1965**, *87*, 3253.

[3] Several heavy analogues of the cyclic polyenes have recently been utilized as ligands in transition-metal complexes; heavy cyclopentadienyl ligands: a) W. P. Freeman, T. D. Tilley, A. L. Rheingold, R. L. Ostrander, *Angew. Chem.* **1993**, *105*, 1841; *Angew. Chem. Int. Ed. Engl.* **1993**, *32*, 1744; b) W. P. Freeman, T. D. Tilley, A. L. Rheingold, *J. Am. Chem. Soc.* **1994**, *116*, 8428; c) J. M. Dysard, T. D. Tilley, *J. Am. Chem. Soc.* **1998**, *120*, 8245; d) J. M. Dysard, T. D. Tilley, *J. Am. Chem. Soc.* **2000**, *122*, 3097; e) J. M. Dysard, T. D. Tilley, *Organometallics* **2000**, *19*, 2671; f) W. P. Freeman, J. M. Dysard, T. D. Tilley, A. L. Rheingold, *Organometallics* **2002**, *21*, 1734; heavy arene ligands: g) N. Nakata, N. Takeda, N. Tokitoh, *Angew. Chem.* **2003**, *115*, 119; *Angew. Chem. Int. Ed.* **2003**, *42*, 115; h) A. Shinohara, N. Takeda, T. Sasamori, T. Matsumoto, N. Tokitoh, *Organometallics* **2005**, *24*, 6141; i) Y. Mizuhata, T. Sasamori, N. Takeda, N. Tokitoh, *J. Am. Chem. Soc.* **2006**, *128*, 1050; heavy cyclobutadiene ligands: j) Y. Kon, K. Sakamoto, C. Kabuto, M. Kira, *Organometallics* **2005**, *24*, 1407; k) K. Takanashi, V. Ya. Lee, T. Matsuno, M. Ichinohe, A. Sekiguchi, *J. Am. Chem. Soc.* **2005**, *127*, 5768.

[4] V. Ya. Lee, K. Takanashi, T. Matsuno, M. Ichinohe, A. Sekiguchi, *J. Am. Chem. Soc.* **2004**, *126*, 4758.

[5] Reported ^{29}Si NMR chemical shifts of double-bonded Si atoms incorporated in Si_4 four-membered rings are in the range $\delta =$ 158.1–182.7 ppm: a) M. Kira, T. Iwamoto, C. Kabuto, *J. Am. Chem. Soc.* **1996**, *118*, 10303; b) N. Wiberg, H. Auer, H. Nöth, J. Knizek, K. Polborn, *Angew. Chem.* **1998**, *110*, 3030; *Angew. Chem. Int. Ed.* **1998**, *37*, 2869; c) A. Sekiguchi, T. Matsuno, M. Ichinohe, *J. Am. Chem. Soc.* **2001**, *123*, 12436; d) see reference [4].

[6] A. F. Hill, *Organotransition Metal Chemistry*, Wiley, New York, **2002**.

[7] The skeletal C atoms of cyclobutadiene derivatives are strongly deshielded: a) $\delta = 172.1$ ppm for tetrakis(trimethylsilyl)cyclobutadiene: A. Sekiguchi, M. Tanaka, T. Matsuo, H. Watanabe, *Angew. Chem.* **2001**, *113*, 1721; *Angew. Chem. Int. Ed.* **2001**, *40*, 1675; b) $\delta = 159.2$ ppm for a 1,2-digermacyclobutadiene derivative: C. Cui, M. M. Olmstead, P. P. Power, *J. Am. Chem. Soc.* **2004**, *126*, 5062.

[8] All theoretical calculations were performed with the GAUSSIAN 98 program at the B3PW91/6-31G(d) level.

[9] Crystal structure analysis of **2a**: Single crystals of **2a** for X-ray diffraction were grown from a hexane solution. The X-ray crystallographic experiments were performed on a MacScience DIP2030 image plate diffractometer equipped with graphite-monochromated $Mo_{K\alpha}$ radiation ($\lambda = 0.71070$ Å). Crystal data for **2a** at 120 K: $M_r = 881.63$, monoclinic, space group $P2_1/c$, $a =$ 8.9380(3), $b = 23.9770(4)$, $c = 23.9410(8)$ Å, $\beta = 94.3610(10)°$, $V = 5115.9(3)$ Å^3, $Z = 4$, $\rho_{calcd} = 1.145$ g cm^{-3}, GOF = 1.039. The final R factor was 0.0420 ($R_w = 0.1196$ for all data) for 11720 reflections with $I_o > 2\sigma(I_o)$. The structure was solved by direct methods and refined by full-matrix least squares with the SHELXL-97 program. CCDC-296097 (**2a**) contains the supplementary crystallographic data for this paper. These data can be obtained free of charge from The Cambridge Crystallographic Data Centre via www.ccdc.cam.ac.uk/data_request/cif.

[10] M. Kaftory, M. Kapon, M. Botoshansky, in *The Chemistry of Organic Silicon Compounds*, *Vol. 2*, Part 1 (Eds.: Z. Rappoport, Y. Apeloig), Wiley, Chichester, **1998**, chapter 5.

[11] J. Y. Corey, J. Braddock-Wilking, *Chem. Rev.* **1999**, *99*, 175.

[12] H. Hashimoto, K. Suzuki, W. Setaka, C. Kabuto, M. Kira, *J. Am. Chem. Soc.* **2004**, *126*, 13628.

[13] J. W. Chinn, M. B. Hall, *J. Am. Chem. Soc.* **1983**, *105*, 4930.

[14] This conformational feature of **2a** is distinctly different from the staggered conformation previously reported by us for the anionic Co complex **5**, in which the Si_4 ring has a rectangular-planar geometry with two long (2.3154(8), 2.3081(8) Å) and two short (2.2570(9), 2.2588(9) Å) skeletal Si–Si bonds: see reference [3k].

[15] In our computations on the model compound [(η^4-H_4Si_4)$Fe(CO)_3$], the structure with a rectangular-planar η^4-H_4Si_4 ligand as a minimum-energy structure was not located, thus confirming that for such neutral complexes, the nearly square-planar geometry of the tetrasilacyclobutadiene ligand is more favorable.

[16] P. von R. Schleyer, C. Maerker, A. Dransfeld, H. Jiao, N. J. R. van E. Hommes, *J. Am. Chem. Soc.* **1996**, *118*, 6317.

 © 2006 Wiley-VCH Verlag GmbH & Co. KGaA, Weinheim

Hemifullerenes

DOI: 10.1002/anie.200503542

$C_{30}H_{12}^{6-}$: Self-Aggregation, High Charge Density, and Pyramidalization in a Supramolecular Structure of a Supercharged Hemifullerene**

Noach Treitel, Tuvia Sheradsky, Lingqing Peng, Lawrence T. Scott, and Mordecai Rabinovitz**

Although C_{60} is readily available from the vaporization of graphite and the combustion of hydrocarbons in fuel-rich flames, these methods are unselective and relatively uncontrollable. Considerable progress has been made over the last few years towards the total synthesis of C_{60} in isolable quantities;[1] however, chemical synthesis in bulk amounts remains elusive and challenging even today. One rational approach is the synthesis of two identical $C_{30}H_{12}$ units, which could then be fused together to form the fullerene.[2–4] Thus, the study and synthesis of buckybowls, potential precursors of fullerenes and larger π systems, is essential, and many of them have attained key positions in the literature.[5–7]

The $C_{30}H_{12}$ geodesic polyarene **1** is one of several possible hemifullerene isomers.[6a,d] Considerable effort has been directed toward studies on the ligating properties and reactivity of the smaller fullerene fragment corannulene, $C_{20}H_{10}$,[8] but hardly any transition-metal complexes of $C_{30}H_{12}$ isomers have been prepared. Only recently was the first π complex of **1** with rhodium[9] isolated, and charging of **1** with alkali metals has never been examined.

Self-aggregation into supramolecular structures has also recently found large interest. Supramolecular chemistry plays roles in molecular and chiral recognition,[10] bioorganics and biomimetics,[10i,11] reactivity and catalysis,[10i–k,11c,d,12] and transport.[10j,k,11b,13] A particularly intriguing facet of this field is the ability of alkali metal ions to act as "electrostatic paste" to hold together two or more organic anions.[14,15] Polycyclic aromatic hydrocarbons (PAHs) constructed in a stack are held together by countercharged metal ions that stabilize high negative charges on the anions. As the total electrostatic interaction between PAH anions and alkali metal cations depends on the square of the degree of reduction, it is clear why some PAHs show an inclination to aggregate only at high charges.[16] The PAH anions that do aggregate are typically unstable in solution and tend to precipitate,[14] so higher order stable aggregates with Li^+ ions, even more so with K^+ ions, are scarce.[17] Herein we describe the self-assembly and structure of a unique tetrameric aggregate of hemifullerene hexaanions with potassium cations that has high charge density, pyramidalization, and surprising stability in solution.

Hemifullerene **1** ($C_{30}H_{12}$, Figure 1a) undergoes an extremely slow charging process with potassium metal to give a hexaanion.[18] Quenching of the hexaanion with water[19] cleanly yields a hexahydro derivative ($C_{30}H_{18}$) that is isomeric with **2**,[20] as verified by desorption chemical ionization high resolution mass spectrometry (DCI-HRMS calcd: 379.1487, found: 379.1519). The absence of any other signal in the *m*/*z* 372–389 region indicates that none of the $\mathbf{1}^{6-}$ was quenched back to **1** and confirms that the degree of charge was indeed hexaanionic. The exact structure of the

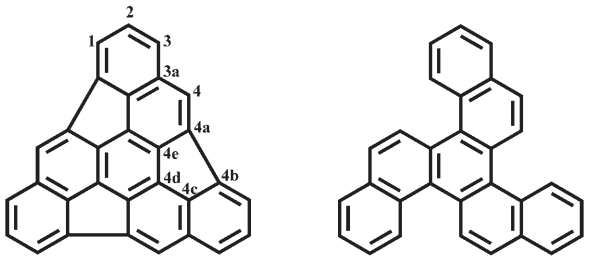

1 **2**

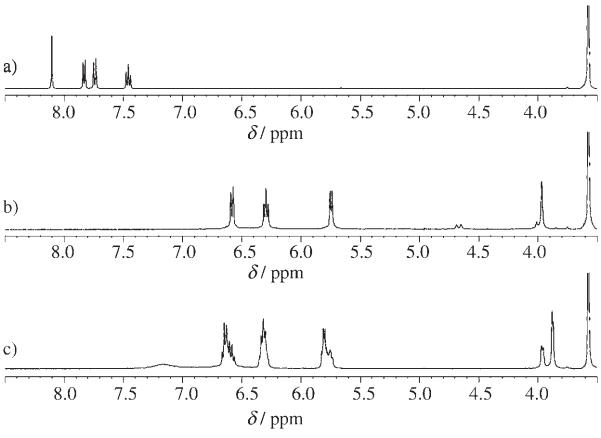

Figure 1. ^{1}H NMR spectra (400.1 MHz, [D$_8$]THF) of a) neutral $C_{30}H_{12}$ (**1**) at 220 K, b) tetramer of $\mathbf{1}^{6-}$ at 270 K, and c) tetramer and additional aggregates of $\mathbf{1}^{6-}$ at room temperature.

[*] N. Treitel, Prof. T. Sheradsky, Prof. M. Rabinovitz
Department of Organic Chemistry and
The Lise Meitner-Minerva Center for Computational Quantum Chemistry
Safra Campus, The Hebrew University of Jerusalem
Givat Ram, Jerusalem 91904 (Israel)
Fax: (+972) 2-652-7547
E-mail: mordecai@vms.huji.ac.il
L. Peng, Prof. L. T. Scott
Department of Chemistry
Boston College
Chestnut Hill, MA 02467-3860 (USA)
Fax: (+1) 617-552-6454
E-mail: lawrence.scott@bc.edu

[**] Financial support from the Lise Meitner-Minerva Center for Computational Quantum Chemistry and the U.S. Department of Energy is gratefully acknowledged. N.T. and M.R. are also indebted to Prof. Silvio Biali for insight and fruitful discussions, Dr. Rachel Perski for assistance with the HRMS experiments, and Dr. David Danovich for support with the computations.

Supporting information for this article is available on the WWW under http://www.angewandte.org or from the author.

 © 2006 Wiley-VCH Verlag GmbH & Co. KGaA, Weinheim

$C_{30}H_{18}$ product obtained is uncertain; however, it is clear from the ^{1}H NMR spectrum that this new species is neither **1** nor **2**.

Reduction of **1** with lithium gives no new diamagnetic species, even after months of contact with the alkali metal, heating, sonication, and/or the aid of corannulene.[21,22] Charging with potassium, on the other hand, gives rise to the stable[23] hexaanion, albeit only after a long period of charging[24] and heating to room temperature (Figure 1b). No other diamagnetic species is observed before the hexaanion is reached.

From molecular orbital calculations on **1**, the LUMO, LUMO+1, and LUMO+2 were found[25] to be effectively degenerate for the neutral hydrocarbon as the degenerate LUMO+1 and LUMO+2 lie only 2.7 kcal mol^{-1} (0.116 eV) above the LUMO. This suggests that every anion from $\mathbf{1}^-$ to $\mathbf{1}^{5-}$ could have significant paramagnetic character and may account for why no other diamagnetic species are observed before the hexaanion.

A hexacharged system for a relatively small carbon framework should not be entirely surprising as $\mathbf{1}^{6-}$ bears six charges over 30 carbon atoms, that is, five carbon atoms per unit charge, precisely as in the corannulene tetraanion[26] (four charges over a C_{20} skeleton). Nevertheless, $\mathbf{1}^{6-}$ does boast a very high absolute degree of charge over a relatively small carbon skeleton and is the smallest PAH hexaanion ever observed.

Charge density calculations from ^{13}C NMR spectroscopy show a K_c value[27,28] for this hexaanion of about 102 ppm/e$^-$. While this value is somewhat smaller than the K_c values derived for other hexacharged systems with aromatic units of similar size,[29,30] one must remember that reduction can induce major changes in the diatropic and/or paratropic ring currents in the molecule, and these also strongly affect the chemical shifts;[28] in such cases K_c may deviate significantly from the "average" value.[28,31]

The new diamagnetic species shows the same number of proton and carbon signals on charging as the neutral compound (four and ten respectively), with a 1:1:1:1 ratio among the proton signals. No lowering of symmetry in the neutral system is seen on charging, no dimerization or aggregation is apparent, and the C_3 symmetry of the system is retained. On reduction, substantial upfield shifts are seen for C-4, H-4, and C-4d (Table 1).

The signal for C-4d is shifted from 147.9 to 95.7, an upfield shift of about 52 ppm, that of H-4 shifts from highly aromatic 8.11 ppm to nonaromatic 3.93 ppm, whereas the corresponding C-4 resonance is shifted upfield by nearly 96 ppm, from the aromatic region of 125.6 ppm to the apparently aliphatic 29.7 ppm. This indicates a charge pattern with extremely high charge density on the above positions. From the ^{13}C NMR spectrum,[27] one calculates nearly a full unit of charge on each of the C-4 carbon atoms, whereas each of the C-4d carbon atoms bears more than 0.5 units of negative charge. Carbon atoms 4d and 4e of the central benzene ring clearly demonstrate the charge-alternation[32] effect (Figure 2). Such

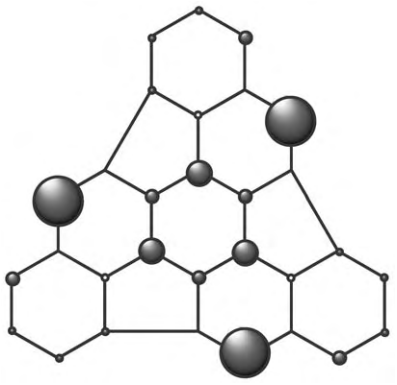

Figure 2. Charge distribution in tetramer of $\mathbf{1}^{6-}$, calculated from ^{13}C NMR shifts.[27] Filled circles represent negative charge, and empty circles positive charge.

a high charge density on the C-4 positions is in fact predicted by DFT calculations at the B3LYP/6-31G*[33–35] level of theory, which show that the HOMO, HOMO−1, and HOMO−2 of $\mathbf{1}^{6-}$ and the LUMO, LUMO+1, and LUMO+2 of **1** all have very large coefficients for the C-4 position.

A striking feature in the NMR spectrum of $\mathbf{1}^{6-}$ is sp^2 coupling for C-1, C-2, and C-3 ($^1J_{CH}$ = 153.3–160.7 Hz) but sp^3 coupling for C-4 ($^1J_{CH}$ = 124.7 Hz). This is the site in the molecule where the chemical shifts of the carbon (29.7 ppm) and hydrogen (3.93 ppm) atoms look more like those of a tetrahedral center than of an unsaturated trigonal center. Together, these data strongly suggest that the C-4 carbon atoms have become pyramidalized[37] in the hexaanion of this $C_{30}H_{12}$.

Table 1: Experimental ^{1}H NMR and ^{13}C NMR shifts for **1** and $\mathbf{1}^{6-}$.[a,b]

	H-1/C-1	H-2/C-2	H-3/C-3	C-3a	H-4/C-4	C-4a	C-4b	C-4c	C-4d	C-4e
^{13}C NMR, neutral	121.1	128.5	127.5	135.6	125.6	144.7	137.8	138.4	147.9	152.8
^{13}C NMR, charged	109.3	118.2	108.1	131.9	29.7	148.6	123.6	155.6	95.7	134.5
$\Delta\delta(^{13}C)$	−11.8	−10.3	−19.4	−3.7	−95.9	+3.9	−14.2	+17.2	−52.2	−18.3
^{1}H NMR, neutral	7.83	7.46	7.74		8.11					
^{1}H NMR, charged	6.56	6.28	5.73		3.93					
$\Delta\delta(^1H)$	−1.27	−1.18	−2.01		−4.18					
Charge on C[36]	−0.115	−0.101	−0.190	−0.036	−0.937	0.038	−0.139	0.168	−0.510	−0.179

[a] 400.1 and 100.6 MHz (^{1}H and ^{13}C NMR, respectively), [D$_8$]THF, 220 K and 270 K for **1** and $\mathbf{1}^{6-}$, respectively. [b] Neutral: $J_{1,2}$ = 7.1, $J_{2,3}$ = 8.1 Hz; hexaanion: $J_{1,2}$ = 7.5, $J_{2,3}$ = 7.2 Hz.

 © 2006 Wiley-VCH Verlag GmbH & Co. KGaA, Weinheim

We considered the possibility that the main factor affecting the C–H coupling is not pyramidalization but rather the presence of an electropositive substituent at this carbon atom (e.g., methyllithium: $^1J_{CH} \approx 98$ Hz vs. methyl chloride: $^1J_{CH} \approx 159$ Hz). However, the small $^1J_{CH}$ in MeLi is derived, at least in part, from a concentration of s-orbital character in the carbon orbital pointing towards the electropositive Li center. This reduces the s-orbital character of the C–H bonds, which in turn reduces $^1J_{CH}$. The rehybridization effect in MeLi is manifested in the strongly contracted H-C-H bond angles (102.3°),[38] which signify amplified pyramidalization at this carbon atom. In light of the $^1J_{CH}$ data for $\mathbf{1}^{6-}$, therefore, it is difficult to avoid the conclusion that the C-4 carbon atoms must have become pyramidalized.

We were initially puzzled by the fact that calculations on bare $\mathbf{1}^{6-}$ at the B3LYP/6-31G* level of theory, with no potassium ions anywhere, show no pyramidalization at any CH site on the rim. The bowl is only slightly flatter than the neutral hydrocarbon, but the C–H bonds do not bend out of the plane defined by the nearest CCC units. Calculations at the same level of theory on $[\mathbf{1}^{6-}/3\,K^+]^{3-}$ with potassium ions "covalently attached" at the three C-4 carbon atoms likewise show no significant pyramidalization at these sites. The potassium ions sit rather far from the carbon atoms, and the C–H bonds do not bend out of plane. From these calculations, it can be inferred that pyramidalization in the hexaanion almost certainly cannot be accounted for by a monomeric species; neither contact-ion pairing nor solvent separation perturbs the planarity of the trigonal carbon atoms. Pyramidalization must therefore be a consequence of some external influence, such as aggregation, in which potassium atoms serve as bridges between hexaanionic units. If the hexaanions do aggregate, however, each unit must be incorporated in the same way relative to the others, so that no new sets of signals are generated in the NMR spectra.

Evidence for aggregation stems not only from the anomalous $^1J_{CH}$ coupling constants but also from the failure of the observed NMR chemical shifts to resemble those expected for a monomeric species. An NMR-GIAO calculation at the B3LYP/6-31G(d) level of theory[33–35,39] on the monomeric hexaanion $\mathbf{1}^{6-}$ with a potassium counterion "covalently attached" (*exo*) at each of the three C-4 positions predicts ^{1}H NMR shifts of $\delta = 5.08$ (H-1), 4.68 (H-2), 5.44 (H-3), and 6.47 ppm (H-4), and ^{13}C NMR shifts of $\delta = 118$ (C-1), 123 (C-2), 127 (C-3), 151 (C-3a), 113 (C-4), 144 (C-4a), 145 (C-4b), 148 (C-4c), 140 (C-4d), and 144 ppm (C-4e). These shifts bear little resemblence to those observed, especially at position 4 (calcd: C-4 113, H-4 6.47; obsd: C-4 29.7, H-4 3.93). NMR-GIAO calculations on the naked hexaanion with no potassium counterions deviate even more from the observed NMR data. Clearly, the NMR spectrum of the observed hexaanion is strongly perturbed by its environment, and the species observed cannot be the simple monomeric hexaanion.

Constructing a concave-concave dimer in which three potassium atoms bridge from the C-4 carbon atoms of one bowl to those of the other yields a complex that is far too crowded to be realistic. A trimer is not possible on graph-theoretical grounds[40] (three bridges emanating from each unit requires an even number of units), but a tetrameric aggregate nicely explains the pyramidalization phenomenon observed in the NMR spectrum. A complex with all concave surfaces facing inward still creates too much crowding, but all concave surfaces facing outward accommodates the experimental results very well (Figure 3). Each potassium cation bonds two hexaanionic units together in a manner that causes the C-4 atoms to pyramidalize. Only in such an aggregate would one expect to find pyramidalization.

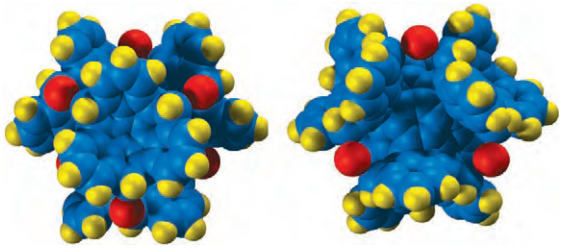

Figure 3. Front and rear views of the proposed tetrameric $[\mathbf{1}^{6-}]_4/24\,K^+$ complex (red K^+, yellow H, blue C). The 18 solvent-separated K^+ ions are not shown.

Note that the data do not exclude the possibility that the observed aggregate could be an even more spectacular superstructure, such as an octamer (cube) or 20-mer (dodecahedron), which are also in agreement with the observed symmetry. However, the tetramer (Figure 3) is the simplest possible structure and should be kinetically more accessible than higher order aggregates (see below).

This picture actually suggests why reduction with potassium yields the hexaanion, whereas reduction with lithium does not: the shorter C–Li distances would draw the bowls much closer together, which is disfavored on both Coulombic and steric grounds. It is also easy to understand from this picture why no intermolecular nuclear Overhauser effects (nOe) are observed; the ionic radius of K^+ is quite large, and since nOe correlates to r^6, one would not expect to see these effects. While six potassium ions are covalently attached (or at least with strong contact-ion character),[41,42] the additional eighteen potassium ions that are not part of the cage are solvent-separated. This structure may also explain why reduction takes so long to give a clean NMR spectrum: the self-assembly process is a slow kinetic phenomenon, and it takes several weeks for the system to sort through all the aggregates and find one that is thermodynamically stable.[43]

Prolonged exposure of $\mathbf{1}^{6-}$ to potassium at room temperature yields additional signals alongside those of the original aggregate. These correspond to at least four-more sets of signals, in a 1:1:1:1 ratio, and with the same symmetry, but at much lower intensity than the original signals. Each set of signals falls extremely close to the original (Figure 1c), and it therefore appears that one or more additional modes of aggregation occur over time. These slowly formed aggregates of $\mathbf{1}^{6-}$ are stable, as is the original tetramer,[23] and once they are formed, reestablishing the tetrameric $\mathbf{1}^{6-}$ alone from them is not possible, even at higher temperatures. Thus, the first aggregate of $\mathbf{1}^{6-}$ observed, although it is the kinetically

 © 2006 Wiley-VCH Verlag GmbH & Co. KGaA, Weinheim

favored species, is not necessarily the thermodynamically most stable aggregate. Quenching this mixture with water or iodine does not lead to an isolable product, as it did with the tetramer $[\mathbf{1}^{6-}]_4/24\,K^+$. Only quenching of the first aggregate alone in water[19] is successful.

In conclusion, experimental evidence from NMR spectroscopy and theoretical evidence from DFT calculations together are best explained by a tetrameric structure for $\mathbf{1}^{6-}$, self-assembled in solution with K^+ counterions and having tetrahedral symmetry. Calculations[33–35,39] on the bare monomeric hexaanion and with three potassium counterions fail to give pyramidalized carbon atoms or to reproduce the observed pattern of NMR shifts. A tetrameric aggregate, however, is in harmony with the symmetry, high charge density, and pyramidalization indicated in the spectra. Each unit in the aggregate is identical to the others, and six potassium ions of contact-ion character serve as an adhesive to simultaneously bond all four units together. Lower aggregates are expected to be more crowded and less stable than the proposed tetramer. The structure of the aggregate as a whole, with potassium cations bridging between hexaanionic units, is responsible for imposing pyramidalization at carbon atoms that should be planar in the bare hexaanion.

The combination of a specific number of hexaanionic units and the particular size of the potassium cation is apparently crucial in forming the supramolecular structure. The fact that no monomer of $\mathbf{1}^{6-}$ is observed and that aggregation is achieved as soon as the hexaanionic state is formed shows, once again, that this is a typical trait of highly charged PAHs.[15,17] In the search for other appropriate PAHs that can self-assemble to anionic aggregates in solution, this discovery of the first polyhedral aggregate may serve as a useful guide.

Received: October 6, 2005
Revised: February 1, 2006
Published online: April 18, 2006

Keywords: alkali metals · anions · density functional calculations · polycycles · self-assembly

[1] a) L. T. Scott, M. M. Boorum, B. J. McMahon, S. Hagen, J. Mack, J. Blank, H. Wegner, A. de Meijere, *Science* **2002**, *295*, 1500; b) L. T. Scott, *Angew. Chem.* **2004**, *116*, 5102; *Angew. Chem. Int. Ed.* **2004**, *43*, 4994.

[2] R. Faust, K. P. C. Vollhardt, *J. Chem. Soc. Chem. Commun.* **1993**, 1471.

[3] F. Diederich, Y. Rubin, *Angew. Chem.* **1992**, *104*, 1123; *Angew. Chem. Int. Ed. Engl.* **1992**, *31*, 1101.

[4] G. H. Narahari, E. D. Jemmis, G. Mehta, S. R. Shah, *J. Chem. Soc. Perkin Trans. 2* **1993**, 1867.

[5] For reviews on bowl-shaped PAHs, see a) P. W. Rabideau, A. Sygula in *Advances in Theoretically Interesting Molecules*, *Vol. 3* (Ed.: R. P. Thummel), JAI, Greenwich, **1995**, p. 1; b) P. W. Rabideau, A. Sygula, *Acc. Chem. Res.* **1996**, *29*, 235; c) S. Hagen, M. S. Bratcher, M. S. Erickson, G. Zimmermann, L. T. Scott, *Angew. Chem.* **1997**, *109*, 407; *Angew. Chem. Int. Ed. Engl.* **1997**, *36*, 406; d) J. S. Siegel, T. J. Seiders, *Chem. Ber.* **1995**, *128*, 313; e) R. Faust, *Angew. Chem.* **1995**, *107*, 1562; *Angew. Chem. Int. Ed. Engl.* **1995**, *34*, 1429; f) L. T. Scott, H. E. Bronstein, D. V. Preda, R. B. M. Ansems, M. S. Bratcher, S. Hagen, *Pure Appl. Chem.* **1999**, *71*, 209.

[6] a) A. H. Abdourazak, Z. Marcinow, A. Sygula, R. Sygula, P. W. Rabideau, *J. Am. Chem. Soc.* **1995**, *117*, 6410; b) P. W. Rabideau, A. H. Abdourazak, H. E. Folsom, Z. Marcinow, A. Sygula, R. Sygula, *J. Am. Chem. Soc.* **1994**, *116*, 7891; c) J. M. Schulman, R. L. Disch, *J. Comput. Chem.* **1998**, *19*, 189; d) S. M. Ferrer, J. M. Molina, *J. Comput. Chem.* **1999**, *20*, 1412.

[7] a) L. T. Scott, *Pure Appl. Chem.* **1996**, *68*, 291; b) L. T. Scott, M. S. Bratcher, S. Hagen, *J. Am. Chem. Soc.* **1996**, *118*, 8743.

[8] See, for example: a) T. J. Seiders, K. K. Baldridge, J. M. O'Connor, J. S. Siegel, *J. Am. Chem. Soc.* **1997**, *119*, 4781; b) M. A. Petrukhina, K. W. Andreini, J. Mack, L. T. Scott, *Angew. Chem.* **2003**, *115*, 3497; *Angew. Chem. Int. Ed.* **2003**, *42*, 3375; c) C. M. Alvarez, R. J. Angelici, A. Sygula, R. Sygula, P. W. Rabideau, *Organometallics* **2003**, *22*, 624.

[9] M. A. Petrukhina, K. W. Andreini, L. Peng, L. T. Scott, *Angew. Chem.* **2004**, *116*, 5593; *Angew. Chem. Int. Ed.* **2004**, *43*, 5477.

[10] For example: a) D. J. Cram, J. M. Cram, *Science* **1974**, *183*, 803; b) J.-M. Lehn, *Pure Appl. Chem.* **1978**, *50*, 871; c) E. Weber, F. Vögtle, *Top. Curr. Chem.* **1981**, *98*, 1; d) D. J. Cram, K. N. Trueblood, *Top. Curr. Chem.* **1981**, *98*, 43; e) J.-M. Lehn, *Science* **1985**, *227*, 849; f) D. J. Cram, *Angew. Chem.* **1986**, *98*, 1041; *Angew. Chem. Int. Ed. Engl.* **1986**, *25*, 1039; g) D. Worsch, F. Vögtle, *Top. Curr. Chem.* **1987**, *140*, 22; h) I. Goldberg, *Top. Curr. Chem.* **1988**, *149*, 1; i) J. Rebek, Jr., *Top. Curr. Chem.* **1988**, *149*, 190; j) H. Dugas, *Bioorganic Chemistry*, Springer, Heidelberg, **1989**; k) C. D. Gutsche, *Calixarenes*, Royal Society of Chemistry, Cambridge, **1989**; l) J.-M. Lehn, *Angew. Chem.* **1990**, *102*, 1347; *Angew. Chem. Int. Ed. Engl.* **1990**, *29*, 1304; m) M. M. Green, N. C. Peterson, T. Sato, A. Teramoto, R. Cook, S. Lifson, *Science* **1995**, *268*, 1860; n) Y. Furusho, T. Kimura, Y. Mizuna, T. Aida, *J. Am. Chem. Soc.* **1997**, *119*, 5267; o) T. Nakano, Y. Satoh, Y. Okamoto, *Macromolecules* **2001**, *34*, 2405.

[11] a) R. M. Kellogg, *Top. Curr. Chem.* **1982**, *101*, 111; b) M. Okahara, Y. Nakatsuji, *Top. Curr. Chem.* **1985**, *128*, 37; c) Y. Matsui, T. Nishioka, T. Fujita, *Top. Curr. Chem.* **1985**, *128*, 61; d) F. P. Schmidtchen, *Top. Curr. Chem.* **1986**, *132*, 101; e) M. Badertscher, M. Welti, P. Portman, E. Pretsch, *Top. Curr. Chem.* **1986**, *136*, 17.

[12] A. E. Strong, B. D. Moore, *J. Mater. Chem.* **1999**, *9*, 1095.

[13] a) G. R. Painter, B. C. Pressman, *Top. Curr. Chem.* **1982**, *101*, 83; b) S. Shinkai, O. Manabe, *Top. Curr. Chem.* **1984**, *121*, 67.

[14] H. Bock, K. Gharagozloo-Hubmann, M. Sievert, T. Prisner, Z. Havlas, *Nature* **2000**, *404*, 267.

[15] A. Ayalon, A. Sygula, P.-C. Cheng, M. Rabinovitz, P. W. Rabideau, L. T. Scott, *Science* **1994**, *265*, 1065.

[16] For example, corannulene forms a dimer sandwich with lithium ions from its tetraanionic units ($[C_{20}H_{10}{}^{4-}]_2/8\,Li^+$).[15]

[17] Recently, a helical tetramer of 2,5,8,11-tetra-*tert*-butylcycloocta[1,2,3,4-*def*;5,6,7,8-*d'e'f'*]bisbiphenylene tetraanion with lithium ions ($[C_{40}H_{44}{}^{4-}]_4 16\,Li^+$) was reported: R. Shenhar, H. Wang, R. E. Hoffman, L. Frish, L. Avram, I. Willner, A. Rajca, M. Rabinovitz, *J. Am. Chem. Soc.* **2002**, *124*, 4685.

[18] Potassium was vacuum-distilled into an NMR tube, previously filled with argon and containing the material (2.5–20 mg). The sample was attached to a vacuum line and flame-dried under vacuum. Dry [D_8]THF ($\approx$0.5 mL) was distilled from a reservoir into the tube. The sample was degassed under vacuum by the freeze–pump–thaw technique and flame-sealed. For lithium samples the same procedure was conducted, except that a freshly produced lithium wire was immediately inserted into the upper part of an extended NMR tube. For several of the lithium samples, a small amount of corannulene was previously added to the tube. Controlled reductions of the samples were carried out by inverting the tubes at low temperature (−30 °C) to bring the

 © 2006 Wiley-VCH Verlag GmbH & Co. KGaA, Weinheim

solutions into contact with the alkali metals. Returning the tubes to their upright positions stopped reductions from progressing.

[19] Two types of quenching reactions were carried out: 1) with water and 2) with iodine. 1) Quenching with water was carried out in a glove bag under oxygen-free conditions. The tube was broken and opened in the glove bag, and after removal of the reduction compartment and excess metal, the reduced compound was introduced into a vial containing distilled water. The characteristic color of the reduced species disappeared instantaneously, and the hexahydro species was formed. The solution was stirred for several minutes at room temperature and was then removed from the glove bag. The organic phase was washed with dichloromethane, and the solvent was evaporated. The product was then characterized by NMR spectroscopy and HRMS. 2) Oxidation with iodine was performed in a glove box. The tube was broken and opened in the glove box under anhydrous conditions, and the reduced compound was immediately added to approximately 10 mol equiv of I_2, upon which oxidation instantly occurred. The solution was stirred for 10 min at room temperature and was then removed from the glove box. Excess iodine was removed by washing with a saturated aqueous solution of sodium dithionite, and the solvent was evaporated. Quenching of $\mathbf{1}^{6-}$ with iodine does not form a new, clean diamagnetic species; rather, it results in apparent polymerization.

[20] Asymmetrical proton addition is likely, as indicated by ^{1}H NMR spectroscopy.

[21] The use of corannulene as an effective "electron shuttle" has been shown: E. Shabtai, A. Weitz, R. C. Haddon, R. E. Hoffman, M. Rabinovitz, A. Khong, R. J. Cross, M. Saunders, P.-C. Cheng, L. T. Scott, *J. Am. Chem. Soc.* **1998**, *120*, 6389.

[22] Although no new diamagnetic species of **1** is seen, the corannulene does undergo its regular reduction: neutral → radical anion → dianion → radical trianion → tetraanion, as observed by ^{1}H NMR spectroscopy.

[23] Standing at room temperature for months in contact with the potassium mirror does not cause decomposition to $\mathbf{1}^{6-}$, aside from the formation of additional aggregates. See text.

[24] Only after weeks of charging at room temperature is a new diamagnetic species formed.

[25] Charge density and molecular orbital calculations were carried out at the DFT level of theory with the Gaussian 98 program package, by employing Becke's three-parameter hybrid density functional with the nonlocal correlation functional of Lee, Yang, and Parr (B3LYP) and the 6-31G* basis set.[33–35]

[26] a) A. Ayalon, M. Rabinovitz, P.-C. Cheng, L. T. Scott, *Angew. Chem.* **1992**, *104*, 1691; *Angew. Chem. Int. Ed. Engl.* **1992**, *31*, 1636; b) M. Rabinovitz, A. Ayalon, *Pure Appl. Chem.* **1993**, *65*, 111.

[27] K_c is a parameter empirically shown to correlate the total change in chemical shift of the ^{13}C NMR spectrum on charging ($\Sigma\Delta\delta$) with the total extra charge added to the π system of the molecule on charging ($\Sigma\Delta q_\pi$), as expressed in the equation $\Sigma\Delta\delta = K_c\Sigma\Delta q_\pi$. In this case, $\Sigma\Delta\delta = 608$ ppm. For reviews on this parameter, see a) S. Braun, H.-O. Kalinowski, S. Berger, *150 and More Basic NMR Experiments: A Practical Course*, Wiley-VCH, Weinheim, **1998**; b) G. Fraenkel, R. E. Carter, A. Mclachlan, J. H. Richards, *J. Am. Chem. Soc.* **1960**, *82*, 5846; c) P. C. Lauterbur, *J. Am. Chem. Soc.* **1961**, *83*, 1838; d) H. Spiesecke, W. G. Schneider, *Tetrahedron Lett.* **1961**, *2*, 468; e) P. C. Lauterbur, *Tetrahedron Lett.* **1961**, *2*, 274; f) R. Schaefer, W. G. Schneider, *Can. J. Chem.* **1963**, *41*, 966; g) D. G. Farnum, *Adv. Phys. Org. Chem.* **1975**, *11*, 123; h) K. Müllen, *Chem. Rev.* **1984**, *84*, 603.

[28] A modification of the above relationship taking into account the anisotropy of π-electron systems was presented by Müllen et al.: B. Eliasson, U. Edlund, K. Müllen, *J. Chem. Soc. Perkin Trans. 2* **1986**, 937.

[29] $C_{30}H_{24}^{6-}$: Z. Di-Nur, M.Sc. Thesis, The Hebrew University of Jerusalem, **1996**.

[30] Hexakis(4-*n*-dodecylbiphenylyl)benzene hexaanion: L. Eshdat, R. E. Hoffman, A. Fechtenkötter, K. Müllen, M. Rabinovitz, *Chem. Eur. J.* **2003**, *9*, 1844.

[31] See also: A. Minsky, A. Y. Meyer, M. Rabinovitz, *Tetrahedron Lett.* **1982**, *23*, 5351.

[32] See, for example a) J. Klein, *Tetrahedron* **1983**, *39*, 2733; b) Y. Cohen, J. Klein, M. Rabinovitz, *J. Am. Chem. Soc.* **1988**, *110*, 4634; c) N. Treitel, M. Deichmann, T. Sternfeld, T. Sheradsky, R. Herges, M. Rabinovitz, *Angew. Chem.* **2003**, *115*, 1204; *Angew. Chem. Int. Ed.* **2003**, *42*, 1172.

[33] Gaussian 98 (Revision A.7): see Supporting Information.

[34] a) C. Lee, W. Yang, R. G. Parr, *Phys. Rev. B* **1988**, *37*, 785; b) A. D. Becke, *J. Chem. Phys.* **1993**, *98*, 5648.

[35] a) P. C. Hariharan, J. A. Pople, *Theor. Chim. Acta* **1973**, *28*, 213; b) W. J. Hehre, R. Ditchfield, J. A. Pople, *J. Chem. Phys.* **1972**, *56*, 2257.

[36] Calculated from ^{13}C NMR shifts, as explained in text and reference [27].

[37] See, for example a) R. C. Haddon, *Acc. Chem. Res.* **1988**, *21*, 243; b) W. T. Borden, *Chem. Rev.* **1989**, *89*, 1095; c) R. C. Haddon, *J. Am. Chem. Soc.* **1990**, *112*, 3385; d) W. Luef, R. Keese, *Top. Stereochem.* **1991**, *20*, 231; e) W. T. Borden, *Synlett* **1996**, 711; f) S. Vázquez, *J. Chem. Soc. Perkin Trans. 2* **2002**, 2100.

[38] O. Kwon, F. Sevin, M. L. McKee, *J. Phys. Chem. A* **2001**, *105*, 913.

[39] a) R. Krishnan, J. S. Binkley, R. Seeger, J. A. Pople, *J. Chem. Phys.* **1980**, *72*, 650; b) A. D. McLean, G. S. Chandler, *J. Chem. Phys.* **1980**, *72*, 5639.

[40] A. T. Balaban, *Chemical Applications of Graph Theory*, Academic Press, London, **1976**.

[41] a) M. Szwarc, *Ions and Ion Pairs in Organic Reactions*, Wiley-Interscience, New York, **1974**; b) C. Reichardt, *Solvents and Solvent Effects in Organic Chemistry*, VCH, Weinheim, **1988**.

[42] See also: a) T. E. Hogen-Esch, J. Smid, *J. Am. Chem. Soc.* **1966**, *88*, 307; b) T. E. Hogen-Esch, J. Smid, *J. Am. Chem. Soc.* **1969**, *91*, 4580; c) A. Ayalon, Ph.D. Thesis, The Hebrew University of Jerusalem, **1993**.

[43] This tetrameric model was found computationally to be an energy minimum. Unfortunately, semiempirical methods, as implemented in Spartan 02 (AM1, PM3, and MNDO) do not handle potassium, and the system is too large to calculate with even higher levels of theory (e.g., ab initio and DFT).

 © 2006 Wiley-VCH Verlag GmbH & Co. KGaA, Weinheim

Polymerization Catalysts

DOI: 10.1002/anie.200600240

Nonconventional Catalysts for Isotactic Propene Polymerization in Solution Developed by Using High-Throughput-Screening Technologies

Thomas R. Boussie, Gary M. Diamond, Christopher Goh, Keith A. Hall, Anne M. LaPointe, Margarete K. Leclerc, Vince Murphy, James A. W. Shoemaker, Howard Turner, Robert K. Rosen, James C. Stevens,* Francesca Alfano, Vincenzo Busico,* Roberta Cipullo, and Giovanni Talarico*

Industrial methods for the manufacture of commodity polyolefins are presently dominated by gas- and slurry-phase processes in which the catalysts are formulated on solid supports.[1] Homogeneous processes in solution offer greater operational flexibility and wider ranges of products, but for technical and economical reasons they operate most effectively at higher temperatures to prevent precipitation of the polymer, with low concentrations of monomer and short catalyst residence times.[2] These restrictions impose a highly demanding set of requirements on the performance of the catalyst, in particular with respect to the thermal stability, the molecular weight capability, and the stereoselectivity (when needed). In the case of ethene polymerization, metallocene and hemi-metallocene catalysts matching the requirements were identified, and solution processes became commercial in the 1990s,[3] yielding an impressive portfolio of high-value ethene/1-alkene copolymers, in particular, that were once thought to be beyond the capability of polyethylene process technology.[4] For propene polymerization, on the other hand, the quest proved to be much more problematic. The performance of C_2-symmetric *ansa*-zirconocenes, which represent the state-of-the-art homogeneous catalysts for isotactic polypropylene,[5] rapidly deteriorates with increasing temperature and decreasing concentration of monomer.[6] Herein, we report on the development, aided by high-throughput-screening (HTS) technologies, of a new family of homogeneous Hf catalysts with non-conventional structure, that are now used commercially for the unprecedented production of materials based on isotactic polypropylene in a high-temperature solution process.[7,8]

The catalyst discovery workflow using the Symyx HTS infrastructure (introduced elsewhere[9]) moves from a microscale high-throughput primary screen (250 μL working volume), in which large arrays of (new) metal–ligand combinations are rapidly surveyed for catalytic activity with 1-octene (a liquid monomer convenient for robotic handling[10]), with automated procedures enabling several hundred experiments per day. Promisingly active metal–ligand combinations thus identified ("hits") are subjected to a secondary screen in which the catalyst performance properties for the targeted application are assessed using larger scales, with less experiments run under more commercially relevant conditions; typically, 48 experiments in parallel are carried out with real-time monitoring in individually controlled high-pressure reactors (Parallel Pressure Reactor Technology (PPR); 5–6 mL working volume). Catalysts that meet predetermined performance criteria ("leads") are then optimized through structural elaboration. Specially developed rapid polymer characterization techniques accommodate the synthetic throughput and assess the nature of the polymer products from primary and secondary screens.[11]

In a previous project on ethene/1-octene copolymerization,[9] a number of new non-metallocene[12] catalysts with remarkable high-temperature stability and molecular weight capability were uncovered. Our attention, in particular, had been raised by the combinations of two closely related pyridyl-amine ligands with $HfBn_4$ (Bn = benzyl), because under primary screening conditions they yielded high-molecular-weight polyoctene with high l-octene conversions. Before evaluating these hits in a secondary screen with propene, a greater number of pyridyl-amine ligands with enhanced structural diversity were synthesized (Figure 1). In designing the expanded ligand array, three convenient positions for structural amplification were identified and are labeled as R^1, R^2, and R^3. The amine substituent R^1 was known to influence catalyst performance dramatically from prior reports of other amide-stabilized systems.[12] Substituent R^2 was chosen to alter the steric and electronic properties of pyridine ligation, while R^3 gave the opportunity to introduce a stereogenic center on the ligand, albeit at a position remote from the propene-binding site in the metal complex, and test whether it can influence the stereoselectivity of the catalyst. In total, 39 pyridyl-amine structures were prepared by using synthetic procedures adapted from known transformations.[13] As can be seen from Figure 1, considerable steric and electronic diversity is represented in this ligand array.

Using previously reported secondary screening protocols,[9] the ligands were complexed in situ with suitable Hf precursors,[14] namely $HfBn_4$ or, for the more sterically hindered ligands, $Hf(NMe_2)_4$ (see Supporting Information). The complexes were then tested in the polymerization of propene at 75 °C in toluene. As many as 34 combinations

[*] F. Alfano, Prof. V. Busico, Dr. R. Cipullo, Dr. G. Talarico
Dipartimento di Chimica
Università di Napoli Federico II
Via Cintia, 80126 Napoli (Italy)
Fax: (+39) 081-674-090
E-mail: busico@unina.it
Dr. T. R. Boussie, Dr. G. M. Diamond, Dr. C. Goh, Dr. K. A. Hall, Dr. A. M. LaPointe, Dr. M. K. Leclerc, Dr. V. Murphy, Dr. J. A. W. Shoemaker, Dr. H. Turner, Dr. R. K. Rosen
Symyx Technologies, Inc.
3100 Central Expressway, Santa Clara, CA 95091 (USA)
E-mail: vmurphy@symyx.com
Dr. J. C. Stevens
The Dow Chemical Company
2301 North Brazosport Blvd., B-3827
Freeport, TX 7754 (USA)
E-mail: jcstevens@dow.com

Supporting information for this article is available on the WWW under http://www.angewandte.org or from the author.

InterScience
© 2006 Wiley-VCH Verlag GmbH & Co. KGaA, Weinheim

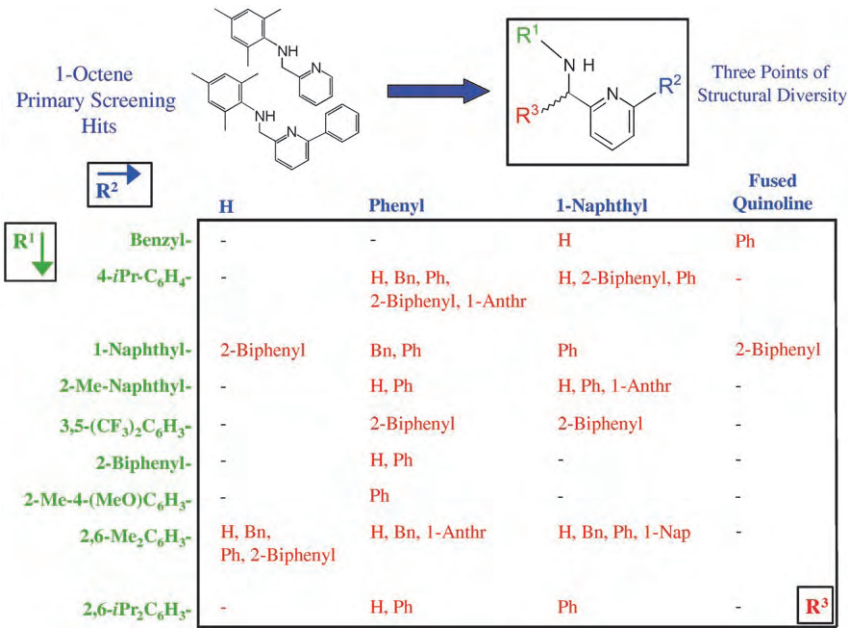

Figure 1. The pyridyl amine ligands used in this study. Bn = benzyl; Anthr = anthracenyl; Nap = naphthyl.

turned out to be active. In the vast majority of cases, the produced polypropylenes came out of the reactor as clear solutions in toluene and were determined by rapid FTIR analysis[9,11] to be stereoirregular (Figure 2). In two reactors, however, opaque suspensions were obtained, which is a clear indication of high-polymer crystallinity, and indeed rapid FTIR analysis indicated an isotactic polypropylene structure. This structure was confirmed by a subsequent NMR spectroscopic characterization of the isolated polymers (see below).

From the members of the library screened in the present study, the two ligands that led to this breakthrough have a very similar structure, with the same R^1 (2,6-*i*$Pr_2C_6H_3$) and R^3 (phenyl) groups, and with R^2 = phenyl in one case (ligand **L1**-H_2) and R^2 = 1-naphthyl in the other (ligand **L2**-H_2). Note that all other substitution patterns in this library, some of which are apparently similar to **L1**-H_2 and **L2**-H_2, resulted in poorly stereoselective or non-stereoselective catalysts. For example, replacing R^1 = 2,6-*i*$Pr_2C_6H_3$ with another 2,6-substituted aryl, such as 2,4,6-Me_3-C_6H_2, resulted in a substantial loss of the stereocontrol. This observation demonstrates that the stereoselectivity is exquisitely sensitive to the nature of the substituents on the ligand, suggesting that the discovery would likely have taken significantly longer without the synthesis of a suitably diverse ligand array coupled with the use of HTS.

The ^{13}C NMR spectrum of the polypropylene sample obtained using ligand **L2**-H_2 is shown in Figure 3. The isotacticity is strikingly high, and the occasional (0.9 mol%) m_xrrm_y (m = *meso* and r = *racemo*) stereodefects are typical of stereocontrol exerted by an intrinsically chiral active species.[15] Low amounts of regiodefects (0.9 mol%) are also seen in the form of isolated head-to-head/tail-to-tail enchainments with an unprecedented stereostructure[5,15] (see Figure 3), which can be attributed to the preference of the catalyst to insert the *same* propene enantioface irrespective of the regiochemistry. Results of ^1H and ^{13}C NMR chain end group analysis on suitable polymer samples indicated that the favored propene insertion mode is 1,2 (primary).[16]

More insight into the novel catalyst class was gained from an investigation of the metal–ligand complexation and alkylation chemistry. The reaction of **L1**-H_2 with $Hf(NMe_2)_4$ (Scheme 1, upper) proceeded smoothly with the elimination of two equivalents of dimethylamine, instead of one as

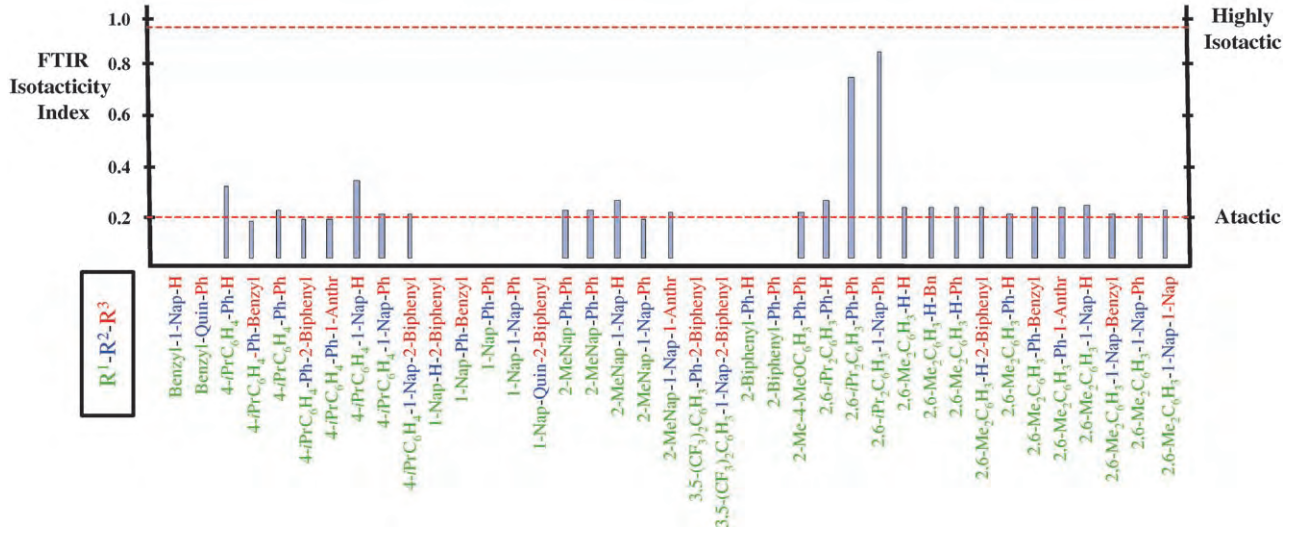

Figure 2. Results from rapid FTIR analysis of polymers obtained from the secondary screening protocol.

 © 2006 Wiley-VCH Verlag GmbH & Co. KGaA, Weinheim

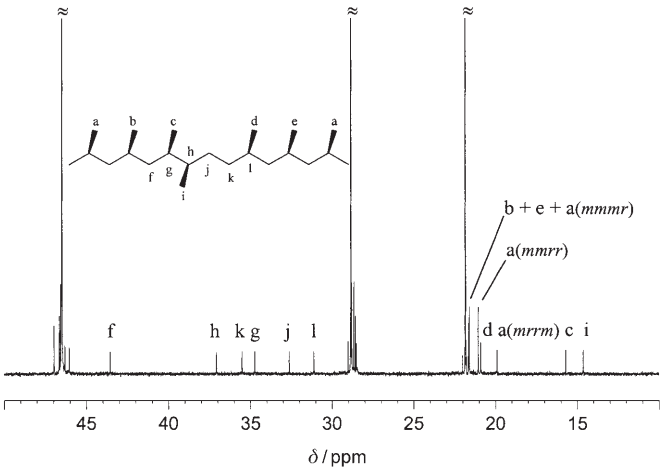

Figure 3. ^{13}C NMR spectrum (100 MHz, $(CDCl_2)_2$, 120 °C; δ scale relative to tetramethylsilane at $\delta = 0$ ppm) of the polypropylene obtained with the in situ combination and activation of **L2**-H_2 with $Hf(NMe_2)_4$, with explicit attributions of peaks owing to regio- and stereodefects. The main peaks of the isotactic polypropylene (marked with ≈) are out of scale.

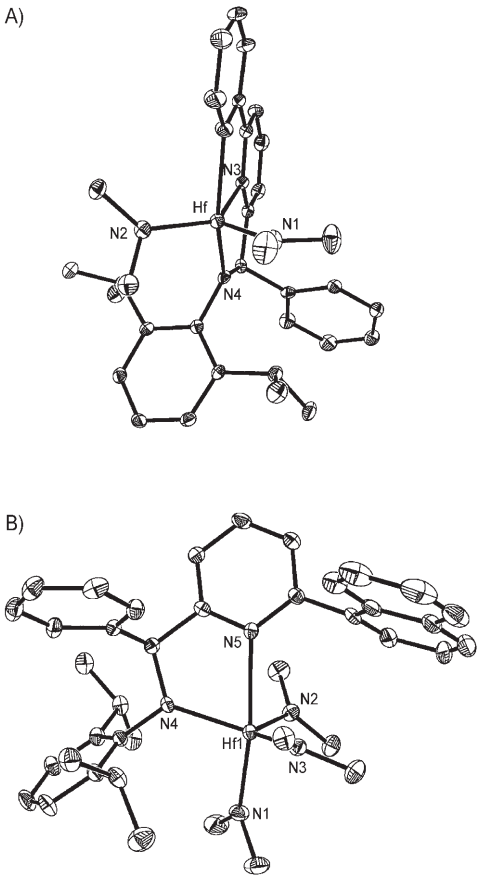

Figure 4. Single-crystal X-ray diffraction structures of A) [{η^3-(N,N,C)-**L1**}$Hf(NMe_2)_2$] and B) [{η^2-(N,N)-**L2**-H}$Hf(NMe_2)_3$].

expected, and the concomitant formation of the pyridyl-amide complex [{η^3-(N,N,C)-**L1**}$Hf(NMe_2)_2$]. ^1H NMR and single-crystal X-ray diffraction data are consistent with the phenyl group at R^2 being the source of the proton necessary for the elimination of the second equivalent of dimethylamine, in addition to that coming from the amine functionality. The structure obtained from single-crystal X-ray studies (see Figure 4A and Supporting Information), in particular, reveals the presence of a Hf–C(aryl) σ bond formed by *ortho*-metalation of the phenyl group[17] and, consequently, tridentate ligation of **L1**. The complex reveals C_1 symmetry, with a highly distorted trigonal-bipyramidal coordination of the Hf center and the two NMe_2 groups that occupy equatorial diastereotopic sites. Alkylation with 10 equivalents of $AlMe_3$[18] gave the dimethyl derivative [{η^3-(N,N,C)-**L1**}$HfMe_2$] (**1**-Me_2), with the protons of the two diastereotopic methyl groups on Hf resonating at $\delta = 0.91$ and 0.61 ppm in the ^1H NMR spectrum.

Less exotically, the reaction of **L2**-H_2 with $Hf(NMe_2)_4$ (Scheme 1, lower) proceeded with the elimination of one equivalent of dimethylamine to give the complex [{η^2-(N,N)-**L2**-H}$Hf(NMe_2)_3$]. In this case, the pyridyl-amide ligand is bidentate, as shown in the single-crystal structure (see Figure 4B and Supporting Information). However, during the subsequent alkylation step with 10 equivalents of $AlMe_3$, the evolution of methane was observed, along with the

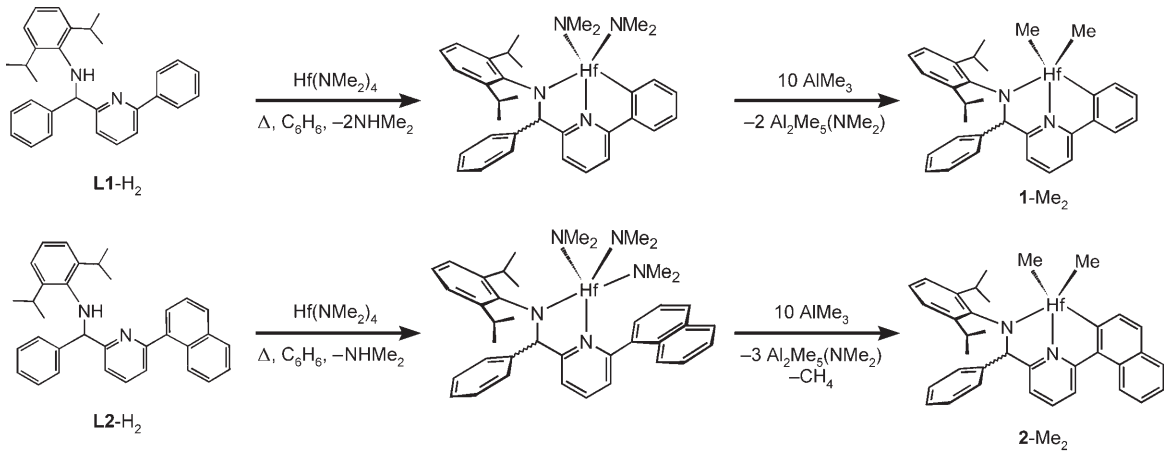

Scheme 1. Reactions of **L1**-H_2 (upper) and **L2**-H_2 (lower) with $Hf(NMe_2)_4$ and concomitant formation of the corresponding pyridyl-amide complexes.

 © 2006 Wiley-VCH Verlag GmbH & Co. KGaA, Weinheim

formation of three equivalents of $Al_2Me_5(NMe_2)$. This observation points to the formation of an *ortho*-metalated dimethyl complex [{η^3-(N,N,C)-**L2**}$HfMe_2$] (**2**-Me_2), strictly similar to the corresponding species with ligand **L1**. Consistently, the ^{1}H NMR spectrum displayed two inequivalent resonances of methyl protons on Hf at $\delta = 0.93$ and 0.65 ppm.

It is plausible to identify **1**-Me_2 and **2**-Me_2 as catalyst precursors, from which cationic active species would be formed by methide abstraction, similar to what is known for metallocenes.[19] Indeed, when **2**-Me_2 was screened in the PPR by activation with $[Me_2PhNH][B(C_6F_5)_4]$ in combination with an alkylaluminum reagent (see Supporting Information for details), propene polymerization led to a highly isotactic polymer, which was identical to that produced starting from an in situ combination of ligand **L2**-H_2 with $Hf(NMe_2)_4$ (when screened under identical conditions). That such cations should be highly isotactic-selective in the polymerization of propene up to very high temperatures, however, is not at all obieous.

The effect of temperature on the stereoselectivity of the catalyst derived from **2**-Me_2 by activation with $[(C_6H_5)_3C][B(C_6F_5)_4]$ in toluene is shown in Figure 5, in which $\ln[\sigma/(1-\sigma)]$ is plotted versus $1/RT$; σ and $1-\sigma$ are the stochastic probabilities of propene insertion in the predominant 1,2 regiochemistry with the two (*re* or *si*) enantiofaces. The limiting cases of $\sigma = 1$ or $\sigma = 0$ correspond to complete enantioselectivity, while $\sigma = 0.5$ corresponds to a complete lack of enantioselectivity. For a single-center isotactic-selective catalytic species with two homotopic active sites (i.e., with local C_2 symmetry), the function is usually a straight line, whose derivative is the difference in activation energy ($\Delta E^{\neq}$) between the two competing diastereomeric propene insertion paths (unless additional routes for the generation of stereodefects, such as growing chain epimerization,[6] are viable), that intercepts at the origin ($\Delta S^{\neq} \approx 0$). The case of interest here is in principle more complicated, because the two active sites of the C_1-symmetric catalytic species are diastereotopic. However, the experimental data points are well interpolated by a straight line through the origin, as if the two active sites were equivalent or, more likely, as if propene insertion occurred predominantly at one of the two, with a robust

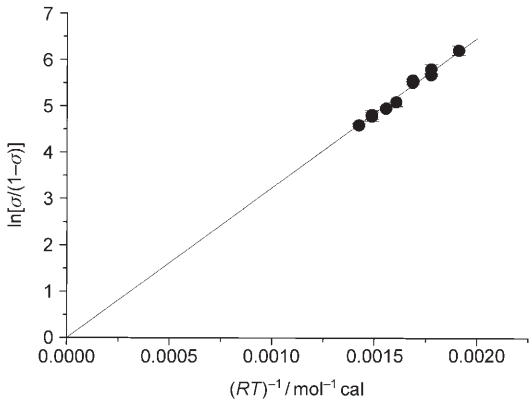

Figure 5. Plot of $\ln[\sigma/(1-\sigma)]$ versus $1/RT$ for propene polymerization with **2**-Me_2/$[(C_6H_5)_3C][B(C_6F_5)_4]$ in toluene (see text for details).

enantioselectivity ($\Delta E^{\neq} = 3.4$ kcal mol^{-1}). Notably, at each given temperature the stereoselectivity turned out to be independent of the concentration of propene (in the explored 0.5–5 M range), which is not always the case for a C_1-symmetric catalyst.[5,15]

A full quantum mechanics study (see Supporting Information) was undertaken on the two diastereoisomers [**2**′-*i*Bu]$^+$ and [**2**″-*i*Bu]$^+$ of a putative active cation [{η^3-(N,N,C)-**L2**}Hf(*i*Bu)]$^+$, with the ligand in R configuration and an isobutyl residue simulating the growing polypropylene chain (Figure 6). In both cases, propene insertion into the Hf–*i*Bu bond was found to proceed according to a standard Cossee-type chain-migratory path,[5,15] and with predominant 1,2 regiochemistry ($G^{\#}_{2,1} - G^{\#}_{1,2} > 2$ kcal mol^{-1}) in agreement with experiment. According to the calculations, for [**2**′-*i*Bu]$^+$ at the transition states the metal is in a distorted trigonal-bipyramidal coordination (Figure 6A,B) and insertion with the *re* enantioface is strongly favored ($G^{\#}_{si} - G^{\#}_{re} = 4.5$ kcal mol^{-1}). The lowest-energy paths for insertion at [**2**″-*i*Bu]$^+$, on the other hand, involve square-pyramidal transition states

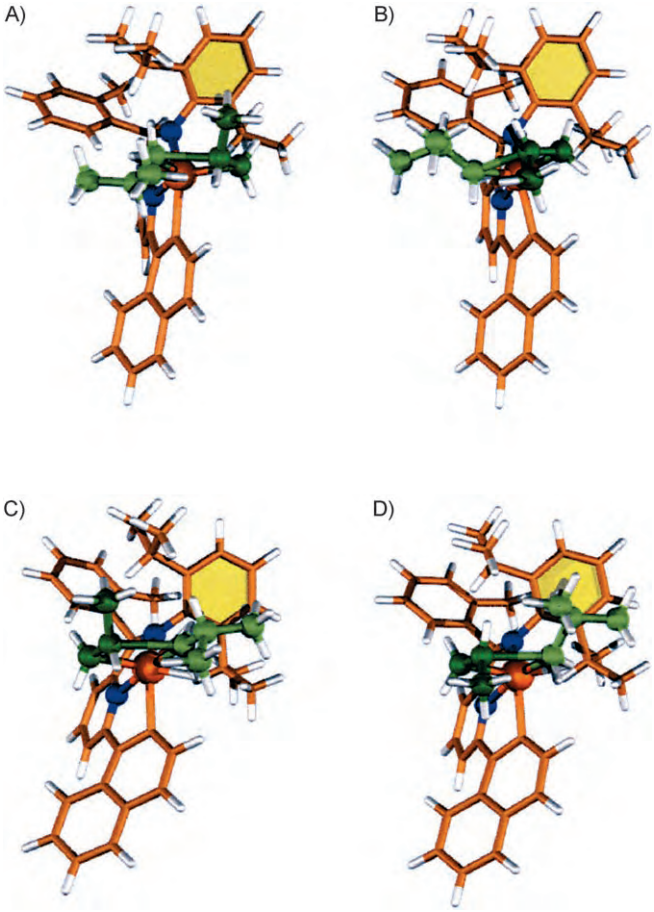

Figure 6. Transition states for 1,2-propene insertion at the two diastereomers of an [{η^3-(N,N,C)-**L2**}Hf(*i*Bu)]$^+$ model cation, as obtained from quantum mechanics calculations (see text for details). Propene dark green, *i*Bu light green, N blue, C(**L2**) orange, H white, Hf orange sphere. A) *re* enantioface (favored) and B) *si* enantioface of [**2**′-*i*Bu]$^+$. C) *si* enantioface (favored) and D) *re* enantioface of [**2**″-*i*Bu]$^+$.

 © 2006 Wiley-VCH Verlag GmbH & Co. KGaA, Weinheim

(Figure 4C,D), and it is the *si* enantioface that is slightly preferred ($G^{\#}_{si} - G^{\#}_{re} = -0.8$ kcal mol^{-1}). In both cases, the flow of chiral information from the active species to the incoming monomer is mediated by the growing polymer chain, as is common in Ziegler–Natta catalysis.[5,15] In brief, the steric hindrance of the ancillary ligand framework reduces the conformational freedom of the chain, which is constrained in a chiral orientation, with the first C–C bond pointing towards the more open of the two accessible quadrants. In turn, 1,2 propene insertion is favored with the enantioface that directs the methyl substituent *anti* to the first C–C bond.

In view of the above, the observed stereoselectivity (Figure 5) can be explained assuming that the monomer inserts in preference at [**2**′-P]$^+$ (P = polymeryl in the place of *i*Bu). The few stereodefects in the polymer can be traced to faults of enantioselection at the same diastereomer and/or to occasional insertions at [**2**″-P]$^+$. This interpretation is consistent with all presently available experimental data, including results of solution-state NMR studies on [**2**-Me][MeB(C_6F_5)$_3$] ion couples showing a single diastereoisomer with the methyl group on Hf at the same site of the *i*Bu group in [**2**′-*i*Bu]$^+$,[20] and of chiral 1-alkene oligomerization with enantiopure [(R)-**2**]-Me_2-based catalysts confirming the preferential uptake of propene with the *re* enantioface,[16] as will be reported in due course. The fact that the stereoselectivity is independent of the concentration of propene suggests that the rate of chain/anion relocation[19,21,22] is fast relative to that of monomer insertion (Curtin–Hammett regime[22]).

It must be added, though, that experimental and quantum mechanics results indicate that monomer insertion into the *ortho*-metallacycle is also viable, leading to an in situ ligand modification.[16] The relevance of this issue for catalysis is currently under investigation.

The performance of the new catalysts in toluene at 90 °C and a partial pressure of propene of 6.9 bar (100 psi) is compared in Table 1 with the state-of-the-art C_2-symmetric metallocene, *rac*-[Me_2Si(2-Me-4-phenyl-1-indenyl)$_2$Zr(η^4-1,4-(phenyl)$_2$-1,3-butadiene)].[23] Strikingly, under the conditions explored, the unoptimized pyridyl-amide catalysts displayed productivities up to 20% of that of the highly optimized metallocene. The complex [{η^2-(N,N)-**L2**-H}Hf(NMe_2)$_3$], moreover, afforded a polypropylene with nearly the same melting temperature (141 vs 142 °C). The metallocene-made polymer, however, revealed an average molecular weight of $M_w \approx 95$ kDa. If it is considered that M_w of typical commercial products is in the range of 300–400 kDa, and that an industrial solution process would operate well above 90 °C at which temperature a further drop of M_w is expected, it is clearly confirmed that the molecular weight capability of this high-performance metallocene is not adequate to the application of interest. The polypropylenes produced with [{η^3-(N,N,C)-**L1**}Hf(NMe_2)$_2$] and [{η^2-(N,N)-**L2**-H}Hf(NMe_2)$_3$], on the other hand, revealed much higher values of M_w with narrow polydispersities; the molecular weight capability of [{η^2-(N,N)-**L2**-H}Hf(NMe_2)$_3$], in particular, with molecular weights of polypropylene above 700 kDa, is truly extraordinary at these polymerization conditions, opening exciting perspectives for a new industrial process.

In fact the readily synthesized pyridyl-amine ligand system facilitated rapid optimization of the catalyst. By further examining the substituent effects at R^1,R^2,R^3 through a positional scanning approach[24] coupled with iterative rounds of secondary screening, we could achieve significant improvements in the catalyst performance. In particular, new catalysts with bulky R^3 substituents such as *ortho*-tolyl, 2-biphenyl, and 2-cyclohexylphenyl were identified, which displayed higher productivity and molecular weight capability. At process temperatures above 100 °C, these catalysts yield isotactic polypropylenes with $T_m \approx 150$ °C and M_w values that are compatible with commercial application. As a result, an industrial high-temperature solution process for the production of new isotactic polypropylene based materials has been introduced in less than four years from the launch of the catalyst discovery program.[7]

Table 1: Typical results of propene polymerization at 90 °C with the new catalysts as well as with metallocene *rac*-[Me_2Si(2-Me-4-phenyl-1-indenyl)$_2$Zr(η^4-1,4-(phenyl)$_2$-1,3-butadiene)], for comparison.

Precatalyst	Productivity[a]	M_w [kDa]	M_w/M_n	T_m [°C][b]
[{η^3-(N,N,C)-**L1**}Hf(NMe_2)$_2$]	1.9	300	2.1	127
[{η^2-(N,N)-**L2**-H}Hf(NMe_2)$_3$]	0.3	710	3.2	141
Zr metallocene	9.2	95	2.0	142

Conditions: toluene (4.4 mL), propene (6.9 bar), Al(*i*Bu)$_2$H (10–30 equiv), [Me_2PhNH][B(C_6F_5)$_4$] (1.1 equiv). See Supporting Information for details. [a] Units: kilograms of polymer per mmol metal per minute. [b] Maximum of the differential scanning calorimetry melting endotherm on the second heating scan (heating rate: 10 °C min^{-1}).

Received: January 19, 2006
Published online: April 18, 2006

Keywords: hafnium · high-throughput screening · nitrogen heterocycles · polymerization · tacticity

[1] G. Fink, R. Muelhaupt, H. H. Brintzinger, *Ziegler Catalysts*, Springer, Berlin, **1995**.
[2] For example, see: *Polymeric Materials Encyclopedia*, *Vol. 8* (Ed.: J. C. Salamone), CRC, Boca Raton, **1996**, p. 5966.
[3] a) H. W. Turner, US Patent 4,752,597, **1988**; b) H. W. Turner, G. G. Hlatki, R. R. Eckman, US Patent 5,470,927, **1995**; c) J. C. Stevens, F. J. Timmers, D. R. Wilson, G. F. Schmidt, P. N. Nickias, R. K. Rosen, G. W. Knight, S.-y. Lay, Eur. Patent Appl. 416 815A2, **1991**; d) J. C. Stevens, D. R. Neithamer, Eur. Patent Appl. 418 044A2, **1991**; e) J. C. Stevens, D. R. Neithamer, US Patent 5,064,802, **1991**; f) J. A. M. Canich, G. F. Licciardi, US Patent 5,057,475, **1991**.
[4] L. F. Albright, *Polym. News* **1997**, *22*, 281–284.
[5] L. Resconi, L. Cavallo, A. Fait, F. Piemontesi, *Chem. Rev.* **2000**, *100*, 1253–1345.
[6] a) V. Busico, R. Cipullo, *J. Am. Chem. Soc.* **1994**, *116*, 9329–9330; b) M. Leclerc, H. H. Brintzinger, *J. Am. Chem. Soc.* **1995**, *117*, 1651–1652; c) V. Busico, R. Cipullo, L. Caporaso, G. Angelini, A. L. Segre, *J. Mol. Catal. A* **1998**, *128*, 53–64, and references therein; d) J. C. Yoder, J. E. Bercaw, *J. Am. Chem. Soc.* **2002**, *124*, 2548–2555.
[7] For details, see: http://www.dow.com/versify
[8] A high-temperature "solution" process for the production of moderately isotactic polypropylene, now discontinued, was run by Eastman. The catalyst, however, was heterogeneous (a

 © 2006 Wiley-VCH Verlag GmbH & Co. KGaA, Weinheim

modified first-generation Ziegler–Natta catalyst). See, for example: H. J. Hagemeyer, D. C. Hull, S. J. Park, US Patent 3,600,463, **1971**.

[9] T. R. Boussie, G. M. Diamond, C. Goh, K. A. Hall, A. M. LaPointe, M. K. Leclerc, C. Lund, V. Murphy, J. A. W. Shoemaker, U. Tracht, H. Turner, J. Zhang, T. Uno, R. K. Rosen, J. C. Stevens, *J. Am. Chem. Soc.* **2003**, *125*, 4306 – 4317.

[10] G. M. Diamond, C. Goh, M. K. Leclerc, V. Murphy, H. W. Turner, WO Patent Appl. 01/98371, **2001**.

[11] a) R. B. Nielson, S. C. Kuebler, J. Bennett, A. Safir, M. Petro, US Patent 6,175,409, **2001**; b) T. R. Boussie, M. Devenney, Eur. Patent Appl. 1-160-262A1, **2001**; c) Z. J. A. Komon, G. M. Diamond, M. K. Leclerc, V. Murphy, M. Okazaki, G. C. Bazan, *J. Am. Chem. Soc.* **2002**, *124*, 15 280 – 15 285.

[12] V. C. Gibson, S. K. Spitzmesser, *Chem. Rev.* **2003**, *103*, 283 – 316, and references therein.

[13] T. R. Boussie, G. M. Diamond, C. Goh, K. A. Hall, A. M. LaPointe, M. K. Leclerc, C. Lund, V. Murphy, WO Patent Appl. 02/38628, **2002**; see also related US Patents: T. R. Boussie, G. M. Diamond, C. Goh, K. A. Hall, A. M. LaPointe, M. K. Leclerc, C. Lund, V. Murphy, US Patent 6,713,577, **2004** and T. R. Boussie, G. M. Diamond, C. Goh, K. A. Hall, A. M. LaPointe, M. K. Leclerc, C. Lund, V. Murphy US Patent 6,750,345, **2004**.

[14] Zr complexes with pyridyl-amine ligands have been reported, see: R. Murray, US Patent 6,103,657, **2000**. In situ combinations of the pyridyl-amine ligands investigated in this study with $ZrBn_4$ and $Zr(NMe_2)_4$ were screened under a variety of activation conditions. However, relative to the Hf homologues, they were significantly less active and the polymers obtained were of much lower average molecular weight.

[15] V. Busico, R. Cipullo, *Prog. Polym. Sci.* **2001**, *26*, 443 – 533, and references therein.

[16] V. Busico, R. Cipullo, R. D. J. Froese, P. D. Hustad, R. L. Kuhlman, G. Talarico, T. T. Wenzel, unpublished results.

[17] Metalation of aryl rings by Group 4 metals is well documented. For a related system, see: S. C. F. Kui, N. Zhu, M. C. W. Chan, *Angew. Chem.* **2003**, *115*, 1666 – 1670; *Angew. Chem. Int. Ed.* **2003**, *42*, 1628 – 1632.

[18] G. M. Diamond, R. F. Jordan, J. L. Peterson, *J. Am. Chem. Soc.* **1996**, *118*, 8024 – 8033.

[19] E. Y.-X. Chen, T. J. Marks, *Chem. Rev.* **2000**, *100*, 1391 – 1434.

[20] A. Macchioni, C. Zuccaccia, personal communication.

[21] P. A. Deck, T. J. Marks, *J. Am. Chem. Soc.* **1995**, *117*, 6128 – 6129.

[22] See, for example: M. Nele, M. Mohammed, S. Xin, S. Collins, M. L. Dias, J. C. Pinto, *Macromolecules* **2001**, *34*, 3830 – 3841.

[23] E. Y.-X. Chen, R. E. Campbell, Jr., D. A. Devore, D. P. Green, B. Link, J. Soto, D. R. Wilson, K. A. Abboud, *J. Am. Chem. Soc.* **2004**, *126*, 42 – 43.

[24] The scan was carried out by maintaining two of the three substituents constant and by systematically varying the third.

 © 2006 Wiley-VCH Verlag GmbH & Co. KGaA, Weinheim

Chemical Protein Synthesis

DOI: 10.1002/anie.200600381

Total Chemical Synthesis, Folding, and Assay of a Small Protein on a Water-Compatible Solid Support**

*Erik C. B. Johnson, Thomas Durek, and Stephen B. H. Kent**

Chemical ligation of unprotected peptides has enabled the successful synthesis of a large number of diverse proteins.[1] The native chemical ligation (NCL) reaction,[2] which proceeds in water at neutral pH to yield a native amide bond at the ligation site, has proven to be the most effective chemistry for the ligation of unprotected peptides. A major limitation of protein synthesis by NCL, and indeed all peptide chemical-ligation methods, is the steady decrease in yield because of losses from intermediate handling and purification. Although recent one-pot schemes[3] for chemical protein synthesis have helped eliminate some intermediate purification steps and, therefore, increased yields, one-pot reactions can, over time and multiple ligations, lead to a large accumulation of by-products that are difficult to purify from the target polypeptide. For certain classes of proteins, such as integral membrane proteins, an additional major problem is the poor solubility of many intermediate polypeptide products in the solvents used for ligation. There is currently no effective and general strategy for solubilizing poorly soluble intermediate polypeptides in ligation buffers without introducing modifications to the peptide building blocks. We aimed to perform protein synthesis by NCL on a cross-linked polymer support to address these limitations.

Polymer-supported synthetic chemistry, originally introduced by Merrifield for peptide synthesis,[4] is known to have a number of advantages over traditional solution-phase chemistry. These advantages include simple purification through

[*] Prof. Dr. S. B. H. Kent
Institute for Biophysical Dynamics
Department of Biochemistry, Department of Chemistry
University of Chicago
929 E. 57th Street, Chicago, IL 60637 (USA)
Fax: (+1) 773-702-0439
E-mail: skent@uchicago.edu

E. C. B. Johnson, Dr. T. Durek
Institute for Biophysical Dynamics
Department of Biochemistry
University of Chicago
929 E. 57th Street, Chicago, IL 60637 (USA)

[**] E.C.B.J. is supported by the MD/PhD Graduate Training in Growth and Development program at the University of Chicago (NIH T32 HD007009). We also gratefully acknowledge support from the Department of Energy Genomes for the Life Genomics Program (Grant DE-FG02-04ER63786).

Supporting information for this article is available on the WWW under http://www.angewandte.org or from the author.

© 2006 Wiley-VCH Verlag GmbH & Co. KGaA, Weinheim

washing the resin-bound product and the consequent possibility of using high concentrations of reactants to achieve rapid reactions. Furthermore, because of the cross-linked nature of the polymer support, molecules that would otherwise be insoluble in a given solvent are well-solvated when attached to the polymer, provided the cross-linked polymer network can swell in the solvent.[5] These properties of the solid phase make it a potentially attractive tool for chemical protein synthesis, and a number of groups have investigated its suitability.[6,7]

We sought to exploit the favorable features of polymer-supported synthesis to make a protein by ligation of unprotected peptides on a water-compatible support. In addition, we wanted to investigate the folding, disulfide formation, and biochemical assay of the protein while it is still covalently attached to the solid support, with an eye towards using chemical protein synthesis to construct protein libraries that can be assayed on-resin. The test system used to explore solid-phase (native) chemical ligation (SPCL) was EETI-II, a trypsin inhibitor isolated from the seeds of the squash plant family.[8] EETI-II is 28 residues in length and is a member of the knottin protein family, all of which contain three disulfide bonds that define the correct tertiary fold of the protein.[9]

The synthetic strategy for EETI-II is shown in Scheme 1. The superpermeable organic combinatorial chemistry (SPOCC) resin[10–12] was used, as studies by our group have shown it to be superior to other water-compatible resins tested for SPCL. This resin consists of a poly(ethyleneoxide) matrix and is, therefore, highly solvated by water and chemically inert. The resin was derivatized with a *para*-hydroxybenzyl alcohol linker, which is labile to strong acids such as trifluoroacetic acid (TFA). The penultimate residue in EETI-II is cysteine, which provided a convenient handle for the attachment of the first unprotected peptide by means of a NCL reaction. The cysteine–glycine dipeptide was synthesized on the SPOCC resin by 9-fluorenylmethoxycarbonyl (Fmoc) chemistry with the cysteine residue protected as (4*R*)-1,3-thiazolidine-4-carboxylic acid (Thz).[13] After removal of the Fmoc group from Fmoc–Thz, the Thz unit was converted into free cysteine by reaction with aqueous 0.8 M methoxylamine·HCl. The resin was then washed with ligation buffer, and the first ligation performed using a 1.5-fold molar excess of EETI-II(19–26)-$^{\alpha}$thioester relative to cysteine attached to the resin, at a concentration of 24 mM. The progress of the reaction was monitored by withdrawal of a small resin sample (5–10 beads), washing with water, cleavage of the peptide from the resin with TFA, redissolving the peptide in acetonitrile/water + 0.1% TFA with tris(2-carboxyethyl)-phosphine hydrochloride (TCEP) added as a reducing agent, and analysis with LC–MS. Analysis of the first ligation step after 1.5 h is shown in Figure 1a. The resin was washed with ligation buffer and water, and the thiazolidine was again converted into cysteine with 0.8 M methoxylamine. EETI-II(9–18)-$^{\alpha}$thioester and EETI-II(1–8)-$^{\alpha}$thioester were ligated in a similar fashion (ligation: 4 h and 6 h, respectively; Figure 1b,c). After multiple ligations, small peaks due to incomplete reaction became apparent. In a second synthesis, the reactions could be driven to completion using a twofold molar excess of peptide relative to immobilized cysteine at a concentration of >20 mM and a reaction time of 2 h per ligation (Figure 1d).

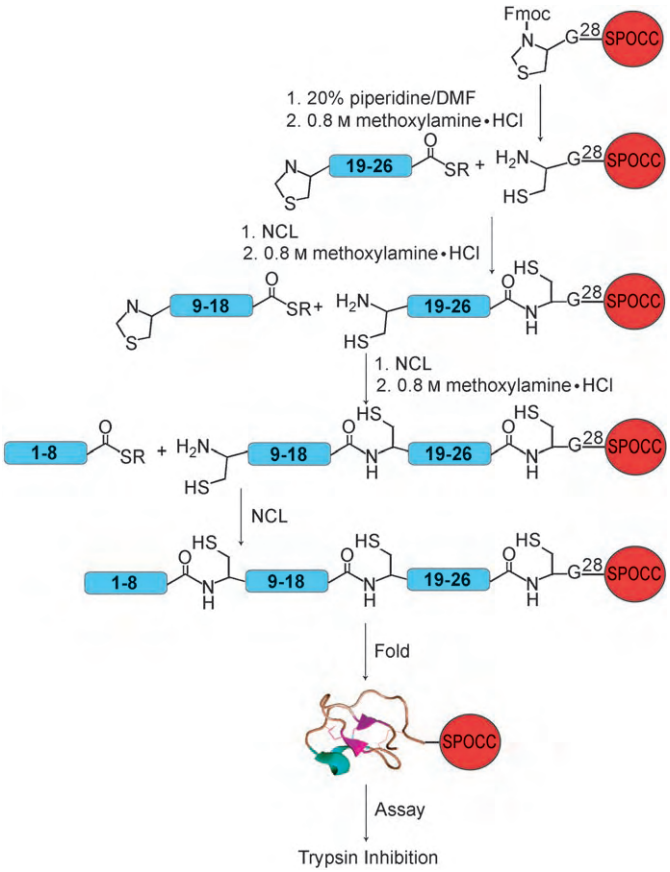

Scheme 1. Strategy for the total chemical synthesis of EETI-II by SPCL, folding, and assay on the solid support. Fmoc-Gly-OH is loaded onto a TFA-labile linker attached to the PEG resin (SPOCC), and Fmoc-Thz-OH is coupled to Gly after Fmoc removal. The N-protecting group is removed from the Fmoc-Thz-peptide-resin, the Thz unit is converted into cysteine, and the first peptide is ligated by NCL. The Thz unit is converted into Cys, and the cycle is repeated until the full-length polypeptide chain has been assembled. The polypeptide is folded into its correct three-dimensional structure while still covalently attached to the resin and assayed for activity. Although the growing polypeptide chain is depicted for simplicity as attached to the surface of the resin, in fact the polypeptide is enmeshed within a swollen interpenetrating PEG polymer network; therefore, all the reagents must diffuse into the resin for the reaction to occur, and the resin must swell further to accommodate the growing polypeptide chain.

After assembly of the polypeptide chain by SPCL, the 28-residue polypeptide product was cleaved by treatment with TFA. Typical recovered yields of EETI-II were 80–90%, based on loading of the resin. The crude material was folded in solution by oxidation with air at pH 8.0 (Figure 2). Folding occurred through the disulfide pathway previously reported for this protein; two disulfides formed quickly, while the third took longer to form.[14] The correctly-folded material was purified by RP-HPLC and tested for inhibitory activity against trypsin (Figure 3). The protein was found to inhibit trypsin in a near 1:1 molar ratio, thus showing the tight-binding affinity which is characteristic of this inhibitor towards trypsin.[15]

 © 2006 Wiley-VCH Verlag GmbH & Co. KGaA, Weinheim

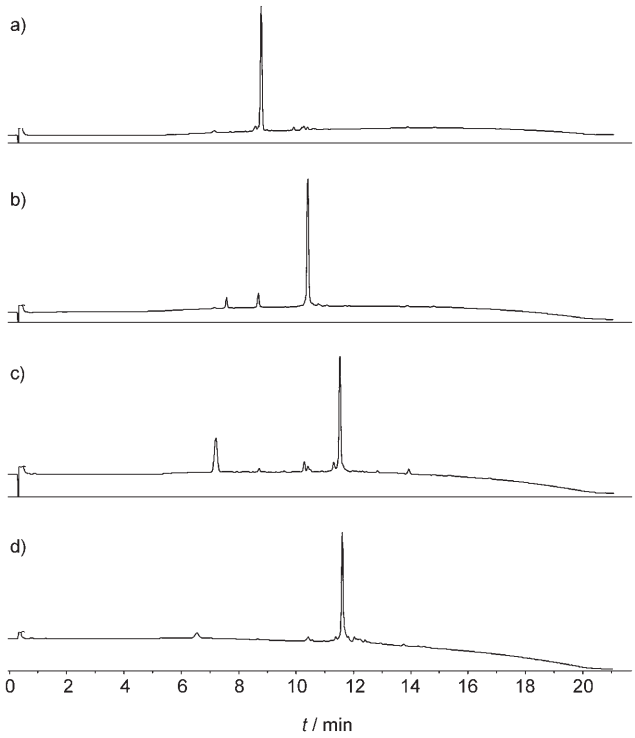

Figure 1. Synthesis of EETI-II by SPCL. Resin samples were withdrawn, the polypeptides cleaved, TFA removed under vacuum, and the crude products redissolved in acetonitrile/water + 0.1% TFA and analyzed by RP-HPLC. a) The crude products after ligation of EETI-II(19–26) for 1.5 h (the peak at 8.7 min corresponds to the expected product). b) The crude products after ligation of residues 9–18 for 4 h (the peak at 10.4 min is the expected product; the peak at 7.6 min is peptide 9–18 ligated to the Cys–Gly (CG) dipeptide, a consequence of incomplete ligation of peptide 19–26 to CG; the peak at 8.7 min is peptide 19–28 incompletely ligated). c) The crude products after ligation of residues 1–8 for 6 h (the peak at 11.6 min is the expected 1–28 product; all other peaks are from incomplete ligation, except for the peak at 7.1 min, which is non-peptidic). d) The final crude products from an SPCL synthesis of EETI-II using a 2-fold molar excess, rather than a 1.5-fold molar excess, of thioester peptides relative to immobilized cysteine peptides (reaction time for each ligation: 2 h).

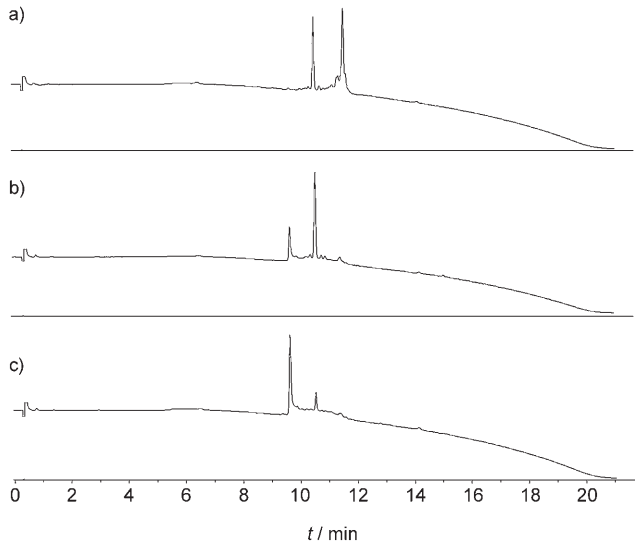

Figure 2. Folding of EETI-II in solution. Fully reduced protein was allowed to fold by air oxidation in 0.2 M phosphate buffer at pH 8.0. Samples were withdrawn during folding and analyzed by RP-HPLC. a) Folding after 2 h (linear EETI-II elutes at 11.6 min; the peak at 10.5 min corresponds to the protein containing two disulfide bonds). b) Folding after 18 h (the peak at 9.6 min corresponds to the folded protein with three disulfide bonds). c) Folding after 36 h.

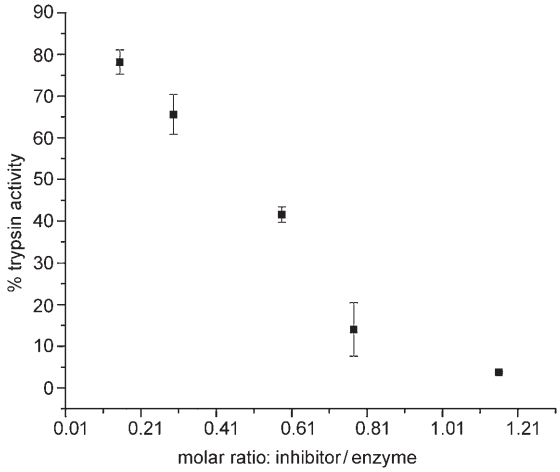

Figure 3. Inhibitor activity against trypsin. Purified EETI-II was assayed for enzymatic inhibition of trypsin. Increasing amounts of synthetic EETI-II reduce the amount of active trypsin available to hydrolyze the substrate BAEE.

The ability to fold a synthetic protein while still covalently attached to the resin would be useful for combinatorial protein synthesis and high-throughput assays, such as enzyme/inhibitor assays, to be performed efficiently. To test whether EETI-II could be folded while the C-terminus was still covalently attached to the resin, the peptide resin was incubated in phosphate buffer at pH 8 while air was bubbled through the solution. Initial folding rates on-resin were noticed to be substantially slower than those in solution, and therefore to speed folding while avoiding potential bacterial contamination, the peptide resin was incubated in water maintained at pH 9. Folding proceeded almost identically as in solution, yet took longer to go to completion (Figure 4).

The SPOCC and similar poly(ethylene glycol) (PEG)-based resins have been shown to allow access of a number of different proteins into the interior of the resin.[10,16–19] A small sample ($\approx$30–50 beads) of the SPOCC–EETI-II resin was incubated with trypsin to test whether trypsin could diffuse into the resin to react with folded EETI-II. A significant decrease in trypsin activity was observed relative to the control (no EETI-II attached to resin) after 10 min of incubation, and the trypsin activity was essentially zero after overnight incubation, thus suggesting that nearly all of the trypsin had diffused into the resin and reacted with EETI-II (Figure 5). We were able to recover trypsin from the resin after washing the resin with water and treating it with TFA to cleave EETI-II from the resin and to dissociate the inhibitor from trypsin (Figure 6).

 © 2006 Wiley-VCH Verlag GmbH & Co. KGaA, Weinheim

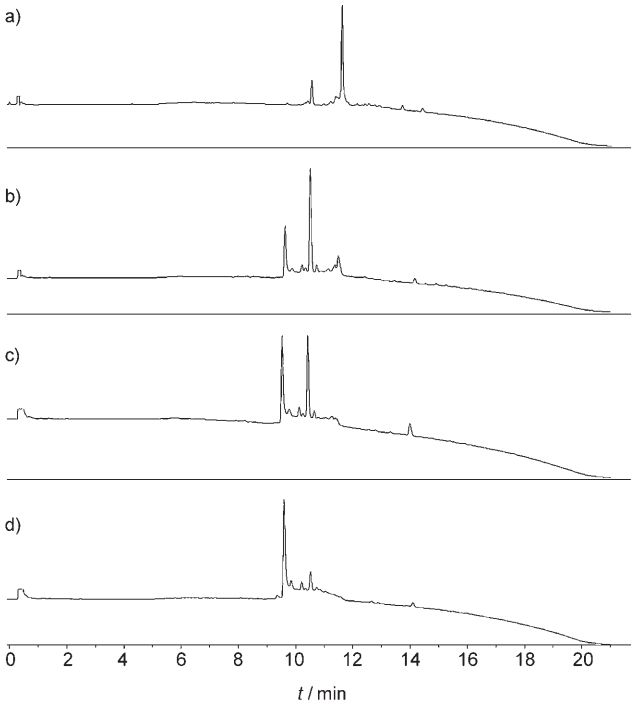

Figure 4. On-resin folding of EETI-II. EETI-II was allowed to fold by air oxidation (unbuffered) while still covalently attached to the PEG resin at the C-terminus. Folding after a) 12 h, b) 5 days, c) 7 days, and d) 10 days. The folding was substantially slower than in solution.

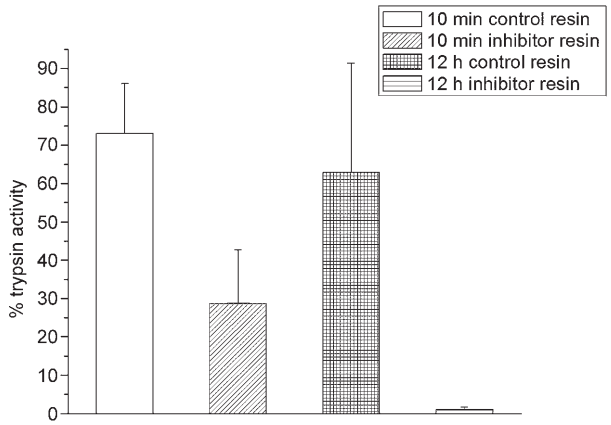

Figure 5. Enzyme inhibition by resin-immobilized EETI-II. Resin with (inhibitor) and without (control) immobilized EETI-II was incubated with trypsin for either 10 min or 12 h, and the solution was then assayed for trypsin activity. EETI-II immobilized on the resin was able to inhibit trypsin activity in a time-dependent fashion.

During preliminary studies on SPCL, it was found that the choice of resin was critical to the quality and success of chemical ligation on the solid phase. The criteria that the polymer support must satisfy include the following: no reactivity towards the conditions used during the synthesis, mechanical stability of the cross-linked network, and the ability to swell in water. Of the resins tested, those that consisted almost exclusively of poly(oxyethylene) were superior to other types of cross-linked polymers, such as cross-linked ethoxylate–acrylate and PEG–polystyrene

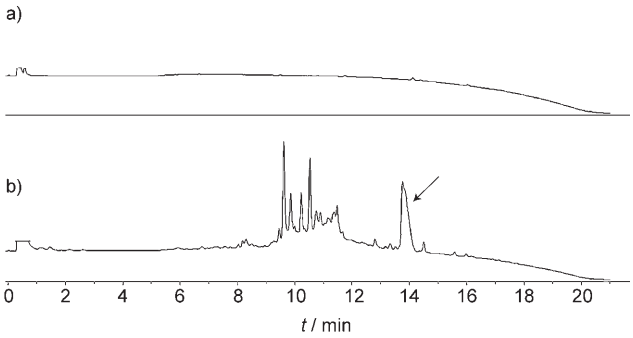

Figure 6. Recovery of trypsin from the resin. a) Control resin lacking immobilized EETI-II was incubated with trypsin overnight at 4 °C, then washed extensively with water, and treated with TFA. After removal of the TFA, the resin was resuspended, any protein products were dissolved in acetonitrile/water + 0.1 % TFA, and the solution was analyzed by RP-HPLC. No trypsin remained in the resin after washing with water. b) As in a), using resin with immobilized EETI-II (the peak at 14.0 min corresponds to trypsin (arrow); the peaks at 9.5–11.5 min correspond to various oxidized forms of EETI-II).

copolymers. This superiority is likely due to the increased swelling properties of cross-linked poly(oxyethylene) over other types of supports.[11] The poly(oxyethylene)–poly(oxetane) copolymer (SPOCC) was also best suited to the synthetic strategy because of its superior swelling in TFA, the solvent used for cleavage of the peptide from the resin.

A well-known aspect of solid-phase chemistry is the requirement for excess reactants to drive the reaction to completion. For precious reagents, such as unprotected peptides, this necessity could present a severe limitation on the use of solid-phase chemistry for protein synthesis. It was possible to achieve near-quantitative ligation with a 1.5-fold molar excess of the thioester peptide as the reactant and complete ligation with a twofold molar excess in a minimal amount of time. The concentrations of these peptides were >20 mM, and less-soluble peptides would likely require longer times for complete ligation. Longer peptides required more time for complete ligation, presumably because of their slower diffusion into the polymer support.

Interestingly, the folding pathway on-resin appeared to be the same as in solution, although the folding kinetics were substantially slowed by immobilizing the protein onto the solid support. The presence of similar amounts of incorrectly folded protein on the solid phase suggests that any misfolding does not involve intermolecular disulfide formation, as the polymer support would be expected to suppress intermolecular aggregation.[5]

The highly permeable nature of the SPOCC resin allows enzymes to diffuse into the polymer matrix and perform chemical reactions.[10,18] It was possible to inhibit the enzymatic activity of trypsin by using EETI-II that had been synthesized and folded on the SPOCC resin, thus demonstrating the ability of trypsin to diffuse into the resin. The enzyme and inhibitor can also be recovered from the resin after TFA cleavage. Because of the permeable nature of the SPOCC resin, it should be possible to perform combinatorial ligations to potentially construct libraries of small proteins which would otherwise be inaccessible through stepwise solid-

 © 2006 Wiley-VCH Verlag GmbH & Co. KGaA, Weinheim

phase peptide synthesis. These highly pure proteins could be assayed for inhibitory activity towards a variety of enzymes by using strategies such as the one-bead-two-compound fluorescence-inhibitor assay.[19–22]

We have demonstrated the synthesis and folding of a small trypsin inhibitor, EETI-II, in rapid fashion and high yield by solid-phase chemical ligation on a PEG-based solid support. We have also shown the ability to perform enzyme assays with the resin-immobilized inhibitor, as well as recovery of both the enzyme and inhibitor from the resin. Because of the good recovery of trypsin from inside the SPOCC resin, it should be possible to assemble polypeptides of >20 kDa by SPCL, fold the polypeptide, and then recover the folded protein from the resin. We are currently working to extend the size limit of proteins synthesized by solid-phase chemical ligation and to perform combinatorial protein synthesis.

Received: January 29, 2006
Published online: April 5, 2006

Keywords: enzymes · native chemical ligation · protein synthesis · proteins · solid-phase synthesis

[1] P. E. Dawson, S. B. Kent, *Annu. Rev. Biochem.* **2000**, *69*, 923.
[2] P. E. Dawson, T. W. Muir, I. Clark-Lewis, S. B. Kent, *Science* **1994**, *266*, 776.
[3] D. Bang, S. B. Kent, *Angew. Chem.* **2004**, *116*, 2588; *Angew. Chem. Int. Ed.* **2004**, *43*, 2534.
[4] B. Merrifield, *Science* **1986**, *232*, 341.
[5] V. K. Sarin, S. B. H. Kent, R. B. Merrifield, *J. Am. Chem. Soc.* **1980**, *102*, 5463.
[6] L. E. Canne, P. Botti, R. J. Simon, Y. J. Chen, E. A. Dennis, S. B. H. Kent, *J. Am. Chem. Soc.* **1999**, *121*, 8720.
[7] A. Brik, E. Keinan, P. E. Dawson, *J. Org. Chem.* **2000**, *65*, 3829.
[8] A. Favel, H. Mattras, M. A. Coletti-Previero, R. Zwilling, E. A. Robinson, B. Castro, *Int. J. Pept. Protein Res.* **1989**, *33*, 202.
[9] D. Le Nguyen, A. Heitz, L. Chiche, B. Castro, R. A. Boigegrain, A. Favel, M. A. Coletti-Previero, *Biochimie* **1990**, *72*, 431.
[10] J. Rademann, M. Grotli, M. Meldal, K. Bock, *J. Am. Chem. Soc.* **1999**, *121*, 5459.
[11] M. Grotli, C. H. Gotfredsen, J. Rademann, J. Buchardt, A. J. Clark, J. O. Duus, M. Meldal, *J. Comb. Chem.* **2000**, *2*, 108.
[12] L. P. Miranda, W. D. Lubell, K. M. Halkes, T. Groth, M. Grotli, J. Rademann, C. H. Gotfredsen, M. Meldal, *J. Comb. Chem.* **2002**, *4*, 523.
[13] M. Villain, J. Vizzavona, K. Rose, *Chem. Biol.* **2001**, *8*, 673.
[14] D. Le-Nguyen, A. Heitz, L. Chiche, M. el Hajji, B. Castro, *Protein Sci.* **1993**, *2*, 165.
[15] D. Le-Nguyen, D. Nalis, B. Castro, *Int. J. Pept. Protein Res.* **1989**, *34*, 492.
[16] M. Meldal, F. I. Auzanneau, O. Hindsgaul, M. M. Palcic, *J. Chem. Soc. Chem. Commun.* **1994**, 1849.
[17] M. Meldal, I. Svendsen, *J. Chem. Soc. Perkin Trans. 1* **1995**, 1591.
[18] M. Renil, M. Ferreras, J. M. Delaisse, N. T. Foged, M. Meldal, *J. Pept. Sci.* **1998**, *4*, 195.
[19] J. Buchardt, C. B. Schiodt, C. Krog-Jensen, J. M. Delaisse, N. T. Foged, M. Meldal, *J. Comb. Chem.* **2000**, *2*, 624.
[20] A. Graven, P. M. St Hilaire, S. J. Sanderson, J. C. Mottram, G. H. Coombs, M. Meldal, *J. Comb. Chem.* **2001**, *3*, 441.
[21] A. Papanikos, M. Meldal, *J. Comb. Chem.* **2004**, *6*, 181.
[22] M. Meldal, *Curr. Opin. Chem. Biol.* **2004**, *8*, 238.

 © 2006 Wiley-VCH Verlag GmbH & Co. KGaA, Weinheim

Zeolite Analogues

DOI: 10.1002/anie.200600455

A Sodalite-like Framework Based on Octacyanomolybdate and Neodymium with Guest Methanol Molecules and Neodymium Octahydrate Ions**

Zhao-Xi Wang, Xiao-Fei Shen, Jun Wang, Peng Zhang, Yi-Zhi Li, Emmanuel N. Nfor, You Song, Shin-ichi Ohkoshi, Kazuhito Hashimoto,* and Xiao-Zeng You**

In the past 15 years, cyanide-bridged dimetallic systems based on the hexacyanometallates $[M^{III}(CN)_6]^{3-}$ (M = Cr, Mn, Fe, Co) have attracted considerable attention in the field of molecular magnetism, owing to their interesting and unique properties. Room-temperature molecule-based magnetism,[1] spin-transition phenomena, and photo-induced magnetism[2] have been reported for analogues of Prussian blue ($Fe^{III}_4[Fe^{II}(CN)_6]_3 \cdot 14H_2O$) with other magnetic first-row transition-metal ions. Recently, pressure-tuned magnetism was observed in compounds of the Prussian-blue family.[3] Synthetic chemists have introduced organic ligands into Prussian-blue analogues to create low-dimensional hybrid materials exhibiting single-molecule magnetism[4] or single-chain magnetism.[5]

With the preparation of the high-spin cluster $Mn^{II}_9[W^{V}(CN)_8]_6$ ($S = 39/2$), which has a unique full-capped cubane structure,[6] the synthesis and magnetic investigation of cyanide-bridged dimetallic complexes were extended to octacyanometallate-based systems with second- or third-row transition metals, and the study of octacyanometallates rapidly became a hot topic in the field of molecular magnetism. This phenomenon may be attributed to the following two points. 1) The octacyanometallates $[M^{V/IV}(CN)_8]^{3-/4-}$ (for example, with M = Nb, Mo, W) are versatile building blocks that can adopt three different spatial configurations (square

[*] Z.-X. Wang, X.-F. Shen, J. Wang, P. Zhang, Y.-Z. Li, E. N. Nfor, Dr. Y. Song, Prof. X.-Z. You
Coordination Chemistry Institute and
the State Key Laboratory of Coordination Chemistry
Nanjing University, Nanjing 210093 (P.R. China)
Fax: (+86) 25-8331-4502
E-mail: yousong@nju.edu.cn
youxz@nju.edu.cn

Prof. Dr. S.-i. Ohkoshi, Prof. Dr. K. Hashimoto
Department of Applied Chemistry, School of Engineering
The University of Tokyo
7-3-1 Hongo, Bunkyo-ku, Tokyo 113-8656 (Japan)
Fax: (+81) 3-5841-1142
E-mail: kazuhito@light.t.u-tokyo.ac.jp

[**] This work was supported by the China Postdoctoral Science Foundation (No. 2004035657), the Jiangsu Postdoctoral Science Foundation, and the National Natural Science Foundation of China.

Supporting information for this article is available on the WWW under http://www.angewandte.org or from the author.

© 2006 Wiley-VCH Verlag GmbH & Co. KGaA, Weinheim

antiprism (D_{4h}), dodecahedron (D_{2d}), or bicapped trigonal prism (C_{2v})), depending on the metal ion and its chemical environment (the surrounding ligands).[7] Thus, assemblies of these units with various dimensionalities (0D,[6,8] 1D,[9] 2D,[10] and 3D[11]) are found in the crystal structures of the octacyanometallates. 2) Because of their flexible molecular structures, octacyanometallate-based complexes can exhibit magnetic properties as varied as those of the hexacyanometallates, for example, photo-induced magnetism,[10b,11d] and single-molecule magnetism.[8b] In recent studies, the investigation of octacyanometallate-based dimetallic systems has mainly focused on first-row transition-metal ions. The synthesis of complexes containing octacyanometallates and lanthanide ions is still challenging. To date, only two examples, with 1D[12] and 2D[13] polymeric structures, respectively, have been reported. Lanthanide–octacyanometallate compounds with 3D structures have not yet been obtained. As lanthanide ions often have higher coordination numbers, complexes containing lanthanide ions can have very complicated structures. The high spins and significant spin–orbit coupling of the lanthanide ions can lead to interesting magnetic properties. For these reasons, we tried to prepare a lanthanide-containing octacyanometallate-based magnet using $[Mo^{V}(CN)_8]^{3-}$ and Nd^{III} as the building blocks. However, the unexpected octacyanomolybdate(IV)-based complex $[\{Nd^{III}(CH_3OH)_4Mo^{IV}(CN)_8\}_3]^{3-}\cdot[Nd^{III}(H_2O)_8]^{3+}\cdot 8\,CH_3OH$ (**1**), which has a unique zeolite-like framework containing guest methanol molecules and $[Nd^{III}(H_2O)_8]^{3+}$ ions, was isolated instead. Herein, we report the preparation and structure of **1**, to our knowledge, the first 3D lanthanide-containing octacyanometallate-based complex. Complex **1** is also the first case of $[Nd^{III}(H_2O)_8]^{3+}$ ions occurring as guests locked in a cagelike framework.

The reaction mixture of $(Bu_3NH)_3[Mo^{V}(CN)_8]$ (Bu_3N = tributylamine) and $Nd^{III}(NO_3)_3\cdot 6H_2O$ in methanol yielded light yellow needles after one day. On keeping the reaction mixture for three months, the needles turned into brown-yellow diamond-shaped crystals of **1**.

Single-crystal X-ray diffraction revealed that **1** is composed of the anionic 3D zeolite-like framework $[\{Nd^{III}(CH_3OH)_4Mo^{IV}(CN)_8\}_3^{3-}]_\infty$, which contains $[Nd^{III}(H_2O)_8]^{3+}$ ions and methanol molecules as guests in its channels. The local environments of the metal ions, all of which are eight-coordinate, are shown in Figure 1. The $\{Mo^{IV}(CN)_8\}$ units have a distorted square-antiprismatic geometry. Four of the molybdenum-bound cyanide ligands (C1N1, C1AN1A, C4N4, and C4AN4A) bridge to neighboring $Nd1^{III}$ ions in the framework, while the four remaining cyanide groups (C2N2, C2AN2A, C3N3, and C3AN3A) are terminal. The Mo–CN bond lengths range from 2.121(4)–2.159(4) Å, and the C–N bond lengths from 1.137(6)–1.150(5) Å. The coordination environment around Nd1 is also a distorted square antiprism. Four oxygen atoms (O1, O1B, O2, and O2B) from methanol molecules occupy four Nd1 coordination sites, in a distorted tetrahedral conformation, and the nitrogen atoms (N1, N1A, N4C, and N4D) of four cyanide groups from neighboring $\{Mo^{IV}(CN)_8\}$ units, also in a distorted tetrahedral conformation, occupy the other four coordination sites. Together, the $\{Mo^{IV}(CN)_8\}$ and $\{Nd^{III}(CH_3OH)_4(NC)_4\}$ units,

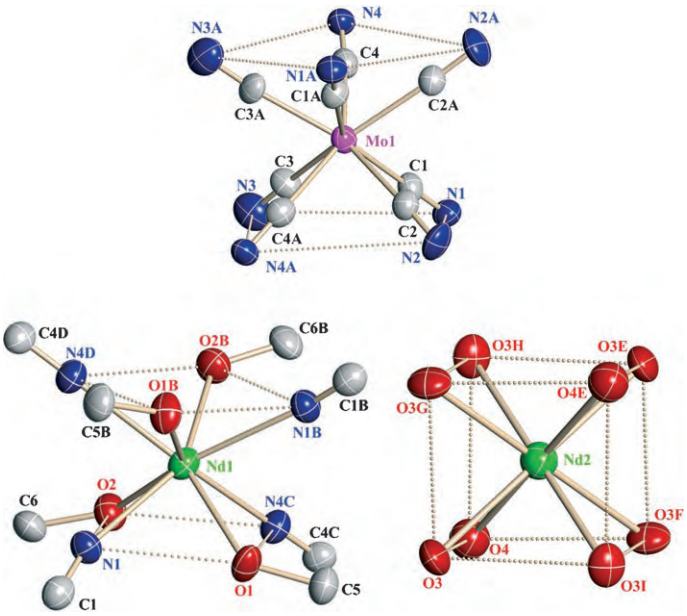

Figure 1. Coordination environments of the metal ions in **1**. Thermal ellipsoids are set at 50% probability. H atoms are omitted for clarity. Symmetry codes: A: $-x, -x+y, 3/2-z$; B: $-1/3+y, 1/3+x, 11/6-z$; C: $1/3-y, 2/3-x, 1/6+z$; D: $1/3-y, 2/3-x, 5/3-z$; E: $4/3-x, 2/3-y, 5/3-z$; F: $1-y, x-y, z$; G: $1/3+y, 2/3-x+y, 5/3-z$; H: $1-x+y, 1-x, z$; I: $1/3+x-y, -1/3+x, 5/3-z$. Selected bond lengths [Å] and angles [°]: C1–Mo1 2.159(4), C2–Mo1 2.159(4), C3–Mo1 2.121(4), C4–Mo1 2.154(5), C1–N1 1.150(5), C2–N2 1.137(6), C3–N3 1.143(6), C4–N4 1.146(6), Nd1–N1 2.543(4), Nd1–N4C 2.535(4), Nd1–O1 2.437(3), Nd1–O2 2.459(3), Nd2–O3 2.388(3), Nd2–O4 2.472(6); N1-C1-Mo1 178.5(4), N2-C2-Mo1 177.1(4), N3-C3-Mo1 173.4(4), N4-C4-Mo1 175.5(4), C1-N1-Nd1 175.0(4), C4C-N4C-Nd1 162.1(3).

connected through their shared cyanide groups, form the zeolite-like skeleton $[\{Nd^{III}(CH_3OH)_4Mo^{IV}(CN)_8\}_3^{3-}]_\infty$ of **1** (capped sticks in Figure 2). The $[Nd^{III}(H_2O)_8]^{3+}$ hydrate ion assumes a slightly distorted cubic geometry. Six symmetry-related O3 atoms and two symmetry-related O4 atoms from water molecules coordinate the Nd2 center at two slightly different Nd–O bond lengths (Figure 1).

In the open zeolite-like framework of **1**, there are two types of channels: regular hexagonal channels run along [001] (Figure 2a), and ellipsoidal hexagonal channels run along [065], [$\bar{6}$05], and [5$\bar{5}$4] (Figure 2b). In fact, the repeating unit of the framework of **1** is the cage shown in Figure 3. The cage is composed of eight 18-membered rings (18-MRs), two of which define the regular hexagonal channels (10.78×10.78 Å^2), and six of which define three ellipsoidal hexagonal channels (9.42×11.62 Å^2). These 18-MRs share their edges with each other and with six square 12-MRs (5.74×5.85 Å^2). All of the cage edges are Mo–CN–Nd linkages. The cage can be visualized as a truncated cube: the eight hexagonal 18-MRs are shaped by "cutting off" small tetrahedra from each of the eight corners of the cube, and the six square 12-MRs are situated at the center of each of the six sides of the cube. Each cage has 14 neighbors: it shares its eight hexagonal faces with eight neighboring cages (Figure 4) and shares its six square faces with six neighboring cages (see Supporting Informa-

 © 2006 Wiley-VCH Verlag GmbH & Co. KGaA, Weinheim

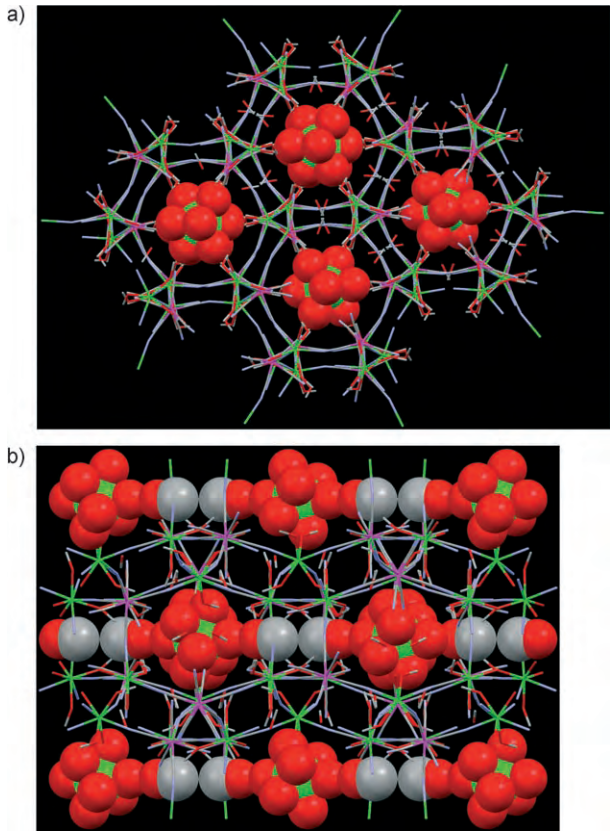

Figure 2. Structure of **1**. The anionic $[\{Nd^{III}(CH_3OH)_4Mo^{IV}(CN)_8\}_3^{3-}]_\infty$ framework (capped sticks) contains hexagonal channels a) along [001], and b) along [065], [$\bar{6}$05], and [5$\bar{5}$4], which are filled with $[Nd^{III}(H_2O)_8]^{3+}$ ions (space-filling spheres) and methanol molecules (capped sticks and space-filling spheres). C gray, N blue, O red, Mo pink, Nd green. H atoms are omitted for clarity.

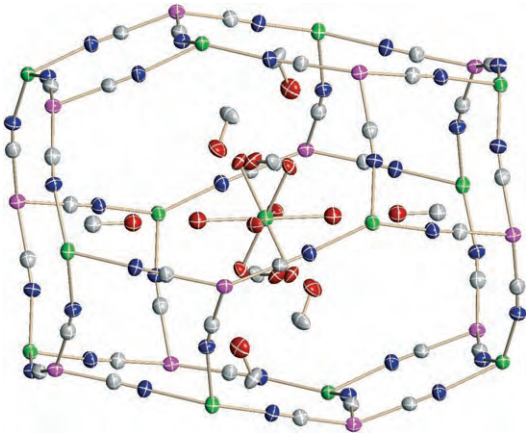

Figure 3. The sodalite-like β-cage of the anionic framework of **1**, which contains one $[Nd^{III}(H_2O)_8]^{3+}$ ion at its center and eight free methanol molecules near the eight hexagonal openings. C gray, N blue, O red, Mo pink, Nd green. H atoms are omitted for clarity.

tion). Even though six of the hexagonal faces in the cages of **1** are distorted, it is still convenient to regard it as a β-cage, the primary building unit of sodalite ($Na_8Cl_2[Al_6Si_6O_{24}]$).[14] Note that all edges of the sodalite-like framework in **1** are

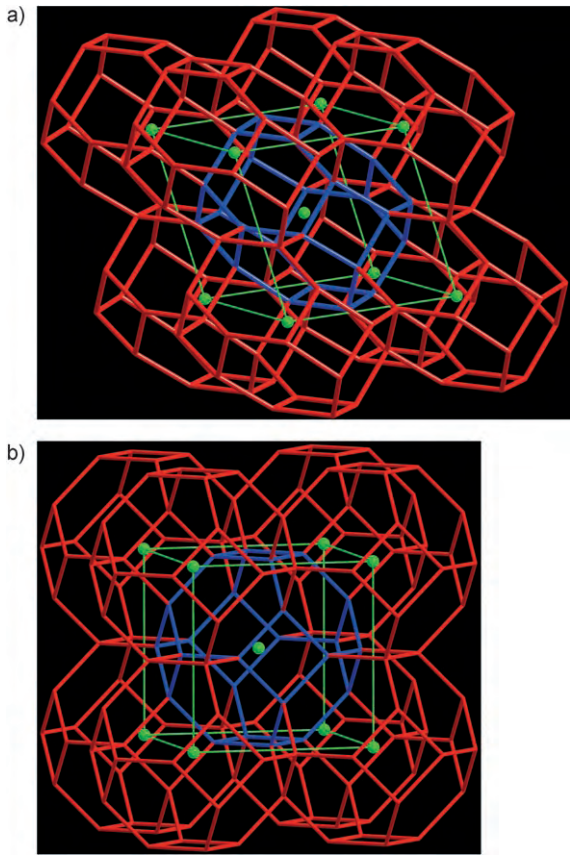

Figure 4. Each β-cage (blue) a) in **1** and b) in sodalite shares its hexagonal faces with eight neighboring β-cages (red).[22] The green spheres represent the Nd (a) or Cl (b) atoms that occupy the centers of the cages in **1** and sodalite, respectively. The green box in (b) represents the unit cell of sodalite; that in (a) is drawn for comparison.

approximately linear, because of the near linearity of the cyanide bridges.

One $[Nd^{III}(H_2O)_8]^{3+}$ ion and eight methanol molecules are encapsulated in the β-cage; the $[Nd^{III}(H_2O)_8]^{3+}$ ion occupies the center of the cage, and four pairs of methanol molecule are located near the eight openings of the four hexagonal channels. Thus, the O4–Nd2–O4A axis of the $[Nd^{III}(H_2O)_8]^{3+}$ ion and the C–O axes of two methanol molecules are aligned along one pseudo-S_6 axis of the cage (Figure 2b). The $[Nd^{III}(H_2O)_8]^{3+}$ ions and methanol molecules are fixed and stabilized within the β-cage by strong hydrogen-bonding interactions. In addition to hydrogen bonds, electrostatic interactions between the metal cation and the anionic cage inhibit the $[Nd^{III}(H_2O)_8]^{3+}$ ions from leaving the channels. The $[Nd^{III}(H_2O)_8]^{3+}$ ion in **1** is a rare example of a solvated lanthanide guest in a 3D cage.[15]

The magnetic properties of **1** were measured for crystalline samples on a SQUID magnetometer in an applied field of 0.1 kOe. The temperature dependence of the magnetic susceptibility from 300–1.8 K is plotted in the forms of $\chi_M(T)$ and $\chi_M T(T)$ in Figure 5. For the free Nd^{III} ion, the ground state of $^4I_{9/2}$ is well separated in energy from the first excited state of $^4I_{11/2}$ (1900 cm^{-1});[16] therefore, only the $^4I_{9/2}$ state is thermally populated at room temperature and below.

 © 2006 Wiley-VCH Verlag GmbH & Co. KGaA, Weinheim

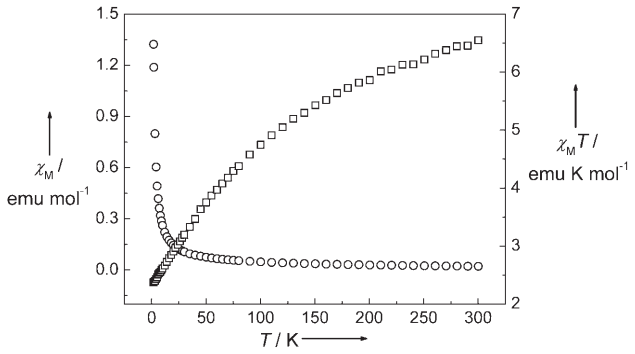

Figure 5. Temperature dependence of the magnetization of **1**, in the forms of $\chi_M(T)$ (left, ○) and $\chi_M T(T)$ (right, □).

Under crystal-field perturbation, the $^4I_{9/2}$ state splits into Stark components.[17] For a Nd^{III} ion in this ground state, the Zeeman factor g_J is equal to 8/11, and the Curie constant is 1.64 emu K mol^{-1}. For **1**, the room-temperature $\chi_M T$ value of 6.55 emu K mol^{-1} is in good agreement with the value of 6.56 emu K mol^{-1} expected for four Nd^{III} ions with $S_{Mo} = 0$.[18] Upon cooling the system, $\chi_M T$ decreases continuously over the whole temperature range and reaches 2.38 emu K mol^{-1} at 1.8 K. This behavior, which is comparable with results reported previously,[19] implies that the magnetic susceptibility of **1** deviates from the Curie law because of the thermal depopulation of Stark levels. The magnetic properties of **1** are consistent with noncoupled magnetic behavior based on four Nd^{III} ions per formula unit.

In summary, we have synthesized the first 3D octacyanomolybdate-based coordination complex of an f-block element. The crystal structure consists of a unique sodalite-like framework with four channels of two types, along [001], and [065], [$\bar{6}$05], and [5$\bar{5}$4], respectively, in which methanol molecules and $[Nd^{III}(H_2O)_8]^{3+}$ ions are encapsulated as guests. The structural and magnetic characterization of **1** indicates that the oxidation state of the molybdenum ion decreases from v to iv with the formation of the anionic host framework, probably to balance the charge of the guest during the self-assembly. The investigation of the magnetic properties of **1** reveals single-ion magnetic behavior for the Nd^{III} ions in this sodalite-like framework.

Experimental Section

1: The starting material $(Bu_3NH)_3[Mo^V(CN)_8]$ was synthesized according to the literature method.[20] To prepare complex **1**, a solution of $Nd^{III}(NO_3)_3{\cdot}6H_2O$ (43.8 mg, 0.10 mmol) in methanol (5 mL) was added to a solution of $(Bu_3NH)_3[Mo^V(CN)_8]$ (93.6 mg, 0.10 mmol) in methanol (5 mL) with gentle stirring. The subsequent addition of a solution of NH_4SCN (22.8 mg, 0.30 mmol) in methanol (3 mL) resulted in a yellow solution. The solution was placed in the dark, and light yellow needles formed after one day. After three months, the needles turned into brown-yellow diamond-shaped crystals of **1** (ca. 28.3 mg, 37% yield). Elemental analysis (%) calcd for **1** ($C_{44}H_{96}Mo_3N_{24}Nd_4O_{28}$): C 23.24, H 4.25, N 14.78; found: C 23.20, H 4.31, N 14.69.

Crystal data for **1**: $C_{44}H_{96}Mo_3N_{24}Nd_4O_{28}$, $M_r = 2274.23$, trigonal, space group $R\bar{3}c$, $a = 20.883(4)$, $c = 32.658(6)$ Å, $V = 12334(4)$ Å^3, $Z = 6$, $\rho_{calcd} = 1.837$ g cm^{-3}, $R_1 = 0.0397$, $wR_2 = 0.0917$, $\mu = 3.004$ mm^{-1}, $S = 1.084$. Data reduction was performed with the Bruker SAINT package. Absorption correction was performed using the SADABS program. The structure was solved by direct methods and refined on F^2 by full-matrix least-squares techniques. Anisotropic displacement parameters were used for all non-hydrogen atoms. Hydrogen atoms were introduced in calculated positions and refined using the riding model. All computations were carried out using the SHELXTL-2000 program package.[21] CCDC-297119 (**1**) contains the supplementary crystallographic data for this paper. These data can be obtained free of charge from The Cambridge Crystallographic Data Centre via www.ccdc.cam.ac.uk/data_request/cif.

Received: February 3, 2006
Published online: April 11, 2006

Keywords: coordination polymers · cyanides · lanthanides · magnetic properties · zeolite analogues

[1] a) T. Mallah, S. Thiébaut, M. Verdaguer, P. Veillet, *Science* **1993**, *262*, 1554; b) M. Verdaguer, T. Mallah, V. Gadet, I. Castro, C. Hélary, S. Thiébaut, P. Veillet, *Conf. Coord. Chem.* **1993**, *14*, 19; c) W. R. Entley, G. S. Girolami, *Science* **1995**, *268*, 397; d) S. Ferlay, T. Mallah, R. Ouahès, P. Veillet, M. Verdaguer, *Nature* **1995**, *378*, 701.

[2] a) N. Shimamoto, S.-i. Ohkoshi, O. Sato, K. Hashimoto, *Inorg. Chem.* **2002**, *41*, 678; b) S.-i. Ohkoshi, T. Matsuda, H. Tokoro, K. Hashimoto, *Chem. Mater.* **2005**, *17*, 81; c) W. Kosaka, K. Nomura, K. Hashimoto, S.-i. Ohkoshi, *J. Am. Chem. Soc.* **2005**, *127*, 8590; d) O. Sato, T. Iyoda, A. Fujishima, K. Hashimoto, *Science* **1996**, *272*, 704; e) S.-i. Ohkoshi, S. Yorozu, O. Sato, T. Iyoda, K. Fujishima, K. Hashimoto, *Appl. Phys. Lett.* **1997**, *70*, 1040.

[3] E. Coronado, M. C. Giménez-López, G. Levchenko, F. M. Romero, V. García-Baonza, A. Milner, M. Paz-Pasternak, *J. Am. Chem. Soc.* **2005**, *127*, 4580.

[4] a) J. J. Sokol, A. G. Hee, J. R. Long, *J. Am. Chem. Soc.* **2002**, *124*, 7656; b) C. P. Berlinguette, D. Vaughn, C. Cañada-Vilalta, J. R. Galán-Mascarós, K. R. Dunbar, *Angew. Chem.* **2003**, *115*, 1561; *Angew. Chem. Int. Ed.* **2003**, *42*, 1523; c) H. J. Choi, J. J. Sokol, J. R. Long, *Inorg. Chem.* **2004**, *43*, 1606; d) S. Wang, J.-L. Zuo, H.-C. Zhou, H. J. Choi, J. R. Long, Y. Ke, X.-Z. You, *Angew. Chem.* **2004**, *116*, 6066; *Angew. Chem. Int. Ed.* **2004**, *43*, 5940.

[5] a) R. Lescouëzec, J. Vaissermann, C. Ruiz-Pérez, F. Lloret, R. Carrasco, M. Julve, M. Verdaguer, Y. Dromzee, D. Gatteschi, W. Wernsdorfer, *Angew. Chem.* **2003**, *115*, 1521; *Angew. Chem. Int. Ed.* **2003**, *42*, 1482; b) S. Wang, J.-L. Zuo, S. Gao, Y. Song, H.-C. Zhou, Y.-Z. Zhang, X.-Z. You, *J. Am. Chem. Soc.* **2004**, *126*, 8900.

[6] Z. J. Zhong, H. Seino, Y. Mizobe, M. Hidai, A. Fujishima, S.-i. Ohkoshi, K. Hashimoto, *J. Am. Chem. Soc.* **2000**, *122*, 2952.

[7] J. G. Leipoldt, S. S. Basson, A. Roodt, *Adv. Inorg. Chem.* **1993**, *40*, 241.

[8] a) J. Larionova, M. Gross, M. Pilkington, H. Andres, H. Stoeckli-Evans, H. U. Güdel, S. Decurtins, *Angew. Chem.* **2000**, *112*, 1667; *Angew. Chem. Int. Ed.* **2000**, *39*, 1605; b) Y. Song, P. Zhang, X.-M. Ren, X.-F. Shen, Y.-Z. Li, X.-Z. You, *J. Am. Chem. Soc.* **2005**, *127*, 3708.

[9] For example: a) P. Przychodzeń, K. Lewiński, M. Bałanda, R. Pełka, M. Rams, T. Wasiutyński, C. Guyard-Duhayon, B. Sieklucka, *Inorg. Chem.* **2004**, *43*, 2967; b) Y. S. You, D. Kim, Y. Do, S. J. Oh, C. S. Hong, *Inorg. Chem.* **2004**, *43*, 6899.

[10] For example: a) R. Podgajny, T. Korzeniak, M. Balanda, T. Wasiutynski, W. Errington, T. J. Kemp, N. W. Alcockc, B. Sieklucka, *Chem. Commun.* **2002**, 1138; b) Y. Arimoto, S.-i.

 © 2006 Wiley-VCH Verlag GmbH & Co. KGaA, Weinheim

Ohkoshi, Z. J. Zhong, H. Seino, Y. Mizobe, K. Hashimoto, *J. Am. Chem. Soc.* **2003**, *125*, 9240.
[11] a) Z. J. Zhong, H. Seino, Y. Mizobe, M. Hidai, M. Verdaguer, S.-i. Ohkoshi, K. Hashimoto, *Inorg. Chem.* **2000**, *39*, 5095; b) Y. Song, S.-i. Ohkoshi, Y. Arimoto, H. Seino, Y. Mizobe, K. Hashimoto, *Inorg. Chem.* **2003**, *42*, 1848; c) T. Kashiwagi, S.-i. Ohkoshi, H. Seino, Y. Mizobe, K. Hashimoto, *J. Am. Chem. Soc.* **2004**, *126*, 5024; d) T. Hozumi, S.-i. Ohkoshi, K. Hashimoto, *J. Am. Chem. Soc.* **2005**, *127*, 3864.
[12] S. Ikeda, T. Hozumi, K. Hashimoto, S.-i. Ohkoshi, *Dalton Trans.* **2005**, 2120.
[13] T. Hozumi, S.-i. Ohkoshi, Y. Arimoto, H. Seino, Y. Mizobe, K. Hashimoto, *J. Phys. Chem. B* **2003**, *107*, 11571.
[14] E. C. Moloy, R. T. Cygan, F. Bonhomme, D. M. Teter, A. Navrotsky, *Chem. Mater.* **2004**, *16*, 2121.
[15] S. Liu, C. E. Plecnik, E. A. Meyers, S. G. Shore, *Inorg. Chem.* **2005**, *44*, 282.
[16] a) R. L. Carlin, *Magnetochemistry*, Springer, Berlin, **1986**; b) M. Andruh, E. Bakalbassis, O. Kahn, J. C. Trombe, P. Porchers, *Inorg. Chem.* **1993**, *32*, 1616.
[17] a) J.-C. G. Bunzli, G. R. Chopin, *Lanthanide Probes in Life, Chemical and Earth Sciences*, Elsevier, Amsterdam, **1989**; b) J.-P. Costes, F. Nicodème, *Chem. Eur. J.* **2002**, *8*, 3442.
[18] a) G. Rombaut, S. Gohen, L. Ouahab, C. Mathonière, O. Kahn, *J. Chem. Soc. Dalton Trans.* **2000**, 3609; b) S.-i. Ohkoshi, N. Machida, Z. J. Zhong, K. Hahsimoto, *Synth. Met.* **2001**, *122*, 523; c) F. Tuna, S. Golhen, L. Ouahab, J.-P. Sutter, *C. R. Chim.* **2003**, *6*, 377.
[19] a) G. Oczko, J. Legendziewicz, M. S. Wickleder, G. Meyer, *J. Alloys Compd.* **2002**, *341*, 255; b) Q.-L. Wang, M. Liang, D.-Z. Liao, S.-P. Yan, Z.-H. Jiang, P. Cheng, *Z. Anorg. Allg. Chem.* **2004**, *630*, 613; c) M. Roger, T. Arliguie, P. Thuéry, M. Fourmigué, M. Ephritikhine, *Inorg. Chem.* **2005**, *44*, 584.
[20] a) J. D. Leipoldt, L. D. C. Bok, P. J. Chilliers, *Z. Anorg. Allg. Chem.* **1974**, *407*, 350; b) L. D. C. Bok, J. D. Leipoldt, S. S. Basson, *Z. Anorg. Allg. Chem.* **1975**, *415*, 81.
[21] Bruker SMART, SAINT, SADABS and SHELXTL, Bruker AXS Inc., Madison, WI, USA, **2000**.
[22] a) I. Hassan, H. D. Grundy, *Acta Crystallogr. Sect. B* **1984**, *40*, 6; b) K. Brandenburg, Diamond Version 2.1c, Crystal Impact, Germany, **1999**.

 © 2006 Wiley-VCH Verlag GmbH & Co. KGaA, Weinheim

Dinitrogen Activation

DOI: 10.1002/anie.200504343

A Co_2N_2 Diamond-Core Resting State of Cobalt(I): A Three-Coordinate Co^I Synthon Invoking an Unusual Pincer-Type Rearrangement**

*Alison R. Fout, Falguni Basuli, Hongjun Fan, John Tomaszewski, John C. Huffman, Mu-Hyun Baik, and Daniel J. Mindiola**

Coordinatively unsaturated transition-metal complexes are expected to be inherently reactive and offer an opportunity to study novel transformations such as homogeneous catalysis[1] and the activation of inert substrates such as N_2.[2] However, generating low-coordinate environments in these systems can often result in degradation or rearrangement of the ancillary ligand. Only in a few cases can reorganization of the ancillary ligand be reversible, thus generating resting states that are capable of behaving as "masked" low-coordinate fragments. For example, Cummins and co-workers reported a reversible β-hydride elimination pathway leading to a masked three-coordinate Mo^{III} fragment capable of reductively cleaving atmospheric nitrogen.[3] A similar reversible β-hydride elimination has also been documented for the complex $[Fe(PMe_3)_5]$, which has been shown to equilibrate with the corresponding iron(II) isomer $[Fe(H)(\eta^2\text{-}CH_2PMe_2)(PMe_3)_3]$ and free trimethylphosphine.[4] In other amphivalent systems, Fink and co-workers[5] discovered that a dinuclear Pd^0 complex containing bridging bidentate phosphine ligands can equilibrate with its mononuclear scaffold. We report herein an unprecedented ligand rearrangement of a pincer-type framework PNP (PNP = $[N\{2\text{-}P(CHMe_2)_2\text{-}4\text{-}MeC_6H_3\}_2]^-$).[6,7] Reorganization of the PNP pincer ligand from a terminal chelating mode to a bridging mode allows for isolation of $[\{(\mu_2\text{-PNP})Co\}_2]$, a complex bearing a Co_2N_2 diamond-core resting state. $[\{(\mu_2\text{-PNP})Co\}_2]$ behaves as a three-coordinate Co^I synthon when treated with substrates

[*] A. R. Fout, Dr. F. Basuli, Dr. H. Fan, Dr. J. Tomaszewski, Dr. J. C. Huffman, Prof. Dr. M.-H. Baik, Prof. Dr. D. J. Mindiola
Department of Chemistry
School of Informatics and Molecular Structure Center
Indiana University, Bloomington, IN 47405 (USA)
Fax: (+1) 812-855-8300
E-mail: mindiola@indiana.edu

[**] This work was supported by Indiana University, the Camille and Henry Dreyfus Foundation (Teacher-Scholar Award to D.J.M.), the Alfred P. Sloan Foundation (Fellowship award to D.J.M.), the National Institutes of Health (HG003894 to M.-H.B.), and the National Science Foundation (CHE-0348941 grant and PECASE award to D.J.M.). A.R.F. acknowledges the Department of Education for a GAANN Fellowship and Dr. Allen R. Siedle for insightful advice. We are also grateful to Prof. Karsten Meyer and Dr. Ingrid Castro-Rodriguez for collecting SQUID data of compound **1**.

Supporting information for this article (including experimental details and crystallographic data) is available on the WWW under http://www.angewandte.org or from the author.

 © 2006 Wiley-VCH Verlag GmbH & Co. KGaA, Weinheim InterScience

such as N_2 and CO. We also report a rare example of a dianionic dinitrogen[8] salt of cobalt(−I), a product likely resulting from overreduction of the "[(PNP)Co]" core under atmospheric nitrogen.

The square-planar complex [(PNP)CoCl] (**1**)[7,9] is a precursor prepared readily from [Li(PNP)][6] and $CoCl_2$ in THF, and displays an irreversible one-electron reduction wave at −2.41 V under N_2.[7] Chemical reduction of **1** with an excess of $NaC_{10}H_8$ in an N_2 atmosphere effected an immediate color change from dark green to black. Upon work up and crystallization from Et_2O at −35 °C, dark crystals of the dianionic cobalt–dinitrogen complex $[\{Na_2(thf)_3\}_2\{(PNP)Co(N_2)\}_2]$ (**2**) were obtained.[7] However, solid samples of **2** were marred with about 5–10% content of another cobalt species (assayed by ^{31}P and ^{15}N NMR spectroscopy, see below). Complex **2** is diamagnetic and displays an intense absorption in the IR spectrum at $\tilde{\nu}_{NN} = 1784\ cm^{-1}$, a value higher in energy than that measured for the isotopomer prepared from $^{15}N_2$ (1732 cm^{-1}). The ^{15}N NMR spectrum of **2** exhibits two broad signals at $\delta = 319$ and 293 ppm, for which no J_{NN} coupling was resolved even upon cooling, an attribute possibly arising from coupling to the ^{59}Co nucleus ($I = 7/2$, 100% abundance). Complex **2** is exceedingly reactive, and solid samples or solutions of **2** become oxidized over several hours with transformation (albeit not cleanly) into $[\{(PNP)Co\}_2(\mu_2\text{-}N_2)]$[7] (**3**), the same by-product observed in the original synthesis of **2** from **1**. Characterization data for **3** include a weak absorption in the IR spectrum at $\tilde{\nu}_{NN} = 2024\ cm^{-1}$, a value blue-shifted from that measured for the $^{15}N_2$ isotopomer (1957 cm^{-1}). In contrast to **2**, the $^{15}N_2$ unit in complex **3** exhibits only one broad ^{15}N NMR resonance at $\delta =$ 306 ppm. Complex **3** can be prepared in greater yield from the one-electron reduction of **1** with *t*BuLi in an N_2 atmosphere or alternatively by addition of two equivalents of **1** to **2**. The latter reaction suggests that **2** is a powerful one-electron reductant and that an unsaturated "[(PNP)Co]" intermediate might play a role in the course of these reactions (Scheme 1). Furthermore, the $^{15}N_2$ isotopomer of **3** slowly exchanges with $^{14}N_2$, as evidenced by a blue shift of the $\tilde{\nu}_{NN}$ stretching frequency in the IR spectrum as well as by the decay of the ^{15}N NMR resonance.

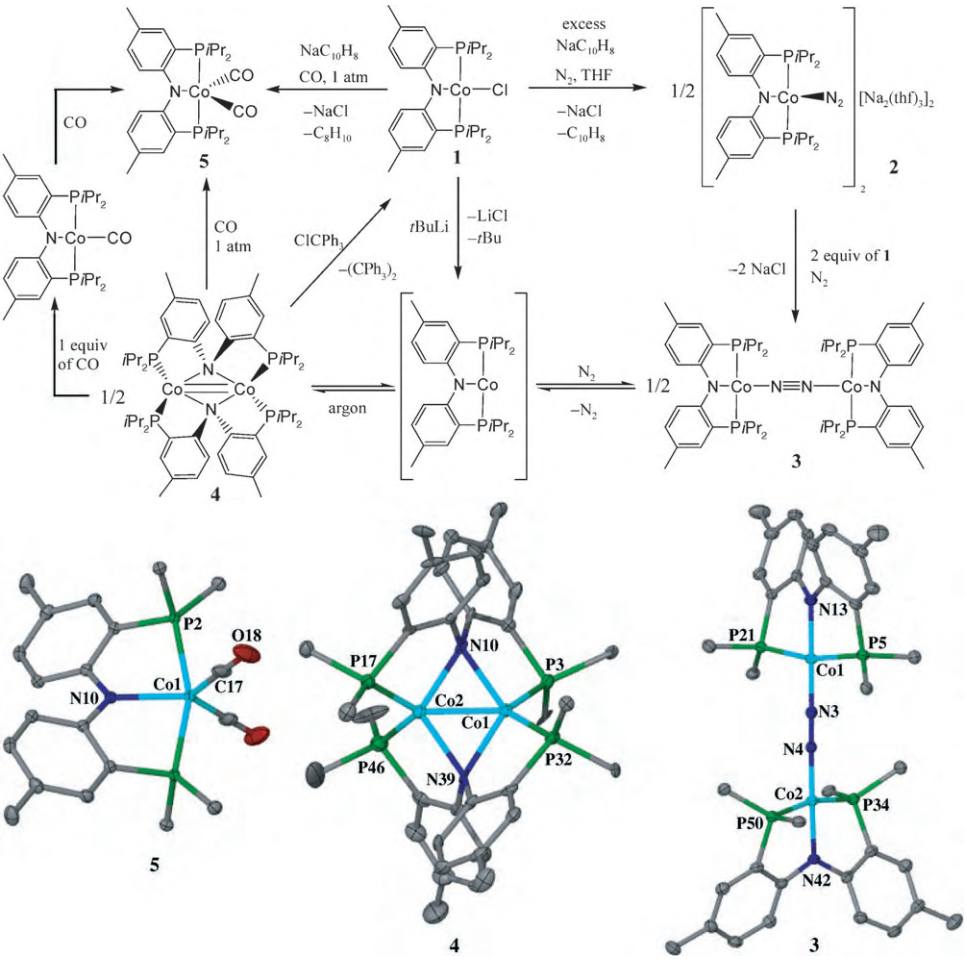

Scheme 1. Synthesis of complexes **2**–**5** and the intermediate [(PNP)Co(CO)]. Molecular structures are depicted with thermal ellipsoids set at 50% probability with H atoms, isopropyl methyl groups, and solvent molecules omitted for clarity.

Single-crystal solid-state structures for compounds **2** and **3** reveal that each system is composed of two cobalt centers (Figure 1 (**2**) and Scheme 1 (**3**)).[7] The molecular structure of **2** exhibits a $Na_2Co_2N_4$ core divided into two topologically linear Co–N–N units which are related by an inversion center (Figure 1). One of the Na^+ centers bridges another $\{(PNP)CoN_2\}$ unit through the adjacent β-N atom to close the $Na_2Co_2N_4$ ring in **2**. If one ignores the Na^+ ions, each Co atom is confined in a highly distorted tetrahedral geometry with the metal atom deviating from the PNP mean plane by about 0.832°. The molecular structure of **2** unarguably depicts a dianionic $\{(PNP)Co(N_2)\}^{2-}$ unit, but the poor quality of the X-ray data prevents us from discussing any specific metrical parameters (Figure 1).[7]

We were able to reproduce the structural features in **2** by using high-level density functional calculations at the B3LYP/6-31G** level of theory.[10] To ascertain more information on the nature of the Co–N bond in **2**, we computed the bond order directly from the molecular structure,[11] and obtained a bond order of 0.898 for the Co–N linkage and a bond order of 2.322 for the N–N linkage. As a result, we tentatively assign a single bond for the Co–N linkage and a triple bond for the N–N linkage.[7] More importantly, when we computed the

 © 2006 Wiley-VCH Verlag GmbH & Co. KGaA, Weinheim

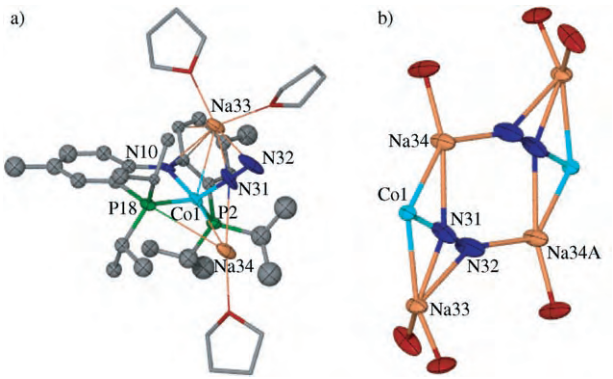

Figure 1. Molecular structure of **2**. The $[\{Na_2(thf)_3\}\{(PNP)CoN_2\}]$ unit (a) and $[\{Na_2(thf)_3CoN_2\}_2]$ core (b) are shown with thermal ellipsoids set at 50% probability. All H atoms in (a) are excluded for clarity, and the disordered thf ligands are depicted with sticks. Only the O atoms (red) of the thf ligands are displayed in (b).

molecular structure of the monomer $[(PNP)Co(N_2)]^{2-}$, the energy of the system fell into a minimum for the analogous geometry observed in the $\{(PNP)Co(N_2)\}^{2-}$ unit of the crystal structure of **2**. As expected for a Co^{-I} species, the five filled orbitals highest in energy (HOMO through HOMO−4) are all metal-based, and the LUMO is *only* ligand-based and comprises the $aryl_{PNP}$ π* orbital (Figure 2).[7] For all these reasons, complex **2** is best described as a dianionic d^{10} cobalt–dinitrogen complex. Compound **2** represents a rare example of a dinitrogen-ligated[8] cobalt(−I) dianion.

In contrast to **2**, the crystal structure of **3** displays a more common Co–N_2–Co linkage (Scheme 1),[8,12] with both cobalt atoms residing in a square-planar geometry in which the two {(*mer*-PNP)Co} units are essentially orthogonal to each other (ca. 93°). The $Co–N_{PNP}$ bond lengths (1.928(2) and 1.935(2) Å) are much longer than the $Co–N_{NN}$ bond lengths (1.763(2) and 1.768(2) Å), and the N–N bond length is short (1.144(3) Å), hence consistent with the topologically linear resonance structure [(PNP)Co–N=N–Co(PNP)].

Interestingly, in vacuum or in an argon atmosphere, compound **3** expels N_2 to afford a green product.[7] The ^1H and ^{31}P NMR spectra both indicate formation of a new diamagnetic material, while the $\tilde{\nu}_{NN}$ stretch originally present in **3** vanishes. The same product can be generated from the one-electron reduction of **1** with *t*BuLi under argon, and when green solutions of the latter material are exposed to N_2, formation of **3** slowly becomes observable (48 h) by NMR and IR spectroscopies. Single-crystal X-ray diffraction analysis of the green material clearly reveals a reorganization of the PNP ligand to give $[\{(\mu_2\text{-PNP})Co\}_2]$ (**4**), in which a dimeric structure with a Co_2N_2 diamond core results from the bridging of the PNP ligand through the amide nitrogen atom. A close Co–Co contact is observed in the Co_2N_2 core in **4**. Unfortunately, the diffraction data originating from single crystals of **4** were weak, hence making the metrical parameters somewhat questionable.[7,13] The gross structural features of **4**, however, are unquestionable and resemble a dinuclear Cu^I system recently reported by Harkins and Peters.[14]

The Co_2N_2 diamond core in **4** behaves as a highly reactive three-coordinate Co^I synthon as it reversibly binds N_2 (in the solid state and in solution) to afford **3** cleanly (see above). Likewise, the π acid CO reacts smoothly with **4** to generate $[(PNP)Co(CO)_2]$ (**5**), which has been characterized by NMR spectroscopy, elemental analysis (CHN), and single-crystal X-ray diffraction analysis.[7,15] Independent synthesis of **5** can be readily accomplished by reduction of **1** with $NaC_{10}H_8$ under CO (Scheme 1). In the conversion of **4** into **5**, an intermediate can be observed by the growth and decay of a ^{31}P NMR resonance ($\delta = 69$ ppm) and an intense IR absorption ($\tilde{\nu}_{CO} = 1901\ cm^{-1}$). Concomitant with the disappearance of these signals is the appearance of a new ^{31}P NMR signal ($\delta = 94$ ppm) and two intense IR absorptions ($\tilde{\nu}_{CO} = 1957$ and $1893\ cm^{-1}$) corresponding to **5**. Under depleted CO (2 equiv per **4**), such a putative intermediate can be isolated and characterized. We speculate the identity of this intermediate to be the monocarbonyl complex [(PNP)Co(CO)],[16] based on a combination of solution NMR (^1H, ^{13}C, and ^{31}P) and IR spectroscopies (Scheme 1).[7] As opposed to π-acid coordination, complex **4** can also be readily oxidized with $ClCPh_3$ to effect dimer cleavage and ligand reorganization to regenerate **1** along with Gomberg's dimer (Scheme 1). Separation of **1** (67% yield) was achieved by fractional crystallization from cold Et_2O.

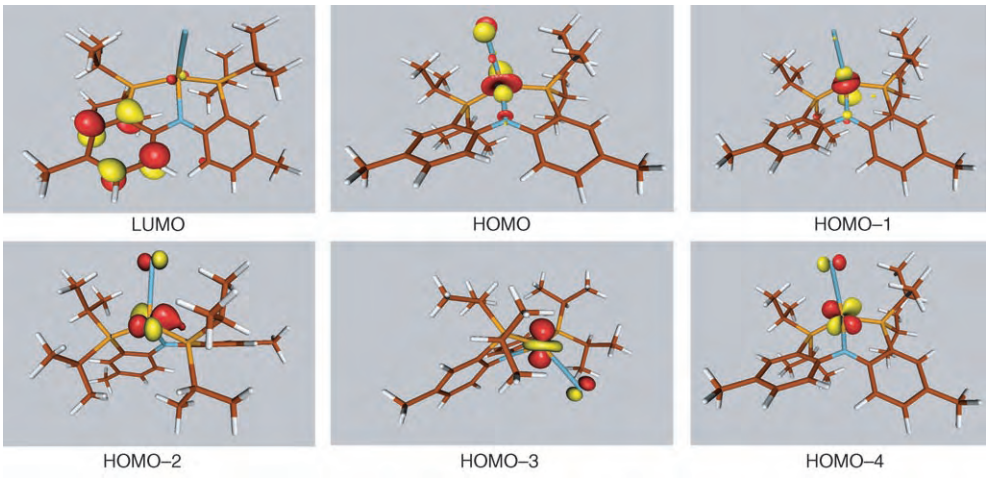

Figure 2. LUMO (π*, ligand-based) and HOMO through HOMO−4 (all cobalt-based) for the full model of the $\{(PNP)Co(N_2)\}^{2-}$ unit of complex **2**.

In summary, we have prepared a dianionic cobalt(−I)–dinitrogen complex as well as a dinuclear Co^I species. For the latter, we have demonstrated the system to be a masked form of a three-coordinate Co^I complex. Most notably, the Co_2N_2 diamond core is highly reactive, which is reflected by its reversible binding of N_2 to afford a cobalt(I)–dinitrogen adduct. Unlike typical Co=Co units reported in the literature,

 © 2006 Wiley-VCH Verlag GmbH & Co. KGaA, Weinheim

the dinuclear complex **4** is a masked form of a low-coordinate Co^{I} species which in the presence of N_2, CO, and $ClCPh_3$ can regenerate the original three-coordinate pincer-type "{(PNP)Co}" framework. We propose that such an unusual ligand rearrangement in complex **4** might be driven by the chelate-enforced nature of the tridentate pincer scaffold, hence preventing the occurrence of metal or ligand disproportionation reactions. The steric crowding imposed by the diisopropyl phosphine substituents might also possibly be a contributing factor to the fragile diamondlike-core resting state in **4**. The mechanism of formation of compounds such as **3**, **5**, and [(PNP)Co(CO)] from compounds possessing cores such as in **4** is currently under scrutiny as ligand reorganization of this kind may play a role in catalytic processes involving pincer-type frameworks.

Received: December 6, 2005
Revised: January 23, 2006
Published online: April 18, 2006

Keywords: chelates · cobalt · ligand effects · N ligands · rearrangement

[1] S. D. Ittel, L. K. Johnson, M. Brookhart, *Chem. Rev.* **2000**, *100*, 1169 – 1204.
[2] C. C. Cummins, *Prog. Inorg. Chem.* **1998**, *47*, 685 – 836.
[3] Y.-C. Tsai, M. J. A. Johnson, D. J. Mindiola, C. C. Cummins, W. T. Klooster, T. F. Koetzle, *J. Am. Chem. Soc.* **1999**, *121*, 10426 – 10427.
[4] a) T. V. Harris, J. W. Rathke, E. L. Muetterties, *J. Am. Chem. Soc.* **1978**, *100*, 6966 – 6977; b) H. H. Karsch, H. F. Klein, H. Schmidbaur, *Chem. Ber.* **1977**, *110*, 2200 – 2212; c) an Ir^{III} analogue $[Ir(H)(\eta^2\text{-}CH_2PMe_2)(PMe_3)_3]^+$ has also been proposed to result from the thermolysis of $[Ir(PMe_3)_4]PF_6$ at elevated temperatures. A. L. Casalnuovo, J. C. Calabrese, D. Milstein, *J. Am. Chem. Soc.* **1988**, *110*, 6738 – 6744.
[5] Y. Pan, J. T. Mague, M. J. Fink, *J. Am. Chem. Soc.* **1993**, *115*, 3842 – 3843.
[6] a) O. V. Ozerov, C. Guo, V. A. Papkov, B. M. Foxman, *J. Am. Chem. Soc.* **2004**, *126*, 4792 – 4793; b) L. Fan, B. M. Foxman, O. V. Ozerov, *Organometallics* **2004**, *23*, 326 – 328.
[7] See the Supporting Information for complete experimental details.
[8] a) J. H. Enemark, B. R. Davis, J. A. McGinnety, J. A. Ibers, *J. Chem. Soc. Chem. Commun.* **1968**, 96 – 97; b) A. Yamamoto, S. Kitazume, L. S. Pu, S. Ikeda, *J. Chem. Soc. Chem. Commun.* **1967**, 79; c) B. R. Davis, N. C. Payne, J. A. Ibers, *Inorg. Chem.* **1969**, *8*, 2719 – 2728; d) R. Hammer, H. F. Klein, U. Schubert, A. Frank, G. Huttner, *Angew. Chem.* **1976**, *88*, 648 – 649; *Angew. Chem. Int. Ed. Engl.* **1976**, *15*, 612 – 613; e) H. F. Klein, K. Ellrich, K. Ackermann, *J. Chem. Soc. Chem. Commun.* **1983**, 888 – 889; f) A. Yamamoto, Y. Miura, T. Ito, H.-L. Chen, K. Irl, F. Ozawa, *Organometallics* **1983**, *2*, 1429 – 1436; g) R. A. Jones, A. L. Stuart, J. L. Atwood, W. E. Hunter, *Organometallics* **1983**, *2*, 1437 – 1441; h) F. Cecconi, C. A. Ghilardi, S. Midollini, S. Moneti, A. Orlandini, M. Bacci, *J. Chem. Soc. Chem. Commun.* **1985**, 731 – 733; i) H. F. Klein, H. König, S. Koppert, K. Ellrich, J. Riede, *Organometallics* **1987**, *6*, 1341 – 1345; j) C. Bianchini, M. Peruzzini, F. Zanobini, *Organometallics* **1991**, *10*, 3415 – 3417; k) J. L. Detrich, R. Konecný, W. M. Vetter, D. Doren, A. L. Rheingold, K. L. Theopold, *J. Am. Chem. Soc.* **1996**, *118*, 1703 – 1712, and references therein; l) V. C. Gibson, M. J. Humphries, K. P. Tellmann, D. F. Wass, A. J. P. White, D. J. Williams, *Chem. Commun.* **2001**, 2252 – 2253; m) T. A. Betley, J. C. Peters, *J. Am. Chem. Soc.* **2003**, *125*, 10782 – 10783; n) A. Yamamoto, S. Kitazume, L. S. Pu, S. Ikeda, *J. Am. Chem. Soc.* **1971**, *93*, 371 – 380; o) A. Misono, Y. Uchida, T. Saito, *Bull. Chem. Soc. Jpn.* **1967**, *40*, 700; p) A. Sacco, M. Rossi, *J. Chem. Soc. Chem. Commun.* **1967**, 361 – 362; q) C. Bianchini, C. Mealli, A. Meli, M. Peruzzini, F. Zanobini, *J. Am. Chem. Soc.* **1988**, *110*, 8725 – 8726.
[9] Crystallographic details for $\mathbf{1}\cdot C_7H_8$: A dark crystal of approximate dimensions $0.15\times0.08\times0.06\ mm^3$ was selected and mounted on a glass fiber. A total of 3711 reflections ($-13\le h\le14$, $-12\le k\le12$, $-18\le l\le11$) were collected at $T=126(2)$ K in the range of 2.54 to 26.68° of which 2335 were unique ($R_{int}=0.0746$); $Mo_{K\alpha}$ radiation ($\lambda=0.71073$ Å). A direct-methods solution was calculated which provided most non-hydrogen atoms from the E-map. A severely disordered toluene molecule was present in the asymmetric unit. All non-hydrogen atoms were refined with anisotropic displacement parameters. All hydrogen atoms not associated with the solvent were located in subsequent Fourier maps and included as isotropic contributors in the final cycles of refinement. No attempt was made to locate the hydrogen atoms on the toluene molecule. The residual peak and hole electron densities were 0.488 and $-0.382\ e\,A^{-3}$. The absorption coefficient was $0.740\ mm^{-1}$. The least-squares refinement converged normally with residuals of $R(F)=0.0432$, $wR(F^2)=0.1036$, and a GOF = 0.707 ($I>2\sigma(I)$). $C_{33}H_{48}ClCoNP_2$, monoclinic, space group $P2/n$, $a=11.530(1)$, $b=9.685(1)$, $c=14.377(4)$ Å, $\beta=90.673(3)°$, $V=1605.3(3)$ Å^3, $Z=2$, $\rho_{calcd}=1.272\ g\,cm^{-3}$, $F(000)=654$.
[10] a) A. D. Becke, *J. Chem. Phys.* **1993**, *98*, 5648 – 5652; b) C. T. Lee, W. T. Yang, R. G. Parr, *Phys. Rev. B* **1988**, *37*, 785 – 789.
[11] I. Mayer, *Chem. Phys. Lett.* **1983**, *97*, 270 – 274.
[12] Crystallographic details for $\mathbf{3}\cdot Et_2O$: A dark green crystal of approximate dimensions $0.26\times0.25\times0.16\ mm^3$ was selected and mounted on a glass fiber. A total of 13329 reflections ($-17\le h\le17$, $-21\le k\le20$, $-21\le l\le20$) were collected at $T=120(2)$ K in the range of 2.42 to 24.60° of which 8607 were unique ($R_{int}=0.0594$); $Mo_{K\alpha}$ radiation ($\lambda=0.71073$ Å). A direct-methods solution was calculated which provided most non-hydrogen atoms from the E-map. All non-hydrogen atoms were refined with anisotropic displacement parameters. An Et_2O molecule was present in the cell. All hydrogen atoms with the exception of those associated with the solvent were located in subsequent Fourier maps and included as isotropic contributors in the final cycles of refinement. Hydrogen atoms on the Et_2O molecule were placed in ideal positions and refined as riding atoms with relative isotropic displacement parameters. The residual peak and hole electron densities were 0.637 and $-0.432\ e\,A^{-3}$. The absorption coefficient was $0.721\ mm^{-1}$. The least-squares refinement converged normally with residuals of $R(F)=0.0412$, $wR(F^2)=0.0806$, and a GOF = 0.821 ($I>2\sigma(I)$). $C_{56}H_{90}Co_2N_4OP_4$, triclinic, space group $P\bar{1}$, $a=13.627(1)$, $b=16.380(2)$, $c=16.593(2)$ Å, $\alpha=60.676(2)$, $\beta=66.601(2)$, $\gamma=87.963(2)°$, $V=2904.4(4)$ Å^3, $Z=2$, $\rho_{calcd}=1.232\ g\,cm^{-3}$, $F(000)=1152$.
[13] The Co–Co separation in complex **4** is 2.254(1) Å, a value shorter than reported Co^{I}=Co^{I} bond lengths. For some Co^{I} dimers containing short Co=Co bond lengths, see: a) S. Stella, C. Floriani, A. Chiesi-Villa, C. Guastini, *New J. Chem.* **1988**, *12*, 621 – 631; b) J. J. Schneider, R. Goddard, S. Werner, C. Kruger, *Angew. Chem.* **1991**, *103*, 1145 – 1147; *Angew. Chem. Int. Ed. Engl.* **1991**, *30*, 1124 – 1126.
[14] S. Harkins, J. C. Peters, *J. Am. Chem. Soc.* **2005**, *127*, 2030 – 2031.
[15] Crystallographic details for **5**: A green crystal of approximate dimensions $0.30\times0.30\times0.25\ mm^3$ was selected and mounted on a glass fiber. A total of 3957 reflections ($-15\le h\le15$, $-13\le k\le9$, $-16\le l\le18$) were collected at $T=122(2)$ K in the range of 2.60 to 29.97° of which 3133 were unique ($R_{int}=0.0514$); $Mo_{K\alpha}$

 © 2006 Wiley-VCH Verlag GmbH & Co. KGaA, Weinheim

radiation ($\lambda = 0.71073$ Å). A direct-methods solution was calculated which provided most non-hydrogen atoms from the E-map. Full-matrix least-squares/difference Fourier cycles were performed to locate the remaining non-hydrogen atoms. All non-hydrogen atoms were refined with anisotropic displacement parameters. The molecule lies on a crystallographic twofold axis. All hydrogen atoms were located in subsequent Fourier maps and included as isotropic contributors in the final cycles of refinement. The residual peak and hole electron densities were 0.555 and $-0.332\ e\,A^{-3}$. The absorption coefficient was $0.778\ mm^{-1}$. The leastsquares refinement converged normally with residuals of $R(F) = 0.0324$, $wR(F^2) = 0.0738$, and a GOF = 0.961 ($I > 2\sigma(I)$). $C_{28}H_{40}CoNO_2P_2$, monoclinic, space group $P2/n$, $a = 11.0228(6)$, $b = 9.3842(6)$, $c = 13.2222(7)$ Å, $\beta = 98.501(2)°$, $V = 1352.7(3)$ Å^3, $Z = 2$, $\rho_{calcd} = 1.334\ g\,cm^{-3}$, $F(000) = 576$.

[16] Four-coordinate Co^I monocarbonyl complexes are scarce (see reference [8k]).

[17] CCDC-291872–291876 (**1**–**5**) contain the supplementary crystallographic data for this paper. These data can be obtained free of charge from The Cambridge Crystallographic Data Centre via www.ccdc.cam.ac.uk/data_request/cif.

 © 2006 Wiley-VCH Verlag GmbH & Co. KGaA, Weinheim

Enzyme Assays

DOI: 10.1002/anie.200504576

Solid-Phase Enzyme Activity Assay Utilizing an Entrapped Fluorescence-Signaling DNA Aptamer**

Nicholas Rupcich, Razvan Nutiu, Yingfu Li, and John D. Brennan**

The immobilization of biomolecules is critical for the fabrication of biosensors and valuable in the development of biological assays.[1–5] Herein, we describe a novel solid-phase assay that uses a fluorescence-signaling DNA aptamer to monitor the catalytic activity of an enzyme, both of which are entrapped in sol-gel derived silica[6–12] and formed either as a single phase or as separate layers containing the aptamer or enzyme. Adenosine deaminase (ADA), whose catalytic function is to convert adenosine to inosine, is used as the model enzyme. We show that the enzymatic action of ADA can be continuously monitored in silica by a fluorogenic DNA aptamer that has a high affinity for adenosine ($K_D \approx 0.5$ mM) and no affinity for inosine. Moreover, we demonstrate that a two-layer silica structure with the ADA layer cast over the signaling-aptamer layer can accurately measure the IC_{50} value of a small-molecule inhibitor. Given the ability to generate a signaling aptamer that can bind to either the substrate or product of an enzymatic reaction, significant potential exists for the development of a multiplexed assay technology that can be applied to multiple pairs of entrapped enzymes and matching signaling aptamers for parallel high-throughput screening of enzyme inhibitors.

Aptamers are highly structured single-stranded DNA (or RNA) molecules that are able to bind a ligand with high affinity and specificity.[13] As nucleic acids, aptamers are inherently capable of recognizing both the cognate non-nucleic acid target for which the aptamer is engineered and an antisense DNA molecule through duplex formation. We have exploited this property for the design and in vitro selection of fluorescent reporters denoted "structure-switching signaling aptamers".[14] Furthermore, we have recently demonstrated that such aptamers can be used as real-time reporters of the action of an enzyme through monitoring the formation of the product produced by the enzyme in solution.[15] These findings set the stage for us to develop the new solid-phase enzyme assay presented in this paper.

The competition-based assay studied in this report is illustrated in Figure 1. In this system, the enzyme, ADA, converts adenosine to inosine and can be inhibited by erythro-9-(2-hydroxy-3-nonyl)adenine hydrochloride (EHNA). A

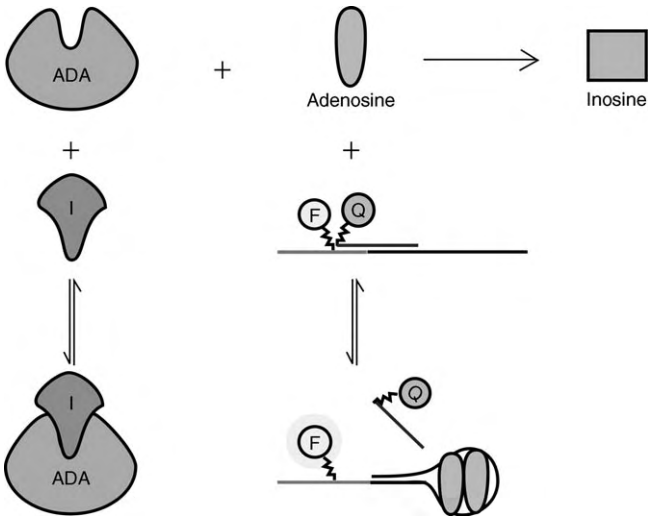

Figure 1. The coupled assay involving ADA, an adenosine-binding DNA aptamer, and a small-molecule inhibitor (I). F and Q represent a fluorophore and a quencher, respectively.

[*] Dr. N. Rupcich, R. Nutiu, Prof. Y. Li, Prof. J. D. Brennan
Department of Chemistry
McMaster University
1280 Main St. W. Hamilton, ON L8S 4M1 (Canada)
Fax: (+1) 905-522-2509
E-mail: liying@mcmaster.ca
brennanj@mcmaster.ca
Prof. Y. Li
Department of Biochemistry and Biomedical Sciences
McMaster University
1280 Main St. W. Hamilton, ON L8N 3Z5 (Canada)
Fax: (+1) 905-522-9033

[**] The authors thank MDS-Sciex, the Natural Sciences and Engineering Research Council of Canada (NSERC), the Canadian Institutes for Health Research (CIHR), the Canada Foundation for Innovation (CFI), and the Ontario Innovation Trust (OIT) for support of this work. Thanks also to Dr. Balu Easwaramoorthy for technical assistance. R.N. holds a CIHR doctoral award. Y.L. is a Canada Research Chair in Nucleic Acids Biochemistry. J.D.B. holds the Canada Research Chair in Bioanalytical Chemistry.

Supporting information for this article is available on the WWW under http://www.angewandte.org or from the author.

© 2006 Wiley-VCH Verlag GmbH & Co. KGaA, Weinheim

structure-switching signaling DNA aptamer exists that has a high affinity for adenosine and no affinity for inosine[16] and hence should be able to monitor the action of ADA. When ADA is fully active, adenosine is depleted rapidly and the aptamer signal should decrease with time. Upon inhibition of ADA by EHNA (I), the adenosine concentration should remain high and the aptamer reporter should remain highly fluorescent.

We first studied the ADA/EHNA/signaling-aptamer system in solution by using three different procedures, 1) a one-step procedure wherein the aptamer, ADA, and EHNA were mixed together prior to the addition of adenosine, 2) a two-step procedure in which the preincubated solution of the aptamer/adenosine and that of ADA/EHNA were made separately and then combined, and 3) a three-step procedure in which ADA was first incubated with EHNA, followed by the addition of adenosine and incubation for 2 min before the addition of the aptamer.

In the one-step procedure (Figure 2a), the initial increase in signal upon the addition of adenosine and ADA was dependent upon the level of EHNA present in the assay. A high level of EHNA resulted in a sustained fluorescence signal, whereas lower inhibitor concentrations resulted in a concentration-dependent decrease in signal intensity that was proportional to the degree of ADA activity. In the two-step procedure (Figure 2b), the signaling system started with a very high fluorescence signal that progressively decreased as adenosine was converted into inosine by ADA. The rate of the fluorescence decrease was reduced as the concentration of EHNA was increased. In the three-step procedure (Figure 2c), because the action of ADA preceded the addition of the aptamer, significant signal changes were only observed for solutions that contained a high concentration of EHNA and hence retained a higher initial concentration of adenosine.

IC_{50} curves (Figure 2d) for the one-step (●), two-step (■), and three-step (▲) assays provided IC_{50} values of 60 ± 6, 84 ± 5, and 86 ± 3 nM, respectively. By using a K_M of 89 μM for adenosine[17] and a substrate concentration of 1 mM, K_I values of 5 ± 1, 6 ± 1, and 6 ± 1 nM were obtained for the one-step, two-step, and three-step assays, respectively (the data analysis is described in the Supporting Information). These values all compare well with the K_I value of 6.5 nM reported in the literature, which was determined by using the standard absorbance based assay.[18]

We next studied the signaling ability of the entrapped ADA/EHNA/signaling aptamer system by using coentrapment (mode A), the aptamer layered on top of the ADA (mode B), and ADA on top of the aptamer (mode C). The mixed and layered silica monoliths were all formed in microwell plates with a well diameter of 5 mm and total thickness of 2.3 mm. The mixed system has a random dispersion of entrapped species within silica, whereas the layered silica system, which is formed by simply casting 1.1 mm thick layers of silica containing different species, allows for segregation of different biomolecules into unique reaction zones. The key to the layered reaction zone system for enzyme-reporter systems is that the biomolecule that is entrapped in the layer nearest to the solution interface receives the initial exposure to the substrate. Thus, the degree

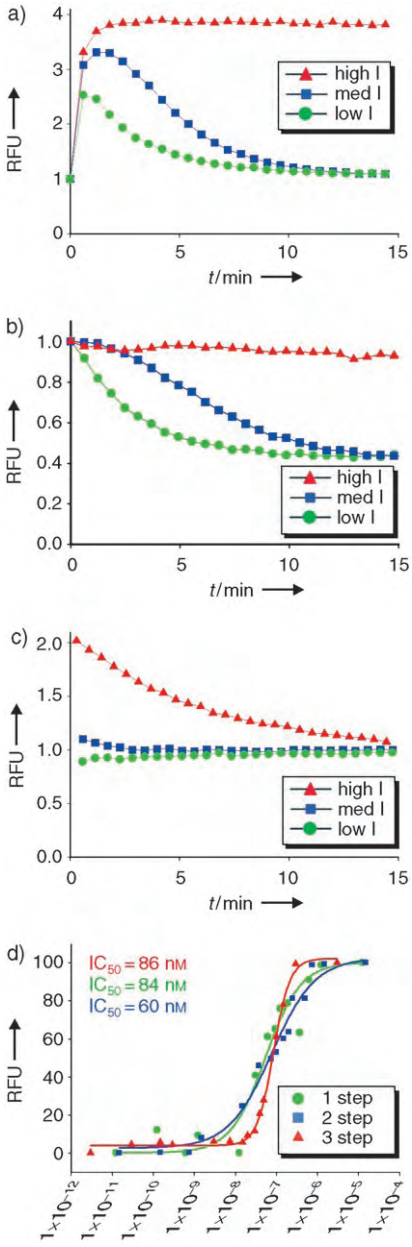

Figure 2. a)–c) Signaling profiles of an ADA/EHNA/signaling aptamer system in solution under one-step, two-step, and three-step procedures, respectively. Samples contained EHNA (I) at 15 μM (△), 150 nM (□), and 15 pM (○) levels. d) Normalized signal responses compared with EHNA concentration in one-step (●), two-step (■), and three-step (▲) solution assays. RFU = relative fluorescence units.

of binding or conversion of substrate in the upper layer determines the level of exposure of the subsequent layer to the substrate.

Entrapment mode A exhibited a fluorescence response pattern (Figure 3a) that was quite similar to that obtained from the one-step solution assay (Figure 2a) except that the rate of the reaction was slowed substantially by the mass-transfer limitations imposed by the silica matrix.[19] We note that full inhibition of ADA (i.e., exposure of the aptamer to 1 mM adenosine) results in a 4-fold increase in fluorescence intensity for the mixed system, whereas fully active ADA

 © 2006 Wiley-VCH Verlag GmbH & Co. KGaA, Weinheim

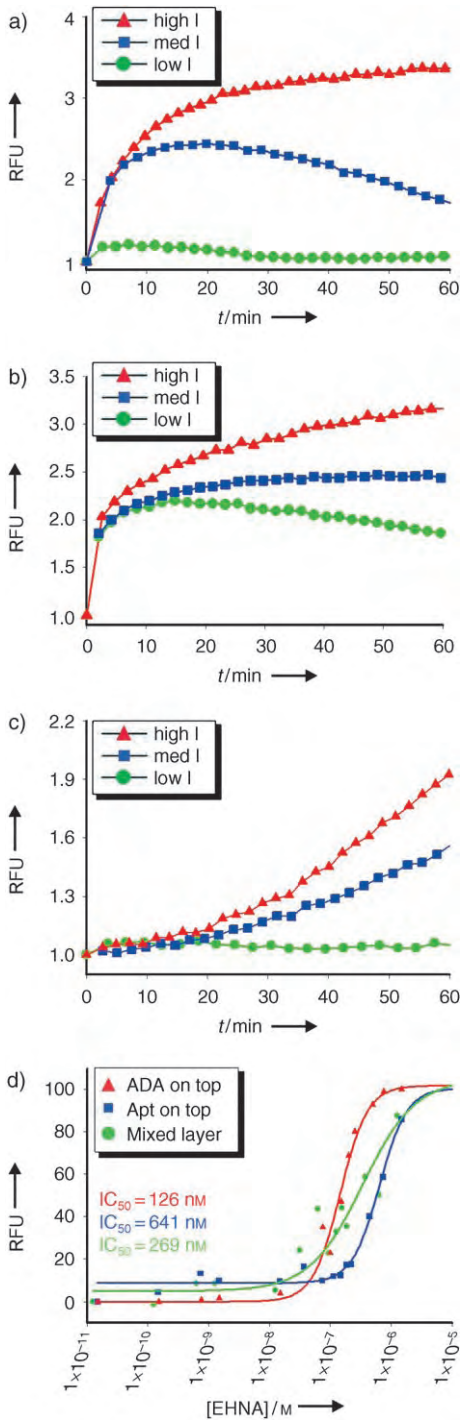

Figure 3. a)–c) Signaling profiles of the ADA/EHNA/signaling aptamer systems entrapped in single mixed layer, aptamer (apt) in the top layer and ADA at the bottom, and ADA on top and aptamer at the bottom, respectively. Samples contained EHNA (I) at 15 μM (△), 150 nM (□) and 15 pM (○) levels. d) Normalized signal responses compared with EHNA concentration in the single layer system (●), aptamer on top (■) and ADA on top (▲).

ultimately results in restoration of the baseline signal, which is consistent with full conversion of adenosine to inosine. For entrapment mode B, the signal increased relatively rapidly in the initial phase (< 10 min) owing to the binding of adenosine to the aptamer in the top layer (Figure 3b). However, at a low level of EHNA (○), ADA remained highly active and led to a relatively rapid conversion of adenosine to inosine and a decrease in the fluorescence signal after 10 minutes. Conversely, at a high level of EHNA (△), the activity of ADA was significantly inhibited, the adenosine concentration remained high, and the signal continued to increase during the incubation period. Entrapment mode C led to no increase in the fluorescent signal over a period of at least 60 min when EHNA was used at a low level (Figure 3c). This is consistent with adenosine being consumed prior to reaching the aptamer layer. Beyond 60 min, there was a very slow increase in fluorescence, suggesting that ADA was not able to fully consume all of the adenosine that was added (data not shown). When ADA was strongly inhibited by EHNA (△), the fluorescence response showed a relatively slow increase over the first 20 min, followed by a more rapid increase in intensity over a period of 40 min as adenosine penetrated into the aptamer layer. The slope of the response increased with increasing inhibitor concentration, reflecting the loss of ADA activity. It is noted that even after 2 h, the system did not show the maximum expected signal, indicating that full equilibration of substrate into the bottom layer likely requires a longer time. The data shown in Figure 3a–c convincingly demonstrate that both ADA and the signaling aptamer remain active within silica and that the signaling aptamer can report the activity of ADA, regardless of which entrapment option is used.

The ability of each entrapment method to generate accurate inhibition constants was assessed by using methods described in the Supporting Information. For entrapment mode A, fitting the fluorescence responses to the concentration change of EHNA (Figure 3d, ●) according to the Hill equation resulted in an IC_{50} value of 269 ± 15 nM (although the quality of the fit was poor, $r^2 = 0.890$). By using a K_M value of 106 μM for ADA entrapped in silica,[2] a K_I value of 26 nM, which is ≈4-fold larger than the literature value, was obtained. We speculate that the increase in the K_I value is most likely owing to the fact that the mixed system never attains equilibrium with respect to either the aptamer/adenosine or ADA/adenosine reactions. This is as a result of the time needed for adenosine to traverse the monolith. Hence, the aptamer and ADA present at the bottom of the monolith may never be exposed to adenosine, whereas the aptamer and enzyme near the top of the monolith will be exposed to the maximum concentration of 1 mM adenosine. This will result in a gradient of IC_{50} values owing to variability in substrate concentration throughout the layer. It is also possible that partitioning effects may alter the K_I value owing to either substrate–silica or inhibitor–silica interactions,[19] although at the ionic strength used (≈130 mM), such interactions are likely to be minimal.[19,20]

Entrapment mode B (■ in Figure 3d) resulted in an IC_{50} of 641 ± 9 nM ($r^2 = 0.980$), which translated to a K_I of 61 nM. Both parameters were significantly different from those measured in solution. The large K_I value was assumed to be the result of the insufficient incubation time for the inhibitor, which would lead to a lower-than-expected inhibitor concentration in the region of the ADA when the enzyme was present in the bottom layer. This would be particularly

 © 2006 Wiley-VCH Verlag GmbH & Co. KGaA, Weinheim

problematic at lower inhibitor concentrations, resulting in the inflated IC_{50} value. To confirm this assumption, the assay was rerun with a 5 h incubation time (data not shown), and resulted in the IC_{50} value dropping somewhat to approximately 550 nM. Although this experiment confirms the temporal dependence of the IC_{50} data when ADA is present in the bottom layer, it also indicates that excessively long incubation times would be needed to overcome this issue. This therefore makes this particular layered construct of limited use for high-throughput screening.

Entrapment mode C (▲ in Figure 3d) produced an IC_{50} of 126 ± 7 nM ($r^2 = 0.987$) and a K_I of 12 nM, both of which were close to the literature value.[18] The better accuracy of these values, when ADA is in the top layer, is most likely owing to the ability of the inhibitor to penetrate through the thinner upper layer (1.1 mm compared with 2.3 mm for the mixed system) and thus establish equilibrium with the enzyme. It should be noted that the data from mode C provided a better fit to the Hill equation than the other two modes. The reason for the better quality of the fit can be attributed to the nature of the signal that is produced. All samples begin with similar background intensities and the response is based on a continuous increase in signal rather than an initial increase followed by a decrease. The improved accuracy may also relate to the fact that the delay in signal evolution allows time for the addition of reagents, loading of plates, and initiation of reading prior to significant signal development. This leads to a more consistent baseline value for the intensity.

In summary, we have reported the first example of a solid-phase enzyme assay that utilizes a coimmobilized DNA aptamer as a reporter. The signaling aptamer can qualitatively report the action of the protein enzyme, regardless of whether the aptamer and enzyme are entrapped in a mixed fashion or separately entrapped into two distinct layers. However, only the layered structure with the protein/enzyme layer on top of the aptamer layer can provide accurate IC_{50} and K_I values in cases where both species compete for the substrate. If the aptamer can be selected to be specific for the product of an enzymatic reaction, it is likely that coentrapment (mode A) may provide a more-accurate assessment of inhibitor potency as issues with substrate competition will not exist.

The advantages of entrapping coupled aptamer/enzyme systems include the potential to reuse the reagents,[21] protection of the entrapped species from nucleases[9] and proteases,[6] and the ability to use the entrapped species to form devices such as microarrays[10] and bioaffinity[2] or bioreactor[3] columns. The use of layered entrapment systems for the separation of coupled assays can offer additional advantages. Firstly, the spatial separation of biomolecules may allow biological species that are incompatible (such as a DNase and a DNA aptamer) to be coimmobilized, which would not be possible when using a single monolith. Secondly, the thickness of each layer can either be increased to introduce a delay time (which provides time to perform multiple assay steps prior to reading), or decreased to accelerate the overall reaction. Finally, the concentration of biomolecules within each layer and the chemical composition of the individual silica layers can also be optimized to ensure that the molar ratio and activity of reagents is optimized.

As aptamers can be generated by in vitro selection for virtually any target of interest,[13] and structure-switching signaling aptamers can be either rationally designed for any known aptamer[14a] or selected directly when there is no existing aptamer,[14c] it is conceivable that many specific signaling aptamer/protein enzyme pairs can be developed in the future. As recently demonstrated by our group,[10,22] protein microarrays can be fabricated by using a sol-gel process and used for enzyme inhibition assays that utilize a 14 nL reaction volume to generate a 12 point IC_{50} curve. Such a device could provide new opportunities for conducting a unique high-throughput screen that simultaneously surveys the same combinatorial library for potential inhibitors to many different protein enzymes based on a single readout method.

Received: December 23, 2005
Revised: February 20, 2006
Published online: April 18, 2006

Keywords: aptamer · enzymes · fluorescence · inhibitors · sol-gel processes

[1] W. H. Scouten, J. H. T. Luong, R. S. Brown, *Trends Biotechnol.* **1995**, *13*, 178–185.
[2] a) R. J. Hodgson, T. R. Besanger, M. A. Brook, J. D. Brennan, *Anal. Chem.* **2005**, *77*, 7512–7519; b) D. C. Schriemer, *Anal. Chem.* **2004**, *76*, 440A–448A; c) B. Zhang, M. M. Palcic, D. C. Schriemer, G. Alvarez-Manilla, M. Pierce, O. Hindsgaul, *Anal. Biochem.* **2001**, *199*, 173–182.
[3] a) R. J. Hodgson, M. A. Brook, J. D. Brennan, *Anal. Chem.* **2005**, *77*, 4404–4412; b) T. Jiang, R. Mallik, D. S. Hage, *Anal. Chem.* **2005**, *77*, 2362–2372; c) W. Clarke, J. D. Beckwith, A. Jackson, B. Reynolds, E. M. Karle, D. S. Hage, *J. Chromatogr. A* **2000**, *888*, 13–22.
[4] C. Fan, G. Li, D. Zhu, *Curr. Top. Anal. Chem.* **2002**, *3*, 233–251.
[5] a) M. Schena, D. Shalon, R. W. Davis, P. O. Brown, *Science* **1995**, *270*, 467–470; b) A. C Pease, D. Solas, E. J. Sullivan, M. T. Cronin, C. P. Holmes, S. P. Fodor, *Proc. Natl. Acad. Sci. USA* **1994**, *91*, 5022–5026.
[6] a) W. Jin, J. D. Brennan, *Anal. Chim. Acta* **2002**, *461*, 1–36; b) I. Gill, *Chem. Mater.* **2001**, *13*, 3404–3421.
[7] J. Livage, T. Coradin, C. Roux, *J. Phys. Condens. Matter* **2003**, *15*, R673-R691.
[8] a) T. R. Besanger, J. D. Brennan, *Anal. Chem.* **2003**, *75*, 1094–1101; b) T. R. Besanger, B. Easwaramoorthy, J. D. Brennan, *Anal. Chem.* **2004**, *76*, 6470–6475.
[9] N. Rupcich, R. Nutiu, Y. Li, J. D. Brennan, *Anal. Chem.* **2005**, *77*, 4300–4307.
[10] N. Rupcich, J. D. Brennan, *Anal. Chim. Acta* **2003**, *500*, 3–12.
[11] R. Obert, B. C. Dave, *J. Am. Chem. Soc.* **1999**, *121*, 12192–12193.
[12] I. Gill, A. Ballesteros, *J. Am. Chem. Soc.* **1998**, *120*, 8587–8598.
[13] a) D. S. Wilson, J. W. Szostak, *Annu. Rev. Biochem.* **1999**, *68*, 611; b) M. Famulok, G. Mayer, M. Blind, *Acc. Chem. Res.* **2000**, *33*, 591–599; c) S. E. Osborne, I. Matsumura, A. D. Ellington, *Curr. Opin. Chem. Biol.* **1997**, *1*, 5–9.
[14] a) R. Nutiu, Y. Li, *J. Am. Chem. Soc.* **2003**, *125*, 4771–4778; b) R. Nutiu, Y. Li, *Chem. Eur. J.* **2004**, *10*, 1868–1876; c) R. Nutiu, Y. Li, *Angew. Chem.* **2005**, *117*, 1085–1089; *Angew. Chem. Int. Ed.* **2005**, *44*, 1061–1065; d) R. Nutiu, Y. Li, *Methods* **2005**, *37*, 16–25; e) R. Nutiu, Y. Li, *Angew. Chem.* **2005**, *117*, 5600–5603; *Angew. Chem. Int. Ed.* **2005**, *44*, 5464–5467.

 © 2006 Wiley-VCH Verlag GmbH & Co. KGaA, Weinheim

[15] R. Nutiu, J. Yu, Y. Li, *ChemBioChem* **2004**, *5*, 1139 – 1144.
[16] D. E. Huizenga, J. W. Szostak, *Biochemistry* **1995**, *34*, 656 – 662.
[17] E. Gabellieri, S. Bernini, L. Piras, P. Cioni, E. Balestreri, G. Cercignani, R. Felicioli, *Biochim. Biophys. Acta* **1986**, *884*, 490 – 496.
[18] R. P. Agarwal, *Pharmacol. Ther.* **1982**, *17*, 399 – 429.
[19] T. R. Besanger, Y. Chen, A. K. Deisingh, R. Hodgson, W. Jin, S. Mayer, M. A. Brook, J. D. Brennan, *Anal. Chem.* **2003**, *75*, 2382 – 2391.
[20] P. Kovarik, R. J. Hodgson, T. Covey, M. A. Brook, J. D. Brennan, *Anal. Chem.* **2005**, *77*, 3340 – 3350.
[21] a) J. A. Cruz-Aguado, Y. Chen, Z. Zhang, M. A. Brook, J. D. Brennan, *Anal. Chem.* **2004**, *76*, 4182 – 4188; b) J. A. Cruz-Aguado, Y. Chen, Z. Zhang, N. H. Elowe, M. A. Brook, J. D. Brennan, *J. Am. Chem. Soc.* **2004**, *126*, 6878 – 6879.
[22] N. Rupcich, J. R. A. Green, J. D. Brennan, *Anal. Chem.* **2005**, *77*, 8013 – 8019.

 © 2006 Wiley-VCH Verlag GmbH & Co. KGaA, Weinheim

Heavy-Oil Desulfurization

DOI: 10.1002/anie.200503660

Towards Clean Fuels: Molecular-Level Sulfur Reactivity in Heavy Oils

Tushar V. Choudhary, Jim Malandra, John Green, Stephen Parrott, and Byron Johnson*

Due to environmental concerns there is a continual worldwide thrust towards clean transportation fuels, with the emphasis on minimization of sulfur content.[1–6] The threshold limit for sulfur in gasoline and diesel is expected to be regulated to 50 ppm of weight (ppmw) or less within the next few years,[1,5,6] and several billion dollars are anticipated to be spent to meet these stricter regulations.[1] Sulfur removal from heavy oil (HO) is an important process for meeting sulfur regulations in transportation fuels.[5,7–11] From an economic viewpoint, it is therefore extremely desirable to increase the efficiency of the HO sulfur removal process. Unfortunately, whereas there is a vast and fundamental understanding of sulfur removal chemistry for gasoline/diesel,[3,5,8] the molecular-level understanding of the ultra-complex HO desulfurization chemistry is inadequate, thereby limiting process/catalyst improvements. Because of its enormous complexity, previous studies have been unable to provide the much needed quantitative molecular-level structure–reactivity information about HO sulfur chemistry.[12–18]

Herein, we present a method that can be used routinely to quantitatively classify the total HO sulfur content into individual sulfur molecular groups. Moreover, we have coupled this sulfur characterization tool with systematic desulfurization experiments in pilot-scale reactors to gain molecular-level insights into the heavy-oil sulfur reaction chemistry. These studies provide a first-ever "reactivity scale" for individual sulfur molecular groups in HO and reveal that the reactivity scale is profoundly influenced by the reaction temperature. This study, which represents a major advance in unraveling the complex sulfur chemistry in HO, is expected to assist the production of clean fuels by opening-up new avenues for process improvements and superior catalyst development.

Our sulfur characterization method can be used to quantitatively discriminate between different sulfur molecular groups present in HO in less than five hours. The content of nonaromatic sulfur compounds is quantitatively determined by chemical analysis, while the remaining compounds are identified chromatographically, as described in detail in the Experimental Section. Figure 1, which shows chromatograms of sulfur compounds in heavy oil 1 (HO1), clearly demonstrates the ability of the method to distinguish between different sulfur compounds in complex heavy oils. Such quantitative resolution over a wide range (carbon range: C_{10}-C_{44}) has never been reported; in fact, prior to this, molecular-level quantification of only around 20% of the total HO sulfur compounds has been reported.[12,14]

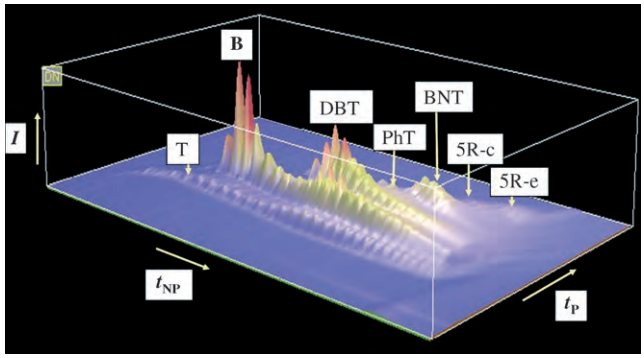

Figure 1. Chromatograms of sulfur compounds in HO1. I = intensity, t_{NP} = retention time on a nonpolar column, t_P = retention time on a polar column; T = thiophenes, b = benzothiophenes, DBT = dibenzothiophenes, PhT = phenanthrothiophenes, BNT = benzonaphthothiophenes, 5R-c = compact five-rings thiophenes, 5R-e = extended five-rings thiophenes. The six-rings thiophenes, although not marked here because of their very low content, are present just beyond the extended five-rings thiophenes.

Each series of peaks in Figure 1 represents a homologous series of aromatic sulfur compounds in HO1. The parent structure for each of the homologous series was identified by mass spectrometric analysis. The corresponding quantitative information for HO1 in a condensed form is summarized in Table 1. Benzothiophenes, dibenzothiophenes, benzonaphthothiophenes, and nonaromatic sulfides are the dominating compounds in HO1, while thiophenes, phenanthrothiophenes, thiophenes with a total of five annulated rings either in compact (compact five-rings thiophenes) or extended form (extended five-rings thiophenes), and thio-

[*] Dr. T. V. Choudhary, Dr. J. Malandra, Dr. J. Green, Dr. S. Parrott, Dr. B. Johnson
ConocoPhillips Company
Bartlesville Technology Center
Bartlesville, OK 74004 (USA)
Fax: (+1) 918-661-8761
E-mail: tushar.v.choudhary@conocophillips.com

© 2006 Wiley-VCH Verlag GmbH & Co. KGaA, Weinheim

Table 1: Sulfur compounds[a] in heavy oils and feed properties.

Compound type[b]/Feed property	HO1[c]	HO2[d]	Parent structure
total sulfur content	32290	11518	
thiophenes (total) (T)	1133	62	
benzothiophenes (total) (B)	9500	2215	
C_0 benzothiophenes	11	0	
C_1 benzothiophenes	154	5	
C_2 benzothiophenes	547	30	
C_3 benzothiophenes	624	61	
C_4 benzothiophenes	616	80	
C_5 benzothiophenes	449	94	
C_{6+} benzothiophenes	7099	1945	
dibenzothiophenes (total) (DBT)	8695	4168	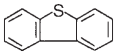
C_0 dibenzothiophenes	96	52	
C_1 dibenzothiophenes	323	193	
C_2 dibenzothiophenes	665	373	
C_3 dibenzothiophenes	1082	571	
C_{4+} dibenzothiophenes	6529	2979	
phenanthrothiophenes (total) (PhT)	1257	412	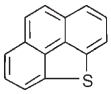
C_0 phenanthrothiophenes	19	0	
C_1 phenanthrothiophenes	39	26	
C_2 phenanthrothiophenes	151	44	
C_{3+} phenanthrothiophenes	1048	342	
benzonaphthothiophenes (total) (BNT)	3806	1767	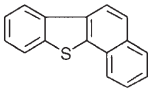
C_0 benzonaphthothiophenes	75	38	
C_1 benzonaphthothiophenes	74	129	
C_2 benzonaphthothiophenes	514	280	
C_{3+} benzonaphthothiophenes	3143	1319	
compact 5-rings thiophenes (total) (5R-c)	489	113	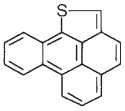
C_0 5R-c	11	0	
C_1 5R-c	57	12	
C_{2+} 5R-c	421	101	
extended 5-rings thiophenes (total) (5R-e)	945	336	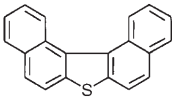
6-rings thiophenes (total) (6R)	44	5	
nonaromatic sulfides (NArS)	6421	2440	
other properties[e]			
API	20.9	21.9	
total nitrogen content [ppmw]	1691	1321	
IBP–FBP [K]	440–815	485–877	
total core aromatic compounds [wt.%]	26.2	21.5	

[a] Sulfur content given in ppmw. [b] C_n indicates the hydrocarbon group(s) containing *n* carbon atoms that are attached to the aromatic ring system; C_{n+} is used for hydrocarbon group(s) containing more than *n* carbon atoms. [c] HO1 is a blend of atmospheric gas oil, vacuum gas oil, coker gas oil, and coker distillate. [d] HO2 is a blend of atmospheric gas oil and vacuum gas oil. [e] API = 141.5/(Specific Gravity at 288.55 K) − 131.5, IBP–FBP = initial boiling point–final boiling point.

phenes with a total of six annulated rings (six-rings thiophenes) are present in much smaller amounts. The sulfur distribution for heavy oil 2 (HO2) is also shown for comparison. From these data, it is apparent that heavy oils can differ appreciably in their total sulfur content and distribution.

HO1 and HO2 were hydrotreated in pilot reactors under an industrially relevant range of process conditions (temperature: 622–655 K; H_2 pressure: 7–14 MPa; catalyst: commercial NiMo). The hydrotreated products obtained from this study were characterized for sulfur distribution. Based on these data, the sulfur molecules were collated into the following seven groups: group 1: thiophenes and benzothiophenes; group 2: C_0/C_1 dibenzothiophenes; group 3: C_{2+} dibenzothiophenes; group 4: phenanthrothiophenes; group 5: benzonaphthothiophenes and compact five-rings thiophenes; group 6: extended five-rings thiophenes and six-rings thiophenes; and group 7: nonaromatic sulfides.

The kinetic parameters for HO1 were determined assuming parallel first-order kinetics (described in the Experimental Section) for the seven groups. Figure 2 shows parity plots for experimental and calculated sulfur contents for individual sulfur groups and for the total sulfur content obtained under different process conditions. The kinetic parameters obtained

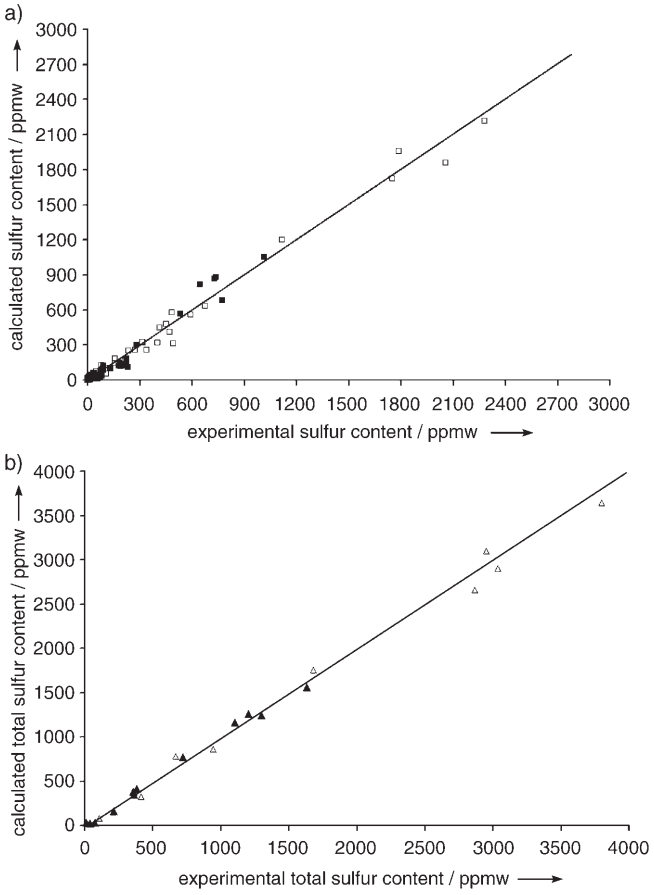

Figure 2. Comparison of calculated and experimental sulfur contents for the individual sulfur groups given in Table 1 (a) and of the total bulk sulfur content (b) for HO1 (filled symbols) and HO2 (open symbols). Process conditions: temperature: 622–655 K; H_2 pressure: 7–14 MPa; liquid hourly space velocity: 1 h^{-1}.

 © 2006 Wiley-VCH Verlag GmbH & Co. KGaA, Weinheim

from the fitting to the experimental data for HO1 (□ in Figure 2a and △ in Figure 2b) were used to predict the sulfur distribution (■) and total sulfur content (▲) for HO2. HO2 has an appreciably different sulfur content/distribution than HO1; furthermore, the nature of the heavy oils is also very different as only one of them contains coker liquids. The excellent predictive ability, as seen from Figures 2a and b, lends substantial credence to the sulfur analysis and kinetic calculations.

The relative reactivities of different sulfur compounds at three temperatures are shown in Figure 3. The relative reactivity in this study is defined as the ratio of the rate constant of a sulfur molecular group at a given temperature to the rate constant of C_0/C_1 dibenzothiophene compounds. The

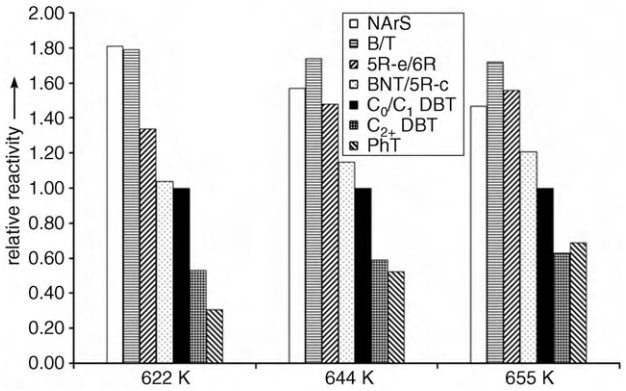

Figure 3. Relative reactivities ($k_{S\,component}/k_{C_0/C_1\,dibenzothiophenes}$) of sulfur molecular groups as a function of desulfurization reaction temperature. For the abbreviations, see Figure 1 and Table 1.

nonaromatic sulfides, thiophenes, benzothiophenes, benzonaphthothiophenes, extended and compact five-rings thiophenes, and six-rings thiophenes are easier to desulfurize than C_0/C_1 dibenzothiophene, while the C_{2+} dibenzothiophenes and phenanthrothiophenes are more difficult to desulfurize at all the temperatures investigated in this study. Since the distribution of the aromatic sulfur compounds (Table 1) is dominated by compounds containing a large number of side-chains, considerable steric hindrance may be expected for these molecules; this decreases the ability of the sulfur compound to interact with the active sites of the catalyst.

Sulfur removal from petroleum fractions is possible by a) direct extraction, which involves sulfur removal in a single hydrogenolysis step, and b) hydrogenation, which involves hydrogenation of the aromatic ring(s) of the sulfur compound prior to the hydrogenolysis step.[19] Hydrogenation of the aromatic ring(s) facilitates the hydrogenolysis step by diminishing the steric hindrance and increasing the electron density on the sulfur atom.

Based on the reactor studies undertaken to examine the influence of hydrogen pressure on the reactivity of the sulfur compounds at 622 K, the following dependence on the hydrogen pressure was observed: nonaromatic sulfides $<$ C_0/C_1 dibenzothiophenes $<$ C_{2+} dibenzothiophenes $<$ benzothiophenes $<$ benzonaphthothiophenes $\approx$ phenanthrothiophenes $\approx$ compact five-rings thiophenes $<$ extended five-rings thiophenes $\approx$ six-rings thiophenes. A higher dependence of the reactivity on hydrogen pressure suggests a relatively greater contribution from the hydrogenation mechanism.

The reactivity scale for the different sulfur compounds (Figure 3) at 622 K is given by: nonaromatic sulfides $>$ thiophenes $\approx$ benzothiophenes $\gg$ extended five-rings thiophenes $\approx$ six-rings thiophenes $>$ benzonaphthothiophenes $\approx$ compact five-rings thiophenes $>$ C_0/C_1 dibenzothiophenes $\gg$ C_{2+} dibenzothiophenes $>$ phenanthrothiophenes.

The low influence of hydrogen partial pressure on the reactivity of the nonaromatic sulfides suggests that they react predominantly by the direct hydrogenolysis route; the high electron density expected on the sulfur atom for these compounds is responsible for their rapid removal. Thiophenes react rapidly due to their low steric hindrance. The high dependence of the reactivity of the benzothiophenes on the hydrogen pressure suggests that the hydrogenation pathway also plays an important role in their removal: the large bond orders for benzothiophenes at the unsaturated bond that needs to be hydrogenated prior to sulfur removal are expected to facilitate rapid hydrogenation,[20] which explains the high reactivity of these compounds. The C_0/C_1 dibenzothiophenes exhibit a weak dependence on hydrogen pressure and react mainly by the direct hydrogenolysis route. The steric hindrance for these dibenzothiophenes is expected to be considerably lower than that for C_{2+} dibenzothiophenes, and hence their reactivity is higher. The C_{2+} dibenzothiophenes show low sulfur reactivity on account of their high steric hindrance and small bond orders (slower hydrogenation).[20]

The multi-aromatic-rings sulfur molecules (more than three rings), such as extended five-rings thiophenes, six-rings thiophenes, benzonaphthothiophenes, and compact five-rings thiophenes, show a higher dependence on hydrogen pressure, thus indicating that the hydrogenation pathway is important for them. Similar compounds are known to have high hydrogenation rates for the first aromatic ring,[21,22] therefore sulfur compounds containing multiple aromatic rings are expected to show higher reactivity (compared to dibenzothiophenes) via the hydrogenation route due to facile hydrogenation of their first aromatic ring.

Figure 3 shows that the reactivity scale is significantly influenced by the reaction temperature. The relative reactivity of the multi-aromatic-rings sulfur compounds increases upon increasing the reaction temperature from 622 to 655 K, whereas the relative reactivity of the nonaromatic sulfides (hydrogenolysis pathway) decreases. This suggests that an increase in reaction temperature assists sulfur removal by the hydrogenation mechanism (by increasing the rate of hydrogenation) to a greater extent than sulfur removal by the direct hydrogenolysis mechanism. In line with this, we observed a large increase in the total experimental hydrogen consumption upon increasing the temperature. The dependence of the hydrogenation rate on temperature is not the same for different compounds,[21] and hence the relative rates are expected to vary to a different extent with temperature.

Surprisingly, the phenanthrothiophenes, despite containing multiple aromatic rings, are the least reactive compounds at 622 K. The hydrogenation of the first ring of phenanthrene

 © 2006 Wiley-VCH Verlag GmbH & Co. KGaA, Weinheim

(hydrocarbon analogue of phenanthrothiophene) is known to be unusually slow,[21,22] in fact it is even slower than the hydrogenation of the first aromatic ring of compounds containing only two aromatic rings. Therefore, at low temperatures (622 K) the phenanthrothiophenes react very slowly due to lower hydrogenation rates. However, increasing the temperature makes the hydrogenation more facile and leads to a considerable increase in reactivity. In contrast, the reactivity of C_{2+} dibenzothiophenes does not increase as much with the reaction temperature as the hydrogenation pathway (based on its relatively lower hydrogen dependence) is less important for these compounds. Therefore, although the reactivity of C_{2+} dibenzothiophenes is higher than that of phenanthrothiophenes at 622 K, their reactivities are similar at 655 K.

We have developed a method for the molecular-level classification of HO sulfur compounds and have demonstrated that the sulfur compounds present in HO exhibit distinctly different reactivity, depending on their structure. Furthermore, their reactivity is a complex function of the process conditions. The nature and distribution of the different sulfur compounds is expected to define the ability to remove sulfur from these feeds. For example, feeds dominated by phenanthrothiophenes and C_{2+} dibenzothiophenes will be more difficult to desulfurize. In the case of the lower-boiling petroleum fraction (distillate range), the nature and distribution of sulfur compounds are known to dictate the selection of the catalyst and the processing conditions to achieve the desired product sulfur.[19] Information about the nature and distribution of the sulfur compounds in HO may similarly be used to maximize the HO desulfurization efficiency. Process innovations and the development of advanced desulfurization catalysts require a deep understanding of the fundamentals of the process under consideration.[19,23,24] The detailed molecular-level information apropos HO sulfur chemistry provided by this study is expected to help in process innovations and desulfurization catalyst ("conventional" and "biocatalyst") improvements.

Experimental Section

Determination of the sulfur content: In the first step, nonaromatic sulfides were selectively oxidized to sulfoxides, which were separated by adsorption on silica gel, thereby avoiding interference in the quantitative analysis of other sulfur compounds. Âs a first step, the sample was heated in an oven at 363 K for 0.5 h. One gram of the heated sample was treated with 0.15 g of tetrabutylammonium periodate in 12 mL of toluene/methanol (5:1, v/v) at 358 K for 1 h, washed with water, and separated into two fractions on a silica gel column. The fraction containing sulfoxides was quantitatively analyzed for the total sulfur content. The presence of sulfoxide groups was confirmed by infrared spectroscopy. The remaining fraction (devoid of sulfoxides) was introduced onto a diphenyl-/dimethylpolysiloxane (5/95) column (nonpolar) and then subsequently onto a diphenyl-/dimethylpolysiloxane (50/50) column (polar). The nonpolar column separates according to boiling point, and a modulator reintroduces the sample onto the second column, which separates according to polarity; a sulfur-chemiluminescence detector (SCD) and flame-ionization detector (FID) were used for sulfur and hydrocarbon detection, respectively. The amounts of sulfur compounds determined by this analysis were combined with the amount of nonaromatic sulfide and normalized to the total sulfur of the sample. The sulfur recovery ranged from 75 to 95%; the average sulfur recovery for feed samples was about 85%, whereas the average recovery for hydrotreated product samples was about 80%. The sulfur loss is due to formation of emulsions during the water-wash. However, the relative concentrations are not altered by this process: Control studies at different recoveries showed that the sulfur analysis is not significantly different for two analyses with considerably different sulfur recovery. This method is applicable to coker gas oils, vacuum gas oils, heavy atmospheric gas oils, heavy cycle oil, and other deashphalted heavy oils.

Hydrotreating experiments: The hydrotreating experiments with a commercial NiMo catalyst were undertaken in pilot units at the Bartlesville Technology Center, ConocoPhillips (COP). The HO feeds used in this study were obtained from COP refineries. Presulfiding was achieved using a distillate feed. Experiments were undertaken at varying reactor temperatures (622–655 K) and pressures (7–14 MPa); the liquid hourly space velocity was maintained constant at 1 h^{-1} and H_2/feed ratio at 356 m^3/m^3. Four pilot units were used to obtain the data in this study. An excellent reproducibility for a range of product properties was obtained between different pilot units for a given HO under identical process conditions.

The parallel first-order kinetics are described by the Equations (1) and (2), where S^f = sulfur content of the feed, x = 1–7 (group

$$\text{total } S_{\text{product}} = \sum [S^{f}_{\text{group}(x)} \exp(-k_{\text{group}\,x}\, P_{H_2}^{\alpha \text{group}\,x}/\text{LHSV})] \quad (1)$$

$$k_{\text{group}\,x} = A_{\text{group}\,x} \exp(-E_{\text{group}\,x}/RT) \quad (2)$$

numbering as given in the text), α = pressure dependence term, LHSV = liquid hourly space velocity, k = rate constant, A = pre-exponential factor, and E = activation energy.

The kinetic parameters were obtained from fitting the kinetic model to the experimental data obtained for HO1 under a range of process conditions. The scatter in the parity plot is mostly within experimental error (arising from pilot reactor operations and sulfur analysis). In order to validate the kinetic analysis, the parameters obtained from the HO1 data were used to predict the desulfurization performance of HO2 under the same process conditions. HO2 was chosen because it has significantly different properties (different source, sulfur content and distribution). Figure 2a provides the data for individual sulfur groups, while Figure 2b provides the corresponding total sulfur content data. Figure 2b has significantly fewer points as each data point represents the sum of the data of individual sulfur groups under a given process condition. In this particular study, the relative inhibition effect from nitrogen compounds is not expected to be important in terms of predictability as both HO1 and HO2 have similar total nitrogen content (Table 1). In a future study, the effect of individual nitrogen molecular groups (molecular composition), if any, on the desulfurization reaction should be determined.

Received: October 15, 2005
Revised: February 20, 2006
Published online: April 5, 2006

Keywords: analytical methods · desulfurization · fuel technology · green chemistry · sulfur

[1] S. F. Venner, *Hydrocarbon Process.* **2000**, *79*, 51–60.
[2] R. T. Yang, A. J. Hernandez-Maldonado, F. H. Yang, *Science* **2003**, *301*, 79–81.
[3] S. Brunet, D. Mey, G. Perot, C. Bouchy, F. Diehl, *Appl. Catal. A* **2005**, *278*, 143–172.
[4] N. Gupta, P. K. Roychoudhary, J. K. Deb, *Appl. Microbiol. Biotechnol.* **2005**, *66*, 356–366.
[5] I. V. Babich, J. A. Moulijn, *Fuel* **2003**, *82*, 607–631.
[6] C. Song, X. L. Ma, *Appl. Catal. B* **2003**, *41*, 207–238.

 © 2006 Wiley-VCH Verlag GmbH & Co. KGaA, Weinheim

[7] S. W. Shorey, D. A. Lomas, W. H. Keesom, *Hydrocarbon Process.* **1999**, *78*, 43 – 51.
[8] C. Song, *Catal. Today* **2003**, *86*, 211 – 263.
[9] V. Bavaro, *World Refrig.* **2000**, *10*, 34 – 37.
[10] C. Botchwey, A. K. Dalai, J. Adjaye, *Energy Fuels* **2003**, *17*, 1372 – 1381.
[11] T. A. Reid, *Akzo Nobel Catalyst Courier* **2002**, no. 42.
[12] X. L. Ma, K. Sakanashi, T. Isoda, I. Mochida, *Fuel* **1997**, *76*, 329 – 339.
[13] N. Ghaloum, G. Michael, Z. Khan, *J. Liq. Chromatogr. Relat. Technol.* **2002**, *25*, 1409 – 1420.
[14] X. L. Ma, K. Sakanashi, I. Mochida, *Ind. Eng. Chem. Res.* **1996**, *35*, 2487 – 2494.
[15] T. M. Schaub, R. P. Rodgers, A. G. Marshall, *Energy Fuels* **2005**, *19*, 1566 – 1573.
[16] J. T. Andersson, S. K. Panda, S. Wolfgang, *Abstr. Pap. ACS*, 230th ACS National Meeting, September **2005**.
[17] F. Ali, Z. H. Khan, N. Ghaloum, *Energy Fuels* **2004**, *18*, 1798 – 1805.
[18] H. Behbehani, M. K. Andari, *Pet. Sci. Technol.* **2000**, *18*, 51 – 61.
[19] K. G. Knudsen, B. H. Cooper, H. Topsoe, *Appl. Catal.* **1999**, *189*, 205 – 215.
[20] X. L. Ma, K. Sakanashi, T. Isoda, I. Mochida, *Energy Fuels* **1995**, *9*, 33 – 37.
[21] A. Stanislaus, B. H. Cooper, *Catal. Rev. Sci. Eng.* **1994**, *36*, 75 – 123.
[22] S. C. Korre, M. T. Klein, R. J. Quann, *Ind. Eng. Chem. Res.* **1995**, *34*, 101 – 117.
[23] M. Breysse, G. Djega-Mariadassou, S. Pessayre, C. Geantet, M. Vrinat, G. Perot, M. Lemaire, *Catal. Today* **2003**, *84*, 129 – 138.
[24] Y. Ishii, S. Kozaki, T. Furuya, K. Kino, K. Kirimura, *Curr. Microbiol.* **2005**, *50*, 63 – 70.

 © 2006 Wiley-VCH Verlag GmbH & Co. KGaA, Weinheim

DNA Assays

DOI: 10.1002/anie.200600124

Multiplexed DNA Detection with Biobarcoded Nanoparticle Probes**

*Savka I. Stoeva, Jae-Seung Lee, C. Shad Thaxton, and Chad A. Mirkin**

High-throughput multiplexed DNA detection is important for gene-expression profiling, as well as the detection of single-nucleotide polymorphism and pathogens such as common infectious diseases and biowarfare agents.[1] DNA microarrays utilize fluorescence readout and have become a core technology for the parallel interrogation of a large number of nucleic acid sequences.[1,2] However, microarray technology coupled with molecular fluorophore probes has limitations; these include the necessity for target amplification, post-amplification fluorophore labeling, slow binding kinetics between target sequence and capture strand, and in the case of multiplexed analysis, overlapping spectral features of the fluorophores, nonuniform photobleaching rates, the need for multiple-laser excitation sources, and complex, expensive instrumentation. The quest for improved and uniform labeling and detection methodologies has led to the development of alternative approaches such as fluorophore-labeled dendrimers,[3] fluorophore-encoded microspheres,[4] optically encoded porous silicon photonic crystals,[5] multimetal microrods,[6] nanowires,[7] and metal and semiconductor nanoparticle labels.[8]

Oligonucleotide-functionalized gold nanoparticles (Au NPs) have a demonstrated advantage in terms of sensitivity and selectivity over conventional probes in a variety of biodetection schemes.[8a–c,9] Their outstanding performance stems from cooperative binding properties, unique optical properties, catalytic properties, and the existence of robust and versatile surface-functionalization methods.[10] The biobarcode assay is based on Au NPs functionalized with a large number of oligonucleotide strands (the barcodes) and a corresponding recognition agent (an antibody in the case of protein detection and a portion of the barcode strand that can recognize the target of interest in the case of nucleic acid detection). This assay is particularly promising as it allows the rapid detection of protein targets at low-attomolar concentrations[11a–c] and nucleic acids at high-zeptomolar levels under optimized conditions.[11d] Significantly, enzymatic amplification of the target sequence prior to detection is not necessary. In the biobarcode assay, the barcode strands are used as a surrogate target and as a means of amplification. For every target molecule recognized and captured in the sandwich assay, about 300 barcodes (particle-probe size 30 nm; the DNA number is determined by fluorophore-probe labeling[9e]) are released. In principle, this is an assay that could be highly multiplexed, but in practice only single-target studies have been developed. Multiplexing is challenging for many assays because of the need to eliminate probe set/target set cross-reactivity, minimize nonspecific binding, and design spectroscopically and chemically unique probes. Herein, we demonstrate for the first time the feasibility of the biobarcode assay to detect multiple oligonucleotide targets simultaneously by using oligonucleotide sequences of 30 to 33 bases associated with a) hepatitis B virus surface-antigen gene (HBV), b) variola virus (small pox, VV), c) Ebola virus (EV), and d) human immunodeficiency virus (HIV) as model systems. The barcode for each target is the sequence-specific nucleotide probe, while the remainder of the sequence is universal for scanometric detection and readout. We demonstrate that these four DNA targets can be detected with high selectivity at mid-femtomolar concentrations. Significantly, the multiplexed biobarcode assay can be performed with a 96-well-plate format in a high-throughput and facile manner.

[*] S. I. Stoeva,[+] J.-S. Lee,[+] C. S. Thaxton, Prof. C. A. Mirkin
Department of Chemistry and the International Institute for Nanotechnology
Northwestern University
2145 Sheridan Road, Evanston, IL 60208-3113 (USA)
Fax: (+1) 847-467-5123
E-mail: chadnano@northwestern.edu

[+] These authors contributed equally to this work.

[**] C.A.M. acknowledges the HSARPA, the DARPA, the AFOSR, the Doris Duke Foundation, and the NIH for support of this research. C.A.M. is also grateful for an NIH Director's Pioneer Award. The authors thank Nanosphere, Inc. for useful discussions and help with microarray construction.

 © 2006 Wiley-VCH Verlag GmbH & Co. KGaA, Weinheim

The multiplexed biobarcode assay utilizes four sets of 30-nm Au-NP probes loaded with barcode DNA sequences specific to a given target (Figure 1a), as well as 2.8-μm magnetic-microparticle (MMP) probes. The MMP probes are

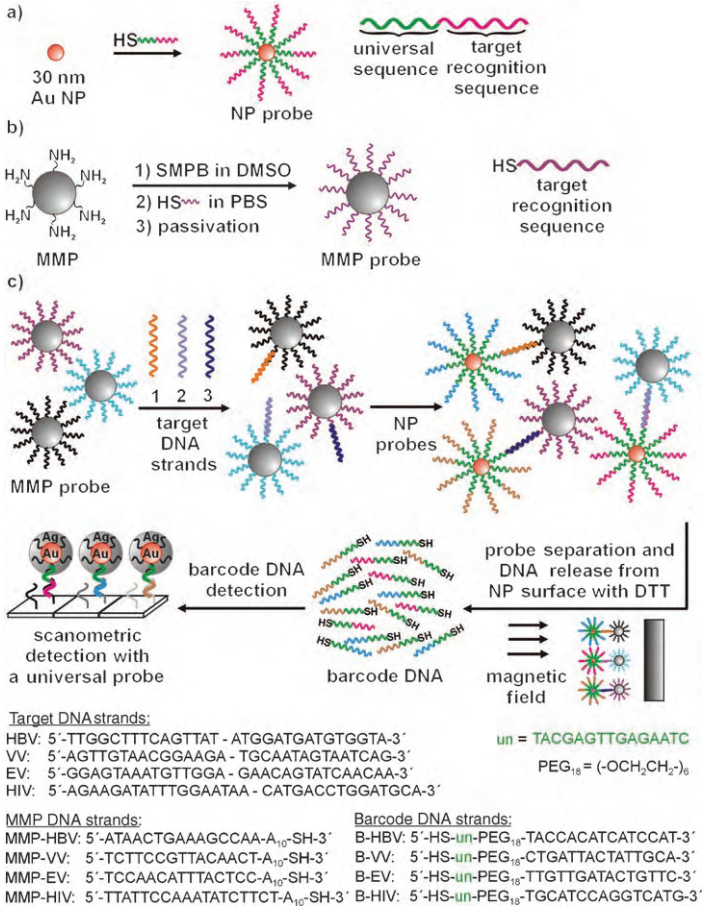

Figure 1. The multiplexed biobarcode assay for DNA detection. a) Preparation of the Au-NP probe; b) preparation of the MMP probe; c) biobarcode assay and scanometric detection of the barcodes. PBS = phosphate buffer saline.

functionalized with oligonucleotides that are complementary to a nucleotide region within the target of interest and different from the region recognized by the NP probes (Figure 1b). Importantly, each of the barcode DNA sequences is terminated with an oligonucleotide sequence (universal sequence; Figure 1a) that is identical for all the barcodes, which allows the use of one type of 13-nm Au-NP chip probe for the chip-based scanometric identification of the barcodes (Figure 1).[9a] Such a barcode design reduces probe-preparation and assay time, required effort, and probe-generation expense. The DNA targets are effectively captured in solution by a sandwich process involving the Au-NP and MMP probes (Figure 1c). The sandwich structures are isolated with a magnetic field, washed, and the barcode DNA strands are released from the NP surface by a ligand-exchange process induced by dithiothreitol (DTT).[11e] The DNA strands are subsequently identified by using the chip-based scanometric method developed in our laboratory and commercialized by Nanosphere, Inc.[9a]

The Au NPs (30-nm diameter) were functionalized with 5′-thiol-modified oligonucleotides following a previously published stepwise salting procedure with a few modifications.[10a] The excess barcode DNA was removed from the NP-probe solutions by repeated centrifugation and washing with assay buffer. The NP probes were used in the assay at a starting concentration of 5 nM. Amino-functionalized MMPs (2.8-μm diameter) were coupled to 3′-thiol-modified target-recognition DNA by using succinimidyl 4-(*p*-maleimidophenyl)butyrate (SMPB), a heterobifunctional cross-linking agent, following a protocol developed by our group (see Experimental Section). The surface of the MMP probes was passivated by acylation of the primary amino groups with sulfosuccinimidyl acetate (sulfo-NHS-acetate) to minimize nonspecific binding. The MMP probes contained on average 3×10^5 DNA strands/particle (determined by UV/Vis spectroscopy). The MMP probes were stored in assay buffer at a concentration of 30 mg mL^{-1}. Prior to the experiment, the MMP probes were washed twice with assay buffer.

To evaluate the selectivity of the system, 10 tests were run with different combinations of the target DNA sequences (Figure 2). In the first combination, all four DNA targets were

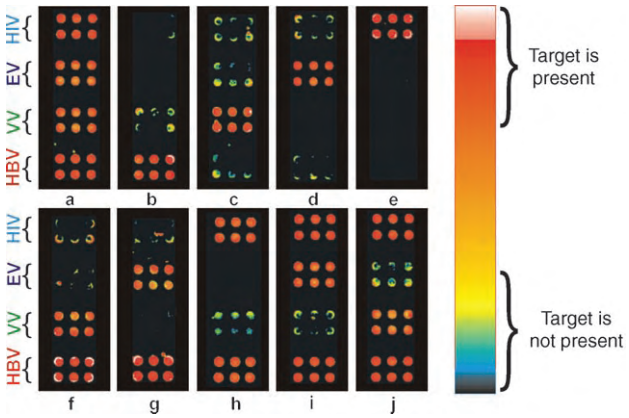

Figure 2. Scanometric detection of the barcode-DNA strands released from the 30-nm Au-NP probes for 10 different samples. a) All targets are present; b) HBV; c) VV; d) EV; e) HIV; f) HBV and VV; g) HBV and EV; h) HBV and HIV; i) HBV, EV and HIV; j) HBV, VV and HIV. The gray-scale images from the Verigene ID system were converted into colored ones using GenePix Pro 6 software (Molecular Devices). The diameter of the spots on the chip is 200 μm.

present. In the next nine tests, we systematically combined targets to evaluate the multiplexing capability of the barcode method. Importantly, the operator did not know the contents of each sample. The concentrations of the target DNA strands were kept constant for all experiments (each final concentration in the assay 500 fM). Prior to the assay, an MMP-probe solution composed of all four MMP probes (MMP multiplexing solution) was prepared by diluting equal volumes of each probe (30 mg mL^{-1}) in assay buffer to a final total MMP concentration of 1.56 mg mL^{-1}. The assay was initiated by mixing assay buffer (150 μL), MMP multiplexing solution (40 μL), and the appropriately mixed target solution (10 μL) in a polymerase-chain-reaction (PCR) tube. The system was

 © 2006 Wiley-VCH Verlag GmbH & Co. KGaA, Weinheim

heated at 45 °C for 30 min, followed by incubation at 25 °C for 3 h under constant vortex to allow hybridization between the MMP probes and the target DNA strands. Next, the reaction tube was placed on a 96-well-plate magnet, and the MMP–target complexes were washed twice with assay buffer (200 μL). An NP-probe solution composed of all four NP probes (NP multiplexing solution) was prepared by diluting equal volumes of each NP probe (5 nM) in assay buffer containing formamide (15 %) to a final total NP concentration of 200 pM. Formamide increases the stringency at which hybridization occurs, and the presence of 15 % formamide in the reaction mixture resulted in optimal selectivity of the system. The NP multiplexing solution (50 μL) was added to the MMP–target complexes, and hybridization was allowed to proceed at 25 °C for 75 min under vortex. The system was washed seven times with assay buffer (200 μL) to remove nonspecifically bound NPs and any free barcode DNA. The barcode DNA strands were then released from the NP probes by the addition of DTT (75 μL, 0.5 M) in scanometric buffer. The DTT-induced release of the barcodes was allowed to proceed at 50 °C for 10 min and at 25 °C for 50 min under vortex. Introduction of a magnetic field removed all MMP probes from the solution, leaving barcode DNA (its concentration is in the high-picomolar to low-nanomolar region) for detection with the chip-based scanometric method. The signal was identified with a Verigene ID system that records the scattered light from the developed spots after silver amplification.[9a]

The scanometric identification of the barcodes in all ten target combinations is presented in Figure 2. High-intensity spots with uniform signals were observed for each of the target DNA markers in each test solution. In some cases, low-intensity background signals were observed for targets that were not present in the test solutions (green/yellow features in Figure 2). However, the high-intensity positive signals were easily differentiated from the low-intensity background signals with the GenePix Pro 6 software used with the scanometric system, thus allowing the "blind" researcher in all ten cases to identify accurately the target composition of each mixture.

In conclusion, we demonstrated that the biobarcode-amplification approach can be used to detect multiple DNA targets in solution with high selectivity without the need for enzymatic target amplification and labeling. This is simply a proof-of-concept demonstration under idealized conditions (buffer). However, given that previously reported Au NP assays have been refined to work with unamplified genomic DNA,[12] it is likely that this multiplexed assay will ultimately enjoy similar capabilities with more complex samples. The biobarcode approach is particularly appealing for multiplexing as a large number of discernable barcode DNA sequences can be designed. In fact, for a 15-mer oligonucleotide sequence, there are more than 1×10^9 possible unique barcodes. Within this set of possible barcodes, a multitude of unique nonoverlapping, nonreactive sequences can be identified for almost any conceivable multiplexing experiment. Therefore, the results described herein are a promising step towards highly multiplexed panel assays for diseases with identified genetic markers.

Experimental Section

Au-NP probes (30 nm): Au NPs with an average diameter of 30 nm (Ted Pella, Inc.) were used at a concentration of ≈330 pM (≈2×10^{11} particles mL^{-1}). The disulfide bonds in all oligonucleotides (Integrated DNA Technologies) were reduced prior to mixing with the Au colloid by soaking in DTT (0.1 M; Pierce Biotechnology, Inc.) in phosphate buffer (0.17 M) at pH 8 for 2 h (10 OD of lyophilized DNA is typically reduced with 150 μL of 0.1 M DTT). The solutions of deprotected DNA were purified through desalting NAP-5 columns (GE Healthcare), and the amount of DNA from each column was determined by reading the absorbance of the solutions at 260 nm. A solution of the freshly deprotected DNA was then added to the Au colloid (final concentration of oligonucleotides 3–4 μM) to functionalize the Au NPs, and the mixture was shaken gently overnight at 10 °C. The colloid was first buffered at pH 7.2 (phosphate (10 mM), sodium dodecylsulfate (SDS; 0.01 %)), and the NaCl concentration was brought to 0.2 M in a stepwise manner over 1 day. After the salting process was completed, the Au probes were stored at 4 °C. Prior to the biobarcode experiment, the Au probes were purified from excess DNA by centrifugation (four times at 10000 rpm at 10 °C for 10 min) and washed each time with assay buffer (NaCl (0.2 M), tween 20 (0.1 %), phosphate buffer (10 mM), pH 7.2). All Au-NP probes were finally redispersed in assay buffer at a concentration of ≈5 nM. The exact Au-NP concentration was determined by reading the absorbance of the colloid at 530 nm. The molar extinction coefficient for 30-nm particles at 530 nm is $3 \times 10^9\ M^{-1}\,cm^{-1}$.

Au-NP chip probes (13 nm): Au NPs with an average diameter of 13 nm were synthesized by the citrate reduction of $HAuCl_4$. The 13-nm Au particles were functionalized with oligonucleotides as with the 30-nm Au particles. The 13-nm Au probe was purified from excess DNA by centrifugation (four times at 14000 rpm at 20 °C for 25 min) and washed each time with scanometric buffer (NaCl (0.5 M), tween 20 (0.01 %), phosphate buffer (10 mM), pH 7.2). The probe was finally redispersed in the same solution at a concentration of ≈10 nM and stored at 4 °C. The exact concentration of Au NPs was determined by reading the absorbance of the colloid at 525 nm. The molar extinction coefficient for 13-nm particles at 525 nm is $2.4 \times 10^8\ M^{-1}\,cm^{-1}$.

MMP probes: Amino-functionalized MMPs (2.8-μm diameter; Invitrogen) were covalently linked to 3′-thiol-modified oligonucleotides with SMPB (Pierce Biotechnology, Inc.). First, the MMPs (30 mg mL^{-1}, 1 mL) were washed twice with anhydrous dimethyl sulfoxide (DMSO; 1 mL). A solution of SMPB (50 mg) in DMSO (15 mL) was prepared prior to the reaction. Caution was taken to prevent the exposure of the solution to light. The SMPB/DMSO solution was added to the magnetic beads, and the reaction between the primary amino group and the *N*-hydroxysuccinimide (NHS) ester of SMPB was allowed to proceed for 4 h with gentle shaking at room temperature. The beads were magnetically separated and washed three times with DMSO (10 mL) and two times with coupling buffer (NaCl (0.2 M), phosphate buffer (100 mM), pH 7.0; 10 mL). The disulfide bonds in all 3′-thiolated oligonucleotides were reduced by DTT prior to mixing with the SMPB-activated MMPs. Solutions (5 μM) of each of the freshly cleaved oligonucleotides were prepared in coupling buffer, and 300 μL of each was added to each of the washed SMPB-activated magnetic beads. The reaction between the maleimide group and the SH group of the DNA was allowed to proceed at 20 °C for 1 h under constant vortex (1400 rpm). Next, the DNA-functionalized beads were placed on a magnet (Polysciences), the supernate was removed, and the beads were washed twice with coupling buffer and then twice with passivation buffer (NaCl (0.15 M), phosphate buffer (150 mM), pH 8.0). The supernate was used to determine the coupling efficiency by measuring the absorbance at 260 nm and comparing it with that before DNA functionalization. There were on average 3×10^5 DNA strands/particle. The surface of the DNA-functionalized MMPs was passivated by adding a freshly prepared solution (40 mL) of sulfo-NHS-acetate (100 mg; Pierce Biotechnology, Inc.) in passivation buffer (40 mL). Sulfo-NHS-

 © 2006 Wiley-VCH Verlag GmbH & Co. KGaA, Weinheim

acetate acylates primary amino groups in basic media. The passivation process proceeded for 30 min at room temperature with mild shaking. The beads were washed twice with passivation buffer, twice with assay buffer, and stored at 4 °C in assay buffer at a concentration of 30 mg mL^{-1}.

DTT-released barcodes: For the scanometric detection of barcode DNA, *N*-hydroxysuccinimide-activated Codelink glass microarray slides (GE Healthcare) were spotted at Nanosphere, Inc. with amine-terminated barcode-capture DNA sequences of the type 5′-H_2N-$(PEG_{18})_2$-DNA (Integrated DNA Technologies) following the manufacturer's protocol. Each DNA sequence was spotted six times. DTT-released barcodes (20 μL) in scanometric buffer were injected into hybridization chambers (Nanosphere, Inc.) attached to a microarray slide. The barcodes were hybridized to the slide in an incubator at 60 °C for 15 min, at 37 °C for 30 min, and at 25 °C for 15 min with mild shaking. The gaskets were disassembled, and the slides were copiously rinsed with scanometric buffer, spin-dried, and reassembled with a hybridization gasket. The universal 13-nm Au-NP chip-probe solution (20 μL; Au NP (500 pM), formamide (10%) in scanometric buffer) was introduced into the hybridization chambers and allowed to hybridize at 37 °C for 45 min. The gaskets were disassembled, washed three times in $NaNO_3$ solution (0.5 M), quickly dipped in cold $NaNO_3$ (0.1 M) and spin-dried. Silver enhancement was performed by applying silver-staining solution (2 mL; Nanosphere, Inc.) on the dried chips for 3 min. The reaction was terminated by washing the slides with Nanopure water (18 MΩ; Barnstead International). The slides were spin-dried and imaged with the Verigene ID system (Nanosphere, Inc.), which records the scattered light from the developed spots.

Received: January 11, 2006
Published online: April 7, 2006

Keywords: barcodes · biosensors · DNA detection · gold · nanoparticles

[1] D. J. Lockhart, E. A. Winzeler, *Nature* **2000**, *405*, 827 – 836.
[2] C. M. Niemeyer, D. Blohm, *Angew. Chem.* **1999**, *111*, 3039 – 3043; *Angew. Chem. Int. Ed.* **1999**, *38*, 2865 – 2869.
[3] Y. Li, Y. T. H. Cu, D. Luo, *Nat. Biotechnol.* **2005**, *23*, 885 – 889.
[4] a) M. Han, X. Gao, J. Z. Su, S. Nie, *Nat. Biotechnol.* **2001**, *19*, 631 – 635; b) F. J. Steemers, J. A. Ferguson, D. R. Walt, *Nat. Biotechnol.* **2000**, *18*, 91 – 94; c) X. Zhao, R. Tapec-Dytioco, W. Tan, *J. Am. Chem. Soc.* **2003**, *125*, 11 474 – 11 475.
[5] F. Cunin, T. A. Schmedake, J. R. Link, Y. Y. Li, J. Koh, S. N. Bhatia, M. J. Sailor, *Nat. Mater.* **2002**, *1*, 39 – 41.
[6] S. R. Nicewarner-Peña, R. G. Freeman, B. D. Reiss, L. He, D. J. Peña, I. D. Walton, R. Cromer, C. D. Keating, M. J. Natan, *Science* **2001**, *294*, 137 – 141.
[7] Y. Cui, Q. Wei, H. Park, C. M. Lieber, *Science* **2001**, *293*, 1289 – 1292.
[8] a) C. A. Mirkin, R. L. Letsinger, R. C. Mucic, J. J. Storhoff, *Nature* **1996**, *382*, 607 – 609; b) N. L. Rosi, C. A. Mirkin, *Chem. Rev.* **2005**, *105*, 1547 – 1562; c) C. M. Niemeyer, *Angew. Chem.* **2001**, *113*, 4254 – 4287; *Angew. Chem. Int. Ed.* **2001**, *40*, 4128 – 4158; d) C. M. Niemeyer, U. Simon, *Eur. J. Inorg. Chem.* **2005**, *18*, 3641 – 3655; e) E. Katz, I. Willner, *Angew. Chem.* **2004**, *116*, 6166 – 6235; *Angew. Chem. Int. Ed.* **2004**, *43*, 6042 – 6108; f) D. Gerion, W. J. Parak, S. C. Williams, D. Zanchet, C. M. Micheel, A. P. Alivisatos, *J. Am. Chem. Soc.* **2002**, *124*, 7070 – 7074; g) D. Gerion, F. Chen, B. Kannan, A. Fu, W. J. Parak, D. J. Chen, A. Majumdar, A. P. Alivisatos, *Anal. Chem.* **2003**, *75*, 4766 – 4772; h) J. Wang, G. Liu, A. Merkoci, *J. Am. Chem. Soc.* **2003**, *125*, 3214 – 3215.
[9] a) T. A. Taton, C. A. Mirkin, R. L. Letsinger, *Science* **2000**, *289*, 1757 – 1760; b) Y. C. Cao, R. Jin, C. A. Mirkin, *Science* **2002**, *297*, 1536 – 1540; c) L. He, M. D. Musick, S. R. Nicewarner, F. G. Salinas, S. J. Benkovic, M. J. Natan, C. D. Keating, *J. Am. Chem. Soc.* **2000**, *122*, 9071 – 9077; d) J. Liu, Y. Lu, *J. Am. Chem. Soc.* **2003**, *125*, 6642 – 6643; e) L. M. Demers, C. A. Mirkin, R. C. Mucic, R. A. Reynolds, R. L. Letsinger, R. Elghanian, G. Viswanadham, *Anal. Chem.* **2000**, *72*, 5535 – 5541.
[10] a) J. J. Storhoff, R. Elghanian, R. C. Mucic, C. A. Mirkin, R. L. Letsinger, *J. Am. Chem. Soc.* **1998**, *120*, 1959 – 1964; b) R. Jin, G. Wu, Z. Li, C. A. Mirkin, G. C. Schatz, *J. Am. Chem. Soc.* **2003**, *125*, 1643 – 1654; c) J. C. Love, L. A. Estroff, J. K. Kriebel, R. G. Nuzzo, G. M. Whitesides, *Chem. Rev.* **2005**, *105*, 1103 – 1169.
[11] a) J.-M. Nam, C. S. Thaxton, C. A. Mirkin, *Science* **2003**, *301*, 1884 – 1886; b) D. G. Georganopoulou, L. Chang, J.-M. Nam, C. S. Thaxton, E. J. Mufson, W. L. Klein, C. A. Mirkin, *Proc. Natl. Acad. Sci. USA* **2005**, *102*, 2273 – 2276; c) B.-K. Oh, J.-M. Nam, S. W. Lee, C. A. Mirkin, *Small* **2006**, *2*, 103 – 108; d) J.-M. Nam, S. I. Stoeva, C. A. Mirkin, *J. Am. Chem. Soc.* **2004**, *126*, 5932 – 5933; e) C. S. Thaxton, H. D. Hill, D. G. Georganopoulou, S. I. Stoeva, C. A. Mirkin, *Anal. Chem.* **2005**, *77*, 8174 – 8178.
[12] a) J. J. Storhoff, A. D. Lucas, V. Garimella, Y. P. Bao, U. R. Müller, *Nat. Biotechnol.* **2004**, *22*, 883 – 887; b) J. J. Storhoff, S. S. Marla, P. Bao, S. Hagenow, H. Mehta, A. Lucas, V. Garimella, T. Patno, W. Buckingham, W. Cork, U. R. Müller, *Biosens. Bioelectron.* **2004**, *19*, 875 – 883.

 © 2006 Wiley-VCH Verlag GmbH & Co. KGaA, Weinheim

RNA Cleavage

DOI: 10.1002/anie.200600164

Reversible Photocontrol of Deoxyribozyme-Catalyzed RNA Cleavage under Multiple-Turnover Conditions**

*Sonja Keiper and Joseph S. Vyle**

Light is a highly effective and well-established bioorthogonal trigger by which the chemical or biochemical reactivities of nucleic acids can be localized in time and space.[1] Typically, photoactivation results from the irreversible removal of a masking group from strategic functionalities and has been utilized for the construction of DNA arrays, the study of RNA

[*] Dr. S. Keiper, Dr. J. S. Vyle
School of Chemistry and Chemical Engineering
Queen's University Belfast
David Keir Building, Stranmillis Road, Belfast BT95AG (UK)
Fax: (+44) 28-9097-6524
E-mail: j.vyle@qub.ac.uk

[**] We thank Prof. R. J. H. Davies, QUB, for help with the illumination setup and L. A. Cooke, J. N. McClean, and J. Buick for providing the starting materials. Prof. A. P. de Silva provided valuable discussions. We gratefully acknowledge financial support by the School of Chemistry and QUESTOR. J.S.V. was supported by a Sir Henry Wellcome Commemorative Award for Innovative Research (050837); S.K. was supported by a postdoctoral fellowship by the Deutscher Akademischer Austauschdienst.

Supporting information for this article is available on the WWW under http://www.angewandte.org or from the author.

WILEY InterScience DISCOVER SOMETHING GREAT
© 2006 Wiley-VCH Verlag GmbH & Co. KGaA, Weinheim

cleavage and folding, the triggering of deoxyribozyme or aptamer activities, and also for the in vivo regulation of gene expression.[2] Alternatively, reversible optical control of DNA recognition has been reported with backbone-substituted azobenzene derivatives.[3] $E \rightarrow Z$ photoisomerization of azobenzenes occurs with high quantum yields at 330–370 nm, is not particularly sensitive to the environment, is fatigue-resistant, and leads to large conformational and polarity changes.[4] Modest discrimination in activities between the so-called irradiated (mainly Z) and more active dark-adapted (mainly E) states of papain modified by nonspecific attachment of azobenzenes to surface lysines was reported in 1991.[5] More recent reports have demonstrated that localization of azobenzenes at strategic residues of transmembrane proteins[6] or DNA-binding oligopeptides,[7] in which the E isomer is inactive, enables highly effective activity modulation by light.

To date, a single report of photoswitchable 8–17 deoxyribozyme-mediated RNA cleavage has been made.[8] However, in this report, only single-turnover behavior with a 200-fold excess of the deoxyribozymes over the substrate is described, highly attenuated activities are shown, and the incorporation of two azobenzene units is required for significant (up to 5.4-fold) light-induced rate modulation. Both the 8–17 and 10–23 RNA-cleaving deoxyribozymes were isolated by in vitro selection from the same library,[9] and have found application in a wide range of roles, for example, as sensors for bacterial rRNA, metal ions, and effector sequences, and for the in vivo regulation of specific mRNA levels.[10] In particular, 10–23 deoxyribozymes can cleave any target purine–pyrimidine motif and have wide tolerance for modifications in the binding arms or catalytic core, thus enabling both substrate affinity and serum stability to be significantly enhanced by chemical modification.[11,12]

Herein, we report the first photoswitchable RNA cleavage by nucleic acid catalysts under multiple-turnover conditions, in which only a single nonconserved residue is substituted by novel, readily accessible nucleotide analogues. Cleavage rates are enhanced up to ninefold following irradiation at 366 nm, thus reaching the rates observed for the unmodified deoxyribozyme.

We prepared 10–23 deoxyribozymes in which a single nucleotide (T8) within the catalytic core was replaced by a 2′-deoxyuridylate analogue. *Ortho*-, *meta*-, or *para*-phenylazobenzoyl moieties were appended to this residue through a 2′-amido linkage (Scheme 1 a). This site was chosen as deletion of T8 or substitution by 2′-*O*-methyluridine has previously been shown to only minimally perturb deoxyribozyme activities.[11] The deoxyribozyme constructs were engineered with short binding arms to promote product release under multiple-turnover conditions.

Modified nucleoside precursors were prepared by reaction of the protected 2′-aminonucleoside[13] with the *N*-hydroxysuccinimidyl ester of the appropriate azobenzene,[14] and subsequently phosphitylated under standard conditions. These precursors were incorporated into model octamers (ACC**1**GGTA) and also 10–23 deoxyribozyme sequences (Scheme 1 b) by automated solid-phase synthesis with extended reaction times for introduction of the modified

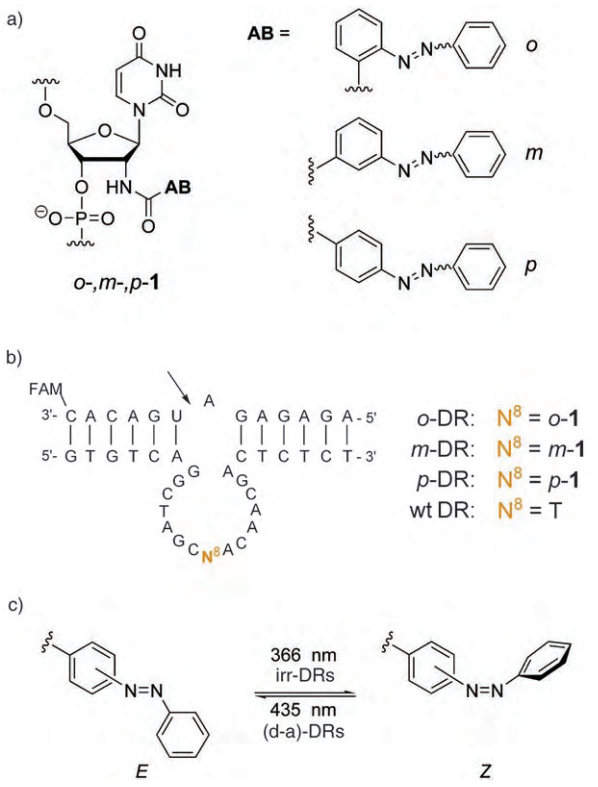

Scheme 1. a) Azobenzene-modified uridylates used in this study. b) The 10–23 deoxyribozymes prepared (FAM = 6-fluoresceinyl; cleavage site indicated by arrow). c) Photoisomerization of the azobenzene unit (irr-DR and (d-a)-DR refer to irradiated and dark-adapted 10–23 deoxyribozymes, respectively).

residue. Coupling yields as monitored by trityl release were greater than 98%. After deprotection under anhydrous conditions, the oligonucleotides were purified by reversed-phase HPLC and their identities were confirmed by MALDI-TOF analysis.

The photoisomerization of oligodeoxynucleotide-appended azobenzenes under irradiation at 366 nm (Scheme 1 c) was investigated by UV/Vis spectroscopy of the model octamers. When the photoswitches were in the thermally stable E configuration, the spectra showed local maxima at 330 (*o*-**1**), 321 (*m*-**1**), and 329 nm (*p*-**1**) that were typical of azobenzene π–π* transitions. Irradiation at 366 nm led to loss of these absorption maxima, with photostationary states being achieved within 8 min. These results were reproduced with deoxyribozymes (DRs) appended to azobenzene, and the $E \rightarrow Z$ conversion yields were measured immediately by HPLC. Peak quantification at 260 nm was used to determine the level of E and Z isomers either directly for *m*-DR and *p*-DR, or by inference using the model octamer sequence containing *o*-**1**. After irradiation, $E \rightarrow Z$ conversion yields of 86% for irr-*o*-DR, 75% for irr-*m*-DR, and 61% for irr-*p*-DR were thus determined. At 26 °C the *ortho* and *meta* photoswitches within both the model sequences and the deoxyribozymes were stable toward $Z \rightarrow E$ thermal back-isomerization. In contrast, *para* photoswitches underwent more rapid thermal reisomerization at this temperature. In all

 © 2006 Wiley-VCH Verlag GmbH & Co. KGaA, Weinheim

cases $Z \rightarrow E$ photoisomerization was complete following irradiation at 435 nm for 2 min.

Both azobenzene-modified and unmodified (wild-type) deoxyribozymes (wt DRs) catalyzed the site-specific cleavage of a 13-mer oligoribonucleotide substrate labeled at its 3′ terminus with a fluoresceinyl moiety (FAM) to yield a labeled hexamer and a 2′,3′ cyclic phosphate-terminated heptamer. The cleavage reactions were thus resolved, visualized, and quantified in a polyacrylamide gel electrophoresis (PAGE) assay (Figure 1 a). Deoxyribozyme solutions were exposed to light at 366 nm for 10 min or at 435 nm for 2 min, and reactions were initiated by the addition of substrate RNA followed by incubation at 26 °C in the absence of light. To assess the cleavage activity of the more thermally labile irr-*p*-DR, continuous irradiation at 366 nm was performed during the assay.

Under multiple-turnover conditions, irradiated azobenzene–deoxyribozymes maintained essentially wild-type activities; thus, irr-*o*-DR, irr-*m*-DR, and irr-*p*-DR showed cleavage rates of 100, 90, and 50%, respectively (Figure 1 b). In contrast, RNA cleavage rates by dark-adapted (d-a) deoxyribozymes were considerably attenuated. The $k_{irr}/k_{d\text{-}a}$ ratios in this assay were determined to be 9:1 for *o*-DR and *p*-DR, and 8:1 for *m*-DR (Figure 1 c). Photocontrol of RNA cleavage by deoxyribozyme–azobenzene conjugates was also demonstrated by using an unlabeled RNA substrate and reversed-phase HPLC analysis.[14] The effects observed in these assays compare well with the results from the PAGE analyses. Thus, the relative rates of substrate cleavage by irr-*o*-DR and irr-*m*-DR are both the same as for the unmodified deoxyribozyme wt DR, and irr-*p*-DR shows 44% of the wild-type activity. Dark-adapted deoxyribozymes give significantly less conversion than the irradiated constructs; $k_{irr}/k_{d\text{-}a}$ discrimination factors of 6 for *o*-DR and 5 for *m*-DR and *p*-DR constructs were observed.

The effect of photoswitching upon catalysis by the azobenzene-conjugated deoxyribozymes was also demonstrated to be reversible under multiple-turnover conditions with either 5 mol% (*o*-DR or *m*-DR) or 10 mol% (*p*-DR) deoxyribozyme (Figure 2). After initial irradiation of deoxyribozyme solutions at 366 nm the reactions were initiated by addition of substrate, and RNA cleavage rates comparable to those previously described were observed. After 120 min the reactions were irradiated at 435 nm for 2 min to afford the dark-adapted deoxyribozymes which gave rise to significantly retarded reaction rates, although these were higher than those previously observed using purified *E*-DRs. Thus, $k_{irr}/k_{d\text{-}a}$ discrimination factors of 3.6 for *o*-DR, 3.8 for *m*-DR, and 4.1 for *p*-DR were observed. This difference might be accounted for by perturbation of the $Z \rightarrow E$ photoisomerization process[4] in the presence of substrate RNA or kinetic

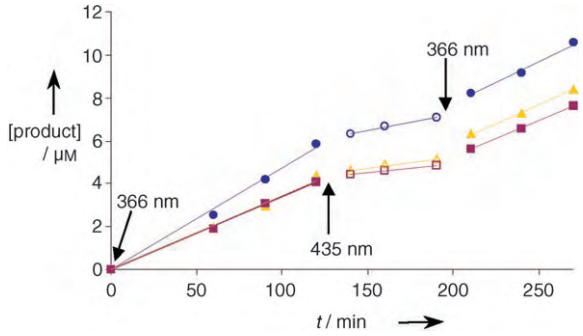

Figure 2. Reversibility of RNA (20 μM) cleavage by 10–23 deoxyribozymes *o*-DR (1 μM), *m*-DR (1 μM), and *p*-DR (2 μM) under multiple-turnover conditions. Key: ○ (d-a)-*o*-DR; ● irr-*o*-DR; △ (d-a)-*m*-DR; ▲ irr-*m*-DR; □ (d-a)-*p*-DR; ■ irr-*p*-DR.

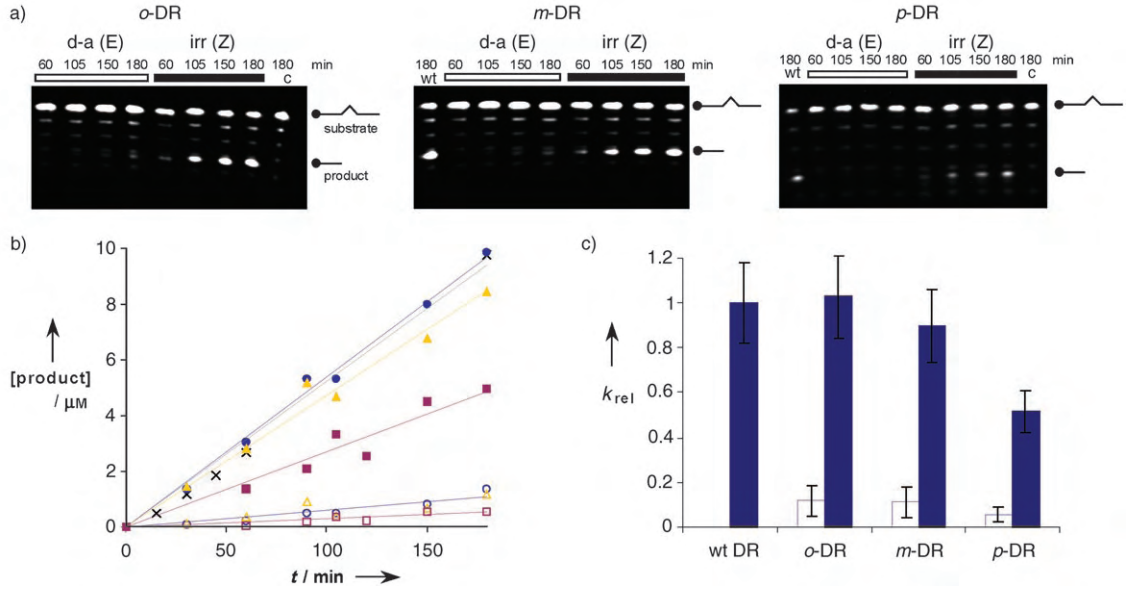

Figure 1. RNA (20 μM) cleavage by 10–23 deoxyribozymes *o*-DR, *m*-DR, *p*-DR, and wt DR under multiple-turnover conditions (10:1 RNA/deoxyribozyme). a) PAGE analysis of 3′-FAM-labeled RNA substrate strands (wt: wt DR RNA cleavage; c: control without DR). b) Quantitative analysis of product formation; key: ○ (d-a)-*o*-DR; ● irr-*o*-DR; △ (d-a)-*m*-DR; ▲ irr-*m*-DR; □ (d-a)-*p*-DR; ■ irr-*p*-DR; × wt DR. c) k_{rel} values for dark-adapted (open bars) and irradiated (filled bars) deoxyribozymes normalized to the unmodified deoxyribozyme reaction.

© 2006 Wiley-VCH Verlag GmbH & Co. KGaA, Weinheim

folding traps, which do not respond to this isomerization.[15] However, the initial cleavage rates were recovered following irradiation at 366 nm (Figure 2).

Large differences in the steric demands and hydrophobic characters of the *E* and *Z* isomers of *para*-azobenzene residues attached to biomolecules are well-described,[16] but we are unaware of any other report in which the *ortho* isomers give similar activity switching. Preliminary NMR spectroscopic investigations indicate that both *E* and *Z* isomers of *p*-**1** reside in the C2′-*endo* furanoside pucker typical of 2′-amido deoxyribonucleoside analogues and their unmodified congeners, and so the active conformation of the catalytic core containing the photoswitch may be modulated in some other fashion.

Our demonstration of photomodulated deoxyribozyme-catalyzed RNA cleavage under multiple-turnover conditions is of particular interest as the irradiated "on" state maintains wild-type cleavage rates. The novel analogues described herein enable incorporation of azobenzene moieties with readily accessible nucleoside derivatives, which have the potential to maintain essential base contacts and the biological activity of nucleic acids. We envisage that the ability to reversibly modulate the catalytic RNA cleavage rates of the 10–23 deoxyribozyme by light will add a useful tool to the repertoire of regulatory biocatalysts. We are currently working toward the development of light-programmable conformational switches within DNA and RNA,[17] and their application to the spatiotemporal control of gene expression and array-based computation.[18]

Received: January 15, 2006
Published online: April 18, 2006

Keywords: azo compounds · deoxyribozymes · enzyme catalysis · photoisomerization · RNA

[1] J. H. Kaplan, B. Forbush, J. F. Hoffman, *Biochemistry* **1978**, *17*, 1929–1935.

[2] a) A. C. Pease, D. Solas, E. J. Sullivan, M. T. Cronin, C. P. Holmes, S. P. A. Fodor, *Proc. Natl. Acad. Sci. USA* **1994**, *91*, 5022–5026; b) S. G. Chaulk, A. M. MacMillan, *Nucleic Acids Res.* **1998**, *26*, 3173–3178; c) C. Höbartner, S. K. Silverman, *Angew. Chem.* **2005**, *117*, 7471–7475; *Angew. Chem. Int. Ed.* **2005**, *44*, 7305–7309; d) P. Wenter, B. Fürtig, A. Hainard, H. Schwalbe, S. Pitsch, *Angew. Chem.* **2005**, *117*, 2656–2659; *Angew. Chem. Int. Ed.* **2005**, *44*, 2600–2603; e) R. Ting, L. Lermer, D. M. Perrin, *J. Am. Chem. Soc.* **2004**, *126*, 12720–12721; f) A. Heckel, G. Mayer, *J. Am. Chem. Soc.* **2005**, *127*, 822–823; g) S. Shah, S. Rangarajan, S. H. Friedman, *Angew. Chem.* **2005**, *117*, 1352–1356; *Angew. Chem. Int. Ed.* **2005**, *44*, 1328–1332; h) H. Ando, T. Furuta, R. Y. Tsien, H. Okamoto, *Nat. Genet.* **2001**, *28*, 317–325; i) W. T. Monroe, M. M. McQuain, M. S. Chang, J. S. Alexander, F. R. Haselton, *J. Biol. Chem.* **1999**, *274*, 20895–20900.

[3] a) H. Asanuma, T. Ito, T. Yoshida, X. G. Liang, M. Komiyama, *Angew. Chem.* **1999**, *111*, 2547–2549; *Angew. Chem. Int. Ed.* **1999**, *38*, 2393–2395; b) A. Yamazawa, X. G. Liang, H. Asanuma, M. Komiyama, *Angew. Chem.* **2000**, *112*, 2446–2447; *Angew. Chem. Int. Ed.* **2000**, *39*, 2356–2357; c) H. Asanuma, D. Tamaru, A. Yamazawa, M. Z. Liu, M. Komiyama, *ChemBioChem* **2002**, *3*, 786–789.

[4] G. A. Woolley, *Acc. Chem. Res.* **2005**, *38*, 486–493.

[5] I. Willner, S. Rubin, A. Riklin, *J. Am. Chem. Soc.* **1991**, *113*, 3321–3325.

[6] a) M. Banghart, K. Borges, E. Isacoff, D. Trauner, R. H. Kramer, *Nat. Neurosci.* **2004**, *7*, 1381–1386; b) M. Volgraf, P. Gorostiza, R. Numano, R. H. Kramer, E. Y. Isacoff, D. Trauner, *Nat. Chem. Biol.* **2006**, *2*, 47–52.

[7] L. Guerrero, O. S. Smart, G. A. Woolley, R. K. Allemann, *J. Am. Chem. Soc.* **2005**, *127*, 15624–15629.

[8] Y. Liu, D. Sen, *J. Mol. Biol.* **2004**, *341*, 887–892.

[9] a) S. W. Santoro, G. F. Joyce, *Proc. Natl. Acad. Sci. USA* **1997**, *94*, 4262–4266; b) S. W. Santoro, G. F. Joyce, *Biochemistry* **1998**, *37*, 13330–13342.

[10] a) H. Suenaga, R. Liu, Y. Shiramasa, T. Kanagawa, *Appl. Environ. Microbiol.* **2005**, *71*, 4879–4884; b) I. H. Chang, J. J. Tulock, J. W. Liu, W. S. Kim, D. M. Cannon, Y. Lu, P. W. Bohn, J. V. Sweedler, D. M. Cropek, *Environ. Sci. Technol.* **2005**, *39*, 3756–3761; c) D. Y. Wang, D. Sen, *J. Mol. Biol.* **2001**, *310*, 723–734; d) S. H. Pun, F. Tack, N. C. Bellocq, J. J. Cheng, B. H. Grubbs, G. S. Jensen, M. E. Davis, M. Brewster, M. Janicot, B. Janssens, W. Floren, A. Bakker, *Cancer Biol. Ther.* **2004**, *3*, 641–650.

[11] a) Z. Zaborowska, S. Schubert, J. Kurreck, V. A. Erdmann, *FEBS Lett.* **2005**, *579*, 554–558; b) Z. Zaborowska, J. P. Furste, V. A. Erdmann, J. Kurreck, *J. Biol. Chem.* **2002**, *277*, 40617–40622.

[12] a) C. R. Dass, E. G. Saravolac, Y. Li, L. Q. Sun, *Antisense Nucleic Acid Drug Dev.* **2002**, *12*, 289–299; b) M. J. Cairns, T. M. Hopkins, C. Witherington, L. Wang, L. Q. Sun, *Nat. Biotechnol.* **1999**, *17*, 480–486; c) S. K. Silverman, *Nucleic Acids Res.* **2005**, *33*, 6151–6163.

[13] D. P. C. McGee, A. Vaughnsettle, C. Vargeese, Y. S. Zhai, *J. Org. Chem.* **1996**, *61*, 781–785.

[14] See the Supporting Information for details.

[15] a) K. Nakayama, M. Endo, T. Majima, *Chem. Commun.* **2004**, 2386–2387; b) A. M. Caamano, M. E. Vazquez, J. Martinez-Costas, L. Castedo, J. L. Mascarenas, *Angew. Chem.* **2000**, *112*, 3234–3237; *Angew. Chem. Int. Ed.* **2000**, *39*, 3104–3107.

[16] C. Dugave, L. Demange, *Chem. Rev.* **2003**, *103*, 2475–2532.

[17] R. Micura, *Angew. Chem.* **2006**, *118*, 32–34; *Angew. Chem. Int. Ed.* **2006**, *45*, 30–31.

[18] M. N. Stojanovic, D. Stefanovic, *Nat. Biotechnol.* **2003**, *21*, 1069–1074.

 © 2006 Wiley-VCH Verlag GmbH & Co. KGaA, Weinheim

Molecular Recognition

DOI: 10.1002/anie.200600354

Crystal Structure of the *Homo sapiens* Cytoplasmic Ribosomal Decoding Site Complexed with Apramycin**

*Jiro Kondo, Boris François, Alexandre Urzhumtsev, and Eric Westhof**

Aminoglycosides are positively charged oligosaccharides with several ammonium and hydroxy groups[1] that bind specifically to bacterial 16S aminoacyl–tRNA (t = transfer) decoding sites (A sites), thereby disturbing the fidelity of the tRNA selection step during protein synthesis.[2,3] Various complexes can be formed between 4,5- and 4,6-disubstituted aminoglycosides and the 30S ribosomal particles[4–7] or oligonucleotides containing the bacterial A-site fragment;[8–12] 3D structures of these complexes were solved by X-ray crystallographic analysis. Comparative structural analysis showed that a) the puckered sugar ring I inserts into the A-site helix, stacks onto the G1491 residue, and forms two hydrogen bonds with the universally conserved A1408 residue; b) the central ring II (2-deoxystreptamine; 2-DOS) forms four conserved hydrogen bonds, N1–H···O4-(U1495), N3–H···N7(G1494), N3–H···O2P-(G1494), and N3–H···O1P(A1493). These six hydrogen bonds help to maintain the A site in a state in which the residues A1492 and A1493 are fully bulged out, thus allowing them to pack their sugar edges into the shallow/minor groove of the first two Watson–Crick base pairs of the codon–anticodon minihelix bound to the 30S ribosome (the A-minor motif).[13] This conformational state induces misreading of the codon.[5]

Although the molecular mechanisms of aminoglycoside-induced miscoding in bacterial cells are now well-investigated, the origins of aminoglycoside toxicity in eukaryotic cells are still debated.[14] Indeed, these compounds are all toxic to mammals,[1,15,16] and the effects in humans are attributed to the binding of aminoglycosides to the *Homo sapiens* cytoplasmic or mitochondrial A sites[17–20] owing to sequence similarities with those of bacteria (Figure 1a).

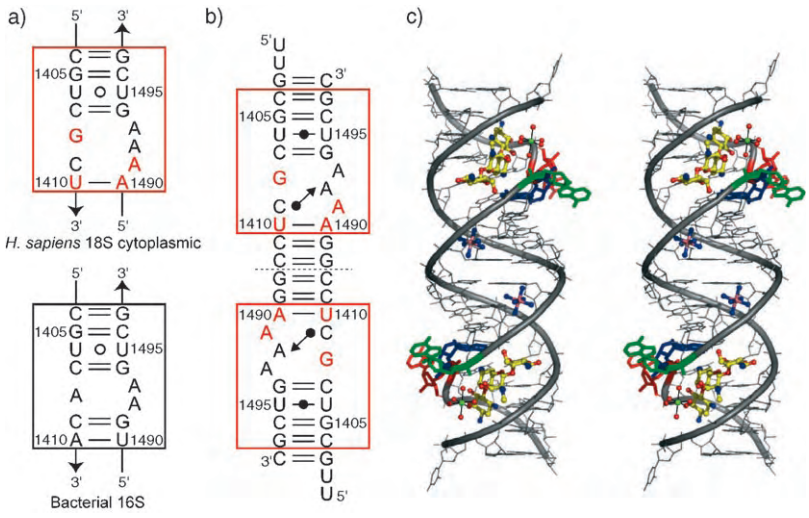

Figure 1. a) Secondary structures of the *H. sapiens* 18S and the bacterial 16S ribosomal decoding A sites. The nucleotides of *H. sapiens* that are different from those in the bacterial A site are in red. b) Secondary structure of the RNA duplex found in the crystal. The unobserved 5′-overhanging uracil residues are in light gray. Geometric nomenclature and symbols for nucleic acid base pairs are according to those in reference [41]. c) Stereoview of the RNA duplex in complex with apramycin. A1491, A1492, and A1493 are in green, blue, and red, respectively.

Apramycin, formerly called nebramycin factor 2,[21] is produced by *Streptomyces tenebrarius*.[22] This antibiotic, officially listed as an aminocyclitol because its unusual structure contains a bicyclic moiety (Figure 2),[23] is also classified as an aminoglycoside owing to its physicochemical properties.[24,25] Apramycin acts against Gram-negative bacteria such as *Escherichia coli* and Gram-positive bacteria such as *Staphylococcus aureus*[24,25] by inhibiting protein synthesis after binding to the bacterial A site.[26] This site-specific binding of apramycin was recently revealed by X-ray crystallographic analysis.[27] Apramycin has good potential

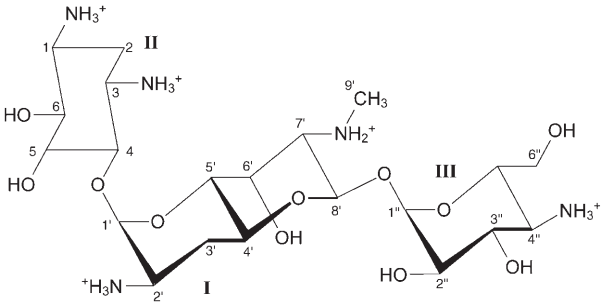

Figure 2. Chemical structure of apramycin.

[*] Dr. J. Kondo, Dr. B. François, Prof. E. Westhof
Institut de Biologie Moléculaire et Cellulaire
Université Louis Pasteur
15 rue René Descartes, 67084 Strasbourg (France)
Fax: (+33) 3-8860-2218
E-mail: e.westhof@ibmc.u-strasbg.fr
Prof. A. Urzhumtsev
Faculté des Sciences
Université Henri Poincaré
Vandoeuvre-lès-Nancy, 54506 Nancy (France)

[**] J.K. is supported by the Japan Society for the Promotion of Science. We are grateful to Dr. B. Masquida, Dr. A. C. Vaiana, Dr. P. Auffinger, and Prof. P. S. Ho for helpful discussions and suggestions. We thank the European Synchrotron Radiation Facility for the use of their facilities and acknowledge the staff of beamline ID14-4.

Supporting information for this article is available on the WWW under http://www.angewandte.org or from the author.

WILEY InterScience DISCOVER SOMETHING GREAT
© 2006 Wiley-VCH Verlag GmbH & Co. KGaA, Weinheim

as an antibiotic; unfortunately, its use in mammals is limited by the relatively high risk of toxicity.[28–31] In fact, it is only used in veterinary medicine and never in humans.[31] Mass-spectrometric studies with RNA model fragments showed that apramycin binds to the eukaryotic 18S ribosomal A site with a higher affinity ($K_d = 0.5$ μM) than to the bacterial 16S site ($K_d = 2 \pm 0.20$ μM).[32] This result strongly suggests that the binding of apramycin to the eukaryotic cytoplasmic A site may be the cause of decreasing translation fidelity and inhibition of translocation of the eukaryotic ribosome. We determined the 3D structure of the *H. sapiens* 18S cytoplasmic A site complexed with apramycin at 2.8-Å resolution by X-ray crystallography.

The asymmetrical loop of the *H. sapiens* cytoplasmic A site was inserted between Watson–Crick pairs in RNA fragments designed to fold as a duplex with two A sites (Figure 1b). Such RNA fragments were previously used as successful models for crystallographic studies to determine the specific interactions between bacterial A sites and aminoglycosides.[8–12] It was shown that A sites inserted into RNA fragments present the same footprint as that of the full 16S rRNA (r = ribosomal).[33–36]

The secondary and overall crystal structure of the RNA fragment in complex with apramycin is shown in Figure 1b and c. Two noncrystallographic-symmetry-related RNA strands form a pseudosymmetrical duplex. The root-mean-square deviation (RMSD) between two A sites is 0.006 Å. The apramycin molecules bind specifically to the deep/major groove of both A sites (Figures 1c and 3). A hexahydrated magnesium ion is held between the two phosphate backbones (Figure 3) and is in contact with the atoms of both apramycin and RNA (Figure 4a). At the center of the duplex, four contiguous Watson–Crick G=C base pairs are formed, and each G/G stack interacts with a hexammine cobalt cation (Figure 1c). Three Watson–Crick G=C base pairs close the stem at both ends. Two of the four overhanging U residues are involved in crystal-packing interactions, with the other two being disordered in the solvent channel. Hereafter, we focus our description on one A site using the numbering of *H. sapiens* cytoplasmic 18S rRNA.

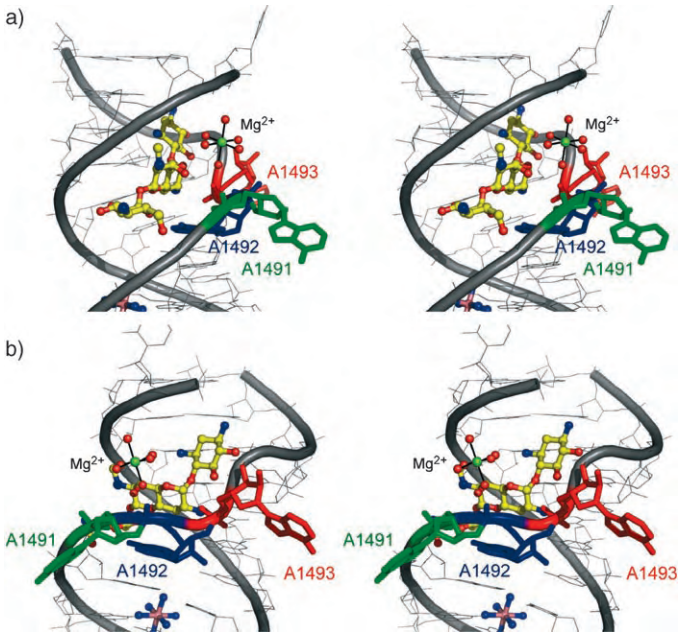

Figure 3. Stereoview of the *H. sapiens* cytoplasmic A site in complex with apramycin from two different angles. A1491 (green) and A1493 (red) are protruding, whereas A1492 (blue) is inside the A-site helix.

At both ends of the internal loop of the cytoplasmic A site, four canonical Watson–Crick pairs, C1404=G1497, G1405=C1496, C1407=G1494, and U1410−A1490, are formed (Figure 4b,c,e,h). The U1406 residue forms a symmetric base pair with U1495 involving the Watson–Crick edges (Figure 4d). The G1408 residue, which is universally conserved in all eukaryotic cytoplasmic A sites, does not form a base pair, but makes two contacts with the phosphate anionic oxygen atom of A1493, that is, N1−H···O2P(A1493) (3.3 Å) and N2−H···O2P(A1493) (2.9 Å) (Figure 4f). Consequently, the A1493 residue protrudes into the solvent region but is not involved in any crystal-packing interaction (Figures 3 and 4f). The C1409 residue forms the Watson–Crick/sugar-edge base pair with A1492 with three hydrogen bonds, O2···H−O2′-(A1492) (3.2 Å), N3···H−O2′(A1492) (3.1 Å), and N4−H···N3(A1492) (3.3 Å) (Figure 4g). The A1492 residue also interacts with the phosphate backbone of A1491 by using its Hoogsteen edge through N6−H···O1P(A1491) (3.5 Å) (Figure 4g). The A1491 residue protrudes and does not contact a symmetrical molecule (Figures 3 and 4g).

Apramycin binds to the deep/major groove of the A site and makes 14 direct and seven water-mediated contacts to the base and phosphate oxygen atoms of the RNA (Figure 4a). Ring II (2-DOS) is oriented flat against the base-pair edges in the deep/major groove of the upper side of the A site (Figure 3) and interacts with C1404=G1497, G1405=C1496, and C1407=G1494 through four direct and two water-mediated contacts (Figure 4a–c,e). The N3 atom of ring II is not involved in any interaction with the A site (Figure 4a). The central bicyclic ring I is perpendicular to the central part of the A site (Figure 3) and makes seven direct and five water-mediated contacts with RNA atoms (Figure 4a). The G1408 residue forms two hydrogen-bond interactions with sugar ring I through O6(G1408)···H−C3′ and O6(G1408)···H−N2′ by using the Watson–Crick edge (Figure 4f). The N2′ atom also interacts with the phosphate backbone of A1493, maintaining it in a bulged-out conformation (Figure 4f). A hexahydrated magnesium ion is wedged between two phosphate-ribose backbones and bridges ring I (O5′ and O6′) to the phosphate oxygen atoms of the C1404, A1492, and G3 residues (Figure 4a). Ring III recognizes the Watson–Crick/sugar-edge C1409−A1492 base pair from the deep/major groove and forms the O5″···H−N6(A1492) hydrogen bond with the Watson–Crick edge of A1492 (Figure 4g). This interaction forces A1492 inside the RNA duplex.

The binding mode of apramycin to the *H. sapiens* cytoplasmic A site is surprisingly different from that observed in the analogous bacterial complex.[27] The orientation of apramycin in the bacterial A site is rotated back to front with respect to that in the *H. sapiens* cytoplasmic A site (see Supporting Information). Apramycin penetrates the internal loop of the bacterial A site from the deep/major to the

 © 2006 Wiley-VCH Verlag GmbH & Co. KGaA, Weinheim

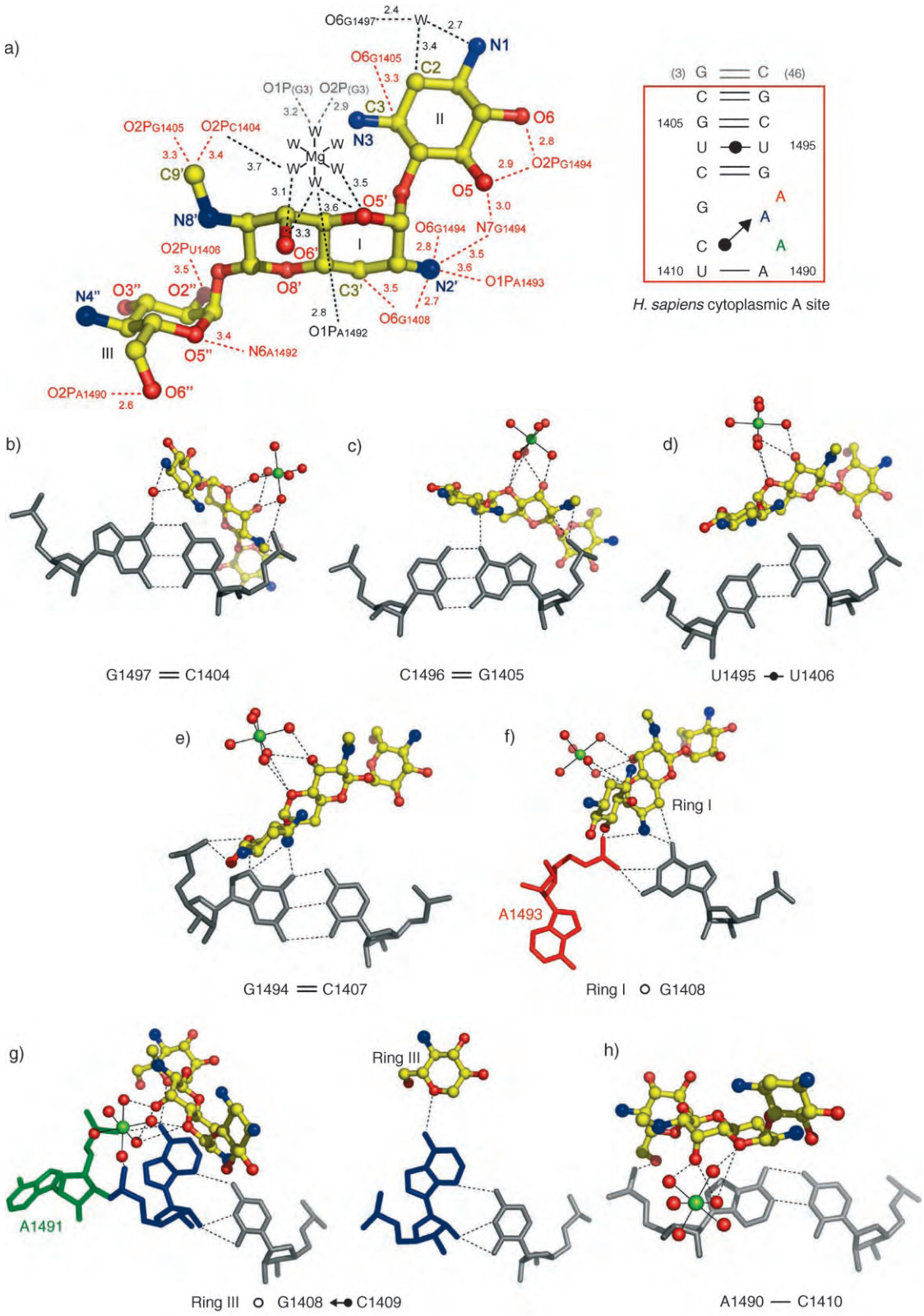

Figure 4. Description and analysis of the contacts between apramycin and the *H. sapiens* cytoplasmic A site. a) Structure adopted by the apramycin molecule inside the *H. sapiens* cytoplasmic A site. Ring numbers (I–III) and atom names are specified. The *H. sapiens* cytoplasmic numbering is used for the RNA atoms; W = water molecule, Mg = magnesium ion. Direct and water-mediated contacts between apramycin and the minimal A site are shown as red and black dashed lines, respectively. b–h) Atomic details of the contacts involving each base pair of the minimal A site interacting with apramycin. A1491, A1492, and A1493 are in green, blue, and red, respectively. Hydrogen bonds are represented by black dashed lines. The C–H···O hydrogen bonds are also indicated.

 © 2006 Wiley-VCH Verlag GmbH & Co. KGaA, Weinheim

shallow/minor groove and forces both A1492 and A1493 to bulge out. The number of direct contacts between apramycin and the bacterial A site (nine) is slightly less than that observed in the *H. sapiens* cytoplasmic complex (14) (Figure 4a and Supporting Information). This result agrees with mass-spectrometric studies, which show that apramycin binds to the eukaryotic 18S ribosomal A site in the absence of magnesium ions with a higher affinity ($K_d = 0.5$ μM) than to the bacterial site ($K_d = 2 \pm 0.20$ μM).[32] Ring II makes three direct contacts with U1406–U1495, C1407=G1494, and the protruding A1493 of the bacterial A site through the N1 and N3 atoms. The O5 atom, which interacts with G1494 in the cytoplasmic A site (Figure 4a,e), is not bound to the bacterial A site. Ring I stacks onto G1491 of the Watson–Crick C1409=G1491 base pair and forms a sugar–base-pair interaction with the universally conserved A1408 of the bacterial A site with O5′···H–N6(A1408) and O6′–H···N1(A1408). In contrast, in the *H. sapiens* cytoplasmic complex, O5′ and O6′ are bound to three of the six hydration water molecules of the magnesium ion. The A1492 and A1493 residues of the bacterial A site are thus forced to protrude from the RNA helix. The N2′ atom, which binds to G1408 of the cytoplasmic A site (Figure 4a,f), is free from any interactions in the bacterial complex. In other words, ring I forms sugar–base-pair interactions with the bacterial A1408 and the cytoplasmic G1408 residues through different edges. The terminal ring III, which forms a sugar–base interaction with the C1409○A1492 base pair of the cytoplasmic A site (Figure 4g), recognizes the C1409=G1491 Watson–Crick base pair of the bacterial A site in the shallow/minor groove through O5″···H–N2(G1491) and O2′···H–O2′(G1491) sugar–base interactions. This comparative structural analysis shows that apramycin specifically recognizes both the bacterial and the *H. sapiens* cytoplasmic A sites, but uses different interaction modes that involve two changes in the sequence: a) A1408 (bacterial) and G1408 (cytoplasmic) for the interactions between ring I and residue 1408; b) the C1409=G1491 (bacterial) and C1409○A1492 (cytoplasmic) pairs for the interactions with ring III. Because of the important contribution of electrostatics to the binding strength of aminoglycosides to RNA,[37,38] it is interesting to compare the contacts made by the positively charged ammonium groups in the two complexes. In both cases, three ammonium groups have no contact with the RNA; of those, N8′ (ring I) and N4″ (ring III) are common. While N3 (ring II) has no contact in the *H. sapiens* cytoplasmic complex and N2′ (ring I) forms several hydrogen bonds, the opposite is observed in the bacterial complex. The N1 atom (ring II) forms either a water-mediated or a direct hydrogen bond with the RNA, albeit not to the same atom. Although the initial concentrations of magnesium ions in the crystallization drops are not much different (1.25 mM in the *H. sapiens* cytoplasmic and 1.00 mM in the bacterial complex), one magnesium ion is clearly trapped only in the *H. sapiens* cytoplasmic complex.

Recently, we reported the crystal structure of the *H. sapiens* cytoplasmic A site without any bound aminoglycosides.[39] In that structure, two conformational states, the "on" (A1492/A1493 bulging out and A1491 tucked in) and "off" (A1491/A1393 bulging out and A1492 tucked in), were observed. The conformation of the cytoplasmic A site in the present RNA/apramycin complex is almost the same as the "off" state of the free structure (RMSD = 1.0 Å). Therefore, it can be concluded that apramycin stabilizes the "off" state of the *H. sapiens* cytoplasmic A site.

In the absence of an eukaryotic cytoplasmic ribosome, superimposition of the *H. sapiens* cytoplasmic A site in complex with apramycin on the crystal structure of the 30S ribosome in complex with mRNA (m = messenger), tRNA, and paromomycin[6] yields some insight into the molecular mechanisms of apramycin toxicity in mammals. The A1493 residue, which monitors the first Watson–Crick base pair of the codon–anticodon helix, protrudes toward the mRNA/tRNA complex (Figure 5). However, A1493 is too far from

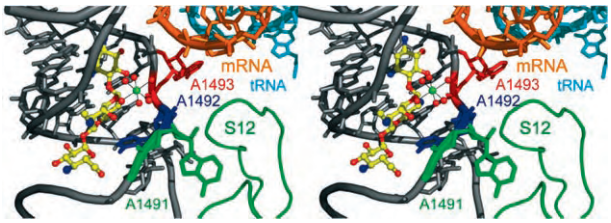

Figure 5. Stereoview of the superimposition of the *H. sapiens* cytoplasmic A site complexed with apramycin (PDB ID: 2G5K) on the 30S ribosomal decoding site (PDB ID: 1IBL).[6] A1491, A1492, and A1493 are colored as in the other figures. Ribosomal protein S12, tRNA, and mRNA are in green, cyan, and orange, respectively.

the codon–anticodon base pairs to form an A-minor motif. Since A1492 is inside the A-site helix in the apramycin complex, it cannot recognize the second Watson–Crick base pair. Furthermore, the bulged-out A1491 residue is in close contact with ribosomal protein S12, which is known as a control element for translocation of the mRNA/tRNA complex (Figure 5).[40] In the bacterial A site, ring III of apramycin is in close contact with S12 and may play the same role as A1491 in the complex of the cytoplasmic A site.[27] Therefore, in 40S cytoplasmic ribosomes, A1491 may disturb the local conformation of a cytoplasmic ribosomal protein, thereby inhibiting translocation of the eukaryotic ribosome.

In a previous paper, we showed how a modification of the aminoglycoside paromomycin led to a conformational change and a better binding mode of the drug to the same conformation of the A site.[11] The present results show how the same drug binds to different conformations of the A site following a change of two nucleotides in the sequence. The observed surprising adaptability of both the binding mode of the drug (aminoglycosides) and the conformation of the target (A site) constitutes a challenge for drug design and the understanding of toxicity.

Received: January 26, 2006
Published online: April 5, 2006

Keywords: aminoglycosides · antibiotics · decoding site · molecular recognition · RNA structures

 © 2006 Wiley-VCH Verlag GmbH & Co. KGaA, Weinheim

[1] C. Walsh, *Antibiotics: Action, Origins, Resistance*, ASM Press, Washington, D.C., **2003**, pp. 51 – 70.
[2] J. Davies, L. Gorini, B. D. Davis, *Mol. Pharmacol.* **1965**, *1*, 93 – 106.
[3] D. Moazed, H. F. Noller, *Nature* **1987**, *327*, 389 – 394.
[4] J. M. Ogle, F. V. Murphy, M. J. Tarry, V. Ramakrishnan, *Cell* **2002**, *111*, 721 – 732.
[5] J. M. Ogle, A. P. Carter, V. Ramakrishnan, *Trends Biochem. Sci.* **2003**, *28*, 259 – 266.
[6] J. M. Ogle, D. E. Broderson, W. M. Clemons, Jr., M. J. Tarry, A. P. Carter, V. Ramakrishnan, *Science* **2001**, *292*, 897 – 902.
[7] A. P. Carter, W. M. Clemons, D. E. Broderson, R. J. Morgan-Warren, B. T. Wimberly, V. Ramakrishnan, *Nature* **2000**, *407*, 340 – 348.
[8] Q. Vicens, E. Westhof, *Structure* **2001**, *9*, 647 – 658.
[9] Q. Vicens, E. Westhof, *Chem. Biol.* **2002**, *9*, 747 – 755.
[10] Q. Vicens, E. Westhof, *J. Mol. Biol.* **2003**, *326*, 1175 – 1188.
[11] B. François, J. Szychowski, S. S. Adhikari, K. Pachamuthu, E. E. Swayze, R. H. Griffey, M. T. Migawa, E. Westhof, S. Hanessian, *Angew. Chem.* **2004**, *116*, 6903 – 6906; *Angew. Chem. Int. Ed.* **2004**, *43*, 6735 – 6738.
[12] B. François, R. J. M. Russell, J. B. Murray, F. Aboul-ela, B. Masquida, Q. Vicens, E. Westhof, *Nucleic Acids Res.* **2005**, *33*, 5677 – 5690.
[13] P. Nissen, J. A. Ippolito, N. Ban, P. B. Moore, T. A. Steitz, *Proc. Natl. Acad. Sci. USA* **2001**, *98*, 4899 – 4903.
[14] E. C. Böttger, B. Springer, T. Prammananan, Y. Kidan, P. Sander, *EMBO Rep.* **2001**, *2*, 318 – 323.
[15] M. P. Mingeot-Leclercq, P. M. Tulken, *Antimicrob. Agents Chemother.* **1999**, *43*, 1003 – 1012.
[16] L. P. Rybak, C. A. Whitworth, *Drug Discovery Today* **2005**, *10*, 1313 – 1321.
[17] J. M. Wilhelm, S. E. Pettitt, J. J. Jessop, *Biochemistry* **1978**, *17*, 1143 – 1149.
[18] J. M. Wilhelm, J. J. Jessop, S. E. Pettitt, *Biochemistry* **1978**, *17*, 1149 – 1153.
[19] S. R. Lynch, D. Puglisi, *J. Mol. Biol.* **2001**, *306*, 1037 – 1058.
[20] S. Bar-Nun, Y. Shneyour, J. S. Beckmann, *Biochim. Biophys. Acta* **1983**, *741*, 123 – 127.
[21] R. Q. Thompson, E. A. Presti, *Antimicrob. Agents Chemother.* **1967**, 332 – 340.
[22] C. E. Higgins, R. E. Kastner, *Antimicrob. Agents Chemother.* **1967**, 324 – 331.
[23] S. O'Conner, L. K. T. Lam, N. D. Jones, M. O. Chaney, *J. Org. Chem.* **1976**, *41*, 2087 – 2092.
[24] G. Ziv, A. Bor, S. Soback, D. Elad, J. F. Nouws, *J. Vet. Pharmacol. Ther.* **1985**, *8*, 95 – 104.
[25] S. Perzynski, M. Cannon, E. Cundliffe, S. B. Chahwala, J. Davies, *Eur. J. Biochem.* **1979**, *99*, 623 – 628.
[26] B. A. Odland, M. E. Erwin, R. N. Jones, *J. Clin. Microbiol.* **2000**, *38*, 453 – 455.
[27] Q. Han, Q. Zhao, S. Fish, K. B. Simonsen, D. Vourloumis, J. M. Froelich, D. Wall, T. Hermann, *Angew. Chem.* **2005**, *44*, 2754 – 2760; *Angew. Chem. Int. Ed.* **2005**, *44*, 2694 – 2700.
[28] D. Pashov, L. Diakov, L. Lashev, *Vet. Med. Nauki* **1987**, *24*, 37 – 42.
[29] D. Pashov, L. Diakov, S. Vangelov, *Vet. Med. Nauki* **1987**, *24*, 41 – 46.
[30] Committee for Veterinary Medicinal Products, the European Agency for the Evaluation of Medicinal Products, *EMEA/CVMP/342/99-corr-FINAL*, **1999**.
[31] Committee for Veterinary Medicinal Products, the European Agency for the Evaluation of Medicinal Products, *EMEA/MRL/526/98-FINAL*, **1999**.
[32] R. H. Griffey, S. A. Hofstadler, K. A. Sannes-Lowery, D. J. Ecker, *Proc. Natl. Acad. Sci. USA* **1999**, *96*, 10129 – 10133.
[33] P. Purohit, S. Stern, *Nature* **1994**, *370*, 659 – 662.
[34] H. Miyaguchi, H. Narita, K. Sakamoto, S. Yokoyama, *Nucleic Acids Res.* **1996**, *24*, 3700 – 3706.
[35] M. I. Recht, D. Fourmy, S. C. Blanchard, K. D. Dahlquist, J. D. Puglisi, *J. Mol. Biol.* **1996**, *262*, 421 – 436.
[36] S. C. Blanchard, D. Fourmy, R. G. Eason, J. D. Puglisi, *Biochemistry* **1998**, *37*, 7716 – 7724.
[37] T. Hermann, E. Westhof, *J. Mol. Biol.* **1998**, *276*, 903 – 912.
[38] Y. Tor, T. Hermann, E. Westhof, *Chem. Biol.* **1998**, *5*, R277-R283.
[39] J. Kondo, A. Urzhumtsev, E. Westhof, *Nucleic Acids Res.* **2006**, *34*, 676 – 685.
[40] A. R. Cukras, D. R. Southworth, J. L. Brunelle, G. M. Culver, R. Green, *Mol. Cell* **2003**, *12*, 321 – 328.
[41] N. Leontis, E. Westhof, *RNA* **2001**, *7*, 499 – 512.

 © 2006 Wiley-VCH Verlag GmbH & Co. KGaA, Weinheim

Synthetic Methods

DOI: 10.1002/anie.200600331

Gold-Catalyzed Intermolecular Hydroamination of Allenes with Arylamines and Resulting High Chirality Transfer

*Naoko Nishina and Yoshinori Yamamoto**

Hydroamination, the formal addition of an N–H bond across a C–C unsaturated bond, is a highly desirable and atom-economical process for the preparation of amine derivatives.[1] It is known that hydroamination of alkenes and alkynes can be catalyzed by 1) organolanthanides,[2] 2) alkali metals,[3] 3) early (Ti, Zr)[4] and 4) late (Pd, Rh, Ru, Ir, Ni, Au)[5] transition metals, and 5) heterogeneous systems.[6] Depending on the catalytic system, an activation of either the C–C multiple bond or the N–H bond takes place; the former activation occurs in the case of (4), and the latter type takes place in the cases of (1)–(3). Concerning the latter type, the N–H bond is converted into either metal–imide intermediates (for example, RN=Ti) or metal–amide intermediates (for example, R_2N–Ln). Two other important aspects of hydroamination are a) the relative difficulty in achieving intermolecular hydroamination as compared to the intramolecular version and b) the relative ease in achieving the hydroamination of alkynes compared to that of alkenes.

Concerning the hydroamination of allenes,[7] the intramolecular reaction is well-studied in comparison with the

[*] N. Nishina, Prof. Dr. Y. Yamamoto
Department of Chemistry
Graduate School of Science
Tohoku University
Sendai 980-8578 (Japan)
Fax: (+81) 22-795-6784
E-mail: yoshi@mail.tains.tohoku.ac.jp

Supporting information for this article is available on the WWW under http://www.angewandte.org or from the author.

WILEY InterScience DISCOVER SOMETHING GREAT
© 2006 Wiley-VCH Verlag GmbH & Co. KGaA, Weinheim

intermolecular reaction. The intramolecular hydroamination of aminoallenes is catalyzed by organolanthanides,[8] Group 4 early transition-metal complexes,[9] and late transition-metal (Pd,[10] Ag,[11] Au[12]) complexes. However, only few examples are known for the intermolecular hydroamination of allenes. Bergman and co-workers reported the Group 4 metal-catalyzed hydroamination of allenes with aryl amines,[13] while Cazes and co-workers[14] and we[15] reported the corresponding palladium-catalyzed hydroamination.

Herein, we report that the intermolecular hydroamination of allenes **1** with aniline **2a** takes place with a gold(III) catalyst at ambient temperature in THF to give the corresponding allylic amines **3** in good to high yields [Eq. (1)]. Furthermore, the axial chirality of allenes **4** can be transferred with very high *ee* values to the products **5** [Eq. (2)].

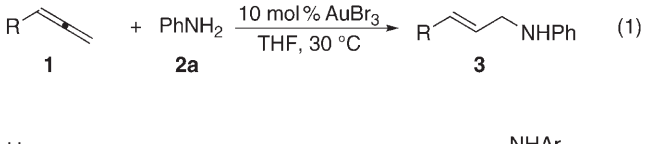

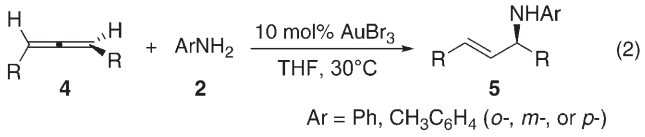

The results are summarized in Table 1. In the presence of 10 mol% $AuBr_3$, the reaction of phenylallene **1a** with two equivalents of aniline **2a** in THF proceeded smoothly at 30 °C, and the corresponding allylic amine **3a** was obtained in 78% yield (Table 1, entry 1). Other catalysts, such as Ag^I, Cu^I, Cu^{II}, Pd^{II}, and Pt^{II} compounds as well as H^+, did not promote the hydroamination at all. In the absence of the gold catalyst, no reaction occurred even after heating at 50 °C. The use of cationic gold catalysts such as [Ph_3PAuCl]/AgOTf and $AuBr_3$/AgOTf gave lower yields of the product **3a**.[16] At high temperature (80–120 °C), $AuBr_3$ lost its catalytic activity.

Monosubstituted aryl- and alkyl allenes **1b**–**1f** proved to be good substrates for the hydroamination (Table 1, entries 2–6). The sterically bulky allene **1g** gave **3g** in lower yield (Table 1, entry 7). The 1,3-disubstituted allenes **1h** and **1j** (Table 1, entries 8 and 10) showed reactivities comparable to the monosubstituted allenes (Table 1, entries 1 and 5); however, the 1,1-disubstituted allenes **1i** and **1k** exhibited extremely low reactivities (Table 1, entries 9 and 11). Interestingly, the hydroamination proceeded very smoothly with the allenes **1m**–**1o**, which bear an olefin moiety tethered by a carbon chain of variable length ($n = 2$–4, Table 1, entries 13–15).[17] However, in the case of $n = 1$ (allylallene, **1l**), the effect of the olefin was not remarkable (Table 1, entry 12). The enhancement of the reactivity may be a result of the coordination of the olefin to a gold species, which would help to bring the two substrates into contact with each other.

To obtain further insight into the mechanism, the hydroamination was investigated with chiral allenes (Scheme 1). The hydroamination of (−)-**1j** with aniline gave (−)-**3j** in 80% yield with 99% *ee*. Similarly, the use of *ortho*-, *meta*-, and *para*-toluidine ($CH_3C_6H_4NH_2$) instead of aniline afforded the corresponding chiral allylic amines in good yields with high *ee* values. The hydroamination of (−)-**1h** with aniline produced (−)-**3h** in 68% yield with 88% *ee*. It should be noted that all four selectivity problems of substituted allenes (positional selectivity, chemoselectivity, regioselectivity, and stereoselectivity)[18] have been solved in the formation of (−)-**3h**. These results strongly suggest that a gold–amine complex is formed, and then the addition to the allene takes place as shown in **A** (Scheme 1). If $AuBr_3$ behaved merely as a Lewis acid, such that the gold center would activate a double bond of the allene and the aniline would attack from the face opposite to gold coordination, then (+)-**3h** would have been obtained. If a gold π-allyl complex was involved as a key intermediate in a similar manner to that of the palladium-catalyzed hydroamination, racemic **3h** would have been obtained.

Table 1: Gold-catalyzed intermolecular hydroamination of allenes with aniline.[a]

Entry	Allene **1**		Product **3**		Yield [%][b]
1	Ar = Ph	**1a**	Ar = Ph	**3a**	78
2	Ar = *p*-$CH_3C_6H_4$	**1b**	Ar = *p*-$CH_3C_6H_4$	**3b**	81
3	Ar = *p*-ClC_6H_4	**1c**	Ar = *p*-ClC_6H_4	**3c**	73
4		**1d**		**3d**	80
5	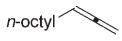	**1e**		**3e**	70
6		**1f**	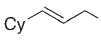	**3f**	75
7		**1g**	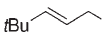	**3g**	34
8	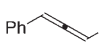	**1h**		**3h**	68[c]
9		**1i**		**3i**	9[d]
10		**1j**	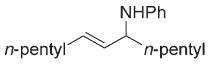	**3j**	80
11	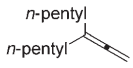	**1k**		**3k**	0
12		$n = 1$, **1l**		**3l**	58[e]
13		$n = 2$, **1m**		**3m**	87[e]
14		$n = 3$, **1n**		**3n**	96[e]
15		$n = 4$, **1o**		**3o**	88[e]

[a] All reactions were performed under the following conditions: a mixture of allene (0.50 mmol), aniline (1 mmol), and $AuBr_3$ (10 mol%) in THF (0.5 mL) was stirred at 30 °C. After 1–5 h, the reaction was filtered through a thin pad of silica gel. [b] Yield of isolated product. [c] A regioisomeric product was not detected. [d] *E*:*Z* ratio was 3:7 (determined by ^1H NMR spectroscopy). [e] Combined yield of the isolated regioisomers (the ratio was about 1:1, as determined by chiral HPLC). Bn = benzyl, Cy = cyclohexyl.

© 2006 Wiley-VCH Verlag GmbH & Co. KGaA, Weinheim

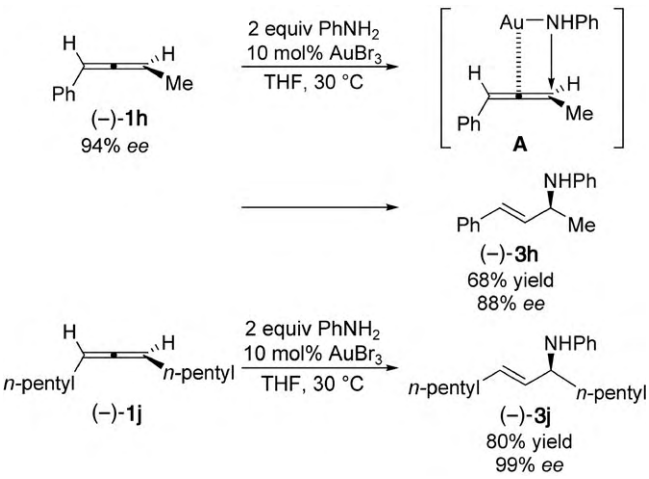

Scheme 1. Chirality transfer in the hydroamination of allenes.

A plausible mechanism, though speculative, is shown in Scheme 2. The catalytic cycle is most probably initiated by the coordination of the allene to the gold–amine complex **B** to afford the intermediate **C**. The presence of the gold–amine

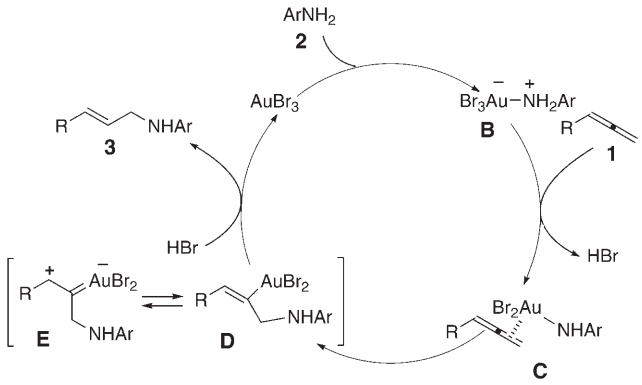

Scheme 2. A plausible mechanism for the hydroamination of **1**.

complex is postulated based on the fact that there was an induction period for the hydroamination, and the yield was decreased when $AuBr_3$ was not exposed to the amine prior to the addition of allene. It should be noted that the 1,1-disubstituted allenes **1i** and **1k** exhibited extremely low reactivities. This is in marked contrast to the palladium-catalyzed hydroamination of 1,1-disubstituted allenes, which proceeded smoothly via a π-allylpalladium intermediate.[19] Consequently, the gold-catalyzed hydroamination must proceed in a manner different from the palladium-catalyzed reaction. Perhaps the amino-auration takes place through **C** to give the gold–alkenyl intermediate **D**, which produces **3** and $AuBr_3$ upon protonation by HBr. It may be argued that **D** should afford *Z* allylamines instead of the *E* isomers **3**. One explanation for the observation of the *E* isomers is that the isomerization may take place through the intermediate **E**. However, formation of the *E* allylamines is alternatively explainable by the attack of the gold species at the more hindered π face of the allene **1**, and this possibility cannot be completely excluded at present.

In conclusion, we have developed a gold-catalyzed intermolecular hydroamination of allenes, which proceeds smoothly at room temperature. In this reaction, the axial chirality of allenes is transferred to the products through the hydroamination to give high *ee* values.

Received: January 26, 2006
Published online: April 18, 2006

Keywords: allenes · allylic compounds · gold · hydroamination

[1] For recent reviews of catalytic hydroamination, see: a) T. E. Müller, M. Beller, *Chem. Rev.* **1998**, *98*, 675–703; b) J. J. Brunet, D. Neibecker in *Catalytic Heterofunctionalization* (Eds.: A. Togni, H. Grützmacher), Wiley-VCH, Weinheim, **2001**, pp. 91–141; c) K. C. Hultzsch, *Adv. Synth. Catal.* **2005**, *347*, 367–391.

[2] For a recent review of hydroamination catalyzed by organolanthanides, see: S. Hong, T. J. Marks, *Acc. Chem. Res.* **2004**, *37*, 673–686.

[3] For a recent review of base-catalyzed hydroamination, see: a) J. Seayad, A. Tillack, C. G. Hartung, M. Beller, *Adv. Synth. Catal.* **2002**, *344*, 795–813; for recent examples of acid-catalyzed hydroamination, see: b) B. Schlummer, J. F. Hartwig, *Org. Lett.* **2002**, *4*, 1471–1474; c) K. Miura, A. Hosomi, *Synlett* **2003**, 143–155.

[4] For recent reviews of hydroamination catalyzed by early transition metals, see: a) I. Bytschkov, S. Doye, *Eur. J. Org. Chem.* **2003**, 935–946; b) S. Doye, *Synlett* **2004**, 1653–1672; c) A. L. Odom, *Dalton Trans.* **2005**, 225–233.

[5] For recent examples of hydroamination catalyzed by late transition metals, see: a) H. M. Senn, P. E. Blöchl, A. Togni, *J. Am. Chem. Soc.* **2000**, *122*, 4098–4107; b) T. E. Müller, M. Grosche, E. Herdtweck, A.-K. Pleier, E. Walter, Y.-K. Yan, *Organometallics* **2000**, *19*, 170–183; c) J. F. Hartwig, *Pure Appl. Chem.* **2004**, *76*, 507–516; d) L. Fadini, A. Togni, *Chem. Commun.* **2003**, 30–31; e) T. Shimada, G. B. Bajracharya, Y. Yamamoto, *Eur. J. Org. Chem.* **2005**, 59–62; f) J. Takaya, J. F. Hartwig, *J. Am. Chem. Soc.* **2005**, *127*, 5756–5757; g) L. D. Field, B. A. Messerle, K. Q. Vuong, P. Turner, *Organometallics* **2005**, *24*, 4241–4250; h) K. Li, P. H. Phua, K. K. Hii, *Tetrahedron* **2005**, *61*, 6237–6242; i) X. Li, A. R. Chianese, T. Vogel, R. H. Crabtree, *Org. Lett.* **2005**, *7*, 5437–5440; for the first example and some recent examples of hydroamination catalyzed by gold, see: j) Y. Fukuda, K. Utimoto, H. Nozaki, *Heterocycles* **1987**, *25*, 297–300; k) A. Arcadi, S. Di Giuseppe, F. Marinelli, E. Rossi, *Adv. Synth. Catal.* **2001**, *343*, 443–446; l) E. Mizushima, T. Hayashi, M. Tanaka, *Org. Lett.* **2003**, *5*, 3349–3352; m) J. Zhang, C.-G. Yang, C. He, *J. Am. Chem. Soc.* **2006**, *128*, 1798–1799.

[6] For recent examples of hydroamination in heterogeneous catalysis, see: a) T. E. Müller, J. A. Lercher, V. N. Nhu, *AIChE J.* **2003**, *49*, 214–224; b) J. Penzien, C. Haeßner, A. Jentys, K. Köhler, T. E. Müller, J. A. Lercher, *J. Catal.* **2004**, *221*, 302–312.

[7] N. Krause, A. S. K. Hashmi, *Modern Allene Chemistry*, *Vol. 2*, Wiley-VCH, Weinheim, **2004**.

[8] a) V. M. Arredondo, F. E. McDonald, T. J. Marks, *J. Am. Chem. Soc.* **1998**, *120*, 4871–4872; b) V. M. Arredondo, F. E. McDonald, T. J. Marks, *Organometallics* **1999**, *18*, 1949–1960; c) V. M. Arredondo, S. Tian, F. E. McDonald, T. J. Marks, *J. Am. Chem. Soc.* **1999**, *121*, 3633–3639.

[9] a) L. Ackermann, R. G. Bergman, *Org. Lett.* **2002**, *4*, 1475–1478; b) L. Ackermann, R. G. Bergman, R. N. Loy, *J. Am. Chem. Soc.* **2003**, *125*, 11956–11963; c) J. M. Hoover, J. R. Petersen, J. H. Pikul, A. R. Johnson, *Organometallics* **2004**, *23*,

 © 2006 Wiley-VCH Verlag GmbH & Co. KGaA, Weinheim

4614 – 4620; d) J. R. Petersen, J. M. Hoover, W. S. Kassel, A. L. Rheingold, A. R. Johnson, *Inorg. Chim. Acta* **2005**, *358*, 687 – 694.
[10] M. Meguro, Y. Yamamoto, *Tetrahedron Lett.* **1998**, *39*, 5421 – 5424.
[11] a) M. Okala Amombo, A. Hausherr, H.-U. Reißig, *Synlett* **1999**, 1871 – 1874; b) N. A. Nedolya, N. I. Schlyakhtina, V. P. Zinov'eva, A. I. Albanov, L. Brandsma, *Tetrahedron Lett.* **2002**, *43*, 1569 – 1571; c) M. Billet, A. Schoenfelder, P. Klotz, A. Mann, *Tetrahedron Lett.* **2002**, *43*, 1453 – 1456.
[12] a) N. Morita, N. Krause, *Org. Lett.* **2004**, *6*, 4121 – 4123; for recent reviews on gold-catalyzed reactions, see: b) A. S. K. Hashmi, *Gold Bull.* **2003**, *36*, 3 – 9; c) A. Hoffmmann-Röder, N. Krause, *Org. Biomol. Chem.* **2005**, *3*, 387 – 391.
[13] a) P. J. Walsh, A. M. Baranger, R. G. Bergman, *J. Am. Chem. Soc.* **1992**, *114*, 1708 – 1719; b) Z. K. Sweeney, J. L. Salsman, R. A. Andersen, R. G. Bergman, *Angew. Chem.* **2000**, *112*, 2429 – 2433; *Angew. Chem. Int. Ed.* **2000**, *39*, 2339 – 2343; c) J. S. Johnson, R. G. Bergman, *J. Am. Chem. Soc.* **2001**, *123*, 2923 – 2924.
[14] L. Besson, J. Goré, B. Cazes, *Tetrahedron Lett.* **1995**, *36*, 3853 – 3856.
[15] M. Al-Masum, M. Meguro, Y. Yamamoto, *Tetrahedron Lett.* **1997**, *38*, 6071 – 6074.
[16] Recently, we found that the intramolecular hydroamination proceeded quantitatively with a variety of gold catalysts (AuCl, $AuCl_3$, and $AuBr_3$): a) L. M. Lutete, PhD thesis, Tohoku University, **2003**, but only $AuBr_3$ effectively catalyzed this intermolecular hydroamination; for *syn* oxy-auration of norbornene, see: b) M. A. Cinellu, G. Minghetti, F. Cocco, S. Stoccoro, A. Zucca, M. Manassero, *Angew. Chem.* **2005**, *117*, 7052 – 7055; *Angew. Chem. Int. Ed.* **2005**, *44*, 6892 – 6895; c) A. S. K. Hashmi, *Angew. Chem.* **2005**, *117*, 7150 – 7154; *Angew. Chem. Int. Ed.* **2005**, *44*, 6990 – 6993.
[17] Recently, we found that the use of olefin enhanced the reaction rate in the platinum-catalyzed intramolecular carboalkoxylation of alkynes; see: I. Nakamura, G. B. Bajracharya, H. Wu, K. Oishi, Y. Mizushima, I. D. Gridnev, Y. Yamamoto, *J. Am. Chem. Soc.* **2004**, *126*, 15423 – 15430.
[18] a) A. S. K. Hashmi, *Angew. Chem.* **2000**, *112*, 3737 – 3740; *Angew. Chem. Int. Ed.* **2000**, *39*, 3590 – 3593; b) A. S. K. Hashmi in *Organic Synthesis Highlights V* (Eds.: H.-G. Schmalz, T. Wirth), Wiley-VCH, Weinheim, **2003**, pp. 56 – 67.
[19] M. Al-Masum, Y. Yamamoto, *J. Am. Chem. Soc.* **1998**, *120*, 3809 – 3810.

 © 2006 Wiley-VCH Verlag GmbH & Co. KGaA, Weinheim

Protein Identification

DOI: 10.1002/anie.200503787

Direct Protein Identification from Nonspecific Peptide Pools by High-Accuracy MS Data Filtering

*Vinh An Thieu, Dieter Kirsch, Thomas Flad, Claudia Müller, and Bernhard Spengler**

A new method of protein identification and biomarker discovery based on the analysis of cleavage peptides formed by endogenous proteolysis or other undetermined processes is described herein. Combining database analysis with highly accurate MS and composition-based de novo sequencing (CBS) now allows rapid and reliable analysis of undefined peptide pools and their originating proteins. With established methods, this can be a highly challenging task if cleavage enzymes, protein size, and the number of originating proteins are unknown.

Peptide pools of undefined formation history are readily found, for example, in blood plasma, pathological samples, or if the enzymatic degradation of biological samples is not actively suppressed. Such peptides are usually hard to characterize with respect to sequence and originating proteins because database (DB)-assisted approaches such as peptide mass fingerprinting requires information on the cleavage enzyme to work well. To understand the specific problems in this kind of analysis, one has to note that standard procedures for protein identification and proteome characterization use specific enzymatic cleavage of individual proteins after 2D-gel separation. Subsequent protein DB search procedures are based on a list of cleavage-peptide masses resulting from the questioned protein. Another alternative approach, called shotgun analysis, uses specific enzymatic cleavage of a complex (unseparated) mixture of proteins followed by 2D-LC fractionation, MS, or MS/MS (fragment ion) analysis of the peptides and DB-assisted protein identification.[1,2] Both methods are commonly used in proteomics studies and are known to work well only if the cleavage step is well defined. Both methods were recently found to nevertheless exhibit a frustratingly poor analytical quality with respect to reproducibility, reliability, completeness of information, and comparability between different instruments or protocols in the field of proteome characterization.[3,4] Furthermore, they are

[*] V. An Thieu, Dr. D. Kirsch, Prof. Dr. B. Spengler
Institut für Anorganische und Analytische Chemie
Justus Liebig Universität
35392 Gießen (Germany)
Fax: (+49) 641-993-4809
E-mail: bernhard.spengler@uni-giessen.de
Dr. T. Flad, Prof. Dr. C. Müller
Sektion für Transplantationsimmunologie und Immunhämatologie
Medizinische Klinik und Poliklinik, Abt. II
Universität Tübingen
72072 Tübingen (Germany)

© 2006 Wiley-VCH Verlag GmbH & Co. KGaA, Weinheim

mostly unsuccessful with nonspecifically formed complex peptide samples.

The key to the limitations of these methods lies in the way in which an individual peptide sequence is determined. If a short sequence tag, a fragmentation pattern, or a set of peptide masses point, in a protein sequence DB, to either a misidentified protein sequence, to an erroneous protein sequence, or to no protein at all, then an incorrect peptide sequence or no sequence at all would be determined. In this case, there is typically no attempt or possibility to quality-control the individual result. A more reliable approach would be to first determine the peptide sequence without DB help and then compare the result with DB protein sequences, or to first list DB hits from standard protein identification approaches and then validate these hits by DB-independent peptide sequencing. This kind of independency in peptide sequence determination and protein identification would result in a much more reliable and quality-controllable method of proteome characterization.

DB-independent, so-called de novo sequencing of peptides is not yet employed in routine proteome analyses owing to limited reliability and long execution times. The CBS approach of de novo sequencing[5] that we recently introduced is able to reliably determine, within milliseconds, amino acid sequences of individual peptides based on high-accuracy Fourier Transform Ion Cyclotron Resonance (FTICR) MS. CBS determines the amino acid compositions of unknown peptides by combinatorial calculations based on accurately measured mass values of precursor ions and respective fragment ions. Instead of probability-based scoring, the algorithm filters sets of mathematically possible compositions of ions and attempts to reduce the intersection to a minimal number of possible amino acid compositions. The correct sequence of the determined composition is subsequently verified by sequence permutation and matching of observed and calculated fragment ion signals. Combining this new approach of de novo sequencing with protein DB information now allows us to analyze undefined peptide pools rapidly and accurately and to identify originating proteins. These peptide pools might even stem from uncontrolled autoproteolysis reactions that allow us to avoid well-defined gel-based or other laborious protein separation and digestion steps that are applied to a native and highly conserved protein sample, as is usually done in proteomics studies. This method appears to be highly successful in the detection of biomarkers in differential studies of easily accessible biofluids or extracts.

The peptide pool is analyzed by nano-LC FTICR MS with a nanoelectrospray ionization (nano-ESI)[6,7] interface. High accuracy MS/MS data were used to search protein DBs resulting in score-based lists of candidate peptides/proteins that are, at this stage, still long and of limited reliability. To reduce and verify the raw list of candidates, CBS analysis was used in parallel to find the correct peptide sequences from the list. The combination of candidate lists of amino acid compositions of peptide precursor ions and of their fragment ions resulted in unequivocal sequence identifications typically within milliseconds. After the peptides were identified with CBS, the corresponding DB-listed proteins were then used to filter and annotate the list of cleavage-peptide signals. The remaining unidentified peptide signals were then investigated in more detail in the following cycle (Figure 1). In general, about two thirds of the top 20 protein raw-list identifications turned out to be false positives before CBS verification. This again demonstrates the need for dedicated validation procedures further to automated proteomics analyses.

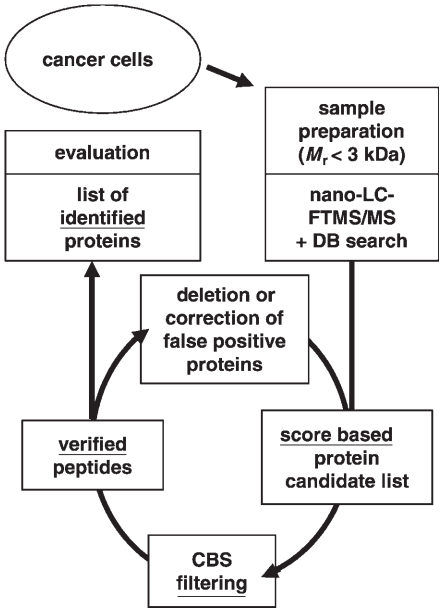

Figure 1. Schematic of the accurate-mass data filtering method for the rapid protein identification from unspecified peptide pools. Nonspecifically cleaved proteins were harvested as complex peptide pools and analyzed by nano-HPLC/nano-ESI-FTICR-MS/MS. Raw candidate lists of proteins were created by a nonspecific DB search. Amino acid composition analysis and sequencing was used to delete false positives from the list while confirmed proteins were digested in silico and used to annotate the original peptide signal lists (see Figure 2).

The above method was applied to directly identify cancer-related cellular proteins. It allowed us to rapidly obtain verified identification and characterization of originating proteins whose cleavage products were acid eluted from cancer cells, without the need for gel separations, enzymatic digestions, or immunoaffinity chromatography.

Identified peptides were found to be mostly representative (proteolytic) fragments that arose from the natural degradation of expressed proteins, including cyclophilin A, galectin-1, S-100 Ca-binding protein, macrophage-migration inhibitory factor (MIF), glyceraldehyde phosphate dehydrogenase (GAPDH), acyl-CoA-binding protein (ACBP), peroxiredoxin, aldolase A, enolase 1, and others. Although most of these proteins belong to well-known ubiquitous cellular house-keeping molecules, some of these proteins (enolase 1, GAPDH, peroxiredoxin) were found in previous proteomics or transcriptional-expression analyses to be up regulated in renal cells that are resistant to oxidative or osmotic stress.[8,9] Alternatively, they were identified as renal-cell carcinoma-associated antigens (galectin-1 and S-100 proteins) with potential relevance for biomarkers in tumor development and novel immunotherapeutic approaches.[8,10,11] A section of

 © 2006 Wiley-VCH Verlag GmbH & Co. KGaA, Weinheim

the annotated peptide map is shown in Figure 2. By using the described method, sophisticated procedures employing well-tuned, empirically determined score cutoff values[12] for each DB search could be avoided.

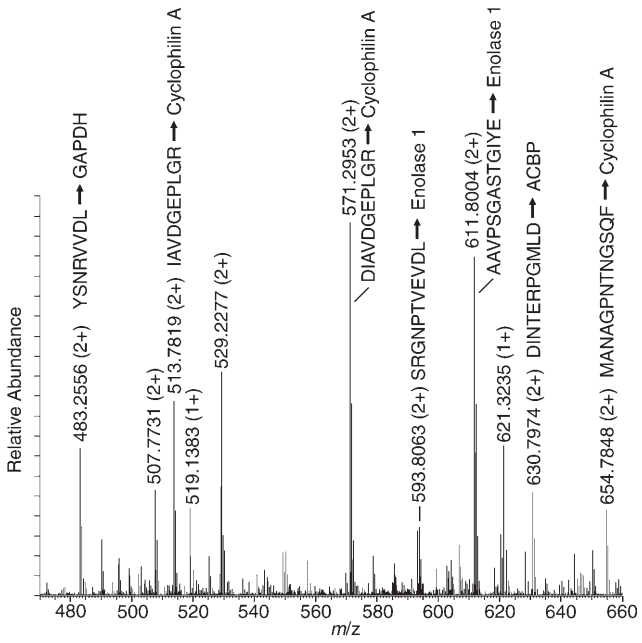

Figure 2. A section of the final annotated peptide map showing that the method allows detection of biomarker proteins that originate from unspecified natural degradation processes. This section is an FT-ICR MS spectrum that was averaged over a time range of 4 min out of a 60 min nano-LC separation. The annotation process is described in Figure 1.

The described method appears to have a high potential for rapid proteome studies based on cleavage products or substance pools (peptides or other biomolecules) originating from natural or other systematic degradation processes. Typically, a one-dimensional, conventional HPLC separation, when performed after a simple acid elution and size-exclusion filtration, was found to be sufficient as sample preparation. The method should be amenable to both qualitative screening studies and more demanding quantitative, differential, or dynamic analyses of biological systems, for example, in biomarker search studies. Furthermore, the described approach can be assumed to be especially useful for posttranslational modification studies, analysis of small proteins, and proteins that are not satisfactorily detected in gel-electrophoretical separations.

Experimental Section

Mild acidic elution of autoproteolytic peptides and other biomolecules[13] from human renal carcinoma cells (cell line A498) was performed by treating the cells with an ice-cold citric-acid-phosphate buffer at pH 3 for 1 min. After centrifugation, the supernatant was prefractionated by reversed-phase HPLC with a C8 column and UV detection. This step was performed to study the extract in more detail and was found to be, in general, unnecessary for the following procedure. To reduce the complexity of these fractions, ultrafiltration membranes with a cut off at 3 kDa were used to obtain only the low-molecular-weight fraction. Nano-LC separation (Ultimate Plus, Dionex Corporation, Idstein, Germany) coupled to FTICR MS/MS (Finnigan LTQ FT, Thermo Electron, Bremen, Germany) was employed. A mass resolution of 100000 at $m/z = 400$ u and a mass accuracy of better than 2 ppm were achieved.

MS/MS data were analyzed by using a common DB search program (Sequest, version 27, revision 12).[14] Precursor ion mass tolerances of 0.01 u and fragment ion tolerances of 0.5 u were selected as program parameters. Different from typical proteomics studies based on tryptic digestion of gel-separated proteins, the cleavage enzyme and the mass range of the originating proteins were not specified in the DB search. Owing to an otherwise extensive reduction in the number of true-positive sequences and therefore failure of protein identifications, the filter parameters for the DB search result list were not set too stringent. The peptide precursor mass range was set to 550–3500 u, and only differing (unique) peptide sequences were displayed in the protein identification lists. These lists of possible proteins contained correct assignments and additionally a large number of false-positive hits. The lists were used as raw lists for further data evaluation. By using CBS analysis, the raw lists were verified, annotated, and filtered by verifying the presumed peptide sequences consecutively, starting from low mass values. Verified proteins were then digested in silico and the resulting theoretical cleavage peptides were marked in the signal list after individual confirmation by CBS. Peptide sequences that remained without protein assignment were, in the end, marked as being of unknown origin.

Received: October 26, 2005
Revised: March 10, 2006
Published online: April 18, 2006

Keywords: high mass accuracy · mass spectrometry · peptide sequencing · protein structures · sequence determination

[1] A. J. Link, J. Eng, D. M. Schieltz, E. Carmack, G. J. Mize, D. R. Morris, B. M. Garvik, J. R. Yates, *Nat. Biotechnol.* **1999**, *17*, 676–682.
[2] M. P. Washburn, D. Wolters, J. R. Yates, *Nat. Biotechnol.* **2001**, *19*, 242–247.
[3] D. Chamrad, H. E. Meyer, *Nat. Methods* **2005**, *2*, 647–648.
[4] J. E. Elias, W. Haas, B. K. Faherty, S. P. Gygi, *Nat. Methods* **2005**, *2*, 667–675.
[5] B. Spengler, *J. Am. Soc. Mass Spectrom.* **2004**, *15*, 703–714.
[6] J. B. Fenn, M. Mann, C. K. Meng, S. F. Wong, C. M. Whitehouse, *Science* **1989**, *246*, 64–71.
[7] M. S. Wilm, M. Mann, *Int. J. Mass Spectrom. Ion Processes* **1994**, *136*, 167–180.
[8] H. Dihazi, A. R. Asif, N. K. Agarwal, Y. Doncheva, G. A. Müller, *Mol. Cell. Proteomics* **2005**, *4*, 1445–1458.
[9] J. Morrison, K. Knoll, M. J. Hessner, M. Y. Liang, *Physiol. Genomics* **2004**, *17*, 271–282.
[10] A. N. Young, M. B. Amin, C. S. Moreno, S. D. Lim, C. Cohen, J. A. Petros, F. F. Marshall, A. S. Neish, *Am. J. Pathol.* **2001**, *158*, 1639–1651.
[11] S. Amatschek, U. Koenig, H. Auer, P. Steinlein, M. Pacher, A. Gruenfelder, G. Dekan, S. Vogl, E. Kubista, K. H. Heider, C. Stratowa, M. Schreiber, W. Sommergruber, *Cancer Res.* **2004**, *64*, 844–856.
[12] J. E. Elias, W. Haas, B. K. Faherty, S. P. Gygi, *Nat. Methods* **2005**, *2*, 667–675.
[13] S. Sugawara, T. Abo, K. Kumagai, *J. Immunol. Methods* **1987**, *100*, 83–90.
[14] J. K. Eng, A. L. McCormack, J. R. Yates, *J. Am. Soc. Mass Spectrom.* **1994**, *5*, 976–989.

 © 2006 Wiley-VCH Verlag GmbH & Co. KGaA, Weinheim

Natural Product Synthesis

DOI: 10.1002/anie.200600458

Total Synthesis of Phoslactomycin B and Its Biosynthetic Deamino Precursor**

*Yong-Gang Wang, Ryuichi Takeyama, and Yuichi Kobayashi**

Phoslactomycins A–F and I are a unique class of compounds that contain a phosphate group and an amino group.[1–3] Similar structures are also seen in phosphazomycins C_1 and C_2,[4] leustroducsins A–C and H,[5] and fostriecin.[6] Antitumor, antibacterial, and antifungal activities have been shown for the phoslactomycins.[1a,2a] Inhibitory activity to human protein phosphatase 2A (PP2A) was later disclosed,[7] and the binding site that interacts with the phoslactomycins through the phosphate group was identified.[8] The carboxylate residue on the cyclohexane ring does not affect the activities, whereas the effect of other parts of the molecule on the activities has not been established. Herein, we describe the synthesis of phoslactomycin B (phospholine; **1**) and its deamino precursor **2**.[9]

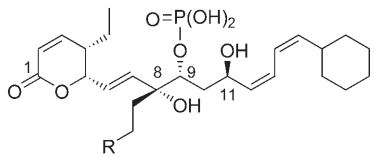

phoslactomycin B (**1**): R = NH_2 (phospholine)
biosynthetic precursor **2**: R = OH

The synthesis of leustroducsin B was recently reported by Fukuyama and co-workers,[10] who introduced the specific *p*-(TBSO)C_6H_4CHO acetal protecting group (TBS = *tert*-butyldimethylsilyl), which was removed during the last stage of the synthesis, for the C8,9-diol unit. On the other hand, the synthesis of fostriecin has been demonstrated by several groups.[11,12] Thus, we initially attempted the synthesis of **1** by applying the transformations developed for the synthesis of fostriecin. However, such efforts were in vain owing to the inefficiency of the transformations[13] and the unexpected instability of the product.[14] We then examined another method that furnished **1** and **2** efficiently, as outlined below.

[*] Y.-G. Wang, R. Takeyama, Prof. Y. Kobayashi
Department of Biomolecular Engineering
Tokyo Institute of Technology
Box B52, 4259 Nagatsuta-cho, Midori-ku
Yokohama 226-8501 (Japan)
Fax: (+81) 45-924-5789
E-mail: ykobayas@bio.titech.ac.jp

[**] We thank Professor H. Osada at RIKEN, Japan, for the generous supply of phoslactomycin B. This work was supported in part by a Grant-in-Aid for Young Scientists from the JSPS.

Supporting information for this article is available on the WWW under http://www.angewandte.org or from the author.

We envisioned that compound **3** would be transformed into **1** by reduction of the triple bond and introduction of the amino and phosphate groups (Scheme 1). To construct **3**, we chose a strategy using chelation-controlled addition of a vinyl anion to ketone **4**, followed by Evans aldol, lactone formation[10] and Sonogashira coupling with vinyl iodide **5**. Thus, the protecting group for the hydroxy group at C9 should be an ether to attain high selectivity in the chelation-controlled reaction and, furthermore, to be discriminated from the other hydroxy groups so as to introduce a phosphate group on it. Among possible candidates, we selected the *p*-methoxybenzyl (PMB) group.[12g]

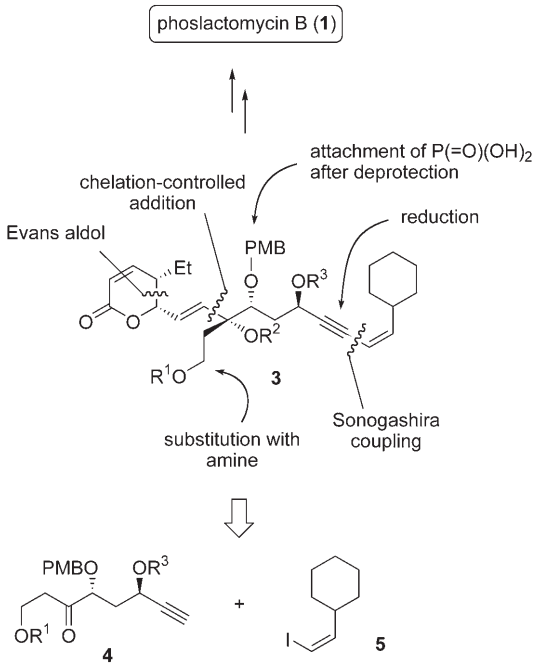

Scheme 1. Retrosynthetic analysis of phoslactomycin B (**1**). PMB = *p*-methoxybenzyl.

The ketone synthon **4** was obtained in the form of compound **12**, and a Sharpless asymmetric epoxidation[15a,c] was used to install conveniently the hydroxy groups at C9 and C11 (Scheme 2). Thus, kinetic resolution of racemic alcohol *rac*-**6** by the asymmetric epoxidation produced (*R*)-**6** (> 97% *ee* by HPLC analysis of the derived benzoate using a chiral column) in 44% yield after easy separation of the epoxy alcohol coproduct (structure not shown). The hydroxy group of (*R*)-**6** was protected to afford the PMB ether, which was transformed into unsaturated ester **8** through a conventional sequence of reactions. Reduction of **8** with DIBAL-H gave the allylic alcohol, which was subjected to the asymmetric epoxidation[15b,c] to give epoxy alcohol **9** as a single diastereomer in 93% yield. The protocol of Yadav et al.[16] was applied to **9**, and subsequent ozonolysis of the resulting compound **10** produced an aldehyde, which upon aldol reaction with $LiCH_2CO_2Et$ followed by reduction with $LiAlH_4$ afforded diol **11** in 64% yield. Finally, selective protection of the primary alcohol as the TBDPS ether followed by Swern oxidation furnished the key ketone **12**.[17]

InterScience DISCOVER SOMETHING GREAT
© 2006 Wiley-VCH Verlag GmbH & Co. KGaA, Weinheim

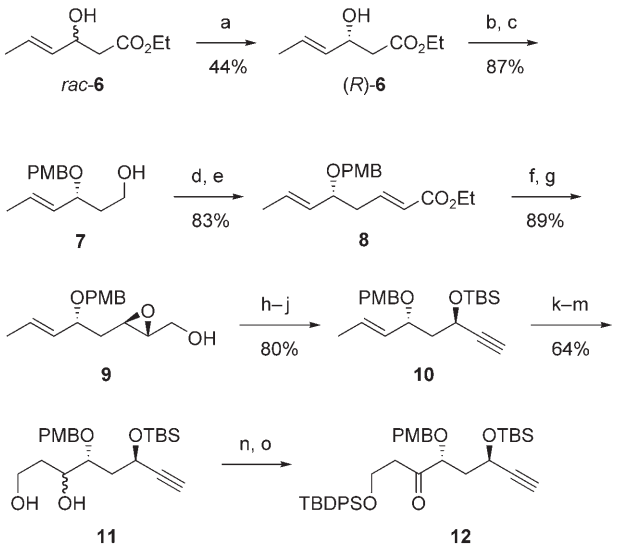

Scheme 2. Synthesis of ketone **12** (synthon **4** in Scheme 1). Reagents and conditions: a) *t*BuOOH (1 equiv), $Ti(O\mathit{i}Pr)_4$ (0.25 equiv), L-(+)-DIPT (0.30 equiv), 4Å M.S., −20°C, 30 h, 44%; b) $PMBOC(=NH)CCl_3$ (2 equiv), CSA (3 mol%); c) $LiAlH_4$ (0.7 equiv), 87% for 2 steps; d) $(COCl)_2$ (1.2 equiv), DMSO (3 equiv), Et_3N (4 equiv); e) $(EtO)_2P(O)CH_2CO_2Et$ (1.2 equiv), DBU (1.25 equiv), LiCl (1.3 equiv), MeCN, 83% for 2 steps; f) DIBAL-H (2.2 equiv), THF, 96%; g) *t*BuOOH (1.5 equiv), $Ti(O\mathit{i}Pr)_4$ (0.30 equiv), D-(−)-DIPT (0.36 equiv), 4-Å M.S. −20°C, 93%; h) PPh_3 (1.2 equiv), $NaHCO_3$ (0.22 equiv), CCl_4, 88%; i) *n*BuLi (3.14 equiv), −78°C, THF; j) TBSCl (1.2 equiv), imidazole (2 equiv), 91% for 2 steps; k) O_3, 2,6-lutidine (1.5 equiv), MeOH; l) $LiCH_2CO_2Et$ from LDA (2.1 equiv) and EtOAc (2.1 equiv), −78°C, THF; m) $LiAlH_4$ (1.5 equiv), THF, 64% for 3 steps; n) TBDPSCl (1.2 equiv), imidazole (2 equiv); o) $(COCl)_2$ (1.2 equiv), DMSO (3 equiv), Et_3N (5 equiv). DIPT = diisopropyl tartrate; M.S. = molecular sieves; CSA = (+)-10-camphorsulfonic acid; DMSO = dimethyl sulfoxide; DBU = 1,8-diazabicyclo[5.4.0]undec-7-ene; DIBAL-H = diisobutylaluminum hydride; TBS = *tert*-butyldimethylsilyl; LDA = lithium diisopropylamide; TBDPS = *tert*-butyldiphenylsilyl.

Construction of the triol **22**, which corresponds to the proposed key intermediate **3** in Scheme 1, was accomplished by the method summarized in Scheme 3. Addition of CH_2=CHMgBr to ketone **12** proceeded cleanly to furnish **13** as the sole product in 87% yield from diol **11**.[18,19] The stereochemistry at C8 was tentatively assigned as depicted, by analogy,[20] and was proved by completion of the synthesis. After protection of the OH group at C8 with TESOTf and 2,6-lutidine, the resulting compound **14** was subjected to ozonolysis in the presence of 2,6-lutidine to produce an aldehyde, which upon Horner–Wadsworth–Emmons reaction furnished α,β-unsaturated ester **15**. Thus, the stage was set for coupling with the remaining partners at the two ends to construct the full carbon skeleton. Installation of the fragment on the right at the acetylene carbon center by Sonogashira reaction[21] with *Z*-vinyl iodide **5** provided enyne **16** in 87% yield. Attachment of the lactone on the left was accomplished by using Evans aldol.[10,22] Thus, ester **16** was reduced to an alcohol and reoxidized to aldehyde **17**. Aldol reaction[23] of **17** with the boron enolate derived from **18** proceeded stereoselectively to afford an aldol, which was converted to lactone **22** by routine reactions through **19**–**21** (see Scheme 3).

Next, zinc-mediated reduction[24] of the triol **22** provided *Z*,*Z*-diene **23** with perfect *cis* selectivity according to ^{1}H NMR spectroscopic analysis. The remaining part of the synthesis involved integration of the amino and phosphate groups on the molecule. As removal of the TES protecting group of the hydroxy group at C8 at the last stage under various conditions was unsuccessful,[14] the more labile TMS group was next studied as the hydroxy-protecting group. Selective protection of the primary and secondary alcohols with TESCl afforded **24** in 85% yield. The remaining tertiary hydroxy group at C8 in **24** was then protected to afford TMS ether **25**, which was exposed to PPTS in THF/MeOH to yield **26** in 53% yield, along with recovered **25** in 38% yield (86% yield of **26** based on recovered **25**). Introduction of the amino group was successfully carried out with $HN(CO_2\text{-allyl})_2$ under Mitsunobu conditions (DIAD, PPh_3)[25] to furnish **27** in 73% yield. To install the phosphate group, the PMB group was removed with DDQ, which proceeded cleanly; subsequent phosphorylation of the resulting alcohol **28** with $(\mathit{i}Pr)_2NP(O\text{-allyl})_2$[26,12f] and 1*H*-tetrazole (then 35% H_2O_2) provided phosphate **29** in good yield. Deprotection of the silyl group (AcCl, CH_2Cl_2/THF/MeOH 5:5:1) produced diol **30** in 95% yield. Finally, all the allyl groups on the nitrogen and phosphorous atoms were removed cleanly by palladium-catalyzed reaction[27,28] with Bu_3SnH and H_2O at 0°C for 1.5 h to afford **1** in 88% yield after preparative TLC (silica gel, normal phase, MeOH/H_2O 8:1). The overall yield of **1** from *rac*-**6** in 38 steps was 0.9% (2% from (*R*)-**6**). Spectral data (^{1}H NMR (500 MHz), ^{13}C NMR (75 MHz), IR), optical rotation ($[\alpha]_D^{28} = +80$ (c = 0.03, MeOH)), and mobility on TLC of synthetic phoslactomycin B were identical in all respects to those reported for the natural material ($[\alpha]_D^{21} = +81$ (c = 1.0, MeOH)).[1b,2]

Next, we turned our attention to the synthesis of the deamino precursor **2**, which is the implicated intermediate in the biosynthesis of **1**.[9] Furthermore, stronger PP2A inhibitory activity was expected from the inhibitory study of the biotin-containing amide derivative at the amino group of **1**.[8] The synthesis started with selective removal of the PMB group of **25** by DDQ followed by assembly of the phosphate group to furnish phosphate **31** in 64% yield (Scheme 4). Desilylation of **31** under acidic conditions provided triol phosphate **32**, which upon palladium-catalyzed deallylation with Bu_3SnH and H_2O at 0°C for 1 h furnished the second target **2** in 77% yield after chromatography on silica gel.

In summary, a highly stereocontrolled and efficient total synthesis of phoslactomycin B (**1**) and its biosynthetic deamino precursor **2** was accomplished by selective protection of the hydroxy group at C9 using the PMB group, which not only provided high selectivity in the construction of the C8 stereocenter but also enabled easy installation of the phosphate group. Furthermore, the successful differentiation of the three other hydroxy groups was demonstrated, thus allowing modification of the functional groups and attachment of another functional group for the study of the structure–activity relationship of **1** and its derivatives and for the execution of chemical biology in this field.

Received: February 3, 2006
Published online: April 18, 2006

 © 2006 Wiley-VCH Verlag GmbH & Co. KGaA, Weinheim

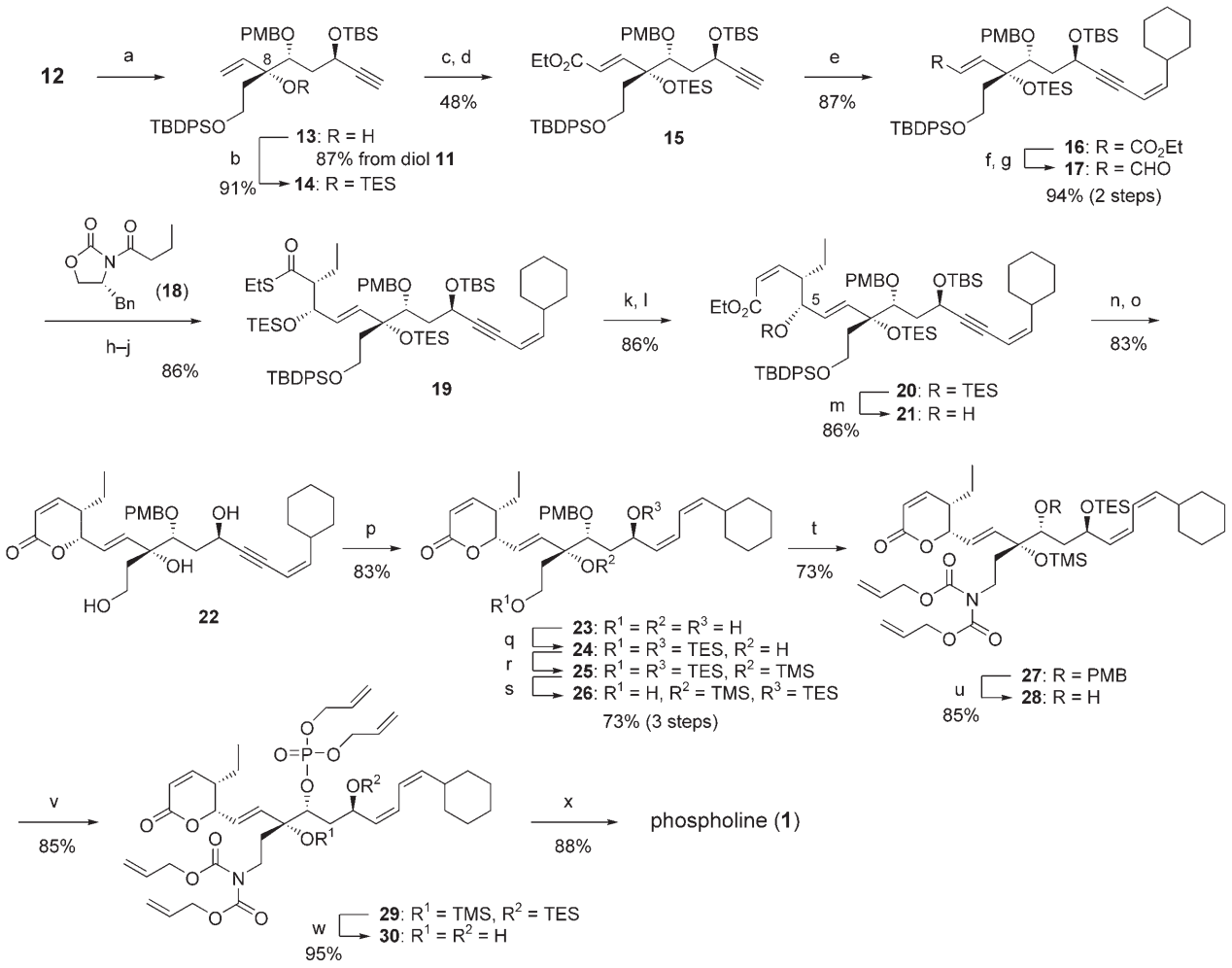

Scheme 3. Synthesis of phoslactomycin B (**1**) through the key intermediate **22** (compare **3** in Scheme 1). Reagents and conditions: a) CH_2=CHMgBr (2 equiv), −78 °C, THF, 87% from diol **11**; b) TESOTf (1.1 equiv), 2,6-lutidine (2 equiv), 91%; c) O_3, 2,6-lutidine (2 equiv), MeOH/*i*PrOH (1:1); d) $(EtO)_2P(O)CH_2CO_2Et$ (2.1 equiv), NaH (2 equiv), THF, 48% for 2 steps; e) **5** (1.2 equiv), $[Pd(PPh_3)_4]$ (5 mol%), CuI (15 mol%), *t*$BuNH_2$ (10 equiv), 87%; f) DIBAL-H (2.5 equiv), THF, 97%; g) $SO_3{\cdot}C_5H_5N$ (3 equiv), DMSO (30 equiv), Et_3N (10 equiv), 97%; h) **18** (1.55 equiv), Bu_2BOTf (1.5 equiv), $(iPr)_2NEt$ (2.2 equiv), −78 °C to RT, CH_2Cl_2; i) TESCl (2 equiv), C_5H_5N (15 equiv), 95% for 2 steps; j) EtSLi from EtSH (5 equiv) and *n*BuLi (3 equiv), 0 °C, 90%; k) DIBAL-H (1.3 equiv), −78 °C, toluene; l) $(PhO)_2P(O)CH_2CO_2Et$ (1.8 equiv), Bu_4NOH (1.75 equiv), THF, 86% for 2 steps; m) PPTS (3 mol%), MeOH/THF (3:1), 86%; n) $Ti(OiPr)_4$ (0.2 equiv), 80 °C, benzene, 94%; o) Bu_4NF (4 equiv), 88%; p) Zn activated with $BrCH_2CH_2Br$, $LiCuBr_2$, EtOH, reflux, 83%; q) TESCl (4 equiv), C_5H_5N (30 equiv), 0 °C, 85%; r) TMSOTf (4 equiv), 2,6-lutidine (30 equiv); s) PPTS (0.1 equiv), THF/MeOH (1:1), 86% for 2 steps based on recovered **25** (38%); t) DIAD (2.6 equiv), PPh_3 (2.4 equiv), $HN(CO_2$-allyl$)_2$ (1.3 equiv), toluene, −78 °C to 0 °C, 73%; u) DDQ (1.5 equiv), CH_2Cl_2/H_2O (19:1), 85%; v) $(iPr)_2NP(O\text{-allyl})_2$ (1.4 equiv), 1*H*-tetrazole (2 equiv) then 35% H_2O_2 (5 equiv), 85%; w) AcCl (0.6 equiv), 0 °C, CH_2Cl_2/THF/MeOH (5:5:1), 95%; x) $[PdCl_2(PPh_3)_2]$ (5 mol%), Bu_3SnH (5 equiv), H_2O (50 equiv), 0 °C, 1.5 h, CH_2Cl_2, 88%. Tf = trifluomethanesulfonyl; TES = triethylsilyl; Bn = benzyl; PPTS = pyridinium *p*-toluenesulfonate; TMS = trimethylsilyl; DIAD = diisopropyl azodicarboxylate; DDQ = 2,3-dichloro-5,6-dicyano-1,4-benzoquinone.

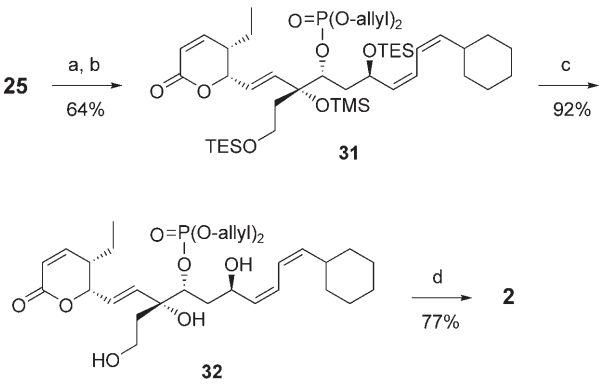

Scheme 4. Synthesis of biosynthetic precursor **2**. Reagents and conditions: a) DDQ (1.2 equiv), CH_2Cl_2/H_2O (19:1), 87%; b) $(iPr)_2NP(O\text{-allyl})_2$ (1.4 equiv), 1*H*-tetrazole (2 equiv) then 35% H_2O_2 (4 equiv), 73%; c) AcCl (0.6 equiv), CH_2Cl_2/THF/MeOH (5:5:1), 0 °C, 92%; d) $[PdCl_2(PPh_3)_2]$ (5 mol%), Bu_3SnH (2.5 equiv), H_2O (30 equiv), CH_2Cl_2, 0 °C, 1 h, 77%.

 © 2006 Wiley-VCH Verlag GmbH & Co. KGaA, Weinheim

Keywords: asymmetric synthesis · natural products · phoslactomycins · phospholine · total synthesis

[1] a) S. Fushimi, S. Nishikawa, A. Shimazu, H. Seto, *J. Antibiot.* **1989**, *42*, 1019–1025; b) S. Fushimi, K. Furihata, H. Seto, *J. Antibiot.* **1989**, *42*, 1026–1036.

[2] a) T. Ozasa, K. Suzuki, M. Sasamata, K. Tanaka, M. Kobori, S. Kadota, K. Nagai, T. Saito, S. Watanabe, M. Iwanami, *J. Antibiot.* **1989**, *42*, 1331–1338; b) T. Ozasa, K. Tanaka, M. Sasamata, H. Kaniwa, M. Shimizu, H. Matsumoto, M. Iwanami, *J. Antibiot.* **1989**, *42*, 1339–1343.

[3] T. Shibata, S. Kurihara, K. Yoda, H. Haruyama, *Tetrahedron* **1995**, *51*, 11999–12012.

[4] T. Tomiya, M. Uramoto, K. Isono, *J. Antibiot.* **1990**, *43*, 118–121.

[5] a) T. Kohama, R. Enokita, T. Okazaki, H. Miyaoka, A. Torikata, M. Inukai, I. Kaneko, T. Kagasaki, Y. Sakaida, A. Satoh, A. Shiraishi, *J. Antibiot.* **1993**, *46*, 1503–1511; b) T. Kohama, T. Nakamura, T. Kinoshita, I. Kaneko, A. Shiraishi, *J. Antibiot.* **1993**, *46*, 1512–1519.

[6] a) D. S. Lewy, C.-M. Gauss, D. R. Soenen, D. L. Boger, *Curr. Med. Chem.* **2002**, *9*, 2005–2032; b) S. B. Buck, C. Hardouin, S. Ichikawa, D. R. Soenen, C.-M. Gauss, I. Hwang, M. R. Swingle, K. M. Bonness, R. E. Honkanen, D. L. Boger, *J. Am. Chem. Soc.* **2003**, *125*, 15694–15695.

[7] a) T. Usui, G. Marriott, M. Inagaki, G. Swarup, H. Osada, *J. Biochem.* **1999**, *125*, 960–965; b) see Reference [6].

[8] T. Teruya, S. Simizu, N. Kanoh, H. Osada, *FEBS Lett.* **2005**, *579*, 2463–2468.

[9] N. Palaniappan, B. S. Kim, Y. Sekiyama, H. Osada, K. Reynolds, *J. Biol. Chem.* **2003**, *278*, 35552–35557.

[10] K. Shimada, Y. Kaburagi, T. Fukuyama, *J. Am. Chem. Soc.* **2003**, *125*, 4048–4049. The total yield is 0.09% in 45 steps, except for the manipulation on the cyclohexane ring.

[11] Reviews: a) see Reference [6]; b) M. Shibasaki, M. Kanai, *Heterocycles* **2005**, *66*, 727–741.

[12] a) D. L. Boger, S. Ichikawa, W. Zhong, *J. Am. Chem. Soc.* **2001**, *123*, 4161–4167; b) J. Cossy, F. Pradaux, S. BouzBouz, *Org. Lett.* **2001**, *3*, 2233–2235; c) Y. K. Reddy, J. R. Falck, *Org. Lett.* **2002**, *4*, 969–971; d) D. E. Chavez, E. N. Jacobsen, *Angew. Chem.* **2001**, *113*, 3779–3782; *Angew. Chem. Int. Ed.* **2001**, *40*, 3667–3670; e) K. Miyashita, M. Ikejiri, H. Kawasaki, S. Maemura, T. Imanishi, *Chem. Commun.* **2002**, 742–743; K. Miyashita, M. Ikejiri, H. Kawasaki, S. Maemura, T. Imanishi, *J. Am. Chem. Soc.* **2003**, *125*, 8238–8243; f) T. Esumi, N. Okamoto, S. Hatakeyama, *Chem. Commun.* **2002**, 3042–3043; g) Y.-G. Wang, Y. Kobayashi, *Org. Lett.* **2002**, *4*, 4615–4618; h) K. Fujii, K. Maki, M. Kanai, M. Shibasaki, *Org. Lett.* **2003**, *5*, 733–736; K. Maki, R. Motoki, K. Fujii, M. Kanai, T. Kobayashi, S. Tamura, M. Shibasaki, *J. Am. Chem. Soc.* **2005**, *127*, 17111–17117; i) B. M. Trost, M. U. Frederiksen, J. P. N. Papillon, P. E. Harrington, S. Shin, B. T. Shireman, *J. Am. Chem. Soc.* **2005**, *127*, 3666–3667.

[13] Ring-closing metathesis of **I** with the Grubbs catalysts (first- and second-generation complexes) under various conditions was unsuccessful.

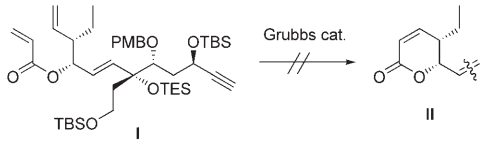

I II

[14] Deprotection of TES ether **III** with AcCl (0.5 equiv) in MeOH afforded a mixture of products, from which **IV** was isolated only in 22% yield. Other conditions (Bu_4NF, HF, $HF{\cdot}C_5H_5N$) resulted in decomposition.

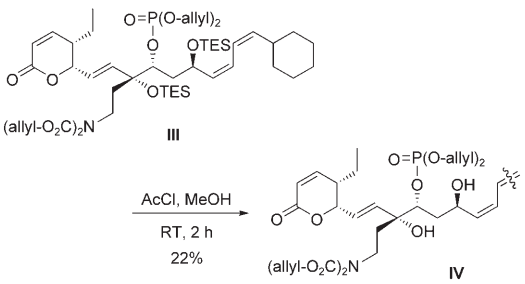

[15] a) V. S. Martin, S. S. Woodward, T. Katsuki, Y. Yamada, M. Ikeda, K. B. Sharpless, *J. Am. Chem. Soc.* **1981**, *103*, 6237–6240; b) T. Katsuki, K. B. Sharpless, *J. Am. Chem. Soc.* **1980**, *102*, 5974–5976; c) Y. Gao, R. M. Hanson, J. M. Klunder, S. Y. Ko, H. Masamune, K. B. Sharpless, *J. Am. Chem. Soc.* **1987**, *109*, 5765–5780.

[16] J. S. Yadav, P. K. Deshpande, G. V. M. Sharma, *Tetrahedron* **1990**, *46*, 7033–7046.

[17] A similar ketone with a TBS protecting group was synthesized from diol **11** and converted into alcohol **V** as well. However, subsequent protection with TESOTf produced a 3:1 mixture of **VI** and **VII** (compare with **13**→**14** in Scheme 3).

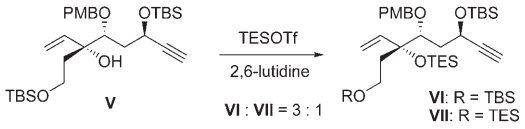

[18] A similar reaction with CH_2=CHLi (CH_2=CH$S n Bu_3$, *n*BuLi) afforded a mixture of products.

[19] Addition of the anion from (*E*)-ICH_2=$CHCH_2OH$ (*n*BuLi then $MgBr_2$) also proceeded stereoselectively. However, this alternative was not adopted owing to the requirement of additional steps for the stereoselective preparation of this alcohol from propargyl alcohol in four steps: 1) CrO_3, H^+; 2) HI; 3) MeOH, H^+; 4) DIBAL-H.

[20] W. C. Still, J. H. McDonald III, *Tetrahedron Lett.* **1980**, *21*, 1031–1034.

[21] a) K. Sonogashira, Y. Tohda, N. Hagihara, *Tetrahedron Lett.* **1975**, *16*, 4467–4470; b) G. Just, B. O'Connor, *Tetrahedron Lett.* **1988**, *29*, 753–756.

[22] D. A. Evans, W. C. Black, *J. Am. Chem. Soc.* **1993**, *115*, 4497–4513.

[23] D. A. Evans, J. Bartroli, T. L. Shih, *J. Am. Chem. Soc.* **1981**, *103*, 2127–2129.

[24] M. H. P. J. Aerssens, R. van der Heiden, M. Heus, L. Brandsma, *Synth. Commun.* **1990**, *20*, 3421–3425.

[25] a) J. C. Arnould, F. Landier, M. J. Pasquet, *Tetrahedron Lett.* **1992**, *33*, 7133–7136; b) O. Mitsunobu, *Synthesis* **1981**, 1–28.

[26] J. W. Perich, R. B. Johns, *Synthesis* **1988**, 142–146.

[27] a) O. Kanno, I. Kawamoto, *Tetrahedron* **2000**, *56*, 5639–5648; b) I. Minami, Y. Ohashi, I. Shimizu, J. Tsuji, *Tetrahedron Lett.* **1985**, *26*, 2449–2452; c) Y. Hayakawa, S. Wakabayashi, T. Nobori, R. Noyori, *Tetrahedron Lett.* **1987**, *28*, 2259–2262.

[28] Deprotection of a model compound, (allyl-$O_2C)_2N(CH_2)_4OP$(=O)(O-allyl)$_2$, using HCO_2H, Et_3N, and a palladium catalyst under standard conditions[27b,c] afforded the Et_3N complex, probably $[H_2N(CH_2)_4OP(O)(OH)(O^-)](Et_3NH^+)$, even after chromatography.

 © 2006 Wiley-VCH Verlag GmbH & Co. KGaA, Weinheim

Polyoxometalate Catalysts

DOI: 10.1002/anie.200600364

Lanthanide Complexes of the Monovacant Dawson Polyoxotungstate $[\alpha_1\text{-}P_2W_{17}O_{61}]^{10-}$ as Selective and Recoverable Lewis Acid Catalysts**

Cécile Boglio, Gilles Lemière, Bernold Hasenknopf, Serge Thorimbert, Emmanuel Lacôte,* and Max Malacria**

Polyoxometalates (POMs) are a large family of metal–oxygen clusters of the early transition metals in high oxidation states, most commonly V^V, Mo^{VI}, and W^{VI}.[1] Their intrinsic chemical properties as electron acceptors or as very strong Brønsted acids (in their protonated form) makes them catalysts in organic transformations,[2] and their ability to form peroxo complexes or to serve as a support for catalytically active metal ions in a high oxidation state is particularly useful in oxidation reactions.[3] Organometallic derivatives of POMs have proven to be effective catalysts in hydrogenation reactions.[4]

To the best of our knowledge, however, no Lewis acid catalysis involving POMs has been reported so far, despite the wide array of transformations that could be addressed. We imagined that lanthanide complexes of monovacant POMs—often called Peacock–Weakley type[5,6]—and in particular of $[\alpha_1\text{-P2W17O61}]^{10-}$ [7–18] would be good candidates for such a task. Some of these compounds have already been studied for their luminescence and magnetic properties provided by the lanthanide ions.[19–21] Hill and co-workers have used the oxidant properties of cerium(IV) in the Keggin derivative $NaH_3[SiW_{11}CeO_{39}]$ as the active site for the aerobic oxidation of formaldehyde.[22] Because lanthanide(III) salts are extremely efficient, water-tolerant Lewis acids, their use in organic reactions has soared over the past ten years.[23–26] However, the quest for more selective and recoverable catalysts remains a challenging task.

The reactivity of lanthanide ions is still present when anionic ligands, such as binaphthyl derivatives, are used to tune the catalytic activity.[27] The use of inorganic polyanionic POMs as ligands should thus also be possible. Indeed, lanthanide complexes with monovacant POMs can be prepared with free coordination sites on the lanthanide ion, which are required to maintain Lewis acid activity. POMs would also bring an additional property: their solubility depends on the counterions. Group 1 metal ions lead to water-soluble complexes that can be used in biphasic catalyst systems,[28] whereas lipophilic ammonium ions solubilize the polyanions in organic solvents. Thus, POMs can be separated easily from small organic molecules by precipitation with diethyl ether or by nanofiltration.[29] Both methods have been applied for the recycling of POM-based oxidation catalysts, and could be extended to the Lewis acidic POM–Ln complexes.

We have chosen to evaluate the lanthanide complexes of the monolacunary Dawson polyoxotungstate $[\alpha_1\text{-}P_2W_{17}O_{61}]^{10-}$. The complexes $(TBA)_5H_2[\alpha_1\text{-}Ln(H_2O)_4\text{-}P_2W_{17}O_{61}]$ (Ln = La, Sm, Eu, Yb; TBA = tetrabutylammonium; Figure 1) are soluble in organic solvents, and the water molecules on the lanthanide ions are labile, thus providing the metal centers with available coordination sites for other ligands.[11,20,30–34] We surveyed catalysts including early, mid, and late lanthanides.

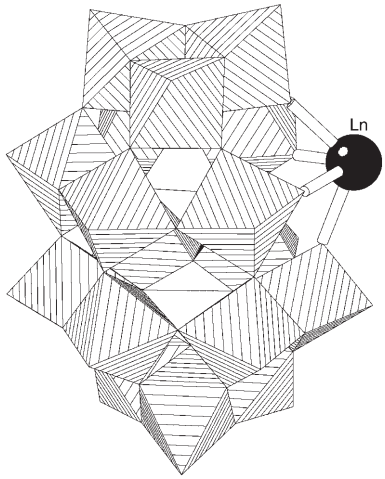

Figure 1. Lanthanide complexes of $[\alpha_1\text{-}P_2W_{17}O_{61}]^{10-}$: the Ln^{3+} ions are coordinated to the vacant site in the lacunary Dawson structure and have four or five open coordination sites.

We first examined Mannich-type reactions of silyl enol ethers with imines[35,36] and found that no reaction occurred with the potassium salts of the POM–Ln complexes, possibly due to solubility issues. We thus switched to complexes that are soluble in organic solvents,[30] especially acetonitrile, and

[*] C. Boglio, G. Lemière, Dr. S. Thorimbert, Dr. E. Lacôte, Prof. M. Malacria
Université Pierre et Marie Curie-Paris 6
Institut de chimie moléculaire (FR 2769)
Laboratoire de chimie organique (UMR CNRS 7611)
case 229, 4 place Jussieu, 75252 Paris cedex 05 (France)
Fax: (+33) 1-4427-7360
E-mail: serge.thorimbert@upmc.fr
lacote@ccr.jussieu.fr
max.malacria@upmc.fr
C. Boglio, Dr. B. Hasenknopf
Université Pierre et Marie Curie-Paris 6
Institut de chimie moléculaire (FR 2769)
Laboratoire de chimie inorganique et matériaux moléculaires (UMR CNRS 7071)
case 42, 4 place Jussieu, 75252 Paris cedex 05 (France)

[**] We thank the CNRS and UPMC for financial support. This work was supported with a UPMC Presidential Young Investigator award (B.H., E.L., S.T.). C.B. thanks the Ministère de l'Enseignement Supérieur et de la Recherche and IUF (of whom M.M. is a senior member) for a grant. Technical support from ICSN (Gif sur Yvette, France) is gratefully acknowledged (HRMS and elemental analyses). We are also indebted to Prof. Lynn C. Francesconi (Hunter College, CUNY (USA)) for fruitful discussions.

Supporting Information for this article is available on the WWW under http://www.angewandte.org or from the author.

InterScience
© 2006 Wiley-VCH Verlag GmbH & Co. KGaA, Weinheim

were able to isolate β-amino ketones **1a–e**, thus proving the catalytic activity of the POM–Ln complexes, although the reaction times were generally longer than those observed with the corresponding lanthanide triflates (two days vs. a few hours). This was expected considering the decreased Lewis acidity of the lanthanides when complexed to the monovacant POM ligand. Nonetheless, the products **1a–e** were isolated in good to excellent yields (Table 1). No reaction occurred when the substrates were mixed in the presence of lacunary $(TBA)_6H_4[\alpha_1\text{-}P_2W_{17}O_{61}]$, which allowed us to exclude a Brønsted acid catalysis for the reaction. Formation of **1a** worked best with the Yb complex as catalyst (Table 1, entry 1), followed by the Sm complex (Table 1, entry 2). La and Eu derivatives were also acceptable (Table 1, entries 3 and 4), although the reactions were slower and the conversion was not optimal. The aldolization is not stereoselective, but neither is it stereoselective with the corresponding triflates.

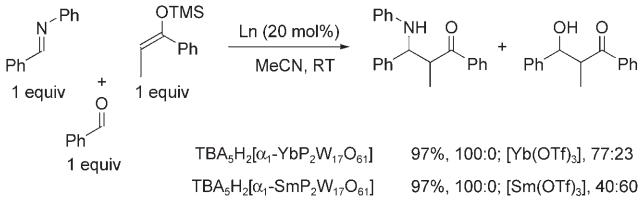

$TBA_5H_2[\alpha_1\text{-}YbP_2W_{17}O_{61}]$ 97%, 100:0; [Yb(OTf)$_3$], 77:23
$TBA_5H_2[\alpha_1\text{-}SmP_2W_{17}O_{61}]$ 97%, 100:0; [Sm(OTf)$_3$], 40:60
$TBA_5H_2[\alpha_1\text{-}LaP_2W_{17}O_{61}]$ 82%, 100:0; [La(OTf)$_3$], 95:5
$TBA_5H_2[\alpha_1\text{-}EuP_2W_{17}O_{61}]$ 96%, 100:0; [Eu(OTf)$_3$], 36:64

Scheme 1. Comparison of the chemoselectivity for POM–Ln catalysts and Ln triflates.

Table 1: POM–Ln-catalyzed aldol reactions of imines.

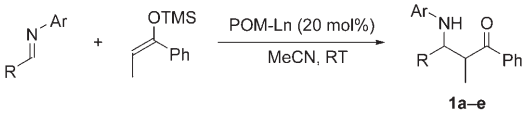

1a–e

Entry	R	Ar	Catalyst	Product	Yield [%]	d.r.
1	Ph	Ph	$(TBA)_5H_2[\alpha_1\text{-}YbP_2W_{17}O_{61}]$	**1a**	96	50:50
2	Ph	Ph	$(TBA)_5H_2[\alpha_1\text{-}SmP_2W_{17}O_{61}]$	**1a**	91	50:50
3	Ph	Ph	$(TBA)_5H_2[\alpha_1\text{-}LaP_2W_{17}O_{61}]$	**1a**	81[a]	50:50
4	Ph	Ph	$(TBA)_5H_2[\alpha_1\text{-}EuP_2W_{17}O_{61}]$	**1a**	71[b]	50:50
5	Ph	*o*-HOC_6H_4	$(TBA)_5H_2[\alpha_1\text{-}YbP_2W_{17}O_{61}]$	**1b**	84	50:50
6	Ph	*p*-$MeOC_6H_4$	$(TBA)_5H_2[\alpha_1\text{-}YbP_2W_{17}O_{61}]$	**1c**	81[c]	60:40
7	*o*-HOC_6H_4	Ph	$(TBA)_5H_2[\alpha_1\text{-}YbP_2W_{17}O_{61}]$	–[d]	–	–
8	CO_2Et	Ph	$(TBA)_5H_2[\alpha_1\text{-}YbP_2W_{17}O_{61}]$	**1d**	70	68:32
9	CO_2Et	*p*-$MeOC_6H_4$	$(TBA)_5H_2[\alpha_1\text{-}YbP_2W_{17}O_{61}]$	**1e**	77	65:35

[a] Yield of isolated product. Conversion was approx. 90%. See Supporting Information for experimental details. [b] Yield of isolated product. Conversion was approx. 80%. [c] Reaction took six days. [d] No conversion was observed.

Except where noted, we decided to proceed with the Yb complex to evaluate the influence of substituents on the imine. Introduction of a hydroxy substituent in the *ortho* position of the aromatic ring attached to the imine carbon totally shut down the reaction, and only the hydrolyzed products were isolated (Table 1, entry 7). We suppose that such a substitution diminishes the electrophilicity of the carbon atom to such an extent that our compounds, which have lower Lewis acidity, are now inactive. On the contrary, the glyoxaldehyde-derived imines reacted much faster, and the reactions were finished in less than an hour (Table 1, entries 8 and 9).

The decreased Lewis acidity of our compounds made them good candidates for chemoselective reactions. Lanthanides favor activation of aldimines over aldehydes, but selectivity is usually achieved only at −23 °C and is not always excellent, particularly with samarium derivatives.[37] We thus ran competition reactions between the benzimine of aniline and benzaldehyde (Scheme 1): only the aldimine reacted at room temperature in the presence of our POM–Ln complexes. The improved selectivities over $Ln(OTf)_3$ were particularly noticeable with $(TBA)_5H_2[\alpha_1\text{-}YbP_2W_{17}O_{61}]$ (selectivity changed from around 3:1 to 100:0), and, most interestingly, with $(TBA)_5H_2[\alpha_1\text{-}SmP_2W_{17}O_{61}]$ and $(TBA)_5H_2[\alpha_1\text{-}EuP_2W_{17}O_{61}]$, which actually brought about an inversion of selectivity. Improvement was still observed with $(TBA)_5H_2[\alpha_1\text{-}LaP_2W_{17}O_{61}]$, a derivative with a lanthanide, whose triflate already greatly favors additions to imines. Overall, the POM–Ln compounds are extremely selective catalysts that are slightly to much better than their parent triflates.

We also carried out a three-component reaction starting from aniline, benzaldehyde, and the same silyl enol ether as before (Scheme 2). Amine **1a** was isolated almost quantitatively, and the reaction proceeded without molecular sieves.

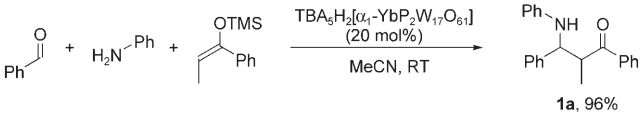

1a, 96%

Scheme 2. The three-component reaction.

We next turned our attention to the imino Diels–Alder reaction of various imines with the Danishefsky diene in the presence of $(TBA)_5H_2[\alpha_1\text{-}YbP_2W_{17}O_{61}]$.[38] Cyclic adducts **2a–d** were isolated in good yields and the reactions proceeded smoothly (Table 2, entries 1–3). Introduction of an *ortho*-hydroxy substituent on the aniline[39a] resulted in a lower yield (57%; Table 2, entry 4), and the use of imines derived from ethyl glyoxalate also proved detrimental (20–30% yield). In this latter case oligomers of the starting materials were also present.

Encouraged by the preceding results, we turned our attention to a variation of the imino Diels–Alder reaction that uses an imine as the aza-diene and an enol ether as the dienophile.[39] Reaction of diphenylimine with ethyl vinyl

 © 2006 Wiley-VCH Verlag GmbH & Co. KGaA, Weinheim

Table 2: POM–Yb-catalyzed imino Diels–Alder reaction with the Danishefsky diene.

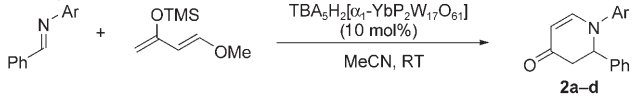

2a–d

Entry	Ar	Product	Yield [%][a]
1	Ph	**2a**	89
2	*p*-$MeOC_6H_4$	**2b**	98
3	*p*-ClC_6H_4	**2c**	76
4	*o*-HOC_6H_4	**2d**	57

[a] See Supporting Information for experimental details.

Table 3: POM–Yb-catalyzed imino Diels-Alder using imines as azadienes.

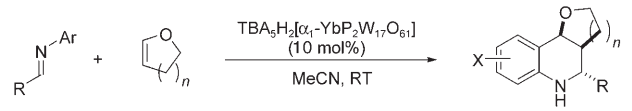

3a–h

Entry	Imine	*n*	Product	Yield [%][a]	d.r.[a]
1		1	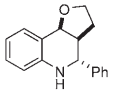	**3a** 67 (80)	60:40 (50:50)
2		2	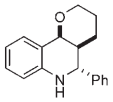	**3b** 79 (89)	80:20 (50:50)
3		1	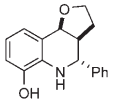	**3c** 63 (74)	90:10 (55:45)
4		2	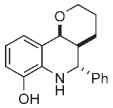	**3d** 39[b] (64)	80:20 (50:50)
5	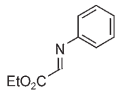	1	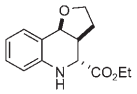	**3e** 39[b,c]	50:50
6	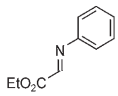	2	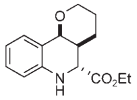	**3f** < 40[b,c]	50:50
7	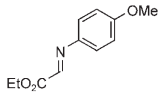	1	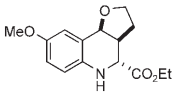	**3g** 67 (48)	50:50 (50:50)
8	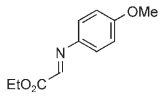	2	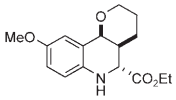	**3h** 62 (<20[b])	50:50 (50:50)

[a] The value in brackets refers to the same reaction using $Yb(OTf)_3$. See Supporting Information for experimental details. [b] Aromatic degradation products were also observed. [c] The starting imine reacted with itself.

ether in the presence of our POM–Yb catalyst was hampered by aromatization of the desired compound into the corresponding quinoline; therefore, in order to limit this decomposition path, we switched to cyclic enol ethers. We selected the same two classes of imines we had used previously, namely the bis-aromatic compounds (Table 3, entries 1–4) and the derivatives of ethyl glyoxalate (Table 3, entries 5–8). The former reacted smoothly, although the yields were slightly lower than those we obtained with $Yb(OTf)_3$. The essential advantage of the POM–Ln catalysts over lanthanide triflates lies in the stereochemical outcome of the reactions: in all examples the diastereoselectivity of the reaction increased noticeably. Given that this increase is most pronounced with *ortho*-hydroxy substrates, we assume that H-bonding interactions between the reactants and the polyanionic ligand exist.[11,12,40] This change in selectivity when the POM–Yb complex is used further indicates that the catalytically active species is not free Yb^{3+}.

In our hands, no significant yields of the tricyclic products could be attained with $Yb(OTf)_3$ and ethyl glyoxalate derivatives (Table 3, entries 5–8) even though we observed rapid consumption of the starting material. We thus thought it might be interesting to use weaker Lewis acids. If our assumption that decomposition is due to an acceleration of the divergent reaction pathways by $Yb(OTf)_3$ was correct, then using the weaker POM–Yb Lewis acid should help. This turned out to be partially the case (Table 3, entries 7 and 8). The stereoselectivity did not vary in these cases, despite possible interactions of the substrates with the polyoxotungstic framework. These intriguing findings show that we need to know more about the POM–Ln–substrate interactions in order to rationalize and fully master their reactivity.

It remained to be shown that the catalysts can be recovered and reused.[29,41] As stated before, we wished to take advantage of the solubility properties of POMs to devise an operationally simple recovery procedure. The complexes we used are soluble in acetonitrile, but not in diethyl ether, in which the vast majority of the adducts are soluble. Indeed, addition of a diethyl ether/ethanol/acetone solution (20:1:1 by volume)[36] to the reaction mixture leading to **1a** (Table 1, entry 1) caused precipitation of a white solid, which was isolated by centrifugation. High-field NMR spectroscopic analysis showed that the solid was pure $(TBA)_5H_2[\alpha_1\text{-}YbP_2W_{17}O_{61}]$, which was isolated quantitatively. We were able to reuse the same catalyst up to ten times with no loss in yield. The following experimental facts made us confident that there had been no leaching of Yb^{3+}: 1) our initial work bears out the decomplexation of Yb^{3+} from the POM upon precipitation;[30] 2) Yb^{3+} is paramagnetic and would influence the NMR spectra of the filtrate, which was not the case (no paramagnetic shift or line broadening); 3) after removal of the POM–Ln complex, the supernatant showed no catalytic activity.

In conclusion, we have discovered a new class of reactions catalyzed by functionalized POMs. The complexation of lanthanide ions by a POM ligand confers essential features, among which a sharply increased chemoselectivity and an increase of the diastereoselectivity in some cases stand out. Furthermore, the catalysts can be easily recovered and reused with no drop in reactivity. Work aimed at further extending the array of possible reactions, understanding the POM–Ln–substrate interactions, which we think provide the basis of diastereoselectivity, as well as examining the enantioselective version of these reactions with additional chiral ligands is

 © 2006 Wiley-VCH Verlag GmbH & Co. KGaA, Weinheim

underway. The POM $[\alpha_1\text{-}P_2W_{17}O_{61}]^{10-}$ itself is chiral and has been used as a racemate throughout this study. Provided an efficient optical resolution method becomes available, our POM–lanthanide complexes could be converted into chiral catalysts without the need for an additional ligand. Progress along these lines will be presented in due course.

Received: January 27, 2006
Published online: April 18, 2006

Keywords: aldol reaction · cycloaddition · lanthanides · Lewis acids · polyoxometalates

[1] a) "Polyoxo anions: Synthesis and Structure": M. T. Pope in *Comprehensive Coordination Chemistry II*, *Vol. 4* (Ed.: A. G. Wedd), Elsevier, Oxford, **2004**, pp. 635–678; b) "Polyoxometalates: Reactivity": C. L. Hill, in *Comprehensive Coordination Chemistry II*, *Vol. 4* (Ed.: A. G. Wedd), Elsevier, Oxford, **2004**, pp. 679–759.

[2] a) M. Misono, *Catal. Today* **2005**, *100*, 95; b) "Applications of Polyoxometalates in Homogeneous Catalysis": R. Neumann, in *Polyoxometalate Molecular Science*, *Vol. 98* (Eds.: J. J. Borras-Almenar, E. Coronado, A. Müller, M. T. Pope), Kluwer, Dordrecht, **2003**, p. 327; c) I. V. Kozhevnikov, "*Heterogeneous Catalysis by Heteropoly Compounds*" in *Polyoxometalate Molecular Science*, *Vol. 98* (Eds.: J. J. Borras-Almenar, E. Coronado, A. Müller, M. T. Pope), Kluwer, Dordrecht, **2003**, p. 351; d) L. E. Briand, G. T. Baronetti, H. J. Thomas, *Appl. Catal. A* **2003**, *256*, 37.

[3] For recent references, see: a) W. Adam, P. L. Alsters, R. Neumann, C. R. Saha-Moeller, D. Seebach, A. K. Beck, R. Zhang, *J. Org. Chem.* **2003**, *68*, 8222; b) I. Bar-Nahum, H. Cohen, R. Neumann, *Inorg. Chem.* **2003**, *42*, 3677; c) T. M. Anderson, W. A. Neiwert, M. L. Kirk, P. M. B. Piccoli, A. J. Schultz, T. F. Koetzle, D. G. Musaev, K. Morokuma, R. Cao, C. L. Hill, *Science* **2004**, *306*, 2074; d) M. Bosing, A. Noh, I. Loose, B. Krebs, *J. Am. Chem. Soc.* **1998**, *120*, 7252; e) D. Kumar, E. Derat, A. M. Khenkin, R. Neumann, S. Shaik, *J. Am. Chem. Soc.* **2005**, *127*, 17712; f) Y. Nakagawa, K. Kamata, M. Kotani, K. Yamaguchi, N. Mizuno, *Angew. Chem.* **2005**, *117*, 5266; *Angew. Chem. Int. Ed.* **2005**, *44*, 5136.

[4] I. Bar-Nahum, R. Neumann, *Chem. Commun.* **2003**, 2690.

[5] R. D. Peacock, T. J. R. Weakley, *J. Chem. Soc. A* **1971**, 1836.

[6] A. B. Yusov, V. P. Shilov, *Radiochemistry* **1999**, *41*, 3.

[7] J.-P. Ciabrini, R. Contant, *J. Chem. Res.* **1993**, 2720.

[8] Q.-H. Luo, R. C. Howell, J. Bartis, M. Dankova, W. D. Horrocks, Jr., A. L. Rheingold, L. C. Francesconi, *Inorg. Chem.* **2002**, *41*, 6112.

[9] J. Bartis, M. Dankova, J. J. Lessmann, Q.-H. Luo, W. D. Horrocks, Jr., L. C. Francesconi, *Inorg. Chem.* **1999**, *38*, 1042.

[10] Q.-H. Luo, R. C. Howell, M. Dankova, J. Bartis, C. W. Williams, W. D. Horrocks, Jr., V. G. Young, A. L. Rheingold, L. C. Francesconi, M. R. Antonio, *Inorg. Chem.* **2001**, *40*, 1894.

[11] M. Sadakane, M. H. Dickman, M. T. Pope, *Inorg. Chem.* **2001**, *40*, 2715.

[12] M. Sadakane, A. Ostuni, M. T. Pope, *J. Chem. Soc. Dalton Trans.* **2002**, 63.

[13] C. Zhang, R. C. Howell, K. B. Scotland, F. G. Perez, L. Todaro, L. C. Francesconi, *Inorg. Chem.* **2004**, *43*, 7691.

[14] C. Zhang, R. C. Howell, Q.-H. Luo, H. L. Fieselmann, L. J. Todaro, L. C. Francesconi, *Inorg. Chem.* **2005**, *44*, 3569.

[15] D. Drewes, B. Krebs, Z. *Naturforsch.* **2006**, in press.

[16] N. Belai, M. H. Dickman, M. T. Pope, R. Contant, B. Keita, I. M. Mbomekalle, L. Nadjo, *Inorg. Chem.* **2005**, *44*, 169.

[17] S. Lis, S. But, G. Meinrath, *J. Alloys Compd.* **2004**, *374*, 366.

[18] J. Y. Niu, J. W. Zhao, D. J. Guo, J. P. Wang, *J. Mol. Struct.* **2004**, *692*, 223.

[19] C. Zhang, R. C. Howell, D. McGregor, L. Bensaid, S. Rahyab, M. Nayshtut, S. Lekperic, L. C. Francesconi, *C. R. Chim.* **2005**, *8*, 1035.

[20] P. Mialane, A. Dolbecq, E. Rivière, J. Marrot, F. Sécheresse, *Eur. J. Inorg. Chem.* **2004**, 33.

[21] X. Fang, T. M. Anderson, C. Benelli, C. L. Hill, *Chem. Eur. J.* **2005**, *11*, 712.

[22] O. A. Kholdeeva, M. N. Timofeeva, G. M. Maksimov, R. I. Maksimovskaya, W. A. Neiwert, C. L. Hill, *Inorg. Chem.* **2005**, *44*, 666.

[23] M. P. Sibi, S. Manyem, J. Zimmerman, *Chem. Rev.* **2003**, *103*, 3263.

[24] S. Kobayashi, M. Sugiura, H. Kitagawa, W. W. L. Lam, *Chem. Rev.* **2002**, *102*, 2227.

[25] K. Mikami, M. Terada, H. Matsuzawa, *Angew. Chem.* **2002**, *114*, 3704; *Angew. Chem. Int. Ed.* **2002**, *41*, 3554..

[26] M. Shibasaki, N. Yoshikawa, *Chem. Rev.* **2002**, *102*, 2187.

[27] S. Kobayashi, H. Ishitani, *J. Am. Chem. Soc.* **1994**, *116*, 4083.

[28] D. Sloboda-Rozner, P. L. Alsters, R. Neumann, *J. Am. Chem. Soc.* **2003**, *125*, 5280.

[29] P. T. Witte, S. R. Chowdhury, J. E. ten Elshof, D. Sloboda-Rozner, R. Neumann, P. L. Alsters, *Chem. Commun.* **2005**, 1206.

[30] C. Boglio, G. Lenoble, C. Duhayon, B. Hasenknopf, R. Thouvenot, C. Zhang, R. C. Howell, B. P. Burton-Pye, L. C. Francesconi, E. Lacôte, S. Thorimbert, M. Malacria, C. Afonso, J.-C. Tabet, *Inorg. Chem.* **2006**, *45*, 1389.

[31] A. Dolbecq, C. Mellot-Draznieks, P. Mialane, J. Marrot, G. Férey, F. Sécheresse, *Eur. J. Inorg. Chem.* **2005**, 3009.

[32] A. Dolbecq, P. Mialane, L. Lisnard, J. Marrot, F. Sécheresse, *Chem. Eur. J.* **2003**, *9*, 2914.

[33] U. Kortz, *J. Cluster Sci.* **2003**, *14*, 205.

[34] P. Mialane, A. Dolbecq, J. Marrot, F. Sécheresse, *Inorg. Chem. Commun.* **2005**, *8*, 740.

[35] S. Kobayashi, M. Araki, H. Ishitani, S. Nagayama, I. Hachiya, *Synlett* **1995**, 233.

[36] See Supporting Information for experimental details.

[37] S. Kobayashi, S. Nagayama, *J. Am. Chem. Soc.* **1997**, *119*, 10049.

[38] S. Kobayashi, H. Ishitani, S. Nagayama, *Synthesis* **1995**, 1195.

[39] a) H. Ishitani, S. Kobayashi, *Tetrahedron Lett.* **1996**, *37*, 7357; b) Y. Ma, C. Qian, M. Xie, J. Sun, *J. Org. Chem.* **1999**, *64*, 6462.

[40] S. Bareyt, S. Piligkos, B. Hasenknopf, P. Gouzerh, E. Lacôte, S. Thorimbert, M. Malacria, *J. Am. Chem. Soc.* **2005**, *127*, 6788.

[41] S. Kobayashi, S. Nagayama, *J. Am. Chem. Soc.* **1998**, *120*, 2985. For a general review on catalyst recovery, see the special: *Chem. Rev.* **2002**, *102*(10).

 © 2006 Wiley-VCH Verlag GmbH & Co. KGaA, Weinheim

Supported Gold Catalysts

DOI: 10.1002/anie.200600552

Gold–Organic–Inorganic High-Surface-Area Materials as Precursors of Highly Active Catalysts**

*Gerolamo Budroni and Avelino Corma**

Gold has always been recognized as a very stable and inert metal. The status of inert and inactive, especially when compared with other noble metals such as Pd and Pt, changed when Haruta et al.[1] observed the extraordinary activity of gold for the oxidation of CO at low temperature. Since then, interest in gold catalysis has grown exponentially and gold catalysts have been successfully applied to a variety of reactions such as hydrogenation of unsaturated substrates,[2] epoxidation of propene,[2d,3] oxidation of alcohols[4] and aldehydes,[5] hydrochlorination of ethyne,[6] and carbon–carbon bond formations,[7] among others.[8] Two factors are believed to convert the "inert gold" into a highly active catalyst: the reduced dimensions of the metal particles ($\leq$5 nm)[9] and a strong interaction with the support.[9b,10] Indeed, selected supports such as Co_3O_4,[2b,9] ZnO,[11] TiO_2,[2b,12] Fe_2O_3,[2b,12] and nanocrystalline Ce_2O_3[13] have been claimed as being adequate for preparing highly active gold supported catalysts, while others such as SiO_2 and Al_2O_3 were considered no good.[14] The poor activity of gold supported on SiO_2 and Al_2O_3 was attributed to the weak metal support interaction obtained with conventional preparation methods and the easy sintering of gold particles on these supports during catalyst activation, as nicely demonstrated by Okamura et al. by supporting the gold through chemical vapor deposition (CVD).[15] It is not then surprising that in order to obtain high gold dispersion, structured high-surface-area mesoporous materials[14a,16] have been used as supports. However, the success obtained up to now with these materials has been modest as their catalytic activity remains, at least, one order of magnitude lower than that for Au/TiO_2 catalysts.

Herein, we present a modified sol–gel approach for the preparation of Au nanoparticles embedded in silica and accessible for catalysis. The material, when properly activated, is highly active for the oxidation of CO at low temperature. The synthesis involves the formation of a three-component metal–organic–inorganic structure composed of Au nanoparticles (AuNPs) that are capped with alkanethiols and partially functionalized with alkoxysilane groups, and polymerized with tetraethyl orthosilicate (TEOS).

Capped AuNPs were prepared in a water-in-oil microemulsion.[17] The ionic gold was reduced with an excess of hydrazine, in the presence of a mixture of 1-dodecanethiol (DT) and 3-mercaptopropyltrimethoxysilane (MPMS) in a molar ratio of 13:1 (see Supporting Information for more details). Alkanethiols reduce the surface energy of the Au particles and consequently their tendency to aggregate.[18] The stable alkanethiol-capped gold nanoparticles were precipitated, washed, and redispersed in ethanol, and then analyzed by transmission electron microscopy (TEM; see Supporting Information). The particles revealed a narrow size distribution centered at approximately 2.0 nm.

The Au–organic–silica material was prepared from AuNPs capped with both DT and MPMS and dispersed in ethanol containing TEOS, followed by the hydrolysis of TEOS catalyzed by NH_4F (see Supporting Information for more details). The presence of the two protecting agents, DT and MPMS, is vital for the preparation as each one plays a specific role during the process to form the Au–organic–silica material. In particular, the alkoxysilane groups of the MPMS promote the hydrolysis and condensation of TEOS around the particle and provide a link between the metal particles and the silica. On the other hand, the inert alkane chains of DT behave as physical spacers between the particles and the silica shell. In the case of nanoparticles capped only with MPMS, the formation of a silica layer around the particle is expected with corresponding occlusion of the metal, whereas capping with DT only should instead limit the hydrolysis around the particle and avoiding the complete embedment of the metal in silica. If we consider that a) the sulfur bond to the gold surface occupies 2.2 gold sites;[19] b) in 2-nm particles about half of the atoms remain on the surface; and c) the molar ratio of DT to MPMS used is 13, then we can calculate that there are, on average, about eight MPMS ligands per gold particle and, therefore, each gold nanoparticle should link to silica through several organic bridges. With all these considerations, the final material would appear as metal particles linked to each other through an organic–inorganic three-dimensional net (Figure 1). The method we propose is then designed to incorporate the nanoparticles into an "open

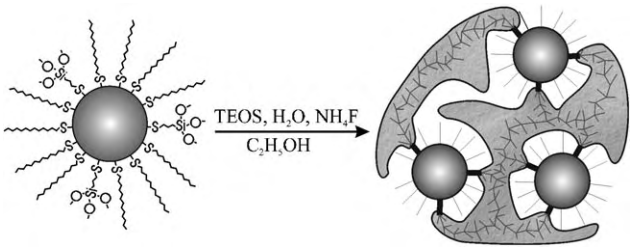

Figure 1. Schematic representation of gold nanoparticles capped with 1-dodecanethiol (DT) and 3-mercaptopropyltrimethoxysilane (MPMS) and the AuNP–organic–SiO_2 structure. MPMS, shown as thick lines on the right-hand side of the figure, provides the organic links between the metal particles and the inorganic mesoporous silica.

[*] Dr. G. Budroni, Prof. A. Corma
Instituto de Tecnología Química, UPV-CSIC
Universidad Politécnica de Valencia
Avda. de los Naranjos s/n, 46022 Valencia (Spain)
Fax: (+34) 96-387-7809
E-mail: acorma@itq.upv.es

[**] We thank the CICyT (MAT-2006) for financial support. G.B. thanks the ITQ for a postdoctoral scholarship.

Supporting information for this article is available on the WWW under http://www.angewandte.org or from the author.

InterScience
© 2006 Wiley-VCH Verlag GmbH & Co. KGaA, Weinheim

shell" of silica that will limit the sintering of the particles at high temperature while preventing a total occlusion of the particles, and consequently favoring accessibility of the catalytic sites to the reactants.

The as-prepared three-component material has a BET surface area of 250 $m^2 g^{-1}$ with a relatively narrow pore size distribution centered at 9 nm (see Supporting Information). Calcination in air at 350 °C removes most of the organic component, with it being fully eliminated at 450 °C (as observed by temperature-programmed desorption with thermal-conductivity and MS detectors). The BET surface area of the sample calcined at 450 °C is 540 $m^2 g^{-1}$. The N_2 adsorption isotherm is typical of a mesoporous material with a relatively narrow distribution of pore sizes, centered at 7 nm (see Supporting Information). It is clear that the accessible surface area strongly increases by removing the organic components by calcination while the pore size decreases.

The resultant materials after calcination at 350 °C and 450 °C were analyzed by TEM (Figure 2), which shows that most of the particles have a diameter between 1.5 and 5 nm, with a few particles with a diameter of 10–30 nm likely originated from an extensive sintering of some Au nanoparticles agglomerated on the surface of the silica that were already observed in the noncalcined Au–organic–inorganic material (see Supporting Information). The particle size distribution plotted in Figure 2 gives an average size of around 3.0 nm for the sample calcined at 350 °C and about 3.5 nm for the sample calcined and reduced at 450 °C.

We can then conclude that in our case, the particle growth during calcination was strongly impeded by the preparation of the metal–organic–inorganic precursor. The thermal sintering was greater with gold deposited on functionalized MCM-41 and SBA-15 (average particles of 5–10 nm)[16a,c] and similar to that of particles incorporated into mesoporous material by reduction of Au^{III} complexes (average particle size of ca. 3 nm).[14a] However, taking into account the particle size and the diameter of the channels of those materials, a partial blocking of the channels may occur with a corresponding inaccessibility of the reactants to some of the gold particles. This, as well as a lower metal–support interaction would be responsible for the relatively low activity shown by these structured mesoporous materials.

Interestingly, the sample that was calcined and reduced (20 % H_2 in N_2) at 450 °C and activated in situ at 150 °C in the presence of 1.7 wt % of gold was already active for the oxidation of CO to CO_2 at temperatures as low as −5 °C (Figure 3 a). Most catalytic data for the oxidation of CO with Au/SiO_2 to date were reported at a reaction temperature of 30 °C or higher. Therefore, we also calculated the specific rate of our catalyst for CO oxidation at 30 °C and obtained a value

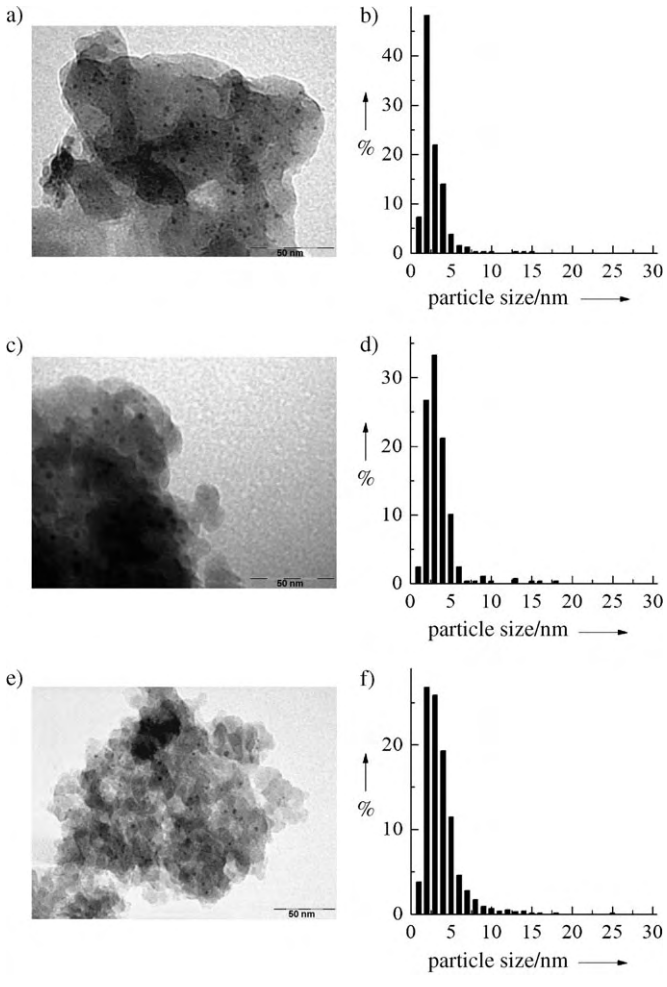

Figure 2. TEM micrographs of the AuNP–organic–SiO_2 precursors (a, c, e) and corresponding particle size distributions (b, d, f) calculated over 250–500 particles. a, b) Sample calcined at 350 °C; c, d) sample calcined at 450 °C; and e, f) sample calcined at 450 °C and subsequently reduced at 450 °C. The average particles size are 2.9, 3.5, and 3.6 nm, respectively. Scale bars: 50 nm.

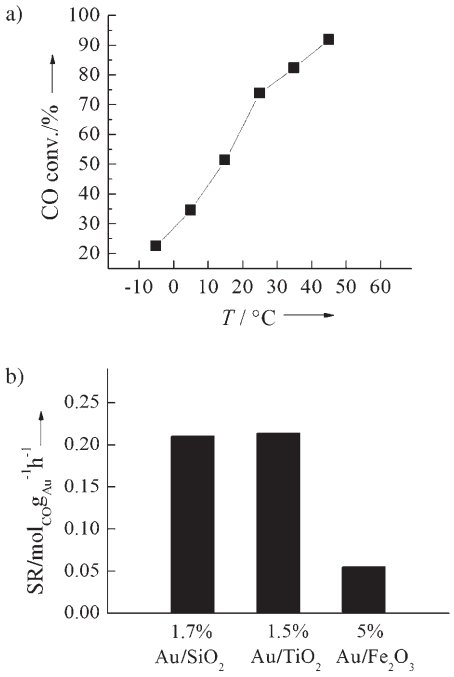

Figure 3. a) Conversion of CO into CO_2 as a function of temperature for the Au/SiO_2 catalyst activated by calcination at 450 °C, treatment at 450 °C in H_2 (20 % flow), and heating in situ at 150 °C for 1 h. b) Histogram showing the specific rate (SR) for CO oxidation at 5 °C of different supported gold catalysts.[13]

 © 2006 Wiley-VCH Verlag GmbH & Co. KGaA, Weinheim

of 0.48 $mol_{CO}\,g_{Au}^{-1}\,h^{-1}$. This result is at least one order of magnitude larger than that obtained with gold on MCM-41 or SBA-15 mesoporous materials[16] and is also higher than the specific rate (0.17 $mol_{CO}\,g_{Au}^{-1}\,h^{-1}$) obtained by Okamura et al. with Au/SiO_2 prepared by CVD[15] at 30 °C (see Table 1).

Table 1: Specific rates for the oxidation of CO to CO_2 with different Au/SiO_2 catalysts at specified temperatures and contact times.[a]

Catalyst preparation	T [°C][b]	Specific rate [$mol_{CO}\,g_{Au}^{-1}\,h^{-1}$]	Contact time [$g_{cat}\,h\,mol_{CO}^{-1}$]	Particle size (T [°C])
AuNPs[c]	30	0.48	93	3.6 (450)
impregnation on SiO_2[15]	300	0.061	113	20 (400)
CVD on SiO_2[15]	30	0.17	113	6.6 (400)
incorporation of Au[d]	125	0.078	124	2.6 (500)
deposition on SBA-15[e]	30	0.017	111	4.5[f] (–)
deposition on MCM-41[g]	80	0.025	570	5.1 (600)
deposition on MCM-48[g]	80	0.014	570	6.9 (600)
deposition on SBA-15[g]	80	0.019	570	5.8 (600)

[a] The average particle size after thermal treatment at the specified temperature for each catalyst are also provided. [b] Reaction temperature. [c] This work. [d] Incorporation of gold into mesoporous through complexation-mediated growth of AuNPs and surfactant-templating synthesis of silica (see Reference [14a]). [e] See Reference [16a]. [f] Sample not calcined. The particle size changed to 10–30 nm after reaction at 160 °C. [g] See Reference [16c].

The specific rate of our catalyst for CO oxidation has been compared with those of Au/TiO_2 and Au/Fe_2O_3 catalysts prepared by the World Gold Council, and the results (Figure 3b) clearly show that our Au/SiO_2 system is as active as the Au/TiO_2 catalyst and much more active than Au/Fe_2O_3. Note that the thermal treatments are crucial for the activation of the material, as both the uncalcined and unreduced catalysts reveal a much lower conversion of between 10 and 15% at 100 °C.

In conclusion, the preparation of hybrid Au–organic–inorganic materials, in which gold nanoparticles are capped with two different thiol molecules, DT and MPMS, leads to high-surface-area Au/SiO_2 catalysts. The metal particles are well stabilized against sintering, even when the samples are calcined and reduced at 450 °C. The synthesis does not require the metal colloid suspension to be prepared "in situ", but instead the AuNPs can be prepared previously, isolated, and stored, thereby lending a strong flexibility to the method. The catalytic activity of these materials for CO oxidation is the same as that obtained with gold on TiO_2, indicating that it is possible to obtain highly active gold–silica catalysts by a liquid-based method, provided that accessible small gold particles and strong metal–support interactions are present. This suggests that despite the active role attributed to supports such as TiO_2, Fe_3O_2, and nanocrystalline CeO_2, gold nanoparticles may have a high intrinsic activity. The high surface area and properties of the three-component catalyst make it an interesting system for further studies in catalyzed organic synthesis reactions.

Received: February 10, 2006
Published online: April 19, 2006

Keywords: gold · heterogeneous catalysis · nanostructures · organic–inorganic hybrid materials · oxidation

[1] a) M. Haruta, T. Kobayashi, H. Sano, N. Yamada, *Chem. Lett.* **1987**, 405–408; b) M. Haruta, N. Yamada, T. Kobayashi, S. Iijima, *J. Catal.* **1989**, *115*, 301–309.
[2] a) P. Mukherjee, C. R. Patra, A. Ghosh, R. Kumar, M. Sastry, *Chem. Mater.* **2002**, *14*, 1678–1684; b) C. Mohr, H. Hofmeister, J. Radnik, P. Claus, *J. Am. Chem. Soc.* **2003**, *125*, 1905–1911; c) C. Mohr, H. Hofmeister, P. Claus, *J. Catal.* **2002**, *213*, 86–94; d) A. K. Sinha, S. Seelan, S. Tsubota, M. Haruta, *Top. Catal.* **2004**, *29*, 95–102; e) C. González-Arellano, A. Corma, M. Iglesias, F. Sánchez, *Chem. Commun.* **2005**, *27*, 3451–3453.
[3] M. P. Kapoor, A. K. Sinha, S. Seelan, S. Inagaki, S. Tsubota, H. Yoshida, M. Haruta, *Chem. Commun.* **2002**, *23*, 2902–2903.
[4] A. Abad, P. Conception, A. Corma, H. Garcia, *Angew. Chem.* **2005**, *117*, 4134–4137; *Angew. Chem. Int. Ed.* **2005**, *44*, 4066–4069.
[5] A. Corma, M. E. Domine, *Chem. Commun.* **2005**, *32*, 4042–4044.
[6] G. J. Hutchings, *Gold Bull.* **1996**, *29*, 123–130.
[7] a) A. Stephen, K. Hashmi, *Angew. Chem.* **2005**, *117*, 7150–7154; *Angew. Chem. Int. Ed.* **2005**, *44*, 6990–6993; b) C. González-Arellano, A. Corma, M. Iglesias, F. Sánchez, *J. Catal.* 2006, 328, 497–501.
[8] a) S. Carrettin, J. Guzman, A. Corma, *Angew. Chem.* **2005**, *117*, 2282–2285; *Angew. Chem. Int. Ed.* **2005**, *44*, 2242–2245; b) A. Stephen, K. Hashmi, Ralph Salathé, T. M. Frost, L. Schwarz, J. H. Choi, *Appl. Catal. A* **2005**, *291*, 238–246; c) A. Hoffmann-Röder, N. Krause, *Org. Biomol. Chem.* **2005**, *3*, 387–391.
[9] a) M. Haruta, S. Tsubota, T. Kobayashi, H. Kageyama, M. J. Genet, B. Delmon, *J. Catal.* **1993**, *144*, 175–192; b) M. Haruta, *Catal. Today* **1997**, *36*, 153–166.
[10] a) M. Haruta, M. Date, *Appl. Catal. A* **2001**, *222*, 427–437; b) L. Guczi, G. Petö, A. Beck, K. Frey, O. Geszti, G. Molnár, C. Daróczi, *J. Am. Chem. Soc.* **2003**, *125*, 4332–4337.
[11] a) F. Boccuzzi, A. Chiorino, M. Tsubota, M. Haruta, *J. Phys. Chem.* **1996**, *100*, 3625–3631; b) M. A. P. Dekkers, M. J. Lippits, B. E. Nieuwenhuys, *Catal. Lett.* **1998**, *56*, 195–197.
[12] S. Tsubota, T. Nakamura, K. Tanaka, M. Haruta, *Catal. Lett.* **1998**, *56*, 131–135.
[13] S. Carrettin, P. Conception, A. Corma, J. M. Lopez Nieto, V. F. Puntes, *Angew. Chem.* **2004**, *116*, 2592–2594; *Angew. Chem. Int. Ed.* **2004**, *43*, 2538–2540.
[14] a) S. H. Overbury, L. Ortiz-Soto, H. Zhu, B. Lee, M. D. Amiridis, S. Dai, *Catal. Lett.* **2004**, *95*, 99–106; b) M. M. Schubert, S. Hackenberg, A. C. van Veen, M. Muhler, V. Plazak, R. J. Behm, *J. Catal.* **2001**, *197*, 113–122.
[15] a) M. Okumura, S. Nakamura, S. Tsubota, T. Nakamura, M. Azuma, M. Haruta, *Catal. Lett.* **1998**, *51*, 53–58; b) M. Okumura, S. Tsubota, M. Haruta, *J. Mol. Catal. A* **2003**, *199*, 73–84.
[16] a) C. M. Yang, M. Kalwei, F. Schüth, K. J. Chao, *Appl. Catal. A* **2003**, *254*, 289–296; b) C. W. Chiang, A. Wang, B. Z. Wan, C. Y. Mou, *J. Phys. Chem. B* **2005**, *109*, 18042–18047; c) Y. S. Chi, H. P. Lin, C. Y. Mou, *Appl. Catal. A* **2005**, *284*, 199–206; d) G. Martra, L. Prati, C. Manfredotti, S. Biella, M. Rossi, S. Coluccia, *J. Phys. Chem. B* **2003**, *107*, 5453–5459; e) A. Q. Wang, J. H. Liu, S. D. Lin, T. S. Lin, C. Y. Mou, *J. Catal.* **2005**, *233*, 186–197.

 © 2006 Wiley-VCH Verlag GmbH & Co. KGaA, Weinheim

[17] a) S. Eriksson, U. Nylen, S. Rojas, M. Boutonnet, *Appl. Catal. A* **2004**, *265*, 207 – 219; b) D. W. Chen, C. J. Chen, *J. Mater. Chem.* **2002**, *12*, 1557 – 1562.
[18] J. E. Martin, J. P. Wilcoxon, J. Odinek, P. Provencio, *J. Phys. Chem. B* **2000**, *104*, 9475 – 9486.
[19] a) A. Badia, S. Singh, L. Demers, L. Cuccia, G. R. Brown, R. B. Lennox, *Chem. Eur. J.* **1996**, *2*, 359 – 363; b) A. Badia, L. Cuccia, L. Demers, F. Morin, R. B. Lennox, *J. Am. Chem. Soc.* **1997**, *119*, 2682 – 2692.

 © 2006 Wiley-VCH Verlag GmbH & Co. KGaA, Weinheim

Polymerization Catalysts

DOI: 10.1002/anie.200600197

Are Aluminoxanes Nanotubular? Structural Evidence from a Quantum Chemical Study

Mikko Linnolahti, John R. Severn, and Tapani A. Pakkanen*

Single-site α-olefin polymerization catalysts hold promise for a rational tailoring of the polymer microstructure and hence its properties. One of the critical components in these systems is the co-catalyst, which can profoundly influence the activity, stereoselectivity, and molecular-weight capability of the catalytic system.[1] The archetypal co-catalyst is a solution of methylaluminoxanes (MAO), the structural characterization of which has remained challenging and elusive. As a consequence, the understanding and control of the polymerization process, together with optimization of the co-catalyst, has been handicapped by the inability to determine the structure of the active component.

Due to the lack of precise crystallographic and spectroscopic characterization, several structural models have been proposed for MAO. The first proposals included chains and rings with three-coordinate, highly Lewis acidic Al centers.[2] The preference for four-coordinate Al and three-coordinate O atoms was demonstrated in 1983 by Atwood et al. by a crystal structure analysis of $[Al_7O_6Me_{16}]^-$.[3] Further progress towards interpretation of polyhedral cages as the most relevant structural alternative was made in the mid-90s by Sinn[4] and Barron et al.[5] Following the synthesis of $[AlO(t\mathrm{Bu})]_n$ cages ($n = 6$–9 and 12),[5] the preference for cage structures over other proposed alternatives was demonstrated by quantum chemical calculations on methyl-substituted[6,7] and unsubstituted[8] aluminoxanes. Herein, we report a HF- and B3LYP-level quantum chemical study of the structures of alkylaluminoxanes.

The structural determination of MAO is further complicated by association of trimethylaluminum[1] into the {AlO(Me)} core. This led us to an unexpected observation while studying the subsequent reactions between the unsubstituted $[AlO(H)]_n$ cages and AlH_3. The products of the reactions for cages with $n = 6$ and 8, which are the unsubstituted counterparts of two cages characterized crystallographically by Barron et al., are illustrated in Figure 1. The

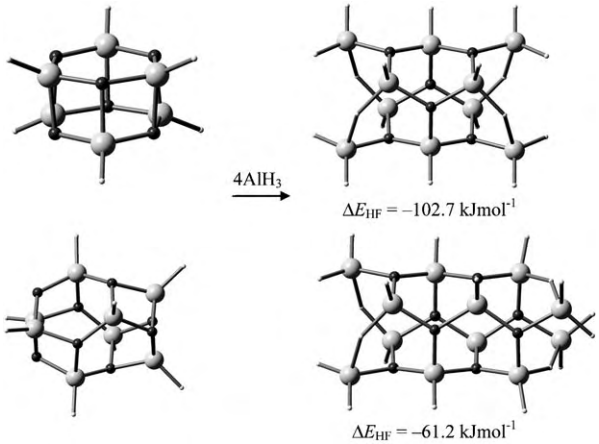

Figure 1. The formation of aluminoxane nanotubes by association of four $\{AlH_3\}$ groups into $[AlO(H)]_6$ and $[AlO(H)]_8$ cages.

AlH_3 units attach to the $[AlO(H)]_n$ core by breaking the Al–O bond between $\{Al_2O_2\}$ squares; the mechanism of this "latent Lewis acidicity"[9] has been described by Zurek and Ziegler.[10] For both cages, the reaction is exothermic for addition of up to four AlH_3 groups,[11] after which all $\{Al_2O_2\}$ squares are opened to form six-membered rings exclusively. The resulting molecular structures are striking, with sections of armchair (2,2) nanotubes capped with two AlH_3 groups at each end. These species do not undergo further reaction with AlH_3. Changing the hydrogen atoms to methyl groups leads a similar, although somewhat more pronounced, result: in the case of the smaller cage the reaction energy increases from $-102.7\ \mathrm{kJ\,mol^{-1}}$ to $-157.2\ \mathrm{kJ\,mol^{-1}}$.

Next, we investigated the cage dimer of $[AlO(H)]_6$, whose methylated counterpart has been proposed as a possible component of MAO.[12] It turns out that this cage dimer is unstable and undergoes a structural deformation. Depending on the orientations of the two cages, the dimer has three isomers; the energetically most favored one, by a margin of over $40\ \mathrm{kJ\,mol^{-1}}$, is shown in Figure 2. This S_4-symmetric isomer, which is favored over two non-interacting cages by $340\ \mathrm{kJ\,mol^{-1}}$, takes the form of a capped (2,2) nanotube. As the dimer is capped with three adjacent $\{Al_2O_2\}$ squares, oligomerization of the cages probably proceeds beyond the dimer. Alternatively, incorporation of trialkylaluminum would terminate the tube growth.

[*] Dr. M. Linnolahti, Prof. T. A. Pakkanen
Department of Chemistry
University of Joensuu
P.O. Box 111, 80101 Joensuu (Finland)
Fax: (+358) 13-251-3390
E-mail: mikko.linnolahti@joensuu.fi
Dr. J. R. Severn
Borealis Polymers Oy
P.O. Box 330, 06101 Porvoo (Finland)

Supporting Information for this article is available on the WWW under http://www.angewandte.org or from the author.

© 2006 Wiley-VCH Verlag GmbH & Co. KGaA, Weinheim

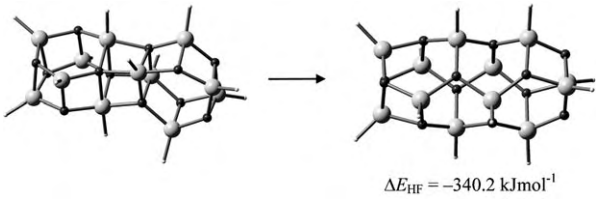

Figure 2. The formation of a capped (2,2) armchair aluminoxane nanotube by dimerization of face-bridged $[AlO(H)]_6$ cages.

Encouraged by these observations, we studied the tubular section of the unsubstituted aluminoxanes by means of periodic ab initio calculations for the open-ended infinite tubes. In analogy with carbon nanotubes,[13] zigzag, armchair, and chiral nanotubes can be derived. The relative stabilities of the tubes are listed in Table 1 using the preferred $[AlO(H)]_n$ cage (*T*-symmetric $Al_{28}O_{28}H_{28}$[8]) as a reference. The favored structures for each family are illustrated in Figure 3.

Table 1: Diameters [nm] and stabilities [kJ mol^{-1}] relative to the preferred cage ($Al_{28}O_{28}H_{28}$[8]) for $[AlO(H)]_n$ nanotubes of infinite length.

$[AlO(H)]_n$ nanotube	Diameter	ΔE (n_{HF})	ΔE (n_{B3LYP})
(2,2)	0.69	−1.4	−3.3
(3,3)	0.87	−2.3	−4.1
(4,4)	1.03	3.3	1.0
(3,0)	0.56	3.8	1.6
(4,0)	0.75	−10.6	−11.5
(5,0)	0.81	−10.6	−11.4
(6,0)	0.95	−7.2	−8.2
(2,1)	0.55	15.7	13.3
(3,1)	0.71	−5.0	−6.5
(3,2)	0.74	−4.4	−6.1
(4,1)	0.79	−8.8	−9.9
(4,2)	0.88	−3.7	−5.3

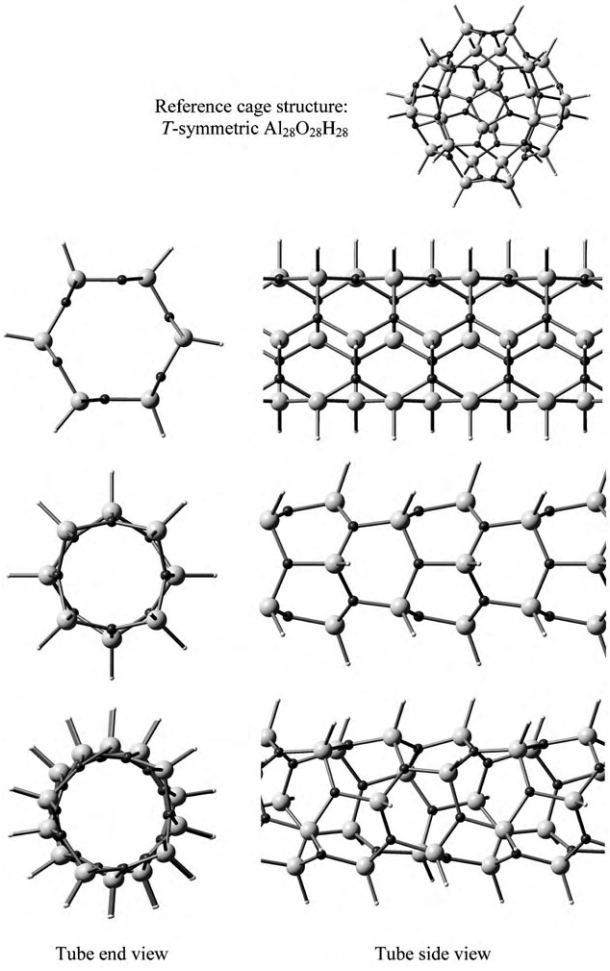

Figure 3. Optimized structures of the favored $[AlO(H)]_n$ nanotubes of infinite length for each family: armchair (3,3) (top), zigzag (4,0) (middle), and chiral (4,1) (bottom).

The aluminoxane nanotubes are favored over the cage whatever the method applied. The tubes reach their energy minimum at diameters somewhat below 1 nm: armchair in (3,3), zigzag in (4,0), and chiral in (4,1). The preference for zigzag tubes is due to the repulsion between the hydrogen substituents. The zigzag arrangement allows the largest separation between the neighboring substituents (3.76 Å in the case of the preferred (4,0), compared to 2.98 Å for armchair (3,3) and 3.27 Å for chiral (4,1)). The preference for relatively thin tubes, on the other hand, is due to the optimal curvature for sp^3-hybridized Al. While the $Al_{28}O_{28}H_{28}$ cage is a representative of optimal curvature, the cages are handicapped by the $\{Al_2O_2\}$ squares necessary for cage closure. In this regard, nanotubular shapes appear more reasonable owing to their larger relative proportion of favorable six-membered rings.

To verify that the preference for the tubular shape is not characteristic for unsubstituted aluminoxanes alone, we repeated the cage dimerization study (Figure 2) for methyl-substituted cages. The substitution pattern does not affect our conclusions, the dimerization energy in the case of methyl substituents being −330 kJ mol^{-1} (compared to −340 kJ mol^{-1} for the unsubstituted case). We then optimized the methyl- and *tert*-butyl-substituted zigzag (4,0) and (3,0) nanotubes, respectively, and compared their stabilities with those of the correspondingly substituted cages. The calculations of Ziegler et al. suggest that $Al_{12}O_{12}Me_{12}$ is the favored $[AlO(Me)]_n$ cage,[6] therefore we selected this as the reference structure. No data for the relative stabilities of *tert*-butyl-substituted cages are available, therefore a cage synthesized by Barron et al., namely $[AlO(tBu)]_6$, was selected as a reference.[5] The optimized structures of the substituted cages and nanotubes, together with their relative stabilities, are given in Figure 4. The methylaluminoxane nanotube, in line with the unsubstituted ones, is clearly favored over the cage, the difference in relative energy being almost 20 kJ mol^{-1} per {AlO(Me)} unit. The opposite is observed for *tert*-butyl substituents, however, as the marked overcrowding due to the vicinity of the bulky substituents results in significant destabilization—the $[AlO(tBu)]_6$ cage is favored by more than 70 kJ mol^{-1} per {AlO(*t*Bu)} unit. One should note that the energy difference is due to destabilization of the tube rather than stabilization of the cage owing to the presence of *tert*-butyl substituents. Preliminary studies on the (4,0) nanotube suggest that the tubes

 © 2006 Wiley-VCH Verlag GmbH & Co. KGaA, Weinheim

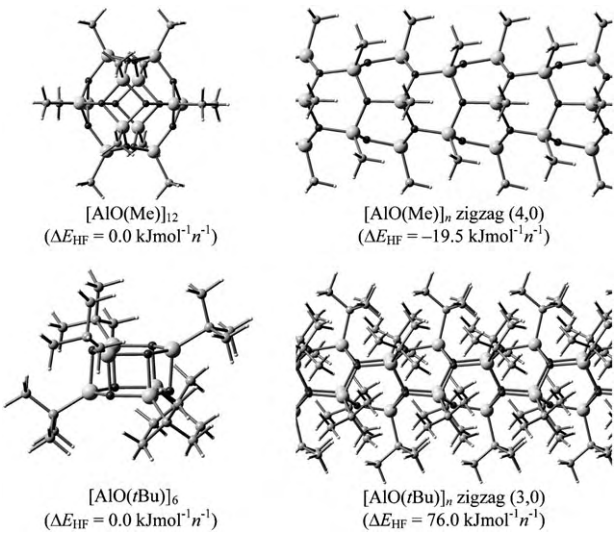

Figure 4. Structures and relative stabilities of selected methyl- and *tert*-butyl-substituted aluminoxane cages and zigzag nanotubes.

become increasingly overcrowded as a function of the tube diameter.

The structural differences between MAO and *tert*-butyl-substituted aluminoxanes can now be discussed in a new light. The $[AlO(tBu)]_n$ cages could actually be considered to be very short tubes for which the tube growth is prematurely interrupted after two or three repetitive cycles as a consequence of repulsion between the bulky substituents. In the case of MAO, no interruption of the tube growth occurs as the repulsion between the methyl groups is insignificant. One should note that the current interpretation of the structure of MAO being in a dynamic equilibrium of variably sized cages[7] is basically based on Barron's *tert*-butyl-substituted polyhedral cages.[5] Taking into account the significantly different structural preferences of methyl- and *tert*-butyl-substituted aluminoxanes, the structure of MAO might involve a dynamic equilibrium mostly between nanotubes of variable lengths and thicknesses, perhaps containing fractions of proposed cages and other structural fragments.

In order to understand the function of nanotubular MAO as a co-catalyst in polymerization catalysis, further studies are required to determine its average molar mass, tube growth mechanism, capping of the tube ends, and association of trimethylaluminum into the AlO(Me) core. As far as the molar mass is concerned, various experimental values have been reported.[1] Recently, the size of the $[Me{-}MAO]^-$ anion was determined from a pulsed field-gradient NMR study by Babushkin and Brintzinger.[14] The observed mean effective hydrodynamic radius of 12.2–12.5 Å, assuming a spherical structure, corresponds to about 150–200 Al atoms in each MAO molecule. Possibly due to its size, catalytic activity declines strongly at MAO concentrations below an Al/Zr ratio of 200–300:1.[15] The sizes of the preferred MAO cages reported previously[7] are about an order of magnitude lower, hence they are unlikely to account for the structure of MAO. Instead, the presence of hundreds of Al atoms in nanotubular shapes could be a plausible explanation. In the case of the zigzag (4,0) tube, 200 Al atoms would correspond to 50 repetitive $\{Al_4O_4Me_4\}$ rings. As the tubular section of MAO is inert towards reactions with trimethylaluminum, it is likely that trimethylaluminum becomes associated into the tube ends (see Figure 1). Building on this theory, one could reason that the functional sites of MAO as a co-catalyst are exclusively at the tube ends, hence a MAO molecule containing hundreds of Al atoms arranged into a nanotubular shape would possess, at most, two active sites, namely both ends of the tube. The relatively few active sites of large MAO molecules given the tasks of the co-catalyst, that is, activation of the catalyst precursor and scavenging of impurities, would explain why thousandfold Al/Zr ratios are generally required in catalytic polymerizations.

In summary, we have provided new evidence concerning the structures of aluminoxanes, among which methylaluminoxane is particularly important due to its application as a co-catalyst in single-site homogeneous polymerization catalysis. The data presented suggest that MAO is nanotubular in shape. The aluminoxanes are capable of adopting armchair, zigzag, and chiral analogues of the well-known carbon nanotubes and prefer diameters of about 1 nm. Trimethylaluminum is likely to become associated at the tube ends, which act as functional sites in MAO.

Methods

All structures, including the periodic ones, were fully optimized. Aluminoxane cages were constrained to the symmetries in question, namely T for $[AlO(H)]_{28}$, T for $[AlO(Me)]_{12}$, and C_{3v} for $[AlO(tBu)]_6$, and were characterized as true minima by frequency calculations. Periodic calculations of unsubstituted aluminoxanes were performed at the HF and B3LYP levels of theory; in all other examples the HF method was applied. Periodic calculations generally require optimized basis sets. The optimized 8-5-11G* and 8-411G* basis sets were used for aluminum and oxygen,[16] respectively, together with the standard 6-31G** basis set for hydrogen, as reported in a previous study.[8] For carbon, a 6-21G* basis set with a modified outer sp exponent was adopted.[17] Identical basis sets were applied for the clusters and the periodic tubes. The calculations were performed with Gaussian 03 software.[18]

Received: January 17, 2006
Published online: April 7, 2006

Keywords: ab initio calculations · aluminoxanes · nanostructures · polymerization · structure elucidation

[1] a) E. Y.-X. Chen, T. J. Marks, *Chem. Rev.* **2000**, *100*, 1391 – 1394; b) J.-N. Pédeutour, K. Radhakrishnan, H. Cramail, A. Deffieux, *Macromol. Rapid. Commun.* **2001**, *22*, 1095 – 1123; c) M. Bochmann, *J. Organomet. Chem.* **2004**, *689*, 3982 – 3998.
[2] S. Pasynkiewicz, *Polyhedron* **1990**, *9*, 429 – 453.
[3] J. L. Atwood, D. C. Hrncir, R. D. Priester, R. D. Rogers, *Organometallics* **1983**, *2*, 985 – 989.
[4] H. Sinn, *Macromol. Symp.* **1995**, *97*, 27 – 52.
[5] a) M. R. Mason, J. M. Smith, S. G. Bott, A. R. Barron, *J. Am. Chem. Soc.* **1993**, *115*, 4971 – 4984; b) C. J. Harlan, M. R. Mason, A. R. Barron, *Organometallics* **1994**, *13*, 2957 – 2969.
[6] E. Zurek, T. K. Woo, T. K. Firman, T. Ziegler, *Inorg. Chem.* **2001**, *40*, 361 – 370.
[7] E. Zurek, T. Ziegler, *Prog. Polym. Sci.* **2004**, *29*, 107 – 148.

 © 2006 Wiley-VCH Verlag GmbH & Co. KGaA, Weinheim

[8] M. Linnolahti, T. N. P. Luhtanen, T. A. Pakkanen, *Chem. Eur. J.* **2004**, *10*, 5977 – 5987.
[9] C. J. Harlan, S. G. Bott, A. R. Barron, *J. Am. Chem. Soc.* **1995**, *117*, 6465 – 6474.
[10] E. Zurek, T. Ziegler, *Inorg. Chem.* **2001**, *40*, 3279 – 3292.
[11] The energy of AlH_3 was taken for its lowest energy form, which is crystalline aluminum hydride. See reference [8] for details. The energy of $AlMe_3$ was taken as being that of its dimer, Al_2Me_6.
[12] P. L. Bryant, C. R. Harwell, A. A. Mrse, E. F. Emery, Z. Gan, T. Cladwell, A. P. Reyes, P. Kuhns, D. W. Hoyt, L. S. Simeral, R. W. Hall, L. G. Butler, *J. Am. Chem. Soc.* **2001**, *123*, 12009 – 12017.
[13] S. Iijima, *Nature* **1991**, *354*, 56 – 58.
[14] D. E. Babushkin, H.-H. Brintzinger, *J. Am. Chem. Soc.* **2002**, *124*, 12869 – 12873.
[15] H.-H. Brintzinger, D. Fischer, R. Mülhaupt, B. Rieger, R. M. Waymouth, *Angew. Chem.* **1995**, *107*, 1255 – 1283; *Angew. Chem. Int. Ed. Engl.* **1995**, *34*, 1143 – 1170.
[16] M. Catti, G. Valerio, R. Dovesi, M. Causà, *Phys. Rev. A* **1994**, *49*, 179 – 187.
[17] M. Catti, A. Pavese, R. Dovesi, V. R. Saunders, *Phys. Rev. B* **1993**, *47*, 9189 – 9198.
[18] Gaussian 03, Revision C.02, M. J. Frisch, et al.; see Supporting Information.

 © 2006 Wiley-VCH Verlag GmbH & Co. KGaA, Weinheim

Anion Transporters

DOI: 10.1002/anie.200504489

Regulating Supramolecular Function in Membranes: Calixarenes that Enable or Inhibit Transmembrane Cl^- Transport**

*Jennifer L. Seganish, Paul V. Santacroce, Kevan J. Salimian, James C. Fettinger, Peter Zavalij, and Jeffery T. Davis**

Self-assembly is an attractive strategy for building synthetic ion channels.[1] Solid-state structures, when combined with functional data, can provide clues about how self-assembly regulates transmembrane ion transport.[2,3] We show that modest changes in the primary structure of a calix[4]arene amide lead to dramatic differences in the transport of chloride ions across phospholipid membranes. Comparison of solid-state structures for partial-cone calix[4]arene (*paco*-H) **1** and its *para*-substituted analogue (*paco*-*t*Bu) **2**, suggested that

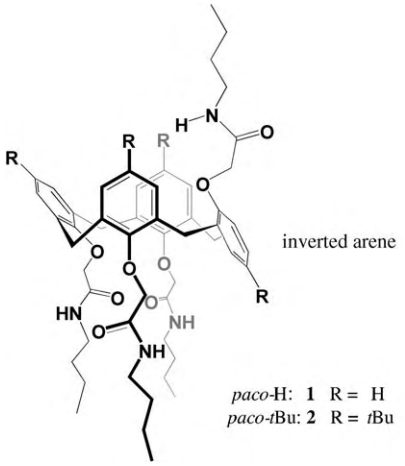

self-association and Cl^- ion transport activity might be controlled by the conformation of the side chain on the inverted arene of the partial cone. Using this structural information as a basis for probing function, we describe a novel regulatory system, wherein the inactive **2** inhibits transmembrane transport of Cl^- ions by *partial-cone* **1**. This last finding is timely, given the interest in regulating the activity of synthetic transporters using external stimuli such as light, temperature, voltage, or ligand-gating to turn ion transport on or off.[4]

Various "small molecules" transport Cl^- ions across phospholipid membranes. These compounds range from ion carriers such as prodigiosins and cholapods,[5,6] to sterols and peptides that self-assemble in the membrane.[7,8] Our contributions to the field have involved calix[4]arenes[9]—scaffolds previously used for synthetic cation channels.[10] We found that a 1,3-*alt*-calix[4]arene tetraamide and an acylic analogue could transport Cl^- ions across liposomal membranes.[11,12] Solid-state structures revealed that amide NH···Cl^- hydrogen bonds mediated self-assembly of the 1,3-*alt*-calix[4]arene tetraamide and voltage clamp experiments confirmed formation of stable ion channels in phospholipid and cell membranes.[11]

We now compare the structure and function of **1** and **2**, both prepared from conformationally fixed esters.[13] Proton NMR titrations showed that both calixarene tetraamides bind tetrabutylammonium chloride weakly in $CDCl_3$, with similar values ($K_a = 10–20\,M^{-1}$).[14,15] Although both compounds bind Cl^- ions in organic solution, only **1** transports Cl^- ions across phospholipid membranes. Figure 1 shows Cl^- transport activity in the presence of **1** or **2** in dipalmitoyl phosphatidylcholine (DPPC) liposomes at 43 °C. Liposomes (100 nm) containing 1 mM of the Cl^--sensitive dye, lucigenin,[16] and 100 mM $NaNO_3$ were suspended in a solution of 100 mM $NaNO_3$ and 10 mM sodium phosphate (pH 6.4). Calixarenes **1** or **2** were added to the liposome suspension to give a 2:100 calixarene:lipid ratio. Evidence for transmembrane transport of Cl^- ions was obtained from the quenching of lucigenin's fluorescence after NaCl was added to give an extravesicular

[*] J. L. Seganish, Dr. P. V. Santacroce, K. J. Salimian, Dr. J. C. Fettinger, Dr. P. Zavalij, Prof. J. T. Davis
Department of Chemistry and Biochemistry
University of Maryland
College Park, MD 20742 (USA)
Fax: (+1) 301-314-9121
E-mail: jdavis@umd.edu

[**] We thank the U.S. Department of Energy for financial support. K.J.S. thanks the University of Maryland's Rollinson Scholars program and HHMI program for fellowships. We thank Frank Kotch and Vladimir Sidorov for discussions, and Prof. Marco Colombini for a preprint of reference [23] before its publication.

Supporting information for this article is available on the WWW under http://www.angewandte.org or from the author.

InterScience
© 2006 Wiley-VCH Verlag GmbH & Co. KGaA, Weinheim

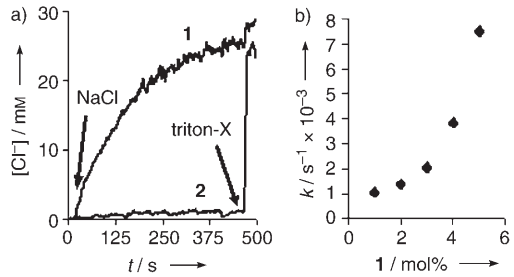

Figure 1. a) Chloride transport assay in DPPC liposomes in 100 mM $NaNO_3$ solution, 10 mM sodium phosphate (pH 6.4) at 43 °C in the presence of 2 mol% of **1** or **2**. A transmembrane Cl^- gradient was initiated by adding NaCl to the extravesicular buffer. The chloride concentration inside the vesicles was calculated from the fluorescence of the lucigenin dye. b) Concentration dependence of the transport of Cl^- ions by **1** in DPPC liposomes at 37 °C.

chloride concentration of 25 mM. Substituents on the calixarene's upper-rim clearly have an effect on the function (Figure 1a); **1** is a potent transporter of Cl^- ions, whereas **2** is inactive. Furthermore, in experiments done at 37 °C (where DPPC is in its gel phase) the rate of Cl^- transport by **1** was nonlinear with concentration, a result that is consistent with the formation of membrane-active aggregates $(\mathbf{1})_n$ (Figure 1b).[17] The difference in Cl^- transport activity for the calixarenes, and the evidence that **1** self-assembles in the DPPC membrane, prompted us to search for a structural basis that might help rationalize this mechanistic data.

Solid-state structures for **1** and **2** were determined from X-ray analysis of single crystals.[18,19] The conformation of the calixarene core was similar in both structures.[20] The most significant conformational difference for **1** and **2** was the orientation of the *n*-butylamide side chain connected to the inverted arene (Figure 2). For paco-H **1** the amide NH proton on this inverted arm forms an intramolecular H bond with its ether oxygen atom and is buried in a pocket formed by two flanking arenes. In this conformation, the amide NH proton on the inverted arene of **1** is unavailable for intermolecular interactions. In contrast, the inverted amide side chain in **2** is rotated 90° relative to the conformation in **1**. Presumably, the *tert*-butyl substituents on the flanking arenes block folding of the amide group into the macrocycle's pocket. Such a conformation ensures that this NH proton in **2** is available for intermolecular interactions, a feature that we think helps regulate the function of **1** (see below).

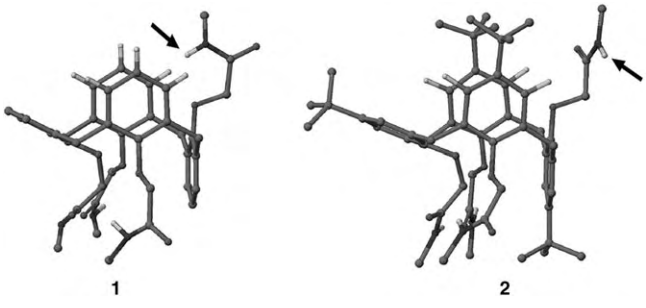

Figure 2. The conformation of the butylamide side chain on the inverted arene is different in solid-state structures of **1** (left) and **2** (right). In **1** the NH proton is buried in a pocket formed by neighboring arenes. In **2** this side chain is rotated 90°, thus making the amide NH proton accessible for intermolecular interactions. The *n*-butyl side chains in **1** and **2** are removed for clarity.

The solid-state conformations for **1** and **2** are retained in solution, as judged by ^{1}H NMR spectroscopic studies (Figure 3). For **1** the shielding environment of the arene pocket caused a significant upfield shift ($\delta = 5.97$ ppm in $CDCl_3$) for the inverted amide NH proton. We also observed a diagnostic NOE interaction between this NH proton and the *ortho* protons on the flanking arenes. The chemical shift for this inverted amide NH proton in **1** was also relatively insensitive to temperature, concentration, and the addition of Cl^- ions, all consistent with the presence of a buried NH proton in solution. In contrast, the chemical shift for the inverted amide NH proton in **2** was shifted relatively far downfield ($\delta = 7.65$ ppm), and had no NOE interactions between the NH group and the arene protons, both consistent with the amide NH group on the inverted arene being exposed to the solvent.

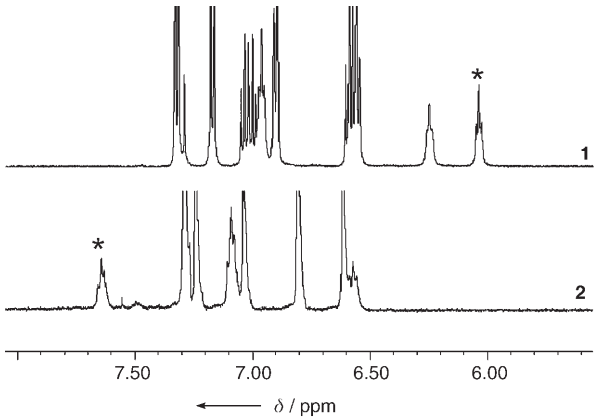

Figure 3. ^{1}H NMR data for **1** and **2**. The signal for the amide NH proton on the inverted arene is marked by an asterisk. Note the upfield shift for this NH proton in **1**, which is consistent with the solid-state conformation shown in Figure 2a, where this NH proton is located within the electron-rich arene pocket.

The conformation of the inverted arene's side chain contributes to different crystal packing for **1** and **2**. As depicted in Figure 4, paco-H **1** forms an extended, parallel-oriented chain of hydrogen bonds by having the downward-pointing amide groups of one molecule interact with the downward-pointing amide groups on neighboring molecules. Since it is buried in the calixarene's cavity, the amide group of the inverted arene is not involved in any intermolecular hydrogen bonding in this self-association of **1**. In marked contrast, the exposed amide group on the inverted arene of **2** forms intermolecular hydrogen bonds with the downward pointing amide groups of adjacent molecules to give an antiparallel, centrosymmetric, "up-down" arrangement of calixarenes in the solid state. This packing of **2** gives chains that are more staggered than the chains observed for **1** (Figure 4). The major point here is that **2** self-associates much differently than does **1**, presumably because the amide NH proton on its inverted arene forms intermolecular hydrogen

 © 2006 Wiley-VCH Verlag GmbH & Co. KGaA, Weinheim

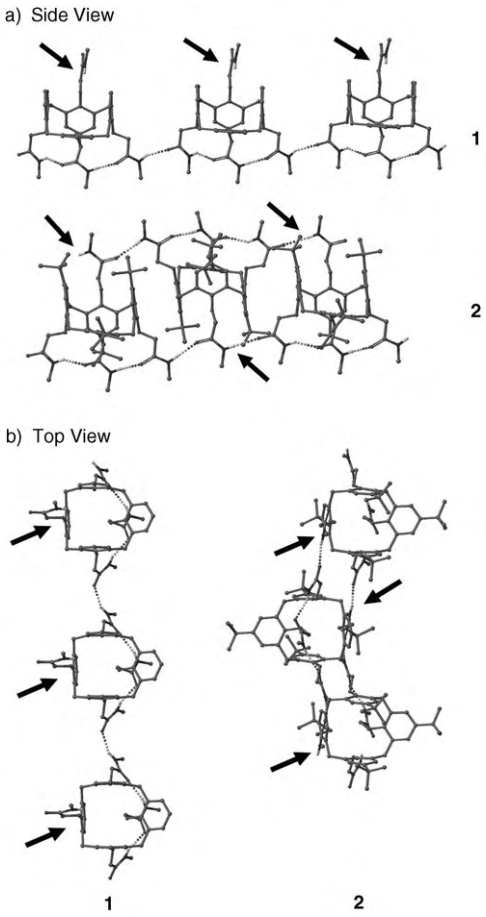

Figure 4. Depiction of the solid-state packing in the crystal structures of **1** and **2** Individual calixarene units in $(\mathbf{1})_n$ are connected by intermolecular hydrogen bonds between the three downward-pointing *n*-butylamide chains of the calixarene. The buried amide NH proton on the inverted arene does not perturb the packing of $(\mathbf{1})_n$. In the self-association of **2**, the amide group on the inverted arene participates in intermolecular interactions with the downward-pointing *n*-butylamide chains of neighboring molecules, thus resulting in a staggered, antiparallel, up-down arrangement of individual calixarenes within the hydrogen-bonded chains of $(\mathbf{2})_n$. Arrows point to the NH amide proton on the inverted arene of **1** or **2**.

bonds. In addition, the *tert*-butyl groups also likely influence the packing geometry for $(\mathbf{2})_n$. The assembly depicted in Figure 4 for $(\mathbf{1})_n$, with its hydrogen-bonded chain, suggests a plausible mechanism for transmembrane transport of Cl^- ions; a solvent-exposed amide NH proton could hydrogen bond to a Cl^- ion at the water–lipid interface and, upon rotation of the side chain, the Cl^- ion could be passed to the next NH group in the chain.

Whether the solid-state structures for **1** and **2** are related to 1) membrane-active structures or to 2) Cl^- transport activity remain open questions. The solid-state structures provided, however, a logical basis for experiments aimed at regulating anion transport using these calixarenes. Since the amide NH proton on the inverted arene of **2** is available for intermolecular interactions, we hypothesized that combining inactive **2** with active **1** might form heteroaggregates $\mathbf{1}_n{\cdot}\mathbf{2}_m$ in the membrane. We also reasoned that such $\mathbf{1}_n{\cdot}\mathbf{2}_m$ heteroaggregates might have attenuated Cl^- transport activity (either enhanced or diminished) relative to any self-assembled structures $\mathbf{1}_n$.[21] In contrast, if **1** functions by a carrier mechanism then one would not expect addition of an inactive analogue such as **2** to influence the transport rate of Cl^- ions. In the experiments, the concentration of active **1** was fixed at a 2:100 ligand-to-DPPC lipid ratio and the concentration of **2** was varied from a 0:100 to a 6:100 ligand:lipid ratio. The anion gradient assay, in which lucigenin was used as an intravesicular sensor,[16] was again used to monitor transmembrane transport of Cl^- ions. As shown in Figure 5, a plot

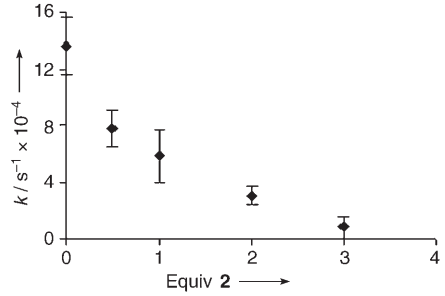

Figure 5. Inhibition of Cl^- transport by the inactive analogue **2**. Pseudo-first-order rate constants for Cl^- transport by **1** (2 mol% to lipid) are plotted against the concentration of **2** (0–6 mol% to lipid). Lucigenin was used in the assays to measure intravesicular [Cl^-] in DPPC liposomes (37°C) suspended in 100 mM $NaNO_3$ and 10 mM sodium phosphate (pH 6.4). A Cl^- gradient was initiated by adding NaCl to give an external concentration of 25 mM.

of pseudo-first-order rate constants versus concentration of **2** shows dose-dependent inhibition of the transport of Cl^- ions. One explanation for this data is that inactive **2** partitions into the membrane in preference to **1**. Another explanation, which we favor, is that **2** and **1** form inactive heteroaggregates $\mathbf{1}_n{\cdot}\mathbf{2}_m$ in the membrane, thus shifting the equilibrium away from active $\mathbf{1}_n$ structures.[22] This type of inhibition within a membrane favors a channel or hopping transport mechanism (versus a carrier mechanism) and it has recent precedent in that self-assembled ceramide ion channels in both liposomes and mitochondria are inhibited by addition of inactive dihydroceramide.[23,24]

Further development of anion transporters, based on results from these inhibition studies, could lead to a "switch" for regulating function if self-assembly could be triggered by reversibly controlling the conformation of compounds such as **1** and **2**. Additionally, our data suggests that the inverted amide side chain is not necessary for transport function in **1**. Thus, this side chain could be used as a connection to make dimeric or oligomeric calixarenes, compounds that may show enhanced transmembrane Cl^- transport activity, especially if a channel mechanism is operative. Such synthetic iterations, based on the structure–function relationships revealed herein, are currently being pursued.

Experimental Section

Preparation of DPPC liposomes: DPPC lipid (50 mg, Avanti) was dissolved in a chloroform/methanol mixture (5% MeOH, 5 mL). The

 © 2006 Wiley-VCH Verlag GmbH & Co. KGaA, Weinheim

resulting solution was evaporated under reduced pressure at 45 °C to produce a thin film that was dried in vacuo for 2 h. The lipid film was hydrated with a solution (1 mL) of 10 mM sodium phosphate (pH 6.4) containing 100 mM $NaNO_3$ and 1 mM lucigenin. After 5 freeze/thaw cycles (thawing and then warming to 45 °C) the liposomes were extruded through a 100-nm polycarbonate membrane 21 times between 45–55 °C. The liposome solution was passed through a sephadex (G-25) column to remove excess dye. The isolated liposomes were diluted in 10 mM sodium phosphate (pH 6.4, 100 mM $NaNO_3$) to give a concentration of 11 mM in DPPC, assuming 100% retention of lipid during the gel filtration process.

Chloride transport assay: In a typical experiment, the stock DPPC liposomes (0.1 mL) were diluted into 10 mM sodium phosphate (2 mL, pH 6.4, 100 mM $NaNO_3$) to give a solution that was 0.5 mM in lipid. A solution of calixarene **1** or **2** in DMSO was added to this solution to give a 2:100 ligand:lipid ratio. The sample was incubated for 10 minutes at either 43 °C or 37 °C. 4.0 M NaCl (20 μL) was added to the cuvette containing the DPPC/calixarene mixture through an injection port to give a final extravesicular Cl^- concentration of 25 mM. The fluorescence of the intravesicular lucigenin was monitored at an excitation wavelength of 372 nm and emission wavelength of 504 nm for 500 s. After 470 s, 10% triton-X detergent (0.04 mL) was added to destroy the liposomes and to determine the maximal fluorescence quenching of lucigenin by Cl^- ions. Experiments at two different temperatures (37 °C and 43 °C) were done in triplicate. Lucigenin fluorescence was converted into chloride concentration by using the Stern–Volmer constant determined under the assay conditions. To measure the Stern–Volmer constant, liposomes prepared as above were lysed immediately with triton-X. 4.0 M NaCl (5 μL) was titrated in every 30 s through the injection port. The slope of a plot of f_0/f versus chloride concentration gave the Stern–Volmer constant for lucigenin.

Received: December 17, 2005
Published online: April 11, 2006

Keywords: calixarenes · ion channels · ion transport · self-assembly · supramolecular chemistry

[1] For reviews of synthetic ion channels, see: S. Matile, A. Som, N. Sorde, *Tetrahedron* **2004**, *60*, 6405; U. Koert, L. Al-Momani, J. R. Pfeeifer, *Synthesis* **2004**, 1129.

[2] Crystal structures provided insight into the function of the K^+ ion channel: R. MacKinnon, *Angew. Chem.* **2004**, *116*, 4363; *Angew. Chem. Int. Ed.* **2004**, *43*, 4264.

[3] Solid-state structures also helped rationalize the function of a synthetic ion channel: J. D. Hartgerink, J. R. Granja, R. A. Milligan, M. R. Ghadiri, *J. Am. Chem. Soc.* **1996**, *118*, 43.

[4] Examples of stimuli-responsive transmembrane transporters: T. M. Fyles, D. Lock, X. Zhou, *J. Am. Chem. Soc.* **1998**, *120*, 2997; C. Goto, M. Yamamura, A. Satake, Y. Kobuke, *J. Am. Chem. Soc.* **2001**, *123*, 12152; V. Gorteau, F. Perret, G. Bollot, J. Mareda, A. N. Lazar, A. W. Coleman, D.-H. Tran, N. Sakai, S. Matile, *J. Am. Chem. Soc.* **2004**, *126*, 13592; W. H. Chen, S. L. Regen, *J. Am. Chem. Soc.* **2005**, *127*, 6538.

[5] P. A. Gale, M. E. Light, B. McNally, K. Navakhum, K. I. Sliwinski, B. D. Smith, *Chem. Commun.* **2005**, 3773; J. L. Sessler, L. R. Eller, W.-S. Cho, S. Nicolaou, A. Aguilar, J. T. Lee, V. M. Lynch, D.J Magda, *Angew. Chem.* **2005**, *117*, 6143; *Angew. Chem. Int. Ed.* **2005**, *44*, 5989; J. L. Seganish; J. T. Davis, *Chem. Commun.* **2005**, 5781.

[6] A. V. Koulov, T. N. Lambert, R. Shukla, M. Jain, J. M. Bood, B. D. Smith, H. Y. Li, D. N. Sheppard, J. B. Joos, J. P. Clare, A. P. Davis, *Angew. Chem.* **2003**, *115*, 5081; *Angew. Chem. Int. Ed.* **2003**, *42*, 4931.

[7] S. Otto, M. Osifchin, S. L. Regen, *J. Am. Chem. Soc.* **1999**, *121*, 7276.

[8] P. H. Schlesinger, R. Ferdani, J. Liu, J. Pajewska, R. Pajewki, M. Saito, H. Shabany, G. W. Gokel, *J. Am. Chem. Soc.* **2002**, *124*, 1848.

[9] For a lead to the extensive calixarene literature, see: V. Böhmer, *Angew. Chem.* **1995**, *107*, 785; *Angew. Chem. Int. Ed. Engl.* **1995**, *34*, 713.

[10] Transmembrane cation transporters from calix[4]arenes or resorcin[4]arenes: Y. Tanaka, Y. Kobuke, M. Sokabe, *Angew. Chem.* **1995**, *107*, 717; *Angew. Chem. Int. Ed. Engl.* **1995**, *34*, 693; J. de Mendoza, F. Cuevas, P. Prados, E. S. Meadows, G. W. Gokel, *Angew. Chem.* **1998**, *110*, 1650; *Angew. Chem. Int. Ed.* **1998**, *37*, 1534; N. Yoshino, A. Satake, Y. Kobuke, *Angew. Chem.* **2001**, *113*, 471; *Angew. Chem. Int. Ed.* **2001**, *40*, 457; A. J. Wright, S. E. Matthews, W. Fischer, P. D. Beer, *Chem. Eur. J.* **2001**, *7*, 3474; M. Mauleucci, F. De Riccardis, B. Botta, A. Casapullo, E. Cressina, E. Fregonese, P. Tecilla, I. Izzo, *Chem. Commun.* **2005**, 1354.

[11] V. Sidorov, F. W. Kotch, G. Abdrakhmanova, R. Mizani, J. C. Fettinger, J. T. Davis, *J. Am. Chem. Soc.* **2002**, *124*, 2267.

[12] V. Sidorov, F. W. Kotch, Y. Lam, J. L. Kuebler, J. T. Davis, *J. Am. Chem. Soc.* **2003**, *125*, 2840.

[13] K. Iwamoto, S. Shinkai, *J. Org. Chem.* **1992**, *57*, 7066.

[14] For reviews on calixarene–anion receptors, see: P. Lhotak, *Top. Curr. Chem.* **2005**, *255*, 65; S. E. Matthews, P. D. Beer, *Supramol. Chem.* **2005**, *17*, 411; P. D. Beer, P. A. Gale, *Angew. Chem.* **2001**, *113*, 502; *Angew. Chem. Int. Ed.* **2001**, *40*, 486.

[15] See the Supporting Information for the NMR titration data. These K_a values (**1**, 28.7 ± 17 and **2**, $31.7 \pm 6\ M^{-1}$) for Cl^- binding by secondary amides in **1** and **2** are consistent with values for *N*-methylacetamide binding tetrabutylammonium chloride (TBACl) in $CDCl_3$: F. Werner, H.-J. Schneider, *Helv. Chim. Acta* **2000**, *83*, 465.

[16] B. A. McNally, A. V. Koulov, B. D. Smith, J. B. Joos, A. P. Davis, *Chem. Commun.* **2005**, 1087.

[17] For examples where concentration dependence indicates membrane-active aggregates with ion-channel characteristics, see: T. M. Fyles, D. Loock, X. Zhou, *J. Am. Chem. Soc.* **1998**, *120*, 2997; A. F. DiGiorgio, S. Otto, P. Bandyopadhyay, S. L. Regen, *J. Am. Chem. Soc.* **2000**, *122*, 11029.

[18] Crystal data for **1** from acetonitrile: $C_{52}H_{68}N_4O_8 \cdot C_2H_3N$, $M_r = 918.16$, dimensions $0.38 \times 0.32 \times 0.13\ mm^3$, triclinic, space group $P\bar{1}$, $a = 12.9335(4)$, $b = 16.6625(5)$, $c = 25.6605(8)$ Å, $V = 5107.6(3)$ Å^3, $Z = 4$, $\rho_{calcd} = 1.1194\ mg\,m^{-3}$, $Mo_{K\alpha} = 0.080\ mm^{-1}$. Data were collected on a Bruker SMART 1000 CCD diffractometer at 173(2) K. The structure was refined to convergence [$\Delta/\sigma \leq 0.001$] with $R(F) = 5.55\%$, $wR(F^2) = 17.73\%$, GOF = 1.095 for all 18,493 reflections. CCDC-293015 contains the supplementary crystallographic data for this paper. These data can be obtained free of charge from The Cambridge Crystallographic Data Centre via www.ccdc.cam.ac.uk/data_request/cif.

[19] Data for **2** from acetone/CH_2Cl_2: $C_{68}H_{100}N_4O_8 \cdot 0.77\,CH_2Cl_2 \cdot C_3H_6O$, $M_r = 1180.27$, dimensions $0.05 \times 0.08 \times 0.380\ mm^3$, triclinic, space group $P\bar{1}$, $a = 13.798(3)$, $b = 14.308(3)$, $c = 18.487(4)$ Å, $V = 3438.1(12)$ Å^3, $Z = 2$, $\rho_{calcd} = 1.140\ mg\,m^{-3}$, $Mo_{K\alpha} = 0.131\ mm^{-1}$. Data collected were at 223(2) K. The structure was refined to convergence [$\Delta/\sigma \leq 0.001$] with $R(F) = 5.93\%$, $wR(F^2) = 13.43\%$, GOF = 1.034 for all 9876 unique reflections. CCDC-293016 contains the supplementary crystallographic data for this paper. These data can be obtained free of charge from The Cambridge Crystallographic Data Centre via www.ccdc.cam.ac.uk/data_request/cif.

[20] *para* Substitution typically has a minor influence on calix conformation: C. D. Gutsche, L. J. Bauer, *J. Am. Chem. Soc.* **1985**, *107*, 6052; P. D. J. Grootenhuis, P. A. Kollman, L. C.

 © 2006 Wiley-VCH Verlag GmbH & Co. KGaA, Weinheim

Groenen, D. N. Reinhoudt, G. J. van Hummel, F. Ugozzoli, G. D. Andreeti, *J. Am. Chem. Soc.* **1990**, *112*, 4165.
[21] Recently, it was shown that oppositely charged calixarenes combine within a lipid layer to form protein sensors that are more sensitive than either of the individual components: R. Zadmard, T. Schrader, *J. Am. Chem. Soc.* **2005**, *127*, 904.
[22] Solution NMR studies shows that **1** and **2** (both 1 mM) interact in CD_2Cl_2, as judged by changes in the chemical shift of the NH proton.
[23] J. Stiban, D. Fistere, M. Colombini, *Apoptosis* **2006**, in press.
[24] This type of inhibition is also similar to that for HIV-1 protease, wherein an inactive subunit when combined with a native subunit gave inactive heterodimers: J. E. Rozzelle, D. S. Dauber, S. Todd, R. Kelley, C. S. Craik, *J. Biol. Chem.* **2000**, *275*, 7080.

 © 2006 Wiley-VCH Verlag GmbH & Co. KGaA, Weinheim

DNA Sensing

DOI: 10.1002/anie.200502151

Feature Multiplexing—Improving the Efficiency of Microarray Devices**

*Matthew J. Schmid, Kalpana Manthiram, Scott M. Grayson, James C. Willson, Jason E. Meiring, Kathryn M. Bell, Andrew D. Ellington, and C. Grant Willson**

Since the genomic sequencing of more than 100 organisms first began, an almost overwhelming compendium of genetic and proteomic targets has been identified. Researchers are now beset with the task of characterizing these targets, as well as identifying and characterizing their extant natural variants. Combinatorial analytical techniques, such as microarray analysis, have emerged as the preferred tools for performing these characterizations and have enabled the recent commercialization of DNA[1–4] and proteomic[5] sensor arrays. A common attribute shared by all of these devices is the convention of distributing each sensor probe onto an exclusive array feature. This methodology imposes the requirement that the arrays possess a number of features equal to the number of probes, thus requiring array designers to investigate miniaturization to enable higher-density array construction.[6,7] However, decreasing the feature size correspondingly reduces the number of sensing molecules per feature, and the reduction of feature size and spacing is fundamentally limited by the array technology (namely, optimized feature spacing is at present on the order of hundreds of microns).

A novel platform-independent probe-loading methodology has been developed that circumvents the need for the continual shrinkage of sensor features. This methodology increases the information density of the array not by miniaturizing the features in the array, but rather by changing the way probes are distributed within the array (see Figure 1).

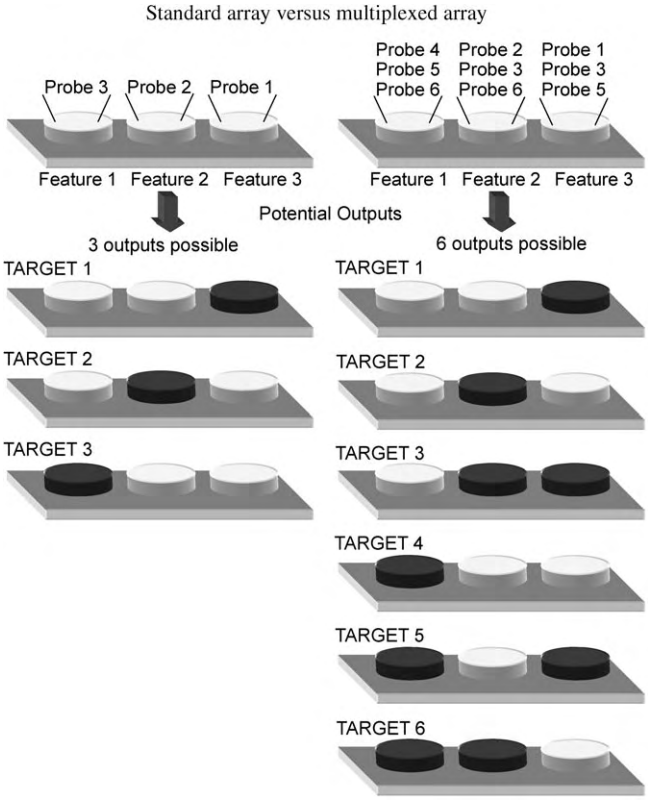

Figure 1. Three-feature standard arrays (with one probe per feature) can only detect three targets, whereas multiplexed arrays can detect six target sequences.

This technique, called feature multiplexing, achieves increases in density by incorporating multiple probes into each feature using a unique encoding system (see Figure 1). The use of this methodology allows a given number of features (n) to be used to deploy a much greater quantity of probes (up to 2^n-2) when sensing for a single analyte. This methodology can dramatically increase the capacity or information density of an array because there is this exponential relationship between the number of array

[*] Dr. M. J. Schmid, K. Manthiram, Dr. S. M. Grayson, Dr. J. E. Meiring, Prof. C. G. Willson
Department of Chemical Engineering
The University of Texas at Austin
Austin, TX 78712 (USA)
Fax: (+1) 512-471-7222
E-mail: willson@che.utexas.edu
J. C. Willson, K. M. Bell, Prof. A. D. Ellington, Prof. C. G. Willson
Department of Chemistry and Biochemistry
The University of Texas at Austin
Austin, TX 787412 (USA)

[**] We acknowledge Benjamen Rathsack and David Johnson for their involvement in developing the shape-indexed MUFFINS platform. We also thank the Welch Foundation, MURI, The Department of Army Research (project DAAD19-99-1-0207), and The Beckman Foundation (project 26-7506-95) for financial support, as well as the NSF/IGERT program (Cellular and Molecular Imaging for Diagnostics and Therapeutics) for academic support (M.J.S.).

Supporting information for this article is available on the WWW under http://www.angewandte.org or from the author.

InterScience
© 2006 Wiley-VCH Verlag GmbH & Co. KGaA, Weinheim

features and the number of probes that the array can accommodate. A demonstration of feature multiplexing in array-based diagnostics is presented herein.

To illustrate the principle of feature multiplexing, a small single-nucleotide-polymorphism (SNP) detection array was constructed and its performance verified in three separate detection assays.[8] Due to the clinical importance of the p53 gene, the array was designed to screen for the presence of 29 potential cancer-causing missense SNPs within a short test section of that gene.[9] The array contained a total of 31 different single-stranded oligonucleotide probes: 29 test probes complementary to the SNPs for which the array had been designed and two reference probes complementary to the different nonoverlapping halves of the "wild-type" (or reference) p53 gene sequence. These 29 test probes were distributed into just five array features by using feature multiplexing, thus constituting an approximate sixfold increase in information density. The reference probes served as controls in our assays; their function and their placement within the array will be discussed in more detail later.

As for all SNP detection arrays, the probe design of a feature-multiplexed array has an enormous impact on the signal-to-noise characteristics of the array. An ideal probe should form a stable double helix with its complement, and only its complement under the hybridization conditions of the detection assay. Thus, a probe set was designed such that a single base-pair mismatch would be sufficient to disrupt duplex formation. Likewise, all of the probes should produce a signal of uniform intensity in response to the detection of their complement. To that end, the probes in this array were carefully designed by a custom software program to all have nearly the same melting temperature ($T_m = 30.8\,°C$, $\sigma = 1.0\,°C$), and hence the same duplex stability under the optimized hybridization conditions (Table 1).

To distinguish the output of one probe from that of another, each probe is indexed by assignation of a unique distribution pattern within the multiplexed features. Although there were many ways of choosing the distribution patterns for these probes, the following procedure was developed for ease of encoding and decoding. All the probes were assigned a number (1–29), and that number was converted into its five-bit binary expression (e.g., probe 21 = 10101). The pattern of "1"s in the five-bit binary expression was used to determine the placement of each probe into a set of multiplexed features (Table 2). For example, probe 21 (or "10101") was placed in features 1, 3, and 5. Likewise, the signal response can be readily interpreted, as each positive response represents a "1" and each

Table 1: Probe sequences used in the detection assays and their positions relative to the reference p53 gene sequence.[a, b]

Probe	Probe sequence[b]	T_m [°C]
1	GTG**A**GTGTTTG	28.7
2	GGTG**G**GTGTT	31.0
3	GTG**T**GTGTTTG	29.9
4	GTGC**A**TGTTTG	30.6
5	GGTGC**C**TGTT	31.9
6	GTGC**T**TGTTTG	30.5
7	GGTGCGT**A**TTT	31.4
8	TGCGT**C**TTTG	29.0
9	TGCGT**T**TTTGT	31.9
10	TGCGTG**A**TTG	29.2
11	CGTG**G**TTGTG	30.6
12	CGTG**C**TTGTG	31.5
13	TGTT**A**GTGCCT	31.4
14	CGTGTT**G**GTG	30.6
15	CGTGTT**C**GTG	31.2
16	CGTGTTT**A**TGC	29.9
17	TGTTT**C**TGCCT	32.5
18	GTGTTT**T**TGCC	30.9
19	TGTTTG**A**GCCT	32.5
20	GTTTG**G**GCCT	31.7
21	TGT**A**CCTGTCC	31.8
22	TGTTTGT**C**CCT	31.6
23	TTGT**T**CCTGTC	29.6
24	TTGTG**A**CTGTC	29.8
25	TTGTG**G**CTGTC	30.2
26	TTGTG**T**CTGTC	29.8
27	TGTGCC**A**GTC	31.5
28	GTGCC**G**GTC	31.2
29	GTGCC**C**GTC	31.2
Ref 1	GTGCGTGTTT	30.3
Ref 2	GTGCCTGTCC	33.2

[a] The 5′-methacrylamide modifications on the probes are not shown; mutant bases are printed in bold. [b] p53 reference gene sequence: 5′-TGAGGTGCGTGTTTGTGCCTGTCCTGG-3′

Table 2: Binary loading patterns for each of the probes used in the array.

Probe		Feature type/shape[a]							
	ID	Sq	Cir	Ch	H	Tra	X[b]	P[b]	T[c]
1	00001					X			
2	00010				X				
3	00011				X	X			
4	00100			X					
5	00101			X		X			
6	00110			X	X				
7	00111			X	X	X			
8	01000		X						
9	01001		X			X			
10	01010		X		X				
11	01011		X		X	X			
12	01100		X	X					
13	01101		X	X		X			
14	01110		X	X	X				
15	01111		X	X	X	X			
16	10000	X							
17	10001	X				X			
18	10010	X			X				
19	10011	X			X	X			
20	10100	X		X					
21	10101	X		X		X			
22	10110	X		X	X				
23	10111	X		X	X	X			
24	11000	X	X						
25	11001	X	X			X			
26	11010	X	X		X				
27	11011	X	X		X	X			
28	11100	X	X	X					
29	11101	X	X	X		X			
Ref 1	N.A.						X		
Ref 2	N.A.							X	

[a] Legend: Sq = square, Cir = circle, Ch = chevron, H = hexagon, Tra = trapezoid, X = cross, P = pentagon, T = triangle. [b] Reference feature. [c] Control feature. N.A. = not applicable.

 © 2006 Wiley-VCH Verlag GmbH & Co. KGaA, Weinheim

negative a "0" in the binary expression of the probe that detected its complement (see Figure 2).

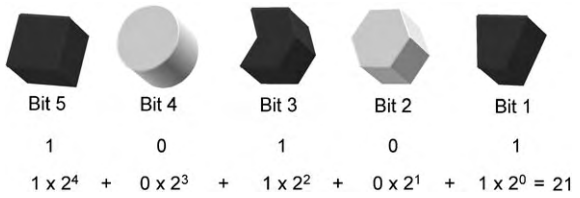

Figure 2. Each multiplexed feature is uniquely shaped and corresponds to a bit in a binary expression. The binary expression (fluorescence = "1" and non-fluorescence = "0") is converted into a number, which identifies the probe that has detected its complement (in this case, probe 21).

In addition to the five multiplexed features, our array also contained three control features that were not multiplexed, the two reference probes, and a control containing no DNA. Because each reference probe was complementary to a different half of the test sequence, their output could be used to determine which portion contained a mutation (see Figure 3), and therefore could corroborate the output of the multiplexed features.

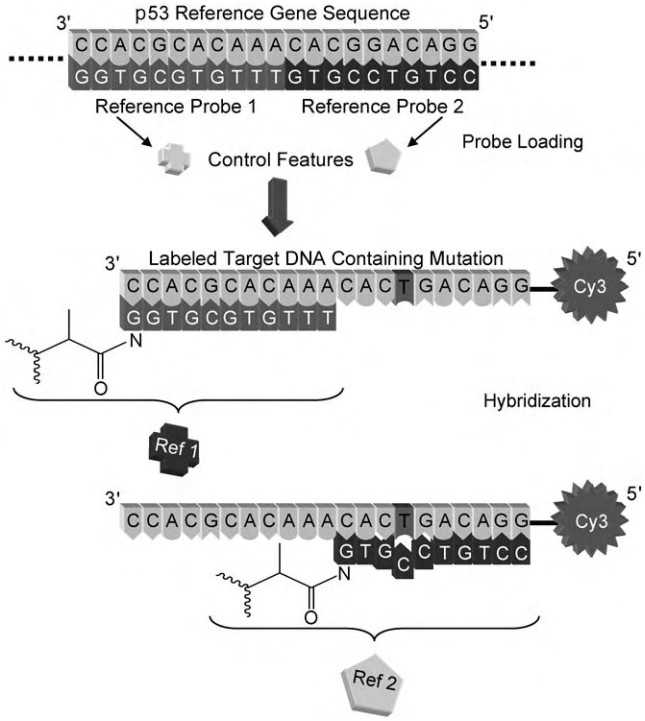

Figure 3. The output from the two reference features verifies which subsection of the target contains a mutation.

The feature multiplexing methodology can be used in a multitude of array platforms, including traditional Cartesian-indexed arrays. However, this demonstration was performed by using a randomly ordered/shape-indexed approach called the MUFFINS (Mesoscale Unaddressed Functionalized Features INdexed by Shape) platform[10] because it offers the opportunity to readily incorporate multiple probes in a single feature. The shape-encoded features were constructed by contact lithography using a photopolymerizable liquid hydrogel prepolymer containing poly(ethylene glycol) diacrylate (PEG-da), water, probe DNA, and trace amounts of a photoinitiator. To covalently attach the probe sequences to the hydrogel matrix, each of the probes used in this demonstration contained a polymerizable 5′-acrydite modification.[10] Each batch of features was uniquely shaped, so as to provide a means of rapidly identifying the function of each feature within the randomly ordered array. The features can be immobilized onto a support matrix, but for this demonstration the array features were in their loose form.

The detection assays were conducted by placing a set of array features (the five multiplexed features and the three control features) in a buffer solution containing fluorescently labeled target DNA. The three assays consisted of two sequences which contained a single base mutation and a third sequence without a mutation, identical to the reference sequence (Table 3). After the features had hybridized with the target analytes, they were rinsed and imaged on a fluorescence microscope. Bright-field and fluorescence micrographs of the arrays are presented in Figure 4. In all cases, the decoded output of each of the detection assays agreed with the known identity of the target sequence.

Table 3: Target sequences used in the detection assay.

Target	Sequence[a]
p53 "wild type"	3′-CCACGCACAAACACGGACAGG-5′-Cy3
Probe 7	3′-CCACGCA**T**AAACACGGACAGG-5′-Cy3
Probe 21	3′-CCACGCACAAACA**T**GGACAGG-5′-Cy3

[a] Mutant bases are printed in bold.

Array designers have focused on decreasing the physical size of the individual sensing features to meet the need for increased information density. Arrays can hold twice as many probes, a linear improvement, by halving the area of each of the features. On the other hand, multiplexing enables exponential increases in information density when sensing a single analyte simply by distributing multiple probes in each feature (see Figure 5). The above proof-of-concept study has demonstrated that this method is capable of yielding a sixfold increase in density with only five multiplexed features. Higher compressions are possible, but require an increase in the number of probes that must be placed at each feature. Feature multiplexing is a very versatile technique, applicable to a variety of sensing chemistries and platforms in which one is attempting to identify a single unknown substance. Virtually any microarray device in which multiple probes can be placed in a single feature can benefit from this technique, thus decreasing the need for further miniaturization and improving the time and cost efficiency of their manufacture.

Received: June 20, 2005
Published online: April 11, 2006

 © 2006 Wiley-VCH Verlag GmbH & Co. KGaA, Weinheim

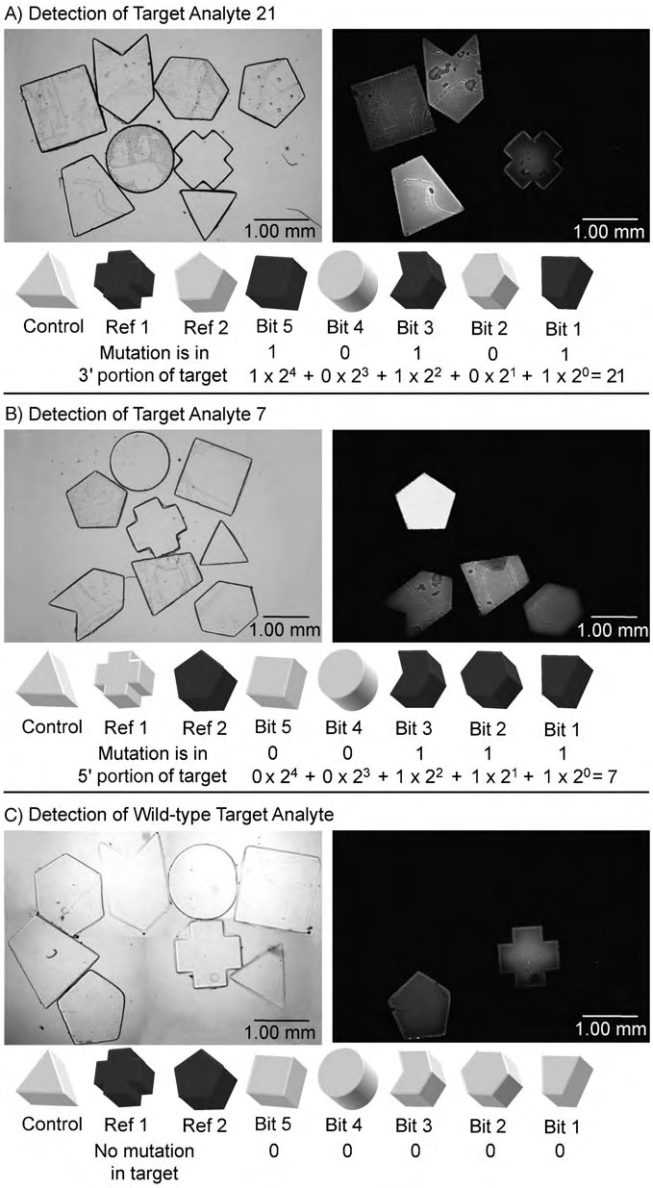

Figure 4. Bright field (left) and fluorescence (right) micrographs of the sensor response during the three detection assays. Below each set of micrographs is a schematic representation that illustrates the decoding process.

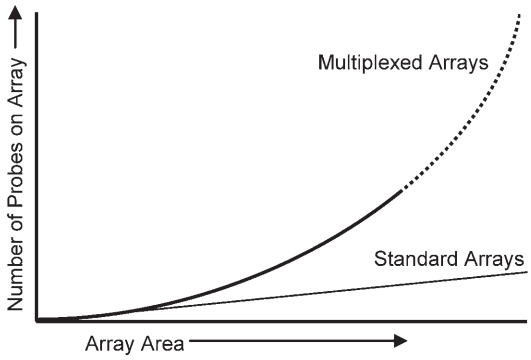

Figure 5. The graph of two trend lines which illustrate the linear improvements gained by decreasing the size of the features relative to the exponential improvements that result from feature multiplexing.

Keywords: DNA · hydrogels · multiplexing · sensors

[1] A. C. Pease, D. Solis, E. J. Sullivan, M. T. Cronin, C. P. Holmes, S. A. Fodor, *Proc. Natl. Acad. Sci. USA* **1994**, *91*, 5022.
[2] M. J. O'Donnell-Maloney, D. P. Little, *Genet. Anal. Tech. Appl.* **1996**, *13*, 151.
[3] F. J. Steemers, J. A. Ferguson, D. R. Walt, *Nat. Biotechnol.* **2000**, *18*, 91.
[4] R. G. Sosnowski, E. Tu, W. F. Butler, J. P. O'Connell, M. J. Heller, *Proc. Natl. Acad. Sci. USA* **1997**, *94*, 1119.
[5] H. Zhu, M. Bilgin, R. Bangham, D. Hall, A. Casamayor, P. Bertone, N. Lan, R. Jansen, S. Bidlingmaier, T. Houfek, T. Mitchell, P. Miller, R. A. Dean, M. Gerstein, M. Snyder, *Science* **2001**, *293*, 2101.
[6] M. O. Reese, R. M. van Dam, A. Scherer, S. R. Quake, *Genome Res.* **2003**, *13*, 2348.
[7] R. J. Lipshutz, S. P. A. Fodor, T. R. Gingeras, D. J. Lockhart, *Nat. Genet.* **1999**, *21*, 20.
[8] Full experimental details are available in the Supporting Information.
[9] Y. Cho, S. Gorina, P. D. Jeffery, N. P. Pavletich, *Science* **1994**, *265*, 346.
[10] J. E. Meiring, M. J. Schmid, S. M. Grayson, B. M. Rathsack, D. M. Johnson, R. Kirby, R. Kannappan, K. Manthiram, B. Hsia, Z. L. Hogan, A. D. Ellington, M. V. Pishko, C. G. Willson, *Chem. Mater.* **2004**, *16*, 5574.

 © 2006 Wiley-VCH Verlag GmbH & Co. KGaA, Weinheim

Molecular Transport

DOI: 10.1002/anie.200504579

Surfactant-Modulated Switching of Molecular Transport in Nanometer-Sized Pores of Membrane Gates

*Riaan Schmuhl, Albert van den Berg, Dave H. A. Blank, and Johan E. ten Elshof**

Molecular and ionic gates through which species can be transported at will under the influence of externally tunable parameters have received considerable attention recently.[1–7] In view of their relevance for application in microfluidic devices, these components are becoming an established

[*] Dr. R. Schmuhl, Prof. D. H. A. Blank, Dr. J. E. ten Elshof
Inorganic Materials Science
MESA+ Institute for Nanotechnology
University of Twente
7500 AE, Enschede (The Netherlands)
Fax: (+31) 53-489-4683
E-mail: j.e.tenelshof@utwente.nl
Prof. A. van den Berg
Laboratory of Biosensors
MESA+ Institute for Nanotechnology
University of Twente
7500 AE, Enschede (The Netherlands)

Supporting information for this article is available on the WWW under http://www.angewandte.org or from the author.

© 2006 Wiley-VCH Verlag GmbH & Co. KGaA, Weinheim

technology in analytical chemistry and biotechnology.[8,9] They may enable new ways of molecular separation, dosing, and analysis.[1–7] The channels or pores of the gate typically have diameters of ≈20 nm or less in order to function properly. The operating principle is based on the presence of 1) a driving force for species transport, usually a concentration or electrical potential gradient over the gate, and 2) an externally controllable switch with which the gate can be opened or closed, or the selectivity of the gate modified.

Martin and co-workers were the first to show the concept of influencing the ion permselectivity of nanoporous nuclear-track-etched polymeric membranes by imposing an electrical bias potential (relative to the feed solution) on the gold-coated inner pore surface of the membrane.[2] We and others demonstrated that the selectivity of a membrane toward anions or cations can also be controlled by adjusting the ionic strength and pH of the system, which results in the electrostatic opening and closing of membrane pores.[1–9] Alternatively, Sweedler, Bohn, and co-workers developed a gateable interconnect for analyte injection in microfluidic devices,[1,4] where transport is driven by electroosmotic flow and the selectivity is determined by the double-layer properties inside the pore. It has also been shown that modification of the membrane surface properties by self-assembled monolayers of amino- or carboxy-functional molecules imparts to the membrane a high dependency of the ionic permeability on the pH value.[10–12]

In a number of recent studies, the transport behavior of ionic species in nanometer-sized pores has been modeled to gain a better understanding of the influence of the double layer and surface charge density on the ion-transport properties.[13–15] However, the control of ionic strength and surface charge to manipulate the permeability of a membrane is limited to dilute conditions under which double-layer overlap inside the channel/pore occurs, that is, at relatively low ionic strengths, when charge exclusion is sufficient to reject ions.[5–7] A much more universal method of tuning the permeability of molecular gates would be the controlled steric blocking of permeating species. By physically blocking or unblocking the channels of a gate, an open/closed system can be created. This concept could also be useful, for instance, when species are present whose structure and function depend on ionic strength and pH, such as enzymes.

We illustrate the concept with a tunable membrane gate, the working principle of which is essentially based on the co-addition of surfactant molecules to a system of ionic probes that are transported through a membrane under the influence of an electrical potential gradient. As a result of their size and ability to adsorb reversibly inside channels and pores, these surfactants can be used to physically open or close nanometer-sized channels and pores of molecular gates by varying their concentration. Thus, the flux of ionic or molecular species can be controlled by an independent, externally tunable variable, without having to manipulate the probe concentration in the feed or the driving force for transport.

A four-region adsorption model has been proposed to explain the adsorption of surfactants at charged interfaces depending on concentration.[16] Adsorption can occur either directly on an oppositely charged interface or through oppositely charged counterions.[17] At an increasing concentration, the adsorption characteristics range from isolated monomers through local aggregates to complete monolayers, bilayers, and ultimately to hemicelles (see Figure 1 a). The application of surfactants thus offers the possibility of chemically modifying the internal channel surface,[18] and of influencing the net electrostatic charge present on the pore walls. The exact structure of the adsorbed surfactant layer determines how pore size, pore chemistry, and surface charge density are affected by adsorption. Three surfactants were used in the present study (Figure 1 b): cetyltrimethylammonium bromide (CTAB), sodium dodecyl sulfate (SDS), and triethylhexylammonium bromide (C6TEA). These compounds have carbon tail lengths of 16, 12, and 6, respectively. An α-alumina-supported γ-alumina membrane gate was placed in a U-shaped tube, and external Pt electrodes were fixed on both sides of the membrane over which the driving force was applied.[6] Ionic probes were introduced on one side (feed) of the gate, and surfactants were added on both the feed and receive sides at the same concentration.

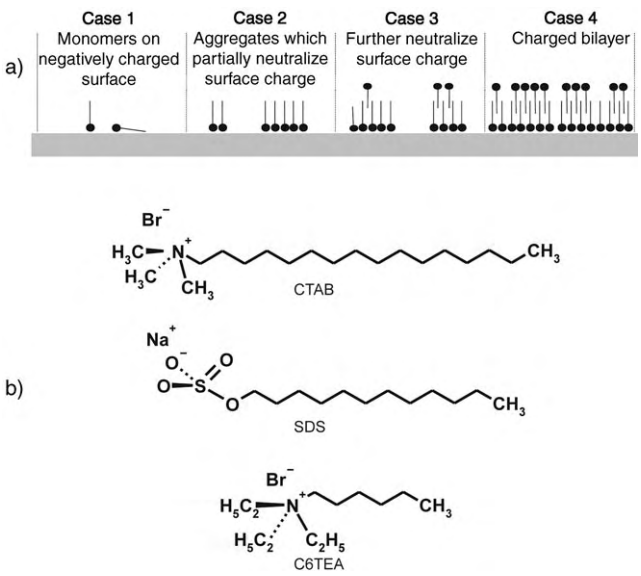

Figure 1. a) Schematic representation of the adsorption behavior of surfactants at varying concentrations according to the four-region adsorption model. b) Structures of the surfactants used: cetyltrimethylammonium bromide (CTAB), sodium dodecyl sulfate (SDS), and triethylhexylammonium bromide (C6TEA).

Figure 2 shows the influence of surfactant concentration on the flux of doubly charged methyl viologen cations (MV^{2+}) and fluorescein anions (Fl^{2-}). The surfactant concentrations were increased at 24-hour intervals after steady-state conditions had been reached. The gray bands in the figure indicate the average steady-state fluxes of probe ions through the gate when no surfactant was present. When long-chain CTAB or SDS were used, the MV^{2+} flux could be suppressed with surfactant concentrations larger than $\approx 10^{-4}$ M. A qualitatively similar, though less pronounced trend was observed in the presence of short-chain C6TEA. When the same surfactants were used together with Fl^{2-} ions, the flux of the

 © 2006 Wiley-VCH Verlag GmbH & Co. KGaA, Weinheim

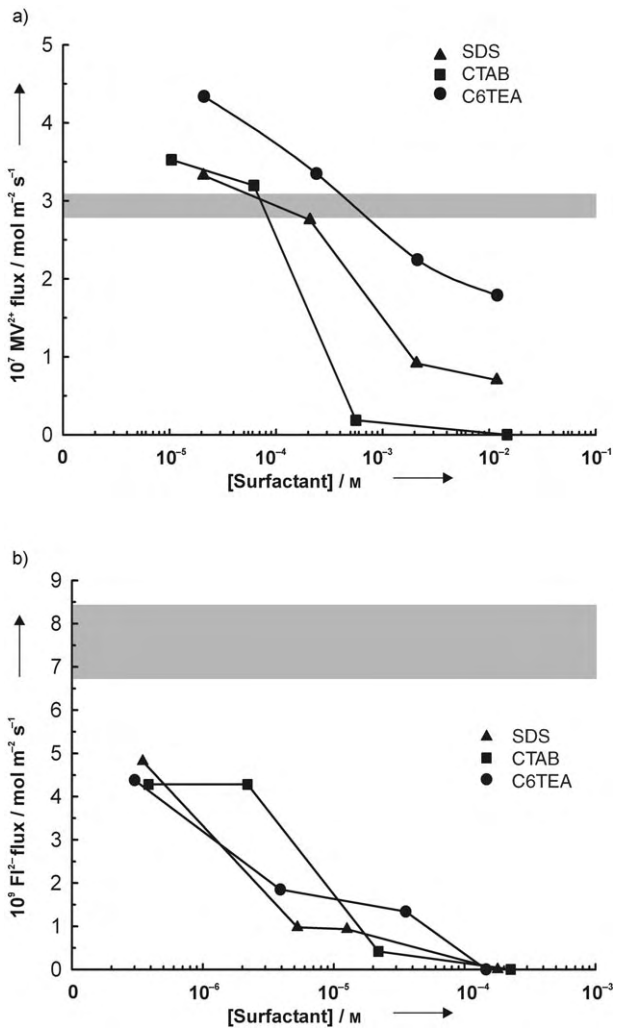

Figure 2. Influence of surfactant concentration on transport rate of a) methyl viologen cations (MV^{2+}) and b) fluorescein anions (Fl^{2-}) through an α/γ-alumina membrane gate. [MV^{2+}] and [Fl^{2-}] at feed side is 8×10^{-4} M. The potential difference ΔV over the membrane is -2 and $+2$ V, respectively. The gray area represents the average flux of the ionic probes when no surfactant was present in the system.

ionic probes decreased in all cases and became virtually zero above 10^{-4} M, irrespective of the type of surfactant used.

The open/close switching ability of the membrane by co-addition of surfactant molecules at the feed side and its effect on the flux of MV^{2+} and Fl^{2-} is illustrated by the enhancement factor R, which is defined as the ratio of the ionic flux in the presence and absence of surfactant. Selected values of R at high and low concentrations are listed in Table 1. Partial or complete pore blocking ($R<1$) was observed for both probe molecules when the surfactant concentration was sufficiently high. The degree to which the flux can be controlled depends on the nature and concentration of the surfactant; however, for both probe molecules the degree of blocking at high concentration increased in the sequence C6TEA < SDS < CTAB. After surfactant removal the transport rates were restored to their original values. Hence, the pores can be reversibly opened and closed for ion transport. The magnitude of the ionic fluxes can be controlled completely by addition of surfactant. The desorption process was somewhat slow and seems to be controlled by a limited mass-transfer rate.

The influence of surfactant on the ionic probes can be exerted through the electrostatic charge of the polar head groups and/or by the length of the hydrophobic tail. When considering the differences between the cationic surfactants CTAB and C6TEA, which have the same head groups, the tail length clearly has an influence: CTAB is more effective than C6TEA in suppressing the MV^{2+} flux at a high surfactant concentration, and is roughly as effective as SDS. This finding suggests that the adsorption of long-chain surfactants causes steric effects to play a substantial role in the blocking process.

However, an alternative explanation could be that the small fluxes at high surfactant concentrations are a result of the formation of molecule–surfactant complexes. To rule out this possibility, MV^{2+} solutions were investigated by UV/Vis spectroscopy in the presence of different concentrations of surfactants. No significant changes were observed in the spectra, except at very high concentrations of SDS ($\approx10^{-2}$ M), in which a shift in the absorption maximum was observed, which indicates that there was some interaction between MV^{2+} ions and SDS. As regards Fl^{2-} ions, fluorescence spectroscopy showed no evidence of a surfactant–Fl^{2-} interaction. Hence, steric hindrance of ion transport by surfactants appears to be the dominant mechanism of permeability control at high concentration.

Surprisingly, an enhancement of the MV^{2+} flux ($R>1$) was observed in the presence of low surfactant concentrations (10^{-6}–10^{-4} M; see Figure 1b and Table 1). Apparently, the mobility and/or local concentration of MV^{2+} ions are affected by a low concentration of adsorbed surfactants. Several factors might play a role, although it seems likely that the rate enhancement is somehow related to a (partial) screening of the native charges present on the alumina surface, and the more aliphatic nature of the pore walls after surfactant adsorption. At the low concentrations of 10^{-4} M or less, at which $R>1$ occurred, a monolayer of surfactant is present on the membrane surface. The formation of surfactant aggregates at $\approx10^{-5}$ M (case 2 in Figure 1a) neutralizes the surface charge and increases the hydrophobicity of the alumina surface.[16,19] As the long-range coulombic interactions between charged surface sites and MV^{2+} lower the mobility of MV^{2+} ions inside the pore, the partial screening of surface charges by adsorbed surfactants will increase the MV^{2+} ionic mobility. In addition, the more aliphatic nature of the pore probably provides more favorable surroundings for MV^{2+} ions than the bulk water phase, so that MV^{2+} partitions preferentially into the membrane, thus leading to a higher concentration inside the pore. Both effects will enhance the ion transport rate. C6TEA was more effective in enhancing the flux of MV^{2+} than CTAB or SDS. This finding is probably explained by the smaller size of C6TEA, as it may be able to adsorb in and around charged surface sites where the larger CTAB and SDS could be sterically hindered. No enhancement factors $R>1$ were observed for Fl^{2-}, which may be related to the fact that it is a less hydrophobic ion than MV^{2+}.

Figure 3 shows the zeta potential of γ-alumina as a function of surfactant concentration.[20] This experiment

 © 2006 Wiley-VCH Verlag GmbH & Co. KGaA, Weinheim

Table 1: Ionic fluxes and enhancement factors (R) of MV^{2+} and Fl^{2-} through a γ-alumina membrane gate upon co-addition of surfactant.[a]

Surfactant	Concentration [M]	MV^{2+}		Fl^{2-}	
		Flux [$mol\,m^{-2}\,s^{-1}$]	R	Flux [$mol\,m^{-2}\,s^{-1}$]	R
None	0	$(2.8–3.2)\times10^{-7}$	1	$(6.9–8.4)\times10^{-9}$	1
SDS	10^{-5}	3.3×10^{-7}	1.11	4.5×10^{-9}	0.59
	10^{-3}			$<7.2\times10^{-15}$	$<10^{-6}$
	10^{-2}	7.8×10^{-9}	0.026		
CTAB	10^{-6}			5.8×10^{-9}	0.76
	10^{-5}	3.5×10^{-7}	1.18		
	10^{-3}			$<7.2\times10^{-15}$	$<10^{-6}$
	10^{-2}	1.8×10^{-9}	0.006		
C6TEA	10^{-5}	4.3×10^{-7}	1.44		
	10^{-4}			5.9×10^{-9}	0.77
	10^{-3}			$<7.2\times10^{-15}$	$<10^{-6}$
	10^{-2}	2.0×10^{-7}	0.68		

[a] The potential difference ΔV over the membrane is -2 and $+2$ V for MV^{2+} and Fl^{2-} ions, respectively. ΔV is defined as $\Delta V = V_{receive} - V_{feed}$, where V_{feed} and $V_{receive}$ are the electrode potentials at the feed and receive sides, respectively. The membrane was placed between the two halves of a U-shaped tube with the oxide layer exposed to the so-called feed side. $[MV^{2+}]$ and $[Fl^{2-}]$ at feed side is 8×10^{-4} M.

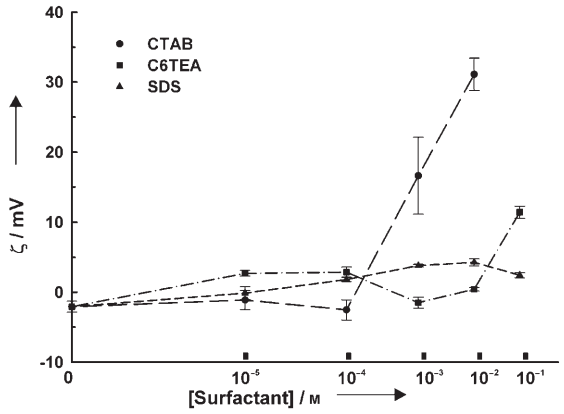

Figure 3. Zeta potential of γ-alumina powder as a function of surfactant concentration in the presence of phosphate buffer (pH 6). Conditions are similar to those for the permeability measurements. Lines serve as a guide to the eye.

provides insight into the effect of surfactant adsorption on alumina surface charge, and may thus help to distinguish steric and charge-blocking effects more clearly. In the absence of surfactant the zeta potential was slightly negative. At low concentrations the potentials varied slightly depending on the concentration and nature of the surfactant. The sudden strong increase of the zeta potential of solutions containing CTAB and C6TEA at concentrations of $\approx10^{-3}$ and 10^{-1} M, respectively, indicates the formation of charged bilayers. The formation of a bilayer in the pores at high concentration (case 4 in Figure 1a) is likely to lead to both an increase of flux-retarding coulombic interactions between the charged surface and probe ion, and an increased steric hindrance of the probe ions inside the nanometer-sized pores because of the presence of a bilayer. In contrast, the zeta potential of SDS shows no indication of a charged bilayer up to at least 10^{-1} M. Yet, the MV^{2+} and Fl^{2-} fluxes at high concentration decrease in the order C6TEA > SDS > CTAB, and so SDS is a more effective transport-blocking surfactant than C6TEA. Apparently, the blocking of the ionic probe by SDS does not occur by an increase of coulombic interactions, but rather by steric hindrance. The data support the findings that SDS and CTAB block ion transport sterically because of their long hydrocarbon tails, and that CTAB and C6TEA block transport by coulombic interactions through a charged bilayer. CTAB is both a steric and coulombic pore blocker, and is thus the most effective surfactant at high concentrations, followed by SDS (mainly steric blocking) and C6TEA (mainly charge blocking).

In summary, a switchable membrane gate for ionic species that operates by co-addition and removal of surfactants was demonstrated. The permeability of the gate for ionic probe molecules could be manipulated by steric and/or coulombic blocking depending on the nature of the surfactant. The blocking and unblocking of pores was reversible, thus demonstrating a membrane gate with in situ tunable permeability. Under specific conditions, cation fluxes higher than in the absence of surfactant were observed. The kinetics of surfactant sorption seem to be controlled by mass transfer. Surface-active species may also complicate transport behavior in some cases. The ability to physically control the transport rate through the membrane gate by an externally tunable variable, which is independent of the probe ion concentration and driving force, provides an interesting approach that could find use in devices such as selective gates for DNA and protein sampling routines, injectors for electrophoretic separations, or on-demand therapeutic agents in microfluidic devices.

Received: December 23, 2005
Published online: April 10, 2006

Keywords: adsorption · membranes · molecular transport · nanopores · surfactants

[1] T.-C. Kuo, L. A. Sloan, J. V. Sweedler, P. W. Bohn, *Langmuir* **2001**, *17*, 6298–6303.
[2] M. Nishizawa, V. P. Menon, C. R. Martin, *Science* **1995**, *268*, 700–702.
[3] C. R. Martin, M. Nishizawa, K. Jirage, M. Kang, S. B. Lee, *Adv. Mater.* **2001**, *13*, 1351–1362.
[4] P. J. Kemery, J. K. Steehler, P. W. Bohn, *Langmuir* **1998**, *14*, 2884–2889.
[5] R. Schmuhl, J. Sekulić, S. Roy Chowdhury, C. J. M. van Rijn, K. Keizer, A. van den Berg, J. E. ten Elshof, D. H. A. Blank, *Adv. Mater.* **2004**, *16*, 900–904.
[6] R. Schmuhl, W. Nijdam, J. Sekulić, S. Roy Chowdhury, C. J. M. van Rijn, A. van den Berg, J. E. ten Elshof, D. H. A. Blank, *Anal. Chem.* **2005**, *77*, 178–184.
[7] R. Schmuhl, K. Keizer, A. van den Berg, J. E. ten Elshof, D. H. A. Blank, *J. Colloid Interface Sci.* **2004**, *273*, 331–338.

 © 2006 Wiley-VCH Verlag GmbH & Co. KGaA, Weinheim

[8] T.-C. Kuo, H.-K. Kim, D. M. Cannon, Jr., M. A. Shannon, J. V. Sweedler, P. W. Bohn, *Angew. Chem.* **2004**, *116*, 1898 – 1901; *Angew. Chem. Int. Ed.* **2004**, *43*, 1862 – 1865.
[9] A. Plecis, R. B. Schoch, P. Renaud, *Nano Lett.* **2005**, *5*, 1147 – 1155.
[10] Z. Hou, N. L. Abbott, P. Stroeve, *Langmuir* **2000**, *16*, 2401 – 2404.
[11] K-Y. Chun, P. Stroeve, *Langmuir* **2002**, *18*, 4653 – 4658.
[12] S. B. Lee, C. R. Martin, *Anal. Chem.* **2001**, *73*, 768 – 775.
[13] A. N. Chatterjee, D. M. Cannon, E. N. Gatimu, J. V. Sweedler, N. R. Aluru, P. W. Bohn, *J. Nanopart. Res.* **2005**, *7*, 507 – 516.
[14] D. N. Petsev, *J. Chem. Phys.* **2005**, *123*, 244 907.
[15] S. Pennathur, J. G. Santiago, *Anal. Chem.* **2005**, *77*, 6772 – 6781.
[16] A. Fan, P. Somasundaran, N. J. Turro, *Langmuir* **1997**, *13*, 506 – 510.
[17] L. J. Crisenti, D. A. Sverjensky, *Am. J. Sci.* **1999**, *299*, 828 – 899.
[18] A. A. Kavitskaya, N. A. Klimenko, A. V. Bildyukevich, A. A. Petrachkov, *Desalination* **2003**, *158*, 225 – 230.
[19] P. Chandar, P. Somasundaran, N. J. Turro, *J. Colloid Interface Sci.* **1987**, *117*, 31 – 46.
[20] W. B. S. de Lint, N. E. Benes, J. Lyklema, H. J. M. Bouwmeester, A. J. van der Linde, M. Wessling, *Langmuir* **2003**, *19*, 5861 – 5868.

 © 2006 Wiley-VCH Verlag GmbH & Co. KGaA, Weinheim

Peptide Enrichment

DOI: 10.1002/anie.200503485

$CaCO_3$–Poly(methyl methacrylate) Nanoparticles for Fast Enrichment of Low-Abundance Peptides Followed by $CaCO_3$-Core Removal for MALDI-TOF MS Analysis**

Weitao Jia, Xuehua Chen, Haojie Lu, and Pengyuan Yang**

Peptide mapping by MALDI-TOF mass spectrometry has encountered some challenges, such as difficulties in peptide preconcentration and isolation from a complex environment in proteomic analysis,[1] although this method has become one of the major tools in proteomics because of its capabilities of high throughput and good sensitivity.[2] Sample loss is unavoidable during normal peptide/protein extraction and the preparation process prior to MALDI-TOF MS analysis; this is especially true for trace-level proteins, such as disease-associated proteins expressed commonly in low abundance.[3] Thus, it would be desireable that an efficient enrichment step could be carried out beforehand for peptide preparation. However, the conventional technique to concentrate peptides through simple evaporation always results in a loss of sample, due mainly to analyte adsorption onto the surface of the container. An additional drawback for the evaporation technique is the simultaneous concentration of interferential components (e.g., salts) or other contaminants in the solution. As a consequence, the sensitivity of detection might not be satisfactory when applying this sample pretreatment. Alternative methods for peptide enrichment by use of reversed-phase resin are complicated and typically suitable for hydrophobic peptides.[4] Therefore, a simple, fast, and universal enrichment step is in strong demand to avoid protein/peptide loss and to concentrate analytes for sample preparation and separation.

In previous works, we have successfully applied nanozeolite materials for selective absorption and separation of desired peptides/proteins or for the enrichment and isolation of low-abundance peptides, based on the high selectivity and strong absorption ability of these materials.[5] One of the biggest advantages observed during those previous works was that the peptides adsorbed on the nanozeolites could be directly analyzed by MALDI-TOF MS. However, these previous methods were relatively time consuming for a 90-min sample-absorption step. Furthermore, the introduction of solid particles on the MALDI target would cause a relatively unstable MS signal due to the inhomogeneity of cocrystallization. Additionally, a careful and experiential process was needed to avoid the aggregation of nanomaterials which would cause spattering and quickly contaminates the ion source chamber.[6]

Herein, we report the development of a particle-free MALDI and "octopus-like" enrichment protocol. In this protocol, we selected nanoparticles of calcium carbonate derivatized with poly(methyl methacrylate) (PMMA) because of its ability to adsorb the peptide/protein. The particle denoted as $CaCO_3$–PMMA has a destroyable core of $CaCO_3$, which can be removed later for a particle-free MALDI analysis. When the $CaCO_3$–PMMA material was added dropwise to the sample solution, the linear chains of PMMA linked on the $CaCO_3$ core would be flexible and would spread out into the solution like the tentacles of an octopus. We have found that $CaCO_3$–PMMA exhibits some remarkable features that are useful in peptide/protein extraction and the related MALDI-TOF MS analysis.

In order to investigate the enrichment efficiency, the $CaCO_3$–PMMA particles were dispersed into a solution of acetonitrile/water/trifluoroacetic acid (TFA; 50:50:0.1) containing three standard peptides (1 fmol μL^{-1}). The peptides were peptide I, PPGFSPFR ($M_w = 903.46$, isoelectric point (pI) = 10.18), peptide II, DRVYLHPFHL ($M_w = 1295.68$,

[*] W. Jia, Prof. Dr. H. Lu, Prof. Dr. P. Yang
Department of Chemistry and Institutes of Biomedical Sciences
Fudan University
Shanghai 200433 (P.R. China)
Fax: (+86) 21-6564-2009
E-mail: luhaojie@shmu.edu.cn
pyyang@fudan.edu.cn
X. Chen
Key Laboratory for Ultrafine Materials of Ministry of Education
East China University of Science and Technology
Shanghai 200237 (P.R. China)

[**] Supported by the National Basic Research Priorities Program (grant no. 2001CB510202), the National Science and Technology Key Project (grant no. 2002BAC11A11), the Shanghai Science and Technology Development Program (grant nos. 03DZ14024 and 04DZ14005), and the National Natural Science Foundation of China (grant nos. 20271013, 20299030, and 20405003).

Supporting information for this article is available on the WWW under http://www.angewandte.org or from the author.

 © 2006 Wiley-VCH Verlag GmbH & Co. KGaA, Weinheim

pI = 6.92), and peptide III, EGVNDNEEGFFSAR (M_w = 1569.67, pI = 4.00). Two standard protein solutions containing horse heart cytochrome *c* (500 fmol μL^{-1}, M_w = 12384, pI = 9.59) or horse heart myoglobin (MYO, 600 fmol μL^{-1}, M_w = 16941, pI = 7.36) were also tested. During a 10-min incubation with continual agitation, the PMMA flexible chains adsorbed peptides or proteins in the solution. After the peptides or proteins adsorbed onto the "spreading tentacles", the solid nanoparticles were isolated completely by a 10-min centrifuge process.

Subsequently, without any additional washing step, acetonitrile (5 μL) containing acetic acid (0.2 μL) was added to the container to dissolve the $CaCO_3$ core. The dissolving step was one of the most crucial steps in the whole enrichment process. All of adsorbed peptides or proteins were effectively redissolved into an acidic acetonitrile solution due to the fully destroyed physical structure of the $CaCO_3$–PMMA particles. Calcium acetate was formed and deposited on the bottom of container during the dissolving step. After a second centrifugation, the supernatant solution containing the peptide and PMMA was mixed with a MALDI matrix (α-cyano-4-hydroxycinnamic acid, α-CHCA) solution on a MALDI plate for MS analysis. For comparison, the original peptide and protein solutions without enrichment were also analyzed

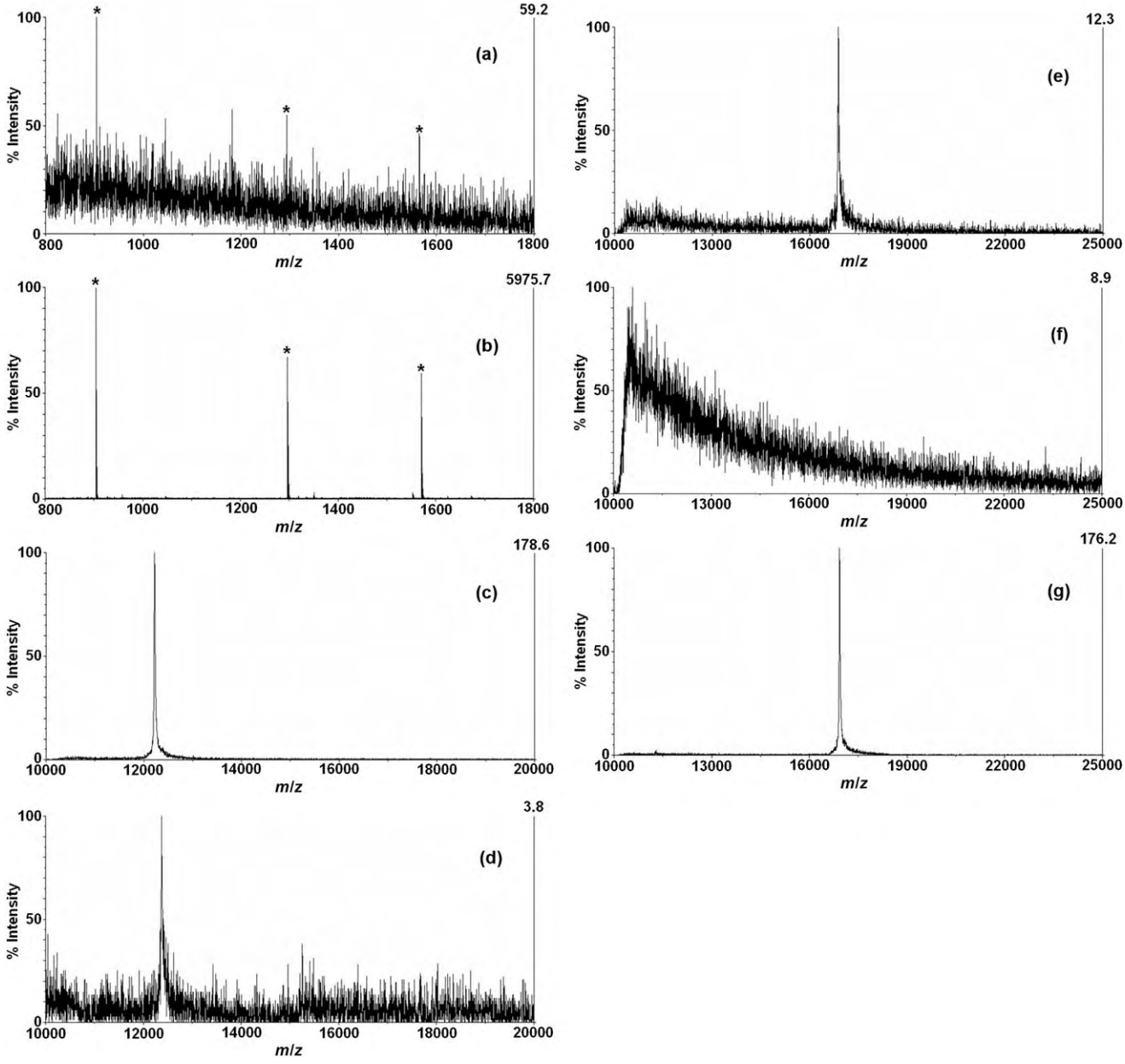

Figure 1. MALDI-TOF mass spectra of the standard peptide mixture (1 fmol μL^{-1}) a) without enrichment and b) with enrichment, cytochrome *c* (500 fmol μL^{-1}) c) with enrichment and d) without enrichment, e) MYO (600 fmol μL^{-1}) without enrichment, f) the supernatant after incubation for 10 min, and g) MYO (600 fmol μL^{-1}) with enrichment. MALDI-TOF MS experiments were performed on a 4700 Proteomics Analyzer (Applied Biosystems, USA), with the Nd-YAG laser at 355 nm, a repetition rate of 200 Hz, and an acceleration voltage of 20 kV. Analysis of peptides and proteins was performed in the reflector and linear TOF detection modes, respectively. All spectra were taken from a signal averaging of 800 laser shots. Asterisks mark the peaks of the standard peptides.

 © 2006 Wiley-VCH Verlag GmbH & Co. KGaA, Weinheim

by MALDI-TOF MS under the same experimental conditions.

The main advantage of this enrichment process is that the $CaCO_3$–PMMA particles can not only remarkably concentrate peptides but can also effectively enrich proteins. MALDI-TOF MS spectra are displayed in Figure 1 for the standard peptides and proteins with or without the $CaCO_3$–PMMA enrichment process. Peptides with concentrations lower than 1 fmol μL^{-1} were hardly detected without any enrichment step (Figure 1 a). However, after the $CaCO_3$–PMMA enrichment process, the peptide signal became stronger in the mass spectrum (Figure 1 b). The signal-to-noise (S/N) ratios of the three tested peptides were increased from 11.7 (m/z: 904.46), 6.8 (m/z: 1296.68), and 5.6 (m/z: 1570.67) to 2808, 1676, and 1450, respectively. In this case, S/N enhancement factors of 240, 246, and 259 could be estimated for the three peptides, respectively. After the enrichment process, the S/N ratio of cytochrome *c* at a concentration of 500 fmol μL^{-1} is increased to 168 (Figure 1 c), while without any enrichment the S/N ratio is 2.8 (Figure 1 d). In this case, a S/N enhancement factor of 60 could be estimated. The S/N ratio of MYO at a concentration of 600 fmol μL^{-1} was 5.1 without any enrichment step (Figure 1 e). After a 10-min incubation and 10-min centrifugation, no assignable signal could be observed in the first supernatant (Figure 1 f), a result indicating that most of the MYO was effectively adsorbed on the $CaCO_3$–PMMA particles. By contrast, the S/N ratio of MYO in the final supernatant was increased to 170 (Figure 1 g). In this case, a S/N enhancement factor of 33 can be estimated.

The second advantage of the enrichment process is its fast absorption speed. The signal intensity for free peptide I (10 fmol μL^{-1}) in the first supernatant decreased rapidly from 430 to 0 as the incubation time progressed from 0 to 9 minutes (see the Supporting Information). The amazing efficiency of this enrichment process was attributed to the large external surface area, high dispersibility, and strong absorption ability of $CaCO_3$–PMMA. More importantly, the original folded PMMA linear chain could unfold and spread into the solution,[7] so the peptides or proteins quickly adsorb on the moveable and flexible PMMA chain.

The third advantage of the enrichment process is that the remaining $CaCO_3$-free PMMA results in a good reproducibility of analyte signals (see the Supporting Information). The prepared sample solution obtained by this novel enrichment protocol contained both PMMA polymer and analytes, while the conventional solid-phase extraction solution only contained analytes.[8] The existence of polymer substrates in solutions is propitious for the formation of well-proportioned, homogeneous, and small cocrystals which ensure a uniform analyte-to-matrix ratio in each valid zone.[9]

The last advantage of the enrichment process is that the coconcentration of salts can be avoided by using $CaCO_3$–PMMA particles in the peptide absorption due to the weak interaction between salts and PMMA. Normally, peptides and proteins come from real proteome samples that always contain salts, while the presence of salts can hardly result in good mass spectra.[10] Therefore, a desalting step is necessary after conventional protein-concentration processes in order to obtain a satisfactory analysis. Without any concentration step, only four peptides could be detected in a MYO-digest solution at a concentration of 5 fmol μL^{-1} (Figure 2 a). In the presence of 100 mM NH_4HCO_3, the signals of the MYO-digest peptides disappeared due to the signal suppression effect of nonvolatile salts (Figure 2 b). After the MYO digest containing 100 mM NH_4HCO_3 was desalted by use of commercial

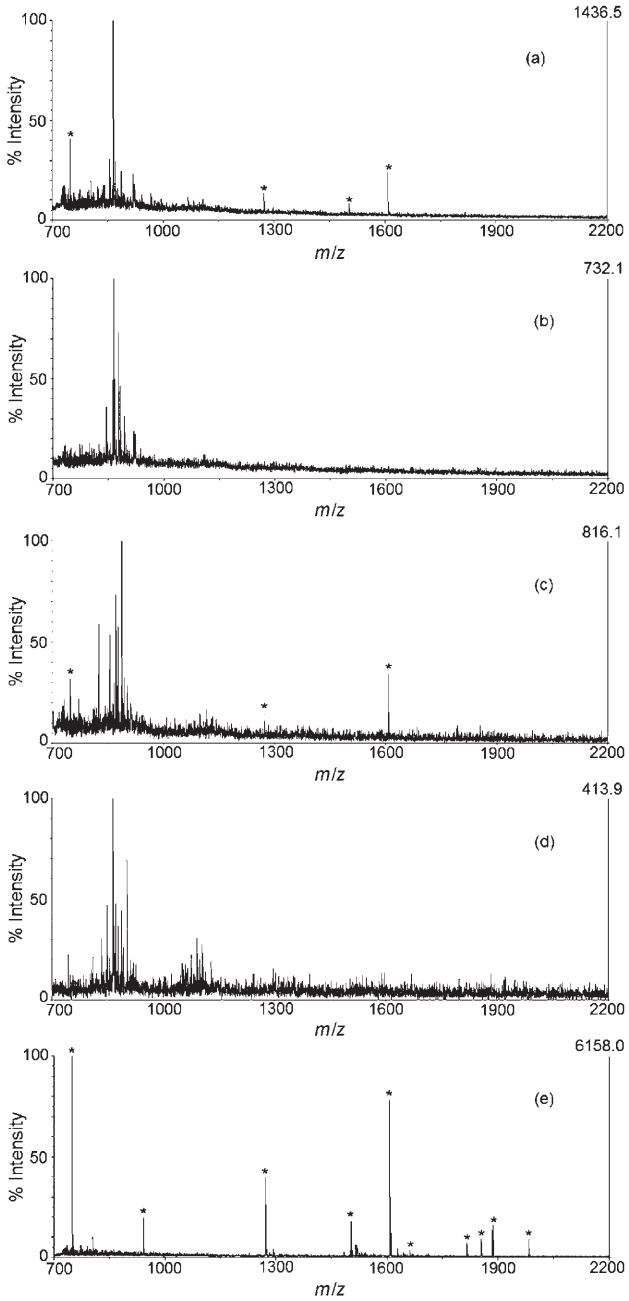

Figure 2. MALDI-TOF mass spectra of a) a normal MYO digest (5 fmol μL^{-1}), b) the MYO digest (5 fmol μL^{-1}) with 100 mM NH_4HCO_3, c) the MYO digest (5 fmol μL^{-1}) with 100 mM NH_4HCO_3 treated by a ZipTipC18 pipette tip, d) the MYO digest (5 fmol μL^{-1}) with 100 mM NH_4HCO_3 concentrated by solvent evaporation, and e) the MYO digest (5 fmol μL^{-1}) with 100 mM NH_4HCO_3 after $CaCO_3$–PMMA enrichment. Asterisks mark peaks assigned to peptides from MYO.

 © 2006 Wiley-VCH Verlag GmbH & Co. KGaA, Weinheim

ZipTipC18 (see the Supporting Information), three peptides were observed with a lower S/N ratio (Figure 2c). Unfortunately, no peaks were observed in the presence of 100 mM NH_4HCO_3 after the conventional solvent-evaporation method, due to the coconcentration of salts and analytes (Figure 2d). However, with the novel enrichment method, 10 peptides could be assigned to MYO with a sequence coverage of 70%, even in the presence of 100 mM NH_4HCO_3 (Figure 2e). It was also noticed that $CaCO_3$–PMMA could enrich various peptides without discrimination.

The proposed enrichment process has been proven to be effective in a real proteomic analysis. Proteins extracted from the blood plasma of Sprague-Dawley (SD) rats were selected and eight protein spots were analyzed after 2D electrophoresis separation. These eight excised protein spots were labeled with Arabic numerals according to the optical intensity (from strong to weak, see the Supporting Information). Results show that the success rate of protein identification was increased with the novel enrichment method (Table 1). For the strongest spots, 1 and 2, the novel enrichment protocol exhibits a performance equivalent to that of the conventional evaporation method. However, for the weaker spots 3–5, the proteins identified by $CaCO_3$–PMMA enrichment protocol display higher scores than those from the evaporation method. For the weakest spots 6–8, the proteins could barely be identified with the solvent-evaporation method due to the adsorption onto the container surface and the interference of contamination. By contrast, the proteins were positively identified with the novel protocol, thereby showing the excellent potential of this method for proteomic applications.

In summary, $CaCO_3$–PMMA nanoparticles were applied for the first time for the enrichment of low-abundance peptides and proteins. The process of enrichment is very quick and efficient. The resulting nanoparticle-adsorbed peptides or proteins can be analyzed by MALDI-TOF MS in the particle-free mode with high reproducibility and good recovery, thereby avoiding sample loss and contamination inside the mass spectrometer. It has been found that $CaCO_3$–PMMA nanoparticles exhibit a strong enriching and desalting ability, which could pave way to novel approach to the enrichment of trace-level proteins or peptides, as well as new applications for $CaCO_3$–PMMA nanoparticles.

Table 1: The proteins identified from eight 2D electrophoresis spots with solvent-evaporation enrichment or $CaCO_3$–PMMA enrichment.[a]

Spot	Protein	Solvent-evaporation enrichment		$CaCO_3$–PMMA enrichment	
		protein score[b]	sequence coverage [%]	protein score[b]	sequence coverage [%]
1	preprohaptoglobin	269	45	269	45
2	preprohaptoglobin	248	51	248	51
3	Ba1-647 (*Rattus norvegicus*)	228	35	262	39
4	α1-macroglobulin	126	9	158	9
5	Ba1-647 (*Rattus Norvegicus*)	145	29	202	31
6	α1-macroglobulin precursor (rat)	51	8	82	12
7	albumin (*Rattus norvegicus*)	48	15	79	20
8	albumin (*Rattus norvegicus*)	33	11	76	20

[a] The proteins were extracted from the blood plasma of healthy SD rats. Search parameters: NCBInr database (Version: July 12, 2005); digest used: Trypsin; maximum of missed cleavages: 1; peptide mass tolerance: 80 ppm; tandem mass tolerance: 0.5 Da. Every extraction solution of protein spots was divided into two portions with equal volume and each portion was enriched either by the conventional solvent-evaporation method or the novel $CaCO_3$–PMMA protocol. GPS Explorer software from Applied Biosystems with Mascot as a search engine was used to identify proteins. All proteins were identified by using the peptide fingerprint mass spectra combined with tandem mass spectra. [b] Protein scores greater than 68 are significant (probability $p < 0.05$).

Experimental Section

$CaCO_3$–PMMA particles were synthesized by in situ polymerization of methyl methacrylate onto the surface of $CaCO_3$ nanoparticles, according to the reported procedures.[11]

A $CaCO_3$–PMMA suspension (10 μL, 10 mg mL^{-1}) was added into a solution (1 mL) containing certain concentrations of peptides or proteins. The solution containing the peptides (or proteins) and $CaCO_3$–PMMA was then agitated for 10 min at 37 °C; this was followed by centrifugation at 16000 rpm for 10 min. After the supernatant was decanted, the residue was dispersed into an acetonitrile solution (5 μL) containing acetic acid (0.2 μL) and the solution was centrifuged at 16000 rpm for 5 min. The supernatant (0.5 μL) was then mixed with a α-cyano-4-hydroxycinnamic acid (0.5 μL) saturated solution (in 50% acetonitrile aqueous solution containing 0.1% TFA) on the MALDI plate and applied for MALDI-TOF MS analysis.

Received: October 2, 2005
Revised: February 7, 2006
Published online: April 7, 2006

Keywords: mass spectrometry · nanoparticles · peptides · protein enrichment · proteins

[1] a) M. Mann, P. Hojrup, P. Roepstorff, *Biol. Mass Spectrom.* **1993**, *22*, 338; b) J. R. Yates, S. Speicher, P. R. Griffin, T. Hunkapiller, *Anal. Biochem.* **1993**, *214*, 397.
[2] a) V. C. Wasinger, S. J. Cordwell, A. Cerpapoljak, J. X. Yan, A. A. Gooley, M. R. Wilkins, M. W. Duncan, R. Harris, K. L. Williams, I. Humpherysmith, *Electrophoresis* **1995**, *16*, 1090; b) S. Fields, *Science* **2001**, *291*, 1221; c) A. Abbott, *Nature* **2001**, *409*, 747.
[3] K. Karlsson, N. Cairns, G. Lubec, M. Fountoulakis, *Electrophoresis* **1999**, *20*, 2970.
[4] M. Kussmann, E. Nordhoff, H. Rahbek-Nielsen, S. Haebel, M. Rossel-Larsen, L. Jakobsen, J. Gobom, E. Mirgorodskaya, A. Kroll-Kristensen, L. Palm, P. Roepstorff, *J. Mass Spectrom.* **1997**, *32*, 593.
[5] a) F. Xu, Y. J. Wang, X. D. Wang, Y. H. Zhang, Y. Tang, P. Y. Yang, *Adv. Mater.* **2003**, *15*, 1751; b) Y. H. Zhang, X. Y. Wang, W. Shan, B. Y. Wu, H. Z. Fan, X. J. Yu, Y. Tang, P. Y. Yang, *Angew. Chem.* **2005**, *117*, 621; *Angew. Chem. Int. Ed.* **2005**, *44*, 615.
[6] S. F. Ren, L. Zhang, Z. H. Cheng, Y. L. Guo, *J. Am. Soc. Mass Spectrom.* **2005**, *16*, 333.
[7] T. Kawauchi, J. Kumaki, E. Yashima, *J. Am. Chem. Soc.* **2005**, *127*, 9950.

 © 2006 Wiley-VCH Verlag GmbH & Co. KGaA, Weinheim

[8] a) T. Herraiz, V. Casal, *J. Chromatogr. A* **1995**, *708*, 209; b) M. A. Strausbauch, J. P. Landers, P. J. Wettstein, *Anal. Chem.* **1996**, *68*, 306; c) D. S. Peterson, T. Rohr, F. Svec, J. M. J. Frechet, *Anal. Chem.* **2003**, *75*, 5328; d) N. G. Hatcher, T. A. Richmond, S. S. Rubakhin, J. V. Sweedler, *Anal. Chem.* **2005**, *77*, 1580.
[9] Y. Kim, G. B. Hurst, M. J. Doktycz, M. V. Buchanan, *Anal. Chem.* **2001**, *73*, 2617.
[10] a) R. Westermeier, T. Naven, *Proteomics in Practice: A Laboratory Manual of Proteome Analysis*, Wiley-VCH, Weinheim, **2002**, p. 263; b) N. Zhang, A. Doucette, L. Li, *Anal. Chem.* **2001**, *73*, 2968; c) A. H. Brockman, B. S. Dodd, N. Orlando, *Anal. Chem.* **1997**, *69*, 4716.
[11] a) Q. Liu, J. Ding, D. E. Chambers, S. Debnath, S. L. Wunder, G. R. Baran, *J. Biomed. Mater. Res.* **2001**, *57*, 384; b) J. L. Luna-Xavier, A. Guyot, E. Bourgeat-Lami, *J. Colloid Interface Sci.* **2002**, *250*, 82; c) P. Meneghetti, S. Qutubuddin, *Chem. Eng. Commun.* **2001**, *188*, 81; d) Y. H. Yang, Y. Dan, *Colloid Polym. Sci.* **2003**, *281*, 794.

 © 2006 Wiley-VCH Verlag GmbH & Co. KGaA, Weinheim

Cross-Coupling

DOI: 10.1002/anie.200600442

Heck Coupling with Nonactivated Alkenyl Tosylates and Phosphates: Examples of Effective 1,2-Migrations of the Alkenyl Palladium(II) Intermediates**

Anders L. Hansen, Jean-Philippe Ebran, Mårten Ahlquist, Per-Ola Norrby, and Troels Skrydstrup**

Considerable efforts have been undertaken by numerous groups in academia and industry over the past decade to expand the repertoire of coupling reagents in palladium(0)-catalyzed cross-coupling reactions.[1] In particular, alkenyl phosphates and tosylates have proven their worth in various cross-coupling reactions, such as the Stille,[2] Suzuki,[2e,f,3] Negishi,[2b] Kumada,[2b,3e,4] Sonogashira,[2b,e,f,5] Buchwald–Hartwig,[4a,6] carbonyl enolate,[3d] and Heck couplings,[7] as effective alternatives to the less stable and typically more expensive alkenyl triflates and nonaflates.[8] However, the majority of this work has focused on the use of activated vinyl phosphates and tosylates, such as α,β-unsaturated systems or α-heteroatom-substituted alkenes, for which the oxidative-addition step is nonproblematic with palladium(0) catalysts bearing aryl phosphine ligands. Less attention has been devoted to nonactivated counterparts, most likely because of the greater difficulty in carrying out the first step of the catalytic cycle, namely the oxidative addition.[3d,4,5,9]

We now report on catalyst systems composed of a palladium complex with a basic, hindered alkyl phosphine that can promote the Heck coupling of nonactivated vinyl tosylates and phosphates with electron-deficient alkenes in good yields, thereby increasing the scope of this important cross-coupling reaction. Furthermore, during these studies we observed an interesting 1,2-isomerization with certain alkenyl tosylates and phosphates under reaction conditions that provide coupling yields as high as 95%. A mechanistic proposal supported by experimental results and DFT calculations is included.

To identify suitable reaction conditions for Heck couplings with nonactivated alkenyl tosylates and phosphates, we examined the use of palladium complexes with the ever increasingly popular bulky electron-rich phosphines.[10] All tosylates and phosphates were prepared from starting ketones by base-promoted proton extraction and reaction with tosyl anhydride (Ts_2O) or $(PhO)_2POCl$, as earlier reported.[4b,11,12] Initial coupling attempts were performed between the tosylate **1** and ethyl acrylate (Scheme 1). After examining a

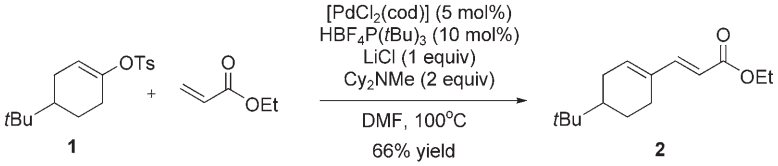

Scheme 1. Heck coupling with a nonactivated vinyl tosylate.

variety of reaction conditions, we noted that a combination of $[PdCl_2(cod)]$ (cod = 1,5-cyclooctadiene; 5 mol%) and the $P(tBu)_3HBF_4$ salt[13] (10 mol%) in the presence of dicyclohexylmethylamine (2 equiv) in dimethylformamide (DMF) at 85°C could furnish the diene **2**, albeit in low yield (approximately 5%). The addition of one equivalent of LiCl, however, had a dramatic effect on the reaction outcome, thus providing a 50% yield of the diene **2** after 24 hours.[14] Increasing the reaction temperature to 100°C improved the coupling yield to 66%. Other reactions conditions, including change of solvent or examination of alternative catalyst combinations, were incapable of promoting the cross-coupling.

To probe the scope of these reaction conditions, we examined the Heck coupling of a variety of alkenyl tosylates

[*] A. L. Hansen, Dr. J.-P. Ebran, Prof. Dr. T. Skrydstrup
The Center for Insoluble Protein Structures (inSPIN)
Department of Chemistry and the Interdisciplinary Nanoscience Center
University of Aarhus
Langelandsgade 140, 8000 Aarhus (Denmark)
Fax: (+45) 8619-6199
E-mail: ts@chem.au.dk
M. Ahlquist, Prof. Dr. P.-O. Norrby
Department of Chemistry, Building 201, Kemitorvet
Technical University of Denmark
DK-2800 Lyngby (Denmark)

[**] We thank the Danish National Science Research Council, the Carlsberg Foundation, and the University of Aarhus for generous financial support of this work.

Supporting information for this article is available on the WWW under http://www.angewandte.org or from the author.

 © 2006 Wiley-VCH Verlag GmbH & Co. KGaA, Weinheim

with electron-deficient alkenes and styrene derivatives catalyzed by the $[PdCl_2(cod)]/P(tBu)_3$ combination in the presence of LiCl (Table 1). Generally, all the reactions were completed after 20 h and provided satisfactory coupling yields

Table 1: Heck coupling with nonactivated vinyl tosylates.

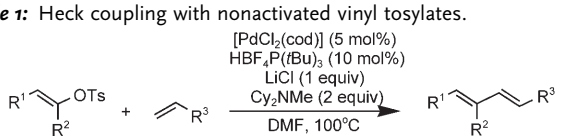

Entry	Vinyl tosylate	t [h]	Product	Yield [%][a]
1	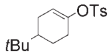	23	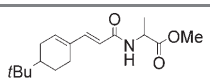	64
2		16	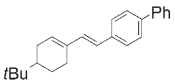	99
3		17	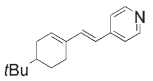	88
4		17	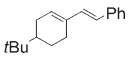	96
5		17	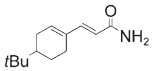	92
6	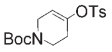	19	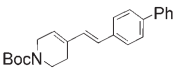	70
7		6	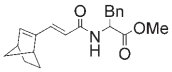	51
8		3	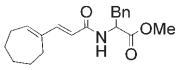	83
9		18	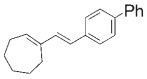	94
10		18	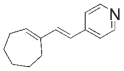	79
11		3	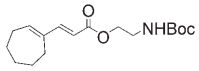	97
12		21	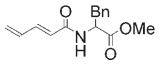	56

[a] Yield of the isolated product.

as high as 99%. Six- and seven-membered cyclic alkenyl tosylates proved particularly effective for these coupling reactions, although reactions with larger rings were unsuccessful. The coupling of the readily available vinyl tosylate to the acrylamide (Table 1, entry 12) demonstrates the potential of this methodology for the simple introduction of a vinyl unit to an α,β-unsaturated amide. Hence, the application of alkenyl tosylates in Heck couplings provides a straightforward means for the preparation of functionalized butadienes from simple starting materials.

Unexpectedly, the normal coupling product was not isolated in the reaction between 1-*tert*-butylvinyl tosylate and styrene. Rather the product from an apparent 1,2-migration of the intermediate alkenyl palladium(II) species was obtained in good yield (79%; Table 2, entry 1).[15] This

Table 2: Heck coupling of alkenyl tosylates with isomerization.

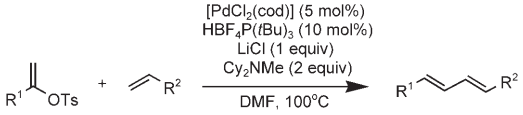

Entry	R^1	t [h]	Product	Yield [%][a]
1	*t*Bu	4	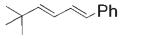	79
2	*t*Bu	20	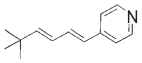	93
3	*t*Bu	23	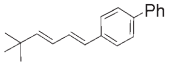	95
4	*t*Bu	20	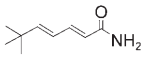	72
5	*t*Bu	3	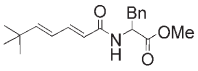	80[b]
6	*t*Bu	24	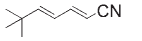	83[c]
7	$SiMe_3$	16	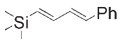	33

[a] Yield of isolated product; unless noted all selectivities of isomerized versus normal Heck products were >95:5. [b] Isomerized/normal products = 10:1. [c] *cis*/*trans* mixture = 1:1.

result is in stark contrast to recent observations by Reissig and co-workers, in which the Heck coupling between the corresponding vinyl nonaflate and methyl acrylate under phosphane-free conditions was reported to give the expected coupling product.[12c] Nevertheless, coupling of the same vinyl tosylate with a variety of alkenes revealed this isomerization to be quite effective with yields attaining 95% and with exclusive *trans* selectivity in all but one case (Table 2, entries 2–6). The use of acrylonitrile (Table 2, entry 6) led to a 1:1 mixture of *cis*/*trans*-isomerized products undoubtedly because of the small size of the nitrile group. One example was attempted with a 1-trimethylsilylvinyl tosylate (Table 2, entry 7). Although its coupling to styrene led to considerable degradation, a 33% yield of the rearranged coupling product could be secured, thus indicating the feasibility of such isomerizations, even with silyl-substituted alkenes, although further optimization is required.[16]

This isomerization–coupling step was also expanded to alkenyl phosphates (Table 3). 1-*tert*-Butylvinyl *O*,*O*-diphenyl phosphate behaved similarly as with the tosylate and coupled effectively to styrene, *p*-phenylstyrene, and 4-vinylpyridine (Table 3, entries 1, 2, and 4, respectively). Interestingly, these reactions proved to be more sensitive to the solvent employed. Whereas dioxane was the solvent of choice in entries 1 and 2, DMF was more adequate in the coupling with the vinyl pyridine. C–C bond formation to the styrene derivatives in DMF only provided coupling yields in the order of 20%. Additional examples with two acrylamides and one acrylate (Table 3, entries 3, 5, and 6) also revealed these substrates to be effective for Heck couplings with isomerization, whereas attempts with acrylonitrile were unsuccessful. In all cases, the diene products were the result of an apparent rearrangement, although in three cases an approximate 9:1 ratio of the isomerized and the normal Heck coupling products was detected (Table 3, entries 3, 5, and 6).

 © 2006 Wiley-VCH Verlag GmbH & Co. KGaA, Weinheim

Table 3: Heck coupling of alkenyl phosphates with isomerization.

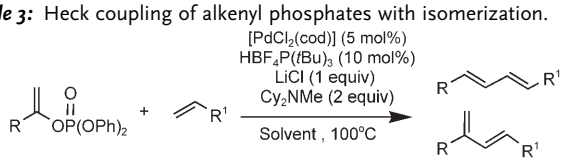

Entry	R	Solvent	*t* [h]	Major product (isomerized/normal)[a]	Yield [%][b]
1	*t*Bu	dioxane	24	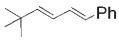	65
2	*t*Bu	dioxane	24	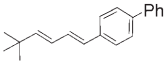	75
3	*t*Bu	DMF	24	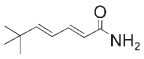	71
4	*t*Bu	DMF	24	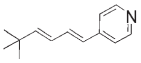 (89:11)	64
5	*t*Bu	DMF	24	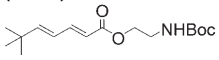 (90:10)	77
6	*t*Bu	DMF	24	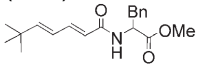 (88:12)	68
7	Ph	dioxane	18	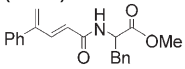	12
8	Ph	DMF	20	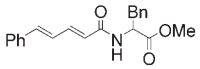 (4:3)	51

[a] Unless noted all selectivities of isomerized versus normal Heck products were > 95:5. [b] Yield of the isolated products.

Finally, a noteworthy solvent effect on the isomerization was observed in the Heck coupling with α-styryl *O*,*O*-diphenylphosphate (Table 3, entries 7 and 8). The reaction of acrylamide with this vinyl phosphate in dioxane was slow but nevertheless afforded 12% yield of the nonisomerized product and recovered starting material after 24 h. In contrast, the same Heck coupling performed in DMF led to a 4:3 mixture of the isomerized and normal Heck products. Recent work by Hartwig and co-workers has shown that isomerization does not take place for Kumada couplings with α-styryl tosylate in toluene.[4b] Hence, it is interesting to note how subtle changes in both structure and solvent can have a marked influence on the isomerization process in these Heck couplings.

A conceivable mechanism for this 1,2-migration involves an initial β-hydride elimination of the palladium(II) species after the oxidative-addition step to give an intermediate alkyne-coordinated palladium hydride species.[17] To gain further insight into the plausibility of this reaction mechanism, a DFT study was conducted for the *tert*-butyl vinyl substrates (Figure 1).[18] The starting point for the calculations was a T-shaped complex **3** that coordinated $P(tBu)_3$, a chloride ion, and the *tert*-butyl vinyl group. Under the experimental reaction conditions, chloride ions are present in the reaction solution; thus, it is likely that a chloride ion displaces the leaving-group anion (tosylate or phosphate). Due to the large steric bulk of the *tert*-butyl alkene and $P(tBu)_3$, they are likely to be positioned *trans* to each other. Palladium(II) complexes containing $P(tBu)_3$ have previously been shown to form tri-coordinate T-shaped complexes rather than the more commonly observed tetra-coordinate square-planar-type complexes.[19] A free coordination site is therefore available to facilitate a potential hydride elimination from any group containing a β hydrogen, as the need for decoordination of a ligand prior to the actual elimination is not present.

From complex **3**, there are then two possibilities, either coordination and insertion of the olefin, or initial 1,2-palladium migration with subsequent coordination and insertion of the olefin. A transition state **TS1** was characterized in which the hydride is transferred to the palladium center, thus yielding the *tert*-butyl acetylene hydride palladium(II) com-

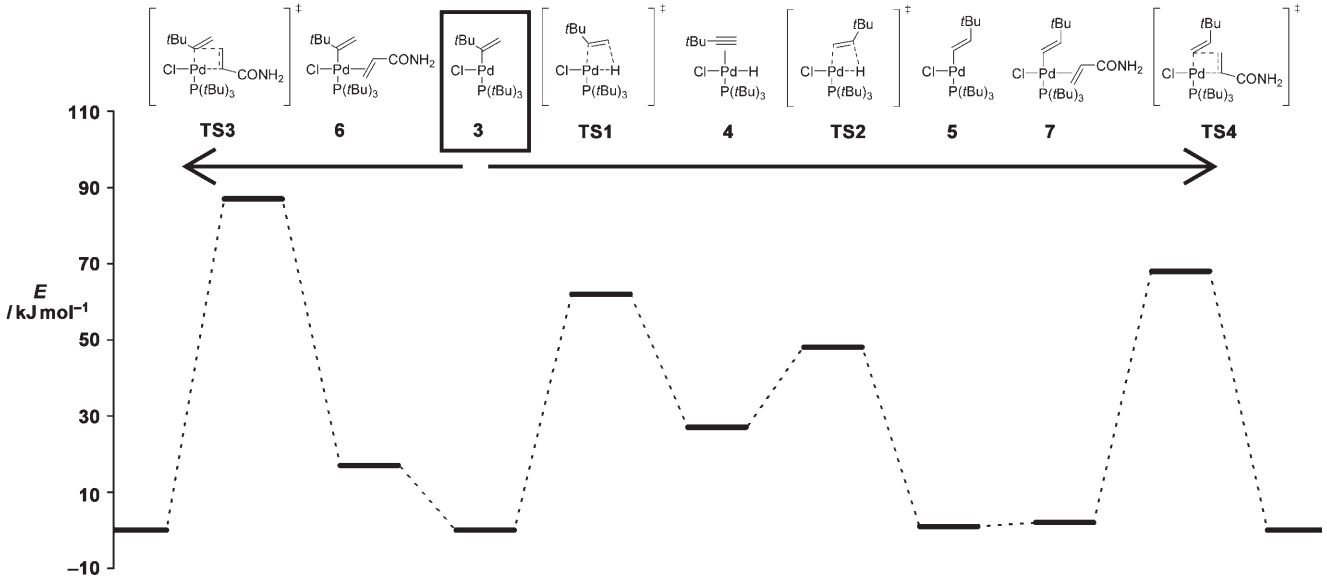

Figure 1. Schematic presentation of the relative energies of the structures **3**–**7** and **TS1**–**TS4**.

 © 2006 Wiley-VCH Verlag GmbH & Co. KGaA, Weinheim

plex **4**. The transformation was calculated to proceed with a barrier of 62 kJ mol^{-1}, and the intermediate **4** was found to be 27 kJ mol^{-1} higher in potential energy than **3**. Subsequent insertion of *tert*-butyl acetylene in the Pd–H bond proceeds via **TS2** to yield the isomeric terminal *tert*-butyl vinyl palladium(II) complex **5**. The barrier from **4** was calculated to be 21 kJ mol^{-1}, and the overall isomerization reaction from **3** to **5** is basically thermoneutral, with **5** having a potential energy 1 kJ mol^{-1} above that of **3**. To conclude, the highest barrier for isomerization between the two isomeric palladium–vinyl intermediates was calculated to be 62 kJ mol^{-1} (**TS1**). With such a low barrier, the reaction is likely to proceed rapidly under the reaction conditions. Still, to observe scrambling it is necessary that the barrier for isomerization is lower than the carbopalladation of the olefin. The difference in energy between the barriers for the insertion step then determines the product outcome, thus representing a typical Curtin–Hammett situation.

Further calculations are in support of this hypothesis. Coordination of an olefin (here acrylamide) with **3** yields the prereactive complex **6**, and subsequent insertion takes place via **TS3** with an overall barrier of 87 kJ mol^{-1} relative to **3**. The barrier for the β-hydride elimination described above was found to be 25 kJ mol^{-1} lower in potential energy and is thus several orders of magnitude more rapid than the insertion of acrylamide.[20] At the isomerized complex **5**, coordination of acrylamide results in complex **7**. The insertion occurs via **TS4** with an overall calculated barrier of 68 kJ mol^{-1}, 19 kJ mol^{-1} lower than **TS3**, from which we conclude that the path that leads to the isomerized product is strongly favored.

Finally, some experimental support for this migration was obtained from a coupling experiment between *p*-phenylstyrene and the dideuterated vinyl tosylate **8** (Scheme 2). Under identical coupling conditions with the nonlabeled tosylate, a 72% yield of the diene **9** was isolated in which migration of one deuterium atom was observed.[21]

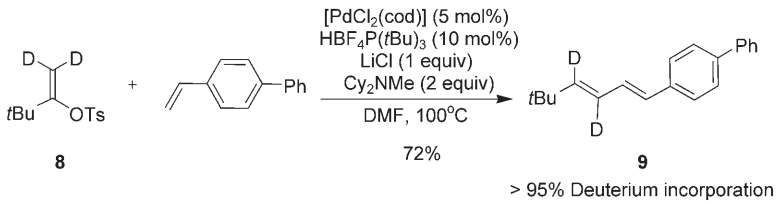

Scheme 2. Isomerization studies with a dideuterated substrate **8**.

In conclusion, we have demonstrated the potential for nonactivated vinyl tosylates and phosphates to be worthy substrates for Heck couplings with electron-poor alkenes and styrene derivatives. Furthermore, effective 1,2-migrations of the alkenyl palladium(II) intermediate has been observed, thus providing a new variation of the Heck coupling. A feasible path for this rearrangement has been located using DFT methods. Further work is currently underway to identify more effective conditions under which the catalyst loading can be lowered and the selectivity to produce either the normal or the isomerized Heck products can be controlled. This work will be reported in due course.

Experimental Section

(*E*)-4-(2-(4-*tert*-Butylcyclohex-1-enyl)vinyl)pyridine: 4-Vinyl pyridine (84 μL, 0.78 mmol), 4-*tert*-butylcyclohex-1-enyl tosylate (60.0 mg, 0.19 mmol), Cy_2NMe (83 μL, 0.38 mmol; Cy = cyclohexyl), LiCl (8.2 mg, 0.19 mmol), and $HBF_4P(tBu)_3$ (5.6 mg, 0.019 mmol) were dissolved in DMF (3 mL). $[PdCl_2(cod)]$ (2.8 mg, 0.0097 mmol) was then added, and the sample vial was fitted with a teflon-sealed screwcap and removed from the glovebox. The reaction mixture was heated for 16 h at 100 °C. After completion, water was added to the crude reaction mixture, followed by extraction with diethyl ether (3 × 25 mL). The organic phases were washed with water (3 × 10 mL) and brine, dried over $MgSO_4$, and concentrated in vacuo. The crude product was purified by flash chromatography on silica gel using ethyl acetate/pentane (1:2) as the eluent, thus affording 41.3 mg of the title compound (88% yield) as a colorless solid. ^{1}H NMR (400 MHz, CD_3CN): $\delta = 8.45$ (d, 2H, $J = 6.4$ Hz), 7.32 (d, 2H, $J = 6.4$ Hz), 7.06 (d, 1H, $J = 16$ Hz), 6.40 (d, 1H, $J = 16$ Hz), 6.05 (t, 1H, $J = 2.8$), 2.47–2.42 (m, 1H), 2.27–2.10 (m, 2H), 2.02–1.93 (m, 2H), 1.32 (ddt, 1H, $J =$ 11.2, 4.8, 1.6 Hz), 1.20 (dq, 1H, $J = 11.2$, 5.2 Hz), 0.90 ppm (s, 9H); ^{13}C NMR (100 MHz, CD_3CN): $\delta = 151.0$, 146.3, 137.2, 136.5, 135.2, 123.31, 121.5, 45.1, 32.8, 28.7, 27.5, 26.5, 24.6 ppm; HRMS $C_{17}H_{23}N$ [M+H$^+$]; calcd: 242.1909; found: 242.1902.

Received: February 2, 2006
Published online: April 11, 2006

Keywords: 1,2-migration · alkenes · Heck reaction · phosphates · tosylates

[1] a) A. de Meijere, F. Diederich, *Metal-Catalyzed Cross-Coupling Reactions*, 2nd ed., Wiley-VCH, Weinheim, **2004**; b) J. Tsuji, *Palladium Reagents and Catalysts, New Perspectives For the 21st Century*, Wiley, Chicester, **2004**; c) *Handbook of Organopalladium Chemistry for Organic Synthesis* (Ed.: E. Negishi), Wiley-Interscience, New York, **2002**.

[2] a) K. C. Nicolaou, G.-Q. Shi, J. L. Gunzner, P. Gärtner, Z. Yang, *J. Am. Chem. Soc.* **1997**, *119*, 5467; b) K. C. Nicolaou, G.-Q. Shi, K. Namoto, F. Bernal, *Chem. Commun.* **1998**, 1757; c) J. Jiang, R. J. DeVita, G. A. Doss, M. T. Goulet, M. J. Wyvratt, *J. Am. Chem. Soc.* **1999**, *121*, 593; d) C. Buon, P. Bouyssou, G. Coudert, *Tetrahedron Lett.* **1999**, *40*, 701; e) F. L. Galbo, E. G. Occhiato, A. Guarna, C. Faggi, *J. Org. Chem.* **2003**, *68*, 6360; f) D. Steinhuebel, J. M. Baxter, M. Palucki, I. W. Davies, *J. Org. Chem.* **2005**, *70*, 10124.

[3] a) F. Lepifre, C. Buon, R. Rabot, P. Bouyssou, G. Coudert, *Tetrahedron Lett.* **1999**, *40*, 6373; b) F. Lepifre, S. Clavier, P. Bouyssou, G. Coudert, *Tetrahedron* **2001**, *57*, 6969; c) J. Wu, L. Wang, R. Fathi, Z. Yang, *Tetrahedron Lett.* **2002**, *43*, 4395; d) H. N. Nguyen, X. Huang, S. Buchwald, *J. Am. Chem. Soc.* **2003**, *125*, 11818; e) U. S. Larsen, L. Martiny, M. Begtrup, *Tetrahedron Lett.* **2005**, *46*, 4261; f) J. M. Baxter, D. Steinhuebel, M. Palucki, I. W. Davies, *Org. Lett.* **2005**, *7*, 215.

[4] a) A. H. Roy, J. F. Hartwig, *J. Am. Chem. Soc.* **2003**, *125*, 8704; b) M. E. Limmert, A. H. Roy, J. F. Hartwig, *J. Org. Chem.* **2005**, *70*, 9364.

[5] D. Gelman, S. L. Buchwald, *Angew. Chem.* **2003**, *115*, 6175; *Angew. Chem. Int. Ed.* **2003**, *42*, 5993.

[6] A. Klapars, K. R. Campos, C.-y. Chen, R. P. Volante, *Org. Lett.* **2005**, *7*, 1185.

[7] a) J. W. Coe, *Org. Lett.* **2000**, *2*, 4205; b) X. Fu, S. Zhang, J. Yin, T. L. McAllister, S. A. Jiang, T. Chou-Hong, K. Thiruvengadam, F. Zhang, *Tetrahedron Lett.* **2002**, *43*, 573; c) A. L. Hansen, T. Skrydstrup, *J. Org. Chem.* **2005**, *70*, 5997; d) A. L. Hansen, T. Skrydstrup, *Org. Lett.* **2005**, *7*, 5585.

 © 2006 Wiley-VCH Verlag GmbH & Co. KGaA, Weinheim

[8] For mechanistic studies on oxidative addition with aryl tosylates, see reference [4a] and A. H. Roy, J. F. Hartwig, *Organometallics* **2004**, *23*, 194.
[9] For a few examples of cross-coupling reactions that employ Ni catalysis, see: a) W. R. Baker, J. K. Pratt, *Tetrahedron* **1993**, *49*, 8739; b) Y. Nan, Z. Yang, *Tetrahedron Lett.* **1999**, *40*, 3321; c) J. Wu, Z. Yang, *J. Org. Chem.* **2001**, *66*, 7875.
[10] For references on the development and application of bulky electron-rich phosphines for cross-coupling reactions, notably through the work of Fu, Buchwald, Hartwig, and Beller, see: A. Zapf, M. Beller, *Chem. Commun.* **2005**, 431.
[11] The synthesis of vinyl tosylates and phosphates was prepared according to reference [4b] through proton abstraction of the required ketones with lithium hexamethyldisilazide (LiHMDS) in THF and subsequent treatment with tosyl anhydride or diphenyl chlorophosphate.
[12] The lithium enolate required for the preparation of vinyl tosylate from Table 1, entry 12 was prepared from cyclofragmentation from lithiated THF; see: a) R. B. Bates, L. M. Kroposki, D. E. Potter, *J. Org. Chem.* **1972**, *37*, 560; b) M. E. Jung, R. B. Blum, *Tetrahedron Lett.* **1977**, *18*, 3791; c) I. M. Lyapkalo, M. Webel, H.-U. Reissig, *Eur. J. Org. Chem.* **2001**, 4189.
[13] M. R. Netherton, G. C. Fu, *Org. Lett.* **2001**, *3*, 4295.
[14] The rate acceleration effect of added halide ions to Pd-catalyzed cross-coupling reactions has been proposed to be a result of a medium effect and a more reactive halide-coordinated Pd^0 species; for a recent discussion on the effect of added halide ions with relevant references, see reference [8]. As our previous results in Heck couplings with activated vinyl tosylates suggest that the tosylate is not bound to the alkenyl palladium(II) species after oxidative addition[7c,d] in solvents such as dioxane and, undoubtedly also, DMF, we suggest that added LiCl assures that the reaction passes through a neutral pathway in these Heck couplings by trapping the Pd^{II} cationic intermediate.
[15] A couple of examples of this migration have been reported in two other cross-coupling reactions, although in modest yield; see reference [4b] and J. Takagi, K. Takahashi, T. Ishiyama, N. Miyaura, *J. Am. Chem. Soc.* **2002**, *124*, 8001.
[16] For a recent review on 1,4-migrations, see: S. Ma, Z. Gu, *Angew. Chem.* **2005**, *117*, 7680; *Angew. Chem. Int. Ed.* **2005**, *44*, 7512; .
[17] Along with a mechanism involving β-hydride elimination, an alternative explanation was proposed by Hartwig and co-workers in the 1,2-migration observed for the Kumada couplings with vinyl tosylates.[4b] The presence of a strong base was suggested to induce elimination of the tosylate, thus leading to an alkyne. We do not believe this mechanism holds for these Heck couplings because of the weak base used in these coupling reactions. N. Frydman, R. Bixon, M. Sprecher, Y. Mazur, *J. Chem. Soc. Chem. Commun.* **1969**, 1044.
[18] DFT calculations were carried out with the Jaguar 4.2 program package from Schrödinger Inc., Portland, Oregon: http://www.schrodinger.com. All the calculations were performed at the B3LYP/LACVP* level. The geometries were fully optimized in solvent and simulated with the PB-SCRF model: B. Marten, K. Kim, C. Cortis, R. A. Friesner, R. B. Murphy, M. N. Ringnalda, D. Sitkoff, B. Honig, *J. Phys. Chem.* **1996**, *100*, 11775. The parameters were set to $\varepsilon = 38$, probe radius = 2.47982 to simulate DMF.
[19] J. P. Stambuli, C. D. Incarvito, M. Bühl, J. F. Hartwig, *J. Am. Chem. Soc.* **2004**, *126*, 1184.
[20] As the β-hydride elimination is a unimolecular process, while the olefin insertion is bimolecular, the β-hydride is also strongly favored entropically. Earlier studies have shown that a value of approximately 40–60 kJ mol^{-1} should be added to account for the change in molecularity; see: a) M. S. Searle, M. S. Westwell, D. H. Williams, *J. Chem. Soc. Perkin Trans. 2* **1995**, *1*, 141; b) T. K. Woo, P. E. Blöchl, T. Ziegler, *J. Phys. Chem. A* **2000**, *104*, 121; c) M. Ahlquist, P. Fristrup, D. Tanner, P.-O. Norrby, *Organometallics* **2006**, DOI: 10.1021/om060126q.
[21] A cross-over experiment was also performed with the 1-*tert*-butylvinyl tosylate by the addition of 1-hexyne representing a less hindered alkyne. No hydropalladation and subsequent coupling to an alkene was observed with this alkyne, thus suggesting that the insertion step is probably faster than dissociation of the *tert*-butylacetylene from the palladium hydride intermediate.

 © 2006 Wiley-VCH Verlag GmbH & Co. KGaA, Weinheim

Asymmetric Catalysis

DOI: 10.1002/anie.200600392

Rhodium-Catalyzed Asymmetric Addition of Aryl- and Alkenylboronic Acids to Isatins**

*Ryo Shintani, Mitsunori Inoue, and Tamio Hayashi**

Oxindoles constitute a common structural motif in various natural products and biologically active compounds.[1] Among them, 3-aryl-3-hydroxy-2-oxindoles are a useful class of compounds found in several drug candidates.[2–4] For example, compound **A** (SM-130686) is a potent growth hormone secretagogue[2] and compound **B** shows a high affinity for the arginine-vasopressin (AVP) V_{1b} receptors and/or the ocytocin (OT) receptors (Figure 1).[3] Owing to the signifi-

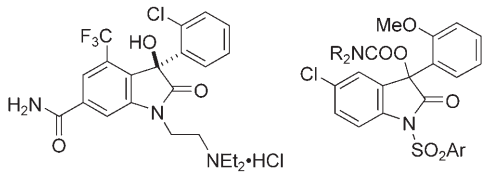

A (SM-130686) **B**

Figure 1. Examples of biologically active 3-aryl-3-hydroxy-2-oxindoles.

cance of this structural motif, the development of a catalytic asymmetric synthesis of these compounds is highly valuable, and the asymmetric arylation of isatins would be the most straightforward approach to this end. To the best of our

[*] Dr. R. Shintani, M. Inoue, Prof. Dr. T. Hayashi
Department of Chemistry
Graduate School of Science
Kyoto University
Sakyo, Kyoto 606-8502 (Japan)
Fax: (+81) 75-753-3988
E-mail: thayashi@kuchem.kyoto-u.ac.jp

[**] Support was provided in part by a Grant-in-Aid for Scientific Research from the Ministry of Education, Culture, Sports, Science, and Technology, Japan (21 COE on Kyoto University Alliance for Chemistry).

Supporting information for this article is available on the WWW under http://www.angewandte.org or from the author.

© 2006 Wiley-VCH Verlag GmbH & Co. KGaA, Weinheim
InterScience

knowledge, however, there have been no examples reported to date that employ this strategy.[5,6] Herein, we report that a Rh/(*R*)-MeO-mop complex catalyzes the addition of aryl- and alkenylboronic acids to isatins **1** under mild conditions, achieving high enantioselectivity [Eq. (1)].[7–10]

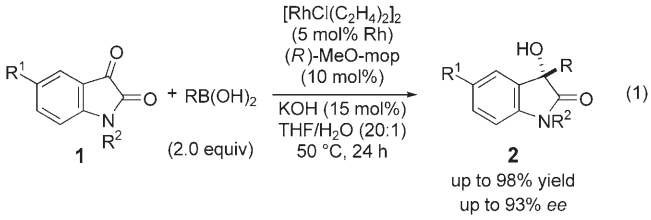

(1)

Initially, we conducted a reaction of isatin **1a** with phenylboronic acid in the presence of 5 mol% rhodium catalyst at 50°C to examine the effect of chiral ligands (Table 1). The use of (*R*)-binap,[11] which is highly effective for the rhodium-catalyzed asymmetric addition of arylboronic acids to various electron-deficient olefins,[12] quantitatively produced addition product **2a**, but with only 24% *ee* (Table 1, entry 1). Other chiral bis(phosphine) ligands such as (*R*)-segphos[13] also turned out to be ineffective in achieving high enantioselectivity (Table 1, entry 2; 19% *ee*). We therefore decided to explore other types of chiral ligands. Unfortunately, the use of (*S*)-ip-phox,[14] a bidentate P,N ligand, did not promote this addition reaction (Table 1, entry 3). The employment of (*S*)-phosphoramidite[15] or (*S*)-(*R*)-ppf-OMe[16] gave compound **2a**, but the enantioselectivity was still unsatisfactory (Table 1, entries 4 and 5; 39–49% *ee*). In contrast, the use of (*R*)-MeO-mop,[17] an axially chiral monophosphine ligand, gave high yields and significantly improved the enantioselectivity (Table 1, entry 6; 92% yield, 90% *ee*).[18]

Under these conditions with (*R*)-MeO-mop as a ligand, various arylboronic acids reacted with isatin **1a** to furnish 3-aryl-3-hydroxy-2-oxindoles **2** in excellent yield and with high enantioselectivity (Table 2, entries 1–6; 90–98% yield, 82–91% *ee*). Although the yield remained high in the addition of *o*-tolylboronic acid, a decrease in the *ee* value was observed

Table 1: Rhodium-catalyzed asymmetric addition of phenylboronic acid to isatin **1a**.[a]

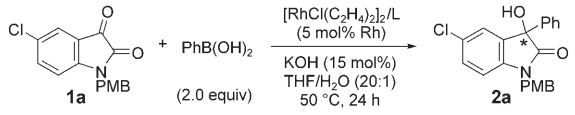

Entry	Ligand (L)	Yield [%][b]	*ee* [%][c]
1	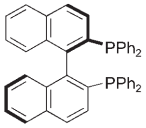 (*R*)-binap	100	24 (*S*)
2	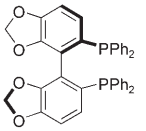 (*R*)-segphos	80	19 (*S*)
3	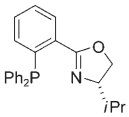 (*S*)-ip-phox	< 2	–
4	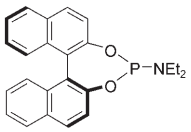 (*S*)-phospor amidite	66	39 (*S*)
5	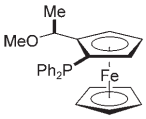 (*S*)-(*R*)-ppf-OMe	43	49 (*R*)
6	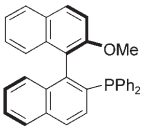 (*R*)-MeO-mop	92	90 (*S*)

[a] Rh/L = 1:1 (entries 1–3); Rh/L = 1:2 (entries 4–6). PMB = *p*-methoxybenzyl. [b] Isolated yield. [c] *ee* values were determined by HPLC on a chiralcel OD-H column with hexane/2-propanol (80:20).

Table 2: Asymmetric addition of arylboronic acids to isatin **1a** catalyzed by Rh/(*R*)-MeO-mop.

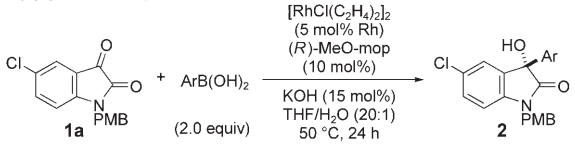

Entry	Product	Yield [%][a]	*ee* [%][b]
1	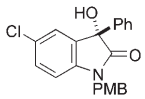 **2a**	92	90
2	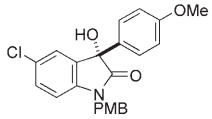 **2b**	90	91
3	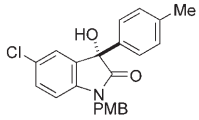 **2c**	96	89
4	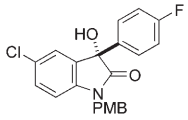 **2d**	95	82
5	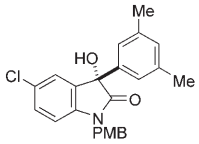 **2e**	98	90
6	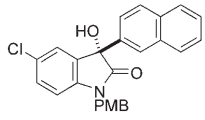 **2f**	96	88
7	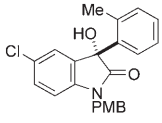 **2g**	93	72

[a] Isolated yield. [b] *ee* values were determined by HPLC on a Chiralcel OD-H column with hexane/2-propanol (80:20).

 © 2006 Wiley-VCH Verlag GmbH & Co. KGaA, Weinheim

(Table 2, entry 7; 93% yield, 72% *ee*). The absolute configurations of these products were assigned as *S* from X-ray crystallographic analysis of compound **2e** (Figure 2).[19,20]

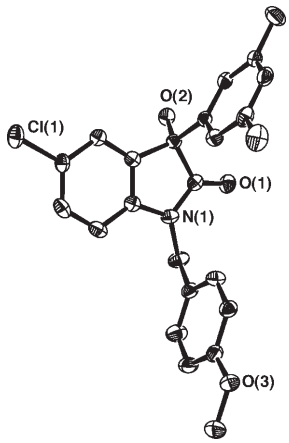

Figure 2. ORTEP illustration of **2e** with thermal ellipsoids drawn at the 50% probability level (hydrogen atoms are omitted for clarity).

Moreover, isatins bearing different substituents on the nitrogen atom and/or the aromatic ring could also be phenylated effectively under these conditions (Table 3, entries 1–4; 78–83% yield, 82–89% *ee*). Even NH isatins underwent the addition reaction with moderate efficiency (Table 3, entry 5; 49% yield, 87% *ee*), in contrast to the copper-catalyzed N-arylation of NH isatins with arylboronic acids.[21]

We also found that the Rh/(*R*)-MeO-mop complex effectively catalyzes the addition of alkenylboronic acids to give tertiary allylic alcohol derivatives in excellent yield and with high *ee* values [Eq. (2); 91–98% yield, 88–93% *ee*].

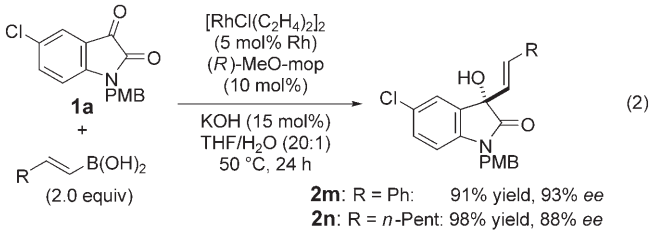

In summary, we have developed a rhodium-catalyzed asymmetric addition of arylboronic acids to isatins to produce biologically relevant 3-aryl-3-hydroxy-2-oxindoles in high yield. High enantioselectivity was achieved by the use of (*R*)-MeO-mop as a ligand, and these conditions can also be used in the addition of alkenyl groups with high enantioselectivity.

Table 3: Asymmetric addition of phenylboronic acid to isatins catalyzed by Rh/(*R*)-MeO-mop.[a]

Entry	Product		Yield [%][b]	*ee* [%][c]
1	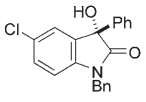	**2h**	80	89[d]
2	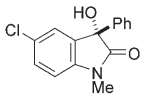	**2i**	83	88
3	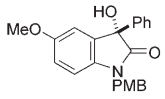	**2j**	78	82
4	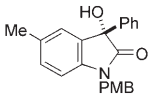	**2k**	79	87
5	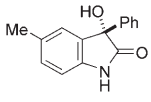	**2l**	49	87

[a] See Table 2 for conditions. [b] Isolated yield. [c] *ee* values were determined by HPLC on a Chiralcel OD-H column with hexane/2-propanol (80:20 or 90:10) unless otherwise noted. [d] *ee* value was determined by HPLC on a Chiralpak AD-H column with hexane/2-propanol (80:20).

Experimental Section

General procedure for reactions described in Tables 2 and 3: A solution of $[RhCl(C_2H_4)_2]_2$ (1.9 mg, 9.8 μmol Rh) and (*R*)-MeO-mop (9.4 mg, 20 μmol) in THF (1.0 mL) was stirred for 10 min at room temperature. KOH (0.10 mL, 30 μmol; 0.3 M aqueous), isatin **1** (0.20 mmol), and $RB(OH)_2$ (0.40 mmol) were added successively with additional THF (1.0 mL), and the resulting mixture was stirred for 24 h at 50 °C. The mixture was then directly passed through a pad of silica gel with Et_2O, and after removing the solvent under vacuum, the residue was purified by preparative thin-layer chromatography on silica gel with EtOAc/$CHCl_3$ to afford the 1,2-adduct **2**.

Received: January 30, 2006
Published online: April 5, 2006

Keywords: asymmetric catalysis · boron · isatins · oxindoles · rhodium

[1] a) M. Somei, F. Yamada, *Nat. Prod. Rep.* **2003**, *20*, 216; b) S. Hibino, T. Choshi, *Nat. Prod. Rep.* **2002**, *19*, 148; c) H. R. Howard, J. A. Lowe III, T. F. Seeger, P. A. Seymour, S. H. Zorn, P. R. Maloney, F. E. Ewing, M. E. Newman, A. W. Schmidt, J. S. Furman, G. L. Robinson, E. Jackson, C. Johnson, J. Morrone, *J. Med. Chem.* **1996**, *39*, 143; d) Y. Koguchi, J. Kohno, M. Nishio, K. Takahashi, T. Okuda, T. Ohnuki, S. Komatsubara, *J. Antibiot.* **2000**, *53*, 105; e) Y.-Q. Tang, I. Sattler, R. Thiericke, S. Grabley, X.-Z. Feng, *Eur. J. Org. Chem.* **2001**, 261; f) H. Suzuki, H. Morita, M. Shiro, J. Kobayashi, *Tetrahedron* **2004**, *60*, 2489.

[2] a) T. Tokunaga, W. E. Hume, T. Umezome, K. Okazaki, Y. Ueki, K. Kumagai, S. Hourai, J. Nagamine, H. Seki, M. Taiji, H. Noguchi, R. Nagata, *J. Med. Chem.* **2001**, *44*, 4641; b) J. Nagamine, R. Nagata, H. Seki, N. Nomura-Akimaru, Y. Ueki, K. Kumagai, M. Taiji, H. Noguchi, *J. Endocrinol.* **2001**, *171*, 481; c) T. Tokunaga, W. E. Hume, J. Nagamine, T. Kawamura, M. Taiji, R. Nagata, *Bioorg. Med. Chem. Lett.* **2005**, *15*, 1789.

[3] A. Di Malta, G. Garcia, R. Roux, B. Schoentjes, C. Serradeil-le Gal, B. Tonnerre, J. Wagnon, PCT Int. Appl. No. WO2003008407, **2003**.

[4] P. Hewawasam, M. Erway, S. L. Moon, J. Knipe, H. Weiner, C. G. Boissard, D. J. Post-Munson, Q. Gao, S. Huang, V. K. Gribkoff, N. A. Meanwell, *J. Med. Chem.* **2002**, *45*, 1487.

 © 2006 Wiley-VCH Verlag GmbH & Co. KGaA, Weinheim

[5] There have been scattered examples of the preparation of enantiomerically enriched 3-aryl-3-hydroxy-2-oxindoles: a) by using an enantiopure substrate: S. Barroso, G. Blay, L. Cardona, I. Fernández, B. García, J. R. Pedro, *J. Org. Chem.* **2004**, *69*, 6821; b) by using an enantiopure reagent: see Ref. [4]; c) through chiral HPLC resolution: see Ref. [2a].

[6] For examples of the catalytic asymmetric preparation of 3-alkyl-3-hydroxy-2-oxindoles from isatins with moderate enantioselectivity, see: a) K. Funabashi, M. Jachmann, M. Kanai, M. Shibasaki, *Angew. Chem.* **2003**, *115*, 5529; *Angew. Chem. Int. Ed.* **2003**, *42*, 5489 (76% *ee*); b) G. Luppi, P. G. Cozzi, M. Monari, B. Kaptein, Q. B. Broxterman, C. Tomasini, *J. Org. Chem.* **2005**, *70*, 7418 (up to 77% *ee*).

[7] For rhodium-catalyzed asymmetric phenylation of aldehydes, see: a) M. Sakai, M. Ueda, N. Miyaura, *Angew. Chem.* **1998**, *110*, 3475; *Angew. Chem. Int. Ed.* **1998**, *37*, 3279; b) K. Suzuki, S. Ishii, K. Kondo, T. Aoyama, *Synlett* **2006**, 648.

[8] Very recently, a rhodium-catalyzed asymmetric alkenylation of α-ketoesters was reported, see: J.-R. Kong, M.-Y. Ngai, M. J. Krische, *J. Am. Chem. Soc.* **2006**, *128*, 718.

[9] For catalytic asymmetric addition of organozinc reagents to ketones, see: a) P. I. Dosa, G. C. Fu, *J. Am. Chem. Soc.* **1998**, *120*, 445; b) L. Pu, *Tetrahedron* **2003**, *59*, 9873; c) J. M. Betancort, C. García, P. J. Walsh, *Synlett* **2004**, 749; d) D. J. Ramón, M. Yus, *Angew. Chem.* **2004**, *116*, 286; *Angew. Chem. Int. Ed.* **2004**, *43*, 284.

[10] For an example of a rhodium-catalyzed non-asymmetric addition of organotin reagents to activated ketones, see: S. Oi, M. Moro, H. Fukuhara, T. Kawanishi, Y. Inoue, *Tetrahedron* **2003**, *59*, 4351.

[11] H. Takaya, K. Mashima, K. Koyano, M. Yagi, H. Kumobayashi, T. Taketomi, S. Akutagawa, R. Noyori, *J. Org. Chem.* **1986**, *51*, 629.

[12] a) Y. Takaya, M. Ogasawara, T. Hayashi, M. Sakai, N. Miyaura, *J. Am. Chem. Soc.* **1998**, *120*, 5579; b) T. Hayashi, M. Takahashi, Y. Takaya, M. Ogasawara, *J. Am. Chem. Soc.* **2002**, *124*, 5052; for reviews, see: c) T. Hayashi, K. Yamasaki, *Chem. Rev.* **2003**, *103*, 2829; d) K. Fagnou, M. Lautens, *Chem. Rev.* **2003**, *103*, 169.

[13] T. Saito, T. Yokozawa, T. Ishizaki, T. Moroi, N. Sayo, T. Miura, H. Kumobayashi, *Adv. Synth. Catal.* **2001**, *343*, 264.

[14] a) P. von Matt, A. Pfaltz, *Angew. Chem.* **1993**, *105*, 614; *Angew. Chem. Int. Ed. Engl.* **1993**, *32*, 566; b) J. Sprinz, G. Helmchen, *Tetrahedron Lett.* **1993**, *34*, 1769; c) G. J. Dawson, C. G. Frost, J. M. J. Williams, S. J. Coote, *Tetrahedron Lett.* **1993**, *34*, 3149.

[15] a) J.-G. Boiteau, A. J. Minnaard, B. L. Feringa, *J. Org. Chem.* **2003**, *68*, 9481; b) B. L. Feringa, *Acc. Chem. Res.* **2000**, *33*, 346.

[16] T. Hayashi, T. Mise, M. Fukushima, M. Kagotani, N. Nagashima, Y. Hamada, A. Matsumoto, S. Kawakami, M. Konishi, K. Yamamoto, M. Kumada, *Bull. Chem. Soc. Jpn.* **1980**, *53*, 1138.

[17] a) T. Hayashi, *Acc. Chem. Res.* **2000**, *33*, 354; b) Y. Uozumi, A. Tanahashi, S.-Y. Lee, T. Hayashi, *J. Org. Chem.* **1993**, *58*, 1945.

[18] The reaction does not proceed in the absence of KOH.

[19] The Flack parameter is 0.00(4) with this configuration (see Supporting Information for details): H. D. Flack, *Acta Crystallogr. Sect. A* **1983**, *39*, 876.

[20] CCDC-293711 contains the supplementary crystallographic data for this paper. These data can be obtained free of charge from The Cambridge Crystallographic Data Centre via www.ccdc.cam.ac.uk/data_request/cif.

[21] a) D. M. T. Chan, K. L. Monaco, R.-P. Wang, M. P. Winters, *Tetrahedron Lett.* **1998**, *39*, 2933; b) P. Y. S. Lam, G. Vincent, C. G. Clark, S. Deudon, P. K. Jadhav, *Tetrahedron Lett.* **2001**, *42*, 3415; c) G. C. H. Chiang, T. Olsson, *Org. Lett.* **2004**, *6*, 3079.

 © 2006 Wiley-VCH Verlag GmbH & Co. KGaA, Weinheim

Synthetic Methods

DOI: 10.1002/anie.200600169

Highly Diastereoselective Silyl-Modified Sakurai Multicomponent Reaction**

*Jiøí Pospíšil, Takuya Kumamoto, and István E. Markó**

Dedicated to Professor Milan Potáček

Multicomponent reactions (MCRs) are some of the most interesting and challenging transformations in organic synthesis.[1–7] The ability to form two or more C–C and/or C–heteroatom bonds with high levels of stereocontrol and in a single operation is one of the most exciting areas of research in chemistry. It has been rapidly recognized that MCRs have not only been sought after for their academic interest but also for their industrial relevance,[8] especially owing to their high atom economy,[9–11] selectivity, and low levels of by-products.

Asymmetric multicomponent reactions (AMCRs) belong to the finest arena of this chemistry.[12] By definition, AMCR is a transformation in which three or more chiral or achiral reagents, placed in single vessel, react together sequentially to form a chiral compound stereoselectively. This adduct should contain portions of all the individual components, and at least one new stereogenic center should be generated.[12]

For some time, we have been interested in the silyl-modified Sakurai reaction (also known as the Sakurai MCR),[13] especially the catalytic and intramolecular version.[14–16] The Sakurai MCR involves the Lewis acid catalyzed condensation of carbonyl derivatives (ketones, aldehydes, ketals, hemiketals, orthoesters, ortholactones) with allylic silanes and alcohols (or silyl ethers), thus yielding the corresponding homoallylic ethers (Scheme 1).

As part of a general program directed towards the preparation of novel antifungal agents,[17–19] it was deemed important to study and develop new strategies for the rapid, efficient, and versatile synthesis of (+)-ambruticin (**5**)[20] and related analogues. To reach this goal, a general and concise route towards dihydropyrans, such as **6**, which would allow a broad spectrum of substitutions at any position of the heterocyclic ring system, was sought after.[21–23]

[*] J. Pospíšil, Prof. I. E. Markó
Département de Chimie
Université Catholique de Louvain
Place Louis Pasteur 1, 1348 Louvain-la-Neuve (Belgium)
Fax: (+32) 010-472-788
E-mail: marko@chim.ucl.ac.be
Dr. T. Kumamoto
Graduate School of Pharmaceutical Sciences
Chiba University
1-33 Yayoi, Inage, Chiba 263-8522 (Japan)

[**] Financial support by the Université Catholique de Louvain, Rhodia Ltd. (studentship to J.P.) and the Japan Society for the Promotion of Sciences (postdoctoral fellowship to T.K.) is gratefully acknowledged. I.E.M. thanks Rhodia for the 2002 Rhodia Outstanding Award.

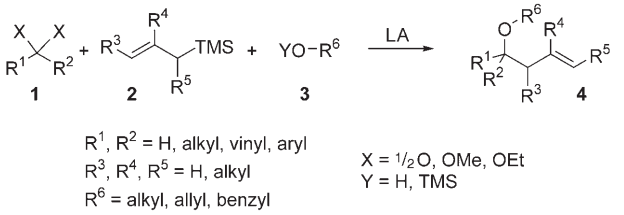

Scheme 1. The Sakurai MCR. LA = Lewis acid, TMS = trimethylsilyl.

Despite a previously successful construction of fragment **6**,[18] a domino Sakurai MCR/metathesis approach was envisioned as the most direct and flexible route towards **6** (Scheme 2).

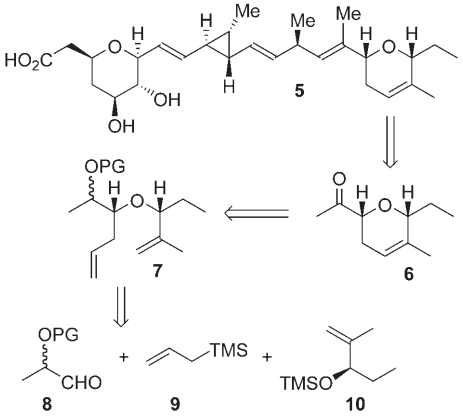

Scheme 2. Retrosynthetic analysis of (+)-ambruticin. PG = protecting group.

Although several examples of using asymmetric Sakurai MCRs with chiral alcohols[24–27] or their derivatives[28–34] to create a new stereogenic center have been reported, to the best of our knowledge, no example using chiral aldehydes or ketones has been disclosed so far. Herein, we present our results for the first chiral-aldehyde-based Sakurai MCR condensation that gives a rapid, versatile, and highly stereoselective access to diastereomerically enriched homoallylic ethers **7**. The synthetic power of this method will be illustrated by the efficient and stereocontrolled assembly of dihydropyran **6** (Scheme 2).

Initially, aldehyde (−)-**8**, prepared from ethyl lactate[35] by a protection/reduction sequence, commercially available allyl silane **9** and silylated alcohol **10**[36] were selected, and the possible influence of the protecting group present in (−)-**8** was examined (Table 1). It was found that bulky substituents, which inhibit the interaction between the Lewis acid and the lone pairs of electrons on the oxygen atom of (−)-**8**, gave adducts **7** in good yields (Table 1, entries 1–3). No deprotection of the *tert*-butyldimethylsilyl (TBS) or *tert*-butyldiphenylsilyl (TBDPS) groups by trimethylsilyl triflate (TMSOTf) was observed in situ. To our surprise, the TBS and TBDPS moieties also exert a dramatic influence on the diastereoselectivity of the reaction. Indeed, (*S*)-Bn-**8** afforded the desired product **7** as a 1:1 mixture of diastereoisomers (Table 1, entry 1), whereas (*S*)-TBS-**8** and (*S*)-TBDPS-**8**

 © 2006 Wiley-VCH Verlag GmbH & Co. KGaA, Weinheim

Table 1: Multicomponent Sakurai condensation—reaction optimization.

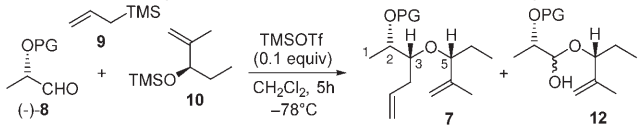

Entry	PG[a]	Workup	Yield[b] [%]	d.r.[c]	Yield of **12**[d] [%]
1	Bn	sat. $NaHCO_3$	18	1:1	56
2	TBS	sat. $NaHCO_3$	56	>95:1	25
3	TBDPS	sat. $NaHCO_3$	62	>95:1	10
4	TBS	pyridine	80	>95:1	11
5	TBDPS	pyridine	81	>95:1	11
6[e]	TBS	pyridine	65	>95:1	<5

[a] PG = protecting group. [b] Yields of the isolated products. [c] Determined by ^{1}H NMR spectroscopic analysis. [d] Determined by GC analysis. [e] Additive 2,6-di-*tert*-butyl-4-methylpyridine.

provided the corresponding 2,3-*syn* adduct **7** in diastereomerically pure form (Table 1, entries 2 and 3). Hemiacetal **12** was identified in some cases as the main side product of this three-component coupling process.

It was thought that **12** could be formed by the hydrolysis of one of the possible reaction intermediates during the workup procedure.[37] Therefore, various quenching methods and additives, which should capture adventitious traces of triflic acid (TfOH), were tested (Table 1, entries 4–6).

As can be seen in Table 1, the addition of pyridine as a trapping agent for TMSOTf and TfOH gave superior results to $NaHCO_3$ (entries 4 and 5). The addition of 2,6-di-*tert*-butyl-4-methyl pyridine (DTBMP) to the reaction mixture successfully suppressed the formation of **12** but led to incomplete conversion and therefore lower yields of the desired product **7** (Table 1, entry 6).

To determine the absolute configuration of the newly formed stereogenic center, **7** was converted into the right-hand fragment **6** of ambruticinfollowing a metathesis/deprotection/oxidation sequence (Scheme 3). All the chemical and physical data for **6** (including $[\alpha]_D^{20} +181°$ ($c = 0.257$, $CDCl_3$); $[\alpha]_D^{23} +172°$ ($c = 0.248$, $CDCl_3$))[23] agree well with those published by Martin et al. and Donaldson and Lukesh.[21–23] To the best of our knowledge, this synthesis of the ambruticin subunit **6** is the shortest one reported, as **6** is furnished in six steps and 59% overall yield from the commercially available (*S*)-ethyl lactate, allyltrimethylsilane, and methacrolein.

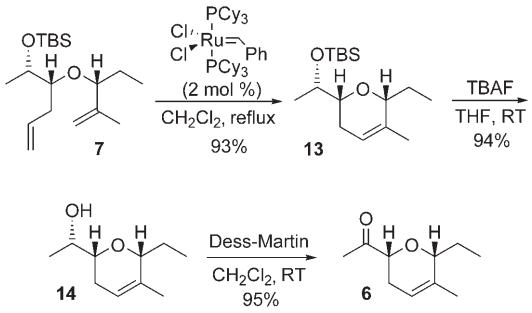

Scheme 3. Synthesis of the right-hand fragment of (+)-ambruticin. cy = cyclohexyl.

To broaden the scope of this multicomponent condensation, with the aim of understanding the origin of the chiral induction, (*S*)-TBDPS-**8** was treated with a variety of silyl ethers and allyl silane **9** in the presence of catalytic amounts of TMSOTf (Table 2).

Table 2: Influence of the silyl ether on the reaction diastereoselectivity.

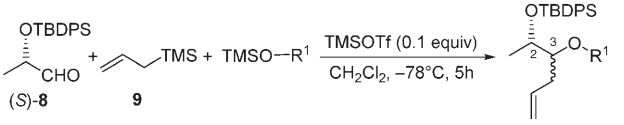

Entry	TMS—OR[1]	Product(s)		Yield[a] [%]
1	TMSO, Ph; **15**	OTBDPS, 2,3-*syn*-**16**	OTBDPS, 2,3-*anti*-**16**	87 (1.2:1 d.r.)
2	OTMS; **17**	OTBDPS, 2,3-*syn*-**18**	OTBDPS, 2,3-*anti*-**18**	79 (1.5:1 d.r.)
3	TMSO; **19**	OTBDPS, 2,3-*syn*-**20**	OTBDPS, 2,3-*anti*-**20**	89 (8:1 d.r.)
4	OTMS; (*S*)-**21**	OTBDPS, 2,3-*syn*-3,5-*syn*-**22**		85
5	OTMS; (*R*)-**21**	OTBDPS, 2,3-*syn*-3,5-*anti*-**22**		84
6	OTMS; **23**	OTBDPS, 2,3-*syn*-**24**		72
7	OTMS; **25**	OTBDPS, 2,3-*syn*-**26**		67

[a] Yields of the isolated products.

Disappointingly, the condensations employing the primary silyl ethers **15** and **17** were not diastereoselective and the desired products were obtained in ratios of 1.2:1–1.5:1 of the 2,3-*syn*/2,3-*anti* isomers, respectively (Table 2, entries 1 and 2). In contrast, adduct **20** was formed in an increased 8:1 *syn*/*anti* ratio when the cyclic secondary silyl ether **19** was employed (Table 2, entry 3). Other silylated secondary and tertiary alcohols gave the 2,3-*syn* diastereoisomer exclusively (Table 2, entries 4–7). It is noteworthy that the stereogenic center present in the silyl ether had no influence on the diastereoselectivity of the reaction (Table 2, entries 4 and 5).

 © 2006 Wiley-VCH Verlag GmbH & Co. KGaA, Weinheim

The lack of a match/mismatch effect in the Sakurai MCR condensation proved to be an unexpected bonus. Indeed, by the judicious choice of the enantiomerically pure aldehyde **8** and silyl ether **10**, all four possible 2,3-*syn*-configured adducts **7** could be prepared in high yield and with complete control of both the relative and absolute configuration of the newly formed stereogenic center (Table 3).

The proposed reaction mechanism of the Sakurai MCR is shown in Scheme 4. It is believed that intermediate **31** is generated under the reaction conditions and equilibrates with the starting aldehyde **8** and the silylated alcohol **10**. The diastereoselectivity observed during this study can be broadly rationalized by invoking an S_N1-type mechanism which involves the oxocarbenium ion **31**. The addition of the allyl silane **9** then proceeds according to the Felkin–Anh transition state **32**, thus delivering the 2,3-*syn* adducts.

In contrast, competing reaction pathways might intervene if primary and cyclic secondary silyl ethers are employed, thus resulting in decreased selectivity.[37]

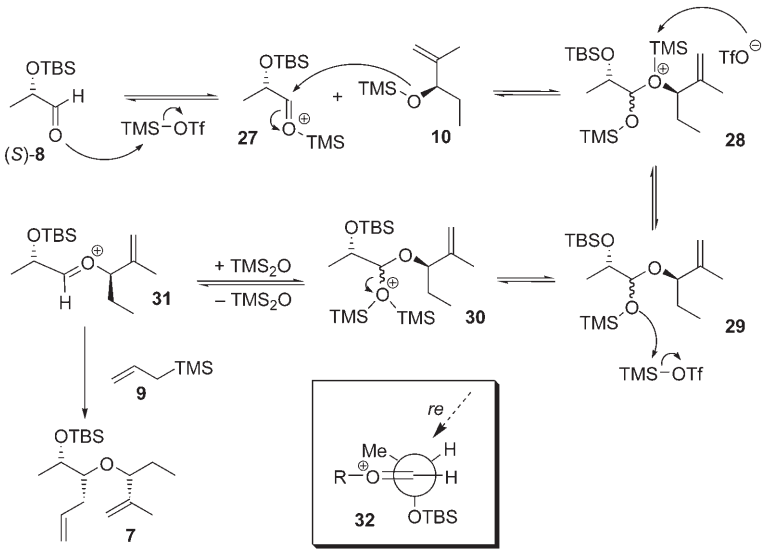

Scheme 4. Proposed reaction mechanism for the Sakurai MCR.

Table 3: The synthesis of the four 2,3-*syn* stereoisomers of **7** (PG = TBDPS).

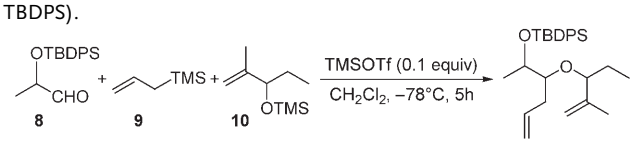

Entry	Aldehyde	Silyl ether	Product	Yield[a] [%]
1	OTBDPS, CHO, (*S*)-**8**	OTMS, (*R*)-**10**	OTBDPS, O, (2*S*,3*R*,5*R*)-**7**	81
2	OTBDPS, CHO, (*S*)-**8**	OTMS, (*S*)-**10**	OTBDPS, O, (2*S*,3*R*,5*S*)-**7**	82
3	OTBDPS, CHO, (*R*)-**8**	OTMS, (*R*)-**10**	OTBDPS, O, (2*R*,3*S*,5*R*)-**7**	75
4	OTBDPS, CHO, (*R*)-**8**	OTMS, (*S*)-**10**	OTBDPS, O, (2*R*,3*S*,5*S*)-**7**	76

[a] Yields of the isolated products.

In summary, we have described the first chiral-aldehyde-based Sakurai MCR, which furnishes the coupled products in good-to-excellent yields (67–87%) and with complete diastereocontrol in the case of secondary and tertiary silyl ethers. These products are versatile building blocks in organic chemistry. To illustrate their utility, the synthesis of the right-hand fragment **6** of (+)-ambruticin has been readily accomplished in six steps and 59% overall yield starting from commercially available products. The scope and limitations of this novel methodology and its application to the synthesis of other challenging intermediates and natural products are currently being actively investigated.

Experimental Section

Typical experimental procedure for the synthesis of (2*S*,3*R*,5*R*)-**7**: A solution of (*S*)-(−)-**8** (7.5 g, 24 mmol, 1.0 equiv), (*R*)-**10** (4.42 g, 25.7 mmol, 1.07 equiv), and **9** (4.20 mL, 26.4 mmol, 1.1 equiv) in dry CH_2Cl_2 (50 mL, 0.5 M, freshly distilled from CaH_2) was cooled to −78 °C and TMSOTf (0.5 mL, 2.40 mmol, 0.1 equiv) was added. The reaction mixture was stirred for 6 h at −78 °C. Pyridine (1.0 mL) was added, and the resulting mixture was stirred for an additional 10 min. A saturated aqueous solution of $NaHCO_3$ (80 mL) was added, and the layers were separated. The aqueous layer was extracted with CH_2Cl_2 (3 × 100 mL), and the pooled organic layers were washed with water (100 mL) and brine (100 mL), dried over $MgSO_4$, and the solvents were carefully evaporated under reduced pressure using a cold water bath. The residue was purified by chromatography on silica gel (∅ = 6.5 cm, 11 cm of SiO_2, 50 mL fractions; petroleum ether/Et_2O 100:1→50:1), thus affording 8.4 g (80%) of the titled compound as a slightly yellow oil.

Received: January 16, 2006
Published online: April 10, 2006

Keywords: diastereoselectivity · heterocycles · multicomponent reactions · Sakurai reaction · total synthesis

[1] a) L. F. Tietze, U. Beifuss, *Angew. Chem.* **1993**, *105*, 137; *Angew. Chem. Int. Ed. Engl.* **1993**, *32*, 131.
[2] L. F. Tietze, *Chem. Rev.* **1996**, *96*, 115.
[3] T.-L. Ho, *Tandem Organic Reactions*, Wiley, New York, **1992**.
[4] P. J. Parsons, C. S. Penkett, A. J. Shell, *Chem. Rev.* **1996**, *96*, 195.
[5] H. M. R. Hoffmann, *Angew. Chem.* **1992**, *104*, 1361; *Angew. Chem. Int. Ed. Engl.* **1992**, *31*, 1332.
[6] K. K. Wang, *Chem. Rev.* **1996**, *96*, 207.

 © 2006 Wiley-VCH Verlag GmbH & Co. KGaA, Weinheim

[7] A. Padwa, M. D. Weingarten, *Chem. Rev.* **1996**, *96*, 223.
[8] H. Bienayme, C. Hulme, G. Oddon, P. Schmitt, *Chem. Eur. J.* **2000**, *6*, 3321.
[9] B. M. Trost, *Science* **1991**, *254*, 1471.
[10] B. M. Trost, *Angew. Chem.* **1995**, *107*, 285; *Angew. Chem. Int. Ed. Engl.* **1995**, *34*, 259.
[11] B. M. Trost, *Acc. Chem. Res.* **2002**, *35*, 695.
[12] D. J. Ramón, M. Yus, *Angew. Chem.* **2005**, *117*, 1628; *Angew. Chem. Int. Ed.* **2005**, *44*, 1602.
[13] T. Jacques, I. E. Markó, J. Pospíšil, *Multicomponent Reactions*, Wiley-VCH, Weinheim, **2005**.
[14] A. Mekhalfia, I. E. Markó, H. Adams, *Tetrahedron Lett.* **1992**, *33*, 4783.
[15] I. E. Markó, R. Dumeunier, C. Leclercq, B. Leroy, J.-M. Plancher, A. Mekhalfia, D. J. Bayston, *Synthesis* **2002**, 958.
[16] B. Leroy, I. E. Markó, *J. Org. Chem.* **2002**, *67*, 8744.
[17] I. E. Markó, D. J. Bayston, *Synthesis* **1996**, 297.
[18] I. E. Markó, D. J. Bayston, *Tetrahedron* **1994**, *50*, 7141.
[19] I. E. Markó, T. Kumamoto, T. Giard, *Adv. Synth. Catal.* **2002**, *344*, 1063.
[20] D. T. Connor, R. C. Greenough, M. von Strandtmann, *J. Org. Chem.* **1977**, *42*, 3664.
[21] T. A. Kirkland, J. Colucci, L. S. Geraci, M. A. Marx, M. Schneider, D. E. Kaelin, Jr., S. F. Martin, *J. Am. Chem. Soc.* **2001**, *123*, 12432.
[22] S. M. Berberich, R. J. Cherney, J. Colucci, C. Courillon, L. S. Geraci, T. A. Kirkland, M. A. Marx, M. F. Schneider, S. F. Martin, *Tetrahedron* **2003**, *59*, 6819.
[23] J. M. Lukesh, W. A. Donaldson, *Tetrahedron Lett.* **2005**, *46*, 5529.
[24] R. Imwinelried, D. Seebach, *Angew. Chem.* **1985**, *97*, 781; *Angew. Chem. Int. Ed. Engl.* **1985**, *24*, 765.
[25] A. Hosomi, H. Sakurai, *Tetrahedron Lett.* **1976**, *17*, 1295.
[26] A. D. Dilman, S. L. Ioffe, *Chem. Rev.* **2003**, *103*, 733.
[27] T. Mukaiyama, M. Ohshima, N. Miyoshi, *Chem. Lett.* **1987**, 1121.
[28] A. Mekhalfia, I. E. Markó, *Tetrahedron Lett.* **1991**, *32*, 4779.
[29] K. Manju, S. Trehan, *Chem. Commun.* **1999**, 1929.
[30] J. Cossrow, S. D. Rychnovsky, *Org. Lett.* **2002**, *4*, 147.
[31] J. R. Huckins, S. D. Rychnovsky, *J. Org. Chem.* **2003**, *68*, 10135.
[32] L. F. Tietze, A. Dolle, K. Schiemann, *J. Am. Chem. Soc.* **1992**, *114*, 1372.
[33] L. F. Tietze, K. Schiemann, C. Wegner, C. Wulff, *Chem. Eur. J.* **1996**, *2*, 1164.
[34] L. F. Tietze, C. Wulff, C. Wegner, A. Schuffenhauer, K. Schiemann, *J. Am. Chem. Soc.* **1998**, *120*, 4276.
[35] L. E. Overman, G. M. Rishton, *Org. Synth.*, Vol. 9, p. 139.
[36] Ether **10** was prepared from methacrolein according to two different protocols, either by kinetic resolution: a) J. Cossy, D. Bauer, V. Bellosta, *Tetrahedron* **2002**, *58*, 5909; or by asymmetric addition: b) X. Zhang, C. Guo, *Tetrahedron Lett.* **1995**, *36*, 4947; c) C. Guo, J. Qiu, X. Zhang, D. Verdugo, M. L. Larter, R. Christie, P. Kenney, P. J. Walsh, *Tetrahedron* **1997**, *53*, 4145.
[37] Detailed discussion of the reaction mechanism will be reported separately.

 © 2006 Wiley-VCH Verlag GmbH & Co. KGaA, Weinheim

Bioactive Surfaces

DOI: 10.1002/anie.200600357

Reactive Polymer Coatings that "Click"**

*Himabindu Nandivada, Hsien-Yeh Chen, Lidija Bondarenko, and Joerg Lahann**

Future advances in the design of biologically active interfaces require novel strategies for the robust and specific attachment of biological ligands onto surfaces.[1] Herein, a new type of biofunctional surface based on alkyne-containing vapor-deposited polymer coatings is reported. These reactive coatings are applicable to a wide range of substrates and can be modified by subsequent spatially directed "click chemistry". Click chemistry represents a family of powerful and efficient chemical reactions, which are modular, widely applicable, relatively insensitive to solvents and pH value, while resulting in stereoselective conversions with high to very high yields.[2] The most widely used click reaction is the Huisgen 1,3-dipolar cycloaddition between azides and terminal alkynes.[3] This coupling reaction has been employed for drug discovery applications[4] and for the target-guided synthesis of enzyme-inhibitors.[5,6] Moreover, Huisgen 1,3-dipolar cycloadditions of azide- and alkyne-functionalized self-assembled monolayers (SAMs) have been used as a versatile tool for tailoring surface functionalities.[7–11] Their bioorthogonality, that is, the dependence on proximity and proper alignment of the reactants make click reactions promising candidates for biointerface design.[12] However, further use is currently hampered by the availability of polymer coatings that can undergo surface-directed dipolar cycloadditions. In the past, chemical vapor deposition (CVD) polymerization of substituted [2,2]paracyclophanes has been instrumental in creating a wide array of functionalized poly-(*p*-xylylenes) with a diverse class of functional groups, such as amines,[13,14] esters,[15–17] aldehydes,[18] and alcohols,[19–21] which enable the immobilization of biomolecules.

To further extend the concept of click-chemistry-based immobilization, we use CVD polymerization for synthesizing alkyne-containing polymer coatings (Scheme 1). Moreover, we demonstrate the applicability of these reactive coatings by

[*] H. Nandivada, H.-Y. Chen, Dr. L. Bondarenko, Prof. J. Lahann
Department of Chemical Engineering
University of Michigan
Ann Arbor, MI-48109 (USA)
Fax: (+1) 734-764-7453
E-mail: lahann@umich.edu

[**] J.L. gratefully acknowledges support from the NSF in form of a CAREER grant (DMR-0449462) and funding from the NSF under the MRI program (DMR-0420785). We thank Prof. Larson, University of Michigan, for use of the fluorescence microscope and Prof. J. Kim, Materials Science and Engineering, University of Michigan, for use of the spectrofluorometer.

Supporting information for this article is available on the WWW under http://www.angewandte.org or from the author.

WILEY InterScience DISCOVER SOMETHING GREAT
© 2006 Wiley-VCH Verlag GmbH & Co. KGaA, Weinheim

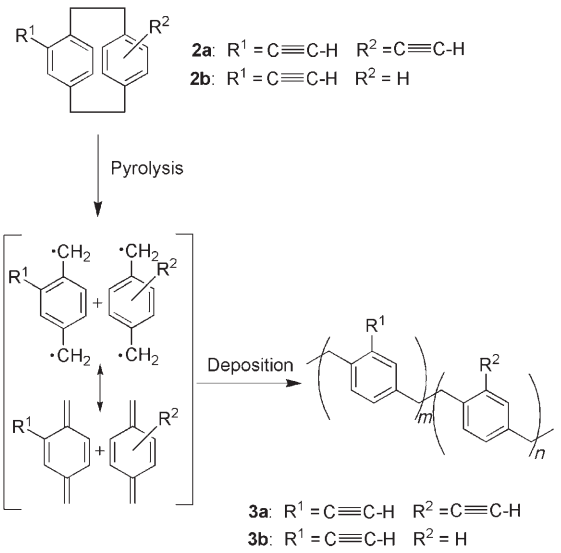

Scheme 1. Synthesis of alkyne-containing polymers by CVD polymerization of diethynyl[2,2]paracyclophane (**2a**) and 4-ethynyl-[2,2]paracyclophane (**2b**).

conducting spatially directed Huisgen 1,3-dipolar cycloaddition on a surface.

Prior to polymer deposition using CVD polymerization, the starting materials diethynyl[2,2]paracyclophane (**2a**) and ethynyl[2,2]paracyclophane (**2b**) were prepared from the commercially available [2.2]paracyclophane (**1**), according to a synthesis recently reported by Hopf and co-workers.[22] Under these conditions, pseudo-*ortho* and pseudo-*meta* derivatives have been reported as the major isomers,[22] but in this case they were not separated for subsequent CVD polymerization.

First, we attempted the CVD polymerization of the dialkyne **2a**, which was expected to yield poly(diethynyl-*p*-xylylene) (**3a**). For this purpose, **2a** was sublimed at 90–110 °C and a reduced pressure of 0.5 mbar. The reactants were then transported into pyrolysis chamber (650 °C) and then into a deposition chamber (15 °C), where the spontaneous formation of a polymer film was observed. However, the FTIR spectrum of polymer films formed under these conditions did not show the band for the alkyne C–H stretch around 3200 cm^{-1}, indicating the absence of alkyne groups. Instead, several side products were formed, which were not further characterized, but could potentially be due to an alkyne–vinylidine rearrangement.[23] Alteration of process conditions, (e.g., pyrolysis temperatures below 550 °C), resulted in alkyne-functionalized polymers, with typical ellipsometric thicknesses of about 50 nm (for 50 mg of the precursor polymerized onto a 4-inch wafer). Nevertheless, these polymer films showed little reactivity, underwent thermal decomposition, and generally had quite poor stability towards organic solvents (see Supporting Information). Thus, they were not pursued further.

Instead, we shifted our focus to the CVD polymerization of the monoalkyne **2b**. In sharp contrast to the dialkyne-containing polymer **3a**, poly(4-ethynyl-*p*-xylylene-co-*p*-xylylene) (**3b**) was prepared without appreciable side reactions, even under very typical CVD conditions[20] (pressure of 0.5 mbar, sublimation, pyrolysis, and substrate temperatures of 90–110 °C, 680 °C, and 15 °C, respectively). Moreover, the FTIR spectrum of **3b** revealed a strong band at 3286 cm^{-1} for the alkyne C–H stretch and a signal at 2100 cm^{-1}, which can be attributed to the carbon–carbon triple bond. Evidence from the FTIR data was reaffirmed by X-ray photoelectron spectroscopy (XPS), which was used to quantify the surface elemental composition of **3b**. The analysis revealed that **3b** contained 1.3 % oxygen, which may be due to contaminations during CVD polymerization or subsequent sample handling. The high resolution C1s spectrum of **3b** further revealed a symmetric and narrow peak centered at 285.6 eV with a full width at half maximum (FWHM) of 1.13 eV. This peak is associated exclusively with the presence of carbon that is bound to carbon or hydrogen.[24] The C1s peak spectrum further showed a smaller signal centered at 291.7 eV, which can be attributed to a π–π^* shake-up signal characteristic of aromatic π electrons. This signal has been observed for similar polymer systems.[19] For polymer **3b**, ellipsometry gave a thickness of 91.81 ± 0.03 nm (for 50 mg of precursor); **3b** is stable in aqueous solutions and organic solvents such as acetone, ethanol, methanol, and chloroform. Probing the adhesiveness of **3b** using the scotch tape test[18] showed that the film had good adhesion to a wide variety of substrates such as glass, poly(dimethylsiloxane) (PDMS), silicon, and gold.

A spectrofluorometer study of the polymer **3b** showed a characteristic excitation peak at 380 nm and a characteristic emission peak at 450 nm. These peaks disappeared after heating the polymer to 150 °C for 3 h, presumably as a result of cross-linking of the polymer (see Supporting Information). To assess the thermal stability of polymer **3b**, we compared the FTIR spectra of samples that were stored at 20 °C, 80 °C, 150 °C, and 250 °C, respectively. The C–H stretch at 3283 cm^{-1} continuously decreased with increasing temperature and was absent in samples stored at 250 °C (Supporting Information). Again, this result suggests that the polymer has limited thermal stability, most likely arising from cross-linking of the ethynyl groups.

To assess whether the reactive coating **3b** can be used for heterogeneous click reactions, its reactivity against azides was studied. Specifically, the Huisgen 1,3-dipolar cycloaddition between **3b** and an azide-containing biotin-based ligand **4** in the presence of copper(II) sulfate and sodium ascorbate was examined (Scheme 2). As described for solvent-based systems, this coupling reaction yielded triazoles.[25] Sodium

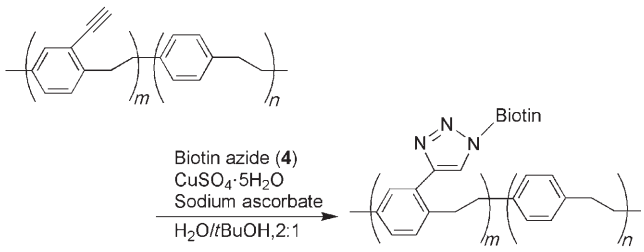

Scheme 2. Huisgen 1,3-dipolar cycloaddition between biotin-based azide-ligand **4** and the polymer **3b**.

 © 2006 Wiley-VCH Verlag GmbH & Co. KGaA, Weinheim

ascorbate acts as a reductant, generating Cu^{I} ions in situ, which then function as the catalyst.[25] The biotin azide **4** was chosen as the representative ligand in this study, because biotin forms a strong noncovalent interaction with streptavidin (which has been widely used for binding biotinylated biomolecules).[15]

To ensure spatial control over the cycloaddition reaction, a microcontact printing (μCP) approach was chosen. For this approach to be successful, the Cu^{I} catalyst and the reductant have to be used independently of each other. Therefore a thin layer of **4** and sodium ascorbate was spread onto a film of **3b** and dried using N_2. Next, a patterned PDMS stamp was inked with a solution of $CuSO_4$ and kept in contact with the substrate for 12–18 h (Figure 1). After rinsing, the patterned

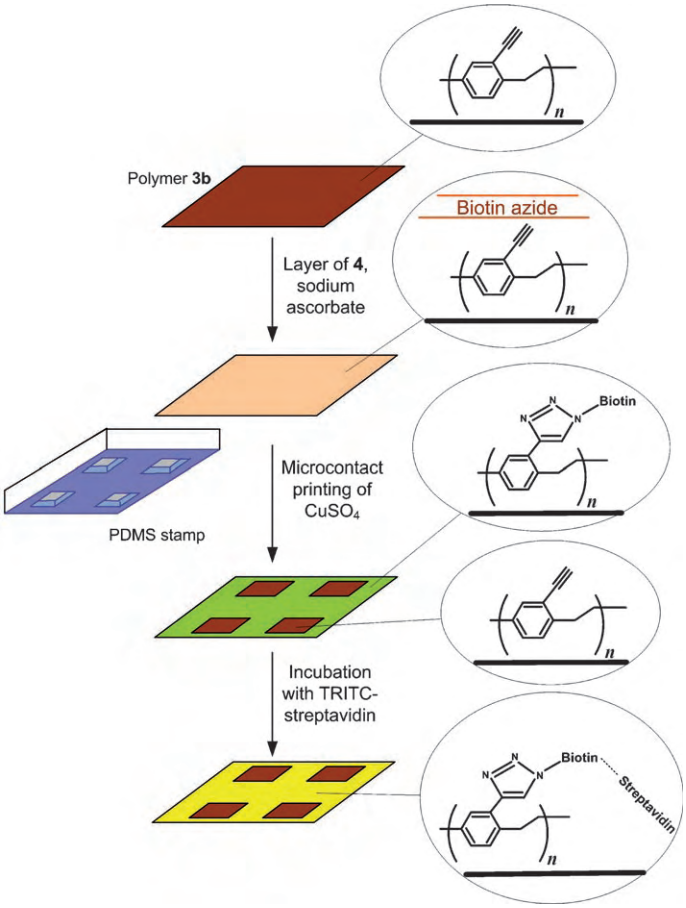

Figure 1. Immobilization of azide-containing ligand on the reactive polymer coating **3b**. Subsequently the $CuSO_4$ catalyst precursor is microcontact printed on a preadsorbed layer of biotin azide ligand **4** on the reactive polymer **3b**.

substrate was incubated with an aqueous solution of rhodamine-labeled streptavidin. Fluorescence microscopy was used to assess the immobilization of **4** onto polymer **3b**. The fluorescence micrographs shown in Figure 2a,c confirm selective protein coupling in the regions where the $CuSO_4$ solution was microcontact printed, thus demonstrating the spatially directed binding of **4** to polymer **3b**. This result shows that the alkyne groups on the polymer surface are

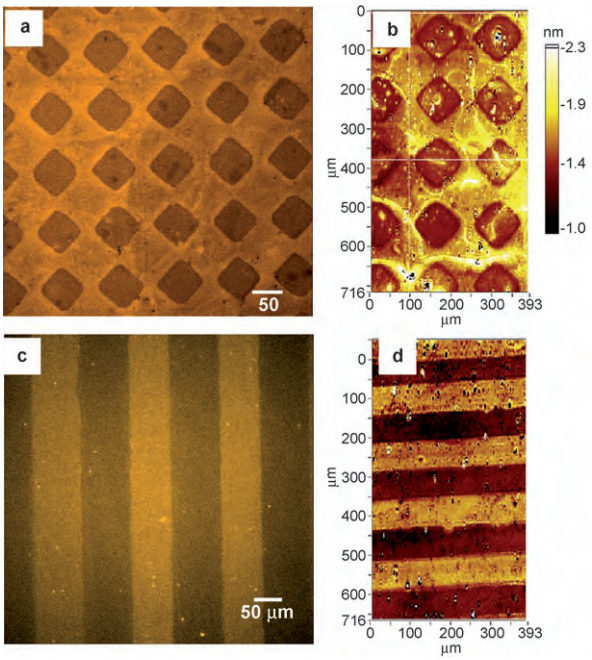

Figure 2. a),c) Fluorescence micrographs showing the binding of TRITC-streptavidin to patterns of biotin azide, b),d) Corresponding ellipsometric images for determining layer thickness. TRITC = tetramethylrhodaminisothiocyanate, PDMS = poly(methylsiloxane).

reactive and can be effectively used as anchoring sites for surface modifications. The two-step approach was found to be superior to the concurrent microcontact printing of catalyst and azide.

To complement the fluorescence study, patterned surfaces were further analyzed by imaging ellipsometry (Figure 2b and d) which revealed protein patterns, which are inline with the corresponding fluorescence patterns. The observed thickness differences of about 1–2 nm between the biotinylated and the non-biotinylated regions after incubation with streptavidin are comparable with the thickness of a protein monolayer.[26]

In conclusion, the alkyne-containing polymer **3b** has been found to show remarkable reactivity towards azides through the chemoselective Huisgen 1,3-dipolar cycloaddition. In contrast to the dialkyne containing polymer **3a**, reactive coating **3b** showed excellent adhesion and stability at elevated temperatures and in solvents. Further work will be directed towards the elucidation of the CVD polymerization mechanism as well as its scope with respect to different cycloadditions. The development of bioactive surfaces is an important step towards advanced biomaterials and biointerfaces. Our regioselective immobilization strategy could be applicable in the design of biofunctional surfaces for diagnostics (e.g. microarrays), biosensors, and biomedical device coatings.

Experimental Section

CVD: **2a** (50 mg) was sublimed at 90–110 °C and 0.5 mbar and carried into the pyrolysis chamber by argon at a flow rate of 20 sccm. After pyrolysis (at different pyrolysis temperatures T_{pyr}), the polymer was

 © 2006 Wiley-VCH Verlag GmbH & Co. KGaA, Weinheim

deposited on the substrate at 15 °C. $T_{pyr} = 650$ °C. IR (grazing angle of 85°): $\tilde{\nu} = 837$, 1039, 1150, 1439, 1505, 1624, 1694, 1910, 2916, 3010, 3048 cm^{-1}. XPS signal (%; referenced to aliphatic C at 285.0 eV): C 96.9, O 3.1; $T_{pyr} = 550$ °C. IR (grazing angle of 85°): $\tilde{\nu} = 839.35$, 877, 922, 1036, 1261, 1439, 1623, 1913, 2100, 2848, 2921, 3013, 3052, 3285 cm^{-1}. XPS signal (%; referenced to aliphatic C at 285.0 eV): C 93.7, O 6.3.

2b: CVD as described above. IR (grazing angle of 85°): $\tilde{\nu} = 833$, 894, 1158, 1251, 1411, 1454, 1493, 1513, 1605, 1699, 1900, 2102, 2859, 2926, 3015, 3286 cm^{-1}; XPS signal (%; referenced to aliphatic Cat 285.0 eV): C 98.7, O 1.3; XPS signals: 285.6 eV (C1 s); 291.7 eV (π–π^*).

Surface Characterization: IR spectroscopy: Nicolet 6700 spectrometer. XPS elemental analyses: Axis Ultra X-ray photoelectron spectrometer (Kratos Analyticals, UK) equipped with a monochromatized $Al_{K\alpha}$ X-ray source.

Height analysis data were recorded using an EP^3-SW imaging ellipsometer (Nanofilm AG, Germany) at a wavelength of 532 nm. Both, nulling (four zones) and mapping experiments were performed at an angle of incidence of 65°. An anisotropic Cauchy parameterization model was used for curve fitting. For the mapping mode, data was recorded by an imaging scanner with a lateral resolution of 1 μm with a field of view of about 100 μm × 500 μm.

Patterning of **4** on polymer films of **3b**: Patterned PDMS stamps were created as described elsewhere.[14] A thin layer of solution of ligand **4** (Photoprobe biotin, Vector labs, 10 $\mu g\,mL^{-1}$) and sodium ascorbate (1 mM) in a 2:1 mixture of water and *tert*-butyl alcohol was spread on **3b** and dried using N_2. The patterned PDMS stamp was oxidized for 20 min using UV-ozone cleaner (Jelight) and inked with $CuSO_4$ solution (1 mM in methanol) adopting an approach reported by Abbott et al.[27]. The stamp was then kept in contact with the polymer substrate for 12–18 h. After stamp removal, the patterned substrate was incubated with rhodamine-labeled streptavidin (50 $\mu g\,mL^{-1}$ in aqueous phosphate buffer PBS containing 0.02% (v/v) Tween 20 and 0.1% (w/v) bovine serum albumin (BSA)) for 1 h. The substrate was then repeatedly washed with the incubating buffer, PBS and finally rinsed with deionized water. The fluorescence micrographs were captured using a Nikon TE200 fluorescence microscope.

Received: January 26, 2006
Published online: April 19, 2006

Keywords: alkynes · chemical vapor deposition · click chemistry · immobilization · reactive coatings

[1] R. Langer, D. A. Tirrell, *Nature* **2004**, *428*, 487–492.
[2] a) H. C. Kolb, M. G. Finn, K. B. Sharpless, *Angew. Chem.* **2001**, *113*, 2056–2075; *Angew. Chem. Int. Ed.* **2001**, *40*, 2004–2021; b) V. D. Bock, H. Hiemstra, J. H. van Maarseveen, *Eur. J. Org. Chem.* **2006**, 51–68.
[3] R. Huisgen, *1,3-Dipolar Cycloaddition Chemistry*, (Ed.: A. Padwa), Wiley, New York, **1984**, pp. 1–176.
[4] H. C. Kolb, K. B. Sharpless, *Drug Discovery Today* **2003**, *8*, 1128–1137.
[5] R. Manetsch, A. Krasinski, Z. Radic, J. Raushel, P. Taylor, K. B. Sharpless, H. C. Kolb, *J. Am. Chem. Soc.* **2004**, *126*, 12809–12818.
[6] a) W. G. Lewis, L. G. Green, F. Grynszpan, Z. Radic, P. R. Carlier, P. Taylor, M. G. Finn, K. B. Sharpless, *Angew. Chem.* **2002**, *114*, 1095–1099; *Angew. Chem. Int. Ed.* **2002**, *41*, 1053–1057; b) A. Dantas de Araújo, J. M. Palomo, J. Cramer, M. Köhn, H. Schröder, R. Wacker, C. Niemeyer, K. Alexandrov, H. Waldmann, *Angew. Chem.* **2006**, *118*, 302–307; *Angew. Chem. Int. Ed.* **2006**, *45*, 296–301.
[7] J. P. Collman, N. K. Devaraj, C. E. D. Chidsey, *Langmuir* **2004**, *20*, 1051–1053.
[8] N. K. Devaraj, G. P. Miller, W. Ebina, B. Kakaradov, J. P. Collman, E. T. Kool, C. E. D. Chidsey, *J. Am. Chem. Soc.* **2005**, *127*, 8600–8601.
[9] J. K. Lee, Y. S. Chi, I. S. Choi, *Langmuir* **2004**, *20*, 3844–3847.
[10] T. Lummerstorfer, H. Hoffmann, *J. Phys. Chem. B* **2004**, *108*, 3963–3966.
[11] X.-L. Sun, C. L. Stabler, C. S. Cazalis, E. L. Chaikof, *Bioconjugate Chem.* **2006**, *17*, 52–57.
[12] J. A. Prescher, C. R. Bertozzi, *Nat. Chem. Biol.* **2005**, *1*, 13–21.
[13] J. Lahann, I. S. Choi, J. Lee, K. Jensen, R. Langer, *Angew. Chem.* **2001**, *113*, 3273–3276; *Angew. Chem. Int. Ed.* **2001**, *40*, 3166–3169.
[14] J. Lahann, H. Höcker, R. Langer, *Angew. Chem.* **2001**, *113*, 746–749; *Angew. Chem. Int. Ed.* **2001**, *40*, 726–728.
[15] J. Lahann, D. Klee, H. Höcker, *Macromol. Rapid Commun.* **1998**, *19*, 441–444.
[16] J. Lahann, M. Balcells, T. Rodon, J. Lee, I. S. Choi, K. F. Jensen, R. Langer, *Langmuir* **2002**, *18*, 3632–3638.
[17] J. Lahann, M. Balcells, H. Lu, T. Rodon, K. F. Jensen, R. Langer, *Anal. Chem.* **2003**, *75*, 2117–2122.
[18] H. Nandivada, H.-Y. Chen, J. Lahann, *Macromol. Rapid Commun.* **2005**, *26*, 1794–1799.
[19] J. Lahann, R. Langer, *Macromol. Rapid Commun.* **2001**, *22*, 968–971.
[20] J. Lahann, R. Langer, *Macromolecules* **2002**, *35*, 11, 4380–4386.
[21] K. Schürmann, J. Lahann, J. Meyer, H. Klosterhalfen, D. Vorwerk, D. Klee, R. W. Günther, *Radiology* **2004**, *230*, 151–162.
[22] L. Bondarenko, I. Dix, H. Hinrichs, H. Hopf, *Synthesis* **2004**, 2751–2759.
[23] J. J. Gajewski, *Hydrocarbon Thermal Isomerizations*, Elsevier, San Diego, **2004**, pp. 13–15.
[24] G. Polzonetti, A. M. Cianciusi, A. Furlani, M. V. Russo, *Synth. Met.* **1989**, *28*, D413–D417.
[25] V. V. Rostovtsev, L. G. Green, V. V. Fokin, K. B. Sharpless, *Angew. Chem.* **2002**, *114*, 2708–2711; *Angew. Chem. Int. Ed.* **2002**, *41*, 2596–2599.
[26] J. Voros, *Biophys. J.* **2004**, *87*, 553–561.
[27] K. L. Yang, K. Cadwell, N. L. Abbott, *Adv. Mater.* **2003**, *15*, 1819–1823.

 © 2006 Wiley-VCH Verlag GmbH & Co. KGaA, Weinheim

Polymer Solar Cells

DOI: 10.1002/anie.200503958

Charge Separation at Self-Assembled Nanostructured Bulk Interface in Block Copolymers**

Stefan M. Lindner, Sven Hüttner, Arnaud Chiche, Mukundan Thelakkat, and Georg Krausch**

Electronic devices made of organic materials, in particular photovoltaic devices, have attracted steadily increasing attention during the last years owing to their potential in terms of cheap processing, their application to large areas, and their compatibility with flexible substrates.[1,2] In contrast to inorganic semiconductors, organic materials do not directly create free charge carriers on illumination; instead, bound electron–hole pairs called excitons are generated.[3] These excitons must be carried towards a donor–acceptor (DA) interface, where they dissociate and then drift towards the electrodes. Unfortunately, excitons travel only a few tens of nanometers before recombination. Therefore the absorption layer should be very thin for all the excitons to reach the DA interface.[4] At the same time the optical absorption length is on the order of a few hundreds of nanometers. Thus, an efficient device also requires a thick absorption layer, which is then not compatible with the very short diffusion length of an exciton. To solve this issue, improvements of the original bilayer heterojunction solar device[4] have been developed by introducing the concepts of multiple heterojunctions[5] and bulk heterojunctions[6–8] (Figure 1 d).

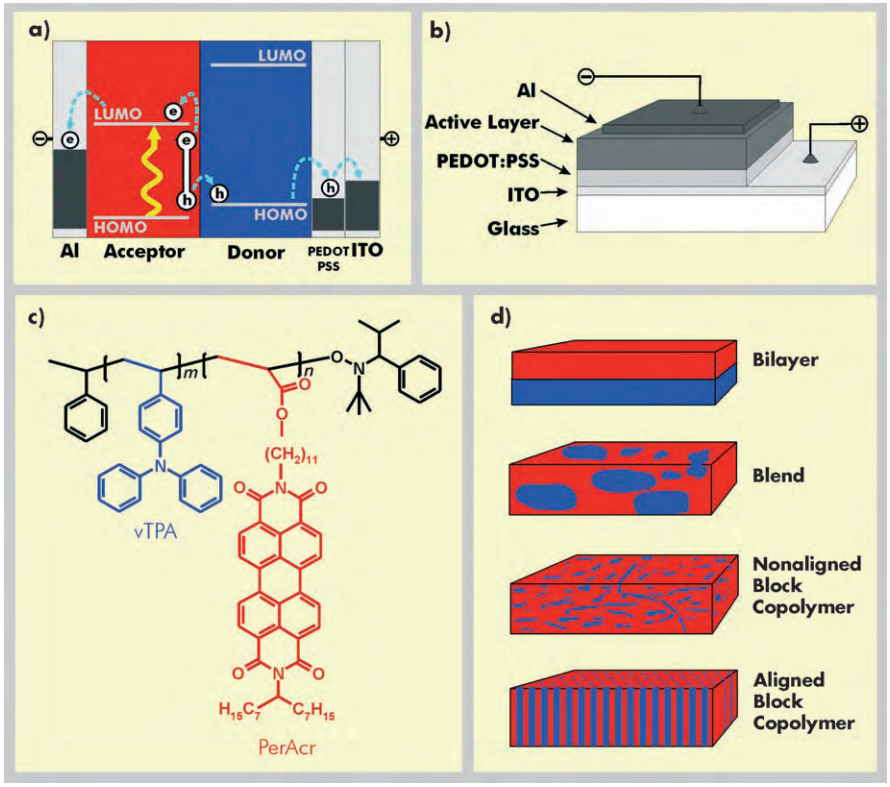

Figure 1. a) The physical processes in a bilayer donor–acceptor solar cell. The absorbed light generates excitons which drift in all directions. Those that reach the DA interface separate into free charges: electrons (e) transfer into the LUMO of the acceptor and holes (h) into the HOMO of the donor. The separated charges are transported by hopping and collected at the respective electrodes. PEDOT = poly(3,4-ethylenedioxythiophene), PSS = poly(styrene sulfonate), ITO = indium tin oxide. b) Schematic representation of a polymer solar cell. c) Chemical structure of the block copolymer PvTPA-*block*-PPerAcr. vTPA = vinyltriphenylamine, PerAcr = acrylate unit with perylene bisimide side group. d) Various morphologies in the active layer that can be utilized to create a DA interface for charge separation.

Polymer blends usually result in macrophase separation, limiting the efficiency of charge separation and power conversion in a photovoltaic device.[9,10] Therefore, generating "nanostructured bulk heterojunctions" that guarantee a proper percolation of charges remains a challenging task.

Nanostructured bulk heterojunctions can be realized by using diblock copolymers made of two covalently linked polymers with suitable electronic properties (donor and acceptor blocks). The interplay between molecular connectivity and immiscibility leads to the spontaneous formation of ordered microdomains of molecular dimensions[11] and solves the issue of exciton transport to the DA interface.

The fundamentals of block copolymer self-assembly in thin films have been the subject of numerous studies throughout the last decade[12] in view of its enormous potential for nanotechnology applications.[13] One important aspect is the macroscopic alignment of the nanostructures by

[*] S. M. Lindner, Priv.-Doz. Dr. M. Thelakkat
Makromolekulare Chemie I
Universität Bayreuth
Universitätsstrasse 30, 95440 Bayreuth (Germany)
Fax: (+49) 921-55-3206
E-mail: mukundan.thelakkat@uni-bayreuth.de
S. Hüttner, Dr. A. Chiche, Prof. G. Krausch
Physikalische Chemie II
Universitätsstrasse 30, 95440 Bayreuth (Germany)
Fax: (+49) 921-55-2059
E-mail: georg.krausch@uni-bayreuth.de

[**] We thank C. Kunert for the TEM images and H. Hänsel and S. Haque, Imperial College, London, for fruitful discussions. This work was supported by the German Research Council (DFG/SFB 481-Project B4). A.C. acknowledges financial support from the European Union's "Marie-Curie Actions" of the "Polyfilm" Research Training Network.

WILEY InterScience DISCOVER SOMETHING GREAT
© 2006 Wiley-VCH Verlag GmbH & Co. KGaA, Weinheim

means of external fields,[14,15] which potentially allows the control of the percolation paths mentioned above (Figure 1d). The obvious advantage of block copolymers for application in electrooptical devices made of organic materials has been recognized.[16–18] To date, however, no working photovoltaic device based on a nanostructured bulk heterojunction has been demonstrated.

Herein we describe a single-active-layer photovoltaic device obtained by the self-assembly of a diblock copolymer bearing all the functionalities required for light absorption, charge separation, and charge transport. The block copolymer self-assembles into a nanostructure, which provides charge-separating interfaces on the nanometer scale. As a proof of concept, we compare the performance of the block-copolymer device with a device made from a blend of the two individual segment polymers of identical thickness and composition. We demonstrate that the photovoltaic properties (short circuit current J_{SC}, open circuit voltage V_{OC}, and power conversion efficiency η) of the block copolymer significantly surpass those of the blend device. As a result of the nanostructured nature of the film, the photovoltaic properties are less dependent on the thickness of the polymer layer, thereby enabling thicker devices with higher optical absorption without significant loss of efficiency. The considerable improvement in performance can be correlated to the nanostructured bulk heterojunction formed in block copolymers by imaging of the active layers through transmission electron microscopy (TEM) and atomic force microscopy (AFM).

Recently, we described the synthesis of fully functionalized tailor-made semicrystalline block copolymers carrying hole-conductor, electron-conductor, and light-absorption functionalities.[19] The hole transport is mediated by a poly(vinyltriphenylamine) segment (PvTPA, HOMO $\approx$5.2 eV), and both electron transport and light absorption occurs in a polyacrylate segment bearing perylene bisimide side groups (PPerAcr, LUMO $\approx$3.7 eV; Figure 1c). The block copolymers were obtained with well-defined molecular weights in the range between 18 and 40 kg mol^{-1}. The composition and dye content can be varied to suit the requirements of light absorption and balanced charge transport. We also showed that such fully functionalized diblock copolymers phase-separate on the nanometer scale. These block copolymers exhibit both a glass transition temperature T_g at about 150 °C owing to the amorphous PvTPA segment and a melting temperature T_m at about 200 °C as a result of stacking of the perylene bisimide side group.

Thin films of the block copolymer PvTPA$_{21}$-*block*-PPerAcr$_{79}$ (79 wt% PPerAcr; M_n = 37710 g mol^{-1}; T_g = 149.5 °C, T_m = 198.0 °C) with thicknesses of around 250 nm were prepared by spin-coating from chloroform solution onto a glass substrate initially coated with indium tin oxide (ITO) and an additional injection layer of PEDOT:PSS, to avoid short-circuiting through the active layer. For comparison, polymer-blend cells were prepared in the same way by mixing homopolymers of PvTPA and PPerAcr (weight fractions: 0.21 and 0.79, respectively).[19] Aluminum electrodes were evaporated on top of the polymer layers by vacuum deposition at 10^{-6} mbar (Figure 1b). The active area of a single device was 0.18 cm^2. These single-layer devices were characterized by current–voltage measurements in the dark and under illumination with a white-light source (AM 1.5 (spectral distribution of sunlight at a zenith angle of 48.2°; AM = air mass; 77 mW cm^{-2}). All measurements were performed at ambient conditions without any encapsulation or protection of the devices against degradation.

Figure 2 compares the current–voltage characteristics of illuminated devices made of the polymer blend and the block copolymer. The data demonstrates quite convincingly that the

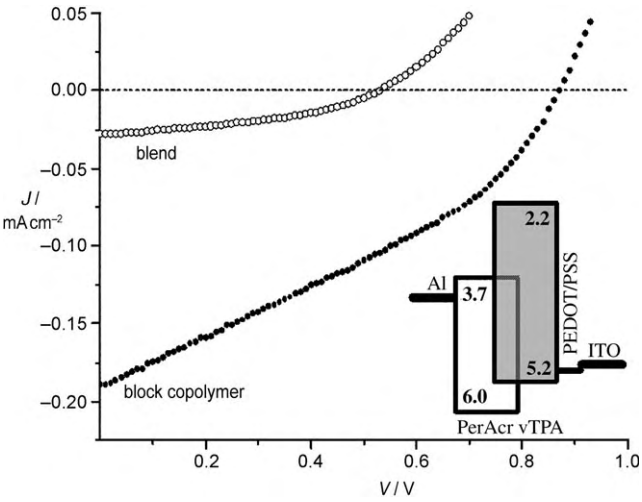

Figure 2. Plot of current density (J) versus voltage (V) for a photovoltaic device constructed from a polymer blend (open symbols) and from a block copolymer (filled symbols). Thickness of active layer: 250 nm; the short circuit current (J_{sc}) and the open circuit voltage (V_{oc}) are 0.028 mA cm^{-2} and 0.525 V for the blend and 0.19 mA cm^{-2} and 0.865 V for the block copolymer, respectively. The power conversion efficiency was also improved by one order of magnitude from 0.007% in the polymer blend to 0.07% in the block-copolymer device. Inset shows the energy-level diagram of the donor and acceptor blocks; the values representing the HOMO and LUMO levels are in eV and were determined by cyclic voltammetry.

block-copolymer device exhibits significantly better performance than the blend device. The short circuit current J_{sc} is 0.028 mA cm^{-2} for the blend and 0.19 mA cm^{-2} for the block copolymer. Accordingly, the open-circuit voltage V_{oc} increases from 525 mV for the blend to 865 mV for the block copolymer. The power conversion efficiency under white-light exposure was improved by one order of magnitude from 0.007% in the polymer blend to 0.07% in the block-copolymer device. The inset in Figure 2 shows the energy-level diagram of the donor and acceptor blocks. The energetic offset at the interface compels the charge separation and the desired flow of electrons to the respective electrodes. The energy values of the HOMO and LUMO given here are determined from cyclic voltammetry measurements in solution.

To rationalize this finding we investigated the phase morphology of the thin films in the solar cells. For this purpose cross-sectional transmission electron microscopy (TEM) studies were carried out on the actual solar cells. As PEDOT:PSS is water soluble, the active layer could be floated onto water, embedded into epoxy resin, and cut to reveal

 © 2006 Wiley-VCH Verlag GmbH & Co. KGaA, Weinheim

vertical cross sections through the active layer of the devices (Figure 3a, b). The dark domains result from stained perylene bisimide.

The polymer blend is characterized by large, micrometer-sized domains, whereas the block-copolymer film exhibits structure in the nanometer range. These results are also supported by the tapping-mode AFM topography images in Figure 3c, d. The characteristic width of the block-copolymer microdomain structure (10–50 nm) is of the same order as the exciton diffusion length observed in similar perylene compounds.[5] This allows the excitons generated in the perylene bisimide domain to reach the DA interface (i.e. the PvTPA segment) more efficiently in a block-copolymer layer than in the blend.

The devices were characterized by addition means to evaluate this explanation. Figure 4a presents the absorption

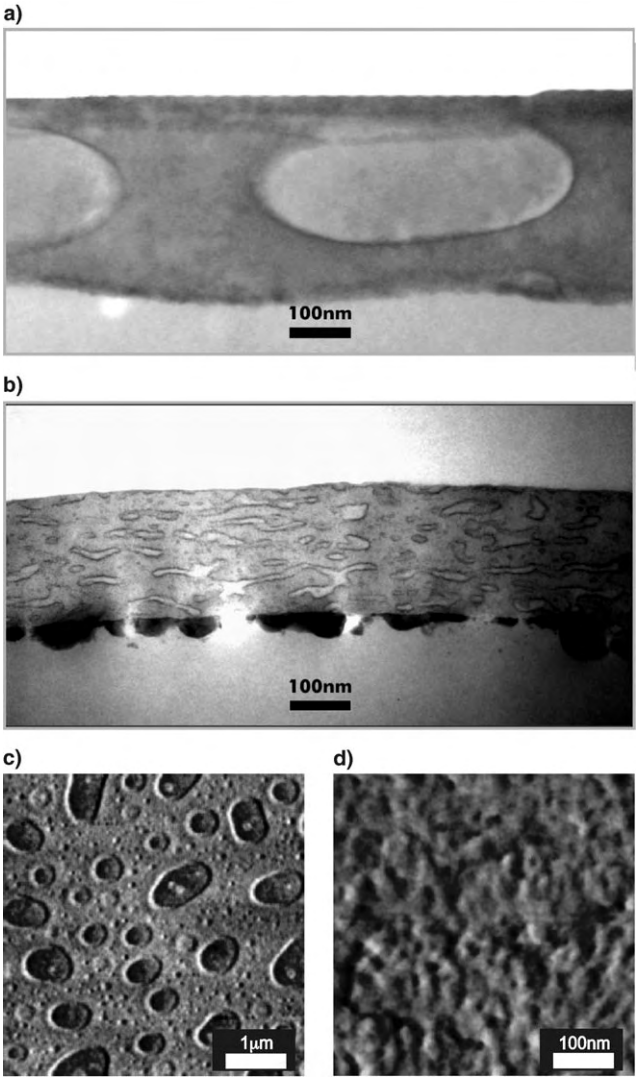

Figure 3. TEM cross sections a) of a polymer-blend device with 21 wt% of PvTPA and 79 wt% of PPerAcr and b) of a block-copolymer device ($PvTPA_{21}$-*block*-$PPerAcr_{79}$). The active layers were floated, embedded into epoxy, and cut for TEM. TEM pictures were taken from the vertical cross sections of the same layers used in the devices. AFM phase images in tapping mode c) of a polymer-blend surface with 21 wt% of PvTPA and 79 wt% of PPerAcr (*z* axis 2.5°) and d) of a block-copolymer surface ($PvTPA_{21}$-*block*-$PPerAcr_{79}$) (*z* axis 5.0°). Note that the scale bars differ by a factor of 10.

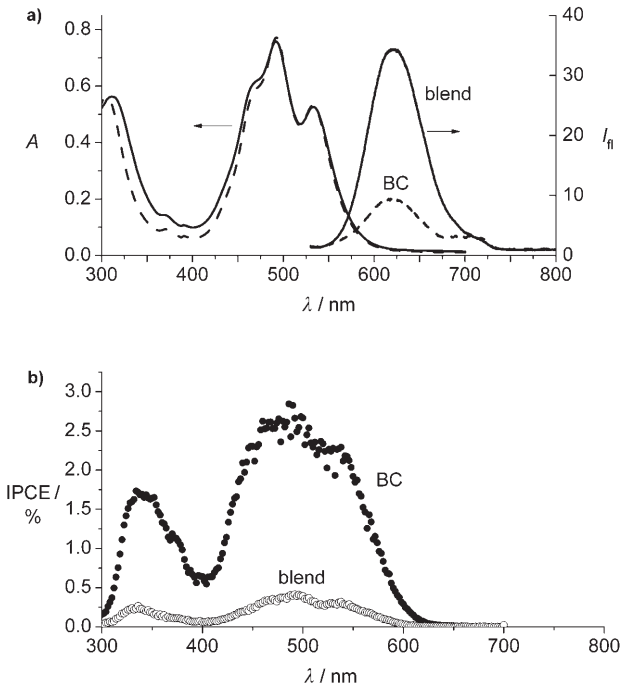

Figure 4. a) Absorption spectrum of the polymer-blend (solid line) and the block-copolymer films (dashed line), and photoluminescence spectra of the polymer-blend (solid line) and block-copolymer films (BC, dashed line) at an excitation wavelength of 470 nm, b) IPCE curves (external quantum efficiency) of the polymer-blend device (open symbols) and the block-copolymer device (BC, filled symbols) in which the active layer has a thickness of 250 nm.

curves of films of the blend and the block copolymer. The perylene dye units show strong aggregation (crystallization in confined nanometer domains resulting from segregation effects of segments in a block copolymer). This actually should favor the transport of electrons in these highly ordered structures and it also favors a small red shift in the absorption, which is desired in solar cells. The fact that the absorption spectra of the block copolymer and the polymer blend are almost identical indicates that the two films contain the same amounts of absorbing material, in this case the vTPA and the perylene bisimide groups. This meets our expectations, as the blend ratio and the ratio of block-copolymer segments are the same, and the films are both around 250 nm thick. The same density of excitons should then be generated in both systems. These excitons can either reach a DA interface (and generate separated charges) or recombine, resulting in photoluminescence (PL). As suggested by the different performances of the cells (Figure 2), more excitons finally result in charge separation in the case of the block copolymer. This is confirmed by the PL-quenching experiments carried out on both the blend and the block copolymer (Figure 4a). The PPerAcr homopolymer exhibits intense PL at 620 nm on excitation with 470-nm light, indicating that radiative decay is the main recombination pathway for the exciton. In the block copolymer the maximum PL intensity is quenched more efficiently than in the blend layer, again indicating the more efficient charge transfer in the nanostructured bulk heterojunction in the block copolymer. This is also supported by the

 © 2006 Wiley-VCH Verlag GmbH & Co. KGaA, Weinheim

wavelength-dependent incident photon to current conversion efficiency (IPCE) measurements. The IPCE curves (Figure 4b) are directly correlated with the absorption in both cases (Figure 4a), but the efficiencies are much lower for the blend devices. These results are also in agreement with the reported values of poor efficiency and quantum yield generally observed in polymer-blend devices.[10]

These are profound findings with positive consequences for devices constructed from polymer films. Using the concept of fully functionalized block copolymers, single active layers can be used for efficient charge separation with the advantage that the majority of generated excitons reach the interface for charge separation. This is a first step towards efficient thicker layer devices designed for higher light absorption. Using a 580-nm-thick block copolymer layer, we have already obtained a similar open circuit voltage V_{OC} (0.88 V) and a reasonable short circuit current J_{SC} (0.09 mA cm^{-2}).

Based on these results, the use of a block copolymer with suitable electronic properties appears to be an elegant and a very promising solution for overcoming the short diffusion length of an exciton formed in an organic semiconductor. Controlling the alignment of the nanodomains is the next challenge for improving the charge conduction toward the device electrodes. Indeed, the block-copolymer domains displayed in Figure 3b do not exhibit a well-aligned structure, and if at all, appear to be preferentially aligned parallel rather than perpendicular to the electrodes. Ideally, one would wish for rather defect-free microdomains aligned perpendicularly to the plane of the film (Figure 1d). The orientation of PPerAcr nanostructures in particular will augment the flow of electrons towards the electrodes considerably.

Current research work is therefore focused on the combination of the above approach with one of the various techniques recently devised for the creation of defect-free block-copolymer structures and alignment of macroscopic domains in thin block-copolymer films. Potentially the most promising route may involve solvent- induced alignment similar to that recently reported by Russell et al. [20] as the films are prepared from solution anyway. Alternatively, electric-field-induced alignment of the domains may be sought, since in most cases reported so far the domains are aligned such that the interfaces lie parallel to the electric field vector.[21,22] In this case, particular care would have to be taken since the block copolymers under study are electrically (semi-) conducting, whereas the materials studied so far were insulators.

While the absolute efficiencies of the devices we have described here are still considerably smaller than the best state-of-the-art organic photovoltaic cells, we were able to give a proof-of-principle clearly showing that the concept of nanostructured bulk heterojunction devices based on block copolymers is a significant breakthrough in the design of more efficient organic devices. Moreover, the method of fabrication is compatible with current processes for preparing devices and with current schemes for removing defects and aligning macroscopic domains. This finding also gives large input into the field of fully functionalized self-organizing molecular devices and molecular electronics in general.

Experimental Section

UV/Vis spectra were recorded on a Hitachi U-3000 spectrometer, and fluorescence spectra were recorded on a Shimadzu RF-5301 PC spectrofluorophotometer.

The photovoltaic devices were prepared by spin-coating PEDOT:PSS dispersion, obtained from Bayer AG, onto precleaned, patterned indium tin oxide substrates (18 Ω per square). The active layer was deposited by spin-coating from a 1.5 wt% $CHCl_3$ solution. The aluminum electrode (100 nm) was deposited by vacuum evaporation at 10^{-6} mbar. The active area of the cell is 0.18 cm^2.

Current–voltage measurements were conducted with white light (77 mW cm^{-2}, AM 1.5; Oriel setup with 150-W xenon arc lamp and suitable filters). This setup was calibrated using a reference Si cell from ISE Freiburg at the same sample position and height.

Incident photon to current conversion efficiency (IPCE) was measured using a monochromator (Spex, Model 1681 B) with a holographic grid (lamp: 300-W xenon arc lamp, model 6259, Oriel) creating homogeneous illumination of a circular spot 3.5 cm in diameter (power: < 1 mW) for the wavelength range from 280 nm to 1000 nm.

Samples for TEM were floated with water, embedded into epoxy resin, cut vertically to get a cross section of the active layer, and stained with RuO_4. The measurements were performed with a Zeiss 902 transmission electron microscope. The AFM measurements were performed with a Dimension 3100 device from Digital Instruments. Images were recorded in the tapping mode.

Received: November 8, 2005
Revised: January 9, 2006
Published online: April 18, 2006

Keywords: block copolymers · electron microscopy · scanning probe microscopy · self-assembly · solar cells

[1] G. Malliaras, R. Friend, *Phys. Today* **2005**, *58*, 53–58.
[2] C. J. Brabec, J. A. Hauch, P. Schilinsky, C. Waldauf, *MRS Bull.* **2005**, *30*, 50–52.
[3] B. A. Gregg, *MRS Bull.* **2005**, *30*, 20–22.
[4] C. W. Tang, *Appl. Phys. Lett.* **1986**, *48*, 183–185.
[5] P. Peumans, A. Yakimov, S. R. Forrest, *J. Appl. Phys.* **2003**, *93*, 3693–3723.
[6] G. Yu, J. Gao, J. C. Hummelen, F. Wudl, A. J. Heeger, *Science* **1995**, *270*, 1789–1791.
[7] C. J. Brabec, N. S. Sariciftci, J. C. Hummelen, *Adv. Funct. Mater.* **2001**, *11*, 15–26.
[8] J. J. M. Halls, C. A. Walsh, N. C. Greenham, E. A. Marseglia, R. H. Friend, S. C. Moratti, A. B. Holmes, *Nature* **1995**, *376*, 498–500.
[9] A. C. Arias, J. D. MacKenzie, R. Stevenson, J. J. Halls, M. Inbasekharan, E. P. Woo, D. Richards, R. H. Friend, *Macromolecules* **2001**, *34*, 6005–6013.
[10] Y. Kim, S. Cook, S. A. Choulis, J. Nelson, J. R. Durrant, D. D. C. Bradley, *Chem. Mater.* **2004**, *16*, 4812–4818.
[11] F. S. Bates, G. H. Fredrickson, *Ann. Rev. Phys. Chem.* **1990**, *41*, 525–557.
[12] C. Park, J. Yoon, E. L. Thomas, *Polymer* **2003**, *44*, 6725–6760.
[13] M. J. Fasolka, A. M. Mayes, *Annu. Rev. Mater. Res.* **2001**, *31*, 323–355.
[14] Z. R. Chen, J. A. Kornfield, S. D. Smith, J. T. Grothaus, M. M. Satkowski, *Science* **1997**, *277*, 1248–1253.
[15] T. Thurn-Albrecht, J. Schotter, G. A. Kastle, N. Emley, T. Shibauchi, L. Krusin-Elbaum, K. Guarini, C. T. Black, M. T. Tuominen, T. P. Russell, *Science* **2000**, *290*, 2126–2129.

 © 2006 Wiley-VCH Verlag GmbH & Co. KGaA, Weinheim

[16] J. Liu, E. Sheina, T. Kowalewski, R. D. McCullough, *Angew. Chem.* **2002**, *114*, 339 – 342; *Angew. Chem. Int. Ed.* **2002**, *41*, 329 – 332.
[17] M. H. van der Veen, B. de Boer, U. Stalmach, K. I. van de Wetering, G. Hadziioannou, *Macromolecules* **2004**, *37*, 3673 – 3684.
[18] J. P. Chen, D. Markiewicz, V. Y. Lee, G. Klaerner, R. D. Miller, J. C. Scott, *Synth. Met.* **1999**, *107*, 203 – 207.
[19] S. M. Lindner, M. Thelakkat, *Macromolecules* **2004**, *37*, 8832 – 8835.
[20] S. H. Kim, M. J. Misner, T. P. Russell, *Adv. Mater.* **2004**, *16*, 2119 – 2123.
[21] T. Thurn-Albrecht, J. DeRouchey, T. P. Russell, H. M. Jaeger, *Macromolecules* **2000**, *33*, 3250 – 3253.
[22] A. Böker, H. Elbs, H. Hänsel, A. Knoll, S. Ludwigs, H. Zettl, V. Urban, V. Abetz, A. H. E. Müller, G. Krausch, *Phys. Rev. Lett.* **2002**, *89*, 135502.

 © 2006 Wiley-VCH Verlag GmbH & Co. KGaA, Weinheim

Electron Transfer

DOI: 10.1002/anie.200504383

σ-Donor and π-Acceptor Stacking Interactions in a *trans*-2-Linked C_{60}–Cobalt(II) Tetraphenylporphyrin Diad**

*Jörg Dannhäuser, Wolfgang Donaubauer, Frank Hampel, Markus Reiher, Boris Le Guennic, Björn Corzilius, Klaus-Peter Dinse, and Andreas Hirsch**

Dedicated to Professor Fred Wudl on the occasion of his 65th birthday

Twofold cyclopropanation of C_{60} with tetraphenylporphyrin bismalonates yields *trans*-1- or *trans*-2-linked diads such as **1** or **2** in high regioselectivity.[1–3] In this way, the two chromophores in these diads are forced into a rigid stacking arrangement. Model calculations showed that there is a van der Waals contact between the two π systems.[1d] The resultant electronic communication expresses itself, for example, in efficient photoinduced electron transfer from the porphyrin moiety to the fullerene.[1–3] In the *trans*-2-linked C_{60}–cobalt(II) tetraphenylporphyrin diad **1**, which we recently reported, the intermolecular interaction between the two chromophores is especially strong.[2] Electrochemical and photophysical investigations proved that the first reduction step, which takes place mainly at the fullerene moiety, occurs more readily than for similar compounds such as the Zn diad **2** and the singly connected system **3**, whereas the first oxidation step, which takes place at the porphyrin moiety, occurs at a more positive potential. Notably, the choice of solvent determines whether the oxidation product is ($Co^{II}Porph^{\bullet+}$)–fullerene or ($Co^{III}Porph$)–fullerene (Porph = porphyrin). We herein present a model based on detailed X-ray, spectroscopic, and quantum-chemical investigations with **1**, in which the C_{60} unit plays the role of an unusual complex ligand, to describe the exceptional fullerene–porphyrin interactions. We also show that analogous intermolecular interactions occur in the solid state that lead to the formation of new linear coordination polymers.

Single crystals of **1** could be obtained by slow evaporation of a solution in dichloromethane.[4] Compound **1** crystallizes in the triclinic space group $P\bar{1}$. The asymmetric unit contains

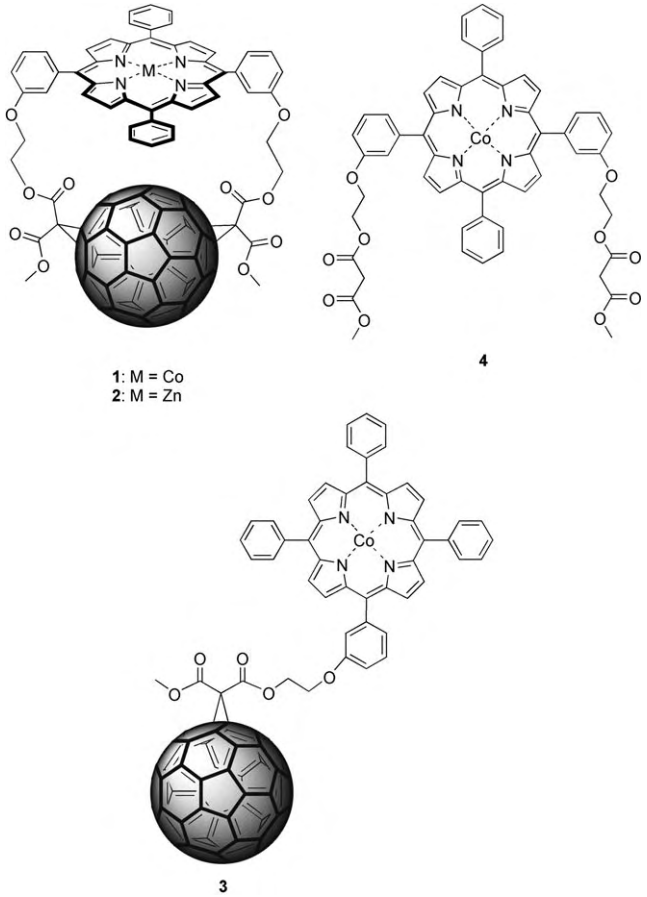

[*] J. Dannhäuser, W. Donaubauer, Dr. F. Hampel, Prof. A. Hirsch
Institut für Organische Chemie
Friedrich-Alexander-Universität Erlangen-Nürnberg
Henkestrasse 42, 91054 Erlangen (Germany)
Fax: (+49) 9131-852-6864
E-mail: andreas.hirsch@chemie.uni-erlangen.de
Prof. M. Reiher, Dr. B. Le Guennic
Laboratorium für Physikalische Chemie
ETH Zürich
Hoenggerberg
8093 Zürich (Switzerland)
B. Corzilius, Prof. K.-P. Dinse
Physikalische Chemie III
Technische Universität Darmstadt
Petersenstrasse 20, 64287 Darmstadt (Germany)

[**] This work was supported by the Deutsche Forschungsgemeinschaft (SFB 583 Redoxactive Metal Complexes—Control of Reactivity via Molecular Architectures). M.R. would like to thank the Fonds der Chemischen Industrie for support by a lecturer's scholarship. We thank Dr. R.-A. Eichel for the assistance with the recording of the HYSCORE spectra.

Supporting information for this article is available on the WWW under http://www.angewandte.org or from the author.

InterScience
© 2006 Wiley-VCH Verlag GmbH & Co. KGaA, Weinheim

two independent molecules of **1** which correspond to the enantiomers of the C_2-symmetric compound with the configurations ^{f}C and ^{f}A (Figure 1). The X-ray crystallographic analysis confirms the existence of the C_2-symmetric *trans*-2

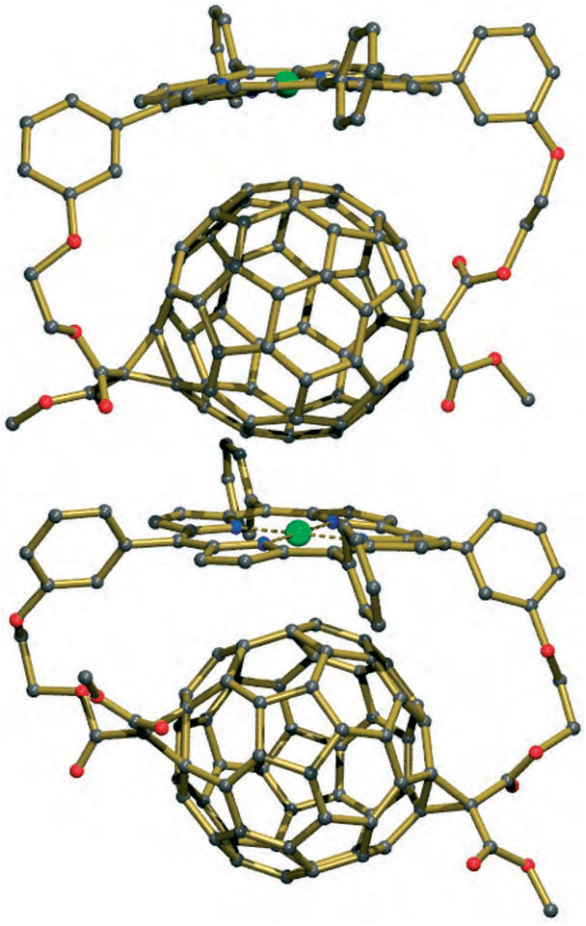

Figure 1. Part of the crystal structure of **1** (asymmetric unit; hydrogen atoms have been omitted). The upper molecule is the ^{f}A-symmetric enantiomer and the lower molecule the ^{f}C-symmetric enantiomer.

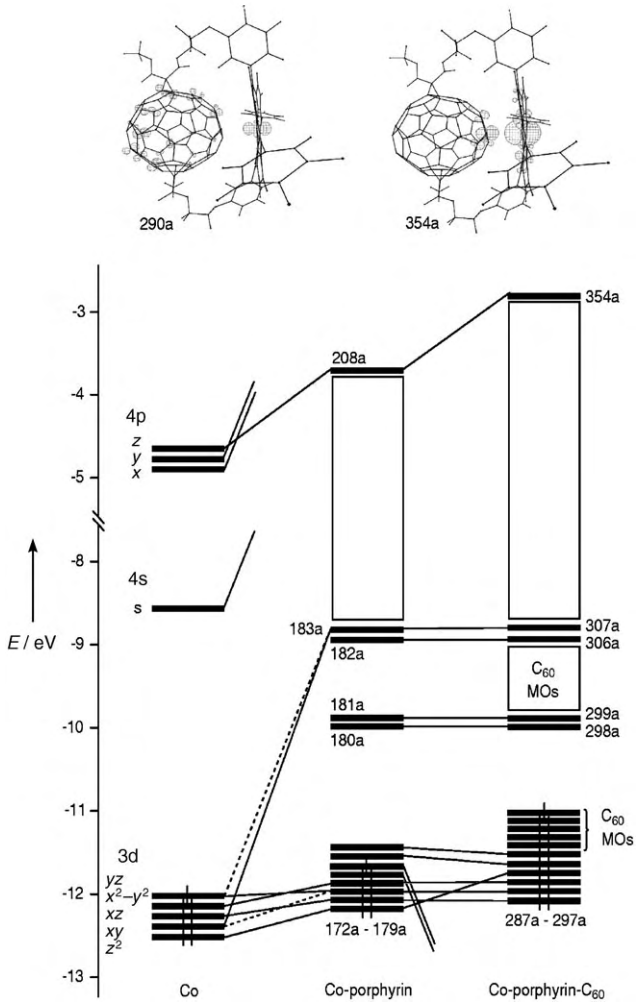

Figure 2. Molecular-orbital correlation diagram for the interaction of the Co center with the porphyrin ligand and the fullerene. The diagram was obtained by an extended Hückel calculation so that the advantages such as occupation-rate-independent molecular orbitals and well-defined decomposition into fragment orbitals could be used. The diagram shows clearly the weak σ donation of the fullerene to the Co (see the Supporting Information for a more detailed discussion).

addition pattern previously deduced from spectroscopic and computational results.[1,2] The short distance between Co and C1 (slightly more than 2.7 Å) is less than the sum of the van der Waals radii and alludes to a weak covalent σ-donor interaction between the fullerene and the singly occupied d_{z^2} orbital of the Co^{II} ion. This supposition is also supported by semiquantitative MO calculations (Figure 2). Similarly short interplanar distances have been found in a series of cocrystals of C_{60} with Fe^{II}, Fe^{III}, and Co^{II} porphyrins.[5,6]

X-band EPR spectra of **1** and **4** were recorded at 10 K, and the ^{59}Co hyperfine components could be resolved (Figure 3). Since good spectral resolution could be obtained only in the high-field range, additional EPR spectra were recorded at 95 GHz (W band). At this Larmor frequency, the *g*-matrix elements were determined with high accuracy independent of the small, initially unknown cobalt hyperfine tensor (see the Supporting Information for the corresponding W-band spectrum of the diad). In contrast to standard detection by field modulation, the EPR absorption spectrum could be recorded directly by detecting the free induction decay (FID) after single-pulse excitation. After the complete *g* matrix was determined, the error in the determination of the small hfs-tensor elements from the X-band data could be minimized. Good fits of the W- and X-band spectra with a single set of parameters were obtained by assuming axial symmetry of the *g* matrix and the hfs tensor (Table 1).

Table 1: Parameters obtained from simulated EPR spectra.

	$g_\perp$	$g_\parallel$	$A_\perp(^{59}Co)$ [MHz]	$A_\parallel(^{59}Co)$ [MHz]	c_1	c_3	K [MHz]	P [MHz]	ρ_{3d}	ρ_{4s}
1	2.447	2.012	210	310	0.079	0.12	469	99	0.68	0.068
4	2.358	2.034	72	265	0.061	0.15	637	−18	0.92	0.054

© 2006 Wiley-VCH Verlag GmbH & Co. KGaA, Weinheim

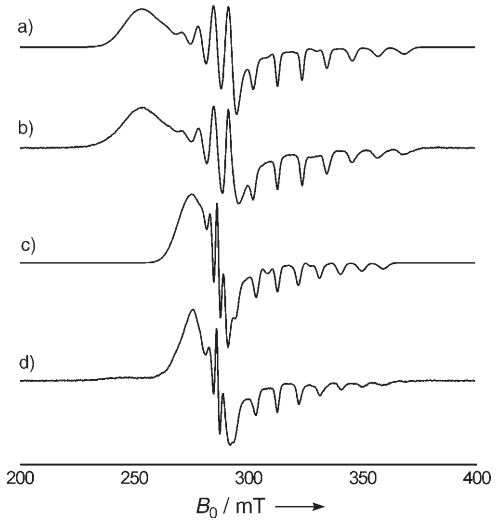

Figure 3. X-band continuous wave EPR spectra of a) **1** and c) **4** in polycrystalline THF at 10 K and the corresponding simulated spectra ((b) and (d)).

HYSCORE experiments were performed to detect the ^{14}N hfs in the porphyrin ring as well. The energy differences between nuclear spin states in different electron spin multiplets can be correlated by this method.[7] These signals, which correspond to the ENDOR frequencies, are broadened in the polycrystalline matrix by anisotropic components of the dipolar and quadrupolar interactions. Surprisingly, well-resolved spectra could be observed in the 2D EPR experiment for both the diad and the precursor molecule (Figure 4). The signals were clearly identified as double-quantum transitions. Transitions between the $m_I = +1$ and $m_I = -1$ states are, as a first approximation, independent of the quadrupole interaction.[8] The line broadening by the dipolar terms can be minimized by orientation selection if the principal axes of the g matrix and the nitrogen hfs tensor are colinear, which seems to be the case for our systems.

The accurately determined frequencies of these double-quantum transitions can be used to determine the main values of the nitrogen hfs tensor [Eq. (1)]. The tensor principal axes are labeled $i = x, y, z$, and the two m_s multiplets are labeled α and β.

$$A_{ii} = \frac{(\nu^{\alpha}_{DQ}(i))^2 - \nu^{\beta}_{DQ}(i))^2}{8\nu_1} \quad (1)$$

Equation (1) is derived from the analytical solution of the simplified electron/nitrogen spin system for the case of the canonical orientation (see the Supporting Information). The orientation can be selected by the choice of the appropriate magnetic field. In our analysis, we have also assumed that all four nuclei are equivalent within the margins of errors. The results are summarized in Table 2. The quadrupole coupling can also be estimated by using the analytical solution and in both cases results in $e^2qQ/h = 2.2(4)$ MHz, in which the field-gradient principal axis is given by the direction of the Co–N bond. This value has a relatively large uncertainty but agrees fairly well with literature values for similar systems (1.75 to 1.80 MHz).[9]

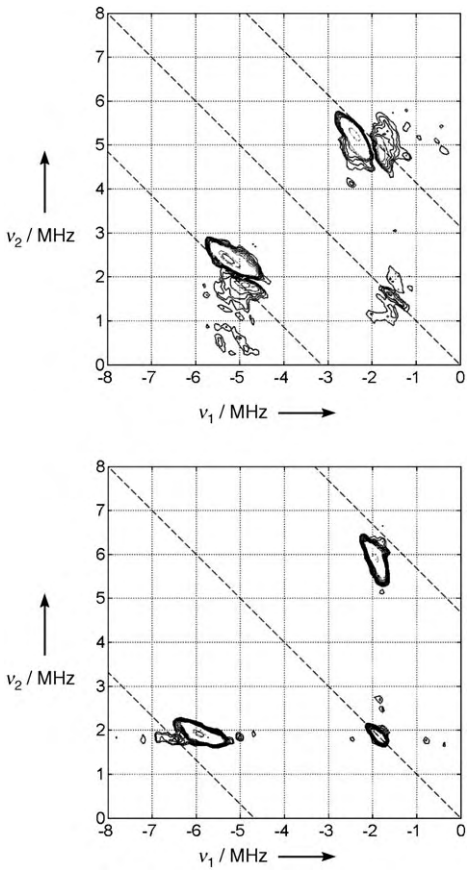

Figure 4. X-band HYSCORE spectra of **4** obtained at 10 K by microwave excitation at 255 mT (top) and 380 mT (bottom). Under these conditions, the orientations parallel and perpendicular to the porphyrin plane, respectively, are selected. Only the (−,+) quadrants of the spectra are shown.

Table 2: ^{14}N hfs parameters obtained from HYSCORE spectra.

	$A_\perp(^{14}N)$ [MHz][a]	$A_\parallel(^{14}N)$ [MHz][a]
1	3.45	3.35
4	3.65	3.54

[a] The principal axes of the axial ^{14}N hfs tensor are presumed to be colinear with the principal axes of the g matrix. The main value is perpendicular to the porphyrin plane.

With the aid of the experimentally determined g-matrix elements and the cobalt hfs data, the changes in the spin-density distribution during the formation of the diad can be estimated. For this purpose, we use the model of McGarvey[10] in combination with the approach of Wayland and Abd-Elmageed,[11] to determine the spin densities at the metal center (see the Supporting Information). We find that the 3d spin density decreases by 20% during the formation of the diad. A comparison of the local BP86 spin density at the Co^{II} ion in the isolated Co porphyrin **4** and in complex **1** shows a decrease of about 0.1 elementary charge units during the formation of the complex with C_{60} (see the Supporting

 © 2006 Wiley-VCH Verlag GmbH & Co. KGaA, Weinheim

Information). This decrease is clearly smaller than the value derived from the McGarvey relation and corresponds much better with the very small decrease observed for the ^{14}N hfs (ca. 200 kHz).

Furthermore, density functional calculations (with the BP86 functional) involving rigorous definitions for the local spin densities[12] at **1** and **4** have been performed to analyze quantitatively the distribution of the spin density in the porphyrin–fullerene complex. The local $\langle S_{zA} \rangle$ expectation values obtained for each atom are depicted in the Supporting Information. (As these local spins are equal to half the difference population of α and β electrons at the center A, the expectation values have been multiplied by a factor of 2.) Spin density is also found to a minor extent at the N atoms of the porphyrin. Importantly, a number of C atoms of the fullerene—located directly next to the π system of the porphyrin and the Co center—show a small but significantly higher spin density relative to the remaining C atoms of the C_{60} cage (and also to those of the porphyrin). These results show that there are both σ-donor and π-acceptor interactions between the fullerene and the porphyrin. The existence of π–π interactions between the two chromophores has been suggested repeatedly [5] and is supported by these investigations.

^1H NMR spectroscopic investigations show a large downfield shift of the signals of the pyrrolic β-H atoms in the Co^{II} compounds **3** ($\delta = 14.70$ ppm) and **4** ($\delta = 15.84$ ppm; Figure 5), as expected for paramagnetic metal porphyrins.[1,2] In contrast, the downfield shift of the corresponding ^1H NMR signal of the paramagnetic diad **1** is noticeably smaller ($\delta =$ 11.81 ppm). This behavior is also a result of partial spin transfer from the porphyrin unit to the fullerene unit.

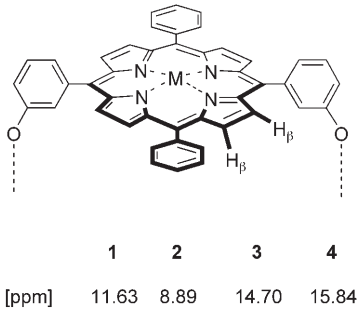

Figure 5. ^1H NMR chemical shifts of the pyrrolic β-H atoms of the compounds **1**–**4**.

From these results, the model depicted schematically in Figure 6 can be derived to describe the intramolecular interactions in **1**: a) The fullerene C atom (C1) nearest to the cobalt center bears a weak coordinative σ-donor interaction with the singly occupied Co d_{z^2} orbital. b) Furthermore, significant back bonding from the π system of the porphyrin to the π system of the fullerene takes place. c) The π-acceptor effect of the fullerene is stronger than its σ-donor effect. This model explains on the one hand why the porphyrin is more difficult to oxidize and on the other hand why the fullerene moiety is easier to reduce.[2] Another reason for the facile reduction is that the already present C1→Co σ-donor interaction promotes the acceptance of an electron to form a completely covalent bond between C1 and Co, thus stabilizing the reduced state. Such covalent bonds with typical Co–C(fullerene) distances of 2.28–2.32 Å can indeed be found in diamagnetic Co^{II}-TPP/fullerene$^-$ complexes (TPP = tetraphenylporphyrin).[6]

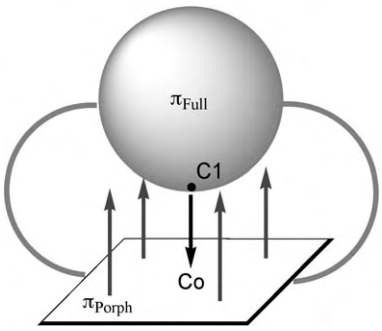

Figure 6. σ-Donor (C1→Co) and π-acceptor ($\pi_{Porph} \rightarrow \pi_{Full}$) stacking interactions in **1**.

Linear stacking arrangements are formed in the crystal of **1** (see the Supporting Information), in which the fullerene moiety of one molecule is located in proximity to the porphyrin moiety of the neighboring molecule. Especially noteworthy is the similarity of the intra- and intermolecular packing motifs. In particular, the shortest fullerene–cobalt distance within a molecule ($d_{C1\text{-}Co} = 2.726$ and 2.713 Å) is nearly the same as the shortest fullerene–cobalt distance between two neighboring molecules ($d_{C\omega\text{-}Co} = 2.726$ Å, Figure 1). The surprising similarity of these packing motifs suggests that the intermolecular stacking is also favored by analogous σ-donor (Cω→Co) and π-acceptor ($Porph_\pi \rightarrow Full_\pi$) interactions. Currently, we are investigating the coordination polymers of **1** in the solid state (see the Supporting Information) and other analogous transition-metal complexes with respect to their potential as novel magnetic materials.

Received: December 9, 2005
Revised: January 19, 2006
Published online: April 19, 2006

Keywords: cobalt · electron transfer · fullerenes · molecular dyads · porphyrinoids

[1] a) E. Dietel, A. Hirsch, E. Eichhorn, A. Rieker, S. Hackbarth, B. Röder, *Chem. Commun.* **1998**, 1981–1982; b) D. M. Guldi, C. Luo, T. Da Ros, M. Prato, E. Dietel, A. Hirsch, *Chem. Commun.* **2000**, 375–376; c) D. M. Guldi, C. Luo, M. Prato, E. Dietel, A. Hirsch, *Chem. Commun.* **2000**, 373–374; d) D. M. Guldi, C. Luo, M. Prato, A. Troisi, F. Zerbetto, M. Scheloske, E. Dietel, W. Bauer, A. Hirsch, *J. Am. Chem. Soc.* **2001**, *123*, 9166–9167.

[2] L. R. Sutton, M. Scheloske, K. S. Pirner, A. Hirsch, D. M. Guldi, J.-P. Gisselbrecht, *J. Am. Chem. Soc.* **2004**, *126*, 10370–10381.

[3] a) J.-P. Bourgeois, F. Diederich, L. Echegoyen, J.-F. Nierengarten, *Helv. Chim. Acta* **1998**, *81*, 1835–1844; b) N. Armaroli, G. Marconi, L. Echegoyen, J.-P. Bourgeois, F. Diederich, *Chem. Eur. J.* **2000**, *6*, 1629–1645.

[4] Crystallographic data: $C_{116}H_{40}CoN_4O_{10}$, $M_r = 1708.51$, $0.25 \times 0.20 \times 0.20$ mm^3, triclinic, space group $P\bar{1}$, $a = 16.5651(3)$, $b =$

 © 2006 Wiley-VCH Verlag GmbH & Co. KGaA, Weinheim

20.56850(10), $c = 26.5555(3)$ Å, $\alpha = 76.8696(11)$, $\beta = 78.0099(12)$, $\gamma = 83.2600(11)°$, $V = 8595.77(19)$ Å^3, $Z = 4$, $\rho_{calcd} = 1.541$ g cm^{-3}, $2\theta_{max} = 50.12°$, index range: $-19 \le h \le 19$, $-24 \le k \le 24$, $-31 \le l \le 28$, $\mu = 0.433$ mm^{-1}, max/min transmission 0.9184/0.8995. The structural data were collected by a Nonius Kappa CCD area detector with $Mo_{K\alpha}$ radiation ($\lambda = 0.71073$ Å) at $T = 173(2)$ K. An empiric absorption correction was performed.[13] 51 862 reflections were collected, 30 094 of which were independent and 17 065 with $I > 2\sigma(I)$. The structure was solved with direct methods and refined by full-matrix least-squares methods on F^2 with 2598 refined parameters.[14] All non-hydrogen atoms were refined anisotropically. The hydrogen atoms were refined as riding atoms on calculated positions ($R1$ ($I > 2\sigma(I)$) = 0.1011; $wR2$ (all data) = 0.3320; GOF = 1.028; max/min residual electron density 1.483/−1.023 e Å^{-3}). The asymmetric unit contained two independent molecules of **1** as well as five molecules of dichloromethane, four molecules of methanol, and one molecule of water. One of the two independent molecules of **1** displayed disorder, which was solved and refined to an occupation ratio of 75:25. The 75% occupied molecule is the ^{f}A-symmetric enantiomer of **1** (Figure 1, upper part). The ^{f}C-symmetric enantiomer is depicted in the lower part of Figure 1. CCDC-292094 contains the supplementary crystallographic data for this paper. These data can be obtained free of charge from The Cambridge Crystallographic Data Centre via www.ccdc.cam.ac.uk/data_request/cif.

[5] For a recent overview, see: P. D. W. Boyd, C. A. Reed, *Acc. Chem. Res.* **2005**, *38*, 235 – 242.

[6] a) D. V. Konarev, S. S. Khasanov, A. Otsuka, Y. Yoshida, G. Saito, *J. Am. Chem. Soc.* **2002**, *124*, 7648 – 7649; b) D. V. Konarev, S. S. Khasanov, G. Saito, R. N. Lyubovskaya, Y. Yoshida, A. Otsuka, *Chem. Eur. J.* **2003**, *9*, 3837 – 3848.

[7] P. Höfer, A. Grupp, H. Nebenführ, M. Mehring, *Chem. Phys. Lett.* **1986**, *132*, 279 – 282.

[8] H. L. Flanagan, D. J. Singel, *J. Chem. Phys.* **1988**, *89*, 2585 – 2586.

[9] S. Van Doorslaer, A. Schweiger, *Phys. Chem. Chem. Phys.* **2001**, *3*, 159 – 166.

[10] B. R. McGarvey, *Can. J. Chem.* **1975**, *53*, 2498 – 2511.

[11] B. B. Wayland, M. E. Abd-Elmageed, *J. Am. Chem. Soc.* **1974**, *96*, 4809 – 4814.

[12] a) A. E. Clark, E. R. Davidson, *J. Chem. Phys.* **2001**, *115*, 7382 – 7392; b) C. Herrmann, M. Reiher, B. A. Hess, *J. Chem. Phys.* **2005**, *122*, 034102.

[13] a) "Collect" data-collection software, Nonius BV, **1998**; b) "Scalepack" data-processing software: "Macromolecular Crystallography, Part A": Z. Otwinowski, W. Minor, *Methods Enzymol.* **1997**, *276*, 307.

[14] SHELX-97: G. M. Sheldrick, SHELX-97, Program for Refinement of Crystal Structures, University of Göttingen, **1997**.

 © 2006 Wiley-VCH Verlag GmbH & Co. KGaA, Weinheim

Fluorescent Probes

DOI: 10.1002/anie.200504210

Structure-Sensitive and Self-Assembled Helical Pyrene Array Based on DNA Architecture**

*Elke Mayer-Enthart and Hans-Achim Wagenknecht**

The generation of defined molecular structures based on functionalized nucleic acids is a research topic of increasing interest with important applications in nanobiotechnology.[1–3] The modification of RNA and DNA by single or dual fluorescent labeling is routinely applied for molecular diagnostics.[4–6] Moreover, the self-assembled and regular structure of duplex DNA provides a supramolecular scaffold that allows the photophysical interaction of more than two fluorophores that are incorporated as surrogates of nucleoside bases.[7–12] Pyrenes have been used successfully for nucleic acid labeling.[13–17] Recently, such a π-array of pyrenes was synthesized along duplex RNA.[18] DNA was also applied as a template for the helical assembly of noncovalently bound chromophores in the minor groove.[19]

With respect to potential applications in DNA analytics, the goal of these research efforts is to enhance and modulate the fluorescence properties by the incorporation of several adjacent fluorophores into DNA. Most importantly, the sequence-selective base-pairing properties of such modified oligonucleotides should be maintained for their application as probes in molecular diagnostics with DNA, for example, for the detection of single nucleotide polymorphism.[20] One suitable and important way to fulfil these requirements is to attach chromophores covalently to natural DNA bases.[4,21]

Recently, we introduced 5-(pyren-1-yl)-2′-deoxyuridine (PydU),[22–24] 1-ethynylpyrene,[25,26] and other chromophores[27] as fluorescent probes and photoinducable electron donors in DNA. Herein, we describe the properties of DNA duplexes that have been functionalized by a helical stack consisting of five adjacent PydU moieties. Using our previously described synthetic protocols,[28,29] we prepared the following DNA duplexes (Scheme 1): **DNA1** contains a single PydU modification site, whereas **DNA3a–d** bear a row of five adjacent chromophore modifications. **DNA2** and **DNA4** represent control duplexes lacking any modification.

It is important to note that in PydU the pyrene chromophore is linked covalently to the uridine by a single C–C

[*] Dipl.-Chem. E. Mayer-Enthart, Prof. H.-A. Wagenknecht
Institute for Organic Chemistry
University of Regensburg
93040 Regensburg (Germany)
Fax: (+49) 941-943-4617
E-mail: achim.wagenknecht@chemie.uni-regensburg.de

[**] This work was supported by the Deutsche Forschungsgemeinschaft, the Volkswagen-Stiftung, the University of Regensburg, and the Fonds der Chemischen Industrie.

Supporting information for this article is available on the WWW under http://www.angewandte.org or from the author.

WILEY InterScience DISCOVER SOMETHING GREAT
© 2006 Wiley-VCH Verlag GmbH & Co. KGaA, Weinheim

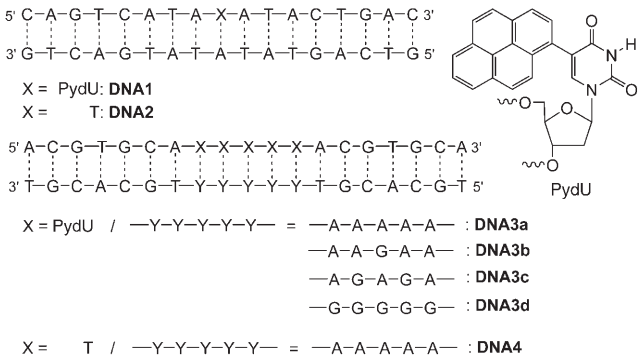

Scheme 1. Sequences of duplexes **DNA1**, **DNA2**, **DNA3 a–d**, and **DNA4**.

bond, yielding a strong electronic coupling. According to our previous studies,[23,24,28–32] the photoinduced intramolecular exciplexes[33,34] of PydU exhibit intense, unstructured fluorescence bands with solvent-dependent maxima. This stands in contrast to similar assays in which pyrene chromophores are attached to the 2′-hydroxy group for base-mismatch detection in RNA.[13–16]

Interestingly, the emission quantity of **DNA3a** is more than ten times that of **DNA1**, and this increase is significantly higher than the fivefold sum of each single PydU chromophore (Figure 1). In fact, the fluorescence enhancement

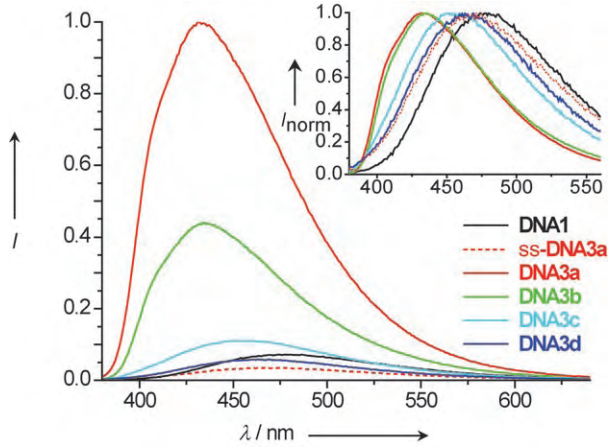

Figure 1. Fluorescence spectra of **DNA1** and **DNA3 a–d** ($\lambda_{ex} = 360$ nm, 2.5 μM DNA in 10 mM sodium phosphate buffer, 250 mM NaCl, pH 7). Inset: Fluorescence spectra with λ_{max} normalized to 1.

(ca. 22-fold) as a result of DNA hybridization is even greater; this can be seen by comparing the single-stranded(ss)-**DNA3a** with the duplex **DNA3a**. Additionally, a shift of the maximum emission occurs from 475 nm in ss-**DNA3a** (similar to **DNA1**) to 445 nm in duplex **DNA3a**. Both results indicate a regular and highly organized structure of the five PydU moieties that is formed upon DNA hybridization and allows strong excitonic interactions among the chromophores.

In the duplexes **DNA3b–d**, one, two, and five adenine bases, respectively, have been replaced by guanines as part of the complementary counterstrand to the PydU-modified oligonucleotide. It is remarkable that the incorporation of these mismatches results in a significant loss of emission quantity. Apparently at least two mismatches are needed to interrupt significantly the electronically coupled organization of the PydU array. The bathochromic shift of the maximum from 445 nm (**DNA3b**) to 465 nm (**DNA3d**) correlates with the increasing number of mismatches. The emission properties of the highly mismatched duplexes **DNA3c**,**d** are similar to that of the single labeled duplex **DNA1**, indicating that the five single PydU chromophores are electronically decoupled. The observed mismatch effect in **DNA3b** compared to that in **DNA3a** is similar to that in existing assays but is accompanied by a more intense fluorescence signal of five pyrene chromophores.[17]

To obtain more information about the secondary structure of the PydU-modified DNA duplexes, we performed CD spectroscopy (Figure 2). Remarkably, a significant exciton-

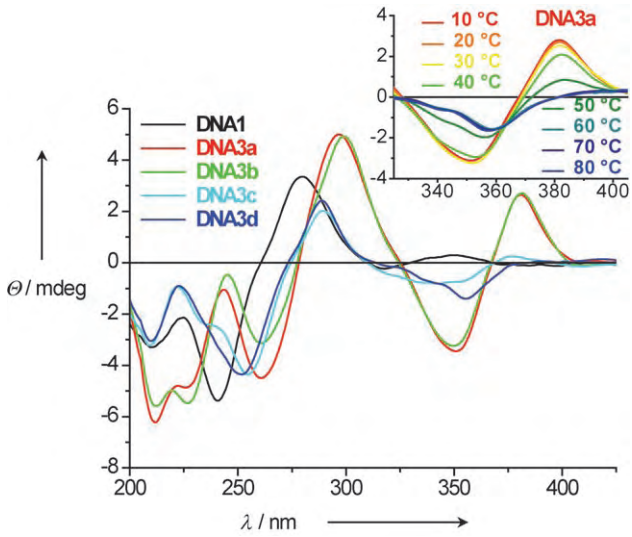

Figure 2. CD spectra of **DNA1** and **DNA3 ad** (2.5 μM DNA in 10 mM sodium phosphate buffer, 250 mM NaCl, pH 7). Inset: Temperature-dependent CD spectra of **DNA3 a**.

coupled CD signal is observed in the case of **DNA3a** in the range of the PydU chromophore (305–425 nm); this signal is not present in the CD spectrum of single-PydU-modified **DNA1**. Apparently the incorporation of just one guanine instead of adenine as the counterbase to the middle chromophore in **DNA3b** seems to be tolerated for the helical arrangement of the PydU chromophores since the corresponding CD spectrum looks very similar to that of **DNA3a**. In contrast, the incorporation of two (**DNA3c**) or five (**DNA3d**) mismatches results in a nearly complete destruction of the CD signal. In the latter duplexes, the highly ordered helical PydU arrangement seems to be perturbed. In agreement with this interpretation stands the observation that the CD spectrum of the duplex **DNA3a** exhibits DNA-typical melting behavior. Above ca. 50 °C, the corresponding CD signal of the fully matched duplex **DNA3a** flattens (see insert in Figure 2). Thus, the CD spectrum of **DNA3a** below the melting temperature (T_m) indicates a right-handed helical

 © 2006 Wiley-VCH Verlag GmbH & Co. KGaA, Weinheim

arrangement of the adjacent PydU chromophores. The CD spectrum of **DNA3a** above T_m looks very similar to that of **DNA3d** at room temperature. This means that the helically arranged conformation of the chromophores breaks down by either the thermally induced denaturation of the DNA duplex scaffold or by the influence of at least two base mismatches within the fivefold PydU array.

If the helical arrangement of the PydU chromophores depends on the presence of the duplex architecture, the corresponding fluorescence properties should also change above T_m. As expected, the characteristic emission enhancement of **DNA3a** and the bathochromic shift of the emission maximum are present only below T_m (Figure 3).

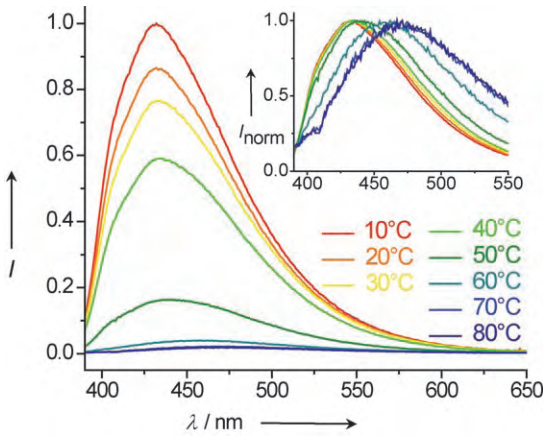

Figure 3. Temperature-dependent fluorescence spectra of **DNA3a** (λ_{exc} = 360 nm, 2.5 μM DNA in 10 mM sodium phosphate buffer, 250 mM NaCl, pH 7). Inset: Fluorescence spectra with λ_{max} normalized to 1.

The T_m values of the modified duplexes were measured and compared with those of the unmodified **DNA2** and **DNA4** (Table 1). The incorporation of a single PydU unit

Table 1: Melting temperatures of **DNA1**, **DNA2**, **DNA3a–d**, and **DNA4**.[a].

Duplex	T_m upwards [°C]	T_m downwards [°C]
DNA1	52	49
DNA2	61	59
DNA3a	56	50
DNA3b	61	50
DNA3c	51	49
DNA3d	–[b]	–[b]
DNA4	71	69

[a] λ = 260 nm, 2.5 μM DNA in 10 mM sodium phosphate buffer, 250 mM NaCl, pH 7. [b] No cooperative melting transition observed (see the Supporting Information).

(**DNA1**) destabilizes the DNA duplex (**DNA2**). But it is interesting to observe that the incorporation of five chromophore units (**DNA3a**) does not destabilize the duplex additionally. Apparently some amount of destabilization can be regained by the hydrophobic interactions between PydU chromophores. The incorporation of a single base mismatch stabilizes the duplex (**DNA3b**), whereas additional mismatches reduce the thermal stability (**DNA3c**) and even disturb the cooperative melting behavior (**DNA3d**).

In conclusion, the architecture of DNA duplexes is suitable as a structural scaffold for the self-assembled helical arrangement of a covalently attached π-stacked array of organic chromophores. In the presented example, the fivefold helical stack exhibits sequence selectivity and therefore represents a highly structure-sensitive probe for DNA. The optical properties of this type of DNA constructs have a high potential for applications in fluorescent DNA analytics, for example, for the base-mismatch detection within a whole codon that translates into a single mutated amino acid in a protein.

Received: November 25, 2005
Revised: January 25, 2006
Published online: April 18, 2006

Keywords: DNA · fluorescent probes · nucleobases · oligonucleotides · pyrene

[1] T. Carell, C. Behrens, J. Gierlich, *Org. Biomol. Chem.* **2003**, *1*, 2221–2228.
[2] J. Wengel, *Org. Biomol. Chem.* **2004**, *2*, 277–280.
[3] J. L. Sessler, J. Jayawickramarajah, *Chem. Commun.* **2005**, 1939–1949.
[4] C. Wojczewski, K. Stolze, J. W. Engels, *Synlett* **1999**, 1667–1678.
[5] M. K. Johansson, R. M. Cook, *Chem. Eur. J.* **2003**, *9*, 3466–3471.
[6] W. Tan, K. Wang, T. J. Drake, *Curr. Opin. Chem. Biol.* **2004**, *8*, 547–553.
[7] A. P. H. J. Schenning, E. W. Meijer, *Chem. Commun.* **2005**, 3245–3258.
[8] J. Gao, S. Watanabe, E. T. Kool, *J. Am. Chem. Soc.* **2004**, *126*, 12748–12749.
[9] D. Ackermann, R. Häner, *Helv. Chim. Acta* **2004**, *87*, 2790–2804.
[10] H. Kashida, H. Asanuma, M. Komiyama, *Angew. Chem.* **2004**, *116*, 6684–6687; *Angew. Chem. Int. Ed.* **2004**, *43*, 6522–6525.
[11] C. Brotschi, G. Mathis, C. J. Leumann, *Chem. Eur. J.* **2005**, *11*, 1911–1923.
[12] I. Bouamaied, E. Stulz, *Chimia* **2005**, *59*, 101–104.
[13] M. Nakamura, Y. Fukunaga, K. Sasa, Y. Ohtoshi, K. Kanaori, H. Hayashi, H. Nakano, K. Yamana, *Nucleic Acids Res.* **2005**, *33*, 5887–5895.
[14] K. Yamana, R. Iwase, S. Furutani, H. Tsuchida, H. Zako, T. Yamaoka, A. Murakami, *Nucleic Acids Res.* **1999**, *27*, 2387–2392.
[15] K. Yamana, H. Zako, K. Asazuma, R, Iwase, H. Nakano, A. Murakami, *Angew. Chem.* **2001**, *113*, 1138–1140; *Angew. Chem. Int. Ed.* **2001**, *40*, 1104–1106.
[16] A. Mahara, R. Iwase, T. Sakamoto, K. Yamana, T. Yamaoka, A. Murakami, *Angew. Chem.* **2002**, *114*, 3800–3802; *Angew. Chem. Int. Ed.* **2002**, *41*, 3648–3650.
[17] A. Okamoto, K. Kanatani, I. Saito, *J. Am. Chem. Soc.* **2004**, *126*, 4820–4827.
[18] M. Nakamura, Y. Ohtoshi, K. Yamana, *Chem. Commun.* **2005**, 5163–5165.
[19] B. A. Armitage, *Top. Curr. Chem.* **2005**, *253*, 55–76.
[20] K. Nakatani, *ChemBioChem* **2004**, *5*, 1623–1633.
[21] R. T. Ranasinghe, T. Brown, *Chem. Commun.* **2005**, 5487–5502.
[22] T. L. Netzel, M. Zhao, K. Nafisi, J. Headrick, M. S. Sigman, B. E. Eaton, *J. Am. Chem. Soc.* **1995**, *117*, 9119–9128.

 © 2006 Wiley-VCH Verlag GmbH & Co. KGaA, Weinheim

[23] M. Raytchev, E. Mayer, N. Amann, H.-A. Wagenknecht, T. Fiebig, *ChemPhysChem* **2004**, *5*, 706 – 712.
[24] P. Kaden, E. Mayer-Enthart, A. Trifonov, T. Fiebig, H.-A. Wagenknecht, *Angew. Chem.* **2005**, *117*, 1662 – 1666; *Angew. Chem. Int. Ed.* **2005**, *44*, 1637 – 1639.
[25] E. Mayer, L. Valis, C. Wagner, M. Rist, N. Amann, H.-A. Wagenknecht, *ChemBioChem* **2004**, *5*, 865 – 868.
[26] C. Wagner, M. Rist, E. Mayer-Enthart, H.-A. Wagenknecht, *Org. Biomol. Chem.* **2005**, *3*, 2062 – 2063.
[27] L. Valis, N. Amann, H.-A. Wagenknecht, *Org. Biomol. Chem.* **2005**, *3*, 36 – 38.
[28] E. Mayer, L. Valis, R. Huber, N. Amann, H.-A. Wagenknecht, *Synthesis* **2003**, 2335 – 2340.
[29] N. Amann, E. Pandurski, T. Fiebig, H.-A. Wagenknecht, *Chem. Eur. J.* **2002**, *8*, 4877 – 4883.
[30] A. Trifonov, I. Buchvarov, H.-A. Wagenknecht, T. Fiebig, *Chem. Phys. Lett.* **2005**, *409*, 277 – 280.
[31] R. Huber, T. Fiebig, H.-A. Wagenknecht, *Chem. Commun.* **2003**, 1878 – 1879.
[32] N. Amann, E. Pandurski, T. Fiebig, H.-A. Wagenknecht, *Angew. Chem.* **2002**, *114*, 3084 – 3087; *Angew. Chem. Int. Ed.* **2002**, *41*, 2978 – 2980.
[33] Z. R. Grabowski, K. Rotkiewicz, W. Rettig, *Chem. Rev.* **2003**, *103*, 3899 – 4031.
[34] T. Fiebig, K. Stock, S. Lochbrunner, E. Riedle, *Chem. Phys. Lett.* **2001**, *345*, 81 – 88.

 © 2006 Wiley-VCH Verlag GmbH & Co. KGaA, Weinheim

Cover Picture

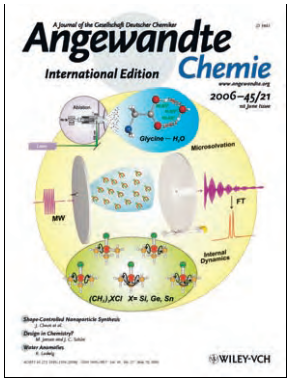

Melanie Schnell, Jens-Uwe Grabow,*

José L. Alonso,* Emilio J. Cocinero, Alberto Lesarri, M. Eugenia Sanz, and Juan C. López

Microsolvation of glycine has been studied by combining impulse supersonic-jet Fourier-transform microwave spectroscopy with laser ablation and the structure of the monohydrated complex derived from rotational spectra. Combining this method with theoretical considerations enables the internal dynamics of multiple large-amplitude motions, such as in $(CH_3)_3XCl$ (X = Si, Ge, Sn), to be revealed. For more details, see the Communications by J.-U. Grabow and J. L. Alonso and co-workers on pages 3465 and 3471 ff.

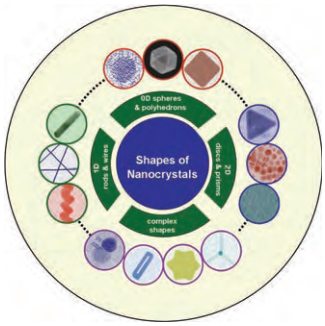

Nanoparticle Synthesis
Inorganic nanocrystals with size- and shape-dependent properties are excellent building blocks for functional nanosystems. Recent developments in the shape-controlled synthesis of colloidal nanocrystals are described by J. Cheon et al. in their Review on page 3414 ff.

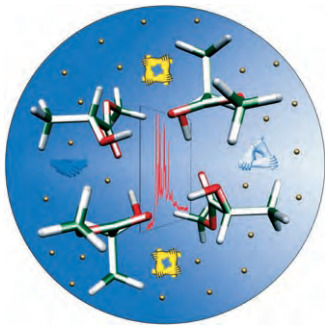

Molecular Recognition
Four methyl lactate molecules with alternating configurations cluster through hydrogen bonds to form a structure unfavored for homoconfigurational tetramers. See the Communication by M. A. Suhm and co-workers on page 3440 ff., for further details.

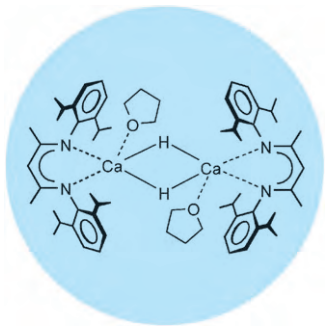

Main-Group Hydrides
Reaction of a calcium amide with phenylsilane leads to the ready formation of a molecular calcium hydride. S. Harder and J. Brettar describe in the Communication on page 3474 ff. their approach to this new class of compound.

Contents

VIP *The following Communications have been judged by at least two referees to be "very important papers" and will be published online at www.angewandte.org soon:*

*C. Burke, Y. Shi**
Regio- and Enantioselective Epoxidation of Dienes by a Chiral Dioxirane: Synthesis of Optically Active Vinyl *cis*-Epoxides

C.-W. So, H. Roesky, J. Magull, R. Oswald*
Synthesis and Characterization of [{PhC(NtBu)$_2$}SiCl]: A Stable Monomeric Chlorosilylene

*H. Yu, S. Huang, H. Chokhawala, M. Sun, H. Zheng, X. Chen**
Highly Efficient Chemoenzymatic Synthesis of Naturally Occurring and Non-Natural α2,6-Linked Sialosides: A *P. damsela* α2,6-Sialyltransferase with Extremely Flexible Donor Substrate Specificity

*D. Rohde, C.-J. Yan, H.-J. Yan, L.-J. Wan**
From Lamellar to Hexagonal Self-Assembly of Bis(dioxaborin) Molecules

News

Inorganic Chemistry: Nöth Recognized — 3398

Biophysics: Sackmann Honored — 3398

Biochemistry: Davies Awarded — 3398

Books

Six-Membered Hetarenes with One Nitrogen or Phosphorus Atom — D. St. C. Black — *reviewed by C. Marazano* — 3399

The Organic Chemistry of Sugars — Daniel E. Levy, Péter Fügedi — *reviewed by V. Wittmann* — 3399

Highlights

Water Anomalies

R. Ludwig* — 3402 – 3405

The Puzzling Properties of Supercooled and Glassy Water

Cold as ice: The anomalies in the properties of water arise from a transformation between two major liquid forms of water in the deeply supercooled region which are proposed to meet at a liquid–liquid critical point. Recent studies of glassy and supercooled water give insight into water's unusual phase-transition behavior.

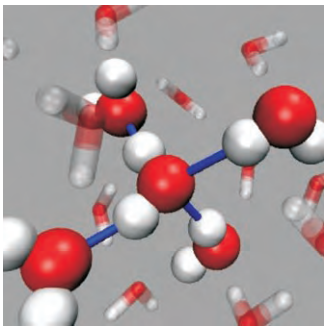

Essays

Design in Chemistry

M. Jansen,* J. C. Schön — 3406 – 3412

"Design" in Chemical Synthesis—An Illusion?

The power of words: According to its generally accepted definition, the process of "design" is the creation of a form that fulfills a given function as well as possible and is also considered aesthetically pleasing. This implies a type of creativity that does not exist in the synthesis of new chemical compounds. This essay discusses the implications of the term "design" in the context of chemistry.

InterScience

© 2006 Wiley-VCH Verlag GmbH & Co. KGaA, Weinheim

Reviews

Nanocrystals get into shape: Recent developments in the shape control of semiconductor and metal oxide nanocrystals have yielded many structurally unprecedented nanocrystals including polyhedrons, rods, wires, plates, prisms, and other complex shapes (see picture). Such specially shaped nanocrystals exhibit novel properties and can be further utilized as key building blocks for the fabrication of nanosystems.

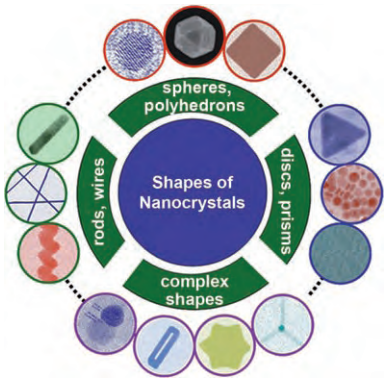

Nanoparticle Synthesis

Y.-w. Jun, J.-s. Choi, J. Cheon* ——— 3414 – 3439

Shape Control of Semiconductor and Metal Oxide Nanocrystals through Nonhydrolytic Colloidal Routes

Communications

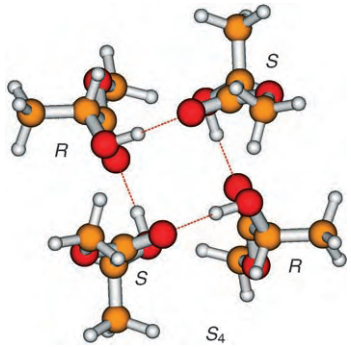

Supersonic jet expansions of racemic methyl lactate show a prominent OH-stretching infrared absorption at 3401 cm^{-1} which is not present in the enantiopure compound. Experimental results and quantum chemical calculations show that the underlying tetrameric cluster has 2:2 stoichiometry of the *R* and *S* isomers and S_4 symmetry (see picture; C orange, O red, H gray).

Chiral Recognition

T. B. Adler, N. Borho, M. Reiher, M. A. Suhm* ——— 3440 – 3445

Chirality-Induced Switch in Hydrogen-Bond Topology: Tetrameric Methyl Lactate Clusters in the Gas Phase

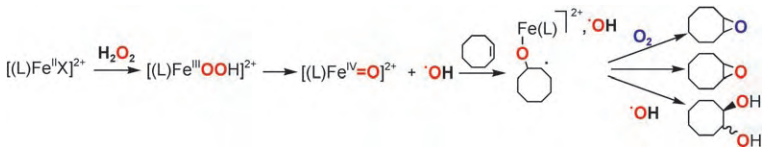

Going ferryl: Fe^{II} complexes with two isomeric bispidine ligands catalyze the oxidation of cyclooctene with H_2O_2 in MeCN under aerobic conditions with high selectivity for the epoxide (see scheme; L = bispidine ligand). An $\{Fe^{IV}{=}O\}$ complex is postulated to be the oxidant, formed by the homolytic cleavage of the O–O bond of an $\{Fe^{III}\text{-}OOH\}$ intermediate. Performing the reaction under argon gives a mixture of *cis* and *trans* diols as well as the epoxide.

Homogeneous catalysis

M. R. Bukowski, P. Comba,* A. Lienke, C. Limberg, C. Lopez de Laorden, R. Mas-Ballesté, M. Merz, L. Que, Jr.* ——— 3446 – 3449

Catalytic Epoxidation and 1,2-Dihydroxylation of Olefins with Bispidine–Iron(II)/H_2O_2 Systems

For the USA and Canada:
ANGEWANDTE CHEMIE International Edition (ISSN 1433-7851) is published weekly by Wiley-VCH PO Box 191161, D 69451 Weinheim, Germany. Air freight and mailing in the USA by Publications Expediting Inc. 200 Meacham Ave., Elmont, NY 11003. Periodicals postage paid at Jamaica NY 11431. US POSTMASTER: send address changes to *Angewandte Chemie*, Wiley-VCH, 111 River Street, Hoboken, NJ 07030. Annual subscription price for institutions: US$ 5685/5168 (valid for print and electronic / print or electronic delivery); for individuals who are personal members of a national chemical society prices are available on request. Postage and handling charges included. All prices are subject to local VAT/sales tax.

© 2006 Wiley-VCH Verlag GmbH & Co. KGaA, Weinheim

The best in chemistry –

for more than a hundred years

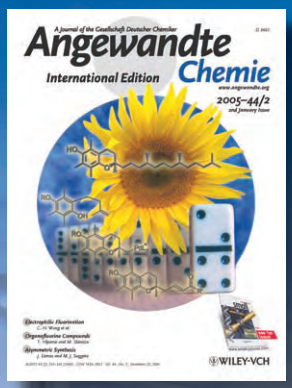

A Journal of the Gesellschaft Deutscher Chemiker

Angewandte
International Edition **Chemie**

www.angewandte.org

1888: ***The beginning of a success story***

Constant Innovations

1962: *First issue of the International Edition*
1976: *Graphical abstracts*
1979: *Cover pictures*
1988: *Centenary of Angewandte*
1989: *Routine use of color*
1991: *New section: Highlights*
1992: *Computerized editorial tracking system*
1995: *Internet service for readers*
1998: *Regular press service; full-text online*
2000: *New section: Essays; EarlyView: Communications available online ahead of the printed version*
2001: *New section: Minireviews*
2002: *Online submission of manuscripts*
2003: *Weekly publication; new section: News; new layout*
2004: *Backfiles (1962-1997); ManuscriptXpress: Online system for authors and referees*

Angewandte's advisors...

Wolfgang A. Herrmann
Technische Universität München

»**Angewandte Chemie** is at home in Germany and successful in the world. This journal has developed as the international community of chemists has grown together. Today, **Angewandte** is of central importance for modern chemists. It is the only journal I afford not to hurry through in the office – it's my "home is my castle journal"!«

Angewandte Chemie International Edition *is a journal of the German Chemical Society (GDCh)*

GDCh

WILEY InterScience® DISCOVER SOMETHING GREAT

WILEY-VCH

1908/1506_gu

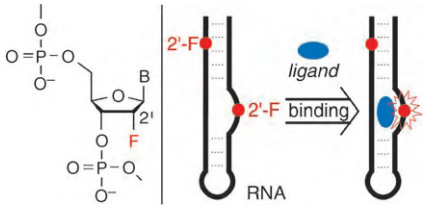

Bound to succeed: Noncovalent binding of ligands to RNA can be analyzed easily by ^{19}F NMR spectroscopy through site-specific fluorine-labeling of the target RNA (see picture; B = adenine, cytosine, guanine, uracil). The proof of concept is provided by RNA aptamer–ligand interactions. The speed and the robustness of this simple approach present major advantages over methods relying on ^{1}H NMR spectroscopy.

Drug Design

C. Kreutz, H. Kählig, R. Konrat,* R. Micura* ——— **3450 – 3453**

A General Approach for the Identification of Site-Specific RNA Binders by ^{19}F NMR Spectroscopy: Proof of Concept

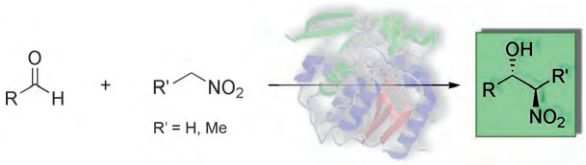

Novel enzyme activity: Biocatalytic Henry reactions with nitromethane and nitroethane yielded the corresponding nitroalcohols with good enantio- and diastereocontrol in the presence of the hydroxynitrile lyase from the tropical rubber tree *Hevea brasiliensis*. Molecular modeling and deuterated starting materials were used in mechanistic investigations.

Enzymatic Syntheses

T. Purkarthofer, K. Gruber, M. Gruber-Khadjawi, K. Waich, W. Skranc, D. Mink, H. Griengl* ——— **3454 – 3456**

A Biocatalytic Henry Reaction—The Hydroxynitrile Lyase from *Hevea brasiliensis* Also Catalyzes Nitroaldol Reactions

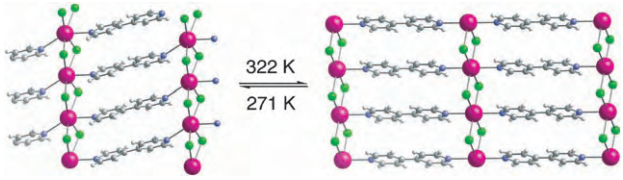

Three structures for the price of one: The room-temperature phase of the 2D network $[Pb(\mu\text{-}Cl)_2(\mu\text{-bipy})]_\infty$ (bipy = 4,4′-bipyridine) undergoes crystal-to-crystal transformations both upon cooling (see picture; Pb pink, Cl green, N blue, C gray, H white) and upon heating. With increasing temperature, decreased packing efficiency is traded for higher symmetry.

Solid-State Structures

C. Hu, U. Englert* ——— **3457 – 3459**

Space Filling Versus Symmetry: Two Consecutive Crystal-to-Crystal Phase Transitions in a 2D Network

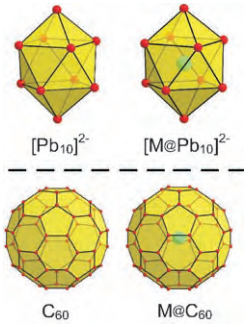

Closed encounters: A closed deltahedral homoatomic cluster, $[Pb_{10}]^{2-}$, is structurally characterized. When this "empty" cluster is considered together with the recently published filled cluster $[Ni@Pb_{10}]^{2-}$, a striking parallel to the fullerenes emerges: Zintl ions form polyhedral cages that can enclose a central atom without any major structural alterations.

"Empty" Metal Clusters

A. Spiekermann, S. D. Hoffmann, T. F. Fässler* ——— **3459 – 3462**

The Zintl Ion $[Pb_{10}]^{2-}$: A Rare Example of a Homoatomic *closo* Cluster

© 2006 Wiley-VCH Verlag GmbH & Co. KGaA, Weinheim

Contents

C–H Activation

H. Ren, P. Knochel* ——— **3462 – 3465**

Chemoselective Benzylic C–H Activations for the Preparation of Condensed N-Heterocycles

Buttoning up: A chemoselective domino reaction including one or two successive C–H activations serves to convert a range of readily available N-arylpyrroles into complex polycondensed N-heterocycles. The reaction is catalyzed by $Pd(OAc)_2$ (5 mol%), and p-Tol_3P (10 mol%) is added as the ligand (see scheme; Tol = tolyl).

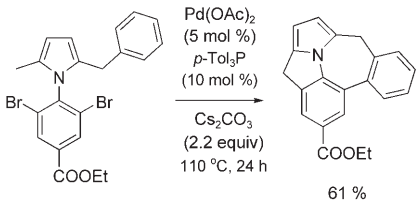

Molecular Dynamics

M. Schnell, J.-U. Grabow* ___ **3465 – 3470**

Multidimensional Large-Amplitude Motion: Revealing Concurrent Tunneling Pathways in Molecules with Several Internal Rotors

Light at the end of the tunnel: Knowledge of the feasible tunneling pathways of a molecule can shed light on the interaction mechanisms that govern its internal dynamics. A combination of rotational spectroscopy, permutation inversion group theory, and multidimensional tunneling formalism has shown that in the series $(CH_3)_3XCl$ (X = Si, Ge, Sn), electrostatic repulsion is gradually reduced and the chemical bond gains importance.

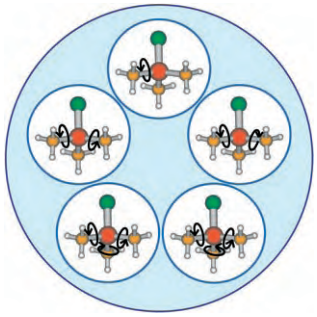

Rotational Spectroscopy

J. L. Alonso,* E. J. Cocinero, A. Lesarri, M. E. Sanz, J. C. López ——— **3471 – 3474**

The Glycine–Water Complex

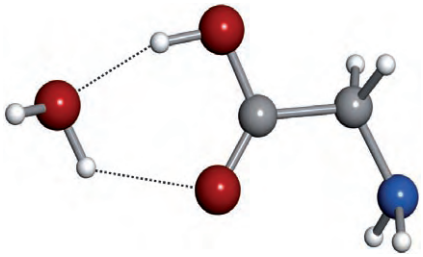

Expanding the possibilities: The hydration of glycine has been observed in a supersonic jet by using laser ablation in combination with Fourier transform microwave spectroscopy. The rotational spectrum reveals that water binds to glycine through two hydrogen bonds, which bridge the carboxylic acid group in a closed planar structure. In the complex, glycine retains the most stable conformer of the parent unhydrated molecule.

Main-Group Hydrides

S. Harder,* J. Brettar ——— **3474 – 3478**

Rational Design of a Well-Defined Soluble Calcium Hydride Complex

A surprisingly simple approach led to the synthesis of a molecular calcium hydride. Reaction of a calcium amide with phenylsilane gives clean conversion into the hydride that crystallizes as a dimer (see structure).

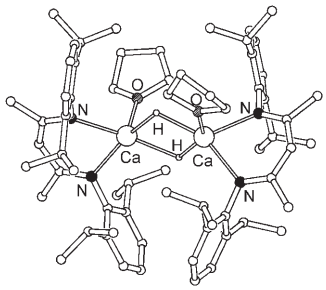

© 2006 Wiley-VCH Verlag GmbH & Co. KGaA, Weinheim

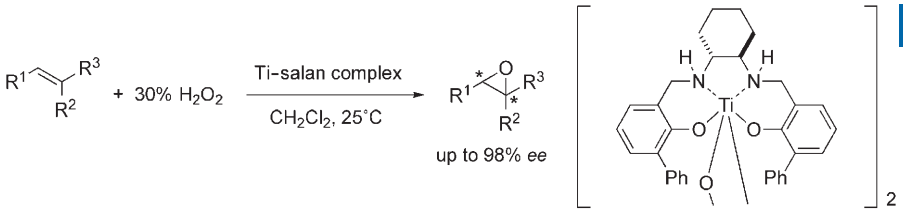

Asymmetric Catalysis

Y. Sawada, K. Matsumoto, S. Kondo, H. Watanabe, T. Ozawa, K. Suzuki, B. Saito, T. Katsuki* ——— **3478 – 3480**

Titanium–Salan-Catalyzed Asymmetric Epoxidation with Aqueous Hydrogen Peroxide as the Oxidant

Keep it simple: A titanium complex with a salan ligand bearing phenyl groups at C3 and C3′ is an efficient catalyst for the enantioselective epoxidation of unfunctionalized olefins with aqueous hydrogen peroxide (see scheme); furthermore, the epoxidation was stereospecific. The C3 and C3′ substituents stabilize this complex and enhance the asymmetric induction.

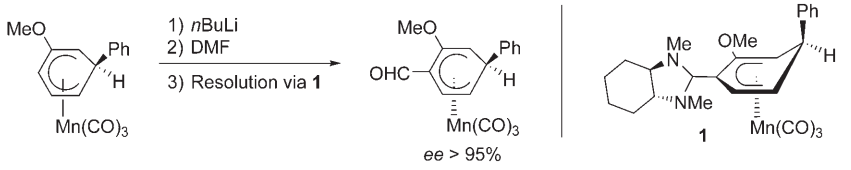

Planar Chirality

B. Jacques, M. Chavarot, F. Rose-Munch,* E. Rose ——— **3481 – 3484**

Lithiation/Electrophilic Quench of [(η^5-Cyclohexadienyl)$Mn(CO)_3$]: Versatile Functionalization and Resolution of Planar Chirality in the Organomanganese Series

Easy does it: A lithiation/electrophilic quench sequence gives efficient access to a large variety of unprecedented complexes. One such complex (**1**; see scheme) can be successfully used in the synthesis of the first enantiopure formyl-substituted [(η^5-cyclohexadienyl)$Mn(CO)_3$] derivatives.

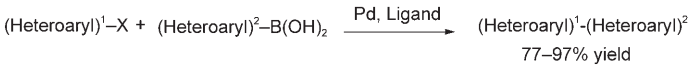

Coupling Reactions

K. L. Billingsley, K. W. Anderson, S. L. Buchwald* ——— **3484 – 3488**

A Highly Active Catalyst for Suzuki–Miyaura Cross-Coupling Reactions of Heteroaryl Compounds

Unprecedented activity: Catalysts derived from Pd and bulky dialkylphosphinobiaryl ligands are shown to be highly stable and active in Suzuki–Miyaura reactions of heteroaryl halides and heteroaryl boronic acids/esters (e.g., 3- or 4-pyridine, indole, and N-protected pyrrole derivatives). Furthermore, this catalyst system is not inhibited by the presence of highly basic aminopyridines or aminopyrimidines.

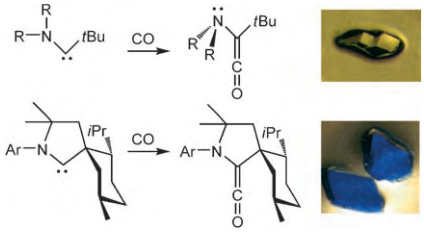

Carbenes

V. Lavallo, Y. Canac, B. Donnadieu, W. W. Schoeller, G. Bertrand* ——— **3488 – 3491**

CO Fixation to Stable Acyclic and Cyclic Alkyl Amino Carbenes: Stable Amino Ketenes with a Small HOMO–LUMO Gap

A quick fix: In contrast to cyclic diamino carbenes, stable alkyl amino carbenes react with CO to give stable ketenes (see scheme, top). Contrary to the acyclic versions, cyclic amino ketenes cannot escape from the destabilizing n–π donation of the nitrogen lone pair, which induces a diradical character and unusual optical (see scheme, bottom and photographs of crystals) and NMR spectroscopic properties.

© 2006 Wiley-VCH Verlag GmbH & Co. KGaA, Weinheim

Contents

Asymmetric Synthesis

H. Takikawa, Y. Hachisu, J. W. Bode, K. Suzuki* ——— **3492 – 3494**

Catalytic Enantioselective Crossed Aldehyde–Ketone Benzoin Cyclization

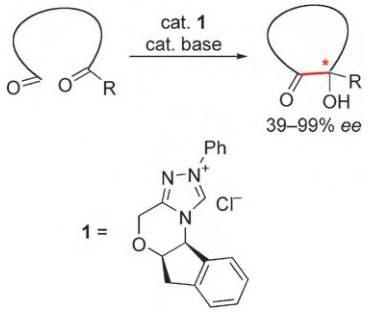

Joining together: The catalytic, asymmetric benzoin cyclization of a wide variety ketoaldehydes using chiral triazolium salts of type **1** has been carried out (see scheme). The corresponding cyclized products were prepared in high yields and with excellent enantioselectivities.

Oxidation

T. Ngouansavanh, J. Zhu* — **3495 – 3497**

Alcohols in Isonitrile-Based Multicomponent Reaction: Passerini Reaction of Alcohols in the Presence of *O*-Iodoxybenzoic Acid

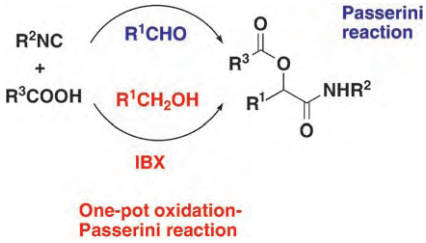

High proof: An alcohol instead of an aldehyde is an effective reaction partner in the Passerini reaction (P-3CR) in the presence of *O*-iodoxybenzoic acid (IBX). Thus, by simply heating a solution of an alcohol, a carboxylic acid, an isonitrile, and IBX at 40 °C, an oxidation/P-3CR sequence occurred smoothly to afford the α-acyloxy carboxamide in good-to-excellent yield.

Microporous Materials

W. Ouellette, M. H. Yu, C. J. O'Connor, D. Hagrman, J. Zubieta* — **3497 – 3500**

Hydrothermal Chemistry of the Copper–Triazolate System: A Microporous Metal–Organic Framework Constructed from Magnetic $\{Cu_3(\mu_3\text{-}OH)(triazolate)_3\}^{2+}$ Building Blocks, and Related Materials

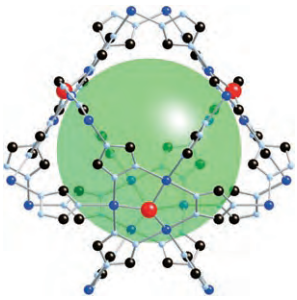

Networking with triazolate: Three new compounds containing networks of Cu^{I} or Cu^{II} ions linked by 1,2,4-triazolate (trz) ligands were prepared by hydrothermal synthesis. The microporous metal–organic framework $\{Cu_3(\mu_3\text{-}OH)(trz)_3(OH)_2(H_2O)_4\}_n$, which is built up from magnetic triangles, forms 17 × 13 × 13 Å³ cavities (see picture; Cu dark blue, O red, N light blue, C black).

Hydrogen Storage

C. P. Baldé, B. P. C. Hereijgers, J. H. Bitter, K. P. de Jong* ——— **3501 – 3503**

Facilitated Hydrogen Storage in $NaAlH_4$ Supported on Carbon Nanofibers

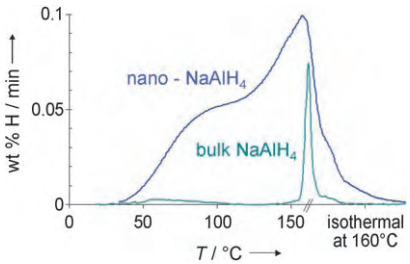

The ins and outs of hydrogen: The hydrogen desorption from and absorption to sodium alanate ($NaAlH_4$) supported on carbon nanofibers are significantly facilitated if its particle size is reduced from the micrometer to the nanometer range (see graph). This improvement is tentatively attributed to the minimization of the solid-state diffusion path length during loading and desorption of hydrogen.

© 2006 Wiley-VCH Verlag GmbH & Co. KGaA, Weinheim

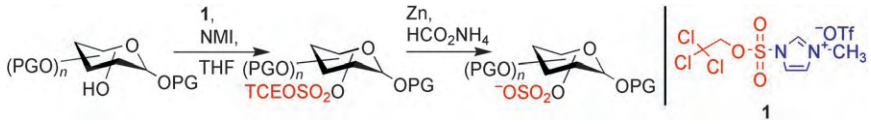

Sweet sulfur: Sulfuryl imidazolium salt **1** represents a new class of highly potent sulfating agents and is very effective for introducing trichloroethyl-protected sulfates into monosaccharides for the synthesis of sulfated oligosaccharides (see scheme; NMI = *N*-methylimidazole, OTf = triflate, PG = protecting group, TCE = 2,2,2-trichloroethyl).

Protecting Groups

L. J. Ingram, S. D. Taylor* — **3503 – 3506**

Introduction of 2,2,2-Trichloroethyl-Protected Sulfates into Monosaccharides with a Sulfuryl Imidazolium Salt and Application to the Synthesis of Sulfated Carbohydrates

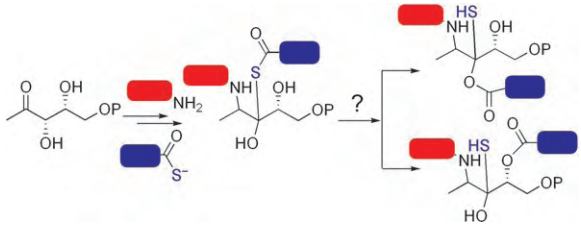

ThiS and that: An alternative substrate for thiazole synthase, namely 1,4-dideoxy-D-xylulose-5-phosphate, was synthesized and used as a mechanistic probe to determine the regiochemistry of the acyl-shift reaction that occurs as an intermediate step in the biosynthesis of thiamin thiazole in *B. subtilis* (see scheme; ThiS protein (blue); ThiG protein (red); OP = phosphate group).

Biosynthesis

A. Chatterjee, X. Han, F. W. McLafferty, T. P. Begley* — **3507 – 3510**

Biosynthesis of Thiamin Thiazole: Determination of the Regiochemistry of the S/O Acyl Shift by Using 1,4-Dideoxy-D-xylulose-5-phosphate

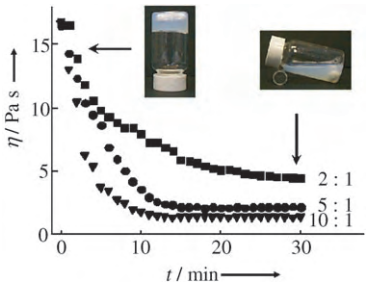

To rub gel into the wound: A thermoresponsive ABA triblock copolymer gelator with A = *N*-isopropylacrylamide and B = 2-(methacryloyloxy)ethyl phosphorylcholine has been synthesized by atom transfer radical polymerization by using a bifunctional disulfide-based initiator. This triblock copolymer forms free-standing peptide-degradable micellar gels under physiologically relevant conditions.

Gels

C. Li, J. Madsen, S. P. Armes,* A. L. Lewis — **3510 – 3513**

A New Class of Biochemically Degradable, Stimulus-responsive Triblock Copolymer Gelators

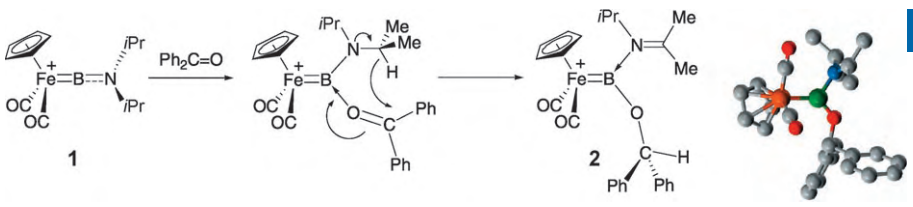

It's all new to B: In the reaction of borylene complex **1** with benzophenone, a Meerwein–Ponndorf β-hydride transfer from the aminoborylene ligand to the coordinated ketone generates **2** (see structure), the first example of an imine-donor-stabilized borylene complex, and the first cationic alkoxyborylene system.

Boron Chemistry

D. L. Kays (née Coombs), J. K. Day, S. Aldridge,* R. W. Harrington, W. Clegg — **3513 – 3516**

Cationic Terminal Borylene Complexes: Interconversion of Amino and Alkoxy Borylenes by an Unprecedented Meerwein–Ponndorf Hydride Transfer

© 2006 Wiley-VCH Verlag GmbH & Co. KGaA, Weinheim

Contents

Host–Guest Chemistry

R. J. Hooley, S. M. Biros, J. Rebek, Jr.* ——— **3517 – 3519**

A Deep, Water-Soluble Cavitand Acts as a Phase-Transfer Catalyst for Hydrophobic Species

Overcoming inhibition: A deep, water-soluble cavitand has been shown to extract various *N*-substituted maleimides into aqueous solution through the hydrophobic effect. These complexes react with a water-soluble thiol to confer water solubility to the product, thus leading to a drastic reduction in binding affinity and allowing this system to function as a phase-transfer catalyst.

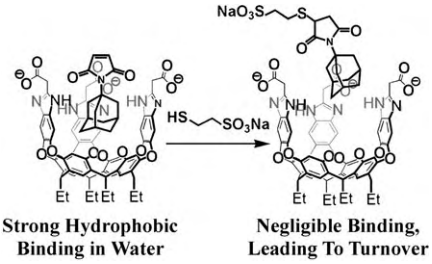

Sulfur Complexes

H. Sugimoto,* R. Tajima, T. Sakurai, H. Ohi, H. Miyake, S. Itoh, H. Tsukube ——— **3520 – 3522**

Reversible Sulfurization–Desulfurization of Tungsten Bis(dithiolene) Complexes

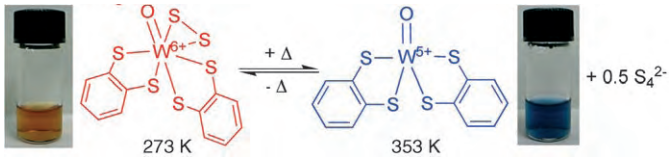

Easy come, easy go: Tungsten bis(dithiolene) complexes undergo reversible sulfurization–desulfurization in which the metal center changes between $\{W^{VI}(S_2)\}$ and $\{W^{V}\}$. The process is effectively controlled by the solution temperature, the solvent, and the electron-donating properties of the dithiolene ligands and results in a distinct color change (see scheme).

DNA Structures

X. Tang, I. J. Dmochowski* **3523 – 3526**

Controlling RNA Digestion by RNase H with a Light-Activated DNA Hairpin

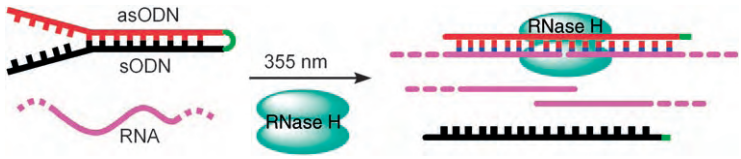

Making sense: A DNA hairpin was synthesized by attaching a 20-mer antisense oligodeoxynucleotide (asODN) to a sense ODN through a bifunctional photocleavable linker. This conjugate became much less stable upon UV photoactivation ($\Delta T_m = -29$ K, $\Delta\Delta G = 4.6$ kcal mol^{-1}), which facilitated binding of the asODN to the complementary RNA. By this strategy, photomodulation of RNase H activity towards a variety of RNA targets was performed.

Colloids

U. T. Gonzenbach, A. R. Studart,* E. Tervoort, L. J. Gauckler — **3526 – 3530**

Ultrastable Particle-Stabilized Foams

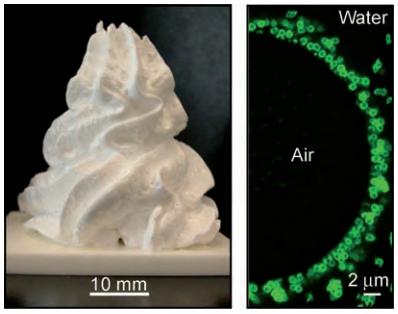

Pump up the volume: Wet foams prepared with surfactants are thermodynamically unstable systems that undergo rapid disproportionation, drainage, and coalescence. Ultrastable foams have now been prepared using colloidal particles as stabilizers (left picture). The stabilization results from the irreversible adsorption at the air–water interface of particles surface-modified with short-chain amphiphiles (right picture).

© 2006 Wiley-VCH Verlag GmbH & Co. KGaA, Weinheim

Well protected: Porphyrins act as a molecular cap (see picture) to selectively stabilize a non-self-complementary non-Watson–Crick DNA structure through additional hydrophobic interactions. At the same time, these porphyrins serve as an efficient internal sensor of the newly formed secondary structure.

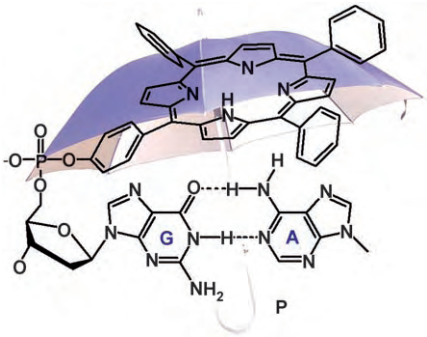

DNA structure

M. Balaz,* B. C. Li, S. Jockusch, G. A. Ellestad, N. Berova* — **3530 – 3533**

Tetraarylporphyrin as a Selective Molecular Cap for Non-Watson–Crick Guanine–Adenine Base-Pair Sequences

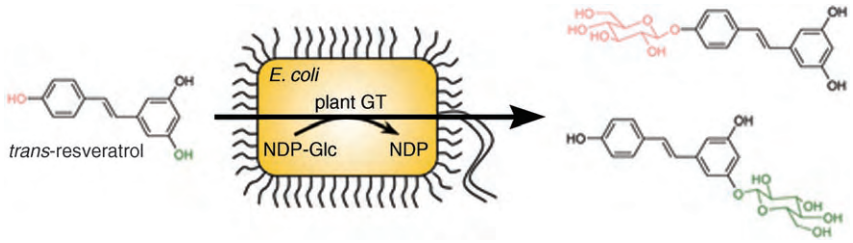

A novel whole-cell screen for the identification of new glucosyltransferase (GT) biocatalysts within a recombinant enzyme library was developed. Following biotransformation, levels of D-glucose were used as a measure of biocatalysis. Twenty five enzymes that transfer D-glucose to *trans*-resveratrol were identified that have the regioselectivity shown in the picture.

Biocatalyst Identification

M. Weis, E. K. Lim, N. Bruce, D. Bowles* — **3534 – 3538**

Regioselective Glucosylation of Aromatic Compounds: Screening of a Recombinant Glycosyltransferase Library to Identify Biocatalysts

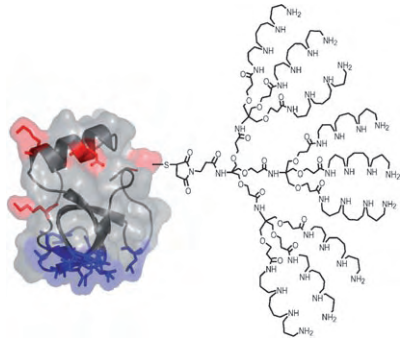

Strength in numbers: Multivalent dendrons that have an *N*-maleimido group at the focal point can be used to construct monodisperse one-to-one protein–dendron conjugates. The second generation polyamine dendron with spermine surface groups clearly imparts its high-affinity DNA binding to a protein of choice.

Protein Functionalization

M. A. Kostiainen,* G. R. Szilvay, D. K. Smith,* M. B. Linder, O. Ikkala — **3538 – 3542**

Multivalent Dendrons for High-Affinity Adhesion of Proteins to DNA

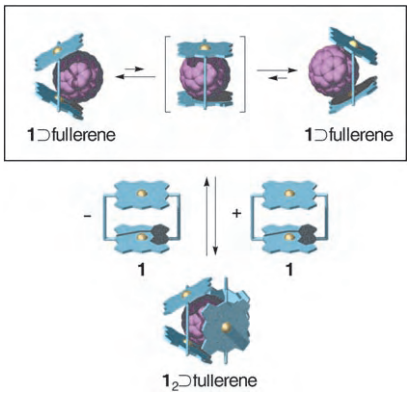

Shake, rattle, and roll: As a guest within a short-spaced cyclic dimer of an organorhodium porphyrin **1**, fullerenes such as C_{60} and C_{70} start to oscillate by slipping through the host cavity. This dynamic motion is substantially prohibited by another molecule of **1** through the formation of capsule-type inclusion complexes. In contrast, a larger fullerene such as C_{76} can hardly slip through the host cavity but is simply encapsulated by two molecules of **1**.

Host–Guest Chemistry

A. Ouchi, K. Tashiro,* K. Yamaguchi, T. Tsuchiya, T. Akasaka, T. Aida* — **3542 – 3546**

A Self-Regulatory Host in an Oscillatory Guest Motion: Complexation of Fullerenes with a Short-Spaced Cyclic Dimer of an Organorhodium Porphyrin

The issues for May 2006 appeared online on the following dates
Issue 17: April 11. · Issue 18: April 21. · Issue 19: April 27. · Issue 20: April 5

© 2006 Wiley-VCH Verlag GmbH & Co. KGaA, Weinheim

Sources

Product and Company Directory

You can start the entry for your company in "Sources" in any issue of *Angewandte Chemie*.

If you would like more information, please do not hesitate to contact us.

Wiley-VCH Verlag – Advertising Department
Tel.: 0 62 01 - 60 65 65
Fax: 0 62 01 - 60 65 50
E-Mail: MSchulz@wiley-vch.de

Service

Keywords ____ *3548*

Authors ____ *3549*

Angewandte's Sister Journals ____ *3550 – 3551*

Vacancies ____ *3397*

Preview ____ *3553*

For more information on ChemMedChem see www.chemmedchem.org

© 2006 Wiley-VCH Verlag GmbH & Co. KGaA, Weinheim

Awarded...

H. Nöth receives Bavarian Medal

Heinrich Nöth (Ludwig Maximilians University of Munich, LMU) received the Bavarian Constitutional Medal in Gold. Nöth served as president of the German Chemical Society (GDCh) in 1988/89 and 1992/93, and of the Bavarian Academy of Sciences and Humanities (BAdW) in 1998–2005. From 1969 to 1999, Nöth guided the progress of the journal *Chemischen Berichte* and its successor, the *European Journal of Inorganic Chemistry*, as an editor.

H. Nöth

Nöth completed his doctoral thesis in 1954 with E. Wiberg at the LMU, and worked at Imperial Chemical Industries Ltd. (UK) in 1956/57. He completed his habilitation at the LMU in 1962 and became a professor there in 1964. In 1966, he moved to the Philips University of Marburg, and he returned to the LMU in 1969, where he remained beyond his formal retirement in 1996. His research has concentrated on boron and aluminum chemistry, as well as on inorganic polymers. He is still an active researcher, as demonstrated by the publication last year of his 257th contribution on boron chemistry, specifically the *N*-lithiation of 2,4,6-triphenylborazine.[1]

E. Sackmann receives Stern–Gerlach Medal

The German Physical Society (DPG) has awarded its highest distinction for experimental physics, the Stern–Gerlach Medal, to Erich Sackmann (Technical University of Munich) for his work on the dynamics of membranes and biopolymer networks, the mechanical properties of membranes, and the interactions between cells and surfaces. This work has established him as a founder of the physics of biosystems. He outlined the origin and perspectives of biophysics in a contribution to a special issue of *ChemPhysChem*,[2] a journal for which he is a member of the editorial board.

E. Sackmann

Sackmann completed his doctoral thesis in 1964 with T. Förster at the University of Stuttgart, and worked as a postdoc at Bell Labs (USA) and at the Max Planck Institute for Biophysical Chemistry in Göttingen, where he completed his habilitation in 1974. He subsequently took up an appointment at the University of Ulm, and in 1980, he moved to the Technical University of Munich. His research began with the spectroscopy of lyotropic liquid crystals and lipids, and then moved increasingly in the direction of biophysics. In the course of this research, he applied resonance and scattering methods to biological systems, and also developed new methods in rheology and microscopy (among others) to understand the self-organization and function of cells on a physical basis.

G. Davies receives Whistler Award

Gideon J. Davies (University of York, UK) was recognized by the International Carbohydrate Organization with the Roy L. Whistler International Award in Carbohydrate Chemistry 2006 for his outstanding contributions to carbohydrate chemistry. The US$ 10000 prize will be awarded at the International Carbohydrate Symposium in Whistler, BC (Canada) in July. Davies' award lecture will have the title "Carbohydrate-Active Enzymes: How Nature Makes and Breaks Glycosides".

Davies completed his PhD in 1990 at the University of Bristol with H. Watson und L. Hall. He then worked as a postdoc at the European Molecular Biology Laboratory Outstation at the DESY synchrotron in Hamburg (K. S. Wilson), as well as in York (G. Dodson), Grenoble, and Uppsala. In 1996, he returned to the University of York, where he has been active as a professor since 2004. The research focus of his group is the structure of enzymes, especially those involved in the synthesis, modification, and degradation of carbohydrates (hydrolases, transferases, lyases, and esterases). In a recent Communication to *ChemBioChem*, he investigates the binding of conformationally restricted inhibitors to a β-glucosidase.[3]

G. Davies

[1] H. Nöth, A. Troll, *Eur. J. Inorg. Chem.* **2005**, 3524.

[2] E. Sackmann, *ChemPhysChem* **2002**, *3*, 237.

[3] T. M. Gloster, R. Madsen, G. J. Davies, *ChemBioChem* **2006**, *7*, 738.

DOI: 10.1002/anie.200601599

InterScience

© 2006 Wiley-VCH Verlag GmbH & Co. KGaA, Weinheim

Water Anomalies

DOI: 10.1002/anie.200601053

The Puzzling Properties of Supercooled and Glassy Water**

*Ralf Ludwig**

Keywords:
amorphous ice · phase transitions · polyamorphism · supercooled water · water anomalies

The relationship between liquid, supercooled, and glassy water is an exciting topic of research.[1–3] The hypothesis of a liquid–liquid critical point for water assumes the existence of two different liquid phases at low temperatures. These two phases are supposed to meet at a second critical point. However, even if this liquid–liquid critical point exists, it would lie in the "no-man's-land" where liquid water cannot be studied by direct experimental means because the low-temperature liquid would freeze. Recent experimental and theoretical studies have improved our knowledge about supercooled and glassy water.[4–11] They deliver further pieces for understanding the puzzling behaviour of liquid water and contribute towards a coherent picture of this ubiquitous substance. Despite significant progress in water research, important questions remain.

Water's Anomalies

Water is a remarkable liquid as it possesses a number of highly unusual properties not displayed by other liquids. The peculiar properties of water are a result of the hydrogen-bonding network between the oxygen and hydrogen atoms of water molecules (Figure 1). Above 320 K water behaves like a "normal" liquid. Upon heating, the density decreases, and the thermal compressibility and the isobaric heat capacity both increase. This behavior is known for "normal" liquids such as liquified noble gases, liquid metals or organic liquids. However, upon cooling the density goes through a maximum at 277 K, and the isothermal compressibility and the isobaric heat capacity pass minima at 319 K and 308 K, respectively (Figure 2).

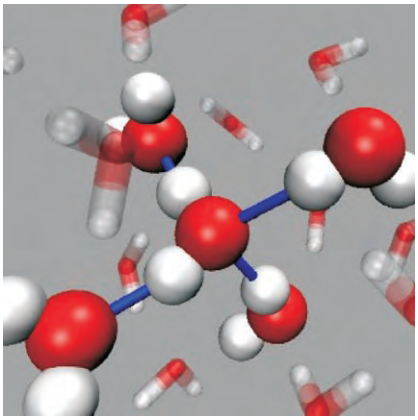

Figure 1. Molecular structure of liquid water. Molecules typically form hydrogen bonds (blue bars) with four neighbors in a tetrahedral fashion. The liquid displays an open, loosely packed, structure. The atoms of the central water molecule and its first neighboring shell are shown as spheres.

Further cooling below these temperatures leads to a strong decrease in density and strong increase for both the thermal compressibility and the isobaric heat capacity. The temperature changes of these water properties become more pronounced in the supercooled region below the melting point. If these properties are extrapolated below the lowest temperatures, they appear to become infinite at the unreachable temperature of $T_s = 228$ K. It is assumed that the explanation of water's anomalies can be found in the metastable water phases.

Supercooled and Glassy water

As mentioned above, water displays maximum density at 277 K, only 4 K above the melting point. Since liquid water's anomalies are quantitatively small at ambient temperature, the behavior of liquid water is investigated at lower temperatures where the anomalies become much more pronounced (Figure 2). Normally water freezes below the melting point T_m to form hexagonal ice I_h, which is the thermodynamically stable phase. But liquid water can exist inside the crystalline domain of stability. This supercooled water represents a metastable liquid (Figure 3).

Minor perturbations can trigger the sudden appearance of the stable crystalline phase. If liquid water is cooled fast enough and freezing can be avoided altogether, then water becomes a non-crystalline solid, which is called a glass. Glassy water can exist when the temperature drops below the glass transition temperature $T_g = 136$ K. Although glassy water is a solid, its structure exhibits a disordered liquidlike arrangement. Initially investigators found two amorphous ice forms: low-density amorphous ice (LDA) and high-density amorphous ice (HDA). The phenomenon that a pure material can exist in more than one amorphous state is called

[*] Prof. Dr. R. Ludwig
Institut für Chemie
Abteilung Physikalische Chemie
Universität Rostock
Dr.-Lorenz-Weg 1
18051 Rostock (Germany)
Fax: (+49) 381-498-6524
E-mail: ralf.ludwig@uni-rostock.de

[**] This work was supported by the Deutsche Forschungsgemeinschaft (Forschergruppe 436, Lu506/5-3).

InterScience
© 2006 Wiley-VCH Verlag GmbH & Co. KGaA, Weinheim

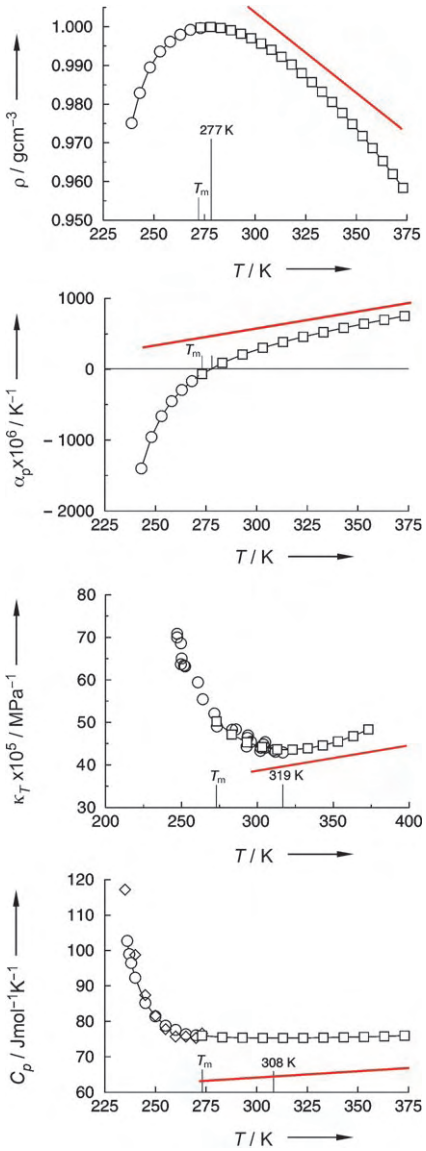

Figure 2. Temperature dependence of a) the density ρ, b) the coefficient of thermal expansion α_p, c) isothermal compressibility κ_T, and d) the constant-pressure specific heat C_p. The anomalous thermodynamics and fluctuations of liquid water are apparent above the melting temperature T_m, and they become much more striking when water is supercooled below T_m. The temperature behavior of "normal" liquids is given by the red lines.

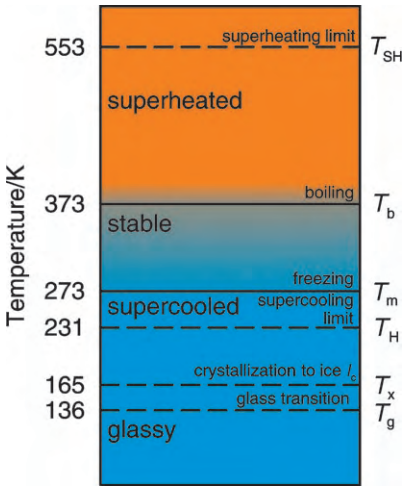

Figure 3. Temperature domains of stability and metastability for liquid and glassy water at atmospheric pressure. Equilibrium transitions are shown as solid lines, kinetically controlled transitions as dotted lines. T_b denotes the boiling point, T_m the melting point, T_H the homogeneous nucleation temperature, and T_g the glass transition temperature. Adapted from references [1] and [3].

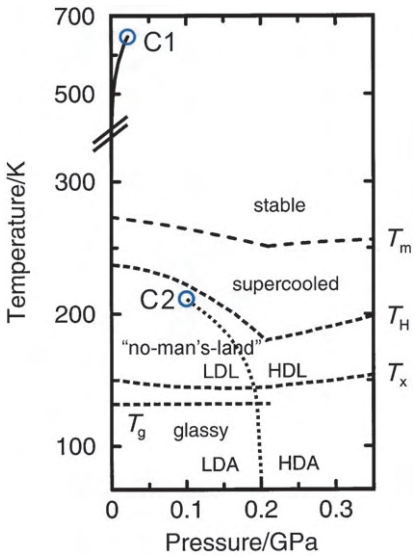

Figure 4. The most probable thermodynamic scenario for the phase behavior of metastable water. In keeping with the hypothesized liquid–liquid phase transition, a first-order phase transition occurs between the LDL and HDL forms of supercooled liquid water. The transition between the HDA and LDA forms of amorphous ice is the low-temperature manifestation of that phase change. The physical properties change smoothly in going from LDL to LDA and from HDL to HDA. The first-order transition terminates at a so-called second critical point C2. The regular critical point C1 terminates the liquid–gas coexistence curve. Unfortunately C2 is expected to be between the homogeneous nucleation curve (T_H) and the crystallization curve to cubic ice ("no-man's-land"). This makes it extremely difficult to observe it experimentally. Adapted from references [1] and [3].

polyamorphism. The two glassy states differ in structure and in bulk properties. Unfortunately glasses are nonequilibrium materials; their physical properties depend on how the glassy states were produced. A sharp and reversible transformation between different glassy forms suggests a thermodynamic phase transition. LDA and HDA can be interconverted by compression and decompression at temperatures below the crystallization temperature. A sharp change in the density of the amorphous sample was observed when LDA was compressed, and hence the transition to HDA was called "first-order-like". On heating, LDA and HDA are thought to undergo a glass transition resulting in highly viscous, supercooled liquids referred to as low-density liquid (LDL) and high-density liquid (HDL), respectively. Thus the transition between LDA and HDA is a low-temperature manifestation of a first-order transition between the two phases of liquid water. At higher temperatures LDL and HDL meet at a second critical point (C2) (Figure 4). The two liquid phases are no longer distinguishable, like the gas and the liquid phases above the liquid–gas critical point (C1 at 647 K). However, the exact connection between the different amorphous ice forms and supercooled liquid water is not clear, in particular since the "no-man's-land" region largely prohibits direct experimental access.

The proposed liquid–liquid critical point is supported experimentally by the changing slope of the metastable melting curves observed for different ice polymorphs[3,12] Further support was recently provided by Klotz et al.,[4] who used neutron scattering diffraction to study the transition between LDA and HDA at 0.3 GPa and 130 K. A progressive transformation of one distinct phase to another, with phase coexistence at constant pressure and temperature, gives direct evidence of a classical first-order transition. Although the results tend to support this intriguing possibility, a second critical point could not be proved.

New Findings

The scenario of two supercooled liquid phases has been recently questioned owing to the discovery of a third disordered modification apparently distinct from HDA and LDA and called, because of its higher density, very-high-

© 2006 Wiley-VCH Verlag GmbH & Co. KGaA, Weinheim

density amorphous ice (VHDA) ice.[13] VHDA is generated by heating HDA under pressure. The resulting glass does not convert back to HDA when it is recovered at ambient pressure at 77 K. The relation between VHDA and HDA phases is important to support the hypothesis that two distinct phases of liquid water, namely LDL and HDL, exist below a critical temperature.

In this context two important questions arise: Which phase, HDA or VHDA, resembles more closely liquid water at high pressure? If there are two different high-density amorphous ices does this imply the existence of more than one form of HDL?

Simulation studies indicate that very-high-density amorphous ice (VHDA) is a more stable form of HDA. Thus VHDA should be considered as the amorphous ice of the quenched liquid-water phase HDL at ambient conditions.[5,6] Koza et al.[7] have demonstrated by using elastic and inelastic neutron scattering that HDA and VHDA are heterogeneous on the length scale of nanometers and that different forms of HDA are obtained, depending on the exact preparation process. Tulk et al. have found by annealing of HDA at normal pressure[14] evidence for the presence of a multitude of (metastable) amorphous ice states.

Very recently Loerting et al.[8] described a stepwise formation process LDA→HDA→VHDA at 125 K; this is the first observation of a stepwise transformation sequence between three amorphous phases. The transition from HDA to VHDA on isothermal compression at 125 K has been found to be similar to the transition from LDA to HDA. The authors suggest the presence of a well-established first-order phase transition between the HDA and VHDA amorphous ices. It may be that the two steps between LDA, HDA, and VHDA are analogues in the glassy state for phase transitions between LDL, HDL, and VHDL, respectively. Conversions between LDA, HDA, and VHDA suggest that densification of amorphous ice occurs as two thermodynamically distinct transitions. However, Loerting et al.[8] could not exclude a kinetically controlled densification process in amorphous ice.

Theoretical calculations on supercooled and amorphous water suggest that a thermodynamic transition between HDA and VHDA is possible by showing that several metastable liquids separated by first-order phase transitions and critical points can be found for various water potentials. Based on computer simulations, Brovchenko et al.[9,15] were the first to conclude that even more than one liquid–liquid transition might exist in supercooled water.

As mentioned above, the search for the predicted first-order liquid–liquid transition line and its end point, the second low-temperature critical point in water, has been hampered by the intervention of homogeneous nucleation, which takes place at 231 K at ambient pressure. However, by confining water in nanopores of mesoporous silica, Liu et al.[10] were able to study the pressure effect on the dynamic behavior of water in the deeply supercooled state without crystallization. They found clear evidence of a fragile-to-strong dynamic transition. The authors related the measured transition temperature line to the liquid–liquid transition line obtained by molecular dynamics simulations. Above a pressure of 1600 bar the characteristic feature of this transition can no longer be discerned. This end point is discussed as possible low-temperature critical point.

Significance

Why is the understanding of supercooled and glassy water so important? Three main reasons can be given: Supercooled water and amorphous metastable water are more than just curiosities since they do exist in many places in the real world. Small droplets of supercooled water exist in stratiform and cumulus clouds. In the processing of solar and terrestrial radiative energy fluxes supercooled water also plays a crucial role.[16] It is also important for life at subfreezing conditions, for the commercial preservation of proteins and cells, and for the prevention of hydrate formation in natural-gas pipelines.[1]

Besides water, other network-forming substances also display anomalies in their densities, isothermal compressibilities, heat capacities, diffusion coefficients, and kinematic viscosities. SiO_2, GeO_2, Si, and Ge also form tetrahedral networks and display at least two different amorphous states.[17] Thus studying supercooled water and amorphous ice is important for the fundamental understanding of the molecular requirements for macroscopically anomalous thermodynamic behavior.

And finally, it has been shown that water's anomalies are more pronounced in the supercooled region. Fluctuations of the entropy and volume increase with decreasing temperature. The existence of two liquid phases, LDL and HDL, terminating in a second critical point could explain water's anomalies easily. In keeping with the hypothesized liquid–liquid critical point, the observed water anomalies are simply the beginning of the transformation of high-density "normal" water to low-density, highly ordered liquid.

Despite the exciting new findings about supercooled and glassy water, we still cannot explain the sharp increase of the thermodynamic properties upon supercooling, the nature of the transitions between LDA, HDA, and VHDA, and the relationship between supercooled and glassy water. Instead of investigating small structural or thermodynamic changes upon water transformation it may be a good idea to study more sensitive properties. Paschek[11] found that the structural transformation of water into a low-density liquid in the supercooled range strongly enhances the solubility of hydrophobic particles. The transformation of water into a tetrahedrally structured liquid is accompanied by a minimum in the hydration entropy and enthalpy.

[1] P. G. Debenedetti, H. E. Stanley, *Phys. Today* **2003**, *56*, 40–46.
[2] P. G. Debenedetti, *J. Phys. Condens. Matter* **2003**, *15*, R1669–R1726.
[3] O. Mishima, H. E. Stanley, *Nature* **1998**, *396*, 329–335.
[4] S. Klotz, T. Strässle, R. J. Nelmes, J. S. Loveday, G. Hamel, G. Rousse, B. Canny, J. C. Chervin, A. M. Saitta, *Phys. Rev. Lett.* **2005**, *94*, 025506.
[5] N. Giovambattista, H. E. Stanley, F. Sciortino, *Phys. Rev. Lett.* **2005**, *94*, 107803.
[6] N. Giovambattista, H. E. Stanley, F. Sciortino, *Phys. Rev. E* **2005**, 72, 0311510.

 © 2006 Wiley-VCH Verlag GmbH & Co. KGaA, Weinheim

[7] M. M. Koza, B. Geil, K. Winkel, C. Köhler, F. Czeschka, M. Scheuermann, H. Schober, T. Hansen, *Phys. Rev. Lett.* **2005**, *94*, 125506.
[8] T. Loerting, W. Schustereder, K. Winkel, C. Salzmann, I. Kohl, E. Mayer, *Phys. Rev. Lett.* **2005**, *96*, 025702.
[9] I. Brovchenko, A. Geiger, A. Oleinikova, *J. Chem. Phys.* **2005**, *123*, 044515.
[10] L. Liu, S.-H. Chen, A. Faraone, C.-W. Yen, C.-Y. Mou, *Phys. Rev. Lett.* **2005**, *95*, 117802.
[11] D. Paschek, *Phys. Rev. Lett.* **2005**, *94*, 217802.
[12] O. Mishima, *Phys. Rev. Lett.* **2000**, *85*, 334–336.
[13] T. Loerting, C. Salzmann, I. Kohl, E. Mayer, A. Hallbrucker, *Phys. Chem. Chem. Phys.* **2001**, *3*, 5355–5357.
[14] C. A. Tulk, C. J. Benmore, J. Urquidi, D. D. Klug, J. Neuefeind, B. Tomberli, P. A. Egelstaff, *Science* **2002**, *297*, 1320–1323.
[15] I. Brovchenko, A. Geiger, A. Oleinikova, *J. Chem. Phys.* **2003**, *118*, 9473–9476.
[16] A. Tabazadeh, Y. S. Djikaev, H. Reiss, *Proc. Natl. Acad. Sci. USA* **2002**, *99*, 15873–15878.
[17] P. F. McMillan, *J. Mater. Chem.* **2004**, *14*, 1506–1512.

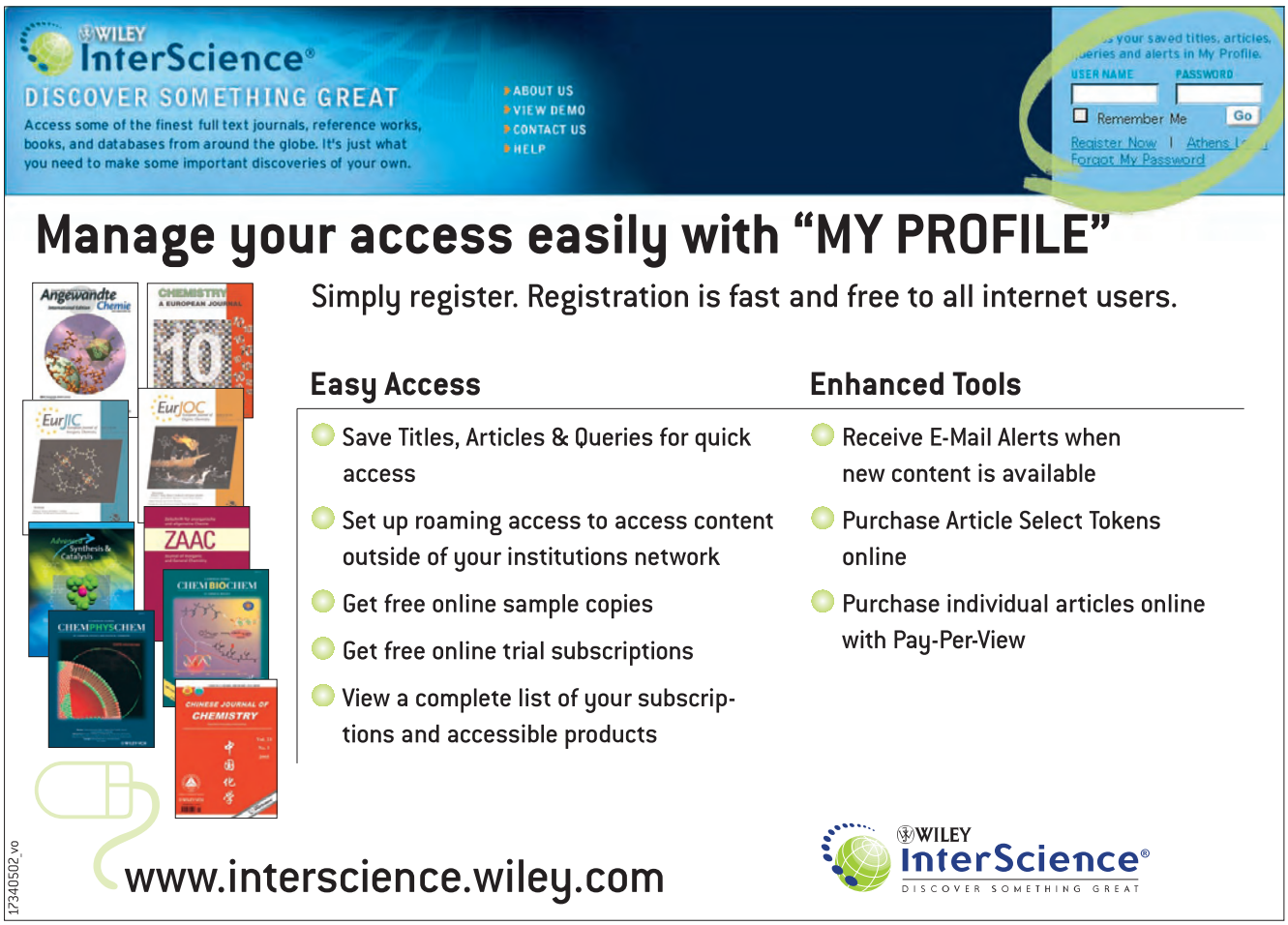

 © 2006 Wiley-VCH Verlag GmbH & Co. KGaA, Weinheim

Design in Chemistry

DOI: 10.1002/anie.200504510

"Design" in Chemical Synthesis—An Illusion?**

Martin Jansen and J. Christian Schön*

Keywords:
chemical synthesis · configuration space · solid-state chemistry · supramolecular chemistry · theory of science

1. Introduction

The development of scientific understanding in the natural sciences proceeds in a stepwise, even hierarchical fashion. At the beginning, a phenomenon is observed and measured, and the results are integrated into the ever increasing foundation of factual knowledge. In the next steps, these individual observations are systematized, and patterns and relations are revealed which are formalized in the language of mathematics. Finally, at the highest level, universally valid laws are derived, allowing us to recognize cause-and-effect relationships. In this sense, the maturity of a scientific field can be related to the degree to which novel experiments can be performed in a controlled and purposeful fashion, or, to say it more generally, to what extent and with what precision events and phenomena in our environment can be correctly predicted. This is the stage where theory begins to challenge the experiment; hypotheses are presented that are to be verified experimentally, and the inductive procedure described above begins to transform into a deductive one.

In chemistry, the inductive approach has proven to be especially successful. If one reduces this field to one of its main goals, that is, the synthesis of new compounds, and tries to evaluate the field's current state, one reaches the conclusion that over the past two centuries great achievements have been made. This progress has predominantly taken place along experimental lines: In important subfields of synthetic chemistry one is able with impressive reliability to both devise still unknown compounds as synthetic targets and plan feasible synthetic routes for their realization. The countless well-documented examples of the nearly complete control of syntheses have led chemists to conjure up appealing terms such as "tailoring" or "synthesis strategy". In recent times the term "design" has also enjoyed great popularity in this context. Here, this term is employed not only in the sense of the "design" of the composition or structure of a new compound but also with respect to the set (or some) of its properties. A small selection of titles of recent publications may serve as evidence: "Turning Down the Heat: Design and Mechanism in Solid-State Synthesis",[6] "Design of Solids from Molecular Building Blocks: Golden Opportunities for Solid-State Chemistry",[7] "Reticular synthesis and the design of new materials",[8] "Looking for design in materials design".[9]

These and many more examples not mentioned here may illustrate how common the use of this term, which immediately commands attention and recognition, has become today. However, speaking of "design" in reference to the synthesis of chemical compounds and, even more, to certain properties of a compound, is the first step toward misleading implications of the ability of chemists to shape a material to their will. Furthermore, the incorrect choice of words is often accompanied by an inaccurate understanding of the basic concepts involved.

According to the generally accepted definition, the process of "design" incorporates the creation of a topology/shape/form, which fulfills a given function as well as possible, and is also considered aesthetically pleasing. An additional fundamental aspect of "design" is that in general it is imbued with an artistic component and thus is associated with the self-expression of the designer. On this basis, classical schools of design, such as the Bauhaus, have developed their specific styles (see Figure 1). Besides this main meaning of "design", which is the same in all languages and cultures, a number of more restrictive definitions exist. In most instances, these deal with the competition, proper weighting, or mutual dependence of functionality and aesthetics. The most restrictive definition of the term acknowledges "design" as a purely technical process of the production of an object according to a sketch, without any valuation of its function or beauty. However, every one of these definitions presupposes the existence of creative freedom, and the mere selection from among given and unchangeable topologies is never

[*] Prof. Dr. M. Jansen,
Priv.-Doz. Dr. J. C. Schön
Max-Planck-Institut für Festkörperforschung
Heisenbergstrasse 1, 70569 Stuttgart (Germany)
Fax: (+49) 711-689-1502
E-mail: jansen@fkf.mpg.de

[**] The authors do not claim to have fully covered the barely surveyable literature that pertains directly or indirectly to the topics discussed in this essay. Instead, representative examples are cited. The essay is based on presentations by M.J. (e.g. M. Jansen, *405th Meeting of the Northrhine-Westphalian Academy of Sciences*, **1994**;[1] M. Jansen, *Egon Wiberg Lecture*, LMU München, **2004**; M. Jansen, Plenary Lecture, *7th International Materials Chemistry Conference*, Edinburgh, **2005**; M. Jansen, *55th Meeting of the Math.-Nat. Sci. Session of the Berlin-Brandenburg Academy of Sciences*, **2005**; M. Jansen, *Berlin Local Meeting of the German Chemical Society*, **2005**); excerpts are published in Refs. [1–5].

WILEY InterScience DISCOVER SOMETHING GREAT
© 2006 Wiley-VCH Verlag GmbH & Co. KGaA, Weinheim

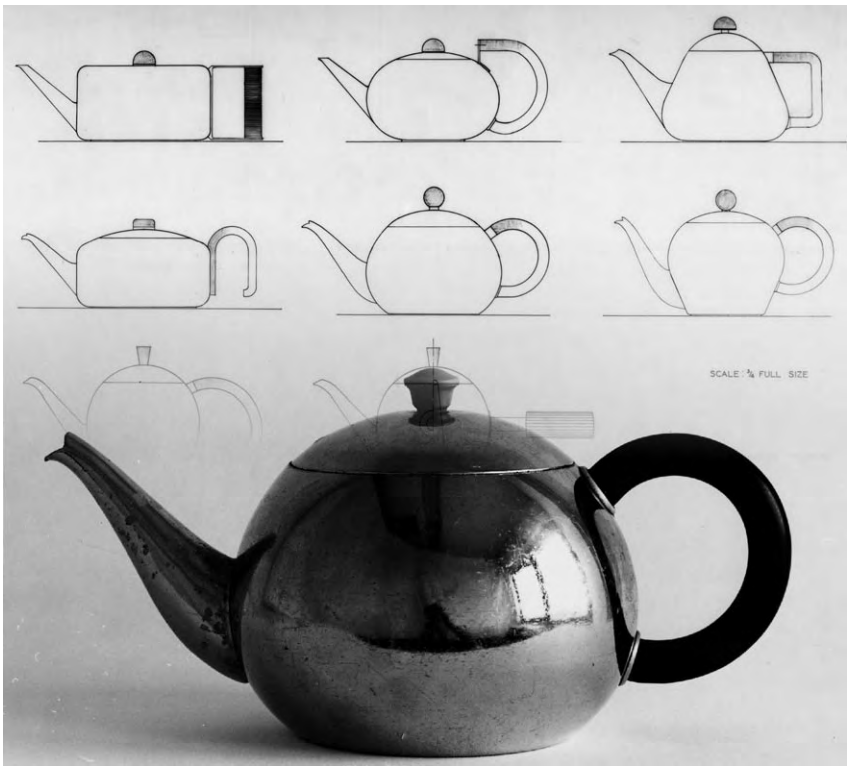

Figure 1. Teapot designs by Walter Gropius for Aluminium Ltd., London, 1935 (background) and the only type of teapot made based on these designs. *Bauhaus-Archiv Berlin.*

associated in any language with the term "design". In the following, we will endeavor to show that this type of freedom in shaping a species does not exist in the context of the synthesis of new chemical compounds.

2. The Concept of the Energy Landscape of Chemical Systems

As a basis for a general discussion (valid for all classes of chemical systems) of the possibility of creative freedom in the sense of "design" available to a synthetic chemist, we refer to our concept of synthesis planning in solid-state chemistry.[1–5] For in contrast to the chemistry of molecules, in particular carbon-based compounds, which commands a great repertoire of efficient methods for the detailed planning of syntheses, one is usually not able to reliably plan the preparation of new solids and thus must still rely on an explorative approach. We have long been occupied with the search for ways and means to improve this unsatisfactory situation, and for the past 14 years we have been following a specific conception. The foundation of our approach is the projection, onto an energy landscape, of the whole world of known compounds as well as those that have not yet been synthesized but are capable of existence.[1–5] In a simplified way, our concept can be elucidated with the help of the configuration space that is defined in the Appendix together with and in relation to several other relevant spaces. As explained there, a point in configuration space corresponds to a configuration of atoms, and the union of all atom configurations that together form a locally ergodic region on the time scale of observation represents a (meta)stable chemical compound capable of existence on this time scale. In particular at low temperatures, the region around each individual local minimum of the potential energy represents a compound that is at least kinetically stable.[1–5] To simplify the nomenclature in the following discussion, we will always refer to minima instead of the more general locally ergodic regions, even though the locally ergodic regions may be large and encompass many local minima.

Such a description of the world of chemical compounds in terms of the configuration space and the energy landscape associated with it leads to immediately accessible fundamental insights.

1) In a unique relation, each local minimum of the energy landscape corresponds to a compound capable of existence, and conversely every synthesized or realizable chemical compound is associated with such a minimum. As a result of this correspondence, this representation of the chemical world is all-encompassing and contains all kinetically and thermodynamically stable compounds, independent of the state of aggregation, the existence or lack of crystalline order, or the particle size (nano-, meso-, or macroscopic). As a welcome side effect, construed contrasts and essentially artificial opposites such as between natural and synthetic compounds,[10] living and nonliving matter, or between solid-state and molecular chemistry, are obviated and vanish or are at least relativized.

2) The question of whether a hypothetical compound is "thermodynamically stable" was often asked reflexively, without much thought, in the past and still today. This question is shown to be inappropriate as far as the compound's realizability is concerned. The only necessary condition for the compound being accessible synthetically is that it is associated with a local minimum, that is, it must be kinetically stable.

3) The structure of the energy landscape associated with the space of all possible configurations of atoms is determined by the laws of nature (by means of the sum of all atomic interactions, cf. Appendix). Thus, for given boundary conditions, the global as well as local minima, and therefore all stable and metastable compounds, are predetermined.

4) The approach discussed here is deductive and thus represents a change in paradigm from the inductive one previously preferred in chemistry.

According to our view, working in the field of synthetic chemistry is equivalent to exploring the landscape of free enthalpy. While in the past this exploration was mostly undertaken by the preparative chemist by way of experiments, today this procedure is joined increasingly by the theoretical exploration, which, understandably, has been developed the furthest for small molecules. These two approaches are not in

 © 2006 Wiley-VCH Verlag GmbH & Co. KGaA, Weinheim

opposition; indeed, they complement each other. In the long run, computational chemistry will be cheaper and faster, and it will be called on to support the preparative-explorative approach on a broad front. Classical preparative chemistry remains indispensable, however, since practical applications of a material can be tested only if it is available in reality. The demands on the synthetic skills of the chemist will most likely increase, for modeling calculations result in truly surprising even exotic structure proposals, and their realization sets tremendous challenges for even the most modern synthesis methods. Furthermore, as a matter of principle, experimental verification remains the final authority for the evaluation of the correctness of a prediction.

The quintessence of these considerations with respect to the topic of this essay is clear: *Owing to the equivalence mentioned above of compounds capable of existence with well-defined, predetermined, locally ergodic regions on the energy landscape of chemical systems, there is no room for either the free or the arbitrary shaping of compositions and/or topologies of chemical systems by human efforts. Thus, "design" is not possible, and "humans are the explorers, and not the creators of chemical worlds".*[2] It is particularly misleading to try to "design" a new material starting with the desired material property,[9,11] since a physical property by itself cannot be a criterion of whether a compound might exist. First of all, one must show that the compound is capable of existence, and thereafter one might derive the set of properties based on its composition and structure.

3. Why Is the Belief in the Possibility of "Designing" Chemical Compounds So Widespread?

In light of these easily understood considerations it is amazing how widely spread and tenaciously the belief persists in the possibility of freedom in shaping a compound, in the sense of "design", by the scientist in chemical synthesis. This view can be understood from a psychologically standpoint perhaps if one considers the truly remarkable degree of control and predictability of syntheses attained in some areas of chemistry. Together with the unimaginable plethora of possible chemical compounds ("combinatorial explosion!"),[4] this can easily convey the impression that one can create ensembles of atoms with a definite structure or even property in a creative act, in analogy to a piece of art. But the landscape of compounds remains discrete even in regions of closely neighboring minima, and the equilibrium topologies are unchangeable, of course. In reality a successful synthetic plan always corresponds to the anticipation (based on a prediction, identification, or intuitive hunch) of a still unknown compound, that is, of a predetermined local minimum on the energy hypersurface. The corresponding structures, including possible isomers and polymorphic modifications, equilibrium distances, and material properties such as, for example, melting points or densities, are inherent to the chemical system and are not accessible to "design".

The differences in sophistication of the tools available for planning a synthesis in the different classes of chemical systems are quite striking. Without any doubt the synthesis of organic compounds is most advanced in this respect. Here one can, with seemingly playful effortlessness, construct the structures of even quite complex molecular compounds capable of existence, without the assistance of complex tools.[12] The reasons for this are manifold. Clearly, the most of the resources available to chemistry over the past two centuries have been devoted to the chemistry of carbon. The resulting rich treasure trove of experience, together with a certain uniformity in the bonding behavior of carbon (e.g. its tendency to form C–C linkages), allow particularly effective extrapolations and thus the prediction of not-yet-synthesized molecular compounds. The physical reason behind this system of practically universally combinable structure increments is that the stereochemistry of carbon and of many other nonmetals is mostly determined by local covalent bonding interactions; long-range forces can be neglected or at least are not dominant in structure formation. For the realization of the particular synthesis goals an effective set of synthesis tools and methods is available.[12–14] The decisive feature is the selectivity through kinetic control, whereby using functional groups, protective groups or auxiliaries the specific desired chemo-, regio-, or stereoselectivity or positional selectivity is achieved. Some subfields of inorganic molecular chemistry can come quite close to this state of the art in those cases in which a particular target configuration can be realized by specific reaction routes based on well-understood procedures, for example, employing electronic or steric effects and the use of reaction steps with high directionality such as salt eliminations.[15]

Currently, the field of "coordination polymers"[16,17] (a term coined already in 1964[18]) is burgeoning worldwide[8,19,20] and boasts truly spectacular results[21,22] (e.g. Figure 1 in Ref. [21]). A particular focus is on open-pored, three-dimensional framework structures, since they are thought to have high potential for important applications such as gas storage and heterogeneous catalysis. For this class of compounds, a nearly inflationary use of the term "design" has developed. As in organic chemistry, one employs a system of independent structure increments that are connected by means of polycondensation or donor–acceptor interactions. The required building units must be stable under the reaction conditions and on the time scale of the reaction, and they must exhibit the necessary correctly matching sites for the interconnection. With a clever choice of increments, a very reliable prediction of the structures is possible, even without a large computational effort. However, since the desired compounds are collective solids, the traditional concepts of molecular chemistry for directing the synthesis process do not apply. Steering the reaction towards the target compound must, in contrast, be controlled by means of the solubility product, and nucleation and growth processes.[4] In this regard, the gap between the control that is claimed and that actually achieved is disturbingly large. Also, one should critically note that typically in those cases in which a synthesis is claimed to have been successfully designed, the design and the actual synthesis are published in the same paper. This does not strike us as very convincing.

 © 2006 Wiley-VCH Verlag GmbH & Co. KGaA, Weinheim

In solid-state chemistry, predictions using classical approaches are possible only in a very restricted fashion. They usually refer to extra- or interpolations of structure families such as perovskites, spinels, or rock-salt variants.[23,24] For particular classes of materials, for example, the oxosilicates, systematizations and predictions have been performed successfully on the basis of the tetrahedral building unit SiO_4.[25] Most difficult by far is the prediction of possible compositions and structures of intermetallic phases.[26,27]

All classes of materials for which "designed" synthesis routes and targets have been claimed have in common that these compounds can be visualized as being divisible into structure increments, from which they can be readily constructed. Such planning and systematizing of chemical compounds in terms of adjoining monomeric and oligomeric building units has a long tradition in chemistry. We mention as examples the hydrocarbons and their isomers, the chemistry of silicates,[25,28] and the description of zeolites by means of secondary building units,[29] where mathematical tools such as graph theory have also been called upon.[30,31] As we have discussed above, this restriction to certain classes of compounds is surmountable, of course, if one proceeds towards the global exploration of the energy landscape of chemical systems.[1–5] While this procedure requires considerably more effort, it is more correct and more inclusive insofar as no building units are fixed a priori and subsequently assumed to be unchangeable during the synthesis process. Strictly speaking, all species in homogeneous systems (such as solutions) participate in systems of interdependent chemical equilibria. Even benzene exchanges hydrogen against deuterium under surprisingly mild conditions, and complex oxometalates can be crystallized in a single phase from mother liquors that contain an plethora of oligomers coupled by dynamic equilibria.[32]

Yet regardless of the degree of perfection of synthesis planning in the different fields of chemistry, it is generally not correct and thus inappropriate to employ the term "design" to describe the process of chemical synthesis. One could argue that the issue of whether words are used according to their correct meaning should be of secondary relevance for our field of science, and should be relegated to the field of linguistics under the heading "semantics". We have only limited sympathy for such an opinion and point out the dangers of incorrect word use. As the well-established Sapir–Whorf hypothesis implies,[33–35] the terminology and associated meaning both reflect and circumscribe our imagination, and thus an incorrect development of terminology can lead to grave misconceptions. In our field of science, too, we can only be successful in the long run, if images and concepts are as "correct" as possible, that is, correspond as closely as possible to reality. And an incorrect linguistic description of scientific concepts proves to be particularly perilous when one deals with nonexperts and, in particular, students and pupils, who might be led to a wrong understanding of the topic at hand.

In fact, one sometimes encounters examples even in the specialist chemical literature, where incorrect terminology appears to go hand in hand with a wrong conceptual understanding. For instance, it has been suggested that one can take a desired physical property as a starting point in order to design a compound that exhibits exactly this property.[9] But this is not possible, in principle, for at least two reasons. Firstly, there is no one-to-one correspondence between a property and compound (a given property can be related to several different compounds). Secondly, a property can never serve as a criterion for the stability of a compound.[11] Similarly, with respect to the synthesis route, formulations are frequently chosen (see e.g. Ref. [36]) that evoke the impression of a goal-oriented operation and complete control, although the desired control of the reaction to give the crystalline product involving nucleation, selection, and growth, is not even remotely achieved. The very commendable elegance of the procedure chosen[36] is actually found in the adroit restriction of the space of chemical configurations. Here one should not forget that besides the "designed" and published topology many others might be accessible by employing all species present in the system and by including additional building principles (e.g. interpenetration of nets) together with modifications of the selection of nuclei for growth (by variation of concentration, solvent, pressure, temperature, etc.).

We consider it particularly risky to compare synthesis planning on the atomic level with planning and realizations in the macroscopic world, though these are sometimes employed to visualize or even justify the use of the term "design" in chemistry. Buildings constructed using bricks that are used as models for three-dimensional solids built from structure increments (e.g. Figure 1 in Ref. [37]) evoke wrong associations in at least two regards. Bricks are continuously adjustable in their dimensions on the length scales envisioned for their function, but chemical structure increments do not possess this property. They are variable, but this variability cannot be influenced by the chemist. Similarly, on a macroscopic scale, there is a wide latitude in the continuously adjustable combination of macroscopic building blocks. In contrast, chemical structure increments can be combined only in particular compositions and for each such combination only in well-defined ways, the particulars of which are beyond human control.

We are sure that essentially all authors (only a few examples are mentioned) who have employed the term "design" in a misleading or even incorrect fashion in the context of their synthesis planning are fully aware of the physico-chemical foundations of their experiments. But quite independently of this, we express with a certain urgency the view that in the interest of progress, one should use as few as possible, but at the same time as "correct" as possible, model pictures and descriptions, and that the limitations of each model should always be clear in one's mind.

4. Where Does Design Begin?

The highest control currently possible with regard to the realization of structures on the microscopic level might be found in the manipulation and localization of single atoms and molecules on surfaces[38] or in the con-

 © 2006 Wiley-VCH Verlag GmbH & Co. KGaA, Weinheim

struction of heterogeneous semiconductor structures in monoatomic layers[39] by molecular-beam epitaxy. Confronted with such purposeful manipulations one might again give in to temptation and assume we are dealing with "design". But here, too, the atoms always occupy discrete equilibrium positions, beyond human influence. Thus the actions of scientists again consist in the selection of one particular equilibrium configuration from among the multitude of possible ones.

Whether one is justified to speak of "design", that is, the presence of latitude for shaping and formation on the part of humans, depends on the length scale of the system. The possibility for "design" is available only if the desired function can be realized by a structure with essentially macroscopic dimensions. Obviously, when macroscopic objects are planned and realized, the materials employed also must be (kinetically) stable in a chemical sense, that is, correspond to minima of the energy landscape of the chemical system, and should at most degrade over long time scales, for example, by corrosion or upon being exposed to high temperatures. Furthermore, these objects should be stable with respect to their shape on the level of continuum mechanics, both with or without applied strains. Yet even with these restrictions the latitude necessary for "free" planning exists, and one can generate arbitrary topologies (see Figure 1) with continually tunable dimensions down to sizes on the order of a few atomic diameters. In our opinion, a suitable criterion for deciding whether a situation permits "design" might be whether structure formation takes place by means of atomic (chemical) or mechanical processes. This drawing of a boundary would, for example, correspond to the distinction between nano- and mesostructures generated in bottom-up vs. top-down processes.

5. On the Role of Human Creativity and the Origin of Chemical Structure Information

Those readers who have been willing to follow our considerations might be feeling disillusioned or even frustrated on hearing that their field of study is restricted to "merely" discovering predetermined worlds without the true freedom of shaping new compounds. Yet though this limitation prevails on a fundamental level, dealing with the unfathomable multitude of possible compositions and structures of chemical compounds[4] sets demands of a type and extent that reach or often far exceed the limits of human intellectual potential. Thus, we do not share the opinion of some philosophers such as George Steiner, who denies the natural sciences all creativity.[40] In their daily encounters chemists must call upon all of their knowledge, imagination, and intuition in order to anticipate and finally synthesize (new) compounds that fulfill their conceptual expectations. More often than not, during these efforts bitter setbacks must be overcome.

If one transfers these considerations to the macroscopic world and reviews the role of creativity in the visual arts, for a designer of everyday objects or an architect conceiving of a building, one quickly notes here the actual possibility for self-expression because within wide boundaries the topologies of the objects can be varied continuously. It is precisely from this that the freedom of formation indispensable for design is derived. Now one can without any contradiction take the attitude that the creative act of, for example, a sculptor, consists in "selecting" exactly one from among the essentially infinite number of sculptures that can be produced from a given block of granite. This view would allow us to relate the activities of synthetic chemists and of artists, as has been proposed, for example, by Roald Hoffmann,[41] however, on a completely different level of reference where one supposes that in both regimes one "only" selects from among a fixed set of possibilities. Yet through this parallel the fundamental difference noted above between the microscopic (atomic) length scale and the macroscopic world is by no means removed.

In the context of the central subject of this essay—the multitude of atomic structures and their variability—the question is often posed, whether structure information is encoded somewhere in the material world,[42] for example, like the genetic building plans contained within the DNA. Often it is suggested that analogous building plans for the structure of matter should have been generated and stored in the moment of the big bang or shortly thereafter. Hans Jonas gives an immediately convincing answer to this problem: "*Information requires for itself already, as its physical substrate, a differentiated and stable system … Information is thus not only the cause but is itself already the result of organization, embodiment, and expression of previous achievements, which are thus perpetuated but not elevated.*"[*][43] With this, one can surely agree, and in our view the structures of chemical compounds follow immediately from the nature of matter and its different interactions. Understanding the origins of these interactions is, however, beyond the authors and probably most of the readers.[44]

Appendix: Energy-Landscape Picture of Chemical Systems

Every chemical system is described on the quantum mechanical level by a time-dependent wave function, which depends on the coordinates of the electrons ($\boldsymbol{r}_1 \ldots \boldsymbol{r}_n$) and nuclei ($\boldsymbol{R}_1 \ldots \boldsymbol{R}_N$). In the Born–Oppenheimer approximation (separation of electronic and nuclear degrees of freedom), the contribution of the electronic degrees of freedom to the total energy is given by the energy of the electronic ground state $E_{\mathrm{el}}(\boldsymbol{R})$ for a given spatial arrangement of the atomic nuclei $\boldsymbol{R} = (\boldsymbol{R}_1 \ldots \boldsymbol{R}_N)$, called an atomic configuration. If one adds to this the electrostatic interaction of the nuclei $E_{\mathrm{KK}}(\boldsymbol{R})$ and the operator of the kinetic energy of the nuclei, one obtains the, still quantum mechanical, energy operator (Hamiltonian) of the atoms.

If tunnel effects, zero-point vibrations, and other typical quantum mechanical effects are neglected, one can perform the transition to the classical energy landscape: Rather than by a

[*] "*Information braucht für sich selbst schon, als ihr physisches Substrat, ein differenziertes und stabiles System... . Information ist also nicht nur Ursache, sondern selber schon Ergebnis von Organisation, Niederschlag und Ausdruck des vorher Erreichten, das dadurch perpetuiert, aber nicht erhöht wird.*

 © 2006 Wiley-VCH Verlag GmbH & Co. KGaA, Weinheim

wave function, the chemical system is now described by the position vectors $\boldsymbol{R}=(\boldsymbol{R}_1 \ldots \boldsymbol{R}_N)$ and the momentum vectors $\boldsymbol{P}=(\boldsymbol{P}_1 \ldots \boldsymbol{P}_N)$ of the N atoms of the system, and the classical energy function is the sum of the kinetic energy of the atoms $E_{\mathrm{kin}}=\Sigma_i \boldsymbol{P}_i^2/2m_i$ and the potential energy $E_{\mathrm{pot}}=E_{\mathrm{el}}(\boldsymbol{R}) + E_{\mathrm{KK}}(\boldsymbol{R})$. One denotes the $3N$-dimensional space of the vectors $\boldsymbol{R}$ as the configuration space, and the $6N$-dimensional space of the vectors $(\boldsymbol{R},\boldsymbol{P})$ as the phase space of the system of N atoms, respectively. The hypersurface of the function $E_{\mathrm{pot}}(\boldsymbol{R})$: $\mathbf{R}^{3N}\rightarrow\mathbf{R}$ defines the landscape of the potential energy, often simply called the energy landscape.

The time evolution of the system is represented by the trajectory $\boldsymbol{R}(t)$ on the energy landscape, which results from the solution of the classical Newtonian equations: $\boldsymbol{F}_i=m_i \mathrm{d}^2\boldsymbol{R}_i/\mathrm{d}t^2$, where m_i is the mass of atom i, and the force on atom i is given by the gradient of the potential energy with respect to $\boldsymbol{R}_i$, $\boldsymbol{F}_i=-\mathrm{grad}_i E_{\mathrm{pot}}(\boldsymbol{R})$. A physical measurement process is given by the time average $\langle O\rangle_t$ of an observable O along the trajectory over the measurement interval t_{obs}, $\langle O\rangle_t=(1/t_{\mathrm{obs}})\int_0^{t_{\mathrm{obs}}} O(\boldsymbol{R}(t))\mathrm{d}t$. If this trajectory explores a region R of the energy landscape on the time scale τ_{eq} so densely that the ensemble average of the observable O, for example, according to the Boltzmann distribution of the configurations k in the region R: $p_{\mathrm{B}}(k)=\exp(-E_k/T)/\Sigma_{l\in R}\exp(-E_l/T)=\exp(-E_k/T)/Z(R)$, over this region R, $\langle O\rangle_{\mathrm{ens}}=\Sigma_{k\in R}p_{\mathrm{B}}(k)O(k)$, equals the time average of O, $\langle O\rangle_{\mathrm{ens}}=\langle O\rangle_t$, then one denotes the region R as locally ergodic, and the system as locally equilibrated on time scales $t_{\mathrm{obs}}>\tau_{\mathrm{eq}}(T)$. In general, the trajectory leaves the region R on a characteristic time scale $\tau_{\mathrm{esc}}(T)$, the so-called escape time. For time scales t_{obs}, for which $\tau_{\mathrm{esc}}\gg t_{\mathrm{obs}}\gg\tau_{\mathrm{eq}}$ holds, the system can be considered as being metastable, and one can compute a local free energy $F(R)=-T\ln Z(R)$.[3,5]

A decisive point is that each of these locally ergodic regions corresponds to a chemical compound that is kinetically stable on the time scale t_{obs} at a temperature T. At $T\neq 0$, a multitude of configurations contribute to the compound—the "structure" of the compound is the appropriate average over these configurations. In particular, at low enough temperatures the basins around local minima of the potential energy constitute locally ergodic regions. Since both τ_{esc} and τ_{eq} are temperature dependent, the resulting landscape of the free energy also depends on temperature.

If one introduces the pressure p as an external thermodynamic variable, one has to replace the landscape of the potential energy by the landscape of the enthalpy $H=E_{\mathrm{pot}}+pV$. On this one, too, one can determine locally ergodic regions, for which on the time scale t_{obs} the free enthalpies $G(R)$ can be computed and the landscape of the free enthalpy can be constructed.[3–5] One now calls the region with the lowest free energy the thermodynamically stable modification of the chemical compound on the time scale t_{obs}, and the remaining regions the metastable ones. In the thermodynamic space, which is described by the variables p,T, etc., there exists therefore for each point (p,T) a plethora of discrete modifications that are kinetically stable on the time scale t_{obs}. Usually, one includes only the thermodynamically stable phase in a phase diagram since one implicitly assumes an essentially infinite observation time $t_{\mathrm{obs}}\rightarrow\infty$, for which the system with highest probability is found in the region with the lowest free energy: $p_{\mathrm{B}}(R)=\Sigma_{k\in R}p_{\mathrm{B}}(k)/\Sigma_l p_{\mathrm{B}}(l)=\exp(-(F(R)-F_{\mathrm{global}}))/T$ takes on its maximum for the region R whose local free energy $F(R)$ is minimal.

This approach to the understanding of chemical systems by the analysis of their energy landscape is valid for molecules as well as for crystalline and amorphous phases of the system. The difference between a crystalline low-temperature phase, which corresponds to the basin around one local minimum, a partially disordered high-temperature phase, where the locally ergodic region encompasses a multitude of structurally related minima, and an amorphous phase, where τ_{esc} and τ_{eq} are of similar size and thus aging phenomena and rate dependence of physical properties are present, is only one of complexity and not of principle.

[1] M. Jansen, *Wege zu Festkörpern jenseits der thermodynamischen Stabilität*, *Vol. N420*, *Proceedings of the North-rhine-Westphalia Academy of Scienes*, Wissenschaftsverlag, Opladen, **1996**.

[2] J. C. Schön, M. Jansen, *Angew. Chem.* **1996**, *108*, 1358–1377; *Angew. Chem. Int. Ed. Engl.* **1996**, *35*, 1286–1304.

[3] J. C. Schön, M. Jansen, *Z. Kristallogr.* **2001**, *216*, 307–325; J. C. Schön, M. Jansen, *Z. Kristallogr.* **2001**, *216*, 361–383.

[4] M. Jansen, *Angew. Chem.* **2002**, *114*, 3896–3917; *Angew. Chem. Int. Ed.* **2002**, *41*, 3746–3766.

[5] J. C. Schön, M. Jansen in *Solid State Chemistry of Inorganic Materials V* (Eds.: J. Li, N. E. Brese, M. G. Kanatzidis, M. Jansen), Materials Research Society, Warrendale, **2005**, pp. 333–344.

[6] A. Stein, S. W. Keller, T. E. Mallouk, *Science* **1993**, *259*, 1558–1564.

[7] O. M. Yaghi, M. O'Keeffe, M. Kanatzidis, *J. Solid State Chem.* **2000**, *152*, 1–2.

[8] O. M. Yaghi, M. O'Keeffe, N. W. Ockwig, H. K. Chae, M. Eddaoudi, J. Kim, *Nature* **2003**, *423*, 705–713.

[9] M. E. Eberhart, D. P. Clougherty, *Nat. Mater.* **2004**, *3*, 659–661.

[10] R. Hoffmann, *The Same and Not the Same*, Columbia University Press, New York, **1995**.

[11] M. Jansen, J. C. Schön, *Nat. Mater.* **2004**, *3*, 838.

[12] E. J. Corey, *Angew. Chem.* **1991**, *103*, 469–479; *Angew. Chem. Int. Ed. Engl.* **1991**, *30*, 455–465.

[13] a) K. C. Nicolaou, E. J. Sorensen, *Classics in Total Synthesis*, Wiley-VCH, Weinheim, **1996**; b) M. B. Smith, J. March, *Advanced Organic Chemistry, 5th ed.*, Wiley-Interscience, New York, **2001**.

[14] I. Ugi, J. Bauer, K. Bley, A. Dengler, A. Dietz, E. Fontain, B. Gruber, R. Herges, M. Knauer, K. Reitsam, N. Stein, *Angew. Chem.* **1993**, *105*, 210–239; *Angew. Chem. Int. Ed. Engl.* **1993**, *32*, 201–227.

[15] C. Elschenbroich, *Organometallchemie*, Teubner, Stuttgart, **2005**.

[16] C. Robl in *Chemistry at the Beginning of the Third Millenium* (Eds.: L. Fabbrizzi, A. Poggi), Springer, Berlin, **2000**, pp. 278–303, and references therein.

[17] C. Janiak, *Dalton Trans.* **2003**, 2781–2804, and references therein.

[18] J. C. Bailar, Jr. in *Preparative Inorganic Reactions* (Ed.: W. L. Jolly), Wiley-Interscience, New York, **1964**, pp. 1–25.

[19] A. K. Cheetham, G. Férey, T. Loiseau, *Angew. Chem.* **1999**, *111*, 3466–3492; *Angew. Chem. Int. Ed.* **1999**, *38*, 3268–3292.

[20] a) C. N. R. Rao, S. Natarajan, R. Vaidhyanathan, *Angew. Chem.* **2004**, *116*, 1490–1520; *Angew. Chem. Int. Ed.* **2004**, *43*, 1466–1496; b) S. Kitagawa, R. Kitaura, S. Noro, *Angew. Chem.* **2004**,

 © 2006 Wiley-VCH Verlag GmbH & Co. KGaA, Weinheim

116, 2388 – 2430; *Angew. Chem. Int. Ed.* **2004**, *43*, 2334 – 2375.
[21] G. Férey, C. Mellot-Draznieks, C. Serre, F. Millange, J. Dutour, S. Surblé, I. Margiolaki, *Science* **2005**, *309*, 2040 – 2042.
[22] A. P. Côté, A. I. Benin, N. W. Ockwig, M. O'Keeffe, A. J. Matzger, O. M. Yaghi, *Science* **2005**, *310*, 1166 – 1170.
[23] U. Müller, *Anorganische Strukturchemie*, Teubner, Stuttgart, **1992**.
[24] S. Andersson, B. G. Hyde, *Inorganic Crystal Structures*, Wiley-Interscience, New York, **1989**.
[25] F. Liebau, *Structural Chemistry of Silicates*, Springer, Berlin, **1985**.
[26] L. Pauling in *Theory of Alloy Phases*, American Society for Metals, Cleveland, **1956**.
[27] R. Nesper, *Angew. Chem.* **1991**, *103*, 805 – 837; *Angew. Chem. Int. Ed. Engl.* **1991**, *30*, 789 – 817.
[28] S. Han, J. V. Smith, *Acta Crystallogr. Sect. A* **1999**, *55*, 332 – 341.
[29] W. M. Meier, D. H. Olson, *Handbook of Zeolite Structure Types 1987*, Butterworth, London, **1987**.
[30] G. Pólya, *Acta Math.* **1937**, *68*, 145 – 254.
[31] S. J. Chung, Th. Hahn, W. E. Klee, *Acta Crystallogr. Sect. A* **1984**, *40*, 42 – 50.
[32] M. T. Pope, A. Müller, *Angew. Chem.* **1991**, *103*, 56 – 70; *Angew. Chem. Int. Ed. Engl.* **1991**, *30*, 34 – 48.
[33] F. Boas, *Race, Language and Culture*, University of Chicago Press, Chicago, **1940**.
[34] E. Sapir, *Language* **1929**, *5*, 207 – 214.
[35] B. L. Whorf, *Language, Thought and Reality*, MIT Press, Cambridge, **1956**.
[36] M. Eddaoudi, J. Kim, N. Rosi, D. Vodak, J. Wachter, M. O'Keeffe, O. M. Yaghi, *Science* **2002**, *295*, 469 – 472.
[37] G. Ferey, *J. Solid State Chem.* **2000**, *152*, 37 – 48.
[38] a) D. M. Eigler, E. K. Schweizer, *Nature* **1990**, *344*, 524 – 526; b) M. F. Crommie, C. P. Lutz, D. M. Eigler, *Science* **1993**, *262*, 218 – 220; c) L. Bartels, G. Meyer, K. H. Rieder, *Phys. Rev. Lett.* **1997**, *79*, 697 – 700.
[39] E. H. C. Parker, *The Technology and Physics of Molecular Beam Epitaxy*, Plenum, New York, **1985**.
[40] G. Steiner, *Grammars of Creation*, Faber & Faber, London, **2001**.
[41] R. Hoffmann, *Am. Sci.* **1990**, *78*, 14 – 15.
[42] A. Müller, *Chemie und Ästhetik – die Formenvielfalt der Natur als Ausdruck der Kreativität*", Zentrum für interdisziplinäre Forschung der Universität Bielefeld, Bielefeld, **1999**, pp. 7 – 21.
[43] H. Jonas in *Philosopische Untersuchungen und metaphysische Vermutungen*, Insel, Frankfurt, **1992**, p. 209.
[44] In the field of physics there have been repeated efforts to derive the form of theoretically possible physical laws or the observed fundamental constants of nature from fundamental concepts such as optimization principles or statistical probability analyses of the laws of physics. The one perhaps most widely known is the so-called weak anthropic principle,[45] which states that the reason that, with a multitude of possible emerging and vanishing universes available, we are living in just that universe with the physical laws and fundamental constants we observe, is precisely that in universes with different laws and constants, no human life could have developed.
[45] J. D. Barrow, F. J. Tipler, *The Anthropic Cosmological Principle*, Oxford University Press, Oxford, **1986**.

 © 2006 Wiley-VCH Verlag GmbH & Co. KGaA, Weinheim

Nanoparticle Synthesis

DOI: 10.1002/anie.200503821

Shape Control of Semiconductor and Metal Oxide Nanocrystals through Nonhydrolytic Colloidal Routes

*Young-wook Jun, Jin-sil Choi, and Jinwoo Cheon**

Keywords:
colloids · metal oxides · nanostructures · semiconductors · shape control

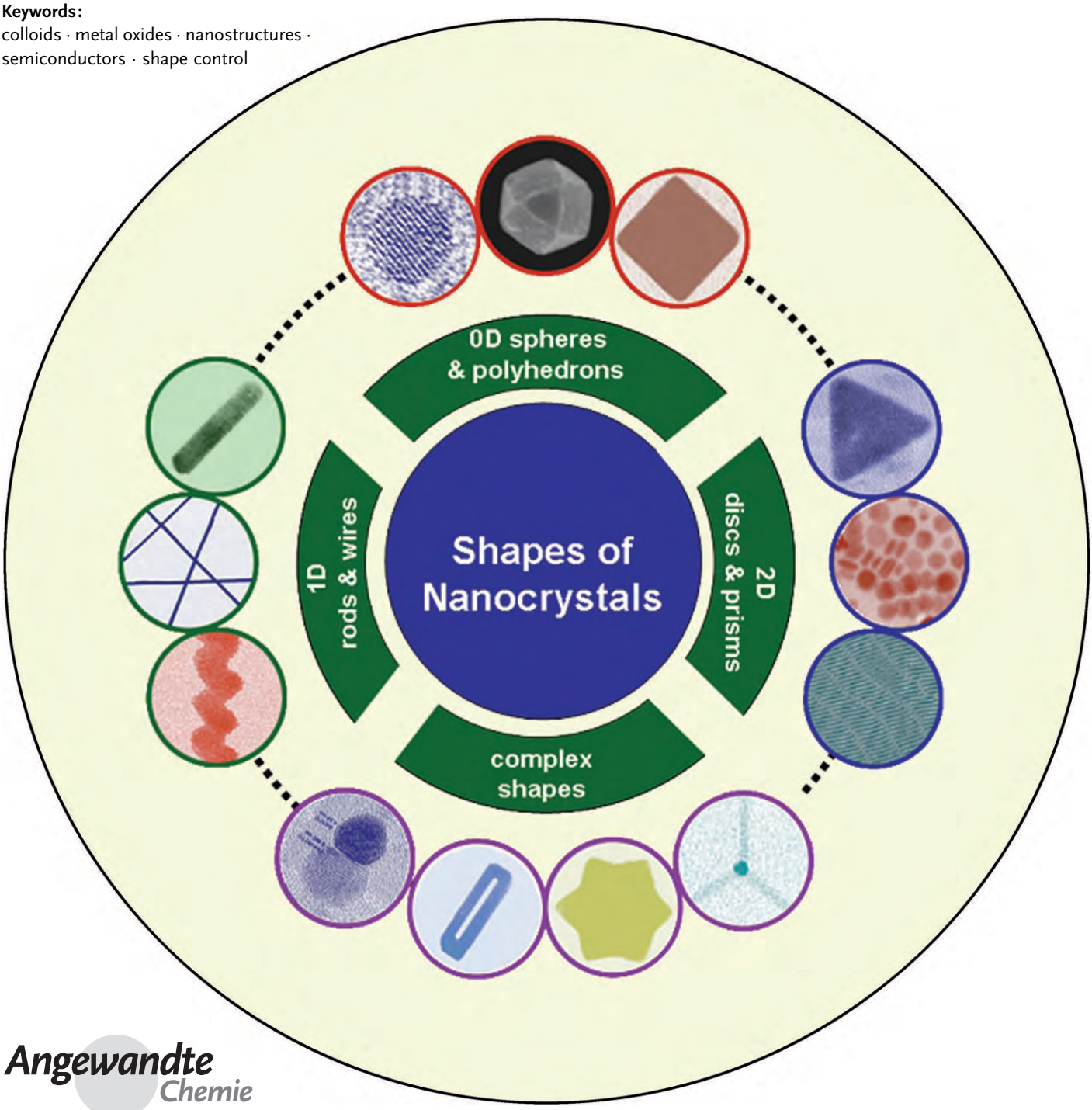

© 2006 Wiley-VCH Verlag GmbH & Co. KGaA, Weinheim

Inorganic nanocrystals with tailored geometries exhibit unique shape-dependent phenomena and subsequent utilization of them as building blocks for the fabrication of nanodevices is of significant interest. Herein, we review the recent developments in the shape control of colloidal nanocrystals with a focus on the scientifically and technologically important semiconductor and metal oxide nanocrystals obtained by nonhydrolytic synthetic methods. Many structurally unprecedented motifs have been discovered including polyhedrons, rods and wires, plates and prisms, and other advanced shapes such as branched rods, stars, inorganic dendrites, and dumbbells. The currently proposed shape-guiding mechanisms are presented and the important pioneering studies on the assembly of shape-controlled nanocrystals into ordered superlattices and the fabrication of prototype advanced nanodevices are discussed.

From the Contents

1. Introduction 3415

2. The Shape Control of Semiconductor and Metal Oxide Nanocrystals 3417

3. Proposed Mechanism for the Anisotropic Growth of Nanocrystrals 3427

4. Nanocrystal Assemblies and Device Applications 3432

5. Summary and Outlook 3435

1. Introduction

The ability to control and manipulate the physical and chemical properties of materials as we desire is one of the challenging issues in chemistry and materials science. Modern chemists are now exploring ways to obtain such control at the nanometer scale. Whereas bulk inorganic crystals possess their own characteristics and innate properties, such as color and melting point, at the nanometer scale, however, these properties can be tailored as desired.[1–15] For example, CdSe semiconductor crystals have characteristic red luminescence, however, on the sub 10-nm scale their luminescence can be tuned continuously from red to blue.[1] Similarly, the melting temperature of 1.6-nm sized gold nanocrystals is significantly lower (approximately 350 °C) than that of bulk gold (1064 °C).[9]

These novel phenomena are strongly related to two crucial nanoscale geometrical parameters: size and shape. Since physical properties of nanocrystals are strongly influenced by the size of the nanocrystals, early investigations focused on the nanoscale size effect.[1,3,7–13] For example, it has been revealed both theoretically and experimentally that the electronic band of a crystal is gradually quantized as the crystal-size is reduced, resulting in an increase in the band-gap energy. The size of the nanocrystals also significantly influences the electron-transport process.

Similarly, the shape of nanocrystals plays a crucial parameter in the determination of their properties.[14,15] The shape of nanocrystals can be simply classified by their dimensionality. Figure 1 illustrates the basic geometrical motifs of inorganic nanocrystals: zero-dimensional (0D) isotropic spheres, cubes, and polyhedrons; 1D rods and wires; and 2D discs, prisms, and plates. The most distinct shape effects are observed in the density of energy states (DOS).[16] The DOS ($\rho(E)$) of inorganic crystals simultaneously evolves from continuous levels into discrete states as the dimensionality is decreased from 3D to 0D as described by the relationship $\rho(E) \approx E^{D/2-1}$ (where D = dimensionality; Figure 2). In 3D crystals, $\rho(E)$ is a smooth square-root function of energy. The 2D crystals confined along a specific

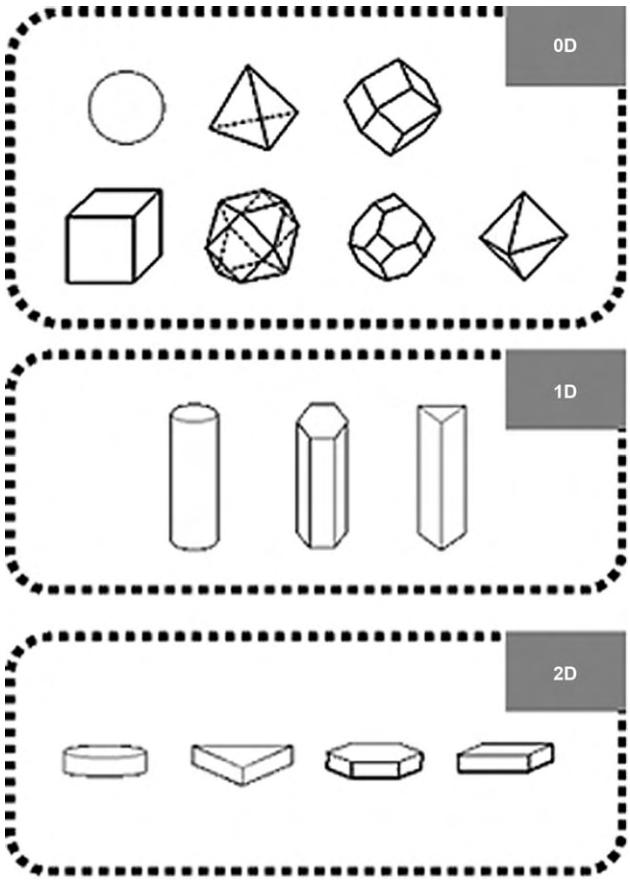

Figure 1. Basic motifs of inorganic nanocrystals: 0D spheres, cubes, and polyhedrons; 1D rods and wires; 2D discs, prisms, and plates.

[*] Y.-w. Jun, J.-s. Choi, Prof. J. Cheon
Department of Chemistry
Yonsei University
Seoul 120–749 (Korea)
Fax: (+82) 2-364-7050
E-mail: jcheon@yonsei.ac.kr

© 2006 Wiley-VCH Verlag GmbH & Co. KGaA, Weinheim

direction (e.g. z axis) and 1D crystals confined along two directions (e.g. x,y direction) show staircase and saw-tooth like DOS, respectively, while 0D crystals show a δ-function-like DOS.

The band-gap energy (E_g) of nanocrystals is also influenced by their shape. The band-gap energy diagram of CdSe nanocrystals with various diameters and lengths, depicted in Figure 3a, clearly exhibits such shape effects.[14] Strong quantum confinement effects are observed as a function of the diameter reduction, while weaker quantum confinement effects are observed as a function of the length reduction. CdSe emission gradually changes from circular to linearly polarized as the nanocrystal shape evolves from spherical to rodlike (Figure 3b).[15]

During the last few years, researchers have been extensively studying efficient synthetic routes to well-defined nanocrystals with controlled size and shape. These methods include gas-phase syntheses utilizing vapor–liquid–solid (VLS) methods,[17–22] chemical vapor deposition (CVD),[23–25] thermal evaporation,[26–28] and liquid-phase colloidal syntheses in aqueous[29–45] or nonhydrolytic[1,5,7,46–121] media. The liquid-phase colloidal synthetic approach is an especially powerful tool for the convenient and reproducible shape-controlled synthesis of nanocrystals not only because this method allows for the resulting nanocrystals to be precisely tuned in terms of their size, shape, and composition on the nanometer scale but also because it allows them to be dispersed in either an aqueous or a nonhydrolytic media. Moreover, these colloidal nanocrystals are often referred to as "molecular nanocrystals" and can be modified by chemical hybridization with other functional materials for applications in electronics and biological systems.[122–132] Simplified colloidal nanocrystal growth processes can be understood by the following three steps (Figure 4): 1) seed formation initiated by a rapid increase in the monomer concentration in the

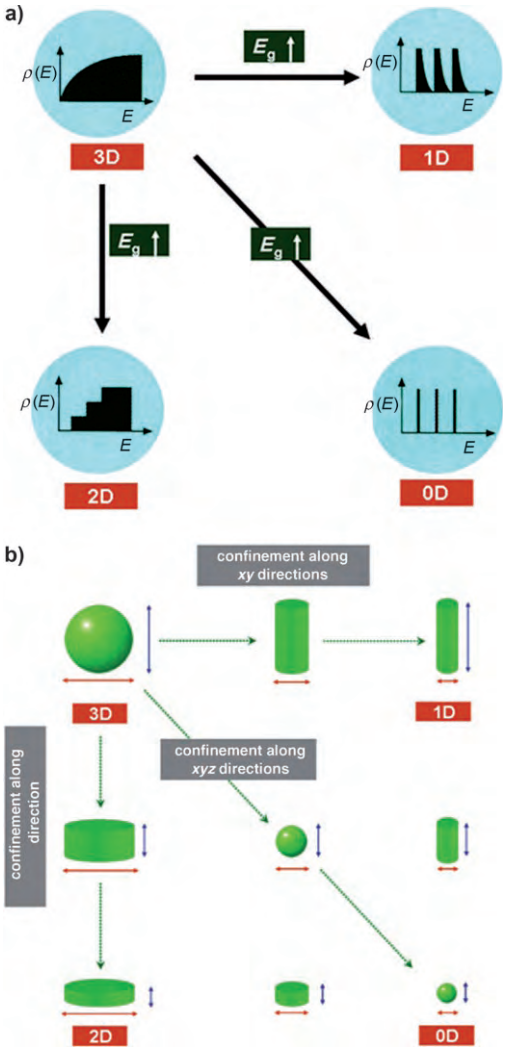

Figure 2. Shape evolution of crystals and their shape-dependent properties. a) The plot of density of state (DOS) versus energy is a continuous curve for 3D crystals and changes to a discrete line for 0D crystals. The band-gap energy of semiconductors and metal oxides gradually increases as the dimensionality and size reduce. b) Confinement of 3D crystals along one- (z), two- (xy), three (xyz) directions results in 2D, 1D, and 0D nanocrystals, respectively.

Young-wook Jun earned his degree in chemistry from Yonsei University (1999) and his PhD from the Korea Advanced Institute of Science and Technology (KAIST) (2005), where he studied the controlled synthesis and assembly of colloidal inorganic nanocrystals under the guidance of Prof. Sang Youl Kim and Prof. Jinwoo Cheon. Currently, he is carrying out postdoctoral studies in Prof. Cheon's group at Yonsei University on smart inorganic nanocrystal–biomolecule hybrid systems for biomedical imaging and sensor applications. He received the IUPAC Honorable Mention Award in 2005.

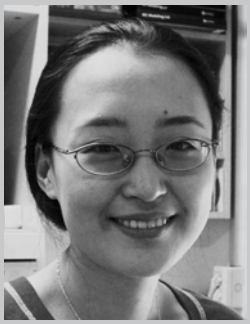

Jin-sil Choi was born in 1980 in Daegu, Korea. She received her degree in chemistry from Yonsei University in 2004 and is now student pursuing her PhD degree at Yonsei University under the supervision of Prof. Jinwoo Cheon. Her current research interests are the fabrication of size-, shape-, and composition-controlled multicomponent inorganic nanocrystals and their biocompatibility and safety evaluation on biological systems.

Jinwoo Cheon is a Professor of Chemistry at Yonsei University and Head of the Nanomaterials Division of the Nano-Medical National Core Research Center of Korea. He studied chemistry at Yonsei University in Seoul, Korea then moved to the University of Illinois, where he earned his PhD with Prof. G. Girolami on organometallic and materials chemistry (1993). After postdocs at Berkeley (Prof. J. Arnold) and UCLA (Prof. J. Zink) he joined the Korea Advanced Institute of Science and Technology (KAIST) as an assistant professor (1998). In 2002, he moved to Yonsei University as a professor of chemistry. His awards include the Korean Chemical Society Award in Inorganic Chemistry (2004), the National Science Prize for Junior Faculty (2002), and the Korean Chemical Society Wiley Young Chemist Award (2001).

© 2006 Wiley-VCH Verlag GmbH & Co. KGaA, Weinheim

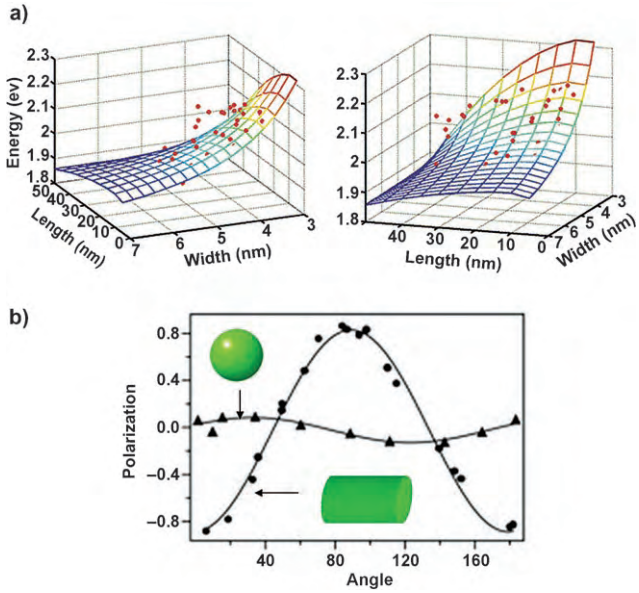

Figure 3. a) Band-gap energy diagram of CdSe nanorods[14] and b) shape-dependent polarized emission of CdSe.[15] CdSe nanorods have linearly polarized emission properties, while circularly polarized emission is observed from spherical CdSe nanoparticles.

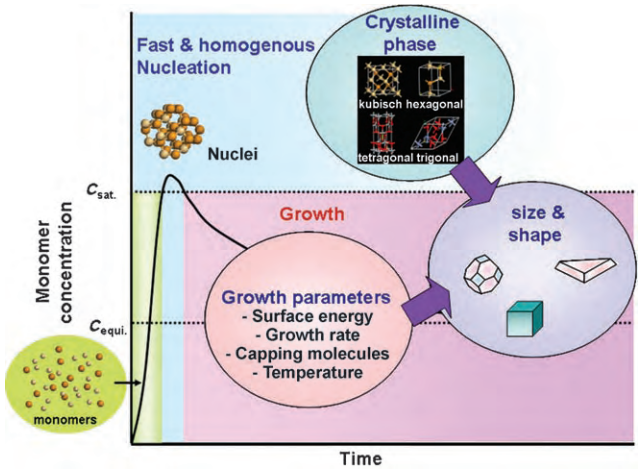

Figure 4. Crystal-growth diagram. When the monomer concentration reaches a supersaturation level, seed nucleation occurs and then monomer continuously aggregates onto the seeds, which results in the gradual decrease of monomer concentration. During these nucleation and growth stages, the control of growth parameters and crystalline phase is critical in determining the final size and shape of nanocrystals. $C_{sat.}$ = saturation concentration, $C_{equi.}$ = equilibrium concentration.

solution to super-saturation levels, 2) crystal growth from seeds by aggregation of monomers on the seed, which results in progressive decrease in the monomers concentration, and 3) surface stabilization of the resulting nanocrystals by surfactants.

In earlier methods of colloidal nanocrystals synthesis, the nanocrystals were usually grown in hydrolytic (i.e. aqueous) media in the presence of structured micelles at room temperature.[29–39] Several semiconductor[29–34] and metal oxide[35–39] nanocrystals have been grown by this method starting from ionic precursors inside organic micelles. However, nanocrystals obtained by this method frequently suffer from relatively poor crystallinity or polydispersity in their size and shape.[30,32,37–39] As an alternative way to relieve some of these problems, a nonhydrolytic high-temperature thermal reaction method in the presence of organic surfactants has been developed.[1] Nanocrystals obtained by this nonhydrolytic colloidal route, in general, exhibit excellent crystallinity and monodispersity. Moreover, this route has several advantages for the shape-controlled synthesis of nanocrystals including facile separation between the nucleation and growth stages, and easier controllability of growth parameters by changing variables, such as the type of surfactant molecules, monomer concentration, and temperature. Herein, we focus on this nonhydrolytic colloidal method which has been utilized for the synthesis of semiconductor and metal oxide nanocrystals with various geometrical motifs.

The ability to rationally assemble such size and shape-controlled nanocrystals enables these crystals to be utilized as key components for the fabrication of advanced nanodevices and nanosystems (Figure 5). By patterning and integrating these nanocrystals, the development of functional nanodevices, such as biosensors,[122,123] single-electron transistors (SET),[124–130] and ferroelectric memory devices,[131–133,170] can be possible. These applications will be further discussed in Section 4.

2. The Shape Control of Semiconductor and Metal Oxide Nanocrystals

2.1. Zero-Dimensional Spheres and Polyhedrons

Spheres are the most basic and symmetric motif among shaped nanocrystals. As the anisotropic shape control of nanocrystals is the main focus of this review, only a brief discussion of 0D nanocrystals will be presented.

Initially, Brus and co-workers successfully synthesized various II–VI semiconductor nanospheres with high colloidal stability in coordinating solvents (e.g. 4-ethylpyridine) but size tunability and monodispersity of these nanocrystals were limited.[7] Bawendi and co-workers later developed a groundbreaking nonhydrolytic method to prepare CdSe nanocrystals by injecting a solution containing dimethyl cadmium and trioctylphosphine selenide (TOPSe) into hot trioctylphosphine oxide (TOPO).[1] The nanocrystals obtained are highly monodisperse and the size of the nanocrystals could be varied from 1.2 to 11.5 nm. Optical spectra clearly demonstrated size-dependent quantum confinement effects indicating high monodispersity and crystallinity. This nonhydrolytic chemical route has been the most widely adopted method for synthesizing high-quality inorganic nanocrystals.[46–55]

Controlled growth of isotropic 0D nanocrystals with distinctly faceted faces has also been demonstrated. Cube-shaped $CoFe_2O_4$ nanocrystals are obtained through thermal reactions of cobalt(II) acetylacetonate and iron(III) acetyla-

 © 2006 Wiley-VCH Verlag GmbH & Co. KGaA, Weinheim

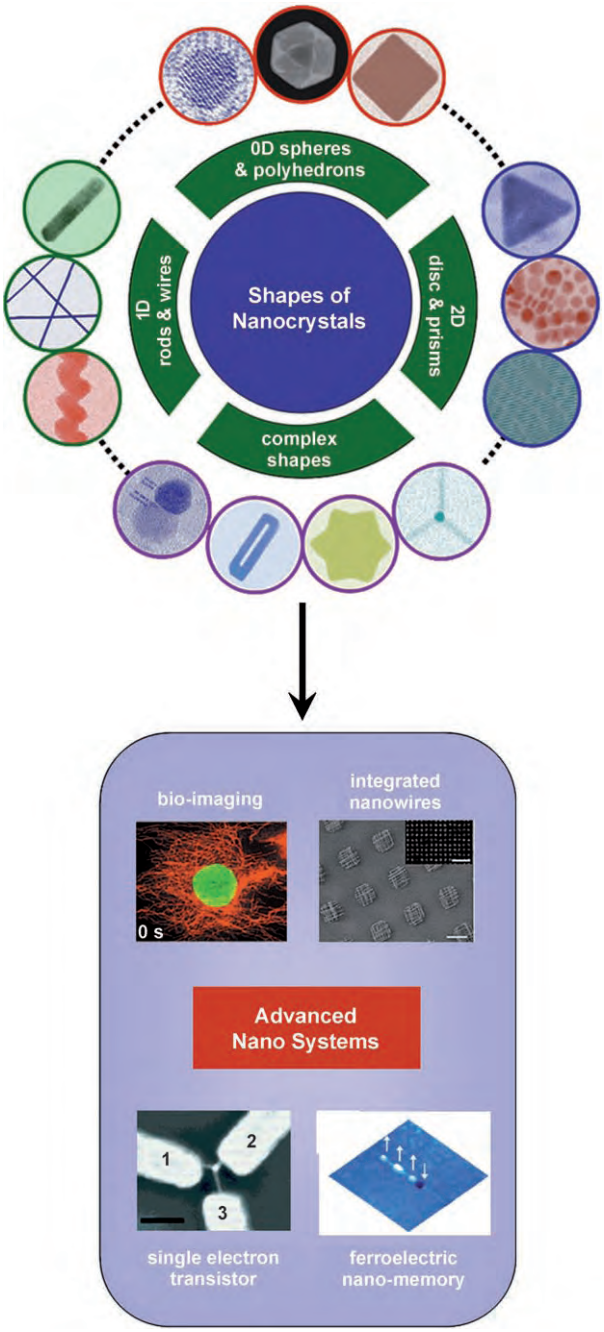

Figure 5. Representative shapes of inorganic nanocrystals developed to date. These kinds of nanocrystals have been utilized as key building blocks for the fabrication of novel nanosystems for biomedical and electronic technologies.

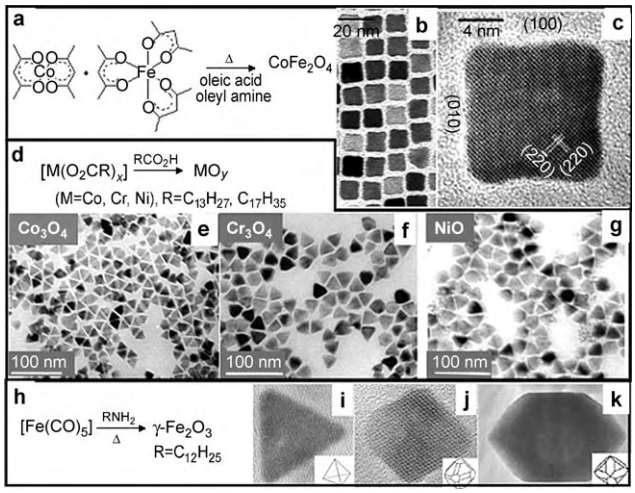

Figure 6. Isotropic 0D nanocrystals with distinctly faceted faces. a–c) $CoFe_2O_4$ nanocubes obtained by thermal decomposition of [Co(acac)$_2$] and [Fe(acac)$_3$] in a surfactant containing organic solution. b) TEM and c) HRTEM images of approximately 13-nm sized nanocubes.[46] d–g) Triangular shapes of metal oxides synthesized through the thermal decomposition of metal carboxylate precursors in a surfactant containing organic solution. TEM images of e) Co_3O_4, f) Cr_2O_3, and g) NiO.[47] h–k) Various shapes of γ-Fe_2O_3 nanocrystals. i) TEM images of triangle, j) diamond, and k) hexagon nanocrystals.[48] These shapes are actually 2D projection of 3D shapes: tetrahedrons (i), truncated octahedrons (j), and icosahedrons, which are truncated by {111} and {110} faces (k, insets).

cetonate in the presence of oleic acid and oleylamine (Figure 6a).[46] Under mild growth conditions with a low precursor concentration and a slow heating rate, cube-shaped $CoFe_2O_4$ nanocrystals are obtained (Figure 6b,c) whereas spherical-shaped nanocrystals are formed under harsh growth conditions (i.e. high temperature and high precursor concentration).

Triangular shapes of transition-metal oxide nanocrystals were also reported by Peng and co-workers (Figure 6d–g).[47] The cobalt stearate ($Co(O_2CC_{17}H_{35})_2$) precursor decomposes thermally in a hot organic solvent containing stearic acid to form triangular Co_3O_4 nanocrystals (Figure 6e). Similarly, triangular crystals of Cr_2O_3 and NiO are obtained from chromium myristate and nickel myristate precursors, respectively (Figure 6f,g).

Other 0D shapes of transition-metal oxide nanocrystals have been reported by Cheon and co-workers (Figure 6h–k).[48] Thermal decomposition of $[Fe(CO)_5]$ in refluxing 1,2-dichlorobenzene containing the surfactant dodecylamine and subsequent air oxidation yields sphere, triangle, diamond, and hexagon nanocrystals of γ-Fe_2O_3. (Figure 6i–k) Triangle, diamond, and hexagon shapes are the 2D projections of 3D structures of tetrahedra, truncated octahedra, and icosahedra, respectively. The dodecylamine surfactant molecules modulate the growth rate along certain directions (e.g. along the $\langle 111 \rangle$ direction of cubic inverse spinel iron oxide), which results in a variety of nanocrystal shapes.

2.2. 1D Rods and Wires

1D nanostructures of semiconductors and metal oxides exhibit unique optical[56,57] and magnetic[58,59] properties which arise from their anisotropic shape. Since CdSe nanorods were first reported,[56] a nonhydrolytic, high-temperature-injection method has been widely utilized for the syntheses of high–quality 1D nanocrystals.

 © 2006 Wiley-VCH Verlag GmbH & Co. KGaA, Weinheim

2.2.1. *Group II–VI, IV–VI, and Transition-Metal Chalcogenide Semiconductors*

Alivisatos and co-workers first reported CdSe nanorods from a thermal reaction of $CdMe_2$ and TOPSe in a hot surfactant mixture of TOPO and hexylphosphonic acid (HPA; Figure 7a).[68] In the absence of HPA, formation of

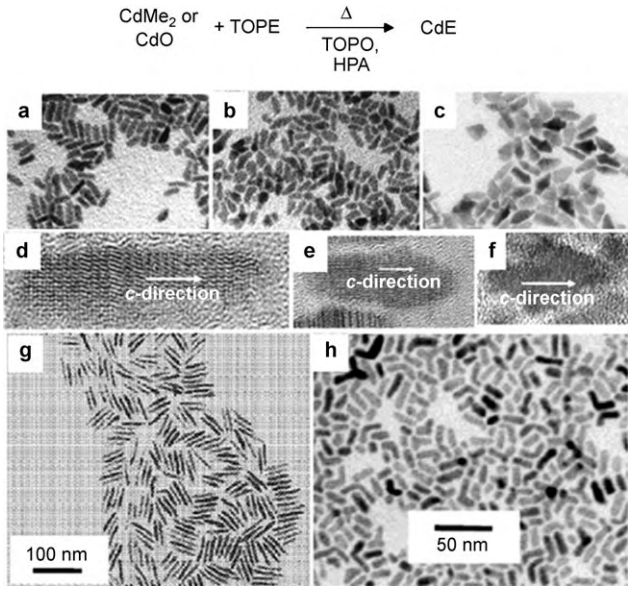

Figure 7. a–f) 1D CdSe nanostructures synthesized through thermal reactions of $CdMe_2$ and TOPSe in the presence of hexylphosphonic acid (HPA) and trioctylphosphine oxide (TOPO) as surfactants.[68] As the HPA concentration is increased, the CdSe nanocrystal shape changes from rods (a) to pencils (b,d), arrows (c,e) and pine-trees (c,f). HRTEM analyses show these nanocrystals are elongated along *c*-axis of wurtzite CdSe (d–f). g) CdSe and h) CdTe nanorods obtained from CdO precursors.[57]

CdSe nanospheres is preferred (see Section 2.1). When HPA is used as a cosurfactant, however, CdSe nanorods elongated along the *c* direction are obtained (for mechanistic details, see Section 3.3). Furthermore, by increasing the concentration of HPA, the shape systematically changes to pencil shaped (Figure 7b,d), arrow shaped (Figure 7c,e), and pine-tree shaped (Figure 7c,f).[68] Peng and co-workers proposed another synthetic method for 1D nanocrystals utilizing less-reactive cadmium precursors.[57,60,61] By using CdO or Cd–fatty-acid precursors rather than highly reactive alkyl cadmium precursors, the environmentally more benign synthesis of Cd-based chalcogenide (CdE, E = S, Se, Te) nanorods is possible (Figure 7g,h). This approach further enables large-scale production of CdE nanorods with better controllability of their size, monodispersity, and aspect ratio. The synthetic method has been successfully applied for the fabrication of other metal chalcogenide semiconductors including ZnO,[62] ZnS,[63,67] ZnSe,[63,64] CdS,[66,67] CdSe,[56,57,65,68] CdTe,[60] $Zn_{1-x}Cd_xS$,[69] and PbSe.[49,70]

A simpler synthetic method using a single-source molecular precursor was reported by Cheon and co-workers (Figure 8a–c).[66,71,115] For example, the injection of Cd-

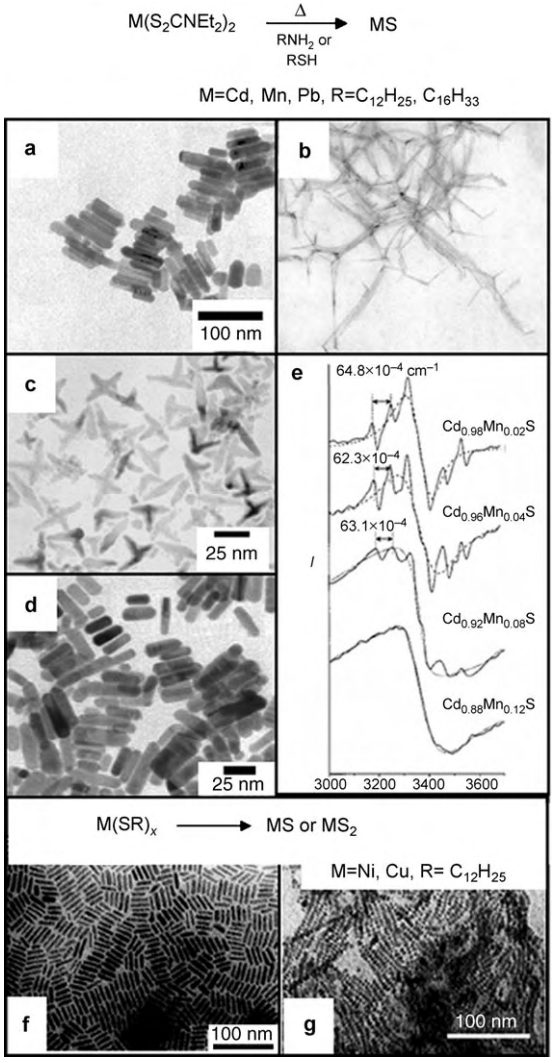

Figure 8. Single-source molecular precursor approaches for the synthesis of metal chalcogenide nanocrystals. Thermal decomposition of a metal *N*,*N*-diethylthiocarbamate precursor leads to the formation of 1D rod structures of a) CdS,[66] b) MnS,[71] c) PbS,[115] and d) $Cd_{0.92}Mn_{0.08}S$ nanorods.[71] e) Electron paramagnetic resonance (EPR) spectra of $Cd_{1-x}Mn_xS$ ($0 < x \leq 0.12$).[71] Similarly, thermal decomposition of $Ni(SR)_x$ and $Cu(SR)_x$ in a hot alkanethiol solution yields f) NiS and g) Cu_2S, respectively.[72–74]

$(S_2CNEt)_2$ into a hot hexadecylamine (HDA) surfactant solution yields well-defined and highly crystalline CdS nanorods (Figure 8a).[66] Thermal decomposition of the single-source molecular precursor produces stable monomers and facilitates the formation of wurtzite CdS nanorods elongated along the *c* direction. Similarly, when $Mn(S_2CNEt)_2$ is used, 2-nm thick MnS nanowires with an aspect ratio of approximately 80 are obtained (Figure 8b).[71] This single-source molecular approach also yields of branched PbS nanocrystals in the rock salt form, elongated along the [100] direction (Figure 8c).[115] Moreover, this method can be successfully applied for the synthesis of 1D $Cd_{1-x}Mn_xS$ diluted magnetic semiconductors (DMS) (Figure 8d).[71] In this case, by utilizing kinetic growth at relatively mild temperature, magnetic Mn could be homogeneously doped to high levels ($\approx 12\%$)

© 2006 Wiley-VCH Verlag GmbH & Co. KGaA, Weinheim

into the 1D CdS nanorod matrix (Figure 8e). Korgel and co-workers successfully demonstrated a metal alkylthiolate approach to produce anisotropic metal sulfide nanocrystals (Figure 8f, g).[72–74] Solventless thermal decomposition of a mixture of nickel alkylthiolate and octadecanoate yields rhombohedral NiS nanorods elongated along the [110] direction (Figure 8f).[74] Similarly, Cu_2S nanorods can be obtained by solventless thermal decomposition of a copper thiolate precursor (Figure 8g).[72,73]

Shape transformation from small nanocrystals to larger nanocrystals by oriented attachment mechanisms is also an efficient route for the synthesis of 1D nanorods and wires (for mechanistic details, see Section 3.2). Weller and co-workers reported the formation of ZnO nanorods by refluxing ZnO nanospheres in methanol solution (Figure 9).[75] Similarly,

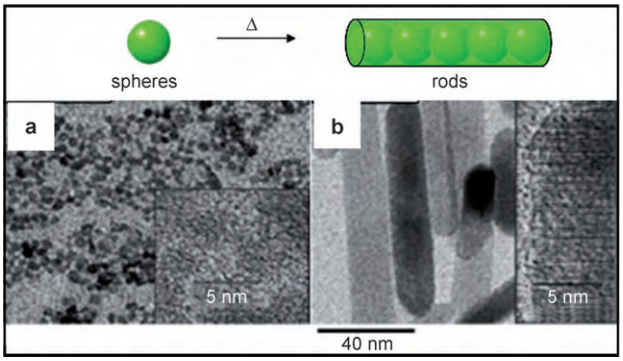

Figure 9. Shape transformation of ZnO nanospheres to ZnO nanorods by an oriented attachment process. HRTEM images of the a) nanospheres and b) nanorods.[75]

Hyeon and co-workers synthesized anisotropic ZnS nanocrystals through shape transformation of 5-nm ZnS nanospheres to nanorods by aging them in an oleylamine solution at 60 °C for 1 day.[76] In contrast, isotropic growth to give 10-nm sized ZnS nanospheres by an Ostwald ripening processes is observed when the nanocrystals are stored in an oleic acid solution. Very recently, single-crystalline PbSe nanowires were synthesized by Murray and co-workers.[77] By changing the type of surfactants, the nanocrystals are assembled through different modes, which results in a variety of 1D nanostructures. Straight PbSe nanowires are obtained from the thermal reaction of lead oleate and TOPSe in diphenyl ether containing oleic acid and tetradecylphosphonic acid (TDPA) surfactants. In contrast, when a mixture of oleic acid and HDA is used, PbSe zigzag nanowires are formed. Nanowire helices are also formed when the straight PbSe nanowires are annealed in the presence of trioctylamine (TOA).

2.2.2. *Group III–V and IV Semiconductors*

Unlike II–VI semiconductor systems, which have been well studied, the shape control of III–V semiconductor nanocrystals has been very limited. The difficulty in the III–V semiconductor nanocrystal formation is most likely due to a greater degree of the covalent bonding and the absence of suitable precursors. Except for metal nitrides, III–V semiconductors favor isotropic zinc blende structures and thus 0D nanocrystal growth is commonly preferred rather than 1D rod growth.[130] We have shown that the crystalline phase of gallium phosphide nanocrystals can be chemically modulated by using suitable surfactants.[78] When a single-molecular precursor, $Ga(PtBu_2)_3$, is injected into a hot trioctylamine (TOA) surfactant solution, 0D GaP nanospheres with a zinc blende crystalline structure are obtained (Figure 10a). In

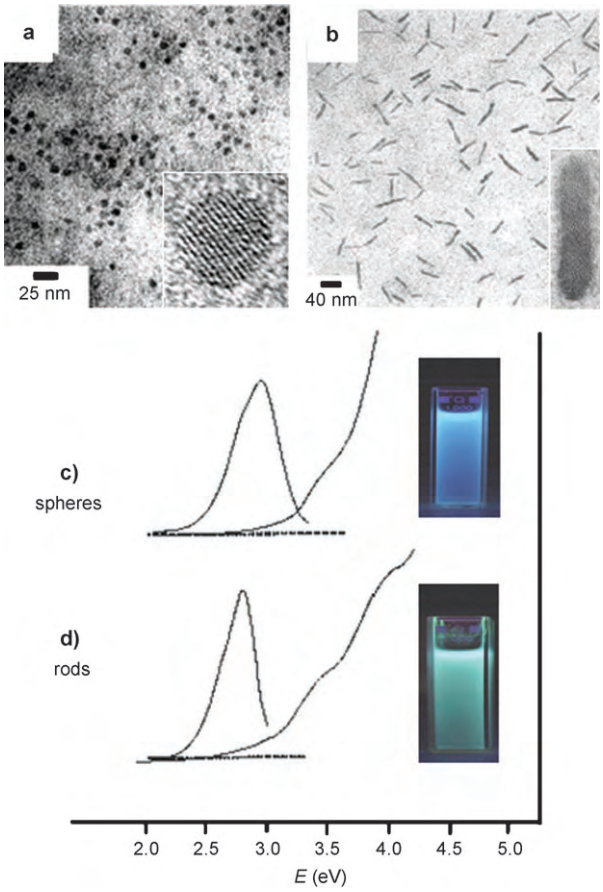

Figure 10. a) Zinc blende GaP nanospheres and b) wurtzite nanorods and their shape-dependant optical spectra (c,d). Although their absorption edges are almost identical, GaP spheres emit a blue fluorescence blue while the rods emit a green fluorescence.[78]

contrast, wurtzite GaP nanorods are formed when a mixed surfactant solution of TOA and HDA (Figure 10b) is used. These resulting nanocrystals show unique shape-dependent spectroscopic features. The absorption spectra exhibit shoulders (3.48 eV for spheres and 3.46 eV for rods) and shallow tails that are attributed to direct and indirect transitions, respectively.[135] The photoluminescence maximum was 2.94 eV for the 8-nm GaP spheres and corresponds to the direct transition, whereas a red shift to 2.79 eV is observed for the rods (8×45 nm), which arises from their shape anisotropy (Figure 10c,d).

It is more difficult to obtain nanorods by a typical solution-based precursor-injection method in the case of

 © 2006 Wiley-VCH Verlag GmbH & Co. KGaA, Weinheim

group IV semiconductor systems. Recently, Ge nanorods synthesized from a tetraethylgermane precursor were reported by Gerion and co-workers.[79] This reaction is performed in a highly pressurized autoclave and produces a mixture of various shaped Ge nanocrystals including spheres, cubes, pyramids, and rods as well as amorphous byproducts.

As an alternative method, seed-mediated growth of nanocrystals through solution–liquid–solid processes (SLS) facilitates the formation of group III–V and IV 1D nanostructures.[80–83] Buhro and co-workers reported the SLS growth of InN, InP, InAs, and GaAs nanowires by thermal decomposition of a single-source molecular precursor, $[t\mathrm{Bu_2M\{\mu\text{-}E(SiMe_3)_2\}}]_2$ (M = In, Ga; E = N, P, As) (Figure 11 a–c).[81–83] When the precursor molecule, for example, $[t\mathrm{Bu_2In\{\mu\text{-}P(SiMe_3)_2\}}]_2$, decomposes, it generates InP monomers and indium metallic seeds by two cycles of In–P bond cleavage and reformation. The monomers subsequently diffuse into the liquid indium seeds and eventually precipitate and crystallize along a specific direction to form 1D InP nanowires when the liquid seeds become supersaturated.

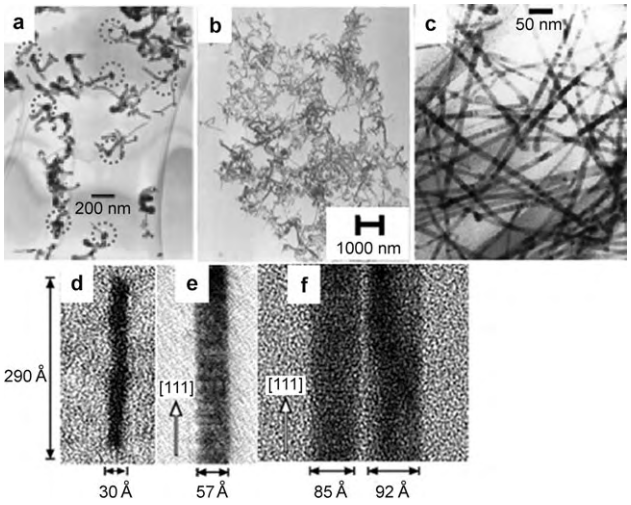

Figure 11. Seed-mediated solution–solid–solution (SLS) growth of group III–V semiconductor nanowires. a–c) Thermal decomposition of a single-source molecular precursor, $[t\mathrm{Bu_2M\{\mu\text{-}E(SiMe_3)_2\}}_2]_2$, generates metallic indium seeds (a, circled) and subsequent ME monomer formation produces InN (a),[81] InP (b),[82] and GaAs (c)[83] nanowires. d–f) SLS growth of InP nanorods through a two precursor system of $[t\mathrm{Bu_2InP(SiMe_3)_2}]_2$ and $[\mathrm{Cl_2InP(SiMe_3)_2}]_2$. Control of the nanorod diameter is possible from 3 nm (d) to 6 nm (e) and 9 nm (f).[84]

A similar approach to synthesize InP nanorods has been employed by Nozik and co-workers.[84] They utilized a two-precursor system of $[t\mathrm{Bu_2InP(SiMe_3)_2}]_2$ and $[\mathrm{Cl_2InP(SiMe_3)_2}]_2$ to separate the seed formation from wire growth processes while the diameter of the nanorods is controlled by the surfactant molecules. Small nanorods with diameters of approximately 3 nm are grown from a mixture of TOA and dodecylamine (DDA) at 250 °C for 3 h (Figure 11 d), and wires with larger diameters (between 5 and several tens of nanometers) are obtained from a mixture of TOPO/TOP depending on the growth time (Figure 11 e, f).

Korgel and co-workers reported another approach, supercritical fluid–liquid–solid (SFLS), which uses high growth temperatures (around 600 °C) and pressures (Figure 12 a).[85–91] Since most semiconductor/metal eutectic temperatures exceed the boiling point of conventional solvents, the use of a supercritical fluid enables SLS growth of highly crystalline group IV semiconductor nanowires. For example, in supercritical hexane, Si nanowires have been successfully synthesized using gold nanocatalysts (Figure 12 b, c).[85] Above 300 °C, Si and Au form an alloy in equilibrium with pure solid Si. The continuous supply of monomers made from the thermal decomposition of Si precursor into the gold nanocatalyst induces Si:Au alloy supersaturation which results in pure solid Si nanowires being expelled from the Au seeds.

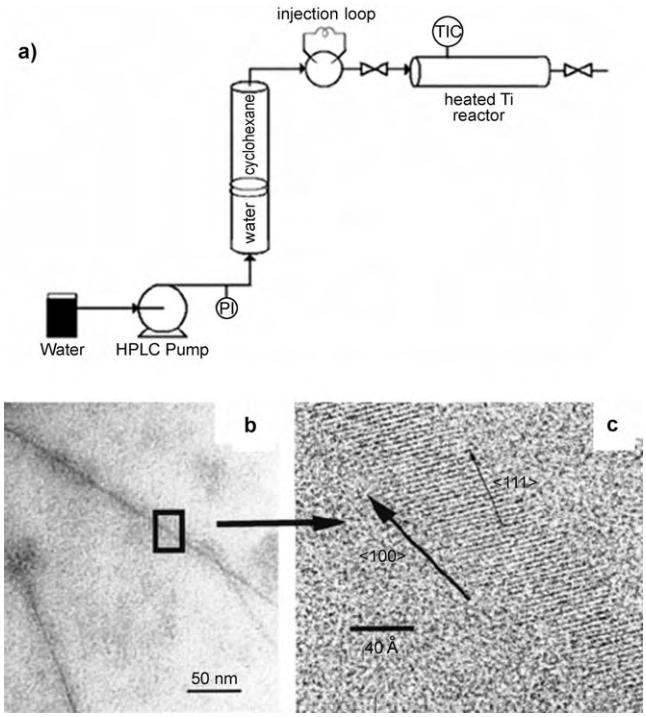

Figure 12. Supercritical-fluid–liquid–solid (SFLS) growth of Si nanowires. a) Schematics of the experimental setup (PI = pressure indicator, TIC = temperature indicator and controllor),[89] b) TEM and c) HRTEM images of Si nanowires.[85]

Banin and co-workers reported a controlled synthesis of InAs nanorods in organic solvents.[92] When a solution containing precursor molecules of $InCl_3$ and $As(TMS)_3$ (TMS = trimethylsilyl) and gold nanocrystals is injected into a hot TOP solution, InAs nanorods form in 3 seconds. The nanorods have mean diameters of 4 nm, which is comparable to the size of initial gold seeds and their mean lengths can be controlled to 9.4 nm, 15.1 nm, or 22.7 nm (Figure 13 a–c). These nanorods exhibit shape-dependent optical properties (Figure 13 d). The gradual red-shift in the photoluminescence spectra accompanied by a significant reduction in the photoluminescence intensity observed as the length of the nanorods

 © 2006 Wiley-VCH Verlag GmbH & Co. KGaA, Weinheim

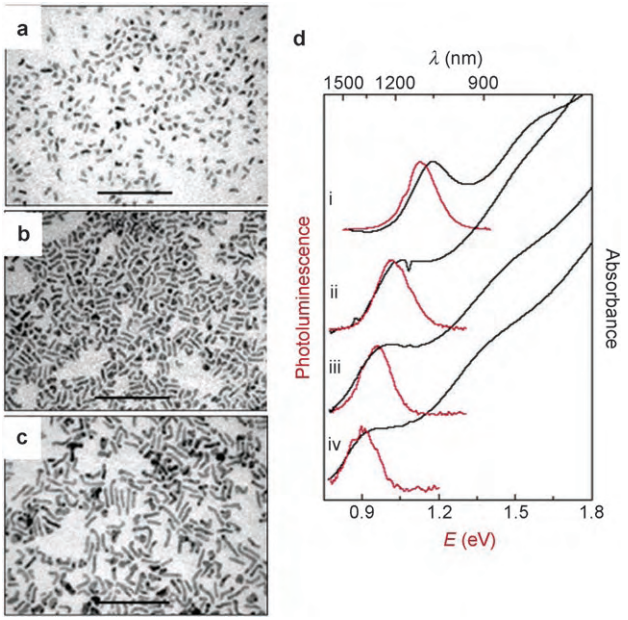

Figure 13. InAs nanorods with different aspect ratios grown by Au nanocrystal catalyzed SLS in a TOPO solution a) 4×9.4 nm InAs, b) 4×15.1 nm InAs, and c) 4×22.7 nm InAs (scale bar in each case: 100 nm). d) Both absorption (black) and luminescence (red) spectra of InAs rods in (a)–(c) (d,ii–iv) shift to lower energy, compared to those of 4-nm spherical InAs particles (d,i).[92]

increases is a signature of a quantum confinement effect along rod axis.

2.2.3. *Transition-Metal Oxides and Phosphides*

Transition-metal oxides are an important group of materials used in white pigments, electronic ceramics, cosmetics, supports in catalysis, and as photocatalysts.[136–139] Bulk materials are typically synthesized through sol–gel processes in aqueous or alcohol media,[140–143] while, for the past few years, the shape-controlled metal oxide and phosphide nanocrystals have been successfully fabricated in high quality through the nonhydrolytic thermal processes.

Non-sol–gel based nonhydrolytic synthesis of transition-metal oxide nanocrystals was first reported by Colvin and co-workers.[93] The alkylhalide elimination reaction of $TiCl_4$ with $Ti(OiPr)_4$ in a hot TOPO solvent produces highly crystalline spherical TiO_2 nanocrystals. This method has been extended to the shape-controlled synthesis of 1D TiO_2 nanorods by Cheon, Alivisatos, and co-workers through a mixed surfactant system of TOPO and lauric acid (LA; Figure 14a).[94] (For more details, see Section 3.3)

Thermal decomposition of a transition-metal alkoxide precursor in a hot organic solvent can also induce the 1D growth of metal oxide nanocrystals. Weller and co-workers reported TiO_2 nanorods synthesized through the thermal decomposition of a $Ti(OiPr)_4$ precursor in the presence of oleic acid (Figure 14b).[95] Similar approaches have been reported by Hyeon and co-workers through an ester elimination reaction of $Ti(OiPr)_4$ and oleic acid, and by Han and co-workers through an aminolysis reaction of $Ti(OiPr)_4$ and

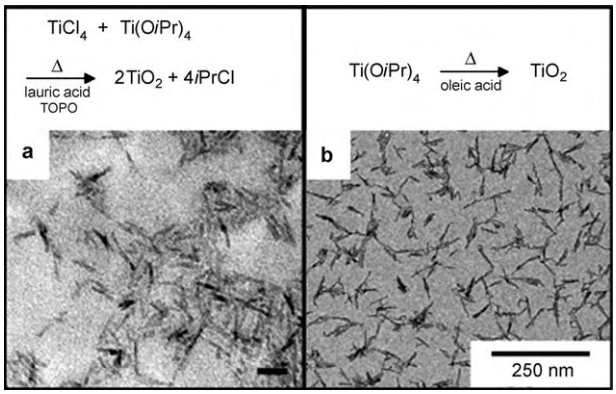

Figure 14. Synthesis of TiO_2 nanorods by a) An alkylhalide elimination reaction of $TiCl_4$ with $Ti(OiPr)_4$ in a mixture of TOPO and lauric acid (LA) yields TiO_2 nanorods (scale bar: 25 nm).[94] b) thermal decomposition of the metal alkoxide precursors.[95]

oleylamine.[96,97] Hyeon and co-workers also reported the reaction of zero-valent metal carbonyl precursors with a chemical oxidant to yield 1D metal oxide nanocrystals: air oxidation of $[Mn_2(CO)_{10}]$ complexes leads to the formation of MnO nanorods (Figure 15a).[98] Similarly, Park and co-workers reported the growth of WO_{3-x} nanorods through the reaction of $[W(CO)_6]$ with Me_3NO in the presence of oleylamine surfactant (Figure 15b).[99]

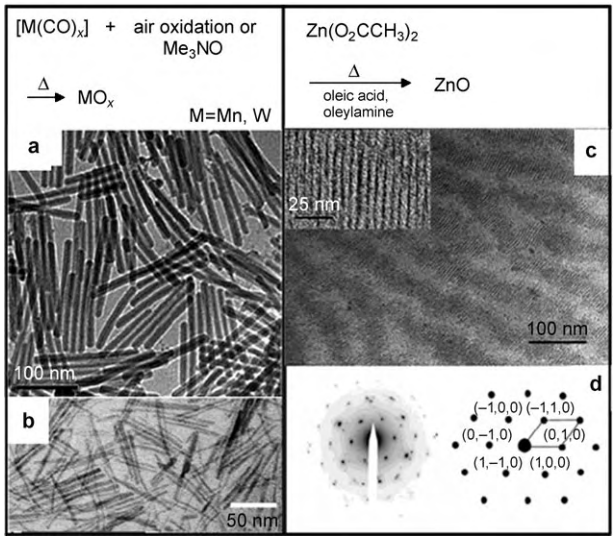

Figure 15. a,b) Transition-metal oxide nanocrystals prepared from metal carbonyl precursors. a) MnO nanorods[98] and b) WO_{3-x} nanorods.[99] c) ZnO nanorods assemblies into close-paced "stacks", d) SAED diagram of the ZnO nanorods in (c).[62]

Metal carboxylic acid complexes in hot organic solvent can also efficiently produce transition-metal oxide nanorods. O'Brien and co-workers synthesized ZnO nanorods through the thermal decomposition of zinc acetate in the presence of oleic acid.[62] The nanocrystals have a high monodispersity for diameter and length. These nanocrystals self-assemble into closely packed "stacks" which align their long axes parallel to

 © 2006 Wiley-VCH Verlag GmbH & Co. KGaA, Weinheim

each other (Figure 15c). Selected area electron diffraction (SAED) patterns confirm that these nanocrystals have a single-crystalline hexagonal structure (Figure 15d). Syntheses of various metal oxide nanocrystals (Fe_3O_4, CoO, and ZnO rods) have been developed by Peng and co-workers through the thermal decomposition of a metal oleate complex (Figure 16a–c).[46] Hyeon and co-workers have also reported a large-scale synthesis of such metals oxide nanocrystals (Co_3O_4 rods, ZnO horns and rods) through a similar approach (Figure 16d–f).[100]

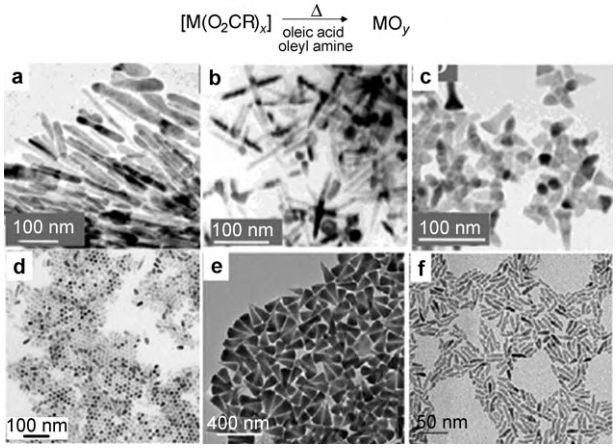

Figure 16. transition-metal oxide nanocrystals prepared form metal fatty acid complexes. a) Fe_3O_4 nanorods, b) CoO nanorods, c) ZnO nanorods, d) Co_3O_4 nanopencils, e) ZnO nanohorns, and f) ZnO nanorods.[47,100]

A generalized synthetic approach for the 1D shapes of transition-metal oxide nanocrystals has been developed through a thermal reaction of metal halides and oleic acid in the presence of an oleylamine surfactant. Cheon and co-workers reported the one-pot synthesis of transition-metal oxide nanorods including TiO_2, $W_{18}O_{49}$, and Mn_3O_4 was carried out through a kinetically driven crystal growth process (Figure 17a,c,d).[101] The acylhalide elimination reaction of metal halides and oleic acid induces an increase of the metal oxide monomer concentration and promotes fast growth of nanocrystals along directions with high surface energy. All nanorods obtained are elongated along their own crystallographically high energy directions (Figure 17b,e,f).

The preparation of 1D ternary perovskite oxides by nonhydrolytic synthesis was demonstrated by Park and co-workers.[102] They synthesized single-crystalline cubic $BaTiO_3$ nanowires through sol–gel reactions of bimetallic precursors, $BaTi(O_2CCH_3)_6$, in a hot organic solvent initiated by injection of aqueous H_2O_2 solution (For more detail, see Section 4.2).

Metal phosphide nanocrystals have been studied because of their unique ferromagnetism, semiconductivity, catalytic, and magnetocaloric properties.[144–150] Brock and co-workers first synthesized colloidal metal phosphide nanospheres by thermal decomposition of metal precursors in the presence of trioctylphosphine (TOP).[103] Continuous addition of precursor molecules into the reaction solution drives anisotropic 1D growth of the metal phosphide nanocrystals (Figure 18). Yang

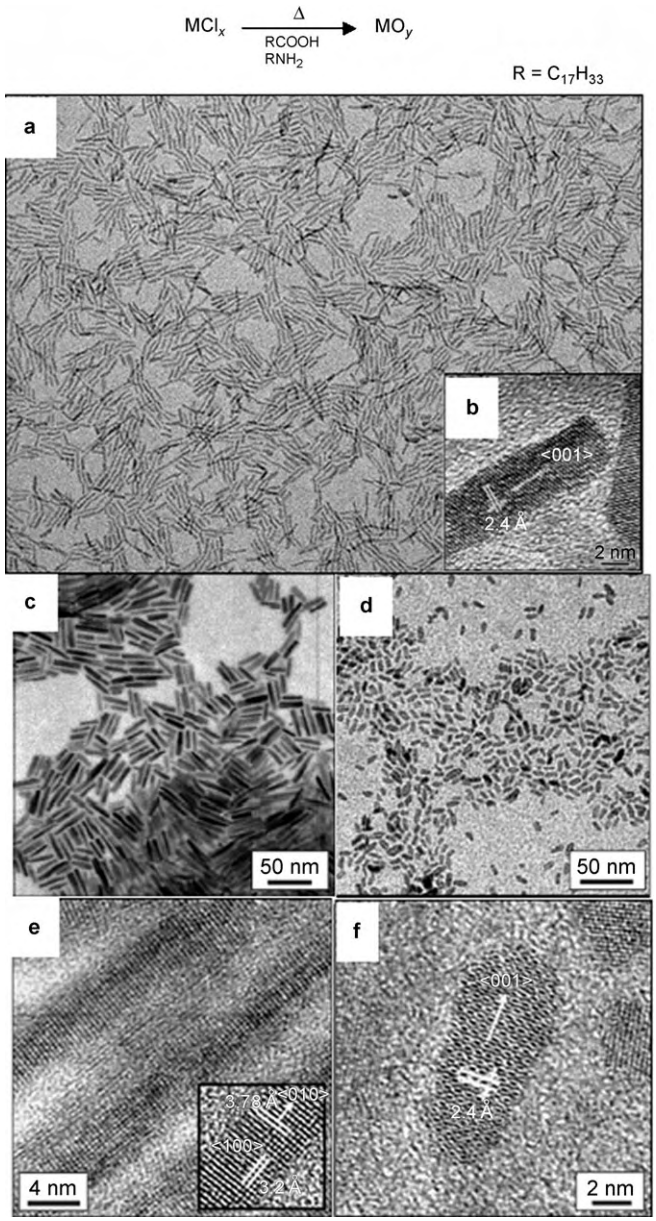

Figure 17. A generalized synthetic approach for 1D transition-metal oxide nanorods through an acylhalide elimination reaction of metal chloride and fatty acid. TEM and HRTEM analyses of a,b) TiO_2, c,e) $W_{18}O_{49}$, and d,f) Mn_3O_4 nanorods. Tetragonal TiO_2 and Mn_3O_4 nanorods are elongated along the [001] direction, and monoclinic $W_{18}O_{49}$ nanorods are elongated along the [010] direction.[101]

and co-workers reported the synthesis of FeP nanorods and nanowires through multiple injections of $[Fe(CO)_5]$ and phosphine mixtures (Figure 18a).[104] A generalized synthetic approach for 1D metal phosphide nanocrystals has been developed by using selective adhesion of surfactants by Hyeon and co-workers (Figure 18b–e).[105] Metal phosphide nanorods including Fe_2P, FeP, MnP, Co_2P, Ni_2P, have been successfully synthesized through continuous delivery of metal phosphine precursor molecules using a syringe pump. In addition, by controlling either the injection rate or the choice of surfactant, the nanocrystal diameter and aspect ratio can be changed. Recently, O'Brien and co-workers reported that

© 2006 Wiley-VCH Verlag GmbH & Co. KGaA, Weinheim

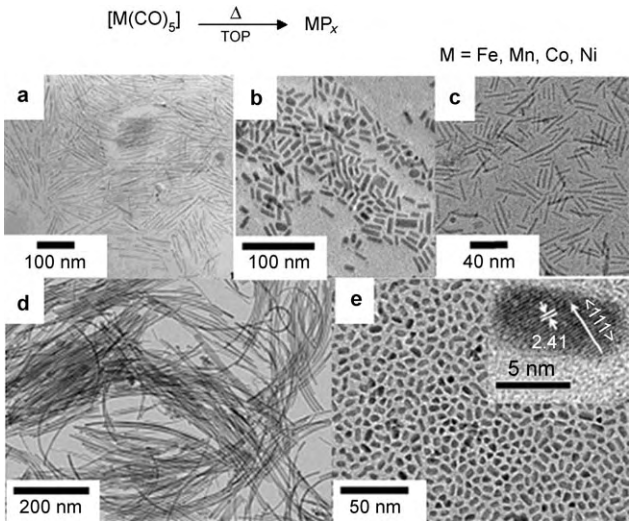

Figure 18. Metal phosphide nanorods and nanowires. a) FeP nanorods synthesized through multiple injection of $[Fe(CO)_5]$ and phosphine mixtures.[104] b–e) Metal phosphide nanorods synthesized through continuous delivery of metal phosphine complex precursor from a syringe pump. TEM images of b) MnP, c) Co_2P, d) FeP, and e) NiP nanorods; inset: HRTEM image of a NiP nanorod.[105]

CoP nanowires can be also synthesized through thermal decomposition of $[Co(acac)_2]$ (acac = acetylacetonate) and tetradecylphosphonic acid in a mixture of TOPO and HDA.[106]

2.3. 2D Discs and Prisms

Unlike 1D rods, the formation of disc-shaped nanocrystals is very rare in colloidal systems. In a kinetically driven growth regime, 1D nanorod growth is typically promoted with faster growth along a specific direction (e.g. *z* axis; Figure 19a). On the other hand, when growth along an axis is blocked and preferential growth occurs along the other two axes (e.g. *x*,*y* axes), the formation of disc-shaped nanocrystals is facilitated (Figure 19b). Such a strategy for the synthesis of 2D nanostructures was utilized for the first time for the synthesis of metallic cobalt nanodiscs.[5,107] While, the Cu_2S hexagonal nanocrystal synthesized through solventless thermolysis of copper alkanethiol precursors is an example of a "nonmetallic" disc-shaped nanostructure.[72,73] In the presence of alkanethiol surfactants, preferential growth along ⟨100⟩ and ⟨110⟩ directions and inhibition of growth along [001] direction results in the formation of Cu_2S nanodiscs (Figure 20a). Similar results are obtained for the synthesis of NiS nanocrystals.[74] Rhombohedral NiS nanoprisms result from inhibition of growth along the ⟨110⟩ direction and fast growth along the directions perpendicular to it (Figure 20b).

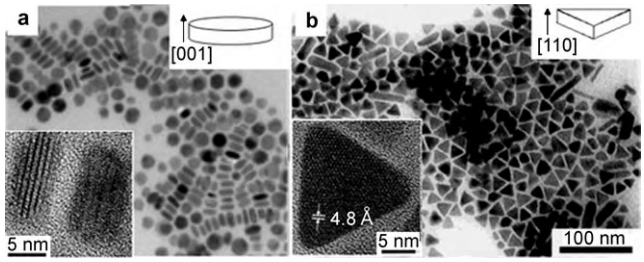

Figure 20. a) Cu_2S discs[72] and b) NiS nanoprisms[74] through solventless thermolysis of metal-alkanethiol complexes. Insets show HRTEM images of the Cu_2S discs (side view) and NiS prisms (top view).

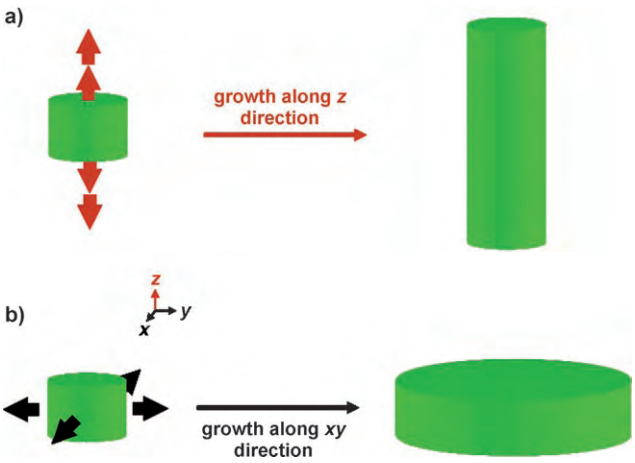

Figure 19. 1D rod versus 2D disc growth. a) Preferential growth along one direction (e.g. *z* axis) of a seed results in rod-shaped nanocrystals, b) growth along two directions (*xy* plane) leads to the formation of disc-shaped nanocrystals.

Disc and plate shapes of lanthanide oxide nanocrystals have also been prepared. For example, Gd_2O_3 nanoplates were synthesized through the thermolysis of the precursor molecule, $Gd(O_2CCH_3)_3$, in a hot octadecene containing oleic acid and oleylamine surfactants (Figure 21a).[108] The nanoplates obtained have a highly crystalline cubic structure with a space group of *Ia*3 and are confined in the [100] direction. These nanoplates assemble into ribbons of stacked plates that stand on their edges (Figure 21b). Extension of such methods to a generalized synthesis of 2D lanthanide oxide nanoplates has been successfully performed by Yan and co-workers.[109] Thermal decomposition of lanthanum bezoylacetylacetonate in a hot mixture of oleic acid and oleylamine produces Ln_2O_3 (Ln = La, Pr, Nd, Sm, Eu, Gd, Tb, Er, Y). All resulting nanocrystals have a cubic symmetry with a space group of *Ia*3 and are plate or disc shapes with a confined direction of either [100] or [111]. Selective adhesion of surfactants may play a critical role in the formation of such 2D nanocrystals (Figure 21c–e).

2.4. Advanced Shapes of Nanocrystals

As described above, shape controls of nanocrystals have been widely studied for 0D spheres, 1D rods, and 2D plates. These basic building blocks have unique geometries and properties and can be used further as components in more complex nanostructures. If the assembly of several compo-

 © 2006 Wiley-VCH Verlag GmbH & Co. KGaA, Weinheim

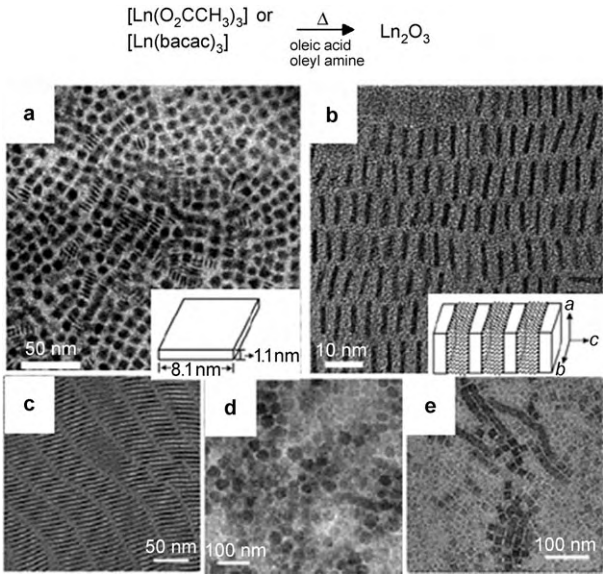

Figure 21. 2D lanthanide oxide nanoplates. a,b) Gd_2O_3 nanoplates synthesized by thermal decomposition of gadolinium acetate precursors. Insets: proposed model for the nanoplates (a) and assembly of nanoplate stacks (b).[108]. TEM images of c) Eu_2O_3 plates d) Er_2O_3 discs, and e) Pr_2O_3 plates[109] prepared from $[Ln(bacac)_3]$.

nents, each with different geometries, can be controlled, the construction of novel nanostructures may be possible. For example, an L-shaped structure can be obtained using two rods and a cube (Figure 22a) while a V-shaped structure can

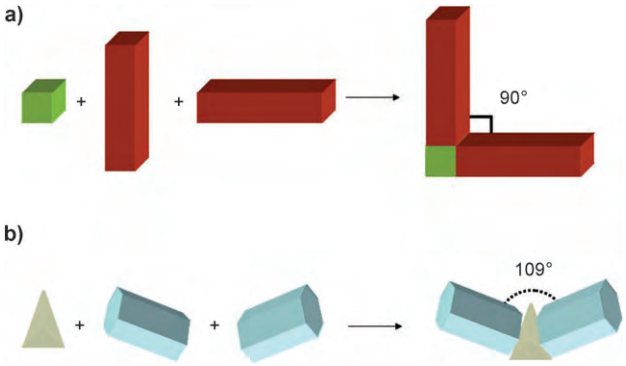

Figure 22. Formation of a) L-shaped and b) V-shaped structures. The L-shaped structure can be formed by assembling a cube and two rods with an angle of 90°, while V-shaped structure can be obtained by assembling a tetrahedron and two rods.

be achieved by assembling two rods on a tetrahedron (Figure 22b). Other examples of such advanced nanostructures are CdSe tetrapods obtained by Alivisatos[68] and the MnS tetrapods from Cheon and co-workers(Figure 23a,b).[71] In these cases, a zinc blende tetrahedron seed truncated with four {111} faces and subsequent growth of wurtzite arms on these four surfaces results in the tetrapod-shaped nanocrystals with tetrahedral (T_d) symmetry (Figure 23c).

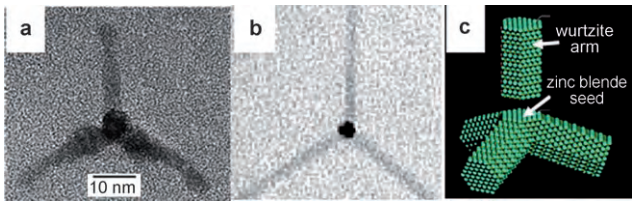

Figure 23. Tetrapod shaped nanocrystals of a) CdSe and b) MnS formed by epitaxial growth of four wurtzite arms on a tetrahedral zinc blende seed results in tetrapod shaped nanocrystals (c).[68, 71, 110]

Formation of novel multipod structures using a tetrahedron and 1D rods was studied with CdS nanocrystals by Cheon and co-workers.[66] Kinetic growth processes can be used to systematically vary the nanocrystal shapes from spheres to 1D rod ($D_{\infty h}$), bipod (C_{2v}), tripod (T_d), and tetrapod (C_{3v}) (Figure 24). When four wurtzite arms grow

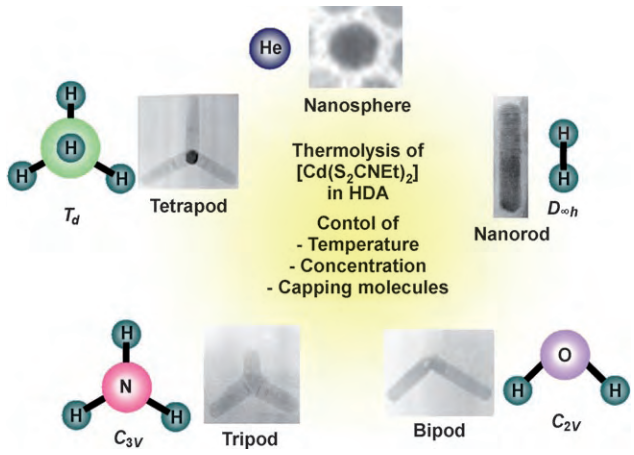

Figure 24. Shape evolution of CdS nanocrystals. By controlling growth parameters such as growth temperature and capping molecules, the nanocrystal shape systematically changes from spheres to rods ($D_{\infty h}$), bipods (C_{2v}), tripods (T_d), and tetrapods (C_{3v}). Bipods and tripods result from nonsynchronous growth of wurtzite arms from four {111} faces of tetrahedral seeds.[66] Small molecules of the same symmetry are also shown for comparison.

equivalently out of the four {111} equivalent faces of a tetrahedral zinc blende seeds, a tetrapod shaped CdS nanocrystal is obtained. However, when the growth rate increases, the equilibrium between growth on the four {111} faces is expected to break, which induces nonsynchronous growth of wurtzite arms from either one-, two-, or three- {111} faces of a tetrahedral seed resulting in the formation of monopods, bipods, and tripods.

Alivisatos and co-workers reported the growth of CdTe tetrapods with controlled lengths and diameters.[110] They found that higher ratios of Cd/Te results in longer arms (Figure 25a), whereas a higher alkylphosphonic acid/Cd ratio yields arms with a larger diameter (Figure 25b). These CdTe tetrapods exhibit shape-dependent optical properties. Tetrapods having comparable arm lengths but different arm

 © 2006 Wiley-VCH Verlag GmbH & Co. KGaA, Weinheim

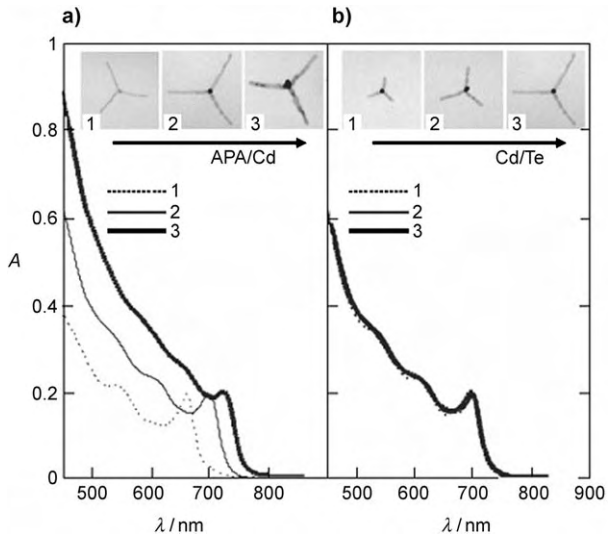

Figure 25. a) Diameter and b) length-controlled synthesis of CdTe tetrapods and their shape-dependent optical spectra. When the ratio of alkylphosphonic acid (APA)/Cd increases, the diameter of CdTe tetrapod arms is increased while higher ratios of Cd/Te result in longer arms. Absorption spectra are red-shifted for tetrapods with thicker diameters (a), but almost identical spectra are observed for a set of tetrapods with arms of comparable diameter but different arm lengths (b).[110]

diameters show significant differences in their absorption spectra (Figure 25a), but almost identical absorption spectra are observed for a set of tetrapods with comparable arm diameters but different arm lengths (Figure 25b).

A similar but different growth process for branched structures through SLS growth of MSe (M = Cd, Pb) has been reported by Kuno and co-workers.[111] A germinate nucleation of seeds of the zinc blende type, grown from metallic seeds, induces the formation of multiply branched MSe nanocrystals including Y-shapes, V-shapes, tripods, and nanowires with higher ordered of branchings.[112]

Secondary crystal growth of wurtzite arms at the ends of a tetrapod can yield inorganic nanocrystals with dendritic structures (Figure 26a). A second injection of $CdMe_2$ and TOPSe into a solution containing CdSe tetrapod leads to the dendritic CdSe (Figure 26b).[113] Similarly, core tetrapod$_{(CdSe)}$–branched tetrapod$_{(CdTe)}$ dendritic structures are also obtained through a second injection of TOPTe into a solution containing CdSe tetrapods (Figure 26c). Very recently, hyperbranched CdSe nanocrystals were reported in which the degree of branching can be controlled. The resulting nanocrystals have morphologies which include thorny balls, tree-like structures, and cobweb-like structures.[114]

Cheon and co-workers reported that systematic geometrical control in the synthesis of PbS nanocrystals is accomplished by controlling the nanocrystal growth parameters, such as temperature, monomer concentration, and surfactant type. The shape evolution of PbS nanocrystals from a cube to a branched rod via a star-shaped structure as a transient species was demonstrated (Figure 27a–c).[115] This star-shaped nanocrystal is a 2D projection of a 3D structure with truncated octahedral cores and six symmetric horns in the

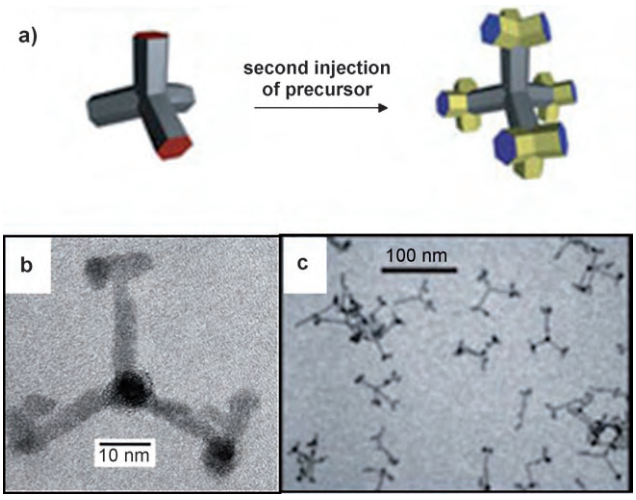

Figure 26. Inorganic nanodendrites. a) In situ second injection of precursor molecules into a solution containing CdSe tetrapods leads to the dendritic shapes. b) CdSe dendrites[68] and c) mixed dendrite with a CdSe tetrapod core and CdTe tetrapod branches.[113]

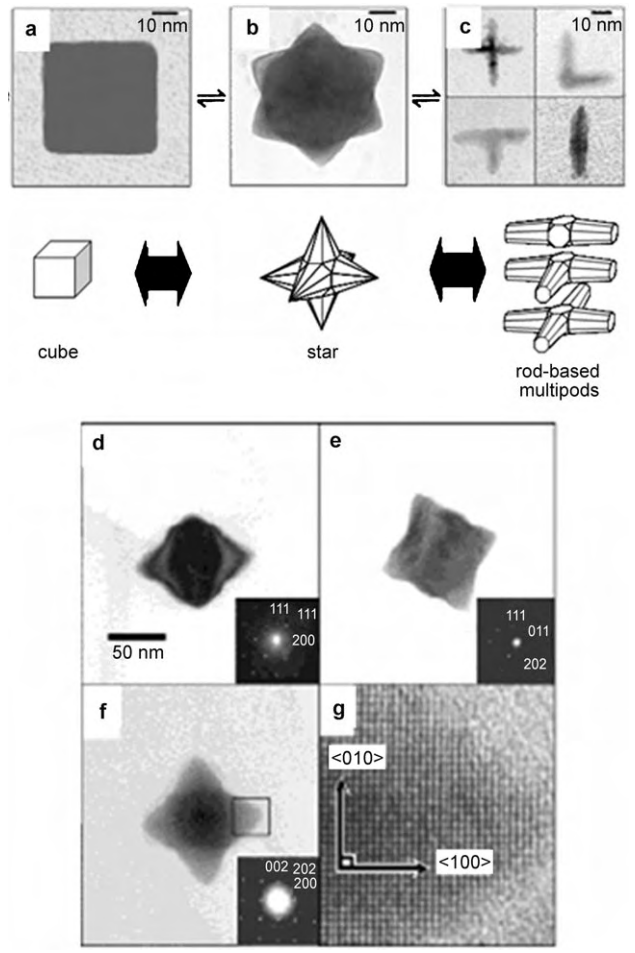

Figure 27. Shape evolution of PbS nanocrystals. By controlling the growth parameters, cubes (a) can be converted via star-shaped nanocrystals (b) into and 1D rod-based multipods (c). TEM zone axis analyses of star-shaped PbS nanocrystals: b) [111], d) [110], e) [112], and f) [100]. g) HRTEM analysis of star-shaped PbS shows that the nanocrystals have rock salt structures with elongated horns along [100] direction.[115]

 © 2006 Wiley-VCH Verlag GmbH & Co. KGaA, Weinheim

[100] directions of PbS (Figure 27g). TEM zone axis analyses clearly shows its 3D stereographic structure (Figure 27d–f). It possesses well-defined geometry and a single crystalline rock salt phase. When the zone axis is changed from [111] to [110], [112], and [100], the structural images and electron diffraction patterns change simultaneously.

Murray and co-workers elegantly demonstrated that radially branched nanowires can be fabricated from star-shaped PbSe nanocrystals by linking the star-shaped nanocrystals together along their [100] direction (Figure 28a–c).[77]

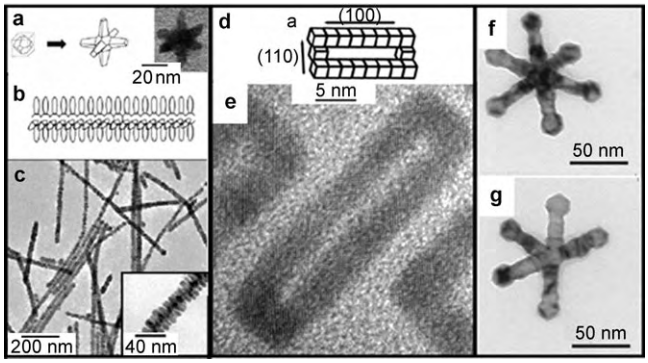

Figure 28. Advanced shapes of PbSe and MnO nanocrystals obtained through an oriented attachment processes. a) Star-shaped PbSe building block, b) schematic structure and c) TEM images of the radially branched nanowires. d) Schematic structure and e) TEM image of PbSe nanorings. Oriented attachment of 0D nanocrystals along both the ⟨100⟩ and ⟨110⟩ directions results in the formation of closed ring shapes.[77] f) MnO hexapods and g) pentapods.[116]

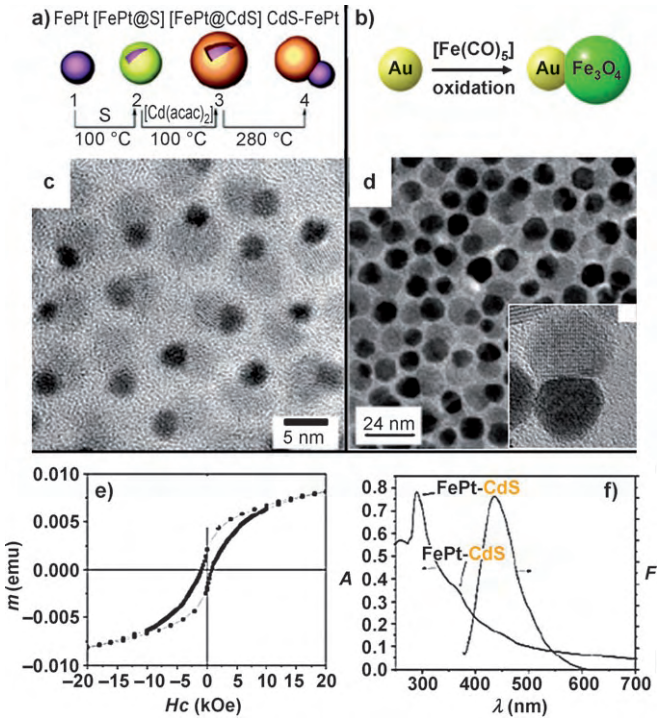

Figure 29. a) Growth processes and c) TEM image of heterodimeric CdS–FePt nanocrystals. When sulfur and $[Cd(acac)_2]$ are added to a hot reaction solution containing FePt nanocrystals subsequent annealing of the resulting solution at 280°C gives heterodimers of CdS–FePt. These heterodimers have dual-functionality: e) magnetic and f) fluorescent properties.[117] b) Synthesis of Au–Fe_3O_4 heterodimers. d) TEM and inset: HRTEM images of Au–Fe_3O_4 heterodimers.[118] Thermal decomposition and subsequent oxidation of the $[Fe(CO)_5]$ precursor in a hot reaction solution containing Au nanocrystals induces epitaxial growth of Fe_3O_4 nanocrystals on the [111] surface of Au nanocrystals.

They also demonstrated that the formation of PbSe nanorings is possible by a similar oriented attachment approach.[77] Since the oriented attachment mechanism strongly depends on the dipole moments of the PbSe nanocrystals, the controlled assembly process of PbSe nanocrystals along different axes would allow for the formation of nanostructures with complex geometries. The attachment of nanocrystals along both the ⟨100⟩ and ⟨110⟩ directions results in the formation of closed ring shapes (Figure 28d,e). Very recently, multipods of MnO nanocrystals were formed by an oriented attachment between initially formed truncated octahedral units (Figure 28f,g).[116]

Multicomponent nanocrystals are a class of advanced nanostructures. Multicomponent nanocrystals not only possess the multi-functionalities of each of their components but also demonstrate new collective properties arising from the interactions between each of these components. Heterodimers formed from semiconducting CdS and magnetic FePt nanocrystals are one such example.[117] Xu and co-workers reported the formation of a CdS shell onto a FePt core and subsequent annealing to form heterodimers of CdS–FePt nanocrystals (Figure 29a,b). These heterodimers exhibit optical fluorescence arising from the CdS component and magnetic behavior from the FePt (Figure 29c,d). Similarly, Sun and co-workers reported heterodimers of Au–Fe_3O_4 nanocrystals (Figure 29e,f).[118] Thermal decomposition of $[Fe(CO)_5]$ precursors and subsequent oxidation in a hot solution containing Au nanocrystals leads to the epitaxial growth of Fe_3O_4 nanocrystals on the {111} surface of Au nanocrystals (Figure 29f, inset).

Multicomponent nanostructures composed of 0D spheres and 1D nanorods have also been generated. Banin and co-workers reported selective growth of gold onto the tips of semiconductor CdSe rods and tetrapods (Figure 30a–c).[119,120] The fluorescent quenching phenomena that are characteristic of these Au–CdSe nanocrystals are observed owing to the strong coupling between the metal and the semiconductor (Figure 30d). Dumbbell-shaped nanostructures from PbSe spheres and CdSe rods were also synthesized by Parak and Manna and co-workers.[121] Significant modification of optical spectra is observed for the dumbbell-shaped nanostructures compared to those of either the initial CdSe nanorods or PbSe nanospheres.

3. Proposed Mechanism for the Anisotropic Growth of Nanocrystrals

To date, several proposals have been made for how to achieve shape control of nanocrystals. In this Section, we will

© 2006 Wiley-VCH Verlag GmbH & Co. KGaA, Weinheim

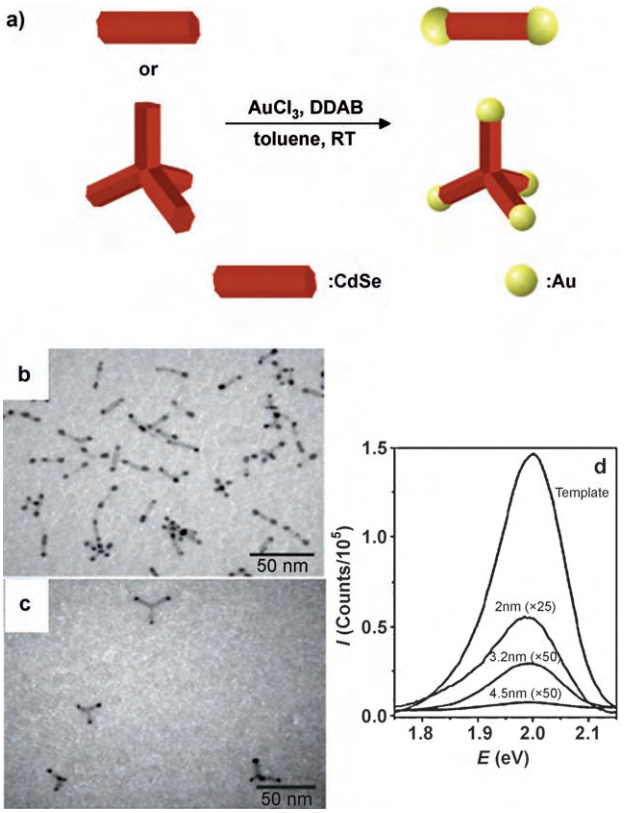

Figure 30. a) Schematic representation of the selective growth of gold tips onto semiconductor CdSe nanorods and tetrapods; DDAB = dodecyldimethylammoniumbromide. b,c) TEM images of the gold-tipped structures in (a). d) Photoluminescence spectra of the nanocrystals show the characteristic fluorescent quenching behavior which results from the strong coupling between the nanocrystal components.[119]

focus on three representative shape-controlling mechanisms (Figure 31):

1) Seed-mediated solution–liquid–solid (SLS) growth.
2) Shape transformation through oriented attachment.
3) Kinetically induced anisotropic growth.

All of these growth mechanisms have the merit of facile separation between the nucleation and growth stages, which is a prerequisite for the shape-controlled nanocrystal fabrication.

3.1. Seed-Mediated Solution–Liquid–Solid (SLS) Growth

Nanocrystals can be useful as seeds and facilitate highly anisotropic crystal growth. Under gas-phase synthetic approaches, such as chemical vapor deposition, 1D silicon and germanium wires are easily obtained on a substrate through a vapor–liquid–solid (VLS) growth mechanism.[12–22] Similar approach can be very useful for the generation of colloidal semiconductor nanowires by a solution–liquid–solid (SLS) process.[80–91] Decomposition of the molecular precursor at high temperature generates monomers in organic media. The monomers diffuse onto the seeds to form an alloy.

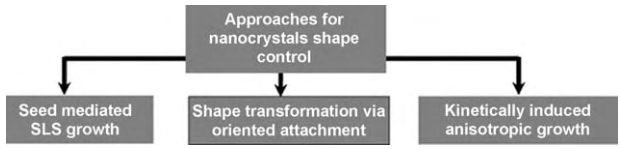

Figure 31. Proposed mechanisms for the shape-controlled synthesis of nanocrystals.

As the dissolution of monomers onto the seed increases, the supersaturated pure solid nanowire grows out of the seed (Figure 32a). Under the supercritical fluid environment, for example, Ge nanowires were obtained by Korgel and co-workers using gold nanocrystal seeds.[89] Above 360 °C, Ge and Au first form an alloy in equilibrium with pure solid Ge (Figure 32b) and, upon supersaturation, pure solid Ge is expelled from the Au seeds in wire form (Figure 32c,d).

3.2. Oriented Attachment

Another approach to obtaining 1D nanorods is based on inorganic self-assembly through an oriented attachment process. Owing to the high surface to volume ratio of

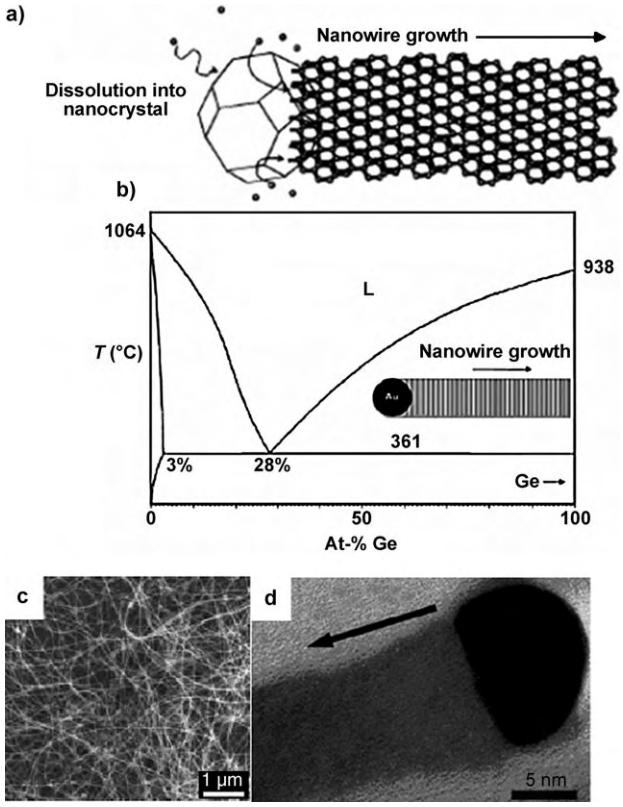

Figure 32. a) Schematic representation of the SLS growth processes.[85] Dissolution of monomers into metallic seeds first forms an alloyed phase. A gradual increase of monomer concentration in the alloy seed to supersaturation level then induces the rod growth along a specific direction. b) Phase diagram of AuGe alloy formation. c) TEM, and d) HRTEM images of Ge nanowires.[89]

 © 2006 Wiley-VCH Verlag GmbH & Co. KGaA, Weinheim

nanocrystals, the surface energy significantly contributes to the total energy. Therefore, as the surface area is reduced by aggregation processes (Figure 33), the total energy of the crystal will decrease. The concept of "oriented attachment" was first demonstrated by Banfield and co-workers in the hydrolytic synthesis of TiO_2 nanocrystals.[152] Truncated diamond-shaped anatase TiO_2 nanocrystals have three different faces: {001}, {121}, and {101}. According to Donnay–Harker rules, the surface energy of the (001) is higher than those of the other surfaces.[153] When there is a sufficient thermal energy in the system, the removal of high-energy surfaces is thermodynamically favorable. Therefore, the fusion of diamond-shaped nanocrystals along the [001] direction is facilitated by the oriented attachment process that results in a necklace-shaped nanocrystal (Figure 33b). Similar observations were made in the cases of both the hydrolytic growth of CdTe nanowires[154] and the nonhydrolytic growth of ZnO,[75] ZnS,[76] and PbSe[77] nanocrystals (see also Section 2.2). Through aging processes, PbSe nanospheres are aligned and fused together along a specific axis (Figure 33c–e) and after surface reconstruction processes result in well-defined nanowires (Figure 33f,g). Variations of either the shapes of the building blocks or the attachment directions yield a variety of nanocrystal shapes including wires, zigzags, helices, branches, and rings (Figure 33h–j).

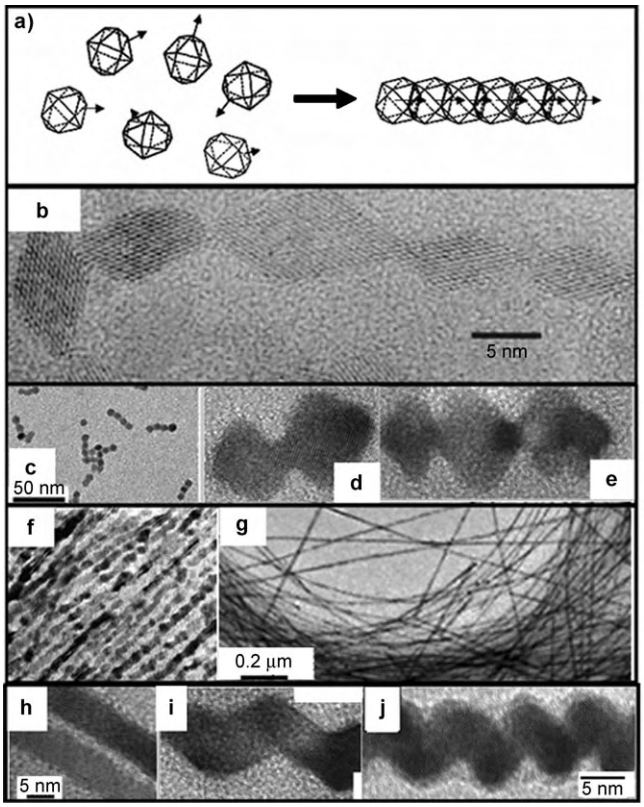

Figure 33. a) Schematic representation of oriented attachment processes. The initial 0D nanocrystals align and come together along their dipole direction. After surface reconstruction to minimize the surface energy, 1D rod-based structures are obtained. b) Aligned diamond-shaped TiO_2 particles.[152] c–e) Aggregated oligomers of PbSe nanocrystals which are intermediates during the oriented attachment processes. f,g) Fused PbSe nanowires before (f) and after (g) surface reconstruction. By controlling the reaction parameters, various shapes of nanocrystals including straight h) PbSe nanowires, i) zigzag chains, and j) helices are obtained.[77]

3.3. Kinetically Induced Anisotropic Growth

The kinetically induced anisotropic growth from molecular precursors is highly effective for producing advanced shapes of nanocrystals. There are three important key factors for determining nanocrystal shape: 1) surface energy and selective adhesion, 2) the influence of the phase of the crystalline seed, 3) thermodynamic or kinetic control of the growth regime.

3.3.1. Surface Energy and Selective Adhesion

The surface energy of the crystallographic faces of a seed strongly affects the anisotropic growth patterns of nanocrystals. For example, the surface energy of the (001) face (e.g. 0.9 $J\,m^{-2}$ for ZnS) is larger than those of other faces such as (100) and (110) (e.g. 0.5 $J\,m^{-2}$; Figure 34).[151] Since the crystal

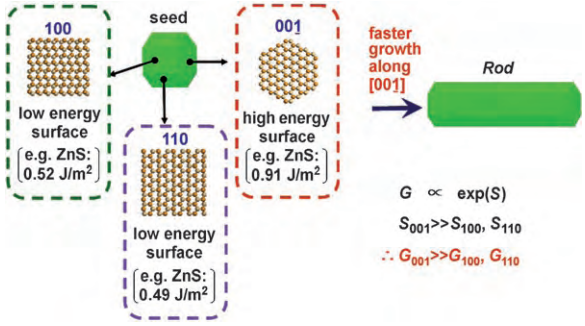

Figure 34. Surface energy of wurtzite ZnS nanocrystals. The (001) surface has the highest surface energy. Since the growth rate is exponentially proportional to the surface energy, the fastest growth occurs along the [001] direction in the kinetic growth regime; G = growth rate, S = surface energy.

growth rate is exponentially correlated to the surface energy, such surface-energy differences induce much faster growth along the [001] direction of ZnS than the other directions, resulting in formation of ZnS nanorod elongated along the [001] direction. Similarly, nanorods of other semiconductors with a wurtzite structure (e.g. ZnO,[62] ZnS,[63,67] ZnSe,[63,64] CdS,[66,67] CdSe,[56,57,65,68] CdTe,[60] MnS,[71] and GaP[78] (see Section 2.2)), or with a tetragonal structure (TiO_2[93–97,101] and Mn_3O_4[101]) elongated along the [001] direction. In a similar way orthorhombic $W_{18}O_{49}$[101] and FeP[103–105] elongated along the [010] direction.

The surface energy of the nanocrystals can be modulated by introducing surfactants that adsorb onto surfaces of growing crystallites.[56,57,68,72–74,96,101] When surfactants stabilize a certain surface by "selective adhesion", the growth rate difference between different crystallographic directions can be accentuated. Selective adhesion of surfactants is critical in the synthesis of CdSe nanorods.[68] When dimethylcadmium

© 2006 Wiley-VCH Verlag GmbH & Co. KGaA, Weinheim

and TOPSe are injected into a hot surfactant mixture of TOPO and HPA, the amount of HPA that selectively binds to the surfaces {100} and {110} of the growing crystallites modulates the growth pattern. At low HPA concentration or in the absence of HPA, only spherical nanocrystals are formed. However, with higher HPA concentrations, nanorods are obtained since the surface-bound HPA molecules serve to reduce the growth along {100} and {110} surfaces (Figure 35a).

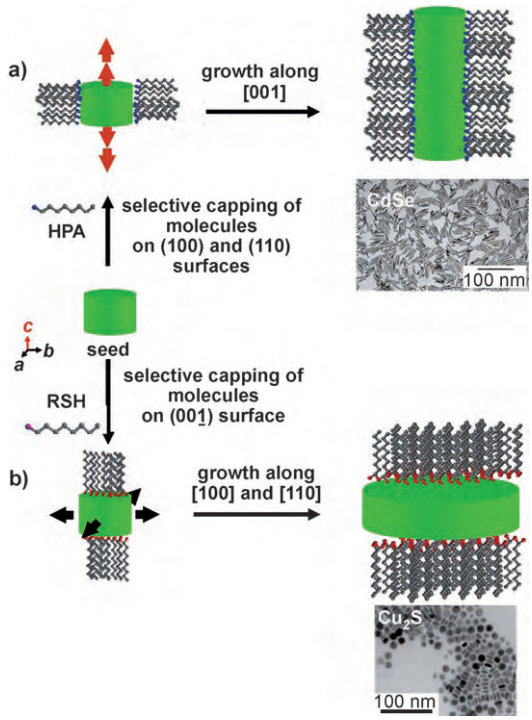

Figure 35. Surface modulation effects induced by surface-selective surfactants on either a) anisotropic rod or b) disc growth. When surfactant molecules specifically bind to the {100} and {110} surfaces of a hexagonal structure, preferential growth along the ⟨001⟩ directions and therefore rod growth is facilitated (a).[68] In contrast, when surfactant molecules bind to the {001} surfaces of a hexagonal structure, it prevents growth along the ⟨001⟩ direction and therefore disc shapes are obtained (b).[72]

Selective adhesion of surfactants can not only induce elongation along a specific axis but it can also induce compression along other axes. The formation of copper sulfide nanodiscs in the presence of surface selective alkanethiol surfactant is a good example.[72] The alkanethiol molecules strongly adsorb on the {001} faces of Cu_2S and, by lowering the surface energy, 2D Cu_2S nanodiscs are formed (Figure 35b).

Anatase TiO_2 nanocrystals are another model system for surfactant-assisted, surface-energy modulated anisotropic growth (Figure 36).[94] TiO_2 anatase has a tetragonal crystal structure with an anisotropic *c*-axis. When TiO_2 with a truncated octahedral, bipyramidal shape terminated by {001} and {101} faces nucleates,[152] fast growth along the high-energy surface {001} induced complete elimination of the {001} surfaces which results in arrow- and diamond-

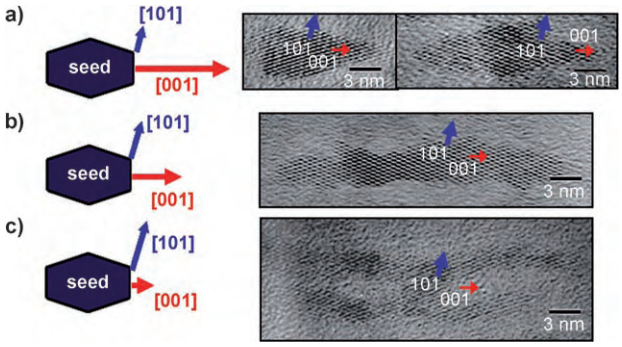

Figure 36. Shape evolution of TiO_2 nanocrystals through the surface-energy modulation effect by using surface selective lauric acid (LA) surfactants. a) Bullet- and diamond-shaped nanocrystals are formed at low LA concentration. b,c) At higher LA concentrations rods (b) and branched rods (c) are formed.[94]

shaped nanocrystals (Figure 36a). However, when lauric acid molecules are involved as surfactants in the reaction, they strongly bind to the {001} faces and reduce the growth rate along the ⟨001⟩ directions.[155] This induces growth along both directions of ⟨001⟩ and ⟨101⟩ whereby the area of the {001} surface remains constant, which finally results in rod formation (Figure 36b). At higher lauric acid concentration, the growth along [101] is facilitated, resulting in the formation of branched rods with a [101] branching direction (Figure 36c).

3.3.2. *Influence of the Crystalline-Seed Phase*

Another parameter responsible for shape control is the crystallographic phase of the nucleated seeds. When seed crystals are of the zinc blende phase, they tend to grow isotropically along the three crystallographic axes (*a*, *b*, and *c* directions), resulting in 0D shapes, such as spheres and cubes. However, when seeds are formed in a wurtzite structure, crystals can grow anisotropically, resulting in shapes such as rods and discs. Hence, control of the key factors affecting the crystalline phases of seeds and subsequent growth is of particular interest. Crystal seeds can potentially have a variety of different crystallographic phases and the stable phase is highly dependent on the environment.[66,71,78,112] For example, by adjusting the temperature during the nucleation processes, the crystalline phase may be controlled. In the case of MnS semiconductor nanocrystals,[71] the seed with a rock-salt phase is preferred at higher temperatures (> 200 °C) and isotropic cubes are easily formed (Figure 37a).[156,157] In contrast, at lower temperature of around 120 °C, where the wurtzite phase is more stable, the growth of nanorods is preferred (Figure 37b).[156,157]

Shapes of CdS nanocrystals can also be adjusted by this temperature-mediated phase control of the initial seeds.[66] At higher temperatures (≈300 °C), CdS seed are in the wurtzite phase and exclusive 1D nanorod formation is observed (Figure 37c), whereas at lower temperatures zinc blende nuclei are preferred and tetrahedral seeds with four {111} faces are formed.[158] The epitaxial growth of wurtzite pods along the [001] direction from the {111} faces occurs and, as a result, CdS bipods are formed (Figure 37d).

 © 2006 Wiley-VCH Verlag GmbH & Co. KGaA, Weinheim

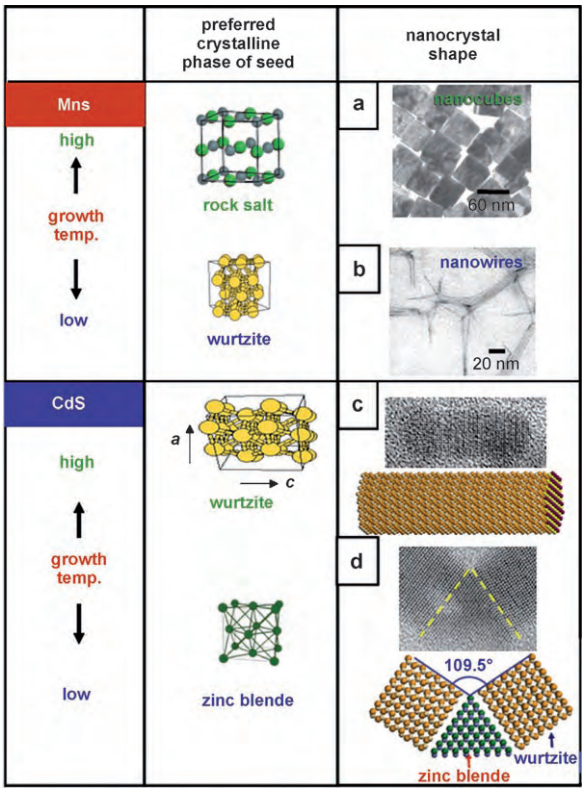

Figure 37. Temperature-mediated crystalline-phase control of a,b) MnS and c,d) CdS nanocrystals. At high temperature the formation of rock salt phase MnS nanocubes is preferred (a), while at low temperature branched MnS nanowires of wurtzite phases are obtained (b).[71] Similarly, at high temperature CdS rods are grown from seeds in the wurtzite phase (c), while at low temperature CdS bipods are grown from zinc blende tetrahedral seeds (d).[66]

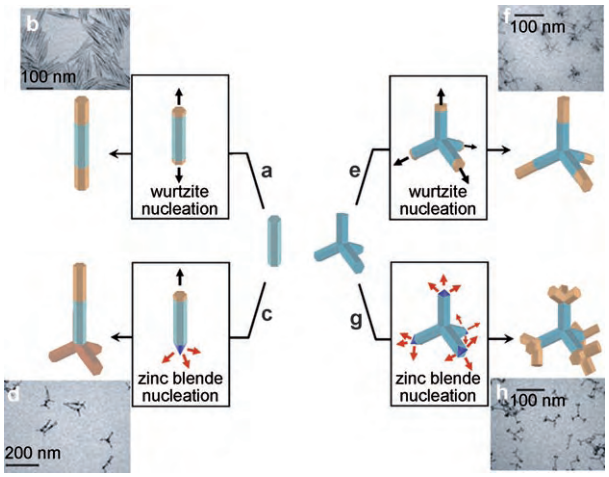

Figure 38. a,b) Heterostructured rods formed by adding CdSe extensions to each end of CdS nanorods. c,d) Branched rods result from the nucleation of zinc blende CdTe on either end of the CdSe nanorods. e,f) Extending each arm of a CdSe tetrapod linearly with wurtzite CdTe yields extended tetrapods. h,g) Branched tetrapods result from the nucleation of zinc blende CdTe branch points on the end of each arm of a CdS tetrapod.[113]

Multiply branched heterostructures can be obtained through a careful control of such crystalline-phase effects. With the addition of TOPE (E = S, Se) to CdE′ nanorods (E′ = Se, Te), heterostructures of CdE-CdE′-CdE are obtained with various morphologies (Figure 38).[113] When wurtzite CdSe is nucleated at the both ends of the rodlike CdS seeds, 1D CdSe growth is favored and therefore extended heterogeneous $rod_{(CdSe)}$–$rod_{(CdS)}$–$rod_{(CdSe)}$ structures are formed (Figure 38a,b). In contrast, when zinc blende CdTe is nucleated on either end of CdSe nanorods, $rod_{(CdTe)}$–$rod_{(CdSe)}$–$tetrapod_{(CdTe)}$ structures result (Figure 38c,d). Similar growth patterns are observed for the growth of secondary materials from core tetrapod seeds, which result in extended tetrapods of $rod_{(CdTe)}$–$tetrapod_{(CdSe)}$–$rod_{(CdTe)}$ (Figure 38e,f) or multiply branched $tetrapod_{(CdTe)}$–$tetrapod_{(CdS)}$–$tetrapod_{(CdTe)}$ heterostructures (Figure 38g,h).

3.3.3. *Control of the Growth Regime*

A balance between the kinetic and the thermodynamic growth regimes strongly governs the final shape of the nanocrystals. Isotropic growth of nanocrystals is preferred under the thermodynamic growth regime that is characterized by a sufficient supply of thermal energy (kT) and a low flux of monomers. In contrast, anisotropic growth along a specific direction is facilitated under a kinetic growth regime that is promoted by a high flux of monomers.

Peng and co-workers proposed a CdSe growth model that is controlled by the diffusion flux of monomers.[61] In their model, the thermal reaction of CdO and alkylphosphonic acids (APAs) generates stable Cd–APA complexes and maintains a high monomer concentration in the diffusion layer of the growing crystallites. CdSe nanocrystals grow through four modes: 1) 1D growth, 2) 3D growth, 3) 1D to 2D ripening, and 4) Ostwald ripening (Figure 39). During a 1D growth stage, a high diffusion flux of monomers into the diffusion layer promotes the preferential 1D growth of monomers on the highest energy (001) surface. As the monomer concentration drops so does the diffusion flux. A relatively low diffusion flux induces an equi-directional growth of the nanocrystals (the 3D growth stage). When the monomer concentration is low, the system reaches equilibrium by dissolution and re-growth of the monomers from the (001)face onto the other faces (the 1D to 2D ripening stage). At very low monomer concentrations, the nanocrystals grow by an interparticular Ostwald ripening process.

Another system suitable for examining such growth-regime effects is the shape evolution of PbS nanocrystals with a symmetric rock salt structure.[115] Rapid injection of a PbS molecular precursor induces the formation of tetrahedral seeds that are terminated by {100} and {111} faces. Subsequent competitive growth between these two different crystalline faces determines the final shape. In the presence of dodecanethiol surfactants, the {100} surface has a higher surface energy than the {111} surface. When excess thermal energy (i.e. high temperature) is supplied, the formation of thermodynamically stable 0D truncated-cube-shaped PbS nanocrystals results (Figure 40a). However, under lower temperature conditions ($\approx$120 °C), the growth process shifts into the

 © 2006 Wiley-VCH Verlag GmbH & Co. KGaA, Weinheim

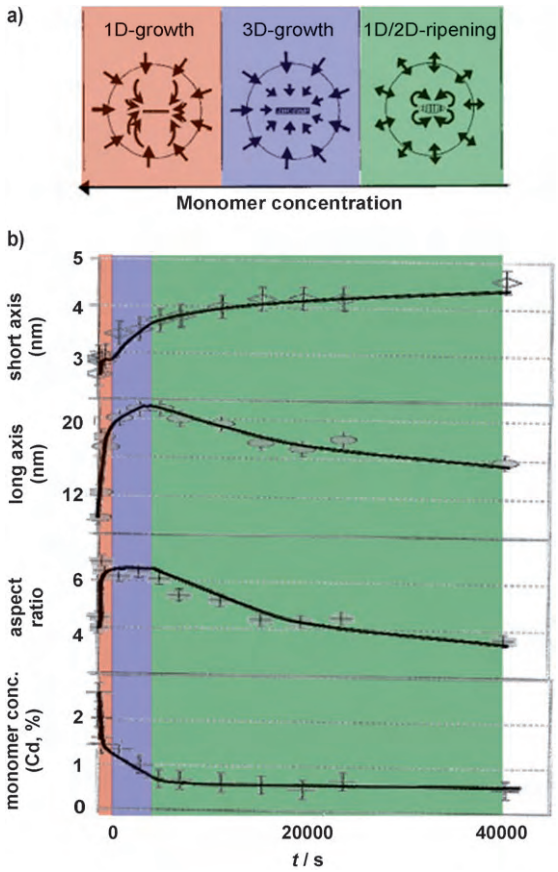

Figure 39. a) Diffusion flux model. Very high monomer concentration results in a high diffusion flux from the surrounding solution to the diffusion layer. The high surface energy of the {001} faces promotes 1D growth. As the monomer concentration decreases so does the diffusion flux, this results in a 3D growth of nanocrystals. During the 1D to 2D ripening stage, dissolution and re-growth of the monomers from the {001} faces with high surface energy onto the other faces occurs. b) Changes in the diameters, lengths, and aspect ratio of CdSe nanorods as a function of growth time.[61]

kinetic regime which results in 1D rods and multipod structures (Figure 40b).

4. Nanocrystal Assemblies and Device Applications

4.1. Superlattices and Assemblies of Inorganic Nanocrystals

The controlled assembly of nanocrystal building blocks is a prerequisite for the generation of nanodevices and nanosystems. In this Section, we will discuss assemblies of anisotropic nanocrystals.

When nanocrystals, coated with long-chain alkane molecules, are formed with highly monodispersed size and shape, slow evaporation of solvent from the nanocrystal solution can lead to highly ordered superlattices of nanocrystals as a result of van der Waals interactions.[159,160] The symmetry of a close-packed array of nanocrystals can be modulated by changing parameters including particle sizes, shape, and interparticle distances. Superlattices of CdSe nanospheres were first

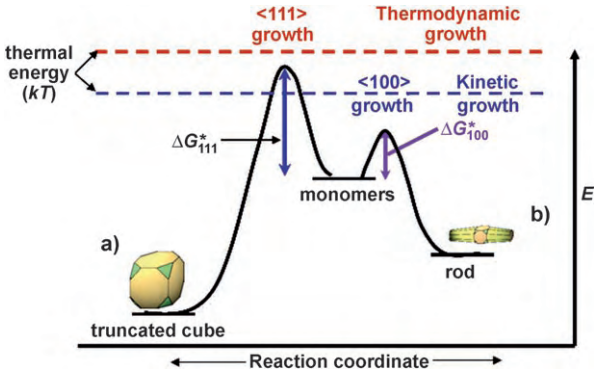

Figure 40. Comparison of a) thermodynamic and b) kinetic growth of PbS nanocrystals. At high temperature, the formation of thermodynamically stable structures (truncated cubes) is preferred. At low temperature, however, a shift of growth regime to the kinetic process results in rod growth.[115]

reported by Bawendi and co-workers who used selective solvent evaporation under reduced pressure of a mixed solution of octane and octanol containing spherical CdSe nanocrystals.[161] Advanced multicomponent superlattices, such as Fe_3O_4/Fe_3Pt,[162] $PbSe/Fe_2O_3$,[163] and PbSe/Pd,[164] have also been fabricated using a similar process.

Interestingly, assemblies of 1D nanostructures can form anisotropic liquid-crystalline phases. Yang and co-workers reported the formation of liquid-crystalline phases of $BaCr_2O_4$ nanorods (Figure 41) through the Langmuir–Blodgett assembly process.[165] By increasing the surface pressure, various liquid-crystalline phases can be obtained ranging from isotropic to 2D nematic, 2D smectic, 3D nematic, and spiral phases. Alivisatos and co-workers demonstrated the liquid-crystalline behavior of CdSe nanorod assemblies through their polarized emission (Figure 42a–c).[166] Slow solvent evaporation from a solution containing CdSe nanocrystals

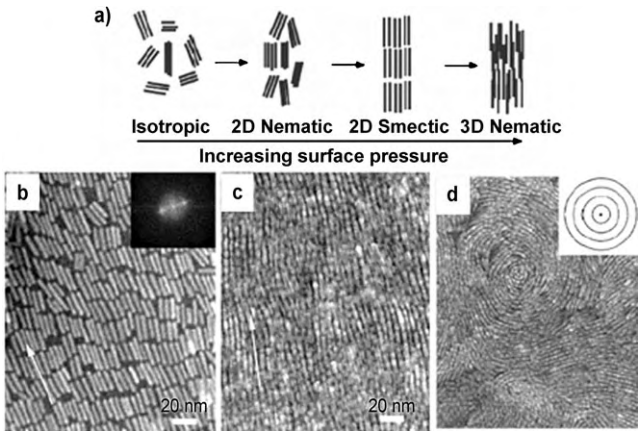

Figure 41. Langmuir–Blodgett assemblies of 1D $BaCr_2O_4$ nanorods. a) Schematic representation of nanorod assembly patterns, b) 2D smectic phase, c) 3D nematic phase, and d) spiral phase. By increasing the surface pressure, the assembly patterns change from isotropic to 2D nematic, 2D smectic, and 3D nematic phases.[165]

 © 2006 Wiley-VCH Verlag GmbH & Co. KGaA, Weinheim

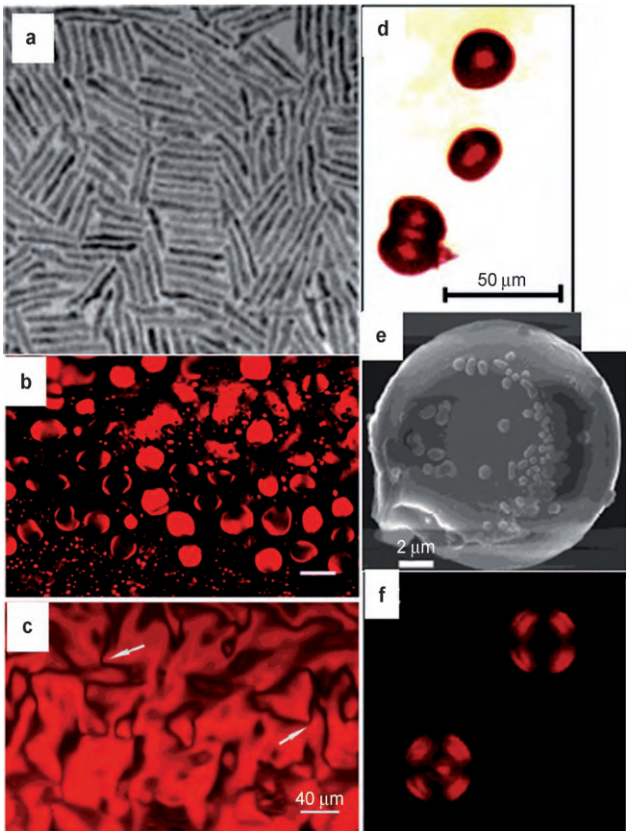

Figure 42. a) TEM image of 1D CdSe nanorods. b,c) Images of the liquid-crystalline phase in a concentrated solution of CdSe nanocrystals under a polarizing optical microscope. The isotropic phase appears black in these images. The red areas in the images correspond to the liquid-crystalline phase, and the dark lines correspond to disclinations (the arrows point to the disclinations),[166] that is, the area where the orientations of the nanorods are parallel to either of the polarizers. Clearly shown are droplets of liquid-crystalline phase mixed with the isotropic phase (b) and Schlieren textures of the liquid-crystalline phase (c). d) Optical microscopic and e) scanning electron microscopic images of the self-assembled platelet-like CdSe nanorod superlattices obtained by a two-phase crystallization method. f) Optical microscopy image of the CdSe nanorod superlattice viewed between crossed polarizers.[166]

forms a variety of liquid-crystalline structures. Droplets (tactoids) are formed from the isotropic phase upon the evaporation of solvent (Figure 42b). Schlieren textures are observed in a later stage (Figure 42c).

Talapin and co-workers utilized another technique that induces the growth of nanorod superlattices by destabilization of a colloidal solution through a two-phase crystallization method.[167] Upon the slow diffusion of. MeOH/*i*PrOH mixture into a toluene dispersion of CdSe nanorods, platelet-like nanorod superlattices nucleate and grow on the surface of ITO-coated glass substrates (Figure 42d,e). These superlattices exhibit a specific birefringence and, under a crossed polarizing light, the superlattices show a Maltese cross with concentric rings (Figure 42f).

The assembly of 2D nanocrystals into superlattices has also been reported. Korgel and co-workers reported superlattices of Cu_2S nanodiscs prepared by the deposition of concentrated dispersion of nanorods onto a substrate.[73] These 2D nanodiscs self-assemble into either 1D chains of stacked discs (Figure 43a) or 3D crystals (Figure 43b). Another example of 2D self-assembly was reported for Gd_2O_3 nanoplates.[108] Superlattices ranging from 1 to 100 μm are generated by slow evaporation of a concentrated dispersion of nanoplates (Figure 43c). Electron-diffraction and X-ray diffraction studies of the superlattices, clearly show the characteristic small-angle diffraction peaks (spots) corresponding to an interparticle distance of 4.2 nm between the nanoplates (Figure 43d,e).

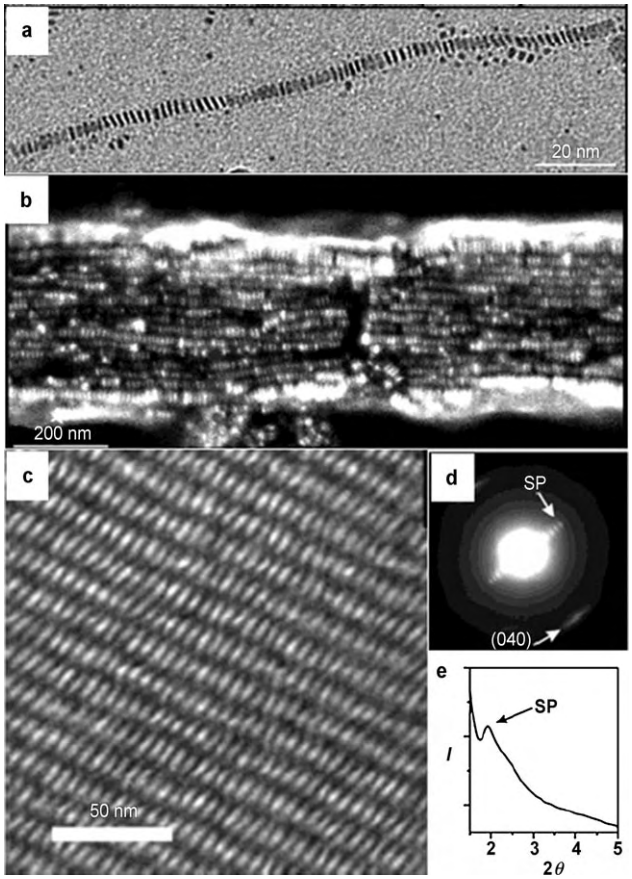

Figure 43. Assemblies of 2D nanodiscs and plates. a) TEM image of a 1D chain structure and b) SEM image of 3D superlattices of Cu_2S nanodiscs.[73] c) TEM image and d) small-angle electron diffraction and e) small-angle X-ray diffraction patterns of superlattices of Gd_2O_3 nanoplates.[108]

Recently, Alivisatos and co-workers reported a new strategy to integrate colloidal nanocrystals into prepatterned templates.[168] They successfully utilized a capillary interaction induced patterning process.[169] When a solution containing colloidal nanocrystals is exposed to a flat substrate that is patterned with trenches and allowed to evaporate, the capillary force directs the nanoparticles into the prepatterned trenches (Figure 44A). Figure 44B and c show scanning electron microscopy (SEM) images of CdTe tetrapods confined in the trenches. Nearly all the tetrapods are well

 © 2006 Wiley-VCH Verlag GmbH & Co. KGaA, Weinheim

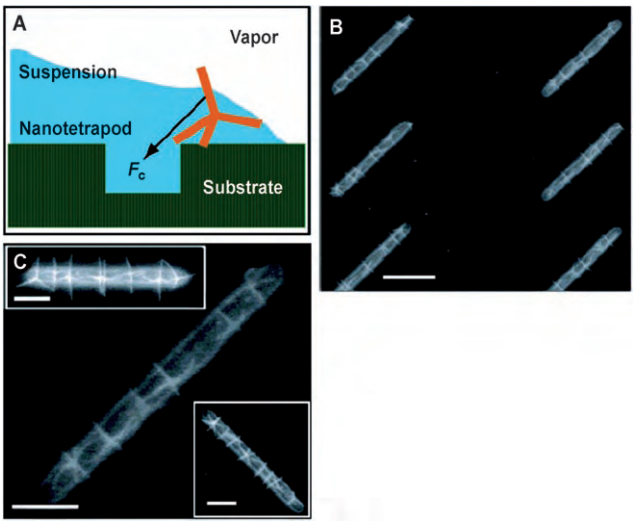

Figure 44. Capillary-force driven positioning of CdTe tetrapods into a lithographically pre-patterned SiO_2 substrate. A) Schematic illustration. B,C) SEM images of CdTe tetrapods confined into trenches. Scale bars: 500 nm (B) and 200 nm (C).[168]

aligned in the trench, with two arms perpendicular to the trench axis and the other two parallel (Figure 44C).

4.2. Nanosystems for Advanced Memory, Optical, and Electronic Devices

It is anticipated that nanocrystals with unique shape-dependent properties will be important for the development new materials for the biomedical and electronic applications. Nanodevices have recently been fabricated by utilizing non-spherical nanocrystals with shape-dependent properties. $BaTiO_3$ nanowires with ferroelectric behavior is one such example.[170] When 1D $BaTiO_3$ nanowires (Figure 45a) are placed on a conductive substrate and an external electric field is applied to the nanowire by the conductive tip of a scanning probe microscope, nonvolatile electric polarization can be induced (Figure 45b). Figure 45c shows electrostatic force microscopic (EFM) images after writing with $V_{tip} = -10$ V and $V_{tip} = +10$ V. Red, white, and blue pixels in the EFM images correspond to resonance frequency shifts of −10, 0, and 10 Hz, respectively, indicating ferroelectric behavior of the $BaTiO_3$ nanowire. In addition, characteristic hysteresis behavior is observed in a plot of voltage versus frequency shift (Figure 45d). Multiple spin polarizations can also be induced in a single nanowire (Figure 45e), which demonstrates the potential use of such materials for ferroelectric memory nanodevices.

1D semiconducting nanorods can be very useful for the fabrication of photovoltaic devices through the combination of CdSe nanorods with P3HT hole transporting polymers (Figure 46).[171] Such a nanorod-based solar-cell device has several advantages over conventional solar cells including efficient charge transfer between high-electron-affinity inorganic semiconductors and relatively low-ionization-potential polymers (Figure 46b). Moreover, they exhibit a higher

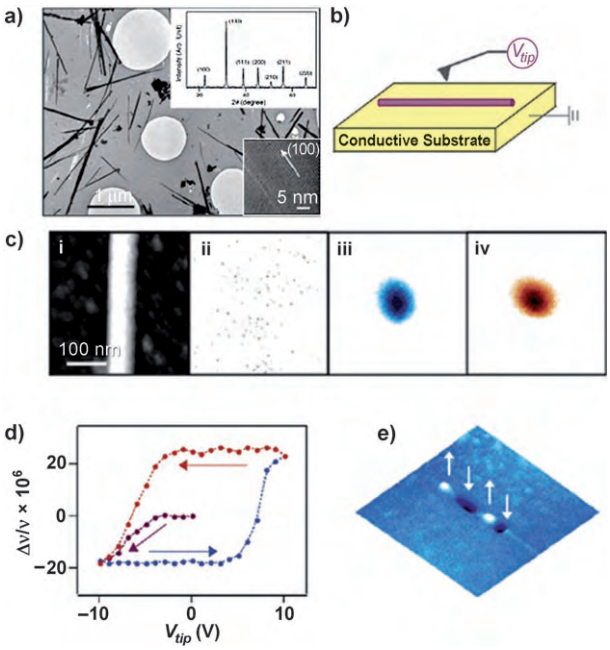

Figure 45. Ferroelectric $BaTiO_3$ nanowire memory. a) TEM image and X-ray diffraction pattern of $BaTiO_3$ nanowires. b) Schematic representation of the device. c) i) Tomographic image of a single nanowire. ii–iv) Electrostatic force microscopic (EFM) images of same nanowire, ii) as deposited, iii) after the writing procedure with $V_{tip} = -10$ V, and iv) with $V_{tip} = +10$ V. d) Ferroelectric hysteresis loop of a single nanowire. e) Three-dimensional EFM image of a single nanowire after the multiple writing procedures (the white arrows indicate the polarization direction).[170]

external quantum efficiency (EQE) of approximately 55% under 0.1 mW cm^{-2} illumination at 485 nm. This high value arises from the efficient charge transport in the conduction band of the hybrid solar cells. For comparison, solar cells based on nanospheres have a EQE of approximately 18% and operate by electron hopping between the particles (Figure 46e). Very recently, another type of solar cell consisting of CdTe and CdSe nanorods was reported.[172]

Multicomponent dumbbell structures of the form $sphere_{(Au)}$–$rod_{(CdSe)}$–$sphere_{(Au)}$ (Figure 47a) have potential for applications in electronic devices.[119] As shown in the conductive atomic force microscopic (C-AFM) image of a single rod (Figure 47b), a small tunneling current is observed to flow through the gold tips of the structure, whereas the central part of the rod, which consists of the semiconductor is nonconductive at a bias of 1.5 to 2.0 V. Since the gold quantum dots can be utilized as contact points while the bridging rods can be a semiconducting island, a single dumbbell shaped nanocrystal can be potentially utilized as a single nanodevice.

The use of tetrapod shaped CdSe nanocrystals enables the development of a new type of single-electron transistor (SET).[173] The CdTe tetrapod nanocrystals are deposited onto an Si_3N_4 surface. Palladium electrodes are then deposited onto the three tetrapod arms in contact with the surface (Figure 48). Carriers can delocalize across the branches or localize and hop between arms depending on their coupling strength to the metallic back-gate. The differential conduc-

 © 2006 Wiley-VCH Verlag GmbH & Co. KGaA, Weinheim

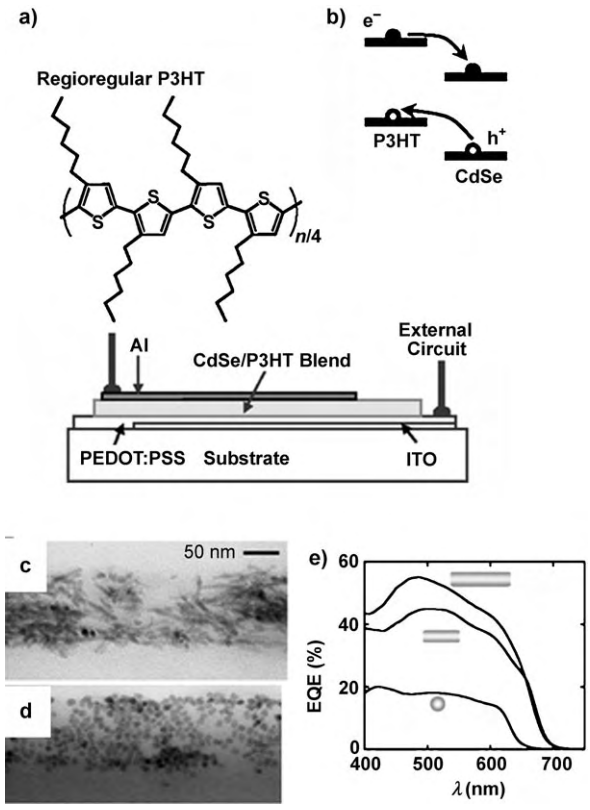

Figure 46. a) Schematic representation of CdSe-nanorod–polymer hybrid solar cells. P3HT polymers are used as the hole-transporting materials and CdSe nanorods are used as photoelectron generating and electron-transporting materials. b) The energy-level diagram for CdSe nanorods and P3HT showing the transfer of electrons to CdSe and holes (h^+) to P3HT. TEM images of c) CdSe nanosphere/P3HT and d) CdSe nanorod/P3HT films. e) External quantum efficiency (EQE) of nanohybrid solar cells depends on the nanocrystal shape (shape shown in gray).[171]

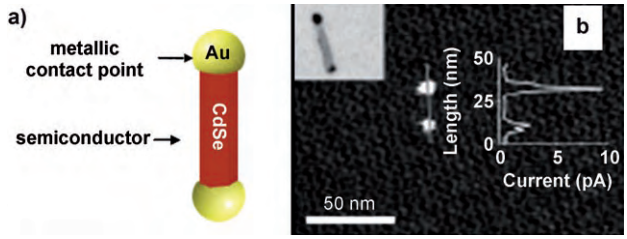

Figure 47. Multicomponent dumbbell shapes of sphere$_{(Au)}$–rod$_{(CdSe)}$–sphere$_{(Au)}$ particles. a) The gold ends can be utilized as metallic contact points and CdSe can be used as semiconductor island. b) Conductivity force microscopic image of a single nanodumbbell. Metallic properties are only observed at the gold ends and the CdSe nanorod is nonconductive.[119]

tance $\partial I/V\partial$ as a function of the source–drain voltage V and the back-gate voltage V_g for these two categories is plotted in Figure 48b. The zero-conductance regions (dark blue) are bound by regions of higher conductance (light blue). The large diamond corresponds to states with a large probability of a charge being localized on the branch point and lower probability of being on the arms while small diamonds

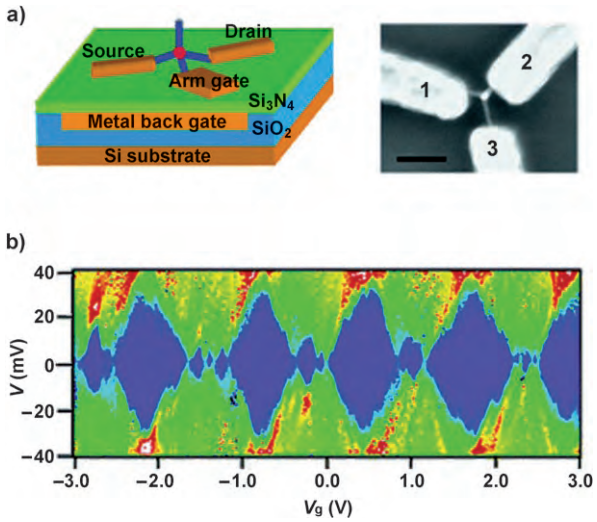

Figure 48. A tetrapod-based single-electron transistor (SET). a) Schematic representation and scanning electron microscopic image of the SET device. b) The differential conductance plot as a function of the source–drain voltage V and the back-gate voltage V_g: zero-conductance regions (blue), higher conductance regions (green).[173] See text for details.

represent states with a large probability of a charge being localized on the arms and low probability of being on the branch.

5. Summary and Outlook

Although there have been many new interesting developments in the shape control of nanocrystals in the past few years, these synthetic methods have mainly focused on 1D nanocrystals and a limited range of materials. Current shape-control strategies depend highly on experimental trial-and-error approaches rather than on a systematic design of synthetic strategies. The next step required for the success of this field is the development of more versatile and reliable but simple synthetic schemes for the tailored architecture of nanocrystals with desired components. Concurrently, a better understanding of the guiding principles of nanocrystal growth should be pursued. This knowledge will enable further fine tuning of the size, shape, and surfaces of nanocrystals.

The ability to assemble novel nanocrystals into nanodevices will be very important to their future applications. For example, to utilize nanocrystals in memory devices and transistors, it is important not only to bring the nanocrystals into the desired position but also to integrate them into a very small substrate structure. Various nanocrystal assembly technologies have been developed, including solvent evaporation,[161–164] organization of nanowire arrays through electric-field induction,[174–176] Langmuir–Blodgett approaches,[165,166,177,178] and the assembly of nanocrystals inside prepatterned organic or inorganic templates.[168,169,179–187] These technologies are still in their infancy but show great potential for applications in integrated nanosystems.

© 2006 Wiley-VCH Verlag GmbH & Co. KGaA, Weinheim

The heterodimers of nanocrystals presented in Section 2.4 are a good example of a prototype multicomponent nanocrystal system. Further extension of such methods for advanced multicomponent nanocrystal systems will provide enhanced multifunctionality and novel phenomena. Furthermore, hybridization of inorganic nanocrystals with other functional materials will extend their utility. Biocompatible 0D quantum dots and magnetic nanocrystals have already shown their potential for biomedical imaging and therapy. The use of anisotropic nanocrystals can then lead to more advanced diagnosis and therapeutic systems.[188–195] For example, 1D quantum rods with linearly polarized emission properties can be used for optical imaging systems.[161]

Inorganic nanocrystals with unique shapes can be used as key components for electronic devices. As presented in Section 4.2, examples are tetrapod-based single-electron transistors[170] and nanowire-based ferroelectric memory elements.[163] Nanocrystal hybrid materials with other inorganic materials or organic polymers will make them potentially useful for energy sources (e.g. fuel cells,[196–198] solar cells,[171,172,199,200] batteries[201,202]) and catalytic systems[203–205] Although current nanocrystal technology and its applications are still in an early stage, many new and as of yet undiscovered nanobuilding blocks will become the key components in nanosystems.

We would like to thank Dr. Y. J. Kim (KBSI) for high voltage TEM (JEM-ARM1300S), H. S. Kwon (KBSI) and J. M. Oh (KBSI-chuncheon) for TEM analysis. This research is supported by the National R&D Project for Nano Science and Technology (M1-0213-12-0001), NCRC (R15-2004-024-02002-0), the National R&D Program for Cancer Control of the Ministry of Health & Welfare (0320250-2), and AOARD (FA520905P0285).

Received: October 28, 2005
Published online: April 27, 2006

[1] C. B. Murray, D. J. Norris, M. G. Bawendi, *J. Am. Chem. Soc.* **1993**, *115*, 8706.
[2] H. Zeng, J. Li, J. P. Liu, Z. L. Wang, S. Sun, *Nature* **2002**, *420*, 395.
[3] A. P. Alivisatos, *Science* **1996**, *271*, 933.
[4] M. A. El-Sayed, *Acc. Chem. Res.* **2004**, *37*, 326.
[5] V. F. Puntes, K. M. Krishnan, A. P. Alivisatos, *Science* **2001**, *291*, 2115.
[6] J.-I. Park, J. Cheon, *J. Am. Chem. Soc.* **2001**, *123*, 5743.
[7] L. E. Brus, *J. Chem. Phys.* **1984**, *80*, 4403.
[8] N. Chestnoy, R. Hull, L. E. Brus, *J. Chem. Phys.* **1986**, *85*, 2237.
[9] M. Steigerwald, L. E. Brus, *Acc. Chem. Res.* **1990**, *23*, 183.
[10] G. Markovich, C. P. Collier, S. E. Henrichs, F. Remacle, R. D. Levine, J. R. Heath, *Acc. Chem. Res.* **1999**, *32*, 415.
[11] C. L. Cleveland, W. D. Luedtke, U. Landman, *Phys. Rev. B* **1999**, *60*, 5065.
[12] Al. L. Efros, A. L. Efros, *Semiconductors* **1982**, *16*, 1209.
[13] D. J. Norris, A. L. Efros, M. Rosen, M. G. Bawendi, *Phys. Rev. B* **1996**, *53*, 16347.
[14] L.-s. Li, J. Hu, W. Yang, A. P. Alivisatos, *Nano Lett.* **2001**, *1*, 349.
[15] J. Hu, L.-s. Li, W. Yang, L. Manna, L.-w. Wang, A. P. Alivisatos, *Science* **2001**, *292*, 2060.
[16] S. V. Gaponenko in *Optical Properties of Semiconductor Nanocrystals*, Cambridge University Press, New York, **1998**, p. 23.
[17] J. Hu, T. W. Odom, C. M. Lieber, *Acc. Chem. Res.* **1999**, *32*, 435.
[18] Y. Xia, P. Yang, Y. Sun, Y. Wu, B. Mayers, B. Gates, Y. Yin, F. Kim, H. Yan, *Adv. Mater.* **2003**, *15*, 353.
[19] E. P. A. M. Bakkers, M. A. Verheijen, *J. Am. Chem. Soc.* **2003**, *125*, 3440.
[20] Z. W. Pan, Z. R. Dai, Z. L. Wang, *Science* **2001**, *291*, 1947.
[21] Y. Saito, T. Matsumoto, *Nature* **1998**, *392*, 237.
[22] P. X. Cao, Z. L. Wang, *J. Phys. Chem. B* **2004**, *108*, 7534.
[23] X. Duan, C. M. Lieber, *Adv. Mater.* **2000**, *12*, 198.
[24] J. Goldberger, R. He, Y. Zhang, S. Lee, H. Yan, H.-J. Choi, P. Yang, *Nature* **2003**, *422*, 599.
[25] W. Y. Kong, Y. Ding, R. S. Yang, Z. L. Wang, *Science* **2004**, *303*, 1348.
[26] Z. W. Pan, Z. R. Dai, L. Xu, S. T. Lee, Z. L. Wang, *J. Phys. Chem. B* **2001**, *105*, 2507.
[27] C. Ma, Y. Ding, D. Moore, X. Wang, Z. L. Wang, *J. Am. Chem. Soc.* **2004**, *126*, 708.
[28] Y. Zhang, L. Wang, X. Liu, Y. Yan, C. Chen, J. Zhu, *J. Phys. Chem. B* **2005**, *109*, 13091.
[29] M. P. Pileni, *Catal. Today* **2000**, *58*, 151.
[30] M. L. Steigerwald, A. P. Alivisatos, J. M. Gibson, T. D. Harris, R. Kortan, A. J. Muller, A. M. Thayer, T. M. Duncan, D. C. Douglass, L. E. Brus, *J. Am. Chem. Soc.* **1988**, *110*, 3046.
[31] B. A. Simmons, S. Li, V. T. John, G. L. McPherson, A. Bose, W. Zhou, J. He, *Nano Lett.* **2002**, *2*, 263.
[32] D. Kim, M. Miyamoto, M. Nakayama, *Phys. Status Solidi* **2003**, *0*, 1233.
[33] B. S. Zou, R. B. Little, J. P. Wang, M. A. El-Sayed, *Int. J. Quantum Chem.* **1999**, *72*, 439.
[34] D.-F. Zhang, L.-D. Sun, J.-L. Yin, C.-H. Yan, *Adv. Mater.* **2003**, *15*, 1022.
[35] C. Liu, B. Zou, A. J. Rondinone, Z. J. Zhang, *J. Phys. Chem. B* **2000**, *104*, 1141.
[36] Y. Lee, J. Lee, C. J. Bae, J.-G. Park, H.-J. Noh, J.-H. Park, T. Hyeon, *Adv. Funct. Mater.* **2005**, *15*, 503.
[37] N. Moumen, P. Bonville, M. P. Pileni, *J. Phys. Chem.* **1996**, *100*, 14410.
[38] C. E. Sjogren, C. Johansson, A. Naevestad, P. C. Sontum, K. Briley-Saebo, A. K. Fahlvik, *Magn. Reson. Imaging* **1997**, *15*, 55.
[39] A. P. Ngo, P. Bonville, M. P. Pileni, *Eur. Phys. J.* **1999**, *9*, 583.
[40] Y. S. Kang, S. Risbud, J. F. Rabolt, P. Stroeve, *Chem. Mater.* **1996**, *8*, 2209.
[41] J. Tang, M. Myers, K. A. Bosnick, L. E. Brus, *J. Phys. Chem. B* **2003**, *107*, 7501.
[42] Z. J. Zhang, Z. L. Wang, B. C. Chakoumakos, J. S. Yin, *J. Am. Chem. Soc.* **1998**, *120*, 1800.
[43] E. Matijevic, *Chem. Mater.* **1993**, *5*, 412.
[44] D. Murphy-Wilhelmy, E. Matijevic, *Colloids Surf.* **1985**, *16*, 1.
[45] T. Ishikawa, E. Matijevic, *Colloid Interface Sci.* **1998**, *123*, 122.
[46] Q. Song, Z. J. Zhang, *J. Am. Chem. Soc.* **2004**, *126*, 6164.
[47] N. R. Jana, Y. Chen, X. Peng, *Chem. Mater.* **2004**, *16*, 3931.
[48] J. Cheon, N.-J. Kang, S.-M. Lee, J.-H. Lee, J.-H. Yoon, S. J. Oh, *J. Am. Chem. Soc.* **2004**, *126*, 1950.
[49] C. B. Murray, S. Sun, W. Gaschler, H. Doyle, T. A. Betley, C. R. Kagan, *IBM J. Res. Dev.* **2001**, *45*, 47.
[50] M. Yin, S. O'Brien, *J. Am. Chem. Soc.* **2003**, *125*, 10180.
[51] E. Kang, J. Park, Y. Hwang, M. Kang, J.-G. Park, T. Hyeon, *J. Phys. Chem. B* **2004**, *108*, 13932.
[52] T. Hyeon, Y. Chung, J. Park, S. S. Lee, Y.-W. Kim, B. H. Park, *J. Phys. Chem. B* **2002**, *106*, 6831.
[53] T. Hyeon, S. S. Lee, J. Park, Y. Chung, H. B. Na, *J. Am. Chem. Soc.* **2001**, *123*, 12798.
[54] K. Woo, J. Hong, S. Choi, H.-W. Lee, J.-P. Ahn, C. S. Kim, S. W. Lee, *Chem. Mater.* **2004**, *16*, 2818.

 © 2006 Wiley-VCH Verlag GmbH & Co. KGaA, Weinheim

[55] T. J. Boyle, S. D. Bunge, T. M. Alam, G. P. Holland, T. J. Headley, G. Avilucea, *Inorg. Chem.* **2005**, *44*, 1309.
[56] X. Peng, L. Manna, W. Yang, J. Wickham, E. Scher, A. Kadavanich, A. P. Alivisatos, *Nature* **2000**, *404*, 59.
[57] Z. A. Peng, X. Peng, *J. Am. Chem. Soc.* **2002**, *124*, 3343.
[58] E. Paperno, I. Sasada, K. Tashiro, *IEEE Trans. Magn.* **2002**, *38*, 3324.
[59] R. S. Turtelli, C. Bormio-Nunes, G. Kumar, R. Grossinger, J. Eckert, L. Schultz, *J. Magn. Magn. Mater.* **2005**, *285*, 395.
[60] Z. A. Peng, X. Peng, *J. Am. Chem. Soc.* **2001**, *123*, 183.
[61] Z. A. Peng, X. Peng, *J. Am. Chem. Soc.* **2001**, *123*, 1389.
[62] M. Yin, Y. Gu, I. L. Kuskovsky, T. Andelman, Y. Zhu, G. F. Neumark, S. O'Brien, *J. Am. Chem. Soc.* **2004**, *126*, 6206.
[63] L. S. Li, N. Pradhan, Y. Wang, X. Peng, *Nano Lett.* **2004**, *4*, 2261.
[64] P. D. Cozzoli, L. Manna, M. L. Curri, S. Kudera, C. Giannini, M. Striccoli, A. Agostiano, *Chem. Mater.* **2005**, *17*, 1296.
[65] L. Qu, Z. A. Peng, X. Peng, *Nano Lett.* **2001**, *1*, 333.
[66] Y. Jun, S.-M. Lee, N.-J. Kang, J. Cheon, *J. Am. Chem. Soc.* **2001**, *123*, 5150.
[67] J. Joo, H. B. Na, T. Yu, J. H. Yu, Y. W. Kim, F. Wu, J. Z. Zhang, T. Hyeon, *J. Am. Chem. Soc.* **2003**, *125*, 11100.
[68] L. Manna, E. C. Scher, A. P. Alivisatos, *J. Am. Chem. Soc.* **2000**, *122*, 12700.
[69] X. Zhong, Y. Feng, W. Knoll, M. Han, *J. Am. Chem. Soc.* **2003**, *125*, 13559.
[70] E. Lifshitz, M. Bashouti, V. Kloper, A. Kigel, M. S. Eisen, S. Berger, *Nano Lett.* **2003**, *3*, 857.
[71] Y. Jun, Y. Jung, J. Cheon, *J. Am. Chem. Soc.* **2002**, *124*, 615.
[72] A. Ghezelbash, B. A. Korgel, *Langmuir* **2005**, *21*, 9451.
[73] M. B. Sigman, Jr., A. Ghezelbash, T. Hanrath, A. E. Sauders, F. Lee, B. A. Korgel, *J. Am. Chem. Soc.* **2003**, *125*, 16050.
[74] A. Ghezelbash, M. B. Sigman, Jr., B. A. Korgel, *Nano Lett.* **2004**, *4*, 537.
[75] C. Pacholski, A. Kornowski, H. Weller, *Angew. Chem.* **2002**, *114*, 1234; *Angew. Chem. Int. Ed.* **2002**, *41*, 1188.
[76] J. Yu, J. Joo, H. M. Park, S.-I. Baik, Y. W. Kim, S. C. Kim, T. Hyeon, *J. Am. Chem. Soc.* **2005**, *127*, 5662.
[77] K.-S. Cho, D. V. Talapin, W. Gaschler, C. B. Murray, *J. Am. Chem. Soc.* **2005**, *127*, 7140.
[78] Y.-H. Kim, Y. Jun, B.-H. Jun, S.-M. Lee, J. Cheon, *J. Am. Chem. Soc.* **2002**, *124*, 12656.
[79] D. Gerion, N. Zaitseva, C. Saw, M. F. Casula, S. Fakra, T. van Buuren, G. Galli, *Nano Lett.* **2004**, *4*, 597.
[80] T. J. Trentler, K. M. Hickman, S. C. Goel, A. M. Viano, P. C. Gibbons, W. E. Buhro, *Science* **1995**, *270*, 1791.
[81] S. D. Dingman, N. P. Rath, P. D. Markowitz, P. C. Gibbons, W. E. Buhro, *Angew. Chem.* **2000**, *112*, 1530; *Angew. Chem. Int. Ed.* **2000**, *39*, 1470.
[82] T. J. Trentler, S. C. Goel, K. M. Hickman, A. M. Viano, M. Y. Chiang, A. M. Geatty, P. C. Gibbons, W. E. Buhro, *J. Am. Chem. Soc.* **1997**, *119*, 2172.
[83] H. Yu, W. E. Buhro, *Adv. Mater.* **2003**, *15*, 416.
[84] S. P. Ahrenkiel, O. I. Micic, A. Miedaner, C. J. Curtis, J. M. Nedeljkovic, A. J. Nozik, *Nano Lett.* **2003**, *3*, 833.
[85] J. D. Holmes, K. P. Johnston, R. C. Doty, B. A. Korgel, *Science* **2000**, *287*, 1471.
[86] F. M. Davidson III, R. J. Wiacek, B. A. Korgel, *Chem. Mater.* **2005**, *17*, 230.
[87] T. Hanrath, B. A. Korgel, *Adv. Mater.* **2003**, *15*, 437.
[88] F. M. Davidson III, A. D. Schricker, R. J. Wiacek, B. A. Korgel, *Adv. Mater.* **2004**, *16*, 646.
[89] T. Hanrath, B. A. Korgel, *J. Am. Chem. Soc.* **2002**, *124*, 1424.
[90] X. Lu, T. Hanrath, K. P. Johnston, B. A. Korgel, *Nano Lett.* **2003**, *3*, 93.
[91] H.-Y. Tuan, D. C. Lee, T. Hanrath, B. A. Korgel, *Nano Lett.* **2005**, *5*, 681.
[92] S. Kan, T. Mokari, E. Rothernberg, U. Banin, *Nat. Mater.* **2003**, *2*, 155.
[93] T. J. Trentler, T. E. Denler, J. F. Bertone, A. Agrawal, V. L. Colvin, *J. Am. Chem. Soc.* **1999**, *121*, 1613.
[94] Y. Jun, M. F. Casula, J.-H. Sim, S. Y. Kim, J. Cheon, A. P. Alivisatos, *J. Am. Chem. Soc.* **2003**, *125*, 15981.
[95] P. D. Cozzoli, A. Kornowski, H. Weller, *J. Am. Chem. Soc.* **2003**, *125*, 14539.
[96] Z. Zhang, X. Zhong, S. Liu, D. Li, M. Han, *Angew. Chem.* **2005**, *117*, 3532; *Angew. Chem. Int. Ed.* **2005**, *44*, 3466.
[97] J. Joo, S. G. Kwon, T. Yu, M. Cho, J. Lee, J. Yoon, T. Hyeon, *J. Phys. Chem. B* **2005**, *109*, 15297.
[98] J. Park, E. Kang, C. J. Bae, J.-G. Park, H.-J. Noh, J.-Y. Kim, J.-H. Park, H. M. Park, T. Hyeon, *J. Phys. Chem. B* **2004**, *108*, 13594.
[99] K. Lee, W. S. Seo, J. T. Park, *J. Am. Chem. Soc.* **2003**, *125*, 3408.
[100] J. Park, K. An, Y. Hwang, E. J.-G. Park, H.-J. Noh, Kang, J.-Y. Kim, J.-H. Park, N.-M. Hwang, T. Hyeon, *Nat. Mater.* **2004**, *3*, 891.
[101] J. Seo, Y. Jun, S. J. Ko, J. Cheon, *J. Phys. Chem. B* **2005**, *109*, 5389.
[102] J. J. Urban, W. S. Yun, Q. Gu, H. Park, *J. Am. Chem. Soc.* **2002**, *124*, 1186.
[103] S. L. Brock, S. C. Perera, K. L. Stamm, *Chem. Eur. J.* **2004**, *10*, 3364.
[104] C. Qian, F. Kim, L. Ma, F. Tsui, P. Yang, J. Liu, *J. Am. Chem. Soc.* **2004**, *126*, 1195.
[105] J. Park, B. Koo, K. Y. Yoon, Y. Hwang, M. Kang, J.-G. Park, T. Hyeon, *J. Am. Chem. Soc.* **2005**, *127*, 8433.
[106] Y. Li, M. A. Malik, P. O'Brien, *J. Am. Chem. Soc.* **2005**, *127*, 16020.
[107] V. F. Puntes, D. Zanchet, C. K. Erdonmez, A. P. Alivisatos, *J. Am. Chem. Soc.* **2002**, *124*, 12874.
[108] Y. C. Cao, *J. Am. Chem. Soc.* **2004**, *126*, 7456.
[109] R. Si, Y.-W. Zhang, L.-P. You, C.-H. Yan, *Angew. Chem.* **2005**, *117*, 3320; *Angew. Chem. Int. Ed.* **2005**, *44*, 3256.
[110] L. Manna, D. J. Milliron, A. Meisel, E. C. Scher, A. P. Alivisatos, *Nat. Mater.* **2003**, *2*, 382.
[111] J. W. Grebinski, K. L. Hull, J. Zhang, T. H. Kosel, M. Kuno, *Chem. Mater.* **2004**, *16*, 5260.
[112] K. L. Hull, J. W. Grebinski, T. H. Kosel, M. Kuno, *Chem. Mater.* **2005**, *17*, 4416.
[113] D. J. Milliron, S. M. Hughes, Y. Cui, L. Manna, J. Li, L.-W. Wang, A. P. Alivisatos, *Nature* **2004**, *430*, 190.
[114] A. G. Kanaras, C. Sonnichsen, H. Liu, A. P. Alivisatos, *Nano Lett.* **2005**, *5*, 2164.
[115] S.-M. Lee, Y.-w. Jun, S.-N. Cho, J. Cheon, *J. Am. Chem. Soc.* **2002**, *124*, 11244.
[116] D. Zitoun, N. Pinna, N. Frolet, C. Belin, *J. Am. Chem. Soc.* **2005**, *127*, 15034.
[117] H. Gu, R. Zheng, X. Zhang, B. Xu, *J. Am. Chem. Soc.* **2004**, *126*, 5664.
[118] H. Yu, M. Chen, P. M. Rice, S. X. Wang, R. L. White, S. Sun, *Nano Lett.* **2005**, *5*, 379.
[119] T. Mokari, E. Tothenberg, I. Popov, R. Costi, U. Banin, *Science* **2004**, *304*, 1787.
[120] T. Mokari, C. G. Sztrum, A. Salant, E. Rabani, U. Banin, *Nat. Mater.* **2005**, *4*, 855.
[121] S. Kudera, L. Carbone, M. F. Casula, R. Cingolani, A. Falqui, E. Snoeck, W. J. Parak, L. Manna, *Nano Lett.* **2005**, *5*, 445.
[122] A. P. Alivisatos, *Nat. Biotechnol.* **2004**, *22*, 47.
[123] R. Elghanian, J. J. Storhoff, R. C. Mucic, R. L. Letsinger, C. A. Mirkin, *Science* **1997**, *277*, 1078.
[124] S.-W. Chung, D. S. Ginger, M. W. Morales, Z. Zhang, V. Chandrasekhar, M. A. Ratner, C. A. Mirkin, *Small* **2005**, *1*, 64.
[125] G. Schmid, Y. P. Liu, *Nano Lett.* **2001**, *1*, 405.
[126] U. Simon, *Adv. Mater.* **1998**, *10*, 1487.

 © 2006 Wiley-VCH Verlag GmbH & Co. KGaA, Weinheim

[127] T. Sato, H. Ahmed, D Brown, B. F. G. Johnson, *J. Appl. Phys.* **1997**, *82*, 696.
[128] W. Lu, Z. Q. Ji, L. Pfeiffer, K. W. West, A. J. Rimberg, *Nature* **2003**, *423*, 422.
[129] O. Millo, D. Katz, Y. W. Cao, U. Banin, *Phys. Rev. B* **2000**, *61*, 16773.
[130] A. Benzyadin, C. Dekker, G. Schmid, *Appl. Phys. Lett.* **1997**, *71*, 1273.
[131] C. T. Black, C. B. Murray, R. L. Sandstrom, S. Sun, *Science* **2000**, *290*, 1131.
[132] S. Sun, C. B. Murray, D. Weller, L. Folks, A. Moser, *Science* **2000**, *287*, 1989.
[133] D. Weller, A. Moser, *IEEE Trans. Magn.* **1999**, *35*, 4423.
[134] C.-Y. Yeh, Z. W. Lu, S. Froyen, A. Zunger, *Phys. Rev. B* **1992**, *46*, 1186.
[135] O. I. Micic, J. R. Sprague, C. J. Curtis, K. M. Jones, J. L Machol, A. J. Nozik, H. Giessen, B. Fluegel, G. Mohs, N. Peyghambarian, *J. Phys. Chem.* **1995**, *99*, 7754.
[136] H. Kominami, S.-y. Murakami, J.-i. Kato, Y. Kera, B. Ohtani, *J. Phys. Chem. B* **2002**, *106*, 10501.
[137] B. O'Regan, M. Grätzel, *Nature* **1991**, *353*, 737.
[138] J. Karch, R. Birringer, H. Gleiter, *Nature* **1987**, *330*, 556.
[139] Y. Zhu, J. Shi, Z. Zhang, C. Zhang, X. Zhang, *Anal. Chem.* **2002**, *74*, 120.
[140] B. L. Bischoff, M. A. Anderson, *Chem. Mater.* **1995**, *7*, 1772.
[141] T. Boyd, *J. Polym. Sci.* **1951**, *7*, 591.
[142] E. A. Barringer, H. K. Bowen, *Langmuir* **1985**, *1*, 414.
[143] R. C. Paul, M. S. Makhni, *Indian J. Chem.* **1971**, *9*, 247.
[144] B. Arinsson, T. Landstrom, S. Rounquist, *Borides, Silicide and Phosphides*, Wiley, New York, **1965**.
[145] N. N. Greenwood, A. Earnshaw, *Chemistry of the Elements*, Pergamon, New York, **1994**.
[146] C. Stinner, R. Prins, T. Wever, *J. Catal.* **2001**, *202*, 187.
[147] S. T. Oyama, *J. Catal.* **2003**, *216*, 343.
[148] E. L. Muetterties, J. C. Sauer, *J. Am. Chem. Soc.* **1974**, *96*, 3410.
[149] C. M. Lukehart, S. B. Milne, S. R. Stock, *Chem. Mater.* **1998**, *10*, 903.
[150] R. S. Ganeshram, T. F. Pedersen, S. Calvert, R. François, *Nature* **2002**, *415*, 156.
[151] H. Zhang, F. Huang, B. Gilbert, J. F. Banfield, *J. Phys. Chem. B* **2003**, *107*, 13051.
[152] R. L. Penn, J. F. Banfield, *Geochim. Cosmochim. Acta* **1999**, *63*, 1549.
[153] J. D. Donnay, D. Harker, *Am. Mineral.* **1937**, *22*, 446.
[154] Z. Tang, N. A. Kotov, M. Giersig, *Science* **2002**, *297*, 237.
[155] R. E. Tanner, Y. Liang, E. I. Altman, *Surf. Sci.* **2002**, *506*, 251.
[156] *Dictionary of Inorganic Compounds*, 1st ed. (Hrsg.: J. E. Macintyre), Chapman & Hall, London, **1992**.
[157] J. Lu, P. Qi, Y. Peng, Z. Yang, W. Yu, Y. Qian, *Chem. Mater.* **2001**, *13*, 2169.
[158] O. Zwlaya-Angel, J. J. Alvaradi-Gel, R. Loxada-Morales, H. Vargas, A. R. Silva, *Phys. Lett.* **1994**, *64*, 291.
[159] R. L. Whetten, M. N. Shafigullin, J. T. Khoury, T. G. Schaaff, I. Vezmar, M. M. Alvarez, A. Wilkinson, *Acc. Chem. Res.* **1999**, *32*, 397.
[160] C. B. Murray, C. R. Kagan, M. G. Bawendi, *Annu. Rev. Mater. Sci.* **2000**, *30*, 545.
[161] C. B. Murray, C. R. Kagan, M. G. Bawendi, *Science* **1995**, *270*, 1335.
[162] H. Zeng, J. Li, J. P. Liu, Z. L. Wang, S. Sun, *Nature* **2002**, *420*, 395.
[163] F. X. Redl, K.-S. Cho, C. B. Murray, S. O'Brien, *Nature* **2003**, *423*, 968.
[164] E. V. Shevchenko, D. V. Talapin, S. O'Brien, C. B. Murray, *J. Am. Chem. Soc.* **2005**, *127*, 8741.
[165] F. Kim, S. Kwan, J. Akana, P. Yang, *J. Am. Chem. Soc.* **2001**, *123*, 4360.
[166] L.-s. Li, J. Walda, L. Manna, P. A. Alivisatos, *Nano Lett.* **2002**, *2*, 557.
[167] D. V. Talapin, E. V. Shevchenko, C. B. Murray, A. Kornowski, S. Forster, H. Weller, *J. Am. Chem. Soc.* **2004**, *126*, 12984.
[168] Y. Cui, M. T. Bjork, J. A. Liddle, C. Sonnichsen, B. Boussert, A. P. Alivisatos, *Nano Lett.* **2004**, *4*, 1093.
[169] Y. Yin, Y. Lu, B. Gates, Y. Xia, *J. Am. Chem. Soc.* **2001**, *123*, 8718.
[170] W. S. Yun, J. J. Urban, Q. Gu, H. Park, *Nano Lett.* **2002**, *2*, 447.
[171] W. U. Huynh, J. J. Dittmer, A. P. Alivisatos, *Science* **2002**, *295*, 2435.
[172] I. Gur, N. A. Fromer, M. L. Geier, A. P. Alivisatos, *Science* **2005**, *310*, 462.
[173] Y. Cui, U. Banin, M. T. Bjork, A. P. Alivisatos, *Nano Lett.* **2005**, *5*, 1519.
[174] Z. Zhong, D. Wang, Y. Cui, M. W. Bockrath, C. M. Lieber, *Science* **2003**, *302*, 1377.
[175] Y. Cui, C. M. Lieber, *Science* **2001**, *291*, 851.
[176] Y. Cui, Q. Wei, H. Park, C. M. Lieber, *Science* **2001**, *293*, 1289.
[177] S. Jin, D. Whang, M. C. McAlpine, R. S. Friedman, Y. Wu, C. M. Lieber, *Nano Lett.* **2004**, *4*, 915.
[178] D. Whang, S. Jin, Y. Wu, C. M. Lieber, *Nano Lett.* **2003**, *3*, 1255.
[179] A. N. Shipway, E. Katz, I. Willner, *ChemPhysChem* **2000**, *1*, 18.
[180] R. E. Schaak, R. E. Cable, B. M. Leonard, B. C. Norris, *Langmuir* **2004**, *20*, 7293.
[181] S. A. Davis, M. Breulmann, K. H. Rhodes, B. Zhang, S. Mann, *Chem. Mater.* **2001**, *13*, 3218.
[182] Q. Y. Lu, F. Gao, D. Y. Zhao, *Nanotechnology* **2002**, *13*, 741.
[183] Y. Cui, M. T. Bjork, J. A. Liddle, C. Sonnichsen, B. Boussert, A. P. Alivisatos, *Nano Lett.* **2004**, *4*, 1093.
[184] M. Bruchez, Jr., M. Moronne, P. Gin, S. Weiss, A. P. Alivisatos, *Science* **1998**, *281*, 2013.
[185] W. C. W. Chan, S. Nie, *Science* **1998**, *281*, 2016.
[186] X. Wu, H. Liu, J. Liu, K. N. Haley, J. A. Treadway, J. P. Larson, N. Ge, F. Peale, M. P. Bruchez, *Nat. Biotechnol.* **2003**, *21*, 41.
[187] B. Dubertret, P. Skourides, D. J. Norris, V. Noireaux, A. H. Brivanlou, A. Libchaber, *Science* **2002**, *298*, 1759.
[188] D. S. Lidke, P. Nagy, R. Heintzmann, D. J. Arndt-Jovin, J. N. Post, H. E. Grecco, E. A. Jares-Erijman, T. M. Jovin, *Nat. Biotechnol.* **2004**, *22*, 198.
[189] S. Kim, Y. T. Lim, E. G. Soltesz, A. M. De Grand, J. Lee, A. Nakayama, J. A. Parker, T. Mihaljevic, R. G. Laurence, D. M. Dor, L. H. Cohn, M. G. Bawendi, J. V. Frangioni, *Nat. Biotechnol.* **2004**, *22*, 93.
[190] L. Josephson, C.-H. Tung, A. Moore, R. Weissleder, *Bioconjugate Chem.* **1999**, *10*, 186.
[191] H.-T. Song, J.-s. Choi, Y.-M. Huh, S. Kim, Y.-w. Jun, J.-S. Suh, J. Cheon, *J. Am. Chem. Soc.* **2005**, *127*, 9992.
[192] Y.-M. Huh, Y.-w. Jun, H.-T. Song, S. Kim, J.-s. Choi, J.-H. Lee, S. Yoon, K.-S. Kim, J.-S. Shin, J.-S. Suh, J. Cheon, *J. Am. Chem. Soc.* **2005**, *127*, 12387.
[193] L. R. Hirsch, R. L. Stafford, J. A. Bankson, S. R. Sershen, B. Rivera, R. E. Price, J. D. Hazle, N. J. Halas, J. L. West, *Proc. Natl. Acad. Sci. USA* **2003**, *100*, 13549.
[194] M. Johannsen, A. Jordan, R. Scholz, M. Koch, M. Lein, S. Deger, J. Roigas, L. Jung, S. Loening, *J. Endourol.* **2004**, *18*, 495.
[195] A. Ito, Y. Kuga, H. Honda, H. Kikkawa, A. Horiuchi, Y. Watanabe, T. Kobayashi, *Cancer Lett.* **1994**, *21*, 167.
[196] K. W. Park, J. H. Choi, B. K. Kwon, S. A. Lee, Y. E. Sung, H. Y. Ha, S. A. Hong, H. Kim, A. Wieckowski, *J. Phys. Chem. B* **2002**, *106*, 1869.
[197] H. Bönnemann, R. M. Richards, *Eur. J. Inorg. Chem.* **2001**, 2455.
[198] A. Crown, H. Kim, G. Q. Lu, I. R. de Moraes, C. Rice, A. Wieckowski, *J. New Mater. Electrochem. Syst.* **2000**, *3*, 275.

 © 2006 Wiley-VCH Verlag GmbH & Co. KGaA, Weinheim

[199] S. Nakade, M. Matsuda, S. Kambe, Y. Saito, T. Kitamura, T. Sakata, Y. Wada, H. Mori, S. Yanagida, *J. Phys. Chem. B* **2002**, *106*, 10004.
[200] Y. X. Weng, L. Li, Y. Liu, L. Wang, G. Z. Yang, *J. Phys. Chem. B* **2003**, *107*, 4356.
[201] D. L. Schulz, C. J. Curtis, R. A. Flitton, H. Wiesner, J. Keane, R. J. Matson, K. M. Jones, P. A. Parilla, R. Noufi, D. S. Ginley, *J. Electron. Mater.* **1998**, *27*, 433.
[202] J. Chen, Z.-L. Tao, S.-L. Li, *Angew. Chem.* **2003**, *115*, 2197; *Angew. Chem. Int. Ed.* **2003**, *42*, 2147.
[203] C. Kim, M. Noh, M. Choi, J. Cho, B. Park, *Chem. Mater.* **2005**, *17*, 3297.
[204] L. N. Lewis, *Chem. Rev.* **1993**, *93*, 2693.
[205] J. A. Widegren, R. G. Finke, *J. Mol. Catal. A* **2003**, *191*, 187.

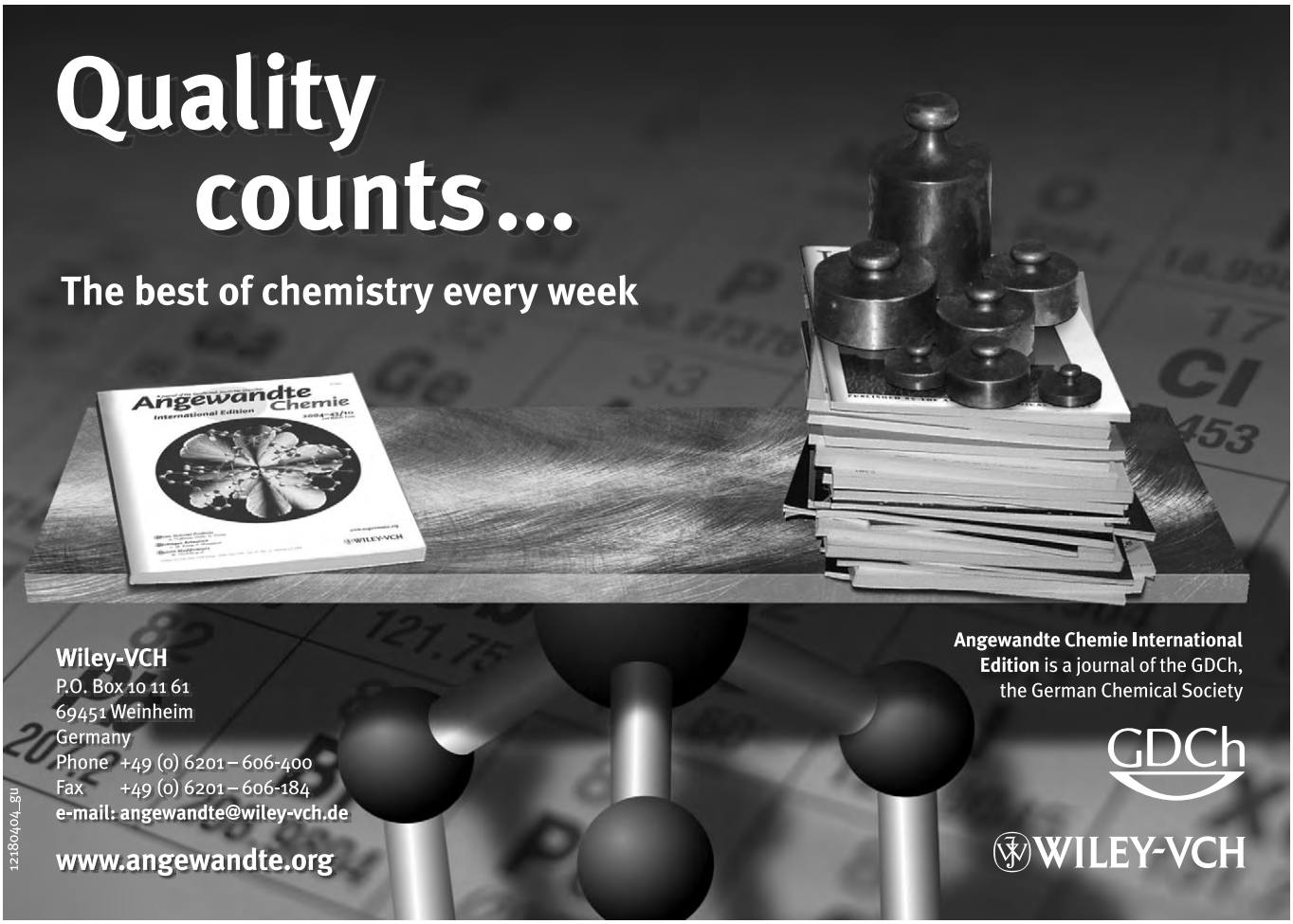

© 2006 Wiley-VCH Verlag GmbH & Co. KGaA, Weinheim

Communications

DOI: 10.1002/anie.200600380

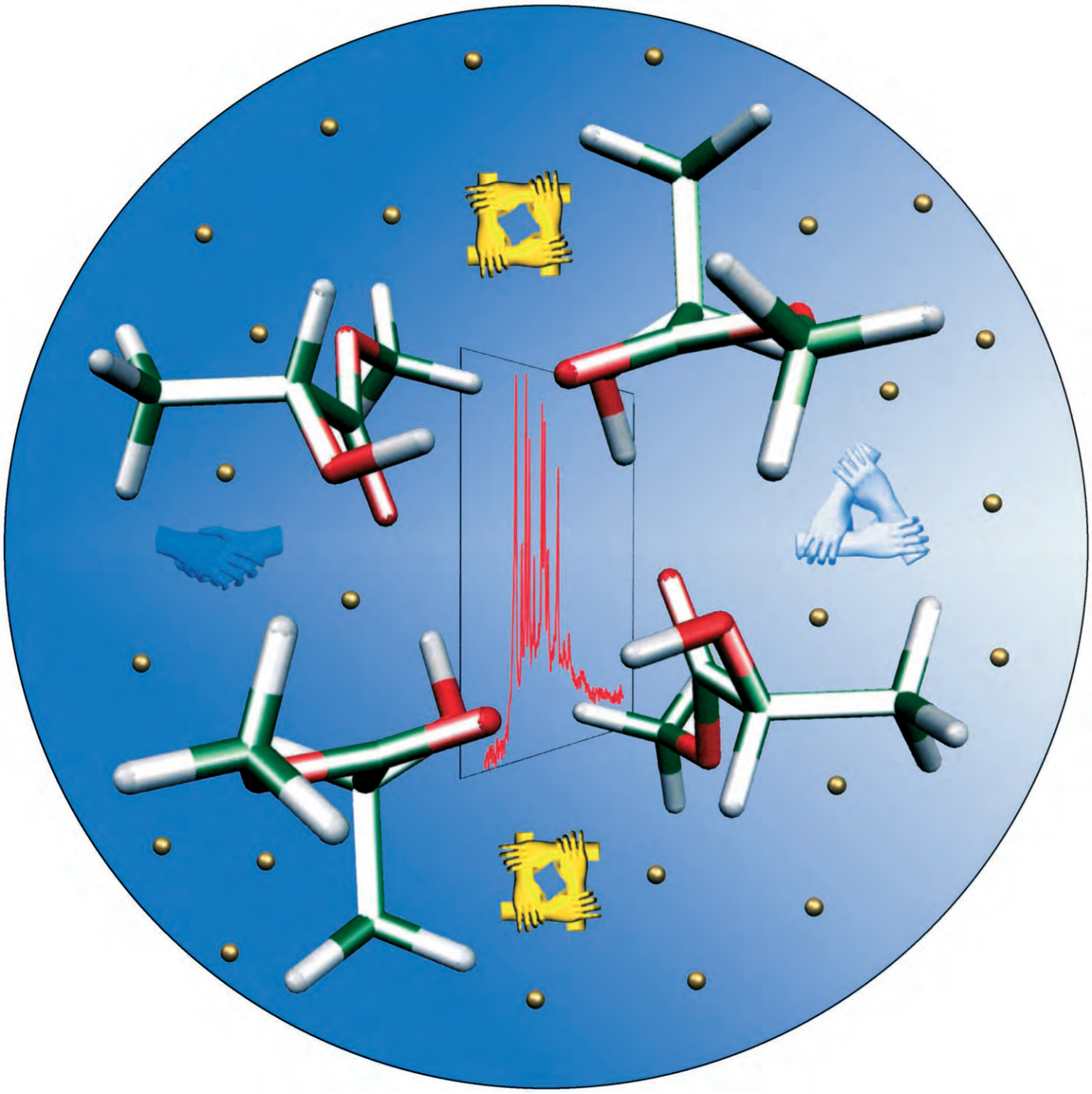

Supersonic-jet FTIR spectra and ab initio calculations show that four methyl lactate molecules with alternating chirality cluster together to form a hydrogen-bond topology that is not favored for homoconfigurational tetramers. For more details, see the Communication by Suhm and co-workers on the following pages.

WILEY InterScience DISCOVER SOMETHING GREAT
© 2006 Wiley-VCH Verlag GmbH & Co. KGaA, Weinheim

Chiral Recognition

DOI: 10.1002/anie.200600380

Chirality-Induced Switch in Hydrogen-Bond Topology: Tetrameric Methyl Lactate Clusters in the Gas Phase**

*Thomas B. Adler, Nicole Borho, Markus Reiher, and Martin A. Suhm**

In memory of Marco Häser

The self-assembly of 20-nanometer-sized virus capsids from a large number of chiral protein building blocks is a complex phenomenon in the solution phase and a considerable challenge for molecular-modeling approaches. We are searching for three-dimensional self-assembly phenomena in vacuo on the 1-nm scale that are amenable to accurate quantum-chemical treatment. These phenomena promise to provide quantitative insights into aspects of intermolecular interactions which are not yet captured adequately in simplified molecular-mechanics approaches. Such model systems may teach us about appropriate quantum-chemical approximations and about how to refine simplified force-field approaches even in solution.

The protonated serine octamer is among the best-studied examples for specific gas-phase self-assembly,[1,2] although it has been postulated that the phenomenon may be more general.[3] It features a strong homoconfigurational (or homochiral, see however reference [4]) preference, as revealed by mass-spectrometric experiments. The presence of an excess charge facilitates its study, while the number of charges correlates with the chiral preference and structure in serine clusters.[3]

Chiral recognition in neutral dimers has also been studied for many years[5–11] and can even lead to chirality-dependent switches in the hydrogen-bond pattern.[10] Our recent spectroscopic observations of neutral methyl lactate clusters and related aggregates beyond dimers[12–16] confirm that a net charge is not necessary for specific and spontaneous self-assembly in the gas phase beyond dimerization. In supersonic jets of methyl lactate, the spectral signatures of a unique homoconfigurational trimer and—even more surprisingly—that of a unique heteroconfigurational tetramer were found.[12] Extensive studies of homologous compounds,[12] achiral variants,[13,15] argon-coated clusters,[12,13] and the stagnation pressure dependence,[12,16] as well as size-selective scattering experiments[16] unambiguously confirmed the phenomenon, but the underlying hydrogen-bond topology has remained elusive. This is due to the complexity of the intermolecular potential-energy (hyper)surface with competing hydrogen-bond patterns, conformational flexibility, and subtle secondary interactions beyond the classical hydrogen-bond contacts.[12]

Whereas lactate dimers are easily characterized in terms of doubly hydrogen-bonded 5- and 8-membered ring structures,[12,17] trimers and tetramers offer a variety of topologies. Herein, we summarize key results of a comprehensive search for homoconfigurational and heteroconfigurational methyl lactate tetramer structures obtained for the RI-BP86 density functional, supplemented by RI-MP2 optimizations and energy calculations. For the first time, a consistent and detailed structural picture of this unusual aggregation phenomenon is found. It explains a wealth of experimental details that have been accumulated in recent years in our group.[12,13]

Supersonic-jet expansions of racemic methyl lactate exhibit a prominent OH-stretching infrared absorption at 3401 cm^{-1} (Qb[18]) that is not present in the enantiopure compound.[12] Figure 1 shows a series of spectra as a function of enantiomeric purity. The spectra were obtained in our filet-jet cluster spectrometer,[19] which features a slit (600 mm × 0.2 mm) pulsed jet expansion into a vacuum chamber (volume 23 m^3). The expansion is probed by a synchronized FTIR spectrometer.[20] The different cluster absorptions are marked D (dimers), T (trimers), Q (tetramers), and C (oligomers $N \geq 4$). They occur at progressively lower wavenumber relative to the internally hydrogen-bonded monomer conformation M. The prominent Qb band at 3401 cm^{-1} shows a characteristic intensity evolution (A_x) with increasing enantiopurity until it vanishes completely. This intensity evolution relative to the initial racemic value (A_0) is plotted in Figure 2 as a function of the fraction x of *S*-lactate. For comparison, the intensities expected for a statistical ensemble of $(R{:}S) = (2{:}2)$ tetramers and $(R{:}S) = (1{:}3)$ tetramers—implying kinetically control cluster formation—are also plotted. The Qb band is dominated by 2:2 tetramers, although a small contribution of 1:3 tetramers beyond $x = 80\,\%$ cannot be ruled out. The much smaller Qd band at 3354 cm^{-1} closely follows the 1:3 statistics in an equivalent analysis. Thus, there is strong evidence for the assignment of the Qb band to a 2:2 racemic tetramer. In the enantiopure limit, little oscillator strength remains in the Qb region, whereas absorptions characteristic for cyclic alcohol tetramers[20] appear (Ca, Cb).

More than one IR-active OH-stretching band may be expected for a racemic tetramer even for the highest conceivable symmetry (S_4). The experimental spectrum is consistent with a single strong absorption and possibly a weak satellite band to higher frequency. This situation is strongly indicative of high cluster symmetry. Furthermore, it suggests uncoupled OH oscillators that are hydrogen-bonded to the carbonyl group rather than cooperatively enhanced OH···OH

[*] T. B. Adler, Dr. N. Borho, Prof. Dr. M. A. Suhm
Institut für Physikalische Chemie
Universität Göttingen
Tammannstrasse 6, 37077 Göttingen (Germany)
Fax: (+49) 551-39-3117
E-mail: msuhm@gwdg.de
Prof. Dr. M. Reiher
Laboratorium für Physikalische Chemie
ETH Zürich
Hoenggerberg, 8093 Zürich (Switzerland)

[**] Support by the DFG research training group GRK 782 and the Fonds der Chemischen Industrie is acknowledged. We are grateful to A. de Meijere for advice on nomenclature, U. Buck, C. Rice, and U. Schmitt for help and discussions, and A. Bochenkova for preliminary MP2 studies.

 © 2006 Wiley-VCH Verlag GmbH & Co. KGaA, Weinheim

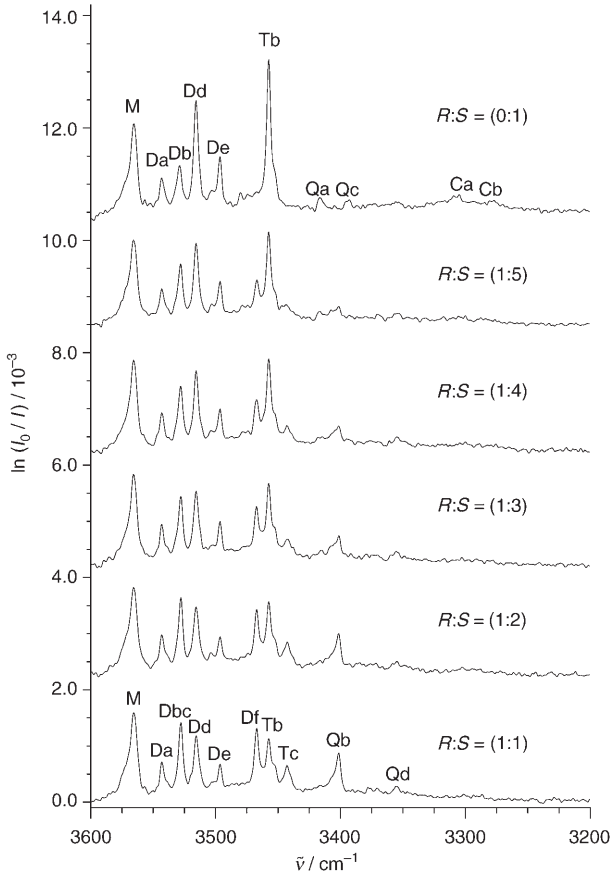

Figure 1. Filet-jet direct absorption spectra of methyl lactate (0.08%, expanded in 1 bar He) in the OH-stretching region for different mixtures of *R* and *S* isomers ranging from racemic (bottom) to enantiopure (top). The labels indicate the cluster size (M = monomer, D = dimers, T = trimers, Q = tetramers[18]) as well as their spectral sequence, a,b,c... in order of decreasing wavenumber.[12]

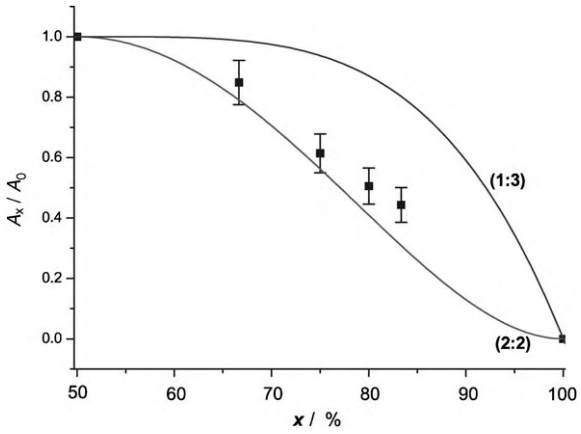

Figure 2. Intensity of the Qb band (squares with error bars) as a function of enantiopurity (mole fraction *x* of (*S*)-methyl lactate) compared with the results expected for the formation of purely statistical (*R*:*S*) = (1:3) and (2:2) tetramer clusters. A_x absorbance of mixture *x*; A_0 absorbance of racemic mixture ($x = 50\%$).

hydrogen bonds. The spectral simplicity further indicates one type of hydrogen bond, that is, an *RSRS* (C_2 or S_4) ringlike pattern rather than an *RRSS* (C_i, C_2) sequence.

In addition to the configurational isomerism, methyl lactate has several conformational degrees of freedom.[12,21] An extensive structural search with emphasis on symmetry was performed in the conformational and configurational subspace of the tetrameric cluster with the Turbomole package.[22,23] Over 30 structures were fully optimized with RI-BP86/TZVP. For the most promising ones, RI-MP2/TZVP-optimized structures were calculated, and RI-MP2/TZVPP energies were evaluated. TZVP and TZVPP represent triple ζ valence basis sets with polarization functions. Harmonic frequencies and transition strengths were calculated seminumerically by using analytical first geometric derivatives and dipole moments for displaced structures, respectively.[24] In some cases, the characteristic C=O and OH stretching vibrations were also directly calculated with the mode-tracking algorithm[25] and turned out to converge within one iteration step (for a detailed analysis of this algorithm, see reference [26]). There is a delicate balance between OH···O=C and OH···OH hydrogen bonds. The former are intrinsically more stable and favored in dimers, whereas the latter profit from cooperative strengthening if more than two of them occur in sequence.

We concentrate our discussion on three particularly stable (RI-BP86/TZVP) symmetric tetramer structures, which may be responsible for the Qb and Ca/Cb spectral features. Structure R_C is racemic, has S_4 symmetry, and involves OH···O=C hydrogen bonds. Structure R_H is also racemic, but involves cooperatively enhanced OH···OH hydrogen bonds, and has C_2 symmetry. Structure E_H is enantiopure, but otherwise similar to R_H. The three structures (BP86) are shown in Figure 3. The OH···O=C hydrogen bonds in the R_C structure have a length of 182 pm and deviate by only $\pm 14°$ from linearity. The hydrogen atoms of the OH groups are tilted $\pm 84°$ out of the backbone plane in the direction of the C_α–H group, thus avoiding the C_α–CH_3 group. The racemic C_2-symmetric structure R_H features OH···OH hydrogen bond lengths of 173 and 172 pm. Secondary CH···O=C and CH_3···O=C interactions can be observed as well. For the enantiopure C_2-symmetric structure E_H, OH···OH hydrogen bond lengths of 172 and 176 pm are found. The α-CH group is involved in weak hydrogen bonds with the carbonyl group. The quoted structural parameters are quite similar for the MP2 structures.

The energies for these three structures are summarized in Table 1 without and with basis-set superposition error (BSSE)

Table 1: Electronic energies (in kJ mol^{-1}, uncorrected (ΔE_u) and corrected (ΔE_c) for basis-set superposition error) for selected methyl lactate tetramer structures (shown in Figure 3) relative to four stable monomers.

Structure				RI-BP86 TZVP		RI-MP2 TZVP		RI-MP2 TZVP//TZVPP	
Code	Config.	Topology	Sym.	ΔE_u	ΔE_c	ΔE_u	ΔE_c	ΔE_u	ΔE_c
R_C	*RSRS*	OH···O=C	S_4	−68.3	−52.3	−179.4	−105.3	−161.5	−117.4
R_H	*RSRS*	OH···OH	C_2	−71.8	−57.0	−160.3	−96.8	−142.5	−104.3
E_H	*RRRR*	OH···OH	C_2	−76.3	−61.0	−169.0	−93.4	−150.4	−106.4

 © 2006 Wiley-VCH Verlag GmbH & Co. KGaA, Weinheim

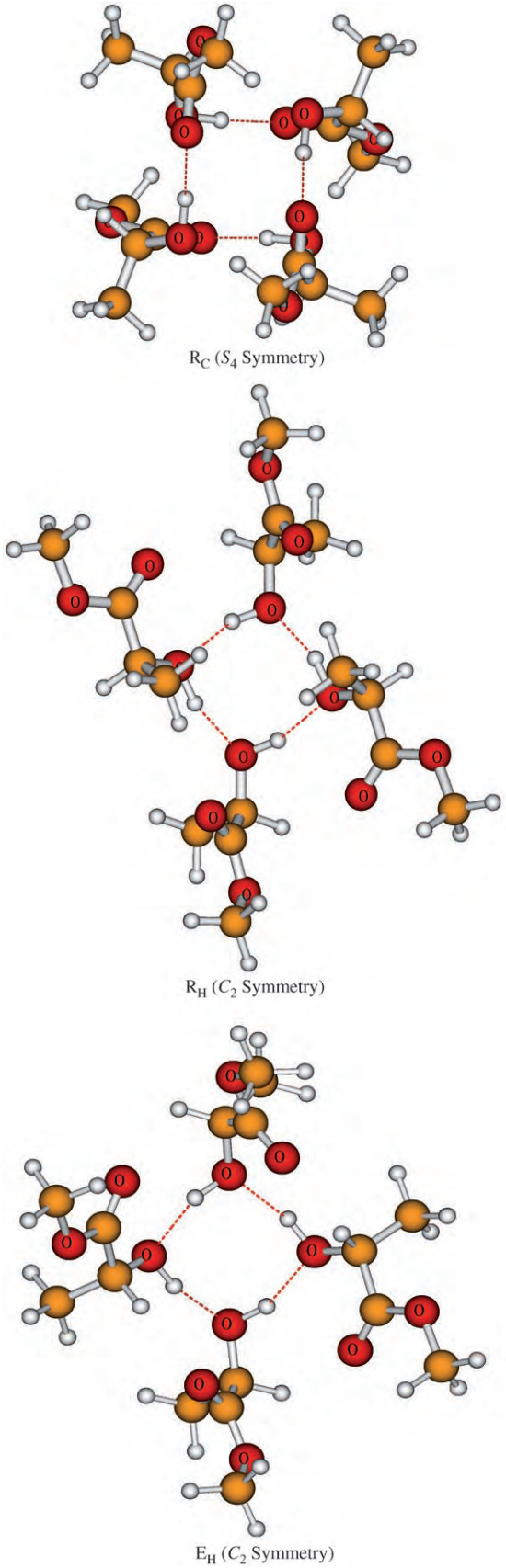

Figure 3. Stable methyl lactate structures (RI-BP86/TZVP) that possibly contribute to the jet spectrum in the Q/C range in Figure 1. Labels: R racemic, E enantiopure, subscripts: C O=C acceptor, H OH acceptor. The E_H structure displayed consists solely of *R* isomers.

correction. The BP86 and MP2 predictions for the relative energy differ substantially. The BP86 homoconfigurational E_H structure is among the deepest minima and the racemic tetramer also favors the OH···OH topology. Within the MP2 approximation, however, the compact racemic R_C structure, about 1 nm in diameter, is clearly the global minimum, even after BSSE correction and basis-set extension. For structures differing in secondary C–H hydrogen bonds and compactness, we consider relative DFT energies to be less reliable than MP2 predictions. The difference between MP2 and BP86 binding energies is striking and also points to serious deficiencies of the BP86 functional in the description of weak interactions such as dispersion. Its detailed analysis is beyond the scope of this article. Test calculations indicate that the RI approximation is not the cause for the discrepancy.

Within the folded OH···O=C hydrogen-bond topology, the depicted *RSRS* S_4 structure is the most stable arrangement even for BP86. This fact is supported by a series of configurational mutations in which the chirality-inducing H and CH_3 groups of one to four lactate units are interchanged, followed by structural minimization. Each mutation increases the energy by about 7 kJ mol^{-1}, partly as a result of a change in the monomer HOC(CH_3) torsional angle from *anti* to *gauche* and partly from intermolecular steric hindrance caused mainly by one C–H bond of the methyl group at the chiral center. Even a single mutation immediately leads to competing OH···OH structures. The systematic preference for cooperative OH···OH structures over compact, but non-cooperative OH···O=C topologies for BP86 makes the unique S_4 structure difficult to locate. The potential-energy surface in the region of OH···OH ringlike topologies is much shallower and has multiple minima. For BP86, not only various homoconfigurational (E_H), but also 1:3-heteroconfigurational and even 2:2-heteroconfigurational tetramers (R_H) attain their presumably global minima for such topologies (see Table 1). Configurational mutations lead to substantially smaller energy penalties. For MP2, this situation is partly reversed, as discussed above.

Figure 4 compares unscaled RI-BP86 absorption spectra for the most stable structures with the experimental anharmonic spectra in the harmonic OH-stretching region. Scaling is obviated by the good match between the experimental anharmonic value for the monomer (3565 cm^{-1}) and the harmonic RI-BP86 value (3554 cm^{-1}). OH bonds are too soft in the BP86 approach, which fortuitously compensates for anharmonicity. All minimum structures within 20 kJ mol^{-1} of the lowest point located on the multidimensional potential-energy hypersurface are included to take into account the expected error in the DFT treatment. The predicted spectra are grouped into homoconfigurational 4:0 and heteroconfigurational 3:1 and 2:2 tetramers.

Only one of the structures in the chosen energy range has OH···O=C connectivity, and it is the only one predicted to absorb near the Qb band. It has one strong IR band and a weak, slightly blue-shifted satellite, which is consistent with the experimental spectrum. All the other structures, irrespective of their relative configuration, involve cooperative OH···OH bonds and are predicted to have absorbance peaks at substantially lower wavenumber. Many have C_2 symmetry

 © 2006 Wiley-VCH Verlag GmbH & Co. KGaA, Weinheim

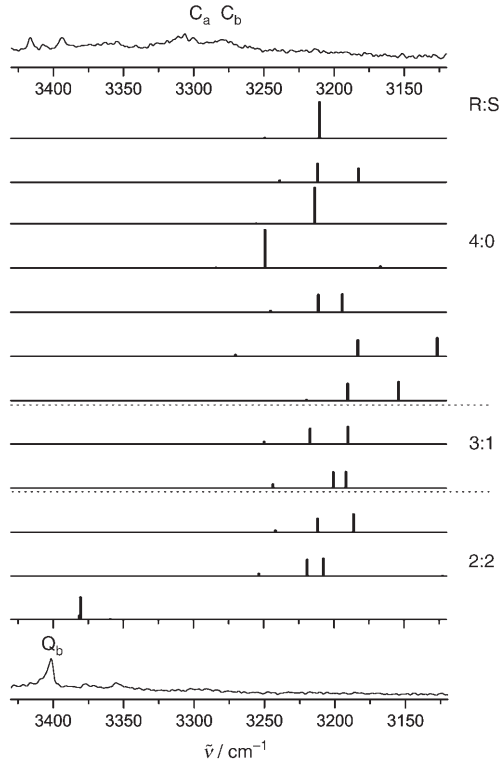

Figure 4. Harmonic RI-BP86 stick spectra of selected tetramer structures compared with the anharmonic experimental spectra of enantiopure (top) and racemic expansions (bottom).

(two strong bands) or C_4 symmetry (one strong band). As expected for DFT calculations, frequency shifts due to cooperative OH hydrogen bonds are far overestimated.[27] Therefore, the predicted OH···OH wavenumbers are fully consistent with the C-band absorptions observed in the spectrum around 3300 cm^{-1}, in view of the superposition of many cluster contributions. The absence of significant C-type absorption in the spectrum of the racemic mixture strongly supports the interpretation of Q- and C-bands as structurally different clusters of the same size.

The observation of a Q-type band in achiral methyl glycolate without C_α methyl group[13] is consistent with the proposed R_C structure. The absence of a Q-type band in methyl α-hydroxyisobutyrate[13] is also plausible, because a second C_α methyl group will lead to steric hindrance in the R_C structure. The slight blue shift of the methyl lactate Qb band upon Ar coating[12] is consistent with a compact, shielded structure, in which Ar atoms cannot compete with the strong hydrogen bonds. Substitution of the methyl ester by an ethyl ester group[12] does not change the Qb band, but it does split the dimer and trimer bands. This observation is consistent with the ester groups in the R_C structure being arranged far away from each other and having no influence on the cluster binding. The fact that the C_α–H unit has no secondary binding function in the R_C structure correlates well with the absence of spectral splitting in the C–H stretching bands for the racemic mixture.[12] In contrast, enantiopure expansions are rich in ringlike OH···OH topologies, which profit from secondary C_α–H hydrogen bonds (see E_H structure in Figure 3). This may cause the splitting in the C–H stretching bands.[12] Finally, the C=O stretching region of the spectrum of methyl lactate clusters differs markedly between enantiopure and racemic expansions.[12] Enantiopure expansions exhibit a strong, blue-shifted C=O peak, which corresponds to reduced hydrogen bonding relative to the internally hydrogen-bonded monomer.[21] This is expected for cooperative OH···OH hydrogen bonds. Conversely, the racemic C=O spectrum is further red-shifted and lacks the extra blue-shifted peak. The experimental difference amounts to approximately 15 cm^{-1}, which correlates well with the theoretical predictions for tetramers of about 30 cm^{-1}. The racemic cluster must therefore contain strong bonds to the carbonyl groups.

In summary, the R_C structure represents a deep minimum on the potential surface of two *R*- and two *S*-methyl lactate units. This structure has no inversion center or symmetry plane and is surrounded by a shallow area of open R_H-like cooperative topologies. The fundamental difference in hydrogen-bond connectivity between R_C and R_H requires a fairly accurate electronic-structure calculation to determine the relative stabilities. The R_C structure has a remarkably small hydrogen-bond-induced red-shift of the OH-stretching band, as it involves non-cooperative hydrogen bonds. An overwhelming number of experimental observations are consistent with the assignment of this R_C structure to the Qb band in the supersonic jet spectrum. This system thus represents a beautiful manifestation of a chirality-induced switch in hydrogen-bond topology for a simple tetrameric model system. The R_C cluster appears to be the principal survivor of OH···O=C hydrogen bonding against the tendency towards cooperative OH···OH interactions in lactates. Beyond the evidence available from mass spectrometry[1,3] and complementary to it, our infrared approach provides detailed structural and dynamic information on the phenomenon of chiral self-recognition[9] in the gas phase. It may also help to understand self-disproportionation phenomena of enantiomers[28] and other dynamical features of chiral molecules.[29]

Received: January 29, 2006
Revised: March 12, 2006

Keywords: chirality · hydrogen bonds · molecular recognition · nanostructures · vibrational spectroscopy

[1] R. G. Cooks, D. Zhang, K. J. Koch, F. C. Gozzo, M. N. Eberlin, *Anal. Chem.* **2001**, *73*, 3646–3655.
[2] R. R. Julian, R. Hodyss, B. Kinnear, M. Jarrold, J. L. Beauchamp, *J. Phys. Chem. B* **2002**, *106*, 1219–1228.
[3] R. R. Julian, S. Myung, D. E. Klemmer, *J. Am. Chem. Soc.* **2004**, *126*, 4110–4111.
[4] G. P. Moss, *Pure Appl. Chem.* **1996**, *68*, 2193–2222.
[5] A. R. Al-Rabaa, E. Bréhéret, F. Lahmani, A. Zehnacker, *Chem. Phys. Lett.* **1995**, *237*, 480–484.
[6] A. Giardini Guidoni, S. Piccirillo, D. Scuderi, M. Satta, T. M. Di Palma, M. Speranza, *Phys. Chem. Chem. Phys.* **2000**, *2*, 4139–4142.
[7] A. K. King, B. J. Howard, *Chem. Phys. Lett.* **2001**, *348*, 343–349.
[8] K. Le Barbu, F. Lahmani, A. Zehnacker-Rentien, *J. Phys. Chem. A* **2002**, *106*, 6271–6278.

 © 2006 Wiley-VCH Verlag GmbH & Co. KGaA, Weinheim

[9] N. Borho, M. A. Suhm, *Phys. Chem. Chem. Phys.* **2002**, *4*, 2721 – 2732.
[10] N. Seurre, J. Sepioł, K. Le Barbu-Debus, F. Lahmani, A. Zehnacker-Rentien, *Phys. Chem. Chem. Phys.* **2004**, *6*, 2867 – 2877.
[11] O. Picazo, I. Alkorta, J. Elguero, O. Mó, M. Yáñez, *J. Phys. Org. Chem.* **2005**, *18*, 491 – 497.
[12] N. Borho, M. A. Suhm, *Org. Biomol. Chem.* **2003**, *1*, 4351 – 4358.
[13] N. Borho, M. A. Suhm, *Phys. Chem. Chem. Phys.* **2004**, *6*, 2885 – 2890.
[14] N. Seurre, K. Le Barbu-Debus, F. Lahmani, A. Zehnacker-Rentien, N. Borho, M. A. Suhm, *Phys. Chem. Chem. Phys.* **2006**, *8*, 1007 – 1016.
[15] M. Fárník, C. Steinbach, M. Weimann, U. Buck, N. Borho, M. A. Suhm, *Phys. Chem. Chem. Phys.* **2004**, *6*, 4614 – 4620.
[16] M. Fárník, M. Weimann, C. Steinbach, U. Buck, N. Borho, T. B. Adler, M. A. Suhm, *Phys. Chem. Chem. Phys.* **2006**, *8*, 1148 – 1158.
[17] I. Alkorta, O. Picazo, J. Elguero, *J. Phys. Chem. A* **2005**, *109*, 3262 – 3266.
[18] The band was named Qb because it belongs to a cluster of four (Latin *quattuor*) molecules and was the second highest frequency band (b) observed for lactate tetramers; we keep this nomenclature for easy reference to earlier work.[12,13]
[19] C. A. Rice, N. Borho, M. A. Suhm, *Z. Phys. Chem. (Munich)* **2005**, *219*, 379 – 388.
[20] T. Häber, U. Schmitt, M. A. Suhm, *Phys. Chem. Chem. Phys.* **1999**, *1*, 5573 – 5582.
[21] A. Borba, A. Gómez-Zavaglia, L. Lapinski, R. Fausto, *Vibrat. Spectrosc.* **2004**, *36*, 79 – 88.
[22] R. Ahlrichs, M. Bär, M. Häser, H. Horn, C. Kölmel, *Chem. Phys. Lett.* **1989**, *162*, 165 – 169.
[23] F. Weigend, M. Häser, H. Patzelt, R. Ahlrichs, *Chem. Phys. Lett.* **1998**, *294*, 143.
[24] J. Neugebauer, M. Reiher, C. Kind, B. A. Hess, *J. Comput. Chem.* **2002**, *23*, 895 – 910.
[25] M. Reiher, J. Neugebauer, *J. Chem. Phys.* **2003**, *118*, 1634 – 1641.
[26] M. Reiher, J. Neugebauer, *Phys. Chem. Chem. Phys.* **2004**, *6*, 4621 – 4629.
[27] D. Zimmermann, T. Häber, H. Schaal, M. A. Suhm, *Mol. Phys.* **2001**, *99*, 413 – 426.
[28] V. A. Soloshonok, *Angew. Chem.* **2006**, *118*, 780 – 783; *Angew. Chem. Int. Ed.* **2006**, *45*, 766 – 769.
[29] M. Quack, *Angew. Chem.* **1989**, *101*, 588 – 604; *Angew. Chem. Int. Ed. Engl.* **1989**, *28*, 571 – 586.

 © 2006 Wiley-VCH Verlag GmbH & Co. KGaA, Weinheim

Homogeneous catalysis

DOI: 10.1002/anie.200504357

Catalytic Epoxidation and 1,2-Dihydroxylation of Olefins with Bispidine–Iron(II)/H_2O_2 Systems**

Michael R. Bukowski, Peter Comba, Achim Lienke, Christian Limberg, Carlos Lopez de Laorden, Rubén Mas-Ballesté, Michael Merz, and Lawrence Que, Jr.**

Non-heme iron-catalyzed oxidation of hydrocarbons has attracted considerable attention in the last decade.[1–4] Mononuclear Fe^{III}–peroxide and –hydroperoxide species are believed to be involved in biological oxygen activation in systems such as those which involve the heme iron enzyme cytochrome P450,[5,6] the non-heme iron antitumor drug bleomycin,[7,8] and the non-heme Rieske dioxygenases.[9–11] Hetero- or homolytic O–O bond cleavage of the end-on-bound Fe^{III}–hydroperoxide complexes yield formally the corresponding {Fe^{V}=O} or {Fe^{IV}=O} compounds, respectively, which are assumed to be the catalytically active species. Homolytic cleavage of the O–O bond also yields oxygen-centered radicals, which may give rise to typical radical reactions. For a number of synthetic, low-molecular-weight model systems with tetra- and pentadentate amine/pyridine-containing ligands there is unambiguous spectroscopic and/or structural evidence for end-on {Fe^{III}-OOH}, side-on {Fe^{III}-(O_2)}, and {Fe^{IV}=O} intermediates,[4,12–19] but evidence for {Fe^{V}=O} complexes is more circumstantial.

The various Fe^{III}–peroxide complexes are generally obtained from the Fe^{II} precursors by oxidation with H_2O_2,[12–14] while oxygen transfer from oxo transfer agents such as peracids or iodosylbenzene is used to produce the ferryl products.[15–19] Direct formation of {Fe^{IV}=O} complexes from the Fe^{II} precursor, using H_2O_2, without formation of the usual Fe^{III} intermediates, is another possible pathway.[20,21] On the basis of spectroscopic and theoretical investigations of low-molecular-weight model complexes, as well as studies of the corresponding reactivities, mechanisms were proposed for the iron-catalyzed olefin oxidation, and pathways for pentadentate ligands as well as strong- and weak-field tetradentate ligands were proposed.[3,4] Systems which were studied in detail include tetradentate (L^1, L^2) and pentadentate derivatives (L^3) of tris(2-pyridylmethyl)amine (tpa). These are shown Scheme 1, together with the two isomeric pentadentate bispidine ligands L^4 and L^5 discussed herein.

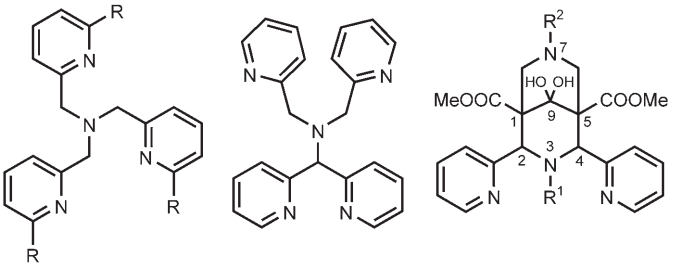

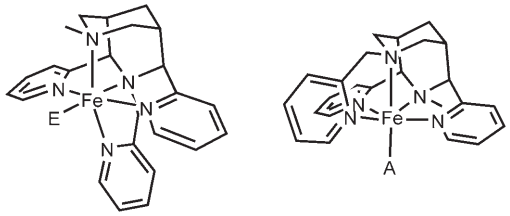

[(L^4)FeX]$^{n+}$, **1** [(L^5)FeX]$^{n+}$, **2**

Scheme 1. Ligands L^1–L^5 as well as two isomeric Fe^{II} complexes of L^4 and L^5 (substituents on the bispidine backbone are omitted); Py = pyridyl,; X = MeCN, MeOH; A = axial X; E = equatorial X.

A wide variety of bispidine ligands are relatively easy to prepare in respectable yields.[22–25] The two isomeric Fe^{II} complexes of the ligands L^4 and L^5 (**1** and **2**, respectively, Scheme 1) have been structurally, spectroscopically, and electrochemically characterized.[22] In **1** the coligand X is coordinated *trans* to N3 (equatorial, E) through a short and strong Fe^{II}–X bond, while in **2** the X ligand is positioned *trans* to N7 (axial, A) through a long and weak Fe^{II}–X bond.[12,22] The structural difference between the two isomers is manifested in their reactions with H_2O_2 in MeOH at −40 °C, which afford spectroscopically distinct iron(III) complexes.[12] The low-spin end-on hydroperoxo- and high-spin side-on peroxo complexes differ in terms of their thermal stability, with that of L^4 being among the most stable species of this class of compounds.[12] Herein we compare the catalytic capabilities of the two [(L^n)Fe^{II}(X)]$^{2+}$ (n = 4 (**1**), 5 (**2**); X = MeCN, MeOH) complexes in the reaction with cyclooctene as the substrate and H_2O_2 as the oxidant.

[*] Prof. Dr. P. Comba, Dr. C. Lopez de Laorden, Dr. M. Merz
Universität Heidelberg
Anorganisch-Chemisches Institut
INF 270, 69120 Heidelberg (Germany)
Fax: (+49) 6226-548-453
E-mail: peter.comba@aci.uni-heidelberg.de
Dr. M. R. Bukowski, Dr. R. Mas-Ballesté, Prof. Dr. L. Que, Jr.
Department of Chemistry and
Center for Metals in Biocatalysis
University of Minnesota
207 Pleasant St. SE, Minneapolis MN 55455 (USA)
E-mail: que@chem.umn.edu
Dr. A. Lienke
Unilever Research and Development
Olivier van Noortlaan 120
3133 AT Vlaardingen (The Netherlands)
Prof. C. Limberg
Institut für Chemie
Humboldt-Universität zu Berlin
Brook-Taylor-Strasse 2, 12489 Berlin (Germany)

[**] Financial support from the German Science Foundation (DFG) and the US Department of Energy (DOE) is gratefully acknowledged.

 InterScience © 2006 Wiley-VCH Verlag GmbH & Co. KGaA, Weinheim

Table 1 lists the product distributions observed in the $[(L^n)Fe^{II}(X)]^{2+}/H_2O_2$/cyclooctene experiments under different reaction conditions. To facilitate comparison with published data[3] the experimental conditions for the oxidation reactions were chosen to resemble those with L^1–L^3 (MeCN, 25.0 °C, catalyst/H_2O_2/substrate = 1:10(100):1000; 30 min reaction time; see *Experimental Section*). Complex **1** yields only about 1 TON (TON = 10 μmol product per μmol {Fe}) of oxidation product in MeCN under aerobic conditions (primarily epoxide; Table 1, entry 4a), a reactivity similar to that of the iron–L^3 complex (Table 1, entry 3). In contrast, **2** affords 5 TON of epoxide exclusively under aerobic conditions (Table 1, entry 5a). At first glance, this comparison might suggest that **1** is a rather poor catalyst, but further experiments show that the picture is more complicated. When the reactions are carried out over 6 h, the product yields increase to about 7 TON with **1** (Table 1, entry 4d) and 8 TON for **2** (Table 1, entry 5d). Data points obtained at intermediate times indicate that, whereas most of the products are formed in the experiments with **2** within the first half hour, the reactions with **1** take about seven times longer to achieve a comparable product yield (Table 1, entries 4a–d and 5a–d). Thus, by this criterion, **1** is almost as effective a catalyst as **2**, but is much slower in activating the H_2O_2 oxidant. When the reactions are carried out for 30 minutes under argon, the product yields decrease by about 20% and 60%, respectively (Table 1, entries 4e and 5e), thus suggesting a greater susceptibility of **2** than **1** to autoxidation.

Table 1: Product distribution (D = diol, E = epoxide).

Entry	Ligand	Experimental conditions[a]	D + E[d,e]	D/E
1	L^1	[b]	7.4	1.2:1
2	L^2	[b]	5.6	7:1
3	L^3	[b]	0.6	0:1
4a	L^4	air (0.5 h)	1.2	0.1:1
4b	L^4	air (1.5 h)	3.3	0.1:1
4c	L^4	air (3.5 h)	6.0	< 0.1:1
4d	L^4	air (6 h)	6.8	< 0.1:1
4e	L^4	argon (0.5 h)	1.0	0.2:1
4f	L^4	PhIO[c], air	1.1	0:1
4g	L^4	PhIO[c], argon	0.6	0:1
5a	L^5	air (0.5 h)	5	0:1
5b	L^5	air (1.5 h)	6.3	0:1
5c	L^5	air (3.5 h)	7.3	0:1
5d	L^5	air (6 h)	8.1	0:1
5e	L^5	argon (0.5 h)	2.0	1:1
5f	L^5	PhIO[c], air	1	0:1
5g	L^5	PhIO[c], argon	0.4	0:1
5h	L^5	MeOH, air	1.9	0:1
5i	L^5	MeOH, argon	1.7	0:1

[a] 1000 equiv cyclooctene, 10 equiv H_2O_2, reaction time 0.5 h under air in MeCN at 298 K unless otherwise noted. [b] Ambient temperature. [c] Oxidant: 1 equiv of {Fe^{IV}=O}; no H_2O_2 used (stoichiometric reaction). [d] TON, 10 = max;[19] the error limit for all data is ca. ±5% (relative) for TON. [e] Diol is exclusively *cis* for L^1 and L^2 and a mixture of *cis* and *trans* for L^4 and L^5, when observed.

A mechanism is proposed in Scheme 2 to rationalize the above observations, in which an {Fe^{III}-OOH} intermediate is formed initially and then undergoes O–O bond homolysis to form an {Fe^{IV}=O} oxidant and HO·, as proposed for the FeL^3-catalyzed hydroxylation of alkanes.[26] The difference in catalyst efficiency between **1** and **2** can be associated with their different structural and electronic properties (Scheme 1). The constraints of the bispidine ligand architecture dictate that the HOO ligand in **1** is *trans* to N3 (that is, in a similar configuration as in the complex with L^3),[26] while that in **2** is *trans* to N7. As noted in a number of other metal complexes of the isomeric ligands L^4 and L^5, the two tertiary amine donors differ in their distances to the metal center.[22,24,25] This probably is related to the π-bonding properties of the two equatorially coordinated pyridine groups and gives rise to a stronger Fe–OOH interaction (π-back-bonding) for the $[(L^4)Fe^{III}OOH]$ intermediate.[18]

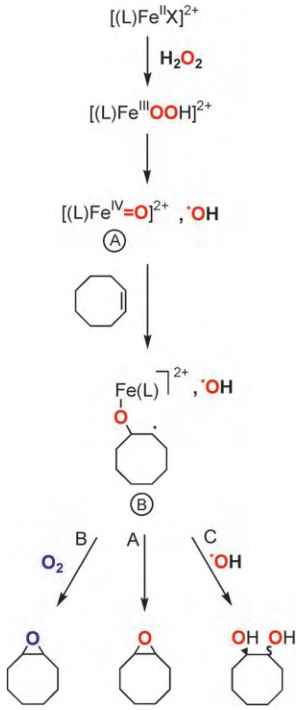

Scheme 2. Proposed mechanisms for the formation of the epoxide and diol. See text for details.

To ascertain the involvement of ferryl species, the {Fe^{IV}=O} complexes of the two ligands L^4 and L^5 were synthesized in situ and their reactivities towards cyclooctene were then compared in the absence of other potential oxidizing species. These complexes were independently prepared by following the method for the synthesis of $[(L^3)Fe^{IV}=O]^{2+}$,[17] by addition of iodosylbenzene to **1** and **2** in MeCN. Formation of the corresponding ferryl complexes was indicated by the appearance of the expected electronic transition in the NIR region ($\varepsilon^{L^4}_{728nm} = 400\,M^{-1}cm^{-1}$, $\varepsilon^{L^5}_{728nm} = 380\,M^{-1}cm^{-1}$, Figure 1), characteristic for this class of complexes.[4] Both $[(L)Fe^{IV}=O]^{2+}$ complexes were generated by addition of PhIO in MeCN and react readily with cyclooctene to afford cyclooctene oxide. Under argon $[(L^4)Fe^{IV}=O]^{2+}$ forms 0.6 TON, and

 © 2006 Wiley-VCH Verlag GmbH & Co. KGaA, Weinheim

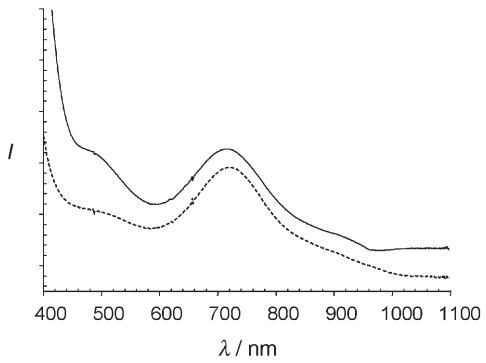

Figure 1. UV/Vis-NIR spectra of the ferryl complexes $[Fe{=}O(L^5)]^{2+}$ (——) and $[Fe{=}O(L^4)]^{2+}$ (----).

$[(L^5)Fe^{IV}{=}O]^{2+}$ 0.4 TON of epoxide, respectively (Table 1, entries 4g and 5g), thus showing that both ferryl complexes are capable of transferring their oxo atom to cyclooctene, as proposed in Scheme 2. The relative efficiencies of this oxo transfer are mirrored by the yields of the cyclooctene oxidation products obtained with H_2O_2 under argon. In air, the epoxide yields increase by 90% to 1.1 TON with L^4 (Table 1, entry 4f) and 150% to 1.0 TON with L^5 (Table 1, entry 5f), thus emphasizing some difference in the susceptibilities of the two systems to radical autoxidation. Taken together, the data support the proposed formation of a radical intermediate, derived from the reaction of the {Fe=O} unit with cyclooctene (intermediate B in Scheme 2), which can either afford epoxide directly (pathway A) or be intercepted by O_2 to generate more epoxide (pathway B). There is precedent for {M=O} complexes that attack double bonds to yield {M-O-C-C}$^{\bullet}$ and subsequently form {M···epoxide} complexes.[27]

Table 2: Labeling data.

Ligand	Experimental conditions[a]	% Epoxide-^{18}O[c]			% 1,2-Diol-^{18}O			
		$H_2{}^{18}O$	$H_2{}^{18}O_2$	$^{18}O_2$	$H_2{}^{18}O$		$H_2{}^{18}O_2$	
					$^{16}O^{16}O$	$^{16}O^{18}O$	$^{16}O^{18}O$	$^{18}O^{18}O$
L^1	H_2O_2, air	9	90	(1)	13[d]	86[d]	97[d]	3[d]
L^2	H_2O_2, air	3	54	(43)	99[d]	1[d]	4[d]	96[d]
L^5	H_2O_2, air	(0)	15	85				
L^5	H_2O_2, argon	18	82	–	70[d]	30[d]	23[d]	77[d]
					50[e]	50[e]	56[e]	44[e]
L^5	PhIO[b], air			55[f]				
L^5	PhIO[b], argon	40[g]						

[a] 1000 equiv cyclooctene, 10 equiv H_2O_2, reaction time 0.5 h under air in MeCN, unless otherwise noted. [b] 1 equiv PhIO used as oxidant to form $\{Fe^{IV}{=}O\}$; no H_2O_2 used. [c] Values in parentheses are calculated by difference. [d] *cis* diol. [e] *trans* diol; *cis*/*trans* = 0.4:0.6. [f] 45% from PhIO. [g] 60% from PhIO.

The oxidation of cyclooctene by **2**/H_2O_2 in MeCN under argon affords 1 TON cyclooctane-1,2-diol (*cis*/*trans* 40:60) in addition to 1 TON epoxide. The diol product was not observed when the reaction was carried out in aerobic MeCN or in MeOH. In the latter solvent, 2 TON of epoxide were obtained, irrespective of whether O_2 was present or not. These results suggest that the precursor to the diol product is also intermediate B (pathway C). The presence of oxygen diverts intermediate B to form more epoxide, while MeOH quenches HO$^{\bullet}$; hence the diol product is only observed in MeCN under argon.

^{18}O-labeling experiments, focusing on the $\{FeL^5\}$-catalyzed reaction (Table 2), support the proposed mechanism (Scheme 2). As expected for pathway A, a large fraction (82%) of the oxygen atom of the epoxide is derived from the $H_2{}^{18}O_2$ oxidant under Ar, with the remainder from $H_2{}^{18}O$, presumably by water exchange with the {Fe=O} unit.[28] On the other hand, the same reaction under aerobic conditions resulted in only 15% of the labeling in the epoxide arising from $H_2{}^{18}O_2$ and the balance derived from $^{18}O_2$, thus supporting the involvement of pathway B. Similar conclusions were reached in labeling experiments using the in situ formed $[(L^5)Fe{=}O]^{2+}$ (Table 2). Pathway B in Scheme 2 consists of the trapping of radical B by O_2 to initiate a radical chain reaction that affords most of the epoxide observed under aerobic conditions. It is well known that the autoxidation of cyclooctene primarily yields epoxide, through the addition of an initially formed alkylperoxy radical to the double bond.[29] However, the autoxidation pathway is apparently quenched in MeOH, as the yield of epoxide is not sensitive to the presence of air.

The labeling experiments also provide insight into the origin of the diol product, which formed (1 TON) only under anaerobic conditions and only in MeCN. The oxygen atoms of the diol mainly originate from $H_2{}^{18}O_2$, but some incorporation from $H_2{}^{18}O$ was also observed. The fact that both *cis* as well as *trans* products were observed indicates that the 1,2-diol must be formed by a pathway different from that proposed for the systems based on L^1 and L^2, which involves a high-valent $[M(L)(O)(OH)]^{n+}$ species that attacks the double bond with high stereoselectivity.[3,4] The fact that no diols are observed in the reaction with directly prepared $\{Fe^{IV}{=}O\}$ suggests that an additional component (H_2O_2 or a H_2O_2-derived species, for example, $^{\bullet}OH$) is also required for formation of the diol. We thus propose that the diol forms by the reaction of adduct B with HO$^{\bullet}$ within the solvent cage of the Fe complex (Scheme 2, pathway C). Such caged radical pairs have been proposed before, for example, in Ref. [30]. The involvement of B in a radical reaction (pathway C) is supported by the loss of stereocontrol in diol formation as well as the absence of any diol formation in the presence of O_2, which reacts with B to form more epoxide (Scheme 2, pathway B), and in reactions in MeOH, which traps and quenches O-based radicals such as HO$^{\bullet}$. The incorporation of oxygen from $H_2{}^{18}O$ into the diol product can be rationalized by solvent exchange of $[(L^5)Fe^{IV}{=}O]^{2+}$, thus supporting the notion that the ferryl species can lead to both epoxide and diol.

Our mechanistic proposal centers around adduct B as a common intermediate for all the observed products. The

 © 2006 Wiley-VCH Verlag GmbH & Co. KGaA, Weinheim

appearance of products other than epoxide depends on the lifetime of adduct B, which is modulated by the supporting ligand. The adduct lifetime for L^5 must be significantly longer than for L^4 to account for the extensive autoxidation of the epoxide observed, as well as its trapping by HO· or related species to form the diol.

In summary, pentadentate bispidine-based Fe^{II} complexes catalyze the oxidation of cyclooctene with H_2O_2 to afford the expected epoxide product, with the reaction rate dependent on the ligand structure. Unexpectedly, *cis*- and *trans*-1,2-diols are also observed but only under anaerobic conditions in MeCN. The accumulated data support a mechanism which involves formation of a low-spin Fe^{III}–hydroperoxo intermediate that produces $\{Fe^{IV}=O\}$. Epoxide is formed both by direct transfer of the ferryl oxygen atom and by a radical-based process with molecular oxygen. Diol formation is proposed to arise from a pathway not previously observed in non-heme iron-based oxidation catalysis.

Experimental Section

Reaction conditions for the cyclooctene oxidation: A 70 mM solution of H_2O_2 in MeCN (or MeOH, 0.3 mL) was delivered by syringe pump over 30 min at 25 °C under argon (or in air) to a vigorously stirred solution of MeCN (or MeOH, 2.7 mL) containing the iron catalyst and the olefin substrate; the resulting concentrations were 0.7 mM iron catalyst, 7.0 mM H_2O_2, and 0.70 M olefin. The solution was stirred for 5 min after the addition of H_2O_2 was complete. 1-Methylimidazole (0.1 mL) and acetic anhydride (1 mL) were added, followed by the addition of ice (these are standard reactions[3] for quenching the reaction and derivatization). After extraction with $CHCl_3$, the organic extract was washed successively with 1M H_2SO_4 (1.0 mL), saturated $NaHCO_3$, and water. Naphthalene was added to the organic extract as an internal standard for GC analysis.

In experiments with $H_2{}^{18}O$, $H_2{}^{18}O$ (42 mL, 0.70 M) was added to the catalyst solution prior to the injection of H_2O_2 (experiments with the same amount of natural abundance H_2O were also made and shown not to have any influence on the product distribution). In experiments with $H_2{}^{18}O_2$, 70.0 mM $H_2{}^{18}O_2$ (diluted with MeCN or MeOH) was used (2% $H_2{}^{18}O_2/H_2O$ solution, $H_2{}^{18}O_2/H_2{}^{16}O_2$ 9:1). Experiments with $^{18}O_2$ were performed with $^{18}O_2$-saturated solutions. Fe^{IV} solutions in MeCN were prepared with excess solid PhIO to afford, after filtration of the remaining PhIO, the desired solutions. The concentration of $\{Fe^{IV}=O\}$ was determined spectrophotometrically.

For comparison with published data, all yields are reported as TON = 10 μmol product) per μmol {Fe}; for most experiments (10 equivalents of H_2O_2), the maximum TON (without autoxidation) was 10.0. All experiments were run at least in duplicate and subjected to GC analysis (GC/MS for the labeling experiments). The GC was calibrated with the pure epoxide and *cis* diols. No other major products were detected, except for the *trans* diol in one set of experiments (see Table 2), and this had the same mass and fragmentation pattern, but a slightly different retention time. The relatively small yields means the error limit for all data is approximately ±5% (absolute) for TON and ±5% (relative) for labeling percentages.

Received: December 8, 2005
Published online: April 25, 2006

Keywords: coordination chemistry · dihydroxylation · epoxidation · homogeneous catalysis · iron

[1] "Metal-Oxo and Metal-Peroxo Species in Catalytic Oxidations": B. Meunier, *Struct. Bonding (Berlin)* **2000**, *97*.
[2] *Biomimetic Oxidations Catalyzed by Transition Metal Complexes* (Ed.: B. Meunier), Imperial College Press, London, **2000**.
[3] K. Chen, M. Costas, L. Que, Jr., *J. Chem. Soc. Dalton Trans.* **2002**, 672.
[4] M. Costas, M. P. Mehn, M. P. Jensen, L. Que, Jr., *Chem. Rev.* **2004**, *104*, 939.
[5] R. Davydov, T. M. Makris, V. Kofman, D. E. Werst, S. G. Sligar, B. M. Hoffman, *J. Am. Chem. Soc.* **2001**, *123*, 1403.
[6] B. Meunier, S. P. de Visser, S. Shaik, *Chem. Rev.* **2004**, *104*, 3947.
[7] R. M. Burger, *Struct. Bonding (Berlin)* **2000**, *97*, 287.
[8] N. Lehnert, F. Neese, R. Y. N. Ho, L. Que, Jr., E. I. Solomon, *J. Am. Chem. Soc.* **2002**, *124*, 10810.
[9] D. T. Gibson, R. E. Parales, *Curr. Opin. Biotechnol.* **2000**, *11*, 236.
[10] B. Kauppi, K. Lee, E. Carredano, R. E. Parales, D. T. Gibson, S. Ramaswamy, *Structure* **1998**, *6*, 571.
[11] A. Karlsson, J. V. Parales, R. E. Parales, D. T. Gibson, H. Eklund, S. Ramaswamy, *Science* **2003**, *299*, 1039.
[12] M. R. Bukowski, P. Comba, C. Limberg, M. Merz, L. Que, Jr., T. Wistuba, *Angew. Chem.* **2004**, *116*, 1303; *Angew. Chem. Int. Ed.* **2004**, *43*, 1283.
[13] G. Roelfes, V. Vrajmasu, K. Chen, R. Y. N. Ho, J. Rohde, C. Zondervan, R. M. la Crois, E. P. Schudde, M. Lutz, A. L. Spek, R. Hage, B. Feringa, E. Munck, L. Que, Jr., *Inorg. Chem.* **2003**, *42*, 2639.
[14] J.-J. Girerd, F. Banse, A. J. Simaan, *Struct. Bonding (Berlin)* **2000**, *97*, 145.
[15] C. A. Grapperhaus, B. Mienert, E. Bill, T. Weyhermüller, K. Wieghardt, *Inorg. Chem.* **2000**, *39*, 5306.
[16] J.-U. Rohde, J.-H. In, M. H. Lim, W. W. Brennessel, M. R. Bukowski, A. Stubna, E. Münck, W. Nam, L. Que, Jr., *Science* **2003**, *299*, 1037.
[17] E. J. Klinker, J. Kaizer, W. W. Brennessel, N. L. Woodrum, C. J. Cramer, L. Que, Jr., *Angew. Chem.* **2005**, *117*, 3756; *Angew. Chem. Int. Ed.* **2005**, *44*, 3690.
[18] J. Kaizer, E. J. Klinker, N. Y. Oh, J.-U. Rohde, W. J. Song, A. Stubna, J. Kim, E. Münck, W. Nam, L. Que, Jr., *J. Am. Chem. Soc.* **2004**, *126*, 472.
[19] V. Balland, M.-F. Charlot, F. Banse, J.-J. Girerd, T. A. Mattioli, E. Bill, J.-F. Bartoli, P. Battioni, D. Mansuy, *Eur. J. Inorg. Chem.* **2004**, 301.
[20] F. Buda, B. Ensing, M. C. M. Gribnau, E. J. Baerends, *Chem. Eur. J.* **2001**, *7*, 2775.
[21] M. L. Kremer, *Phys. Chem. Chem. Phys.* **1999**, 3595.
[22] H. Börzel, P. Comba, K. S. Hagen, M. Merz, Y. D. Lampeka, A. Lienke, G. Linti, H. Pritzkow, L. V. Tsymbal, *Inorg. Chim. Acta* **2002**, *337*, 407.
[23] H. Börzel, P. Comba, K. S. Hagen, M. Kerscher, H. Pritzkow, M. Schatz, S. Schindler, O. Walter, *Inorg. Chem.* **2002**, *41*, 5440.
[24] P. Comba, M. Merz, H. Pritzkow, *Eur. J. Inorg. Chem.* **2003**, 1711.
[25] P. Comba, C. Lopez de Laorden, H. Pritzkow, *Helv. Chim. Acta* **2005**, *88*, 647.
[26] G. Roelfes, M. Lubben, R. Hage, L. Que, Jr., B. L. Feringa, *Chem. Eur. J.* **2000**, *6*, 2152.
[27] C. Limberg, *Angew. Chem.* **2003**, *115*, 6112; *Angew. Chem. Int. Ed.* **2003**, *42*, 5932.
[28] M. S. Seo, J.-H. In, S. O. Kim, N. Y. On, J. Hong, J. Kim, L. Que, Jr., W. Nam, *Angew. Chem.* **2004**, *116*, 2417; *Angew. Chem. Int. Ed.* **2004**, *43*,2417.
[29] D. E. van Sickle, F. R. Mayo, R. M. Arluck, *J. Am. Chem. Soc.* **1965**, *87*, 4824.
[30] Y. Mekmouche, S. Ménage, C. Toia-Duboc, M. Fontecave, J.-B. Galey, C. Lebrun, J. Pécaut, *Angew. Chem.* **2001**, *113*, 975; *Angew. Chem. Int. Ed.* **2001**, *40*, 949.

 © 2006 Wiley-VCH Verlag GmbH & Co. KGaA, Weinheim

Drug Design

DOI: 10.1002/anie.200504174

A General Approach for the Identification of Site-Specific RNA Binders by ^{19}F NMR Spectroscopy: Proof of Concept**

Christoph Kreutz, Hanspeter Kählig, Robert Konrat, and Ronald Micura**

Dedicated to Professor Bernhard Kräutler on the occasion of his 60th birthday

Ribonucleic acid (RNA) has been recognized as a potential candidate for drug discovery since RNA plays essential functional roles in the lifecycles of cells—traditionally associated with mRNA maturation and ribosomal protein synthesis—and in the progression of viral diseases.[1–3] In these processes, aminoglycosides represent the most prominent class of validated RNA effectors.[4] More recent discoveries on important regulatory functions of non-coding RNAs (ncRNA),[5] such as small interfering RNAs, microRNAs, and riboswitches, make RNA an increasingly attractive target in the development of novel RNA-binding drugs.

Several approaches are used to identify ligands for RNA. One approach relies on mass-spectrometry-assisted screening, as has been recently described for a 23S rRNA target.[6] Another approach is based on fluorescence spectroscopy, using either fluorescently labeled RNAs[7,8] or labeling of the potential ligands.[9] Alternatively, surface plasmon resonance (SPR) has been utilized to detect the binding of small molecules to immobilized RNA.[10] Over the past few years, NMR spectroscopy has also been established as a powerful and reliable means for identifying lead molecules, predominantly in the context of protein targets.[11–13] Very recently, the potential of ^{19}F detection for NMR-based binding and functional screenings has been recognized. Experiments such as FAXS (fluorine chemical shift anisotropy and exchange for screening)[14] and 3-FABS (three fluorine atoms for biochemical screening)[15] are particularly suitable because these methods are rarely subject to experimental artifacts. When this method is combined with cryogenic probe technology optimized for ^{19}F detection, the low sensitivity of the instrumentation can be diminished.[14]

Here, we present a novel concept for the identification of RNA binders by ^{19}F NMR spectroscopy. The approach relies on site-specific labeling of RNA with 2′-deoxy-2′-fluoro (2′-F) nucleosides, thereby replacing the 2′-hydroxy group with a fluorine atom. Our aim to verify ligand binding should be feasible if the 2′-F label is positioned at the binding site (Figure 1). Since most of the RNA ligands known follow the concept of adaptive recognition,[16] their binding alters the local RNA conformation to a certain extent. Because the chemical environment of the 2′-F atom is expected to be different for the free versus complexed RNA, we expect different chemical shift values for the corresponding resonances. In this sense, a key feature of the approach relies on the strategic positioning of the individual 2′-F labels within the RNA sequence of interest. Such an approach is particularly powerful because of simultaneous accessibility of an internal reference, represented by a fluorine label placed, for example, within a double-helical region where no binding is expected, and consequently, no resonance shift is anticipated.

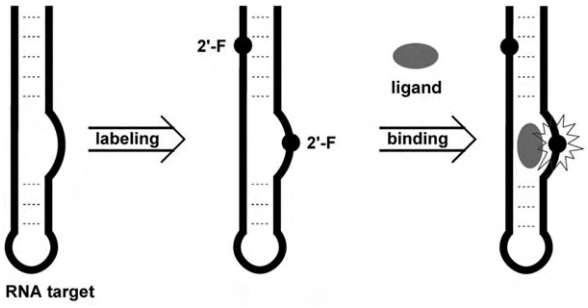

Figure 1. Concept for the identification of RNA binders by ^{19}F NMR spectroscopy. The RNA drug target is site-specifically modified with a "sensor" (2′-F-adenosine, 2′-F-cytidine, 2′-F-guanosine, 2′-F-uridine) in the suspected region of interaction ("sensor"). When a ligand is bound, the local environment is changed and results in a resonance shift of the sensor. A second 2′-F nucleoside positioned in a region where no binding is expected serves as internal reference.

Figure 2 illustrates the realization of our concept with the ^{19}F NMR spectra of the structurally well characterized tobramycin RNA aptamer system.[17] The RNA sequence was labeled with a 2′-fluoroadenosine label in the loop, which is known to bind the aminoglycoside tobramycin with a nanomolar dissociation constant ($\approx$10 nM), and a 2′-fluorocytidine was placed in the stem, which is not involved in the binding event. At submillimolar concentration, two distinct ^{19}F NMR signals were observed for the free RNA that were

[*] Prof. Dr. R. Konrat
Institute of Biomolecular Structural Chemistry
University of Vienna, Max Perutz Laboratories
Vienna Biocenter Campus 5, 1030 Vienna (Austria)
Fax: (+43) 1-4277-53099
E-mail: robert.konrat@univie.ac.at
Mag. C. Kreutz, Prof. Dr. R. Micura
Leopold Franzens University
Institute of Organic Chemistry, Center for Molecular Biosciences
Innrain 52a, 6020 Innsbruck (Austria)
Fax: (+43) 512-507-2892
E-mail: ronald.micura@uibk.ac.at
Dr. H. Kählig
Institute of Organic Chemistry
University of Vienna
Währingerstrasse 38, 1090 Vienna (Austria)

[**] Financial support from the Austrian Science Fund FWF (P17864 to R.M. and SFB17, project part F1719 to R.K.), the Tiroler Wissenschaftsfonds TWF (GZ: UNI0404/39 to R.M), bm:bwk (GEN-AU project cluster, "Non-coding RNAs", to R.M.) the Wiener Wissenschafts- und Technologiefonds WWTF (LS162 to R.K.) is gratefully acknowledged.

Supporting information for this article is available on the WWW under http://www.angewandte.org or from the author.

InterScience
© 2006 Wiley-VCH Verlag GmbH & Co. KGaA, Weinheim

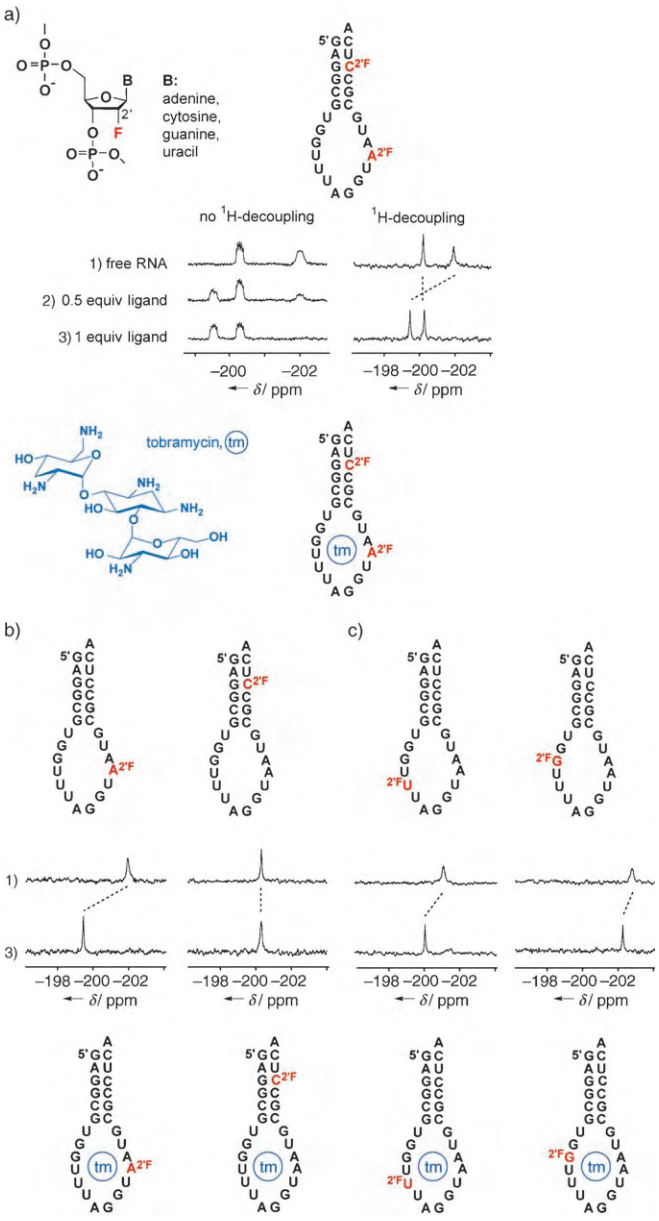

Figure 2. Site-specific binding of the high-affinity binder tobramycin to its 27-nt RNA aptamer. a) RNA aptamer containing two 2′-F nucleoside labels: Ligand binding followed by non-proton-decoupled (Varian Inova 500 MHz) and proton-decoupled ^{19}F NMR spectroscopy (Bruker DRX 400 MHz). A pronounced shift and a decrease in linewidth of the ^{19}F resonance from the loop were observed while the ^{19}F resonance from the stem remained unaffected upon ligand binding. b) Assignment of 2′-F resonances by reference aptamers with a single 2′-F label. c) Alternative positions of the 2′-F label in the loop showed the same spectroscopic behavior upon ligand binding. Conditions: 0.2 or 0.4 mM strand concentrations, H_2O/D_2O 9:1, 25 mM sodium phosphate buffer, pH 6.5, 298 K. ^{19}F resonances relative to external CCl_3F.

easily assigned by reference sequences containing one or the other 2′-F label (Figure 2b).

When the RNA sequence was titrated with aliquots of tobramycin, one of the resonances decreased while a novel signal appeared downfield indicating that ligand binding occurred in the slow-exchange mode; the binding was complete after addition of one equivalent (see also the Supporting Information). Importantly, the chemical shift of the resonance originating from the 2′-F label positioned in the stem remained unaffected. Therefore, our expectation that fluorine labeling is sensitive to minor local conformational changes induced upon ligand binding was confirmed. We intended to further strengthen our approach by arbitrarily choosing two other nucleoside positions for labeling within the 14-nt loop (Figure 2c). Although the effect was less pronounced, we observed a distinct downfield shift of the resonance upon ligand binding. Remarkably, for all three fluorine labels in the loop, we observed a clear decrease of linewidth, indicating that the RNA has a more rigid structure in the bound state.

With the intention to identify novel ligands for the tobramycin RNA aptamer, we extended our studies towards various classes of aminoglycosides (e.g. neomycin B, paromomycin, ribostamycin, streptomycin, and spectinomycin)[18] and investigated their interaction with the aptamer (Figure 3 and the Supporting Information). Upon addition of stoichiometric amounts of neomycin B, a significant broadening of the resonance assigned to the loop fluorine label was observed, but the change in chemical shift was marginal, indicating weak loop-specific interaction. The same behavior was found upon addition of stoichiometric amounts of paromomycin or ribostamycin. A 2.5-fold excess of these aminoglycosides resulted in extremely increased linewidths of the 2′-F loop resonances, or in broadening to such an extent that they were no longer observable, while the reference 2′-F stem resonances remained unaffected (Supporting Information). In the case of streptomycin, slight broadening and a defined shift of the loop fluorine resonance reflected a well-behaved fast-exchange ligand–RNA interaction, and the dissociation constant K_d could be determined with accuracy. Figure 3 shows how the chemical shift of the particular 2′-F adenosine resonance moved steadily downfield upon titration with streptomycin, as well as the curve obtained from fitting the data to a simple one-site binding equation. The calculated K_d value was 350 μM, which corresponds to a weak affinity interaction (see the Supporting Information).

To complement our studies, we investigated an RNA interaction with a ligand type other than aminoglycosides. In the presence of Mg^{2+} ions, flavine mononucleotide (FMN) is known to bind to the in vitro selected RNA bulge motif depicted in Figure 4a with a nanomolar dissociation constant ($\approx$0.5 μM).[19] The free FMN RNA aptamer comprising a 2′-F uridine label at the bulge site displayed a single ^{19}F resonance. Addition of Mg^{2+} ions resulted in a slightly shifted and broadened signal, indicating increased flexibility of the particular region in the bulge. Upon addition of one equivalent of FMN, a significant shift of the ^{19}F resonance and a decrease in its linewidth were observed, confirming the typical behavior of a high-affinity binder.

We expanded our studies to the 53-nt RNA depicted in Figure 4b (and the Supporting Information) to demonstrate that our approach works reliably for larger RNAs, for which binding assays based on ^{1}H NMR spectroscopy (imino protons) [20,21] suffer from signal overlap and the labor-intensive signal assignment. The sequence contained both the tobra-

 © 2006 Wiley-VCH Verlag GmbH & Co. KGaA, Weinheim

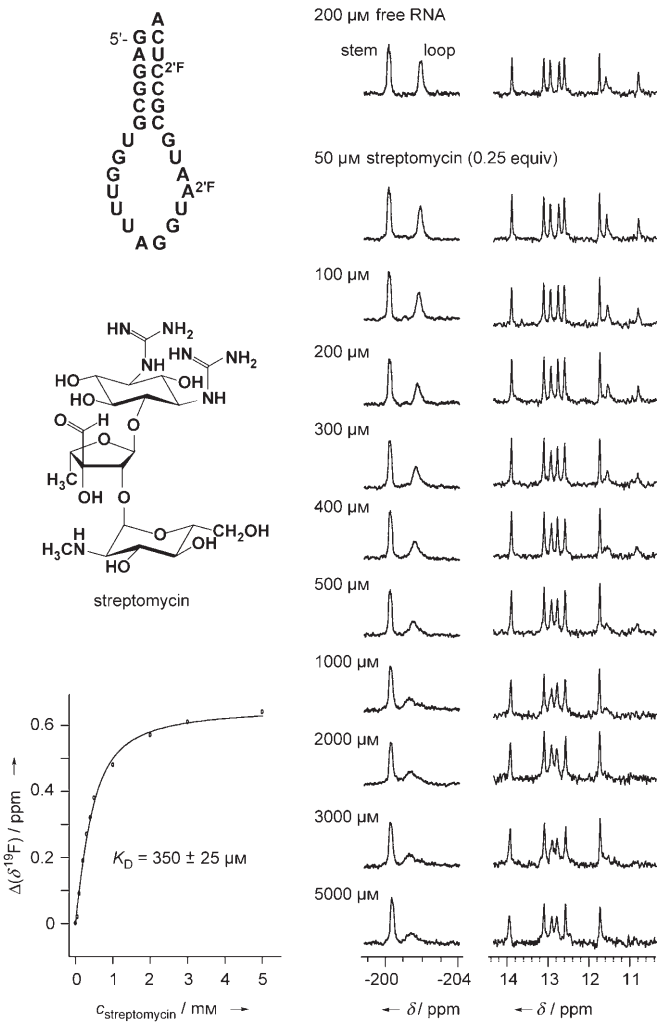

Figure 3. Identification of a low-affinity binder (streptomycin) to the tobramycin RNA aptamer. Titrations followed by non-proton-decoupled ^{19}F NMR and ^{1}H NMR (imino proton) spectroscopy. The dissociation constant was determined by fitting the loop 2′-F chemical shift as a function of ligand concentration according to a two-site second-order exchange process (free state and ligand-bound state, respectively) as displayed in the plot on the bottom (see also the Supporting Information). Conditions: 0.2 mM strand concentrations, H_2O/D_2O 9:1, 25 mM sodium phosphate buffer, pH 6.5, 298 K. ^{19}F resonances relative to external CCl_3F.

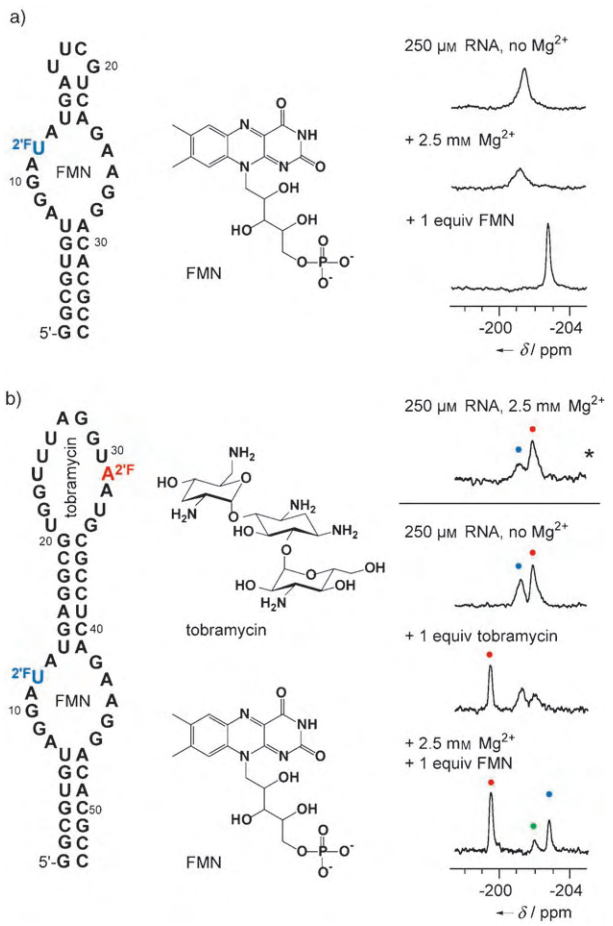

Figure 4. a) Binding of FMN to its 35-nt RNA aptamer followed by ^{19}F NMR spectroscopy. b) RNA (53-nt) containing two binding sites, one for tobramycin and one for FMN. Upon consecutive addition of the ligands, their selective binding was monitored by ^{19}F NMR spectroscopy. The signal assignment was based on the individual aptamer ligand interactions (see Figure 2 and Figure 4a). The additional, low-intensity signal around −202 ppm in the final spectrum when both ligands were present (bottom right; green dot) was associated with a partly misfolded FMN binding pocket or a second binding mode for FMN. All spectra except the one marked with an asterisk were recorded without proton decoupling. Conditions: 0.25 mM strand concentration, H_2O/D_2O 9:1, 25 mM sodium phosphate buffer, pH 6.5, 298 K. ^{19}F resonances relative to external CCl_3F.

mycin and the FMN recognition site, each labeled with a ribose 2′-F atom at a position previously investigated for the individual aptamers. Successive addition of tobramycin, and Mg^{2+} ions together with FMN reflected the site-specific binding events by pronounced shifts and decreases in linewidths of the corresponding resonances. Binding of tobramycin to the 53-nt RNA seemed to be comparable with the individual aptamer–ligand interaction and the same was true for a major population concerning FMN. Interestingly, an additional low-intensity ^{19}F resonance was observed at −202 ppm which did not correlate to the reference aptamers and which was associated to the fluorine label positioned in the FMN site based on integral analysis. This resonance might reflect a minor population of a second binding mode for FMN to its recognition site, or otherwise, a partly misfolded FMN binding pocket in the 53-nt RNA. An excess of both ligands over the RNA or reversed addition of the ligands did not alter the final, observed signal pattern. The precise reason for the low-intensity ^{19}F signal remains to be clarified.

We point out that the majority of the ^{19}F NMR experiments concerning the 35-nt FMN aptamer and the 53-nt RNA construct were recorded without proton decoupling since the linewidths of ^{19}F resonances reached values comparable to the sizes of $^{1}H/^{19}F$ couplings (Figure 4). Also, the weak nonspecific binding of the various aminoglycosides investigated in context with the tobramycin aptamer could be easily detected without proton decoupling (see Figure 3 and the Supporting Information). We consider this feature a strength of the approach that makes it accessible in most organic chemistry laboratories possessing standard NMR hardware.

 © 2006 Wiley-VCH Verlag GmbH & Co. KGaA, Weinheim

The ^{19}F nucleus has 100% natural abundance, possesses an intrinsic NMR sensitivity almost as high as that of protons, and most importantly offers a chemical-shift dispersion that is 100 times greater than that of protons. These properties make fluorine an ideal candidate to monitor functionally important transitions. With respect to nucleic acids, these properties have been exploited to some extent for studies on metal-ion binding,[22] hairpin–duplex transitions,[23] hammerhead ribozyme folding,[24] DNA methylation,[25] and oligonucleotide hybridization.[26,27] Most of these ^{19}F NMR studies on nucleic acids utilize nucleotides that have been modified with fluorine at the nucleobase,[28–32] but a few reports also document ribose 2′-F labeling.[27,33] Of particular interest here is that the introduction of a fluorine in the 2′-position favors ribose C3′-*endo* conformation. This can influence the monomer/dimer equilibrium slightly and may have consequences on the structural integrity as shown for a 10-nt hairpin that, upon labeling with six ribose 2′-fluorines, was observed to form a minor population of the duplex.[27] In the present study, we have no indication for such behavior, which might be a result of the lower number of labels used within the RNAs. Moreover, for the tobramycin aptamer system, the melting profiles of unmodified and 2′-F modified RNAs were compared in detail and they did not indicate an impairment of the native structure (see the Supporting Information).

The recent improvements in the chemical synthesis of RNA make ribose 2′-F labeling available for all four standard nucleobases, and significantly expands the scope of promising applications in RNA research.[34] One example is the verification of RNA folding equilibria that we have reported recently.[35] The approach presented here is another application. The identification of RNA ligands is easily achieved by 2′-F ribose labeling and ^{19}F NMR spectroscopy. Although it cannot be excluded a priori that the replacement of a 2′-OH by 2′-F may affect RNA–ligand interactions, this chemical modification seems to be well tolerated for a majority of RNA ligands. RNA usually provides multiple specific recognition contacts and if these are located at the major groove face of nucleobases or at the phosphate backbone, the 2′-F modification has little effect. Caution might be exercised, however, for the identification of binders to the RNA minor groove.

Thus far, we have predominantly investigated known RNA–ligand interactions to obtain a proof of principle; however, we consider this approach promising for the screening of small combinatorial libraries to identify novel RNA binders.[36]

Received: November 23, 2005
Revised: February 27, 2006
Published online: April 19, 2006

Keywords: drug design · NMR spectroscopy · noncovalent interactions · RNA · solid-phase synthesis

[1] S. J. Sucheck, C.-H. Wong, *Curr. Opin. Chem. Biol.* **2000**, *4*, 678–686.
[2] J. Gallego, G. Varani, *Acc. Chem. Res.* **2001**, *34*, 836–843.
[3] H. Schwalbe, M. Göbel, G. Wess, *ChemBioChem* **2003**, *4*, 915–917.
[4] J. Poehlsgaard, S. Douthwaite, *Nat. Rev. Microbiol.* **2005**, *3*, 870–881.
[5] A. Hüttenhofer, P. Schattner, N. Polacek, *Trends Genet.* **2005**, *21*, 289–297.
[6] E. E. Swayze, E. A. Jefferson, K. A. Sannes-Lowery, L. B. Blyn, L. M. Risen, S. Arakawa, S. A. Osgood, S. A. Hofstadler, R. H. Griffey, *J. Med. Chem.* **2002**, *45*, 3816–3819.
[7] B. Llano-Soleto, E. F. Azucena, L. P. Kotra, S. Mobashery, C. S. Chow, *Chem. Biol.* **2002**, *9*, 455–463.
[8] J. R. Thomas, J. C. DeNap, M. L. Wong, P. J. Hergenrother, *Biochemistry* **2005**, *44*, 6800–6808.
[9] J. B.-H. Tok, R. R. Rando, *J. Am. Chem. Soc.* **1998**, *120*, 8279–8280.
[10] C.-H. Wong, M. Hendrix, D. D. Manning, C. Rosenbohm, W. A. Greenberg, *J. Am. Chem. Soc.* **1998**, *120*, 8319–8327.
[11] J. R. Huth, C. Sun, D. R. Sauer, P. J. Hajduk, *Methods Enzymol.* **2005**, *394*, 549–587.
[12] L. Feelding, *Curr. Top. Med. Chem.* **2003**, *3*, 39–53.
[13] F. Rastinejad, C. Evilia, P. Lu, *Methods Enzymol.* **1995**, *261*, 560–575.
[14] C. Dalvit, N. Mongelli, G. Papeo, P. Giordano, M. Veronesi, D. Moskau, R. Kümmerle, *J. Am. Chem. Soc.* **2005**, *127*, 13380–13385.
[15] C. Dalvit, E. Ardini, M. Flocco, G. P. Fogliatto, N. Mongelli, M. Veronesi, *J. Am. Chem. Soc.* **2003**, *125*, 14620–14625.
[16] T. Hermann, D. J. Patel, *Science* **2000**, *287*, 820–825.
[17] L. Jiang, D. J. Patel, *Nat. Struct. Biol.* **1998**, *5*, 769–774.
[18] F. Walter, Q. Vicens, E. Westhof, *Curr. Opin. Chem. Biol.* **1999**, *3*, 694–704.
[19] P. Fan, A. K. Suri, R. Fiala, D. Live, D. J. Patel, *J. Mol. Biol.* **1996**, *258*, 480–500.
[20] L. Yu, T. K. Oost, J. M. Schkeryantz, J. Yang, D. Janowick, S. W. Fesik, *J. Am. Chem. Soc.* **2003**, *125*, 4444–4450.
[21] M. Mayer, T. L. James, *J. Am. Chem. Soc.* **2004**, *126*, 4453–4460.
[22] M. Olejniczak, Z. Gdaniec, A. Fischer, T. Grabarkiewicz, L. Bielecki, R. W. Adamiak, *Nucleic Acids Res.* **2002**, *30*, 4241–4249.
[23] J. R. P. Arnold, J. J. Fisher, *J. Biomol. Struct. Dyn. Biomol. Struct. Dyn.* **2000**, *18*, 843–856.
[24] C. Hammann, D. G. Norman, D. M. J. Lilley, *Proc. Natl. Acad. Sci. USA* **2001**, *98*, 5503–5508.
[25] S. Klimasauskas, T. Szyperski, S. Serva, K. Wüthrich, *EMBO J.* **1998**, *17*, 317–324.
[26] J.-F. Trempe, C. J. Wilds, A. Y. Denisov, R. T. Pon, M. J. Damha, K. Gehring, *J. Am. Chem. Soc.* **2001**, *123*, 4896–4903.
[27] B. Reif, V. Wittmann, H. Schwalbe, C. Griesinger, K. Wörner, K. Jahn-Hoffmann, J. Engels, W. Bermel, *Helv. Chim. Acta* **1997**, *80*, 1952–1971.
[28] A. Fischer, Z. Gdaniec, E. Biala, M. Lozynski, J. Milecki, R. W. Adamiak, *Nucleosides Nucleotides* **1996**, 477–488.
[29] W. H. Gmeiner, R. T. Pon, J. W. Lown, *J. Org. Chem.* **1991**, *56*, 3602–3608.
[30] L. G. Scott, B. H. Geierstanger, J. R. Williamson, M. Hennig, *J. Am. Chem. Soc.* **2004**, *126*, 11776–11777.
[31] W. C. Chu, J. Horowitz, *FEBS Lett.* **1991**, *295*, 159–162.
[32] W. C. Chu, J. Horowitz, *Nucleic Acids Res.* **1989**, *17*, 7241–7252.
[33] B. Luy, J. P. Merino, *J. Biomol. NMR* **2001**, *20*, 39–47.
[34] R. Micura, *Angew. Chem.* **2002**, *114*, 2269–2373; *Angew. Chem. Int. Ed.* **2002**, *41*, 2265–2267.
[35] C. Kreutz, H. Kählig, R. Konrat, R. Micura, *J. Am. Chem. Soc.* **2005**, *127*, 11558–11559.
[36] J. R. Thomas, X. Liu, P. J. Hergenrother, *J. Am. Chem. Soc.* **2005**, *127*, 12434–12435.

 © 2006 Wiley-VCH Verlag GmbH & Co. KGaA, Weinheim

Enzymatic Syntheses

DOI: 10.1002/anie.200504230

A Biocatalytic Henry Reaction—The Hydroxynitrile Lyase from *Hevea brasiliensis* Also Catalyzes Nitroaldol Reactions**

*Thomas Purkarthofer, Karl Gruber, Mandana Gruber-Khadjawi, Kerstin Waich, Wolfgang Skranc, Daniel Mink, and Herfried Griengl**

Hydroxynitrile lyases (HNLs) are a family of versatile enzymes that catalyze the reversible cleavage of α-hydroxy nitriles and are utilized for the production of enantiopure cyanohydrins from aldehydes or ketones and HCN.[1] Several HNLs from different sources have been identified, and the HNL-catalyzed synthesis of a large number of cyanohydrins with *R* and *S* configuration with excellent stereoselectivity has been demonstrated.[2] In trying to expand the synthetic applicability of the HNL methodology we considered replacing HCN by other nucleophiles to be added to carbonyl compounds catalyzed by these enzymes. Based on the mechanism of this biotransformation[3] crucial parameters for such alternative reagents would be the molecular size and the pK_a of the CH-acidic portion, which should be similar to that of HCN (p$K_a \approx 9$). One important substance class that meets these criteria are nitroalkanes. Their reaction with carbonyl compounds—known as the nitroaldol or Henry reaction—constitutes a carboligation process of high synthetic value. The Henry reaction furnishes vicinal nitroalcohols, which can easily be transformed to a series of valuable intermediates such as, for example, 1,2-aminoalcohols and α-hydroxycarboxylic acids.[4]

First, we examined the addition of nitromethane to aldehydes in the presence of the hydroxynitrile lyase from *Hevea brasiliensis* (*Hb*HNL). The reaction of benzaldehyde with nitromethane gave 2-nitro-1-phenylethanol in 63% yield with an enantiomeric excess of 92% (Table 1). Besides the expected nitroalcohol product, small amounts (10–15%) of the corresponding elimination product, 1-nitro-2-phenylethene, was detected as the only by-product. By comparing optical rotation data of the product with literature values the absolute configuration of the product was determined to be *S*,[5] which is in agreement with the known stereopreference of *Hb*HNL in cyanohydrin reactions.

Table 1: Stereoselective addition of nitromethane to aldehydes in the presence of *Hb*HNL.[a]

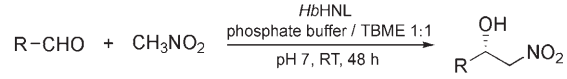

R	Yield [%]	*ee* [%][b]
	63	92
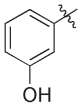	46	18
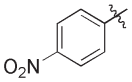	77	28
	57	72
$CH_3(CH_2)_5$	25	89

[a] TBME = *tert*-butyl methyl ether. [b] The absolute configuration of the products was assigned by comparison of the sign of optical rotation with literature data (see the Supporting Information).

Although the nitroaldol reaction has been known for more than a century,[6] stereoselective protocols started to evolve only a few decades ago. In these studies various nonenzymatic catalysts have been utilized.[7] Our results represent the first example of a biocatalytic asymmetric Henry reaction.

The *Hb*HNL-catalyzed addition of nitromethane to benzaldehyde was carried out under standard conditions after adjustment of the aqueous enzyme solution to pH 7.[8] The yields and selectivity are comparable when either *tert*-butyl methyl ether (TBME) or toluene are used as the organic phase. In contrast to *Hb*HNL-catalyzed cyanohydrin reactions, spontaneous unselective product formation does not play a crucial role even at elevated pH values. This can be explained in part by the fact that the partition coefficient of nitromethane in the water/organic phase system is lower than that of HCN, owing to the reduced solubility of nitromethane in the aqueous phase.[9] On the other hand, this also constitutes a limiting factor since the amount of nitro compound available for the enzyme in the aqueous phase cannot be increased arbitrarily.

The productivity of *Hb*HNL in the nitroaldol reaction is much lower than its activity in cyanohydrin reactions. On average several hundred units of enzyme are sufficient to transform carbonyl compounds into the corresponding α-hydroxy nitriles within a few hours, whereas 4000 units are

[*] Dr. T. Purkarthofer, Prof. K. Gruber, Dr. M. Gruber-Khadjawi, DI K. Waich, Prof. H. Griengl
Research Centre Applied Biocatalysis
Petersgasse 14, 8010 Graz (Austria)
Fax: (+43) 316-873-8740
E-mail: office.orgc@tugraz.at
Dr. W. Skranc
DSM Fine Chemicals Austria
R & D Center Linz
St.-Peter-Strasse 25, 4021 Linz (Austria)
Dr. D. Mink
DSM Research
Advanced Synthesis Catalysis & Development
P.O. Box 18, 6160 MD Geleen (The Netherlands)

[**] We thank Prof. Bernard Golding, University of Newcastle, for his fruitful contributions to this project. The Österreichische Forschungsförderungsgesellschaft (FFG), the Province of Styria and the Styrian Business Promotion Agency (SFG), and the city of Graz—within the framework of the K*plus* programme—are acknowledged for financial support.

Supporting information for this article is available on the WWW under http://www.angewandte.org or from the author.

InterScience © 2006 Wiley-VCH Verlag GmbH & Co. KGaA, Weinheim

required to perform nitroaldol reactions and reach acceptable yields within 48 h. Regarding the scope of the reaction with respect to the carbonyl acceptor, several representative aldehydes were converted into the corresponding nitroalcohols in the presence of *Hb*HNL (Table 1).

The corresponding addition of nitroethane to benzaldehyde introduces two new stereocenters simultaneously (Table 2) and requires good control of the diastereoselectivity, which has been shown to be difficult in Henry reactions.[10] In the *Hb*HNL-catalyzed reaction of nitroethane and benzaldehyde we obtained a diastereomeric mixture of 2-nitro-1-phenylpropanol (**1a**–**4a**) in 67% yield (Table 2).

Table 2: *Hb*HNL-catalyzed stereoselective addition of nitroethane to benzaldehyde.[a]

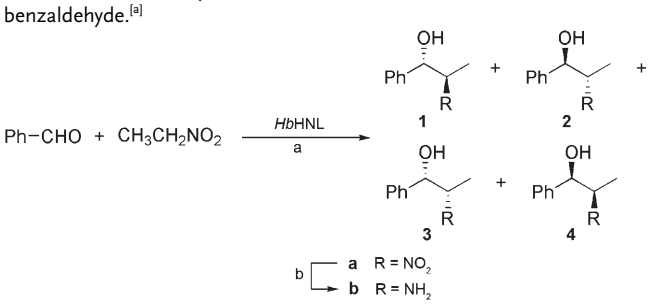

		Config.	Relative yield [%]	*ee* [%]
anti	**1a**	1*S*,2*R*	88	95
	2a	1*R*,2*S*	2	
syn	**3a**	1*S*,2*S*	8	53
	4a	1*R*,2*R*	2	

[a] Reaction conditions: a) *Hb*HNL, phosphate buffer (pH 7)/TBME 1:1, RT, 48 h, 67%; b) H_2, Pd/C, EtOH, RT, 6 h, 90%.

The absolute configuration of the products **1a**–**4a** was determined by reduction to aminoalcohols **1b**–**3b** followed by derivatization to give oxazolines **5**–**7** (Scheme 1); these were compared to reference compounds of known configuration.

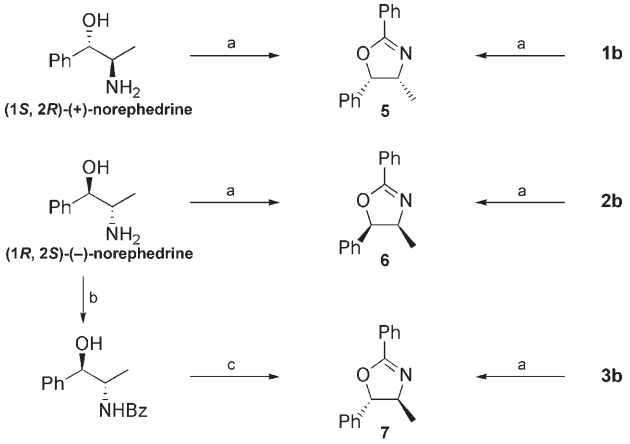

Scheme 1. Determination of the absolute configuration of aminoalcohols **1b**, **2b**, **3b**. Conditions: a) triethyl orthobenzoate, trifluoroacetic acid, 1,2-dichloroethane, reflux, 3 h, 74%; b) Et_3N, PhCOCl, CH_2Cl_2, RT, 3 h, 80%; c) diisopropyl azodicarboxylate, PPh_3, THF, RT, 16 h, 63%.

Optically pure reference compounds were prepared starting from commercially available *anti*-norephedrins. To get access to the *syn* series we inverted the configuration at C-1 via the corresponding benzamide to give oxazoline **7** (Scheme 1). Based on this analysis, the main product of the *Hb*HNL-catalyzed addition of nitroethane to benzaldehyde is (1*S*,2*R*)-2-nitro-1-phenylpropanol (**1a**). Nitroalcohols **1a**–**4a** were obtained with an *anti*/*syn* ratio of 9:1 and an enantiomeric excess of the *anti* isomer **1a** of 95%. Thus, the product mixture contains almost 90% of the main product (1*S*,2*R*)-**1a**. Assignment of the absolute configuration of the *anti* isomers using a similar derivatization method was accomplished recently.[11]

Possible binding modes of 2-nitro-1-phenylethanol to the active site of *Hb*HNL were investigated by molecular modeling. *Hb*HNL has been studied extensively with respect to its three-dimensional structure[12] and mechanism of catalysis.[13] A wealth of experimental structural information on substrate complexes of this enzyme is available.[3,13a,14] Complexes of *Hb*HNL with both enantiomers of 2-nitro-1-phenylethanol were modeled by molecular docking simulations.[15] In analogy to studies with cyanohydrins, these calculations predicted the *S* enantiomer to bind more favorably to the enzyme than the corresponding *R* enantiomer. In the complex with the *S* enantiomer, the substrate OH group forms hydrogen bonds to the side chains of Ser80 and Thr11 and the nitro group interacts with Lys236 (Figure 1, yellow structure). Thus, all mechanistically important polar interactions with active-site residues are preserved.[3] The phenyl ring is bound in the same hydrophobic pocket as that observed in the complex with mandelonitrile.[14] The nitro and phenyl groups occupy similar positions in the complex with the *R* enantiomer as in the complex with the *S* enantiomer, but the crucial hydrogen bond with Ser80 is lost (data not shown).

As a result of the equivalent substrate binding modes and the conservation of important polar interactions, the mechanism for the transformation of cyanohydrins by *Hb*HNL very likely applies to the nitroaldol reaction as well. The

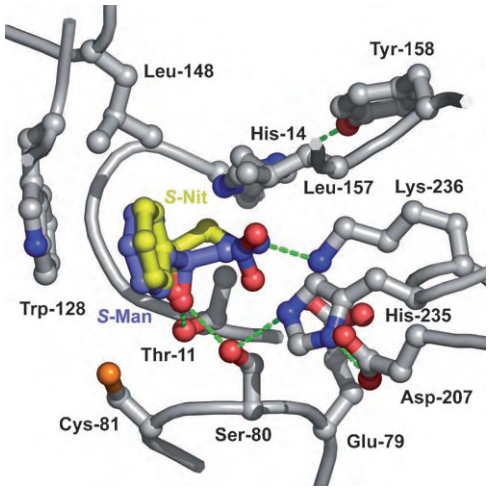

Figure 1. Modeled complex of *Hb*HNL with (*S*)-2-nitro-1-phenylethanol (yellow) in comparison with the binding mode of (*S*)-mandelonitrile (blue) observed experimentally.

© 2006 Wiley-VCH Verlag GmbH & Co. KGaA, Weinheim

nitroalcohol would then be deprotonated at the hydroxy function by the catalytic triad Ser80/His235/Asp207 in the cleavage direction, and the positive charge contributed by Lys236 would facilitate the deprotonation of the nitroalkane in the synthesis direction.[3] Whether enzyme kinetics follow an ordered "uni–bi" mechanism as observed for cyanohydrin substrates[16] is under investigation. The substrate binding site of *Hb*HNL is spacious enough to accept the more voluminous nitro compounds in a similar fashion to the binding of the corresponding cyanohydrins (Figure 1). Steric interactions, however, may still be responsible for the observed reduced catalytic rate.

For more information about the mechanism of the enzymatic Henry reaction, we carried out experiments using deuterated nitroalkanes. Although definitive conclusions will have to await results from proper kinetics experiments, the reduced yield obtained for the addition of [1,1-D_2]nitroethane to benzaldehyde already indicates the existence of a kinetic isotope effect and suggests the deprotonation of the nitroalkane to be the rate-limiting step. In contrast, in the *Hb*HNL-catalyzed cyanohydrin reaction, the C–C bond formation was found to be rate limiting.[17] In enzyme kinetics studies of nitroalkane oxidases, true kinetic isotope effects of 8–9 were measured for the formation of a nitroethane anion.[18] This is in reasonable agreement with our rough estimate for the equivalent effect—on the order of 10—for the *Hb*HNL-catalyzed Henry reaction. These findings are also in line with the well-known nitroalkane anomaly, which describes the fact that the deprotonation rate of nitroalkanes is lower than that expected based on their pKa value.[19] Thus, a combination of steric and electronic effects may explain the reduced rate of the *Hb*HNL-catalyzed Henry reaction compared to the rate of cyanohydrin formation.

In summary, Henry reactions catalyzed by the hydroxynitrile lyase from *Hevea brasiliensis* involving aldehydes and either nitromethane or nitroethane yielded the corresponding nitroalcohols in good yields and reasonable-to-high enantiomeric excess. In the case of the reaction with nitroethane, two stereocenters are generated simultaneously with good diastereo- and enantioselectivity, granting access to substances of the ephedrine family. We are currently testing other carbonyl compounds and nitroalkanes as starting materials for this reaction, and studies to improve the efficiency of the process with respect to both yields and stereoselectivity are underway.

Received: November 28, 2005
Published online: April 24, 2006

Keywords: biocatalysis · Henry reaction · hydroxynitrile lyase · molecular modeling · nitroalcohols

[1] a) P. Pöchlauer, *Chim. Oggi* **1998**, *16*, 15–19; b) D. V. Johnson, A. A. Zabelinskaja-Mackova, H. Griengl, *Curr. Opin. Chem. Biol.* **2000**, *4*, 103–109; c) "Enzymatic Synthesis of Cyanohydrins": M. H. Fechter, H. Griengl in *Enzyme Catalysis in Organic Synthesis* (Eds.: K. Drauz, H. Waldmann), Wiley-VCH, Weinheim, **2002**, pp. 974–989; d) M. Sharma, N. N. Sharma, T. C. Bhalla, *Enzyme Microb. Technol.* **2005**, *37*, 279–294.

[2] a) K. Gruber, C. Kratky, *J. Polym. Sci. Part A* **2004**, *42*, 479–486; b) F. Effenberger, *Angew. Chem.* **1994**, *106*, 1609–1619; *Angew. Chem. Int. Ed. Engl.* **1994**, *33*, 1555–1564; c) R. J. H. Gregory, *Chem. Rev.* **1999**, *99*, 3649–3682; d) H. Griengl, H. Schwab, H. Fechter, *Trends Biotechnol.* **2000**, *18*, 252–256; e) M. North, *Tetrahedron: Asymmetry* **2003**, *14*, 147–176; f) M. H. Fechter, H. Griengl, *Food Technol. Biotechnol.* **2004**, *42*, 287–294.

[3] K. Gruber, G. Gartler, B. Krammer, H. Schwab, C. Kratky, *J. Biol. Chem.* **2004**, *279*, 20501–20510.

[4] a) N. Ono, *The Nitro Group in Organic Synthesis*, Wiley-VCH, New York, **2001**; b) F. A. Luzzio, *Tetrahedron* **2001**, *57*, 915–945.

[5] a) B. M. Trost, V. S. C. Yeh, *Angew. Chem.* **2002**, *114*, 889–891; *Angew. Chem. Int. Ed.* **2002**, *41*, 861–863; b) D. A. Evans, D. Seidel, M. Rueping, H. W. Lam, J. T. Shaw, C. W. Downey, *J. Am. Chem. Soc.* **2003**, *125*, 12692–12693.

[6] L. Henry, *C. R. Hebd. Seances Acad. Sci.* **1895**, *120*, 1265.

[7] a) C. Palomo, M. Oiarbide, A. Mielgo, *Angew. Chem.* **2004**, *116*, 5558–5560; *Angew. Chem. Int. Ed.* **2004**, *43*, 5442–5444; b) C. Palomo, M. Oiarbide, A. Laso, *Angew. Chem.* **2005**, *117*, 3949–3952; *Angew. Chem. Int. Ed.* **2005**, *44*, 3881–3884, and references therein; c) M. Shibasaki, N. Yoshikawa, *Chem. Rev.* **2002**, *102*, 2187–2209; d) M. Shibasaki, H. Gröger in *Comprehensive Asymmetric Catalysis*, *Vol. III* (Eds.: E. N. Jacobsen, A. Pfalz, H. Yamamoto), Springer, Berlin, **1999**, pp. 1075–1090; e) T. Marcelli, R. N. S. van der Haas, J. H. van Maarseveen, H. Hiemstra, *Angew. Chem.* **2006**, *118*, 943–945; *Angew. Chem. Int. Ed.* **2006**, *45*, 929–931.

[8] General procedure: Wt-*Hb*HNL (4000 U mmol^{-1} aldehyde; activity determined for the cleavage of mandelonitrile; the enzyme was kindly provided by DSM) was stirred in phosphate buffer (pH 7, 50 mM) and TBME (1:1) until an emulsion was established. Freshly distilled aldehyde (1–10 mmol) was added to the mixture. The mixture was stirred for 5 min before the nitroalkane (10 mmol mmol^{-1} aldehyde) was added. The reaction mixture was stirred for 48 h at room temperature. After centrifugation and separation of the layers, the aqueous phase was extracted with TBME. The combined organic phases were dried over Na_2SO_4 and concentrated in vacuo. The crude products were purified by column chromatography.

[9] R. M. Stephenson, *J. Chem. Eng. Data* **1992**, *37*, 80–95.

[10] B. Lecea, A. Arrieta, I. Morao, F. P. Cossio, *Chem. Eur. J.* **1997**, *3*, 20–28.

[11] T. Ooi, K. Doda, K. Maruoka, *J. Am. Chem. Soc.* **2003**, *125*, 2054–2055.

[12] a) U. G. Wagner, M. Hasslacher, H. Griengl, H. Schwab, C. Kratky, *Structure* **1996**, *4*, 811–822; b) K. Gruber, M. Gugganig, U. G. Wagner, C. Kratky, *Biol. Chem.* **1999**, *380*, 993–1000.

[13] a) J. Zuegg, K. Gruber, M. Gugganig, U. G. Wagner, C. Kratky, *Protein Sci.* **1999**, *8*, 1990–2000; b) K. Gruber, *Proteins Struct. Funct. Genet.* **2001**, *44*, 26–31.

[14] G. Gartler, C. Kratky, K. Gruber, *J. Biotechnol.* **2006**, in press.

[15] See the Supporting Information.

[16] M. Bauer, H. Griengl, W. Steiner, *Biotechnol. Bioeng.* **1999**, *62*, 20–29.

[17] W.-M. Ching, R. G. Kallen, *J. Am. Chem. Soc.* **1978**, *100*, 6119–6124.

[18] M. P. Valley, P. F. Fitzpatrick, *J. Am. Chem. Soc.* **2004**, *126*, 6244–6245.

[19] a) R. G. Pearson, R. L. Dillon, *J. Am. Chem. Soc.* **1953**, *75*, 2439–2443; b) F. G. Bordwell, W. J. Boyle, J. A. Hautala, K. C. Yee, *J. Am. Chem. Soc.* **1969**, *91*, 4002–4003; c) F. G. Bordwell, J. E. Bartmess, J. A. Hautala, *J. Org. Chem.* **1978**, *43*, 3107–3113; d) J. R. Keeffe, J. Morey, C. A. Palmer, J. C. Lee, *J. Am. Chem. Soc.* **1979**, *101*, 1295–1297; e) N. Agmon, *J. Am. Chem. Soc.* **1980**, *102*, 2164–2167; f) H. Yamataka, S. C. Ammal, *Arkivoc* **2003**, 59–68.

 © 2006 Wiley-VCH Verlag GmbH & Co. KGaA, Weinheim

Solid-State Structures

DOI: 10.1002/anie.200504460

Space Filling Versus Symmetry: Two Consecutive Crystal-to-Crystal Phase Transitions in a 2D Network**

*Chunhua Hu and Ulli Englert**

Dedicated to Professor Minqin Chen on the occasion of his 67th birthday

Phase transitions with the retention of single-crystal character directly reflect the relationship between the solids involved. These processes are rare, and normally occur smoothly through minor movements of atoms in the vast diffusionless environment of the crystal. The first examples were provided by the photodimerization of small organic molecules;[1,2] this field has recently been reviewed.[3] Later, other reaction types, such as polymerizations[4–6] or racemizations[7–10], were also shown to proceed in a topochemical way, and the relevance of topochemistry to photodimerization and photopolymerization in diolefinic crystals was likewise discussed.[11] Studies on crystal-to-crystal transformations involving coordination polymers and networks are more recent.[12–18] Herein, we report an unprecedented system: two consecutive reversible phase transitions occur in a single crystal of the 2D coordination compound $[Pb(\mu\text{-}Cl)_2(\mu\text{-bipy})]_\infty$ (bipy = 4,4′-bipyridine). These transformations relate the highly distorted low-temperature structure **1α**, via the intermediate room-temperature phase **1β**, to the arrangement of maximum symmetry **1γ**, the so-called aristotype (Scheme 1).[19]

The underlying topology of the 2D network is maintained in all three phases. Figure 1 shows a section of the room-temperature structure **1β**. This phase has not yet been described for $[Pb(\mu\text{-}Cl)_2(\mu\text{-bipy})]_\infty$; it is, however, isotypic to the crystal structures of the analogous bromo[21] and iodo derivatives.[22] In this structure, the chloro ligands form a nearly symmetrical bridge between the metal cations, which occupy sites of symmetry 2/*m*. The resulting strands of metal and chlorine atoms extend along the crystallographic *c* axis and are crosslinked by bipy ligands in the *b* direction. The striking feature of the 2D network **1β** is its ability to undergo crystal-to-crystal phase transitions, both upon cooling and heating: three crystal structures could be determined from the same sample.

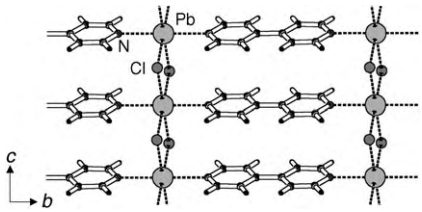

Figure 1. PLUTON[20] representation of one layer of **1β**. The view direction is slightly tilted from [100].

low-temp. phase	322 K ⇌ 271 K	room-temp. phase	423 K ⇌ 422 K	high-temp. phase
1α		**1β**		**1γ**
$P\bar{1}$		*C*2/*m*		*Cmmm*
space filling 0.744		space filling 0.716		space filling 0.678

Scheme 1. Structures determined by single-crystal X-ray diffraction on the same sample of $[Pb(\mu\text{-}Cl)_2(\mu\text{-bipy})]_\infty$. The three phases, which differ in their symmetry and space filling (the fraction of the cell volume that is occupied by the van der Waals spheres of the atoms), interconvert at the transition temperatures indicated.

When solid **1β** is exposed to temperatures below 271 K, it adopts a highly distorted structure of low symmetry and high space filling (Scheme 1). Single crystals of the room-temperature structure **1β** are converted into twins of **1α**. This low-temperature phase was also obtained by Nordell et al. under hydrothermal conditions;[23] these authors studied the phase at room temperature and did not observe any indication of a phase transition.

In the course of the solid-state transformation of **1β** to **1α**, one nitrogen atom of each bipy ligand shifts in the *c* direction to the next lead atom in the chloro-bridged chain (Figure 2). This process, which occurs in each 2D layer, can be understood as the cleavage of the bond between each lead atom and one ligand nitrogen atom, the movement of the bridging bipy ligands, and the subsequent formation of new Pb–N bonds within an almost unchanged matrix of lead and chlorine atoms. The alternative process, namely a shift of entire $\{Pb(\mu\text{-}Cl)_2\}_\infty$ chains throughout the crystal without bond cleavage, would require an extensive movement of all atoms and is, therefore, an unrealistic scenario for a crystal-to-crystal transformation. In addition to this intralayer process, a displacement of neighboring layers results in a slightly different stacking sequence in the third dimension in **1α** and **1β**.

The strong distortion of the low-temperature structure **1α** is reflected by the asymmetric coordination environment of the lead centers, and the unusual disposition of the metal atoms out of the planes of the pyridine rings (Figure 3). This arrangement, however, increases the density and space filling: the distance between neighboring bipy bridges (and thus, the shortest lattice constant) is reduced from 4.11 to 3.95 Å.

Remarkably, $[Pb(\mu\text{-}Cl)_2(\mu\text{-bipy})]_\infty$ also undergoes a topotactic transformation in the opposite direction: when a single crystal of **1β** is heated to 423 K, it reversibly converts into yet another phase, **1γ**, in the space group *Cmmm*, a supergroup of the *C*2/*m* space group of **1β** (Scheme 1, Figure 4). The atomic

[*] Dr. C. Hu, Prof. Dr. U. Englert
Institut für Anorganische Chemie
RWTH Aachen
Landoltweg 1, 52074 Aachen (Germany)
Fax: (+49) 241-809-2288
E-mail: ullrich.englert@ac.rwth-aachen.de

[**] We thank Dr. A. Fischer and D. Lischke, Grünenthal GmbH Aachen, and Dr. K. Beckerle, RWTH Aachen, for help with the DSC measurements. I. Kalf, RWTH Aachen, is acknowledged for help with the IR spectroscopic studies. We are grateful to Prof. Dr. M. U. Schmidt and Dr. J. Glinnemann, Universität Frankfurt, for help with the variable-temperature powder diffraction studies.

© 2006 Wiley-VCH Verlag GmbH & Co. KGaA, Weinheim

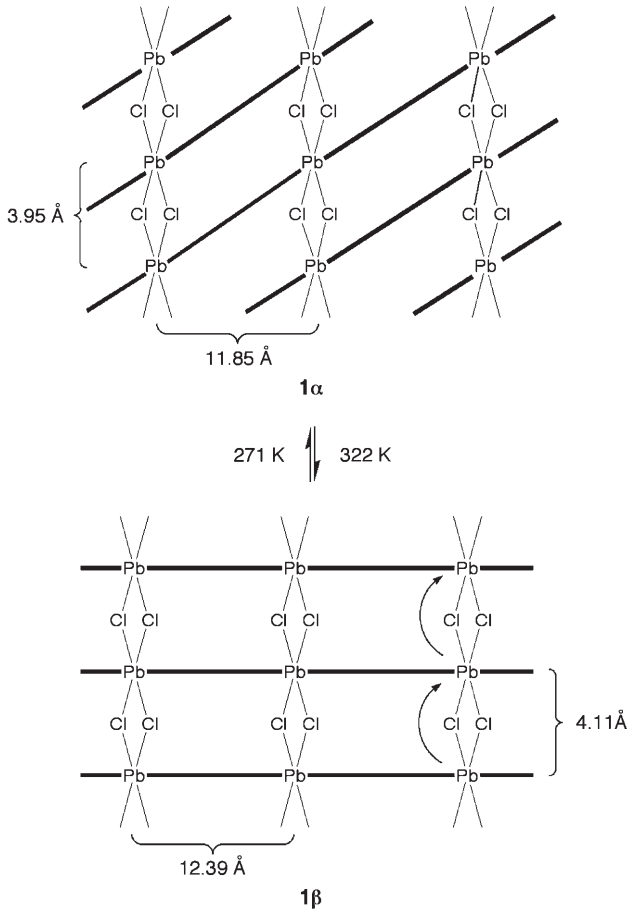

Figure 2. Process for the transition between the phases **1α** and **1β**. The indicated intralayer Pb···Pb distances (equivalent to the in-plane cell parameters) are similar in both structures. The bipy ligands are represented by thick lines.

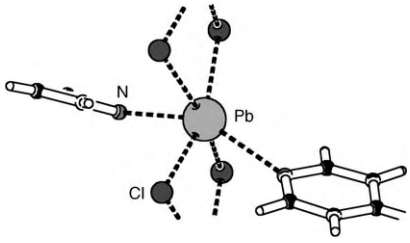

Figure 3. Distorted coordination environment of the lead atoms in **1α**.

arrangement in **1γ** corresponds to the highest possible symmetry for a 2D network of composition $[M(\mu\text{-}X)_2(\mu\text{-bipy})]_\infty$ (M = metal, X = halogen) and has not been documented previously for $[Pb(\mu\text{-}Cl)_2(\mu\text{-bipy})]_\infty$. Analogous structures have been reported for other divalent metals.[24–28]

The lead atoms in **1γ** occupy positions of *mmm* site symmetry, which necessitates that the six-membered rings of the bipy ligands be coplanar and oriented perpendicular to the direction of the $\{Pb(\mu\text{-}Cl)_2\}_\infty$ chains. As a consequence, short intermolecular contacts occur along the *b* axis between hydrogen atoms in adjacent polymer layers. The lattice parameter *b* in **1γ** is, therefore, longer than the corresponding

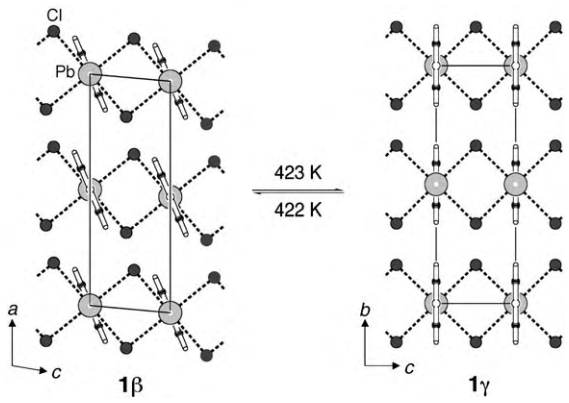

Figure 4. Views of **1β** and **1γ** along the bridging bipy ligands.

cell constant *a* in **1β**, and this difference is the main reason for the larger cell volume of the high-temperature form **1γ**. The movement of atoms that results in the **1γ** structure is largely due to the conformational change within the 2D nets; neighboring layers are only slightly displaced relative to one another.

In conclusion, the presumably rigid 2D network $[Pb(\mu\text{-}Cl)_2(\mu\text{-bipy})]_\infty$ consecutively undergoes two reversible crystal-to-crystal transformations, which lead from a highly distorted low-temperature structure, via a room-temperature intermediate, to the aristotype. In agreement with the topochemical principle, essential features of the layer structure are conserved during both processes. Increased packing efficiency is exchanged for higher symmetry.

Experimental Section

Single crystals of **1β** suitable for X-ray diffraction were prepared by three-layer diffusion: in a 25-mL test tube, a solution of $PbCl_2$ (0.05 mmol, 14 mg) in water (8 mL) was layered with 2-propanol (5 mL); a third layer of 4,4′-bipyridine (0.05 mmol, 7.8 mg) in diethyl ether (8 mL) was added carefully. Colorless platelets of the product formed at the water/2-propanol interface.

Powder X-ray diffraction experiments (STOE STADI P powder diffractometer equipped with a position-sensitive image-plate detector and an Oxford Cryosystems Series 700 temperature controller) showed that the phase transitions described for single crystals also occur in macroscopic powder samples and lead to monophasic products.

The crystal-to-crystal transformations described are reversible; up to five phase transitions were performed with the same sample. We note, however, that the data-collection temperature required for **1γ** is relatively close to the decomposition temperature of the sample, which is well below 500 K; at 450 K, samples are only stable for a few hours. The phase transitions were monitored not only by X-ray diffraction, but also optically (with the integrated CCD camera of the diffractometer, at limited resolution). No visible changes were associated with the transition between **1α** and **1β**, whereas the onset of the decomposition of the crystals is clearly visible at 450 K; the decomposition starts at the crystal face exposed to the warm nitrogen stream.

Single-crystal structure determinations: Intensity data were collected with a Bruker Smart APEX CCD detector on a D8 goniometer ($Mo_{K\alpha}$ radiation, $\lambda = 0.71073$ Å, graphite monochromator). The temperature during the data collection was controlled with an Oxford Cryosystems Series 800 instrument. The intensity data

 © 2006 Wiley-VCH Verlag GmbH & Co. KGaA, Weinheim

were integrated with SAINT[29] and corrected for absorption with SADABS.[30] The structures were solved by direct methods (SHELXS-97)[31] and refined on F^2 (SHELXL-97).[32] The three consecutive structure determinations were performed on the same crystal.

Crystal data for **1α**: triclinic space group $P\bar{1}$, $a = 3.9490(13)$, $b = 11.853(4)$, $c = 12.324(4)$ Å, $\alpha = 94.094(7)$, $\beta = 93.195(7)$, $\gamma = 93.396(7)°$, $V = 573.3(3)$ Å^3, $Z = 2$, $T = 200$ K. The crystals of **1α**, obtained by cooling the room-temperature phase **1β**, are nonmerohedral twins. The refinement of 77 parameters on the basis of 2831 independent reflections (of a total of 7225) converged at $R1 = 0.0676$, $wR2 = 0.1514$, and GOF = 1.053.

Crystal data for **1β**: monoclinic space group $C2/m$, $a = 11.7878(9)$, $b = 12.3863(10)$, $c = 4.1107(3)$ Å, $\beta = 95.217(4)°$, $V = 597.71(8)$ Å^3, $Z = 2$, $T = 293$ K. The refinement of 39 parameters on the basis of 777 independent reflections (of a total of 2776) converged at $R1 = 0.0305$, $wR2 = 0.0586$, and GOF = 1.057.

Crystal data for **1γ**: orthorhombic space group $Cmmm$, $a = 12.333(2)$, $b = 12.2648(18)$, $c = 4.0991(7)$ Å, $V = 620.05(17)$ Å^3, $Z = 2$, $T = 450$ K. The refinement of 28 parameters on the basis of 478 independent reflections (of a total of 2770) converged at $R1 = 0.0352$, $wR2 = 0.0646$, and GOF = 1.017.

CCDC-292650 (**1α**), CCDC-292651 (**1β**), and CCDC-292652 (**1γ**) contain the supplementary crystallographic data for this paper. These data can be obtained free of charge from The Cambridge Crystallographic Data Centre via www.ccdc.cam.ac.uk/data_request/cif.

Received: December 15, 2005
Published online: April 19, 2006

Keywords: coordination polymers · crystal-to-crystal transitions · lead · phase transitions · topochemistry

[1] M. D. Cohen, G. M. J. Schmidt, *J. Chem. Soc.* **1964**, 1996.
[2] M. D. Cohen, G. M. J. Schmidt, F. I. Sonntag, *J. Chem. Soc.* **1964**, 2000.
[3] T. Friscic, L. R. MacGillivray, *Z. Kristallogr.* **2005**, *220*, 351.
[4] M. Yalpani, R. Boese, D. Bläser, *Chem. Ber.* **1983**, *116*, 3338.
[5] J. Xiao, M. Yang, J. W. Lauher, F. W. Fowler, *Angew. Chem.* **2000**, *112*, 2216; *Angew. Chem. Int. Ed.* **2000**, *39*, 2132.
[6] X. Ouyang, F. W. Fowler, J. W. Lauher, *J. Am. Chem. Soc.* **2003**, *125*, 12400.
[7] Y. Ohashi, K. Yanagi, T. Kurihara, Y. Sasada, Y. Ohgo, *J. Am. Chem. Soc.* **1982**, *104*, 6353.
[8] A. Uchida, J. D. Dunitz, *Acta Crystallogr. Sect. B* **1990**, *46*, 45.
[9] Y. Takenaka, Y. Ohashi, T. Tamura, A. Uchida, Y. Sasada, Y. Ohgo, S. Baba, *Acta Crystallogr. Sect. B* **1993**, *49*, 272.
[10] Y. Ohashi, Y. Sakai, A. Sekine, A. Arai, Y. Ohgo, N. Kamiya, H. Iwasaki, *Bull. Chem. Soc. Jpn.* **1995**, *68*, 2517.
[11] M. Hasegawa, *Adv. Phys. Org. Chem.* **1995**, *20*, 117, and references therein.
[12] J. D. Ranford, J. J. Vittal, D. Wu, *Angew. Chem.* **1998**, *110*, 1159; *Angew. Chem. Int. Ed.* **1998**, *37*, 1114.
[13] J. D. Ranford, J. J. Vittal, D. Wu, X. Yang, *Angew. Chem.* **1999**, *111*, 3703; *Angew. Chem. Int. Ed.* **1999**, *38*, 3498.
[14] M. P. Suh, J. W. Ko, H. J. Choi, *J. Am. Chem. Soc.* **2002**, *124*, 10976.
[15] C. Hu, U. Englert, *Angew. Chem.* **2005**, *117*, 2321; *Angew. Chem. Int. Ed.* **2005**, *44*, 2281.
[16] C.-L. Chen, A. M. Goforth, M. D. Smith, C.-Y. Su, H.-C. zur Loye, *Angew. Chem.* **2005**, *117*, 6831; *Angew. Chem. Int. Ed.* **2005**, *44*, 6673.
[17] Q. Chu, D. C. Swenson, L. R. MacGillivray, *Angew. Chem.* **2005**, *117*, 3635; *Angew. Chem. Int. Ed.* **2005**, *44*, 3569.
[18] T. K. Maji, G. Mostafa, R. Matsuda, S. Kitagawa, *J. Am. Chem. Soc.* **2005**, *127*, 17152.
[19] H. Bärnighausen, *MATCH* **1980**, *9*, 139.
[20] A. L. Spek, Program PLATON, Universiteit Utrecht, The Netherlands, **2004**.
[21] Y. Cui, J. Ren, G. Chen, W. Yu, Y. Qian, *Acta Crystallogr. Sect. C* **2000**, *56*, e552.
[22] Y.-J. Shi, Y. Xu, Y. Zhang, B. Huang, D.-R. Zhu, C.-M. Jin, H.-G. Zhu, Z. Yu, X.-T. Chen, X.-Z. You, *Chem. Lett.* **2001**, 678.
[23] K. J. Nordell, K. N. Schultz, K. A. Higgins, M. D. Smith, *Polyhedron* **2004**, *23*, 2161.
[24] M. A. Lawandy, X. Huang, R.-J. Wang, J. Li, J. Y. Lu, T. Yuen, C. L. Lin, *Inorg. Chem.* **1999**, *38*, 5410.
[25] N. Masciocchi, P. Cairati, L. Carlucci, G. Mezza, G. Ciani, A. Sironi, *J. Chem. Soc. Dalton Trans.* **1996**, 2739.
[26] L. Pan, N.-W. Zheng, Y. Wu, S. Wu, X.-Y. Huang, *Acta Crystallogr. Sect. C* **1999**, *55*, 343.
[27] For the space-group ambiguity between *Pban* and *Cmmm* for complexes of the type $[M(\mu\text{-}X)_2(\mu\text{-bipy})]_\infty$, see A. M. Chippindale, A. R. Cowley, K. J. Peacock, *Acta Crystallogr. Sect. C* **2000**, *56*, 651.
[28] C. Hu, Q. Li, U. Englert, *CrystEngComm* **2003**, *5*, 519.
[29] SAINT+ (version 6.02), Program for reduction of data collected on a Bruker CCD area detector diffractometer, Bruker AXS Inc., Madison, WI, **1999**.
[30] G. M. Sheldrick, SADABS, Program for empirical absorption correction of area-detector data, Universität Göttingen, Germany, **1996**.
[31] G. M. Sheldrick, SHELXS-97, Program for solution of crystal structures, Universität Göttingen, Germany, **1997**.
[32] G. M. Sheldrick, SHELXL-97. Program for refinement of crystal structures, Universität Göttingen, Germany, **1997**.

 © 2006 Wiley-VCH Verlag GmbH & Co. KGaA, Weinheim

"Empty" Metal Clusters

DOI: 10.1002/anie.200503916

The Zintl Ion $[Pb_{10}]^{2-}$: A Rare Example of a Homoatomic *closo* Cluster**

*Annette Spiekermann, Stephan D. Hoffmann, and Thomas F. Fässler**

Dedicated to Professor Hansgeorg Schnöckel on the occasion of his 65th birthday

Wade's rules were originally developed to describe the polyhedral structures of boranes (Figure 1).[1] Their application to ligand-free polyhedra of the atoms of Groups 13–15 is possible, but has been the subject of controversy. The isolobal replacement of the B–H units, which each donate two

[*] A. Spiekermann, Dr. S. D. Hoffmann, Prof. Dr. T. F. Fässler
Department Chemie
Technische Universität München
Lichtenbergstrasse 4, 85747 Garching (Germany)
Fax: (+49) 89-289-13186
E-mail: thomas.faessler@lrz.tum.de

[**] We would like to thank Christian Benda for his help with the synthetic work.

© 2006 Wiley-VCH Verlag GmbH & Co. KGaA, Weinheim

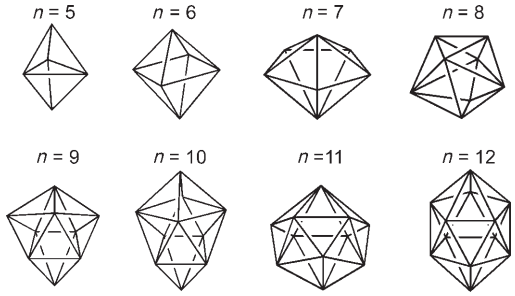

Figure 1. Deltahedral frameworks: *closo*-hydridoborates $[B_nH_n]^{2-}$ are known for $n = 6$–12; ligand-free homoatomic *closo* clusters $[E_n]^{2-}$ of Group 14 elements are only known for $n = 5$ (E = Si–Pb) and $n = 9$ (E = Si).

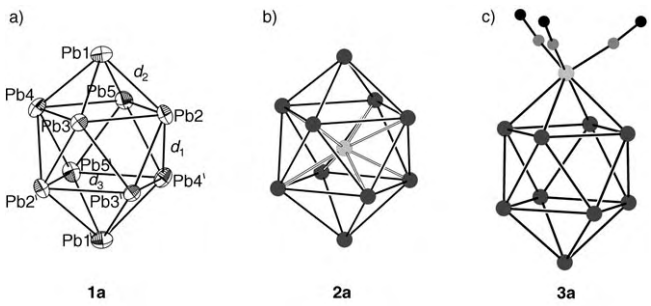

Figure 2. a) Bicapped-square-antiprismatic structure of the anion $[Pb_{10}]^{2-}$ (**1a**); thermal ellipsoids are set at 50% probability. For comparison, the structures of b) $[Ni@Pb_{10}]^{2-}$ (**2a**)[20] and c) $[Pb_9Mo(CO)_3]^{4-}$ (**3a**)[13] are also shown. Average interatomic Pb–Pb distances [Å] between the square planes of the antiprisms and the capping atoms (d_2; only one square face is capped with a Pb atom in **3a**): **1a** 3.074, **2a** 3.094, **3a** 3.051; between the square planes (d_1): **1a** 3.082, **2a** 3.135, **3a** 3.136; within the square planes (d_3): **1a** 3.310, **2a** 3.405, **3a** 3.320.

electrons to the skeletal framework of the polyhedral boranes, with an atom E from Group 14 (E = Si, Ge, Sn, Pb) leads to an electronic situation that is only roughly comparable to that of the boranes. Each E atom must be described as having a nonbonding electron pair with an outward orientation. The lone-pair states of E_n clusters are relatively higher in energy, with respect to the bonding skeletal orbitals, than are the external B–H bonds in borane clusters. The chemical availability of the free electron pairs is demonstrated for E = Ge and Sn by the anions $[\{E[Cr(CO)_5]\}_6]^{2-}$, in which each E atom of the octahedral $\{E_6\}^{2-}$ cluster framework is coordinated to a $\{Cr(CO)_5\}$ group.[2,3] External ligands are also known to influence the number of bonding skeletal orbitals in the boranes. For example, replacing the borane H atoms with more electronegative Cl (or Br) atoms in the 18-skeletal-electron cluster B_9Cl_9 (or B_9Br_9) leads to a tricapped trigonal-prismatic structure (Figure 1, $n = 9$) that is predicted for 20 bonding skeletal electrons according to Wade's rules.[4,5]

Furthermore, a number of the ligand-free clusters of Group 14 elements have structures that deviate considerably from the expected polyhedral structures.[6,7] The structural characterization of numerous $[E_9]^{4-}$ ions has revealed that in many cases distortions from the expected *nido* polyhedral structure (monocapped square antiprism) occur, as has also been observed for the electron-deficient clusters $[E_9]^{3-}$.[7] The unambiguous assignment of a framework structure to a given number of bonding skeletal electrons is, therefore, not always possible.[8] If the *nido* clusters $[E_9]^{4-}$ are completed by a transition-metal fragment, which according to the isolobal concept, does not contribute any electrons to the polyhedral framework, the resulting heteroatomic *closo* polyhedra are nearly undistorted (with respect to the homoatomic contacts), as observed for the structurally characterized compounds $[E_9M(CO)_3]^{4-}$ (E = Sn, and M = Cr, Mo, W;[9–11] E = Pb, and M = Cr, Mo (**3a**);[10,12,13] Figure 2c). The structure of the recently described *closo* cluster $[Si_9]^{2-}$ also deviates considerably from that of a tricapped trigonal prism with D_{3h} symmetry.[14]

At present, significantly more examples of *closo*-hydridoborates $[B_nH_n]^{2-}$ ($n = 6$–12)[15] than of the corresponding homoatomic anions $[E_n]^{2-}$, which are only known for $n = 5$ and E = Si, Ge, Sn, Pb,[16–19] or for $n = 9$ and E = Si,[14] have been structurally characterized. Homoatomic $[E_6]^{2-}$ ions have only been isolated as derivatives stabilized by Lewis acids. In addition, two representatives of homoatomic cluster anions enclosing an additional heteroatom have recently been characterized: the deltahedral clusters $[Ni@Pb_{10}]^{2-}$ (**2a**; Figure 2b)[20] and $[Pt@Pb_{12}]^{2-}$ each contain an interstitial transition-metal atom. In the latter compound, only weak interactions occur between the orbitals of the central Pt atom and those of the cluster atoms,[21] which leads to the formulation $[Pt^0@Pb_{12}]^{2-}$. Hence, the "empty" homoatomic clusters of the Group 14 elements should also be stable, but they have not yet been described. It has been speculated that larger electron-precise clusters can only be formed with endohedral atoms or templates.[22]

After oxidation of a solution of $[Pb_9]^{4-}$ ions in ethylene diamine with Au^I in the form of $[P(C_6H_5)_3AuCl]$ as the oxidizing agent, the compound $[\{K(2.2.2\text{-crypt})\}_2Pb_{10}]$ (**1**; 2.2.2-crypt = 4,7,13,16,21,24-hexaoxa-1,10-diazabicyclo-[8.8.8]hexacosane) was isolated, allowing the first structural characterization of a 10-atom *closo* cluster of a Group 14 element. During the redox reaction, some of the starting material is oxidized to Pb^0, which at the end of the reaction forms a voluminous precipitate that surrounds the nearly black crystals of **1** at the bottom of the reaction container [Eq. (1)].

$$2\,[Pb_9]^{4-} + 6\,Au^+ \rightarrow [Pb_{10}]^{2-} + 8\,Pb^0 + 6\,Au^0 \qquad (1)$$

Crystals of **1** and their intensely colored brown solutions in ethylene diamine or dimethyl formamide (DMF) are extremely sensitive to air and moisture. A qualitative energy dispersive X-ray (EDX) analysis of the crystals indicates the presence of K and Pb, but not Au.

A single-crystal X-ray structure analysis of **1** reveals that five symmetry-independent Pb atoms form a $[Pb_{10}]^{2-}$ ion (**1a**; Figure 2a) with a bicapped-square-antiprismatic structure of nearly perfect D_{4d} symmetry.[23] The presence of two $[K(2.2.2\text{-crypt})]^+$ ions per cluster indicates that the deltahedron is a dianion. As according to Wade's rules, each Pb atom contributes two electrons to the cluster framework, the $[Pb_{10}]^{2-}$ polyhedron contains 22 bonding skeletal electrons

 © 2006 Wiley-VCH Verlag GmbH & Co. KGaA, Weinheim

$(10\times2+2)$. Therefore, $[Pb_{10}]^{2-}$ is the first empty 10-atom *closo* cluster of a Group 14 element that has been unambiguously characterized.

The shortest Pb–Pb contacts occur between the atoms of opposite square planes in the **1a** antiprism ($3.068(1)\le d_1\le 3.093(2)$ Å, $\varnothing(d_1)=3.082$ Å), as well as between these atoms and the capping atoms ($3.036(1)\le d_2\le 3.109(1)$ Å, $\varnothing(d_2)=3.074$ Å). The Pb–Pb distances within the square planes ($3.294(1)\le d_3\le 3.339(1)$ Å, $\varnothing(d_3)=3.310$ Å) are considerably longer; therefore, the $[Pb_{10}]^{2-}$ cage can be described as a slightly compressed bicapped square antiprism. The distance sequence $d_1\approx d_2<d_3$ is similar to that found in the $[B_{10}H_{10}]^{2-}$ ion.[24] Moreover, the structure of **1a** is comparable to that of the binary cluster $[Ni@Pb_{10}]^{2-}$ (**2a**) recently published by Eichhorn et al. (Figure 2b).[20] With respect to the shortest average bond length $\varnothing(d_2)$of **1a**, the relative lengths d_1:d_2:d_3 are 1.00:1:1.08 for **1a** and 1.01:1.02:1.11 for **2a**. The endohedral nickel atom widens the cage ever so slightly (by less than 3% for d_3). The similarity of the anions is also reflected in the fact that **1** can be described as a defect variant of $[\{K(2.2.2\text{-crypt})\}_2NiPb_{10}]$ (**2**).[20]

Apart from the $[Si_9]^{2-}$ ion, which is significantly distorted from the expected D_{3h} symmetry, only two other *closo* clusters with $n>5$ have been described for the Group 14 elements. However, owing to unclear charge distribution ($[Ge_9]^{2-}$), or inadequate structural characterization ($[Ge_{10}]^{2-}$),[25] these clusters do not allow a concrete correlation between the number of bonding skeletal electrons and the polyhedral structure. The anion described as *closo*-$[Ge_9]^{2-}$ has a structure that deviates significantly from the ideal tricapped-trigonal-prismatic structure (one of the three edges of the prism is considerably longer than the others) and is only found in salts that also contain the $[Ge_9]^{4-}$ ion.[26] As many of the compounds containing two different E_9 anions (E = Ge, Sn, Pb) are paramagnetic,[27,28] the charge distribution $[Ge_9]^{2-}$/$[Ge_9]^{4-}$ is not certain. The only example of a 12-atom cluster of a Group 14 element is found in the form of the endohedrally filled anion $[Pt@Pb_{12}]^{2-}$.[21]

Thus, the $[Pb_{10}]^{2-}$ ion is not only the first unambiguously characterized representative of its class, but owing to its similarity with the filled analogue $[Ni@Pb_{10}]^{2-}$, is also an attestation that the Ni–Pb bonds are not necessary for the formation of a stable 10-atom Pb cluster. The existence of main-group-element polyhedra in both empty and endohedrally filled states, had previously only been demonstrated for the fullerenes.[29] The $[Pb_{10}]^{2-}$ ion described herein offers striking evidence that this characteristic is also encountered in Zintl ions. Remarkably, clusters of the heaviest member of Group 14, namely Pb, are involved, despite the fact that these cages are considered to be far less rigid than the fullerenes.[30] The existence of empty as well as filled Zintl anions of Group 14 elements, thus, represents yet another striking parallel between the fullerene cages and the polyhedral Zintl ions.[21,22,31]

Experimental Section

All manipulations and reactions were performed in an Ar atmosphere, using standard Schlenk techniques. Solids were weighed in an Ar-filled glove box. The metallic compound of nominal composition "K_4Pb_9" was synthesized by heating the elements at 350 °C for 8 h in a stainless-steel tube. X-ray diffraction analysis showed that, apart from amorphous components, "K_4Pb_9" consists of a mixture of the phases K_4Pb_9 and KPb. Ethylene diamine (Merck) was distilled over calcium hydride and used immediately after collection. $[P(C_6H_5)_3AuCl]$ was synthesized from $HAuCl_4$ (ChemPur) and $P(C_6H_5)_3$ (Merck), according to a known procedure,[32] and dried under vacuum for 8 h. The cryptand 2.2.2-crypt (Merck) was also dried under vacuum for 8 h. The "K_4Pb_9" compound (303 mg, 0.15 mmol) and 2.2.2-crypt (162 mg, 0.4 mmol) were dissolved in ethylene diamine (4 mL) and stirred for 2 h. The red-brown solution was separated from the insoluble residue by filtration onto $[P(C_6H_5)_3AuCl]$ (75 mg, 0.15 mmol), stirred for 1 h, and collected after filtration through tightly packed glass wool. EDX analysis (JEOL-SEM 5900LV) of the filtration residue indicated the presence of Pb and Au. After 2 days, dark brown to black platelike crystals formed in the dark red solution (ca. 15% yield). The crystals of **1** are embedded in a voluminous Pb sponge. Attempts to obtain ^{207}Pb NMR spectra of the intensely colored brown DMF solutions that result from the digestion of the solid have not yet been successful.

Received: November 4, 2005
Published online: April 19, 2006

Keywords: cluster compounds · cryptands · lead · Wade's rules · Zintl anions

[1] K. Wade, *Adv. Inorg. Chem. Radiochem.* **1976**, *18*, 1.
[2] P. Kirchner, G. Huttner, K. Heinze, G. Renner, *Angew. Chem.* **1998**, *110*, 1754; *Angew. Chem. Int. Ed.* **1998**, *37*, 1664.
[3] B. Schiemenz, G. Huttner, *Angew. Chem.* **1993**, *105*, 295; *Angew. Chem. Int. Ed. Engl.* **1993**, *32*, 297.
[4] M. B. Hursthouse, J. Kane, A. G. Massey, *Nature* **1970**, *228*, 659.
[5] W. Hönle, Y. Grin, A. Burkhardt, U. Wedig, M. Schultheiss, H. G. von Schnering, *J. Solid State Chem.* **1997**, *133*, 59.
[6] J. D. Corbett, *Struct. Bonding (Berlin)* **1997**, *87*, 158.
[7] T. F. Fässler, *Coord. Chem. Rev.* **2001**, *215*, 347.
[8] L. Kloo, T. F. Fässler, J. Rosdahl, *Inorg. Chem. Eur. J.* **2005**, *14*, 2888.
[9] B. W. Eichhorn, R. C. Haushalter, *J. Am. Chem. Soc.* **1988**, *110*, 8704.
[10] B. W. Eichhorn, R. C. Haushalter, *J. Chem. Soc. Chem. Commun.* **1990**, 937.
[11] B. Kesanli, J. Fettinger, B. Eichhorn, *Chem. Eur. J.* **2001**, *7*, 5277.
[12] J. Campbell, H. P. A. Mercier, H. Franke, D. P. Santry, D. A. Dixon, G. J. Schrobilgen, *Inorg. Chem.* **2002**, *41*, 86.
[13] L. Yong, S. D. Hoffmann, T. F. Fässler, *Eur. J. Inorg. Chem.* **2005**, *18*, 3363.
[14] J. M. Goicoechea, S. C. Sevov, *Inorg. Chem.* **2005**, *44*, 2654.
[15] A. F. Hollemann, N. Wiberg, *Lehrbuch der anorganischen Chemie*, de Gruyter, Berlin, **1995**.
[16] J. M. Goicoechea, S. C. Sevov, *J. Am. Chem. Soc.* **2004**, *126*, 6860.
[17] J. Campbell, G. J. Schrobilgen, *Inorg. Chem.* **1997**, *36*, 4078.
[18] P. A. Edwards, J. D. Corbett, *Inorg. Chem.* **1977**, *16*, 903.
[19] M. Somer, W. Carrillo-Cabrera, E. M. Peters, K. Peters, M. Kaupp, H. G. von Schnering, *Z. Anorg. Allg. Chem.* **1999**, *625*, 37.
[20] E. N. Esenturk, J. Fettinger, B. W. Eichhorn, *Chem. Commun.* **2005**, 247.
[21] E. N. Esenturk, J. Fettinger, Y.-F. Lam, B. Eichhorn, *Angew. Chem.* **2004**, *116*, 2184; *Angew. Chem. Int. Ed.* **2004**, *43*, 2132.
[22] T. F. Fässler, S. D. Hoffmann, *Angew. Chem.* **2004**, *116*, 6400; *Angew. Chem. Int. Ed.* **2004**, *43*, 6242.
[23] a) Single crystals of **1** were fixed on glass capillaries. The structure was solved by direct methods (SHELXS-97[23b]) and refined by full-matrix least-squares calculations against F^2

 © 2006 Wiley-VCH Verlag GmbH & Co. KGaA, Weinheim

(SHELXL-97[23c]). All non-H atoms were refined with anisotropic displacement parameters. Crystal size: $0.2\times0.1\times0.006$ mm; cell parameters at 135 K: $a=24.682(2)$, $b=11.862(1)$, $c=21.271(2)$ Å, $\beta=97.23(1)°$, $V=6178(1)$ Å^3; space group $C2/c$ (No. 15), $Z=4$, $\rho_{calcd}=3.121$ g cm^{-3}, $\mu=27.322$ mm^{-1}, numerical absorption correction ($T_{min}=0.07$, $T_{max}=0.85$); data collection: Oxford Diffraction Xcalibur3 diffractometer, $Mo_{K\alpha}$ radiation, $2\theta_{max}=25.31°$, 34647 measured reflections, 5628 independent reflections, $R_{int}=0.058$; $R_1=0.059$ and $wR_2=0.130$ for $I>2\sigma(I)$, $R_1=0.089$ and $wR_2=0.145$ for all data. CCDC-288640 (**1**) contains the supplementary crystallographic data for this paper. These data can be obtained free of charge from The Cambridge Crystallographic Data Centre via www.ccdc.cam.ac.uk/data_request/cif; b) G. M. Sheldrick. SHELXS-97, Program for the Solution of Crystal Structures, Universität Göttingen, **1997**; c) G. Sheldrick. SHELXL-97, Program for the Refinement of Crystal Structures, Universität Göttingen, **1997**.

[24] S. Chitsaz, H. Folkerts, J. Grebe, T. Grob, K. Harms, W. Hiller, M. Krieger, W. Massa, J. Merle, M. Mohlen, B. Neumuller, K. Dehnicke, *Z. Anorg. Allg. Chem.* **2000**, *626*, 775.

[25] The structure of the only previously characterized compound containing a 10-atom *closo* cluster of a Group 14 element, $[Ge_{10}]^{2-}$,[33] has not been satisfactorily determined, owing to a threefold rotational disorder of the cluster. Analysis of crystals with similar cell parameters and symmetry has also led to an alternative description of this compound as containing disordered $[Ge_9]^{2-}$ clusters.[14,28]

[26] C. H. E. Belin, J. D. Corbett, A. Cisar, *J. Am. Chem. Soc.* **1977**, *99*, 7163.

[27] T. F. Fässler, M. Hunziker, *Z. Anorg. Allg. Chem.* **1996**, *622*, 837.

[28] T. F. Fässler, M. Hunziker, M. Spahr, H. Lueken, *Z. Anorg. Allg. Chem.* **2000**, *626*, 692.

[29] H. Shinohara, *Rep. Prog. Phys.* **2000**, *63*, 843.

[30] ^{207}Pb NMR spectra of the anions $[Pb_9]^{4-}$ and $[Ni@Pb_{10}]^{2-}$ show only one signal: R. W. Rudolph, W. L. Wilson, F. Parker, R. C. Taylor, D. C. Young, *J. Am. Chem. Soc.* **1978**, *100*, 4629, and ref. 20.

[31] T. F. Fässler, *Angew. Chem.* **2001**, *113*, 4289; *Angew. Chem. Int. Ed.* **2001**, *40*, 4161.

[32] S. Ahrland, K. Dreisch, B. Norén, Å. Oskarsson, *Mater. Chem. Phys.* **1993**, *35*, 281.

[33] C. Belin, H. Mercier, V. Angilella, *New J. Chem.* **1991**, *15*, 931.

 © 2006 Wiley-VCH Verlag GmbH & Co. KGaA, Weinheim

C–H Activation

DOI: 10.1002/anie.200600111

Chemoselective Benzylic C–H Activations for the Preparation of Condensed N-Heterocycles**

*Hongjun Ren and Paul Knochel**

Dedicated to Professor Siegfried Blechert on the occasion of his 60th birthday

The preparation of complex polycyclic heterocycles is an important synthetic goal because of the utility of these molecules as potential pharmaceuticals.[1] One of the most efficient approaches for preparing polycyclic molecules is to use domino reactions.[2] Especially attractive are reaction sequences that involve C–H activation reactions[3] since such reactions preclude the presence of additional functionalities in the substrate. A range of Ru-,[4] Rh-,[5] Pt-,[6] and Pd-[7] catalyzed C–H activations for heterocycle synthesis have been recently described.[8] Since a variety of 2-bromoanilines **1** can be readily converted into N-arylpyrrole derivatives of type **2** by the reaction with a 1,4-diketone **3**, we envisaged that a subsequent C–H activation would afford condensed heterocycles of type **4** (Scheme 1).

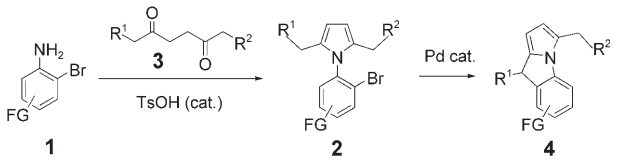

Scheme 1. Preparation of tricyclic N-heterocycles of type **4**. FG = functional group; Ts = 4-toluenesulfonyl.

We therefore heated pyrrole **2a** with $Pd(OAc)_2$ (5 mol%) and various ligands in toluene and in the presence of a base for trapping HBr (100 °C, 20 h, Table 1). Preliminary experiments showed that polar solvents such as DMF led to complex reaction mixtures, but nonpolar solvents such as toluene gave much better results. Strongly chelating ligands such as dppe and dppp did not lead to the formation of **4a**; however, PPh_3 (10 mol%) led to the 9*H*-pyrrolo[1,2-*a*]indole **4a** with 45% conversion after 20 h at 100 °C, (entries 1–3 in Table 1). When

[*] Dipl.-Chem. H. Ren, Prof. Dr. P. Knochel
Ludwig-Maximilians-Universität München
Department Chemie und Biochemie
Butenandtstrasse 5–13, Haus F, 81377 München (Germany)
Fax: (+49) 89-2180-77680
E-mail: paul.knochel@cup.uni-muenchen.de

[**] We thank the Fonds der Chemischen Industrie and Merck Research Laboratories for financial support. We also thank Chemetall GmbH (Frankfurt) and BASF AG (Ludwigshafen) for the generous gift of chemicals.

Supporting information for this article is available on the WWW under http://www.angewandte.org or from the author.

© 2006 Wiley-VCH Verlag GmbH & Co. KGaA, Weinheim

Table 1: Pd-catalyzed cyclization of the pyrrole derivative **2a** leading to the tricyclic heterocycle **4a**.

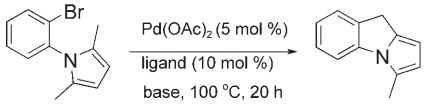

2a **4a**

Entry	Ligand[a]	Base	Conv. [%][b]
1	dppe	Cs_2CO_3	0
2	dppp	Cs_2CO_3	0
3	PPh_3	K_2CO_3	45
4	PPh_3	Cs_2CO_3	73
5	*o*-Tol_3P	Cs_2CO_3	0
6	*o*-$Furyl_3P$	Cs_2CO_3	8
7	*m*-Tol_3P	K_2CO_3	27
8	*m*-Tol_3P	Cs_2CO_3	100
9	*p*-Tol_3P	K_2CO_3	15
10	*p*-Tol_3P	Cs_2CO_3	100[c]
11	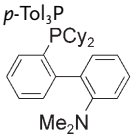	Cs_2CO_3	67

[a] dppe = ethane-1,2-diylbis(diphenylphosphane); dppp = propane-l,2-diylbis(diphenylphosphane); Tol = tolyl; Cy = cyclohexyl. [b] The conversion was determined by GC analysis of reaction aliquots. [c] Conversion after 12 h at 110°C.

K_2CO_3 was replaced by Cs_2CO_3 (1.2 equiv), the conversion increased to 73% (entry 4, Table 1). Sterically hindered ligands such as *o*-Tol_3P and *o*-$Furyl_3P$ were not suitable (entries 5 and 6, Table 1), but *m*-Tol_3P afforded 27% conversion in the presence of K_2CO_3 and 100% conversion with Cs_2CO_3. The best result was obtained with *p*-Tol_3P; reaction in the presence of Cs_2CO_3 gave 100% conversion within 12 h at 110°C (entries 7–10, Table 1). Interestingly, when the hindered phosphine 2-dicyclohexylphosphino-2′-(*N*,*N*-dimethylamino)biphenyl was used,[9] we observed a conversion of 67% (entry 11, Table 1).

Based on these optimized reaction conditions, we prepared a large range of 9*H*-pyrrolo[1,2-*a*]indoles (Table 2). The 2-iodo- and 2-bromo-*N*-arylpyrrole derivatives **2b** and **2c** underwent ring closure smoothly providing the tricyclic product **4b** in 81% and 83% yield, respectively, showing that the use of aryl iodides and bromides leads to similar results (entries 1 and 2 in Table 2). The ester function was well tolerated in this ring closure. Also, the cyano-substituted iodide **2d** and bromide **2e** furnished the expected product **4c** in 70% and 60% yield, respectively (entries 3 and 4, Table 2) under the standard conditions. Trifluoromethyl-substituted substrates, which may be of importance for the preparation of pharmaceutically relevant heterocycles, reacted readily and led to the tricyclic products **4d** (77%) and **4e** (65%) (entries 5 and 6, respectively). Only a nitro substituent complicated the reaction and furnished the 9*H*-pyrrolo-[1,2-*a*]indole **4f** in only 33% yield (entry 7, Table 2).

In the case of unsymmetrical 2,5-disubstituted derivatives, an interesting selectivity was observed. Thus, the N-arylpyrrole derivative **5** underwent preferentially a chemoselective activation of the phenyl ring over the methyl substituent,

Table 2: Preparation of 9*H*-pyrrolo[1,2-*a*]indoles of type **4**.

Entry	Product of type **2**	Product of type **4**	Yield [%][a]
	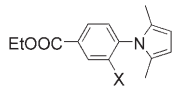	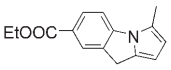	
1	**2b**: X = I	**4b**	81
2	**2c**: X = Br	**4b**	83
	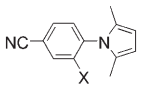	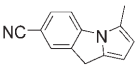	
3	**2d**: X = I	**4c**	70
4	**2e**: X = Br	**4c**	60
	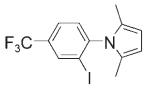	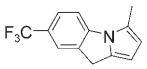	
5	**2f**	**4d**	77
	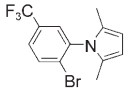	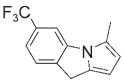	
6	**2g**	**4e**	65
	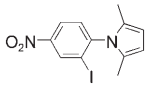	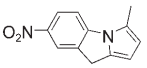	
7	**2h**	**4f**	33

[a] Yield of isolated, analytically pure product.

leading to the pyrrolo[1,2-*f*]phenanthridine derivative **6** in 85% yield (Scheme 2). A stepwise cyclization was observed with the dibromo derivative **7**. Under the standard conditions only the phenyl C–H bond was activated, resulting in formation of a seven-membered ring (**8**, 62%). Forcing reaction conditions (110°C, 24 h) led to a second cyclization with the formation of the pentacyclic compound **9** in 61% yield (Scheme 2).

These results show that the activation of a methyl substituent is not easy and is not facilitated by the presence of a further phenyl substituent; the benzyl substituent of compound **7** did not undergo a C–H activation at the benzylic position but on the phenyl ring despite the formation of a seven-membered ring. The additional phenyl ring has rather a deleterious steric influence. These considerations led us to propose the following tentative reaction sequence for the cyclization reaction. The *N*-(2-haloaryl)pyrrole derivative **10** undergoes first an oxidative addition of Pd^0 generated in situ, leading to the Pd^{II} species **11** (Scheme 3). Concomitant C–H activation and HX elimination provides the palladacycle **12**, which after reductive elimination provides the 9*H*-pyrrolo-[1,2-*a*]indole **4a**.

Remarkably, this activation of the 2-methyl substituent of pyrroles[10] can be extended to *N*-acyl-2,5-pyrrole derivatives such as **13a–c**. Under the usual conditions, these readily available amides are converted to the pyrrolo[1,2-*b*]isoquinolines **14a–c** in yield of 75–81% (Scheme 4). Nonaromatic N-acylpyrroles such as **15a–c** undergo the same type of

 © 2006 Wiley-VCH Verlag GmbH & Co. KGaA, Weinheim

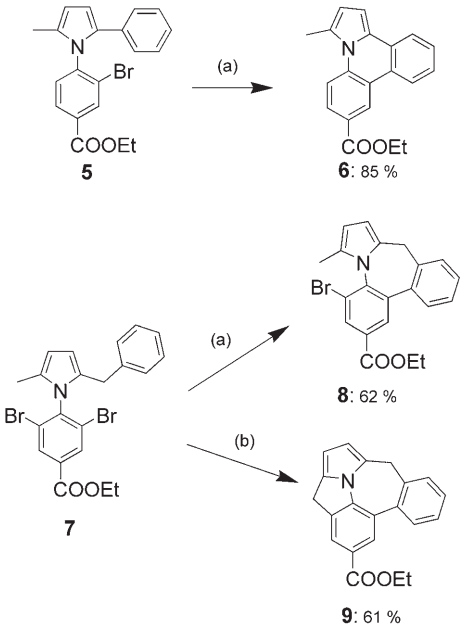

Scheme 2. Chemoselective C–H activation. Reaction conditions: a) $Pd(OAc)_2$ (5 mol%), *p*-Tol_3P (10 mol%), Cs_2CO_3 (1.2 equiv), 110°C, 12 h; b) $Pd(OAc)_2$ (5 mol%), *p*-Tol_3P (10 mol%), Cs_2CO_3 (2.2 equiv), 110°C, 24 h.

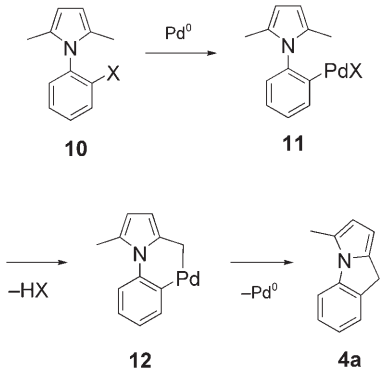

Scheme 3. Tentative reaction sequence for the ring closure.

cyclization with a C–H activation, leading to the heterocycles **16a–c** in 74–85% yield and demonstrating the broad scope of this type of ring closure (Scheme 4).

In summary, we have reported new Pd-catalyzed cyclizations leading to condensed N-heterocycles. The key step of these ring closures is a chemoselective intramolecular C–H activation of a methyl group at position 2 of a pyrrole ring. Further studies on the reaction mechanism and scope are currently underway in our laboratories.

Experimental Section

Synthesis of **4b** starting **2c** (entry 2 of Table 2): A mixture of the aryl bromide **2c** (322 mg, 1.0 mmol), $Pd(OAc)_2$ (11 mg, 5 mol%), tri(*p*-tolyl)phosphine (30 mg, 10 mol%), and Cs_2CO_3 (391 mg, 1.2 mmol) was heated at 110°C in toluene (5 mL) under N_2 in a sealed tube for 12 h. After the reaction mixture had cooled to room temperature,

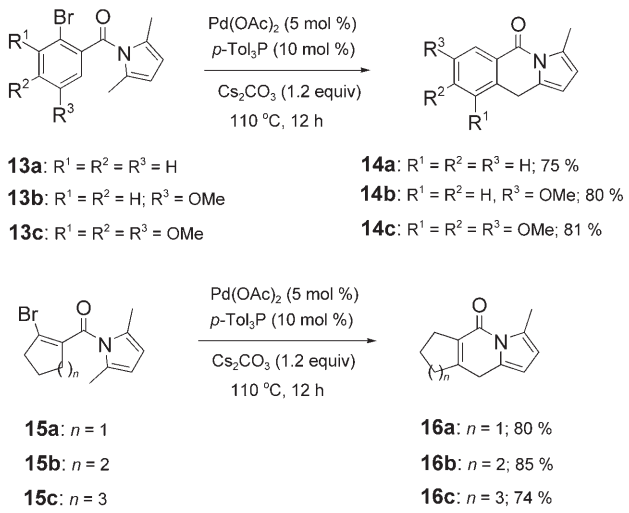

Scheme 4. Preparation of tricyclic heterocycles starting from N-acylpyrroles.

water (10 mL) was added. The mixture was extracted with diethyl ether (3 × 30 mL), and the combined extracts were washed with brine, dried over Na_2SO_4, and concentrated in vacuo. Purification by flash chromatography (hexane/diethyl ether 10:1) provided **4b** (200 mg, 83% yield) as a white solid, m.p. 77.9–78.9°C.

Received: January 11, 2006
Published online: April 25, 2006

Keywords: C–H activation · domino reactions · nitrogen heterocycles · palladium

[1] a) T. L. Gilchrist, *Heterocyclic Chemistry*, Longman, **1998**; b) T. Eicher, S. Hauptmann, *The Chemistry of Heterocycles*, Wiley-VCH, **2003**.

[2] a) L. F. Tietze, N. Rackelmann, *Pure Appl. Chem.* **2004**, *76*, 1967; b) A. de Meijere, P. von Zezschwitz, S. Bräse, *Acc. Chem. Res.* **2005**, *38*, 413; c) A. Padwa, *Pure Appl. Chem.* **2003**, *75*, 47; d) B. Breit, *Chem. Eur. J.* **2000**, *6*, 1519; e) S. Ikeda, *Acc. Chem. Res.* **2000**, *33*, 511.

[3] "Activation of C–H bonds: catalytic reactions": a) F. Kakiuchi, S. Murai, *Top. Organomet. Chem.* **1999**, *3*, 47; b) G. Dyker, *Angew. Chem.* **1999**, *111*, 1808; *Angew. Chem. Int. Ed.* **1999**, *38*, 1698; c) A. E. Shilov, G. B. Shul'pin, *Chem. Rev.* **1997**, *97*, 2879; d) V. Ritleng, C. Sirlin, M. Pfeffer, *Chem. Rev.* **2002**, *102*, 1731; e) C. Jia, T. Kitamura, Y. Fujiwara, *Acc. Chem. Res.* **2001**, *34*, 633; f) C.-J. Li, *Acc. Chem. Res.* **2002**, *35*, 533; g) S. Ma, Z. Gu, *Angew. Chem.* **2005**, *117*, 7680; *Angew. Chem. Int. Ed.* **2005**, *44*, 7512.

[4] a) C. S. Yi, S. Y. Yun, I. A. Guzei, *J. Am. Chem. Soc.* **2005**, *127*, 5782; b) C. S. Yi, S. Y. Yun, *J. Am. Chem. Soc.* **2005**, *127*, 17000; c) N. Chatani, T. Asaumi, S. Yorimitsu, T. Ikeda, F. Kakiuchi, S. Murai, *J. Am. Chem. Soc.* **2001**, *123*, 10935; d) F. Kakiuchi, S. Murai, *Acc. Chem. Res.* **2002**, *35*, 826; e) L. Ackermann, *Org. Lett.* **2005**, *7*, 3123.

[5] a) B. DeBoef, S. J. Pastine, D. Sames, *J. Am. Chem. Soc.* **2004**, *126*, 6556; b) R. K. Thalji, J. A. Ellman, R. G. Bergman, *J. Am. Chem. Soc.* **2004**, *126*, 7192; c) K. L. Tan, R. G. Bergman, J. A. Ellman, *J. Am. Chem. Soc.* **2001**, *123*, 2685; d) K. L. Tan, A. Vasudevan, R. G. Bergman, J. A. Ellman, A. J. Souers, *Org. Lett.* **2003**, *5*, 2131; e) K. L. Tan, S. Park, J. A. Ellman, R. G. Bergman, *J. Org. Chem.* **2004**, *69*, 7329; f) H. M. L. Davies, Q. Jin, P. Ren,

 © 2006 Wiley-VCH Verlag GmbH & Co. KGaA, Weinheim

A. Y. Kovalevsky, *J. Org. Chem.* **2002**, *67*, 4165; g) R. K. Thalji, K. A. Ahrendt, R. G. Bergman, J. A. Ellman, *J. Am. Chem. Soc.* **2001**, *123*, 9692.

[6] a) J. A. Johnson, N. Li, D. Sames, *J. Am. Chem. Soc.* **2002**, *124*, 6900; b) J. A. Johnson, D. Sames, *J. Am. Chem. Soc.* **2000**, *122*, 6321.

[7] a) B. Sezen, R. Franz, D. Sames, *J. Am. Chem. Soc.* **2002**, *124*, 13372; b) B. D. Dangel, K. Godula, S. W. Youn, B. Sezen, D. Sames, *J. Am. Chem. Soc.* **2002**, *124*, 11856; c) J. L. Portscheller, H. C. Malinakova, *Org. Lett.* **2002**, *4*, 3679; d) Q. Huang, A. Fazio, G. Dai, M. A. Campo, R. C. Larock, *J. Am. Chem. Soc.* **2004**, *126*, 7460; e) E. J. Hennessy, S. L. Buchwald, *J. Am. Chem. Soc.* **2003**, *125*, 12084; f) D. Shabashov, O. Daugulis, *Org. Lett.* **2005**, *7*, 3657; g) A. R. Dick, K. L. Hull, M. S. Sanford, *J. Am. Chem. Soc.* **2004**, *126*, 2300; h) V. G. Zaitsev, O. Daugulis, *J. Am. Chem. Soc.* **2005**, *127*, 4156; i) O. Daugulis, V. G. Zaitsev, *Angew. Chem.* **2005**, *117*, 4114; *Angew. Chem. Int. Ed.* **2005**, *44*, 4046; j) M. D. K. Boele, G. P. F. van Strijdonck, A. H. M. de Vries, P. C. J. Kamer, J. G. de Vries, P. W. N. M. van Leeuwen, *J. Am. Chem. Soc.* **2002**, *124*, 1586; k) D. Kalyani, N. R. Deprez, L. V. Desai, M. S. Sanford, *J. Am. Chem. Soc.* **2005**, *127*, 7330; l) M. A. Campo, Q. Huang, T. Yao, Q. Tian, R. C. Larock, *J. Am. Chem. Soc.* **2003**, *125*, 11506; m) C. Bour, J. Suffert, *Org. Lett.* **2005**, *7*, 653; n) L.-C. Campeau, M. Parisien, M. Leblanc, K. Fagnou, *J. Am. Chem. Soc.* **2004**, *126*, 9186; o) L.-C. Campeau, M. Parisien, A. Jean, K. Fagnou, *J. Am. Chem. Soc.* **2006**, *128*, 581; p) T. Okazawa, T. Satoh, M. Miura, M. Nomura, *J. Am. Chem. Soc.* **2002**, *124*, 5286.

[8] For various of C–H activation reactions, see: a) O. Baudoin, A. Herrbach, F. Guéritte, *Angew. Chem.* **2003**, *115*, 5914; *Angew. Chem. Int. Ed.* **2003**, *42*, 5736; b) Y. Kuninobu, A. Kawata, K. Takai, *J. Am. Chem. Soc.* **2005**, *127*, 13498; c) G. Karig, M.-T. Moon, N. Thasana, T. Gallagher, *Org. Lett.* **2002**, *4*, 3115; d) M. Catellani, E. Motti, S. Ghelli, *Chem. Commun.* **2000**, 2003; e) A. Diefenbach, F. M. Bickelhaupt, *J. Phys. Chem. A* **2004**, *108*, 8460.

[9] D. W. Old, J. P. Wolfe, S. L. Buchwald, *J. Am. Chem. Soc.* **1998**, *120*, 9722.

[10] For other Pd-mediated activations of pyrrole rings, see: a) A. L. Bowie, Jr., C. C. Hughes, D. Trauner, *Org. Lett.* **2005**, *7*, 5207; b) J. H. Rigby, M. E. Mateo, *Tetrahedron* **1996**, *52*, 10569.

 © 2006 Wiley-VCH Verlag GmbH & Co. KGaA, Weinheim

Molecular Dynamics

DOI: 10.1002/anie.200600201

Multidimensional Large-Amplitude Motion: Revealing Concurrent Tunneling Pathways in Molecules with Several Internal Rotors**

*Melanie Schnell and Jens-Uwe Grabow**

The study of internal rotation in molecules as well as the magnitude and origin of the forces that impede free internal rotation has interested chemists for a long time. Internal rotation is understood as the rotation of one or several parts of a molecule, such as a methyl group, about a single bond relative to the remaining part of the molecule. Besides smaller molecules, such as ethane, internal rotations are also important for larger molecules such as proteins and nucleic acids. The different contributions to internal-rotation barriers are not yet completely understood and are still subject to intensive controversial discussions in the literature: In a recent study, Weinhold and co-workers[1–3] argue on the basis of natural bond orbital (NBO) calculations that the preference of the staggered over the eclipsed conformation in ethane is of electronic origin, since the adjacent carbon–hydrogen bonding orbitals σ_{CH} and σ^*_{CH} have the greatest overlap and hence lead to stronger interactions. In contrast to this, Bickelhaupt and Baerends found that their electronic-structure calculations support the interpretation that the barrier is caused by steric repulsion between vicinal C–H bonds.[4]

If a molecule exhibits more than one rotatable group (also referred to as a top), the internal motions can interact, that is, they can communicate to each other their orientation with respect to the rest of the molecule (the molecular frame). A distinction is drawn between top–top communication through space resulting from electrostatic repulsion of electron clouds of neighboring groups, and communication through chemical bonds, which is determined mainly by the character of the chemical bond that connects the top with the molecular frame

[*] Dr. M. Schnell,[+] Dr. J.-U. Grabow
Universität Hannover
Institut für Physikalische Chemie und Elektrochemie
Lehrgebiet A, Callinstrasse 3–3a, 30167 Hannover (Germany)
Fax: (+49) 511-762-4009
E-mail: jens-uwe.grabow@pci.uni-hannover.de

[+] Present address:
Fritz-Haber-Institut der Max-Planck-Gesellschaft
Abteilung Molekülphysik
Faradayweg 4–6, 14195 Berlin (Germany)

[**] We thank the state of Lower Saxony and the Deutsche Forschungsgemeinschaft for financial support, as well as F. J. Lovas for helpful discussions. M.S. is grateful for support from the Berlin-Brandenburgische Akademie der Wissenschaften through an Akademiestipendium 2005. We are also particularly thankful to Jon T. Hougen for fruitful scientific discussions.

Supporting information for this article is available on the WWW under http://www.angewandte.org or from the author.

© 2006 Wiley-VCH Verlag GmbH & Co. KGaA, Weinheim

and seems to be not yet well understood. In revealing the feasible tunneling pathways of the molecule and determining the corresponding barriers to internal rotation with microwave spectroscopy, we want to gain insight into the interaction mechanisms governing internal molecular dynamics.

We chose to investigate the series $(CH_3)_3XCl$ (X = Si, Ge, Sn), whose central atoms systematically increase in size, so that electrostatic repulsion, and thus top–top communication through space, is gradually reduced in the order Si > Ge > Sn and, consequently, the relative contribution of the character of the chemical bond X–CH_3 (X = Si, Ge, Sn) becomes more important and leads to dramatic differences in the internal molecular dynamics. Furthermore, although belonging to the same main group in the periodic table, the elements carbon, silicon, germanium, and tin are quite different. For example, the covalent radii of the central atoms in this series change significantly from 1.17 Å for Si and 1.22 Å for Ge to 1.40 Å for Sn. It is also well known[5] that molecular Si and Ge compounds show similar chemical properties, whereas the analogous Sn compounds differ. For example, significant Lewis acidity was found for $(CH_3)_3SnCl$, whereas $(CH_3)_3SiCl$ and $(CH_3)_3GeCl$ show essentially no Lewis acidity.[6]

Table 1 summarizes the calculated distances (B3LYP/6-311G** and ecp-46-mwb (Sn))[7] of closest approach between hydrogen atoms connected to neighboring CH_3 groups for the case of one, two, and three CH_3 tops rotated out of their equilibrium position by 60°. For three rotated methyl groups, the hydrogen atoms of neighboring CH_3 groups come as close as 2.5 Å for $(CH_3)_3SiCl$, whereas they approach only 3.1 Å for $(CH_3)_3SnCl$. A comparison of these results with the van der Waals radius for hydrogen ($r_{vdW}(H) = 1.2$ Å) indicates that electrostatic repulsion has a major influence on the internal dynamics of $(CH_3)_3SiCl$, but a noticeably smaller influence for $(CH_3)_3SnCl$.

Table 1: Calculated[a] distances of closest approach for hydrogen atoms of neighboring methyl groups when either one, two, or three methyl groups are rotated out of the local minimum position by 60° as well as calculated barriers to internal rotation ΔE.

n[b]		$(CH_3)_3SiCl$	$(CH_3)_3GeCl$	$(CH_3)_3SnCl$
1	r(H–H) [Å]	3.0	3.1	3.6
2	r(H–H) [Å]	2.5	2.7	3.1
3	r(H–H) [Å]	2.5	2.7	3.1
	ΔE [kJ mol^{-1}]	6.4	4.2	2.1

[a] B3LYP/6-311G**, X = Sn: ecp-46-mwb (Sn). [b] Number of CH_3 tops rotated.

The calculated torsional barriers to internal rotation of one CH_3 group at a time for $(CH_3)_3XCl$ are also given in Table 1. These values have been calculated by keeping the internal rotation angles for the three CH_3 groups fixed while allowing all other geometric parameters to relax in the course of the optimization process. The barrier is calculated to be highest for $(CH_3)_3SiCl$ (6.4 kJ mol^{-1}), whereas it is about 2 and 4 kJ mol^{-1} lower for $(CH_3)_3GeCl$ (4.2 kJ mol^{-1}) and $(CH_3)_3SnCl$ (2.1 kJ mol^{-1}), respectively. Furthermore, the conformers with two or three CH_3 tops rotated by 60° relative to the equilibrium conformation are higher in energy than the equilibrium structures by 13.5 and 21.5 kJ mol^{-1}, respectively, for $(CH_3)_3SiCl$, and 10.1 kJ mol^{-1} and 15.4 kJ mol^{-1}, respectively, for $(CH_3)_3GeCl$. As described below, the differences in the barrier heights not only scale the tunneling splittings in the recorded spectra, but we observed completely different-looking torsion–rotation spectra for the three species, which then demand different considerations for their analysis. A recent microwave spectroscopy study[8] gave a barrier of $V_3 = 6.9$ kJ mol^{-1} for $(CH_3)_3SiCl$. The rotational spectrum of $(CH_3)_3GeCl$ has also been recorded previously but the torsion–rotation splittings were not observed.[9]

To study internal rotation in molecules, a combination of experimental techniques and theoretical methods is often employed. We have used high-resolution rotational spectroscopy[10] along with permutation-inversion (PI) group theory. Pure rotational spectra of polar molecules provide very precise molecular data such as the geometrical structure, the barriers to internal rotation, and, in combination with Stark-effect measurements, the molecular dipole moment. Furthermore, bonding parameters can be estimated from an analysis of the nuclear quadrupole coupling constants. To analyze the additional spectral features caused by internal rotation (i.e., torsion–rotation splittings) and to extract information about the top–top communication for these molecules we combine PI group theory with multidimensional tunneling theory. In PI group theory, the symmetry operations of a molecule are described by permutations and inversions instead of by rotations and reflections as in point-group theory.[11] The advantage of PI group theory over point-group theory is that it permits the group-theoretical description of rotations of part of the molecule, such as a methyl group, relative to the remaining part of the molecule. The appropriate PI group for the molecules of the series $(CH_3)_3XCl$ (X = Si, Ge, Sn) is G_{162},[12–14] which consists of 162 elements and is not isomorphic with any point group. Generally, these PI groups can become quite large (for a more detailed description of the molecular symmetry group G_{162}, see reference [15]).

The multidimensional tunneling formalism provides a description of the internal rotation in terms of tunneling pathways. As another prominent example, the inversion motion of the NH_3 molecule can be described by a single tunneling pathway passing through a planar transition state. For molecules with more than one rotatable group, several internal motions that can be described by more complicated tunneling pathways are possible. For $(CH_3)_3XCl$, in particular, 351 different tunneling motions between 27 equivalent equilibrium conformations ("frameworks") are possible. It can be shown by group theory that because of the high symmetry of the $(CH_3)_3XCl$ molecules (C_{3v} in their rigid equilibrium geometry) many pathways are topologically equivalent. Only five pathways remain chemically distinct: internal rotation of one methyl top (H_R), internal rotation of two methyl groups, differentiating between geared (H_G, opposite sense of rotation) and anti-geared motion (H_A, the same sense of rotation), as well as internal rotation of three methyl groups at a time, with the three methyl tops either rotating all with the same direction (H_L) or with one rotating in the opposite direction (H_E).

 © 2006 Wiley-VCH Verlag GmbH & Co. KGaA, Weinheim

The diagonalization of a tunneling Hamiltonian matrix constructed with matrix elements H_j associated with the five different tunneling pathways yields the torsional splitting pattern and the energy ordering for $K=0$ rotational transitions $J+1\leftarrow J$ (see the Supporting Information). We consider only tunneling pathways involving the internal rotation of a single methyl group (H_R) at a time for $(CH_3)_3SiCl$, since we expect the barriers for simultaneous internal rotation of two or even three methyl groups to be too high to be feasible on the timescale of our experiment (for the concept of feasibility, see references [11,16]). This leads to a characteristic splitting pattern (center column of Figure 1) of four multiply degenerate groups at constant separation denoted by the torsional species I_3 and E_2 (8-fold degenerate), I_1 and I_4 (12-fold degenerate), I_2 (6-fold degenerate), and A_1 (non-degenerate), respectively. The left of Figure 1 shows the hypothetical 27-fold degenerate J_0 symmetric rotor energy level that occurs when the internal rotation is frozen.

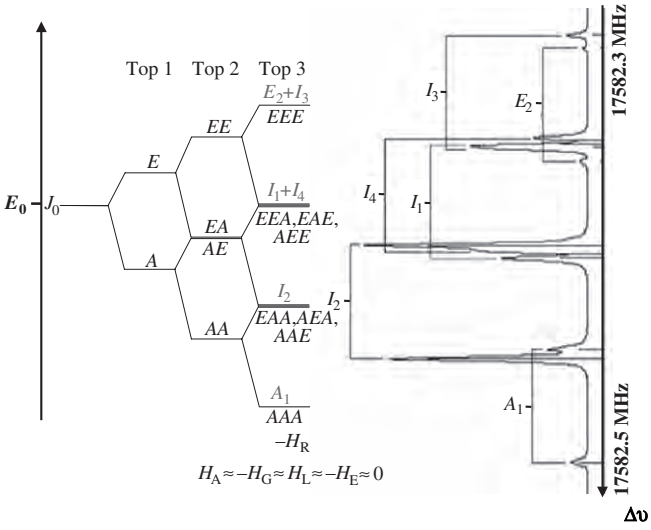

Figure 1. Torsional splitting pattern of the $J_K=J_0$ rotational level for $(CH_3)_3SiCl$ obtained with the high-barrier torsion–rotation tunneling formalism. Only internal rotation of one methyl group is included at a time (H_R). The torsion–rotation levels (denoted E_2, I_3, I_4, I_1, I_2, and A_1) are shown in the center of the figure. A description of these same levels by local mode theory (*AAA*, *AAE*, *AEA*, *EAA*, *EEA*, *EAE*, *AEE*, and *EEE*) is given on the left (see text and the Supporting Information). The relative ordering of the energy levels predicted by theory is compared with the observed splitting pattern in the rotational spectrum for the $4\leftarrow 3$ transition ($K=0$, $F'\leftarrow F=3.5\leftarrow 3.5$,[8]) on the right of the figure.

Also on the left of Figure 1, we show the torsional splitting pattern obtained by local mode theory, in which the methyl groups are treated independently at first (see the Supporting Information). As expected, local mode theory and the high-barrier tunneling formalism including only H_R matrix elements give the same splitting pattern for $(CH_3)_3SiCl$.

The right part of Figure 1 shows the measured rotational spectrum of the $J+1\leftarrow J=4\leftarrow 3$ transition ($K=0$, $F'\leftarrow F=3.5\leftarrow 3.5$ chlorine hyperfine transition) for $(CH_3)_3SiCl$,[8] which exhibits only small splittings because of a high barrier that results from severe steric hindrance. Each line consists of two Doppler components because of the coaxial beam resonator arrangement (COBRA)[10,17] of the Fourier transform microwave spectrometer. The actual transition frequency is given by the frequency of the center of the doublets, as indicated by the bars in Figure 1. It was shown by Hougen and Ohashi[18] that for $K=0$ the relative energy ordering of the torsional energy levels of a rotational state resembles the frequency ordering of the different torsional components in the $J+1\leftarrow J$ rotational spectrum, but with opposite directions; that is, we expect the $J+1,A_2\leftarrow J,A_1$ transition to be located at the high-frequency end of the $K=0$ series, since the A_1 torsional level is shifted to the lowest energy in the splitting pattern. The corresponding matrix elements H_j for the different molecular species are given in the Supporting Information. Both theoretical approaches (local mode theory and multidimensional tunneling formalism) show very good agreement with the experimental results for $(CH_3)_3SiCl$, which indicates that the concerted internal rotation of two or even three CH_3 tops is not feasible.

The distance between two neighboring hydrogen atoms is only somewhat larger in $(CH_3)_3GeCl$ than in $(CH_3)_3SiCl$. However, the barrier for $(CH_3)_3GeCl$ is predicted to be about 50% lower than for the Si species (Table 1). In accordance with the lower barrier, we obtain not only a quantitatively more widely spread but also a qualitatively more complicated torsion–rotation spectrum with additional splittings (Figure 2). To understand these observations physically and describe them theoretically, we also had to include tunneling

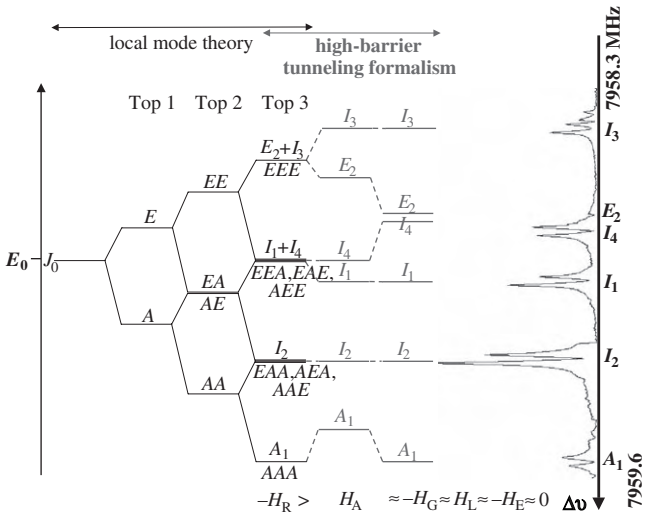

Figure 2. Torsional splitting pattern of the $J_K=J_0$ rotational level for $(CH_3)_3GeCl$ obtained with the high-barrier torsion–rotation tunneling formalism. The internal rotation of one and two methyl groups at a time are included (H_R, H_A, H_G). Tunneling pathways involving internal rotation of three methyl groups at a time (H_E, H_L) have a negligible contribution and are not shown. The torsion–rotation levels (denoted E_2, I_3, I_4, I_1, I_2, and A_1) are shown in the center of the figure. On the left, a description of the same levels by local mode theory is given. The relative ordering of the energy levels predicted by theory is compared with the observed splitting pattern in the rotational spectrum for the $2\leftarrow 1$ transition ($K=0$, $F'\leftarrow F=7\leftarrow 5=5\leftarrow 3$) on the right of the figure.

 © 2006 Wiley-VCH Verlag GmbH & Co. KGaA, Weinheim

pathways with two methyl tops internally rotating (H_G and H_A). When these tunneling pathways become important, the local mode theory can no longer be expected to reproduce the torsional splitting in the rotational spectrum. In contrast, very good agreement is obtained between the high-barrier tunneling formalism including two-top concerted motions and the experimental data for $(CH_3)_3GeCl$, which proves that multidimensional tunneling can no longer be neglected for this member of the series. When the similar chemical properties of silicon and germanium are taken into account, the difference in internal dynamics between $(CH_3)_3GeCl$ and $(CH_3)_3SiCl$ can be attributed primarily to the change in the borderline steric situation.

The calculated barrier for $(CH_3)_3SnCl$ is quite low (2.1 kJ mol^{-1}; Table 1), which leads to large torsional splittings and immense shifts in the frequencies of rotational transitions (Figure 3). Furthermore, the splitting patterns appear far more complicated, and to facilitate the assignments of the torsion–rotation transitions we employed Stark-effect measurements[19] to differentiate between the different torsion–rotation transitions by their Stark effect (linear or quadratic).[15] At the low barriers encountered for the tin compound, all five tunneling pathways must be considered to be feasible. The theoretical results are displayed in Figure 3 together with the measured $J+1\leftarrow J=1\leftarrow 0$ transition ($K=0$) in the range 3225–3380 MHz. The torsional transition spreads over about 155 MHz, so that overlaps occur since the transition is split further by chlorine quadrupole coupling ($F'\leftarrow F=3\leftarrow 3$, $5\leftarrow 3$, $1\leftarrow 1$ with splittings of about 20 MHz for the $J+1\leftarrow J=1\leftarrow 0$ transition) and by the existence of seven tin isotopomers (^{124}Sn (5.98% natural relative abundance), ^{122}Sn (4.71%), ^{120}Sn (32.97%), ^{119}Sn (8.58%), ^{118}Sn (24.01%), ^{117}Sn (7.57%), ^{116}Sn (14.24%); splitting about 5 MHz).[15]

The contributions from H_L and H_E (tunneling pathways describe the concerted internal rotation of three methyl tops) are of the order of several hundred kHz (see the Supporting Information) and are thus important in reproducing the measured transition frequencies with experimental accuracy (1–4 kHz). The contributions of H_R, H_A, and H_G are all of the same order of magnitude in $(CH_3)_3SnCl$, which results in large changes in the relative ordering of the torsional energy levels compared with $(CH_3)_3SiCl$ and $(CH_3)_3GeCl$. In particular, the frequency of the $E_2\leftarrow E_2$ transition is shifted from the higher frequency end of the spectrum in $(CH_3)_3SiCl$ to the lower frequency end in $(CH_3)_3SnCl$. In general, the overall splitting pattern of the torsion–rotational transitions for $(CH_3)_3SnCl$ appears strikingly different from those for $(CH_3)_3SiCl$ and $(CH_3)_3GeCl$.

On the basis of these assignments supported by PI group theory, the barriers to internal rotation can be determined from the torsional splitting patterns of the rotational spectra by using the fitting program XIAM,[20] which employs the internal-axis method to account for top–top coupling. The results are summarized in Table 2 along with the chlorine quadrupole coupling constants eQq(^{35}Cl) and derived bonding parameters. A complete analysis of the rotational spectra of $(CH_3)_3GeCl$ and $(CH_3)_3SnCl$ is

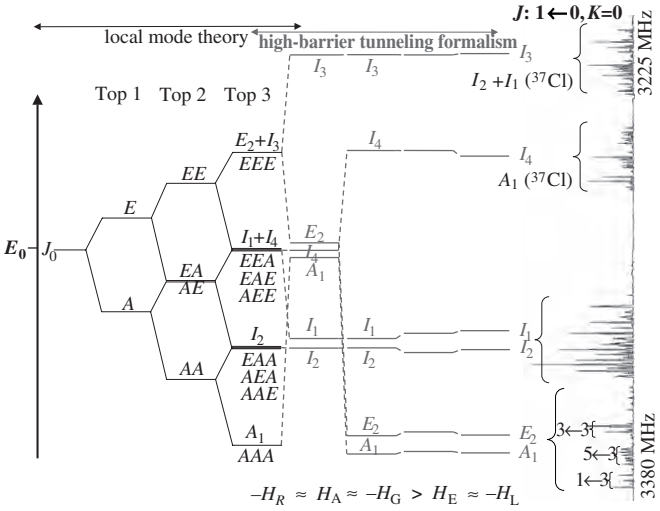

Figure 3. Torsional splitting pattern of the $J_K=J_0$ rotational level for $(CH_3)_3SnCl$ obtained with the high-barrier torsion–rotation tunneling formalism including tunneling pathways for one (H_R), two (H_G, H_A), and three methyl tops (H_E, H_L) rotating internally. The torsion–rotation levels (denoted E_2, I_3, I_4, I_1, I_2, and A_1) are shown in the center of the figure. The contributions for H_R, H_A, and H_G are of similar order of magnitude, which leads to large splittings and shifts of the energy levels; this is most noticeable for E_2. The relative ordering of the energy levels predicted by theory is compared with the observed splitting pattern in the rotational spectrum[15] for the $1\leftarrow 0$ transition ($K=0$) on the right of the figure. The different torsional transitions are split further as a result of chlorine nuclear quadrupole coupling ($F'\leftarrow F=3\leftarrow 3$, $5\leftarrow 3$, $1\leftarrow 1$) and the existence of seven tin isotopomers, as discussed in the text.

Table 2: Threefold hindering potential V_3 and chlorine quadrupole coupling constants eQq(^{35}Cl) for $(CH_3)_3SiCl$, $(CH_3)_3GeCl$, and $(CH_3)_3SnCl$, obtained with XIAM[20] from the torsion–rotation spectra, along with the corresponding data for $(CH_3)_3CCl$[29, 30] and the derived parameters[23–24] for the X–Cl and X–CH_3 bonds (X = C, Si, Ge, Sn).

	$(CH_3)_3CCl$	$(CH_3)_3SiCl$	$(CH_3)_3GeCl$	$(CH_3)_3SnCl$
V_3(exptl) [kJ mol^{-1}]	–	6.91(1)[8]	4.449(5)	1.774(6)
eQq(^{35}Cl) [MHz]	−67.312(3)[30]	−34.81134(83)[8]	−40.0711(14)	−35.776(81)
Cl–X(CH_3)$_3$ bond:				
X(CH_3)$_3$ group EN	2.44	1.97	1.93	1.79
ionic contribution	0.354	0.198	0.376	0.518
σ contribution	0.646	0.485	0.465	0.395
π contribution	0[a]	0.317	0.159	0.087
H_3C–X(CH_3)$_2$Cl bond:				
X(CH_3)$_2$Cl group EN	2.53	1.97	1.96	1.83
ionic contribution	0.095	0.185	0.190	0.255
σ contribution	0.905	0.815	0.810	0.745
π contribution	0[a]	0[a]	0[a]	0[a]

[a] Parameter kept constant.

 © 2006 Wiley-VCH Verlag GmbH & Co. KGaA, Weinheim

presented elsewhere.[15,21] In fair agreement with the calculations (Table 1), the experimentally determined threefold hindering potential V_3 decreases from 6.91(1) kJ mol^{-1} for $(CH_3)_3SiCl$ to 4.449(5) kJ mol^{-1} for $(CH_3)_3GeCl$ to 1.774(6) kJ mol^{-1} for $(CH_3)_3SnCl$. Since the steric repulsion should only play a minor role for $(CH_3)_3SnCl$, it can be assumed that the origin of the internal rotation barrier in $(CH_3)_3SnCl$ arises mainly from the properties of the Sn–C bond.

Although the direct connection between bond character and internal rotation barrier is still not completely understood, we can utilize the Townes–Dailey model,[22] to evaluate the ionic versus covalent character of the Cl–X$(CH_3)_3$ bond (X = C, Si, Ge, Sn) and (using Gordy's approach[23]) the H_3C–X$(CH_3)_2$Cl bond from the $eQq(^{35}Cl)$ values. For this estimation, the electronegativity (EN) values of the substituent groups X$(CH_3)_3$ and X$(CH_3)_2$Cl (X = C, Si, Ge, Sn) have to be determined[24] by taking into account the atomic electronegativities and the partial charges of the atoms. For comparison, we also included $(CH_3)_3CCl$ in this study. On the basis of these data, the Cl–X$(CH_3)_3$ bond character can be estimated from the $eQq(^{35}Cl)$ values (Table 2). For the series $(CH_3)_3XCl$ (X = Si, Ge, Sn), the relative ionic contributions to the X–Cl bond character increase with decreasing ability of the central atom X to perform π back-bonding into its empty d orbitals. Since this ability decreases with increasing size of X, the largest ionic contribution to the X–Cl bond character is found for $(CH_3)_3Sn$–Cl. Since π bonding is not possible for $(CH_3)_3C$–Cl, the C–Cl bond is dominated, as expected, by covalent σ bonding, whereas the ionic character resulting from the high electronegativity of the chlorine amounts to about 35 %.

Similar considerations can be made for the H_3C–X-$(CH_3)_2$Cl bond. The electronegativities of the X$(CH_3)_2$Cl group are somewhat larger than for X$(CH_3)_3$ because of the electronegative chlorine atom, but the general ordering for X = C, Si, Ge, Sn is preserved. Furthermore, no π back-bonding is possible for the H_3C–X bond in any species. Consequently, the X–CH_3 bond character is virtually identical for $(CH_3)_3SiCl$ and $(CH_3)_3GeCl$. Thus, it can be deduced that the change in barrier height between $(CH_3)_3SiCl$ and $(CH_3)_3GeCl$ is due mainly to reduced steric repulsion in $(CH_3)_3GeCl$; the influence of a change in the H_3C–X bond character is presumed to be small. In contrast, both factors become important for the internal dynamics in $(CH_3)_3SnCl$: The larger covalent radius of Sn relative to Si and Ge resulting in less steric repulsion together with a significant increase in the ionic character of the H_3C–Sn bond.

In summary, Fourier transform microwave (FTMW) spectroscopy in combination with PI group theory and multidimensional tunneling theory allows the detection and analysis of complex molecular internal dynamics. As we have shown, the internal dynamics for the three related molecules $(CH_3)_3SiCl$, $(CH_3)_3GeCl$, and $(CH_3)_3SnCl$ are significantly different and can be understood and described by up to five topologically distinct tunneling pathways. The observed torsional splitting patterns of the rotational spectra reflect the dramatic changes in property in going from Ge to Sn as the central atom. The complex internal dynamics in $(CH_3)_3SnCl$ is influenced not only by the significantly reduced electrostatic repulsion, but also by the change of the bonding situation for Sn–C bonds. The character of the Cl–X$(CH_3)_3$ and H_3C–X$(CH_3)_2$Cl bonds (X = C, Si, Ge, Sn) could be estimated from an analysis of the quadrupole coupling constants eQq and used to gain a better understanding of the different barrier heights of these species. It is interesting that the decrease in the barrier height V_3 from $(CH_3)_3GeCl$ to $(CH_3)_3SnCl$ (2.6 kJ mol^{-1}) is approximately the same as that from $(CH_3)_3SiCl$ to $(CH_3)_3GeCl$ even though the distances between hydrogen atoms of the neighboring methyl groups in $(CH_3)_3SnCl$ are already large enough to minimize electronic repulsion of the C–H bond orbitals. This observation suggests that the internal rotation barrier in $(CH_3)_3SnCl$ originates largely from the character of the Sn–C bond.

Experimental Section

$(CH_3)_3GeCl$ and $(CH_3)_3SnCl$ (98 % and 97 % pure, respectively) were purchased from Sigma–Aldrich and used without further purification. An argon flow was saturated from a liquid reservoir of $(CH_3)_3GeCl$ and expanded supersonically into a microwave resonator by using a pulsed nozzle. A mixture of about 1 % od the volatile $(CH_3)_3SnCl$ in neon was used at stagnation pressures between 50 and 100 kPa to record its rotational spectrum. The $J+1 \leftarrow J$ transitions with $J = 1,\ldots,5$ of the rotational spectrum of $(CH_3)_3GeCl$ were recorded at the NIST by using two FTMW spectrometers with pulsed molecular beams.[25–28] With argon as the carrier gas, the uncertainty in the transition frequency is about 4 kHz. To determine the $J+1 \leftarrow J=1 \leftarrow 0$ rotational transition of $(CH_3)_3GeCl$ and the complete rotational spectrum of $(CH_3)_3SnCl$, we used the broadband (2–26.5 GHz) high-resolution FTMW spectrometer at the University of Hannover.[10] The line widths at half height (resolving powers) are about 1 kHz (3 kHz) for argon and about 1.5 kHz (5 kHz) for neon as the carrier gas.[10]

Received: January 18, 2006

Keywords: microwave spectroscopy · molecular dynamics · nuclear quadrupole coupling · theoretical chemistry

[1] F. Weinhold, *Nature* **2001**, *411*, 539 – 541.
[2] L. Goodman, V. Pophristic, F. Weinhold, *Acc. Chem. Res.* **1999**, *32*, 983 – 993.
[3] F. Weinhold, *Angew. Chem.* **2003**, *115*, 4320 – 4326; *Angew. Chem. Int. Ed.* **2003**, *42*, 4188 – 4194.
[4] F. M. Bickelhaupt, E. J. Baerends, *Angew. Chem.* **2003**, *115*, 4315 – 4320; *Angew. Chem. Int. Ed.* **2003**, *42*, 4183 – 4188.
[5] A. F. Hollemann, *Lehrbuch der Anorganischen Chemie*, de Gruyter, Berlin, **1995**.
[6] J. N. Spencer, S. W. Barton, B. M. Cader, C. D. Corsico, L. E. Harrison, M. E. Mankuta, C. H. Yoder, *Organometallics* **1985**, *4*, 394 – 396.
[7] M. J. Frisch, G. W. Trucks, H. B. Schlegel, G. E. Scuseria, M. A. Robb, J. R. Cheeseman, Jr., J. A. Montgomery, T. Vreven, K. N. Kudin, J. C. Burant, J. M. Millam, S. S. Iyengar, J. Tomasi, V. Barone, B. Mennucci, M. Cossi, G. Scalmani, N. Rega, G. A. Petersson, H. Nakatsuji, M. Hada, M. Ehara, K. Toyota, R. Fukud, J. Hasegawa, M. Ishida, T. Nakajima, Y. Honda, O. Kitao, H. Nakai, M. Klene, X. Li, J. E. Knox, H. P. Hratchian, J. B. Cross, V. Bakken, C. Adamo, J. Jaramillo, R. Gomperts, R. E. Stratmann, O. Yazyev, A. J. Austin, R. Cammi, C. Pomelli, J. W. Ochterski, P. Y. Ayala, K. Morokuma, G. A. Voth, P. Salvador, J. J. Dannenberg, V. G. Zakrzewski, S. Dapprich, A. D. Daniels,

 © 2006 Wiley-VCH Verlag GmbH & Co. KGaA, Weinheim

M. C. Strain, O. Farkas, D. K. Malick, A. D. Rabuck, K. Raghavachari, J. B. Foresman, J. V. Ortiz, Q. Cui, A. G. Baboul, S. Clifford, J. Cioslowski, B. B. Stefanov, G. Liu, A. Liashenko, P. Piskorz, I. Komaromi, R. L. Martin, D. J. Fox, T. Keith, M. A. Al-Laham, C. Y. Peng, A. Nanayakkara, M. Challacombe, P. M. W. Gill, B. Johnson, W. Chen, M. W. Wong, C. Gonzalez, J. A. Pople. Gaussian 03, Gaussian, Inc., Wallingford, **2004**.

[8] I. Merke, W. Stahl, S. Kassi, D. Petitprez, G. Wlodarczak, *J. Mol. Spectrosc.* **2002**, *216*, 437 – 446.

[9] J. R. Durig, K. L. Hellams, *J. Mol. Struct.* **1975**, *29*, 349 – 356.

[10] J.-U. Grabow, W. Stahl, H. Dreizler, *Rev. Sci. Instrum.* **1996**, *67*, 4072 – 4084.

[11] P. R. Bunker, P. Jensen, *Molecular Symmetry and Spectroscopy*, 2nd ed., NRC, Ottawa, **1998**.

[12] K. D. Möller, H. G. Andresen. *J. Chem. Phys.* **1963**, *39*, 17 – 22.

[13] K. K. Lehmann, B. H. Pate, *J. Mol. Spectrosc.* **1990**, *144*, 443 – 445.

[14] P. Groner, *Spectrochim. Acta Part A* **1993**, *49*, 1935 – 1946.

[15] M. Schnell, J.-U. Grabow, J. T. Hougen, unpublished results.

[16] H. C. Longuet-Higgins, *Mol. Phys.* **1963**, *6*, 445 – 460.

[17] J.-U. Grabow, W. Stahl, *Z. Naturforsch. A* **1990**, *45*, 1043 – 1044.

[18] J. T. Hougen, N. Ohashi, *J. Mol. Spectrosc.* **1993**, *159*, 363 – 387.

[19] M. Schnell, D. Banser, J.-U. Grabow, *Rev. Sci. Instrum.* **2004**, *75*, 2111 – 2115.

[20] H. Hartwig, H. Dreizler, *Z. Naturforsch.* **1996**, *51*, 923 – 932.

[21] M. Schnell, J.-U. Grabow, *Phys. Chem. Chem. Phys.*, DOI: 10.1039/b600682e.

[22] C. H. Townes, A. L. Schawlow, *Microwave Spectroscopy*, Dover, New York, **1975**.

[23] W. Cook, *Phys. Rev.* **1946**, *69*, 604 – 607.

[24] W. Gordy, R. L. Cook, *Microwave Molecular Spectra*, 3rd ed., Wiley, New York, **1984**.

[25] T. J. Balle, W. H. Flygare, *Rev. Sci. Instrum.* **1981**, *52*, 33 – 45.

[26] R. D. Suenram, F. J. Lovas, W. Pereyra, G. T. Fraser, A. R. Hight Walker, *J. Mol. Spectrosc.* **1997**, *181*, 67 – 77.

[27] F. J. Lovas, N. Zobov, G. T. Fraser, R. D. Suenram, *J. Mol. Spectrosc.* **1995**, *171*, 189 – 199.

[28] R. D. Suenram, J.-U. Grabow, A. Zuban, I. Leonov, *Rev. Sci. Instrum.* **1999**, *70*, 2127 – 2135.

[29] D. R. Lide, M. Jen, *J. Chem. Phys.* **1963**, *38*, 1504 – 1507.

[30] M. C. Ellis, A. C. Legon, C. A. Rego, D. J. Millen, *J. Mol. Struct.* **1989**, *200*, 353 – 359.

 © 2006 Wiley-VCH Verlag GmbH & Co. KGaA, Weinheim

Rotational Spectroscopy

DOI: 10.1002/anie.200600342

The Glycine–Water Complex**

José L. Alonso, Emilio J. Cocinero, Alberto Lesarri, M. Eugenia Sanz, and Juan C. López*

The solvation of biomolecular building blocks is an essential biochemical process with relevance for a variety of fundamental phenomena such as molecular recognition and proton transport. The hydration in amino acids is known to trigger the transformation from the neutral form observed in the gas phase[1–7] to the charged zwitterion ($NH_3^+CH(R)COO^-$)[8,9] present in condensed media. A detailed understanding of these effects requires the characterization of the isolated clusters formed between biomolecules and water in the gas phase. Herein we present the first experimental observation of the monohydrated cluster of the prototypical amino acid glycine (NH_2CH_2COOH). The glycine–water complex provides the simplest molecular model of the biologically important amino acid/water interactions and represents the initial step of the hydration process. Fundamental questions addressed in this study include how water molecules bind to amino acids and whether conformational changes are induced by hydration.

Hydrated clusters can be generated by a supersonic expansion[10,11] of a solute/water gas mixture diluted in a light carrier gas. The cooling that accompanies the expansion favors the formation of complexes in which the solute and water molecules interact through hydrogen bonding. Furthermore, the jet expansion provides the conditions of virtual isolation necessary to probe the complexes spectroscopically. The jet-cooled hydrated clusters can be investigated through their rotational spectra by using molecular-beam Fourier-transform microwave spectroscopy (MB-FTMW).[12,13] Microwave spectroscopy is particularly adapted to this task since it has an inherent high resolution and is exceptionally sensitive to the molecular-mass distribution and geometry; the rotational spectrum is thus a unique identifier of the structure. However, until the introduction of laser-ablation techniques, gas-phase spectra were only available for solids with sufficient vapor pressure and thermal stability. Hence, there was a lack of information on the structures of most amino acids and microsolvation clusters because of the vaporization difficulties associated with their high melting points and thermal instability. Suenram et al.[14] and Walker and Gerry[15] independently developed laser-ablation devices in combination with molecular-beam Fourier-transform microwave spectroscopy (LA-MB-FTMW) to investigate the rotational spectra of metal oxides and halides. The first device was also applied to the structural study of glycine in the gas phase, but it was reported that the classical heating method was more reliable.[1b] We recently developed a LA-MB-FTMW spectrometer[16] (Figure 1) dedicated to the investigation of the rotational spectra of biomolecules. This technique has been applied successfully to analyze the shape of the neutral form of several amino acids[2–7] and identify their energetically accessible conformers under isolation conditions. The knowledge of the gas-phase structure has provided important insight into the intramolecular interactions that determine their conformation. Herein we have extended this experimental method to observe the microsolvation of biomolecules.

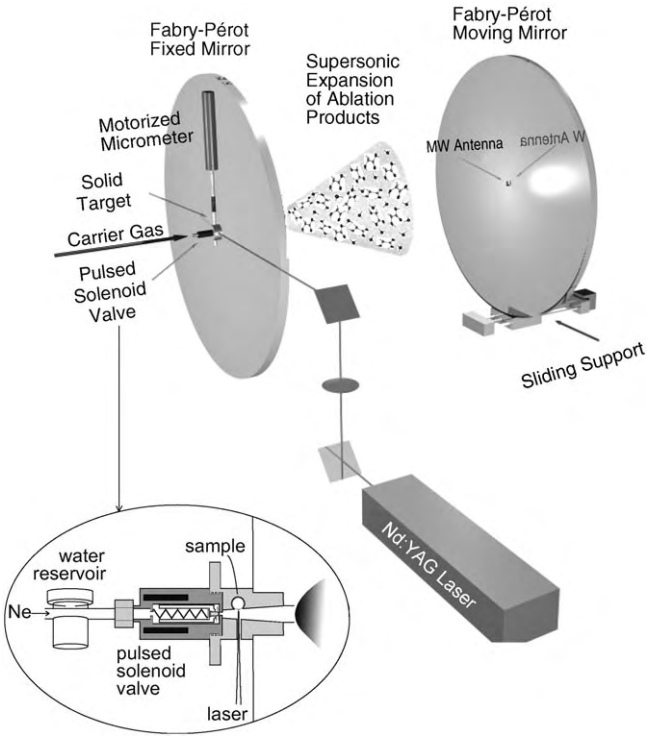

Figure 1. Schematic diagram of the laser-ablation system and Fabry–Pérot resonator of the LA-MB-FTMW spectrometer used to observe the glycine–water complex.

Previous studies of glycine in the gas phase[1] identified two conformers of the neutral molecule, which differ in the intramolecular hydrogen bonds that stabilize the amino acid skeleton. Conformer I is stabilized by a bifurcated hydrogen bond between the amine and carbonyl groups (N–H···O=C) and has a *cis*-COOH interaction, whereas conformer II exhibits a hydrogen bond from the hydroxy group to the lone pair of electrons on the nitrogen atom (N···H–O) and has

[*] Prof. J. L. Alonso, Dr. E. J. Cocinero, Prof. A. Lesarri, Dr. M. E. Sanz, Prof. J. C. López
Grupo de Espectroscopía Molecular (GEM)
Departamento de Química Física y Química Inorgánica
Facultad de Ciencias Universidad de Valladolid
47005 Valladolid (Spain)
Fax: (+34) 983-423-204
E-mail: jlalonso@qf.uva.es

[**] We would like to thank the Ministerio de Ciencia y Tecnología (grant BQU2003-03275) and the Junta de Castilla y León (grant VA012-C05) for financial support. M.E.S. thanks the Ministerio de Ciencia y Tecnología for cofunding within the Ramón y Cajal program.

Supporting information for this article is available on the WWW under http://www.angewandte.org or from the author.

© 2006 Wiley-VCH Verlag GmbH & Co. KGaA, Weinheim

a *trans*-COOH configuration. A third low-energy conformer III (N–H···O–H) has not been observed in jet experiments because of its conformational relaxation to conformer I.[17] In the hydrated clusters, intermolecular hydrogen-bonding interactions can drive the amino acid into conformations that are not favorable for the parent molecule. The issue of how the solvent influences the conformational preferences in the hydrated molecule can be addressed by making comparisons between the structures of the parent molecule and those observed in the microsolvated clusters. For this reason, the experimental study of the interaction of glycine with H_2O started with ab initio predictions[18] of the spectroscopic constants at the MP2/6-311++G(d,p) level (Table 1) for the two lower-energy 1:1 structures.[19,20] These structures are denoted as conformers Ia and IIIa since they originate from glycine conformations I and III, respectively. All other conformers of the complex are predicted to be much higher ($>14\,kJ\,mol^{-1}$) in energy. A survey of the microwave spectrum was then performed in the regions where the most intense transitions of conformers Ia and IIIa were expected. After the transitions corresponding to the monomers of glycine I and II[1] had been discarded from the spectrum, a detailed search revealed the presence of a new set of rotational transitions corresponding to a near-prolate asymmetric rotor. These lines disappeared when either the laser or the admixing water were removed, thus confirming that they belong to a complex formed between glycine and water. Furthermore, all the transitions were split into several close hyperfine components as a result of a nuclear quadrupole coupling originating from a ^{14}N nucleus ($I=1$), thus indicating that they arise from a molecular species containing a nitrogen atom. A total of 30 observed hyperfine transition frequencies have been fit to a least-squares procedure with a semirigid rotor Hamiltonian[21] in Watson's asymmetric (A) reduction ($\boldsymbol{H}_R^{(A)}$), supplemented with a nuclear quadrupole coupling[22,23] interaction term ($\boldsymbol{H}_Q$) [Eq. (1)].

$$\boldsymbol{H} = \boldsymbol{H}_R^{(A)} + \boldsymbol{H}_Q \tag{1}$$

The semirigid Watson Hamiltonian is given by Equation (2),

$$\begin{aligned}\boldsymbol{H}_R^{(A)} &= A\boldsymbol{P}_a^2 + B\boldsymbol{P}_b^2 + C\boldsymbol{P}_c^2 - \Delta_J\boldsymbol{P}^4 - \Delta_{JK}\boldsymbol{P}^2\boldsymbol{P}_a^2 \\ &- \Delta_K\boldsymbol{P}_a^4 - 2\delta_J\boldsymbol{P}^2(\boldsymbol{P}_b^2 - \boldsymbol{P}_c^2) - \delta_K[\boldsymbol{P}_a^2(\boldsymbol{P}_b^2 - \boldsymbol{P}_c^2) + (\boldsymbol{P}_b^2 - \boldsymbol{P}_c^2)\boldsymbol{P}_a^2]\end{aligned} \tag{2}$$

where the coefficients A, B, and C represent the rotational constants and Δ_J, Δ_{JK}, Δ_K, δ_J, and δ_K are the quartic centrifugal distortion constants. The term $\boldsymbol{H}_Q$ accounts for the interaction energy of the ^{14}N electric quadrupole moment (Q) with the molecular electric field gradient ($q_{\alpha\beta} = \partial^2 V/\partial\alpha\partial\beta$; α,β = a, b, c) at the nitrogen nucleus. The determinable spectroscopic parameters are the elements of the nuclear quadrupole coupling tensor $\boldsymbol{\chi}$ which are linearly related to the electric field gradient by $\boldsymbol{\chi} = -eQ\boldsymbol{q}$. The resulting rotational and quadrupole coupling constants (Table 1) provide conclusive evidence for the nature of the glycine–water complex detected in the supersonic expansion (the centrifugal distortion constants are given in the Supporting Information). A comparison of the experimental parameters with the predicted ab initio values is a first suggestion that the conformation of the glycine–water complex corresponds to that of conformer Ia, which is predicted to be the global minimum. The structure of conformer Ia was used to calculate the isotopic shifts of the isotopomers ^{15}N-glycine···H_2O and ^{15}N-glycine···$H_2{}^{18}O$, which were investigated using enriched samples. The observation of their rotational spectra close to the predicted frequencies definitively confirms the presence of conformer Ia of the glycine–water complex in the jet (the spectroscopic parameters also given in Table 1).

The planar moment of inertia P_c ($=1/2\,(I_a+I_b-I_c) = \Sigma_i m_i c_i^2$), which gives the mass extension out of the *ab* principal inertial plane, was initially considered in order to derive an experimental structure for the glycine–water complex. The almost equal values of P_c for the three observed isotopomers of the glycine–water complex (parent: $3.199\,u\,Å^2$) establishes that the nitrogen and the water oxygen atoms are lying on the *ab* inertial plane of the complex. A comparison with the value for conformer I of the parent glycine ($2.860\,u\,Å^2$) further indicates that the water

Table 1: Theoretical predictions of the rotational parameters for the two lower-energy conformers of glycine–water complexes, compared with the experimental values for the observed isotopomers of the complex.

	Ab initio[a]		Experiment[b]		
	conformer Ia	conformer IIIa	parent glycine···H_2O	^{15}N-glycine···H_2O	^{15}N-glycine···$H_2{}^{18}O$
	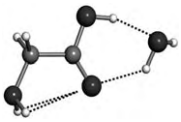	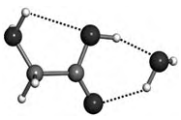			
A [MHz][c]	8440	7978	8437.979(149)	8401.068(109)	8374.891(113)
B [MHz]	1614	1654	1613.41327(71)	1579.66148(61)	1500.69207(52)
C [MHz]	1379	1404	1378.06131(51)	1352.44092(45)	1293.54511(39)
P_c [u Å^2]	3.26	4.47	3.19871(67)	3.20301(51)	3.20776(51)
χ_{aa} [MHz]	−3.57	−3.95	−3.285(27)	–[d]	–
χ_{bb} [MHz]	1.69	2.14	1.694(67)	–	–
χ_{cc} [MHz]	1.88	1.80	1.590(67)	–	–
ΔE [kJ mol^{-1}]	0.0	4.7			

[a] Second-order Møller–Plesset perturbation theory (MP2) and 6-311++G(d,p) basis set. The predicted relative energy (ΔE) does not include zero-point vibrational energy corrections. [b] The full set of experimental spectroscopic parameters is given in the Supporting Information. [c] *A*, *B*, *C* represent the rotational constants. $P_c(=1/2\ (I_a+I_b-I_c) = \Sigma_i m_i c_i^2)$ is the planar moment of inertia. $\chi_{\alpha\beta}(\alpha,\beta$=a,b,c) are elements of the nuclear quadrupole coupling tensor. [d] The isotopomers with ^{15}N ($I=1/2$) do not exhibit nuclear quadrupole coupling hyperfine effects.

 © 2006 Wiley-VCH Verlag GmbH & Co. KGaA, Weinheim

oxygen atom in the complex lies essentially on the heavy atom plane of glycine, since the small increment in the value of P_c in the hydrated complex can be attributed to the contribution of out-of-plane hydrogen atoms and/or zero-point vibrational effects. These arguments give a description of the structure of the complex consistent with the theoretical predictions for conformer Ia. In this conformer, water interacts through the carboxy group, simultaneously acting as a proton donor to the carbonyl oxygen atom and accepting a proton from the hydroxy group. This configuration benefits from two intermolecular hydrogen bonds, with water bridging the carboxylic acid group in a cyclic planar structure. The water hydrogen atom not participating in the intermolecular hydrogen bonds is predicted to lie out of the plane of the glycine skeleton.

An effective structure[22,24] for the glycine–water complex has been derived here from the isotopical information assuming that complexation does not alter significantly[25,26] the structure of the individual monomers of glycine I and water. Since no experimental structure was reported for glycine I, the rotational spectrum of this conformer was first reinvestigated, which resulted in the new assignment of the $^{15}NH_2CH_2{}^{13}COOH$ species and new measurements on the $^{15}NH_2CH_2COOH$ isotopomer. The rotational data from these species, together with previous data from the other four isotopomers found in the literature,[1] allowed us to calculate the effective structure of glycine I (see the Supporting Information). The structure of the glycine–water complex was then obtained from a least-squares fit of the nine rotational constants of the complex in Table 1 to the three parameters $r[O_B\cdots H_W]$, $\measuredangle[H_W\cdots O_B{=}C]$, and $\measuredangle[O_W\text{-}H_W\cdots O_B]$ giving the relative orientation of the two subunits of the adduct. The dihedral angle $\tau[H_V\text{-}O_W\text{-}H_W\cdots O_B]$ which defines the elevation of the water hydrogen atom not involved in the intermolecular hydrogen bond could not be determined from the least-squares fit. A value of τ around 140° reproduces the ground-state value of the P_c planar moment and yields the effective structural parameters of the glycine–water complex given in Table 2.

The experimental effective structure provides relevant chemical information on the nature of the hydrogen-bonding interactions stabilizing the adduct. Binding of a single water molecule to glycine proceeds through the carboxylic acid group and gives rise to a closed ring structure in which the water bridge benefits from an enhancing cooperative effect.[27] The structure of conformer Ia of the glycine–water cluster retains the preferred conformation I (NH···O=C, *cis*-COOH) of unsolvated glycine, so the water molecule in the complex does not enter into competition with the intramolecular hydrogen bonds in glycine, further stabilizing the complex. The distance of the $O_A\text{-}H_A\cdots O_W$ interaction (1.806 Å, Table 2) is significantly shorter than that of $O_W{-}H_W\cdots O_B$ distance (2.073 Å). In addition, the nonlinearity of the $O_W{-}H_W\cdots O_B$ bond (126.4°) is much more pronounced than that of the $O_A{-}H_A\cdots O_W$ bond (161.8°). If we acknowledge that a shorter H···O distance and a more linear O–H···O arrangement are indicative of a greater hydrogen bond strength, our structure shows that the acidic character of the OH group of the carboxylic acid dominates the interaction between water and glycine.

The lack of observation of conformer IIIa of the glycine–water cluster can not be attributed to small dipole moment components since these are predicted to be almost equal to those of conformer Ia. It is well known that molecular adducts are formed by three-body collisions in the first steps of the supersonic expansion. The formation of conformer IIIa might require the presence of conformer III as one of the collisional partners in the jet. However this conformer of glycine,[17] as occurs with other aliphatic α-amino acids,[2–4] has never been observed in supersonic jets because of its collisional relaxation to the most stable conformer I of glycine. This collisional relaxation can take place also for the glycine–water complex and thereby contribute to the lack of formation of conformer IIIa. Additionally it is also possible that a low concentration of glycine III in the jet would limit the formation of glycine–water complex IIIa.

The structural studies of biomolecules have entered a new stage with the use of LA-MB-FTMW spectroscopy. It is now possible to place nonvolatile biomolecules in the gas phase and explore the most stable conformers and their hydrated clusters generated in a supersonic expansion. Future studies will be directed toward the investigation of larger molecules or more complex systems with additional water molecules. In this sense, the potentialities of LA-MB-FTMW spectroscopy are remarkable and surpass the limitations of other techniques which, lacking rotational resolution, can not provide unequivocal structural assignments, or require the presence, as in the case of rotationally resolved LIF, of absorbing chromophore groups.

Table 2: The structure of the glycine–water complex.

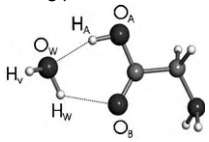

$r(H_W\cdots O_B)$ [Å]	2.073(2)
$r(O_W\cdots H_A)$ [Å]	1.806(1)
$\measuredangle(H_W\cdots O_B{=}C)$ [°]	112.4(1)
$\measuredangle(O_W{-}H_W\cdots O_B)$ [°]	126.4(5)
$\measuredangle(H_A\cdots O_W{-}H_W)$ [°]	91.4(7)
$\measuredangle(O_A{-}H_A\cdots O_W)$ [°]	161.8(1)
τ $(H_V{-}O_W{-}H_W\cdots O_B)$ [°]	140.0

Experimental Section

The laser-ablation pulsed nozzle system is shown in Figure 1. Briefly, a cylindrical target rod of the solid sample obtained by pressing glycine powder is attached to a motorized support at the pulsed valve exit. The sample is rotated and translated so that a fresh sample area is always exposed to the green nanosecond pulses of a focused Q-switched Nd:YAG laser with a wavelength of 532 nm. In each laser pulse the vaporized glycine is entrained into a flow of Ne that expands adiabatically to produce a supersonic jet. A heatable water reservoir was placed before the gas valve to add water to the inert carrier gas, with stagnation pressures af about 8 bar. The clusters of glycine and water were formed in the jet and later probed with a short polarizing microwave pulse. After the excitation pulse, the free-induction-decay

 © 2006 Wiley-VCH Verlag GmbH & Co. KGaA, Weinheim

(FID) corresponding to molecular relaxation was recorded in the time domain. The Fourier transformation of the FID transient signal yielded the resonant frequencies of the rotational transitions.

Received: January 26, 2006
Revised: March 29, 2006

Keywords: amino acids · hydrogen bonds · rotational spectroscopy · solvation

[1] a) P. D. Godfrey, R. D. Brown, *J. Am. Chem. Soc.* **1995**, *117*, 2019; b) F. J. Lovas, Y. Kawashima, J.-U. Grabow, R. D. Suenram, G. T. Fraser, E. Hirota, *Astrophys. J.* **1995**, 455, L201; c) S. J. McGlone, P. S. Elmes, R. D. Brown, P. D. Godfrey, *J. Mol. Struct.* **1999**, *485–486*, 225.
[2] S. Blanco, A. Lesarri, J. C. López, J. L. Alonso, *J. Am. Chem. Soc.* **2004**, *126*, 11675.
[3] A. Lesarri, E. J. Cocinero, J. C. López, J. L. Alonso, *Angew. Chem.* **2004**, *116*, 615; *Angew. Chem. Int. Ed.* **2004**, *43*, 605.
[4] A. Lesarri, R. Sánchez, E. J. Cocinero, J. C. López, J. L. Alonso, *J. Am. Chem. Soc.* **2005**, *127*, 12952.
[5] A. Lesarri, S. Mata, E. J. Cocinero, S. Blanco, J. C. López, J. L. Alonso, *Angew. Chem.* **2002**, *114*, 4867; *Angew. Chem. Int. Ed.* **2002**, *41*, 4673.
[6] A. Lesarri, E. J. Cocinero, J. C. López, J. L. Alonso, *J. Am. Chem. Soc.* **2005**, *127*, 2572.
[7] A. Lesarri, E. J. Cocinero, J. C. López, J. L. Alonso, *ChemPhysChem* **2005**, *6*, 1559.
[8] G. Albrecth, R. B. Corey, *J. Am. Chem. Soc.* **1939**, *61*, 1087.
[9] H. A. Levy, R. B. Corey, *J. Am. Chem. Soc.* **1941**, *63*, 2095.
[10] D. H. Levy, *Annu. Rev. Phys. Chem.* **1980**, *31*, 197.
[11] *Jet Spectroscopy and Molecular Dynamics* (Eds.: J. M. Hollas, D. Phillips), Blackie, London, **1995**.
[12] T. J. Balle, W. H. Flygare, *Rev. Sci. Instrum.* **1981**, *52*, 33.
[13] J. L. Alonso, F. J. Lorenzo, J. C. López, A. Lesarri, S. Mata, H. Dreizler, *Chem. Phys.* **1997**, *218*, 267.
[14] R. D. Suenram, F. J. Lovas, G. Fraser, K. Matsumura, *J. Chem. Phys.* **1990**, *92*, 4724.
[15] K. A. Walker, M. C. L. Gerry, *J. Mol. Spectrosc.* **1997**, *182*, 178.
[16] A. Lesarri, S. Mata, J. C. López, J. L. Alonso, *Rev. Sci. Instrum.* **2003**, *74*, 4799.
[17] P. D. Godfrey, R. D. Brown, F. H. Rodgers, *J. Mol. Struct.* **1996**, *376*, 65.
[18] Gaussian 03, Revision B.04, M. J. Frisch et al., see the Supporting Information.
[19] H. Basch, W. J. Stevens, *Chem. Phys. Lett.* **1990**, *169*, 275.
[20] W. Wang, W. Zheng, X. Pu, N.-B. Wong, A. Tian, *J. Mol. Struct.* **2002**, *618*, 235.
[21] J. K. Watson in *Vibrational Spectra and Structure*, *Vol. 6* (Ed.: J. R. Durig), Elsevier, Amsterdam, **1977**, pp. 1–89.
[22] W. Gordy, R. L. Cook, *Microwave Molecular Spectra*, Wiley, New York, **1984**.
[23] H. M. Pickett, *J. Mol. Spectrosc.* **1991**, *148*, 371.
[24] H. D. Rudolph, *Struct. Chem.* **1991**, *2*, 581.
[25] S. Blanco, A. Lesarri, J. C. López, J. L. Alonso, *Chem. Eur. J.* **2002**, *8*, 1603.
[26] M. E. Sanz, V. M. Sanz, J. C. López, J. L. Alonso, *Chem. Phys. Lett.* **2001**, *342*, 31.
[27] a) G. A. Jeffrey, *An introduction to Hydrogen Bonding*, Oxford University Press, Oxford, **1997**; b) G. A. Jeffrey, W. Saenger, *Hydrogen Bonding in Biological Structures*, Springer, New York, **1991**.

 © 2006 Wiley-VCH Verlag GmbH & Co. KGaA, Weinheim

Main-Group Hydrides

DOI: 10.1002/anie.200601013

Rational Design of a Well-Defined Soluble Calcium Hydride Complex**

Sjoerd Harder and Julie Brettar*

There is a wealth of information on transition-metal hydride complexes, a field driven by numerous applications in catalytic processes.[1] Recently, significant progress has also been made in the syntheses of lanthanide hydride complexes.[2] The area of main-group metal hydride complexes is biased in the sense that *p*-block metal hydrides are much better documented[3] than *s*-block metal hydrides, for which only few examples have been reported.[4] There are two important reasons for this imbalance: 1) relatively small bond energies in these predominantly ionic complexes allow for facile ligand exchange and thus formation of ligand-free metal hydride (this holds especially for the larger metals) and 2) very high lattice energies for early-main-group metal hydrides result in immediate precipitation of $[MH_x]_\infty$. Consequently, the few examples of early-main-group metal hydrides all show the hydride encapsulated in mixed aggregates. A well-defined Li-Al-hydride[4a] cluster, a lithium amide-hydride aggregate[4b,c] and the alkoxide-hydride cluster $(t\text{BuOLi})_{16}(\text{LiH})_{17}$[4d] have been described. A magnesium hydride was found in an "inverse crown ether", that is, encapsulated in a ring that also contains metal ions (**1**).[4e,f]

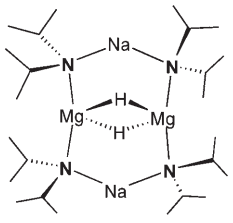

1

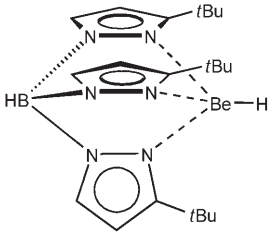

2

Also a beryllium hydride stabilized with a scorpionate ligand (Tp^{tBu}) has been reported (**2**).[4g] Although soluble arylcalcium hydrides (prepared by activation of the C–H bond with calcium vapor) have been reported,[4h,i] no NMR spectroscopic or structural proof was available. Herein we describe the synthesis and characterization of a well-defined soluble calcium hydride complex.

[*] Prof. Dr. S. Harder, Dr. J. Brettar
Anorganische Chemie
Universität Duisburg-Essen
Universitätsstrasse 5, 45117 Essen (Germany)
Fax: (+49) 201-183-2621
E-mail: sjoerd.harder@uni-due.de

[**] We kindly acknowledge H. Bandmann for measurement of 500 MHz NMR spectra. We are grateful to Prof. Dr. R. Boese and D. Bläser for measuring some of the X-ray diffraction data sets.

WILEY InterScience DISCOVER SOMETHING GREAT
© 2006 Wiley-VCH Verlag GmbH & Co. KGaA, Weinheim

Our first approach was based on the synthesis of **1**, a mixed-metal hydride that was obtained by β-hydrogen elimination in an iPr$_2$N-complex (iPr$_2$N$^-$ → iPrN=CMe$_2$ + H$^-$). Since preliminary results indicated that such an elimination is also possible in calcium chemistry,[5] we converted the heteroleptic benzylcalcium complex **3** into the heteroleptic amide **4** according to Scheme 1. This calcium amide

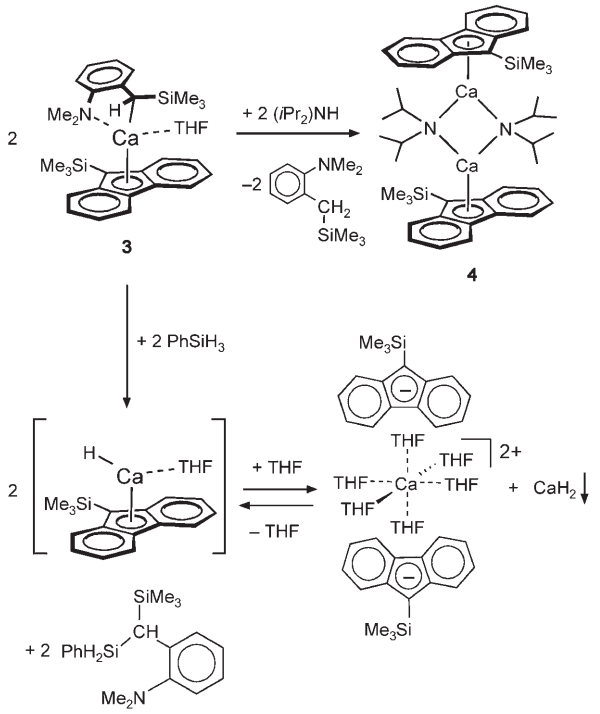

Scheme 1.

compound crystallizes as a dimer with terminal 9-Me$_3$Si-fluorenyl ligands and bridging iPr$_2$N$^-$ ions (Figure 1). There are no precedents for iPr$_2$N–Ca complexes, but the Ca–N bond lengths in **4** (average: 2.399(5) Å) are significantly shorter than those for the bridging (Me$_3$Si)$_2$N$^-$ ions in

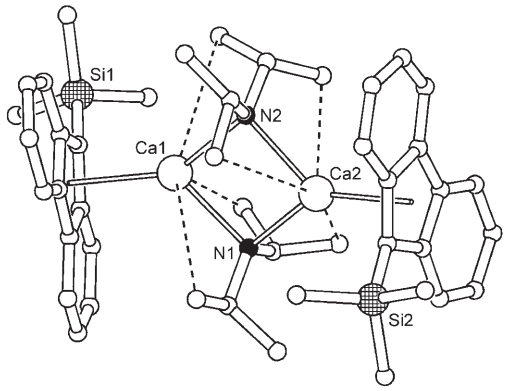

Figure 1. Crystal structure of **4**; hydrogen atoms omitted for clarity. Selected bond lengths [Å] and angles [°]: Ca1–ring 2.716(6)–2.806(6), Ca2–ring 2.724(6)–2.814(7), Ca1–N1 2.385(5), Ca1–N2 2.420(5), Ca2–N1 2.395(5), Ca2–N2 2.394(5); N1-Ca1-N2 86.3(2), N1-Ca2-N2 86.7(2). Agostic Me···Ca interactions are indicated by dashed lines: Ca···H distances range from 2.57–2.80 Å.

[((Me$_3$Si)$_2$N)$_2$Ca]$_2$ (average: 2.475(6) Å).[6] This situation is in line with the higher basicity and smaller steric bulk of the iPr$_2$N$^-$ ion. The crystal structure reveals several short agostic Me···Ca contacts (indicated in Figure 1) similar to those observed in the dimer [iPr$_2$NK·TMEDA]$_2$ (TMEDA = *N*,*N*′,*N*′-tetramethyl-1,2-ethanediamine).[7] Heating benzene or THF solutions of **4** in closed NMR-tubes for several days at 100 °C only showed small amounts of decomposition products which could be neither identified nor isolated. The high stability of **4** is remarkable and strongly contrasts with that of iPr$_2$NK.[7]

A second approach to generate metal hydride complexes is the reaction of a nucleophilic metal complex with phenylsilane (Scheme 1). Although this method is well-established in lanthanide chemistry,[2] it surprisingly has not been applied in early-main-group chemistry. The validity of this metathesis reaction is suggested by a new class of alkene hydrosilylation catalysts based on early-main-group metals.[8] Reaction of the heteroleptic complex **3** with phenylsilane was monitored by ^{1}H NMR spectroscopy: clean conversion into the expected benzylsilane (Scheme 1) was observed and broad signals for a fluorenyl species appeared in the spectrum. A crystalline product could only be obtained by addition of small amounts of THF. The product was analyzed as the homoleptic complex [9-trimethylsilylfluorenyl$^-$]$_2$ [Ca^{2+}·(THF)$_6$].[9] The additional observation of small amounts of a white precipitate during the reaction suggests that the hydride precipitated in the form of CaH$_2$.

Heteroleptic calcium hydrides will possibly only be stable if the Schlenk equilibrium is steered exclusively to the heteroleptic side. Strongly bonding bulky ligands are therefore an absolute prerequisite. The bulky scorpionate ligand Tp$^{t\mathrm{Bu}}$ (as in **2**) seemed promising for two reasons: 1) the attempted synthesis of its homoleptic Ca complex was not possible even under extreme conditions: reaction of two equivalents of Tp$^{t\mathrm{Bu}}$Tl with CaI$_2$ only produced Tp$^{t\mathrm{Bu}}$CaI[10] and 2) stable monomeric Tp$^{t\mathrm{Bu}}$ZnH has been reported;[11] the Ca^{2+} ion is approximately 0.15 Å larger than the Zn^{2+} ion.

Heteroleptic Tp$^{t\mathrm{Bu}}$CaN(SiMe$_3$)$_2$, earlier reported by Chisholm,[10] gave, after reaction with phenylsilane, clean conversion into PhH$_2$SiN(SiMe$_3$)$_2$ which indicated concommitant formation of Tp$^{t\mathrm{Bu}}$CaH. However, crystallization of the presumed product gave a batch of large, colorless crystals that were determined to be (Tp$^{t\mathrm{Bu}}$)$_2$Ca (**5**) by X-ray diffraction (Figure 2a). Although a space-filling model of the Tp$^{t\mathrm{Bu}}$Ca unit (Figure 2b) suggests that it is impossible that two ligands can coordinate at one metal center, both Tp$^{t\mathrm{Bu}}$ units coordinate as tridentate ligands: one is coordinated as a (κ^3 *N*,*N*′,*N*″)-ligand whereas the other is bonded through two pyrazole nitrogen atoms and a B-H unit. Two rings in the (κ^3 *N*,*N*′,*N*″)-ligand are tilted towards each other creating space for the two bulky pyrazole rings of the (κ^3 *N*,*N*′,*BH*)-ligand (Figure 2b). Steric crowding in (Tp$^{t\mathrm{Bu}}$)$_2$Ca is underscored by the relatively long Ca–N bonds: the Ca–N bonds for the (κ^3 *N*,*N*′,*N*″)-ligand (average: 2.481(1) Å) are significantly longer than those in Tp$^{t\mathrm{Bu}}$Ca(O-2,6-iPr$_2$C$_6$H$_3$) which range from 2.412(1) to 2.437(1) Å.[10] The Ca–N bonds for the (κ^3 *N*,*N*′,*BH*)-ligand (average: 2.521(1) Å) are even longer. The B–H···Ca contact of 2.47(2) Å is also considerably longer than

 © 2006 Wiley-VCH Verlag GmbH & Co. KGaA, Weinheim

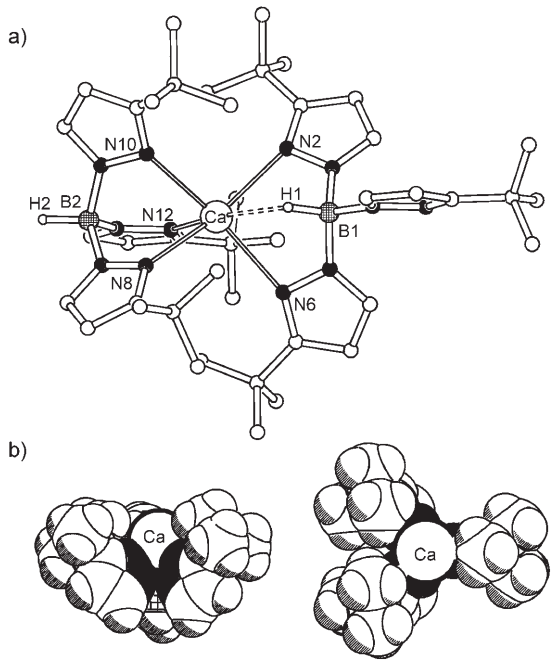

Figure 2. a) Crystal structure of $(Tp^{tBu})_2Ca$ (**5**); hydrogen atoms omitted for clarity. Selected interatomic distances [Å] and angles [°]: Ca–N2 2.510(1), Ca–N6 2.531(1), Ca–N8 2.493(1), Ca–N10 2.483(1), Ca–N12 2.468(1), Ca···H1 2.47(2), B1–H1 1.14(2), B2–H2 1.12(2); N2-Ca-N6 92.73(4), N2-Ca-H1 64.6(4), N6-Ca-H1 63.5(4), Ca···H1-B1 109(1), N8-Ca-N10 69.99(4), N8-Ca-N12 92.53(4), N10-Ca-N12 91.32(4). b) Space-filling models of part of the structure showing the (κ^3 *N*,*N*′,*N*″)Tp^{tBu} ligand bonded to Ca.

that of 2.21(4) Å in (1,2,4-Me_3Si-Cp)Ca($HBEt_3$).[12] Few cases of tridentate coordination using a polarized $B^{\delta+}$–$H^{\delta-}$ unit instead of a pyrazole nitrogen have been reported.[13] This coordination mode is a good alternative in ionic complexes, since the negative charge in the scorpionate anion is largely on the atoms directly attached to boron. The β-diketiminate anion, in which the charge is mainly on the nitrogen atoms, could, despite its lower denticity, be a stronger ligand than a scorpionate ligand.

Reaction of (DIPP-nacnac)CaN($SiMe_3$)$_2$(thf) (**6**)[10] ((DIPP-nacnac = (2,6-*i*$Pr_2C_6H_3$)NC(Me)C(H)C(Me)N(2,6-*i*$Pr_2C_6H_3$)) with phenylsilane in hexane (Scheme 2) gave, after cooling, a batch of large colorless crystals. The crystal structure shows the heteroleptic dimer: [(DIPP-nacnac)CaH-(thf)]$_2$ (**7**; Figure 3). The hydride atoms, which could be located in the difference Fourier map and were refined isotropically, bridge symmetrically between the two Ca^{2+} ions which are separated by 3.524(4) Å. The Ca–H bonds are in the range of 2.09(4)–2.21(3) Å and thus considerably longer than the Mg–H bonds in **1** (1.94(2) Å)[4e] and the Be–H bond in **2** (1.23(7) Å).[4g]

The hydride complex **7** dissolves in benzene and shows a remarkable stability. Even under reflux conditions no disproportionation to (DIPP-nacnac)$_2$Ca and insoluble $[CaH_2]_8$ is observed. This result is the more remarkable since we have shown that homoleptic (DIPP-nacnac)$_2$Ca is a rather stable complex on account of Me_2C-H···π(aryl)-bonding.[14] NMR spectroscopic investigations suggest that the structure of **7** is

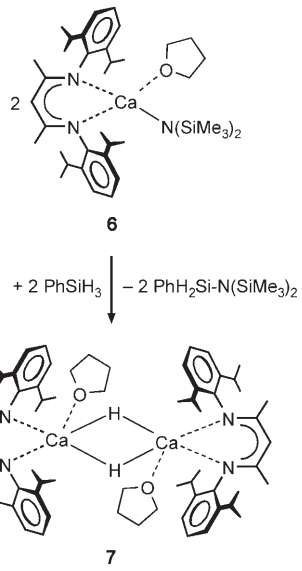

Scheme 2.

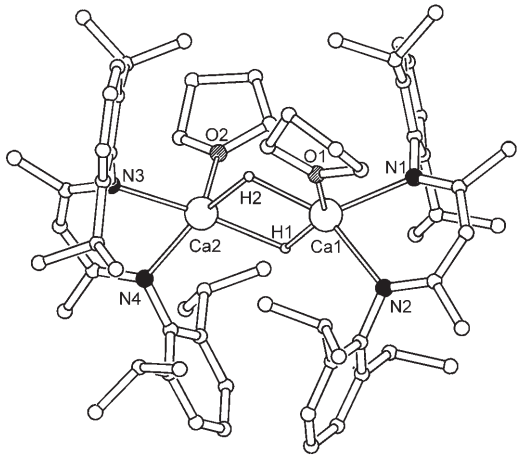

Figure 3. Crystal structure of **7**; hydrogen atoms omitted for clarity. Selected bond lengths [Å] and angles [°]: Ca1–H1 2.10(3) Ca1–H2 2.09(4), Ca2–H1 2.21(3), Ca2–H2 2.20(4), Ca1–O1 2.391(1), Ca2–O2 2.355(1), Ca1–N1 2.384(1), Ca1–N2 2.372(1), Ca2–N3 2.396(1), Ca2–N4 2.390(1); Ca1-H1-Ca2 109.7(11), Ca1-H2-Ca2 110.4(17), H1-Ca1-H2 71.8(13), H1-Ca2-H2 67.8(13).

retained in benzene solution. The *i*Pr-methyl groups are inequivalent as a result of hindered rotation around the N–C(aryl) bond and give two doublets. The outer methyl groups give strong NOE cross peaks with the methyl groups in the backbone, whereas for the inner methyl groups strong NOE cross peaks are observed with the α-CH_2 of THF and with the hydride. Although the ^{1}H NMR signals for the interstitial hydride in mixed metal complexes[4a–c] have not been observed, we find a relatively sharp singlet at $\delta = 4.45$ ppm. This is downfield of the ^{1}H resonance for the hydride in the inverse crown ether **1** ($\delta = 3.70$ ppm)[4e] but upfield of that in **2** ($\delta = 5.00$ ppm).[4g] ^{1}H NMR chemical shifts for the bridging hydride in numerous dimeric yttrium hydride complexes are spread over a large range: $\delta = 1.85$–8.31 ppm.[15]

In summary, we have prepared the first well-defined soluble calcium hydride by metathesis of a calcium amide

 © 2006 Wiley-VCH Verlag GmbH & Co. KGaA, Weinheim

with phenylsilane. This method, which was shown to function equally well with benzylic calcium, strontium, and potassium precursors,[8] could give impetus to the hydride chemistry of the early-main-group metals in general. We are currently exploring the reactivity and applications of soluble calcium hydride complexes.

Experimental Section

All experiments were carried out using standard Schlenk techniques and freshly dried solvents. Diisopropylamine was distilled from CaH_2 prior to use. Phenylsilane was used as received. The following compounds were prepared according to literature methods: **3**,[16] $Tp^{tBu}CaN(SiMe_3)_2$[10] and (DIPP-nacnac)$CaN(SiMe_3)_2$(thf) (**6**).[10]

4: Dry iPr_2NH (86 mg, 0.85 mmol) was added to a solution of **3** (400 mg, 0.72 mmol) in toluene (5.0 mL). The resulting solution was heated to 60 °C for 30 min, concentrated to 2.5 mL, and slowly cooled to −30 °C. A crop of orange plate-like crystals was isolated (185 mg, 68 %). Elemental analysis (%) calcd for $C_{22}H_{31}CaNSi$ (M_r = 377.67): C 69.97, H 8.27; found: C 69.58, H 8.21. ^{1}H NMR (250 MHz, [C_6D_6], 20 °C): δ = 0.35 (d, ^3J(H,H) = 6.0 Hz, 12 H; *i*Pr), 0.46 (s, 9 H; Me_3Si), 1.86 (sept, ^3J(H,H) = 6.0 Hz, 2 H; *i*Pr), 7.00 (t, ^3J(H,H) = 7.6 Hz, 2 H; fluorenyl), 7.22 (t, ^3J(H,H) = 7.5 Hz, 2 H; fluorenyl), 7.86 (d, ^3J(H,H) = 7.6 Hz, 2 H; fluorenyl), 7.95 ppm (d, ^3J(H,H) = 7.5 Hz, 2 H; fluorenyl). ^{13}C NMR (75 MHz, [C_6D_6], 20 °C): δ = 2.3 (Me_3Si), 26.3 (*i*Pr), 48.1 (*i*Pr), fluorenyl: 87.0, 117.3, 121.5, 122.0, 123.7, 124.8, 141.6 ppm.

5: Phenylsilane (30 mg, 0.28 mmol) was added to a solution of $Tp^{tBu}CaN(SiMe_3)_2$ (163 mg, 0.28 mmol) in benzene (3.0 mL). After stirring for 3 h at 60 °C, all solvent was removed. Crystallization of the oily product from pentane at −30 °C gave a crop of large colorless blocks (51 mg, 45 %). Elemental analysis (%) calcd for $C_{42}H_{68}B_2CaN_{12}$ (M_r = 802.79): C 62.84, H 8.54; found: C 62.49, H 8.43. ^{1}H NMR (250 MHz, [C_6D_6], 20 °C): δ = 1.12 (s broad, 54 H; *t*Bu), 5.82 (s broad, 3 H; pyrazole), 5.91 (s broad, 3 H; pyrazole), 7.46 (s broad, 3 H; pyrazole), 8.19 ppm (s broad, 3 H; pyrazole). ^{13}C NMR data could not be obtained owing to severe line-broadening.

7: Phenylsilane (140 mg, 1.29 mmol) was added to a solution of (DIPP-nacnac)$CaN(SiMe_3)_2$(thf) (**6**; 900 mg, 1.30 mmol) in hexane (5.0 mL). The solution was stirred for 1 h at 60 °C and then slowly cooled to −30 °C giving **7** in the form of colorless crystals (419 mg, 61 %). Elemental analysis (%) calcd for $C_{33}H_{50}CaN_2O$ (M_r = 530.86): C 74.67, H 9.49; found: C 74.32, H 9.58. ^{1}H NMR (250 MHz, [C_6D_6], 20 °C): δ = 1.06 (d, ^3J(H,H) = 6.8 Hz, 12 H; *i*Pr), 1.24 (d, ^3J(H,H) = 6.9 Hz, 12 H; *i*Pr), 1.40 (m, 4 H; THF), 1.65 (s, 6 H; Me), 3.14 (sept, ^3J(H,H) = 6.8 Hz, 4 H; *i*Pr), 3.57 (m, 4 H; THF), 4.45 (s, 1 H, Ca-H), 4.72 (s, 1 H, H-backbone), 7.05–7.15 ppm (m, 6 H, aryl). ^{13}C NMR (75 MHz, [C_6D_6], 20 °C): 24.5 (*i*Pr-Me), 24.6 (Me-backbone), 25.2 (THF), 25.7 (*i*Pr-Me), 28.0 (*i*Pr-CH), 69.3 (THF), 93.6 (backbone), 123.5 (Ar), 123.9 (Ar), 141.9 (Ar), 146.6 (Ar), 164.9 ppm (backbone).

Crystal data for **4**.[17,18] Monoclinic, space group $P2_1/c$, a = 10.235(9), b = 18.714(13), c = 33.958(10) Å, β = 97.70(8), V = 6446(8) Å^3, formula $C_{44}H_{62}Ca_2N_2Si_2$, Z = 6, R = 0.0738, $wR2$ = 0.2614, GOF = 0.98, ρ_{max} = 0.86 e Å^{-3}, ρ_{min} = −0.89 e Å^{-3}. Measurement on an Enraf Nonius CAD4 at −90 °C, $Mo_{K\alpha}$, $2\theta_{max}$ = 50°, 12 019 reflections measured, 11 333 independent reflections (R_{int} = 0.046), 6643 reflections observed with $I > 2\sigma(I)$. All hydrogen atoms were placed on calculated positions and refined in a riding mode. The asymmetric unit comprises a dimer with no overall symmetry in a general position, and a centrosymmetric dimer severely disordered in the amide part. Since no effective disorder model could be found, these atoms have high anisotropic displacement factors. The discussion on bond lengths relates only to the ordered dimer, which is structurally similar to the disordered dimer.

Crystal data for **5**.[17,18] Orthorhombic, space group $P2_12_12_1$, a = 11.2161(2), b = 18.9172(4), c = 22.1466(5) Å, V = 4699.0(2) Å^3, formula $C_{42}H_{68}B_2CaN_{12}$, Z = 4, R = 0.0416, $wR2$ = 0.0975, GOF = 1.04, ρ_{max} = 0.40 e Å^{-3}, ρ_{min} = −0.26 e Å^{-3}. The Flack parameter refined to −0.005(19). Measurement on a Siemens SMART CCD diffractomer at −90 °C, $Mo_{K\alpha}$, $2\theta_{max}$ = 58.8°, 185 322 reflections measured, 13 005 independent reflections (R_{int} = 0.051), 11 354 reflections observed with $I > 2\sigma(I)$. All hydrogen atoms were placed on calculated positions and refined in a riding mode.

Crystal data for **7**.[17,18] Monoclinic, space group $C2/c$, a = 47.9796(17), b = 12.5912(4), c = 22.2426(8) Å, β = 103.069(2)°, V = 13089.2(8) Å^3, formula $C_{66}H_{100}Ca_2N_4O_2$, Z = 8, R = 0.0455, $wR2$ = 0.1354, GOF = 1.02, ρ_{max} = 0.70 e Å^{-3}, ρ_{min} = −0.38 e Å^{-3}. Measurement on a Siemens SMART CCD diffractomer at −90 °C, $Mo_{K\alpha}$, $2\theta_{max}$ = 62°, 433851 reflections measured, 20 768 independent reflections (R_{int} = 0.038), 15 482 reflections observed with $I > 2\sigma(I)$. The hydride atoms, like nearly all other H atoms, were located and refined isotropically; few *i*Pr-hydrogen atoms were placed on calculated positions and refined in a riding fashion. Ring puckering disorder in THF was resolved. Slight disorder in one of the *i*Pr groups was treated by anisotropic refinement.

CCDC-601651–601653 contain the supplementary crystallographic data for this paper. These data can be obtained free of charge from The Cambridge Crystallographic Data Centre via www.ccdc.cam.ac.uk/data_request/cif.

Received: March 14, 2006
Published online: April 25, 2006

Keywords: alkaline-earth metals · amides · calcium · hydrides · scorpionate ligands

[1] a) G. G. Hlatky, R. H. Crabtree, *Coord. Chem. Rev.* **1985**, *65*, 1; b) S. Sabo-Etienne, B. Chaudret, *Chem. Rev.* **1998**, *98*, 2077; c) A. J. Hoskin, D. W. Stephan, *Coord. Chem. Rev.* **2002**, *233–234*, 107.

[2] a) M. Ephritikhine, *Chem. Rev.* **1997**, *97*, 2193; b) S. Arndt, J. Okuda, *Chem. Rev.* **2002**, *102*, 1953; K. C. Hultzsch, P. Voth, T. P. Spaniol, J. Okuda, *Z. Anorg. Allg. Chem.* **2003**, *629*, 1272; c) Z. Hou, Y. Zhang, O. Tardif, Y. Wakatsuki, *J. Am. Chem. Soc.* **2001**, *123*, 9216.

[3] a) J. J. Jegier, W. L. Gladfelter, *Coord. Chem. Rev.* **2000**, *206*, 631; b) "Science of Synthesis": A. J. Clark, *Houben-Weyl Methods of Molecular Transformations*, *Vol. 5* **2003**, p. 205; c) H.-J. Himmel, *Dalton Trans.* **2003**, 3639; d) N. W. Mitzel, *Angew. Chem.* **2003**, *115*, 3984; *Angew. Chem. Int. Ed.* **2003**, *42*, 3856; e) S. S. Kumar, H. W. Roesky, *Dalton Trans.* **2004**, 3927; f) H.-J. Himmel, *Z. Anorg. Allg. Chem.* **2005**, *631*, 1551.

[4] a) H. Nöth, A. Schlegel, J. Knizek, H. Schwenk, *Angew. Chem.* **1997**, *109*, 2754; *Angew. Chem. Int. Ed. Engl.* **1997**, *36*, 2640; b) D. R. Armstrong, W. Clegg, R. P. Davies, S. T. Liddle, D. J. Linton, P. R. Raithby, R. Snaith, A. E. H. Wheatley, *Angew. Chem.* **1999**, *111*, 3568; *Angew. Chem. Int. Ed.* **1999**, *38*, 3367; c) S. R. Boss, M. P. Coles, R. Haigh, P. B. Hitchcock, R. Snaith, A. E. H. Wheatley, *Angew. Chem.* **2003**, *115*, 5751; *Angew. Chem. Int. Ed.* **2003**, *42*, 5593; d) D. Hoffmann, T. Kottke, R. J. Lagow, R. D. Thomas, *Angew. Chem.* **1998**, *110*, 1630; *Angew. Chem. Int. Ed.* **1998**, *37*, 1537; e) D. J. Gallagher, K. W. Henderson, A. R. Kennedy, C. T. O'Hara, R. E. Mulvey, R. B. Rowlings, *Chem. Commun.* **2002**, 376; f) P. C. Andrikopoulos, D. R. Armstrong, A. R. Kennedy, R. E. Mulvey, C. T. O'Hara, R. B. Rowlings, *Eur. J. Inorg. Chem.* **2003**, 3354; g) R. Han, G. Parkin, *Inorg. Chem.* **1992**, *31*, 983; h) K. Mochida, Y. Hiraga, H. Takeuchi, H. Ogawa, *Organometallics* **1987**, *6*, 2293; i) J. P. Dunne, M. Tacke, C. Selinka, D. Stalke, *Eur. J. Inorg. Chem.* **2003**, 1416.

[5] Addition of two equivalents of *i*PrNH to a benzene solution of bis(2-Me_2N-α-Me_3Si-benzyl)calcium(thf)$_2$ gave, after heating to

 © 2006 Wiley-VCH Verlag GmbH & Co. KGaA, Weinheim

reflux, a white THF-insoluble solid that reacts with water under vigorous evolution of a flammable gas. We presume the precipitate is CaH_2.
[6] M. Westerhausen, W. Schwarz, *Z. Anorg. Allg. Chem.* **1991**, *604*, 127.
[7] W. Clegg, S. Kleditzsch, R. Mulvey, P. O'Shaughnessy, *J. Organomet. Chem.* **1998**, *558*, 193.
[8] F. Buch, J. Brettar, S. Harder, *Angew. Chem.* **2006**, *118*, 2807; *Angew. Chem. Int. Ed.* **2006**, *45*, 2741.
[9] S. Harder, F. Feil, T. Repo, *Chem. Eur. J.* **2002**, *8*, 1991.
[10] M. H. Chisholm, J. C. Gallucci, K. Phomphrai, *Inorg. Chem.* **2004**, *43*, 6717.
[11] R. Han, I. B. Gorrell, A. G. Looney, G. Parkin, *J. Chem. Soc. Chem. Commun.* **1991**, 717.
[12] M. J. Harvey, T. P. Hanusa, M. Pink, *Chem. Commun.* **2000**, 489.
[13] a) J. C. Calabrese, P. J. Domaille, J. S. Thompson, S. Trofimenko, *Inorg. Chem.* **1990**, *29*, 4429; b) A. Kremer-Aach, W. Kläui, R. Bell, A. Strerath, H. Wunderlich, D. Mootz, *Inorg. Chem.* **1997**, *36*, 1552; c) I. Lopes, G. Y. Lin, A. Domingos, R. McDonald, N. Marques, J. Takats, *J. Am. Chem. Soc.* **1999**, *121*, 8110.
[14] S. Harder, *Organometallics* **2002**, *21*, 3782.
[15] K. C. Hultzsch, P. Voth, K. Beckerle, T. P. Spaniol, J. Okuda, *Organometallics* **2000**, *19*, 228.
[16] S. Harder, F. Feil, K. Knoll, *Angew. Chem.* **2001**, *113*, 4391; *Angew. Chem. Int. Ed.* **2001**, *40*, 4261.
[17] G. M. Sheldrick, *SHELXL-97*, *Programs for the Determination of Crystal Structures*, Universität Göttingen, Germany, **1997**.
[18] A. L. Spek, *PLATON*, *A Multipurpose Crystallographic Tool*, Utrecht University, Utrecht, The Netherlands, **2000**.

 © 2006 Wiley-VCH Verlag GmbH & Co. KGaA, Weinheim

Asymmetric Catalysis

DOI: 10.1002/anie.200600636

Titanium–Salan-Catalyzed Asymmetric Epoxidation with Aqueous Hydrogen Peroxide as the Oxidant**

*Yuji Sawada, Kazuhiro Matsumoto, Shoichi Kondo, Hisayuki Watanabe, Tomoyuki Ozawa, Kenji Suzuki, Bunnai Saito, and Tsutomu Katsuki**

Oxidation reactions are at the core of methods for the conversion of bulk chemicals into useful and high-value materials.[1] Although many economical and highly selective methods for oxidation have been developed, more atom-efficient approaches that can be carried out under mild conditions are strongly desired from the viewpoint of protecting the environment and conserving resources. The choice of oxidant is an important factor in the enhancement of the efficiency of the oxidation reaction. Among the oxidants known, aqueous hydrogen peroxide is almost ideal, because it is relatively cheap, commercially available, and easy to handle; moreover, only water is generated as the by-product. Thus, the development of a catalyst for oxidation reactions with hydrogen peroxide has been a central theme in oxidation chemistry.[2] In particular, much effort has been directed toward the development of a chiral catalyst for epoxidation because of the high utility of optically active epoxides as versatile chiral building blocks.[3,4] However, a general and highly enantioselective epoxidation of unfunctionalized olefins with hydrogen peroxide has not been developed.

Recently, we developed a chiral di-μ-oxo titanium–salalen (salalen[5,6]: hybrid salan/salen tetradentate (ONNO)-type ligand; salan: *N*,*N*,-bis(*o*-hydroxybenzyl)-1,2-diaminoethane, salen: *N*,*N*'-bis(salicylidene)ethylenediamine) complex that was able to catalyze the epoxidation of unfunctionalized olefins using aqueous hydrogen peroxide with high enantioselectivity and a high turnover number of the catalyst.[7] The robustness and the unique catalysis of the titanium–salalen complex are in marked contrast with the ineffectiveness of the corresponding di-μ-oxo titanium–salen complex as an epoxidation catalyst. These distinctive features of the former complex have been attributed to hydrogen bonding between the amino proton and the oxygen atom of a putative peroxo species (Scheme 1). Although the complex is currently one of the most efficient catalysts for asymmetric epoxidation, it has a rather elaborate structure and its synthesis using Meerwein–Ponndorf–Verley reduction in situ has less flexibility in tuning the structure. Construction of an efficient catalyst that has a much simpler structure and that can be prepared from readily available compounds is a worthy challenge. A requirement for such a catalyst is the ability to efficiently enhance the reactivity of a putative peroxo species and to regulate its orientation in an asymmetric atmosphere. Thus, we newly introduced a series of di-μ-oxo titanium–salan complexes and examined their catalysis, because salan ligands and the corresponding titanium–salan complexes can be readily synthesized,[8] and the catalysis of the titanium–salan complex could be tuned by introducing an appropriate substituent to the ligand. Moreover, the complexes also possess amino protons to activate a putative peroxo species.

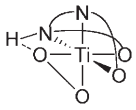

Scheme 1. A putative peroxo species activated by hydrogen bonding.

The experimental procedure for the synthesis of the di-μ-oxo titanium–salan complexes is shown in Scheme 2. Salan ligands **1a–d** were prepared by reduction of the corresponding salen ligands with $NaBH_4$. $[Ti(O\mathit{i}Pr)_4]$ was added to a solution of the salan ligand in dichloromethane, and subsequent treatment with water gave the di-μ-oxo titanium–salan complexes **2a–d**.[9]

First, asymmetric epoxidation of 1,2-dihydronaphthalene with 30% hydrogen peroxide in the presence of 5 mol% of a

[*] Y. Sawada, K. Matsumoto, Dr. B. Saito, Prof. T. Katsuki
Department of Chemistry
Faculty of Science
Graduate School, Kyushu University
Hakozaki, Higashi-ku, Fukuoka 812-8581 (Japan)
Fax: (+81) 92-642-2607
E-mail: katsuscc@mbox.nc.kyushu-u.ac.jp
Dr. S. Kondo, Dr. H. Watanabe, T. Ozawa, K. Suzuki
Nissan Chemical Industries, Ltd. (Japan)

[**] Financial support was provided by CREST and the Japan Science and Technology Agency. We are indebted to JEOL Ltd. for the coldspray ionization mass-spectrometric (CSI-MS) measurements. K.M. is grateful for a JSPS Research Fellowship for Young Scientists.

InterScience © 2006 Wiley-VCH Verlag GmbH & Co. KGaA, Weinheim

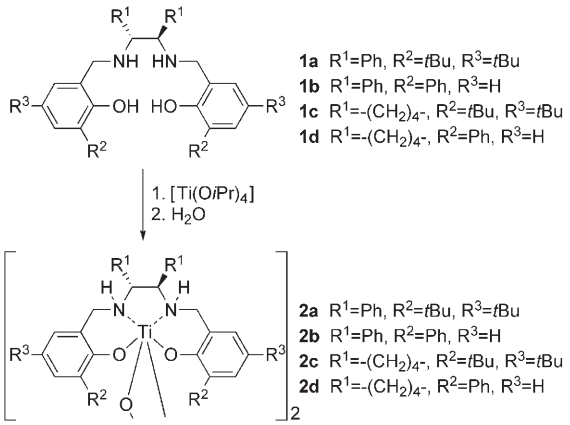

Scheme 2. Synthesis of di-μ-oxo titanium–salan complexes **2a**–**d**.

di-μ-oxo titanium–salan complex was investigated (Table 1). Titanium–salan complexes (**2a** and **2b**) with a diphenylethylenediamine moiety were found not to be efficient catalysts (entries 1 and 2). On the other hand, the complexes (**2c** and **2d**) bearing a cyclohexanediamine moiety showed the desired catalysis (entries 3 and 4). The presence of a cyclohexane ring was considered to provide a more suitable structure for hydrogen bonding of the amino proton with the oxygen atom of the peroxo group. Furthermore, introduction of a phenyl substituent at C3 and C3′ was found to remarkably enhance catalytic activity and improve enantioselectivity (entry 4). The use of 1.5 equivalents of hydrogen peroxide improved the yield to some extent (entry 5). Lowering the reaction temperature to 0 °C slightly increased enantioselectivity, although the yield was decreased somewhat (entry 6). Moreover, the catalyst prepared in situ from $[Ti(OiPr)_4]$ and ligand **1d** gave an almost comparable enantioselectivity to the pre-made catalyst **2d**, but slightly diminished yield was obtained (entry 7).[10] Although prolonged reaction time led to ring-opening of the epoxide to give a mixture of the corresponding 1- or 2-hydroperoxy 2- or 1-alcohol and 1,2-diol, the enantiomeric excess of the remaining epoxide did not change. Furthermore, when hydrogen peroxide was added to the reaction medium with a syringe pump over 4 h, a significant amount of ring-opened products was obtained (entry 8). These results suggested that **2d** decomposed under the reaction conditions into a Lewis acid complex that did not carry the salan ligand and did not promote epoxidation but ring-opening.

The substrate scope of the epoxidation using **2d** was investigated using 1.5 equivalents of hydrogen peroxide (Table 2). The epoxidation of terminal, *cis*-disubstituted, and trisubstituted olefins proceeded with high enantioselectivity. It is noteworthy that the epoxidation was stereospecific and no formation of the *trans* epoxide was detected in the epoxidation of *cis*-1-phenylpent-3-en-1-yne (entry 4). How-

Table 1: Asymmetric epoxidation of 1,2-dihydronaphthalene (**3**) with a Ti–salan complex as the catalyst.[a]

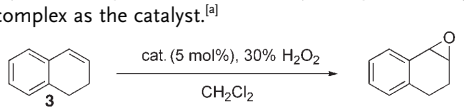

Entry	Catalyst	*t*	*T* [°C]	Yield [%][b]	*ee* [%][c]	Config.[d]
1	**2a**	24	25	NR		
2	**2b**	24	25	< 5	44	1*S*,2*R*
3	**2c**	24	25	19	82	1*S*,2*R*
4	**2d**	6	25	73	95	1*S*,2*R*
5[e]	**2d**	6	25	87	96	1*S*,2*R*
6[e]	**2d**	24	0	79	98	1*S*,2*R*
7[e]	**2d**[f]	6	25	80	94	1*S*,2*R*
8[e,g]	**2d**[h]	5	25	24 (30, 21)	95	1*S*,2*R*

[a] Reaction conditions: catalyst (5 μmol), 1,2-dihydronaphthalene (0.1 mmol), and aqueous H_2O_2 (30%, 0.12 mmol) in CH_2Cl_2 (1.0 mL). [b] Determined by ^1H NMR (400 MHz) spectroscopic analysis; the yields of the ring-opened products (1,2-diol, 1- or 2-hydroperoxy 2- or 1-alcohols) are given in brackets. [c] Determined by HPLC analysis on a chiral stationary-phase column (Daicel chiralcel OB-H, hexane/*i*PrOH = 99:1). [d] Determined by comparison of the elution order with that of the authentic sample in HPLC analysis. [e] Amount of aqueous H_2O_2 = 1.5 equivalents. [f] The catalyst was generated in situ. [g] Hydrogen peroxide was added with a syringe pump over 4 h. [h] Amount of complex **2d**: 3 μmol. NR = no reaction.

Table 2: Asymmetric epoxidation catalyzed by **2d**.[a]

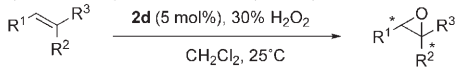

Entry		Substrate	Yield [%][b]	*ee* [%]	Configuration[c]
1[d]	**4**		72	95[e]	1*S*,2*R*
2	**5**	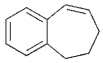	44	97[f]	5*S*,6*R*
3	**6**		47	82[g]	*S*
4	**7**	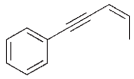	69	90[h]	2*R*,3*S*
5	**8**	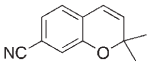	77	99[i]	3*S*,4*S*
6[d]	**9**		55	95[j]	1*R*,2*S*
7	**10**	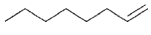	25	55[k]	*R*

[a] Reaction conditions: catalyst **2d** (5 μmol), olefin (0.1 mmol), and aqueous H_2O_2 (30%, 0.15 mmol) in CH_2Cl_2 (1.0 mL) at 25 °C for 24 h. [b] Determined by ^1H NMR (400 MHz) spectroscopic analysis. [c] Determined by comparison of the elution order with that of the authentic sample in HPLC analysis and/or comparison of the chiroptical data with the literature value. [d] Reaction time was 5 h. [e] Determined by HPLC analysis on a chiral stationary-phase column (Daicel Chiracel OB-H; hexane/*i*PrOH = 90:10). [f] Determined by HPLC analysis on a chiral stationary-phase column (Daicel Chiralpak AS-H; hexane/*i*PrOH = 99.9:0.1). [g] Determined by HPLC analysis on a chiral stationary phase column (Daicel Chiracel OD-H; hexane/*i*PrOH = 99.9:0.1). [h] Determined by HPLC analysis on a chiral stationary phase column (Daicel Chiracel OD-H; hexane/*i*PrOH = 99:1). [i] Determined by HPLC analysis on a chiral stationary phase column (Daicel Chiracel OJ-H; hexane/*i*PrOH = 70:30). [j] Determined by HPLC analysis on a chiral stationary-phase column (Daicel Chiracel OB-H; hexane/*i*PrOH = 99:1). [k] Determined by ^1H NMR spectroscopic analysis using a chiral shift reagent [Eu(hfc)$_3$] (hfc = 3-(heptafluoropropylhydroxymethylene)-D-camphorate).

 © 2006 Wiley-VCH Verlag GmbH & Co. KGaA, Weinheim

ever, the reaction of a nonconjugated terminal olefin was slow (entry 7).

The reaction mechanism is unclear at present. It is, however, of note that the catalyst prepared in situ from $[Ti(OiPr)_4]$ and an *N*,*N*′-dimethylated derivative of **1d** did not show any catalytic activity for the epoxidation of styrene. This result agreed with our proposal that a titanium–peroxo species is activated through hydrogen bonding. Moreover, when a solution of **2d** in dichloromethane was treated with aqueous hydrogen peroxide, a new species was obtained. Analysis by cold-spray ionization mass-spectrometry (CSI-MS) indicated a μ-peroxo-μ-oxo species ($M_r = 1097.3$); however, this species was also detected by CSI MS in the presence of hydrogen peroxide and 1,2-dihydronaphthalene. Accordingly, it is very likely that the active species is not the dimeric μ-peroxo-μ-oxo species but a monomeric peroxo or dimeric di-μ-peroxo species.

In summary, the titanium–salan-catalyzed asymmetric epoxidation of unfunctionalized olefins using aqueous hydrogen peroxide has been developed. High enantioselectivity of up to 98% *ee* was achieved for several olefins. We have demonstrated that a more efficient catalyst of lower molecular weight could be constructed for asymmetric epoxidation using hydrogen peroxide as the oxidant by appropriately considering the mechanism of activation of a peroxo species. Further improvements in the catalytic activity and detailed mechanistic studies are now in progress.

Experimental Section

2d: $[Ti(OiPr)_4]$ (1.3 mmol) was added to a solution of salan ligand **1d** (1.2 mmol) in dichloromethane (3.5 mL), and the solution was stirred at room temperature. A few drops of H_2O were added after 5 h, and the resultant mixture was stirred overnight. Volatiles were removed under reduced pressure, and the residue was recrystallized from dichloromethane to give the desired complex **2d** in 46% yield. Elemental analysis (%) for $C_{64}H_{64}N_4O_6Ti_2{\cdot}H_2O{\cdot}1.5\,CH_2Cl_2$: C 64.15, H 5.67, N 4.57; found: C 64.03, H 5.49, N 4.55; CSI MS: *m*/*z*: calcd for $C_{64}H_{64}N_4O_6Ti_2$: 1080.38; found: 1081.32 $[M^+ + H]$.

Typical procedure for epoxidation using a pre-made catalyst: Titanium complex **2d** (5 μmol) and 1,2-dihydronaphthalene (0.1 mmol) were dissolved in dichloromethane (1.0 mL) in an nitrogen atmosphere. The resultant mixture was stirred at room temperature after 30% aqueous hydrogen peroxide (0.15 mmol) had been added. The solvent was removed in vacuo, and the residue was purified by column chromatography on silica gel (pentane/Et_2O, 40:1) to give the corresponding epoxide. The *ee* value was determined by HPLC on a chiral stationary phase.

Typical procedure for epoxidation using a catalyst prepared in situ: Salan ligand **1d** (10 μmol) was added to a solution of $[Ti(OiPr)_4]$ (10 mmol) in dichloromethane (1.0 mL, 10 mM), and the solution was stirred at room temperature. A drop of water was added after 30 min, and the resultant mixture was stirred for 30 min. The reaction mixture was stirred at room temperature for 6 h after 1,2-dihydronaphthalene (0.1 mmol) and 30% aqueous hydrogen peroxide (0.15 mmol) were added. The solvent was removed in vacuo, and the residue was purified by column chromatography on silica gel (pentane/Et_2O 40:1) to give the corresponding epoxide. The *ee* value was determined by HPLC on a chiral stationary phase.

Received: February 17, 2006
Published online: April 24, 2006

Keywords: asymmetric catalysis · enantioselectivity · epoxidation · hydrogen peroxide · titanium

[1] *Comprehensive Organic Synthesis*, *Vol. 7* (Eds.: B. M. Trost, I. Fleming), Pergamon, Oxford, **2001**.
[2] a) B. S. Lane, K. Burgess, *Chem. Rev.* **2003**, *103*, 2457–2474; b) R. Noyori, M. Aoki. K. Saito, *Chem. Commun.* **2003**, 1977–1986.
[3] a) E. N. Jacobsen, M. H. Wu in *Comprehensive Asymmetric Catalysis*, *Vol. II* (Eds.: E. N. Jacobsen, A. Pfaltz, H. Yamamoto), Springer, Heidelberg, **1999**, chap. 21, pp. 649–677; b) T. Katsuki in *Comprehensive Coordination Chemistry II*, *Vol. 9* (Ed.: J. McCleverty), Elsevier Science, Oxford, **2003**, chap. 9.4, pp. 207–264.
[4] a) S. Juliá, J. Masana, J. C. Vega, *Angew. Chem.* **1980**, *92*, 968–969; *Angew. Chem. Int. Ed. Engl.* **1980**, *19*, 929–931; b) S. Colonna, H. Molinari, S. Banfi, S. Juliá, J. Masana, A. Alvalez, *Tetrahedron* **1983**, *39*, 1635–1641; c) P. Pietikäinen, *Tetrahedron* **1994**, *50*, 941–944; d) R. Irie, N. Hosoya, T. Katsuki, *Synlett* **1994**, 255–256; e) A. Berkessel, M. Frauenkron, T. Schwenkreis, A. Steinmetz, G. Baum, D. Fenske, *J. Mol. Catal. A* **1996**, *113*, 321–342; f) P. Pietikäinen, *Tetrahedron* **1998**, *54*, 4319–4326; g) S. Arai, H. Tsuge, T. Shioiri, *Tetrahedron Lett.* **1998**, *39*, 7563–7566; h) L. Shu, Y. Shi, *Tetrahedron* **2001**, *57*, 5213–5218; i) R. I. Kureshy, N. H. Khan, S. H. R. Abdi, S. Singh, I. Ahmed, R. S. Shunkla, R. V. Jasra, *J. Catal.* **2003**, *219*, 1–7; j) M. K. Tse, C. Döbler, S. Bhor, M. Klawonn, W. Mägerlein, H. Hugl, M. Beller, *Angew. Chem.* **2004**, *116*, 5367–5372; *Angew. Chem. Int. Ed.* **2004**, *43*, 5255–5260.
[5] A. Yeori, S. Gendler, S. Groysman, I. Goldberg, M. Kol, *Inorg. Chem. Commun.* **2004**, *7*, 280–282.
[6] B. Saito, T. Katsuki, *Angew. Chem.* **2005**, *117*, 4676–4678; *Angew. Chem. Int. Ed.* **2005**, *44*, 4600–4602.
[7] K. Matsumoto, Y. Sawada, B. Saito, T. Katsuki, K. Sakai, *Angew. Chem.* **2005**, *117*, 5015–5019; *Angew. Chem. Int. Ed.* **2005**, *44*, 4935–4939.
[8] a) J. Balsells, P. J. Carroll, P. J. Walsh, *Inorg. Chem.* **2001**, *40*, 5568–5574; b) J. Sun, C. Zhu, Z. Dai, M. Yang, Y. Pan, H. Hu, *J. Org. Chem.* **2004**, *69*, 8500–8503; c) A. Yeori, S. Groysman, I. Goldber, M. Kol, *Inorg. Chem.* **2005**, *44*, 4466–4468; d) Z. Dai, C. Zhu, M. Yang, Y. Zheng, Y. Pan, *Tetrahedron: Asymmetry* **2005**, *16*, 605–608.
[9] CCDC-297268 (for complex **2d**) contains the supplementary crystallographic data for this paper. These data can be obtained free of charge from The Cambridge Crystallographic Data Centre via www.ccdc.cam.ac.uk/data_request/cif.
[10] A catalyst prepared in situ from $[Ti(OiPr)_4]$ and a salan ligand with other substituents at C3 gave inferior results (H: 36%, 93% *ee*; Me: 69%, 93% *ee*; *t*Bu: 15%, 83% *ee*).

 © 2006 Wiley-VCH Verlag GmbH & Co. KGaA, Weinheim

Planar Chirality

DOI: 10.1002/anie.200600689

Lithiation/Electrophilic Quench of [(η^5-Cyclohexadienyl)Mn(CO)$_3$]: Versatile Functionalization and Resolution of Planar Chirality in the Organomanganese Series**

Béatrice Jacques, Murielle Chavarot, Françoise Rose-Munch, and Eric Rose*

The coordination of a transition-metal center to an arene modifies the reactivity of the arene ligand in several distinct ways. Among them, the increased acidity of the ring protons, which strongly facilitates direct proton abstraction from the arene, is remarkable. The first lithiation of the arene in an [(η^6-arene)Cr(CO)$_3$] complex was reported in 1968,[1] and since then this reaction has seen extensive development and has been the subject of several reviews.[2] Very surprisingly, no report has appeared concerning isoelectronic π complexes of manganese, although these have become increasingly important in organometallic and organic syntheses.[3] Particularly interesting are the neutral [(η^5-cyclohexadienyl)Mn(CO)$_3$] complexes, which are of strategic importance to provide access to a wide range of organometallic or organic target structures (Scheme 1). Rearomatization of the η^5-cyclohexadienyl complex occurs upon hydride abstraction by [CPh_3]-[BF_4] (Scheme 1, path a, $R^1 = H$), thus delivering the corresponding cationic η^6-arene–Mn complex, whereas treatment with a nucleophile R^2 followed by oxidation results in the formation of highly functionalized cyclohexadienes (Scheme 1, path b).[3a,c,4]

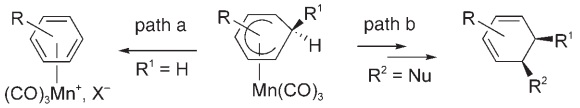

Scheme 1. General reactivity patterns of [(η^5-cyclohexadienyl)Mn(CO)$_3$] complexes. Nu = nucleophile.

The first *cine* and *tele* nucleophilic substitutions of [(η^5-cyclohexadienyl)Mn(CO)$_3$] complexes were developed in 1996 by treatment with hydrides and a proton source,[5] and their mechanism was shown to be very close to the *cine* and *tele* aromatic nucleophilic substitution (SN_{Ar}) described for [(η^6-arene)Cr(CO)$_3$] complexes.[3d] The discovery of Pd cross-coupling reactions in the η^5-cyclohexadienyl–Mn series[6] enabled ready access to a large variety of substituted η^5 complexes bearing double or triple bonds, aryl, or keto groups linked to the π system. This latter work established that the presence of the tricarbonyl–Mn fragment dramatically activates the carbon–halogen bonds in η^5-cyclohexadienyl–Mn complexes in the same way the tricarbonyl–Cr entity does in η^6-arene–Cr complexes, for which Pd-catalyzed reactions have been well documented for many years.[7] The similarities in reactivity properties between the η^5-cyclohexadienyl–Mn and η^6-arene–Cr series raised the possibility that lithiation at the organomanganese complexes could provide a new strategy to further extend the scope of their utility. We report herein a general method for the functionalization of these compounds by a lithiation/electrophilic quench sequence. Its potential application to the synthesis of enantiopure η^5-cyclohexadienyl–Mn complexes is illustrated by the resolution of one of the unprecedented planar chiral complexes synthesized by this strategy.

The [(η^5-cyclohexadienyl)Mn(CO)$_3$] complexes **1**–**4** (Scheme 2) used as starting materials in this study were readily obtained by nucleophilic addition of PhMgCl onto the corresponding [(η^6-arene)Mn(CO)$_3$]$^+$ complexes.[6,8] Chloro- and/or methoxy-substituted arenes were used for their good *ortho*-directing properties in the lithiation step,[9] either as a result of an inductive electron-withdrawing effect (Cl) or a lithium coordination (OMe).[2d]

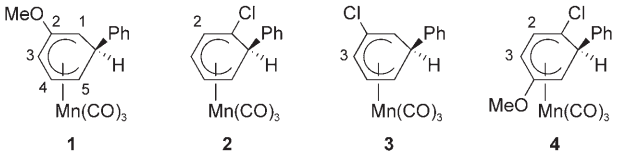

Scheme 2. Structure and numbering of the [(η^5-cyclohexadienyl)-Mn(CO)$_3$] complexes.

The lithiation/electrophilic quench of these complexes was effected by reaction with *n*-butyllithium (*n*BuLi) at −78 °C, followed by addition of the electrophile at the same temperature. Trimethylsilylchloride (TMSCl) was chosen as the reference electrophile.

These reactions give efficient access to the silylated products with yields that range from 62 to 88% (Table 1). No competing halogen–lithium exchange occurred and a high degree of regiocontrol was observed. NMR spectroscopic characterization of products **5**–**8** confirmed that the trimethylsilyl group is located *ortho* to the Cl or OMe substituent in all these examples. The 2-methoxy derivative **1**, which gives the 3-trimethylsilylated complex **5** (entry 1), is less reactive than the chloro-substituted derivatives **2** and **3**, which afford the 2- and the 3-trimethylsilylated complexes **6** and **7** (Table 1, entries 2 and 3); thus, in this case, the addition of tetramethylethylenediamine (TMEDA) was needed to ensure complete conversion of the substrate **1**. Complex **4** appears to be the most reactive η^5-cyclohexadienyl complex, probably because of a synergic effect of the two activating groups.

[*] B. Jacques, Dr. M. Chavarot, Dr. F. Rose-Munch, Dr. E. Rose
Université Pierre et Marie Curie – Paris 6
Laboratoire de Chimie Organique (UMR CNRS 7611)
Institut de Chimie Moléculaire (FR 2769)
Case 181, 4 Place Jussieu, 75252 Paris Cedex 05 (France)
Fax: (+33) 144-275-504
E-mail: rosemun@ccr.jussieu.fr

[**] This work was supported by the CNRS and MRES. A. Eloi is gratefully acknowledged for preliminary results and P. Herson (CIM^2, UMR 7071, Université P. et M. Curie, Paris) for the X-ray structure analysis.

 © 2006 Wiley-VCH Verlag GmbH & Co. KGaA, Weinheim

Table 1: Lithiation/silylation sequence applied to complexes **1–4**.

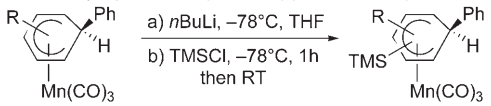

1–4 **5–8**

Entry	Substrate	Product	Position	Yield [%]
1	**1**[a]	**5**	C3	86
2	**2**[b]	**6**	C2	62
3	**3**[b]	**7**	C3	81
4	**4**[c]	**8a** + **8b**	C2 + C3[d]	88

[a] Addition of TMEDA, reaction time = 1 h. [b] Reaction time = 1 h. [c] Reaction time = 15 min. [d] Ratio = 90:10.

The reaction required only 15 min at −78 °C without TMEDA for complete conversion (entry 4). When both the C1 and C3 positions are available adjacent to the C2 substituent, as in **1** or **3**, the competition between C1 and C3 is fully controlled by *selective lithiation at the C3 position* (Table 1, entries 1 and 3). This selectivity arises from the greater sp^2 character of C3 with respect to C1[10] and likely from steric factors, as C1 is adjacent to the phenyl-substituted sp^3 C6 center. Furthermore, when two *ortho*-directing groups are present, as in **4**, there is a substantial preference for *ortho* lithiation at C2 adjacent to the more strongly activating chloro group (entry 4).

Complex **1** was chosen as the model compound to carry out further investigations with various electrophiles under the previously optimized conditions (Table 2). The results establish the general applicability of the lithiation/electrophilic quench sequence which led to a large variety of derivatives in good-to-excellent yields (68–95 %) with complete regiocontrol. These results show that the reaction is efficient for the introduction of alkyl, benzylic alcohol, and ester groups (Table 2, entries 1–3, respectively). It should be pointed out that we also introduced ester groups into [(η^5-chlorocyclohexadienyl)$Mn(CO)_3$] complexes by using the C–Cl reactivity towards Pd-catalyzed coupling reactions under a CO atmosphere.[6] Herein, the procedure does not affect the substituents of the starting material, and consequently when a chlorine atom is present, as in **2**, **3**, or **4**, it remains available for subsequent functionalization. This new approach is therefore complementary to the Pd-catalyzed method developed in this series a few years ago.[6] Finally, more strategically important products with wide scope for further transformation were formed by reaction with tributyltin chloride, 1,2-diiodoethane, or dimethylformamide (DMF; Table 2 entries 4–6, respectively), thus introducing tributylstannyl, iodo, and formyl groups (resulting in complexes **12–14**, respectively) adjacent to the methoxy group. Whereas [(η^5-chlorocyclohexadienyl)$Mn(CO)_3$] complexes have been well documented, to our knowledge only one synthesis of a bromo derivative has been reported[11] and no iodo-substituted complexes, which could exhibit a rich and varied chemistry, have been reported until now. Pleasingly, monocrystals of **13** were readily obtained for X-ray diffraction studies.[12] The ORTEP view indicates that the iodine atom is indeed located adjacent to the methoxy group (Figure 1) and does not modify the η^5 structure. There are five coplanar sp^2 carbon atoms, while the remaining sp^3 carbon atom is located 43.77° above this plane. The conformation of the {$Mn(CO)_3$} tripod is in agreement with what is usually observed, with the sp^3 carbon atom being eclipsed by one Mn–CO bond.

Table 2: Functionalization of complex **1** by various electrophiles.

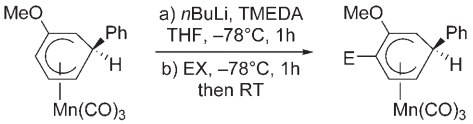

1 **9–14**

Entry	Reagent (EX)	E–	Product	Yield [%]
1	MeI	Me–	**9**	82
2	Ph_2CO	$Ph_2C(OH)$–	**10**	83
3	$ClCO_2Et$	EtO_2C–	**11**	72
4	nBu_3SnCl	nBu_3Sn–	**12**	87
5	$I(CH_2)_2I$	I–	**13**	95
6	DMF	OHC–	**14**	68

E = electrophile.

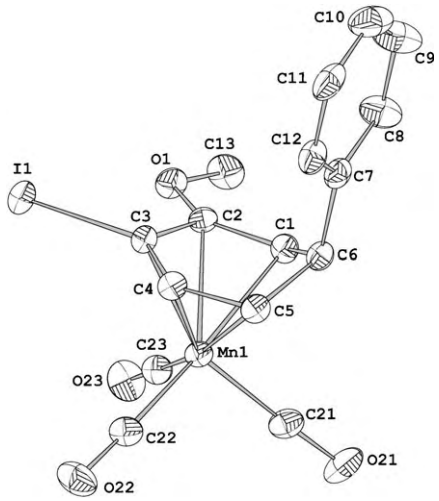

Figure 1. ORTEP view of complex **13**.

The efficient formylation procedure with DMF as the electrophile provided the first example of a formyl-substituted [(η^5-cyclohexadienyl)$Mn(CO)_3$] complex; thus, we developed a strategy for the resolution of such planar chiral racemic complexes. To our knowledge, no general methodology to synthesize enantiopure [(η^5-cyclohexadienyl)$Mn(CO)_3$] complexes is available despite a number of attempts by using different approaches, which demonstrates the undoubted interest in these planar chiral entities. Miles et al. reported the addition of chiral non-racemic enolates to achiral cationic η^6-arene–Mn complexes to generate η^5-cyclohexadienyl complexes.[13] By a similar approach, Pearson et al. studied the addition of various nucleophiles to η^6-arene complexes bearing a chiral amino auxiliary.[14] Despite good diastereoselectivities, this class of compound has limited applications because it is not straightforward to remove the

 © 2006 Wiley-VCH Verlag GmbH & Co. KGaA, Weinheim

chiral auxiliary from the final product. More recently, Chung and co-workers developed an approach specifically devoted to enantioenriched acetoxy-substituted η^5-cyclohexadienyl complexes by the addition of nucleophiles to [(η^5-oxocyclohexadienyl)$Mn(CO)_3$] in the presence of chiral ligands.[15] Some time ago, we described the resolution of *ortho*-substituted (η^6-benzaldehyde)tricarbonylchromium complexes with chiral diamines with a C_2 symmetry axis.[16] Thus, we decided to test the potential of such a chiral diamine for the resolution of a racemic mixture of [(η^5-formylcyclohexadienyl)$Mn(CO)_3$] (**14**).

After reaction of (*rac*)-**14** with enantiopure (*R*,*R*)-*N*,*N*′-dimethylcyclohexane-1,2-diamine, two diastereomeric aminals (*R*,*R*,*pR*)-**15** and (*R*,*R*,*pS*)-**15** were obtained (Scheme 3). Separation of the mixture by careful chromatography on neutralized silica gel afforded the two diastereoisomers both in 33 and 32% yield with > 95 and 85% *de*, respectively.

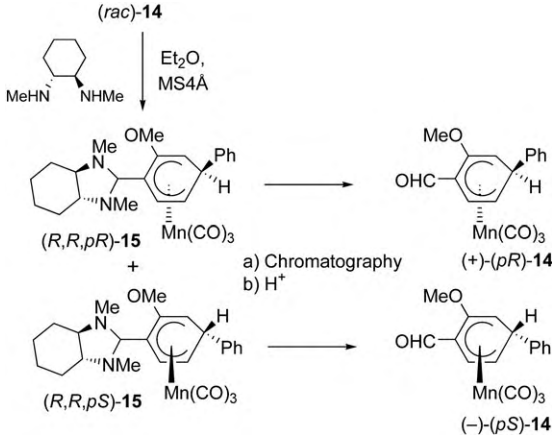

Scheme 3. Diastereoselective resolution of complex (*rac*)-**14**. MS = molecular sieves.

The diastereomeric composition was readily determined by ^{1}H NMR spectroscopic analysis because the aminalic proton of each compound resonates at $\delta = 4.19$ and 5.17 ppm, a difference of almost $\delta = 1$ ppm. These aminals were readily converted by acid-catalyzed hydrolysis into the pure enantioenriched aldehydes (*pR*)- and (*pS*)-**14** in 93 and 99% yield after chromatography and with > 95 and 85% *ee*, respectively.[17]

The assignment of the configuration[18] of the planar chiral η^5-cyclohexadienyl moiety was possible through X-ray analysis[19] of suitable crystals of one of the diastereomeric aminals **15** (> 95% *de*, $\delta_{\text{H aminal}} = 4.19$ ppm). Indeed, a *pR* configuration associated with the *R*,*R* configuration of the aminal was observed for this diastereoisomer (Figure 2). On this basis, the absolute configurations of the formyl derivatives (*pR*)- and (*pS*)-**14** could also be unambiguously assigned.

In conclusion, we have reported a highly efficient general pathway to functionalized [(η^5-cyclohexadienyl)$Mn(CO)_3$] complexes through a lithiation/electrophilic quench sequence. For the first time, a remarkable resolution of a planar chiral formyl-substituted derivative has been achieved for this class of complex through the formation of the corresponding aminal from a chiral diamine. This procedure led to the synthesis of enantiopure [(η^5-cyclohexadienyl)$Mn(CO)_3$] complexes bearing an aldehyde function, which gives a new perspective on the application of η^5-manganese complexes in organometallic and organic asymmetric syntheses.

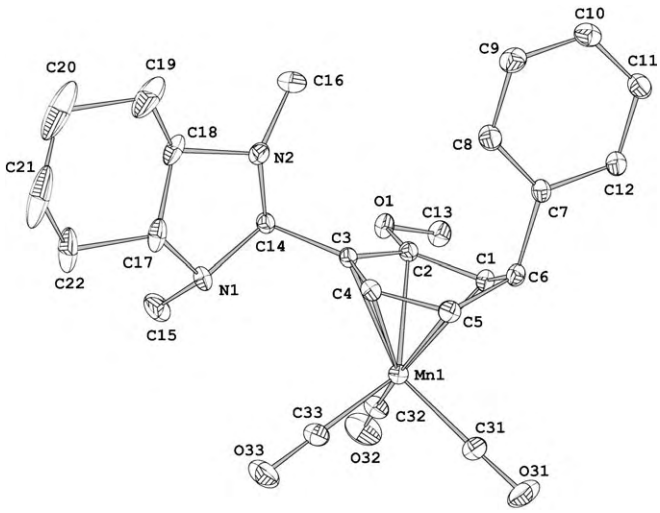

Figure 2. ORTEP view of complex (*R*,*R*,*pR*)-**15**.

Experimental Section

Typical procedure for the lithiation/electrophilic quench sequence: A solution of **1** (1 mmol) and freshly distilled TMEDA (1.6 equiv) in THF (10 mL) was cooled to −78 °C. A solution of *n*BuLi (1.6 M in hexanes; 1.6 equiv) was slowly added. The mixture was stirred for 1 h at −78 °C before the addition of the electrophile (2 equiv). The reaction mixture was stirred for another hour at −78 °C before warming to room temperature and quenching by the addition of H_2O. After extraction of the reaction mixture with Et_2O, the combined organic layers were washed with a saturated aqueous solution of NaCl and dried over $MgSO_4$. After concentration in vacuo, the crude mixture was purified by flash chromatography on silica gel to afford the pure functionalized η^5-cyclohexadienyl complex.

Received: February 21, 2006
Published online: April 26, 2006

Keywords: arene ligands · electrophilic addition · enantiopure complexes · lithiation · manganese

[1] A. N. Nesmeyanov, N. E. Kolobova, K. N. Anisimov, Y. V. Markarov, *Izv. Akad. Nauk. SSSR Ser. Khim.* **1968**, 2665 – 2665.
[2] For recent reviews, see: a) M. F. Semmelhack in *Comprehensive Organometallic Chemistry II*, *Vol. 12* (Eds.: E. W. Abel, F. G. A. Stone, G. Wilkinson), Pergamon, Oxford, **1995**, pp. 1017 – 1038; b) F. Rose-Munch, E. Rose, *Curr. Org. Chem.* **1999**, *3*, 445 – 467; c) A. Berger, J.-P. Djukic, C. Michon, *Coord. Chem. Rev.* **2002**, *225*, 215 – 238; d) M. F. Semmelhack, A. Chlenov, *Top. Organomet. Chem.* **2004**, *7*, 21 – 42.
[3] For recent reviews, see: a) K. F. McDaniel in *Comprehensive Organometallic Chemistry II*, *Vol. 6* (Eds.: E. W. Abel, F. G. A. Stone, G. Wilkinson), Pergamon, Oxford, UK, **1995**, pp. 93 – 107; b) R. D. Pike, D. A. Sweigart, *Coord. Chem. Rev.* **1999**, *187*, 183 – 222; c) A. R. Pape, K. P. Kaliappan, E. P. Kündig, *Chem. Rev.*

 © 2006 Wiley-VCH Verlag GmbH & Co. KGaA, Weinheim

2000, *100*, 2917 – 2940; d) F. Rose-Munch, E. Rose, *Eur. J. Inorg. Chem.* **2002**, 1269 – 1283.
[4] T. Y. Lee, Y. K. Kang, Y. K. Chung, R. D. Pike, D. A. Sweigart, *Inorg. Chim. Acta* **1993**, *214*, 125 – 134.
[5] F. Balssa, V. Gagliardini, F. Rose-Munch, E. Rose, *Organometallics* **1996**, *15*, 4373 – 4382.
[6] A. Auffrant, D. Prim, F. Rose-Munch, E. Rose, S. Schouteeten, J. Vaissermann, *Organometallics* **2003**, *22*, 1898 – 1913.
[7] a) J. F. Carpentier, F. Petit, A. Mortreux, V. Dufaud, J. M. Basset, J. Thivolle-Cazat, *J. Mol. Catal.* **1993**, *81*, 1 – 15; b) D. Prim, B. Andrioletti, F. Rose-Munch, E. Rose, F. Couty, *Tetrahedron* **2004**, *60*, 3325 – 3347.
[8] Y. K. Chung, P. G. Williard, D. A. Sweigart, *Organometallics* **1982**, *1*, 1053 – 1056.
[9] The directed *ortho* metalation is a well-known methodology in organic synthesis; see for example: a) V. Snieckus, *Chem. Rev.* **1990**, *90*, 879 – 933; b) M. C. Whisler, S. MacNeil, V. Snieckus, P. Beak, *Angew. Chem.* **2004**, *116*, 2256 – 2276; *Angew. Chem. Int. Ed.* **2004**, *43*, 2206 – 2225.
[10] R. Hoffmann, P. Hofmann, *J. Am. Chem. Soc.* **1976**, *98*, 598 – 604.
[11] P. L. Pauson, J. A. Segal, *J. Chem. Soc. Dalton Trans.* **1975**, 1677 – 1682.
[12] Crystal data for **13**: $C_{16}H_{12}IMnO_4$, $M_r = 450.10$, yellow parallelepipedic crystals, $T = 250$ K, monoclinic, space group $C2/c$, $a = 26.524(3)$, $b = 9.7720(6)$, $c = 12.6332(18)$ Å, $V = 3274.2(5)$ Å^3, $Z = 8$, $\rho_{calcd} = 1.83$ g.cm^{-3}, $2\theta_{max} = 60°$, $\mu(Mo_{K\alpha}) = 27.05$ cm^{-1}, 4767 independent reflections, $R = 0.0209$, $wR = 0.0241$. The structure was solved by direct methods using SHELXS86 and refined with full-matrix least-squares technique on F using the CRYSTALS programs. CCDC-298751 contains the supplementary crystallographic data for this paper. These data can be obtained free of charge from the Cambridge Crystallographic Data Centre *via* www.ccdc.cam.ac.uk/data request/cif.
[13] W. H. Miles, P. M. Smiley, H. R. Brinkman, *J. Chem. Soc. Chem. Commun.* **1989**, 1897 – 1899.
[14] a) A. J. Pearson, P. Y. Zhu, W. J. Youngs, J. D. Bradshaw, D. B. McConville, *J. Am. Chem. Soc.* **1993**, *115*, 10376 – 10377; b) A. J. Pearson, A. V. Gontcharov, P. Y. Zhu, *Tetrahedron* **1997**, *53*, 3849 – 3862.
[15] S. U. Son, K. H. Park, S. J. Lee, H. Seo, Y. K. Chung, *Chem. Commun.* **2002**, 1230 – 1231.
[16] A. Alexakis, P. Mangeney, I. Marek, F. Rose-Munch, E. Rose, A. Semra, F. Robert, *J. Am. Chem. Soc.* **1992**, *114*, 8288 – 8290.
[17] (*pR*)-**14**: $[\alpha]_D + 171°$ ($c = 0.21$, $CHCl_3$); (*pS*)-**14**: $[\alpha]_D -145°$ ($c = 0.23$, $CHCl_3$).
[18] The planar chirality was assigned according to the extended Cahn–Ingold–Prelog (CIP) rules.
[19] Crystal data for (*R*,*R*,*pR*)-**15**: $C_{25}H_{29}MnN_2O_4$, $M_r = 476.44$, yellow parallelepipedic crystals, $T = 250$ K, orthorhombic, space group $P2_12_12_1$, $a = 10.5344(14)$, $b = 13.9240(8)$, $c = 16.439(2)$ Å, $V = 2411.3(3)$ Å^3, $Z = 4$, $\rho_{calcd} = 1.31$ g cm^{-3}, $2\theta_{max} = 60°$, $\mu(Mo_{K\alpha}) = 5.80$ cm^{-1}, 6866 independent reflections, $R = 0.0303$, $wR = 0.0321$. The structure was solved by direct methods using SHELXS86 and refined with full-matrix least-squares technique on F using the CRYSTALS programs. CCDC-298752 contains the supplementary crystallographic data for this paper. These data can be obtained free of charge from The Cambridge Crystallographic Data Centre via www.ccdc.cam.ac.uk/data_request/cif.

 © 2006 Wiley-VCH Verlag GmbH & Co. KGaA, Weinheim

Coupling Reactions

DOI: 10.1002/anie.200600493

A Highly Active Catalyst for Suzuki–Miyaura Cross-Coupling Reactions of Heteroaryl Compounds**

*Kelvin L. Billingsley, Kevin W. Anderson, and Stephen L. Buchwald**

In the past two decades, the Suzuki–Miyaura cross-coupling reaction has evolved into one of the most widely employed carbon–carbon bond-forming processes.[1,2] Its impact on organic synthesis is largely attributed to the fact that it provides a general and applicable method for the formation of biaryls, which are found in polymers,[3] biologically active compounds,[4] ligands,[5] and various materials.[6] In recent years, work by numerous groups has resulted in the production of highly active catalyst systems, which allow for couplings to occur with more challenging substrates, such as unactivated aryl chlorides and hindered boronic acids.[7]

Despite these advances, limitations of the method, to date, include its inability to maintain the efficacy exhibited in simple aryl–aryl bond formation when employing nitrogen heterocycles as one or both of the coupling partners (e.g., heteroaryl halides and/or heteroaryl boronic acids/esters).[8] Nitrogen-based heterocycles are ubiquitous in biologically active compounds, but inclusion of these heterocyclic motifs have been particularly detrimental to catalyst activity when palladium is used.[4] In addition, for exceptionally challenging substrates, such as chloroaminopyridines and chloroaminopyrimidines, protection of the free $-NH_2$ group or the need to employ chelating ligands, which prevent competitive binding of the substrate, have been reported to be essential to the success of the transformation.[9,10] Given the importance of the Suzuki–Miyaura reaction, particularly in the area of drug development, an efficient method for the coupling of nitrogen-containing heterocyclic substrates would make a significant impact.

Herein, we report that extremely active catalysts composed of Pd and dialkylbiphenylphosphino ligands **1** or **2** provide a general system for the Suzuki–Miyaura reaction of

[*] K. L. Billingsley, K. W. Anderson, Prof. Dr. S. L. Buchwald
Department of Chemistry, Room 18-490
Massachusetts Institute of Technology
Cambridge, MA 02139 (USA)
Fax: (+1) 617-253-3297
E-mail: sbuchwal@mit.edu

[**] We thank the National Institutes of Health (GM 46059) and the National Cancer Institute (Cancer Training Grant GM 5-T32-CAO9112-30) for support of this work. We are grateful to Merck, Amgen, and Englehard ($Pd(OAc)_2$) for additional support. The Bruker Advance 400 MHz instrument used was purchased with funding from the National Institutes of Health (GM 1S10RR13886-01).

Supporting information for this article is available on the WWW under http://www.angewandte.org or from the author.

WILEY InterScience DISCOVER SOMETHING GREAT
© 2006 Wiley-VCH Verlag GmbH & Co. KGaA, Weinheim

challenging heterocyclic substrates, such as aminoheteroaryl halides (chloroaminopyridines and chloroaminopyrimidines) and/or heteroaryl boronic acids/esters (e.g., 3- and 4-pyridineboronic acids, pyrrole boronate esters, and indole boronic acids). After our work was completed, Fu and co-workers reported that a catalyst system comprised of Pd/PCy_3 (Cy = cyclohexyl) was particularly effective in coupling aryl/heteroaryl halides and heteroaryl boronic acids.[11]

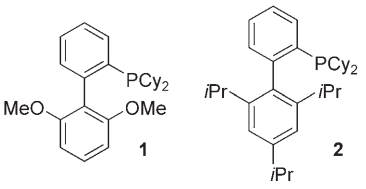

Only a few reports can be found on the successful Suzuki–Miyaura coupling of substrates that possess unprotected amino groups on a heteroaryl moiety.[9,12] Traditionally, to circumvent the problems associated with this functional group array, the free amino group is protected prior to the cross-coupling process and must, correspondingly, be deprotected following the organometallic reaction.[10] Past studies suggest that binding of the free $-NH_2$ group to the metal center can retard the catalytic cycle; therefore, the basicity of the aminoheteroaryl moiety should directly correlate to the efficacy of the Pd-catalyzed process (Scheme 1).[9a,13] Although previous reports suggest that chelating ligands are a necessity for the efficient coupling of unprotected aminoheteroaromatic compounds,[9a] our group has established that Suzuki–Miyaura reactions that employ the dialkylmonophosphino biaryl **1** as the supporting ligand display unprecedented reactivity while maintaining a broad substrate scope. Thus, in our initial studies, we utilized a catalyst based upon $Pd(OAc)_2$/**1** for the coupling of aryl boronic acids with chloroaminoheterocycles.

A catalyst system that employs **1** as the supporting ligand proved to be highly active for the cross-coupling of a range of chloroaminopyridines and chloroaminopyrimidines with aryl boronic acids that possess functional groups. For example, the reaction of 3-amino-2-chloropyridine with 2-methoxyphenylboronic acid smoothly produced the desired biaryl in 99% yield (Table 1, entry 1). In addition, the sterically hindered 2,6-dimethylphenylboronic acid reacted in 82% yield with 5-amino-2-chloropyridine (Table 1, entry 2), and similarly electron-deficient boronic acids also react in good yield under the derived conditions (Table 1, entry 4). Also, it is interesting to note that 4-amino-2-chloropyridine, which is the most basic among these substrates, reacts in excellent yield with phenylboronic acid (Table 1, entry 5). To the best of our knowledge, this result represents the highest yielding Suzuki–Miyaura coupling with a highly basic chloroaminopyridine.[9a]

Similar to the results found for chloroaminopyridines, the $Pd(OAc)_2$/**1** catalyst system was highly active for the couplings of chloroaminopyrimidines (Table 1, entries 6–8). These reactions proceed in greater than 90% yield for both sterically encumbered heteroaryl halides and aryl boronic acids. In addition, the reaction of the electron-deficient boronic acid, 3-acetylphenylboronic acid, with the 4-amino-5-chloro-2,6-dimethylpyrimidine proceeds smoothly to produce the highly substituted heterobiaryl in

Table 1: Suzuki–Miyaura coupling of chloroaminoheterocycles using ligand **1**.[a]

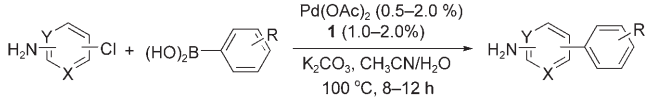

Entry	Aryl chloride	Boronic acid	Product	Yield [%][b]
1		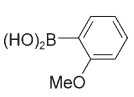	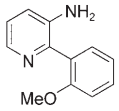	99
2	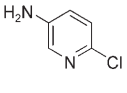	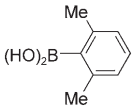	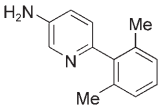	82
3	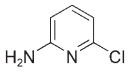	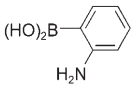	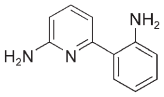	95
4	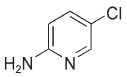	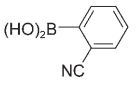	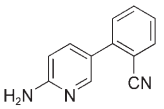	79[c]
5	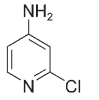	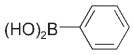	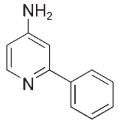	92
6	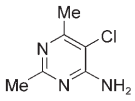	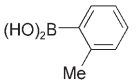	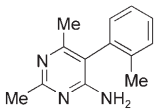	97
7	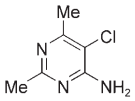	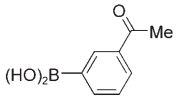	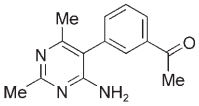	96
8	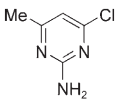	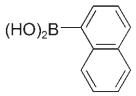	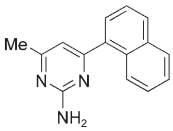	92[c]

[a] Reaction conditions: heteroaryl halide (1.0 equiv), aryl boronic acid (1.2–1.5 equiv), K_2CO_3 (2.0–3.0 equiv), CH_3CN (1.5 mL mmol^{-1} halide), H_2O (1.0 mL mmol^{-1} halide), cat. = $Pd(OAc)_2$, L/Pd = 2:1. [b] Yield of isolated product based upon an average of two runs. [c] Reaction was conducted using K_3PO_4 and 1,4-dioxane (2.5 mL mmol^{-1} halide).

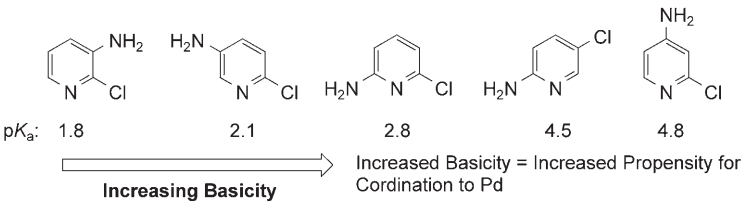

Scheme 1. Basicity of selected aminopyridines.

 © 2006 Wiley-VCH Verlag GmbH & Co. KGaA, Weinheim

96% yield (Table 1, entry 7). This protocol corresponds to the only method whereby chloroaminopyrimidines are coupled to hindered aryl boronic acids.

Pyridines are the most common heterocyclic motif found in pharmaceutically active compounds.[14] Thus, preparative methods of pyridine derivatives remain an essential research topic in organic synthesis. Despite efforts by numerous groups, pyridine-derived boronic acids have proved to be a particularly difficult class of substrate for the Suzuki–Miyaura reaction.[11,15] The $Pd(OAc)_2$/**1** catalyst system provided good yields for the reaction of pyridine boronic acids with activated heteroaryl chlorides. For example, the reaction of 3-chloro-2,5-dimethylpyrazine with 4-pyridineboronic acid provided an 83% yield of the desired heterobiaryl (Table 2, entry 5).

Table 2: Suzuki–Miyaura coupling of pyridine boronic acids using ligands **1** or **2**.[a]

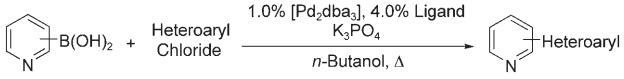

Entry	Boronic acid	Aryl chloride	Product	Ligand	*T* [°C]	Yield [%][b]
1	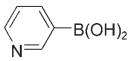	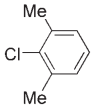	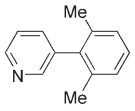	**2**	100	81
2	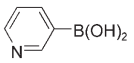	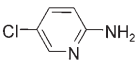	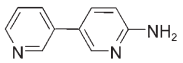	**2**	120	95
3	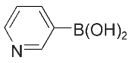	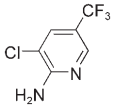	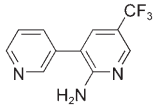	**2**	120	95
4	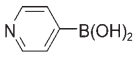	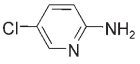	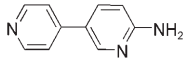	**2**	120	95
5	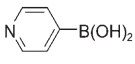	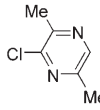	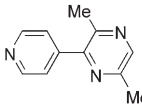	**1**	100	83[c,d]
6	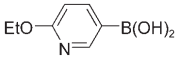	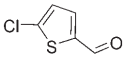	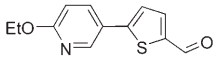	**2**	100	91
7	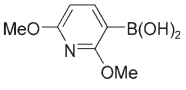	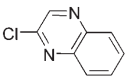	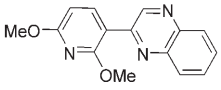	**2**	100	91[e]

[a] Reaction condiitons: aryl or heteroaryl chloride (1.0 equiv), boronic acid (1.5 equiv), K_3PO_4 (2.0 equiv), *n*-butanol (2 mL mmol^{-1} halide), cat. = [Pd_2dba_3], L/Pd = 2:1. [b] Yield of isolated product based upon an average of two runs. [c] $Pd(OAc)_2$ was used instead of [Pd_2dba_3]. [d] Reaction was conducted in *s*-butanol. [e] Reaction was conducted in *tert*-amyl alcohol.

However, the catalyst proved to be far less efficacious for the reaction of unactivated aryl and heteroaryl chlorides.

We have established that a catalyst system based upon [Pd_2dba_3] (dba = dibenzylideneacetone) and the more-hindered ligand **2** afforded good-to-excellent yields for the cross-coupling of a variety of aryl and heteroaryl chlorides with pyridine-based boronic acids. We speculate that use of **2** maximizes the concentration of [$L_1Pd(Ar)X$] (X = halide) intermediates, which may be particularly important in these cases. Pyridine boronic acids reacted efficiently with sterically hindered aryl chlorides, as the coupling of 2-chloro-*m*-xylene with 3-pyridineboronic acid provided the biaryl in 81% yield (Table 2, entry 1). In addition, a range of aminopyridines was effectively coupled in excellent yield to 3- and 4-pyridineboronic acids (Table 2, entries 2–4). Similarly, commercially available alkoxypyridine boronic acids reacted in greater than 90% yield with an electron-deficient heteroaryl chloride (Table 2, entry 6). This protocol represents a general method for the coupling of pyridine-derived boronic acids with heteroaryl chlorides.

The first report of a pyrrole boronic acid was in 1991,[16] and currently a limited number of citations are found on the synthesis and utility of pyrrole-based boronic acids and borane derivatives.[17] As pyrroles are found in a variety of biological systems, we found this lack of precedent to be of particular interest. We discovered that employing a boronate ester instead of the boronic acid allowed for facile purification of the pyrrole reagent and its increased stability under the reaction conditions. Thus, **A** was synthesized in 79% yield from pyrrole by protection, selective bromination, and subsequent palladium-catalyzed boronation (Scheme 2).

Initial studies that employed pyrrole boronate esters proved to be unsuccessful as significant reduction of the aryl halide was detected. However, the addition of extraneous water to the reaction mixture minimized the amount of by-product and increased the overall yield. These conditions proved to be highly efficient for the coupling with heteroaryl bromides and activated heteroaryl chlorides at low catalyst loadings. The reaction of **A** with 5-bromoindole (Table 2, entry 1) and 2-bromopyridine (Table 2, entry 2) smoothly produced the heterobiaryls in greater than 90% yield at Pd loading of 0.25 mol%. In addition, **A** was also coupled to 2-bromothiophene in nearly quantitative yield with relatively high turnover numbers (Table 2, entry 3).

To examine the differences between the 2- and 3-boronated positions of the pyrrole unit, *N*-Boc-pyrrole-2-boronic acid (Boc = *tert*-butoxycarbonyl) was prepared by the known directed metalation strategy.[18] Significant dimerization or protodeboronation of the boronic acid was not readily detected under these conditions in contrast to what was previously repor-

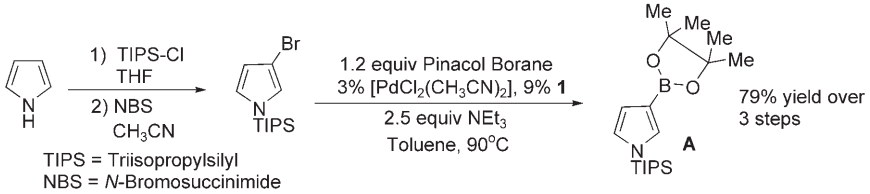

Scheme 2. Synthesis of *N*-(TIPS)-3-pyrrole pinacol borane.

 © 2006 Wiley-VCH Verlag GmbH & Co. KGaA, Weinheim

ted.[17b] Under the standard conditions, *N*-Boc-pyrrole-2-boronic acid was combined with the sterically encumbered substrate 2-bromomesitylene to afford the desired product in 89% yield (Table 3, entry 4). In addition, this boronic acid reacted in good yield with a variety of heteroaryl halides. The coupling of *N*-Boc-pyrrole-2-boronic acid with 5-chloro-2-thiophene carboxaldehyde and 4-bromoisoquinoline afforded the heterobiaryls in 84 and 95% yield, respectively (Table 3, entries 5 and 6). This method is the first general protocol through which 2- and 3-pyrrole organoboranes may serve as the nucleophilic component in the Suzuki–Miyaura reaction.

Indoles have been of interest for over a century because of the biological activity displayed by many of its derivatives.[19] Several studies have been conducted on the reactivity of indole-derived boronic acids under Suzuki–Miyaura conditions.[20] However, to date, there are only a few general methods for the cross-coupling of these derivatives with heteroaryl chlorides.[11] The reaction of 5-indoleboronic acid with a range of heteroaryl chlorides proceeded in good-to-excellent yields. The $Pd(OAc)_2$/**1** catalyst system was highly active for the reaction of activated heteroaryl chlorides. The coupling of *N*-methyl-5-indoleboronic acid with 5-chloro-2-thiophene carboxaldehyde resulted in 96% yield of the biaryl at a Pd loading of 0.25 mol% (Table 3, entry 7). In addition, this indole boronic acid smoothly reacted with 3-chloro-2,5-dimethylpyrazine to afford the heterobiaryl in 90% yield (Table 3, entry 8). As suggested in other reports, no significant difference in reactivity for the unprotected heteroaryl boronic was observed.[21] 5-Indoleboronic acid was coupled to several unactivated heteroaryl chlorides in $\geq$75% yield (Table 3, entries 9 and 10). In these cases, the temperature of the reaction had to be raised to 120 °C to facilitate the complete conversion of the heteroaryl chloride. The reaction of 5-indoleboronic acid with 5-chlorobenzoxazole and 2-amino-5-chloropyridine produced the desired heterobiaryl in 91 and 77% yields, respectively (Table 3, entries 9 and 10). This protocol represents the only current method by which indole boronic acids can be coupled to unactivated heteroaryl chlorides.

In summary, we have demonstrated that use of catalysts comprised of Pd and ligands **1** or **2** provide highly stable and active catalysts for the Suzuki–Miyaura coupling of pyridine, pyrrole, and indole boronic acids/esters. We also have shown that this catalyst is not inhibited by the presence of highly basic aminopyridines or aminopyrimidines, again demonstrating its high catalytic activity. Further work in applying these catalytic systems to a wider array of heteroaryl substrates will be reported in due course.

Table 3: Suzuki–Miyaura coupling of pyrrole and indole boranes using ligands **1** or **2**.[a]

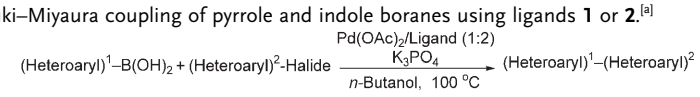

Entry	Boronic acid	Aryl chloride	Product	Ligand	Pd [mol%]	Yield [%][b]
1	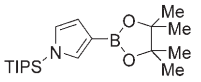	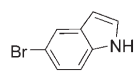	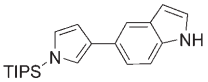	**1**	0.25	97[c]
2	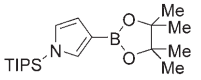	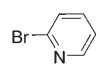	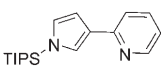	**1**	0.25	91[c]
3	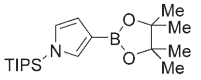		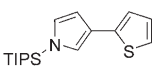	**1**	0.25	99[c]
4	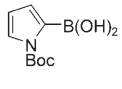	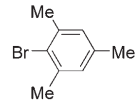	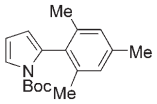	**1**	2.0	89
5	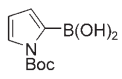	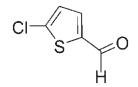	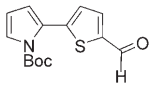	**1**	2.0	84
6	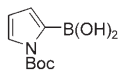	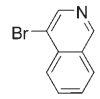	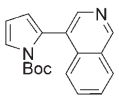	**1**	2.0	95
7	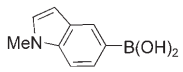	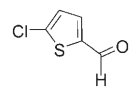	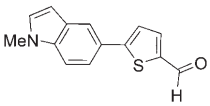	**1**	0.25	96
8	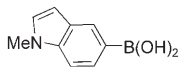	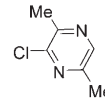	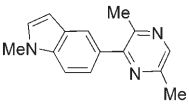	**1**	2.0	90[e]
9	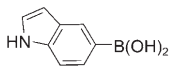	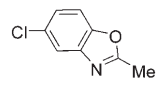	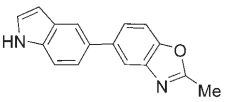	**2**	2.0	91[d]
10	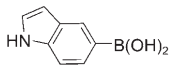	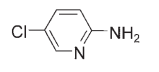	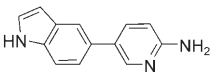	**2**	2.0	77[d]

[a] Reaction conditions: aryl or heteroaryl chloride (1.0 equiv), boronic acid (1.5 equiv), K_3PO_4 (2.0 equiv), *n*-butanol (2 mL mmol^{-1} halide), cat. = [Pd_2dba_3], L/Pd = 2:1. [b] Yield of isolated product based upon an average of two runs. [c] [Pd_2dba_3] was used instead of $Pd(OAc)_2$. [d] Reaction was conducted at 120 °C. [e] *s*-Butanol was used as the solvent.

Received: February 6, 2006
Published online: April 26, 2006

Keywords: amines · boronic acids · cross-coupling · heteroaryl halides · Suzuki–Miyaura reaction

 © 2006 Wiley-VCH Verlag GmbH & Co. KGaA, Weinheim

[1] A. de Meijere, F. Diederich, Eds. *Metal-Catalyzed Cross-Coupling Reactions*, *Vol. 2*, Wiley-VCH, Weinheim, **2004**.

[2] a) N. Miyaura, *Top. Curr. Chem.* **2002**, *219*, 11; b) A. Suzuki, *Organomet. Chem.* **1999**, *28*, 147.

[3] M. Kertesz, C. H. Choi, S. Yang, *Chem. Rev.* **2005**, *105*, 3448.

[4] a) A. Markham, K. L. Goa, *Drugs* **1997**, *54*, 299; b) R. Capdeville, E. Buchdunger, J. Zimmermann, A. Matter, *Nat. Rev. Drug Discovery* **2002**, *1*, 493; c) J. Boren, M. Cascante, S. Marin, B. Comin-Anduix, J. J. Centelles, S. Lim, S. Bassilian, S. Ahmed, W. N. Lee, L. G. Boros, *J. Biol. Chem.* **2001**, *276*, 37747.

[5] H. Tomori, J. M. Fox, S. L. Buchwald, *J. Org. Chem.* **2000**, *65*, 5334.

[6] S. Lightowler, M. Hird, *Chem. Mater.* **2005**, *17*, 5538.

[7] a) T. E. Barder, S. D. Walker, J. R. Martinelli, S. L. Buchwald, *J. Am. Chem. Soc.* **2005**, *127*, 4685; b) T. E. Barder, S. L. Buchwald, *Org. Lett.* **2004**, *6*, 2649; c) S. D. Walker, T. E. Barder, J. R. Martinelli, S. L. Buchwald, *Angew. Chem.* **2004**, *116*, 1907; *Angew. Chem. Int. Ed.* **2004**, *43*, 1871; d) H. N. Nguyen, X. Huang, S. L. Buchwald, *J. Am. Chem. Soc.* **2003**, *125*, 11818; e) J. Yin, M. P. Rainka, X.-X. Zhang, S. L. Buchwald, *J. Am. Chem. Soc.* **2002**, *124*, 1162; f) R. Singh, M. S. Viciu, N. Kramareva, O. Navarro, S. P. Nolan, *Org. Lett.* **2005**, *7*, 1829; g) A. F. Littke, C. Dai, G. C. Fu, *J. Am. Chem. Soc.* **2000**, *122*, 4020.

[8] a) I. Kondolff, H. Doucet, M. Santelli, *Synlett* **2005**, 2057; b) A. E. Thompson, G. Hughes, A. S. Batsanov, M. R. Bryce, P. R. Parry, B. Tarbit, *J. Org. Chem.* **2005**, *70*, 388; also see references [7a–d].

[9] A few direct cross-coupling reactions that involve heteroaryl moieties with unprotected NH_2 groups have been disclosed; see: ref. [8b] and a) T. Itoh, T. Mase, *Tetrahedron Lett.* **2005**, *46*, 3573; b) T. Itoh, K. Sato, T. Mase, *Adv. Synth. Catal.* **2004**, *346*, 1859; c) P. Gunda, L. M. Russon, M. K. Lakshman, *Angew. Chem.* **2004**, *116*, 6532; *Angew. Chem. Int. Ed.* **2004**, *43*, 6372; d) L. A. Agrofoglio, I. Gillaizeau, Y. Saito, *Chem. Rev.* **2003**, *103*, 1875; e) T. Tagata, M. Nishida, *J. Org. Chem.* **2003**, *68*, 9412; f) M. Feuerstein, H. Doucet, M. Santelli, *J. Organomet. Chem.* **2003**, *687*, 327.

[10] For examples in which it was essential to protect the amino-heterocycle, see: a) S. Caron, S. S. Massett, D. E. Bogle, M. J. Castaldi, T. F. Braish, *Org. Process Res. Dev.* **2001**, *5*, 254; b) J. A. Miller, R. P. Farrell, *Tetrahedron Lett.* **1998**, *39*, 6441.

[11] N. Kudo, M. Perseghini, G. C. Fu, *Angew. Chem.*, **2006**, *118*, 1304; *Angew. Chem. Int. Ed.* **2006**, *15*, 1282.

[12] During the production of this manuscript, Guram et al. reported that the use of $[PdCl_2\{PtBu_2(p\text{-}RPh)\}_2]$ ($R = H, NMe_2, CF_3$) were quite effective as catalysts in the Suzuki–Miyaura coupling of amino-heteroaryl/heteroaryl chlorides and aryl boronic acids, see: A. S. Guram, A. O. King, J. G. Allen, X. Wang, L. B. Schenkel, J. Chan, E. E. Bunel, M. M. Faul, R. D. Larsen, M. J. Martinelli, P. J. Reider, *Org. Lett* **2006**, ASAP.

[13] S. Wagaw, S. L. Buchwald, *J. Org. Chem.* **1996**, *61*, 7240.

[14] V. Bonnet, F. Mongin, F. Tre'court, G. Breton, F. Marsais, P. Knochel, G. Que'guiner, *Synlett* **2002**, 1008.

[15] a) M. Ishikura, M. Kamada, M. Terashima, *Heterocycles* **1984**, *22*, 265; b) P. R. Parry, C. Wang, A. S. Batsanov, M. R. Bryce, B. Tarbit, *J. Org. Chem.* **2002**, *67*, 7541; c) G. A. Molander, B. Biolatto, *J. Org. Chem.* **2003**, *68*, 4302; d) C. L. Cioffi, W. T. Spencer, J. J. Richards, R. J. Herr, *J. Org. Chem.* **2004**, *69*, 2210; e) P. B. Hodgson, F. H. Salingue, *Tetrahedron Lett.* **2004**, *45*, 685; f) T. E. Barder, S. L. Buchwald, *Org. Lett.* **2004**, *6*, 2649.

[16] S. Martina, V. Enkelmann, G. Wegner, A. D. Schluter, *Synthesis* **1991**, 613.

[17] a) A. Alzarez, A. Guzmen, A. Ruiz, E. Velards, J. Muchowski, *J. Org. Chem.* **1992**, *57*, 1653; b) C. Johnson, G. Stemp, N. Anand, S. Stephen, T. Gallagher, *Synlett* **1998**, 1025.

[18] B. Bray, P. Mathies, R. Naef, D. Solas, T. Tidwell, D. Artis, J. Muchowski, *J. Org. Chem.* **1990**, *55*, 6317.

[19] *Indoles* (Ed.: W. J. Houlihan), Wiley-Interscience, New York, **1972**.

[20] Y. Yang, A. R. Martin, *Heterocycles* **1992**, *34*, 1395.

[21] M. Prieto, E. Zurita, E. Rosa, L. Munoz, P. Lloyd-Williams, E. Giralt, *J. Org. Chem.* **2004**, *69*, 6812.

 © 2006 Wiley-VCH Verlag GmbH & Co. KGaA, Weinheim

Carbenes

DOI: 10.1002/anie.200600987

CO Fixation to Stable Acyclic and Cyclic Alkyl Amino Carbenes: Stable Amino Ketenes with a Small HOMO–LUMO Gap**

*Vincent Lavallo, Yves Canac, Bruno Donnadieu, Wolfgang W. Schoeller, and Guy Bertrand**

Reactive intermediates play a central role in modern chemistry.[1] Since 1900, and the discovery by Gomberg of a stable radical,[2] many species that were thought to be too short-lived for observation have been isolated. The availability of stable versions of reactive intermediates has allowed for a superior control of their reactivity and a better understanding of the mechanism of chemical reactions. Even more importantly, new applications of these species have been found, for example, the successful use of stable carbenes as ligands for transition-metal catalysts,[3] and even as organic catalysts.[4]

There are still several families of synthetically important reactive intermediates, the preparation of which has been impeded by the belief that they are incapable of existence, or has eluded the synthetic skills of investigators. Because of their very high reactivity, ketenes are key intermediates in synthetic organic chemistry, and have even found industrial applications.[5–7] Despite the isolation of diphenylketene as early as the beginning of the 20th century,[8] most ketenes are intrinsically unstable and cannot be isolated.[5] Calculations have predicted that σ-electron-withdrawing substituents, as well as π-donor groups destabilize ketenes.[9] Accordingly, alkoxy ketenes have only been characterized at low temper-

[*] V. Lavallo, Dr. Y. Canac, B. Donnadieu, Prof. G. Bertrand
UCR-CNRS Joint Research Chemistry Laboratory (UMI 2957)
Department of Chemistry
University of California
Riverside, CA 92521-0403 (USA)
Fax: (+1) 951-827-2725
E-mail: gbertran@mail.ucr.edu
Prof. W. W. Schoeller
Fakultät für Chemie der Universität Bielefeld
Postfach 100131, 33615 Bielefeld (Germany)

[**] We are grateful to the NIH (R01 GM 68825) and NSF (CHE-0518675) for financial support of this work.

Supporting information for this article is available on the WWW under http://www.angewandte.org or from the author.

WILEY InterScience DISCOVER SOMETHING GREAT
© 2006 Wiley-VCH Verlag GmbH & Co. KGaA, Weinheim

ature or by fast-spectroscopic methods,[10] whereas amino ketenes have never been observed.[11]

Transient triplet carbenes, such as methylene, react with CO to give the corresponding ketenes.[12] In contrast, although the carbonylation of singlet carbenes is spin-allowed, there are very few examples of ketene formation using this route.[13] In 1994 it was claimed that the imidazol-2-ylidene **1a** reacts with carbon monoxide to give the stable diamino ketene **2a** (Scheme 1).[14] However, a year later Arduengo et al.[15] were

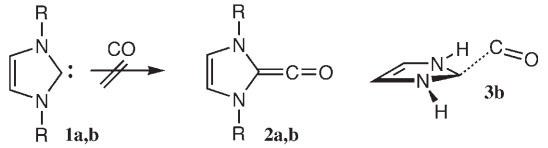

Scheme 1. N-heterocyclic carbenes (NHCs) do not react with CO; the structure of van der Waals complex **3b**.

not able to duplicate these experimental results. They demonstrated computationally that the parent compound **2b** is not even a transition state, and found that there is no stable structure associated with the combination of **1b** and CO, other than "a non-bonded weakly interacting (van der Waals) complex" **3b** (scheme 1). Moreover, the calculations showed that the CO addition leading to **2b** is not favored thermodynamically [$\Delta H(298\,K) = +15.9$ kcal mol^{-1}].[15]

Herein we report that, in marked contrast with cyclic diamino carbenes **1**, stable acyclic **4a**[16] and **4b**, and cyclic alkyl amino carbenes (CAACs) **6**[17] react with CO to afford amino ketenes **5a**,**b** and **7**, respectively (see Scheme 2), which are indefinitely stable at room temperature both in solution and in the solid state. We show that the ring structure forces the planarization of the amino fragment of **7**, and therefore causes the destabilizing n–π donation from the amino group. Consequently, the HOMO of the ketene **7** is raised and the singlet–triplet gap considerably reduced, which induces unusual optical and NMR spectroscopic properties.

According to calculations,[16] the singlet–triplet gap (26.7 kcal mol^{-1}) and the HOMO (−4.3 eV) for acyclic alkyl amino carbenes **4** are much smaller and higher in energy, respectively, than for NHCs **1** (79.6 kcal mol^{-1} and −5.4 eV).[18] Consequently, carbenes **4** are more nucleophilic but also more electrophilic than NHCs **1**, and are therefore better candidates for a carbonylation reaction. Indeed, when carbon monoxide was bubbled at room temperature through a THF solution of acyclic carbene **4a**, a clean reaction occurred, and after evaporation of the solvent under vacuum, ketene **5a** was obtained in good yield as a pale yellow oil (Scheme 2). The IR spectrum of **5a** shows a very strong C=C=O stretching vibration at 2066 cm^{-1}, and the ^{13}C NMR signals for the ketene group appear at $\delta = 213.95$ (*C*CO) and 60.90 (*C*CO) ppm; all these values are expected for a ketene bearing a σ-electron-withdrawing group.[9] Only one set of NMR signals was observed for the isopropyl substituents, which suggests free rotation around the N–CCO bond.

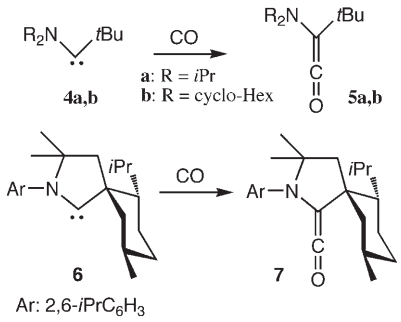

Scheme 2. Addition of CO to carbenes **4a**,**b** and **6**.

Starting from carbene **4b**, which has cyclohexyl instead of isopropyl groups, ketene **5b** was isolated as pale yellow crystals (m.p.: < 20 °C) suitable for X-ray diffraction (Figure 1).[19] Interestingly, the N–C1 bond (ca. 1.43 Å) is much longer than in carbene **4a** (1.30 Å), suggesting again the absence of interaction between the nitrogen lone pair and the CCO fragment. Indeed, molecule **5b** escapes the destabilizing n–π donation, by pyramidalization of the amino group (sum of the angles: 347.7°), and by directing the nitrogen lone pair 180° away from the CCO moiety. Consequently, the observed geometric parameters of the CCO fragment of **5b** are very similar to those calculated for the parent ketene H_2CCO (Table 1).[20]

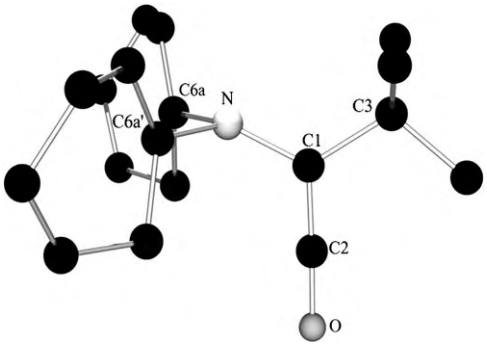

Figure 1. Molecular view of the crystal structure of **5b**. Selected bond lengths [Å] and angles [°]: N–C1 1.426(4), C1–C2 1.310(5), C2–O 1.174(4), C1–C3 1.517(4), N–C6a 1.417(7); N-C1-C3 122.6(3), C3-C1-C2 119.2(3), N-C1-C2 118.2(3), C6a-N-C1 127.7(3), C6a′-N-C1 127.7(3), C6a′-N-C6a 92.3(5).

Table 1: Comparison of the spectroscopic data, geometric parameters, and singlet–triplet (S/T) energy gap for ketenes.

Ketene	^{13}C CCO [ppm]	^{13}C CCO [ppm]	IR ν_{CCO} [cm^{-1}]	UV λ_{max} [nm]	Σ_N[a] [°]	N–C1 [Å]	C1–C2 [Å]	C2–O [Å]	S/T gap [Kcal mol^{-1}]
H_2CCO	194.0[23]	2.5[23]	2151[24]	329[20]			1.315[20]	1.173[20]	51.8[20]
Ph_2CCO	201.2[23]	47.6[23]	2105[25]	405[25]					
5a	213.9	60.9	2066	381					
5b	214.7	62.3	2066	380	347.7	1.426	1.310	1.174	
5c$_{pyr}$[20]	209.1	35.6		370	336.4	1.443	1.326	1.176	23.9
5c$_{pla}$[20]	288.1	53.7		673	360	1.409	1.322	1.186	17.0
7	278.0	81.4	2073	598	357.3	1.405	1.334	1.186	

© 2006 Wiley-VCH Verlag GmbH & Co. KGaA, Weinheim

The next challenge was to synthesize an amino ketene in which the nitrogen lone pair would be forced to stay parallel to the C=C π system. We have recently shown that despite the reluctance of phosphorus to be planar (inversion barrier 35 kcal mol^{-1} for PH_3 compared to 5 kcal mol^{-1} for NH_3), its incorporation into a ring, in addition to the use of bulky substituents, allowed us to force its planarization.[21,22] Applying the same concept, the CAAC **6** (Scheme 2)appeared to be the ideal precursor. As soon as carbon monoxide was bubbled at room temperature through a THF solution of CAAC **6**, a very deep blue color appeared. After evaporation of the solvent under vacuum, ketene **7** crystallizes from hexane at −20 °C as blue crystals (65 %, m.p.: 95–97 °C) suitable for X-ray diffraction (Figure 2).[19] As expected, the nitrogen atom is

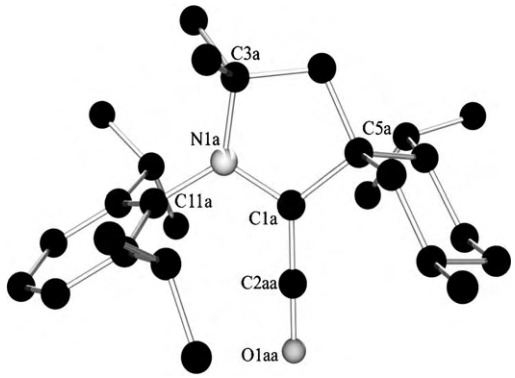

Figure 2. Molecular view of the crystal structure of **7**. Selected bond lengths [Å] and angles [°]: N1a–C1a 1.405(2), C1a–C2aa 1.334(5), C2aa–O1aa 1.186(5) C1a–C5a 1.524(2), N1a–C11a 1.437(2); N1a-C1a-C5a 110.80(14), C5a-C1a-C2aa 125.6(2), N1a-C1a-C2aa 122.8(2), C11a-N1a-C1a 119.27(13), C11a-N1a-C3a 125.63(14), C3a-N1a-C1a 112.41(13).

in a planar environment (sum of the angles: 357.3°), and the lone pair is coplanar with the C=C π system. Although the N1a−C1 bond (ca. 1.40 Å) is much longer than that of carbene **6** (1.31 Å), it is similar to that observed for ketene **5b**. Similarly, in the IR spectrum, the C=C=O stretching vibration for **7** is at 2073 cm^{-1}, very close to that observed for **5** ($\Delta\nu$ = 7 cm^{-1}). These results suggest only a weak interaction between the nitrogen lone pair and the CCO fragment. However, compared to other ketenes, a dramatic red-shifted UV absorption is observed (very intense band from 500 to 700 nm, λ_{max} 598 nm), as well as a spectacular downfield shift of the ^{13}C NMR signal of the *C*CO carbon of **7** ($\delta \approx 278$ ppm; Table 1).

To gain further insight into the electronic structure of amino ketenes **5** and **7**, density functional theory (DFT) calculations at triple-zeta basis set quality[20] were performed on the parent acyclic amino ketenes $\mathbf{5c_{pyr}}$ and $\mathbf{5c_{pla}}$ (Scheme 3), which feature a nitrogen atom in a pyramidal (pyr) and planar (pla) environment, respectively. The calculated geometry and NMR chemical shifts for $\mathbf{5c_{pyr}}$ are similar to those observed experimentally for **5a**,**b** (Table 1). Of particular interest, the lone pair of $\mathbf{5c_{pyr}}$ is also directed 180° away from the CCO fragment. Forcing the nitrogen to be in a planar geometry, with the lone pair parallel to the C=C

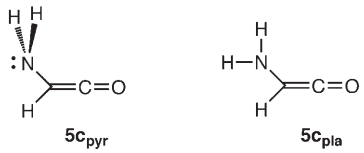

$\mathbf{5c_{pyr}}$ $\mathbf{5c_{pla}}$

Scheme 3. Schematic representations of the calculated parent amino ketenes $\mathbf{5c_{pyr}}$ and $\mathbf{5c_{pla}}$.

π system, costs 6.8 kcal mol^{-1}, and $\mathbf{5c_{pla}}$ is not even an energy minimum on the electronic hypersurface. In $\mathbf{5c_{pla}}$ the π-conjugation of the amino group with the adjacent C=C π bond has a drastic effect on the frontier orbitals. It raises the HOMO (π-C=C) while the LUMO (π*-C=O), is not affected. The resulting smaller HOMO–LUMO gap is in line with the smaller value of the adiabatic singlet–triplet energy separation, which decreases from 23.9 for $\mathbf{5c_{pyr}}$ to 17.0 kcal mol^{-1} for $\mathbf{5c_{pla}}$. In other words, forcing the π-conjugation with the adjacent amino substituent, as in the calculated $\mathbf{5c_{pla}}$ and observed ketenes **7**, induces a biradical character. The reduction of the HOMO–LUMO energy gap readily explains the red-shift of the π(C=C)-→π*(C=O) optical transition. The small singlet–triplet energy gap leads to the enhancement of the paramagnetic term, and therefore the downfield shift of the ^{13}C NMR signal of the CO carbon of $\mathbf{5c_{pla}}$ and **7**.

In conclusion, cumulenes **5** and **7** are the first ketenes prepared from CO fixation to stable carbenes. When compared to the parent ketene (H_2CCO), the presence of a pyramidal amino group as in **5** reduces the singlet–triplet energy gap by about 50 %, and the planarization of the amino group as in **7** induces another 30 % reduction to reach 17 kcal mol^{-1}. The small HOMO–LUMO energy gap induces unusual optical and NMR spectroscopic properties.[26] The design of ketenes featuring an even more pronounced diradical character is under active investigation.

Experimental Section

All manipulations were performed under an inert atmosphere of argon using standard Schlenk techniques. Dry, oxygen-free solvents were employed. ^{1}H and ^{13}C NMR spectra were recorded on Varian Inova 300, 500, and Bruker Avance 300 spectrometers.

5a,**b** and **7**: Carbon monoxide was bubbled (30 min) at room temperature through a THF solution (20 mL) of the appropriate carbene **4a**,**b** and **6** (4.7 mmol). After evaporation of the solvent under vacuum and extraction with hexane (10 mL), ketene **5a** was obtained as a yellow oil (82 % yield), whereas **5b** and **7** were isolated by crystallization in hexane at −20 °C as yellow (80 % yield) and blue crystals (65 % yield), respectively. **5a**: ^{1}H NMR (C_6D_6, 300 MHz, 25 °C): δ = 3.08 (sept, 2H, C*H*CH$_3$, J = 6.7 Hz), 1.01 (s, 9H, C(C*H*$_3$)$_3$), 0.99 ppm (d, 12H, CHC*H*$_3$, J = 6.7 Hz); ^{13}C NMR ([D$_8$]THF, 100 MHz, 25 °C): δ = 213.95 (*C*CO), 60.90 (*C*CO), 53.02, 30.71, 29.00, 21.99 ppm; IR (CH_2Cl_2): $\tilde{\nu}$(CO) 2066 cm^{-1}; UV (hexane): λ_{max} 381 nm; DCI-MS *m*/*z* 170 [carbene + H$^+$]. **5b**: m.p. < 20 °C; ^{1}H NMR (C_6D_6, 500 MHz, 25 °C): δ = 2.71 (m, 2H, C*H*), 1.02–1.90 (m, 20H, C*H*$_2$), 1.05 ppm (s, 9H, C(C*H*$_3$)$_3$); ^{13}C NMR (C_6D_6, 125 MHz, 25 °C): 214.68 (*C*CO), 63.64, 62.26 (*C*CO), 34.31, 31.80, 29.92, 27.38, 26.61 ppm; IR (CH_2Cl_2): $\tilde{\nu}$(CO) 2066 cm^{-1}; UV (hexane): λ_{max} 380 nm. **7**: m.p. 95–97 °C; ^{1}H NMR (C_6D_6, 500 MHz, 25 °C): δ = 7.25–7.35 (m, 3H, H_{ar}), 3.92 (sept, 1H, C*H*CH$_3$, J = 7.0 Hz), 3.88 (sept, 1H, C*H*CH$_3$, J = 6.5 Hz), 2.74 (d, 1H, J = 13.0 Hz), 2.56 (d, 2H, J = 13.0 Hz), 1.58–1.78 (m, 4H), 1.47 (d, 3H, CHC*H*$_3$, J = 6.5 Hz),

 © 2006 Wiley-VCH Verlag GmbH & Co. KGaA, Weinheim

1.46 (d, 3H, CHCH_3, J = 7.0 Hz), 1.44 (3H, CHCH_3, J = 6.5 Hz), 1.35–1.42 (m, 12H), 1.24 (d, 3H, CHCH_3, J = 7.0 Hz), 1.16 (d, 3H, CHCH_3, J = 7.5 Hz), 1.07 (d, 3H, CHCH_3, J = 6.5 Hz), 0.94 ppm (m, 1H); ^{13}C NMR (C_6D_6, 125 MHz, 25 °C): 277.96 (*C*CO), 152.27, 151.97, 134.57, 128.93, 125.01, 124.94, 81.40 (*C*CO), 64.55, 55.04, 53.76, 49.89, 49.79, 35.17, 31.49, 30.99, 30.66, 29.17, 29.11, 28.36, 27.13, 26.49, 25.71, 24.87, 24.21, 23.80, 23.02, 18.65 ppm; IR (CH_2Cl_2): $\tilde{\nu}$(CO) 2073 cm^{-1}; UV (hexane): λ_{max} 598 nm; DCI-MS m/z 383 [carbene + H$^+$].

Received: March 13, 2006
Published online: April 25, 2006

Keywords: carbenes · carbon monoxide fixation · ketenes · optical properties · radicals

[1] *Reactive Intermediate Chemistry* (Eds.: R. A. Moss, M. S. Platz, M. Jones, Jr.), Wiley-Interscience, Hoboken, NJ, **2004**.
[2] a) M. Gomberg, *Ber. Dtsch. Chem. Ges.* **1900**, *33*, 3150; b) M. Gomberg, *J. Am. Chem. Soc.* **1900**, *22*, 757.
[3] For recent reviews on stable carbenes as ligands for transition-metal catalysts, see: a) N. M. Scott, S. P. Nolan, *Eur. J. Inorg. Chem.* **2005**, 1815; b) E. Peris, R. H. Crabtree, *Coord. Chem. Rev.* **2004**, *248*, 2239; c) C. M. Crudden, D. P. Allen, *Coord. Chem. Rev.* **2004**, *248*, 2247; d) V. César, S. Bellemin-Laponnaz, L. H. Gade, *Chem. Soc. Rev.* **2004**, *33*, 619; e) W. A. Herrmann, *Angew. Chem.* **2002**, *114*, 1342; *Angew. Chem. Int. Ed.* **2002**, *41*, 1290; f) D. Bourissou, O. Guerret, F. P. Gabbaï, G. Bertrand, *Chem. Rev.* **2000**, *100*, 39.
[4] For recent reviews on stable carbenes as organic catalysts: a) D. Enders, T. Balensiefer, *Acc. Chem. Res.* **2004**, *37*, 534; b) V. Nair, S. Bindu, V. Sreekumar, *Angew. Chem.* **2004**, *116*, 5240; *Angew. Chem. Int. Ed.* **2004**, *43*, 5130.
[5] For recent general reviews on ketenes: a) T. T. Tidwell, *Angew. Chem.* **2005**, *117*, 5926; *Angew. Chem. Int. Ed.* **2005**, *44*, 5778; b) *Ketenes* (Ed.: T. T. Tidwell), Wiley, Hoboken, NJ, **2006**; c) *Science of Synthesis Houben-Weyl Methods of Molecular Transformations*, *Vol 23* (Eds.: R. L. Danheiser, D. Bellus), Thieme, Stuttgart, **2006**; d) C. M. Temperley in *Comprehensive Organic Functional Group Transformations II*, *Vol. 3* (Eds.: A. R. Katritzky, R. J. K. Taylor), Elsevier, Amsterdam, **2005**, p. 573.
[6] For recent reports on the reactivity of ketenes: a) T. T. Tidwell, *Eur. J. Org. Chem.* **2006**, 573; b) J. Louie, *Curr. Org. Chem.* **2005**, *9*, 605; c) T. T. Tidwell, *Angew. Chem.* **2005**, *117*, 6973; *Angew. Chem. Int. Ed.* **2005**, *44*, 6812; d) C. Schaefer, G. C. Fu, *Angew. Chem.* **2005**, *117*, 4682; *Angew. Chem. Int. Ed.* **2005**, *44*, 4606; e) E. Martin-Zamora, A. Ferrete, J. M. Llera, J. M. Munoz, R. R. Pappalardo, R. Fernandez, J. M. Lassaletta, *Chem. Eur. J.* **2004**, *10*, 6111; f) A. R. Far, *Angew. Chem.* **2003**, *115*, 2442; *Angew. Chem. Int. Ed.* **2003**, *42*, 2340.
[7] For industrial applications of ketenes: a) "Ketenes": R. Miller, C. Abaecherli, A. Said, *Ullman's Encyclopedia of Industrial Chemistry*, *Vol. A15*, 6th ed., **2002**, pp. 63–75; b) A. Reiser, H.-Y. Shih, T.-F. Yeh, J.-P. Huang, *Angew. Chem.* **1996**, *108*, 2610; *Angew. Chem. Int. Ed. Engl.* **1996**, *35*, 2428; c) A. Reiser, J. P. Huang, X. He, T. F. Yeh, S. Jha, H. Y. Shih, M. S. Kim, Y. K. Han, K. Yan, *Eur. Polym. J.* **2002**, *38*, 619; d) F. Xu, J. D. Armstrong III, G. X. Zhou, B. Simmons, D. Hughes, Z. Ge, E. J. J. Grabowski, *J. Am. Chem. Soc.* **2004**, *126*, 13002.
[8] H. Staudinger, *Ber. Dtsch. Chem. Ges.* **1905**, *38*, 1735.
[9] a) L. Gong, M. A. McAllister, T. T. Tidwell, *J. Am. Chem. Soc.* **1991**, *113*, 6021; b) M. A. McAllister, T. T. Tidwell, *J. Org. Chem.* **1994**, *59*, 4506.
[10] See for examples: a) A. V. Fedorov, E. O. Danilov, A. G. Merzlikine, M. A. J. Rodgers, D. C. Neckers, *J. Phys. Chem. A* **2003**, *107*, 3208; b) Y. Wang. J. P. Toscano, *J. Am. Chem. Soc.* **2000**, *122*, 4512; c) M. Barra, T. A. Fisher, G. J. Cernigliaro, R. Sinta, J. C. Scaiano, *J. Am. Chem. Soc.* **1992**, *114*, 2630.
[11] Note that the phthalimido-*tert*-butylketene has been isolated, but because of the presence of the carbonyl group, the nitrogen lone pair is not active: S. Winter, H. Pracejus, *Chem. Ber.* **1966**, *99*, 151.
[12] a) W. Sander, G. Bucher, S. Wierlacher, *Chem. Rev.* **1993**, *93*, 1583; b) W. Sander R. Hubert, E. Kraka, J. Grafenstein, D. Cremer, *Chem. Eur. J.* **2000**, *6*, 4567.
[13] a) P. Visser, R. Zuhse, M. W. Wong, C. Wentrup, *J. Am. Chem. Soc.* **1996**, *118*, 12598; b) J. R. Ammann, R. Subramanian, R. S. Sheridan, *J. Am. Chem. Soc.* **1992**, *114*, 7592.
[14] S. N. Lyashchuk, Y. G. Skrypnik, *Tetrahedron Lett.* **1994**, *35*, 5271.
[15] D. A. Dixon, A. J. Arduengo III, K. D. Dobbs, D. V. Khasnis, *Tetrahedron Lett.* **1995**, *36*, 645.
[16] V. Lavallo, J. Mafhouz, Y. Canac, B. Donnadieu, W. W. Schoeller, G. Bertrand, *J. Am. Chem. Soc.* **2004**, *126*, 8670.
[17] V. Lavallo, Y. Canac, C. Prasang, B. Donnadieu, G. Bertrand, *Angew. Chem.* **2005**, *117*, 5851; *Angew. Chem. Int. Ed.* **2005**, *44*, 5705.
[18] Similar values have been reported for NHCs by other groups: a) D. A. Dixon, A. J. Arduengo III, *J. Phys. Chem.* **1991**, *95*, 4180; b) C. Heinemann, W. Thiel, *Chem. Phys. Lett.* **1994**, *217*, 11.
[19] CCDC-600953 (**5b**), and CCDC-600954 (**7**) contain the supplementary crystallographic data for this paper. These data can be obtained free of charge from The Cambridge Crystallographic Data Centre via www.ccdc.cam.ac.uk/data_request/cif.
[20] The Turbomole 5.7.1 program system was used: R. Ahlrichs et al.: http://www.turbomole.com. The geometry optimizations were performed at the RI-BP86/TZVP level (without symmetry constraints), and the NMR spectroscopy parameters at the RI-BP86/TZVPP//RI-BP86 level.
[21] D. Martin, A. Baceiredo, H. Gornitzka, W. W. Schoeller, G. Bertrand, *Angew. Chem.* **2005**, *117*, 1728; *Angew. Chem. Int. Ed.* **2005**, *44*, 1700.
[22] For reviews on the influence of the substituents on the planarization of phosphorus, see: a) L. Nyulaszi, *Tetrahedron* **2000**, *56*, 79; b) L. Nyulaszi, *Chem. Rev.* **2001**, *101*, 1229.
[23] H. R. Seikaly, T. T. Tidwell, *Tetrahedron* **1986**, *42*, 2587.
[24] W. F. Arendale, W. H. Fletcher, *J. Chem. Phys.* **1956**, *26*, 793.
[25] S. Nadzhimutdinov, N. A. Slovokhotova, V. A. Kargin, E. P. Cherneva, Y. A. Cherbukov, *Zh. Giz. Khim.* **1957**, *41*, 1829.
[26] D. E. Perepichka, M. R. Bryce, *Angew. Chem.* **2005**, *117*, 5504; *Angew. Chem. Int. Ed.* **2005**, *44*, 5370.

 © 2006 Wiley-VCH Verlag GmbH & Co. KGaA, Weinheim

Asymmetric Synthesis

DOI: 10.1002/anie.200600268

Catalytic Enantioselective Crossed Aldehyde–Ketone Benzoin Cyclization**

*Hiroshi Takikawa, Yoshifumi Hachisu, Jeffrey W. Bode, and Keisuke Suzuki**

Despite the exceptionally long history of the benzoin reaction in the toolbox of organic methodology,[1] it has found only limited use in the synthesis of complex molecules. Two major limitations have stymied advances in synthetic applications. First, catalytic reaction conditions are usually limited to the synthesis of homobenzoins. Second, the resulting products are often labile, even when the desired reactivity can be obtained.[2] It is thus not surprising that recent innovations in this area have focused on new methods for the selective generation of acyl anions,[3,4] novel applications of the catalyst-bound Breslow intermediate,[5,6] and expansion of the scope of the electrophilic reaction partners[7] to include electron-deficient olefins,[8] imines,[9] disulfides,[10] and aryl fluorides.[11]

In the context of our studies on the selective synthesis of natural products with α-keto tertiary alcohols, such as eucomol (**1**),[12] we recently reported the viability of benzoin cyclizations of ketoaldehydes with thiazolium catalysts, thus affording the desired structure under mild conditions.[13] With the hope of opening an enantioselective access to these and other natural products, we were attracted to chiral, non-racemic azolium salts as precatalysts for this synthetically valuable process.[14] Enders et al. reported chiral triazolium salts for intramolecular Stetter reactions[15] and, in an impressive advance, the utility of chiral triazolium salt **6** as a precatalyst for enantioselective intermolecular benzoin homodimerizations.[16] Contemporaneously, Rovis and co-workers developed a class of triazolium salts derived from amino alcohols and documented their remarkable application to highly diastereo- and enantioselective intramolecular Stetter reactions[17] and to catalytic, enantioselective redox esterifications of α,α-dichloroaldehydes.[18]

Although it was initially believed that the intramolecular aldehyde–ketone benzoin[19] reaction was limited to preorganized substrates as a result of competing homobenzoin and intramolecular aldol processes, we[20a] and Enders and Niemeier[20b] recently showed that the thiazolium-catalyzed benzoin cyclization is a general process for the formation of five- and six-membered α-hydroxyketones. Just recently, Enders et al. disclosed a chiral γ-lactam-derived triazolium salt that effects catalytic, enantioselective aldehyde–ketone benzoin cyclizations of three substrate classes in 67–98% *ee*.[21] Prompted by this report, we report herein the use of Rovis' aminoindanol-derived chiral triazolium salts as exceptional catalysts for a highly enantioselective aldehyde–ketone benzoin cyclization of a wide variety of substrates in up to 99% *ee* (Scheme 1).[22]

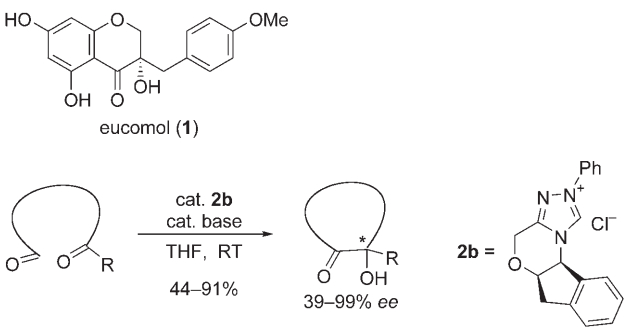

Scheme 1. Catalytic, enantioselective ketoaldehyde benzoin cyclizations.

Our studies began with a survey of the chiral heterocyclic salts for the catalytic cyclization of a model ketoaldehyde **3**, which is readily obtained by the cyclocondensation of an aryl nitrile oxide and 1,3-diketone[23] [Eq. (1)]. Although trials with the enantiomerically pure thiazolium salt **5**[24] were disappointing, significant asymmetric induction was observed with chiral triazolium salts **6**,[16] **7**,[25] **2a**, and **2b**[17c] (Table 1, entries 1–5). Further studies revealed optimal conditions in terms of base (1,8-diazabicyclo[5.4.0]undec-7-ene (DBU),

Table 1: Optimization of the selective benzoin cyclization of **3**.[a]

Entry	Cat. (mol%)	Base (mol%)	*t* [h]	Yield [%]	*ee* [%]
1[b]	**5** (10)	DBU (10)	4	24	58 (*S*)
2	**6** (40)	KO*t*Bu (40)	44	13	98 (*R*)
3	**7** (10)	KO*t*Bu (10)	6.5	86	87 (*R*)
4	**2a** (10)	KO*t*Bu (10)	8	28	99 (*R*)
5	**2b** (10)	KO*t*Bu (10)	8	44	99 (*R*)
6	**2b** (10)	NEt_3 (10)	24	8	99 (*R*)
7	**2b** (10)	DBU (10)	14.5	87	99 (*R*)

[a] Unless otherwise indicated, all reactions were performed on a 1.0-mmol scale at a concentration of 0.3 M in THF at room temperature; the enantiomeric excess was determined by HPLC analysis on chiralpak AD-H. [b] The reaction was performed in *t*BuOH at 40 °C.

[*] H. Takikawa, Y. Hachisu, Dr. J. W. Bode,[+] Prof. Dr. K. Suzuki
Department of Chemistry
Tokyo Institute of Technology
SORST-JST Agency
2-12-1 O-okayama, Meguro-ku, Tokyo 152-8551 (Japan)
Fax: (+81) 3-5734-2788
E-mail: ksuzuki@chem.titech.ac.jp

[+] Present address:
Department of Chemistry and Biochemistry
University of California
Santa Barbara, CA 93106-9510 (USA)

[**] We thank Prof. Dr. Dieter Enders for the generous donation of catalyst **6**; Banyu Pharmaceutical Co., Ltd. for the gift of (1*S*,2*R*)-1-amino-2-indanol; and Dr. Hidehiro Uekusa and Sachiyo Kubo for the X-ray analysis. This study was partially supported by the 21st Century COE program (Tokyo Institute of Technology), Grants-in-Aid for Scientific Research (JSPS), and Research Fellowships for Young Scientists (from JSPS to H.T.).

Supporting information for this article is available on the WWW under http://www.angewandte.org or from the author.

InterScience
© 2006 Wiley-VCH Verlag GmbH & Co. KGaA, Weinheim

entries 5–7), which led to product formation in high yield and with 99% *ee* in favor of the *R* enantiomer.[26]

A substrate screen revealed the broad substrate scope of the reaction. Various ketoaldehydes underwent highly enantioselective cyclization under the catalytic conditions (Table 2).[26] Entry 1 shows the reaction of an aliphatic ketoaldehyde **8**, which cyclized with excellent selectivity. Alkyl aryl ketoaldehydes **9** and **10** are also viable substrates. The selectivity was excellent for six-membered ring formation (entry 2), whereas the selectivity was substantially lower for five-membered ring formation (entry 3).

Biaryl ketoaldehydes (entries 4–6) proved to be good substrates for the enantioselective cyclizations, but careful studies on the absolute configuration of the products revealed that the facial selectivity was opposite to that observed for all other substrate classes. The origin of this unexpected reversal is under investigation, but may be due to changes in the enol geometry of the Breslow intermediate. The enantiomeric excess varied according to the size of the substituent at the ketone moiety, thus giving 39% *ee* (*S*) for the methyl ketone, 90% *ee* (*S*) for the ethyl ketone, and 85% *ee* (*S*) for the isopropyl ketone (entries 4–6, respectively).

In anticipation of the application of the Rovis catalysts to the synthesis of complex anthraquinoid and naphthoquinoid structures, we were pleased to find that isoxazole substrates **14** and **15** cyclized in good yield and with high enantioselectivity (entries 7 and 8). Further studies on the application of this process to the synthesis of natural products are ongoing.

Table 2: Enantioselective cyclization of ketoaldehydes.[a]

Entry	Keto aldehyde		Products		*t* [h]	Yield [%]	*ee* [%]
1[b]	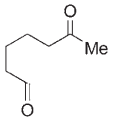	**8**		**16**	24	44	96
2	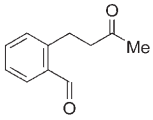	**9**	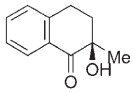	**17**	7	70	96
3[c]	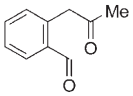	**10**	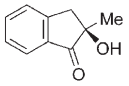	**18**	0.5	69	60
4[d]	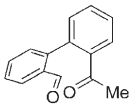	**11**	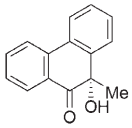	**19**	15	73[e]	39
5	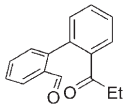	**12**	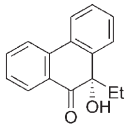	**20**	18	47[e]	90
6	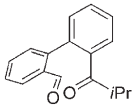	**13**	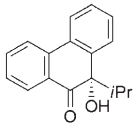	**21**	19	74[e]	85
7[d]	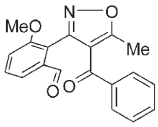	**14**	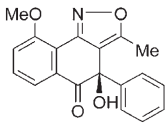	**22**	6	91	98
8[f]	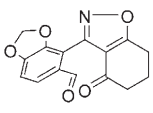	**15**	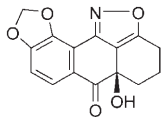	**23**	19	73	99

[a] Unless otherwise indicated, all reactions were performed with 20 mol% **2b** and 20 mol% DBU in THF at room temperature; the enantiomeric excess was determined by HPLC analysis on chiralpak AD-H or chiralcel OD-H; the absolute configuration was confirmed by X-ray analysis of the corresponding (*S*)-camphanyl esters.[26] [b] The corresponding homobenzoin product was obtained (28%); the enantiomeric excess of **16** was determined by GC analysis on a chrompak chirasil-dex CB. [c] The reaction was performed with 25 mol% **2b** and 20 mol% KO*t*Bu. [d] The reaction was performed with 10 mol% **2b** and 20 mol% DBU. [e] The corresponding intramolecular aldol products were also obtained (entry 4: 18%, entry 5: 37%, entry 6: 8%). [f] The reaction was performed with 40 mol% **2b** and 40 mol% DBU; the crude product was acetylated prior to analysis.

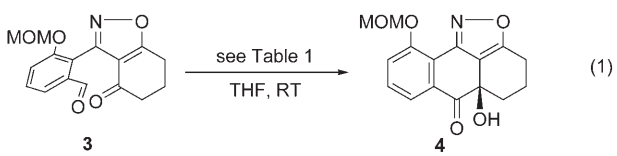

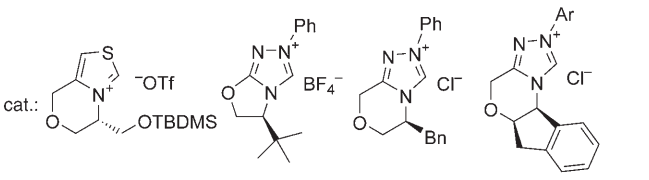

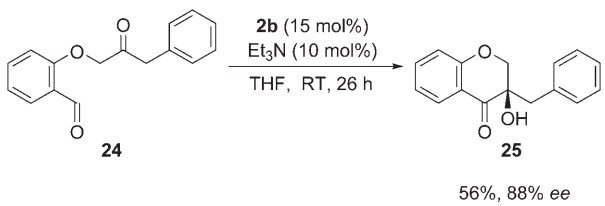

Scheme 2. Enantioselective synthesis of the eucomol core.

Scheme 2 shows the application of this approach to the asymmetric synthesis of 4-chromanones, a key structural

© 2006 Wiley-VCH Verlag GmbH & Co. KGaA, Weinheim

motif in natural products, including (−)-eucomol (**1**). In addition to providing a concise entry to this interesting class of natural products, the successful enantioselective cyclization of readily enolizable ketone **24** demonstrated the uniquely mild reaction conditions for enantioselective carbon–carbon bond formation.

Received: August 17, 2004
Revised: January 21, 2006
Published online: April 25, 2006

Keywords: asymmetric synthesis · C—C coupling · cyclization · N-heterocyclic carbenes · tertiary alcohols

[1] M. Pohl, B. Lingen, M. Müller, *Chem. Eur. J.* **2002**, *8*, 5289 – 5295.
[2] "The benzoin and related acyl anion equivalent reactions": A. Hassner, K. M. L. Rai in *Comprehensive Organic Synthesis, Vol. 1* (Eds.: B. M. Trost, I. Fleming), Pergamon, Oxford, **1991**, pp. 541 – 577.
[3] For the development of crossed benzoin-type reactions of acyl silanes and aldehydes, see: a) X. Linghu, J. S. Johnson, *Angew. Chem.* **2003**, *115*, 2638 – 2640; *Angew. Chem. Int. Ed.* **2003**, *42*, 2534 – 2536; b) X. Linghu, J. R. Potnick, J. S. Johnson, *J. Am. Chem. Soc.* **2004**, *126*, 3070 – 3071; c) X. Linghu, C. C. Bausch, J. S. Johnson, *J. Am. Chem. Soc.* **2005**, *127*, 1833 – 1840.
[4] The exquisite specificity of enzymes has enabled the development of a highly enantioselective crossed-benzoin reaction that employs 2-substituted benzaldehydes as activated aldehyde precursors: P. Dünkelmann, D. Kolter, A. Nitsche, A. S. Demir, P. Siegert, B. Lingen, M. Puhl, M. Müller, *J. Am. Chem. Soc.* **2002**, *124*, 12084 – 12085.
[5] For the seminal work of Breslow on the mechanism of thiazolium-catalyzed benzoin reactions, see: R. Breslow, *J. Am. Chem. Soc.* **1958**, *80*, 3719 – 3725.
[6] K. Zeitler, *Angew. Chem.* **2005**, *117*, 7674 – 7678; *Angew. Chem. Int. Ed.* **2005**, *44*, 7506 – 7510.
[7] For recent highlights and reviews, see: a) J. S. Johnson, *Angew. Chem.* **2004**, *116*, 1348 – 1350; *Angew. Chem. Int. Ed.* **2004**, *43*, 1326 – 1328; b) D. Enders, T. Balensiefer, *Acc. Chem. Res.* **2004**, *37*, 534 – 541; c) M. Christmann, *Angew. Chem.* **2005**, *117*, 2688 – 2690; *Angew. Chem. Int. Ed.* **2005**, *44*, 2632 – 2634.
[8] H. Stetter, H. Kuhlmann, *Org. React.* **1991**, *40*, 407 – 496.
[9] a) J. A. Murry, D. E. Frantz, A. Soheili, R. Tillyer, E. J. J. Grabowski, P. J. Reider, *J. Am. Chem. Soc.* **2001**, *123*, 9696 – 9697; b) for an enantioselective variant, see: S. M. Mennen, J. D. Gipson, Y. R. Kim, S. J. Miller, *J. Am. Chem. Soc.* **2005**, *127*, 1654 – 1655.
[10] W. H. Rastetter, J. Adams, J. W. Frost, L. J. Nummy, J. E. Frommer, K. B. Roberts, *J. Am. Chem. Soc.* **1979**, *101*, 2752 – 2753.
[11] Y. Suzuki, T. Toyota, F. Imada, M. Sato, A. Miyashita, *Chem. Commun.* **2003**, 1314 – 1315.
[12] a) C. Tamm, *Fortschr. Chem. Org. Naturst.* **1981**, *40*, 105 – 152; b) F. A. Davis, M. C. Weismiller, *J. Org. Chem.* **1990**, *55*, 3715 – 3717; c) S.-S. Jew, H.-A. Kim, J.-H. Kim, H.-G. Park, *Heterocycles* **1997**, *46*, 65 – 70.
[13] Y. Hachisu, J. W. Bode, K. Suzuki, *J. Am. Chem. Soc.* **2003**, *125*, 8432 – 8433.
[14] For pioneering studies on catalytic, asymmetric benzoin reactions with chiral thiazolilum salts, see: J. C. Sheehan, D. H. Hunneman, *J. Am. Chem. Soc.* **1966**, *88*, 3666 – 3667.
[15] D. Enders, K. Breuer, J. Runsink, J. H. Teles, *Helv. Chim. Acta.* **1996**, *79*, 1899 – 1902.
[16] D. Enders, U. Kallfass, *Angew. Chem.* **2002**, *114*, 1822 – 1824; *Angew. Chem. Int. Ed.* **2002**, *41*, 1743 – 1745.
[17] a) M. S. Kerr, J. Read de Alaniz, T. Rovis, *J. Am. Chem. Soc.* **2002**, *124*, 10298 – 10299; b) M. S. Kerr, T. Rovis, *Synlett* **2003**, *12*, 1934 – 1936; c) M. S. Kerr, T. Rovis, *J. Am. Chem. Soc.* **2004**, *126*, 8876 – 8877; d) J. Read de Alaniz, T. Rovis, *J. Am. Chem. Soc.* **2005**, *127*, 6284 – 6289; e) M. S. Kerr, J. Read de Alaniz, T. Rovis, *J. Org. Chem.* **2005**, *70*, 5725 – 5728.
[18] N. T. Reynolds, T. Rovis, *J. Am. Chem. Soc.* **2005**, *127*, 16406 – 16407.
[19] Although the resulting products are more appropriately labeled acyloins rather than benzoins, we have adopted the term benzoin reaction as a general rubric for the nucleophilic addition of aldehydes to carbonyl compounds by the transient intermediacy of an acyl anion equivalent. Although imperfect, this nomenclature avoids confusion with the acyloin reaction, a fundamentally different process that affords otherwise identical products.
[20] a) Y. Hachisu, J. W. Bode, K. Suzuki, *Adv. Synth. Catal.* **2004**, *346*, 1097 – 1100; b) D. Enders, O. Niemeier, *Synlett* **2004**, 2111 – 2114.
[21] D. Enders, O. Niemeier, T. Balensiefer, *Angew. Chem.* **2006**, *118*, 1491 – 1495; *Angew. Chem. Int. Ed.* **2006**, *45*, 1463 – 1467.
[22] This work was presented in full at the Pacifichem Conference 2005 in Honolulu, Hawaii, USA, December 20, **2005** and the 85th CSJ Spring Meeting in Kanagawa University, Japan, March 26, **2005**.
[23] For the preparation of the ketoaldehyde substrates, see: a) J. W. Bode, Y. Hachisu, T. Matsuura, K. Suzuki, *Tetrahedron Lett.* **2003**, *44*, 3555 – 3558; b) J. W. Bode, K. Suzuki, *Tetrahedron Lett.* **2003**, *44*, 3559 – 3563; c) T. Matsuura, J. W. Bode, Y. Hachisu, K. Suzuki, *Synlett* **2003**, *11*, 1746 – 1748.
[24] R. L. Knight, F. J. Leeper, *Tetrahedron Lett.* **1997**, *38*, 3611 – 3614.
[25] R. L. Knight, F. J. Leeper, *J. Chem. Soc. Perkin Trans. 1* **1998**, 1891 – 1893.
[26] The absolute configurations of the tertiary alcohols were confirmed by X-ray analysis of the derived (*S*)-camphanyl esters following studies to confirm the chiral integrity of benzoin products under the esterification conditions (see the Supporting Information for details).

 © 2006 Wiley-VCH Verlag GmbH & Co. KGaA, Weinheim

Oxidation

DOI: 10.1002/anie.200600588

Alcohols in Isonitrile-Based Multicomponent Reaction: Passerini Reaction of Alcohols in the Presence of *O*-Iodoxybenzoic Acid**

*Tifelle Ngouansavanh and Jieping Zhu**

In memory of Pierre Potier

The carbonyl compound is one of the most important reactants in isonitrile-based multicomponent reactions (MCRs) because of the pronounced reactivity of the divalent isonitrile carbon atom towards the C(sp^2) electrophilic center.[1] A prominent example is the Passerini reaction (P-3CR),[2] which produces α-acyloxy carboxamide **1** in one pot from aldehyde **2**, isonitrile **3**, and carboxylic acid **4** [Scheme 1, Eq. (1)]. Together with the Ugi four-component reaction (U-4CR),[3] which involves **2**, **3**, **4**, and an amine to lead to an α-acylamino amide, these reactions have been the subject of

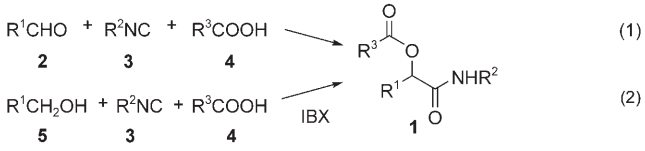

Scheme 1. Alcohols in the Passerini reaction.

intensive research over recent decades. Through the application of these MCRs, many different scaffolds are now readily accessible, as shown in a large collection of examples.[4] Aside from the commercially available aldehydes, most of the in-house-prepared carbonyl compounds are obtained by oxidation of the corresponding alcohols. It is evident that the direct use of alcohols would significantly increase the versatility and overall synthetic efficiency of these MCRs, which would be particularly true when the aldehydes are unstable or difficult to handle. Although a few tandem processes initiated by an oxidation reaction have been developed,[5] an isonitrile-based MCR of alcohols under oxidative conditions is, to the best of our knowledge, unknown. We report herein the first examples of P-3CR mediated by *O*-iodoxybenzoic acid (IBX) with alcohol **5** as one of the reaction partners[6] [Scheme 1, Eq. (2)].

Though conceptually simple, some intrinsic problems persisted with the projected oxidative Passerini reaction. Indeed, besides the alcohol functionality, the isonitrile group undergoes facile α-addition with both the nucleophile and electrophile and is readily oxidized on going from a divalent to tetravalent carbon atom. Furthermore, putative intermediates such as **6**, **7**, and **8** of the P-3CR (Scheme 2) contain

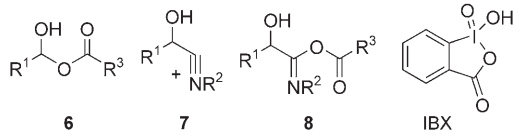

Scheme 2. Putative intermediates of the Passerini reaction.

functional groups that can also be oxidized, thus interrupting the desired reaction sequence. Following the pioneering work of Taylor et al. on the MnO_2-promoted oxidative tandem processes,[5] we initially examined the reaction of benzyl alcohol (**5a**, R^1 = Ph), acetic acid (**4a**, R^3 = Me), and *tert*-butylisonitrile (**3a**, R^2 = *t*Bu) with MnO_2 as the oxidant. The reaction indeed occurred in CH_2Cl_2 to afford the Passerini adduct **1a** (R^1 = Ph, R^2 = *t*Bu, R^3 = Me) in 33% yield after prolonged stirring at 40 °C. However, these conditions turned out to be limited in scope as no reaction occurred when 2-phenylethanol (**5b**) was used, even under forcing conditions. The failure of MnO_2 to oxidize unactivated alcohols is, nevertheless, not unexpected.[7]

We next examined IBX as the oxidant using nonactivated alcohol **5b**, benzoic acid (**4b**), and **3c** as test substrates (Scheme 3).[8–10] In light of the observation of More and Finney that IBX is an effective oxidant in solvents other than

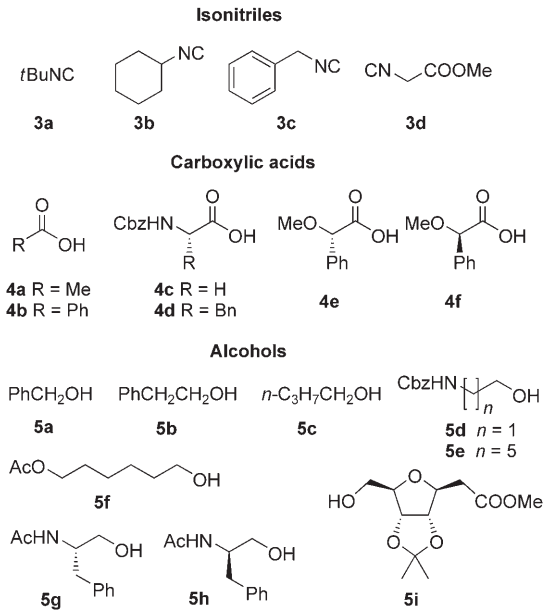

Scheme 3. Structures of the starting materials. Cbz = phenylmethoxycarbonyl.

[*] T. Ngouansavanh, Dr. J. Zhu
Institut de Chimie des Substances Naturelles
CNRS
91198 Gif-sur-Yvette Cedex (France)
Fax: (+33) 1-6907-7247
E-mail: zhu@icsn.cnrs-gif.fr

[**] Financial support from the CNRS and the Institut de Chimie des Substances Naturelles is gratefully acknowledged. We thank Dr. A. Plant of (Syngenta) and Professor R.J.K. Taylor (York University, UK) for fruitful discussions.

Supporting information for this article is available on the WWW under http://www.angewandte.org or from the author.

© 2006 Wiley-VCH Verlag GmbH & Co. KGaA, Weinheim

dimethyl sulfoxide (DMSO),[11] conditions for the oxidative P-3CR were screened in common organic solvents that are known to be good reaction media for the P-3CR (Table 1).[12] As seen, 2-phenylethanol (**5b**) effectively participated in the

Table 1: IBX-promoted oxidative Passerini reaction: a survey of the reaction conditions.[a]

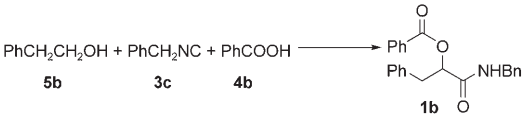

Entry	Solvent	*T* [°C]	*t* [h]	Yield [%] of **1b**[b]
1	CH_2Cl_2	40	5.5	64
2	Et_2O	40	24	49
3	toluene	40	7	55
4	THF	40	24	93
5	THF	60	6	57
6	DCE	40	6	63
7	EtOAc	40	48	51
8	MeCN	40	25	58

[a] General conditions: **3c**/**5b**/**4b**/IBX = 1:1.5:1.5:2.0, concentration = 0.5 M. [b] Yields refer to pure isolated compound after chromatography on silica gel.

P-3CR in the presence of IBX in a variety of solvents, including dichloromethane, diethyl ether, toluene, dichloroethane (DCE), ethyl acetate, and acetonitrile, while THF is the solvent of choice (entries 4 and 5). Control experiments indicated that oxidative polymerization of THF remained minimal at temperatures below 40 °C[13] and that the isonitrile is stable upon exposure to IBX in THF. It is worth noting that IBX is poorly soluble in THF and, consequently, the oxidative P-3CR was realized under heterogeneous conditions. Excess of IBX, as well as its reduced form iodosobenzoic acid (IBA), were removed by a simple filtration through a short pad of celite.

Using IBX as the oxidant and THF as the solvent, the scope of this oxidative Passerini reaction was examined with nine representative alcohols, four isonitriles, and six carboxylic acids (Scheme 3). The α-acyloxy carboxamides **1** synthesized by this protocol are given in scheme 4. In all cases, the Passerini adducts were obtained in good-to-excellent yields except for benzyl alcohol. This is not unexpected as the same compounds **1a** and **1c** were obtained in low yields from benzaldehyde under classic Passerini conditions.[14] Functionalized isonitriles, such as α-isocyano acetate **3d**, participated in the reaction without event to afford **1f** in 62 % yield. When chiral *N*-acetyl α-amino alcohol **5g** or its antipode **5h** were used, two diastereomers were produced in a ratio of 1:1.5. Chiral HPLC analysis of two pairs of enantiomers **1q**/**1s** and **1r**/**1t** indicated that little, if any, racemization occurred. Similarly, the reaction proceeded without racemization when chiral *N*-Cbz-phenylalanine (**4d**) or mandelic acid derivatives **4e** and **4f** were used as the acid components. Glucofuranose derivative **5i** was a stringent test of our protocol, as the corresponding aldehyde is known to be unstable.[15] To our delight, **5i** was converted under our oxidative conditions into the corresponding α-acyloxy carboxamide **1u** as a mixture of

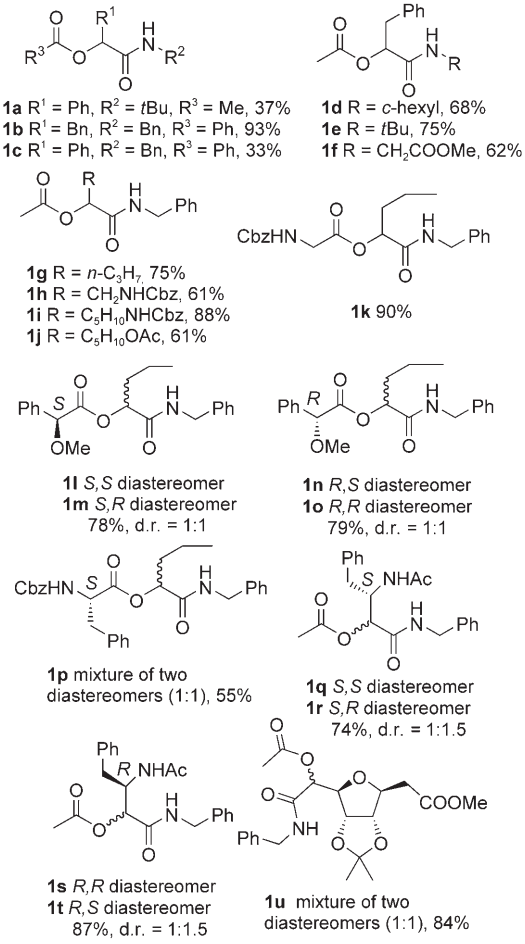

Scheme 4. Structures of α-acyloxy amides.

two diastereomers in 84 % yield. This result clearly indicated the advantage of the present one-pot domino oxidation/P-3CR process relative to the classic two-step sequence. Intrinsic to P-3CR, the diastereoselectivity of these oxidative P-3CRs involving chiral starting materials remained low.[16,17]

In conclusion, we have documented for the first time that an alcohol is an effective reaction partner in the Passerini reaction in the presence of IBX and demonstrated the utility of such a process when the corresponding aldehyde is unstable. In view of the large number of known isonitrile-based MCRs, the possibility of performing these reactions with an alcohol instead of an aldehyde should broaden the scope and versatility of these already powerful reactions tremendously. Work is in progress to extend this concept to other MCRs and will be reported in due course.[18]

Received: February 14, 2006
Published online: April 25, 2006

Keywords: isonitriles · multicomponent reaction · *O*-iodoxybenzoic acid · oxidation · Passerini reaction

[1] *Multicomponent Reaction* (Eds.: J. Zhu, H. Bienaymé), Wiley-VCH, Weinheim, **2005**.

 © 2006 Wiley-VCH Verlag GmbH & Co. KGaA, Weinheim

[2] a) M. Passerini, *Gazz. Chim. Ital.* **1921**, *51*, 126 – 129; b) M. Passerini, *Gazz. Chim. Ital.* **1922**, *52*, 432 – 435; for an excellent review, see: c) L. Banfi, R. Riva in *Org. React.*, *Vol. 65* (Ed.: A. B. Charette), Wiley, **2005**, pp. 1 – 140.
[3] A. Dömling, I. Ugi, *Angew. Chem.* **2000**, *112*, 3301 – 3344; *Angew. Chem. Int. Ed.* **2000**, *39*, 3168 – 3210.
[4] a) C. Hulme, V. Gore, *Curr. Med. Chem.* **2003**, *10*, 51 – 80; b) R. V. A. Orru, M. De Greef, *Synthesis* **2003**, 1471 – 1499; c) J. Zhu, *Eur. J. Org. Chem.* **2003**, 1133 – 1144; d) A. Dömling, *Chem. Rev.* **2006**, *106*, 17 – 89.
[5] For a recent overview, see: R. J. K. Taylor, M. Reid, J. Foot, S. A. Raw, *Acc. Chem. Res.* **2005**, *38*, 851 – 869.
[6] For a highlight on the recent applications of IBX, see: T. Wirth, *Angew. Chem.* **2001**, *113*, 2893 – 2895; *Angew. Chem. Int. Ed.* **2001**, *40*, 2812 – 2814.
[7] MnO_2 can oxidize unactivated alcohol when it is performed in the presence of Wittig reagent; see: L. Blackburn, X. Wei, R. J. K. Taylor, *Chem. Commun.* **1999**, 1337 – 1338.
[8] For the oxidation of alcohols, see: M. Frigerio, M. Santagostino, S. Sputore, G. Palmisano, *J. Org. Chem.* **1995**, *60*, 7272 – 7276.
[9] For other applications of IBX, see: a) K. C. Nicolaou, Y. L. Zhong, P. S. Baran, *Angew. Chem.* **2000**, *112*, 636 – 639; *Angew. Chem. Int. Ed.* **2000**, *39*, 625 – 628; b) K. C. Nicolaou, P. S. Baran, R. Kranich, Y. L. Zhong, K. Sugita, N. Zou, *Angew. Chem.* **2001**, *113*, 208 – 212; *Angew. Chem. Int. Ed.* **2001**, *40*, 202 – 206; c) R. Mazitschek, M. Mülbaier, A. Giannis, *Angew. Chem.* **2002**, *114*, 4216 – 4218; *Angew. Chem. Int. Ed.* **2002**, *41*, 4059 – 4061; d) K. C. Nicolaou, C. J. N. Mathison, T. Montagnon, *J. Am. Chem. Soc.* **2004**, *126*, 5192 – 5201, and references therein.
[10] For tandem oxidation/Wittig reactions initiated by Dess–Martin periodinane (DMP) or IBX, see: a) C. C. Huang, *J. Labelled Compd. Radiopharm.* **1987**, *24*, 676 – 681; b) A. G. M. Barrett, D. Hamprecht, M. Ohkubo, *J. Org. Chem.* **1997**, *62*, 9376 – 9378; c) D. Crich, X. S. Mo, *Synlett* **1999**, 67 – 68.
[11] J. D. More, N. S. Finney, *Org. Lett.* **2002**, *4*, 3001 – 3003.
[12] IBX used in this study was synthesized according to M. Frigerio, M. Santagostino, S. Sputore, *J. Org. Chem.* **1999**, *64*, 4537 – 4538; **Caution**! IBX, like other hypervalent iodine oxidants, can explode on impact or heating; see: J. B. Plumb, D. J. Harper, *Chem. Eng. News* **1990**, *68*(29), 3 – 3.
[13] IBX is able to oxidize THF at elevated temperatures (80 °C and above); see references [9b] and [11].
[14] M. Passerini, *Gazz. Chim. Ital.* **1921**, *51*(II), 181 – 188.
[15] Oxidation of **5i** with IBX (in THF or DMSO) or under Swern conditions led only to the decomposition of the starting material.
[16] For a few diastereoselective P-3CRs, see: a) S. Marcaccini, D. Miguel, T. Torroba, M. Garcia-Valverde, *J. Org. Chem.* **2003**, *68*, 3315 – 3318; b) R. Frey, S. G. Galbraith, S. Guelfi, C. Lamberth, M. Zeller, *Synlett* **2003**, 1536 – 1538; c) G. Cuny, R. Gámez-Montaño, J. Zhu, *Tetrahedron* **2004**, *60*, 4879 – 4885.
[17] For enantioselective P-3CRs, see: a) S. E. Denmark, Y. Fan, *J. Am. Chem. Soc.* **2003**, *125*, 7825 – 7827; b) U. Kusebauch, B. Beck, K. Messer, E. Herdtweck, A. Dömling, *Org. Lett.* **2003**, *5*, 4021 – 4024; c) P. R. Andreana, C. C. Liu, S. L. Schreiber, *Org. Lett.* **2004**, *6*, 4231 – 4233.
[18] Experimental procedures, product characterization, and ^1H and ^{13}C NMR spectra of **1a**–**1u** are provided in the Supporting Information.

 © 2006 Wiley-VCH Verlag GmbH & Co. KGaA, Weinheim

Microporous Materials

DOI: 10.1002/anie.200504128

Hydrothermal Chemistry of the Copper–Triazolate System: A Microporous Metal–Organic Framework Constructed from Magnetic $\{Cu_3(\mu_3\text{-}OH)(triazolate)_3\}^{2+}$ Building Blocks, and Related Materials**

*Wayne Ouellette, Ming Hui Yu, Charles J. O'Connor, Douglas Hagrman, and Jon Zubieta**

The significant contemporary interest in metal–organic frameworks reflects their widespread applications in areas as diverse as sensing, gas storage, separation, and catalysis.[1–5] In the specific case of zeolite mimics, the frameworks must be architecturally robust, so that upon removal of the guest molecules, the pore structure is maintained, and the interior volume is fully accessible to sorbate molecules. The most common synthetic strategy for the design of open-framework hybrid materials is the node and spacer approach,[6] which exploits metal ions as sites of attachment for dipodal or multipodal linkers. Stable architectures have also been obtained by using metal clusters, rather than single metal ions as nodes.[7,8]

While multitopic carboxylate and pyridine ligands have been most extensively exploited as linkers,[9] ligands offering alternative tether lengths, charge-balance requirements, or orientations of donor groups may afford advantages in the design of materials. The polyaza heterocycle 1,2,4-triazole (Htrz) is one such ligand, which can bridge metal ions to afford polynuclear complexes and also has a superexchange capacity that is reflected in the unusual magnetic properties of its complexes.[10–17]

As part of our investigation of strategies for the construction of organic–inorganic hybrid materials from molecular building blocks,[18] we have investigated the ligand trz as a component of Cu^{II}–trz coordination cations in the construction of complex bimetallic oxides.[19] The effectiveness of trz as a tridentate bridging group and the facile formation of triangular Cu^{II} clusters of the type $\{Cu_3(\mu_3\text{-}OH)(N{-}N)_3\}$[11] encouraged us to investigate the $\{Cu_3(\mu_3\text{-}OH)(trz)_3\}^{2+}$ cluster as a molecular building block under hydrothermal conditions.

[*] W. Ouellette, D. Hagrman, Prof. J. Zubieta
Department of Chemistry
Syracuse University, Syracuse, NY 13244 (USA)
Fax: (+1) 315-443-4070
E-mail: jazubiet@syr.edu
M. H. Yu, Prof. C. J. O'Connor
Advanced Materials Research Institute
University of New Orleans, New Orleans, LA 70148 (USA)

[**] This work was supported by grants from the National Science Foundation (CHE-0242153) and from the Defense Advanced Research Agency (MDA972-04-0029).

Supporting information for this article is available on the WWW under http://www.angewandte.org or from the author.

© 2006 Wiley-VCH Verlag GmbH & Co. KGaA, Weinheim

The hydrothermal reaction of $CuSO_4 \cdot 5H_2O$, Htrz, and H_2O, in the molar ratio 0.90:1.00:801, at 200 °C for 48 h gave $[Cu^{II}_3(trz)_3(OH)_3(H_2O)_4] \cdot 4.5H_2O$ (**1**·4.5 H_2O), as dark blue crystals in 90 % yield. The deprotonation of Htrz upon its coordination to metal ions, in the absence of strong bases, is not uncommon;[20,21] furthermore, the shift in pKa for Htrz occurs in a manner analogous to that for H_2O to promote deprotonation.[22]

As shown in Figure 1 a, the structure of **1**·4.5 H_2O consists of a 3D metal–organic framework encompassing a considerable solvent accessible volume.[23] The framework is constructed from the linking of trinuclear triangular $\{Cu_3(\mu_3\text{-}OH)(trz)_3(OH)_2(H_2O)_4\}$ building blocks (Figure 1 b) through the N4 atoms of the trz ligands. The coordination environment of the Cu^{II} sites is a "4+2" distorted octahedron: two N donors from trz groups in the cluster, the μ_3-OH^- group, and a N atom from the trz ligand of an adjacent trinuclear cluster define the equatorial plane, and either two H_2O ligands, or an H_2O ligand and an OH^- group occupy the axial positions. The covalent connectivity produces a $\{Cu_3N_6\}$ ring. As illustrated schematically in Figure 1 c, each triangular building block links to six adjacent triangular subunits through six Cu^{II}–N interactions involving the three Cu^{II} ions and the three N4 atoms of the trz groups in each cluster. The connectivity pattern generates channels of approximate dimensions 17 × 13 × 13 Å^3, corresponding to 41.4 % of the unit-cell volume, which are occupied by H_2O molecules of crystallization.

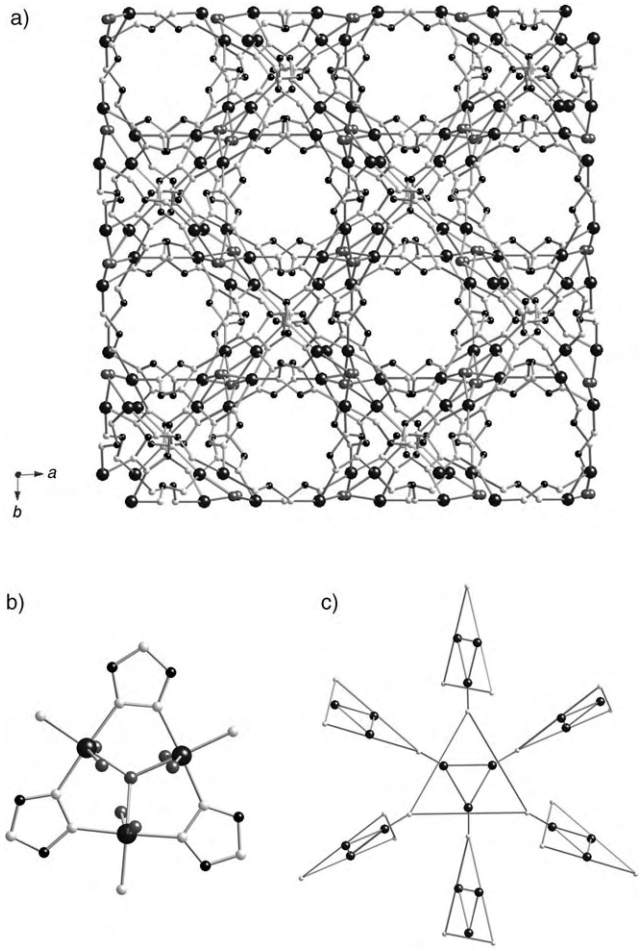

Figure 1. a) A view down the *c* axis of the $\{Cu_3(\mu_3\text{-}OH)(trz)_3\}^{2n+}_n$ framework (coordinated H_2O and terminal OH^- groups omitted for clarity) of **1**·4.5 H_2O. b) The trinuclear $\{Cu_3(\mu_3\text{-}OH)(trz)_3(OH)_2(H_2O)_4\}$ building block of the framework. c) Linking of the trinuclear building blocks (represented by large triangles defined by the N4 atoms of the three trz ligands, which contain smaller triangles defined by the three Cu atoms) in the framework. Cu large black, O dark gray, N light gray, C small black; H atoms omitted for clarity.

The thermogravimetric profile of **1**·4.5 H_2O exhibits a 15 % weight loss between room temperature and 150 °C, which corresponds to the loss of the H_2O molecules of crystallization (see Supporting Information). The coordinated H_2O and the organic components are lost in two steps between 300–340 °C and between 500–620 °C. The green product of the first dehydration step, **1**, reverts to blue upon exposure to moisture. The X-ray thermodiffractograms of **1**·4.5 H_2O reveal no significant structural changes below 300 °C (see Supporting Information), indicating that the framework is maintained upon the first dehydration. Samples of the dehydrated material **1** that have been rehydrated to **1**·4.5 H_2O produce diffraction profiles identical to those of freshly prepared **1**·4.5 H_2O. The temperature dependence of the magnetic susceptibility of **1**·4.5 H_2O, shown in Figure 2, is

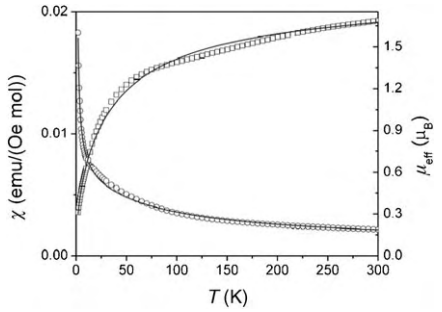

Figure 2. The temperature dependence of the magnetic susceptibility χ (left axis, ○) and the effective magnetic moment μ_{eff} (right axis, □) of **1**·4.5 H_2O. The lines drawn through the data are the fits to the trimer equilateral-triangle model.

consistent with the presence of both intra- and intercluster antiferromagnetic coupling. The effective moment of $\mu_{eff} = 1.68\ \mu_B$ at 300 K for three Cu^{II} ions ($S = 1/2$) is appreciably lower than the theoretical value of $\mu_{eff} = 3.0\ \mu_B$ for three uncoupled $S = 1/2$ spins. The effective moment for **1**·4.5 H_2O at 2 K is $\mu_{eff} = 0.31\ \mu_B$. The best description of the experimental results was obtained using the trimer equilateral-triangle model, which takes intercluster exchange interactions into account.[24–27] The best fit gave values of $J/k_B = -569$ K and $zJ'/k_B = -149$ K, which are consistent with those determined for other $\{Cu^{II}_3(\mu_3\text{-}OH)L_3\}$ cores.[11,12,27]

When CuBr is used in place of $CuSO_4 \cdot 5H_2O$ as the Cu source, the hydrothermal reaction produces $[Cu^{II}_3(trz)_3OH]$-$[Cu^{I}_2Br_4]$ (**2**) as black crystals in 30 % yield. As shown in Figure 3, the cationic substructure $\{Cu_3(\mu_3\text{-}OH)(trz)_3\}^{2n+}_n$ of **2** is the same as the framework found in **1**·4.5 H_2O, but without

 © 2006 Wiley-VCH Verlag GmbH & Co. KGaA, Weinheim

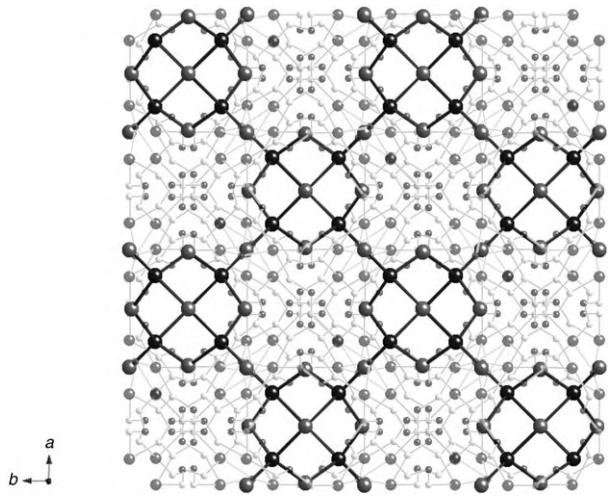

Figure 3. A view down the *c* axis of the structure of **2**; the cationic $\{Cu_3(\mu_3\text{-}OH)(trz)_3\}_n^{2n+}$ framework (Cu large dark gray, O medium gray, N light gray, C small dark gray; H atoms omitted for clarity) contains the anionic $\{CuBr_2\}_n^{n-}$ substructure (highlighted; Cu black, Br dark gray).

the axial OH^- and H_2O ligands.[23] In contrast to **1**·4.5 H_2O, the interframework domain of **2** is occupied by the 3D anionic substructure $\{CuBr_2\}_n^{n-}$, which consists of adamantoid $\{Cu_4Br_6\}^{2-}$ rings, each linked to four adjacent rings by Br^- ions. Consequently, the structure of **2** may be described as being composed of two different and inextricably interpenetrating 3D substructures, the cationic component containing Cu^{II} sites, and the anionic component containing Cu^{I} sites.

The triangular $\{Cu_3(\mu_3\text{-}OH)(trz)_3\}^{2+}$ building blocks of **1**·4.5 H_2O and **2** do not persist when $CuCl_2$·2 H_2O is used as the Cu source in the hydrothermal chemistry. As shown in Figure 4a, the structure of $[Cu^I_3(trz)_2][Cu^I_2(trz)Cl]Cl$·3 H_2O (**3**·3 H_2O) is constructed from layer and chain substructures, both containing Cu^I sites.[23] Within the $\{Cu_3(trz)_2\}_n^{n+}$ layers, shown in Figure 4b, each Cu^I ion is two-coordinate, and each trz ligand bonds to three Cu^I ions to produce a herringbone pattern based on $\{Cu_6(trz)_6\}$ rings. The chain substructure $\{Cu_2(trz)Cl\}_n$, shown in Figure 4c, contains two distinct Cu^I sites. One Cu^I ion is bonded to the N1 and N4 atoms of adjacent trz ligands in the chain. The second Cu^I ion is linked to the remaining N2 atom and to a Cl^- ligand, and projects outward from the chain axis in a pendant geometry. The $\{Cu_3(trz)_2\}_n^{n+}$ layers stack along the *b* axis, while the chains, which run along the *a* axis, occupy the interlamellar domains. The charge-balancing Cl^- ions and the H_2O molecules of crystallization occupy the interlamellar region between adjacent chains.

The Cu–trz system exhibits an unusually rich coordination chemistry based on framework, layer, and chain substructures. Compound **1** exhibits microporous properties, as well as unusual magnetic behavior, while compound **2** demonstrates the robust nature of the $\{Cu_3(\mu_3\text{-}OH)(trz)_3\}_n^{2n+}$ framework, which persists for guests as different as H_2O and $\{CuBr_2\}_n^{n-}$. Compound **3** suggests that the identity of the counterion may dramatically influence the structures of the building blocks in the resulting network.

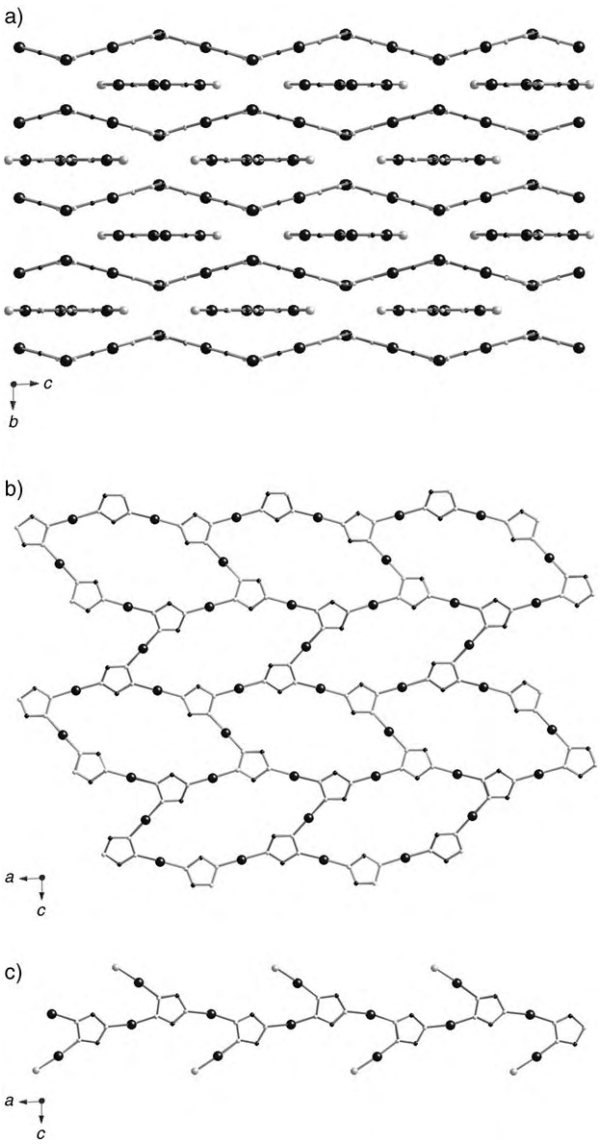

Figure 4. a) A view down the *a* axis of the $\{Cu_3(trz)_2\}_n^{n+}$ and $\{Cu_2(trz)Cl\}_n$ substructures of **3**·3 H_2O. Views down the *b* axis of b) the $\{Cu_3(trz)_2\}_n^{n+}$ layer, and c) the $\{Cu_2(trz)Cl\}_n$ chain. Cu large black, Cl medium gray, N light gray, C small black; H atoms omitted for clarity.

Experimental Section

1·4.5 H_2O: A solution of $CuSO_4$·5 H_2O (0.163 g, 0.628 mmol), Htrz (0.048 g, 0.694 mmol), and H_2O (10.00 g, 556 mmol), in the molar ratio 0.90:1.00:801, was stirred briefly before heating at 200 °C for 48 h. Blue crystals of **1**·4.5 H_2O, suitable for X-ray diffraction, were isolated in 90 % yield. IR (KBr pellet): $\tilde{\nu}$ = 3479 (b), 3142 (w), 1629 (m), 1515 (s), 1298 (m), 1170 (s), 1104 (s), 1000 (w), 881 (m), 663 (m), 617 cm^{-1} (m); elemental analysis (%) calcd for $C_6H_{26}Cu_3N_9O_{11.5}$: C 12.0, H 4.34, N 21.0; found: C 11.7, H 4.22, N 20.2.

2: A mixture of CuBr (0.081 g, 5.58 mmol), Htrz (0.205 g, 2.97 mmol), and H_2O (10.00 g, 556 mmol), in the molar ratio 1.88:1.00:187, was heated at 180 °C for 48 h. IR (KBr pellet): $\tilde{\nu}$ = 3447 (b), 3132 (v), 1507 (s), 1288 (s), 1171 (m), 1035 (s), 988 (m), 861 (m), 652 cm^{-1} (m); elemental analysis (%) calcd for $C_6H_7Br_4Cu_5N_9O$: C 8.42, H 0.82, N 14.7; found: C 7.95, H 0.66, N 14.2.

3·3 H_2O: A mixture of $CuCl_2$·2 H_2O (0.283 g, 1.66 mmol), Htrz (0.233 g, 3.373 mmol), and H_2O (10.00 g, 556 mmol), in the molar

 © 2006 Wiley-VCH Verlag GmbH & Co. KGaA, Weinheim

ratio 0.49:1.00:165, was heated at 200 °C for 48 h. IR (KBr pellet): $\tilde{\nu}$ = 3435 (b), 3111 (v), 1507 (m), 1278 (s), 1156 (s), 1075 (m), 988 (m), 861 (w), 657 cm^{-1} (m); elemental analysis calcd for $C_6H_{12}Cl_2Cu_5N_9O_3$: C 11.1, H 1.86, N 19.5; found C 11.0, H 1.69, N 19.1.

Magnetic measurements: The temperature-dependent magnetic data were recorded for a 54.8-mg polycrystalline sample in the 2–300 K temperature range under an applied magnetic field of H = 1000 Oe, using a Quantum Design MPMS-5S SQUID magnetometer. Full details may be found in reference [25].

Received: November 19, 2005
Revised: February 15, 2006
Published online: April 20, 2006

Keywords: copper · hydrothermal synthesis · magnetic properties · microporous materials · N ligands

[1] J. F. Eubank, R. D. Walsh, M. Eddaoudi, *Chem. Commun.* **2005**, 2095–2097, and references therein.
[2] O. Ohmori, M. Kawano, M. Fujita, *Angew. Chem.* **2005**, *117*, 1998–2000; *Angew. Chem. Int. Ed.* **2005**, *44*, 1962–1964.
[3] C.-D. Wu, W. Lin, *Angew. Chem.* **2005**, *117*, 1994–1997; *Angew. Chem. Int. Ed.* **2005**, *44*, 1958–1961.
[4] A. C. Sudhik, A. R. Millward, N. W. Ockwig, A. P. Côté, J. Kim, O. M. Yaghi, *J. Am. Chem. Soc.* **2005**, *127*, 7110–7118.
[5] J. Seo, D. Whang, H. Lee, S. Jun, J. Oh, Y. Jeon, K. Kim, *Nature* **2000**, *404*, 982–986.
[6] A. Erxleben, *Coord Chem. Rev.* **2003**, *246*, 203–228, and references therein.
[7] M. Eddaoudi, J. Kim, N. Rose, D. Vodak, J. Wachter, M. O'Keeffe, O. M. Yaghi, *Science* **2002**, *295*, 469–472, and references therein.
[8] O. M. Yaghi, M. O'Keeffe, N. W. Ockwig, H. K. Chae, M. Eddaoudi, J. Kim, *Nature* **2003**, *423*, 705–714.
[9] The literature on organic–inorganic hybrid materials is voluminous. Some recent reviews and representative articles include: a) S. Kitagawa, S. Noro in *Comprehensive Coordination Chemistry II*, *Vol. 7* (Eds. J. A. McCleverty, T. J. Meyer), Elsevier, Amsterdam, **2003**, pp. 231–261; b) C. N. R. Rao, S. Natarajan, R. Vaidhyanathan, *Angew. Chem.* **2004**, *116*, 1490–1521; *Angew. Chem. Int. Ed.* **2004**, *43*, 1466–1496; c) O. M. Yaghi, M. O'Keeffe, N. W. Ockwig, H. K. Chae, M. Eddaoudi, J. Kim, *Nature* **2003**, *423*, 705–714; d) J. Y. Lu, *Coord. Chem. Rev.* **2003**, *241*, 327–347; e) S. L. James, *Chem. Soc. Rev.* **2003**, *32*, 276–288.
[10] M. H. Klingale, S. Brooker, *Coord. Chem. Rev.* **2003**, *241*, 119–132.
[11] U. Beckman, S. Brooker, *Coord. Chem. Rev.* **2003**, *245*, 17–29.
[12] J. G. Haasnoot, *Coord. Chem. Rev.* **2000**, *200–202*, 131–185.
[13] O. Kahn, C. J. Martinez, *Science* **1998**, *279*, 44–48, and references therein.
[14] J.-P. Zhang, Y.-Y. Lin, X.-C. Huang, X.-M. Chen, *J. Am. Chem. Soc.* **2005**, *127*, 5495–5506.
[15] J.-P. Zhang, S. L. Zhang, X.-C. Huang, X.-M. Chen, *Angew. Chem.* **2004**, *43*, 208–211; *Angew. Chem. Int. Ed.* **2004**, *43*, 206–209.
[16] S. Ferrer, F. Lloret, I. Bertomeu, G. Alzuet, J. Borrás, S. García-Granda, M. Liu-González, J. G. Haasnoot, *Inorg. Chem.* **2002**, *41*, 5821–5830.
[17] J. P. Zhang, Y.-Y. Lin, W.-X. Zhang, X.-M. Chen, *J. Am. Chem. Soc.* **2005**, *127*, 14162–14163.
[18] E. Burkholder, V. Golub, C. J. O'Connor, J. Zubieta, *Inorg. Chem.* **2004**, *43*, 7014–7029, and references therein.
[19] a) D. Hagrman, J. Zubieta, *Chem. Commun.* **1998**, 2005–2006; b) P. J. Hagrman, C. Bridges, J. E. Greedan, J. Zubieta, *J. Chem. Soc. Dalton Trans.* **1999**, 2901–2903.
[20] G. Yang, R. G. Raptis, *Chem. Commun.* **2004**, 2058–2059.
[21] D. J. Chesnut, A. Kusnetzow, R. Birge, J. Zubieta, *Inorg. Chem.* **1999**, *38*, 5484–5494.
[22] F. H. Sweeton, R. E. Mesmer, C. F. Baes, Jr., *J. Solution Chem.* **1974**, *3*, 191–214.
[23] **1**·4.5 H_2O: $C_6H_{26}Cu_3N_9O_{11.5}$, M_r = 598.98, cubic, $Fd\bar{3}c$, a = 24.7233(4) Å, V = 15111.9(4) $Å^3$, Z = 32, ρ_{calcd} = 2.106 $g\,cm^{-3}$, $R1$ = 0.0317, $wR2$ = 0.0798 (855 reflections, all data). The diffuse disordered H_2O molecules of crystallization were modeled using the SQUEEZE routine of the program PLATON.[28] The μ_3-OH^- group is disordered across the Cu_3 plane. **2**: $C_6H_7Br_4Cu_5N_9O$, M_r = 858.54, cubic, $Fd\bar{3}c$, a = 24.5326(6) Å, V = 14764.9(6) Å, Z = 32, ρ_{calcd} = 3.086 $g\,cm^{-3}$ (ρ_{found} = 3.10 $g\,cm^{-3}$ by flotation), $R1$ = 0.0694, $wR2$ = 0.1630 (690 reflections, all data). The $\{CuBr_2\}_n^{n-}$ subunit is disordered over two sets of sites. **3**: $C_6H_{12}Cl_2Cu_5N_9O_3$, M_r = 646.84, orthorhombic, *Pnma*, a = 11.6389(6), b = 9.9663(5), c = 12.3013(6) Å, V = 1426.9(1) $Å^3$, Z = 4, ρ_{calcd} = 3.670 $g\,cm^{-3}$, $R1$ = 0.0570, $wR2$ = 0.1451 (1787 reflections, all data). The diffuse disordered H_2O of crystallization was modeled using the SQUEEZE routine of the program PLATON.[28] Full experimental details are provided in the Supporting Information. CCDC-289564 (**1**·4.5 H_2O), CCDC-289565 (**2**), and CCDC-289566 (**3**·3 H_2O) contain the supplementary crystallographic data for this paper. These data can be obtained free of charge from The Cambridge Crystallographic Data Centre via www.ccdc.cam.ac.uk/data_request/cif.
[24] The temperature-dependent magnetic data were fit to Equations (1)–(3). The best fit gave g = 2.15, J/k_B = −569 K, zJ'/k_B = −149 K, χ_{TI} = 0.0009 emu Oe^{-1} mol^{-1}, and p = 0.017. The coefficient of determination for the least-squares fitting was R^2 = 0.99925.

$$\chi = (1-p)\chi'_{tri} + p\frac{3N_A g^2 \mu_B^2}{4k_B T} + \chi_{TI} \quad (1)$$

$$\chi'_{tri} = \frac{\chi_{tri}}{1 - 2zJ'\chi_{tri}/N_A g^2 \mu_B^2} \quad (2)$$

$$\chi_{tri} = \frac{N_A g^2 \mu_B^2}{4k_B T}\frac{1 + 5\exp\left(\frac{3J}{k_B T}\right)}{1 + \exp\left(\frac{3J}{k_B T}\right)} \quad (3)$$

[25] C. J. O'Connor, *Prog. Inorg. Chem.* **1982**, *29*, 203–283.
[26] E. Sinn, C. M. Harris, *Coord. Chem. Rev.* **1969**, *4*, 391–422.
[27] T. Chivers, Z. Fu, L. K. Thompson, *Chem. Commun.* **2005**, 2339–2341.
[28] A. L. Spek, *J. Appl. Cryst.* **2003**, *36*, 7–13.

 © 2006 Wiley-VCH Verlag GmbH & Co. KGaA, Weinheim

Hydrogen Storage

DOI: 10.1002/anie.200504202

Facilitated Hydrogen Storage in $NaAlH_4$ Supported on Carbon Nanofibers**

*Cornelis P. Baldé, Bart P. C. Hereijgers, Johannes H. Bitter, and Krijn P. de Jong**

Hydrogen is regarded as a suitable energy carrier for sustainable energy schemes. However, the reversible storage of hydrogen is still a major challenge, especially for mobile applications. Several storage media have been considered, for example, clathrate structures,[1] metal–organic frameworks,[2] and lithium nitride/amide[3,4] as well as physisorption on carbon or zeolites,[5–7] and alanates.[8] Sodium alanate ($NaAlH_4$) is promising because of its high reversible hydrogen storage capacity and optimal thermodynamic stability for reversible hydrogen storage at medium temperatures. Nevertheless, kinetic barriers restrict hydrogen desorption rates. Furthermore, reloading of undoped $NaAlH_4$ is also slow and not possible under practical conditions.[9,10] It has been found that Ti additives improve the kinetics of hydrogen absorption and desorption, but high pressures ($P > 100$ bar) and long times are still needed to reload depleted sodium alanate.[10–13] Further improvement of the kinetics requires new strategies and methods. A possible strategy is to decrease the particle size to the nanometer range, for which it is known that physicochemical properties of such particles may deviate considerably from the bulk properties.[13–17] By using nanosized sodium alanate, the phase segregation to micrometer-sized NaH and Al during hydrogen extraction from these materials will be prevented,[18,19] which might lead to enhanced rates of hydrogen desorption and absorption.

Therefore we prepared, for the proof of the principle, nanosized $NaAlH_4$ particles supported on a surface-oxidized carbon nanofiber support (CNF_{ox}) and investigated their hydrogen desorption and absorption properties in relation to the structural properties of the materials. The $NaAlH_4$ (9 wt %) supported on carbon nanofibers was obtained by impregnation and drying techniques (see the Experimental Section for details) and is referred to here as $NaAlH_4/CNF_{ox}$. A physical mixture of bulk $NaAlH_4$ and CNF_{ox} of identical gross composition was included in the study as a reference sample.

Figure 1 displays the X-ray diffraction (XRD) patterns of CNF, $NaAlH_4/CNF_{ox}$, and the physical mixture prior to hydrogen extraction. The diffractograms of CNF and $NaAlH_4/CNF_{ox}$ are identical. In contrast, the XRD pattern of the physical mixture showed sharp intense diffraction peaks that could be attributed to $NaAlH_4$ and intense broad peaks from the CNF. Thus, the crystallinity of the $NaAlH_4$ changed when impregnated on the support, and the $NaAlH_4$ was most probably present in a highly dispersed and/or amorphous phase, for example, as a thin film or as small particles. After desorption of the hydrogen, typically above 250 °C, the diffractogram of desorbed $NaAlH_4/CNF_{ox}$ only showed the presence of CNF diffraction peaks while the desorbed physical mixture showed intense narrow peaks of crystalline domains of Al and NaH (Figure 1). This observation indicates that in the case of the supported sample the NaH and Al were also present in a highly dispersed or amorphous phase after desorption.

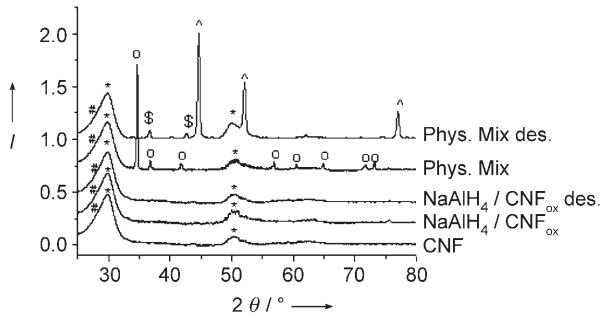

Figure 1. XRD pattern of Phys Mix, $NaAlH_4/CNF_{ox}$ and CNF, measured under a perspex cup. # = perspex, ⋆ = CNF, ○ = $NaAlH_4$, ^ = Al, and $ = NaH. Phys. Mix = physical mixture, des. = after desorption.

To investigate the details of the NaH and Al phases a desorbed sample of $NaAlH_4/CNF_{ox}$ was passivated with O_2 and studied by transmission electron microscopy (TEM). Figure 2 shows a representative bright-field TEM micrograph and scanning transmission electron microscopy energy dis-

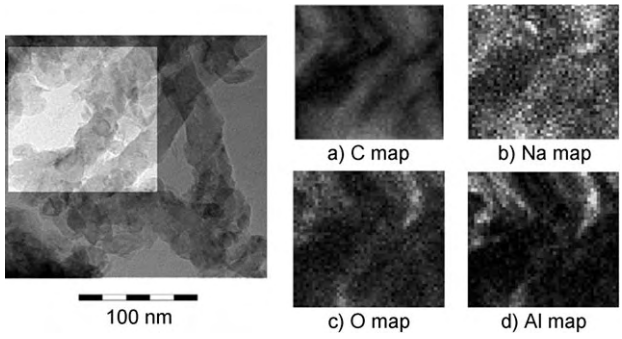

Figure 2. Left: TEM micrograph of "$NaAlH_4/CNF_{ox}$" after complete desorption and O_2 passivation. Right: EDX maps of C, Na, O, and Al of the highlighted region.

[*] Drs. C. P. Baldé, B. P. C. Hereijgers, Dr. J. H. Bitter, Prof. Dr. K. P. de Jong
Department of Chemistry
Group of Inorganic Chemistry and Catalysis
Utrecht University
Sorbonnelaan 16, 3584 CA, Utrecht (The Netherlands)
Fax: (+31) 30-253-7400
E-mail: k.p.dejong@chem.uu.nl

[**] This research was funded by ACTS (project number 053.61.002). We would like to acknowledge Hans Stil from the Shell Research and Technology Centre in Amsterdam for the H_2 absorption experiment. We would also like to thank Cor van der Spek and John Geus for the TEM and STEM studies.

Supporting information for this article is available on the WWW under http://www.angewandte.org or from the author.

 © 2006 Wiley-VCH Verlag GmbH & Co. KGaA, Weinheim

persive analysis by X-rays (STEM-EDX) elemental maps of the highlighted region. The C map in Figure 2a followed the structure of the CNF. It can be seen in Figure 2b that the Na map coincided quite well with the C map, thus indicating that Na was highly dispersed on the fibers. In contrast, the Al was present in distinct areas on the support, which shows that the Al had segregated into nanometer-sized domains (Figure 2d). These observations differ from those obtained with unsupported alanates, where it is known that Na and Al segregate into micrometer-sized domains after desorption.[18,19] It can therefore be concluded that the phase segregation has been limited to the nanometer range in the desorbed $NaAlH_4/CNF_{ox}$. From the size of the Al domains (5–20 nm) observed in Figure 2d, one may expect a detectable XRD pattern. The absence of such a pattern (Figure 1) indicates, in our opinion, that either the Al was amorphous or the average crystallite size was much smaller.

The hydrogen desorption profiles of $NaAlH_4$ samples have been measured by temperature-programmed desorption (TPD). Hydrogen was desorbed by heating a sample to 160 °C at 2 °C min^{-1}, that is, below the melting point of $NaAlH_4$ (180 °C), thereby minimizing possible sintering. The H_2 desorption curves of $NaAlH_4/CNF_{ox}$ and the physical mixture are shown in Figure 3. Quantification of the H_2 released

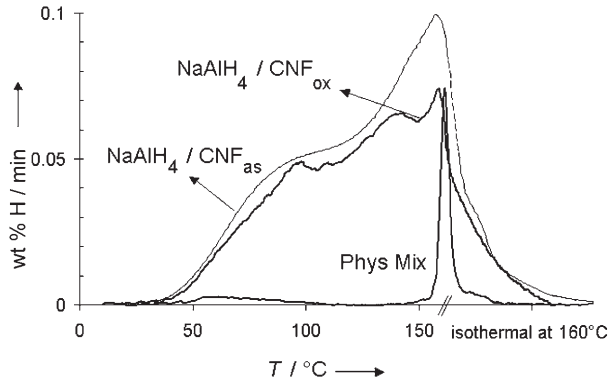

Figure 3. First desorption curve of $NaAlH_4/CNF_{ox}$, $NaAlH_4/CNF_{as}$, and the physical mixture. Heating rate 2 °C min^{-1} to 160 °C.

revealed that 2.9 wt % H_2 was desorbed from $NaAlH_4/CNF_{ox}$ (normalized to the amount of $NaAlH_4$), while only 0.15 wt % H_2 was desorbed from the physical mixture under identical conditions. Moreover, the $NaAlH_4/CNF_{ox}$ released H_2 starting from 40 °C, whereas the physical mixture started from 150 °C. This result clearly illustrates that the desorption kinetics have been significantly improved by using nanosized $NaAlH_4$.

The total hydrogen capacity for $NaAlH_4/CNF_{ox}$ was determined to be 3.6 wt % H_2 (normalized to the amount of $NaAlH_4$) by a temperature-programmed desorption to 300 °C. Since the theoretical hydrogen content is 5.6 wt %, it was concluded that 2 wt % H_2 was lost during the synthesis. To limit the hydrogen loss, $NaAlH_4$ was deposited on non-oxidized CNF (called CNF_{as}). It was found for $NaAlH_4/CNF_{as}$ that the hydrogen desorption capacity was 3.7 wt % H_2 up to 160 °C and 4.8 wt % H_2 for temperatures up to 300 °C. The hydrogen desorption profile is shown in Figure 3 and showed similar features as $NaAlH_4/CNF_{ox}$.

After the desorption step at 160 °C, the $NaAlH_4/CNF_{ox}$ was reloaded for 48 h at $T = 115$ °C and $P_{H_2} = 90$ bar, that is, under typical reloading conditions. The desorption curve (see the Supporting Information) reveals that 0.74 wt % H_2 had been reabsorbed at temperatures lower than 160 °C, which is 26 % of the originally desorbed H_2. Apparently, nanosized $NaAlH_4/CNF_{ox}$ can store hydrogen in a reversible manner under relatively mild conditions without the need for a catalyst, which to the best of our knowledge has never been observed for bulk, undoped alanates.[10–12]

The reversibility in this nanosized $NaAlH_4$ is tentatively attributed to a physical limitation of the phase segregation, which occurs when hydrogen is desorbed. In bulk $NaAlH_4$ phase segregation results in micrometer-sized Al and NaH domains,[18,19] whereas in nanosized $NaAlH_4$ the NaH and Al domains are limited to the nanometer range. Consequently, restoring the $NaAlH_4$ structure in the latter system is facilitated as a result of a decreased solid-state diffusion path length.

In summary, nanosized $NaAlH_4$ displayed improved hydrogen absorption and desorption characteristics compared to bulk alanates. The hydrogen desorption temperature decreased considerably and significant amounts of hydrogen could be desorbed at $T \leq 160$ °C with nanosized $NaAlH_4$. Moreover, reloading of the material was easier compared to bulk material, that is, hydrogen storage became partly reversible. This reversibility was facilitated most likely by the physical limitation of phase segregation when nanosized $NaAlH_4$ was desorbed. The approach, namely, deposition of nanosized clusters on a support material, opens up the possibility to study particle-size effects on kinetic, thermodynamic, and optical properties of complex metal hydrides in general. Nanosized alanates comprise a promising direction for developing a material that meets the requirements needed for the reversible storage of hydrogen.

Experimental Section

All syntheses were carried out by using Schlenk techniques. Handling and storage of the samples was carried out in a glovebox in an inert atmosphere. $NaAlH_4$ (Sigma–Aldrich; 90 % purity) was purified by dissolving it in dried THF and removing the insoluble species by filtration. Crystallization by evaporation of the THF under vacuum led to the isolation of $NaAlH_4$ as a white powder.

The CNF support materials were synthesized by using 5 wt % Ni/SiO_2 growth catalyst with syngas at 550 °C for 12 h as described elsewhere.[20] The growth catalyst (SiO_2 and non-encapsulated Ni) was removed by heating the sample at reflux in 1 M KOH, and in concentrated HNO_3 (CNF_{ox}) or concentrated HCl (CNF_{as}), respectively. Prior to the deposition of $NaAlH_4$, the supports were dried at 200 °C in N_2. Deposition was carried out by incipient wetness impregnation of a solution of $NaAlH_4$ in THF. For CNF_{ox}, the sample was dried in a vacuum to 10 mbar, and around 9 wt % of $NaAlH_4$ was deposited on the CNF_{ox}. For CNF_{as}, the sample was dried at −40 °C in a vacuum and the residual THF was evaporated at 0 °C.

Temperature-programmed desorption (TPD) measurements were performed on an AutoChem II 2920 in an Ar flow of 25 mL min^{-1}. The hydrogen concentration was measured using a calibrated thermal conductivity detector. The hydriding capacity was

 © 2006 Wiley-VCH Verlag GmbH & Co. KGaA, Weinheim

measured using a Sieverts' apparatus purchased from the Hydro-Quebec Company at the Shell Research and Technology Centre. Powder X-ray diffraction (XRD) patterns were obtained at room temperature in an inert atmosphere from $2\theta = 10$–$100°$ with a Philips D-8 setup using $Co_{K\alpha}$ radiation. Transfer of the samples from the glovebox to the instrument was done in a special airtight sample holder. HR-TEM and STEM images were obtained on a Tecnai 20 microscope operating at 200 kV and equipped with an EDX and high-angle annular dark field (HAADF) detector.

Received: November 25, 2005
Published online: April 24, 2006

Keywords: adsorption · hydrides · hydrogen · nanostructures · sodium alanate

[1] H. Lee, J. Lee, D. Y. Kim, J. Park, Y. T. Seo, H. Zeng, I. Moudrakovski, C. I. Ratcliffe, J. A. Ripmeester, *Nature* **2005**, *434*, 743 – 746.
[2] J. L. C. Rowsell, O. M. Yaghi, *Angew. Chem.* **2005**, *117*, 4748 – 4758; *Angew. Chem. Int. Ed.* **2005**, *44*, 4670 – 4679.
[3] P. Chen, Z. T. Xiong, J. Z. Luo, J. Y. Lin, K. L. Tan, *Nature* **2002**, *420*, 302 – 304.
[4] K. Miwa, N. Ohba, S. Towata, Y. Nakamori, S. Orimo, *Phys. Rev. B* **2005**, 71, 195109.
[5] A. Zecchina, S. Borgida, J. G. Vitillo, G. Ricchiardi, C. Lamberti, G. Spoto, M. Bjørgen, K. P. Lillerud, *J. Am. Chem. Soc.* **2005**, *127*, 6361 – 6366.
[6] M. G. Nijkamp, J. E. M. J. Raaymakers, A. J. van Dillen, K. P. de Jong, *Appl. Phys. A* **2001**, 72, 619 – 623.
[7] J. Weitkamp, M. Fritz, S. Ernst, *Int. J. Hydrogen Energy* **1995**, *20*, 967 – 970.
[8] L. Schlapbach, A. Zuttel, *Nature* **2001**, *414*, 353 – 358.
[9] Sodium alanate decomposes upon heating according to the following steps: $NaAlH_4 \leftrightarrow \frac{1}{3}Na_3AlH_6 + \frac{2}{3}Al + H_2$ and $Na_3AlH_6 \leftrightarrow 3\,NaH + Al + 1\frac{1}{2}H_2$. By applying elevated hydrogen pressures $NaAlH_4$ is restored through the reverse reactions.
[10] B. Bogdanovic, M. Schwickardi, *J. Alloys Compd.* **1997**, *253*–254, 1 – 9.
[11] C. M. Jensen, R. Zidan, N. Mariels, A. Hee, C. Hagen, *Int. J. Hydrogen Energy* **1999**, *24*, 461 – 465.
[12] D. Sun, S. S. Srinivasan, T. Kiyobayashi, N. Kuriyama, C. M. Jensen, *J. Phys. Chem. B* **2003**, *107*, 10176 – 10179.
[13] F. Schüth, B. Bogdanivic, A. Taguchi (MPI Mülheim, Germany), patent application WO2005014469.
[14] X. He, D. M. Antonelli, *Angew. Chem.* **2002**, *114*, 222 – 238; *Angew. Chem. Int. Ed.* **2002**, *41*, 214 – 229.
[15] J. D. Aiken, R. G. Finke, *J. Mol. Catal. A* **1999**, *145*, 1 – 44.
[16] A. Gutowska, L. Li, Y. Shin, C. M. Wang, X. S. Li, J. C. Linehan, R. S. Smith, B. D. Kay, B. Schmid, W. Shaw, M. Gutowski, T. Autrey, *Angew. Chem.* **2005**, *117*, 3644 – 3648; *Angew. Chem. Int. Ed.* **2005**, *44*, 3578 – 3582.
[17] R. W. P. Wagemans, J. H. van Lenthe, P. E. de Jongh, A. J. van Dillen, K. P. de Jong, *J. Am. Chem. Soc.* **2005**, *127*, 16675 – 16680.
[18] B. Bogdanovic, R. A. Brand, A. Marjanovic, M. Schwickardi, J. Tolle, *J. Alloys Compd.* **2000**, *302*, 36 – 58.
[19] M. Felderhoff, K. Klementiev, W. Grunert, B. Spliethoff, B. Tesche, J. M. B. von Colbe, B. Bogdanovic, M. Hartel, A. Pommerin, F. Schüth, C. Weidenthaler, *Phys. Chem. Chem. Phys.* **2004**, *6*, 4369 – 4374.
[20] M. L. Toebes, E. M. P. van Heeswijk, J. H. Bitter, A. J. van Dillen, K. P. de Jong, *Carbon* **2004**, *42*, 307 – 315.

 © 2006 Wiley-VCH Verlag GmbH & Co. KGaA, Weinheim

Protecting Groups

DOI: 10.1002/anie.200600153

Introduction of 2,2,2-Trichloroethyl-Protected Sulfates into Monosaccharides with a Sulfuryl Imidazolium Salt and Application to the Synthesis of Sulfated Carbohydrates**

*Laura J. Ingram and Scott D. Taylor**

Sulfated polysaccharides are widespread in nature. These compounds are implicated in a wide variety of important biological processes such as blood clotting, cell adhesion, and cell–cell communication.[1] However, detailed characterization of their specific biological roles has proved very challenging. One reason for this is that the synthesis of even relatively small sulfated oligosaccharides still remains a considerable challenge. The current approach to their synthesis involves first protecting the hydroxy groups in the monosaccharide building blocks. The hydroxy groups that bear the sulfate groups in the final product are protected in a manner orthogonal to those that are not sulfated. After assembly of the oligosaccharide, the hydroxy groups to be sulfated are deprotected. These groups are then sulfated, usually with a sulfur trioxide–amine or –amide complex, following which all other protecting groups are removed to give the desired product.[2] There are several drawbacks to this approach. First, intensive manipulation of protecting groups is required at the end of the synthesis. Second, the sulfated products are highly polar and can be difficult to purify and manipulate for subsequent deprotections. Finally and most significantly, good yields of the sulfation reactions can be difficult to attain especially when multiple sulfations are necessary. Such difficulties can potentially be removed and/or diminished by the introduction of the sulfate groups at the monosaccharide stage as protected sulfate diesters; this strategy would avoid the need for selective hydroxy deprotections and sulfations at the end of the synthesis. Although this alternative approach could be highly effective in the synthesis of sulfated carbohydrates, it has received little attention, most probably because of the difficulties in developing protecting groups for sulfate monoesters. Perlin and Penney used phenyl chlorosulfate to introduce phenyl-protected sulfate groups into monosaccharides.[3] However, no further reports on the use of this protecting group in the synthesis of sulfated monosaccharides or higher carbohy-

[*] L. J. Ingram, Prof. Dr. S. D. Taylor
Department of Chemistry, University of Waterloo
200 University Ave. West, Waterloo, ON N2L3G1 (Canada)
Fax: (+1) 519-746-0435
E-mail: s5taylor@sciborg.uwaterloo.ca

[**] This research was supported by a Discovery Grant to S.D.T. from the Natural Sciences and Engineering Research Council (NSERC) of Canada.

Supporting information for this article is available on the WWW under http://www.angewandte.org or from the author.

 © 2006 Wiley-VCH Verlag GmbH & Co. KGaA, Weinheim

drates have appeared in the literature, possibly owing to low or variable yields during removal of the phenyl group. Proud et al. later introduced the trifluoroethyl (TFE) group as a protecting group for sulfated carbohydrates,[4] but there are two disadvantages to this approach. TFE was introduced by treating sulfate monoesters with trifluorodiazoethane, a reagent that must be freshly prepared and is highly toxic and potentially explosive. Moreover, its removal requires somewhat harsh conditions, that is, refluxing with KO*t*Bu/HO*t*Bu. Karst et al. recently demonstrated that deprotection of the sulfate groups proceeds in low or moderate yields when using fully protected disaccharides as substrates.[5]

Recently, we described the use of the 2,2,2-trichloroethyl (TCE) group as the first protecting group developed for aryl sulfates.[6] The TCE-protected sulfate esters were prepared in a single step by the reaction of phenols with 2,2,2-trichloroethyl chlorosulfate (TCECS) in the presence of triethylamine. The resulting protected sulfates were stable to a variety of conditions, but were readily deprotected in excellent yields under neutral conditions with Pd/C–ammonium formate or zinc–ammonium formate. These studies prompted us to examine the TCE group as a protecting group for sulfated carbohydrates. Herein we describe the first synthesis of a sulfuryl imidazolium salt, an entirely new class of sulfating agents. We demonstrate that this reagent is highly effective for introducing TCE-protected sulfates into carbohydrates. We also show that the TCE group can be removed in excellent yields and that this group shows outstanding potential as a valuable tool for the synthesis of sulfated carbohydrates.

Incorporation of the TCE-protected sulfate group into carbohydrates was first examined with diisopropylidene-D-galactose (**1**) as a model substrate. Reaction of **1** with TCECS under a wide variety of conditions generally gave the desired product **2** in very low yields (Scheme 1);[7] the dominant product was often chlorosugar **3**. In an attempt to decrease the amount of chloride-displacement product, the reactions were performed in the presence of

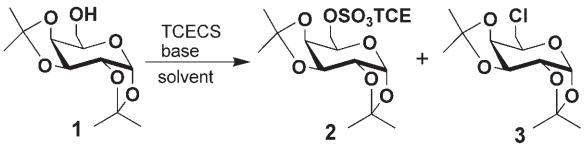

Scheme 1. Reaction of **1** with TCECS.

various silver salts. After some experimentation, it was found that the reaction of **1** in the presence of AgCN, Et_3N, and 4-dimethylaminopyridine (DMAP) in THF gave the desired product **2** in approximately 50% yield. However, **3** still accounted for a significant proportion of the products (Scheme 1). Moreover, applying these conditions to other monosaccharides such as benzyl 2,4,6-tri-*O*-benzyl-β-D-galactopyranoside (**4**) gave little or no sulfodiester product. Nevertheless, these results suggest that the desired compounds could be formed in good yield if a highly reactive sulfating agent that did not liberate a nucleophilic species such as chloride ion could be developed. O'Connell and Rapoport reported the synthesis of aryl sulfonamides and sulfonates with highly reactive sulfonyl imidazolium triflates **5**

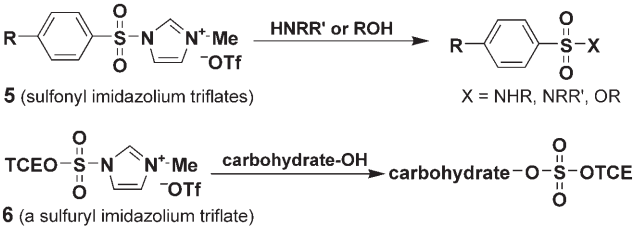

5 (sulfonyl imidazolium triflates)

6 (a sulfuryl imidazolium triflate)

Scheme 2. Sulfonyl and sulfuryl imidazolium triflates.

(Scheme 2).[8] These reagents were particularly useful for preparing sterically hindered sulfonates and sulfonamides, as well as certain primary sulfonates that were difficult to prepare with sulfonyl chlorides owing to the formation of alkyl chloride by-products. On the basis of these studies, we anticipated that sulfuryl imidazolium triflate[9] **6** would be a highly effective sulfating agent and would be particularly useful for introducing TCE-protected sulfate esters into carbohydrates (Scheme 2). Although sulfuryl imidazolium salts have never been reported, we found that **6** was readily constructed. Reaction of TCECS (**7**)[6] with imidazole gave sulfuryl imidazole **8** in 86% yield (Scheme 3). Reaction of **8**

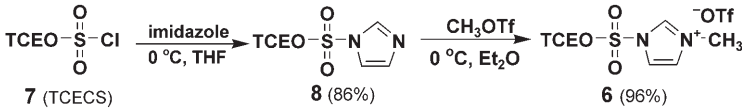

7 (TCECS) **8** (86%) **6** (96%)

Scheme 3. Synthesis of sulfuryl imidazolium triflate **6**.

with methyl triflate in dry diethyl ether resulted in the precipitation of **6**, which was isolated in almost quantitative yield by filtration of the reaction mixture (Scheme 3).[10] No further purification of **6** was necessary. Imidazolium salt **6** is stable and does not require storage under an inert atmosphere. It can be stored at room temperature for weeks or at −20 °C for months without any detectable decomposition.

Imidazolium salt **6** was treated with a variety of monosaccharides that bear an array of hydroxy protecting groups in the presence of *N*-methylimidazole (NMI) in THF (Table 1). In most cases, primary and secondary hydroxy groups were sulfated in good to excellent yields by subjecting them to **6** (2.0–4.7 equiv) and NMI (2.5–6.0 equiv) in THF at room temperature for 16–48 h.[10] In the case of **12**, 10.5 equivalents of **6**, 11.6 equivalents of NMI, and 72 h were required to allow 90% yield. The presence of NMI was essential for all the reactions. Other bases (Et_3N, Hünig base, pyridine, 2,6-lutidine, piperidine) were considerably less effective.

The TCE group was removed from **2** and **14**–**19** in very good yields by employing zinc–ammonium formate in methanol (Table 1).[10] Apart from the presence of $ZnCl_2$, $(HCO_2)_2Zn$, and NH_4Cl, the crude material was essentially

 © 2006 Wiley-VCH Verlag GmbH & Co. KGaA, Weinheim

Table 1: Synthesis of TCE-protected sulfocarbohydrates with **6** and deprotection of the sulfate group with Zn–HCO_2NH_4.

	Substrate		Sulfodiester product	Protection yield[a,b] [%]		Deprotected product	Deprotection yield[b,h] [%]
1	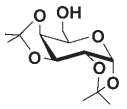	**2**	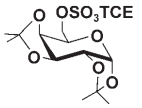	87[c]	**20**	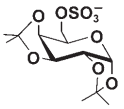	99
4	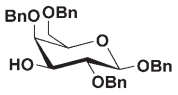	**14**	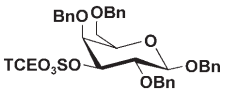	94[c]	**21**	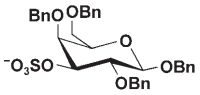	94
9	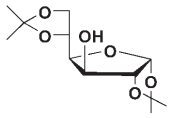	**15**	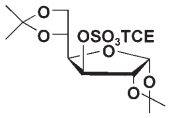	90[c]	**22**	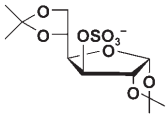	97
10	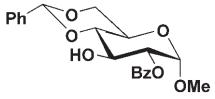	**16**	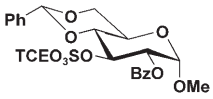	94[d]	**23**	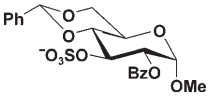	96
11	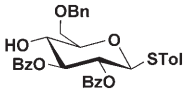	**17**	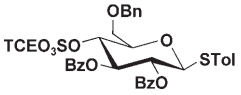	91[e]	**24**	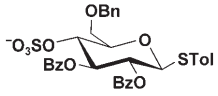	96
12	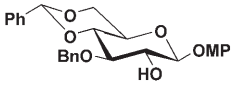	**18**		90[f]	**25**	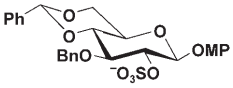	91
13	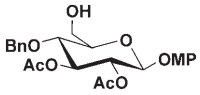	**19**	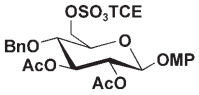	81[g]	**26**	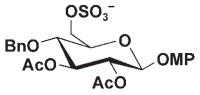	94

[a] All reactions were conducted with the carbohydrate (0.22–0.26 M) in THF. [b] Yield of isolated pure product. [c] 2 equiv **6**, 2.5 equiv NMI. [d] 4.7 equiv **6**, 5.3 equiv NMI. [e] 4.3 equiv **6**, 5.2 equiv NMI. [f] 10.5 equiv **6**, 11.6 equiv NMI. [g] 3.7 equiv **6**, 6 equiv NMI. [h] HCO_2NH_4 (6 equiv), Zn dust (7.6 equiv), carbohydrate (0.1 M) in MeOH. Bn = benzyl, Bz = benzoyl, MP = *p*-methoxyphenyl, Tol = *p*-tolyl.

pure. These impurities were easily removed by passing the product through a short column of silica with CH_2Cl_2/MeOH/NH_4OH (20:4:1) as eluent. Deprotection studies were also performed with Pd/C–ammonium formate; however, the yields were slightly lower than those with Zn.

Preliminary studies indicate that the TCE-protected sulfates are stable to many of the conditions commonly encountered in carbohydrate chemistry (Table 2).[10] Selective 6-O-debenzylation and acetylation of **14** with $ZnCl_2$/AcOH/Ac_2O gave **27** in 95% yield. Subjection of **27** to catalytic NaOMe in MeOH gave the deacetylated product **28** in 85% yield. Benzylidene ring opening of **16** with either TfOH (Tf = trifluoromethanesulfonyl) or $PhBCl_2$ in the presence of Et_3SiH gave **29**, which bears a free 4-OH group, or **30**, which bears a free 6-OH group, in 96% and 87% yield, respectively. Complete cleavage of the benzylidene group of **16** was obtained in 94% yield with TsOH (Ts = *p*-toluenesulfonyl). Subjection of **17** to *N*-bromosuccinimide (NBS) in acetone/water gave **32**, with a free anomeric OH group, in 74% yield. Reaction of **32** with trichloroacetonitrile in the presence of catalytic 1,8-diazabicyclo[5.4.0]undec-7-ene (DBU) gave the trichloroacetimidate **33** in 80% yield. Attempts to remove the benzyl group in **19** selectively with H_2 and Pd catalyst, without affecting the TCE-protected sulfate group, were unsuccessful. However, the benzyl group in **19** was selectively cleaved to give **34** in 91% yield by irradiation with a 250-W lamp in the presence of NBS and $CaCO_3$.[11]

As mentioned earlier, Karst et al. removed the TFE moiety from sulfate groups in fully protected disaccharides with low to moderate yields.[5] We anticipated that this would not be an issue with the TCE group as it is removed under very mild conditions. To illustrate this, **30** was coupled to **33** (Scheme 4) in the presence of TMSOTf (TMS = trimethylsilyl) to give disaccharide **35** in 68% yield (unoptimized). Deprotection of **35** with zinc–ammonium formate gave the sulfo-deprotected product **36** in 92% yield (Scheme 4).[10]

In summary, the first synthesis of a sulfuryl imidazolium salt **6** is reported. This compound represents a new class of highly potent sulfating agents.[12] Compound **6** was very effective in introducing TCE-protected sulfates into monosaccharides. The TCE-protected sulfates were stable to many of the reaction conditions commonly encountered in carbo-

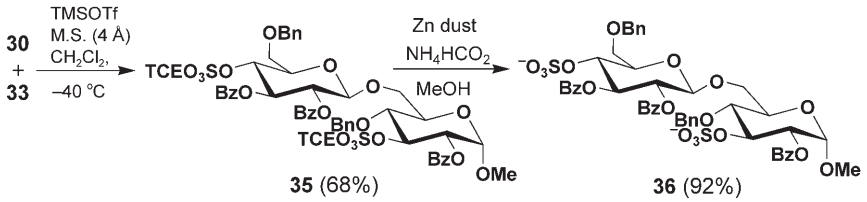

Scheme 4. Glycosylation and TCE cleavage. M.S. = molecular sieves.

 © 2006 Wiley-VCH Verlag GmbH & Co. KGaA, Weinheim

Table 2: Cleavage of selected hydroxy protecting groups from TCE-protected sulfocarbohydrates.

	Substate		Product	Yield [%][a]
14	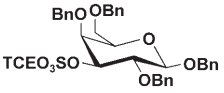	27	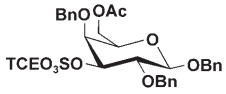	95[b]
27	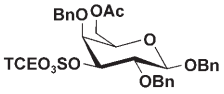	28	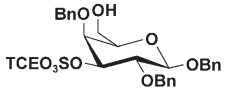	85[c]
16	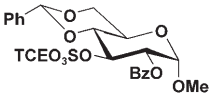	29	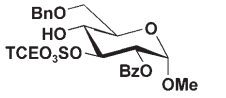	96[d]
16	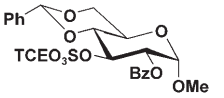	30	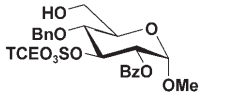	87[e]
16	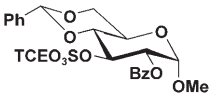	31	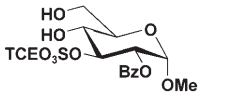	94[f]
17	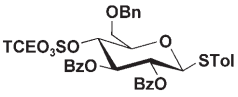	32	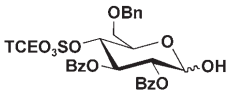	74[g]
32	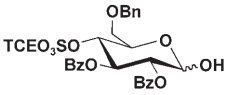	33	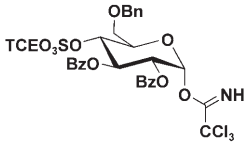	80[h]
19	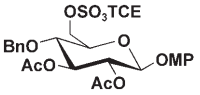	34	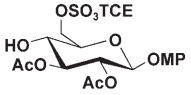	91[i]

[a] Yield of isolated pure product. [b] $ZnCl_2$ (3.7 equiv), $AcOH/Ac_2O$, 3 h. [c] NaOMe (0.16 equiv) in MeOH, 3 h. [d] TfOH (3.4 equiv), Et_3SiH (3.0 equiv), 4-Å molecular sieves, −78 °C, CH_2Cl_2, 1 h. [e] $PhBCl_2$ (3.4 equiv), Et_3SiH (3.0 equiv), 4-Å molecular sieves, −78 °C, CH_2Cl_2, 1 h. [f] TsOH (0.1 equiv), CH_2Cl_2/MeOH, 45 °C, 16 h. [g] NBS (3.0 equiv), acetone/H_2O, 0 °C, 20 min. [h] DBU (0.2 equiv), Cl_3CCN (16 equiv), −40→−10 °C, CH_2Cl_2, 3 h. [i] NBS (3.5 equiv), $CaCO_3$ (5 equiv), CCl_4/H_2O, 250-W incandescent lamp.

hydrate chemistry. Deprotection of the sulfate group with zinc–ammonium formate proceeded in outstanding yields. This methodology should have a significant impact on the synthesis of sulfated carbohydrates. More studies on the scope of this methodology and its application to the synthesis of complex sulfated oligosaccharides are in progress and will be reported in due course.

Received: January 13, 2006
Published online: April 24, 2006

Keywords: carbohydrates · imidazolium · protecting groups · sulfates · sulfation

[1] T. Toida, A. Chaidedgumjorn, R. J. Linhardt, *Trends Glycosci. Glycotechnol.* **2003**, *15*, 29–46.
[2] For examples, see: a) K. C. Nicolaou, N. J. Bockovich, D. R. Carcanague, *J. Am. Chem. Soc.* **1993**, *115*, 8843–8844; b) K. Singh, A. Fernandez-Mayoralas, M. Martin-Lomas, *J. Chem. Soc. Chem. Commun.* **1994**, 775; c) A. Lubineau, R. Lemoine, *Tetrahedron Lett.* **1994**, *35*, 8795–8796; d) W. Stahl, U. Sprengard, G. Kretzschmar, D. W. Schmidt, H. Kunz, *J. Prakt. Chem.* **1995**, *337*, 441–445.
[3] C. L. Penney, A. Perlin, *Carbohydr. Res.* **1981**, *93*, 241–246.
[4] A. D. Proud, J. C. Prodger, S. L. Flitsch, *Tetrahedron Lett.* **1997**, *38*, 7243–7246.
[5] N. A. Karst, T. F. Islam, F. Y. Avci, R. J. Lindhardt, *Tetrahedron Lett.* **2004**, *45*, 6433–6437.
[6] Y. Liu, I. F. Lien, S. Ruttgaizer, P. Dove, S. D. Taylor, *Org. Lett.* **2004**, *6*, 209–212.
[7] The initial intention of Proud et al.[4] was to use TCE protection. Although they anticipated that the TCE group would be easily removed under very mild conditions using Zn/HOAc, they reported that the yields of TCE-protected sulfated monosaccharides with unspecified reagents and reaction conditions were very poor. Therefore, the TFE group was examined. However, the reaction of 2,2,2-trifluoroethylchlorosulfate with carbohydrates proceeded in poor yields and gave a number of unspecified by-products, hence the use of trifluorodiazoethane. We found that deprotection of the TCE-protected sulfocarbohydrates described herein with Zn–HOAc results in the formation of desulfated products.
[8] J. F. O'Connell, H. Rapoport, *J. Org. Chem.* **1992**, *57*, 4775–4777.
[9] Although the terms sulfonyl and sulfuryl are often used interchangeably, we designated **6** a sulfuryl imidazolium salt. We use the term sulfuryl to differentiate it from sulfonyl imidazolium salts, which is the term used by O'Connell and Rapoport to describe their sulfonating agents.[8]
[10] For experimental details, see the Supporting Information.
[11] a) R. W. Binkley, D. G. Hehemann, *J. Org. Chem.* **1990**, *55*, 378–380; b) J. G. Riley, T. B. Grindley, *J. Carbohydr. Chem.* **2001**, *20*, 159–169.
[12] We have also prepared the TFE, phenyl, and other analogues of **6**. Their synthesis and sulfating properties will be reported elsewhere.

 © 2006 Wiley-VCH Verlag GmbH & Co. KGaA, Weinheim

Biosynthesis

DOI: 10.1002/anie.200504614

Biosynthesis of Thiamin Thiazole: Determination of the Regiochemistry of the S/O Acyl Shift by Using 1,4-Dideoxy-D-xylulose-5-phosphate**

*Abhishek Chatterjee, Xuemei Han, Fred W. McLafferty, and Tadhg P. Begley**

Thiamin pyrophosphate is an essential cofactor in all living systems, where it plays a key role in the metabolism of amino acids and carbohydrates.[1,2] The biosynthesis of this cofactor is complex and involves separate syntheses of the thiazole and the pyrimidine moieties, which are then linked to form the cofactor.[3–6] The biosynthesis of thiamin thiazole in *Bacillus subtilis* involves five enzymes and is different from any of the known chemical or biochemical thiazole syntheses.[7–12] In this biosynthesis, ThiF and a cysteine desulfurase catalyze the formation of the sulfide carrier protein thiocarboxylate (**4**, ThiS-COS$^-$), glycine oxidase (ThiO) catalyzes the oxidation of glycine to the glycine imine **10**, and thiazole synthase (ThiG) catalyzes the formation of thiazole from ThiS-COS$^-$, the glycine imine **10**, and 1-deoxy-D-xylulose-5-phosphate (**1**, DXP; see Scheme 1).

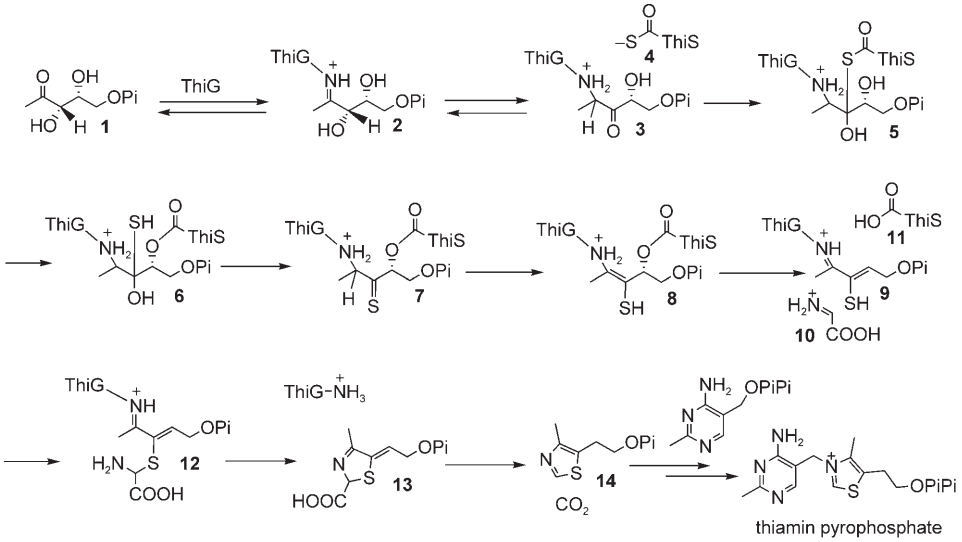

Scheme 1. Proposed mechanism for the formation of the thiazole phosphate moiety of thiamin pyrophosphate. Pi = phosphate.

In the current mechanistic proposal for this reaction[7–12] (Scheme 1), DXP (**1**) forms an imine with Lys96 of ThiG. Tautomerization to **3** followed by addition of ThiS-COS$^-$ (**4**) to the resulting ketone gives **5**. An O/S acyl shift followed by loss of water gives thioketone **7**, which then tautomerizes and eliminates ThiS-COO$^-$ to give **9**. Addition of this thioenol to the glycine imine **10**, formed in a separate step by ThiO-catalyzed oxidation of glycine, followed by transimination and decarboxylation, completes the formation of the thiazole moiety.

This mechanism is supported by the trapping of imine **2**,[11] by the observation of enzyme-catalyzed H/D exchange at C3 and carbonyl oxygen exchange at C2 of DXP (**1**),[11] by the demonstration that one of the carboxy terminal oxygen atoms of ThiS-COO$^-$ (**11**) is derived from an oxygen atom from either C3 or C4 of DXP,[9] and by the trapping of thioenol **9**.[9] Modeling of intermediate **5** into the active site of the ThiG/ThiS-COO$^-$ complex revealed that this enzyme has a remarkably simple active site, using only Asp182 and Glu98 to catalyze the conversion of **2** into thiazole phosphate **14**.[10]

The regiochemistry of the acyl shift (**5**→**6**) has not yet been experimentally established. While it is clear that the carboxy-terminal oxygen atom of ThiS-COO$^-$ (**11**) is not derived from the reaction buffer, the DXP used to demonstrate the direct oxygen transfer from the carbohydrate to ThiS-COO$^-$ was labeled at both C3 and C4, leaving open the possibility that the O/S acyl shift from **5** could occur to the C3 oxygen substituent rather than to the C4 oxygen atom as depicted in Scheme 1. While acyl transfer to the C3 hydroxy group seemed less plausible to us, as it requires the formation of a strained four-membered cyclic intermediate, it could not be excluded on these grounds because several examples of enzyme-catalyzed reactions are known in which four-membered cyclic structures are formed involving analogous tetrahedral intermediates.[13–18] It was therefore necessary to experimentally differentiate between the two pathways for the cleavage of thioester **5**.

Herein, we resolve this ambiguity by using 1,4-dideoxy-D-xylulose-5-phosphate (**15**, DDXP) as an alternative substrate for ThiG. If this analogue is a substrate, it will form the imine **16**, which will then tautomerize to the ketone **17** (Scheme 2). Addition of ThiS-thiocarboxylate (**4**) to this ketone will give **18**. The subsequent reactivity of this intermediate will then reveal the regiochemistry of the acyl-transfer reaction: If the acyl transfer occurs to the C3 oxygen atom, **18** will convert into **19**, which will then lose ThiS-COO$^-$ to give thioketone **20**. Reduction of this thioketone with sodium borohydride will result in the stable incorporation of the ThiS-COS$^-$ sulfur

[*] A. Chatterjee, X. Han, Prof. F. W. McLafferty, Prof. T. P. Begley
Department of Chemistry and Chemical Biology
Cornell University
Ithaca, NY 14853 (USA)
Fax: (+1) 607-255-7133
E-mail: tpb2@cornell.edu

[**] This research was supported by grants from the National Institutes of Health to T.P.B. (DK44083) and to F.W.M. (GM16609).

Supporting information for this article, including experimental details, is available on the WWW under http://www.angewandte.org or from the author.

© 2006 Wiley-VCH Verlag GmbH & Co. KGaA, Weinheim

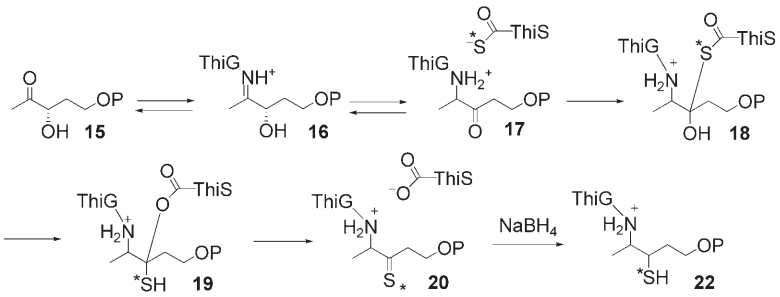

Scheme 2. Strategy for the use of 1,4-dideoxy-D-xylulose-5-phosphate (DDXP, **15**) to determine the regiochemistry of the S/O acyl shift involved in thiazole formation. P = phosphate.

atom into the thiazole synthase, as we have previously demonstrated in our successful trapping of intermediate **9** (Scheme 1). In contrast, if the acyl transfer occurs to the C4 oxygen atom, the reaction will be blocked at **18**. Intermediate **18** will be stable to borohydride reduction and will collapse to **17** upon protein denaturation. Therefore, if this experiment is carried out using [^{35}S]ThiS-COS$^-$, we predict the stable, DDXP-mediated incorporation of ^{35}S into ThiG if the acyl shift occurs to the C3 oxygen atom and no incorporation of ^{35}S into ThiG if the acyl shift occurs to the C4 oxygen center.

To establish the validity of DDXP (**15**) as a mechanistic probe of the ThiG-catalyzed reaction, it was first necessary to demonstrate that it binds to the enzyme in a catalytically competent manner. We used a combination of ThiG-catalyzed H/D exchange (on C3) and carbonyl oxygen exchange (on C2) on DDXP and the demonstration that ThiG forms an active-site imine with DDXP catalytically, to determine if ThiG can process this substrate analogue.

DDXP (**15**) was prepared in five steps from α-hydroxy-γ-butyrolactone as reported previously.[19] To test for the formation of imine **16**, ThiG was treated with DDXP followed by reduction with sodium borohydride. Analysis of this reaction mixture by high-resolution ESI-FTMS (electrospray ionization Fourier transform mass spectrometry) demonstrated the complete conversion of the enzyme into a new species with an additional mass of 182 Da corresponding to reduced **16** (Figure 1). Extensive fragmentation of this new species localized the imine formation on Lys96, the active-site lysine. We therefore conclude that DDXP binds to thiazole synthase and forms an active-site imine.

To test for ThiG-catalyzed exchange of the carbonyl oxygen atom of DDXP with buffer, carbonyl-labeled [^{18}O]DDXP was treated with the enzyme and the exchange reaction was monitored by mass spectrometry. Incubation of [^{18}O]DXP with thiazole synthase showed the expected enzyme-catalyzed exchange (Figure 2 A). Incubation of an equimolar mixture of [^{18}O]DXP and [^{18}O]DDXP with thiazole synthase demonstrated almost equal rates of exchange for the two compounds (Figure 2 B and C). Exchange of the carbonyl oxygen atom of DXP and DDXP was much slower in the absence of the enzyme (Figure 2 D), which demonstrates that thiazole synthase can catalyze the reversible formation of imine **16** with DDXP and that DDXP competes with DXP for the ThiG active site.

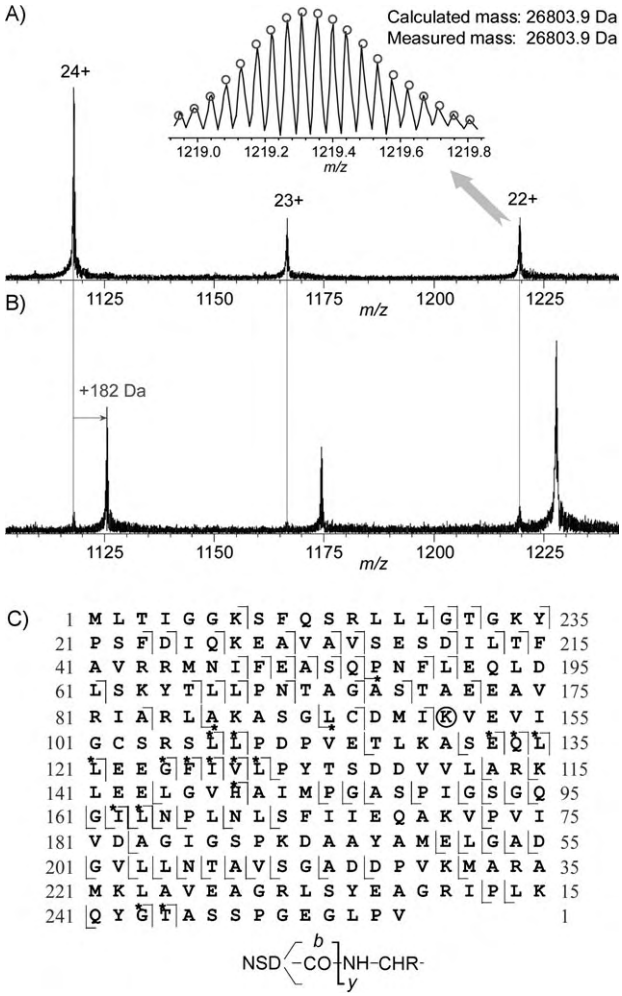

Figure 1. ESI-FTMS analysis of thiazole synthase modification using DDXP. A) Mass spectrum of unmodified thiazole synthase after reduction using borohydride. B) Mass spectrum of thiazole synthase treated with DDXP followed by reduction using borohydride: The adduct, with an extra mass of 182 Da, has a mass that is consistent with reduced **16**. C) Extensive fragmentation of the ThiG–DDXP adduct localizes this imine formation to K96, the active-site lysine. The asterisks indicate the peptide fragments with the covalent modification. Nozzle-skimmer dissociation (NSD) yields amino-terminal containing *b* ions and carboxy-terminal containing *y* ions.

Incubation of DDXP with ThiG in deuterated buffer for 10 h resulted in the partial exchange of the proton at C3. Figure 3 A shows the ^{1}H NMR spectrum of DDXP incubated overnight in reaction buffer, and Figure 3 B shows an identical reaction mixture in the presence of ThiG in which the resonance for the C3 proton decreases in intensity relative to that of the C5 proton, which does not exchange and can therefore be used as an internal standard. The rate of this exchange is considerably slower than the corresponding rate of exchange of the C3 proton of DXP, which is complete in about 1 h under identical reaction conditions. This slower exchange rate is likely due to a combination of factors: the intrinsically lower acidity of the C3 proton of imine **16** relative to imine **2**, and non-optimal orientation of the C3 proton with respect to the active-site base (Asp182) resulting from the loss of the orientating effect of the C4 hydroxy group.

 © 2006 Wiley-VCH Verlag GmbH & Co. KGaA, Weinheim

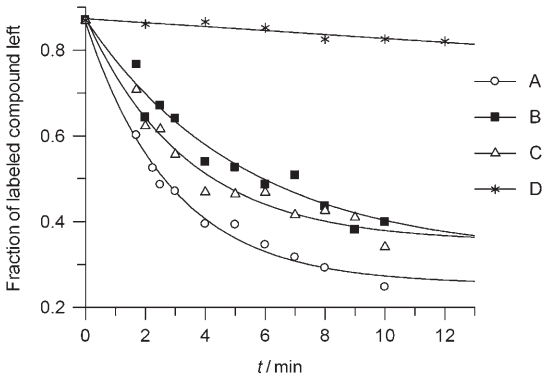

Figure 2. Time courses from ESI-MS analysis of the thiazole synthase catalyzed exchange of [^{18}O]DXP and [^{18}O]DDXP: A) the enzyme-catalyzed exchange of [^{18}O]DXP, B) the enzyme-catalyzed exchange of [^{18}O]DXP in the presence of [^{18}O]DDXP, C) the enzyme-catalyzed exchange of [^{18}O]DDXP in the presence of [^{18}O]DXP, and D) the exchange of [^{18}O]DDXP in the absence of enzyme. The rates for ^{18}O exchange in parts (B) and (C) were measured simultaneously, after an equimolar mixture of labeled DXP and DDXP was added to ThiG.

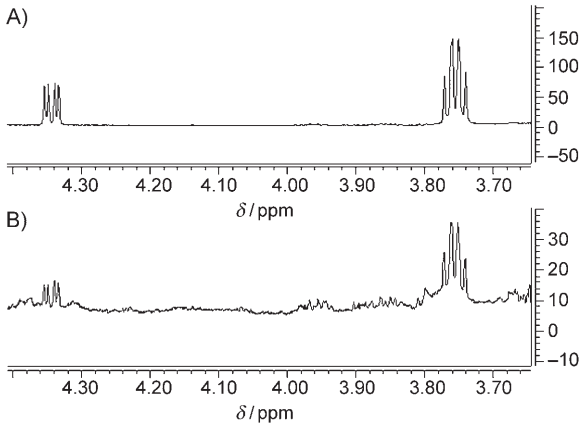

Figure 3. ^{1}H NMR spectroscopic analysis of the H/D exchange at C3 of DDXP incubated for 10 h in deuterated buffer: A) in the absence of thiazole synthase; B) in the presence of thiazole synthase. The proton at C3 and those at C5 resonate at $\delta = 4.35$ and 3.76 ppm, respectively.

The experiments described above demonstrate that this substrate analogue binds to the active site of ThiG in a catalytically competent manner. DDXP is therefore a valid probe to differentiate the two mechanisms shown in Scheme 2.

Incubation of [^{35}S]ThiS-COS$^-$ with DXP in the presence of ThiG demonstrated the stable incorporation of ^{35}S into the ThiG (Figure 4 A, lane 2). When the same experiment was carried out using DDXP, only a trace of sulfur transfer to ThiG was detected. (Figure 4 A, lane 3). This low level of sulfur transfer did not increase after incubation overnight (Figure 4 A, lane 5), suggesting that failure to form **22** is caused by the absence of the acyl acceptor at C4 and not due to a retardation of the O/S acyl-shift reaction. The very low level of DDXP-mediated incorporation of ^{35}S into ThiG shown in lane 3 is likely to arise from low levels of hydrolysis of the thioester **18** during treatment with borohydride. We

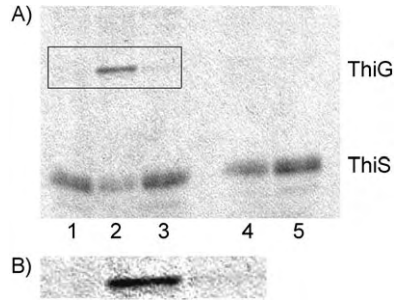

Figure 4. Analysis of the transfer of ^{35}S from [^{35}S]ThiS-COS$^-$ to thiazole synthase (ThiG) by SDS-PAGE/autoradiography. A) Lane 1: ThiG + [^{35}S]ThiS-COS$^-$, 30 min; lane 2: ThiG + [^{35}S]ThiS-COS$^-$ + DXP, 30 min; lane 3: ThiG + [^{35}S]ThiS-COS$^-$ + DDXP, 30 min; lane 4: ThiG + [^{35}S]ThiS-COS$^-$, 12 h; lane 5: ThiG + [^{35}S]ThiS-COS$^-$ + DDXP, 12 h. B) Magnified image of the region highlighted in part (A).

therefore conclude that the S/O acyl transfer occurs to the C4 hydroxy group of DXP during thiazole formation.

The experiments described herein demonstrate that DDXP is an alternative substrate for thiazole synthase and can be used as a mechanistic probe to demonstrate that the ThiS acyl-shift reaction occurs to the C4 oxygen atom and not to the C3 oxygen center of DXP (**5**→**6** in Scheme 1). These studies also suggest that DDXP may be useful for the structural characterization of the active site of thiazole synthase.

Received: December 29, 2005
Revised: March 1, 2006
Published online: April 20, 2006

Keywords: acyl shift · biosynthesis · enzyme catalysis · isotopic labeling · vitamins

[1] R. F. Butterworth, *Nutr. Res. Rev.* **2003**, *16*, 277.
[2] F. Jordan, *Nat. Prod. Rep.* **2003**, *20*, 184.
[3] T. P. Begley, D. M. Downs, S. E. Ealick, F. W. McLafferty, A. P. G. M. Van Loon, S. Taylor, N. Campobasso, H.-J. Chiu, C. Kinsland, J. J. Reddick, J. Xi, *Arch. Microbiol.* **1999**, *171*, 293.
[4] I. D. Spenser, R. L. White, *Angew. Chem.* **1997**, *109*, 1096; *Angew. Chem. Int. Ed. Engl.* **1997**, *36*, 1032.
[5] B. Estramareix, S. David, *New J. Chem.* **1996**, *20*, 607.
[6] T. P. Begley, *Nat. Prod. Rep.* **1996**, *13*, 177.
[7] J.-H. Park, P. C. Dorrestein, H. Zhai, C. Kinsland, F. W. McLafferty, T. P. Begley, *Biochemistry* **2003**, *42*, 12430.
[8] E. C. Settembre, P. C. Dorrestein, J.-H. Park, A. M. Augustine, T. P. Begley, S. E. Ealick, *Biochemistry* **2003**, *42*, 2971.
[9] P. C. Dorrestein, H. Zhai, F. W. McLafferty, T. P. Begley, *Chem. Biol.* **2004**, *11*, 1373.
[10] E. C. Settembre, P. C. Dorrestein, H. Zhai, A. Chatterjee, F. W. McLafferty, T. P. Begley, S. E. Ealick, *Biochemistry* **2004**, *43*, 11647.
[11] P. C. Dorrestein, H. Zhai, S. V. Taylor, F. W. McLafferty, T. P. Begley, *J. Am. Chem. Soc.* **2004**, *126*, 3091.
[12] H. Zhai, P. C. Dorrestein, A. Chatterjee, T. P. Begley, F. W. McLafferty, *J. Am. Soc. Mass Spectrom.* **2005**, *16*, 1052.
[13] D. C. Aldridge, D. Giles, W. B. Turner, *J. Chem. Soc. Perkin Trans. 1* **1971**, *23*, 3888.
[14] L. Mayol, V. Piccialli, D. Sica, *Tetrahedron Lett.* **1987**, *28*, 3601.
[15] L. R. Dick, A. A. Cruikshank, L. Grenier, F. D. Melandri, S. L. Nunes, R. L. Stein, *J. Biol. Chem.* **1996**, *271*, 7273.

 © 2006 Wiley-VCH Verlag GmbH & Co. KGaA, Weinheim

[16] B. O. Bachmann, R. Li, C. A. Townsend, *Proc. Natl. Acad. Sci. USA* **1998**, *95*, 9082.
[17] M. T. Miller, B. Gerratana, A. Stapon, C. A. Townsend, A. C. Rosenzweig, *J. Biol. Chem.* **2003**, *278*, 40996.
[18] B. Gerratana, A. Stapon, C. A. Townsend, *Biochemistry* **2003**, *42*, 7836.
[19] J.-F. Hoeffler, D. Tritsch, C. Grosdemange-Billiard, M. Rohmer, *Eur. J. Biochem.* **2002**, *269*, 4446.
[20] S. V. Taylor, L. D. Vu, T. P. Begley, U. Schoerken, S. Grolle, G. A. Sprenger, S. Bringer-Meyer, H. Sahm, *J. Org. Chem.* **1998**, *63*, 2375.
[21] S. C. Beu, M. W. Senko, J. P. Quinn, F. M. Wampler III, F. W. McLafferty, *J. Am. Soc. Mass Spectrom.* **1993**, *4*, 557.
[22] H. Zhai, X. Han, K. Breuker, F. W. McLafferty, *Anal. Chem.* **2005**, *77*, 5777.
[23] D. M. Horn, R. A. Zubarev, F. W. McLafferty, *J. Am. Soc. Mass Spectrom.* **2000**, *11*, 320.

 © 2006 Wiley-VCH Verlag GmbH & Co. KGaA, Weinheim

Gels

DOI: 10.1002/anie.200600324

A New Class of Biochemically Degradable, Stimulus-Responsive Triblock Copolymer Gelators**

Chengming Li, Jeppe Madsen, Steven P. Armes, and Andrew L. Lewis*

There is increasing interest in biocompatible hydrogels for various biomedical applications.[1] Stimulus-responsive hydrogels are of particular interest as the formation of space-filling gels within complex cavities in situ is important for certain applications, for example, wound dressings.[2] Increasing attention is also being paid to biochemically responsive hydrogels. For example, Miyata et al. reported a new class of hydrogels, cross-linked by a specific antigen–antibody interaction, that swell in response to excess antigen in solution.[3] Similarly, Plunkett et al. recently demonstrated that polyacrylamide hydrogels prepared by using a tetrapeptide cross-linker are degraded in the presence of α-chymotrypsin.[4a] A number of other examples of enzyme-responsive hydrogels have also been reported.[4b,c] However, we are not aware of any reports of hydrogels that are both biochemically responsive (with respect to degradation) and stimulus responsive (with respect to gelation). Disulfide–thiol chemistry is well known to protein chemists and is becoming increasingly popular in conventional polymer syntheses. Recent papers describe the use of disulfide-based divinyl monomers and initiators to prepare degradable gels, hydrogels, microgels, and branched copolymers.[5] One advantage of this approach is that the disulfide bond can be cleaved specifically under mild conditions by using reagents such as dithiothreitol (DTT).[6] Recently, we reported the synthesis of new biocompatible, thermo-responsive ABA triblock copolymer gelators[7] by atom transfer radical polymerization[8] (ATRP). A bifunctional diethyl-*meso*-2,5-dibromoadipate (DEDBA) initiator was used to polymerize first 2-(methacryloyloxy)ethyl phosphorylcholine (MPC) followed by *N*-isopropylacrylamide (NIPAM). In the present study we replaced DEDBA with the disulfide-based initiator (bis[2-(2-bromoisobutyryloxy)ethyl] disulfide or $(BiBOE)_2S_2$), which was previously reported by Tsarevsky and Matyjaszewski (Figure 1).[9]

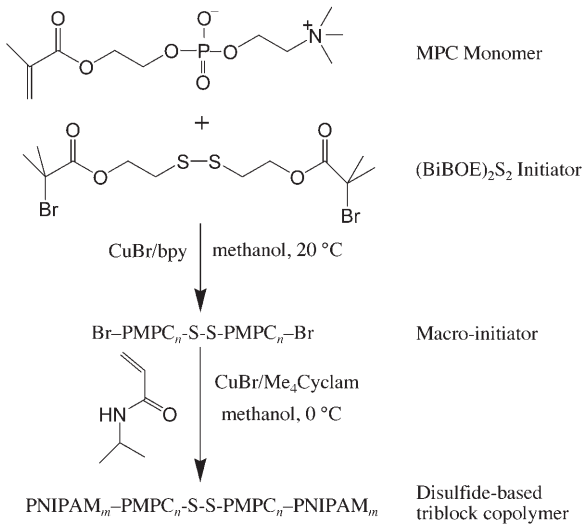

Figure 1. Synthesis of the $PNIPAM_{80}$–$PMPC_{125}$-S-S-$PMPC_{125}$–$PNIPAM_{80}$ triblock copolymer by ATRP through the use of a disulfide-based bifunctional ATRP initiator ($(BiBOE)_2S_2$).

The $PNIPAM_{80}$–$PMPC_{125}$-S-S-$PMPC_{125}$–$PNIPAM_{80}$ triblock copolymer was synthesized by using essentially the same ATRP protocol as that previously described for the DEDBA initiator (see the Supporting Information).[7] Self-blocking experiments confirmed that the efficiency of the Br–$PMPC_m$-S-S-$PMPC_m$–Br macro-initiator was high, hence the triblock copolymer architecture was expected to be well defined. Gel permeation chromatography (GPC) studies in a 3:1 chloroform/methanol mixed eluent at 40 °C with a series

[*] C. Li, J. Madsen, Prof. S. P. Armes
Dainton Building
Department of Chemistry
The University of Sheffield
Brook Hill, Sheffield, South Yorkshire, S3 7HF (UK)
Fax: (+44) 0114-222-9346
E-mail: S.P.Armes@sheffield.ac.uk
A. L. Lewis
Biocompatibles Ltd.
Chapman House
Farnham Business Park
Weydon Lane, Farnham, Surrey, GU98QL (UK)

[**] EPSRC is thanked for a post-doctoral grant to support C.L. (Platform Grant GR/S25845). S.P.A. is the recipient of a Royal Society–Wolfson Research Merit Award. Biocompatibles are thanked for funding a PhD CASE studentship for J.M. and also for supplying the MPC monomer. The reviewers of this manuscript are thanked for their helpful comments.

Supporting information for this article is available on the WWW under http://www.angewandte.org or from the author.

InterScience
© 2006 Wiley-VCH Verlag GmbH & Co. KGaA, Weinheim

of near-monodisperse poly(methyl methacrylate) calibration standards indicated an M_n of 88,000 and an M_w/M_n of 1.34 for the final $PNIPAM_{80}$–$PMPC_{125}$-S-S-$PMPC_{125}$–$PNIPAM_{80}$ triblock copolymer.

The PMPC homopolymer is highly hydrophilic and dissolves molecularly in aqueous solution over a wide temperature range. In contrast, the solubility of the PNIPAM homopolymer in aqueous solution is temperature dependent: it dissolves molecularly at 20 °C but precipitates above its lower critical solution temperature (LCST) of approximately 32 °C.[10] Thus the $PNIPAM_{80}$–$PMPC_{125}$-S-S-$PMPC_{125}$–$PNIPAM_{80}$ triblock copolymer chains formed a free-standing gel under physiologically relevant conditions at a copolymer concentration above approximately 8% *w*/*v*. Chemical intuition, combined with variable temperature dynamic light scattering (DLS) and ^{1}H NMR spectroscopic studies (see the Supporting Information), suggest that this copolymer forms a gel at 37 °C that is comprised of interconnected PNIPAM-core "flower" micelles (Figure 2).[11] Variable angle DLS studies were conducted on these "flower" micelles yielding apparent micelle diameters ranging from 168–207 nm. However, we emphasize that these micelles are strongly interacting (ultrafiltration of these aqueous solutions proved very difficult) even in highly dilute solutions (0.06%). The validity of the Stokes-Einstein equation is, therefore, questionable and such particle sizing data should be treated with caution.

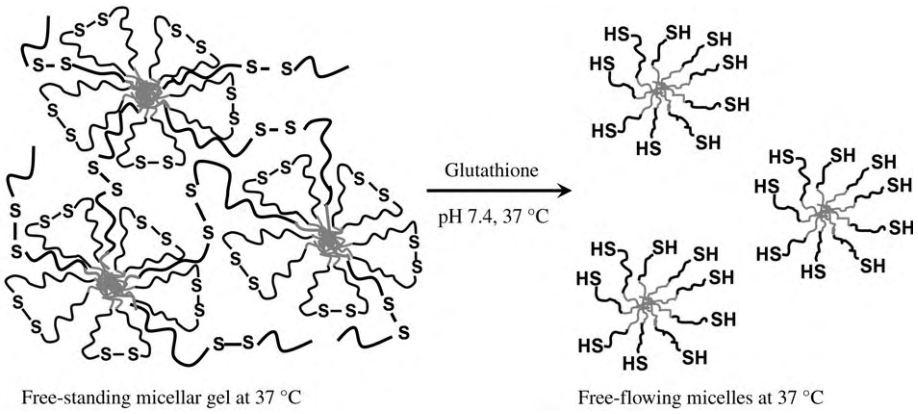

Figure 2. Biochemical degradation of the free-standing micellar gel formed by the $PNIPAM_{80}$–$PMPC_{125}$-S-S-$PMPC_{125}$–$PNIPAM_{80}$ triblock copolymer after cleavage of the disulfide bonds by using the naturally occurring tripeptide, glutathione.

These copolymer gels are purely physical in nature as they revert to free-flowing liquids below 37 °C. Rheological studies of the gelation behavior of this triblock copolymer in aqueous solution are summarized in the Supporting Information. Relatively soft, albeit free-standing, physical gels are formed at around 35 °C. This is essentially the same behavior as that reported previously for the analogous PNIPAM–PMPC–PNIPAM triblock copolymers prepared by using a non-disulfide-based initiator.[7] If the central disulfide bond is cleaved, the triblock chains are converted into $PNIPAM_{80}$–$PMPC_{125}$-SH diblock chains of half the original copolymer molecular weight. More importantly, the intermicelle bridges in the 3D gel network would be destroyed, which should lead to rapid gel dissolution. Hence the disulfide bond was expected to act as a "keystone" for the gel. As far as we are aware, changing the block copolymer architecture to induce degelation is a new paradigm in polymer science. As disulfide bonds can be selectively cleaved under mild conditions by using various naturally occurring reagents such as oligopeptides, this new class of gels should be both biochemically responsive and thermoresponsive. This hypothesis is evaluated herein.

The reductive degradation of a Br–$PMPC_{125}$-S-S-$PMPC_{125}$–Br macro-initiator was initially attempted by using DTT (10% *w*/*v* aqueous solution; pH 7.4). The use of a DTT/disulfide molar ratio of 100:1 led to almost 100% cleavage within 2 h at 37 °C: aqueous GPC studies confirmed that the M_w of the final cleaved $PMPC_{125}$-SH homopolymer was, as expected, approximately 50% of the M_n of the original macroinitiator. The $PNIPAM_{80}$–$PMPC_{125}$-S-S-$PMPC_{125}$–$PNIPAM_{80}$ triblock copolymer formed a free-standing gel at 10% *w*/*v* and 37 °C: the gel dissolved completely at this temperature within 0.5 h of adding a 100-fold excess of DTT. After disulfide bond cleavage, the resulting $PNIPAM_{80}$–$PMPC_{125}$-SH diblock copolymer ($M_n = 49\,000$, $M_w/M_n = 1.32$ compared with poly(methyl methacrylate) calibration standards) was no longer a gelator: only a free-flowing liquid was obtained even at 20% *w*/*v* copolymer and elevated temperatures (up to 60 °C). DLS studies of the diluted diblock copolymer solution indicated an intensity-average diameter of 96 nm on heating to 37 °C. Thus the $PNIPAM_{80}$–$PMPC_{125}$-SH diblock copolymer chains still underwent temperature-induced micellar self-assembly but now formed noninteracting conventional PNIPAM-core micelles, rather than interconnected "flower" micelles (see Figure 2). Angular dependence DLS studies indicated that the former micelles were approximately spherical and noninteracting. A similarly dilute aqueous solution of the original triblock copolymer, however, contained significantly larger, more-polydisperse, and non-spherical micellar structures, which is consistent with weakly interacting micelles.

Glutathione is an important tripeptide antioxidant that is commonly found within cells at millimolar concentrations.[12] Like DTT, the reduced form of glutathione contains a thiol group that exchanges with the disulfide bond: successful cleavage using this tripeptide was expected to herald a new class of biochemically degradable stimulus-responsive gels. The kinetics of degelation of the $PNIPAM_{80}$–$PMPC_{125}$-S-S-$PMPC_{125}$–$PNIPAM_{80}$ copolymer (9.2% *w*/*v* aqueous solution) using glutathione/disulfide molar ratios of 2:1, 5:1, and 10:1 at 37 °C in PBS buffer were assessed by monitoring the solution viscosity using a rheometer operating at a fixed shear stress of

 © 2006 Wiley-VCH Verlag GmbH & Co. KGaA, Weinheim

5.0 Pa and a shear frequency of 1 rad sec^{-1} (see Figure 3). In each case, the gel viscosity decreased monotonically from around 17 Pa s to a limiting value of approximately 1–5 Pa s within 12–30 min. Faster rates of degelation and lower

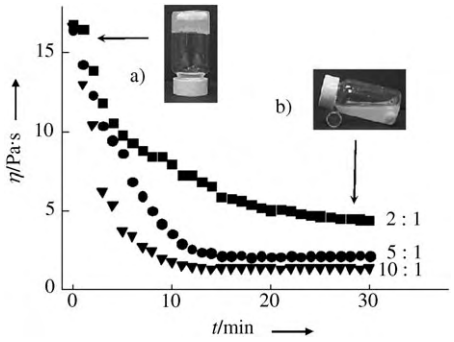

Figure 3. Viscosity versus time curves obtained at a constant applied stress of 5.0 Pa for varying glutathione/disulfide molar ratios at 37 °C. Initially, a 9.2 % aqueous solution of the $PNIPAM_{80}$–$PMPC_{125}$-S-S-$PMPC_{125}$–$PNIPAM_{80}$ triblock copolymer formed a free-standing gel (see inset a)). Reductive cleavage by the glutathione causes gel dissolution and leads to a free-flowing liquid (see inset b)) as the disulfide bonds in the intermicelle bridges are cleaved to produce $PNIPAM_{80}$–$PMPC_{125}$-SH diblock copolymer chains (see also Figure 2).

limiting viscosities were obtained, as expected, at higher glutathione/disulfide molar ratios. After disulfide cleavage, each free-standing gel had become a free-flowing liquid that no longer gelled under any conditions. In a control experiment, a 10 % gel prepared by using the same triblock copolymer remained free-standing in phosphate-buffered saline solution after 8 h at 37 °C (longer time scales over days/weeks led to partial gel dehydration) in the absence of glutathione. This indicates that the majority of the disulfide bonds remained intact, hence aerial oxidation must be negligible on this time scale under the stated conditions.

At this early stage, we do not have clinical data as to how these proof-of-concept experiments relate to the future use of these gels as advanced biomaterials. However, we anticipate that if these gels were loaded with cell nutrients or drugs, they would degrade and release their payloads in direct and proportionate response to the in situ environment. For example, if these gels were to be used as wound dressings, the payload could be delivered faster if the local biochemical environment was more aggressive as reagents such as hydrogen peroxide or peracetic acid (whivh are often associated with local inflammation) can readily cleave the disulfide bonds and hence cause gel dissolution.

Gel degradation in situ must involve the diffusion of the glutathione (or other reagent required for disulfide cleavage) into and through the gel. Given that these gels comprise at least 90 % water, this diffusion is not expected to be retarded. However, in our proof-of-concept gel degradation experiments, glutathione was added to the free-flowing solution prior to gelation, which means that the glutathione is uniformly distributed within the gel (i.e. there is no diffusional time lag). Moreover, the glutathione concentration in situ is most likely at least an order of magnitude lower than that found in living cells. Thus, we anticipate that gel degradation in situ is expected to proceed on a time scale of hours to days rather than tens of minutes. We expect that such longer time scales are more likely to be of therapeutic value.

In summary, a new type of disulfide-based thermoresponsive triblock copolymer gelator is reported. Cleavage of the central disulfide bond causes irreversible dissolution of the micellar gel. Unlike the hydrolytically degradable poly(amidoamine) hydrogels reported by Ferruti et al., this new "keystone" strategy means that no small-molecule by-products are produced during gel degradation.[13] This degradation can be achieved under physiologically relevant conditions by using naturally occurring oligopeptides such as glutathione, hence such copolymers constitute a new class of injectable gelators that are both biochemically responsive and thermoresponsive.

Received: January 25, 2006
Revised: March 9, 2006
Published online: April 24, 2006

Keywords: biomimetic synthesis · copolymers · gels · micelles · peptide-induced degradation

[1] a) K. Yamamoto, T. Serizawa, Y. Muraoka, M. Akashi, *Macromolecules* **2001**, *34*, 8014; b) C. Wang, J. Kopecek, R. J. Stewart, *Biomacromolecules* **2001**, *2*, 912; c) J. T. Zhang, S. X. Cheng, S. W. Huang, R. X. Zhou, *Macromol. Rapid Commun.* **2003**, *24*, 447; d) K. A. Davis, K. S. Anseth, *Crit. Rev. Ther. Drug Carrier Syst.* **2002**, *19*, 385; e) K. Nam, J. Watanabe, K. Ishihara, *J. Biomater. Sci. Polym. Ed.* **2002**, *13*, 1259; f) K. S. Soppimath, T. M. Aminabhavi, A. M. Dave, S. G. Kumbar, W. E. Rudzinski, *Drug Dev. Ind. Pharm.* **2002**, *28*, 957; g) A. Hatefi, B. J. Amsden, *J. Controlled Release* **2002**, *80*, 9; h) Y. Luo, M. S. Shoichet, *Nat. Mater.* **2004**, *3*, 249; i) A. S. Hoffman, *Adv. Drug Delivery Rev.* **2002**, *43*, 3.

[2] a) J. P. Schneider, D. Pochan, J. B. Ozbas, K. Rajagopal, L. Haines, J. Kretsinger, *J. Am. Chem. Soc.* **2002**, *124*, 15030; b) Y. Ma, Y. Tang, N. C. Billingham, S. P. Armes, A. L. Lewis, *Biomacromolecules* **2003**, *4*, 864; c) Z. Yang, S. Pickard, N. J. Deng, R. J. Barlow, D. Attwood, C. Booth, *Macromolecules* **1994**, *27*, 2371; d) G. Chen, A. S. Hoffman, *Nature* **1995**, *373*, 49; e) F. Illman, T. Tanaka, E. Kokufuta, *Nature* **1991**, *349*, 400.

[3] T. Miyata, N. Asami, T. Uragami, *Nature* **1999**, *399*, 766.

[4] a) K. N. Plunkett, K. L. Berkowski, J. S. Moore, *Biomacromolecules* **2005**, *6*, 632; b) M. Kurishawa, N. Yui, *Macromol. Chem. Phys.* **1998**, *199*, 705; c) M. Kurishawa, Y. Matsuo, N. Yui, *Macromol. Chem. Phys.* **1998**, *199*, 2613.

[5] a) H. A. Aliyar, P. D. Hamilton, N. Ravi, *Biomacromolecules* **2005**, *6*, 204; b) Y. Li, S. P. Armes, *Macromolecules* **2005**, *38*, 8155; c) Y. Liu, X. Shu, G. D. Prestwich, *Biomaterials* **2005**, *26*, 4737; d) X. Shu, Y. Liu, Y. , Y. Luo, M. C. Roberts, G. D. Prestwich, *Biomacromolecules* **2002**, *3*, 1304; e) L. Bromberg, M. Temchenko, V. Alakhov, T. A. Hatton, *Langmuir* **2005**, *21*, 1590; f) K. N. Plunkett, M. L. Kraft, Q. Yu, J. S. Moore, *Macromolecules* **2003**, *36*, 3960.

[6] D. J. Cline, S. E. Redding, S. G. Brohawn, J. N. Psathas, J. P. Schneider, C. Thorpe, *Biochemistry* **2004**, *43*, 15195.

[7] C. Li, Y. Tang, S. P. Armes, C. J. Morris, S. F. Rose, A. W. Lloyd, A. L. Lewis, *Biomacromolecules* **2005**, *6*, 994.

[8] a) J. Wang, K. J. Matyjaszewski, *J. Am. Chem. Soc.* **1995**, *117*, 5614; b) J. Wang, K. Matyjaszewski, *Macromolecules* **1995**, *28*, 7572; c) K. Matyjaszewski, J. Xia, *Chem. Rev.* **2001**, *101*, 2921.

 © 2006 Wiley-VCH Verlag GmbH & Co. KGaA, Weinheim

[9] a) N. V. Tsarevsky, K. Matyjaszewski, *Macromolecules* **2002**, *35*, 9009; b) N. V. Tsarevsky, K. Matyjaszewski, *Macromolecules* **2005**, *38*, 3087.
[10] C. Wu, X. Wang, *Phys. Rev. Lett.* **1998**, *80*, 4092.
[11] a) N. P. Balsara, M. Tirrelli, T. P. Lodge, *Macromolecules* **1991**, *24*, 1975; b) M. Nguyen-Misra, W. L. Mattice, *Macromolecules* **1995**, *28*, 1444; c) A. Semenov, J. F. Joanny, A. R. Khokhlov, *Macromolecules* **1995**, *28*, 1066; d) B. Xu, L. Li, A. Yekta, Z. Masoumi, S. Kanagalingam, M. A. Winnik, K. Zhang, P. M. Macdonald, S. Menchen, *Langmuir* **1997**, *13*, 2447.
[12] S. Carelli, A. Ceriotti, A. Cabibbo, G. Fassina, M. Ruvo, R. Sitia, *Science* **1997**, *277*, 1681.
[13] P. Ferruti, S. Bianchi, E. Ranucci, F. Chiellini, A. M. Piras, *Biomacromolecules* **2005**, *6*, 2229.

 © 2006 Wiley-VCH Verlag GmbH & Co. KGaA, Weinheim

Boron Chemistry

DOI: 10.1002/anie.200600714

Cationic Terminal Borylene Complexes: Interconversion of Amino and Alkoxy Borylenes by an Unprecedented Meerwein–Ponndorf Hydride Transfer**

Deborah L. Kays (née Coombs), Joanna K. Day, Simon Aldridge, Ross W. Harrington, and William Clegg*

Dedicated to Professor Tony Downs on the occasion of his 70th birthday

The fundamental reactivity of transition-metal complexes containing metal–boron double bonds has recently become an area of considerable research activity,[1] reflecting both the development of viable synthetic approaches to such systems (for example, terminal borylene complexes $L_nM{=}BX$),[2–4] and the desire to compare patterns of reactivity with other multiply bonded second-period ligand systems (for example, carbenes and alkylidenes).[5] Within this area, diverse chemistries are emerging, ranging from simple nucleophilic substitution and addition processes dominated by the electrophilic character of the two-coordinate boron center,[4] to synthetically valuable borylene-transfer chemistry involving both transition-metal and wholly organic substrates.[2b,g,6] We have recently demonstrated the first examples of M=B metathesis chemistry; reaction of the cationic aminoborylene complex $[CpFe(CO)_2{=}B(N\mathit{i}Pr_2)]^+[BAr^f{}_4]^-$ (**1**; $Cp = C_5H_5$; $Ar^f = 3,5\text{-}(CF_3)_2C_6H_3$) with $Ph_3E{=}X$ ($E = P$, As; $X = S$, O) yields $[CpFe(CO)_2(EPh_3)]^+[BAr^f{}_4]^-$ and $[XB(N\mathit{i}Pr_2)]_n$ ($X = O$, $n = 3$; $X = S$, $n = 2$).[7]

The widespread application of metathesis processes involving substrates with multiple bonds to carbon[5b,c] has led us to explore the reactivity of **1** towards C=E multiple bonds. Given that the key step in M=B metathesis towards P=O, P=S, and As=O linkages has been shown to be the precoordination of the oxygen or sulfur donor center to boron,[7] it seemed logical to first examine the reactivity of **1** towards polar C=E bonds, such as those present in ketones or imines. Such an investigation also probes the extent to which borylene reactivity can be tuned by modification of the pendant X substituent; the arylborylene complex $[Cp^*Fe(CO)_2{=}B(C_6H_2Me_3\text{-}2,4,6)]^+$ ($Cp^* = C_5Me_5$) has been shown to react with ketones by substitution of the borylene ligand at the iron center, yielding for example, $[Cp^*Fe(CO)_2(\eta^1\text{-}OCPh_2)]^+$.[4b] The reaction of **1** with benzophenone proceeds by neither metathesis nor ligand displacement, but by an entirely unprecedented ligand transformation process: Meerwein–Ponndorf β-hydride transfer from an isopropyl substituent of the aminoborylene ligand to the coordinated ketone generates the first example of an imine-donor-stabilized borylene complex, and the first cationic alkoxyborylene system.

The reaction of **1** with benzophenone (Scheme 1) proceeds by an initial coordination of the ketone at the electrophilic boron center, yielding the thermally fragile intermediate $[CpFe(CO)_2B(N\mathit{i}Pr_2)(OCPh_2)]^+[BAr^f{}_4]^-$ (**2**). Although **2** is labile even at −30 °C, its multinuclear NMR spectra at −50 °C are consistent with an adduct of the type $[CpFe(CO)_2B(N\mathit{i}Pr_2)(OEPh_n)]^+[BAr^f{}_4]^-$.[7] Thus, for example, the detection of inequivalent isopropyl groups by ^1H and ^{13}C NMR spectroscopy (in contrast to the equivalent isopropyl groups in **1**), and of a significantly upfield-shifted ^{11}B NMR resonance (**2**: $\delta_B = 49.0$ ppm; **1**: $\delta_B = 93.5$ ppm) are consistent with the formation of a trigonal-planar boron center (from the linear two-coordinate boron center of **1**) by coordination of the Ph_2CO Lewis base. Very similar spectroscopic changes are observed on formation of the crystallographically characterized boron-bound Ph_3PO adduct $[CpFe(CO)_2B(N\mathit{i}Pr_2)(OPPh_3)]^+[BAr^f{}_4]^-$ (**3a**; Scheme 2): a ^{11}B NMR resonance at $\delta_B = 48.9$, and two ^1H NMR signals for the methyl substituents of the inequivalent isopropyl groups at $\delta_H = 1.06$ and 1.20 ppm.[7]

On warming to room temperature, quantitative conversion of intermediate **2** is detected, and the species formed (**4**) displays a more complex pattern of two doublets (both integrating to three hydrogen atoms), two singlets (also both integrating to three hydrogen atoms), and a septet (integrating to one hydrogen atom) in the alkyl region of its ^1H NMR spectrum. Such a pattern is consistent with the formation of a

[*] Dr. D. L. Kays (née Coombs), J. K. Day, Dr. S. Aldridge
Centre for Fundamental and Applied Main Group Chemistry
School of Chemistry, Cardiff University
Main Building, Park Place, Cardiff, CF10 3AT (UK)
Fax: (+44) 2920-874-030
E-mail: AldridgeS@cardiff.ac.uk
Dr. R. W. Harrington, Prof. W. Clegg
School of Natural Sciences (Chemistry)
Bedson Building, University of Newcastle
Newcastle upon Tyne, NE1 7RU (UK)

[**] We thank the EPSRC for funding (including that for the National Crystallography Service) and for access to the National Mass Spectrometry Facility, and the CCLRC for the award of synchrotron beamtime.

Supporting information for this article is available on the WWW under http://www.angewandte.org or from the author.

 © 2006 Wiley-VCH Verlag GmbH & Co. KGaA, Weinheim

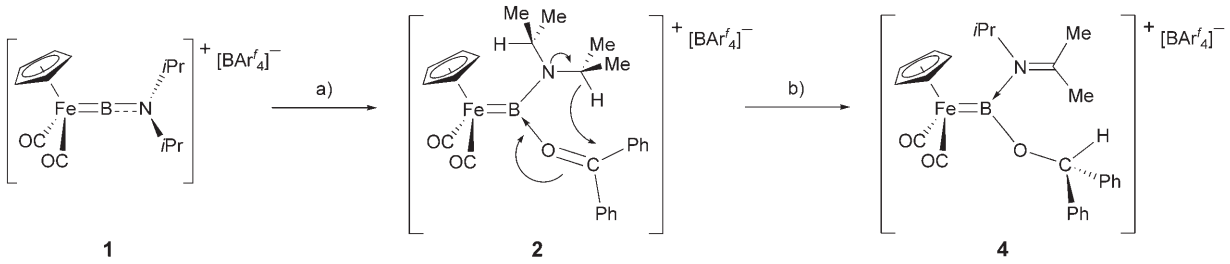

Scheme 1. Reaction of **1** with benzophenone. Reaction conditions: a) **1**, benzophenone (1 equiv), CH_2Cl_2, −78 to −50 °C; b) subsequent warming to room temperature, sonication for 1.5 h, 36% isolated yield.

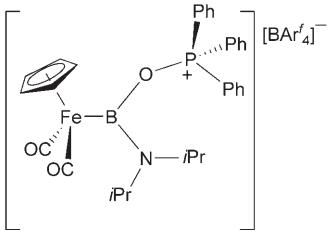

3a

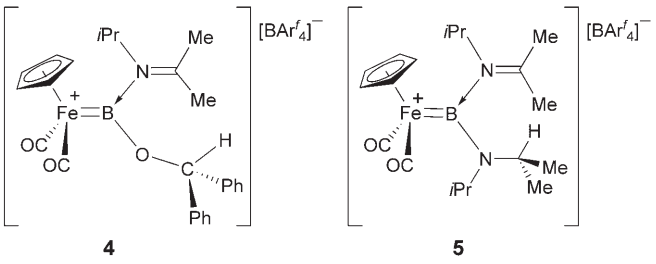

Scheme 2. Contrasting predominant resonance forms for **3a** and imine-stabilized complexes **4** and **5**.

coordinated imine (*i*PrN=CMe$_2$). Compared to the ^{1}H NMR spectrum of the "free" imine ($\delta_H = 1.10$ (d, 6H), 1.85 (s, 3H), 2.00 (s, 3H), 3.60 ppm (sept, 1H)),[8] the chemical shift differences and the splitting of the isopropyl methyl resonances in the alkyl region of the spectrum of **4** are consistent with the electronic and steric effects of coordination. Furthermore, the OC(H)Ph$_2$ fragment implied by the hydride-transfer process that gives rise to the coordinated imine (Scheme 1) is evidenced by signals at $\delta_H = 6.24$ ppm and $\delta_C =$ 89.3 ppm in the ^{1}H and ^{13}C NMR spectra of **4** (compare to $\delta_H = 5.92$ ppm and $\delta_C = 74.2$ ppm for Ph$_2$C(H)OH). The ^{11}B NMR chemical shift for the boron center in the cation of **4** ($\delta_B = 64.0$ ppm) is also consistent with a base-stabilized borylene complex (compare to $\delta_B = 52.1$ ppm for the pyridine-stabilized ethoxyborylene complex Os[B(NC$_5$H$_4$NH)(OEt)]Cl(CO)(PPh$_3$)$_2$[3b]). The carbonyl stretching frequencies ($\tilde{\nu}$(CO) = 2012, 1969 cm^{-1}) in the IR spectrum of **4** are intermediate between those observed for base-free cationic iron–carbonyl complexes with two-coordinate aminoborylene ligands (**1**: $\tilde{\nu}$(CO) = 2070, 2028 cm^{-1};[7] [CpFe(CO)$_2$=B(NCy$_2$)]$^+$[BAr$^f_4$]$^-$ (Cy = C$_6$H$_{11}$): $\tilde{\nu}$(CO) = 2070, 2021 cm^{-1} [9]) and those for neutral complexes with three-coordinate aminoboryl ligands (for example, CpFe(CO)$_2${B(N*i*Pr$_2$)Cl}: $\tilde{\nu}$(CO) = 2001, 1941 cm^{-1} [7]). Although the mass spectrum of **4** contains only peaks due to ions without a coordinated imine group (for example, [CpFe(CO)$_2$B{OC(H)Ph$_2$}]$^+$ ([M−N(*i*Pr)CMe$_2$]$^+$) at $m/z = 371.1$), the loss of a weakly bound ligand under such conditions is amply precedented. Furthermore, the structure of **4**·CH_2Cl_2 in the solid state has subsequently been determined, and it confirms the formulation of **4** as [CpFe(CO)$_2$B{OC(H)Ph$_2$}{N(*i*Pr)CMe$_2$}]$^+$[BAr$^f_4$]$^-$ (Figure 1).

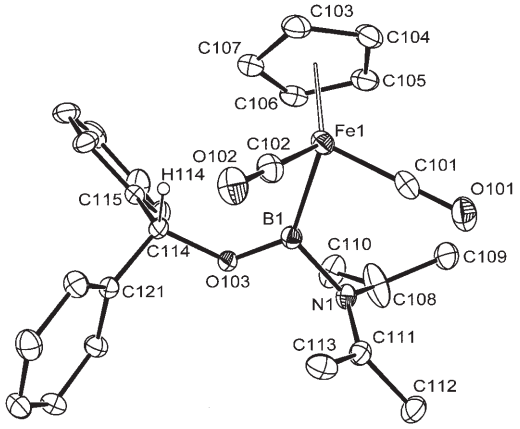

Figure 1. Molecular structure of one of the two crystallographically independent cations in **4**·CH_2Cl_2. Thermal ellipsoids are set at 50% probability. Hydrogen atoms (with the exception of H114) are omitted for clarity. Selected bond lengths [Å] and angles [°]: Fe1−B1 2.000(4), Fe1−C101 1.752(4), B1−O103 1.343(4), O103−C114 1.454(3), B1−N1 1.570(4), N1−C111 1.281(4), N1−C108 1.494(4); Fe1-B1-N1 122.1(2), Fe1-B1-O103 131.6(2), N1-B1-O103 106.2(3), N1-C111-C112 124.5(3), N1-C111-C113 119.9(3), C112-C111-C113 115.6(3), O103-C114-C115 109.5(2), O103-C114-C121 106.7(2), C115-C114-C121 114.7(2).

The solid-state structure of **4**·CH_2Cl_2 not only confirms the gross structural features implied by the spectroscopic data, but also suggests that a description of **4** as a base-stabilized borylene complex (that is, one involving significant contributions from a resonance form incorporating Fe=B and N=C double bonds) is most appropriate (Scheme 2). As such, **4** represents only the second example of a terminal alkoxyborylene complex,[3b] and the first such cationic species; it also represents the first example of an imine-donor-stabilized borylene complex. The bonding in **4** contrasts with that found in the superficially similar complex [CpFe(CO)$_2$B(N*i*Pr$_2$)(OPPh$_3$)]$^+$[BAr$^f_4$]$^-$ (**3a**), which has been shown to best be viewed as a boryl species in which the positive charge is

 © 2006 Wiley-VCH Verlag GmbH & Co. KGaA, Weinheim

largely localized on the pendant phosphorus center (Scheme 2).[7] Thus, the two sets of C–N distances for the *i*PrN=CMe$_2$ fragment in **4** are consistent with the distinct C=N double (1.281(4) and 1.283(4) Å, for the two distinct cations in the asymmetric unit) and C–N single bonds (1.494(4) and 1.508(4) Å) implied by a coordinated imine moiety. In addition, the B–N distances (1.570(4) and 1.575(5) Å) associated with this fragment are significantly longer than the B–N distances typically found for conventional aminoboryl complexes (for example, CpFe(CO)$_2${B(N*i*Pr$_2$)Cl}: 1.389(5) Å[7]), being much more akin to those found for donor–acceptor adducts of imines with borane Lewis acids (for example, Ph(H)C=N(CH$_2$Ph)·B(C$_6$F$_5$)$_3$: 1.627(3) Å[10]). The Fe–B distances for **4** (2.000(4) and 2.001(4) Å) are shorter than those found in either neutral or cationic boryl systems featuring the B(N*i*Pr$_2$) moiety (for example, CpFe(CO)$_2${B(N*i*Pr$_2$)Cl}: 2.054(4) Å; **3a**: 2.057(4) Å[7]), but are somewhat longer than those found in base-free systems featuring a two-coordinate boron center and a M=B double bond (for example, [CpFe(CO)$_2$=B(NCy$_2$)]$^+$[BAr$^f_4$]$^-$: 1.859(6) Å[9]). The smaller extent of bond-length contraction (compared to M–B single bonds) on formation of a M=B double bond in a base-stabilized borylene complex, however, reflects trends previously observed for related osmium–borylene systems.[3] Finally, the metric parameters for the BOC(H)Ph$_2$ unit are indicative of O–B and O–C single bonds;[11] the presence of the hydrogen atom at C114 is reflected in the narrowing of the O-C-C$_{ipso}$ and C$_{ipso}$-C-C$_{ipso}$ angles (sum of angles = 330.6° (mean)) compared to those of benzophenone (sum of angles = 360°).[12]

The contrasting reactivity of **1** towards E=O (E = P, As) and C=O bonds presumably reflects the differing electronic structures of the first-formed boron-bound adducts [CpFe(CO)$_2$B(N*i*Pr$_2$)(OEPh$_n$)]$^+$[BAr$^f_4$]$^-$ (Scheme 3). In contrast to the Ph$_3$PO (**3a**) and Ph$_3$AsO (**3b**) adducts of **1**,[7] the corresponding benzophenone adduct (**2**) possesses a pendant atom E (the carbonyl carbon) with significant electrophilic character. In essence, the cationic borylene complex **1** serves as a Lewis acid to activate the benzophenone carbonyl group to nucleophilic attack, in this case by the β hydride of a proximal isopropyl group from the amino substituent. As such, this chemistry represents an unprecedented ligand modification by a Meerwein–Ponndorf reduction.[13] The degree of electrophilic character at the carbonyl carbon atom can be shown to be a key factor in facilitating hydride transfer. Thus, the reaction of **1** with *i*PrN=CMe$_2$ leads to the formation of the imine adduct [CpFe(CO)$_2$B(N*i*Pr$_2$){N(*i*Pr)CMe$_2$}]$^+$[BAr$^f_4$]$^-$ (**5**; see Supporting Information for crystallographic data). In this case, however, no hint of hydride transfer is observed by ^{1}H NMR spectroscopy, even at 100 °C, presumably owing to the less electrophilic nature of the imine substrate compared to benzophenone.

The reactivity of aminoborylene complex **1** towards benzophenone contrasts markedly with that of the related cationic arylborylene complex [Cp*Fe(CO)$_2$B(C$_6$H$_2$Me$_3$-2,4,6)]$^+$[BAr$^f_4$]$^-$ towards ketones, which has been shown to proceed by attack at the transition-metal center and displacement of the borylene ligand to give [Cp*Fe(CO)$_2$(η^1-OCR$_2$)]$^+$ (R = Ph, Me).[4b] The differing reactivities of **1** and [Cp*Fe(CO)$_2$B(C$_6$H$_2$Me$_3$-2,4,6)]$^+$[BAr$^f_4$]$^-$ towards C=O double bonds provide convincing evidence of the crucial role played by the electronic properties of the borylene ligand in determining the chemistry of the metal complex. Further comparative studies involving substrates with C=S, C=N, C=P, and C≡P bonds will be reported in due course.

Experimental Section

Reaction of **1** with benzophenone (intermediate **2**): The reaction of **1** (0.071 g, 0.062 mmol) with benzophenone (1 equiv) in CD$_2$Cl$_2$ (2 cm^3) in a J. Young NMR tube on warming from −78 °C to room temperature was monitored by multinuclear (^{1}H, ^{11}B, ^{13}C, and ^{19}F) NMR spectroscopy. On warming to −50 °C, the borylene (δ_B = 93.5 ppm) and isopropyl methyl (δ_H = 1.39 ppm) signals assigned to **1** were quantitatively replaced by a broad resonance at δ_B = 49.0 ppm and by two doublets at δ_H = 1.15 and 1.18 ppm. Further warming to room temperature led to a second set of changes in the ^{1}H and ^{11}B NMR spectra: the resonance at δ_B = 49.0 ppm converted into a signal at δ_B = 64.0 ppm, and the two methyl signals of the isopropyl group were replaced by a more complex pattern of two doublets (δ_H = 1.28 and 1.44 ppm) and two singlets (δ_H = 2.05 and 2.37 ppm). The thermally labile first-formed intermediate was identified as **2**, on the basis of multinuclear NMR spectroscopy at −50 °C, whereas the final product **4** can be prepared in yields of ca. 36 %. **2**: ^{1}H NMR (300 MHz, CD$_2$Cl$_2$, −50 °C): δ = 1.15 (d, J = 6.5 Hz, 6H, CH$_3$ of *i*Pr), 1.18 (d, J = 6.5 Hz, 6H, CH$_3$ of *i*Pr), 3.44 (sept, J = 6.5 Hz, 1H, CH of *i*Pr), 3.96 (sept, J = 6.5 Hz, 1H, CH of *i*Pr), 4.26 (s, 5H, Cp), 7.36–8.11 (br m, 10H, Ph$_2$CO), 7.48 (s, 4H, *p*-CH of [BAr$^f_4$]$^-$), 7.69 ppm (s, 8H, *o*-CH of [BAr$^f_4$]$^-$); ^{13}C NMR (76 MHz, CD$_2$Cl$_2$, −50 °C): δ = 21.6 (CH$_3$ of *i*Pr), 24.6 (CH$_3$ of *i*Pr), 47.9 (CH of *i*Pr), 53.7 (CH of *i*Pr), 85.1 (Cp), 118.4 (*p*-CH of [BAr$^f_4$]$^-$), 125.3 (q, $^1J_{CF}$ = 272 Hz, CF$_3$ of [BAr$^f_4$]$^-$), 129.6 (q, $^2J_{CF}$ = 31 Hz, *m*-C of [BAr$^f_4$]$^-$), 131.0 (*m*-CH of Ph$_2$CO), 132.7 (*p*-CH of Ph$_2$CO), 135.5 (*o*-CH of [BAr$^f_4$]$^-$), 136.8 (*o*-CH of Ph$_2$CO), 141.3 (*ipso*-C of Ph$_2$CO), 162.6 (q, $^1J_{CB}$ = 50 Hz, *ipso*-C of [BAr$^f_4$]$^-$), 215.1 ppm (CO), carbonyl carbon of Ph$_2$CO not observed; ^{11}B NMR (96 MHz, CD$_2$Cl$_2$, −50 °C): δ = −7.8 ([BAr$^f_4$]$^-$),

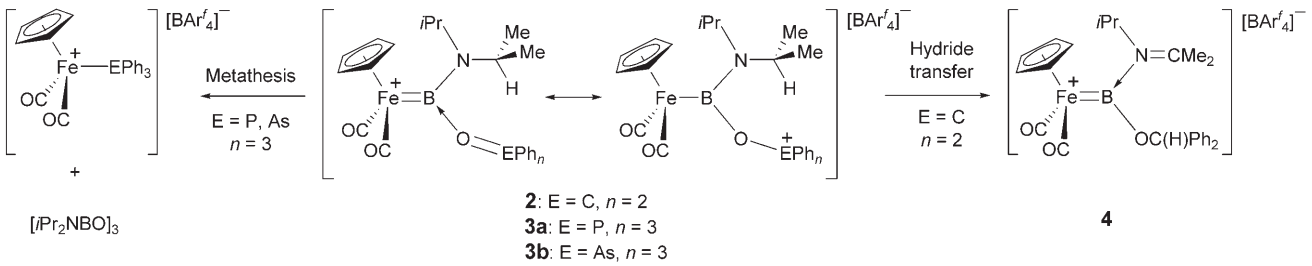

Scheme 3. Contrasting metathesis and β-hydride-transfer reactions for adducts of the type [CpFe(CO)$_2$B(N*i*Pr$_2$)(OEPh$_n$)]$^+$[BAr$^f_4$]$^-$.

 © 2006 Wiley-VCH Verlag GmbH & Co. KGaA, Weinheim

49.0 ppm (br, fwhm 1700 Hz, borylene); ^{19}F NMR (283 MHz, CD_2Cl_2, −50 °C): $\delta = 61.7$ ppm (CF_3).

4: **1** (0.285 g, 0.248 mmol) and benzophenone (1 equiv) were dissolved in CH_2Cl_2 at −78 °C, and the stirred reaction mixture was warmed to room temperature over 2 h. Sonication for a further 1.5 h drove the reaction to completion (as judged by ^{11}B NMR spectroscopy). Filtration and concentration of the reaction mixture, followed by layering with hexanes and storage at −30 °C led to the formation of **4** as colorless crystals suitable for X-ray diffraction. Isolated yield: 0.120 g, 36 %. ^{1}H NMR (400 MHz, CD_2Cl_2): $\delta = 1.28$ (d, $J = 6.9$ Hz, 3H, CH_3 of *i*Pr), 1.44 (d, $J = 6.9$ Hz, 3H, CH_3 of *i*Pr), 2.05 (s, 3H, CH_3 of N=CMe_2), 2.37 (s, 3H, CH_3 of N=CMe_2), 4.07 (sept, $J = 6.9$ Hz, 1H, CH of *i*Pr), 4.81 (s, 5H, Cp), 6.24 (s, 1H, CH of Ph_2CHO), 7.19–7.32 (m, 10H, Ph of Ph_2CO), 7.47 (s, 4H, *p*-CH of $[BAr^f_4]^-$), 7.64 ppm (s, 8H, *o*-CH of $[BAr^f_4]^-$); ^{13}C NMR (76 MHz, CD_2Cl_2): $\delta = 21.0$, 21.1 (CH_3 of *i*Pr), 23.8, 27.3 (CH_3 of N=CMe_2), 55.1 (CH of *i*Pr), 85.0 (Cp), 89.3 (CH of Ph_2CHO), 117.5 (*p*-CH of $[BAr^f_4]^-$), 124.7 (q, $^1J_{CF} = 272$ Hz, CF_3 of $[BAr^f_4]^-$), 125.8, 125.9 (*p*-CH of Ph_2CHO), 128.9 (q, $^2J_{CF} = 31$ Hz, *m*-C of $[BAr^f_4]^-$), 128.8, 129.0 (*m*-CH of Ph_2CHO), 129.2, 129.4 (*o*-CH of Ph_2CHO), 134.8 (*o*-CH of $[BAr^f_4]^-$), 140.2, 140.4 (*ipso*-C of Ph_2CHO), 161.8 (q, $^1J_{CB} = 50$ Hz, *ipso*-C of $[BAr^f_4]^-$), 182.1 (C of N=CMe_2), 212.7, 213.8 ppm (CO); ^{11}B NMR (96 MHz, CD_2Cl_2): $\delta = -7.6$ ($[BAr^f_4]^-$), 64.0 ppm (br, fwhm ca. 450 Hz, borylene); ^{19}F NMR (283 MHz, CD_2Cl_2): $\delta = -62.7$ ppm (CF_3); IR (CD_2Cl_2): $\tilde{\nu}$(CO) = 2012, 1969 cm^{-1}; MS (CI): *m*/*z* (%): 371.1 (8) $[M-N(iPr)CMe_2]^+$. A reproducible elemental analysis for **4** could not be obtained, possibly owing to the presence of CH_2Cl_2 solvent in the crystal lattice. Crystallographic data for **4**·CH_2Cl_2: $C_{59}H_{43}B_2Cl_2F_{24}FeNO_3$, $M_r = 1418.3$, triclinic, $P\bar{1}$, $a = 12.7448(9)$, $b = 19.0873(14)$, $c = 25.3695(19)$ Å, $\alpha = 86.511(2)$, $\beta = 85.645(2)$, $\gamma = 85.320(2)$°, $V = 6123.9(8)$ Å^3, $Z = 4$, $\rho_{calcd} = 1.538$ Mg m^{-3}, $T = 120(2)$ K, synchrotron radiation, $\lambda = 0.6712$ Å, 50972 reflections collected, which were used in all calculations, $R_1 = 0.0623$, $wR_2 = 0.1607$ ($F^2 > 2\sigma(F^2)$), $R_1 = 0.0838$, $wR_2 = 0.1797$ (all data), max./min. residual electron density 0.91/−1.03 e Å^{-3}. CCDC-296849 (**4**·CH_2Cl_2) contains the supplementary crystallographic data for this paper. These data can be obtained free of charge from The Cambridge Crystallographic Data Centre via www.ccdc.cam.ac.uk/data_request/cif.

5: The imine *i*PrN=CMe_2 (0.039 mL, 1 equiv) was added to a solution of **1** (0.338 g, 0.294 mmol) in CH_2Cl_2 at −78 °C, and the reaction mixture was warmed to room temperature over 20 min. At this point, the reaction was judged to be complete by ^{11}B NMR spectroscopy. Filtration of the reaction mixture, followed by layering with hexanes and storage at −30 °C led to the formation of **5** as pale yellow crystals suitable for X-ray diffraction. Isolated yield: 0.110 g, 30 %. ^{1}H NMR (400 MHz, CD_2Cl_2): $\delta = 1.26$ (d, $J = 7.0$ Hz, 3H, CH_3 of *i*Pr), 1.31 (d, $J = 7.1$ Hz, 3H, CH_3 of *i*Pr), 1.35 (d, $J = 7.2$ Hz, 3H, CH_3 of *i*Pr), 1.38 (d, $J = 7.2$ Hz, 3H, CH_3 of *i*Pr), 1.56 (d, $J = 6.7$ Hz, 3H, CH_3 of *i*Pr), 1.58 (d, $J = 6.6$ Hz, 3H, CH_3 of *i*Pr), 2.23 (s, 3H, CH_3 of N=CMe_2), 2.47 (s, 3H, CH_3 of N=CMe_2), 3.66 (sept, $J = 7.0$ Hz, 1H, CH of *i*Pr), 4.00 (sept, $J = 6.9$ Hz, 1H, CH of *i*Pr), 4.52 (sept, $J = 7.1$ Hz, 1H, CH of *i*Pr), 4.91 (s, 5H, Cp), 7.51 (s, 4H, *p*-CH of $[BAr^f_4]^-$), 7.66 ppm (s, 8H, *o*-CH of $[BAr^f_4]^-$); ^{13}C NMR (76 MHz, CD_2Cl_2): $\delta = 21.3$, 21.5, 24.4, 24.7, 25.1, 25.8 (CH_3 of *i*Pr), 24.3, 28.5 (CH_3 of N=CMe_2), 51.6, 55.1, 55.4 (CH of *i*Pr), 85.0 (Cp), 117.6 (*p*-CH of $[BAr^f_4]^-$), 124.7 (q, $^1J_{CF} = 272$ Hz, CF_3 of $[BAr^f_4]^-$), 128.9 (q, $^2J_{CF} = 31$ Hz, *m*-C of $[BAr^f_4]^-$), 134.9 (*o*-CH of $[BAr^f_4]^-$), 161.8 (q, $^1J_{CB} = 50$ Hz, *ipso*-C of $[BAr^f_4]^-$), 183.8 (C of N=CMe_2), 222.4 ppm (CO); ^{11}B NMR (96 MHz, CD_2Cl_2): $\delta = -7.6$ ($[BAr^f_4]^-$), 53.7 ppm (borylene); ^{19}F NMR (283 MHz, CD_2Cl_2): $\delta = -62.7$ ppm (CF_3); IR (CD_2Cl_2): $\tilde{\nu}$(CO) = 2007, 1951 cm^{-1}; elemental analysis (%) calcd: C 48.99, H 3.55, N 2.24; found: C 48.51, H 3.39, N 2.17. Crystallographic data for **5** included in Supporting Information.

Received: February 23, 2006
Published online: April 24, 2006

Keywords: boron · borylene ligands · hydrogen transfer · imines · iron

[1] For recent reviews of borylene chemistry see: a) H. Braunschweig, M. Colling, *Eur. J. Inorg. Chem.* **2003**, 393 – 403; b) S. Aldridge, D. L. Coombs, *Coord. Chem. Rev.* **2004**, *248*, 535 – 559; c) H. Braunschweig, *Adv. Organomet. Chem.* **2004**, *51*, 163 – 192; d) H. Braunschweig, D. Rais, *Heteroat. Chem.* **2005**, *16*, 566 – 571.

[2] a) H. Braunschweig, C. Kollann, U. Englert, *Angew. Chem.* **1998**, *110*, 3355 – 3357; *Angew. Chem. Int. Ed.* **1998**, *37*, 3179 – 3180; b) H. Braunschweig, M. Colling, C. Kollann, H. G. Stammler, B. Neumann, *Angew. Chem.* **2001**, *113*, 2359 – 2361; *Angew. Chem. Int. Ed.* **2001**, *40*, 2298 – 2300; c) H. Braunschweig, M. Colling, C. Kollann, K. Merz, K. Radacki, *Angew. Chem.* **2001**, *113*, 4327 – 4329; *Angew. Chem. Int. Ed.* **2001**, *40*, 4198 – 4200; d) H. Braunschweig, M. Colling, C. Hu, K. Radacki, *Angew. Chem.* **2003**, *115*, 215 – 218; *Angew. Chem. Int. Ed.* **2003**, *42*, 205 – 208; e) H. Braunschweig, K. Radacki, D. Scheschkewitz, G. R. Whittell, *Angew. Chem.* **2005**, *117*, 1685 – 1688; *Angew. Chem. Int. Ed.* **2005**, *44*, 1658 – 1661; f) H. Braunschweig, D. Rais, K. Uttinger, *Angew. Chem.* **2005**, *117*, 3829 – 3832; *Angew. Chem. Int. Ed.* **2005**, *44*, 3763 – 3766; g) H. Braunschweig, K. Radacki, D. Rais, F. Seeler, *Angew. Chem.* **2006**, *118*, 1087 – 1090; *Angew. Chem. Int. Ed.* **2006**, *45*, 1066 – 1069.

[3] a) G. J. Irvine, C. E. F. Rickard, W. R. Roper, A. Williamson, L. J. Wright, *Angew. Chem.* **2000**, *112*, 978 – 980; *Angew. Chem. Int. Ed.* **2000**, *39*, 948 – 950; b) C. E. F. Rickard, W. R. Roper, A. Williamson, L. J. Wright, *Organometallics* **2002**, *21*, 4862 – 4872.

[4] a) D. L. Coombs, S. Aldridge, C. Jones, D. J. Willock, *J. Am. Chem. Soc.* **2003**, *125*, 6356 – 6357; b) D. L. Coombs, S. Aldridge, A. Rossin, C. Jones, D. J. Willock, *Organometallics* **2004**, *23*, 2911 – 2926.

[5] See for example: a) W. A. Nugent, J. M. Mayer, *Metal Ligand Multiple Bonds*, Wiley Interscience, New York, **1988**; b) R. R. Schrock, *J. Chem. Soc. Dalton Trans.* **2001**, 2541 – 2550; c) T. M. Trnka, R. H. Grubbs, *Acc. Chem. Res.* **2002**, *35*, 18 – 29.

[6] H. Braunschweig, T. Herbst, D. Rais, F. Seeler, *Angew. Chem.* **2005**, *117*, 7627 – 7629; *Angew. Chem. Int. Ed.* **2005**, *44*, 7461 – 7463.

[7] D. L. Kays, J. K. Day, L.-L. Ooi, S. Aldridge, *Angew. Chem.* **2005**, *117*, 7623 – 7626; *Angew. Chem. Int. Ed.* **2005**, *44*, 7457 – 7460.

[8] M. Newcomb, T. Varick, S. H. Goh, *J. Am. Chem. Soc.* **1990**, *112*, 5186 – 5192.

[9] S. Aldridge, C. Jones, D. L. Kays, T. Gans-Eichler, manuscript in preparation.

[10] J. M. Blackwell, W. E. Piers, M. Parvez, R. McDonald, *Organometallics* **2002**, *21*, 1400 – 1407.

[11] D. L. Coombs, S. Aldridge, C. Jones, *Appl. Organomet. Chem.* **2003**, *17*, 356 – 360.

[12] a) E. B. Fleischer, N. Sung, S. Hawkinson, *J. Phys. Chem.* **1989**, *93*, 4311 – 4312; b) H. Kutzke, H. Klapper, R. B. Hammond, K. J. Roberts, *Acta Crystallogr. Sect. B* **2000**, *56*, 486 – 496.

[13] For a recent review encompassing aspects of the Meerwein–Ponndorf reduction see: P. H. M. Budzelaar, G. Talarico, *Struct. Bonding (Berlin)* **2003**, *105*, 141 – 165.

 © 2006 Wiley-VCH Verlag GmbH & Co. KGaA, Weinheim

Host–Guest Chemistry

DOI: 10.1002/anie.200600405

A Deep, Water-Soluble Cavitand Acts as a Phase-Transfer Catalyst for Hydrophobic Species**

*Richard J. Hooley, Shannon M. Biros, and Julius Rebek, Jr.**

Product inhibition is generally a problem for catalysis by synthetic receptors.[1] Supramolecular catalysts do not show the exquisite recognition of transition structures versus products required for high turnover and, with few exceptions,[2,3] their reactions slow down, then stop. We have now encountered cases of phase-transfer catalysis[4] with the water-soluble tetracarboxylate cavitand **1** (Scheme 1).[5] The reactions produce anionic products that are replaced with a neutral reactant, thus forcing high turnover. The results suggest that moving beyond shape complementarity in the recognition event can lead to efficient catalysts.

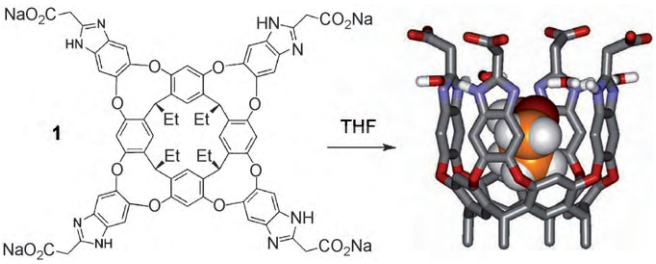

Scheme 1. Water-soluble synthetic receptor **1** and a representation of the complex of **1** with THF (Maestro v7.0.2; AMBER forcefield;[6] some groups are omitted for clarity).

Normal alkanes, which are essentially insoluble in water, can be extracted into aqueous solutions containing **1** and form stoichiometric 1:1 complexes.[7] Hydrophobic stabilization drives this binding and leads to very high association constants. The open-ended nature of the receptor exposes a portion of the guest to the aqueous environment. When the guest gains a water-soluble functionality by chemical transformation, the hydrophobic stabilization of the guest is decreased along with the binding affinity. This allows the guest to be replaced by the starting material, thus leading to turnover and the use of the cavitand as a phase-transfer catalyst (Figure 1). For example, sodium decyl sulfate (SDS) is a good guest for **1** below its critical micelle concentration,[8] but no binding is observed at higher concentrations; the guest only binds if dissolution in water is unfavorable.[9]

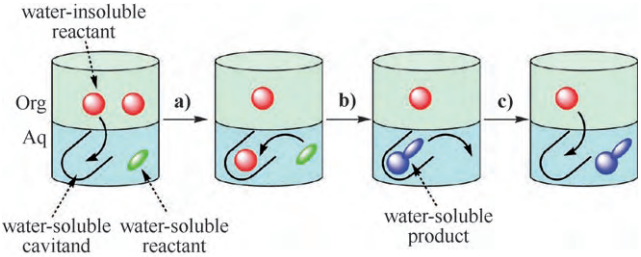

Figure 1. The phase-transfer process. a) The water-insoluble guest is extracted into aqueous solution by cavitand **1**. b) The bound guest, with its reactive group protruding from the cavity, reacts with an aqueous partner. c) The product of this union gains water solubility and leaves the cavitand, thus allowing for turnover and catalysis. Org = organic phase, Aq = aqueous phase.

We used a "two-part" reactant to effect the process: a hydrophobic anchor (to provide water insolubility and shape complementarity for the cavitand) and a reactive functionality, *N*-substituted maleimides. Species such as *N*-adamantylmaleimide **3** show no water solubility by NMR spectroscopic analysis, yet maleimides **3–9** are all extracted into a solution of **1** in D_2O. Their NMR spectra show that the hydrocarbon portions of substrates **3–9** are bound inside the cavity, whereas the maleimide function is exposed to the solvent.

A water-soluble coupling partner that reacts well with the maleimide and confers water solubility on the product was found in the commercially available thiol **2**. Reaction of **2** with maleimide **3** proceeds smoothly to completion in less than 10 minutes in a homogeneous THF/H_2O solution to give product **10**. Water-soluble succinimide **10** shows no affinity for **1**, thus promising that the product would be displaced from the cavitand by the starting material.

Table 1 shows the results of the addition of thiol **2** to various *N*-substituted maleimides **3–9** in a two-phase (CD_2Cl_2/D_2O) system in the presence and absence of **1** as the catalyst. The reactions in the presence of 2 mol% **1** showed a significant rate enhancement relative to the uncatalyzed process. The lack of affinity of the water-soluble products for **1** allows the use of only 2 mol% catalyst, thus suggesting that very little (if any) product inhibition occurs.

The larger maleimides required longer times for completion of the reaction, and the rate acceleration was correspondingly greater. Only *N*-*n*-octylmaleimide **7** was a poor substrate for the reaction, with the starting material still present after 2 days. Maleimide **7** was almost completely insoluble in water, and even the anionic product **14** was only sparingly soluble. The background rate for this reaction was very slow; less than 1% completion was observed after 51 h, and only 3% conversion occurred after 220 h. Both *N*-

[*] Dr. R. J. Hooley, S. M. Biros, Prof. J. Rebek, Jr.
The Skaggs Institute for Chemical Biology and
Department of Chemistry
The Scripps Research Institute
10550 North Torrey Pines Road, La Jolla, CA 92037 (USA)
Fax: (+1) 858-784-2876
E-mail: jrebek@scripps.edu

[**] We are grateful to the Skaggs Institute and the National Institutes of Health (GM 27932) for financial support and to Dr. L.B. Pasternak and Dr. D-H. Huang for NMR assistance. R.J.H. is a Skaggs Postdoctoral fellow.

Supporting information for this article is available on the WWW under http://www.angewandte.org or from the author.

© 2006 Wiley-VCH Verlag GmbH & Co. KGaA, Weinheim

Table 1: Scope of the phase-transfer process.[a]

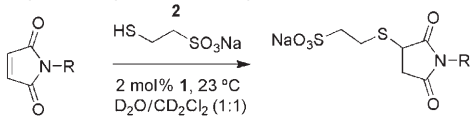

3-9 10-16

Maleimide		*t* [h]	Yield [%][b] (2 mol% **1**)	Yield [%] (0 mol% **1**)[b]
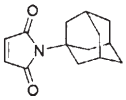	**3**	24	81	13
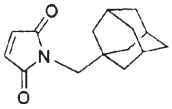	**4**	4.5	82	1
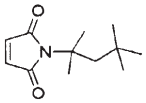	**5**	9	76	7
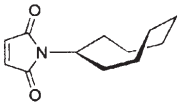	**6**	4.5	80	15
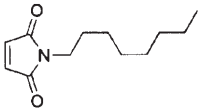	**7**	51	25	1
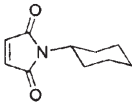	**8**	2	98	12
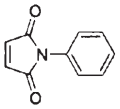	**9**	1	78	60

[a] Maleimide (70 mM in CD_2Cl_2) was combined with **1** (1.4 mM) and **2** (100 mM) in D_2O and stirred at 23 °C. [b] Yields determined by dilution with a stock solution (6.2 mM) of dipotassium 1,2-benzenedisulfonate in D_2O and comparison of integrals in the ^{1}H NMR spectrum.

cyclohexylmaleimide (**8**) and *N*-phenylmaleimide (**9**) reacted quickly, but showed relatively high background reaction rates because of their partial solubility in water. A competition experiment between **3** and **8** showed that selectivity was possible. When reacted in a two-phase system in the presence of 2 mol% **1**, significant selectivity (>8:1) for the reaction of **8** over **3** was observed. When the reaction was performed in the absence of catalyst under homogeneous conditions (1:1 THF/H_2O), the ratio of products was 1:1.

A good turnover was achieved with 2 mol% catalyst, but lower concentrations of catalyst were also effective. The reaction of **6** and **2** for 2 h in the presence of 1 and 0.5 mol% **1** gave yields of 31 and 15%, respectively. The conversion observed at 0.2 mol% catalyst (8%) was not significantly greater than that of the background reaction.

Why do the rates vary so much for processes with very similar reactants? There are two steps to the phase-transfer process which could contribute to the observed differences: the transfer from the organic phase to the aqueous phase (Figure 1, step a) and the reaction (step b). The relative rate of the nucleophilic addition step was determined by treating a preformed complex of **1** and **3** (1 mM) with an equimolar amount of **2**. Complete conversion into the product was observed in less than 1 minute, thus indicating that the second-order nucleophilic addition step is much faster than the overall process. The rates of addition for each of the complexed maleimides should be approximately the same. A similarly rapid rate was observed when a 1 mM aqueous solution of *N*-methylmaleimide was treated with **2**.

The rate of the overall process is determined by the transfer rate of the maleimide reactant into the aqueous layer. The innate water solubility of the maleimide and its affinity for the cavitand are responsible for the differences in the transfer rates. Certain fast-reacting species, namely, **8** and **9**, are slightly water soluble, and so the effectiveness of their phase transfer is not determined solely by binding affinity (they have poor shape complementarity for **1**). However, as the size of the alkyl substituent increases, the water solubility drops to a level at which it no longer dominates the phase-transfer process. These larger species **3**–**7** are transferred in accordance with their binding properties.

The rate difference between **3** and **4** is surprising; the addition of only one methylene unit causes a significant increase in reaction rate. The ^{1}H NMR spectra of the complexes give an illustration of the relative positions of the maleimide group when bound in **1** (see the Supporting Information for the ^{1}H NMR spectra). The chemical shift for the olefinic protons in *N*-methylmaleimide in D_2O ($\delta =$ 6.88 ppm) can be used as a reference to approximate the extent to which the maleimide is unaffected by the magnetic anisotropy of the cavitand. The further upfield the olefinic protons of the guest are shifted, the "deeper" the maleimide resides in the cavity. These signals of the longer guests **4**, **6**, and **7** were essentially unshifted ($\delta = 6.83$, 6.80, and 6.96 ppm, respectively), thus showing that the large alkyl substituent fills the cavity and leaves the maleimide near the rim of the cavitand. Maleimides **5** and **8** are bound more deeply because of their small size, with olefinic CH shifts of $\delta = 6.74$ and 6.73 ppm, respectively, but the olefinic protons of **3** were much more highly shifted ($\delta = 6.58$ ppm), thus indicating that the guest is located even deeper than the small cyclohexylmaleimide **8**.[10] These $\Delta\delta$ values are not large and indicate that the maleimide function is situated at the cavitand opening, well positioned for reaction.

Table 1 shows that **4** is far more reactive in the phase-transfer process than **3**, even though their sizes (and water solubilities) are similar. The major difference between the two is that **4** is a far better guest for **1** than **3**. When an equimolar mixture of solids **4** and **3** is exposed to a solution of **1**, **4** is preferentially encapsulated by a ratio of 6:1 (Figure 2). As discussed above, the maleimide moiety is positioned deeper in the cavity in **3** as opposed to **4**. The adamantyl group has good shape complementarity for **1**, but the binding of *N*-adamantylmaleimide (**3**) evidently forces the carbonyl groups of the maleimide too close to the benzimidazole walls, thereby lowering the binding affinity. In the case of **4**, the maleimide group is positioned further from the walls, and so binding affinity (and consequently the rate of phase transfer) is increased. Figure 2 shows molecular models of the complexes

 © 2006 Wiley-VCH Verlag GmbH & Co. KGaA, Weinheim

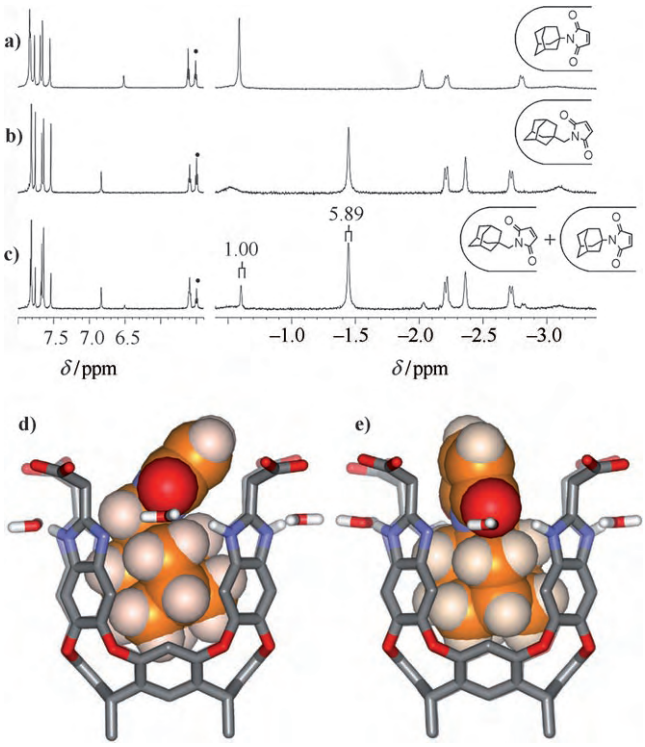

Figure 2. ^{1}H NMR spectra of the complexes of cavitand **1** (1 mM, D_2O) and a) *N*-adamantylmaleimide (**3**), b) *N*-adamantylmethylmaleimide (**4**), and c) an equimolar mixture of **3** and **4** (●, peak from "free" cavitand **1** binding THF). Representations of the complexes of **1** with d) **4** and e) **3** (Maestro v7.0.2; AMBER forcefield;[6] some groups are omitted for clarity).

3·**1** and **4**·**1**, from which the relative positions of the maleimide oxygen atoms may be seen.

The cavitand is also useful to effect transfer between the solid and liquid phases. When solid **3** was added to a solution of **2** and 2 mol% **1**, no dissolution was observed; the maleimide merely floated on top of the solution. After 2 hours of vigorous stirring, quantitative consumption of starting material had occurred, thus yielding product **10**, as observed in the solid–liquid cases described above. In the absence of the catalyst, the maleimide was present even after 4 days of stirring. Quantitative analysis of this process proved difficult, however, as the rate of the reaction was highly dependent not only upon the rate of stirring, but also on the physical nature of the solid maleimide: recrystallized maleimide and maleimide purified by chromatography on silica gel, identical by ^{1}H NMR spectroscopic analysis, gave large variances in rate (the large acceleration in the presence of the catalyst was still observed in each case). The slow rate of reaction for the uncatalyzed process (relative to the rapid conversion observed in THF/H_2O) suggests that this reaction is not an example of acceleration "on water", as described recently.[11]

In conclusion, water-soluble tetracarboxylate cavitand **1** extracts insoluble maleimides into the aqueous phase, whereupon reaction with thiol **2** occurs. The anionic products are released from the cavitand and replaced by the reactant, thus allowing catalytic phase-transfer processes with little-to-no observed product inhibition. The efficiency of these reactions is governed by both the intrinsic solubility of the reactants and the binding affinity of the substrates for the cavitand. Accordingly, selective reactions can be conceived for suitably sized molecules bearing a hydrophobic "handle". Further studies on the applications of **1** to promote reactions of such species are underway.

Received: January 30, 2006
Published online: April 20, 2006

Keywords: aqueous reactions · hydrophobic effect · molecular recognition · NMR spectroscopy · phase-transfer catalysis

[1] F. Hof, S. L. Craig, C. Nuckolls, J. Rebek, *Angew. Chem.* **2002**, *114*, 1556–1578; *Angew. Chem. Int. Ed.* **2002**, *41*, 1488–1508.
[2] a) J. M. Kang, G. Hilmersson, J. Santamaria, J. Rebek, *J. Am. Chem. Soc.* **1998**, *120*, 3650–3656; b) J. Chen, J. Rebek, *Org. Lett.* **2002**, *4*, 327–329; c) B. W. Purse, A. Gissot, J. Rebek, *J. Am. Chem. Soc.* **2005**, *127*, 11222–11223.
[3] Some successful examples of supramolecular catalysis include: a) W. L. Mock, T. A. Irra, J. P. Wepsiec, T. L. Manimaran, *J. Org. Chem.* **1983**, *48*, 3619–3620; b) A. McCurdy, L. Jiminez, D. A. Stauffer, D. A. Dougherty, *J. Am. Chem. Soc.* **1992**, *114*, 10314–10321; c) J. M. Kang, J. Santamaria, G. Hilmersson, J. Rebek, *J. Am. Chem. Soc.* **1998**, *120*, 7389–7390; d) D. Fiedler, R. G. Bergman, K. N. Raymond, *Angew. Chem.* **2004**, *116*, 6916–6919; *Angew. Chem. Int. Ed.* **2004**, *43*, 6748–6751; e) H. Ito, T. Kusukawa, M. Fujita, *Chem. Lett.* **2000**, 598–599.
[4] a) R. Breslow, S. D. Dong, *Chem. Rev.* **1998**, *98*, 1997–2011; b) S. Shimizu, T. Suzuki, S. Shirakawa, Y. Sasaki, C. Hirai, *Adv. Synth. Catal.* **2002**, *344*, 370–378; c) M. Baur, M. Frank, J. Schatz, F. Schildbach, *Tetrahedron* **2001**, *57*, 6985–6991.
[5] S. M. Biros, E. C. Ullrich, F. Hof, L. Trembleau, J. Rebek, *J. Am. Chem. Soc.* **2004**, *126*, 2870–2876.
[6] F. Mohamadi, N. G. J. Richards, W. C. Guida, R. Liskamp, M. Lipton, C. Caufield, G. Chang, T. Hendrickson, W. C. Still, *J. Comput. Chem.* **1990**, *11*, 440–467.
[7] R. J. Hooley, S. M. Biros, J. Rebek, *Chem. Commun.* **2006**, *5*, 509–510.
[8] L. Trembleau, J. Rebek, *Science* **2003**, *301*, 1219–1220.
[9] L. Trembleau, J. Rebek, *Chem. Commun.* **2004**, 58–59.
[10] Under the conditions used to form the complexes, *N*-phenylmaleimide (**9**) was hydrolyzed to *N*-phenylmaleamic acid as a result of the extra lability of the C–N amide bond. In the phase-transfer process, no products from hydrolysis were detected. The nucleophilic addition of **2** is evidently much faster than the competing hydrolysis.
[11] S. Narayan, J. Muldoon, M. G. Finn, V. G. Fokin, H. C. Kolb, K. B. Sharpless, *Angew. Chem.* **2005**, *117*, 3339–3343; *Angew. Chem. Int. Ed.* **2005**, *44*, 3275–3279.

 © 2006 Wiley-VCH Verlag GmbH & Co. KGaA, Weinheim

Sulfur Complexes

DOI: 10.1002/anie.200600640

Reversible Sulfurization–Desulfurization of Tungsten Bis(dithiolene) Complexes

Hideki Sugimoto, Reiko Tajima, Takashi Sakurai, Hiromi Ohi, Hiroyuki Miyake, Shinobu Itoh, and Hiroshi Tsukube*

Reversible redox reactions between transition-metal complexes and small molecules are one of the most intriguing chemical events, and are usually accompanied by drastic changes in structure, color, and magnetism of the complexes. These reactions have significantly contributed to the development of catalysts for atom transfers, such as oxygenation/hydrogenation/sulfurization, models for metal protein active sites, and molecular switching devices.[1] The reversible oxygenation[2a,b] and hydrogenation[2c,d] of metal complexes have been extensively developed from both industrial and biological points of view. However, the reversible sulfurization–desulfurization of metal complexes has yet to be accomplished. Because of the numerous oxidation states of sulfur (elemental sulfur (S_8^0), sulfide (S^{2-}), polysulfides (S_n^{2-}) and polysulfur radicals ($S_n^{\bullet}$)) and its numerous coordination modes, unfortunately, transition-metal complexes containing sulfur species exhibit numerous structures which are irreversibly changed by photochemical, electrochemical, and thermal stimuli.[3,4] The thermodynamic stability of both sulfur-bound and sulfur-nonbound structures are required to design a metal-complex system promoting a reversible sulfurization.

Dianionic dithiolene ligands stabilize mononuclear five-coordinate tungsten(IV)/(V) complexes, and tungsten(VI) complexes are stabilized by coordination of a sixth ligand to the five-coordinate tungsten centers,[7] therefore, a series of oxo-tungsten bis(dithiolene) complexes may be promising candidates for metal complexes that do not undergo irreversible structural changes as a response to external stimuli. We report herein the first example of a metal complex promoting reversible sulfurization–desulfurization. Novel tungsten persulfide complexes were prepared with bdt (benzene-1,2-dithiolate) and $S_2C_6H_8$ (cyclohexene-1,2-dithiolate) giving $(Ph_4P)_2[W^{VI}O(S_2)(bdt)_2]$ (**1**) and $(Et_4N)_2[W^{VI}O(S_2)(S_2C_6H_8)_2]$ (**4**), respectively (Scheme 1, and Supporting Information). A reversible reaction between the $\{W^{VI}(S_2)\}$ and $\{W^{V}\}$ structures is demonstrated and discussed, in which the electron-donating property of the dithiolene ligands plays an important role.

[*] Dr. H. Sugimoto, R. Tajima, T. Sakurai, H. Ohi, Prof. Dr. H. Miyake, Prof. Dr. S. Itoh, Prof. Dr. H. Tsukube
Department of Chemistry
Graduate School of Science
Osaka City University
Sumiyoshi-ku, Osaka, 558-8585 (Japan)
Fax: (+81) 6-6605-2522
E-mail: sugimoto@sci.osaka-cu.ac.jp

Supporting information for this article is available on the WWW under http://www.angewandte.org or from the author.

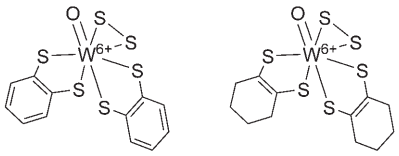

1 4

Scheme 1. Structures of the $[W^{VI}O(S_2)(dithiolene)_2]^{2-}$ complexes **1** and **4**.

Complex **1** was prepared as red crystals by mixing $(Et_4N)_2[W^{IV}O(bdt)_2]$ (**2**), elemental sulfur (as S_8^0), and PPh_4Br in a 1:2:2 ratio in MeCN. The structure of the anionic part of **1** is shown in Figure 1.[8]

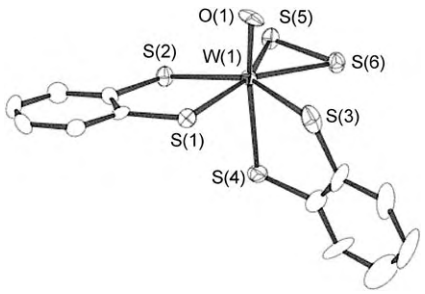

Figure 1. Crystal structure of anion of **1**, thermal ellipsoids are set at 50% probability. The hydrogen atoms are omitted for clarity.

The tungsten center is coordinated by one oxygen atom from one oxo ligand and by six sulfur atoms from one persulfide group and two bdt ligands. The O(1)-W(1)-S(4) angle of 169.0(2)° indicates that the tungsten center adopts a distorted pentagonal-bipyramid structure. The tungsten centers similarly coordinated with one oxygen and six sulfur atoms are also observed in $(Et_4N)_2[W^{VI}O(S_2)(mnt)_2]$ (**7**, mnt = maleonitrile-1,2-ethylenedithiolate)[9] and $[W^{VI}O(S_2)(S_2CNEt_2)_2]$ (**8**, S_2CNEt_2 = diethyl dithiocarbanate).[10] The W(1)–O(1), W(1)–S(5), and W(1)–S(6) bonds of **1** at 1.737(5), 2.417(2), and 2.437(2) Å are somewhat longer than the corresponding bonds in **7** (1.689(4), 2.389(2), and 2.420(2) Å) and **8** (1.706(3), 2.372(1), and 2.388(1) Å). This finding suggests that the W(1)=O(1), W(1)–S(5), and W(1)–S6 bonds in **1** are weakened by the stronger *trans* influence of the bdt compared with that of the mnt and S_2CNEt_2 ligands of **7** and **8**.

The temperature dependent electronic spectral change of **1** in MeCN:EtCN (70:30) is shown in Figure 2. At 253 K, the MeCN:EtCN solution exhibited absorption bands with peak maxima at 413 and 480 nm, and an ESI-MS spectrum with a pattern arising from $[WO(S_2)(bdt)_2]^{2-}$ (m/z 277). As the solution temperature was increased from 253 to 353 K, the intensity of the absorption bands at 413 and 480 nm decreased, with the concomitant appearance of a new band at 613 nm. The λ_{max} and ε values of the absorption spectrum recorded at 353 K were identical to those of $[W^{V}(O)(bdt)_2]^{-}$ (**3**).[7b] The solution changed from a deep red to a deep blue, therefore, the reaction could be detected by observing this color change (Scheme 2). The progress of the reaction was

InterScience
© 2006 Wiley-VCH Verlag GmbH & Co. KGaA, Weinheim

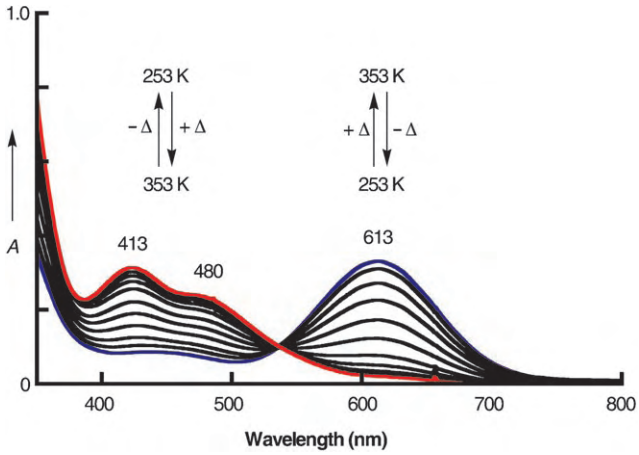

Figure 2. Temperature dependence of the electronic spectrum of a MeCN:EtCN (70:30) solution of **1** (1.0×10^{-4} M) recorded at 253 (red), 263, 273, 283, 293, 303, 313, 323, 333, 343, and 353 (blue) K.

Scheme 2. Reversible sulfurization–desulfurization in bdt complexes **1** and **3**. (The concentration of the solutions shown in the photographs is 6.3×10^{-4} M, and the solution temperatures are 273 (left) and 353 (right) K, respectively.)

monitored by ^{1}H NMR spectroscopy and ESI-MS. As the temperature of the CD_3CN solution was increased, the ^{1}H NMR signals assigned to the bdt ligands of **1** became broad, the ESI-MS peak pattern for $[WO(S_2)(bdt)_2]^{2-}$ disappeared, and that for $[WO(bdt)_2]^-$ (m/z 480) appeared.

Interestingly, when the temperature of the solution decreased from 353 to 253 K, the initial absorption spectrum of **1** at 253 K was completely regenerated. Since Figure 2 shows a clear isosbestic point at 536 nm, the W^{VI} complex **1** and the W^V complex **3** are thought to exist in equilibrium.

Additions of DMF or EtCN to the MeCN solutions of **1** also resulted in dissociation of the S_2 unit in **1**, thus indicating that this reaction is not only subject to a thermal-dependent equilibrium, but also a solvent-dependent equilibrium. Because the desulfurization of **1** did not yield **2**, but rather **3**, the reaction of **3** with Na_2S_4 in a 2:1 ratio at 273 K was examined as the back reaction.[11] As shown in the Supporting information, **3** was confirmed to change to **1** upon treatment with S_4^{2-}, and the isosbestic point at 536 nm was obtained. Thus, the mechanism in Scheme 3 is suggested: 1) The $\{W^{VI}(S_2^{2-})\}$ unit in **1** dimerizes with tetrasulfide (S_4^{2-}) as a result of temperature and solvents effects, forming a bridged dinuclear W^V complex as an intermediate, $[\{W^VO(bdt)_2\}_2(\mu\text{-}S_4)]$; 2) dissociation of the tetrasulfide (S_4^{2-}) from the W^V centers results in the formation of **3** and S_4^{2-}.[13]

Interestingly, **4** underwent a reversible reaction in a lower temperature range than **1**.[14] The complex **4** was stable in MeCN:EtCN (70:30) at 223 K, and its desulfurization occurred to give the $[W^VO(S_2C_6H_8)_2]^-$ (**6**) at 293 K, as monitored by the reversible electronic spectral change (Supporting Information).[15,16] The observed reactivity difference between **1** and **4** can be ascribed to the W–S bond strengths in the WS_2 rings. Since the crystal structure of **4** was not determined, ln K values for the reaction Scheme 2 were plotted against $1/T$ for **1** and **4** (Figure 3). A smaller ΔH value (43 kJ mol^{-1}) was

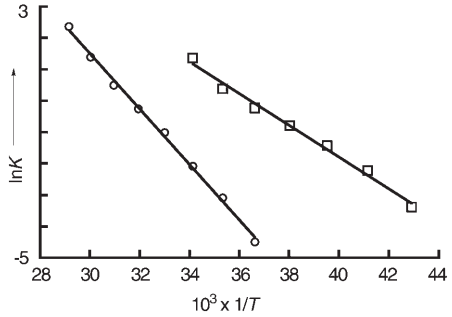

Figure 3. Plots of ln K (from the reaction in Scheme 2) versus $1/T$ for **1** (○) and **4** (□).

obtained for the desulfurization from **4** to **6** as compared with that (74 kJ mol^{-1}) from **1** to **3**, suggesting that the W–S bonds in the WS_2 ring of **4** are weaker than those of **1** and the weaker W–S bonds make the desulfurization more facile. In fact, **7**[9] which has stronger W–S bonds in the WS_2 ring than **1** (as indicated by its short W–S bond lengths) did not undergo desulfurization.[17] The electronic spectrum of **7** in MeCN:EtCN (70:30) was unchanged on increasing the temperature and adding DMF to the solution.[18]

Thus, the electron-donating properties of the dithiolene ligands employed are thought to play a crucial role in controlling the reversible reaction. The present reversible sulfurization–desulfurization proceeds with temperature- and solvent-dependent changes in color (deep red/deep blue) and

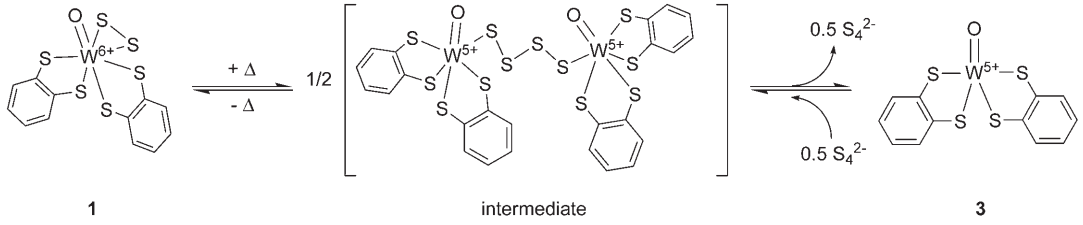

Scheme 3. Proposed mechanism for desulfurization of **1** to **3**.

© 2006 Wiley-VCH Verlag GmbH & Co. KGaA, Weinheim

in the spin-state of the tungsten center (diamagnetism/paramagnetism). Thus, our system offers a promising design for novel types of molecular-sized devices as well as sulfur-transfer catalysts.

Experimental Section

The complexes were synthesized under a dinitrogen atmosphere. Complexes **2**,[7b] **3**,[7b] and **7**[9] were prepared as described in the literature.

1·1.5 H_2O: A THF solution (1 mL) of S_8 (23 mg, 8.5 μmol) was added to a MeCN solution (20 mL) of **2** (25 mg, 0.034 mmol). Addition of Ph_4PBr (29 mg, 0.068 mmol) to the resulting red solution gave a red microcrystalline powder, **1**, which was collected by filtration and recrystallized from MeCN/diethyl ether. Yield: 21 mg (50 %). ^{1}H NMR (300 MHz, [D$_3$]MeCN): $\delta = 6.33$ (t, $J = 4.3$ Hz, 1H, bdt), 6.39 (d, $J = 4.4$ Hz, 1H, bdt), 6.44 (t, $J = 4.4$ Hz, 1H, bdt), 6.68 (qui, $J = 4.2$ Hz, 2H, bdt), 7.06 (d, $J = 4.1$ Hz, 1H, bdt), 7.16 (t, $J = 4.4$ Hz, 2H, bdt), 7.6–7.7 (m, 32H, Ph_4P), 7.92 ppm (t, $J = 4.1$ Hz, 8H, Ph_4P). Elemental analysis (%) calcd for $C_{60}H_{48}OP_2S_6W$·1.5 H_2O (M_r: 1250.26): C 57.64, H 4.11; found: C 57.32, H 3.78.

5·0.5 H_2O was prepared in the same manner as $(Et_4N)_2[MoO(S_2C_6H_8)_2]$ by using a tungsten starting material, $[W(CO)_3(CH_3CN)_3]$, instead of $[Mo(CO)_3(CH_3CN)_3]$.[19] Yield: 77 %. Elemental analysis (%) calcd for $C_{28}H_{56}N_2OS_4W$·0.5 H_2O (M_r: 757.88): C 44.38, H 7.58, N 3.70; found: C44.34, H 7.56, N 3.68. UV/Vis spectrum (CH_3CN): 240 (ε: 22000 dm^3 mol^{-1} cm^{-1}, sh), 288 (7700, sh), 366 (1700), 458 (430), 688 (40). IR (KBr): $\tilde{\nu} = 899$ cm^{-1} ($\nu_{(W=O)}$).

Received: February 17, 2006
Published online: April 24, 2006

Keywords: desulfurization · dithiolene ligands · sulfur · sulfurization · tungsten

[1] a) C. Tard, X. Liu, S. K. Ibrahim, M. Bruschi, L. D. Gioia, S. C. Davices, X. Yang, L.-S. Wang, G. Sawers, C. J. Pickett, *Nature* **2005**, *433*, 610; b) J. T. York, E. C. Brown, W. B. Tolman, *Angew. Chem.* **2005**, *117*, 7923; *Angew. Chem. Int. Ed.* **2005**, *44*, 7745; c) E. Evangelio, D. Ruiz-Molina, *Eur. J. Inorg. Chem.* **2005**, 2957; d) M. L. Kuhlman, T. B. Rauchfuss, *Angew. Chem.* **2004**, *116*, 6910; *Angew. Chem. Int. Ed.* **2004**, *43*, 6742; e) Y. Peng, H. Fan, V. Jancik, H. W. Roesky, R. Herbst-Irmer, *Angew. Chem.* **2004**, *116*, 6316; *Angew. Chem. Int. Ed.* **2004**, *43*, 6190; f) T. B. Rauchfuss, *Inorg. Chem.* **2004**, *43*, 14.

[2] a) G. A. Abakumov, A. I. Poddel'sky, E. V. Grunova, V. K. Cherkasov, G. K. Fukin, Y. A. Kurski, L. G. Abakumova, *Angew. Chem.* **2005**, *117*, 2827; *Angew. Chem. Int. Ed.* **2005**, *44*, 2767; b) L. M. Mirica, M. Vance, D. J. Rudd, B. Hedman, K. O. Hodgson, E. I. Solomon, T. D. P. Stack, *Science* **2005**, *308*, 1890; c) P. Marie, T. Buttner, F. Breher, P. L. Floch, H. Grützmacher, *Angew. Chem.* **2005**, *117*, 6477; *Angew. Chem. Int. Ed.* **2005**, *44*, 6318; d) J. W. Peters, W. N. Lanzilotta, B. J. Lemon, L. C. Seefeldt, *Science* **1998**, *282*, 1853.

[3] a) F. A. Cotton, G. Wilkinson, C. A. Murillo, M. Bochmann, *Advanced Inorganic Chemistry*, 6th ed., Wiley, New York, **1999**, p. 920; b) D. Coucouvanis, K. D. Demadis, S. M. Malinak, P. E. Mosier, M. A. Tyson, L. Laughlin in *Transition Metal Sulfur Chemistry* (Eds.: E. I. Stiefel, K. Matsumoto), American Chemical Society, Washington, DC, **1996**, p. 117; c) D. Ian, F. Keith, *Prog. Inorg. Chem: Metal Chalcogenide Cluster Chemistry*, *Vol. 41* (Ed.: K. D. Karlin), Wiley, New Jersey, **1990**, p. 637.

[4] Some complexes of $[M(dithiolene)_3]^{n-}$ (M = Mo, W; dithiolene = dimethylethylene-1,2-dithiolate, benzene-1,2-dithiolate, and 3,6-dichloro-benzene-1,2-dithiolate) underwent reversible redox reactions between $n = 0$–2).[5] $[Fe(N\text{-MeIm})_6]S_8$ (*N*-MeIm = *N*-methyl-imidazole) also changed into $[Fe(N\text{-MeIm})_6][Fe_2S_{12}]$ by addition of $[Fe(CO)_5]$, and its back reaction occurred on addition of S_8 in *N*-MeIm solutions.[6]

[5] a) D. V. Fomitchev, B. S. Lim, R. H. Holm, *Inorg. Chem.* **2001**, *40*, 645; b) H. V. Huynh, T. Lügger, F. E. Hahn, *Eur. J. Inorg. Chem.* **2002**, 3007; c) C. S. Isfort, T. Page, F. E. Hahn, *Eur. J. Inorg. Chem.* **2005**, 2607; d) H. Sugimoto, Y. Furukawa, M. Tarumizu, H. Miyake, K. Tanaka, H. Tsukube, *Eur. J. Inorg. Chem.* **2005**, 3088.

[6] T. B. Rauchfuss, S. Dev, S. R. Wilson, *Inorg. Chem.* **1992**, *31*, 154.

[7] a) J. H. Enemark, J. J. A. Cooney, J.-J. Wang, R. H. Holm, *Chem. Rev.* **2004**, *104*, 1175; b) H. Oku, N. Ueyama, A. Nakamura, *J. Am. Chem. Soc.* **1992**, *114*, 7310.

[8] Crystallographic data for **1**: $C_{50}H_{48}OP_2S_6W$, $M_r = 1071.03$, 0.10 × 0.08 × 0.06 mm, monoclinic, $P2_1/a$ (no. 14), $a = 19.530(4)$, $b = 12.861(2)$, $c = 23.199(4)$ Å, $\beta = 117.463(4)°$, $V = 5170.6(16)$ Å^3, $Z = 4$, $\rho_{calcd} = 1.376$ g cm^{-3}, $\mu = 25.34$ cm^{-1} min./max. transmission = 0.641/0.859, $2\theta_{max} = 55°$, 10082 independent reflections, $R1 = 0.0602$, $wR2 = 0.1065$ against F^2 (6585 reflections, $I > 2.20\sigma(I)$), 679 parameters, max./min. residual electron density = 2.46/−6.04 e Å^{-3}; **5**: $C_{30}H_{59}N_3OS_4W$, $M_r = 789.91$, 0.30 × 0.20 × 0.20 mm, orthorhombic, $Pna2_1$ (no. 33), $a = 18.0767(8)$, $b = 18.0767(8)$, $c = 10.9458(8)$ Å, $V = 3576.7(3)$ Å^3, $Z = 4$, $\rho_{calcd} = 1.467$ g cm^{-3}, $\mu = 34.93$ cm^{-1}, min./max. transmission = 0.339/0.497, $2\theta_{max} = 55°$, 58186 measured reflections, 4573 independent reflections, $R1 = 0.0320$, $wR2 = 0.0570$ against F^2 (3635 reflections, $I > 2.00\sigma(I)$), 393 parameters, max./min. residual electron density = 0.73/−0.97 e Å^{-3}. For crystallographic details of **1** and **5**, see Supporting Information. CCDC-297773 and CCDC-297774 contain the supplementary crystallographic data for this paper. These data can be obtained free of charge from The Cambridge Crystallographic Data Centre via www.ccdc.cam.ac.uk/data_request/cif.

[9] S. K. Das, D. Biswas, R. Maiti, S. Sarker, *J. Am. Chem. Soc.* **1996**, *118*, 1387.

[10] J. A. Broomhead, J. H. Enemark, B. Hammer, R. B. Ortega, W. Pienkowski, *Aust. J. Chem.* **1987**, *40*, 381.

[11] Because Na_2S_4 is barely soluble in the employed MeCN:EtCN solution, its absorption spectrum was not measured. In ref. [12] the homolysis of S_6^{2-} was reported to give $2\,S_3^-$.

[12] R. G. Teller, L. J. Krause, R. C. Haushalter, *Inorg. Chem.* **1983**, *22*, 1809.

[13] A preliminary kinetic experiment revealed that desulfurization proceeds by second-order kinetics with respect to the complex concentration, thus supporting the mechanism proposed in Scheme 3.

[14] For example, the temperatures that gave $K([W^VO][S_4]^{1/2}/[W^{VI}OS_2]) = 1$ were 310 and 268 K for **1** and **4**, respectively.

[15] Complex **4** was prepared in situ by the reaction of $(Et_4N)_2[W^{IV}O(S_2C_6H_8)_2]$ (**5**; see Supporting Information) with 1/4 S_8.

[16] IR and ESI-MS spectra of the solution recorded at 293 K exhibited a $\nu(W^V{=}O)$ band (936 cm^{-1}) and a peak pattern (m/z 488) that indicate the formation of **6**.

[17] The thermodynamic stability of $[W^V(O)(dithiolene)_2]^-$ is also a factor involved in promoting the reversible reaction. Values for the $[W(O)(dithiolene)_2]^{-/2-}$ couple (where dithiolene is bdt = −0.63 V,[7b] $S_2C_6H_8 = -0.91$ V, and mnt = + 0.25 V[9] vs. saturated calomel electrode (SCE)) indicate that the stability of the W^V complexes increases in the order of mnt ≪ bdt < $S_2C_6H_8$.

[18] The red solution of **7** gave an absorption spectrum with λ_{max} at 385 and 478 nm, which was originated from the $(Et_4N)_2[WO(S_2)(mnt)_2]$ complex, and the ESI-MS spectrum gave a peak pattern arising from $\{[WO(S_2)(mnt)_2]^{2-} + [Et_4N]^+\}^-$.

[19] H. Sugimoto, M. Harihara, M. Shiro, K. Sugimoto, K. Tanaka, H. Miyake, H. Tsukube, *Inorg. Chem.* **2005**, *44*, 6386.

 © 2006 Wiley-VCH Verlag GmbH & Co. KGaA, Weinheim

DNA Structures

DOI: 10.1002/anie.200600954

Controlling RNA Digestion by RNase H with a Light-Activated DNA Hairpin**

*XinJing Tang and Ivan J. Dmochowski**

Many gene silencing technologies have focused on targeting mRNA by using ribozymes, DNAzymes, and complementary RNA or DNA oligonucleotides. It is attractive that mRNA is accessible during transcription, processing (e.g., 5′-capping, intro-exon splicing, polyadenylation, nuclear export), and ribosomal binding and translation. Hybridization of an "antisense" oligodeoxynucleotide (asODN) to a target mRNA inhibits translation by sterically blocking the ribosome and/or recruiting endogenous ribonucleases. In mammalian cells, mRNA/asODN duplex formation activates RNase H-mediated hydrolysis of mRNA. Antisense ODNs have proven effective in gene silencing[1] in many experimental systems and are being evaluated as treatments for cancer and other diseases in human clinical trials. It was recently reported that the stability of DNA hairpins relative to their corresponding RNA/DNA hybrids influenced the extent of RNA degradation by RNase H.[2] Based on this principle, we designed a light-activated DNA hairpin to control this enzymatic reaction (Figure 1 A).

Photoinduced generation of nucleic acid strand breaks has been reported by several groups.[3] However, most studies have focused on mimicking genomic lesions, whereas our strategy is based on the photorelease of DNA for controlling biological processes. Light-activated methods for controlling the binding of asODNs to target mRNA would permit the reduction of protein expression in a cell or tissue-specific fashion and thereby limit systemic toxicity.[4] Recent efforts to increase the specific activity of asODNs have focused on improving delivery to cells and nuclease resistance.[5] Stability within cells can be enhanced considerably by modifying the backbone of the oligonucleotide, as exemplified by phosphorothioate,[6] peptide,[7] morpholine,[8] and "locked"[9] nucleic acids. However, there are few reports about regulating the activity of asODNs.[10,11]

In a pioneering example, Matsunaga et al. recently applied the UV-mediated *trans*→*cis* isomerization of azobenzene to control RNA digestion by RNase H.[10] By attaching five azobenzenes to a 20-mer sense DNA strand, the binding of a complementary asODN decreased upon UV irradiation: *trans*, $T_m = 60.8\,^{\circ}C$; *cis*, $T_m = 42.6\,^{\circ}C$. The less conformationally extended *cis* isomer sterically blocked DNA duplex formation. Based on this difference in melting temperature, $\Delta T_m = 18\,K$, it was possible to regulate the hybridization of the asODN to a complementary RNA target.

However, the photoefficiency was greatly reduced by the requirement for five azobenzenes. For DNA modified with n moieties, each with a photoquantum efficiency of 50%, the irradiation time required to generate the fully active molecule should scale as 2^n. In fact, prolonged UV irradiation leads to side reactions that lower the yield of the active molecule and cause cytotoxicity. For cell experiments, prolonged irradiation reduces temporal as well as spatial resolution due to diffusion. Moreover, the use of a reversible, photoisomerizable blocking group is problematic as mRNA is an abundant and persistent target.

In related studies, DNA hybridization was recently photomodulated between 14% (blocked) and 80% (activated) by using an average of 14–16 nitrophenyl adducts per 20-mer asODN.[11] Further precedent exists for the control of

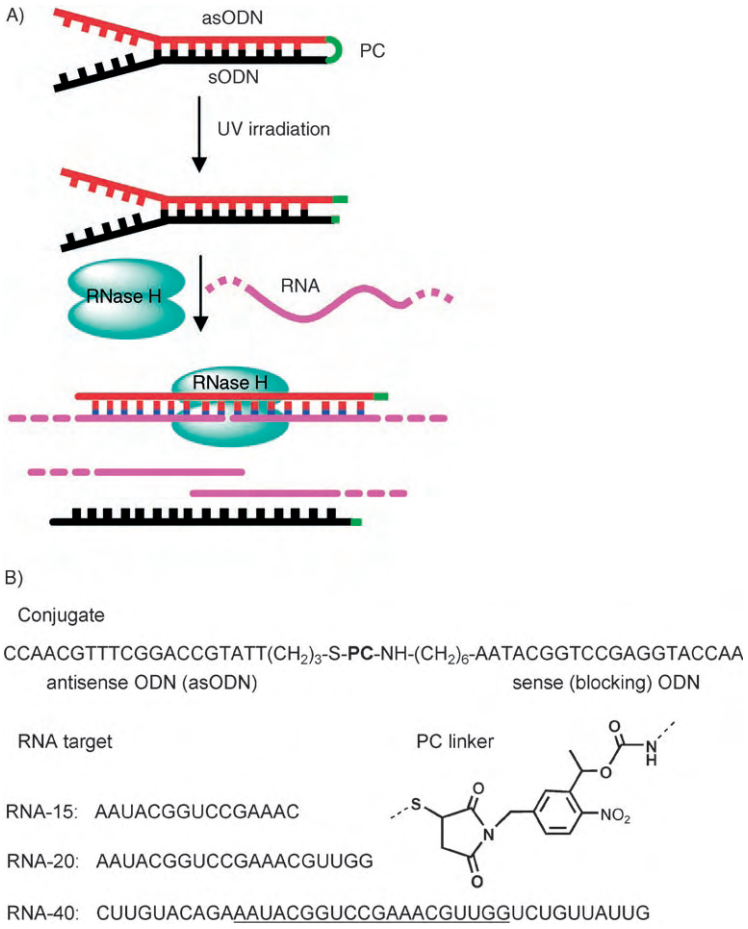

Figure 1. A) Strategy for regulating RNA digestion by RNase H by using a light-activated DNA hairpin. B) Sequences of the asODN-sODN conjugate and RNA targets; structure of the heterobifunctional photocleavable linker, PC. Underlined bases in RNA-40 are identical to RNA-20.

[*] X. Tang, Prof. I. J. Dmochowski
Department of Chemistry
University of Pennsylvania
231 South 34th Street, Philadelphia, PA 19104-6323 (USA)
Fax: (+1) 215-898-2037
E-mail: ivandmo@sas.upenn.edu

[**] This work was supported by a Camille and Henry Dreyfus New Faculty Award, the University of Pennsylvania Genomics Institute (PGI) and Institute for Medicine and Engineering (IME). We thank Jim Eberwine, Feng Gai, and Eric Meggers for access to instrumentation. Alan Gewirtz is acknowledged for valuable discussions.

Supporting information for this article is available on the WWW under http://www.angewandte.org or from the author.

© 2006 Wiley-VCH Verlag GmbH & Co. KGaA, Weinheim

DNA and RNA activity with light.[12] However, the use of multiple photoactive groups in most cases has limited the utility of these methods for biological investigations. Our strategy for photoregulating DNA involves the incorporation of a single, maximally effective blocking group.

We synthesized a light-activated DNA hairpin by covalently attaching a 20-mer asODN to an ODN with 12 complementary bases through a heterobifunctional photocleavable linker (PC, Figure 1). This 1-(5-(*N*-maleimidomethyl)-2-nitro-phenyl)ethanol *N*-hydroxysuccinimide ester was designed to react with thiol and amine functionalities on opposite ends of the linker (Figure 1 B). PC was synthesized in four steps in a 14% yield. Its dual reactivity made it even more versatile for bioconjugation reactions than the 1-(5-(aminomethyl)-2-nitrophenyl)ethanol linker used previously.[13,14] Covalent attachments of the thiolated asODN to the maleimido group and the amino-ODN to the *N*-hydroxysuccinimide ester occurred in good yields. Purification of the conjugated DNA hairpin was achieved by ion exchange chromatography at 40 °C. This step was particularly important because any unreacted asODN would readily form a duplex with the target RNA and thus promote RNase H activity.

The DNA hairpin exhibited a high melting temperature, $T_m = 80$ °C. Upon UV illumination, the carbamate linkage was broken and the asODN/ODN duplex became much less stable, $T_m = 51$ °C. Photocleavage was confirmed by HPLC and MALDI-TOF mass spectrometry. This large difference in thermal stability, $\Delta T_m = 29$ K, allowed the photomodulation of RNA/asODN duplex formation, thereby regulating RNA hydrolysis by RNase H (Figure 1 A).

RNase H activity was studied with RNA oligomers of varied length, RNA-15 (15-mer), RNA-20 (20-mer), and RNA-40 (40-mer). Digestion of each RNA target was compared between solutions containing the control single-stranded asODN (CCAACGTTTCGGACCGTATT) or the DNA hairpin. Figure 2 shows hydrolysis of 45% of the total

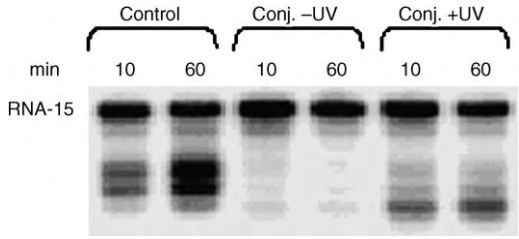

Figure 2. Denaturing PAGE (20%) analysis of RNA-15 digestion by RNase H at 37 °C. Lanes 1–2, asODN; Lanes 3–4, conjugate (conj.−UV); Lanes 5–6, UV-activated conjugate (conj.+UV).

RNA-15 target after photoactivation as compared with only 4.6% for the conjugate in a 1 h experiment with 1 unit of enzyme. Under the same conditions, 66% RNA degradation for the control single-stranded asODN was observed. The UV light used in these experiments had no effect on the enzyme or RNA stability. Control experiments confirmed that RNase H hydrolyzed RNA only when hybridized with asODN.

RNase H assays were also performed with RNA-20 and RNA-40. After photolysis of the DNA hairpin, RNA-20 and RNA-40 digestion increased by a factor of 1.3 ± 0.2 and 4.4 ± 0.4, respectively, versus a 9.0 ± 1.0-fold increase for RNA-15 (Figure 3). Three units of fresh RNase H gave nearly com-

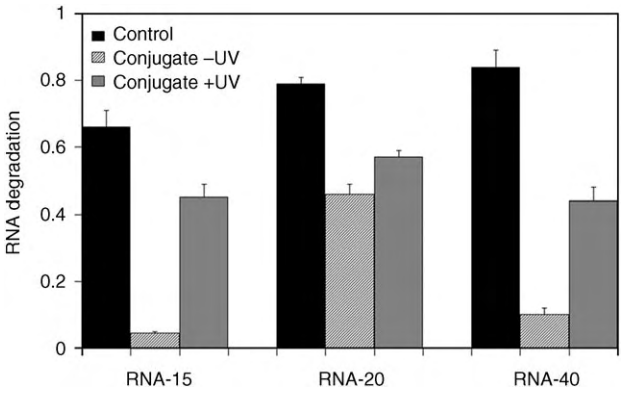

Figure 3. RNase H assays showing degradation of RNA-15, RNA-20, and RNA-40 target sequences in 60 min at 37 °C with 1 unit of RNase H. Error bars signify the variation from two separate trials. The control lanes show hydrolysis of RNA hybridized to asODN.

plete digestion of RNA-15 (98%), RNA-20 (88%), and RNA-40 (84%) in 1 h in the presence of the control asODN or photolyzed conjugate. This compared favorably with the consumption of only 49% of RNA-15, 70% of RNA-20, and 27% of RNA-40 by using the DNA hairpin (see the Supporting Information). RNA-40 is more representative of cellular mRNA, which has secondary structure that can limit nonspecific DNA hybridization and RNase H digestion. Within a cell, where each mRNA molecule can template the synthesis of several thousand proteins per hour,[15] the ability to photomodulate target mRNA between 73% and 16% of basal levels, as was shown for RNA-40, would produce a large effect.

The observed photomodulation efficiency was controlled predominantly by the relative thermodynamic stabilities of the conjugate, pre- and postphotolysis, and the RNA/asODN duplexes. The melting temperatures for duplexes of asODN with RNA-15 and RNA-20 were 63 and 70 °C, respectively. For these two RNA targets, the increases in RNase H activity upon photoactivation arose from the greater stability of the DNA hairpin ($\Delta T_m = 17$, 10 °C) compared with the RNA/asODN duplexes. Free-energy calculations gave ΔG values for asDNA/sDNA, asDNA/RNA-15, and asDNA/RNA-20 at 37 °C in RNase H buffer of −12.4, −14.5, and −16.3 kcal mol^{-1}, respectively.[16] For the conjugate, $\Delta G = -17.0$ kcal mol^{-1} was calculated by determining the changes in enthalpy and entropy upon duplex formation, ΔH_d and ΔS_d, respectively, from the concentration dependence of the melting equilibria by using the van't Hoff expression (see the Supporting Information). Binding RNA-15 or RNA-20 to the DNA hairpin was disfavored thermodynamically, $\Delta\Delta G = 2.5$ and 0.7 kcal mol^{-1}, respectively. The decrease in $\Delta\Delta G$ with increasing RNA oligomer length helps to explain the higher background levels of RNA-20 digestion, before photolysis.

 © 2006 Wiley-VCH Verlag GmbH & Co. KGaA, Weinheim

RNase H has been shown to promote the formation and cleavage of RNA/DNA duplexes, even under conditions where RNA/DNA hybridization is thermodynamically disfavored.[17] After photolysis, the activated asODN/sODN hybrid readily converted to asODN/RNA-15 and asODN/RNA-20 ($\Delta\Delta G = -2.1$ and -3.9 kcal mol^{-1}, respectively).

In addition to thermodynamic considerations, the higher background level of RNase H activity for RNA-20 was owing to the nature of the blocking group. The 12 complementary bases on the sense ODN were designed to block the binding and degradation of RNA targets with the same 12-base recognition motif. However, the eight mismatched bases of the asODN in the DNA hairpin were able to base pair with RNA-20 and recruit RNase H. Although RNA-20 should be one of the most difficult sequences for this DNA hairpin to photodiscriminate against, the photomodulation efficiency (1.3 ± 0.2) was slightly greater than background levels.

The DNA hairpin exhibited the highest photomodulation efficiency towards the RNA-15 substrate. Contributing factors were the stability of the DNA hairpin relative to the asODN/RNA-15 duplex ($\Delta\Delta G = -2.5$ kcal mol^{-1}), proper complementarity of the blocking strand (slightly shorter than the target), and the structure of the RNA itself, which limited nonspecific DNA hybridization. The RNA melting temperatures of RNA-15, RNA-20, and RNA-40 were 51 °C, 54 °C, and 63 °C, respectively. The expected correlation between increasing RNA strand length and structure was interesting in view of the higher photomodulation efficiency for RNA-40 than RNA-20. These targets had the same 20 bases complementary to asODN and yet RNA-40 exhibited much lower background levels of hydrolysis. Evidently, for targets such as RNA-40, it is important that the asODN has a high degree of complementarity to compete with the stable RNA stem-loop structure. To test this hypothesis, a RNA 40-mer was employed with only 15 complementary bases (CUUGUACAGAAAUACGGUCCGAAACCAACCUCUGUUAUUG, underlined bases are identical to RNA-15). No RNase H activity was observed towards this substrate by using the photolyzed DNA hairpin, and only 13 % digestion was seen with the control asODN. The results with the four RNA substrates provide guidelines for designing photoactive DNA hairpins against a specific RNA target.

Notably, in the earlier azobenzene example, a small ΔT_m of 18 K required a 10-fold excess of sense ODN relative to asODN to limit RNA/asODN duplex formation.[10] This strategy is not practical for most biological applications as the sense ODN can diffuse away or become degraded inside the cell. Furthermore, introducing an organic chromophore in the middle of an ODN typically lowers the DNA duplex melting temperature only by a few degrees Celsius per blocking group.[10,11,14] We demonstrated herein that a much larger ΔT_m can be achieved by conjugating the sense ODN to the asODN through a single photocleavable linker. The PC linker plays a role in stabilizing the conjugate.

In conclusion, a DNA hairpin was designed that efficiently regulates DNA/DNA and DNA/RNA duplex formation by using a single photoactive group. The stability of the DNA hairpin, proper complementarity of the blocking group, and RNA structure were important factors affecting RNA hydrolysis by RNase H. This represents the most efficient method for photomodulating this enzyme activity. Oligonucleotide conjugates can be designed to photoregulate many other processes for biotechnological and cellular applications.

Experimental Section

The standard procedure for RNase H assay: The DNA conjugate was annealed in the 1 × ribonuclease H reaction buffer (Tris-HCl (20 mM), KCl (20 mM), $MgCl_2$ (10 mM), ethylenediaminetetraacetic acid (EDTA; 0.1 mM), dithiothreitol (DTT; 0.1 mM); pH 8.0) by heating to 95 °C, then slowly cooling to 70 °C. The temperature was held at 70 °C for 10 min to melt nonspecific DNA structures, before further slow cooling to 37 °C. [γ-^{32}P]-labeled RNA oligonucleotide was added and incubated at 37 °C for 20 min to allow RNA/DNA duplex formation. RNase H was added to the mixture and incubated at 37 °C. The total reaction volume was 10 μL and the final concentrations of conjugate or control (asODN), and RNA (RNA-15, RNA-20, or RNA-40) were 0.01 μM and 2 μM, respectively. Time points were taken at 10 and 60 min by sampling 4 μL of the reaction mixture, adding 6 μL loading buffer (EDTA (50 mM), formamide (90 %)), and heating to 95 °C for 3 min to terminate the reaction. Finally, 5 μL of the resulting solution was subject to electrophoresis on a polyacrylamide gel containing 7 M urea. RNA imaging was performed by using a Storm phosphorimager and quantified with IMAGEQUANT software (Amersham Biosciences). To measure RNA degradation after photoactivation, the annealed DNA hairpin was illuminated (Xe lamp with monochromator, 355 nm, 36 mW cm^{-2}, 10 min) and [γ-^{32}P]-labeled RNA oligonucleotide was then added and incubated for 20 min. RNA degradation by RNase H was determined as described above. See the Supporting Information for further experimental details.

Received: March 10, 2006
Published online: April 24, 2006

Keywords: DNA structures · oligonucleotides · photoactivation · RNase H

[1] a) C. Cazenave, C. Stein, N. Loreau, N. Thuong, L. Neckers, C. Subasinghe, C. Helene, J. Cohen, J. Toulme, *Nucleic Acids Res.* **1989**, *17*, 4255; b) M. Kozak, *Proc. Natl. Acad. Sci. USA* **1986**, *83*, 2850; c) J. B. Opalinska, B. Machalinski, J. Ratajczak, M. Z. Ratajczak, A. M. Gewirtz, *Clin. Cancer Res.* **2005**, *11*, 4948.
[2] J. Li, B. Bourdelat-Parks, J. H. Boatright, R. M. Wartell, *Biochemistry* **2003**, *42*, 10945.
[3] a) A. Dussy, C. Meyer, E. Quennet, T. A. Bickle, B. Giese, A. Marx, *ChemBioChem* **2002**, *3*, 54; b) P. Ordoukhanian, J.-S. Taylor, *Bioconjugate Chem.* **2000**, *11*, 94; c) K. Zhang, J.-S. Taylor, *J. Am. Chem. Soc.* **1999**, *121*, 11579; d) P. Ordoukhanian, J.-S. Taylor, *J. Am. Chem. Soc.* **1995**, *117*, 9570; e) M. C. Pirrung, X. Zhao, S. V. Harris, *J. Org. Chem.* **2001**, *66*, 2067.
[4] T. L. H. Jason, J. Koropatnick, R. W. Berg, *Toxicol. Appl. Pharmacol.* **2004**, *201*, 66.
[5] M. Rubenstein, P. Tsui, P. Guinan, *Drugs Future* **2004**, *29*, 893.
[6] W. Stec, G. Zon, W. Egan, B. Stec, *J. Am. Chem. Soc.* **1984**, *106*, 6077.
[7] J. C. Hanvey, N. J. Peffer, J. E. Bisi, S. A. Thomson, R. Cadilla, J. A. Josey, D. J. Ricca, C. F. Hassman, M. A. Bonham, K. G. Au, S. G. Carter, D. A. Bruckenstein, A. L. Boyd, S. A. Noble, L. E. Babiss, *Science* **1992**, *258*, 1481.
[8] J. Summerton, *Biochim. Biophys. Acta* **1999**, *1489*, 141.
[9] L. Wang, C. J. Yang, C. D. Medley, S. A. Benner, W. Tan, *J. Am. Chem. Soc.* **2005**, *127*, 15664.

 © 2006 Wiley-VCH Verlag GmbH & Co. KGaA, Weinheim

[10] D. Matsunaga, H. Asanuma, M. Komiyama, *J. Am. Chem. Soc.* **2004**, *126*, 11452.
[11] B. Ghosn, F. R. Haselton, K. R. Gee, W. T. Monroe, *Photochem. Photobiol.* **2005**, *81*, 953.
[12] a) L. Kröck, A. Heckel, *Angew. Chem.* **2005**, *117*, 475; *Angew. Chem. Int. Ed.* **2005**, *44*, 471; b) S. Shah, S. Rangarajan, S. H. Friedman, *Angew. Chem.* **2005**, *117*, 1352; *Angew. Chem. Int. Ed.* **2005**, *44*, 1328; c) H. Ando, T. Furuta, R. Y. Tsien, H. Okamoto, *Nat. Genet.* **2001**, *28*, 317; d) A. Yamazawa, X. Liang, H. Asanuma, M. Komiyama, *Angew. Chem.*. **2000**, *112*, 2446; *Angew. Chem. Int. Ed.* **2000**, *39*, 2356.
[13] a) X. Bai, Z. Li, S. Jockusch, N. J. Turro, J. Ju, *Proc. Natl. Acad. Sci. USA* **2003**, *100*, 409; b) X. Tang, J. L. Richards, A. E. Peritz, I. J. Dmochowski, *Bioorg. Med. Chem. Lett.* **2005**, *15*, 5303.
[14] X. Tang, I. J. Dmochowski, *Org. Lett.* **2005**, *7*, 279.
[15] Y. Arava, Y. Wang, J. D. Storey, C. L. Liu, P. O. Brown, *Proc. Natl. Acad. Sci. USA* **2003**, *100*, 3889.
[16] ΔG was determined by using an Excel spreadsheet (http://www.biochem.umd.edu/biochem/kahn/teach_res/thermsim.xls) for simulating the melting curves of non-self-complementary DNA.
[17] E. Zamaratski, P. I. Pradeepkumar, J. Chattopadhyaya, *J. Biochem. Biophys. Methods* **2001**, *48*, 189.

 © 2006 Wiley-VCH Verlag GmbH & Co. KGaA, Weinheim

Colloids

DOI: 10.1002/anie.200503676

Ultrastable Particle-Stabilized Foams**

Urs T. Gonzenbach, André R. Studart, Elena Tervoort, and Ludwig J. Gauckler*

Aqueous foams are important in a variety of different applications, ranging from food and cosmetics to oil recovery, blast mitigation, and fire extinguishing.[1] Well-established and emerging applications that use foams as an intermediate structure to produce macroporous materials are also widely used in the field of engineering to fabricate thermal insulating materials and low-weight structures, as well as in medicine to produce artificial implants and scaffolds for drug delivery and tissue engineering.[2–4] The thermodynamically unstable nature of liquid foams is a critical issue in all these applications. Foam instability arises from the high energy associated with the gas–liquid interface, and constitutes a driving force for decreasing the total interfacial area of the foam through coalescence and disproportionation (Ostwald ripening) of the bubbles. Such processes can be partially hindered by using long-chain surfactants or biomolecules such as lipids and proteins to adsorb at the air–bubble surface and reduce the gas–liquid interfacial energy.[1] In addition to surfactants and biomolecules, colloidal particles have long been exploited to stabilize oil droplets in Pickering emulsions.[5–7] However, it was only recently recognized that partially hydrophobic particles can also attach to gas–liquid interfaces and stabilize air bubbles in surfactant-free diluted suspensions.[7–10] The attachment of particles at the gas–liquid interface requires an optimum balance between the solid–liquid, solid–gas, and liquid–gas interfacial tensions and is therefore dependent on the wetting behavior at the particle surface (Figure 1 a,b).[7]

A number of approaches have been described to change the lyophobicity and wetting properties of solid particles so as to favor their attachment at gas–liquid interfaces. In the flotation industry, for example, wetting is usually controlled through the adsorption of long-chain surfactants (typically >10 carbon atoms) on the particle surface.[11–15] Hydrophobic silane species have also been deliberately grafted on to the surface of silica nanoparticles to enable model investigations in the absence of surfactants to be performed.[7–10,16–20] However, in all the particle-stabilized foams reported so far, the concentration of modified particles in the liquid medium is not sufficiently high to stabilize a large gas–liquid interfacial area. Therefore, the initially aerated suspension undergoes extensive drainage and creaming before a stable floating foam is achieved on top of the liquid phase.[7–10,16,20] The stabilization of a high concentration of sub-millimeter-sized air bubbles that do not undergo drainage or creaming would, however, be highly advantageous in many foam applications.

We report here a simple and versatile approach to prepare ultrastable particle-stabilized foams that percolate throughout the entire liquid phase and exhibit no drainage or creaming effects. The novelty of our method is the fact that it enables the surface modification of a high concentration of colloidal particles in the liquid phase, thus allowing the stabilization of a large gas–liquid interfacial area against disproportionation, coalescence, drainage, and creaming. Herein we describe and discuss: 1) our approach to surface-modify a large number of particles in the liquid phase, 2) the resulting attachment of lyophobized particles at a gas–liquid interface, 3) the foaming behavior after surface modification, and finally 4) the foam stability achieved. The examples described herein illustrate the universal nature of the method, which in principle can be extended to any type of oxide or non-oxide particles regardless of their initial wetting behavior.

Colloidal particles of various chemical compositions (Figure 1 c) were surface-lyophobized through the adsorption of short-chain amphiphilic molecules on to the particle surface. A key feature of our approach is the use of short amphiphiles (typically <8 carbon atoms) which exhibit high solubility and high critical micelle concentrations in the aqueous phase. This is a primary requisite to enable the

[*] U. T. Gonzenbach, Dr. A. R. Studart, Dr. E. Tervoort, Prof. Dr. L. J. Gauckler
Department of Materials
ETH Zurich
Wolfgang-Pauli-Strasse 10, HCI G 539
8093 Zurich (Switzerland)
Fax: (+41) 44-632-1132
E-mail: andre.studart@mat.ethz.ch

[**] We thank Benedikt Seeber for synthesizing the fluorescent silica particles, Dr. Gabor Csucs for the CLSM images, and Prof. Paul Smith for the encouraging and fruitful suggestions.

Supporting information for this article is available on the WWW under http://www.angewandte.org or from the author.

InterScience DISCOVER SOMETHING GREAT
© 2006 Wiley-VCH Verlag GmbH & Co. KGaA, Weinheim

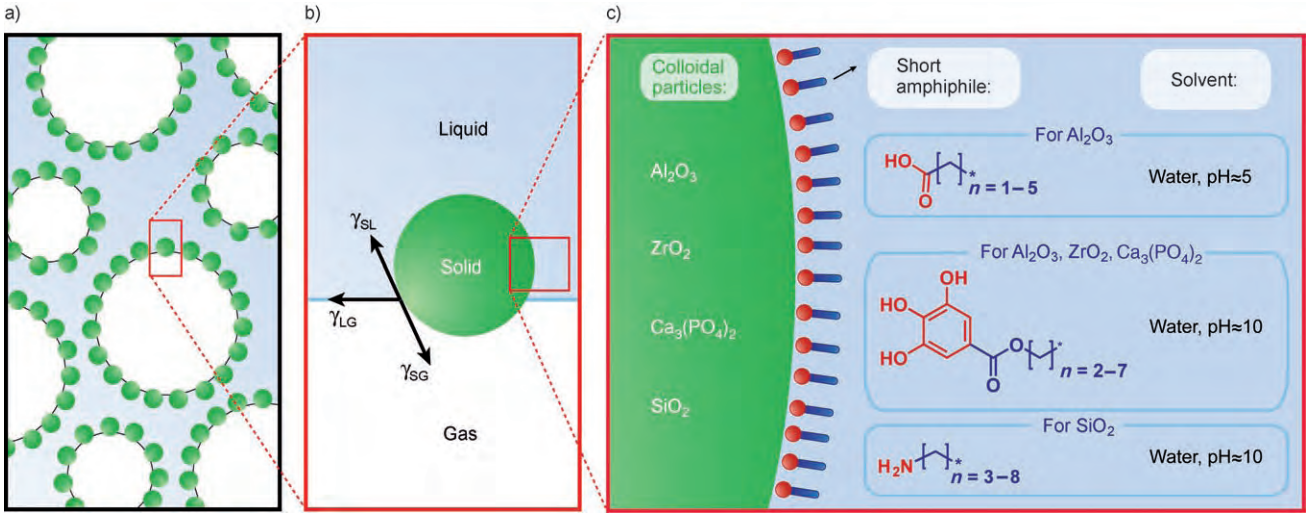

Figure 1. Possible approaches to attach colloidal particles at gas–liquid interfaces by tuning their surface-wetting properties. a) Schematic illustration of the stabilization of gas bubbles with colloidal particles (the particle size is exaggerated for clarity). b) The adsorption of partially lyophobic particles at the gas–liquid interface, illustrating the balance in tension (γ) responsible for the attachment of particles. c) The approaches used to tune the wetting properties of originally hydrophilic particles to illustrate the universality of the foaming method developed. The same principles can be easily extended to other types of particles, by using different surface modifiers as well as liquid and gaseous phases.

surface modification of a high concentration of colloidal particles in the liquid phase. By choosing appropriate anchoring groups and pH conditions (Figure 1c), particles were surface-lyophobized through the adsorption of short amphiphiles through electrostatic interactions (carboxylates and amines) and ligand-exchange reactions (gallates).[21] Figure 2a shows an example of the electrostatic-driven adsorption of anionic carboxylate amphiphiles onto positively charged alumina particles in a suspension under acidic conditions (Figure 1c). The lyophobization achieved by adsorption of the amphiphile was confirmed by contact-angle measurements of aqueous solutions of valeric acid (0.05 mol L^{-1}; pH 4.75) deposited on polycrystalline alumina substrates: angles of approximately 60° were measured through the aqueous phase. Lyophobization occurs as a result of the relatively strong interaction between the anchoring group and the particle surface, thus leaving the amphiphile's hydrophobic tail in contact with the aqueous solution. In the case of the example shown in Figure 2a, the adsorption of negatively charged carboxylate ions on to the alumina surface screened the surface positive charge at acidic pH values, thereby reducing the zeta potential of the particle in water. Therefore, addition of carboxylate amphiphiles beyond the concentrations depicted in Figure 2a led to strong coagulation of the particles as a result of van der Waals and hydrophobic attractive forces.[22–25]

The attachment of the resulting partially lyophobic particles at the air–water interface was indirectly evidenced by surface-tension measurements on a droplet of the suspension at various concentrations of added amphiphilic molecules (Figure 2b). A relatively abrupt decrease in surface tension was observed for amphiphile additions above a certain critical concentration. Since a fraction of the added amphiphiles does not adsorb at the particle surface (Figure 2a), part of the observed reduction in the surface tension was caused by the adsorption of free amphiphilic molecules at the air–water interface. To investigate this issue, the individual contributions of the free amphiphiles and of the partially lyophobic particles to the reduction in the overall surface tension was measured. Figure 3 shows as an example the case of suspensions with butyric acid. The contribution of the amphiphile alone was evaluated by measuring the surface tension of aqueous solutions containing amphiphile concentrations corresponding to the fraction of non-adsorbed molecules given in Figure 2a. The results shown in Figure 3 indicate that the contribution of amphiphiles ($\Delta\gamma_{amph}$) to the overall surface tension increases steadily below the critical amphiphile concentration, whereas the contribution of modified particles ($\Delta\gamma_{part}$) remains constant. However, a drastic increase in the contribution of modified particles to the overall surface tension is observed for amphiphile concentrations above the critical point. This finding indicates that a significant fraction of modified particles attach at the air–water interface at amphiphile concentrations beyond the critical condition. This result was also evidenced by the formation of a thin stiff skin on the surface of suspensions prepared with amphiphiles above this critical concentration.

The presence of partially lyophobized particles in the suspension enabled the preparation of foams simply by incorporating air bubbles through mechanical frothing. Foams prepared by vigorous mechanical shearing of concentrated alumina suspensions (35 vol% solids) showed a five- to sixfold increase in volume at optimum concentrations of carboxylic acid (Figure 2c). This volume increase corresponds to an amount of incorporated air of approximately 85% air with respect to the total volume of the foam. A bubble-size distribution ranging typically from 10 to 100 μm is formed through this foaming process under conditions that produce the maximum amount of foam. Narrower bubble-size distributions are achieved by increasing the particle lyophobicity.

 © 2006 Wiley-VCH Verlag GmbH & Co. KGaA, Weinheim

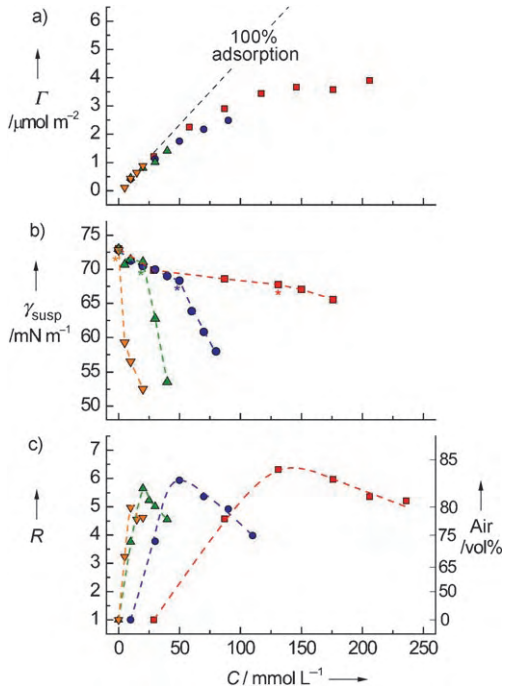

Figure 2. Example of surface lyophobization and foaming behavior using alumina particles and short fatty acids as amphiphiles (■: propionic acid (C_3), ●: butyric acid (C_4); ▲: valeric acid (C_5), ▼: enanthic acid (C_7)). a) Surface lyophobization of colloidal particles accomplished through the electrostatic-driven adsorption of negatively charged carboxylic acids on to positively charged alumina particles. The symbols Γ and C denote the amount of amphiphile adsorbed per unit surface area of alumina and the initial concentration of the amphiphile added to the suspension, respectively. b) The ability of lyophobized particles to attach at air–water interfaces results in a significant decrease in the surface tension of colloidal suspensions (γ_{susp}). The asterisks (*) indicate the critical concentration at which the particles are supposed to attach at the gas–liquid interface. c) The decrease in surface tension resulted in remarkably high foamability upon high mechanical shearing. R is the foam expansion ratio given by the volume of foam divided by the volume of the initial suspension. The volume percentage of air incorporated in the foams is also indicated on the right y-axis in (c). All data were obtained from 35 vol% alumina suspensions at pH 4.75.

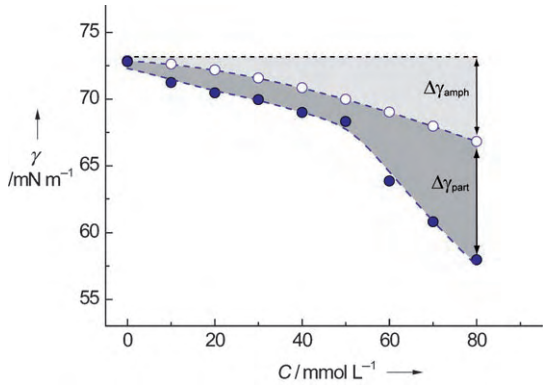

Figure 3. Reduction in surface tension resulting from free amphiphiles (open symbols) and by the combined effect of surface-modified particles and free amphiphiles (filled symbols). Butyric acid is the amphiphile used in this example. The graph illustrates the individual contribution of the free non-adsorbed amphiphiles ($\Delta\gamma_{amph}$) and that of the modified particles ($\Delta\gamma_{part}$) to the overall decrease in the surface tension of the suspension. All data were obtained at pH 4.75, either from 35 vol% alumina suspensions (filled symbols) or aqueous solutions of butyric acid containing the concentration of non-adsorbed amphiphiles depicted in Figure 2a (open symbols).

A further increase in the surface lyophobicity leads, however, to strong coagulation between particles in the liquid media, thus hindering the attachment of particles at the gas–liquid interface and thus hindering the foaming process.

In general, foam formation was favored by increasing the particle concentration or decreasing the particle size in the initial suspension. Such trends are explained by the fact that an increase in particle concentration and a decrease in particle size reduce the time required for the modified particles to diffuse and adsorb on to the surface of the air bubble.[26–28] For the particle size used in the example reported in Figure 2 (diameter: ca. 200 nm), a minimum colloid concentration of 15 vol% was necessary to obtain relatively stable, high-volume foams. However, this lower concentration limit could be reduced to approximately 5 vol% by using highly mobile partially lyophobized nanoparticles (diameter: ca. 70 nm) as foam stabilizers (see the Supporting Information). The production of fresh bubbles at very high rates during air incorporation was also observed to be crucial for the preparation of foams that can percolate throughout the entire volume of the initial suspension. The aforementioned general foaming behavior was observed for all the examples outlined in Figure 1c (see the Supporting Information).

The adsorption of lyophobic particles at the air–water interface of our foams was also confirmed by confocal microscopy images of air bubbles obtained from the dilution of concentrated fluorescent silica foams. A large number of extremely stable air bubbles or hollow colloidosomes[29] were produced upon dilution of the foam (Figure 4). Small clusters of particles were adsorbed at the air–water interface, thus suggesting the existence of an attractive colloidal network around the air bubbles.

The stability of our high-volume particle-stabilized foams was compared to that of foams known to be very stable in cosmetic and food applications. No liquid drainage, creaming, or bubble disproportionation was observed in the particle-stabilized foams four days after their preparation (see the Supporting Information). Highly stable foams were actually only produced with amphiphile additions higher than the critical concentrations depicted in Figures 2b and 3, thus indicating that the stable foams prepared in this work are indeed stabilized by partially lyophobized colloidal particles. The outstanding stability of the particle-stabilized foams contrasts to the markedly higher drainage and disproportionation rates of food and cosmetic wet foams. Liquid foams containing conventional long-chain surfactants adsorbed at the air–water interface collapse much faster—typically within a couple of minutes—than the foams investigated here.[10] The remarkable resistance of our particle-stabilized foams to coalescence and disproportionation is most likely imparted by the strong attachment of particles at the air–water interface (Figure 4) and by the formation of an attractive particle network at the interface and throughout the foam lamella.[8,9]

 © 2006 Wiley-VCH Verlag GmbH & Co. KGaA, Weinheim

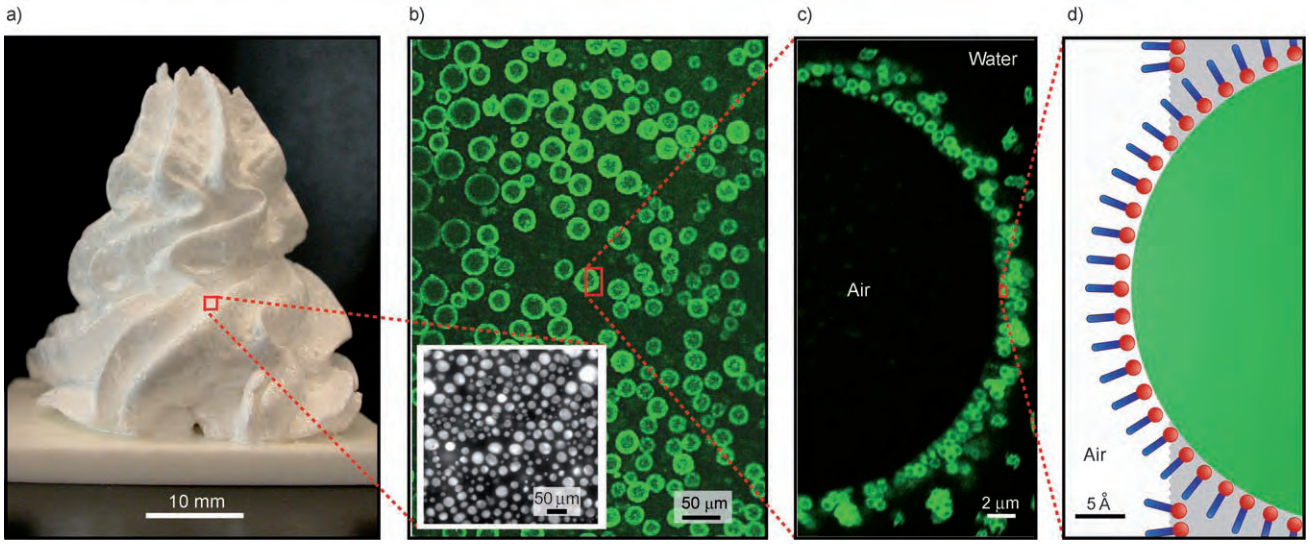

Figure 4. Hierarchical features of the particle-stabilized foams containing short amphiphilic molecules. High-volume macroscopic foams (a) with bubble sizes within the range 10–50 μm (b) are formed through the adsorption of submicrometer-sized colloidal particles at the air–liquid interface (c). Particles attach at the air–water interface as a result of the surface hydrophobicity imparted by the adsorbed amphiphilic molecules, as indicated schematically in (d). The confocal images shown in (b) and (c) were obtained after dilution of concentrated foams (inset in b) containing fluorescently labeled silica particles and hexylamine as amphiphile.

The unique colloidal architecture responsible for the long-term stability of the foam depicted in Figure 4 is based on the sequential assembly of amphiphiles on the surface of the particles and of particles on the surface of air bubbles, which leads to a hierarchical structure spanning over more than five orders of magnitude in length scale. Foam assembly involves a high degree of synergism between the individual components of different length scales, which lead ultimately to the intricate hierarchical structure depicted in Figure 4.

High-volume wet foams with remarkable long-term stability and bubble size as small as 10–100 μm can be prepared for cosmetic and food applications by using the described method. The strong attachment of particles at the air–water interface also enables the fabrication of an enormous number of hollow colloidosomes (Figure 4b) for a variety of emerging applications.[29] Additionally, the outstanding stability of the foam has allowed us to fabricate bulk macroporous structures with a variety of different ceramic, polymeric, and metallic materials by drying and heat treating the wet foams (see the Supporting Information). Macroporous materials prepared by this simple and straightforward method can be used as low-weight structural components, porous media for chemical and biological separation, thermal and electrical insulating materials, catalyst supports, refractory filters for molten metals, and scaffolds for tissue engineering and medical implants.[2–4] Therefore, we expect this novel technique to open up new opportunities in a wide number of areas, including food, cosmetics, engineering, biology, and medicine.

Received: October 17, 2005
Revised: March 10, 2006
Published online: April 26, 2006

Keywords: amphiphiles · colloids · interfaces · surface chemistry

[1] A. J. Wilson in *Springer Series in Applied Biology* (Ed.: A. W. Robards), Springer, Berlin, **1989**, p. 233.
[2] M. Scheffler, P. Colombo, Wiley-VCH, Weinheim, **2005**, p. 645.
[3] M. Ashby, A. Evans, N. A. Fleck, L. J. Gibson, J. W. Hutchinson, H. N. G. Wadley, *Metal Foams: A Design Guide*, Butterworth-Heinemann, Oxford, **2000**.
[4] L. L. Hench, J. M. Polak, *Science* **2002**, *295*, 1014.
[5] S. U. Pickering, *J. Chem. Soc.* **1907**, *91*, 2001.
[6] R. Aveyard, B. P. Binks, J. H. Clint, *Adv. Colloid Interface Sci.* **2003**, *100*, 503.
[7] B. P. Binks, *Curr. Opin. Colloid Interface Sci.* **2002**, *7*, 21.
[8] Z. P. Du, M. P. Bilbao-Montoya, B. P. Binks, E. Dickinson, R. Ettelaie, B. S. Murray, *Langmuir* **2003**, *19*, 3106.
[9] E. Dickinson, R. Ettelaie, T. Kostakis, B. S. Murray, *Langmuir* **2004**, *20*, 8517.
[10] B. P. Binks, T. S. Horozov, *Angew. Chem.* **2005**, *117*, 3788; *Angew. Chem. Int. Ed.* **2005**, *44*, 3722.
[11] B. M. Moudgil, P. K. Singh, J. J. Adler in *Handbook of Applied Surface and Colloid Chemistry, Vol. 1* (Ed.: K. Holmberg), Wiley, West Sussex, **2002**, p. 591.
[12] J. Shibata, D. W. Fuerstenau, *Int. J. Miner. Process.* **2003**, *72*, 25.
[13] T. W. Healy, P. Somasundaran, D. W. Fuerstenau, *Int. J. Miner. Process.* **2003**, *72*, 3.
[14] D. W. Fuerstenau, M. Colic, *Colloids Surf. A* **1999**, *146*, 33.
[15] S. C. Lu, S. X. Song, *Colloids Surf.* **1991**, *57*, 49.
[16] Y. Q. Sun, T. Gao, *Metall. Mater. Trans. A* **2002**, *33*, 3285.
[17] S. I. Kam, W. R. Rossen, *J. Colloid Interface Sci.* **1999**, *213*, 329.
[18] G. Kaptay, *Colloids Surf. A* **2003**, *230*, 67.
[19] B. S. Murray, R. Ettelaie, *Curr. Opin. Colloid Interface Sci.* **2004**, *9*, 314.
[20] R. G. Alargova, D. S. Warhadpande, V. N. Paunov, O. D. Velev, *Langmuir* **2004**, *20*, 10371.
[21] P. C. Hidber, T. J. Graule, L. J. Gauckler, *J. Eur. Ceram. Soc.* **1997**, *17*, 239.
[22] I. Ametov, C. A. Prestidge, *J. Phys. Chem. B* **2004**, *108*, 12116.
[23] H. K. Christenson, P. M. Claesson, *Adv. Colloid Interface Sci.* **2001**, *91*, 391.
[24] J. Israelachvili, R. Pashley, *Nature* **1982**, *300*, 341.

 © 2006 Wiley-VCH Verlag GmbH & Co. KGaA, Weinheim

[25] J. L. Parker, P. M. Claesson, P. Attard, *J. Phys. Chem.* **1994**, *98*, 8468.
[26] R. Miller, P. Joos, V. B. Fainerman, *Adv. Colloid Interface Sci.* **1994**, *49*, 249.
[27] D. Beneventi, B. Carre, A. Gandini, *Colloids Surf. A* **2001**, *189*, 65.
[28] A. H. Martin, K. Grolle, M. A. Bos, M. A. Stuart, T. van Vliet, *J. Colloid Interface Sci.* **2002**, *254*, 175.
[29] A. D. Dinsmore, M. F. Hsu, M. G. Nikolaides, M. Marquez, A. R. Bausch, D. A. Weitz, *Science* **2002**, *298*, 1006.
[30] D. Mobius, R. Miller in *Studies in Interface Science*, *Vol. 11* (Eds.: D. Mobius, R. Miller), Elsevier, Amsterdam, **2001**, p. 521.
[31] A. Vanblaaderen, A. Vrij, *Langmuir* **1992**, *8*, 2921.

 © 2006 Wiley-VCH Verlag GmbH & Co. KGaA, Weinheim

DNA structure

DOI: 10.1002/anie.200504431

Tetraarylporphyrin as a Selective Molecular Cap for Non-Watson–Crick Guanine–Adenine Base-Pair Sequences**

Milan Balaz, Benjamin C. Li, Steffen Jockusch, George A. Ellestad, and Nina Berova**

Dedicated to Professor Koji Nakanishi on the occasion of his 80th birthday

Noncovalent interactions between aromatic molecules are an important factor in maintaining the structural integrity of many biological macromolecules.[1] Owing to its crucial role in the preservation of genetic information, DNA is perhaps the most important. Although hydrogen bonding is responsible for base-pair specificity, it is hydrophobic forces that stabilize the DNA molecule into its double-helical structure.[2] Most of the studies on DNA structures have so far focused on the traditional B-form DNA. However, DNA can exist in many other unique forms,[3] such as Z-DNA,[4] hairpins,[5] cruciform,[6] and triple helices.[7] Some of these secondary structures are difficult to study because they exist only within a narrow range of biophysical conditions. Therefore, chemical probes that trap and/or stabilize such structures can play an important role in their study and/or detection.[8]

The use of molecular probes for the study of the structure and dynamics of nucleic acids has attracted widespread attention. There are four known ways in which small molecules bind DNA: intercalation, groove binding, electrostatic binding to the backbone, and capping.[9] Unlike the first three binding modes, the latter not only specifies the binding position of the molecule, but can stabilize the oligonucleotide through π–π-stacking interactions of the adjacent terminal base pairs.[10,11] Capping is carried out by covalently linking a small molecule to the termini of the DNA oligonucleotides and is base-pair specific.[11,12] Based on the above, we chose to use porphyrin-based molecular caps as a tool to explore the effect of capping on DNA structures. Owing to their unique electronic and spectroscopic properties,[13] these compounds have been used as a selective circular dichroic reporter group for detecting secondary structural changes of oligodeoxynucleotides (ODNs)[14] or as molecular caps to enhance duplex-DNA thermal stability.[15]

Herein, we report the stabilization of a non-self-complementary ODN duplex with continuous noncanonical Watson–Crick guanine–adenine (G–A) base pairs by covalently linked terminal porphyrins. The noncharged hydrophilic tetraaryl-

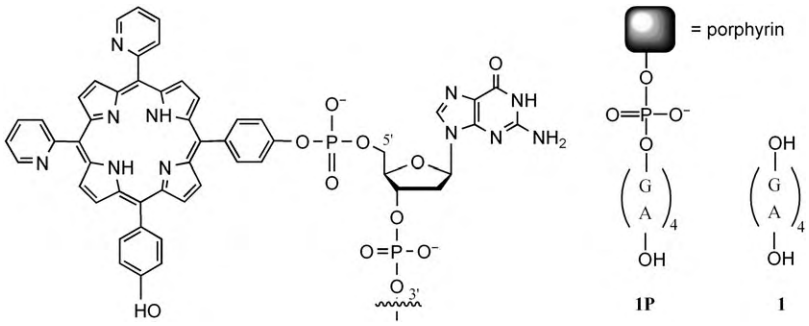

Scheme 1. Representation of the attachment of porphyrin to the guanine unit, and the structures of end-capped porphyrin–ODN conjugate **1P** and unmodified sequence **1**.

porphyrin was attached to the 5′ end of the ODN 5′-GAGAGAGA-3′ through a short but flexible phosphate linker according to a previously reported methodology (Scheme 1).[16,17]

The circular dichroism (CD) of the non-self-complementary and unmodified sequence OH-$(GA)_4$-OH **1** shows the expected weak CD spectrum with a negative band at 285 nm and a positive band at 250 nm (Figure 1, dotted line). Surprisingly, the CD of porphyrin–$d(GA)_4$ **1P** in Figure 1 shows a spectrum characteristic of a highly ordered structure with A-like features. According to Johnson, such a strong and characteristic CD spectrum is directly associated with an organized secondary structure in which the bases are in

[*] Dr. M. Balaz, B. C. Li, Dr. S. Jockusch, Dr. G. A. Ellestad, Prof. N. Berova
Department of Chemistry
Columbia University
3000 Broadway, New York, NY 10027 (USA)
Fax: (+1) 212-932-1289
E-mail: milan.balaz@chem.ox.ac.uk
nbd1@columbia.edu

[**] We thank the National Science Foundation (CHE04-10655, S.J.) and the National Institutes of Health (GM 36564, N.B.) for financial support. We thank Dr. Y. Itakagi for MALDI-TOF measurements. M.B. thanks Dr. S. V. Dzyuba for very creative and helpful discussions.

Supporting information for this article is available on the WWW under http://www.angewandte.org or from the author.

InterScience
© 2006 Wiley-VCH Verlag GmbH & Co. KGaA, Weinheim

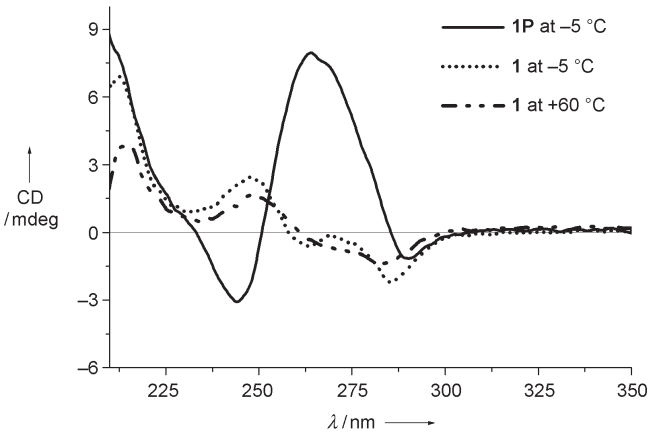

Figure 1. CD spectra of porphyrin–ODN **1P** and porphyrin-free ODN 5′-$(GA)_4$-3′ **1** at −5 and +60 °C in potassium phosphate (50 mM, pH 7.0; $c_{ODN} \approx 10^{-5}$ M).

proximity and can interact with each other.[18] Indeed, the spectrum with a strong positive band at 264 nm and two weak negative bands at 290 and 240 nm (Figure 1, solid line) is strikingly similar to those observed previously for a number of $d(GA)_n$, including highly ordered single strands, hairpins, parallel and antiparallel homoduplexes, and triplexes and tetraplexes.[19] However, the conditions under which these structures are formed (dimethyl sulfoxide (DMSO), ethanol, salt, various pH values) are quite different from the neutral potassium phosphate buffer used in this study. Molecular structures have not been established for any of these forms, although intrastrand guanine–guanine stacking seems to play an important role in all of these forms and evidently accounts for the strong positive band at 260 nm.[19d,20]

Figure 2 shows the variable-temperature CD data for **1P** (melting experiments). The CD spectrum of the porphyrin conjugate **1P** at −5 °C consists of two regions: the ODN CD spectrum below 320 nm and a bisignate curve in the porphyrin Soret band absorption region. The exciton couplet curve (a positive band at 425 nm and a negative band at 407 nm) is evidence for the dipole–dipole through-space long-range electronic interaction between the two porphyrin chromophores.[14,21] Upon increasing the temperature from −5 to 60 °C, the CD signal changes dramatically. The positive band at 264 nm and the negative one at 240 nm disappear, thus indicating a loss of ODN secondary structure because of strand separation (denaturation). The porphyrin bisignate curve disappears at temperatures higher than 30 °C. As expected, the CD spectrum of porphyrin-free sequence **1** varied only slightly on heating from −5 to 60 °C (see the Supporting Information).

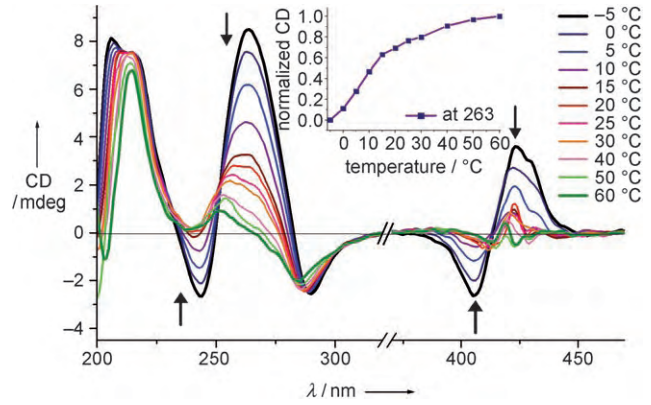

Figure 2. CD spectra of porphyrin–ODN **1P** ($c_{ODN} \approx 10^{-5}$ M) at different temperatures (−5–60 °C) in potassium phosphate buffer (50 mM, pH 7.0). Inset: melting curve detected at 263 nm.

The inset in Figure 2 illustrates the non-cooperative melting curve of porphyrin–ODN **1P** with the melting temperature (T_m) equal to approximately 7 °C. It also shows the increase in the T_m value of the porphyrin-modified sequence **1P** by more than 10 °C. The melting CD experiments run at half concentration ($c = 5.10^{-6}$ M) still show stabilization of the secondary structure but with a decrease in the T_m value to approximately 0 °C ($\Delta T_m = 7$ °C; see the Supporting Information).

The bisignate CD signal in the porphyrin Soret band absorption region (Figure 2) is strongly indicative of a porphyrin–porphyrin long-range interaction because of an antiparallel duplex structure of **1P**. The porphyrin bisignate CD curve also excludes the existence of a hairpin, organized single-strand, or tetraplex structure. An organized single strand and hairpin can also be ruled out because of the concentration dependency of T_m. In addition, the 8-mer sequence in **1P** is too short to form any reasonable hairpin structure as any hairpin of an 8-mer cannot have more than two base pairs. A tetraplex structure is unlikely for **1P** given that the $(GA)_n$ strands have not been observed to associate into a tetraplex.[19c] Thus, we propose that the CD in Figure 2 reflects an antiparallel homoduplex structure with porphyrins at each end that serve as molecular caps (Figure 3).

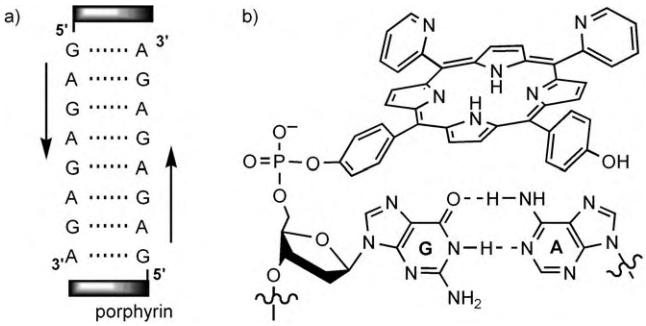

Figure 3. a) Schematic representation of the antiparallel duplex **1P** with porphyrins serving as molecular caps. b) Diagram demonstrating the overlap of the porphyrin with a guanine–adenine base pair.

Guanine–adenine repeat strands ($d(GA)_n$) are well known for their conformational polymorphism and are known to self-associate into parallel- and antiparallel-stranded homoduplexes depending on environmental factors, such as solvent and counterions. But it is remarkable that porphyrin end-capping induces such a highly ordered antiparallel duplex structure. This behavior is in contrast to the lack of self-association of uncapped ODN **1** under identical conditions.[19]

 © 2006 Wiley-VCH Verlag GmbH & Co. KGaA, Weinheim

Upon increasing the temperature from −4 to 60 °C, the UV absorbance band at 260 nm exhibited the hyperchromicity well associated with a double-to-single strand transition (see the Supporting Information). In the Soret band absorption region, hyperchromicity and an isosbestic point (412 nm) are clearly observed upon heating **1P** from −4 to 60 °C (Figure 4). Similar hyperchromism has previously been

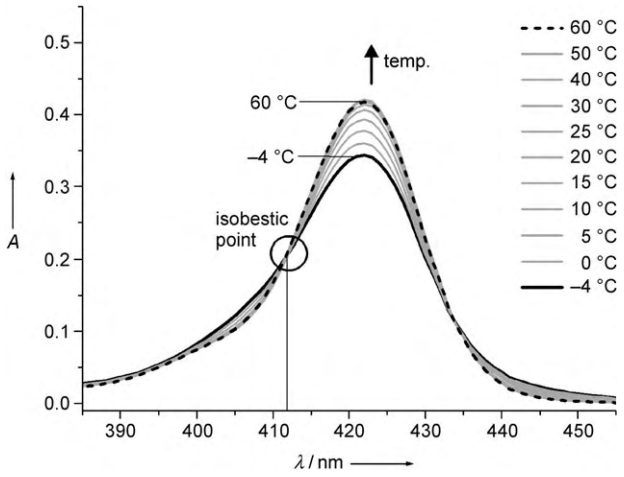

Figure 4. The Soret band absorption region of the porphyrin 5′ end-capped ODN **1P** at different temperatures (−4–60 °C) in potassium phosphate buffer (50 mM, pH 7.0). $c_{1P} \approx 5.10^{-6}$ M.

observed when the porphyrin is no longer bound outside the DNA or intercalated into the DNA base pairs.[22] In the current study, the position and length of the selected phosphate linker prevents intercalation. The presence of a single isosbestic point suggests that only two forms of porphyrin–ODN **1P** (double- and single-stranded DNA) are in equilibrium.

Fluorescence spectroscopy was employed to give additional evidence of the porphyrin-induced stabilization of the non-self-complementary DNA sequence. This porphyrin probe shows fluorescence bands centered at approximately 650 nm. It is expected that the spectral shape and/or intensity of the porphyrin fluorescence changes upon dimerization of **1P** because of the change in the local environment. Figure 5 shows the fluorescence spectra of **1P** at different temperatures, at which a clear difference between the spectra at −2 and 60 °C is observable. The fluorescence intensity increases, the intensity ratio between the vibronic peaks change, and a bathochromic shift (2 nm) is observed with increasing temperature. This behavior indicates once again closer interactions between the porphyrin and the base pairs at lower temperatures (organized structure: double strand) than at higher temperatures (unorganized structure: single strand).

The time-dependent CD experiment shows that the porphyrin-stabilized secondary structure comes apart slowly at 0 °C (see the Supporting Information). Eight hours after the initial measurement, the intensity of the CD signal in the 200–300-nm region drops marginally, thus corresponding to a decrease of less than 15 % (detected as a change of CD signal

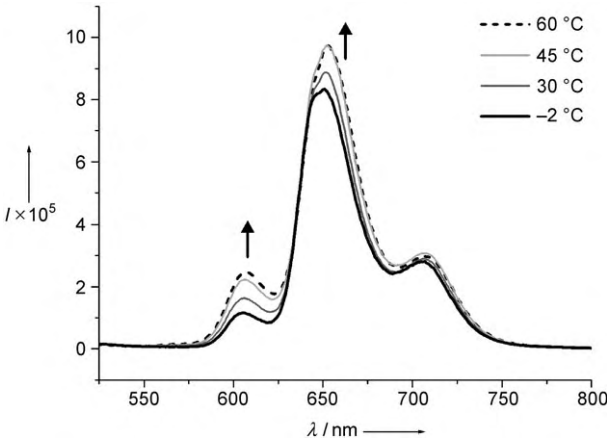

Figure 5. The steady-state fluorescence spectra of **1P** at different temperatures (−2–60 °C) in potassium phosphate buffer (50 mM, pH 7.0; $c_{1P} \approx 10^{-6}$ M).

at 262 nm), and the shape of the CD signal in the DNA region stays the same. However, a more complicated situation is observed in the porphyrin Soret band region. Although the intensity of the bisignate curve decreases by a proportionate 20 %, a change in the shape of the signal is also observed. In the 8-hour measurement, the original simple bisignate curve is transformed into a "trisignate" curve with negative bands at 440 and 405 nm and a positive band at 423 nm. This behavior suggests the progressive aggregation of the porphyrin–ODN units into more complex structures, thus representing an irreversible "aging" phenomenon of the porphyrin-stabilized secondary structure. Similar behavior has been previously observed.[23] The changes are more rapid at 15 °C: the signal decreases gradually and the positive band at 420 nm disappears completely within 2 hours.

Significantly, no stabilization of the secondary structure was observed in a previous study when the porphyrin was attached to the non-self-complementary ODN sequence 5′-CTCTCTCT.[17] Moreover, in the case of the self-complementary ODN sequence 5′-porphyrin–CGCGCGCG no increase in the T_m value was observed.[17] This result is not surprising as molecular models indicate that the tetraarylporphyrin overlaps better with the larger purine–purine G–A base pairs than with the traditional Watson–Crick G–C base pair (purine–pyrimidine), thus resulting in a higher degree of stabilization through hydrophobic interactions.

In conclusion, this study reveals the propensity of tetraarylporphyrins to serve as selective molecular caps for the stabilization of the non-self-complementary non-Watson–Crick 5′-GAGAGAGA-3′ DNA sequence reminiscent of an A-form-like DNA antiparallel helix. More importantly, the porphyrin not only acts as a specific DNA cap, but as a result of its unique spectroscopic features, it can also serve as an internal and highly sensitive CD reporter group of the newly formed secondary structure and allow the first spectroscopic discrimination between parallel and antiparallel homoduplexes. Further studies are in progress to understand this unusual duplex-like form of DNA as well as to enhance the stabilization effect of the porphyrin molecular cap.

 © 2006 Wiley-VCH Verlag GmbH & Co. KGaA, Weinheim

Experimental Section

All the measurements were made in potassium phosphate buffer (50 mM, pH 7.0). The concentration of the ODNs was 10^{-5}–10^{-6} M. CD spectra were recorded on a JASCO J-810 spectrophotometer using quartz cuvettes with an optic path of 1 cm. Fluorescence emission spectra were recorded on a SPEX Fluorolog-3 spectrometer FL3-22 (J. Y. Horiba, Edison, NJ) at an excitation wavelength of 420 nm using quartz cuvettes with an optical path length of 1 × 1 cm. Absorbance spectra were recorded on an Agilent 8456 spectrophotometer with quartz cuvettes with an optic path of 1 cm.

Received: December 13, 2005
Revised: March 1, 2006
Published online: April 20, 2006

Keywords: circular dichroism · DNA structures · fluorescence · mismatched base pairs · porphyrinoids

[1] a) J. SantaLucia, R. Kierzek, D. H. Turner, *Science* **1992**, *256*, 217; b) C. Tanford, *J. Am. Chem. Soc.* **1962**, *84*, 4240.
[2] a) C. Brotschi, A. Haberli, C. J. Leumann, *Angew. Chem.* **2001**, *113*, 3101; *Angew. Chem. Int. Ed.* **2001**, *40*, 3012; b) K. M. Guckian, B. A. Schweitzer, R. X.-F. Ren, C. J. Scheils, P. L. Paris, D. C. Tahmassebi, E. T. Kool, *J. Am. Chem. Soc.* **1996**, *118*, 8182; c) E. T. Kool, J. C. Morales, K. M. Guckian, *Angew. Chem.* **2000**, *112*, 1046; *Angew. Chem. Int. Ed.* **2000**, *39*, 990; d) T. J. Martray, E. T. Kool, *J. Am. Chem. Soc.* **1998**, *120*, 6191; e) T. J. Martray, E. T. Kool, *Nature* **1999**, *399*, 704; f) M. Petersheim, D. H. Turner, *Biochemistry* **1983**, *22*, 256; g) B. A. Schweitzer, E. T. Kool, *J. Am. Chem. Soc.* **1995**, *117*, 1863.
[3] P. Belmont, J. F. Constant, M. Demeunyck, *Chem. Soc. Rev.* **2001**, *30*, 70.
[4] a) A. Rich, S. Zhang, *Nat. Rev. Genet.* **2003**, *4*, 566; b) A. Herbert, A. Rich, *Genetica* **1999**, *106*, 37.
[5] a) F. D. Lewis, T. Wu, Y. Zhang, R. L. Letsinger, S. R. Greenfield, M. R. Wasielewski, *Science* **1997**, *277*, 673; b) P. Tattersall, D. C. Ward, *Nature* **1976**, *263*, 106.
[6] a) K. Mizuuchi, M. Mizuuchi, M. Gellert, *J. Mol. Biol.* **1982**, *156*, 229; b) N. Panayotatos, R. D. Wells, *Nature* **1981**, *289*, 466.
[7] a) G. Felsenfeld, D. R. Davies, A. Rich, *J. Am. Chem. Soc.* **1957**, *79*, 2023; b) J. Robles, A. Grandas, E. Pedroso, F. J. Luque, R. Eritja, M. Orozco, *Curr. Org. Chem.* **2002**, *6*, 1333.
[8] a) M. Balaz, M. De Napoli, A. E. Holmes, A. Mammana, K. Nakanishi, N. Berova, R. Purrello, *Angew. Chem.* **2005**, *117*, 4074; *Angew. Chem. Int. Ed.* **2005**, *44*, 4006; b) S. Hikishima, N. Minakawa, K. Kuramoto, Y. Fujisawa, M. Ogawa, A. Matsuda, *Angew. Chem.* **2005**, *117*, 602; *Angew. Chem. Int. Ed.* **2005**, *44*, 596; c) G. H. Clever, K. Polborn, T. Carell, *Angew. Chem.* **2005**, *117*, 7370; *Angew. Chem. Int. Ed.* **2004**, *44*, 7204; d) Y. Xu, Y. X. Zhang, H. Sugiyama, T. Umano, H. Osuga, K. Tanaka, *J. Am. Chem. Soc.* **2004**, *126*, 6566; e) J. A. Brazier, J. Fisher, R. Cosstick, *Angew. Chem.* **2006**, *118*, 120; *Angew. Chem. Int. Ed.* **2006**, *45*, 114.
[9] a) R. J. Fiel, *J. Biomol. Struct. Dyn.* **1989**, *7*, 1259; b) O. P. Kryatova, W. H. Connors, C. F. Bleczinski, A. A. Mokhir, C. Richert, *Org. Lett.* **2001**, *3*, 987; c) S. Narayanan, J. Gall, C. Richert, *Nucleic Acids Res.* **2004**, *32*, 2901; d) F. D. Lewis, X. Liu, Y. Wu, X. Zuo, *J. Am. Chem. Soc.* **2003**, *125*, 12729; e) R. F. Pasternack, E. J. Gibbs, *ACS Symp. Ser.* **1989**, *402*, 59.
[10] a) W. H. Connors, S. Narayanan, O. P. Kryatova, C. Richert, *Org. Lett.* **2003**, *5*, 247; b) Z. Dogan, R. Paulini, J. A. Rojas Stutz, S. Narayanan, C. Richert, *J. Am. Chem. Soc.* **2004**, *126*, 4762; c) K. Fujimoto, Y. Yoshimura, T. Ikemoto, A. Nakazawa, M. Hayashi, I. Saito, *Chem. Commun.* **2005**, 3177.
[11] J. Tuma, R. Paulini, J. A. Rojas Stutz, C. Richert, *Biochemistry* **2004**, *43*, 15680.
[12] a) M. Salunkhe, T. Wu, R. L. Letsinger, *J. Am. Chem. Soc.* **1992**, *114*, 8768; b) J. Tuma, W. H. Connors, D. H. Stitelman, C. Richert, *J. Am. Chem. Soc.* **2002**, *124*, 4236.
[13] a) G. Pescitelli, S. Gabriel, Y. K. Wang, J. Fleischhauer, R. W. Woody, N. Berova, *J. Am. Chem. Soc.* **2003**, *125*, 7613; b) X. F. Huang, K. Nakanishi, N. Berova, *Chirality* **2000**, *12*, 237.
[14] M. Balaz, A. E. Holmes, M. Benedetti, P. C. Rodriguez, N. Berova, K. Nakanishi, G. Proni, *J. Am. Chem. Soc.* **2005**, *127*, 4172.
[15] H. Morales-Rojas, E. T. Kool, *Org. Lett.* **2002**, *4*, 4377.
[16] M. Balaz, A. E. Holmes, M. Benedetti, G. Proni, N. Berova, *Bioorg. Med. Chem.* **2005**, *13*, 2413.
[17] M. Balaz, J. D. Steinkruger, G. A. Ellestad, N. Berova, *Org. Lett.* **2005**, *7*, 5613.
[18] C. Johnson in *Circular Dichroism: Principles and Applications* (Eds.: N. Berova, K. Nakanishi, R. W. Woody), Wiley-VCH, New York, **2000**, p. 703.
[19] a) N. G. Dolinnaya, J. R. Fresco, *Proc. Natl. Acad. Sci. USA* **1992**, *89*, 9242; b) D. Huertas, L. Bellsolell, J. M. Casasnovas, M. Coll, F. Azorin, *EMBO J.* **1993**, *12*, 4029; c) I. Kejnovska, J. Kypr, M. Vorlickova, *Chirality* **2003**, *15*, 584; d) M. Vorlickova, I. Kejnovska, J. Kovanda, J. Kypr, *Nucleic Acids Res.* **1998**, *26*, 1509; e) M. Vorlickova, I. Kejnovska, J. Kovanda, J. Kypr, *Nucleic Acids Res.* **1999**, *27*, 581.
[20] J. Kypr, M. Vorlickova, *Biopolymers* **2002**, *67*, 275.
[21] a) N. Berova, K. Nakanishi in *Circular Dichroism: Principles and Applications* (Eds.: N. Berova, K. Nakanishi, R. W. Woody), Wiley-VCH, New York, **2000**, pp. 337; b) F. D. Lewis, Y. Wu, L. Zhang, X. Zuo, R. T. Hayes, M. R. Wasielewski, *J. Am. Chem. Soc.* **2004**, *126*, 8206.
[22] D. R. McMillin, A. H. Shelton, S. A. Bejune, P. E. Fanwick, R. K. Wall, *Coord. Chem. Rev.* **2005**, *249*, 1451.
[23] a) N. Angelini, N. Micali, P. Mineo, E. Scamporrino, V. Villari, D. Vitalini, *J. Phys. Chem. B* **2005**, *109*, 18645; b) J.-O. Kim, Y.-A. Lee, B. Jin, T. Park, R. Song, S. K. Kim, *Biophys. Chem.* **2004**, *111*, 63; c) J. R. Dunetz, C. Sandstrom, E. R. Young, P. Baker, S. A. Van Name, T. Cathopolous, R. Fairman, J. C. de Paula, K. S. Akerfeldt, *Org. Lett.* **2005**, *7*, 2559.

 © 2006 Wiley-VCH Verlag GmbH & Co. KGaA, Weinheim

Biocatalyst Identification

DOI: 10.1002/anie.200504505

Regioselective Glucosylation of Aromatic Compounds: Screening of a Recombinant Glycosyltransferase Library to Identify Biocatalysts**

*Markus Weis, Eng-Kiat Lim, Neil Bruce, and Dianna Bowles**

The chemical synthesis of glycosides requires glycosyl activation and involves multiple steps of protection/deprotection to control regioselectivity. This can often reduce the yield of the final product.[1] Glycosyltransferases (GTs) offer a potential solution to this problem[2] as the enzymes use unprotected aglycones in aqueous solution and their catalytic activity is chemo-, regio- and enantioselective.[3] However, to date, the availability of characterized enzymes has been limited and their use as biocatalysts is constrained by the need to supply activated sugars for the synthesis of the glycosides. Recently, a large multigene family of GTs has been identified in *Arabidopsis thaliana*[4] and expressed as recombinant enzymes in *Escherichia coli*. This strategy has enabled new catalytic activities towards small aromatic molecules to be identified in vitro.[5,6] Studies have shown that plant GTs are capable of recognizing compounds beyond those found in plants.[7] The need to add activated sugars has been successfully overcome by the use of recombinant GTs in a whole-cell biocatalysis system.[8] Based on this system, we have developed an assay method in which an entire library of GTs can be screened against potential substrates without the requirement of recombinant protein purification and supplementary activated sugars, thereby allowing rapid identification of relevant biocatalysts for future use in chemical synthesis or fermentation. The method is in contrast to those previously reported including liquid chromatography (LC), LC–MS, or radiometric detection,[9] which were developed for analyzing the activity of purified recombinant GTs.

Herin, we wanted to apply the whole-cell biocatalysis system in a format that would enable us to screen simultaneously a library consisting of multiple GTs. Thus, single colonies of *E. coli*, each expressing an individual GT, were cultured in 96-well titer plates. The screen for catalytic activity needed to be independent of aglycone if the method was to be generic. Therefore, we used a colorimetric detection system for D-glucose,[10] which is experimentally released from glucosides formed during the biocatalysis. The principle aim of the study has been to provide a rapid assessment of GTs to detect those with a high potential for development into whole-cell biocatalysts. This provides the foundation for the subsequent detailed analysis and choice of enzyme to use or improve for the synthesis of aromatic glucosides.

The method, illustrated in Scheme 1, was established and optimized for a 96-well plate format by using the conversion of the hydroxycoumarin, scopoletin (**1**), into scopolin (**2**) as a model system. In vitro catalysis had already demonstrated that the substrate was recognized by multiple recombinant arabidopsis GTs.[6] Cells were cultured in standard media before transferring to D-glucose-minus medium in which L-arabinose was the carbon source. Following induction, addition of substrate, and incubation, cells were separated and the media from each well were collected and samples either analyzed directly by using reverse-phase (RP) HPLC or treated with β-glucosidase, filtered through polyvinyl-

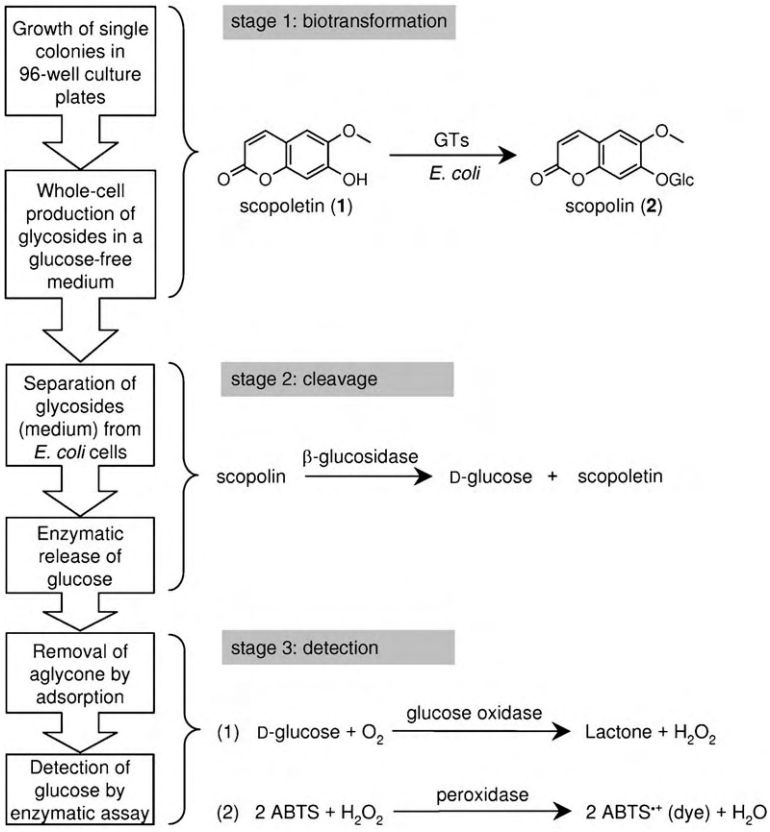

Scheme 1. Design of the rapid-screening method. This method consists of three stages: aglycone biotransformation (stage 1), cleavage of the glucoside (stage 2), and detection of the released D-glucose in a coupled enzymatic assay (stage 3).

[*] M. Weis, Dr. E. K. Lim, Prof. N. Bruce, Prof. D. Bowles
CNAP, Department of Biology
University of York
York YO10 5DD (UK)
Fax: (+44) 1904-328-772
E-mail: djb32@york.ac.uk

[**] This work was supported by The Garfield Weston Foundation. We thank Dr. David Ashford, Dr. Gideon Grogan, and members of the group for helpful discussions.

Supporting information for this article is available on the WWW under http://www.angewandte.org or from the author.

InterScience
© 2006 Wiley-VCH Verlag GmbH & Co. KGaA, Weinheim

polypyrrolidone (PVPP) to remove remaining aglycone, and the levels of D-glucose then detected in an enzymatic assay. Figure 1 illustrates the GT activities towards scopoletin and demonstrates a linear relationship between the amount of scopolin formed in each reaction and D-glucose detection. The whole-cell biocatalysis and screen identified 45 GTs with activity towards scopoletin, confirming and extending the earlier data from in vitro catalysis. Invariably, a negative result in the D-glucose detection assay correlated with a negative result in the RP-HPLC analysis.

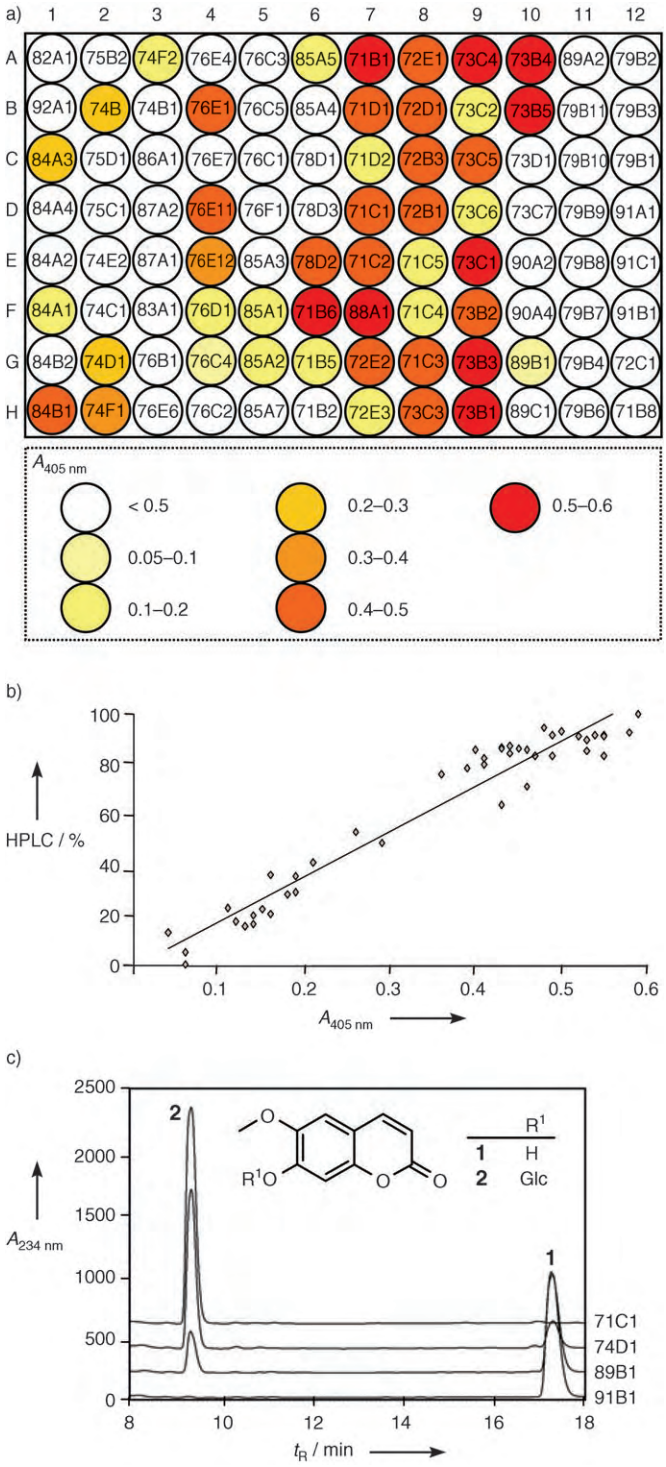

Figure 1. Screening of a GT library against the aglycone scopoletin. a) The readings at A_{405nm} for D-glucose detection are presented in a color-code format. b) The correlation of the colorimetric detection at A_{405nm} and the HPLC analysis. HPLC quantification of glucosides are normalized on the strongest peak and annotated in percentage. c) Examples of RP-HPLC chromatographs of active and non-active GTs in whole-cell biocatalysis are illustrated.

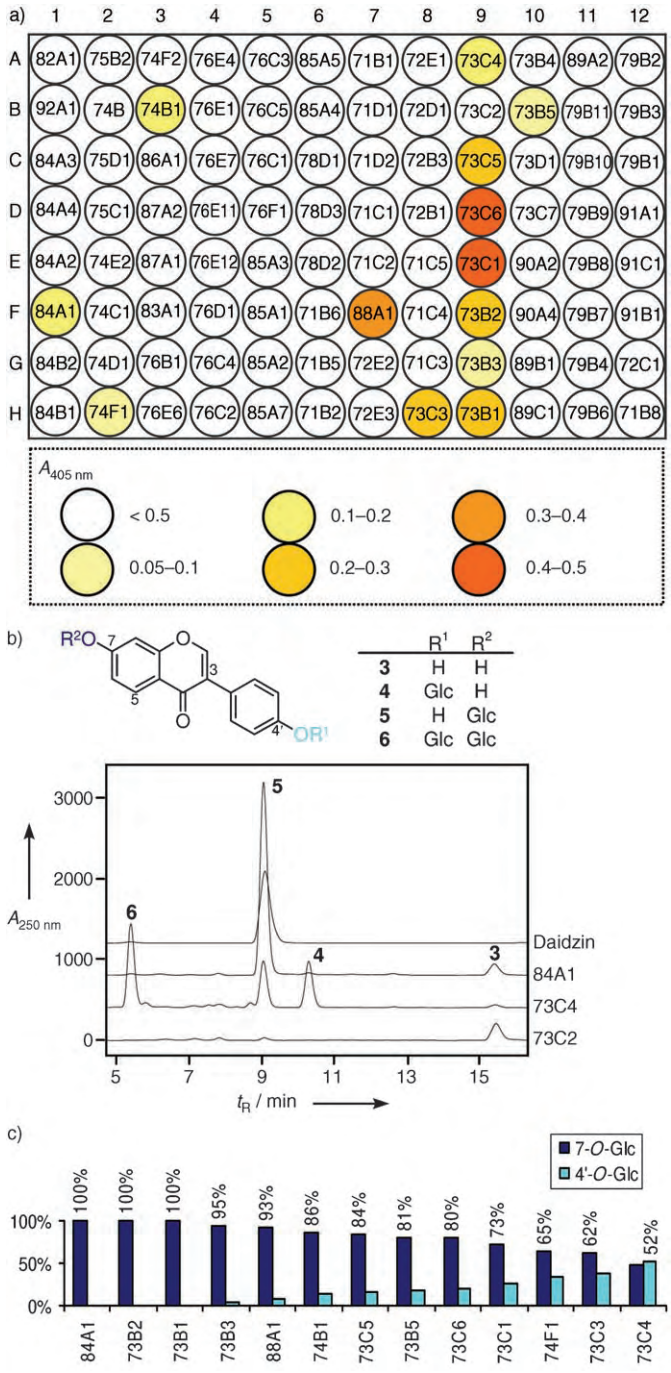

Figure 2. Screening of a GT library against the aglycone daidzein. a) The readings at A_{405nm} for D-glucose detection are presented in a color-code format. b) Examples of RP-HPLC traces of active and non-active GTs in whole-cell biocatalysis are illustrated. c) The regioselectivity of the active GTs towards daidzein, defined by the percentage of a regiospecific glucoside in the total amount of monoglucosides formed.

© 2006 Wiley-VCH Verlag GmbH & Co. KGaA, Weinheim

The utility of the method to discover novel biocatalysts was investigated by using the isoflavone, daidzein (**3**), and the stilbene, *trans*-resveratrol (**7**). Both compounds exist as glucosides, have attracted considerable pharmaceutical interest,[11] and chemical synthesis of their different glycosides has been attempted but resulted in poor yields and lack of regioselective discrimination.[12] Daidzein, as well as other isoflavones, occurs naturally in legumes as the 7- and 4′-β-*O*-glucosides (**4** and **5**, respectively).[13] *trans*-Resveratrol, a naturally occurring hydroxystilbene, is found as glucosides[14] and methoxides.[15] Piceid (3-β-*O*-glucoside; **8**) and resveratroloside (4′-β-*O*-glucoside **9**) are the most abundant conjugates. Bioactivity of these compounds has been reported in relation to cancer prevention,[16] coronary heart disease,[17] antioxidant activity,[18] and estrogenic activity[19] As neither daidzein nor *trans*-resveratrol is reported to occur in arabidposis, they represent non-natural substrates for the GT screen.

The utility of the screening method and regioselective biocatalysis by the GTs are illustrated in Figure 2 and Figure 3. 13 GTs recognized daidzein and 25 GTs were identified that glucosylated *trans*-resveratrol. As previously described for scopoletin, RP-HPLC quantification of the glucosides formed in the biocatalysis revealed a linear correlation to D-glucose detection for both substrates (see the Supporting Information). The mono- and diglucosides of daidzein (**4**–**6**) and *trans*-resveratrols (**8**–**10**), which eluted earlier than the two aglycones under the RP-HPLC conditions used (Figure 2b and Figure 3b), were identified by using external standards when available, or by electrospray LC–MS. ^{1}H NMR analysis was used to confirm the structure of the monoglucosides (see the Supporting Information). From the 13 GTs that recognized daidzein, three (GTs 84A1, 73B2, and 73B1) were found to be 100% regioselective for the 7-OH; the remaining enzymes glucosylated the 4′-OH and 7-OH positions to varying degrees, and one GT, 73C4, produced the diglucoside in addition to the monoglucosides (Figure 2b). Similarly, regioselective glucosylation of *trans*-resveratrol was observed. From the 25 enzymes that recognized the substrate, five GTs were specific for the 3-OH position (GTs 71D1, 71C2, 88A1, 72D1 and 71C4) and one GT 74B1 was specific for the 4′-OH position (Figure 3b). Only trace levels of a diglucoside were observed under the reaction conditions used. As before, for the biotransformation of both daidzein and *trans*-resveratrol, the D-glucose-based detection system did not miss any positive enzyme activities; however, in these assays, two false positives in screens of each compound were observed in which an intense absorption was

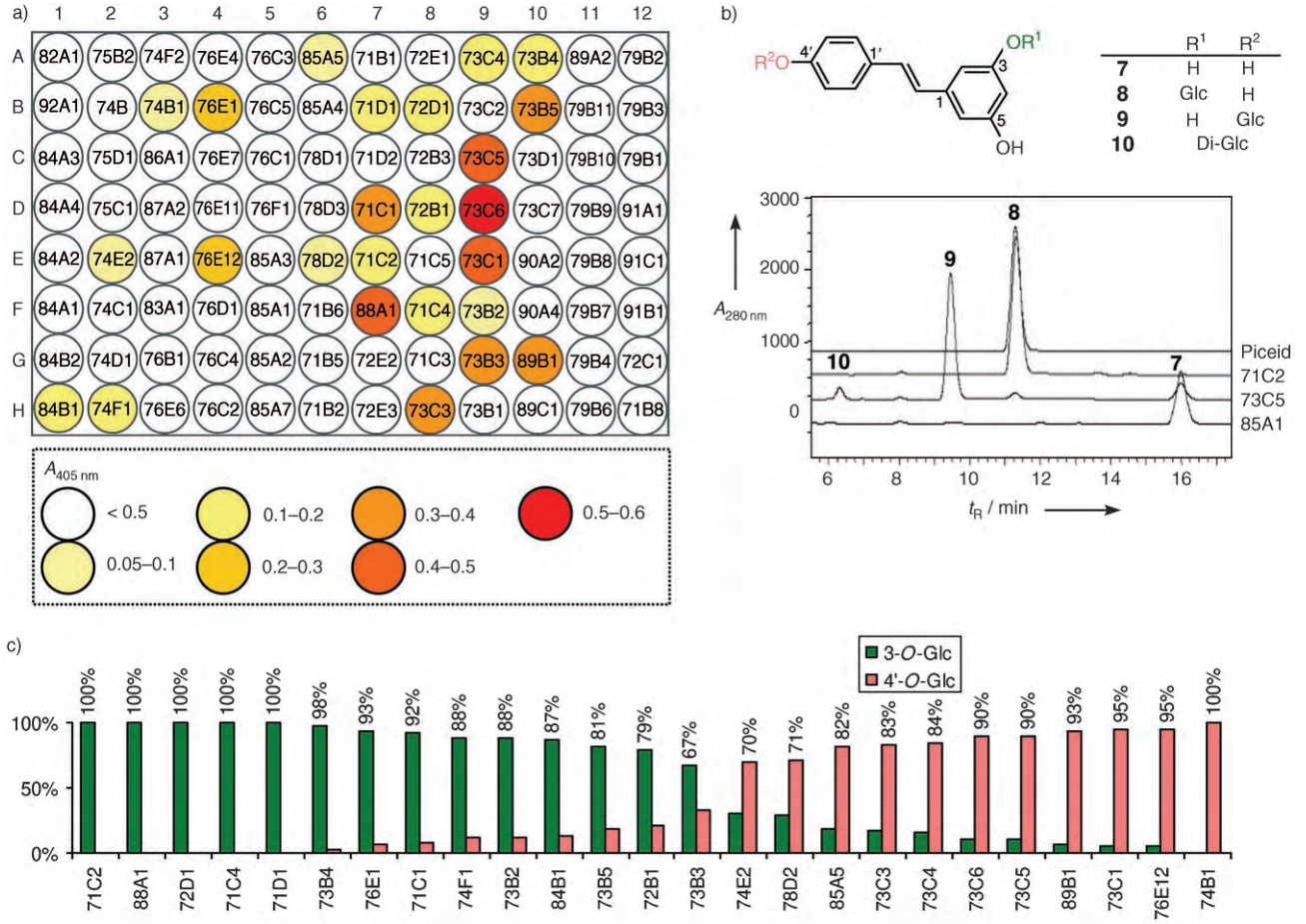

Figure 3. Screening of a GT library against the aglycone *trans*-resveratrol. a) The readings at A_{405nm} for D-glucose detection are presented in a color-code format. b) Examples of RP–HPLC traces of active and non-active GTs in whole-cell biocatalysis are illustrated. c) The regioselectivity of the active GTs towards *trans*-resveratrol (defined by the percentage of a regiospecific glucoside in the total amount of monoglucosides formed).

 © 2006 Wiley-VCH Verlag GmbH & Co. KGaA, Weinheim

not associated with any product formation. To confirm that the GT activity detected in the whole-cell system remain after purification, the activity of a number of individual recombinant GTs were also analyzed in vitro. The GT activities detected in the whole-cell screen were confirmed in vitro and their specific activities determined (see the Supporting Information).

The potential of GTs for use in preparative synthesis of daidzein and *trans*-resveratrol glucosides was explored on a fermenter scale by using bacterial cells expressing GT 73B1 and GT 73C6, respectively. This confirmed that GTs offer major opportunities for preparative-scale biotransformations as the glucosides could readily be obtained in significant quantities (see the Supporting Information).

The use of this screening method in whole-cell biocatalysis can be readily extended for the detection of other glycosides. This can be achieved by combining, for example, xylosidase and pyranose oxidase[20] to detect xylosides, or galactosides through the use of galactosidase and galactose oxidase.[21]

In conclusion, we have successfully developed a generic screen to determine the activity of recombinant GT libraries towards aromatic compounds in whole-cell biocatalysis. We have demonstrated that the method provides the means to rapidly identify GTs of high utility that can be further developed for use in biotransformations or chemo-enzymatic synthesis of small-molecule glycosides. The regio- and enantioselectivity of GT biocatalysts offers a useful complement to classical chemical approaches.

Experimental Section

Stage 1, biotransformation: Single colonies of the GT library grown on Lauria Bertani (LB)–agar plates overnight were transferred to individual wells in a 96-well bacterial culture plate containing 2 × YT medium (400 μL; bacto tryptone (16 g L^{-1}), yeast extract (10 g L^{-1}), NaCl (5 g L^{-1})) and ampicillin (50 μg mL^{-1}). The plate was covered with an adhesive plate seal (ABgene, U.K.) and incubated at 37 °C (250 rpm). The bacterial growth was monitored at 595 nm by a plate reader (Bio-Tec Instruments Inc., U.S.A). After 4 h, the cultures had reached the exponential phase. The plate was centrifuged (4000 g, 10 min), the supernatants discarded, and cell pellets were resuspended in isopropyl-β-D-thiogalactopyranoside (IPTG, 1 mM), 2-(*N*-morpholino) ethanesulfonic acid (MES, 50 mM, pH 7.0), ampicillin (50 μg mL^{-1}), L-arabinose (10 g L^{-1}), and 500 μM of aglycone to a total whole-cell reaction volume of 400 μL per well. The 96-well plate was closed with a gas-permeable adhesive plate seal, wrapped in aluminium foil for light protection, and incubated at 25 °C (250 rpm). After 44 h, the cultures were centrifuged (4000 g, 15 min) and the supernatants analyzed.

Stage 2, cleavage: Supernatants (100 μL) were transferred to a microtiter plate, β-glucosidase (1 μL, 1 U mL^{-1}) was added and the plate incubated for 90 min at 37 °C.

Stage 3, detection: The reaction mix (50 μL) was transferred to a 96-well filtration plate (ABgene, U.K.), mixed with an equal volume of PVPP aqueous suspension (25 g L^{-1}), and shaken for 1 h at 25 °C before centrifugation (1000 g, 5 min). To each filtrate, MES (50 mM; pH 7.0), 2,2'-azino-bis(3-ethylbenzthiazoline-6-sulfonic acid) (ABTS; 4 mM), peroxidase (2 U mL^{-1}), and glucose oxidase (2 U mL^{-1}) were added to a final volume of 125 μL. The formation of the green dye was monitored at 405 nm for 30 min by using a plate reader.

Other experimental details and analytical methods as well as physical data were included as Supporting Information.

Received: December 19, 2005
Published online: April 24, 2006

Keywords: enzymes · glycosides · glycosylation · regioselectivity · screening

[1] a) H. Pellissier, *Tetrahedron* **2005**, *61*, 2947–2993; b) K. C. Nicolaou, H. J. Mitchell, *Angew. Chem.* **2001**, *113*, 1624–1672; *Angew. Chem. Int. Ed.* **2001**, *40*, 1576–1624; c) S. Hanessian, B. L. Lou, *Chem. Rev.* **2000**, *100*, 4443–4463.

[2] a) S. L. Flitsch, *Curr. Opin. Chem. Biol.* **2000**, *4*, 619–625; b) B. G. Davis, V. Boyer, *Nat. Prod. Rep.* **2001**, *18*, 618–640; c) P. Sears, C. H. Wong, *Science* **2001**, *291*, 2344–2350; d) Z. Nahalka, Y. Liu, X. Chen, P. G. Wang, *Chem. Eur. J.* **2003**, *9*, 373–377; e) E. K. Lim, D. J. Bowles, *EMBO J.* **2004**, *23*, 2915–2922; f) K. M. Koeller, C. H. Wong, *Chem. Rev.* **2000**, *100*, 4465–4493.

[3] a) E. Garcia-Junceda, J. F. Garcia-Garcia, A. Bastida, A. Fernandez-Mayoralas, *Bioorg. Med. Chem.* **2004**, *12*, 1817–1834; b) E. K. Lim, *Chem. Eur. J.* **2005**, *11*, 5486–5494.

[4] Y. Li, S. Baldauf, E. K. Lim, D. J. Bowles, *J. Biol. Chem.* **2001**, *276*, 4338–4343.

[5] a) B. Hou, E. K. Lim, G. S. Higgins, D. J. Bowles, *J. Biol. Chem.* **2004**, *279*, 47822–47832; b) E. K. Lim, C. J. Doucet, Y. Li, L. Elias, D. Worrall, S. P. Spencer, J. Ross, D. J. Bowles, *J. Biol. Chem.* **2002**, *277*, 586–592; c) E. K. Lim, C. J. Doucet, B. Hou, R. G. Jackson, S. R. Abrams, D. J. Bowles, *Tetrahedron: Asymmetry* **2005**, *16*, 143–147.

[6] E. K. Lim, S. Baldauf, Y. Li, L. Elias, D. Worrall, S. P. Spencer, R. G. Jackson, G. Taguchi, J. Ross, D. J. Bowles, *Glycobiology* **2003**, *13*, 139–145.

[7] a) C. Loutre, D. P. Dixon, M. Brazier, M. Slater, D. J. Cole, R. Edwards, *Plant J.* **2003**, *34*, 485–493; b) B. Poppenberger, F. Berthiller, D. Lucyshyn, T. Sieberer, R. Schuhmacher, R. Krska, K. Kuchler, J. Glossl, C. Luschnig, G. Adam, *J. Biol. Chem.* **2003**, *278*, 47905–47914; c) T. Hefner, J. Arend, H. Warzecha, K. Siems, J. Stockigt, *Bioorg. Med. Chem.* **2002**, *10*, 1731–1741; d) B. Messner, O. Thulke, A. R. Schaffner, *Planta* **2003**, *217*, 138–146.

[8] a) V. Kren, J. Thiem, *Chem. Soc. Rev.* **1997**, *26*, 463–473; b) S. Koizumi, T. Endo, K. Tabata, A. Ozaki, *Nat. Biotechnol.* **1998**, *16*, 847–850; c) E. K. Lim, D. A. Ashford, B. Hou, R. G. Jackson, D. J. Bowles, *Biotechnol. Bioeng.* **2004**, *87*, 623–631; d) S. Koizumi, *Trends Glycosci. Glycotechnol.* **2003**, *15*, 65–74; e) J. Arend, H. Warzecha, T. Hefner, J. Stockigt, *Biotechnol. Bioeng.* **2001**, *76*, 126–131.

[9] a) M. Yang, M. Brazier, R. Edwards, B. G. Davis, *ChemBioChem* **2005**, *6*, 346–357; b) A. Di Marco, M. D'Antoni, S. Attaccalite, P. Carotenuto, R. Laufer, *Drug Metab. Dispos.* **2005**, *33*, 812–819; c) M. M. Palcic, K. Sujino, *Trends Glycosci. Glycotechnol.* **2001**, *13*, 361–370; d) J. Wongkongkatep, Y. Miyahara, A. Ojida, I. Hamachi, *Angew. Chem.* **2006**, *118*, 681–684; *Angew. Chem. Int. Ed.* **2006**, *45*, 665–668; B. Schwartz, J. A. Markwalder, S. P. Seitz, Y. Wang, R. L. Stein, *Biochemistry* **2002**, *41*, 12552; e) C. Deng, R, Chen, *Anal. Biochem.* **2004**, *330*, 219–226; f) H. C. Hang, C. Yu, M. R. Pratt, C. R. Bertozzi, *J. Am. Chem. Soc.* **2004**, *126*, 6–7; g) H. Liu, T. K. Ritter, R. Sadamoto, P. S. Sears, M. Wu, C.-H. Wong, *ChemBioChem* **2003**, *4*, 603–609.

[10] a) D. C. Williams, G. F. Huff, W. R. Seitz, *Clin. Chem.* **1976**, *22*, 372–374; b) N. P. Groome, *J. Clin. Chem. Clin. Biochem.* **1980**, *18*, 345–349.

[11] a) G. Galati, P. J. O'Brien, *Free Radical Biol. Med.* **2004**, *37*, 287–303; b) S. Barnes, J. Prasain, *Curr. Opin. Plant. Biol.* **2005**, *8*, 324–328; c) L. Fremont, *Life Sci.* **2000**, *66*, 663–673; d) P.

 © 2006 Wiley-VCH Verlag GmbH & Co. KGaA, Weinheim

Signorelli, R. Ghidoni, *J. Nutr. Biochem.* **2005**, *16*, 449 – 466; e) J. Reynaud, D. Guilet, R. Terreux, M. Lussignol, N. Walchshofer, *Nat. Prod. Rep.* **2005**, *22*, 504 – 515; f) K. D. R. Setchell, A. Cassidy, *J. Nutr.* **1999**, *129*, 758S-767S.

[12] a) P. W. Needs, G. Williamson, *Carbohydr. Res.* **2001**, *330*, 511 – 515; b) F. Orsini, F. Pelizzoni, B. Bellini, G. Miglierini, *Carbohydr. Res.* **1997**, *301*, 95 – 109; c) P. T. Lewis, K. Wahala, *Tetrahedron Lett.* **1998**, *39*, 9559 – 9562.

[13] Y. Shibuya, S. Tahara, Y. Kimura, J. Miyzutani, *Z. Naturforsch. C* **1991**, *46*, 513 – 518.

[14] D. M. Goldberg, E. Ng, A. Karumanchiri, E. P. Diamandis, G. J. Soleas, *Am. J. Enol. Vitic.* **1996**, *47*, 415 – 420.

[15] P. Langcake, C. A. Cornford, R. J. Pryce, *Phytochemistry* **1979**, *18*, 1025 – 1027.

[16] a) H. Adlercreutz, M. Yaghoob, K. Hoeckerstedt, *Acta Oncol.* **1992**, *350*, 115 – 181; b) M. Jang, L. Cai, G. O. Udeani, K. V. Slowing, C. F. Thomas, C. W. Beecher, H. H. Fong, N. R. Farnsworth, A. D. Kinghorn, R. G. Mehta, R. C. Moon, J. M. Pezzuto, *Science* **1997**, *275*, 218 – 220; c) D. Ingram, K. Sanders, M. Kolybaba, D. Lopez, *Lancet* **1998**, *350*, 990 – 994.

[17] a) S. Samman, P. Lyons-Wall, N. Cook, *Antioxid. Health Dis.* **1998**, *7*, 469 – 481; b) P. Nestel, T. Yamashita, T. Sasahara, S. Pomeroy, A. Dart, P. Komesaroff, A. Owen, A. Abbey, *Arterioscler. Thromb. Vasc. Biol.* **1997**, *17*, 3392 – 3398.

[18] a) M. Begona-Ruiz-Larrera, A. Moham, G. Paganga, N. Miller, G. Bolwell, C. Rice-Evans, *Free Radical Res.* **1997**, *26*, 63 – 70; b) M. J. Tikkanen, K. Wahala, S. Ojala, V. Vihma, H. Adlercreutz, *Proc. Natl. Acad. Sci. USA* **1998**, *95*, 3106 – 3110.

[19] a) S. D. Garrett, H. A. Lee, M. R. A. Morgan, *Nat. Biotechnol.* **1999**, *17*, 1219 – 1222; b) B. D. Gehm, J. M. McAndrews, P. Y. Chien, J. L. Jameson, *Proc. Natl. Acad. Sci. USA* **1997**, *94*, 14138 – 14143.

[20] K. Wagschal, D. Franqui-Espiet, C. C. Lee, G. H. Robertson, D. W. S. Wong, *Appl. Environ. Microbiol.* **2005**, *71*, 5318 – 5323.

[21] a) K. Schmid, R. Schmitt, *Eur. J. Biochem.* **1976**, *67*, 95 – 104; b) G. Avigad, D. Amaral, C. Asensio, B. L. Horecker, *J. Biol. Chem.* **1962**, *237*, 2736 – 2743; c) C. S. Frings, H. L. Pardue, *Anal. Chem.* **1964**, *36*, 2477 – 2478.

 © 2006 Wiley-VCH Verlag GmbH & Co. KGaA, Weinheim

Protein Functionalization

DOI: 10.1002/anie.200504540

Multivalent Dendrons for High-Affinity Adhesion of Proteins to DNA**

Mauri A. Kostiainen, Géza R. Szilvay, David K. Smith,* Markus B. Linder, and Olli Ikkala*

Protein functionalization constitutes a particularly interesting target for biopharmaceutical applications, which increasingly rely on monodisperse protein–polymer conjugates with controllable therapeutic properties.[1] Proteins modified with precisely controlled polymeric materials have the potential to exhibit a wide range of improved biological effects—for example, high-affinity binding to various biomolecules or tissues, or intracellular targeting by multivalent binding to cell-surface receptors,[2] improved circular half-life,[3] and switching of enzyme activity.[4] Linear polymers have been studied as part of protein–polymer hybrids, however, they induce a degree of heterogeneity in the form of both the attached polymer and the protein attachment sites,[5,6] resulting in varying biochemical properties.[7] Dendritic macromolecules offer several advantages over linear polymers, for example, a precisely defined branched structure with a high density of functional surface groups that can offer multiple simultaneous interactions leading to enhanced binding—the principle known as multivalency.[8] The assembly of dendritic building blocks is of considerable current interest,[9] and for

[*] M. A. Kostiainen, Prof. O. Ikkala
Department of Engineering Physics and Mathematics and
Center for New Materials
Helsinki University of Technology
P.O. BOX 2200, 02015 HUT, Espoo (Finland)
E-mail: kostiainen@focus.hut.fi

Dr. D. K. Smith
Department of Chemistry
University of York
Heslington, York, YO105DD (UK)
E-mail: dks3@york.ac.uk

G. R. Szilvay, Dr. M. B. Linder
VTT Biotechnology
Tietotie 2, P.O. BOX 1500, FIN-02044 VTT (Finland)
(G.R.S.) Institute of Biotechnology
Research Program in Structural Biology and Biophysics
P.O. Box 65, FIN-00014 University of Helsinki (Finland)

[**] This work was supported by the Finnish National Graduate School in Nanoscience (M.A.K.), the Informational and structural biology graduate school (G.R.S.), and partly carried out in the Centre of Excellence of the Academy of Finnland (Bio- and Nanopolymers Research Group, 77317) and Academy of Finnland project 205997. The National Technology Agency of Finnland is acknowledged for project funding. The Finnish Chemical Society is gratefully acknowledged for a study grant. D.K.S acknowledges EPSRC for financial support (EP/C534395/1). We acknowledge Dr. Roman Tuma, Dr. Juho Helaja, Katri Laurikainen and Jari Kavakka for discussions and support.

Supporting information for this article is available on the WWW under http://www.angewandte.org or from the author.

WILEY InterScience DISCOVER SOMETHING GREAT
© 2006 Wiley-VCH Verlag GmbH & Co. KGaA, Weinheim

this reason, protein functionalization by using dendritic macromolecules is an intriguing target.

There have been only a few studies of protein–dendron conjugates. For example, dendritic bisphosphonic acid acts as a bone-targeting unit for proteins.[10] Other reports have looked to the development of dendritic proteins with applications in immunochemistry[11] or neutron capture therapy.[12] In general, dendritic molecules are conjugated to proteins by using nonspecific methods resulting in conjugation at multiple sites. Interestingly, Hayashi and co-workers achieved controlled "dendron-like" functionalization of the heme propionate groups of myoglobin and used the resultant anionic conjugate to bind to the cationic surface of cytochrome c.[13,14] Furthermore, an important study appeared recently reporting native chemical ligation as a method to prepare dendrimers with exactly one copy of recombinant protein.[15]

One of the emerging goals of nanotechnology is the self-assembly of functional biological nanostructures.[16] With this in mind, DNA binding is an important prerequisite for the function of various biomolecules.[17] For example, many proteins exhibit natural DNA-binding ability that is essential for DNA replication, transcription, and modification. Recently, it was shown that modifying the heme propionates of myoglobin with DNA-binding peptides endowed myoglobin with the ability to bind DNA.[18] We reasoned that by using site-directed mutagenesis methods, a low-molecular-weight dendron could be grafted onto any protein of choice, modifying its properties and enabling it to self-assemble with DNA. High-affinity binding of DNA with proteins is ultimately useful for DNA modification, protection, and delivery.[19] To date, protein modification for this purpose has not been fully employed.

We have previously reported a series of dendrons that utilize the Newkome dendritic scaffold and display multiple spermine units on the dendritic surface. These dendrons were capable of high-affinity multivalent DNA binding by using their surface groups in a generation-dependent manner,[20] and showed modest gene delivery profiles.[21] Herein, we describe the modification of the focal point of the dendrons with an *N*-maleimide group, thus allowing their site-specific conjugation to a model protein. The resultant protein–dendron conjugates were then studied for their ability to bind DNA at the surface of the dendron. This communication highlights a straightforward coupling and purification of well-defined one-to-one protein–dendron conjugates and their unique DNA-binding ability.

Polyamine dendrons with spermine surface groups and a benzyloxycarbonyl (Cbz)-protected core were synthesized by using a divergent methodology as reported previously; all data were in agreement with those previously published.[20] We then used standard synthetic methods to construct target compounds **A** and **B** (Scheme 1, full details of the synthesis can be found in the Supporting Information). Deprotection of the Cbz-protected amino core by using catalytic hydrogenation yielded the free amine, which was subsequently reacted with an excess of 3-maleimidopropionic acid to afford a cysteine reactive dendron. Deprotection of the spermine groups by using HCl then yielded highly water-soluble target dendrons **A** and **B** with an intact *N*-maleimido group at the core. All synthetic steps were high yielding and all target compounds and intermediates were fully characterized by standard methods (see the Supporting Information).

Class II hydrophobin (**HFBI**), a mesoscale surfactant protein from *Trichoderma reesei*, was chosen as a model protein for the protein–dendron conjugation reactions.[22] Mesoscale surfactants are interesting in terms of their unique properties[23] in surface adhesion, surface activity, and self-assembly.[24–26] Furthermore, it is known that amphiphilic structures promote self-assembly with DNA.[27] The complex natural structure of proteins offers many possible sites for attachment, however, we wanted to develop multivalent conjugates with well-defined molecular structures. Site-directed mutagenesis was therefore used to construct a protein variant of **HFBI** with a free sulfhydryl group for site-specific conjugation. The protein variant, termed NCys–**HFBI**, was produced in its homologous production host *Trichoderma reesei* and purified from the fermentation biomass. Purification was achieved by using the methodology of Linder et al. yielding a partially oxidized covalent dimer of NCys–**HFBI**.[28]

After purification, disulfide bridged NCys–**HFBI** dimers were reduced to monomers (**HFBI**) with dithiothreitol. The reduced **HFBI** was conjugated to the first and second generation dendrons in buffered aqueous solution at neutral pH by using an excess of dendron. The high hydrophilicity of the dendrons allowed easy purification of the target conjugates (**HFBI–G1** and **HFBI–G2**) by semipreparative reverse phase HPLC. Peaks were fractionated, pooled, and finally lyophilized to yield the products as white solids. Analytical data for **HFBI–G2** are presented in Figure 1 (see the Supporting Information for **HFBI–G1** CD and MS data). Purification by semipreparative HPLC showed good separation between the **HFBI–G2** conjugate (first eluted peak) and unreacted **HFBI**/side products (second eluted peak). High purity after pooling was confirmed by analytical HPLC, which shows a single symmetric peak. Analysis by MALDI-TOF MS shows a clear signal at m/z 11782.752, which is in good accordance with the calculated mass of the conjugate: 11781.992 g mol^{-1}. This result shows that this is a convenient method to prepare exact one-to-one dendron–protein conjugates in good yield (> 80%) and could also be applicable to other functionalized dendrons and different proteins. CD measurements (see the Supporting Information) were used to confirm that the protein tertiary structure was not drastically changed by the attached dendron.

We then turned to an assessment of the DNA-binding ability of **HFBI** and its dendron conjugates. The DNA binding abilities of **HFBI**, **HFBI–G1**, and **HFBI–G2** were determined by using an ethidium bromide fluorescence quenching displacement assay, which is commonly employed to study nucleic acid binding behavior.[29] This assay employs competition between the compound of interest and ethidium bromide for DNA binding. When ethidium bromide is displaced from the DNA duplex by an effective DNA-binding compound, its fluorescence is quenched (Figure 2). Such a study leads to the determination of c_{50} and CE_{50} values (Table 1). c_{50} values are defined as the concentration of the added compound that leads to a 50% reduction in the

 © 2006 Wiley-VCH Verlag GmbH & Co. KGaA, Weinheim

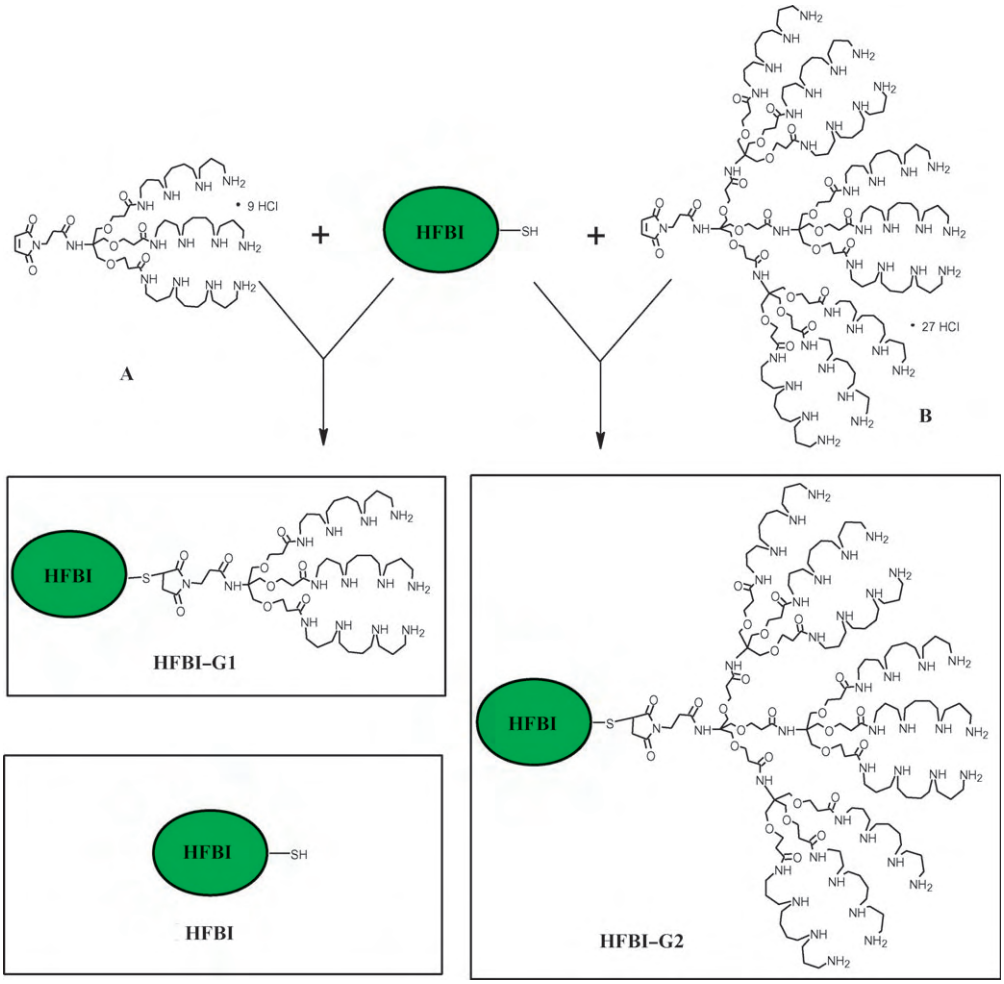

Scheme 1. Target dendrons for protein modification (**A** and **B**) and preparation of protein–dendron conjugates (**HFBI–G1** and **HFBI–G2**). Reaction conditions: H_2O, pH 7.

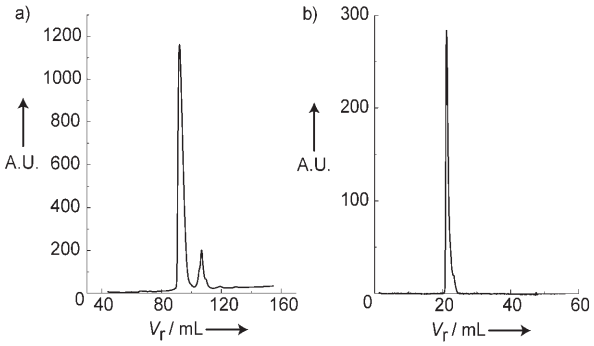

Figure 1. a) Semipreparative HPLC chromatogram of the **HFBI–G2** reaction mixture. b) Analytical HPLC chromatogram of purified **HFBI–G2**. V_r = retention volume.

fluorescence intensity of DNA saturated with ethidium. CE_{50} values represent the "charge excess"[30] required to achieve the same 50% reduction in fluorescence. We used two different salt concentrations (9.4 and 150 mM NaCl) at a physiologically relevant pH value of 7.2. Spermine was used as a reference compound, and importantly its binding behavior was in good agreement with literature data.[29]

Under low-salt conditions (9.4 mM NaCl), a large excess of **HFBI** would have been required to achieve 50% quenching of ethidium bromide fluorescence. Only negligible quenching was observed under both salt conditions, indicating that **HFBI** does not bind to DNA and thus no c_{50} or CE_{50} values are available. This was expected, as **HFBI** does not contain any DNA-binding motifs or significant surface positive charge and should therefore only exhibit weak electrostatic interactions with polyanionic DNA. However, the protein–dendron conjugates showed significantly enhanced DNA binding. Under low-salt conditions **HFBI–G1** and **HFBI–G2** showed similar binding affinity (**HFBI–G1**: $c_{50} = 66$ nM, $CE_{50} = 0.59$; **HFBI–G2**: $c_{50} = 23$ nM, $CE_{50} = 0.61$). Both compounds displaced ethidium bromide effectively from DNA owing to the strong electrostatic interactions between the protonated dendron and the polyanionic DNA. Similar trends were observed under physiological salt conditions (150 mM NaCl). **HFBI–G1** binding was somewhat affected by the increase in salt concentration as the first generation dendron failed to fully compete with Na^+ ions but still showed reasonable binding ($c_{50} = 100$ nM, $CE_{50} = 0.90$). **HFBI–G2** exhibited an extremely strong affinity for DNA even under high salt concentrations ($c_{50} = 17$ nM, $CE_{50} = 0.47$) as the binding affinity was not adversely affected by the

 © 2006 Wiley-VCH Verlag GmbH & Co. KGaA, Weinheim

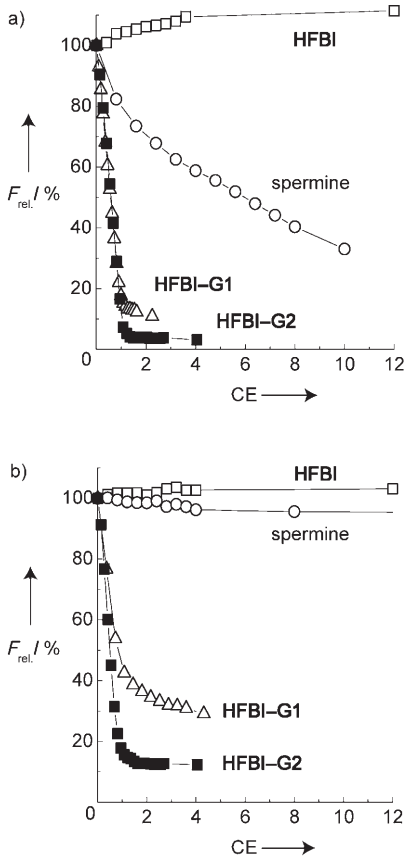

Figure 2. Fluorescence titration profiles for the addition of spermine, **HFBI**, **HFBI–G1**, or **HFBI–G2** to a solution of 1 μM DNA and 1.26 μM ethidium bromide in buffer solution (pH 7.2) in the presence of 9.4 mM (a) and 150 mM NaCl (b). $F_{rel.}$ = relative fluorescence intensity.

Table 1: Results for spermine, **HFBI**, **HFBI–G1**, and **HFBI–G2** from an ethidium bromide displacement assay.[a]

Compound	NaCl [mM]	Nominal charge	c_{50} [μM]	CE_{50}
Spermine	9.4	4+	1.5	6
HFBI	9.4	(4+)[b]	>50	>200
HFBI–G1	9.4	9+	0.066	0.59
HFB1–G2	9.4	27+	0.023	0.61
Spermine	150	4+	>100	>400
HFBI	150	(4+)[b]	>50	>200
HFBI–G1	150	9+	0.1	0.9
HFB1–G2	150	27+	0.017	0.47

[a] Conditions: buffer solution pH 7.2 (2 mM 2-[4-(2-hydroxyethyl)-1-piperazinyl]ethanesulfonic acid (HEPES), 0.05 mM ethylenediaminetetraacetic acid (EDTA)). DNA (1 μM) and ethidium bromide (1.26 μM) concentrations were kept constant. The total added polyamine solution did not exceed 5% of the total volume, therefore corrections were not made for sample dilution. Results are an average of three titrations. [b] According to protein amino acid sequence and the number of protonatable side chains, four positive charges were assumed.

competitive Na^+ ions—an effect of multivalency of the second-generation dendron.

The values measured for protein–dendron conjugates are in close agreement with, if not slightly better than, those measured for the dendrons alone. The binding of protein–dendron conjugates is therefore largely independent of the protein, proving that the high binding affinity of these low-molecular-weight dendrons is fully and directly transferred to larger nanoscale bioconjugates. Indeed, **HFBI–G2** shows remarkably high, salt-independent DNA affinity. In this way, the dendron acts to promote adhesion between a protein of choice and DNA.

Quartz crystal microbalance (QCM) studies were used to further investigate the surface adhesion and DNA binding properties of the protein and its dendron modified conjugate. Both **HFBI** and **HFBI–G2** were immobilized on hydrophobic polystyrene coated crystals. Figure 3 shows the adsorbtion of

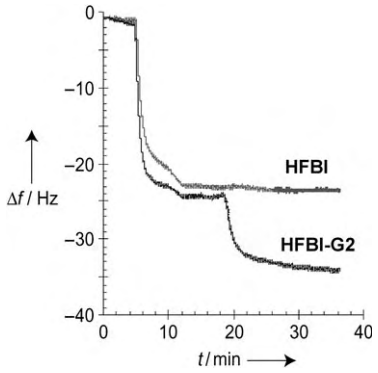

Figure 3. QCM sensograms: surface adhesion and DNA binding properties of **HFBI** and **HFBI–G2** as measured by the change in resonance frequency. **HFBI** or **HFBI–G2** were added after 3 min, DNA was added after 16 min.

both compounds at a concentration of 50 $\mu g\,mL^{-1}$. Both compounds adsorb rapidly in a similar manner, reaching the maximum level almost instantly, as would be expected for amphiphilic proteins (flow between 3–10 min, see Figure 3). This indicates that the dendron does not dramatically modify the surface adhesion and film formation properties of the protein. Washing with buffer solution (2 mM HEPES, 0.05 mM EDTA, pH 7.2) did not reduce the amount of surface bound compound. After immobilization and washing of the functionalized sensor crystals, the interaction with DNA was examined. DNA was allowed to flow into the sample chamber after 16 min in the same buffer system with a 0.2 mM nucleotide concentration. As expected, **HFBI** did not show any interaction with DNA and no shift in resonance frequency was observed. **HFBI–G2**, however, showed a clear shift in frequency, indicating DNA binding.

In conclusion, we have demonstrated the successful synthesis of multivalent protein–dendron conjugates in which the dendron imparts its properties onto the protein to which it is attached: that is, high-affinity DNA binding. It is therefore possible to convey DNA affinity to proteins that do not have natural DNA binding ability. Notably, by using this approach, **HFBI–G2** is one of the strongest DNA-binding proteins ever reported. Furthermore, we have demonstrated that the protein can also play an active role in the conjugate by promoting adhesion onto a hydrophobic surface. We expect that the union between proteins and multivalent synthetic compounds opens a route to nanobiotechnological research. It is possible to "fine-tune" the functionality of the

 © 2006 Wiley-VCH Verlag GmbH & Co. KGaA, Weinheim

dendron periphery by means of organic synthesis and to further control the interactions between molecules and the self-assembly of nanoscale bioconjugates. Also, the protein functionality can be varied simply by choosing a different protein. Work towards these structures and applications is currently being carried out.

Received: December 21, 2005
Revised: March 3, 2006
Published online: April 26, 2006

Keywords: dendrimers · DNA · multivalency · protein modifications · self-assembly

[1] R. Duncan, *Nat. Rev. Drug Discovery* **2003**, *2*, 347 – 360.
[2] R. Weissleder, K. Kelly, E. Y. Sun, T. Shtatland, L. Josephson, *Nat. Biotechnol.* **2005**, *23*, 1418 – 1423.
[3] G. G. Kochendoerfer, S. Y. Chen, F. Mao, S. Cressman, S. Traviglia, H. Y. Shao, C. L. Hunter, D. W. Low, E. N. Cagle, M. Carnevali, V. Gueriguian, P. J. Keogh, H. Porter, S. M. Stratton, M. C. Wiedeke, J. Wilken, J. Tang, J. J. Levy, L. P. Miranda, M. M. Crnogorac, S. Kalbag, P. Botti, J. Schindler-Horvat, L. Savatski, J. W. Adamson, A. Kung, S. B. H. Kent, J. A. Bradburne, *Science* **2003**, *299*, 884 – 887.
[4] Z. L. Ding, R. B. Fong, C. J. Long, P. S. Stayton, A. S. Hoffman, *Nature* **2001**, *411*, 59 – 62.
[5] B. S. Lele, H. Murata, K. Matyjaszewski, A. J. Russell, *Biomacromolecules* **2005**, *6*, 3380 – 3387.
[6] F. M. Veronese, *Biomaterials* **2001**, *22*, 405 – 417.
[7] P. Bailon, A. Palleroni, C. A. Schaffer, C. L. Spence, W.-J. Fung, J. E. Porter, G. K. Ehrlich, W. Pan, Z.-X. Xu, M. W. Modi, A. Farid, W. Berthold, *Bioconjugate Chem.* **2001**, *12*, 195 – 202.
[8] A. Mulder, J. Huskens, D. N. Reinhoudt, *Org. Biomol. Chem.* **2004**, *2*, 3409 – 3424.
[9] D. K. Smith, A. R. Hirst, C. S. Love, J. G. Hardy, S. V. Brignell, B. Huang, *Prog. Polym. Sci.* **2005**, *30*, 220 – 293.
[10] G. Bansal, J. E. I. Wright, C. Kucharski, H. Uludag, *Angew. Chem.* **2005**, *117*, 3776 – 3780; *Angew. Chem. Int. Ed.* **2005**, *44*, 3710 – 3714.
[11] L. J. Cruz, E. Iglesias, J. C. Aguilar, L. J. Gonzalez, O. Reyes, F. Albericio, D. Andreu, *Bioconjugate Chem.* **2004**, *15*, 112 – 120.
[12] G. Wu, R. F. Barth, W. Yang, M. Chatterjee, W. Tjarks, M. J. Ciesielski, R. A. Fenstermaker, *Bioconjugate Chem.* **2004**, *15*, 184 – 194.
[13] T. Hayashi, Y. Hitomi, H. Ogoshi, *J. Am. Chem. Soc.* **1998**, *120*, 4910 – 4915.
[14] Y. Hitomi, T. Hayashi, K. Wada, T. Mizutani, Y. Hisaeda, H. Ogoshi, *Angew. Chem.* **2001**, *113*, 1132 – 1135; *Angew. Chem. Int. Ed.* **2001**, *40*, 1098 – 1101.
[15] I. van Baal, H. Malda, S. A. Synowsky, J. L. J. van Dongen, T. M. Hackeng, M. Merkx, E. W. Meijer, *Angew. Chem.* **2005**, *117*, 5180 – 5185; *Angew. Chem. Int. Ed.* **2005**, *44*, 5052 – 5057.
[16] For a review of the ways in which protein modification can give rise to new host–guest processes on protein surfaces, see: I. Hamachi, J.-i. Watanabe, R. Eboshi, T. Hiraoka, S. Shinkai, *Biopolymers* **2000**, *55*, 459 – 468.
[17] H. Yan, S. H. Park, G. Finkelstein, J. H. Reif, T. H. LaBean, *Science* **2003**, *301*, 1882 – 1884.
[18] S. Sakamoto, K. Kudo, *Bull. Chem. Soc. Jpn.* **2005**, *78*, 1749 – 1756.
[19] I. M. Verma, N. Somia, *Nature* **1997**, *389*, 239 – 242.
[20] M. A. Kostiainen, J. G. Hardy, D. K. Smith, *Angew. Chem.* **2005**, *117*, 2612 – 2615; *Angew. Chem. Int. Ed.* **2005**, *44*, 2556 – 2559.
[21] J. G. Hardy, M. A. Kostiainen, D. K. Smith, N. P. Gabrielson, D. W. Pack, *Bioconjugate Chem.* **2006**, *17*, 172 – 178.
[22] M. B. Linder, G. R. Szilvay, T. Nakari-Setälä, M. E. Penttilä, *FEMS Microbiol. Rev.* **2005**, *29*, 877 – 896.
[23] D. Chandler, *Nature* **2005**, *437*, 640 – 647.
[24] M. Linder, G. R. Szilvay, T. Nakari-Setälä, H. Söderlund, M. Penttilä, *Protein Sci.* **2002**, *11*, 2257 – 2266.
[25] A. Paananen, E. Vuorimaa, M. Torkkeli, M. Penttilä, M. Kauranen, O. Ikkala, H. Lemmetyinen, R. Serimaa, O. Ikkala, M. Linder, *Biochemistry* **2003**, *42*, 5253 – 5258.
[26] M. Torkkeli, R. Serimaa, O. Ikkala, M. Linder, *Biophys. J.* **2002**,*83*, 2240 – 2247.
[27] D. Joester, M. Losson, R. Pugin, H. Heinzelmann, E. Walter, H. P. Merkle, F. Diederich, *Angew. Chem.* **2003**, *115*, 1524 – 1528; *Angew. Chem. Int. Ed.* **2003**, *42*, 1486 – 1490.
[28] M. Linder, K. Selber, T. Nakari-Setälä, Q. Mingqiang, M.-R. Kula, M. Penttilä, *Biomacromolecules* **2001**, *2*, 511 – 517.
[29] B. F. Cain, B. , C. Baguley, W. A. Denny, *J. Med. Chem.* **1978**, *21*, 658 – 668.
[30] Charge excess is defined as the nominal "number of positive charges" of the polyamine divided by the "number of negative charges" present on the DNA. A molecular weight of $330\ g\,mol^{-1}$ and one negative charge per nucleotide were assumed.

 © 2006 Wiley-VCH Verlag GmbH & Co. KGaA, Weinheim

Host–Guest Chemistry

DOI: 10.1002/anie.200600478

A Self-Regulatory Host in an Oscillatory Guest Motion: Complexation of Fullerenes with a Short-Spaced Cyclic Dimer of an Organorhodium Porphyrin

Ayako Ouchi, Kentaro Tashiro, Kentaro Yamaguchi, Takahiro Tsuchiya, Takeshi Akasaka, and Takuzo Aida**

The association of fullerenes with metalloporphyrins has attracted considerable attention,[1] not only for the basic understanding of π-electronic interactions between extended

[*] A. Ouchi, Dr. K. Tashiro, Prof. Dr. T. Aida
Department of Chemistry and Biotechnology
School of Engineering
The University of Tokyo
7-3-1 Hongo, Bunkyo-ku, Tokyo 113-8656 (Japan)
Fax: (+81) 3-5841-7310
E-mail: aida@macro.t.u-tokyo.ac.jp
Prof. Dr. K. Yamaguchi[+]
Department of Pharmaceutical Technology
Faculty of Pharmaceutical Sciences at Kagawa Campus
Tokushima Bunri University
Shido, Sanuki, Kagawa 769-2193 (Japan)
Dr. T. Tsuchiya,[$] Prof. Dr. T. Akasaka[$]
Center for Tsukuba Advanced Research Alliance
University of Tsukuba
Tsukuba, Ibaraki 305-8577 (Japan)
[+] Responsible for ESI mass-spectrometric measurements.
[$] Responsible for the synthesis of ^{13}C-enriched C_{76}.

Supporting information for this article is available on the WWW under http://www.angewandte.org or from the author.

WILEY InterScience DISCOVER SOMETHING GREAT
© 2006 Wiley-VCH Verlag GmbH & Co. KGaA, Weinheim

π-conjugated molecules, but also for possible application to the design of functional carbon-rich materials.[2] Whereas these studies have mostly been done in the solid state or constrained media,[1,2a,c] we have discovered that a strong fullerene–metalloporphyrin interaction can occur even in solution when cyclic dimers of metalloporphyrins with flexible alkylene spacers are used as the host molecules.[3,4] For example, cyclic metalloporphyrin dimers with C_6 alkylene spacers, such as **4** and **5** (Scheme 1), in aromatic and

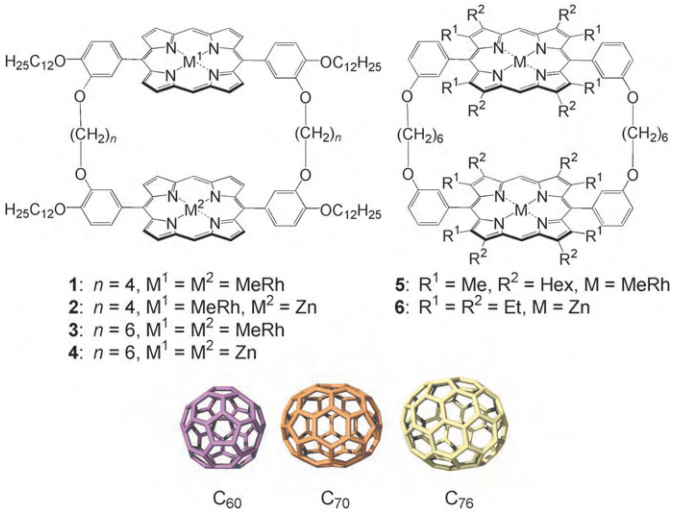

Scheme 1. Molecular structures of cyclic hosts **1**–**6** and fullerene guests C_{60}, C_{70}, and C_{76}.

halogenated solvents form highly stable 1:1 inclusion complexes with fullerenes such as C_{60}, C_{70}, and C_{120},[3b,5] along with even higher fullerenes.[6] A crystallographic study of an inclusion complex of **6** with C_{60} has indicated that the C_6 alkylene spacers are slightly too long but are folded to adjust the porphyrin–porphyrin distance to 12.4 Å.[3b] This observation prompted us to investigate the inclusion behavior of analogous host molecules with shorter alkylene spacers. For example, a Corey–Pauling–Kultun (CPK) model study predicted that host molecule **1** with C_4 alkylene spacers (Scheme 1) could furnish a maximum porphyrin–porphyrin distance of 11.8 Å, even when the spacers are fully extended. However, to our surprise, this short-spaced host is able to bind fullerenes such as C_{60}, C_{70}, and even C_{76} by tilting its metalloporphyrin disks and eventually forms capsule-type 2:1 host/guest inclusion complexes. Herein, we report details of this unexpected inclusion phenomenon and also highlight a self-regulatory behavior of **1** in a slip-through oscillatory motion of the included guests in the host cavity (Scheme 2).

We chose a methylrhodium porphyrin as the building block for the host molecule, because a C_6-alkylene-spaced analogue of **1** (**5**) has been revealed to bind fullerenes very strongly, with association constants (K_{assoc}) larger than $10^7\,M^{-1}$.[3b] Furthermore, the axial methyl groups of **1** are expected to serve as a sensitive probe for NMR spectroscopic analysis of the complexation. As the first survey of a possibility of the host/guest complexation, we conducted electrospray ionization mass-spectrometric (ESI MS) analysis

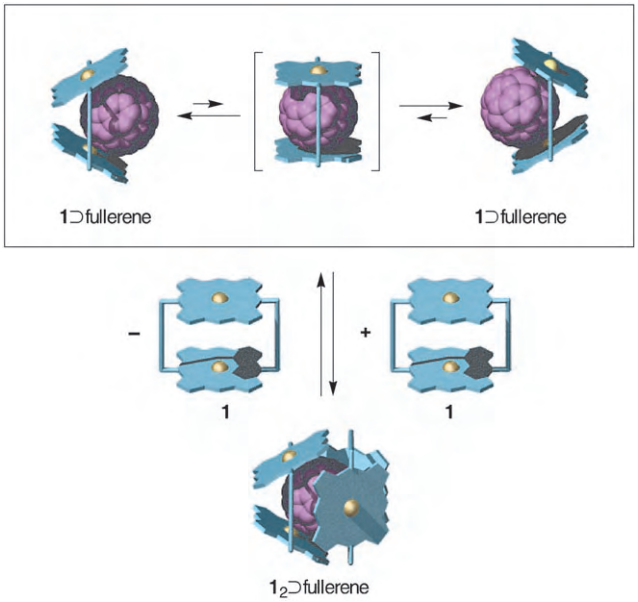

Scheme 2. Schematic representation of the complexation behavior of **1** with fullerenes and their dynamics.

of **1** in the presence of C_{60} to investigate if **1** and C_{60} form such host/guest complexes that are tolerant to mass-spectrometric conditions. Upon ionization at 50 °C, a 2:1 mixture of **1** (3.7×10^{-4} M) and C_{60} in CH_2Cl_2/MeOH (3:1) displayed two peaks at 4852.3 ($[\mathbf{1}_2+C_{60}]^+$) and 2786.0 ($[\mathbf{1}+C_{60}]^+$) assignable to the 2:1 ($\mathbf{1}_2\supset C_{60}$) and 1:1 ($\mathbf{1}\supset C_{60}$) host/guest complexes, respectively (Figure 1a). ESI mass-spectrometric analysis of a mixture of **1** and C_{70} or C_{76} resulted in a similar mass spectrum that exhibited molecular-ion peaks as a result of 2:1 and 1:1 host/guest complexes (Figure 1a). Electronic absorption spectroscopic analysis of a solution of **1** in toluene at 20 °C showed a red shift of the Soret absorption band with a decrease in intensity upon mixing with C_{60}, C_{70}, or C_{76},[7] thus indicating that the complexation between **1** and these fullerenes takes place by a π-electronic interaction. Job plots (400 nm) upon mixing solutions of **1** and C_{70} in toluene at 20 °C displayed the typical signature pattern for the competitive formation of the 1:1 and 2:1 host/guest complexes.[7]

A 2:1 mixture of **1** (1.0×10^{-3} M) and ^{13}C-enriched (10–15 %) C_{60} in [D_8]toluene displayed an intense ^{13}C NMR signal at $\delta=136.1$ ppm and a minor signal at $\delta=139.7$ ppm at −20 °C, both of which were shifted upfield from that of host-free C_{60} ($\delta=143.1$ ppm).[7] As the host/guest ratio was changed from 2:1 to 1:1, the minor signal became pronounced at the expense of the major signal. Considering also the electronic and magnetic ring-current effects of the metalloporphyrin units, the former signal of $\Delta\delta=-7.0$ ppm ($\Delta\delta=\delta_{obsd}-\delta_{host\text{-}free}$) can be assigned to C_{60} in $\mathbf{1}_2\supset C_{60}$, whereas the latter with a less negative $\Delta\delta$ value ($\Delta\delta=-3.4$ ppm) is attributable to C_{60} in $\mathbf{1}\supset C_{60}$.[7] We also found that the chemical shift of the Me–Rh signal of **1** is dependent on the stoichiometry of the host/guest complexation. Complex $\mathbf{1}\supset C_{60}$ in [D_8]toluene, predominantly formed at [**1**]/[C_{60}] = 1:2 ([**1**] = 5.0×10^{-4} M), showed a single Me–Rh signal at $\delta=$

 © 2006 Wiley-VCH Verlag GmbH & Co. KGaA, Weinheim

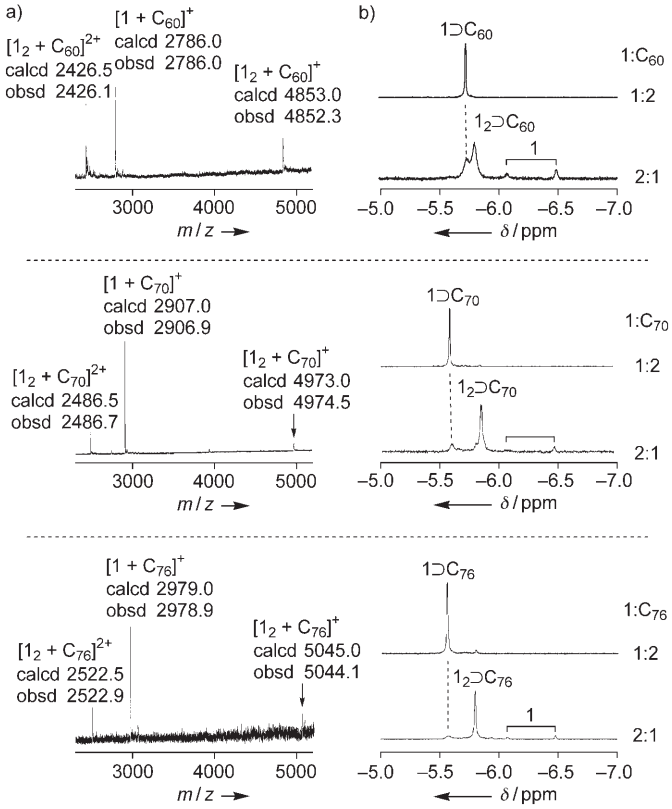

Figure 1. a) ESI mass spectra ([**1**] = 3.7×10^{-4} M; in CH_2Cl_2/MeOH (3:1); ionized at 50 °C) and b) ^{1}H NMR spectra of **1** ($\delta = -7.0$ to -5.0 ppm) ([**1**] = 5.0×10^{-4} M; in [D_8]toluene at −20 °C) in the presence of C_{60}, C_{70}, and C_{76}.

−5.73 ppm at −20 °C (Figure 1b). On the other hand, mixing of **1** and C_{60} at a molar ratio of 2:1 under otherwise identical conditions to the above resulted in the predominant formation of $\mathbf{1}_2\supset C_{60}$, whose Me–Rh signal was observed at $\delta = -5.80$ ppm, with minor signals at $\delta = -5.73$ ppm, as a result of $\mathbf{1}\supset C_{60}$, and $\delta = -6.06$ and −6.49 ppm, which are characteristic of conformational isomers of guest-free **1** (Figure 1b).[3b] Similar trends were observed for **1** upon complexation with larger fullerenes C_{70} and C_{76} (Figure 1b).

For the 1:1 complexation of C_{60} with **1**, an absorption-spectral titration at 20 °C in toluene allowed the evaluation of the association constant (K_{assoc}) for $\mathbf{1}\supset C_{60}$ as $2.1\times10^5\ M^{-1}$.[7] On the other hand, a ^{13}C NMR titration experiment at −20 °C in [D_8]toluene showed that resultant $\mathbf{1}\supset C_{60}$ binds **1** with a K_{assoc} value of $5.2\times10^3\ M^{-1}$ for $\mathbf{1}_2\supset C_{60}$,[7] which is two orders of magnitude smaller than that for $\mathbf{1}\supset C_{60}$. Considering also the molecular models, the much smaller affinity of $\mathbf{1}\supset C_{60}$ than C_{60} toward **1** is most likely because of an electronic effect, rather than a steric effect, of the first-bound host **1**. As reported previously,[3b] cyclic dimers of zinc porphyrins have lower affinities than methylrhodium porphyrin analogues toward fullerenes. When host **2**[7] (Scheme 1), a hybrid version of these two metalloporphyrin hosts, was allowed to interact with C_{60} in [D_8]toluene, only 1:1 complex $\mathbf{2}\supset C_{60}$ ($\delta =$ 139.6 ppm) was detected by ^{13}C NMR spectroscopy over a wide temperature range (down to −80 °C), even when two equivalents of **2** with respect to C_{60} were present.[7] Therefore, in the formation of electronically less favored $\mathbf{1}_2\supset$fullerene complexes, the inherently large affinity of organorhodium porphyrins toward fullerenes plays a significant role.

^{1}H NMR spectroscopy was also informative about the relative orientation of the metalloporphyrin units upon complexation of **1** with fullerenes. Before complexation, each methylrhodium porphyrin unit in **1** possesses one set of two equivalent meso protons and two sets of four equivalent pyrrole β protons. However, ^{1}H NMR spectroscopic analysis of $\mathbf{1}_2\supset C_{60}$, prepared by mixing **1** (5.0×10^{-3} M) and C_{60} in a 2:1 ratio at −20 °C, showed splitting of each of the above sets of signals (Figure 2a), whereas no such splitting was displayed for the Me–Rh proton signal. Considering also the stoichiometry of the complexation with the absorption and ^{13}C NMR spectra, such a ^{1}H NMR spectral pattern indicates that host **1** dimerizes to form a supramolecular capsule which includes one C_{60} molecule, in which the two metalloporphyrin units in each host molecule adopt a nonparallel, tilted geometry with respect to one another on the NMR timescale (Figure 2a). In contrast with $\mathbf{1}_2\supset C_{60}$, 1:1 host/guest complex $\mathbf{1}\supset C_{60}$, prepared by mixing **1** (5.0×10^{-4} M) and C_{60} in a 1:2 ratio in [D_8]toluene, showed an ordinary ^{1}H NMR spectral profile without any particular splitting at −20 °C (Figure 2b). However, when cooled further to −90 °C, a splitting signature was displayed, as observed for $\mathbf{1}_2\supset C_{60}$ at −20 °C (Figure 2a), in which the meso and pyrrole β protons both showed two sets of signals with an integral ratio of unity (Figure 2b). This spectral profile is in sharp contrast with that of reference host molecule **3** with longer C_6 alkylene spacers (Scheme 1),[7] in which $\mathbf{3}\supset C_{60}$ exhibited only one set of signals for each of the corresponding protons under identical conditions.[7] By reference to crystallographically defined $\mathbf{6}\supset C_{60}$,[3b] the fullerene guest in $\mathbf{3}\supset C_{60}$ is most likely located in the center of the parallel-oriented two metalloporphyrin units. Therefore, the splitting signature, observed for the ^{1}H NMR spectral profile of $\mathbf{1}\supset C_{60}$ at −90 °C (Figure 2b), again indicates that the two metalloporphyrin units in short-spaced host **1** adopt a tilted geometry with respect to one another to accommodate C_{60}.

Quite interestingly, variable-temperature (VT) ^{1}H and ^{13}C NMR spectroscopic analysis of $\mathbf{1}\supset C_{60}$ revealed a slip-through motion of C_{60} in the cavity of **1**. The split pairs of the meso and pyrrole β proton signals, observed at −90 °C, coalesced at around −80 °C and became simplified upon further heating, thus displaying one set of two equivalent meso protons and two sets of four equivalent pyrrole β proton signals (Figure 2b). For this coalescence phenomenon, the following two dynamic events are considered to be responsible: 1) a rapid guest exchange of $\mathbf{1}\supset C_{60}$ (disassembly/reassembly dynamics) and 2) a rapid slip-through motion of guest C_{60} in $\mathbf{1}\supset C_{60}$ (Scheme 2). Although these dynamic events are both capable of causing a ^{1}H NMR site exchange for nonequivalent meso and pyrrole β protons in $\mathbf{1}\supset C_{60}$, event (1) can separately be evaluated by VT ^{13}C NMR spectroscopic analysis of a mixture of $\mathbf{1}\supset C_{60}$ and free C_{60}.[5] ^{13}C NMR spectroscopic analysis of ^{13}C-enriched C_{60} in [D_8]toluene in the presence of 0.5 equivalents of **1** (5.0×10^{-4} M) at −90 °C exhibited two signals at $\delta = 142.9$ and 139.5 ppm as a result of host-free and complexed C_{60}, respectively.[7] Interestingly, these two signals did not coalesce over a wide temperature

 © 2006 Wiley-VCH Verlag GmbH & Co. KGaA, Weinheim

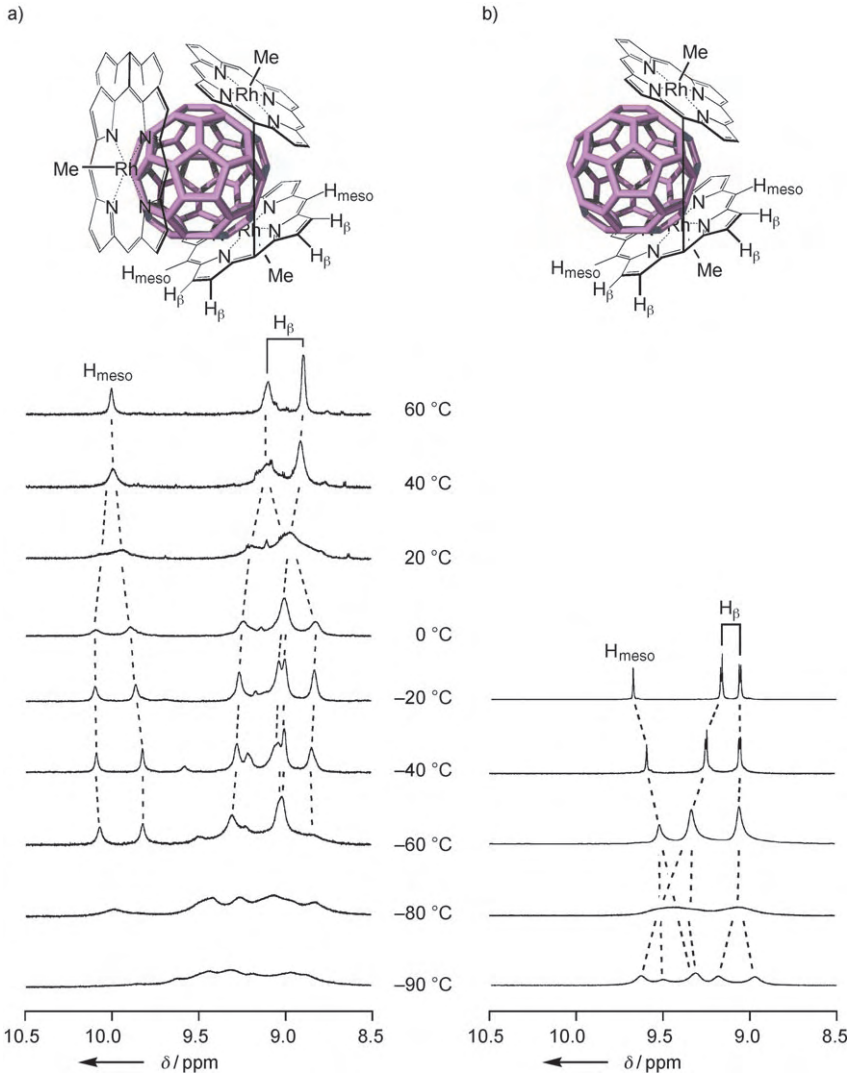

Figure 2. VT ^{1}H NMR spectral profiles ($\delta = 8.5$–10.5 ppm) of a) 2:1 and b) 1:2 mixtures of **1** and C_{60} in [D_8]toluene. [**1**] $= 5.0\times10^{-3}$ and 5.0×10^{-4} M for (a) and (b), respectively. The meso-aryl groups of the porphyrin units in the structures are omitted for clarity.

range up to −20 °C,[7] thus indicating a rather slow guest-exchange dynamic of **1**⊃C_{60}. To make a quantitative evaluation of these two dynamic events, NMR line-shape analysis was conducted using the DNMR5 program.[5,8] Consequently, we found that the ^{1}H NMR site exchange with respect to the pyrrole β protons occurs at a rate constant ($k_{\text{site exchange}}$) of 340 s^{-1} at −80 °C, whereas the guest exchange of **1**⊃C_{60}, as observed by VT ^{13}C NMR spectroscopy, takes place at a rate constant ($k_{\text{guest exchange}}$) of 5 s^{-1}. As the latter is roughly two orders of magnitude smaller than the former, guest C_{60} in **1**⊃C_{60} most likely slips through the cavity of **1** (Scheme 2). If this interesting oscillatory motion indeed takes place, the coalescence temperature would be affected by the size of the guest fullerene. In fact, the VT ^{1}H NMR spectral profile of **1**⊃C_{70} showed a coalescence temperature for the site-exchange event at −40 °C, which is, as expected, notably higher than that of **1**⊃C_{60} (−80 °C; see Figure 2b and the Supporting Information). Furthermore, when C_{76} was used as the guest, no coalescence for the ^{1}H NMR site exchange took place, even at 0 °C.[7]

As the site-exchange and guest-exchange dynamics that involved C_{76} were both too slow to evaluate at −80 °C, the ^{1}H and ^{13}C NMR line-shape analyses were conducted at a higher temperature, such as −20 °C, for all the three fullerene systems (Figure 3). The $k_{\text{site exchange}}$ value of **1**⊃C_{70} was evaluated at −20 °C to be 9000 s^{-1}, which dropped enormously to 3 s^{-1} when the fullerene guest was replaced with C_{76} (**1**⊃C_{76}). Although the $k_{\text{site exchange}}$ value of **1**⊃C_{60} was too large to evaluate accurately at −20 °C, it must be larger than that of **1**⊃C_{70}, considering the fact that the ^{1}H NMR coalescence temperature of **1**⊃C_{60} (−80 °C) is obviously lower than that of **1**⊃C_{70} (−40 °C; see before). On the other hand, compared with $k_{\text{site exchange}}$, $k_{\text{guest exchange}}$ was much less dependent on the guest size and became monotonically smaller from 30 to 13 to 7 s^{-1} as the guest fullerene became larger from C_{60} to C_{70} to C_{76} (Figure 3).[9] Once again, it should be noted that the ^{1}H NMR site exchange can take place as a consequence of the slip-through motion and exchange of fullerene guests. When host **1** binds relatively smaller guests, such as C_{60} and C_{70}, $k_{\text{site exchange}}$ is much greater than $k_{\text{guest exchange}}$. In contrast, when **1** binds the largest guest C_{76}, $k_{\text{site exchange}}$ is as small as $k_{\text{guest exchange}}$. These observations allow us to conclude that relatively small fullerenes C_{60} and C_{70} can slip through a small cavity of **1** and oscillate much more frequently than the guest-exchange event (Scheme 2),[10] whereas C_{76} is too large to slip through the cavity of **1**. On the other hand, the VT ^{1}H NMR spectra of the 2:1 host/guest complexes with C_{60} and C_{70} were much less temperature-dependent than those of the corresponding 1:1 complexes (see Figure 2 and the Supporting Information), thus indicating that capping of the 1:1 host/guest complexes with the second host molecule substantially prohibits the slip-through dynamic motion of the guest fullerenes (Scheme 2).

In conclusion, we have demonstrated that newly synthesized short-spaced metalloporphyrin cyclic dimer **1** bearing C_4 alkylene spacers can form 1:1 and 2:1 complexes with fullerenes such as C_{60}, C_{70}, and even C_{76}, in which the two metalloporphyrin units in the host adopt a nonparallel, tilted geometry with respect to one another to accommodate these fullerene guests. When the fullerene guest is relatively small (C_{60}, C_{70}), the resulting 1:1 complex undergoes a unique dynamic motion (Scheme 2). Namely, the fullerene guest slips through the small cavity of **1**, rather than disassembles, and

 © 2006 Wiley-VCH Verlag GmbH & Co. KGaA, Weinheim

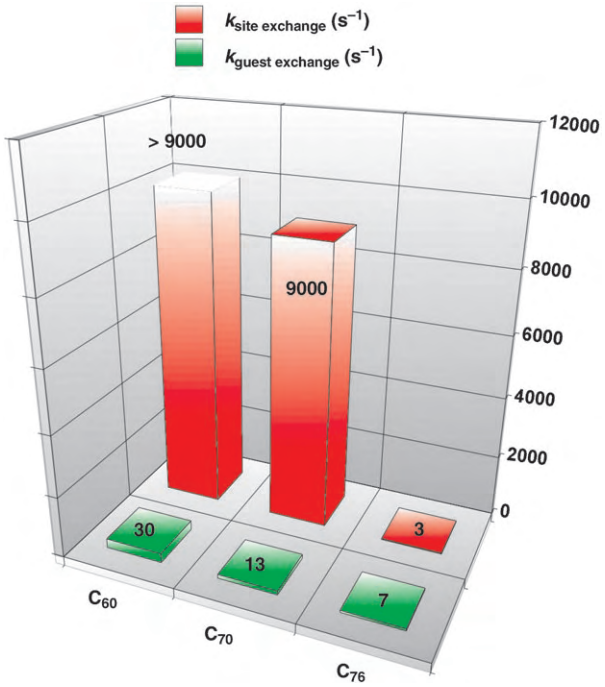

Figure 3. Dynamic motions of **1**⊃fullerenes. Site-exchange rate constants $k_{site\ exchange}$ for two nonequivalent pyrrole β protons (red square poles) and guest-exchange rate constants $k_{guest\ exchange}$ (green square poles) at −20 °C in [D_8]toluene, as evaluated by line-shape analysis of VT ^{1}H and ^{13}C NMR spectra of **1**/fullerene mixtures (1:2), respectively, using the DNMR5 program.

oscillates with an inversion of the tilted geometry of the metalloporphyrin disks. However, this dynamic motion is substantially frozen when the second host molecule caps the 1:1 complex to form a capsule-type 2:1 inclusion complex. We have reported that **5** bearing C_6 alkylene spacers allows a simple oscillatory motion of C_{120} in its cavity.[5] Compared with **5**, short-spaced host **1** behaves much more interestingly in that it can self-regulatorily operate in the oscillatory guest motion. The capsule-type 2:1 host/guest complexes are considered an elementary model of hetero "bucky onions",[11] whose electronic properties, along with their covalent stabilization, deserve further studies.

Received: February 6, 2006
Published online: April 20, 2006

Keywords: fullerenes · host–guest chemistry · inclusion compounds · oscillation · porphyrinoids

[1] a) M. M. Olmstead, D. A. Costa, K. Maitra, B. C. Noll, S. L. Phillips, P. M. Van Calcar, A. L. Balch, *J. Am. Chem. Soc.* **1999**, *121*, 7090; b) P. D. W. Boyd, M. C. Hodgson, C. E. F. Rickard, G. A. Oliver, L. Chaker, P. J. Brothers, R. D. Bolskar, F. S. Tham, C. A. Reed, *J. Am. Chem. Soc.* **1999**, *121*, 10487; c) P. D. W. Boyd, C. A. Reed, *Acc. Chem. Res.* **2005**, *38*, 235.

[2] a) M. Kimura, Y. Sato, K. Ohta, K. Hanabusa, H. Shirai, N. Kobayashi, *J. Am. Chem. Soc.* **2002**, *124*, 5274; b) T. Yamaguchi, N. Ishii, K. Tashiro, T. Aida, *J. Am. Chem. Soc.* **2003**, *125*, 13934; c) T. Hasobe, H. Imahori, P. V. Kamat, S. Fukuzumi, *J. Am. Chem. Soc.* **2003**, *125*, 14962; d) S. Yoshimoto, E. Tsutsumi, Y. Honda, Y. Murata, M. Murata, K. Komatsu, O. Ito, K. Itaya, *Angew. Chem.* **2004**, *116*, 3106; *Angew. Chem. Int. Ed.* **2004**, *43*, 3044.

[3] a) K. Tashiro, T. Aida, J.-Y. Zheng, K. Kinbara, K. Saigo, S. Sakamoto, K. Yamaguchi, *J. Am. Chem. Soc.* **1999**, *121*, 9477; b) J.-Y. Zheng, K. Tashiro, Y. Hirabayashi, K. Kinbara, K. Saigo, T. Aida, S. Sakamoto, K. Yamaguchi, *Angew. Chem.* **2001**, *113*, 1909; *Angew. Chem. Int. Ed.* **2001**, *40*, 1857; c) H. Sato, K. Tashiro, H. Shinmori, A. Osuka, Y. Murata, K. Komatsu, T. Aida, *J. Am.* Chem. *Soc.* **2005**, 127, 13086.

[4] For examples of a fullerene–monomeric metalloporphyrin interaction in solution, see: a) N. Solladié, M. E. Walther, M. Gross, T. M. F. Duarte, C. Bourgogne, J.-F. Nierengarten, *Chem. Commun.* **2003**, 2412; b) H. Sasabe, N. Kihara, Y. Furusho, K. Mizuno, A. Ogawa, T. Takata, *Org. Lett.* **2004**, *6*, 3957.

[5] K. Tashiro, Y. Hirabayashi, T. Aida, K. Saigo, S. Sakamoto, K. Yamaguchi, K. Fujiwara, K. Komatsu, *J. Am. Chem. Soc.* **2002**, *124*, 12086.

[6] Y. Shoji, K. Tashiro, T. Aida, *J. Am. Chem. Soc.* **2004**, *126*, 6570.

[7] See the Supporting Information.

[8] a) M. J. Sanger, R. J. Angelici, *Organometallics* **1994**, *13*, 1821; b) G. Hilmersson, Ö. Davidsson, *J. Org. Chem.* **1995**, *60*, 7660.

[9] The order of the observed $k_{guest\ exchange}$ values is consistent with our expectation from the guest size-dependent stabilities of inclusion complexes of **4** and **5** with fullerenes (Refs. [3b] and [6]).

[10] Eyring plots of the rate constant of the oscillatory motion of C_{70}, as estimated from $k_{site\ exchange} - k_{guest\ exchange}$, gave a positive value ($+57.8 \pm 8.0\ J\,K^{-1}\,mol^{-1}$) for $\Delta S^{\neq}$ (see the Supporting Information); therefore, analogous to the oscillation of C_{120} in **5** (Ref. [5]), the oscillatory motion of fullerenes in **1** is likely driven by an entropic gain for the desolvation of C_{70} in the transition state.

[11] D. Ugarte, *Nature* **1992**, *359*, 707.

 © 2006 Wiley-VCH Verlag GmbH & Co. KGaA, Weinheim